PROCEEDINGS OF THE FOURTEENTH INTERNATIONAL SYMPOSIUM ON ARTIFICIAL LIFE AND ROBOTICS

(AROB 14th'09)

Feb.5 - Feb.7, 2009
B-Con Plaza, Beppu, Oita, JAPAN

Supported by Japan Society for the Promotion of Science (JSPS)
International Meeting Series

Editors: Masanori Sugisaka and Hiroshi Tamaka
ISBN 978-4-9902880-3-7

Program of The Fourteenth International Symposium on

ARTIFICIAL LIFE AND ROBOTICS

(AROB 14th '09)

Feb. 5 - Feb.7, 2008
B-Con Plaza, Beppu, Oita, Japan,

Editors: Masanori Sugisaka and Hiroshi Tanaka

©ISAROB 2009

THE FOURTEENTH INTERNATIONAL SYMPOSIUM ON ARTIFICIAL LIFE AND ROBOTICS

(AROB 14th '09)

ORGANIZED BY

Organizing Committee of International Symposium on Artificial Life and Robotics
(Department of Mechanical and Electrical Engineering, Nippon Bunri University, Japan)

SPONSORED BY

Japan Society for Promotion of Science (JSPS)
Mitsubishi Electric Corporation Advanced Technology R&D Center
Oita Gas Co., Ltd.
ME System Co., Ltd.
SANWA SHURUI Co.,Ltd

CO-OPERATED BY

Santa Fe Institute (SFI, USA)
The Robotics Society of Japan (RSJ, Japan)
The Institute of Electrical Engineers of Japan (IEEJ, Japan)
Institute of Control, Robotics and Systems (ICROS, Korea)
Chinese Association for Artificial Intelligence (CAAI, P. R. China)
The Institute of Systems, Control and Information Engineers (ISCIE)
The Institute of Electronics, Information and Communication Engineers (IEICE)
The Institute of Electrical and Electronics Engineers, Inc. (IEEE Japan Council)
Japan Robot Association (JARA)
The Society of Instrument and Control Engineers (SICE, Japan)

SUPPORTED BY

Kyushu Bureau of Economy, Trade and Industry, Ministry of Economy, Trade and Industry
OITA PREFECTURE
Oita City
BEPPU CITY
Oita Chamber of Commerce and Industry
The Oita Prefectural Organization of the Industrial Groups
Kyodo News
JIJI PRESS
Oita Godo Shimbunsya
The Asahi shimbun
The Mainichi Newspaper Co., Ltd.
THE YOMIURI SHIMBUN SEIBUHONSHA
The Nishinippon Shimbun
THE NIKKAN KOGYO SHIMBUN, LTD
Japan Broadcasting Corporation Oita Station
Oita Broadcasting System
Television Oita System Corporation
Oita Asahi Broadcasting co., ltd.

©ISAROB 2009

ADVISORY COMMITTE CHAIRMAN

F. Harashima (Tokyo Denki University, Japan)

GENERAL CHAIRMAN

M. Sugisaka (Nippon Bunri University, Japan)

PROGRAM CHAIRMAN

H. Tanaka (Tokyo Medical & Dental University, Japan)

VICE-CHAIRMAN

J. J. Lee (KAIST, Korea)
J. L. Casti (Institute for Applied Systems Analysis and The Kenos Circle, Austria)
Y. G. Zhang (Academia Sinica, P. R. China)

ADVISORY COMMITTEE

T. Fukuda (Nagoya University, Japan)
F. Harashima (Tokyo Denki University, Japan)
H. Kimura (RIKEN, Japan)
M. Tomizuka (University of California Berkeley, USA)

INTERNATIONAL ORGANIZING COMMITTEE

K. Aihara (The University of Tokyo, Japan)
C. Barrett (Los Alamos National Laboratory, USA)
M. Bedau (Reed College, USA)
J. L. Casti (Institute for Applied Systems Analysis and The Kenos Circle, Austria)
M. Eaton (University of Limerick, Ireland)
J. M. Epstein (The Brookings Institution, USA)
T. Fukuda (Nagoya University, Japan)
H. Hashimoto (The University of Tokyo, Japan)
D. J. G. James (Coventry University, UK)
K. Kyuma (Mitsubishi Electric Corporation, Japan)
J. J. Lee (KAIST, Korea)
M. H. Lee (Pusan National University, Korea)
S. Rasmussen (Santa Fe Institute, USA)
T. S. Ray (University of Oklahoma, USA)
M. Sugisaka (Nippon Bunri University, Japan) (Chairman)
C. Taylor (University of California-Los Angeles, USA)
W. R. Wells (University of Nevada-Las Vegas, USA)
Y. G. Zhang (Academia Sinica, P. R. China)

INTERNATIONAL PROGRAM COMMITTEE

K. Abe (Nihon University, Japan)
K. Aihara (The University of Tokyo, Japan) (Co-chairman)
T. Arita (Nagoya University, Japan)
M. Bedau (Reed College, USA)
R. Belew (University of California-San Diego, USA)
S. M. Chen (National Taiwan University of Science and Technology, Taiwan)
Y. I. Cho (The University of Suwon, Korea)
Y. Y. Fan (University of California-Davis, USA)
S. H. Han (Kyungnam University, Korea)
H. Hashimoto (The University of Tokyo, Japan) (Co-chairman)
N. Homma (Tohoku University, Japan)
S. Ishikawa (Kyushu Institute of Technology, Japan)
T. Ito (Ube National College of Technology, Japan)
T. Iwamoto (Mitsubishi Electric Corporation, Advanced Technology R&D Center, Japan)
J. Johnson (The Open University, UK)
O. Katai (Kyoto University, Japan)
H. Kawamura (Hokkaido University, Japan)
M. Kono (University of Miyazaki, Japan)
S. Kumagai (Osaka University of Economics and Law, Japan)
K. Kurashige (Muroran Institute of Technology, Japan)
J. M. Lee (Pusan National University, Korea)
H. H. Lee (Waseda University, Japan)
H. H. Lund (Technical University of Denmark, Denmark)
M. Nakamura (Saga University, Japan)
K. Nakano (The University of Electro-Communications, Japan)
K. Naitoh (Waseda University, Japan)
W. Nistico (University of Dortmund, Germany)
K. Ohnishi (Niigata University, Japan)
M. Okamoto (Kyushu University, Japan)
S. Omatu (Osaka Prefecture University, Japan)
H. Oogai (Waseda University, Japan)
M. Osano (Aizu University, Japan)
M. Oswald (Vienna University of Technology, Austria)
R. Pfeifer (University of Zurich-Irchel, Switzerland)
L. Pagliarini (Technical University of Denmark, Denmark)
T. S. Ray (University of Oklahoma, USA) (Co-chairman)
S. Sagara (Kyushu Institute of Technology, Japan)
P. Sapaty (National Academy of Sciences of Ukraine, Ukraine)
T. Sawaragi (Kyoto University, Japan)
T. Shibata (AIST, Japan)
K. Shimohara (Doshisha University, Japan)
K. Sugawara (Tohoku Gakuin University, Japan)
M. Sugisaka (Nippon Bunri University, Japan)
H. Suzuki (The University of Tokyo, Japan)
H. Tanaka (Tokyo Medical & Dental University, Japan) (Chairman)
M. Tanaka-Yamawaki (Tottori University, Japan)
K. Uosaki (Fukui University of Technology, Japan)
H. Umeo (Osaka Electro-Communication University, Japan)
K. Watanabe (Saga University, Japan)
T. Yamamoto (Tokushima College of Technology, Japan)
H. Yanagimoto (Osaka Prefecture University, Japan)
M. Yano (Tohoku University, Japan)

Y. Yin (The Beijing University of Science and Technology, P. R. China)
M. Yokota (Fukuoka Institute of Technology, Japan)

LOCAL ARRANGEMENT COMMITTEE

F. Dai (Matsue National College of Technology, Japan)
M. Ito (Maizuru National College of Technology, Japan)
R. Mamat (TATI University Colledge, Malaysia)
M. Rizon (King Saud University, Saudi Arabia)
S. Sagara (Kyushu Institute of Technology, Japan)
M. Sugisaka (Nippon Bunri University, Japan) (Chairman)
J. Wang (Alife Robotics Co., Ltd., Japan)
X. Wang (Niihama National College of Technology Japan)

HISTORY

This symposium was founded in 1996 by the support of Science and International Affairs Bureau, Ministry of Education, Culture, Sports, Science and Technology, Japanese Government. Since then, this symposium has been held every year at B-Con Plaza, Beppu, Oita, Japan except in Oita, Japan (AROB 5th '00) and in Tokyo, Japan (AROB 6th '01). The Fourteenth symposium will be held on 5– 7 February, 2009, at B-Con Plaza, Beppu, Oita, Japan. This symposium invites you all to discuss development of new technologies concerning Artificial Life and Robotics based on simulation and hardware in the twenty first century.

OBJECTIVE

The objective of this symposium is the development of new technologies for artificial life and robotics which have been recently born in Japan and are expected to be applied in various fields. This symposium will discuss new results in the field of artificial life and robotics.

GENERAL SESSION TOPICS

Artificial intelligence
Artificial living
Bioinformatics
Chaos
Complexity
DNA computing
Fuzzy control
Human-machine cooperative systems
Innovative Computations
Mobile vehicles
Nano-biology
Neural networks
Robotics
Virtual reality
Artificial life
Artificial mind research
Brain Science
Cognitive Science
Computer graphics
Evolutionary computations
Genetic algorithms
Human-welfare robotics
Micromachines
Multi-agent systems
Nano-robotics
Pattern recognition
Robust Virtual Engineering
Others

ORGANIZED SESSION TOPICS

Intelligent Control
Robotics and Control
Bioinformatics and Intelligent Classification (1)
Soft Robotics
Dynamical Information Processing in the Brain
Bio-inspired Theory and Application
Intuitive Human-System Interaction
Biomimetic Machines and Robots
Intelligent Control and Robotics
Intelligent Robot
Automata and Control
Bioinformatics and Intelligent Classification (2)
Learning and Robotics
Measurement and Control
Session of Economics and Management
Intelligent Systems
Embracing Complexity in Natural Intelligence

COPYRIGHTS

Accepted papers will be published in the proceeding of AROB and some of high quality papers in the proceeding will be requested to re-submit their papers for the consideration of publication in an international journal ARTIFICIAL LIFE AND ROBOTICS and APPLIED MATHEMATICS AND COMPUTATION. All correspondence related to the symposium should be addressed to AROB Secretariat.

AROB Secretariat
ALife Robotics Corporation Ltd.
301 Koopo Nagaoka 1385-1 Miyazaki, Oita 870-1133, JAPAN
TEL/FAX：+81-97-594-0181
E-MAIL：arobsecr@alife-robotics.co.jp
Home Page：http://alife-robotics.co.jp/

ADDRESS

Sadayoshi Suga
Bunri Gakuen Educational Foundation
Nippon Bunri University
Chairman/Chancellor

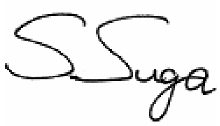

Sadayoshi Suga
Bunri Gakuen Educational Foundation
Nippon Bunri University
Chairman/Chancellor

It is my great pleasure to welcome you all to The Fourteenth International Symposium on Artificial Life and Robotics. I would like to offer my sincere thanks and respect to the many people who have helped make this yearly event possible.

Last year, Nippon Bunri University invited Professor Sugisaka to lead the symposium's team, and with his help we have undertaken this new venture.

As well as being a great venue to meet specialists in many fields, I also feel it's an important platform for presenting research and giving Universities the opportunity to support such research.

As Chairman of this University, I feel great pleasure in working with such outstanding educators who have, on so many occasions, presented their research to the world.

It's my sincere wish that advances in Artificial Life and Robotics Research, in cooperation with the Medical Sciences, Information Systems and other technological fields will lead to improvements in all of our lives.

During your stay here in Beppu, please take time to enjoy the beautiful scenery, relaxing hot springs, and healthy Japanese cuisine that Oita Prefecture has to offer. It's my heartfelt hope that when you leave here, you do so with fresh enthusiasm and motivation.

MESSAGES

Fumio Harashima
Advisory Committe Chairman
(Professor, Tokyo Denki University)

Fumio Harashima
Advisory Committee Chairman of AROB

The science and technology (S&T) on Artificial Life and Robotics was born in 1996, and it's been providing human being with happiness. This S & T is not only important but also necessary for people living in the world to maintain high quality of life. Research is heart and desire of human being and the S&T is going toward clarifying tool to achieve our objective.

I would like to congratulate researchers who work in the fields on Artificial Life and Robotics.

Masanori Sugisaka
General Chairman
(Professor, Nippon Bunri University, Japan
Visiting Professor, Waseda University, Japan)

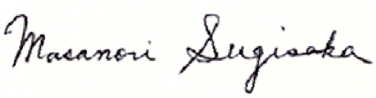

Masanori Sugisaka
General Chairman of AROB

It is my great honor to invite you all to the Fourteenth International Symposium on Artificial Life and Robotics (AROB 14th '09).

The symposium from the first (1996) to the Thirteenth (2008) were organized by Oita University under the sponsorship of the Science and Technology Policy Bureau, the Ministry of Education, Science, Sports, and Culture (Monbusho), presently, the Ministry of Education, Culture, Sports, Science, and Technology (Monkasho), Japanese Government, Japan Society for the Promotion of Science (JSPS), The Commemorative Organization for the Japan World Exposition ('70), Air Force Office of Scientific Research, Asian Office of Aerospace Research and Development (AFOSR/AOARD), USA.

This symposium is organized by Nippon Bunri University under the sponsorship of JSPS and is co-operated by the Santa Fe Institute (USA), RSJ, IEEJ, ICASE (Now ICROS) (Korea), CAAI (P. R. China), ISCIE, IEICE, IEEE (Japan Council), JARA, and SICE.

The AROB symposium has grown up by the supports from many people who attended the former AROB symposiums. Now, the age of the AROB Symposium became 14 years old since it was born in 1996. The AROB symposium is growing up by absorbing many new knowledge and technologies into it. The future of the AROB symposium is brilliant from a point of view of yielding new technologies to human society in 21st century.

I would like to express my sincere thanks to not only Monkasho, JSPS, the Commemorative Organization for the Japan World Exposition ('70) but also Japanese companies for their repeated support.

This Fourteenth symposium is sponsored by both JSPS and Japanese companies (Mitsubishi Electric Corporation Advanced Technology R&D Center, Oita Gas Co., Ltd., ME System Co., Ltd., Sanwa Shurui Co., Ltd.). I would like to express special thanks to companies stated above.

The symposium invites you to discuss developments and applications of new technologies in the 21st century concerning Artificial Life and Robotics, based on software and hardware.

I hope that fruitful discussions between researchers who have different specific ideas will yield new merged technologies and, hence, AROB 14th '09 will facilitate the establishment of an international joint research institute on Artificial Life and Robotics in future.

I hope that you will obtain fruitful results from exchange of ideas between researchers during the symposium.

Hiroshi Tanaka
Program Chairman
(Professor, Tokyo Medical and Dental University)

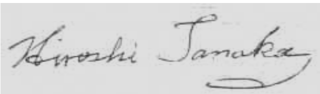

Hiroshi Tanaka
Program Chairman of AROB

On behalf of the program committee, it is my great pleasure and honor to invite you all to the Fourteenth International Symposium on Artificial Life and Robotics (AROB 14th '09). This symposium is made possible owing to the cooperation of Nippon Bunri University and Santa Fe Institute. We are also debt to Japanese academic associations such as SICE, RSJ, and several private companies. I would like to express my sincere thanks to all of those who make this symposium possible.

As is needless to say, the Alife or biologically-inspired Robotics approach now attracts wide interests as a new paradigm of science and engineering. Taking an example in the field of bioscience, the accomplishment of HGP (Human Genome Project) and subsequent post-genomic comprehensive "Omics data" such as transcriptome, proteome and metabolome, bring about vast amount of bio-information. However, as a plenty of omics data becomes available, it becomes sincerely recognized that the framework by which these omics data can be understood to make a whole picture of life is critically necessary. Thus, in the post-genomic era, biologically-inspired systems approach like Alife is expected to give one of new alternative ideas to integrate this vast amount of bio-data.

This example shows the Alife approach is very promising and may exert a wide influence on the effort to develop a new paradigm for next generation of life science. We hope this symposium becomes a forum for exchange of the ideas of the attendants from various fields, including the life science field, who are interested in the future possibility of biologically-inspired computation and systems approach.

I am looking forward to meeting you in Beppu, Oita.

Ju-Jang Lee
Vice Chairman
(Professor, KAIST)

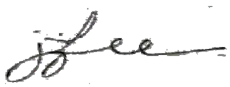

Ju-Jang Lee
Vice Chairman of AROB

The Fourteenth International Symposium on Artificial Life and Robotics (AROB) will be held in Beppu, Oita, Japan from Feb. 5th to 7th, 2009. This year's Symposium will be held amidst the high expectation of the increasingly important role of the new interdisciplinary paradigm of science and engineering represented by the field of artificial life and robotics that continuously attracts wide interests among scientist, researchers, and engineers around the globe.

Since the time of the very first AROB meeting in 1996, each year, distinguished researchers and technologists from around the world are looking forward to attending and meeting at AROB. AROB is becoming the annual excellent forum that represents a unique opportunity for the academic and industrial communities to meet and assess the latest developments in this fast growing artificial life and robotics field. AROB enables them to address new challenges, share solutions, discuss research directions for the future, exchange views and ideas, view the results of applied research, present and discuss the latest development of new technologies and relevant applications.

In addition, AROB offers the opportunity of hearing the opinions of well known leading experts in the field through the keynote sessions, provides the bases for regional and international collaborative research, and enables to foresee the future evolution of new scientific paradigms and theories contributed by the field of artificial life and robotics and associated research area. The twenty-first century will become the century of artificial life and intelligent machines in support of humankind and AROB is contributing through wide technical topics of interest that support this direction.

It is a great for me as the Vice Chairman of the 14th AROB 2009 to welcome everyone to this important event. Also, I would like to extend my special thanks to all authors and speakers for contributing their research works, the participants, and the organizing team of the 14th AROB.

Looking forward to meeting you at the 14th AROB in Beppu-Oita and wishing you all the best.

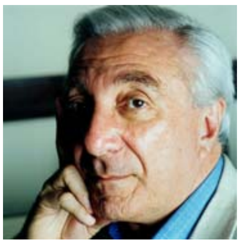

J. Casti
Vice Chairman
(Professor, International Institute for Applied Systems Analysis and The Kenos Circle)

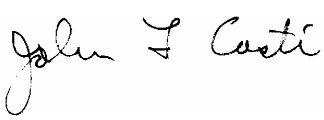

John Casti
Vice Chairman of AROB

Since its inception, the AROB has become the most important meeting in Asia each year for the fields of artificial life and robotics. Many of the significant advances in these areas have first been announced at the AROB, including robot football (the MIROSOT). So as a member of the Scientific Committee of this meeting since it began, it is my great pleasure to wish Professor Sugisaka and all participants another successful event in this long sequence of informative meetings in the lovely surroundings of Beppu.

Y. G. Zhang
Vice Chairman
(Professor, Academia Sinica)

Yongguang Zhang

Y. G. Zhang
Vice Chairman of AROB

Dear all friends and all participants,

Here I would like to show my warm welcome to you all attending the Fourteenth International Symposium on Artificial Life and Robotics (AROB ’09). As you know, this annual symposium was founded in 1996 by the support of Science and International Affairs Bureau, Ministry of Education, Science, Sports, and Culture (currently, Ministry of Education, Culture, Sports, Science and Technology) of Japan. Since then AROB is gradually become worldwide famous international symposium. Now AROB is already not an “academic baby”, but “academic teenage”, and AROB also owns an international journal, named the “Journal of Artificial Life and Robotics” published by Springer in decade.

The objective of AROB is aimed to develop new technologies for Artificial Life and Robotics which have been born recently. The important devotion of AROB is not only to pay attention to the development of theory on Artificial Life, but also expected to apply the principle to various fields, especially, the combination of both the Artificial Life and Robotics together. So far there are only few international symposiums or conference on artificial life, however, AROB is the only one that to explore the new generation of Robotics in far-sight with artificial life principle. In fact, some intelligent toys and intelligent systems have already been developed, although they have not completed knowledge construction and no evolution. Obviously, this is a very great and difficult career, and need continuous and consistent efforts of more and more scientists and engineers. In recent years, to our pleasure, many young professors and researchers join our team and bring significant outcomes of their work focusing on intelligent robots that we believe applies to the concepts of artificial life and artificial brain. We’d like to welcome and encourage more challenges like these for we are also devoting to the same target.

Beppu, the place of held most AROB symposium, is very charming city in Japan, she has variety of hot spring (jigoku), beautiful bay and colorful mountains. Her phantasmagoric visual change in various season attract many tourists. I hope all of you enjoy and appreciate her.

Finally, I would like to show my great thanks to all people who are working for this AROB ’09, including all staffs of AROB Lab, secretariat, and students, the successful holding of AROB symposium is dependent on the contributions of you all.

TIME TABLE

Date	Time	RoomA	RoomB	RoomC
2/4 (Wed)	13:00	Registration (Registration Desk)		
	17:00	Welcome Party (at Hotel ARTHUR)		
2/5 (Thur)	8:00	Registration (Registration Desk)		
	8:40	OS 8 (6) Chair H. H. Lee	OS 13 (6) Chair M. Yokota	OS 1 (6) Chair C- N. Ko
	10:10	Coffee Break		
	10:30	Ceremony		
	10:55	Plenary Talk PT1 A. H. Abbass Chair Y. G. Zhang		
	11:45	Lunch		
	12:40	GS 2 (5) Chair H. Yamamoto	Invited Talks session IT1 H. H. Lund IT2 L. Pagliarini Chair A. Grzech will end at 14:10	OS2 (6) Chair K- L. Su will end at 14:10
	13:55	Coffee Break		
	14:20	GS 12 (7) Chair C. E. Taylor	GS 14 (7) Chair J. Shim	GS 5 (5) Chair D. H. Kim will end at 15:35
	16:05	OS 17 (6) Chair J. B. Park	GS 1 (3) Chair S-C Heudin will end at 16:50	OS 14 (5) Chair S. Jung will end at 16:50
			GS 8 (3) Chair K-H Hsia	GS 4 (4) Chair K. Ohnishi will end at 17:50
	17:35			

GS: General Session OS: Organized Session

GS1 Artificial Intelligence, Artificial Living & Artificial Mind Research
GS2 Artificial Life
GS3 Bioinformatics & Cognitive Science
GS4 Brain Science, Chaos & DNA computing
GS5 Complexity
GS6 Computer Graphics, Micromachines & Robust Virtual Engineering
GS7 Evolutionary Computations
GS8 Fuzzy Control & Genetic Algorithms
GS9 Human-machine cooperative systems & Innovative Computations
GS10 Mobile Vehicles- Ⅰ
GS11 Mobile Vehicles- Ⅱ
GS12 Multi-agent systems
GS13 Neural Networks
GS14 Pattern recognition
GS15 Robotics- Ⅰ
GS16 Robotics- Ⅱ
GS17 Robotics-Ⅲ
GS18 Robotics-Ⅳ
GS19 Robotics- Ⅴ
GS20 Virtual Reality, Nano-biology & Nano-robotics
OS1 Intelligent Control
OS2 Intelligent Robot
OS3 Robotics and Control
OS4 Automata and Control
OS5 Bioinformatics and Intelligent Classification (1)
OS6 Bioinformatics and Intelligent Classification (2)
OS7 Soft Robotics
OS8 Learning and Robotics
OS9 Dynamical Information Processing in the Brain
OS10 Measurement and Control
OS11 Bio-inspired Theory and Application
OS12 Session of Economics and Management
OS13 Intuitive Human-System Interaction
OS14 Intelligent Systems
OS15 Biomimetic Machines and Robots
OS16 Embracing Complexity in Natural Intelligence
OS17 Intelligent Control and Robotics

		RoomA	RoomB	RoomC
2/6	8:00	Registration (Registration Desk)		
(Fri)	8:40	GS 10 (4) Chair M. H. Lee	GS 15 (4) Chair H. Ogai	OS 16 (4) Chair Y. Ishida
	9:40	GS 11 (4) Chair J-M. Lee	Invited Talk IT3 A. Grzech Chair H. H. Lund will end at 10:25	GS 20 (4) Chair N. Homma
	10:40	Coffee Break		
	10:50	GS 7 (5) Chair J. J. Lee	GS 3 (5) Chair K. Naitoh	GS 17 (5) Chair S. Jung
	12:05	Lunch		
	13:05	GS 13 (7) Chair H. Kinjo	Invited Talk IT4 J. Swiatek Chair L. Pagliarini will end at 13:50	GS 6 (5) Chair S. Omatu will end at 14:20
	14:50	Poster Session PS1, PS2, PS3, PS4	OS 3 (7) Chair M. Uchida	GS 19 (5) Chair H. H. Lee
	15:35	Coffee Break		
	15:50	Plenary Talk PT2 K. Aihara Chair J. J. Lee		
	16:40	GS 9 (4) Chair M. Yokota	OS 9 (4) Chair H. Suzuki	OS 7 (4) Chair H. Kinjo
	17:40 18:20	AROB Award Ceremony (Chair K. Naitoh) Banquet – Hotel Shiragiku (Chair Y. G. Zhang)...... Welcome Address C. Zhang / M. Oswald/ H. H. Lund/ L. Pagliarini		
	20:30			

GS: General Session OS: Organized Session

GS1 Artificial Intelligence, Artificial Living & Artificial Mind Research
GS2 Artificial Life
GS3 Bioinformatics & Cognitive Science
GS4 Brain Science, Chaos & DNA computing
GS5 Complexity
GS6 Computer Graphics, Micromachines & Robust Virtual Engineering
GS7 Evolutionary Computations
GS8 Fuzzy Control & Genetic Algorithms
GS9 Human-machine cooperative systems & Innovative Computations
GS10 Mobile Vehicles- Ⅰ
GS11 Mobile Vehicles-Ⅱ
GS12 Multi-agent systems
GS13 Neural Networks
GS14 Pattern recognition
GS15 Robotics- Ⅰ
GS16 Robotics-Ⅱ
GS17 Robotics-Ⅲ
GS18 Robotics-Ⅳ
GS19 Robotics-Ⅴ
GS20 Virtual Reality, Nano-biology & Nano-robotics
OS1 Intelligent Control
OS2 Intelligent Robot
OS3 Robotics and Control
OS4 Automata and Control
OS5 Bioinformatics and Intelligent Classification (1)
OS6 Bioinformatics and Intelligent Classification (2)
OS7 Soft Robotics
OS8 Learning and Robotics
OS9 Dynamical Information Processing in the Brain
OS10 Measurement and Control
OS11 Bio-inspired Theory and Application
OS12 Session of Economics and Management
OS13 Intuitive Human-System Interaction
OS14 Intelligent Systems
OS15 Biomimetic Machines and Robots
OS16 Embracing Complexity in Natural Intelligence
OS17 Intelligent Control and Robotics

	RoomA	RoomB	RoomC
2/7 (Sat) 8:00	Registration (Registration Desk)		
8:40	OS 12 (5) Chair T. Ito	Invited Talk IT5 M. H. Lee Chair M. Oswald will end at 9:25	OS 4 (4) Chair M. Kono will end at 9:40
9:55	OS 11 (6) Chair I. Yoshihara	Invited Talk IT6 J. Shim Chair M. Oswald will end at 10:10	OS 5 (4) Chair M. Yoshioka will end at 10:40
		GS16 (6) Chair J. Wang will end at 11:40	OS 6 (4) Chair S. Omatu will end at 11:40
11:25	Coffee Break		
11:50	Plenary Talk PT3 C- S. Zhang Chair H. Tanaka		
12:40	Lunch		
13:25	GS 18 (5) Chair S. Sagara	OS 15 (6) Chair K. Watanabe will end at 14:55	OS 10 (5) Chair Y. Yoshitomi
14:55	Farewell Party (Room A)		
15:45			

GS: General Session OS: Organized Session

GS1 Artificial Intelligence, Artificial Living & Artificial Mind Research
GS2 Artificial Life
GS3 Bioinformatics & Cognitive Science
GS4 Brain Science, Chaos & DNA computing
GS5 Complexity
GS6 Computer Graphics, Micromachines & Robust Virtual Engineering
GS7 Evolutionary Computations
GS8 Fuzzy Control & Genetic Algorithms
GS9 Human-machine cooperative systems & Innovative Computations
GS10 Mobile Vehicles-Ⅰ
GS11 Mobile Vehicles-Ⅱ
GS12 Multi-agent systems
GS13 Neural Networks
GS14 Pattern recognition
GS15 Robotics-Ⅰ
GS16 Robotics-Ⅱ
GS17 Robotics-Ⅲ
GS18 Robotics-Ⅳ
GS19 Robotics-Ⅴ
GS20 Virtual Reality, Nano-biology & Nano-robotics
OS1 Intelligent Control
OS2 Intelligent Robot
OS3 Robotics and Control
OS4 Automata and Control
OS5 Bioinformatics and Intelligent Classification (1)
OS6 Bioinformatics and Intelligent Classification (2)
OS7 Soft Robotics
OS8 Learning and Robotics
OS9 Dynamical Information Processing in the Brain
OS10 Measurement and Control
OS11 Bio-inspired Theory and Application
OS12 Session of Economics and Management
OS13 Intuitive Human-System Interaction
OS14 Intelligent Systems
OS15 Biomimetic Machines and Robots
OS16 Embracing Complexity in Natural Intelligence
OS17 Intelligent Control and Robotics

TECHNICAL PAPER INDEX

February 5 (Thursday)

Room A

10:55~11:45 Plenary Talk
Chair Y. G. Zhang (Academia Sinica, P. R. China)

PT1 *The pareto operating curve for risk minimization in life and robotics*
H. Abbass (University of New South Wales, Australia)

Room B

12:40~14:10 Invited Talks Session
Chair A. Grzech (Wroclaw University of Technology, Poland)

IT1 *Modular robotic system as multisensory room in children's hospital*
H. H. Lund (Technical University of Denmark, Denmark)

IT2 *Modular robotic wearable*
L. Pagliarini (Technical University of Denmark, Denmark)

February 6 (Friday)

Room A

15:50~16:40 Plenary Talk
Chair J. J. Lee (KAIST, Korea)

PT2 *Mathematical modelling of complex systems and its possible applications*
K. Aihara (The University of Tokyo, Japan)

Room B

9:40~10:25 Invited Talk
Chair H. H. Lund (Technical University of Denmark, Denmark)

IT3 *Optimal monitoring for distributed intrusion detection system*
A. Grzech (Wroclaw University of Technology, Poland)

13:05~13:50 Invited Talk
Chair L. Pagliarini (Technical University of Denmark, Denmark)

IT4 *Making decision in two-stage identification system with knowledge updating*
J. Swiatek (Wroclaw University of Technology, Poland)

February 7 (Saturday)

Room A

11:50~12:40 Plenary Talk
Chair H. Tanaka（Tokyo Medical and Dental University, Japan）

PT3 *Graph based semi-supervised learning*
C-S. Zhang (Tsinghua University, P. R. China)

©ISAROB 2009

Room B

8:40~9:25 Invited Talk

Chair M. Oswald (Vienna University of Technology, Austria)

IT5 *On the observability and estimability analysis of the global positioning system (GPS) and inertial navigation system (INS)*
M- H. Lee (Pusan National University, Korea)

9:25~10:10 Invited Talk

Chair M. Oswald (Vienna University of Technology, Austria)

IT6 *A design of brain sensory monitoring thinking activity inside the knowledge system*
J. Shim (Kangnam University, Korea)

February 5 (Thursday)

8:00~Registration

Room A

8:40~10:10 OS8 Learning and Robotics
Chair: H. H. Lee (Waseda University, Japan)
Co-Chair: H. Ogai (Waseda University, Japan)

OS8-1 *Modeling of traffic flow using cellular automata and traffic signal control by Q-learning*
K. Umemoto, J-S. Shin, T. Ohshita, Y. Osuki (Waseda University, Japan)
M. Miyazaki (Kanto-Gakuin University, Japan)
H-H. Lee (Waseda University, Japan)

OS8-2 *Humanoid robot's motion planning using genetic network programming*
Y. X. Sun, H. Ogai (Waseda University, Japan)

OS8-3 *On-line tuning PID parameters in idle-speed engine based on modified BP neural network by particle swarm optimization*
J-M. Yin, J-S. Shin, H-H. Lee (Waseda University, Japan)

OS8-4 *Traffic signal control based on predicted distribution of traffic jam*
C-Y. Cui, J-S. Shin (Waseda University, Japan)
F. Shoji (Fukuoka Institute of Technology, Japan)
H-H. Lee (Waseda University, Japan)

OS8-5 *Pipe inspection robot using wireless communication system*
H. Ogai, Y. Yeh, D. Wu (Waseda University, Japan)
K. Hirai, T. Abe (Hakutsu Technology Corporation, Japan)
G. Sato (Wave Professional Inc., Japan)

OS8-6 *Production adjusting method based on predicted distribution of production and inventory using dynamic bayesian network*
Y-H. Park, J-S. Shin, K-Y. Woo (Waseda University, Japan)
F. Shoji (Fukuoka Institute of Technology)
H-H. Lee (Waseda University, Japan)

12:40~14:10 GS2 Artificial Life
Chair: H. Yamamoto (Gifu University, Japan)

GS2-1 *Research on softman cooperation mechanism and algorithms*
D. Ai, H-T. Xiong, G. Zeng,Y. Yue (University of Science and Technology Beijing, P. R. China)

GS2-2 *The effects of the trophic level on the stability of food webs*
H. Ochiai, R. Suzuki, T. Arita (Nagoya University, Japan)

GS2-3 *Evolutionary acquisition of behaviors building structural objects by virtual creatures*
K. Oomiya, K. Nakamura (Future University – Hakodate, Japan)
K. Suzuki (Hokkaido University, Japan)

GS2-4 *Agent based approach for homeostatic plasticity in neuronal activities*
S. Fernando, Y. Nakamura, S. Matsuzaki, A. Marasinghe (Nagaoka University of Technology, Japan)

GS2-5 *Adaptive sensor arrays for acoustic monitoring of bird behavior and diversity: Preliminary results on source identification using support vector machines*
E. E. Vallejo (ITESM, México)
C. E. Taylor (UCLA, USA)

14:20~16:05 GS12 Multi-agent systems
Chair: C. E. Taylor (University of California, Los Angeles, USA)

GS12-1 *The PSP practice support system using multiagent techniques and manipulation analysis data*
D. Yamaguchi, K. Otsuka, F. Katayama, M. Takahashi (Toin University of Yokohama, Japan)

GS12-2 *Use of multiobjective genetic rule selection for examining the effectiveness of inter-vehicle communication in traffic simulations*
Y. Hamada, Y. Nojima, H. Ishibuchi (Osaka Prefecture University)

GS12-3 *Web news summary system with clustering algorithm to identify same article*
A. Niimi, Y. Saito, O. Konishi (Future University-Hakodate, Japan)

GS12-4 *Evolution of cooperative behavior among heterogeneous agents with different strategy representations in an iterated prisoner's dilemma game*
H. Ohyanagi, Y. Wakamatsu, Y. Nakashima, Y. Nojima,
H. Ishibuchi (Osaka Prefecture University)

GS12-5 *Moving robots' mind of autonomous decentralized FMS and mind change control*
H. Yamamoto, H. Kikuchi (Gifu University, Japan)
T. Yamada, M. A. Jamali (Universite du Quebec, Canada)

GS12-6 *High survivability of a large colony through a small world relationship*
M. Kubo, H. Sato, T. Matsubara (National Defense Academy, Japan)
C. Melhuish (Bristol Robotic Laboratory, UK)

GS12-7 *An evolutionary nano-agent control architecture for intelligent artificial creatures*
J-C. Heudin (IIM Interactive Media Lab., France)

16:05~17:35 OS17 Intelligent Control and Robotics
Chair: J. B. Park (Yonsei University, Korea)
Co-Chair: Y. H. Choi (Kyonggi University, Korea)

OS17-1 *Fault location estimation using estimator residual*
C. K. Lee, S. H. Doo, J. B. Park (Yonsei University, Korea)
T. S. Yoon (Changwon National University, Korea)

OS17-2 *Observer-based fuzzy control for nonlinear networked control system with pack drop*
G. B. Koo, J. B. Park (Yonsei University, Korea)
Y. H. Joo (Kunsan National University , Korea)

OS17-3 *Formation control of mobile robots with disturbances*
B. S. Park, S. K. Song, J. B. Park (Yonsei University, Korea)
Y. H. Choi (Kyonggi University, Korea)

OS17-4 *Grasping control of thumb-index finger model: Lyapunov stability approach*
S. K. Song, J. B. Park (Yonsei University, Korea)
Y. H. Choi (Kyonggi University, Korea)

OS17-5 *Intelligent diagnosis system for transmission line: Fuzzy-bayesian cassifier approach*
H. C. Sung, J. B. Park (Yonsei University, Korea)
Y. H. Joo (Kunsan National University, Korea)

OS17-6 *Linear frequency estimation for motor application with quadratic constrained condition*
G. H. Choi (Yonsei University, Korea)
T. S. Yoon (Changwon University, Korea)
J. B. Park (Yonsei University, Korea)

Room B

8:40~10:10 OS13 Intuitive Human-System Interaction
Chair: M. Yokota (Fukuoka Institute of Technology, Japan)
Co-Chair: T. Oka (Fukuoka Institute of Technology, Japan)

OS13-1 *A method for top-down control of robotic attention based on mental-image description language,* L_{md}
M. Yokota, K. Sasaki, R. Kaida, T. Oka, K. Sugita (Fukuoka Institute of Technology)

OS13-2 *Problem finding and solving based on mental-image description language,* L_{md}
M. Yokota, T. Tomezuka, Y. Takubo, T. Oka, K. Sugita (Fukuoka Institute of Technology)

OS13-3 *Success rates in a multi-modal command language for home robot users*
T. Abe, T. Oka, K. Sugita, M. Yokota (Fukuoka Institute of Technology, Japan)

OS13-4 *Multi-modal command interface with remote home robots*
T. Abe, T. Oka, K. Sugita, M. Yokota (Fukuoka Institute of Technology, Japan)

OS13-5 *Some consideration on user adaptive interface for universal multimedia access*
Y. Maeda, E. Tsujimura, K. Sugita, T. Oka, M. Yokota (Fukuoka Institute of Technology, Japan)

OS13-6 *Control of damping with reinforcement learning for power-assisted positioning task*
T. Morizono (Fukuoka Institute of Technology, Japan)
M. Higashi (Toyota Technological Institute, Japan)

14:20~16:05 GS14 Pattern recognition
Chair: J. Shim (Kangnam University, Korea)

GS14-1 *Unsupervised learning method for support vVector machine and its application to surface-electromyogram recognition*
S. Kawano, H. Tamura, K. Tanno (University of Miyazaki, Japan)

GS14-2 *A method for extraction of arbitrary curve using one-dimensional histogram*
S. Nakashima, S. Serikawa (Kyushu Institute of Technology, Japan)

GS14-3 *Covariance-based recognition using incremental learning approach*
E. O. Hassab (Tokyo Institute of Technology, Japan)

GS14-4 *Elimination of un-uniformed image distortion using LCD*
K. Miyazaki (Kumamoto Prefectural College of Technology, Japan)
K. Kawasue (University of Miyazaki, Japan)

GS14-5 *Incorporation of user preference into multiobjective genetic fuzzy rule selection for pattern classification problems*
Y. Nojima, H. Ishibuchi (Osaka Prefecture University)

GS14-6 *Feature map sharing hypercolumn model for shift invariant face recognition*
S. Aly (Kyushu University, Japan)
N. Tsuruta (Fukuoka University, Japan)
R. Taniguchi (Kyushu University, Japan)

GS14-7 *A moving object tracking based on color information employing a particle filter algorithm*
B. Sugandi, H. Kim, J. K. Tan, S. Ishikawa (Kyushu Institute of Technology, Japan)

16:05~16:50 GS1 Artificial Intelligence, Artificial Living & Artificial Mind Research
Chair: J-C. Heudin (Pôle Universitaire Léonard de Vinci, France)

GS1-1 *Correlation-based similarity metrics in MBR for ordered data*
D. Nakahigashi, H. Tsuji (Osaka Prefecture University, Japan)

GS1-2 *Hybrid system based emotion recognition and novel emotion engine*
D. H. Kim (Hanbat National University, S. Korea)

GS1-3 *Group feature extraction based on matrix factorization from long-range office-logging data*
I. Kita, T. Shibata, K. Ikeda, (Nara Institute of Science and Technology, Japan)
Y. Kamiya, D. Kato, K. Kunieda, K. Yamada, (CCIL, NEC Corporation, Japan)

16:50~17:35 GS8 Fuzzy Control & Genetic Algorithms
Chair: K-H. Hsia (Far East University, Taiwan)

GS8-1 *Robust stability analysis for uncertain T-S fuzzy systems with a time-varying delay*
I-S. Song, J-W. Shin, J-W. Ko, P-G. Park (Pohang University of Science & Technology, Korea)

GS8-2 *Optimization of the sensor network using genetic algorithm*
T. Minamino, K. Ito (Hosei University, Japan)

GS8-3 *A novel genetic algorithm with different structure selection for circuit design optimization*
Z. Bao, T. Watanabe (Waseda University, Japan)

Room C

8:40~10:10 OS1 Intelligent Control
Chair: Chia-Nan Ko (Nan-Kai University of Technology, Taiwan)
Co-Chair: Li-Chun Lai (Chung Chou Institute of Technology, Taiwan)

OS1-1 *A PSO method with nonlinear time-varying evolution for optimal design of PID controllers in a pendubot system*
P-Y. Chen, C-J. Wu (National Yunlin University of Science and Technology, Taiwan)
Y-Y. Fu, C-N. Ko (Nan-Kai University of Technology, Taiwan)
L-C. Lai (Chungchou Institute of Technology, Taiwan)

OS1-2 *Support vector regression for initialization of radial basis function networks for a multi-input multi-output system*
P-Y. Chen, C-J. Wu (National Yunlin University of Science and Technology, Taiwan)
Y-Y. Fu, C-N. Ko (Nan-Kai University of Technology, Taiwan)
J-T. Jeng (National Formosa University, Taiwan)

OS1-3 *ARRBFNs with SVR for prediction of chaotic time series with outliers*
Y-Y. Fu, C-J. Wu (National Yunlin University of Science and Technology, Taiwan)
C-N. Ko (Nan Kai University of Technology, Taiwan)
J-T. Jeng (National Formosa University, Taiwan)
L-C. Lai (Chung Chou Institute of Technology, Taiwan)

OS1-4 *A fast identification algorithm with outliers under box-cox transformation-based annealing robust radial basis function networks*
P-Y. Chen, C-J. Wu (National Yunlin University of Science and Technology, Taiwan)
C-N. Ko (Nan Kai University of Technology, Taiwan)
J-T. Jeng (National Formosa University, Taiwan)

OS1-5 *Develop a module based security system for intelligent home*
K-L. Su (National Yunlin University of Science & Technology, Taiwan)
S-H. Chia (Wu-Feng Institute of Techonlogy, NYUST, Taiwan)
S-V. Shiau, J-H. Guo (National Yunlin University of Science & Technology, Taiwan)

OS1-6 *Synchronous reluctance motor speed drive using sliding mode controller based on gaussian radial basis function neural network*
C-A. Chen, H-K. Chiang (National Yunlin University of Science and Technology, Taiwan)
W-B. Lin (Far East University, Taiwan)

12:40~14:10 OS2 Intelligent Robot
Chair: Kuo-Lan Su (National Yunlin University of Science & Technology, Taiwan)
Co-Chair: Jyh-Hwa Tzou (Wu-Feng Institute of Technology, Taiwan)

OS2-1 *Detection system of security robot using multisensor fusion algorithms*
T-L. Chien, J-H. Tzou (Wu-Feng Institute of Technology, Taiwan)
C-C. Wang (Chienkuo Technology University, Taiwan)
K-L. Su (National Yunlin University of Science & Technology, Taiwan)

OS2-*2 High-speed laser localization for restaurant service mobile robot*
J-H. Tzou (Wu-Feng Institute of Technology, Taiwan)
K-L. Su (National Yunlin University of Science and Technology, Taiwan)

OS2-3 *PSO-based potential field method for a mobile robot motion planning in an unknown environment*
L-C. Lai (Chung Chou Institute of Technology, Taiwan)
C-J. Wu (National Yunlin University of Science and Technology, Taiwan)
J-T. Jeng (National Formosa University, Taiwan)
C-N. Ko, Y-Y. Fu (Nan Kai University of Technology, Taiwan)

OS2-4 *Motion planning of mobile robots using laser range finder*
J-H. Guo, K-L. Su, C-J. Wu, S-V. Shiau (National Yunlin University of Science & Technology, Taiwan)

OS2-5 *Image-guided searching for landmark*
C. C. Wang (Chienkuo Technology University, Taiwan)
S. F. Lien (National Yunlin University of Science and Technology, Taiwan)
K. H. Hsia (Far East University, Taiwan)
J. P. Su (National Yunlin University of Science and Technology, Taiwan)

OS2-6 *Design and implementation of human machine interface surveillance systems for tracked robots*
C. C. Wang (Chienkuo Technology University, Taiwan)
K-L. Su (National Yunlin University of Science and Technology, Taiwan)

14:20~15:35 GS5 Complexity
Chair: D. H. Kim (Hanbat National University, Korea)

GS5-1 *Harmonic oscillations in lotka-volterra-type dynamic systems: A new approach from a matrix operator equation system*
K. Ohnishi (Niigata University, Japan)

GS5-2 *Chemical reaction simulations using abstract rewriting system on multisets with Lattice Boltzmann method*
M. Umeki, Y. Suzuki (Nagoya University, Japan)

GS5-3 *A design of algorithms for real-time generation of linear-recursive sequences on cellular automata*
N. Kamikawa, H. Umeo (University of Osaka Electro-Communication, Japan)

GS5-4 *Towards a brief proof of the four-colour theorem without using computer: Basic theorems and a bird-eye's view*
K. Ohnishi (Niigata University, Japan)

GS5-5 *Simulating the behaviour of cellular automata by extended spiking neural P systems*
A. Binder, R. Freund, (Vienna University of Technology, Austria)
M. Oswald (Vienna University of Technology, Hungarian Academy of Sciences, Austria)

15:35~16:50 OS14 Intelligent Systems
Chair: S. Jung (Chungnam National University, Korea)
Co-Chair: J-J. Lee (KAIST)

OS14-1 *Memory retention strategy by balancing neutral energy point*
J. Shim (kangnam University, Korea)

OS14-2 *Target-adjusted model for kernel-based tracker*
J-G. Choe, J-H. Seok, J-J. Kim, J-J. Lee (KAIST, Korea)

OS14-3 *Human arm-like surgical robot system with force reflection measurement for minimally invasive surgery*
K-Y. Kim, H-S. Song, J-W. Suh, J-J. Lee (KAIST, Korea)

OS14-4 *A novel compact genetic algorithm using offspring survival evolutionary strategy*
J-H. Seok, T-Y. Choi, J-J. Lee (KAIST, Korea)

OS14-5 *Neural network based smith predictor design for a time delay of a tele-operated control system*
H. J. Choi, S. Jung (Chungnam National University, Korea)

16:50~17:50 GS4 Brain Science, Chaos & DNA computing
Chair: S. Ohnishi (Niigata University, Japan)

GS4-1 *Artificial realization of an adaptive expert knowledge database for automatic sleep stage determination in clinical practice*
B. Wang, T. Sugi (Saga University, Japan)
F. Kawana (Toranomon Hospital, Japan)
X. Wang (East China University of Science and Technology, P. R. China)
M. Nakamura (Saga University, Japan)

GS4-2 *Reliable EOG signal based control approach with EEG signal judgement*
T. Zhang, C. Chen (Tsinghua University, P. R. China)
M. Nakamura (Saga University, Japan)

GS4-3 *AKP energy levels by a simple shooting scheme for a periodic orbit*
K. Kubo, T. Shimada (Meiji University, Japan)

GS4-4 *Synchronization and periodic windows in the globally coupled map lattice*
T. Moriya, K. Kubo, T. Shimada (Meiji University, Japan)

February 6 (Friday)

8:00~ Registration

Room A

8:40~9:40 GS10 Mobile Vehicles- I
Chair: M. H. Lee (Pusan National University, Korea)

GS10-1 *Stability analysis of the wheeled humanoid robot*
H-U. Ha, S-W. Ryu, J-M. Lee (Pusan National University, Korea)

GS10-2 *Trajectory tracking control of mobile robots without using longitudinal velocity measurement*
K. Maeda, M. Oya, Q. Wang (Kyushu Institute of Technology, Japan)
K. Okumura (Fukuoka Industrial Technology Center, Japan)

GS10-3 *Integration of stereo vision system and laser range finder for autonomous obstacle avoidance and map construction*
Y-Z. Chang, J-F. Hou (Chang Gung University, Taiwan)
Y-P. Chang (Chung-Shan Institute of Science & Technology, Taiwan)

GS10-4 *Concurrent localization of multiple robots*
J-H. Park, J-Y. Cheong, T-K. Yang, J-M. Lee (Pusan National University, Korea)

9:40~10:40 GS11 Mobile Vehicles-Ⅱ
Chair: J-M. Lee (Pusan National University, Korea)

GS11-1 *Yawing control of a single wheel robot*
B-H. Ahn, J-M. Hwang, J-B. Son, J-M. Lee (Pusan National University, Korea)

GS11-2 *Robust oscillation control of wheeled mobile robots*
Y. Tsuchida, M. Oya, N. Takagi, Q. Wang (Kyushu Institute of Technology, Japan)

GS11-3 *Workspace mapping based on multi-sensor information fusion using heterogeneous onboard sensors*
M. Miyake, H. Takai (Hiroshima City University)
K. Tachibana (Osaka Gakuin University)

GS11-4 *Simultaneous localization and mapping of wheel basedAutonomous vehicle with ultrasonic sensors*
S-Y. Jung, J-M. Kim, J-M Heo, S-S. Kim (Pusan National University, Korea)
J-I. Bae (Pukyong National University, Korea)

10:50~12:05 GS7 Evolutionary Computations
Chair: J. J. Lee (KAIST, Korea)

GS7-1 *Hybridization of evolutionary multiobjective optimization algorithmsby the adaptive use of scalarizing fitness functions*
N. Tsukamoto, Y. Sakane, Y. Nojima, .H. Ishibuchi (Osaka Prefecture University, Japan)

GS7-2 *Development of programming language espace and its application to parallel and distributed evolutionary computation*
T. Iwakawa, S. Ono, S. Nakayama (Kagoshima University, Japan)

GS7-3 *Competitive coevolutionary algorithms can solve function optimization problems*
T. Sato, T. Arita (Nagoya University, Japan)

GS7-4 *Pareto-optimal fuzzy rule mining with EMO algorithms and its improvement by heuristic initialization*
I. Kuwajima, Y. Nojima, H. Ishibuchi (Osaka Prefecture University, Japan)

GS7-5 *Robust optimization using multi-objective particle swarm optimization*
S. Ono, Y. Yoshitake, S. Nakayama (Kagoshima University, Japan)

13:05~14:50 GS13 Neural Networks
Chair: H. Kinjo (University of the Ryukyus, Japan)

GS13-1 *Three-dimensional medical image recognition of cancer of the liver by the revised radial basis function (RBF) neural network algorithm*
M. Nakagawa, T. Kondo, T. Kudo, S. Takao, J. Ueno (Tokushima University, Japan)

GS13-2 *Remarks on tracking method of neural network weight change for learning type neural network feedforward feedback controller*
T. Yamada (Ibaraki University, Japan)

GS13-3 *Multiple self-organizing maps for visuo-motor system that uses multiple cameras with different field of views*
N. Okada, J. Qiu, K. Nakamura, E. Kondo (Kyushu University, Japan)

GS13-4 *Three-dimensional medical image analysis of the heart by the revised GMDH-type neural network self-selecting optimum neural network architecture*
C. Kondo (Kyushu University, Japan)
T. Kondo (Tokushima University, Japan)

GS13-5 *Modeling artificial neural networks using a visual programming paradigm*
K. J. Mackin (Tokyo University of Information Sciences, Japan)

GS13-6 *Neuro-based olfactory model for artificial organoleptic tests*
Z. Soh, T. Tsuji, N. Takiguchi (Hiroshima University, Japan)
H. Ohtake (Osaka University, Japan)

GS13-7 *Revised GMDH-type neural network algorithm self-selecting optimum neural network architecture*
C. Kondo (Kyushu University, Japan)
T. Kondo (Tokushima University, Japan)

14:50~15:50 Poster Session & Coffee Break

PS1 *Pheromone-oriented transmission for load-balanced data gathering in wireless sensor networks*
E. Orito, A. Utani, H. Yamamoto (Musashi Institute of Technology, Japan)

PS2 *A study on object observation by large-scale wireless sensor network and autonomous mobile robot*
K. Matsumoto, A. Utani, H. Yamamoto (Musashi Institute of Technology, Japan)

PS3 *Discrete particle swarm optimization selecting forwarding nodes for query dissemination in wireless sensor networks*
J. Nagashima, A. Utani, H. Yamamoto (Musashi Institute of Technology, Japan)

PS4 *Logistic regression analysis for mutation data of hemophilia B*
M. Utsunomiya, M. Sakamoto, H. Furutani (University of Miyazaki, Japan)

16:40~17:40 GS9 Human-machine cooperative systems & Innovative Computations
Chair: M. Yokota (Fukuoka Institute of Technology, Japan)

GS9-1 *Real-time estimation system of gaze angle based on electrooculogram*
X. Zhang, T. Sugi (Saga University, Japan)
X. Wang (East China University of Science and Technology, P. R. China)
M. Nakamura (Saga University, Japan)

GS9-2 *A study on a postural optimization for bicycle's exercise based on electromyography*
S. Matsumoto, T. Tokuyasu, S. Iwao, H. Taniguchi, S. Adachi, S. Shiga, K. Ohba
(Oita National College of Technology, Japan)

GS9-3 *A movie rating prediction system based on personal propensity analysis*
S. Lee, T. Jeon, G. Baek, J. Cho, S. Kim (Pusan National University, Korea)

GS9-4 *Electric wheelchair control with gaze direction and eye blinking*
D. Purwanto, R. Mardiyanto (Institut Teknologi Sepuluh Nopember, Indonesia)
K. Arai (Saga University, Japan)

Room B

8:40~9:40 GS15 Robotics- I
Chair: H. Ogai (Waseda University, Japan)

GS15-1 *Construction of the robot control system which understands voice and pointing action*
Y. Takenaka, N. Abe, Y. Tabuchi (Kyushu Institute of Technology, Japan)
H. Taki (Wakayama University, Japan)
S. He (VuCOMP, USA)

GS15-2 *Effective RFID tag positioning strategy for mobile robot with indoor mapping*
J. Shin, M. Chang, G. Lee (Pohang University of Science and Technology, Korea)
W. Kang, Y. Kim, J. An (Daegu Techopark Venture 2nd Plant, Korea)
P. Park (Pohang University of Science and Technology, Korea)

GS15-3 *A new grasp quality measure considering physical limits of robot hands*
H. Jeong, J. Park, J. Cheong (Korea University, Korea)

GS15-4 *Generation of a pick and place trajectory model for the tip of a robotic manipulator arm for an loading and unloading operation*
T. C. Manjunath (NHCE, India)
I. Mishra (NIST, India)
A. K. Satapathy (General Motors, India)

10:50~12:05 GS3 Bioinformatics & Cognitive Science
Chair: K. Naitoh (Waseda University, Japan)

GS3-1 *Mathematical modeling for morphogenesis of leaf with employing cell automata and reaction-diffusion equation*
K. Ishii, H. Hamada, M. Okamoto (Kyushu University, Japan)

GS3-2 *An abstract model for investigating the adaptivity of misperception*
J. Akaishi (Yatsushiro National College of Technology, Japan)
T. Arita (Nagoya University, Japan)

GS3-3 *Prediction of human eye movements in facial discrimination tasks*
S. Nishida, T. Shibata, K. Ikeda (Nara Institute of Science and Technology, Japan)

GS3-4 *Origin of the word-initial consonant system of the Japanese-Ryukyuan (JR) language from Oceanic consonant system: Elucidation by JR-Oceanic consonant correspondence laws*
K. Ohnishi, M. Kiriyama (Niigata University, Japan)

GS3-5 *A study on effect of morphological filters on computer-aided medical image diagnosis*
N. Homma, S. Shimoyama, Y. Kawai, T. Ishibashi, M. Yoshizawa (Tohoku University, Japan)

13:50~15:35 OS3 Robotics and Control
Chair: M. Uchida (The University of Electro-Communications, Japan)
Co-Chair: H. Asano (Aoyamga Gakuin University, Japan)

OS3-1 *Group behavior of agents with emotional model*
S. Hiroshige, H. Asano (Aoyama Gakuin University, Japan)
M. Uchida (The University of Electro-Communications)
H. Ide (Aoyama Gakuin University, Japan)

OS3-2 *Basic examination concerning multi agent cooperation with entrainment*
H. Asano, H. Suzuki (Aoyama Gakuin University, Japan)
M. Uchida (The University of Electro-Communications)
H. Ide (Aoyama Gakuin University, Japan)

OS3-3 *Basics study about cooperation movement of human and agent with entrainment*
M. Saito, H. Asano (Aoyama Gakuin University, Japan)
M. Uchida (The University of Electro-Communications)
H. Ide (Aoyama Gakuin University, Japan)

OS3-4 *Man-machine interface for modular robot system*
T. Goto, M. Uchida (University of Electro-Communications)
H. Asano (Aoyama Gakuin University)
A. Nozawa (Meisei University)
H. Onogaki (Kogakuin University)
T. Mizuno (AIST)
H. Ide (Aoyama Gakuin University)
S. Yokoyama (Kogakuin University)

OS3-5 *Autonomous reconfiguration of robot shape by using Q-learning*
S. Shiba, M. Uchida (The University of Electro-Communications)
A. Nozawa (Meisei University)
H. Asano (Aoyama Gakuin University)
H. Onogaki (Kogakuin University)
T. Mizuno (AIST)
H. Ide (Aoyama Gakuin University)
S. Yokoyama (Kogakuin University)

OS3-6 *Current control of PWM power amplifier by approximate 2-degree-of-freedom digital controller*
K. Fujita, K. Higuchi, K. Nakano (The University of Electro-Communications, Japan)
K. Matsushita, F. Chino (NF Corporation, Japan)

OS3-7 *Vibration suppression control of a flexible arm using non-linear observer with simultaneous perturbation stochastic approximation*
J. I. M. Martinez (The University of Electro-Communications, Japan)
U. Sawut (Nikki Co. Ltd, Japan)
K. Nakano (The University of Electro-Communications, Japan)

16:40~17:40 OS9 Dynamical Information Processing in the Brain
Chair: H. Suzuki (The University of Tokyo, Japan)
Co-Chair: T. Kohno (The University of Tokyo, Japan)

OS9-1 *Multiple cell assemblies and multi-step computation in neural networks*
M. Oku (The University of Tokyo, Japan)
K. Aihara (ERATO, JST, The University of Tokyo, Japan)

OS9-2 *Possible roles of pre-synaptic connections in neural circuits*
H. Watanabe (University of Tokyo, Japan)
K. Aihara (University of Tokyo, ERATO Aihara Complexity Modeling Project, JST, Japan)

OS9-3 *Self-organization of orientation selective and ocular dominance maps through spike-timing-dependent plasticity*
K. Iwayama, H. Suzuki, K. Aihara (The University of Tokyo, Japan)

OS9-4 *Integrative bayesian model of two opposite types of sensory adaptation*
Y. Sato (University of Tokyo, Japan)
K. Aihara (The University of Tokyo, ERATO, JST, Japan)

Room C

8:40~9:40 OS16 Embracing Complexity in Natural Intelligence
Chair: Y. Ishida (Toyohashi University of Technology, Japan)
Co-Chair: K. Harada (Toyohashi University of Technology, Japan)

OS16-1 *A hub gene in a HIV-1 gene regulatory network is a promising target for anti-HIV-1 drugs*
K. Harada, Y. Ishida (Toyohashi University of Technology, Japan)

OS16-2 *Reverse engineering of spatiotemporal patterns in spatial prisoner's dilemma*
T. Ueda, Y. Ishida (Toyohashi University of Technology, Japan)

OS16-3 *Using spatial strategies to model agents' commitments for a protocol formation*
N. D. Thien, Y. Katsumata, M. Tokumitsu, Y. Ishida (Toyohashi University of Technology, Japan)

OS16-4 *A time-dependent threshold condition to determine an onset of AIDS*
K. Harada, Y. Ishida (Toyohashi University of Technology, Japan)

9:40~10:40 GS20 Virtual Reality, Nano-biology & Nano-robotics
Chair: N. Homma (Tohoku University, Japan)

GS20-1 *Quadruped virtual robot simulation in virtual environment obeying physical law*
K. Miyoshi, N. Abe, Y. Tabuchi (Kyusyu Institute of Technology, Japan)
H. Taki (Wakayama University, Japan)
S. He (VuCOMP, USA)

GS20-2 *Modeling and deforming virtual dense elastic object with haptic device PHANToM*
H. Takada, N. Abe (Kyushu Institute of Technology, Japan)
Y. Kinoshita (Munakata Suikokai General Hospital, Japan)
H. Taki (Wakayama University, Japan)
T. Tokuyasu (Oita National College of Technology, Japan)
S. He (VuCOMP, USA)

GS20-3 *Study on communication system between haptic-device*
Y. Uchida, N. Abe (Kyushu Institute of Technology, Japan)
Y. Kinoshita (Munakata Suikokai General Hospital, Japan)
S. He (VuCOMP, USA)
H. Taki (Wakayama University, Japan)
T. Tokuyasu (Oita National College of Technology, Japan)

GS20-4 *Detection of brain aneurysm and route searching to brain aneurysm aim at the development of operation simulation system*
T. Miyagi, N. Abe (Kyushu Institute of Technology, Japan)
Y. Kinoshita (Munakata Suikokai General hospital, Japan)
T. Tokuyasu (Oita National College of Technology, Japan)
H. Taki (Wakayama University, Japan)
S. He (VuCOMP, USA)

10:50 ~12:05 GS17 Robotics-Ⅲ
Chair: S. Jung (Chungnam National University, Korea)

GS17-1 *Development of indoor navigation system for monocular-vision-based autonomous mobile robot*
T. Kinoshita, E. Hayashi (Kyushu Institute of Technology, Japan)

GS17-2 *An effective localization and navigation method based on sensor fusion for mobile robot moving in unknown indoor environment*
I-S. Kim, W-K. Hyun, J-J. Yu (Honam University, Korea)
S-S. Park (Korea Digital Co., Korea)

GS17-3 *An indoor autonomously mobile robot with laser sSensor and image processing approach*
A. Fujiwara, N. Abe, Y. Tabuchi (Kyushu Institute of Technology, Japan)
H. Taki (Wakayama University, Country)
S. He (VuCOMP, USA)

GS17-4 *Development of a desktop swarm robot system based on pheromone communication*
N. Kitamura, Y. Nakamichi (Anan National College of Technology, Japan)
K. Fukuda (Gifu National College of Technology, Japan)

GS17-5 *Subsea fiber optic cable maintenance using ROV based flux leakage expert system*
Md. R. Hedayati (Scientific-Applied Faculty of Post and Telecommunication, Iran)

13:05~14:20 GS6 Computer Graphics, Micromachines & Robust Virtual Engineering
Chair: S. Omatu (Osaka Prefecture University, Japan)

GS6-1 *Development of a finger pointing interpretation and speech recognition system to operate virtual world*
T. Shiofuku, N. Abe, Y. Tabuchi (Kyushu Institute of Technology, Japan)
H. Taki (Wakayama University, Japan)
S. He (VuCOMP,, USA)

GS6-2 *Entire shape recovery employing virtual see-through cameras*
K. Mori, T. Sone, J. K. Tan, H. Kim, S. Ishikawa (Kyushu Institute of Technology, Japan)

GS6-3 *Autonomous control of mobile robots by image data processing and development of the simulation system*
R. Mizokami, Y. Tabuchi, N. Abe (Kyushu Institute of Technology)
H. Taki (Wakayama University)
S. He (VuCOMP)

GS6-4 *Construction of super-micro sense of force feedback and visual for micro objects -Develop the haptic device-*
R. Uehara, E. Hayashi (Kyushu Institute of Technology, Japan)

GS6-5 *Microorganic engine*
K. Naitoh, R. Kubo (Waseda University, Japan)
R. Miyagawa, (Waseda University, Japan until March of 2008)
K. Ogata, A. Suzuki (Waseda University, Japan)

14:20~15:35 GS19 Robotics-Ⅴ
Chair: H. H. Lee (Waseda University, Japan)

GS19-1 *A unified motion planning method for a multifunctional underwater robot*
K. Shiraishi, H. Kimura (Kyushu University, Japan)

GS19-2 *Image data processing for an autonomously moving robot using network*
M. Sato, Y. Tabuchi, N. Abe (Kyushu Institute of Technology, Japan)
H. Taki (Wakayama University, Japan)
S. He (VuComp, U.S.A)

GS19-3 *Cooperative manipulation of a floating object by some space robots with joint velocity controller*
-Application of a tracking control method using transpose of generalized jacobian matrix-
S. Sagara (Kyushu Institute of Technology, Japan)
Y. Taira (National Fisheries University, Japan)

GS19-4 *Determinate the time to contact using compound eye sensor*
Y. Kaneta, Y. Katsuyama, K. Ito (Hosei University, Japan)

GS19-5 *Systematization of error recovery in skill-based manipulation*
A. Nakamura, T. Kotoku (National Institute of Advanced Industrial Science and Technology, Japan)

16:40~17:40 OS7 Soft Robotics
Chair: H. Kinjo (University of the Ryukyus, Japan)
Co-Chair: N. Oshiro (University of the Ryukyus, Japan)

OS7-1 *Generating function of color information detection using genetic programming*
T. Ogawa, N. Oshiro, H. Kinjo (University of the Ryukyus, Japan)

OS7-2 *Swing up control of a 3-DOF acrobot using evolutionary approach*
R. Fukushima, E. Uezato (University of the ryukyus, Japan)

OS7-3 *Intelligent control of a three-DOF planar underactuated manipulator*
S. C. Duong, H. Kinjo, E. Uezato (University of the Ryukyus, Japan)
T. Yamamoto (Tokushima Technology College, Japan)

OS7-4 *Optimal suppression control of load swing with disturbance for rotary crane system using neuro-controller*
K. Nakazono, K. Tamanoi, K. Ozaki (University of the Ryukyus, Japan)
K. Ohnishi (Keio University, Japan)

February 7 (Saturday)

8:00~ Registration

Room A

8:40~9:55 OS12 Session of Economics and Management
Chair: T. Ito (Ube National College of Technology, Japan)
Co-Chair: S. Matsuno (Ube National College of Technology, Japan)

OS12-1 *Japanese companies and those introductions of the american management technique*
S. Fujii (Hiroshima University, Japan)

OS12-2 *A consideration of management of the value co-creation with customers:A case of the grocery retailers*
Y. Fujioka (Hiroshima University, Japan)

OS12-3 *A relationship analysis between centrality and module production in the keiretsu of Mazda*
H. Kimura, T. Ito (Ube National College of Technology, Japan)
Z. Xia (Wenzhou University, P. R. China)

OS12-4 *H marketing strategy with introduction of customer relationship management -Case of Japanese financial institutions-*
T. Yamaguchi (Okayama University of Science, Japan)

OS12-5 *An empirical investigation of the determinants of IS outsourcing in Japan*
S. Matsuno, T. Ito (Ube National College of Technology, Japan)
Z. Xia (Wenzhou University, P. R. China)

9:55~11:25 OS11 Bio-inspired Theory and Application
Chair: I. Yoshihara (University of Miyazaki, Japan)
Co-Chair: M. Yasunaga (University of Tsukuba, Japan)

OS11-1 *Study of genetic algorithms with mutation by Markov chains and diffusion model*
Y-A. Zhang, M. Sakamoto, H. Furutani (University of Miyazaki, Japan)

OS11-2 *A visual-inspection system using self-organizing map*
K. Ikeda, M. Yasunaga, Y. Yamaguchi (University of Tsukuba, Japan)
Y. Yamamoto (Yamamoto System Design Corporation, Japan)
I. Yoshihara (University of Miyazaki, Japan)

OS11-3 *Development of physiological activity estimation method of foods using amplitude extended neural networks*
T. Kuno, M. Kamiguchi, K. Yamamori, I. Yoshihara (University of Miyazaki, Japan)
K. Nagahama (Miyazaki Prefectural Industrial Foundation, Japan)

OS11-4 *Roll of rhythmic component in proactive controll of human hand*
Y. Hayashi (NPO natural science, Tohoku Institute of Technology, Japan)
Y. Tamura (Tohoku Gakuin University, NPO natural science, Japan)
F. Ishida (The University of Electro-Communications, Japan)
K. Sugawara (Tohoku Gakuin University, Japan)
Y. Sawada (Tohoku Institute of Technology)

OS11-5 *Modeling of patrol behavior of diacamma gamergate*
K. Yaegashi (Tohoku University, Japan)
K. Sugawara (Tohoku Gakuin University, Japan)
Y. Hayashi (natural science NPO, Japan)

OS11-6 *Analysis and modeling of diacamma workers' behavior*
M. Yuki (Tohoku Gakuin University, Japan)
Y. Hayashi (natural science NPO, Japan)
K. Sugawara (Tohoku Gakuin University, Japan)

13:25~14:40 GS18 Robotics-Ⅳ
Chair: S. Sagara (Kyushu Institute of Technology, Japan)

GS18-1 *Modeling and robostic control of reduction car using the ultrasonic satellite system*
H-J. Park, S-M. Yoon, S-Y. Kim, J-I. Bae, M-H. Lee (Pusan National University, Korea)

GS18-2 *Development of an autonomous-drive personal robot (Self-position recognition by characteristic point detection)*
S. Matsuura, E. Hayashi (Kyushu Institute of Technology, Japan)

GS18-3 *The recognition of multiple people using an ocellus camera*
S. Tanaka, E. Hayashi (Kyushu Institute of Technology, Japan)

GS18-4 *Robust object instance registration to robot-centered knowledge framework*
D-S. Lee, G-H. Lim, I-H. Suh (Hanyang University, Korea)

GS18-5 *Developing high-level management facilities for distributed unmanned systems*
P. Sapaty (National Academy of Science, Ukraine)
K-D. Kuhnert (University Siegen, Germany)
M. Sugisaka (Nippon Bunri University, Japan)
R. Finkelstein (Robotic Technology Inc., USA)

Room B

10:10~11:40 GS16 Robotics-Ⅱ
Chair: J. Wang (Alife Robotics Co., Ltd., Japan)

GS16-1 *USAT (ultrasonic satellite system) and gyro integrated system using kalman filter*
Y-S. Yeom, J-H. Kang, S-Y. Kim, J-I. Bae, M-H. Lee (Pusan National University, Korea)

GS16-2 *Development of an autonomous flexible robot that uses no explicit sensors or controllers*
R. Anzai, K. Ito (Hosei University, Japan)

GS16-3 *Development of an autonomous-drive personal robot "object recognition system using a monocular camera"*
Y. Moritaka, E. Hayashi (Kyushu Institute of Technology, Japan)

GS16-4 *An algorithm for automatic generation of assembly process of modular fixture parts*
T. Yamada, K. Kuroda (Nagoya Institute of Technology, Japan)
Y. Funahashi (Chukyo University, Japan)
H. Yamamoto (Gifu University, Japan)

GS16-5 *Optimization of robot path using off-line simulation and method for changing tool using a wireless communication device*
I. Mishra, M. Abhro (NIST, India)
G. Ajay (Difacto Robotics, India)
A K. Satapathy (General Motors, India)
T. C. Manjunath (NHCE, India)

GS16-6 *Implementation of ant colony system for DNA sequence optimization*
Z. Ibrahim, T. B. Kurniawan, N. K. Khalid (Centre for Artificial Intelligence and Robotics, Malaysia)
M. Khalid (Universiti Teknologi Malaysia, Malaysia)

13:25~14:55 OS15 Biomimetic Machines and Robots
Chair: K. Watanabe (Saga University, Japan)

OS15-1 *Understanding user commands by evaluating fuzzy linguistic information based on visual attention*
B. Jayasekara, K. Watanabe, K. Izumi (Saga University, Japan)

OS15-2 *Biomimetic intelligent creatures and artificial muscles*
M. K. Habib (The American University in Cairo and Saga University, Egypt)
K. Watanabe, K. Izumi (Saga University, Japan)

OS15-3 *Voice-based control of a robotic forceps by using displayed image and auxiliary information*
K. Watanabe, T. Tokunaga, K. Izumi (Saga University, Japan)

OS15-4 *Unconstrained and noninvasive measurement of bioelectric signals from small fish*
M. Terawaki, A. Hirano, Z. Soh, T. Tsuji (Hiroshima University, Japan)

OS15-5 *Three-dimensional human motion modeling by back projection based on image-based camera calibration*
S. Masaoka, J. K. Tan, H. Kim, S. Ishikawa (Kyushu Institute of Technology, Japan)

OS15-6 *Research on the intelligent control algorithm for a soft joint actuated by McKibben muscles*
E. Jiang (zhengzhou university, P. R. China)
H. Zhao (Shanghai Institute of Technology, P. R. China)
M. Sugisaka (Nippon Bunri University, Japan)
F. Dai (Matsue National College of Technology, Japan)
W. Quan (Fudan University, P. R. China)

Room C

8:40~9:40 OS4 Automata and Control
Chair: M. Kono (University of Miyazaki, Japan)
Co-Chair: N. Takahashi (University of Miyazaki, Japan)

OS4-1 *Cooperating systems of three-dimensional finite automata*
T. Matsukawa, M. Sakamoto (University of Miyazaki, Japan)
Y. Uchida (Ube National College of Technology, Japan)
A. Taniue, M. Fukuda, K. Kajisa, S. Okatani (University of Miyazaki, Japan)
T. Ito (Ube National College of Technology, Japan)
H. Furutani, M. Kono (University of Miyazaki, Japan)

OS4-2 *Hierarchies based on the number of cooperating systems of three-dimensional finite automata*
Y. Uchida (Ube National College of Technology, Japan)
M. Sakamoto, S. Okatani, K. Kajisa, M. Fukuda, T. Matsukawa, A. Taniue (University of Miyazaki, Japan)
T. Ito (Ube National College of Technology, Japan)
H. Furutani, M. Kono (University of Miyazaki, Japan)

OS4-3 *Robust l-infinity preview control for biped walking pattern generation*
S. Kunimatsu, T. Fukuda, M. Kumon, M. Ishitobi (Kumamoto University, Japan)

OS4-4 *Robust control method for the inverted pendulum system with structured uncertainty caused by measurement error*
N. Takahashi, T. Morikubo, O. Sato, M. Kono (University of Miyazaki, Japan)

9:40~10:40 OS5 Bioinformatics and Intelligent Classification (1)
Chair: S. Omatu (Osaka Prefecture University, Japan)
Co-Chair: M. Yoshioka (Osaka Prefecture University, Japan)

OS5-1 *Gene subset selection using an iterative approach based on genetic algorithms*
M. S. Mohamad, S. Omatu (Osaka Prefecture University, Japan)
S. Deris (Universiti Teknologi Malaysia, Malaysia)
M. Yoshioka (Osaka Prefecture University, Japan)

OS5-2 *Particle swarm optimization for gene selection in classifying cancer classes*
M. S. Mohamad, S. Omatu (Osaka Prefecture University, Japan)
S. Deris (Universiti Teknologi Malaysia, Malaysia)
M. Yoshioka (Osaka Prefecture University, Japan)

OS5-3 *An analysis of expression data using support vector machine and feature selection methods*
M. Yoshioka, N. Shimoda, S. Omatu (Osaka Prefefecture University, Japan)

OS5-4 *Audio-signal separation by independent component analysis*
M. Yoshioka, S. Omatu (Osaka Prefecture University)

10:40~11:40 OS6 Bioinformatics and Intelligent Classification (2)
Chair: M. Yoshioka (Osaka Prefecture University, Japan)
Co-Chair: S. Omatu (Osaka Prefecture University, Japan)

OS6-1 *Crack detection method using rotational morphology*
M. Yoshioka, S. Omatu (Osaka Prefefecture University, Japan))

OS6-*2 Estimation of the optimal image resolution using SIFT*
M. Yoshioka, Y. Maeda, S. Omatu (Osaka Prefecture university, Japan)

OS6-*3 Smell classification by neural networks*
M. Yoshioka (Osaka Prefecture University, Japan)
T. Fujinaka (Hirishima University, Japan)
S. Omatu (Osaka Prefecture University, Japan)

OS6-4 *Bill money classification by neural networks*
S. Omatu, M. Yoshioka (Osaka Prefecture University, Japan)
T. Kosaka (Glory Ltd, Japan)

13:25~14:40 OS10 Measurement and Control
Chair: Y. Yoshitomi (Kyoto Prefectural University, Japan)
Co-Chair: Y. Hitaka (Kitakyushu National College of Technology, Japan)

OS10-1 *Motion analysis of tripod parallel mechanism*
Y. Hikata, Y. Tanaka (Kitakyushu National College of Technology, Japan)
Y. Tanaka (Hosei University, Japan)
K. Ichiryu (Kikuchi Seisakusho, Kikuchi Seisakusho, Japan)

OS10-2 *Development of a new positioning system for underwater robot based on sensor network*
B. Fu, F. Zhang, M. Ito (Tokyo University of Marine Science and Technology, Japan)
Y. Watanabe, T. Aoki (JAMSTEC, Japan)

OS10-3 *Motion estimation based on optical flow and ANN*
J. Zhang, F. Zhang, M. Ito (Tokyo University of Marine Science and Technology, Japan)

OS10-4 *Development for on-board use anti-tilting table with horizontally slider type parallel link mechanism−−analysis on Inverse kinematics and work-space of the mechanism*
Y. Zhang, E. Shimizu, F. Zhang, M. Ito (Tokyo University of Marine Science and Technology, Japan)

OS10-5 *A method for expressing human posture as 3DCG using thermal image processing and 3D model fitting*
T. Asada, Y. Yoshitomi (Kyoto Prefectural University, Japan)

The Fourteenth International Symposium on Artificial Life and Robotics 2009 (AROB 14th '09),
B-Con Plaza, Beppu, Oita, Japan, February 5 - 7, 2009

The Pareto Operating Curve for Risk Minimization in Life and Robotics

Hussein A. Abbass
School of Information Technology and Electrical Engineering,
University of New South Wales, Australian Defence Force Academy,
Canberra, ACT 2600, Australia

Abstract

The use of non-dominance in multi-objective search has traditionally focused on generating the set of non-dominated solutions and choosing an element of this set to implement. In this paper, I will show the richness of the non-dominated set when the objectives (in the multi-objective search problem) represent complexity measures. I will present the concept of Pareto Operating Curves, whereby a system operates along these operating curves based on the risk, complexity and required trade-off it encounters in the environment. Key fundamental features these systems possess are robustness and the ability to adapt in different environments.

1 introduction

The concept of non-dominance has been associated in the evolutionary multi-objective computation (EMO) literature with multi-objective optimization problems (MOP). The topology of the set of non-dominated solutions in the objective space shapes up a curve that is known as the Pareto curve. An optimization problem is traditionally seen in terms of objectives - representing the performance measures of the system - and a set of constraints.

In this paper, we wish to expand the use of the Pareto curve from being a set of trade-off "independent" solutions to an operating curve, where the environment will dictate which solution from this set will be used. Risk is traditionally defined as the impact of uncertainty on objectives. The uncertainty that this paper is concerned with, is the uncertainty in the operating environment. In this case, the objective functions need to reflect the performance of a solution in an operating environment. We will call this operating curve as the Pareto Operating Curve (POC). This paper is the first to discuss the concept of POC.

In the rest of this paper, we will introduce some basic definitions in MOP, followed by discussions of some of my work where the POC was used - although not necessarily discussed explicitly.

2 Multi-objective optimization

Consider a *multi-objective optimization problem* (MOP) as presented below:-

$$\textbf{Optimize } F(\vec{x} \in \Upsilon) \tag{1}$$

$$\textbf{Subject to: } \Upsilon = \{\vec{x} \in R^n | G(\vec{x}) \leq 0\} \tag{2}$$

Where $\vec{x}$ is a vector of decision variables $(x_1, \ldots, x_n)$ and $F(\vec{x} \in \Upsilon)$ is a vector of objective functions $(f_1(\vec{x} \in \Upsilon), \ldots, f_K(\vec{x} \in \Upsilon))$. Here $f_1(\vec{x} \in \Upsilon), \ldots, f_K(\vec{x} \in \Upsilon)$, are functions on R^n and Υ is a nonempty set in R^n. The vector $G(\vec{x})$ represents a set of constraints.

The aim is to find the vector $\vec{x}^* \in \Upsilon$ which optimizes $F(\vec{x} \in \Upsilon)$. Without any loss of generality, we assume that all objectives are to be minimized. We note that any maximization problem can be transformed to a minimization one by multiplying the former by -1.

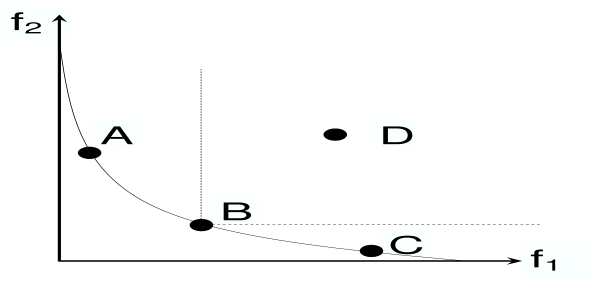

Figure 1: The concept of dominance in multi-objective optimization. Assuming that both f_1 and f_2 are to be minimized, D is dominated by B since B is better than D when measured on all objectives. However, A, B and C are non–dominated since none of them is better than the other two when measured on all objectives.

The principle of dominance (Figure 1) in *multi-objective optimization problem* (MOP) allows a partial order relation

©ISAROB 2009

that works as follows: a solution does not have an advantage to be included in the set of optimal solutions unless there is no solution that is better than the former when measured on all objectives. A non–dominated solution is called Pareto. A MOP can be solved in different ways. Evolutionary algorithms (EAs) [8, 10], being population based, they are able to generate a set of near-Pareto solutions in a single run. In addition, they do not require assumptions of convexity, differentiability, and/or continuity as traditional optimization problems do. EAs with local search are usually used to improve the performance of EAs to get closer to the actual optimal or, the Pareto set in the case of MOPs.

3 The Pareto Operating Curve

In many situations, the Pareto curve can be seen as the single solution to the problem. Take for example a problem where there is a need to evolve controllers for a robot. The objective functions can potentially be to minimize energy consumption and minimize the robot's performance error. In this case, a solution on the Pareto curve for this problem is just one possible trade-off that can be made between the previous two objectives. However, this robot is likely to encounter a number of situations where it needs to trade-off differently between these two objectives over time. As such, the Pareto Curve can be seen as an Operating Curve, as the level of trade-off needed changes over time, a solution moves from one location to another on that curve (See Figure 2).

Definition 3.1 Pareto Operating Curve *A Pareto Operating Curve (POC) is a Pareto Curve for a problem where the trade-off between the objectives to be optimized varies over time; thus a solution selected along this curve at one point of time needs to move to a different solution at another point of time to minimize the impact of uncertainty on objectives (i.e. risk).*

We need to differentiate between adaptive feedback control with the concept of Pareto Operating Curve. In traditional adaptive feedback control, a controller adjusts its parameters in response to changes in the environment. The Pareto Operating Curve provides the most efficient set of models to be operated in different environments to minimize the risk. Each member in this set is optimal in a particular environment in the sense that each environment represents a specific level of trade-off and there is a solution in the efficient set which is optimal on that required level of trade-off. One can then imagine the existence of a switch or a decision maker that senses the environment, determines the optimal level of trade-off needed, then selects the corresponding non-dominated solution from the efficient set. Each time a solution is selected from the non-dominated set, it defines a movement on the Pareto curve. This movement may be constrained in terms of its cost or characteristics, thus bounds the impact of the risk mitigation strategy. We now provide examples where this concept is successfully demonstrated.

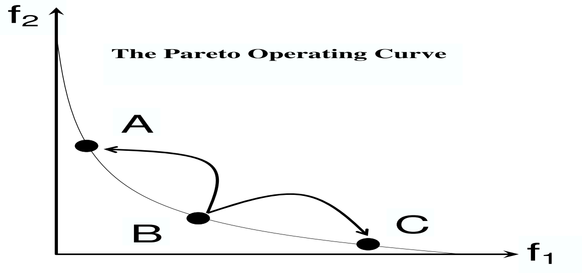

Figure 2: The Pareto Operating Curve. Solution B can be the best solution for a specific level of trade-off between objective function f_1 and f_2 at time t. When the required level of trade-off changes, this solution may need to move along the curve to become, for example, solution A or C.

4 The Pareto Operating Curve and Evolution

The majority of research in decision making and engineering has focused on selecting a single solution. Recent research showed the benefits in viewing problems in the eyes of multi-objective search. For example, in single objective optimization, one can simply benefit from transforming it into multi-objective as being demonstrated in [6].
To discuss the concept of POC in an artificial life context, it would be less attractive to do so without discussing its biological roots and impact. Although this is the first time this concept is introduced in this paper, we can trace some seeds for this concept in the literature. Darwin wrote:

> It seems clear that organic beings must be exposed during several generations to new conditions to cause any great amount of variation; and that, when the organisation has once begun to vary, it generally continues varying for many generations" (from [9] P25).

What is interesting about Darwin's quote is the emphasis he placed on variations. According to Darwin, any organization is in a constant state of flux. But we know from

common sense and decision sciences that each state of flux is likely to require different levels of trade-offs. The Pareto curve represents the optimal set of solutions in the sense that for any level of trade-off required, there is a solution in that set that is the optimal solution for the single objective optimization problem derived from the utilities associated with the required level of trade-off. Therefore, evolution does not necessarily need to be an optimizer, but for evolution to work, it needs to maintain diversity along the Pareto curve. In so doing, evolution can move from one trade-off to another. Evolution is not an optimizer from traditional optimization point of view, while from multi-objective optimization point of view, I will make the assertion that evolution is a multi-objective optimizer. In fact, I would claim that this is the evolutionary strategy for risk mitigation. The objectives that evolution optimizes include for example adaptive capacity, robustness, and survivability. In a number of situations, such as in viruses where the level of unpredictability in the change in the environment is high, we should accept that random selection can be an efficient strategy for risk minimization in such environment. Once the signal to noise ratio is high, random selection fails as a strategy and other types of selection mechanisms become more appropriate.
Not so long after Darwin's writing, Pareto wrote:

> If, as has generally been the case, it is held that, for a people, utility is coterminous with its material prosperity and its moral and intellectual development, then we have a criterion for making comparisons between different people. But there still remains a difficulty, deriving from the fact that society has to be considered as a complex whole, as a system, as an organism. [12].

Well said before its time, Pareto pointed us to the right direction, that an organism is a system of systems (SoS), evolution is, the mind is, and society is. As such, each sub-system (which is a system in its own right) has its own utilities which can be in conflict. For example, material prosperity can be in conflict with intellectual development. These competing objectives on the sub-system level, along with the different levels of trade-off possessed by each subsystem (representing their own individual biases) generate the diversity required for the system as a whole to operate and function.

5 The Pareto Operating Curve and Complexity

In [14, 15], we have shown for the first time the relationship between Pareto and Complexity. The essence of this work is that complexity of species is not a single measure. Moreover, combining many measures of complexity using some index into a single measure, not only hides information because of the strict order bias generated by a weighted sum approach, it also violates the essence of what complexity is. Thus, complexity should be defined as a strict partial order rather than a linear strict order. In these papers, we introduced the following definition of complexity:

- **Complexity** is a strict partial order relation.

This definition moves away from what the majority of literature in Engineering attempts to do; that is, to come up with a quantitative measure (single number) of complexity to establish a linear rank. This single number hides information of its constituent parts and the level of trade-offs required on the sub-system level. It also assumes that one must unify dimensionality and scale before combining the different complexity measures. Pareto's view to complexity, however, accepts the existence of many different quantitative measures of complexity but it rejects the idea of combining them as a single measure. Pareto optimality does not satisfy reflexivity; that is, a solution cannot dominate itself. It also acts as a filter of these measures since a measure is redundant if it is not in conflict (i.e. it produces identical order) with an existing measure. Pareto optimality, thus, imposes a complexity hierarchy on the set of objects/solutions.

6 The Pareto Operating Curve and Robotics

The use of Pareto-based Evolutionary Multi-objective (EMO) Search techniques in computational intelligence - particularly fuzzy inferencing and neural networks, is a relatively new literature. The work on Pareto-based EMO for fuzzy inferencing was pioneered in a number of papers, particularly [11], while the work on Pareto-based EMO for neural networks was pioneered in [1, 2, 5]. Work on neuro-ensemble was then introduced in a number of papers including [3, 4].
Traditionally, one would search for a learning machine - such as a neural network - that performs well on the average on all environmental conditions it may encounter. However, there are many applications where this average performance is not acceptable. For example, imagine a walk-gate performed by a neural network. Imagine that we want the robot to walk in different environments. Here, we can use the concept of Pareto optimality to optimize along different environmental conditions. The objective functions represent the robot performance in different environmental conditions. For example, one objective can represent the robot's speed while the second represents the friction in the

©ISAROB 2009

terrain. The set of non-dominated solutions for this problem represents a trade-off between performance (speed) and complexity (nature of the terrain). Every solution in this set represents the optimal solution on the corresponding terrain's friction. As such, the whole set can be used within a robot with a switch attached to a sensor that senses the friction between the robot's leg and the terrain. One can then imagine that at any particular point of time, the robot is operating in one area of the Pareto curve and as the environmental conditions change, it moves to other areas.
The previous concept was used in [13], where the two objectives were distance travelled and the size of the controller. The resultant robots trade-off, the size of the controller and the Pareto curve clearly demonstrated a smooth transition from no-walking behavior to a robot that jumps. Another application of this concept was in the area of Air Traffic Management [7]. Different algorithms for conflict detection work better in specific environments. Once more, one can imagine the Pareto Operating Curve as the set of environmental conditions where an algorithm would fail. By combining these conditions using a switch/gate, one would minimize the overall failure of the aircraft detection mechanism and the risk associated with that by combining different detection algorithms.

7 Conclusion

In this paper, I introduced the concept of Pareto Operating Curve, whereby the decision making process is seen as a set of movements along the curve to minimize risk. The roots of this concept were traced in evolution, and its relationship with complexity and robotics were discussed. As a new concept, the doors are open to adopt it to many applications including data mining, robotics or decision theory.

Acknowledgement

This work is supported by an Australian Research Council (ARC) discovery grant No. DP0667123.

References

[1] H.A. Abbass. A memetic Pareto evolutionary approach to artificial neural networks. In M. Stumptner, D. Corbett, and M. Brooks, editors, *AI'01, LNAI 2256*, pages 1–12. Springer-Verlag, Berlin, 2001.

[2] H.A. Abbass. An evolutionary artificial neural network approach for breast cancer diagnosis. *Artificial Intelligence in Medicine*, 25(3):265–281, 2002.

[3] H.A. Abbass. Pareto neuro-ensemble. In *AI'03, LNAI 2903*, pages 554–566. Springer-Verlag, Berlin, 2003.

[4] H.A. Abbass. Pareto neuro-evolution: Constructing ensemble of neural networks using multi-objective optimization. In *Proceedings of the IEEE Congress on Evolutionary Computation (CEC2003)*, number 3, pages 2074–2080. IEEE-Press, 2003.

[5] H.A. Abbass. Speeding up back-propagation using multiobjective evolutionary algorithms. *Neural Computation*, 15(11):2705–2726, 2003.

[6] Hussein A. Abbass and Kalyanmoy Deb. Searching under multi-evolutionary pressures. In C.M. Fonseca et. al., editor, *EMO'03, LNCS 2632*, pages 391–404. Springer-Verlag, Berlin, 2003.

[7] S. Alam, K. Shafi, H.A. Abbass, and M. Barlow. An ensemble approach for conflict detection in free flight by data mining. *Transportation Research Part C*, In Press.

[8] C.A. Coello Coello, D.A. Van Veldhuizen, and G.B. Lamont. *Evolutionary Algorithms for Solving Multi-Objective Problems*. Kluwer Academic, New York, 2002.

[9] C.H. Darwin. *The origins of species by means of natural selection*. London, Penguin Classics, 1859.

[10] K. Deb. *Multi-objective Optimization using Evolutionary Algorithms*. John Wiley & Sons, Chicester, UK, 2001.

[11] H. Ishibuchi, T. Murata, and IB Türkşen. Single-objective and two-objective genetic algorithms for selecting linguistic rules for pattern classification problems. *Fuzzy Sets and Systems*, 89(2):135–150, 1997.

[12] V. Pareto. *Cours d'ėconomie politique professė à l'universitė de Lausanne*, volume 1,2. F. Rouge, Laussanne, 1896.

[13] J. Teo and H.A. Abbass. Automatic generation of controllers for embodied legged organisms: A Pareto evolutionary multi-objective approach. *Evolutionary Computation*, 12(3):355–394, 2004.

[14] J. Teo and H.A. Abbass. Multi-objectivity and complexity in embodied cognition. *IEEE Transactions on Evolutionary Computation*, 9(4):337–360, 2005.

[15] Jason Teo, Minh Ha Nguyen, and Hussein A. Abbass. Multi-objectivity as a tool for constructing hierarchical complexity. In E. Cantu-Paz et. al., editor, *GECCO'03, LNCS 2723*, pages 483–494. Springer-Verlag, Berlin, 2003.

©ISAROB 2009

Modular Robotic System as Multisensory Room in Children's Hospital

Henrik Hautop Lund[1,2] Anders Henningsen[2] Rasmus Nielsen[2]
[1]Center for Playware, Technical University of Denmark, Kgs. Lyngby, Denmark
[2]Entertainment Robotics, Albani Torv 4, 5000 Odense C, Denmark
info@e-robot.dk
www.playware.dk www.e-robot.dk

Abstract
We developed a system composed of different modular robotic devices, which can be used e.g. as a multi-sensory room in hospital settings. The system composed of the modular robotic devices engage the user in physical activities, and should motivate to perform physical activities by providing immediate feedback based upon physical interaction with the system. The modularity, ease of use and the functionality of the devices such as modular robotic tiles and cubic I-BLOCKS suit well into these kinds of scenarios, because they can provide feedback in terms of light, vibration, sound and possibly many other ways, since the devices are fairly generic, which means that they can be augmented with other sensors or actuators. It is therefore possible to create applications with different stimuli and to dynamically change parameters to provide immediate feedback to the users. A main finding of the tests conducted here at a children's hospital, is that it was found to be very important to create feedback that was easily recognised by the users, and it was found that the interaction was boring if the feedback was too implicit (subtle) and not well understood by the user. Instead, users appreciated *explicit immediate feedback* very much because it was obvious and understandable, and did not require any a priori knowledge of the application.

Introduction
In recent developments, some research has focussed on the development of modular robotic devices that act as playware. We define *playware* as the use of technology to create the kind of leisure activities we normally label play, i.e. intelligent hardware and software that aims at producing play and playful experiences among users and of which e.g. computer games are a sub-genre [1].
The aim of the research is to combine robotic systems, artificial intelligence and play culture to produce new products that can be used in play, sports, health, rehabilitation, music, architecture, art and learning. The collaboration strongly combines the forces of both technical and human art research to focus on how new products can be designed, and to gain further knowledge on areas such as play culture and how this is evolving as our life becomes digital.

Fig. 1. The playground tiles used in a city square.

An outcome of earlier research in playware is electronic tiles (see playground tiles on fig. 1), which were developed as a new product that could stimulate the youth to engage in more physical active games to fight obesity and other life-style related diseases [2]. The tiles consist of a microprocessor, LED lights, force-sensitive sensor and means of communicating with 4 other devices. The tiles can be put together in large playgrounds, with wires providing for power and communication, and are controlled by a central computer. 6 of these playgrounds have been installed at 6 institutions (kindergartens, elementary schools and youth clubs) in Odense. In [3] research was conducted, to find out if it was possible to dynamically adapt the games for the users, while they were using the playground. The idea was to even out the difference among the users, to create an equally challenging experience with no regards to speed or other factors that would be beneficial to win a game. For instance, if speed is a key, the game would require a faster response from fast children than it would from slower children. This would be determined dynamically by classifying each individual and then adapt the game accordingly.
Further, we developed the modular robotic tiles, which are more suitable for applications, where it should be

©ISAROB 2009

easy to change the topology. The initial generation of these flexible tiles are interconnected by magnets, and they communicate by using IR diodes. 8 LED's are placed in a ring surrounding the FSR sensor, and thus, it is more intuitive, where the user should press the tile to activate it [4].

Whereas the playground tiles were mostly used for playgrounds, the modular robotic tiles have been used in various therapeutic setups. At the Rehabilitation Central in Odense, physiotherapists are using the tiles to create exercise games that are costumed for each individual patient by changing the topology and various application parameters (such as time, speed and FSR activation level). They have a wide range of patients, but most of them are recovering from surgery, and needs to regain strength and manoeuvrability. Because of the diversity of the patients, they need to facilitate many different tools and machines, so that every need can be satisfied. It is investigated if the modular robotic tiles can be used in various setups to help the training process of the patients. The applications on the tiles were originally developed for Sygehus Fyn (a hospital in Svendborg), which works with recovering heart patients [5].

Fig. 2. Modular robotic tiles for cardiac rehabilitation at the hospital Sygehus Fyn Svendborg.

Further, at Hôpital de la Salpetriere in Paris, Jacqueline Nadel is using the tiles to stimulate and motivate children with autism spectrum disorder (ASD). Due to ASD, the children have social impairments, and do not explore their environment for novel artefacts or events. By using the tiles, they hope to generate a feeling of self-efficiency in the children, by encouraging the children to push the tiles. When they do so, the lights will change from blue to red (and vice-versa), which is an immediate effect and hopefully the child will recognise this event as being his/hers responsibility. Finally, at the Robots at Play festival [6] we have demonstrated, how the tiles can be used in music and sport applications.

Fig. 3. The modular robotic tiles used as an interactive goal for soccer training and entertainment.

Research in modular robotics has also spawned projects such as ATRON, Odin and the cubic I-BLOCKS. The cubic IBLOCKS are interesting as playware, since they are used in education and entertainment areas. The first prototype consisted of LEGO Duplo bricks, which were equipped with a microprocessor and various sensors. By assembling the bricks, different applications could be built. The newest prototype (see figure 6) is developed and maintained by Jacob Nielsen, and is currently used in the RoboMusicKidz project [7]. The hardware is very similar to the hardware in the modular robotic tiles, so basically it is only the physical form that differs and the extension possibilities.

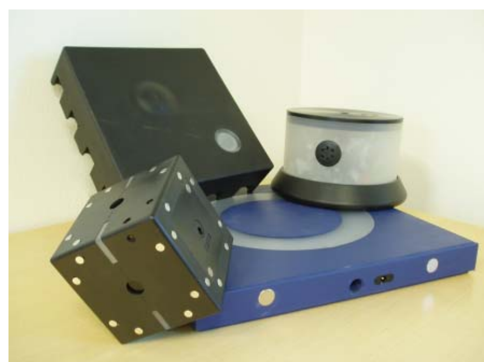

Fig. 4. Examples of modular robotic devices that should use the same protocol for easy integration and flexible configuration.

The modular robotic tiles and the cubic I-BLOCKS can be used in very flexible applications, since it is very easy to arrange them differently on run-time. Changing the topology can be done very easily, since they attach to each other using magnets, and there are no wires or mechanical connections, that would make it more difficult to rearrange the individual devices.

Changing the topology of a setup can be one way of interacting with the application. Also, it allows the user

to customize the setup before use, and it makes it easy to adapt the application to whatever need the user has.
For instance, there seems to be numerous opportunities for investigating the use of modular robotic playware devices as part of multi-sensory environments, which are used at hospitals and other institutions to stimulate patients and to provoke different reactions due to the stimulation. The range of patients is wide and different kinds of tools and remedies are available to provide the stimulating experiences. The most common tools are providing visual stimuli in terms of light, auditory stimuli in terms of sound effects or soothing music or physical stimuli, which can be a vibrating or massaging device.
Producing the sensations can also be done by using the actuators of the robotic modules. All the modules have built-in light capabilities, and by embedding other types of actuators, it is possible to provide sound and physical stimuli. From this point of view, there should be no trouble in using the robotic modules in a multisensory environment. Furthermore, by utilising the computing power and the sensors, it is possible to provide feedback to the user that is determined from combining the sensory input with some knowledge about the use. In other words, it is possible to interact with the user in an intelligent way, which might help to provide even better stimulation.
The development of multisensory room with modular robotic devices was studied for a different user group, namely elderly dementia patients in a hospital in Italy [8, 9] and modular robotic devices have been developed for children with different abilities [10]. Also, the MEDIATE project studied the development of an electronic multisensory room [11, 12]. In that case, there was no use of modular robotics, and hence the set-up seemed fixed with less flexibility than what is investigated here. Also, in general, most other interactive walls or floors are all quite static set-ups that do not allow for the user to perform physical reconfigurations at run-time (e.g. products such as t-Wall and LightSpace).
In order to allow for flexible use of the different modular robotic devices in the multi-sensory environment, Anders Henningsen and Rasmus Nielsen developed a generic and versatile communication protocol and framework for the modular robotic devices described below.

Modular robotic devices

Modular Robotic Tiles

The modular robotic tiles are created to be mobile, even when the application is running so that the topology can be changed by any user, even at run-time. The modular robotic tile consists of a square tile, in PUR, with a circular cover. The cover is made of a transparent satiniced plate and a centre made of PUR, such that the light from the 8 RGB LEDs, used for output on the printed circuit board (PCB), are uniformly distributed and the FSR in the center of a tile could easily be activated. Two tiles are connected via the two magnets on each side of the tiles, and they could be mounted on a magnetic surface like a metal wall or a radiator, because 4 magnets are built into the back of the tile.
The hardware on the modular robotic tile is based on the ATmega1280, which internally has 4 USARTs that is used for the IR transceivers where the tile is communicating with its neighbours through. These tiles are also prepared for communication through a XBee module, which make them able to communicate wirelessly across multiple platforms. The modular robotic tile also has a 2-axis accelerometer, which senses the inclination compared to gravity.

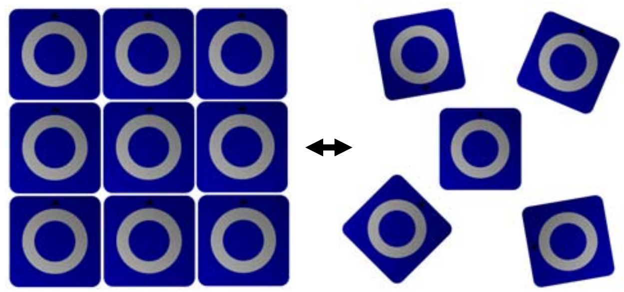

Fig. 5. The modular robotic tiles can be physically reconfigured by any user at run-time.

This new generation of tiles is much more distributed than the former playground tiles. It is not only the battery power supply in each tile that makes this tile suitable for distributed applications, but also the way they are coupled together and communicating with each other. Last but not least, these tiles are not preprogrammed, like the Playground tile, to start in a bootloader, where they are waiting for a given message to start the application.
Summary of the modular robotic tiles:

- Based on the ATmega1280
- 4 communication channels (IR light)
- Opportunity for wireless communication (XBee)
- 8 RGB LEDs, placed under the circular cover
- 1 FSR sensor
- a 2-axis accelerometer

I-BLOCKS

Similarly to the modular robotic tiles, we have developed modular building blocks such as I-BLOCKS and the new Cubic I-BLOCKS. Their hardware are by intention much alike the hardware in the modular robotic tiles, they are also based on the ATmega1280 and are communicating via IR light, with their neighbours. They have a 3-axis accelerometer and 4 RGB LEDs are used for output. The

hardware of the cubic I-BLOCKS is created so that it can be expanded with an extra internal PCB, which can be used for different sensors or actuators. There already exist different expansion boards with e.g. display, ultrasonic sound, USB connector and a XBee module.
Summary of the cubic I-BLOCKS:

- Based on the ATmega1280
- 4 communication channels (IR light)
- Opportunity for expansion, e.g. display, XBee or USB
- 4 RGB LEDs
- a 3-axis accelerometer

MidiBox
The MidiBox is created as a tool for receiving or transmitting MIDI commands, through the internal XBee module. The MidiBox is then interfaced to another MIDI device, a PC, MIDI keyboard etc., which could send notes or generate the given sounds. The MidiBoxes have been used in different applications. Recently they are being used in the RoboMusicKidz project by Jacob Nielsen and was used in the interactive concert with Funkstar De Luxe [13].

Fig. 6. Children creating music with the cubic I-BLOCKS.

In general, the devices are very alike with regard to the hardware and the choice of the sensors and actuators. They are created such that distributed applications are suitable. The XBee module is chosen as a link for three of the mentioned devices, which make them perfect in applications where they all are used at the same time.

Application environments

We have tested the modular robotic tiles in a number of applications environments. We describe briefly these environments below.

Odense Rehabilitation Central
At the Rehabilitation Central in Odense, physiotherapists are working with patients that are recovering from surgery and needs to regain strength and manoeuvrability. They receive a wide range of patients with different needs, and need to facilitate many kinds of machines and exercise equipments, and are using many different kinds of exercises to help their patients. It is very important, that they can supervise the patients, so that they do not overstrain themselves, which could possibly be dangerous after a comprehensive surgery. The therapists have been using the modular robotic tiles, which they have incorporated in some of their training programs. The applications on the tiles, was originally developed to Sygehus Fyn, who works with heart patients. They have a permanent setup of tiles on the wall, and a bunch of tiles, that they can set up on the floor in any configuration, that they desire (see Fig. 2).
There are several possibilities for developing applications for this target group. On one hand, they need exercises that increase the pulse of the patient in a controllable way, and on the other hand, they need exercises where the patients are supposed to move a specific limb in a specific way. Both classes of exercises must be configurable, so that they are suited for each individual patient.

Nadel Group, Paris
Jacqueline Nadel from CNRS is working with children who suffer from ASD, which causes impairments in their social skills. One of their methods for therapy, uses familiar objects (such as sunglasses, cowboy hats, umbrellas and so on) and arrange these in a setting with the child. All items are duplicated, so the therapist can use one object, while the child uses an object of the same type. Some of the children do not explore their environment, and do not initiate interaction with these objects, so the therapist has to initiate, and try to encourage the child to imitate his behaviour. By using the modular robotic tiles, they will try to show the children, that a physical interaction with these tiles can result in feedback such as light and sounds, which then hopefully will generate a feeling of self-efficiency in the child, because the child was responsible for the feedback. The first simple application in test, simply changes the light from blue to red (or vice versa), when the tile is pushed.
The best setups for these therapists are simple applications – possibly run on different types of modules – that they use with the children. It should be easy to use, and no comprehensive control of the application is necessary. Again, there is lots of possibilities for using multiple types of modules, since there are no restrictions on how the children physically interact with the modules.

Handicapafsnittet Odense
At Handicapafsnittet (a center for treatment of handicapped children in Odense), the physiotherapists are

©ISAROB 2009

dealing with children with both physical and mental handicaps. Some of the diagnoses are:

- ASD
- Physical handicaps
- Development problems
- Different kinds of syndromes

They have tested the modular robotic tiles with the same applications that are in use at the rehabilitation center in Odense. However, it seems that those particular (rehab) games are not motivating for these children, and some refinement will be necessary for this group of users. Some of the therapist requests are:

- Games that will enforce cooperation among the children.
- Application control should be entirely in the hands of the therapists.
- Educational games (spelling, math)
- Games that resembles common children plays (jigsaw puzzles, twister)
- The ability to change the appearance of the module

Fig. 7. A child with autism playing with the modular robotic tiles [4].

H. C. Andersen Children's Hospital

The H. C. Andersen Children's Hospital was official inaugurated April 2nd 2008 in Odense by HRH Prince Joachim. The responsibility of the hospital is to treat children and infants. It is mostly patients, who cannot get treated in the county hospitals and children with urgent needs or rare and complex conditions. The hospital also works as an educational institution as a part of the University of Southern Denmark. The hospital contains a multi-sensory environment, which are used for many different kinds of patients and for various purposes. The room provides different tools and means for stimulation, and is often visited by children and their family, when staying at the hospital for a longer period of time.

There are many possibilities in using this target group, and the robotic devices will be very easy to use in the room. The therapists have shown great interest in the devices, and are very open for a test setup, that is more dynamic than the current equipment in the room.

General Protocol

In order to obtain a versatile system, we developed a protocol which

- Is device independent
- Supports for multiple platforms
- Supports for both centralised and distributed applications
- Can utilise of the modular devices in a dynamic environment
- Is easy to integrate and use

The framework has to be device independent. The meaning of this requirement is that different devices could be used in the same application, without changing the code in the application or protocol. The framework has to be implemented, and designed, in a way such that the protocol and the application is working no matter what communication lines and drivers, that are used.

The devices that we use are modular devices, which are created so that they can be used without other devices. When a single device is used, the applications are limited, but a single device could be seen as a platform in a larger perspective. E.g. instead of creating a field of devices (e.g. tiles) which always are rectangular or another shape where all devices are connected locally, it should be possible to spread out the devices without changing the application. The devices will in these applications have to communicate through a wireless link, which specifies new requirements for the communication in the protocol.

In some cases, all the devices may need to know the full exact topology. This specifies not only large requirements about the design of the new framework, but also about the memory available. A full knowledge about the total topology could take up a large amount of the memory. One of the biggest problems is to maintain the topology in every device in a dynamic environment.

Since a lot of the devices are modular, and easy to connect and disconnect, the framework has to handle changes in the topology, since this could give opportunities, for new interesting applications, where the devices need to be moved around to interact with the system.

The last requirement for the protocol is that it has to be easy to integrate, not only in a new application, but also on a new device related to the other devices. If the

©ISAROB 2009

protocol can be compiled into a new project, it has to be easy to use, which means that the initialisation and the methods in the protocol are simple and understandable. Compiling the applications and protocol is also relevant, when it has to be easy to integrate, this require an understandable structure of the files, code, makefiles etc. that are used in the project, and a simple toolchain. An easy way of programming the devices is also preferable.

Mechanisms in the Protocol

Different mechanisms have to be implemented to fulfil the requirements. The design of the most important issues is described in this section.

Using Alive Signals to Spot Topology Changes

Alive signals is one of the most important mechanisms when modular devices like these have to be used like it was intended, namely in applications where the changes in the topology is an interaction with the system. Without alive signals or a similar mechanism, it would not be possible to spot these topology changes, know which devices that are active in the system, how these are reached and keep all the routing tables up to date. A lot of these information depend on the alive signals and the parameters regarding this.

The actual alive signal is quite simple. When a given interval has elapsed, the device then transmits an alive packet on the concerned channel, every channel has its own counter. When another device, a neighbour, receives this packet it reacts compared to whether this device was known or unknown. If the device has not been seen before, it updates its routing table and transmits a new broadcast packet, describing the new device, and how they are connected.

If the alive signal was received on a local channel, the device which receives the packet resets its own alive interval on this channel to the half of the original interval.

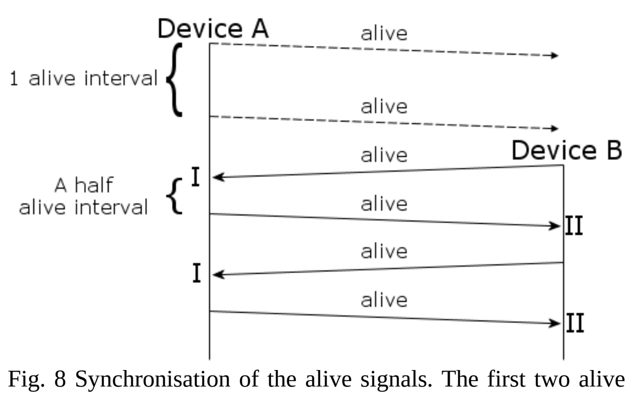

Fig. 8 Synchronisation of the alive signals. The first two alive signals send from device A are not received because there is no neighbour. When device B is connected, this will send an alive signal, which synchronises the timer of device A. Device A is synchronised on I while device B is on II.

This way the alive signals will be synchronized, and they will take turn to send alive signals to each other. Remote channels will never be synchronized, because the alive signals are transmitted as broadcasts, and every device that receives the alive signal would then be synchronized the same way, which would result that they all would send their alive signals almost at the same time.

The alive signals also contain a checksum of the routing table on the current device. This way two neighbour devices could verify whether they have identical tables or not, and react on this, e.g. by exchanging their tables. The routing tables have to be the same on the whole platform, so it is possible to reach all the devices, and the shortest paths in the system can be found. If a packet is received, with an unknown receiver address, the packet will be discarded, and never reach the intended device. Maintaining the routing tables is an important task on the network layer in the protocol.

Routing Tables

Routing tables are used in the protocol to store all the devices that are active in the system. An entry in the routing table consists of the address of the represented device, the channel needed for the shortest path, the address of the next device on the path and the total cost, which is the length of the path to the device. The cost is created such that it is possible to weight the different channels, e.g. by having a cost of 5 on a wireless channel and a cost of 1 on a local channel. The system will then choose to send a packet through 4 local channels than 1 wireless.

Every device will have its own routing table, and will have the responsibility to maintain it, by updating it when the device receives new alive signals, they disappear or special messages are received regarding changes in the topology.

History for Loop Detection

Loops in the communication paths could be a problem when working with these devices, because of the position of the communication channels. To ensure that packets not will loop forever, a circular history is used in every device, which remembers which packets that have been seen before. If a packet is received twice, the packet is then deleted and not processed or forwarded. A history could only work if all packets are unique, this is done by saving the address of the sending device, which already is unique, and allocating a frame number to every new packet. These two values, which will be a part of every packet, will create unique frames and they will be stored in the history. A single byte is used for frame numbers in the packets, and when this increasing number reaches it maximum, which is 2541, it will start all over again from 0, packets could then be similar to earlier transmitted packets, but an aging system of the entries in the history, ensures that these entries are expired when this happens, if the entries not already have been overwritten by newer entries.

Bootloaders
Bootloaders are implemented for the therapy tiles and cubic I-BLOCKS, to ease the transmission of the program code to the devices. Instead of programming all the devices one at a time with the JTAG, it is now possible to transmit the program code to a device through one of its communication channels, local or remote. When this device is programmed, it will distribute the code to all its local neighbours, which do the same until all the devices on the given platform are programmed.

Experimental Setup at HCA Children's Hospital

The purpose of the enhanced multisensory room is to use the devices as tools for various stimuli, and to create dynamic applications, that can adapt to the users by processing the information from the interaction of the devices. By examining the behaviour of the users, it might be possible to provide a more directed stimulus, which is tailored to each individual or to a group of users. We used the modular robotic tiles and the cubic I-BLOCKS, because they are very flexible and easy to handle. The Playground Tiles was disregarded, because they take up too much space, and are not very easy to move around, which is a general requirement for artifacts in the room due to cleaning conditions. The modular robotic tiles and the cubic I-BLOCKS can be used for different kinds of stimuli, and we will consider how to utilise this in our application proposal.
It should be noted, that during the test period by Anders Henningsen and Rasmus Nielsen, the nurses and other groups of therapist announced their strike action at the same time as the collaboration with the hospital was started. The impact was that only high-priority patients were available at the hospital and the majority was not able to test our equipment in the sensory room, due to their condition. For this reason it was very difficult to make larger tests of the application to collect a lot of data for analysis. It also affected the types of patients, who were available. The sensory room are normally used by children with disabilities, who have preference of the room, because they do not have the same opportunities as healthy children in terms of playgrounds and ways of being activated. But during the strike action, only children that do not suffer from any physical disabilities and do not have any development problems, were available at the hospital.

Application
We created an application that allowed for:

- immediate feedback to the user when an action has been taken.
- various types of stimuli that can be controlled by the system.
- simple application that is susceptible to quick updates and adjustments.
- autonomous application which exhibit behaviours without the intervention of the user.

We decided to use the modular robotic tiles as components in an interactive light-wall. By placing 16 tiles in a 4 by 4 square on the wall, we were able to provide a very powerful light stimulus, by showing various patterns in different colours. The light-wall is also sensitive to pressure, and provides one way of interacting with the wall. The tangible cubic I-BLOCKS are used for interaction with the system, and are themselves able to provide direct feedback in terms of light and vibration. The cubic I-BLOCKS make use of a 3D accelerometer to detect the orientation with respect to gravity, and it is also possible to detect if the user is shaking the cube. They communicate locally through IR channels, and by using our protocol stack, topology changes can easily and quickly be detected. All of these behaviours can be integrated into the software as a way of interacting with the system.

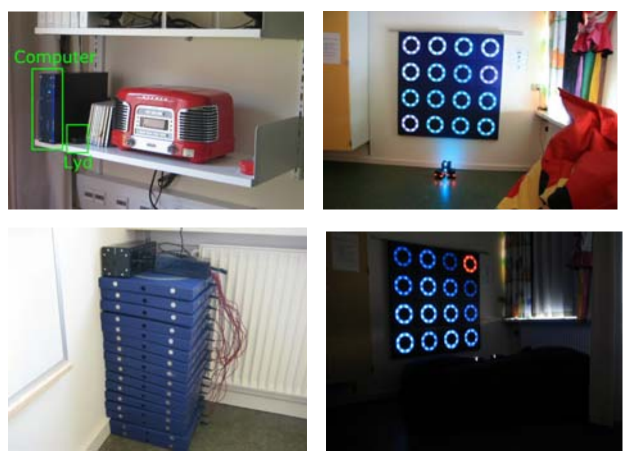

Fig. 9. Easy Storage (lower left) and set-up for sound (upper left) in the multisensory room of HCA Children's hospital.

We developed a light wave application which is completely distributed, and the purpose is to create so-called lightwaves on the tiles. A random tile will light up in a random colour, and then propagate this colour to its direct neighbours and eventually fade its own colour out. The same behaviour applies for the neighbours, who all also will light up, propagate the colour to their neighbours, fade out, and so on (see fig. 10).

The design of the lightwave application is based very much on visual stimuli, and it is the hope that it can draw some attention, because of the moving colours. If the room is dark, the lightwaves may be very clear and eye-catching.
The cubic I-BLOCKS can be used for controlling the lightwaves in different ways and by turning, shaking or assembling/disassembling the cubes, different events can be generated, that will have an immediate observable effect. Suggestions for variable parameters are:

- the propagation speed of the lightwaves.
- the trail of the lightwave (e.g. how long each tile is showing the color, before fading out.)
- the intensity of the lightwaves.
- the amount of lightwaves.
- the color of the lightwaves.

The computer can be used for logging the events, and for controlling sound effects and background music. Together with musician Kasper Falkenberg, we made some soothing background music, and for each lightwave, there would be sound effect, e.g. a note from some instrument.
The final setup consists of the following equipment (also see Fig. 9):

- 16 modular robotic tiles (at least one with a XBee RF module).
- 1 Whiteboard for holding the Therapy Tiles.
- 3 cubic I-BLOCKS with XBee RF modules inside.
- A charger with room for 15 devices.
- A small computer with a XBee2USB dongle.
- 2 satellite speakers with 1 subwoofer.

In the corner of the multi-sensory environment, they have collected all control-related equipment, so that the therapists have easy access to control the various tools. We have placed the computer and the loudspeakers in this corner, and the only thing, the therapists have to do, is to push 2 buttons to turn on the computer and the speaker system.

Lightwave Parameters
The modular robotic tiles are able to receive several commands that affect the parameters for the lightwaves. These commands are:
Duration Time: the duration time is a time value in milliseconds, and can in the time of writing be a value between 200 and 1500 ms. It affects how long each tile should be lid up, before fading out. The longer the duration time is, the longer trails will be drawn from the lightwaves.
Forward Time: the forward time is a time value in milliseconds, and can in the time of writing be a value between 200 and 1500 ms. It controls the propagation speed, and how fast it should spread from tile to tile.
Start Interval: the start interval controls how often a lightwave should occur. The values can be between 5000 and 1500 ms. For instance, if the start interval is 5000 ms, the lightwaves will occur randomly with a maximum of 5 seconds between each lightwave.
The above three commands are controlled by three cubic I-BLOCKS. Using the 6 orientations of a cubic I-BLOCK, we can provide 6 levels for each parameter. The LEDs on the cubic I-BLOCKS are used for both indicating the purpose of the cubic I-BLOCK and the current level for the specific parameter.
For a later implementation, we changed the parameter START_INTERVAL to be a FORWARD_WAVE instead. This allowed the users to create lightwaves themselves in their own colours.

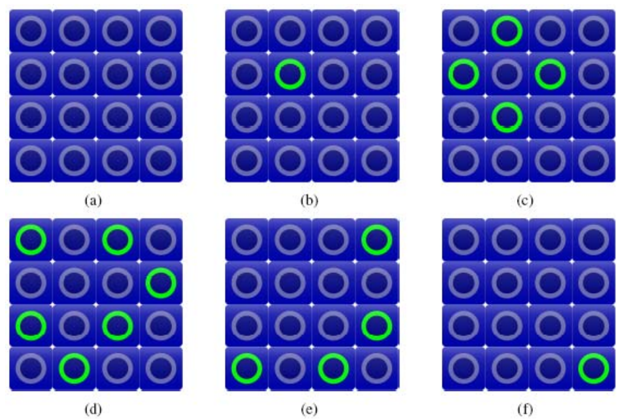

Fig. 10. The propagation of a lightwave starting from square (2,2) in the upper left. The start position could e.g. be random or based on a hand pressure on the tile.

HCA Controller
The HCA Controller is the software, that is running on the computer. It runs on top of the protocol framework and provides logging capabilities into a persistent data storage, and it also provides means of controlling music and sound effects. The controller is using the ProtocolStack from the protocol framework, and it is implementing the ProtocolListener interface, so that it will receive any incoming data that is destined for the application. The AudioCenter provide means of playing different notes with three different instruments. It can also create a WAVPlayer, which can read any wav files and it is possible to control the volume of the music.
The controller uses the HSQLDB relational database engine, which are based entirely on Java. It provides a fast and easy-to-use database, which can be integrated into the HCA Controller and log all the incoming events for further analysis. The DataContainer class is a wrapper

for the data that is contained in a single event. When the system is started, the controller will create a new database and provide it with a timestamp. A table for the events are also created, and it contains 7 fields: id, command, 3 columns for integer arguments, 1 column for a string-type argument, the address of the sending device and finally a timestamp. The argument columns are used to store the values, that are changed when an event occurs.

Tests

The multisensory room with the modular robotic devices was developed and tested over three iterations as described below.

Fig. 11. A child and her father in the multi-sensory room.

First Iteration test

The first iteration covers the first application that was developed and deployed at the hospital. The first feedback that we received was that the tiles and cubes were very easy to use, and they had no trouble in starting and shutting down the system. However, they requested some kind of user guide, so that the children and their parent could use the system on their own.

The lightwall was very much appreciated and the colours and lightwaves were attracting the attention of both the personnel and the children and their parents. The sound of bubbles was also working well, and the children found it amusing. However, they did not understand the purpose of the cubic I-BLOCKS, and was not able to see the effects on the lightwall, when changing from one level to a subsequent level. It was possible to convince them of the effect, when changing from the highest level to the lowest level with a given cube, because this impacts on the parameter the most, but all the intermediate levels were not observable, or at least not as obvious. Of course, this was not our intention.

The use of cubic I-BLOCKS was also appreciated and they had made some interesting observations regarding the physical structure and use of the cubes. The children had fun turning the cubic I-BLOCKS around, so that the colour would change, and for some children it was almost a challenge to disconnect them due to the strong forces of the magnets, that hold the cubic I-BLOCKS together. The hospital staff observed that the use of the modular devices stimulated physical movement, which could be used for some groups of children. Children with bowel problems are encouraged to move around, and it was found, that the cubic I-BLOCKS could be a tool for stimulating physical movement. This could be done, by placing the cubic I-BLOCKS around the child with enough space between each of them, so that the child would have to move the body to reach the cubes. Another child had been through a rough period of time due to cancer, but was recovering again. She was physical weak after the exhausting period, and she had trouble in disconnecting the cubic I-BLOCKS. But the therapists observed that she expressed self-confidence and happiness, when she finally disconnected the two cubic I-BLOCKS.

Second Iteration Test

In the second iteration, we changed the number of levels for each parameter, so that (hopefully) it was easier to see the effects on the lightwall, when orientating a cubic I-BLOCK. From 6 levels, we went down to 3 and made the span between the lowest and highest level wider, so each level would be significantly different from the other levels. Since the cubic I-BLOCKS have 6 sides, each level was represented by two different sides.

To encourage further use of the cubic I-BLOCKS, we provided the therapists with new cubic I-BLOCKS with vibrators, which were supposed to replace the old cubes. By turning the cubic I-BLOCK, it would then provide visual stimuli (changing colour of the LEDs) and it would vibrate for half a second. We also added the possibility for the users to shake the cubic I-BLOCKS, which would change the volume of either the bobble sound effect, or the volume of the background music, which also was added in this iteration. The background music was composed by Kasper Falkenberg and is a very relaxing and calm piece of music.

After creating user guides for the personnel and changing the number of levels for the parameters, the staff and children were able to observe the immediate feedback from turning the cubic I-BLOCKS. The vibrating stimulus was found very amusing, and it further encouraged the use of the cubic I-BLOCKS.

We also received positive feedback regarding the background music. The children quickly realised, that by shaking the cubic I-BLOCKS, it was possible to alter the volume of either the bubble sound effect or the music.
The hospital staff noticed that some children were searching for specific colours. For instance, one girl only liked the purple colour, so she would turn the cubic I-BLOCKS in various ways to get the purple lightwaves. This indicates two things: she has not understood the purpose of the cubic I-BLOCKS, since they do not control the colour of the lightwaves, and it indicates, that we should provide the possibility for letting the user controlling the colours as well. From the feedback, it was clear, that the children have a favourite colour, and that this could be integrated in the system.

Third Iteration Test

For this iteration, we changed the function of cubic I-BLOCK, because changing the start interval parameter did not seem very obvious to the users. Instead, there was a bigger interest in better control for the lightwaves and the colours, which the user had no control of in the former iterations. Cubic I-BLOCK now functions as a wave generator, and each side of the cube controls a unique colour for the lightwave, which yields 6 possible colours. We did not change any of the sound effects or the background music, because it seemed to work fine at this point.
The change of I-BLOCK was very much appreciated, because it provided the users with (a more obvious) immediate feedback, and it was now possible to create lightwaves in a desired colour. However, in some cases problems regarding the wireless communication ruined the feeling of immediate feedback from using the cubic I-BLOCKS, since the commands were not properly received by the lightwall. This was quickly fixed, but initially this was a demotivating factor for the users, because of the lack of feedback from the system. But in general, the *explicit immediate feedback* provided a clear change in the user behaviour.

Data collection and evaluation

Each time the computer is turned on, a new database is created and associated with a timestamp. We did not provide any means for the therapists, to enter any information about the user (such as an ID), because it was very important to keep the equipment simple and easy to start. It was reckoned, that by including a screen and a keyboard, the therapists would be less motivated for using the system in the sensory room. Also, due to the striking action, it has been hard for the therapists to schedule appointments in the sensory room with the patients, so a majority of the data represents spontaneous and short sessions of therapy in the room.
The consequences of this, is that most of the gathered data has no direct association with the individual users, and it is not possible to determine if two sets of data have been gathered from the same user. The data is still of use, since it can be used for detecting patterns or certain behaviours, but it is not possible to recognize individual users and associate datasets with users, since any matches can not be confirmed.
A standard test protocol has been defined for the controlled tests, to ensure uniform datasets that can be compared: For the tests that we conducted, we defined the following protocol:

- A minimum of 3 tests should be conducted with the same individual.
- Each test must be of approximately 4 minutes.
- For the first test, the user will get an introduction of how to interact with the system, but will not receive an explanation of the feedback from each action taken on the system.
- Between the first and second test, the user is interviewed and asked questions about the system, to find out if the user had discovered the connection between a certain action and the feedback of the system.
- Before the second test, the user gets an explanation of the connection between the actions and the feedback.
- The third test should be conducted at a later time if possible (e.g. the next day), so that the user enters the room and uses the system with a fresh mind.

In general, the lightwall was popular, because of the very strong and eye-catching lightwaves that emerged in many different colours. When the curtains were pulled and the light turned off, the lightwall had a strong effect.
The use of the cubic I-BLOCKS was also well received, but initially the function of each cube was not as obvious as we wanted it to be. They did impact on the lightwaves, but the feedback from the first two iterations of the project clearly showed us, that the functionality was too *implicit*. The children (and staff) were very focused on the cubic I-BLOCKS when interacting with them, and missed the feedback on the lightwall, which should have indicated to the user, that they just changed something in the system. Also, the definition of turning a cubic I-BLOCK was misinterpreted a couple of times. It was necessary to turn the cubic I-BLOCK 90 degrees to either direction, before it would activate, but some of the users were rotating in smaller angles, which meant that there was no feedback and this lead to a demotivation of the user for using the cubic I-BLOCKS.
The parameters (DURATION_TIME, FORWARD_TIME, START_INTERVAL) that were changed, were

too subtle and we should have chosen more powerful effects instead. This was also indicated when we switched the START_INTERVAL parameter with the FORWARD_WAVE, as it was more obvious, what happened when turning the cubic IBLOCK. A similar switch to more *explicit feedback* should be done and investigated with the remaining two cubic I-BLOCKS.

One suggestion of how the functionality of the cubic IBLOCKS should have been implemented instead of the chosen solution would be letting each cubic I-BLOCK represent a colour (red, green or blue). If a cubic I-BLOCK was turned, it would create a lightwave in that particular colour on the lightwall. If two cubic I-BLOCKS were to be connected, this would mix the colours, e.g. red and blue would create purple, and by turning these cubic I-BLOCKS, it would also create a lightwave on the lightwall and in that composite colour (e.g. purple). This scenario reminds a bit of the colour mix setup that we used when working with autistic children and the therapy tiles [4]. That work used three colour tiles (red, green and blue), that were emitting colour packets to their neighbours when connected, and the colours would blend.

We could still use the old parameters (such as propagation speed and time on each tile for each colour) to create an adaptive application. For instance, measurements such as how often the cubic I-BLOCKS are turned or the actual speed of the rotation, can be used to adjust the lightwaves on the lightwall. From the feedback we have received, we estimate that this would have been a better solution and more attractive for the children at the hospital.

The use of sound and music could have been more extensively, but there was not time to test this further. The current setup plays simple tones for each lightwave, it plays a sound of bubbles and it provides soothing background music. When the user shakes one of the cubic I-BLOCKS, it will turn up the volume for the bubbles or the music. It was discussed, if there should have been an attempt to create multiple sound universes, e.g. music with different atmospheres and tempi. Then it would have been possible to associate the activity and aggression of the user with a suitable sound universe. Imagine, that it is detected that the user is highly active (even too active) and the system tries to calm the user by playing some relaxing and down-tempo music. The ways of combining the activity of the user with universes is many, and various effects could be obtained.

Conclusion

Compared to the equipment, which is normally found in a sensory room, it is argued that the robotic devices can provide much of the same stimuli to the users. The modularity, ease of use and the functionality of the devices suits perfectly into these kinds of scenarios, because they can provide light, vibration, sound and there are many other possibilities. These devices are fairly generic, which means that they can be augmented with other sensors or actuators. However, it can be argued that the physical form factor of the cubic I-BLOCKS is not perfectly suited for the little children, who barely can grasp them, and the strong magnetic force that is used for connecting the cubic I-BLOCKS may be too much compared to the strength of some visitors of the room. This has not been a main issue for the project, but the staff has made comments about it and we have observed a little boy, who was struggling with the cubic I-BLOCKS, because he was only able to use one hand.

The lightwave application provided powerful light stimuli, and the possibility of dynamically changing parameters to provide immediate feedback to the users. In the tests conducted here, it was found to be very important to create feedback that was recognised by the users, and it was found that the interaction was boring if the feedback was too implicit (subtle) and not well understood by the user. When we changed the behaviour of one of the cubic I-BLOCKS to allow the users to create lightwaves, the users suddenly appreciated this *explicit immediate feedback* because it was much more obvious and understandable, and did not require any a priori knowledge of the dynamics of a lightwave.

Acknowledgements

C. Jessen, J. Nielsen, R. Nielsen, L. Pagliarini, and K. Falkenberg collaborated on developing the concept and technology. Thanks to the staff and children at the Hans Christian Andersen Children's Hospital, especially pedagogue Mette Sorang Kjær, and to the Feelix Growing project.

References

[1] H. H. Lund and C. Jessen. Playware - Intelligent Technology for Childrens play. Technical Report 1, The Maersk Mc-Kinney Moller Institute, SDU, June 2005.

[2] H. H. Lund, T. Klitbo, and C. Jessen. Playware Technology for Physically Activating Play, *Artificial Life and Robotics Journal, 9:4,* 165-174, 2005

[3] A. Derakhshan, F. Hammer, and H. H. Lund. Adapting Playgrounds for Children's Play Using Ambient Playware. In Proceedings of IEEE Intelligent Robots and Systems (IROS'06), IEEE Press, Hong Kong, 2006

[4] H. H. Lund, M. D. Pedersen, and R. Beck. Modular Robotic Tiles – Experiments for Children with Autism.

©ISAROB 2009

In Sugisaka and Takaga (eds.) Proceedings of 13th International Symposium on Artificial Life and Robotics (AROB'13), ISAROB, Oita, 2008.

[5] Robotic Therapy Tiles Help Patients Play Their Way to Health. *WIRED*, 02/10/2007 http://www.wired.com/medtech/health/news/2007/10/therapy_tiles

[6] H. H. Lund. *Robots at Play*. ISBN 978-87-992302-0-4, 160 pages, Odense, 2007.

[7] J. Nielsen, N. K. Bærendsen, C. Jessen. RoboMusicKids – Music Education with Robotic Building Blocks. In Second IEEE International Conference on Digital Games and Intelligent Toys Based Education, IEEE Press, 149-156, 2008

[8] P. Marti, H. H. Lund, M. Bacigalupo, L. Giusti, and C. Mennecozzi. A Multi-sensory Environment for the Treatment of Dementia Affected Subjects. *Journal of Gerontechnology*, *6(1)*, 33-41, 2007

[9] H. H. Lund, P. Marti, A. Derakhshan, R. Beck, T. Klitbo, and J. Nielsen. Modular Robotics for Novel Tools in Dementia Treatment. In Proceedings of 15th IEEE International Symposium on Robot and Human Interactive Communication (RO-MAN 06), IEEE Press, 655-661, 2006.

[10] H. H. Lund, and P. Marti. Designing Manipulative Technologies for Children with Different Abilities. Artificial Life and Robotics Journal, 9:4, 175-187, 2005.

[11] N. Parés, A. Carreras, J. Durany, J. Ferrer, P. Freixa, D. Gomez, O. Kruglanski, R. Parés, J. I. Ribas, M. Soler, A. Sanjurjo. MEDIATE: An interactive multisensory environment for children with severe autism and no verbal communication. Proceedings of the Third International Workshop on Virtual Rehabilitation (IWVR'04). EPFL, Lausanne, Switzerland. 2004.

[12] N. Parés, A. Carreras, M. Soler. Non-invasive attitude detection for full-body interaction in MEDIATE, a multisensory interactive environment for children with autism. Proceedings of Vision, Modeling, and Visualization 2004 (VMV'04). Stanford, USA, 2004.

[13] H. H. Lund, and M. Ottesen. RoboMusic – A Behavior-Based Approach, Artificial Life and Robotics Journal, 12: 1-2, 18-23, 2008.

Modular Robotic Wearable

Luigi Pagliarini[1,2] Henrik Hautop Lund[1]

[1] Centre for Playware, Technical University of Denmark, 2800 Kgs. Lyngby, Denmark
[2] Academy of Fine Arts of Bari, Via Gobetti, 8. 70125 Bari, Italy

luigi@artificialia.com info@e-robot.dk

Abstract
In this concept paper we trace the contours and define a new approach to robotic systems, composed of interactive robotic modules which are somehow worn on the body. We label such a field as *Modular Robotic Wearable* (MRW). We describe how, by using modular robotics for creating wearable, it is possible to obtain a flexible wearable processing system, where freely inter-changeable input/output modules can be positioned on the body suit in accordance with the task at hand. We describe the first rough prototypes and show an artistic application, as well as some drawing of future works and projects. Finally, by focusing on the intersection of the combination modular robotic systems, wearability, and bodymind we attempt to explore the theoretical characteristics of such approach and exploit the possible playware application fields.

Introduction
The Modular Robotic Wearable (MRW) thought was born in 2007 from both the research line in electronic and robotic art – called *The SuperAvatars*. This work was based upon our research tradition on *modular robotics* since the mid 1990's with the development of LEGO robots, embodied AI humanoids, intelligent robotic building blocks such as I-Blocks, African I-Blocks, robotic playground tiles and robotic therapy tiles.

Fig.1. Fatherboard, The SuperAvatar *(The mask, 2007)*

Besides that, the concept derives, somehow, from both artistic and scientific-technological fields.
Indeed, MRW inherits the knowledge coming from either the old *Wearable Electronic Art* works (see *Gutai Bijutsu Kyokai*, Gutai Art Association), such as Atsuko Tanaka's Electricdress (Fig. 2), and the old Steampunk and Cyberpunk [2] lines of thinking.
These, indeed, are consistent electronic art branches that are expressed in different styles (cyborgs, humanoids, exoskeletons, etc.) and through prestigious authors (Stelarc, Marcel.li Antúnez Roca, Bill Vorn, Chico MacMurtrie, Martin Spanjaard, Ulrike Gabriel, etc.). In the last few decades, they have explored the possibility of augmenting the body through modern digital technologies.

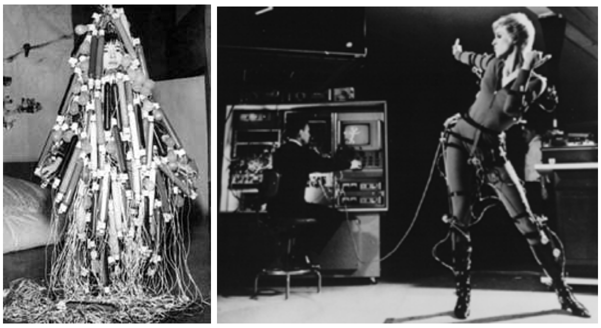

Fig. 2. Classical examples of wearable for artistic performance. Left: Atsuko Tanaka *(Electricdress, 1956)*, Right: The Steampunk.

Under the scientific point of view, MRW is inspired by and related to *Wearable Computing* or *WearComp* – a branch of research on forms of human-computer interaction comprising a small body-worn computer (e.g. user programmable device) that is always on and always ready and accessible, as defined by Steve Mann in 1997 [3].

Despite of these evident similarities, MRW approach proposes alternative and innovative paths, also thanks to the close relation established with modular robotics.
.

Towards Modular Robotic Wearable
Differently from the above mentioned works, MRW aim at making no use of mechatronic devices (as, for example, in Cyberpunk and related research branches) and mostly relies on "simple" plug-and-play circuits, ranging from pure sensors-actuators schemes to artefacts with a smaller level of elaboration complexity. Indeed, MRW focuses on enhancing the body perception and proprioperception by trying to substitute all of the traditional exoskeletons perceptive functions - in most of the cases strongly rigid, cabled and centralized - through the use of local sensing circuits. In MRW we do so keeping the weight load as light as possible, while preserving a high level of modules interchangeability, as well as efficiency and flexibility.
Indeed, the MRW concept that derives from the *Polymorphic Intelligence* theory [4] has as a major goal

to focus on human-machine interaction pushing it to such an extreme in which interaction can be called and considered (human-machine) interrelation. This is because it takes into deep consideration certain aspects of body action/reaction which might be partially or fully unconscious. Therefore, although the MRW is thought as a non-invasive technology, the goal of such a research approach is to push the borders of machine mediated movements and sensing to unknown limits, and develop tools for investigating psychological and psychosomatic aspects, such as gestural and postural persons' attitudes and body automatisms.
Therefore, besides being an excellent method for expressing multimedia art aesthetics, MRW might represent a fascinating instrument for exploring such fields as neural robotics, and playware, as well. In fact, the MRW approach focuses both on pre-existing and well known psychosomatic aspects - a body re/appropriation [5] - and on body/hi-tech relationship, bringing along new discoveries and potential research fields on exploring body action and reaction, limits and capabilities.
Evidently, and more simply, MRW can also be seen as a means for augmenting human interfaces both from virtual realities to the body and from the physical body to virtual realities.

Fig. 3. *Fatherboard*, performing [13] (*The suite, 2007).*

MRW Definition

We define *Modular Robotic Wearable* (MRW) as a robotic system composed of interactive robotic modules which is worn on the body.

- By wearable we intend that the system has to be worn on the body and interact with the body as part of the surrounding environment of the system.
- By a robotic module we intend an entity with a physical expression which is able to process and communicate with its surroundings. The communication can be directed towards neighbouring modules and/or via sensory input and actuation output to the surroundings (i.e. interactive robotic modules). A modular robotic system is constructed from many such robotic modules.

Modular Robotic Wearable combines the wearable with the modular robotics and exploits the intersection of this combination.
By exploiting modular robotics for creating wearable, it is possible to obtain a flexible wearable processing system, where input/output modules (robotic modules) are freely interchangeable and freely can be positioned on the body suit in accordance with the task at hand. As with any modular robotic system, the design of the individual module is crucial for the performance of the modular robotic wearable. Design issues include attachment mechanism, communication method, size, form, material, and energy as well as the definition of processing, input and output capabilities.

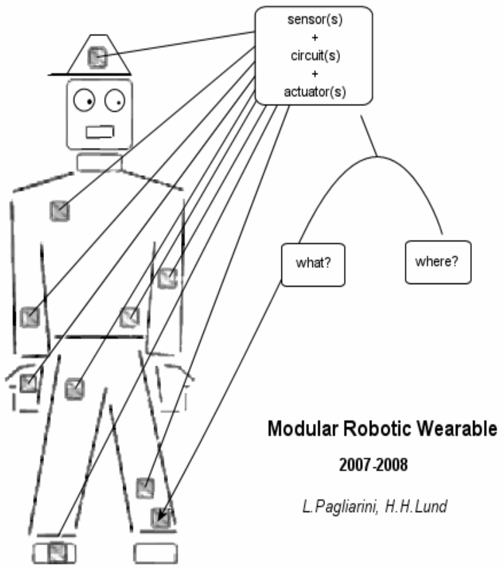

Fig. 5 Modular Robotic Wearable
(original schemata, 2007)

There are two categories of module attachment in modular robotic wearable, namely

- Direct attachment, where modules attach and communicate directly to each other;
- Indirect attachment, where modules attach to, and communicate to each other through, the body (suit).

The direct attachment is similar to most modern modular robotic systems, where the modules can attach directly to each other, whereas the indirect attachment resembles the use of discrete grid systems in some early modular robotic systems and simulations. In traditional modular robotic systems most research strives towards developing a connection as free as possible with no constraints imposed from the surrounding environment.
However, in wearable the situation is often somewhat different, and there may be advantages in developing modular robotic wearable with indirect attachment through a predefined grid system. Often, for full-body

wearable, a body suit is needed in order to create the wearable system and this body suit may form the grid system. Hence, in such a system, the modules attach directly to the body suit in any position formed by the grid system on the body suit.
Communication between modules in the modular robotic wearable can be categorised into:

- Local neighbour-to-neighbour communication (wired or wireless)
- Global communication from one module to a module further away (wireless)

And the way to perform the communication can be either wired (e.g. by direct connection or through the body suit) or wireless (e.g. by IR or radio). So, for instance, the communication possibilities in a modular robotic wearable may be as enlisted in Table 1.

Communication	**Wired**	**Wireless**
Local	Physical connection	IR or radio
Global	Body suit	Radio

Table 1. Communication possibilities in modular robotic wearable.

Several experiences with human – modular robot interaction [6,7,8,9,10] tell that the design of the individual modules is crucial for the easy understanding and manipulation with the modular robotic system. For instance, development of African i-BLOCKS showed the need for particular module attachment design to facilitate 3D building possibilities needed by users in the local context of schools and hospitals in rural areas of Tanzania [11], and strength of magnetic attachment in modular robotic therapy tiles were defined by the capabilities of autistic children in the therapy use [12].

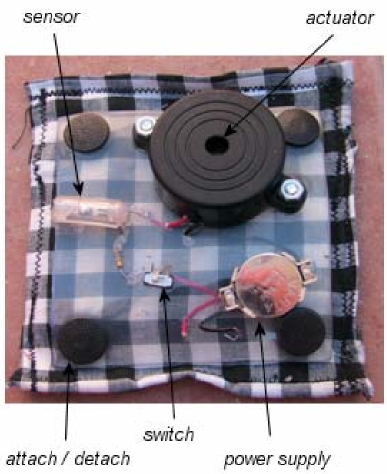

Fig. 6 MRW Module example
(early prototype, 2008)

Similarly, for modular robotic wearable, it is important to understand the use and use context when designing the individual modules. With wearable as the context, the modules must be designed to be flexible in order to fit the body and the free body motion. For instance, in one of our early prototypes we experimented the use of pure electronic circuits (with no PIC or digitalization, see Fig. 6) in order to run quick and inexpensive tests while optimizing on the input-output reaction time. In synthesis, we allow any possible input (sensors of acceleration, temperature, movement, vibration, and etc.) to mediate body actions and reaction directly activating (either in a discrete or analogical fashion), a given actuator (sound, light, etc.), as in a shortcut.

MRW Modules and Playfield characteristics
A further important aspect concerning a good MRW prototype is conceiving wearable robotic modules that are as "flexible" as possible in terms of functionality or displacement (on the bodysuit) , as well as the proper "*playfield*" (surface) for such modules.
As mentioned above, MRW easily allows to explore and study existing relationship amongst psyche (mental states, wishes and wills) and body (movements and parameters), as well as it easily enhance body language capabilities. Therefore, in the MRW a central part of the research is focused on catching (experimenting) relationships between routinary, as well as unusual body movements and possible robotic circuits, in which the input-output flow highlight, improve or detect special characteristics of human body (or body-movement) in space. Such an achievement (i.e. high level of experimentation and exploitation of MRW technology) can only be reached by building modules that follows certain rules:

- each circuit is fully autonomous energetically and electronically, although a circuit can be thought as 'eventually' connected to others MRW modules or any other computer interface;
- although there can be exceptions, each single circuit is conceived independently from the body-part (either suits or accessories) where it will be positioned;
- a MRW circuit applies to the whole body host and should not be limited to any single and specific application.

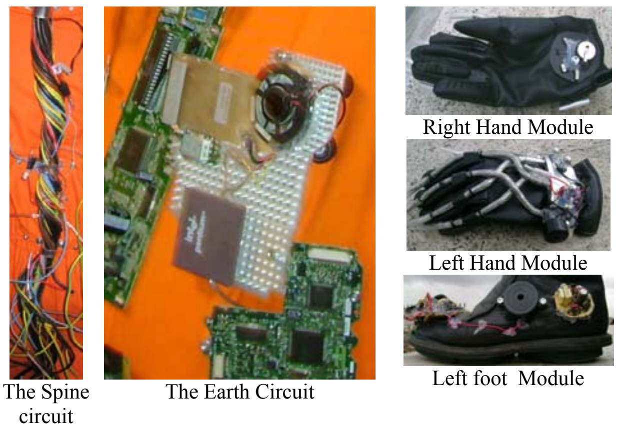

Fig. 7 Few Fatherboard Modules

Although, when building the first prototypes, we become aware that the development of a good MRW bodysuit or "playfield" is crucial to achieve the best results out of a MRW system, at the present, we only ran a couple tests.

The first one was produced for the very initial prototype, Fatherboard (Fig. 3) and was basically a rough start point with all circuits fixed on the tissue or the suite accessories (see Fig. 3 and Fig. 7).

Indeed, the pilot project run on the "*Fatherboard, The Superavatar*" art project [13] was the β-version for MRW - that has been successfully exhibit in different prestigious locations, as the Fondazione Bevilacqua La Masa in Venice [14], Palazzo Strozzi in Florence [15], Piemonte Share Festival in Turin [16], Expocoruña, La Coruña [17], Fondazione D'Ars XXV Oscar Signorini Pize, "Robotic Art", Milan [18], and etc. In the Fatherboard costume we installed about 15 different circuits made out of sound (buzzers, beepers, etc.) and visual (led, digits, etc.) outputs. Since the intention was to run a preliminary study on basic wearable robotics, the circuits were fixed on the suit (or accessories) and although most of them were energetically autonomous, some shared a central battery.

The second prototype (i.e.: Phonotron), still under development, represents a much better approach and, somehow, foresee what will be the basis of future MRW playfield and applications. As shown in Fig. 6, in this prototype the modules are becoming fully autonomous in terms of power supply and functionality and - thanks to a (females) spring buttons system - easily attachable-detachable. In this second prototype we are building a suit that, as for a chessboard, contains all the matching spring buttons (males).

With this new system we plan to test the MRW concept with a wider and more complex set of situations trying to exploit all the following potential interfaces:

1. Body-reality;
2. Body – Virtual Reality (Avatars, SL, any VW);
3. VR - Body

and apply the concept to different potential application fields, such as:

1. Sport
2. Health
3. Entertainment

Indeed, we believe that further than the artistic performances use, the MRW concept with its tight body coupling holds promise for new uses of *playware* (intelligent hardware and software that create play and playful experiences [8]) where the body motions are used to create feedback that motivates playful interactions in several application domains, e.g. for sports training, health rehabilitation and its documentation, and in entertaining play and games.

Conclusion

This concept paper presented the Modular Robotics Wearable technique as a new approach to robotic systems to wear on the body. By using the basic principles of modular robotics, the MRW method creates a large variety of flexible wearable artefacts with freely inter-changeable input/output modules that can be positioned all over the body suit (and accessories). We described a couple prototypes and tried to depict a line of research and the potentiality of the method. Finally, we focused on the intersection of the combination modular robotic systems, wearability, and body-mind theory to highlight the theoretical characteristics of such approach.

Acknowledgements

The authors wish to thanks the sculptor Demian Battisti for his essential contribution in building the first prototypes and the Superavatar suit and mask. Also thanks to the Centre for Playware colleagues for discussions of the concept presented here.

References

[1]. Jeter K.W. *Morlock Night*, DAW. 1979.

[2]. Gibson W. *Neuromancer*. NY: Ace Books, 1984.

[3]. Steve Mann. *Wearable computing*: A first step toward personal imaging. IEEE. *Computer*, 30(2):25–32, Feb. 1997.

[4]. Pagliarini L., Polymorphic Intelligence. In proceedings of *The Twelfth International Symposium on Artificial Life and Robotics*. AROB 12th '07. Oita, Japan, 2007.

[5]. Dychtwald K., *Bodymind*. Penguin Group, 1986

[6]. H. H. Lund. *Robots at Play*. ISBN 978-87-992302-0-4, 160 pages, Odense, 2007.

[7]. H. H. Lund. Intelligent Artefacts. In Sugisaka and Tanaka (eds.) *Proceedings of 8th International Symposium on Artificial Life and Robotics*. pp. I11-I14, ISAROB, Oita, 2003.

[8]. H. H. Lund, T. Klitbo, and C. Jessen. Playware Technology for Physically Activating Play, *Artificial Life and Robotics Journal, 9:4,* 165-174, 2005

[9]. H. H. Lund, P. Marti, A. Derakhshan, R. Beck, T. Klitbo, and J. Nielsen. Modular Robotics for Novel Tools in Dementia Treatment. In *Proceedings of 15th IEEE International Symposium on Robot and Human Interactive Communication (RO-MAN 06)*, IEEE Press, 655-661, 2006.

[10]. H. H. Lund, and P. Marti. Designing Manipulative Technologies for Children with Different Abilities. *Artificial Life and Robotics Journal, 9:4*, 175-187, 2005.

[11]. H. H. Lund, M. D. Pedersen, and R. Beck. Modular Robotic Tiles – Experiments for Children with Autism. In *Proceedings of 13th International Symposium on Artificial Life and Robotics (AROB'13)*, ISAROB, Oita, 2008.

[12]. H. H. Lund, and M. Vesisenaho. I-Blocks in an African Context. In *Proceedings of 9th International Symposium on Artificial Life and Robotics*. pp. I-7 – I-12. ISAROB, Oita, 2004.

[13]. *Fatherboard, The Superavatar*, http://www.artificialia.com/Fatherboard

[14]. *http://www.bevilacqualamasa.it/*

[15]. http://www.strozzina.org/

[16]. http://www.toshare.it/

[17]. http://www.expocoruna.com/

[18]. http://www.dars.it/eventi/comunicato.asp?id=938&archivio=1

Mathematical Modelling of Complex Systems and its Possible Applications

Kazuyuki Aihara

Institute of Industrial Science, University of Tokyo
4-6-1 Komaba, Meguro-ku, Tokyo153-8505, Japan
and
Aihara Complexity Modelling Project, ERATO, JST
(Tel : 81-3-5452-6691; Fax : 81-3-5452-6692)
aihara@sat.t.u-tokyo.ac.jp

Abstract: In this plenary talk, I review our recent studies on mathematical modelling of complex systems and its possible applications.

Keywords**:** mathematical modelling, complex systems

This plenary talk is to review our studies on mathematical modelling of complex systems and its possible applications, which have been carried out by the Aihara Complexity Modelling Project, ERATO, JST (Japan Science and Technology Agency). In this research project, we have been developing mathematical theory and analysis methodology for modelling complex systems in general, and simultaneously applying such modelling to individual real-world complex systems. The applications include (1) dynamical information processing of biological systems like neural networks ([1]-[6]) and genetic networks ([7]-[13]), (2) a new kind of computation by complex systems and its hardware and wetware implementations ([14]-[17]), and (3) modelling of diseases like new influenza and prostate cancer ([18]-[21]). These applications show that mathematical modelling is useful for understanding and controlling various complex systems in this real world.

REFERENCES

[1] Taro Toyoizumi, Jean-Pascal Pfister, Kazuyuki Aihara, and Wulfram Gerstner: "Generalized Bienenstock-Cooper-Munro Rule for Spiking Neurons that Maximizes Information Transmission," Proc. Natl. Acad. Sci. USA, Vol.102, No.14, pp.5239-5244 (2005).

[2] Kenji Morita, Kunichika Tsumoto, and Kazuyuki Aihara: "Possible Effects of Depolarizing $GABA_A$ Conductance on the Neuronal Input-output Relationship: A Modeling Study," Journal of Neurophysiology, Vol.93, pp.3504-3523 (2005).

[3] Taro Toyoizumi, Kazuyuki Aihara, and Shun-ichi Amari: "Fisher Information for Spike-based Population Decoding," Physical Review Letters, Vol.97, 098102 (2006).

[4] Kenji Morita, Kunichika Tsumoto, and Kazuyuki Aihara: "Bidirectional Modulation of Neuronal Responses by Depolarizing GABAergic Inputs," Biophysical Journal, Vol.90, No.6, pp.1925-1938 (2006).

[5] Kenji Morita, Rita Kalra, Kazuyuki Aihara, and Hugh P.C. Robinson: "Recurrent Synaptic Input and the Timing of Gamma-frequency-modulated Firing of Pyramidal Cells During Neocortical "UP" States," Journal of Neuroscience, Vol.28, pp.1871-1881 (2008).

[6] Yoshito Hirata, Yuichi Katori, Hidetoshi Shimokawa, Hideyuki Suzuki, Timothy A. Brenkinsop, Eric J. Lang, and Kazuyuki Aihara: "Testing a Neural Coding Hypothesis using Surrogate Data," Journal of Neuroscience Methods, Vol.172, pp.312-322 (2008).

[7] Tianshou Zhou, Luonan Chen, and Kazuyuki Aihara: "Molecular Communication through Stochastic Synchronization Induced by Extracellular Fluctuations," Physical Review Letters, Vol.95, 178103 (2005).

[8] Dorjsuren Battogtokh, Kazuyuki Aihara, and John J. Tyson: "Synchronization of Eukaryotic Cells by Periodic Forcing," Physical Review Letters, Vol.96, 148102 (2006).

[9] Chunguang Li, Luonan Chen, and Kazuyuki Aihara: "Transient Resetting: A Novel Mechanism for Synchrony and Its Biological Examples," PLoS Computational Biology, Vol.2, No.8, pp.0925-0931 (2006).

[10] Chunguang Li, Luonan Chen, and Kazuyuki Aihara: "Stability of Genetic Networks with SUM Regulatory Logic: Lur'e System and LMI Approach," IEEE Trans. on Circuits and Systems-I: Regular Papers, Vol.53, No.11, pp.2451-2458 (2006).

©ISAROB 2009

[11] Chunguang Li, Luonan Chen, and Kazuyuki Aihara: "A Systems Biology Perspective on Signal Processing in Genetic Network Motifs," IEEE Signal Processing Magazine, Vol.24, No.2, pp.136-147 (2007).
[12] Hirokazu Tozaki, Tetsuya J. Kobayashi, Hiroyuki Okano, Ryo Yamamoto, Kazuyuki Aihara, and Hidenori Kimura: "Reconstructing the Single-cell-level Behavior of a Toggle Switch from Population-level Measurements," FEBS Letter, Vol.582, No.7, pp.1067-1072 (2008).
[13] Ruiqi Wang, Chunguang Li, Luonan Chen, and Kazuyuki Aihara: "Modeling and Analyzing Biological Oscillations in Molecular Networks," Proceedings of the IEEE, Vol.96, pp.1361-1385 (2008).
[14] Takashi Kohno and Kazuyuki Aihara: "A MOSFET-based model of a Class 2 Nerve membrane," IEEE Transactions on Neural Networks, Vol.16, No.3, pp.754-773 (2005).
[15] Yoshihiko Horio, Tohru Ikeguchi, and Kazuyuki Aihara: "A Mixed Analog/Digital Chaotic Neuro-computer System for Quadratic Assignment Problems," INNS Neural Networks, Vol.18, No.5-6, pp.505-513 (2005).
[16] Yoshihiko Horio and Kazuyuki Aihara: "Analog computation through high-dimensional physical chaotic neuro-dynamics," Physica D, Vol.237, Issue 9, pp.1215-1225 (2008).
[17] Masashi Aono, Masahiko Hara, and Kazuyuki Aihara: "Amoeba-based Neurocomputing with Chaotic Dynamics," Communications of the ACM, Vol. 50, No. 9, pp.69-72 (2007).
[18] Naoki Masuda, Norio Konno, and Kazuyuki Aihara: "Transmission of Severe Acute Respiratory Syndrome in Dynamical Small-world Networks," Physical Review E, 69, 031917 (2004).
[19] Nobuaki Sugimine, Naoki Masuda, Norio Konno, and Kazuyuki Aihara: "On Global and Local Critical Points of Extended Contact Process on Homogeneous Trees," Mathematical Bioscience, Vol.213, No.1, pp.13-17 (2008).
[20] Aiko Miyamura Ideta, Gouhei Tanaka, Takumi Takeuchi, and Kazuyuki Aihara: "A Mathematical Model of Intermittent Androgen Suppression for Prostate Cancer," Journal of Nonlinear Science (in press).
[21] Gouhei Tanaka, Kunichika Tsumoto, Shigeki Tsuji, and Kazuyuki Aihara: "Bifurcation Analysis on a Hybrid Systems Model of Intermittent Hormonal Therapy for Prostate Cancer," Physica D, Vol.237, No.20, pp.2616-2627 (2008).

Optimal Monitoring for Distributed Intrusion Detection System

Adam Piotr Grzech

Institute of Computer Science, Wroclaw University of Technology
Wybrzeze Wyspianskiego 27, 50-370 Wroclaw, Poland
(tel: +48 71 320 35 89; fax: +48 71 320 38 84)
(adam.grzech@pwr.wroc.pl)

Abstract: Distributed intrusion detection systems, which consist of spatially distributed monitoring elements, may be applied to detect intrusions in real-time manner based on the analysis of collected data. This paper is devoted to present and discuss some selected aspects of detection systems architecture and efficiency. In the first part detection capabilities as dependent on distributed computer communication system parameters are discussed. The aim of the second part is to present an idea of hierarchical architecture of distributed intrusion detection systems and to discuss quality of monitoring performed at the lower layer of detection system hierarchical architecture.

Keywords: computer networks, distributed IDS, monitoring

I. INTRODUCTION

Intrusion Detection System (IDS), being a system monitoring a stream of events for attacks and taking countermeasures, is defined as the process of intelligently monitoring the events occurring in a computer system, analysing them for signs of violation of the security policy. The security policies are in general designed and applied as services composed of contemplery parts and organized according applied security measures: avoidance and intrusion detection, restrictive and preventive measures, detection and forensic measures. IDS implemented in gain to protect the availability, confidentiality and integrity of networked systems by misuse or anomaly detection, are defined by both the method used to detect attack, and the placement of the IDS on the network [2,3,7,8].

IDS may be classifeied in different manners, but the most common is to classify them based on analysed IDS events sources, i.e., host-based IDS (HIDS) or network-based IDS (NIDS) and application-based IDS (AIDS). Most of them are distributed intrision detection systems (DIDS) utilizing the concept of specialized distributed agents community representing agents with the same purpose for detecting anomalies [3].

DIDS based on anomalies detection, and commonly called as intelligent IDS (IIDS), often requires extensive training data for artificial learning algorithms and are computationally expensive. In intelligent IDS various machine learning algorithms belonging to stochastic learning, rule-based learning, neural learning and empirical learning classes are frequently applied.

Architectures, structures and effectiveness of DIDS are optimized based on various criteria [5-10].

The paper is devoted to present some concepts relating to anomalies detecting capabilities (section II), an idea of DIDS monitoring system quality (section III) and to discuss the limitations of the proposed solutions, as well as suggest further research (section IV).

II. ANOMALIES DETECTION SYSTEMS SENSITIVITY

The decision about the intrusion detection (traffic monitoring) devices location can be dependable on several aspects: the possibility of detecting a large number of intrusions, expected loss of functionality of the monitored computer system due to intrusions and mutual location of devices. It is assumed that number and location of network traffic monitoring devices impact amount of data available for decision making and cost of the data delivery, and that the latter directly influence functionality of the DIDS measured by proposed indexes.

It is assumed that a topology of system is modeled by directed graph $G=(V,E)$, where the given set of nodes $V=\{1,...,n\}$ represents distinguishable parts of monitored system and $E \subseteq \{(u,v): u,v \in V, u \neq v\}$ is a set of ordered pairs of distinct nodes each representing a communication channel used to exchange messages in the computer system. Each node can send and receive messages that are: the results of typical work of that computer system or the messages that are being intrusions, which can violate confidentiality, integrity, or availability of data in the monitored system.

It is also assumed that in each network node an intrusion detection device, that can monitor both in-coming and out-coming traffic, may be located. Location

©ISAROB 2009

of intrusion detection device in node i ($1 \le i \le n$) is denoted by binary variable x_i, where $x_i = 1$ ($x_i = 0$) means that there is (there is not) an intrusion detection device in node i. The number of available intrusion detection devices in the system is given and equal to m.

The number of devices and their location should guarantee the security policy established for monitored system. In this paper three measures defining the security level and loss of performance of monitored system are proposed: intrusion detection accuracy, speed and the overall overhead caused by the communication of devices with each other.

Intrusion detection accuracy is a measure indicating the percentage value of detected intrusions by DIDS to the overall number of intrusions occurred in the monitored computer system. Intrusion detection speed is measured in the number of hops between a node where intrusion where generated and a node with intrusion detection device where that intrusion was detected. Overall overhead is a measure that specifies the overall number of hops needed for communication among all intrusion detection devices.

Location of intrusion detection devices based on the value characterizing the possibility of detecting a large number of intrusions points out to the desire of detect as many intrusion as it is possible. For any node i in the graph, $1 \le i \le n$, it can be estimated using data gathered during the work of the system (e.g. we can use traffic size passed through that node or number of intrusions in that node), using some subjective characterization of node sets up by security experts or even using degree of the node. Location of detection devices based on the value characterizing the possibility of detecting a large number of intrusions can be presented as:

$$x_1, x_2, \ldots, x_m \leftarrow \min_{x_1, x_2, \ldots, x_m} w^T x \tag{1}$$

where $w^T = [w_1, w_2, \ldots, w_n]^T$ and $w_i \in [0,1]$, $1 \le i \le n$ characterizes the inverse possibility of detecting large number of intrusions (i.e. the higher the value of w_i, the less intrusions are to be detected in that node).

Expected loss of functionality of the monitored computer system is connected with the administrators and users wishes of protecting the most valuable parts of monitored computer system. Quantity of expected loss can be characterized by the lost performance due to unavailability of some parts of the computer system, full cost recovery of attacked node, etc.

Location of intrusion detection devices which minimizes the excepted loss can be denoted as follows:

$$x_1, x_2, \ldots, x_m \leftarrow \min_{x_1, x_2, \ldots, x_m} s^T (\overline{1} - x) \tag{2}$$

where $s^T = [s_1, s_2, \ldots, s_n]^T$ and $s_i \in [0,1]$ for $1 \le i \le n$ characterizes the expected loss for node i and $\overline{1}$ is a column vector of size n.

Mutual location of intrusion detection devices affects to the communication cost among intrusion detection devices and the speed of intrusion detection. Both quantities can be defined based on the conception of distance matrix $D = [d_{ij}]$ where $d_{i,j} \in [0,1]$ characterizes the shortest distance between node i and node j (e.g. the proportion of the shortest distance in hops between these two nodes to the longest possible distance in graph G). Then the location of intrusion detection devices which satisfies the minimum value of communication cost among all intrusion detection devices can be described as follows (where m is equal to the number of used intrusion detection devices):

$$x_1, x_2, \ldots, x_m \leftarrow \min_{x_1, x_2, \ldots, x_m} \frac{1}{m(m-1)} x^T D x \tag{3}$$

It is also possible to calculate locations maximizing speed of intrusion detection (e.g. can be measured in hops as a distance traveled from the node where the intrusion was generated to the node where it was detected for the first time). Optimal detection devices location can be defined as:

$$x_1, x_2, \ldots, x_m \leftarrow \min_{x_1, x_2, \ldots, x_m} \frac{1}{m(n-m)} x^T D(\overline{1} - x) \tag{4}$$

Suggested criteria (1) - (4) give possibility to set up the location of detection devices. To indicate relative importance of the criteria coefficients ω_1, ω_2, ω_3 and ω_4 ($\omega_1, \omega_2, \omega_3, \omega_4 \ge 0$, $\omega_1 + \omega_2 + \omega_3 + \omega_4 = 1$) may be applied. Introduction of such coefficients leads to definition of optimization task, i.e., location of intrusion detection devices in network that minimizes the following function:

$$f(x) = \omega_1 w^T x + \omega_2 s^T (\overline{1} - x) + \\ + \omega_3 \frac{1}{m(m-1)} x^T D x + \omega_4 \frac{1}{m(n-m)} x^T D(\overline{1} - x) \tag{5}$$

subject to:

$$x_1 + x_2 + \ldots + x_n = m \tag{6}$$

with respect to $x = [x_1, x_2, \ldots, x_n]^T$ defining location of intrusion detection devices in the monitored network.

The above binary quadratic programming problem is an optimization NP-hard problem solved effciently by optimal and approximate algorithms or heuristics used.

III. HIERARCHICAL DISTRIBUTED INTRUSION DETECTION SYSTEM

Efficiency of DIDS, in which data are collected and transferred for decision making purposes, depends on number and location of monitoring elements, amount of collected and transmitted data and the location, where the data are processed.

Lower layer of the DIDS is responsible for local monitoring of distributed system and consists of monitored elements - software applications or hardware systems that collect data about the state of linked network devices. Any of the monitored element is local to the network device which entail negligible delay in exchanging data between them. Monitored elements are next grouped into areas (called monitoring areas). All monitored elements from the same monitoring area send its data in specified time intervals to the same middle layer element for the intrusion detection analysis.

The middle layer of the DIDS consists of monitoring elements that gather data from all monitored elements within their monitoring areas. The data between monitored elements of the lower layer and monitoring elements of the middle layer are sent through the same distributed system communication channels that are used for users' traffic exchange in the distributed system. A monitoring element itself can be a software application or hardware system which analyses data collected from all monitored elements within its monitoring area in order to detect intrusions. The amount of sent data for an analysis, as well as users' data results from the ordinary distributed system functionality impacts on delay of the network traffic. In this paper it is assumed that monitoring element can be located locally to any of the network device.

The highest layer of DIDS consists of a correlation element which is responsible for gathering data from all monitoring elements from the middle layer for the intrusion detection analysis within the whole distributed system. The controlling element can also derive dynamic properties of detected intrusions which can be next used to prevent their spread throughout the distributed system.

Quality of local and global decisions (DIDS higher layers functionality) depends on quality of distributed monitoring system [5].

Hierarchical architecture of the DIDS allows the division of functionality that improves the scalability and reliability of distributed intrusion detection system as well as simplifies the design and implementation phase of such a system comparing to the architecture of centralized intrusion detection system. In addition, such architecture fulfills several important features [4,7], like it imposes the minimum overhead on the distributed system in order to avoid interference with its ordinary functionality and is easy to deploy. Therefore the quality of DIDS depends on the quality of monitoring system.

3.2. Basic notations

A distributed system is modeled as an undirected graph $G(V,E)$, where $V=\{v_1,v_2,...,v_N\}$ represents a set of nodes, where each node $v_i \in V$ $(1 \le i \le N)$ depicts a location in which network devices are localized, and $E=\{e_{ij}\}$ defines a set of communication channels between these nodes with given capacity. Knowledge of networks topological structure, traffic requirements, channel capacities and applied routing algorithm leads to knowledge of traffic flows over all networks channels.

A monitoring devices can be located in any node $v_j \in V$ $(1 \le i \le N)$. For each monitoring element located in node v_i there is defined a corresponding monitoring area Λ_i which is a subset of nodes from which data for an analysis is sent to this monitoring element.

It is also assumed that there exists a finite set of possible network device classes $U=\{u^{(1)},u^{(2)},...,u^{(k)}\}$ possible to locate in any node of the graph. A monitoring devices can be located in any node $v_j \in V$ $(1 \le j \le N)$. For each monitoring element located in node $v_j \in V$ there is defined a corresponding monitoring area Λ_i; all monitoring devices located in nodes belonging to the distinguished are send data to distinguished node $v_i \in \Lambda_i \subset V$ $(i=1,2,...,m)$. The total number of monitoring nodes (m) may be given, or selected in gain to optimise selected performance measure.

The set of all Λ_i ($\Lambda_1 \cup \Lambda_2 \cup ... \cup \Lambda_m = V$), where set which is a subset of nodes from which data for an analysis is sent to this monitoring element.

The number of network devices belonging to the distinguished classes, located in the particular node $v_j \in \Lambda_i \subset V$ and transferring monitoring data to the node $v_i \in \Lambda_i \subset V$ is $L_{ji}=\{l_{ji}^{(1)},l_{ji}^{(2)},...,l_{ji}^{(k)}\}$. It is the set of all monitoring devices, located in the j-th node, and delivering monitoring data to the i-th node ($v_i \in \Lambda_i$).

Moreover, it is assumed that each network device class has its own data generation intensity $\alpha^{(k)}$ $(1 \le k \le K)$ which quantitively depicts the amount of data generated and relayed to the linked monitored element. The network device which belongs to class k $(1 \le k \le K)$ together with its locally monitored element located in node $v_j \in \Lambda_i$ sends monitoring data to a monitoring node $v_i \in V$; amount of transferred data in time interval τ with the data sending rate $\beta_{ji}^{(k)}$ equals to $\alpha_{ji}^{(k)}(\tau)=\alpha^{(k)}\beta_{ji}^{(k)}\tau$. Total amount of data transferred from the $v_j \in \Lambda_i$ node to the $v_i \in V$ node equals to:

$$\alpha_{ji}(\tau)=l_{ji}^{(1)}\alpha_{ji}^{(1)}(\tau)+l_{ji}^{(2)}\alpha_{ji}^{(2)}(\tau)+...+l_{ji}^{(K)}\alpha_{ji}^{(K)}(\tau).$$

Therefore, the total amount of data generated within the particular monitoring area Λ_i equals to:

$$\alpha_i(\tau)=\alpha_{ji}^{(1)}(\tau)+\alpha_{ji}^{(2)}(\tau)+...+\alpha_{ji}^{(K)}(\tau).$$

3.3. Distributed monitoring system quality

In the hierarchical DIDS, the functionality of higher layers is based on the functionality of lower layers, therefore the intrusion detection capabilities depends on the monitoring system quality.

The quality of the monitoring system is influenced both by the amount and delay of data collected for intrusion detection analysis: having more data with small enoygh delay it is possible to take a better decision .

Therefore, it is assumed that the impact of data intended for an analysis in amount of $\alpha_{ji}(\tau)$ on the monitoring system quality is complied by a penalty function. Penalty function can be calculated for all the given or calculated monitoring area Λ_i :

$$p(\Lambda_i) = \frac{1}{\alpha_i(\tau)} \sum_{v_j \in \Lambda_i} \alpha_{ji}(\tau) \cdot p_{ji}(\alpha_{ji}(\tau)) \qquad (7)$$

Similarly to penalty function, a collected data delay can be calculated for all the given or calculated monitoring area Λ_i :

$$d(\Lambda_i) = \frac{1}{\alpha_i(\tau)} \alpha_{ji}(\tau) \cdot \sum_{v_j \in \Lambda_i} d_{ji}(\alpha_{ji}(\tau)) \qquad (8)$$

A monitoring system quality which depicts the quality of the lower layer of distributed intrusion detection system depends on the localization and number of monitoring elements, form of monitoring areas and amount of data that is sent for intrusion detection analysis and can be calculated a sum of delay and penalty function:

$$Q\left(\Gamma, \Lambda_i, \beta_{ji}^{(k)}\right) = \sum_{v_j \in \Lambda_i} \left(d(\Lambda_i) + p(\Lambda_i)\right) \qquad (9)$$

The optimization task of monitoring system quality can be formulated, analyzed and solved based on all possible parameters defining monitoring system quality (5), namely localization and a number of monitoring elements, form of monitoring areas, amount of monitoring data determined by data sending rate and amount of users' network traffic.

In the discussed quality of monitoring system, depending on amount of monitoring data and the data communication costs, delivery costs of locally made decisions may be included.

Fot example, the data sending rate optimization task is formulated as below:

$$Q^*\left(\beta_{ji}^{(k)}\right) = \min_{\beta_{ji}^{(k)}, v_j \in \Lambda_i, k=1..K;} \sum_{v_j \in \Lambda_i} \left(d(\Lambda_i) + p(\Lambda_i)\right) \qquad (9)$$

In this case the monitoring system quality depends on the data sending rate.

IV. CONCLUSIONS

In this paper some selected issues concering optimal architecture of DIDS are discussed; intrusion detection capabilities depending on parameters describing distributed computer communication systems and quality of distributed monitoring system.

Quality and amount of data,collected and transferred for decision making purposes in DIDS, may be important to control quality of decisions produced by the system. It is also important to manage the trade-off between cost of collecting and transferring monitoring data and the quality of detection.

As in the paper many additional assumptions were made, in the future work more detailed analysis is going to be provided as well as the analysis of real appliance for distributed and intrusion detection systems will be presented and the impact of monitoring system quality on the distributed intrusion system quality will be examined thoroughly. The presented concept will be further enhanced for more complex dynamic computer networks.

The optimisation problem of monitoring devices localization and amount of data exchanged among monitoring and monitored data as well as quality of the distributed monitoring issues, discussed in the paper, is a part of work devoted to investogate interdependencies between quality of monitoring systems and two-stage decision making system. The gain of the latter is to produce decisions, quality of which are usually measured by the probability for undetected attacks.

REFERENCES

[1] Bar-ilan J., Kortzars G., Peleg D. (1993), How To Allocate Network Centers, Journal of Algorithms (15/3).

[2] Bashah N., Shanmugam B., Ahmed A.M. (2005), Hybrid intelligent detection system, Proceedings of World Academy of Science, Engineering and Technology (vol. 6): 291 - 294.

[3] Benattou M., Tamine E. K. (2005), Intelligent agents for distributed intrusion detection system, Proceedings of World Academy of Science, Engineering and Technology (vol. 6): 190 - 193.

[4] Chebrolu S., et.al. (2004), Feature deduction and ensemble design of Intrusion Detection Systems, Computer & Security.

[5] Grzech A. (2006), Anomaly detection in distributed computer communication systems, Cybernetics and Systems (37/6).

[6] Hentea M. (2007), Intelligent system for information security management: Architecture and design issues, Issues in Information Science and Information Technology (vol. 4): 29 – 43.

[7] Neumann P., Porras P. (1997), Event Monitoring Enabling Responses to Anomalous Live Disturbances.

[8] Ozsoy F., Pinar M. (2006), An exact algorithm for the capacitated vertex p-center problem, Computers and Operations Research (33/5).

[9] Peddabachgari S., Abraha A., Grosan C., Thomas J. (2005), Modeling intrusion detection system using hybrid intelligent systems (www.sciencedirect.com).

[10] Snapp S., et.al. (1991), Distributed Intrusion Detection System – Motivation, Architecture and an Early Prototype, NCSC.

Making Decision in Two-Stage Identification System with Knowledge Updating

J. Swiatek, K. Brzostowski
Wroclaw University of Technology
Institute of Informatics
Wyb. Wyspianskiego 27, 50-370 Wroclaw, Poland

Abstract

In the paper an algorithm for knowledge updating in adaptive system to select scenario has been proposed. Taking into account specific character of the process, two-stage identification approach is used. The first stage is built for diagnostic purpose i.e. estimated parameters of the first-stage's relationship is utilised to make a decision at the second stage. Proposed algorithms to select scenario, at the second stage, rests on extracted knowledge from human expert and effects of diagnosis.

1 Introduction

Most of real control plants are strongly non-linear and uncertain due to measurement disturbances. Hence, it is difficult or sometimes even impossible to work out an exact mathematical model of the plant. Nowadays many approaches to control or support making decision do not require direct description of the process in order to work properly. We pay attention to those which are based on expert's knowledge.

Another way to cope with non-linearity and uncertainty is application of adaptive techniques in designing systems. In spite of the fact that it has been proposed three decades ago, it is still widely used.

1.1 Support making decision system

In the article the problem of building rehabilitation plan for patients is considered. The tasks can be decomposed into few stages which are shown in Fig. 1 and described in details in next paragraphs.

The first stage (*O1*) is used to asses the current state of the object and referring to biomedical problem of the paper and can be connected with making diagnosis.
Object at this stage is described by the vector of parameters $\mathbf{a_1}(k_1)$ and model $\Phi_1(y(k_1-1), \pi_1(k_1); \mathbf{a_1}(k_1))$. Measured signals $\pi_1(k_1)$ and $y(k_1)$

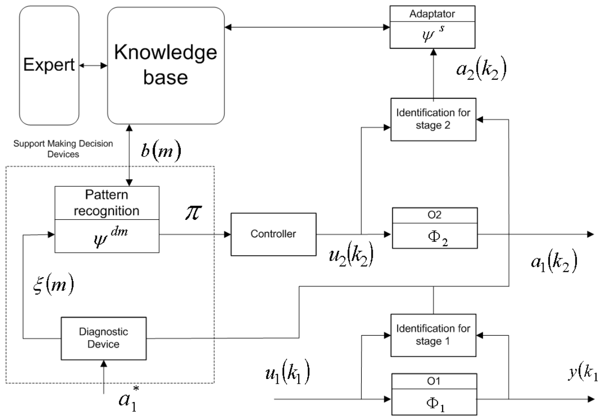

Figure 1: Support making decision system with knowledge updating and two-stage identification approach

are used only to determine values of model's parameters $\mathbf{a_1}(k_1)$ (identification at the first stage).

The second one (denoted as *O2*) plays the role in establishing the relationship between stimulation (exercises) and internal muscle's parameters $\mathbf{a_1}(k_1)$ which are calculated at the first stage. As it was mentioned proposed algorithms to select scenario based on *pattern recognition* approach and to make a proper decision the learning sequence is needed.

The main goal is to bring values of these parameters to desired $\mathbf{a_1^*}$. In order to do this, process at the second stage is employed. Its control action is denoted by $\pi_2(k_2)$ and model $\Phi_2(\mathbf{a_1}(k_1-1), \pi_2(k_2); \mathbf{a_2}(k_2))$ describes its influence on values of parameters $\mathbf{a_1}(k_1)$ of the model $\Phi_1(\cdot, \cdot; \cdot)$. We assume that model $\Phi_2(\cdot, \cdot; \cdot)$ (dependent on parameters $\mathbf{a_1}(k_2)$) approximates real relation between $\pi_2(k_2)$ and $\mathbf{a_1}(k_2)$. Controller performs sequence of actions $\pi_2(k_2)$ (scenario) chosen by the decision making device. Decision about scenario to be used is made on the basis of difference $\xi(k_2)$ between current values of parameters $\mathbf{a_1}(k_1)$ and desired ones $\mathbf{a_1^*}$. Scenario is selected from the knowledge base containing set of prespecified scenarios together

©ISAROB 2009

with rules describing suggestions of their usage. For different current values of $\mathbf{a_1}(k_1)$ and desired $\mathbf{a_1^*}$, different control scenarios are proposed by well-known *kNN* rule.

Presented scheme has straightforward interpretation as a rehabilitation process. Model on the first stage represents a patient [2], model on the second stage describes influence of rehabilitation exercises on the state of the patient, decision maker together with knowledge base represents a physician and controller is a therapist. Adaptation and knowledge updating means that physician learns by experience.

2 Problem formulation

Let us consider that a set of accessible control actions (which are called *scenarios*) is denoted as Π and has a following form:

$$\Pi = \{\pi_1, \pi_2, \ldots, \pi_H\}, \tag{1}$$

where H is the number of all scenarios.

Each scenario is composed by make the most of instructions stored in finite set: $U_2 = \{u_{21}, u_{22}, \ldots, u_{2L}\}$. Where L is the number of all available instructions.

Taking into account it is possible to show the structure of single scenario: $\pi = \left(u_{2l_1}, u_{2l_2}, \ldots, u_{2l_M}\right)$. Where M is the instructions' number used to combine scenario.

Now, let us define function $d^{dm}(\cdot,\cdot)$ to measure distance between current value $\mathbf{a_1}(k_1)$ and desired $\mathbf{a_1^*}$:

$$\xi(k_2) = d^{dm}\big(\mathbf{a_1^*}, \mathbf{a_1}(k_1)\big). \tag{2}$$

It was supposed that the value of the parameter $\mathbf{a_1}(k_1)$ is known and was determined as a result of resolving identification task at the first stage [2].

Process of planning rehabilitation for spastic people can be formulated as the making decision problem. As a result of solving the multi-stage decision process it is gained following sequence:

$$\big(\pi(1), \ldots, \pi(K_2-1); \xi(1), \ldots, \xi(K_2)\big). \tag{3}$$

It is clear that the number of all admissible sequences may be large. The problem is to rate them and choose optimal by using performance index. Let us define following performance index Q^{dm} written below:

$$Q^{dm}\Big(\pi(1), \pi(2), \ldots, \pi(K_2-1); \xi(1), \xi(2), \ldots \\ \ldots, \xi(K_2)\Big) = \sum_{k_2=1}^{K_2} q^{dm}\Big(\pi(k_2), \xi(k_2)\Big), \tag{4}$$

where $q^{dm}\Big(\pi(k_2); \xi(k_2)\Big)$ is local assessment of decision in $k_2 - th$ stage for $\xi(k_2)$.

Applied defined criterion function (4) for sequence (3) leading to optimisation task:

$$Q^{pd}\Big(\pi^*(1), \pi^*(2), \ldots \\ \ldots, \pi^*(K_2-1); \xi(1), \xi(2), \ldots, \xi(K_2)\Big) = \\ = \min_{\pi^*(1),\pi^*(2),\ldots,\pi^*(K_2-1)\in\Pi} Q^{pd}\big(\pi(k_2), \xi(k_2)\big), \tag{5}$$

and for stochastic plant:

$$\mathbb{E}\Big[Q^{pd}\Big(\pi^*(1), \pi^*(2), \ldots \\ \ldots, \pi^*(K_2-1); \tilde{\xi}(1), \tilde{\xi}(2), \ldots, \tilde{\xi}(K_2)\Big)\Big] = \\ = \min_{\pi^*(1),\pi^*(2),\ldots,\pi^*(K_2-1)\in\Pi} \mathbb{E}\Big[Q^{pd}\big(\pi(k_2), \tilde{\xi}(k_2)\big)\Big], \tag{6}$$

where $\tilde{\xi}(k_2) = g_w\Big(\xi(k_2), w(k_2)\Big)$. Function $g_w\Big(\cdot,\cdot\Big)$ describes influence of the disturbance $w(k_2)$ on $\xi(k_2)$. In consequence, as a solution of formulated above optimisation task (5 and 6) it is given decision making algorithm written below:

$$\pi^*(k_2) = \psi^{dm}\Big(\xi(k_2); \mathbf{b}\Big), \tag{7}$$

where $\xi(k_2) \in D^*_{\xi(k_2)}$:

$$D^*_{\xi(k_2)} = \Big\{\xi(k_2) : Q^{dm}\Big(\pi^*(k_2); \xi(k_2)\Big) < \\ < Q^{dm}\Big(\pi(k_2); \xi(k_2)\Big) \qquad \forall_{\pi\in\Pi}\Big\}. \tag{8}$$

For stochastic plant algorithm to select scenario has form similar to (7) i.e.:

$$\pi^*(k_2) = \psi^{dm}\Big(\tilde{\xi}(k_2); \mathbf{b}\Big), \tag{9}$$

In this paper classical formulation of the decision process has been shown, where the horizon K_2 is finite.

3 Pattern recognition in decision support process

Practically, determining solution for task (5) or (6) may be expensive and time consuming. To resolve described problem, the pattern recognition algorithm with knowledge updating was proposed. To design the proper decision making procedure in this case it is

©ISAROB 2009

required to fix the learning sequence which is denoted by $X^{K_{dm}}$ and has following form:

$$X^{K_{dm}} = \Big\{ \Big(\xi^{(1)}, (\pi^*)^{(1)}\Big), \Big(\xi^{(2)}, (\pi^*)^{(2)}\Big), \ldots \\ \ldots, \Big(\xi^{K_{dm}}, (\pi^*)^{K_{dm}}\Big) \Big\}. \quad (10)$$

General form of knowledge-based algorithm is shown below:

$$\left(\tilde{\pi}^*(1), \tilde{\pi}^*(2), \ldots, \tilde{\pi}^*(K_2 - 1)\right) = \\ = \psi^{pd}_{PR}\Big(\xi(k_2), X^{K_{dm}}; \mathbf{b}\Big), \quad (11)$$

where (10) is updated in each *m-th* step of process i.e.: $X^{K_{dm}}(m) = X^{K_{dm}}(m-1)$.

4 Algorithm for knowledge updating

There are many different approaches in adaptive control or support decision systems to apply learning process. One of them is *adaptation through identification* where parameters of the algorithm $\psi^{dm}\Big(\xi(k_2); \mathbf{b}\Big)$ or $\psi^{dm}\Big(\tilde{\xi}(k_2); \mathbf{b}\Big)$ are updating step-by-step as a result of identification of the object's model.

In the expert systems another methodology can be applied. It is connected with concept of storing information in the system. Instead of changing algorithm's parameters it is possible to update and validate knowledge which is embedded in the knowledge base.

In the considered problem knowledge which is collected in *knowledge base* is used to support decision process and it is possible to update it if necessary. In real tasks frequently is needed to update expert's knowledge because it has been obsoleted or was not correctly prepare before had been applied to the system.

Discussed system uses knowledge base (10) which can be updated or validated at each m-th step of the adaptation process: $X^{K_{dm}}(m) = X^{K_{dm}}(m-1)$.

In the paper two different algorithms have been proposed. First approach is characterised, by using *performance index* (4) one new item to add to learning sequence is selected. Below the algorithm of updating knowledge is listed:

Algorithm 1:

(1) Put control sequence $\{\pi(k_2)\}_{k_2^M=1}^{K_2^M}$ and measure output $\{a_1(k_2)\}_{k_2^M=1}^{K_2^M}$ and $\{\xi(k_2)\}_{k_2^M=1}^{K_2^M}$ for object at the second stage. K_2^M is the length of the measured sequence;

(2) For each error $\xi(k_2^M)$ where $k_2^M = 1, 2, \ldots, K_2^M$, calculate value of the *performance index* (4) in k_2-th step;

(3) Select error value $\xi(k_2^M)$ for which control action has been done and value of *performance index* is the smallest;

(4) Add new item $\Big(\xi^{K_{dm}+1}, (\pi^*)^{K_{dm}+1}\Big)$ to learning sequence $X^{K_{dm}}$.

The second version of the updating method is as follows: at the first step new element is selected (by using *performance index* (4)) and - in the second step - the worst from knowledge based is chosen as well. Then, new item in the learning sequence is not added but replace the worst one. Algorithm for the second version is as follows:

Algorithm 2:

(1) to (4) the same as for **Algorithm 1**;

(5) Replace it by new one (from step 3).

5 Simulation studies

In order to test proposed algorithms to select scenario with knowledge updating modification simulation environment has been built. There is a straight relation to biomedical application. In [4] a model of fatigue in human skeletal muscles has been proposed. The mathematical relationship allow us to model activation of muscle by physical exercises and produced force. Having set of different scenarios (exercises routes) it is possible to select them in the right order during training cycle to reach the aim of control. This aim can be defined as a desired value of force which is produced by athletes during exercises.

In Fig. 2 effect of support of making decision has been shown for which value of the performance index $Q^{dm} = 0.0086$. In figures 3 and 4 the same process has been conducted but for algorithm with knowledge updating. Value of $Q^{dm} = 0.0081$ for the second approach and for first $Q^{dm} = 0.0075$.

6 Summary

In the paper adaptive system to select scenario has been considered. The main idea is connected with utilisation of pattern recognition approach and expert's knowledge. In general, for proposed algorithm only suboptimal solution can be found. To improve performance of the proposed system in process of selecting scenarios to plan rehabilitation for spastic people

©ISAROB 2009

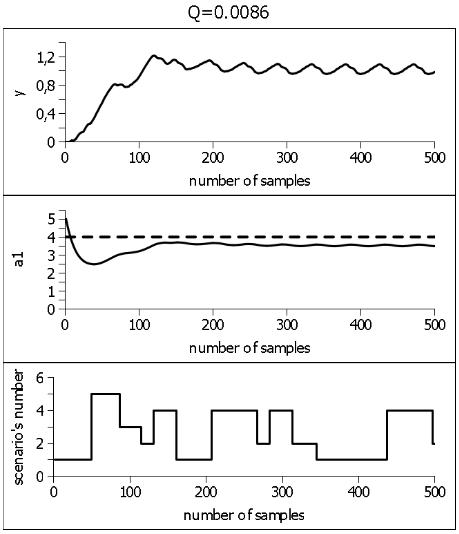

Figure 2: Effect of support decision making process for algorithm of scenario selecting based on *kNN* rule

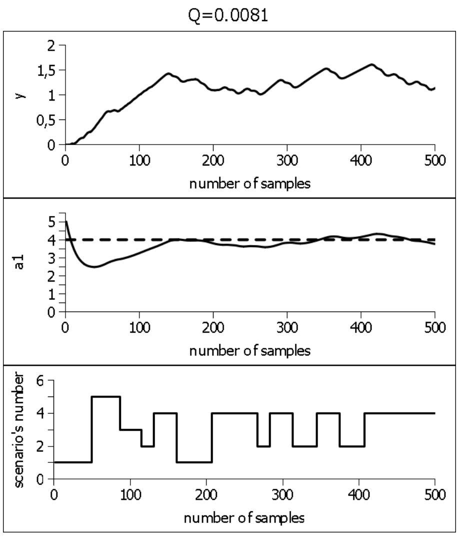

Figure 3: Effect of support decision making process for algorithm of scenario selecting based on *kNN* rule with make the most of knowledge updating rule in first version

adaptive techniques have been applied.

It worth stressing that the computational cost of application additional algorithms are not very high so the total efficiency is still low and lowest that for exact algorithms of the optimisation task (5) or (6) defined in section 2.

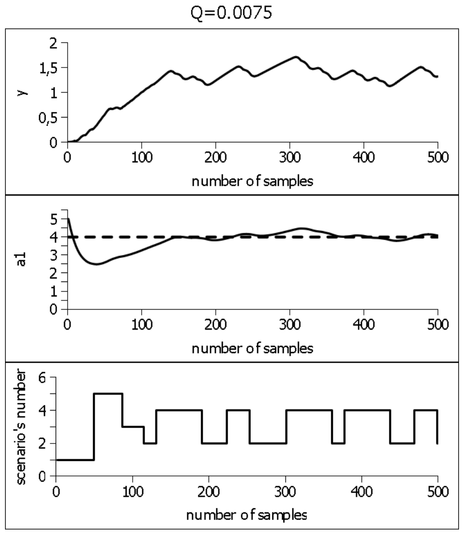

Figure 4: Effect of support decision making process for algorithm of scenario selecting based on *kNN* rule with make the most of knowledge updating rule in second version

References

[1] K. Brzostowski and J. Swiatek, "Selecting Scenario in Adaptive System with Neuro-fuzzy Decision Maker" *Proceedings of Nineteenth International Conference on Systems Engineering*, pp. 195 - 200, 2008.

[2] K. Brzostowski, "Some Problems of Neuromuscular System Identification Using Two-Stage Principle" *Proceedings of the 16th International Conference on Systems Science ICSS*, pp. 467 - 476, 2007.

[3] Z. Bubnicki, "Learning process in a class of knowledge-based systems" *Kybernets*, Vol. 29, pp. 1016 - 1028, 2000.

[4] L. Frey Law and R. Shields, "Mathematical models use varying parameter strategies to represent paralyzed muscle force properties: a sensitivity analysis" *Journal of Neuroengineering Rehabil*, 2005.

[5] J. Swiatek, *Two Stage Identification and its Technical and Biomedical Applications*, Scientific Papers of the Institute of Control and Systems Engineering of the Wroclaw Technical University, 1987. (in polish)

Graph Based Semi-supervised Learning

Changshui Zhang
Department of Automation
Tsinghua University
Beijing 100084 P.R.China

Fei Wang
Department of Automation
Tsinghua University
Beijing 100084 P.R.China

Abstract

The recent years have witnessed a surge of interests in graph based semi-supervised learning. However, two of the major problems in graph based semi-supervised learning are: (1) how to set the hyperparameter in the Gaussian similarity; (2) how to make the algorithm scalable. In this talk, we will introduce a general framework for graph based learning. First, we proposed a method called linear neighborhood propagation which can automatically construct the optimal graph, second, we introduce a novel multilevel scheme to make our algorithm scalable for large data sets. The applications of our algorithm on various real world problems are also demonstrated.

1 Introduction

Semi-Supervised Learning, which aims at learning from labeled and unlabeled data, has aroused considerable interests in data mining and machine learning fields since it is usually hard to collect enough labeled data points in practical applications. Various semi-supervised learning methods have been proposed in recent years and they have been applied to a wide range of areas including text categorization, computer vision, and bioinformatics (see [6][22] for recent reviews). Moreover, it has been shown recently that the significance of semi-supervised learning is not limited to utilitarian considerations: *humans perform semi-supervised learning too* [8][12][21]. Therefore, to understand and improve semi-supervised learning will not only help us to get a better solver for real world problems, but also help us to to better understand how natural learning come about.

One key point for understanding the semi-supervised learning approaches is the *cluster assumption* [6], which states that [19] (1) nearby points are likely to have the same label (local consistency); (2) points on the same structure (such as a cluster or a submanifold) are likely to have the same label (global consistency). It is straightforward to associate cluster assumption with the *manifold analysis* methods developed in recent years [2][9] (note that these methods are also in accordance with the ways that the humans perceive the world [10]). The manifold based methods first assume that the data points (nearly) reside on a low-dimensional manifold (which is called *manifold assumption* in [6]), and then try to discover such manifold by preserving some local structure of the dataset. It is well known that graphs can be viewed as discretizations of manifolds [1], consequently, numerous *graph based SSL* methods have been proposed in recent years, and graph based *SSL* has been becoming one of the most active research area in semi-supervised learning community [6].

However, in spite of the intensive study of graph based *SSL* methods, there are still some open issues which have not been addressed properly, such as:

1. How to select an appropriate similarity measure between pairwise data automatically;

2. How to speed up these algorithms for handling large-scale dataset (since they usually require the computation of matrix inverse).

To address the first issue, in this talk we will first present a novel method called *Linear Neighborhood Propagation* (*LNP*) [15]. The *LNP* algorithm approximates the whole graph by a series of overlapped linear neighborhood patches, and the edge weights in each patch can be solved by a standard quadratic programming procedure. After that all the edge weights will be aggregated together to form the weight matrix of the whole graph. We prove theoretically that the *Laplacian* matrix of this "pasted" graph can approximate the *Laplacian* matrix of a standard weighted undirected graph. Therefore, this approximated *Laplacian* matrix can be used as a smooth matrix as in standard graph-based semi-supervised learning algorithms.

Second, we present a fast multilevel graph learning algorithm. In our method, the data graph is first

©ISAROB 2009

coarsened level by level based on the *similarity* between pairwise data points (which has a similar spirit with grouping, such that for each group, we only select one representative node), then the learning procedure can be performed on a graph with a much small size. Finally the solution on the coarsened graph will be *refined* back level by level to get the solution of the initial problem. Moreover, as unsupervised learning can be viewed as a special case of semi-supervised learning, we will show that our multilevel method can easily be incorporated into the graph based clustering methods. Our experimental results show that this strategy can improve the speed of graph based semi-supervised learning algorithms significantly. And we also give a theoretical guarantee on the performance of our algorithm.

2 Linear Neighborhood Propagation

In this section we will present the detailed algorithm of *linear neighborhood propagation*. First let's introduce some notations. $\mathcal{X} = \{\mathbf{x}_1, \mathbf{x}_2, \cdots, \mathbf{x}_l, \mathbf{x}_{l+1}, \cdots, \mathbf{x}_n\}$ represents a set of n data objects in $\mathbb{R}^d$, and $\mathcal{L} = \{1, -1\}$ is the label set (we consider the two-class case for the moment). The first l points $\mathcal{X}_L = \{\mathbf{x}_i\}_{i=1}^{l}$ are labeled as $t_i \in \mathcal{L}$ and the remaining points $\mathcal{X}_U = \{\mathbf{x}_u\}_{u=l+1}^{n}$ are unlabeled.

we propose to use the neighborhood information of each point to construct $\mathcal{G}$. For computational convenience, we assume that all these neighborhoods are linear, *i.e.* each data point can be optimally reconstructed using a linear combination of its neighbors [9]. Hence our objective is to minimize

$$\varepsilon = \sum_i \left\| \mathbf{x}_i - \sum_{i_j : \mathbf{x}_{i_j} \in \mathcal{N}(\mathbf{x}_i)} w_{ii_j} \mathbf{x}_{i_j} \right\|^2 \qquad (1)$$

where $\mathcal{N}(\mathbf{x}_i)$ represents the neighborhood of $\mathbf{x}_i$, $\mathbf{x}_{i_j}$ is the j-th neighbor of $\mathbf{x}_i$, and w_{ii_j} is the contribution of $\mathbf{x}_{i_j}$ to $\mathbf{x}_i$. We further constrain $\sum_{i_j \in \mathcal{N}(\mathbf{x}_i)} w_{ii_j} = 1$, $w_{ij} \geqslant 0$. Obviously, the more similar $\mathbf{x}_{i_j}$ to $\mathbf{x}_i$, the larger w_{ii_j} will be (as an extreme case, when $\mathbf{x}_i = \mathbf{x}_{i_k} \in \mathcal{N}(\mathbf{x}_i)$, then $w_{ii_k} = 1$, $w_{ii_j} = 0$, $i_j \neq i_k$, $\mathbf{x}_{i_j} \in \mathcal{N}(\mathbf{x}_i)$ is the optimal solution). Thus w_{ii_j} can be used to measure how similar $\mathbf{x}_{i_j}$ to $\mathbf{x}_i$. One issue should be addressed here is that usually $w_{ii_j} \neq w_{i_j i}$. It can be easily inferred that

$$\varepsilon_i = \sum_{i_j, i_k : \mathbf{x}_{i_j}, \mathbf{x}_{i_k} \in \mathcal{N}(\mathbf{x}_i)} w_{ii_j} G^i_{i_j i_k} w_{ii_k} \qquad (2)$$

where $G^i_{i_j i_k}$ represents the (j,k)-th entry of the *local Gram matrix* $\mathbf{G}^i$ where $K = |\mathcal{N}(\mathbf{x}_i)|$ is the size of $\mathbf{x}_i$'s neighborhood. Thus the reconstruction weights of each data object can be resolved by the following n standard quadratic programming problems

$$\begin{aligned} min_{w_{ii_j}} \quad & \sum_{i_j, i_k : \mathbf{x}_{i_j}, \mathbf{x}_{i_k} \in \mathcal{N}(\mathbf{x}_i)} w_{ii_j} G^i_{i_j i_k} w_{ii_k} \\ s.t. \quad & \sum_{i_j} w_{ii_j} = 1, \ w_{ii_j} \geqslant 0. \end{aligned} \qquad (3)$$

After all the reconstruction weights are computed, we will construct a sparse matrix $\mathbf{W}$ by $W(i,j) = w_{ij}$. Intuitively, this $\mathbf{W}$ can be treated as the weight matrix of $\mathcal{G}$. And the way we construct the whole graph is to first shear the whole graph into a series of overlapped linear patches, and then pasted them together.

After the graph has been constructed, we have to make use of it to predict the labels of the unlabeled vertices. Here we label propagation scheme, which can iteratively propagate the labels of the labeled data to the remaining unlabeled data $\mathcal{X}_U$ on the constructed graph.

Let $\mathcal{F}$ denote the set of classifying functions defined on $\mathcal{X}$, $\forall\ f \in \mathcal{F}$ can assign a real value f_i to every point $\mathbf{x}_i$. The label of the unlabeled data point $\mathbf{x}_u$ is determined by the sign of $f_u = f(\mathbf{x}_u)$ (let's only consider the two-class case for the time being).

In each propagation step, we let each data object *absorbs* a fraction of label information from its neighborhood, and *retains* some label information of its initial state. Therefore the label of $\mathbf{x}_i$ at time $m+1$ becomes

$$f_i^{m+1} = \alpha \sum_{j : \mathbf{x}_j \in \mathcal{N}(\mathbf{x}_i)} w_{ij} f_j^m + (1-\alpha) t_i \qquad (4)$$

where $0 < \alpha < 1$ is the fraction of label information that $\mathbf{x}_i$ receives from its neighbors. Let $\mathbf{t} = (t_1, t_2, \cdots t_n)^T$ with $t_i \in \mathcal{L}$ $(i \leqslant l)$, $u_u = 0$ $(l+1 \leqslant u \leqslant n)$. $\mathbf{f}^m = (f_1^m, f_2^m, \cdots, f_n^m)^T$ is the prediction label vector at iteration t and $\mathbf{f}^0 = \mathbf{t}$. Then we can rewrite our iteration equation as

$$\mathbf{f}^{m+1} = \alpha \mathbf{W} \mathbf{f}^m + (1-\alpha)\mathbf{t} \qquad (5)$$

We will use Eq.(5) to update the labels of each data object until convergence, here "convergence" means the predicted labels of the data will not change in several successive iterations.

3 A Multilevel Scheme

Below we will introduce a novel *multilevel* scheme [17] for semi-supervised learning on graphs. The scheme is composed of three phases: (1) *graph coarsening*; (2) *initial classification*; (3) *solution refining.*

3.1 Graph Coarsening

In the following we will describe the first coarsening step. Starting from graph $\mathcal{G}^0 = \mathcal{G}$ (the superscript represents the level of graph scale), we first split $\mathcal{V}^0 = \mathcal{V}$ into two sets, $\mathcal{C}^0$ and $\mathcal{F}^0$, subject to $\mathcal{C}^0 \cup \mathcal{F}^0 = \mathcal{V}^0$, $\mathcal{C}^0 \cap \mathcal{F}^0 = \Phi$. The set $\mathcal{C}^0$ will be used as the node set of the coarser graph of the next level, *i.e.* $\mathcal{V}^1 = \mathcal{C}^0$. And the nodes in $\mathcal{C}^0$ are called *$\mathcal{C}$-nodes*, which is defined as:

Definition 1. ($\mathcal{C}$-nodes and $\mathcal{F}$-nodes) Given a graph $\mathcal{G}^l = (\mathcal{V}^l, \mathcal{E}^l)$, we split $\mathcal{V}^l$ into two sets, $\mathcal{C}^l$ and $\mathcal{F}^l$ satisfying $\mathcal{C}^l \cup \mathcal{F}^l = \mathcal{V}^l$, $\mathcal{C}^l \cap \mathcal{F}^l = \Phi$, $\mathcal{C}^l = \mathcal{V}^{l+1}$. And each node in $\mathcal{C}^l$ must satisfy one of the following conditions:
(1) it is labeled;
(2) it *strongly influences* at least one node in $\mathcal{F}^l$ on level l.
We will call the nodes in $\mathcal{C}^l$ *$\mathcal{C}$-nodes*, and the nodes in $\mathcal{F}^l$ *$\mathcal{F}$-nodes*.

Here *strongly influence* means

Definition 2. (Strongly Influence) A node $\mathbf{x}_i$ *strongly influences* $\mathbf{x}_j$ on level l means that

$$w_{ij}^l \geqslant \delta \sum\nolimits_k w_{kj}^l \tag{6}$$

where $0 < \delta < 1$ is a control parameter, and w_{ij}^l is the weight of the edge linking $\mathbf{x}_i$ and $\mathbf{x}_j$ on $\mathcal{G}^l$.

In fact, $z_{ij}^l = w_{ij}^l / \sum_k w_{kj}^l$ measures how much $\mathbf{x}_j$ depends on $\mathbf{x}_i$. Since $\mathbf{x}_j$ only connects to its neighborhood, a larger z_{ij} implies a larger dependency of $\mathbf{x}_j$ to $\mathbf{x}_i$. Intuitively, if $\mathbf{x}_j$ depends too much on $\mathbf{x}_i$, then we only need to retain $\mathbf{x}_i$. The normalization is to make z_{ij} a relative measure which is independent of the data distributions.

Let $\mathbf{f}^0 = \mathbf{f}$ be an *classification vector* we want to solve, and $\mathbf{f}^1$ be its *corresponding classification vector* on $\mathcal{G}^1$ (hence the dimensionality of $\mathbf{f}^1$ should be equivalent to n^1, the cardinality of $\mathcal{V}^1$). The same as in other multilevel methods [13], we assume that $\mathbf{f}^0$ can be approximately interpolated from $\mathbf{f}^1$, that is[1]

$$\mathbf{f}^0 \approx \mathbf{P}^{[0,1]}\mathbf{f}^1, \tag{7}$$

where $\mathbf{P}^{[0,1]}$ is the interpolation matrix of size $n^0 \times n^1$ ($n^0 = n$), subject to $\sum_j \mathbf{P}_{ij}^{[0,1]} = 1$. Moreover, we have the following theorem:

Theorem 1. The edge weights on graph $\mathcal{G}^{l+1}$ can be computed from the edge weights on $\mathcal{G}^l$ by

$$w_{uv}^{l+1} = \frac{1}{2}\sum\nolimits_{i,j} w_{ij}^l (P_{jv}^{[l,l+1]} - P_{iv}^{[l,l+1]})(P_{iu}^{[l,l+1]} - P_{ju}^{[l,l+1]}). \tag{8}$$

An issue should be addressed here is that for computational efficiency, the above coarsening weight equation can be somewhat simplified to the following *Iterated Weighted Aggregation* strategy [13], which compute w_{uv}^{l+1} by

$$w_{uv}^{l+1} = \frac{1}{2}\sum\nolimits_{i,j} P_{iu}^{[l,l+1]} w_{ij}^l P_{jv}^{[l,l+1]} \tag{9}$$

It can be shown that Eq.(9) can provide a good approximation to Eq.(8) in many cases [11].

3.1.1 Initial Classification

Assuming the data graph $\mathcal{G}$ has been coarsened recursively to some level s, then the semi-supervised classification problem defined on $\mathcal{G}^s$ is to minimize

$$\begin{aligned} \mathcal{J}(\mathbf{f}^s) \quad = \quad & \mathbf{f}^{sT}\mathbf{P}^{[s,s-1]}\cdots\mathbf{P}^{[1,0]}\mathbf{S}\mathbf{P}^{[0,1]}\cdots\mathbf{P}^{[s-1,s]}\mathbf{f}^s \\ & +\gamma\|\mathbf{P}^{[0,1]}\cdots\mathbf{P}^{[s-1,s]}\mathbf{f}^s - \mathbf{y}\|^2, \end{aligned}$$

where $\mathbf{P}^{[i,i-1]} = \left(\mathbf{P}^{[i-1,i]}\right)^T$, and $\mathbf{S}$ is the smoothness matrix. Therefore, let $\frac{\partial \mathcal{J}(\mathbf{f}^s)}{\partial \mathbf{f}^s} = 0$, then

$$\begin{aligned} \frac{\partial \mathcal{J}(\mathbf{f}^s)}{\partial \mathbf{f}^s} \quad = & \quad (\mathbf{L}^s)\,\mathbf{f}^s - \gamma\mathbf{P}^{[s,s-1]}\cdots\mathbf{P}^{[1,0]}\mathbf{y} = 0 \\ \Longrightarrow & \quad \mathbf{f}^s = \gamma\,(\mathbf{L}^s)^{-1}\,\mathbf{P}^{[s,s-1]}\cdots\mathbf{P}^{[1,0]}\mathbf{y}. \end{aligned}$$

Here $\mathbf{I}$ is the $n \times n$ identity matrix. Moreover, we have the following theorem

Theorem 2. The matrix $\mathbf{L}^s = \mathbf{P}^{[s,s-1]}\cdots\mathbf{P}^{[1,0]}(\mathbf{S} + \gamma\mathbf{I})\mathbf{P}^{[0,1]}\cdots\mathbf{P}^{[s-1,s]}$ is invertible.

Based on the above theorem, we can compute the *initial classification vector* using Eq.(10), in which we only need to compute the inverse of an $n^s \times n^s$ matrix, and usually n^s is much smaller than n.

3.1.2 Solution Refining

Having achieved the *initial classification vector* from Eq.(10), we have to refine it level by level to get a classification vector on the initial graph $\mathcal{G}^0 = \mathcal{G}$. As stated in section 3.1, we assume that the classification vector on graph $\mathcal{G}^l$ can be linearly interpolated from $\mathcal{G}^{l+1}$, *i.e.* $\mathbf{f}^l = \mathbf{P}^{[l,l+1]}\mathbf{f}^{l+1}$. Here $\mathbf{P}^{[l,l+1]}$ is an $n^l \times n^{l+1}$ interpolation matrix subject to $\sum_j \mathbf{P}_{ij}^{[l,l+1]} = 1$.

[1] Actually, as we have analyzed after definition 3, the nodes in $\mathcal{V}^0/\mathcal{V}^1$ are largely dependent on the nodes in $\mathcal{V}^1$. Therefore what we define in Eq.(7) is just to model such a dependence rule. The interpolation rule is simple and efficient, and it has also been widely used in the multilevel or multigrid methods for solving *Partial Differential Equations*[5][13], that's the reason why we apply it here.

©ISAROB 2009

Based on the simple geometric intuition that the label of a point should be similar to the label of its neighbors (which is also consistent with the cluster assumption we introduced in section **??**), we propose to compute $P_{iI(j)}^{[l,l+1]}$ by

$$P_{iI(j)}^{[l,l+1]} = \begin{cases} w_{ij}^l / \sum_{k\in\mathcal{C}^l} w_{ik}^l & i \notin \mathcal{C}^l \\ 1 & i = j \\ 0 & \mathbf{x}_i \in \mathcal{C}^l,\ i \neq j \end{cases} \quad (10)$$

In the above equation, subscripts i, j, k are used to denote the index of the nodes in $\mathcal{V}^l$. We assume that node j has been selected as a $\mathcal{C}$-*node*, and $I(j)$ is the index of j in $\mathcal{V}^{l+1}$. It can be easily inferred that $\mathbf{P}^{[l,l+1]}$ has full rank.

4 Summary

We present a general framework for graph based semi-supervised learning. The framework first use linear neighborhood propagation to automatically construct the optimal graph, then we apply a multilevel scheme to make the whole algorithm more efficient.

References

[1] Belkin, M., Matveeva, I., Niyogi, P. Regularization and Semi-supervised Learning on Large Graphs. In *Proceedings of the 17th Conference on Learning Theory*, 2004.

[2] Belkin, M., Niyogi, P. Laplacian Eigenmaps for Dimensionality Reduction and Data Representation. *Neural Computation*, vol. 15, no. 6, 1373-1396, 2003.

[3] Belkin, M. and Niyogi, P. Semi-Supervised Learning on Riemannian Manifolds. *Machine Learning*, 56: 209-239, 2004.

[4] Blum, A., and Chawla, S. Learning from labeled and unlabeled data using graph mincuts. *Proceedings of the 18th International Conference on Machine Learning*, 2001.

[5] Brandt, A., and Ron, D. Multigrid Solvers and Multilevel Optimization Strategies. in: J. Cong, J.R. Shinnerl (*Eds.*), *Multilevel Optimization and VLSICAD*, Kluwer, 2002.

[6] Chapelle, O., *et al.* (eds.): *Semi-Supervised Learning.* MIT Press: Cambridge, MA. 2006.

[7] Gloub, G. H., Vanloan, C. F. *Matrix Computations.* Johns Hopking UP,Baltimore, 1983.

[8] Graf Estes, K., Evans, J. L., Alibali, M. W., and Saffran, J. R. Can Infants Map Meaning to Newly Segmented Words? Statistical Segmentation and Word Learning. *Psychological Science*. 2006.

[9] Roweis, S. T. and Saul, L. K.: Noninear Dimensionality Reduction by Locally Linear Embedding. *Science*: vol. 290: 2323-2326, 2000.

[10] Seung, H. S. and Lee, D. D. The Manifold Ways of Perception. *Science* vol. 290: 2268-2269, 2000.

[11] Sharon, E., Brandt, A., Basri, R. Fast Multiscale Image Segmentation. In *Proceedings IEEE Conference on Computer Vision and Pattern Recognition*, I:70-77, South Carolina, 2000.

[12] Stromsten, S. B. Classification Learning from Both Classified and Unclassified Examples. *Ph.D. Dissertation*, Stanford. 2002.

[13] Trottenberg, U., Oosterlee, C.W., and Schler, A. *Multigrid.* with guest contributions by Brandt, A., Oswald, P. and Sten, K. San Diego, Calif. London, Academic, 2001.

[14] Vapnik, V. N. *The Nature of Statistical Learning Theory.* Berlin: Springer-Verlag, 1995.

[15] Wang, F., Zhang, C. Label Propagation Through Linear Neighborhoods. In *Proceedings of the 23rd International Conference on Machine Learning.* 2006.

[16] Wang, F., Zhang, C. Label Propagation Through Linear Neighborhoods. In *IEEE Transactions on Knowledge and Data Engineering.* 2006.

[17] Wang, F., Zhang, C. Fast Multilevel Transduction on Graphs. In *The 7th SIAM International Conference on Data Mining.* 2007.

[18] Wertheimer, M. Gestalt Theory. In W. D. Ellis (ed.), *A Source of Gestalt Psychology*, 1-11. New York: The Humanities Press. 1924/1950.

[19] Zhou, D., Bousquet, O., Lal, T. N. Weston, J., & Schölkopf, B. Learning with Local and Global Consistency. *Advances in Neural Information Processing Systems 16.* Thrun, S., Saul, L., and Schölkopf, B. (eds.), pp. 321-328, 2004.

[20] Zhu, X. *Semi-Supervised Learning with Graphs.* Ph.D. Thesis. Language Technologies Institute, School of Computer Science, Carnegie Mellon University. May, 2005.

[21] Zhu, X., Rogers, T., Qian, R., and Kalish, C. Humans Perform Semi-Supervised Classification Too. In *Proc. of the Twenty-Second AAAI Conference on Artificial Intelligence* (*AAAI*), 2007.

[22] Zhu, X. Semi-supervised learning literature survey. Technical Report 1530, Univ. Wisconsin-Madison. 2005.

On the Observability and Estimability Analysis of the Global Positioning System (GPS) and Inertial Navigation System (INS)

Man Hyung Lee *, Sinpyo Hong **, Jeong Hyun Moon***, Ho-Hwan Chun****,

* School of Mechanical Engineering, Pusan National University, Busan 609-735, Korea
** General Marine Business Inc, Ulsan 680-819, Korea
*** Graduate School of Mechanical Engineering, Pusan National University,
Busan 609-735, Korea (Tel : 82-51-510-1456; Fax : 82-51-512-9835)
**** Advanced Ship Engineering Research Center, Pusan National University, Busan 609-735, Korea

Abstract In this paper a brief review on the observability and estimability analysis of GPS/INS is presented. There have been various analysis results on the observability of INS errors. However different INS error dynamics models and reference frames of INS mechanization have been used in the observability analysis. Moreover, the analysis framework was not unique. In this paper, known observability analysis results are summarized first. Then relatively general analysis tools to handle system model perturbation on the observability and estimability is given.

Keywords Observability, estimability, measure, GPS, INS

1. Introduction

The observability of measurement systems has been studied to understand the behavior of error estimators in the aided inertial navigation systems (INS) [1, 2, 3, 4, 5]. For the observability study of INS, error covariance matrices or observability matrices have usually been investigated. Error covariance has been considered to be related to the degree of observability in the Kalman filter applications [6]. The error covariance test is also an efficient means of statistical study on the behavior of estimators [7]. In the analytic studies, the rank of the observability matrix was mainly investigated [3, 8, 9, 10, 11, 12]. Analytical approaches to the observability study provide insights on the estimator behavior in a more systematic way.

In the error covariance test, error covariance matrices are considered to give useful information on the degree of observability. However, the behavior of error covariance can be sensitive to the initial error covariance and the relation between the observability and the error covariance can be misleading [13]. On the other hand, in the rank test on the observability matrix, the rank does not provide the degree of observability. It only decides if a system is observable or not. In addition, the rank of a matrix can be sensitive to perturbation. Moreover, it is usually quite difficult to decide the rank of an observability matrix analytically except for very simple system models [3, 9, 10, 11, 12]. To study the degree of observability analytically, several measures of observability have been proposed. Frequency domain observability measures for time invariant systems were suggested in [14, 15]. The condition number of the observability matrix for single-output time-varying systems was considered as a measure of observability in [16]. However, these measures are not suitable for time-varying multi-input/multi-output systems. In this paper, observability measures are considered for a wider class of systems.

Measures of observability for a wider class of systems were introduced to study the degree of observability in [17]. The measure indicates how far, in the sense of 2-norm, the information matrix is from rank-deficient matrices. The measures are less sensitive to perturbation and applicable to time-varying multi-input/multi-output systems.

The concept of estimability was introduced to characterize the behavior of state estimation in [18]. Estimability measures were also introduced to indicate the ratio of error covariance decrease to the initial error covariance in [17]. It was shown that the sensitivity of the measures to perturbation depends on the size of initial error covariance.

2. Observability Analysis of GPS/INS

An INS consists of 3-axis accelerometers, 3-axis gyros, and a computer. The computer calculates position, velocity, and attitude by integrating the inertial sensor measurements. Due to the initial errors and sensor measurement uncertainty, the results of computer calculation contain errors that grow as time elapses.

If a position or velocity measurement is taken, some of the errors can be eliminated or estimated. The error that can be estimated depends upon the motion of a vehicle in which the INS is installed. The effect of the measurement on the navigation state error

©ISAROB 2009

estimation has usually been studied with the behavior of error covariance matrix in the Kalman filter [6].

The first control theoretic study on the observability analysis on the INS errors was attempted by an piece-wise constant systems modeling in [3]. For the vehicle that moves with a constant speed on the horizontal plane with velocity measurement, the paper showed that the three components of attitude are unobservable. The paper also showed that the components of errors in attitude and gyro bias that are orthogonal to the direction of the acceleration change are made observable.

A more detailed observability analysis on the aided INS is given in [11]. In the paper, estimation of INS errors and the lever arm between the inertial sensors and the GPS antenna is studied with a simplified INS error dynamics model. For a vehicle with the horizontal constant speed motion, it is shown that the attitude as well as the lever and the vertical component of gyro bias are unobservable. It is also shown that acceleration changes enhance the estimates of attitude and gyro bias. The components of errors in attitude and gyro bias that are orthogonal to the direction of the acceleration change are made observable. The changes in angular rate also improve the estimate of the lever arm.

The vertical component of gyro bias is known to be nearly unobservable or weakly observable from experiences. It is interesting to note that the observability analysis with the simplified INS error dynamics model in [11] confirms the experience. However, in the observability study with relatively exact INS error dynamics model [3], the vertical component of gyro bias is observable.

3. Observability and Estimability Measures

In this section, observability and estimability measures and their properties in [17, 19] are introduced. With the measures, sensitivity of observability and estimability to perturbation in the system model can be analyzed. The influence of the initial error covariance on the error covariance is studied in detail.

Consider the following system:

$$x_i = \Phi_{i,0} x_0 \tag{1}$$

$$y_i = H_i x_i + v_i \tag{2}$$

where $x_i \in \mathbb{R}^n$ is the state vector at the time step *i*, $x_0 \in \mathbb{R}^n$ is the initial state vector, $\Phi_{i,0} \in \mathbb{R}^{n\times n}$ is the state transition matrix from the time step 0 to the time step *i*, $y_i \in \mathbb{R}^m$ is the measurement vector at the time step *i*, $v_i \in \mathbb{R}^m$ is the measurement noise vector at the time step *i*, and $H_i \in \mathbb{R}^{m\times n}$ is the measurement matrix at the time step *i*. Assume that $x_0 \sim N(\bar{x}_0, P_0)$ with $P_0 > 0$, $v_i \sim N(0, R_i)$ with $R_i > 0$ for $i = 1, 2, \cdots$, $E\left[v_i v_j^T\right] = 0$ for $i \neq j$, and $E\left[v_i x_0^T\right] = 0$ for all *i*. The optimal estimation problem considered in this section is as follows: Given a set of measurements $\{y_0, y_1, \cdots, y_k\}$ find the optimal estimate of x_0, $\hat{x}_{0,k}$, that minimizes the cost function

$$J = \frac{1}{2}\left\{\left(x_0 - \bar{x}_0\right)^T P_0^{-1}\left(x_0 - \bar{x}_0\right) + \sum_{i=0}^{k}\left(y_i - H_i x_i\right)^T R_i^{-1}\left(y_i - H_i x_i\right)\right\}$$

The above weighted-least-squares estimate is identical to the conditional expected-value estimate that is also the minimum variance or maximum-likelihood estimate [20,21]. The optimal estimate is given as

$$\hat{x}_{0,k} = \left(P_0^{-1} + L_{0,k}\right)^{-1}\left(K_{0,k} + P_0^{-1}\bar{x}_0\right) \tag{3}$$

with

$$L_{0,k} = \sum_{i=0}^{k} \Phi_{i,0}^T H_i^T R_i^{-1} H_i \Phi_{i,0},\ K_{0,k} = \sum_{i=0}^{k} \Phi_{i,0}^T H_i^T R_i^{-1} y_i \tag{4}$$

where $L_{0,k}$ is the observability gramian or information matrix. Note that if the measurements do not have noise, then the system is deterministic and the corresponding observability gramian is

$$\mathcal{L}_{0,k} = \sum_{i=0}^{k} \Phi_{i,0}^T H_i^T H_i \Phi_{i,0} \tag{5}$$

Thus, observability gramians for stochastic and deterministic systems differ only in scaling due to R_i. Therefore, a stochastic system is observable if and only if the corresponding deterministic system is observable. The above stochastic system is observable on [0,*k*] if and only if $L_{0,k} > 0$ [22]. If the system is unobservable, then a vector x_u, called an unobservable state, exists such that $L_{0,k} x_u = 0$. The null space of $L_{0,k}$ is called the unobservable subspace.

Let $\tilde{x}_{0,k} = \hat{x}_{0,k} - x_0$. Then, the error covariance matrix is defined as

$$P_{0,k} \triangleq E\left[\tilde{x}_{0,k}\tilde{x}_{0,k}^T\right] \tag{6}$$

Then, we have

$$\left(P_{0,k}\right)^{-1} = P_0^{-1} + L_{0,k} \tag{7}$$

Since

$$\left(P_0 - P_{0,k}\right)\left(P_0\right)^{-1} = P_{0,k} L_{0,k} \tag{8}$$

the null spaces for $L_{0,k}$ and $\left(P_0 - P_{0,k}\right)$ can be different. Thus, the error covariance of an unobservable state can experience a decrease

For the observability study, consider the following measure for $M, \Delta \in \mathbb{R}^{r\times s}, r \geq s$:

$$\underline{\mu}(M) \triangleq \min_{rank(M-\Delta)<s} \|\Delta\|_2 \tag{9}$$

It indicates the magnitude of the smallest perturbation in *M* that makes *M* rank-deficient. For a matrix $M \in \mathbb{R}^{r\times s}$ with $r \geq s$, $\sigma_1(M), \sigma_1(M), \cdots, \sigma_s(M)$ denote the singular values of *M* such that $\sigma_1(M) \geq \sigma_2(M) \geq \cdots \geq \sigma_s(M) \geq 0$. Let $\bar{\sigma}(\bullet)$ and $\underline{\sigma}(\bullet)$ be the largest and the smallest singular values of a matrix, respectively. Then the following theorem essentially comes from Theorem 2.5.3 in [23]:

Theorem 1: Let $M \in \mathbb{R}^{r\times s}, r \geq s$. Then $\underline{\mu}(M) = \underline{\sigma}(M)$.

It is well-known that singular values of a matrix are well-conditioned to perturbation such that

$$\left|\sigma_i(M+E) - \sigma_i(M)\right| \leq \bar{\sigma}(E) \tag{10}$$

for $i=1,2,\cdots,s$, and $E\in\mathbb{R}^{r\times s}$ [23,24] So, if we define an observability measure for a system with $\underline{\mu}\left(L_{0,k}\right)$, then $\underline{\sigma}\left(L_{0,k}\right)$ indicates how far the system is from the rank-deficient matrices. The measure is less sensitive to perturbation due to errors in the system model or the numerical computation.

In many estimation applications, the measure of observability for a subspace can be quite convenient to predict or understand the behavior of the subspace of the state-space. For this purpose, the following norm can be useful to define the measure:

$$\mu\left(M,z\right)\triangleq\min_{(M-\Delta)z=0}\left\|\Delta\right\|_2 \tag{11}$$

where $M,\Delta\in\mathbb{R}^{r\times s}, r\geq s$ and $z\in\mathbb{R}^s$. With the definition, we have the following theorems:

Theorem 2: Let $M\in\mathbb{R}^{r\times s}, r\geq s, z\in\mathbb{R}^s$ with $\left\|z\right\|_2=1$. Then

$$\mu\left(M,z\right)=\left\|Mz\right\|_2 \tag{12}$$

Proof: See [17].

Theorem 3: Let $M,E\in\mathbb{R}^{r\times s}, r\geq s$ and $z\in\mathbb{R}^s$ with $\left\|z\right\|_2=1$. Then,

$$\left|\mu\left(M+E,z\right)-\mu\left(M,z\right)\right|\leq\bar{\sigma}\left(E\right) \tag{13}$$

Proof: See [17]

Theorem 3 shows that $\mu\left(M,z\right)$ is also well-conditioned to the perturbation in *M*.

The other observability measure can be defined with $\mu\left(L_{0,k},z\right)$. This measure indicates the magnitude of the smallest perturbation in the information matrix that makes the subspace spanned by the vector *z* unobservable. Let the singular value decomposition (SVD) of $L_{0,k}$ be $U_k\Sigma_kU_k^T$ where $U_k=\left[u_1u_2\cdots u_n\right]$ is an orthogonal matrix composed of singular vectors and $\Sigma_k=diag\left(\sigma_1,\sigma_2,\cdots,\sigma_n\right)$ is a diagonal matrix whose diagonal elements are the singular values of $L_{0,k}$ such that $\sigma_1\geq\sigma_2\geq\cdots\geq\sigma_n\geq 0$. Since $\mu\left(L_{0,k},z\right)=\left\|\Sigma_kU_k^Tz\right\|_2$,

$$\mu\left(L_{0,k},u_i\right)=\sigma_i\left(L_{0,k}\right) \tag{14}$$

Therefore, a singular value of the information matrix can be considered as the measure of observability for the subspace spanned by the corresponding singular vector. A large singular value implies that a large change in the information matrix is necessary to make the subspace spanned by the corresponding singular vector unobservable. It is apparent that the system observability measure is the smallest subspace observability measure over the whole state-space. Thus, we have the following relation:

$$\underline{\mu}\left(L_{0,k}\right)=\min_{z\in\mathbb{R}^n}\mu\left(L_{0,k},z\right) \tag{15}$$

In estimation applications, the behavior of the error covariance is one of the main concerns of estimator designers. To characterize estimator performance, the term 'estimability' will be used. A system is called estimable if $P_0-P_{0,k}>0$. The null space of $P_0-P_{0,k}$ is referred to as an unestimable subspace. Then, a measure of estimability for a subspace may be defined with

$$\nu\left(L_{0,k},P_0,u\right)=\frac{u^T\left(P_0-P_{0,k}\right)u}{u^TP_0u} \tag{16}$$

for $u\in\mathbb{R}^n$. It indicates the ratio of the decrease in the error covariance of a state in the direction of *u* to the initial error covariance of the same state. The concept of estimability that is used in this paper is similar to that in [18]. However, estimability in [18] is concerned with the error covariance rather than the initial error covariance. The connection between the observability and estimability can be found in (8). From this equation it can be shown that a system is observable if and only if the system is estimable. If the span of a vector *u* is unobservable, then $\text{span}\left\{P_0^{-1}u\right\}$ is unestimable. Then, the following theorem shows the the estimability measure is less sensitive to perturbation in the information matrix if the magnitude of the initial error covariance matrix is not excessively large:

Theorem 4: Let $E\in\mathbb{R}^{n\times n}$, $r\triangleq 1+\underline{\sigma}\left(L_{0,k}\right)\underline{\sigma}\left(P_0\right)>\bar{\sigma}(E)$, and $u\in\mathbb{R}^n$. Then,

$$\left|\nu\left(L_{0,k}+E,P_0,u\right)-\nu\left(L_{0,k},P_0,u\right)\right|\leq\frac{\bar{\sigma}\left(E\right)\bar{\sigma}\left(P_0\right)}{r\left(r-\bar{\sigma}\left(E\right)\right)} \tag{17}$$

Proof: See [19].

Let the SVD of $\sqrt{P_0}L_{0,k}\sqrt{P_0}$ be $U_{pl}\Sigma_{pl}U_{pl}^T$ where Σ_{pl} is $\text{diag}\left(\sigma_{pl,1},\sigma_{pl,2},\cdots,\sigma_{pl,n}\right)$ and $U_{pl}=\left[u_{pl,1}u_{pl,2}\cdots u_{pl,n}\right]$. Let $d_{pl,i}=\sigma_{pl,i}\big/\left(1+\sigma_{pl,i}\right)$, i=1,2,$\cdots$,$n$. Then,

$$\nu\left(L_{0,k},P_0,u\right)=\frac{u^T\sqrt{P_0}U_{pl}D_{pl}U_{pl}^T\sqrt{P_0}u}{u^TP_0u} \tag{18}$$

where $D_{pl}=\text{diag}\left(d_{pl,1},d_{pl,2},\cdots,d_{pl,n}\right)$. Thus, SVD of $\sqrt{P_0}L_{0,k}\sqrt{P_0}$ gives useful information on the estimability measure.

4. Conclusions

The exact model of INS error dynamics is nonlinear and highly complicated. Observability study of GPS/INS usually involves simplification of the INS error model. The observability analysis by rank test is sensitive to the system model perturbation. Observability anaysis of GPS/INS by covariance analysis can be statistically convenient. However, the error covariance behavior is highly influenced by the choice of initial error covariance and can give misleading results on the observability.

With the proposed observability and estimability measures, a straight forward analysis on the characteristics of the observability and estimability of GPS/INS error is possible. The observability analysis results are insensitive to system model perturbation. The estimability measures show that the sensitivity of error covariance to system model perturbation can be influenced by the choice of the initial error covariance.

Acknowledgement

This work was supported by the Korea Science and Engineering Foundation through the Advances Ship Engineering Research Center and the brain Korea 21 Project at Pusan National University

Reference

[1] A. A. Sutherland Jr., "The Kalman filter in transfer alignment of inertial guidance systems," *Journal of Spacecraft and Rockets*, Vol. 5, 1968, pp. 1175-1180.

[2] I. Y. Bar-Itzhack and B. Porat, "Azimuth observability enhancement during inertial navigation system in-flight alignment," *Journal of Guidance and Control*, Vol. 3, 1981, pp. 337-344.

[3] D. Goshen-Meskin and I. Y. Bar-Itzhack, "Observability analysis of piece-wise constant systems-Part II: Application to inertial navigation In-Flight Alignment," *IEEE Transactions on Aerospace and Electronic Systems*, Vol. 28, No. 4, 1992, pp. 1068-1075.

[4] S. Hong, M. H. Lee, S. H. Kwon, and H. H. Chun, "A Car Tests for the Estimation of GPS/INS Alignment Errors," *IEEE Transactions on Intelligent Transportation Systems*, Vol. 5, No. 3, 2004, pp. 208-218.

[5] S. Hong, M. H. Lee, H. H. Chun, S. H. Kwon, and Jason L. Speyer, "Experimental Study on the Estimation of Lever Arm in GPS/INS," *IEEE Transactions on Vehicular Technology*, Vol. 55, No. 2, 2006, pp.431-448.

[6] F. M. Ham and R. G. Brown, "Observability, Eigenvalues, and Kalman Filtering," *IEEE Transactions on Aerospace and Electronic Systems*, Vol. 19, No. 2, 1983, pp. 269-273.

[7] P. S. Maybeck, *Stochastic Models, Estimation, and Control, Vol. I* . New York, Academic Press, 1979.

[8] I. Y. Bar-Itzhack and N. Berman, "Control T heoretic Approach to Inertial Navigation Syste ms," *Journal of Guidance and Control*, Vol. 11, No. 3, 1988, pp. 237-245.

[9] Y. F. Jiang and Y. P. Lin, "Error Estimation of INS Ground Alignment Through Observability Analysis," *IEEE Transactions on Aerospace and Electronic Systems*, Vol. 28, No. 1, 1992, pp. 92-97.

[10] S. Hong, M. H. Lee, J. A. Rios, and J. L. Speyer, "Observability Analysis of INS with a GPS Multi-Antenna System," *International Journal of the Korean Society of Mechanical Engineers (KSME)*, Vol. 16, No. 11, 2002, pp. 1367-1378.

[11] S. Hong, M. H. Lee, H. H. Chun, S. H. Kwon, and J. L. Speyer, "Observability of Error States in GPS/INS Integration," *IEEE Transactions on Vehicular Technology*, Vol. 54, No. 2, 2005, pp.731-743.

[12] M. K. Lee, S. Hong, M. H. Lee, S. H. Kwon, and H. H. Chun, "Observability Analysis of Alignment Errors in GPS/INS," *Journal of Mechanical Science and Technology (KSME international Journal)*, Vol. 19, No. 6, 2005, pp. 1253-1267.

[13] S. Hong and H. H. Chun, "Singular Value Decomposition Approach to Observability Analysis of GPS/INS," *Proc. of IAIN/GNSS 2006*, Jeju, Korea, October 18-20, 2006, pp. 133-138.

[14] D. K. Lindner, J. Babendreier, and A. M. Hamdan, "Measures of Controllability and Observability and Residues," *IEEE Transactions on Automatic Control*, Vol. 34, No. 6, June 1989, pp.648-650.

[15] M. Tarokh, "Measures for Controllability, Observability, and Fixed Modes," *IEEE Transactions on Automatic Control*, Vol. 37, No. 8, August 1992, pp.1268-1273.

[16] Z. Chen, "Local Observability and Its Application to Multiple Measurement Estimation," *IEEE transactions on Industrial Electronics*, Vol. 38, No. 6, December 1991, pp. 491-496.

[17] S. Hong, H. H. Chun, S. H. Kwon, and M. H. Lee, "Observability Measures and Their Application to GPS/INS," *IEEE Transactions on Vehicular Technology*, Vol. 57, No. 1, 2008, pp.97-106.

[18] Y. Baram and T. Kailath, "Estimability and Regulability of Linear Systems," *IEEE Transactions on Automatic Control*, Vol. 33, No. 12, December 1988, pp.1116-1121.

[19] J. H. Moon, S. Hong, H. H. Chun, and M. H. Lee, "Estimability Measures and Their Application to GPS/INS," *Journal of Mechanical Science and Technology*, Vol. 22, 2008, pp.905-913.

[20] A. H. Jazwinski, *Stochastic Process and Filtering Theory*, Academic Press, New York, 1970.

[21] A. E. Bryson, Jr., and Y.-C. Ho, *Applied Optimal Control*, Hemisphere Publishing Co., Washington, 1975.

[22] F. M. Callier and C. A. Desoer, *Linear System Theory*, Springer-Verlag, New York, 1991.

[23] G. H. Golub and C. F. Van Loan, *Matrix Computations*, 3rd Ed., The Johns Hopkins University Press, Baltimore and London, 1996.

[24] G. W. Stewart, *Introduction to Matrix Computations*, Academic Press Inc, Orlando, 1973.

©ISAROB 2009

The Fourteenth International Symposium on Artificial Life and Robotics 2009 (AROB 14th '09),
B-Con Plaza, Beppu, Oita, Japan, February 5 - 7, 2009

A Design of Brain Sensory monitoring Thinking Activity inside the Knowledge System

JeongYon Shim
Div. of GS, Computer Science, Kangnam University, Kugal Dong 111, KiHeung Gu, YongIn Si, KyeongKi Do, Korea
(Tel : +82-31-280-3736; E-mail: mariashim@kangnam.ac.kr)

Abstract: For several recent years many studies adopting the brain functions have been studied for making efficient system in the dynamic complex environment. As one of brain based research, in this paper the new concept of Brain sensory was defined as 6th sensory organ and brain sensory monitoring thinking activity is designed which has various functions including selective sensory input signals, recalling the related knowledge and retrieving thinking chains. Especially DTAM (Dynamic Thinking Association Map) was designed for conditioned learning process and Emotional Switching concept for activating the matched knowledge from the large well structured memory with the control signal was proposed. The functions of DTAM and Emotional Switching make dynamic selective thinking chain retrieval possible. This system was applied to the virtual memory and tested with sample data.

Keywords: Brain Sensory, Thinking Activity,Emotional Switching

1. INTRODUCTION

For recent several years the studies in the brain inspired system have been activated and are rising as an area of blue ocean part. The main reason lies in the fact that brain is the final product which has been survived and evolved in the dynamic complex environments for several million years. The brain has developed the optimal structure of being adapted for the dynamic complex circumstances. The brain not only controls whole living system but also takes part in sensing, learning, memorizing,recalling and thinking process. And it is also known that the brain creates mind and emotion. According to the studies of emotion, emotion is closely related to the survival. Positive emotion makes the whole body system opened and be ready for production. On the contrary, negative emotion makes the body system closed and ready for defense. It means that the emotion plays a very important role of decision making. There are occurring many thinking activities as well as many kinds of emotion inside the brain when the brain is activated. During this phase the emotional factor performs an important functions. From this point of view, brain theory gives many clues for solving the complex problems surrounding human beings. Especially in the huge dynamic internet circumstance its functions can be usefully adopted and inspired to the process of implementing the artificial intelligent system.

Focusing on the activities inside the brain, in this paper as one of studies of brain inspired system the concept of 'Brain Sensory' is defined as 6th sensory organ which is monitoring Thinking Activity inside brain. Especially Dynamic Thinking Activity Map(DTAM) was designed as a space for containing the information about temporal associative relation related to the conditioned learning and Dynamic Thinking chaining threads extracted from the memory. For occurrence of Thinking Activity memory recalling process is necessary. In this system the concept of Emotional Switching is defined and used for activating the related knowledge in memory during the memory recalling process by Type matching Strategy. That is, Emotional switching takes part in the function of selecting the extracted thinking chaining thread. The knowledge based data in the virtual memory was applied to test this system and the processing step of monitoring the brain sensor was investigated.

2. THE OVERVIEW OF BRAIN SENSORY

It is known that Human being has five organs for sensing the external signals. But in our work,we define 'Brain Sensory' as the 6th new sensory which senses Thinking activities occurred inside the brain. We always experience that many thinking streams appear and disappear during the thinking process. There occur several thinking streams in parallel. They sometimes combine together or conflict with each other. The brain sensory is monitoring these thinking activity from the sensory input data to the occurring thinking streams inside brain. As shown in Fig.1,Brain Sensory is designed for monitoring whole process of Thinking Activity. Starting from the stimulus signal of input data which came from the five sensory organs, Thinking activity occurs in DTAM (Dynamic Thinking Activity Map) using Memory recalling mechanism from the knowledge Networks of the memory. DTAM consists of TAR(Temporal Associative Relation) and Thinking chaining thread space. TAR contains Associative Relations obtained by Conditioned learning temporally and is used for extracting the thinking threads. The Knowledge extracting strategy based on DTAM is described in detail in the paper[1].

3. THINKING CHAINING THREAD EXTRACTION AND EMOTIONAL SWITCHING

3.1 The structure of knowledge network in memory

The structure and its mechanism of knowledge network composing the memory is very important to design

©ISAROB 2009

the efficient system. The knowledge network consists of knowledge nodes and their associative relations. It is represented as

$\langle$K-node$_i$, R_{ij},$K - node_j$ $\rangle$

where $K - node_i$ is the name of knowledge node and R_{ij} is connection strength between two knowledge nodes. R_{ij} is calculated by equation (1).

$$R_{ij}=P(K - node_i \mid K - node_j) \quad (1)$$

Knowledge node is an basic atom composing the Knowledge Network. It contains 'ID','Type','Emotional Factors' attributes which can identify itself. Knowledge node is represented as a form of 'struct'.

struct k-node$_i\langle ID, Type, EmotionalFactors\rangle$

Emotional Factors has three terms representing emotional state and are described in the next section.

3.2 Thinking chaining Thread extraction by Type Matching Strategy

The system extracts the related knowledge from the memory and makes Thinking chaining Threads using Type Matching Rule which is a proposed criteria of selecting the knowledge. Starting from the idea that everything has its own property,'Qualia',we define 'Type' as a factor representing the property of a thing. In this system, five types, M,F,E,K and S are defined. These five types can be flexibly designed according to the application area. Type Matching rule which is representing matching relations is also defined. There exists attractive force or repulsive force between two things. The attractive force means that two properties of things are matched well and the repulsive force says that they are mismatched and rejecting each other. The following tables depicts Attractive relation and Repulsive relation respectively.The knowledge extraction method using Type matching strategy is described in the paper in detail[2].

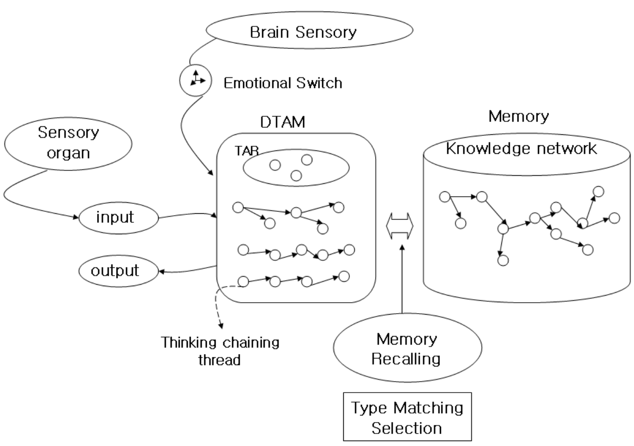

Fig. 1 Brain Sensory

Table 1. Type Matching Rule

Attractive Relation	Attractive degree d_i
M $\oplus\gg$ F	d_1=0.5
F $\oplus\gg$ E	d_2=0.5
E $\oplus\gg$ K	d_3=0.5
K $\oplus\gg$ S	d_4=0.5
S $\oplus\gg$ M	d_5=0.5
Repulsive Relation	**Repulsive degree d_i**
M $\ominus\gg$ E	d_1=-0.5
E $\ominus\gg$ S	d_2=-0.5
S $\ominus\gg$ F	d_3=-0.5
F $\ominus\gg$ K	d_4=-0.5
K $\ominus\gg$ M	d_5=-0.5

The matching rule 'M $\oplus\gg$(0.5) F' means that M type helps F type with attracting degree 0.5. The value d_s of 'M $\oplus\gg(d_s)$ S' is derived from 'M $\oplus\gg$(0.5) F $\oplus\gg$(0.5) E $\oplus\gg$(0.5) K $\oplus\gg$(0.5) S'. The attractive degree of multiple relation is calculated by the following equation(2).

$$d_s=\begin{cases} \prod_{i=1}^{n}(-1)^{n+1}d_i & \text{if } Type_i \neq Type_j \\ 1 & \text{otherwise} \end{cases} \quad (2)$$

If the value of d_s is positive, it is attractive relation. Otherwise, the minus value means repulsive relation.

3.3 Emotional Switching

During the process of Thinking Chaining thread extraction, several thinking threads are occurred. Brain sensor monitoring Thinking Activity checks the current emotional state activates the Thinking chaining thread selected by Emotional switching.

'Emotion' is represented by three dimensional values of E_{X_i},E_{Y_i} and E_{Z_i}. That is, emotional state of i-th thread E_i is :

$$E_i = (E_{X_i},E_{Y_i},E_{Z_i}) \quad (3)$$

As shown in Fig.2, E_{X_i},E_{Y_i} and E_{Z_i} represent the emotional states and have a value of [-1,+1].

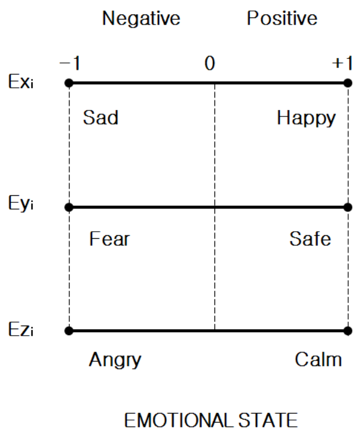

Fig. 2 Emotional State

The value of Emotional vector, $V(E_i)$, is calculated by equation (4).

$$V(E_i) = P * \sqrt{{E_{X_i}}^2 + {E_{Y_i}}^2 + {E_{Z_i}}^2} \quad (4)$$

$$P = \begin{cases} 1 & \text{if } t > 1 \\ -1 & \text{otherwise} \end{cases} \quad (5)$$

$$t = E_{X_i} + E_{Y_i} + E_{Z_i} \quad (6)$$

- **Thinking thread selection by Emotional Switching**

Based on calculating the value of emotion Brain Sensory checks whole emotion state of $E_0 = (E_{X_0}, E_{Y_0}, E_{Z_0})$. It turns on Emotional switch and activates the selected Thinking chaining Thread. During Emotional switching process Thinking thread is selected by the following equation (7) and activated.

$$Active(T) = argmin_k \frac{\sum_{i=1}^{n} \sqrt{{E'_X}^2 + {E'_Y}^2 + {E'_Z}^2}}{n} \quad (7)$$

where $E'_X = E_{X_i} - E_{X_0}$, $E'_Y = E_{Y_i} - E_{Y_0}$, $E'_Z = E_{Z_i} - E_{Z_0}$

where n is the number of chained knowledge nodes of Thinking thread k.

4. EXPERIMENTS

In this experiment, the designed Brain Sensory was applied to the Virtual memory and its monitoring process was tested. Fig. 3 shows the initial state of testing knowledge network composing the Virtual memory. As shown in Table 2 the knowledge node has the Emotional factors which represents the current Emotional state.

Table 2. Emotional factor of Knowledge node

$K - node_i$	E_{X_i}	E_{Y_i}	E_{Z_i}
K_1	0.7	0.8	0.9
K_2	0.8	0.7	0.5
K_3	0.8	0.7	0.5
K_4	0.9	0.4	0.7
K_5	1.0	0.2	0.3
K_6	1.0	0.3	0.4
K_7	0.2	0.0	0.1
K_8	0.1	0.1	0.2
K_9	0.2	0.1	0.2
K_{10}	0.1	0.0	0.0
K_{11}	-0.7	0.1	-0.5
K_{12}	-0.8	-0.7	-0.5
K_{13}	-0.6	-0.3	-0.2
K_{14}	-0.9	-0.2	-0.1
K_{15}	-1.0	0.0	0.1

Fig. 4 depicts the process of Type Matching Selection from the initial knowledge network. In the case of Input type,'M',the matched knowledge nodes with type 'M' were selected and activated. Using Type Matching Selection strategy,three Thinking chaining threads were extracted in the experiment as shown in Fig.5. Especially Fig.6 describes the result of Thinking Chaining Thread Selection by Emotional Switching. In the case of Emotional state which has Emotional factor E0, namely, Ex0=0.9,Ey0=0.7 and Ez0=0.6, Thinking chaining thread 1 was selected. Fig.7 also shows the changing results of Emotional Switching according to the current Emotional state of whole system,E01,E02,E03,E04 and E05.

Table 3. Emotional state of whole system

E-state	$E0i_{X_i}$	$E0i_{Y_i}$	$E0i_{Z_i}$	E-value
E01	0.900000	0.700000	0.600000	1.288410
E02	0.500000	0.500000	0.500000	0.866625
E03	0.000000	0.000000	0.000000	1.191385
E04	-0.300000	-0.400000	-0.500000	-0.707107
E05	-0.800000	-0.300000	-0.500000	-1.024695

As a result of experiments we could find that Brain sensory performs the monitoring function focusing on thinking chaining monitoring Thinking chaining thread extraction by emotional switching successfully.

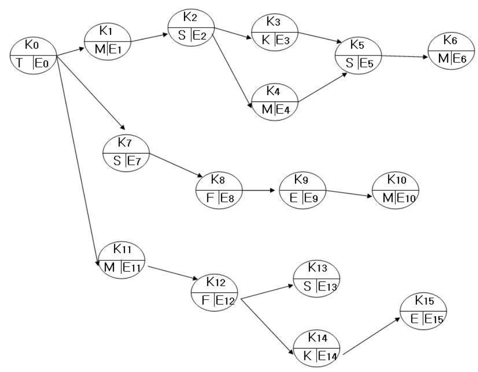

Fig. 3 The initial state of testing knowledge network

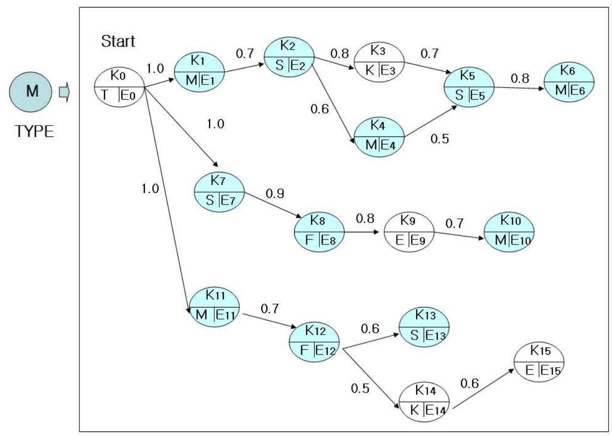

Fig. 4 Type Matching : Type= M

5. CONCLUSION

In this paper, Brain sensory monitoring Thinking Activity was designed. It is very meaningful that Emotional state was defined and the strategy of Thinking chaining thread extraction by Emotional switching was designed. This strategy was applied to the virtual memory and experimented with sample testing data and got the good testing results. This strategy can be usefully applied to design and construct core artificial brain of the Intelligent

System.

REFERENCES

[1] JeongYon Shim, **A Design of Brain Sensory Ensemble Structure for Intelligent system** ICCAS2008.

[2] JeongYon Shim, **Personal Knowledge Network Reconfiguration Based on Brain like function using Self Type Matching Strategy** IDEAL, volumn 5326, Springer,2008.

[3] Jean-Marc Fellous, Michael A. Arbib, **Who needs Emotions?** Oxford University press,2005.

[4] JeongYon Shim, **Knowledge Network Management System with medicine Self Repairing strategy** ICES2007,LNCS4684,pp119-128,Springer Verlag,Berlin Heidelberg2007.

[5] JeongYon Shim, **The design of Self Internal Entropy Balancing System with Incarnation process** LSMS2007,LNCS4688,pp55-62,Springer Verlag,Berlin Heidelberg2007.

[6] JeongYon Shim, **Intelligent capsule Design for the multi functional aspects** LSMS2007,LNCS4688,pp719-725,Springer Verlag,Berlin Heidelberg2007.

[7] E. Bruce Goldstein, **Sensation and Perception** Fifth edition,Brooks/Cole Publishing Company,1999.

[8] Michael A. Arbib, Jeffrey S. Grethe, **Computing the brain : A guide to Neuroinformatics** Academic Press,2001.

[9] Ning Zhong, Jiming Liu, **Intelligent Technologies for Information Analysis** Springer,2004.

[10] Paol Giudici, **Applied Data Mining : Statistical Method for Bussiness and Industry** Wiley 2003.

[11] Daniel L. Schacter, Elaine Scarry, **Memory, Brain, and Belief** Harvard University Press, Cambridge, Massachusetts, London/2000.

[12] Luc De Raedt Arno Siebes, **Principles of Data Mining and Knowledge Discovery** Springer 2001.

[13] Ian Cloete and Kacek M. Zurada, **Knowledge Based Neuro Computing** MIT press 2000.

[14] Sushmita Mitra, Tinku Acharya, **DATA MINING Multimedia, Soft Computing and Bio Informatics** Wiley Inter Science 2003.

[15] Tamraparni Dasu, Theodore Johnson, **Exploratory Data Mining and Data Cleaning** Wiley Inter Science 2003.

[16] Pierre Baldi,Paolo Frasconi, Padhraic Smyth, **Modeling the Internet and the Web - Probabilistic Methods and algorithms** Wiley Inter Science 2003.

```
Knowledge Extraction stage ...

Input Type(M/F/E/K/S)? M

Knowledge Extraction starts...

K0 1.0 K1 0.7 K2 0.6 K5 0.8 K6 0.0 Null
K0 1.0 K1 0.7 K2 0.6 K4 0.5 K5 0.8 K6 0.0 Null
K0 1.0 K7 0.9 K8 0.6 K10 0.0 Null
K0 1.0 K11 0.7 K12 0.6 K13 0.0 Null
```

Fig. 5 Thinking Chaining Thread Extraction:Type=M

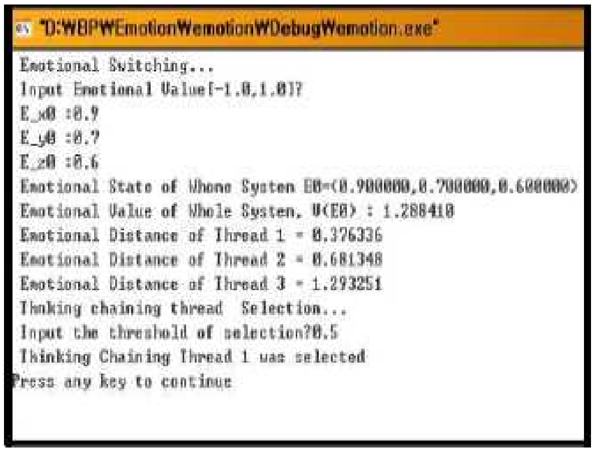

Fig. 6 Thinking Chaining Thread Selection by Emotional Switching

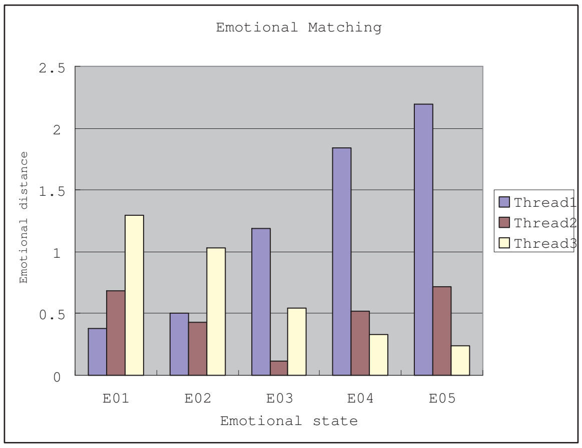

Fig. 7 The changing Emotional distance according to the current Emotional states, E01,E02,E03,E04 and E05

The Fourteenth International Symposium on Artificial Life and Robotics 2009 (AROB 14th '09),
B-Con Plaza, Beppu, Oita, Japan, February 5 - 7, 2009

Modeling of Traffic Flow using Cellular Automata and Traffic Signal Control by Q-learning

Kiyoshi Umemoto, Ji-Sun Shin, Tomofumi Ohshita, Yohei Osuki (Waseda Univ.),

Michio Miyazaki (Kanto Gakuin Univ.), and Hee-Hyol Lee (Waseda Univ.)

(Tel: 093-692-5017; Fax: 093-692-5021)
(Email address: tumsk_osaka@yahoo.co.jp)

Abstract: Recently, the flow of traffic has increased in the cities, and it has caused problems because of CO_2 emissions due to traffic jams. The traffic signal control is a typical counter measures for the congestion easing. The traffic signal control method includes the point control, the series control, and the wide area control, and the cycle time, the split, and the offset are used as the control parameters of the traffic signal. The offset is the difference of the start for the green signal between adjoining crossroads. The existing researches to generate the offset automatically are the cycle-less control technique, the real-time simulation using GA, and the optimization technique by the inclination method.

First, the traffic flow is modeled to reproduce the movement of the vehicle on the road in this paper. There are two models of the traffic flow being developed now: one is to model the traffic flow as a continuous style, and the other is to regard the vehicle as the individual movement and to form the whole flow. The traffic flow is modeled using the cellular automata as the latter case here. A traffic signal is consisted as an agent and the agent learns the control parameters of the traffic signal, which are the split and the offset under the fixed cycle length, using Q-learning method. In this paper, the offset of the signal agent is deduced using Q-learning method considering the adaptation for the dynamic change of the traffic flow.

Keywords: Traffic Flow, Traffic Signal Control, Offset, Q-learning, Cellular Automata, Agent

I. INTRODUCTION

The traffic signal control is a typical counter measures for the congestion easing. The traffic signal control method includes the point control, the series control, and the wide area control, and the cycle time, the split, and the offset are used as the control parameters of the traffic signal. The traffic signals are generated by an autonomous agent, and each signal agent studies the control parameter independently.

In this paper, a traffic signal control by the multi agent type is proposed. The traffic flow of the road network including crossroads is modeled by the traffic flow cellular automata. Under the cycle of the signal interval is constant, the control parameter of the signal agent are adjusted by Q-learning method.

II. MODELING OF TRAFFIC FLOW USING CELLULAR AUTOMATA

As the model of the traffic flow, a typical Elementary CA [1] of Wolfram by one dimension cellular automata is developed to a two dimensional model including crossroads here. The road is divided into two or more cells, and the cell where a vehicle exists is shown as "1", and the cell where a vehicle does not exist is shown as "0". An individual vehicle moves using the rule-184 [2]: advance one mass only when a forward cell empties. The updating time of the rule-184 is shown as,

$$U_j^{t+1} = U_j^t + \min(U_{j-1}^t, 1 - U_j^t) - \min(U_j^t, 1 - U_{j+1}^t) \qquad (1)$$

t: time, j: position of cell

U_j^t : state of position j at time t

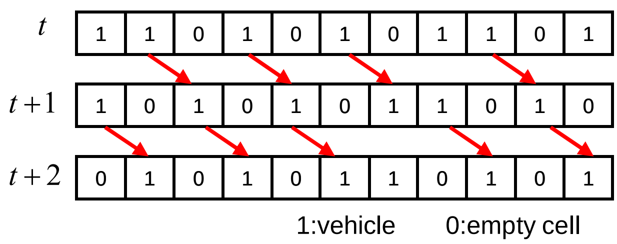

Fig.1 Movement of vehicles by rule-184

The movement of the vehicles by the rule-184 is shown in Fig.1. This model can be extended to a two-dimensional model which includes crossroads.

III. TRAFFIC SIGNAL CONTROL BY Q-LEARNING

The signal agent is composed of the State observer, the Learning, and the Select action as shown in Fig.2.

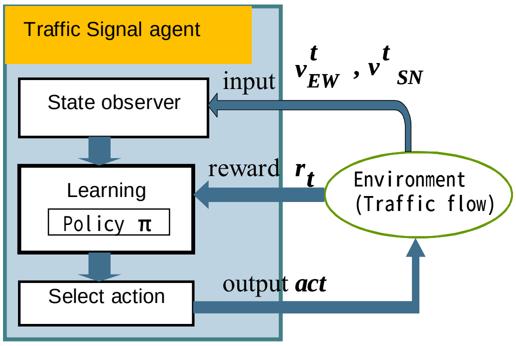

Fig.2 Structure of Traffic Signal agent

The State observer measures the number of the inflowing and outflowing vehicles from/to the crossroad and the stationary vehicles between adjoining crossroads.

The number of the stationary vehicles is denoted as follows:

v^t_{EW} : Vehicles existed on the road in the direction of east and west at time t

v^t_{SN} : Vehicles existed on the road in the direction of south and north at time t

The Learning carries out the update for the parameters of the traffic signal using the Q-learning which is an environmental identification type.

The action value function is defined as $Q(v^t_{EW}, v^t_{SN}, act)$.

act: control parameter which yields the passage in direction of east and west

Q value is updated every two cycles. When the number of the stationary vehicles between adjoining crossroads increases more than the number of the stationary vehicles of the previous cycle, the signal agent gets a penalty r, and the penalty is calculated for each inflowing road. Moreover, when the number of the stationary vehicles decreases, a reward is given. Therefore, the updating of Q value is defined as

$$Q(v^t_{EW}, v^t_{SN}, act_t) \leftarrow Q(v^t_{EW}, v^t_{SN}, act_t) + \alpha[r_t + \gamma \max_{a \in A} Q(v^{t+1}_{EW}, v^{t+1}_{SN}, act_{t+1}) - Q(v^t_{EW}, v^t_{SN}, act_t)] \quad (2)$$

α : learning rate ($0 < \alpha \leqq 1$),

γ : discount rate ($0 \leqq \gamma < 1$)

The ε-greedy selection is used for the Select action. It acts randomly at the probability ε, and except for this situation, the agent acts according to the Q values memorized in the learning machine.

IV. SIMULATION

1. Field of Simulation and Q-learning Process

The overview of a road network consisted from three crossroads will be targeted in this simulation as shown in Fig.3. There is a road with two lanes including a right turn lane (6 cells, 43m) on Rikimaru, Kitakyushu-city. The distance between adjoining crossroads is 64 cells (480m). The number of the traffic density for the crossroads area was measured between 17:00 and 19:00 on January 17th, 2008. Based on the measured date, the following probabilities are supposed: the vehicles flow into the road network from the two ends of east-west direction and the six ends of north-south direction with probabilities 0.35 and 0.1, respectively; the vehicles flow outside of the road network with probability 0.8; the vehicles flow into the crossroads from the straight path, the left turn, and the right turn in the direction of north-south with probabilities 0.2, 0.7, and 0.1, respectively, and in the direction of east-west with probabilities 0.8, 0.15, and 0.05, respectively.

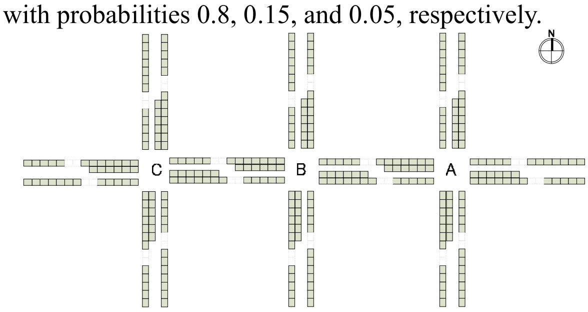

Fig.3 Gridiron

The splits in the signal of crossroads A, B, and C are assumed to be the same ratio. The behaviors of the signal agent are assumed to be the following:

Action = {10%, 20%, 30%, 40%, 50%, 60%, 70%, 80%, 90%}

Fig.4 shows the procedure of the simulation by Q learning for the splits.

Initialize $Q(s, a)$ arbitrarily;
Repeat (for each episode);
  Repeat (for each step of episode);
    Observe a state observation *st* ;
    Choose *at* from *st* using policy derived from Q value;
    Take action *at*, observe *rt*, *st*+1;
    Q value is updated by the following update equation;

$$Q(s_t, a_t) \leftarrow Q(s_t, a_t) + \alpha\{r_t + \gamma \max_{a_{t+1}} Q(s_{t+1}, a_{t+1}) - Q(s_t, a_t)\}$$

$t \rightarrow t+1$
until *st* is terminal;
until all episodes are finished;
where α : Learning rate ($0 < \alpha \leqq 1$)
γ : Discount rate ($0 \leqq \gamma < 1$)

Fig.4 flow of procedure

The offset values of the crossroads A and B are defined based on the crossroad C. The amount of the change of the absolute offset value assumes 1/4 or less [3] of the cycle length 250(steps), and calculates each signal as the offset= {0, 20, 40, 60} (steps). Moreover, one cycle is 60 steps, and in the finish time of one split, all the traffic signals are red light during two steps.

2. Result of Simulation

The average number of the stationary vehicles between adjoining crossroads A and B is decreased about 1/4 for the east-west split 70% compared with the east-west splits 50% and 80% on 300,000 advanced steps as shown in Fig.5. Through the learning, the traffic signal agent can obtain the split to reduce the traffic jam.

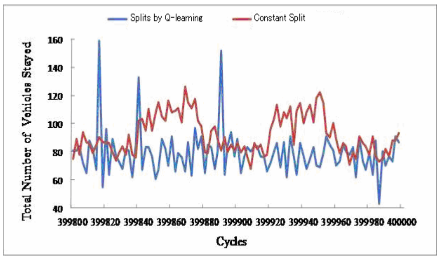

Fig.5 Total number of the vehicles stayed (Offset=0)
Average: 81.6 vehicles
Standard Variance: 12.9

The number of the east-west splits selected during the learning for the traffic signal agent on the crossroad A is shown in Fig.6, and the most selected split is 60%.

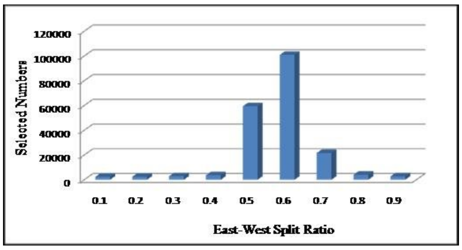

Fig.6 Selected numbers of East-West Sprit Ratio

Table1 Sprit

		Standing vehicles in the direction of North-South									
		10 ~19	20 ~29	30 ~39	40 ~49	50 ~59	60 ~69	70 ~79	80 ~89	90 ~99	100 ~109
Standing vehicles in the direction of East-West	10～19	50	50	50	50	40	50	50	50	50	50
	20～29	80	30	60	20	50	10	20	50	30	30
	30～39	70	60	70	80	40	60	50	30	40	40
	40～49	60	60	30	10	70	50	60	30	40	50
	50～59	60	60	60	30	80	50	50	40	40	40
	60～69	50	60	40	60	40	40	40	30	70	50
	70～79	50	60	50	30	30	80	40	50	50	50
	80～89	50	50	60	10	40	60	50	20	20	90
	90～99	50	60	40	50	50	50	50	30	70	60
	100～109	50	60	40	50	50	30	50	50	50	10
	110～119	60	60	50	50	50	30	40	40	60	80
	120～129	70	60	50	50	50	50	40	50	70	60
	130～139	60	60	60	50	50	40	50	80	10	90
	140～149	60	70	50	50	70	60	50	10	90	70
	150～159	60	60	50	50	70	50	50	80	40	80
	160～170	60	60	50	50	50	50	80	70	20	50

The splits of each stationary vehicle in the directions of east-west and north-south are shown in table1, and the total number of the stationary vehicles using the splits obtained by Q-learning and the constant split(50%) for each offset 20, 40, and 60 are shown in Fig.7, Fig.8, and Fig.9. As the result, the average of the stationary vehicles for the offset 20 is smaller than the other offsets.

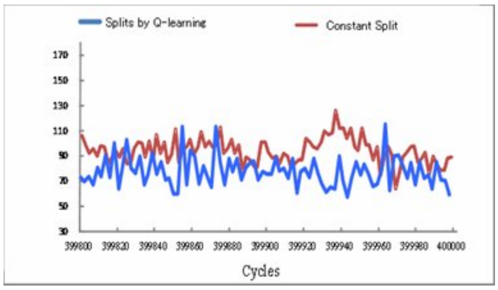

Fig.7 Total number of the vehicles stayed (Offset=20)
Average: 78.3 vehicles
Standard Variance: 13.6

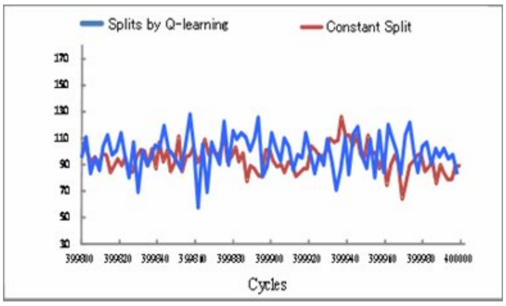

Fig.8 Total number of the vehicles stayed (Offset=40)
Average: 98.8 vehicles
Standard Variance: 12.8

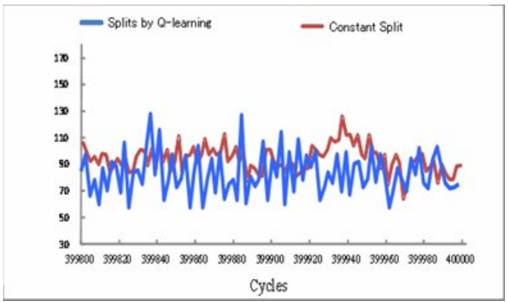

Fig.9 Total number of the vehicles stayed (Offset=60)
Average: 82.6 vehicles
Standard Variance: 14.8

REFERENCES

[1] S.Wolfrm, Theory and application of cellular automata, World Scientific, Singapore (1986)
[2] Naofumi Yamamoto, Shin Morishita, Simulation of Traffic Flow by Cellular Automata and its Control (In Japanese), Transactions of the Japan Society of Mechanical Engineers, Series C, Vol. 65, No. 637, pp.75-80 (1999)
[3] Satoshi Igaue, Mamoru Hisai, Real-Time Control of Coordinated Traffic Signal Systems through Sequential Formation of Offsets (In Japanese), Memoirs of the Faculty of Engineering, Yamaguchi University, Vol.56, No.1, pp.53-61 (2005)

The Fourteenth International Symposium on Artificial Life and Robotics 2009 (AROB 14th ’09),
B-Con Plaza, Beppu, Oita, Japan, February 5 - 7, 2009

Humanoid Robot’s Motion Planning using Genetic Network Programming

Y.X. Sun and H. Ogai

Ogai Research Lab., Graduate School of Information, Production and Systems, Waseda University
2-7 Hibikino, Wakamatsu-ku, Kitakyushu-shi, Fukuoka 808-0135, Japan
(Tel : +81-090-9581-4495)
(sand_sun@ruri.waseda.jp)

Abstract: We have developed the program for humanoid robot's whole body motion planning using Genetic Network Programming (GNP). First we introduce the main idea and the way constructing GNP, then the method of applying GNP to robot's whole body motion planning, and give the result of our research as a conclusion.

Keywords: Genetic Network Programming, population, individual, node, evaluation function

I. INTRODUCTION

Research on humanoid robot's motion planning has been drawing attentions since long ago. So far, there have already been many different methods solving this problem. These methods are mainly divided into three classes: motion planning based on motion capture technology; one using pin/drag interface based on Graphical User Interface (GUI); and motion planning in multi-dimensional space by specifying the initial posture and the final posture, then the system generates continues motions connecting these two, a typical method is rapid-exploring random trees (RRT) [1].

In the meantime, professor K.Hirasawa proposed an evolutionary algorithm: Genetic Network Programming (GNP) in the year of 2000 [2] and it's been gradually applied in various research fields to solve different kinds of practical problems like double-deck elevator group supervisory control systems, data mining, stock trading rules’ generation and comprehensible control rules for real robots [3].

Inspired from these achievements, we tried effort to develop a control system for humanoid robots’ motion planning using GNP. Basically, the goal is to generate control rules that manipulate robot's movements connecting a preset initial posture and a final posture, which in other words, is to find a new solution in the 3rd class of motion planning.

This paper is going to present the latest research progress. It is organized as follows: firstly, give a brief introduction to GNP in Section 2, then in Section 3, bring out the research model built based on MATLAB and detailed methods applying GNP to motion planning. Finally, give the result of our research and relative analysis as a conclusion.

II. GENETIC NETWORK PROGRAMMING

Nowadays, control systems are becoming large and complex that it is not easy for us human beings to figure out a clear and precise control rule in advance, so an idea of developing an intelligent system that could find optimal rules automatically popped out, and then, inspired from GP and GA, GNP was proposed.

1. Structure of GNP

The fundamental elements that construct a network for GNP are called nodes. Basically, two classes of nodes are required: processing node and judgment node.

Processing nodes describe the actions of GNP and judgment nodes judge the information from the environment and choose to take actions according to the judged result. They connect with each others to form a control network. This kind of network is called an individual. Fig.1 shows a typical structure of one individual of GNP.

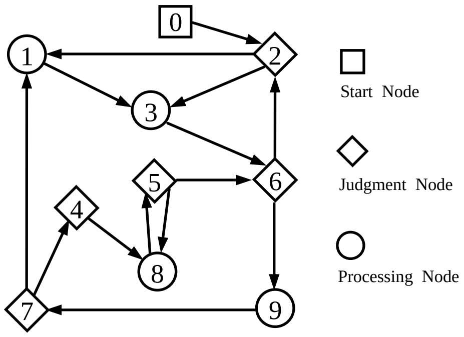

Fig.1 Basic structure of GNP

Fig.1 illustrates the phenotype of GNP's network structure, while Fig.2 shows the genotype of it:

Node 0	0	0	0	2	0		
Node 1	2	1	5	3	0		
Node 2	1	1	1	3	0	1	0
Node 3	2	2	5	6	0		
Node 4	1	1	1	2	0	8	0
Node 5	1	3	1	8	0	6	0
Node 6	1	2	1	9	0	2	0
Node 7	1	2	1	1	0	4	0
Node 8	2	1	5	5	0		
Node 9	2	2	5	7	0		

NT_i	FID_i	d_i	C_{i1}	d_{i2}	……	C_{in}	d_{in}

Fig.2 Genotype of Fig.1

We use a two-dimensional array to establish the gene structure of an individual. Each row represents one node, could either be a processing node or a judgment node, it depends on the value of the first element in the row array: NT_i. In the above table, for example, NT_i equals 1 meaning a judgment node while 2 meaning a processing node.

FID_i describes the function of the i^{th} node and d_i presents the time cost (delay) for the node to carry out its action or judgment.

After deciding the node's type, function and delay time, we need to decide which node does the present node connect. Here C_{in} denotes the connections and d_{in} denotes the connection time delay. Note that if the node is a processing node, it can only have one connection and if it is a judgment node, the number of connections can be more than one.

2. Genetic Operations in GNP

There are three types of the genetic operations in GNP: **selection**, **crossover** and **mutation**.

Selection: Individuals are initialized randomly at the beginning of the program. After mutation or crossover, apparently the population becomes larger. The selection operation can help the program select the individuals with better performance among the population and keep it within a fit size.

We take two ways to carry out selection operation: tournament selection and elite selection. Tournament selection is carried out between any two individuals. The program calculates two individuals' fitness and dumps the low valued one. Elite selection calculates all individuals' fitness and sets a bottom line of it. Ones that are higher than the line are chosen and the rest are discarded.

Crossover exchanges the sub-network of two parent individuals to create new individuals. Here the sub-network can be several nodes which connect each other, can be only one point, or just several points which are randomly chosen from parents.

Mutation takes effect in a single individual. It is used to change one node's connection branches, the function, or even its node type. This is another way of producing new kind of individuals.

Both crossover and mutation offers new individuals in a population for selection to select better ones.

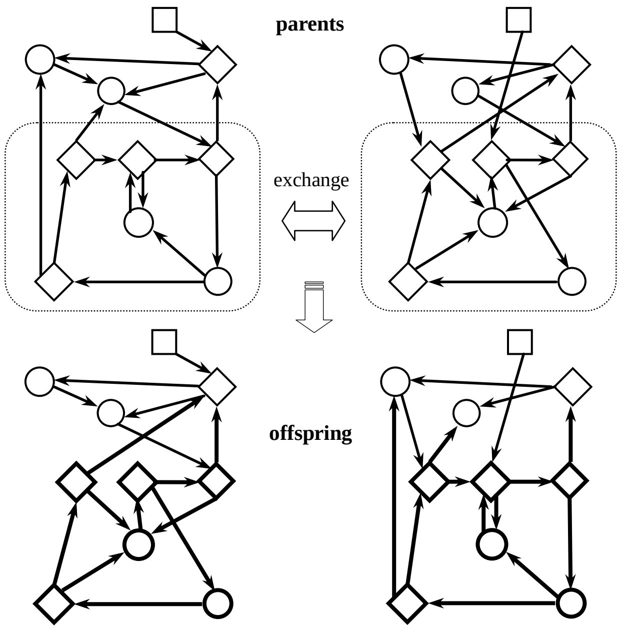

Fig.3 Crossover in GNP

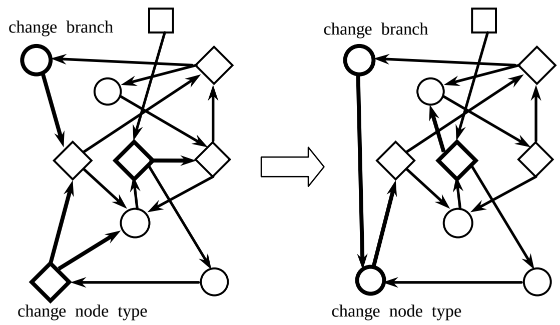

Fig.4 Mutation in GNP

III. MODEL AND APPLICATION DESIGN

1. Modeling

We built a model of humanoid robot which is illustrated in Fig.5. It has 19 degrees of freedom and each joint's range of rotatable angle has been specified generally according to human beings.

The data structure of the robot is a tree structure, each joint has a sister branch and a child branch. Start from the head, we can use forward kinematics to calculate the posture of the model robot. Besides, with the mass of each joint set during the initialization, calculation of the robot's center of mass is possible.

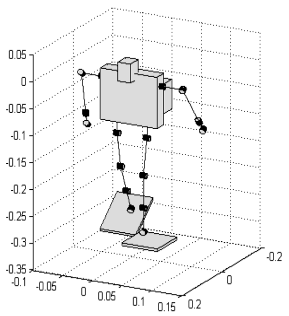

Fig.5 Model of a humanoid robot

2. Application Design

In this chapter, we are to develop an application that can find optimal control rules to generate motion series which connecting the preset initial posture and final posture. We start from designing the various nodes (type and related functions) that are intended for constructing individuals.

A. Processing Node

Since the model we built has 19 degrees of freedom, the actions that processing nodes take are to manipulate the joint angles of these 19 joints. Each node takes charge of one joint and can only choose to adjust its angle to plus or minus a certain value. So if we want the entire body of the robot be controlled, at least 38 kinds of processing nodes are needed (2 nodes, respectively, doing plus and minus for each joint).

For more adaptive control, even the step length of the adjustments can have many choices, like one degree per action or two. But by doing this, the kinds of processing node grow extremely large and system becomes complex, so here in our research, we just take the simplest way: 38 kinds of processing nodes.

In order to make sure that the robot can finally reach the desired posture, we set a constant command in all processing nodes, that is: after taking its action, the joint is forced to get closer by one degree to its final value.

B. Judgment Node

During the robot's movement, the most important thing is to keep balanced. Here we suppose our robot's movement is slow and steady, so the momentum which might affect the robot's balance is not considered. Then, the only element relative to balance is the center of mass (CoM). So we design the judgment conditions to be: which quadrant does the CoM locate in X-Y coordinate system, and then choose actions according to the judged result.

Table.1 Node Assignment

Node Type	**Functions**		
Processing Node	Joint 1 + 1°		Joint 1 - 1°
	Joint 2 + 1°		Joint 2 - 1°
	… …		… …
	Joint 19 + 1°		Joint 19 - 1°
Judgment Node	**Node Kind**	**X-Axis**	**Y-Axis**
	1	+	+
	2	+	-
	3	-	+
	4	-	-

C. Evaluation Function

The evaluation function is used to calculate the fitness of each individual. There are two parts that add up to present the fitness value: one is the total steps that the robot's all 19 joints took to perform the desired motion; the other is the CoM's average deviation from the track connecting the CoM at start and the one at the end, which is easy to understand by referring to Fig.6.

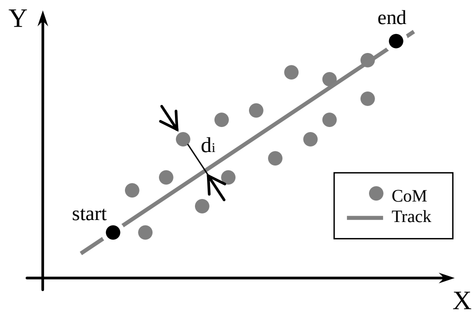

Fig.6 Deviation of CoM from desired track

Evaluation Function:

$$\text{fitness} = n * \alpha + \frac{\sum d_i}{n} * \beta$$

where n denotes the step count, $\sum d_i / n$ calculates the average deviation, and α, β are weight coefficients.

One point should be clarified is that, the desired track of the CoM is not necessarily to be a straight line, a curve might do better in some circumstances. Here in our experiment, we take the track as a straight line.

Once all the three elements are decided, the genetic operations can be carried out. Fig.8 illustrates the flow chart of the application.

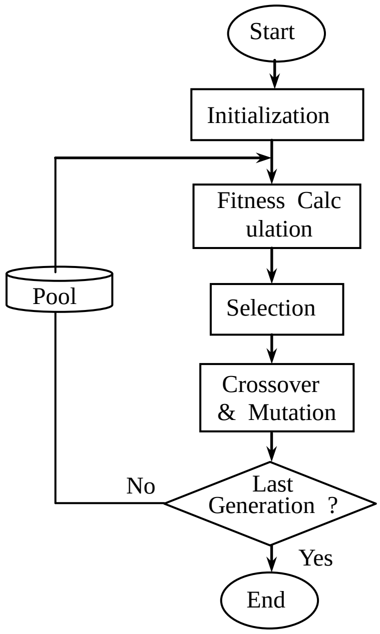

Fig.7 Flow Chart of Program

In case that too many individuals were discarded after selection, we here set a data pool storing randomly generated individuals to relief the population crisis that might happen in chance.

IV. EXPERIMENT RESULT

Considering that the number of node functions is large, during the initialization period, if we directly let the computer generate all the individuals randomly, maybe none of them has the ability to simply control all the joints. Though after genetic operations, there might be several ideal individuals produced, we decided to help accelerate the evolution procedure by adding several man-made individuals that has the ability to control all the joints. Then let the genetic operations be carried out. Table.2 shows the parameters of the program:

Table.2 Parameters Specifications

Selection Rate	0.24
Crossover Rate	0.08
Mutation Rate	0.08
Population(Individuals)	25
Judgment Node	20
Processing Node	80
Starting Node	1
Generation	30

After trained the population using the above parameters by several target motions, we obtained some individuals that can control the robot to perform some simple movements. Then we went on to train these individuals for a test motion, we found that there is still space for improvement referring to Fig.8 which shows the fitness value curve as generations grow.

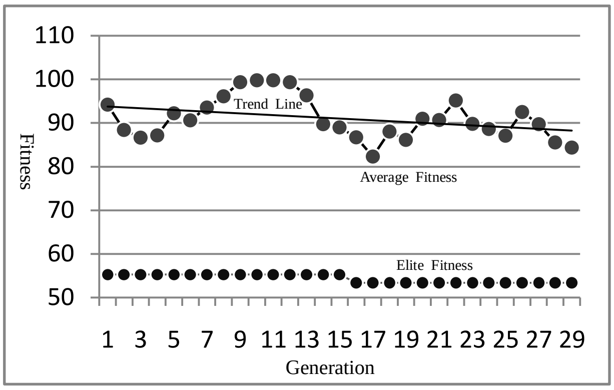

Fig.8 Fitness Curve

Using the elite individual selected from the last generation, we control the model robot to perform a simple motion of "kick" whose snapshots are shown in Fig.9.

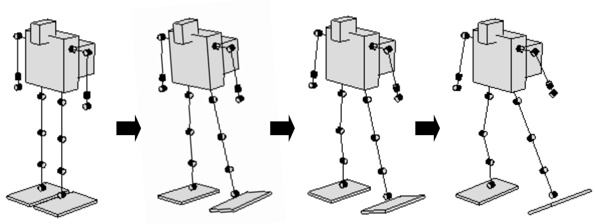

Fig.9 Snapshots of "kick"

V. CONCLUSION

So far, we have developed an application using GNP algorithm to generate control rules for a humanoid robot. But there is still space for improvements: to generate complex motions by setting several transitional key postures; to add new kinds of judgment node judging momentum and as mentioned in Section.4: in the initialization phase, we still have to help computer generate the first generation, or it will take too much time to finally obtain a usable individual, so how to improve the efficiency during initialization phase will also be our future research target.

REFERENCES

[1] Kajita S (2005), Humanoid Robot (in Japanese). pp.163-170

[2] Katagiri H, Hirasawa K, Hu J (2000), Genetic Network Programming – Application to Intelligent Agents. IEEE pp.3829-3834

[3] Murata T and Okada D (2006), Using Genetic Network Programming to Get Comprehensible Control Rules for Real Robots. 2006 IEEE Congress on Evolutionary Computation, pp.1983-1988

©ISAROB 2009

The Fourteenth International Symposium on Artificial Life and Robotics 2009 (AROB 14th '09),
B-Con Plaza, Beppu, Oita, Japan, February 5 - 7, 2009

On-line Tuning PID Parameters in Idle-speed Engine based on Modified BP Neural Network by Particle Swarm Optimization

Jia-Meng Yin, Ji-Sun Shin, Hee-Hyol Lee

Graduate School of Information, Production and Systems, Waseda University,
2-7 Hibikino, Wakamatsu-ku, Kitakyushu, Fukuoka
(Tel: 81-937-692-5164; Fax: 81-93-692-5164)
yinjm1983@moegi.waseda.jp

Abstract: PID control systems are widely used in many fields, and many methods to tune parameters of PID controller are known. When the characteristics of the object are changed, the traditional PID control should be adjusted by empiri cal knowledge. It may bring a worse performance to the system. In this paper, a new method to tune PID parameters cal led as the modified back propagate network by Particle swarm optimization is proposed. This algorithm combines the c onventional PID control with the back propagate neural network (BPNN) and the particle swarm optimization (PSO). T his method is demonstrated in the engine idle-speed control problem; the proposed method provides prominent perform ance benefits over the traditional controller in this simulation.

Keywords: BP neural network, Particle swarm optimization; PID control; Engine idle-speed control.

I. INTRODUCTION

Vehicle is a symbol of modern civilization. It doesn't only bring comfortable life to people, but also promotes the economic and social progress. For whole automobile, the engine system is the most important component of the vehicle. Following statistics of some research, the spark ignition engine spends a large percentage of their operation in the idle-speed region. In this condition the engine management system aims to maintain a constant idle speed in the presence of alterable situation. The engines are inherently nonlinear, incorporating variable, time delays, and discontinuity which make to model to be difficult. Because of this reason, some researches, for example neural network approach, are well known to fit for the engine control system. Neural network is well fit for engine control system.

In the last decades, the conventional PID control has been largely applied to many fields. Because of its versatility, PID strategy still remains the most common control algorithm in modern industry. When the idle-speed engine system occupies in the alterable situation, the rapid and accurate response of the controller is necessary. In this research, a learning type PID control system using modified BP network by particle swarm optimization is designed which will bring prominent performance benefits over a traditional controller in this application.

II. Modified BP network by Particle Swarm Optimization

1. Back Propagate Neural Network

BP network is widely used in many fields. It is proposed by Rumelhart in 1986. The BPNN is a multi-layers network that consists of the input layer, the hidden layer, and the output layer. The standard structure will be shown in Fig 2.1.

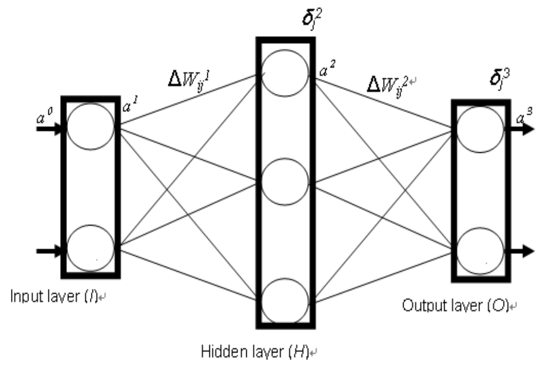

Fig 2.1.Structure of BP network

BP algorithm step:

Firstly, the actual output of BPNN will obtain from the actual outputs as eq. (2.1). It is forward progress.

$$a^{m+1} = f^{m+1}(w^{m+1} * a^m + b^m), m = 0,1,\ldots,M-1 \tag{2.1}$$

a: output of each layer
w: weight value
b: bias value
m: number of layer

©ISAROB 2009

Secondly, the error will be generated at the output layer by comparing between the actual output and the target output. The error function at output layer is defined as

$$Ep = \frac{1}{2}\sum_{k=1}^{M}(T_k - A_k)^2 \quad (2.2)$$

T_k : reference output

A_k : actual output

The total error function of neural network is shown in eq. (2.3).

$$E = \sum_{p=1}^{p} Ep \quad (2.3)$$

P: total numbers of pattern

Thirdly, the gradient descent method is utilized to calculate the weight of network and adjusts the weight of interconnections to minimize the output error. The gradient descent algorithm adopts the weights according to the gradient error, which is given by eq. (2.4).

$$\Delta W_{ij} = -\eta \times \frac{\partial E}{\partial W_{ij}} \quad (2.4)$$

η : Learning rate

The general form of ∂E/ ∂W is expressed as the following eq. (2.5).

$$\frac{\partial E}{\partial W_{ij}} = -\delta_j^n \times A_i^{n-1} \quad (2.5)$$

A: output value of each layer

W: connective weight

δ: error signal

n: layer number of BP network

Substituting (2.4) into (2.5), the gradient error is expressed as

$$\Delta W_{ij} = \eta \times \delta_j^n \times A_i^{n-1} \quad (2.6)$$

ΔW adjusts the weight value between the input layer nodes to the output layer nodes from output layer to the input layer. This is known as the back propagates progress. According to these adjustments, the error will decrease until the small set point. However, there are some disadvantages in BP algorithm. It is easy to converge to local minimum point; and it means the long time to convergence and training are needed.

2. Particle Swarm Optimization

Particle swarm optimization is a stochastic population-based evolutionary computer algorithm for solving problem. It is one of intelligence algorithm based on social-psychological principles. It provides insights into social behavior, as well as contributing to engineering applications. The particle swarm optimization algorithm was firstly described in 1995.

$$v_i = w*v_i + c_1*r_1*(pbest - x_i) + c_2*r_2*(gbest - x_i) \quad (2.7)$$

$$x_i = x_i + v_i \quad (2.8)$$

x: position of particle;

v: velocity of particle;

Pest: personnel best position of particle swarm;

Gbest: global best position of particle swarm

C: learning rate;

r: random number;

w: inertial factor;

Eq. (2.7) and (2.8) are learning rule of particle swarm optimization.

Flow chart of particle swarm optimization is shown in Fig. 2.2.

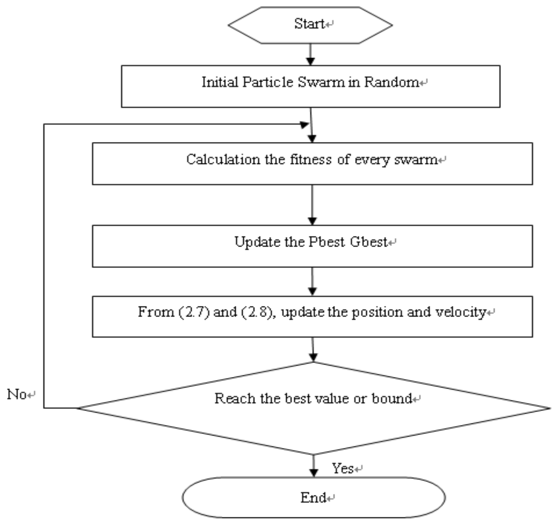

Fig 2.2.Flow Chart of Particle Swarm Optimization

There are three points why the PSO is choice to combine with BP network.

—Particle swarm optimization is a type of the global optimal method. It will find the global minimum point.

—The speed of search in PSO is much faster than the genetic algorithm.

—PSO has the simple structure to program.

3. Modified BP network by PSO

A new algorithm to combine BP network and PSO is proposed to overcome the disadvantages of BP network. The whole BP network training process consists of two Phases:

Phase 1: The global optimization procedure
(Particle swarm optimization)

Step1.1 To design a group of swarm this represents the weight and bias of BP network.

Step1.2 To calculate by forward progress in BP network to evaluate warm by error rate.

Step1.3 To operate particle swarm optimization

Phase 2: Refining the learning procedure.
(Traditional BP algorithm training)

Step2.1 To train BP network by traditional method.

In this method, some groups of particle swarm will be generated randomly. They represent the weight value and bias of BP network. Then these values will be taken into BP network and calculated in BP's forward progress. The function is shown in eq. (2.1). Comparing with actual output, the error of each group will get as eq. (2.2). Eq. (2.2) will be choice as the cost function of particle swarm optimization. After some steps, eq. (2.7) and eq. (2.8) will be used to calculate. This is the optimization process by PSO. During the many times of the optimization, Ep will reach the expected value. Then the best particle swarm will be generated. Next step is to take the optimized weight value and bias into BP network, and train BP network as traditional BP algorithm. The following figure will demonstrate the computational steps in detail for 2-3-1 structure network as an example.

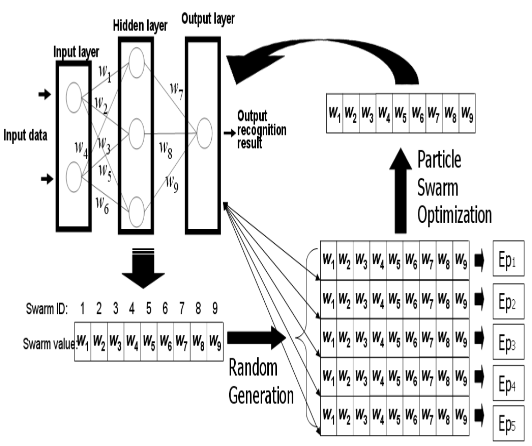

Fig 2.3.Schematic diagram of new algorithm

According to these procedures, it has proven that the new algorithm gets much faster convergence and more powerful calculation.

III. Idle-Speed Engine System

To compare with the traditional PID control scheme, the new algorithm is simulated on a simple generic engine model. The engine system changes throttle angle to keep the engine speed on fixed idle speed in alterable load demands. The following figure illustrates the model of the engine. In this simulation, 800Nm has been choice as a reference value of the idle-speed.

Dynamic block of components are taken as

$$Gi(s) = \frac{9000}{(0.05s+1)} \qquad Ga(s) = 0.85e^{-0.1s}$$

$$Gr(s) = \frac{20}{(3.5s+1)} \qquad Kn = 1*10^{-4}$$

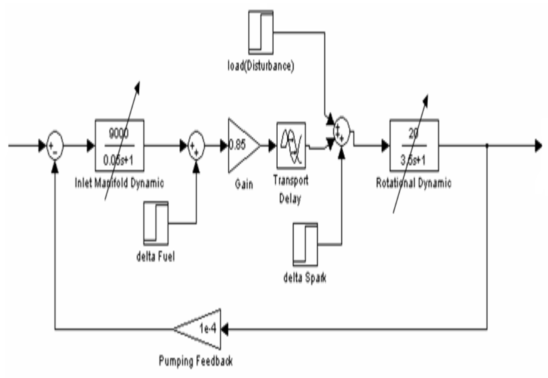

Fig 3.1.Engine idle-speed model

IV. Simulation and Comparison

1. Experiment Settings

In this section, the new algorithm will be compared with the traditional PID control scheme and PID control with BPNN control scheme in the idle-speed engine system. There are two cases of the experiment for the idle-speed engine. The one is to increase the gain of Gi. Gi represents the inlet manifold dynamic block. Because of the carbon deposition and dust, it will make the gain of Gi to be increased. The other is to increase the gain of Gr. Gr represents the power-train rotational dynamic block. When the loads are increased, the gain of Gr will follow the increment. In these two situations, three algorithms are adopted to keep the idle speed of engine to be stable.

The three methods of PID control law adopt the increment PID form shown in eq. (4.1).

$$u(k) = u(k-1) + Kp[e(k) - e(k-1)] + Kie(k) + Kd[e(k) + e(k-2) - 2e(k-1)] \qquad (4.1)$$

©ISAROB 2009

2. Structure and Parameters setting

In the traditional PID control system, there are so many method to determine the PID parameters, including Ziegler Nicolas Method, pole placement, Nyquist based design, and so on. The parameters of PID controller are determined here by Ziegler-Nicolas method.

In modified BP network by PSO control system, the structure of the modified BP network by PSO control system is shown in Fig.4.1.

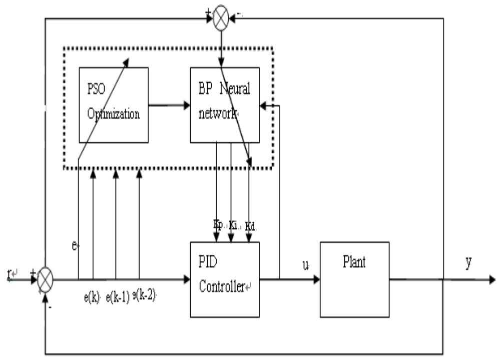

Fig 4.1.Structure of new self-tuning PID control system

It consists of four parties: the conventional PID controller, BP neural network, the particle swarm optimization and plant, where Kp, Ki, Kd are the coefficients of the proportion, the integral and the differential.

The learning algorithm of the new PID control system is as that:

—For the BPNN, there are 4 nodes in the input layer, 4 nodes in the hidden layer, and 3 nodes in the output layer. $\eta = 0.5$;

—Observe y(k) and r(k), e(k)=y(k)-r(k)

—Generate the groups of the particle randomly, the PSO optimizes the initial weights of BPNN and gets the initial value of parameters.

—Inputs and outputs of each layer of BPNN are calculated and three parameters of PID will be obtained.

—Calculate the output of the controller from eq. (4.1).

In the BPNN with PID control system, the structure of BPNN is same with the new method, and the difference is calculated just only BPNN without PSO optimization. In next section, the advantages of the new algorithm will be shown by the simulation.

3. Simulation Result

In the experiment 1, the gain of Gr is changed from 20 to 35 in 20 seconds shown in Fig.4.2 (a). The responses of the control systems are shown as follows. Fig.4.2 (b) is the result of the traditional PID control. When the gain of Gr increases up to 30, the divergence response is shown. Obviously, it is unexpected. In the Fig.4.2(c), the response of BP network control system is shown. It has improved but the steady state error is remained. When PSO is adopted to optimize the BP network in control system, the response is shown in Fig.4.2 (d). The output of the control system has improved dramatically. The state error has eliminated. Fig.4.3. (e) shows the update of Kp, Ki and Kd. The solid line is for the new algorithm and the dashed line is for the BP network. The red curve is the parameter Kp; The green curve is the parameter Ki; The blue curve is the parameter Kd.

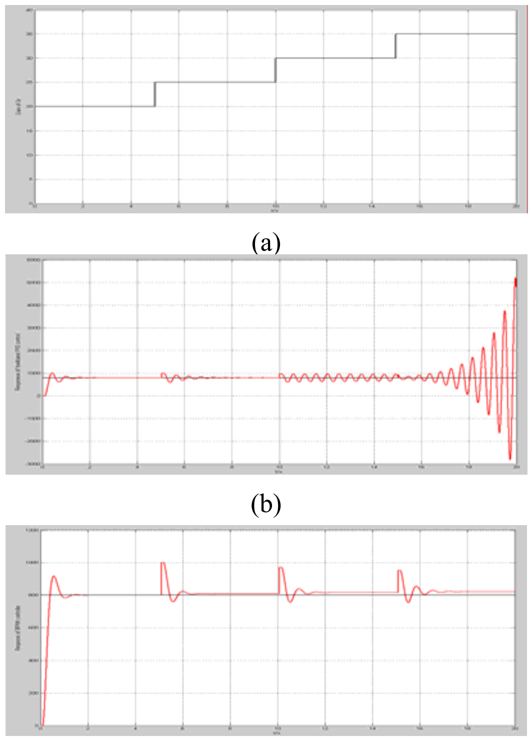

(a)

(b)

(c)

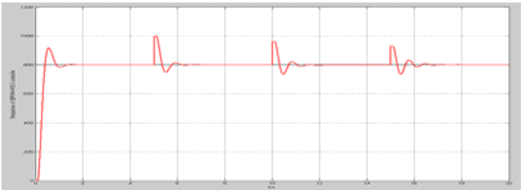

(d)

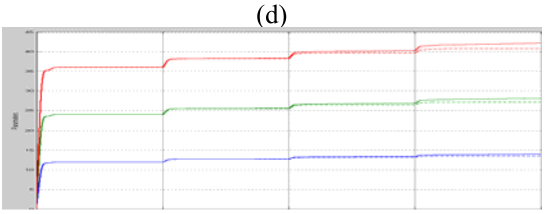

(e)

Fig 4.2.Experiment for the increment of Gr

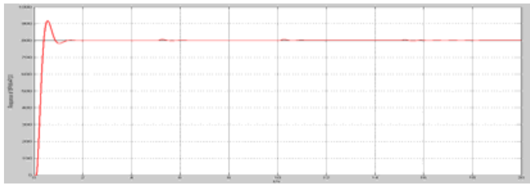

(d)

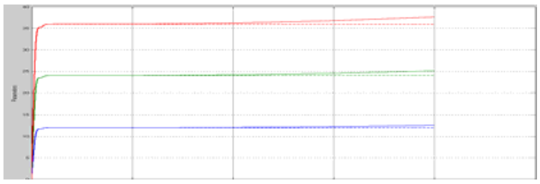

(e)

Fig 4.3.Experiment for the increment of Gi

In the experiment 2, the gain of Gi is changed from 9000 to 18000 in 20 seconds shown in Fig. 4.3(a). The responses of the control systems are shown as follows. Fig.4.3 (b) shows the response of traditional PID control. When the gain of Gi increases up to 15000, output of system is unstable. In Fig.4.3(c), it is response of BP network control system. It has improved greatly, but there is steady state error. In Fig.4.3 (d), the output of modified BP network by PSO control system is shown, and the state error is eliminated. Meanwhile, the response of the control system is much faster and higher accuracy. Fig4.3. (e) shows the update of parameters of BP network and BP with PSO method. Because of combining with PSO, the modified BP network is more effective for the update of the parameters.

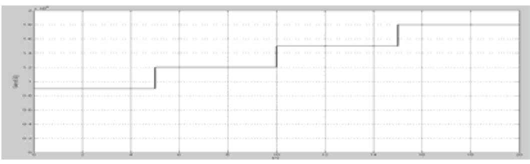

(a)

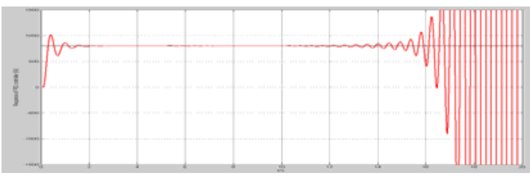

(b)

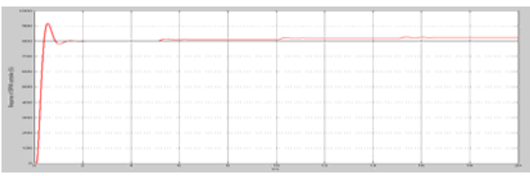

(c)

V. Conclusion

In this paper, an effective approach to tune PID parameters by on line is proposed. The PID controller based on BPNN and PSO improves the level of intelligent decision making and can adapt to various working requirements. PSO will improve BP network greatly, and it makes BP network faster convergence, and avoid local minimum point. According to procedure proposed in this paper, the new algorithm has shown not only powerful calculation but also strong robustness. The satisfactory simulation result has proven that the proposed algorithm is effective for the idle-speed control problem.

REFERENCES

[1] J. Chen, A study of Neurocontrol Theory and Its Industrial Applications, Ph. D. Dissertation, Zhejiang University, Hangzhou, China 1996

[2] W. T. Miller III, R. S. Sutton, and P. J. Werbos, Neural Network for Control (MIT Press, Cambridge, MA, 1990)

[3] Nørgaard N, Ravn O, Poulsen N K, et al. Neural networks for modeling and control of dynamic systems. London: Springer Verlag, 2000

[4] Hagan M T, Demuth H B, Beale M H. Neural network design. PWS publishing company, 1995

[5] Tohru Takahashi, Takashi Ueno, Aklto Yamamoto etc. A simple Engine Model for Idle Speed Control [R]. SAE 850291, 1985. 2.769-2.776

[6] Cook, J. A., & Powell, B. K. (1988). Modeling of an internal combustion engine for control analysis. IEEE Control Systems Magazine, 8(4), 20-26

[7] Wei Yang. Q. QangLi, "Summarization of PSO," Chinese Engineering of science, 2004, 6(5): 87-94

[8] J.C. Zeng, Jing Jie, Z. H. Cui, "The Algorithm of Particle Swarm," Beijing: The press of Science, 2004

[9] The MathWorks Inc. Neural network toolbox-User's guide2.0. 2005

©ISAROB 2009

Traffic Signal Control Based on Predicted Distribution of Traffic Jam

Cui cheng-You, Shin ji-Sun(Waseda University), Shoji Fumihiro(Fukuoka Institute of Technology),
Lee Hee-Hyol(Waseda University)
Graduate School of Information and Systems, Waseda University
2-7 Hibikino, Wakamatsu-ku,Kitakyushu,Fukuoka, 808-0135, Japan
(Tel : 81-93-692-5164; Fax : 81-93-692-5164)
(cuichengyou@ruri.waseda.jp)

***Abstract*:** In this paper, we propose a new method of a traffic signal control based on the predicted distribution of the traffic jam. First, we built a forecasting model to predict the probability distribution of vehicles for traffic jam during the each period of traffic signal. As the forecasting model, the Dynamic Bayesian Network is used and predicted the probability distribution of the amount of the standing vehicle in traffic jam. According to calculation by the Dynamic Bayesian network, the prediction of probability distribution of the amount of standing vehicles in each time will be obtained, and a control rule to adjust the split and the cycle of the signal to maintain the probability of a lower limit and a ceiling of the standing vehicles is deduced. Through the simulation using the actual traffic data of a city, the effectiveness of our method is shown.

Keywords: Traffic Jam, Traffic Signal Control, Dynamic Bayesian Network, Forecasting model, probabilistic distribution

I. INTRODUTION

In recent years, the traffic congestion has become serious problem, with the number of automobiles increased significantly. The traffic signal control is one of the effective ways to solve the problem.

The traffic forecasting has been known as an important part of the traffic signal control, and the Random walk method, Neuron Network, and Bayesian Network are known as the methods, however these methods do not use the information for neighboring roads.

In this paper, a Dynamic Bayesian networks (DBN) model to predict the probability distribution of standing vehicles is constructed based on the information of the neighboring roads, and the traffic signal control method is proposed.

II. FORECASTING MODEL AND PREDICT PROBABILITY DISTRIBUTION

1. DBN Model

The Bayesian network is a directed and acyclic graphical model, and each node represents variables of the given problem. The relationship between each variable is evaluated quantitatively using the conditional probability.

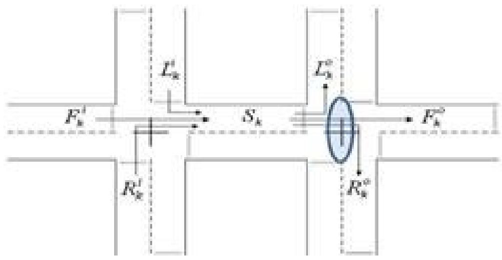

Fig.1 Crossroads and random variables

Here, we consider the two crossroads as shown in Fig.1. The random variables of the inflows and the outflows of the crossroad and the standing vehicles between the two roads are represented as nodes. The Bayesian network model of the standing vehicles is shown in Fig.2.

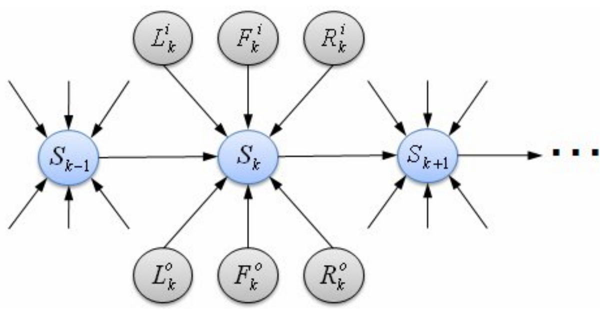

Fig.2 DBN model of standing vehicle

The number of the standing vehicles of k cycle can be calculated as eq.(1).

$$S_k = S_{k-1} + F_k^o + L_k^o + R_k^o - F_k^i - L_k^i - R_k^i \tag{1}$$

S_k : Standing vehicles of k cycle

S_{k-1} : Standing vehicles of k - 1 cycle

F_k^o : Outflowing straight vehicles of k cycle

L_k^o : Outflowing left turn vehicles of k cycle

R_k^o : Outflowing right turn vehicles of k cycle

F_k^i : Inflowing straight vehicles of k cycle

L_k^i : Inflowing left turn vehicles of k cycle

R_k^i : Inflowing right turn vehicles of k cycle

The probabilistic distribution of the standing vehicles is obtained by summing over all joint probability distribution of the other variables. With the chain rule, the joint probabilistic distribution is represented as the product of conditional probability as following,

$$\begin{aligned} &P(S_k, S_{k-1}, F_k^o, L_k^o, R_k^o, F_k^i, L_k^i, R_k^i) = \\ &P(S_k \mid S_{k-1}, F_k^o, L_k^o, R_k^o, F_k^i, L_k^i, R_k^i) P(S_{k-1}) \\ &\times P(F_k^o) P(L_k^o) P(R_k^o) P(F_k^i) P(L_k^i) P(R_k^i) \end{aligned} \tag{2}$$

And according to the d-separation, eq.(2) can be represented as

$$\begin{aligned} P(S_k) = &\sum_{S_{k-1}} \sum_{F_k^o} \sum_{L_k^o} \sum_{R_k^o} \sum_{F_k^i} \sum_{L_k^i} \sum_{R_k^i} \\ &P(S_{k-1}) P(F_k^o) P(L_k^o) P(R_k^o) P(F_k^i) P(L_k^i) P(R_k^i) \end{aligned} \tag{3}$$

According to above equation, the probabilistic distribution of the standing vehicle is calculated.

2. Predicted Probabilistic Distribution of Standing Vehicle

The priori probability of each variable is calculated from previous data firstly. And the probabilistic distribution of the standing vehicle at k cycle is calculated using the standing vehicle in proceeding cycle and the observed inflows and outflows of each direction. Next, the probabilistic distributions of the inflows, the outflows, and the standing vehicles at the cycle k+1, k+2,…, are predicted.

The splits and cycle of the traffic signal will be changed by the adjust rule which will be described at next session.

First, the passage ratio is calculated using the split and the cycle time at k cycle as

Passage ratio=traffic flow / (split*cycle time)

and, the future traffic flow is calculated using the fixed cycle and split. Then the probabilistic distributions of the future standing vehicle are predicted.

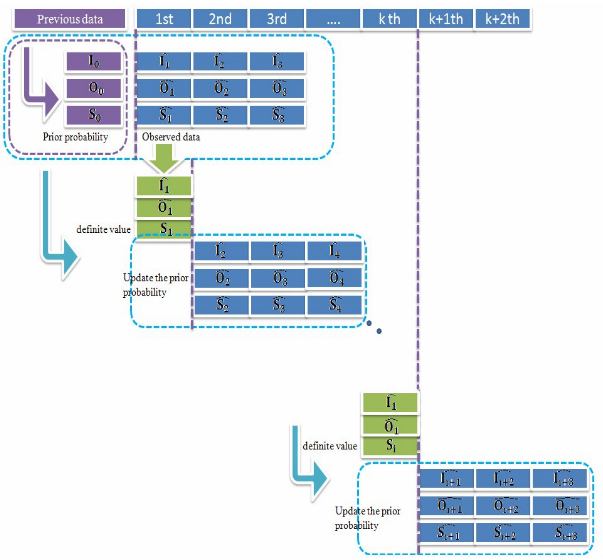

Fig.3 Flowchart of prior probability update

III. TRAFFIC SINGNAL CONTROL

1. Adjust Algorithm of Traffic Signal Control

According to the DBN model the probabilistic distribution of the standing vehicle is obtained. The split and cycle time of the traffic signal are controlled using the predicted probabilistic distribution of the standing vehicles. The control procedure is followed as that:

Step1: Predict the probabilistic distribution of the standing vehicles using the Dynamic Bayesian model to the 3rd cycle.

Step2: Calculate the probabilities Smax or above and Smin or below of the standing vehicles.

Step3: Compare these probabilities with the desired values.

Step4: Adjust the split and the cycle time until the probabilities for Smax and Smin satisfy the desired values.

The flowchart of the procedure for the traffic signal control is shown in Fig.4.

The probabilistic distribution will be change by the increase and decrease of the procedure. The two patters are considered.

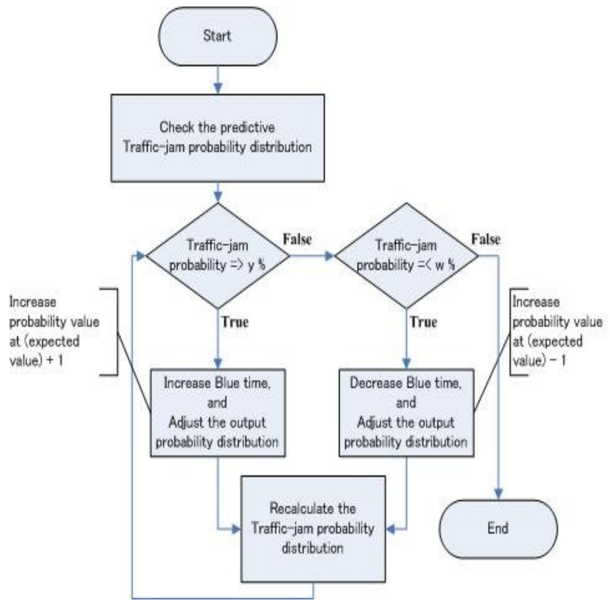

Fig.4 Flowchart of algorithm

2. Updated Patterns of Outflows Probability Distribution

The altered traffic signals will change the probabilities of the outflowing vehicles. To treat this situation, two patterns are considered here. As shown in Fig.5, the pattern 1 is to shift the probability distribution according to change of green time. The pattern 2 is to shift probability distribution as pattern 1, and increase probability of neighboring expectation and reduces others. In the simulation, pattern 2 to change the probabilistic distribution of the outflows is adopted.

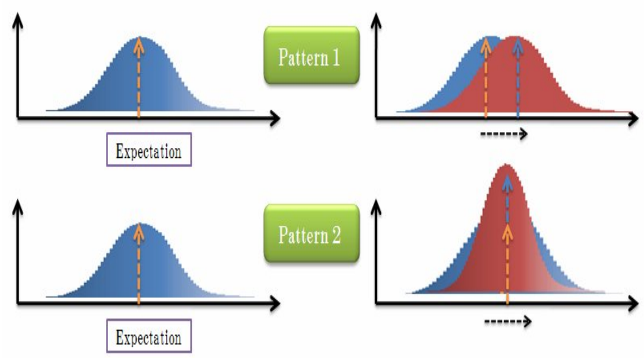

Fig.5 Update patterns

IV. SIMULATION

To prove the effective of the proposed method, a simulation was carried out based on the actual data at Tutuyimati, Kitakyushu on January 17th. 2007.

The parameters of the simulation are as: cycle length: 60-150[s]; split: 50-70%; Smax=75, Smi=35, α=0.1, β=0.1

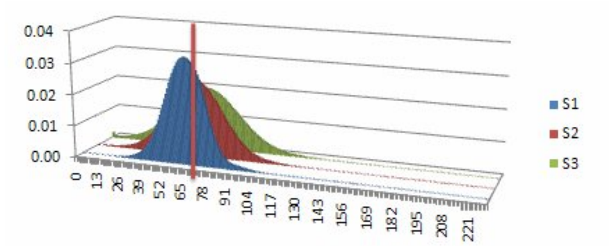

(a)

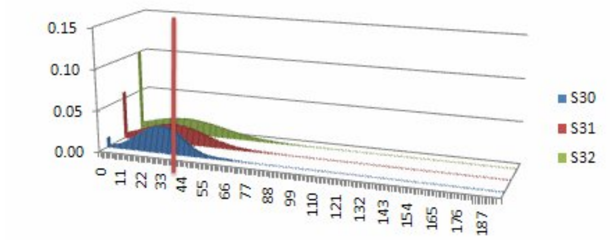

(b)

Fig.6 Predictive probabilistic distribution

Fig.6 shows the predicted probabilistic distribution of the number of standing vehicles from the cycle 1 to 3 and 30 to 32. We can see that probability of more than Smax is bigger than α in Fig.6(a), and the probability of less than Smin is bigger than β in Fig.6(b) .

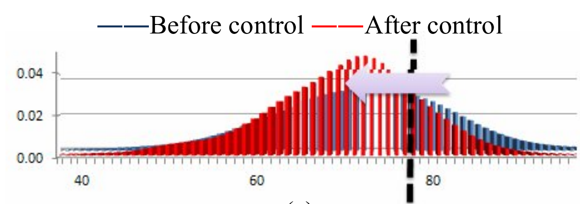

(a)

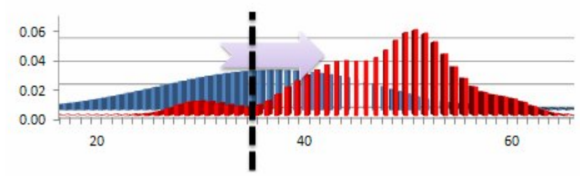

(b)

Fig.7 Probabilistic distribution of before and after control

Fig.7 is the probabilistic distribution of the standing vehicles before and after control at the cycle 1 and 30. By the extension of the green time, the probabilities of the more than Smax and less than Smin are updated to be small.

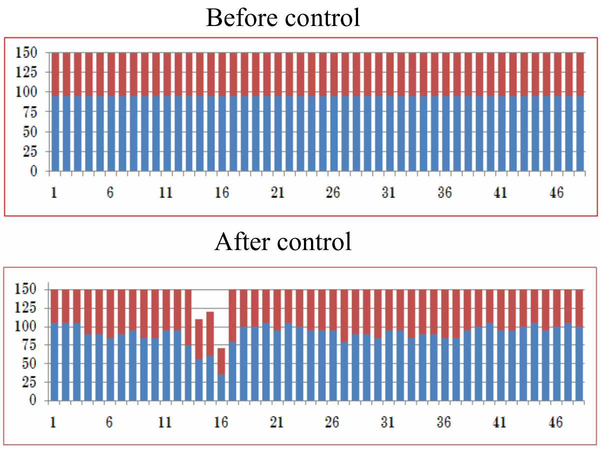

Fig.8 Split and Cycle time before and after control

The result of the splits and cycle time of the traffic signal by the control procedure is illustrated in Fig.8. The numbers of the standing vehicles on the main and minor roads before and after control are shown in Fig.9. In the main road, the numbers of the standing vehicles are within the desired numbers from 35 to 70.

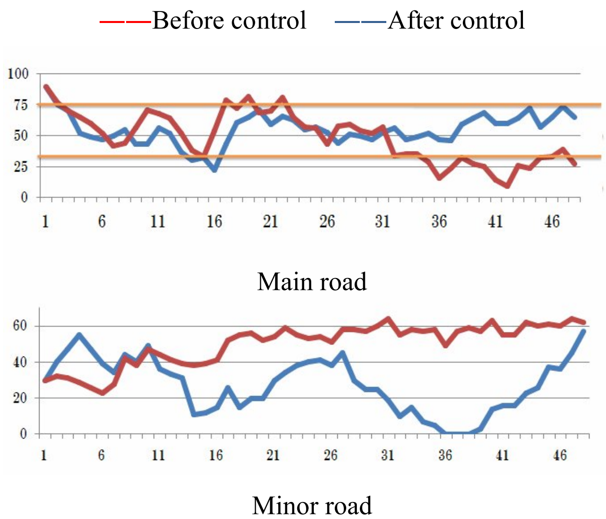

Fig.9 Standing vehicles of main road and minor road

The sum of the main and minor roads is compared before and after control in Fig.10. The number of standing vehicles by the proposed traffic signal control is decreased by 16% compared with the fixed traffic signal.

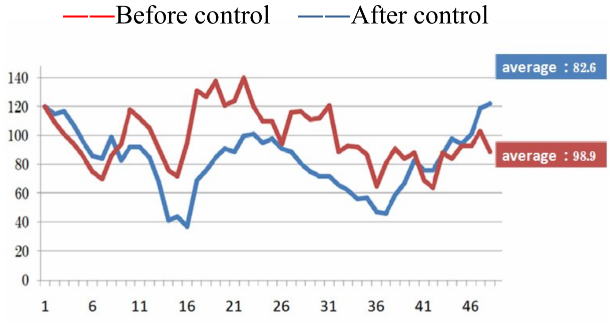

Fig.10 Standing vehicles of before and after control

V. CONCLUSIONS

In this paper, DBN model to predict the probabilistic distribution of the standing vehicles was built. And the adjust algorithm to control the cycle and the split of the traffic signal is proposed. Through the simulation using the actual data, the effectiveness of the new method is shown.

For the future research, the processing time of the adjusting algorithm will be reduced to achieve real-time control.

REFERENCES

[1] Keinosuke Matsumoto, Koichi Kise, Naoki Mori (2002), Introduction to Intelligent Systems Engi neering(in japannese). 4:69-78
[2] Lianwen Zhang, Haipeng Guo(2006) Introduction to Bayesian networks(in chinese). 2:62-65
[3] Shiliang Sun, Changshui Zhang, Guoqiong Yu(2 006), A Bayesian Network Approach to Traffic Flow Forecasting
[4] Japan Society of Traffic Engineers(2006)
[5] Richard E. Neapolitan(2003), Learning Bayesian Networks

The Fourteenth International Symposium on Artificial Life and Robotics 2009 (AROB 14th '09),
B-Con Plaza, Beppu, Oita, Japan, February 5 - 7, 2009

Pipe Inspection Robot using Wireless Communication System

H. Ogai[1], Y.Yeh[1], D. Wu [1], K.Hirai[2], T. Abe[2] and G. Sato[3]

[1]Graduate school of Information, Production and Systems, Waseda University, Japan
(Tel: +81-93-672-5147; Fax: +81-93-672-5147)
(E-mail: ogai@waseda.jp,dongmei_wu2008@yahoo.co.jp)
[2]Kawasaki office, Hakutsu Technology Corporation, Kanagawa, Japan
[3]Kawasaki office, Wave Professional Inc., Kanagawa, Japan

Abstract: Recently many plants become old, and then the pipe lines in the plant also become old. For that reason, it is necessary to develop a flexible pipe inspection robot using wireless communication system. In this research, we have studied the wireless communication system. And we know that the communication system can steadily transfer image data at high speed. Therefore, we developed a new pipe inspection robot with wireless communication system for drain pipe. With this new system, we can control the movement of the robot and inspect the defect or trouble inside the steel pipe or ceramic pipe and also we can transfer the image information inside the pipe in real time.

Keywords: Pipe inspection robot, wireless communication system, image information, real time

I. INTRODUCTION

Recently many plants become old and pipe lines in the plant also become old. In order to inspect and repair these pipes [1], a flexible automotive inspection robot is needed, beside, for controlling the inspection robot and transmitting the collected data to terminal institute, wireless communication system need to be applied together with the inspection robot.

In 2005, radio wave transmission property in steel pipe line had been measured, as for the measurement, if we use wireless LAN with OFDM-2.4GHz or 5.2GHz in the steel pipe, more than 10Mbps information could be transmitted, provide the measured pipe diameter is 20-40cm, and its length within 100m.

Besides, transmission property for ceramic pipe line was also tested, radio transmission property was greatly affected by pollutant, provided the pipe has little pollutant, information data could be transmitted to a long distance.

We have studied the wireless communication system. The wireless communication system can steadily transfer the image data at high speed. Therefore, in this research, we developed a new pipe inspection robot with wireless communication system for drain pipe. With this system, we can control the movement of the robot and inspect the defect or trouble inside the steel pipe or ceramic pipe, and also we can transfer the image information inside the pipe in real time.

II. PIPE INSPECTION SYSTEM

1. Transmission Test in the Steel Pipe

Steel pipe with 30cm diameter and 10 m length is shown in Fig.1. The transmission loss from transmitting antenna input to receiving antenna output is $14 \pm 6dB$ in 2.4GHz band (as Fig.2 shown), $23 \pm 7dB$ in 5.2 GHz band (as Fig.3 shown). So we can transmit [2].

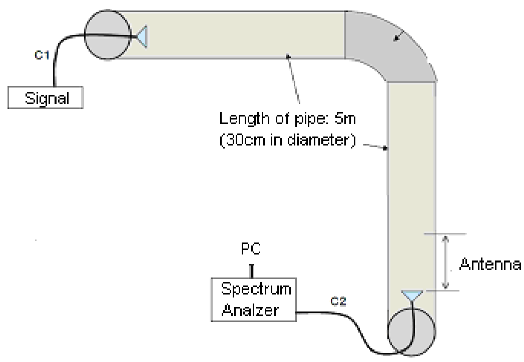

Fig.1. Wireless communication property measurement in the steel pipe

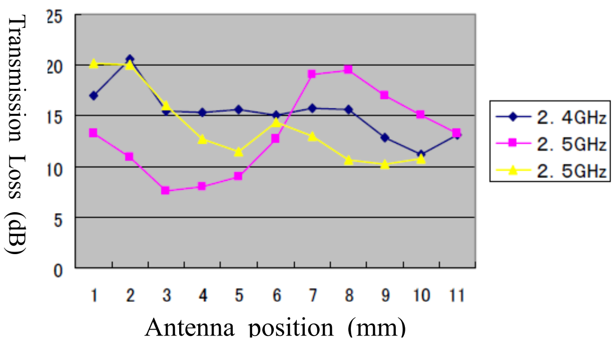

Fig.2. Wireless communication property (Transmission Loss) in Steel Pipe (2.4 GHz)

©ISAROB 2009

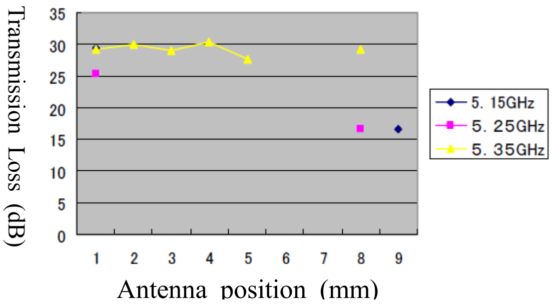

Fig. 3 Wireless communication property (Transmission Loss) in Steel Pipe (5.2 GHz)

2. Transmission Test in the Ceramic Pipe

As for the ceramic pipe with 25cm diameter and 7m length(as shown in Fig.4), the transmission loss was $84 \pm 2.5dB$ in 2.4GHz band, $52 \pm 1.5dB$ in 5.2GHz. Fig.5 shows the relative electric field strength between ceramic pipe and free space. 5.2Ghz band have a good performance in ceramic pipe.

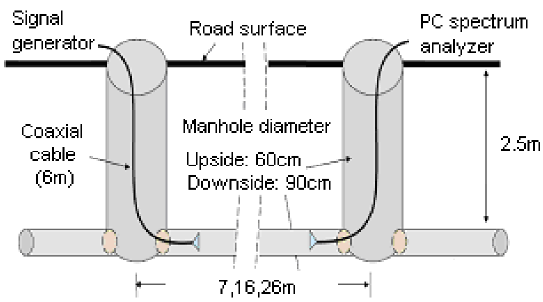

Fig.4. Wireless communication property measurement in the ceramic pipe

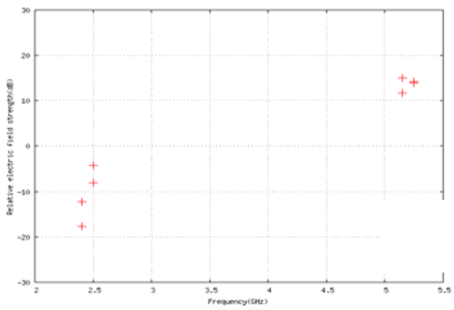

Fig.5. Wireless communication property Result in Ceramic Pipe

III.ROBOT TEST AND TRANSMISSION LOSS MEASUREMENT

We did robot test and transmission loss measurement in actual drain pipe at Yahata in Kitakyushu city in 2007.

1. Robot Test

The wireless robot could run inside the pipe with 20m length and transmitted the inside image data in real time.

Fig.6 shows pipe inspection robot system.

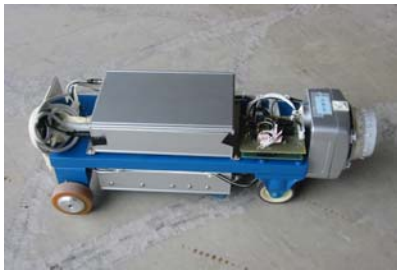

Fig.6. Pipe inspection robot system

2. Transmission Loss Specification

Specifications of transmission loss are explained as the following:

- Measured frequency: 5.25GHz,
- Transmit output: 17dBm,
- Receiver antenna: each 13dBi, total 26 dB,
- Receive cable loss: 6dB.

Fig.7 shows date transmitting and receiving schematic system.

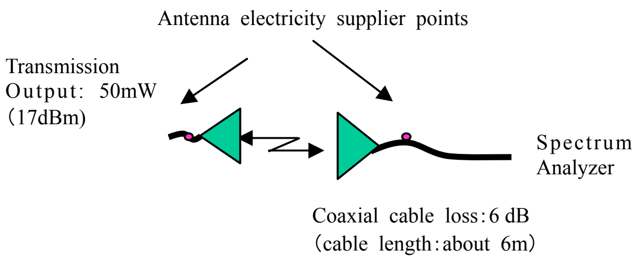

Fig.7. Transmit and receive theoretical schematic

3. Transmission Loss Measurement

The measurement is conducted under the following conditions:

The pipe is ceramic pipe, and well cleaned,

The pipe length is 19m,

There are two type ceramic pipes with different diameter as 25cm and 30cm.

Fig. 8 is the schematic diagram for transmission loss measurement system.

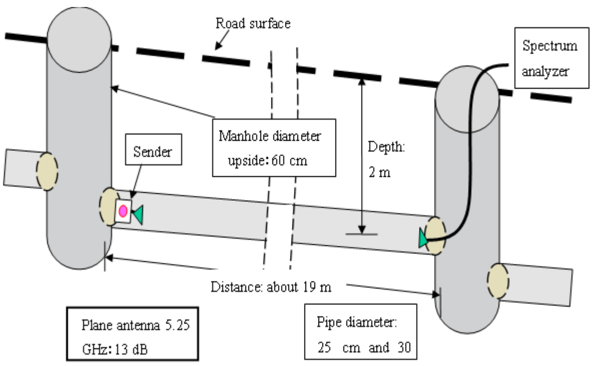

Fig.8. Transmission loss measurement system

4. Measurement Results

Measured data were processed with different method, transmission loss and the approximate equation for 25cm and 30cm diameter pipe are shown in Fig.9, and Fig.10 shows the transmission loss between antenna points, which is measured on the desk indoors.

As for these figures, it is found that transmission loss can be explained using approximate linear equation.

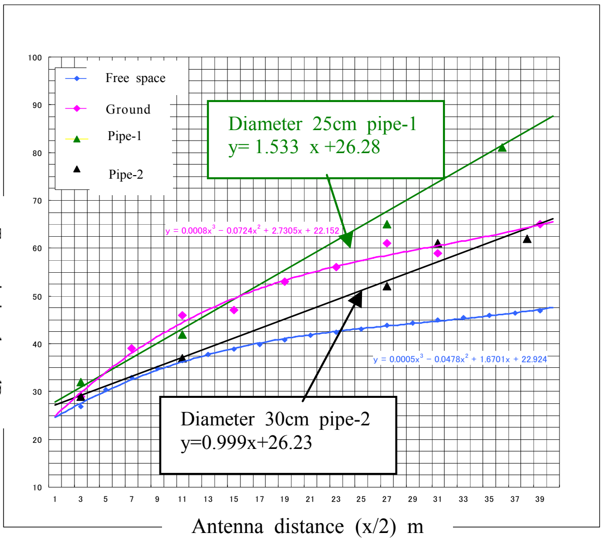

Fig.9. Transmission property

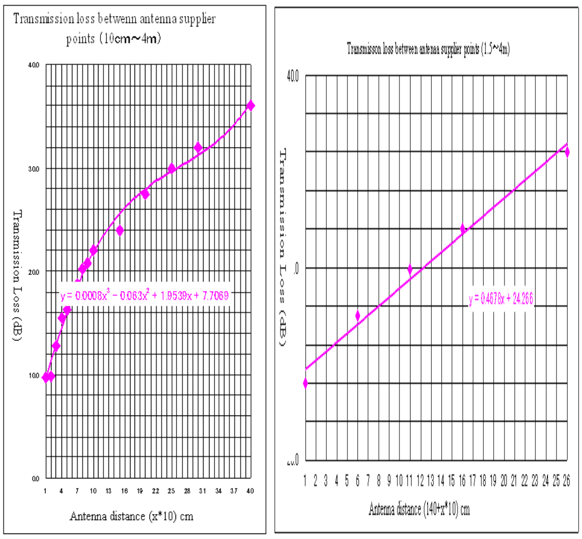

Fig.10. Transmission loss between antenna points

5. Result Discussion

(1) Considering the ground transmission property, measured result in close range, and error, we can use approximate equation in Fig.9 to predict transmission loss in pipe.

(2) The measured data is arranged to Table.1.

Table.1. Approximate Transmission Loss in Pipe line

distance (m)	transmission loss (dB)	
	25cm	30cm
1	27.8	27.2
2	30.9	29.2
5	40.1	35.2
10	55.5	45.2
20	86.2	65.2
30	116.9	85.2

Transmission loss in pipe can be explained by the following equations:

As for diameter 25cm pipe, transmission loss L:

$$L = 3.07 \times d + 24.75 \qquad (1)$$

As for diameter 25cm pipe, transmission loss L:

$$L = 2.00 \times d + 25.22 \qquad (2)$$

From these equations, it is found that the transmission loss (dB) is proportional to the pipe line length, as shown in Fig.11.

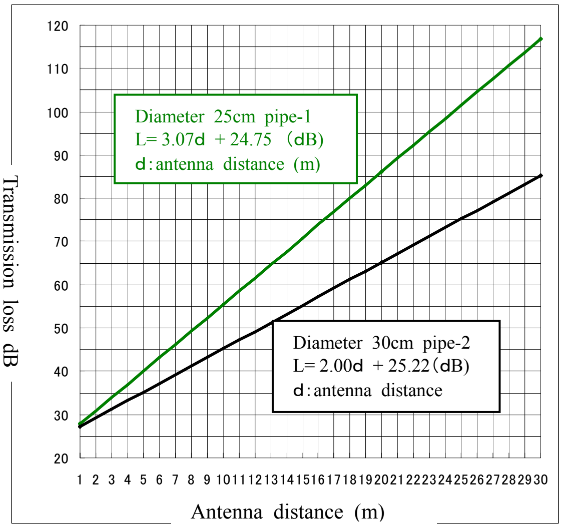

Fig.11. Transmission loss property between antenna electricity supplier points (Antenna distance more than 1m)

(3) Transmission loss property is obtained: if the antenna distance more than 1.5km, transmission loss would increase 3.07dB/m for 25cm diameter pipe, and 2.0dB/m for 30cm diameter pipe.

IV. WIRELESS PIPE INSPECTION SYSTEM

The aforesaid robot inspection system is a testing one, considering real environment, a new robot is applied, besides, wireless communication system would be introduced into the robot, for data transmission and robot control.

1. Wireless Robot System Diagram

Fig.12 shows the small size wireless robot system.

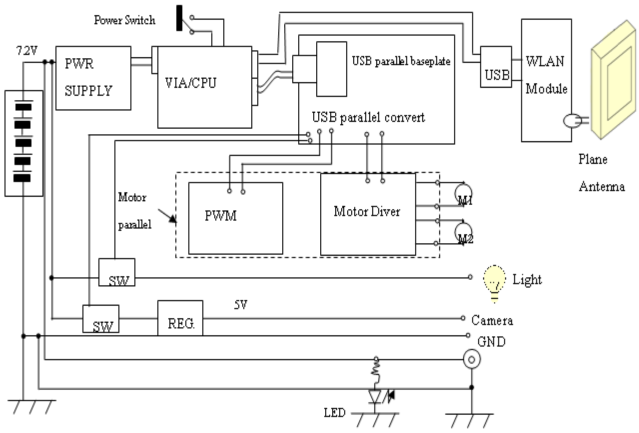

Fig.12. Small size wireless robot system

2. Inspection Robot

The inspection robot applied is Mogurinko by Ishikawa Tekkousyo, as shown below.

Fig.13. Inspection robot (Mogurinko)

Specifications of the inspection robot:

- Moving speed: 13.7m/min,
- Driveling mode: double motor,
- Electric Power: rechargeable batteries 7.2V.
- Wireless frequency: apply to 2.4/5 GHz and Data transmission by 100 base-T Ethernet.

3. Wireless Communication System

There are two type wireless communication system in long distance pipe or manhole.

In order to ensure the information transmission which passes manhole, the two-way amplifier between antennas is introduced (type-1 shown in Fig.14). As for the type-2 wireless communication system (shown in Fig.15), it could realize 200-300m information transmission, besides, it is possible to be applied to mesh cable and parallel two-wire cable.

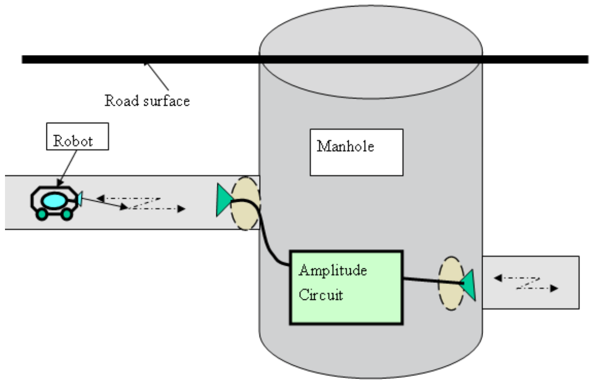

Fig.14. Wireless system type-1(two-way transmission type)

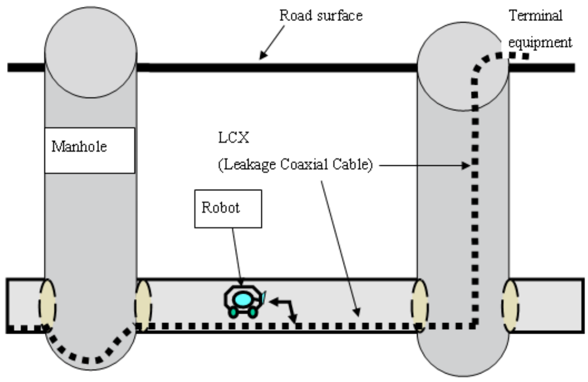

Fig.15. Wireless communication system type-2

V. CONCLUSION

We studied the wireless communication system in the pipe, and developed new robot system which would be used in pipe inspection robot system. We tested transmission loss in ceramic pipe, and got the transmission property.

Because of different pipe materials and service condition, maximum transmission length would be determined for wireless communication system.

REFERENCES

[1] Kosuke Wada (2007), Wireless Radio Communication System for Pipe Inspection Robot and Bridge Diagnosis Data. Waseda University, Master's thesis,

[2] Harutoshi Ogai, Kosuke Wada, Katsumi Hirai, et al (2007), Wireless Radio Communication System for a Pipe Inspection Robot, International Conference on Control, Automation, and System, October 17-20, Korea.

©ISAROB 2009

Production Adjusting Method based on Predicted Distribution of Production and Inventory using Dynamic Bayesian Network

Yeong-Hwa Park*, Ji-Sun Shin, Ki-Yun Woo(Waseda University)
Fumihiro Shoji(Fukuoka Institute of Technology), Hee-Hyol Lee(Waseda University)

Graduate School of Information, Production and Systems, Waseda University
2-7 Hibikino, Wakamatsu-ku, Kitakyushu, Fukuoka, 808-0135, Japan
(*Tel & Fax: 81-93-692-5164*)
(*Email address: parkyh@akane.waseda.jp*)

Abstract: In general, the production quantities and the delivered goods are changed randomly, and then the total stock is also changed randomly. This paper deals with the production and inventory control of an automobile production part line using the Dynamic Bayesian Network. Bayesian Network indicates the quantitative relations between the individual variables by the conditional probability. The probabilistic distribution of the total stock is calculated through the propagation of the probability on the network. Moreover, an adjusting rule of the production quantities to maintain the probability of the lower bound value and the upper bound value of the total stock to certain values is shown.

Keywords: Dynamic Bayesian Network, Production Adjusting Method, Predicted Distribution, Delivery data

I. INTRODUCTION

In the manufacturing business, the delivery guarantee of quantities is a prerequisite for improving the credit of corporation and securing profit. However, the delivery quantity, the production quantity, and the inventory is changed according to various unexpected reasons. Then the prediction of production inventory which can cope with such irregular fluctuations is required. This paper deals with an adjusting production method using the Dynamic Bayesian Network (DBN) for all factors which influence the production quantity, the delivery quantity, and the inventory quantity for an automobile part production process. This study also provides an adjusting production schedule algorithm that adjusts sequentially the production schedule for appropriate guarantee of the deadline. Furthermore, an adjusting rule of the production quantities to maintain the delivery guarantee is provided.

II. CONSTRUCTION OF DBN MODEL FOR PRODUCTION AND INVENTORY CONTROL IN AN AUTOMOBILE PARTS PRODUCTION PROCESS

The production quantities and the delivered goods are changed randomly in real problem, and then the total stock is also changed irregularly under these conditions.

Dynamic Bayesian Network is applied to the production and inventory control of the automobile part that calculate the probabilistic distribution of the total stock through the propagation of the probability on the network. The target production system is as that:

· Item of the production: :
Automobile engine valve lifter
· Max of production quantity: 1,000,000ea/month
· Actual data period: JAN.2003 ~ DEC.2005

Production quantity for each month is decided by the inventory of previous month and the delivery quantity of the month. However, the production quantity must take into consideration the conditions at the production site. The reason is that the production quantity can be changed according to the trouble of equipments and the outbreak cancels, etc. And, the delivered goods is also assumed that it can be changed randomly according to the order-change, the control of inventory quantities, and the manufacturing trouble, etc. The production process is as follows.

· Production quantities : A_t
· Delivery quantities : D_t
· Total stock : S_t
· Its forecast and an adjustment period of the production schedule hold between m months
($t=1,2,...,l$ l : forecast adjustment months).
· Factors for the production quantities
$RA\alpha_t$: ($\alpha=A,B,\ldots,Z$ α: factors)
$RA\alpha\beta_t$: ($\beta=A,B,\ldots,Z$ β: factors)
$RA\alpha\beta\gamma_t$: ($\gamma=A,B,\ldots,Z$ γ: factors)
$RA\alpha\beta\gamma\zeta_t$: ($\zeta=A,B,\ldots,Z$ ζ: factors)
$RA\alpha\beta\gamma\zeta^i{}_t$: ($i=1,2,...,m$ m:The number of factors)
· Probabilistic change factor of the delivery quantities
$RD\kappa_t$: ($\kappa=A,B,\ldots,Z$ κ: factors)
$RD\kappa\lambda_t$: ($\lambda=A,B,\ldots,Z$ λ: factors)
$RD\kappa\lambda\mu_t$: ($\mu=A,B,\ldots,Z$ μ: factors)
$RD\kappa\lambda\mu\nu_t$: ($\nu=A,B,\ldots,Z$ ν: Factors)

©ISAROB 2009

$RD\kappa\lambda\mu v^j_t$: (j=1,2,...,n n:The number of factors)

· Production quantity of every month : $A_t \leq A_{max}$

Thus, the total stock of the product S_t of tth month can be expressed as eq. (1)

$$S_t = S_{t-1} + A_t - D_t \tag{1}$$

The stochastic model of the production and the inventory control considering the practical dependence of the productions, deliveries, and inventories changed randomly is illustrated in Fig.1. In addition, each factor which corresponds to each node is shown in Table 1.

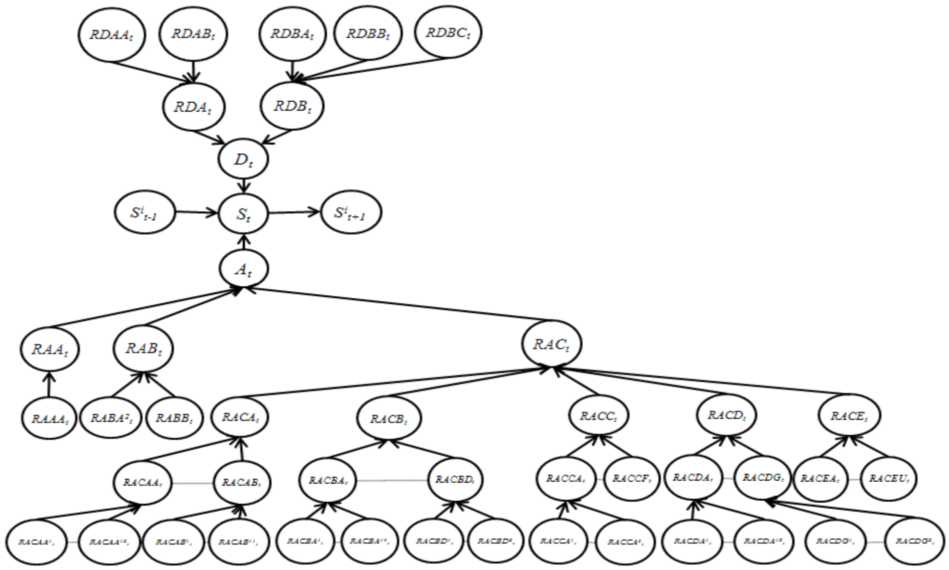

Fig. 1. Stochastic model of production and inventory by Dynamic Bayesian Network

Table1. The stochastic variable of delivered goods and production

$\boldsymbol{S_t}$	**Inventory quantities**	$RACAF_t$	An external diameter processing
$\boldsymbol{D_t}$	**Delivered goods**	$\boldsymbol{RACB_t}$	Inferior of B2
$\boldsymbol{RDA_t}$	The cause of external	$RACBA_t$	Lathe processing
$RDAA_t$	A poor outbreak process	$RACBB_t$	Dimensional check
$RDAB_t$	A poor delivery inspection	$RACBC_t$	An external diameter processing
$\boldsymbol{RDB_t}$	The cause of in-company	$RACBD_t$	The inside diameter processing
$RDBA_t$	Strike of customer	$\boldsymbol{RACC_t}$	Inferior of DPL
$RDBB_t$	Order-change of A/S products	$RACCA_t$	DPL-lathe processing
$RDBC_t$	Change of production schedule	$RACCB^t$	Crowning
$\boldsymbol{A_t}$	**production quantities**	$RACCC_t$	Hole-processing
$\boldsymbol{RAA_t}$	The cause of external	$RACCD_t$	An external diameter processing
$RAAA_t$	Order-change	$RACCE_t$	Hole polishing
$\boldsymbol{RAB_t}$	The cause of in-company	$RACCF_t$	An external diameter processing
$RABA_t$	Control of Inventory quantity (+)	$\boldsymbol{RACD_t}$	Inferior of assembling
$RABB_t$	Control of Inventory quantity (-)	$RACDA_t$	HOLE -CHECK
$\boldsymbol{RAC_t}$	Inferior a manufacturing process	$RACDB_t$	CLIP Insertion
$RACA_t$	Inferior of B1	$RACDC^t$	DPL-assembling
$RACAA_t$	Body-lathe processing	$RACDD_t$	Stratification
$RACAB_t$	Hole-processing	$RACDE_t$	Stratification
$RACAC_t$	An external diameter processing	$RACDF_t$	Assembling
$RACAD_t$	Crowning	$RACDG_t$	OIL-pouring
$RACAE_t$	Swaging	$\boldsymbol{RACE_t}$	Product inspection

©ISAROB 2009

III. MAINTENANCE OF APPROPRIATE INVENTORY THROUGH PRODUCTION ADJUSTING ALGORITHM

1. Prior Probabilistic Distribution

Actual data on the production and delivery for 36 months are shown in Fig.2. Also, Fig.3 represents all factors related to the production and delivery.

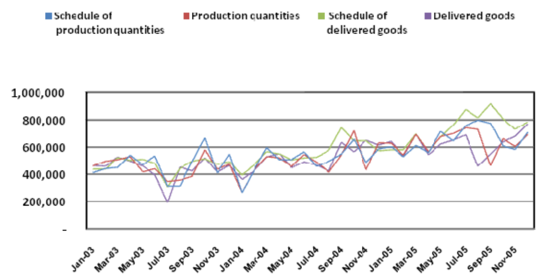

Fig.2. Schedule and actual data of production, delivered good and inventory quantities

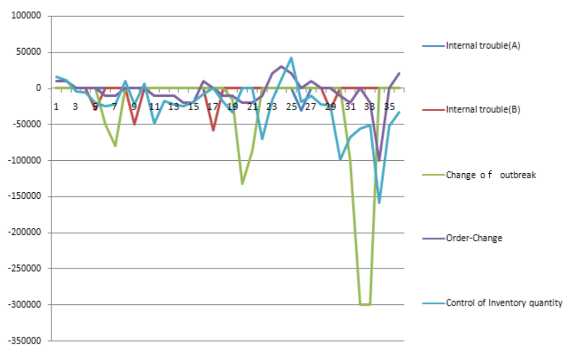

Fig. 3. Main cause of change

Delivery quantity is changed according to various factors such as the order-change and the manufacturing trouble postponement of delivery. Here, the prior probability on the change of delivery quantity is calculated based on the actual data from January 2003 to December 2005 (36 months). The prior probability is calculated using the quantity and frequency of each factor, and is set as shown in Fig4.

The prior probability of the internal trouble is shown in Fig.7, and the prior probability of the order change can be founded shown in Fig.8. In addition, the actual production quantity for each month has to take account of the change which results from various factors including the order change, the inventory control and the defect in the process. These prior probabilities are calculated based on the past data as shown in Fig.9, Fig.10, and Fig.11.

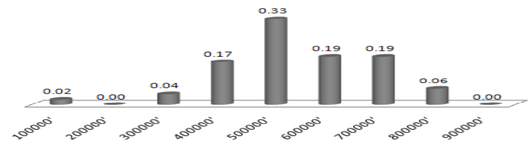

Fig.4. Prior probability of delivered goods

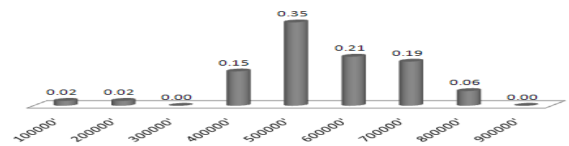

Fig.5. Prior probability of production quantities

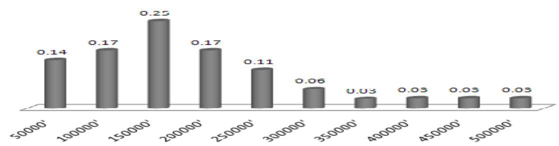

Fig.6. Prior probability of inventory quantities

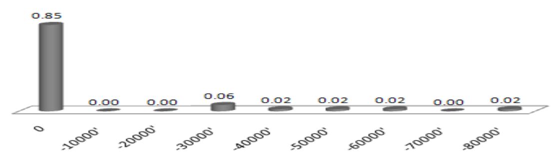

Fig.7. Prior probability of internal trouble

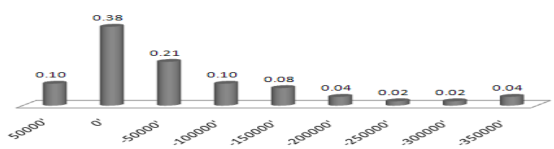

Fig.8. Prior probability of change of outbreak

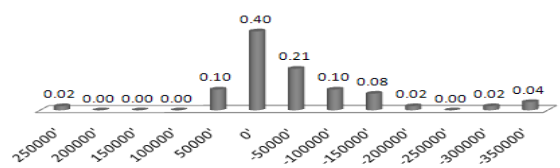

Fig.9. Prior probability of order change

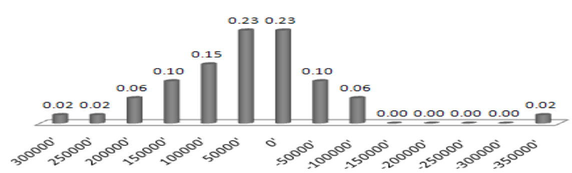

Fig.10. Prior probability of control inventory quantity

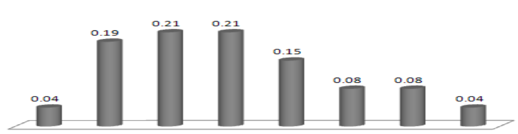

Fig.11. Prior probability of trouble-amount

Therefore, the probability distribution for the amount of the product A_i in stock of the ith month can be calculated as that:

$$P(S_t^i) = \sum_{S_{t-1}^i}\sum_{A_t^i}\sum_{D_t^i}\sum_{RA\alpha_t}^{C}\sum_{RD\kappa_t}^{B}\sum_{RA\alpha\beta}^{E}\sum_{RD\kappa\lambda_t}^{C}\sum_{RA\alpha\beta\gamma_t}^{U}\sum_{RA\alpha\beta\gamma\zeta_t}^{G} P(S_t^i, S_{t-1}^i, A_t^i, D_t^i, RA\alpha_t, RD\kappa_t, RA\alpha\beta_t, RD\kappa\lambda_t, RA\alpha\beta\gamma_t, RA\alpha\beta\gamma\zeta_t) \quad (2)$$

$$\begin{aligned}
&P(S_t^i, S_{t-1}^i, A_t^i, D_t^i, RA\,\alpha_t, RD\,\kappa_t, RA\,\alpha\beta_t, RD\,\kappa\lambda_t, RA\,\alpha\beta\gamma_t, , RA\,\alpha\beta\gamma\zeta_t) \\
&= P(S_t^i \mid S_{t-1}^i, A_t^i, D_t) P(S_{t-1}^i) P(A_t^i) P(D_t^i) \\
&\times P(A_t^i \mid RA\,\alpha_t, RA\,\alpha\beta_t, RA\,\alpha\beta\gamma_t, RA\,\alpha\beta\gamma\zeta_t) \\
&\times P(D_t^i \mid RD\,\kappa_t, RD\,\kappa\lambda_t) \\
&\times P(RA\,\alpha_t \mid RA\,\alpha\beta_t, RA\,\alpha\beta\gamma_t, RA\,\alpha\beta\gamma\zeta_t) P(RA\,\alpha_t) \\
&\times P(RD\,\kappa_t \mid RD\,\kappa\lambda_t) P(RD\,\kappa_t) \\
&\times P(RA\,\alpha\beta_t \mid RA\,\alpha\beta\gamma_t, RA\,\alpha\beta\gamma\zeta_t) \\
&\times P(RA\,\alpha\beta_t) P(RD\,\kappa\lambda_t) \\
&\times P(RA\,\alpha\beta\gamma_t \mid RA\,\alpha\beta\gamma\zeta_t) P(RA\,\alpha\beta\gamma_t) P(RA\,\alpha\beta\gamma\zeta_t)
\end{aligned} \quad (3)$$

$$\begin{aligned}
P(S_t^i) &= \sum_{S_{t-1}^i}\sum_{A_t^i}\sum_{D_t^i}\sum_{RA\,\alpha_t}^{C}\sum_{RD\,\kappa_t}^{B}\sum_{RA\,\alpha\beta}^{E}\sum_{RD\,\kappa\lambda_t}^{C}\sum_{RA\,\alpha\beta\gamma_t}^{U}\sum_{RA\,\alpha\beta\gamma\zeta_t}^{G} P(S_t^i, S_{t-1}^i, A_t^i, D_t^i, RA\,\alpha_t, RD\,\kappa_t, RA\,\alpha\beta_t, RD\,\kappa\lambda_t, RA\,\alpha\beta\gamma_t, RA\,\alpha\beta\gamma\zeta_t) \\
&= \sum_{S_{t-1}^i}\sum_{A_t^i}\sum_{D_t^i}\sum_{RA\,\alpha_t}^{C}\sum_{RD\,\kappa_t}^{B}\sum_{RA\,\alpha\beta}^{E}\sum_{RD\,\kappa\lambda_t}^{C}\sum_{RA\,\alpha\beta\gamma_t}^{U}\sum_{RA\,\alpha\beta\gamma\zeta_t}^{G} P(S_t^i \mid S_{t-1}^i, A_t^i, D_t) \\
&\times P(A_t^i \mid RA\,\alpha_t, RA\,\alpha\beta_t, RA\,\alpha\beta\gamma_t, RA\,\alpha\beta\gamma\zeta_t) \\
&\times P(D_t^i \mid RD\,\kappa_t, RD\,\kappa\lambda_t) \\
&\times P(RA\,\alpha_t \mid RA\,\alpha\beta_t, RA\,\alpha\beta\gamma_t, RA\,\alpha\beta\gamma\zeta_t) \\
&\times P(RA\,\alpha\beta_t \mid RA\,\alpha\beta\gamma_t, RA\,\alpha\beta\gamma\zeta_t) \\
&\times P(RA\,\alpha\beta\gamma_t \mid RA\,\alpha\beta\gamma\zeta_t) P(RD\,\kappa_t \mid RD\,\kappa\lambda_t) \\
&\times P(S_{t-1}^i) P(A_t^i) P(D_t^i) P(RA\,\alpha_t) P(RA\,\alpha\beta_t) \\
&\times P(RA\,\alpha\beta\gamma_t) P(RA\,\alpha\beta\gamma\zeta_t) P(RD\,\kappa_t) P(RD\,\kappa\lambda_t)
\end{aligned} \quad (4)$$

Eq.(2) is simplified as eq.(3) by the D-separation which is the feature of Dynamic Bayesian Network. Therefore, the probability distributions of the inventory quantity are calculable from eq.(4).

2. Adjusting Algorithm of Production Schedule

The total stock is decided by an amount of stock of the previous month, delivered goods, and production quantities on the month. But, it is necessary to consider a large amount of the shipment after the month, and to keep more than a certain amount. Then, an adjusting rule of the production schedule to maintain the probability of the lower limit and upper limit value of the total stock to a certain value is necessary.

As an example, the production schedule is improved as that the probabilities of more than the lower limit and upper bound of the total stock don't exceed 5%. Here the lower limit and the upper bound of the amount for the total stock A_t are 100,000 and 1,000,000, respectively.

The algorithm of the improvement rule is shown in Fig.12. The production schedule can be updated automatically by the algorithm.

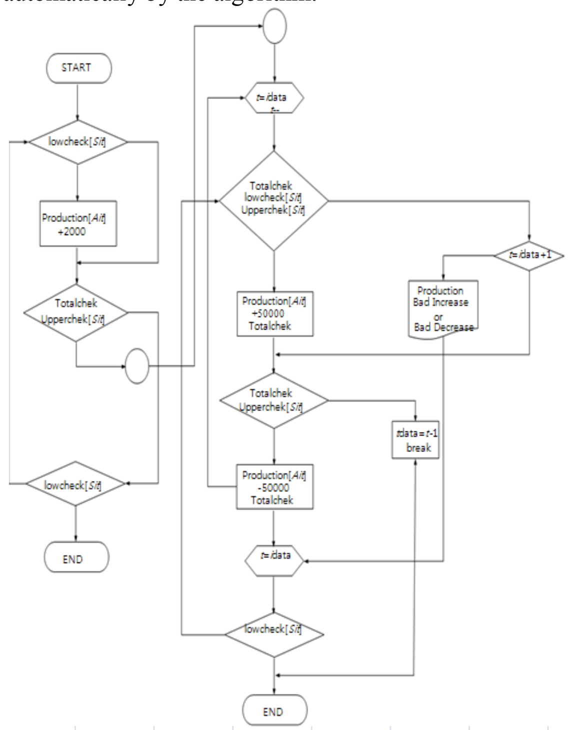

Fig.12. Adjusting rule of flow chart

3. Predictive Distribution of Inventory

The probability distribution of the total stock of one year(2006) based on the initial production schedule of Table 2 is shown in Fig.13.

Table 2. Schedule of production (2006year)

Month-Year	Jan-06	Feb-06	Mar-06	Apr-06
Schedule of Delivered goods	800,000	500,000	500,000	600,000
Schedule of Production	**550,000**	**500,000**	**500,000**	**500,000**
Month-Year	**May-06**	**Jun-06**	**Jul-06**	**Aug-06**
Schedule of Delivered goods	750,000	700,000	100,000	550,000
Schedule of Production	**450,000**	**500,000**	**300,000**	**450,000**
Month-Year	**Sep-06**	**Oct-06**	**Nov-06**	**Dec-06**
Schedule of Delivered goods	600,000	750,000	700,000	700,000
Schedule of Production	**750,000**	**700,000**	**400,000**	**450,000**

The production schedule updated by the adjusting algorithm based on the prior probabilities is shown in Fig.14. The new probabilistic distribution of the total stock by this corrected production schedule is as shown in Fig.15.

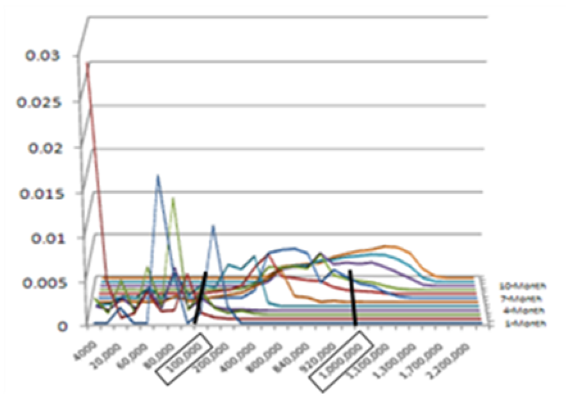

Fig.13. Probability distribution of production schedule

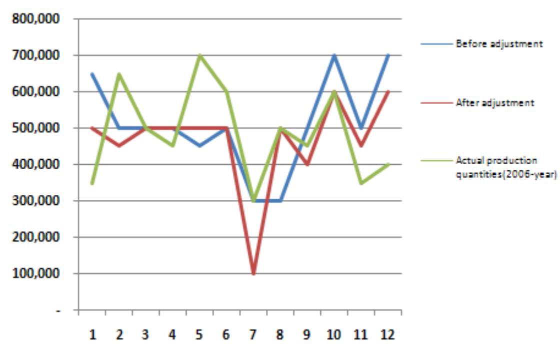

Fig.14. Adjustment of production schedule

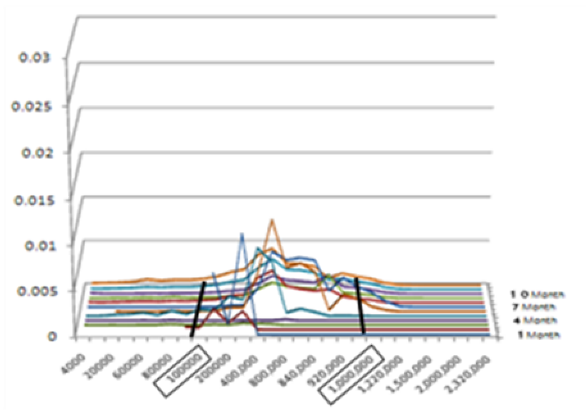

Fig.15. Adjustment of probability distribution of production schedule

As the results, it is understood that the probability for the stock to be 100,000 or less has become small more than 5% as shown in Fig.16. And also the probability for the stock to be 1,000,000 or more has become small more than 5% as shown in Fig.16.

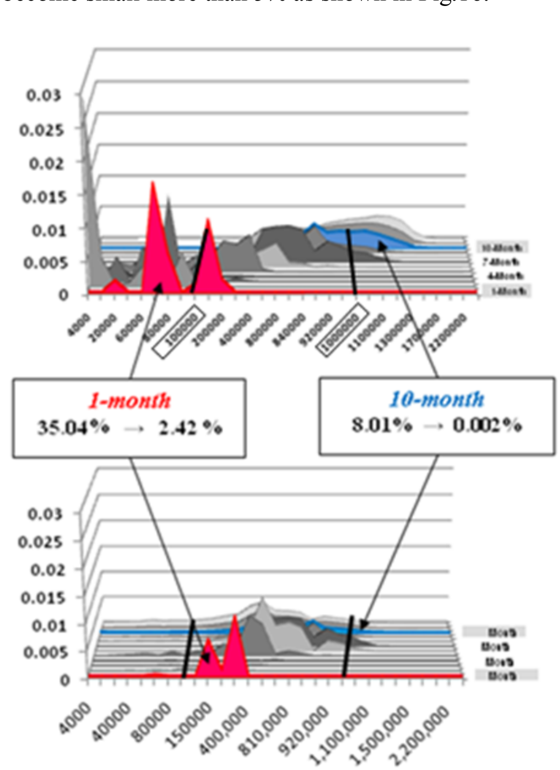

Fig.16. Adjustment of the lower limit

The inventory quantity before adjustment and after adjustment are compared with no adjustment as shown in Fig.17. As the results, the actual inventory dose not exceed target inventory (200,000 ~ 300,000 products). Therefore, the delivery guarantee goods and the maintenance of appropriate inventory can be achieved by considering the probabilistic changes in the delivery quantity and production quantity using the adjusting production algorithm.

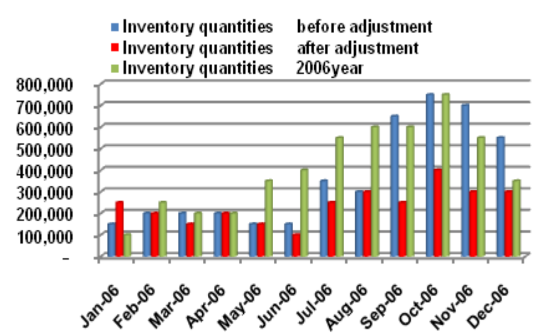

Fig.17 Inventory quantities of adjusted production and Actual production

VI. CONCLUSION

This paper dealt with the production and inventory control of the automobile part process using the Dynamic Bayesian Network. We consider the real situation in which the production quantities and delivered goods are changed randomly, then the total stock is also changed randomly.

Firstly, the probabilistic distribution of the total stock was calculated through the propagation of the probability on the network. Furthermore, the adjusting rule of the production quantities to maintain the probability of the lower limit and upper bound value of the total stock to a certain value was deduced.

As the result, the production schedule could be updated so as not to exceed the probability of the lower bound value and upper bound value of the amount of stock specified. By this method, the reduction in costs from the excessive production and the expense of the inventory management expense can be expected.

REFERENCES

[1] A. Biedermann, F. Taron, Bayesian networks and probabilistic reasoning about scientific evidence when there is a lack of data, Forensic Science International 157(2006)

[2] P. Seferlis N. F. Giannelos: A Tow-lauered Optimization-based Control Strategy for Multi-echelon Supply Chain Networks, Computers and chemical Engineering, Vol.28, pp.799-809, 2004

[3] Takao SUGURO, Mitsuru KURODA: Safety Stock and Reorder Pont for Reordering Pont System with Variable Lead Times, Journal of Japan Inustrial Management Association, vol.55, 89-94 (2004)

[4] Richard E.Neapolitan : Learning Bayesian Networks , Prentice Hall (2003)

[5] Tsuchiya K (1995), Model dynamics and function of a complex system (in Japanese). Control inf 39(1):29-34

[6] Han-Ying Kao, Shia-Hui Huang, Han-Lin Li : Supply chain diagnostics with dynamic Bayesian Networks. Computers &Industrial Engineering Vol.49, pp.339-347, (2005)

[7] Edward A. Siver et al. ：Inventory Managemaent and Production Planning and Scheduling, John Wiley & Sons Inc (1998)

[8] Tsuchiya K (1995), Model dynamics and function of a complex system (in Japanese). Control inf 39(1):29-34

The Fourteenth International Symposium on Artificial Life and Robotics 2009 (AROB 14th '09),
B-Con Plaza, Beppu, Oita, Japan, February 5 - 7, 2009

Research on softman Cooperation Mechanism and Algorithms[1]

Dongmei Ai[1,2], Hai-tao Xiong[1], Guangping Zeng[1] ,Yang Yue[1]

[1](School of Information Engineering, University of Science and Technology Beijing, Beijing, 100083, China)
(School of Applied science , University of Science and Technology Beijing, Beijing, 100083, China)
(Tel : 86-01-62332349; Fax : 86-01-62334071)
(aidongmei@sina.com)

Abstract: Based on contract net model and acquaintance model for softman cooperation, a new model which based on the acquaintance coalition and softman's service centre is proposed. According to the acquaintance decision-making function and service center decision-making function, an effective collaboration softman can be quickly accessed. At the same time , using the two update strategies of acquaintance and service centre, the softman's mind parameters can reflect changes in the environment. The new model make it more efficiency in searching cooperator and more reliable in cooperation process.

Key words: Softman; contract net protocol; acquaintance model; task cooperation

I. INTRODUCTION

Softman is a sort of Software Artificial Life with human-intimated intelligence and ability to live on computer network. That is to say, it is a kind of "virtual robots"[1][2][3]. A single softman's ability is limited, so he often faces tasks that he can not finish only by himself. In this situation, a number of softmen's cooperation will be needed[3].

At present, the research on distribution model of softman system cooperation method is mainly divided into two types: contract net cooperation method and acquaintance cooperation method:

(1) Contract net cooperation method

Document[4] proposes a contract net protocol: when a softman needs to determine a cooperator, firstly he will broadcast the task tender to all of the softmen in the system. On receipt of the task tender, the softmen will make assessment according to their own resources and abilities, and decide whether they tender or not. if they decide to tender, they need to send their bids to the sender and the sender will evaluate all of the bids he collected and determine the most suitable cooperator. As the contract net protocol needs broadcasting tenders to all of the softmen in the system, communication abilities and resources of the system are put high demands.

Centralized coordination support is a common way to reduce the system's communication costs .This way is to set up a special center coordinating softman to take charge of saving and coordinating all the other softmen's information[5]. In application of this method are Lashkari cooperation framework[6],and Genesereth and Ketchpel[7] alliance systems. The former uses the bulletin board softman, while the latter uses the Communication service softman, to function as the center coordinating softman. Centralized coordination support lowers the cost of communication, but still requires a large amount of communication expenses to ask center coordinating softman for search of cooperating softmen[8].

(2) Acquaintance model cooperating method

Roda and Jennings ,etc, put forward an acquaintance model[9][10][11] to get access to the basic information of cooperating softmen. In this architecture, they design a "model of self" to indicate the information of softman himself and a "model of acquaintance" to indicate the information of other softmen in terms of resources and capacities .If he needs to determine a cooperating softman, he will first of all assess the abilities of his acquaintances, and then choose the most suitable cooperator. This approach reduces the cost of system's communication. Through the acquaintance model, other softmen's information can be accessed, but the acquaintance's information is fixed and can not timely reflect the current state of each softman in the system. Besides, the acquaintance' ability will directly have an impact on the softman.

Through the above analysis, we can conclude that the contract net model is a kind of approximately global optimum allocation method, while the acquaintance model is a local optimum allocation approach. This paper, for the limitation of the above two models, proposes a softman cooperating model which is based on acquaintance collection and service-center. This model solves the problems of cooperator-searching

---

[1]This work is supported by NNSF of China(No.60375038)

©ISAROB 2009

efficiency, as well as the reliability of cooperators. This model is improved in the following aspects:

(1) An acquaintance collection is added to the softman system. Through the acquaintance decision making function, the cooperator is determined. As in the softman system, the cost of communication is much larger than the cost of calculating. Through the introduction of acquaintance collection, the cost of system' communication is reduced, and then the price of looking for cooperators is also lowered.

(2) An service center softman is added to the softman system, who is to maintain the snapshots of softmen with collaborating abilities in the system. When softman can not find a suitable cooperator in the acquaintance collection , he can look for his cooperator in the service center according to talent service center decision-making function. The introduction of service center increases the solution space for softman to look for his cooperator, and avoids the problem that, in the process of cooperation, softman can only search for local solutions in the acquaintance collection.

(3) It defines a acquaintance collection updating strategy, which makes the acquaintance collection of softman system reflect the current state of the system, strengthens the adaptive capability of softman system, and increases the reliability that the cooperator can be found.

II. COOPERATION MODEL STRUCTURE

According to the characteristics of contract net model and acquaintance model, this article builds a hybrid model structure, based on acquaintance collection and talent service center. The model structure diagram is as follows:

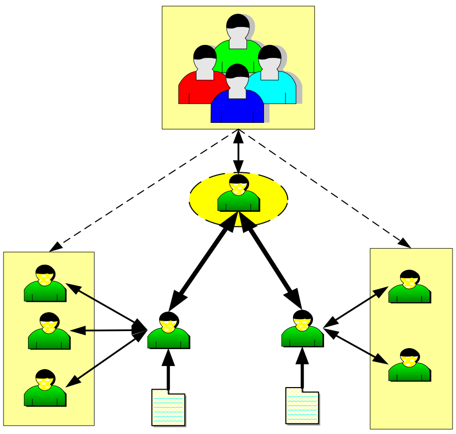

Fig.1. Cooperation model based on the acquaintance collection and service center

According to the different roles in the system, softmen can be divided into two types:

(1) service center softman: Service Center softman is a special kind of softman. It is the intermediary of softman system, responsible for keeping the softman name list who is willing to cooperate. The softman with cooperative wish voluntarily registers at the service center, and the service center records the softman's mailing address, ability description keywords. At the same time, the service center is also responsible for maintaining the evaluation information made by the system to this softman.

Service center softman, indicated with SMS, can be formulated as:

$$SMS = \{< SM_k, SMB_k, SC_k > | k = 1, 2, ..., m\}$$

Of which, m says the number of softmen in the service center, SM_K says the mailing address of the No.K softman. SMB_K says the ability vector of the No.K softman. SC_K says the evaluation level of the No.K softman.

(2) Implementary softman: the implementary softman , the core of the system, is responsible for the realization of specific issues. He receives tasks from the user or other softmen, and then makes different decisions according to different tasks:

a) If $SMB_k \ge TB_i$, the implementary softman will treat the task seperately.

b) If $SMB_k < TB_i$, that is ,for the tasks that the softman can not finish alone, he will firstly sub-divide the tasks into a series of tasks, and then search for cooperators to do it together. Meanwhile, he will also be in charge of unified planning and coordination of the cooperators.

III. THE SOFTMAN'S COOPERATING PROCESS

By means of acquaintance collection and service center softman, this article improves the classic contract net cooperating process[4][12][13]. When the softman invites bids, in accordance with the acquaintance collection decision-making function and the talent service center decision-making function, the bidders could either come from acquaintance collection or service center .Meanwhile, by means of its updating strategy, the softman acquaintance collection could timely reflect the changes of environment.

1. Acquaintance collection decision-making function

After receiving the task Ti, softman SM_k needs to select a suitable acquaintance to cooperate through an acquaintance evaluation. The acquaintance could be screened with two indicators: the first is the acquaintance's implementary capability SMBj; the second is the acquaintance's credibility Trust (SMk, SMj).The following decision-making function is introduced:

FS(SMk,Ti)={SMj|SMBj>=TBi, Trust(SMk,SMj)>=TH(SMk,SMj),j=0,1,2…,M} (1)

Of which, M says the number of acquaintances.

2. Acquaintance collection's decision-making function: Remove and fill

(1) filling operation (fill) :

In an acquaintance collection,when the number of acquaintances is smaller than the size of sliding window, the softman will operate to fill .The filling operation is shown as follows:

```
while(sizeof(Friend(SM_K))<sizoef(FW(SW_j))
{
    SM=fetchCooperator(SMS)
    add(SM_K,SM_j)
}
```

(2) Removing operation(remove):

When the number of acquaintances is larger than the size of sliding window, or when the credibility of acquaintances is smaller than the number ξ, a removing operation is needed now. The pseudo-code of removing operation is indicated as follows:

```
if(sizeof(Friend(SM_K))<sizoef(FW(SMj))
{
   sortFriendByTrust(Friend(SM_K))
   SM=fetchLastFriend(SM_K)
   remove(SM)
}else
if(Trust(SM_K, SM_j)<ξ
{
   remove(SM)
}
```

3. Service center decision-making function

When softman SMk chooses his cooperator in the service center to fulfill task Ti, he will screen the cooperators mainly by two indicators: the first is the acquaintance's implementary capability SMBj ;the second is the acquaintance's credibility Trust (SMk, SMj).The following decision-making function is introduced:

S(SMk,Ti)={SMj|SMBj×SMEj>=TBi, SMEj>=THE,j=0,1,…,M} (2)

Of which, M says the number of registered softmen in the service center.

4. Bid-winning decision-making function

The traditional bid-winning decision-making function adopts different strategies for problems of different areas. More representative are the weighted average method, the maximum / minimum, the maximum density (dichotomy), etc.

This paper, combined with the above-mentioned softman trust parameters, introduces the following task decision-making function :

V(SMk,Ti)'= V(SMk,Ti)×Trust(SMk) (3)

Of which, V (SMk, Ti) says the returned bid value by bidders. Trust equals to discount rate given by bidders. The higher the trust is, the less discount of bid value the bidders offer.

IV. EXPERIMENTAL DESIGN AND THE RESULTS

This article will use the experimental design and data analysis to clarify that ,in the softman system, the introduction of acquaintance collection and talent service center will have influence on the softman collaboration. The experiment is made on the platform[14] JADE (Java Agent Development Framework). We have materialized two different softman cooperating processes on this platform.

In order to simplize the model analysis, the softman's ability is indicated with two-dimensional vector as: SMB (HZ, QS), of which, HZ says the softman's calculating speed.QS says the size of available mission queue in the softman.

In the experiment, there are 6 mission executives, one mission manager. The mission executives are of the selfish type. Their probability of mission success are 1.0,0.8,0.6,0.4,0.2,0. Experimental data are shown in Figure 2 and Figure 3:

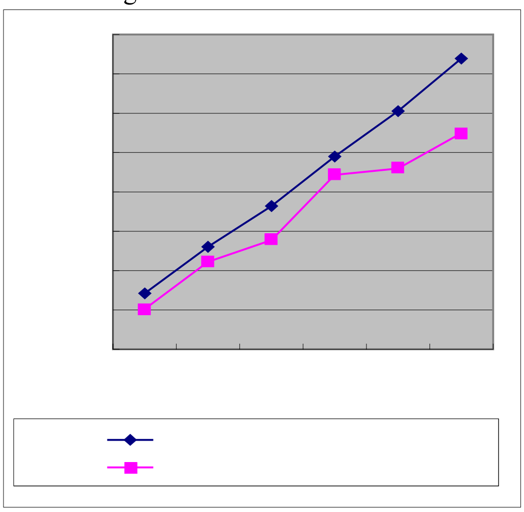

Fig 2. Cooperating mission –time diagram

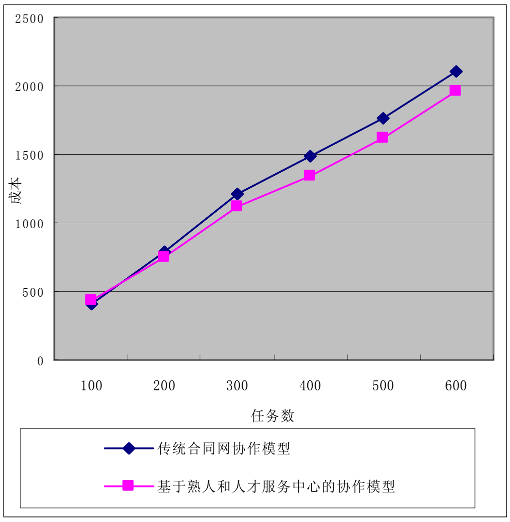

Fig 3. Cooperating mission-cost diagram

In Figure 2, due to the softman's selfishness, the number of negotiation failure ,which is based on the contract net cooperation model, increases evidently. It leads to an increase of mission implementing time. The improved cooperation model, through the updated strategies of acquaintance collection credibility and talent service center, makes the selected cooperators have high success rate of implementation. Especially when the number of mission increases and acquaintance collection stablizes, the mission implementing time will reduce significantly. In Figure 3, with the mission number increasing, the improved cooperating method costs far less than the traditional contract net cooperating method.

V. CONCLUSION

A softman cooperating method is proposed in this paper, which is based on an acquaintance collection and service center, and solves the problems of cooperator-searching efficiency and the credibility of cooperators in the process of cooperation. The softman uses acquaintances collection and service center, according to acquaintance decision-making function, to quickly have access to the softman who can supply effective cooperation. At the same time, by means of acquaintance updating strategies, softman system could timely reflect the changes of system environment. The result shows that the softman cooperating method, could significantly improve the cooperating efficiency of softman .

REFERENCES

[1] ZENG Guang-ping,TU Xu-yang.SoftMan[c]. China Institute of artificial intelligence at the 10th Annual Proceedings of the National,2003.697-702.
[2] Zeng Guang-ping,Tu Xu-yang,Wang Hong-bo. Research on Softman and its application[M]. Beijing: Science Press, 2007.
[3] TU Xu-yan, TANG Tao. Intelligent autonomous decentralized system(IADS)[C].Proceedings of the 2nd Internation Workshop of IEEE Compute Society on Autonomous Decentralized Sysntem,2002.10-15.
[4] R G Smith. The contract net protocol：High-level communication and control in a distributed problem solver. IEEE Trans on Computer, 1980, C229 (12) ： 1104-1113.
[5] K Decker, K Sycara, M Williamson. Middle-agents for the Internet. The 15th Int'l Joint Conf on Artificial Intelligence (IJCAI97) , Nagoya , 1997.
[6] Y Lashkari, M Metral , P Maes. Collaborative interface agents. In : Proc of the 12th National Conf on Artificial Intelligence. Seattle : AAAI Press , 1994 .444-449.
[7] M Inverno, M Luck. A formal view of social dependence networks. In : Proc of the 1st Australian Workshop on DAI. Berlin: Springer-Verlag, 1996 1 115-1295.
[8] O Shehory. A scalable agent location mechanism. In : MWooldridge, YLesperance eds. Lecture Notes in Artificial Intelligence, Intelligent Agents VI1 Berlin : Springer-Verlag , 1999.162-172.
[9] H.Chi Wong, Katia Sycars. A Taxonmoy of Middle-Agents for the Internet, Fourth International Conference on Multi-agent Systems (ICMAS'00),2001. 465-469.
[10] Ramchure S,Jenning N,Sierra C. Devising a trust model for multi-agent interactions using confidence and reputation[J] .Applied artificial intelligence, 2004, 18 (9/10) :833-852.
[11] Klush M,Gerber A. Dynamic coalition formation among rational Agents .IEEE Intelligent Systems, 2002, 17 (3) :42-47.
[12] TAO Hai-jun,WANG Ya-dong,GUO Mao-zu. A Multi-Agent Negotation Model Based on Acquaintance Coalition and Extended Contract Net Protocol. Journal of Computer Research and Development, 2006 , 43(7)：1155-1160.
[13] ZENG Guang-zhou,YANG Gong-ping,WANG Xiao-lin. Study of Task Allocation Problem Based on Agent Ability Confidence. Chinese Journal of Computers, 2007,11-15.
[14] Krzysztof Chmiel, Maciej Gawinecki, Pawel K aczmarek.Efficiency of JADE Agent Platform.JADE Workshop at AAMAS 2005.

The effects of the trophic level on the stability of food webs

Hirofumi Ochiai   Reiji Suzuki   Takaya Arita
Graduate School of Information Science, Nagoya University
Furo-cho, Chikusa-ku, Nagoya 464-8601, Japan
E-mail: ochiai@alife.cs.is.nagoya-u.ac.jp, reiji@is.nagoya-u.ac.jp, arita@nagoya-u.jp

Abstract

The study of food webs has long been a central topic of ecological research, but structural effects of a trophic level on their stability are still not clear. The work described here addresses the influence of a restriction arising from the trophic level on the network topology of food webs, which affects their global behaviors. We propose a network model of food webs in which the degree of the effects of the trophic level on speciation can be adjusted continuously by a single parameter. The restriction limits the number of species on each level and the establishment of prey-predator relationships between distant levels. Experimental results show that the restriction contributes to the stability of the ecosystem. It is because the strong restriction kept less robust species at the lower levels abundant by making the distribution of the number of species at each level flat, while the distribution became a inverse-pyramidal structure without restriction. On the other hand, we found that the several features of the network such as the power-law distribution of coextinction sizes and the number of predators do not depend on the degree of restriction. We also show several comparisons of the experimental data with empirical data of fossil records.

Keywords: Food web, trophic level, mass extinction, restriction, power-law, fossil record, artificial life.

1 Introduction

In ecology, the various types of models on food webs have been proposed by ecologists, mathematicians and physicists for understanding the mechanism of ecological dynamics. The models on food webs fall roughly into two categories. The first group of the models has a fixed structure of food webs and the second group of the models has a dynamic growth structure. Amaral and Meyer's model [1] is known as one of the latter ones. They constructed a network model for large scale extinction and evolution of species, in which there exists a strong restriction arising from the trophic level that limits the number of the species on each level and the establishment of prey-predator relationships between distant levels. The results showed a power-law distribution of coextinction sizes, in good agreement with available data from the fossil records [1, 3, 4, 8]. Recently, this model was reconsidered by Pekalski *et al.* [8]. They investigated the dependence of the system behavior on the maximum number of the species at each level and on the maximum number of preys per predator, then showed that the food web may collapse if either or both are too small. However, it is still unclear how the restriction arising from the trophic level can affect the global behaviors of ecological networks.

We clarify how the restriction based on the trophic level can affect the evolution and extinction of food webs. We propose a network model of food webs in which the degree of the effects of trophic level on evolution can be adjusted continuously by a single parameter θ. Amaral and Meyer's model is thus equivalent to our model with a specific setting of this parameter.

Experimental results have shown that the restriction contributes to the stability of the ecosystem, but the several features of the network such as the a power-law distribution of coextinction sizes and the number of predators do not depend on the degree of the restriction. We also show several comparisons of the experimental data with the empirical data of fossil records.

2 Model

Fig. 1 shows an example of food webs in our model. There is one special node termed the sun which is the permanent energy source. The other nodes represent the species. The directed link represents the energy flow from one species or the sun to another species.

The trophic level of the species is defined as the minimum distance from the sun whose trophic level is defined as 0. The species at the level 1 corresponds to the autotrophic species, and the other ones correspond to heterotrophic species. It is because the former cannot exist without incoming links from the sun and the latter cannot exist without incoming links from the other species. The dynamics of the web is driven by the speciation and extinction of species. The model starts with N_0 species at the level 1 and evolves according to the following rules:

(*i*) Speciation. — Every existing species tries to speciate with a probability μ. For each speciating species at the trophic level l ($1 \leq l \leq L$), it performs the following speciation event with a probability θ as shown in Fig. 1 (restricted speciation). In this case, it creates a new node at the level l-1, l or l+1

©ISAROB 2009

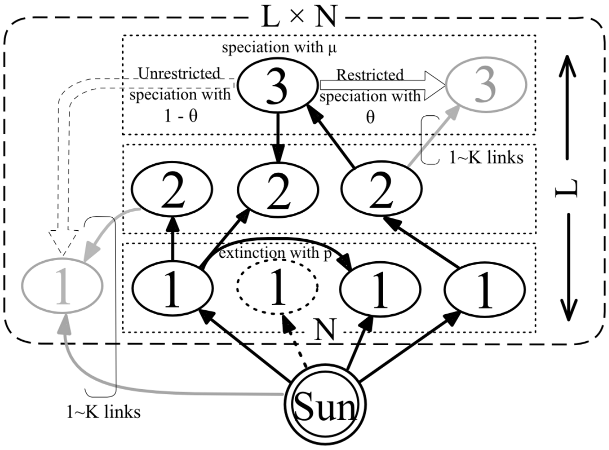

Figure 1: Schematic representation of the model for K=3, L=3 and N=4.

which receives the links from randomly selected number ($1 \leq k \leq K$) of nodes at the level l-2, l-1, or l respectively. This event occurs only when the level of the new node is from 1 up to L and the number of nodes at the same level l is smaller than N.

Otherwise, with a probability 1-θ, it creates a new node which receives the links from a randomly selected number ($1 \leq k \leq K$) ones from all species as shown in Fig. 1 (unrestricted speciation). This event occurs only when the number of nodes in the system is smaller than $L \cdot N$.

(*ii*) Extinction. — Only autotrophic species can trigger the avalanche (chains of extinction) as is the case with Amaral and Meyer 's model. When a species goes extinct, all the links from it to other species are removed. The extinction occurs on all species which have lost all incoming links recursively.

3 Experiments

We use the canonical set of parameters used in [1], namely, the maximum trophic level L=6, the extinction probability p=0.01, the probability of speciation μ=0.02, and the maximum number of preys K=3. These values came from the data of statistical investigation [5]. Although Amaral and Meyer used N=1000 in the simulations, we use N=100 because the total size of the experimentally observed food webs does not have such large number of species according to [8].

We shall investigate how is the system influenced by the parameter θ for the restriction of the choice of level and feeds. The results obtained will be compared to the empirical data coming from investigations of the fossil records [6].

3.1 Basic Dynamics

At the beginning, we discuss the basic dynamics of the system which was commonly observed across the whole range of θ. Amaral and Meyer's model, which is basically equivalent to our model in the case of θ=1.0[1], leads to a power-law (i.e., scale-free) distribution of extinction avalanche sizes which form $p(x) \propto x^{-\tau}$ and a strong correlation between the number of speciation and extinction events [1]. Irrespective of the parameter θ, we observed identical results except for the exponent value of power-law τ. As a typical example, we focus on the results in the case of θ=0.6. Fig. 2 (top) shows the transitions of the number of entire species, speciation and extinction. From the figure, we see the number of entire species fluctuated around the maximum value 600 and its drastic decreases often happened. We also observed the extinction of entire species as seen at the 11,000 step in the figure. It is because we used the lower value of the parameter N in the experiments compared to the original one as explained above, and also used the intermediate value of the parameter θ as described later. We also see that the number of speciation and extinction have a strong correlation. This trends are in good agreement with empirical data [1]. Fig. 2 (bottom) shows the distribution of the frequency of the extinction size in a single run. The extinction size means the number of extinct species at each step. We see that the shape of the distribution is approximately a straight line, which

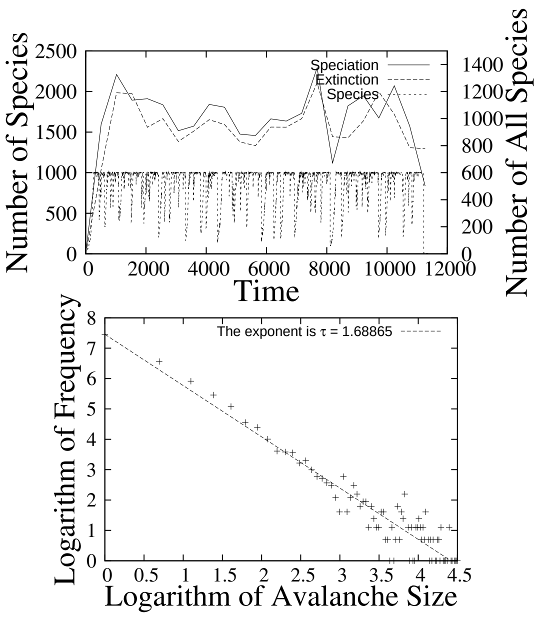

Figure 2: Time sequence of the number of species, speciation and extinctions events for θ= 0.6 (top). The number of speciation or extinction is the total number of speciation or extinction events during consecutive non-overlapping intervals of 512 time steps. Avalanche size for θ=0.6 (bottom). Both axes are in logarithmic scale (to base 10) on the vertical and horizontal axis.

[1]To be exact, there is a small difference between our model and Amaral and Mayer's in the sense that we adopted the probabilistic occurrence of extinction which was used in [2], and the random choice of the number of preys in a speciation event. But the global behaviors of the system was basically the same.

©ISAROB 2009

θ		0.00	0.20	0.40	0.60	0.80	1.00
Survival Time		626	1071	1575	3001	10930	50000
Number of Species		291	320	397	501	537	565
Variance of the Number of Species		218	236	224	163	124	69
Maximum Outdegree		8.79	1.34×10	1.68×10	1.83×10	1.38×10	1.03×10
Exponent of Avalanche size	τ	3.11×10^{-1}	3.50×10^{-1}	1.67	1.69	1.73	1.96
Exponent of Species Lifetime	α	-	-	-	1.30	1.78	1.86
Exponent of Outdegree	β	2.65	3.37	3.32	3.72	3.33	4.41

Table 1: Effects of θ on the system behavior. The first four values were the averages taken over 20 runs and the rest were calculated from a randomly selected run. When $\theta \leq 0.40$, the distribution of the species lifetime did not follow a power-law, which is expected to be due to the short survival time and the small number of species.

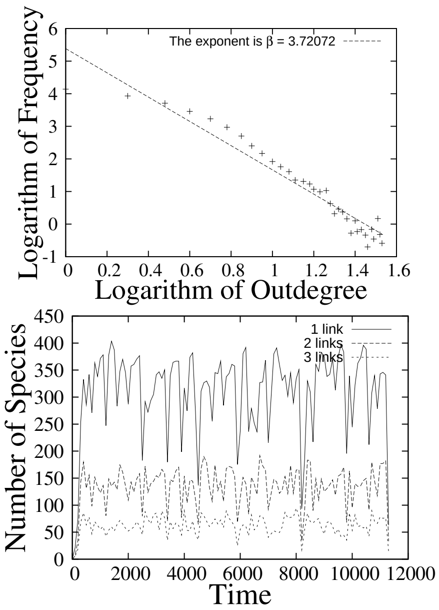

Figure 3: Outdegree distribution for θ=0.6 (top). The axes are in logarithmic scale (to base 10) on the vertical and horizontal axis. Time sequence of the indegree for θ=0.6 (bottom).

means that it is a power-law (i.e., scale-free) distribution which form $p(x) \propto x^{-\tau}$. The result also agreed with the fossil records [6]. Here, we further focus on the topology of the network. Fig. 3 (top) show the distribution of the number of outdegree (predators) for each species. It is approximately a straight line which form $p(t) \propto t^{-\beta}$. It is interesting that the distribution of the number of outdegree follows such a power-law, because it means that the system is composed of a scale-free network [2]. Fig. 3 (bottom) shows the transition of the distribution of indegrees (preys) for each species. The order of the number of links was unchanged, and the species with one indegree held the maximum number. This indicates that most of the species had a single prey.

3.2 Effects of θ on the overall dynamics

Table 1 summarizes the results of the experiments in the various cases of θ. As the parameter θ decreased, the survival time[2] and the average number of species decreased and the variance of the number of species increased. This means that the system tended to be small and unstable, and easily become extinct in the range of lower values of θ. The average maximum outdegree was largest when θ=0.6, which means there were preys predated by larger number of species in the case of intermediate restriction.

Here, we explain the relationship between the stability of the entire system and the restriction of the trophic level from the standpoint of the network structure and the robustness of species. Fig. 4 (top) illustrates the rate of species at each level averaged over 20 runs. In the cases of lower θ, it became the system an inverse-pyramidal structure, which means that the species at higher trophic levels were more populated than the lower ones. On the other hand, in the higher cases of θ, it became a flat structure in the sense that there were almost the same rate of species at every level. The species at the higher level tends to be more robust against the avalanche of extinction as a general trend, because the potential routes from the sun to the target species can become more diverse. Thus, we could see the frequency of species became higher as the level increased in the case of smaller restriction from the Fig. 4 (top). On the other hand, we could also see the constant frequency of species through the whole level in the case of larger restriction. This is clearly due to the restriction of the maximum number of species at each level N.

Fig. 4 (bottom) shows the average robustness of species at each level. The robustness of species is defined as the number of different species at the level 1 which exist in all the routes from the sun to the target species. Basically, there was a trend that the robustness increased with the increasing the level in all the cases of restriction. We observed clearly this trend when the parameter θ was highest. The condition of the system was basically static in that the number of

[2] The elapsed time before all the species went extinct.

©ISAROB 2009

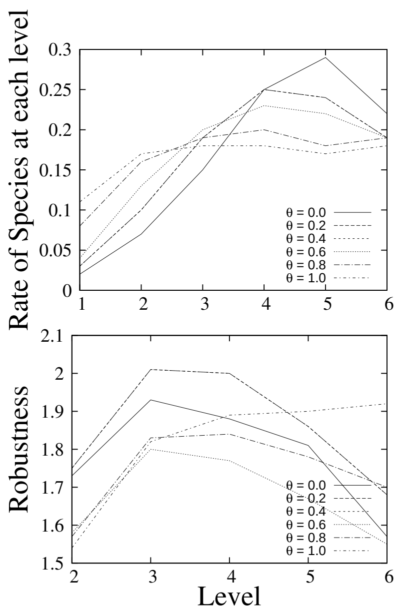

Figure 4: The rate of species at levels (top) and the rate of species robustness at levels (bottom). The averages was taken over 20 runs.

species saturated at any level, because the restriction made less robust species at the lower levels abundant. On the other hand, the robustness had a peak at an intermediate level (3 or 4) in the cases of lower value of the parameter θ. This is because the whole system grows and collapses many times with dynamic change in its system size. In the growth stage, there is a trend that the robustness of the higher level becomes slightly smaller due to a time lag between the appearance of the species at the higher level and the increase in its robustness.

After all, we can say that the restriction of the trophic level contributes to the stability of the whole system because it makes less robust species at the lower levels abundant by making the distribution of the number of species at each level flat.

Also, Table 1 shows the exponent of the distribution of avalanche size and species lifetime were proportional to the parameter θ. The fossil records of marine animals appears to have a power-law distribution of the extinction size with an exponent τ=2.0 $\pm$ 0.2 [9]. We found that the distribution of the extinction sizes in the case of θ=1.0 was in the best agreement with the fossil records among these results. The distribution of the genus lifetime appears to follow a power-law with an exponent α=1.7 $\pm$ 0.3 [9]. Its distribution was in the best agreement with the fossil records when θ=0.8. On the other hand, there were no clear trends in the effect of θ on the exponent of outdegree.

In addition, we observed that the fraction of highly connected species (omnivores) significantly increased just before the extinction of the whole species when $\theta < 0.4$ (not shown). It was reported in [8] that the similar phenomenon can occur when N is very small.

4 Conclusion

We have discussed the influence of the restriction arising from the trophic level on the global behavior of food webs, which were neglected in previous studies. From the experimental results, we found that the network structure and the stability of the ecosystem strongly depended on the degree of the restrictions. With decreasing the degree of the restriction, the distribution of the species at each trophic level changed from flat to inverse-pyramidal, and its stability became more unstable. This is because the restriction maintains the number of less robust species at lower levels in abundance. On the other hand, we found the features that the distribution of the extinction sizes and the outdegrees followed a power-law regardless of the degree of the restrictions.

References

[1] L. A. N. Amaral and M. Meyer, "Environmental changes, coextinction, and patterns in the fossil record", *Phys. Rev. Lett.*, Vol. 82, pp. 652-655, 1999.

[2] A. L. Barabási and R. Albert, "Emergence of scaling in random networks", *Science*, Vol. 286, pp. 509-512, 1998.

[3] J. Camacho and R. V. Solé, "Extinction and taxonomy in a trophic model of coevolution", *Phys. Rev. E*, Vol. 62, pp. 1119-1123, 2000.

[4] B. Drossel, "Extinction events and species lifetimes in a simple ecological model", *Phys. Rev. Lett.*, Vol. 81, pp. 5011-5014, 1998.

[5] M. Lassin, U. Bastolla, S. C. Manrubia and A. Valleriani, "Shape of ecological networks", *Phys. Rev. Lett.*, Vol. 86, pp. 4418-4421, 2001.

[6] M. E. J. Newman and R. G. Palmer, *Modeling Extinction*, Oxford University Press, 2003.

[7] M. E. J. Newman and P. Sibani, "Extinction, diversity and survivorship of taxa in the fossil record", *Biological Science*, Vol. 266, No. 1428, pp. 1593-1599, 1999.

[8] A. Pekalski, "Extinction risk and structure of a food web model", *Phys. Rev. E*, Vol. 77, 031917 (8 pages), 2008.

[9] J. J. Sepkosk, Jr, "A compendium of fossil marine animal families, 2nd edition", *Milwaukee Public Museum Contributions to Biology and Geology*, Vol. 83, pp. 1-156, 1992.

The Fourteenth International Symposium on Artificial Life and Robotics 2009 (AROB 14th '09),
B-Con Plaza, Beppu, Oita, Japan, February 5 - 7, 2009

Evolutionary Acquisition of Behaviors Building Structural Objects by Virtual Creatures

Kenta OOMIYA[*1], Keisuke NAKAMURA[*1] and Keiji SUZUKI[*2]

[*1]*Future University - Hakodate, Kameda-Nakano 116-2, Hakodate Hokkaido, Japan*
(g3107001@fun.ac.jp)

[*2]*Hokkaido University, Graduate School of Information Science Technology*

Abstract: One of our purposes is to develop virtual creatures which can acquire behaviors building structural objects in 3D physical simulation. In this paper, we show influences of behaviors on structural objects which is built by virtual creatures. Many creatures can change their environments for their better by building structural objects, for example nests. In the field of Artificial Life, there are many studies about virtual creatures which change their bodies and acts to suit their environments. In contract, there are few studies about virtual creatures which build structural objects. As natural lives, virtual creatures need physical interaction between their bodies and its environments. Therefore, our purpose is to develop the framework of autonomous acquiring behaviors which builds structural objects in 3D physical simulation. In order to develop it, at first, we studied on evolutionary acquisition of behaviors building structural objects, nest for predation, by one simple behavior, throwing blocks. As a result, we show the possibility which virtual creatures can acquire the building behaviors evolutionarily.

Keywords: Evolution, Virtual Creatures, Building structural objects, Artificial Life, 3D physical simulation

I. INTRODUCTION

One of our purposes is to develop virtual creatures which can acquire behaviors building structural objects in 3D physical simulation. In this paper, we show evolutionary acquisition of behaviors on structural objects which is built by virtual creatures.

Many creatures can change their environments for their better by building structural objects, for example nests. Spiders and ant-lions build their nests for predation and beavers and ants build their nests for barriers against enemies, for example. In the field of Artificial Life, there are many studies about virtual creatures which change their bodies and acts to suit their environments. In 1994, Karl Sims proposed new simulation which virtual creatures can evolutionarily acquire its suitable body structures and behaviors in order to suit their environments [1] [2]. In contract, there are few studies about virtual creatures which build structural objects. Funes and Pollack proposed the method which can evolutionarily acquire the construction diagrams of structural objects with Lego Bricks such as long bridges, scaffolds and cranes [3]. However processes of building structural objects were not considered in the studies. Therefore, Rieffel and Pollack proposed the method which can acquire processes of structural objects by an agent building those objects [4] [5]. However, these processes were not considered physical interaction between agents and environments. That is, they are manipulated in symbolic form. Therefore, our purpose is to develop the framework of autonomous acquiring behaviors which build structural objects in 3D physical simulation. In order to develop it, at first, we studied on evolutionary acquisition of behaviors building structural objects, a nest for predation, by one simple behavior, throwing blocks. As a result, we show the possibility which virtual creatures can acquire the building behaviors evolutionarily.

II. FRAMEWORK OF THE SIMULATION

1. Schematic View

In this paper, we do an experiment about evolutionary acquisition of behaviors building a structural object by using Genetic Algorithm [6].

In that experiment, a virtual creature, a predator, builds a nest for predation by throwing blocks. Then the nest is evaluated by a fitness function. Behaviors building a nest are decided by its gene of the virtual creature. Therefore to evaluate the nest is equal to evaluate the behaviors. By using genetic algorithm, the behaviors are improved and the virtual creature finally acquires effective behaviors and an effective nest for predation. Figure 1 shows a framework of this simulation.

©ISAROB 2009

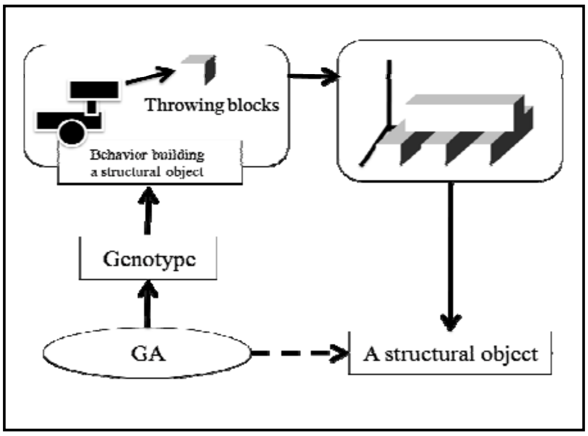

Fig. 1. A Framework of this simulation

2. Gene Structure

Figure 2 shows the gene structure which represents behaviors throwing a block. The gene consists of a number of information sets. One set consists of a position, an angle and a speed value when a block is thrown.

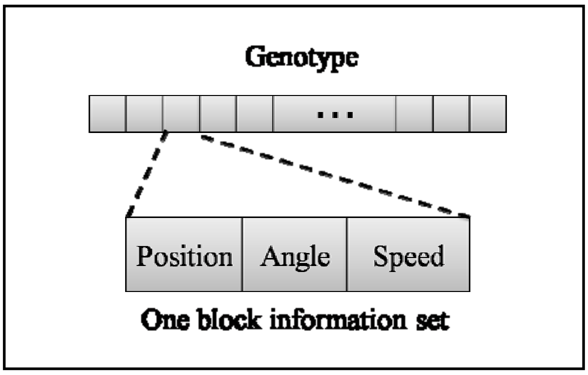

Fig. 2. Genotype of virtual creatures in this simulation

III. THE EXPERIMENT OF PREDATION

The purpose of a virtual creature, a predator, is to capture preys by navigation with blocks which the virtual creature throws.

1. Schematic View

Figure 3 shows the environment of this experiment. Figure 4 (a) shows a predator. Figure 4 (b) shows a prey.

In this environment, there are one predator and some preys. A predator can move only 4 tiles around the center of the environment and throw blocks forward any 8 directions with arbitrary power which is indicated by its gene. These blocks are generated in front of the virtual creature in turn. The preys are one of simple reflexive agents. They can avoid obstacles with a vision

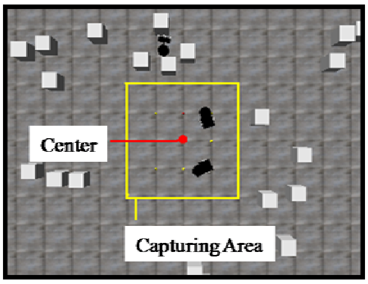

Fig. 3. The environment of this experiment

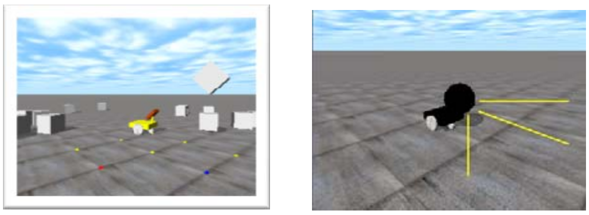

(a) A predator (b) A prey

Fig. 4. Virtual Creatures

sensor which can measure direction and distance to objects. Their simple avoidance rule is as follows:

1. If they do not sense any obstacles, they go straight.
2. While they sense an obstacle, they turn around.

They simultaneously start to move from the one side to the contrary side. If they enter the capturing area where is in 4 tiles around the center of the environment, it is considered that they are captured by the predator. It is like a nest of spiders. The fitness of the nest is as follows:

$$Fitness = \alpha C + \beta \sum_{j=0}^{S-C} 1/d_j \qquad (1)$$

where, S specifies the number of the preys, C specifies the number of captured preys, d_j is distance between prey j and the center and alpha and beta are constant. The first term means rewards which is proportional to the number of captured preys. The second term evaluates gathering performance on preys which is not captured.

2. Gene Structure of the Predator

Figure 4 shows that gene structure of the predator. The gene consists of block information. Each block information sets includes position, a direction and a speed when the predator throws a block.

3. Result

The parameters of the experiment are as follows: the number of blocks is 50, the number of the preys S is 16. Population of the genes is 200, generation is repeated until 140. Elitist preserve strategy and Roulette wheel strategy are employed.

Figure 5 shows transitions of the fitness values and Figure 6 shows the handmade nest for us to compare nests built by the predator. The uppermost line (dotted line) is fitness values of the handmade nest. The line below the uppermost line (thick line) is fitness values of the predator. The other line (thin line) is fitness values of random behaviors. The nests built by the predator are not better than the handmade nest. However, we slightly show that evolutionary acquisition of behaviors building an effective structural object for predation. Figure 9 shows distribution maps of blocks. Figure 7 (a) shows a nest before evolution (in 0th generation). Figure 7 (b) shows a nest after evolution (in the last generation). These maps mean how nests are built by the predator. The nest before evolution has a barrier in front of the capturing area. Preys moving from the right side avoided the barrier and the capturing area. That is, the nest leads the prey to outside. In contract, the nest after evolution has entryway to the capturing area. That is, the nest can capture the preys effectively.

As a result, we show evolutionary acquisition of behaviors building an effective structural object.

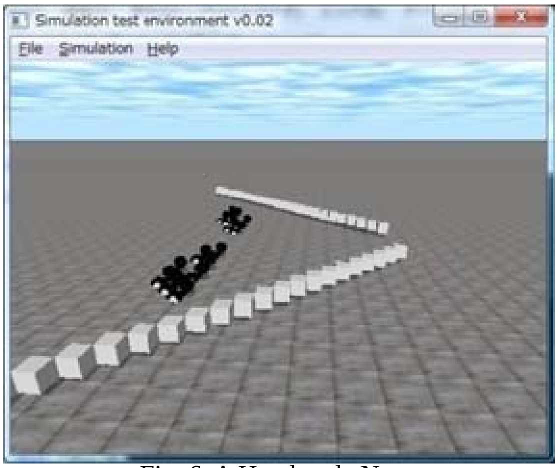

Fig. 6. A Handmade Nest

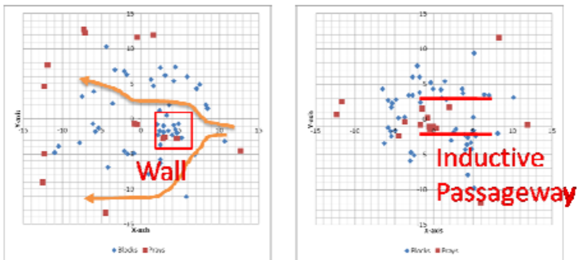

(a) Before Evolution (b) After Evolution

Fig. 7. Distribution maps of Nests

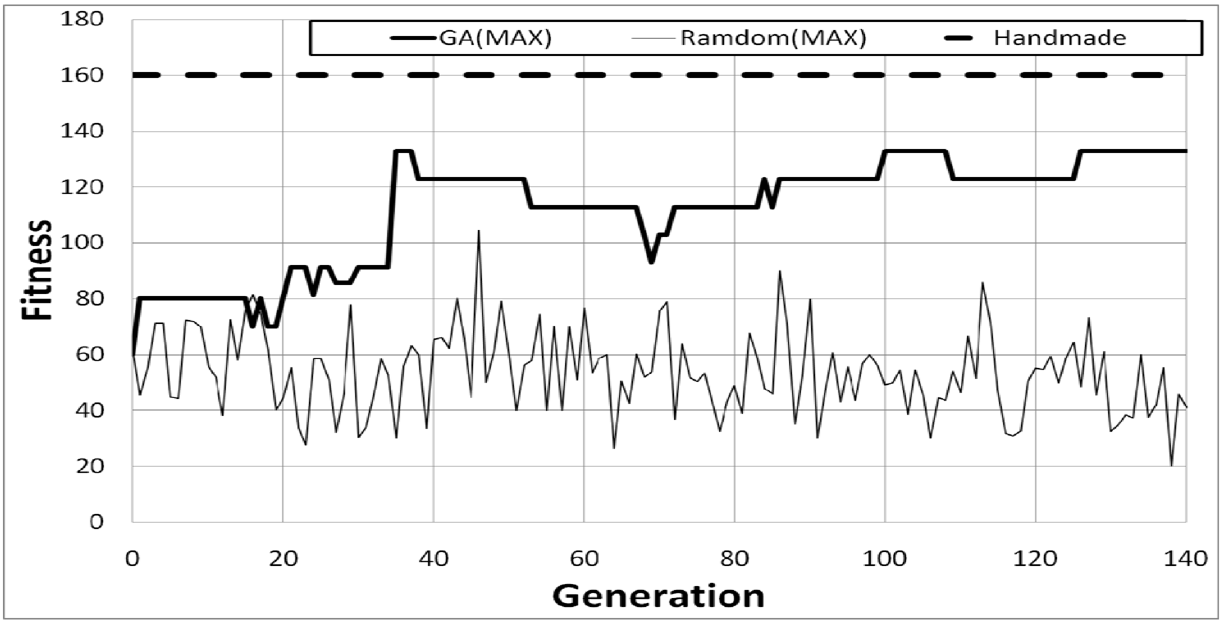

Fig. 5. Transition of fitness values

IV. CONCLUSION

Our purpose is to propose a virtual creature which acquires behaviors building a structural object evolutionarily in 3D physical simulation. As the first step, we show the simulation of a virtual creature which evolutionarily acquires behaviors building a structural object by simple behaviors, throwing blocks. However, there are many problems to solve. In order to build more complicated structural objects, a virtual creature needs more various behaviors and methods to generate new behaviors by combining simple behaviors.

REFERENCES

[1] Karl Sims (1994), Evolving Virtual Creatures. SI GGRAPH: 15-22

[2] Karl Sims (1994), Evolving 3D Morphology and Behavior by Competition. ALIFE1(4): 353-372

[3] Pablo J. Funes and Jordan B. Pollack (1999), Computer Evolution of Buildable Objects. Evolutionary Design by Computers: 387-403

[4] John Rieffel and Jordan B. Pollack (2005), Evolving Assembly Plans for Fully Automated Design and Assembly. Evolvable Hardware 2005: 165-170

[5] John Rieffel and Jordan B. Pollack (2005), Evolutionary Fraction: the emergence of novel assembly methods in artificial ontogenesis. GECCO Workshop 2005: 265-272

[6] John H. Holland (1975), Adaptation in Natural and Artificial Systems. MIT PRESS

©ISAROB 2009

The Fourteenth International Symposium on Artificial Life and Robotics 2009 (AROB 14th '09),
B-Con Plaza, Beppu, Oita, Japan, February 5 - 7, 2009

Agent based approach for homeostatic plasticity in neuronal activities

Subha Fernando, Yuichi Nakamura, Shuichi Matsuzaki, Ashu Marasinghe

Nagaoka University of Technology,
Niigata-ken, Nagaoka-shi, Kamitomiokmachi 1603-1
(Tel: 81-258-47-9372; Fax: 81-258-47-9350)
(subha_fernando@yahoo.com)

Abstract: **The capability of re-establishing to its normal rhythm over an excitation while adapting to external or internal stimuli is a process of complexity. We propose an agent based framework to model the homeostatic plasticity in neuronal activity incorporating the concept of self-organization. Our model provides the ability for neuro-agents to adapt themselves as a series of activities over the excitements of synaptic inputs as similar to the nervous systems, hence allowing the creation of diversification and competitive environment.**

Keywords: Agent, Homeostasis, Self-organization

I. INTRODUCTION

The capability of re-establishing to its normal rhythm over an excitation while adapting to external or internal stimuli is a process of complexity which is characterized by self-organization, non-linearity, chaos dynamics and emergent properties, Kirshbaum [1]. According to the researches, if the system is complex enough it will trigger changes automatically and naturally within the system in order to improve the system efficacy. These changes are mainly accomplished by its elements as a responds to the external and internal inputs. Especially these elements reorganize and resettle them-selves, to accomplish the overall system goal. This process is known as self-organization of a complex system.

As similar to other complex systems like social system, echo system, politic systems etc, nervous systems also adapt to the changes in the environment over a time period. Depending on the time scale of this adaption, different terms, such as plasticity, potentiation, augmentation, etc have been used. Apart from the short-term adaption, long-term adaptions are also possible in the nervous system which can be varied from couple of seconds to couple of days, Burrone and Murthy [2]. However, all these adaption or self-organization is required when the nervous system is being pushed away from its operational range, to bring back to its normal rhythm. So we can interpret, this behavior as a behavioral rule of the nervous system, refer rule 1,

Rule 1: neurons reorganize and resettle them-selves, to accomplish the overall system goal.

According to the empirical researches, this is accomplished through process of homeostatic plasticity, where neurons monitor their own activity levels and transduce the information to regulate changes in excitability. This adaption should not prevent the neuronal excitements or changes because it is identified that neurons are learning through these excitability, Davis and Bezprozvanny [3]. Therefore, nervous systems are subject two opposite requirements, adaption to the change and maintain the stability. Researches into biology have identified that; these changes are accomplished in the form of activity dependent alteration, by modifying,

Rule 2: The number of synaptic connections, and

Rule 3: The strength of synaptic connections,

to regulate the synaptic firing rate, Turrigiano [4]. According to the researchers, Turrigiano [4] and Burrone and Murthy [2], Homeostatic plasticity allows,

Rule 4: continuous and steady modifications to neural network elements by making neurons to stabilize their excitability while keeping relative differences in individual strengths of synapses.

Rule 5: The overall activity of the network is controlled as a set of rules; these rules either can be local or global rules.

As such, neurons fluctuate constantly their electrical, morphological and synaptic properties, Turrigiano [4]. According to the biology, neurons electrical properties are determined by the ca^{+2} ionic concentrations. For example,

Rule 6: if the synaptic firing rate is very low then neurons close their ca^{+2} gates which in turn increase the

©ISAROB 2009

synaptic firing rates. On the other hand, as similar to the previous scenario,

Rule 7: neurons open their ca^{+2} ionic gates to bring down the synaptic firing rates when it is high,

Gazzaniga, Ivry and Mangun [5]. Apart from the regulations of ionic channels, neurons also regulate their synaptic strength in order to control their synaptic firing rates. According to the Turrigiano [4],

Rule 8: As the firing rates increase, associated activities of homeostatic plasticity put down synaptic strength by allowing pre and post synaptic neurons to grow and contact others to form trial synapses.

Rule 9: If the firing rate is very low, neuron strength and stabilize the appropriate connections by making inappropriate connections to be lost, and this will be achieved through by halting synaptic growth.

Information about neuronal activity (synaptic strength) and neuronal size, (number of synaptic connections) are known to be monitored through neurons monitors, which are seem to be located inside the neuronal cell.

Rule 10: These sensors, inside the neurons report the deviation of a particular neuron from its equilibrium point.

The deviation will be fed back to the neuron as an error signal to bring it back to the equilibrium point Davis and Bezprozvanny [3] and Davis [6]. Simply, homeostatic plasticity can be viewed as a feedback system, Turrigiano [1].

The rest of the paper organized as follows: section II discusses the applicability of homeostatic plasticity in neural networks while highlighting the issues in applications. Section III describes our approach of implementing homeostatic plasticity and section IV evaluates the first result of the approach and paper concludes with section V discussing the applications, limitations, advantageous and further work.

II. APPLICATIONS OF HOMEOSTATIC PLASTICITY

According the current review on Homeostatic plasticity, current researches are now attempting to apply this mechanism as a supportive plasticity mechanism for Hebbian synaptic plasticity, because Hebbian rules allows (a) unconstraint growth of synaptic weights in neural networks when correlation of input and output is positive and (b) when correlation is negative, it causes strength of synaptic to move towards the zero level. Finally this is ended up in losing the network sensitivity. The network to be sensitive to the input, the signals generated by that input should propagate through the network, Vogels, Rajan and Abbott [7]. Therefore researches are now attempting to implement the homeostatic plasticity as a feedback system, either (a) to modify excitability of total synaptic strength at a constant level or (b) to modify the synapse number to produce changes in synaptic strength. Especially these researches are into applications of Continuous Time Recurrent Neural Network (CTRNN), which are capable of approximate output of any dynamical system when appropriately parameterized, Funahashi and Nakamura [8].

In CTRNN each node is described in terms of differential equation as shown in (1), where u_i represents the internal state of the i^{th} neuron, τ_I – the time constant of the i^{th} neuron, I_i – external input (or threshold) of the i^{th} neuron, w_{ij} – connection weight from j^{th} neuron to the i^{th} neuron and σ -output function as shown in (2).

$$\frac{du_i(t)}{dt} = -\,{}^{1}\!/_{\tau_i}\, u_i(t) + \sum_j w_{ij}\sigma(u_j(t)) + I_i \qquad (1)$$

$$\sigma(x) = {}^{1}\!/_{(1+\exp(-x))} \qquad (2)$$

The shape of the sigmoid function causes the node firing rate to be saturated when the neuron potential is very high and low. When the firing rate is saturated there are no fluctuations in firing rate, therefore the sensitivity of the network is lost. To avoid this saturation, researches are now trying to apply homeostatic plasticity on CTRNN in terms of weight plasticity or as a process that affecting the excitability of individual neurons, Williams and Noble [9] and Williams [10]. Some of these researches are being concluded with even homeostatic plasticity improves the signal propagation; it acts as barrier for creating evolvers, Williams [10].

Our interpretation on these conclusions are, either (a) approach for modeling homeostatic plasticity might be wrong or (b) current view on CTRNN may not be supported to the homeostatic plasticity. With align to the part (b) some researchers are being carried out to solve the evolvability of CTRNN with fixed weight concepts by viewing the learning as interactions between the multiple timescale dynamics, Izquierdo-Torres and Harvey [11]. On their research they are being able to demonstrate, for the smallest CTRNN network, with the concept of two-time scale, slow-time and fast-time scale, that it is possible to make the CTRNN to be evolved. However, still, they are not being able to exhibit it for large neural networks with proper time delays. Therefore, developing reliable and evolvable CTRNN networks are not being solved. With align to part (b) we understand the nervous system as a network of network, where each node on the network has self-organization ability. Our approach is Artificial Life approach which define the complexity as it could be rather than as we know it.

III. OUR APPROACH

We understand the nervous system, as a network of self-organizing network, in other terms, as a network of simple agents, called neuro-agents, where they organize and re-settle themselves to accomplish the overall system goals, refer to rule (1). As a process of organizing, it has the ability to control its own excitation by changing the size which in turn changes its strength, refer to rules (2) and (3). This is promoted through the structure of the neuro-agent, which consists of large number of receivers and transmitters which can be in either active or inactive status. At the same time, neurons are able to monitor their own deviations through the monitors inside the soma, refer rule (10). Based on the retrieved information, neuron can change the selected number of active transmitters and receivers, since information can be transferred from active transmitter to active receivers. So if neuron is over excited it changes the selected number of inactive receivers and inactive transmitters to be active to weak the strength as similar to the rule (8). And if the neurons is inhibited it make selected number of active transmitters and active receivers to be inactive as similar to the rule (9). As such, our model neuron can be viewed as in figure 1.

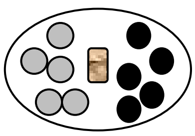

Fig. 1: The model of neuro-agent, light-color circles represent the receivers, dark-color circles represent the transmitters, and square represent the soma.

However, over all behavior of the system as a self-organizing network is controlled through the set of global rules imposed to the entire network, refer to rule (5). As a mechanism of signal propagation, all the neurons should always adhere to the following four rules, Fernando, Matsuzaki, Nakamura, et al [12].

Rule A: Only active transmitter can transmit the signal to the active receiver.

Rule B: Only active receiver can receive the signal.

Rule C: Once active transmitter transmit the signal it should become inactive (as similar to the refectory period) and inactive receiver in the same neuron become active (similar to Na^{+2} ionic concentration).

Rule D: Once active receiver receives the signal it should becomes inactive and inactive transmitter in the same neuron becomes active.

Therefore, the number of active transmitters within the neuron determines the volume of the signal that is transmitted by a particular neuro-agent. There are neither fixed connections between receivers and transmitters nor among the neurons. The active transmitter can transmit the signal to the active receiver in the same neuron or active receiver in another neuron. Therefore, our network somewhat looks like Recurrent neural network (RNN) as shown in figure 2.

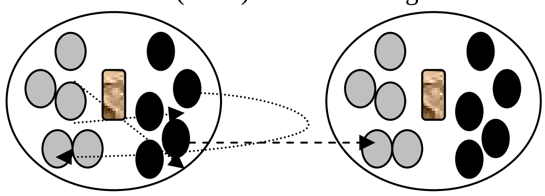

Fig. 2: The model of the proposed neural network, signal can be transmitted through active transmitters to active receivers on the same or different neuron.

As communication mechanisms, neurons are monitored through the concepts of central controller, which implements as a set of rules, in order to guarantee homeostatic plasticity is achieved. As a first step of the proposed model, we developed a network of network, simply having three model neurons, where each one having only receivers and transmitters. We evaluate the system, in terms of implementing above for rules as described in the next section.

IV. EVALUATION OF THE SYSTEM FROM FIRST RESULT

We model the system with three neurons (N1, N2 and N3) where each neuron consists of 10,000 receivers and 10,000 transmitters. At the onset only half of the transmitters and receivers are set to active. The number of active transmitters and receivers may be changed

©ISAROB 2009

accordingly as neuro-agents response to the external or internal stimuli. Active transmitters within the neuron emit signals in iterations of 100 steps. Experiment was divided into five stages; each stage consists of 5000 steps. Emission interval for N2 was set to 200 steps in stage 4, indicating that activity of N2 was decreased in that stage. Similarly, the interval for N3 was set to 50 steps in stage 3 and 10steps in stage 3 and 4 indicating that activity was increased.

When the neurons attained to its dynamic equilibrium, signaling patterns between the neurons was observed to fluctuate in different stages as shown figure 3, while individual neurons change their active transmitters and receivers in response to the manipulations.

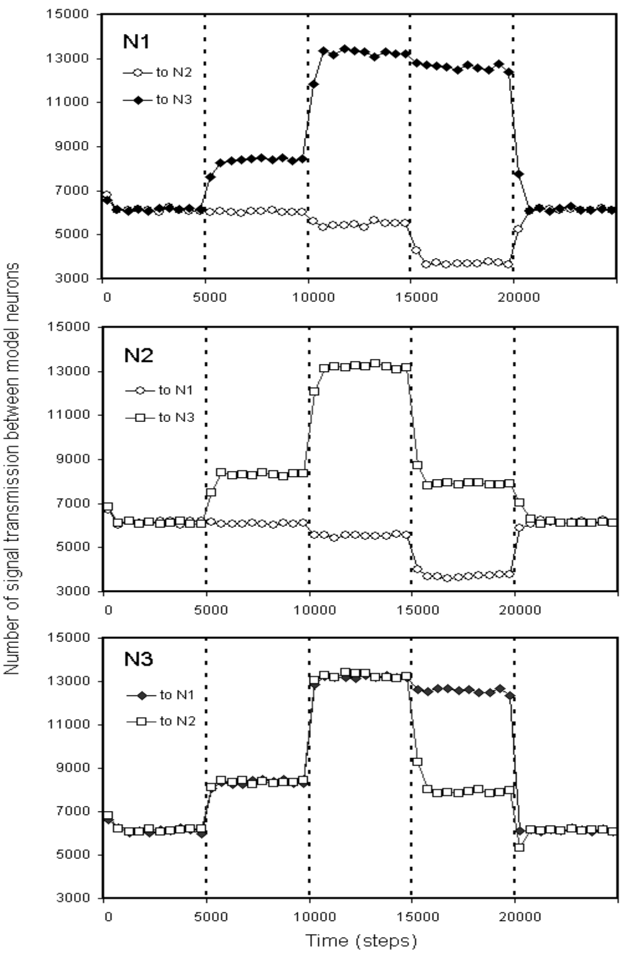

Figure 3: Signal propagation from one neuron to others.

IV. CONCLUSION

We demonstrated the preliminary version of homeostatic plasticity as a communication between self-organizing neuro-agents. The self-organization, in this case was merely achieved through very simple four rules, which set up as a global or environmental rules. The system has sown it is possible to achieve the homeostatic plasticity as a means of signal propagation without updating of internal parameters.

However, real implementation of homeostatic plasticity attach to the environmental input as a self-organizing agent networks still to be tested. If the propose model able to demonstrate the homeostatic plasticity as a smooth process then it will open up the new direction for the modeling nervous system. At the same time, it will open up new challenge for the research; demonstration of learning, evolving with the homeostatic plasticity.

REFERENCES

[1]. Kirshbaum D (2002), Introduction to Complex Systems, retrieved from http://www.calresco.org/ intro.htm #def on September 2008.
[2]. Burrone J and Murthy V.N, (2003), Synaptic gain control and homeostasis, Current Opinion in Neurobiology, 13, 560-567.
[3]. Davis G.W and Bezprozvanny I, (2001), Maintaining the stability of Neural Function: A Homeostatic Hypothesis, Annual Review of Physiology 63, 847-869.
[4]. Turrigiano G.G, (1999), Homeostatic plasticity in neuronal networks: the more things change, the more they stay the same, Trends in Neuroscience, 22, 221-227.
[5]. Gazzaniga M.S, Ivry R.B and Mangun, G.R, (2002), Cognitive Neuroscience: The biology of mind, ch 2.
[6]. Davis G.W, (2006), Homeostatic control of Neural Activity: From Phenomenology to Molecular Design, Annual Review of Neuroscience, 29, 307-323.
[7]. Vogels, T.P, Rajan K. and Abbott L.F. (2005), Neural Network Dynamics, Reviews in Advance, 18:15.
[8] Funahashi K and Nakamura Y, (1993), Approximation of Dynamical Systems by Continuous Time Recurrent Neural Networks, Neural Networks, 6, 801-806.
[9]. Williams H. and Noble J, (2005), Homeostatic plasticity improves signal propagation in continuous-time recurrent neural networks, Biosystems, 87 (2-3), 252-259.
[10]. Williams H, (2005) Homeostatic plasticity improves continuous-time recurrent neural network as a behavioral substrate, Adaptive Motions in Animals and Machines.
[11]. Izquierdo-Torres E and Harvey I, (2007), Hebbian learning using fixed weight evolved dynamical neural networks, IEEE Symposium on Artificial Life.
[12]. Fernando S, Matsuzaki S, Nakamura Y, Marasinghe A, (2008), Simulation of Neuronal Activity using Molecular Reaction, Human and Computer 2008.

Adaptive sensor arrays for acoustic monitoring of bird behavior and diversity: Preliminary results on source identification using Support Vector Machines

Edgar E. Vallejo
Computer Science Dept.
ITESM, Campus Estado de México
Atizapán de Zaragoza, 52926, México
vallejo@itesm.mx

Charles E. Taylor
Dept. of Ecology and Evolutionary Biology
University of California, Los Angeles
Los Angeles, CA, 90095, USA
taylor@biology.ucla.edu

Abstract

We summarize the work in our laboratories toward developing adaptive sensor arrays for monitoring bird vocalizations. We have focused on four species of antbirds in a tropical rainforest of Mexico. Preliminary results on individual identification using Support Vector Machines are presented. Also, we describe our initial attempts at higher order processing of information about the identification and localization of each source.

1 Introduction

Adaptive sensor arrays provide excellent platforms for testing hypothesis on different aspects of adaptive behavior such as collective and social behavior, communication and language, emergent structures and behaviors, among others. This technology holds the potential to produce a major paradigm shift in the way we interact with the physical environment. Furthermore, understanding the capabilities and limitations of sensor arrays will be important for guiding the construction of artifacts that possess problem-solving abilities.

In this study we are concerned with developing acoustic sensor arrays so that they will be useful for observing and analyzing bird diversity and behavior. We would like each sensor to see and "understand" part of the situation – depending on its own location – then to fuse their experiences with other such sensors to form a single, coherent understanding by the ensemble [1]. The ideal is that the array will act something like a living membrane, sensitive to what is going on within it, around it and passing through it.

Toward that goal we have developed and tested sensor arrays that can identify their own location and sense bird vocalizations in real-world settings. We have developed filters to identify species (in some instances individual birds) and software tools to localize those individuals in natural environments. More recently, we are beginning to explore how we can identify the meaning of these vocalizations in the social context of the vocalizing animals. Separate aspects of this work has been described elsewhere, indicated below. In this paper we will briefly touch on those topics, but focus on the issue of individual recognition by Support Vector Machines [2].

2 Methods and tools

2.1 Biological context

The principal field site for our work has been the rainforest environment at the Estación Chajul, Reserva de la Biósfera Montes Azules, in Chiapas México (approximately $16°6'44''$ N and $90°56'27''$ W). The species of birds in our analysis have been the Barred Antshrike (BAS) (*Thamnophilus doliatus*), Dusky Antbird (DAB) (*Cercomacra tyrannina*), Great Antshrike (GAS) (*Taraba major*), and the Mexican Antthrush (MAT) (*Formicarius analis*). A sonogram of two MATs is in Figure 1, below, and those for the other species are illustrated in [3]. Examples of the songs from these species are posted on http://taylor0.biology.ucla.edu/al/bioacoustics/.

2.2 Sensor arrays

We have developed and tested an acoustic platform with small microphone sub-arrays that can be deployed 10-30m apart. They are automatically calibrated, to determine their location and orientation, then activated to perform streaming event recognition, and acquire data when triggered by animal vocalizations. Details on the development and implementation of the Acoustic ENSBox platform are described in [4].

©ISAROB 2009

2.3 Event recognition

Event recognition a critical first step to processing that follows, triggering source recognition and localization. We find that streaming adaptive statitical classifiers are a good approach in most cases.

We have implemented a marmot alarm call detector which runs in real time on the Acoustic ENSBox platform. Since the nodes are connected to each other via wireless ethernet, we make one additional improvement. If one node detects an event, that node tells all the others to trigger. In this way, the thresholds can be set quite high since only the node nearest to the event needs to detect it. Specific performance results are reported in [5].

2.4 Acoustic bird species recognition

We have developed filters to identify species, and individual birds in natural environments. We have taken several approaches. We have obtained promising results by extracting a sonogram of the vocalization, then look at particular features of those sonograms that might be particular to the species.

We have found it most helpful is to adapt methods from human voice recognition to create a Markov Transition Matrix appropriate to the vocalizations of each individual or species. We are also looking at other methods that appear promising, especially data mining and Self-Organizing Maps.

Trifa [3] describes in detail our experience with using HMMs to discriminate among different species of antbirds. In general, discrimination is at least 90% successful. We are currently directing efforts at identifying individuals, with quite positive preliminary results.

Similarly, we have explored with the use of data mining for the classification of bird species. The main goal has been to understand the importance of particular features of the acoustic signal that are distinctive for the accurate discrimination of bird species. A secondary goal has been to reduce the dimensionality of the acoustic signal in order to minimize the computational resources required for its manipulation and analysis [6].

Escobar [7] employed Self-Organizing Maps (SOMs) for the acoustic classification of bird species. The overall goal has been to examine the scope in which unsupervised learning is capable of conferring meaningful categorization abilities and increasing autonomy to sensor arrays.

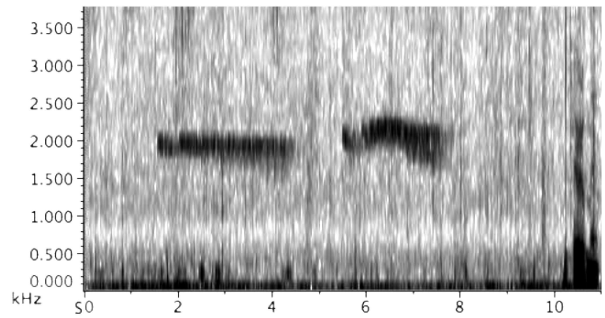

Figure 1: Spectrograms for two MATs from one territory

2.4.1 Acoustic bird individual recognition

It is sometimes possible to distinguish individual singers. For example, Figure 1 shows sonograms for the songs of we inferred to be two MATs singing on the same territory. Songs were recorded from each of 10 birds during December 2006, by Martin Cody. The identitication of each singer was inferred from timing and location. Samples of 20 - 50 songs from each of the 6 territories they occupied were included. The sonogram of each song was measured for 20 traits, including length and maximum or minimum frequency at various parts of the song, so that each song was represented by a vector. The standardized variance-covariance matrix for all songs was calculated and principal components extracted. Each song is plotted in the first two principal axes of Figure 2. The convex hull of songs for what we identified as each individual shows the clustering. It is apparent that some individuals are clearly distinguished while others are much less so, at least when plotted in these two dimensions. We are currently exploring ways to automate this procedure and increase the power of discrimination, with the goal of identification being done in real time on each node in the array.

Particularly, we have recently explored with the use of Support Vector Machines (SVMs) for the classification of individual MATs. Using feature selection we reduced the dimensionality of the original vector to 7

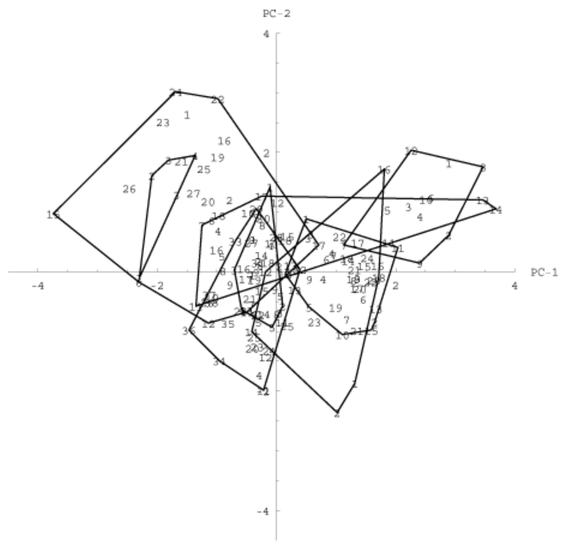

Figure 2: Convex hulls of principal component scores from 10 putatively individual MATs

individual	samples	training	testing
PMPa	28	21	7
PMPb	22	16	6
LGEa	12	9	3
PBEa	25	19	6
AVEa	38	30	8
LCNb	17	13	4
SNWa	20	15	5

Table 1: Individual MATs data set

features. Additional data selection yielded the data set used in our experiments with SVMs (Table 1).

We conducted simple scaling to the data (z-scores). A radial basis function (RBF) kernel was used for the experiments. N-fold cross-validation was conducted to find appropriate kernel parameters. Training was performed using the obtained kernel parameters on the training set. Testing was conducted using data samples not included in the training set. This procedure is fully described in [8].

The classification results obtained in our preliminary experiments are presented in Table 2.

2.5 Localizing sound sources

When an array of sound sensors are employed, localizing the source of a sound should be possible in any of several ways – including comparison of sound energy, comparison of time of arrival of the sounds, and analysis of phase relations of the sound waves. In the rainforest, comparing sound energy is difficult because of reflection and interference from the vegetation. Comparing time of arrival is made difficult when sensors are widely spaced because of drifting time synchronization among widely spaced processors that need to process the sounds. Consequently, we have focused our efforts on comparing phase relations among the several microphones on the sub-arrays described in section 2.2 above. Within the sub-array there are expected to be differences in the phases that arrive at the several sensors, but time synchronization is achieved by using the same or closely coupled processors. While not permitting localization as such, this method does permit estimation of direction of arrival (DOA) to any one sub-array. Triangulation of estimated DOA from several sub-arrays can then be used to identify the location, itself, of the source.Our colleague Kung Yao and his students have developed algorithms for estimating DOA in these circumstances. Their method, termed "Approximate Maximum Likelihood" (AML), is described in [9] and [5].

procedure	accuracy	classified	misclassified
training	94.30	116	7
testing	84.62	33	6

Table 2: Classification results

2.6 Emergent understanding

Our long term goal is to provide sensor arrays with the adaptation capabilities required to identify the meaning of bird vocalizations in the social context of the vocalizing animals. This requires event recognition, symbol grounding and adaptive communication in order for the array to arrive at a collective understanding [10]. Previous studies have established plausible scenarios for the emergence of these capabilities in sensor arrays [11].

Symbol grounding, identifying and binding semantically meaningful events to symbols, then communicating that information among parts of the arrays is of great importance. We are currently examining methods based on information theory [12].

Once events have been recognized then we can use self-organizing maps to categorize the songs . A problem has been that new events might be attached to one symbol in one part of the array, but to another symbol

©ISAROB 2009

in other parts of the array. We have determined, to some extent, the conditions under which the different "meanings" will converge or remain separate [13].

Finally, we are developing the linguistic structure that is necessary to describe these songs and events in an expressive, learnable manner, based on the ideas developed by Stabler [14].

3 Conclusions

Overall, adaptive sensor arrays seem promising platforms for habitat monitoring applications. In the near future, our efforts will be directed towards enabling sensor arrays with increasing adaptability and cognitive abilities. To accomplish this we will build largely on the results reported here.

Acknowledgements

This work was supported by the US National Science Foundation under Award Number 0410438 and by Consejo Nacional de Ciencia y Tecnología under Award Number REF:J110.361/2007. The authors would like to thank Martin L. Cody, Kung Yao, Edward P. Stabler, Lewis Girod and Travis C. Collier for their invaluable contribution to this paper.

References

[1] Taylor, C. E., From cognition in animals to cognition in superorganisms, In M. Bekoff, C. Allen and G. Gurghardt, (eds.), *The Cognitive Animal. Empirical and Theoretical Perspectives on Animal Cognition* The MIT Press, 2002.

[2] Cristianini, N. and Shawe-Taylor, J., *An Introduction to Support Vector Machines.* Cambridge University Press, 2000.

[3] Trifa, V. M., Kirschel, A. N., Taylor, C. E., Vallejo, E. E: Automated species recognition of antbirds in a Mexican rainforest using hidden Markov models, *The Journal of Accoustical Society of America* (In press)

[4] Girod, L., Lukac, M., Trifa, V., Estrin, D., The Design and Implementation of a self-calibrating distributed acoustic sensing platform, In *ACM SenSys, 2006.*

[5] Ali, A. M. S., Asgari, T. C. Collier, M. Allen, L. Girod, R. E. Hudson, K. Yao, C. E. Taylor, Blumstein, D. T., An empirical study of collaborative acoustic source localization *Wireless Sensor Networks*, 2008.

[6] Vilches, E., Escobar, I. A., Vallejo, E. E., Taylor, C. E., Data mining applied to acoustic bird species recognition, In *18th International Conference on Pattern Recognition, ICPR 2006* Volume 3, pp. 400-403., IEEE, 2006.

[7] Escobar, I. A., Vilches, E., Vallejo, E. E., Cody, M. L., Taylor, C. E., Self-organizing acoustic categories in sensor arrays, In F. Almeida e Costa, M. L. Rocha, E. Costa et al (eds.) *Advances in Artificial Life, 9th European Conference, ECAL 2007.* LNAI 4648, pp. 1161-1160, Springer-Verlag, 2007.

[8] Chang, C.-C. and Lin, C.-J., LIBSVM a library for support vector machines, 2001. `http://www.csie.ntu.edu.tw/~cjlin/libsvm`

[9] Chen, C. E., Lorenzelli, F., Hudson, R. E. and Yao, K. Acoustic source DOA estimation using the cross-entropy method, In ICASSP, 2007.

[10] Lee Y., Riggle, J., Collier, T.C. et al., Adaptive communication among collaborative agents: Preliminary results with symbol grounding, In M. Sugisaka, H. Tanaka (eds), *Proceedings of the Eighth International Symposium on Artificial Life and Robotics* (AROB8th), 2003.

[11] Collier, T. C., Taylor C.E.: Self-Organization in Sensor Networks. *Journal of Parallel and Distributed Computing* **64**:7 (2004) pp.866–873.

[12] Kobele, G. M., J. Riggle, R. Brooks, D. Friedlander, C. Taylor, E. Stabler., Induction of Prototypes in a Robotic Setting Using Local Search MDL, in M. Sugisaka and H. Tanaka, (eds.), *Proceedings of the Ninth International Symposium on Artificial Life and Robotics*, (AROB9th), 2004.

[13] Vallejo, E. E. and Taylor, C. E., A simple model for the evolution of a lexicon, In M. Sugisaka and H. Tanaka, (eds.), *Proceedings of the International Symposium on Artificial Life and Robotics* (AROB9th), 2004.

[14] Stabler, E. P., Collier, T. C., Kobele, G. M., et al, The learning and emergence of mildly context sensitive languages, In W. Banzhaf, T. Christaller, P. Dittrich, et al (Eds.) *Advances in Artificial Life, 7th European Conference, ECAL 2003.* Springer-Verlag, 2003.

©ISAROB 2009

The Fourteenth International Symposium on Artificial Life and Robotics 2009 (AROB 14th '09),
B-Con Plaza, Beppu, Oita, Japan, February 5 - 7, 2009

The PSP Practice Support System Using Multiagent Techniques and Manipulation Analysis Data

Daisuke Yamaguchi
Dept. of Electric and Information
Faculty of Engineering
Toin University of Yokohama
1614, Kurogane-Cho, Aoba-Ku,
Yokohama, 225-8502, JAPAN

Kyouhei Otsuka
Dept. of Electric and Information
Faculty of Engineering
Toin University of Yokohama
1614, Kurogane-Cho, Aoba-Ku,
Yokohama, 225-8502, JAPAN

Fumiyo Katayama
Dept. of Electric and Information
Faculty of Engineering
Toin University of Yokohama
1614, Kurogane-Cho, Aoba-Ku,
Yokohama, 225-8502, JAPAN

Muneo Takahashi
Dept. of Electric and Information
Faculty of Engineering
Toin University of Yokohama
1614, Kurogane-Cho, Aoba-Ku,
Yokohama, 225-8502, JAPAN

Abstract

Multiagent technologies enable us to explore their sociological and psychological foundations.

Personal Software Process (PSP) support system is built using this.

Moreover, We think that the data inputted can acquire software development process by sorting out using a user action record table.

In this paper, the PSP system of programming is built and the analysys data of Multiagents learning method.

The data of the prostates cancer offered by the medical institution and a renal cancer was used for verification of a system.

Keyword:

Multiagent System, Personal Software Process ,Practis Support System

1 Introduction

An agent is a computational entity such as a software program or a robot, and can be viewed as perceiving and acting upon its environment. This agent is autonomous in that its behavior at least partially depends on its own experience.

Multiagent systems have the capacity to play an important role in developing and analyzing models and theories of interactivity in human societies. Humans interact in various ways and at many levels: for instance, they observe and model one another, they request and provide information, they observe and model one another, they request and provide information, they negotiate and discuss, they develop shared views of their environment, they detect as terms, committees, and economies. Many interactive processes among humans are still poorly understood, although they are an integrated part of our everyday life. Multiagent technologies enable us to explore their sociological and psychological foundations.

PSP support system is built using this. Moreover, We think that the data inputted can acquire software development process by sorting out using a user action record table.

In this paper, the PSP system of programming is built and the analysys data of Multiagents learning method. Generally, software process data is complicated, and when building a support system using such data including some action time, the calculation with expression is difficult in many cases. Then, the PSP systems configuration from a data pattern is effective using the Machine Learning who is excellent in pattern recognition to such a problem.

Furthermore, in order to treat effectively the error

©ISAROB 2009

included in data, a Rough Neural Network is formed using the extended type Rough Neuron defined from Rough Aggregate Theory. Moreover, change of the diagnostic accuracy by using Genetic Programming to changing the number and combination of the data inputted is seen. Back Propagation generally used in a Neural Network is used for study of a network.

The data of the prostates cancer offered by the medical institution and a renal cancer was used for verification of a system.

2 Intelligent Agents and Multiagent System

Artificial Intelligence (AI) has made great strides in computational problem solving using explicitly represented knowledge extracted from the task. If we continue to use explicitly represented knowledge exclusively for computational problem solving, we may never computationally accomplish a level of problem solving performance equal to humans. From this idea, the paper describes the development of a multiagent system that can be used to support the assessment of design performance in the cellular automata model. Agents represent objects or people with their own behavior, and take the structure of cellular automata lattice.

Intelligent agents and multiagent systems are one of the most important emerging technologies in computer science today [1]. The advent of multiagent systems has brought together many disciplines in an effort to build distributed, intelligent, and robust applications. They have given us a new way to look at distributed systems and provided a path to more robust intelligent applications.

Multiagent systems deal with coordinating intelligent behavior among a collection of autonomous agents. Emphasis is placed on how the agents coordinate their knowledge, goals, skills, and plans jointly to take action or to solve problems. Constructing the multiagent systems is difficult [2, 3]. They have all the problems of traditional distributed and concurrent systems plus the additional difficulties that arise from flexibility requirements and sophisticated interactions.

3 Personal Software Process

The Personal Software Process (PSP) is a self-improvement process that helps you to control, manage, and improve the way you work. It is a structured framework of forms, guidelines, and procedures for developing software [4]. Properly used, the PSP provides the data you need to make and meet commitments, and it makes the routine elements of your job more predictable and efficient.

The PSP's sole purpose is to help you improve your software engineering skills. It is a powerful tool that you can use in many ways. For example, it will help you manage your work, assess your talents, and build your skills. It can help you to make better plans, to precisely track your performance, and to measure the quality of your products. Whether you design programs, develop requirements, write documentation, or maintain existing software, the PSP can help you to do better work.

Rather than using one approach for every job, you need an array of tools and methods and the practiced skills to use them properly. The PSP provides the data and analysis techniques you need to determine which technologies and methods work best for you.

The PSP also provides a framework for understanding why you make errors and how best to find, fix, and prevent them. You can determine the quality of your reviews, the defect types you typically miss, and the quality methods that are most effective for you.

After you have practiced the exercises in this book, you will be able to decide what methods to use and when to use them. You will also know how to define, measure, and analyze your own process. Then, as you gain experience, you can enhance your process to take advantage of any newly developed tools and methods.

The PSP is not a magical answer to all of your software engineering problems, but it can help you identify where and how you can improve. However, you must make the improvements yourself.

PSP write several program using the evolving process shown Figure 1.

PSP0 and PSP0.1 hierarchy include introduces process discipline and measurement. PSP1 and PSP1.1 hierarchy include introduces estimating and planning. PSP2 and PSP2.1 hierarchy include Introduces quality management and design. Team Software Process exist over the PSP hierarchies. Because, PSP occupies an important part in the software engineering.

4 The PSP Practis support system using Multiagent

In this section, we study combined as it occurs in genetic Techniques into agent learner. We used as a tool for searching wide and complex solution space in Intelligent agent learns data. Intelligent agent using

The Fourteenth International Symposium on Artificial Life and Robotics 2009 (AROB 14th '09),
B-Con Plaza, Beppu, Oita, Japan, February 5 - 7, 2009

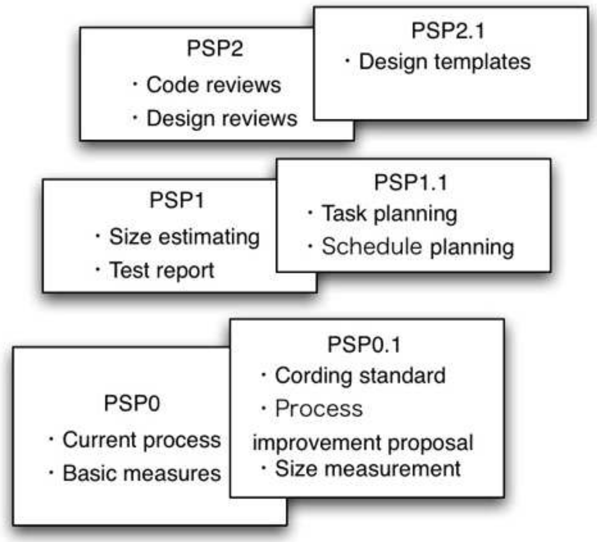

Figure 1: **PSP Process Evolution**

complex techniques of related research. Multiagent is state in a filed shown Figure 2.

Figure 2 depicts the Agent Communication Module and shared Information Data. The Agent make filed in order to shared information data from Agent communication filed. These fields include other Learner kept in Intelligent Agent shown Figure 3.

Figure shows the Agent between communication module in other communicate method. In this case, Intelligent Agent support the PSP time and size measures record to user manipulation data. Agent Controller select over Intelligent Agent Information Data Share (AiD-S) over Agent Information Data Delivery (AiD-D).

Other Learner support anything AI techniques of input data. Intelligent Agent has made combined these techniques into the Machine Learning. Machine Learning include same function of standard algorithm using user analyses data. These techniques supported by analysis data in time sheet that retrieval of start and end point.

Table 1 shows the PSP record form Time Measures and Size Measures [4].

In the PSP, engineers use the time recording log to measure the time spent in each process phase. In this log, they note the time they started working on a task, the time when they stopped the task, and any interruption time. For example, an interruption would be a phone call, a brief break, or someone interrupting to ask a question. By tracking time precisely, engineers

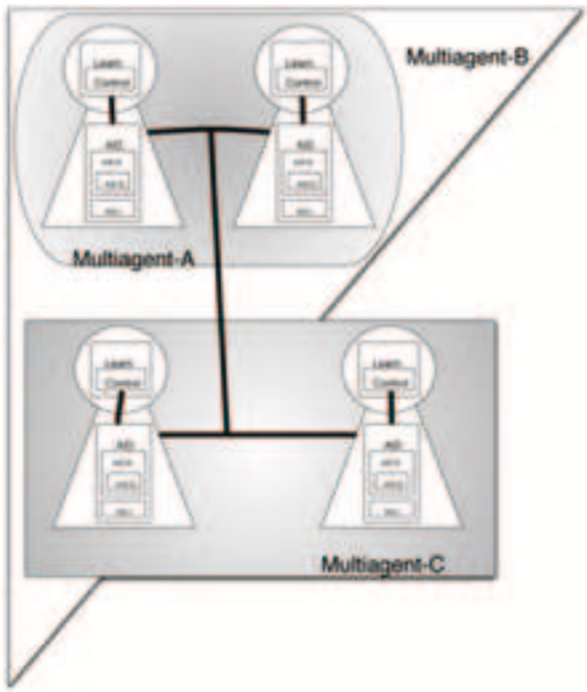

Figure 2: **Support System Communication of Multiagent**

Figure 3: **The Configuration of Agent Module**

©ISAROB 2009

Table 1: The scale of program size categories

	Plan	Results	Accumulation
Base			
Added			
Modified			
Deleted			
New and Changed			
Reused			
New Reused			
Total			

track the effort actually spent on the project tasks. Since interruption time is essentially random, ignoring these times would add a large random error into the time data and reduce estimating accuracy.

Since the time it takes to develop a product is largely determined by the size of that product, when using the PSP, engineers first estimate the sizes of the products they plan to develop. Then, when they are done, they measure the sizes of the products they produced. This provides the engineers with the size data they need to make accurate size estimates. However, for these data to be useful, the size measure must correlate with the development time for the product. While lines of code (LOC) is the principal PSP size measure, any size measure can be used that provides a reasonable correlation between development time and product size. It should also permit automated measurement of actual product size.

So, This any measure record to support Intelligent Agent consider with using this Agent Learner expanded of PSP support. A person engaging in a person who experienced PSP and software development for many years is not very worried about a form record-keeping work. Record-keeping is vague, and what is performed of a person pressed by a work still increases. Necessity to perform automatically is important in a soldier, remission of an activity and process assay to record an activity precisely.

Therefore I record all activities, and a support system shares the documentary information, and an Intelligent agent examines to whether be content which documentary information to shows personal characteristic of difference with an another person.

5 Conclusion and Future Work

In this research we build Multiagent complex system sensing user working data. We were able to searching user experience data. We create agent learner data in user working analyses system.

For future works, we will consider methods quick running of agent learner in communication data and user experience data. We try to delete user missing work date filter on experience data. We consider to that delete missing work filter on experience data.

Future versions of this model will aim to show how the system in communication response in a more natural, unscripted scenario, involving multiple parts in addition to other forms of process and contingency.

References

[1] Weiss, G. (1999), Multiagent Systems, A Modern Approach to Distributed Artificial Intelligence, the MIT Press.

[2] Abul, O., Polat, F., and Alhajj, R. (2000), Multiagent Reinforcement Learning Using Function Approximation, IEEE Transaction on systems, man, and cybernetics-part c: application and reviews, Vol. 30, No. 4, pp. 485-497.

[3] Khosla, R., and Dillon, T. (1997), Engineering Intelligent Hybrid Multi-Agent Systems, Kluwer Academic Publishers.

[4] Watts S. Humphrey (2005), PSP - A Self-Improvement Process for Software Engineers, Addison-Wesley.

The Fourteenth International Symposium on Artificial Life and Robotics 2009 (AROB 14th '09),
B-Con Plaza, Beppu, Oita, Japan, February 5 - 7, 2009

Use of Multiobjective Genetic Rule Selection for Examining the Effectiveness of Inter-Vehicle Communication in Traffic Simulations

Yoshihiro Hamada, Yusuke Nojima, and Hisao Ishibuchi

Graduate School of Engineering, Osaka Prefecture University
1-1 Gakuen-cho, Naka-ku, Sakai, Osaka 599-8531, Japan
(Tel : 81-072-254-9198; Fax : 81-072-254-9915)
({hamada@ci., nojima@, hisaoi@}cs.osakafu-u.ac.jp)

Abstract**:** Recently, Inter-Vehicle Communication (IVC) has actively been studied to avoid traffic congestion. In this paper, we propose an idea of using fuzzy rules to examine the effectiveness of IVC. In the proposed approach, we first collect travel records (e.g., travel time, travel path, traffic volume) of vehicles with IVC from our cellular automata-based traffic simulator. Various kinds of available information for vehicles with IVC are used in the antecedent part of our fuzzy rules. The level of the effectiveness of IVC is discretized into four categories (i.e., four classes) in this paper. The consequent class of each fuzzy rule is one of those four classes. Next we generate a large number of fuzzy rules from the collected data. Then we select only a small number of fuzzy rules by multiobjective genetic rule selection. We use three objectives: to maximize the accuracy, to minimize the number of selected rules, and to minimize the total rule length (i.e., the total number of antecedent conditions). Our approach can find a number of non-dominated fuzzy rule-based systems with respect to their accuracy and complexity. Finally we analyze the effectiveness of IVC using fuzzy rules in the obtained fuzzy rule-based systems through their linguistic interpretation.

Keywords: Multiobjective genetic rule selection, fuzzy rules, inter-vehicle communication, traffic simulation.

I. INTRODUCTION

Vehicles are widely used as a means of useful transportation in the mobility society where the demand for road traffic is expanding year by year. At the same time, chronic traffic congestion has become a social problem. To solve this problem, several studies [2], [3] have pointed out and discussed the potential ability of direct wireless communication between vehicles, usually referred to as Inter-Vehicle Communication (IVC). IVC has several advantages: no need of huge public infrastructure investment and little time lag on transmitting traffic information. This is because vehicles can directly communicate traffic information to each other.

In this paper, we propose an idea of examining the effectiveness of IVC using fuzzy rules generated from traffic simulations. During our simulations, we collect time-series data from each vehicle such as the traffic volume and the route of each vehicle. We use fuzzy rules selected by multiobjective genetic rule selection to examine the effectiveness of IVC. A large number of fuzzy rules are generated from the collected data from vehicles. Only a small number of fuzzy rule are selected by multiobjective genetic rule selection. A number of non-dominated fuzzy systems can be obtained with respect to their accuracy and complexity. Using the selected fuzzy rules, we can manually analyze how each vehicle can predict the travel time for each route based on the available information through IVC.

This paper is organized as followed. First we explain our traffic simulator in Section II. Next we explain a route guidance method based on the traffic information sharing among neighboring vehicles through IVC in Section III. Then we explain multiobjective genetic rule selection in Section IV. In Section V, we examine the effect of IVC through computational experiments on our traffic simulator. Experimental results show that the selected fuzzy if-then rules can explain how each vehicle chooses a route using the available information through IVC. Finally Section VI concludes this paper.

II. TRAFFIC SIMULATOR

In this section, we explain our traffic simulator. This model is used in Section IV to examine the effect of IVC through computational experiments.

Traffic simulators can be divided into macroscopic and microscopic models. In this paper, we develop a microscopic traffic simulator using cellular automata [6]. Figure 1 shows the road map of our traffic simulator. The simulation area is divided into squared cells. In our simulator, we assume that the road map is treated as a directed graph where a node and a link correspond to an intersection and a road between intersections, respec-

©ISAROB 2009

tively. A link is represented by a sequence of gray cells in Fig. 1. The origin and the destination of a driver are assigned randomly to any cell on any link in Fig. 1. When a driver arrives at its destination, a new destination is assigned randomly.

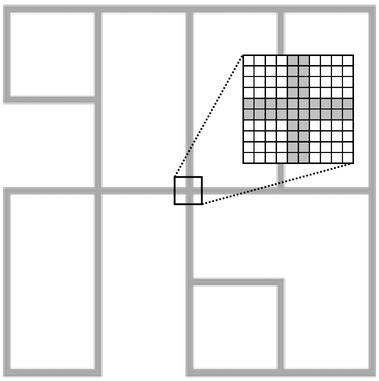

Fig. 1. Road map of our traffic model.

The positions of all vehicles running in the simulator are updated synchronously. At every state transition time, each vehicle stays at the current cell or jumps to its next cell according to a local transition rule. Our local transition rule is simply stated as "a vehicle moves only when its next cell towards its destination is empty".

III. INTER-VEHICLE COMMUNICATION

In this section, we explain a route selection method based on available information for vehicles through IVC. Our method chooses a route for a driver from its origin to its destination based on available information, and revises the selected route whenever the driver approaches an intersection. In this paper, we represent the traffic information for each link by a link weight. For example, if a link weight is large, a vehicle on the link needs long travel time to pass the link. We employ Dijkstra's algorithm [1] to search for the route with the minimal sum of link weights (i.e., the fastest route).

Each driver has its own weight for each link. The actual travel time of the driver is assigned as the weight to the corresponding link. There are two cases where the weight of a link is updated. One is when the driver travels the link. When the driver arrives at a node (i.e., intersection), the weight of the corresponding link is updated to the actual travel time. The update time for the link weight is set as well. The other is the case in which another vehicle is in the range of IVC. Each vehicle compares the update times for all weights with those of another vehicle. Figure 2 shows an example in which a vehicle A passes on another vehicle B on the opposite lane. They can communicate with each other through IVC. Traffic information to be shared by these two vehicles consists of the travel time (i.e., weight) and the update time for each link. It should be noted that each vehicle has its own travel time and update time for each link. More specifically, the newer information for each link is shared by these two vehicles by updating the older one for each link. Closely adjacent vehicles in the same lane also communicate directly with each other in the same manner as in the above-mentioned situation.

A

# of link	Travel time	Update time
1	7	7
2	5	12
3	8	20
4	3	23

# of link	Travel time	Update time
1	5	25
2	6	20
3	8	20
4	3	23

B

# of link	Travel time	Update time
1	5	25
2	6	20
3	9	14
4	5	5

# of link	Travel time	Update time
1	5	25
2	6	20
3	8	20
4	3	23

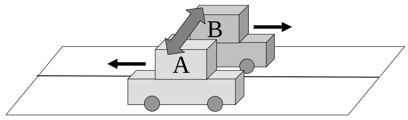

Fig. 2. An example of inter-vehicle communication.

IV. MULTIOBJECTIVE RULE SELECTION

In this section, we briefly explain fuzzy rules, fuzzy reasoning, and multiobjective genetic rule selection.

1. Pattern Classification Problem

Let us assume that we have m training (i.e., labeled) patterns $\mathbf{x}_p = (x_{p1}, ..., x_{pn})$, $p = 1, 2, ..., m$ from M classes in the n-dimensional continuous pattern space where x_{pi} is the attribute value of the p-th training pattern for the i-th attribute ($i = 1, 2, ..., n$). For the simplicity of explanation, we assume that all the attribute values have already been normalized into real numbers in the unit interval [0, 1]. That is, $x_{pi} \in [0, 1]$ for $p = 1, 2, ..., m$ and $i = 1, 2, ..., n$.

2. Fuzzy Rules for Pattern Classification

We use fuzzy rules of the following type for our n-dimensional problem:

$$\text{Rule } R_q : \text{If } x_1 \text{ is } A_{q1} \text{ and ... and } x_n \text{ is } A_{qn} \text{ then Class } C_q \text{ with } CF_q, \qquad (1)$$

where R_q is the label of the q-th fuzzy rule, $\mathbf{x} = (x_1, ..., x_n)$ is an n-dimensional pattern vector, A_{qi} is an antecedent fuzzy set ($i = 1, 2, ..., n$), C_q is a class label, and CF_q is a certainty grade.

We use multiple fuzzy partitions with different granularities in rule extraction. In this paper, we use four homogeneous fuzzy partitions with triangular fuzzy sets in Fig. 3. In addition to the 14 fuzzy sets in Fig. 3, we also use the domain interval [0, 1] as an antecedent fuzzy set in order to represent a *don't care* condition. That is, we use the 15 antecedent fuzzy sets for each attribute in our computational experiments. Thus the total number of possible fuzzy rules is 15^n.

For each of those 15^n combinations of the antecedent fuzzy sets, the consequent class and the certainty grade can be easily specified based on compatible training patterns [4]. Using a fuzzy rule evaluation measure in fuzzy data mining [4], we generate a prespecified number of fuzzy rules.

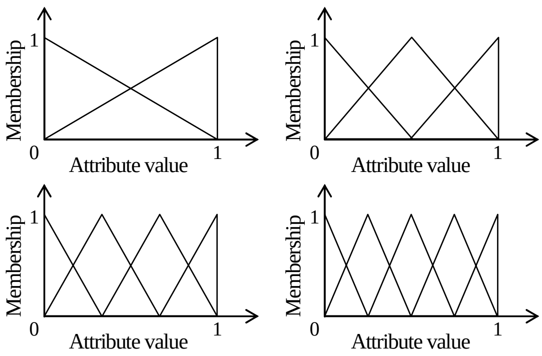

Fig. 3. Four fuzzy partitions used in our experiments.

3. Multiobjective Genetic Rule Selection

Let us assume that N candidate rules have already been extracted. Multiobjective genetic rule selection tries to find an accurate and compact rule set from the N candidate rules. Any subset S of the N candidate rules can be represented by a binary string of length N as $S = s_1 s_2 s_3 \cdots s_N$ where $s_i = 1$ and $s_i = 0$ mean that the i-th candidate rule is included in and excluded from the rule set S, respectively. Such a binary string is used as an individual in multiobjective genetic rule selection.

We use an evolutionary multiobjective optimization (EMO) algorithm to search for non-dominated fuzzy rule sets with respect to the three objectives: to maximize the number of correctly classified training patterns by S, to minimize the number of fuzzy rules in S, and to minimize the total rule length of S.

Since each individual is represented by a binary string, we can use any EMO algorithm with standard genetic operations. In our computational experiments, we used NSGA-II together with uniform crossover and bit-flip mutation. The execution of NSGA-II was terminated at the prespecified number of generations. See [5] for details on multiobjective genetic rule selection.

V. COMPUTATIONAL EXPERIMENTS

1. Data Preparation

In this subsection, we explain how to prepare training data with class labels from the travel records in our traffic simulator. There exist 300 vehicles in our simulation environment in Fig. 1. The termination condition of traffic simulations was that each vehicle reached the goals at least 50 times. Each vehicle can communicate with another vehicle in the eight neighborhood cells.

Let us assume that a vehicle travels from node A to B and then chooses a route from node B to C in Fig. 4. In this case, a training pattern $\mathbf{x} = (x_1, \ldots, x_{10})$ is collected at the node B. In the following, each element of this training pattern is explained in detail.

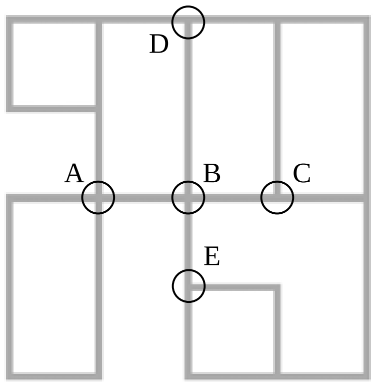

Fig. 4. An example of *link connection density*.

The first three elements x_1, x_2, and x_3 are *link connection density* of node A, B, and C, respectively. *Link connection density* is a sum of the number of links that the neighbor nodes have. For example, x_2 is *link connection density* of node B, which is a sum of the number of links that the neighboring nodes (i.e., A, C, D, and E) have. That is, x_2 is 13 (i.e., 4+3+3+3). When the *link connection density* of a node is high, the node can be viewed as a hub of the neighboring nodes. That is, a large number of vehicles must be likely to pass the node.

The fourth element x_4 is the traffic volume in the current lane (i.e., A to B), x_5 is the traffic volume in the current opposite lane (i.e., B to A), x_6 is the traffic volume in the next lane (i.e., B to C), and x_7 is the traffic volume in the next opposite lane (i.e., C to B). A large traffic volume of a link means heavy traffic where each vehicle can communicate with each other very often. It also suggests possible traffic congestion.

The other elements x_8, x_9, x_{10} are the number of links of nodes A, B, and C, respectively. They are related to the traffic volume and the frequency of communication.

Next we explain how to define the class label of each training pattern, which shows the effectiveness of IVC. We focus on the freshness of traffic information held by each vehicle and the accuracy of the predicted travel time from available information. We use the following four class labels:

Class 1: The update time of the weight of the chosen link held by a vehicle is old, and the vehicle could not correctly predict the travel time of the chosen link.

Class 2: The update time is old, but the vehicle could correctly predict the travel time.

Class 3: The update time is new, but the vehicle could not correctly predict the travel time.

Class 4: The update time is new, and the vehicle could correctly predict the travel time.

2. Experimental Results

First we generated 250 fuzzy rules for each class from the collected training patterns. Those fuzzy rules were used as candidate rule in multiobjective genetic rule selection where NSGA-II with the population size 200 was executed fro 5000 generations.

We obtained a number of fuzzy systems with different accuracy-complexity tradeoffs from a single run of NSGA-II. In order to manually analyze the effectiveness of IVC, we chose a very simple fuzzy system with only a single rule per class in Fig. 5 where DC means *don't care* and the real number in the parentheses shows the certainty grade of each fuzzy rule. The selected fuzzy rules in Fig. 5 are linguistically interpreted as follows:

R_1: If a vehicle came from a node with high *link connection density* and the traffic volume in the current link is moderate, it cannot obtain new traffic information and cannot predict the travel time.

R_2: If a vehicle is about to go to a node with moderate *link connection density* and the traffic volume in the current link is very large, it can obtain new traffic information but cannot predict the travel time.

R_3: If a vehicle is on a link with a very light traffic, the vehicle cannot obtain new traffic information but can predict the travel time correctly.

R_4: If a vehicle came from a node with small *link connection density* and is on a link with a somewhat heavy traffic, it can use new traffic information and can predict the travel time correctly.

From these fuzzy rules, we can see that there exist situations where vehicles cannot obtain new traffic information by IVC. We can also see that there are some cases in which vehicles cannot predict their travel times even when they have new information.

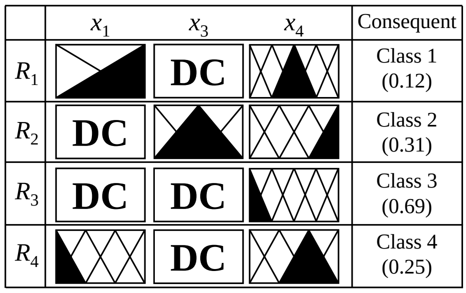

Fig. 5. One example of extracted knowledge.

VI. CONCLUSION

We proposed an idea of using fuzzy rules to examine the effectiveness of Inter-Vehicle Communication (IVC). Through computational experiments, we demonstrated that we can obtain linguistic descriptions from fuzzy rules about the characteristic features of IVC with respect to the availability of new traffic information and the accuracy of predicted travel times for vehicles.

This work was partially supported by the Grant-in-Aid for Exploratory Research: KAKENHI (18650055).

REFERENCES

[1] E. W. Dijkstra (1959), A note on two problems inconnexion with graphs, in *Numeriche Mathematik* 1:269-271

[2] K. Ohara, Y. Nojima, H. Ishibuchi (2007), A study on traffic information sharing through inter-vehicle communication, in *Proc. of 2007 Multi-conference on Systems and Control*: 670-675

[3] S. Kato, N. Minobe, and S. Tsugawa (2003), Applications of inter-vehicle communications to driver assistance system, in JSAE Review, (24)1: 9-15.

[4] H. Ishibuchi, T. Nakashima, M. Nii (2005), *Classification and Modeling with Linguistic Information Granules*, Springer-Verlag

[5] H. Ishibuchi, Y. Nojima, I. Kuwajima (2008), Evolutionary multiobjective design of fuzzy rule-based classifiers, J. Fulcher, L.C. Jain (eds.) *Computational Intelligence: A Compendium*: 641-685, Springer, Berlin

[6] S. Wolfram (1986), Theory and application of cellular automata, *World Scientific*

©ISAROB 2009

Web News Summary System with Clustering Algorithm to Identify Same Article

Ayahiko Niimi
Department of Media Architecture
Future University-Hakodate
116-2 Kamedanakano-cho, Hakodate-shi,
Hokkaido 041-8655, JAPAN

Yusaku Saito
Department of Complex Systems
Future University-Hakodate
116-2 Kamedanakano-cho, Hakodate-shi,
Hokkaido 041-8655, JAPAN

Osamu Konishi
Department of Complex Systems
Future University-Hakodate
116-2 Kamedanakano-cho, Hakodate-shi,
Hokkaido 041-8655, JAPAN

Abstract

We propose the system that offers only the article that is the relation to topics to the user in this research. When the user wants to read the article that is the relation to topics, the user must click the link to the article. Therefore, it is difficult for the user to read only the article related to topics. Moreover, there is the article that is similar to each other content or article. Therefore, user must read the article that is similar to other article. We propose the algorithm to find similar articles. For the proposed system, we use the feature of reported articles. There is an outline of the entire article at the beginning of reported articles.

Keyword:

Web news, Natural Language Processing, Morphological Analysis, Summary Generation

1 Introduction

The web news sites become popular, but they are not understood easily. On the other hand, the newspaper and the television are comprehensible. We think that it is a cause that the web news is not arranged. The portal site (such as Yahoo JAPAN News, etc) is news collection site. If news is a little related to other news, it becomes related news and is made a link to related news. Moreover, the portal site publishes the article on a lot of newspapers and news agencies. Therefore, there are a lot of related contents, but it is difficult to read articles that user actually wants to read.

We propose the system that offers only the article that is the relation to topics to the user in this research. When the user wants to read the article that is the relation to topics, the user must click the link to the article. Therefore, it is difficult for the user to read only the article related to topics. Moreover, there is the article that is similar to each other content or article. Therefore, user must read the article that is similar to other article. We propose the algorithm to find similar articles. For the proposed system, we use the feature of reported articles. There is an outline of the entire article at the beginning of reported articles.

2 Morpheme Analysis

A morphological analysis is to divide the input sentence into the morpheme which is a minimum unit with the meaning in linguistics, to decide the part of speech of each morpheme, and to allocate the prototype to the morpheme to which the transformation of the word of use. [4, 7]

A morphological analysis is important for Japanese documents, because Japanese sentence is not divide words by blank. In English, a morphological analysis is used to analyze end of a word transformation (tense, single or plural), suffix, prefix, etc.

For instance, it is analyzed that the morphological analysis is done by the sentence "Happyoukai wo okonaitai." (This sentence means "I want to hold a symposium"). (Refer to table 1)

Table 1: Examples of Morphological Analysis

Happyou	Happyou:	Noun
kai	Kai:	Noun
wo	Wo:	particle
okonai	Okonau:	verb-independent
tai	Tai:	auxiliary verb
.	.	symbol-period

The word divided by the morphological analysis is called an element-term. It comes to be able to do the frequency analysis and filtering to a specific part of speech by dividing into the element-term.

3 Proposed System

This chapter describes a proposed algorithm for low related articles and similar articles are deleted from the list of the news of topics.

This system extracts only a high relativity article from the article list including high/low relativity articles about topics that the user wants to learn. Moreover, the article on a similar contents are searched out, and deleted. In this paper, we decide a high relativity article which includes main content as related to topics. Moreover, we think that same information of the article with the high similarity is contained in other articles.

For the necessity for confirming the content clicking the link to the article to know the relativity of the article to exist, and to read only a high relativity article, it can be said that it is inconvenient under the present situation. Moreover, because a lot of similar articles exist, too the possibility of reading the article on almost the same content is high. It is thought that the site where a lot of volume of information with high possibility that the problem becomes a relief exists is the best for the verification of this system. Yahoo! JAPAN news has a lot of topics, and its source are from many newspaper sites. So, in this paper, we discuss "Yahoo! JAPAN news" site for experiment. It paid attention to the tendency that the entire summary was written in the part at the beginning about the news article when the proposed system was designed. Because the point of the entire article has been brought together in the sentence at the beginning, the outline can be understood. Therefore, we use beginning sentences of article for analysis. The system is mounted by the Java application.

Figure 1: Topics list of Yahoo! JAPAN News

We describe the proposed algorithm of extracting high relativity article from the article group of topics of Yahoo! JAPAN news, and deleting URL of a similar article.

The flow of the algorithm is shown below.

1. input top-page URL of topics
2. get the beginning sentence and the delivery date
3. process morphological analysis using MeCab
4. extract keywords
5. extract high relativity articles
6. delete similar articles
7. outout results

The user acquires URL of topics that the user wants to learn from the top page of topics of news and the program outputs URLs to the text file. At this time, we think the article only in the image thought that the content is low relativity, then that URL is excluded. Moreover, the link is not acquired when there is a page such as other newspapers because it targets only Yahoo! JAPAN news in this paper.

It accesses acquired URL, and the sentence to the punctuation of the start of the text and the delivery date is acquired. Because the noun decreases when one sentence of the start is short, the following punctuation is acquired in addition, and it outputs it to the text file for 20 characters or less. Moreover, delivery time of the article is acquired, and it outputs it to the text file with URL of the article. But, for the situation that there is no abstract sentences at the beginning. Then, when the sentences are not extracted when it is fewer than the threshold number at the beginning with the number of strokes to the punctuation of the sentence, we extract sentences until the following punctuation. It sets it to 25 characters as a result of experimenting on the number of strokes that becomes a standard.

Using MeCab that is the morphological analysis tool, the morphological analysis of the sentence is done at the beginning, and the result of the acquired each article is output to one text file.

The part of speech that doesn't show the feature of the article easily is excluded from the text file that does the morphological analysis and is output, and only a part of noun is extracted. The extracted part of speech is output to the text file.

The extracted part of speech is sorted to the lexical order, and a lot of consecutive nouns are found. It thinks this noun to be a noun that characterizes the relativity of topics, and only the article with this noun is output to the text file. However, when the same in one article two nouns or more exist, it counts with one. Moreover, the article not extracted is output to another text file. We use of the expression agreement technique to consider the number of extracted words. The following equation is used for the expression agreement technique. [9] In the equation, x is a number of words of sentences X that become standards, y is a number of words of sentences Y that become the object of comparisons, and m is a number of words that appears in both X and Y. It experimented to set the evaluation value as well as algorithm 1. As a result, if Score(X, Y) is larger than 60%, it is judged that two articles are similar , and deletes an old article.

$$\text{Score(X,Y)} = \frac{\frac{m}{x} + \frac{m}{y}}{2} \times 100 \qquad (1)$$

We think that it is rare that same topics exist in two days or more. It is based on the newest article in the extracted relativity and high article. Nouns that are to the article on the day before are compared. If the noun more than the evaluation value of nouns that exist in the article that became a standard exists in the article on the object of comparison, it is judged that two articles are similar and deletes an old article. Next, a new similar article is secondarily operated, and repeated this operation. We show its example. In Table 2, the alphabet presents one article. If D and E, G and H, J and K, L and M are judged as same contents. In Table 2, "similer to" means"judged as same contents". Using our proposed algorithm, the comparison is done in order of (A,B) → (A,C) → (A,D) → (A,E) → (A,F) → (B,D) → (B,E) → (B,G) → (H,I) → (L,M). When (A,C), (A,D), (A,F), (D,E), and (D,G) are compared, the article on C, D, F, E, and G is deleted. Therefore, A, B, D, H, I, J, K, L, and M are extracted. The extracted article is output to the text file. Moreover, the deleted article is output to another text file.

Table 2: date and articles

date	articles	similer to
12, Feb.	A	-
12, Feb.	B	-
11, Feb.	C	A
11, Feb.	D	-
11, Feb.	E	D
11, Feb.	F	A
10, Feb.	G	D
9, Feb.	H	D
8, Feb.	I	-
6, Feb.	J	A
31, Jan.	K	A
15, Jan.	L	B
15, Jan.	M	B

As an output result, the extracted URLs are written to the html file with the title of the article, newspaper site name in delivery origin, delivery date, extracted nouns and opening sentences. Moreover, URL of low relativity articles and similar articles are output to the text file respectively. (See Fig. 2)

4 Experimental Results

This section describes the experimental methodology and the results. We use two topics, " the damage

Figure 2: Output of proposed system

of crops by chemicals hepatitis C lawsuit" and "the Aegis destroyer collision in the experiment".

64 articles existed in topics of the damage of crops by chemicals hepatitis C prosecution when experimenting. 59 pieces in 64 pieces have been extracted because it was judged that five pieces were image links.

Using the topics of the Aegis destroyer collision in the experiment, as a result of the URL extraction, 336 URL has been extracted. However, 20 articles have been deleted from making the system work to doing this verification. The article that has been deleted is disregarded in the experiment. Therefore, it experimented assuming that 316 URL was extracted.

4.0.1 Result of "the damage of crops by chemicals hepatitis C lawsuit"

The ratio of the total of the number of articles to be able to delete the number and the relativity of the article to which relativity was able to be extracted high low became 67% among the numbers of URL extracted to the start. Moreover, the ratio of the total of the number of articles that were able to be deleted by a similar article became 100% with the number of articles that were able to be extracted in an article not similar among the numbers of articles that were judged that relativity was high and extracted. (See Table 3)]

Table 3: Extracted result of " the damage of crops by chemicals hepatitis C lawsuit"

	correct	miss
high related articles extract	67 %	33 %
similar articles extract	100 %	0 %

4.0.2 Result of "aegis destroyer collision"

The ratio of the total of the number of articles to be able to delete the number and the relativity of the article to which relativity was able to be extracted high low became 79% among the numbers of URL extracted to the start. Moreover, the ratio of the total of the number of articles that were able to be deleted by a similar article became 79% with the number of articles that were able to be extracted in an article not similar among the numbers of articles that were judged that relativity was high and extracted. (See Table 4) Moreover, the execution time from the input of URL to the output of the result was 55 seconds of two minutes. (We used a notePC with Intel Core2 Duo CPU(1.2GHz, 1GB RAM, Windows XP.)

Table 4: Extracted result of "aegis destroyer collision"

	correct	miss
high related articles extract	79 %	21 %
similar articles extract	79 %	21 %

5 Discussions

It can be said that the algorithm of the relativity judgment proposes in the present study was able surely to pick up the noun that becomes the key to topics. However, there was a difference at the positive detection rate of a relativity judgment of the result of targeted damage of crops by chemicals hepatitis C lawsuit and Aegis destroyer collision because of being only not existing at the beginning in the sentence, and the logic that one noun had extracted of the deletion. Similarly, there was a difference at the positive detection rate of the similarity judgment in the algorithm of the similarity judgment. There was information that had been described only to the deleted old article though this system was an algorithm that old when nouns were compared, and it was judged that it resembled it deletes the article, too. The method such as deleting a short article is devised as an idea that improves this problem in consideration of the entire amount of the sentence of each article.

6 Future Works

It is thought that the extraction result in which accuracy is high can be generated by considering the shake of the synonym and the mark of the morpheme not considered in the algorithm of this system, and the appearance order. In assumption as the logic considered that relativity is high if the noun that becomes a standard is expanded because only it doesn't exist at the beginning in the sentence, and the logic in a relativity judgment that one noun extracted of the deletion, and there is one, is the false detection that deletes a relativity and high article?It is thought that it is possible to eliminate it. Moreover, it compares after the noun of frequent occurrence is excluded when similar judged, and there is a possibility to understand the noun that the content of the article on the object or more characterizes.

References

[1] Ichimura, Y., Hasegawa, T., Watanabe, I., Sato, M.: Text Mining: Case Studies, Journal of Japanese Society for Artificial Intelligence, Vol.16 No.2,pp.192–200 (2001). (In Japanese)

[2] Nasukawa, T., Kawano, H., Arimura, H.: Base Technology for Text Mining, Journal of Japanese Society for Artificial Intelligence, Vol.16,No.2,pp.201–211 (2001). (In Japanese)

[3] Nagata, M., Taira, H.: Text Classification - Showcase of Learning Theories -, IPSJ Magazine, Vol.42 No.1,pp.32–37 (2001). (In Japanese)

[4] Matsumoto, Y., Kitauchi, A., Yamashita, T., Hirano, Y., Matsuda, H., Takaoka, K., Asahara, M.: Morphological Analysis System ChaSen version 2.2.1 Manual (2000). [Online] Available: http://chasen.aist-nara.ac.jp/chasen/bib.html.en

[5] Yahoo! NEWS, http://headlines.yahoo.co.jp/hl

[6] Juman, http://nlp.kuee.kyoto-u.ac.jp/nl-resource/juman.html

[7] MeCab, http://mecabsourceforge.jp/

[8] Ohtake, K., Okamoto, D., Kodama, M., Masuyama, S.: A Summarization System YELLOW for Japanese Newspaper Articles, IPSJ Magazine, Vol.43 No.SIG02, TOD13,pp.37–47 (2002). (In Japanese)

[9] Fujie, Y., Watabe, H., Kawaoka, T.: Article classification method using the calculation of the degree of association between articles and category attributes extracted from Web information, The 21st Annual Conference of the Japanese Society for Artificial Intelligence, 1G3-5 (2007). (In Japanese)

[10] Iguchi, T., Kaminaga, H., Yokomaya, S., Miyadera, Y., Nakamura, S.: Proposal of a Web Exploring Support Method Focusing on Topic Transition Processes, IEICE Technical Report, ET2007-54, pp.33–38 (2007). (In Japanese)

[11] Matsuo,. Y., Ishizuka, M.: Keyword Extraction from a Document using Word Co-occurrence Statistical Information, Journal of Japanese Society for Artificial Intelligence, Vol.17,No.3,pp.217–223 (2002). (In Japanese)

[12] Toda, H., Kataoka, R., Kitagawa, H.: Clustering News Articles using Named Entities, IPSJ SIG Technical Report, 2005-DBS-137, pp.175-181 (2005). (In Japanese)

[13] KNP, http://nlp.kuee.kyoto-u.ac.jp/nl-resource/knp.html

The Fourteenth International Symposium on Artificial Life and Robotics 2009 (AROB 14th '09),
B-Con Plaza, Beppu, Oita, Japan, February 5 - 7, 2009

Evolution of Cooperative Behavior among Heterogeneous Agents with Different Strategy Representations in an Iterated Prisoner's Dilemma Game

Hiroyuki Ohyanagi, Yoshihiko Wakamatsu, Yusuke Nakashima, Yusuke Nojima, and Hisao Ishibuchi

Osaka Prefecture University, 1-1 Gakuen-cho, Naka-ku, Sakai, Osaka 599-8531, Japan
(Phone: +81-72-254-9198; Fax: +81-72-254-9915)
({ohyanagi@ci., wakamatsu@ci., ysknksm@ci., nojima@, hisaoi@}cs.osakafu-u.ac.jp)

Abstract: The iterated prisoner's dilemma (IPD) game has been frequently used to examine the evolution of cooperative behavior among agents. When the effect of representation schemes of IPD game strategies was examined, the same representation scheme was usually assigned to all agents. That is, a population of homogeneous agents was usually used in computational experiments in the literature. In this paper, we focus on a slightly different situation where each agent does not necessarily use the same representation scheme. That is, a population can be a mixture of heterogeneous agents with different representation schemes. In computational experiments, we use binary strings of different length (i.e., three-bit and five-bit strings) for representing IPD game strategies. We examine the evolution of cooperative behavior among heterogeneous agents in comparison with the case of homogeneous ones for the standard IPD game with the typical payoff values 0, 1, 3 and 5. Experimental results show that the evolution of cooperative behavior is slowed down by the use of heterogeneous agents. It is also demonstrated that the faster evolution of cooperative behavior is achieved among majority agents than minority ones in a heterogeneous population.

Keywords: Iterated prisoner's dilemma (IPD) game, evolution of cooperative behavior, evolution of game strategies, genetic algorithms, representation, coding schemes.

I. INTRODUCTION

The evolution of cooperative behavior among agents in the iterated prisoner's dilemma (IPD) game has been discussed in many studies since the late 1980s [1] and the early 1990s [2], [3]. A player's strategy, which can be represented in various manners such as a binary string, a real-number string, a finite-state machine and a neural network, is evolved by selection, crossover and mutation in those studies. The fitness of a player in a population is defined by its average payoff obtained in iteratively playing the prisoner's dilemma game against other players in the same population. Various techniques and concepts have been introduced to the IPD game such as the speciation of strategies [4], individual recognition [5], and partner selection [6]. The IPD game has also been extended to various cases such as a multi-player version [7], [8], a spatial version [9], [10], stochastic strategies [11], [12], and random paring [13], [14]. See [15] for various studies on the evolution of cooperative behavior among agents in the IPD game.

Recently the IPD game has been used for examining the effect of the choice of a representation scheme on the evolution of game strategies [16], [17]. Those studies compared various representation schemes such as finite-state machines, cellularly encoded finite-state machines, feed-forward neural networks, if-skip-action lists, parse trees storing two types of Boolean functions, lookup tables, Boolean function stacks, and Markov chains. Experimental results showed that the choice of a representation scheme had a dominant effect on the evolution of game strategies.

When the effect of the choice of a representation scheme was examined, the same representation scheme was usually assigned to all agents in a population. That is, a population of homogeneous agents was usually used in computational experiments. In this paper, we focus on a slightly different situation where each agent does not necessarily use the same representation scheme. For example, some agents can use binary strings as their game strategies even when all the others use feed-forward neural networks. That is, a population can be a mixture of heterogeneous agents. Our aim is to show the effect of mixing different representation schemes.

II. IPD GAME AND GAME STRATEGIES

In this paper, we examine the evolution of cooperative behavior among heterogeneous agents in comparison with the case of homogeneous ones through computational experiments on the standard IPD game with the typical payoff values 0, 1, 3 and 5 (see Table 1).

©ISAROB 2009

The prisoner's dilemma game with the payoff matrix in Table 1 is played for a prespecified number of rounds (100 rounds in our computational experiments) between a pair of randomly selected agents from the current population. The random choice of two agents and the game playing between them are repeated in each generation until every agent plays the IPD game against a prespecified number of opponents (five opponents in our computational experiments). The fitness of each agent is defined by the average payoff per round obtained in the current population. New strategies for the next generation are generated by genetic operations.

We use three-bit and five-bit binary strings for representing IPD game strategies. Examples of those binary strings are shown in Table 2 and Table 3. Table 2 shows a three-bit binary string "101" which represents the so-call TFT (Tit-for-Tat) strategy. The same strategy is represented by a five-bit binary string in Table 3. One of these two representation schemes is assigned to each agent in our computational experiments.

Table 1. Payoff matrix of our IPD game.

Player's Action	Opponent's Action	
	C: Cooperate	D: Defect
C: Cooperate	Player: 3 Opponent: 3	Player: 0 Opponent: 5
D: Defect	Player: 5 Opponent: 0	Player: 1 Opponent: 1

Table 2. A three-bit binary string (TFT)

Player's First Action: Cooperate		1
Opponent's Action on the preceding Round	Suggested Action	
D: Defect	D: Defect	0
C: Cooperate	C: Cooperate	1

Table 3. A five-bit binary string (TFT)

Player's First Action: Cooperate			1
Actions on the Preceding Round		Suggested Action	
Player	Opponent		
D: Defect	D: Defect	D: Defect	0
C: Cooperate	D: Defect	D: Defect	0
D: Defect	C: Cooperate	C: Cooperate	1
C: Cooperate	C: Cooperate	C: Cooperate	1

When we use both representation schemes, the current population is a mixture of three-bit and five-bit binary strings. The game playing between binary strings with different length involves no additional difficulties. Thus we assume no restriction on the choice of two agents for the game playing. That is, a pair of strings (i.e., agents) is randomly selected from the current population for the game playing with no restriction.

On the other hand, we always choose a pair of strings of the same length for crossover. That is, we use a mating restriction where binary strings of different length are never recombined. The current population can be viewed as two sub-populations: One with three-bit binary strings and the other with five-bit binary strings. Genetic operations are separately performed in each sub-population to generate the next sub-population. That is, the current population can be viewed as two separate sub-populations in the genetic operation phase whereas it is handled as a single population in the IPD game playing phase in our computational experiments.

In each sub-population, a pair of binary strings is selected based on the following selection probability:

$$P(s_i) = \frac{fitness(s_i) - f_{\min}(\Psi)}{\sum_{j \in \Psi} (fitness(s_j) - f_{\min}(\Psi))}, \tag{1}$$

where s_i is the i-th string, $fitness(s_i)$ is the average payoff of s_i obtained by the IPD game in the current population, Ψ is a sub-population including s_i, and $f_{\min}(\Psi)$ is the minimum average payoff among strings in the sub-population Ψ. Eq.(1) is a standard roulette wheel selection with the linear scaling based on the minimum fitness value. It should be noted that the selection is separately performed in each sub-population.

We apply the standard one-point crossover operation to the selected pair of strings (with the probability 1.0 in our computational experiments). One of the generated two strings by the crossover operation is randomly chosen as an offspring. The standard bit-flip mutation operation is applied to the selected offspring (with the probability 0.002 per bit). By iterating the selection, crossover and mutation, we generate the same number of offspring as the sub-population size. The current sub-population is entirely replaced with the newly generated offspring. Thus the sub-population size is constant throughout the evolution of IPD game strategies.

III. COMPUTATIONAL EXPERIMENTS

We examined the following five situations in our computational experiments:

(1) Homogeneous case with 100% three-bit strings,
(2) Homogeneous case with 100% five-bit strings,
(3) 25% three-bit strings and 75% five-bit strings,
(4) 50% three-bit strings and 50% five-bit strings,
(5) 75% three-bit strings and 25% five-bit strings.

We used the following conditions in computational experiments in this paper:

[Overall computational experiment setting]

Number of runs: 1000 for each case.

[Genetic algorithm setting]

Population size: 100,
Initial strings: Randomly generated binary strings,
Selection: Roulette wheel selection in Eq.(1),
Crossover probability: 1.0 (One-point),
Mutation probability: 0.002 per bit (Bit-flip),
Generation gap: 100% (i.e., no elite individuals),
Termination condition: 1000 generations.

[IPD game setting]

Number of opponents: 5 (Randomly chosen),
Number of rounds: 100 (between the same agents).

First we compare the two homogeneous cases with each other in Fig. 1 where the average payoff at each generation is shown. This figure shows the effect of the choice of a representation scheme on the evolution of cooperative behavior. In Fig. 1, slightly faster evolution of cooperative behavior was achieved by shorter strings (i.e., by three-bit than five-bit). Since the representation schemes are very similar to each other, we obtained similar results in Fig. 1. The choice of a representative scheme, however, often has a dominant effect [16], [17]. We used these very similar representation schemes in order to highlight the effect of mixing them.

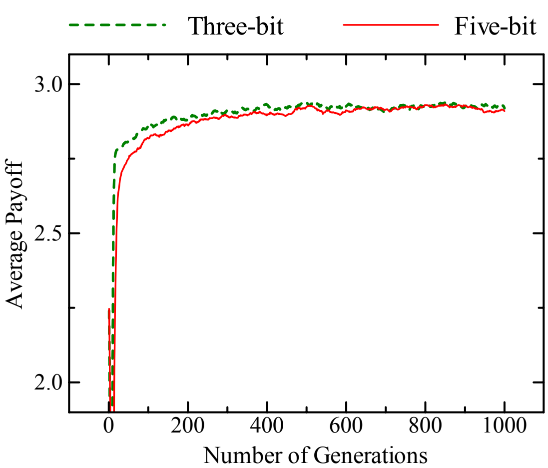

Fig. 1. Average payoff from homogeneous populations.

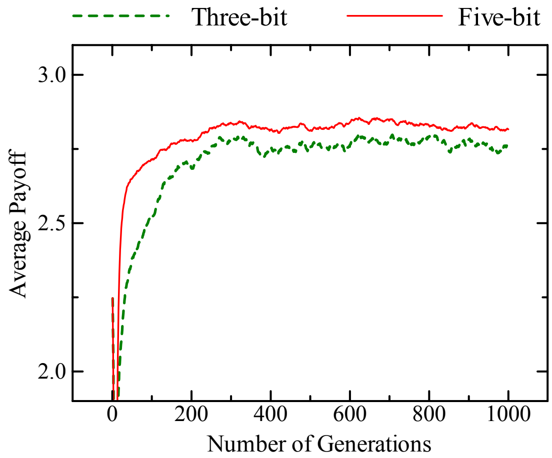

Fig. 2. Average payoff from inhomogeneous populations with 25% three-bit strings and 75% five-bit strings.

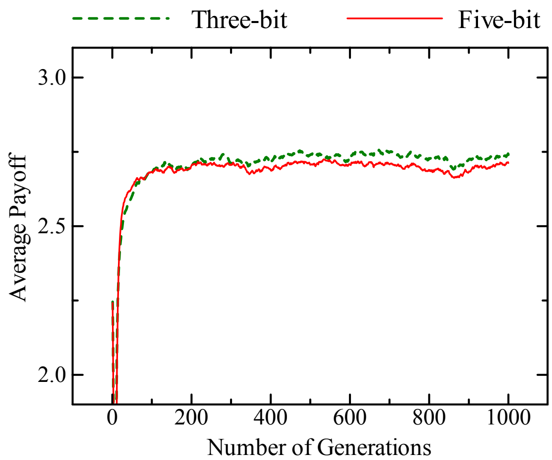

Fig. 3. Average payoff from inhomogeneous populations with 50% three-bit strings and 50% five-bit strings.

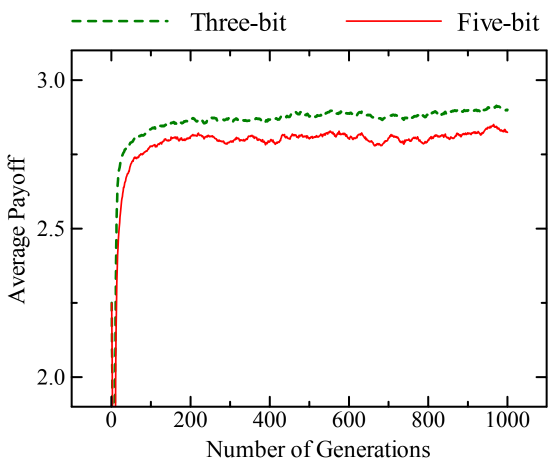

Fig. 4. Average payoff from inhomogeneous populations with 75% three-bit strings and 25% five-bit strings.

Experimental results on the three inhomogeneous cases are shown in Figs. 2-4. The average payoff was calculated in each sub-population in these figures. From the comparison of Fig. 1 with Figs. 2-4, we can see that cooperative behavior was more easily evolved among homogeneous agents in Fig. 1 than heterogeneous ones in Figs. 2-4. That is, mixing different representation schemes in a population slowed down the evolution of cooperative behavior. This negative effect was the most severe in Fig. 3 where the number of agents with each representation scheme was the same. An interesting observation is that better results were always obtained by majority agents (i.e., five-bit strings in Fig. 2 and three-bit strings in Fig. 4) when the number of agents with each representation scheme was different. Another interesting observation is that much better results were obtained in Fig. 4 than Fig. 2 whereas there was no large difference in Fig. 1 between the two schemes.

VI. CONCLUSION

In this paper, we examined the effect of mixing different representation schemes on the evolution of cooperative behavior in the IPD game. We used very similar representation schemes: three-bit and five-bit binary strings. We obtained similar results from these two representation schemes when they were separately used in homogeneous populations. Their simultaneous use in a single population, however, clearly slowed down the evolution of cooperative behavior. This negative effect of mixing different representation schemes affected the minority agents more severely. The worst results (i.e., the most severe negative effect) were obtained when the number of agents with each representation scheme was the same. As future research, we are planning to further examine the effect of mixing different representation schemes on the evolution of cooperative behavior in various situations such as using more than two types of agents and/or totally different representation schemes. We will also discuss potential positive effects of mixing different representation schemes on the evolution of IPD game strategies.

REFERENCES

[1] R. Axelrod, "The evolution of strategies in the Iterated Prisoner's Dilemma," in L. Davis (ed.), *Genetic Algorithms and Simulated Annealing*, Morgan Kaufmann, Los Altos, pp. 32-41, 1987.

[2] K. Lindgren, "Evolution phenomena in simple dynamics," in C. G. Langton, C. Taylor, J. D. Farmer, and S. Rasmussen (eds.), *Artificial Life II*, Addison-Wesley, Reading, pp. 295-312, 1991.

[3] D. B. Fogel, "Evolving behaviors in the Iterated Prisoner's Dilemma," *Evolutionary Computation*, vol. 1, no. 1, pp. 77-97, 1993.

[4] P. Darwen and X. Yao, "Automatic modularisation by speciation," *Proc. of 3rd IEEE International Conference on Evolutionary Computation*, pp. 88-93, Nagoya, Japan, May 1996.

[5] P. H. Crowley, L. Provencher, S. Sloane, L. A. Dugatkin, B. Spohn, L. Rogers, and M. Alfieri, "Evolving cooperation: The role of individual recognition," *BioSystems*, vol. 37, no. 1, pp. 49-66, 1996.

[6] D. Ashlock, M. D. Smucker, E. A. Stanley, and L. Tesfatsion, "Preferential partner selection in an evolutionary study of Prisoner's Dilemma," *BioSystems*, vol. 37, no. 1, pp. 99-125, 1996.

[7] S. Bankes, "Exploring the foundations of artificial societies: Experiments in evolving solutions to Iterated *N*-player Prisoner's Dilemma," in R. A. Brooks and P. Maes (eds.), *Artificial Life IV*, MIT Press, Cambridge, pp. 237-242, 1994.

[8] X. Yao and P. Darwen, "An experimental study of *N*-person Iterated Prisoner's Dilemma games," *Informatica*, vol. 18, no. 4, pp. 435-450, 1994.

[9] M. A. Nowak, R. M. May, and K. Sigmund, "The arithmetics of mutual help," *Scientific American*, pp. 50-53, 1995.

[10] A. L. Lloyd, "Computing bouts of the Prisoner's Dilemma," *Scientific American*, pp. 80-83, 1995.

[11] P. Grim, "Spatialization and greater generosity in the stochastic Prisoner's Dilemma," *BioSystems*, vol. 37, no. 1, pp. 3-17, 1996.

[12] K. Brauchli, T. Killingback, and M. Doebeli, "Evolution of cooperation in spatially structured populations," *Journal of Theoretical Biology*, vol. 200, no. 4, pp. 405-417, 1999.

[13] H. Ishibuchi and N. Namikawa, "Evolution of cooperative behavior in the iterated prisoner's dilemma under random pairing in game playing," *Proc. of 2005 Congress on Evolutionary Computation*, pp. 2637-2644, Edinburgh, UK, 2005.

[14] H. Ishibuchi and N. Namikawa, "Evolution of iterated prisoner's dilemma game strategies in structured demes under random pairing in game playing," *IEEE Trans. on Evolutionary Computation*, vol. 9, no. 6, pp. 552-561, 2005.

[15] L. A. Dugatkin, *Cooperation among Animals - An Evolutionary Perspective*, Oxford University Press, New York, 1997.

[16] D. Ashlock, E. Y. Kim, and N. Leahy, "Understanding representational sensitivity in the iterated prisoner's dilemma with fingerprints," *IEEE Trams. on Systems, Man, and Cybernetics: Part C,* vol. 36, no. 4, pp. 464-475, 2006.

[17] D. Ashlock and E. Y. Kim, "Fingerprinting: visualization and automatic analysis of prisoner's dilemma Strategies," *IEEE Trans. on Evolutionary Computation*, vol. 12, no. 5, pp. 647-659, 2008.

Moving Robots' Mind of Autonomous Decentralized FMS and Mind Change Control

Hidehiko Yamamoto[1], Kikuchi Hiroyuki[2], Takayoshi Yamada[3] and M. Anouar Jamali[4]

[1]*Department of Human and Information Systems, Gifu University, Japan*
(yam-h@gifu-u.ac.jp)
[2]*Graduate School of Engineering, Gifu University, Japan*
(m3128013@edu.gifu-u.ac.jp)
[3] *Department of Human and Information Systems , Gifu University, Japan*
[4]*Industrial Engineering Department, Universite du Quebec a Trois-Rivieres, Canada*
(jamali@uqtr.ca)

Abstract: This paper describes the control of the moving robots in an autonomous decentralized FMS by moving robots' mind change. In Autonomous Decentralized Flexible Manufacturing System where a lot of moving robots operate, there are problems of path interference. There is an existing method we have developed, called AAA used to evade from these interference problems. However, using this method, it is very difficult to grasp entirely the innumerable path interference situations that really occur. Therefore, to evade these unexpected situations flexibly, we propose the mind model which is the complicated expression of combinations from the three elements: Stimulation Vector, Unit and Load. Even if a same situation happens, moving robots take different actions when the mind is changed.

Keywords: Robot moving collision, FMS, AGV, path interference, mind

I. INTRODUCTION

Today; the actions of the robots are made by pre-decided control rules. When many robots try to perform complicated tasks, it is very difficult for them to cooperate with each other by using the pre-decided control rules.

On the other hand, human beings can perform such complicated tasks by an analyze based thinking. It is because the human beings have a mind that enables them to think by themselves [1].

Instead of using the pre-decided control rules, if we can provide a mind to the robots, they can cooperate themselves to perform complicated operations and will be able to adapt in every situation.

In Autonomous Decentralized Flexible Manufacturing System (AD-FMS), a lot of moving robots called Automated Guided Vehicles (AGVs) are operated [2-3]. In AD-FMS, AGVs move individually and have a high possibility to collide with each other.

In this paper, we propose the mind whose functions include mind change in order that AGVs do not collide. We will also present 6 models of AGVs mind, basic model, model of majority decision, model of mind that is hard to carry out mind change and other 3 models of mind that are easy to carry out mind change.

The effectiveness of these models are evaluated with production simulations in a AD-FMS virtual factory.

II. ELEMENTS OF MIND

It is said that mind is not constantly decided but changes ambiguously. And decision-making standards are different from each other.

Considering these factors, we propose the mind model which is the combination of three elements: Stimulation Vector, Unit and Load. The mind model can deal with mind change.

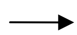

Fig.1 Stimulation vector

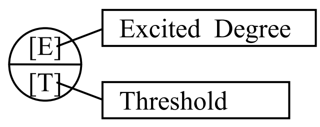

Fig.2 Unit

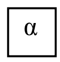

Fig.3 Load

The function of the Stimulation Vector shown in Fig.1 is to link between the Unit and the Load. If the stimulation signal is sent to the Stimulation Vector, the stimulation signal is either sent to the Unit or Load to indicate the arrow direction.

©ISAROB 2009

Fig.2 shows the schematic figure of the Unit which has the variable called Excited Degree [E] and the threshold value [T]. [E] of the Unit A is shown as A[E]. In the later sentences, Unit A is shown as just A. Similarly, [T] of A is shown as A[T]. [E] increases and decreases by various stimulations. If [E] exceeds [T], it is decreased to [T] and the Unit will send an output stimulation signal in the direction of the Stimulation Vector arrow. In this way, the Unit function will receive an input stimulation signal and send an output stimulation signal. When the [E] and [T] are equal, the Unit state is called Excited. Meanwhile, when [E] is lower than the [T], the Unit is said to be on Calm state. These two states can be changed and the change corresponds to mind change.

The Load shown in Fig. 3 has one numerical value plus or minus called Control Value. The Load is linked with the Unit by the Stimulation Vector following an arrow direction. If a stimulation signal is sent to the Load, [E] of the Unit is added or reduced by Control Value of the Load.

The mind change is expressed by the change of state of the Unit. Even if the same situation happens twice, AGVs can take different actions whether the mind has same state or not. The state of mind changes by sending a stimulation signal to Units or Loads from the result.

III. AGV WITH MIND

1. AD-FMS

Fig.4 shows the AD-FMS model. The AD-FMS consists of AGVs, machining centers that process parts, the parts warehouse that supplies many parts to machining centers and the products warehouse that stores finished parts. These correspond to agents.

2. Problems of AGV moving control

In the AD-FMS, when many AGVs operate, there are problems of path interference. There is an existing method we have developed called AAA used to evade from these interference problems by knowledge exchange [4-5]. Even if, this method is used, it is very difficult to grasp entirely the innumerable path interference situations that really occur. Therefore, to evade these unexpected situations flexibly, we use the mind model.

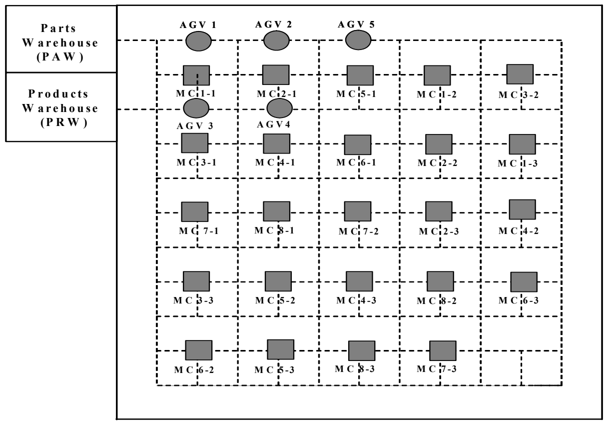

Fig.4 Model of AD-FMS

3. Basic models of AGVs' mind

Fig.5 shows the basic model of AGVs' mind (model (1)) that consists of 3 Stimulation Vectors, 2 Units (A,B) and a Load α with random numerical values of minus.

Fig.6 shows the work of model (1). In AD-FMS environment, AGVs can grasp each other's positions by exchanging their information [4-5].

When a certain AGV-1 gets closer to the other AGV, the information for possibility of the path interference is input into A of the mind. Then, the model (1) of AGV-1 outputs one of the following actions by the two states of its A, Calm and Excited. In this way, AGVs mind can also be divided into arrogant and modest states by the states of A.

Calm : Go to the destination
→ Arrogant AGV
Excited : Make way for other AGV
→ Modest AGV

When the arrogant AGV and the modest AGV gets closer, the arrogant AGV forces to go ahead. At the same time, the modest AGV clears the path so that the arrogant AGV can pass.

When the two arrogant AGVs get closer and path interference occurs, AGVs stimulate their individual mind by sending A the signal to increase A[E]. A gets Excited when A[E] reaches to A[T]. As a result, one of the AGVs becomes modest and both AGVs can evade path interference.

On the other hand, when the two modest AGVs get closer and try to make mutual concession of the path, AGVs stimulate their individual mind by sending B the signal to increase B[E]. B gets Excited when B[E] reaches to B[T] and sends a signal to α. α sends A and B the stimulations that decrease A[E] and B[E] by random integers from 1 to A[T] and from 1 to B[T]. As a result, A and B become Calm together and one of the AGVs becomes arrogant.

In this way, as for A, the state of A changes (Excited ⇔ Calm) by the action result (path interference or mutual concessions). This change corresponds to mind change. In addition, it can be said that the model (1) can express two states of mind, arrogant and modest.

When many AGVs get closer, AGVs evade path interference by repeating the mind change.

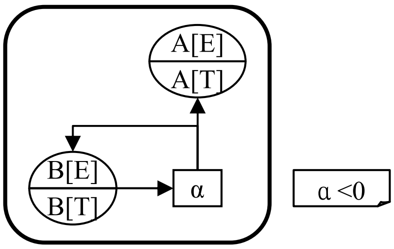

Fig.5 Basic model of AGVs' mind

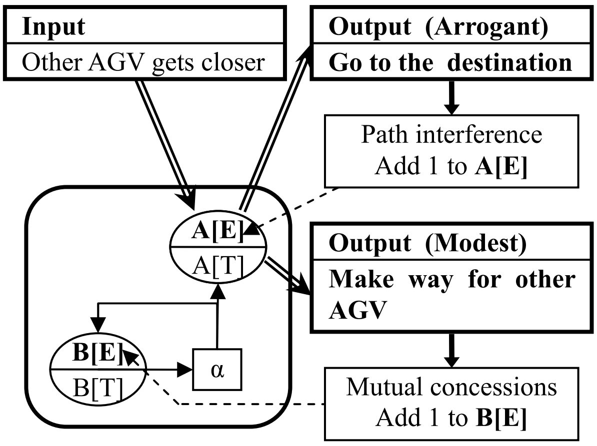

Fig.6 Work of model (1)

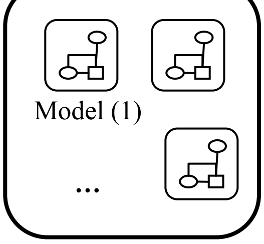

Fig.7 Model (2)

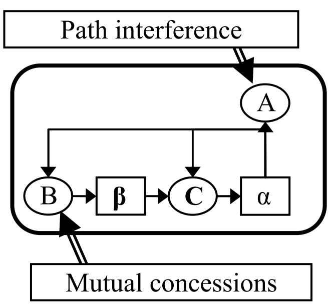

Fig.8 Model (3)

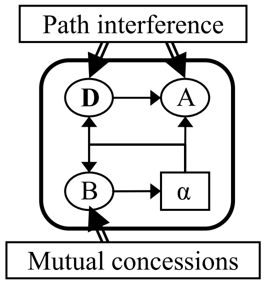

Fig.9 Model (4)

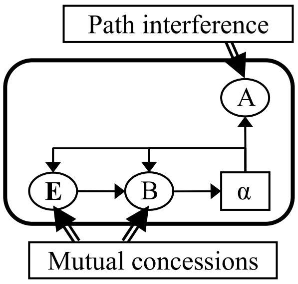

Fig.10 Model (5)

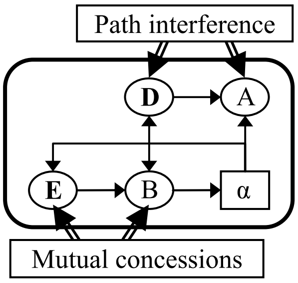

Fig.11 Model (6)

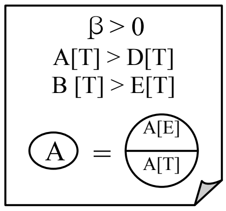

Fig.12 Condition and formulas of the models

4. More complicated models

To express various personalities of AGVs, it is necessary to increase the number of internal elements of the model of mind (1). We will present 5 more complicated models of mind (model (2)-(6)).

Fig.7 shows the model (2). Inside this model, there are a few model (1) and the state of mind is decided by majority decisions.

Fig.8 shows the model (3). It is the model that adds C and β between B and α of model (1). β takes random positive integers from 1 to C(T). The process that A gets Excited is similar to model (1). We will explain the process that A gets calm. When β gets Excited, C is stimulated. When C gets Excited, α is stimulated. As a result, α changes all states of A, B and C from Excited to Calm. It can be said that model (2) is harder to change mind than model (1).

Fig.9, 10 and 11 show the model (4), (5) and (6) respectively. These models are those who add D and E to the model (1).

In case of model (4), when path interference occurs, A[E] and D[E] increase. Because when A[T] > D[T], D becomes Excited faster than A and D sends A the signal to increase A[E]. Therefore, it can be said that the model (4) is easy to become modest because A is easier to get Excited than model (1).

Table 1. The simulation results

Item \ Model	(1)	(2)	(3)	(4)	(5)	(6)	Random
Volume of Production	256.6	256.1	253.6	257.9	258.3	257.9	143.3
Average Efficiency	25.79	25.7	25.44	25.84	25.92	25.92	14.79
Path Interference	1108	1113	1116	851	1110	891	11985

In model (5), when AGVs try to make mutual concession of the path, E gives B simulations. Because of it, the model (5) is easy to become arrogant. That means A is easier to get Calm than model (1).

Model (6) has the characteristics of both models (4) and (5).

Let's pay attention to the numerical values of A[T] and D[T]. The smaller they are, the more easily A gets Excited. That is the mind easily becomes modest. On the other hand, the larger they are, the more difficult mind becomes modest. Similarly, let's pay attention to numerical values of B[T], C[T] and E[T]. The smaller they are, the more easily A gets Calm. That is the mind easily becomes arrogant.

Various characters can be expressed by combining the above-mentioned features. For instance, when a certain model of mind has small values for A[T] and B[T], this model expresses the mind that are easy to change mind.

Fig.12 shows the condition and formulas of the models.

IV. SIMULATION RESULTS

In this paper, we applied all of mind models (model (1)-(6)) that we have presented to AGVs in AD-FMS which is built on a computer and carried out simulations. In addition, to compare the various conditions of the models, the simulation with the condition that randomly changes mind states were also carried out.

Table 1 shows the simulations results (the volume of production, average efficiency of machining centers, and the number of path interference).The results of model (2)-(6) are compared with that of model (1).

The results shown in table.1 reveal that the state of a mind changes randomly, the volume of production and average efficiency of machining centers fell remarkably, and the number of path interference increased 10 times than that of model (1). Therefore, it can be said that moving control with a mind change is effective.

Both the volume of production and the average efficiency of machining centers of model (4)-(6) were slightly better than that of model (1). The models can reduce time spent for evading path interference because these models are easy to change their states. Moreover, number of path interference of model (4) and (6) could be reduced 20% more than that of model (1).

V. CONCLUSIONS

In this paper, we proposed the various mind models of AGVs that can flexibly evade unexpected path interference situations not using the pre-decided control rules. Comparing the proposed mind model with the basic mind model, we could obtain the better result that reduced the number of path interference by 23.2%.

REFERENCES

[1] Scassellati B (2002), Theory of Mind for a Humanoid Robot. Autonomous Robots 12:13–24
[2] Kaighobadi M and Venkatesh K (1994), Flexible Manufacturing Systems: an overview, International Journal of Operations & Production Management, 14:.26-49
[3] Kost G G and Zdanowicz R (2005), Modeling of manufacturing systems and obot motions, Journal of Materials Processing Technology, 164-165:1369-1378
[4] Yamamoto H and Ramli R (2006), Real-time Decision Making of Agents to Realize Decentralized Autonomous FMS by Anticipation, International Journal of Computer Science and Network Security, 6(12):7-17
[5] Ramli R, Abu Qudeiri J and Yamamoto H (2007), Anticipating Action Decisions of Automated Guided Vehicle in an Autonomous Decentralized Flexible Manufacturing System. Internation Journal of Intelligent Technology, 2(1):21-27

The Fourteenth International Symposium on Artificial Life and Robotics 2009 (AROB 14th '09),
B-Con Plaza, Beppu, Oita, Japan, February 5 - 7, 2009

High Survivability of a Large Colony Through a Small World Relationship

Masao KUBO
Computer Science
National Defense Academy of Japan
Yokosuka, Japan

Hiroshi SATO
Computer Science
National Defense Academy of Japan
Yokosuka, Japan

Takashi MATSUBARA
Computer Science
National Defense Academy of Japan
Yokosuka, Japan

Chris MELHUISH
Bristol Robotic Laboratory
Univ. of the West of England,Univ. of Bristol
Bristol,UK

Abstract

In this paper, energy tophallaxis, distributed autonomous energy management methodology inspired by social insects and bat behaviour, and its advantage is shown by a series of computer simulations to address the survivability of organized agents group under dynamics environment with uncertainty. Uncertainty of organizational agent's behaviour is represented by 2 Lévy distributions. By controlling energy donation behaviour based on these distributions carefully, the survivability of a larger group that traditional works cannot analyze is examined. As a result, a only small friendship over organization makes the group's survivability improved dramatically.

1 INTRODUCTION

This paper proposes a basic methodology for resource assingnment problem in a multiple agents system with uncertainty. There is a lot of papers which discuss resource assingnment problem under conditions of complete infomation. Meanwhile, growing in popularity of Internet and robotic technology on our daily life has been accompanied by a marked difficulty of its efficient management. For example, let us think about the energy management of many mobile robots. Usually, their batties are charged by being plugged in. When the number of plug is restricted or there is not enough time to be charged, how should we manage them? It is not easy question because of uncertainty. Of course, the group of robots are desiged carefully for some specific tasks but their behaviour is not 100% known beforehand. Especially, it seems to be very difficult to predict their energy consumption when they engage in jobs to interact directly with human. As we know, human changes its mind frequently. However, even if there is this innate difficulty, it is undeniable fact that some methodology that can design resource allocation under such uncertainty is required.

We have focused attention on trophallaxis. Trophallaxis is mouth-to-mouth food sharing among ants[1], bats[5], and other some social animals. Basically, traditional energy management of robots have been based on nest like "central sharing", that is difficult to share their energy by congestion. On the other hand, this new energy sharing strategy, *energy trophallaxis*, can provide more flexible energy flow so that they can survive longer and stable[3][2].

In this paper, we discuss the survivability of a arger group with trophallaxis type energy sharing. When the colony is small, the hypothesis that each agent can transfer its energy to any member directory is reasonable, because the travel cost for reaching a recipient is negligible. Therefore, when the feeding success rate, the probability of getting energy from the environment, is independent, the larger the colony, the easier it is for its members to survive [3][6].

However, in general, it is difficult to assume this condition when the colony is large because some agent pairs must pay considerable travel costs. We show that this difference is sufficiently critical to result in members in larger colonies having a shorter life. By simulation, we show that an increase in the colony size makes it difficult for agents in a common organization to survive. Despite this counterproductive scale effect, we show that trophallaxis is still a good strategy for a large colony to achieve high survivability, by the law of large numbers. The scale effect can be solved by small world trait, which is normally found in ordinary

©ISAROB 2009

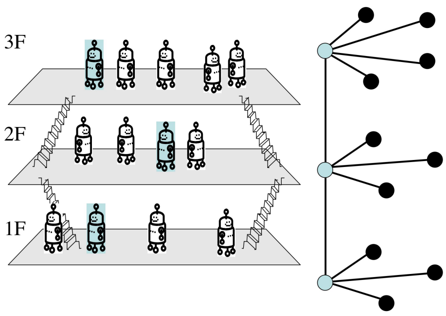

Figure 1: An example of high correlation between behaviour in the workspace and the organization.

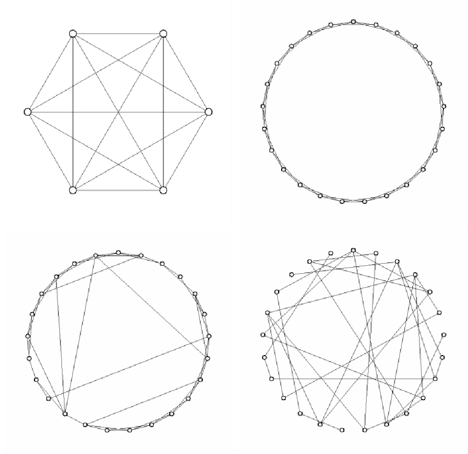

Figure 2: Networks used as organizational structures :(a) Complete Graph, (b) Regular Graph, (c)Beta Graph, (d) Random Graph

relationships with friends.

This paper is composed as follows. In the next section, we propose our approach for handling large colony sizes. Two static networks are introduced: organization network and friend network. In our framework, agents meet others statistically. We suppose that all agents belong to the same organization, and an agent meets others according to a rendezvous probability, based on the topological distance of the organization network. When a pair of agents meet, the richer decides whether it donates energy to the poorer according to a permission probability, based on the topological distance of the relationships with friends in the friend network. Using these two probability distributions and networks, we can examine a variety of organizational structures.

In section 3, we briefly explain the trophallaxis model. We proposed an extension of the vampire bat energy model [6]. This model is useful because it is simpler than those of other related works [2][3].

In section 4, using simple computer simulation, the emerging properties are discussed.

2 THE ORGANIZATIONAL STRUCTURE

2.1 Organizational network

This paper examines a large colony. In this case, the travel cost for some agent pairs is not negligible, so we assume that energy transfer is conducted when a pair of agents happen to meet. When the agents rendezvous, one decides whether to donate energy to the other.

We suppose that the rendezvous frequency depends on the relationship of the agent pair on the organization of their colony. Obviously, the frequency of rendezvous is also determined by behaviour, however, in this paper, we are not interested in particular practical robot behaviour and tasks. Therefore, we introduce colony organization, rather than some concrete behaviour to approximate the frequency of rendezvous. When a colony is well organized, the organizational structure seems to provide a strong correlation between the working area of the members and the topological relationship of the organization, as shown in Fig.1. This figure shows a robot system that the designer wants to realize. The agents on each floor must work cooperatively, so these agents will have strong relationships. Obviously, these agents will meet frequently, therefore, the designer will assign the appropriate number of robots to build an effective robotic system. When a well-organized structure is provided, it is reasonable that the frequency of rendezvous can be estimated from the topological distance of the organization structure.

We assume that this each rendezvous takes place following by a probabilistic function based on their relative distances within the organizational structure. The organizational structure is represented by a graph with undirected links. Each node represents an agent. We suppose that the distance is the shortest link distance in the network. Also, the network is static, and there are no changes during trials. For example, if an agent is completely exhausted, the corresponding agent's node is not alive. However, this void node does not change the shortest distance calculation for

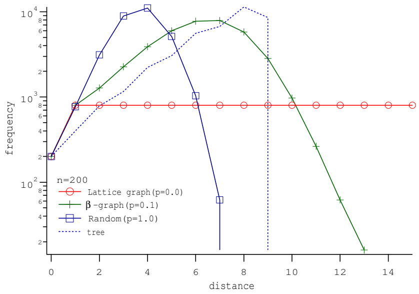

Figure 3: Shortest distance distribution of the networks adopted in this paper.

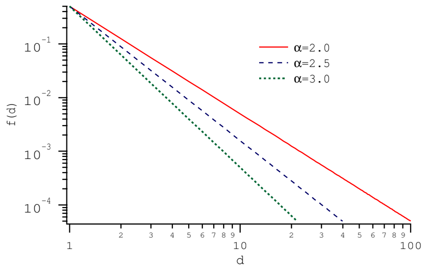

Figure 4: Rendezvous probability of α

other agents. Note that two different networks are introduced - one for the rendezvous and the other is for permission probability of donating. However, both networks use the same notation and distance calculation method. Later, we describe the details of the network for judging whether to donate. The organization network $\mathbf{S}$ gives its adjacency matrix $\mathbf{A}$ of C. Now, when a colony $C = \{i \in \{1, \cdots, n\}\}$ is given, if there is a link between agent i and j, the element a_{ij} of $\mathbf{A}$ is 1, otherwise it is 0.

The distance between a pair of agents is calculated as the shortest distance of $\mathbf{A}$. Let the distance of agent i and j be $d(i,j)(= d(j,i))$. The shortest distance is then deduced by the Dijkstra method.

This paper adopts a complete graph, a lattice graph (a kind of regular graph), a random graph, and a β-graph[4], as shown in Fig.2. Figure 3 illustrates the shortest distance distribution of these graphs for n=200.

The complete graph corresponds to a small, well organized structure. Each agent has links to all others (Fig.2a), therefore, the distance from any agent to any other member is 1, which is shortest. This suggests that they all work together in a vicinity.The lattice graph is introduced to represent organizations in which the members interact well locally. As shown in Fig.2b, each agent has L equal number of links to its neighbours. When L=2, they connect as a ring. This means that there is a less well marked global structure, but there are strong relationships among neighbours. Figure 3 shows the shortest distance distribution for L=4. There are a constant number of agents located in a range from very close to very far away. The random graph represents an unorganized organization structure (Fig.2d). The distance distribution is similar to a normal distribution. The β-graph [4] is generated by applying the random rewiring procedure to the lattice graph noted above. A link of the lattice graph, selected by probability p, is removed and reconnected to another node. This process is called random rewiring. Even if this probabilistic procedure causes the network to lose strong connectivity, there is no special compensation algorithm. Obviously, the graph with the random rewiring probability of p=0 is the original lattice graph, and the graph with a random rewiring probability of p=1 is same as the random graph. This parameter changes the characteristics, in particular for the graph with a probability of around p=0.1 is known, as it has small world characteristics[4]. This property means that the average distance is slowly increased as $\log(n)$. In Fig.3, the β-graph is made from an L=4 regular graph, and p=0.1 is shown. The degree distribution at L=4 is like that of the original lattice graph, whereas the distance distribution is completely different from the original.

2.2 Rendezvous probability based on the organization network

Let the distance of agent i and j in a given organization network be $d_o(i,j)(= d_o(j,i))$. Now we suppose that the rendezvous probability is defined as the power function fo of distance $d_o(i,j)$ as follows.

$$f(d_o(i,j)) = m/d_o(i,j)^{\alpha_o} \tag{1}$$

In the remainder of this paper, m=0.5. α_o is a control parameter. This function has been well studied in many areas, for example, the Lévy flight probabilistic procedure. In Fig.4, the probability distributions $\alpha_o = \{2.0, 2.5, 3.0\}$are shown. If α_o is small (α_o¡2), agents too far away still have a high probability of meeting; when α_o is large, for example, α_o¿3.0, agents only meet their closer neighbours.

3 ENERGY SHARING MODEL AND ITS EVALUATION

3.1 The Vampire Bat Energy Sharing Model

This section explains the trophallaxis energy exchange procedure. When a pair of agents meet according to the rendezvous probability in eq.1, they have a chance to exchange energy. We adopt a model proposed by [6] for this exchange procedure. This model is simple and well-grounded because it simulates the energy exchange procedure of the common vampire bat, which is a famous example of for trophallaxis [5].

The essence of the model is that each agent tries to get food once every 24 steps. The feeding success probability is called the $feederate$. Now, if agent i succeeds, its energy e_i is fully increased.

$$e_i(t) = e_{max}. \tag{2}$$

Each agent consumes ecycle per step. If $e_i < 0$, it is dead. If $e_i < e_{need}$, agent i requests donations from richer agents - those who have more energy than e_{have}. If a rich agent accepts the request, the recipient receives thave energy per donation. The exchange loss during transfer is represented by $e_{efficiency}$. For example, if $e_{efficiency}$=100, the energy which a donor loses is the same as that obtained by the recipient; if the recipient receives no energy, then $e_{efficiency}$=0. That is,

$$e_{donor}(t+1) = e_{donor}(t) - t_{have}. \tag{3}$$

$$e_{recipient}(t+1) = e_{recipient}(t) + t_{have}e_{efficiency}/100. \tag{4}$$

These parameters are set as follows: e_{cycle}=1, e_{max}=60, e_{need}=24, e_{have}=28, $t_{transfer}$=3, $e_{efficiency}$=80, $feederate$ =0.7. These are reflected in the vampire bat. Under this parameter set, a donor cannot be a recipient after single donation because

$$e_{have} - t_{transfer} > e_{need}. \tag{5}$$

Therefore, this is called the stable condition.

3.2 Permission probability on the friend network and donor selection

When an agent is starving ($e < e_{need}$), it makes havelisti which is a set of donor candidates.

As mentioned previously, two networks are introduced in this paper: the organization network, which controls the rendezvous probability, and the friend network. The judgment as to whether an agent donates energy when a pair of agents meet is determined by the permission probability based on the distance between them in this network. The notation of the friend network is same as for the organization network. Also, the same network types are adopted.

Let the distance of agent i and j in the friend network be $d_f(i,j)(= d_f(j,i))$. Now we suppose that the permission probability is also defined as the power function f_f of distance $d_f(i,j)$ as follows.

$$f(d_f(i,j)) = m/d_f(i,j)^{\alpha_f}. \tag{6}$$

In the rest of this paper, m=0.5. α_f is a control parameter. When a pair of agents meet, if one is starving and the other has enough energy to satisfy the stable condition (see eq.5), the richer one joins the recipient's *havelist* with the probability $f_f(d_f(i,j))$.

When there is more than one rich agent ($e > e_{have}$) in a recipient's *havelist*, their order can cause another problem. In this model, a donor is selected randomly. The trophallaxis is executed repeatedly until there are no starving agents or there are no rich agents in the starving agent's *havelist*.

3.3 Evaluation criteria:*survivability*

In this model, survivability is employed as the evaluation criterion. Each simulation is executed for 10×365×24 steps, which corresponds to 10 years - a sufficiently long span. The ratio of survivors to the number of initial members is evaluated as the *survivability*.

4 COMPUTER SIMULATION

In this section, we show the characteristics of a large size colony by employing colony size n, the rendezvous probability of α_o, based on the organization network, and the permission probability of α_f, based on the friend network.

4.1 Complete graph organization with trophallaxis

First, we conduct a simulation to address the affect of scale on trophallaxis. We use four somewhat small different sized colonies with trophallaxis $n = \{15, 20, 25, 35\}$, and a colony of size n=35 without trophallaxis. All colonies with trophallaxis adopt the complete graph as their organization and friend

©ISAROB 2009

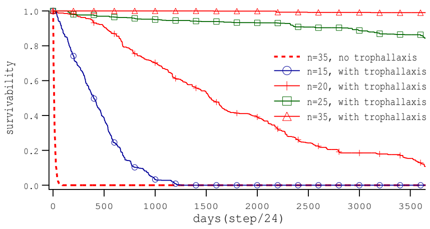

Figure 5: Survivability of a small colony.

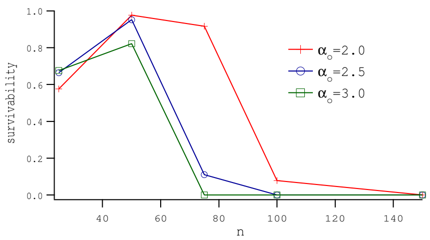

Figure 6: Size effect of lattice organization colony.

networks, so that a member can get energy from any other member. Each colony is examined for at least 50 trials and the average survivability for each day is shown in Fig.5.

The dotted line indicates the survivability of the colony of 35 agents without trophallaxis. The x axis is the time (day=step/24) and the y axis is the survivability. As you see, survivability drops quickly. There was no trial in which at least one agent survived over 150 days.

The solid lines illustrate the results for the colonies with trophallaxis. When n=15, the colony can survive longer than the colony without trophallaxis but for no trial among 20 trials did at least one agent survive more than 1250 days. However, colonies larger than 30 agents can survive over 10 years.

This result can be understood as follows. In this exchange model, each individual's feeding success rate is independent and this model assumes that the total amount of food in the environment is unlimited. In this case, the number of agents who get food converges at $n \cdot feederate$ when n becomes infinite, by the law of large numbers theorem. Consequently, the probability of the occurrence of the "less food" state goes to zero. Therefore, we can say that trophallaxis offers a great advantage for survival if agents can exchange energy with any other agent at any time.

4.2 Lattice graph organizations with trophallaxis

In the previous subsections, we conducted a set of experiments to address the survivability of trophallaxis of ideal colony. In this successive subsections, lattice networks with L=20 for a more practical large colony are used mainly. In section 4.2.2, the organizational structure adopts a lattice graph and a friend network that is a β-graph network, based on the lattice graph.

4.2.1 Lattice graph friend network with lattice organization

When a pair of agents meet and one is able to donate energy, first the donor candidate decides whether it will donate, based on its permission probability $f_f(d)$ (see eq.6.). The parameter α_f controls the range of the donation. When α_f is smaller than α_o, in eq.1, the agent gives energy agents who it rarely meets. If α_f is larger than α_o, however, it does not donate to agents who it meets frequently. First, we conduct a simulation to bring out the effect of the colony size, n. We used 15 colonies by combining colonies of different sizes, $n = \{25, 50, 75, 100, 150\}$ and three different organization networks $\alpha_o = \{2.0, 2.5, 3.0\}$. The friend network parameter α_f of all of these is 2.5. Figure 6 shows the survivability. When the colony size is small (n=25), they partially survive. Survivability improves with an increase of n until some limit. After the limit, it becomes worse, depending on α_o.

We think this result is very important because it indicates that the colony size has an adverse affect on survival. Even if the feeding success rate is independent, the survivability becomes worse as the colony size increases, when the organizational structure is a lattice graph.

The reason could be that, in such an organization, every agents has 20 links to their neighbours. Therefore, a donor can give its energy to a recipient 10 units away from it. Obviously, the speed of the diffusion of energy in this case is faster than for a network with a smaller number of links, for example L=2 or 3. Thus, surplus energy moves away from its donor quickly. Therefore, in the long term, its donation does not make its neighbour and itself rich. When the colony size is not too large, namely n=50, as shown in Fig.6, we suppose that the diffused energy comes back before it vanishes due to exchange losses, $e_{efficiency}$. because it takes few exchanges to make a circuit of the organization. Therefore, survivability is improved. When

©ISAROB 2009

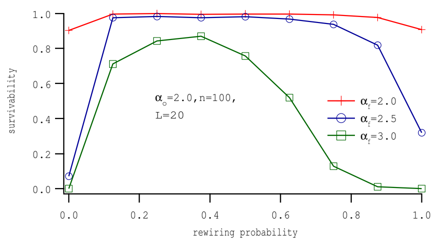

Figure 7: β-graph friend network over a dense lattice organization (α_o=2.0).

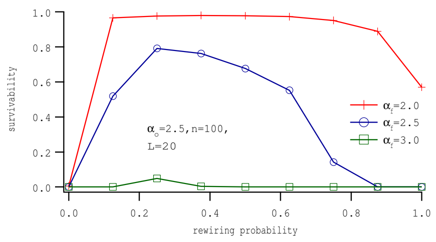

Figure 8: β-graph friend network over a sparse lattice organization (α_o=2.5).

the colony is too large, the scale effect is lost. More work is needed to clarify this issue.

4.2.2 β-graph friend network over a lattice organization

The last section showed that trophallaxis does not work well in a large lattice graph organizational structure. We suggested the reason is the quick diffusion of energy. In this section, we conduct a simulation addressing this trend. In generally speaking, a β-graph with a small rewiring probability has high clustering coefficient. This means that there are many small triangles in the organization. Therefore, it is reasonable to ask whether this helps retain surplus energy. Figures 7 and 8 show the survivability of a β-graph friend network with L=20 over lattice graph organization network with L=20, n=100, and $\alpha_o = \{2.0, 2.5\}$. In both graphs, the x axis is the rewiring probability.

The effect is impressive. Of all these situations, the colony with a small rewiring probability, p=0.125, can survive more consistently than that of one with a rewiring probability of p=0.0. Although more work is require to clarify the details of this mechanism, this high survivability ensures that we can say that the rewiring procedure can produce successful trophallaxis.

5 CONCLUSION

In this paper, the survivability of large colonies with trophallaxis energy transfer is examined by introducing two networks: an organization, and a friend network. In a large colony, the travel cost for some agent pairs is not negligible, so that energy transfer is conducted when a pair of agents happen to meet. The probability of a rendezvous is determined by the organization network. After a pair of agents meet, one decides whether to donate energy, based on its permission probability, which is defined by the friend network. By this simplified approach, we can examine the characteristics of survivability for a large colony with trophallaxis, for example, the scale effects and unfavourable issues.

Several computer simulations produced the following observations: 1) In general, if the colony is small, survivability improves with an increase of members. However, even if their feeding success rate is independent, their survivability becomes worse with an increase in colony size when their organization structure is a lattice graph; and, 2) it is possible to deal with this unfavourable characteristic using the random rewiring procedure of β-graph, which yields a small world phenomenon.

References

[1] Holdobler B., Wilson E.D. , The Ants, Springer-Verlag, 1990.

[2] Kubo M., Melhuish C., "Robot Trophallaxis: Managing Energy Autonomy in Multiple Robots," Proceedings of Towards Autonomous Robotic Systems 2004. Department of Computer Science University of Essex Technical Report Series,CSM-415,2004

[3] Melhuish C., Kubo M., "Collective Energy Distribution: Maintaining the Energy Balance", Proceedings of 7th International Symposium of Distributed Autonomous Robotic Systems (DARS04),pp. 261-270, 2004

[4] Watts D.,J.,Small Worlds: The Dynamics of Networks between Order and Randomness, Princeton University Press, 1999.

[5] Wilkinson, G.S., "Food sharing in vampire bats", Scientific American,pp. 64-70, 1990

[6] Witkowski N., "Energy sharing for swarms modelled on the common vampire bat", Adaptive Behavior,Vol. 15, No. 3, pp. 307-328, 2007

The Fourteenth International Symposium on Artificial Life and Robotics 2009 (AROB 14th '09),
B-Con Plaza, Beppu, Oita, Japan, February 5 - 7, 2009

An Evolutionary Nano-Agent Control Architecture for Intelligent Artificial Creatures

Jean-Claude Heudin

IIM Interactive Media Lab.
Pôle Universitaire Léonard de Vinci – 92916 Paris La Défense, France
(Jean-Claude.Heudin@devinci.fr)

Abstract: This paper describes a new multi-agent architecture for the Evolutionary Virtual Agent project. It introduces the nano-agent bio-inspired control architecture and its nanoScheme programming language. A typical application consists of one or more nano-agents, and possibly up to a large number if necessary as in natural swarms. As an example, it describes an online self-animated character that uses natural language and emotional expressions. This virtual character is based on a "schizophrenic" model composed of multiple distinct personalities, each with its own pattern of perceiving and interacting with the user.

Keywords: artificial creature, intelligence, nano-agent, schizophrenic architecture

I. INTRODUCTION

Recent advances in robotics and artificial life make now possible to develop a growing number of real-world applications in various fields. However, these applications require a new generation of open software architecture that combines such technologies with lightweight design and portability for onboard and online applications. This paper proposes a new evolutionary nano-agent control architecture designed for intelligent artificial creatures. This software environment takes advantages of our past experiences in distributed artificial intelligence with the Knowledge-based Operating System (KOS) [1], multi-expert applications such as the Electronic Copilote project for combat aircrafts [2], and the more recent Evolutionary Virtual Agent (EVA) applications [3].

In the first part of the paper, we introduce the nano-agent bio-inspired architecture and its programming language called nanoScheme. The second part describes an application developed using this software environment: an online self-animated character that can interact using natural language and emotional expressions. This virtual character is based on a "schizophrenic" model in which the character has multiple distinct personalities, each with its own pattern of perceiving and interacting with the user. The qualitative efficiency of this prototype is then compared with the ALICE conversational engine [4]. The paper concludes by outlining future developments and some possible applications.

II. ARCHITECTURE OVERVIEW

1. Nano-agent architecture

We propose a multi-agent bio-inspired architecture that does not try to *simulate* a specific organism but rather integrates several artificial life features in order to *implement* machine life and intelligence. A typical application consists one or more *nano-agents*, and possibly up to a large number if necessary as in natural swarms. Nano-agents can run on a standalone machine or can be distributed on a network of computers depending on the application requirements. We call them "nano" because of their small size and resource requirement compared to most existing software environments. In the current implementation, the core technology is implemented in Java and its weight is less than 25 Kilo-bytes. Most applications require a small set of knowledge-base and behavioral scripts text files, thus resulting in lightweight applications that are well-suited for web-based, mobile phone, robots and embedded environments.

2. The nanoScheme language

The behavior of each nano-agent is programmed using a user-friendly language, called nanoScheme, based on the Scheme programming language. It includes a reduced set of primitive functions which is a subset of the R4RS specification [5]. This subset is given in table 1. Most of the missing features of the Scheme specification could be added by programming them directly in nanoScheme. This provides the

©ISAROB 2009

application developer a high-level interactive language which is embedded in each nano-agent.

Table 1. The nanoScheme core primitives

+ - * / = < > <= >=
cos sin acos asin log expt round
number? integer? even? string? symbol?
string=?eqv? pair? null? procedure?
string->number number->string
string->symbol symbol->string
substring string-length string-append
cons car cdr set-car! set-cdr!
quote eval apply load
define lambda set! begin if

3. Artificial life primitives

The nanoScheme language includes also a reduced set of bio-inspired primitive functions. They have been designed in the same spirit of Tom Ray's Tierran assembly language [6]. That is, the production of synthetic organisms based on a computer metaphor of organic life in which CPU time is the "energy'" resource and memory is the "material" resource. These functions are the following in the current implementation :

Table 2. Bio-inspired functions in nanoScheme

reproduce: create a new nano-agent.
terminate: kill the current nano-agent.
diffuse: diffuse a message to other nano-agents in the local environment.
rule: define a new behavior rule consisting of condition and action expressions, and a priority.
engine: make an inference loop on the current behavior rule base.
crossover: genetic programming crossover operator.
mutate: genetic programming mutate operator and random code generator.
random: return a random real number.
time: return the current real time.
stress: return a "stress" value based on the current available memory and computing resources.
plugin: dynamically load a new package of dedicated primitive functions.
message: hook invoked when the nano-agent receives a message.
lifepulse: hook for implementing periodic behaviors.

Since all code, behavior rules, and messages are basically S-expressions (i.e. lisp expressions), the use of genetic programming seems natural in this environment [7]. Also, the remote execution of code on distant nano-agents is a natural feature by simply sending messages containing S-expressions. These expressions are then evaluated by all nano-agents. This approach enables an easy implementation of distributed algorithms on nano-agents.

4. Natural language interaction

Each nano-agent can be specialized to a given task by dynamically loading an appropriate dedicated package using the *plugin* primitive function. A typical example is the natural language package providing the developer natural language processing features [8] such as categories extraction, template expressions, etc. These functions allow the design of efficient behavior rules for implementing natural language interactions with the user. Table 3 gives a simple example of such a rule that handles the way to answer to most kinds of "bye" expressions.

Table 3. Example of a behavior rule

```
(rule "example" 2
    ; condition part
    '(or   (find? *categories* "BYE")
           (find? *user-input* "see you"))
    ; action part
    '(begin
           (show HAPPY 0.5)
           (random-template "BYE")))
```

III. THE EXPERIMENT

1. The experimental prototype

We describe an experiment that illustrates the use of the nano-agent architecture: an online self-animated character that interacts using natural language and emotional expressions. This experiment uses multiple nano-agents for the natural language processing part, plus an animated 3D character agent, a text-to-speech agent and a "chat" agent for interactions with the user. Figure 1 shows the graphical interface.

2. The "schizophrenic" character model

The virtual character is based on a "schizophrenic" model in which the character has multiple distinct identities or personalities, each with its own pattern of

©ISAROB 2009

perceiving and interacting with the user. Note that a more accurate psychological term is Dissociative Identity Disorder rather than schizophrenia [9]. Each personality is implemented as one or more nano-agents that reacts to the user's inputs by computing an answer using their behavior rules and diffusing messages containing answers. Then, a dedicated nano-agent "reconnects" the identities of the disparate alters into a single functioning identity by selecting the "thought" with the highest evaluation. In this prototype we used a straightforward priority-based scoring approach.

The different personalities are based on stereotypes used in story telling for creating believable characters [10]. There are four basic personalities:

- The *Protagonist* is essentially the principal driver of the effort to achieve the goal.
- The *Antagonist* is the personality which is opposed to the Protagonist's end goal and tries to undermine his success.
- The *Logic* personality is calm, perhaps even cold. He makes decisions and takes actions wholly on the basis of logic.
- The *Emotion* personality is reactive, seemingly uncontrolled, disorganized, mainly driven by feelings and moods.

As in story telling, additional secondary personalities could be added to complete the character such as an *Obstacle* personality which tries to block the ways or a *Sidekick* which is a faithful supporter of any of the other personalities. In our experiment, we have only implemented the four main personalities. The emotion one is based on both the previous emotional model of Eva [3] and the ALMA hierarchical model [11].

3. Memory and web mining

They are two additional groups of nano-agents that implement memory and web mining functionalities. The memory group is responsible for storing and retrieving information when needed. It stores all interactions with the user in log files and an indexer periodically parses these log files and extracts keywords. A dedicated plugin package adds to nanoScheme a small set of functions for retrieving information in the memory [12]. When the character has no information on a specific question, the web mining group tries to find a pertinent answer by searching information on the web [12].

Fig.1. The virtual character interface.

IV. RESULTS AND DISCUSSION

In this section, we discuss a typical interaction experiment with Alice [4] and Eva on the same simple interaction scenario. We obtained the following result with Alice:

(1) User: hi
Alice: Hello there.
(2) User: how are you today?
Alice: My logic and cognitive functions are normal.
(3) User: what is your name?
Alice: My name is ALICE.
(4) User: how old are you?
Alice: I am the product of over five years' research.
(5) User: Can you help me?
Alice: What kind of help would you like?
(6) User: What are clinical trials?
Alice: Have you tried a web search?
(7) User: Thank you.
Alice: you are quite welcome.
(8) User: bye
Alice: Sayonara.

We can note the quality of answers in the classical introductory and concluding discussion phase. However, even if its knowledge base includes a lot of general culture information, Alice was not able to answer to the very specific question about clinical trials and suggest the user to try a web search.

We obtained the following result with the multiple personalities of Eva :

(1) User: hi
Eva: Hello.
(2) User: how are you today?
Eva: Not too bad for a virtual creature.
(3) User: what is your name?
Eva: You may call me Eva.
(4) User: how old are you?
Eva : Just an advice: never ask such a question to a woman.
(5) User: Can you help me?
Eva: I will do my best. What do you want?
(6) User: What are clinical trials? […]
Eva: Researchers use interventional clinical trials to test hypotheses about the effect of a particular intervention upon a pathological disease condition.
(7) User: Thank you.
Eva: You're welcome.
(8) User: bye
Eva: Goodbye.

As for Alice, the Eva introductory and concluding phases are good. In (1), (3), (5), (7) and (8) the Protagonist personality answers have been selected, while in (2) and (4), the answers were from the Emotion personality. The question (6) has been processed by the web mining nano-agents through a search using Wikipedia. The answer in this specific case is very pertinent. However, for a more ambiguous question, the answer is not so convincing [12]. Another problem is that, in most cases, the user must wait for few seconds between his questions and the answer (shown by […] in the interaction). This delay is due to the time required to access Internet, make the search query and compute the answer. This could be solved by enabling the schizophrenic model to continue interactions with the user while searching on the web. Another evident critic is that the interaction case reported here is too short and simple to let all the personalities express themselves in the flow of conversation.

V. CONCLUSION

Eva is a long term open architecture project for designing artificial creatures [13]. Future works include (1) a deeper study of the schizophrenic model for creating rich believable characters, (2) enabling interactions not only with the user but between the multiple personalities, (3) adding much more personalities to create a swarm. Another direction is to develop more robust web mining and memory functionalities using evolutionary programming and swarm algorithms. Our goal is to reduce the amount of programming required by learning information from the flow of conversation and from the web rather than coding a large amount of predefined knowledge.

The Eva bio-inspired architecture has obvious applications for designing intelligent agents for commercial web sites and marketing studies. However, its lightweight nano-agent architecture enables a wider spectrum of applications. We like to imagine virtual assistants on mobile phones, assistants for lone aged and/or sick people, for learning foreign languages, virtual characters in video games and, of course, for robotic and embedded applications.

REFERENCES

[1] Heudin JC, Burg B, Zavidovique B (1986), A flexible operating system for distributed process control. 4th SPIE Conf. on Applications of AI
[2] Gilles A, Lebiannic Y, Montet P, Heudin JC (1991), A parallel architecture for the Electronic Copilote. 11th EC2 Int. Conf. on Expert Systems Applications
[3] Heudin JC (2004), Evolutionary Virtual Agent. ACM/WIC/IEEE Intelligent Agent Technology Conf. 93-98
[4] http://www.alicebot.org
[5] Clinger W, Rees J (Eds.) (1991), Revised(4) Report on the Algorithmic Language Scheme
[6] Ray TS (1991), An approach to the synthesis of life. Artificial Life II, Addison-Wesley, 371-408
[7] Koza JR (1992), Genetic programming. MIT Press.
[8] Heudin JC (2007), Evolutionary Virtual Agent at an exhibition. Virtual Systems and Multimedia Conf.
[9] http://en.wikipedia.org/wiki/Schizophrenia
[10] Masterson L (2000), Casting your character. http://www.fictionfactor.com
[11] Gebhard P (2005), ALMA: A layered model of affect. 4th Int. Joint Conf. on Autonomous Agents and Multi-agent Systems, 29-36
[12] Millet P, Heudin JC (2007), Web mining in the EVA intelligent agent architecture. ACM/WIC/IEEE Intelligent Agent Technology Conf.
[13] http://www.artificial-creature.com

The Fourteenth International Symposium on Artificial Life and Robotics 2009 (AROB 14th '09),
B-Con Plaza, Beppu, Oita, Japan, February 5 - 7, 2009

Fault Location Estimation using Estimator Residual

C. K. Lee , S. H. Doo and J. B. Park
Dept. of Electrical and Electronic Engineering
Yonsei University
Seoul, 120-749

T. S. Yoon
Dept. of Electrical Engineering
Changwon National University
Changwon, 641-773

Abstract

Reflectometry is a kind of cable fault diagnosis. There are various kinds of reflectometries such as time domain reflectometry(TDR), frequency domain reflectometry(FDR), and joint time-frequency domain reflectometry(TFDR). In this paper, we propose a new fault location estimation method using residual of AR coefficient estimation. Proposed fault distance estimation method models the reference signal as a simple second order AR coefficient, and estimates reference signal and reflected signal via robust weighted least square(RWLS) estimator. Using residual of estimation, proposed fault distance estimator estimates the fault location of the cable. The performance of the proposed method is verified by simulations and experiments.

1 Introduction

Defected cable may cause fatal disaster. In order to prevent disaster, fault detection method is needed. There are many kinds of cable fault diagnosis. The reflectomery that stems from sonar and radar system is one of the cable fault diagnosis. There are various reflectometries, such as TDR, FDR, and TFDR. Each reflectometry has different analysis method and characteristics[1]. However, main idea of reflectometry is the same. At the fault location of cable, transmitted reference signal is reflected due to the impedance miss matching. Fault location is estimated based on the time delay between the reference signal and the reflected signal.

The Gaussian enveloped linear chirp signal is adopted as a reference signal on the TFDR method. In the TFDR, the joint time-frequency energy distribution of the reference signal and reflected signals is computed. And the time-frequency cross correlation is computed using the joint time-frequency distribution. The time delay information is obtained from the time-frequency cross correlation[1]. Accurate fault distance estimation in the TFDR is possible due to the time-frequency cross correlation function. However, the computational burden is a fatal obstruct to do the real-time implementation. From the view point of the estimator for the time delay between the reference signal and the reflected signal, cable fault diagnosis is interpreted as a signal modeling and estimation problem. In time of arrival estimation problem, the reflected signal is modeled as an attenuated and time delayed version of the reference signal, and use the least square(LS) estimator to estimate the time delay[4]. In this paper, we introduce another approach to time delay estimation. Reference signal is modeled with second order AR coefficients for minimizing the computational burden. The RWLS[2] estimator is designed to estimate the AR coefficients. When the reference signal or the reflected signal is detected, residual has peak amplitude that is due to the conversions rate of the RWLS estimator. Using this phenomenon, we are able to estimate the time delay.

2 AR Modeling for Chirp Signal

The reflected signal in reflectometry is assumed as an attenuated and time delayed version of the reference signal. If reference signal is modeled via AR coefficient, the reflected signal also satisfies the AR modeling coefficients because the reflected signal is a replica of the reference signal. In this paper, the reference signal is a linear chirp signal that has linearly increasing frequency. The linear chirp signal is represented as follows,

$$
\begin{aligned}
s_k =& M e^{j(\frac{1}{2}\beta(T_s k)^2+\omega_0(T_s k)-\frac{\pi}{2})} \qquad (1)\\
=& M[cos(\frac{1}{2}\beta(T_s k)^2+\omega_0(T_s k)-\frac{\pi}{2})\\
&+jsin(\frac{1}{2}\beta(T_s k)^2+\omega_0(T_s k)-\frac{\pi}{2})],
\end{aligned}
$$

©ISAROB 2009

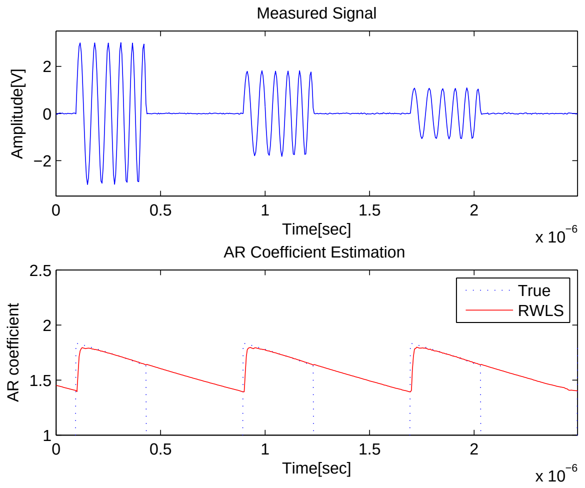

Figure 1: AR coefficient estimation : 100.08m

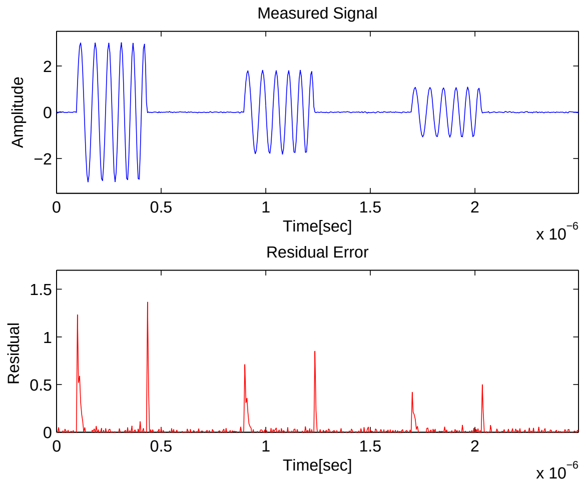

Figure 2: Residual of AR coefficients estimation: 100.08m

where M is the amplitude of linear chirp signal, β is frequency sweep rate, T_s is sampling interval and ω_0 is start frequency. For notational convenience, θ_k is defined as follows:

$$\theta_k = (\frac{1}{2}\beta(T_s(k))^2 + \omega_0(T_s(k)) - \frac{\pi}{2}). \tag{2}$$

Using the θ_k, s_{k-1} and s_{k-2} are given by,

$$s_{k-1} = M[cos(\theta_{k-1}) + jsin(\theta_{k-1})]. \tag{3}$$
$$s_{k-2} = M[cos(\theta_{k-2}) + jsin(\theta_{k-2})]. \tag{4}$$

For deriving the AR coefficients equation, s_k is rewritten by,

$$\begin{aligned} & s_k + s_{k-2} \\ =& 2Mcos(-\beta T_s^2(k-1) - \omega_0 T_s) \\ & \times [cos(\frac{1}{2}\beta T_s^2)\{cos(\theta_{k-1}) + jsin(\theta_{k-1})\} \\ & + jsin(\frac{1}{2}\beta T_s^2)\{cos(\theta_{k-1}) + jsin(\theta_{k-1})\}] \\ =& 2cos(-\beta T_s^2(k-1) - \omega_0 T_s) \\ & \times \Big(cos(\frac{1}{2}\beta T_s^2) + jsin(\frac{1}{2}\beta T_s^2)\Big) s_{k-1} \end{aligned} \tag{5}$$

For notational convenience, A_k is defined as follows:

$$A_k = -\beta T_s^2(k-1) - \omega_0 T_s. \tag{6}$$

Equation(5) is can be rearranged by,

$$\begin{aligned} s_k =& 2cos(A_k) \\ & \times \Big(cos(\frac{1}{2}\beta T_s^2) + jsin(\frac{1}{2}\beta T_s^2)\Big) s_{k-1} - s_{k-2}. \end{aligned} \tag{7}$$

Complex signal s_k can be represented by the real and imaginary terms. So we represent the complex signal s_k as follows:

$$s_k = a_k + jb_k, \tag{8}$$

where a_k is real part of s_k and b_k is imaginary part of s_k. We assume that $cos(\frac{1}{2}\beta T_s^2) \approx 1$ without loss of generality. Real part of complex signal s_k is only used. Therefore, signal can be modeled as follows:

$$a_k = 2cos(A_k)a_{k-1} - a_{k-2} \tag{9}$$

3 Robust Weighted Least Square Estimator

In this section, the RWLS is used to estimate the coefficients of the AR model. Transient equation can be defined as follows,

$$x_{k+1} = F_k x_k + w_k, \tag{10}$$

where $x_k \triangleq 2cos(A_k)$, F_k is transient matrix, and w_k is zero mean white Gaussian noise. We define stochastic signal $\tilde{a}_k$ before defining the measurement equation. The measured signal contains not only noise uncorrupted signal a_k but also noise signal. In order to represent the noise corrupted measurement signal, we denote as,

$$\tilde{a}_k = a_k + \bar{v}_k, \tag{11}$$

©ISAROB 2009

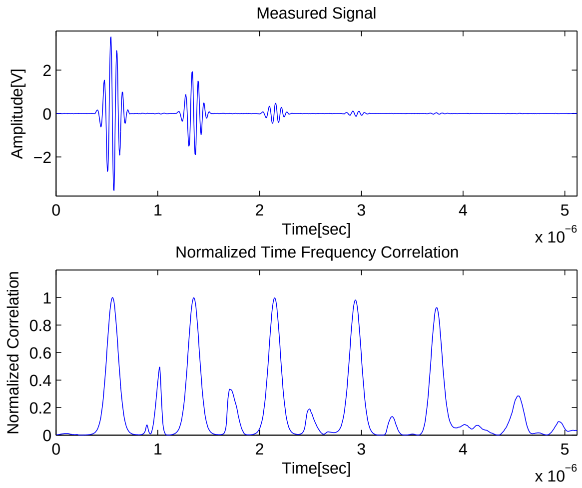

Figure 3: TFDR experiment on 10C-HFBT: 100m

where $\tilde{a}_k$ is noise corrupted measured signal and $\bar{v}_k$ is zero mean white Gaussian noise. Equation(9) is rewritten as follows:

$$\tilde{a}_k + \tilde{a}_{k-2} = 2cos(A_k)(\tilde{a}_{k-1} - \bar{v}_{k-1}) + (\bar{v}_k + \bar{v}_{k-2}) \tag{12}$$

and then the measurement equation can be defined as follows,

$$y_k = [\tilde{H}_k - \Delta H_k]x_k + v_k, \tag{13}$$

where

$$y_k \triangleq \tilde{a}_k + \tilde{a}_{k-2}, \qquad v_k \triangleq \bar{v}_k + \bar{v}_{k-2},$$
$$\tilde{H}_k \triangleq \tilde{a}_{k-1}, \qquad \Delta H_k \triangleq \bar{v}_{k-1}.$$

Measurement matrix $\tilde{H}_k$ is measured from sensor. We can only obtain measurement matrix $\tilde{H}_k$ that contains uncertainty. The RWLS estimator successfully eliminates the scale factor error and the bias error that is due to the stochastic uncertainty in the measurement matrix[3]. State-space equation can be obtained as follows:

$$x_{k+1} = F_k x_k + w_k,$$
$$y_k = [\tilde{H}_k - \Delta H_k]x_k + v_k.$$

It is assumed that the stochastic uncertainty ΔH_k is stationary, and ΔH_k and v_k are mutually uncorrelated in the RWLS.

$$E[\Delta H_k^T \cdot \Delta H_k] \triangleq \bar{R}_{k-1}, \tag{14}$$
$$E[\Delta H_k \cdot v_k] \triangleq 0,$$
$$E[\Delta H_k \cdot w_k] \triangleq 0.$$

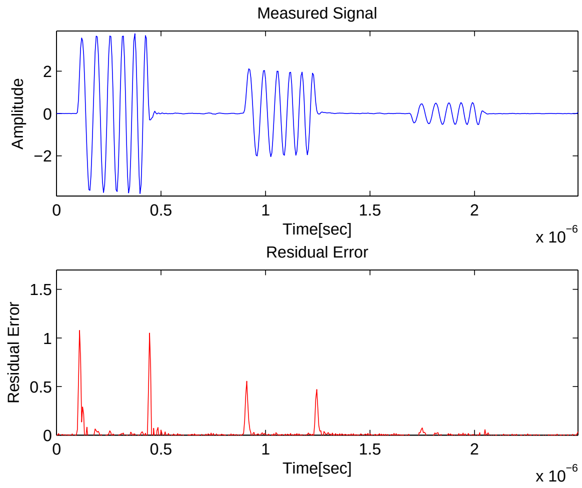

Figure 4: Proposed fault estimator experiment on 10C-HFBT: 100m

The equations of RWLS are written as follows,

$$\mathcal{P}_{k|k}^{-1} = \lambda \mathcal{P}_{k|k-1}^{-1} + \tilde{H}_k^T \tilde{H}_k - \bar{R}_{k-1}, \tag{15}$$
$$\hat{x}_{k|k} = (I + \mathcal{P}_{k|k}\bar{R}_k)\hat{x}_{k|k-1} \tag{16}$$
$$+ \mathcal{P}_{k|k}\tilde{H}_k^T(y_k - \tilde{H}_k \hat{x}_{k|k-1}), \tag{17}$$
$$\mathcal{P}_{k+1|k} = F_k \mathcal{P}_{k|k} F_k^T, \tag{18}$$
$$\hat{x}_{k+1|k} = F_k \hat{x}_{k|k}. \tag{19}$$

where λ is the forgetting factor and $\mathcal{P}_{k|k}$ is the Gramian matrix. The existence condition of RWLS is given by,

$$\mathcal{P}_{k|k}^{-1} \triangleq (\mathcal{H}^k)^T \Lambda^k \mathcal{H}^k - (\Phi^k)^T \mathcal{R}^k \Phi^k > 0 \tag{20}$$

where Λ^k is the weighting matrix. The AR coefficient, $2cos(A_k)$, is estimated by the RWLS estimator.

4 Fault Distance Estimation via Residual

In this section, the fault distance estimation method via residual of the RWLS is presented. Not only the RWLS but also all estimator takes some time to converges at the true state. This is due to the convergence rate of estimator. If state is suddenly changed, residual is increased steeply. As the estimated state converges to the true state, residual is also decreased. We use this characteristics of estimator that residual is increased at the wide variation point of state to estimate the fault distance. In fault distance estimation, state is suddenly changed at the boundaries of the reference and the reflected signals. Residual has peak values at the boundaries of the reference and the reflected signals. Using the peak points of residual, fault distance is estimated. Residual can be defined as follows:

$$\begin{aligned} r_k &= y_k - \hat{y}_k \\ &= (\hat{a}_k + \hat{a}_{k-2}) - [\tilde{H}_k - \Delta H_k]x_k. \end{aligned} \tag{21}$$

5 Simulation Results

For the simulation, we use the linear chirp signal. In simulation, frequency range is 13 $\sim$ 19.7MHz, time duration is 340nsec, amplitude of the linear chirp signal is $6V_{pp}$, sampling rate is 200Msps and the length of cable is 100.08m. Velocity of propagation and noise standard deviation that are extracted from experiments are 2.502×10^8m/s, 0.013 respectively. Measured signal, true AR coefficients, and AR coefficient estimation are shown in Fig.1. In Fig.1, upper graph represents the measured signal. The first signal is the reference signal and the other signals are the reflected signals. Below graph represents the true AR coefficient by dotted line and estimation result by solid line. In Fig.1, true AR coefficient steeply changes at the boundaries of the reference and reflected signals. AR coefficient is properly estimated by the RWLS. However at the boundaries of the reference and reflected signal, estimation result does not follow the true AR coefficient. At the boundaries of the reference and reflected signals, residual will be steeply increased. This fact is shown in Fig.2. In Fig.2, below graph represents the residual. Peak locations of residual is coincident with the boundaries of the reference and reflected signals. The fault distance is computed by peak locations. In this simulation, estimated fault distance is 100.08m.

6 Experimental Results

In this section, the proposed fault distance estimator is compared with the conventional TFDR. Cable is 10C-HFBT 100m. Experimental set consists of arbitrary waveform generator(NI-PXI 5422), digital storage oscillator(NI-PXI 5124) and connector. Arbitrary waveform generater generates the Gaussian enveloped linear chirp signal that has the same time duration and frequency range of the linear chirp signal used in simulation. However, the Gaussian envelope is chirp signal. This reference signal flows with the conductor of cable via connector. The reference signal is reflected at the end of the cable that is open fault. Reflected signal is measured by digital storage oscilloscope.

In the same noisy environment, fault distance estimation is performed. The experimental results of TFDR and the proposed method are shown in Fig.3 and Fig.4. The fault distance of TFDR is 100.07m and the proposed method gives the fault distance as 100.08m. From these results, proposed estimator offers reliable estimation results. The Proposed fault distance estimator reduces the computational burden of TFDR because the proposed estimator uses the RWLS and residual instead of cross correlation and joint time-frequency energy distribution. Therefore the proposed fault distance estimator is suitable to real-time implementation.

Acknowledgements

This study was supported by the Brain Korea 21 Project in 2008.

This work was supported by Manpower Development Program for Energy & Resources of MKE with Yonsei Electric Power Research Center (YEPRC) at Yonsei University, Seoul, Korea.

References

[1] Y. J. Shin, J. Powers, T. S. Choe, C. Y. Hong, E. S. Song, J. G. Yook, and J. B. Park, "Application of Time-Frequency Domain Reflectometry for Detection and Localization of a Fault on a Coaxial Cable", *IEEE Transactions on Instrumentation and Measurement*, Vol. 54, No. 6, Dec. 2005.

[2] W. S. Ra, I. H. Whang, and J. B. Park, "Robust Weighted Least Squares Range Estimation for UAV Applications", *SICE Annual Converence 2008*, pp. 251-255, Aug. 2008.

[3] G. H. Choi, W. S. Ra, T. S. Yoon and J. B. Park, "Low-Cost Tachometer based on the Recursive Frequency Estimation for Automotive Applications", *SICE Ann. Conf.*, pp. 46-49, Sep. 2007.

[4] R.J Vaccaro,C.S Ramalingam, D.W.Tufts, R.L.Field "Least-squares time-delay estimation for transient signals in a multipath environment",*J.Acoust.Soc.Am* Vol. 92, No 1, pp.210-218, July 1992.

©ISAROB 2009

Observer-based fuzzy control for nonlinear networked control system with pack drop

Geun Bum Koo[1], Jin Bae Park[1] and Young Hoon Joo[2]

[1] *Department of Electrical and Electronic Engineering, Yonsei University, Seodaemun-gu, Seoul, 120-749, Korea*
(Tel : 82-2-2123-2773; Fax : 82-2-362-4539)
(Email: {milbam, jbpark}@yonsei.ac.kr)
[1] *School of Electronic and Information Engineering, Kunsan National University, Kunsan, Chonbuk, 573-701, Korea*
(Tel : 82-63-469-4706)
(Email: yhjoo@kunsan.ac.kr)

Abstract: In this paper, an observer-based fuzzy controller is proposed for the nonlinear networked control systems (NCSs) with packet drop. Using Takagi-Sugeno (T-S) fuzzy model, the nonlinear NCS is represented by a fuzzy system, and the observer-based controller is design in the fuzzy form. The stochastic stability condition of the closed-loop system is obtained by Lyapunov functional. Its sufficient condition is represented to the linear matrix inequality (LMI) form and the observer and control gains are obtained by LMI. An example is given to demonstrate the verification discussed throughout the paper.

Keywords: nonlinear networked control system, stochastic stability, fuzzy observer-based control, packet drop, linear matrix inequality

I. INTRODUCTION

During the recent years, due to increasing of the ubiquitous computing, the importance of the networked control system (NCS) is grown and many people have concerned about stability and stabilization of system. The NCS offers many advantages in the economy and efficiency, and has applications in wireless networked system, internet-based control, automation technology, communication technique and so on. However, it has some problem such as packet drop, time delay, and sampling. To solve these problems, many papers have been published[1-8].

The packet drop is one of the main problems in NCS. It needs a stochastic approach to solve the packet drop problem. Thus, traditional deterministic stabilization method is not useful in packet drop problem. Moreover, if NCS includes the nonlinearity, uncertainty, time delay, and so on, it is more difficult to obtain the stability condition.

In a few number of research concerned stability problem of NCS[4-8]. Wang[6] studied the robust control method for NCS with packet drop. Hu[7] developed the optimization problem of packet dropping margin. But they did not considered the nonlinearity problem in NCS. Zhang[8] designed the fuzzy controller for nonlinear systen with packet drop. This paper used the state feedback method, which needs the information of all states, but it is impossible in NCS.

In this paper, we aim to solve the problem of stability of a fuzzy NCS with output packet drop, input transmission failure and Gaussian noise. An observer-based controller is proposed for the stochastic stability. Using a Lyapunov functional, the sufficient condition for stability is offered in the linear matrix inequality (LMI) format. A numerical example is presented to demonstrate the effectiveness of the proposed controller and theorem.

II. PRELMINIRIES

Consider a fuzzy networked control system, in which the i th IF-THEN rule is represented as follows:

$$\begin{aligned}&Plant\ \ Rule\ \ i:\\&IF\ \ z_1\ \ is\ \ \Gamma_1^i,\cdots,\ and\ \ z_p\ \ is\ \ \Gamma_p^i\\&THEN\begin{cases}x_{k+1}=A_ix_k+B_iu_k+D_ix_k\omega_k,\\ y_k=\alpha_kCx_k, \qquad (1\le i\le r)\end{cases}\end{aligned} \tag{1}$$

where x_k is state variable, u_k is input, y_k is output, and ω_k is a scalar zero-mean Gaussian white noise with $\mathrm{E}\{\omega_k^2\}=\gamma^2$. Γ_q^i is a fuzzy set for $1\le q\le p$, r is the number of fuzzy rules, A_i, B_i, C, D_i are nominal system matrices, α_k is a stochastic variable which determines the packet drop of output part. This stochastic variable is a Bernoulli process as the following probability:

$$\begin{aligned}\mathrm{Prob}\{\alpha_k = 1\} &= \mathrm{E}\{\alpha_k\} = \hat{\alpha} \\ \mathrm{Prob}\{\alpha_k = 0\} &= 1 - \mathrm{E}\{\alpha_k\} = 1 - \hat{\alpha}\end{aligned}$$

Using the center-average defuzzification, product inference, and singleton fuzzifier, the T-S fuzzy system (1) is inferred as follows:

$$\begin{aligned}x_{k+1} &= \sum_{i=1}^{r} \theta_i (A_i x_k + B_i u_k + D_i x_k \omega_k) \\ y_k &= \alpha_k C x_k\end{aligned} \tag{2}$$

where

$$\theta_i = \left(\prod_{q=1}^{p} \Gamma_q^i(z_q)\right) \Bigg/ \left(\sum_{i=1}^{r}\left(\prod_{q=1}^{p} \Gamma_q^i(z_q)\right)\right)$$

and $\Gamma_q^i(z_q)$ is the degree of the membership function.

Hence, we consider a observer-based fuzzy controller for fuzzy networked control system in the following form:

$$\begin{aligned}&\mathit{Controller\ \ Rule\ \ i}: \\ &\mathit{IF}\ \ z_1\ \ \mathit{is}\ \ \Gamma_1^i, \cdots, \mathit{and}\ \ z_p\ \ \mathit{is}\ \ \Gamma_p^i \\ &\mathit{THEN} \begin{cases}\hat{x}_{k+1} = A_i \hat{x}_k + B_i u_k + L_i (y_k - \hat{y}_k), \\ \hat{y}_k = \hat{\alpha} C \hat{x}_k \\ u_k = \beta_k K_i \hat{x}_k \qquad\qquad (1 \le i \le r)\end{cases}\end{aligned} \tag{3}$$

where $\hat{x}_k$ is an estimation of state variable, L_i and K_i are observer and controller gains, respectively. β_k is a stochastic variable which determines the transmission failure of input part. This stochastic variable is a Bernoulli process as the following probability:

$$\begin{aligned}\mathrm{Prob}\{\beta_k = 1\} &= \mathrm{E}\{\beta_k\} = \hat{\beta} \\ \mathrm{Prob}\{\beta_k = 0\} &= 1 - \mathrm{E}\{\beta_k\} = 1 - \hat{\beta}\end{aligned}$$

The input-output form of the controller is then

$$\begin{aligned}\hat{x}_{k+1} &= \sum_{i=1}^{r} \theta_i (A_i \hat{x}_k + B_i u_k + L_i (y_k - \hat{y}_k)) \\ \hat{y}_k &= \hat{\alpha} C x_k \\ u_k &= \sum_{i=1}^{r} \theta_i \beta_k K_i \hat{x}_k\end{aligned} \tag{4}$$

Assumption 1. The stochastic variable of the output packet drop α_k, the stochastic variable of the input transmission failure β_k, and the Gaussian noise ω_k are independent.

$$\mathrm{E}\{\alpha_k \beta_k \omega_k\} = \mathrm{E}\{\alpha_k\}\,\mathrm{E}\{\beta_k\}\,\mathrm{E}\{\omega_k\}$$

Assumption 2. The output matrix C has full row rank, i.e., there exists the inverse of CC^T.

Consider the estimation error as follows

$$e_k = x_k - \hat{x}_k \tag{5}$$

Substituting (4) into (2) and (5), we obtain the following closed-loop system:

$$\begin{bmatrix} x_{k+1} \\ e_{k+1} \end{bmatrix} = \sum_{i=1}^{r}\sum_{i=1}^{r} \theta_i \theta_j (\Phi_{ij} + \varepsilon_k \Lambda_{ij} + \hat{D}_i \omega_k) \begin{bmatrix} x_k \\ e_k \end{bmatrix} \tag{6}$$

where

$$\Phi_{ij} = \begin{bmatrix} A_i + \hat{\beta} B_i K_j & -\hat{\beta} B_i K_j \\ 0 & A_i + \hat{\alpha} L_i C \end{bmatrix},$$

$$\varepsilon_k = \begin{bmatrix} (\beta_k - \hat{\beta}) I & 0 \\ 0 & (\alpha_k - \hat{\alpha}) I \end{bmatrix},$$

$$\Lambda_{ij} = \begin{bmatrix} B_i K_j & -B_i K_j \\ -L_i C & 0 \end{bmatrix}, \qquad \hat{D}_i = \begin{bmatrix} D_i & 0 \\ D_i & 0 \end{bmatrix}$$

The objective of this paper is to obtain the stability condition of the closed-loop system (6). But system (6) includes the stochastic variable, it is not impossible to guarantee the traditional deterministic stable condition. We solve this problem in next section.

III. MAIN RESULTS

For the fuzzy networked control system with stochastic variable, we need to define the notion of stochastic stability.

Definition 1. The equilibrium point $x_k = 0$ of the closed-loop networked control system (6) is said to be stochastically stable if, for each $\mu > 0$, there is $\delta = \delta(\mu) > 0$ such that

$$\|x_0\| < \delta \Rightarrow \|x_k\| < \mu, \quad \forall k \ge 0$$

In order to derive the stability condition in the LMI form, we need the following lemmas.

Lemma 1[9]. If there exist a Lyapunov functional $V(x_k)$ and a nondecreasing convex function $a(\eta)$, such that $a(0)=0$ and $a(\eta)>0$ for $\eta>0$, satisfying the following three conditions:

1) $V(0)=0$
2) $a(\|x_k\|)\le V(x_k)$
3) $\mathrm{E}\{V(x_{k+1})\}-\mathrm{E}\{V(x_k)\}<0$

then the equilibrium point $x_k=0$ of the fuzzy networked control system (6) is stochastically stable.

Lemma 2[10]. For any real matrices X_i, Y_i for $1\le i\le n$, and $S\succ 0$ with appropriate dimensions, we have

$$2\sum_{i=1}^{n}\sum_{j=1}^{n}\sum_{k=1}^{n}\sum_{l=1}^{n}h_ih_jh_kh_lX_{ij}^TSY_{kl} \le \sum_{i=1}^{n}\sum_{j=1}^{n}h_ih_j\left(X_{ij}^TSX_{kl}+Y_{ij}^TSY_{kl}\right)$$

where $h_i\left(1\le i\le n\right)$ is defined as $h_i\ge 0$, $\sum_{i=1}^{n}h_i=1$

Lemma 2[13]. Given constant symmetric matrices N, O and L of appropriate dimensions, the following inequalities

$$O\succ 0,\qquad N+L^TOL\prec 0$$

are equivalent to the following inequality

$$\begin{bmatrix} N & L^T \\ L & -O^{-1}\end{bmatrix}\prec 0 \quad \text{or} \quad \begin{bmatrix} -O^{-1} & L \\ L^T & N\end{bmatrix}\prec 0$$

The sufficient condition is provided for the stochastic stability of the closed-loop system (6) in the following theorem.

Theorem 1. If there exist some symmetric and positive definite matrix Q, some matrices W_i, N_i, such that the following LMIs are satisfied, then the networked closed-loop system (6) is stochastically stable.

$$\begin{bmatrix} -Q & * & * & * & * & * & * \\ 0 & -Q & * & * & * & * & * \\ \Omega_{ii} & -\hat{\beta}B_iW_i & -Q & * & * & * & * \\ 0 & \Psi_i & 0 & -Q & * & * & * \\ \tilde{\beta}B_iW_i & -\tilde{\beta}B_iW_i & 0 & 0 & -Q & * & * \\ -\tilde{\alpha}N_iC & 0 & 0 & 0 & 0 & -Q & * \\ \gamma D_i & 0 & 0 & 0 & 0 & 0 & -2Q \end{bmatrix}\prec 0 \tag{7}$$

$$\begin{bmatrix} -Q & * & * & * & * & * & * \\ 0 & -Q & * & * & * & * & * \\ \Omega_{ij}+\Omega_{ji} & -\hat{\beta}\tilde{W}_{ij} & -Q & * & * & * & * \\ 0 & \Psi_i+\Psi_j & 0 & -Q & * & * & * \\ \tilde{\beta}\tilde{W}_{ij} & -\tilde{\beta}\tilde{W}_{ij} & 0 & 0 & -Q & * & * \\ -\tilde{\alpha}\tilde{N}_{ij} & 0 & 0 & 0 & 0 & -Q & * \\ \gamma D_i & 0 & 0 & 0 & 0 & 0 & -2Q \end{bmatrix} \prec 0 \tag{8}$$

and

$$CQ=MC \tag{9}$$

for $1\le i,\ j\le r$ and $i\ne j$.

where

$$W_i=K_iQ,\qquad N_i=L_iM$$
$$\tilde{\alpha}=\sqrt{(1-\hat{\alpha})\hat{\alpha}},\qquad \tilde{\beta}=\sqrt{(1-\tilde{\beta})\tilde{\beta}}$$
$$\Omega_{ij}=A_iQ+\hat{\beta}B_iW_j,\qquad \Psi_i=A_iQ+\hat{\alpha}N_iC$$
$$\tilde{W}_{ij}=B_iW_j+B_jW_i,\qquad \tilde{N}_{ij}=N_iC+N_jC$$

and $*$ denotes the transposed element in symmetric position. The observer gain and control gain are obtain by the following equations:

$$K_i=W_iQ^{-1},$$
$$L_i=N_i\left\{CQC^T(CC^T)^{-1}\right\}^{-1}$$

Proof) It is omitted in this paper.

IV. SIMULATION

Consider a fuzzy system which is represented in the following form:

$$x_{k+1}=\sum_{i=1}^{2}\theta_i(A_ix_k+B_iu_k+D_ix_k\omega_k)$$
$$y_k=\alpha_kCx_k$$

where

$$x_k=\begin{bmatrix}x_{k1} & x_{k2}\end{bmatrix}^T,$$
$$A_1=\begin{bmatrix}0.8 & 0.6\\ 0.4 & 0.7\end{bmatrix},\qquad A_2=\begin{bmatrix}0.9 & 0.2\\ 0.3 & 0.8\end{bmatrix}$$
$$B_1=\begin{bmatrix}1\\ 0\end{bmatrix},\qquad B_2=\begin{bmatrix}1.2\\ 0\end{bmatrix},\qquad C=\begin{bmatrix}1 & 0\end{bmatrix}$$
$$D_1=\begin{bmatrix}0.2 & 0\\ 0 & 0.1\end{bmatrix},\qquad D_2=\begin{bmatrix}0.1 & 0\\ 0 & 0.2\end{bmatrix}$$
$$\theta_1=\exp\left[-2x_{k1}^2\right],\qquad \theta_2=1-\theta_1$$

We assume the stochastic variables as follows:

$$\mathrm{E}\left\{\omega_k^2\right\}=1$$
$$\Pr ob\left\{\alpha_k=1\right\}=\Pr ob\left\{\beta_k=1\right\}=0.2$$

©ISAROB 2009

Using LMIs (7) and (8), The observer gain and control gain is obtained.

$$K_1 = \begin{bmatrix} -0.8657 & -0.6188 \end{bmatrix},$$
$$K_2 = \begin{bmatrix} -0.5657 & -0.3087 \end{bmatrix},$$
$$L_1 = \begin{bmatrix} 0.8399 \\ 0.6484 \end{bmatrix}, \quad L_1 = \begin{bmatrix} 0.7059 \\ 0.3933 \end{bmatrix}$$

Time responses for each state are shown in Fig.1 and Fig.2 with the initial condition $x_k = \begin{bmatrix} 1 & 1 \end{bmatrix}^T$.

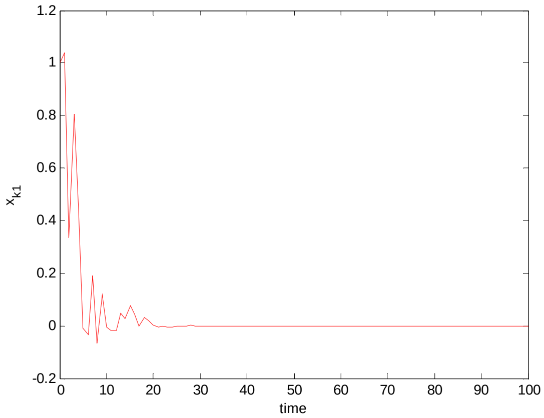

Fig.1. Time response of x_{k1}

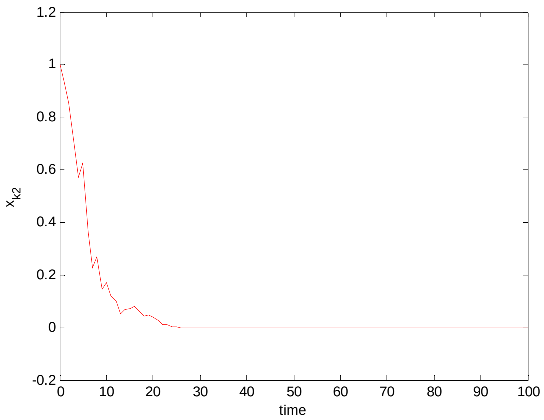

Fig.2. Time response of x_{k2}

V. CONCLUSION

In this paper, the observer-based fuzzy controller has been proposed for the nonlinear networked control systems with packet drop. The controller is designed in the T-S fuzzy system form and sufficient conditions for stochastic stabilization of the closed-loop system are designed in the LMI format. The numerical example has been shown to prove the advantage of the developed method.

ACKNOWLEDGEMENT

This work was supported by the Brain Korea 21 Project in 2008 and Manpower Development Program for Energy & Resources of MKE with Yonsei Electric Power Research Center (YEPRC) at Yonsei University, Seoul, Korea

REFERENCES

[1] W. Zhang, M. S. Branicky and S. M. Phillips (2001), Stability of networked control system. IEEE Control Systems Magazine 21(1): 84-99

[2] G. C. Walsh, H. Ye and L. G. Bushnell (2002), Stability analysis of networked control systems. IEEE Control Systems Technology 10(3): 436-446

[3] D. Huang and S. K. Nguang (2008), State feedback control of uncertain networked control systems with random time delays. IEEE Trans. on Automatic Control 53(3): 829-834

[4] J. Xiong and J. Lam (2007), Stabilization of linear systems over networks with bounded packet loss. Automatica 43: 80-87

[5] J. Wu and T. Chen (2007), Design of networked control systems with packet dropouts. IEEE Trans. on Automatic Control 52(7): 1314-1319

[6] Z. Wang, F. Yang, D. W. C. Ho and X. Liu (2007), Robust H_∞ control for networked systems with random packet losses. IEEE Trans. on Systems, Man, and Cybernetics – Part B: Cybernetics 37(4): 916-924

[7] S. Hu and W. Y. Yan (2007), Stability robustness of networked control systems with respect to packet loss. Automatica 43: 1243-1248

[8] X. Zhang, Y. Zheng, H. Tang and G. Lu (2006), A stochastic fuzzy system approach to networked control systems with data dropout. Proceeding of the 25th Chinese Control Conference: 2189-2193

[9] B. Chen, Z. Wang, H. Shu and G. Wei (2008), On nonlinear H_∞ filtering for discrete-time stochastic systems with missing measurements. IEEE Trans. on Automatic Control. 53(9): 2170-2180

[10] X. P. Guan and C. L. Chen (2004), Delay-dependent guaranteed cost control for T-S fuzzy systems with time delay. IEEE Trans. on Fuzzy Systems 12(2): 236-249

[11] L. Xie (1996), Output feedback H_∞ control of systems with parameter uncertainties. Int. J. Contr 63(4): 741-750

The Fourteenth International Symposium on Artificial Life and Robotics 2009 (AROB 14th '09),
B-Con Plaza, Beppu, Oita, Japan, February 5 - 7, 2009

Formation Control of Mobile Robots with Disturbances

B. S. Park and J.B. Park
Department of Electrical
and Electronic Engineering
Yonsei University
Seoul, Korea, 120-749

Y. H. Choi
School of Electronic
Engineering
Kyonggi University
Suwon, Korea, 443-760

Abstract

This paper proposes a formation control method for nonholonomic mobile robots in the presence of disturbances. We use the kinematic model based on the leader-following approach for the formation control of multiple robots. However, unlike many researches considering only the kinematic model, we also consider the dynamic model to obtain the torque input because it is more realistic to use the torque as the input than the velocity. Moreover, the sliding mode control method is used to deal with disturbances acting on the mobile robots. The system stability and the convergence of tracking errors are proven using Lyapunov stability theory.

1 Introduction

Over the past decade, the formation control of multiple robots has been studied by many researchers because of its usefulness in many applications, such as automated transportation, spacecraft interferometry, mitigation of natural and man-made disasters, surveillance, mapping, and border patrol [1]. Various approaches have been proposed for the formation control of multiple robots in the literature. These are roughly categorized as behavior-based [2], virtual structure [3], and leader-following [4].

In the leader-following approach, the referenced robot, called a leader, tracks the predefined trajectory, and the other robots, the followers, maintain the desired distance and angle with respect to the leader. This approach has been adopted by many researchers because of the simplicity, scalability, and reliability. Desai et al. [5] presented a feedback linearization control method for the formation of multiple mobile robots. Li et al. [6] proposed a kinematic model using Cartesian coordinates and applied a backstepping technique to the formation control of multiple mobile robots. Shao et al. [7] introduced a virtual robot to keep the relative position between the leader and followers. However, these methods only consider the kinematic model of mobile robots and do not consider the disturbances acting on the robots. The control input of the controller for the kinematic model is the velocity, but it is more realistic that the input is a torque [8]. In addition, in practice, we have to deal with unstructured uncertainties, noise, and disturbances. To solve these problems, Sanchez and Fierro [9] proposed a sliding mode controller for the leader-following robot formation. However, since the control law requires the derivative of the absolute value, it has a drawback that it is difficult to obtain the control input.

Motivated by these observations, we propose a sliding mode formation control method based on the leader-following approach.

2 Problem Statement

2.1 Kinematics and Dynamics of Mobile Robots

We consider the two-wheeled mobile robot. The posture of the mobile robot can be described by three parameters (x, y, θ) where x and y are position variables, θ is a heading direction angle. It is assumed that the driving wheels of the mobile robot purely roll and do not slip. This nonholonomic constraint can be expressed as $\dot{x}\sin\theta - \dot{y}\cos\theta = 0$. Then, the kinematic equation in Cartesian coordinates is derived as follows:

$$\begin{bmatrix} \dot{x} \\ \dot{y} \\ \dot{\theta} \end{bmatrix} = \begin{bmatrix} \cos\theta & 0 \\ \sin\theta & 0 \\ 0 & 1 \end{bmatrix} \begin{bmatrix} v \\ \omega \end{bmatrix} \tag{1}$$

where v and ω are the linear and angular velocities of the mobile robot.

The dynamic equation of the mobile robot with nonholonomic constraints can be described by Euler-

©ISAROB 2009

Lagrange formulation as

$$M(q)\ddot{q} + V(q,\dot{q})\dot{q} + G(q) = B(q)\tau - A^T(q)\lambda \quad (2)$$

where $q \in \mathbb{R}^n$ is generalized coordinates, $\tau \in \mathbb{R}^r$ is a control input vector, $\lambda \in \mathbb{R}^m$ is a vector of constraint forces, $M(q) \in \mathbb{R}^{n\times n}$ is a symmetric, positive definite inertia matrix, $V(q,\dot{q}) \in \mathbb{R}^{n\times n}$ is the centripetal and coriolis matrix, $G(q) \in \mathbb{R}^n$ is the gravitational vector, $B(q) \in \mathbb{R}^{n\times r}$ is an input transformation matrix, and $A(q) \in \mathbb{R}^{m\times n}$ is a matrix related with nonholonomic constraints.

Using $A(q)\dot{q} = 0$ and $A(q)J(q) = 0$ obtained by the nonholonomic constraints, an r-dimensional vector z exists such that $\dot{q} = J(q)z$ where $J(q) \in \mathbb{R}^{n\times r}$ consists of linearly independent vectors in the null space of $A(q)$.

Substituting the equation $\dot{q} = J(q)z$ into (2) yields

$$H(q)\dot{z} + F(q,z) = \tau \quad (3)$$

where $H(q) = (J^T(q)B(q))^{-1}J^T(q)M(q)J(q)$ and $F(q,z) = (J^T(q)B(q))^{-1}J^T(q)(M(q)\dot{J}(q) + V(q,\dot{q})J(q))z$. If the bounded disturbance τ_d exists in the mobile robot, the actual dynamic equation of the mobile robot can be rewritten as

$$H(q)\dot{z} + F(q,z) + \tau_d = \tau \quad (4)$$

where $\tau_d = H(q)f$, $f = [f_1 \quad f_2]^T$, $|f_i| \le f_{mi}$, $i = 1,2$, and $\tau = [\tau_l \quad \tau_r]^T$ is a torque vector applied to the left and right driving wheels.

Property 1 *The matrix $H(q)$ is bounded and invertible.*

2.2 Formation Model Based on the Leader-Following Approach

To design the sliding mode formation controller, we use the leader-following model. For the follower, we consider a virtual follower R_h which locates a distance D_f from the center of the follower R_f, where $D_f = \rho^d \cos\varphi^d$, ρ^d is a desired distance, and φ^d is a desired angle. The virtual follower R_h is defined as follows [7]:

$$\begin{aligned} x_h &= x_f + D_f \cos\theta_f \\ y_h &= y_f + D_f \sin\theta_f \\ \theta_h &= \theta_f \end{aligned} \quad (5)$$

where (x_f, y_f, θ_f) denotes the position and the orientation of the follower. Then, on the basis of (1), the derivative of (5) is calculated as

$$\begin{bmatrix}\dot{x}_h\\ \dot{y}_h\\ \dot{\theta}_h\end{bmatrix} = \begin{bmatrix}\cos\theta_f & -D_f\sin\theta_f\\ \sin\theta_f & D_f\cos\theta_f\\ 0 & 1\end{bmatrix}\begin{bmatrix}v_f\\ \omega_f\end{bmatrix} \quad (6)$$

where v_f and ω_f are the linear and angular velocities of the follower.

We also assume that there exists a virtual leader R_v, which locates a distance D_l from the center of the leader R_l, where $D_l = \rho^d \sin\varphi^d$. The virtual leader R_v is defined as follows:

$$\begin{aligned} x_v &= x_l + D_l\cos(\theta_l - \frac{\pi}{2}) = x_l + D_l\sin\theta_l \\ y_v &= y_l + D_l\sin(\theta_l - \frac{\pi}{2}) = y_l - D_l\cos\theta_l \\ \theta_v &= \theta_l \end{aligned} \quad (7)$$

where (x_l, y_l, θ_l) denotes the position and the orientation of the leader. The derivative of (7) can be obtained as

$$\begin{bmatrix}\dot{x}_v\\ \dot{y}_v\\ \dot{\theta}_v\end{bmatrix} = \begin{bmatrix}\cos\theta_l & D_l\cos\theta_l\\ \sin\theta_l & D_l\sin\theta_l\\ 0 & 1\end{bmatrix}\begin{bmatrix}v_l\\ \omega_l\end{bmatrix} \quad (8)$$

where v_l and ω_l are the linear and angular velocities of the leader.

Assumption 1 *The linear velocity v_l of the leader is not zero.*

3 Main Results

The objective of the formation control problem is to keep a relative pose (ρ^d, φ^d) between the leader and the follower. For this, we use the virtual follower R_h and the virtual leader R_v. That is, our control objective is to steer the virtual follower R_h so as to track the virtual leader R_v. If the virtual follower can track the virtual leader exactly, then the follower can maintain the relative pose (ρ^d, φ^d) with respect to its leader.

The tracking errors between R_h and R_v are chosen as

$$x_e = x_h - x_v, \quad y_e = y_h - y_v, \quad \theta_e = \theta_h - \theta_v \quad (9)$$

To guarantee the convergence of (9), we define the following variables as

$$s_x = \dot{x}_e + k_1 x_e, \quad s_y = \dot{y}_e + k_2 y_e, \quad s_\theta = \dot{\theta}_e + k_3\theta_e \quad (10)$$

where k_i is a positive constant, $i = 1,2,3$.

Redefine (6) and (8) as follows:

$$M_1(\theta_h, D_f)\dot{R}_h = z \quad (11)$$

$$M_2(\theta_v, D_l)\dot{R}_v = z_l \quad (12)$$

©ISAROB 2009

Table 1: Initial positions for four mobile robots

	$[x(0),\ y(0),\ \theta(0)]$
Leader	[0, 0, 0]
Follower 1	[0, -0.5, 0]
Follower 2	[1, 0.5, 0]

where

$$M_1(\theta_h, D_f) = \begin{bmatrix} \cos\theta_h & \sin\theta_h & 0 \\ -\alpha\sin\theta_h & \alpha\cos\theta_h & 1-\alpha D_f \end{bmatrix},$$
$$M_2(\theta_v, D_l) = \begin{bmatrix} \cos\theta_v & \sin\theta_v & -D_l \\ 0 & 0 & 1 \end{bmatrix},$$
$$z = [v_f\ \omega_f]^T,\ z_l = [v_l\ \omega_l]^T,\ \alpha = \tanh(v_l/\kappa_1). \tag{13}$$

Here, κ_1 is a positive constant. Based on (13), we propose the sliding surface S as follows:

$$S = M_1(\theta_h, D_f) \times \begin{bmatrix} s_x + (1-\alpha D_f)\sin\theta_h s_\theta \\ s_y - (1-\alpha D_f)\cos\theta_h s_\theta + \tanh(y_e s_\theta)s_\theta \\ \alpha s_\theta \end{bmatrix} \tag{14}$$

where $S = [s_1 \quad s_2]^T$.

By using the computed-torque method, we can choose the torque control input as follows:

$$\tau = H(q)\dot{z}_l + F(q,z) + H(q)u \tag{15}$$

where $u = [u_1 \quad u_2]^T$ is a control law. Substituting (15) into (4), we have

$$\dot{z} + f = \dot{z}_l + u. \tag{16}$$

In this paper, we propose the control law u as follows:

$$u = \Upsilon(R_h, R_v) - LS - P\mathrm{sgn}(S) \tag{17}$$

where $L = \mathrm{diag}[l_1, l_2] > 0$, $P = \mathrm{diag}[p_1, p_2] > 0$, and $\mathrm{sgn}(S) = [\mathrm{sgn}(s_1), \mathrm{sgn}(s_2)]^T$. $\Upsilon(R_h, R_v)$ is represented as follows:

$$\begin{aligned}\Upsilon(R_h, R_v) =& \\ &\dot{M}_1(\theta_h, D_f)\begin{bmatrix} -k_1x_e + \dot{x}_v \\ -k_2y_e + \dot{y}_v \\ \dot{\theta}_e - \alpha s_\theta + \dot{\theta}_v \end{bmatrix} \\ &+ M_1(\theta_h, D_f)\begin{bmatrix} -k_1\dot{x}_e + \ddot{x}_v \\ -k_2\dot{y}_e + \ddot{y}_v \\ \ddot{\theta}_e - \dot{\alpha}s_\theta - \alpha\dot{s}_\theta + \ddot{\theta}_v \end{bmatrix} \\ &- \dot{M}_2(\theta_v, D_l)\begin{bmatrix} \dot{x}_v \\ \dot{y}_v \\ \dot{\theta}_v \end{bmatrix} - M_2(\theta_v, D_l)\begin{bmatrix} \ddot{x}_v \\ \ddot{y}_v \\ \ddot{\theta}_v \end{bmatrix} \\ &- \begin{bmatrix} \frac{d}{dt}\{\sin\theta_h\tanh(y_e s_\theta)s_\theta\} \\ \frac{d}{dt}\{-\alpha(1-\alpha D_f)s_\theta + \alpha\cos\theta_h\tanh(y_e s_\theta)s_\theta\} \end{bmatrix}.\end{aligned} \tag{18}$$

Theorem 1 *Consider the dynamic model* (4) *of the mobile robot with disturbances controlled by the proposed control law* (17). *Under Property 1 and Assumption 1, the control law* (17) *stabilizes the sliding surface S. Then, x_e, y_e, and θ_e converge to zero.*

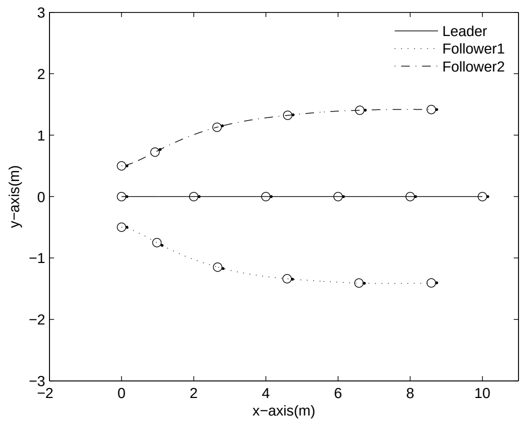

Figure 1: Trajectories of the leader and two followers for the straight line path case.

4 Simulation Results

In this section, we demonstrate the effectiveness of the proposed controller. Design parameters for the proposed controller are chosen as $k_1 = k_2 = 1$, $k_3 = 0.002$, $l_1 = l_2 = 0.5$, $\kappa_1 = 0.01$, and $p_1 = p_2 = 1$. The external disturbances are chosen to be normally distributed random noises with the upper bounds

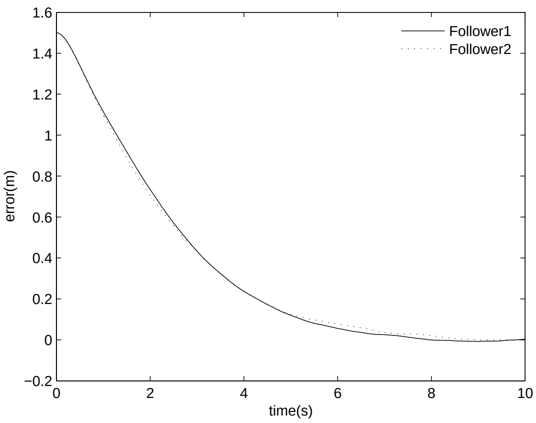

(a)

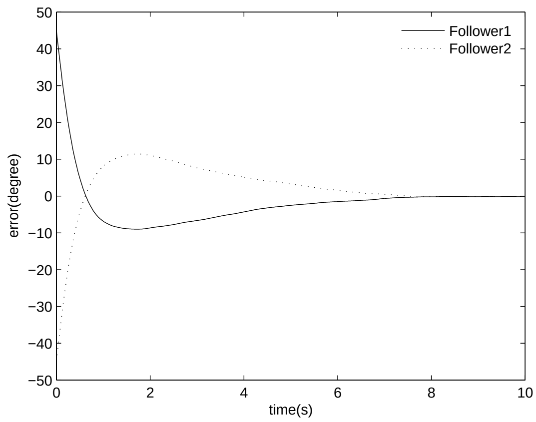

(b)

Figure 2: Tracking errors (a) $\rho_d - \rho$ (b) $\varphi_d - \varphi$

$f_{m1} = f_{m2} = 0.5$. To simulate the formation control, we assume that there exist three mobile robots. The initial positions for three mobile robots are presented in Table I. The leader is moving on a straight line with velocities [v_l, ω_l]=[1 m/s, 0 rad/s]. The desired relative poses of followers with respect to leader are $\rho^d_{1,2} = 2\ m$, $\varphi^d_1 = \pi/4\ rad$, and $\varphi^d_2 = -\pi/4\ rad$. Figs. 1 and 2 show the trajectories of the leader and followers and tracking errors, respectively.

5 Conclusions

In this paper, a new sliding mode formation controller for nonholonomic wheeled mobile robots with external disturbances has been proposed. The kinematic model based on the leader-following approach has been considered. The dynamic model has also been considered to obtain the control law at the torque level. The system stability and the convergence of tracking errors have been proven using Lyapunov stability theory.

Acknowledgements

This work was supported in part by Yonsei University Institute of TMS Information Technology, a Brain Korea 21 program.

References

[1] O. A. A. Orqueda, X. T. Zhang, and R. Fierro, "An output feedback nonlinear decentralized controller for unmanned vehicle coordination", *Int. J. Robust Nonlinear Control*, vol. 17, pp. 1106-1128, 2007.

[2] T. Balch, and R. C. Arkin, "Behavior-based formation control for multirobot teams", *IEEE Trans. Robot. Automat.*, vol. 14, pp. 926-939, Dec. 1998.

[3] K. D. Do, and J. Pan, "Nonlinear formation control of unicycle-type mobile robots", *Robot. Auton. Syst.*, vol. 55, pp. 191-204, 2007.

[4] J. P. Desai, J. Ostrowski, and V. Kumar, "Modeling and control of formations of nonholonomic mobile robots", *IEEE Trans. Robot. Automat.*, vol. 17, pp. 905-908, Dec. 2001.

[5] J. P. Desai, J. P. Ostrowski, and V. Kumar, "Controlling formations of multiple mobile robots", in *Proc. 1998 IEEE Int. Conf. Robotics and Automation*, Leuven, Belgium, May 1998, pp. 2864-2869.

[6] X. Li, J. Xiao, and Z. Cai, "Backstepping based multiple mobile robots formation control", in *Proc. IEEE Int. Conf. Intelligent Robots and Systems*, 2005, pp. 887-892.

[7] J. Shao, G. Xie, and L. Wang, "Leader-following formation control of multiple mobile vehicles", *IET Control Theory Appl.*, vol. 1, pp. 545-552, 2007.

[8] T. Fukao, H. Nakagawa, and N. Adachi, "Adaptive tracking control of a nonholonomic mobile robot", *IEEE Trans. Robot. Automat.*, vol. 16, pp. 609-615, Oct. 2000.

[9] J. Sanchez, and R. Fierro, "Sliding mode control for robot formations", in *Proc. IEEE Int. Symposium on Intelligent Control*, Houston, Texas, Oct. 2003, pp. 438-443.

©ISAROB 2009

Grasping Control of Thumb-Index Finger Model: Lyapunov Stability Approach

S. K. Song and J. B. Park
Dept. of Electrical and Electronic Engineering
Yonsei University
Seoul, 120-749

Y. H. Choi
School of Electronic Engineering
Kyonggi University
Suwon, 443-760

Abstract

This paper is concerned with the dynamics and control of grasping and regulating motion generated by a thumb index finger robot. Thumb index finger model is the optimized model to manipulate an object without joint redundancy. To manipulate an object, the overall motion of the finger needs to be restricted by the object states. Therefore, we derive the kinematics of model governed by the object states by using four constraints which are based on the nonslipping assumption between the rigid fingertips and the surface of an object. Then, the control input is derived via Lyapunov stability analysis including the dynamics of the overall system. Further, we propose a solution of the contact forces between the fingertips and an object via physical analysis, which can not be solved mathematically. Finally, computer simulations are presented to verify the effectiveness of the proposed concept and method.

1 Introduction

Since the beginning of robotics research, the fingered hand robots have been designed to mimic human hand which has the capability of dexterous manipulations and elaborate operations. In the history of development of the fingered hand robots, various hand models with four or five fingers with two or three joints were reported [1]-[3]. They are so far used only in the open-loop control system which do not consider the relationship between the fingers and an object, because there is no way to estimate the forces between them.

In order to overcome the disadvantages of open-loop control system, Arimoto *et al.* [4]-[5] suggested a pair of robot fingers with hemispherical finger-ends using sensory motor coordination. The basic theory of this work is the passivity. The passivity means that the energy variation of the overall system, which is composed of the fingers and an object is caused by the torque generated from a joint motor. In this paper, we employ the thumb-index model which is optimized to manipulate an object such as shifting, rotating and changing contact position without joint redundancy. By the kinematic constraints of the posture of the object, The overall joint angles are dependent. Adding the dynamics of the finger model based on this properties, the control input can be calculated. The control input, however, compared to previous approach which is based on passivity, should accompany with calculating the contact force between the fingertips and an object. We propose a contact forces based on physical insight, which are impossible to be calculated mathematically. Using the kinematics and dynamics of the overall system and the contact forces, the control input is finally determined via Lyapunov stability analysis.

This paper is organized as follows. In Section II, a set of dynamics and kinematics of the fingers and an object is derived on the basis of Hamilton's principle. In Section III, the method for designing the control input is proposed and the contact forces are derived via physical analysis. Simulation results are presented to verify the effectiveness of the proposed method in Section IV.

2 Dynamics and Kinematics of Thumb Index Model

2.1 Dynamics

For the sake of physical simplicity, we assume that a 3-joint dual finger robot shown in Fig. 1 moves on a horizontal plane to ignore the gravitational force. Further, we only deal with a solid rectangular object with hard spherical fingertips.

Applying Hamilton's principle to the following

©ISAROB 2009

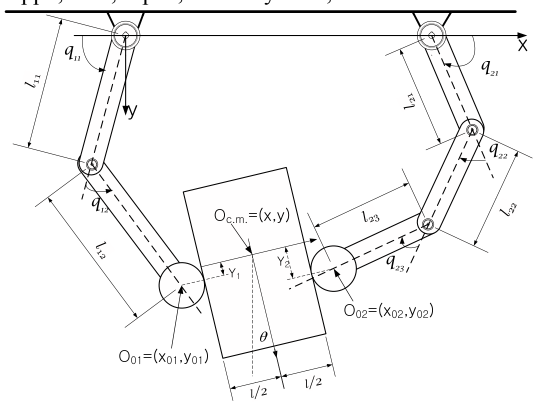

Figure 1: Thumb index finger robot system

equation,

$$\int_{t_0}^{t_1} \{\delta(K+Q+R) + u_1\delta q_1 + u_2\delta q_2\}\, dt = 0$$

we can obtain the dynamics of the fingers and an object described as follows:

$$H_i\ddot{\mathbf{q}}_i + \Gamma_i\dot{\mathbf{q}}_i + (-1)^i J_{0i}^T \begin{bmatrix} -\cos\theta \\ \sin\theta \end{bmatrix} f_i - \left\{ J_{0i}^T \begin{bmatrix} \sin\theta \\ \cos\theta \end{bmatrix} - r_i \begin{bmatrix} 1 & 1 & 1 \end{bmatrix}^T \right\}\lambda_i = u_i, \quad i = 1,2 \tag{1}$$

$$\begin{aligned} M\ddot{x} &= (f_1 - f_2)\cos\theta - (\lambda_1+\lambda_2)\sin\theta, \\ M\ddot{y} &= -(f_1 - f_2)\sin\theta - (\lambda_1+\lambda_2)\cos\theta, \\ I\ddot{\theta} &= f_1Y_1 - f_2Y_2 - \frac{l}{2}(\lambda_1 - \lambda_2), \end{aligned} \tag{2}$$

where Γ_1 and Γ_2 stand for the coefficient of $\dot{\mathbf{q}}_i$ including coriolis, centrifugal forces and differential functions of inertia moment. M and I are the mass and the inertia moment of an object, respectively. Further, f_i and λ_i stand for the normal and tangential contact forces, which are exerted on an object for secure grasp and dexterous movements, respectively.

2.2 Kinematics

The transformed equations from kinematic constraints are represented as follows:

$$l_{12}\cos\phi_{12} + l_{11}\cos\phi_{11} = -x + (\frac{l}{2} + r_1)\cos\theta - Y_1\sin\theta, \tag{3}$$

$$l_{12}\sin\phi_{12} + l_{11}\sin\phi_{11} = y + (\frac{l}{2} + r_1)\sin\theta + Y_1\cos\theta, \tag{4}$$

$$\phi_{12} = \frac{Y_1 - Y_1(0)}{r_1} + \theta, \tag{5}$$

$$l_{23}\cos\phi_{23} + l_{22}\cos\phi_{22} + l_{21}\cos\phi_{21} = x + (\frac{l}{2} + r_2)\cos\theta + Y_2\sin\theta - L, \tag{6}$$

$$l_{23}\sin\phi_{23} + l_{22}\sin\phi_{22} + l_{21}\sin\phi_{21} = y - (\frac{l}{2} + r_2)\sin\theta + Y_2\cos\theta, \tag{7}$$

$$\phi_{23} = \frac{Y_2 - Y_2(0)}{r_2} - \theta, \tag{8}$$

where,

$$\begin{aligned} \phi_{i1} &= q_{i1}, \\ \phi_{i2} &= q_{i2} + q_{i3}, \\ \phi_{i3} &= q_{i1} + q_{i2} + q_{i3}, \quad i = 1,2. \end{aligned}$$

Numerically, we can find a solution of $\mathbf{q}_1$ and $\mathbf{q}_2$ by solving a set of nonlinear equations as from (3) to (8). However, we need the differential forms to derive the control input of the overall dynamic system. The differential form of the kinematics of the fingers can be derived as follow:

$$A_i\ddot{\Phi}_i = B_i\ddot{\mathbf{z}} + C_i\dot{\Phi}_i + D_i \quad i = 1,2, \tag{9}$$

where,

$$\Phi_i = \begin{bmatrix} \phi_{i1} & \phi_{i2} & \phi_{i3} \end{bmatrix}^T, \qquad \mathbf{z} = \begin{bmatrix} \mathbf{x}^T & \mathbf{y}^T \end{bmatrix}^T,$$

$$A_1 = \begin{bmatrix} l_{11}\cos\phi_{11} & l_{12}\cos\phi_{12} - r_1\cos\theta \\ l_{11}\sin\phi_{11} & l_{12}\sin\phi_{12} - r_1\sin\theta \end{bmatrix},$$

$$A_2 = \begin{bmatrix} l_{i1}\cos\phi_{21} & l_{22}\cos\phi_{22} & l_{23}\cos\phi_{23} \\ l_{21}\sin\phi_{21} & l_{22}\sin\phi_{22} & l_{23}\sin\phi_{23} \\ 0 & 0 & r_2 \end{bmatrix},$$

$$B_1 = \begin{bmatrix} 0 & 1 & \left(\frac{l}{2} + r_1\right)\cos\theta - Y_1\sin\theta & \cos\theta & 0 \\ 1 & 0 & \left(\frac{l}{2} + r_1\right)\sin\theta - Y_1\cos\theta & \sin\theta & 0 \end{bmatrix},$$

$$B_2 = \begin{bmatrix} 0 & 1 & -\left(\frac{l}{2} + r_2\right)\cos\theta - Y_2\sin\theta & 0 & \cos\theta \\ -1 & 0 & \left(\frac{l}{2} + r_2\right)\sin\theta - Y_2\cos\theta & 0 & -\sin\theta \\ 0 & 0 & -r_2 & 0 & 1 \end{bmatrix},$$

$$C_1 = \begin{bmatrix} l_{11}\sin\phi_{11}\ \dot{\phi}_{11} & l_{12}\sin\phi_{12}\dot{\phi}_{12} \\ -l_{11}\cos\phi_{11}\ \dot{\phi}_{11} & -l_{12}\cos\phi_{12}\dot{\phi}_{12} \end{bmatrix},$$

©ISAROB 2009

$$C_2 = \begin{bmatrix} l_{21}\sin\phi_{21}\dot{\phi}_{21} & l_{22}\sin\phi_{22}\dot{\phi}_{22} & l_{23}\sin\phi_{23}\dot{\phi}_{23} \\ -l_{21}\cos\phi_{21}\dot{\phi}_{21} & -l_{22}\cos\phi_{22}\dot{\phi}_{22} & -l_{23}\cos\phi_{23}\dot{\phi}_{23} \\ 0 & 0 & 0 \end{bmatrix},$$

$$D_i = \begin{bmatrix} -2\dot{Y}_i\sin\theta\dot{\theta} - \dot{\theta}^2\Big(\big(\frac{l}{2}+r_i\big)\sin\theta + Y_i\cos\theta\Big) \\ 2\dot{Y}_i\cos\theta\dot{\theta} + \dot{\theta}^2\Big(\big(\frac{l}{2}+r_i\big)\cos\theta + (-1)^i Y_i\sin\theta\Big) \\ 0 \end{bmatrix}.$$

3 Design of Control Input

3.1 Control Input

The control input should consist of the states of an object because the objective of control is to manipulate an object using the dynamics of fingers.

Substituting (9) into (1), we can obtain

$$H_iT^{-1}A_i^{-1}B_i\ddot{\mathbf{z}} + H_iT^{-1}A_i^{-1}(C_iT\dot{q}_i + D_i) + \Gamma_i\dot{q}_i + (-1)^iJ_{0i}^T\begin{bmatrix}-\cos\theta\\ \sin\theta\end{bmatrix}f_i - \left\{J_{0i}^T\begin{bmatrix}\sin\theta\\ \cos\theta\end{bmatrix} - r_i\begin{bmatrix}1 & 1 & 1\end{bmatrix}^T\right\}\lambda_i = u_i, \qquad i=1,2. \tag{10}$$

For regulating the posture and position of an object, the states $\mathbf{z}$ should be guaranteed to converge to the desired states $\mathbf{z_d}$.

Theorem 1 *Assume that the control input is formulated as follows:*

$$\begin{aligned} u_i =& \Gamma_i\dot{q}_i + (-1)^iJ_{0i}^T\begin{bmatrix}-\cos\theta\\ \sin\theta\end{bmatrix}f_i \\ &- \left\{J_{0i}^T\begin{bmatrix}\sin\theta\\ \cos\theta\end{bmatrix} - r_i\begin{bmatrix}1 & 1 & 1\end{bmatrix}^T\right\}\lambda_i \\ &+ H_iT^{-1}A_i^{-1} \\ &\times\Big[C_iT\dot{q}_i + D_i - B_i\{(P_{\mathbf{z}}+1)\dot{\mathbf{z}} + P_{\mathbf{z}}(\mathbf{z}-\mathbf{z}_d)\}\Big], \end{aligned} \tag{11}$$

where, $P_{\mathbf{z}} = diag[P_x, P_y, P_\theta, P_{Y_1}, P_{Y_2}]$, and P_x, P_y, P_θ, P_{Y_1}, P_{Y_2} are strictly positive constant. Then, the states $\mathbf{z}$ are guaranteed to converge to the desired states $\mathbf{z_d}$.

3.2 Contact Forces

We have designed the control input u_i for $i = 1, 2$. However, the control input u_i is imperfect to control the overall system because of the lack of information about the normal and tangential contact forces such as f_1, f_2, λ_1, and λ_2. Before obtaining the contact forces, defining of $\ddot{\mathbf{x}}$ should be preceded so as to obtain those from (2). It is also necessary to define Y_1 and Y_2.

We need to redefine the Lyapunov candidate function to define the state space of $\mathbf{z}$.

Theorem 2 *If the state equation of $\mathbf{z}$ is formulated as follows:*

$$\ddot{\mathbf{z}} = -(P_{\mathbf{z}} + I)\dot{\mathbf{z}} - P_{\mathbf{z}}(\mathbf{z}-\mathbf{z}_d), \tag{12}$$

Then, these states are asymptotic stable.

Even though we have calculated (12) and we still should find one more condition to get the contact forces from (2), because (2) is not enough to obtain the contact forces. We can find this condition from the physical meaning of an object motion. To grasp an object securely, the desired normal force f_d should be exerted continuously. Only the additional force $\Delta f = M \times (\ddot{x}\cos\theta - \ddot{y}\sin\theta)$ is added to accelerate and decelerate an object.

With the condition in Table I and (12), finally we can calculate the contact forces from (2) as follows:

$$f_1 = f_d + \frac{1}{2}\big\{\Delta f + \Delta f sgn(\Delta f)\big\}, \tag{13}$$

$$f_2 = f_d + \frac{1}{2}\big\{-\Delta f + \Delta f sgn(\Delta f)\big\}, \tag{14}$$

$$\lambda_1 = \Lambda_1\ddot{\mathbf{x}} + \frac{f_d}{l}(Y_1 - Y_2), \tag{15}$$

$$\lambda_2 = \Lambda_2\ddot{\mathbf{x}} - \frac{f_d}{l}(Y_1 - Y_2), \tag{16}$$

where,

$$\Lambda_1 = \begin{bmatrix} \frac{M}{l}\Big(\frac{Y_1+Y_2}{2} + \frac{Y_1-Y_2}{2}\mathbf{sgn}(\Delta f)\Big)\cos\theta - \frac{M}{2}\sin\theta \\ -\frac{M}{l}\Big(\frac{Y_1+Y_2}{2} + \frac{Y_1-Y_2}{2}\mathbf{sgn}(\Delta f)\Big)\sin\theta - \frac{M}{2}\cos\theta \\ -\frac{I}{l} \end{bmatrix}^T,$$

$$\Lambda_2 = \begin{bmatrix} -\frac{M}{l}\Big(\frac{Y_1+Y_2}{2} + \frac{Y_1-Y_2}{2}\mathbf{sgn}(\Delta f)\Big)\cos\theta - \frac{M}{2}\sin\theta \\ \frac{M}{l}\Big(\frac{Y_1+Y_2}{2} + \frac{Y_1-Y_2}{2}\mathbf{sgn}(\Delta f)\Big)\sin\theta - \frac{M}{2}\cos\theta \\ \frac{I}{l} \end{bmatrix}^T,$$

Table 1: normal contact forces

Condition	$\ddot{x}\cos\theta - \ddot{y}\sin\theta > 0$	$\ddot{x}\cos\theta - \ddot{y}\sin\theta < 0$
Normal Forces	$f_1 = f_d + \Delta f$ $f_1 = f_d$	$f_2 = f_d$ $f_2 = f_d - \Delta f$

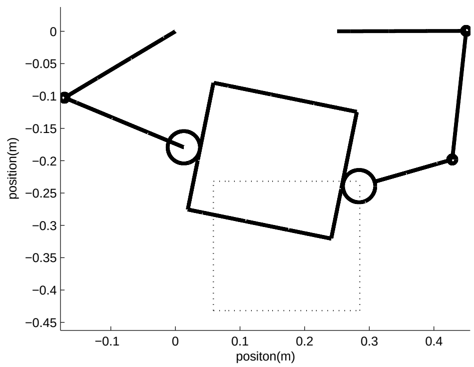

Figure 2: Final posture

Substituting (13) to (16) into (11), The overall system can be controlled by the control inputs $\mathbf{x_d}$, $\mathbf{Y}_d$ and f_d as shown in Fig. 2.

4 SIMULATION RESULTS

We carry out computer simulations in Matlab. From Fig. 2, we can confirm that the proposed control system performs secure grasp and manipulation such as shifting and changing the contact position simultaneously. From the result of Fig. 3, we can confirm that the normal contact forces f_1 and f_2, which accelerates and decelerates an object, respectively, are induced in order and converge to the desired force f_d eventually within a second. We can also confirm that the tangential contact forces λ_1 and λ_2 are induced to shift an object toward y-axis direction and eventually converge to zero. Thus, the simulation results reconfirm the effectiveness of the proposed control method.

5 Conclusion

This paper dealt with a thumb-index finger robot for grasping and regulating the posture and position of an object. We derived and analyzed the dynamics of a setup of the model with spherical fingertips pinching a rigid object. In order to calculate the kinematics of fingers, we used four geometric constraint based on the assumption of nonslipping condition between the fingertips and an object. To design the control input, we proposed the contact forces for manipulating an object, which were derived via physical insight. The computer simulation results verified the effectiveness of our proposed method.

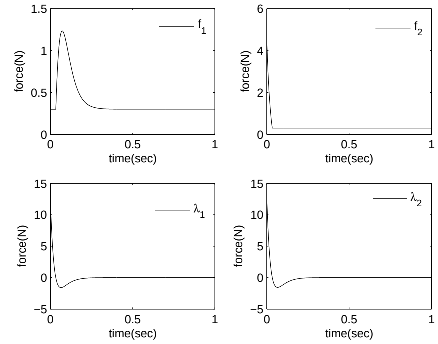

Figure 3: Normal and tangential contact forces by fingertips

Acknowledgements

This study was supported by the Brain Korea 21 Project in 2008.

This work was supported by Manpower Development Program for Energy & Resources of MKE with Yonsei Electric Power Research Center (YEPRC) at Yonsei University, Seoul, Korea.

References

[1] K. B. Shimoga, "Robot grasp synthesis algorithms: a survey", *Int. J. of Robotics System,* vol. 13, no. 3, 1996, pp. 230-266.

[2] A. M. Okamura, N. Smaby and M. R. Cutkosky, "An overview of dexterous manipulation", *in Proc. of 2000 IEEE Int. Conf. on Robotics and Automation,* San Francisco, CA, vol. 1, 2000, pp. 255-262.

[3] A. Bicchi, "Hand for dexterous manipulation and robust grasping: a difficult road toward simplicity", *IEEE Trans. on Robotics and Automation,* vol. 16, no. 6, 2000, pp. 652-662.

[4] S. Arimoto, K. Tahara, J. H. Bae, M. Yoshida, "A stability theory on a manifold: concurrent realization of grasp and orientation control of an object by a pair of robot fingers", *Robotica,* vol. 21, no. 2, 2003, pp. 163-178.

[5] S. Arimoto, M. Yoshida, J. H. Bae, K. Tahara, "Dynamic force/torque closure of 2D polygonal objects by a pair of rolling contacts and sensory-motor coordination", *Int. J. of Robotics System,* vol. 20, no. 9, 2003, pp. 517-537.

©ISAROB 2009

Intelligent Diagnosis System for Transmission Line: Fuzzy-Bayesian Classifier Approach

Hwa Chang Sung[1], Jin Bae Park[1], and Young Hoon Joo[2]

[1]Department of Electrical and Electronic Engineering, Yonsei University, Seoul, Korea
(Tel : 81-97-554-7831; Fax : 81-97-554-7841)
({casfirsper, jbpark}@yonsei.ac.kr)
[2]School of Electronic and Information Engineering, Kunsan National University, Kunsan, Korea
(Tel : 81-97-554-7831; Fax : 81-97-554-7841)
(yhjoo@kunsan.ac.kr)

Abstract: We develop an intelligent diagnosis system which is based on fuzzy-classifier. The term of intelligent diagnosis system (IDS) is a real-time fault monitoring system for transmission line. Based on the Time-Frequency Domain Reflectometry (TFDR) algorithm, we implement the wire detecting system which shows the condition of the wires. The concrete processes are represented as follows: 1) the reflected signals which are sent from the fault of wires are obtained and saved in main server; 2) IDS classifies the fault type of the wires into damage and normal. For classifying the fault type efficiently, we use the fuzzy-Bayesian classifier which is merged the IF-THEN rules with Bayesian algorithms. Simulation results convincingly validate the effectiveness of our algorithms.

Keywords: Intelligent diagnosis system (IDS), fuzzy-Bayesian classifier, time-frequency domain reflectometry (TFDR).

I. INTRODUCTION

Detecting fault for transmission lines is very important because the main origins of electric accidents are faults of wires. In [1], the importance of aging electrical wiring and associated faults in aircraft has been highlighted. Generally, there become known to three kinds of the fault detection algorithm – time domain reflectometry (TDR), frequency domain reflectometry (FDR) and time-frequency domain reflectometry (TFDR). However, the resolution and accuracy of the TDR and FDR are limited by the rise/fall time and frequency sweep bandwidth, respectively.

In order to supplement the weak points of TDR and FDR, Shin *et. al.* propose a new high-resolution reflectometry technique that operates simultaneously in both the time and frequency domains [1]. The TFDR algorithms have shown better accuracy in fault localization than the TDR in the same experimental conditions. However, each fault detecting experiment has performed respectively so that it is hard to recognize the fault types of real-used wires. In other words, it is necessary to group the each type of faults for electric wires.

The conventional classifiers are needed for the classification of the highly complex real data such as the sensory data and the signal data. Among the many classifiers, a fuzzy classifier which is to translate domain expert's knowledge in a linguistic form into discriminant function is very popular because of its usefulness [2-5]. However, fuzzy methods are cumbersome to use in high dimensions problems. For solving that, some researchers attempted to merge the fuzzy classifier and others, especially statistical ones, and improve the capability of the pattern classification problem [7], [9-11]. Among them, Bayesian decision theory is a fundamental statistical technique. The main idea of the Bayes classifier is to capture all information about class membership available from the set of conditional probability densities. Reference [2] introduces the new fuzzy rule-based classifier equipped with a Bayes rule consequent which is known as fuzzy-bayesian classifier.

Generally, the result of the detecting signals which are sent from the faults of transmission lines is represented as highly nonlinear appearance. For classifying these complex signals, we propose an intelligent diagnosis system (IDS) [8]. When unknown faults are detected by TFDR algorithm, we are able to recognize the kinds of faults through the IDS. For classifying the faults efficiently, we use the fuzzy-Bayesian classifier which is represented as IF-THEN rule. Finally, to show the feasibility of the proposed algorithm, computer simulations are provided.

This paper is organized as follows: Section 2 fuzzy-Bayesian algorithms are developed. In Section 3, we formulate the IDS. An example is shown in Section 4. This paper concludes with Section 5

II. Fuzzy-Bayesian Classifier

2. 1 Fuzzy Classifier

Generally, the fuzzy rule-based classifier is

©ISAROB 2009

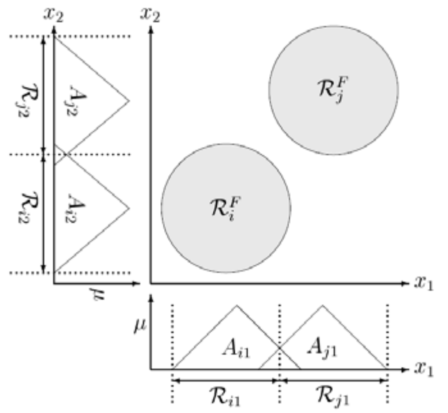

Fig. 1. The decision regions R_1 and R_2 of the fuzzy classifier

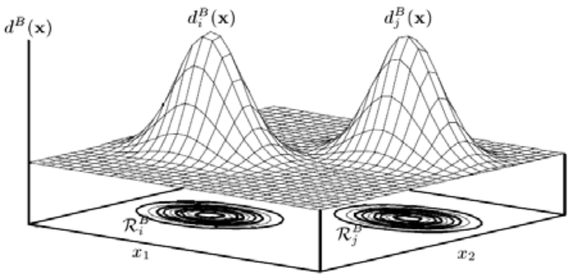

Fig. 2. The decision regions R_1 and R_2 of the Bayesian classifier

represented as following form:

$$R_i : \text{If } x_1(t) \text{ is } A_{i1} \text{ and} \ldots \text{and } x_n(t) \text{ is } A_{in} \quad \text{the class is } i, \tag{1}$$

where R_i is the i th fuzzy rule, x_j is the j th feature variable, and A_{ij} is the fuzzy set. The output of (1) is obtained as

$$Y(x(t)) = \frac{\sum_{i=1}^{p} h_i(x(t)) y_i}{\sum_{i=1}^{p} h_i(x(t))} \tag{2}$$

where $h_i(x(t)) = \prod_{j=1}^{m} \mu_{M_{ij}}(x_j)$, $\mu_{M_{ij}} \in [0, 1]$. The conjunction rule to transform the fuzzy sets into a discriminant function is

$$w_i = \mu_{A_{i1}} \times \cdots \times \mu_{A_{in}} \tag{3}$$

where w_i perform to divide the feature space R^n into the decision regions $R_1, \ldots, R_m$. Therefore, the fuzzy classifier is to assign a feature variable vector x to class C_{i1} , if

$$w_{i_1} > w_{i_2}, \quad \forall i_2 \neq i_1, \quad i_2 \in I_m \tag{4}$$

Fig. 2 shows the decision regions of the fuzzy classifier.

2.2 Bayesian Classifier

Using the prior probabilities $P(x)$ and the conditional densities $P(x \mid C_i)$, especially, the multivariate Gaussian model, the Bayesian classifier is designed by the following discriminant functions [2]:

$$d_i(x) = \frac{1}{(2\pi)^{\frac{2}{n}} \left| \Sigma_i \right|^{\frac{1}{2}}} e^{-\frac{1}{2}(x-m_i)^T \Sigma_i^{-1} (x-m_i)} P(C_i) \tag{5}$$

where x is n-component column vector, m_i is the n-component mean vector, Σ_i is the $n \times n$ covariance matrix, C_i, is the i th class, and $|\Sigma_i|$ and Σ_i^{-1} are its determinant and inverse, respectively. As shown in Fig. 3, the Bayesian classifier is said to assign a feature vector x to class C_{i_1} , if

$$d_{i_1}(x) > d_{i_2}(x), \quad \forall i_2 \neq i_1, \quad i_2 \in I_m . \tag{6}$$

2.3 Fuzzy-Bayesian Classifier

Despite of the existence of good point of previous researches, it is necessary to develop new algorithm. In spite of the many advantages, the fuzzy classifier has the following limitations: fuzzy methods are cumbersome the use in high dimensions or on complex problems or in problems with dozens of hundreds of features. Also, Bayesian classifier has the following drawbacks: it is drawback to determine and compute $P(x \mid C_i)$. Specifically, in the design of Bayesian classifiers, particularly in the design of Gaussian normal classifiers, a frequently made assumption about the normal form of $P(x \mid C_i)$ governing of patterns is not necessarily true for real data.

Motivated by above observation, we suggest a method to identify the fuzzy classifier and to effectively reduce the dimension of Bayesian classifier for implementing the intelligent diagnosis system. The concrete algorithms are represented as following three steps:

Step 1: Construct the initial fuzzy-Bayesian classifier by using the MIMO fuzzy model.
Step 2: Through the fuzzy set analysis, prune the feature variables.
Step 3: Finely tune the premise parameters for the misclassified feature vectors.

III. Intelligent Diagnosis System

IDS is the classification system which is based on the fuzzy-Bayesian classifier. Generally, it is difficult to classify the result of the detecting signals which are sent from the faults of transmission lines. See the following two TFDR results:

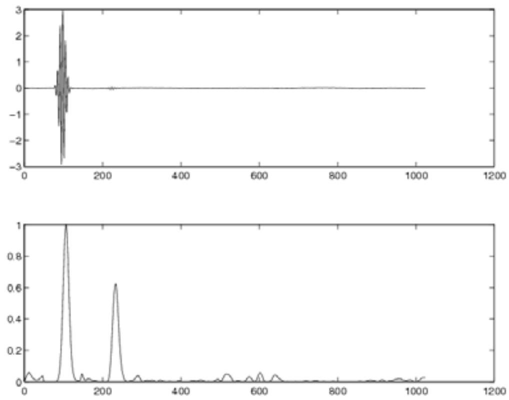

Fig. 3. TFDR result signal (normal)

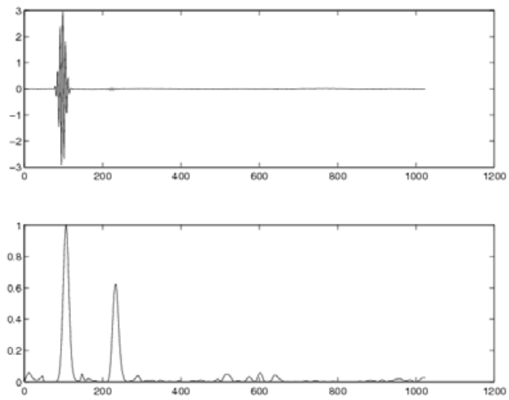

Fig. 4. TFDR result signal (fault)

Figure 3 and 4 are represented as the TFDR result signal, the one is normal condition and the other has the fault in the transmission line. As you shown these two figures, it is very difficult to classify the condition of the transmission line. In order to solve this problem, we propose the IDS which is based on the fuzzy-Bayesian classifier.

VI. Simulation Result

The purpose of the intelligent diagnosis system is to classify the condition of 220V transmission line. As shown in Fig 3 and 4, the magnitude of the reflected signal is very small so that it is too difficult to classify the each condition.

In this paper, we classify the condition of transmission line. The simulation process is represented as follows:

Cable Type: VCTF 1.5
Input Signal: linearly modulated chirp signal with a Gaussian envelope
Time Duration: 50*ns*
Frequency Bandwidth: 100 *MHz (*400*MHz* ~ 500*MHz)*
Frequency Sweep: Linearly increasing
($\beta / 2\pi = 100$ *MHZ/*50*ns*)

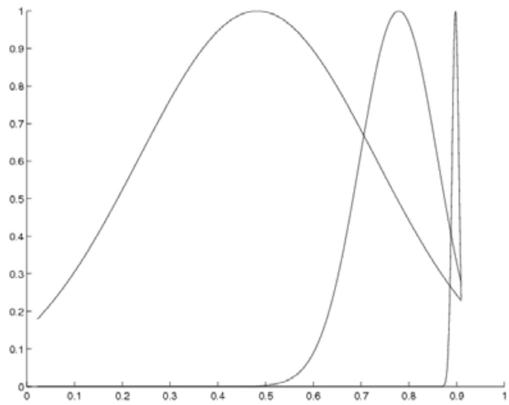

Fig. 5. Membership function of R_1

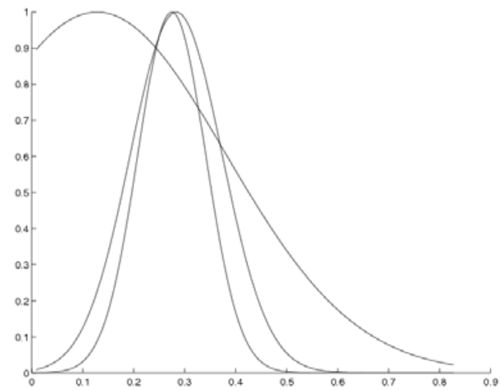

Fig. 6. Membership function of R_2

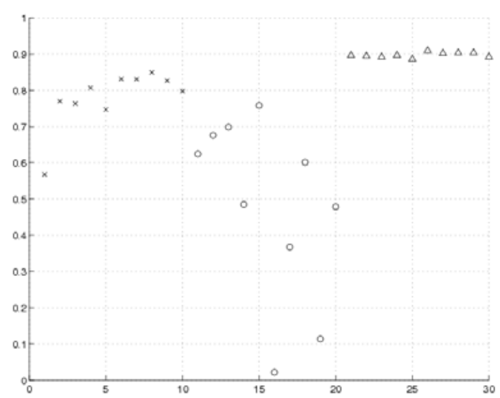

Fig. 7. The classification result

Figure 5 and 6 are the membership function of each fuzzy rule and Figure 7 represents the classification result of TFDR signal. A symbol 'x' means the normal condition, 'o' means the connected with fan, '△' means the fault of transmission line.

V. Conclusion

We have proposed IDS which is based on the fuzzy-Bayesian classifier for transmission. Based on the TFDR algorithm, the wire detecting system shows the condition of the cable and transmission line. We analyze the reflected signal which is sent from the wire detecting system and classify the fault type of the wires by using intelligent diagnosis system. For classifying the fault type efficiently, we use the fuzzy-Bayesian classifier. The simulation results for the transmission line (VCTF 1.5) are shown the excellence of the proposed algorithm.

ACKNOWLEDGMENT

This research was funded by the Korea Electrical Safety Corporation (KESCO), Project #R-2006-1-229, "Implementation of real-time fault monitoring system for transmission line."

REFERENCES

[1] Y. J. Shin, T. S. Choe, C. Y. Hong, E. S. Song, J. G. Yook, and J. B. Park, "Application of time-frequency domain reflectometry for detection and localization fault on a coaxial cable," IEEE Trans. Instrumentation and measurement, vol 54, no. 6, Dec. 2005. .
[2] M. H. Kim, J. B. Park, W. G. Kim, and Y. H. Joo, "Identification of T-S fuzzy classifier via linear matrix inequalities," LNAI 3809, pp. 1134-1137, 2005.
[3] M. Setnes, and H. Roubos "GA fuzzy modeling and classification: complexity and performance," IEEE Trans. Fuzzy Syst., vol. 8, pp. 509-522, 2000.
[4] Y. H. Joo, H. S. Hwang, K. B. Kim, and K. B. Woo, "Linguistic model identification for fuzzy system," Electron. Letter. vol. 31, pp. 330-331, 1995.
[5] T. P. Wu and S. M. Chen, "A new method for constructing membership functions and fuzzy rules from training examples," IEEE Trans. Syst., Man, Cybern. B. , vol. 29, pp. 25-40, 1999.
[6] H. Roubos and M. Setnes, "Compact transparent fuzzy models and classifiers through iterative complexity reduction," IEEE Trans. Fuzzy Syst., vol. 9, no. 4, pp. 516-524, 2001.
[7] Y. Shi, R. Eberhart, and Y. Chen, "Implementation of evolutionary fuzzy systems," IEEE Trans. Fuzzy Syst,, vol. 7, pp. 109-119, 1999.
[8] H. C. Sung, J. B. Park, and Y. H. Joo, "Implementation of intelligent diagnosis system based on fuzzy-Bayesian classifier," SCIS & ISIS 2008, pp. 570-573, 2008.

The Fourteenth International Symposium on Artificial Life and Robotics 2009 (AROB 14th '09),
B-Con Plaza, Beppu, Oita, Japan, February 5 - 7, 2009

Linear Frequency Estimator for Motor Application with Quadratic Constrained Condition

Ga Hyung Choi*, Tae Sung Yoon** and Jin Bae Park*

**Department of Electrical Engineering, Yonsei Unversity, Seoul, Korea*
(Tel : 82-2-2123-2773)
(E-mail: choigh99@yonsei.ac.kr, jbpark@yonsei.ac.kr)
***Department of Electrical Engineering, Changwon National University, Changwon, Korea*
(Tel : +82-55-213-3633)
(E-mail: tsyoon@changwon.ac.kr)

Abstract: Conventional linear prediction algorithm with sinusoidal signal for the estimation of motor's speed has a limitation in the range of low speed. If an estimator can get additional information then its performance is able to be improved. A sinusoidal signal has the natural property which is quadratic equation so called Pythagorean identity. However, since the equation was nonlinear form, it needs change to a linear constrained condition. Adding it to the measurement equation, it is possible to derive a linear state space equation which has more information without additional sensor. The experimental results and the computer simulations show that the performance of the proposed algorithm in this study is better than that of the conventional algorithm. It supports that the additional constrained condition can improve the estimator's performance.

Keywords: Linear Hall sensor, Linear estimator, Motor speed, Frequency estimation, Constrained condition**.**

I. INTRODUCTION

Angular velocity is a necessary information for motor control. If a system is under the condition which is a varying velocity or repeated running and stopping, it is more important for motor control to get the velocity. Motor's angular velocity can be obtained by various sensors like tachometer, latch type Hall sensor, linear type Hall sensor, current sensor and shunt resistor [1]. Among these sensors, the shunt resistor has the best cost advantage. However, since an estimator using the shunt resistor can be derived from the motor parameters, it is not suitable for the common device. One of the methods not using the motor parameters is to use the linear Hall sensor. Its output signal represents the motor's rotation. The signal is a continuous sinusoidal wave. Therefore, an estimator using the linear Hall sensor can estimate motor's speed precisely. The linear Hall sensor's output is represented by a sinusoidal signal and an additive noise in [2]. And using linear prediction, a linear state space equation is derived. With this equation, one can estimate motor's speed and it shows good performance as tachometer but not in the low speed range. The motor can be operated at various velocities. And it is able to repeat running and stopping. Therefore, the estimator needs additional information to complement the error at low speed.

The additional information like a constrained condition can improve the accuracy of the estimator [3]. The sinusoidal signal has natural constrained condition. When one has two sinusoidal waves which are delayed 90 degree in phase each other, the square of the sine plus the square of the cosine is always 1 which is called Pythagorean identity. With this quadratic constrained condition, the estimator in [2] can enhance the accuracy at low speed. To adopt this condition into the linear state space equation, it needs the change from the quadratic form to a linear form. The linear constrained condition can be used like additional measurement information as in [3].

In this paper, we set sinusoidal signal with additive white noise to measurement data and estimate the frequency of these data. To solve the low speed problem, $\cos(\alpha)$ is multiplied to the measurement data so that state space equation has $\cos(w_k)$ and $\sin(w_k)$ in state values. Since each state has 90 degree phase delay, these two states must satisfy the Pythagorean identity. This gives another information without additional sensor. To change Pythagorean identity to a linear form constraint, we use the past estimated value. The derived linear constraint is added into the measurement equation of the linear state space equation. The linear constraint is not the same as the original constraint. It causes error in the measurement matrix. Therefore, we use the Robust Least Square (RLS) algorithm to compensate these measurement uncertainties [4]. To prove the performance of the proposed algorithm, the motor installed in a car window system is used and its rotation is obtained from the linear Hall sensor. With the sensor data, we estimated motor's speed and compared the results with those of [2]. The proposed algorithm shows enhanced performance not only in the low speed range but also the high range. When the motor was stopped, the proposed algorithm estimated the speed with lower error than [2]. We also simulated the proposed algorithm under varying frequencies. The analysis by the mean of estimation error and the root mean square error shows that the additional constrained condition can improve the performance of the estimation.

II. LINEAR STATE SPACE MODEL

The sinusoidal signal obtained from the linear Hall sensor which has stationary DC offset can be represented by linear prediction method [5].

$$d_k = A_k \cos(w_k k) + v_k \tag{1}$$

$$d_k + d_{k-2} = 2\cos(w_k)\{d_{k-1} - v_{k-1}\} + v_k + v_{k-2} \tag{2}$$

where A_k is amplitude of the Hall sensor, w_k is angular velocity and v_k is white noise having the zero mean and the variance of R_k. With multiplying $\cos(\alpha)$ to (2), one can derive the following equation contained sine and cosine function.

$$\begin{aligned}(d_k + d_{k-2})\cos(\alpha) &= 2\cos(w_k)\cos(\alpha)\{d_{k-1} - v_{k-1}\} \\ &\quad + (v_k + v_{k-2})\cos(\alpha) \\ &= 2\{d_{k-1} - v_{k-1}\}\{\cos(w_k+\alpha) + \sin(w_k)\sin(\alpha)\} \\ &\quad + (v_k + v_{k-2})\cos(\alpha)\end{aligned} \tag{3}$$

(2) and (3) represent linear state space equation which the measurement matrix has uncertainty,

$$\begin{aligned} x_{k+1} &= x_k + w_k \\ y_k &= (\tilde{H}_k - \Delta H_k)x_k + \bar{v}_k \end{aligned} \tag{4}$$

where

$$x_k = \begin{bmatrix} \cos(w_k) \\ \cos(w_k+\alpha) \\ \sin(w_k) \end{bmatrix}$$

$$y_k = \begin{bmatrix} d_k + d_{k-2} \\ (d_k + d_{k-2})\cos(\alpha) \end{bmatrix}$$

$$\tilde{H}_k = \begin{bmatrix} 2d_{k-1} & 0 & 0 \\ 0 & 2d_{k-1} & 2d_{k-1}\sin(\alpha) \end{bmatrix} \tag{5}$$

$$\Delta H_k = \begin{bmatrix} 2v_{k-1} & 0 & 0 \\ 0 & 2v_{k-1} & 2v_{k-1}\sin(\alpha) \end{bmatrix}$$

$$\bar{v}_k = \begin{bmatrix} v_k + v_{k-2} \\ (v_k + v_{k-2})\cos(\alpha) \end{bmatrix}$$

and w_k is modeling error under the assumptions of white and zero mean. (5) shows the state variable x_k that has two sinusoid signals which are delayed 90 degree in phase each other.

III. QUADRATIC CONSTRAINED CONDITION

The two state variables, $\cos(w_k)$ and $\sin(w_k)$, have following constraint naturally in (5).

$$\cos^2(w_k) + \sin^2(w_k) = 1 \tag{6}$$

(6) can be considered another measurement information without additional sensor. However, since (6) is quadratic form, it is not suitable for the linear state equation. To change (6) to linear form, one can use a past estimation result as follows:

$$\begin{aligned} 1 &= \left\{\cos(\hat{w}_{k-1}) + \varepsilon_{c_k}\right\}\cos(w_k) \\ &\quad + \left\{\sin(\hat{w}_{k-1}) + \varepsilon_{s_k}\right\}\sin(w_k) \end{aligned} \tag{7}$$

With (7), the quadratic constraint becomes another measurement. With augmenting (7) to (4), (4) can be re-written

$$\begin{aligned} x_{k+1} &= x_k + w_k \\ y_{a_k} &= (\tilde{H}_{a_k} - \Delta H_{a_k})x_k + \bar{v}_{a_k} \end{aligned} \tag{8}$$

where

$$y_{a_k} = \begin{bmatrix} d_k + d_{k-2} \\ (d_k + d_{k-2})\cos(\alpha) \\ 1 \end{bmatrix}$$

$$\tilde{H}_{a_k} = \begin{bmatrix} 2d_{k-1} & 0 & 0 \\ 0 & 2d_{k-1} & 2d_{k-1}\sin(\alpha) \\ \cos(\hat{w}_{k-1}) & 0 & \sin(\hat{w}_{k-1}) \end{bmatrix} \tag{9}$$

$$\Delta H_{a_k} = \begin{bmatrix} 2v_{k-1} & 0 & 0 \\ 0 & 2v_{k-1} & 2v_{k-1}\sin(\alpha) \\ -\varepsilon_{c_{k-1}} & 0 & -\varepsilon_{s_{k-1}} \end{bmatrix}$$

$$\bar{v}_{a_k} = \begin{bmatrix} v_k + v_{k-2} \\ (v_k + v_{k-2})\cos(\alpha) \\ 0 \end{bmatrix}$$

The augmented equation (8) has also uncertainty in measurement matrix. To obtain a compensated estimation results from these uncertainties, we use the RLS algorithm in [4].

IV. LINEAR FREQUENCY ESTIMATOR

The RLS algorithm in [4] can be summarized as follows:

Measurement update:

$$\begin{aligned} P_{k|k}^{-1} &= \lambda P_{k|k-1}^{-1} + \tilde{H}_{a_k}^T \tilde{H}_{a_k} - W_k \\ \hat{x}_{k|k} &= (I + P_{k|k}W_k)\hat{x}_{k|k-1} + P_{k|k}\tilde{H}_k^T(y_{a_k} - \tilde{H}_{a_k}\hat{x}_{k|k-1}) \end{aligned} \tag{10}$$

Time update:

©ISAROB 2009

$$\begin{aligned} P_{k+1|k} &= F_k P_{k|k} F_k^T \\ \hat{x}_{k+1|k} &= F_k \hat{x}_{k|k} \end{aligned} \tag{11}$$

where λ is weight parameter which is able to adjust along the system characteristic and W_k is stochastic property of the measurement uncertainty, ΔH_{a_k}. The stochastic property of ΔH_{a_k} can be represented by definition in (8) as follows:

$$\begin{aligned} W_k &= E\left[\Delta H_{a_k}^T \Delta H_{a_k}\right] \\ &= \begin{bmatrix} 4R_k + A_k & 0 & B_k \\ 0 & 4R_k & 4R_k \sin(\alpha) \\ B_k & 4R_k \sin(\alpha) & 4R_k \sin^2(\alpha) + C_k \end{bmatrix} \end{aligned} \tag{12}$$

where

$$E\left(\begin{bmatrix} \varepsilon_{c_{k-1}} \\ \varepsilon_{s_{k-1}} \end{bmatrix} \begin{bmatrix} \varepsilon_{c_{k-1}} \\ \varepsilon_{s_{k-1}} \end{bmatrix}^T\right) = \begin{bmatrix} A_k & B_k \\ B_k & C_k \end{bmatrix} \tag{13}$$

(13) is covariance of error which caused by transforming quadratic equation (6) to linear constraint (7). The error covariance matrix is also tuning parameter like λ.

V. EXPERIMENTAL RESULTS

To prove the performance of the proposed algorithm, the motor installed in a car window system is used and its rotation is obtained from the linear Hall sensor. With the sensor data, we estimated motor's speed and compared the results with those of [2]. Since the algorithm in [2] showed good performance as tachometer, we did not compare with tachometer in these experiments. Parameters of the estimator are as follows:

$$\begin{aligned} &\lambda = 0.95 \\ &R_k = 0.000049339[V^2] \\ &P_{0|-1} = \begin{bmatrix} 10^3 & 0 & 0 \\ 0 & 10^3 & 0 \\ 0 & 0 & 10^3 \end{bmatrix} \\ &\begin{bmatrix} A_k & B_k \\ C_k & D_k \end{bmatrix} = \begin{bmatrix} 10^{-12} & 0 \\ 0 & 10^{-12} \end{bmatrix} \\ &\cos(\alpha) = 0.809, \quad \alpha = \frac{\pi}{5}[rad] \end{aligned} \tag{14}$$

The linear Hall sensor output is represented in Fig. 1. At the around 3000 step and the around 6000 step, there was a speed change. The motor was stopped at around 7200 step. The estimated motor's speed obtained from the linear Hall sensor data was shown in Fig. 2. The proposed algorithm had the lower error than [2] at both the low and the high speed range. However, in stopped condition, proposed algorithm showed bias error. The approximation of the linear constrained condition from quadratic equation might cause these errors.

The computer simulation results along varying frequencies were represented in Fig. 3 and Fig. 4. The mean of the estimation error in Fig. 3 showed both two algorithms increased bias error as frequency decreased. Root means square of estimation error in Fig. 4 showed also both two algorithms decrease performance as frequency come down. However, in both two cases, the proposed algorithm was better than [2]. Therefore, the results supported that the additional constrained condition can improve the estimator's performance.

VI. CONCLUSION

To estimate motor's speed from the sinusoidal signal obtained by the linear Hall sensor, we established linear state pace equation reflecting the constraint and used the RLS algorithm to cope with the measurement uncertainty. Since a conventional linear prediction algorithm has a limitation of the range in the low speed, we gave the additional information to estimator which is quadratic equation so called Pythagorean identity that is natural property in sinusoidal signal. However, since the equation is a nonlinear form, we change it to a linear constrained condition. Adding it to the measurement equation, it is possible to derive another linear state space equation which has more information without additional sensor. The experimental results and the computer simulations show that the performance of the proposed algorithm is better than that of the conventional algorithm. Moreover, it supports that the additional constrained condition can improve the estimator's performance

ACKNOWLEDGEMENT

This work has been supported by Korea Sanhak Foundation.

REFERENCES

[1] Raj Mohan Bharadwaj and Alexander G. Parlos, "Neural speed filtering for induction motors with anomalies and incipient faults," *IEEE/ASME trans. Mechatronics*, vol. 9, no. 4, pp. 679-688, Dec. 2004.

[2] G. H. Choi, W. S. Ra, T. S. Yoon, J. B. Park, " Low-cost tachometer based on the recursive frequency estimation for automotive applications," *SICE Annual Conference 2007*, Sep. 17-20, 2007, Kagawa University, Japan, 2007.

[3] Gupta Nachi, "Kalman filtering in the presence of state space equality constraints," *Proc. of the 26th*

Chinese control conference, Jul. 26-31, 2007, Zhangjiajie, Hunan, China, 2007.

[4] W. S. Ra, I. H. Whang, and J. B. Park, "Robust weighted least quares range estimator for UAV applications," *SICE Annual Conference 2008,* Aug. 20-22, 2008, Electro-Communications University, Japan, 2008.

[5] H. C. So. and P. C. Ching, "Adaptive algorithm for direct frequency estimation", *IEE Proc.-Radar Sonar Navig.*, vol. 515, no. 6, pp. 359-364, 2004.

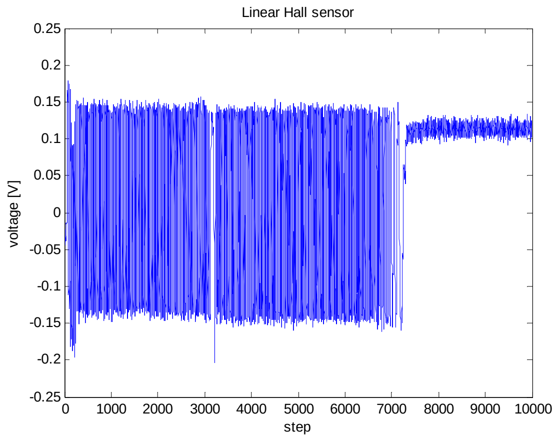

Fig 1. Linear Hall sensor output

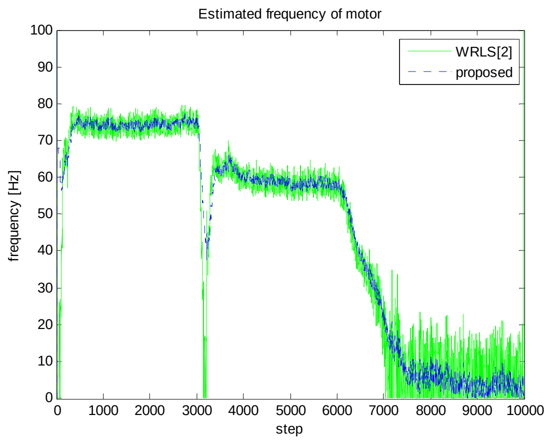

Fig 2. Frequency estimation results from linear Hall sensor

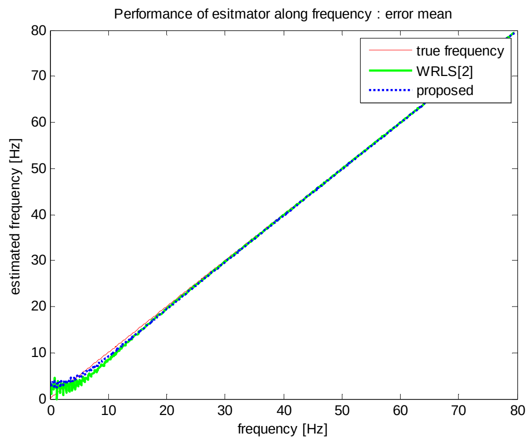

Fig 3. Performance of estimator along frequency : mean of estimation error

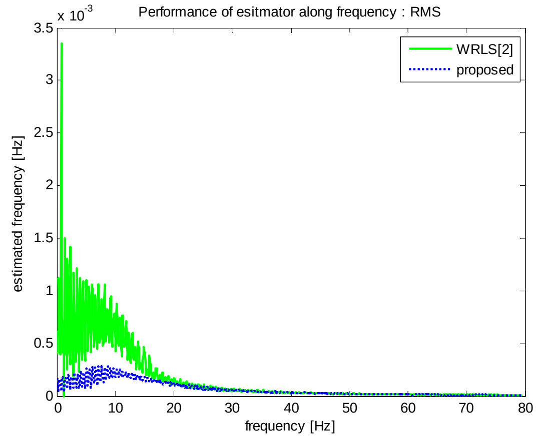

Fig 4. Performance of estimator along frequency : root mean square of estimation error

The Fourteenth International Symposium on Artificial Life and Robotics 2009 (AROB 14th '09),
B-Con Plaza, Beppu, Oita, Japan, February 5 - 7, 2009

A method for top-down control of robotic attention based on Mental-image Description Language, L_{md}

Masao Yokota, Kenji Sasaki, Reiichi Kaida, Tetsushi Oka and Kaoru Sugita

Fukuoka Institute of Technology, 3-30-1 Wajiro-higashi, Higashi-ku, Fukuoka-shi, 811-0295, Japan
(Tel : 81-92-606-5897; Fax : 81-92-606-8923)
(yokota@fit.ac.jp)

Abstract: Mental Image Directed Semantic Theory (MIDST) has defined the semantic content (i.e., concept) of a spatiotemporal expression as a certain generalized mental image of its referents in the physical world and proposed a method to model mental images as "loci in attribute spaces" formalized in the formal language L_{md}. The most remarkable feature of L_{md} is its capability of formalizing spatiotemporal events based on a hypothesis of human attention mechanism. This paper presents a systematic method for top-down control of robotic attention by L_{md} representation with some computer simulation results.

Keywords: Natural language, Multimedia understanding, Robotic sensation and action.

I. INTRODUCTION

The authors have been working on integrated multimedia understanding for intuitive human-robot interaction, that is, interaction between non-expert or ordinary people and home robots as shown in Fig.1 [1-4]. In such a situation, natural language is the leading information medium for their communication as well as for the communication between ordinary people because it can convey the exact intention of the sender to the receiver due to its syntax and semantics common to its users, which is not necessarily the case for another medium such as gesture or so.

For such an intuitive human-robot interaction intended here, it is essential to develop a systematically computable knowledge representation language (KRL) as well as representation-free technologies such as neural networks for processing unstructured sensory/motory data. This type of language is indispensable to *knowledge-based* processing such as *understanding* sensory events, *planning* appropriate actions and *knowledgeable* communication with ordinary people in natural language, and therefore it needs to have at least a good capability of representing spatiotemporal events that correspond to human/robotic sensations and actions in the real world.

Most of conventional methods have provided robotic systems with such quasi-natural language expressions as 'move(*Velocity*, *Distance*, *Direction*)', 'find(*Object*, *Shape*, *Color*)' and so on for human instruction or suggestion, uniquely related to computer programs to deploy sensors/ motors [e.g., 5, 6]. These expression schemas, however, are too linguistic or coarse to represent and compute sensory/motory events in such an integrated way as intended here.

Mental Image Directed Semantic Theory (MIDST) [1] has proposed a model of human attention-guided perception yielding omnisensory images that inevitably reflect certain movements of the focus of attention of the observer (FAO) scanning certain matters in the world. More analytically, these omnisensory images are associated with spatiotemporal changes (or constancies) in certain attributes of the matters scanned by FAO and modeled as temporally parameterized "loci in attribute spaces", so called, to be formulated in a formal language, L_{md} (Mental-image Description Language). This language is employed for predicate logic and has already been implemented on several types of computerized intelligent systems [1-4].

This paper presents a systematic method for top-down control of robotic attention by L_{md} representation with some computer simulation results.

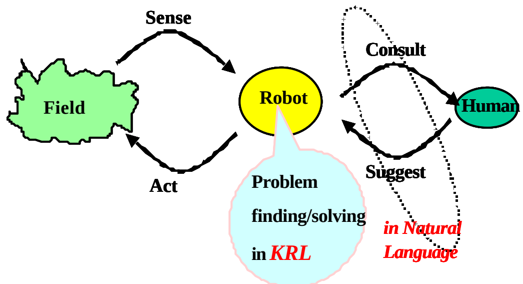

Fig.1. Intuitive human-robot interaction

II. IMAGE, ATTENTION AND L_{md}

MIDST models omnisensory mental images as "Loci in Attribute Spaces". An attribute space corresponds with a certain measuring instrument just like a barometer, thermometer or so and the loci represent the movements of its indicator.

For example, the moving gray triangular object shown in Fig.2-Left is assumed to be perceived as the loci in the three attribute spaces, namely, those of 'Location', 'Color' and 'Shape' in the observer's brain. A general locus is to be articulated by "Atomic Locus" as depicted in Fig.2-Right and formulated as (1).

$$L(x,y,p,q,a,g,k) \quad (1)$$

The intuitive interpretation of (1) is given as follows.

©ISAROB 2009

"Matter 'x' causes Attribute 'a' of Matter 'y' to keep (p=q) or change (p ≠ q) its values temporally (g=Gt) or spatially (g=Gs) over a time-interval, where the values 'p' and 'q' are relative to the standard 'k'."

When $g=G_t$, the locus indicates monotonic change or constancy of the attribute in time domain and when $g=G_s$, that in space domain, respectively. The former is called 'temporal event' and the latter, 'spatial event'. For example, the motion of the 'bus' represented by S1 is a temporal event and the ranging or extension of the 'road' by S2 is a spatial event whose meanings or concepts are formulated as (2) and (3), respectively, where 'A_{12}' denotes the attribute 'Physical Location'. These two formulas are different only at the term 'Event Type'.

(S1) The bus runs from Tokyo to Osaka.

$$(\exists x,y,k)L(x,y,Tokyo,Osaka,A_{12},G_t,k) \wedge bus(y) \quad (2)$$

(S2) The road runs from Tokyo to Osaka.

$$(\exists x,y,k)L(x,y,Tokyo,Osaka,A_{12},G_s,k) \wedge road(y) \quad (3)$$

The formal language L_{md} has employed 'tempo-logical connectives (TLCs)' representing both logical and temporal relations between loci. Articulated loci are combined with tempo-logical conjunctions, where 'SAND ($\wedge_0$)' and 'CAND ($\wedge_1$)' are most frequently utilized, standing for 'Simultaneous AND' and 'Consecutive AND', conventionally symbolized as 'Π' and '•', respectively. For example, the expression (4) is the definition of the English verb concept 'fetch' depicted as Fig.3-Left. This implies such a temporal event that 'x' goes for 'y' and then comes back with it.

$$(\lambda x,y)fetch(x,y)$$
$$\leftrightarrow (\lambda x,y)(\exists p1,p2,k)L(x,x,p1,p2,A12,Gt,k) \bullet$$
$$((\underline{L(x,x,p2,p1,A12,Gt,k)\Pi L(x,y,p2,p1,A12,Gt,k)})$$
$$\wedge x \neq y \wedge p1 \neq p2 \quad (4)$$

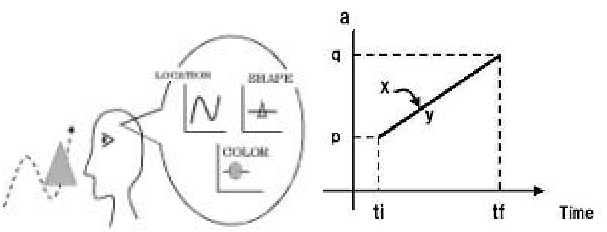

Fig.2. Mental image model (Left) and Atomic Locus in Attribute Space (Right).

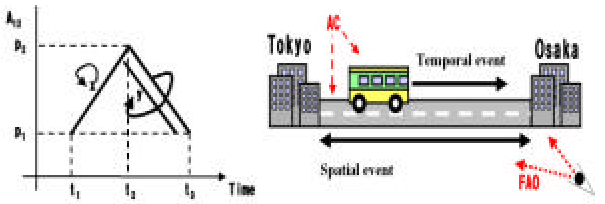

Fig.3. Image of 'fetch'(Left) and Event types (Right).

It has been often argued that human active sensing processes may affect perception and in turn conceptualization and recognition of the physical world. The difference between temporal and spatial event concepts can be attributed to the relationship between the Attribute Carrier (AC) and the Focus of the Attention of the Observer (FAO). To be brief, the FAO is fixed on the whole AC in a temporal event but *runs* about on the AC in a spatial event. Consequently, as shown in Fig.3-Left, the *bus* and the FAO move together in the case of S1 while the FAO solely moves along the *road* in the case of S2. That is, ***all loci in attribute spaces correspond one to one with movements or, more generally, temporal events of the FAO. This implies that L_{md} expression can suggest a robot what and how should be attended to in its environment.*** And this is why S3 and S4 can refer to the same scene in spite of their appearances, where what 'sinks' or 'rises' is the FAO and whose conceptual descriptions are given as (5) and (6), respectively, where 'A13', '↑' and '↓' refer to the attribute 'Direction' and its values 'upward' and 'downward', respectively. Such a fact is generalized as '***Postulate of Reversibility of a Spatial Event*** (PRS) ' that can be one of the principal inference rules belonging to people's common-sense knowledge about geography. These pairs of conceptual descriptions are called ***equivalent in the PRS***, and the paired sentences are treated as ***paraphrases*** each other.

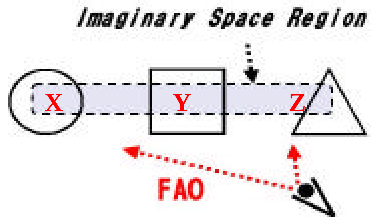

Fig.4. Spatial event 'row' and FAO movement.

(S3) The path *sinks to* the brook.

$$(\exists x,y,p,z,k_1,k_2)L(x,y,p,z,A_{12},G_s,k_1)\Pi$$
$$L(x,y,\downarrow,\downarrow,A_{13},G_s,k_2) \wedge path(y)$$
$$\wedge brook(z) \wedge p \neq z \quad (5)$$

(S4) The path *rises from* the brook.

$$(\exists x,y,p,z,k_1,k_2)L(x,y,z,p,A_{12},G_s,k_1)\Pi$$
$$L(x,y,\uparrow,\uparrow,A_{13},G_s,k_2) \wedge path(y)$$
$$\wedge brook(z) \wedge p \neq z \quad (6)$$

For another example of spatial event, Fig.4 concerns the perception of the formation of multiple isolated objects, where FAO runs along an imaginary object so called 'Imaginary Space Region (ISR)'. This spatial event can be verbalized as S5 using the preposition 'between' and formulated as (7) or (8), corresponding also to such concepts as 'row', 'line-up', etc.

(S5) Y is between X and Z.

$$(\exists x,y,p,q,k_1,k_2)(L(x,y,X,Y,A_{12},G_s,k_1)\Pi$$
$$L(x,y,p,p,A_{13},G_s,k_2))\bullet(L(x,y,Y,Z,A12,G_s,k_1)\Pi$$
$$L(x,y,q,q,A_{13},G_s,k_2)) \wedge ISR(y) \wedge p=q \quad (7)$$

$$(\exists x,y,p,k_1,k_2)(L(x,y,Z,Y,A_{12},G_s,k_1)\bullet$$
$$L(x,y,Y,X,A_{12},G_s,k_1))\Pi L(x,y,p,p,A_{13},G_s,k_2) \wedge ISR(y) \quad (8)$$

©ISAROB 2009

At our best knowledge, there is no other theory or method [e.g., 7, 8] that can provide spatiotemporal expressions with semantic interpretation in such a systematic way where both temporal and spatial events are simply and adequately formulated by controlling the term of Event Type of the atomic locus formula reflecting FAO movement. Table 1 shows about 50 attributes extracted exclusively from English and Japanese words of common use contained in certain thesauri [9]. Most of them (i.e., A01-A45) correspond to the sensory receptive fields in human brains. For example, those marked with '*' in this table can be associated to the sense 'sight'. Correspondingly, six categories of standards shown in Table 2 have been extracted that are necessary for representing relative values of each attribute in Table 1. ***These tables imply that ordinary people live their casual life, attending to tens of attributes of the matters in the world to cognize them in comparison with several kinds of standards. That is, without any verbal hint, it is extremely difficult for a robot to understand which part of its environment is significant or not for people because there are too many things to attend to as it is.***

Table 1. List of attributes

Code	Attribute [Property†] (words/phrases
*A01	PLACE OF EXISTENCE [N] (*happen,*
*A02	LENGTH [S] (*long, shorten, close, away*)
*A03	HEIGHT [S] (*high, lower*)
*A04	WIDTH [S] (*widen, narrow*)
*A05	THICKNESS [S] (*thick, thin*)
*A06	DEPTH1 [S] (*deep, shallow*)
*A07	DEPTH2 [S] (*deep, concave*)
*A08	DIAMETER [S] (*across, in diameter*)
*A09	AREA [S] (*square meters, acre*)
*A10	VOLUME [S] (*litter, gallon*)
*A11	SHAPE [N] (*round, triangle*)
*A12	PHYSICAL LOCATION [N] (*move, stay*)
*A13	DIRECTION [N] (*turn, wind, left*)
*A14	ORIENTATION [N] (*orientate, command*)
*A15	TRAJECTORY [N] (*zigzag, circle*)
*A16	VELOCITY [S] (*fast, slow*)
*A17	MILEAGE [S] (*far, near*)
A18	STRENGTH OF EFFECT [S] (*strong,*
A19	DIRECTION OF EFFECT [N] (*pull, push*)
A20	DENSITY [S] (*dense, thin*)
A21	HARDNESS [S] (*hard, soft*)
A22	ELASTICITY [S] (*elastic, flexible*)
A23	TOUGHNESS [S] (*fragile, stiff*)
A24	TACTILE FEELING [S] (*rough, smooth*)
A25	HUMIDITY [S] (*wet, dry*)
A26	VISCOSITY [S] (*oily, watery*)
A27	WEIGHT [S] (*heavy, light*)
A28	TEMPERATURE [S] (*hot, cold*)
A29	TASTE [N] (*sour, sweet, bitter*)
A30	ODOUR [N] (*pungent, sweet*)
A31	SOUND [N] (*noisy, silent, loud*)
*A32	COLOR [N] (*red, white*)
A33	INTERNAL SENSATION [N] (*tired,*
A34	TIME POINT [S] (*o'clock, elapse*)
A35	DURATION [S] (*hour, minute, long, short*)
A36	NUMBER [S] (*ten, quantity, number*)
A37	ORDER [S] (*first, last*)
A38	FREQUENCY [S] (*sometimes, frequent*)
A39	VITALITY [S] (*alive, dead, vivid*)
A40	SEX [S] (*male, female*)
A41	QUALITY [N] (*make, destroy*)
A42	NAME [V] (*name, token*)
A43	CONCEPTUAL CATEGORY [V] (*mammal*)
*A44	TOPOLOGY [V] (*in, out, touch*)
*A45	ANGULARITY [S] (*sharp, dull, rectangle*)
B01	WORTH [N] (*improve, praise, deny, alright*)
B02	LOCATION OF INFORMATION [N] *tell,*
B03	EMOTION [N] (*like, hate*)
B04	BELIEF VALUE [S] (*believe, trust*)
	…………………………..

†S: scalar value, N: non-scalar value. *Attributes concerning the sense of sight.

Table 2. List of standards

Categories	Remarks
Rigid Standard	Objective standards such as denoted by measuring *units* (meter, gram, etc.).
Species Standard	The *attribute value ordinary* for a species. A *short train* is ordinarily longer than a *long pencil*.
Proportional Standard	'*Oblong*' means that the width is greater than the height at a physical object.
Individual Standard	*Much* money for one person can be too *little* for another.
Purposive Standard	One room large enough for a person's *sleeping* must be too small for his *jogging*.
Declarative Standard	The origin of an order such as 'next' must be declared explicitly just as 'next *to him*'.

III. ATTENTION CONTROL BY L_{md}

The description of an event in L_{md} is compared to a movie film recorded through a floating camera because it is necessarily grounded in FAO's movement over the event. ***That is to say in short, L_{md} expression suggests a robot what and how should be attended to in its environment.*** Therefore, the robotic attention can be controlled in a top-down way based on L_{md} expression.

For example, consider such a suggestion to a robot as S6 whose semantic interpretation is given by (26), where 'avoid' is defined as 'keep Topology (A_{44}) Disjoint (=***Dis***)'. In this case, unless the robot is aware of the existence of a certain box between the stool and the desk, such semantic understanding as the underlined part of (26) and such a semantic definition of the word 'box' as (27) are very helpful for it. The attributes A_{12} (Location), A_{13} (Direction), A_{32} (Color), A_{11} (Shape) and the spatial event on A_{12} in these L_{md} expressions indicate that the robot has only to activate its vision system in order to search for the box from the stool to the desk during the pragmatic understanding. That is, the robot can attempt to understand pragmatically the words of objects and events in an integrated top-down way.

(S6) Avoid <u>the green box between the stool and the desk</u>.

$$(\exists x_1,x_2,x_3,x_4,x_5,x_6,y_1,y_2,p,k_1,k_2,k_3,k_4)$$
$$L(x_6,x_5,\boldsymbol{Dis},\boldsymbol{Dis},A_{44},G_t,k_4)\Pi L(x_6,x_5,x_2,x_6,A_{12},G_s,k_1)\Pi$$
$$(\underline{L(y_1,x_4,x_1,x_2,A_{12},G_s,k_1)\bullet L(y_1,x_4,x_2,x_3,A_{12},G_s,k_1)})\Pi$$
$$L(y_1,x_4,p,p,A_{13},G_s,k_2)\Pi L(y_2,x_2,Green,Green,A_{32},G_t,k_3)$$
$$\wedge stool(x_1)\wedge box(x_2)\wedge desk(x_3)\wedge ISR(x_4)\wedge ISR(x_5)$$
$$\wedge robot(x_6) \tag{26}$$

$$(\lambda x)box(x)\leftrightarrow(\lambda x)(\exists y,k)L(y,x,\mathbf{Hexahedron},\mathbf{Hexahedron},A_{11},G_t,k)\wedge container(x) \tag{27}$$

Figure 5 shows the simulated action of a virtual robot to the command S7. The robot's pragmatic understanding of this command is given as (28), where, '$Robot_0$' refers to the virtual robot itself, 'D_c' is the direction from '$Rectangle_1$' to '$Triangle_1$' calculated from their locations, and P_c and P_g are the current and the goal locations of '$Robot_0$', respectively.

(S7) Go to between the rectangle and the triangle, avoiding the pentagon.

$$L(Robot_0,Robot_0,P_c,P_g,A_{12},G_t,\_)$$
$$\Pi L(Robot_0,ISR_2,Disjoint,Disjoint,A_{44},G_t,\_)$$
$$\Pi(L(\_,ISR_1,Rectangle_1,P_g,A_{12},G_s,\_)\bullet$$
$$L(\_,ISR_1,P_g,Triangle_1,A_{12},G_s,\_))$$
$$\Pi L(Robot_0,ISR_1,D_c,D_c,A_{13},G_s,\_)$$
$$\Pi L(Robot_0,ISR_2,Pentagon_1,Robot_0,A_{12},G_s,\_) \tag{28}$$

The process flow for this simulation is roughly as follows [1-4].

[STEP1] Syntactic interpretation: production of a surface dependency structure (SDS) from S7.

[STEP2] Semantic understanding: production of a generalized (conceptual) interpretation U_s based on the SDSs and the semantic definitions of the words included in S7.

[STEP3] Pragmatic understanding: production of such a concrete interpretation as (28) by grounding the variables of U_s onto the matters in the environment.

[STEP4] Behavioralization: production of the action to S7 so as to satisfy the conditions indicated in (28) in the top-down way controlled by the attributes involved.

The text understanding process above is completely reversible except that multiple paraphrases can be generated by tempological reasoning as shown in Fig.6 because event patterns are sharable among multiple word concepts, where text-generation is also controlled in a top-down way in use of attributes involved.

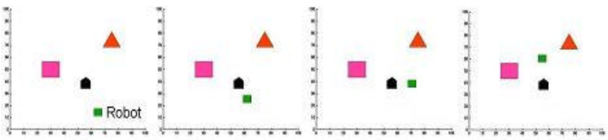

Fig. 5. Simulation in Matlab of the command 'Go to between the rectangle and the triangle, avoiding the pentagon'.

(Input)

With the long red stick Tom precedes Jim.

(Output)

Tom with the long red stick goes before Jim goes.
Jim goes after Tom goes with the long red stick.
Jim follows Tom with the long red stick.
Tom carries the long red stick before Jim goes.
The stick moves simultaneously when Tom goes.
………………….

Fig.2. Text paraphrasing by tempological reasoning.

IV. CONCLUSION

Yokota,M. has analyzed a considerable number of spatiotemporal event terms over various kinds of English words such as prepositions, verbs, adverbs, etc. categorized as 'Dimensions', 'Form' and 'Motion' in the class 'SPACE' of the Roget's thesaurus [9], and found that almost all the concepts of spatiotemporal event terms can be defined in exclusive use of six kinds of attributes for FAOs, namely, 'Physical location (A12)', 'Direction (A13)', 'Trajectory (A15)', 'Velocity (A16)', 'Mileage (A17)' and 'Topology (A44)'. This fact implies that L_{md} expression can control robotic attention mechanism very efficiently in a top-down way in the physical world.

REFERENCES

[1] Yokota M (2005), An Approach to Integrated Spatial Language Understanding Based on Mental Image Directed Semantic Theory. Proc. of 5th Workshop on Language and Space, Bremen, Germany, Oct.

[2] Yokota M & Capi G (2005), Cross-media Operations between Text and Picture Based on Mental Image Directed Semantic Theory. WSEAS Trans. on Information Science and Applications, 10-2:1541-1550

[3] Yokota,M., Sugita,K. & Oka,T. (2008), Natural language understanding based on mental image description language L_{md} and its application to language-centered robot manipulation. Artificial Life and Robotics, 13:84-88

[4] Yokota,M. (2008), In Lazinica,A. (Ed.), Humanoid Robots, I-Tech Education and Publishing, 333-362

[5] Coradeschi, S. & Saffiotti, A.: "An introduction to the anchoring problem", Robotics and Autonomous Systems, 43, pp.85–96, 2003.

[6] Drumwright,E. Ng-Thow-Hing,V. & Mataric,M.J. "Toward a vocabulary of primitive task programs for humanoid robots", *Proceedings of International Conference on Development and Learning (ICDL06)*, Bloomington IN, May 2006.

[7] Sowa JF (2000), Knowledge Representation: Logical, Philosophical, and Computational Foundations, Brooks Cole Publishing Co., Pacific Grove, CA

[8] Miller GA & Johnson-Laird PN (1976), Language and Perception, Harvard University Press

[9] Roget P (1975), Thesaurus of English Words and Phrases, J.M.Dent & Sons Ltd., London

The Fourteenth International Symposium on Artificial Life and Robotics 2009 (AROB 14th '09),
B-Con Plaza, Beppu, Oita, Japan, February 5 - 7, 2009

Problem finding and solving based on Mental-image Description Language, L_{md}

Masao Yokota, Taiki Tomezuka, Yusuke Takubo, Tetsushi Oka and Kaoru Sugita

Fukuoka Institute of Technology, 3-30-1 Wajiro-higashi, Higashi-ku, Fukuoka-shi, 811-0295, Japan
(Tel : 81-92-606-5897; Fax : 81-92-606-8923)
(yokota@fit.ac.jp)

Abstract: Mental Image Directed Semantic Theory has proposed a formal language named "Mental-image Description Language, L_{md}". This language can provide intermediate knowledge representation and has already been applied to the integrated multimedia understanding system IMAGES-M that can perform cross-media translation, question-answering, etc. This paper describes a systematic method based on L_{md} for intelligent robots to find and solve problems in their environments.
Keywords: Knowledge representation language, Problem finding, Problem solving.

I. INTRODUCTION

In recent years, there have been developed various types of real or virtual robots as artificial partners. However, they are to play their roles according to programmed actions to stimuli and have not yet come to perform as natural as ordinary people. In order to realize such artificial partners, it is very important to develop a systematically computable knowledge representation language [1] as well as connectionism-based technologies for unstructured data processing [2]. This type of language is indispensable to *knowledge-based* processing such as *understanding* sensory events, *planning* appropriate actions and *knowledgeable* communication even with ordinary people, and therefore it needs to have at least a good capability of representing spatiotemporal events that correspond to humans' or robots' sensations and actions in the real world. Most of conventional methods have provided robotic systems with such quasi-natural language expressions as 'move(*Velocity*, *Distance*, *Direction*)', 'find(*Object*, *Shape*, *Color*)', etc. for human instruction or suggestion, uniquely related to computer programs for deploying sensors/motors as their semantics [e.g., 3,4]. These expression schemas, however, are too linguistic or coarse to represent and compute sensory/motory events. This is also the case for AI planning ("action planning") which deals with the development of representation languages for planning problems and with the development of algorithms for plan construction [5].

In order to solve this problem, Yokota, M. has employed the formal language so called 'Language for Mental-image Description (L_{md})' proposed in his original semantic theory 'Mental Image Directed Semantic Theory (MIDST)' [e.g., 6]. L_{md} was originally proposed for formalizing the natural semantics, that is, the semantics specific to humans, but it is general enough for the artificial semantics, that is, the semantics specific to each artificial device such as robot. This language has already been implemented on several types of computerized intelligent systems [e.g., 7] and there is a feedback loop between them for their mutual refinement, unlike other similar ones [e.g., 8].

This paper describes a systematic method based on L_{md} for intelligent robots to find and solve problems in their environments.

II. BRIEF DESCRIPTION OF L_{md}

MIDST treats word meanings in association with mental images, not limited to visual but omnisensory, modeled as "Loci in Attribute Spaces". An attribute space corresponds with a certain measuring instrument just like a barometer, a map measurer or so and the loci represent the movements of its indicator. A general locus is to be articulated by "Atomic Locus" and formalized as the expression (1). This is a formula in many-sorted first-order predicate logic, where "L" is a predicate constant with five types of terms: "Matter" (at 'x' and 'y'), "Attribute Value" (at 'p' and 'q'), "Attribute" (at 'a'), "Event Type" (at 'g') and "Standard" (at 'k').

$$L(x,y,p,q,a,g,k) \qquad (1)$$

This formula is called 'Atomic Locus Formula' and its intuitive interpretation is given as follows, where 'matter' refers to 'object' or 'event'.

"Matter 'x' causes Attribute 'a' of Matter 'y' to keep (p=q) or change ($p \neq q$) its values temporally (g=Gt) or spatially (g =Gs) over a time-interval, where the values 'p' and 'q' are relative to the standard 'k'."

When $g=Gt$, the locus indicates monotonic change or constancy of the attribute in time domain and when $g=Gs$, that in space domain. The former is called a temporal event and the latter, a spatial event.

For example, the motion of the 'bus' represented by S1 is a temporal event and the ranging or extension of the 'road' by S2 is a spatial event whose meanings or concepts are formalized as (2) and (3), respectively,

©ISAROB 2009

where the attribute is “physical location ” denoted by ‘A12’.

(S1) The bus runs from Tokyo to Osaka.

(S2) The road runs from Tokyo to Osaka.

$(\exists x,y,k)L(x,y,Tokyo,Osaka,A12,Gt,k)\wedge bus(y)$ (2)

$(\exists x,y,k)L(x,y,Tokyo,Osaka,A12,Gs,k)\wedge road(y)$ (3)

In order to represent both logical and temporal relations between loci, MIDST has employed ‘tempo-logical’ connectives [9] such that are defined by (4), where t_i, c and K refer to one of the temporal relations indexed by ‘i’, locus, and an ordinary binary logical connective such as the conjunction ‘$\wedge$’, respectively.

$$c_1 K_i c_2 \leftrightarrow (c_1 K c_2) \text{ Ù } t_i(c_1, c_2) \qquad (4)$$

Table 1 shows the definition of τ_i, where the conventional 13 types of temporal relations between two intervals are discriminated by the suffix ‘i’(-6≤ i ≤6). For example, the expression (5) is the conceptual description of the English verb “fetch”, depicted in Fig.4, implying such a temporal event that ‘x’ goes for ‘y’ and then comes back with it, where ‘Π(=$\wedge_0$)’ and ‘•(=$\wedge_1$)’ are instances of the tempo-logical connectives, ‘SAND’ and ‘CAND’, standing for “Simultaneous AND” and “Consecutive AND”, respectively. In general, a series of atomic locus formulas with such connectives is called ‘Locus formula’.

$$(\lambda x,y)fetch(x,y)\leftrightarrow(\lambda x,y)(\exists p1,p2,k)L(x,x,p1,p2,A12,Gt,k)\bullet(\underline{(L(x,x,p2,p1,A12,Gt,k)\Pi L(x,y,p2,p1,A12,Gt,k)})\wedge x\neq y\wedge p1\neq p2 \qquad (5)$$

As indicated by the underline at (5), an event ‘fetch(x,y)’ is necessarily *finished by* an event ‘carry(x,y)’. This fact can be formulated as (6), where ‘$\supset_{-4}$’ is the ‘*implication* ($\supset$)’ furnished with the temporal relation ‘*finished-by* (τ_{-4})’ (See Table 1).

$$fetch(x,y) \supset_{-4} carry(x,y) \qquad (6)$$

Table 1. List of temporal relations†

Definition of τ_i		Allen’s notation [10]
$t_{11}=t_{21} \wedge t_{12}=t_{22}$	$\tau_0(\chi_1, \chi_2)$	equals(χ_1,χ_2)
	$\tau_0(\chi_2, \chi_1)$	equals(χ_2, χ_1)
$t_{12}=t_{21}$	$\tau_1(\chi_1, \chi_2)$	meets(χ_1, χ_2)
	$\tau_{-1}(\chi_2, \chi_1)$	met-by(χ_2, χ_1)
$t_{11}=t_{21} \wedge t_{12}<t_{22}$	$\tau_2(\chi_1, \chi_2)$	starts(χ_1, χ_2)
	$\tau_{-2}(\chi_2, \chi_1)$	started-by(χ_2, χ_1)
$t_{11}>t_{21} \wedge t_{12}<t_{22}$	$\tau_3(\chi_1, \chi_2)$	during(χ_1, χ_2)
	$\tau_{-3}(\chi_2, \chi_1)$	contains(χ_2, χ_1)
$t_{11}>t_{21} \wedge t_{12}=t_{22}$	$\tau_4(\chi_1, \chi_2)$	finishes(χ_1, χ_2)
	$\tau_{-4}(\chi_2, \chi_1)$	finished-by(χ_2, χ_1)
$t_{12}<t_{21}$	$\tau_5(\chi_1, \chi_2)$	before(χ_1, χ_2)
	$\tau_{-5}(\chi_2, \chi_1)$	after(χ_2, χ_1)
$t_{11}<t_{21}\wedge t_{21}<t_{12} \wedge t_{12}<t_{22}$	$\tau_6(\chi_1, \chi_2)$	overlaps(χ_1, χ_2)
	$\tau_{-6}(\chi_2, \chi_1)$	overlapped-by(χ_2, χ_1)

†The durations of χ_1 and χ_2 are [t_{11}, t_{12}] and [t_{21}, t_{22}], respectively.

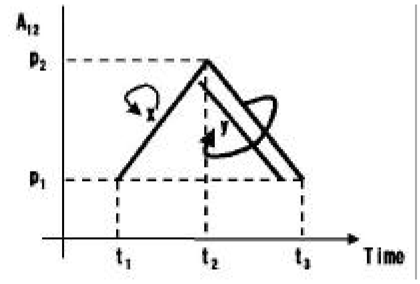

Fig.4. Locus of ‘fetch’.

III. COMPUTATION ON L_{md}

Our intelligent system IMAGES-M [7] working on L_{md} is one kind of expert system equipped with five kinds of user interfaces for multimedia communication, that is, Sensor Data Processing Unit (SDPU), Speech Processing Unit (SPU), Image Processing Unit (IPU), Text Processing Unit (TPU), and Action Data Processing Unit (ADPU) besides Inference Engine (IE) and Knowledge Base (KB). Each processing unit in collaboration with IE performs mutual conversion between each type of information medium and locus formulas.

The fundamental computations on L_{md} by IMAGES-M are to detect semantic anomalies, ambiguities and paraphrase relations. These are performed as inferential operations on locus formulas at IE. Detection of semantic anomalies is very important to avoid succession of meaningless computations or actions. For an extreme example, consider such a report from certain sensors as (7) represented in L_{md}, where ‘…’ and ‘A29’ stand for descriptive omission and the attribute ‘Taste’. This locus formula can be translated into the English sentence S3 by TPU, but it is semantically anomalous because a ‘desk’ has ordinarily no taste.

$$(\exists x,y,k)L(y,x,Sweet,Sweet,A29,Gt,k)\wedge desk(x) \qquad (7)$$

(S3) The desk is sweet.

These kinds of semantic anomalies can be detected in the following processes.

Firstly, assume the postulate (8) as the commonsense or default knowledge of “desk”, stored in KB, where ‘A39’ is the attribute ‘vitality’. The special symbol ‘*’ represents ‘always’ as defined by (9), where ‘ε(t1,t2)’ is a simplified atomic locus formula standing for time elapsing with an interval [t1,t2]. Furthermore, ‘_’ and ‘/’ are anonymous variables employed for descriptive simplicity and defined by (10) and (10’), respectively.

$$(\lambda x)\ desk(x) \leftrightarrow (\lambda x)\ (\ldots L^*(\_,x,/,/,A29,Gt,\_)\wedge \ldots \wedge L^*(\_,x,/,/,A39,Gt,\_) \wedge \ldots) \qquad (8)$$

$$X^*\leftrightarrow(\forall t1,t2)X\Pi\varepsilon(t1,t2) \qquad (9)$$

$$X(\_)\leftrightarrow (\exists u)\ X(u) \qquad (10)$$

$$X(/)\leftrightarrow \sim(\exists u)\ X(u) \qquad (10')$$

Secondly, the postulates expressed by (11) and (12) in KB are utilized. The formula (11) means that ***if one of two loci exists every time interval, then they can coexist***. The formula (12) states that ***a matter has never different values with a standard of an attribute at a time***.

$$X \wedge Y^* .\supset. X \Pi Y \quad (11)$$

$$L(x,y,p,q,a,g,k) \Pi L(z,y,r,s,a,g,k) .\supset. p=r \wedge q=s \quad (12)$$

Lastly, IE detects the semantic anomaly of "sweet desk" by using (8)-(12). That is, the formula (13) below is finally deduced from (8)-(12), which violates the postulate (8), that is, " *Sweet* ≠ / ".

$$L(\_,x,Sweet,Sweet,A29,Gt,\_) \Pi L(z,x,/,/,A29,Gt,\_) \quad (13)$$

These processes above are also employed for dissolving syntactic ambiguities in people's utterances such as S4. IE rejects 'sweet desk' and eventually adopts 'sweet coffee' as a plausible interpretation.

(S4) Bring me the coffee on the desk, which is very sweet.

If multiple plausible interpretations of a text or another type of information are represented in different locus formulas, it is semantically ambiguous. In such a case, IMAGES-M will ask for further information in order for disambiguation.

Furthermore, if two different representations are interpreted into the same locus formula, they are paraphrases of each other. The detection of paraphrase relations is very useful for deleting redundant information, for cross-media translation, etc. [11].

IV. PROBLEM FINDING & SOLVING

Problems can be classified roughly into two categories as follows [11].

(CP) Creation Problem:
House building, food cooking, etc.

(MP) Maintenance Problem:
Fire extinguishing, room cleaning, etc.

An MP is relatively simple one that a robot can find and solve autonomously while a CP is relatively difficult one that is given to the robot, possibly, by humans and to be solved in cooperation with them.

A robot must determine its task to solve a problem in the world. The robot needs to interpolate some transit event X_T between the two events, namely, 'Current Event (X_C)' and 'Goal Event (X_G)' as shown in (14).

$$X_C \bullet X_T \bullet X_G \quad (14)$$

According to this formalization, a problem X_P is defined as $X_T \cdot X_G$ and a task for the robot is defined as its realization.

The events in the world are described as loci in certain attribute spaces and a problem is to be detected by the unit of atomic locus. For example, employing such a postulate as (15) implying 'Continuity in attribute values', the event X in (16) is inferred as (17).

$$L(x,y,p1,p2,a,g,k) \bullet L(z,y,p3,p4,a,g,k) .\supset. p3=p2 \quad (15)$$

$$L(x,y,p1,p2,a,g,k) \bullet X \bullet L(z,y,p3,p4,a,g,k) \quad (16)$$

$$L(z',y,p2,p3,a,g,k) \quad (17)$$

Consider a verbal command such as S5 uttered by a human. Its interpretation is given by (18) as the goal event X_G concerning the attribute of 'Height (A03)'. If the current event X_C is given by (19), then (20) with the transit event X_T underlined can be inferred as the problem corresponding to S5.

(S5) Keep 'balloon C7' flying 5-6 meters high.

$$L(z,C7,q,q,A03,Gt,k) \wedge balloon(C7) \wedge 5m \le q \le 6m \quad (18)$$

$$L(x,C7,p,p,A03,Gt,k) \wedge balloon(C7) \quad (19)$$

$$\underline{L(z1,C7,p,q,A03,Gt,k)} \bullet L(z,C7,q,q,A03,Gt,k) \wedge balloon(C7) \wedge 5m \le q \le 6m \quad (20)$$

For this problem, the DIRN is to execute a task deploying a certain height sensor and actors 'z1' and 'z'. The selection of 'z' is a task in case of MP described below while the actor 'z1' is selected as follows:

If 6m-p <0 then z1 is a sinker, otherwise
if 5m-p >0 then z1 is a raiser, otherwise
5m£p£6m and no actor is deployed as z1.

The goal event X_G for an MP is that for another CP such as S5 given possibly by humans and solved by the robot in advance. That is, the task in this case is to autonomously restore the goal event X_G created in advance to the current event X_C as shown in (21), where the transit event X_T is the reversal of such X_{-T} that has been already detected as 'abnormal' by the DIRN.

For example, if X_G is given by (18) in advance, X_T is also represented as the underlined part of (20) while X_{-T} as (22). Therefore the task here is quite the same that was described in the previous section.

$$X_G \bullet X_{-T} \bullet X_C \bullet X_T \bullet X_G \quad (21)$$

$$L(z1,C7,q,p,A03,Gt,k) \wedge balloon(C7) \quad (22)$$

At present, IMAGES-M, installed on a personal computer, can deploy SONY AIBOs, dog-shaped robots, as actors and gather information about the physical world through their microphones, cameras and tactile sensors. Communications between IMAGES-M and humans are performed though the keyboard, mouse, microphone and multicolor TV monitor of the personal computer.

Consider such a verbal command as S6 uttered to the robot, SONY AIBO, named 'John'.

(S6) John, walk forward and wave your left hand.

Firstly, late in the process of cross-media translation from text to AIBO's action, this command is to be interpreted into (23) with the attribute 'shape (*A11*)' and the values '*Walkf-1*' and so on at the standard of '*AIBO*', reading that John makes himself walk forward and wave his left hand. Each action in AIBOs is defined as an ordered set of shapes (i.e., time-sequenced snapshots of the action) corresponding uniquely with the positions of their actuators determined by the rotations of the joints. For example, the actions 'walking forward (*Walkf*)' and 'waving left hand (*Wavelh*)' are defined as (24) and (25), respectively.

L(John,John,Walkf-1,Walkf-m,A11,Gt,AIBO) ∧
L(John,John,Wavelh-1,Wavelh-n,A11,Gt,AIBO) (23)

Walkf={Walkf-1,Walkf-2,…,Walkf-m} (24)

Wavelh={Wavelh-1,Wavelh-2,…,Wavelh-n} (25)

Secondly, an AIBO cannot perform the two events (i.e., actions) simultaneously and therefore the transit event between them is to be inferred as the underlined part of (26) which is the goal event here.

L(John,John,Walkf-1,Walkf-m,A11,Gt,AIBO)•
<u>L(John,John,Walkf-m,Wavelh-1,A11,Gt,AIBO)</u>•
L(John,John,Wavelh-1,Wavelh-n,A11,Gt,AIBO) (26)

Thirdly, (27) is to be inferred, where the transit event, underlined, is interpolated between the current event and the goal event X_G (=(26)).

L(John,John,p1,p2,A11,Gt,AIBO)
<u>• L(John,John,p2,Walkf-1,A11,Gt,AIBO)•</u> X_G (27)

Finally, (26) is interpreted into a series of the joint angles in the AIBO. Figure 9 shows AIBO's standing up and turning right that cannot be done simultaneously.

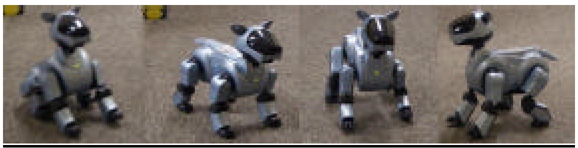

Fig.9. AIBO behaving in accordance to the command 'Stand up and turn right.'

V. CONCLUSION

This paper described about a novel method of problem finding and solving based on the formal language L_{md} where a problem is defined as the combination of a goal event X_G and a transit event X_T between the current event X_C and the goal event. The task sharing and assignment among sensors and actors are executed based on the information of a problem described as locus formulas in L_{md}. The most useful keys to task assignment are the attributes involved. About 50 kinds of attributes have been found in association with natural languages [6]. Furthermore, most of computations on L_{md} are simply for unifying (or identifying) atomic locus formulas and for evaluating arithmetic expressions such as '$p=q$', and therefore we believe that our formalismcan reduce the computational complexities of the others [e.g., 12,13] when applied to the same kinds of problems described here.

Our future work will include establishment of learning facilities for automatic acquisition of word concepts from sensory data and human-robot interaction by natural language under real environments.

REFERENCES

[1] Minsky,M.: "A Framework for Representing Knowledge," Report AIM--306, Artificial Intelligence Laboratory, Massachusetts Institute of Technology, 1974.
[2] Brooks, R. A.: "A robust layered control system for a mobile robot", IEEE Journal of Robotics and Automation, Vol.RA-2, pp.14-23, 1986.
[3] Coradeschi, S. & Saffiotti, A.: "An introduction to the anchoring problem", Robotics and Autonomous Systems, 43, pp.85–96, 2003.
[4] Drumwright,E. Ng-Thow-Hing,V. & Mataric,M.J. "Toward a vocabulary of primitive task programs for humanoid robots", *Proceedings of International Conference on Development and Learning (ICDL06),* Bloomington IN, May 2006.
[5] Wilkins, D.E. & Myers K.L.: "A common knowledge representation for plan generation and reactive execution", *Journal of Logic and Computation*, Vol.5, No.6, pp.731-761, 1995.
[6] Yokota,M.: "An approach to natural language understanding based on a mental image model," Proc. of the 2nd International Workshop on Natural Language Understanding and Cognitive Science, pp.22-31, 2005.
[7] Yokota,M. & Capi,G.: "Cross-media Operations between Text and Picture Based on Mental Image Directed Semantic Theory," WSEAS Transactions on Information Science and Applications, 10-2, pp.1541-1550, 2005.
[8] Zarri,G.P.: "NKRL, a Knowledge Representation Tool for Encoding the 'Meaning' of Complex Narrative Texts", Natural Language Engineering - Special Issue on Knowledge Representation for Natural Language Processing in Implemented Systems, 3,pp.231-253, 1997.
[9] Yokota,M.: "Towards Intuitive Spatiotemporal Communication between Human and Ubiquitous Intelligence Based on Mental Image Directed Semantic Theory - A General Theory of Tempo-logical Connectives -", Proc. of the 4th International Conference on Ubiquitous Intelligence and Computing (UIC-07)(LNCS), pp.1066-1078, Hong Kong, China, July, 2007.
[10] Allen,J.F.: "Towards a general theory of action and time," Artificial Intelligence, *23-2*, pp.123-154, 1984.
[11] Yokota,M.: "Towards a Universal Language for Distributed Intelligent Robot Networking," Proc. of IEEE International Conference on Systems, Man and Cybernetics (SMC06)(Invited paper), pp. 2784-2789, Taipei, Oct. 2006.
[12] Shoham,Y.: "Time for actions: on the relationship between time, knowledge, and action," Proc. of IJCAI¥89, pp.954-959, 1989.
[13] P.Haddawy:"A logic of time, chance, and action for representing plans," Artificial Intelligence, 80-2,pp.243-308, 1996.

©ISAROB 2009

The Fourteenth International Symposium on Artificial Life and Robotics 2009 (AROB 14th '09),
B-Con Plaza, Beppu, Oita, Japan, February 5 - 7, 2009

Success Rates in a Multi-modal Command Language for Home Robot Users

T. Abe[1], T. Oka[2], K. Sugita[2], and M. Yokota[2]

[1]*Graduate School of Fukuoka Institute of Technology, 3-30-1, Wajiro-higashi, Higashi-ku, Fukuoka, 811-0295, Japan*
[2]*Fukuoka Institute of Technology, 3-30-1, Wajiro-higashi, Higashi-ku, Fukuoka, 811-0295, Japan*
Tel : 81-92-606-4813; Fax : 81-92-606-0754
mdm07001@bene.fit.ac.jp, {oka, sugita, yokota}@fit.ac.jp

Abstract: This paper discusses success rates in a multi-modal command language for home robot users. In the command language, one specifies action types and action parameter values to direct robots in multiple modes such as speech, touch and gesture. Success rates of commands in the language can be estimated by user evaluation in several ways. This paper presents some user evaluation methods and results from recent studies on command success rates. The results show that the language enables users without much training to command home robots at success rates of as high as 88-100%. It is also shown that multi-modal commands combining speech and button press actions included fewer words and were significantly more successful than single-modal spoken commands.

Keywords: Home robot, multi-modal, command language, success rate, human-robot interaction

I. INTRODUCTION

In recent years, home robots for various purposes have been developed, some of which are already in the market. It is predicted that in near future they find their places to help people in homes in many ways achieving various tasks with or without their users at home. There is no doubt that such multi-purpose home robots should be easily directed by a wide range of untrained non-experts.

The authors proposed to design and use an artificial command language for home robot users, in order to enable non-experts to direct home robots without much training [1,2]. RUNA [2], a multi-modal command language for home robot users is designed to be learned and used by a wide range of users without effort. This language allows users to direct robots in multiple modes such as speech, touch and gesture. It is so carefully designed that one can realize a command interpreter which can interpret multi-modal command without much computational cost for speech and language understanding or gesture detection.

The authors have developed some real and simulated robots that can be directed in RUNA and conducted user studies. Some of the studies showed that novice users who had never directed robots were able to give valid commands in RUNA [2, 3]. However, some users had communication problems and were confused during commanding a robot in RUNA. Some commands given by them were too early and ignored; some were misrecognized due to speech recognition errors and the robot responded with "I don't understand!" or "I cannot do that!" Success rates of those users were low especially in the beginning. However, even those users might be able to improve their success rates in a short period of time with some training if the communication problems can be removed or reduced.

Based on the above discussion, the user evaluation systems were modified in order to reduce all sorts of communication problems including speech recognition errors and improve overall command success rates. This paper presents some user evaluation methods to estimate command success rates and results from recent studies on command success rates. The results show that the language enables users without much training to command home robots at success rates of as high as 88-100%. It is also shown that multi-modal commands combining speech and button press actions included fewer words and were significantly more successful than single-modal spoken commands.

II. MULTIMODAL COMMANDS

In RUNA, users specify an action type and action parameter values for each action command. For instance, to command a robot to turn, one should convey an action type, *turn,* and action parameter values (direction, angle, and speed). In the language, there are 24 action classes; each action type belongs to one of the action classes and has its own parameters. Table 1 shows some of the action classes of RUNA and parameters required.

In the command language, one can direct a robot in a spoken command, verbally specifying an action type and parameters: e. g. "Turn left by 45 degrees very slowly!" Parameter values can be left out: e. g. just saying "Turn left!" or "Turn slowly!" because each action parameter has a default value and this value will be set if not specified. Therefore, users need not mention every parameter and can reduce speech recognition errors.

The multi-modal language also allows users to give a parameter value using a gesture, pressing a button, or touching the robot they are commanding. For example, they can touch the robot's left shoulder for a short while and then say "Turn quickly!" to make the robot turn left (direction) by about 10 degrees (angle).

The authors are interested in how quickly users can learn the command language, how well they can command robots, and the success rate of their multi-modal commands.

Table 1 Action classes, types, and parameters

Class	Type	Parameters
3	*look ,turnto, lookAround*	*speed, target*
4	*turn*	*speed, directionlrni, angle*
5	*sidestep*	*speed, directionlrni, distance*
6	*move*	*speed, directionni, distance*
7	*handshake, highfive*	*speed, handde*
8	*punch*	*speed, handed, directionni*
9	*kich*	*speed, footde, directionni*

III. COMMAND SUCCESS RATES

To command robots in RUNA, users should have a clear purpose in mind. They should decide what action type and action parameter values to specify before giving a command to a robot. The command is successful if and only if the robot executes it correctly. Note that user intention is not observable although it is possible to guess action types and parameter values in spoken commands, gestures, touches, button press actions, etc. One should also note that novice users may not have some of action parameters clearly in mind.

Multi-modal commands must be valid to be correctly interpreted by robots. More specifically, spoken commands must be grammatical, and gestures, touches on robots, and button press actions must be presented to robots so that action types and action parameter values should be precisely recognized. Therefore, novice users must learn the multi-modal language to be successful in directing robots.

Users will make errors and give invalid commands, which cause a lower success rate, even after learning the language. This means that in order to realize a higher success rate with little learning effort, the command language should be carefully designed.

Even valid and reasonable commands can fail, since robots cannot always execute them as users give. First, robots may fail to understand spoken commands due to speech recognition problems or noises. Secondly, non-verbal messages can be misunderstood or ignored due to gesture recognition errors etc. Thirdly, robots may fail to execute even correctly recognized commands for physical reasons; they may fail to pick up a glass or stumble taking three steps forward.

False alarms by speech recognizers and gesture detectors can confuse users, making it harder for them to learn the language, and result in lower success rates. False non-verbal events can set a wrong parameter value. For example, a false alarm of a gesture to indicate "a very low speed" will cause an unwanted very slow action.

As stated above, the command is successful if and only if the robot executes it correctly. Thus, a success rate is determined by the number of successful commands in a set of multi-modal commands. However, as user intention is not observable, one must watch a user giving a command and guess what action type and parameter values were in mind. The problem, however, is that the user might have made a slip of the tongue or an error in non-verbal parameter specifications. Therefore, asking what a user intended and asking users to give particular commands are essential to discuss success rates in user evaluation.

IV. MULTI-MODAL LANGUAGE

The multi-modal language, RUNA, comprises a set of grammar rules and a lexicon for spoken commands and communication cues, and a set of non-verbal events detected using various sensors on robots and buttons on computers, mobile phones, controllers, etc. The spoken language enables users to command home robots in Japanese utterances, completely specifying an action to be executed. Commands in the spoken language can be modified by non-verbal events.

In RUNA, there are two types of commands, action commands and modifier commands. An action command consists of an action *type* such as *walk, turn, pickup,* and *lowertemp (for lowering the temperature setting)* and action *parameters* such as *speed, direction, angle, object* and *temperature*. Table 2 shows examples of action types and commands in RUNA.

Table 2 Examples of action commands

Type	Command	English Utterance
walk	*walk_s_3steps*	Take 3 steps slowly!
turn	*turn_f_l_30deg*	Turn 30°left quickly!
move	*move_m_r_2steps*	Move 2 steps right!
look	*look_f_l*	Look left quickly!

The action types of RUNA are categorized into 24 classes based on the way action parameters are specified in Japanese (Table 1). In other words, actions of different classes are commanded with different modifiers.

There are more than 300 generative rules for the latest full version of RUNA (Table 3). These rules allow Japanese speakers to command robots actions in a natural way by speech alone. In RUNA, a spoken action command is an imperative utterance including a verb to determine the action type and other words to specify action parameters. For instance, a spoken command, "Yukkuri 2 metoru aruke! (Walk 2m slowly!)", indicates an action type *walk* and distance *2m* (Fig. 1). The third rule in Table 3 generates an action command of class 2 (AC2) which has *speed* and *distance* (SD) as parameters. The word category PE is for noise, silence or hesitation voice allowed between parameters. This category was introduced lately to solve some problems and would help speech recognition and command interpretation.

There are more than 250 words, categorized into about 100 groups identified by non-terminal symbols (Table 4). Because the language is simple, well-defined and based on the Japanese language, Japanese speakers would not need long training to learn it. Note that in user test sessions, a reduced set of grammar rules and words can be employed to improve success rate.

In RUNA, non-verbal events modify the meaning of spoken commands. They convey information about parameters of action commands. For instance, users can use keypad buttons to give action parameters values instead of mentioning them. This will reduce average number of words in a command and speech recognition errors. If a non-verbal event has been arrived within a short period of time, a spoken command will be modified (see Table 5 for examples of mappings of button event parameters to action parameters).

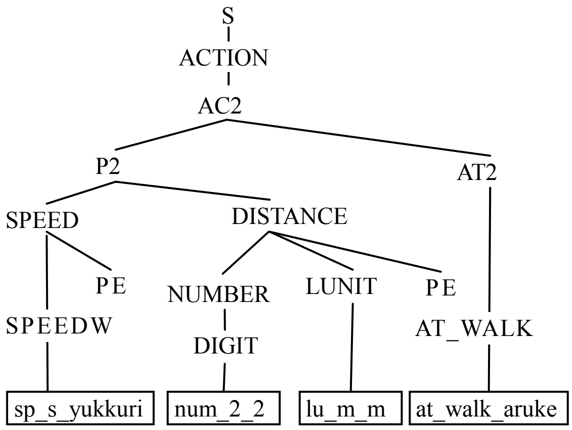

Fig. 1 An example parse tree for a spoken command

Table 3 Grammar rules of RUNA

Rule	Description
S → ACTION	Action command
S → MODIFIER	modifier command
ACTION → SD AC2	class 2 command
AC2 → AT2	Action type (class 2)
P2 → SPEED	speed (parameter)
P2 → DISTANCE SPEED	distance + speed
P2 → SPEED DISTANCE	speed + distance
SPEED → SPEEDW PE	one word for speed
DIST → NUMBER LUNIT PE	number + length unit
MODIFIER → REPEAT	Repeat last action

Table 4 Part of RUNA's lexicon

Non-terminal	Terminal	Pronunciation
AT_WALK	at_walk_hokou	h o k o:
REPEAT	md_repeat_moikkai	m o: i q k a i
SPEED	sp_fast_isoide	i s o i d e
LUNIT	lu_cm_cm	s e N ch i
DIR_LR	dir_left_hidari	h i d a r i
AUNIT	au_degree_do	d o
PEND	mk_pe_q mk_pe_a:	q (pause) a: (hesitation)
NI	joshi_ni_ni	n i

Table 5 Button event and action parameters

action type	duration	count	Key
move	distance	distance	speed / direction
turn	angle	angle	speed / direction
walk	distance	distance	Speed
look	-	-	speed/direction

V. METHODS

There are several ways to estimate command success rates of novice and trained users. One can teach users exactly how to give commands and then let them give the same commands. For spoken commands, one can show them a printed list of utterances presenting every word. Users can be tested given some general instructions and a set of actions, with a type and parameters for each, to be commanded in RUNA or a set of goals to be achieved by commanding a robot in the language.

The authors have developed a command recognition system on top of a multi-agent architecture [4] which interprets multi-modal commands in RUNA, integrating a grammar-based speech recognition engine [5], a gesture detector using the OpenCV library for computer vision (http://www.intel.com), a button press event detector, a tactile event detector, and a command interpreter which utilizes an action database [2, 3]. Recently, a speech synthesizer was added to the system to repeat valid spoken commands to help untrained users. This system has been applied to some test beds to direct real small humanoids and simulated robots on Webots5 simulator (http://www.cyberbotics.com) [6].

Each of 14 novice users, mostly high school students who visited Fukuoka Institute of Technology, gave 25 spoken commands to a small humanoid robot on a table in a noisy environment with many people (Test A). Each verbal command was displayed on a computer screen and the users were given an opportunity of practice before giving each command. We videotaped the users and logged all the system events including non-verbal events, speech recognition results and command interpretations. These users were tested using a reduced grammar with 148 rules and 133 words.

Another 14 novice users of a wider range who visited one of the authors' offices were given a three-page note which explains how to operate robots in RUNA (Test B). After a five minute practice of giving commands in the language, they were asked to remotely operate a humanoid in a simulated environment on Webots5 through a microphone and a keypad to explore a room monitoring images from the camera until they can answer three questions about the room: "Is there a note on the refrigerator?", "Is one of the drawers near the sink open?" and "Is there anything on the floor in front of the sink?" We recorded time to complete the task, multi-modal commands given by the users, and all the system events. We also video-recorded the users while they were giving commands to the simulated robot. The users were tested with a smaller grammar including 110 rules and 92 words.

VI. RESULTS

Some results of the former test (Test A) are shown in Table 6: each user's success rate of spoken commands on the screen (SR), speech recognition rate (RR), and word error rate (WER). Some of the commands were misrecognized by the speech recognizer but successful without errors in action types and parameter values for some reasons. There were one ungrammatical command (0.29%) and two grammatical commands which were slightly different from the command displayed on the screen (0.57%).

Table 6 Success rates of listed spoken commands

User	SR(%)	RR(%)	WER(%)
A1-A5	100	100	0
A6,A7	96.0	96.0	2.5
A8	96.0	92.0	3.7
A9	96.0	92.0	4.9
A10	96.0	88.0	3.7
A11,A12	92.0	92.0	4.9
A13	92.0	88.0	6.2
A14	92.0	84.0	6.2

Table 7 Success rates when achieving a goal

user	SRA(%)	RR(%)	WER(%)	SRM(%)
B1-B5	100	100	0	100
B6	100	97.2	1.7	100
B7	96.9	96.9	3.8	100
B8	95.4	95.4	2.2	97.5
B9	94.4	94.4	4.2	100
B10	93.7	93.7	6.9	94.7
B11	91.9	91.9	6.1	-
B12	90.7	88.9	11.1	100
B13	90.5	90.5	7.2	100
B14	88.0	88.0	14.8	75.0

Table 7 summarizes the results of the latter test (Test B): each user’s success rate of valid commands (SRA), speech recognition rate (RR), word error rate (WER), and success rate of valid multi-modal commands comprising speech and button press actions (SRM). The first five users in Table 7 succeeded in every command they gave with no speech recognition errors although there were a few false alarms per user. For several users, the success rate of multi-modal commands was higher than that of single-modal spoken commands. User B11 gave only spoken commands and user B14 was more successful in giving spoken commands. The users gave 17 to 79 (38.9 on average) valid commands in RUNA and it took about five to thirteen minutes for them to complete their task. Eight of them gave one or two invalid (ungrammatical) commands, which were 2% of all the user commands.

On average, 98.1 % of multi-modal commands and 91.3 % of single-modal spoken commands were successful. The difference is proved to be statistically significant ($p=0.0012$). The average success rate of the 14 users was 95.1%. The average command length of the multi-modal commands was 1.14 words which was significantly shorter than 2.28 words for the spoken commands.

VII. DISCUSSION AND SUMMARY

The facts that in the both user tests more than 95 percent of commands were successful and that there were little invalid commands imply that the users learned how to command robots in RUNA in a very short period of time. In Test B, multi-modal commands were more successful, presumably because multi-modal commands included fewer spoken words and numerical phrases such as “25 cm” or “45 degrees.” The user were more successful, even in a noisier place, than the users described in the authors’ previous work (78%) [3], partly because of the repetitions of spoken commands using the speech synthesizer, short practice, and the new grammar rules for hesitations and pauses. The users learned the language, how to effectively use the microphone, and how loud they should speak very quickly thanks to the speech feedback. In fact, there were much less frequent communication problems in Test B than in user in earlier studies [2, 3]. Using grammars for speech recognition for a specific purpose, the word error rates in most of the users’ commands were as low as 0-8%.

The users in Test B commanded the robot spontaneously without words on paper or the screen which might have slightly lowered their success rates although the grammar was a smaller one. Another hypothesis implied by the data is that young users can adapt to the system more quickly than older users including B11 and B14.

In summary, the results of two user tests show that the language enables users without much training to command home robots at high success rates. It is also shown by the results that multi-modal commands combining speech and button press actions included fewer words and were significantly more successful than single-modal spoken commands.

ACKNOWLEDGMENT

This work was supported by KAKENHI Grant-in-Aid for Scientific Research (C) (19500171).

REFERENCES

[1] Oka T, Yokota M (2007) Designing a multi-modal language for directing multipurpose home robots. Proceedings of the 12th International Symposium on Artificial Life and Robotics (AROB ’07), Beppu, Japan
[2] Oka T, Abe T, Sugita K, Yokota M (2009) RUNA: a multi-modal command language for home robot users. Journal on Artificial Life and Robotics 13-2 (to appear)
[3] Oka T, Abe T, Shimoji M, Nakamura T, Sugita K, Yokota M (2008) Directing humanoids in a multi-modal command language. The 17th International Symposium on Robot and Human Interactive Communication
[4] Cheyer A & Martin D (2001), The open agent architecture. Journal of Autonomous Agents and Multi-Agent Systems, 4-1/2:143-148, March
[5] Lee A, Kawahara A, Shikano K (2001) Julius --- an open source real-time large vocabulary recognition engine. Proceedings of the 7th European Conference on Speech Communication and Technology, Aalborg, Denmark
[6] Michael O (2004) Cyberbotics Ltd – Webots™: Professional Mobile Robot Simulation. International Journal of Advanced Robotic Systems 1-1:39-42

The Fourteenth International Symposium on Artificial Life and Robotics 2009 (AROB 14th '09),
B-Con Plaza, Beppu, Oita, Japan, February 5 - 7, 2009

Multi-modal Command Interface with Remote Home Robots

T. Abe[1], T. Oka[2], K. Sugita[2], and M. Yokota[2]

[1]Graduate School of Fukuoka Institute of Technology, 3-30-1, Wajiro-higashi, Higashi-ku, Fukuoka, 811-0295, Japan
[2]Fukuoka Institute of Technology, 3-30-1, Wajiro-higashi, Higashi-ku, Fukuoka, 811-0295, Japan
Tel : 81-92-606-4813; Fax : 81-92-606-0754
mdm07001@bene.fit.ac.jp, {oka, sugita, yokota}@fit.ac.jp

Abstract: This paper describes a multi-modal command interface with remote home robots based on a simple interaction model using a multi-modal command language and an animated humanoid communicator for multi-modal reactions. The interface can be realized using a mobile phone or a portable computer, and allows one to give multi-modal commands to a remote home robot through a microphone and buttons looking at pictures from home and the animated humanoid on the screen. It is designed to enable users unfamiliar with computers or robots to check rooms and operate appliances away from home. A test bed for user evaluation has been implemented on PCs based on a multi-agent platform, a speech recognition engine, and a robot simulator.

Keywords: Home robot, multi-modal interface, command language, animated humanoid, human-robot interaction

I. INTRODUCTION

In recent years, home robots for various purposes have been developed, some of which are already in the market. It is predicted that in near future they find their places to work as a new kind of interface with home appliances and achieve various tasks with or without their users at home. There are many kinds of potential tasks for those robots while their users are away from home. It would be desirable if tasks and commands could be given to them by remote users via a mobile phone or a small portable computer.

Some remote command interfaces with remote home robots have been recently developed. Typical examples of robots controlled by such an interface are Banryu and Roborior from Tmsuk (http://www.tmsuk.co.jp/), which can be operated pressing buttons on mobile phones. However, it is difficult to build a usable interface using only a small number of buttons. Another example is BlogAlpha developed by Toshiba [1] which allows users to type and send natural language commands and queries using a web browser. However, it is not appropriate for operating robots in real time and does not suit users unfamiliar with computers. Besides, such conventional interfaces have disadvantages on small mobile devices in general.

Voice-activated interfaces with robots [2, 3] have some advantages for our purpose. Even users with little training will be able to give spoken commands without trouble. However, speech recognition errors and background noises deteriorate command success rates and usability.

For the above reasons, the authors propose a new kind of input method combining spoken commands and button press actions, based on a multi-modal command language [4] in order for users to be able to intuitively operate robots without frequent errors in command recognition after a very short period of training.

Obviously, it is very difficult to operate a remote robot in real time if one cannot see the robot or its surroundings at all. Pictures from on-site cameras would help to give the robot tasks and see what is happening. Therefore, the proposed interface displays pictures from a camera on the operated robot on its screen. In addition, an animated humanoid robot appears on the screen and makes gestures to report what the real robot is doing.

The following part of this paper describes an overview of the multi-modal interface, an interaction model, the multi-modal command language, and the animated communicator designed for smooth and desirable multi-modal interaction.

II. MULTIMODAL INTERFACE

The multi-modal interface proposed in this paper can be realized using a mobile phone with a screen and a head set or a small portable computer. Fig. 1 illustrates a typical example of the interface, which displays pictures from a camera on a remote home robot and an animated humanoid "communicator" which speaks and makes gestures to communicate with users.

Using this multi-modal interface, one can command a home robot through a microphone and twelve buttons monitoring the screen and listening to the communicator. This interface is based on an interaction model described in the next section in order for users to command robots without confusion or communication problems.

Fig. 1 Multi-modal interface using a mobile phone

©ISAROB 2009

III. INTERACTION MODEL

1. Interaction states

Fig. 2 depicts the proposed interaction model for remote operation of home robots. This simple model has four interaction states, S1, S2, S3, and S4. In S1, the interface waits for a cue from a user without listening for a command. It listens for a new command in S2. If a valid command arrives, a transition to S3 will occur and the command will be interpreted. If executable, the command will be executed in S4. Otherwise, a transition back to S1 will occur.

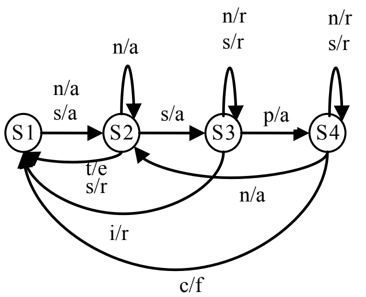

Fig. 2 Interaction model

2. User and system events

The interface is driven by user events and events generated by the interface itself. For instance, the transition from S1 to S2 in Fig. 2 is triggered by a non-verbal user event (n) or a speech event (s) from a user. A system event is either a possible action event (p), an impossible action event (i), a time out event (t), or a completion event (c).

3. Transition signals

In the interaction model, the system sends out transition signals whenever a state transition occurs. Transition signals include acceptance signals (a), rejection signals (r), finish signals (f), and empty signals (e). For example, in S3, a possible action event (p) will trigger a transition to S4 and an acceptance signal (a) sent to the user (hence, **p/a**, see the arrow from S3 to S4 in Fig. 2).

4. Multi-modal commands and communication cues

In the model, users give their robots multi-modal commands and communication cues through a microphone and buttons, generating speech and non-verbal events. Here, a multi-modal command is a series of non-verbal events followed by a speech event arising in S2 of the model. A cue is any user event generated in S1, S3, or S4. Therefore, users can give communication cues only when the system is not listening, in which case user events are recognized as communication cues rather than components of a multi-modal command.

IV. MULTI-MODAL LANGUAGE

The multi-modal language, RUNA, comprises a set of grammar rules and a lexicon for spoken commands and communication cues, and a set of non-verbal events detected using buttons on a mobile phone, a keypad etc. The spoken language enables users to command home robots in Japanese utterances, completely specifying an action to be executed. Commands in the spoken language can be modified by non-verbal events. Speech and non-verbal events are also used as communication cues as described in the previous section. When the robot is unaware of the user, any button event can cue the robot to listen for a command.

In the version of RUNA for the remote interface, there are two types of commands, action commands and modifier commands. An action command consists of an action *type* such as *walk, turn, report,* and *lowertemp (for lowering the temperature setting)* and action *parameters* such as *speed, direction, angle, object* and *temperature*. Table 1 shows examples of action types and commands in RUNA.

The action types of RUNA are categorized into 24 classes based on the way action parameters are specified in Japanese. In other words, actions of different classes are commanded with different modifiers.

There are more than 300 generative rules for the latest full version of RUNA (Table 2). These rules allow Japanese speakers to command robots actions in a natural way by speech alone and to give communication cues. In RUNA, a spoken action command is an imperative utterance including a verb to determine the action type and other words to specify action parameters. For instance, a spoken command, "Yukkuri 2 metoru aruke! (Walk 2m slowly!)", indicates an action type *walk* and distance *2m* (Fig. 3). The third rule in Table 3 generates an action command of class 2 (AC2) which has *speed* and *distance* (SD) as parameters. The word category PE is for noise, silence or hesitation voice allowed between parameters. This helps speech recognition and command interpretation.

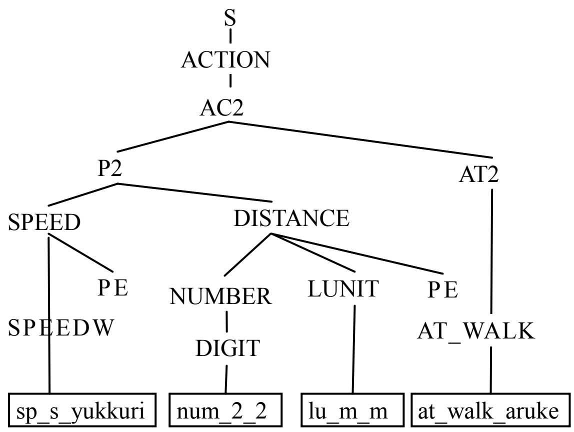

Fig. 3 An example parse tree for a spoken command

There are more than 250 words, categorized into about 100 groups identified by non-terminal symbols (Table 3). Because the language is simple, well-defined and based on the Japanese language, Japanese speakers would not need long training to learn it. Note that in user test sessions, a reduced set of grammar rules and words can be employed to improve speech recognition performance.

Table 1 Examples of action commands

Type	Command	English Utterance
walk	*walk_s_3steps*	Take 3 steps slowly!
turn	*turn_f_l_30deg*	Turn 30°left quickly!
move	*move_m_r_2steps*	Move 2 steps right!
look	*look_f_l*	Look left quickly!
raisetemp	*raisetemp_room_2deg*	Raise the temperature of the room by 2 degrees!
settemp	*settemp_aircon_22deg*	Set the air-conditioner temperature around 22 degrees!
query	*query_aircon_all*	Report the status of the air-conditioner!

Table 2 Grammar rules of RUNA

Rule	Description
S → ACTION	action command
S → MODIFIER	modifier command
ACTION → SD AC2	class 2 command
AC2 → AT2	action type (class 2)
P2 → SPEED	speed (parameter)
P2 → DISTANCE SPEED	distance + speed
P2 → SPEED DISTANCE	speed + distance
SPEED → SPEEDW PE	one word for speed
DIST → NUMBER LUNIT PE	number + length unit
MODIFIER → REPEAT	repeat last action

Table 3 Part of RUNA's lexicon

Non-terminal	Terminal	Pronunciation
AT_WALK	at_walk_hokou	h o k o:
REPEAT	md_repeat_moikkai	m o: i q k a i
SPEED	sp_fast_isoide	i s o i d e
LUNIT	lu_cm_cm	s e N ch i
DIR_LR	dir_left_hidari	h i d a r i
TUNIT	tu_degree_do	d o
AIRCON	dev_aircon_eakon	e a k o N
AUNIT	au_degree_do	d o
PEND	mk_pe_q	q (pause)
	mk_pe_a:	a: (hesitation)
NI	joshi_ni_ni	n i

In RUNA, non-verbal events modify the meaning of spoken commands. They convey information about parameters of action commands. Table 4 shows examples of non-verbal events. For the remote interface, users can use keypad buttons to specify action parameters values instead of mentioning them. This reduces average number of words in a command and speech recognition errors. One can command a robot saying "Turn!" and pressing a button simultaneously instead of saying "Turn 33 degrees left slowly!" Furthermore, multi-modal commands are often more natural than spoken commands: e. g. pointing a glass and saying "Pick this up!" or saying "Lower the temperature!" pressing a button.

If a button event has been arrived within a short period of time, a spoken command will be modified as shown in Table 4. The twelve buttons are assigned to specific parameter values (Fig. 4). For example, the direction and speed of a turning action command are determined by the key pressed most recently by the user. If the key has been pressed once, the turning angle will be determined based on the duration of the key press event. If the key has been pressed more than once, a fixed angle value will be employed. Likewise, if a key has been pressed *twice* before a spoken command "Raise the room temperature!" the preset temperature will be *two* degrees higher.

Finally, the repeat button and query button allow users to command robots without speaking. The empty button helps to send a cue without specifying action parameters.

Table 4 Button event and action parameters

action type	duration	count	key
sidestep walk etc.	distance	distance	speed / direction
turn etc.	angle	angle	speed / direction
look etc.	-	-	speed/target
raisetemp settemp	-	temperature	-

← left	↑ up	→ right	Fast
← left		→ right	Moderate
← left	↓ down	→ right	Slow
empty	query	repeat	Cue

Fig. 4 Key assignment for action parameters

V. HUMANOID COMMUNICATOR

The animated humanoid communicator of the remote interface (hereinafter referred to as *communicator*) displays the current communication state of the interface changing his pose and sends out transition signals speaking and using gestures. When the system is not listening for a command, i.e. when it is in S3, the communicator looks the other way; he looks straight when the system is listening in S2 (Fig. 5). When the home robot is executing the action (S4), the communicator imitates the home robot's motion.

The communicator uses gestures to provide transition signals (Fig. 6) so that users give commands at the right moment. He repeats spoken commands like a parrot when he understands them (in S2 of Fig. 2). If the command is an executable one, the communicator nods and says okay. He bows and says "I cannot do that!" if the command cannot be executed. Table 5 lists spoken messages and gestures on state transitions in Fig. 2.

Table 5 Gestures and spoken messages

transition	gesture	Message
S2 → S3	-	(repeat spoken command)
S2 → S1	shrug	"I don't understand!"
S3 → S4	nod	Okay!"
S4 → S1	salute	"I completed!"
S4 → S2	straighten up	"I stopped the action!"
S1 → S1	glimpse	"You cannot command
S3 → S3	shake hand	now!"
S4 → S4	cross arms	"I cannot stop now!"
S3 → S1	bow	"I cannot do that!"

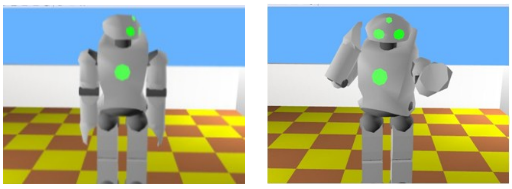

Fig. 5 Poses for S1 (left) and S2

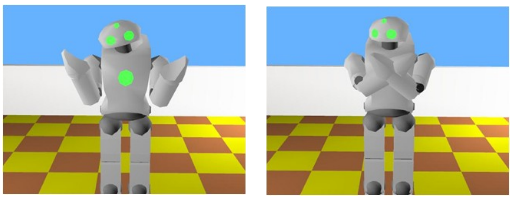

Fig. 6 Gestures for transition signals

Fig. 7 Simulated home environment on Webots5

VI. USER EVALUATION

1. Test bed

The remote interface has been implemented on top of the Open Agent Architecture (OAA) [5]. Speech events are detected by Julian, a grammar based version of a speech recognition engine [6], using a recognition grammar for RUNA. A command interpreter identifies the action type and parameter values mentioned in a spoken command; it determines unspecified parameter values using non-verbal events and default parameter values. Description of the multi-modal command interpreter in more detail can be found in some of the authors' previous papers [4, 7].

The communicator was built on Webots5.8.0 robot simulator (http://www.cyberbotics.com) and a free speech synthesizer. A simulated humanoid robot capable of execute actions in RUNA and a home environment were also created on the same robot simulator for user evaluation using a simulated home (Fig.7).

2. Methods

The remote interface can be evaluated in several ways. In user evaluation, potential users will be asked to achieve various tasks such as navigating the home robot, looking into rooms, operating home appliances and checking their status. Also, they will be asked to give one command at once from a command list for testing. It is planned that the simulated home robot system will be tested with more than 50 users.

VII. CONCLUSION

A multi-modal interface with remote home robots was presented. A test bed for user evaluation has been implemented based on a multi-agent architecture, a speech recognition engine, and a robot simulator. Future work includes full user evaluation using the test bed and implementation on portable devices.

AKNOWLEDGMENT

This work was supported by KAKENHI Grant-in-Aid for Scientific Research (C) (19500171).

REFERENCES

[1] Cho K, Kawamura T (2007) Home Security Robot Using Life Ontology and Blog Interface. Toshiba Review 62-12:50-53 (in Japanese)
[2] Prasad R, Saruwatari H, Shikano K (2004) Robots that can hear, understand and talk. Advanced Robotics 18-5:533-564
[3] Bos J, Oka T (2007) A spoken language interface with a mobile robot. Journal of Artificial Life and Robotics 11-1:42-47
[4] Oka T, Abe T, Sugita K, Yokota M (2009) RUNA: a multi-modal command language for home robot users. Journal on Artificial Life and Robotics 13-2 (to appear)
[5] Cheyer A & Martin D (2001), The open agent architecture. Journal of Autonomous Agents and Multi-Agent Systems, 4-1/2:143-148, March
[6] Lee A, Kawahara A, Shikano K (2001) Julius --- an open source real-time large vocabulary recognition engine. Proceedings of the 7th European Conference on Speech Communication and Technology, Aalborg, Denmark
[7] Oka T, Abe T, Shimoji M, Nakamura T, Sugita K, Yokota M (2008) Directing humanoids in a multi-modal command language. The 17th International Symposium on Robot and Human Interactive Communication

Some consideration on user adaptive interface for universal multimedia access

Yusaku Maeda[1], Eriko Tsujimura[2], Kaoru Sugita[2], Tetsushi Oka[2], and Masao Yokota2

[1]Graduate School of Fukuoka Institute of Technology, 3-30-1, Wajiro-higashi, Higashi-ku, Fukuoka, 811-0295, Japan
[2]*Fukuoka Institute of Technology, 3-30-1, Wajiro-higashi, Higashi-ku, Fukuoka, 811-0295, Japan*
Tel : 81-92-606-4965; Fax : 81-92-606-4965
mgm08004@bene.fit.ac.jp, {sugita, oka, yokota}@fit.ac.jp

Abstract: We have already proposed a new concept of 'universal multimedia access' intended to narrow the digital divide by providing appropriate multimedia expressions according to users' (mental and physical) abilities, computer facilities and network environments. In this paper, we redefine switching functions for our new concept of universal design based multimedia access and discuss its user interface to support the users in accordance with their abilities, computer facilities and network environments.

Keywords: Multimedia system, User interface, Digital divide.

I. INTRODUCTION

Recently, immense multimedia information has come to be exchanged on the Internet, where 3DCG, video, image, sound, and text are involved in various circumstances with terminal devices, networks and users different in their competences and performances. This fact may easily lead to 'digital divide' so called unless any special support is given to the weaker.

The universal design concept is proposed to support handicapped people in their social activities [1]. In the computer science field, the universal web [2] has been proposed to evolve this concept. However, this does not support to switch the contents, media and its quality of service (QoS) function to work the devices and network environments in their full performances. On the other hand, many studies about the QoS function proposed to optimize the video quality to give priority on users' requests [3]. These studies focused on performances of devices and network environments but neither users' abilities nor contents. Of course, there were also several studies on 'universal multimedia access (UMA)' but they could not narrow the digital divide because they concerned 'content switching' only [4].

Considering this fact, we have already proposed a new concept of UMA and its switching functions [5] intended to narrow the digital divide by providing appropriate multimedia expressions according to users' (mental and physical) abilities, computer facilities and network environments. In this paper, we redefine these switching functions and propose a concept of user adaptive interface for UMA.

II. UNIVERSAL MULTIMEDIA ACCESS

The digital divide is caused by the differences in users' personal competences, computer facilities and network environments with such detailed items as follows.

(1) Personal competence: sight ability, hearing ability, handling ability, language ability, computer skill and culture,

(2) Computer facility: processing power, resolution, color quality, sound quality and battery life,

(3) Network environment: bandwidth availability, specification and transfer mode.

Therefore, multimedia information is necessarily accompanied by switching user interface, media and QoS parameters reflecting these differences. Here, we present a new approach to UMA for handicapped people to work their devices and network environments in full performances. Our purpose is exclusively to develop a new mechanism for switching appropriately user interfaces, media and QoS parameters based on such a concept as shown in Fig.1.

III. SWITCHING FUNCTIONS

UMA is to selectively provide three kinds of switching function, namely, user interface switching (UIS), media switching (MS) and QoS switching (Q S). Fig.2 shows these switching functions working as follows:

(SF1) UIS: switch to user interface s (UI) appropriate for users' competences and display devices,

(SF2) MS: switch to media appropriate for users' competences, performances of terminal devices and networks,

(SF3) QS: control media qualities appropriate for users' competences and terminal devices.

These functions are applied in the ascending order (from SF1 to SF3) at beginning to play multimedia information or in the descending order at playing.

1. User Interface Switching

UIS sets up the following items using Table 1 and Table 2.

(U1) Writing style appropriate for language ability,

(U2) UI type and annotation option appropriate for computer skill,

(U3) Media size, font size, number of media and number of characters appropriate for display device size.

Additionally, I/O function is reflected by the users' disability.

2. Media Switching

MS switches to appropriate media according to their priorities after determining usable media types and QoS parameters by logical multiplication of Tab.1 and Tab.2. Numbers and types of media are selected by UIS and such priority as shown in Table.3. Media and its quality are limited by performances both of terminal devices and networks. When MS could not continue to play media by overload of CPU or network, MS is switched to UIS for reducing this load.

3. QoS Switching

QS controls media size and media rate with QoS parameters to measure performances both of terminal devices and networks. The QoS parameter 'Size' means as follows:

(S1) Video – Put priority on the frame size

(S2) Audio – Put priority on the sampling resolution and stereo sound

(S3) Image - Put priority on the size of image

(S4) Text – Enlarge the character

The QoS parameter 'Rate' means as follows:

(R1) Video – Put priority on the frame rate

(R2) Audio – Put priority on the sampling rate

(R3) Image - Put priority on the display timing

(R4) Text – Take priority over any other medias

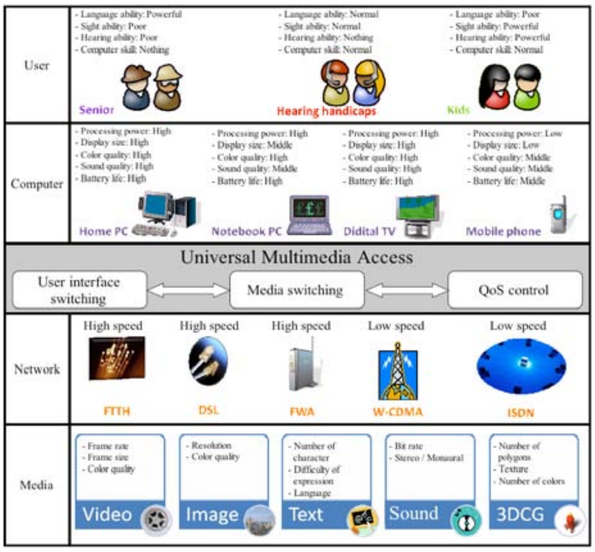

Fig.1. Universal multimedia access

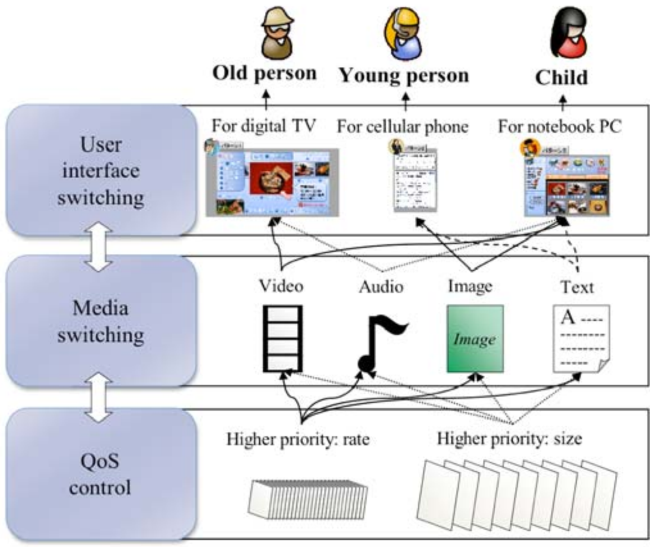

Fig. 2. Switching functions

Table 1. Users' abilities vs. multimedia expressions

		Parameter	Powerful	Normal	Poor	Nothing
Language ability	Expression of media		Advanced text	Simple text	Audiovisual	Nothing
Sight ability	Media	Text	○	○	×	×
		Image	○	○	○	×
		Audio	○	○	○	○
		Video	○	○	○	×
	QoS	Rate	○	○	×	×
		Size	○	○	○	○
Hearing ability	Media	Text	○	○	○	○
		Image	○	○	○	○
		Audio	○	○	×	×
		Video	○	○	○	○
	QoS	Rate	○	○	○	×
		Size	○	○	×	×
Computer skill	Userinterface		Interactive page	Hypertext	On demand	Broadcast
	Annotation		Nothing	Nothing	Abailable	Always

©ISAROB 2009

Table 2. Performances of terminal devices vs. multi media expressions

	Parameter		High	Middle	Low	Nothing
Processing power	Media	Text	○	○	○	×
		Image	○	○	○	×
		Audio	○	○	×	×
		Video	○	○	×	×
	QoS	Rate	○	○	○	×
		Size	○	○	○	×
Display size	Media	Text	○	○	○	×
		Image	○	○	×	×
		Audio	○	○	○	○
		Video	○	○	×	×
	QoS	Rate	○	○	○	○
		Size	○	○	○	○
Sound quolity	Media	Text	○	○	○	○
		Image	○	○	○	○
		Audio	○	○	×	×
		Video	○	○	○	○
	QoS	Rate	○	○	○	○
		Size	○	○	○	○
Battery life	Media	Text	○	○	○	×
		Image	○	○	○	×
		Audio	○	○	×	×
		Video	○	○	×	×
	QoS	Rate	○	○	×	×
		Size	○	○	×	×

Table 3. Network bandwidth vs. multimedia expression

	Nallowband	Broadband
Text	1	4
Image	2	3
Audio	3	2
Video	Nothing	1

When QS could not keep the quality by overload of CPU or network, QoS control is switched to MS for reducing this load.

IV. USER INTERFACE

UI consists of a template, layout and media expression with such detailed items as follows.

(1) Template includes type of UI and annotation

(2) Layout has media size, number of media, font size, number of characters,

(3) Expression uses writing style.

1. Template for User Interface

Template works to select a primitive UI and annotation option with computer skill. Computer skill is classified by following levels.

Level 1: start up application software,

Level 2: select to play media,

Level 3: display a Web page to input URL,

Level 4: find a desired Web page with search engine.

UI is different at each level because of different computer skill. Examples are shown in Fig.3. Broadcast UI is selected for level 1 not to operate as much as possible and to play media according to time schedule. The user could get information just like TV because it is not necessary to operate application software fundamentally. But the user could only get information according to the time schedule. On-demand UI is selected for level 2 to play selectable media. The user could play media only to click a desired media. But it takes user a much time to select from a lot of media. Hypertext UI is selected for level 3 to get information like a general Web page. The user could get information to input URL or click media with hyper link. But the user needs to understand these operations and gets addresses for desired information previously. Interactive page UI is selected for level 4 to support a search function and customize function. The user could search by keywords and customize both display region and visibility options to use customize functions.

2. Layout of Media

A layout is used to put media on UI and specified display position, display size and number of media for resolution of terminal device and each media. Typical resolution of terminal devices is shown in Fig.4 and available number of media is shown from Tab.4 to Tab.6. Using these relations, a layout is specified to display position after display size and number of media for resolution of terminal device and each media.

Fig. 3. Typical examples of user interface

Table 4. Number of characters for specification of resolution

	Resolution		8pt(11x11)			10.5pt(14x14)			12pt(16x16)			16pt(22x22)			18pt(24x24)		
Standard	Width [pixel]	Height [pixel]	Horizontality [Number of characters]	Verticality [Number of characters]	Total [Number of characters]	Horizontality [Number of characters]	Verticality [Number of characters]	Total [Number of characters]	Horizontality [Number of characters]	Verticality [Number of characters]	Total [Number of characters]	Horizontality [Number of characters]	Verticality [Number of characters]	Total [Number of characters]	Horizontality [Number of characters]	Verticality [Number of characters]	Total [Number of characters]
QVGA	320	240	29	21	609	22	17	374	20	15	300	14	10	140	13	10	130
VGA	640	480	58	43	2494	45	34	1530	40	30	1200	29	21	609	26	20	520
SVGA	800	600	72	54	3888	57	42	2394	50	37	1850	36	27	972	33	25	825
XGA	1024	768	93	69	6417	73	54	3942	64	48	3072	46	34	1564	42	32	1344
SXGA	1280	1024	116	93	10788	91	73	6643	80	64	5120	58	46	2668	53	42	2226
UXGA	1600	1200	145	109	15805	114	85	9690	100	75	7500	72	54	3888	66	50	3300
QXGA	2048	1536	186	139	25854	146	109	15914	128	96	12288	93	69	6417	85	64	5440
WQXGA	2560	1600	232	145	33640	182	114	20748	160	100	16000	116	72	8352	106	66	6996

Table 5. Number of images for specification of resolution

	Resolution		Image for cellular phone (96x120)			Image for cellular phone (320x240)			Image for 80 mega pixel digital still camera (1024x768)			Image for 300 mega pixel digital still camera (2048x1536)			Image for 800 mega pixel digital still camera (3264x2448)		
Standard	Width [pixel]	Height [pixel]	Horizontality [Number of images]	Verticality [Number of images]	Total [Number of images]	Horizontality [Number of images]	Verticality [Number of images]	Total [Number of images]	Horizontality [Number of images]	Verticality [Number of images]	Total [Number of images]	Horizontality [Number of images]	Verticality [Number of images]	Total [Number of images]	Horizontality [Number of images]	Verticality [Number of images]	Total [Number of images]
QVGA	320	240	3	2	6	1	1	1	0	0	0	0	0	0	0	0	0
VGA	640	480	6	4	24	2	2	4	0	0	0	0	0	0	0	0	0
SVGA	800	600	8	5	40	2	2	4	0	0	0	0	0	0	0	0	0
XGA	1024	768	10	6	60	3	3	9	1	1	1	0	0	0	0	0	0
SXGA	1280	1024	13	8	104	4	4	16	1	1	1	0	0	0	0	0	0
UXGA	1600	1200	16	10	160	5	5	25	1	1	1	0	0	0	0	0	0
QXGA	2048	1536	21	12	252	6	6	36	2	2	4	1	1	1	0	0	0
WQXGA	2560	1600	26	13	338	8	6	48	2	2	4	1	1	1	0	0	0

Table 6. Number of videos for specification of resolution

	Resolution		QCIF(176x144)			CIF(352x288)			DV(720x480)			720p(1280x720)			1080i(1920x1080)		
Standard	Width [pixel]	Height [pixel]	Horizontality [Number of videos]	Verticality [Number of video]	Total [Number of video]	Horizontality [Number of videos]	Verticality [Number of video]	Total [Number of video]	Horizontality [Number of videos]	Verticality [Number of video]	Total [Number of video]	Horizontality [Number of videos]	Verticality [Number of video]	Total [Number of video]	Horizontality [Number of videos]	Verticality [Number of video]	Total [Number of video]
QVGA	320	240	1	1	1	0	0	0	0	0	0	0	0	0	0	0	0
VGA	640	480	3	3	9	1	1	1	0	1	0	0	0	0	0	0	0
SVGA	800	600	4	4	16	2	2	4	1	1	1	0	0	0	0	0	0
XGA	1024	768	5	5	25	2	2	4	1	1	1	0	1	0	0	0	0
SXGA	1280	1024	7	7	49	3	3	9	1	2	2	1	1	1	0	0	0
UXGA	1600	1200	9	8	72	4	4	16	2	2	4	1	1	1	0	1	0
QXGA	2048	1536	11	10	110	5	5	25	2	3	6	1	2	2	1	1	1
WQXGA	2560	1600	14	11	154	7	5	35	3	3	9	2	2	4	1	1	1

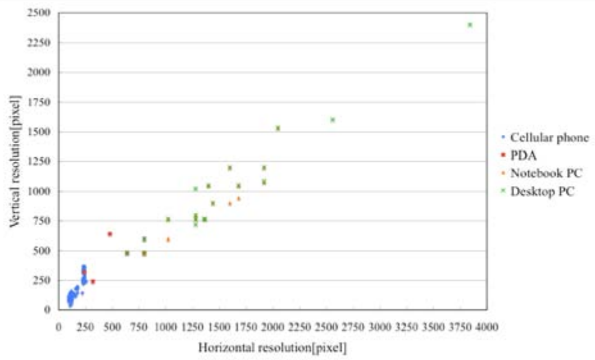

Fig.4. Resolution of terminal device

3. Expression of Media

An expression includes a difficulty of writing style, Kana-Kanji option, alternative media and language. They are determined by language ability and applied to following examples.

(Ex.C1) For children (language ability is low): simple kana text with notes

(Ex.C2) For old person (language ability is high): replacement a loan word with Japanese word

In addition, difficult text is substituted for another media. Also, there are filtered harmful contents from multimedia information.

V. CONCLUSION

In this paper, we redefined switching functions for universal design based multimedia access and discussed its user interface. UMA applies the switching functions to multimedia information according to users' (mental and physical) abilities, computer facilities and network environments. Especially, UIS employs functions to select a template, set up for layout and expressions. Currently, we are implementing a framework for our proposed concept. In the future, we will define rules and transport protocols for each switching function and propose a multimedia markup language for UMA.

REFERENCES

[1] Ronald L. Mace, Graeme J. Hardie, and Jaine P. Place (1996), Accessible Environments: Toward Universal Design. AUED

[2] Kazuhiko Yamazaki (2001), Achievement of universal Web (1) (in Japanese). Design study research 48:330-331

[3] Mohan, R, Smith, J.R and Chung-Sheng Li (1999), Adapting multimedia Internet content universal access, IEEE Multimedia Transcations 1(1):104-114

[4] Fernando Pereira and Ian Burnett (2003), Universal Multimedia Experience for tomorrow, IEEE Signal Proccesing Magazine, IEEE 20(2): 63-73

[5] Y. Maeda, K. Sugita, T. Oka, and M. Yokota (2008), Proposal of a New Concept of Universal Multimedia Access, Proc. 13th International symposium on ARTIFICIAL LIFE AND ROBOTICS (AROB 13th '08), OS7-6.

The Fourteenth International Symposium on Artificial Life and Robotics 2009 (AROB 14th '09),
B-Con Plaza, Beppu, Oita, Japan, February 5 - 7, 2009

Control of Damping with Reinforcement Learning for Power-assisted Positioning Task

Tetsuya Morizono[1] and Masatake Higashi[2]

[1]Fukuoka Institute of Technology, 3-30-1, Wajiro-higashi, Higashi-ku, Fukuoka, 811-0295, Japan
morizono@fit.ac.jp
[2]Toyota Technological Institute, Tempaku-ku, Nagoya, Japan

Abstract: Finding an appropriate reference of kinetic characteristic is a major problem of an impedance-controlled power-assist robot. In this paper, autonomous adjustment of damping (viscosity) based on subjective operational feeling of an operator is discussed. For autonomous adjustment, reinforcement learning is utilized. For adaptation of the robot to a positioning task including multi goal positions, a method for inference of the goal position is developed. Experimental results show that the method developed in this paper is capable of adjusting viscosity of the robot so that dissipation of kinetic energy of the robot assists positioning of an operator at the goal position.

Keywords: Control, Damping, Reinforcement Learning, Power-assist, Positioning, Operational feeling

I. INTRODUCTION

When a power-assist robot is controlled by the impedance control, a major problem is how to find a reference of mechanical impedance appropriate for assistance of an operator. Many studies prefer variable impedance control where control parameters (desired mass, viscous coefficient and/or stiffness) are variable (for example [1]), and operational force and even stiffness of the operator's arm was used as reference signals for adjustment of the control parameters [2][3].

In contrast with those studies, Yamada et al. proposed a scheme for adjustment of control parameters named "Field Impedance Equalizer (FIE)" [4]. The study assumed a repetitive power-assisted positioning task, and the proposed scheme aimed at tune up of the parameters in interaction between an operator and a power-assist robot. Experimental results showed that the viscous coefficient could be adjusted so that an operator obtained a good subjective operational feeling of a robot. However, autonomous adjustment of the coefficient has not been well studied. Therefore, the authors have proposed a method of autonomous adjustment of the viscous coefficient based on FIE [5].

The previous study assumes that the operational distance of a positioning task is constant. However, many tasks existing in factories (an assembly task of automobiles, for example) include different goal positions between operations, and the goal position is often determined by a worker in real time. To extend the previous studies to the case where the operational distance is different between operations and the distance is determined in real time, this paper proposes EFDA (Enhanced Field Damping Adjuster).

II. FIE AND PARAMETER ADJUSTMENT

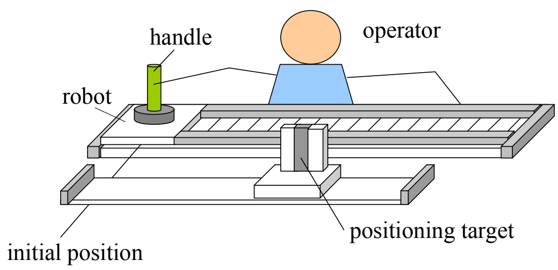

Fig. 1 A 1-DOF power-assist robot

The study in this paper considers a repetitive positioning task with a 1-DOF power-assist robot, as shown in Fig. 1. One task includes repetition of operations from the initial position to the goal position. An operation is one-way; after the robot is positioned at the goal position, return of the robot to the initial position is automatic.

If the goal position is fixed throughout the task, the operating distance is fixed. In this case, the distance can be divided into several sections with constant lengths. The previous study by Yamada et al. [4] defined each of the sections as a "field". *Impedance* parameters of mass, viscous coefficient and stiffness were defined dependent on the field, and tuned (*equalized*) based on operational feeling of the robot. This is the framework of FIE.

Based on FIE, the authors proposed a method of autonomous adjustment. The method adjusted the viscous coefficient, and reinforcement learning was applied for autonomous adjustment. In the method, the state and the action of the agent was defined as the field number and the value of the viscous coefficient, respectively. The action value functions $Q(i, d_i)$ of all the fields were updated by Q-learning, here i and d_i denote the field number and the value of the viscous coefficient at the field i (the field with the number i).

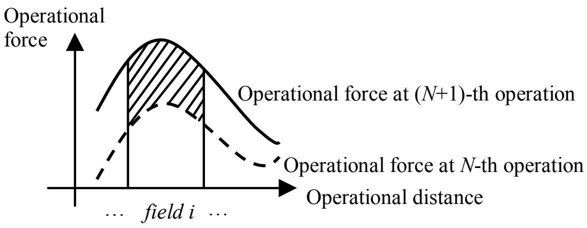

Fig. 2 Profiles (operational force)

If the reward r_i is calculated based on evaluation of operational feeling, $Q(i, d_i)$ reflects the evaluation through learning, here r_i is the reward when the robot passes the field i. In the previous study [5], the evaluation was measured by the degree of convergence between the profiles at the field i obtained in the N-th and (N+1)-th operations. Here, the profile means the plot of the operational force or the velocity of the robot where the operational distance of the robot is assigned to the horizontal axis, as explained in Fig. 2. The degree of convergence at the field i was calculated by the area formed by the plots and the boundary lines of the field i, and a smaller area provided a larger reward at the field i of (N+1)-th operation. This evaluation was based on the assumption that the profile was convergent when a good operational feeling is obtained, and the assumption was based on an experimental observation in the study by Yamada et al. [4]

III. EXTENTION TO EFDA

Operational feeling from the initial position through a goal position is determined by a sequence of viscous coefficients from the first field (the field where the initial position locates) through the goal field (the field where the goal position locates). If we consider extension of the previous study described in the previous section to the case where the number of goal positions which can be selected by an operator is n (n>1), n sequences of viscous coefficients are required and should be learned. In addition, if selection of a goal position is made by an operator in real time, a function of inferring the goal position is necessary, because the goal position cannot be told to the robot in advance before an operation.

To the above problems, the study in this paper considers the extension of the previous study, referred to as EFDA.

1. Sequence of viscous coefficient

When the goal field is the field j, the sequence of viscous coefficients is defined as

$$D_j = \{d_{j1}, \cdots, d_{ji}, \cdots, d_{jj}\}, \tag{2}$$

where $i = 1, \cdots, j$ denotes the field number and $j = 2, \cdots, J$. The field J denotes the field where the farthest goal position from the initial position locates. d_{ji} denotes the viscous coefficient chosen by an agent at the field i when the goal field is the field j.

2. Inference of the goal field

Accurate inference of the goal position is a difficult problem in general. However, adjustment of viscous coefficients is "field-dependent" in the study in this paper. Therefore, the adjustment can be performed if the goal field is inferred. Although several types of algorithms (using Hidden Markov Model, for example) can be considered for inference, this paper considers a simple method.

At the initial stage, an operator is asked to perform *one* operations of positioning to each of all the fields used in a positioning task. By the operations, an initial profile of velocity is obtained for each field, and the robot memorizes the profiles.

In each operation of positioning, the profile of the velocity for the current operation is updated with the measured velocity when the robot enters a new field. The entrance also cues comparison between the updated profile and the profiles memorized in the robot. Integrations of absolute errors between the profiles are calculated, and the field of which profile in the robot gives the smallest value of integration is treated as the goal field at the timing of the entrance. The comparison is repeated until the robot is stopped at the goal field.

After each operation, the profile in the robot is updated. If the robot is stopped at the field k, the profile of the goal field k is replaced with the profile obtained in the current operation. This replacement is important because it is thought that the profile varies according to improvement of skill and fatigue of an operator.

3. Choice of viscous coefficient

If the inferred goal field is the field j when the robot enters the field i, the agent chooses d_{ji} in D_j for control of operational feeling. Furthermore, if the inferred goal field in the next field is the field *j'*, the agent changes choice of the sequence to $D_{j'}$ and select $d_{j'(i+1)}$.

4. Update of the action value function

We assume that the goal field of an operation is the field *k*, and the inferred goal fields from the fields 1 through *k* includes an inference error at the field *i*. If the incorrect inference is the field *k'*, the selection of the viscous coefficients for this operation is $\{d_{k1}, \cdots, d_{k'i}, \cdots, d_{kk}\}$. In this case, the action value function of not $Q(i, d_{ki})$ but $Q(i, d_{k'i})$ is updated for the field *i*.

This update is natural in the context of the theory of reinforcement learning. However, the authors think that an inference error affects learning process. In the above example, if the inferred goal field is correct in the field *i* at the next operation to the goal field *k*, d_{ki} which is not learned in the previous operation to the goal field *k* is selected for the field *i*. This is a problem needed to be discussed. In this paper, the result of experimental investigation is reported in the next section.

IV. EXPERIMENT

1. Setup

Experimental investigation was carried out with the experimental setup as shown in Fig. 1 and some operators. The length of a field was 0.1[m] and seven fields (the fields 1 through 7) were prepared. The task included six goal positions located in the range of 0.2 to 0.7[m] from the initial position at the interval of 0.1[m]. In each of operation, one of goal positions was randomly indicated to the operator by a positioning target. Here, the target position was not told to the robot.

The desired mass and stiffness of the robot were fixed to 10[kg] and 0[N/m], respectively. The desired viscous coefficients prepared for choice by the agent were nine values, ranging from 10 to 50[Ns/m] at the interval of 5[Ns/m]. Adjustment was not applied to the field 1 (including the initial position) and the viscous coefficient of the field (namely, d_{21}, d_{31}, $\cdots$, d_{71}) was fixed to 10[Ns/m], which was the minimum value of the choice. The value was determined based on a well-known result of power-assist devices that a smaller viscous coefficient is preferable in the initial position of an operation.

2. Task

An operator was asked to position the robot at the goal position indicated by the target. After each operation, the operator was also asked to judge whether a preferable operational feeling was obtained or not. If the operator thought that the operational feeling was preferable, adjustment of viscous coefficients to the goal position was finished, and the goal position was excluded from the indication after the next operation.

The operation and the judgment described above were repeated until operational feelings to all the goal positions became preferable for the operator.

3. Results

Table 1 shows the viscous coefficients obtained by one of operators after adjustment. Note again that the field 1 was not included in adjustment. From Table 1, two observations are made. The first is that the values of viscous coefficients around the goal field are larger than those at the field 1. This observation suggests that dissipation of kinetic energy by larger viscosity around the goal field assists positioning of the operator, and the observation is similar to that reported in other studies of power-assist devices. The second observation is that the sequences of viscous coefficients are categorized into two groups: the sequences to the fields 2 and 3, and those to the fields 4 through 7. In the former group, the value of viscous coefficient at the field 2 is 35[Ns/m], whereas its values are 10 and 15[Ns/m] in the latter group.

Table 1 Viscous coefficients after adjustment

goal	field						
field	1	2	3	4	5	6	7
2	10	35	-	-	-	-	-
3	10	35	25	-	-	-	-
4	10	10	20	35	-	-	-
5	10	10	20	25	20	-	-
6	10	15	20	25	20	25	-
7	10	15	15	20	25	25	25

For further consideration of the second observation, correct rates of inference are shown in Table 2. It is observed that high correct rates are marked around the goal field, whereas moderate rates are observed in the field far from the goal field. Especially, the rates at the field 2 when the goal fields are the fields 4 through 7 are in the range of 20.0 to 66.7[%]. This indicates that inaccuracy of inference at the field 2 induces random choice of viscous coefficient, and d_{42}, d_{52}, d_{62} and d_{72} are equally learned to some extent.

Table 2 Correct rates of inference [%]

goal field	field						
	1	2	3	4	5	6	7
2	75.0	100	-	-	-	-	-
3	50.0	66.7	100	-	-	-	-
4	26.7	66.7	80.0	93.3	-	-	-
5	20.0	20.0	80.0	100	100	-	-
6	11.1	22.2	44.4	55.6	77.8	100	-
7	22.2	55.6	77.8	55.6	77.8	100	100

The above consideration suggests that inaccuracy of inference has an influence on learning process. The authors think that the inaccuracy can be taken into account for improved design of the agent, and the design is one of future work.

4. Evaluation of operational feeling

For further study of EFDA in future, the authors attempted to evaluate operational feeling from a viewpoint of energy. The index for evaluation was $J = E_2/E_1$, where E_1 denotes the energy which an operator exerts on the robot in one operation, and E_2 denotes the energy dissipated by the operator in the operation. The energy is calculated by integration of the product of operational force and velocity throughout the operation. Here, the velocity is always positive because one-way operation is assumed in this paper. Therefore, E_1 and E_2 are obtained by the integrations where the operational force is positive and negative, respectively.

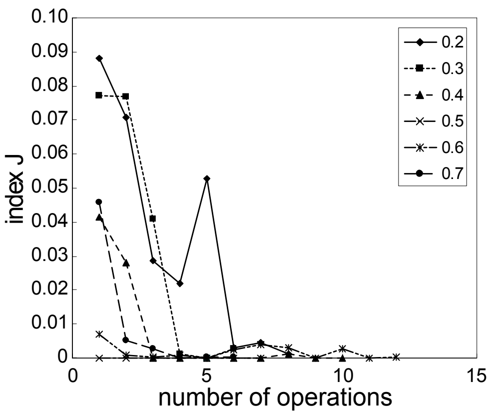

Fig. 3 Transitions of the index J

Figure 3 shows the transitions of J, where the values of $j \times 0.1$ denote the goal position located in the field j. The horizontal axis denotes the number of operations to each goal position. The plots shows that J for all the goal positions become small values (under 5×10^{-3}) at finish of adjustment. However, the plots also indicate that process to finish of adjustment is different between the positions. These observations suggest possibility of measuring preference to operational feeling by energy. However, necessity of another index is also suggested for evaluation of the adjustment process.

V. CONCLUSION

This paper discussed autonomous adjustment of viscosity of a power-assisted positioning task from a viewpoint of operational feeling. Under the assumption that an operator selected one of multi goal positions in real time for an operation, EFDA (Enhanced Field Damping Adjuster) was proposed for realization of preferable operational feelings to all the goal positions, and a function of inferring a goal position and an adjuster using reinforcement learning were developed.

Experimental results showed that adjustment of viscosity was processed so that dissipation of kinetic energy of the robot assisted positioning at the goal position, and also that inaccurate inference of goal positions affected learning process. Considering an improved design of the agent is one of future work.

The study in this paper was supported by Grant-in-Aid for Young Scientists (B) 17760216, and was a part of High-tech Research Center Project (Toyota Technological Institute, 2003-2007).

REFERENCES

[1] R. Ikeura and H. Inoue (1995), Variable Impedance Control of a Robot for Cooperation with a Human, Proc. 1995 IEEE Int. Conf. on Robotics and Automation, 3097-3102

[2] O. M. Al-Jarrah and Y. F. Zheng (1997), Arm-Manipulator Coordination for Load Sharing Using Variable Compliance Control, Proc. 1997 IEEE Int. Conf. on Robotics and Automation, 895-900

[3] T. Tsumugiwa, R. Yokogawa and K. Hara (2002), Variable Impedance Control Based on Estimation of Human Arm Stiffness for Human-Robot Cooperative Calligraphic Task, Proc. 2002 IEEE Int. Conf. on Robotics and Automation, 2002

[4] Y. Yamada, Y. Umetani, H. Daitoh et al. (1999), Construction of a Human/Robot Coexistence System Based on A Model of Human Will - Intention and Desire, Proc. 1999 IEEE Int. Conf. on Robotics and Automation, 2861-2867

[5] T. Morizono, H. Kohno, M. Higashi et al. (2004), A Preliminary Study for Realization of Field Impedance Equalizer with an Automatic Adjusting Function, Proc. 13th IEEE International Workshop on Robot and Human Interaction, 407-412

Unsupervised Learning Method for Support Vector Machine and its Application to Surface-Electromyogram Recognition

Shuji KAWANO Hiroki TAMURA Koichi TANNO

Faculty of Engineering, University of MIYAZAKI
1-1 Gakuken kibanadai-nishi, Miyazaki-shi, 889-2192 Japan
(Email:htamura@cc.miyazaki-u.ac.jp)

Abstract

Support Vector Machine (abbr. SVM) is known as one of the most influential and powerful tools for solving classification and regression problems. But original SVM does not have online learning technique. Therefore, online learning techniques of SVM were introduced by many researchers. In this paper, we propose unsupervised online learning method using self organized map for SVM. Furthermore, the proposed method has the technique of reconstruction of SVM. We compare it performance with the original SVM, supervised learning method of SVM, neural network, and also test our propose method on surface electromyogram recognition problems.

keywords: Surface-Electromyogram, Support Vector Machine, Self-Organizing Map, Pattern Classification Problem

1 Introduction

Surface electromygram signals (abbr. s-EMG) are detected over the skin surface and are generated by the electrical activity of the muscle fibers during contraction [1]. The load of s-EMG that rests upon the user for non-erosion is less than that of other biological signals. Therefore the application that uses s-EMG is actively developed. s-EMG recognition of using the conventional neural network is a method which learns the relation between s-EMG patterns and is reproduced using a neural network. In the recognition system, there are some problems that the s-EMG changes by the muscle wasting. In general, the muscle wasting will cause a decrease in the frequency of s-EMG and the tension. This is assumed to be the one due to the decrease at the muscle fiber conduction velocity [2]. Therefore, an additional learning function that corresponds to the muscle wasting is necessary for the s-EMG application. Support Vector Machine is known as one of the most influential and powerful tools for solving classification and regression problems [3]. But original SVM does not have online learning technique. Therefore, online learning techniques of SVM were proposed by many researchers [4] [5] [6].

In this paper, we propose unsupervised online learning method using self organized map (abbr. SOM) [7] for SVM. Furthermore, the proposed method has the technique of restructuring of SVM. Our proposed method has the advantage of small required memory size and small computational complexity. We test our proposed method to the s-EMG recognition problems.

2 Proposed Method

In this section, we introduce SVM and propose unsupervised learning method for SVM based on SOM.

2.1 Introduction of SVM

In this subsection, we summarize support vector machines for two-class problems. Assume the training sample $S = ((\mathbf{x}_i, y_i), ..., (\mathbf{x}_i, y_i))$ consisting of vectors $\mathbf{x}_i \in R$ with $i = 1, ..., N$, and each vector $\mathbf{x}_i$ belongs to either of the two classes. Thus it is given a label $y_i \in \{-1, 1\}$. The pair of $(\mathbf{w}, b)$ defines a separating hyper-plane of equation as follows:

$$(\mathbf{w}, \mathbf{x}) + b = 0 \tag{1}$$

However, Eq.(1) can possibly separate any part of the feature space, therefore one needs to establish an optimal separating hyper-plane (abbr. OSH) that divides S leaving all. The points of the same class are accumulated on the same side while maximizing the margin which is the distance of the closest point of S. The closest vector $\mathbf{x}_i$ is called support vector (abbr. SV) and the OSH $\mathbf{w}', b'$ can be determined by solving an optimization problem. We explain how to select candidates for SV. The solution of this optimization problem is given by the saddle point of the Lagrangian.

©ISAROB 2009

$$\begin{array}{ll} \text{Maximize margin} & \frac{1}{2}(\mathbf{w}, \mathbf{w}) \\ \text{Subject to} & y_i((\mathbf{w} \cdot \mathbf{x}_i) + b) \geq 1 \end{array}$$

to solve the case of nonlinear decision surfaces, the OSH is carried out by nonlinearly transforming a set of original feature vectors $\mathbf{x}_i$ into a high-dimensional feature space by mapping $\Phi : \mathbf{x}_i \rightarrow \mathbf{z}_i$ and then performing the linear separation. However, it requires an enormous computation of inner products $(\Phi(\mathbf{x}) \cdot \Phi(\mathbf{x}_i))$ in the high-dimensional feature space. Therefore, using a Kernel function which satisfies the Mercer's theorem given in Eq.(2) significantly reduces the calculations to solve the nonlinear problems. In this paper, we used the Gaussian kernel given in Eq.(3) as the kernel function. The SVM decision function $g(\mathbf{x})$ and output of SVM are as given in Eq.(4) and Eq.(5).

$$(\Phi(\mathbf{x}) \cdot \Phi(\mathbf{x}_i)) = K(\mathbf{x}, \mathbf{x}_i) \tag{2}$$

$$K(\mathbf{x}, \mathbf{x}_i) = \exp \frac{-||\mathbf{x} - \mathbf{x}_i||}{2\sigma^2} \tag{3}$$

$$g(\mathbf{x}) = \sum_{i=0}^{N} w_i K(\mathbf{x}, \mathbf{x}_i) + b \tag{4}$$

$$O = sign(g(\mathbf{x})) \tag{5}$$

2.2 Unsupervised Learning Method

The SOM algorithm was introduced by Kohonen [7]. SOM is a kind of artificial neural network that is trained using unsupervised learning. In the basic version, only one map winner at a time is activated corresponding to each input. And, the vector corresponding to the map vector who is called a reference vector was adjusted by learning rule. This model and its variants have been very successful in several real application areas. In this paper, the training vector is used as learned object instead of the reference vector. When SVM maps input data to a nonlinear space, training vectors have very important action. However, the changing input data cannot be correctly mapped using SVM with the training vector at the beginning. The recognition mistake happens when the recognition data changes in the time series like the muscle wasting of s-EMG. To solve this problem, the training vectors are adjusted sequentially according to the SOM algorithm. The possibility of not satisfying the solution of the condition of the margin maximization that is the feature of SVM is caused by updating SOM algorithm. Therefore, this problem is solved by retraining SVM based on changing SV. Moreover, the number of training vectors must be limited for real problems of memory size. Then, we proposed unsupervised online learning method using SOM for SVM and restructure technique.

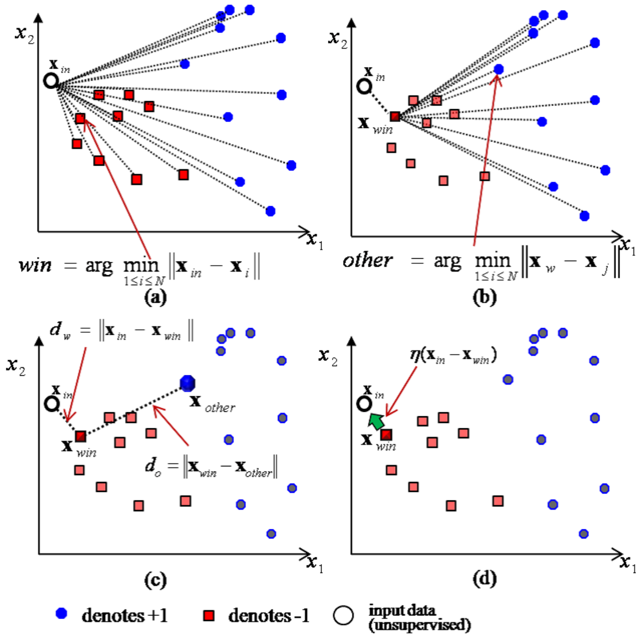

Figure 1: The flow of proposed method using SOM

Let the input space be denoted by $\mathbf{x}_{in} \in R$. The training vectors are included in kernel function, $\mathbf{x}_i$ with $i = 1, ..., N$, belongs to either of the two classes. Thus it is given a label $y_i \in \{-1, 1\}$. Each training vector has the same dimension of input space. To find the best match of the input vector $\mathbf{x}_{in}$ with the training vectors $\mathbf{x}_i$, the euclidean distance between $\mathbf{x}_{in}$ and each $\mathbf{x}_i$ is computed (Fig.1.a). Then the $\mathbf{x}_{in}$ with the smallest distance is selected as

$$win = arg \min_{1 \leq i \leq N} ||\mathbf{x}_{in} - \mathbf{x}_i|| \tag{6}$$

The particular processing element that satisfies this condition is called the winning training vector $\mathbf{x}_{win}$, for the input vector $\mathbf{x}_{in}$. d_w is the euclidean distance between $\mathbf{x}_{in}$ and $\mathbf{x}_{win}$. Next, find the best match of the $\mathbf{x}_{win}$ with the training vectors $\mathbf{x}_j$, the euclidean distance $\mathbf{x}_{win}$ and each $\mathbf{x}_j$ is computed (Fig.1.b). However, $\mathbf{x}_j$ should be a different class from $\mathbf{x}_{win}$. The $\mathbf{x}_j$ which becomes the smallest distance is selected. This selected training vector is called $\mathbf{x}_{other}$, and d_o is the euclidean distance between $\mathbf{x}_{win}$ and $\mathbf{x}_j$. If d_w is condition of rule of Eq.(7), $\mathbf{x}_{win}$ is updated according to the learning rule of Eq.(8) (Fig.1.c and Fig.1.d).

$$d_w \leq \zeta \times d_o \tag{7}$$

$$\mathbf{x}_{win}^{new} = \mathbf{x}_{win}^{old} + \eta(\mathbf{x}_{in} - \mathbf{x}_{win}^{old}) \tag{8}$$

©ISAROB 2009

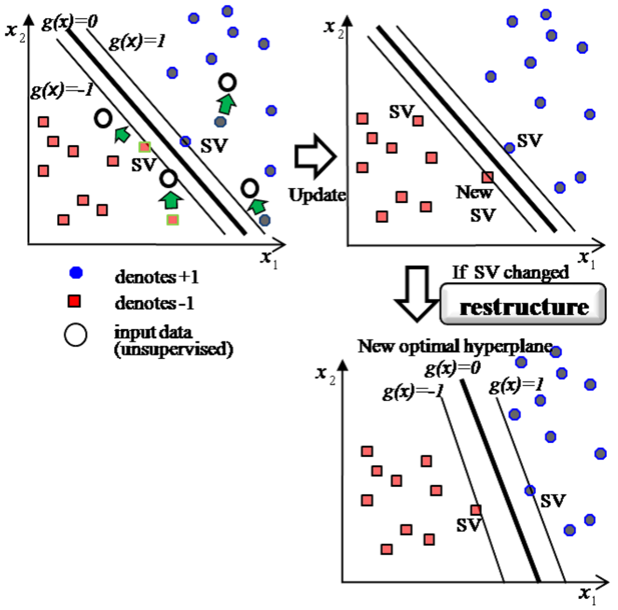

Figure 2: The technique of restructuring of SVM

Parameter ζ is allowable parameter. Parameter η is update parameter. In this paper, we used parameter $\zeta = 0.7$, and $\eta = 0.1$. If SV changed after the update, SVM is restructured with the updated training vectors (Fig.2).

3 Computer Simulations

In this section, the system configuration for recognition experiments of forearm motions using s-EMG is explained. Next, the result of computer simulations is described.

3.1 Experimental Condition

The construction of proposed s-EMG pattern recognition system is shown in Fig.3. The system consists of an input part, a feature extraction part and pattern classification and learning part. S-EMG of each movement pattern is measured with electrode sensors, and the feature quantity is extracted from the s-EMG. The feature quantity is given to the recognition machine as an input and each movement pattern that generates s-EMG is presumed. The feature quantity uses minimum-maximum (abbr. min-max) values and integration values [8]. Paper [8] showed that technique of min-max values and integration values are more easy and superior than FFT processing. The sampling frequency of the measurement data is 1 KHz. And the band is from 0 KHz to 500 KHz.

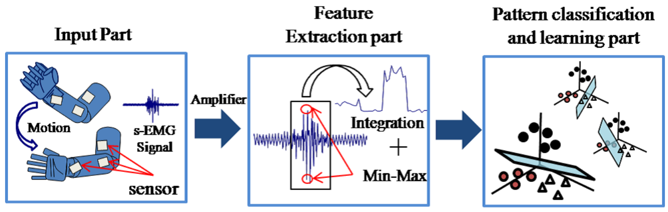

Figure 3: Structure of the EMG recognition system

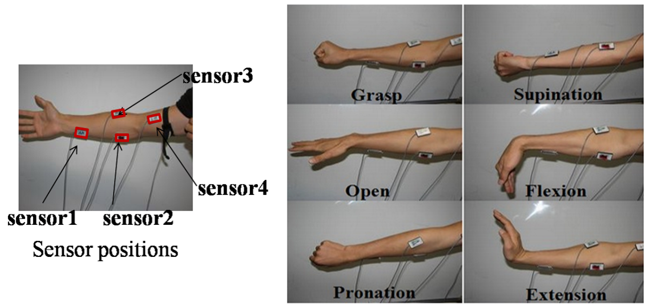

Figure 4: Image figure of forearm motion

3.2 Experiments of Forearm Muscles

We experimented on the effectiveness of the proposed method by the s-EMG recognition problem that the feature quantity changes by the muscle wasting. We compared proposed method performance with the original SVM, MLP, supervised learning method [9] and other unsupervised learning method. Supervised learning method of paper [9] is a method of adjusting threshold b of SVM (Eq.(4)) by online additional learning. This technique was effective to s-EMG recognition problem. In this paper, SOM only method (without part of restructured technique) and every time restructured SVM (SOM with restructured technique when training vectors were updated) are used as additional unsupervised learning method to compare the effectiveness of proposed method. The experimental subject is healthy man (S.K). The subjects sit on a chair. The recognition experiment of the 6 motions pattern is conducted by using s-EMG obtained from four sensors set in the arm of the right hand (Fig.4). Moreover, the input given to the identification machine is eight inputs. The experiments are conducted for three days.

The experiment method, first acquires the training data from s-EMG concerning the movement of forearm. Next, SVM and MLP learn the relation between s-EMG and motion from the training data. And, each motion is identified 20 times. Next, the subject trains few minutes with watching the recognition result on the display. Afterwards, additional supervised learning data is obtained from each motion. The experi-

©ISAROB 2009

ment repeats the measurement nine times.

3.3 Experimental Result

We performed with each method and the simulation results are Fig.5. Proposed method is better than original SVM. And, proposed method had better performance in unsupervised learning method, because the recognition calculation of the proposal method is fast. The 3 days average of muscle wasting experiment results MLP was 86.7%, original SVM was 85.7%, supervised learning method was 89.2%, every time restructured using SOM was 90.4%, SOM only 89.5%, and proposed method was 90.1%. We compared proposed method with total restructuring frequencies, proposed method was 16, every time restructured method was 601. We approached t-test (significance level of 5%) that changed parameter ζ and η. The t-test had a similar tendency of the results of Fig.5. The simulation results showed that the recognition rate of proposed method has improved by unsupervised learning method and original SVM.

4 Conclusion

In this paper, we proposed unsupervised learning method using SOM for SVM corresponding to s-EMG recognition problems. The experiment results showed that the proposed method was effective to s-EMG recognition problem.

Acknowledgements

This research has been supported by TATEISHI Science and Technology Foundation (No.1081019).

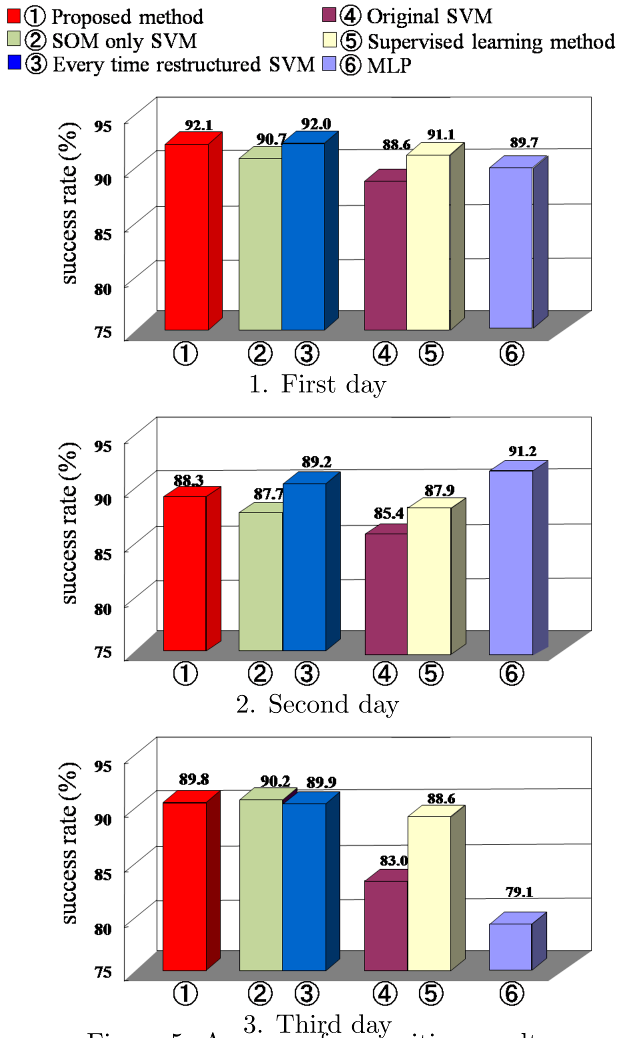

Figure 5: Average of recognition results

References

[1] Kizuka Tomohiro, Masuda Tadashi, Kiryu Tohru and Sadoyama Tsugutake, " Practical Usage of Surface Electromyogram ",Biomechanism Library, 2006.

[2] De Luca C.J. and Knaflitz M, Surface Electromyography:What 's New?, CLUT Publishers, Torino,Italy, 1992.

[3] C.Cortes and V.N. Vapnik, " Support Vector Networks ",Machine Learning, 20(3), pp. 273-297, 1995.

[4] C.J.C Burges, " A Tutorial on Support Vector Machine for Pattern Recognition ",Data Mining and Knowledge Discovery, vol.2, no.2, 1998.

[5] Nello Cristianini, John Shawe-Taylor, " An Introduction to Support Vector Machines and Other Kernel-based Learning Methods ",Cambridge University Press, 2000.

[6] Nobuhiko Ogura, Sumio Watanabe, " Online Learning for Support Vector Machine using Necessity Estimation ",Techinical report of IEICE PRMU,Vol,99,No,182,pp. 45-52,1999.(Japanese)

[7] Teuvo Kohonen. " Self-Organizing Maps ". Springer-Verlag Tokyo, 1996. Translation of Self-Organizing Maps by Teuvo Kohonen, Springer-Verlag Berlin Heidelberg,1995.

[8] Hiroki Tamura, Takafumi Gotoh, Dai Okumura, Hisashi Tanaka, and Koichi Tanno, " A Study on the s-EMG Pattern Recognition using Neural Network ",2008 International Symposium on Intelligent Informatics (ISII 2008).(acceptance)

[9] Shuji Kawano, Hiroki Tamura, Dai Okumura, Hisasi Tanaka, and Koichi Tanno, " Online Learning Method using Support Vector Machine for Surface-Electromyogram Recognition ", AROB2008 (CD-ROM) pp. 227-230, 2008.

©ISAROB 2009

A method for extraction of arbitrary curve using one-dimensional histogram

Shota NAKASHIMA and Seiichi SERIKAWA

Department of Electrical Engineering
Kyushu Institute of Technology
1-1 Sensui-cho, Tobata-ku, Kitakyushu-shi, Fukuoka, 804-8550, JAPAN
(Tel : 81 −93 −884 −3008 ; Fax : 81-93 −844 −3015)
(nakashima@boss.ecs.kyutech.ac.jp)

Abstract: An extraction of a specific curve in image has basic problems in intelligent image sensing. The generalized Hough Transform method (GHT) is the representative method to extract arbitrary curves which are rotated and enlarged or reduced. Many the improvement models were also proposed. However, for extraction of arbitrary curves, it takes much processing time and needs much memory space. In addition, it is impossible to apply the GHT to curves including branches. For an improvement of the problems, a new method to extract arbitrary curve using one-dimensional histogram is proposed in this study. The method utilizes the Polytope method which is one of minimization algorithms. For the extraction of curves, one-dimensional histogram is used. The histogram has two characteristics. (1) The distribution of histogram changes if the parameters representing curve changes. (2) The best parameters are gotten, if the value of most frequency of histogram becomes maximum. Therefore, by using the Polytope method, the best parameters are searched so that the value of most frequency can be maximum. Unlike conventional method, the memory space is very small, processing time is very short and curves including branches can be extracted. In addition, this method is effective for an extraction of arbitrary curve with different aspect ratio.

Keywords: image processing, Polytope method, Generalized Hough Transform, one-dimensional histogram

I. INTRODUCTION

An autonomy robot needs to have an ability of space notation, because it moves and recognizes an object. Especially, a moving robot needs to recognize it fast. Thus the fast image processing has been studied [1]. An extraction of straight line and circle is one of the basic problems of image processing. The Hough Transform method (HT) is the representative method [2][3][4]. It can extract line and circle which are rotated and enlarged or reduced. For the extraction of arbitrary curves, the generalized Hough Transform method (GHT) is usually used [5]. It is an improved method of HT. However, for extraction of arbitrary curves, it takes much processing time and needs much memory space. For the improvement of the problems, many improved models were proposed [6]. In spite of the improvement, these still takes much processing time and needs much memory space. In addition, it is impossible to apply the extraction of curves including branches. We had proposed a method to extract line and circle using one-dimensional histogram and the Polytope method [7]. In comparison with HT, the method takes very small memory space and the processing time is very short. In this study, a new method to extract arbitrary curve is proposed. The method is the extension of the method for line and circle extractions. This is a generalized model. The basic algorithm is the same as those of line, circle and ellipse extractions. Unlike conventional method, the memory space is extremely small, and processing time is greatly short. In addition, it is tough against noise and curves including branches can be extracted. This method can also extract arbitrary curve with different aspect ratio.

II. EXTRACTION OF FIGURES USING ONE-DIMENSIONAL HISTOGRAM

A proposed method utilizes the Polytope method and one-dimensional histogram. An application of the Polytope method to extract figures and a procedure of extraction of figures using one-dimensional histogram are mentioned as follows.

1. Application of the Polytope method

In this study, one-dimensional histogram is generated from image. The histogram has two characteristics. (1) The distribution of histogram changes if the parameters representing curve changes. (2) The best parameters are gotten, if the value of most

©ISAROB 2009

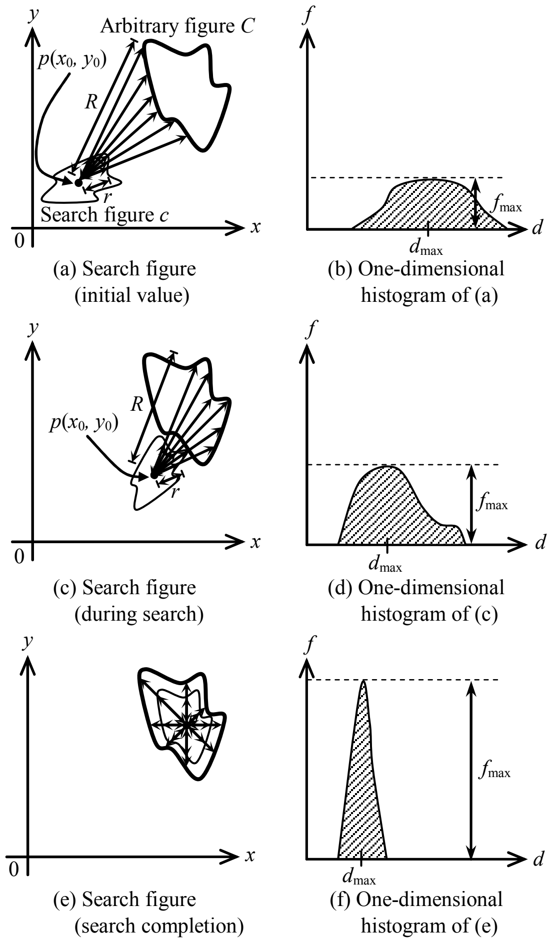

(a) Search figure (initial value)
(b) One-dimensional histogram of (a)
(c) Search figure (during search)
(d) One-dimensional histogram of (c)
(e) Search figure (search completion)
(f) One-dimensional histogram of (e)

Fig. 1. Outline of search for extraction of arbitrary figure.

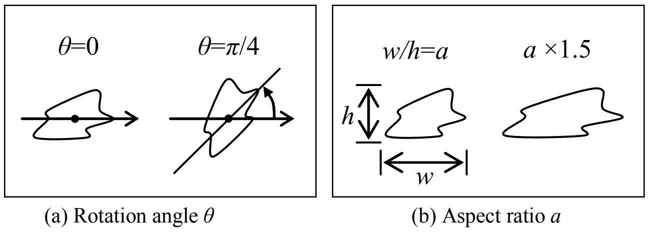

(a) Rotation angle θ
(b) Aspect ratio a

Fig. 2. Rotation angle and aspect ratio.

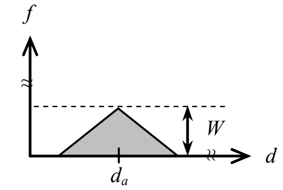

Fig. 3. Weight of voting W

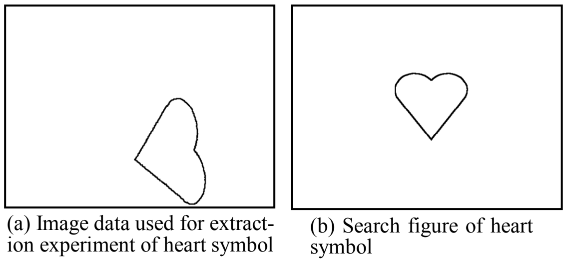

(a) Image data used for extraction experiment of heart symbol
(b) Search figure of heart symbol

Fig. 4. Experiment for extraction of heart symbol.

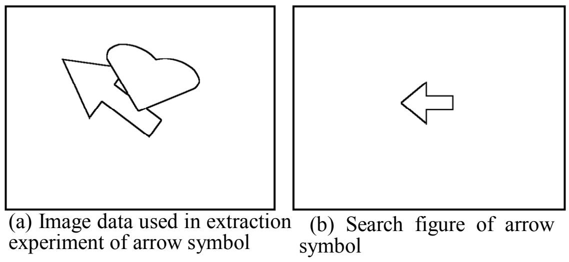

(a) Image data used in extraction experiment of arrow symbol
(b) Search figure of arrow symbol

Fig. 5. Experiment for extraction of arrow symbol.

frequency of histogram becomes maximum (see Sect.II-2 for details). By using the Polytope method, the best parameters are searched so that the value of most frequency can be maximum.

The Polytope method is one of minimization algorithms. Since it can get a minimum value no using derived function different from the Newton's method, the concept can be used for search of histogram. In addition, the program size is small. For more details, see Ref. [8] and [9]. For the use, the "initial values" must be set because this method is available for only a single-peak function. If these are not suitable, the optimum value may not be obtained.

2. Procedure to extract figure using one-dimensional histogram

A procedure to extract figure using one-dimensional histogram is mentioned here. A template figure (search figure c) is prepared for extraction of arbitrary figure C as shown in Fig. 1(a). To represent arbitrary figure as parameters, gravity point $p(x_0, y_0)$, aspect ratio a(height h / width w), and rotation angle θ are defined as shown in Fig. 1(a) and Fig. 2 are defined. The arbitrary figure defined by the above is called "search figure" c. Let the distance between gravity point $p(x_0, y_0)$ of search figure and a point on arbitrary figure C be R, let the distance of search figure to the direction of a point on C be r, and let R/r be the distance ratio d. The value of d is calculated for all pixels on arbitrary figure C. Thus, one-dimensional histogram about d is obtained as shown in Fig. 1(b). It corresponds to the relationship between d and frequency f.

If the parameters of search figure c which are represented by $p(x_0, y_0)$, a and θ are much different from those of arbitrary figure C, the deviation of distance ratio d is large. As a result, the distribution of

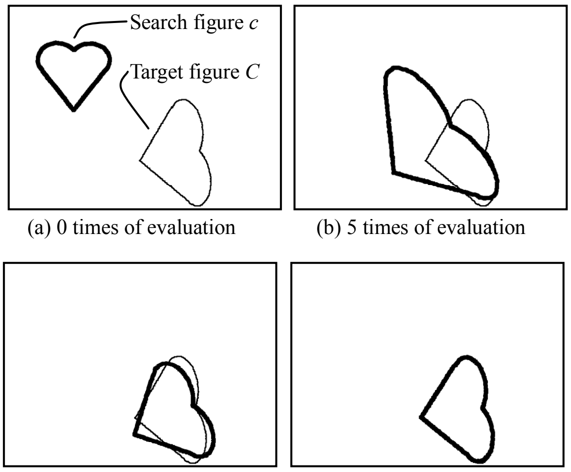

(a) 0 times of evaluation (b) 5 times of evaluation

(c) 40 times of evaluation (d) 188 times of evaluation (search result)

Fig. 6. Search figure c agrees with those of target figure C according as the number of times of the search increases using Polytope method.

the histogram is gentle. In consequence, the value of most frequency f_{max} is low as shown in Fig. 1(b). Here, let the value of d at the position of most frequency f_{max} be d_{max}. According as the parameters of search figure c approach those of arbitrary figure C, the deviation of d becomes small. Then, the value of most frequency f_{max} becomes high as shown in Fig. 1(d). If the parameters of search figure c agree with those of arbitrary figure C as shown in Fig. 1(f), the value of most frequency f_{max} is the highest. At the case, the width w in Fig. 2(b) of arbitrary figure C is obtained as d_{max}, and the height h corresponds to $a \times d_{max}$.

In this way, the arbitrary figure C is gotten, if the value of most frequency f_{max} of histogram becomes maximum. We define the following evaluation function E to evaluate the histogram.

$$E = 1 - \frac{f_{max}}{C_{ir} \times W} \tag{1}$$

where, C_{ir} is the perimeter, which is obtained as perimeter of search figure $c_{ir} \times d_{max}$ when the value of f_{max} is the highest. Symbol W means a weight which is used when d is voted to one-dimensional histogram. The weight has a distribution. The example is shown in Fig. 3. Let a distance ratio d of a pixel on arbitrary figure C be d_a. First, the frequency at the position of d_a is set to be W. According as the distance ratio d is away from d_a, the frequency is reduced one by one. The function E is the lowest when the value of f_{max} is the highest. By the use of the Polytope method, $p(x_0,\ y_0)$, a, and θ of

Table1. Experimental result.

	x	y	a	θ
initial value	150	150	1.0	0
final value	400.0	350.0	1.43	81.0
correct value	400	350	1.5	90

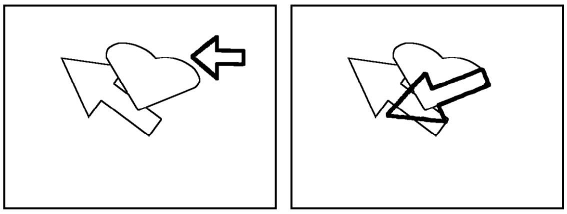

(a) Initial search of arrow symbol (b) Extraction of arrow symbol

Fig. 7. Experiment result for extraction of arrow symbol.

arbitrary figure C are searched so that the function E is the lowest.

III. EXPERIMENTAL EXTRACTION OF A RBITRARY FIGURE

1. Experimental conditions

Image data in Fig. 4(a), which is used in this experiment, includes a heart symbol. The search figure is shown in Fig. 4(b). Another image which includes a heart symbol and an arrow symbol is also prepared as shown in Fig. 5(a). The search figure is shown in Fig. 5(b).

The image consists of 640 × 480 pixels. For the experiments, we used a personal computer (Dell, OptiPlex GX520, OS: Windows XP, CPU: Pentium4 - 3.2GHz). In the case of this experiment, the "initial values" of $p(x_0,\ y_0)$ are set to both 150, a and θ are set to 0 and 0 respectively. The scale factor of $p(x_0,\ y_0)$ are set to 200, a and θ are set to 1 and 1 respectively for the Polytope method.

2. Experimental results

An experimental result for Fig. 4(a) is shown in Fig. 6. Here, the target for extraction is called "target figure" C. In Fig. 6, "search figure" c is also drawn for reference. The parameters of the search figure before the search and it after the search are listed in Table 1. As for extraction of a heart symbol, memory space is 3.2[KB] (for one-dimensional histogram, horizontal axis d[=800Byte] ×vertical axis f[=4Byte]). In this study, memory space is the same as 3.2[kB] for any image data. The processing time of them are 0.9[s].

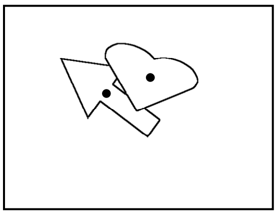

(a) Gravity points of arrow symbol and heart symbol

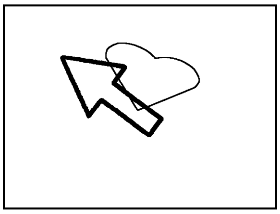

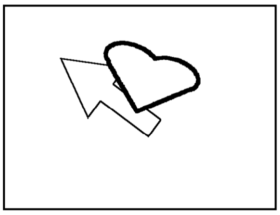

(b) Extraction of arrow symbol (c) Extraction of heart symbol

Fig.8. Experimental result using improved method.

As understood from Fig. 6, the search figure c agrees with target figure C according as the number of times of the search increases. As a result, the heart symbol is correctly extracted in this experiment. In Table 1, the parameters of search figure c (final value) almost agree with those of target figure C (correct value).

In contrast to Fig. 6, the extraction in Fig. 7 is not correct. This is attributed to "initial values" as mentioned in Sect. II-1. The Polytope method is available for only a single-peak function, so the determination of initial values is important for use of multi-peak function. If the values are not suitable, the optimum value may not be obtained. For initial values, it is desirable that the values of parameters of search figure c are as near as those of target figure C possible.

IV. DISCUSSION

1. Initial values of parameters

As understood from the above results, the success of figure extraction depends on "initial value". If most frequency $f_{\max}$ of the one-dimensional histogram becomes highest, a gravity point of $p(x_0, y_0)$, target figure C, rotation angle θ and aspect ratio a are estimated by proposed method. Therefore, we examine the relationship between "initial value" of $p(x_0, y_0)$, θ, and a, and most frequency $f_{\max}$. If $p(x_0, y_0)$ of search figure c are much different from those of target figure C, the value of $f_{\max}$ is not high even if θ and a agree with those of C. In contrast, if $p(x_0, y_0)$ of c agrees with those of C, the value of $f_{\max}$ is relatively high even if θ and a are quite different from those of C. Thus, if the "initial value" of $p(x_0, y_0)$ of c is inappropriate, most frequency $f_{\max}$ does not become high. That is to say, it falls into a local minimum. Thus, the "initial value" of $p(x_0, y_0)$ is much correlated with most frequency $f_{\max}$ more than θ and a.

The "initial value" of $p(x_0, y_0)$ is important especially. The method to determine "initial value" of $p(x_0, y_0)$ is mentioned the followings.

2. How to determine initial value of gravity point of search figure

The success of figure extraction may depend on "initial value" of gravity point p (x_0, y_0). For avoiding the failure of extraction, we roughly estimate the gravity candidate point $p(x_0, y_0)$ of target figure C before the practice of proposed method. The roughly estimated point is regarded as initial value of gravity point $p(x_0, y_0)$ in this study. The procedures are as follows.

1) Enlargement operation：The line which broke off is connected. After binarization, closed lines are sometimes broke off by noise. The lines are connected by "enlargement operation".
2) Extraction of small regions： If a size of region is more than threshold value t_1, the region is removed. Large sizes of noises are removed by "extraction of small regions".
3) Extraction of large regions： If a size of region is less than threshold value t_2, the region is removed. Small sizes of noises are removed by "extraction of large regions".
4) Extraction of gravity point： From closed curves, the gravities are extracted.

By the above procedures, some gravities are extracted. We utilize the gravities as the "initial value" of the search figure.

3. A method improved to extract arbitrary figure using one-dimensional histogram

In this experiment, Fig. 5(a) is used as image data. Fig. 4(b) and Fig. 5(b) are used as search figures to detect the heart symbol and the arrow symbol, respectively. The dots (●) in Fig. 8(a) show the gravities extracted from Fig. 5(a) according as the above procedures. The points are regarded as initial values of $p(x_0, y_0)$. The other initial values are the same as those of Sect. III-2. However, scale factor of $p(x_0, y_0)$ is

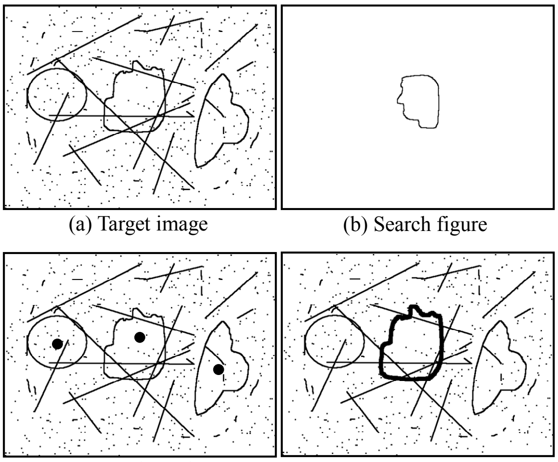

(a) Target image (b) Search figure

(c) Gravity points (d) Experimental result

Fig. 9. Example of other experiment (1).

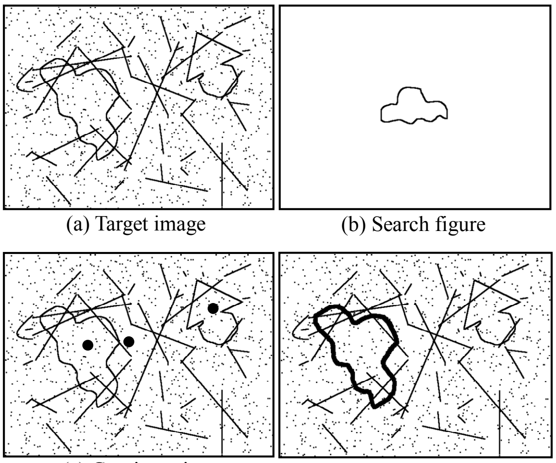

(a) Target image (b) Search figure

(c) Gravity points (d) Experimental result

Fig. 10. Example of other experiment (2).

changed to 10, θ and a are changed to 0.5, which are smaller than those of Sect. III-2. This is because it is easily estimated that the initial points are near the correct gravity points as shown in Fig. 8(a), so large size of scale factor does not need. The extraction is practiced twice as for Fig. 5(a), because two gravities are extracted in Fig. 8(a). After twice extractions, the minimum value of evaluation function E is selected, and the parameters are regarded as final values.

The results are shown in Figs. 8(b) and (c). In these figures, the thick curves show the extracted figures. As understood from these figures, the heart symbol and the arrow symbol are correctly extracted in this experiment. In spite of including branches, the symbols are correctly extracted. As for extraction of gravities, the processing time is 0.2[s]. As for extraction of symbol, it takes

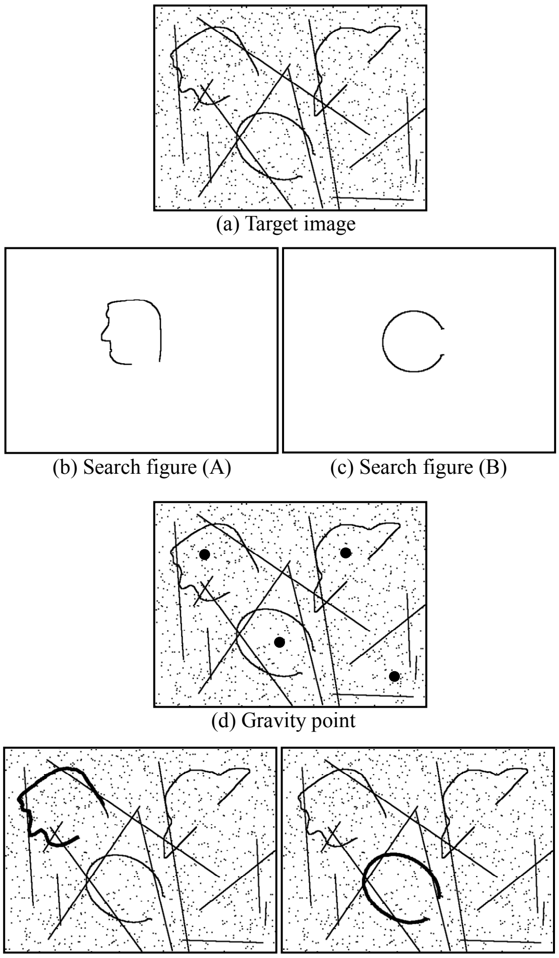

(a) Target image

(b) Search figure (A) (c) Search figure (B)

(d) Gravity point

(e) Experimental result (A) (f) Experimental result (B)

Fig. 11. Experiment for extraction of opened curve

1.8[s] for the heart symbol, and 1.4[s] for the arrow symbol.

Examples of other experiments are shown in Fig. 9, Fig. 10 and Fig. 11. In Fig. 9(c), Fig.10 (c) and Fig.11 (b), the extracted gravities are shown as dots (●). In case of the number of dots is 3, the extraction is practiced three times. The search figures are shown in Fig. 9(b), Fig. 10(b), Fig. 11(c) and Fig. 11(d). The results are shown in Fig. 9(d), Fig. 10(d), Fig. 11(e) and Fig. 11(f). In these figures, the thick curves show the extracted curves. As understood from these figures, each symbol is correctly extracted in this experiment. Although target images include many noises, correct symbols are extracted. Thus, the proposed method has tough against noise. As for extraction of gravities, processing time is 0.2[s] for Fig. 9(c), 0.2[s] for Fig.10 (c), and 0.2[s] for Fig.11(d), respectively. As for extraction of symbol, it takes 4.3[s] for Fig. 9(d), takes 4.7[s] for Fig. 10(d), takes 4.6[s] for Fig. 11(e), and takes 5.5[s] for Fig. 11(f).

©ISAROB 2009

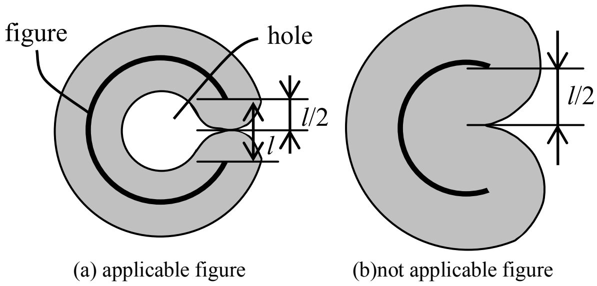

Fig. 12. Extractive condition of gravity point for opened curve

4. Extraction of gravity point for opened curve

The proposed method can be applied to the extraction of opened curve as shown in shown Fig. 11. It can not be, however, applied for all opened curves. It has a limitation. As mentioned in *Sect*. IV-2, enlargement operation is used for the extraction of gravity point. A gravity point is not extracted if a hall does not exist within a curve. The example is shown in Fig. 12. In Fig. 12(a), a hall exists after enlargement operation, while it does not exist in Fig. 12(b). The proposed method can not be applied for an opened curve such as Fig. 12(b).

V. CONCLUDION

A new method to extract arbitrary curve using one-dimensional histogram and the Polytope method are proposed in this study. Unlike conventional method, the memory space is very small, processing time is very short, it is tough against noise and figures including branches can be extracted. In addition, this method is effective for an extraction of arbitrary figure with different aspect ratio.

This research was partly supported by Grant-in-Aid for Scientific Research(C), 19500478.

REFERENCES

[1] Saji Motoki, Ueno Atsushi, Takeda Hideaki (2000) A Robot System to Recognize and Manage Unfixable Objects in the Office Environment.IEI-CE technical report. Vol.99. No.717:1-8

[2] Toshi Minami, Osamu Nakamura (2000). Image engineering. Corona Publishing Co.:103-106

[3] Bahram Javidi, Joseph L.Horner(1994).REAL-TIME OPTICAL INFORMATION PROCESSING. Academic Press:56-57

[4] Eilliam K.Pratt (1991). DIGITAL IMAGE PROCESSING–Second Edition. wiley&Sons:613-614

[5] D.H. Ballard (1981), Generalizing the Hough Transform to detect arbitrary shapes, Pattern Recognition, Vol. 13, No. 2 : 111-122.

[6] Akio Kimura, Takashi Watanabe (2001) Generalized Hough Transform to be Extended as an Affine-Invariant Detector Arbitrary Shapes, IEICE, Vol. J84-D-II, No. 5 :789-798.

[7] Shota Nakashima, Seiichi Serikawa (2009), Artificial Life and Robotics vol.13, (accepted)

[8] Haruhiko Okumura (2006). An algorithm encyclopedia using C. Gijutsu-Hyohron Co.:262

[9] W. H. Press, B. P. Flannery, S. A. Teulolsky, W. T. Vetterling (1987). Numerical Recipes-The Art of Scientific Computing. Cambridge University Press:289-293

The Fourteenth International Symposium on Artificial Life and Robotics 2009 (AROB 14th '09),
B-Con Plaza, Beppu, Oita, Japan, February 5 - 7, 2009

Covariance-based Recognition Using Incremental Learning Approach

HASSAB ELGAWI Osman
Image Science and Engineering Laboratory, Tokyo Institute of Technology, Japan
Email: osman@isl.titech.ac.jp

Abstract

We propose an on-line machine learning approach for object recognition, where new images are continuously added and the recognition decision is made without delay. Random forest (RF) classifier has been extensively used as a generative model for classification and regression applications. We extend this technique for the task of building incremental component-based detector. First we employ object descriptor model based on bag of covariance matrices, to represent an object region then run our on-line RF learner to select object descriptors and to learn an object classifier. Experiments of the object recognition are provided to verify the effectiveness of the proposed approach. Results demonstrate that the propose model yields in object recognition performance comparable to the benchmark standard RF, AdaBoost, and SVM classifiers.

1 Introduction

Object recognition is one of the core problems in computer vision, and it turns out to be extremely difficult for reproduce in artificial devices, simulated or real. Specifically, an object recognition system must be able to detect the presence or absence of an object, under different illuminations, scales, pose, and under differing amounts of background clutter. In addition, the computational complexity is required to be kept minimum, in order for those algorithms to be applicable for real-life applications. Based on "strongly supervised" approach and "weakly supervised" method (*without using any ground truth information or bounding box during the training*), considerable progress has been made for detection of objects. Several studies also have shown that supervised component-based approach is more robust to natural pose variations, than

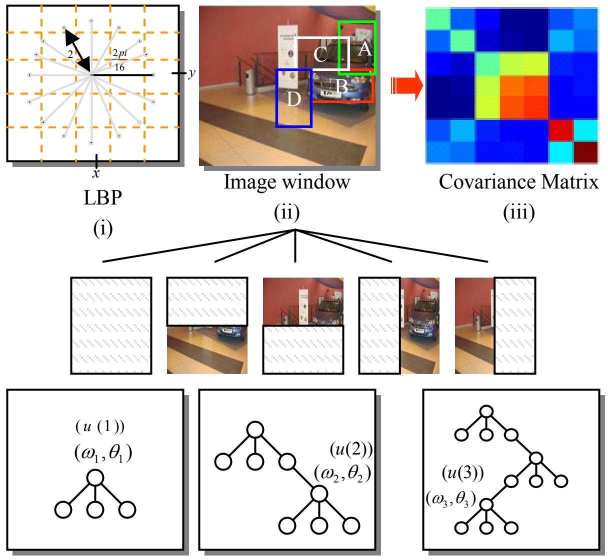

Figure 1: (i) Points sampled to calculate the LBP around a point (x, y). (ii) Rectangles [A, B, C and D] are examples of possible regions for histogram features. (iii)Any region can be represented by a covariance matrix. Size of the covariance matrix is proportional to the number of features used

the traditional global holistic approach. However, supervised learning is usually carried out batch on the entire training set, often is not optimal in a dynamic recognition tasks. In this paper we consider instead how machine learning models for object recognition categories, can be build 'incrementally' or 'on-line' so that new images are continuously added and the recognition decision is made without delay. The process consists of two stages. First we employ object descriptor model based on bag of covariance matrices, to represent an image window then run our on-line random forest (RF) learning algorithm [3]. RF technique has been extend in this paper for the task

©ISAROB 2009

of building incremental component-based detector, for attacking the problem of recognizing generic object categories, such as bikes, cars or persons purely from object descriptors that combines histograms and appearance model.

1.1 Our Object Descriptor Approach

We have used bag of covariance matrices, to represent an object region. Let I be an input color image. Let F be the $W \times H \times d$ dimensional feature image extracted from I

$$F_{W,H,d}(x, y) = \phi(I, x, y) \tag{1}$$

where the function ϕ can be any feature maps (such as intensity, color, etc). For a given region $R \subset F$, let $\{z_k\}_{k=1\cdots n}$ be the d dimensional feature points inside R. We represent the region R with the $d \times d$ covariance matrix C_R of feature points.

$$C_R = \frac{1}{n-1}\sum_{k=1}^{n}(z_k - \mu)(z_k - \mu)^T \tag{2}$$

where μ is the mean of the point. Fig. 1 (i) depicts the points that must be sampled around a particular point (x, y) in order to calculate the LBP at (x, y). In our implementation, each sample point lies at a distance of 2 pixels from (x, y), instead of the traditional 3×3 rectangular neighborhood, we sample neighborhood circularly with two different radii (1 and 3). The resulting operators are denoted by $LBP_{8,1}$ and $LBP_{8,1+8,3}$, where subscripts tell the number of samples and the neighborhood radii. In Fig. 1 (ii), different regions of an object may have different descriptive power and hence, difference impact on the learning and recognition. We follow [4] and represent an object with five covariance matrices $C_{i=1\cdots5}$ of the feature computed inside the object region, as shown in the second row of Fig.1. A bag of covariance which is necessary a combination of Ohta color space histogram ($I_1 = R+G+B/3$, $I_2 = R-B$, $I_3 = (2G-R-B)/2$), LBP and appearance model of different features of an image window is presented in Fig.1 (iii). We use this representation to automatically detect any target in images. We then apply on-line RF learner to select object descriptors and to learn an object classifier.

2 Machine Learning Approach

In the following we introduce the on-line random forests learning algorithm [3] for object recognition based on Breiman's random forest (RF) [1]. Details discussion of Breiman's random forest learning algorithm is beyond the scope of this paper, however, in order to simplify the further discussion, we will need to define some fundamental terms:

Random Forests (RF) is a tree-based ensemble prediction technique combining properties of an efficient classifier and feature selection [1]. Briefly, it is an ensemble of two sources of randomness to generate base decision trees; bootstrap replication of instances for each tree and sampling a random subset of features at each node.

Decision tree. For the k-th tree, a random vector C_k is generated, independent of the past random vectors $C_1, \ldots, C_{k-1}$, and a tree is grown using the training set positive and negative image I and covariance feature C_k. The decision generated by a decision tree corresponds to a covariance feature selected by learning algorithm. Each tree casts a unit vote for a single matrix from the bag of covariance matrices.

Base classifier. Given a set of M decision trees, a base classifier selects exactly one decision tree classifier from this set, resulting in a classifier $h(I, C_k)$.

Forest Given a set of N base classifiers, a forest is computed as ensemble of these tree-generated base classifiers $h(I, C_k)$, $k = 1, \ldots, n$. Finally, a forest detector is computed as a majority vote.

2.1 On-line Learning Random forest (RF)

To obtain an on-line algorithm, each of the steps described above must be on-line, where the current classifier is updated whenever a new sample arrives. In particular on-line RF works as follows: First, the fixed set tree K is initialized. In contrast to off-line random forests, where the root node always represents the object class in on-line mode, for each training sample, the tree adapts the decision at each intermediate node (nonterminal) from the response of the leaf nodes, which characterized by a vector (w_i, θ_i) with $\|w_i\| = 1$. Root node numbered as 1, the activation of two child nodes $2i$ and $2i+1$ of node i is given as

$$u_{2i} = u_i.f(w_i^{'}I + \theta_i) \tag{3}$$

$$u_{2i+1} = u_i.f(-w_i^{'}I + \theta_i) \tag{4}$$

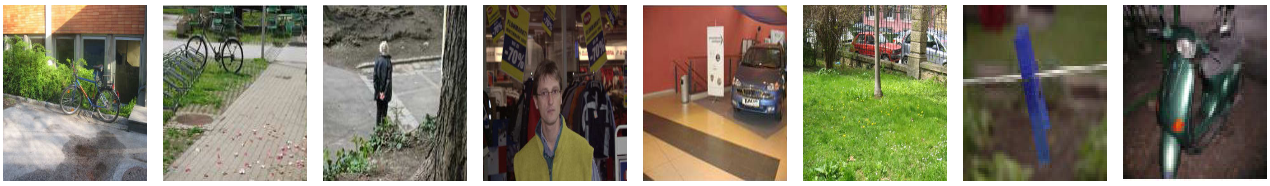

Figure 2: Examples from GRAZ02 dataset [2] for four different categories: bikes (1st pair), people (2nd pair), cars (3rd pair), and background (4th pair).

where I is the input image, u_i represents the activation of node i, and $f(.)$ is chosen as a sigmoidal function. Consider a sigmoidal activation function $f(.)$, the sum of the activation of all leaf nodes is always unity provided that the root node has unit activation. The forest consist of fully grown trees of a certain depth l. The general performance of the on-line forests depends on the depth of the tree. However, we found that the number of trees one needs for good performance eventually tails off as new data vectors are considered. Since after a certain depth, the performance of on-line forest does not vary to a great extent, the user may choose K (the number of trees in forest) to be some fixed value or may allow it to grow up to the maximum possible which is at most $|T|/N_k$, where N_k the tree size chosen by the user.

3 Object Recognition

Given a feature set and a sample set of positive (contains the object relevant to the class) and negative (does not contain the object) images, to detect a specific object, e.g. human, in a given image, we train a random forests learner (detector) offline using covariance descriptors of positive and negative samples. We start by evaluation feature from input image I after the detector is scanned over it at multiple locations and scales. This has to be done for each object. Then for feature in I, we want to find corresponding covariance matrix for estimating a decision tree. Each decision tree learner may explore any feature f, we keep continuously accepting or rejecting potential covariance matrices. We then apply the on-line random forests at each candidate image window to determine whether the window depicts the target object or not. The on-line RF detector was defined as a 2 stage problem, with 2 possible outputs in each stage: In the first one, we build a detector that can decide if the image contains an object, and thus must be recognized, or if the image does not contain objects, and can be discarded, saving processing time. In the second stage, based on selected features the detector must decide which object descriptor should be used. There are two parameters controlling the learning recognition process: The depth of the tree, and the least node. It is not clear how to select the depth of the on-line forests. One alternative is to create a growing on-line forests where we first start with an on-line forest of depth one. Once it converges to a local optimum, we increase the depth. Thus, we create our on-line forest by iteratively increasing its depth.

Table 1: Number of images and objects in each class in the GRAZ02 dataset.

Dataset	Images	Objects
Bikes	373	511
Cars	420	770
Persons	460	785
Total	1253	2066

4 Experiments and Evaluation

To evaluate and validate our approach we used data derived from the GRAZ02[1] dataset [2], a collection of 640×480 24-bit color images and illustrated in Figure 2. As can be seen in Table 1, this dataset has three object classes, bikes (373 images), cars (420 images) and persons (460 images), and a background class (270 images).

4.1 Experimental settings

For testing our framework we used the datasets described above and run it against three state of the art

[1] available at *htt://www.emt.tugraz.at/pinz/data/*

Table 2: Mean AUC performance of four classifiers on the Bikes vs. Background dataset, by amount of training data. Performance of on-line RF is reported for different Depths

	On-line RF					RF	AdaB	SVM
	D3	D4	D5	D6	D7			
10%	0.85	0.86	0.81	0.85	0. 85	0.86	0.81	0.82
50%	0.91	0.90	0.89	0.91	0.92	0.90	0.89	0.90
90%	0.92	0.90	0.91	0.92	0. 92	0.91	0.90	0.91

Table 3: Mean AUC performance of four classifiers on the Cars vs. Background dataset, by amount of training data. Performance of on-line RF is reported for different Depths

	On-line RF					RF	AdaB	SVM
	D3	D4	D5	D6	D7			
10%	0.77	0.79	0.75	0.78	0.73	0.79	0.75	0.73
50%	0.85	0.84	0.82	0.82	0.84	0.85	0.82	0.80
90%	0.86	0.82	0.83	0.85	0.86	0.85	0.83	0.82

Table 4: Mean AUC performance of four classifiers on the Persons vs. Background dataset, by amount of training data. Performance of on-line RF is reported for different Depths

	On-line RF					RF	AdaB	SVM
	D3	D4	D5	D6	D7			
10%	0.84	0.84	0.83	0.80	0.83	0.84	0.77	0.80
50%	0.88	0.86	0.88	0.88	0.88	0.88	0.84	0.86
90%	0.90	0.86	0.89	0.90	0.90	0.90	0.86	0.89

classifiers (offline RF, AdaBoost, and SVM). Each of the classifiers used in our experimentation were trained with varying amounts (10%, 50% and 90% respectively) of randomly selected training data. All image not selected for the training split were put into the test split.

5 Experimental Results

GRAZ02 images contain only one object category per image so the recognition task can be seen as a binary classification problem: bikes vs. background, people vs. background, and car vs. background. The well known statistic measure; the Area Under the ROC Curve (AUC) is used to measure the classifiers performance in these object recognition experiments.

5.1 Mean AUC Performance

Tables 2, 3, and 4 give the mean AUC values across all runs to 2 decimal places for each of the classifier and training data amount combinations, for the bikes, cars ad people datasets respectively. For on-line RF we report the results for different depths of the tree. As can be seen, our algorithm always performs significantly better than the offline RF. We found that the differences in performance are (avg. $= 1.2 \pm 15\%$).The improvement when we varying the tree depth are relatively small. This makes intuitive sense: when an image is characterized by high geometric variability, it is difficult to find useful global features.

6 Conclusions

In this paper we have presented an on-line learning framework for object recognition categories that avoids hand labeling of training data. We have demonstrated that on-line learning obtain comparable results to offline learning. Moreover, the proposed framework is quite general (i.e, it can be used to learn completely different objects) and can be extended in several ways.

References

[1] Leo Breiman, "Random Forests," *Machine Learning*, 45(1):5.32, 2001.

[2] Oplet A., Fussenegger M., Pinz A. and Auer P. "Generic object recognition with boosting," *IEEE Transactions on Pattern Analysis and Machine Intelligence* 28(3) pp. 416-431, 2006.

[3] Hassab Elgawi Osman, "Online Random Forests based on CorrFS and CorrBE," *In Proc.IEEE workshop on online classification, CVPR*, 2008.

[4] O. Tuzel, F. Porikli, and P. Meer. "Region covariance: A fast descriptor for detection and classification," *In Proc. ECCV*, 2006.

Elimination of Un-uniformed Image Distortion Using LCD

Koji Miyazaki[1] and Kikuhito Kawasue[2]

[1]Kumamoto Prefectural College of Technology,
4455-1 Haramizu, Kikuyo-town, Kumamoto, 869-1102, Japan
(Tel: 81-96-232-9834; Fax: 81-96-232-9292)
(Email: miyazaki@kumamoto-pct.ac.jp)
[2]University of Miyazaki, 1-1 Gakuen Kibanadai-Nishi, Miyazaki, 889-2192, Japan

Abstract: An image calibration method involving the use of a liquid crystal display (LCD) placed in the observation medium is presented. The calibration is important for these image-based measurement techniques such as particle image velocimetry (PIV) since it influences the accuracy of measurements. One important task in calibration is to eliminate distortions, especially for images in water. In PIV, distortions have to be eliminated on every change of the target since the distortion caused by refraction varies depending on the shape of the water tank. In this paper, the proposed method is demonstrated to correctly eliminate distortion due the refraction effects of the tank and water. The method is based on the construction of a calibration table using patterns of dots displayed on the LCD in the tank, and provides excellent measurement accuracy.

Keywords: Calibration, Distortion, Measurement, Image processing, PIV

I. INTRODUCTION

Calibration is important task to extract the accurate quantitative data from captured images in computer vision. This task requires estimating the relationship between the camera image and the scene prior to performing a measurement. Moreover, the calibration procedure must eliminate any distortion in the captured image.

Distortions can originate from either the characteristics of the camera lens or from the refraction of light. The distortion caused by the lens is isotropic and can be corrected relatively easily by methods such as that of Tsai [1]. Radial distortion caused by lens characteristics has also been investigated in a number of studies [2][3]. However, eliminating distortions due to refractions in the scene requires complex procedures, such as tracing the optical path by accounting for refractive index variations [4]. Due to the difficulty of such procedures, we proposed simple and useful method to eliminate the distortion caused by reflection in water, in this paper. The need for distortion correction is particularly important in particle image velocimetry (PIV) for water flow, which is a non-contact, image-based measurement technique that allows the instantaneous velocity field of flow to be determined from the translational displacement of tracer particles. In PIV of water systems, image distortion due to refraction, which is related to the shape of the water tank, must be eliminated in order to obtain quantitative measurement results.

In this study, a novel calibration technique based on the use of a liquid crystal display (LCD) [5] is applied to eliminating distortions. In this method, a waterproof LCD is placed in the water volume targeted for measurement, and a known dot pattern is displayed to allow construction of a calibration table. The experimental results demonstrate the feasibility of the proposed method for eliminating image distortion due to refraction effects.

II. LCD-BASED CALIBRATION METHOD

Figure 1 shows a schematic diagram of the proposed calibration system. The LCD is set in the scene, and a pattern of dots is displayed. The LCD plane is set accurately on the laser plane used for PIV or slit-ray projection method, and the scene image is acquired using a complementary metal oxide semiconductor (CMOS) or charge-coupled device (CCD) camera. The dots are programmed to blink on and off according to a predefined time series, synchronized with the camera timing. An example of the encoded 4-bit dot pattern is shown in Table 1. A total of 15 patterns are possible with 4-bit encoding, and 1023 patterns can be defined with 10 bits. The dots in the acquired images are labeled according to the pattern number, and cross-referenced to the predefined dot coordinates. This decoding is performed by processing consecutive images. The world coordinates in the scene and the corresponding

©ISAROB 2009

image coordinates of the dots are then tabulated. Conversion functions for each local area in the image are determined, and a final conversion table for the entire image is constructed. The mathematical details of the conversion functions are given in the next section. The constructed calibration table is used to convert positions from the camera image into world coordinates. Table 2 shows the calibration table, which is used as a look-up table (LUT). This calibration method is very effective for defining conversion from a distorted image to undistorted world coordinates.

There are two major benefits of using an LCD for calibration. First, thousands of reference marks (dots on the LCD) can be recognized very quickly. The time required to capture 11 images is approximately 350 ms, and even with processing for decoding of the dot patterns, the total time is less than 1 s. Second, the number, size, and display interval of reference marks can be easily changed according to the measurement environment.

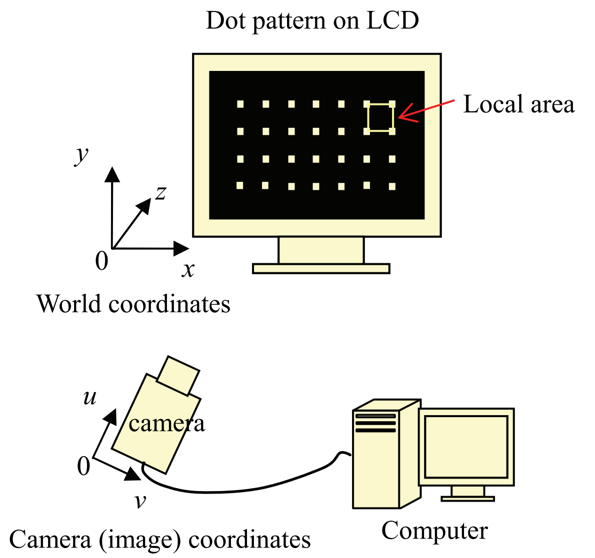

Fig.1 Schematic diagram of the calibration

Table 1. The encoded dot pattern for 4 bits

(1: On, 0: Off)

	T_0	T_1	T_2	T_3	Number
Dot 1	0	0	0	1	$(1)_{10}$
Dot 2	0	0	1	0	$(2)_{10}$
:	:	:	:	:	:
Dot 15	1	1	1	1	$(15)_{10}$

Table 2. Calibration table

Image coordinates (Pixel)		World coordinates (Actual scale)	
u_1	v_1	x_1	y_1
u_2	v_2	x_2	y_2
:	:	:	:
u_n	v_n	x_n	y_n

III. LOCAL PROJECTION MATRIX

In the pinhole camera model, the relationship between camera coordinates (u,v) and world coordinates (x,y,z) (see Fig. 1) is given by

$$\lambda[u \quad v \quad 1]^T = P[x \quad y \quad z \quad 1]^T \tag{1}$$

where λ is a coefficient and P is the perspective projection matrix within intrinsic and extrinsic camera parameters [6]. Elements of the projection matrix are often simply referred to as camera parameters. With $z = 0$ for a two-dimensional LCD plane, eq. (1) can be rewritten as

$$\lambda\begin{bmatrix} u \\ v \\ 1 \end{bmatrix} = \begin{bmatrix} p_{11} & p_{12} & p_{13} \\ p_{21} & p_{22} & p_{23} \\ p_{31} & p_{32} & 1 \end{bmatrix}\begin{bmatrix} x \\ y \\ 1 \end{bmatrix} \tag{2}$$

where p_{11} to p_{32} are elements of the projection matrix. Solving this equation to eliminate λ then affords the following relationships.

$$\begin{cases} p_{11}x + p_{12}y + p_{13} - p_{31}ux - p_{32}uy = u \\ p_{21}x + p_{22}y + p_{23} - p_{31}vx - p_{32}vy = v \end{cases} \tag{3}$$

Equations (3) consist of one set of world coordinates and the image coordinates with reference marks, comprising a total of eight unknown variables. Therefore, eight equations, or four reference marks, are required to solve the projection matrix. This process yields the following set of simultaneous equations.

$$\begin{bmatrix} x_1 & y_1 & 1 & 0 & 0 & 0 & -u_1x_1 & -u_1y_1 \\ 0 & 0 & 0 & x_1 & y_1 & 1 & -v_1x_1 & -v_1y_1 \\ \vdots & \vdots & \vdots & \vdots & \vdots & \vdots & \vdots & \vdots \\ x_4 & y_4 & 1 & 0 & 0 & 0 & -u_4x_4 & -u_4y_4 \\ 0 & 0 & 0 & x_4 & y_4 & 1 & -v_{i4}x_4 & -v_4y_4 \end{bmatrix}\begin{bmatrix} p_{11} \\ p_{12} \\ \vdots \\ p_{31} \\ p_{32} \end{bmatrix} = \begin{bmatrix} u_1 \\ v_1 \\ \vdots \\ u_4 \\ v_4 \end{bmatrix} \tag{4}$$

Note that eq. (4) is linear, whereas the distortion due to the refraction of light is a nonlinear phenomenon. Therefore, as eq. (4) cannot be applied directly, it is assumed that the image can be divided up into a large number of sufficiently small local areas exhibiting linear behavior that can be modeled by eq. (4). The local areas are defined as each area enclosed by four reference marks, as shown in Fig. 1. The projection matrix for each local area is then determined by eq. (4) and denoted as the local projection matrix. Conversion from the image coordinates to the world coordinates is then executed for all image pixels using eq. (2) and the local projection matrixes.

IV. EXPERIMENT

An experiment was performed to evaluate the performance of the proposed calibration system as shown in Fig. 2. The waterproof LCD was placed in a tank half-filled with water. The LCD displayed the dot pattern for calibration, and a checkered-flag pattern. A CMOS camera (640×480 pixel) was used as the capture device. To demonstrate the feasibility of this method, a low-distortion lens was used, and two shapes of water tank were tested: a cube and a cylinder. After calibration, the checkered flag pattern is measured using the constructed calibration table as an LUT, and the accuracy of measurement is evaluated.

1. Case 1: Cubic water tank

Figure 3 shows the captured and corrected images for the cubic water tank with flat plane shown in Fig. 2. In Fig. 3(a), the flag pattern has been distorted in water; it should be the same size and shape with that in air. Although some distortion remains near the water surface, the corrected pattern in water conforms to that expected in air (Fig. 3(b)). This result indicates that the image distortion caused by water has been corrected for appropriately.

2. Case 2: Cylindrical water tank

Figure 4 shows the cylindrical water tank used in the second test. The diameter of the tank tapers from the top to the base, and the distortion caused by the tank and water is expected to be more severe than in case 1. Figure 5 shows the captured and corrected images. The distortion in this case is much more severe than for the cubic tank. Whereas no distortion occurs in the air region in the cubic tank, distortion is apparent in both air and water in the cylindrical tank (Fig. 5(a)). This can also be seen in the captured image of the dot pattern as shown in Fig. 6. Unevenness in the glass forming the cylindrical tank is indicated by the small-scale displacements of the dots. The distortion transformation is thus more complicated than in case 1. After correction, most of the flag pattern was well reconstructed, as in case 1, although some distortion remains at the water surface (Fig. 5(b)). These results indicate that distortion in both water and air can be corrected simultaneously, and that the proposed method provides robust correction even for complex shapes and complicated transformations.

.

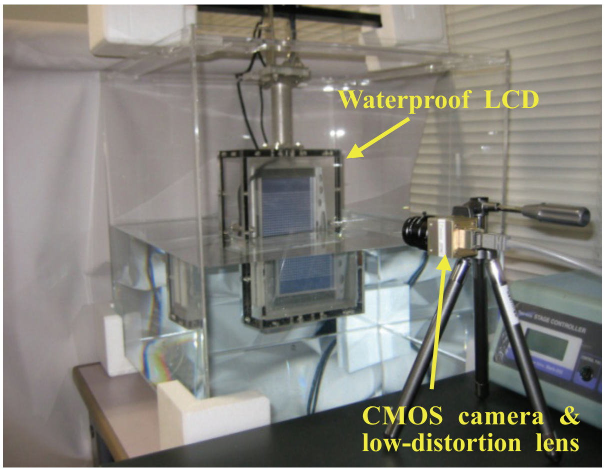

Fig. 2 Calibration in a cubic tank

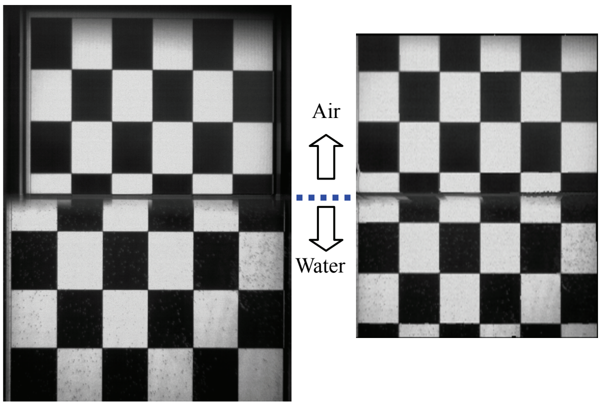

(a) (b)

Fig. 3 (a) Captured image and (b) corrected image of flag pattern acquired in a cubic tank

©ISAROB 2009

3. Accuracy of measurements

The measurement accuracy was evaluated by measuring the length of a side of the flag pattern in case 2. The original captured image and constructed calibration table were used to calculate the final measurements. The world coordinates of two neighboring vertices were found from the calibration table and used to determine the actual length by computing the distance between two points. The accuracy of measurements was thus found to be 0.17 mm in the water region and 0.21 mm in the air region. These values are equivalent to 1.4 % and 1.8% of total length, respectively. The measurement accuracies in both water and air are thus approximately the same.

V. CONCLUSION

A new LCD-based calibration technique was demonstrated to correctly eliminate image distortion due to external refractions in both water and air simultaneously. Excellent correction results were obtained even for complex tank shapes, and the measurement accuracy was shown to be adequate. The proposed technique is considered highly effective for PIV in water, and is potentially applicable to the shape measurement of objects in water using the slit-ray projection method. This technique was applied in the present study for two-dimensional measurements. However, if the position of the laser illumination plane and the camera can be fixed and the object moved, it will also be possible to apply this technique to three-dimensional measurements.

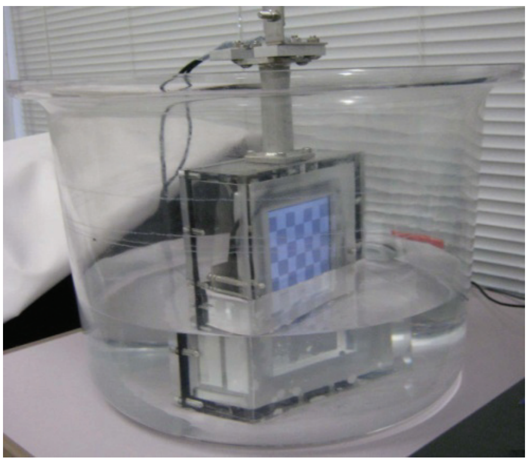

Fig. 4 Calibration in a cylindrical tank

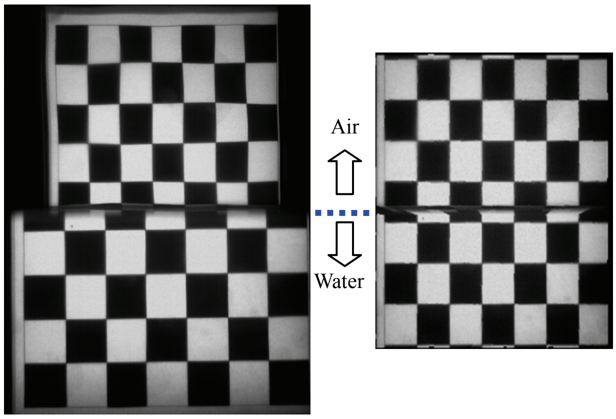

(a) (b)

Fig. 5 (a) Captured image and (b) corrected image of flag pattern acquired in a cylindrical tank

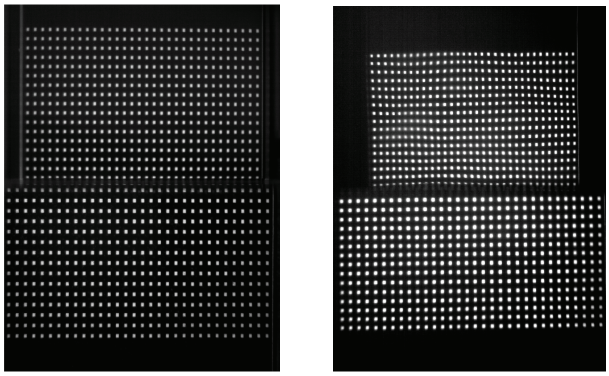

(a) Case 1 (b) Case 2

Fig. 6 Captured images of dots pattern in (a) the cubic tank and (b) the cylindrical tank

REFERENCES

[1] R Tsai (1987), A Versatile Camera Calibration Technique for High-Accuracy 3D Machine Vision Metrology Using Off-the-Shelf TV Cameras and Lenses, IEEE Journal of Robotics and Automation, Vol.3, No.4, pp.323-344.

[2] R. Strand, E. Hayman (2005), Correcting radial distortion by circle fitting, British Machine Vision Conference.

[3] S. Kang (2001), Radial Distortion Snakes, IEICE transactions on information and systems, Vol.E84-D, No.12, pp.1603-1611

[4] Yamashita A, Hayashimoto E, Kaneko T (2006) , 3-D Shape Measurement of Objects in Liquid with a Laser Range Finder (in Japanese), Transactions of the Japan Society of Mechanical Engineers. C, Vol.72, No.717, pp. 1506-1513.

[5] Kawasue K, Sakai S, Wakiyama T, et al (2008), Sewer Pipe Measurement Robot Using Parallel Laser Sheets, Transactions of the Japan Society of Mechanical Engineers. C, Vol.74, No.737, pp. 90-97.

[6] DA. Forsyth, J. Ponce (2002), Computer Vision: A Modern Approach, Prentice Hall.

Incorporation of User Preference into Multiobjective Genetic Fuzzy Rule Selection for Pattern Classification Problems

Yusuke Nojima and Hisao Ishibuchi

Department of Computer Science and Intelligent Systems,
Graduate School of Engineering, Osaka Prefecture University,
1-1 Gakuen-cho, Naka-ku, Sakai, Osaka 599-8531, Japan
(Tel : +81-72-254-9198; Fax : +81-72-254-9915)
({nojima@, hisaoi@}cs.osakafu-u.ac.jp)

***Abstract*:** In the design of fuzzy rule-based systems, we have two conflicting objectives: accuracy maximization and interpretability maximization. As a measure of interpretability, a number of criteria have been proposed in the literature. Most of those criteria have been incorporated into fitness functions in order to automatically find accurate and interpretable fuzzy systems by genetic algorithms. Interpretability is, however, very subjective and is hardly defined for any users beforehand. In this paper, we propose the incorporation of user preference into multiobjective genetic fuzzy rule selection for pattern classification problems. User preference is represented by a preference function which is changeable according to user's direct manipulation during evolution. The preference function is used as one of objective functions in multiobjective genetic fuzzy rule selection. The effectiveness of the proposed method is examined through some case studies for the design of fuzzy rule-based classifiers.

***Keywords*:** Multiobjective genetic fuzzy systems, fuzzy rule-based systems, user preference, interactive genetic algorithms, pattern classification problems.

I. INTRODUCTION

Fuzzy rule-based systems have been widely used for pattern classification, function approximation, modeling, forecasting, and control. One advantage of fuzzy rule-based systems over other nonlinear systems such as neural networks is their linguistic interpretability. That is, each fuzzy rule is linguistically interpretable when fuzzy rule-based systems are designed by using linguistic knowledge of human experts. Linguistic knowledge, however, is not always available, especially for high dimensional data. Thus various approaches have been proposed for extracting fuzzy rules from numerical data in the literature since the early 1990s. Evolutionary algorithms can be used not only for parameter tuning but also for discrete optimization such as input selection, rule generation and rule selection [1]. Most of fitness functions were based on only the maximization of the accuracy of fuzzy rule-based systems. Since the late 1990s, the importance of interpretability maintenance in the design of fuzzy rule-based systems has been pointed out by many studies. Interpretability maximization as well as accuracy maximization was taken into account in order to design accurate and interpretable fuzzy rule-based systems [2]. The number of fuzzy rules in a system has been mostly used as one of the complexity measures. In the literature, other measures are the total number of condition parts, transparency, compactness, and so on. Interpretability is, however, very subjective and hardly specified beforehand without actual users.

For the design of simple and accurate fuzzy rule-based classifiers, we have already proposed multiobjective genetic fuzzy rule selection [3]. We have used two objective functions: to maximize the number of correctly classified training patterns and to minimize the number of fuzzy rules in a fuzzy rule-based classifier. In this paper, considering user preference on the interpretability of fuzzy rule-based classifiers, we propose the incorporation of user preference represented by a preference function into multiobjective genetic fuzzy rule selection for pattern classification problems. During evolution, the preference function can be interactively changed and is used as one of the objective function. That is, our method can find non-dominated solutions (fuzzy rule-based classifiers) in terms of three objectives: accuracy maximization, complexity minimization, and preference maximization. Through some case studies, we examine the effectiveness of the proposed idea.

II. GENETIC FUZZY RULE SELECTION WITH USER PERFERENCE

In this section, we explain fuzzy rule-based classifiers and multiobjective genetic fuzzy rule selection. We

©ISAROB 2009

also explain user preference and a preference function proposed in this paper.

1. Fuzzy rule-based classifiers

Let us assume that we have m training (i.e., labeled) patterns $\mathbf{x}_p = (x_{p1}, ..., x_{pn})$, p = 1, 2, ..., m from M classes in an n-dimensional pattern space where x_{pi} is the attribute value of the pth pattern for the ith attribute (i = 1, 2, ..., n). For the simplicity of explanation, we assume that all the attribute values have already been normalized into real numbers in the unit interval [0, 1]. Thus the pattern space of our classification problem is an n-dimensional unit-hypercube $[0, 1]^n$.

For our n-dimensional pattern classification problem, we use fuzzy rules of the following type:

$$\text{Rule } R_q: \text{ If } x_1 \text{ is } A_{q1} \text{ and ... and } x_n \text{ is } A_{qn} \text{ then Class } C_q \text{ with } CF_q, \quad (1)$$

where R_q is the label of the qth fuzzy rule, $\mathbf{x} = (x_1, ..., x_n)$ is an n-dimensional pattern vector, A_{qi} is an antecedent fuzzy set (i = 1, 2, ..., n), C_q is a class label, and CF_q is a rule weight. We denote the antecedent fuzzy sets of R_q as a fuzzy vector $\mathbf{A}_q = (A_{q1}, A_{q2}, ..., A_{qn})$.

We use 14 fuzzy sets in four fuzzy partitions with different granularities in Fig. 1. In addition to those 14 fuzzy sets, we also use the domain interval [0, 1] itself as an antecedent fuzzy set in order to represent a *don't care* condition.

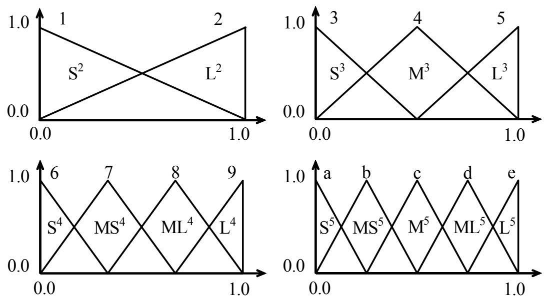

Fig. 1. Membership functions used in this paper.

The consequent class C_q and the rule weight CF_q of each fuzzy rule R_q are specified from training patterns compatible with its antecedent part $\mathbf{A}_q = (A_{q1}, A_{q2}, ..., A_{qn})$ in the following heuristic manner. First we calculate the confidence of each class for the antecedent part $\mathbf{A}_q$ as

$$c(\mathbf{A}_q \Rightarrow \text{Class } h) = \frac{\sum_{\mathbf{x}_p \in \text{Class } h} \mu_{\mathbf{A}_q}(\mathbf{x}_p)}{\sum_{p=1}^{m} \mu_{\mathbf{A}_q}(\mathbf{x}_p)}, \quad h = 1, 2, ..., M. \quad (2)$$

Then the consequent class C_q is specified by identifying the class with the maximum confidence:

$$c(\mathbf{A}_q \Rightarrow \text{Class } C_q) = \max_{h=1,2,...,M} \{c(\mathbf{A}_q \Rightarrow \text{Class } h)\}. \quad (3)$$

In this manner, we generate the fuzzy rule R_q with the antecedent part $\mathbf{A}_q$ and the consequent class C_q.

The rule weight CF_q of each fuzzy rule R_q is specified by the confidence values:

$$CF_q = c(\mathbf{A}_q \Rightarrow \text{Class } C_q) - \sum_{h=1, h \neq C_q}^{M} c(\mathbf{A}_q \Rightarrow \text{Class } h). \quad (4)$$

We do not use the fuzzy rule R_q as a candidate rule if the rule weight CF_q is not positive (i.e., if its confidence is not larger than 0.5).

As confidence, support is also often used for evaluating the interestingness of individual rules. Support can be calculated as follows:

$$s(R_q) = s(\mathbf{A}_q \Rightarrow \text{Class} C_q) = \frac{\sum_{\mathbf{x}_p \in \text{Class } C_q} \mu_{\mathbf{A}_q}(\mathbf{x}_p)}{m}. \quad (5)$$

Let S be a set of fuzzy rules of the form in (1). When an input pattern $\mathbf{x}_p$ is to be classified by S, first we calculate the compatibility grade of $\mathbf{x}_p$ with the antecedent part $\mathbf{A}_q$ of each fuzzy rule R_q in S using the product operation. Then a single winner rule is identified using the compatibility grade and the rule weight of each fuzzy rule. The input pattern $\mathbf{x}_p$ is classified as the consequent class of the winner rule.

2. Multiobjective genetic fuzzy rule selection

Multiobjective genetic fuzzy rule selection is a two-step method. In the first step, a prespecified number of promising fuzzy rules are generated from training patterns as candidate rules. In the second step, an EMO algorithm is used to search for non-dominated fuzzy rule-based classifiers (i.e., non-dominated subsets of the generated candidate rules in the first step).

Since we use the 14 antecedent fuzzy sets in Fig. 1 and a *don't care* for each attribute of our n-dimensional classification problem, the total number of possible fuzzy rules is 15^n. Among these possible rules, we examine only short fuzzy rules with a small number of antecedent conditions (i.e., short fuzzy rules with many *don't care* conditions) to generate candidate rules. In this paper, we examine fuzzy rules with three or less antecedent conditions. For prescreening candidate rules, we use the product of the support $s(R_q)$ and the confidence $c(R_q)$. That is, we choose a prespecified number of the best candidate rules for each class with respect to $s(R_q) \cdot c(R_q)$.

Let us assume that we have N candidate rules (i.e., N/M candidate rules for each of M classes). Any subset S of the N candidate rules can be represented by a binary string of length N: $S = s_1 s_2 \ldots s_N$ where $s_j = 1$ and $s_j = 0$ mean the inclusion and the exclusion of the jth candidate rule R_j in the subset S, respectively ($j = 1, 2, \ldots, N$). Such a binary string S is used as an individual (i.e., a fuzzy classifier) in an EMO algorithm for multiobjective genetic fuzzy rule selection.

Each fuzzy rule-based classifier S is evaluated by the following three objectives:

$f_1(S)$: the number of correctly classified training patterns,
$f_2(S)$: the number of selected fuzzy rules,
$f_3(S)$: user preference.

That is, our multiobjective genetic fuzzy rule selection is written as

$$\text{Maximize } f_1(S) \text{ and } f_3(S), \text{ and minimize } f_2(S). \tag{6}$$

We use NSGA-II of Deb et al. [4] to search for non-dominated fuzzy rule-based classifiers with respect to these three objectives. In this paper, uniform crossover and bit-flip mutation were used in NSGA-II. In order to efficiently decrease the number of fuzzy rules in S, a larger mutation probability is assigned to the mutation from 1 to 0 than that from 0 to 1. Besides, the unnecessary fuzzy rules which were not selected as a winner rule were removed from S after calculating the first objective.

3. User preference on interpretability

Interpretability is very subjective and hardly specified without actual users. One approach may be to use various interpretability measures as objective functions. But current evolutionary multiobjective optimization algorithms are not appropriate for the problems with more than four objectives [5]. For these reasons, we combine multiple interpretability criteria into a single preference function. Then users change the priority of criteria in the preference function during evolution of multiobjective genetic fuzzy rule selection.

We specify an interval for internal evaluations. During this interval, the preference function is not changed. After the interval, the user checks some of non-dominated classifiers and changes the priority of criteria in the preference function. Then another internal evaluation process starts. By repeating this interactive process, the user can modify the preference function and find the classifier with the high user preference value.

In this paper, we use three criteria for representing user preference: average confidence, average support, and the number of used attributes. Confidence and support have been often used to examine the interestingness of individual rules [6]. Of course, we can use other criteria in the preference function.

III. USER INTERFACE

We developed a user interface for presenting a fuzzy rule-based classifier to the user and incorporating his/her preference (Fig. 2). The antecedent part of each fuzzy rule is shown together with its consequent class, confidence, and support. Closed triangles and open rectangles mean membership functions and *don't care* conditions, respectively. The accuracy of the classifier is shown at the right-bottom of the classifier. The bottom gray zone of the interface is a user manipulation area.

Individual preference and its priority on each criterion are represented by a fitness function with two segments: A-B and B-C in Fig. 3. Three points A, B, and C are (-0.05, 0.0), (V_x, V_y), and (1.05, 0.0), respectively. Users can change the preference and the priority of each criterion by moving the point B (V_x, V_y) in $0 \le V_x \le 1$ and $0 \le V_y \le 1$. If the value of some criterion is 0.8 in Fig. 3, the fitness value on the criterion is 0.5.

A preference function is composed of the three fitness functions as in Fig. 3. In this paper, the simple sum of the fitness values is used as the satisfaction degree of user preference on the interpretability of fuzzy classifiers.

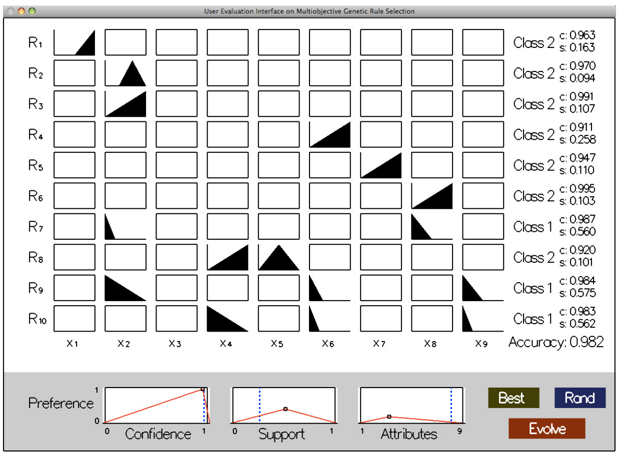

Fig. 2. A user interface for the proposed method.

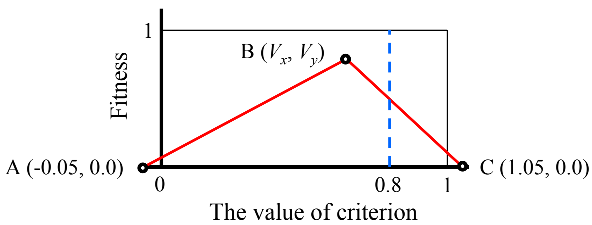

Fig. 3. Fitness functions for interpretability criteria.

©ISAROB 2009

Each vertical dashed line of fitness functions represents the actual values of three criteria for the displayed classifier. Thus, users can refer this information and change the position of the vertices of the triangles. That is, users can modify the preference function (i.e., fitness functions) according to their impression from some displayed classifiers.

There are three buttons at the right-bottom corner. The button "Best" is to show the best classifier in terms of user preference. The button "Rand" is to show three classifiers randomly selected among non-dominated ones. The button "Evolve" is to start another internal evaluation process with a prespecified number of generations.

IV. CASE STUDIES

In this section, we show two case studies s in which two users have different preference on interpretability. We used Wisconsin breast cancer data (683 patterns, 9 attributes, 2 classes) which is available from UCI machine learning repository. Parameter setting is as follows:

Number of extracted rules per class: 300,
Population size: 200,
Number of generations: 500,
Interval for internal evaluations: 50 generations.

Case 1: We assumed that a user prefers a very simple rule set. At the 250th generation, the user specified the fitness functions in Fig. 4. The obtained classifier with the highest user preference value is shown in Fig. 5. Each rule has somewhat high confidence and support. The total number of used attributes is only one. This is a very simple rule set which means "if the value of *Bare Nuclei* is high, the sample is malignant" and "if the value of *Bare Nuclei* is small, the sample is benign".

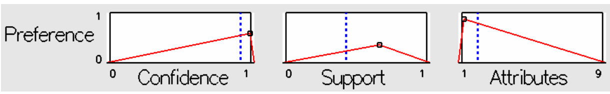

Fig. 4. Fitness functions in Case 1.

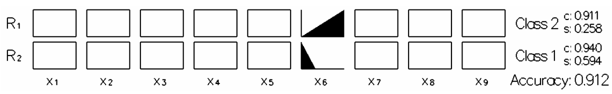

Fig. 5. Non-dominated classifier with the highest user preference value in Case 1.

Case 2: We assumed that a user prefers very accurate rules. As in Case 1, at the 250th generation, the user specified the fitness functions in Fig. 6. The obtained classifier with the highest user preference value is shown in Fig. 7. We can see that each rule has a very high confidence value comparing with the rules in Case 1.

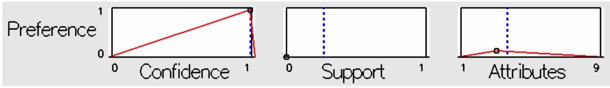

Fig. 6. Fitness functions in Case 2.

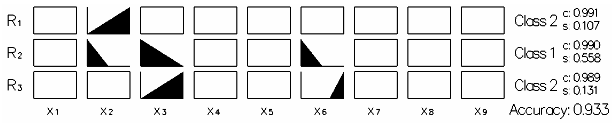

Fig. 7. Non-dominated classifier with the highest user preference value in Case 2.

V. CONCLUSION

In this paper, we proposed the incorporation of user preference into multiobjective genetic fuzzy rule selection. We used a preference function for representing user preference as an additional objective in the multiobjective problem. Through some case studies, we demonstrated that our method can obtain non-dominated fuzzy rule-based classifiers in terms of accuracy and interpretability considering user preference. As a future work, we have to further examine the effect of changing the preference function on the search performance of our method.

This work was partially supported by Grand-in-Aid for Young Scientists (B): KAKENHI (18700228).

REFERENCES

[1] Cordon O, Herrera F, Hoffmann F, Magdalena L (2001) *Genetic Fuzzy Systems*, World Scientific, Singapore.
[2] Ishibuchi H, Nozaki K, Yamamoto N, Tanaka H (1995) Selecting fuzzy if-then rules for classification problems using genetic algorithms. *IEEE Trans. on Fuzzy Systems* 3: 260-270.
[3] Ishibuchi H, Murata T, Turksen IB (1997) Single-objective and two-objective genetic algorithms for selecting linguistic rules for pattern classification problems. *Fuzzy Sets and Systems* 89: 135-150.
[4] Deb K, Pratap A, Agarwal S, Meyarivan T (2002) A fast and elitist multiobjective genetic algorithm: NSGA-II. *IEEE Trans. on Evolutionary Computation* 6: 182-197.
[5] Ishibuchi H, Tsukamoto N, Nojima Y (2008) Evolutionary many-objective optimization: A short review, *Proc. of 2008 IEEE Congress on Evolutionary Computation*: 2424-2431.
[6] Bayardo Jr. RJ, Agrawal R (1999) Mining the most interesting rules, *Proc. of 5th ACM SIGKDD International Conference on Knowledge Discovery and Data Mining*: 145–153.

©ISAROB 2009

The Fourteenth International Symposium on Artificial Life and Robotics 2009 (AROB 14th '09),
B-Con Plaza, Beppu, Oita, Japan, February 5 - 7, 2009

Feature Map Sharing Hypercolumn Model for Shift Invariant Face Recognition

Saleh Aly [1], Naoyuki Tsuruta[2], Rin-Ichiro Taniguchi[1]
[1] Department of Intelligent Systems, Kyushu University
744, Motooka, Nishi-ku, Fukuoka, 819-0395
Email: {aly,rin}@limu.is.kyushu-u.ac.jp

[2] Department of Electronics Engineering and Computer Science, Fukouka University
8-19-1, Nanakuma, Jonan-ku, Fukuoka 814-0180
Email: tsuruta@tl.fukuoka-u.ac.jp

Abstract

In this paper, we propose a shift invariant pattern recognition mechanism using feature sharing Hypercolumn model (FSHCM). To improve the recognition rate of Hypercolumn model (HCM) a shared map among a set of locally neighborhood maps is constructed in the feature extraction and feature integration layers. The shared maps help the network to increase its ability to deal with wide translation and distortion variations. The proposed framework uses FSHCM neural network to perform feature extraction step, and linear support vector machine for recognition task. The effectiveness of proposed approach is verified by using the misaligned ORL face database.

1 Introduction

Most face recognition algorithms assume aligned face images by facial features (e.g. by eye centers). In many applications, automatic alignment by facial features is still open problem. As the misalignment problem remains a bottleneck to the performance of face recognition, we propose a shift invariant pattern recognition mechanism using Hypercolumn model neural network.

Understanding how visual cortex recognize objects is a critical and essential task to design and implement an invariant pattern recognition system. Because humans and primates outperform the best machine vision systems with respect to almost any measure. Building a system that emulates object recognition in cortex has always been an attractive area of research.

Hierarchical models have been shown to outperform single-template object recognition systems [1]. There are two well-known models, which are developed to emulate the structure and behavior of visual cortex, neocognitron (NC) [2] and Standard model (SM) [3]. The complex structure of these models is one reason for its unpopularity. The Neocognitron (NC) is a massively parallel hierarchical neural network, designed primarily for 2-D pattern recognition. It was inspired by Hubel and Wiesel's serial model of biological vision [4]. It has been experimented on character recognition and show a shift and distortion tolerance. The standard model (SM) composed of a hierarchy of feedforward layers of neuron-like units, which perform either (1) a tuning computation (weighted linear sum or Gaussian template matching) to increase feature selectivity or (2) a nonlinear pooling operation based on a maximum operation to increase response invariance to translation and scaling.

Recently, applications of artificial neural networks have been expanded into general image recognition problems such as face recognition and visual surveillance. In these applications, there are three factors should be taken into consideration in order to achieve high recognition rate:

1. *Dimensionality reduction:* the distribution of visual objects in the original image space almost lies in a low-dimension subspace, which is always lower than the dimension of image space. Therefore, it is necessary to reduce the dimensions in order to eliminate the redundancy in the data.

2. *Invariance:* the appearance of the objects almost affected by many kinds of image variations. These variations may occur separately or simultaneously such as scale, shift, rotation, illuminations, pose variations. Therefore robust object recognition system should show some invariance against these factors.

3. *Network parameters:* there are two different pa-

©ISAROB 2009

rameters associated with designing an efficient neural network for object recognition problem, which are structure and training parameters. Deciding the appropriate parameters is highly depend on the distribution of the training data and the kind of required invariance.

Solving these problems is the target of Hypercolumn model. Hypercolumn model [5] has a similar architecture with Neocognitron and standard model. However, the learning strategy of the network is based on Kohonen learning algorithm. Self-organizing map (SOM) [6] is the fundamental component in building the Hypercolumn network.

The main contribution in this paper, is to replace the small-size neighbor maps in feature extraction and feature integration layers with one large shared map. The feature map is trained to share among a set of neighbor maps. This large feature map can be created by two different methods. In the first method, shared features are learned from the aggregation of all training examples covered by all shared maps. While the second method learn the shared map by applying neighborhood learning technique among neighbor maps.

The remainder of the paper is organized as follows: In section 2, the structure and the learning algorithm of HCM neural network is presented. Section 3 describes methods of creating shared feature maps. Experimental results, and conclusions are given in the following two sections,.

2 Hypercolumn model

2.1 HCM structure

The HCM network shown in Figure (1) is derived from the NC by replacing each C-cells and the lower directly connected S-cells with a two-layer hierarchical self-organizing map HSOM network [7]. The first map in the HSOM cell stands for feature extraction with size N_n^{FEL}, while the second one is used for feature integration with size N_n^{FIL}. The number of HSOM in X and Y directions are denoted by N_{HSOM}^X and N_{HSOM}^Y respectively. The input field for each feature extraction map is slightly shifted and overlapped by a certain number of neurons. Feature integration layer is an SOM map, whose input is the index of the winner in the lower feature extraction map. In the feature integration map, therefore, all shifted and distorted patterns are mapped to the same neuron, since the number of neurons in the feature integration map is

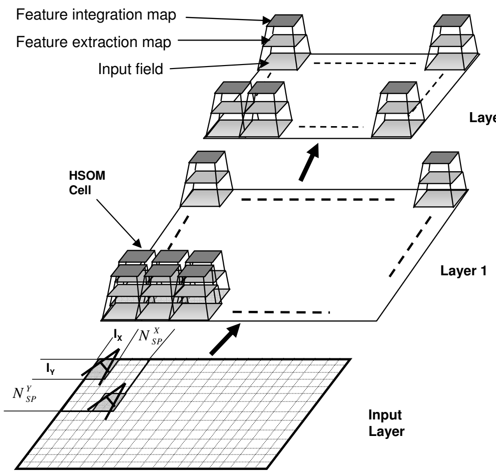

Figure 1: HCM Network structure

smaller than the number of neurons in the feature extraction map. Consequently, the index of the winners from lower feature integration maps are presented to the next higher feature extraction map. These local features are pilled up hierarchically in the higher layers to tolerate image scale, shift, rotation, and distortion variations.

2.2 HCM Training

The HCM uses the unsupervised learning algorithm of the competitive neural networks to construct its feature maps. The learning process is applied layer-by-layer starting from the bottom layer, where the normal learning algorithm of the HSOM is used to train each unit in the map. All HSOMs in the same layer can be trained in parallel. After presenting the input pattern to the HCM network, the training algorithm find the best matching winner from the first feature extraction map. Each feature extraction layer has a local input field with the size of $(I_X \times I_Y)$. The competition step in the feature extraction layer is slightly different than the original competitive step in the Kohonen algorithm. In which the competition is performed through all shifted patterns, the shift step size and the number of shifts in X and Y directions are denoted as $N_S^X \times N_S^Y$ and $N_{SS}^X \times N_{SS}^Y$ respectively. The winner pattern used to update the weights of the winner neuron and its neighbors. The input field for the next HSOM is overlapped with the input field of the neighbor HSOMs, and the size of overlapping in both X and Y directions are decided by the parameters $N_{OP}^X \times N_{OP}^Y$. These parameters are decided experimentally to tolerate shift, scale and distortion

©ISAROB 2009

variations for the HCM network. The feature map for each HSOM cell is constructed by learning all patterns from the region covered by the shifted input field, however, due to expression and rotation variations these features may be repeated in the nearest feature maps. To solve this problem, the feature map for all neighbors HSOM should share one large feature map.

3 Feature map sharing implementation

In order to deal with wide shift and distortion variations in the local features, a shared feature map among a set of neighbor maps is constructed. There are two proposed methods for implementation, In the first one, all training examples presented to the neighbor maps are used to train one shared map with a sufficiently large number of neurons. The second method, apply the idea of neighborhood learning to train neighbor maps.

3.1 Method 1: Training examples aggregation

A shared map is constructed among set of neighbor maps by learning from all examples presented to the neighbor maps. Therefore the training algorithm repeat the original SOM learning algorithm for each input pattern in the region covered by all shared maps.

1. Find the best matching neuron c using a similarity measure between the input and all the map's neurons, where c is the desired winner and should satisfy:

$$\|x_i - w_c\| = arg\min_j(\|x_i - w_j\|) \tag{1}$$

2. Update the weight vector of the winner c and also all its topological neighborhood in the map towards the prevailing input according to the rule:

$$w_j(t+1) = w_j(t) + h_{cj}(t)[x_i(t) - w_j(t)] \tag{2}$$

$$h_{cj}(t) = \alpha(t).\exp\left(-\frac{\|r_c - r_i\|}{2\sigma^2(t)}\right) \tag{3}$$

where $h_{cj}(t)$ is the neighborhood kernel function around the winner c at time $t, \alpha(t)$ is the learning rate and is decreased gradually toward zero and $\sigma^2(t)$ is a factor used to control the width of the neighborhood kernel.

As the learning process finished the constructed feature map is copied to all neighbor maps. We have to mention that each map has its different input field although they shared the same map.

3.2 Method 2: Neighborhood map learning

The main idea for the second method, is to construct the shared feature map by applying the neighborhood learning trick in the feature map level. Which implies that there are two neighborhood learning, the original neighborhood learning in the Kohonen algorithm among neurons in the map and the proposed one between neighbor maps. Therefore the second training algorithm differ than the first method, and can be summarized as follows.

- Find the best matching unit as stated in equation (1). Moreover, the shift mechanism in the HCM is applied to find the winner pattern and the winner neuron by including all shifted patterns in the competition step.
- Update the winner neuron using the winner pattern by applying equation (2).
- Update the neuron at the same position in all neighbor maps by the winner pattern using small learning rate.

The above steps are repeated for each HSOM cell in the HCM network and for every map in the HSOM cells, (i.e. feature extraction map and feature integration map).

4 EXPERIMENTAL RESULTS

4.1 ORL Face Database

The ORL database was collected between 1992 and 1994 [8]. It contains ten different images of each of 40 distinct subjects. For some subjects, the images were taken at different times, varying the lighting, facial expressions (open / closed eyes, smiling / not smiling) and facial details (glasses / no glasses). All the images were taken against a dark homogeneous background with the subjects in an upright, frontal position (with tolerance for some side movement).

4.2 Face recognition using misaligned face database

The aim of this experiment is to determine the performance of FSHCM algorithm to solve misaligned face recognition problem. In this experiment, ORL face database is divided into two halves; one-half used as a training data and the other part for blind test.

The training data for HCM consists of 200 images, the first five images for each person. All images in the database are scaled to the size 48×48 pixels and photometrically normalized with histogram equalization method without any geometric normalization.

The proposed face recognition system consists of 2−layers HCM neural network for feature extraction stage and linear SVM classifier at the top of the network for recognition stage. Table (1) summarizes the parameters used in the training of HCM. In our experiment, the first method is used to construct all shared maps in the first layer of HCM neural network. This system give 89% recognition accuracy using features extracted from the first layer of HCM network. However, the second layer features give slightly lower accuracy rate (88.5%) than the first layer features. The decrease in the accuracy due to the utilization of cropped input image in the test phase, however, for coarse cropped faces the features from second layer expected to give better performance than features from first layer.

4.3 Shift invariant feature extraction

In this experiment, the capability of FSHCM neural network to deal with affine transformed input images is examined. A set of artificial face images is generated using affine transformed training data. The scaling parameter for the transformed test data has the following values $\{0.95, 0.97, 1.05, 1.07\}$, rotation parameter has values of $\{2°, 4°, -2°, -4°\}$, and the translation parameter take the values $\{1, 2, -1, -2\}$ pixels in both X and Y directions. The recognition accuracy for all affine transformed face images using the same network structure in the previous experiment is 98%. This higher rate of accuracy indicate that FSHCM features exhibit large tolerance to affine transformed input images. As the number of shifted pixels due to scale, rotation, and translation variations are more than 10% of the image size.

5 CONCLUSION

A modified version of Hypercolumn model has been proposed. Shared feature maps are proposed to recover wide variation in shift and distortion. In order to perform the classification step in the final stage of our pattern recognition system, a simple linear classifier such as linear SVM algorithm is used to classify the extracted features. The performance of the modified network shows a reasonable results to deal with affine transformed images from ORL face database.

Table 1: HCM Training Parameters

Parameter	Layer 1	Layer 2
$I_X \times I_Y$	3×3	2×2
$N^X_{HSOM} \times N^Y_{HSOM}$	23×23	11×11
$N^X_S \times N^Y_S$	2×2	0×0
$N^X_{SS} \times N^Y_{SS}$	1×1	0×0
$N^X_{OP} \times N^Y_{OP}$	2×2	2×2
N^{FEL}_n	30×16	40×28
N^{FIL}_n	8×6	12×10

References

[1] B. Heisele, T. Serre, M. Pontil, T. Vetter, and T. Poggio. Categorization by learning and combining object parts. *Advances in Neural Information Processing Systems*, 14, 2002.

[2] K. Fukushima. Neocognitron. *Biological Cybernetics*, 36(4):193–202, 1980.

[3] T. Serre, L. Wolf, S. Bileschi, M. Riesenhuber, and T. Poggio. Robust object recognition with cortex-like mechanisms. *IEEE Trans. Pattern Analysis and Machine Intelligence*, 29(3):411–426, 2007.

[4] D. Hubel and T. Wiesel. Receptive fields, binocular interaction and functional architecture in the cats visual cortex. *J. of Physiology*, 160:105–154, 1962.

[5] N. Tsuruta, R. Taniguchi, and M. Amamiya. Hypercolumn model: A combination model hierarchical self- organizing maps and neocognitron for image recognition. *System and Computer in Japan*, 31(2):49–61, 2000.

[6] T. Kohonen. *Self-Organizing Maps.* Springer, 1997.

[7] J. Lampinen and E. Oja. Clustering properties of hierarchical self organizing maps. *Journal of Math. Imaging and Vision*, 2(2-3):261–272, 1992.

[8] F. Sammaria and A. Harter. Parameterization of a stochastic model for human face identification. *In 2nd IEEE workshop on applications of computer vision*, 1994.

©ISAROB 2009

The Fourteenth International Symposium on Artificial Life and Robotics 2009 (AROB 14th '09),
B-Con Plaza, Beppu, Oita, Japan, February 5 - 7, 2009

A moving object tracking based on color information employing a particle filter algorithm

Budi Sugandi, Hyoungseop Kim, Joo Kooi Tan and Seiji Ishikawa

Graduate School of Engineering, Kyushu Institute of Technology
1-1 Sensui, Tobata, Kitakyushu, Fukuoka, Japan
Tel : +81-93-884-3185; Fax :+ 81-93-861-1159
budi@kimlab.cntl.kyutech.ac.jp

Abstract: In this paper, we present a new algorithm to track a moving object based on color information employing a particle filter algorithm. Recently, particle filter has been proven very successful for non-linear and non-Gaussian estimation problems. It approximates a posterior probability density of the state such as the object position by using samples which are called particles. The probability distribution of the state of the tracked object is approximated by a set of particles, where each state is denoted as the hypothetical state of the tracked object and its weight. The particles are propagated according to a state space model. In this paper, the state is treated as the position of the object. The weight is considered as the likelihood of each particle. For this likelihood, we consider the similarity between the color histogram of the tracked object and the region around the position of each particle. The Bhattacharya distance is used to measure this similarity. And finally, the mean state of the particles is treated as the estimated position of the object. The experiments are performed to confirm the effectiveness of this method to track the moving object.

Keywords: object tracking, color information, particle filter.

I. INTRODUCTION

Tracking objects through the frames of an image sequence is an elementary task in online and offline image-based applications including surveillance, human-machine interface, motion capture, and medical imaging, etc. Many researches of tracking object motion in image sequences have been proposed based on image subtraction such as background subtraction and inter-frame difference, optical flow, skin color extraction and probabilistic methods such as Kalman filter and particle filter. Recently, probabilistic methods become popular method among many researches. Kalman filter is a common approach for dealing with target tracking in the probabilistic framework. But it cannot resolve the tracking problem when the model is nonlinear and non-Gaussian. The extended Kalman filter can deal to this problem, but still has a problem when the nonlinearity and non-Gaussian cannot be approximated accurately.

Recently, particle filter has been proven very successful for non-linear and non-Gaussian estimation problems [1-4]. It approximates a posterior probability density of the state such as the object position by using samples which are called particles. As for one of the particle filters, the Condensation algorithm was introduced by M. Isard et al. [1]. This algorithm has been typically used for tracking problems of moving object contours. For another particle filter, Monte Carlo filter was introduced by Kitagawa [2] and Bayesian bootstrap filter was introduced by Gordon et al. [3].

The most important step in tracking based on color information is to establish color distribution model, which provides a basis for weight updating and target state estimation. There are different approaches to build the target model. McKenna et al. [5] use adaptive color threshold to distinguish the target from background, Olson et al. [6] use model intensity of each pixel of the target with a normal distribution and Isard et al. [7] use a mixture of Gaussian distribution to model pixel value. But in practical application, all these methods cannot provide robust and computationally efficient solutions when the background and target are in a complicated condition.

Comparatively, a color histogram has many advantages for target tracking as it is robust to partial occlusion, rotation and scale invariant, and is also easy to be implemented [8-9]. In this paper, we employ a particle filter to track a moving object based on color information. A target model is tracked using the particle filter by comparing its histogram with the histogram of every sample using the Bhattacharyya distance which

©ISAROB 2009

makes the measurement matching and weight updating more reasonable.

The remaining of this paper is organized as following. In section 2, we describe a dynamic model of our system and the color histogram of the tracked object. The implementation of color histogram into particle filter is presented in section 3. Section 4 present some experimental results and finally section 5 is the conclusion of the paper.

II. TRACKING AND COLOR DISTRIBUTION MODEL

2.1. Tracking Model

We consider the motion of a target as the discrete time 2 dimensional motion with constant velocity. The state vector at a time step k is denoted by $\boldsymbol{x}_k$, which usually contains information about the coordinate of the current position of the object and the differential of it. Our dynamical model is described as

$$\boldsymbol{x}_k = F\boldsymbol{x}_{k-1} + G\boldsymbol{w}_k \tag{1}$$

where F is the transition matrix, G is the system noise matrix and $\boldsymbol{w}_k$ is a Gaussian noise vector. This dynamical model is used in the sampling step of particle filters. With the assumption that the object moves in constant velocity (uniform motion), we can describe the motion as following equations:

$$\begin{aligned} x_{k+1} &= x_k + (x_k - x_{k-1}) \\ y_{k+1} &= y_k + (y_k - y_{k-1}) \end{aligned} \tag{2}$$

where x_k, y_k represent the center of the target region at time step k, respectively. From this, the state vector $\boldsymbol{x}_k^{(i)}$ of the i-th particle at time step k, system matrices F and G and noise vectors $\boldsymbol{w}_k$ are defined respectively as follows:

$$\mathrm{x}_k^{(i)} = \left[x_k^{(i)}, y_k^{(i)}, x_{k-1}^{(i)}, y_{k-1}^{(i)}\right]^T \tag{3}$$

$$F = \begin{bmatrix} 2 & 0 & -1 & 0 \\ 0 & 2 & 0 & -1 \\ 1 & 0 & 0 & 0 \\ 0 & 1 & 0 & 0 \end{bmatrix}, \quad G = \begin{bmatrix} 1 & 0 \\ 0 & 1 \\ 0 & 0 \\ 0 & 0 \end{bmatrix} \tag{4}$$

$$\boldsymbol{w}_k^{(i)} = \left[w_{xk}^{(i)}, w_{yk}^{(i)}\right]^T \tag{5}$$

2.2. Color Distribution Model

To achieve robustness against mixed color, rotation and variant illumination condition, we focus on weighted color histograms to represent the target model. The color histogram is used as the discretized color distribution. Let m be the number of segments of the segmented color space. The histograms are produced from the function $h(\boldsymbol{x}_i)$ that assign the color at location $\boldsymbol{x}_i$ to the corresponding bin. In this paper, we use RGB color space with $8\times8\times8$ bins.

We determine the color distribution of the object inside a rectangular region. To increase the reliability of the target model, smaller weight are assigned to the pixels that are further away from region center by employing a weighting function

$$g(r) = \begin{cases} 1 - r^2 & r < 1 \\ 0 & otherwise \end{cases} \tag{6}$$

Here, r is the distance from the center of the region.

The color histogram $p_{\boldsymbol{y}} = \left\{p_{\boldsymbol{y}}^{(u)}\right\}_{u=1,\dots,m}$ at location $\boldsymbol{y}$ is calculated as

$$p_{\boldsymbol{y}}^{(u)} = f \sum_{j=1}^{I} g\left(\frac{\left\|\boldsymbol{y} - \boldsymbol{x}_j\right\|}{a}\right)\delta\left[h\left(\boldsymbol{x}_j\right) - u\right] \tag{7}$$

Where I is the number of pixels in the region, $\boldsymbol{x}_j$ is the position of pixels in the region, δ is the Kronecker delta function, a is the normalization factor, and f is the scaling factor defined as

$$f = \frac{1}{\sum_{i=1}^{I} g\left(\frac{\left\|\boldsymbol{y} - \boldsymbol{x}_i\right\|}{a}\right)} \tag{8}$$

to ensures that $\sum_{u=1}^{m} p_{\boldsymbol{y}}^{(u)} = 1$.

The similarity between two color histograms $\boldsymbol{p} = \left\{p^{(u)}\right\}_{u=1,\dots,m}$ and $\boldsymbol{q} = \left\{q^{(u)}\right\}_{u=1,\dots,m}$ is measured using Bhattacharyya distance defined as

$$d = \sqrt{1 - \rho[\boldsymbol{p}, \boldsymbol{q}]} \tag{9}$$

where

$$\rho[\boldsymbol{p}, \boldsymbol{q}] = \sum_{u=1}^{m} \sqrt{p^{(u)} q^{(u)}} \tag{10}$$

From this equation, the larger ρ shows the more similar the distributions. For two identical histograms we obtain ρ=1, indicating a perfect match.

Fig.1. shows an example of reference color histogram at time step k_o and the candidate color histogram at time step k with hypothesized state $\boldsymbol{x}_k$.

©ISAROB 2009

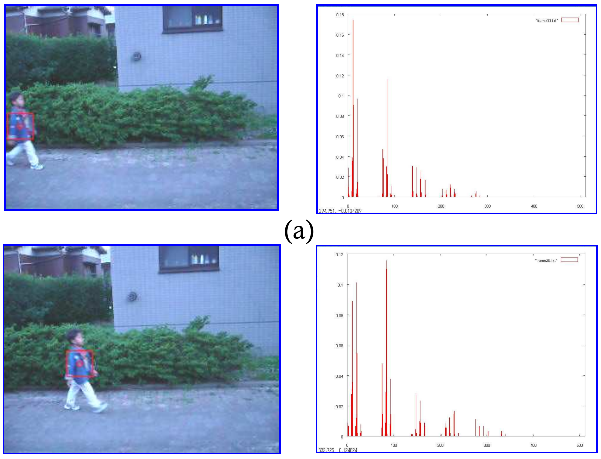

(a)

(b)

Fig.1. Color histogram used for tracking. (a) a reference color histogram at time step k_o (b) candidate color histogram at time step k

III. IMPLEMENTATION OF PARTICLE FILTER

In the particle filter, the probability distribution of the state of the tracked object is approximated by a set of particles $\boldsymbol{s}^{(i)}=\{\boldsymbol{x}^{(i)}, \pi^{(i)}\}$ $(i=1,2,\ldots,N)$ where each $\boldsymbol{x}^{(i)}$ is denoted as the hypothetical state of the tracked object and $\pi^{(i)}$ is its weight. In this paper, the state is treated as the position of the object. The particles are propagated according to a system model. Then, the mean state of the particles is treated as the estimated position of the object. The weight is considered as the likelihood of each particle. For this likelihood, we consider the similarity between the color distributions of the tracked object and the region around the position of each particle using Bhattacharya distance.

The weight $\pi^{(i)}$ of i-th state $\boldsymbol{x}^{(i)}$ is calculated as

$$\begin{aligned}\pi^{(i)} &= \frac{1}{\sqrt{2\pi\sigma}}\exp\left(-\frac{d^2}{2\sigma^2}\right)\\ &= \frac{1}{\sqrt{2\pi\sigma}}\exp\left(-\frac{\left(1-\rho\left[\boldsymbol{p}\left(\boldsymbol{x}^{(i)}\right),\boldsymbol{q}\right]\right)}{2\sigma^2}\right)\end{aligned} \tag{11}$$

Where $\boldsymbol{p}(\boldsymbol{x}^{(i)})$ and $\boldsymbol{q}$ are the color histogram of sample and target, respectively. From this equation we can see that small Bhattacharya distance corresponds to large weight. During resample step of particle filter, samples with a high weight may be chosen several times leading to identical copies, while others with relatively low weights may be ignored.

The proposed tracking algorithm is performed by four steps as following:

1. Initialization:
   - Given the color histogram of tracked object:
     $$\boldsymbol{q} = \left\{q^{(u)}\right\} u = 1,\ldots,m$$
   - Initialize the N particles.

2. Important sampling : For each particle do the following:
   - Propagate each sample according to system model of Eq. (1).
   - Calculate the color histogram $\boldsymbol{p}^{\boldsymbol{u}}_{\boldsymbol{x}_k^{(i)}}$ from Eq. (7).
   - calculate the Bhattacharya coefficient
     $$d_{\boldsymbol{x}_k^{(i)}} = \sqrt{1-\rho[\boldsymbol{p}\left(\boldsymbol{x}_k^{(i)}\right),\boldsymbol{q}]}$$
   - calculate the weight
     $$\pi_k^{(i)} = \frac{1}{\sqrt{2\pi\sigma}}\exp\left(-\frac{\left(1-\rho\left[\boldsymbol{p}\left(\boldsymbol{x}_k^{(i)}\right),\boldsymbol{q}\right]\right)}{2\sigma^2}\right)$$

3. Estimated position of $\boldsymbol{x}_k$ according to mean estimate :
   $$E(\boldsymbol{x}_k) = \sum_{i=1}^{N}\pi_k^{(i)}\boldsymbol{x}_k^{(i)}$$

4. Resampling : Generate a new set of samples
   $$\left\{\boldsymbol{x}_k^{(i)}, \pi^{(i)}\right\} i = 1,\ldots, N$$
   - Calculate the normalized cumulative probability $c_k^{'(i)}$:
     $$c_k^{(0)} = 0,\ c_k^{(i)} = c_k^{(i-1)} + \pi_k^{(i)},\ c_k'^{(i)} = \frac{c_k^{(i)}}{c_k^{(N)}}$$
   - Generate Uniformly distributed number $r\in[0,1]$. Find, by binary search, the smallest j for which $c_k^{'(j)} \geq r$ and set $\boldsymbol{x}_k^{(i)} = \boldsymbol{x}_k^{(j)}$

IV. EXPERIMENTAL RESULT

We have done the experiment to track a moving object with our proposed method. The experiments are implemented on Pentium IV with 2.53 GHz CPU and 512 MB RAM. The resolution of each frame is 320×240 pixels image.

Initially, we prepared the color histogram of the tracked object and the region to make the histogram was set to 30×30 pixels. We performed the experiment using 100 and 300 particles. Fig.2 and Fig.3 show the experimental results of the tracking object. The red circle shows the estimated position of the tracking object and the red square shows the region of the tracked object used in color histogram. As shown in those figure, the accuracy of the tracking result using 100 particles is lower than using 300 particles. However, in both case, satisfactory experimental results are achieved with RMSE for each case is 6.48 and 2.28, respectively.

V. CONCLUSION

This paper presented a new method to track the moving object based on color information employing particle filter algorithm. The experimental results showed the satisfactory performance on each frame.

Furthermore, the performance of the tracking of the moving object needs more improvement. There are many aspects in tracking the moving object that are not considered yet in this paper. The problem of occlusions between object and speed up the computational time are examples of related studies conducted by existing researchers. Taking them into consideration could lead to some improvement. These are remaining for our future works.

REFERENCES

[1] M. Isard and A. Blake (1998), CONDENSATION –Conditional Density Propagation for Visual Tracking, Intl. J. of Computer Vision, 29(1): 5-28.
[2] G. Kitagawa (1996), Monte Carlo filter and smoother for non-Gaussian nonlinear state space models, J. Comput. and Graph. Stat. 5(1):1–25.
[3] N.J. Gordon, D.J. Salmon and A.F.M. Smith (1993), Novel approach to nonlinear/non-Gaussian Bayesian state estimation, IEE Proceeding on Radar and Signal Processing, 140(2):107-113.
[4] P. Li and T. Zhang (2003), Visual contour tracking based on particle filters, Image and Vision Computing, 21(1):111–123.
[5] S. McKenna, Y. Raja, S. Gong (1999), Tracking color objects using adaptive mixture models, Image and Vision Computing, 17: 225–231.
[6] T. Olson and F. Brill (1997), Moving object detection and event recognition algorithm for smart cameras, Proceeding of the DARPA Image Understanding Workshop, 159-175.
[7] M. Isard and J. McCormick (2001), A Bayesian multiple-blob tracker, International Conference on Computer Vision, 2:34–41.
[8] K. Nummiaro, E. Koller, L.V. Gool (2002), A color-based particle filter, 1st Intl. WS on GMBV, 53–60.
[9] P. Perez, C. Hue, J. Vermaak et al [2002], Color-based probabilistic tracking, Proceeding of the 7th European Conference on Computer Vision, 661–675.

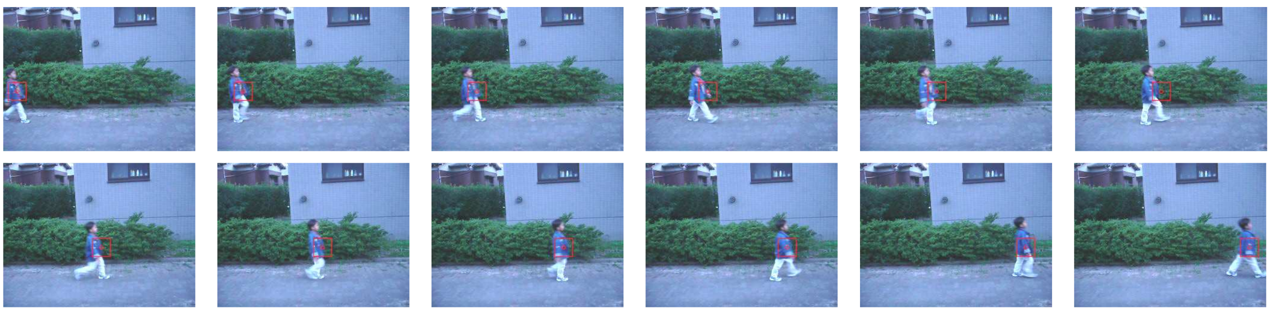

Fig.2. Tracking result using 100 particles

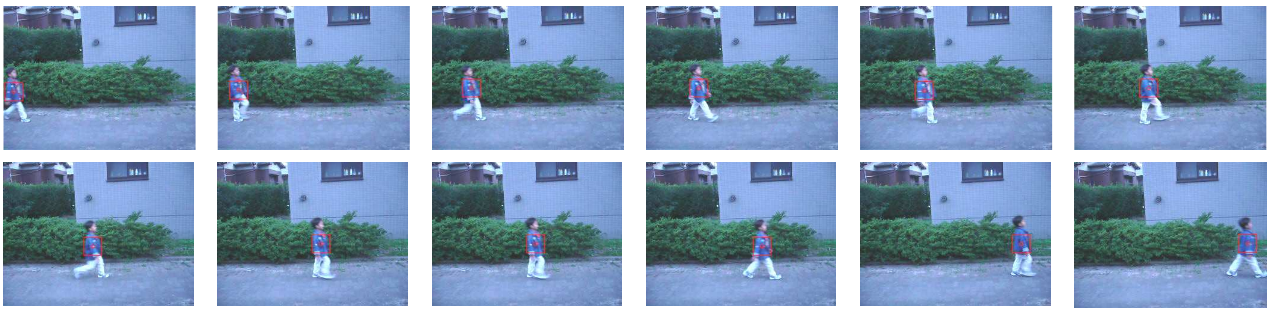

Fig.3. Tracking result using 300 particles

Correlation-based similarity metrics in MBR for ordered data

Daiki Nakahigashi, Hiroshi Tsuji

Osaka Prefecture University, 1-1, Gakuencho Naka-ku, Sakai, Osaka, Japan
(Tel : +81-72-254-9353; Fax : +81-72-254-9915)
(nakahigashi@mis.cs.osakafu-u.ac.jp, tsuji@cs.osakafu-u.ac.jp)

Abstract: To improve the precision of memory-based reasoning for ordered data, this paper presents correlation-based similarity metrics. The basic idea under this research is intuitive assumption: if the correlation between an answer and a feature in example data set is large, the weight of the feature for predication should be large. To validate the proposal, this paper has promoted "Leave-One-Out-Cross-Validation" for fifty three examples which are collected from Japanese client companies who outsource offshore vendor companies. Three measures "mean absolute error, variance of error and precision" are compared among the proposed method, PCD, PFC, ACF and CCF. The Wilcoxon matched-pairs signed-ranks test is also discussed.

Keywords: Memory-Based Reasoning, Expert System, Similarity Metrics, Prediction, Estimation.

I. INTRODUCTION

Memory-Based Reasoning (MBR) is a one of the data mining technique [1]. The technique based on the idea of storing some pairs of features and answer in the data base, and when a new question is given, searching similar examples and predicting the answer of question from the answers of similar examples. Prediction by MBR strongly depends on the definition of the similarity.

While the Euclid distance is a typical example for similarity for ratio data, the conditional probability is another example for nominal data [2]. However, they might not work for ordered data because both of them miss the correlation between features and answer.

To solve the prediction problem for project success/failure based on ordered data [3], this paper proposes a feature weighting method based on the correlation. Comparing the proposed method with the traditional methods, this paper validates the proposal.

II. Overview of Memory-Based Reasoning

MBR is a data mining technique that does not extract rules from the examples data but uses the examples as it is. The basic idea is to store the examples of pair of features and answer as training examples, and when new question is given, to search similar examples from the database and to predict the answer by referring to similar examples (Fig.1). This idea allows relieving bottlenecks of knowledge acquisition like cost when there are contradiction among the extracted rules.

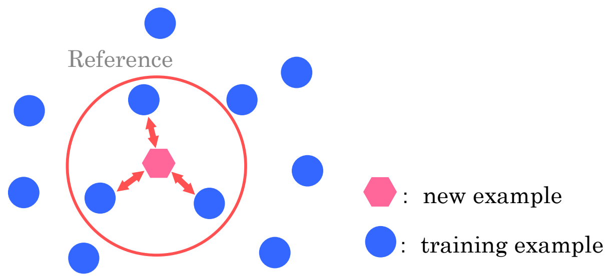

Fig.1. Memory-based Reasoning (MBR)

MBR has following advantages:

- Adding/deleting example does not give side effect,
- Explanation of answers is based on real examples,
- It is possible to apply to ordered data as well as nominal data and ratio data,
- High parallelism is possible.

Because of these advantages, MBR is applied to many domains such as translation [4] and weather forecasting [5]. On the other hand, MBR has following disadvantages:

- No ability to generate the answer that does not exist in the examples data base,
- Prediction accuracy strongly depends on the definition of similarity.

The main step of MBR is shown below (Fig.2):

1. Calculation of similarity

   When a new example is given as a question, the similarity between the example and each training example is calculated.

2. Decision of neighborhood

   The neighborhood is decided based on the similarity for generating answer.

©ISAROB 2009

3. Predicting answer by the combination function

The answer for new example is predicted from neighborhoods by the combination function.

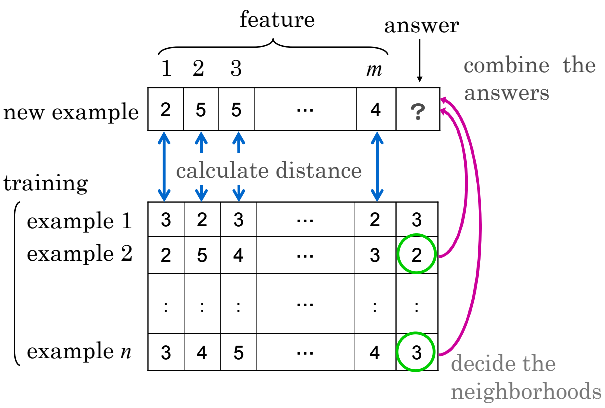

Fig.2. The main step of MBR

III. Traditional method for Nominal Data

1. Feature weighting methods

The precision in MBR strongly depends on the definition of the similarity. Therefore, a variety of feature weighting methods were proposed [2][4][5], while the Euclid distance is a simply way. For nominal data, there are four methods based on conditional probability as follows [2]:

- PCF (Per-Category Future importance)

$$w(a,c)=P(c\mid a) \tag{1}$$

- PFC (Per-Feature Category importance)

$$w(a,c)=P(a\mid c) \tag{2}$$

- ACF (Averaged Category Feature importance)

$$w(a,c)=\frac{P(c\wedge a)}{P(c)\cdot P(a)} \tag{3}$$

- CCF (Cross-Category Feature importance)

$$w(a,c)=w(a)=\sum_{c=1}^{N_c}P(c\mid a)^2 \tag{4}$$

where c : the answer category of training example
a : the feature of the example
N_c: the number of the answer

2. Similarity metrics

There are three metrics for the similarity:

- SUM (Summation Metric)

$$Similarity(u,v)=\sum_i w(a_i,c_u)f(u_i,v_i) \tag{5}$$

- MAX (Maximize Metric)

$$Similarity(u,v)=\underset{i}{MAX}\left(w(a_i,c_u)f(u_i,v_i)\right) \tag{6}$$

- ERROR (Error Minimize Metric)

$$Similarity(u,v)=1-\prod_i\left(1-w(a_i,c_u)f(u_i,v_i)\right) \tag{7}$$

where u : the training examples
v : the new examples
a_i: the feature i
c_u: the answer category of training example u

$$f(x,y)=\begin{cases}1 & (x=y)\\ 0 & (\text{others})\end{cases}$$

As SUM is a metric considers sum of matched feature weights as similarity, it can reflect all feature of the example into similarity. On the other hand, MAX can reflect only distinguishing feature of the example into similarity.

ERROR has both property of SUM and MAX. Although it considers all feature weights, if there is a matched feature (=1), the similarity should be equal to 1.

IV. Correlation-based feature weighting method

The traditional similarity metrics for nominal data may not work well for ordinal data because they only check whether the features between the new example and training example are the same or not. We expect the prediction accuracy can be improved if we modify the weight function for ordinal data.

Let us focus on the correlation between each feature and answer. It is reasonable to consider that the similarity becomes larger if the correlation is large. Then the proposal weighting can be defined as follows:

$$w(a)=\begin{cases}|Corr(a)| & (\ |Corr(a)|\geq t\ )\\ 0 & (\ |Corr(a)|\geq t\ )\end{cases} \tag{8}$$

where $Corr(a)$: correlation coefficient between feature "a" and answer
t: threshold value

As smaller distance means higher similarity, the distance function is defined as follows:

$$d(u,v)=\sum_i w(a_i)f(u_i,v_i) \tag{9}$$

where u : the training examples
v : the new examples
a_i: the feature i
$f(u_i,v_i)=(u_i-v_i)^2$

The function is essentially the same as SUM although it considers the spacing between feature values by calculating the square of difference.

©ISAROB 2009

V. Numerical experimentation

To compare the proposal method with traditional methods, numerical experimentation has been done. The application problem is given as follows [3]:

Predict the success rate (risk) for new offshore software project when its features are given. At that time there are small sizes of examples where each includes fourteen attributes and its result. Each feature is labeled from 1 to 5. The result is also labeled from 1 (Critical Failure) to 5 (Great Success). The example features are "software complexity and scale", "vendor communication skill" and "deadline urgency".

1. Data set

In this experimentation, there are fifty three questionnaire responses as the training examples. The features for project which are classified into three properties are shown in Table 1.

The responses came from the experienced project managers. The questionnaire is consisted of questions about "fourteen features defining the development" and "success or failure". The former is independent variable and the latter is a dependent variable in our experimentation.

Each independent variable is evaluated on a scale of one to five in the questionnaire. Note that there are small sized of training data while the problem space expands to 5^{14} varieties. Then it is expected that MBR works well for the thick subspace while it might not do for the thin subspace.

Table 1. Features of offshore development

Features		Correlation Coefficient
Software Property	Software complexity and scale	0.13
	Software quality measurability	0.21
	Requirement specifiablity	0.12
	Requirement volatility	0.02
Vendor Property	Communication skill	0.54
	Project management capability	0.40
	Vendor flexibility on specification changes	0.24
	Attrition rate	0.20
	Long-term relationship strategically	0.20
Project Property	Deadline urgency	0.14
	Relative cost advantage	0.23
	Client side technical expertise	0.10
	Strategic importance for related project	0.15
	Ability to monitor vendor behavior	0.48
Success or failure of development		

2. Evaluation methodology

To validate our proposal, LOOCV (Leave-One-Out Cross-Validation) test was carried out. The counter methods are four traditional methods (PCF, PFC, ACF and CCF) as described in III.1. LOOCV is one of cross-validations that predict answer by assuming one of examples as a test example (a new example) and the rest (in our case, fifty two examples) as training examples, and repeats the prediction fifty three times for all examples.

While there might be variety of condition parameters, this paper describes the result for the following conditions in the limited pages:

- The number of neighborhood is three for any case,
- The threshold value of correlation coefficient is 0.2,
- The combination function used when the answer is predicted is defined by following formula:

$$c_v = \frac{\sum_{u\in N} Similarity(u,v) c_u}{\sum_{i\in N} Similarity(u,v)} \tag{10}$$

where c_u: the answer category of training example u

$$Similarity(u,v) = \frac{1}{d(u,v)}$$

The intention of this function is to emphasize the answers of high similarity. Although the original answer alternative should be integer (1, 2, 3, 4 or 5), the prediction could take real number. Then we need not round the prediction because the answer alternatives are prepared for responder convenience.

We used following three evaluation indices:

- *Mean of absolute error* between prediction answer and answer of training example. The smaller value is, the more the prediction is accurate,
- *Variance of error* between prediction answer and answer of training example,
- *Precision* which is concordance rate between prediction answer rounded off and answer of training example.

To verify the significant differences between proposal method and traditional methods, two kinds of statistical tests are measured: the Wilcoxon matched-pairs signed-ranks test for mean of absolute error and F-test for variance of error.

3. Experimental result

The mean absolute error, variance of error and precision for five methods are shown in Table 2. Table 2 shows the proposed method obtains the lower value than every traditional method about both mean absolute

©ISAROB 2009

error and variance of error. And the proposed method obtains the higher value than all traditional methods about precision.

Table 2. Three Evaluation Indices among Methods

	Proposal method	PCF	PFC	ACF	CCF
Mean absolute error	0.521	0.714	0.766	0.805	0.766
Variance of error	0.515	0.873	1.061	1.027	1.009
Precision	0.604	0.509	0.453	0.415	0.377

Table 3. Wilcoxon matched-pairs signed-ranks test

	PCF	PFC	ACF	CCF
z-statistics	1.645	2.377	3.112	3.446
p-value	0.050	0.009	0.001	0.000

Table 4. F-test

	PCF	PFC	ACF	CCF
F-statistics	1.686	2.049	1.982	1.948
p-value	0.031	0.005	0.008	0.009

Table 3 and Table 4 are results of Wilcoxon matched-pairs signed-ranks test for mean of absolute error and F-test for variance of error respectively. Those indicate that there are the significant differences between the proposed method and traditional methods.

The p-value in Table 3 shows that there are significant differences about absolute error: (1) at 5% level between the proposed method and PCF, and (2) at 1% level between the proposed method and the other methods. At the same time, the p-value in Table 4 also shows that there are significant differences about variance of error: (1) at 5% level between the proposed method and PCF, and (2) at 1% level between proposal method and the other methods.

These results have proven the proposed method could perform more precise than the traditional methods to the prediction problem of offshore software development's success or failure. It is also expected that the proposed method might work well for any similarity metrics for ordered data.

VI. Conclusion

This paper has described correlation-based similarity metrics in Memory-Based Reasoning. The basic motivation of this research is to improve performance of predication for ordinal data. The problem was project prediction on failure risk which has fourteen features and fifty three examples.

To verify the effect of the proposed method, this paper has used three indices for leave-one-out-cross-validation: mean absolute error, variance of error and precision. Comparing the proposed similarity metrics to the traditional conditional probability based metrics (PCF, PFC, ACF and CCF), this paper found that there are significant differences among them statistically.

There are some issues for future research. Some features might be not useful because of the magnitude of their correlation coefficient, so this paper select the features to be used for predication. The control parameter such as threshold and combination function should be accepted sensitivity analysis.

Future, while there are problems with ordered data, there are also problems which include mixed data: nominal data, numerical data and ordered data. Therefore, the combination of similarity metrics will be discussed as future research.

ACKNOWLEDGEMENTS

The authors would like to give sincere thanks to the members of Joint Forum for Strategic Software Research (SSR) who contributed to collect responses of questionnaire and all the respondents who answered the questionnaire carefully.

REFERENCES

[1] Adriaans P and D Zantinge (1996), "Data Mining". Addison-Wesley Pub.
[2] Wettschereck D, David W. Aha and T Mohri (1997), "A Review and Empirical Evaluation of Feature Weighting Methods for a Class of Lazy Learning Algorithms". Artificial Intelligence Review, vol.11, No.1-5, pp.273-314
[3] Tsuji H, et al. (2007), "Questionnaire-based Risk Assessment Scheme for Japanese Offshore Software Outsourcing". Lecture Notes on Computer Science 4716, B. Meyer and M. Joseph (Eds.), pp.114-127, Sprinter-Verlag Berlin Heidelberg
[4] Sato S (1990), "MBT1: Example-Based Word Selection (in Japanese)". Journal of Japanese Society for Artificial Intelligence, Vol.6, No.4, pp.592-600
[5] Mohri T, M Nakamura and H Tanaka (1993), "Weather Forecasting Using Memory-Based Reasoning". Second International Workshop on Parallel Processing for Artificial Intelligence, pp.40-45

©ISAROB 2009

The Fourteenth International Symposium on Artificial Life and Robotics 2009 (AROB 14th '09),
B-Con Plaza, Beppu, Oita, Japan, February 5 - 7, 2009

Hybrid system based emotion recognition and novel emotion engine

Dong-Hwa Kim

Dept. of Instrumentation and Control Eng., Hanbat National University, Daejeon City, Korea

(Tel : 82-42-821-1170; Fax : 82-42-821-1164)
(kimdh@hanbat.ac.kr)

Abstract: In this paper, we propose a method for recognizing the human's emotion using hybrid learning system by PSO, agent machine learning. The most general method uses neural networks to classify emotion by using speech and face image data for human's emotion recognition. But high-dimension and large size of this data cause low-speed learning of neural networks. The main idea of the proposed method is to learn emotion by hybrid system and to express emotion by novel emotion engine. Experimental result shows that this method can achieve better performance for human's emotion recognition than others and express emotion.

Keywords: Agent machine learning, Human's emotion Recognition, Advanced Robotics, PSO.

I. INTRODUCTION

Recently artificial intelligence has been interested in many areas, such as intelligent computing, intelligent transportation, and intelligent home. Especially, many researchers have been interesting intelligent robotic system to express like human being. In that case, we have to consider emotional technology to robotic system. The creation of robots with emotions, namely 'emotional robots' is recently attracting to provide a novel test-bed for theories of biological emotion.

Of course, to do that, the state of the art on current robot technology should be overviewed, and recent work on the neurobiology of emotions have to be examined to ground our suggestions for a scientific framework in which to approach robot 'emotions'.

'Emotional robots' being used to test theories of biological emotion is of great interest in intelligent robot.

Because of different kinds of emotions such as, a wide spectrum of feelings, it is not easy to implement creation the emotional robotics. That is, cognitive awareness might be linked to feeling the 'heat'of love, sorrow, anger, and so on. We have here to define emotions in our functional context for human being like emotions in robot.

We analyze emotion in two main senses:

(1) The level of expression of emotion in robot.

(2) Learning method for emotion of behavior (action selection, attention and learning).

How might they enter robot design? Both robot technologies and emotional express methods need to express efficiently. Key functions of express are robotic technology, emotion technology, and AI technology. A scream is not much in information and exact expression, but its impact on others is high. Many researchers have proposed explicit functions for emotions in robot. Therefore, we have to think how the understanding of such tradeoffs affects our ideas about robot control.

This paper introduces intelligent learning algorithm to explain emotion effectively.

II. Hybrid Learning Machine Algorithm

1. The Multi-agent Architecture

The architecture is composed of six systems (see Figure 1). Each system expresses for resources of their emotion. Action node selects six motions to carry out commands from the input system. The input system (vision or signal) is responsible for identifying and tracking the goal. Finally, the action system is responsible for choosing higher level emotion (robot motions) to move the robot control system to a specified goal. In this system, these six systems must cooperate to achieve the overall task of reaching the goal control goal or position (robot). The systems are also competing—there are some trade-offs between them. For example, both the sad and the angry system compete for the action system. The sad system needs input for action, while the angry system needs sad level for target detection and tracking. For this cooperation and competition, each system generates bids for the information offered from the input and action system.

The information actually executed by each system depends on the winning bid at each point in time.

The emotion itself is implemented as a multiagent system. This system is composed of six agents with the emotion functions.

©ISAROB 2009

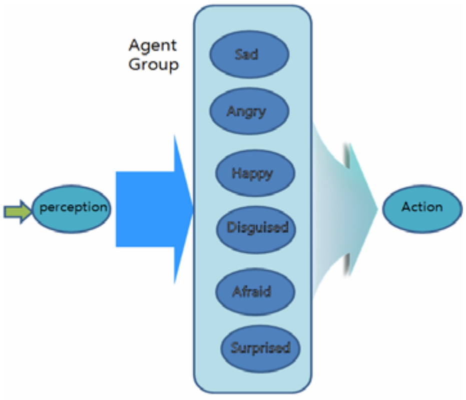

Fig. 1 Architecture of agent system for emotion.

2. PSO Based Optimization for Agent system

A population of particles is initialized with random positions $\vec{k_i}$ and velocities $\vec{v}_i$, and a function, *f*, is evaluated, using the particle's positional coordinates as input values. Positions and velocities are adjusted, and the function evaluated with the new coordinates at each time-step. When a particle discovers a pattern that is better than any it has found previously, it stores the coordinates in a vector $pbest_j$. The difference between $pbest_j$ (the best point found by *i* so far) and the individual's current position $gbest$ is stochastically added to the current velocity, causing the trajectory to oscillate around that point. Further, each particle is defined within the context of a topological neighborhood comprising itself and some other particles in the population. The stochastically weighted difference between the neighborhood's best position $gbest$ and the individual's current position is also added to its velocity, adjusting it for the next time-step. These adjustments to the particle's movement through the space cause it to search around the two best positions.

We used the position and velocity vector of PSO as follows [105-107]:

$$v_{f,g}^{(t+1)} = w\cdot v_j^{(t)} + c_1^* Rand()^*\left(pbest_{j,g} - k_{j,g}^{(t)}\right) + c_2^* Rand()^*\left(gbest_g - k_{j,g}^{(t)}\right)$$
$$j = 1,2,\ldots,n.$$
$$g = 1,2,\ldots,m.$$
$$k_{j,g}^{(t+1)} = k_{j,g}^{(t)} + v_{j,g}^{(t+1)}, \quad k_g^{\min} \le k_{j,g}^{(t+1)} \le k_g^{\max} \tag{1}$$

n : The number of agent in each group
m : The number of member in each group
t : Number of reproduction steps
$v_{j,g}^{(t)}$: The velocity vector of agent *j* in reproduction step of t^{th}. $V_g^{\min} \le v_{j,g}^{(t)} \le V_g^{\max}$
$k_{j,g}^{(t)}$: The position vector of agent *j* in reproduction step of t^{th}.
w : Weighting factor
$c1, c2$: Acceleration constant
$rand(), Rand()$: Random value between 0 and 1
$pbest_j$: Optimal position vector of agent j
$gbest$: Optimal position vector of the group of agents

The variables $c_1^* Rand()^*$ and $c_2^* Rand()^*$ are random positive numbers, drawn from a uniform distribution and defined by an upper limit $c_2^* Rand()^*_{\max}$ which is a parameter of the system. In this version, the term variable $w\cdot v_j^{(t)}$ is limited to the range $k_g^{\max}$, for reasons which will be explained below. The values of the elements in $gbest_g$ are determined by comparing the best performances of all the members of *i*'s topological neighborhood, defined by indexes of some other population members, and assigning the best performer's index to the variable *g*. Thus $gbest_g$ represents the best position found by any member of the neighborhood.

The random weighting of the control parameters in the algorithm results in a kind of explosion or a "drunkard's walk" as particles' velocities and positional coordinates careen toward infinity. The explosion has traditionally been contained through implementation of a $k_g^{\max}$ parameter, which limits the step-size or the velocity. The current section, however, demonstrates that the implementation of properly defined constriction coefficients can prevent explosion; further, these coefficients can induce particles to converge on local optima.

An important source of the swarm's search capability comes from the interactions among particles as they react to one another's findings. Analysis of interparticle effects is beyond the scope of this section, which focuses on the trajectories of single particles.

The value of position vector and velocity vector is determined by the acceleration constants $c1$ and $c2$. If these values are large, each agent moves on to the target position with high speed and fast variation. If vice versa, agents wander about target place. As weighting factor w is for the searching balance of agent, the value for optimal searching is given by [2]

©ISAROB 2009

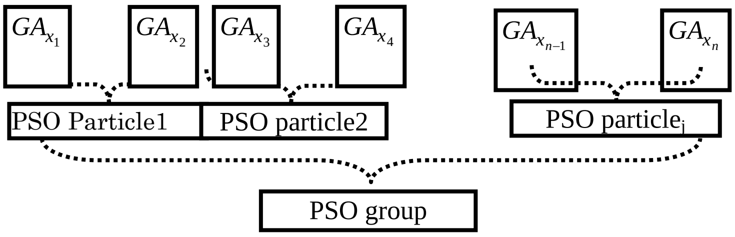

Fig. 2 Individual structure that combines PSO and GA.

$$w = w_{\max} - \frac{w_{\max} - w_{\min}}{iter_{\max}} \times iter , \qquad (2)$$

where $w_{\max}$: max mum value of w (0.9),

$w_{\min}$: minimum value of w (0.4),

$iter_{\max}$: the maximum number of iterative,

$iter$: the number of current iterative.

The velocity vector is limited by $V_g^{\min} \le v_{j,g}^{(t)} \le V_g^{\max}$. In this research, the value of velocity vector for each agent is limited to 1/2 to avoid abrupt variation of affinity

position vector. Calculation process for each step is given in Figure 3.8.

[Step 1] Initialize each variable of GA.

[Step 2] Initialize each variable of PSO.

[Step 3] Calculate affinity of each agent for condition of optimal solution of GA. At this point, optimal position condition of PSO is introduced into GA.

[Step 4] Arrange the group of PSO and agent in GA as shown in Figure 3.9.

[Step 5] Update the position vector $pbest$ and the speed vector $gbest$.

[Step 6] Perform crossover in GA using Euclidian distance and position vector of PSO.

[Step 7] Perform mutation in GA.

[Step 8] If condition of GA is satisfied with the target condition (iteration number or target value), reproduction procedure is halted. Otherwise, it goes to step 3. In Figure 3.9, IG, ED, PV, and SV refers to initial group, Euclidean distance, position vector, and speed vector, respectively.

In this section, initially, positions of individuals are calculated by Euclidean distance based method and then mutation and crossover are performed to improve the running speed and to obtain global optimal solutions. Generally, computing procedure in GA is given as [step 1]→[step 6]→[step 7]→[step 8]. But in this paper, PSO procedure such as step 3, step 4, and step 5 are added in GA procedure. Therefore, information can be exchanged in computing process. Generally, when we obtain an optimal solution by using GA, because each individual operates separately, they (individuals) cannot each other give and take information which computing results and optimal solution, and how much the computed data is useful in system. Therefore, sometimes local optimization or local optimization can become. But the hybrid system GA-PSO suggested, it is possible to communicate with individuals each other even GA (Genetic Algorithm) through PSO (Particle Swarm Optimization). So, we can obtain total optimization and faster learning time and better learning performance.

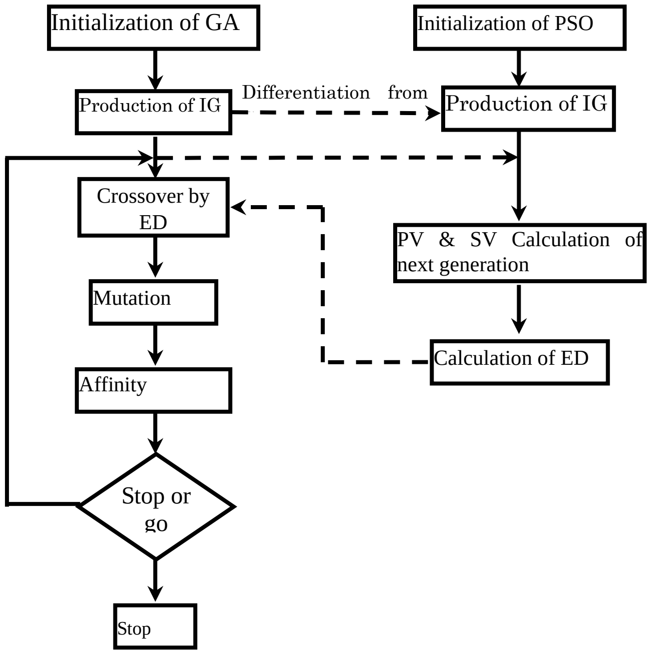

Fig. 3 Calculation process of the combined GA-PSO algorithm.

III. CONCLUSION

In this paper, we proposed a hybrid emotion recognition system using Agent, hybrid system GA and PSO to search for the optimal recognition. The proposed method consists of two parts, a emotion detecting part and an optimization part. In the emotion detecting part, all emotional function are detected from input such as signal and image to produce the optimal emotion function (happiness, sadness, anger, surprise, fear, dislike) properly. We expect that the proposed method had better generalization performance than previous others.

©ISAROB 2009

REFERENCES

[1] I. Essa and A. Pentland(1995), Facial expression recognition using a dynamic model and motion energy. Int. Conf. on Computer Vision.
[2] D. Lin and J. Chen(1999), Facial expressions classification with hierarchical radial basis function networks. Int. Conf. on Neural Information Processing.
[3] Y. Yoshitomi, S. Kim, T. Kawano and T. Kitazoe(2000), "Effect of sensor fusion for recognition of emotional states using voice, face image and thermal image of face," IEEE Int. Workshop on Robot and Human Interactive Communication.
[4] Carole Bernon, "Applications of Self-Organising Multi-Agent Systems: An Initial Framework for Comparison," Informatica 30 (2006) 73–82.
[5] Madhur Ambastha, Dídac Busquets, Ramon López de Màntaras, Carles Sierra, "Evolving a Multiagent System for Landmark-Based Robot Navigation, INTERNATIONAL JOURNAL OF INTELLIGENT SYSTEMS, VOL. 20, 523–539 (2005)
[6] Dong Hwa Kim, TIT(Tokyo Institute of Technology) Thesis (Genetic Algorithm Combined with Particle Swarm Optimization/Bacterial Foraging and Its Application to PID Controller Tuning), Tokyo, Japan, 2006.

The Fourteenth International Symposium on Artificial Life and Robotics 2009 (AROB 14th '09),
B-Con Plaza, Beppu, Oita, Japan, February 5 - 7, 2009

Group Feature Extraction based on Matrix Factorization from Long-range Office-logging Data

Kita, I., Shibata, T., Kamiya, Y., Kato, D., Kunieda, K.,
Yamada, K. and Ikeda, K.
Graduate School of Information Science, NAIST
8916-5 Takayama, Ikoma, Nara, 630-0192
{izumi-k, tom, kazushi}@is.naist.jp
C&C Innovation Research Laboratories, NEC Corporation
{y-kamiya@fn, daishi@cb, k-kunieda@ak, kg-yamada@cp}.jp.nec.com

Abstract

To increase the productivity of knowledge workers, it is necessary to manage their organization so that workers are motivated to collaborate with each other for their synergy. It is, however, di cult for managers to grasp explicit interactions of workers in the organization all the time. Due to advanced communications technology and reduced size and improved capabilities of computers, we are able to record group behaviors as logging data in the o ce. The aim of this study is to extract features of the group behavior from long-range o ce-logging data. We apply principal component analysis to the data matrix whose element is the mean travel velocity calculated from an individual's trajectory per a day. Results demonstrate the feasibility of our approach such that nontrivial informative group features can be extracted.

1 Introduction

Recently, increasing the productivity of knowledge workers has been demanded. For this purpose, it is necessary to manage their organization so that workers are motivated to collaborate with each other for their synergy [2]. It is, however, di cult for managers to grasp explicit interactions of workers in the organization all the time, and also there is no common quantitative measures. Due to advanced communications technology and reduced size and improved capabilities of computers, we are able to record individual behavioral information as logging data in the o ce. One of the typical behavioral data is workers' trajectory (location) information in their o ce. There were studies on data-mining social relationship using the trajectory information. Suzuki et al. detected abnormal behavior of a customer in convenience stores. They fitted hidden Markov models and fit them to individual's trajectory [3]. Kobayashi also used the trajectory data in the o ce and obtained relationship between members [1].

These studies, however, focused on the individual-individual relationship, and did not investigate the individual-group or the group-group relationship.

The aim of this study is to extract features of the group behavior from the long-range o ce-logging data. Our approach is to apply principal component analysis (PCA), a representative matrix factorization method, to the data matrix whose element is mean travel velocity (MTV) of an individual's trajectory data per a day.

2 Methods

2.1 Data Acquisition

The trajectory data of the members have been continuously recorded at C&C Innovation research Laboratories (CCIL) in NEC Corporation. This laboratory employs an infrared location management system. In this system, each user terminal receives the location of the closest ID transmitter position and the recording time. The recorded data is sent to the server at regular intervals. These ID transmitters are attached to the ceiling from 1.5 to 2 meters as a grid, and send individual coordinate of position every second to the user terminal which researchers take along all the time.

Fig. 1 shows an example of one's trajectory of in a day. This figure is over view and shows there are two rooms in the o ce: Room A is in the upper area and Room B is in the lower area. In this case, the member actively moved not only inside each room but

©ISAROB 2009

	K	Y	D	G
1	0	0	0	1
2	1	1	1	0
3	6	4	3	1
4	4	1	0	0

Table 1: The organizational information of the CCIL

Fig. 1: Sample trajectory data

also across the rooms. Furniture and fixtures such as desks and chairs are written in the roomB. The furniture are not fixed.

In this study, we used the data of 23 participants (members of CCIL) from 8/9/2008 to 8/10/2008 (31 days). The reason why we selected this period was because the system became much stabler from around this period after extensive improvement on the system.

As a member attribute, Tbl. 1 presents the organizational information of the CCIL. The member of CCIL consists of a director with a secretary, 3 laboratory heads, 13 researchers, and 5 internship students. In this table, the first three column correspond with three laboratories indicated by K, Y, and D. The final column, indicated by G, is for the director and the secretary. The rows presents the hierarchical information of the CCIL organization. The first row is for the director, the second is for the laboratory heads, and so on. Although this study takes a data-mining approach, one could hypothesize that some organizational feature would be retrieved from the data.

2.2 Preprocessing

Because (1) our focus is on the group feature extraction from the viewpoint of long-range variation rather than the short-term variation such as the one within a day, and (2) the raw-data is high-dimensional, i.e., more than two million dimensions for each person, a feature extraction that follows

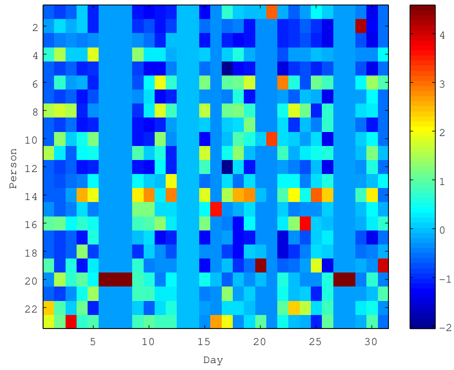

Fig. 2: The data matrix used in this study

$$\sum_{t=1}^{N} \|\mathbf{x}_{t+1} - \mathbf{x}_t\| \Big/ \sum_{t=1}^{N} |T_{t+1} - T_t| \qquad (1)$$

was applied to the raw-data of each person as a preprocessing. Here, t denotes sample number, $\mathbf{x}_t$ denotes person's location [m] at sample t, N indicates the number of samples for a person in a day, and T_t denotes the actual time [s] when $\mathbf{x}_t$ was sampled. In fact, this preprocessing provides mean travel velocity (MTV) [m/s] of a person in a day.

Fig. 2 shows the whole data we used in this study. The data was treated in the form of a 23×31 matrix $\mathbf{X}$. The column and the row corresponds to the day and the member, respectively. As shown in this figure, the elements in this data matrix was not restricted to be positive. In fact, the original MTVs were standardized so that the mean and the standard deviation over each dimension (day) took zero and one, respectively.

It is worth noting here that Fig. 2 showing member's activity in normalized MTV already presents a salient group behavior for taking holidays, and a member No. 20 often did not take holidays.

2.3 Group feature extraction

For group feature extraction, we employed a representative matrix factorization algorithm, principal component analysis (PCA). We also employed a representative clustering algorithm, k-means algorithm, which minimizes a different cost function with PCA, to see the difference.

In general, matrix factorization is the method that factorizes the data matrix $\mathbf{x} \in \mathcal{R}^{n \times m}$ into low-rank matrices $\mathbf{Z} \in \mathcal{R}^{n \times k}$ and $\mathbf{W} \in \mathcal{R}^{k \times m}$ $(n \leq m, k < n)$ so that

$$\mathbf{X} \simeq \mathbf{Z}\mathbf{W}. \qquad (2)$$

©ISAROB 2009

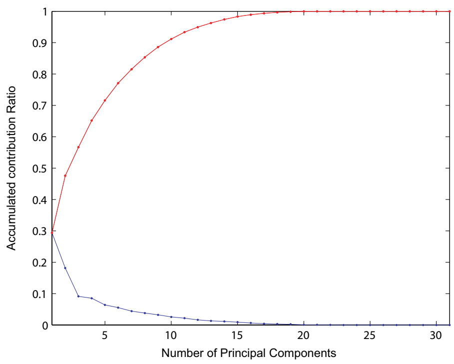

Fig. 3: Contribution ratio

Among possible factorizations, PCA performs the following optimization

$$[\mathbf{Z}, \mathbf{W}] = \arg\min_{\mathbf{Z},\mathbf{W}} \|\mathbf{X} - \mathbf{Z}\mathbf{W}\|^2_{Fro}, \tag{3}$$

and scores of samples and principal components are stored in $\mathbf{Z}$ and $\mathbf{W}$, respectively. The principal components are expected to represent features of group behaviors.

K-means clustering minimizes the different cost function from PCA as

$$J = \sum_{n=1}^{N} \sum_{k=1}^{K} r_{nk} \|\mathbf{y}_n - \boldsymbol{\mu}_k\|^2, \tag{4}$$

Here, $\mathbf{y}_n$ is n-th sample, $\boldsymbol{\mu}_k$ is the centroid of k-th cluster. r_{nk} is a binary variable under 1-of-K coding. Thus, $r_{nk} = 1$ means that $\mathbf{x}_n$ is classified into the k-th cluster. In addition, K-means algorithm is also expected to extract k group features as centroids $\boldsymbol{\mu}_k$.

3 Results

Fig. 3 shows the relationship between the number of principal components and their accumulated contribution ratio. The blue line is contribution ratio, and the red line is accumulated contribution ratio. The contribution ratio is defined by $e_i/(\Sigma_j^N e_j)$ where e_i is the eigenvalue of the i-th principal component. In this figure, the accumulated contribution ratio gets over 80% with seven principal components, which means the subspace spanned by the seven principal components covers rich information of the original data matrix. Note, however, that we are interested in the featured extracted by a couple of principal components instead of having many principal components for accurate reconstruction.

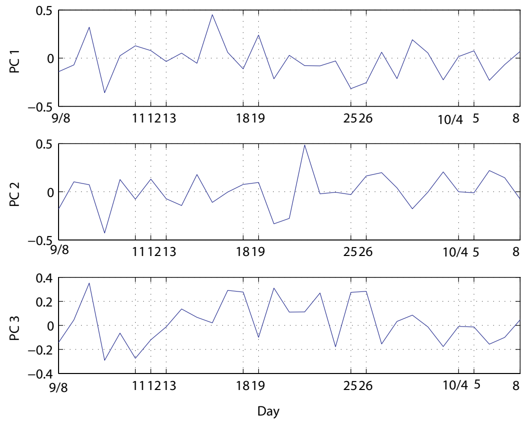

Fig. 4: The first three principal components

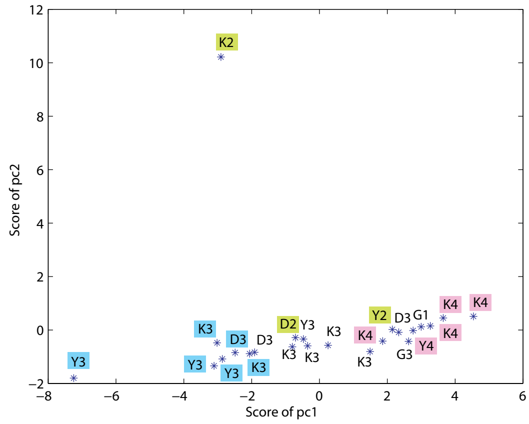

Fig. 5: Scores of each member in the space spanned by the first two principal components

Fig. 4 presents the first three principal components. One of our expected feature was some component would capture some periodicity caused by weekdays and weekends, but it is not possible to interpret such a factor in these three components.

We then looked into the score of all members. Fig. 5 plots the scores using the first two principal components, indicating that the second principal component distinguished K2, the head of laboratory K, from the other members, which was mostly predicted in section 2.2. The interpretation of the first principal component was not easy, as the scores does not completely follow a na ve hypothesis that clusters would represent organization of NEC-CCIL presented in Tbl. 1.

We, however, found the following three interesting facts:

1. The laboratory heads are classified into mutually different classes,

2. All internship students are classified into the same

©ISAROB 2009

Class	Member Attributes
1	K2
2	K3 K3 K4 K4 K4 K4 Y2 Y4 D3 G1 G3
3	K3 K3 K3 K3 Y3 Y3 Y3 Y3 D2 D3 D3

Class	Member Attributes
1	K2
2	Y3
3	K3 K4 K4 K4 K4 Y2 Y4 D3 G1 G3
4	K3 K3 K3 K3 K3 Y3 Y3 Y3 D2 D3 D3

Fig. 6: Clustering results

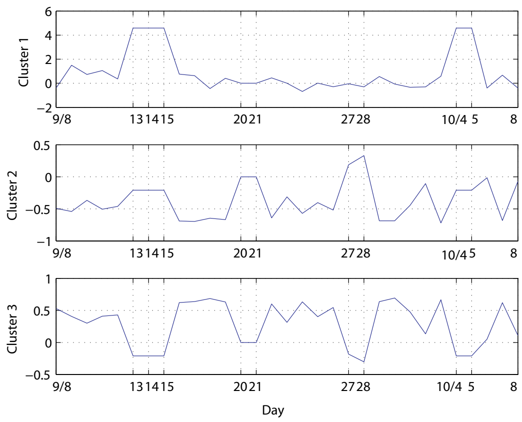

Fig. 7: Acquired centroids in the three-classes case

class,

3. All members who joined NEC within 2 years are classified into the same class but different from the class described in (1) and (2),

which are represented by yellow shades in Fig. 6. In this figure, red, blue, and green shades indicate member attributes that are internship students, members who joined NEC within two years, and laboratory heads, respectively. In fact, additional application of k-means clustering, with the number of clusters were three and four, to the two-dimensional score vectors result in Fig. 6.

We also attempted to apply k-means algorithm to the raw-data, and obtained the same clustering result shown in Fig. 6. Fig. 7 shows the centroids acquired in the case that the number of classes was specified to three. In this figure, μ_1 (the centroid in the top panel) has different pattern from the other centroids. In fact, the only one member was classified into class 1 and the member was the head of laboratory K. In contrast, μ_2 and μ_3 roughly mirror each other, suggesting the internship students and the members who joined NEC within two years had different group behaviors.

Another peculiar feature which was not found by PCA was periodicity caused by weekdays and weekends.

4 Conclusion

This paper addressed unsupervised feature extraction of the group behavior from long-range o ce-logging data. More specifically, a representative matrix factorization algorithm, principal component analysis (PCA), was applied to one month of 23 persons' trajectory data recorded at C&C Innovation research Laboratories (CCIL) in NEC Corporation. As the raw data was impractically high-dimensional and our focus was on long-range group feature rather than the short-term one, we made a heuristic feature extraction, as a preprocessing, which was mean travel velocity (MTV). Application of PCA to the data extracted two feature vectors, the first two principal components, that lead to successful mining of three clusters in which (1) the laboratory heads are classified into mutually different classes, (2) all internship students are classified into the same class, and (3) all members who joined NEC within 2 years are classified into the same class but different from the class described in (1) and (2).

The feature extraction in an unsupervised way, which is the case presented in this study, could be combined with supervised learning for further investigation in order to increase the productivity of knowledge workers, i.e., CCIL members in this study. Incorporating longer-term data and higher-dimensional data including another features and modalities are also our future work.

References

[1] J. Kobayashi. Personal identification and visualization of human-relationship by using human trajectories. Master's thesis, Graduate School of Information Science, NAIST, 2 2008.

[2] N. Moriwaki, N. Sato, Y. Wakisaka, S. Tsuji, N. Okubo, and K. Yano. Business microscope system for organizational activity visualization. *Technical report of IEICE. HCS*, 107(241):31–36, 2007.

[3] N. Suzuki, K. Hirasawa, K. Tanaka, Y. Kobayashi, Y. Sato, and Y. Fujino. Detection of abnormal behavior and patterns by human trajectories analysis. *IEICE TRANSACTIONS on Information and Systems*, J91-D(6):1550–1560, 2008.

©ISAROB 2009

The Fourteenth International Symposium on Artificial Life and Robotics 2009 (AROB 14th '09),
B-Con Plaza, Beppu, Oita, Japan, February 5 - 7, 2009

Robust stability analysis for uncertain T–S fuzzy systems with a time-varying delay

In-sun Song, Jae Wook Shin, Jeong-Wan Ko and PooGyeon Park
{weedsis, shinshingo, hrp26, ppg}@postech.ac.kr

Electrical and Computer Engineering Division,
Pohang University of Science and Technology,
San 31, Hyojadong, Namgu, Pohang, Kyungbuk, 790-784, Korea

Abstract

In this paper, we adopt fuzzy weighting-dependent free variables in the system dynamics elimination and fuzzy weighting-dependent kernel matrices in the integral inequality lemma to maximize the allowable delay bounds that guarantee the stability of Takagi-Sugeno (T–S) fuzzy systems with time-varying delays. The resulting quadratic *Parameterized Linear Matrix Inequalities* (PLMIs) are further relaxed by introducing some free variables for the weighting parameters conditions itself. A simple example is given to demonstrate the effectiveness of the proposed criterion.

keywords

Fuzzy delayed systems, Uncertainty, Constraint elimination, Stability.

1 Introduction

T–S fuzzy systems, characterized by linearity of the local dynamics in different fuzzy sets of fuzzy rules, have been studied widely and applied to various fields of industrial applications [1–5]. Among many attracting topics, we shall focus on the stability analysis of the fuzzy system that has delay elements in the local dynamics.

A general continuous T–S fuzzy control system with a time-varying delay can be described as

$$\dot{x}(t) = A(t)x(t) + A_h(t)x(t-h(t)) + B(t)u(t) \quad (1)$$

$$= \sum_{i=1}^{r} \theta_i(t)\{A_i x(t) + A_{h,i}x(t-h(t)) + B_i u(t)\}, \quad (2)$$

$$\sum_{i=1}^{r} \theta_i(t) = 1 \ \text{ and } \ \theta_i(t) \geq 0, \ i \in \{1, \cdots, r\}, \quad (3)$$

where $\{\theta_i(t)\}$ may depend on some premise variables. Up to now, the usual stability criteria have been represented by way of PLMIs with an affine dependence on $\{\theta_i(t)\}$. To make use of the efficient convex optimization tools, the structure of the decision variables that are multiplied by $\{A(t), A_h(t), B(t)\}$ has been restricted to be independent from the fuzzy weighting functions. See, for example, the free-weighting matrices in the constraint elimination method [1–3] and the kernel matrices in the quadratic Lyapunov function [1–5], etc. Recently, [6, 7] reported the conservativeness of these methods and suggested a relaxation method of handling PLMIs that are not affinely dependent on $\{\theta_i(t)\}$. The resulting nonlinear parameter conditions, usually quadratic functions, could be properly relaxed but the information of (3) could be preserved faithfully.

In this paper, we adopt these constraint relaxation techniques to maximize the allowable delay bounds that guarantee the stability of the T–S fuzzy systems. Both the free variables in the constraint elimination of (1)–(2) [3, 8–10] and the kernel matrices in the integral inequality lemma [11, 12] are modeled as fuzzy weighting-dependent functions. The resulting quadratic PLMIs are further relaxed by introducing some free variables for the weighting parameter conditions in (3). Our approach essentially reduces the conservatism of the existing methods.

The paper is organized as follows. Section 2 will consider a robust stability criterion for T–S fuzzy systems with time-varying delays. Section 3 will show a simple example for verification of the criterion.

2 Main Results

Let us consider the following T–S fuzzy delayed system with model uncertainty:

$$\dot{x}(t) = A(t)x(t) + A_h(t)x(t-h(t)) + Dp(t), \ t \geq 0, \quad (4)$$

$$q(t) = E(t)x(t) + E_h(t)x(t-h(t)), \ t \geq 0, \quad (5)$$

$$x(t) = \phi(t), \ -\bar{h} \leq t \leq 0, \quad (6)$$

$$[A(t) \ A_h(t) \ E(t) \ E_h(t)] = \sum_{i=1}^{r} \theta_i(z(t))[A_i \ A_{h,i} \ E_i \ E_{h,i}], \quad (7)$$

where $h(t) \in [0, \ \bar{h}]$, $p(t) = \Delta(t)q(t)$, $\Delta^T(t)\Delta(t) \leq$

©ISAROB 2009

$\gamma^{-2}I$, and $\phi(t) \in \mathcal{C}^1(\bar{h})$, the set of continuously differentiable functions in the domain $[-2\bar{h}, 0]$. Here, $\{\theta_i(z(t))\}$ denote the normalized fuzzy weighting functions that satisfy

$$0 \le \theta_i(z(t)) \le 1, \ \forall\ i, \text{ and } \sum_{i=1}^{r} \theta_i(z(t)) = 1, \qquad (8)$$

where r is the number of fuzzy rules and $z(t)$ is a premise variable vector that may depend on states in many cases. Let us define $\chi(t) \in \mathcal{R}^{l\times 1}$ as $\chi(t) \triangleq [x^T(t)\ x^T(t-h(t))\ x^T(t-\bar{h})\ \dot{x}^T(t)\ p^T(t)]^T$ and the corresponding block entry matrices as $e_i,\ i \in \{1, \cdots, 5\}$ such that the system (4) can be written as $0 = (A(t)e_1^T + A_h(t)e_2^T - e_4^T + De_5^T)\chi(t)$.

We shall choose the Lyapunov-Krasovskii functional as follows:

$$V(t) \triangleq V_1(t) + V_2(t) + V_3(t), \qquad (9)$$
$$V_1(t) = x^T(t)Px(t),\ P > 0, \qquad (10)$$
$$V_2(t) = \int_{t-\bar{h}}^{t} x^T(\alpha)Q_0x(\alpha)d\alpha,\ Q_0 > 0, \qquad (11)$$
$$V_3(t) = \int_{-\bar{h}}^{0}\int_{t+\alpha}^{t} \dot{x}^T(\beta)S_0\dot{x}(\beta)d\beta d\alpha,\ S_0 > 0 \qquad (12)$$

such that

$$\dot{V}_1(t) = 2\dot{x}^T(t)Px(t) = 2\chi^T(t)e_4Pe_1^T\chi(t), \qquad (13)$$
$$\dot{V}_2(t) = \chi^T(t)\{e_1Q_0e_1^T - e_3Q_0e_3^T\}\chi(t), \qquad (14)$$
$$\dot{V}_3(t) = \bar{h}\chi^T(t)e_4S_0e_4^T\chi(t) - \int_{t-\bar{h}}^{t}\dot{x}^T(\alpha)S_0\dot{x}(\alpha)d\alpha. \qquad (15)$$

Then, by the integral inequality lemma [11, 12], for

$$\begin{bmatrix} Y_{11}(t) & Y_{12}(t) \\ Y_{12}^T(t) & Y_{22}(t) \end{bmatrix} \ge 0, \quad \begin{bmatrix} Z_{11}(t) & Z_{12}(t) \\ Z_{12}^T(t) & Z_{22}(t) \end{bmatrix} \ge 0, \qquad (16)$$

we have

$$\begin{aligned} 0 &\le \int_{t-h(t)}^{t} \begin{bmatrix} \chi(t) \\ \dot{x}(\alpha) \end{bmatrix}^T \begin{bmatrix} Y_{11}(t) & Y_{12}(t) \\ Y_{12}^T(t) & Y_{22}(t) \end{bmatrix} \begin{bmatrix} \chi(t) \\ \dot{x}(\alpha) \end{bmatrix} d\alpha \\ &= \chi^T(t)\{Y_{12}(t)(e_1 - e_2)^T + (e_1 - e_2)Y_{12}^T(t) \\ &\quad + h(t)Y_{11}(t)\}\chi(t) + \int_{t-h(t)}^{t}\dot{x}^T(\alpha)Y_{22}(t)\dot{x}(\alpha)d\alpha, \\ 0 &\le \int_{t-\bar{h}}^{t-h(t)} \begin{bmatrix} \chi(t) \\ \dot{x}(\alpha) \end{bmatrix}^T \begin{bmatrix} Z_{11}(t) & Z_{12}(t) \\ Z_{12}^T(t) & Z_{22}(t) \end{bmatrix} \begin{bmatrix} \chi(t) \\ \dot{x}(\alpha) \end{bmatrix} d\alpha \\ &= \chi^T(t)\{Z_{12}(t)(e_2 - e_3)^T + (e_2 - e_3)Z_{12}^T(t) \\ &\quad + (\bar{h} - h(t))Z_{11}(t)\}\chi(t) + \int_{t-\bar{h}}^{t-h(t)}\dot{x}^T(\alpha)Z_{22}(t)\dot{x}(\alpha)d\alpha, \end{aligned}$$

so that $\dot{V}(t)$ can be upper-bounded by the following quantity:

$$\dot{V}(t) \le \chi^T(t)\Omega_1\chi(t) + \Omega_2,$$

where Ω_i denote

$$\begin{aligned} \Omega_1 = &\ h(t)Y_{11}(t) + (\bar{h} - h(t))Z_{11}(t) + \bar{h}e_4S_0e_4^T \\ &+ Y_{12}(t)(e_1 - e_2)^T + (e_1 - e_2)Y_{12}^T(t) \\ &+ Z_{12}(t)(e_2 - e_3)^T + (e_2 - e_3)Z_{12}^T(t) \\ &+ e_1Q_0e_1^T - e_3Q_0e_3^T + e_4Pe_1^T + e_1Pe_4^T, \end{aligned} \qquad (17)$$

$$\begin{aligned} \Omega_2 = &-\int_{t-\bar{h}}^{t-h(t)}\dot{x}^T(\alpha)(S_0 - Z_{22}(t))\dot{x}(\alpha)d\alpha \\ &-\int_{t-h(t)}^{t}\dot{x}^T(\alpha)(S_0 - Y_{22}(t))\dot{x}(\alpha)d\alpha. \end{aligned} \qquad (18)$$

Clearly, if it holds that $S_0 – Z_{22}(t) \ge 0$ and $S_0 – Y_{22}(t) \ge 0$, Ω_2 is non-positive definite, *i.e.* $\Omega_2 \le 0$. As for Ω_1, since $h(t)Y_{11}(t) + (\bar{h} - h(t))Z_{11}(t)$ is a convex combination of the matrices $Y_{11}(t)$ and $Z_{11}(t)$ on $h(t)$, it can be handled non-conservatively by two corresponding boundary LMIs: one for $h(t) = \bar{h}$ and the other for $h(t) = 0$. Furthermore, we can remove the constraints of the model dynamics itself in (4) by introducing free variables $M(t)$ as $0 \equiv \chi^T(t)M(t)(A(t)e_1^T + A_h(t)e_2^T - e_4^T + De_5^T)\chi(t)$ like [8–10], and the additional uncertainty constraint (5):

$$\begin{aligned} 0 &\le q^T(t)q(t) - \gamma^2p^T(t)p(t) \\ &= \chi^T(t)\{(e_1E^T(t) + e_2E_h^T(t))(E(t)e_1^T + E_h(t)e_2^T) \\ &\quad - \gamma^2e_5e_5^T\}\chi(t), \end{aligned} \qquad (19)$$

which can be handled through the so called $\mathcal{S}$-procedure [13]. Then, we can state the following theorem for robust stability of the delayed T–S fuzzy system.

Theorem 1 *For a given γ, the delayed uncertain T–S fuzzy system (4)–(7) is asymptotically stable if there exist matrices P, Q_0, S_0, $Y_{11}(t)$, $Y_{12}(t)$, $Y_{22}(t)$, $Z_{11}(t)$, $Z_{12}(t)$, $Z_{22}(t)$, and $M(t)$ such that the following conditions hold:*

$$P > 0, Q_0 > 0, S_0 > 0, S_0 \ge Z_{22}(t), S_0 \ge Y_{22}(t), \qquad (20)$$

$$\begin{bmatrix} Y_{11}(t) & Y_{12}(t) \\ Y_{12}^T(t) & Y_{22}(t) \end{bmatrix} \ge 0, \begin{bmatrix} Z_{11}(t) & Z_{12}(t) \\ Z_{12}^T(t) & Z_{22}(t) \end{bmatrix} \ge 0, \qquad (21)$$

$$\begin{aligned} 0 > &\ M(t)(A(t)e_1^T + A_h(t)e_2^T - e_4^T + De_5^T) \\ &+ (e_1A^T(t) + e_2A_h^T(t) - e_4 + e_5D^T)M^T(t) \\ &+ (e_1E^T(t) + e_2E_h^T(t))(E(t)e_1^T + E_h(t)e_2^T) \\ &+ Y_{12}(t)(e_1 - e_2)^T + (e_1 - e_2)Y_{12}^T(t) \\ &+ Z_{12}(t)(e_2 - e_3)^T + (e_2 - e_3)Z_{12}^T(t) \\ &+ \bar{h}e_4S_0e_4^T + e_1Q_0e_1^T - e_3Q_0e_3^T + e_4Pe_1^T + e_1Pe_4^T \\ &+ \bar{h}(\delta(1,k)Y_{11}(t) + \delta(2,k)Z_{11}(t)) - \gamma^2e_5e_5^T \end{aligned} \qquad (22)$$

for $k = 1, 2$, where $\delta(i,i) = 1$ and $\delta(i,j) = 0,\ i \ne j$.

Let us model both the free variables employed for the constraint elimination of (4) [3, 8–10] and the kernel matrices in the integral inequality lemma for the double integral terms of the Lyapunov-Krasovskii functionals [11, 12] as fuzzy weighting $\{\theta_i(z(t))\}$-dependent functions:

$$M(t) = \sum_{i=1}^{r} \theta_i(z(t)) M_i, \tag{23}$$

$$\begin{bmatrix} Y_{11}(t) & Y_{12}(t) \\ Y_{12}^T(t) & Y_{22}(t) \end{bmatrix} \triangleq \sum_{i=1}^{r} \theta_i(z(t)) \begin{bmatrix} Y_{11,i} & Y_{12,i} \\ Y_{12,i}^T & Y_{22,i} \end{bmatrix}, \tag{24}$$

$$\begin{bmatrix} Z_{11}(t) & Z_{12}(t) \\ Z_{12}^T(t) & Z_{22}(t) \end{bmatrix} \triangleq \sum_{i=1}^{r} \theta_i(z(t)) \begin{bmatrix} Z_{11,i} & Z_{12,i} \\ Z_{12,i}^T & Z_{22,i} \end{bmatrix}, \tag{25}$$

$$\begin{bmatrix} Y_{11,i} & Y_{12,i} \\ Y_{12,i}^T & Y_{22,i} \end{bmatrix} \geq 0, \begin{bmatrix} Z_{11,i} & Z_{12,i} \\ Z_{12,i}^T & Z_{22,i} \end{bmatrix} \geq 0, \ \forall\, i. \tag{26}$$

Unfolding the $\{\theta_i(z(t))\}$-dependent time-varying matrices, we can rewrite (22) as a quadratic function of $\Theta(t) \triangleq [I \ \theta_1(z(t))I \ \cdots \ \theta_r(z(t))I]^T \in \mathcal{R}^{(r+1)\cdot l \times l}$:

$$0 > \Theta^T(t)\Omega_{1,k}\Theta(t), \quad k = 1, 2, \tag{27}$$

where $\Omega_{1,k}$ are $(r+1) \times (r+1)$-block time-invariant symmetric matrices. Finally, the constraints elimination method [6, 7] for (8) gives

$$\Theta^T(t)N_{0,k}F\Theta(t) + \Theta^T(t)F^T N_{0,k}^T\Theta(t) = 0, \tag{28}$$

$$F \triangleq [-I \ I \ I \ \cdots \ I] \in \mathcal{R}^{l \times (r+1)\cdot l} \tag{29}$$

for arbitrary $N_{0,k} \in \mathcal{R}^{(r+1)\cdot l \times l}$ and

$$\theta_i(z(t))\theta_i(z(t))N_{1,k,i} \geq 0, \tag{30}$$

$$\theta_i(z(t))\theta_j(z(t))(N_{2,k,ij} + N_{2,k,ij}^T) \geq 0, \tag{31}$$

$$\theta_i(z(t))(1 - \theta_i(z(t)))(N_{3,k,i} + N_{3,k,i}^T) \geq 0 \tag{32}$$

for

$$N_{1,k,i} \geq 0, \ N_{2,k,ij} + N_{2,k,ij}^T \geq 0, \ N_{3,k,i} + N_{3,k,i}^T \geq 0, \tag{33}$$

where $1 \leq i \leq r$, $i < j \leq r$ and $k = 1, 2$. Then, we can obtain the following PLMIs-based stability criterion for delayed T–S fuzzy systems.

Theorem 2 *For a given γ, the delayed uncertain T–S fuzzy system (4)–(7) is asymptotically stable if there exist matrices P, Q_0, S_0, $Y_{11,i}$, $Y_{12,i}$, $Y_{22,i}$, $Z_{11,i}$, $Z_{12,i}$, $Z_{22,i}$, M_i, $N_{0,k}$, $N_{1,k,i}$, $N_{2,k,ij}$ and $N_{3,k,i}$, $1 \leq i \leq r$, $i < j \leq r$, $k = 1, 2$ such that the following conditions hold:*

$$P > 0, Q_0 > 0, S_0 > 0, S_0 \geq Z_{22,i}, S_0 \geq Y_{22,i}, \tag{34}$$

$$0 > \Omega_{1,k} + N_{0,k}F + F^T N_{0,k}^T, \tag{35}$$

$$\begin{bmatrix} Y_{11,i} & Y_{12,i} \\ Y_{12,i}^T & Y_{22,i} \end{bmatrix} \geq 0, \begin{bmatrix} Z_{11,i} & Z_{12,i} \\ Z_{12,i}^T & Z_{22,i} \end{bmatrix} \geq 0, \tag{36}$$

$$N_{1,k,i} \geq 0, N_{2,k,ij} + N_{2,k,ij}^T \geq 0, N_{3,k,i} + N_{3,k,i}^T \geq 0, \tag{37}$$

where $\Omega_{1,k}$ are $(r+1)\times(r+1)$-block symmetric matrices whose elements are

$$\begin{aligned}
\Omega_{1,k}(1,1) =& e_4 P e_1^T + e_1 P e_4^T + e_1 Q_0 e_1^T - e_3 Q_0 e_3^T \\
&+ \bar{h} e_4 S_0 e_4^T - \gamma^2 e_5 e_5^T, \\
\Omega_{1,k}(1,i+1) =& (e_5 D^T - e_4) M_i^T + N_{3,k,i} \\
&+ \frac{\bar{h}}{2}(\delta(1,k)Y_{11,i} + \delta(2,k)Z_{11,i}) \\
&+ (e_1 - e_2)Y_{12,i}^T + (e_2 - e_3)Z_{12,i}^T, \\
\Omega_{1,k}(i+1,i+1) =& M_i(A_i e_1^T + A_{h,i}e_2^T) + (e_1 A_i^T + e_2 A_{h,i}^T)M_i^T \\
&+ (e_1 E_i^T + e_2 E_{h,i}^T)(E_i e_1^T + E_{h,i}e_2^T) \\
&+ N_{1,k,i} - N_{3,k,i} - N_{3,k,i}^T, \\
\Omega_{1,k}(i+1,j+1) =& M_i(A_j e_1^T + A_{h,j}e_2^T) + (e_1 A_i^T + e_2 A_{h,i}^T)M_j^T \\
&+ (e_1 E_i^T + e_2 E_{h,i}^T)(E_j e_1^T + E_{h,j}e_2^T) + N_{2,k,ij}.
\end{aligned}$$

3 Examples

Example 1 Consider the uncertain T–S fuzzy delayed system (4)–(7) with two fuzzy rules. The following parameters are used.

$$A_1 = \begin{bmatrix} -1.0 & 0.4 \\ 0.0 & -0.5 \end{bmatrix}, \ A_{h,1} = \begin{bmatrix} 0.3 & -0.4 \\ 0.0 & 0.0 \end{bmatrix}, \tag{38}$$

$$E_1 = \begin{bmatrix} -0.2 & 0.0 \\ 0.0 & 0.3 \end{bmatrix}, \ E_{h,1} = \begin{bmatrix} 0.3 & 0.0 \\ 0.0 & 0.0 \end{bmatrix}, \tag{39}$$

$$A_2 = \begin{bmatrix} -0.5 & 0.0 \\ 0.5 & -1.0 \end{bmatrix}, \ A_{h,2} = \begin{bmatrix} 0.4 & 0.0 \\ 0.4 & 0.3 \end{bmatrix}, \tag{40}$$

$$E_2 = \begin{bmatrix} 0.0 & 0.3 \\ 0.0 & 0.1 \end{bmatrix}, \ E_{h,2} = \begin{bmatrix} 0.1 & -0.1 \\ 0.0 & 0.0 \end{bmatrix}, \tag{41}$$

$$D = \begin{bmatrix} 0.1 & 0.0 \\ 0.0 & 1.5 \end{bmatrix}, \ \gamma = 1. \tag{42}$$

By Theorem 2, the improvement of this paper is shown in Table 1.

Table 1: maximum $\bar{h}$ comparison with some previous results

methods	[1]	[2]	[3]	[4]	[5]	Theorem 2
$\bar{h}$	0.639	0.639	0.801	0.808	0.836	1.328

4 Conclusion

In this paper, we adopted fuzzy weighting-dependent free variables in the system dynamics elimination and fuzzy weighting-dependent kernel matrices in the integral inequality lemma to maximize the allowable delay bounds that guarantee the stability of T–S fuzzy systems with time-varying delays. The resulting quadratic PLMIs were further relaxed by introducing some free variables for the weighting parameters conditions itself. A simple example was given to demonstrate the effectiveness of the proposed criterion.

Acknowledgements

This work was supported by the Brain Korea 21 Project in 2008. This research was supported by Ministry of Knowledge and Economy, Republic of Korea, under the ITRC (Information Technology Research Center) support program supervised by IITA(Institute for Information Technology Advancement)." (IITA-2008-C1090-0801-0004)

References

[1] Lien, C., Yu, K., Chen, W., Wan, Z., and Chung, Y. (2007) *IET Control Theory & Applications* **1(3)**, 764–769.

[2] Lien, C.-H. (2006) *Chaos, Solitons and Fractals* **28(2)**, 422–427.

[3] Chen, B., Liu, X., Lin, C., and Liu, K. (2008) *Fuzzy Sets and Systems* available online.

[4] Peng, C., Tian, Y.-C., and Tian, E. (2008) *Fuzzy Sets and Systems* **159(20)**, 2713–2729.

[5] Liu, X. (2008) *Nonlinear Analysis* **68(5)**, 1352–1361.

[6] Park, P. and Choi, D. J. (2001) *International Journal of Robust and Nonlinear Control* **11(14)**, 1343–1363.

[7] Choi, D. J. and Park, P. (2003) *IEEE Transactions on Fuzzy Systems* **11(2)**, 271–278.

[8] He, Y., Wu, M., She, J.-H., and Liu, G.-P. (2004) *Systems & Control Letters* **51(1)**, 57–65.

[9] He, Y., Wu, M., She, J.-H., and Liu, G.-P. (2004) *IEEE Transactions on Automatic Control* **49(5)**, 828–832.

[10] Wu, M., He, Y., She, J.-H., and Liu, G.-P. (2004) *Automatica* **40(8)**, 1435–1439.

[11] Park, P. (1999) *IEEE Transactions on Automatic Control* **44(4)**, 876–877.

[12] Moon, Y. S., Park, P., Kwon, W. H., and Lee, Y. S. (2001) *International Journal of Control* **74(14)**, 1447–1455.

[13] Boyd, S., Ghaoui, L. E., Feron, E., and Balakrishnan, V. (1994) Linear Matrix Inequalities in System and Control Thoery, SIAM, Philadelphia.

©ISAROB 2009

The Fourteenth International Symposium on Artificial Life and Robotics 2009 (AROB 14th '09),
B-Con Plaza, Beppu, Oita, Japan, February 5 - 7, 2009

Optimization of the sensor network using genetic algorithm

T. Minamino and K. Ito

Department of Systems and Control Engineering, Hosei University, 3-7-2 Kajino-cho, Koganei, Tokyo, Japan
(Tel : + 81-42-387-6093; Fax : +81-42-387-6381)
(tomoko.minamino.s3@gs-eng.hosei.ac.jp, ito@hosei.ac.jp)

***Abstract*:** Recently, with the advancement of the aging society, robots that operate in homes and hospitals have attracted much attention, and robots that have flexible artificial skins have been developed. Usually, they have to touch human bodies while performing their jobs. So, many touch sensors are required for the surface of the whole body. However, it is difficult to allocate limited number of sensors to suitable positions, because frequency of stimulus applied to the body is different by the locations, and in addition necessary resolution is different by the locations. In this paper, we consider design of sensor networks for robots, and we distribute limited resources to the sensors and the communication channels by genetic algorithm. Simulations have been conducted, and as a result, in case of noisy environment, many resources have been distributed to communication channels for realizing enough rate of information throughput. And in case of noiseless environment, many resources have been distributed for sensors because each communication channel has enough speed in the noiseless environment. From the results we have confirmed that number of sensors and communication channels has been adjusted and optimal sensor networks have been obtained.

***Keywords*:** Genetic Algorithms, sensor network, touch sensor

I. INTRODUCTION

Recently, with the advancement of the aging society, robots that operate in homes and hospitals have attracted much attention, and robots that have flexible artificial skins have been developed [1]-[4]. Usually, the robots have to touch human bodies while performing their jobs. So, many touch sensors are required for the surface of the whole body. However, it is difficult to allocate limited number of sensors to suitable positions, because frequency of stimuli applied to the body are different by the locations, and necessary resolution is also different by the locations. Moreover, there is a trade-off between resolution and communication cost. By increasing the number of sensors, we can enhance the space resolution, but communication cost is also increased. So, even if we install large number of sensors to the robot, the robot can not utilize information from the sensors because of the lack of the rate of information throughput. So, we have to distribute limited resources adequately to the sensors and the communication channels.

On the other hand, animals have adequate touch sensors on their whole body, and the number of sensors is adjusted based on the locations. For example, human being has many touch sensors on their hand than their foot. It is considered that the distribution is designed by the evolution.

In this paper, we consider design of sensor networks for robots, and we distribute limited resources to the sensors and the communication channels, and in addition, we allocate sensors adequately based on the stimulus from the environment by Genetic Algorithms.

II. PROBLEM DOMAIN

In this paper, we consider the distribution of limited resources to sensors and their communication channels. We assume that there is noise in the environment, and positions of the stimuli are set randomly.

In the environment, amount of information that can be transmitted by a communication channel is given by equation (1), by Shannon− Hartley theorem.

$$C = \log_2(1 + \frac{S}{N}) \qquad \cdots(1)$$

Where, C is the communication channel capacity, S is the total signal power, N is the total noise power.

III. GENETIC ALGORITHM

To realize optimal distribution, we employ genetic algorithm [5]. Fig. 1 shows the flowchart of the genetic algorithm.

First, initial individuals are created randomly, and then, crossover and mutation are conducted and new population is produced. From the population, individuals that survive to the next generation are selected. By repeating this cycle, evolution is realized.

©ISAROB 2009

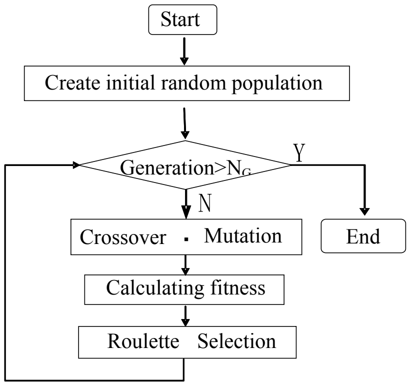

Fig. 1 Flow chart of Genetic Algorithm

IV. ENCODIN METHOD

Fig. 2 shows a sensor network that we consider in this paper. The circles show sensors, and lines are communication channels. Every sensor has own exclusive communication channel, and one communication channel is composed of multiple cables. Rate of information throughput of each communication channel is determined by the number of its cables and noise by equation (1) and (2). The position of the sensors and the number of the cables are given by genetic algorithm.

$$C_{ch}[i] = C \times N_c[i]$$
$$y[i] = \begin{cases} C_{ch}[i] & (C_{ch}[i] \le U) \\ U & (C_{ch}[i] > U) \end{cases} \qquad \cdots(2)$$

Where, C is information throughput of each cable and is given by equation (1). C_{ch}[i] is information throughput of i-th communication channel, N_c[i] is the number of cables of the i-th communication channel, U is input from each sensor, y[i] is output of the i-th communication channel.

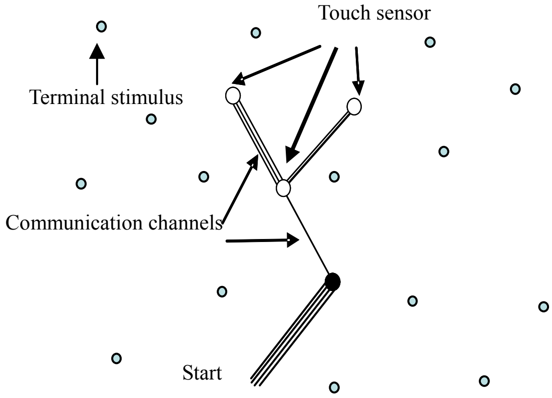

Fig.2 Sensors and communication channels

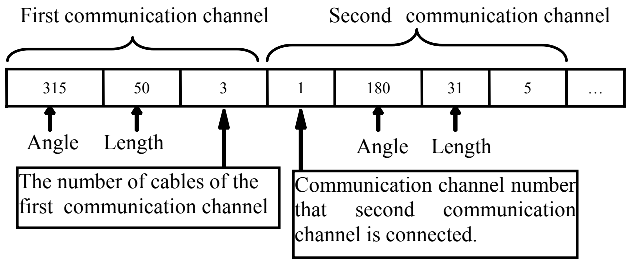

Fig.3 Encoding of sensor network

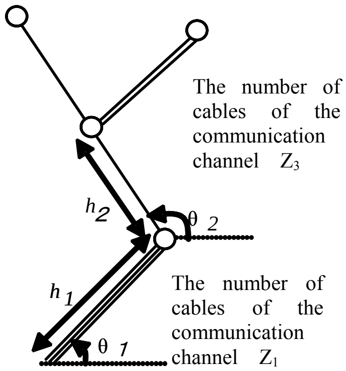

Fig.4 Phenotype

Fig. 3 shows the genotype of the sensor network and Fig. 4 shows the phenotype of that.

In Fig. 3, first gene means the angle from the horizontal axis to the first communication channel as shown in Fig. 4. The angle is selected from 0 to 360 degrees and its step size is one degree. The second gene means the length of the first communication channel. The value is selected from 0 to 50 and its step size is one. The third gene means the number of cables of the first communication channel. The value is selected from 1 to 10 and its step size is one. Fourth gene means communication channel number that second communication channel is connected. Fifth gene means the angle from the horizontal axis to the second communication channel.

By repeating this cycle, whole sensor network is described.

V. FITNESS

We calculate the fitness of the sensor network by total amount of transmitted information.

We input many stimuli to the sensor network. The positions of the stimuli are set randomly and are observed by the nearest sensor. The information of the stimulus is transmitted to the origin by its communication channel. The rate of information throughput of each communication channel is determined by the number of its cables and noise as shown section II and section IV.

From the amount of transmitted information, we calculate fitness as shown in equation (4).

$$fit = \frac{\sum_{i=1}^{n} y[i]}{\sum_{i=1}^{n} (Cs + Ct \times N_c[i])} \quad \cdots(4)$$

Where, n is the number of communication channel, Cs is the cost of each sensor, Ct is the cost of each cables for the communication channel, $N_c[\mathrm{i}]$ is the number of cables of the i-th communication channel.

The numerator of the equation (4) means total amount of transmitted information, and the denominator means total cost.

In the setting that we consider in this paper, as the amount of the resources is limited, if rate of information throughput becomes high, the number of sensors becomes small. In this case, if amount of information that is sent from a sensor is smaller than its rate of information throughput, the communication channel is not utilized efficiently, and the value of the fitness becomes small.

By the same token, if the number of sensors becomes large, then the rate of information throughput becomes low, and it becomes impossible to send all information from the sensors to the origin, because of the lack of the rate of information throughput. So, in this case, the value of the fitness becomes small too.

Thus, by maximizing the fitness, the trade-off of the resolution and the communication cost is solved, and the optimal sensor network is realized.

VI. SIMULATION

We conduct simulations to demonstrate the effectiveness of the proposed approach. We employ three different cases. Table 1 shows the common setting of GA, and Table 2, 3and 4 show the setting of each case.

Table1.The setting of GA

Number of individuals	50
Number of generations	10000
Probability of crossover	50%
Probability of mutation	1%
Amount of information that is sent from each terminal stimulus	10
Cost of the sensor (Cs)	10
Cost of the communication channel (Ct)	1

Table2. The setting of case 1 (In Fig.7)

Gene length (the number of communication channel)	400 (100)
The number of terminal stimulus	100
Signal to noise ratio	2000

Table3. The setting of case 2 (In Fig.8)

Gene length (the number of communication channel)	400 (100)
The number of terminal stimulus	100
Signal to noise ratio	40

Table4. The setting of case 3 (In Fig.9)

Gene length (the number of communication channel)	1200 (300)
The number of terminal stimulus	100
Signal to noise ratio (0≦Y coordinate＜350)	2000
Signal to noise ratio (350≦Y coordinate≦700)	40

Fig. 6 shows the average and the maximum vale of the fitness. Fig. 7, 8 and 9 show examples of the acquired sensor networks.

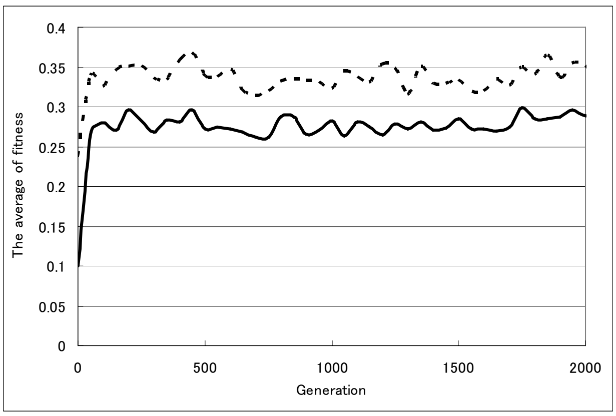

Fig. 6 The average and the maximum vale of the fitness

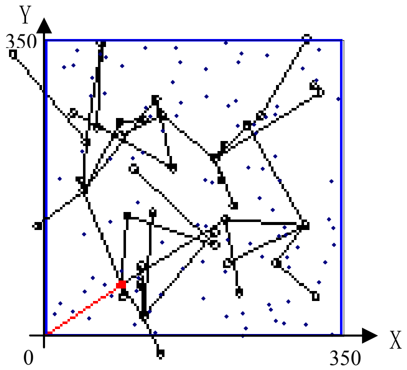

Fig. 7 Acquired sensor network (S/N=2000)

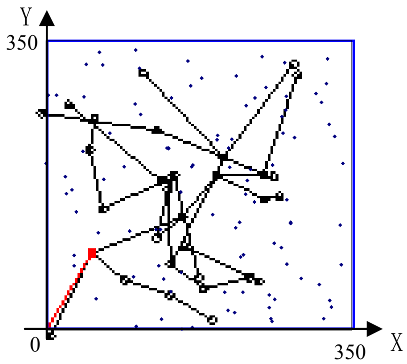

Fig. 8 Acquired sensor network (S/N=40)

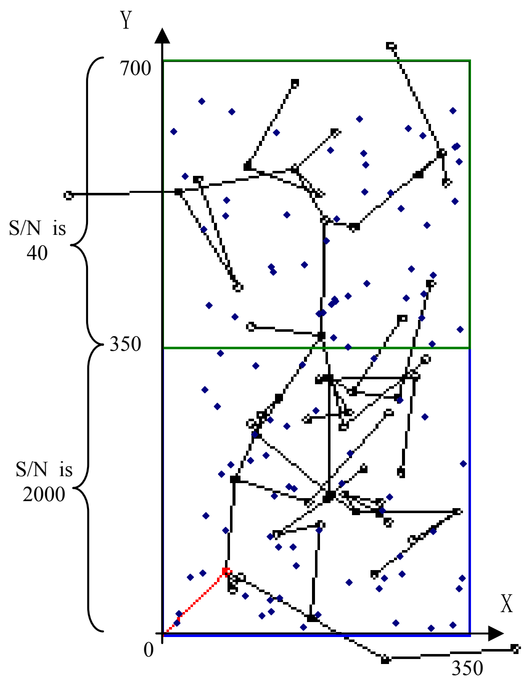

Fig. 9 Acquired sensor network

From Fig. 6, we can find that the fitness increases and evolution has been conducted successfully.

In case of noisy environment, many resources have been distributed for communication channels for acquiring enough rate of information throughput (Fig. 8). And in case of noiseless environment, many resources have been distributed for sensors, because each communication channel has enough rate of information throughput in the noiseless environment (Fig. 7).

From Fig. 9, we can find that even if there are different conditions in the environment, the sensor network is adapted for each condition adequately.

From the results, we can confirm that number of sensors and communication channels are adjusted and optimal sensor networks are obtained.

VII . CONCLUSION

In this paper, we consider design of sensor networks for robots and we distribute limited resources to the sensors and the communication channels. And in addition, we allocate sensors adequately based on the stimulus from the environment.

To demonstrate the effectiveness of the proposed approach, simulations in which noise is taken into consideration have been demonstrated. And as a result, in case of noisy environment, many resources have been distributed for communication channels to acquire enough rate of information throughput. And in case of noiseless environment, many resources have been distributed for the sensors because each communication channel has enough speed in the noiseless environment. From the results, we have confirmed that number of sensors and communication channels has been adjusted and optimal sensor networks have been obtained.

REFERENCES

[1] Noguchi E, Yamamoto H, Miyazaki H(2002), Robot Business on Welfare : A Spoken Dialogue Robot System for the Aged with Communication (in Japanese), RSJ20(7):687-691
[2] Nagakubo A, Alirezaei H, Kuniyoshi Y(2007), A Tactile Distribution Sensor Based on Inverse Problem Theory (in Japanese), RSJ25(6):960-969
[3] Shinoda H(2000), Tactile Sensing for Dexterous Hand (in Japanese), RSJ18(6):767-771
[4] Shinoda H(2001), Artificial Skin for Soft Machines (in Japanese), RSJ 19(7):814-817
[5] Kitano H(1992),Genetic Algorithms(in Japanese), Journal of Japan Society for Artificial Intelligence 7(1):26-37

The Fourteenth International Symposium on Artificial Life and Robotics 2009 (AROB 14th '09),
B-Con Plaza, Beppu, Oita, Japan, February 5 - 7, 2009

A Novel Genetic Algorithm with Different Structure Selection for Circuit Design Optimization

Zhiguo Bao and Takahiro Watanabe
Graduate School of Information Production and Systems
Waseda University
Kitakyushu-shi, Japan
Email: baozhiguo@moegi.waseda.jp

Abstract

Evolvable Hardware (EHW) is a new research field about the use of Genetic Algorithm (GA) to synthesize an optimal circuit. In traditional GA, the tournament selection for crossover and mutation is based on fitness of individuals. It can make convergence easily, but maybe lose some useful genes. In selection, besides fitness, we consider the different structure from individuals comparing to elite one. First, select some individuals with more different structures, then cross over and mutate these ones to generate new individuals. By this way, GA can increase diversification to searching spaces, so that it can find better solution. We propose optimal circuit design by using GA with different structure selection (GAdss) and with fitness function composed of circuit complexity, power and signal delay. Its effectiveness is shown by simulations. From the results, we can see that the best elite fitness, the average value of fitness of correct circuits and the number of correct circuits of GAdss are better than GA. The best case of optimal circuits generated by GAdss is 8.1% better in evaluating value than the circuit of GA.

Keywords

GA, EA, Circuit Optimization, EHW

1 Introduction

In artificial intelligence, Evolutionary Algorithm (EA) is a generic population-based heuristic optimization algorithm. It uses some mechanisms inspired by biological evolution: selection, crossover, mutation and reproduction. Genetic Algorithm (GA) [1][2] is one of the typical evolutionary algorithms.

In traditional GA, the tournament selection for crossover and mutation is based on fitness of individuals. It can make convergence easily, but maybe lose some useful genes. In tournament selection, besides fitness, we consider the different structure from individuals comparing to elite one, because the offspring with more different structure can enhance diversification to searching spaces. The value of different structure is defined by the sum of absolute value of difference of genes between two individuals. First, select some individuals with more different structures, then cross over and mutate these ones to generate new individuals. By this way, GA can increase diversification to searching spaces, so that it can find better solution.

While GA technologies are developed, Evolvable Hardware Systems (EHW) [3][4] is researched, inspired by the Evolution theory. EHW was first proposed in the early 1990s' for hardware design. It is classified into two categories: original design and adaptive systems. Original design uses EA to design a system that meets a predefined specification, and adaptive systems reconfigure an existing design to adapt to a variable operational environment. EHW can be used as an alternative to conventional hardware design methodology. The application of the EHW technique appears to be successful and promising, because it could automatically generate digital circuits by using EA. However, there still remain critical issues such as scalability, maintainability and generalization [5][6] to apply EHW for practical design problems. One of them is a circuit design optimization problem, where mixed design constraints are subjected.

In this paper, we propose a new approach for circuit design optimization by GA with Different Structure Selection (GAdss), where mixed constraints on circuit complexity, power and signal delay are considered. First, we introduce the evaluating value about correctness, complexity, power and signal delay to the fitness function in order to get an optimal circuit. The fitness function used in the experiments aims at accepting solutions with 100% correctness of the target circuit, and with maximal evaluating values about complexity, power and signal delay. Then GAdss can autonomously synthesize a circuit that is equivalent to a conventional design in functionality, but is simpler and has better performance. As a result, GAdss can find a better circuit, compared to GA. To verify an effectiveness of our approach, a simple 2-bit half adder circuit is experi-

©ISAROB 2009

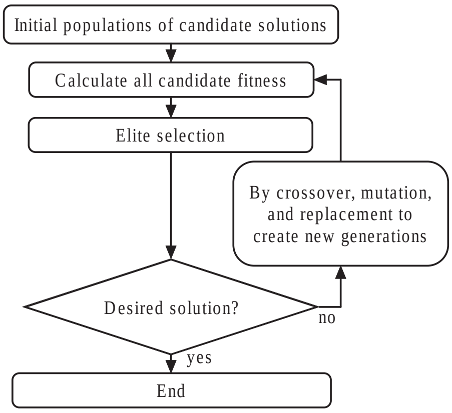

Figure 1: The evolutionary process of GA.

mentally synthesized.

In the next section, a brief overview of GAdss is described. Section 3 describes the use of GAdss as a new approach for the automatic design of an optimized circuit. Section 4 shows experiments on a 2-bit half adder circuit design as an example. Finally, the paper concludes with a summary of the results in section 5.

2 Genetic Algorithm with different structure selection

2.1 Genetic Algorithm

GA is a search technique used to find exact or approximate solutions to optimization and search problems. Figure 1 shows a graphical representation of the GA mechanisms. GA involves a search from a population of individuals.

In the initialization of a GA population, each individual is randomly generated. In the evaluation, GA evaluates each candidate according to a fitness function, which indicates how well a candidate satisfies the design specification. In each generation, the elite individuals are preserved and the rest of the individuals are replaced by the new ones generated by crossover and mutation. GA continues to evolve until it finds the best individual.

2.2 Genetic Algorithm with different structure selection

In traditional GA, elite selection and tournament selection are based on the fitness of individuals. This is good for GA to find the local best solution, but it maybe premature convergence. To avoid premature convergence, we consider the different structure of individuals compared to elite one. The value of different structure is defined by the sum of absolute value of difference of genes between two individuals. We select some individuals with different structure to do crossover and mutation, to generate some new individuals to the next populations. This method can extend diversification to search spaces, so can be fond a better solution.

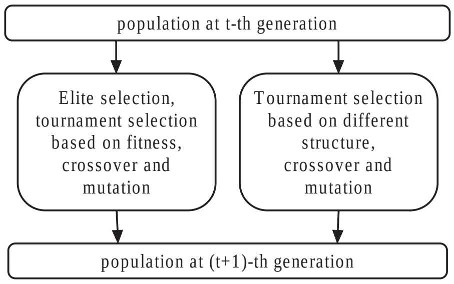

Figure 2: The reproduction of GAdss.

Figure 2 shows a graphical representation of the reproduction of GAdss. In each generation, the elite individuals are preserved. In selecting some individuals, half of them are processed by tournament selection based on fitness, and another half are processed by tournament selection based on different structure. Then crossover and mutation are performed to create new ones for next generation.

$< Crossover >$

The crossover is operated between two parents, and two new individuals are generated. The procedure of the crossover is as follows.

(1) Select two individuals as parents using tournament selection. (2) Some bits in the parents are selected as the crossover bits with the probability of Pc. (3) Two parents exchange the corresponding selected bits with each other. (4) The two new individuals become the individuals of the next generation.

$< Mutation >$

Mutation is executed in one parent and a new individual is generated. The procedure of mutation is as follows.

(1) Select one individual as a parent using tournament selection. (2) Some bits are selected with the probability of Pm. The selected bits are changed randomly and the new individual is generated. (3) The new individual becomes the individual of the next generation.

Here, tournament selection runs a "tournament" among two individuals chosen at randomly from the population, and selects the winner which with the better fitness or has more different structure.

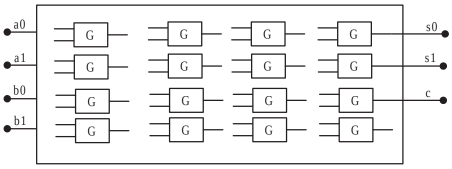

Figure 3: An initial 4*4 array with the input/output functionality for a 2-bit half adder.

3 Circuit Design Optimization using GAdss

3.1 Objective

The overall objective is to discover new and novel solutions by the application of GA in the circuit design process. The target circuit has to provide identical functional behavior equivalent to the specification but require less complexity, less power and less signal delay.

In this section, we will demonstrate the principle of GAdss in the design process using a 2-bit half adder as a sample logic circuit.

3.2 Genetic encoding

To process a genetic encoding easily, the logic circuit under consideration is assumed to be organized on a two dimensional array of cells, which was proposed in [3]. Each cell accepts two inputs and produces one output. The cells in the first column of the array are set with predefined inputs. For the purpose of this experiment, the combinatorial circuit takes four primary inputs. Therefore there are 16 input patterns of the circuit. Cells in the following columns receive outputs from cells in the previous columns. The chromosome is a string of integers where each three continuous genes embody a cell. Each triplet in the chromosome encodes the two inputs and the type of a cell respectively. In this experiment, the last cell is not used, so the chromosome length is calculated by the following formula:

$$3 * ((numberofcolumns) * (numberofrows) - 1). \quad (1)$$

In the experiment, the array is a fixed size of 4*4 cells (shown in Figure 3), thus the length of the chromosome is 45 ($3 * (4 * 4 - 1)$). The inputs of each cell in the first column of the array can take the value of any integer in the range of [0 to $(max\_number\_inputs - 1)$]. Cells in all other columns can take any integer value in the range of [0 to $((now\_column - 1) * (numberofrows) - 1)$]. As for the third gene in the triplet, cell type is defined as shown in Table 1, which was proposed in [7].

A typical chromosome then can be a sequence of triplets such as:

([0-X],[0-X],[0-9])...([0-X],[0-X],[0-9]).

Here, X is 3 in the first four cells (in the first column); X is $((now\_column - 1) * 4 - 1)$ in the other columns, now_column is the number of (2,3,4) column where the cell is placed.

Table 1: Information of cells

CT[a]	LF[b]	GC[c]	EC[d]	power	EP[e]	GSD[f]	ESD[g]
0	NAND	4	6	3	7	4	6
1	NOR	4	6	3	7	4	6
2	XNOR	8	2	4	6	6	4
3	NOT(in1)	2	8	2	8	3	7
4	NOT(in2)	2	8	2	8	3	7
5	WIRE(in1)	0	10	6	4	8	2
6	WIRE(in2)	0	10	6	4	8	2
7	AND	6	4	5	5	7	3
8	OR	6	4	5	5	7	3
9	XOR	8	2	4	6	6	4
-	(not used)	0	20	0	20	0	20

[a] cell type
[b] logical function
[c] gate complexity
[d] evaluating gate complexity
[e] evaluating gate power
[f] gate signal delay
[g] evaluating gate signal delay

3.3 Fitness Function

The fitness function in this experiment aims to accept solutions with 100% correctness of the target circuit, and with maximal evaluating values about complexity, power and signal delay. We use two functions F_1 and F_2. The former is a ratio of correct outputs to all test data, and the latter is an evaluating function of circuit complexity, power and signal delay. The following shows how the fitness of individuals is calculated, which was proposed in [7]:

$$F_1 = \frac{num\_rightout * 100}{num\_testdata}. \quad (2)$$

- $num\_rightout$: the number of correct outputs from circuit individuals.
- $num\_testdata$: the number of all test data.

$$F_2 = (\sum_{i \in N} ecv_i) * \alpha_c + (\sum_{i \in N} epv_i) * \alpha_p + (\sum_{j \in Cols} (\min_{k \in Rows} edv_{jk})) * \alpha_d. \quad (3)$$

©ISAROB 2009

- ecv_i : evaluating complexity value of cell i.
- epv_i : evaluating power value of cell i.
- $edv_{j,k}$: evaluating signal delay value of cell in column j and row k in an array.
- a_c : the coefficient about complexity (set to 1 here).
- a_p : the coefficient about power (set to 1 here).
- a_d: the coefficient about signal delay (set to 1 here).
- N : the number of all the cells.
- $Cols$: all the columns of the array.
- $Rows$: all the rows of the array.

$$Fitness = \begin{cases} F_1, & if(F_1 < 100) \\ F_1 + F_2, & otherwise. \end{cases} \qquad (4)$$

The first part F_1 of the fitness function compares the output response of the evolved circuit with the desired ones from truth table. If all matching, then the fitness value for the correctness is 100. The second fitness F_2 searches for the most optimum solution in terms of complexity, power and signal delay. This is done by designating gates with different evaluating values about complexity, power and signal delay (shown in Table 1).

In order to judge the difference of the complexity, power and signal delay between different gates, we assign values about complexity, power and signal delay to each gates. In the evolution of GA, the larger the fitness is, the better the circuit is. So we use evaluating values about complexity, power and signal delay in fitness function. In Table 1, "GC" is the complexity about CMOS circuit of one gate, "EC" equals to $(10 - GC)$. "power" is the value about power of one gate, "EP" equals to $(10 - power)$. "GSD" is the value about signal delay of one gate, and "ESD" equals to $(10 - GSD)$. When a cell is not used in a circuit, then its evaluating values are set to 20.

4 Experiments

This experiment aims to verify circuit optimization by GAdss. Table 2 shows the parameters of the evolution of GAdss. There is no fixed method to define the number of generations, population size, crossover probability and mutation probability. Therefore some preliminary experiments were performed in advance to decide parameters suitable for our experiment.

Table 2: Conditions for evolution

Number of Generation : 500
Population Size : 1210 Elite Size : 10 Crossover Size : 600 Mutation Size : 600
Crossover Probability (Pc) : 0.2, 0.5 Mutation Probability (Pm) : 0.023

Table 3: The results of different GA

item	GA(0.2)[a]	GAdss(0.2)[b]	GA(0.5)[c]	GAdss(0.5)[d]
best	447	465	471	501
quality	-	5.2%	-	8.1%
average	428.4	438	464.4	500.4
quantity	3	7	14	16
time(m)	19	19	25	25

[a] GA with $(Pc : 0.2)$
[b] GAdss with $(Pc : 0.2)$
[c] GA with $(Pc : 0.5)$
[d] GAdss with $(Pc : 0.5)$

The proposed method has been implemented in Eclipse SDK 3.1.1 with jre 1.6.0; and tested on a PC with Inter(R) Core(TM)2 CPU at 2.67GHz and 2.0GB RAM.

Table 3 shows the results of different GA. For each GA, we select the successful results over 60 independent trials. In Table 3, "best" means the best elite fitness value; "quality" the percent of better in evaluating value of best individual compared to one of GA; "average" the average fitness value of top three individuals; "quality" the number of correct individuals over 60 independent trials; "time" the running time of 60 trials.

From the results, we can see that the best elite fitness, the average fitness value of top three correct circuits, and the number of correct circuits of GAdss are better than GA. Compared to GA, GAdss consider the different structure from individuals comparing to elite one, then it can enhance diversification to searching spaces, so that it can find better solution.

In the experiments, the optimized circuit with fitness 501 was obtained by the GAdss (Pc:0.5). This chromosome is as follows:

(0,2,2)(0,2,7)(1,3,1)(1,3,2)(3,2,5)(0,0,5)(3,0,5)(1,3,1)
(1,6,9)(4,2,6)(3,6,1)(5,7,4)(0,6,3)(1,3,2)(2,7,1)

The graphical representation of this chromosome is shown in Figure 4. In this figure, we show the useful gates

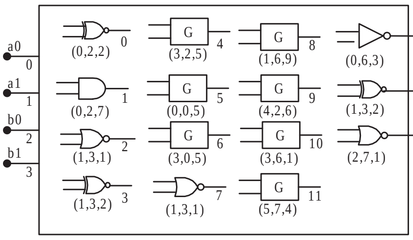

Figure 4: The graphical representation of chromosome (501).

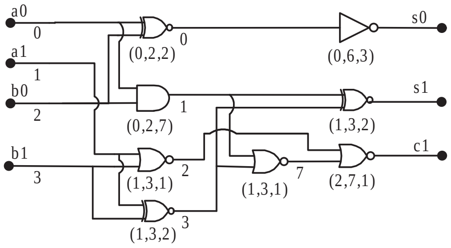

Figure 5: The optimized circuit after removing unnecessary gates (501).

with logic gates symbols. Figures 5 and 6 show the optimized circuits with fitness 501 and fitness 471 respectively, after removing unnecessary gates. The circuit in Figure 5 is obviously better than the one in Figure 6, because the former is composed of less gates, so that the lager fitness can produce a circuit with less complexity, less power and less signal delay.

5 Conclusion

This paper proposed GAdss and its application to autonomous design optimization for combinatorial circuits. By evolution, GAdss can find optimized circuits with less complexity, less power and less signal delay than GA .

We can also apply GAdss to autonomous design circuits for more complex functional requirements, and enhance more exact information about circuit to fitness function. In the future, we will develop the adaptive systems which reconfigure an existing design to adapt to a variable operational environment.

Acknowledgements

This research was supported by "Ambient SoC Global COE Program of Waseda University" of the Ministry of Education, Culture, Sports, Science and Technology, Japan.

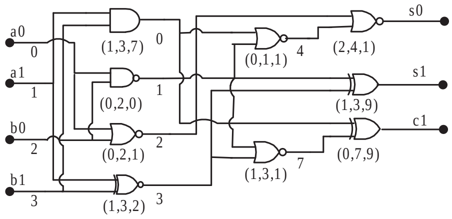

Figure 6: The optimized circuit after removing unnecessary gates (471).

References

[1] J. H. Holland, "Adaptation in Natural and Artificial systems," Ann Arbor, MI: The University of Michigan Press, 1975.

[2] Y. Chen, J. Hu and K. Hirasawa et al, "Solving Deceptive Problems Using A Genectic Algorithm with Reserve Selection," Proc. of IEEE Congress on Evolutionary Computation 2008 (CEC2008), pp.884-889, Hongkong, Jun., 2008.

[3] J. D. Lohn and G. S. Hornby, "Evolvable hardware: using evolutionary computation to design and optimize hardware systems," Computational Intelligence Magazine, IEEE, pp. 19-27, Feb., 2006.

[4] E. Benkhelifa, A. Pipe and G. Dragffy et al, "Towards evolving fault tolerant biologically inspired hardware using evolutionary algorithms," Proc. of IEEE Congress on Evolutionary Computation 2007 (CEC2007), pp. 1548-1554, Sept., 2007.

[5] X. Yao and T. Higuchi, "Promises and Challenges of Evolvable Hardware," IEEE Trans. on Systems, Man, and Cybernetics, Part C: Applications and Reviews, Vol. 29, No. 1, pp. 87-97, Feb., 1999.

[6] V. K. Vassilev and J. E. Miller, "Scalability problems of digital circuit evolution evolvability and efficient designs," Proc. of the Second NASA/DoD Workshop on Evolvable Hardware, pp. 55-64, Palo Alto, CA, USA, Jul., 2000.

[7] Z. Bao and T. Watanabe, "A New Approach for Circuit Design Optimization using Genetic Algorithm," Proc. of International SoC Design Conference 2008 (ISOCC2008), Busan, Korea, Nov., 2008.

A PSO Method with Nonlinear Time-Varying Evolution for Optimal Design of PID Controllers in a Pendubot System

Pi-Yun Chen[1], Chia-Ju Wu[2], Yu-Yi Fu[3], Chia-Nan Ko[4], and Li-Chun Lai[5]

[1]Graduate School of Engineering Science and Technology, National Yunlin University of Science and Technology
Douliou, Yunlin 640, Taiwan
[2]Department of Electrical Engineering, National Yunlin University of Science and Technology
Douliou, Yunlin 640, Taiwan
[3,4]Department of Automation Engineering, Nan-Kai University of Technology
Tasotun, Nantou 542, Taiwan
[5]Department of Electrical Engineering, Chungchou Institute of Technology
Yuanlin, Changhua 510, Taiwan
(E-mail: [1]g9310820@yuntech.edu.tw; [2] wucj@yuntech.edu.tw ; [3] t098@nkut.edu.tw ; [4] t105@nkut.edu.tw;
[5]lclai@dragon.ccut.edu.tw)

Abstract: A particle swarm optimization method with nonlinear time-varying evolution (PSO-NTVE) is employed in designing an optimal PID controller for asymptotical stabilization of a pendubot system. In the PSO-NTVE method, parameters are determined by using matrix experiments with an orthogonal array, in which a minimal number of experiments would have an effect that approximates the full factorial experiments. The PSO-NTVE method and other PSO methods are then applied to design an optimal PID controller in a pendubot system. Comparing the simulation results, the feasibility and the superiority of the PSO-NTVE are verified.

Keywords: Particle swarm optimization, orthogonal array, nonlinear time-varying evolution, PID controllers, pendubot system.

I. INTRODUCTION

A pendubot is a two-link (two-degree-of-freedom) underactuated system and it includes two links rotating on two joints, in which the first link (shoulder) is actuated and the second link (elbow) is not actuated. This system is a simple underactuated mechanical system to permit complete dynamic analyses, but complex enough for investigating many advanced nonlinear control methods. Therefore, it is widely used as a benchmark in the study of underactuated systems [1-4].

In order to stabilize the pendubot to the unstablely inverted equilibrium position, a two-stage control strategy is always used. In the first stage, swing-up control is used to move the pendubot close to the equilibrium manifold. Then in the second stage, the swing-up controller is replaced by a balance controller for position control. Many methods such as the partial feedback linearization technique[1,2], the energy based controller[3], and the bang-bang controller[4] have been conducted for swing-up control of the pendubot. Once both links are swung up, the problem of balancing the pendubot about the unstable equilibrium was investigated. A linear quadratic regulator was proposed for the balance control[1,4]. Furthermore, the hybrid controller and the energy based controller[2,3] were presented.

Particle swarm optimization (PSO) has evolved recently as an important branch of stochastic techniques to explore the search space for optimization[5]. Nowadays, PSO has been developed to be real competitors with other well-established techniques for evolutionary-based optimization methods[6-10]. In this paper, a PSO-NTVE method is employed in the designing of an optimal PID controller in a pendubot system since it can effectively deal with continuous nonlinear programming problems and generate high quality solutions. From the simulation results of the illustrative examples, the feasibility and the validity of the PSO-NTVE are verified.

II. PSO-NTVE-BASED PID CONTROLLERS

1. Review of some PSO methods

In PSO algorithm, each particle keeps track of its own position and velocity in the problem space. The initial position and velocity of a particle are generated randomly. At each iteration, the new positions and velocities of the particles are updated using the following two equations:

$$P_i(k+1) = P_i(k) + V_i(k+1) \quad \text{for } i = 1, 2, \cdots, m \tag{1}$$

$$V_i(k+1) = V_i(k) + c_1 \cdot r_1 \cdot (P_i^l(k) - P_i(k)) + c_2 \cdot r_2 \cdot (P^g - P_i(k)) \tag{2}$$

where m is the number of particles in a population, k is the number of current iteration, c_1 and c_2 are acceleration coefficients, r_1 and r_2 are random numbers between 0 and 1, $P_i(k)$, $P_i^l(k)$, and $V_i(k)$ are the position, the local best, and the velocity of ith particle at iteration k, P^g is the global best of all particles.

Since the introduction of the PSO method in 1995, researchers have put much effort to improve the original version of PSO. Shi and Eberhart[11] used a linearly varying inertia weight over iterations. The mathematical representations of this PSO method are given as shown in (1) and

©ISAROB 2009

$$V_i(k+1)=\omega(k)\cdot V_i(k)+c_1\cdot r_1\cdot(P_i^l(k)-P_i(k)) + c_2\cdot r_2\cdot(P^g-P_i(k)) \ \text{ for } \ i=1,\ 2,\cdots,\ m \tag{3}$$

where the acceleration coefficients c_1 and c_2 are fixed, r_1 and r_2 are two random numbers. The inertia weight starts with a high value $\omega_{\max}$ and linearly decreases to $\omega_{\min}$ at the maximal number of iterations. From hereafter, this PSO algorithm will be referred to as the time-varying inertia weight factor method (PSO-TVIW).

Eberhart and Shi[12] found that the PSO-TVIW method is not very effective in tracking dynamic systems. Considering the dynamic nature of real-world applications, they proposed a random inertia weight factor to track dynamic systems. In their method, the representations are the same as those in the PSO-TVIW method except that the inertia weight factor changes randomly. In the rest of this paper, this algorithm will be referred to as the PSO-RANDW method.

An automation strategy for the PSO with time-varying acceleration coefficients was proposed[13]. The objective is to enhance the global search in the early part of the optimization and to encourage the particles to converge toward the global optimum at the end of the search. In their method, the representations are the same as those in the PSO-TVIW method except that the acceleration coefficients change according to linear time-varying evolution. From hereafter, this algorithm will be referred to as the PSO-TVAC method.

A time-varying nonlinear function modulated inertia weight adaptation was proposed by Chatterjee and Siarry[14]. In this method, the acceleration coefficients are also fixed. However, the inertia weight starts with a high value $\omega_{\max}$ and nonlinearly decreases to $\omega_{\min}$ at the maximal number of iterations. This means that the representations are the same as those in the PSO-TVIW method except that the inertia weight factor changes according to

$$\omega(k)=\omega_{\min}+\left(\frac{iter_{\max}-iter}{iter_{\max}}\right)^{\alpha}\cdot(\omega_{\max}-\omega_{\min}) \tag{4}$$

where $iter_{\max}$ is the maximal number of iterations and $iter$ is the current number of iterations.

2. PSO-NTVE method based on orthogonal arrays

In this section, based on the concept presented[13,14], a PSO-NTVE method is proposed. In the proposed PSO method, the inertia weight is given as described in (4). The gnitive parameter c_1 starts with a high value $c_{1\max}$ and nonlinearly decreases to $c_{1\min}$. Meanwhile, the social parameter c_2 starts with a low value $c_{2\min}$ and nonlinearly increases to $c_{2\max}$. This means that the mathematical expressions are given as shown in (1), (4), and

$$V_i(k+1)=\omega(k)\cdot V_i(k)+c_1(k)\cdot r_1\cdot(P_i^l(k)-P_i(k)) + c_2(k)\cdot r_2\cdot(P^g-P_i(k)) \ \text{ for } \ i=1,\ 2,\cdots,\ m \tag{5}$$

$$c_1(k)=c_{1\min}+\left(\frac{iter_{\max}-iter}{iter_{\max}}\right)^{\beta}\cdot(c_{1\max}-c_{1\min}) \tag{6}$$

$$c_2(k)=c_{2\max}+\left(\frac{iter_{\max}-iter}{iter_{\max}}\right)^{\gamma}\cdot(c_{2\min}-c_{2\max}) \tag{7}$$

where α, β, and γ are constant coefficients.

The proposed PSO method will encourage particles to wander through the entire search space, instead of clustering around a local optimum, during early iterations of the optimization. On the other hand, the algorithm will expedite convergence toward the global optimum during latter iterations. In this manner, the optimal solution should be obtained in a computation-efficient way.

To determine the optimal combination of α, β, and γ, all combinations must be tested. For example, if it is assumed that α, β, and γ are all within the set $\{0.5, 1, 1.5, 2, 2.5\}$. Then there are 5^3 possible combinations for the values of α, β, and γ. However, if α, β, and γ have many possible values, then it may not be possible to perform the experiments of all combinations. An $L_{25}(5^6)$ is an orthogonal array that can deal with at most six variables in five possible values with 25 experiments[15,16]. Instead of 5^3 possible combinations, one only needs to perform 25 experiments to determine the optimal combination of α, β, and γ.

3. PSO-NTVE tuning PID controllers

In a PID control system, the time-domain form of a PID controller is usually expressed as

$$u(t)=K_{P1}e_1(t)+K_{I1}\int e_1(t)dt+K_{D1}\dot{e}_1(t) + K_{P2}e_2(t)+K_{I2}\int e_2(t)dt+K_{D2}\dot{e}_2(t) \tag{8}$$

where $u(t)$ is the control signal, $e_1(t)$, $e_2(t)$ and $\dot{e}_1(t)$, $\dot{e}_2(t)$ are the error signals and their derivatives, and $K_{P1}, K_{I1},\cdots, K_{D2}$ denote the proportional gain, the integral gain, and the derivative gain, respectively. In the PSO, a particle contains these gains. The optimal values of these gains are obtained by the PSO-NTVE method according to a defined fitness.

III. A SIMULATION EXAMPLE

1. Pendubot system

The general dynamic model of underactuated mechanisms with m actuated joints from a total of n joint can be expressed as follows[17]:

$$\boldsymbol{M}(\boldsymbol{q})\ddot{\boldsymbol{q}}+\boldsymbol{C}(\boldsymbol{q},\ \dot{\boldsymbol{q}})\dot{\boldsymbol{q}}+\boldsymbol{G}(\boldsymbol{q})=\boldsymbol{\tau} \tag{9}$$

where $\boldsymbol{q}\in R^n$ is the position vector indicating link angles, $\boldsymbol{M}(\boldsymbol{q})$ denotes the $n\times n$ inertia matrix, $\boldsymbol{C}(\boldsymbol{q},\ \dot{\boldsymbol{q}})\dot{\boldsymbol{q}}\in R^n$ is the vector of damping, coriolis, and centrifugal torques, $\boldsymbol{G}(\boldsymbol{q}) \in R^n$ represents the gravitational term and $\boldsymbol{\tau} \in R^n$ is the vector of control torque which has $(n-m)$ zero components. For the pendubot system in Fig. 1, let m_1 and m_2 denote the distributed mass of the actuated link (link 1) and the unactuated link (link 2), respectively. Mean- while, let q_1 and q_2, l_1 and l_2, l_{1c} and l_{2c}, and I_1 and I_2 denote the angles, the lengths, the distances to the center of mass, the moments of inertia about their centroids of link 1 and link 2, respectively.

Since the inertia matrix $\boldsymbol{M}(\boldsymbol{q})$ is positive definite for all $\boldsymbol{q}$, the dynamics of the Pendubot in (10) can be written as

$$\ddot{\boldsymbol{q}} = \boldsymbol{M}^{-1}(\boldsymbol{q})[\boldsymbol{\tau} - \boldsymbol{C}(\boldsymbol{q},\ \dot{\boldsymbol{q}})\dot{\boldsymbol{q}} - \boldsymbol{G}(\boldsymbol{q})] \tag{10}$$

$$\boldsymbol{M}(\boldsymbol{q}) = \begin{bmatrix} M_{11} & M_{12} \\ M_{21} & M_{22} \end{bmatrix},\ \ \boldsymbol{C}(\boldsymbol{q},\ \dot{\boldsymbol{q}}) = \begin{bmatrix} C_{11} & C_{12} \\ C_{21} & C_{22} \end{bmatrix},$$

$$\boldsymbol{G}(\boldsymbol{q}) = \begin{bmatrix} G_1 \\ G_2 \end{bmatrix},\ \ \boldsymbol{q} = \begin{bmatrix} q_1 \\ q_2 \end{bmatrix},\ \ \boldsymbol{\tau} = \begin{bmatrix} \tau_1 \\ 0 \end{bmatrix} \tag{11}$$

where

$$M_{11} = m_1 l_{c1}^2 + m_2(l_1^2 + l_{c2}^2 + 2 l_1 l_{c2} \cos q_2) + I_1 + I_2$$
$$M_{12} = m_2(l_{c2}^2 + l_1 l_{c2} \cos q_2) + I_2$$
$$M_{21} = M_{12},\quad M_{22} = m_2 l_{c2}^2 + I_2$$
$$C_{11} = -m_2 l_1 l_{c2} \dot{q}_2 \sin q_2$$
$$C_{12} = -m_2 l_1 l_{c2}(\dot{q}_1 + \dot{q}_2) \sin q_2$$
$$C_{21} = m_2 l_1 l_{c2} \dot{q}_1 \sin q_2 + K_d,\quad C_{22} = K_d$$
$$G_1 = (m_1 g l_{c1} + m_2 g l_1) \cos q_1 + m_2 g l_{c2} \cos(q_1 + q_2)$$
$$G_2 = m_2 g l_{c2} \cos(q_1 + q_2)$$

where K_d denotes the damping coefficient.

When the configuration is at equilibrium state; that is, pendubot balances at a state $\dot{q} = 0$ and $\ddot{q} = 0$, the following can be derived from (9).

$$(m_1 g l_{c1} + m_2 g l_1) \cos q_1 + m_2 g l_{c2} \cos(q_1 + q_2) = \tau_1 \tag{12}$$

$$m_2 g l_{c2} \cos(q_1 + q_2) = 0 \tag{13}$$

In the natural equilibriums of the pendubot, which means $\tau_1 = 0$, the solutions of (12) and (13) can be $q_1 = \pi/2$, $q_2 = 0$. In this manner, both link 1 and link 2 are in their upper positions. From the analysis, one can realize that the control of the pendubot system is not an easy task. Therefore, in the following sections, it will be shown how to design a PID controller to asymptotically drive the pendubot to the equilibrium state.

2. Fitness

In the time domain, the fitness function of a PID controller can include performance criteria such as the overshoot, the rise time, the settling time, and the steady-state error[18,19]. In general, the PID controller design method using the integrated absolute error (IAE), or the integral of squared-error (ISE), or the integrated of time-squared-error (ITSE) is often employed in control system designs. In this paper, the ITSE performance criterion is adopted to evaluate the PID controller. The performance criteria can be included in the same fitness as follows:

$$f = \frac{1}{\int t[e_1^2(t) + e_2^2(t)]\, dt} \tag{14}$$

From the definition (16), the fitness value can be calculated to evaluate the performance of the PID controller and a higher fitness value denotes a better performance.

IV. SIMULATION RESULTS

The parameters of the pendubot system shown in Fig. 1 are chosen as $m_1 = 2.0$ kg, $m_2 = 1.5$ kg, $l_1 = 0.3$ m, $l_2 = 0.5$ m, $l_{1c} = 0.15$ m, $l_{2c} = 0.25$ m, $g = 9.8$ m/s^2. The initial state and the desired final state of the pendubot system are $[q_1, \dot{q}_1, q_2, \dot{q}_2] = [-\pi/2,\ 0,\ 0,\ 0]$ and $[q_1, \dot{q}_1, q_2, \dot{q}_2] = [\pi/2,\ 0,\ 0,\ 0]$. Meanwhile, the input torque $\tau(t)$ of the motor is assumed to be within the range $[-8$ Nm, 8 Nm$]$.

In the proposed algorithm, the population size and the maximal iteration number are chosen to be 40, 10000, respectively. Moreover, the particles in PSO methods are all chosen as real numbers in the range $[-10, 10]$. In the proposed PSO-NTVE method, the values of α, β, and γ in (4), (6), and (7) are 0.5, 1.0, and 2.5 determined by experiments of orthogonal arrays. The average values of the optima PID gains and fitness for 20 trials are shown in Table 1.

From the results, it is clear that most considered in this paper are competitive in finding the optimal solution. Hoever, the performance of PSO-NTVE was found to be relatively better than other PSO methods in finding the optimal PID gains.

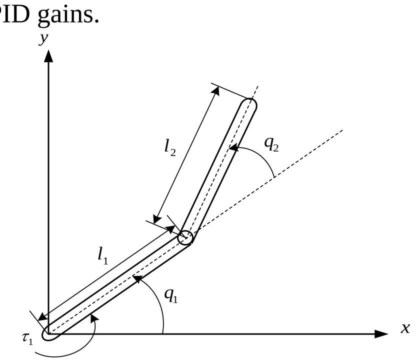

Fig. 1. Dynamics of the pendubot system

©ISAROB 2009

V. CONCLUSION

A PSO-NTVE method is presented in the designing of an optimal PID controller for a pendubot system. An orthogonal array is adopted to determine the parameters of the proposed PSO method. Then, this PSO-NTVE method is applied to design an optimal PID controller for asymptotically stabilizing the pendubot system. The simulation results verify the feasibility and the validity of the proposed PSO-NTVE method in the design of an optimal PID controller of a pendubot system.

Table 1 Average values of the optimal PID gains and fitness (14) for 20 trials.

PSO method	PID gains						Fitness(x10^{-2})
	K_{P1}	K_{I1}	K_{D1}	K_{P2}	K_{I2}	K_{D2}	
PSO-TVIW	1.373742	-0.521886	-1.959868	-9.999187	-0.207341	-2.865347	**8.638798**
PSO-RANDW	0.151508	0.063432	-8.694078	-9.991733	0.014415	-9.999336	**8.588553**
PSO-TVAC	0.912552	-0.760333	-2.479824	-9.999038	-0.307233	-3.409042	**8.638881**
PSO-NTVE	1.751383	-0.103256	-3.467748	-9.227502	-0.045068	-4.446959	**8.765612**

ACKNOWLEDGMENT

This work was supported in part by the National Science Council, Taiwan, R.O.C., under grant NSC96-2628-E-224-007-MY2.

REFERENCES

[1] Spong MW, Block DJ (1995), The Pendubot: a mechatronic system for control research and education. Proceedings of the 34th IEEE conference on decision and control, pp. 555-556
[2] Zhang M, Tarn TJ (2002), Hybrid control of the Pendubot. IEEE/ASME Trans on Mechatronics (1):79-86
[3] Fantoni I, Lozano R, Spong MW (2000), Energy based control of Pendubot. IEEE Trans on Automatic Control 45(4):725-729
[4] Zhao D, Yi J (2003), Swing up Pendubot with a GA-tuned bang-bang controller. Proceedings of the IEEE International Conference on Robotics, Intelligent Systems and Signal Processing, pp. 752-757
[5] Kennedy J, Eberhart R (1995), Particle swarm optimization. Proceedings of the IEEE International Conference on Neural Networks, pp. 1942-1948
[6] Gaing ZL (2004), A particle swarm optimization approach for optimum design of PID controller in AVR system. IEEE Trans on Energy Conversion 19(2):384-391
[7] Eberhart RC, Shi Y (1998), Comparison between genetic algorithms and particle swarm optimization. Proceedings of the IEEE International Congress on Evolutionary Computation, pp. 611-616
[8] Boeringer DW, Werner DH (2004), Particle swarm optimization versus genetic algorithms for phased array synthesis. IEEE Trans on Antennas and Propagation 52(3):771-779
[9] Mendes R, Kennedy J, Neves J (2004), The fully informed particle swarm: Simpler, maybe better. IEEE Trans on Evolutionary Computation 8(3):204-210
[10] Elbeltagi E, Hegazy T, Grierson D (2005), Comparison among five evolutionary-based optimization algorithms. Advanced Engineering Informatics 19(1):43-53
[11] Shi Y, Eberhart RC (1998), A modified particle swarm optimizer. Proceeding of the IEEE International Conference on Evolutionary Computation, pp. 69-73
[12] Eberhart RC, Shi Y (2001), Tracking and optimizing dynamic systems with particle swarms. Proceeding of the IEEE International Congress on Evolutionary Computation, pp. 94-100
[13] Ratnaweera A, Halgamuge SK, Watson HC (2004), Self-organizing hierarchical particle swarm optimizer with time-varying acceleration coefficients. IEEE Trans on Evolutionary Comput 8(3):240-255
[14] Chatterjee A, Siarry P (2006), Nonlinear inertia weight variation for dynamic adaptation in particle swarm optimization. Computers and Operations Research 33:859-871
[15] Montgomery DC (1991), Design and Analysis of Experiments, third edition. Wiley, New York
[16] Hicks CR (1993), Fundamental Concepts in the Design of Experiments, fourth edition. Saunders College, Texas
[17] Spong MW, Vidyasagar M (1989), Robot dynamics and control. Wiley, New York
[18] Krohling RA, Jaschek H, Rey JP (1997), Designing PI/PID controllers for a motion control system based on genetic algorithms. Proceedings of the IEEE International Symmetric Intelligent Control, pp. 125-130
[19] Ogata K (2002), Modern control engineering, fourth edition. Prentice-Hall, New Jersey

Support Vector Regression for Initialization of Radial Basis Function Networks for a Multi-input Multi-output System

Pi-Yun Chen[1], Chia-Ju Wu[2], Yu-Yi Fu[3], Chia-Nan Ko[4], and Jin-Tsong Jeng[5]
[1]Graduate School of Engineering Science and Technology, National Yunlin University of Science and Technology
Douliou, Yunlin 640, Taiwan
[2]Department of Electrical Engineering, National Yunlin University of Science and Technology
Douliou, Yunlin 640, Taiwan
[3,4]Department of Automation Engineering, Nan-Kai University of Technology
Tasotun, Nantou 542, Taiwan
[5]Department of Computer Science and Information Engineering, National Formosa University
Huwei, Yunlin 632, Taiwan
(E-mail: [1]g9310820@yuntech.edu.tw; [2] wucj@yuntech.edu.tw ; [3] t098@nkut.edu.tw ; [4] t105@nkut.edu.tw; [5]tsong@nfu.edu.tw)

Abstract: When a radial basis function network (RBFN) is used for identification of a nonlinear multi-input multi-output (MIMO) system, the number of hidden layer nodes, the initial parameters of the kernel, and the initial weights of the network must be determined first. For this purpose, a systematic way that integrates the support vector regression (SVR) and the least squares regression (LSR) is proposed to construct the initial structure of the RBFN. First, determine the number of hidden layer nodes and the initial parameters of the kernel by the SVR method. Then the weights of the RBFN are determined by solving a minimization problem based on the concept of LSR. After initialization, an annealing robust learning algorithm (ARLA) is then applied to train the RBFN. With the proposed initialization approach, one can find that the designed RBFN has a fast convergent speed. To show the feasibility and superiority of the annealing robust radial basis function networks (ARRBFNs) for identification of MIMO system, one example is included.

Keywords: Radial basis function networks, Support vector regression, Multi-input multi-output, Least square regression

I. INTRODUCTION

In industry, multi-input multi-output (MIMO) system is applied widely. Structural identification and parameter estimation of nonlinear MIMO system are very important but rather difficult issues in system identification. Radial basis function networks (RBFNs) are widely used for system modeling recently since they have only one hidden layer and have fast convergence speed. RBFNs are often referred to as model-free estimators since they can be used to approximate functions without requiring a mathematical description of how the outputs functionally depend on the inputs. This means that they can build systems from input–output patterns directly, or they learn from examples without any knowledge of the model type.

When RBFNs are used for system identification, the number of hidden nodes, the initial parameters of the kernel, and the initial weights of the network must be determined first. In the past few years, several initializations for RBFNs have been proposed. First, the number of hidden nodes is fixed, and then all kinds of algorithms (such as genetic algorithms and gradient descent method) is used to optimize all the parameters, namely the initial parameters of the kernel, and the initial weights of the network. However, a systematic way to determine the initial structure of a RBFNs for a MIMO system is still not established. Therefore, based on support vector regression (SVR), a least square regression method is proposed to solve this problem in this paper. Given the sample set that describes the input-output relation of a function, the first step of the proposed method is to solve an SVR problem for one input-output of an MIMO system. Then the weights of RBFNs for another input-output can be obtained by using least square regression (LSR). From the SVR results, the initial structure of an RBFN can be determined. After initialization, annealing learning algorithms can then be applied to train the RBFNs. With the proposed initialization method, the MIMO system has fewer neurons and the designed RBFNs have fast convergence speed. To show the feasibility and superiority of the proposed method, simulation results are included for illustration.

II. RBFNS FOR IDENTIFICATION OF NONLINEAR MIMO SYSTEMS

In general, the input-output relation of a nonlinear MIMO system can be expressed as

$$\begin{aligned}\mathbf{y}(t+1) = \mathbf{f}(&\mathbf{y}(t), \mathbf{y}(t-1), \cdots, \mathbf{y}(t-n_y), \\ &\mathbf{x}(t), \mathbf{x}(t-1), \cdots, \mathbf{x}(t-n_u)),\end{aligned} \tag{1}$$

where $\mathbf{f}(t) = [f_1(t), f_2(t), \cdots, f_p(t)]^{\mathrm{T}}$ denotes the nonlinear relation to be estimated. $\mathbf{x}(t) = [x_1(t), x_2(t), \cdots, x_m(t)]^{\mathrm{T}}$ is the input vector, $\boldsymbol{y}(t) = [y_1(t), y_2(t), \cdots, y_p(t)]^{\mathrm{T}}$ is the output vector, n_u and n_y are the maximal lags in the input and output, respectively.

One can use a neural network to estimate the input-output relation of a nonlinear MIMO system. In this paper, an RBFN will be adopted since it has a simple structure. When the Gaussian function is chosen as the radial basis function, an RBFN can be expressed in the form

$$\hat{y}_j(t+1) = \sum_{i=1}^{L} G_i w_{ij} = \sum_{i=1}^{L} w_{ij} \exp\left(-\frac{\|\hat{\mathbf{x}} - \mathbf{m}_i\|^2}{2\sigma_i^2}\right), \quad \text{for } j = 1, \cdots, p \tag{2}$$

where $\hat{\mathbf{x}}(t) = [\hat{x}_1(t), \hat{x}_2(t), \cdots, \hat{x}_m(t)]^{\mathrm{T}}$ is the input vector, $\hat{\mathbf{y}}(t) = [\hat{y}_1(t), \hat{y}_2(t), \cdots, \hat{y}_p(t)]^{\mathrm{T}}$ is the output vector, w_{ij} is the synaptic weight, G_i is the Gaussian function, $\mathbf{m}_i$ and σ_i are the center and width of G_i, respectively, and L is the number of the Gaussian functions, which is also equal to the number of hidden layer nodes.

Given a set of training input-output pairs $(\mathbf{x}^{(k)}, \mathbf{y}^{(k)})$, $k = 1, 2, \cdots, N$, where the identification problem of the nonlinear MIMO system is to determine the values of L, w_{ij}, $\mathbf{m}_i$, and σ_i, to minimize the following performance index

$$J = \sum_{k=1}^{N} \left\| \mathbf{y}^{(k)} - \hat{\mathbf{y}}^{(k)} \right\|^2, \tag{3}$$

where $\hat{\mathbf{y}}^{(k)}$ is the corresponding output of the RBFN when the input $\hat{\mathbf{x}}$ to the network is equal to $\mathbf{x}^{(k)}$.

In usual cases, the initial values of L, w_{ij}, $\mathbf{m}_i$, and σ_i are chosen first. Then a training algorithm is applied to the RBFN to search for the optimal combination of these values in an iterative manner. However, as mentioned above, there is no way to choose the initial values of L, w_{ij}, $\mathbf{m}_i$, and σ_i systematically. Therefore, in the following section, an SVR approach will be proposed to serve for this purpose.

III. INITIAL STRUCTURE OF RBFNS

1. SVR-based method to determine L, $\mathbf{m}_i$, and σ_i

The proposed SVR-based method can approximate an unknown function. Without loss of generality, an output of the RBFN, say y_1, and its corresponding training pairs, $(\mathbf{x}^{(k)}, y_1^{(k)})$, $k = 1, 2, \cdots, N$, will be used for demonstration. Meanwhile, assume that a set of basis functions, $g_l(\mathbf{x})$, $l = 1, 2, \cdots, M$, is given. Then the problem of function approximation is transformed into finding the parameters of the following basis linear expansion

$$f(\mathbf{x}, \boldsymbol{\theta}) = \sum_{l=1}^{M} \theta_l g_l(\mathbf{x}) + b, \tag{4}$$

where $\boldsymbol{\theta} = (\theta_1, \theta_2, \cdots, \theta_M)$ is a parameter vector to be identified and b is a constant to be determined.

From Vapnik[1], one can find that the solution is to find $f(\mathbf{x}, \boldsymbol{\theta})$ that minimizes

$$R(\boldsymbol{\theta}) = \frac{1}{N} \sum_{i=1}^{N} L_\varepsilon(y_i - f(\mathbf{x}_i, \boldsymbol{\theta})), \tag{5}$$

subject to the constraint

$$\|\boldsymbol{\theta}\|^2 < C, \tag{6}$$

where $L_\varepsilon(\cdot)$ is the ε -insensitive loss function defined as

$$L_\varepsilon(e) = \begin{cases} 0 & \text{for } |e| \le \varepsilon \\ |e| - \varepsilon & \text{otherwise} \end{cases}, \ \varepsilon > 0. \tag{7}$$

By using the Lagrange multiplier method, it was shown that the minimization of (5) leads a dual optimization problem[1].

In this paper, since the Gaussian function is used as the kernel function, (12) can be rewritten as

$$f(\mathbf{x}, \lambda) = \sum_{l=1}^{\#SV} \lambda_l \exp\left(-\frac{\|\mathbf{x} - \mathbf{x}_l\|^2}{2\sigma_l^2}\right) + b, \tag{8}$$

where $\mathbf{x}_l$ denotes *support vectors* (SVs), $\#SV$ is the number of SVs. Comparing (8) with (2), $\#SV$, l, λ_l, and $\mathbf{x}_l$ in (8) can be regarded as the L, i, w_{i1}, and $\mathbf{m}_i$ in (2), respectively. From the above derivation, the number of hidden layer nodes L, the initial parameters w_{i1}, $\mathbf{m}_i$, and σ_i of the RBFNs can be determined.

2. LSR-based method to determine the synaptic weights

In the above section, the initial values of $w_{11}, w_{21}, \cdots, w_{L1}$ are determined. However, one still needs to determine the initial values of w_{ij}, $1 \le i \le L$, $2 \le j \le p$. Based on the concept of LSR[2], these values can be determined by solving the following problem:

Given L, $w_{11}, w_{21}, \cdots, w_{L1}$, $\mathbf{m}_i$, $1 \le i \le L$, and σ_i, $1 \le i \le L$, determine w_{ij}, $1 \le i \le L$, $2 \le j \le p$, to minimize the following performance index

©ISAROB 2009

$$J_{\mathrm{LSR}} = \sum_{k=1}^{N} \left\| \mathbf{y}^{(k)} - \hat{\mathbf{y}}^{(k)} \right\|^2 - \sum_{k=1}^{N} \left(y_1^{(k)} - \hat{y}_1^{(k)} \right)^2, \tag{9}$$

At first glance, this problem is very similar to the one in (3). However, since the values of L, $w_{11}, w_{21}, \cdots, w_{L1}$, $\mathbf{m}_i$, $1 \le i \le L$, and σ_i, $1 \le i \le L$, are already given, this problem will be very easy to be solved based on the concept of LSR.

IV. ANNEALING ROBUST LEARNING ALGORITHM FOR RBFNS

In the training procedure of the proposed RBFN, the annealing concept[3] in the cost function of robust back-propagation learning algorithm[4] was adopted to overcome the existing problems in robust back-propagation learning algorithm. A cost function for the ARLA is defined here as

$$J_j(h) = \frac{1}{N} \sum_{k=1}^{N} \rho \left[e_j^{(k)}(h); \beta(h) \right], \text{ for } j = 1, 2, \cdots, p \tag{10}$$

where

$$e_j^{(k)}(h) = y_j^{(k)} - \sum_{i=1}^{L} w_{ij} \exp\left(- \frac{\left\| \mathbf{x}^{(k)} - \mathbf{m}_i \right\|^2}{2\sigma_i^2} \right), \tag{11}$$

h is the epoch number, $e_j^{(k)}(h)$ is the error between the kth desired output and the kth output of the ARRBFN at epoch h for the jth input-output training data in an MIMO system, $\beta(h)$ is a deterministic annealing schedule acting like the cut-off point, and $\rho(\cdot)$ is a logistic loss function defined as

$$\rho[e_j^{(k)}; \beta] = \frac{\beta}{2} \ln \left[1 + \frac{(e_j^{(k)})^2}{\beta} \right], \text{ for } j = 1, 2, \cdots, p \tag{12}$$

Based on the gradient-descent kind of learning algorithms, the synaptic weights w_{ij}, the centers $\mathbf{m}_i$, and the widths σ_i of Gaussian functions are updated as

$$\Delta w_{ij} = -\eta \frac{\partial J_j}{\partial w_{ij}} = -\eta \sum_{k=1}^{N} \varphi_j(e_j^{(k)}; \beta) \frac{\partial e_j^{(k)}}{\partial w_{ij}}, \tag{13}$$

$$\Delta \mathbf{m}_i = -\eta \frac{\partial J_j}{\partial \mathbf{m}_i} = -\eta \sum_{j=1}^{p} \sum_{k=1}^{N} \varphi_j(e_j^{(k)}; \beta) \frac{\partial e_j^{(k)}}{\partial \mathbf{m}_i}, \tag{14}$$

$$\Delta \sigma_i = -\eta \frac{\partial J_j}{\partial \sigma_i} = -\eta \sum_{j=1}^{p} \sum_{k=1}^{N} \varphi_j(e_j^{(k)}; \beta) \frac{\partial e_j^{(k)}}{\partial \sigma_i}, \tag{15}$$

$$\varphi_j(e_j^{(k)}; \beta) = \frac{\partial \rho(e_j^{(k)}; \beta)}{\partial e_j^{(k)}} = \frac{e_j^{(k)}}{1 + (e_j^{(k)})^2 / \beta(h)}, \tag{16}$$

where η is a learning constant, $\varphi(\cdot)$ is usually called the influence function. In the ARLA, the annealing schedule $\beta(h)$ has the convergent properties [4].

V. SIMULATION RESULTS

The identification scheme of a nonlinear MIMO system is depicted in Fig. 1. In this scheme, the training input-output data are obtained by feeding a signal $\mathbf{x}(k)$ to the MIMO system and measure its corresponding output $\mathbf{y}(k+1)$. Then subject to the same input signal, the objective of identification is to construct a suitable network model, which produces an output $\hat{\mathbf{y}}(k+1)$ to approximate $\mathbf{y}(k+1)$ as closely as possible.

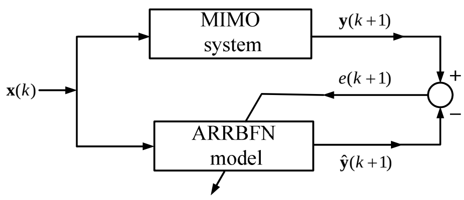

Fig. 1 The proposed identification scheme for an MIMO system

In this section, a two-input two-output nonlinear MIMO systems are used to verify the feasibility of the proposed approach. The root mean squares error (*RMSE*) of the testing data is used to measure the performance of the learning network and is defined as

$$RMSE = \sqrt{\frac{\sum_{k=1}^{N} \left(y_j^{(k)} - \hat{y}_j^{(k)} \right)^2}{N}} \quad \text{for} \quad j = 1, 2 \tag{17}$$

where $y_j^{(k)}$ is the desired output and $\hat{y}_j^{(k)}$ is the output of the ARRBFN.

Example :

In this example, the nonlinear MIMO system to be identified is described as[5]

$$\begin{bmatrix} y_1(k+1) \\ y_2(k+1) \end{bmatrix} = \begin{bmatrix} \dfrac{y_2(k)}{1 + y_1^2(k)} \\ \dfrac{y_1(k)}{1 + y_1^2(k)} \end{bmatrix} + \begin{bmatrix} x_1(k) \\ x_2(k) \end{bmatrix} \tag{18}$$

where

$$(x_1(k), x_2(k)) = (\cos(\frac{2\pi k}{100}), \sin(\frac{2\pi k}{100})) \text{ for } 0 \le k \le 300$$

and the 301 training input-output data are generated by substituting into (18) sequentially.

With the training data and following the procedure of the proposed method, the value of L is found to be 15. Meanwhile, the initial values of w_{ij}, $\mathbf{m}_i$, and σ_i can also be determined. When applying the proposed SVR method, the parameters in (6) and (7) are chosen as $C = 1$ and $\varepsilon = 0.2$, respectively. After initialization, the ARLA is then applied to train the RBFN. After 1000 epochs, the *RMSE* values of y_1 and y_2 are found to be 0.0102 and 0.0144, respectively. The details of the simulation results are shown in Fig. 2 through Fig. 7, respectively.

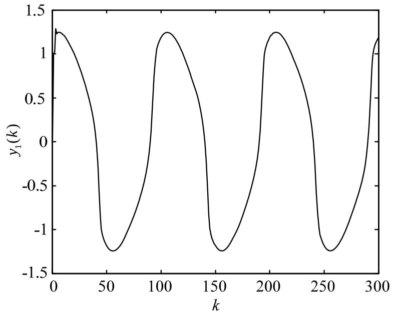

Fig.2 The desired output for y_1

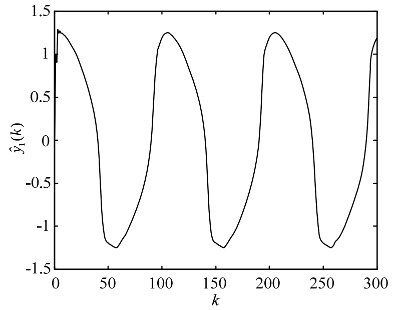

Fig. 3 The final output for y_1 after 1000 epochs

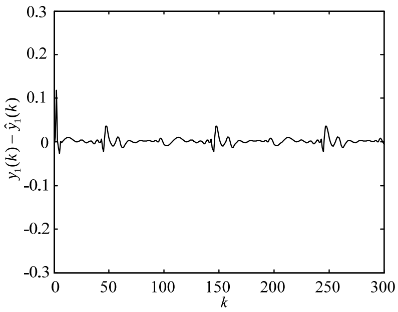

Fig. 4 The plot of $y_1(k)-\hat{y}_1(k)$ after 1000 epochs

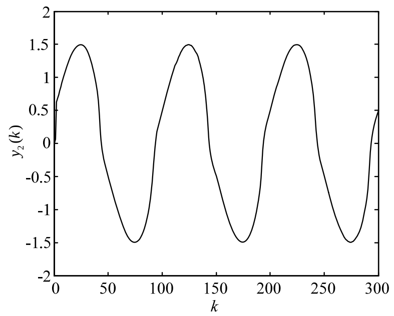

Fig. 5 The desired output for y_2

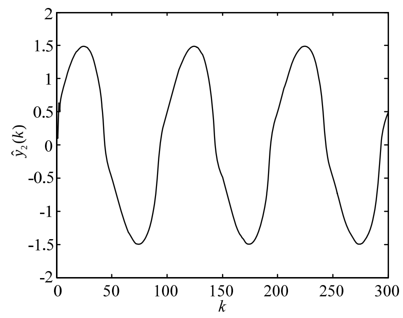

Fig. 6 The final output for y_2 after 1000 epochs

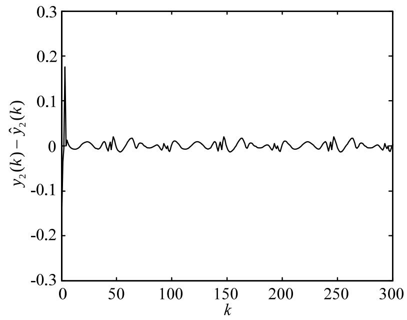

Fig. 7 The plot of $y_2(k)-\hat{y}_2(k)$ after 1000 epochs

7. Conclusion

With the integration of SVR, LSR, and the annealing robust algorithm, an RBFN is used for identification of an MIMO system. The proposed SVR approach has good performance in determining the number of hidden layer nodes and the initial parameters of the kernel. Then based on the values obtained by the SVR method, the synaptic weights can also be determined by using the technique of the LSR. After initialization, the annealing robust learning algorithm is adopted to adjust the parameters of the RBFN to approximate the MIMO system as closely as possible. The simulation results indicated that the proposed method can be used as a reliable technique for identification of nonlinear MIMO systems.

Acknowledgment

This work was supported in part by the National Science Council, Taiwan, R.O.C., under grants NSC96-2628-E-224-007-MY2.

References

[1] Vapnik VN (1995), The Nature of statistical learning Theory. Springer, New York

[2] Larson R, Edwards BH, Falvo DC (2004), Elementary linear algebra, fifth edition. Houghton Mifflin Company, New York

[3] Chuang CC, Jeng JT, Lin PT (2004), Annealing robust radial basis function networks for function approximation with outliers. Neurocomputing 56:123-139

[4] Chuang CC, Su SF, Hsiao CC (2000), The annealing robust backpropagation (BP) learning algorithm. IEEE Trans on Neural Networks 11(5):1067-1077

[5] Purwar S, Kar IN, Jha AN (2007), On-line system identification of complex systems using Chebyshev neural networks. Applied Soft Computing 7:364-372

©ISAROB 2009

ARRBFNs with SVR for prediction of chaotic time series with outliers

Yu-Yi Fu[1], Chia-Ju Wu[2], Chia-Nan Ko[3], Jin-Tsong Jeng[4] and Li-Chun Lai[5]

[1]Graduate School of Engineering Science and Technology, National Yunlin University of Science and Technology
Douliou, Yunlin 640, Taiwan
[2]Department of Electrical Engineering,National Yunlin University of Science and Technology
Douliou, Yunlin 640, Taiwan
[3]Department of Automation Engineering, Nan Kai University of Technology
Tsaotun, Nantou 542, Taiwan
[4]Department of Computer Science and Information Engineering, National Formosa University
Huwei, Yunlin 632, Taiwan
[5]Department of Electrical Engineering, Chung Chou Institute of Technology
Yuanlin, Changhua 510, Taiwan
(email:[1]t098@nkut.edu.tw;[2]WUCJ@yuntech.edu.tw;[3]t105@nkut.edu.tw;[4]tsong@nfu.edu.tw;[5]lclai@dragon.ccut.edu.tw)

Abstract: In this paper, the annealing robust radial basis function networks (ARRBFNs) which consist of a radial basis function networks and a support vector regression (SVR) and an annealing robust learning algorithm (ARLA) are proposed for the prediction of chaotic time series with outliers. In order to overcome the initial structure problems of the proposed neural networks, the SVR is utilized to determine the number of hidden nodes, the initial parameters of the kernel and the initial weights for the proposed ARRBFNs. Then, the ARLA that can against the outliers is applied to tune the parameters of the kernel and the weights in the proposed ARRBFNs under the initial structure with SVR. From the simulation results of Mackey–Glass time series show that the proposed approach with different SVR can overcome outliers and fast learning speed. Besides, results of simulation are also given to demonstrate the validity of proposed method for the chaotic time series with outliers.

Keywords: Chaotic time series; Outliers; Support vector regression; Annealing robust learning algorithm.

I. INTRODUCTION

The prediction of time series is a very important application including weather forecast, economic plan, behavior-based intelligent mobile robot, etc. With the character of nonlinear system, chaotic time series presents sensitive dependence on initial conditions and unstable activities. Hence, many approaches with neural networks are proposed recently.

Gu and Wang [1] used recursive least square algorithm with singular value decomposition to estimate the parameters of fuzzy model. Zhang et al. [2] used genetic algorithm and particle swarm optimization to model chaotic time series. Harpham and Dawson [3] developed a chaotic time series prediction based on radial basis function networks (RBFNs). RBFNs can be used to approximate the desired outputs without needing a mathematical explanation of how the outputs functionally depend on the inputs. However, these approaches haven't a methodical way to determine the number of hidden nodes, the initial parameters of the kernel and the initial weights of the networks. Besides, the data we obtained sometimes contain outliers. Outliers may occur due to improper measurements or noisy data. When outliers occur there is overfitting problem that appears in the learning of these neural networks approaches [4].

Support vector regression (SVR) approach was proposed by Vapnik [5], by the insensitive loss function can make use of a small subset of the training data, called the support vectors (SVs), to approximate the desired outputs within a tolerance band. The selection of the hyper-parameters for SVR lacks systematic way to determine [6], and could not do with learning mechanism to update the weights and the parameters of kernel. In this paper, in order to overcome the above problem, an annealing robust radial basis function networks (ARRBFNs) based on different SVR is proposed to predict Mackey–Glass time series with outliers. First, an ε or ν SVR is used to determine the number of hidden nodes, the initial parameters of the kernel, and the initial weights of the ARRBFNs. Then the ARLA is applied to tune the parameters of radial basis functions and the synaptic weights. It is expected that the proposed approach has fast convergence speed and the ability facing outliers can predict perfectly.

II. THE PROPOSED ARRBFNS FOR PREDICTION OF CHAOTIC TIME SERIES WITH OUTLIERS

In this paper, the Mackey-Glass time series is used to simulation, and is defined as

$$\dot{x} = \frac{\alpha x(t-\tau)}{1+x^{\gamma}(t-\tau)} - \beta x(t). \qquad (1)$$

The problem is how to utilize the past values of x to predict the future value $x(t+\Delta t)$, as following

$$x(t+\Delta t) = f(x(t), x(t-\Delta t), \cdots, x(t-n\Delta t)), \qquad (2)$$

where Δt is the sampling interval. In general, outliers occur due to various reasons, such as improper

©ISAROB 2009

measurements or noisy data. Our purpose is to find a suitable nonlinear identification model

$$\hat{x}(t+\Delta t) = \hat{f}(x(t), x(t-\Delta t), \cdots, x(t-n\Delta t)) \qquad (3)$$

of the time series, where $\hat{x}(t+\Delta t)$ is the output of the neural network and $\hat{f}$ is the estimate of f, which when subjected to the same past values of x, produces an output $\hat{x}(t+\Delta t)$ which approximates $x(t+\Delta t)$ as close as possible.

When the radial basis functions are chosen as Gaussian functions, an ARRBFNs can be expressed as the form

$$\hat{x}_l(t+\Delta t) = \sum_{j=0}^{L} \omega_{jl} G_j = \sum_{j=0}^{L} \omega_{jl} \exp\left(-\frac{\|\boldsymbol{x}-\boldsymbol{m}_j\|^2}{2\sigma_j^2}\right),$$
$$\text{for } l = 1, 2, \cdots, p, \qquad (4)$$

where $\hat{x}_l$ is the lth output of the neural networks, $\boldsymbol{x} = (x(t), x(t-\Delta t), \cdots, x(t-n\Delta t))$ is the input to the neural networks, w_{jl}, $0 \le j \le L$, $1 \le l \le p$, are the synaptic weights, $G_j, 0 \le j \le L$, are the Gaussian functions, $\boldsymbol{m}_j, 0 \le j \le L$, and $\sigma_j, 0 \le j \le L$, are the centers and the widths of G_j, respectively, and L is the number of the Gaussian functions, in which we can find that L also denotes the number of hidden nodes.

When utilizing an ARRBFNs for the identification of time series, the goal is to minimize the index as

$$J_N(h) = \frac{1}{N}\sum_{i=1}^{N} \rho\left[e_i(h); \beta(h)\right], \qquad (5)$$

where

$$e_i(h) = x_i(t+\Delta t) - \hat{x}_i(t+\Delta t), \qquad (6)$$

h is the epoch number, $e_i(h)$ is the error between the ith desired output and the ith output of the ARRBFNs at epoch h and $\rho(\cdot)$ is a logistic loss function and defined as

$$\rho[e_i; \beta] = \frac{\beta}{2}\ln\left[1 + \frac{(e_i)^2}{\beta}\right], \qquad (7)$$

where $\beta(h)$ is a deterministic annealing schedule acting like the cut-off points. Hence the ARRBFNs are proposed to overcome the issues while the time series in equation (1) facing with outliers and have faster learning speed than the traditional RBFNs to attain perfect prediction. In the following section, it will be shown how to use SVR approaches to choose these initial values methodically.

III. INITIAL STRUCTURE OF ARRBFNS BY DIFFERENT SVR APPROACH

An SVR approach is used to approximate an unknown function from a set of (input, output) samples $\{ (\boldsymbol{x}_i, x_i(t+\Delta t)), i = 1, \cdots, N \}$. Suppose that a set of basis functions $\{g_k(\boldsymbol{x}), k = 1, 2, ..., m\}$ is given, there exists a family of functions that can be expressed as a linear expansion of the basis functions. The theme is then be changed into finding the parameters of the following basis linear expansion

$$g(\boldsymbol{x}, \boldsymbol{\theta}) = \sum_{k=1}^{m} \theta_k g_k(\boldsymbol{x}) + b \quad , \qquad (8)$$

where $\boldsymbol{\theta} = (\theta_1, \theta_2, ..., \theta_m)$ is a parameter vector to be identified and b is a constant to be found. The derivation of ARRBFNs for initial structure with the different SVR will be derived in the following sections.

1. Initial Structure of the ARRBFNs by the ε-SVR Approach

Vapnik[5] firstly proposed the ε-SVR approach. The solution for the theme is to find $g(\boldsymbol{x}, \boldsymbol{\theta})$ that minimizes

$$R(\boldsymbol{\theta}) = \frac{1}{n}\sum_{i=1}^{n} L_\varepsilon(u_i - g(\boldsymbol{x}_i, \boldsymbol{\theta})) \quad , \qquad (9)$$

subject to the constraint

$$\|\boldsymbol{\theta}\|^2 < C, \qquad (10)$$

where $L_\varepsilon(\cdot)$ is the ε-insensitive loss function defined as

$$L_\varepsilon(e) = \begin{cases} 0 & \text{for } |e| \le \varepsilon \\ |e| - \varepsilon & \text{otherwise}, \end{cases} \qquad (11)$$

for some previously chosen nonnegative number ε.

By using the Lagrange multiplier method, proposed by Vapnik[5] and Smola et al. [7] and the inner product of basis function $g_k(\boldsymbol{x}_r)$ is replaced via the kernel function

$$K(\boldsymbol{x}_r, \boldsymbol{x}_s) = \sum_{k=1}^{m} g_k(\boldsymbol{x}_r) g_k(\boldsymbol{x}_s) . \qquad (12)$$

It was shown in Vapnik [5] that the solution of the SVR approach is in the form of the following linear expansion of kernel function

$$g(\boldsymbol{x}, \alpha, \alpha^*) = \sum_{k=1}^{m} (\alpha_k^* - \alpha_k) K(\boldsymbol{x}, \boldsymbol{x}_k) + b . \qquad (13)$$

This means that the parameter θ_i in equation (8) can be represented as $\sum_{i=1}^{m} (\alpha_k^* - \alpha_k) g(\boldsymbol{x}_i)$. Note that only some of $(\alpha_k^* - \alpha_k)$'s are not zeros and the corresponding vectors $\boldsymbol{x}_k$'s are called support vectors (SVs). The derivation of ARRBFNs for initial structure with the ε-SVR will be derived in next section.

2. Initial Structure of the ARRBFNs by the ν-SVR Approach

©ISAROB 2009

As it is hard to select a suitable ε, the ν-support vector machine is proposed by Schölkopf et al. [8], a new parameter ν is introduced and one can control the number of SVs and training errors. By the inner product of basis function $g_k(\boldsymbol{x}_r)$ is replaced via the kernel function, the issue is to find the parameters ν ($0 \le \nu \le 1$) and C to have the solution of the approach is in the form of the following linear expansion of kernel function

$$g(\boldsymbol{x},\alpha,\alpha^*) = \sum_{k=1}^{m} (\alpha_k^* - \alpha_k) K(\boldsymbol{x},\boldsymbol{x}_k) + b \, . \qquad (14)$$

In this paper, the Gaussian function is used as the kernel function. Hence, (13) and (14) can be rewritten as

$$g(\boldsymbol{x},\lambda) = \sum_{k=1}^{\#SV} \lambda_k \exp(-\frac{\|\boldsymbol{x}-\boldsymbol{x}_k\|^2}{2\sigma_k^2}) + b \quad , \qquad (15)$$

where $\#SV$ is the number of SVs, $\lambda_k = (\alpha_k^* - \alpha_k) \neq 0$ and $\boldsymbol{x}_k$ are SVs. Let $\exp(-\frac{\|\boldsymbol{x}-\boldsymbol{x}_0\|^2}{2\sigma_0^2}) = 1$ and $\lambda_0 = b$, (15) can be rewritten as

$$f(x,\lambda) = \sum_{k=0}^{\#SV} \lambda_k \exp(-\frac{\|\boldsymbol{x}-\boldsymbol{x}_k\|^2}{2\sigma_k^2}). \qquad (16)$$

As mentioned above and comparing (16) with (4), $\#SV$, k, λ_k, $\boldsymbol{x}_k$ and σ_k in (16) can be regarded as the L, j, w_{jl}, $\boldsymbol{m}_j$ and σ_j, in (4), respectively. From the above derivation, we can find that the number of hidden node L, the initial weights w_{jl}, $\boldsymbol{m}_j$, and σ_j, of the ARRBFNs are determined via the ε-SVR and ν-SVR approach.

IV. ARLA FOR THE ARRBFNS

In this paper, the ARLA is applied to train the proposed ARRBFNs. Using the annealing concept in the cost function of robust back-propagation (BP) learning algorithm, can overcome the existing issues in robust BP learning algorithm. A cost function for ARLA is defined here as (5), where $\beta(h)$ is a deterministic annealing schedule acting like the cut-off points to decide that how large errors can be considered as outliers. The proposed ARRBFNs with the ARLA can overcome the problems of initialization and can deal with the time series with outliers. In the ARLA, the properties of the annealing schedule $\beta(h)$ have [4]:

(A) β_{initial}, $\beta(h)$ for the first epoch, has large values;

(B) $\beta(h) \to 0^+$ for $h \to \infty$;

(C) $\beta(h) = k/h$ for any h epoch, where k is a constant.

Based on the gradient-descent kind of learning algorithms, the synaptic weights w_{jl}, the centers $\boldsymbol{m}_j$ and the width σ_j of Gaussian function are updated as

$$\Delta w_{jl} = -\eta \frac{\partial J_N}{\partial w_{jl}} = -\eta \sum_{i=1}^{N} \varphi(e_i;\beta) \frac{\partial e_i}{\partial w_{jl}}, \qquad (17)$$

$$\Delta \boldsymbol{m}_j = -\eta \frac{\partial J_N}{\partial \boldsymbol{m}_j} = -\eta \sum_{i=1}^{N} \varphi(e_i;\beta) \frac{\partial e_i}{\partial \boldsymbol{m}_j}, \qquad (18)$$

$$\Delta \sigma_j = -\eta \frac{\partial J_N}{\partial \sigma_j} = -\eta \sum_{i=1}^{N} \varphi(e_i;\beta) \frac{\partial e_i}{\partial \sigma_j}, \qquad (19)$$

$$\varphi(e_i;\beta) = \frac{\partial \rho(e_i;\beta)}{\partial e_i} = \frac{e_i}{1+(e_i)^2 / \beta(h)}, \qquad (20)$$

where η is a learning constant.

The learning algorithm of the ARRBFNs for the chaotic time series with outliers is summarized as follows:

Algorithm A :

Step 1: Generate the data from chaotic time series.

Step 2: Using an ε-SVR approach that is depicted by equations (7) through (13), or using an ν-SVR approach that is described by equations (14), to get the initial structure of ARRBFNs.

Step 3: Compute the estimated output and its error by equation (6) for all training data.

Step 4: Decide the values of annealing schedule $\beta(h) = k/h$ for each epoch, where k is set as $2 \cdot max\{|e_i|_{\text{initial}}\}$.

Step 5: Update w_{jl}, $\boldsymbol{m}_j$ and σ_j of Gaussian function iteratively updated by equations (17) through (20). In this step, the outliers are presented.

Step 6: Compute the robust cost function J_{N} defined by equation (5).

Step 7: If the termination conditions are not satisfied, then go to Step 3; otherwise stop the learning process.

V. SIMULATION RESULTS

In this section, the root mean square error (RMSE) of the testing data is used to measure the performance of the learned networks. The RMSE is defined as

$$RMSE = \sqrt{\frac{\Sigma_{i=1}^{N} \left(x_i(t+\Delta t) - \hat{x}_i(t+\Delta t) \right)^2}{N}} \, , \qquad (21)$$

where $x_i(t+\Delta t)$ is the desired output and $\hat{x}_i(t+\Delta t)$ is the output of the proposed ARRBFNs.

Example:

Mackey–Glass time series is defined as equation (1). The initial values of the system are $x(0) = 1.2$, $\alpha = 0.2$, $\beta = 0.1$, $\gamma = 10$. τ is the time-delay parameter. If $\tau \ge 17$, the time series show the chaotic phenomenon. Compare with Gu and Wang [1] for being convenient, the proposed networks are chose as

$$\hat{x}(t+6) = \hat{f}(x(t), x(t-6), x(t-12), x(t-18)), t \geq 19 \,. \quad (22)$$

That is, $x(t), x(t-6), x(t-12), x(t-18)$ are selected as the input variables of the ARRBFNs, and $x(t+6)$ as the output variable of the ARRBFNs.

1000 simulation data points are generated from equation (1), the former 500 points with five artificial outliers are selected as the training data points to build the proposed ARRBFNs of the Mackey–Glass time series, and the rest 500 points as the testing data to test the validity of the proposed ARRBFNs. The parameters in ε-SVR are set as C=10, the Gaussian kernel function with $\varepsilon = 0.35$, $\sigma = 0.15$, with the hidden nodes (i.e. the number of SVs) is obtained as 10. Based on the initial structure of the ARRBFNs and the learning constant is 0.05, after 2000 epochs training, the final training output, the error, the prediction output and the corresponding error are shown in Fig. 1 (a) ~ (d), and the final RMSE is 0.0094. Another initial structure is obtained by an ν-SVR approach, the parameters are set as C=1, $\nu = 0.0009$ and $\sigma = 0.15$, with the hidden nodes is obtained as 10. Based on the above initial structure, the learning constant is 0.05, after 2000 epochs training, the results are shown in Fig. 2 (a) ~ (d), and the final RMSE is 0.0096. From the simulation results show that the proposed ARRBFNs can overcome the outliers and attain a good training and prediction.

VI. CONCLUSIONS

In this paper, an ε or ν SVR based the ARRBFNs with ARLA for the prediction of chaotic time series with outliers is developed. We firstly utilize the SVR approaches to determine the number of hidden nodes, the initial parameters of the kernel and the initial weights of the proposed ARRBFNs. Then the ARLA is applied to tunes the parameters of the kernel and the weights of the time series that can against outliers. From the results indicated that the proposed method can be used as a reliable technique for the prediction of chaotic time series with outliers.

ACKNOWLEDGMENTS

This work was supported in part by the National Science Council, Taiwan, R.O.C., under grants NSC96-2628-E-224-007-MY2.

REFERENCES

[1] Gu H, Wang H (2007), Fuzzy prediction of chaotic time series based on singular value decomposition. Applied Mathematics and Computation 185: 1171–1185

[2] Zhang W, Wu ZM, Yang GK (2005), Genetic programming modeling on chaotic time series. Acta Electronica Sinica 33(4):748-751

[3] Harpham C, Dawson CW (2006), The effect of different basis functions on a radial basis function network for time series prediction: A comparative study. Neurocomputing 69:2161–2170

[4] Chuang CC, Su SF, and Hsiao CC (2000), The annealing robust backpropagation (BP) learning algorithm. *IEEE Trans. Neural Networks* 11(5): 1067–1077

[5] Vapnik V (1995), *The Nature of Statistical Learning Theory*, Springer, Berlin

[6] Jeng JT (2006), Hybrid approach of selecting hyper-parameters of support vector machine for regression. *IEEE Trans. on Systems, Man, and Cybernatics* B36:699-709

[7] Smola AJ, Schölkopf B (1998), From regularization operators to support vector kernels. *Neural Inf. Process System* 10:343–349

[8] Schölkopf B, et al. (1997), Comparing support vector machines with Gaussian kernels to radial basis function classifiers. *IEEE Trans. Signal Process* 45(11): 2758–2765

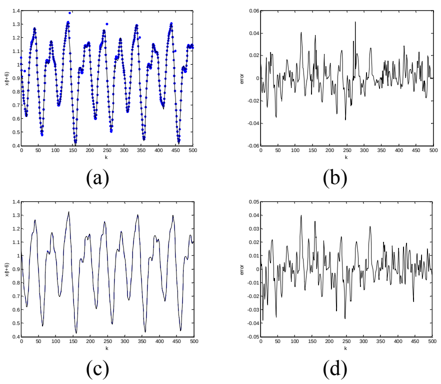

Fig. 1. (a) The final output, (b) the error, (c) the prediction output and (d) the error of prediction for the proposed structure with ε-SVR based under the training data sets contain five artificial outliers

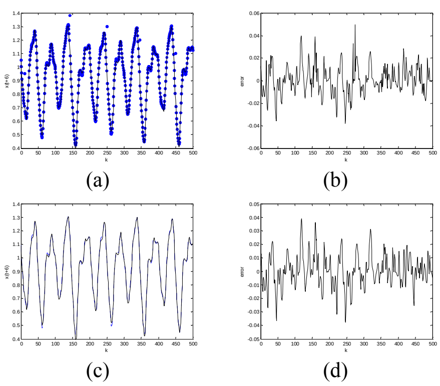

Fig. 2. (a) The final output, (b) the error, (c) the prediction output and (d) the error of prediction for the proposed structure with ν-SVR based under the training data sets contain five artificial outliers

©ISAROB 2009

A fast identification algorithm with outliers under box-cox transformation-based annealing robust radial basis function networks

Pi-Yun Chen [1], Chia-Ju Wu[2], Chia-Nan Ko [3] and Jin-Tsong Jeng[4]

[1]Graduate School of Engineering Science and Technology, National Yunlin University of Science and Technology
Douliou, Yunlin 640, Taiwan
[2]Department of Electrical Engineering,National Yunlin University of Science and Technology
Douliou, Yunlin 640, Taiwan
[3]Department of Automation Engineering, Nan Kai University of Technology
Tsaotun, Nantou 542, Taiwan
[4]Department of Computer Science and Information Engineering, National Formosa University
Huwei, Yunlin 632, Taiwan
(email:[1]g9310820@yuntech.edu.tw;[2]WUCJ@yuntech.edu.tw;[3]t105@nkut.edu.tw;[4]tsong@nfu.edu.tw)

Abstract: In this paper, a Box–Cox transformation-based annealing robust radial basis function networks (ARRBNFs) is proposed for the identification algorithm with outliers. Firstly, a fixed Box–Cox transformation-based ARRBFNs model with support vector regression (SVR) is derived to determine the initial structure. Secondly, the results of the SVR are used as initial structure in the fixed Box–Cox transformation-based ARRBFNs for the identification algorithm with outliers. At the same time, an annealing robust learning algorithm (ARLA) is used as the learning algorithm for the fixed Box–Cox transformation-based ARRBFNs, and applied to adjust the parameters and weights. Hence, the fixed Box–Cox transformation-based ARRBFNs with ARLA have fast convergence speed for the identification algorithm with outliers. Finally, the proposed algorithm and its efficacy are demonstrated with an illustrative example in comparison with Box–Cox transformation-based radial basis function networks.

Keywords: identification algorithm, Box–Cox transformation, outliers, annealing robust radial basis function networks

I. INTRODUCTION

The standard radial basis function networks (RBFNs) consists of three layers; namely, the input layer, the hidden layer, and the output layer. Due to the RBFNs structural simplicity, it has been widely used for nonlinear function approximation [1] and system identification [2]. For the different applications the learning algorithms of the RBFN are designed with different optimization criteria. One of the main applications that the RBFNs has been applied to system dynamic modeling [2]. Besides, it is well known that the well conditioning of a model base is critically important in order to obtain good parameter estimators for the identification problem. Hence, identification algorithm has many important applications including nonlinear control systems, robotic systems, etc.

In general, the Box-Cox transformation on the system output is one of the major statistical techniques Box and Cox [3] to reduce heteroscedasticity when the distribution of the dependent variable is unknown. Hong [4] proposed that a RBFNs model base is derived based on a rank revealing orthogonal matrix triangularization; namely, QR decomposition Hong and Pan [5]. Besides, the identification algorithm uses Gauss-Newton method to derive the Box-Cox transformation parameter. For a large data set, using the QR decomposition increases computational expense for model structure. On the other hand, for the scientific and engineering applications, the obtained training data are always subject to outliers. The intuitive definition of an outlier Hawkins [6] is "*an observation which deviates so much from other observations as to arouse suspicions that it was generated by a different mechanism.*" However, outliers may occur due to various reasons, such as erroneous measurements or noisy data from the tail of noise distribution functions. When the outliers are exists, there still exist some problems in the algorithm of Hong [4].

In this paper, a fast identification algorithm with outliers is introduced for the Box-Cox transformation-based ARRBFNs. Firstly, the support vector regression (SVR) is derived to determine the initial structure. Because of a SVR approach is equivalent to solving a linear constrained quadratic programming problem under a fixed structure of SVR, the number of hidden nodes, the initial parameters and the initial weights of the ARRBFNs are easy obtained via the SVR approach. Secondly, an annealing robust learning algorithm (ARLA) is used as the learning algorithm for the fixed Box–Cox transformation-based ARRBFNs, and applied to adjust the parameters and weights.

II. BOX-COX TRANSFORMATION-BASED ARRBFNS

Given a data set $\{(\vec{x}_i, y_i), i = 1,2,\cdots,N\}$, where $\vec{x}_i$ is the system input vector and y_i is the positive system output. N is the number of data samples. The objective of Box-Cox transformation is usually to make residuals more homogeneous in regression, or transform data to be normally distributed. The well known Box-Cox version of power transformation Box and Cox [4] is formed as

©ISAROB 2009

$$z(y,\lambda)=\begin{cases}\dfrac{y^{\lambda}-1}{\lambda\tilde{y}^{\lambda-1}}, & \text{if } \lambda\neq 0\\ \tilde{y}\log y, & \text{if } \lambda=0\end{cases}, \tag{1}$$

where λ is the transformation parameter and $\tilde{y}=\sqrt[N]{\prod_{i=1}^{N} y_i}$ is the geometric mean of the system output. For a given λ, an RBFN with a single output can be represent as Hong [4]

$$z(y,\lambda)=f(\vec{x},W)+e=\sum_{j=1}^{L} w_j G_j(\vec{x})+b+e, \tag{2}$$

where $f(\vec{x})$ is the output of the Box-Cox transformation-based ARRBFNs Chuange et al [7], e is model error, $W=[w_1,w_2,\cdots,w_L]^T$ is the synaptic weight vector, and L is the number of hidden layer in the Box-Cox transformation-based ARRBFNs. The radial basis functions G_j are chosen as Gaussian functions that it can be express in the form

$$G_j(\vec{x})=\exp\left\{\frac{-\left\|\vec{x}-m_j\right\|^2}{2\sigma_j^2}\right\}, \tag{3}$$

where m_j and σ_j are the center and width of Gaussian functions, respectively. Hence, the $f(\cdot)$ can be rewritten as

$$f(\vec{x},W)=\sum_{j=1}^{L} w_j \exp\left\{\frac{-\left\|\vec{x}-m_j\right\|^2}{2\sigma_j^2}\right\}+b, \tag{4}$$

Note that

$$\lim_{\lambda\to 0} z(y,\lambda)=\lim_{\lambda\to 0}\left[\frac{y^{\lambda}-1}{\lambda\tilde{y}^{\lambda-1}}\right]=\tilde{y}\log y \tag{5}$$

and the inverse of Box-Cox transformation upon $f(\vec{x},W)$ for given $\lambda\neq 0$ and W is

$$\hat{y}=z^{-1}(f(\vec{x},W))=\sqrt[\lambda]{1+\lambda\tilde{y}^{\lambda-1}f(\vec{x},W)}. \tag{6}$$

That is, when $\lambda=0$, $\hat{y}=\exp\left(\dfrac{f(\vec{x},W)}{\tilde{y}}\right)$ in the proposed approach. The proposed structure is shown in Fig. 1.

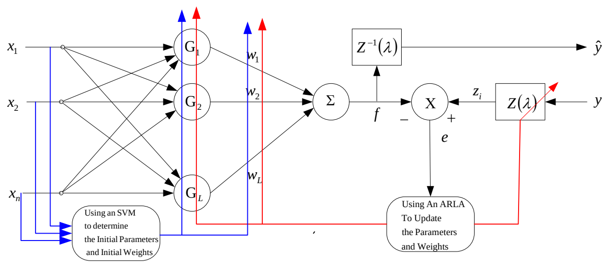

Fig.1. Box-Cox transformation-based ARRBFNs.

2.1 The initial structure of Box-Cox transformation-based ARRBFNs by the SVR approach

An SVR approach is used to approximate an unknown function from a set of samples $\{(\vec{x}_i,z_i), i=1,2,\cdots,N\}$, where the system output y_i is replaced by the normalized transformed response z_i. Assuming that a set of basis functions $\{g_k(\vec{x}), k=1,2,\cdots,m\}$ is given, there exists a family of functions that can be expressed as a linear expansion of the basis function. Then, the problem of function approximation transforms into that finding the parameters of the following basis function linear expansion:

$$f(\vec{x},\vec{\theta})=\sum_{k=1}^{m}\theta_k g_k(\vec{x})+b \tag{7}$$

where $\vec{\theta}\in(\theta_1,\ldots,\theta_m)$ is a parameter vector to be identified and b is a constant. Then, the solution for the problem is to find f that minimizes

$$R(\vec{\theta})=\frac{1}{n}\sum_{i=1}^{n}L_\varepsilon\left(y_i-f(\vec{x}_i,\vec{\theta})\right), \tag{8}$$

subject to the constraint

$$\left\|\vec{\theta}\right\|^2<C, \tag{9}$$

where $L_\varepsilon(\cdot)$ is the ε-insensitive loss function and defined as

$$L_\varepsilon(e)=\begin{cases}0, & \text{for } |e|\le\varepsilon,\\ |e|-\varepsilon, & \text{otherwise,}\end{cases} \tag{10}$$

for some previously chosen nonnegative number ε. In (9), the constraint is imposed to trade off the complexity of the solution.

By using the Lagrange multiplier method, it can be shown Vapnik [8] that the minimization of (8) leads to the following dual optimization problem, minimize

$$\begin{aligned}Q(\alpha,\alpha^*)=&\ \varepsilon\sum_{r=1}^{N}(\alpha_r+\alpha_r^*)-\sum_{r=1}^{N}y_r(\alpha_r^*-\alpha_r)\\ &+\frac{1}{2}\sum_{r,s=1}^{N}(\alpha_r^*-\alpha_r)(\alpha_s^*-\alpha_s)\left[\sum_{k=1}^{m}g_k(\vec{x}_r)g_k(\vec{x}_s)\right],\end{aligned} \tag{11}$$

subject to the constraint

$$\sum_{r=1}^{N}\alpha_r^*=\sum_{r=1}^{N}\alpha_r,\quad 0<\alpha_r,\alpha_r^*<C\quad \text{for } r=1,\ldots,N. \tag{12}$$

In (11), the inner product of basis functions $g_k(\vec{x})$ is replaced via the kernel function

$$K(\vec{x}_r,\vec{x}_s)=\sum_{k=1}^{m}g_k(\vec{x}_r)g_k(\vec{x}_s). \tag{13}$$

The kernel function determines the smoothness properties of solutions and should reflect a prior knowledge of the data. In the literature, the polynomials, B-spline and Gaussian kernel function often used Vapnik et al [9]. Hence the optimization of (11) is rewritten as

$$\begin{aligned}Q(\alpha,\alpha^*)=&\ \varepsilon\sum_{r=1}^{N}(\alpha_r+\alpha_r^*)-\sum_{r=1}^{N}y_r(\alpha_r^*-\alpha_r)\\ &+\frac{1}{2}\sum_{r,s=1}^{N}(\alpha_r^*-\alpha_r)(\alpha_s^*-\alpha_s)K(\vec{x}_r,\vec{x}_s),\end{aligned} \tag{14}$$

It was shown in Vapnik et al [9] that the solution of the SVR approach is in the form of the following linear expansion of kernel functions (i.e. the parameter θ_i in

©ISAROB 2009

(8) can be represented as $\sum_{i=1}^{m}(\alpha_k^* - \alpha_k) g(\vec{x}_i)$),

$$f(\vec{x}, \alpha, \alpha^*) = \sum_{k=1}^{m} (\alpha_k^* - \alpha_k) K(\vec{x}_r, \vec{x}_s) + b \,. \tag{15}$$

Note that only some of $(\alpha_k^* - \alpha_k)$'s are not zeros and the corresponding vectors $\vec{x}_k$'s are called SVs. In this paper, the Gaussian function is used as the kernel function. Hence, (15) can be rewritten as

$$f(\vec{x}, \vec{\upsilon}) = \sum_{k=1}^{SV} \upsilon_k \exp\left\{ \frac{-\|\vec{x} - \vec{x}_k\|^2}{2\sigma^2} \right\} + b \,, \tag{16}$$

where SV is the number of SVs, $\upsilon_k = (\alpha_k^* - \alpha_k) \neq 0$ and $\vec{x}_k$ are SVs. On comparing (16) with (4), the SV, k, υ_k and $\vec{x}_k$ in (16) can be regarded as the L, j, w_j and m_j in (4), respectively. That is, based on Eqs. (4) and (16), the initial weight w_j, the number of hidden node L, and the parameters of the proposed neural network in Fig. 1 can be determined via an SVR method.

2.2 The annealing robust learning algorithm of Box-Cox transformation-based ARRBFNs

In the Box-Cox transformation-based ARRBFNs, an ARLA is proposed as a learning algorithm. An important feature of the ARLA that adopts the annealing concept in the cost function of robust back-propagation learning algorithm is proposed in Chuang et al [10]. Hence, the ARLA can overcome the existing problems in robust back-propagation learning algorithm. A cost function for the ARLA is defined here as

$$E(\vec{x}_i, t) = \frac{1}{N} \sum_{i=1}^{N} \rho[e_i(\vec{x}_i, t); \beta(t)], \tag{17}$$

where

$$e_i(\vec{x}_i, t) = z_i(y, \lambda) - \sum_{j=1}^{N} w_j \exp\left\{ \frac{-\|\vec{x}_i - m_j\|^2}{2\sigma_j^2} \right\}, \tag{18}$$

t is the epoch number, $e_i(\vec{x}_i, t)$ is the error between the ith Box-Cox transformation of desired output and the ith output of the proposed approach at epoch t, $\beta(t)$ is a deterministic annealing schedule acting like the cut-off points and $\rho(\cdot)$ is a logistic loss function and defined as

$$\rho[e_i; \beta] = \frac{\beta}{2} \ln\left[1 + \left(\frac{e_i^2}{\beta} \right) \right]. \tag{19}$$

Based on the gradient-descent kind of learning algorithms, the synaptic weights w_j, centers m_j, width σ_j of Gaussian function and λ_j of Box-Cox transformation parameter are updated as

$$\Delta w_j = -\eta \frac{\partial E}{\partial w_j} = -\eta \sum_{i=1}^{N} \varphi(e_i; \beta) \frac{\partial e_i}{\partial w_j} \,, \tag{20}$$

$$\Delta m_j = -\eta \frac{\partial E}{\partial m_j} = -\eta \sum_{i=1}^{N} \varphi(e_i; \beta) \frac{\partial e_i}{\partial m_j} \,, \tag{21}$$

$$\Delta \sigma_j = -\eta \frac{\partial E}{\partial \sigma_j} = -\eta \sum_{i=1}^{N} \varphi(e_i; \beta) \frac{\partial e_i}{\partial \sigma_j} \,, \tag{22}$$

$$\Delta \lambda_j = \frac{\partial z(y, \lambda_j)}{\partial \lambda_j} \,, \tag{23}$$

$$\varphi(e_i; \beta) = \frac{\partial \rho(e_i; \beta)}{\partial e_i} = \frac{e_i}{1 + e_i^2 / \beta(t)} \,, \tag{24}$$

where η is a learning constant and $\varphi(\cdot)$ is usually called the influence function. When outliers exist, they have a major impact on the approximated results. Such an impact can be understood through the analysis of the influence function. The learning algorithm of the proposed approach is summarized as follows:

Step 1: Using Box-Cox transformation by (1) to form the transformed output.

Step 2: Initialize the Box-Cox transformation-based ARRBFNs structure using an SVR approach that is described by (16) with the given Gaussian kernel functions, the ε -insensitive function and the constant C.

Step 3: Compute the Box-Cox transformation z_i and its error by (18) for all training data.

Step 4: Update the synaptic weights w_j, the centers m_j, the width σ_j of Gaussian function and the λ_j of the Box-Cox transformation parameter are iteratively updated by (20)~(24), respectively. In this process, the influence of the outliers is detected and discriminated.

Step 5: Determine the values of the annealing schedule $\beta(t) = k/t$ for each epoch, where k is set as $2 \cdot \max\{|e_i|_{initial}\}$.

Step 6: Compute the robust cost function E defined by (17).

Step 7: If the termination conditions are not satisfied, then go to *Step* 3; otherwise terminate the learning process.

Step 8: The inverse of the Box-Cox transformation (6) is applied to the Box-Cox transformation-based ARRBFNs model output as the system output predictions $\hat{y}$.

III.SIMULATION RESULTS

The simulations were conducted in the *Matlab* environment. The root mean square error (RMSE) of the testing is used to measure the performance of the learned networks. The RMSE is defined as

$$\text{RMSE} = \sqrt{\frac{\sum_{i=1}^{N} (\hat{y}_i - y_i)^2}{N}} \,, \tag{25}$$

where y_i is the desire value at x_i and $\hat{y}_i$ is the output of the Box-Cox transformation-based ARRBFNs.

Example. The *sinc* function is considered and defined as

$$y(x) = \left(\frac{\sin x}{x} + \xi \right) + 5 \,, \quad -10 \le x \le 10 \,. \tag{26}$$

Because the output y must be positive in the Box-Cox transformation, the output of *sinc* function must shifts up 5. Ten hundred training data $y(x)$ were generated by using uniformly distributed random $x \in [-10, 10]$. Besides, the noise is a normal disturbance with $N(0,1)$ and one hundred artificial outliers are added to the *sinc* function. Firstly, an initial structure of the Box-Cox transformation-based ARRBFNs is obtained by an SVR approach. The parameters in the SVR are set as $C = 3$, Gaussian kernel function with $\sigma = 0.3$ and $\varepsilon = 0.05$. The initial structure of the Box-Cox transformation-based ARRBFNs with the hidden nodes (i.e. the number of SVs) are obtained as 149. Secondly, the parameters of the Box-Cox transformation-based ARRBFNs are adjusted by the ARLA. After 100 epochs using the ARLA, the testing RMSE of the Box-Cox transformation-based ARRBFNs is 0.0263, as shown in Fig. 2. For a comparison study, a Box–Cox transformation-based radial basis function networks Hong [4] was constructed for the same data, but the testing RMSE is 0.4704, as shown in Fig. 3. Besides, the results of comparison with different training data and artificial outliers are shown in Table 1. From the simulation results, the proposed robust learning algorithms could indeed improve the learning performance as the training data contain outliers.

Table 1: The results with different training data and artificial outliers are shown.

The number of training data	The number of artificial outliers	RMSE	
		Box-Cox transformation-based RRBFNs	Box-Cox transformation-based RBFNs Hong [8]
100	10	0.0549	0.4721
1000	100	0.0263 (Fig.2)	0.4704 (Fig.3)
5000	500	0.0270	0.5131
8000	800	0.0254	Out of memory
10000	1000	0.0434	Out of memory

IV. CONCLUSIONS

In this paper, we proposed a fast identification algorithm with outliers, namely the fixed Box-Cox transformation-based ARRBFNs. Using an SVR approach determines the number of hidden nodes, the initial parameters of the kernel, and the initial weights of the proposed neural networks. At the same time, an ARLA is applied to adjust the parameters and weights. Finally, from the simulation results show that the fixed Box–Cox transformation-based ARRBFNs with ARLA have fast convergence speed for the identification algorithm with outliers.

ACKNOWLEDGMENTS

This work was supported in part by the National Science Council, Taiwan, R.O.C., under grants NSC96-2628-E-224-007-MY2.

REFERENCE

[1] Hong X (2007), Modified radial basis function neural network using output transformation, IET Control Theory & Applications 1(1): 1-8.
[2] Hong X, Harris CJ (2003), Experimental design and model construction algorithms for radial basis function networks, Int. J. Syst. Sci. 34(14-15): 733-745.
[3] Box GEP, Cox DR (1964), An analysis of transformation (with discussion), Journal of the Royal Statistical Society, Series B, 26(2):211-252.
[4] Hong X (2006), A fast identification algorithm for Box-Cox transformation based radial basis function neural network, IEEE Trans. Neural Networks 17(4):1064-1069.
[5] Hong YP, Pan CT (1992), Rank-revealing QR factorizations and the singular value decomposition, Math. Comput. 58(192):213-232.
[6] Hawkins DM (1980), Identification of Outliers, Chapman and Hall.
[7] Chuange CC, Jeng JT, Lin PT (2004), Annealing robust radial basis function networks for function approximation with outliers, Neurocomputing, 56(1):123-139.
[8] Vapnik V (1995), The Nature of Statistical Learning Theory, Springer, Berlin.
[9] Vapnik V, Golowich S, Smola AJ (1997), Support vector method for function approximation, regression estimation, and signal processing, Neural Inf. Process. Syst. 9:281-287.
[10] Chuang CC, Su SF, Hsiao CC (2000), The annealing robust backpropagation (BP) learning algorithm, IEEE Trans. Neural Networks 11(5):1067-1077.

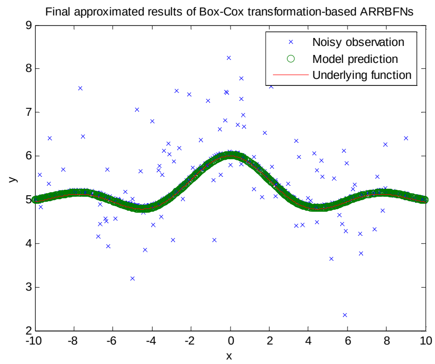

Fig.2. The final output of the proposed approach after 100 epochs uses the ARLA for Example (RMSE=0.0263).

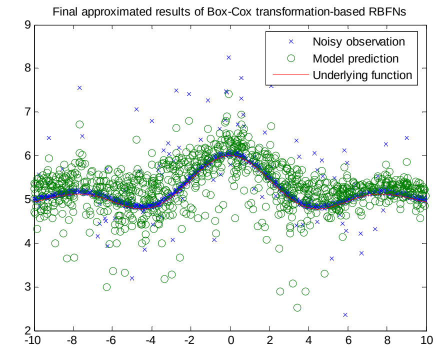

Fig.3. The final output of the Box-Cox transformation-based RBFNs for Example (RMSE =0.4704).

Develop a Module Based Security System for Intelligent Home

Kuo-Lan Su[1,3], Song-Hiang Chia[2,3], Sheng-Ven Shiau[3], Jr-Hung Guo[3],

[1]*Department of Electrical Engineering, National Yunlin University of Science & Technology, Yunlin, Taiwan*

[2]*Department of Electronic Engineering, Wu-Feng Institute of Techonlogy, Chia-Yi, Taiwan*

[3]*Graduate school Engineering Science and technology, National Yunlin University of Science & Technology*

sukl@yuntech.edu.tw, csh@mail.wfc.edu.tw

Abstract: The security detection system of intelligent building, home is important, to human life. An unlucky event was often caused by the negligence of humans. We have developed a module based security system for home automation. The structure of the security system contains many modules. Each module has two variety interfaces (wireless RF and speech). There are active and passive modules in the security system. The active security module is smart robot. We have designed many types' smart robots for the security system. The passive security modules contain fire security module, intruder security module, environment security module, gas security module, AC power security module and appliance control module. In the security module, we use multisensor fusion algorithms to decide an exact output. In these modules, we use two-wire communication method through wireless RF interface, and use voice alarm for event condition, and transmit the real-time status to the supervised computer. In the smart robot system, we have designed many types smart robot for the security system. We have designed a general user interface (GUI) for the intelligent security system. The user interface can supervise these modules and smart robots using wireless RF device, and remote supervised using wireless Internet and cell phone, too.

Keywords: home automation, wireless RF, general user interface.

1. INTRODUCTION

Intelligent buildings and home can provide safety, convenience and welfare for human living in the 21st century, and allow effective management of resource with minimum life-time costs at the same time. The most important role of the intelligent home is security system. In the security system, redundant and complementally information results can enhance system reliability and certainty of intelligent home using multisensor fusion method. In generally, the price of the intelligent home system is very expensive. We want to develop a cheap and flexibility system for the intelligent, and he system is very easy operation and convenience for the user.

Wang and So [1] presented the history of development of building automation system (BAS). The structure of features of a modern BAS was introduced and future trends of BAS are discussed. Azegami and Fujiyoshi [2] described a systematic approach to intelligent building design. Kujuro and Yasuda [3] discussed the systems evolution in intelligent building. The quality of building services can be enhanced by updated information processing and communications functions of building automation systems. Finley et al. [4] presented a survey of intelligent building and reviews issues such as system perspective, subsystem services, multi-tenant building. Flax [5] discussed components and cost benefits of the intelligent building. Chung and Fu expect to set up the standard of appliances and communication protocols, and propose a complete system architecture with integrate control kernel to construct an intelligent building system [6, 7].

The paper is organized as follows: section II describes the system structure of the security system for intelligent home. Section III explains detection methods and algorithms for these detection modules of the security system. Section IV describes the user interface of the intelligent home. Section V presents the experimental results using these modules for the home security system. The brief concluding comments are described in Section VI.

2. SYSTEM ARCHITECTURE

The system architecture of the intelligent home security system is shown in Fig 1. The system contains many subsystems. The supervise computer and the intelligent mobile robot can receive the status of security modules and appliance control modules using wireless RS232 interface. The security modules and the appliance control module use two-way communication with the supervised computer and smart robots. The intelligent mobile robot and the supervised computer can communicate with GSM modern using RS232 interface, and can communicate with remote supervised computer using wireless Internet.

The display panel of the supervise computer is television. We develop the user interface using Visual Basic language for the intelligent security system. The

©ISAROB 2009

supervised computer can control smart robots using wireless RF interface, and control the intelligent mobile robot using wireless Internet. The user can acquire image signals from intelligent mobile robot, supervised computer and IPCAM through Internet. The supervised computer can acquire image signals from smart robots and CCD through wireless RF interface. In the paper, we are interesting in security modules, appliance control module, smart robots, and user interface.

In the architecture, there are many modules in the system, and it's equipped with a microcomputer (HT46R24) as the controller. These modules are independent and autonomous, and can work concurrently, each module can transmits the sensory data, parameter values and detection results to the mobile robot and the supervised computer through wireless series interface (RS232), and transmits detection results to PDA and 3G mobile phone using GSM module, too. These modules can speech Chinese on real-time measured data using voice module. We develop a general user interface for the home security system. The security system communicates with mobile phone using GSM (Global System for Mobile) modular. The GSM modular (WMOD2) was made by Wavecom. The modular is a seft-contained E-GSM900/GSM1800 (or E-GSM900/GSM1900) dual band module.

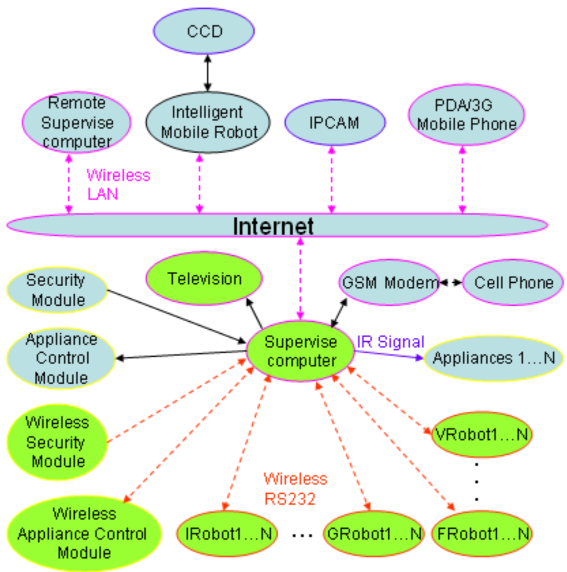

Fig. 1 The overview of the home security system

3. DETECTION MODULES

We develop some intelligent security detection modules for home automation system based on the multi-models fusion architecture. They contain active and passive security modules in the security system. We design some smart robots that are embedded detection devices to detect environment status in the active security modules. In the passive security system, there are fire security module, intruder security module, environment security module, power security module and gas security module. These modules can detect surrounding of the intelligent home using sensors and wireless RF interface. We list sensory type of these security modules in Table I.

Table I. Sensors of security system

Module	Sensors
Fire security module	Three flame sensors,
Intruder security module	Touch sensor, magnetic sensor, IR sensor and body sensor.
Environment security module	humidity sensor, illumination sensor and temperature sensor
Power security module	Four current sensors.
Gas security module	CO sensor, smoke sensor, gas sensor and alcohol sensor
Smart robot	Flame sensor, gas sensor and body sensor

- **Fire security module**

In the fire detection module, we use three flame sensors to detect fire source, and use the weighted average method to decide event. We set the same weight value for these sensors. The prototype of the fire detection module is shown in Fig. 2. The decision rule is according to equation (1) and (2). Then we set a threshold for the fire security module. The average value $\bar{x}$ is over than threshold, and we can say to be fire event. Otherwise we can say no fire condition. The ith measurements value of n sensors is presented x_i , and the weight must be satisfied $0 \le \omega_i \le 1$ is

$$\bar{x} = \sum_{i=1}^{n} \omega_i x_i \qquad (1)$$

$$\sum_{i=1}^{n} \omega_i = 1 \qquad (2)$$

- **AC Power security module**

We proposed a power detection and diagnosis method using four current measured values in the AC power security module, and use a multilevel multisensor fusion method to decide the exact power of the intelligent home. The redundant management method is developed for the power security module. The proposed method is not only to detect power value, but also to diagnose

©ISAROB 2009

sensory status [8]. We can find the estimate value of the measured parameter is obtained by the following equation at that sample time.

$$\hat{x} = \frac{\sum_{i=1}^{l} m_i I_i}{\sum_{i=1}^{l-j} I_i} \tag{3}$$

$$Ii = \sum_{j=1}^{l} f\left[\left|m_i - m_j\right| \le \left(b_i + b_j\right)\right] \quad i = 1,2,\cdots l \tag{4}$$

$$f[*] = \begin{cases} 0, & if \quad * \quad is \quad true \\ 1, & if \quad * \quad is \quad false \end{cases} \tag{5}$$

m_i and m_j are measured values of the ith and jth sensors, and I_i is the indicator function of the ith sensor.

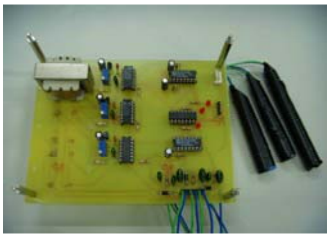

Fig. 2 The prototype of the fire detection module

- **Smart robots**

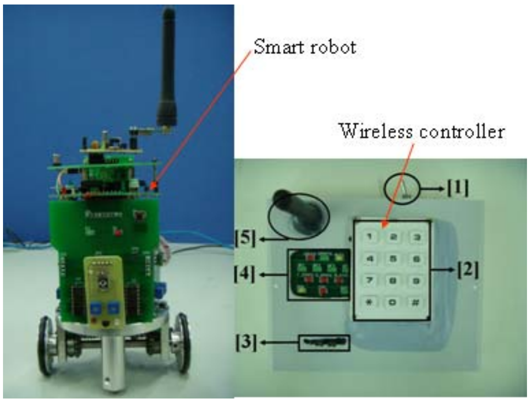

Fig. 3 The smart robots and remote controller

The smart robot has four levels to be embedded hardware devices. The smart robot has the shape of cylinder and its diameter, height and weight is 8cm, 15cm and 2kg. They are shown in Fig. 3. The power of the smart robot is three Li batteries, and connects with parallel arrangement. It has three IR sensors to avoid obstacle. The controller of the smart robot is HT46R24, and can acquire the detection signal from sensors through I/O pins, and receives the command from the supervised computer and remote controller through wireless RF interface. The controller of the smart robot can transmits the detection result to the remote controller and the supervised computer through wireless RF interface.

4. USER INTERFACE

The user interface of the intelligent security system is shown in Fig. 4. There are four regions in the supervised interface. This is the graphic supervised monitor for the intelligent security system in the region 1. The user can program the status of security modules and appliance control modules, and receive the status from these modules by wireless RF interface. The user can move any module (security module and appliance control module) of the region 2 to the region using mouse.

The region 2 can display the arrangement of these security modules and appliance control modules. It can display the real-time measured values of these security modules, and the user can set the threshold value by the supervised computer, and transmit the set value to the module using wireless RF interface. In the region 3, the user can program the output response for any security signal input. For example, if the intruder event happened, we can program alarm, and hazard, and control the appliance module, and transmit the status to the user by the remote supervised computer, PDA or 3G mobile phone through Internet or GSM modern in the region. The user can program the status of each floor of the building in the region 4.

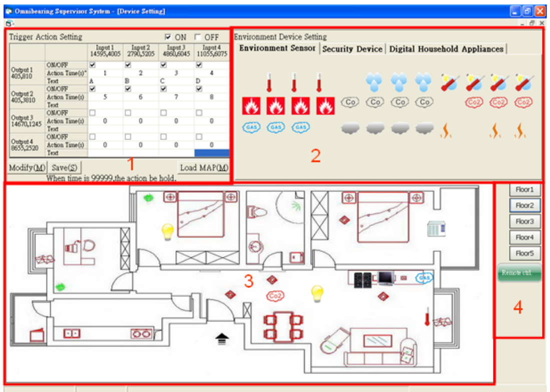

Fig. 4 The user interface of the supervised system

5. EXPERINMENTAL RESULTS

In the intruder security module, we use magnetic sensor to detect the intruder. The intruder detection module can transmit the decision results to the supervised computer and the remote supervised computer (or mobile phone) through the wireless RF interface and Internet (or GSM modern). The experimental results are shown in Fig. 5. The user put off the magnetic sensor from the intruder detection (from Fig. 5(a) to (b)). The module can transmit the signal to the supervised computer, and the supervised computer can transmits the intruder status to the user using GSM modern to be shown in Fig 5(c). The module can speak "intruder" use Chinese language. There are many experimental results in the reference.

The smart robot can move autonomous according to environment using IR sensors. The user can supervise the smart robot for forward, backward, turn right, turn left and stop through wireless RF interface. The smart robot can receive the detection signal from the security module through wireless RF interface, and move to the event place. It can transmit the image signal and the real-time data to the supervised computer and remote controller. The user can control CCD device to catch the event using wireless RF interface. The experimental result is shown in Fig. 6

(a) (b) (c)

Fig. 5 The experimental result for intruder detection

Fig. 6 The fire detection experimental result

6. CONCLUSION

We have presented an intelligent security system applying in the intelligent home. The security system contains active security module (smart robot) and passive security module. These security modules have two interfaces, one is wireless RF interface, and the other is voice interface. It can speak Chinese language according to the environment status. The security system contains five detection modules, one application control modules and smart robots. The detection methods of these modules have weighted average method, statistical method and redundancy management method. These smart robots can detect environment status, and transmit the event signal and real-time image to the wireless RF controller and the supervised computer. The user can control these smart robots through wireless RF interface by the wireless controller and the supervised computer, and supervise these devices using remote supervised computer, PDA and 3G mobile phone.

ACKNOWLEDGMENT

This work was supported by the project "The Development of Module Based Smart Robot" under Industrial Development Bureau Ministry of Economic Affair of Taiwan, R. O. C.

REFERENCES

[1] C. W. Wang and A. T. P. So, "Building Automation In The Century," in proceedings of the 4-th International Conference on Advance on Advances in Power System Control, Operation Management, APCOM-97, Hong Kong, November 1997, pp.819-824.

[2] M. Azegami and H. Fujixoshi, "A systematic Approach to Intelligent Building Design," IEEE Communications Magazine, October 1993, pp.46-48.

[3] Kujuro and H. Yasuda, "Systems Evolution in Intelligent Building," IEEE Communication Magazine, October 1993, pp.22-26.

[4] Marion R. Finley, Jr. Ancilla Karajura and Raphael Nbogni, "Survey of Intelligent Building Concepts," IEEE Communication Magazine, April 1991, pp.18-20.

[5] M. Fiax, "Intelligent Building," IEEE Communication Magazine, April 1991, pp.24-27.

[6] W. Y. Chung, L. C. Fu and S. S. Hung, "A Flexible, Hierarchical and Distributed Control Kernel Architecture for Rapid Resource Integration of Intelligent System", IEEE International Conference on Robotics Automation, Seoul, Korea, May 21-26, 2001, pp.1981-1987.

[7] L. C. Fu and T. J. Shih, "Holonic Supervisory Control and Data Acquisition Kernel for 21st Century Intelligent Building System", IEEE International Conference on Robotics and Automation, San Francisco CA, April 2000, pp.2641-2646.

[8] Kuo L. Su Jyh H. Tzou and Chien C. Liu, "Development of a Multisensor-Based Residual Power Prediction System for Mobile Robots," IEEE Workshop on Advanced Robotics and its Social Impacts 2007 (ARSO '07), Hsinchu, Taiwan, December 9-11, 2007, pp.114-119.

Synchronous Reluctance Motor Speed Drive Using Sliding Mode Controller Based on Gaussian Radial Basis Function Neural Network

Chien-An Chen[1], Huann-Keng Chiang [2] and Wen-Bin Lin[1,3]
[1] *Graduate School of Engineering Science & Technology, National Yunlin University of Science & Technology, Taiwan*
[2] *Department of Electrical Engineering, National Yunlin University of Science & Technology, Taiwan*
[3] *Department of Optoelectronic Engineering, Far East University, Taiwan*
Fax :+886-5-5312065
E-mail: Chianghk@yuntech.edu.tw

Abstract: In this paper, a sliding mode control (SMC) design based on Gaussian radial basis function neural network (GRBFNN) is proposed for the synchronous reluctance motor (SynRM) system robust stabilization and disturbance rejection. This method utilizes Lyapunov function and the steep descent rule to guarantee the convergence of the SynRM drive system asymptotically. Finally, we employ the experiments to validate the proposed method.

Keywords: Sliding Mode Control, Radial Basis Function Neural Network, synchronous reluctance motor, Lyapunov function.

I. INTRODUCTION

In recent decade years, the SynRM [1,2] has been a renewed interesting research subject. The rotor circuit of the SynRM is opened such that the flux linkage of SynRM is directly proportional to the stator currents.

The fast and no error dynamic response is a primary topic in control systems. In real worlds, the real servo systems always include parameter variations and external load disturbances. The sliding mode control [3] has been proven as an effective and robust control technology to overcome the uncertainties in the SynRM [4,5]. The uncertainties, parameter variations and/or external disturbances can be rejected for the sliding mode control when the upper lump uncertainty boundary of the systems is known. In real applications, uncertainty boundaries can easily exceed the assumed magnitude range, under which the sliding mode can not be used. Using high gain control to improve disturbance rejection has been proposed [6]. However, it produces unnecessary deviations from the switching manifold and causes chattering in the control system. Serious chattering can reduce by using the boundary layer which the signum function is replaced by the saturation function. However, it produces the steady state errors. In recent years, some researchers [7,8] proposed the methods to find the uncertainty upper boundaries and reduce the steady state error. Their major concept is to estimate the bounded uncertainties in real-time for the controlled system. Hence, the control signal of the controller is smaller than the conventional sliding mode controller and the chattering phenomenon is also reduced.

In recent years, the neural network of intelligent control has been applied in some motor speed control systems [9,10]. The neural network control does not require mathematical model to approximate nonlinear systems. The radial basis function neural network (RBFNN) theory [11] employs local receptive fields to perform function mapping based on biological receptive fields. The RBFNN is a multilayer perceptron (MLP) feedforward neural network structure. It has been successfully employed in the area of motor control field [12,13]. The RBFNN control1er is an effective method when the systems mathematical model is unknown, or known with uncertainties.

RBFNN [14] is a three-layer feedforward neural network structure. It has the nonlinear transformation of Gaussian basis function in the hidden layer and output layer is the linear combination of hidden layer responses. We proposed the SMC design based on RBFNN concept of SynRM system which the upper lump uncertainty system doesn't know. The SMC is replaced by RBFNN which the sliding surface function S and system control u is the mapping input and output function, respectively. The RBFNN doesn't use the signum function control element. Hence, this system reduces chattering phenomenon and has the response more smooth.

II. MODELING OF THE SYNRM

The d-q equivalent voltage equations of the SynRM with the synchronously rotating rotor reference frame are represented as

$$V_{ds} = R_s i_{ds} + L_{ds}\frac{di_{ds}}{dt} - \omega_r L_{qs} i_{qs} \quad \textbf{(1)}$$

$$V_{qs} = R_s i_{qs} + L_{qs}\frac{di_{qs}}{dt} + \omega_r L_{ds} i_{ds} \quad \textbf{(2)}$$

where the V_{ds} and V_{qs} are direct and quadrature axis terminal voltages, respectively. The i_{ds} and i_{qs} are, respectively, direct axis and quadrature axis terminal currents or the torque producing current. The L_{ds} and L_{qs} are the direct and quadrature axis magnetizing inductances, respectively. The R_s is the stator resistance and ω_r is the speed of the rotor.

The corresponding electromagnetic torque T_e and m otor dynamic equation are given as following

$$T_e = \frac{3}{2}P(L_{ds} - L_{qs})i_{ds}i_{qs} \quad \textbf{(3)}$$

$$T_e - T_L = J\frac{d\omega_r}{dt} + B\omega_r \quad \textbf{(4)}$$

where P , T_L , J and B are the pair of poles, the torque load, the inertia moment of rotor and the viscous friction coefficient, respectively.

The current angle for the maximum power factor control (MPFC) strategy is $\phi = \pm\tan^{-1}(\sqrt{L_{ds}/L_{qs}})$ [2]. Therefore by electromagnetic torque (3), we can find the torque current command as following

$$I_s = \sqrt{i_{ds}^2 + i_{qs}^2} \quad \textbf{(5)}$$

$$i_{ds}^* = \sqrt{\frac{|T_e^*|}{\frac{3}{4}P(L_{ds} - L_{qs})}}\cos(\tan^{-1}(\sqrt{L_{ds}/L_{qs}})) \quad \textbf{(6)}$$

$$i_{qs}^* = sign(T_e^*)\sqrt{\frac{|T_e^*|}{\frac{3}{4}P(L_{ds} - L_{qs})}}\sin(\tan^{-1}(\sqrt{L_{ds}/L_{qs}})) \quad \textbf{(7)}$$

III. SLIDING MODE CONTROL (SMC)

We can rewrite the motor dynamic equation of (4) as follows:

$$\begin{aligned}\dot{\omega}_r &= (-\frac{B_m}{J_m})\omega_r + (\frac{1}{J_m})(T_e - T_L)\\ &= a\omega_r + b(T_e - T_L) \quad \textbf{(8)}\\ &= a_o\omega_r + b_o(u(t) + f)\end{aligned}$$

where

$$a \equiv -\frac{B_m}{J_m} = a_o + \Delta a$$

$$b \equiv \frac{1}{J_m} = b_o + \Delta b$$

$$u \equiv T_e$$

$$f \equiv \frac{1}{b_o}(\Delta a\omega_r + \Delta b u(t) - bT_L)$$

$$J_m \equiv J_{mo} + \Delta J_m$$

$$B_m \equiv B_{mo} + \Delta B_m$$

The subscript index "o" indicates nominal system value; "Δ" symbol expresses uncertainty, and f is the lump uncertainty. Defining the velocity error $e(t) = \omega_{ref} - \omega_r$, ω_{ref} is the velocity command.

The sliding function is defined as

$$S = e(t) + c\int_{-\infty}^{t} e(\tau)d\tau,\ c > 0 \quad \textbf{(9)}$$

The input control $u(t)$ (the electromagnetic torque T_e) can be defined

$$u(t) = u_{eq}(t) + u_n(t) \quad \textbf{(10)}$$

To satisfy equivalent control concept $\dot{S}(e) = 0$, we get

$$\dot{S} = (\dot{\omega}_{ref} - a_o\omega_r - b_o u_{eq} + ce) - b_o(u_n + f) \quad \textbf{(11)}$$

Let $|f| \le K$, we set

$$u_{eq} = \frac{1}{b_o}(\dot{\omega}_{ref} - a_o\omega_r + ce) \quad \textbf{(12)}$$

$$u_n = Ksign(S) \quad \text{or} \quad u_n = Ksat(S) \quad \textbf{(13)}$$

Hence, the sliding condition $S(e)\dot{S}(e) < 0$ can be guaranteed. The chattering phenomenon exists in the $sign(\cdot)$ function and steady state error exists in $sat(\cdot)$ function

IV. SLIDING MODE CONTROLLER BASED ON RBFNN

In real world, most of the physical systems have certain nonlinear and various uncertainties. However, specific and reliable system uncertainty boundaries are difficult obtained for practical applications. Therefore, a model-free neural network (NN) control [15] was employed for controlling dynamic absorbers without knowing the systems model. The error back propagation NN has the disadvantages of slower learning speed and local minimal convergence. Hence, we use the RBFNN to solve these problems and develop a model-free controller structure based on RBFNN. The structure of the SMC based on RBFNN model is shown in Fig. 1. The RBFNN model has j receptive field units. We select the Gaussian function $\varphi_j(S) = \exp\left(-\left(S - c_j\right)^2/(2b_j^2)\right)$ as the receptive field units, where S is the sliding surface function and c_j, b_j are the spread factor and central position of the Gaussian function, respectively. j is the number of hidden layer neurons. The output u of the RBFNN is the sum of weights which the output can be described as

$$u = \sum_{j=1}^{5} w_j\varphi_j(S) \quad \textbf{(14)}$$

$$\varphi_j(S) = \exp\left(-\frac{\left(S - c_j\right)^2}{2b_j^2}\right), \quad j = 1,\cdots,5 \quad \textbf{(15)}$$

where

$$\theta = \left[\varphi_1(S), \varphi_2(S), \cdots, \varphi_5(S)\right]^T, \quad W = [w_1, w_2, \cdots, w_5]^T$$

©ISAROB 2009

$$c_1 = \frac{2000\pi}{6}, c_2 = \frac{2000\pi}{12}, c_3 = 0, c_4 = -\frac{2000\pi}{12}, c_5 = -\frac{2000\pi}{6}$$

$$b_1 = b_2 = b_3 = b_4 = b_5 = 500\pi$$

According the SMC reaching condition $S\dot{S} < 0$, the adaptive rules of this structure derive from the steep descent method to minimize the value of the performance index $S\dot{S}$ with the weight w_j as follows:

$$\dot{w}_j = -\eta \frac{\partial S\dot{S}}{\partial w_j} = -\eta \frac{\partial S\dot{S}}{\partial u} \frac{\partial u}{\partial w_j} = \eta \cdot S \cdot b_o \cdot \varphi_j(S) \qquad \textbf{(16)}$$

where η is the learning rate.

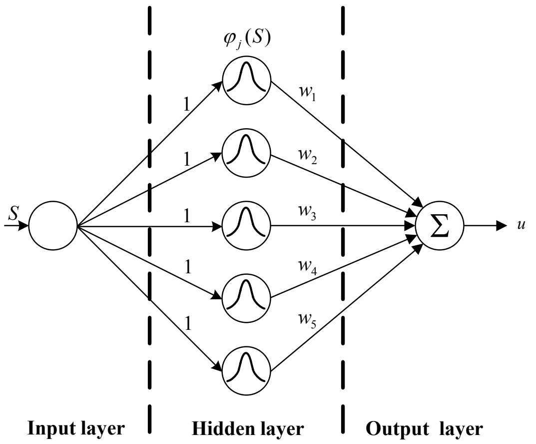

Fig. 1. The structure of the RBFNN model

V. EXPERIMENTAL RESULTS

The block diagram of the experimental SynRM system is shown in Fig. 2. The controller is adopted by a dSPACE DS1104 control board. The nominal parameters of 0.37 KW three-phase SynRM are shown in Table 1. The sampling period of control rules is set as 0.3 $m\sec$. The reference model transfer function of Fig. 2 is set as $\frac{\omega_{ref}(s)}{\omega_r^*(s)} = \frac{81}{s^2 + 18s + 81}$, where s is the Laplace operator. Fig. 3 shows the response for the reference command of is $\omega_r^* = 500\,\text{rev/min}$ under a 0.3 Nt-m machine load at the beginning. In Fig. 4, the reference command is $\omega_r^* = 500\,\text{rev/min}$ under a 0.3 Nt-m machine load at the beginning and a 1.0Nt-m load disturbance is added at *t*=5 sec. From Fig. 3 and 4, the proposed controller has good velocity performance.

Table 1. The parameters of SynRM (0.37KW)

$R_s = 4.2\Omega$	$P = 1$
$L_{ds} = 0.328\,H\ (f = 60Hz)$	$L_{qs} = 0.181\ \text{H}\ (f = 60\text{Hz})$
$J_{mo} = 0.00076\ kg\text{-}m^2$	$B_{mo} = 0.00012\ Nt\text{-}m/rad/sec$
$c = 6$	$\eta = 0.0086$

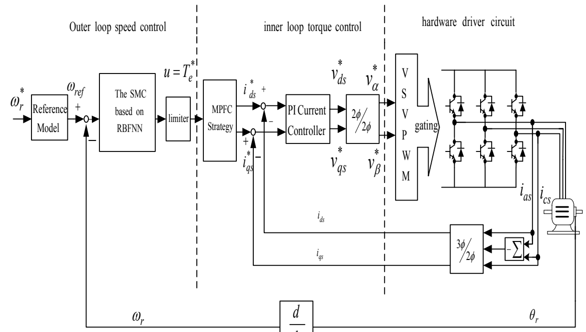

Fig. 2. The block diagram of the experimental SynRM drive system

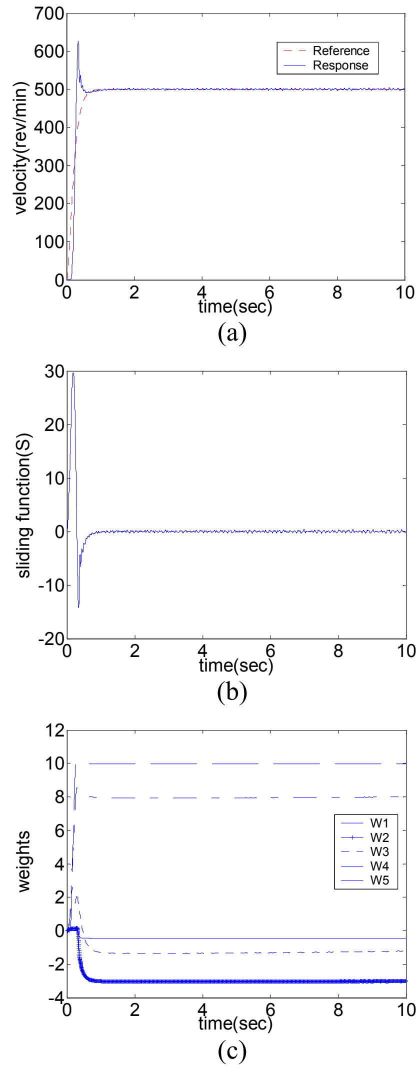

Fig. 3. Experimental results of the SMC based on RBFNN due to $\omega_r^* = 500$ rev/min under a 0.3 Nt-m machine load at the beginning (a) rotor velocity (b) sliding function (c) weights

©ISAROB 2009

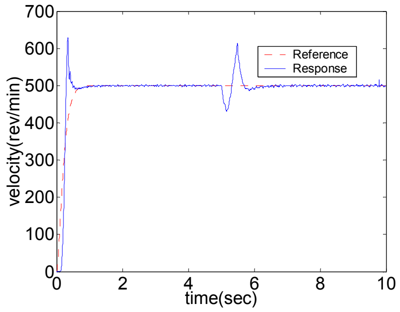

(a)

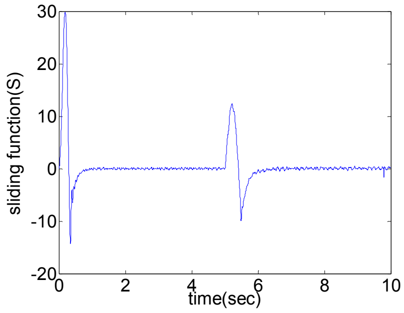

(b)

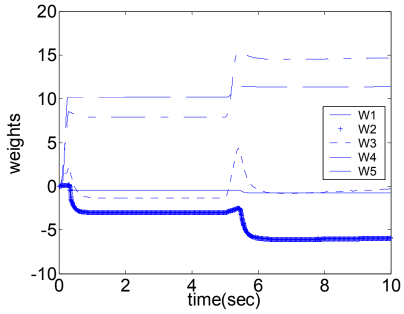

(c)

Fig. 4. Experimental results of the SMC based on RBFNN due to $\omega_r^* = 500$ rev/min under 0.3Nt-m to 1.0Nt-m load torque step disturbance. (a) rotor velocity (b) sliding function (c) weights

VI. CONCLUSION

In this paper, a complete model analysis for the sliding mode controller based on radial basis function neural network of SynRM speed drive is presented. The proposed RBFNN is employed to model the relationship between the sliding function and the systems control law in real-time which has the adaptive rules. It derives from the steep descent method to minimize the value of the performance index $S\dot{S}$. Hence, the chattering problem can be minimized with the proposed control. Finally, we employ the experimental results to validate the proposed method.

ACKNOWLEDGMENT

This work is supported by the National Science Council in Taiwan, Republic of China, through grant NSC97-2221-E- 224-065.

REFERENCES

[1] Miller TJE, et al. (1991), Design of a synchronous reluctance motor drive. IEEE Transactions on Industry Applications 27(4):741-749
[2] Betz RE, Lagerquist R and Jovanovic M (1993), Control of synchronous reluctance machines. IEEE Transactions on Industry Applications 29:1110-1121
[3] Utkin VI, Guldner J, and Shi J (1999), Sliding mode control in electromechanicals systems. Taylor & Francis
[4] Shyu KK, Lai CK, and Tsai YW (2000), Optimal position control of synchronous reluctance motor via totally invariant variable structure control. IEE Proceedings-control Theory and Applications 147(1):28-36
[5] Chiang HK and Tseng CH (2004), Design and implementation of a grey sliding mode controller for synchronous reluctance motor drive. Control Engineering Practice 12(2):155-163
[6] Asada H and Slotine JJ (1986), Robot analysis and control. Wiley, New York
[7] Chiang HK and Tseng CH (2004), Integral variable structure controller with grey prediction for synchronous reluctance motor drive. IEE Proceedings-Electric Power Applications 151(3):349-358
[8] Lin FJ, et al. (2000), Decoupled stator-flux-oriented induction motor drive with fuzzy neural network uncertainty observer. IEEE Transactions on Industrial Electronics 47(2):356-367
[9] Chen TC and Sheu TT (2002), Model reference neural network controller for induction motor speed control. IEEE Trans Energy Conversion 17(2):157-163
[10] Lin Z, et al (2007), Online modeling for switched reluctance motors using B-spline neural networks. IEEE Transactions on Industrial Electronics 54(6):3317-3322
[11] Jang JSR and Sun CT (1993), Functional equivalence between radial basis function networks and fuzzy inference systems. IEEE Transactions on Neural Networks 4(1):156-159
[12] Lin FJ, Teng LT and Shieh PH (2007), Intelligent sliding-mode control using RBFN for magnetic levitation system. IEEE Transactions on Industrial Electronics 54(3):1752-1762
[13] Park JW, Venayagamoorthy GK and Harley RG (2005), MLP/RBF neural-networks-based online global model identification of synchronous generator. IEEE Transactions on Industrial Electronics 52(6):1685-1695
[14] Huang SJ, Huang KS and Chiou KC (2003), Development and Application of a Novel Radial Basis Function Sliding Mode Controller. Mechatronics 13: 313-329
[15] Huang SJ and Lian RJ (1996), A combination of fuzzy logic and neural network algorithms for ac tive vibration control. Proceedings of the institution o f mechanical engineers 210:153-167

©ISAROB 2009

The Fourteenth International Symposium on Artificial Life and Robotics 2009 (AROB 14th '09),
B-Con Plaza, Beppu, Oita, Japan, February 5 - 7, 2009

Detection System of Security Robot Using Multisensor Fusion Algorithms

Ting-Li Chien[1], Jyh-Hwa Tzou[2], Chun-Chieh Wang[3], Kuo-Lan Su[4]

1. Department of Electronic Engineering, Wu-Feng Institute of Technology, Taiwan
2. Department of Mechanical Engineering, Wu-Feng Institute of Technology, Taiwan
3. Department of Electronic Engineering Chienkuo Technology University, Taiwan
4. Department of Electrical Engineering, National Yunlin University of Science & Technology, Taiwan
E-mail: cdl@mail.wfc.edu.tw sukl@yuntech.edu.tw

Abstract: The paper develops detection system of the module based intelligent security robot that has uniform interface. The detection system contains power detection module、gas detection module、environment detection module and fire detection module. The control unit of these modules is HOLTEK microchip. These modules can communicate with master module using I2C interface. The master module communicates with main controller of the security robot using RS232 interface. The main controller of the security robot system is industry personal computer (IPC). It can display status of these modules on the monitor. These modules can enhance the detection results using multisensory fusion algorithms. The user can add or remove the detection modules in any time, and the main controller can acquires sensor signals from these detection modules on real-time. Finally, we present some experimental results using these detection modules, and integrate these modules in the robot system that executes some scenario.
Keywords: module based robot system**,** I2C, robot

I. INTRODUCTION

With the robotic technologies development with each passing day, robot systems have been widely employed in many applications. Nowadays, robot systems have been applied in factory automa Recently, more and more research takes interest in the robot which can help people in our daily life, such as service robot, office robot, security robot, and so on. In the future, we believe that robot will play an important role in our daily life.

In the past literatures, many experts research in the security robot. Some research addressed in developing target-tracking system of mobile robot [1,2], such as Hisato Kobayashi et al. proposed a method to detect human being by an autonomous mobile guard robot [3]. Yoichi Shimosasa et al. developed Autonomous Guard Robot [4] witch integrate the security and service system to an Autonomous Guard Robot, the robot can guide visitors in daytime and patrol in the night. D. A. Ciccimaro developed the autonomous security robot – "*ROBART III*" which equipped with the non-lethal-response weapon [5, 6]. Moreover, some research addressed in the robot has the capability of fire fighting [7, 8].

The hardware and software of these robots are complexity, and are not easy to maintain and repair. How to operate these robots is very difficult for the user. The development and adaptability of robot systems have limited. To increase their development and adaptability, the concept of the module-based robot system (MBRS) has been studied in the robotic field since 1980s. Many robot systems have been designed [9-12].

The paper is organized as follows: Section II describes the system architecture and the interface of the detection system for the module based intelligent security robot. Section III explains the function of the detection module, and it describes the fusion algorithms of the detection module. Section IV presents the experimental results for these detection modules and user interface. Section VI presents brief concluding remarks.

II. SYSTEM ARCHITECTURE

The system architecture of the module based intelligent security mobile robot is shown in Fig. 1. The module based security robot has three parts. There are detection system, motion control system and others. We are focus on the detection system in the paper. The interface of the master module and detection modules is Inter IC (I2C). The master module connects with some detection modules. These modules can use two-way communicate with master module, and the master module communicate with the main controller of the mobile robot by series interface (RS232). These modules are connecting with the master module, and the master can detect which module to be connected, and transmit the module ID to the main controller. On the other hand, the user can adds and removes the module from the mobile robot system. The master can detect which module will be added and removed, and transmit the module ID to the main controller. The main controller of the module based intelligent security robot can know how much modules on line and it can acquire data from these modules.

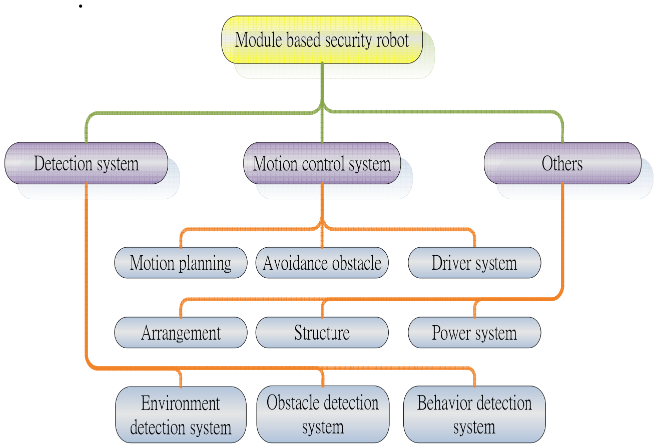

Fig. 1 The system architecture

The controller of these modules is HOLTEK microprocessor. The detection modules have fire detection module, environment

©ISAROB 2009

detection module, gas detection module, remote IR and wireless RF module, power supply module, compass module, acceleration module, power detection module, inclement detection module, obstacle detection module (IR sensors and ultrasonic sensors), master module and DC servomotor driver module. We arrange an ID to each module, and identify the module function by the ID. These modules can be equipped in the intelligent mobile robot. The prototype of the module based intelligent mobile robot is shown in Fig. 2.

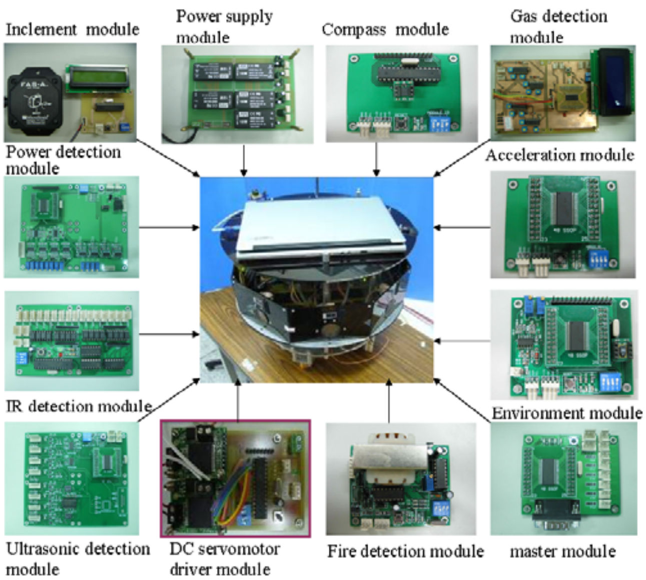

Fig. 2 The prototype of the module based intelligent robot

These modules can acquire sensory signal and processes these signal using amplifier and calibrate circuits and transmits sensory data to the master module using I2C interface. We list these sensors of the detection modules to be tabulated in Table 1.

Table 1 Sensors in these detection modules

Module	Sensors	Examples
Environment detection module	humidity sensor	SHT1x
	temperature sensor	SHT1x
	illumination sensor	S1133
Fire detection module	Flame sensor	R2868
Power detection module	Current sensor	LA-55P
Gas detection module	Carbon monoxide sensors	HS-134 TGS203
	Air pollution	HS135
	Alcohol sensor	TGS822
	Gas sensor	TGS800

III. DETECTION MODULES

The detection system of the module based intelligent mobile robot has some detection modules and one master module. These detection modules contain Environment detection module 、Fire detection module、Power detection module and Gas detection module. Some of the detection modules can calculate the exact measured value using multisensor fusion algorithm, and transmit measured values and decision output to the master module using I2C interface. The controller of these modules is HOLTEK microchip.

- **Power detection module**

In the power detection module, we use four current sensors to measure the current variety of the module based security robot. The block diagram of the power detection module is shown in Fig. 3. The module can measure current and voltage values on the power variety of mobile robots. We use two multisensor fusion methods (redundant management method and a statistical prediction method) to detect current sensor and voltage signals status. In the redundant management method, we can get an exact measured value for power detection, and isolate faulty signal from current sensor and voltage signal [13, 14]. Then we can calculate the residual power of the mobile robot, and decide the residual time to work using second-order polynomial regression for the mobile robot [15].

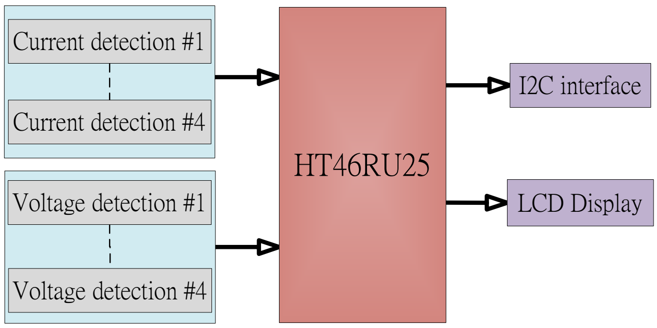

Fig. 3 The block diagram of the power detection module

In the intelligent power detection module, we use redundant management method to estimate the exact values on current and voltage on the power of the mobile robot. The value of the measured parameter is obtained by the following equation at that sample time k

$$\hat{x}(k) = \frac{\sum_{i=1}^{l} m_i(k) I_i(k_i)}{\sum_{i=1}^{l} I_i(K)} \tag{1}$$

Where I_i is a weighted value for the each measurement m_i at the given sample time k . So we can define indicator function Ii is

$$Ii = \sum_{j=1}^{l} f\left[\left|m_i(k) - m_j(k)\right| \le \left(b_i(k) + b_j(k)\right)\right] \quad i = 1,2,\cdots l \tag{2}$$

$$f[*] = \begin{cases} 1, & if \quad * \quad is \quad true \\ 0, & if \quad * \quad is \quad false \end{cases} \tag{3}$$

In the redundant management method and statistical signal method, we can get an exact measured value for power detection, and isolate faulty signal from current sensor and voltage signal. Then we want to predict the residual power of the mobile robot. First we must fit the curve from the power detection value of the mobile robot. Next the user can set the critical power value for the mobile robot. The main controller of the mobile robot can calculate the extrapolation value from the critical power value, and can calculate the residual working time for the mobile robot. The mobile robot must move to the charging station in the residual time.

In the paper, we fit a second-order polynomial regression using the power estimated value.

$$y = a_0 + a_1 x + a_2 x^2 + e \tag{3}$$

The sum of the squares of the error is

$$S_r = \sum_{i=1}^{n} (y_i - a_0 - a_1 x_i - a_2 x_i^2)^2 \tag{4}$$

To generate the least squares fit, we take the derivative of Equation (4) with respect to each of the unknown coefficient (a_0, a_1 and a_2) of the polynomial, and we can get

$$\begin{aligned} na_0 + (\sum x_i)a_1 + (\sum x_i^2)a_2 &= \sum y_i \\ (\sum x_i)a_0 + (\sum x_i^2)a_1 + (\sum x_i^3)a_2 &= \sum x_i y_i \\ (\sum x_i^2)a_0 + (\sum x_i^3)a_1 + (\sum x_i^4)a_2 &= \sum x_i^2 y_i \end{aligned} \tag{5}$$

Finally we can calculate $a_0, a_1,$ and a_2 using numerical analysis method from Equation (5). Then we set the power critical value to be P_S and

$$a_2 x^2 + a_1 x + a_0 = P_S \tag{6}$$

We can calculate the x value (the unit is second) from Equation (6). The sample time of the power system is 1 second.

- **Gas detection module**

In the gas detection module, there are two carbon monoxide sensors (HS134 and TGS203), air pollution sensor (HS135), alcohol sensor (TGS822) and gas sensor (TGS800). The HS134 and TGS203 sensor elements have high sensitive, long life, reliable stability and good selectivity to low carbon monoxide concentration. The TGS203 has low sensitivity to alcohol and hydrogen. The HS135 sensor element has long period stability and widely detecting scope. It should be suitable for detecting of smoke, SO2, CO2, isobutance, alcohol, etc.. The sensing element of the sensor TGS822 is a tin dioxide (SnO2) semiconductor which has low conductivity in clear air. It has high stability and reliability over a long period, and high sensitivity to organic solvent vapors. The block diagram of the gas detection module is similarity to Fig. 3.

We can use sensor elements HS134 、TGS203 and HS135 to detect CO_2 density of the environment, and compare these measurement values. We can use the logical filter method to decide the CO_2 density to be over the threshold. In the otherwise, we can use TGS822 and HS135 sensors to detect alcohol density to be over the threshold using the same method, too. In the logical filter method, we can use AND or OR filter on the gas detection module. Then we can calculate the system reliability of AND filter (R_S) and OR filter (R_P)

$$R_S = \prod_{i=1}^{n} R_i(t) \tag{7}$$

$$R_P = 1 - \prod_{i=1}^{n} [1 - R_i(t)] \tag{8}$$

$R_i(t)$ is the reliability of each sensor of the gas detection module.

- **Environment module**

The environment detection module contains humidity detection, illumination detection and temperature detection. The sensor element of the humidity and temperature detection is SHT1x, and the sensor element of the illumination is S1133. The environment information can be extracted using equation (9) to (12). The humidity measurement value is RH_{true}, and the temperature measurement value is T. The module can be applied in smart home and greenhouse, too.

$$T_C = 0.01(SO_T) - 40 \tag{9}$$

$$RH_{linear} = -0.28 \times 10^{-6} (SO_{RH})^2 + 0.0405(SO_{RH}) - 4 \tag{10}$$

$$RH_{true} = (T_C - 23)(0.01 + 0.00008(SO_{RH})) + RH_{linear} \tag{11}$$

$$T = -40 + 0.04(SO_T) \tag{12}$$

IV. EXPERIMENTAL RESULT

In the power detection module, we use redundant management method and statistical prediction method to calculate the exact power [14, 15]. Then we can compute the standard deviation of each sensor to find out the error sensor for the module. If the standard deviation is bigger than threshold, we can say the current sensor to be broken. We must isolate the measured value of the current sensor, and replace it with other current sensor.

Now in the power detection module, the measured value of current sensor #4 to be broken. We can see the standard deviation (145.9) is bigger than threshold, and the standard deviation is bigger than others. We can diagnose the current sensor to be broken, and we can isolate the measured value. The experimental result is shown in Fig 4. Finally we can use these measured values of the other current sensors (#1, #2 and #4) to calculate the exact current value.

In the residual power prediction experiment, the user can set the critical power. The proposed method can calculate the residual time, and the power of the mobile robot down to the critical value.

In the Fig. 5, the user set the critical power to be 26 W. first, the mobile robot can fit the second-order curve using polynomial regression method. Then it can compute the residual time, display on the bottom of the monitor.

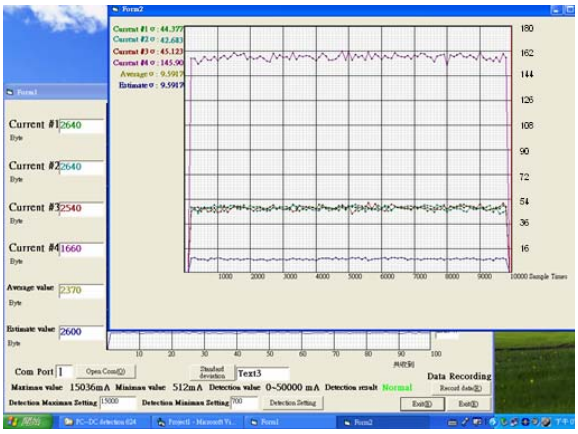

Fig. 4 The standard deviation variety of case II

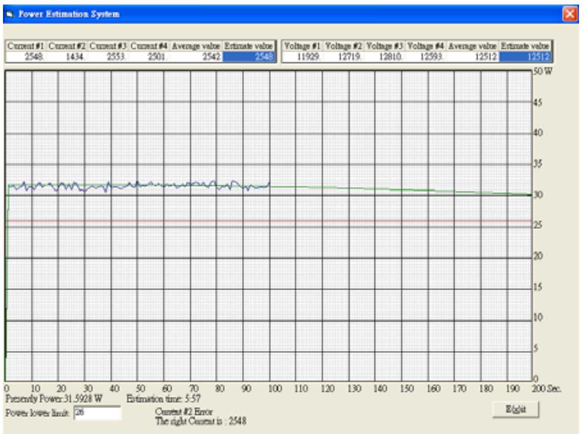

Fig. 5 The residual power prediction for 26W

V. CONCLUSION

We have presented a module-based security robot. These modules have environment module, fire detection module, gas detection module, master module and power detection module. The controller of these modules is HOLTEK microchip. we want to develop multisensor fusion algorithms to enhance the detection results through these detection modules. In the power detection module, we use redundant management method and statistical signal detection method to isolate faulty sensor, and estimates a exact current detection value for mobile robot. The module can transmits really current and voltage values and detection results to main controller (IPC) of the security robot using series interface (RS232). The main controller of the security robot can fit a second-order polynomial curve using auto-regression method. Then the user can select the critical power value to prediction the residual time on real-time for the security robot moving in free space.

ACKNOWLEDGMENT

This work was supported by the National Science Council of Taiwan, R. O. C. under Grand NSC 97- 2221- E-224-071-.

.

REFERENCE

[1] S. O. Lee, Y. J. Cho, M. H. Bo, B. J. You and S. R. Oh , "A stable target-tracking control for unicycle mobile robots," Proceedings of the IEEE/RSJ International Conference on Intelligent Robots and Systems, (IROS 2000) , Vol.3 , 2000 , pp.1822-1827.

[2] L. E. Parker and B. A. Emmons, "Cooperative multi-robot observation of multiple moving targets", Proceedings of the IEEE International Conference on Robotics and Automation,, vol.3, 1997, pp.2082-2089.

[3] H. Kobayashi and M. Yanagida, "Moving object detection by an autonomous guard robot", Proceedings of the 4th IEEE International Workshop on Robot and Human Communication, 1995, TOKYO, pp.323-326.

[4] Y. Shimosasa, J. Kanemoto, K. Hakamada, H. Horii, T. Ariki, Y. Sugawara, F. Kojio, A. Kimura and S. Yuta, "Some results of the test operation of a security service system with autonomous guard robot," 26th Annual Conference of the IEEE on Industrial Electronics Society, 2000 (IECON 2000), Vol.1, pp.405-409.

[5] Gilbreath, G. A., Ciccimaro, D. A., and H. R. Everett, "An Advanced Telereflexive Tactical Response Robot," Proceedings, Workshop 7: Vehicle Teleoperation Interfaces, IEEE International Conference on Robotics and Automation, ICRA2000, San Francisco, CA, 28 April, 2000.

[6] Ciccimaro, D. A., H. R. Everett, M. H. Bruch and C.B. Phillips, "A Supervised Autonomous Security Response Robot,", American Nuclear Society 8th International Topical Meeting on Robotics and Remote Systems (ANS'99), Pittsburgh, pp, 25-29 April, 1999.

[7] A. Bradshaw, "The UK Security and Fire Fighting Advanced Robot project,' IEE Colloquium on Advanced Robotic Initiatives in the UK, 1991, pp.1/1-1/4.

[8] Kuo L. Su, "Automatic Fire Detection System Using Adaptive Fusion Algorithm for Fire Fighting Robot," IEEE International Conference on System, Man and Cybernetics (SMC 2006), Grand Hotel, Taipei, Taiwan, October 2006, pp966-971. (EI)

[9] C. Pozna, "Modular Robots Design Concepts and Research Directions," The 5th International Symposium on Intelligent System and Information (SISY 2007), pp.113-118.

[10] Z. Dehuai, X. Gang Z. Jinming and L. Li, "Development of a Mobile Platform for Security Robot," Proceeding of the IEEE International Conference on Automation and Logistics, pp.1262-1267.

[11] Z. M. Bi and S. Y. T. Lang, "General Modular Robot Architecture and Configuration Design," Proceeding of the IEEE International Conference on Mechatronics & Automation, pp.268-273.

[12] E. Edwan and R. Fierro, "A Low Cost Modular Autonomous Robot Vehicle," Proceeding of the 38th Southeastern Symposium on System Theory, pp.245-249.

[13] R. C. Luo, K. L. Su and C. W Deng,"Power Supply Diagnosis System Using Redundant Sensor for Intelligent Security Robot," IEEE International Conference ON Industrial Electronic, Control,and Instrumentation(IECON2003),PP.2500-2506

[14] Ren C. Luo, Kuo L. Su, "Multilevel Multisensor Based Intelligent Recharging System for Mobile Robot," IEEE Transaction on Industry Electronic. Vol.55, No.1, January, 2008, pp.270-279.

[15] Kuo L. Su Jyh H. Tzou and Chien C. Liu, "Development of a Multisensor-Based Residual Power Prediction System for Mobile Robots," IEEE Workshop on Advanced Robotics and its Social Impacts 2007 (ARSO '07), Hsinchu, Taiwan, December 9-11, 2007, pp.114-119.

The Fourteenth International Symposium on Artificial Life and Robotics 2009 (AROB 14th '09),
B-Con Plaza, Beppu, Oita, Japan, February 5 - 7, 2009

High-speed laser localization for restaurant service mobile robot

Jyh-Hwa Tzou[1] and Kuo L. Su [2]

[1.] *Department of Mechanical Engineering, Wu-Feng Institute of Technology, Taiwan*
(tzoujyh@mail.wfc.edu.tw)
(Tel: 886-5-2267125ext22265; Fax : 886-5-2263723)

[2.] *Department of Electronical Engineering, National Yunlin University of Science and Technology, Taiwan*
(sukl@yuntech.edu.tw)

Abstract: Nowadays, service robots are very popular in robot family. The objective of this paper is to develop a restaurant service mobile robot. This service mobile robot can transfer dishes in the restaurant. It also can show the customers to the unoccupied table. The service efficiency of the restaurant service can be increased with this service robot. This service mobile robot is equipped with "Laser positioning system" The laser positioning system is used for rapid and precise positioning and guidance of the mobile robot.

Keywords: restaurant service mobile robot, Laser positioning system, mobile robot.

I. INTRODUCTION

There are many types of service robots, such as cleaning and house keeping robots, surveillance robots, edutainment robots, rehabilitation robots and so on [1-8]. It is hard to find the autonomous service robots to be used in a restaurant. L. Acosta et al. [9] a highly specialized autonomous robot. The task of the robot is the setting and clearing of tables in a controlled environment. The "Robot Kitchen" restaurant in Hong Kong is conducting a two week feasibility test featuring three robotic employees including a large robot that is equipped to take customer orders, transmit them to the kitchen, and deliver the meals to the customer's table [10]. Another Canadian robo-waiter developed for the 2001 Robo-Cup hosted by the American Association for Artificial Intelligence, Jose, is shown below serving a muffin to Minister of Industry Brian Tobin [11].

The restaurant service robots can help the waiters or waitresses to do many jobs, such as guiding customers, ordering dishes, and delivering meals. The restaurant service robots not only can assist the humanity to finish some jobs, but also they can dance or sing songs to amuse the customers. The service robots can play an important role in a "Robot" restaurant.

In this research, we have developed a restaurant service robot which is equipped with laser positioning system. The target or the motion path of the service robot can be easily changed.

II. HARDWARE STRUCTURE OF THE RESTAURANT SERVICE ROBOT

The restaurant service robot is equipped with laser positioning system. The target or the motion path of the service robot can be easily changed. The subsystems will be explained as the following contents. The structure and the photo of the second generation restaurant service robot is shown in Fig. 1.

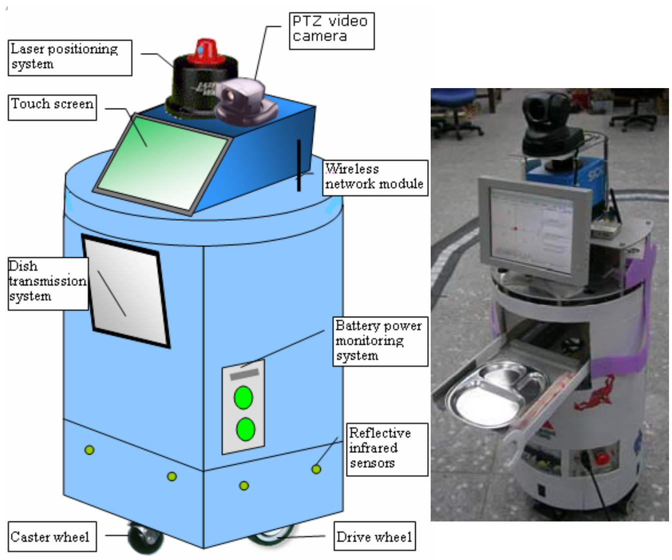

Fig 1. Structure of the second generation restaurant service robot

2.1 Design of the robot mechanism

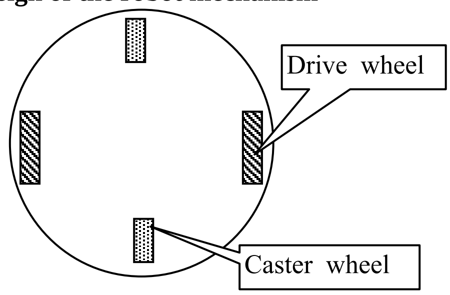

Fig 2. The differential drive system

The main body of the service robot is consisted with five layers of 40 cm circular aluminum alloy board. As shown in Fig. 2, the differential drive system is used in the robot platform. The drive wheels are placed on each side of the robot platform. Two DC servo motors with internal gear reduction are connected to the driving wheels. The caster wheels (non-driven wheels) with

©ISAROB 2009

spring damper are placed in front and rear sides of the robot platform.

2.2 Five layers structure of the service robot

(1) First layer (Bottom layer)

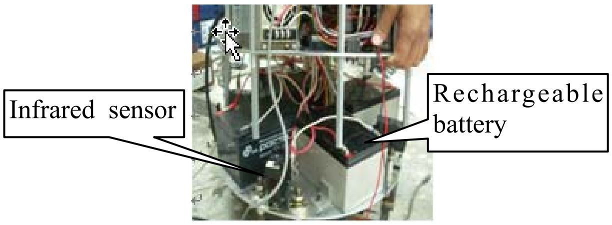

Fig 3. Layout of the bottom layer

Layout of the bottom layer is shown in Fig. 3. Four rechargeable batteries are placed on top of the bottom layer. Eight reflective type infrared sensors are attached around the bottom layer for obstacle avoidance.

(2) Second layer

The following subsystems (Fig. 4) are placed in the second layer:

- Switching power: transfer DC 24V(battery) to DC 5V, 12V
- Sensors signal transfer board: transfer the sensors output (DC 24V) to TTL signal level (DC 5V)
- Panel of the I/O card
- Voltage and current meter: monitoring the batteries power consumption
- DC servo motor drivers
- Emergency STOP button

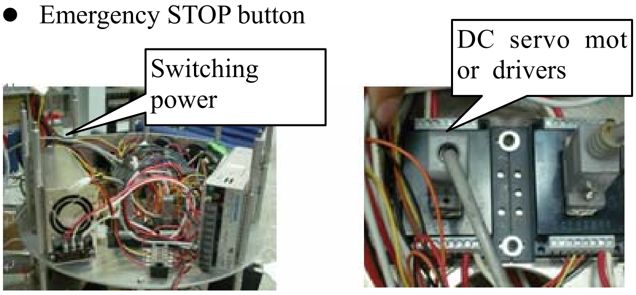

Fig 4. Layout of the second layer

(3)Third layer

The following subsystems (Fig. 5) were placed in the second layer:

- PC based robot controller
- Sensors data acquisition card (I/O card)
- USB to RS232 converter

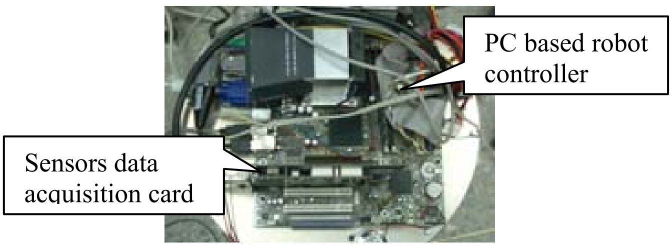

Fig 5. Layout of the third layer

(4) Fourth layer

The dish transmission system is put on the fourth layer. The dish transmission system consists of geared DC motor, chain, linear guides, limit switches, and dish plate. The dish plate is mounted on the linear guides. With the chain mechanism, the geared DC motor can move the dish plate forward and backward until it touches the limit switches.

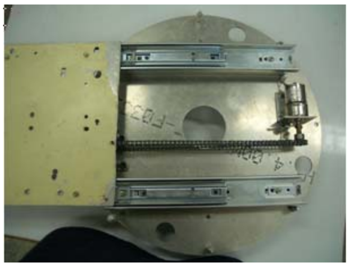

Fig 6. The dish transmission system (fourth layer)

(5)Fifth layer (Top layer)

The following subsystems (Fig. 7) were placed in the second layer:

- Touch screen
- Wireless network module
- Pan/Tilt/Zoom (PTZ) video camera
- Speaker
- Laser positioning system

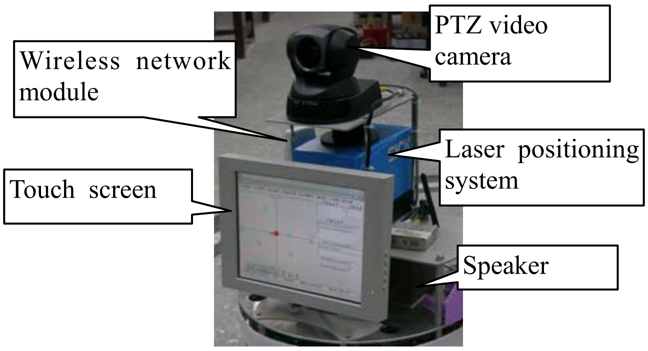

Fig 7. Layout of the top layer

2.3 Web based video monitoring system

Through the web based video monitoring system, the live image of the PTZ CCD camera on the robot can be transferred to the video server. As shown in Fig. 8, the staff on the counter can see the live image before the robot. Additional CCD cameras around the restaurant also can be integrated in this system for monitoring the robot or restaurant.

Fig 8. Web based video monitoring system

2.4 Obstacle avoidance system

As shown in Fig. 9, eight reflective infrared sensors are placed around the robot on the bottom layer for obstacle avoidance. Eight infrared sensors are numbered from 1 to 8 in a clockwise direction. If the obstacle is in front of the robot or on the left hand side, it will turn right. If the obstacle is on the right hand side, it will turn left.

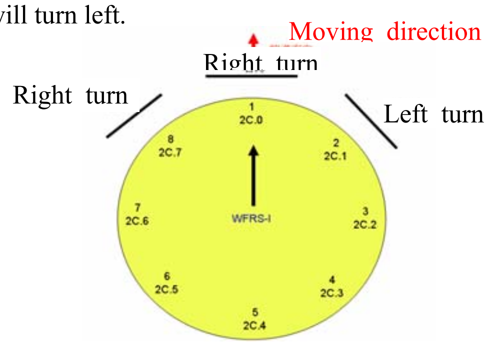

Fig 9. Eight reflective infrared sensors are placed around the robot on the bottom layer

If the robot moving forward, only part of the infrared sensors (No. 1, 2, 3, 7, 8) in front the robot are used to detect the obstacle. The other infrared sensors (No. 4, 5, 6) are used to detect free space behind the robot. The obstacle avoidance algorithm is shown in Fig. 10. In this figure, number "1" represents the infrared sensor detecting an obstacle. If all this five infrared sensors (No. 1, 2, 3, 7, 8) detect obstacles and the other infrared sensors (No. 4, 5, 6) do not detect any obstacle

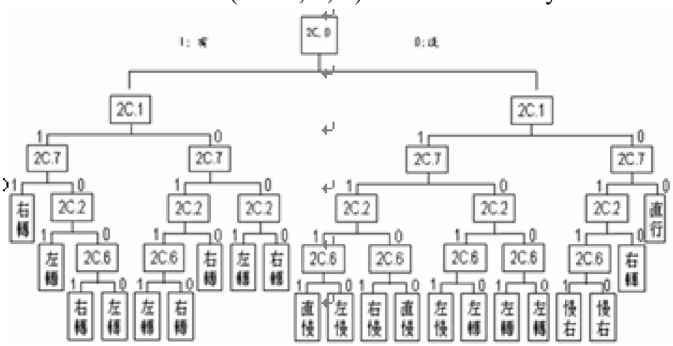

Fig 10. Obstacle Avoidance algorithm

2.5 Laser positioning system

As shown in Fig. 11, the laser positioning system is a component of a navigation system. It continuously supplies current positional data to the robot's computer, which makes course corrections based on this positional data. It scans its surroundings two-dimensionally through 360 . by means of its rotational movement and detects fixed, defined, reflector marks. The system has a serial interface for connecting to the computer of the service robot.

The laser positioning system's position and orientation is continuously calculated on the basis of the reflector positions known to the positioning system in an absolute "world co-ordinate system", and prepared for transfer. The movement of the positioning system itself is taken into account by continuous application of the speed vector, i.e. the system provides position and orientation data extrapolated to the point in time when the data was requested.

Fig 11. Laser positioning system

The laser positioning system operates like optical radar that has the task of detecting fixed reflectors within the surrounding area. The detection of three reflectors is sufficient to determine its position. Within this co-ordinate system, the laser positioning system determines its current absolute position in the x- and y-directions, including its angular position in the co-ordinate system (orientation).

Fig. 12 shows the relationship between the absolute and the local coordinate systems. The axes labeled Xl and Yl show the sensor's "local co-ordinate system" that moves around with it. The sensor zero point is at the rotational axis of the scanning head. The local coordinate system of the laser positioning system moves within a world co-ordinate system defined by the user:

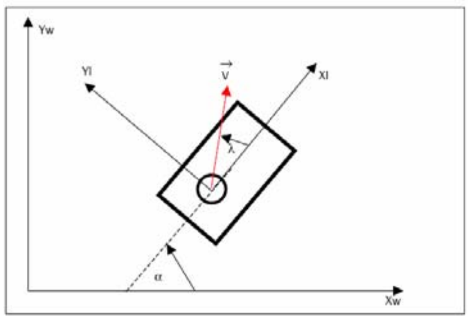

Fig. 12. Coordinate system of the laser positioning system

where:

(Xw, Yw) – World coordinate system

(Xl,Yl) – Local co-ordinate system of the laser positioning system

α= direction in the world co-ordinate system

V= speed vector

For example:

Transformation of the speed vector from local co-ordinate system in the world co-ordinate system:

$$
\begin{aligned}
Vx &= Vxl \times \cos\alpha - Vyl \times \sin\alpha \\
Vy &= Vxl \times \sin\alpha + Vyl \times \cos\alpha
\end{aligned} \qquad (1)
$$

III. EXPERIMENTAL RESULTS

3.1 Wander with obstacle avoidance

As shown in Fig.13 (a) - Fig.13 (e), the robot wanders with obstacle avoidance using the infrared sensors. From the experimental results, the robot can detect the static or dynamic obstacle. The robot dodges the obstacles without collision.

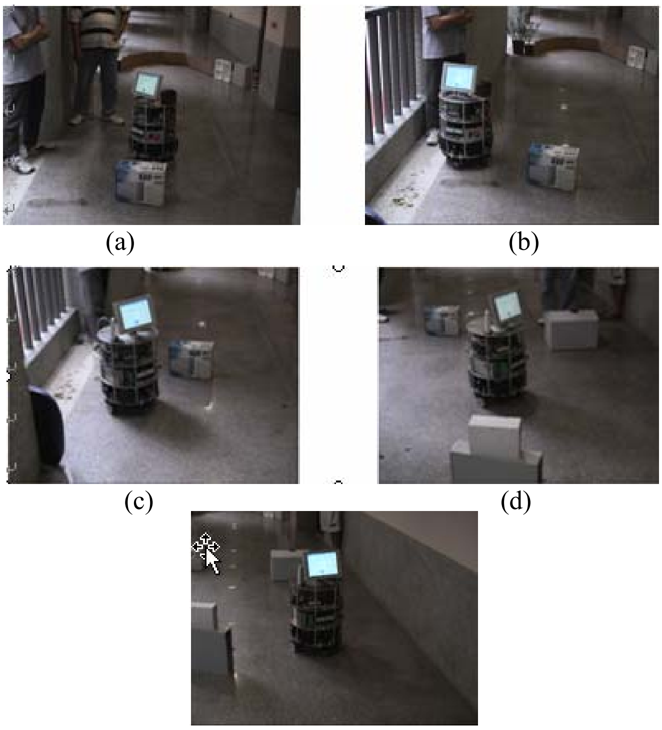

(a) (b) (c) (d) (e)

Fig 13. Wander with obstacle avoidance

3.2 Escape from dead-end zone

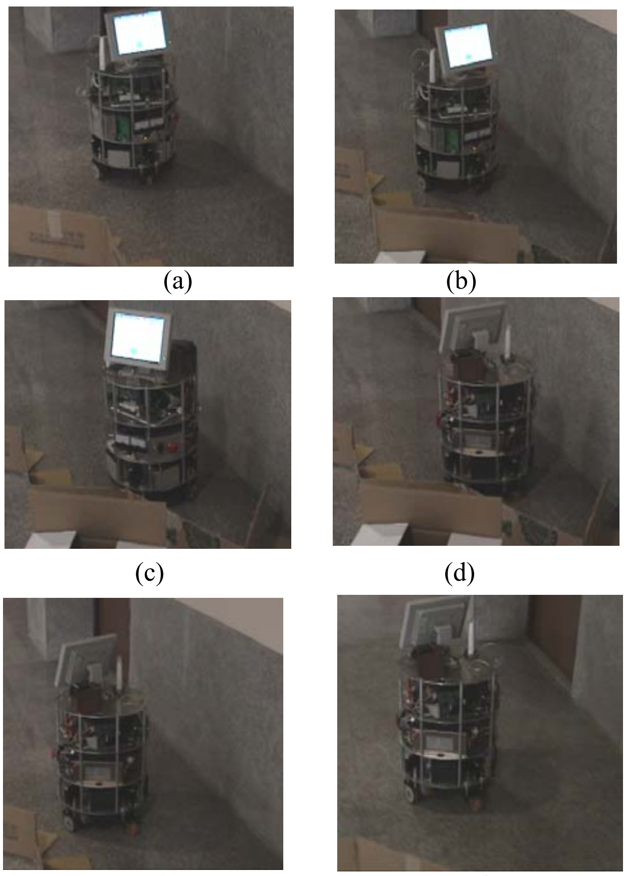

(a) (b) (c) (d) (e) (f)

Fig 14. Escape from dead-end zone

In this experiment, we will test the robot using obstacle avoidance algorithm to escape from dead-end zone. If all this five infrared sensors (No. 1, 2, 3, 7, 8) detect obstacles and the other infrared sensors (No. 4, 5, 6) do not detect any obstacle behind the robot, robot will make an 180° turn and then move straight. As shown in Fig. 14, the robot can escape from dead-end zone successfully.

IV. CONCLUSION

Service robots assist human beings, typically by performing a job that is dirty, dull, distant, dangerous or repetitive. Integration of robots with service industry is an important trend for now and the future. In this research, we have developed a restaurant service robot which is equipped with laser positioning system. The target or the motion path of the service robot can be easily changed.

The proposed restaurant service robot can transfer dishes in the restaurant. It also can show the customers to the unoccupied table. The service efficiency of the restaurant service can be increased with this service robot. This service mobile robot is equipped with "Laser positioning system". The laser positioning system is used for rapid and precise positioning and guidance of the mobile robot.

REFERENCES

[1] http://www.elibrary.com.tw/index.asp
[2] http://news.xinhuanet.com/it/2004-03/09/content_1354062.htm
[3] http://159.226.2.5:89/gate/big5/www.kepu.net.cn/gb/technology/robot/index.html
[4] http://www.stdaily.com/gb/innovation/2005-07/25/content_413157.htm
[5] http://www-1.expo2005.or.jp/cn/index.html
[6] http://www.sina.com.cn
[7] http://isci.cn.nctu.edu.tw/index.html
[8] http://www.ia.ee.ccu.edu.tw
[9] L. Acosta, E.J. González, J.N. Rodríguez, A.F. Hamilton, J.A. Méndez, S. Hernéndez, M. Sigut, and G.N. Maricha, "Design and implementation of a service robot for restaurant", International Journal of Robotics and Automation , Vol. 21, 2006.
[10] http://www.robots-dreams.com/2006/07/hong_kong_resta.html
[11] http://www.technovelgy.com/ct/Science-Fiction-News.asp?NewsNum=771

The Fourteenth International Symposium on Artificial Life and Robotics 2009 (AROB 14th '09),
B-Con Plaza, Beppu, Oita, Japan, February 5 - 7, 2009

PSO-Based Potential Field Method for a Mobile Robot Motion Planning in an Unknown Environment

Li-Chun Lai[1], Chia-Ju Wu[2], Jin-Tsong Jeng[3], Chia-Nan Ko[4], and Yu-Yi Fu[5]

[1]Department of Electrical Engineering, Chung Chou Institute of Technology
Yuanlin, Changhua 510, Taiwan
[2]Department of Electrical Engineering, National Yunlin University of Science and Technology
Douliou, Yunlin 640, Taiwan
[3]Department of Computer Science and Information Engineering, National Formosa University
Huwei, Yunlin 632, Taiwan
[4]Department of Automation Engineering, Nan Kai University of Technology
Tasotun, Nantou 542, Taiwan
[5]Department of Automation Engineering, Nan Kai University of Technology
Tasotun, Nantou 542, Taiwan
(email:[1]lclai@dragon.ccut.edu.tw; [2]WUCJ@yuntech.edu.tw;[3]tsong@nfu.edu.tw; [4]t105@nkut.edu.tw;[5]t098@nkut.edu.tw)

***Abstract*:** Based on a particle swarm optimization (PSO) algorithm to adjust attractive factor of potential function, a method is proposed to navigate a mobile robot from a given initial configuration to a desired final configuration in an unknown environment filled with obstacles. The potential field method has some problems that include oscillations in the presence of obstacles and oscillations in narrow passages. Thus, the paper uses PSO algorithm to adjust attractive factor and repulsive factor which is a fixed constant. By the attractive factor and repulsive factor of the potential function, the navigational path of the mobile robot is smooth and the shortest. To show the feasibility of the proposed method, the simulation results are included for illustration.

Keywords: Particle swarm optimization (PSO) algorithm; Mobile robot; Potential field method; Motion planning**.**

I. INTRODUCTION

Motion planning is an important issue in mobile robotics. In an environment with obstacles, the aim of path planning is to find a suitable collision-free path for a mobile robot to move from a given initial configuration to a desired final configuration.

The earliest algorithms for motion planning problems of robots deal with navigation of a robot in a completely known environment filled with stationary obstacles (Conte et al [1], Ge and Cui [2], Tsourveloudis et al [3], and Song and Kumar [4]). Another kind of motion planning algorithms deals with navigation of a robot in a completely unknown environment (Lee et al [5], Mester [6], and Toibero et al [7]). Since the environment is unknown to the mobile robot, different sensors such as computer vision, ultrasonics, and odometers will be used in these algorithms, and each of these algorithms shows its feasibility in different application areas.

The basic concept is to fill the working space of the robot with an artificial potential field in which the robot is attracted to its goal position and is repulsed away from the obstacles (Latombe [8]). This potential field method is particularly attractive because of its mathematical elegance and simplicity, and has been studied extensively for mobile robot motion planning in the past decade (Ge and Cui [2], Tsourveloudis et al [3], Song and Kumar [4], Latombe [8], and Lai et al [9]). However, this method has some problems, such as oscillations in the presence of obstacles and oscillations in narrow passages. Particle Swarm Optimization (PSO) algorithm proposed by Kennedy and Eberhart [10] is another kind of evolutionary computation techniques. This method was based on the simulation of simplified animal social behaviors such fish schooling and bird flocking. In PSO searching space, each single solution acts as a flying bird, which we call it a particle. The PSO algorithm works on a social behavior of particles in the swarm. It finds the global best solution by simply

©ISAROB 2009

adjusting the trajectory of each particle its own best particle and toward the best particle of the entire swarm at each generation. The PSO algorithm has been used in solving many optimization problems successfully. Compared with GA, the advantage of PSO is that it is easier to implement and there are fewer parameters to be adjusted. In this paper, The PSO algorithm is proposed to determine attractive factor of the potential field function, then the path of the mobile robot is smooth and shortest from a given initial configuration to a desired final configuration in an unknown environment.

The remaining sections of this paper are organized as follows. Section 2 shows the potential field method. Section 3 presents a PSO-based potential field method for robot navigation in an unknown environment. Simulations are performed in Section 4 to confirm the feasibility of the proposed algorithm. Section 5 concludes the paper.

II. POTENTIAL FIELD FOR MOTION PLANNING

1. Potential Field Method

In the previous research of potential field methods, for simplicity, a robot is usually treated as a point. If the position of the robot is denoted by $[x_r, y_r]$, then the most commonly used attractive potential field between a robot and an obstacle takes the following form Latombe [8]

$$U_{att} = \frac{1}{2}\xi[(x_r - x_g)^2 + (y_r - y_g)^2] \quad (1)$$

where ξ is a positive scaling factor and $[x_g, y_g]$ denotes the position of the goal point. The corresponding attractive force is then given by the negative gradient of the attractive potential field

$$\mathbf{F}_{att} = -\nabla U_{att} = \xi \begin{bmatrix} x_g - x_r \\ y_g - y_r \end{bmatrix} \quad (2)$$

which converges linearly toward zero as the robot approaches the goal.

On the other hand, one commonly used repulsive potential field between a robot and an obstacle takes the following form Latombe [8]

$$U_{rep} = \begin{cases} \frac{1}{2}\eta\left(\frac{1}{\sqrt{(x_r - x_{obs})^2 + (y_r - y_{obs})^2}} - \frac{1}{\rho}\right)^2, & \text{if } \sqrt{(x_r - x_{obs})^2 + (y_r - y_{obs})^2} \le \rho \\ 0, & \text{otherwise} \end{cases} \quad (3)$$

where η is a positive scaling factor, ρ is a positive constant denoting the distance of influence of the obstacle, and $[x_{obs}, y_{obs}]$ denotes the point on the obstacle such the distance $\sqrt{(x_r - x_{obs})^2 + (y_r - y_{obs})^2}$ is minimal. The corresponding repulsive force is then given by

$$\mathbf{F}_{rep} = -\nabla U_{rep} = \begin{cases} \begin{bmatrix} F_{rep,x} \\ F_{rep,y} \end{bmatrix}, & \text{if } \sqrt{(x_r - x_{obs})^2 + (y_r - y_{obs})^2} \le \rho \\ 0, & \text{otherwise} \end{cases} \quad (4)$$

where

$$F_{rep,x} = \eta\left(\frac{1}{\sqrt{(x_r - x_{obs})^2 + (y_r - y_{obs})^2}} - \frac{1}{\rho}\right) \cdot \frac{(x_r - x_{obs})}{\sqrt{(x_r - x_{obs})^2 + (y_r - y_{obs})^2}} \cdot \frac{1}{(x_r - x_{obs})^2 + (y_r - y_{obs})^2} \quad (5)$$

$$F_{rep,y} = \eta\left(\frac{1}{\sqrt{(x_r - x_{obs})^2 + (y_r - y_{obs})^2}} - \frac{1}{\rho}\right) \cdot \frac{(y_r - y_{obs})}{\sqrt{(x_r - x_{obs})^2 + (y_r - y_{obs})^2}} \cdot \frac{1}{(x_r - x_{obs})^2 + (y_r - y_{obs})^2} \quad (6)$$

The total force applied to the robot is the sum of the attractive force and the repulsive force

$$\mathbf{F}_{total} = \mathbf{F}_{att} + \mathbf{F}_{rep} \quad (7)$$

which will determine the movement of the robot.

2. Kinematics of the Mobile Robot

By assuming that the wheels do not slip, the kinematics of the mobile robot as shown in (8).

$$\begin{aligned} x_r(k+1) &= x_r(k) + \Delta d \cos\theta(k) \\ y_r(k+1) &= y_r(k) + \Delta d \sin\theta(k) \\ \theta(k+1) &= \mathbf{F}_{total} \end{aligned} \quad (8)$$

where Δd is the moving distance in sampling interval k.

III. DETERMINATION OF ATTRACTIVE FACTOR WITH PSO METHOD

The attractive factor ξ plays an important role in the proposed potential field method. If its value is very large, then only the influence of the attractive force will be taken into account. On the other hand, if its value is quite small, then the attractive force will be neglected. However, there is no systematic way to determine it. Therefore, the PSO is used to serve for this purpose. The mathematic description of PSO is as the follow:

Suppose the dimension of the searching space is D, the number of particle is n. Vector $\vec{x}_i = (x_{i1}, x_{i2}, \ldots, x_{iD})$ represents the position of the i-th particle and $P_i = (p_{i1}, p_{i2}, \ldots, p_{iD})$ is the best position searched by now, and the whole particle swarm's best position is represented as $P_g = (p_{g1}, p_{g2}, \ldots, p_{gD})$ Vector $\vec{v}_i = (v_{i1}, v_{i2}, \ldots, v_{iD})$ is the position change rate of the i-th particle. Each particle updates its position according to the following formulas:

$$v_{id}(k+1) = w \times v_{id}(k) + c_1 \times rand(\,) \times (p_{id}(k) - x_{id}(k)) + c_2 \times rand(\,) \times (p_{gd}(k) - x_{id}(k)) \tag{9}$$

$$x_{id}(k+1) = x_{id}(k) + v_{id}(k+1) \tag{10}$$

Where c_1 and c_2 are positive constant parameters called acceleration coefficients. The $rand(\,)$ is a random function with the range [0,1]. w is called the inertia weight and is less than 1.

The fitness function of PSO algorithm is defined as

$$fitness = \frac{1}{\lambda d_{rg} + 1} \tag{11}$$

where $d_{rg} = \sqrt{(x_r - x_g)^2 + (y_r - y_g)^2}$ and the value λ (12) prevents the mobile robot through the obstacle to the goal point.

$$\lambda = \begin{cases} a, & \text{if } \sqrt{(x_r - x_{obs})^2 + (y_r - y_{obs})^2} \le \rho \\ 1, & \text{otherwise} \end{cases} \tag{12}$$

where a is a large value.

The details of the determination of the attractive factor can be summarized as follows:

Algorithm A:

Step 1: Define the problem space.

Step 2: Initialize an array of particles with random positions and velocities.

Step 3: Evaluate the desired fitness function of the particles using equation (11).

Step 4: Determine the best personal position visited so far by each particle.

Step 5: Determine the best global position visited so far by all the particles.

Step 6: Update velocities using Eq. (9).

Step 7: Update particles' positions using Eq. (10).

Step 8: Repeat the procedure in Step 3 through Step 7 until all the particles have attained their desired fitness.

IV. SIMULATION RESULTS

Example 1:

In this simulation example, it will be shown how to apply Algorithm A to determine the attractive factor ξ when performing the proposed navigation algorithm, the value Δd and ρ are chosen to 0.1m and 0.5m, respectively. The initial position and final position of the mobile robot are (1m, 1m) and (9m, 7.5m) in a completely unknown environment. The attractive factor and repulse factor of the potential field method are chosen to be 5 and 5; the simulation result is shown in Fig. 1. It is applying Algorithm A in Fig. 2, the value c_1, c_2, the inertia weight, and a are chosen to be 2, 2, 0.8, and 100000, respectively. The fitness function is defined as in (11). The navigation distance of mobile robot is 13.6m and 11.8m in Fig. 1 and Fig. 2, respectively. The shortest path of the mobile robot is obtained in Fig. 2 with algorithm A.

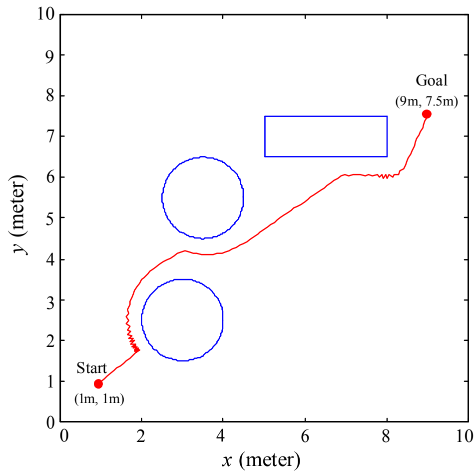

Fig. 1 The navigation distance of mobile robot is 13.6m from the initial configuration (1m, 1m) to the final configuration (9m, 7.5m) with the attractive factor and repulse factor of the potential field method are chosen to be 5 and 5.

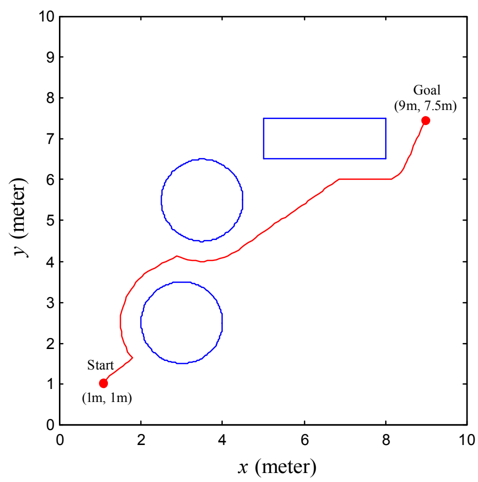

Fig. 2 The navigation distance of mobile robot is 11.8m from the initial configuration (1m, 1m) to the final configuration (9m, 7.5m) with Algorithm A.

©ISAROB 2009

Example 2:

In this simulation example, the narrow passage is shown in Fig. 3. The value Δd and ρ are chosen to 0.1m and 0.5m, respectively. The initial position and final position of the mobile robot are (1m, 6.1m) and (9m, 6.1m) in a completely unknown environment. The attractive factor and repulse factor of the potential field method are chosen to be 5 and 5; the simulation result is shown in Fig. 3. It is applying Algorithm A in Fig. 4, the value c_1, c_2, the inertia weight, and a are chosen to be 2, 2, 0.8, and 100000, respectively. The fitness function is defined as in (11). The mobile robot can not reach the final position in Fig. 3. The navigation path of the mobile robot can reach the final position in Fig. 4 with algorithm A.

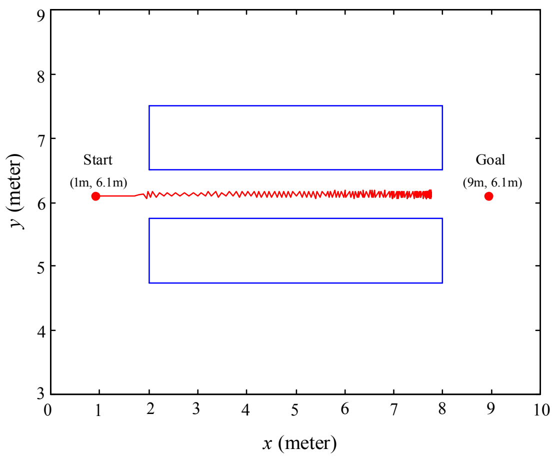

Fig. 3 The mobile robot can not reach the final configuration from the initial configuration (lm, 6.1m) to the final configuration (9m, 6.1m) with the attractive factor and repulse factor of the potential field method are chosen to be 5 and 5.

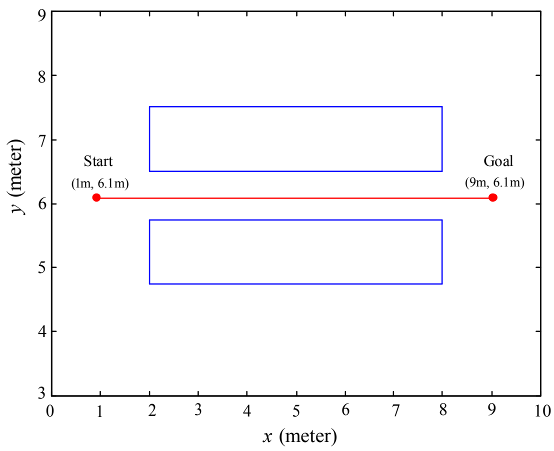

Fig. 4 The navigation distance of mobile robot is 8m from the initial configuration (lm, 6.1m) to the final configuration (9m, 6.1m) with Algorithm A.

V. CONCLUSIONS

The paper uses PSO algorithm to adjust attractive factor of potential function, a method is proposed to navigate a mobile robot from a given initial configuration to a desired final configuration in an unknown environment filled with obstacles. Compared with most other potential field function, the PSO algorithm can solve oscillations in the presence of obstacles and oscillations in narrow passages problems. The simulation results can show the feasibility of the proposed method.

ACKNOWLEDGMENTS

This work was supported in part by the National Science Council, Taiwan, R.O.C., under grants NSC96-2628-E-224-007-MY2.

REFERENCES

[1] Conte G, Longhi S, Zulli R (1996), Robot motion planning for unicycle and car-like robots. International Journal of Systems Science 27: 791–798

[2] Ge SS, Cui YJ (2000), New potential function for mobile robot path planning. IEEE Trans. on Robotics and Automation 16(5):615–620

[3] Tsourveloudis NC, Valavanis KP, Hebert T (2001), Autonomous vehicle navigation utilizing electrostatic potential fields and fuzzy logic. IEEE Trans. on Robotics and Automation 17(4):490–497

[4] Song P, Kumar V (2002), A potential field based approach to multi-robot manipulation. Proceedings of the IEEE International Conference on Robotics and Automation 2:1217–1222

[5] Lee TL, Lai LC, Wu CJ (2005), A fuzzy algorithm for navigation of mobile robots in unknown environments. IEEE International Symposium on Circuits and Systems 4:3039–3042

[6] Mester G (2007), Obstacle avoidance of mobile robots in unknown environments. 5th International Symposium on Intelligent Systems and Informatics, pp. 123–127

[7] Toibero JM, Carelli R, Kuchen B (2007), Switching control of mobile robots for autonomous navigation in unknown environments. IEEE International Conference on Robotics and Automation, pp. 1974–1979

[8] Latombe J (1991), Robot Motion Planning. Kluwer, Boston, MA, USA

[9] Lai LC, Wu CJ, Shiue YL (2007), A potential field method for robot motion planning in unknown environments. Journal of the Chinese Institute of Engineers 30(3):369–377

[10] Kennedy J, Eberhart R (1995), Particle swarm optimization. IEEE International Conference on Neural Network, pp. 1942–1948

The Fourteenth International Symposium on Artificial Life and Robotics 2009 (AROB 14th '09),
B-Con Plaza, Beppu, Oita, Japan, February 5 - 7, 2009

Motion Planning of Mobile Robots Using Laser Range Finder

Jr-Hung Guo[2], Kuo-Lan Su[1], Chia-Ju Wu[1], Sheng-Ven Shiau[2],

[1]Department of Electrical Engineering, National Yunlin University of Science & Technology, Yunlin, Taiwan

[2]Graduate school Engineering Science and technology, National Yunlin University of Science & Technology

sukl@yuntech.edu.tw, g9610808@yuntech.edu.tw

Abstract: We design a mobile robot with distribution structure for the intelligent life space. The mobile robot is constructed using aluminum frame. The mobile robot has the shape of cylinder and its diameter, height and weight is 40 cm, 80cm and 40kg. There are six systems in the mobile robot, including structure, avoidance obstacle and driver system, software development system, detection module system, remote supervise system and others. In the avoidance obstacle and driver system, we use NI motion control card to drive two DC servomotors of the mobile robot, and detect obstacle using laser range finder and laser positioning system. Finally, we control the mobile robot using NI motion control card and MAXON driver according the programmed trajectory. The mobile robot can avoid obstacle using laser range finder, and follow the programmed trajectory. We develop the user interface with four functions for the mobile robot. In the security system, we design module based security devices to detect dangerous event, and transmit the detection results to the mobile robot using wireless RF interface. The mobile robot can move the event position using laser positioning system.

Keywords: Mobile robot、NI motion control card、Laser range finder、Laser positioning system

1. INTRODUCTION

With the robotic technologies development with each passing year, Mobile robots have been widely applied in many fields. Such as factory automation dangerous environment detection, office automation, hospital, entertainment, education, space exploration, farm automation, military and security system. Recently more and more research takes interest in the field especially intelligent mobile robot. There are some successful examples, ASIMO, KHR, QRIO, WABIAN-2R and AIBO. In our lab, we have been designed a mobile robot (ISLR-I) to fight fire source [1, 2].

The autonomous mobile robot and automatic guide vehicle are a growing interest and a popular subject. They have been implemented widely in many areas. But in the real world, the surrounding environment is unconstructive and complex. So how to program the motion trajectory and obstacle avoidance problem is fundamental, yet the important part of the autonomous or the semi-autonomous navigates mobile robot. How to plan the mobile robot efficiently to complete missions is an important task in the home and building.

In the recently, many exports research in the autonomous mobile robot. Some researches addressed in developing intelligent system of mobile robots [3, 4, 5]. Javier Minguez et al. proposed a navigation method to drive an autonomous mobile robot in unknown or uncertain environment [5]. Yoichi Shimosasa et al. developed autonomous guard robot [6, 7] which integrate the security and service system, the robot can guide visitors in daytime and patrol at the night. There are many methods to be developed in the motion trajectory of mobile robots. In the paper, we use laser range finder to avoid obstacle on the mobile robot, and locate the position of the mobile robot using laser position device.

The paper is organized as follows: Section II describes the system structure of the mobile robot, and describes the avoidance obstacle and position system using laser range finder and laser positioning device. Section III presents the principle of the motion planning of the mobile robot according to the programmed trajectory. The user interface is described in section IV. Section V presents the experimental results of the proposed method. Section VI presents brief conclusion remark.

2. SYSTEM ARCHITECTURE

The mobile robot is constructed using aluminium frame. The contour of the mobile robot is cylinder. The diameter is 40 cm, and height is about 80cm. Fig. 1 shows the hardware configuration of the mobile robot (ISLR.-I). The main controller of the mobile robot is industry personal computer (IPC). In the paper, we are interesting in the motion trajectory planning, avoidance obstacle and security detection of the mobile robot.

The hardware devices of the mobile robot have GSM modern, batteries, NI motion control card, MAXON drivers, laser range finder, laser positioning system,

©ISAROB 2009

wireless LAN interface, alarm device, GSM modem, detection module, touch screen, remote supervised computer, wireless RF interface, driver system and some hardware devices [8]. The mobile robot can communicate with the remote supervised computer through wireless Internet.

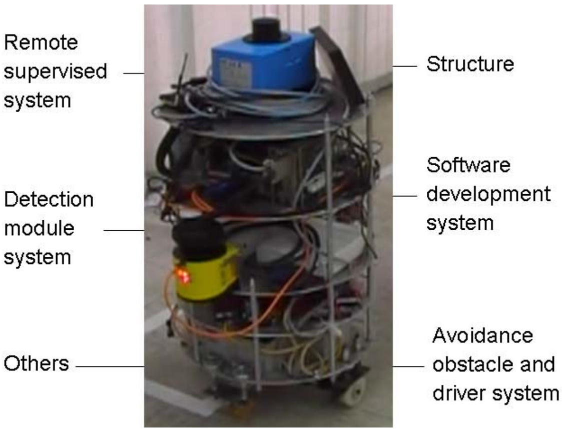

Fig. 1 The structure of the mobile robot

In the motion control function, the user can orders command to control two DC servomotors through motion control card and MAXON driver devices. In the avoidance obstacle function, the mobile robot can use laser range finder to detect obstacle, and locate the position of the mobile robot using laser positioning system. In the detection system, there are fire detection device, gas detection device, digital input device, power detection device and environment detection device, etc. The transmission interface between the detection device and the mobile robot is wireless RF interface (RS232), and the transmission interface between the mobile robot and the remote supervised computer and the mobile robot is wireless Internet.

3. THE MOTION PLANNING

The obstacle detection device of the mobile robot is laser range finder. The type is S200 that is produced by SICK. The device S200 is an optical sensor that its surroundings in two dimensions using infrared laser beams. The maximum distance is about 30 m. The location device of the mobile robot use laser positioning system. The type is NAV200 that is produced by SICK, too. The NAV200 laser positioning system continuously determines its own position and orientation with an industrial area using fixed reflectors. The measured range is about 30m.

How to locate the position of the mobile robot? We can use the geometry relation to calculate the orientation and displacement of the mobile robot. We can define the initial position of the mobile robot is at the start point (x_i, y_i), and move to the next point (x_{i+1}, y_{i+1}). It is shown in Fig. 2. The mobile robot can acquire the position axis (x, y) from the laser positioning system. We can use the equation (1) to modify the orientation angle of the mobile robot, and control the mobile robot move to the next point (x_{i+1}, y_{i+1}).

$$\theta = Tan^{-1}\frac{y - y_i}{x - x_i} - Tan^{-1}\frac{y_{i+1} - y}{x_{i+1} - x} \quad (1)$$

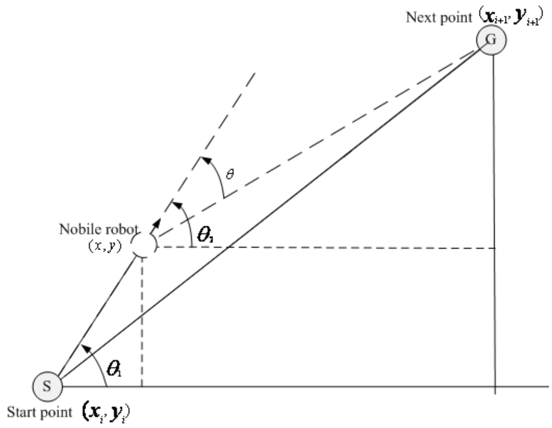

Fig. 2 The structure of the mobile robot

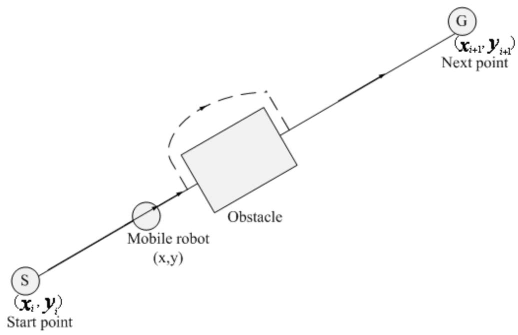

Fig. 3 The structure of the mobile robot

The motion trajectory of the mobile robot has obstacle, and the mobile robot must avoid obstacle using laser range finder. It is shown in Fig. 3. The mobile robot can measure the distance between the mobile robot and the obstacle using laser range finder. The distance is small than threshold, and the mobile robot can turn left about $\pi/2$. Then it can walk following the obstacle with fixed distance using laser range finder. Otherwise the mobile robot moves forward to the next point. The mobile robot arrives at the motion trajectory according to the laser position system, and it can turn left about $\pi/2$. Next it can move forward to the next point (x_{i+1}, y_{i+1}).

4. USER INTERFACE

The user interface of the mobile robot has four functions to be shown in Fig. 4. It contains obstacle detection interface, environment detection interface, motion planning interface and location interface. The obstacle detection interface is shown in Fig. 4(a). It can display surrounding status using laser range finder on the left side of the monitor. The right side of the monitor can display the measured values of the ultrasonic sensors and reflected infrared sensors. We can use these sensory data to enhance the accuracy using multisensor fusion algorithms.

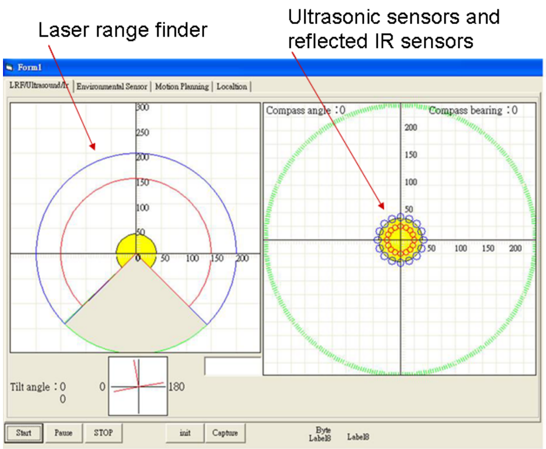

(a) The obstacle detection interface

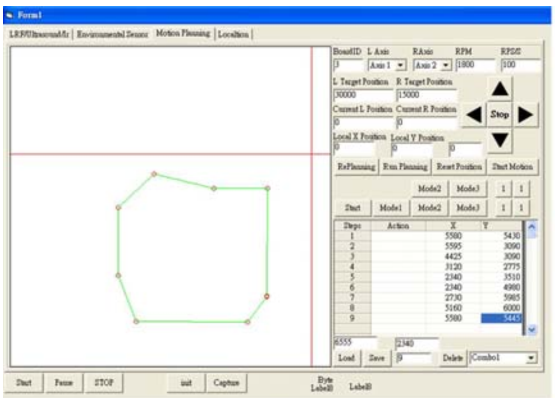

(b) The motion planning interface
Fig. 4 The user interface of the supervised system

The motion planning interface of the mobile robot is shown in Fig. 4(b). The user can program the motion trajectory on the left side of the monitor, and the position axis of the intersection can be listed in the right side. The parameter setting values of the motion planning function are programmed on the right side. The user can control the mobile robot on manual in the region.

5. EXPERINMENTAL RESULTS

We design two experimental scenarios for the motion planning function of the mobile robot. The first term is motion trajectory experiment. We set the trajectory to be rectangle. It is shown in Fig.5(a). The other is avoidance obstacle experiment to be shown in Fig. 5(b). The mobile robot can be programmed the motion trajectory according to the Fig 5(a). Then we make a test using the mobile robot. First the mobile robot stops at the start point, and move to the goal point according to the proposed method. It can acquire the position axis and orientation angle using the laser positioning system, and modify the orientation using the equation (1). Then it can move to the next intersection. The mobile robot turn left, and modifies the error angle. The mobile robot can face to the next intersection. Finally it can move to the goal point. The experimental results are shown in Fig. 6.

Next we place four obstacles in the motion trajectory of the mobile robot. The mobile robot can measure the distance from the obstacle using laser range finder. The distance is small than the threshold, the mobile robot can turn left about $\pi/4$, and walk following the obstacle to the next position. The experimental scenario is shown in Fig. 7.

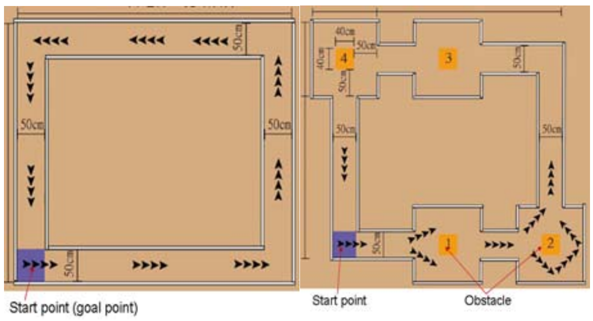

(a) (b)
Fig. 5 The user interface of the supervised system

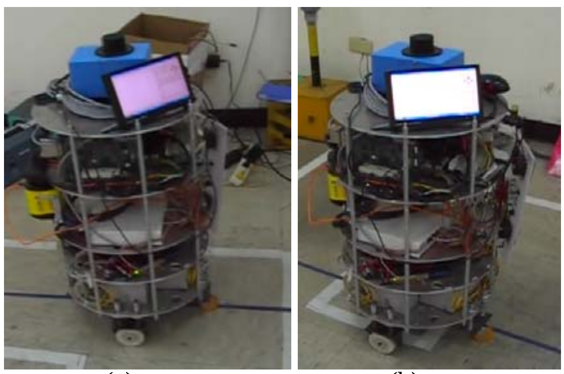

(a) (b)

©ISAROB 2009

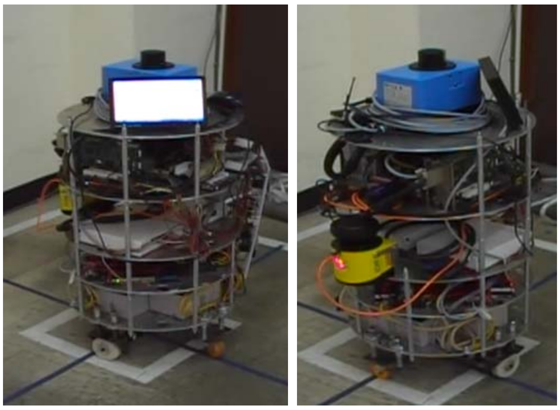

(c) (d)

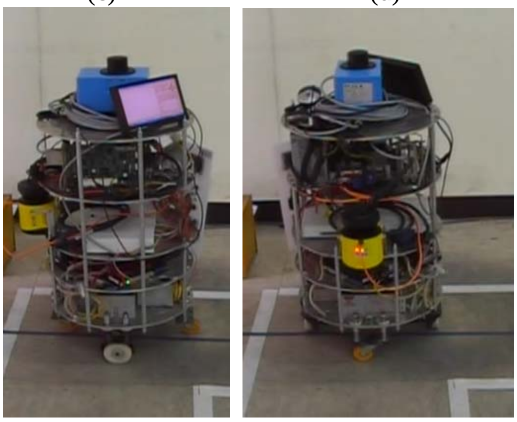

(e) (f)

Fig. 6 The motion trajectory experiment

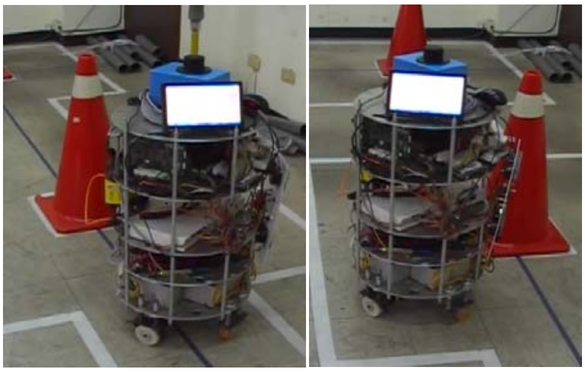

(a) (b)

Fig. 7 The avoidance obstacle experiment

6. CONCLUSION

We design an intelligent mobile robot for perfect life on home automation, and present a motion trajectory problem of the four-wheeled mobile robot using laser range finder and laser positioning device. The mobile robot has six system, including structure, avoidance obstacle and driver system, software development system, detection module system, remote supervise system and others. The motion trajectory of the mobile robot is programmed using kinematic method. The major advantage of the proposed method is that the motion trajectory of mobile robot is easily programming, and can be used in obstacle avoidance system. The main controller can establish the control command to the NI motion control card, and control the mobile robot move along the programmed trajectory. Then we use the mobile robot applying in the security system of the home automation.

ACKNOWLEDGMENT

This work was supported by the project "Design of the platform for intelligent Robot" under Ministry of Education of Taiwan, R. O. C. (97-E-03-064).

REFERENCES

[1] T. L. Chien, J. H. Guo, K. L. Su and S. V. Shiau, "Develop a Multiple Interface Based Fire Fighting Robot," IEEE International Conference on Mechatronics (ICM 2007), Kumamoto, Japan, WA1-B-3, May 8-10, 2007.

[2] K. L. Su, "Automatic Fire Detection System Using Adaptive Fusion Algorithm for Fire Fighting Robot," IEEE International Conference on System, Man and Cybernetics (SMC 2006), Grand Hotel, Taipei, Taiwan, pp966-971, October 2006.

[3] S. O. Lee, Y. J. Cho, H. B. Myung, B. J, You and S. R. Oh, "A Stable Target-Tracking Control for Unicycle Mobile Robot," International Conference on Intelligent Robots and Systems (IROS), Vol. 3, pp.1822-1827, 2000.

[4] J. Minguez and L. Montano, "Nearness Diagram (ND) Navigation: Collision Avoidance in Troublesome Scenarios," IEEE Transaction on Robotics and Automation, Vol. 20, pp.45-49, 2004.

[5] H. Kobayashi, and M. Yanagida, "Moving Object Detection by An Autonomous Guard Robot", IEEE International Workshop on Robot and Human Communication, Tokyo, pp.323-326, 1995.

[6] Y. Shimosasa, J. Kanemoto, K. Hakamada, H. Horii, T. Ariki and Y. Sugawara, F. Kojio, A. Kimura and S. Yuta, "Some Results of The Test Operation of a Security Service System With Autonomous Guard Robot," IEEE International Conference on Industrial Electronic, Control, and Instrumentation(IECON2000), pp.405-409.

[7] Y. Shimosasa, J. Kanemoto, K. Hakamada, H. Horii, T. Ariki and Y. Sugawara, F. Kojio, A. Kimura and S. Yuta, "Security Service System Using Autonomous Mobile Robot," IEEE International Conference on System, Man, and Cybernetics, (SMC1999), pp.825-829.

[8] K. L. Su, T. L. Chien and J. H. Guo, "Design a Low Cost Security Robot Applying in Family," International Conference on Autonomous Robots and Agents, December 13-15, 2004, Palmerston North, NZ, pp.367-372.

©ISAROB 2009

The Fourteenth International Symposium on Artificial Life and Robotics 2009 (AROB 14th '09),
B-Con Plaza, Beppu, Oita, Japan, February 5 - 7, 2009

Image-Guided Searching for Landmark

C.C. Wang[1], S.F. Lien[2], K.H. Hsia[3] and J.P. Su[4]

[1]*Department of Electronic Engineering, Chienkuo Technology University*
No. 1, Chieh Shou N. Rd., Changhua City, Taiwan, R.O.C.
(Tel : 886-4-7111111ext3350; Fax : 886-4-7111139)
(Email address: jasonccw@ctu.edu.tw)
[2]*Graduate School of Engineering Science & Technology (Doctoral Program)*
National Yunlin University of Science & Technology
[3] *Department of Management Information System, Far East University*
[4]*Department of Electrical Engineering, National Yunlin University of Science & Technology*

Abstract: A novel image-guided structure is proposed in this paper for searching any apron. The key feature of the presented structure is the introduction of a stationary camera placed beneath the helicopter so that it can arrive at the right top of any apron by image-guided searching. The validity of the proposed image-guided structure is verified by means of a practical testing on an experimental Ball & Plate apparatus. The experimental results validate the superiority and practicality of the image-guided searching for landmarks.

Keywords: Image-Guided Searching, Landmark, Ball & Plate Platform.

I. INTRODUCTION

Over the past twenty years, the machine vision has been successfully used for robotic development and servo-position control. For example, pneumatic robotic arm controlled by on-off valves for automatic harvesting based on vision localization [1], automatic micro-indentation and inspection system by piezo driven micro robot with multiple inner sensors [2], and localization and error correction for mobile robot with an image sensor [3] etc., deal with positioning problems via machine vision. However, as regards image-guided control, few researchers delve into flying robots. In 2007, Kei Watanabe et al. presented an image-based visual servo control for a micro helicopter [4]. A stationary camera is placed on the ground, and it obtains image features of the helicopter. This visual servo system enables the helicopter to enter a stationary hover procedure, but it still does not apply to anyplace.

In this paper, we place a stationary camera beneath the helicopter so that it can arrive at the right top of any apron by image-guided searching. To illustrate the effectiveness of the design, the proposed method will be verified through practical testing on an experimental setup, called Ball and Plate system. The experimental results validate the superiority and practicality of the image-guided searching for landmarks.

II. IMAGE-GUIDE ALGORITHM

To obtain a relative location of the landmark to the helicopter, an image-guided searching algorithm will be used to evaluate the center of the landmark and the moving vector. These procedures for the image processing are shown in Fig. 1.

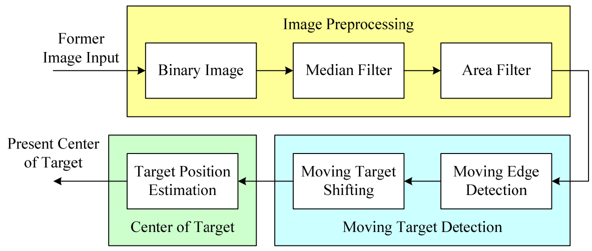

Fig. 1. Procedures for image processing

2.1 Image Preprocessing

The image preprocessing contains binarization and filtering with the aim of distinguishing the object from the background. To reduce the data, the three-dimensional RGB-image information is transformed into a one-dimensional colour axis in this paper. Unfortunately, the regulation of the threshold value usually produces noises. To improve image quality, the median and area filter will be used to reduce these noises.

2.2 Moving Target Detection

A. Sobel Filter

To detect the edge of a binarized picture, Sobel filter is the most common and very useful tool. The following two matrices are used as the filtering operators:

$$G_x = \begin{bmatrix} -1 & 0 & 1 \\ -2 & 0 & 2 \\ -1 & 0 & 1 \end{bmatrix} \tag{1}$$

$$G_y = \begin{bmatrix} 1 & 2 & 1 \\ 0 & 0 & 0 \\ -1 & -2 & 1 \end{bmatrix}, \tag{2}$$

where G_x and G_y are used for edge detection along x-direction and y-direction, respectively. These two 3x3

©ISAROB 2009

convolution masks are applied to each pixel. The result of each convolution is treated as a vector representing the edge through the current pixel. If the magnitude of the sum of these two orthogonal vectors is greater than any user-specified threshold, the pixel is marked in black as an edge. Otherwise, the pixel is set to white.

B. Moving Edge Detection

To extract the background automatically, enough number of successive structures must be available for processing. The procedures for moving edge detection are shown in Fig. 2. First, three successive structures (I_t , I_{t+1} , I_{t+2}) will be taken from CCD and the differences $D[I_{t+2}-I_{t+1}]$ and $D[I_{t+1}-I_t]$ can be calculated. Logical AND operation can be used to evaluate the difference product. Hence the moving vector of I_{t+1} can be obtained.

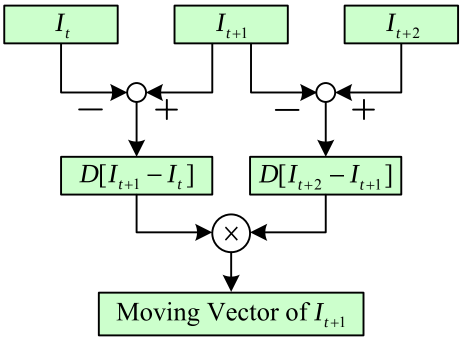

Fig. 2. Moving edge detection

C. Moving Target Shifting

As shown in Fig. 3, to overcome image-delay, the moving target shifting method will be used to get the new landmark *M2*. Compare $D[I_{t+2}-I_{t+1}]$ with *M1*, the shift values X_d and Y_d can be estimated as follows.

$$\begin{cases} X_d = (C1-C2)+(A1-A2) \\ Y_d = (B1-B2)+(D1-D2) \end{cases} \tag{3}$$

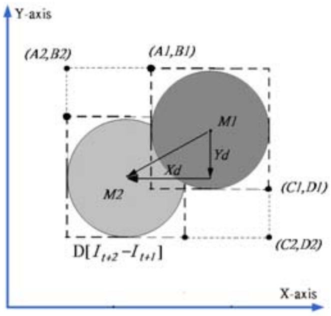

Fig. 3. Moving target shifting

2.3 The Central Point of Landmark

In this paper, 0 and 1 gray-level images are regarded as the background and the landmark, respectively. If the maximum and minimum values of projection are found in x-axis and y-axis, respectively, then the center point will be obtained (see Fig. 4).

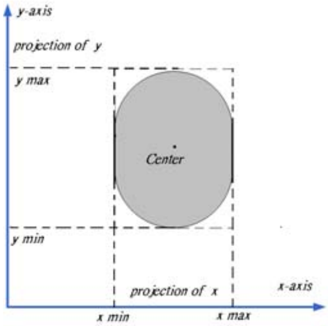

Fig. 4. Central point of the landmark

III. BALL & PLATE APPARATUS [5]

To experimentally justify the validity of the proposed algorithms described above, a test device, called Ball & Plate apparatus (see Fig. 5-a), is constructed. It is a dynamic system with two inputs and two outputs. Its system configuration is shown on from the Fig. 5-b. Moreover, the system consists of a plate pivoted at its center such that the slope of the plate can be manipulated in two perpendicular directions. A servo system consisting of motor controller card and two stepper motors is used for tilting the plate. Ball position and target location are measured by a vision system which is composed mainly of a CCD camera and an FG 201 Structure Grabber PC add-on card. Afterwards, the PWM signal will be transmitted by MF614 multifunction card. The time period for updating the ball position measurement is set to 40ms. The basic control task is to control the position of a ball freely rolling on the plate.

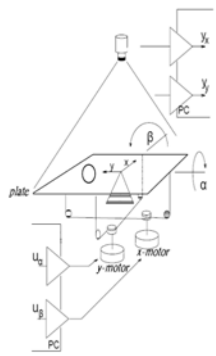

5-a Actual picture 5-b Schematic diagram

Fig. 5. The Ball & Plate Apparatus

IV. EXPERIMENTAL DESIGN

To completely show the effectiveness of the design, a situation flowchart has to be planned, shown in Fig. 6. Once we find the coordinates of the landmark via image-guided algorithm, the flying direction of the helicopter will be changed by tuning the swashplate.

Step 1. As shown in Fig. 7, let A and B be regarded as the landmark and the location of the projection of the helicopter, respectively. Once A and B are laid overlapping each other, the helicopter will be steered to arrive at the right top of landmark.

Step 2. Calculate the moving vector and the central coordinates of the landmark.

Step 3. To further control the servo motors of swashplate, the central coordinates and the moving vector will be transferred to the control signals. Fig. 8 shows the relationship between the motion of the swashplate and the flying direction of the helicopter.

The swashplate can be regarded as the X-Y plane and the ball, freely rolling on the plate, an apron. In addition, the arbitrary set-point can be viewed as the projection of the helicopter. The experimental goal is to control the servo motors of the swashplate such that the ball can arrive at the assigned point as rapidly as possible.

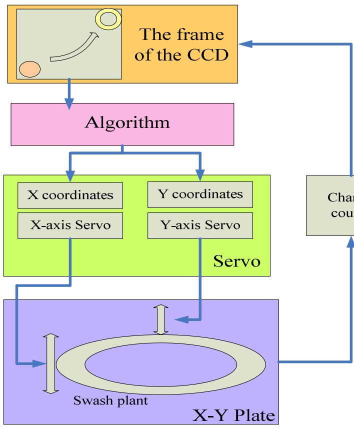

Fig. 6. Flow chart of image-guided searching for landmark

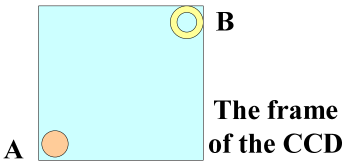

Fig. 7. Schematic diagram of the structure of the CCD

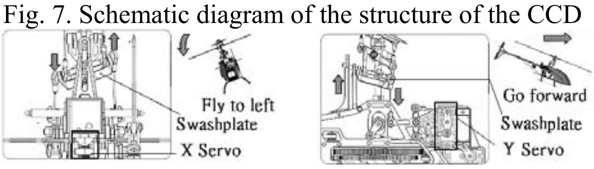

Fig. 8. The relationship between the motion of the swashplate and the flying direction of the helicopter

V. EXPERIMENTAL RESULTS

The location picture, taken from CCD, is shown in Fig. 9. The range of X-Y coordinates is between -1 and +1. To simulate the different tracking situation, 5 set-points are dispersedly over the plate. The initial point of the ball is set to be (.79,.91) due to the restriction of the physical size of the ball and the edge-wall of the plate.

Fig. 10-14 shows the tracking responses, where the targets are arbitrary with the same initial point. The corresponding actual responses are shown in Fig. 15-19, respectively, where the point in each structure is the default target.

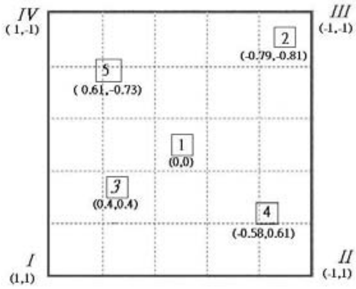

Fig. 9. Locations of the set-points

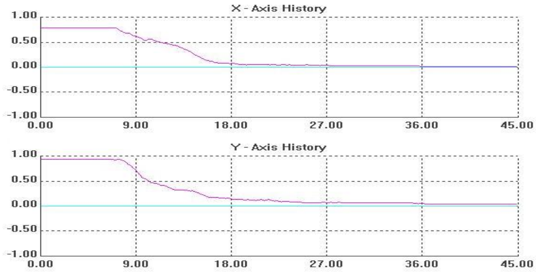

Fig. 10. Tracking responses from (.79,.91) to (0,0)

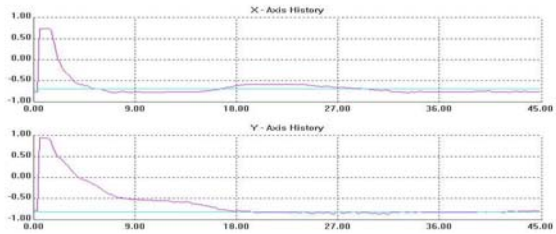

Fig. 11. Tracking responses from (.79,.91) to (−.79,−.81)

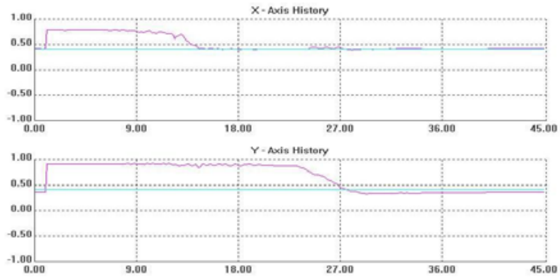

Fig. 12. Tracking responses from (.79,.91) to (.4,.4)

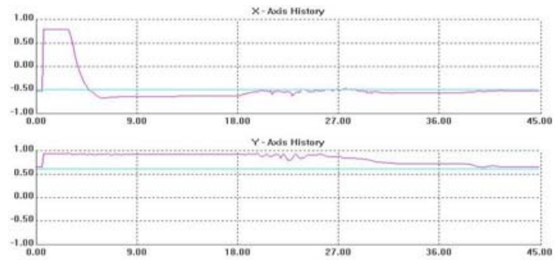

Fig. 13. Tracking responses from (.79,.91) to (.58,.61)

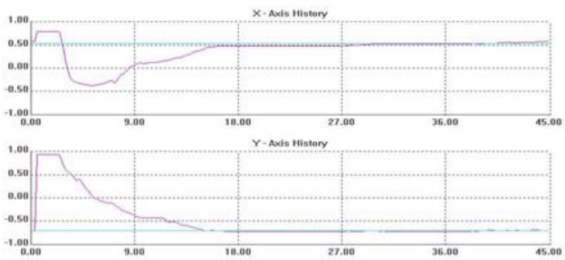

©ISAROB 2009

Fig. 14. Tracking responses from (.79,.91) to (.61,−.73)

15-a

15-b

15-c

15-d

Fig. 15. Actual responses from (.79,.91) to (0,0)

16-a

16-b

16-c

16-d

Fig. 16. Actual responses from (.79,.91) to (−.79,−.81)

17-a

17-b

17-c

17-d

Fig. 17. Actual responses from (.79,.91) to (.58,.61)

18-a

18-b

18-c

18-d

Fig. 18. Actual responses from (.79,.91) to (.61,−.73)

19-a

19-b

19-c

19-d

Fig. 19. Actual responses from (.79,.91) to (.4,.4)

VI. CONCLUSION

In this paper, a novel image-guided structure is proposed for searching any apron. The key feature of the presented structure is the introduction of a stationary camera placed on the helicopter so that it can arrive at the straight top of any apron by image-guided searching. To verify the effectiveness of the design, the proposed method will be verified through practical testing on an experimental setup, called Ball and Plate system. The experimental results validate the superiority and practicality of the image-guided searching for landmarks.

REFERENCES

[1] Carducci G., Foglia M., Gentile A., Giannoccad N.I., and Messha A. (2004), Pneumatic robotic arm controlled by on-off valves for automatic harvesting based on vision localization, IEEE International Conference on Industrial Technology, 1017-1022.

[2] Fuchiwaki O., Tobe N., Aoyama H., Misaki D., and Usuda T. (2005), Automatic micro-indentation and inspection system by piezo driven micro robot with multiple inner sensors, Proceedings of the IEEE International Conference on Mechatronics & Automation, Niagara Falls, Canada, 83-88.

[3] Nagai I. and Tanaka Y. (2006) ,Localization and error correction for mobile robot with an image sensor, SICE-ICASE International Joint Conference, Busan, Korea, 5373-5377.

[4] Watanabe K., Yoshihata Y., Iwatani Y., and Hashimoto K. (2007), Image-based visual PID control of a micro helicopter using a stationary camera, SICE Annual Conference, 3001-3006.

[5] Horáček P. (1996), ball & plate apparatus user's technical manual, third revision, Humusoft.

Design and Implementation of Human Machine Interface Surveillance Systems for Tracked Robots

Chun-Chieh Wang[1] and Kuo-Lan Su[2]

[1]*Department of Electronic Engineering Chienkuo Technology University*
No. 1, Chieh Shou N. Rd., Changhua City, Taiwan, R.O.C.
(Tel : 886-4-7111111ext3350; Fax : 886-4-7111139)
(Email address: jasonccw@ctu.edu.tw)
[2]*Department of Electrical Engineering, National Yunlin University of Science & Technology*

Abstract: A tracked robot with one five-axle robotic arm is implemented in this paper. The key feature is the application of a LabVIEW platform applied to design a human machine interface (HMI) so that the robot can be guided by ZigBee based remote control. Moreover, VHDL and 8051 microprocessor will be used to design the controller and decode ASCII code, respectively, such that the remote monitoring and control system (RMCS) can be constructed successfully. The experimental results validate the practicality of LabVIEW platform applied for tracked robots.

Keywords: LabVIEW Platform, ZigBee, Human Machine Interface Surveillance Systems, Tracked Robots, Five-Axle Robotic Arm.

I. INTRODUCTION

Nowadays, the human machine interface surveillance systems have been successfully used for robotic development. For example, toward a generic human machine interface for assistive robots: the AMOR project [1], development of human-machine interface in disaster-purposed search robot systems that serve as surrogates for human [2], and bi-directional human machine interface via direct neural connection [3] etc., deal with positioning problems via human machine interface surveillance systems. However, as regards HMI-guided control, few researchers use LabVIEW platform to delve into tracked robots. In 2001, Priya Olden et al. presented an open-loop motor speed control with LabVIEW [4]. In 2006, Prasanna Ballal et al. proposed a LabVIEW based test-bed with off-the-shelf components for research in mobile sensor networks [5].

In this paper, we first implement a tracked robot with one five-axle robotic arm. Second, a LabVIEW platform will be applied to design a HMI so that any vehicle can be guided by ZigBee based remote control. In addition, VHDL and 8051 microprocessor are used to design the controller and decode ASCII code, respectively, such that the RMCS can be constructed successfully. Finally, to illustrate the effectiveness of the HMI surveillance system, the implemented tracked robot will be a test setup.

The experimental results validate the practicality of LabVIEW platform applied for tracked robots.

II. TRACKED ROBOTS

2.1 Disposition of The Self-Made Tracked Robot

Fig. 1 shows the self-made tracked robot. The apparatus consists of a stationary camera, placed in front of the vehicle, one five-axle robotic arm, placed beside of the camera, and a solar energy supply board, placed at the back of the vehicle. The solar energy supply board is designed to partly power the system by collecting energy from the solar panel.

The mobile vehicle is about 98 cm × 64 cm × 31 cm dimension. In this paper, the worth mentioning is that all devices are self-made except the camera and the solar energy supply board.

Fig. 1. Actual picture of the tracked robot

2.2 Five-Axle Robotic Arm

The actual picture of the self-made five-axle robotic arm is shown in Fig. 2. The robot consists of two middle-sized RC servo motors and five small-sized ones. The stretched arm is nearly 64 cm and the load is about 150-200 kgw.

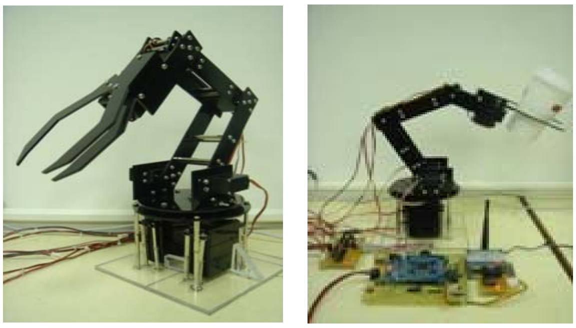

Fig. 2. Self-made five-axle robotic arm

III. IMAGE DETECTION

The procedures for the image transmission and the schematic diagram of the image transmission are shown in Fig. 3 and Fig. 4, respectively. The system consists of an image receiver, a TMS320DM642-PCI board, a wireless camera, and a servo motor (see Fig. 5-Fig. 7).

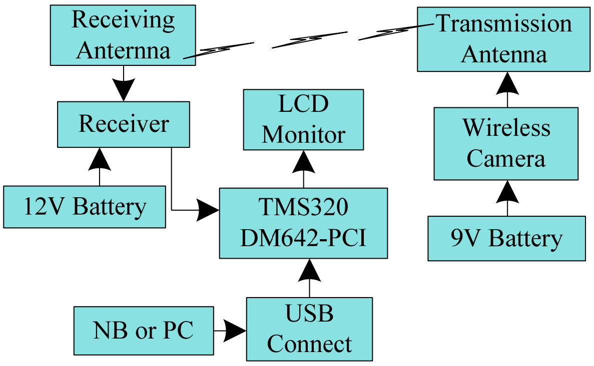

Fig. 3. Procedures for the image transmission

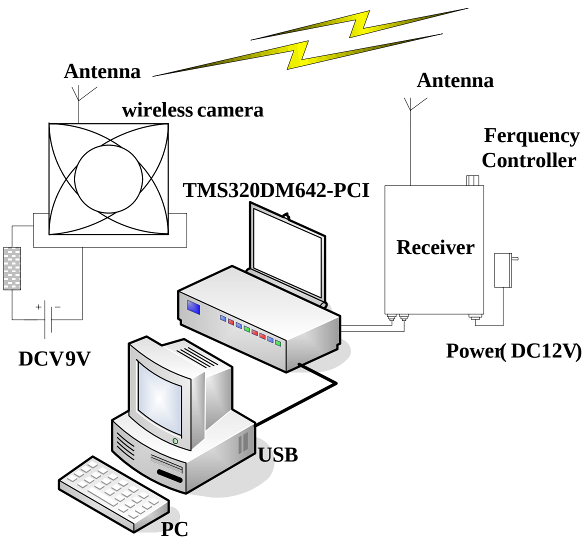

Fig. 4. Schematic diagram of the image transmission

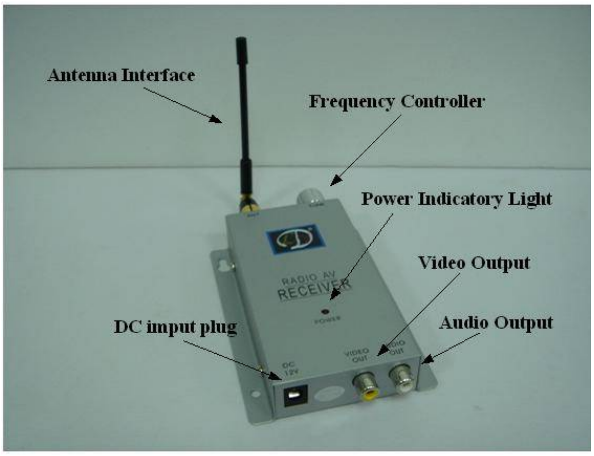

Fig. 5. Image receiver

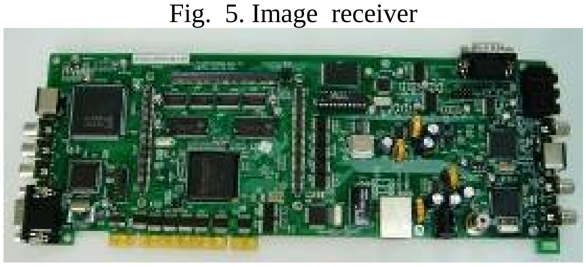

Fig. 6. TMS320DM642-PCI board

Fig. 7. Wireless camera and servo motor

IV. DESIGN OF HUMAN MACHINE INTERFACE SURVEILLANCE SYSTEMS

In this paper, we use LabVIEW graphical programming to design a human machine interface surveillance system. From the transmission of RS-232 and ZigBee modules, the command will be delivered to the controller, placed on the tracked robot so that the vehicle will be arrive at assigned place. Fig. 8 shows The LabVIEW block diagram. The LabVIEW front panel is shown in Fig. 9, where contains four parts. Block 1 can set the buad rate and I/O pins. Block 2 displays the pressed key. Block 3 is the panel for transforming strings into ASCII codes. Block 4 is the urgent stop button.

As regards ZigBee, it is established by IEEE 802.15.4 and ZigBee alliance. The ZigBee structure consists of PHY, MAC, network, security, API, and application. By the requirement, the ZigBee module can be a transmitter or a receiver. In this paper, the ZigBee module is used to deliver the data (see Fig. 11).

©ISAROB 2009

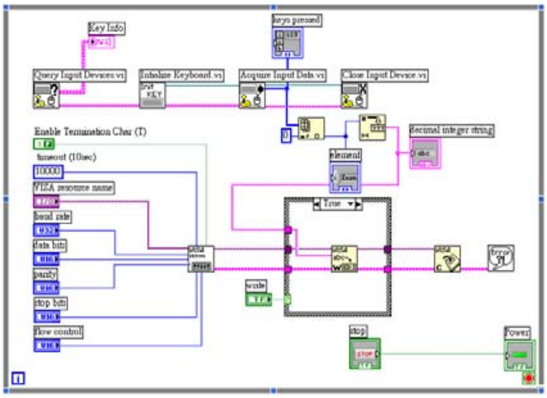

Fig. 8. LabVIEW block diagram

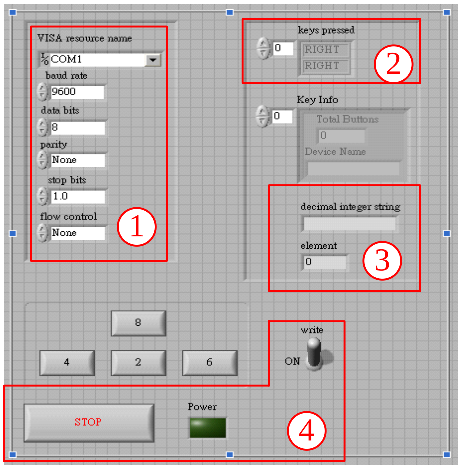

Fig. 9. LabVIEW front panel

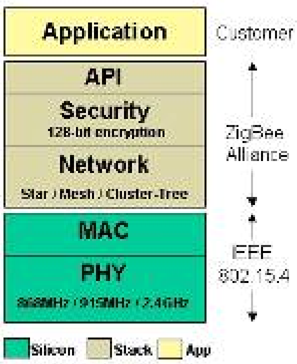

Fig. 10. ZigBee Structure diagram

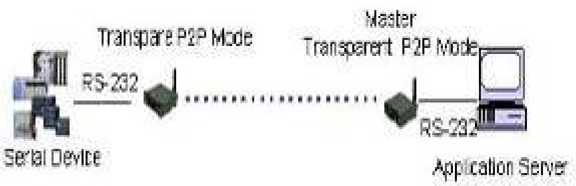

Fig. 11. Transparent P2P mode

V. EXPERIMENTAL RESULTS

The system structure block diagram is shown in Fig. 12. The supervisor can monitor the situation nearby the tracked robot via image-surveillance system, so that so that the robot can be guided by ZigBee based remote control. Fig. 13 shows the actual responses. The experimental results validate the practicality of LabVIEW platform applied for tracked robots.

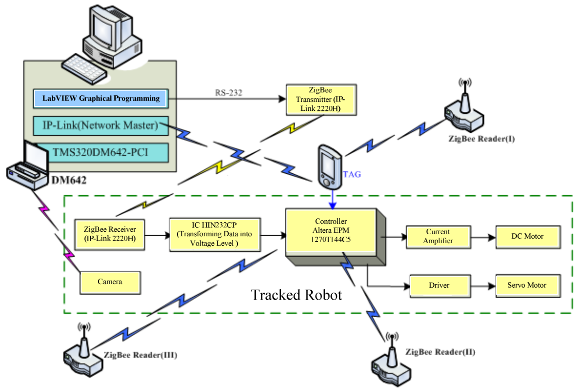

Fig. 12. The system structure block diagram

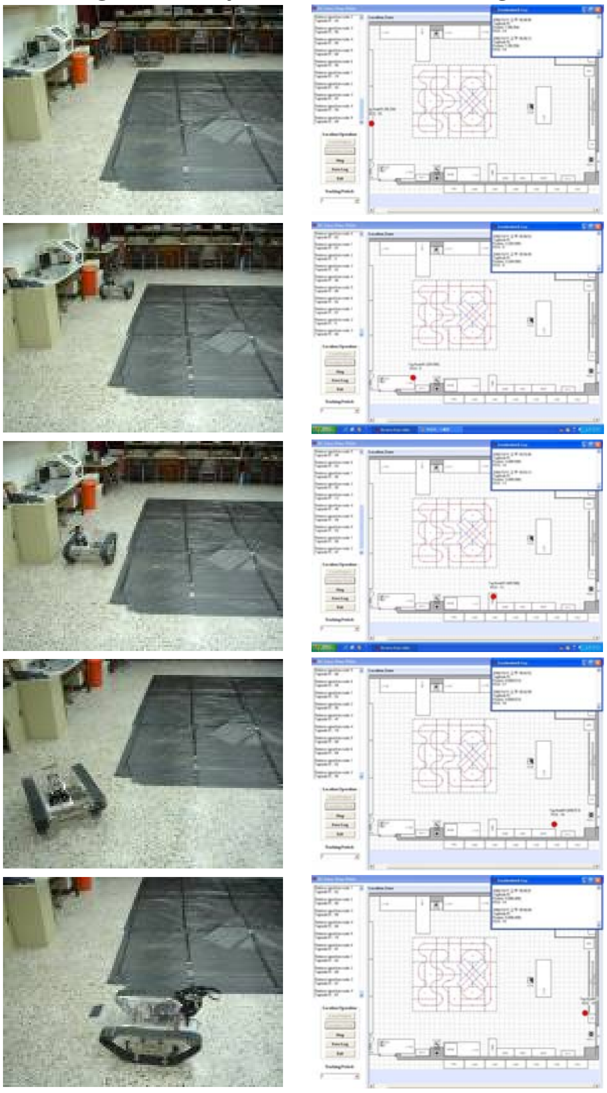

Fig. 13. Actual responses

VI. CONCLUSION

In this paper, a tracked robot with one five axle robotic arm is implemented. The key feature is the application of a LabVIEW platform applied to design a HMI so that the robot can be guided by ZigBee based remote control. Furthermore, VHDL and 8051 microprocessor will be used to design the controller and decode ASCII code, respectively, such that the RMCS can be constructed successfully. The experimental results validate the practicality of LabVIEW platform applied for tracked robots.

REFERENCES

[1] Ghorbel M., Haariz M., Grandjean B., and Mokhtari M. (2005), Toward a generic human machine interface for assistive robots: the AMOR project, Proceedings of the 2005 IEEE 9th International Conference on Rehabilitation Robotics, 168-172.

[2] Zheng X.Z., Tsuchiya K., Sawaragi T., Osuka K., Tsujita K., Horiguchi Y., and Aoi S. (2004), Development of human-machine interface in disaster-purposed search robot systems that serve as surrogates for human, Proceedings of the 2004 IEEE International Conference on Robotics & Automation, 225-230.

[3] Gasson M., Hutt B., Goodhew I., Kyberd P., and Warwick K. (2002), Bi-directional human machine interface via direct neural connection, Proceedings of the 2002 IEEE International Workshop on Robot and Human Interactive Communication, 265-270.

[4] Olden P., Robinson K., Tanner K., Wilson R., and Basher A.M.H. (2001), Open-loop motor speed control with LabVIEW, Proceedings of 2001 IEEE Southeast Conference, 259-262.

[5] Ballal P., Giordano V., Dang P., Gorthi S., Mireles J., and Lewis F. (2006), A LabVIEW based test-bed with off-the-shelf components for research in mobile sensor networks, Proceedings of the 2006 IEEE International Symposium on Intelligent Control, 112-118.

The Fourteenth International Symposium on Artificial Life and Robotics 2009 (AROB 14th '09),
B-Con Plaza, Beppu, Oita, Japan, February 5 - 7, 2009

Harmonic oscillations in Lotka-Volterra dynamic systems: A new approach from a matrix operator equation system

Koji Ohnishi

Department of Biology, Faculty of Science, Niigata University,
Ikarashi-2, Nishi-Ku, Niigata, 950-2181, Japan
(Tel : 81-25-262-6268; Fax : 81-25-262-611) (E-mail: ohnishi@sc.niigata-u.ac.jp)

Abstract: **A 2x2 matrix operator $F=(a_{ij})$, satisfying a harmonic oscillation-type operator equation, $F^2x=-\omega^2x$, (where $x={}^t(x_1(t), x_2(t))$), was obtained by letting $a_{22}= -a_{11}$ and $a_{12}a_{21} = -(\omega^2+a_{11}^2)$. For a_{ij} = const. or = $a_{ij}(t)$, and for some cases of $a_{ij} = a_{ij}(x_1, x_2, t)$, general solutions of $F^2x= -\omega^2x$ were obtained, discussed, and applied to some cases. Mathematical relationship between $F^2x = -\omega^2x$ and $d^2x/dt^2 = -\omega^2x$, where $dx/dt = Fx$, was also analyzed. An application was made to Lotka-Voltera dynamic system, where $a_{11} = r_1-\alpha x_1-\beta x_2$, $a_{12}= -ax_1$, $a_{21} = a'x_{21}$, $a_{22} = -a_{11}$. Finally, this type of Lotka-Volterra operator equation was found to have a trajectory given by an ellipse (for $C > 0$), $(X_1 - X_{10})^2/(C/\kappa_1) + (X_2 - X_{20})^2/(C/\kappa_2) =1$, where $X_i = \pm[\{(\alpha^2-\beta^2+\sigma_1\sqrt{D_0})/(2h)\}x_1+x_2]/\sqrt{\kappa_i\sqrt{D_0}/h^2}$, (i=1,2), in which $(\sigma_1,\sigma_2)= (1,-1)$, $h = \alpha\beta - aa'$, $D_0=(\alpha^2+\beta^2)^2 + 4h^2$, $\kappa_i =(\alpha^2+\beta^2+D_0^{1/2})/2$, $C= (r_1^2/4)\{(\alpha v_{11} +\beta v_{21})^2/\kappa_1 + (\alpha v_{12}+\beta v_{22})^2/\kappa_2 \} - (r_1^2 + \omega^2)$. Schroedinger equation was also discussed from this aspect of generalized harmonic oscillation.**

***Keywords*:** harmonic oscillator system, operaror equation, Lotka-Volterra equation.

1. Introduction

Lotka-Volterra differential equation system has long been analyzed from various aspects in many different and interdisciplinary scientific fields (Reijenge, 2002; Hofbauer & Sigmund, 1998). A well-known typical differential equation system of Lotka-Volterra type is given by

$$(d/dt)x \equiv \begin{pmatrix} dx_1/dt \\ dx_2/dt \end{pmatrix} = \begin{pmatrix} rx_1 - ax_1x_2 \\ a'x_1x_2 - r'x_2 \end{pmatrix} \quad \text{[Eq.1]}$$

where $x = {}^t(x_1, x_2)$, and

$$r = r_1 - \alpha_1 x_1 - \beta_1 x_2, \quad \text{[Eq.1b]}$$

$$r' = r_2 - \alpha_2 x_1 - \beta_2 x_2,. \quad \text{[Eq.1c]}$$

In Eqs.1-1b, x_1 and x_2 denote the number of individuals of preys and predators, respectively, and, r and $-r'$ denote the rate of the increase in the number of prey and predator individuals, respectively, both of which depend on t. For $i =1$ and 2, $r_i, a, a', \alpha_i, \beta_i$ are constants.

In order to analyze this system in relation to harmonic oscillation system, let us consider a 2 x 2 real matrix operator F, given by

$$F = (a_{ij})_{2,2} \overset{d}{=} {}^t(\ (a_{11},a_{12}),\ (a_{21},a_{22})\ ) = \begin{pmatrix} a_{11}, a_{12} \\ a_{21}, a_{22} \end{pmatrix} \quad \text{[Eq.2]}$$

and

$$Q = (q_{ij})_{2,2} = F^2, \quad \text{[Eq.3]}$$

satisfying

$$Qx = F^2x = -\omega^2x,\ (\omega^2 > 0) \quad \text{[Eq.4]}$$

in which x denotes a real vector, $x= {}^t(x_1(t),x_2(t))$, where ^{t} denotes transpose, and a_{ij} are either constants (in simpler cases) or functions of $x_1(t)$, $x_2(t)$, and/or t (i.e., $a_{ij}=a_{ij}(x_1,x_2,t)$, in more general cases). Eq.4 means that $-\omega^2$ (< 0) is an eigenvalue or eigenfunction of Q.

From Eqs.2-4, eigenequation of Q is given by

$$\begin{aligned} g(\kappa) &= g(-\omega^2) \\ &= \begin{vmatrix} (a_{11}^2 + a_{12}a_{21}) + \omega^2, & a_{12}(a_{11}+a_{22}) \\ a_{21}(a_{11}+a_{22}), & (a_{22}^2 + a_{12}a_{21}) + \omega^2 \end{vmatrix} \\ &= (a_{11}+a_{22})^2\omega^2 + \{\omega^2 - (a_{11}a_{22} - a_{12}a_{21})\}^2 \\ &= 0, \end{aligned} \quad \text{[Eq.5]}$$

where κ $(=-\omega^2)$ is an eigenvalue of Q $(= F^2)$. Accordingly, the necessary and sufficient condition for the existence of non-zero solution x of the operator equation, Eq.4, is given by Eq.5.

Since $\omega^2 > 0$, we find, from Eq.5 and Eq.6, that

$$a_{11} + a_{22} = 0, \quad \text{[Eq.6]}$$

and

$$\omega^2 - (a_{11}a_{22} - a_{12}a_{21}) = 0. \quad \text{[Eq.7]}$$

Eqs.6-7 bring about

$$\omega^2 + (a_{11}^2 + a_{12}a_{21}) = 0. \quad \text{[Eq.8]}$$

We easily find

$$a_{12} \neq 0, a_{21} \neq 0, \quad \text{[Eq.9]}$$

because $Q = F^2 = {}^t(\ (a_{11}^2,0),\ (0,a_{22}^2)\ )$ does not satisfy Eq.4.

Notice that Eqs.5-9 can be obtained not only for the case of a_{ij} = const. or = $a_{ij}(t)$ (*i.e.*, functions of t), but also for the general case of $a_{ij} = a_{ij}(x_1,x_2,t)$ or for other cases where a_{ij} are arbitrarily selected functions. This is because the processes from Eq.2 to Eq.4 do not include any operation of "differentiation" (such as d/dt), and consist exclusively of multiplications by a matrix F.

From Eqs.6-9, we finally obtain

©ISAROB 2009

$$F = \begin{pmatrix} a_{11}, & a_{12} \\ -(a_{11}{}^2 + \omega^2)/a_{12}, & -a_{11} \end{pmatrix}. \qquad \text{[Eq.10]}$$

Notice that Eq.4 is completely satisfied by Eq.10, even if ω is any real function of t and/or other variables such as $\omega = \omega(t)$ or $\omega = \omega(x_1(t), x_2(t), t, \ldots)$, the latter being an explicit function of x_1 and x_2.

For special cases where $a_{11} = 0$, and where $a_{11} = 0$, $a_{12} = -\omega$, Eq.10 means

$$F = {}^t((0,a_{12}), (-\omega^2/a_{12},0)), \qquad \text{[Eq.11]}$$

and

$$F = {}^t((0,-\omega),(\omega,0)) = \omega\,{}^t((0,-1),(1,0)), \qquad \text{[Eq.11a]}$$

respectively. Noticing that Eq.12a gives

$$F = {}^t((0,-1),(1,0)), \ (=I, \text{ as below.}), \qquad \text{[Eq.11b]}$$

if $\omega = 1$, F in Eq.11b can be considered to be a further generalization of $I = {}^t((0,-1),(1,0))$ (satisfying $I^2 = -E$), which is often used as a matrix operator expression of the imaginary unit $\boldsymbol{i}$ $(=\sqrt{-1})$. Accordingly, an alternative definition for matrix operator expression of $(-1)^{1/2}$,

$$I = \begin{pmatrix} a_{11}, & a_{12} \\ -(a_{11}{}^2+1)/a_{12}, & -a_{11} \end{pmatrix}, \qquad \text{[Eq.12]}$$

can satisfy $I^2 = -E$, and would be expected to have some useful characteristics not possessed by the conventional matrix operator expression given in Eq.11b, since Eq.11b is considered to be a special case of Eq.12, which is again a special case of F defined byEq.11.

2. Mathematical relations of a matrix equation, $F^2x = -\omega^2x$, to a differential equation, $d^2x/dt^2 = -\omega^2x$ (where $dx/dt=Fx$)

The matrix operator equation, $F^2x = -\omega^2x$ (Eq.4), is a kind of generalization of

$$D^2u(t) \stackrel{d}{=} (d^2/dt^2)u(t) = -\omega^2u(t),$$

which gives a harmonic oscillation of a scalar function $u(t)$, with an angular frequency ω, where D is a differential operator, $D = d/dt$.

In this section, by letting $x={}^t(x_1(t),x_2(t))$ and $F = (a_{ij})_{2,2}$ be a real number vector and a real number matrix, we shall compare the relation between a harmonic oscillator-like matrix operator equation given by

$$F^2x = -\omega^2x$$

and a simultaneous differential equation,

$$Dx = Fx, \qquad \text{[Eq.13a]}$$

satisfying a harmonic oscillator equation,

$$D^2x \stackrel{d}{=} {}^t(D^2x_1,D^2x_2) = -\omega^2x. \qquad \text{[Eq13b]}$$

Here we consider a generalized case of Eq.4, where a_{ij} are either constants or functions of $x_1(t)$, *and* $x_2(t)$, and t, *i.e.,*

$$a_{ij} = a_{ij}(x_1,x_2,t). \qquad \text{[Eq.14]}$$

Then we have,

$$Fx = \begin{pmatrix} a_{11}x_1 + a_{12}x_2 \\ a_{21}x_1 + a_{22}x_2 \end{pmatrix}, \qquad \text{[Eq.14a]}$$

$$F^2 = \begin{pmatrix} (a_{11}{}^2 + a_{12}a_{21})x_1 + a_{12}(a_{11}+a_{22})x_2 \\ a_{21}(a_{11}+a_{22})x_1 + (a_{22}{}^2 + a_{12}a_{21})x_2 \end{pmatrix}. \qquad \text{[Eq.14b]}$$

A simultaneous differential equation, given by

$$Dx \stackrel{d}{=} {}^t(Dx_1,Dx_2) = \begin{pmatrix} a_{11}x_1 + a_{12}x_2 \\ a_{21}x_1 + a_{22}x_2 \end{pmatrix}, \qquad \text{[Eq.15]}$$

is now considered for comparison with Eqs.14a,b. From Eq.14a and Eq.15, we first find

$$Dx = Fx.$$

On the other hand,

$$D^2x = D(Dx) = D\,{}^t(Dx_1,Dx_2)$$

$$= D\begin{pmatrix} a_{11}x_1 + a_{12}x_2 \\ a_{21}x_1 + a_{22}x_2 \end{pmatrix}$$

$$= \begin{pmatrix} (a_{11}Dx_1 + a_{12}Dx_2) + ((Da_{11})x_1 + (Da_{12})x_2) \\ (a_{21}Dx_1 + a_{22}Dx_2) + ((Da_{21})x_1 + (Da_{22})x_2) \end{pmatrix}$$

$$= \begin{pmatrix} a_{11}, a_{12} \\ a_{21}, a_{22} \end{pmatrix}\begin{pmatrix} Dx_1 \\ Dx_2 \end{pmatrix} + \begin{pmatrix} (Da_{11})x_1 + (Da_{12})x_2 \\ (Da_{21})x_1 + (Da_{22})x_2 \end{pmatrix}. \qquad \text{[Eq.16]}$$

$$= F(Dx) + \begin{pmatrix} (Da_{11})x_1 + (Da_{12})x_2 \\ (Da_{21})x_1 + (Da_{22})x_2 \end{pmatrix}.$$

Since $F(Dx) = F(Fx) = F^2x$, then

$$D^2x = F^2x + \begin{pmatrix} (Da_{11})x_1 + (Da_{12})x_2 \\ (Da_{21})x_1 + (Da_{22})x_2 \end{pmatrix} \qquad \text{[Eq.17]}$$

$$= F^2x + \begin{pmatrix} Da_{11}, Da_{12} \\ Da_{21}, Da_{22} \end{pmatrix}\begin{pmatrix} x_1 \\ x_2 \end{pmatrix} \qquad \text{[Eq.18]}$$

$$= F^2x + (DF)x. \qquad \text{[Eq.18a]}$$

From Eqs.17-18, we finally have

$$Da_{11}/Da_{12} = Da_{21}/Da_{22} (= -x_2/x_1),$$

or

$$Da_{11}Da_{22} = Da_{12}Da_{21}, \qquad \text{[Eq.19]}$$

as the necessary and sufficient condition for obtaining

$$D^2x = F^2x. \qquad \text{[Eq.20]}$$

Under the condition of Eq.7, we find

$$Da_{22} = -Da_{11}, \qquad \text{[Eq.21a]}$$

and therefore Eq.19 leads to

$Da_{12}Da_{21} = -(Da_{11})^2$. [Eq.21b]

Accordingly, we now get the following theorem;

[Theorem 1.]

Let x and F be a real vector and a real matrix operator, respectively given by $x = {}^t(x_1(t), x_2(t))$ and $F=(a_{ij})_{2,2}$, where $a_{ij} = a_{ij}(x_1,x_2,t)$. If $F^2x = -\omega^2 x$, $Dx = Fx$, and $Da_{12}Da_{21} = -(Da_{11})^2$, (where $D=d/dt$), then we get a harmonic oscillator, $D^2x = -\omega^2 x$, which further gives

$$D^2x\ (=d^2x/dt^2) = F^2x = -\omega^2 x. \quad \text{[Eq.22]}$$

[Proof] From $F^2x = -\omega^2 x$, we find $a_{22}=-a_{11}$ and $a_{21}=-(a_{11}^2+\omega^2)$, which further gives Eq.22 under the condition of $Dx = Fx$ and $Da_{12}Da_{21}= -(Da_{11})^2$, as described above.

From Eq.21b, it is evident that

$$Da_{11}= Da_{12}=0 \quad \text{[Eq.21c]}$$

(which means that a_{11} and a_{12} are constants.) is sufficient for obtaining Eq.22, if we have $F^2x = -\omega^2 x$ and $dx/dt =Fx$. It is also quite evident that

$$Da_{ij} = 0,\ (i,j = 1,2) \quad \text{[Eq.21d]}$$

(i.e., a_{ij} : constants) give harmonic oscillation of $x(t)$ given by Eq.22, under the similar conditions.

In case of Lotka-Volterra system in Eqs.1-1b, where $a_{12}=ax_1$, $a_{21}= -a'x_2$, $a_{11}= r_1-\alpha x_1-\beta x_2$, $a_{22}=-a_{11}$, Eq.21b is written as

$$(\alpha Dx_1+\beta Dx_2)^2= aa'Dx_1Dx_2, \quad \text{[Eq.23]}$$

if $Dr_1 =0$ (*i.e., r_1*: constant). Eq.23 is rewritten as

$$\alpha^2(Dx_1/Dx_2)+\beta^2(Dx_2/Dx_1)=-(aa'-2\alpha\beta), \quad \text{[Eq.23a]}$$

or as

$$\{(\alpha Dx_1+\beta Dx_2)/(\alpha+\beta)\}^2/(Dx_1Dx_2)=aa'/(\alpha+\beta)^2. \quad \text{[Eq.23b]}$$

3. Towards finding general solutions of $F^2x = -\omega^2 x$

In this section, we will attempt to get a general solution of the operator equation given by Eq.4.

Let G_1 *and* G_2 be 2 X 2 matrix operators defined by

$$G_1 = e^{tF}, \quad G_2 = e^{-tF}, \quad \text{[Eq.24]}$$

where F is given by Eqs.2-4, satisfying Eq.11. Then we find, by noticing $F^2 = -\omega^2 E$, that

$$G_1 = e^{tF} = \sum_{k=0}^{\infty} c_k (tF)^n$$
$$= \sum_{m=0}^{\infty}\{c_{2m}(tF)^{2m} + c_{2m+1}(tF)^{2m+1}\}$$
$$= \sum_{m=0}^{\infty}\{c_{2m}t^{2m}(F^2)^m + c_{2m+1}t^{2m+1}(F^2)^m F\}$$
$$= \sum_{m=0}^{\infty}\{c_{2m}t^{2m}(-\omega^2 E)^m + c_{2m+1}t^{2m+1}(-\omega^2 E)^m F\}$$
$$= \{\sum_{m=0}^{\infty} c_{2m}(\omega t)^{2m}(-1)^m\}E$$
$$+ \omega^{-1}\{\sum_{m=0}^{\infty} c_{2m+1}(\omega t)^{2m+1}(-1)^m\}F$$
$$= (\cos\omega t)E + (\omega^{-1}\sin\omega t)F\ ,$$

where $c_k = 1/k!$.

By similar consideration on G_2, we finally obtain

$$G_1 = e^{tF} = (\cos\omega t)E + (\omega^{-1}\sin\omega t)F\ , \quad \text{[Eq.25.1a]}$$

$$= \begin{pmatrix} \cos\omega t + a_{11}\omega^{-1}\sin\omega t, & a_{12}\omega^{-1}\sin\omega t \\ a_{21}\omega^{-1}\sin\omega t, & \cos\omega t + a_{22}\omega^{-1}\sin\omega t \end{pmatrix}, \quad \text{[Eq.25.1b]}$$

$$G_2 = e^{-tF} = (\cos\omega t)E - (\omega^{-1}\sin\omega t)F \quad \text{[Eq.25.2a]}$$

.

$$= \begin{pmatrix} \cos\omega t - a_{11}\omega^{-1}\sin\omega t, & -a_{12}\omega^{-1}\sin\omega t \\ -a_{21}\omega^{-1}\sin\omega t, & \cos\omega t - a_{22}\omega^{-1}\sin\omega t \end{pmatrix}, \quad \text{[Eq.25.2b]}$$

where $a_{22} = -a_{11}$, and $a_{12} = -(a_{11}^2+\omega^2)/a_{12}$.

By letting $C_k= {}^t(C_{k1},C_{k2})$, where C_{ki} , ($k,i = 1,2$) are real constants selectable arbitrarily, it is easily found that the two solutions (Eq.26) written below satisfy Eq.4 and are lineally independent solutions (singular solutions) of the operator equation Eq.4, if a_{ij} = const. or = $a_{ij}(t)$, which are not explicit functions of x_1 and x_2;

$$x(k)= {}^t(x_{k1},x_{k2}) = G_kC_k$$
$$= e^{\sigma(k)tF}C_k$$
$$= \begin{pmatrix} C_{k1}\cos\omega t + (C_{k1}a_{11} + C_{k2}a_{12})\omega^{-1}\sin\omega t \\ C_{k2}\cos\omega t + (C_{k1}a_{21} + C_{k2}a_{22})\omega^{-1}\sin\omega t \end{pmatrix},$$

(k=1,2, and $\sigma(1)=1, \sigma(2)=-1$, $a_{22}=-a_{11}$). [Eq.26]

Accordingly, general solution of Eq.4 is given by

$$x = {}^t(x_1, x_2)$$
$$= A_1x(1)+A_2x(2) \quad \text{[Eq.27a]}$$
$$= A_1e^{tF}C_1 + A_2e^{-tF}C_2 \quad \text{[Eq.27b]}$$
$$= A_1\begin{pmatrix} C_{11}\cos\omega t + (C_{11}a_{11} + C_{12}a_{12})\omega^{-1}\sin\omega t \\ C_{12}\cos\omega t + (C_{11}a_{21} + C_{12}a_{22})\omega^{-1}\sin\omega t \end{pmatrix}$$
$$+ A_2\begin{pmatrix} C_{21}\cos\omega t + (C_{21}a_{11} + C_{22}a_{12})\omega^{-1}\sin\omega t \\ C_{22}\cos\omega t + (C_{21}a_{21} + C_{22}a_{22})\omega^{-1}\sin\omega t \end{pmatrix} \quad \text{[Eq.27c]}$$

$$= \begin{pmatrix} b_{11}\cos\omega t + (b_{12}a_{11} + b_{22}a_{12})\omega^{-1}\sin\omega t \\ b_{21}\cos\omega t + (b_{12}a_{21} + b_{22}a_{22})\omega^{-1}\sin\omega t \end{pmatrix}, \quad \text{[Eq.28]}$$

where $a_{22} = -a_{11}$, and $a_{12} = -(a_{11}^2+\omega^2)/a_{12}$,

and further, b_{ij} are given by

$$b_{11}= A_1C_{11}+ A_2C_{21},\quad b_{12}= A_1C_{11}- A_2C_{21},$$
$$b_{21}= A_1C_{12}+ A_2C_{22},\quad b_{22}= A_1C_{12}- A_2C_{22}. \quad \text{[Eq.28a]}$$

The four equations in Eq.28a mean that the four constants b_{ij} can be arbitrarily selected since the

©ISAROB 2009

four constants C_{ij} and the two consonants A_1, A_2 are arbitrarily selectable ones.

Eq.28 elucidates a general solution of the operator equation, Eq.4, if a_{ij} in Eq.28 are constants or functions (for example, of t) other than explicit functions of $x_1(t)$ and/or $x_2(t)$. In those cases where some of a_{ij} are explicit function(s) of $x_1(t)$ and/or $x_2(t)$, Eq.28 gives a simultaneous equation of $x_1(t)$ and $x_2(t)$, on which solvability concerning $x_1(t)$ and $x_2(t)$ depends. In those cases where some of a_{ij} are linear combination(s) of $x_1(t)$ and/or $x_2(t)$, Eq.28 might be a solvable simultaneous equation from which general solutions could be deduced, as will be shown later in Lotka-Volterra systems. If Eq.21b or Eq.23 is satisfied, the general solution Eq.28 and that of the simultaneous differential equation Eq.15 are identical.

Eq.28 is rewritten as

$$x_1 = B_{11}\cos \omega t + B_{12}\sin \omega t, \qquad \text{[Eq.29a]}$$

$$x_2 = B_{21}\cos \omega t + B_{22}\sin \omega t, \qquad \text{[Eq.29b]}$$

where

$$B_{11} = b_{11}, \quad B_{12} = (b_{12}a_{11}+b_{22}a_{12})/\omega,$$

$$B_{21} = b_{21}, \quad B_{22} = (b_{12}a_{21}+b_{22}a_{22})/\omega.$$

and where $a_{22} = -a_{11}$, and $a_{12} = -(a_{11}^2+\omega^2)/a_{12}$.

Thus we have

$$\cos \omega t = (B_{22}x_1 - B_{12}x_2) /(B_{11}B_{22} - B_{12}B_{21}),$$

$$\sin \omega t = (-B_{21}x_1 + B_{11}x_2) / (B_{11}B_{22} - B_{12}B_{21}),$$

and therefore it reveals that

$$(B_{22}x_1 - B_{12}x_2)^2 + (-B_{21}x_1 + B_{11}x_2)^2 = (B_{11}B_{22} - B_{12}B_{21})^2, \qquad \text{[Eq.30a]}$$

which further brings about a quadratic equation:

$$(B_{22}^2+B_{21}^2)\, x_1^2 - 2(B_{12}B_{22} + B_{21}B_{11})\, x_1x_2 + (B_{11}^2 + B_{12}^2)\, x_2^2 - (B_{11}B_{22} - B_{12}B_{21})^2=0. \qquad \text{[Eq.30b]}$$

Eq.30b gives a trajectory of Eq.4 ($F^2x = -\omega^2x$; $\omega^2 > 0$) in (x_1, x_2)-plane, which is a conic curve, if B_{ij} are constants.

From Theorem 1, Eq.30b generates a harmonic oscillation given by $D^2x = F^2x = -\omega^2x$ (in Eq.21), if $Dx = Fx$, and $(\alpha Dx_1+ \beta Dx_2)^2 = aa' Dx_1Dx_2$.

4. Lotka-Volterra harmonic oscillations: Mathematical consideration

Lotka-Volterra differential equation in Eq.1 is comparable to the following matrix operator equation.

$$Fx=\begin{pmatrix} a_{11}, a_{12} \\ a_{21}, a_{22} \end{pmatrix}\begin{pmatrix} x_1 \\ x_2 \end{pmatrix}$$

$$=\begin{pmatrix} \mathrm{r}_1 - \alpha_1\mathrm{x}_1 - \beta_1 x_2, & -ax_1 \\ a'x_2, & -(\mathrm{r}_2 - \alpha_2\mathrm{x}_1 - \beta_2 x_2) \end{pmatrix}\begin{pmatrix} x_1 \\ x_2 \end{pmatrix}$$

$$= \begin{pmatrix} (\mathrm{r}_1 - \alpha_1\mathrm{x}_1 - \beta_1 x_2)x_1 - ax_1x_2, \\ a'\mathrm{x}_1x_2 - (\mathrm{r}_2 - \alpha_2\mathrm{x}_1 - \beta_2 x_2)x \end{pmatrix}. \qquad \text{[Eq.4.1]}$$

If the matrix operator F satisfies Eq.4,

$$F^2x = -\omega^2x,$$

then we have Eqs.7-11,and therefore it follows that, by letting $a_{22} = -r' (= \mathrm{r}_2 - \alpha_2\mathrm{x}_1 - \beta_2 x_2)$,

$$-r' = -a_{11} = -(\mathrm{r}_1 - \alpha_1\mathrm{x}_1 - \beta_1 x_2)\,, \qquad \text{[Eq.4.2]}$$

and

$$(\mathrm{r}_1 - \alpha_1\mathrm{x}_1 - \beta_1 x_2)^2 + \omega^2 = aa' x_1x_2\,, \qquad \text{[Eq.4.3a]}$$

the latter being rewritten as a quadratic equation:

$$g(x_1, x_2) = \alpha^2 x_1^2 + 2hx_1x_2 + \beta^2 x_2^2 - 2r_1(\alpha_1\mathrm{x}_1 + \beta_1 x_2) + (r_1^2 - \omega^2) = 0\,, \qquad \text{[Eq.4.3b]}$$

where $\quad h = \alpha\beta - aa'\,. \qquad$ [Eq.4.3c]

Eq.4.3b represents a conic curve, which is a trajectory of Eq.4.1 satisfying $F^2x = -\omega^2x$.

Hessian matrix of $g(x_1,x_2)$ is

$$H = \begin{pmatrix} \alpha^2, & h, & -r_1\alpha \\ h, & \beta^2, & -r_1\beta \\ -r_1\alpha, & -r_1\beta, & r_1^2 - \omega^2 \end{pmatrix}. \qquad \text{[Eq.4.4]}$$

By letting

$$H_0 = \begin{pmatrix} \alpha^2, & h \\ h, & \beta^2 \end{pmatrix} = \begin{pmatrix} \alpha^2, & \alpha\beta - aa' \\ \alpha\beta - aa', & \beta^2 \end{pmatrix}.$$

and

$$L = (-r_1\alpha, -r_1\beta)\,,$$

Eq.4.3b is written as

$$g(x_1,x_2) = {}^t x H_0 x + Lx + (r_1^2 - \omega^2) =0, \qquad \text{[Eq.4.3c]}$$

and we then have

$$|H_0| = \alpha^2\beta^2 - h^2 = -aa'(2\alpha\beta - aa')\,. \qquad \text{[Eq.4.3d]}$$

By letting κ be eigenvalue of H_0, κ satisfies a simultaneous equation;

$$(H_0-\kappa E)x = \begin{pmatrix} (\alpha^2-\kappa)x_1 + hx_2 \\ hx_1 + (\beta^2-\kappa)x_2 \end{pmatrix} = \begin{pmatrix} 0 \\ 0 \end{pmatrix}, \quad \text{[Eq.4.4]}$$

and an eigenequation is

$$|H_0-\kappa E| = (\alpha^2-\kappa)(\beta^2-\kappa) - h^2 = 0,$$

i.e.,

$$\kappa^2 - (\alpha^2+\beta^2)\kappa + (\alpha^2\beta^2 - h^2) = 0. \quad \text{[Eq.4.5]}$$

Thus eigenvalues (κ) of H_0 are given below;

$$\kappa_i = \{\alpha^2+\beta^2+\sigma_i D_o^{1/2}\}/2,\ (i = 1,2), \quad \text{[Eq.4.6]}$$

where

$$D_o = (\alpha^2-\beta^2)^2 + 4h^2, \quad \text{[Eq.4.6a]}$$

and $(\sigma_1, \sigma_2) = (1,-1)$. [Eq.4.6b]

Eigenvectors v_i $(= {}^t(v_{i1}, v_{i2}))$ of H_0, satisfying

$$v_{i1}^2 + v_{i2}^2 = 1, \quad \text{[Eq.4.7]}$$

and corresponding to κ_i ($i=1,2$) are therefore found as

$$v_i = \begin{pmatrix} \{(\kappa_i - \beta^2)/h^2\}t_i \\ t_i \end{pmatrix}, \quad \text{[Eq.4.8]}$$

where

$$t_i = (\kappa_i D_0^{1/2}/h^2)^{-1/2},$$
$$(i=1,2),\ (\kappa_i > 0), \quad \text{[Eq.4.9]}$$

which can be obtained as below;

$$\begin{aligned} t_i &= \{(\kappa_i-\beta^2)^2/h^2+1\}^{-1/2} \\ &= \{(\alpha^2-\beta^2+\sigma_i D_0^{1/2})^2/(4h^2)+1\}^{-1/2} \\ &= [(\alpha^2-\beta^2+\sigma_i D_0^{1/2})^2+4h^2\}/(4h^2)]^{-1/2} \\ &= [\{(\alpha^2-\beta^2)^2+4h^2\}+D_0+2\sigma_i(\alpha^2-\beta^2)D_0^{1/2}\} \\ &\quad /(4h^2)]^{-1/2} \\ &= [D_0+D_0+2\sigma_i(\alpha^2-\beta^2)D_0^{1/2}\}/(4h^2)]^{-1/2} \\ &= [\{(\alpha^2-\beta^2+\sigma_i D_0^{1/2})/2\}D_0^{1/2}/h^2]^{-1/2} \\ &= (\kappa_i D_0^{1/2}/h^2)^{-1/2},\ (i=1,2). \end{aligned}$$

Thus we find an orthogonal matrix, P, for diagonalizing H_0, as below:

$$P = (p_{ij}) = \begin{pmatrix} v_{11}, v_{21} \\ v_{12}, v_{22} \end{pmatrix}. \quad \text{[Eq.4.10]}$$

Letting $X = {}^t(X_1,X_2)$, P satisfies

$$x = PX. \quad \text{[Eq.4.11]}$$

Thus we have

$$\begin{aligned} x_1 &= p_{11}X_1 + p_{12}X_2 \\ &= v_{11}X_1 + v_{21}X_2 \\ x_2 &= p_{21}X_1 + p_{22}X_2 \\ &= v_{12}X_1 + v_{22}X_2 \end{aligned}$$

Since $P^{-1} = {}^tP$, it follows that

$$X = P^{-1}x = {}^tPx \quad \text{[Eq.4.12]}$$

$$= \begin{pmatrix} v_{11}, v_{12} \\ v_{21}, v_{22} \end{pmatrix}\begin{pmatrix} x_1 \\ x_2 \end{pmatrix}$$

$$= \begin{pmatrix} v_{11}x_1 + v_{12}x_2 \\ v_{21}x_1 + v_{22}x_2 \end{pmatrix}. \quad \text{[Eq.4.12a]}$$

Accordingly, for $i = 1, 2$, we have

$$X_i = v_{i1}x_1 + v_{i2}x_2 \quad \text{[Eq.4.13]}$$

$$= \{(\kappa_i - \beta^2)/h\}t_i x_1 + t_i x_2 \quad \text{[Eq.4.13a]}$$

$$= [\{(\alpha^2-\beta^2+\sigma_1\sqrt{D_0})/(2h)\}x_1 + x_2]t_i$$

$$= \pm[\{(\alpha^2-\beta^2+\sigma_1\sqrt{D_0})/(2h)\}x_1 + x_2] \Big/ \sqrt{\kappa_i\sqrt{D_0}/h^2}. \quad \text{[Eq.4.13b]}$$

Furthermore, we find

$$LPX = (-r_1\alpha, -r_1\beta)\begin{pmatrix} v_{11}, v_{21} \\ v_{12}, v_{22} \end{pmatrix}\begin{pmatrix} x_1 \\ x_2 \end{pmatrix}$$

$$= (-r_1\alpha, -r_1\beta)\begin{pmatrix} v_{11}x_1 + v_{21}x_2 \\ v_{12}x_1 + v_{22}x_2 \end{pmatrix}$$

$$= -r_1\{(\alpha v_{11} + \beta v_{12})x_1 + (\alpha v_{21} + \beta v_{22})x_2\} \quad \text{[Eq.4.14]}$$

By letting $K = {}^t((\kappa_1,0),(0,\kappa_2))$, now we have

$${}^tXKX + LPX + (r_1^2 - \omega^2) = 0, \quad \text{[Eq.4.15]}$$

meaning that

$$\kappa_1 X_1^2 + \kappa_2 X_2^2 - r_1\{(\alpha v_{11} + \beta v_{21})x_1 + (\alpha v_{12} + \beta v_{22})x_2\} + (r_1^2 + \omega^2) = 0. \quad \text{[Eq.4.15a]}$$

Based on the above analyses, this equation is rewritten by

$$(X_1 - X_{10})^2/(C/\kappa_1) + (X_2 - X_{20})^2/(C/\kappa_2) = 1 \quad \text{[Eq.4.16]}$$

where

$$X_{10} = r_1(\alpha v_{11} + \beta v_{21})/(2\kappa_1),$$
$$X_{20} = r_1(\alpha v_{12} + \beta v_{22})/(2\kappa_2),$$
$$C = (r_1^2/4)\{(\alpha v_{11} + \beta v_{21})^2/\kappa_1 + (\alpha v_{12} + \beta v_{22})^2/\kappa_2\} - (r_1^2 + \omega^2).$$

Since $\kappa_1\kappa_2 > 0$, if ω does not depends neither on t nor on x_i, this equation (Eq.4.16) represents an ellipse with semi-axis' lengths, $(C/\kappa_1)^{1/2}$ and $(C/\kappa_2)^{1/2}$, when $C > 0$, and a hyperbola when $C < 0$. These conic curves are trajectories represented by (X_1, X_2) which are obtained by the orthogonal transformation, Eq.4.12a, from the trajectories represented by Eq.4.3b. Thus both Eq.4.3b and Eq.4.16 represents the same conic curve being a trajectory of Eq.4.1 satisfying $F^2x = -\omega^2 x$. If $C > 0$, this conic curve trajectory is an ellipse, meaning that $F^2x = -\omega^2 x$ represents a harmonic oscillation. If $C < 0$, on the other hand, the corresponding trajectory is a hyperbola, meaning that harmonic oscillation does not occur..

In more general cases where $C\ (> 0)$ depends on t (*i.e.*, $C= C(t)$), the long and short diameters of the ellipse varies depending on t, *confirming that* X_1 *and* X_2 (and therefore, x_1 and x_2) give *a generalized harmonic oscillation.*

5. Harmonic oscillations in Schrödinger equation

This section describes something about the harmonic oscillation in Schrödinger equation, from a viewpoint of the above-mentioned matrix operator equation.

Schrödinger equation is given by

$$-i\hbar\partial\psi/\partial t = -\{\hbar^2/(2m)\}\partial^2\psi/\partial x^2 + V(x)\psi \quad \text{[Eq.6.1]}$$

As is well-known, by letting

$$\psi(x,t) = u(x)f(t),$$

$\psi(x,t)$ can be separated to a t-dependent portion $f(t)$ and an x-dependent portion $u(x)$, satisfying

$$\frac{i\hbar}{f(t)}\frac{df(t)}{dt} = \frac{1}{u(x)}\left(-\frac{\hbar^2}{2m}\frac{d^2u(x)}{dx^2} + V(x)u(x)\right) = E \quad \text{[Eq.6.2]}$$

where E is a constant. It therefore follows that

$$i\hbar\frac{df(t)}{dt} = Ef(t)\cdot \quad \text{[Eq.6.3]}$$

Eq.6.3 is rewritten as

$$Df(t) = -i(E/\hbar)f(t) = -i\omega f(t) \quad \text{[Eq.6.4a]}$$

in which $D=d/dt$ and $\omega = E/\hbar$, and further written as;

$$(D + i\omega)f(t) = 0\,. \quad \text{[Eq.6.4b]}$$

By using another operator, $(D + i\omega)$, we have

$$(D - i\omega)(D + i\omega)f(t) = 0, \quad \text{[Eq.6.5a]}$$

meaning that

$$(D^2 + \omega^2)f(t) = 0, \quad \text{[Eq.6.5b]}$$

or,

$$d^2f(t)/dt^2 = -\omega^2 f(t)\,. \quad \text{[Eq.6.5c]}$$

From Theorem 1 and Eq.21b (in Section 2), if we use $F = (a_{ij})$ hitherto discussed and $f_0(t) = {}^t(f_1(t), f_2(t))$, Eq.6.5c means that, under the condition of $(da_{12}/dt)(da_{21}/dt)=-(da_{11}/dt)^2$ (Eq.21b), (e.g., a_{ij} are constants), we have

$$D f_0(t) = F f_0(t), \quad \text{[Eq.6.7a]}$$

$$F^2 f_0(t) = \begin{pmatrix} a_{11}, & a_{12} \\ -\dfrac{a_{11}{}^2 + \omega^2}{a_{12}}, & -a_{11} \end{pmatrix}^2 \begin{pmatrix} f_1(t) \\ f_2(t) \end{pmatrix}$$

$$= -\omega^2 \begin{pmatrix} f_1(t) \\ f_2(t) \end{pmatrix}. \quad \text{[Eq.6.7b]}$$

Thus Eqs.6.7a/b elucidates that

$$d^2f_1(t)/dt^2 = -\omega^2 f_1(t), \quad \text{[Eq.6.8a]}$$

$$d^2f_2(t)/dt^2 = -\omega^2 f_2(t)\,. \quad \text{[Eq.6.8b]}$$

Experimental data satisfying Eq.6.4a have hitherto been accumulated during the long history of quantum mechanics, which suggests Eqs. 6.5a/b, whose solutions are $f_1(t)$ and $f_2(t)$ in Eqs.6.8a/b. $f_1(t)$ is considered to be related to the probability of the existence of quantum element, whereas $f_2(t)$ does not seem to have been directly analyzed. Theoretical analyses mentioned above in this paper seem to suggest that we may need to find what $f_2(t)$ could really be. Could $f_2(t)$ be related to some unknown matter or element or some unknown phenomenon other than those we presently know ? The relationship between F and the so-called "spin matrix" or something like might have some essence for answering this question.

REFERENCES:

[1] Anton, H. (1991): *Elementary Linear Algebra, Sixth ed.*, Wiley & Sons, New York.

[2] Reijenge, K.A., et al.(2002): *Biophys. J.* 82:99-108.

[3] Hofbauer and Sigmond (1998): *Evolutionary Games and Population Dynamics,* Cambridge Univ. Press, Cambridge.

[4] Haberman, R.(1977): *Mathematical Model: Population Dynamics.* Printice Hall.

[5] Ohnishi,K. (2008): A preliminary considera-tion on the origin of life as a cognitive system: Evolution from a simple harmonic oscillator system to chaotic learning oscillator machines. *Proc.of the 13th Int. Conf. on Artificial Life & Robotics (AROB 13th '08),* pp.686-689, Beppu, Oita.

Chemical reaction simulations using Abstract Rewriting System on Multisets with Lattice Boltzmann Method

Mai UMEKI and Yasuhiro SUZUKI
Department of Complex Systems Science,
Graduate School of Infromation Science
Nagoya University
Furocho, Chikusa, Nagoya, 464-8603 JAPAN

Abstract

We have composed a simulation method for the reaction-diffusion-convection model of chemical reactions by synthesizing ARMS and the Lattice Boltzmann Method (LBM); LBM is a discrete expression of the Navier-Stokes Equation. **keywords:** Artificial Chemistries, Reaction diffusion and convection system, Lattice Boltzmann Method, Belousov Zhaboyinskii reaction, Abstract Rewriting System on Multisets (ARMS)

Abstract Rewriting System on Multisets, ARMS

ARMS proposed in 1996 [7], it relates to theoretical chemistry[2] and computational algebra [6], [5] An ARMS is a construct $= (A, w, R)$, where A is an alphabet, w is a multiset present in the initial configuration of the system, and R is the set of multiset rewriting rules.

Let A be an *alphabet* (a finite set of abstract symbols). A *multiset* over A is a mapping $M : A \mapsto \mathbf{N}$, where $\mathbf{N}$ is the set of natural numbers; 0, 1, 2,.... For each $a_i \in A$, $M(a_i)$ is the *multiplicity* of a_i in M, we also denote $M(a_i)$ as $[a_i]$. We denote by $A^{\#}$ the set of all multisets over A, with the empty multiset, $\emptyset$, defined by $\emptyset(a) = 0$ for all $a \in A$. A multiset $M : A \mapsto \mathbf{N}$, for $A = \{a_1, \ldots, a_n\}$ is represented by the state vector $w = (M(a_1), M(a_2), \ldots, M(a_n))$, w. The union of two multisets $M_1, M_2 : A \mapsto \mathbf{N}$ is the addition of vectors w_1 and w_2 that represent the multisets M_1, M_2, respectively. If $M_1(a) \leq M_2(a)$ for all $a \in A$, then we say that multiset M_1 is included in multiset M_2 and we write $M_1 \subseteq M_2$. A *reaction rule* r over A can be defined as a couple of multisets, (s, u), with $s, u \in A^{\#}$. A set of reaction rules is expressed as R. A rule $r = (s, u)$ is also represented as $r = s \to u$. Given a multiset $s \subseteq$, the application of a rule $r = s \to u$ to the multiset w produces a multiset w' such that $w' = w - s + u$. Note that s and u can also be zero vector (empty). The *reaction vector*, ν_{ji} denotes the change of the number of a_i molecules produced by one reaction of rule r_j.

f Algorithm of DARMS In Deterministic Abstract Rewriting System on multisets (DARMS), reaction rules are applied in maximally parallel and deterministic way. Hence, the DARMS accommodates P Systems, while it has background in theoretical chemistry [8].

Step 0(Initialization). The time t is set to 0 and the set of vectors $V = (\delta_1, \delta_2, ..., \delta_N)$ $(j = 1, 2, ..., m)$, expressing the stoichiometric change of each species, are initialized. Then all inputs of the system are assigned to their respective variables, $X(a_1), X(a_2), ..., X(a_N)$ are set to the initial quantities of species; $k_1, ..., k_m$ to set m rate constants corresponding to the m reactions; t_{stop} to the ending instant of simulation; set the value of ; *Step 1*(Calculation of state change vector $_t$). According to reaction rules, stoichiometric change of each specie λ_i is calculated as well as the state change vector; $_t = (\lambda_1, \lambda_2, ..., \lambda_N)$ is calculated, where $\lambda_i = \sum_{j=1}^{m} \nu_{ji} v_j \mathbf{x}(t)$.
Step 2(System update and branching). The quantity of each species and t is updated, by using $_t$ and : $\mathbf{x}(t) = \mathbf{x}(t - \ ) + \ _{t-\Delta}, t := t +$. If $t \geq t_{stop}$ or if there are no reactions left in the reactor, the simulation is stopped and the results are sent to the output stream. Otherwise, the simulation returns to *Step 1*. In order to simulate pattern formation, we compose cellular automata by using the ARMS and call it Cellular Automata of Abstract Rewriting System on Multisets (CARMS)[8]. As for the calculation of diffusion, we use conventional explicit scheme

©ISAROB 2009

of difference method to solve partial differential equation of diffusion and for the calculation of convection, we use the Lattice Boltzmann Method [4].

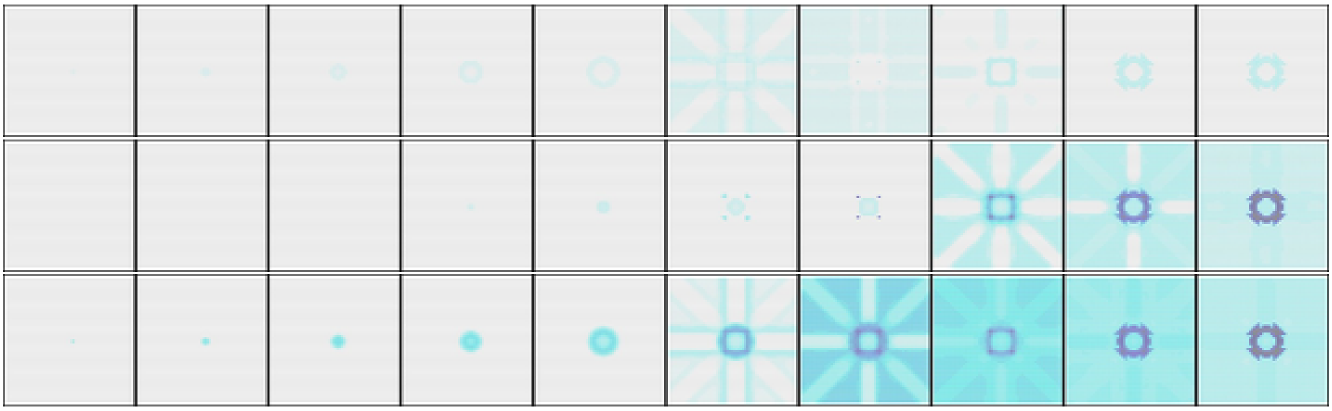

Figure 1: **Time evolution of chemicals**: Each line composed of the difference of the time evolution of concentration of X (top), Y (middle) and Z (bottom) in the CARMS, where, time evolution starts from right toward left. Blue illustrates that the concentration is high, while white, low and $\tau = 1.0 \times 10^4$

Lattice Boltzmann Method (LBM)

The lattice Boltzmann equation (LBE) method is emerging as a physically accurate and computationally viable tool for simulating laminar and turbulent flows. On the theoretical front, rigorous mathematical proof now exists demonstrating that the lattice Boltzmann method (LBM) is a special finite difference scheme of the Boltzmann equation that governs all fluid flows (the Navier-Stokes equation also has its basis in the Boltzmann equation).

The basic LBE for a single-component medium consists of two basic steps: collision and advection. The particle distribution function is thermalized locally through collision processes and advection to the closest neighboring sites occurs according to a small set of discrete particle velocities. The LBE proposed here is the lattice Boltzmann scheme with BGK approximation [8]; $n_\alpha(\mathbf{x} + e_\alpha\delta_t, t + \delta_t) = n_\alpha(\mathbf{x}, t) - \frac{1}{\tau}[n_\alpha(\mathbf{x}, t) - n_\alpha^{(eq)}(\mathbf{x}, t)]$ where n_α is the number density distribution function with discrete velocity e_α, $n_\alpha^{(eq)}$ is the equilibrium distribution function and τ is the relaxation time (towards equilibrium) which determines the viscosity. The time-step size is δ_t, which is the time taken for the advection process to be completed. For the sake of simplicity without losing generality, we adopt the nine-velocity model. Then the equilibrium distribution function for isothermal field is given as $n_\alpha^{(eq)} = w_\alpha n[1 + \frac{1}{c_s^2}(e_\alpha \cdot \mathbf{u}) \times \frac{1}{2c_s^4}(e_\alpha \cdot \mathbf{u})^2 - \frac{1}{c_s^2}u^2]$ in which the discrete particle velocities e_α and the weighting factor w_α (α = 0,1,2,· · ·,8) are

$$e_\alpha = \begin{cases} (0,0) & \alpha = 0 \\ (cos[(\alpha-1)\pi/2]), sin[(\alpha-1)\pi/2] & \alpha = 1,2,3,4 \\ (cos[(\alpha-4)\pi/4]), sin[(\alpha-5)\pi/2 + \pi/4] & \alpha = 5,6,7,8 \end{cases} \tag{1}$$

and

$$e_\alpha = \begin{cases} 4/9 & \alpha = 0 \\ 1/9 & \alpha = 1,2,3,4 \\ 1/36 & \alpha = 5,6,7,8 \end{cases} \tag{2}$$

respectively. The sound speed is $w_\alpha = 1/\sqrt{3}(\delta_x/\delta_t)$ with δ_x being the lattice constant of the underlying square lattice. The macroscopic quantities, such as particle density n, mass density ?? and mass velocity $\mathbf{u}$ are given by $n = \sum_\alpha n_\alpha$ $\rho = mn$ $\rho\mathbf{u} = m\sum n_\alpha e_\alpha$ where m is the molecular weight (for more detail of the LBM, refer [4]).

©ISAROB 2009

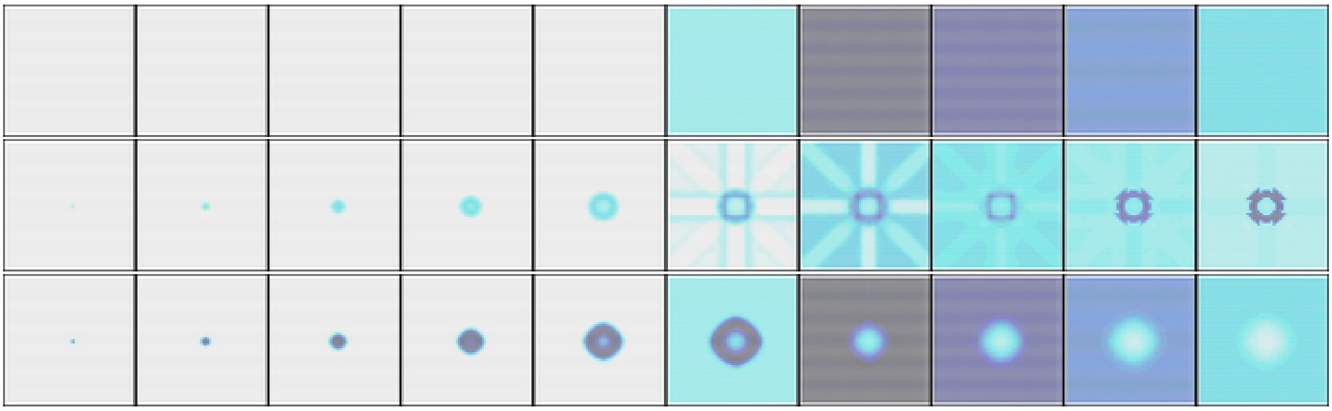

Figure 2: **Effectiveness of the convection** The difference of the time evolution of concentration of Z in the CARMS, where time evolution starts from right toward left. Blue illustrates that the concentration is high, while white, low. The effect of convection is changed; the value of τ denotes the degree of effectiveness of the convection, as the τ is getting large, the effectiveness becomes large. Each line illustrates when $\tau = 10$ (top), $\tau = 1.0 \times 10^4$ (middle), $\tau = 1.0 \times 10^7$ (bottom), respectively

$$
\begin{array}{lcl}
X, Y, H & \stackrel{k_1}{\rightarrow} & 2W : (r_1), \\
A, Y, 2H & \stackrel{k_2}{\rightarrow} & X, W : (r_2), \\
2X & \stackrel{k_3}{\rightarrow} & A, W, H : (r_3), \\
A, X, H & \stackrel{k_4}{\rightarrow} & 2X, 2Z : (r_4), \\
B, Z & \stackrel{k_5}{\rightarrow} & 0.5Y : (r_5).
\end{array}
$$

Table 1: Oregonator

Lattice Boltzman Equations for Reaction flow In a reacting flow, the state of the fluid at any given point in space and time can be completely specified in terms of fluid velocity, composition vector (either in terms of mass fraction or concentration). We will need to develop the LBE for all these variables. For generating a background flow, the conventional LBM sub-steps of collision (relaxation) and streaming (convection) are used. However for the concentration fields, there is an extra sub-step between collision and streaming sub-steps to account for reaction-diffusion and convection. This is identical to the time-splitting approach used in continuum methods for chemically reacting flows.

Flow FIeld The background flow-field is obtained using the following stencil for partial pressure $p_\alpha(\mathbf{x}+e_\alpha, t+1) = p_\alpha(\mathbf{x}, t) - \frac{1}{\tau_p}[p_\alpha(\mathbf{x}, t) - p_\alpha^{(eq)(\mathbf{x},t)}]$ where $p_\alpha^{(eq)} = w_\alpha p[1 + 3(e_\alpha \cdot \mathbf{u}) + \frac{9}{2}(e_\alpha \cdot \mathbf{u})^2 - \frac{3}{2}u^2]$ The total pressure $p(= \rho c_s^2)$ and the fluid velocity are calculated using $p = \sum_\alpha p_\alpha u = \frac{1}{p}\sum_\alpha e_{alpha} p_\alpha$ This is the velocity used for determining the equilibrium distribution functions in temperature and concentration fields.

Concentraton elds For concentration field, there is an extra computational sub-step, reaction and diffusion by using the DARMS and CARMS besides conventional computational sub-steps of collision and advection. **Collision of chemical specie** i $Y_\alpha^i(\mathbf{x}, t) = Y_\alpha^i(\mathbf{x}, t) - \frac{1}{\tau_i}[Y_\alpha^i(\mathbf{x}, t) - Y_\alpha^{i(eq)(\mathbf{x},t)}]$ where Y^i denotes the concentration of chemical specie i, $Y_\alpha^{i(eq)} = w_\alpha Y^i[1 + 3(e_\alpha \cdot u) + \frac{9}{2}(e_\alpha \cdot) u)^2 - \frac{3}{2}u^2]$ and $Y^i = \sum_\alpha Y_\alpha^i$, Relaxation time-constant τ is determined by thermal diffusivity and τ_i's are determined by the diffusivity of corresponding species.

Simulation of the Oregonator

The Oregonator scheme is outlined in Table 1: In this paper, a combination of Tyson's "Lo" and Field-Főrsterling values (TFF parameter) are used [8]: $k_1 : 10^6 M^{-2}S^{-1}, k_2 : 2M^{-3}S^{-1}, k_3 : 2 \times 10^3 M^{-1}S^{-1}, k_4 : 10M^{-2}S^{-1}, k_5 : B \times 2 \times 10^{-2}S^{-1}$, where M stands for one molar, and S stands for a second.

©ISAROB 2009

Results of the simulation We take the non-slip boundary condition (the velocities of particles which hit the wall are inverted after the collision). The condition of the simulation is described as follows; the amount of computation steps is 20,000, $= 0.01$, $\tau = 10, 1.0 \times 10^4, 1.0 times 10^7$, the diffusion constants D obtained by chemical experiments [8]; (cm^2 / sec.) of X, D_X and Z, D_Z are 1.5×10^{-5} and $D_X = 0.9 \times 10^{-5}$.

It is assumed that the size of reactor in the CARMS is a 6cm × 6cm square, where 50 × 50 DARMSes are placed. So, the distance between DARMSes is $x = \frac{6}{50}$cm. In the chemical experiment of BZ reaction, usually a excitation point is generated by stinging a sliver stick, which evokes oxidation reaction. In order to express the generation of the excitation point, we change the concentration of X and Y are smaller, while that of Z is 100 times larger.

The results of simulation of the Oregonator illustrate that the CARMS with reaction, diffusion and convection exhibits typical chemical wave spatial pattern of the Oregonator on every chemical specie X, Y and Z.

Next, we change effectiveness of the convection. Since the value of τ denotes the effectiveness, we change $\tau = 10$ (the effectiveness is strong), $\tau = 1.0 \times 10^4$ (middle) and $\tau = 1.0 \times 10^7$ (weak). And we confirmed that the effectiveness of the convection change the spatio-temporal pattern of chemical reaction (figure 2). When the effectiveness is strong (the top line in the figure 2), since the convection was strong, the reactor was well stirred and spatial patterns were excluded, but temporal patterns were preserved. And when the effectiveness is middle (the middle line in the figure), there emerged spatio-temporal pattern, however, its pattern was different from the case when the effectiveness is weak. When the effectiveness of convection is weak, it is almost same to the system only with reaction and diffusion. We confirmed that when the effectiveness of convection is weak, its pattern (the bottom line in the figure) is similar to the ARMS with reaction-diffusion.

References

[1] Bhatnagar, P.L., Gross, E.P., Krook, K. (1954). A model for collision processes in gases. Phys. Rev. 94: 511.524.

[2] D.T. Gillespie, A General Method for Numerically Simulating the Stochastic Time Evolution of Coupled Chemical Reactions, J. Comp. Phys., 22:403-434, 1976.

[3] D.T. Gillespie, Approximate accelerated stochastic simulation of chemically reacting systems, J. Chem. Phys, 115(4), 1716-1733, 2001.

[4] Huidan Y., L.S. Luo, S. S. Girimaji, Scalar mixinig and chemical reaction simulations using lattice boltzmann method, International Journal of Computational Engineering Science Vol. 3, No. 1 (2002) 73-87, Imperial College Press. Boltzmann Method, J. Comput. Phys. 118, 329-347 1995.

[5] V. Manca, String rewriting and metabolism: a logical perspective, in Computing with Bio-Molecules. Theory and Experiments, 36-60, Springer Verlag, Singapore, 1998.

[6] G. Păun, Computing with membrane, J. Comput. Systems Sci., 61(1):108-143, Elsevier, 2001.

[7] Y. Suzuki, S. Tsumoto, and H. Tanaka, Analysis of Cycles in Symbolic Chemical System based on Abstract Rewriting System on Multisets. Proceedings of Artificial Life V, pp. 482-489. MIT press, 1996.

[8] M. Umeki and Y. Suzuki, A Simple Membrane Computing Method for Simulating Bio-Chemical Reactions, Computer and Informatics, 27, 529-550, 2008.

©ISAROB 2009

The Fourteenth International Symposium on Artificial Life and Robotics 2009 (AROB 14th '09),
B-Con Plaza, Beppu, Oita, Japan, February 5 - 7, 2009

A Design of Algorithms for Real-Time Generation of Linear-Recursive Sequences on Cellular Automata

Naoki Kamikawa
Graduate School of Engineering
Univ. of Osaka Electro-Communication
Neyagawa-shi, Hatsu-cho 18-8,
Osaka, 572-8530, Japan

Hiroshi Umeo
Graduate School of Engineering
Univ. of Osaka Electro-Communication
Neyagawa-shi, Hatsu-cho 18-8,
Osaka, 572-8530, Japan

Abstract

A model of cellular automata (CA) is considered to be a non-linear model of complex systems in which an infinite one-dimensional array of finite state machines (cells) updates itself in a synchronous manner according to a uniform local rule. We study a sequence generation problem on the CA and propose several state-efficient real-time sequence generation algorithms for non-regular sequences. We show that Fibonacci sequence can be generated in real-time by a CA with 5 states. We also study infinite linear-recursive sequences, such as tribonacci, tetranacci and pell sequences generated on the CA.

1 Introduction

A model of cellular automata (CA) was devised originally for studying self-reproduction by John von Neumann. It is now studied in many fields such as complex systems. We study a sequence generation problem on the CA. Arisawa[1], Fischer[2], Korec[3] and Kamikawa and Umeo[5], [6] studied generation of a class of natural numbers on CA. In this paper, we show that Fibonacci sequence can be generated in real-time by a CA with 5 states. We also study infinite linear-recursive sequences, such as tribonacci sequence, tetranacci sequence and pell sequence generated on the CA. We show a design of algorithm for real-time generation of linear-recursive sequences on CA.

2 Real-time sequence generation problem on CA

A cellular automaton consists of an infinite array of identical finite state automata, each located at a positive integer point (See Figure 1).

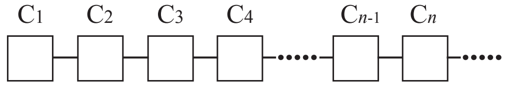

Figure 1: Cellular automaton.

Each automaton is referred to as a cell. A cell at point i is denoted by C_i, where $i \geq 1$. Each C_i, except for C_1, is connected to its left- and right-neighbor cells via a communication link. Each cell can know state of its left- and right-neighbor cells via communication link. One distinguished leftmost cell C_1, the communication cell, is connected to the outside world. A cellular automaton (abbreviated by CA) consists of an infinite array of finite state automata $A = (Q, \delta, F)$, where

1. Q is a finite set of internal states.
2. δ is a function defining the next state of a cell, such that δ: $Q \times Q \times Q \to Q$, where $\delta(\mathtt{p}, \mathtt{q}, \mathtt{r}) = \mathtt{s}$, $\mathtt{p}$, $\mathtt{q}$, $\mathtt{r}$, $\mathtt{s} \in Q$ has the following meaning: We assume that at step t the cell C_i is in state $\mathtt{q}$, the left cell C_{i-1} is in state $\mathtt{p}$ and the right cell C_{i+1} is in state $\mathtt{r}$. Then, at the next step $t+1$, C_i assumes state $\mathtt{s}$. The leftmost cell C_1 is connected to the outside world. The outside world is expressed by $*$. A quiescent state $\mathtt{q} \in Q$ has a property such that $\delta(\mathtt{q}, \mathtt{q}, \mathtt{q}) = \mathtt{q}$.
3. $F \subseteq Q$ is a special subset of Q. The set F is used to specify a designated state of C_1 in the definition of sequence generation.

We now define the **sequence generation problem** on CA. Let M be a CA and $\{t_n | n = 1, 2, 3, ...\}$ be an infinite monotonically increasing positive integer sequence defined natural numbers, such that $t_n \geq n$ for any $n \geq 1$. We then have a semi-infinite array of cells, as shown in Figure 1, and all cells, except for C_1, are in the quiescent state at time $t = 0$. The communication cell C_1 assumes a special state $\mathtt{r}$ in Q for initiation of the sequence generator. We say that M generates a sequence $\{t_n | n = 1, 2, 3, ...\}$ in k *linear-time* if and only if the leftmost end cell of M falls into a special state in $F \subseteq Q$ at time $t = k \cdot t_n$, where k is a positive integer. We call M a *real-time* generator when $k = 1$.

3 Generation Algorithms of Linear-Recursive Sequences

In this section, we propose generation algorithm of linear-recursive sequences. First, we show a design of algorithm for real-time generation of linear-recursive sequences on CA. Next, we show that Fibonacci sequence can be generated on a CA with 5 states.

©ISAROB 2009

3.1 A Design of Algorithm

Let m be any natural number, such that $m \geq 1$. Let k be natural number given, such that $k \geq 1$, $k < m$. Let $b_1, b_2, \ldots, b_k, c_1, c_2, \ldots, c_k$ be natural number given, such that $b_1, b_2, \cdots, b_k \geq 1$, $c_1 < c_2 < \cdots < c_k$. Let a_m be kth order linear-recursive sequences, such that $a_m = b_1 \cdot a_{m-1} + b_2 \cdot a_{m-2} + \cdots + b_k \cdot a_{m-k}$, $a_1 = c_1$, $a_2 = c_2$, $\ldots$, $a_k = c_k$. We show a design of algorithm for real-time generation of sequence a_m on CA.

3.2 First Order Linear-Recursive Sequences

We propose the generation algorithm for $k = 1$. It is approved that $a_m = b_1 \cdot a_{m-1}$, $a_1 = c_1$. However, it is limited to $b_1 \geq 2$. Because all terms take c_1 for $b_1 = 1$, and a_m is not an infinite monotonically increasing positive integer sequence. Figure 2 shows a time-space diagram for generation of the term a_m, when the term a_{m-1} is an even number.

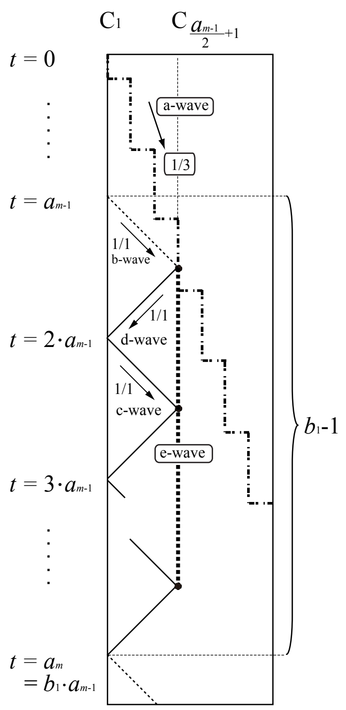

Figure 2: Time-space diagram for generation of the term a_m (when the term $a_{m\;1}$ is an even number).

	1	2	3	4	5	6	7	8	9
0	A3	Q	Q	Q	Q	Q	Q	Q	Q
1	W1	A1	Q	Q	Q	Q	Q	Q	Q
2	W2	A2	Q	Q	Q	Q	Q	Q	Q
3	W3	A3	Q	Q	Q	Q	Q	Q	Q
4	W4	R	A1	Q	Q	Q	Q	Q	Q
5	W5	R	A2	Q	Q	Q	Q	Q	Q
6	G	R	A3	Q	Q	Q	Q	Q	Q
7	Q	B	R	A1	Q	Q	Q	Q	Q
8	Q	R	B	A2	Q	Q	Q	Q	Q
9	Q	R	R	E1	Q	Q	Q	Q	Q
10	Q	R	D	E2	A1	Q	Q	Q	Q
11	Q	D	R	E2	A2	Q	Q	Q	Q
12	t1	R	R	E2	A3	Q	Q	Q	Q
13	t2	C	R	E2	R	A1	Q	Q	Q
14	t2	R	C	E2	R	A2	Q	Q	Q
15	t2	R	R	D	R	A3	Q	Q	Q
16	t2	R	D	R	R	R	A1	Q	Q
17	t2	D	R	R	R	R	A2	Q	Q
18	G	R	R	R	R	R	A3	Q	Q
19	Q	B	R	R	R	R	R	A1	Q
20	Q	R	B	R	R	R	R	A2	Q

Figure 3: A con guration of generation of the term a_m (when the term $a_{m\;1}$ is an even number).

Generation of the term a_m is described in terms of 6 waves: *a-wave*, *b-wave*, *c-wave*, *d-wave*, *e-wave* and *o-wave*. The a-wave is generated on C_1 at time $t = 0$. Figure 3 shows a number of snapshots of the cell configuration at the propagation of the a-wave shown in Figure 2. In Figure 3, state `A1`, `A2` and `A3` advance toward the right at speed 1-cell/3-step in cell space. Therefore, state `A1`, `A2` and `A3` which propagate in cell space is called a-wave. A sequence generation algorithm is designed geometrical by using wave which propagates in cell space. The a-wave propagates in the right direction at 1/3 speed. Figure 3 shows a number of snapshots of the cell configuration at the propagation of the a-wave. The a-wave moves to cell C_2 at time $t = 1$. Afterwards, the a-wave moves by one cell every 3 steps. When we assume $P_a(t)$ to be a function whitch shows the position of the a-wave at time t, it is approved that $P_a(t) = \lceil \frac{t}{3} \rceil + 1$. At time $t = a_{m-1}$, cell C_1 is in a state included F and the b-wave is generated on C_1. The b-wave propagates in the right direction at 1/1 speed, and the b-wave reaches the a-wave. When the a-wave collides with the b-wave, the a-wave keeps propagating, the b-wave is eliminated, the d-wave is generated and the e-wave is generated. When a_{m-1} is an even number, the b-wave collides with the second state of 3 states to compose the a-wave and the e-wave is generated (See Figure 3). Let r be natural number. When the cell which collides the a-wave with the b-wave is assumed to be cell C_r, it is approved that $r = P_a(a_{m-1} + r - 1) = \frac{a_{m-1}}{2} + 1$. Therefore, the e-wave is generated on cell $C_{\frac{a_{m-1}}{2}+1}$ at time $t = a_{m-1} + \frac{a_{m-1}}{2}$. The e-wave keeps staying on cell $C_{\frac{a_{m-1}}{2}+1}$. The d-wave propagates in the left direction at 1/1 speed, and the d-wave reaches the leftmost cell C_1 at time $t = 2 \cdot a_{m-1}$. When the d-wave collides with the leftmost cell C_1, the d-wave is eliminated and the c-wave is generated. The c-wave propagates in the right direction at 1/1 speed, and the c-wave reaches the e-wave at time $t = 2 \ldots a_{m-1} + \frac{a_{m-1}}{2}$. When the c-wave collides with the e-wave, the b-wave is eliminated and the d-wave is generated. The d-wave propagates in the left direction at 1/1 speed. The d-wave reaches cell C_1 at time $t = 3 \cdot a_{m-1}$. Therefore, Time where the b-, c- and d-waves reciprocate between the leftmost cell C_1 and the e-wave is a_{m-1} steps. The b-, c- and d-waves reciprocate $b_1 - 1$ times between the leftmost cell C_1 and the e-wave (See Figure 2). When the d-wave of times $b_1 - 1$ reaches the cell C_1, a state of C_1 changes to a state included F at time $t = b_1 \cdot a_{m-1}$.

Figure 4 shows a time-space diagram for generation of the term a_m, when the term a_{m-1} is an odd number. When a_{m-1} is an odd number, the o-wave is generated by the collision of the a-wave and the b-wave. The b-wave collides with the third state of 3 states to compose the a-wave and the o-wave is generated (See Figure 5). When the cell which collides the a-wave with the b-wave is assumed to be cell C_r, it is approved that $r = P_a(a_{m-1}+r-1) = \lfloor \frac{a_{m-1}}{2} \rfloor + 1$. Because a_{m-1} is an odd number, it is approved that $r = \frac{a_{m-1}-1}{2} + 1$. Therefore, the o-wave is generated on cell $C_{\frac{a_{m-1}-1}{2}+1}$. he c-wave propagates in the right direction at 1/1 speed, and the c-wave reaches the o-wave at time $t = a_{m-1} + \frac{a_{m-1}-1}{2}$. When the c-wave collides with the o-wave, the b-wave is eliminated. The d-wave is generated after 1 step. The d-wave propagates in the left direction at 1/1 speed. The d-wave reaches

©ISAROB 2009

cell C_1 at time $t = a_{m-1} + \frac{a_{m-1}-1}{2} + 1 + \frac{a_{m-1}-1}{2} = 2 \cdot a_{m-1}$. Therefore, Time where the b-, c- and d-waves reciprocate between the leftmost cell C_1 and the o-wave is a_{m-1} steps. The b-, c- and d-waves reciprocate $b_1 - 1$ times between the leftmost cell C_1 and the o-wave (See Figure 4). When the d-wave of times $b_1 - 1$ reaches the cell C_1, a state of C_1 changes to a state included F at time $t = b_1 \cdot a_{m-1}$.

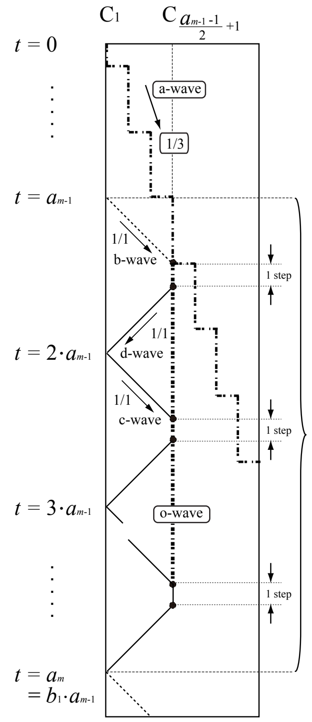

Figure 4: Time-space diagram for generation of the term a_m (when the term $a_{m\ 1}$ is an odd number).

	1	2	3	4	5	6	7	8	9
0	A3	Q	Q	Q	Q	Q	Q	Q	Q
1	W1	A1	Q	Q	Q	Q	Q	Q	Q
2	W2	A2	Q	Q	Q	Q	Q	Q	Q
3	W3	A3	Q	Q	Q	Q	Q	Q	Q
4	W4	R	A1	Q	Q	Q	Q	Q	Q
5	W5	R	A2	Q	Q	Q	Q	Q	Q
6	W6	R	A3	Q	Q	Q	Q	Q	Q
7	G	R	R	A1	Q	Q	Q	Q	Q
8	Q	B	R	A2	Q	Q	Q	Q	Q
9	Q	R	B	A3	Q	Q	Q	Q	Q
10	Q	R	R	O1	A1	Q	Q	Q	Q
11	Q	R	R	O2	A2	Q	Q	Q	Q
12	Q	R	D	O3	A3	Q	Q	Q	Q
13	Q	D	R	O3	R	A1	Q	Q	Q
14	t1	R	R	O3	R	A2	Q	Q	Q
15	t2	C	R	O3	R	A3	Q	Q	Q
16	t2	R	C	O3	R	R	A1	Q	Q
17	t2	R	R	O4	R	R	A2	Q	Q
18	t2	R	R	D	R	R	A3	Q	Q
19	t2	R	D	R	R	R	R	A1	Q
20	t2	D	R	R	R	R	R	A2	Q
21	G	R	R	R	R	R	R	A3	Q
22	Q	B	R	R	R	R	R	R	A1

Figure 5: A con guration of generation of the term a_m (when the term $a_{m\ 1}$ is an odd number).

The first term $a_1 = c_1$ is generated in an internal state. A state of the leftmost cell C_1 is changed a state included F at time $t = c_1$ by counting the $c_1 - 1$ step by using an internal state. And the b-wave is generated. Therefore, 1st Order Linear-Recursive Sequences can be generated on CA in real-time. In Figure 6, we show a number of snapshots of the configuration for $b_1 = 3$ and $c_1 = 3$ from $t = 0$ to 29.

3.3 Second Order Linear-Recursive Sequences

Next, we consider the case of $k = 2$. We propose the generation algorithm of second order linear-recursive sequences which enhance the algorithm described in section 3.2. It is approved that $a_m = b_1 \cdot a_{m-1} + b_2 \cdot a_{m-2}$, $a_1 = c_1$, $a_2 = c_2$. Figure 7 shows a time-space diagram for generation of a second order linear-recursive sequence. The a-wave is generated on C_1 at time $t = 0$. We assume that the e- or o-wave is generated on cell $C_{\lfloor \frac{a_{m-2}}{2} \rfloor + 1}$. At time $t = a_{m-1}$, cell C_1 is in a state included F and the b-wave is generated on C_1. The b-wave propagates in the right direction at $1/1$ speed, and the b-wave reaches the e- or o-wave generated on cell $C_{\lfloor \frac{a_{m-2}}{2} \rfloor + 1}$. When the e- or o-wave collides with the b-wave, the b-wave keeps propagating and the d-wave is generated. The b-wave propagates, and the b-wave reaches the a-wave. When the a-wave collides with the b-wave, the b-wave is eliminated and the e- or o-wave is generated on cell $C_{\lfloor \frac{a_{m-1}}{2} \rfloor + 1}$. The d-wave propagates in the left direction at $1/1$ speed, and the d-wave reaches the leftmost cell C_1 at time $t = a_{m-1} + a_{m-2}$. The b-, c- and d-waves reciprocate b_2 times between the leftmost cell C_1 and the e- or o-wave generated on cell $C_{\lfloor \frac{a_{m-2}}{2} \rfloor + 1}$. When the e- or o-wave generated on cell $C_{\lfloor \frac{a_{m-2}}{2} \rfloor + 1}$ collides with the b- or c-wave b_2 times, the e- or o-wave is eliminated. At the next, The c- and d-waves reciprocate $b_1 - 1$ times between the leftmost cell C_1 and the e- or o-wave generated on cell $C_{\lfloor \frac{a_{m-1}}{2} \rfloor + 1}$. When The b-, c- and d-waves reciprocate b_2 times between cell C_1 and the e- or o-wave generated on cell $C_{\lfloor \frac{a_{m-2}}{2} \rfloor + 1}$ and reciprocate $b_1 - 1$ times between cell C_1 and the e- or o-wave generated on cell $C_{\lfloor \frac{a_{m-1}}{2} \rfloor + 1}$, a state of the leftmost cell C_1 changes a state included F. The first some terms and some e- and o-waves are generated in an internal state. For example, Figure 8 shows generation of pell sequence ($a_m = 2 \cdot a_{m-1} + a_{m-2}, a_1 = 1, a_2 = 2$).

	1	2	3	4	5	6	7	8	9	10	11	12
0	A3	Q	Q	Q	Q	Q	Q	Q	Q	Q	Q	Q
1	W1	A1	Q	Q	Q	Q	Q	Q	Q	Q	Q	Q
2	W2	A2	Q	Q	Q	Q	Q	Q	Q	Q	Q	Q
3	G	A3	Q	Q	Q	Q	Q	Q	Q	Q	Q	Q
4	Q	O1	A1	Q	Q	Q	Q	Q	Q	Q	Q	Q
5	Q	O2	A2	Q	Q	Q	Q	Q	Q	Q	Q	Q
6	t1	O3	A3	Q	Q	Q	Q	Q	Q	Q	Q	Q
7	t2	O4	R	A1	Q	Q	Q	Q	Q	Q	Q	Q
8	t2	D	R	A2	Q	Q	Q	Q	Q	Q	Q	Q
9	G	R	R	A3	Q	Q	Q	Q	Q	Q	Q	Q
10	Q	B	R	R	A1	Q	Q	Q	Q	Q	Q	Q
11	Q	R	B	R	A2	Q	Q	Q	Q	Q	Q	Q
12	Q	R	R	B	A3	Q	Q	Q	Q	Q	Q	Q
13	Q	R	R	R	O1	A1	Q	Q	Q	Q	Q	Q
14	Q	R	R	R	O2	A2	Q	Q	Q	Q	Q	Q
15	Q	R	R	D	O3	A3	Q	Q	Q	Q	Q	Q
16	Q	R	D	R	O3	R	A1	Q	Q	Q	Q	Q
17	Q	D	R	R	O3	R	A2	Q	Q	Q	Q	Q
18	t1	R	R	R	O3	R	A3	Q	Q	Q	Q	Q
19	t2	C	R	R	O3	R	R	A1	Q	Q	Q	Q
20	t2	R	C	R	O3	R	R	A2	Q	Q	Q	Q
21	t2	R	R	C	O3	R	R	A3	Q	Q	Q	Q
22	t2	R	R	R	O4	R	R	R	A1	Q	Q	Q
23	t2	R	R	R	D	R	R	R	A2	Q	Q	Q
24	t2	R	R	D	R	R	R	R	A3	Q	Q	Q
25	t2	R	D	R	R	R	R	R	R	A1	Q	Q
26	t2	D	R	R	R	R	R	R	R	A2	Q	Q
27	G	R	R	R	R	R	R	R	R	A3	Q	Q
28	Q	B	R	R	R	R	R	R	R	R	A1	Q
29	Q	R	B	R	R	R	R	R	R	R	A2	Q

Figure 6: A con guration of real-time generation of a rst order linear-recursive sequence ($a_m = 3\ a_{m\ 1}, a_1 = 3$).

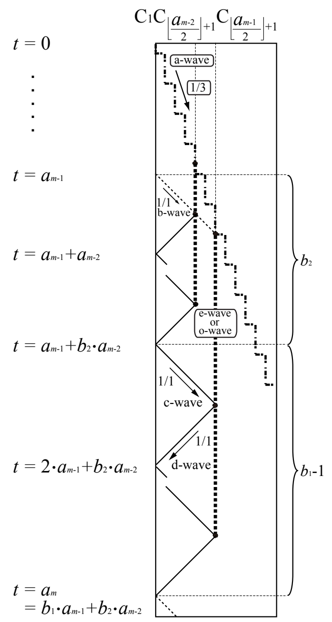

Figure 7: Time-space diagram for generation of a second order linear-recursive sequence.

©ISAROB 2009

	1	2	3	4	5	6	7	8	9	10	11	12
0	A3	Q	Q	Q	Q	Q	Q	Q	Q	Q	Q	Q
1	G	A1	Q	Q	Q	Q	Q	Q	Q	Q	Q	Q
2	G	A2	Q	Q	Q	Q	Q	Q	Q	Q	Q	Q
3	W3	E3	Q	Q	Q	Q	Q	Q	Q	Q	Q	Q
4	W4	E3	A1	Q	Q	Q	Q	Q	Q	Q	Q	Q
5	G	E3	A2	Q	Q	Q	Q	Q	Q	Q	Q	Q
6	Q	E4	A3	Q	Q	Q	Q	Q	Q	Q	Q	Q
7	t1	R	O1	A1	Q	Q	Q	Q	Q	Q	Q	Q
8	t2	C	O1	A2	Q	Q	Q	Q	Q	Q	Q	Q
9	t2	R	O2	A3	Q	Q	Q	Q	Q	Q	Q	Q
10	t2	R	O3	R	A1	Q	Q	Q	Q	Q	Q	Q
11	t2	D	O4	R	A2	Q	Q	Q	Q	Q	Q	Q
12	G	R	O4	R	A3	Q	Q	Q	Q	Q	Q	Q
13	Q	C	O4	R	R	A1	Q	Q	Q	Q	Q	Q
14	Q	R	O5	R	R	A2	Q	Q	Q	Q	Q	Q
15	Q	R	D	B	R	A3	Q	Q	Q	Q	Q	Q
16	Q	D	R	R	B	R	A1	Q	Q	Q	Q	Q
17	t1	R	R	R	R	B	A2	Q	Q	Q	Q	Q
18	t2	C	R	R	R	R	E1	Q	Q	Q	Q	Q
19	t2	R	C	R	R	R	E1	A1	Q	Q	Q	Q
20	t2	R	R	C	R	R	E1	A2	Q	Q	Q	Q
21	t2	R	R	R	C	R	E1	A3	Q	Q	Q	Q
22	t2	R	R	R	R	C	E1	R	A1	Q	Q	Q
23	t2	R	R	R	R	R	E2	R	A2	Q	Q	Q
24	t2	R	R	R	R	D	E3	R	A3	Q	Q	Q
25	t2	R	R	R	D	R	E3	R	R	A1	Q	Q
26	t2	R	R	D	R	R	E3	R	R	A2	Q	Q
27	t2	R	D	R	R	R	E3	R	R	A3	Q	Q
28	t2	D	R	R	R	R	E3	R	R	R	A1	Q
29	G	R	R	R	R	R	E3	R	R	R	A2	Q
30	Q	C	R	R	R	R	E3	R	R	R	A3	Q

Figure 8: A con guration of real-time generation of pell sequence ($a_m = 2 \cdot a_{m-1} + a_{m-2}, a_1 = 1, a_2 = 2$).

3.4 kth Order Linear-Recursive Sequences

Next, we generalize the generation algorithm described in section 3.3, and propose the generation algorithm of kth Order Linear-Recursive Sequences. Figure 9 shows a time-space diagram for generation of a kth order linear-recursive sequence. The a-wave is generated on C_1 at time $t = 0$. We assume that the e- or o-waves are generated on cell $C_{\lfloor \frac{a_{m-k}}{2} \rfloor +1}$, $C_{\lfloor \frac{a_{m-k+1}}{2} \rfloor +1}$, $\cdots$, $C_{\lfloor \frac{a_{m-3}}{2} \rfloor +1}$ and $C_{\lfloor \frac{a_{m-2}}{2} \rfloor +1}$. At time $t = a_{m-1}$, cell C_1 is in a state included F and the b-wave is generated on C_1. The b-wave propagates in the right direction at 1/1 speed, and the b-wave reaches the e- or o-wave generated on cell $C_{\lfloor \frac{a_{m-k}}{2} \rfloor +1}$. When the e- or o-wave collides with the b-wave, the b-wave keeps propagating and the d-wave is generated. The b-wave propagates by passing the e- or o-waves generated on cell $C_{\lfloor \frac{a_{m-k+1}}{2} \rfloor +1}$, $\cdots$, $C_{\lfloor \frac{a_{m-3}}{2} \rfloor +1}$, and the b-wave reaches the a-wave. When the a-wave collides with the b-wave, the b-wave is eliminated and the e- or o-wave is generated on cell $C_{\lfloor \frac{a_{m-1}}{2} \rfloor +1}$. The d-wave propagates by passing the e- or o-waves in the left direction at 1/1 speed, and the d-wave reaches the leftmost cell C_1 at time $t = a_{m-1} + a_{m-k}$. The b-, c- and d-waves reciprocate b_k times between the leftmost cell C_1 and the e- or o-wave generated on cell $C_{\lfloor \frac{a_{m-k}}{2} \rfloor +1}$. When the e- or o-wave generated on cell $C_{\lfloor \frac{a_{m-k}}{2} \rfloor +1}$ collides with the b- or c-wave b_k times, the e- or o-wave is eliminated. At the next, The c- and d-

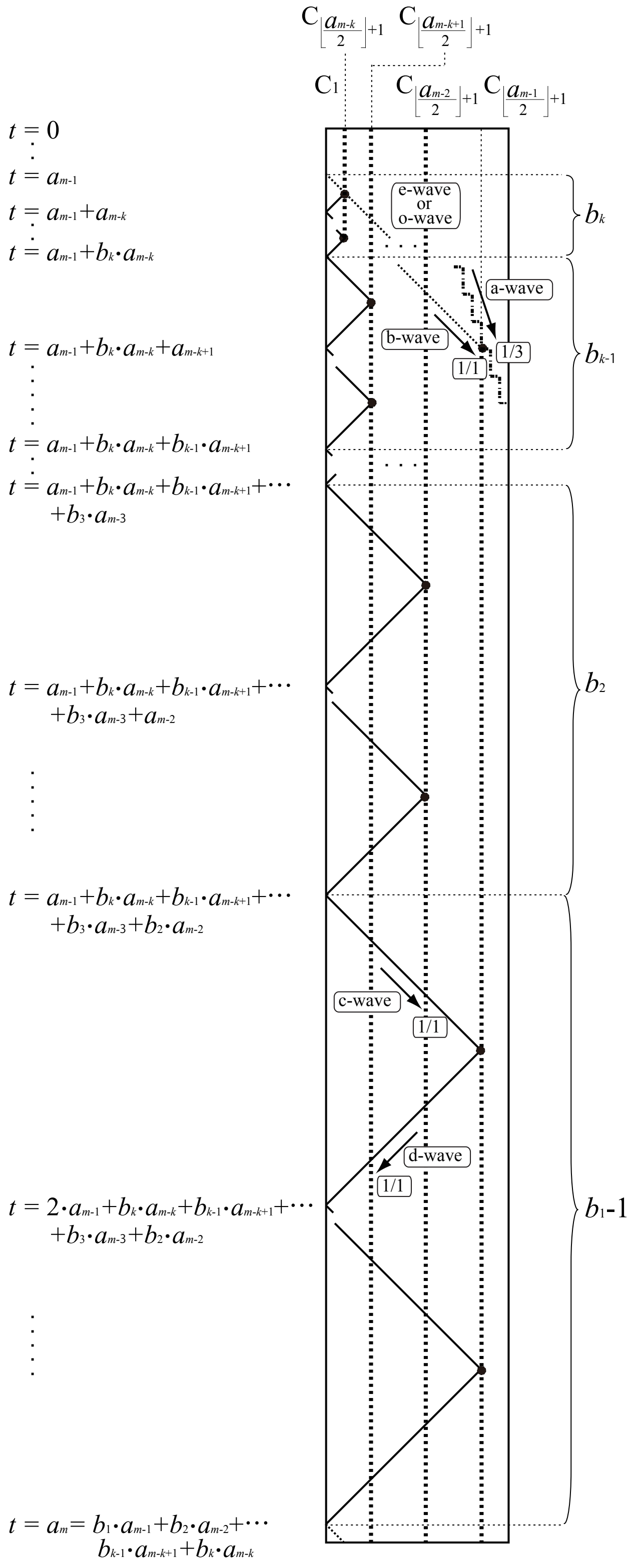

Figure 9: Time-space diagram for generation of a kth order linear-recursive sequence.

waves reciprocate b_{k-1} times between the leftmost cell C_1 and the e- or o-wave generated on cell $C_{\lfloor \frac{a_{m-k+1}}{2} \rfloor +1}$, reciprocate b_{k-2} times between the leftmost cell C_1 and the e- or o-wave generated on cell $C_{\lfloor \frac{a_{m-k+2}}{2} \rfloor +1}$, $\cdots$, reciprocate b_2 times between the leftmost cell C_1 and the e- or o-wave generated on cell $C_{\lfloor \frac{a_{m-2}}{2} \rfloor +1}$ and reciprocate $b_1 - 1$ times between the leftmost cell C_1 and the e- or o-wave generated on cell $C_{\lfloor \frac{a_{m-1}}{2} \rfloor +1}$. At time $t = a_m = b_1 \cdot a_{m-1} + b_2 \cdot a_{m-2} + \cdots + b_k \cdot a_{m-k}$, a state of the leftmost cell C_1 changes a state included F. The first some terms and some e- and o-waves are generated in an internal state. For example, Figure 10 shows generation of tetranacci sequence ($a_m = a_{m-1} + a_{m-2} + a_{m-3} + a_{m-4}, a_1 = 1, a_2 = 2, a_3 = 4, a_4 = 8$).

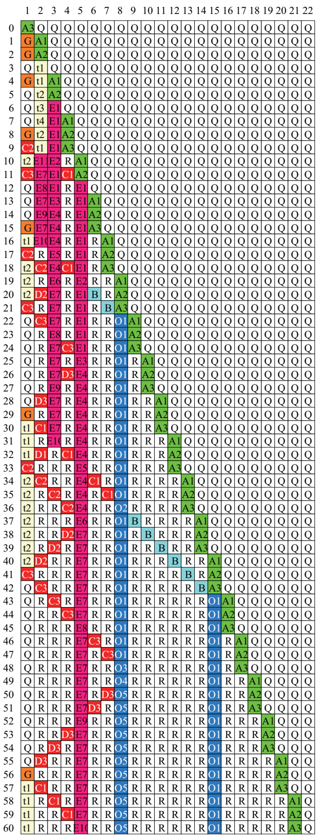

Figure 10: A con guration of real-time generation of tetranacci sequence ($a_m = a_m \; _1 + a_m \; _2 + a_m \; _3 + a_m \; _4, a_1 = 1, a_2 = 2, a_3 = 4, a_4 = 8$).

3.5 Fibonacci Sequence

In this section, we show real-time generation algorithm of Fibonacci sequence. In a past research, Arisawa showed that Fibonacci sequence can be generated in 2 linear-time by a CA with 9 states. However, real-time generation algorithm of Fibonacci sequence on CA is not exist. A consists of an infinite array of finite state automata $A = (Q, \delta, F)$, where $Q = \{\mathtt{Q}, \mathtt{A}, \mathtt{B}, \mathtt{C}, \mathtt{D}\}$, $F = \{\mathtt{A}\}$. We show that Fibonacci sequence can be generated in real-time by a CA with 5 states that is given in Table 1. In Figure 11, we show a time-space diagram for real-time generation of Fibonacci sequence.

Table 1: Transition rules for real-time generation of Fibonacci sequence.

Q (Left State \ Right State)	Q	A	B	C	D
Q	Q	Q	Q	C	Q
A	B		Q	D	
B	Q				
C	Q			D	
D	B				
*	Q	Q		A	Q

A (Left State \ Right State)	Q	A	B	C	D
Q		Q	Q		Q
A			A	C	
B				A	
C				D	
D	A	B	A	A	A
*	Q		A	A	Q

B (Left State \ Right State)	Q	A	B	C	D
Q				B	D
A	C	C	C	D	
B	C				
C	C		B		
D	C	B	B	B	B
*					

C (Left State \ Right State)	Q	A	B	C	D
Q	D	D	Q		D
A	D		Q	C	C
B	D			C	C
C	D		C	C	C
D	A		D	D	D
*					

D (Left State \ Right State)	Q	A	B	C	D
Q				C	C
A	C	A	A		A
B	D		C		
C	C			D	D
D	B	D	D	D	D
*	A				

Real-time generation of Fibonacci sequence is described in terms of 5 waves: *a-wave*, *b-wave*, *d-wave*, *we-wave*, *wo-wave*. Fibonacci sequence is 2nd linear-recursive sequence. Therefore, When each the we- or wo-wave collide with the b- or c-wave 1 time, the we- or wo-wave is eliminated. The initial configuration is the leftmost cell C_1 takes state $\mathtt{D}$ and other cells take a quiescent state $\mathtt{Q}$. At time $t = 0$, the a-wave is generated on the leftmost cell C_1. The a-wave propagates in the right direction at 1/3 speed. State $\mathtt{B}$, State $\mathtt{C}$ and State $\mathtt{D}$ are used for the propagation of the a-wave. At time $t = 0$, $\delta(\mathtt{C}, \mathtt{Q}, \mathtt{Q}) = \mathtt{B}$ are applied in cell C_2. At the next step, a state of C_2 changes to $\mathtt{B}$. At time $t = 1$, $\delta(\mathtt{A}, \mathtt{B}, \mathtt{Q}) = \mathtt{C}$ are applied in cell C_2. At the next step, a state of C_2 changes to $\mathtt{C}$. At time $t = 2$, $\delta(\mathtt{A}, \mathtt{C}, \mathtt{Q}) = \mathtt{D}$ are applied in cell C_2. At the next step, a state of C_2 changes to $\mathtt{D}$. At time $t = 3$, $\delta(\mathtt{D}, \mathtt{Q}, \mathtt{Q}) = \mathtt{B}$ are applied in cell C_3. At the next step, a state of C_3 changes to $\mathtt{B}$. The a-wave propagates by repeating the application of these transition rules. State $\mathtt{A}$ and State $\mathtt{D}$ are used for the propagation of the b-wave. State $\mathtt{C}$ is used for the propagation of the d-wave. The first 5 terms, the we-wave generated on cell C_5 and the d-wave to generate the 6th term are generated with an internal state. At time $t = 11$, the d-wave is generated on cell C_3. The d-wave propagates in the left direction at 1/1 speed, and reaches the leftmost cell C_1. When the d-wave reaches the leftmost cell C_1, $\delta(*, \mathtt{Q}, \mathtt{C}) = \mathtt{A}$ are applied in cell C_1. At time $t = 13$, a state of C_1 changes to $\mathtt{A}$, and the b-wave is generated. The b-wave propagates in

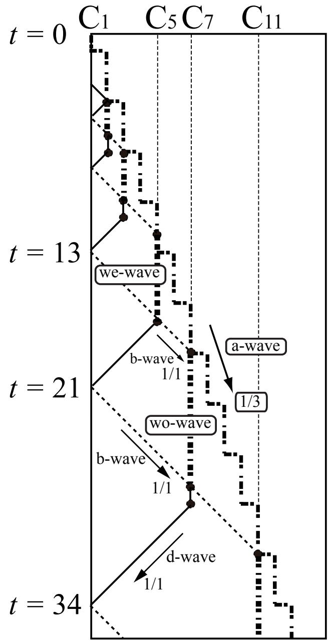

Figure 11: Time-space diagram for real-time generation of Fibonacci sequence.

	1	2	3	4	5	6	7	8	9	10	11	12	13	14	15
0	D	Q	Q	Q	Q	Q	Q	Q	Q	Q	Q	Q	Q	Q	Q
1	A	B	Q	Q	Q	Q	Q	Q	Q	Q	Q	Q	Q	Q	Q
2	A	C	Q	Q	Q	Q	Q	Q	Q	Q	Q	Q	Q	Q	Q
3	A	D	Q	Q	Q	Q	Q	Q	Q	Q	Q	Q	Q	Q	Q
4	Q	C	B	Q	Q	Q	Q	Q	Q	Q	Q	Q	Q	Q	Q
5	A	Q	C	Q	Q	Q	Q	Q	Q	Q	Q	Q	Q	Q	Q
6	Q	D	D	Q	Q	Q	Q	Q	Q	Q	Q	Q	Q	Q	Q
7	Q	C	B	B	Q	Q	Q	Q	Q	Q	Q	Q	Q	Q	Q
8	A	Q	B	C	Q	Q	Q	Q	Q	Q	Q	Q	Q	Q	Q
9	Q	Q	B	D	Q	Q	Q	Q	Q	Q	Q	Q	Q	Q	Q
10	Q	Q	D	D	B	Q	Q	Q	Q	Q	Q	Q	Q	Q	Q
11	Q	Q	C	D	C	Q	Q	Q	Q	Q	Q	Q	Q	Q	Q
12	Q	C	D	D	A	Q	Q	Q	Q	Q	Q	Q	Q	Q	Q
13	A	D	D	D	A	B	Q	Q	Q	Q	Q	Q	Q	Q	Q
14	Q	A	D	D	A	C	Q	Q	Q	Q	Q	Q	Q	Q	Q
15	Q	Q	A	D	A	D	Q	Q	Q	Q	Q	Q	Q	Q	Q
16	Q	Q	Q	A	A	C	B	Q	Q	Q	Q	Q	Q	Q	Q
17	Q	Q	Q	Q	C	Q	C	Q	Q	Q	Q	Q	Q	Q	Q
18	Q	Q	Q	C	D	D	D	Q	Q	Q	Q	Q	Q	Q	Q
19	Q	Q	C	D	D	D	B	B	Q	Q	Q	Q	Q	Q	Q
20	Q	C	D	D	D	D	B	C	Q	Q	Q	Q	Q	Q	Q
21	A	D	D	D	D	D	B	D	Q	Q	Q	Q	Q	Q	Q
22	Q	A	D	D	D	D	B	D	B	Q	Q	Q	Q	Q	Q
23	Q	Q	A	D	D	D	B	C	C	Q	Q	Q	Q	Q	Q
24	Q	Q	Q	A	D	D	B	C	D	Q	Q	Q	Q	Q	Q
25	Q	Q	Q	Q	A	D	B	C	C	B	Q	Q	Q	Q	Q
26	Q	Q	Q	Q	Q	A	B	C	C	C	Q	Q	Q	Q	Q
27	Q	Q	Q	Q	Q	Q	D	C	C	D	Q	Q	Q	Q	Q
28	Q	Q	Q	Q	Q	Q	C	D	C	C	B	Q	Q	Q	Q
29	Q	Q	Q	Q	Q	C	D	D	D	C	C	Q	Q	Q	Q
30	Q	Q	Q	Q	C	D	D	D	D	D	D	Q	Q	Q	Q
31	Q	Q	Q	C	D	D	D	D	D	D	B	B	Q	Q	Q
32	Q	Q	C	D	D	D	D	D	D	D	B	C	Q	Q	Q
33	Q	C	D	D	D	D	D	D	D	D	B	D	Q	Q	Q
34	A	D	D	D	D	D	D	D	D	D	B	D	B	Q	Q
35	Q	A	D	D	D	D	D	D	D	D	B	C	C	Q	Q
36	Q	Q	A	D	D	D	D	D	D	D	B	C	D	Q	Q

Figure 12: A con guration of real-time generation of Fibonacci sequence.

the left direction at 1/1 speed, and reaches the we-wave generated on cell C_5 at time $t = 17$. When the we-wave collides with the b-wave, the we-wave is eliminated, the d-wave is generated and the b-wave keeps propagating. The d-wave reaches the a-wave. When the a-wave collides with the b-wave, the b-wave is eliminated, the wo-wave is generated. The d-wave generated on cell C_5 reaches the leftmost cell C_1 at time $t = 21$. When the d-wave reaches the leftmost cell C_1, a state of C_1 changes to A, and the b-wave is generated. Therefore, Fibonacci sequence can be generated by repeating the propagation of 5 waves. We have implemented the algorithm on a computer. We have tested the validity of the rule set from $t = 0$ to $t = 20000$ steps. We obtain the following theorem. In Figure 12, we show a number of snapshots of the configuration from $t = 0$ to 36.

4 Conclusions

We have studied a sequence generation problem on CA. A design of algorithm for real-time generation of linear-recursive sequences on CA has been given. We have shown that Fibonacci sequence can be generated in real-time by a CA with 5 states. A future study in sequence generation problem on CA is to compare sequence generation power of CA and sequence generation power of 1-bit inter-cell-communication CA.

References

[1] M. Arisawa; On the generation of integer series by the one-dimensional iterative arrays of finite state machines (in Japanese), The Trans. of IECE, 71/8 Vol. 54-C, No.8, pp.759-766, (1971).

[2] P. C. Fischer; Generation of primes by a one-dimensional real-time iterative array. *J. of ACM*, Vol.12, No.3, pp.388-394, (1965).

[3] I. Korec; Real-time generation of primes by a one-dimensional cellular automaton with 9 states. *Proc. of MCU '98*, pp.101-116, (1998).

[4] N. Kamikawa and H. Umeo; Some Algorithms for Real-Time Generation of Non-Regular Sequences on One-Bit Inter-Cell-Communication Cellular Automata, SICE Annual Conference 2007, pp.953-958, (2007).

[5] N. Kamikawa and H. Umeo : Some state-efficient algorithms for real-time generation of non-regular sequences on cellular automata. The Thirteenth International Symposium on Artificial Life and Robotics (AROB 13th '08), pp.47-50, (2008).

[6] N. Kamikawa and H. Umeo : A Note on Sequence Generation Power of Two-States Cellular Automata. SICE Annual Conference 2008, pp.3315-3320, (2008).

©ISAROB 2009

The Fourteenth International Symposium on Artificial Life and Robotics 2009 (AROB 14th '09),
B-Con Plaza, Beppu, Oita, Japan, February 5 - 7, 2009

Towards a Brief Proof of the Four Colour Theorem: Theorems to be used for proving the Four Colour Theorem

Koji Ohnishi

Department of Biology, Faculty of Science, Niigata University,
Ikarashi-2, Nishi-Ku, Niigata, 950-2181, Japan
(Tel : 81-25-262-6268; Fax : 81-25-262-6116)
(E-mail: ohnishi@sc.niigata-u.ac.jp)

Abstract: In order to prove the Four-Colour theorem (FCT) without using computer, basic definitions and theorems useful for proving the FCT are presented and a bird-eye's view of the brief proof is described and discussed. A complete proof will appear elsewhere in near future.

Keywords: Four colour conjecture, Appel & Haken's proof, complete triangulation graph, Four-faced quadrilateral, vertex-reducing complete triangulation series, necessary and sufficient condition.

I. INTRODUCTION

Francis Frederick's observation concerning map-clouring was first submitted by his younger brother, Frederic Guthrie, as a mathematical conjecture later called the *Four-Colour Problem*, to his professor, August de Morgan in 1852 [1-4]. Since then, the Four-Colour Conjecture has long been considered to be a most difficult unsolved problem until Appel and Haken's (1972, [5,6]) success in proving this conjecture by using computer. The question whether or not the Four-Colour theorem (FCT) could be proved without using computer has since been the next important problem remaining to be answered, although *Robertson et al.* (1996) have considerably simplified Appel and Haken's proof [7,8].

In this communication, theorems most possibly useful for proving the FCT with no use of computer were presented and discussed towards prospecting and achieving the final proof. A most plausible final proof of the FCT without using computer will be published elsewhere from this aspect, which is now under reviwing (Ohnishi [9,10].).

II. PRELIMINARIES: BASIC DEFINITIONS

In this section, some basic definitions useful for proving the FCT are described. "▌" denotes the end of each definition or theorem, whereas "█" denotes the end of each proof.

[Definition 2.1](Jordan curve): *Jordan curve QQ'* is defined as a portion of a closed Jordan curve, *C*, cut off by two different points *Q* and *Q'*, which are called *end-points* of the Jordan curve *QQ'*. ▌

The next theorem is well known, and is described below without proof.

[**Theorem 2.1]** (internal and external domains): If *C* is a closed Jordan curve on S^2, then we have $S = int\ C + C + ext\ C$, where *int C* and *ext C* denote internal and external domains of *C*, respectively. Let closed internal and external domains be defined by $Int\ C = int\ C + C$, and $Ext\ C = ext\ C + C$, respecttively, then we have $S^2 = Int\ C + Ext\ C - C$. ▌
[Proof] See Ore (1967) [11]. █

[Definition 2.2] (graph, spherical graph): Graph Γ is defined as a set consisting of a finite set of vertices and a finite setof edges. *Vertex* is defined as a point, and *edge* is defined as a Jordan curve connecting and including two vertices (which are end-points) *P* and *P'*. An edge *e*, connecting two vertices *P* and *P'* is written as $e = [P,P']$. $<e>$ is defined by $<e>=e-P-P'$. A vertex *P* is called to be *adjacent* to *P'*, if a graph Γ has an edge,$[P,P']$. If a graph *G* is embeddable onto a sphere S^2, *G* is called a spherical graph and is written as $G(S^2)$. ▌

[Definition 2.3] (valency): If a vertex *P* is a common end-point of different *m* edges, then *m* is called *valency* (or *degree*) of *P*, and is written as $m = val\ P$. ▌

[Definition 2.4] (s-cycle, s-gon, s-path): A (*s*-) cycle is defined by a *s*-vertex-graph, $C=C^s=C^s(e_{12}, e_{23},...,e_{s,1}) = P_1 + <e_{12}> + P_2 + <e_{23}> + ... + <e_{s-1,s}> + P_s + <e_{s,1}>$. A (*s*-)path is defined by $U(P_1,P_s) = U^s(P_1,P_s)= C^s(e_{12},e_{23},...,e_{s,1}) - e_{s,1}$. C^s is also called *s*-gon (=*s*-hedron) (poly-gon, di-gon, tri-angle, tetrahedron=quadrilateral, pentagon, etc.). ▌

From the Definitions 2.1~2.5, $U(P_1,P_s)$ is a Jordan curve connecting P_1 and P_s, and a cycle is a closed Jordan curve.

[Definition 2.5] (connected graph): If a path $U(P, P')$ of a given graph Γ can be found for any pair of vertices, *P* and *P'*, which belong to Γ, Γ is called *"connected graph"*. ▌

[Definition 2.6] (face): If $G(S^2)$ has a *s*-cycle (= *s*-gon), C^s, *where* $int\ C^s = \emptyset$, $Int\ C^s$ (= $int\ C^s + C^s$) is called *face* (or *s-gon face*). ▌

Thus we find $S^2 = int\ C^s + C^s + ext\ C^s$.

[Definition 2.7]((complete) triangulation): If $G(S^2)$

©ISAROB 2009

is a connected graph dividing S^2 into exclusively triangular faces, G is called *"complete triangulation (of S2)"*. If $G(S^2) = C^s$ satisfies *ext* $C^s = ø$, and if G divides *Int* C^s into exclusively triangular faces, G is called *"triangulation of s-gon,* C^s*"*. ■

Let P be a vertex of complete triangulation of S^2, then we easily find $val\ P \geq 2$.

[Definition 2.8] (ν-colourable): Graph Γ is called "*vertex ν-colourable*" (or simply, *ν-colorable*), if every vertex is coloured with one of the given ν colours so that any two vertices adjacent to each other are coloured with different colours. If a ν-colourable graph G is coloured with μ colours ($\mu \leq \nu$), the coloured graph is *here* called *"ν-coloured graph"*, and is written as $col^{\nu}(G)$. For an vertex $P \in G$, *"$col^{\nu}(P) = a$"* is defined for denoting that the vertex P is coloured with a, in $col^{\nu}(G)$. If a ν-colourable graph, G, is not colourable with ν - 1 colours, G is called *"ν-chromatic"*. ■

The next theorem (Theorem 2.2) is well-known [2,4,11], and is given here without describing proof.

[Theorem 2.2] Let $T(S^2)$ be an arbitrarily selected complete triangulation of S^2. The four-colour theorem (FCT) is equivalent to that "*Proposition A* is true", where *Proposition A* is given by;

Proposition A: $T(S^2)$ is vertex four-colourable. ■

[Definition 2.9] (Two-faced quadrilateral, Figure 1): "*Two-faced quadrilateral* with a diagonal edge e_{13}" is defined as a subgraph of $G(S^2)$, and is given by $Q^{2f} = C^4{}_0 + \langle e_{13} \rangle \subseteq G$, where $C^4{}_0 = C^4(e_{12}, e_{23}, e_{34}, e_{41}), e_{ij} = [P_i, P_j]$, $e_{13} \subseteq Int\ C^4{}_0$, and e_{13} is a Boundary edge dividing $Int\ C^4$ into two triangular faces. Q^{2f} is written as $Q^{2f} = Q^{2f}(C^4{}_0; e_{13})$. If Q^{2f} in $G(S^2)$ has any edge, e'_{13} or e'_{24}, satisfying $e'_{13} = [P_1, P_3] \subseteq Ext\ C^4{}_0$, or $e'_{24} = [P_2, P_4] \subseteq Ext\ C^4{}_0$, then the Q^{2f} is called *"incomplete quadrilateral"*, whereas it is called *"complete quadrilateral"* if there is none of such edges. *$G(S^2)$ having its subgraph* $Q^{2f}{}_0 = Q^{2f}(C^4{}_0; e_{13})$ is written as $G = G(Q^{2f}{}_0; C^4{}_0)$. ■

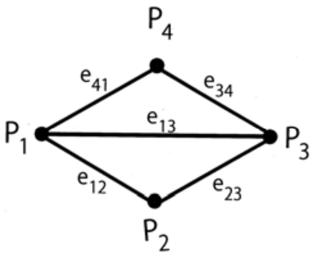

Figure 1. Two-faced quadrilateral, $Q^{2f}(C^4{}_0; e_{13})$, where $C^4{}_0$ is a 4-cycle (= quadrilateral) given by $C^4{}_0 = C^4(e_{12}, e_{23}, e_{34}, e_{41})$, $e_{ij} = [P_i, P_j]$, $e_{13} \subseteq Int\ C^4{}_0$. $\{Q^{2f}\}$ is an unavoidable (one-element-)set of $T_k(S^2)$, a complete triangulation of S^2 with k vertices ($k \geq 4$). See Definition 2.9 and Lemma3.2.1.

[Definition 2.10] (4-coloued graph, Kempe block): Let $col^4{}_o(G)$ denote a 4-coloured graph of $G(S^2)$, coloured with 4 or 3 of the given 4 colours, a, b, c, and d. $col^4{}_o(G)$ is also called *"4-colouration of G"*. Furthermore, *ab-Kempe block*s (= *ab-Kempe chains*), $K_{ab}(P_i)$ and $K_{ab}(P_i, P_j)$, are defined as connected two-coloured sub-graphs of G, respectively having maximum numbers of vertices including P_i (for $K_{ab}(P_i)$), and both of P_i and P_j (for $K_{ab}(P_i, P_j)$), where P_i and P_j are different two vertices of G. ■

If P is coloured with a in $col^4{}_o(G)$, and is not adjacent to any vertex coloured with b, $K_{ab}(P)$ consists of exclusively one vertex P.

III. BASIC THEOREMS

The following basic theorems are useful for proving the FCT. Detailed proofs will be given in Ohnishi (submitted, 2009a, 2009b).

[Theorem 3.1] For $K_{ab}(P_i, P_j)$ in Definition 2.10, there exists a 2-coloured path $U_{ab}(P_j, P_j)$ as a sub-graph of the 2-coloured graph, $K_{ab}(P_i, P_j)$. ■

[Proof] Evident from the definitions of connected graph (Definition 2.5) and vertex 2-coloured graph (Definition 2.8). ■

This theorem means that P_i and P_j are connected by a *2-coloured Jordan curve*, $U_{ab}(P_j, P_j)$.

[Theorem 3.2] Let $T_k(S^2)$ be a complete triangulation of S^2, having k vertices ($k \geq 4$). Then there exists a quadrilateral given by $Q^{2f}{}_{k,0} = Q^{2f}(C^4{}_{k,0}; e_{13}) \subset T_k$, where $C^4{}_{k,0} = C^4(e_{12}, e_{23}, e_{34}, e_{41})$, $\langle e_{13} \rangle \subset int\ C^4{}_{k,0}$, and $e_{ij} = [P_i, P_j]$. Furthermore, $Q^{2f}{}_{k,0}$ satisfies $val\ P_1 \geq 3$, $val\ P_3 \geq 3$, $val\ P_2 \geq 2$, and $val\ P_4 \geq 2$. ■

[Proof] See Ohnishi [9]. ■

[Lemma 3.2.1] In Theorem 3.2, a set, $\{Q^{2f}{}_k\}$ is an unavoidable set (See [4] for definition.) of $T_k(S^2)$, and consists of only one element being a quadrilateral. ■

[Proof] Evident from Theorem 3.2.1. ■

[Theorem 3.3] Let $T_k(S^2)$, $C^4{}_{k,0} = C^4(e_{12}, e_{23}, e_{34}, e_{41})$, and $Q^{2f}{}_{k,0} = Q^{2f}(C^4{}_{k,0}; e_{13}) \subset T_k$, ($k \geq 4$) be defined as same as in Theorem 3.2, with an additional condition that T_k is 4-colourable. If $col^4{}_0(T_k) = col^4(T_k; Q^{2f}{}_{k,0})$ is a four-cloured complete triangulation graph of T_k coloured with a, b, c, and d, then we can consider, without losing generality, a coloration satisfying $col^4{}_0(P_1) = a$, $col^4{}_0(P_2) = b$, $col^4{}_0(P_3) = c$, and $col^4{}_0(P_4) = c$ or d. We find that $col^4{}_0(T_k)$ belongs to either one of the following two cases;

case I: There exists $K_{ac}(P_1, P_3)$ ($\subset col^4(T_k; Q^{2f}{}_0)$).

case II: There does not exist $K_{ac}(P_1, P_3)$ ($\subset col^4(T_k; Q^{2f}{}_0)$). ■

[Proof] See Ohnishi [9]. ■

[Definition 3.1] (case I and case II 4-colorations) Let $col^4{}_{\mathrm{I}}(T_k; Q^{2f}{}_0)$ and $col^4{}_{\mathrm{II}}(T_k; Q^{2f}{}_0)$ respectively denote case I and case II 4-coloured complete triangulation graph described in Theorem 3.3.

IV. VERTEX-REDUCING COMPLETE TRIANGULATION LINEAGE

[Theorem 4.1] Let $T_k(S^2)$, $C^4_{k,0} = C^4(e_{12},e_{23},e_{34},e_{41})$, and $Q^{2f}_{k,0}=Q^{2f}(C^4_0;e_{13}) \subset T_k$, ($k \geq 4$) be defined as same as in Theorem 3.2. Then $Q^{2f}_{k,0}$ belongs to either one of the following three types;

type A: $Q^{2f}_{k,0}$ is a complete two-faced quadrilateral. ($val\ P_1 \geq 4,\ val\ P_3 \geq 4,\ val\ P_2 \geq 3,\ val\ P_4 \geq$)

type B: $Q^{2f}_{k,0}$ is an incomplete two-faced quadrilateral, in which there exists $e'_{13}=[P_1,P_3] \subseteq Ext\ C^4_{k,0}$. ($val\ P_1 \geq 4,\ val\ P_3 \geq 4,\ val\ P_2 \geq 2,\ val\ P_4 \geq 2$)

type C: $Q^{2f}_{k,0}$ is an incomplete two-faced quadrilateral, in which there exists $e'_{24}=[P_2,P_4] \subseteq Ext\ C^4_{k,0}$. ($val\ P_1 \geq 3,\ val\ P_3 \geq 3,\ val\ P_2 \geq 3,\ val\ P_4 \geq 3$). ▌

[Proof] See Ohnishi [10]. ▌

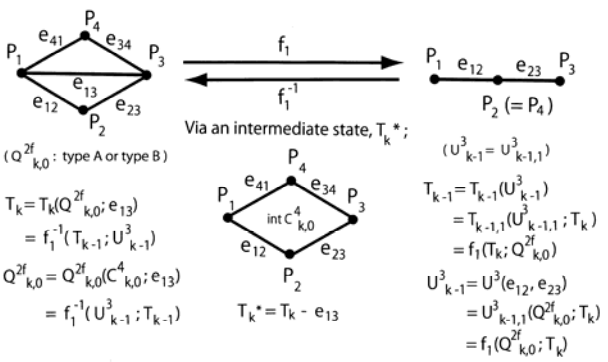

Figure 2. Vertex-reducing operation f_1 and its in verse operation, f_1^{-1}. See Definition 4.1 and Ohni shi [10] for dertails.

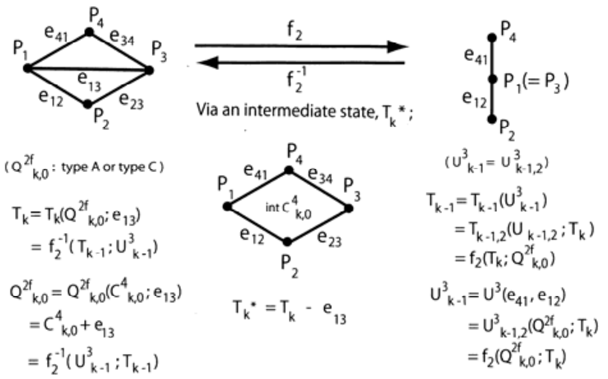

Figure 3. Vertex-reducing operation f_2 and its inverse operation, f_2^{-1}. See Definition 4.1. and Ohnishi [10] for dertails.

[Definition 4.1] (Vertex-reducing operations of quadrilaterals): For type A and type B quadrilaterals ($Q^{2f}_{k,0}$) of $T_k(S^2)$, a vertex-reducing operations f_1 which converts $T_k(S^2)=T_k(Q^{2f}_{k0};e_{12})$ to $T_{k-1}(S^2)=T_{k-1,1}(U^3_{k-1,1};\ T_k)$ are defined as illustrated in Figure 2. Similarly, for type A and type C quadrilaterals, a vertex-reducing operation f_2, which converts $T_k(S^2)= T_k(Q^{2f}_{k,0};e_{12})$ to $T_{k-1}(S^2) = T_{k-1,2}(U^3_{k-1,2};T_k)$, are defin edas illustrated in Figure 3. Since it is evident that

These operations are reversible via an intermediate state ($T_k{*} = T_k - e_{13}$) shown in the figures 2 and 3, there exist inverse operations f_1^{-1} and f_2^{-1} converting T_{k-1} to T_k. These relations are expressed by;

$$T_{k-1} = f_i(T_k),\ T_k = f_i^{-1}(T^k),\ (i = 1,2), \quad [\#4.1]$$

or,

$$T_k \overset{f_i/f_i^{-1}}{\longleftrightarrow} T_{k-1} \quad (i = 1,2), \quad [\#4.2]$$

where $T_{k-1} = T_{k-1,i}(U^3_{k-1,i};\ T_k)$, $T_k = T_k(Q^{2f}k;\ e_{13})$, and $U^3_{k-1,i} = fi(Q^{2f}_k;\ e_{13})$.

More simply, we write [#4.2] as ;

$$T_k \overset{f/f^{-1}}{\longleftrightarrow} T_{k-1} \quad (i = 1,2). \quad [\#4.3]$$

▌

Thus we have reached the next theorem;

[Theorem 4.2] (See Figure 2 and Figure 3): Let $T_k(S^2) = T_k(Q^{2f}_{k,0};e_{13})$, $C^4_{k,0} = C^4(e_{12},e_{23},e_{34},e_{41})$, and $Q^{2f}_{k,0}=Q^{2f}(C^4_0;e_{13}) \subset T_k$, ($k \geq 4$) be defined as same as in Theorem 3.2. Then we have;

(1) If $Q^{2f}_{k,0}$ is type A or type B (in this case, $val\ P_1 \geq 4,\ val\ P_3 \geq 4$): A type 1 vertex-reducing complete triangulation $T_{k-1,1}$ is obtained by f_1;

$$T_{k-1,1} = T_{k-1,1}(U^3_{k-1,1};T_k) = f_1(T_{k-1};\ Q^{2f}_{k,0}),$$

where $T_{k-1,1}(U^3_{k-1,1};T_k)$ denotes that the *type 1* complete triangulation $T_{k-1,1}$ [$= f_1(T_k;\ Q^{2f}_{k,0})$] has a 2-path given by $U^3_{k-1,1} = U^3(e_{12},\ e_{23}) = f_1(Q^{2f}_{k0};\ T_k)$, meaning that $U^3_{k-1,1}$ is generated from $Q^{2f}_{k,0}$ by f_1., as shown in Figure 2. In $T_{k-1,1}$, $val\ P_1 \geq 2,\ val\ P_3 \geq 2,\ val\ P_2 \geq 2\ val\ P_4 \geq 2$.

(2) [Figure 2]: If $Q^{2f}_{k,0}$ is type A or type C (in this case, $val\ P_2 \geq 3,\ val\ P_4 \geq 3$): A type 2 vertex-reducing complete triangulation $T_{k-1,1}$ is obtained by f_1;

$$T_{k-1,2} = T_{k-1,2}(U^3_{k-1,2};T_k) = f_2(T_{k-1};\ Q^{2f}_{k,0}),$$

where $T_{k-1,2}(U^3_{k-1,21};T_k)$ denotes that the *type 2* complete triangulation $T_{k-1,2}$ [$= f_2(T_k;\ Q^{2f}_{k,0})$] has a 2-path given by $U^3_{k-1,2} = U^3(e_{12},\ e_{23}) = f_2(Q^{2f}_{k0};\ T_k)$, meaning that $U^3_{k-1,2}$ is generated from $Q^{2f}_{k,0}$ by f_2., as shown in Figure 2. In $T_{k-1,2}$, $val\ P_1 \geq 2,\ val\ P_3 \geq 2,\ val\ P_2 \geq 2\ val\ P_4 \geq 2$.

Thus we finally have;

(i) If $Q^{2f}_{k,0}$ is type A (i.e.,complete quadrilateral), then we have

$$T_{k-1,1} = f_1(T_k;\ Q^{2f}_{k,0}) = T_{k-1,1}(U^3_{k-1,1};T_k),$$
$$T_{k-1,2} = f_2(T_k;\ Q^{2f}_{k,0}) = T_{k-1,2}(U^3_{k-1,2};T_k).$$

(ii) If $Q^{2f}_{k,0}$ is type B, then we have only

$$T_{k-1,1} = f_1(T_k;\ Q^{2f}_{k,0}) = T_{k-1,1}(U^3_{k-1,1};T_k),$$

(iii) If $Q^{2f}_{k,0}$ is type C, then we have only

$$T_{k-1,2} = f_2(T_k;\ Q^{2f}_{k,0}) = T_{k-1,2}(U^3_{k-1,2};T_k).$$

The vertex-reductions, $T_{k-1,i} = f_i(T_k\ ;Q^{2f}_{k,0}) = T_{k-1,i}(U^3_{k-1,i};T_k\ )\ (i = 1,2)$ in (i),(ii),(iii) are all reversible by $T_k = T_k\ (Q^{2f}_{k,0}\ ;\ e_{13}) = f_i^{-1}(T_{k-1,i};\ U^3_{k-1,i})$. *Thus* $T_k\ (Q^{2f}_{k,0}\ ;\ e_{13})$ *can be reconstructed from* $T_{k-1,i}(U^3_{k-1,i};\ T_k\ )$ *by either or both of* f_1^{-1} *and* f_2^{-1}. ▌

[Proof] Evident from the definitions and theorems descibed above. See also Ohnishi [10]. ▌

[Lemma 4.2.1] For $T_k(S^2) = T_k(Q^{2f}_{k,0};e_{13})$ ($k \geq 4$)

in Theorem 4.2, we find

$$T_k \overset{f_i/f_i^{-1}}{\longleftrightarrow} T_{k-1} \qquad [\#4.3a]$$

where $T_{k-1} = T_{k-1,i} = f_i(T_k)$ for at least either one of *i=1 and i=2.*
and

$$T_k \overset{f_{i(k)}/f_{i(k)}^{-1}}{\longleftrightarrow} T_{k-1} \overset{f_{i(k-1)}/f_{i(k-1)}^{-1}}{\longleftrightarrow} T_{k-2} \overset{f_{i(k-2)}/f_{i(k-2)}^{-1}}{\longleftrightarrow} \ldots\ldots \overset{f_{i(k-s+1)}/f_{i(k-s+1)}^{-1}}{\longleftrightarrow} T_{k-s}$$

$$(1 \leq s \leq k-3) \quad [\#4.4]$$

where $i(k-j) = 1$, *and/or* 2, $j = 1,2,\ldots,s$. ■

[Proof] Easily proven from #4.2 and Theorem 4.2. See Ohnishi [10]. ■

[Lemma 4.2.1] In Lemma 4.2.1, we find

$$T_k \overset{f_{i(k)}/f_{i(k)}^{-1}}{\longleftrightarrow} T_{k-1} \overset{f_{i(k-1)}/f_{i(k-1)}^{-1}}{\longleftrightarrow} T_{k-2} \overset{f_{i(k-2)}/f_{i(k-2)}^{-1}}{\longleftrightarrow} \ldots\ldots \overset{f_{i(4)}/f_{i(4)}^{-1}}{\longleftrightarrow} T_3$$

$$[\#4.5]$$

where $i(k-j) = 1$, *and/or* 2, $j = 1,2,\ldots,k-4$, *and* $T_{k-j-1} = f_{i(k-j)}(T_{k-j}; Q^{2f}_{k-j,0})$, $T_{k-j} = f_{i(k-j)}^{-1}(T_{k-j-1}; U^3_{k-j-1})$. ■

[Proof] Proven by letting $s = k-3$, in [#4.4]. ■

V. TOWARDS FINAL PROOF OF THE FOUR COLOUR THEOREM

[Theorem 5.1] A necessary and sufficient conditio n for that an arbitrary complete triangulation $T_k(S^2)$ (with k vertices, $k \geq 4$) is vertex 4-colourable is as below;

Under the assumption that T_{k-j} is vertex 4-colourable, there exists a 4-coloured graph, $col^4{}_0(T_{k-j-1})$, $(j= 1,2,\ldots,j-3)$, which can be derived from a hypothetical 4-coloured graph of T_{k-j}, given by $col^4{}_0(T_{k-j})$, where $T_{k-j-1}= f(T_{k-j}; Q^{2f}_{k-j,0})$, $f = f_1$ or f_2 (defined by Definition 4.1) and $Q^{2f}_{k-j,0} = Q^{2f}(C^4_{k-j,0}; e^{(k-j)}_{13})$. Here

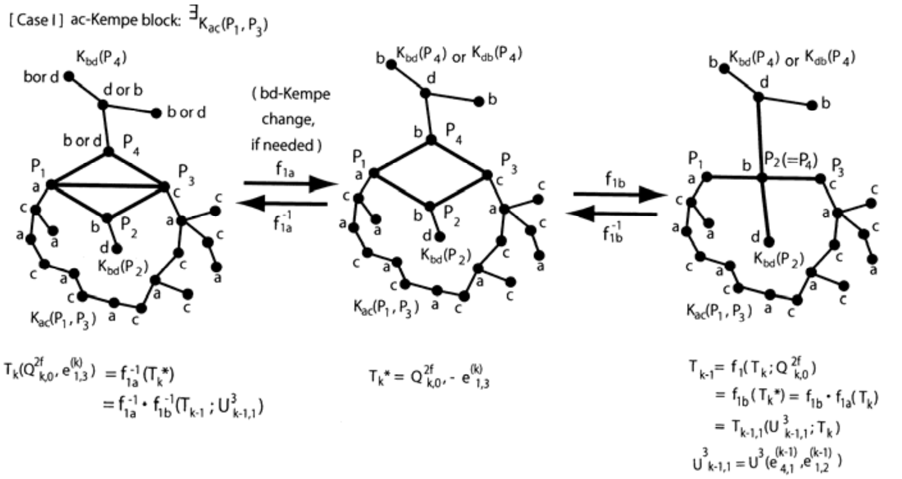

Figure 4. Vertex-reduction of a 4-coloured complete triangulation graph, $col^4{}_0(T_k\ ;\ Q^{2f}_{k,0})$ in case I. See text and Ohnishi [10] for details.

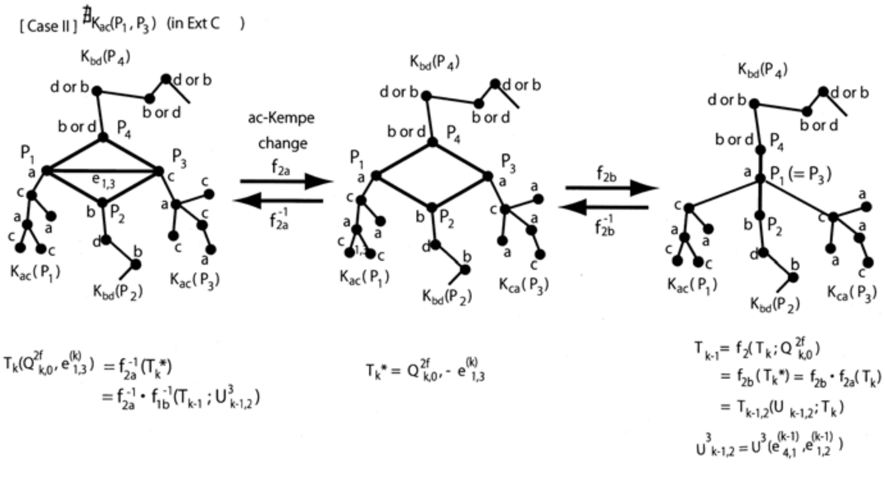

Figure 4. Vertex-reduction of a 4-coloured complete triangulation graph, $col^4{}_0(T_k\ ;\ Q^{2f}_{k,0})$ in case II. See text and Ohnishi [10] for details.

$C^4_{k-j,0}$ is a 4-cycle of T_{k-j}, and $Q^{2f}(C^4_{k-j,0}\ ;e^{(k-j)}_{13})$ is a quadrilateral consisting of $C^4_{k-j,0} = C^4(e^{(k-j)}_{12}, e^{(k-j)}_{23}, e^{(k-j)}_{34}, e^{(k-j)}_{41})$, and $e^{(k-j)}_{i1,i2} = [P^{(k-j)}_{i1}, P^{(k-j)}_{i2}]$. ∎

[Proof] For j = 0, we need to proof

$$col^4{}_0(T_k) \xleftrightarrow{f/f^{-1}} col^4{}_0(T_{k-1}). \qquad [\#4.6]$$

From Theorem 3.3 and Definition 3.1, we find

$col^4{}_0(T_k) = col^4{}_{\mathrm{I}}(T_k;Q^{2f}{}_{k,0})$ *(for case I)* *[Eq.*
or $col^4{}_{\mathrm{II}}(T_k;Q^{2f}{}_{k,0})$. *(for case II ,*

and we can consider that $col^4{}_0\ (P^{(k)}{}_1)=a$, $col^4{}_0(P^{(k)}{}_2) = b$, $col^4{}_0\ (P^{(k)}{}_3) = c$, *and* $col^4{}_0\ (P^{(k)}{}_4) = b$ *or* d, without losing generality.

[I] (See Figure 4) In *case I,* $^{\exists}K_{ac}(P^{(k)}{}_1,\ P^{(k)}{}_3) \subseteq Ext\ C^4{}_{k-j,0}$, and then there exists a *ac*-coloured Jordan curve path *connecting* $P^{(k)}{}_1$ to $P^{(k)}{}_3$. Accordingly, $K_{bd}(P^{(k)}{}_4)$ can be changed into $K_{db}(P^{(k)}{}_4)$, if $col^4{}_0\ (P^{(k)}{}_4) = d$. *Thus we have a 4-colouring of* T_k^* $(= T_k - e^{(k)}{}_{13})$ *with both* $P^{(k)}{}_2$ and $P^{(k)}{}_4$ with b. Let f_{1a} denote the operation converting $col^4{}_{\mathrm{I}}(T_k;Q^{2f}{}_{k,0})$ *to this 4-colouring,* $col^4{}_{\mathrm{I},1\alpha}(T_k^*;C^4{}_{k,0}\ )$, then we have $col^4{}_{\mathrm{I},1\alpha}(T_k^*;C^4{}_{k,0}\ ) = f_{1a}[col^4{}_{\mathrm{I}}(T_k;Q^{2f}{}_{k,0})]$. *It is evident that this operation is reversible, and therefore,* $col^4{}_{\mathrm{I}}(T_k\ ;\ Q^{2f}{}_{k,0}) = f_{1a}{}^{-1}[col^4{}_{\mathrm{I},1}(T_k^*;C^4{}_{k,0}\ )]$.

Since $col^4{}_0(P^{(k)}{}_2) = col^4{}_0(P^{(k)}{}_4) = b$, $col^4{}_{\mathrm{I},1}(T_k^*;C^4{}_{k,0})$ can be further modified to the four coloured graph, $col^4{}_0(T_{k-1};U^3{}_{k-1,1})$, where $U^3{}_{k-1,1} = U^3(e^{(k-1)}{}_{4,1},\ e^{(k-1)}{}_{12})$. Let f_{1b} denote the operation converting $col^4{}_{\mathrm{I}}(T_k;Q^{2f}{}_{k,0})$ *to* $col^4{}_0(T_{k-1};U^3{}_{k-1,1})$, as shown in Figure 4. Then we have $col^4{}_0(T_{k-1};U^3{}_{k-1,1}) = f_{1b}[col^4{}_{\mathrm{I},1\alpha}(T_k^*;C^4{}_{k,0}\ )] = f_{1b}[f_{1a}[col^4{}_{\mathrm{I}}(T_k;Q^{2f}{}_{k,0})]\ ] = f_{1b} \circ f_{1a}[col^4{}_{\mathrm{I}}(T_k;Q^{2f}{}_{k,0})] = f_1[col^4{}_{\mathrm{I}}(T_k;Q^{2f}{}_{k,0})]$, $(\ f_1 \equiv f_{1b} \circ f_{1a})$. Note that every vertex in $T_{k-1,1}$ shows *valency* ≥ 2, since $Q^{2f}{}_{k,0}$ is type A or type B (from Theorem 4.1).

It is also evident that f_{1b} is also reversible, and we have $col^4{}_{\mathrm{I},1\alpha}(T_k^*;C^4{}_{k,0}\ ) = f_{1b}{}^{-1}[col^4{}_0(T_{k-1};U^3{}_{k-1,1})]$, and therefore, $col^4{}_{\mathrm{I}}(T_k;Q^{2f}{}_{k,0}) = f_{1a}{}^{-1}[col^4{}_{\mathrm{I},1\alpha}(T_k^*;C^4{}_{k,0}\ )] = f_{1a}{}^{-1}[f_{1b}{}^{-1}[col^4{}_0(T_{k-1};U^3{}_{k-1,1})]] = f_{1a}{}^{-1} \circ f_{1b}{}^{-1}[col^4{}_0(T_{k-1};U^3{}_{k-1,1})] = f_1{}^{-1}[col^4{}_0(T_{k-1};U^3{}_{k-1,1})]$. Thus for *case I, where* $col^4{}_0\ (T_k) = col^4{}_{\mathrm{I}}(T_k;Q^{2f}{}_{k,0})$, we find

$$col^4{}_0\ (T_k) \xleftrightarrow{f_1/f_1^{-1}} col^4{}_0(T_{k-1}), \qquad [\#4.7]$$

although $col^4{}_0(T_{k-1};U^3{}_{k-1,})$ is defined as derived from $col^4{}_0\ (T_k;\ Q^{2f}{}_{k,0})$. In other words, for a given $T_k(Q^{2f}{}_{k,0};\ e^{(k)}{}_{1,3})$ really exists as proven in Theorem 4.2., but the existence of $col^4{}_0\ (T_k)$ is an assumption, and therefore, the relation [#4.7] could have some meaning only if $col^4{}_0(T_{k-1})$ could exist.

[II] (See Figure 5) In *case II,* there does not exist any *ac*-Kempe block satisfying $K_{ac}(P^{(k)}{}_1, P^{(k)}{}_{33}) \subseteq Ext\ C^4{}_{k-j,0}$, which means no existence of any *ac*-coloured Jordan curve path *connecting* $P^{(k)}{}_1$ to $P^{(k)}{}_3$. Accordingly, in T_k^*, a conversion of $K_{ac}(P_3)$ to $K_{ca}(P_3)$ *generates* P_3 *and* P_1 *to be coloured with the same colour, a.* Thus, as similarly as in case I, we find, for *case II, where* $col^4{}_0\ (T_k) = col^4{}_{\mathrm{II}}(T_k;Q^{2f}{}_{k,0})$, we find

$$col^4{}_0\ (T_k) \xleftrightarrow{f_2/f_2^{-1}} col^4{}_0(T_{k-1}), \qquad [\#4.8]$$

although $col^4{}_0(T_{k-1})$ is defined as deried from $col^4{}_{\mathrm{II}}(T_k;Q^{2f}{}_{k,0})$ (See Figure 5).

Since $col^4{}_0\ (T_k;Q^{2f}{}_{k,0}) = col^4{}_{\mathrm{I}}\ (T_k;Q^{2f}{}_{k,0})$ *and/or* $col^4{}_{\mathrm{II}}(T_k;Q^{2f}{}_{k,0})$, *#4.7 and #4.8 means #4.6 is true, if* $col^4{}_0(T_{k-1})$ could exist.

By converting *k into k-j,* #4.8 proves the Theorem 5.1,

$$col^4{}_0\ (T_{k-j}) \xleftrightarrow{f_2/f_2^{-1}} col^4{}_0(T_{k-j1}). \qquad [\#4.8a] \ ∎$$

However, it is important to note that we do not know whether or not $col^4{}_0\ (T_{k-1})$ could exist in #4.8. If $col^4{}_0\ (T_{k-1})$ exists, then we similarly find

$$col^4{}_0(T_{k-1}) \xleftrightarrow{f/f^{-1}} col^4{}_0(T_{k-2}). \qquad [\#4.6a]$$

By repeating similar considerations, we easily find an important Theorem;

[Theorem 5.2] If T_k(S2) mentioned in Theorem 4.1 is fourcolourable, we find the followings, #4.9 ~ #4.10a;

$$col^4{}_0(T_{k-j}) \xleftrightarrow{f/f^{-1}} col^4{}_0(T_{k-j-1}), \qquad [\#4.9]$$
$$(\ j = 0,1,2,\ \ldots,\ k\text{-}s\text{-}1),\ (s \leq k\text{-}4),$$

or,

$$col^4{}_0(T_k) \xleftrightarrow{f/f^{-1}} col^4{}_0(T_{k-1}) \xleftrightarrow{f/f^{-1}} col^4{}_0(T_{k-2}) \xleftrightarrow{f/f^{-1}} \ldots \xleftrightarrow{f/f^{-1}} col^4{}_0(T_{s+1}) \xleftrightarrow{f/f^{-1}} col^4{}_0(T_s), \qquad [\#4.9a].$$

where

$$col^4{}_0(T_s) = f[col^4{}_0(T_{s+1})] = f^2[col^4{}_0(T_{s+1})] = \ \ldots = f^{k-s}[col^4{}_0(T_k)], \qquad [\#4.10]$$

$$col^4{}_0(T_k) = f^{-1}[col^4{}_0(T_{k-1})] = (f^{-1})^2[col^4{}_0(T_{k-1})] = \ \ldots = (f^{-1})^{k-s}[col^4{}_0(T_s)]. \qquad [\#4.10a]$$

In #4.9/#4.9a, we do not know $col^4{}_0(T_s)$, although we can obtain, from Lemma 4.2.1, a s-vertex complete triangulation graph, T_s, deduced from T_k.

[Lemma 5.2.1] *Based on Theorem 5.2, it follows;*

$$col^4{}_0(T_k) \xleftrightarrow{f^{k-s}/(f^{-1})^{k-s}} col^4{}_0(T_s),\quad (s \leq k\text{-}4), \qquad [\#4.10]$$

or, $col^4{}_0(T_s) = f^{k-s}[col^4{}_0(T_k)]$, $col^4{}_0(T_k) = (f^{-1})^{k-s}[col^4{}_0(T_s)]$. ∎

[Proof] Evoident from above descriptions. ∎

Thus we have reached the Final Theorem;

[Theorem 5.3] (The Four Colour Theorem): Every complete triangulation of S^2, $T_k(S^2)$, is vertex four colourable *(k ≥ 3)*. ∎

[Proof] For k *(k ≥ 4)*, let s = 3 in Lemma 5.2.1, we find;

$$col^4{}_0(T_k) \xleftrightarrow{f^{k-s}/(f^{-1})^{k-3}} col^4{}_0(T_3), \qquad [\#4.11]$$

or, $\quad col^4{}_0(T_3) = f^{k-3}[col^4{}_0(T_k)], \qquad [\#4.11a]$

$\quad col^4{}_0(T_k) = (f^{-1})^{k-3}[col^4{}_0(T_3)]. \qquad [\#4.11b]$

#4.11 ~ #4.11b is a special case of Lemma 5.2.1, where $col^4{}_0(T_3)$ really exists as one of the possible *4x3x2 (=24) 4*-colourings of a triangle, $T^3(S^2)$, by appropriately naming vertices.

Thus we can safely conclude that;

(1) The necessary and sufficient condition for the existence of a 4-coloured complete triangulation, $col^4{}_0(T_k)$, is the existence of $col^4{}_0(T_3)$, satisfying $col^4{}_0(T_3) = f^{k-3}[col^4{}_0(T_k)]$.

(2) “The $col^4{}_0(T_3)$” really exists.

From (1) and (2), Theorem 5.3 is proved. $\blacksquare$

VI. CONCLUTION

The essential portion of the proof of the FCT is briefly presented. The entire, complete proof will be published elsewhere. It is most important that the essence of the enormous complexity of the FCT is beautifully found in the series of the necessary a nd sufficient conditions given in #4.9a (for $s=3$).

REFERENCES

[1] Guthrie, F. (1880), Note on the colouring of maps, *Proc.royal Soc.Edinburgh*, 10: 727-728.

[2] Saaty, T. and Kainen, P. (1977), *The four-color problem*, Assaults and conquest, McGraw-Hill International Book Company, New York.

[3] Frisch, R.and Frisch, G. (1994), *Der Vierfarbensatz,* Bibriographisches Institut & F.A.Brockhaus, 1994.

[4] Wilson, R.(2002), *Four Colours Suffice: How the Map Problem Was Solved,* Penguin Books Ltd..

[5] Appel, K., Haken, W.and Koch, J.(1977), Every planar map is four-colorable, Part I: Discharging, *Illinois J.Math.*, 21, 429-489.

[6] Appel, K.and Haken, W. (1977), Every planar map is four-colorable, Part II: Reducibility, *Illinois J.Math.*, 21, 490-567.

[7] Robertson, N., Sanders, D.P., Seymour, P.D.and Thomas, R. (1996), A new proof of the four colour theorem, *Electron.Res.Announc.Amer.math.Soc.*2, 17-25 (electronic).

[8] Thomas, R. (1998), An update on the four colour theorem. *Notices of the Am.math.Soc.*45 (7), 848-859.

[9] Ohnishi, K., A Brief proof of the four-colour theorem. Part I. Basic definitions and theorems (In Japanese with summary, figures and legends in English). *IPSJ Journal (Nihon Joho-Shori Gakkai Ronbun-shi)* (An official Journal of the Information-Processing Society of Japan (IPSJ)), Submitted in Jan., 2009 (Under reviewing).

[10] Ohnishi, K., A Brief proof of the four-colour theorem. Part II. Final proof of the four-colour theorems. (In Japanese with summary, figures and legends in English).*IPSJ Journal (Nihon Joho-Shori Gakkai Ronbun-shi)* (An official Journal of the Information-Processing Society of Japan (IPSJ)), Submitted in Jan., 2009 (Under reviewing).

[11] Ore, O. (1967), *The four color problem*, Academic Press, New York.

The Fourteenth International Symposium on Artificial Life and Robotics 2009 (AROB 14th '09),
B-Con Plaza, Beppu, Oita, Japan, February 5 - 7, 2009

Simulating the behaviour of cellular automata by extended spiking neural P systems

Aneta BINDER[1] Rudolf FREUND[1] Marion OSWALD[1,2]

[1]Faculty of Informatics
Vienna University of Technology
Vienna, Austria

[2]Computer and Automation Research Institute
Hungarian Academy of Sciences
Budapest, Hungary

ani@emcc.at rudi@emcc.at marion@emcc.at

Abstract

In cellular automata, the cells evolve depending on their own state and the states in their neighborhood, whereas the cells in extended spiking neural P systems act according to the number of spikes within the cells at each discrete time step. In this paper, we show how the looking for the states of the surrounding cells from a cell of a cellular automaton can be simulated by extended spiking neural P systems receiving specific numbers of spikes from the neighboring cells by using suitable encodings.

1 Introduction

Cellular automata are a well-established model for investigating and simulating the behavior of complex biological systems in discrete time steps and in a parallel way. Just recently, (extended) spiking neural P systems have been introduced (e.g., see [1]) arising from the idea of modeling the signal transmission between neuronal cells in the brain, e.g., see [2] as well as [6], [8] and [9]. Whereas the cells in cellular automata evolve depending on their own state and the states in their neighborhood, the cells in extended spiking neural P systems act according to the number of spikes within the cells at each discrete time step. Classic variants of cellular automata are based on a k-dimensional grid structure of the cells, e.g., we mention Conway's famous game of life (we also refer to [14] for a thorough discussion of two-dimensional cellular automata). Spiking neural P systems in principle were defined to work on arbitrary underlying graph structures, which more resembles the concept of generalized automata networks, e.g., see [3] and especially [13]. Extended spiking neural P systems are a special variant of membrane systems (see [10]; for the actual state of the art in this area, we refer to [15]). Inspired by the idea of signal transmission in the human brain, spikes are sent along the axons between cells (neurons), e.g., see [5] and especially [7] and [11]. The number of spikes sent to the surrounding cells depends on the actual contents (the number of spikes) in a specific cell. A spiking neural P system to be finite means that, at any moment, the number of spikes in any cell cannot exceed a given bound. The cells evolve in parallel at any time step, and depending on the actual number of spikes, each cell consumes some spikes and sends different numbers of spikes to its neighboring cells which are accumulated there to be considered in the next time step. Using suitable encodings, we can simulate the looking for the states of the surrounding cells from a cell of a cellular automaton by receiving specific numbers of spikes from these neighbor cells in the corresponding cell of the simulating extended spiking neural P system. In that way, the function and the behavior of a cellular automaton can exactly be simulated by a corresponding extended spiking neural P system, no matter which is the underlying connection structure. Extensions of the classic models of cellular automata can be simulated by suitable extended spiking neural P systems as well.

2 Definitions

For the basic elements of formal language theory needed in the following, we refer to any monograph in this area, in particular, to [12]. We just list a few notions and notations:

©ISAROB 2009

$\mathbb{N}$ denotes the set of non-negative integers. The interval of non-negative integers between k and m is denoted by $[k..m]$. For a finite set N, $|N|$ denotes the cardinality of N.

2.1 ESNP systems with total spiking

We here give a definition of a particular kind of extended spiking neural P systems, i.e., ESNP systems with total spiking (see [4]). For some original definitions we refer to [7] and [1].

An *extended spiking neural P system with total spiking* (*ESNP$_t$ system* for short) is a construct

$$\Pi = (V, S, R)$$

where

- V is a set of *cells* (or *neurons*); if V is a finite set, then the neurons are uniquely identified by a number between 1 and m;
- S describes the *initial configuration* by assigning an initial value (of spikes) to each cell;
- R is a set of *rules* of the form $(i, E/ \to P)$ such that $i \in V$ (specifying that this rule is assigned to cell i), E is a regular *checking set* (the current number of spikes in the cell has to be from E if this rule shall be executed), and P is a (possibly empty) set of *productions* of the form (l, w) where $l \in V$ (thus specifying the target cell), and $w \in \mathbb{N}$ is the *weight* of the energy (i.e., the number of spikes) sent along the axon from cell i to cell l.

Starting from the initial configuration given by S, a transition to the next configuration is performed by applying one rule $(i, E/ \to P)$ in each cell, if the current contents of the corresponding cell coincides with E. (Note that the whole contents of the neuron is lost as soon as a spiking rule $(i, E/ \to P)$ can be applied in neuron i). If there are more rules to be applied in one cell, then one is non-deterministically chosen. Hence, the system works in a sequential way on the level of the cells, but in a parallel way at the level of the whole system.

In the following, we will mainly consider *bounded* ESNP$_t$ systems, where for every cell, the number of cells from which it may receive an input is bounded and where at any moment, the number of spikes in it cannot exceed a bound specific for this cell. The cells evolve in parallel at any time step, and depending on the actual number of spikes, each cell consumes all of its spikes and sends different numbers of spikes to its neighboring cells which are accumulated there to be considered in the next time step. An ESNP$_t$ is called *finite*, if it is bounded and, moreover, V is finite.

2.2 Generalized automata networks and cellular automata

In the following, instead of the basic model of cellular automata (e.g., see [14]), we will consider a more general model based on the generalized automata networks (GAN) as described in [13].The main difference lies in the network topology: while the topology of CA is a d-dimensional lattice, GAN are built on an arbitrary directed graph.

Here, we define a GAN as a construct

$$A_G = (G, Q, f)$$

where

- $G = (V, E)$ is a directed graph, V is a set of vertices also called *cells*, and E is a set of edges,
- Q is a set of *states*,
- $f = \{f_i \mid i \in V\}$ is the *transition function*, where f_i is the local transition function of cell i which, depending on the states of the cells j with $(j, i) \in E$, determines the new state of cell i.

For a GAN A_G, a configuration at time t is defined as

$$C(t) = (q_1(t), q_2(t), ..., q_k(t)),$$

where $q_i(t) \in Q$ is the state of cell i at time t. The evolution of the GAN in time is then given by the iteration of the *evolution operator* $\Phi : C(t) \to C(t+1)$ for $t = 0, 1, ...$, through the simultaneous application in each cell of the local transition rule f.

Usually we assume the set of states Q to be finite, i.e., the cells can only choose from a bounded number of states, and, moreover, that the in-degree as well as the out-degree of every vertex (cell) in the graph G is finite, too; then such a GAN is called *bounded*. If, moreover, V is finite, too, then the GAN is called *finite*.

Example 1 *Consider the GAN $A_G = ((V, E), Q, f)$ with $V = \{1, ..., n\}$ for some $n \in \mathbb{N}$, $E = \{(i, i+1) \mid 1 \leq i < n\} \cup \{(n, 1)\}$, let Q be a finite set of states, f be the transition function with $f_i(q) = q$, and let S describe the* initial configuration *assigning an initial value from Q to each cell. The cells are connected in a simple ring structure by the edges in E,and the local transition function f_i just takes over the state q from* *cell $i+1$ to cell i (from cell n to cell 1). Hence, the time evolution of the GAN is periodic with $C(t) \to C(t+n)$ for $t = 0, 1, ...$, with $C(0) = S$. The in-degree of every cell is 1, hence, with V and Q being finite, A_G is finite.*

Obviously, in order to allow for a finite description, the graph structure as well as the local transition functions for the cells must follow specific restricted rules. The most typical example for a GAN with uniform rules is a (bounded, uniform) *cellular automaton* A_C (CA for short), which is defined on a d-dimensional grid, i.e., $V = \mathbb{N}^d$, $d \in \mathbb{N}$ is the dimension of A_C,

$$E = \{(i, i), (i + r_1, i), ..., (i + r_{n-1}, i) \mid i \in \mathbb{N}^d\},$$

where n is a fixed parameter determining the neighborhood size, and the r_j, $1 \le j \le n-1$, are fixed vectors in the d-dimensional space. Hence, instead of the graph $G = (V, E)$ we may simply define the so-called *neighborhood*

$$U = \{r_1, r_2, ..., r_{n-1}\}$$

and thus write a CA as

$$A_C = (d, Q, U, f)$$

where the *transition function* $f : Q^n \to Q$ maps the state of each cell $i \in \mathbb{N}^d$ to another state from Q as a function of the states of cell i and the cells in the neighborhood $U_i = \{i + r_1, i + r_2, ..., i + r_{n-1}\}$ of cell i. If Q – as it is usually assumed – is finite, then, by the definition given above, the CA A_C is bounded, but not finite. Obviously, there are also many variants of finite CA taking only a finite subspace of $\mathbb{N}^d$ as the underlying set of cells, but we do not go into such details here, as the main result established in the succeeding section holds true for such a variant just as a special case of a GAN.

Example 2 *Consider the CA $A_C = ((2, \{0, 1\}, \{(1, 1)\}, f)$ with $f(q) = q$ as in the first example. The uniform environment $\{(1, 1)\}$ corresponds with*

$$E = \{((i, i), (i + 1, i + 1)) \mid i \in \mathbb{N}^2\},$$

hence, the CA A_C corresponds with the GAN $A_G = ((\mathbb{N}^2, E), \{0, 1\}, f)$,which is bounded, but not finite. The local transition function f_i just takes over the state q from cell $(i + 1, i + 1)$ to cell (i, i). Hence, the time evolution of the CA given by the evolution operator $\Phi : C(t) \to C(t + 1)$ for $t = 0, 1, ...$, can be described by saying that the initial pattern given at time $t = 0$ is shifted one position to the right and one position up in every time step.

3 Results

We now present our main result, showing that the function and the behavior of a bounded generalized automata network or a cellular automaton can exactly be simulated by a corresponding extended spiking neural P system with total spiking (ESNP$_t$ system), independent of the underlying connection structure of the GAN.

Using suitable encodings, we can simulate the looking for the states of the surrounding cells from a cell of a GAN by receiving specific numbers of spikes from these neighbor cells in the corresponding cell of the simulating ESNP$_t$ system.

Theorem 1 *Any bounded generalized automata network (GAN) — independent of its underlying connection structure – can be simulated by a bounded extended spiking neural P system with total spiking (ESNP$_t$ system). If the GAN is finite, then the ESNP$_t$ system is finite, too.*

Proof. The GAN $A_G = ((V, E), Q, f)$ with the initial configuration S can be simulated by an ESNP$_t$ system $\Pi = (V, S', R)$ in the following way:

First, we need an encoding function that allows us to encode all the information that may influence the state of a specific cell, i.e., we have to encode the state of the cell itself as well as the states of all cells from which it gets the information about their states due to the connections defined by E.

Now let n denote the cardinality of Q, i.e., n is the number of states used in A_G. These n states in Q can be ordered in a sequence $1, ..., n$, and each of these n numbers can be represented as a string representing the corresponding number between 1 and n in the dual system. Let $d(n)$ denote the number of digits needed to represent the number n in the dual system.

For a specific cell i, let the number of input cells for cell i be denoted by m_i and let these input cells j with $(j, i) \in E$ be written in a sequence $(j_{i,1}, ...j_{i,m_i})$. The current states of all these m_i input cells of cell i now have to be represented by a number of spikes which uniquely determines this specific situation from another one with these cells of Π being in other states. One specific way to represent the states of these m_i input cells $(j_{i,1}, ...j_{i,m_i})$ of cell i now is to concatenate the $\{0, 1\}$-strings representing the state of each by $d(n)$ digits (i.e., with leading zeroes to have a string with exactly $d(n)$ digits for each cell $j_{i,l}$, $1 \le l \le m_i$). This string (of exactly $d(n) * m_i$ digits 0 or 1) corresponds with a number that in the ESNP$_t$ system Π is the number of spikes representing the states of all its input cells in a cell i.

©ISAROB 2009

Now let us start with the initial configuration S' which in each cell i contains exactly that number of spikes which represents the state of cell i in S. The ESNP_t system Π evolves simulating the transitions in the given GAN A_G by suitable rules in R for each cell i implementing the local transition function f_i: let y be the number of spikes in cell i and $x = y/2^{d(n)m_i}$; for $f_i(x_1, ..., x_{m_i})$ and with x being interpreted as the number encoding the states $x_1, ..., x_{m_i}$ as described above we use $(i, \{x\}/ \to P)$ with P being the set of productions containing the production $\left(i, f_i(x_1, ..., x_{m_i})2^{d(n)m_i}\right)$ – sending the information about its new state to cell i itself – as well as $\left(j, f_i(x_1, ..., x_{m_i})2^{d(n)(p(i,j)-1)}\right)$ for every cell j which has to receive the information about the state of cell i, i.e., with $(i, j) \in E$; $p(i, j)$ denotes the position of cell i in the sequence of input cells for cell j. In that way, the information about the new states of the cells in the given GAN A_G is propagated as the corresponding number of spikes in the ESNP_t system Π. At any moment, in each cell i of the ESNP_t system Π the corresponding state of the underlying GAN can be recovered from the number of spikes y by dividing y by $2^{d(n)m_i}$.

Obviously, if the underlying GAN A_G is finite, then by the construction of the ESNP_t system Π given above, Π is finite, too. $\square$

As a special consequence of the preceding theorem we obtain the result that the evolution of cellular automata can be simulated by ESNP_t systems.

4 Conclusion

We have shown how cellular automata or even generalized automata networks can be simulated by ESNP_t systems, where the states of the cells are represented by the corresponding number of spikes.

It is an open question how such a simulation could also be done by other variants of extended spiking neural P systems as, for example, by ESNP systems with decay or thresholds (see [4]).

References

[1] Alhazov A, Freund R, Oswald M, Slavkovik M (2007) Extended spiking neural P systems generating strings and vectors of non-negative integers, in Hoogeboom HJ, Păun Gh, Rozenberg G (eds.), Membrane Computing, 7th International Workshop, WMC7, Springer, Berlin, 123–134

[2] Buarque de Lima Neto F, de Wilde P (2006) Venn-like models of neo-cortex patches, International Joint Conference on Neural Networks, 89–96.

[3] Csuhaj-Varjú E (2001) Networks of language processors, Current Trends in Theoretical Computer Science. World Scientific, 771–790

[4] Freund R, Ionescu M, Oswald M (2008) Extended spiking neural P systems with decaying spikes and/or total spiking, Intern J Found Computer Sci 19(5), 1223–1234

[5] Martín-Vide C, Pazos J, Păun Gh, Rodríguez-Patón A (2002) A new class of symbolic abstract neural nets: Tissue P systems, in Proceedings of COCOON 2002, Singapore, Lecture Notes in Computer Science 2387, Springer-Verlag, Berlin, 290–299

[6] Gerstner W, Kistler W (2002) Spiking Neuron Models. Single Neurons, Populations, Plasticity. Cambridge Univ. Press

[7] Ionescu M, Păun Gh, Yokomori T (2006) Spiking neural P systems, Fundamenta Informaticae 71, 2–3:279–308

[8] Maass W (2002) Computing with spikes. Special Issue on Foundations of Information Processing of TELEMATIK 8, 1:32–36

[9] Maass W, Bishop C (eds) (1999) Pulsed Neural Networks. MIT Press, Cambridge

[10] Păun Gh (2002) Computing with Membranes: An Introduction. Springer, Berlin

[11] Păun Gh, Pérez-Jiménez MJ, Rozenberg G (2006) Spike trains in spiking neural P systems, Intern J Found Computer Sci 17(4), 975–1002

[12] Rozenberg G, Salomaa A (eds) (1997) Handbook of Formal Languages (3 volumes). Springer, Berlin

[13] Tomassini M (2006), Generalized Automata Networks, Yacoubi S El, Chopard B, Bandini S (Eds.), ACRI 2006, Lecture Notes in Computer Science 4173, Springer, Berlin, 14–28

[14] Wolfram S (2002), A new kind of science, Wolfram Media

[15] The P Systems Web Page, `http://ppage.psystems.eu`

©ISAROB 2009

Memory Retention strategy by balancing Neutral Energy Point

JeongYon Shim

Div. of GS, Computer Science, Kangnam University, Kugal Dong 111, KiHeung Gu, YongIn Si, KyeongKi Do, Korea
(Tel : +82-31-280-3736; E-mail: mariashim@kangnam.ac.kr)

Abstract: As Internet related technologies are developing at high speed, the importance of smart Intelligent system which can process dynamic complex information from the data flood is getting high. It has already became a hot issue how to process efficiently huge amount of data having features of large scale, dynamics and complex. In this paper, focusing on the memory management, memory retention and Retrieval strategy by balancing Neutral Energy point adopting the brain function is proposed. This system was applied to the virtual memory and tested with sample data.

Keywords: memory retention,Neutral energy point, Type Matching Data selection, knowledge network

1. INTRODUCTION

The success of the digital revolution and the growth of the Internet have ensured that huge volumes of high-dimensional multimedia data are available all around us. This information is often mixed, involving different data types. It has the characteristics of dynamics,complex and huge amount of data. According to Moore's law, the number of transistors in a single microchip is doubled every 18 months. We can correlate this with a similar observation from the data and information domain. It has already became a hot issue how to process efficiently huge amount of data having features of large scale, dynamics and complex. Many studies for making smarter Intelligent system have been made for many recent years. As one of these branches, the researches adopting the natural phenomena or brain functions have been progressing actively. Especially, the studies of Brain technology are very meaningful from the point of view that human brain is a final product which has been survived and evolved in the dynamic complex environments for several million years. That is, it means that human brain has the optimum structure and functions for facing the dynamic complex environment. Focusing on the memory management, it is known that the brain maintains the optimum status in the neural networks during the process of information storing, retaining, cleaning and retrieving.

In this paper,finding a clue from the brain functions of maintaining the memory, the memory is designed to be composed of knowledge networks with knowledge nodes. Knowledge node has three components of ID name, Type and Internal Energy. Neutral Energy point is also defined and Memory Retention and Retrieval strategy introducing the concept of Neutral Energy point is proposed. This strategy was applied to the virtual memory and experimented with sample testing data.

2. MEMORY DESIGN AND ACTIVATION

In this proposed system, memory was designed to be composed of Knowledge Network which consists of knowledge nodes and their associative relations. Knowledge node has three values of ID name, Type and Self Energy. Fig. 1 shows Memory activation and retention process. The Entering input,I_i, activates type matched knowledge nodes in the Knowledge Network using Type Matching Selection mechanism and changes its value of Self Energy as a memory retention process. Through this activating process, the system extracts the thinking chains related to the Type matched selected knowledge nodes.

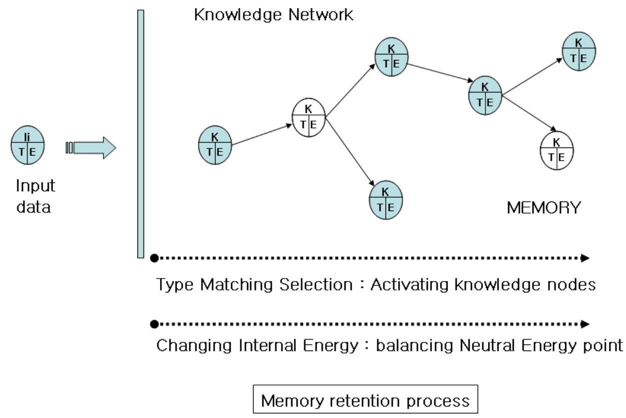

Fig. 1 Memory activation and retention

2.1 The representation of knowledge node and knowledge network

•knowledge node

Knowledge node is an basic atom composing the Knowledge Network. It contains 'Name','Type','Energy' attributes which can identify itself. Knowledge node is represented as a form of 'struct'.

struct k-node$_i\langle Name, Type, Energy\rangle$

The term of Energy describes Self Energy value of [-1.0,1.0] inside the individual knowledge node. The minus value means a negative state and the plus value means a positive state. If the value of Self Energy is zero, it is on the neutral point which represents the balanced state.

•Knowledge Network

Knowledge Network is connected by associative relations between Knowledge nodes and contain the informa-

©ISAROB 2009

tion. It is represented as

$\langle$K-node$_i$, R_{ij},$K-node_j$ $\rangle$

where $K-node_i$ is the name of knowledge node and R_{ij} is connection strength between two knowledge nodes. R_{ij} is calculated by equation (1).

$$R_{ij}=P(K-node_i \mid K-node_j) \quad (1)$$

2.2 Type Matching Selection

Type is defined as a factor representing the property of a thing and is classified to five types, M,F,E,K and S. These five types can be flexibly designed for the application area. We also defined Type matching rule. Type matching rule is used for selecting the knowledge from master Knowledge Network. There are two types of matching relations,Attracting Relation and Rejecting Relation[1].

Attraction Relation	Attracting degree d_i
M $\oplus \gg$ F	d_1=0.5
F $\oplus \gg$ E	d_2=0.5
E $\oplus \gg$ K	d_3=0.5
K $\oplus \gg$ S	d_4=0.5
S $\oplus \gg$ M	d_5=0.5

Rejecting Relation	Rejecting degree d_i
M $\ominus \gg$ E	d_1=-0.5
E $\ominus \gg$ S	d_2=-0.5
S $\ominus \gg$ F	d_3=-0.5
F $\ominus \gg$ K	d_4=-0.5
K $\ominus \gg$ M	d_5=-0.5

The matching rule 'M $\oplus$ $\gg$(0.5) F' means that M type helps F type with attracting degree 0.5. The value d_s of 'M $\oplus$ $\gg$(d_s) S' is derived from 'M $\oplus$ $\gg$(0.5) F $\oplus$ $\gg$(0.5) E $\oplus$ $\gg$(0.5) K $\oplus$ $\gg$(0.5) S'. The attracting degree of multiple relation is calculated by the following equation(2).

$$d_s=\begin{cases} \prod_{i=1}^{n}(-1)^{n+1}d_i & \text{if } Type_i \neq \text{Type}_j \\ 1 & \text{otherwise} \end{cases} \quad (2)$$

If the value of d_s is positive, it is attracting relation. Otherwise, the minus value means rejecting relation.

3. MEMORY RETENTION STRATEGY OF BALANCING NEUTRAL ENERGY POINT IN THE KNOWLEDGE NETWORK

3.1 Self Energy and Neutral Energy Point

AS described in section 2,a knowledge node has its Self Energy. We define Self Energy as an internal energy which represents energy degree determining the activated state. Fig. 2 shows the gauge of energy which has a value between -1 and +1. The plus value means positive energy and the minus value means negative energy. The value 0 represents the balanced Neutral point. This value of Self Energy is continuously adjusted by activating state caused by entering Energy of input facts.

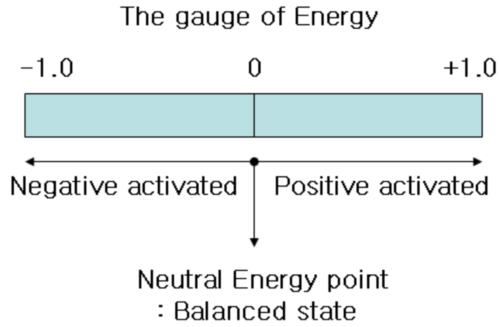

Fig. 2 Neutral Energy point

In the initial state, Self Energy, S_{E_i} of a knowledge node K_i has a value 0 on the balanced neutral energy point. But during repeated processing of Input facts, the value of Self Energy is continuously adjusted by activating state caused by entering Energy. If a input fact comes in and its type is matched with type of knowledge node, that knowledge node is selected and activated. Its Temporal Energy value,T_{E_i} of knowledge node is changed and calculated by equation (4). If the type of input fact is not matched with the type of knowledge node which it finds,the node can't be selected and has no effects on the node.

$$T_i = S_{E_i} + I_{E_i} \quad (3)$$

where S_{E_i} is Self Energy value and I_{E_i} is the energy value of Input fact, I_i.

$$T_{E_i} = \frac{1-exp(-T_i)}{1+exp(-T_i)} \quad (4)$$

The temporal energy value is temporally made value and used for the knowledge retrieving process. Its temporal value effects on adjusting the value of Self Energy. Self Energy S_{E_i} is calculated by following equation (5).

$$S_{E_i} = f(S_{E_i}^{old} + (T_{E_i})^2) \quad (5)$$

$$f(x) = \begin{cases} x & \text{if } -1 <= x <= 1 \\ 1 & \text{if } x > 1 \\ -1 & \text{otherwise} \end{cases} \quad (6)$$

3.2 Memory cleaning by balancing Neutral Energy point : Forgetting

As the activating mechanism is progresses, the value of Self Energy is accumulated and getting higher. Then in the final state, the knowledge network arrives at the state which is easy to be activated by even tiny stimulus. For the efficient precise knowledge retrieval, this state not only cause inaccuracy but also may cause serious problems. For this reason, memory retention process by balancing the neutral energy point is needed.

To adjust the balancing Neutral Point, the system should calculate the total value of Self Energy of Knowledge nodes composing the knowledge network. Total Energy value,B_P is calculated by equation (6).

$$B_p = \frac{\Sigma_{i=1}^{n} S_{E_i}}{n} \quad (7)$$

©ISAROB 2009

where n is the number of knowledge nodes.

For making the memory retention process, we designed the concept of Balancing Threshold,θ, as a retaining critical point. If Total Energy value is greater than or equal to the Balancing threshold, the knowledge nodes not frequently used are removed step by step according to the forgetting gauge,f, and the Self Energy value of survived knowledge nodes are reset as a value of the neutral point energy, zero.

Base on the Balancing Threshold, memory retaining process is performed by following algorithm.

Algorithm 1 : Memory Retaining Mechanism

STEP1 input θ,f;
STEP2 i=0;
STEP3 Calculate B_p
STEP4 If($(B_P)^2 \geq \theta$)
while(queue != Empty) do{
If (f == on){
{Remove the node;
i++;}
Else{
If (S_{E_i}=0)
Mark "Cleaning" flag;
Else S_{E_i}=0;
i++; }}
STEP5 : Stop.

4. EXPERIMENTS

We apply Memory retaining strategy to the example of virtual memory as following Fig.3 and tested with simple knowledge network. This knowledge network has 8 knowledge nodes and 7 associative relations connecting two nodes. The description about Type matching mechanism is abbreviated here because it is described in detail in the referred paper [1]. In this paper, the test for investigating the variation of Self Energy value inside the knowledge node was performed. We made an observation on activated state and the changes effected by 8 input facts which have values of Type and Energy. Fig.4, Fig.5 and Fig.6 show the result of changing Self Energy value according to the Balancing threshold. The cases of Balancing threshold = 0.3,Balancing threshold = 0.5 and Balancing threshold = 0.7. were investigated respectively. Fig.7, Fig.8 and Fig.9 show the changing value of Internal Self Energy value in the graphic form. From the graphic form we can easily distinguish the fact that the smaller the value of Balancing threshold is, the shorter the time span of Balancing Neutral Energy point.

This memory retaining strategy can be applied for not only memory cleaning process but also used for controlling the activation level from the memory. And this system can be also applied to construct core brain like frame of Intelligent System.

5. CONCLUSION

In this paper, Memory Retention strategy by balancing Neutral Energy Point was proposed. Finding a clue from the brain functions of maintaining the memory, the memory is designed to be composed of knowledge networks with knowledge nodes. Knowledge node has three components of ID name, Type and Internal Energy. Neutral Energy point is also defined and Memory Retention and Retrieval strategy introducing the concept of Neutral Energy point is proposed. This strategy was applied to the virtual memory and experimented with sample testing data. As a result of experiments we could observed the successful changing process of Internal Self Energy by Type Matching mechanism and memory activation. This strategy can be applied to design and construct core brain like frame of Intelligent System.

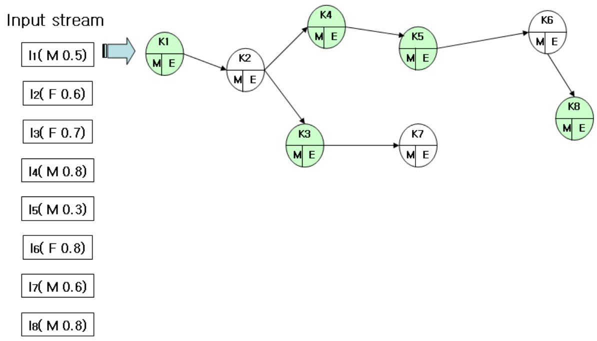

Fig. 3 Testing knowledge network

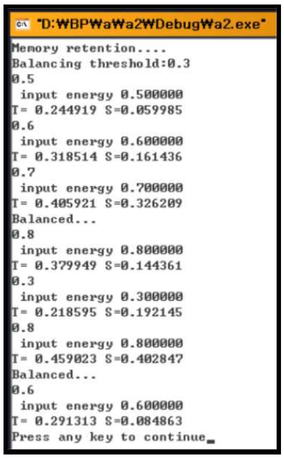

Fig. 4 Balancing threshold=0.3

REFERENCES

[1] JeongYon Shim, **Personal Knowledge Network Reconfiguration Based on Brain like function using Self Type Matching Strategy** IDEAL, volumn 5326, Springer,2008.

[2] Jean-Marc Fellous, Michael A. Arbib, **Who needs Emotions?** Oxford University press,2005.

[3] JeongYon Shim, **Knowledge Network Management System with medicine Self Repairing strategy** ICES2007,LNCS4684,pp119-128,Springer Verlag,Berlin Heidelberg2007.

[4] JeongYon Shim, **The design of Self Internal Entropy Balancing System with Incar-**

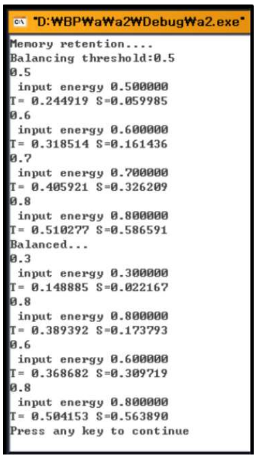

Fig. 5 Balancing threshold=0.5

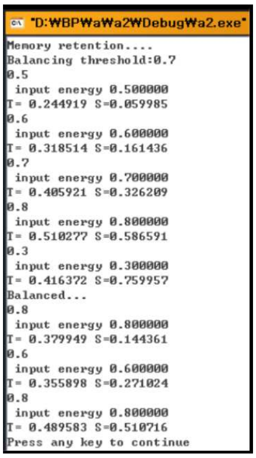

Fig. 6 Balancing threshold=0.7

nation process LSMS2007,LNCS4688,pp55-62,Springer Verlag,Berlin Heidelberg2007.

[5] JeongYon Shim, **Intelligent capsule Design for the multi functional aspects** LSMS2007,LNCS4688,pp719-725,Springer Verlag,Berlin Heidelberg2007.

[6] E. Bruce Goldstein, **Sensation and Perception** Fifth edition,Brooks/Cole Publishing Company,1999.

[7] Michael A. Arbib, Jeffrey S. Grethe, **Computing the brain : A guide to Neuroinformatics** Academic Press,2001.

[8] Ning Zhong, Jiming Liu, **Intelligent Technologies for Information Analysis** Springer,2004.

[9] Paol Giudici, **Applied Data Mining : Statistical Method for Bussiness and Industry** Wiley 2003.

[10] Daniel L. Schacter, Elaine Scarry, **Memory, Brain, and Belief** Harvard University Press, Cambridge, Massachusetts, London/2000.

[11] Luc De Raedt Arno Siebes, **Principles of Data Mining and Knowledge Discovery** Springer 2001.

[12] Ian Cloete and Kacek M. Zurada, **Knowledge Based Neuro Computing** MIT press 2000.

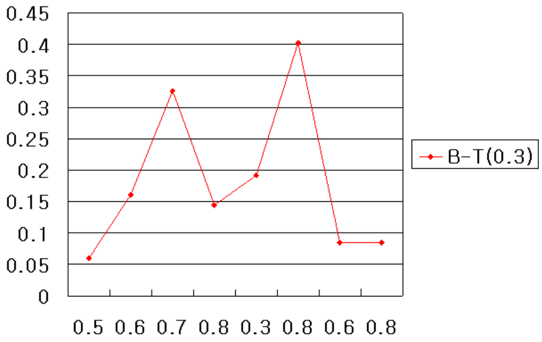

Fig. 7 Balancing threshold=0.3

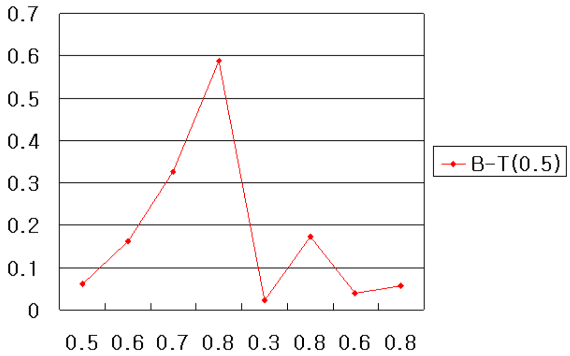

Fig. 8 Balancing threshold=0.5

[13] Sushmita Mitra, Tinku Acharya, **DATA MINING Multimedia, Soft Computing and Bio Informatics** Wiley Inter Science 2003.

[14] Tamraparni Dasu, Theodore Johnson, **Exploratory Data Mining and Data Cleaning** Wiley Inter Science 2003.

[15] Pierre Baldi,Paolo Frasconi, Padhraic Smyth, **Modeling the Internet and the Web - Probabilistic Methods and algorithms** Wiley Inter Science 2003.

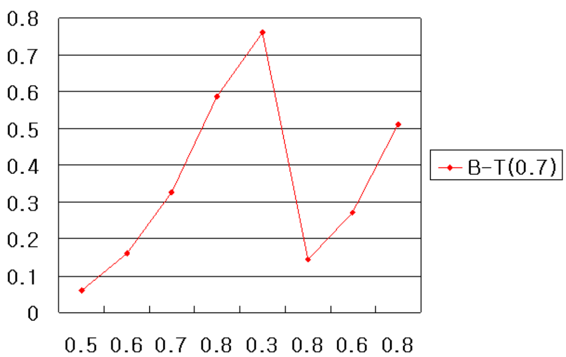

Fig. 9 Balancing threshold=0.7

Target-Adjusted Model for Kernel-Based Tracker

Jeehyun Goya Choe[1], Joon-Hong Seok[2] , Jeong-Jung Kim[2] and Ju-Jang Lee[2]
[1] Robotics Program, Korea Advanced Institute of Science and Technology, Daejeon, Korea
(Tel : +82-42-869-8032; E-mail: goya@kaist.ac.kr)
[2] Electrical Engineering and Computer Science, Korea Advanced Institute of Science and Technology, Daejeon, Korea
(Tel : +82-42-869-3432; E-mail: seokjh@kaist.ac.kr, jjlee@ee.kaist.ac.kr)

Abstract:
Kernel-based tracker shows robust performances in various object tracking technologies. Due to its robustness and accuracy, Kernel-based tracker using Mean-shift algorithm is regarded as one of the best ways to apply in object tracking technology in computer vision fields. However, it has a drawback. It fails tracking when faced with a speedy object moving beyond its window size within one image frame interval time. These failures are reduced with the use of Target-adjusted kernel models proposed in this paper. These models are designed to reflect the previously known target information. Same to the conventional kernel model in kernel-based object tracker, this model also contains the target information of both the color and the distance. Experimental results show that the time required for the calculations in tracking process is lessened so that causing lesser failures by applying this Target-adjusted model. Building a Target-adjusted model requires the previously known color data of the target. The model is designed to focus on the colors in the target object by using look-up tables. These look-up tables enable to reduce the size of the color bins in a model so that unnecessary trivial computations can be regarded.

Keywords: Kernel-based object tracking, Target-adjusted model, LUT(Look Up Table)

1. INTRODUCTION

There are many tracking algorithms which perform well in finding targets accurately in the sequence of image frames. However, most of them require expensive processing of the entire image pixels. Such algorithms do not solve the focus of attention problem, where the only place of interest to the observer lies around the object itself.

To address the focus of attention problem, using only local pixels around the previous target area by Kernel-based Mean-shift tracker has been proposed by Comaniciu and Ramesh (see [2]). An obvious advantage of the Mean-shift tracker over the conventional methods is the elimination of a brute force search, and the computation of the translation of the object patch in a small number of iterations (see [4]).

The original Kernel-based object tracking, analyzed in Section 2, performs real-time target image tracking without any prior information of the target. In this paper, tracking of the specific target--a metal cup--is implemented using a specified target model, the Target-adjusted model. The way to design a Target-adjusted model is described in detail in Section 3.

There are many well-known methods that elaborately represent object information. Those methods show good performance in object recognition and detection but are not appropriate for tracking. Delicate and fine representation of target object models, used in recognition or detection, costs too much computation. It gives poor tracking performance especially when the motions are unreliable and unexpected.

In this paper, Target-adjusted models with newly generated bins is implemented with the advantage of specially designed LUT and proved to be suitable for tracking.

2. KERNEL-BASED TRACKER

The Kernel-based tracker specifies how to combine a set of color values of pixels in local neighborhood with a proper kernel profile k(x) to produce a new location that tracks the center of the target in the image.

Prior to the computation of Mean-shift vector, color models that present the current window and the previously saved original window should be established. Those models should reflect both the color value and the color intensity rate of each color channel. The target model and the target candidate are represented by each pdf which can be estimated from the data in color space (see [2]). The target model with the color u=1…m is obtained as $\hat{\boldsymbol{q}} = \{\hat{q}_u\}_{u=1\ldots m}$,

$$\hat{q}_u = C\sum_{i=1}^{n} k(\|x_i^*\|^2)\delta[b(x_i^*) - u],$$

where x_i^* is the normalized pixel locations of the target model, $b(x_i^*)$ is the index of bin in the quantized color space. The target candidate with the color u=1…m at location y is computed as $\hat{\boldsymbol{p}}(y) = \{\hat{p}_u(y)\}_{u=1\ldots m}$

$$\hat{p}_u(y) = C_h\sum_{i=1}^{n_h} k(\left\|\frac{y - x_i}{h}\right\|^2)\delta[b(x_i) - u]\,,$$

where x_i are the normalized pixel locations of the target candidate, centered at y in the current frame.

The heart of the Mean-shift algorithm is computation of a new location $\hat{y}_1$ from location $\hat{y}_0$ according to the

Mean-shift vector

$$\hat{y}_1 = \frac{\sum_{i=1}^{n_h} x_i w_i g\left(\left\|\frac{\hat{y}_0 - x_i}{h}\right\|^2\right)}{\sum_{i=1}^{n_h} w_i g\left(\left\|\frac{\hat{y}_0 - x_i}{h}\right\|^2\right)},$$

where $g(x) = -k`(x)$, h is the bandwidth of $k(x)$, w_i is given by

$$w_i = \sum_{u=1}^{m} \sqrt{\frac{\hat{q}_u}{\hat{p}_u(\hat{y}_0)}}\,\delta[b(x_i) - u],$$

where w_i is sample weight[2].

3. TARGET-ADJUSTED MODEL

The two most important factors affecting the efficiency of any algorithm using *color space* processing are the color space being chosen and its *quantization*[4]. In this paper, color space and quantization level are fixed for consistency. For the color space, RGB color channel, the most frequently used color space, was used instead of many other available color spaces.

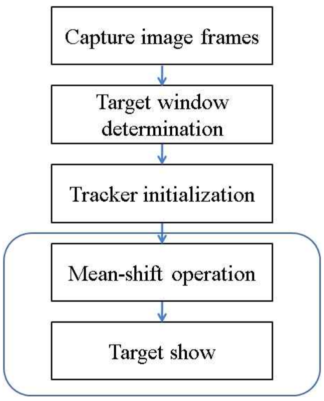

Figure 1. Flow chart of Kernel-based tracker

The chart above shows the main 5 steps in implementing Mean-shift tracker to a real-time video. The target model is built once in Tracker initialization process, while target candidate is periodically built in Mean-shift operation process updating the current window's color distribution. Among 5 steps, the last two steps--Mean-shift operation and Target Show processes--are the ones operated in every video frame. It is clear that improvement of speed is closely related to the time taken in building a target candidate and deriving a Mean-shift vector.

In Mean-shift algorithm, image pixels distributed in a 2-dimensional space are transformed to 1-dimensional bins. In this modeling process, two kinds of information of the target are delivered-color information and the distance information. In implementation, the color models, target model and target candidate, are represented as 1-dimensional arrays.

The number of length of the array is *(number of color-bins)*^{3} for 3 RGB channels. A usual image frame with 256 color-levels for each RGB channel would have 256^3 color-bins. This is a tremendous amount and when trying to directly implement in a practical use, the computer memory easily gets out of control. So in practice, the color-levels are uniformly quantized into 16-levels or less (see [6]).

Performance gets better with higher color-levels (see [1]). Models with larger number of bins represent the same target with more information so that tracking can be more accurate. A uniform quantization with smaller color-levels causes lowering of performance since lesser information is used for tracking. However, its computation time is short. In this paper, 16-level quantization is used for every experiment.

Following figure is an example of a kernel model. This target mainly consists of two colors, pink and white.

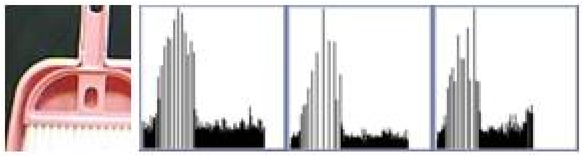

Figure 2. Target image and its RGB plot

The reason that we concentrate on the kernel model rather than the RGB channels is that because it is not easy to extract the common feature from the RGB channel plots. RGB color histograms do not reflect the distance information but only the color frequencies. Therefore they are very sensitive to light, as well as background colors. By observing the sequence of RGB plots in real-time tracking system, it is discovered that the characteristics of histograms vary from time to time (see [1]). Kernel model, on the other hand, usually gives specific distributions regardless of the various poses, orientations or lights. The kernel model of the object shown in Figure 2 is shown below.

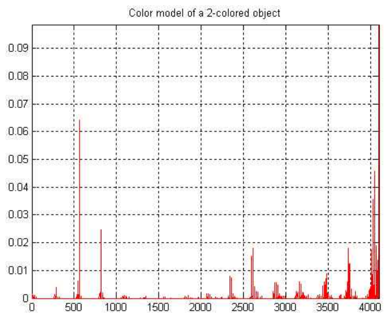

Figure 3. Kernel model with 16^3 color bins

As the Figures 2 and 3 show, the target image usually can be specified with certain number of dominant colors. Some dominant color-bins as well as empty bins are discovered. If we can design the model bins to focus on the meaningful information and discard the unnecessary ones, the implementation of the tracking system would be much simple and efficient.

3-1. Designing a Target-adjusted model

If a uniform quantization of the color model is implemented, there are many unused bins causing memory waste. These unnecessary bins are likely to have noise values, and cause unnecessary calculations.

Extracting an essential data from the target image can be efficiently realized by using the prior knowledge of the target model.

Figure 4 Target selection in the image frame

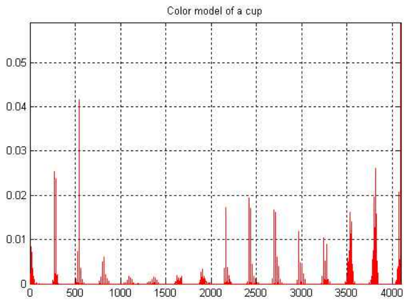

Figure 5. Kernel model of a cup with 16^3 color bins

The image given in Figure 4 is the raw image from the camera, and the selected target region is shown at the right top. Mean-shift kernel model is displayed together with the selected local image. Since this snapshots are from uniform quantization program with 16 *bins per channel*(bpc) the number of bins in x-axis of the Mean-shift model graph is $16^3 = 4096$.

To have a non-uniform quantization of the color-levels, there should be prior model of the target.

As can be seen from the figures, there are some dominant colors, weak colors and very weak colors, practically without any value in its bin, are detected. In the operation that is held for every single frame, every bin value in target candidate should work both as a divider and a multiplier for every bin value in the previously saved target model.

To ignore the bins that have no meaning in tracking the target object, bins with zero color values were mostly discarded and reduced to a small amount of bins.

In the Mean-shift tracker, each color value in target model and target candidate is always used together. Therefore when either target model value or target candidate value is zero, the values calculated from target model and target candidate are always zero. This means if we know that some color levels in target model or target candidate have poor possibility to emerge in the target, discarding that color levels makes no difference to the resulting Mean-shift vectors.

The implementation of establishing a Target-adjusted model is done by observing the target models and target candidates from many samples. Target models--in the form of kernel model in Mean--shift tracker-are sampled from various poses and motions. From the stored sample values, the color levels with frequent zero values can be noticed.

By memorizing only the value-existing color bins, a lookup table can be made. The size of a lookup table is one array with the length same as that of the number of bins in original color model.

The effect of reducing the number of bins is great since there are always more than one iteration per a frame, and usually are more than 6 iterations especially when the target movement is large.

4. EXPERIMENTS

The proposed approach was implemented in the C programming language. The experiment was held in the environment of real-time video system, so the consistency of speed and motion could have had some slight uneven cases. For all experiments, the same set of parameter values, as shown below, were used.

1) The size of each image frame is 320*240 pixels
2) The window size for mean-shift tracking is fixed to 90*104 pixels, thus the bandwidth of the local image is all the same in these experiments.
3) BPC is fixed to 16 bins per one color channel
4) 3 color channels used (red, green and blue)
5) A metal cup was used as a target object

The metal cup used as the target here basically contains three colors. However, the color of the metal surface is very sensitive to the pose, orientation and light.

A. Uniform quantization

5 different speeds of motions were experimented for each type of motion.

Table 1 Experimental variables

Variables	
Types of motions	Linear Rectangular Circular
Speeds of motions	Use of relative motions from 1 to 5

B. Same experiment using the Target-adjusted model

Since the number of bins is critical factor in mean-shift process, we can discard much of the bins from the target model if the bin is empty. Target-adjusted model is built as a Lookup table of important bin numbers. It allocates new indexes to selected bins reducing the amount of bins to a smaller quantity.

5. DISCUSSIONS AND COMPARISONS

A. Uniform quantization

For each case, the total time taken in Mean-shift process was checked and recorded. The results are shown below.

Table 2 Experiment using uniform quantization

Approx. Relative Speed	Computation time for 150 frames (sec)		
	linear motion	rectangular motion	circular motion
1	2.246	2.281	4.374
2	2.841	3.18	4.67
3	3.549	3.531	5.578
4	4.743	4.254	5.8
5	4.9	4.967	6.162

As the speed gets higher, the more calculation time is needed. Also, more time is needed for tracking big motions than tracking small motions. It is noticeable that along with the number of bins, amount of motion path is also a critical factor for calculation speed.

B. Target-adjusted model

The same experiments done in uniform quantization were implemented using the Target-adjusted model.

Table 3 Experiment using LUT

Approx. Relative Speed	Computation time for 150 frames (sec)		
	In linear motion	In rectangular motion	In circular motion
1	1.802	1.977	4.003
2	2.471	2.527	4.511
3	3.096	2.935	5.003
4	3.937	3.992	5.492
5	4.016	3.998	5.588

The result of linear motions is plotted below. Dashed line is the result of using the LUT, and the solid line is the result of uniform quantization. The graph clearly shows that the time needed for computing in the uniform quantization case is longer than that of the LUT case.

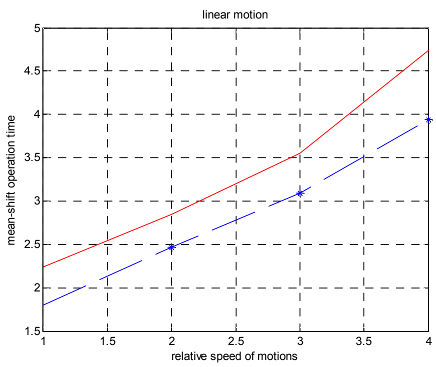

Figure 6 Linear motion with different speeds

These results show the tendency of computing time. It depends on the existence of using Target-adjusted model. Target information helps to reduce the tracking process.

At the relative speed of about 7 in linear motion, the Target-adjusted tracking system had no problem in tracking the target but the conventional Kernel-based tracker repeatedly failed.

6. CONCLUSION

In Target-adjusted tracking system, the time (or the number of calculation) required for tracking process within a frame was reduced without any significant effect on performance.

Extensive simulation and experimental results verified the efficacy and robustness of the proposed algorithm. Tracking failures were reduced. The reduction in processing time also substantiates this conclusion.

Further, this adjusted model scheme can be applied to many other non-rigid objects that have few dominant color values.

REFERENCES

[1] J. G. Choe, J. Seok, J. Lee, "Mean-shift Tracker with Face-adjusted Model", *International Conference on Control, Automation and Systems*, October 2008.

[2] D. Comaniciu, V. Ramesh, P. Meer, "Kernel-based object tracking", IEEE Trans. *Pattern Analysis and Machine Intelligence*, vol25 (5), pp. 564-577, August 2003.

[3] R. T. Collins, "Mean-shift Blob Tracking through Scale Space", IEEE Computer Society Conference on *Computer Vision and Pattern Recognition*, 2003.

[4] A. Yilmaz, O. Javed, M. Shah, "Object Tracking: A Survey", ACM Computing Surveys, 2006.

[5] F. Ennesser, "Finding Waldo, or Focus of Attention Using Local Color Information", IEEE Trans. *Pattern Analysis and Machine Intelligence*, August 1995.

[6] Iain Wallace, *A mean-shift tracker: implementations in C++ and Hume*, 2005.

[7] S. Jeong, M. Lee, Computer Vision programming using OpenCV (in Korean), Hongneung Science Publisher, 2007.

Human arm-like Surgical Robot System with Force Reflection Measurement for Minimally Invasive Surgery

Ki-Young Kim[2], Ho-Seok Song[2], Jung-wook Suh[2] and Jung-Ju Lee[1]
[1] Department of Mechanical Engineering, KAIST, Daejeon 407, Republic of Korea
(LEEJUNGJU@kaist.ac.kr)
[2] Department of Mechanical Engineering, KAIST, Daejeon 407, Republic of Korea
(thine0715@kaist.ac.kr, Hosek@kaist.ac.kr,sjwook@kaist.ac.kr)

Abstract -*The concept design of the suggested robotic surgical system is to measure the position and orientation of the surgeon's arm and to develop the surgical manipulator same 7 degree of freedom as the human arm. The kinematic configuration of the surgeon's arm is obtained by using the hand tool and the elbow supporter. Then the surgical manipulator tracks the movement of the surgeon's arm similarly by using the measured data in real time. The inverse kinematic solution of an additional degree of freedom is derived by using the angle data of the surgeon's elbow joint. And the force measurement system using a fiber bragg grating sensor was developed. The method to measure the 3 axial force applied on the surgical tool was described.*

Keywords: *surgical robot, minimally invasive surgery, robotic surgical system*

1 Introduction

Laparoscopic surgery are less pain, less need for post-surgical pain medication, less scarring and less likelihood for incisional complications [1]. But there is a constraint of degree of freedom (DoF) because tools are inserted through incision points. The surgical tools lose 2 DoF because of this incision points and surgeons have more fatigue and feel more tired than performing open surgery due to the lack of the dexterity.

To solve these problems, the robotic surgical systems are appeared. Zeus and da Vinci system appeared in the late 1990s and da Vinci system is widely used for general surgical applications nowadays [2]. Zeus system has a 4 DoF robot arm but da Vinci system has a 6 DoF robot arm. Surgeons using da Vinci system perform minimally invasive surgical techniques quicker and more efficiently than traditional minimally invasive techniques [3].

Mitsuishi in Japan developed 6DoF surgical systems and link-driven surgical tools. The force applied to the tooltip can be measured by using strain gauge and the force-feedback modes in each surgical task are developed. [4] In this work, we suggest a human arm-like robotic surgical system for laparoscopic surgery. The developed surgical manipulator can mimic the motion of a human arm. If the surgical manipulator to perform surgical tasks moves like the motion of the human arm, the surgeon can predict the motion of the surgical manipulator more easily and intuitively. And we can expect the less time and more agility for performing surgical tasks.

2 Design Concept

The concept design of a suggested system is to make the surgical manipulator perform surgical tasks as if the human arm does. The surgical manipulator has two parts because the surgical tool must be exchanged during laparoscopic surgery. One is the robot base which has 3 DoF and the other is the surgical tool, 4 DoF. The proximal 3 DoF corresponds to the shoulder joint of human arm, 3 DoF. And the distal 4 DoF is correspondent to the elbow joint and the wrist joint of a human arm. This means that the surgical manipulator has additional DoF like human arm. Then if the tooltip of the surgical manipulator is fixed, the manipulator has various configurations. However, if the surgical manipulator has a similar configuration like a human arm, we need position of a human arm in real time. To do this, master system can measure the position of the wrist and elbow of a surgeon. If we assume that the position of the surgeon's shoulder is almost fixed during surgery, we know the configuration of the surgeon's arm by the master system in real time.

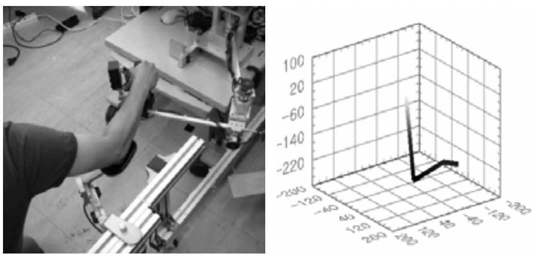

Fig.1.The master system and the obtained kinematic configuration of the human arm

©ISAROB 2009

A. Design of the master system

Master system has a display panel to show the view of the laparoscope and a console which is consisted of a hand tool and an elbow supporter. The hand tool has 6 DoF and it can measure the position and orientation of the surgeon's wrist joint. The elbow supporter has 2 DoF and it supports the weight of the surgeon's arm. And also it can measure the position of the surgeon's elbow joint. (Fig.1)

The hand tool can measure the position of the surgeon's wrist joint by using proximal 3 DoF joints and also the orientation of the surgeon's wrist joint by using the distal 3 DoF joints. If we assume that the position of the surgeon's shoulder is nearly fixed during surgery, we set the virtual position of shoulder joint fixed in Cartesian space. Then we can calculate the kinematic configuration of the surgeon's arm. In other words, by measuring the position of the wrist joint and the elbow joint with reference to the shoulder joint, we can construct the kinematic configuration of the surgeon's arm. The kinematic modeling of the surgeon's arm is like Fig.1.

The surgical manipulator in the slave system can follow the configuration of the surgeon's arm in real time. The tooltip of the surgical manipulator is corresponded to the position of the hand and the kinematic base of the manipulator is corresponded to the position of the surgeon's shoulder joint. Although we assume the position of the surgeon's shoulder joint as a virtual reference point, the position of the hand is measured accurately by the hand tool so we can realize the accurate tracking of the surgical manipulator.

B. Design of the slave system

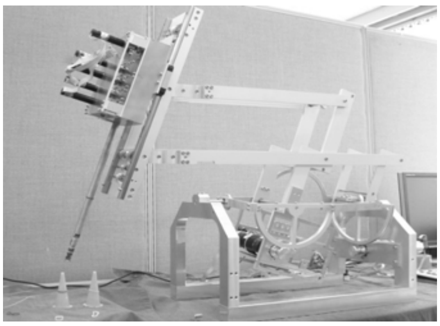

Fig.2 The developed surgical manipulator

The slave system has a laparoscope and a surgical manipulator. The suggested surgical manipulator has 7 DoF that has an additional DoF like a human arm. (Fig.2) The proximal portion adopts double parallelogram which has a remote center so it can avoid the constraint of the incision point. The proximal portion of the surgical manipulator has 2 revolute joints and 1 translational joint, whereas the human's shoulder joint has 3 revolute joints. This is because the translational joint can make the surgical tool move into or out of the abdomen more conveniently and easily than revolute joint does. The surgical tool inserted into abdomen has an elbow joint and roll-pitch-yaw joints to change the orientation of the tooltip. And the surgical tool can be attached to the proximal portion of the surgical manipulator in order to exchange various kinds of tools. Cable-pulley mechanism is used to mechanize the surgical tool and the tension control device is designed for holding the tension of the wire.

3 The Kinematics of the System

A. Kinematics of the master system

The forward kinematics of the hand tool and the elbow supporter is obtained by Denavit-Hartenberg (D-H) parameters. The D-H parameter of the hand tool and the elbow supporter is described in Table.1, 2

The handle and grip are attached to the distal end of the hand tool and the position and orientation of the handle are matched to those of the surgeon's wrist joint. Then we can calculate the kinematic configuration of the surgeon's arm using the measured data. The lengths of the upper and lower arm are simply obtained as described below.

$$L_{upper\ arm} = \sqrt{(x_e - x_o)^2 + (y_e - y_o)^2 + (z_e - z_o)^2}$$

$$L_{lower\ arm} = \sqrt{(x_w - x_e)^2 + (y_w - y_e)^2 + (z_w - z_e)^2}$$

Table1. D-H parameter of 6 DoF hand tool

i	α (i-1)	a(i-1)	d(i)	θ(i)
1	0	0	0	θ1
2	0	L1	0	θ2
3	0	0	-L2	0
4	270	0	0	θ3
5	90	L3	0	θ4
6	90	0	L4	0
7	0	0	0	90
8	180	L5	0	-90+θ5
9	0	L6	0	-45
10	90	L7	0	90
11	270	L8	0	90+θ6

Table2. D-H parameter of 2 DoF elbow supporter

i	α (i-1)	a(i-1)	d(i)	θ(i)
1	0	0	0	θ1
2	0	L9	0	θ2

Where (x_o, y_o, z_o) is the position of the shoulder joint, $(x_e,$

©ISAROB 2009

y_e, z_e) is the position of the elbow joint and (x_w, y_w, z_w) is the position of the wrist joint. The angles of the shoulder joints of the surgeon's arm can be obtained algebraically by using the transformation matrix of the human arm.

$$ {}^0_1T\,{}^1_2T\,{}^2_3T\;{}^3P_{elbow} = {}^0P_{elbow} $$

$$ \theta_1 = Atan2(y_e, z_e) $$

$$ \theta_2 = Atan2(x_e, \pm\sqrt{y_e^2 + z_e^2}) $$

The θ_3, which is the rotation angle along the shaft of the upper arm, is not considered. This is because there is no revolute joint of θ_3 in the surgical manipulator. The revolute joint is replaced to a translational joint in the surgical manipulator. And the angle of the elbow joint is also obtained algebraically.

$$ \theta_{elbow} = $$

$$ \cos^{-1}\left[\frac{(x_e, y_e, z_e)\cdot\{(x_e - x_e), (x_e - x_e), (x_e - x_e)\}}{|L_{upper\ arm}||L_{lower\ arm}|}\right] $$

The rolls, pitch, yaw of the wrist joint are corresponded to the 3 DoF joints of the distal hand tool. The roll angle of the wrist joint is obtained by 6DoF hand tool.

$$ \theta_{roll} = \theta_6 $$

The pitch and yaw angle at wrist joint are calculated approximately. Each O, A, B points are elbow, wrist, hand position. Lines OEF, OCD are projections of OAB. Then we find approximate yaw and pitch angle. (Fig.3)

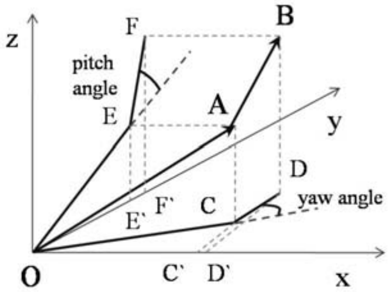

Fig.3 Vector notation of human arm

So we can obtain the kinematic configuration of the surgeon's arm described Fig.1 by measuring the position of the wrist joint and elbow joint using the hand tool and the elbow supporter.

4 Force measurement system

Fig.7 Sensing Element

One of the major limitations of the robotic surgery is the lack of the haptic information. Especially, appropriate applied forces are critical in creating knots firm enough to hold, but do not break sutures or damage tissue. In the robotic surgery, attenuation of the haptic information is unavoidable, because it is helpful for the surgeon to know the information about the forces between the tool and the tissue or the thread to be knotted. Therefore, it is necessary to measure the force applied on the tool.

The 3-axial forces applying on the tooltip can be measured by the sensing element shown Fig.7. For measuring the 3-axial forces, the several assumptions are suggested below.

Ⅰ. 3 moments do not apply on the tooltip of the robot arm

Ⅱ. 3 axial forces always act on the middle of the tooltip.

Ⅲ. The wires driving wrist joint and grip don't slip and elongate.

Ⅳ. Sensor is affected by only F_{zs}, M_{xs} and M_{ys}

The wrist joint rotates θ_1 about axis X, and θ_2 about axis Y and then the forces and moments matrix applying on the middle of the sensor is obtained as described Fig.8. The matrix can be simplified because the sensor is affected by only F_{zs}, M_{xs} and M_{ys}.

$$ \begin{bmatrix} F_{zs} \\ M_{xs} \\ M_{ys} \end{bmatrix} = \begin{bmatrix} -C_1S_2 & -S_1 & C_1C_2 \\ S_1S_2d_s & -C_1d_s - d_1 - d_2C_2 & -S_1C_2d_s \\ C_1C_2d_1 + C_1d_2 + C_2d_s & S_1S_2d_2 & C_1S_2d_1 + S_2d_s \end{bmatrix} \begin{bmatrix} F_x \\ F_y \\ F_z \end{bmatrix} $$

θ_1, θ_2, d_1, d_2 and d_s are variables already we know. So, the F_x, F_y and F_z is derived by using linear algebra. The strain of four beams constituting the sensor is obtained by the strain gages, but electrical strain gages have a lot of limitations to use in the operating room. In order to sterilize, sensor has to be protected from water or the other liquids. Moreover, because of the space limitation induced by the narrow tool, number of electrical lines has to be minimized. These problems can be overcome by the use of the fiber bragg grating (FBG) sensor.

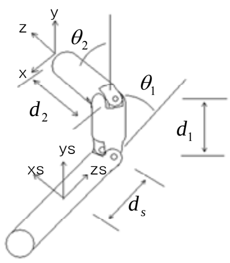

Fig. 8 Kinematic diagram for sensing

©ISAROB 2009

FBG sensors aren't affected by electro-magnetic field and fluidic environment. As the input and the output light are transmitted in one optical fiber, this FBG sensor system requires only simple wiring. So the FBG sensor system can be utilized more effectively.

The basic principle of an FBG-based sensor system lies in the monitoring of the wavelength shift of the returned Bragg-signal (Bragg wavelength), as a function of the measurand (e.g. strain, temperature, and force)

The intensity of the reflected optical signal is a function of the Bragg grating wavelength, which is related to the applied strain on the FBG. Therefore, the dynamic strain can be derived from the intensity change measurement as a function of the wavelength of the reflected optical signal. The operation of an FBG is based on a periodic, refractive index change that is produced in the core of an optical fiber. This grating structure results in the reflection of the light at a specific narrow band wavelength, called the Bragg wavelength. The Bragg condition is given by

$$\lambda_B = 2n_e\Lambda$$

Where λ_B the Bragg wavelength of the FBG, n_e is the effective index of the fiber core, and Λ is the grating period. If there is no temperature change, the mechanical strain detecting the wavelength shift can be measured by

$$\Delta\varepsilon = \frac{1}{(1-P_e)}\frac{\Delta\lambda_B}{\lambda_B}$$

Therefore, the change of the strain can be calculated by measuring the change of wavelength.

5 Conclusion

In the developed master-slave system, the surgical manipulator tracks the movement of the surgeon's arm similarly by using the measured data about the position and orientation of the surgeon's arm. The inverse kinematic solution of an additional DoF is derived by using the angle data of the surgeon's elbow joint. Additionally, the force measurement system using fiber bragg grating (FBG) sensor was developed.

Acknowledgement

This work was supported by the SRC/ERC program of MOST/KOSEF. (grant #R11-1999-008)

6 References

[1] A.J.Madhani, G. Niemeyer and J.K.Salisbury Jr., "Design of teleoperated surgical instruments for minimally invasive surgery," Ph.D Thesis MIT, 1998.

[2] Fobannes Bonder, Florian Augustin, "The da Vinci robotic system for general surgical applications: a critical interim appraisal," SWISS MED WKLY 2005.

[3] G.Hubens, H.Coveliers, "A performance study comparing manual and robotically assisted laparoscopic surgery using the da Vinci system," Surg Endosc Vol.17,pp. 1595-1599,2003.

[4] M.Mitsuishi, N.Sugita, P.Pitakwatchara, "Force-Feedback Augmentation Modes in the Laparoscopic Minimally Invasive Telesurgical System", IEEE/ASME Transactions on Mechatronics, Vol.12, No.4, pp.447-454, 2007.

[8] Won-ho shin, Dong-soo Kwon, "Development of a 5-DoF laparoscopic assistant robot," International journal of assistive robotics and mechatronics, Vol.7, No.4, pp.21-28, 2006.

[9] Ho-seok Song, Jung-ju Lee, "Develoment of a 5 DoF dexterous manipulator executable inside abdomen for minimally invasive surgery," International journal of assistive robotics and mechatronics, Vol.7, No.4, pp. 3-8, 2006.

[10]A.J.Hodgson,R.A. Pantazopol, M.D.Visser, S.E.Salcudean and A.G.Nagy, "Assessing potential benefits of enhanced dexterity in laparoscopic surgery," Proc. IEEE/EMBS, Oct.1997, pp.1966-1969.

[11] Se Jin Park, Soo Chan Park, Jin Ho Kim, Chae-Bogk Kim, "Biomechanical parameters on body segments of Korea adults," International Journal of Industrial Ergonomics, Vol.23, pp.23-31, 1999,

A Novel Compact Genetic Algorithm using Offspring Survival Evolutionary Strategy

Joon-Hong Seok, Tae-Yong Choi and Ju-Jang Lee

Department of Electrical Engineering and Computer Science
Korea Advanced Institute of Science and Technology (KAIST)
Tel: 82-42-350-8032; Fax: 82-42-350-5432
Email: seokjh@kaist.ac.kr

***Abstract*:** This paper describes a compact genetic algorithm (cGA) with the offspring survival evolutionary strategy. The cGA is required less memory and can be easily implemented because of no genetic operators tuning. However, the cGA requires a large amount of fitness evaluation to provide acceptable solutions in the problems involving higher-order building blocks (BBs). So as to reduce the number of fitness evaluation, a higher selection pressure is applied to the cGA. Generally, the elitism is used to increase a higher selection pressure. The elitism-based cGA shows the less number of the fitness evaluation to provide solutions. However, the elitism may lead to premature convergence as the order of BBs becomes higher. In this paper, using offspring survival evolutionary strategy, we propose the cGA which is balanced between the selection pressure and genetic diversity. The usefulness of the proposed cGA is verified by comparing with the original cGA and the elitism-based cGAs using well known benchmark functions.

Keywords: Compact genetic algorithms, Offspring survival evolutionary strategy.

I. INTRODUCTION

The compact genetic algorithm (cGA) is a part of estimation of distribution algorithms (EDA) that generate offspring chromosomes using the estimated probabilistic model [1]. The cGA is useful in memory-constrained problem because the cGA memorizes just the probability vector, not overall population. The cGA mimics the order-one behavior of a simple genetic algorithm (sGA) using a constrained memory.[1]

The original cGA can provide reasonable optimum values in the case of easy problems involving the low order building blocks (BBs). However the original cGA requires a large amount of fitness evaluation to provide acceptable solutions in the problems involving higher-order building blocks (BBs), because the dependency between the variables isn't considered at all in the original cGA [2]. Since the real-world problems are almost the problems involving the higher order BBs, there have been many attempts in order to improve the performance of the original cGA.

The representative way is the use of elitism to increase a selection pressure [2]. If a selection pressure increases, then the convergence speed of the probability vector increases. As a result of the convergence speed increment, The elitism-based cGA shows the less number of the fitness evaluation to provide solutions. However, the elitism may lead to premature convergence [3]. If elite chromosome is near the local optimum, the elitism-based cGAs provide the low quality of solutions.

In this paper, we propose the new cGA with offspring survival evolutionary strategy (os-ES). The offspring survival evolutionary strategy maintains a balance between a selection pressure and a genetic diversity. The high selection pressure lead the fast speed of convergence, and then it leads to fewer number of fitness evaluation. On the other hand, the genetic diversity leads a lot of random search on the solution space, thus it supports to increase the possibility to find the global optimum.

Section II briefly describes the original cGA and the elitism-based cGAs. Section III introduces the proposed cGA using os-ES. Section IV shows the simulation results on well-known benchmark functions. Section V presents the summary of the results.

Step 1.	Initialize probability vector
	For *i*:=0 to *l* do
	p[*i*]=0.5;

Step 2.	Generate two chromosomes from the probability vector.
	achrom := generate(*p*);
	bchrom := generate(*p*);

Step 3.	Let them evaluate and compete. *Winner*, *loser* : compete(*achrom*,*bchrom*);
Step 4.	Update the probability vector For i:=1 to *l* do /* *n* : population size*/ If winner[*i*]==1 then *p*[*i*] := *p*[*i*]+1/*n*; Else *p*[*i*] := *p*[*i*]-1/*n*;
Step 5.	Check if the probability vector has converged Go to **Step2**, if it is not satisfied
Step 6.	The probability vector represents the final solution

Fig. 1. Pseudo-code of the original cGA.

II. THE COMPACT GENETIC ALGORITHMS (cGA)

1. **The original cGA**

The cGA represents the population using a probability vector as a probability distribution. Fig. 1 describes a pseudo-code of the original cGA, where *l* is the number of bits of a chromosome [2].

First of all, every bits of the probability vector, *p*[i], are initialized by 0.5. Two chromosomes are generated by probability vector *p*. The *p*[*i*] denotes the probability of *i*th bit of a chromosome is 1. Each bit of a chromosome is randomly chosen according to probability value in the vector. Two chromosomes are competed each other. Winner and loser are determined according to fitness evaluation. After winner and loser are selected, the result of competition should be updated for getting a better selection. Each bit of winner is compared with each bit of loser, only if that of winner is different from that of loser, then update that bit of the probability vector. The terminal condition of original cGA is that all bits of the probability vector converge into 0 or 1. There is no possibility to change all bits although more iterations. If the terminal condition is not satisfied, then go back to the **Step 2**.

In the original cGA, two chromosomes are generated by probability vector, so fitness evaluation is needed twice in each generation while the probability vector is only updated once each generation. As a result of generation two chromosome in each generation, the total number of the fitness evaluation is increased. If a lot of chromosomes are generated, then the genetic diversity is incremented and the probability to find the global optimum is also increased. However, if the improvement of the performance is not proportionate with the additional time or cost, we consider the way to reduce the number of fitness evaluation in each generation, then we can save the evaluation time or cost to get solutions.

2. The elitism-based cGAs

There are two elitism-based cGAs : non-persistent elitism-based cGA (ne-cGA) and persistent elitism-based cGA (pe-cGA). The pe-cGA uses strong elitism scheme whereas the ne-cGA maintains a genetic diversity using the length of inheritance. The ne-cGA generally shows the better performance than the pe-cGA, but it needs one more parameter, the length of inheritance. The pseudo-codes of these cGAs are in [2].

Commonly the elitism is allowed to copy the best chromosome into the next generation. It provides a way to increase a selection pressure. If a selection pressure is increased, then the survival probability of the better chromosomes gets higher. Consequently the better chromosome so far survives longer than the original cGA. Because the elite chromosome may lead the probability vector to converge with its gene information, the convergence speed is very fast. Thus compared with the original cGA, the elitism-based cGAs make the number of fitness evaluation decreased [2].

However, these elitism-based cGAs have a critical weakness, because elitism may lead to premature convergence due to the higher selection pressure [4]. The selection of pressure of cGA should be proportional to the order of BBs [2]. However, in the multimodal function case, the number of local optimum also increases exponentially with the dimensionality of the problem [4]. In other words, elitism in the cGA has too high selection pressure. Too high selection pressure leads to stall near the local optimums easily.

III. COMPACT GENETIC ALGORITHM USING OFFSPRING SURVIVAL EVOLUTIONARY STRATEGY

This section describes the offspring survival compact GA (os-cGA) using the offspring survival evolution strategy (os-ES).

The os-ES is similar with a (1, λ) evolutionary strategy (ES), where λ equals 1. However, the os-ES is strictly differ from (1,1)-ES. In fact, (1,1)-ES cannot be "evolutionary strategy". If λ equals 1, an offspring always becomes a parent without any competition and we can't update information for evolution to get a better offspring. On the other hand, the os-ES is composed of a parent, an offspring and a memory for writing results of the competition between a parent and an offspring. If a parent and an offspring are competed each other, then winner and loser are determined from fitness values. Winner leaves the information in the memory for evolution to make better chromosomes. After the information update, a parent always dies and an offspring becomes a new parent. New offspring is generated by both a new parent and the information of the memory or only the information of the memory. In the os-cGA, the offspring is only generated by the information of memory. In next generation, new parent and new offspring are competed each other, winner leaves the information again. In the cGA, there is a memory called a probability vector to determine how to generate an offspring. Therefore, we can apply the os-ES to the cGA.

There is main objective to apply the os-ES to the cGA : the balance between the convergence speed using less number of the fitness evaluation and genetic diversity for guarantee to find global optimum. A pseudo-code of the proposed cGA is shown in Fig. 2.

In the initial generation, a parent and an offspring chromosome are generated by initial probability value 0.5. Parent and offspring are competed each other. Winner and loser are determined from the competition result. Probability vector update is done by winner's gene information. In second generation, current parent is eliminated and offspring becomes parent. And then just offspring chromosome is generated by probability vector. Winner and loser are determined by the result of competition and repeat until all the probability vector converges to 0 or 1.

Main difference from the original cGA, elitism-based cGA and os-cGA are following: both winner and loser

```
          /* Other steps is same as the original cGA*/
Step 2.   Generate one chromosome from
          the probability vector. Offspring becomes parent.
            If the first generation then
              pchrom := generate(p);
            else then
              pchrom := ochrom;
            ochrom:=generate(p);

          /*Augmented scheme*/
          If one bit of probability vector only doesn't
          converge, an offspring is generated by the other
          part of a parent. Update the remaining bit of the
          probability vector according to the competition
          between two.

          /*Purification*/
          If a parent and an offspring have a same fitness
          value, then
              θ++;
              If  θ>= 0.05*n, then
                  /* with initial probability vector 0.5*/
                  ochrom := regenerate(p);
                  θ=0;
          else
Step 3.       θ=0;
          Let them evaluate and compete.
          Winner, loser : compete(pchrom,ochrom);
```

Fig. 2. Pseudo-code of the proposed os- cGA.

are eliminated in the original cGA, only loser is eliminated in elitism-based cGA and only parent regardless of winner or loser is eliminated in os-cGA. In the os-cGA, each chromosome at least competes twice with different chromosomes during two generations. As an offspring, a chromosome leaves the information through the competition with its parent, and then as a parent, a chromosome leaves the information through the competition with new offspring generated by a probability vector, resulting in bigger selection pressure than the original cGA. Therefore, the number of fitness evaluation can be reduced than the original cGA. Moreover, compared with the elitism-based cGAs, the os-cGA memorizes only an offspring regardless of winner or loser. Thus, the genetic diversity is wider than the elitism-based cGA and the quality of solutions are higher than the elitism-based cGA.

When a parent and an offspring are identical chromosomes, there is no probability vector update, and when a parent and an offspring have same fitness value but different chromosome, a parent always picked up as a winner. In the os-cGA, an offspring always becomes a parent at next generation, so the probability vector is stalled by two probability values. This problem is called as probability vector stall problem. We should apply two modifications to avoid probability vector stall problem. One is augmented scheme [5]. When one bit of the probability vector is not converged, the augmented scheme checks two cases and then converge that bit to 0 or 1. The other is the purification in Fig.2. Picking up an offspring as the random chromosome in the solution space, the purification scheme solves the stall problem.

TABLE I
Test function

$f_1(x) = \sum_{i=1}^{D} x_i^2$
$f_2(x) = \sum_{i=1}^{D} \lvert x_i \rvert + \prod_{i=1}^{D} \lvert x_i \rvert$
$f_3(x) = \max_i \{\lvert x_i \rvert, 1 \le i \le D\}$
$f_4(x) = \sum_{i=1}^{D} x_i \sin(\sqrt{\lvert x_i \rvert})$
$f_5(x) = (\sum_{i=1}^{D} x_i^2)^{1/4} [\sin^2(50(\sum_{i=1}^{D} x_i^2)^{1/10}) + 1.0]$
$f_6(x) = \sin^2(\sqrt{\sum_{i=1}^{D} x_i^2}) / (1.0 + 0.001(\sum_{i=1}^{D} x_i^2))$

IV. NUMERICAL EXPERIMENTS

In this section, we show the effect of this proposed os-cGA using some well-known 6 benchmark functions [4]. It is compared with the original cGA, pe-cGA, and ne-cGA. Test functions are given in Table I. D denotes the dimensionality of the test functions and equals 10. Functions f1~f3 are unimodal continuous functions, and functions f4~f6 are multimodal functions. The brief descriptions of all the test functions can be offered from the original references [2] [4] . The fitness values and the number of function evaluations are obtained by 100 independent runs. The input value range of f1~f4 is -5.12~5.11 and that of f5~f6 is -20.48~20.47. The population size is fixed by 200 that the other cGA also show the reasonable performance. Based on the literature [2], the length of inheritance η is defined as $0.1n$ where n is the population size. Figure 4 shows the average best fitness curves of the test functions.

The figure of merit is considered as the intersection area below the elitism-based cGA and the original cGA and above the os-cGA. From Fig. 3(a), (b), (d), (e) shows the good performance of the proposed os-cGA because of the large figure of merit. The ne-cGA and pe-cGA show the fast converge speed, but they are easily in the local scope. While the original cGA shows usually better performance than the proposed os-cGA at last, it is necessary to evaluate fitness functions so many times. The os-cGA shows that converge speed is as fast as elitism-based cGA and the performance of finding the global optimum is as exact as the original cGA in the many cases. The figure of merit of os-cGA may be reduced, because these problems are well suitable for the elitism-based cGA from Fig. 3(c) and (f) [2]. However, in the most case, the os-cGA shows the good performance.

The result shows the os-cGA makes a balance between the selection pressure and the genetic diversity. The os-cGA shows higher selection pressure than the original cGA and higher genetic diversity than the elitism-based cGAs. As previously mentioned, by memorizing an offspring chromosome and by competing twice, the os-cGA has a higher selection pressure than the original cGA. Moreover, by memorizing an offspring chromosome regardless of winner or loser, the os-cGA has a higher genetic diversity than the elitism-based cGA.

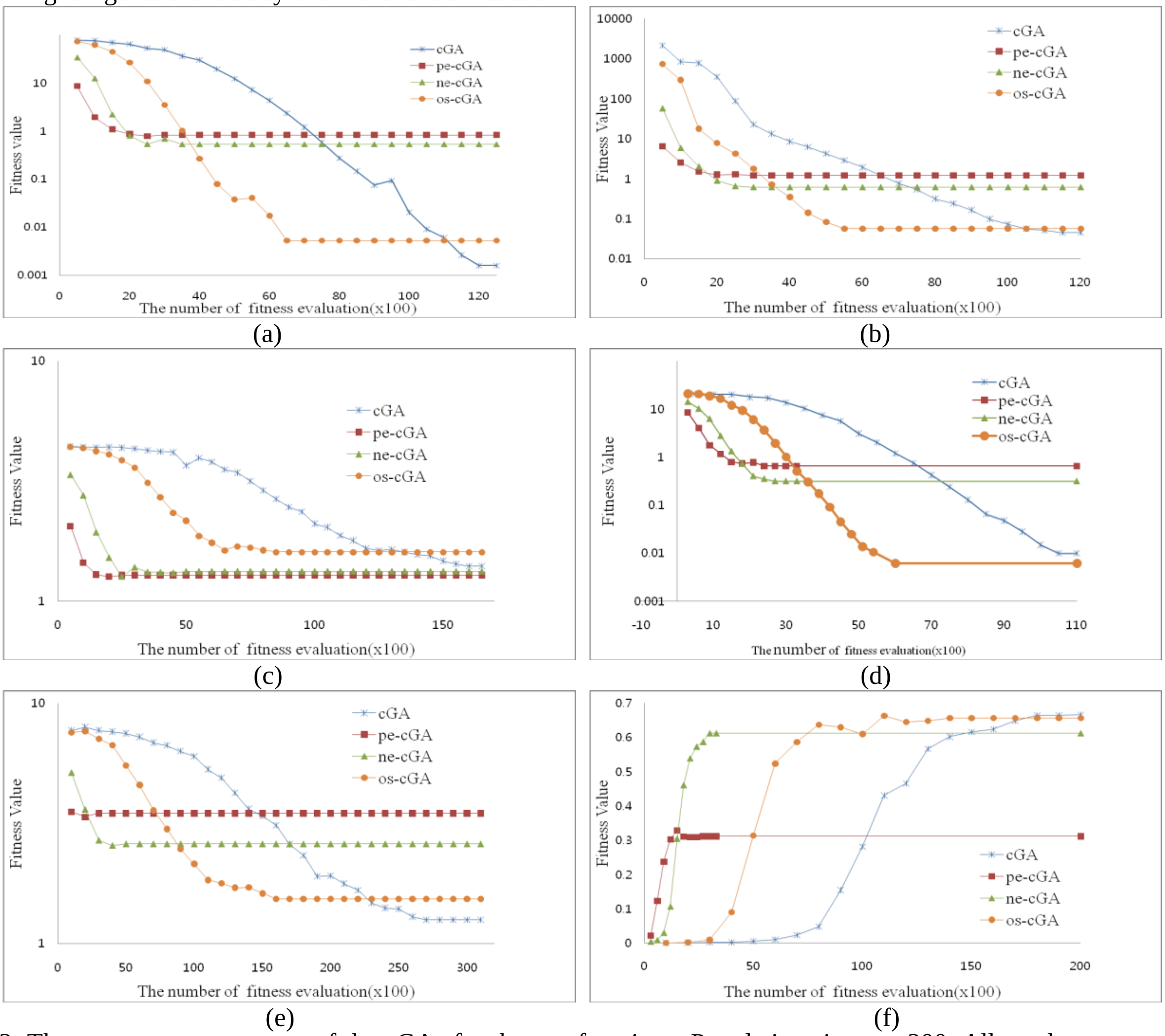

Fig. 3. The convergence property of the cGAs for the test functions. Population size n = 200. All results are averaged over 100 runs. For the ne-cGA, $\eta = 0.1n$. (a) For the test function f_1. (b) For the test function f_2. (c) For the test function f_3. (d) For the test function f_4. (e) For the test function f_5. (f) For the test function f_6.

V. CONCLUSION

In this paper, we showed the novel cGA using the offspring survival evolution strategy. The conventional cGAs have a difficulty to find the global optimum in the case of higher order problem with restricted time or cost. Simulation studies showed that the performance of the proposed os-cGA using os-ES was better than the other cGAs in terms of both quality of solutions and the convergence speed in the problems involving the high order BBs. The os-ES provided a balance between a selection pressure and genetic diversity through offspring survival, thus it was good evolutionary strategy to apply to the cGAs.

We will apply the proposed scheme to real world optimization problems and other type of cGAs as a future work.

References

[1] G. Harik, F. G. Lobo, and D. E. Goldberg. "The Compact Genetic Algorithm." *IEEE. Trans. Evol. Comput. vol.3*, pp. 287-297, Nov. 1999.

[2] C. W Ahn and R. S. Ramakrishna. "Elitism-Based Compact Genetic Algorithms." *IEEE Trans. Evol. Comput., vol. 7, no.4*, pp. 367-385 , Aug. 2003.

[3] G. Rudolph, "Self-adaptive mutations may lead to premature convergence," *IEEE Trans. Evol. Comput.*, vol.5, pp. 410-414, Aug. 2001.

[4] J. Y Lee, S. M Im and J.J Lee, "Bayesian Network-based Non-parametric Compact Genetic Algorithm", *IEEE International Conference on Industrial Informatics*, pp. 359-364, Jul. 2008.

[5] C. W Ahn and R. S. Ramakrishna, "Augmented Compact Genetic Algorithm", Lecture Notes in Computer Science, 2004 – Springer, pp. 560-565, 2004

The Fourteenth International Symposium on Artificial Life and Robotics 2009(AROB 14th '09),
B-Con Plaza, Beppu, Oita, Japan, Feb. 5- Feb.7, 2009

Neural Network Based Smith Predictor Design for a Time Delay of a Tele-operated Control System

H. J. Choi and S. Jung

Intelligent Systems and Emotional Engineering Lab., Department of Mechatronics Engineering, Chungnam National University, Daejeon, Korea 305-7864
(Tel : 82-42-821-6876; Fax : 82-42-823-4919)
(Email address:jungs@cnu.ac.kr)

Abstract: The paper presents a methodology of compensating for time-delayed effects in tele-operated control systems. Compensation can be done by neural network. The tele-operated system consists of a master robot to give commands and a slave robot to work with environment. The positional command by the master robot is transferred to the slave robot, and contact force from the environment back to the master. The structure of the Smith predictor is modified by replacing with neural network. Neural network identifies the slave model to deal with non-linearities in the system. Simulation studies have been conducted.

Keywords: Time-delayed system, Smith predictor, neural network

I. INTRODUCTION

Tele-operation control has become an important technique in robotics research. Recent robotics research focuses more on the development of unmanned systems, but robots are controlled remotely in the space. Most of tele-operated control systems are required to operate under the environment where is harmful to humans, difficult to access, and unexpected environment.

Specially, in the tele-operated robotic systems, haptic is an important terminology to be concerned. The suitable haptic operation requires that the operator feels the same force that the slave feels from the environment. The most popular application of the haptic is the tele-operated surgery. Force feedback from the slave robot has to be delivered to the master robot in a real-time fashion. For stable operation, a time-delay problem has to be solved.

It is well known that there exist time-delays in communication channels when implementing a tele-operated control system. The effect of the time-delay is critical that the tracking performance of the system is poor, even the system becomes unstable if the delay time is severe. Many researches to solve time-delay problems have been presented[1-4].

In linear systems, the time-delay effect has been solved by introducing the Smith predictor that eliminates time-delay terms in the system to make the system stable under the condition that the exact plant model and delayed time are known *a priori*.

However, in nonlinear systems, plant models cannot be exactly modeled and the even delayed time is varying so that control performance by the linear Smith predictor may be degraded. The time varying time-delay has been considered. Nonlinear uncertainties have been estimated by designing disturbance observers.

In this paper, for the nonlinear system, the nonlinear Smith predictor is designed using neural network. The neural network indentifies the slave model, and passes parameters to the master side through communication channels. Simulation results show that the neural network based Smith predictor performs better than that of the linear Smith predictor.

II. SMITH PREDICTOR

The Smith predictor has been known for a cure for the time-delayed systems. The predictor requires the slave plant model and the delayed time to cancel out the delay terms in the characteristic equation. Fig. 1 shows the control block diagram of the linear plant with a time-delay.

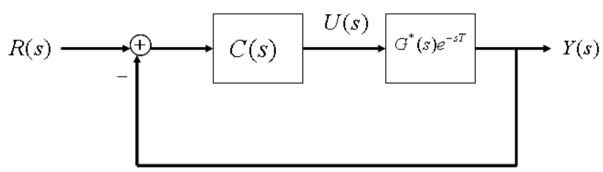

Fig. 1. Time-delayed control system

The closed loop transfer function is

$$T(s) = \frac{G^*(s)C(s)e^{-sT}}{1+G^*(s)C(s)e^{-sT}} \tag{1}$$

©ISAROB 2009

where $G^*(s)$ is a nominal plant and T is a delay time. Thus the system becomes easily unstable.

Fig. 2 shows the structure of the Smith predictor. The time delay is fed back to the controller input. Fig. 3 shows another structure of the Smith predictor that gives the same transfer function.

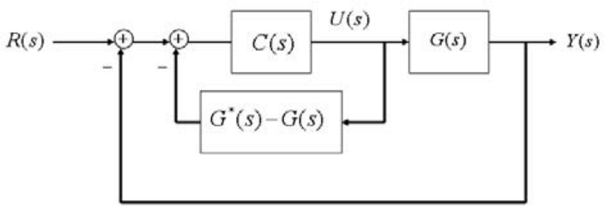

Fig. 2. Smith predictor structure I

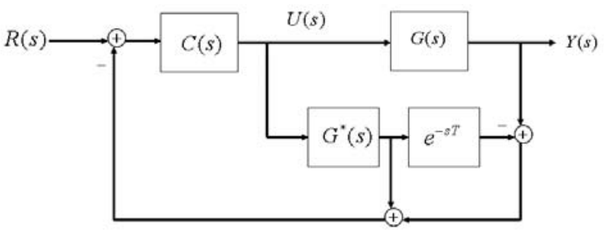

Fig. 3. Smith predictor structure II

The closed loop transfer function for Fig. 2 and 3 is given as

$$T(s) = \frac{G(s)C(s)}{1 + G^*(s)C(s)} \tag{2}$$

where the plant has the delay term, $G(s) = G^*(s)e^{-sT}$. The delay term is eliminated and does not appear in the characteristic equation of (2). Thus, a time-delay effect is minimized.

III. TELEOPERATED CONTROL SYSTEM

One sided tele-operation control system has no feedback from the slave, which is a one port system. There is one time delay from the master to the slave. The master robot sends the position command to the slave robot to follow.

In a two port system, bilateral transmission is required. There is a force feedback from the slave robot so that the operator can feel the force as he/she operates the slave robot directly. There are two time delays, one from the master to the slave and the other from vice versa.

Fig. 4 shows the simple two port tele-operated control system.

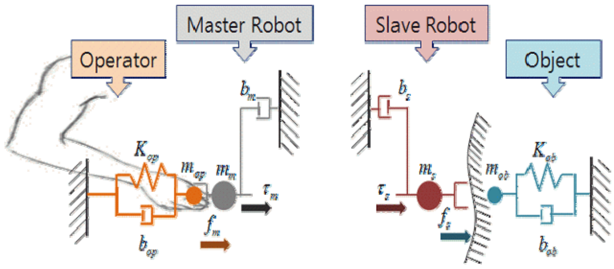

Fig. 4. Tele-operation control

The dynamics of the simple one degrees-of freedom system is given as

$$m_m \ddot{x}_m + b_m \dot{x}_m = f_m + u_m \tag{3}$$

$$m_s \ddot{x}_s + b_s \dot{x}_s = f_s - u_s \tag{4}$$

where m_m, b_m are mass and damping of the master robot, m_s, b_s are mass and damping of the slave robot, and u_m, u_s are nonlinear terms that cannot be modeled. The control block diagram can be described as Fig. 5. The desired force F_h by the operator is an input command to the master robot.

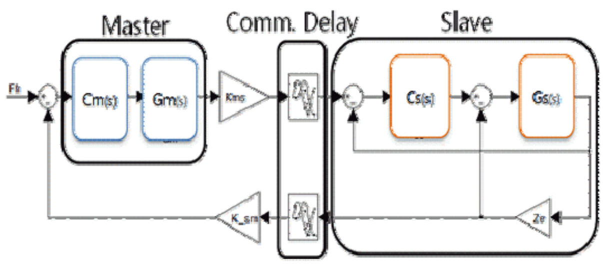

Fig. 5. Tele-operation control block diagram

The transfer function of the slave robot is

$$\frac{X_s(s)}{X_m(s)} = \frac{G_s(s)C_s(s)Z_e}{1 + G_s(s)Z_e + G_s(s)C_s(s)} e^{-sT_f} \tag{5}$$

where T_f is the time delay from the master to the slave and Z_e is the impedance of the environment . Let us denote the slave transfer function as

$$\hat{G}_s(s) = \frac{G_s(s)C_s(s)Z_e}{1 + G_s(s)Z_e + G_s(s)C_s(s)} \tag{6}$$

Then the transfer function from the master to the slave can be described as

$$\frac{F_e(s)}{F_h(s)} = \frac{G(s)C_m(s)e^{-sT_f}}{1+G(s)C_m(s)e^{-s(T_f+T_b)}} \tag{7}$$

where $F_e(s)$ is the force feedback from the slave and T_b is the time delay from the master to the slave and $G(s) = G_m(s)\hat{G}_s(s)$.

Thus, the equivalent block diagram of the Fig. 5 is shown in Fig. 6.

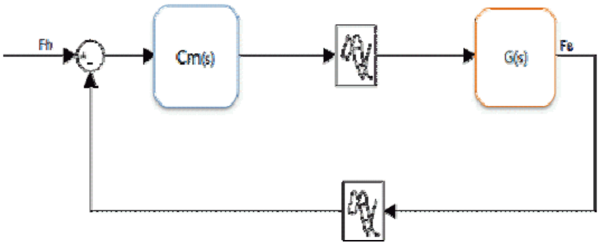

Fig. 6. Equivalent block diagram of Fig. 6

IV. SMITH PREDICTOR WITH NEURAL COMPENSATION

1. Neural network based Smith predictor

Now, we apply the Smith predictor to Fig. 6. However, as in Fig. 2 and 3, the model cannot be known exactly if the plant is nonlinear. To model a nonlinear plant, a nonlinear estimator is preferred. Neural network has been used as a powerful nonlinear estimator. Fig. 7 shows the neural network based Smith predictor. Two neural networks are used, one for estimating a slave model and the other for copying the estimator.

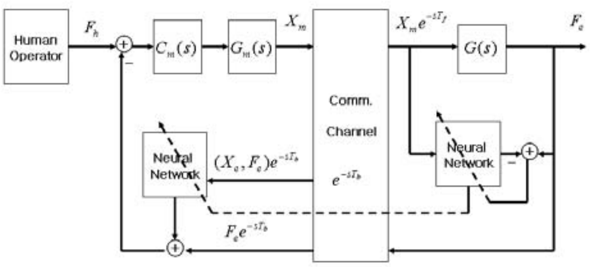

Fig. 7. Neural compensation for the Smith predictor

2. Learning

The radial basis function network is used for the neural network. The back-propagation learning algorithm is used for updating parameters. Fig. 8 shows the learning structure.

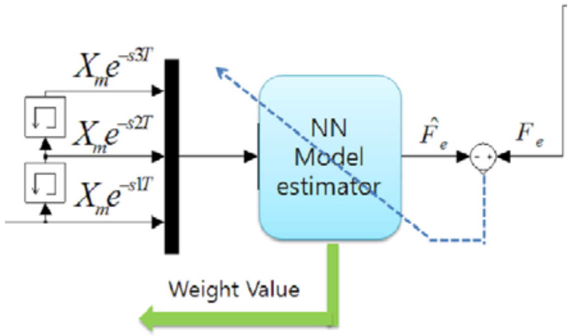

Fig. 8. Neural estimator learning

The structure of the radial basis function network is shown in Fig. 9.

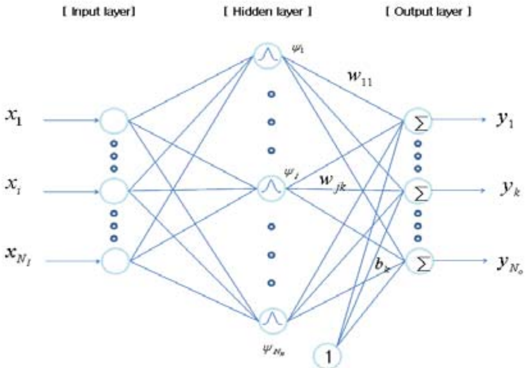

Fig. 9. RBF neural network structure

The nonlinear function $\psi_j(X_{IN})$ is given by

$$\psi_j(X_{IN}) = \exp\left(-\frac{\| X_{IN} - \mu_j \|^2}{\sigma_j^2}\right), \tag{8}$$

where X_{IN} is the input vector, μ_j is the center value, and σ_j is the width of the jth neuron in the hidden layer.

$$y_k = \sum_{j=1}^{N_H} \psi_j w_{jk} + b_k, \tag{9}$$

V. SIMULATION RESULTS

The first simulation study is to test the response when the Hunt-Crossley impedance model is used as an input command.

$$F_h = kx^n + \lambda x^n \dot{x} \tag{10}$$

where k, λ, n are 110, 40, and 1.2, respectively. Fig. 10 shows the responses of different time delays. We see that tracking performances by the neural network based Smith predictor are better than those of the linear Smith predictor. As the delay time is getting larger, the

©ISAROB 2009

deviation error of the linear Smith predictor also becomes larger as shown in Fig. 10 (b).

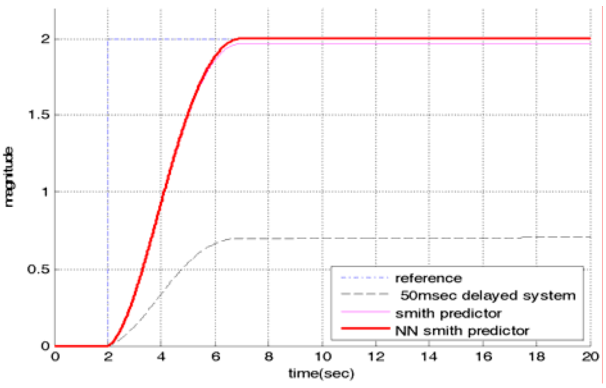

(a) 50ms time delay

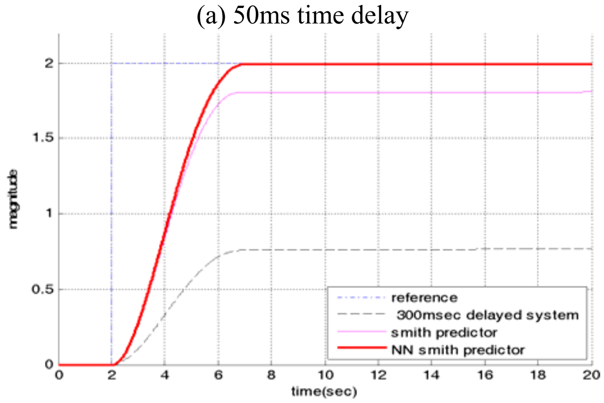

(b) 300ms time delay

Fig. 10. The response to Hunt-Crossley model

The other simulation test is when the force step command is given to the master robot. The force step responses are obtained with different time-delays, 100ms and 300ms. We see from Fig. 11 that performances of both Smith predictors are getting worse as the delay time is longer. Comparing performance between two predictors, the performance of the neural network based Smith predictor is better than that of the linear predictor.

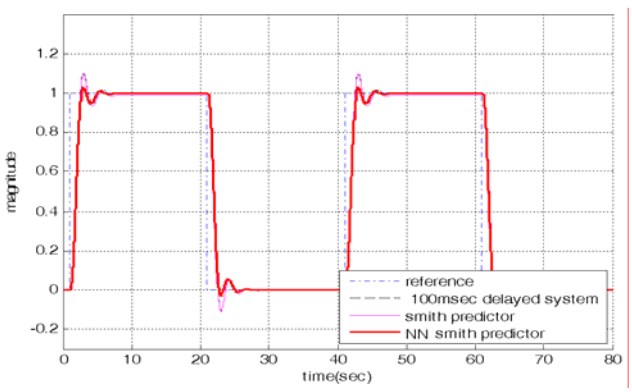

(a) 100ms time delay

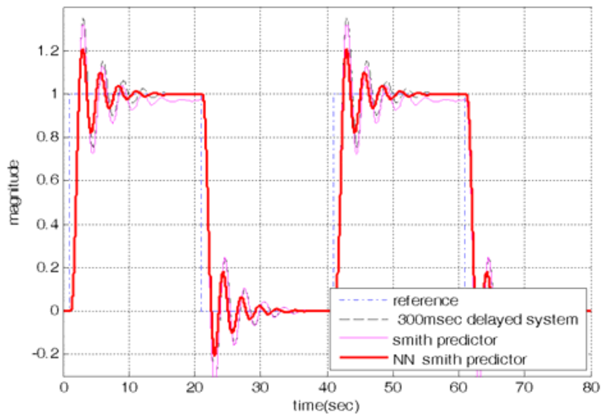

(b) 300ms time delay

Fig. 11. The force step response

VI. CONCLUSION

Neural network is used as a nonlinear estimator to identify the slave plant model by forming the Smith predictor structure to deal with time-delays in tele-operated system. Simulation results show that performances of the neural network based Smith predictor is better than that of the linear predictor because the modeling error due to the nonlinearity degrades the performance. Future research is to confirm the neural network based predictor by conducting experiments.

ACKNOWLEDGEMENT

This research has been financially supported by the Samsung Tales Company. The authors thank you for their kin support

REFERENCES

[1] Y. Yokokohji, T. Imaida, and T. Yoshikawa, "Bilateral control with energy balance monitoring under time-varying communication delay", IEEE Conf. on Robotics and Automations, pp. 2684-2689, 2000

[2] W. H. Zhu and S. E. Sacudean, "Stability guaranteed teleoperation: an adaptive motion/force control approach", IEEE Trans. on Automatic Control, vol. 45, no.11, pp. 1951-1969, 2000

[3] H. Arioui, S. Mammar, and T. Hamel, "A Smith-prediction based haptic feedback controller for time delayed virtual environments systems", American control conference, pp. 4303-4308, 2002

[4] O. M. Palafox, D.J.Lee and M.W.Spong, I. Lopez,and C. T. Abdallah, "Bilateral teleoperation of mobile robot over delayed communication network: implementation", IEEE IROS, pp.4193-4198, 2006

Artificial Realization of an Adaptive Expert Knowledge Database for Automatic Sleep Stage Determination in Clinical Practice

Bei Wang[1, 4], Takenao Sugi[2], Fusae Kawana[3], Xingyu Wang[1] and Masatoshi Nakamura[4]

[1]*Department of Automation, East China University of Science and Technology, Shanghai 200237, China*
(Tel: +86-2164253581; wangbeish@gmail.com)
[2]*Department of Electrical and Electronic Engineering, Saga University, Saga 840-8502, Japan*
(Tel: +81-952-288643; sugi@cntl.ee.saga-u.ac.jp)
[3]*Department of Clinical Physiology, Toranomon Hospital, Tokyo 105-8470, Japan*
(Tel: +81-3-3588-1111; kawana@toranomon.gr.jp)
[4]*Department of Advanced Systems Control Engineering, Saga University, Saga 840-8502, Japan*
(Tel: +81-952-288644; nakamura@cntl.ee.saga-u.ac.jp)

***Abstract*:** Artificial realization of an adaptive expert knowledge database for the sleep data from clinics was investigated. The ultimate purpose is to develop automatic sleep stage determination technique for variable cases of sleep data in hospitals. The automatic sleep stage determination algorithm is designed by using probabilistic method based on conditional probability. In order to make algorithm flexible for variable sleep data, an adaptive expert knowledge database is constructed based on a set of fundamental and optional parameters. The parameters, which can improve the accuracy of sleep stage recognition for the training data, are selected. The adaptive expert knowledge database is consisting of the probability density functions of fundamental parameters and selected optional parameters. The overnight sleep data of 4 subjects from Toranomon hospital, Tokyo, Japan were utilized for analysis. The automatic sleep stage determination results were compared with the visual inspection by clinician. Finally, satisfied results of close agreement with the visual inspection were obtained. The developed automatic sleep stage determination by adaptive expert knowledge database can be an effective tool for clinical practice.

Keywords: Adaptive expert knowledge database, Parameter selection, Conditional probability, Automatic sleep stage determination

I. INTRODUCTION

Sleep can be described by awake stage, rapid eye movement stage (REM) and non rapid eye movement (NREM) stage of I, II, III and IV. The sleep data recorded from real clinics is complex and variable. The staging criteria containing typical waveforms for healthy persons are insufficient to deal with the various cases of sleep data in hospitals and institutions [1], [2]. The conventional rule-based automatic sleep stage determination methods, which have been designed according to the staging criteria, have the similar limitation for clinical practice [3], [4]. An expert knowledge-based method was developed in our previous study which can overcome the limitations of rule-based methods [5]. The expert knowledge is the visual inspection by qualified clinician, which considers the actual surrounding circumstances in hospitals. The expert knowledge database includes probability density functions of parameters for various sleep stages. However, the probability density function of defined parameters may not be efficient enough for the variable sleep data in real clinics. Therefore, an adaptive expert knowledge database is necessary to be developed.

In this study, we are investigating on the artificial realization of adaptive expert knowledge database. The ultimate purpose is to develop an effective automatic sleep stage determination technique for clinical practice. In order to make an adaptive expert knowledge database, an automatic parameter selection algorithm is developed. A set of fundamental parameters and optional parameters are defined. The optional parameters, which can improve the accuracy of sleep stage recognition for training data, are selected. The adaptive expert knowledge database is consisting of the probability density functions of the selected parameters together with the fundamental parameters. The sleep stage is determined based on the conditional probability.

II. METHODS

1. Subjects and data acquisition

All the sleep data were recorded at the department of Clinical Physiology, Toranomon Hospital in Tokyo,

©ISAROB 2009

Japan. Totally four subjects were participated, having an average age of 50 years old. They were suffered by breathing disorders during sleep (Sleep Apnea Syndrome). Their overnight sleeping data were recorded after the treatment of Continuous Positive Airway Pressure (CPAP) based on the polysomnographic (PSG) measurement. The PSG measurement at Toranomon Hospital includes four EEG recordings, two EOG recordings and one EMG recording. EEGs were recorded on central lobes and occipital lobes with reference to opposite earlobe electrode (C3/A2, C4/A1, O1/A2 and O2/A1) according to the International 10-20 system. EOGs were derived on Right Outer Canthus and Left Outer Canthus with reference to earlobe electrode A1 (LOC/A1 and ROC/A1). EMG was obtained from muscle areas on and beneath chin which was termed as chin-EMG. Initially, EEGs and EOGs were recorded under a sampling rate of 100 Hz. Chin-EMG was recorded under a sampling rate of 200Hz.

2. Probabilistic method by conditional probability

Sleep stage scoring was considered as a multi-valued decision making problem in the field of clinics. The automatic sleep stage determination algorithm was designed by probabilistic method based on conditional probability.

Sleep data were divided into 30-second epochs and each epoch was subdivided into 5-second segments for sleep stage determination. The automatic sleep stage determination is carried out based on conditional probability as,

$$P_{k|k}(\zeta^i) = \frac{f(y_k \mid \zeta^i) P_{k|k-1}(\zeta^i)}{\sum_{j=1}^{n} f(y_k \mid \zeta^j) P_{k|k-1}(\zeta_j)}, \qquad (1)$$

where $f(y_k|\zeta^i)$ is the probability density function of parameters y_k for sleep stage ζ^i and $P_{k|k-1}\ (\zeta^i)$ is the predicted probability of previous segment. The conditional probability indicates the possibility of the occurrence of sleep stage ζ^i for current segment k. The sleep stage which has the maximum value of conditional probabilities was decided as the result for current segment k.

The predicted probability of first segment for various sleep stages shared the probability equally with a value of $1/n$, where n is the number of the types of sleep stages. The calculation algorithm was repeated by conditional probability and predicted probability among the consecutive segments. The sleep stage for an epoch is determined by choosing the stage which takes up the major portion among the consisting segments within one epoch.

3. Adaptive expert knowledge database

In order to realize the automatic sleep stage determination algorithm, probability density functions of parameters were required. The adaptive expert knowledge database construction was a learning process to obtain the probability density function of parameters for various sleep stages.

A.Visual inspection

A qualified clinician made visual inspection of sleep stage scoring on the training data. The overnight sleep recording was divided into consecutive 30-scond epochs. The clinician made visual inspection through an epoch-by-epoch approach. Totally, seven types of sleep stages were visually inspected, including awake with eyes closed, awake with eyes opened, REM sleep and non-REM sleep of stage I, II, III and IV. Stage awake was classified into open eyes state and close eyes state according to the alpha activity (8-13Hz) on EEGs of O1/A2 and O2/A1 channels and the existence of eye movements on EOGs. Stage I and II were identified as light sleep. Deep sleep of stage III and IV were scored based on a relatively different presence of slow wave activity within an epoch.

B.Probability density function

The epochs were classified into sleep stage groups according to the visual inspection. Each epoch was assigned to a single sleep stage based on the visual inspection of clinician and described by a set of parameters values. For each sleep stage, the values of parameters are counted to make the histograms.

The probability density function is approximately evaluated using histograms with Cauchy distribution as

$$f(y \mid \zeta) = \frac{b}{\pi((y-a)^2 + b^2)}, \qquad (2)$$

where a is the location parameter and b is the scale parameter. The values of a and b are determined by applying least square method on the histograms.

In addition, a transitional probability matrix of sleep stage change was calculated. The transitional probability between sleep stages designated the probabilities of sleep stage transition between two conjoint segments.

C.Parameter selection

Since the sleep data may be variable from hospitals and institutions, a set of fundamental parameters and optional parameters were extracted from the periodogram of sleep EEGs, EOGs and EMG.

According to the sampling rate, the periodogram was derived by taking 512-point FFT (Fast Fourier Transform) for EEGs and EOGs, whereas 1024-point FFT for EMG. The parameters were defined by certain frequency bands of ratio, amplitude and amount. The equations of parameters were given in Table 1. The parameter type of "F" indicates fundamental parameters and "O" indicates optional parameters. The corresponding frequency bands were listed in the notation under Table 1.

The automatic sleep stage determination algorithm was firstly applied on the fundamental parameters. The accuracy was evaluated comparing with the visual inspection by clinician as,

$$ACC_f = \frac{n_f}{N}, \tag{3}$$

where n_f is the number of epochs which have the consistent determination result with visual inspection and N is the total number of epochs.

When one of the optional parameters brought best determination accuracy together with the fundamental parameters, this parameter would be selected. The selected parameter was added into the fundamental parameter set for next selection. The selection process was repeated until there was no parameter can improve the accuracy comparing with the current fundamental parameter set. The adaptive expert knowledge database was constructed to include the probability density functions of those parameters.

Table 1. Parameter description

	Parameter	Type
Ratio (%)	$R_{s1} = max\left\{\frac{S_{s1}(C3)}{S_T(C3)} \times 100\%, \frac{S_{s1}(C4)}{S_T(C4)} \times 100\%\right\}$	F
	$R_{s2} = max\left\{\frac{S_{s2}(C3)}{S_T(C3)} \times 100\%, \frac{S_{s2}(C4)}{S_T(C4)} \times 100\%\right\}$	O
	$R_{s3} = max\left\{\frac{S_{s3}(O1)}{S_T(O1)} \times 100\%, \frac{S_{s3}(O2)}{S_T(O2)} \times 100\%\right\}$	F
	$R_{s4} = max\left\{\frac{S_{s4}(C3)}{S_T(C3)} \times 100\%, \frac{S_{s4}(C4)}{S_T(C4)} \times 100\%\right\}$	O
	$R_{s5} = max\left\{\frac{S_{s5}(C3)}{S_T(C3)} \times 100\%, \frac{S_{s5}(C4)}{S_T(C4)} \times 100\%\right\}$	O
Amplitude (μV)	$A_{s1} = max\left\{6 \times \sqrt{S_h(C3)}, 6 \times \sqrt{S_h(C4)}\right\}$	O
	$A_{s2} = max\left\{6 \times \sqrt{S_h(C3)}, 6 \times \sqrt{S_h(C4)}\right\}$	F
	$A_{s3} = max\left\{6 \times \sqrt{S_h(O1)}, 6 \times \sqrt{S_h(O2)}\right\}$	O
	$A_{s4} = max\left\{6 \times \sqrt{S_h(C3)}, 6 \times \sqrt{S_h(C4)}\right\}$	O
	$A_{s5} = max\left\{6 \times \sqrt{S_h(C3)}, 6 \times \sqrt{S_h(C4)}\right\}$	O
Amount (μV^2)	$S_{LOC}(LOC)$	F
	$S_{ROC}(ROC)$	F
	$S_{L-R}(LOC-ROC)$	O
	$S_{chin-EMG}(Chin-EMG)$	F

*EEG: *s1* (0.5-2 Hz); *s2* (2-7 Hz); *s3* (8-13 Hz); *s4* (13-25 Hz); *s5* (25-50 Hz). EOG: *LOC, ROC, L-R* (2-10 Hz). EMG: *chin-EMG* (50-100 Hz).

III. RESULTS

The overnight sleep recording of 2 subjects were utilized as the training data. The parameter selection process is illustrated in Table 2. (A) is for fundamental parameters. The number of the fundamental parameters was increased during the parameter selection process. The accuracy value indicates the agreement epochs between the sleep stage determination and visual inspection by clinician. (B) is for the optional parameters. The accuracy value indicates the determination result by using each optional parameter together with the fundamental parameters. For each column, those accuracies in (B) were compared with the accuracy by fundamental parameters in (A). "↑" indicates increased accuracy and "↓" indicates decreased accuracy. The optional parameter which had the highest increased accuracy was selected and added into the fundamental parameter set for next comparison. Finally, three optional parameters were selected. Those were R_{s5}, S_{LR}, and R_{s4}. The combination of the fundamental parameters and those selected optional parameters was utilized for automatic sleep stage determination.

Another two subjects different from the training subjects were tested and analyzed. The accuracy of stage awake, stage REM, light sleep (stage I and II) and deep sleep (III and IV) were calculated and evaluated. The average accuracy of stage awake was 92.41%, stage REM was 58.91%, light sleep was 80.90% and deep sleep was 94.96%. The results for stage awake, light sleep and deep sleep were satisfied. Stage REM showed lower accuracy comparing with other sleep stages.

©ISAROB 2009

Table 2. Parameter selection

(A) Fundamental parameters	**Accuracy**	**Accuracy** (+ R_{s5})	**Accuracy** (+ R_{s5}, S_{LR})	**Accuracy** (+ R_{s5}, S_{LR}, R_{s4})
R_{s1}, R_{s3}, A_{s2}, S_{LOC}, S_{ROC}, $S_{chin\text{-}EMG}$	80.69%	81.61%	82.62%	82.72%
(B) + Optional parameters	**Accuracy**	**Accuracy**	**Accuracy**	**Accuracy**
+ R_{s2}	79.27% ↓	80.08% ↓	81.81% ↓	81.91% ↓
+ R_{s4}	80.59% ↓	78.46% ↓	82.72% ↑	
+ R_{s5}	81.61% ↑			
+ A_{s1}	78.15% ↓	79.67% ↓	82.42% ↓	80.89% ↓
+ A_{s3}	80.96% ↑	79.27% ↓	82.22% ↓	79.78% ↓
+ A_{s4}	77.24% ↓	77.95% ↓	82.01% ↓	80.18% ↓
+ A_{s5}	81.10% ↑	79.17% ↓	82.11% ↓	80.18% ↓
+ S_{LR}	80.89% ↑	82.62% ↑		

IV. DISCUSSION

In real clinics, sleep data adopts long-term recording. It is inevitably being affected by various artifacts. Individual differences are also commonly existed, even under the same recording condition. For the patients with sleep-related disorders, their sleep data has particular characteristics. The conventional rule-based methods are insufficient to deal with the recorded sleep data which containing complex and stochastic factors. We adopt an expert knowledge-based method. The expert knowledge of visual inspection covered staging criteria and considered the actual circumstance in clinics.

The fundamental parameters were defined according to the traditional definition of sleep stages. The optional parameters were defined to cover the frequency bands of the periodogram of sleep EEGs (0.5-50 Hz) together with the fundamental parameters. Even the frequency characteristic is differed from the typical definition of fundamental parameters, the characteristics can be reflected by optional parameters. Additionally, the optional parameter can provide indicators for special cases of sleep disorder which are different from the requirements in hospitals and institutions.

VI. CONCLUSION

An adaptive expert knowledge database was developed by fundamental and optional parameters. The probability density functions of parameters for sleep stage determination were flexible to variable cases of sleep data. The developed automatic sleep stage determination by using adaptive expert knowledge database can be effective for clinical practice.

ACKNOWLEDGMENT

This study is partly supported by Nation Nature Science Foundation of China 60543005, 60674089, and Shanghai Leading Academic Discipline Project, Project number: B504.

REFERENCES

[1] Rechtschaffen A and Kales KK, Manual of standardized terminology, techniques and scoring system for sleep stages of human subject, *California Brain Information Service*, USA, 1968.

[2] Himanen SL, Hasan J (2000), "Limitations of Rechtschaffen and Kales". *Sleep Med Rev.* 4(2):149-167

[3] Smith JR, Karakan I and Yang M (1978), "Automated analysis of the human sleep EEG, waking and sleeping", *Electroenceph. clin. Neurophysiol*, 2:75-82

[4] Smith JR and Karakan I (1971), "EEG sleep stage scoring by an automatic hybrid system", *Electroencephalogr Clin Neurophysiol*, 31(3):231-237

[5] Wang B, Sugi T, Kawana F, Wang X and Nakamura M (2008), "Multi-Valued Decision Making of Sleep Stages Determination Based on Expert Knowledge", *Proceedings of International conference on Instrumentation, Control, and Information Technology*, SICE Annual Conference 2008, Chofu, Japan.

Reliable EOG Signal Based Control Approach with EEG Signal Judgement

T. Zhang, C. Chen
Department of Automation
Tsinghua University
Beijing 100086, CHINA

M. Nakamura
Department of Advanced Systems Control Engineering
Saga University
Saga 840-8502, JAPAN

Abstract

This paper proposes a reliable EOG signal based control approach with EEG signal judgement. In this method, raw bio-neurological signals (including EOG and EEG) are first extracted and segmented in the pre-processing. The processed bio-neurological signals will be then evaluated by calculating feature parameters of these signals. Since in bio-neurological signals they may be contaminated by various kinds of artifacts, by means of feature parameters of bio-neurological signals, some artifacts of bio-neurological signals can be indicated. Thus, the bio-neurological signals contaminated with artifacts can not be adopted to generate control signals and judge the correctness of control signals. In the proposed method, in order to generate reliable control signal based on the EOG signal, EEG signal is adopted to assist to make judgement about the valid of EOG signal. With the proposed method, an EOG signal based control software platform has been implemented. By use of this platform, simulation work has been carried out to control the behavior of a robot. The simulation results verified the effectiveness of the proposed method.

1 Introduction

From human body there have many kinds of bio-neurological signals, which are adopted for diseases diagnosis, such as electroencephalogram (EEG), electromyogram (EMG), electrooculogram (EOG), electrocardiogram (ECG), and so on. In recent decades of years, many researchers are engaged in a new field of study, i.e., Brain-Computer Interface (BCI). The main task of this field is to control robot by means of various kinds of bio-neurological signals [1].

There already have plenty of researches on this topic. Many proposed methods use bio-neurological signals to control different robots. For example, Craig[2] proposed a method of using EEG to control hand of the disabled. Nakamura[3] introduced a method to control meal assistant robot by means of EEG. However, most of control methods are just using one type of bio-neurological signals which has limitation to reach high accuracy of control performance, because bio-neurological signal is too week and very hard to be exact clearly signals. Therefore, the reliable control request is still a most important issue in BCI. So far, we have already carried out a lot of works for proposing effective methods to evaluate various bio-neurological signals [4]. Therefore, it is possible to improve the reliability of control by means of bio-neurological signals.

In this research, we propose a reliable EOG signal based control approach with EEG signal judgement. In this method, raw bio-neurological signals (including EOG and EEG) are first extracted and segmented in the pre-processing. The processed bio-neurological signals will be then evaluated by calculating feature parameters of these signals. Since in bio-neurological signals they may be contaminated by various kinds of artifacts, by means of feature parameters of bio-neurological signals, some artifacts of bio-neurological signals can be indicated. Thus, the bio-neurological signals contaminated with artifacts can not be adopted to generate control signals and judge the correctness of control signals. In the proposed method, in order to generate reliable control signal based on the EOG signal, EEG signal is adopted to assist to make judgement about the valid of EOG signal. With the proposed method, an EOG signal based control software platform has been implemented. By use of this platform, simulation work has been carried out to control the behavior of a robot. The simulation results verified the effectiveness of the proposed method.

In this paper, the proposed method are explained in detail in section 2, including the bio-neurological signals acquisition and pre-processing, evaluation of processed EOG signals and generation of control signals, and judgement by EEG signals. In section 3, control platform for the proposed method is introduced. In the section 4, simulation work was explained to con-

©ISAROB 2009

trol a robot by use of the developed platform.

2 Method

2.1 Bio-neurological signals acquisition and pre-processing

In the proposed method, it first needs to automatically record raw bio-neurological signals (including EOG and EEG) from subject and make some pre-processing. According to the standard, EOG signals can be obtained from the electrodes Fp1, Fp2, F7 and F8 pasted on the human face new eyes. EEG signals can be obtained from the electrodes Fp1, Fp2, F3, F4, F7, F8, C3, C4, P3, P4, O1, O2, T3, T4, T5, T6 pasted on the human head. According to the request, raw continuous bio-neurological signals are segmented in each short time period. For example, a continuous bio-neurological signal can be divided into a set of segments and each segment may have 5 second long. Therefore, it will be helpful to make the further processing. This segmentation work can be automatically made by the system in online.

In the pre-processing of bio-neurological signals, bio-neurological signals need to store into the data file. Additionally, it can automatically generate the name of data file, indicate the types of signals, an instruction file including important information about the signals, and so on.

2.2 Evaluation of bio-neurological signals and generation of control signals by EOG signals

In the proposed method, evaluation of processed bio-neurological signals is very important for generating control signals. In the evaluation of the processed bio-neurological signals, it needs calculate parameters, indicate artifacts and find out qualified signals.

2.2.1 Parameters calculation

The parameter calculation is essential for the evaluation of bio-neurological signals. For example, the features of bio-neurological records in each channel can be expressed by the periodogram parameters.

- Amplitude [μV]: $A_z(x) = 6\ \sqrt{S_z(x)}$
- Symmetry [%]: $P_z(x,y) = 6\sqrt{S_z(x-y)}/6\sqrt{S_z(x+y)} \times 100$
- Asymmetry [%]: $G_z(x,y) = 6\sqrt{S_z(x+y)}/6\sqrt{S_z(x-y)} \times 100$
- Extension [%]: $E_z(x,y) = 6\sqrt{S_z(y)}/6\sqrt{S_z(x)} \times 100$
- Duration [%]: $D_z(x) = S_z(x)/S_T(x) \times 100$
- Central frequency [Hz]: $F_z(x) = f_z^c(x)|_{P_{max}}, P_{max} = \max_{f_{lower} \leq f_z(x) \leq f_{upper}} P(f_z(x))$
- Normalization of parameter: $\Phi_z^Q(i) = (Q_z(i) - \min Q_z(i))/(\max Q_z(i) - \min Q_z(i))$

where x, y both represent each electrode of Fp1, F3, C3, P3, O1, Fp2, F4, C4, P4, O2, F7, T3, T5, F8, T4, T6; z denotes the respective signal components: L(0-0.5 Hz), (0.5-4 Hz), (4-8 Hz), (8-13 Hz), (13-25 Hz), T(0.5-25 Hz), H(35-50 Hz); $f_z(x)$ is the frequency within the frequency band of z in channel x; $f_z^c(x)$ is the central frequency within the frequency band of z in channel x and corresponding to the maximal power spectrum; f_{lower} is the lower limit of the frequency band; f_{upper} is the upper limit of the frequency band; and i is the segment number.

The following items are employed in the parameters definition:

- $S_z(x)$ is the amount of signal components calculated by the summation of periodogram with the frequency band of z in channel x;
- $S_T(x)$ is the amount of signal components calculated by the summation of periodogram with the frequency band of 0.5-25 Hz in channel t;
- $S_z(x-y)$ is the amount of signal components calculated by the summation of periodogram with the frequency band of z in channels x and y, in which the signal time series of channel y is subtracted from that of the channel x;
- $S_z(x+y)$ is the amount of signal components calculated by the summation of periodogram with the frequency band of z in channels x and y, in which the signal time series of channel x adds that of the channel y.

As the first step, in the proposed method, the parameters for EEG and EOG are calculated. When implementing the proposed method, the parameters will be displayed on the screen of computer so that the user can understand the change of the parameters in real time.

©ISAROB 2009

2.2.2 Artifacts indication

Based on the parameter calculation, artifacts contaminating in the bio-neurological signals can be indicated. Normally, there are two types of artifacts. One is technical artifact, including electrode artifact, base line drift artifact, etc. Another is physiological artifact, including blink artifact, EMG artifact, horizontal eye movement (HEM) artifact, etc. For each type of artifact, it has criteria to judge the existence of this artifact. For example, for EOG signals, blink artifact is one of main artifacts always existed in the EOG signals. Its criteria are as below [4].

- **Existence of δ component**:
  $A_\delta(F_{P1}) \geq 25[\mu V], \quad A_\delta(F_{P2}) \geq 25[\mu V]$
- **Symmetry of the waveform**:
  $A_\delta(F_{P1}+F_{P2}) \geq 50[\mu V], \quad P_\delta(F_{P1}, F_{P2}) \leq 55[\%]$
- **Extension to central region**:
  $E_\delta(F_{P1}, F_3) \leq 85[\%], \quad E_\delta(F_{P2}, F_4) \leq 85[\%]$
  $E_\delta(F_{P1}, C_3) \leq 78[\%], \quad E_\delta(F_{P2}, C_4) \leq 78[\%]$

When implementing the proposed method, there always use two ways to indicate the artifacts by the computer. One is using different color for the parameters displaying on the screen of computer. Another is making alarm voice to notice the user. Therefore, it will be very helpful for user to understand the artifacts in real time.

2.2.3 Control signals generation based on qualified EOG signals

Based on the above parameters and artifacts indication method, the qualified signals can be picked up. Since the qualified EOG signals will be adopted to generate control signals in the proposed method, the criteria of judgement of qualified EOG signals for generating control signals are as below. The qualified EOG signals for generating control signals do not mean that the EOG signals have no any artifacts. In contrast, the qualified EOG signals for generating control signals are defined that they should have blink artifact and HEM artifact. Particularly, these two types of artifacts should occur at the same time. It means that the subject shows this manner to express his intention to control object. If these two artifacts are existing separately in EOG signals, these EOG signals are defined unqualified records.

Concerning about the control signals generated by qualified EOG signals, it can be defined based on user's requirement. For example, it can be a kind of pulse.

2.3 Judgement by EEG signals

In the proposed method, although the control signals are generated by qualified EOG signals, it still exists the phenomenon that the subject status is not appropriate for control. For example, the status of subject is drowsy while recording the EOG signals. The EOG signals may be qualified, but the control signals generated by the current EOG signals can not be adopted to fulfill the control task. Therefore, EEG signals can be adopted to judge the status of the subject in order to determine the correctness of the control signals.

Normally, the evaluation of α wave in EEG signals is always adopted to judge the vigilance level of the subject under the relaxed situation. If the relative ratio of α wave is high, the vigilance level is high and therefore the subject status is satisfied with the requirement. The control signals generated by EOG signals at this moment are correct to control object. Due to the page limitation, the calculation method about relative ration of α wave will not be introduced in detail and you can find it in [4].

It should be noticed that the qualified EEG signals adopted for judgement can only judge the correctness of control signals generated by qualified EOG signals which are synchronized with qualified EEG signals.

3 Control platform for the proposed method

The proposed method has been implemented by developing a real time evaluation software system. This system not only can process EOG and EEG signals, but also can generate control signals by qualified EOG signals and make judgement by qualified EEG signals in real time. Fig.1 illustrates the interface of the real time evaluation system.

Basically, this system is developed by C language and includes about three functions, i.e., preprocessing, evaluation and output. For each function, it has a software module. Through AD/DA converter, this system can connected with bio-neurological signals recording machine. The recorded signals can put into the computer running the proposed system. The evaluation results can be displayed on the screen of the computer and saved into the data file in real time. As above explained, two different types of output ways can be both implemented by the proposed system. One is to store useful information into the data file. Another is directly to output control signal to control actual system, such as a robot.

©ISAROB 2009

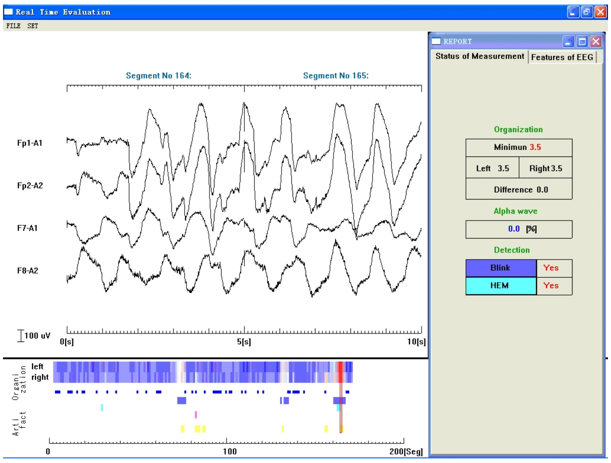

Figure 1: Interface of the control platform

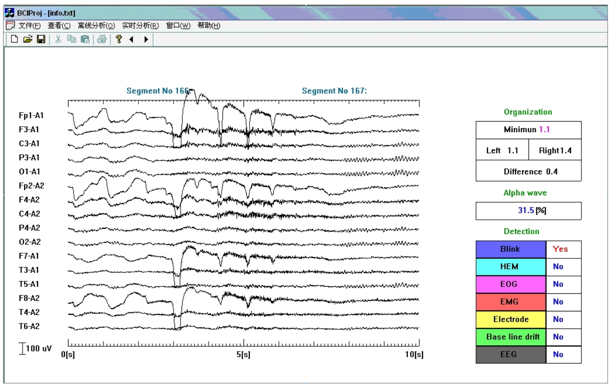

Figure 2: Unqualified EOG signals with blink

4 Simulation of the proposed method

In order to demonstrate the effectiveness of the proposed method, simulation work has been done to control the behavior of a robot by bio-neurological signals. We adopt EOG signals to control the movement of a mobile robot. If the subject blinks his eyes, the mobile robot will start to move or stop. If the subject's eye-ball is horizontal moving, the mobile robot will rotate with an angle. The following Fig.2 illustrates the unqualified EOG signals with blink. Fig.3 illustrates the qualified EOG signals.

5 Summary

This paper proposes a reliable EOG signal based control approach with EEG signal judgement. In this

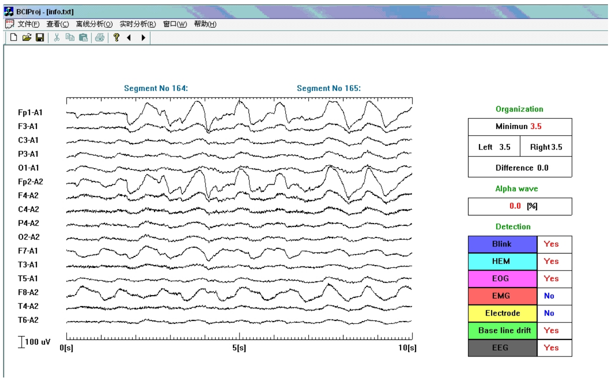

Figure 3: Qualified EOG signals for generating control signals

method, EOG signals are adopted to generate control signals. EEG signals are adopted to assist to make judgement about the valid of EOG signal. With the proposed method, an EOG signal based control software platform has been implemented. By use of this platform, simulation work has been carried out to control the behavior of a robot. The simulation results verified the effectiveness of the proposed method. Actually, the application of the proposed method can be extended to the wide fields.

References

[1] J. R. Wolpaw, N. Birbaumer, D. J. McFarland, G. Pfurtscheller, T. M. Vaughan, "Brain-computer interfaces for communication and control," *Clinical Neurophysiology*, Vol. 113, pp. 767-791, 2002.

[2] A. Craig, P. McIsaac, Y. Tran, L. Kikup, A. Seale, "Alphawave reactivity following eye closure - a potential method of remote hands free control for the disabled," *Technology and Disability*, Vol. 10, pp.187-194, 1999.

[3] M. Nakamura and T. Zhang, "Human assistance robot following the human intention extracted from bio-neurological signals", *Proceedings of the Sixteenth International Conference on Systems Engineering*, pp.506-511, 2003.

[4] M. Nakamura, Q. Chen, T. Sugi, A. Ikeda, H. Shibasaki, "Technical quality evaluation of EEG recording based on electroencephalographers' knowledge," *Medical Engineering and Physics*, Vol. 27, pp. 93-100, 2005.

©ISAROB 2009

The Fourteenth International Symposium on Artificial Life and Robotics 2009 (AROB 14th '09),
B-Con Plaza, Beppu, Oita, Japan, February 5 - 7, 2009

Energy Levels by a Simple Shooting Scheme for a Periodic Orbit

Kazuhiro Kubo, Tokuzo Shimada
Department of Physics, Meiji University
Higashi-Mita 1-1, Kawasaki, Kanagawa 214, Japan

We revisit the periodic orbit theory for anisotropic Kepler problem, which is an important playground for the quantum chaos. In order to explore the periodic orbit Gutzwiller devised an iteration scheme, which computes Fourier coefficients of the orbit iteratively. Here we note in a nutshell all one needs is the primary periodic orbit. We propose an alternative scheme taking account for the symmetry of the target trajectory and the scaling property of the AKP equation of motion. We show a simple shooting scheme gives almost immediately the final periodic orbit.

Key words: quantum chaos, anisotropic Kepler problem, shooting method, periodic orbit theory

I. INTRODUCTION

Recently by the advent of nano-scale devices the handling of various quantum systems in a laboratory becomes viable. A good example is a quantum dot, which confines electrons in a two dimensional region of several hundreds nano-meters in size. This device, under an external magnetic field and at low temperatures, exhibits electric conductance depending on the shape of the region of confinement; it depends whether the region allows regular classical orbit or the region induces the chaotic orbit. Then, natural question arises; if the classical theory for a system involves chaos, does it somehow affect the quantum behavior of the system? The solution of this question will give a clue for the real foundation of quantum theory.

Two possible approaches to this problem may be envisaged; random matrix theory (RMT) and periodic orbit theory (POT). In RMT, the Hamiltonian of the system is approximated by a matrix whose elements are random numbers. The symmetry of the system dictates the type of the ensemble of the random matrices. For instance, for large nuclei, the nearest neighbor spacing distribution of the energy level agrees well with that of a real symmetric random matrix (rather than a simple Poisson distribution). Then, in POT, based on the Feynman's path integral, the quantum characteristics in the semi-classical regime is estimated from classical orbits. Therefore, it is suited to investigate the classical-quantum correspondence. For instance, it is a vital tool for the analysis of the shell effect in the total energy of nuclei.

In a series of works [2–4], Gutzwiller studied various spherically symmetric potentials. These are all integrable cases because the separation of variables is possible; the classical orbits are regular. These may be regarded as a preparation for the next step towards the POT. In a seminal work [5], Gutzwiller extended the work to a non-integrable Hamiltonian system, whose classical trajectory is chaotic. Gutzwiller's quantization condition is

$$S(E) = 2\pi\hbar(n + \ell(E)/4). \tag{1}$$

Here, E is the total energy of the chosen periodic orbit and S is the action integral

$$S(E) = \oint p_i dq_i, \tag{2}$$

along the periodic orbit for one period, and ℓ is a number of conjugate points along the periodic orbit. The energy levels E_n are given by solving the condition (1). The condition (1) is then applied to anisotropic Kepler problem (AKP) and the resulting energy levels are in good agreement with those by solving the Schrödinger equation.

As is well known, the energy levels of an ordinary Kepler problem are given by $-1/n^2$ in appropriate units with the principal quantum number n. In AKP, the energy levels turn out again to be proportional to $-1/n^2$, and the anisotropy affects the proportionality coefficient γ^2. ($\gamma = 1$ for the Kepler problem). In order to compute the value of γ for a certain anisotropy, it is necessary to find a periodic orbit as a solution of the equation of motion of AKP. In [5], a fundamental periodic orbit and its γ are calculated using an iteration scheme. However, this iteration scheme is somewhat elaborated and requires large computation time.

In this paper, we present an alternative scheme to find the fundamental periodic orbit by a simple shooting scheme. In our method a scaling property of the system is fully accounted and the symmetry of the orbit shape helps to reduce the shooting analysis to only one-dimensional. The resulting γ is in good agreement with the Gutzwiller's value.

II. ANISOTROPIC KEPLER PROBLEM

The AKP is a Kepler problem with an anisotropic mass tensor. It includes the motion of an electron confine in a semiconductor. The Hamiltonian of the two-dimensional AKP is

$$H(p,\ q) = \frac{p_1^2}{2m_1} + \frac{p_2^2}{2m_2} - \frac{e^2}{\kappa\sqrt{q_1^2 + q_2^2}}. \tag{3}$$

with $(q_1,\ q_2)$ the position of the electron and $(p_1,\ p_2)$ the conjugate momentum. The m_1, m_2 are the diagonal elements of the electronic mass tensor and we choose $m_1 > m_2$ (q_1 is 'the heavy axis').

©ISAROB 2009

The dimensionless variables for energy, length, frequency are respectively defined in the units

$$E_0 = \frac{m_0 e^4}{2\kappa^2\hbar^2},\ a_0 = \frac{\kappa\hbar^2}{m_0 e^2},\ \omega_0 = \frac{m_0 e^4}{\kappa^2\hbar^3} \tag{4}$$

with $m_0 = \sqrt{m_1 m_2}$. Dimensionless coordinates and temporal parameter are respectively defined by

$$\xi \equiv \frac{q_1}{\sqrt{\mu}a_0},\ \eta \equiv \frac{q_2}{\sqrt{\nu}a_0},\ \tau \equiv \omega_0 t. \tag{5}$$

In order to write the Hamiltonian (and action) with the dimensionless variables, it is convenient to pass through the Lagrangian formalism. The Lagrangian in terms of the dimensionless variables is obtained as

$$\mathcal{L} \equiv \frac{L}{E_0} = \xi'^2 + \eta'^2 + \frac{2}{\sqrt{\mu\xi^2 + \nu\eta^2}} \tag{6}$$

where the prime indicates the derivative with respect to τ and the relation $d/dt = \omega_0 d/d\tau$ is used. The dimensionless conjugate momentum is

$$p_\xi = \frac{\partial\mathcal{L}}{\partial\xi'} = 2\xi', \quad p_\eta = \frac{\partial\mathcal{L}}{\partial\eta'} = 2\eta', \tag{7}$$

and therefore the dimensionless Hamiltonian is given by

$$h \equiv \frac{H}{E_0} = \frac{p_\xi^2}{4} + \frac{p_\eta^2}{4} - \frac{2}{\sqrt{\mu\xi^2 + \nu\eta^2}}, \tag{8}$$

with $\mu = 1/\nu = \sqrt{m_2/m_1} < 1$. The Hamilton equation in the dimensionless variables is

$$\begin{aligned} \xi' &= \frac{\partial h}{\partial p_\xi} = \frac{p_\xi}{2}, \quad p'_\xi = -\frac{\partial h}{\partial \xi} = -\frac{2\mu\xi}{(\mu\xi^2+\nu\eta^2)^{3/2}}, \\ \eta' &= \frac{\partial h}{\partial p_\eta} = \frac{p_\eta}{2}, \quad p'_\eta = -\frac{\partial h}{\partial \eta} = -\frac{2\nu\eta}{(\mu\xi^2+\nu\eta^2)^{3/2}}. \end{aligned} \tag{9}$$

The energy conservation equation calculated from Eq. (8) with Eq. (7) is

$$\xi'^2 + \eta'^2 - \frac{2}{\sqrt{\mu\xi^2 + \nu\eta^2}} = \epsilon. \tag{10}$$

Only the bound states are discussed below, hence $\epsilon < 0$ and trajectories in the $\xi\eta$ plane are all limited inside an ellipse

$$\mu\xi^2 + \nu\eta^2 = \left(\frac{2}{\epsilon}\right)^2. \tag{11}$$

The form of the energy in (10) is quadratic in ξ' and η' and it is homogeneous in ξ and η. Therefore we can use the virial theorem to write the action from Eq. (2) as

$$\frac{S}{\hbar} = \int (\xi'^2 + \eta'^2) d\tau = -\epsilon\frac{2\pi}{\omega}. \tag{12}$$

Here, ω is the dimensionless angular frequency in the unit ω_0.

In the case of ordinary Kepler problem, the shapes of trajectories in bound states are all elliptic except the radial motion. In the units (4), the total energy for the elliptic orbit is represented by

$$\epsilon = -\bar{\alpha}^2\bar{\omega}^2. \tag{13}$$

Dimensionless variables $\bar{\alpha}$ and $\bar{\omega}$ ()correspond to the major radius and angular frequency of the elliptic orbit respectively. Similarly, the Kepler's third law is given by

$$\bar{\alpha}^3\bar{\omega}^2 = 1. \tag{14}$$

These relations (13), (14) can be extended to the case of AKP. The energy is

$$\epsilon = -\alpha^2\omega^2. \tag{15}$$

Again these are the dimensionless energy, size, frequency of the AKP in the units (4).

The counterpart of Eq. (14) is introduced by

$$\gamma \equiv \alpha^3\omega^2. \tag{16}$$

For each periodic orbit, γ takes a different value which depends only on $m = (\mu - \nu)/(\mu + \nu)$, the degree of the anisotropy. It should be noted that for a non-anisotropic case, i.e. $m = 0$, a relation $\gamma(0) = 1$ is satisfied, which is the Kepler's third law.

By the change of variables from (α, ω) to (ϵ, γ), the action in Eq. (12) is rewritten as

$$S = 2\pi\hbar\frac{\gamma(m)}{\sqrt{|\epsilon|}}. \tag{17}$$

By the help of the quantization condition (1), the energy levels of the AKP turn out to be

$$\epsilon_n = -\frac{\gamma^2}{n + \frac{\ell}{4}{}^2}. \tag{18}$$

According to Eq. (18), if the value of γ and the number of conjugate points are known for the particular periodic orbit, then the energy levels of the AKP can be estimated when the degree of anisotropy m is fixed.

For the fundamental periodic orbit discussed below, ℓ equals to 2 and 4 for the two and three dimensional cases respectively [5].

III. GUTZWILLER'S ITERATION SCHEME

In order to compute the value of γ, the search of the periodic orbit is needed. The target is the primary periodic orbit. Its shape is oval; mirror symmetric about both ξ, η axes. For $m = 0$ (the ordinary Kepler problem), the shape is simply a circle, while with anisotropy, one cannot derive the exact solution analytically. To search this orbit, an iteration scheme is devised in [5]. In this scheme complex coordinates are expanded in Fourier series as

$$\xi + i\eta = \alpha\sum_{-\infty}^{\infty}\alpha_j z^{2j+1},$$

$$\xi - i\eta = \alpha\sum_{-\infty}^{\infty}\beta_j z^{2j+1},\ \beta_j = \alpha_{-j-1} \in \mathcal{R}$$

with $z = \exp(i\omega\tau)$. Because the coefficients are calculated by a fixed algorithm below, the scale factor α is needed. The iteration starts from an initial configuration $\alpha_0 = 1, \alpha_1 = \alpha_2 = \cdots = 0$ corresponding to a circle, which is a primary orbit for a Kepler problem without anisotropy. At each step of the iteration procedure, the higher mode Fourie coefficients are computed from the lower by a couple of recurrence relations (derived from the equation of motion and the energy conservation). As the iteration proceeds, the set of Fourie coefficients is thus improved towards the final solution and the circle at the initial time is deformed to the primary orbit of AKP. At the end of the iteration the value of γ is calculated from the Fourie coefficients.

This scheme is advantageous in that the orbit is always closed and the symmetry is respected in every step. However, the number of Fourier coefficients grows exponentially. Therefore it is necessary to truncate the small higher frequency terms. In order to improve both the accuracy huge memory space and long computation time are then required. The decision of whether sufficient convergence is reached or not is difficult, because the convergence is slow and oscillatory as we will reproduce below [7].

IV. PERIODIC ORBIT SEARCH BY A SIMPLE SHOOTING SCHEME

Now let us propose an alternative scheme which uses a shooting method integrating (9). The symmetry of the target orbit simplifies the search; a one-dimensional search is sufficient.

From Eqs. (15), (16) we obtain

$$\gamma = \frac{|\epsilon|^{\frac{3}{2}}}{\omega}, \quad \alpha = \frac{\sqrt{|\epsilon|}}{\omega}. \tag{19}$$

Therefore, γ and α can be worked out by measuring the period ($T = 2\pi/\omega$) of the final orbit with energy ϵ. (The energy can be chosen at an arbitrary value under the scaling). All we need is the precise determination of the period, that is, the precise determination of initial conditions in the shooting scheme. Therefore, this scheme is free from the problems of convergence and huge memory.

A. Choice of energy and the families of trajectories

Let us consider the scaling property of the AKP equation of motion. It is form invariant under the transformation

$$\begin{aligned} \xi(\tau) &\to \tilde{\xi}(\tilde{\tau}) = s \cdot \xi(\tau), \\ \eta(\tau) &\to \tilde{\eta}(\tilde{\tau}) = s \cdot \eta(\tau), \\ \epsilon &\to \tilde{\epsilon} \quad = s^{-1} \cdot \epsilon \\ \tau &\to \tilde{\tau} = s^{\frac{3}{2}} \cdot \tau. \end{aligned} \tag{20}$$

Accordingly the period is scaled as $T \to s^{3/2} \cdot T$. For the scale of the orbit, $\alpha \to s \cdot \alpha$ just like ξ and η.

This scaling property implies that there is a one-parameter (s) family of orbits. What we need is to determine the family to which the primary periodic orbit belongs as a member. Therefore we can pick an arbitrary ϵ for the shooting. Another choice of ϵ will search out another orbit but in the same family. Since the combination $\gamma \equiv \alpha^3\omega^2$ is scale invariant, any member in the same family will give the same γ.

B. The shooting scheme

Let us show that the search for the primary orbit (with reflection symmetry with respect to both ξ and η axes) requires only a one dimensional shooting scheme. From the symmetry, it definitely passes through the ξ axis. So we can choose the initial point on the ξ axis $(\xi_0, 0)$. That is, we choose the ξ axis as a Poincaré surface of section. From the symmetry it suffices to take $\xi_0 > 0$. Also from the symmetry the initial momentum must be then at right angles to the ξ axis; p_ξ must be vanishing ($(p_\xi)_0 = 0$). Furthermore, p_η is computed from ξ_0 via the energy conservation (10). Thus, the initial condition is given by

$$(\xi,\ \eta,\ p_\xi,\ p_\eta) = (\xi_0,\ 0,\ 0,\ p_\eta(\xi_0)). \tag{21}$$

with $p_\eta = 2\sqrt{\frac{2}{\sqrt{\mu}\xi_0} + \epsilon}$. Therefore one-dimensional search, varying ξ_0 as a parameter, is sufficient. The bound for ξ_0 is $0 < \xi_0 < \xi_{max} \equiv 2/\sqrt{\mu}|\epsilon|$.

From this initial point the Hamilton equation is integrated until the trajectory crosses again the Poincaré surface of section ($\eta = 0$). We call this first intersection (after the initial point) as the final point.

The constraint in the shooting scheme is two-fold

$$\xi_1 = \xi_0, \quad (p_\xi)_1 = 0. \tag{22}$$

The integration preserves the energy so that the condition $(p_\eta)_1 = (p_\eta)_0$ automatically follows from $\xi_1 = \xi_0$. The integration is iteratively repeated until the differences $\delta\xi \equiv \xi_1 - \xi_0$ and $(p_\xi)_1$ reach zero.

The constraint (22) is put on the first crossing of the Poincaré section so that it is strong enough to single out the primary orbit. In fact there is (at least) one other solution which is symmetric with respect to both ξ and η axes, but it is oscillatory and after many crossings it comes back to the starting point.

C. The initial value ξ_0^* of the primary orbit and the γ in the shooting scheme

To be explicit let us choose the anisotropy $m = 0.899$ ($\mu = 0.231$) (the germanium) and pick $\epsilon = -0.1$. Fig. 1 is a plot of $\delta\xi$ and $(p_\xi)_1$ as functions of ξ_0. We observe $\delta\xi$ changes the sign as ξ_0 passes a critical value of $\xi_0^* \approx 4.9$. This ξ_0^* is the initial value of the primary periodic orbit. Using the bi-section method for ξ_0^*, we obtain more precise value $\xi_0^* = 4.893087$. The period of

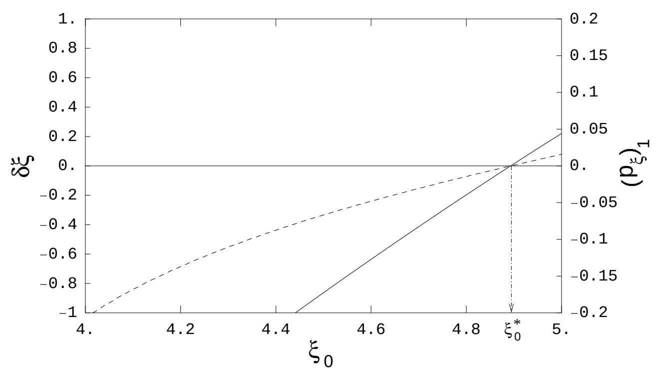

FIG. 1: ξ(solid line), $(p_\xi)_1$(dashed line) versus ξ_0. $\epsilon =$ 0.1.

this solution turns out $T = 151.2541$ and the angular frequency is $\omega = 4.154059 \times 10^{-2}$.

With this ω and $\epsilon = -0.1$ we obtain from (19)

$$\gamma = 0.7612500, \quad \alpha = 7.612500. \tag{23}$$

V. COMPARISON BETWEEN THE TWO SCHEMES

Let us reproduce the computation in [5]. The fundamental periodic orbit and γ may be computed at every iteration step, and hence we can compare them with those by our scheme.

1) *The comparison of orbits.* In Fig. 2, the orbits at several steps of the iteration scheme are compared with the orbit obtained by our shooting scheme. The latter is normalized by the scale factor α in Eq. (23). The zeroth step orbit is a unit circle; as the iteration proceeds, it approaches oscillatory the orbit obtained by the shooting scheme.

2) *Comparison of the parameter γ.* As seen in Fig. 3, γ in the iteration scheme decreases in oscillation, but after the 17th step, the decrease becomes slower and the oscillation remains. Therefore it is difficult to judge the convergence. The asymptote may be slightly above γ determined by the shooting scheme, but it may also be in agreement if iteration is continued further. But the necessary number of the Fourier coefficients is approximately 2^{n+1} in the n-th iteration step and such calculation is practically difficult.

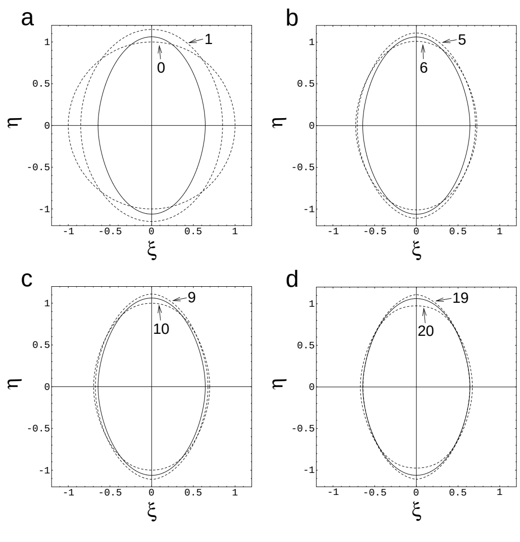

FIG. 2: The orbits from the iteration scheme (dashed lines) as compared with the one from the shooting scheme (the solid line). Numbers indicate the iteration steps.

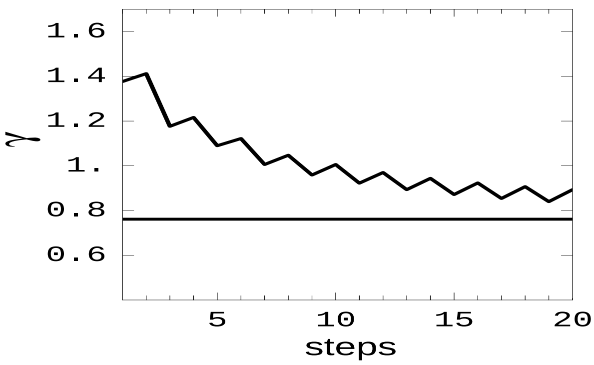

FIG. 3: Comparison of iteration result with that by shooting (23)(horizontal line) up to 20th step. $m = 0.899$ (Ge case).

In Summary, in Gutzwiller's scheme one has to compute exponentially increasing number of Fourier coefficients at each step of the iteration, while in our shooting scheme, it is just sufficient to integrate the orbit from the initial point to the first Poincaré section at each step of the iteration.

[1] R. P. Feynman, Rev. Mod. Phys. **20**, 367 (1948).
[2] M. C. Gutzwiller, J. Math. Phys. **8**, 1979 (1967).
[3] M. C. Gutzwiller, J. Math. Phys. **10**, 1004 (1969).
[4] M. C. Gutzwiller, J. Math. Phys. **11**, 1791 (1970).
[5] M. C. Gutzwiller, J. Math. Phys. **12**, 343 (1971).
[6] R. A. Faulkner, Phys. Rev. **184**, 713 (1969).
[7] This is remedied by a prescription [5]; make the variation small at chosen intervals.

©ISAROB 2009

The Fourteenth International Symposium on Artificial Life and Robotics 2009 (AROB 14th '09),
B-Con Plaza, Beppu, Oita, Japan, February 5 - 7, 2009

Synchronization and Periodic Windows in Globally Coupled Map Lattice

Tokuzo Shimada, Kazuhiro Kubo, Takanobu Moriya
Department of Physics, Meiji University
Higashi-Mita 1-1, Kawasaki, Kanagawa 214, Japan

A globally coupled map lattice (GCML) is an extension of a spin glass model. It consists of a large number of maps with a high nonlinearity and evolves iteratively under averaging interaction via their mean field. It exhibits various interesting phases under the conflict between randomness and coherence. We have found that even in its weak coupling regime, effects of the periodic windows of element maps dominate the dynamics of the system, and the system forms periodic cluster attractors. This may give a clue to the efficient pattern recognition by the brain. We analyze how the effect systematically depends on the distance from the periodic windows in the parameter space.

Key words: synchronization, cluster attractors, periodicity manifestation, globally coupled maps

I. INTRODUCTION

GCML devised by Kaneko [1, 2] is an unfailing source of ideas on the behavior of a complex system composed of many chaotic elements. In its simplest form, it is a model of coupled N logistic maps $f_a(x) = 1 - ax^2$ and evolves in an iteration of a process described by

$$x_i(n+1) = (1-\varepsilon)f_a(x_i(n)) + \frac{\varepsilon}{N}\sum_{i=1}^{N} f(x_i(n)) \quad (1)$$

in discrete time n. The nonlinearity of the map f, controlled by a, generally magnifies the variance among the maps, while the averaging interaction, controlled by ε, focuses the maps to the mean field $h(n) = \sum_{i=1}^{N} f(x_i(n))/N$ and introduce coherence into the maps. Under the conflict between the opposite tendencies the maps exhibit various interesting phases on the a, ε parameter plane [1]. In 90's and early 00's there was important progress concerning the weak coupling regime of the model. Firstly hidden coherence and collective chaos were found [1, 3, 4] in the desynchronized state. Even if the coupling is set to be very weak, maps are not independent random numbers, and consequently the law of large numbers may be violated; there is a long time scale motion which couples the step by step evolution of the maps in a bootstrap. Then, it was found that, even if the coupling is set very weak, the maps systematically synchronize and form various cluster attractors [5, 6] provided that certain tuning condition between the a and ε is satisfied. These were called as periodicity manifestations (PM's) in the turbulent regime and their stability were verified analytically [6]. The most remarkable PM's are the maximally symmetric cluster attractors (MSCA's). Let us denote by p and c the periodicity of the cluster attractor and the number of clusters in the attractor respectively. A period $(p, c = p)$ MSCA is induced by the period p window of the $f_a(x)$ and consists of $c = p$ clusters of maps with almost equal population each other, which oscillate in period p around the mean field with phases ($\exp(2\pi j/p)$, $j = 0, 1, \cdots, p-1$). Such a MSCA is in general associated by a sequence of cluster attractors; $(p, c = p-1) \to (p, c = p-2) \to \cdots$, which are produced in order with the increase of the coupling ε. A basic tool to detect the GCML state is the mean square deviation of the mean field $h(n)$ in time defined by

$$\mathrm{MSD} \equiv \frac{1}{T}\sum_{n_1}^{n_1+T} (h(n) - \overline{h})^2, \quad (2)$$

where n_1 denotes appropriate truncation, and $\overline{h}$ is an average of $h(n)$ during n_1 to $n_1 + T$. At MSCA, the symmetry of the population between clusters is high and accordingly the MSD of the mean field $h(n)$ in evolution is very small. On the other hand, the MSD becomes very high due to the lack of one or more clusters in the case of $p, c < p$ cluster attractors. The coexistence of various PM's were reported in AROB [7]. Universality in the formation of such PM's in various coupled maps was clarified in [8].

In this article we present new observations on the formation of PM's in a resurgence of synchronization study of GCML.

To begin with, let us recapitulate how the windows of element maps control the dynamics of GCML. There is *a curve of equivalent* (a, ε) *points* [6]. That is, if a is increased and ε is *accordingly* increased, GCML should exhibit (qualitatively) the same behavior as before, essentially because the PM's are realized on the balance of randomness and coherence. Then, such curves make altogether a one-parameter family of curves on the (a, ε) plane as depicted in Fig. 1 . To derive these curves let us consider one of the MSCA's with period p. In MSCA the mean field is kept constant (say h^*) for its stability; then all maps obey the same time-independent map

$$x_i(n+1) = (1-\varepsilon)(1 - ax_i^2(n)) + \varepsilon h^*, \ i = 1, \cdots, N. \quad (3)$$

This can be transformed by a scale transformation [9]

$$y_i(n) = \frac{1}{1 - \varepsilon + \varepsilon h^*} x_i(n) \quad (4)$$

©ISAROB 2009

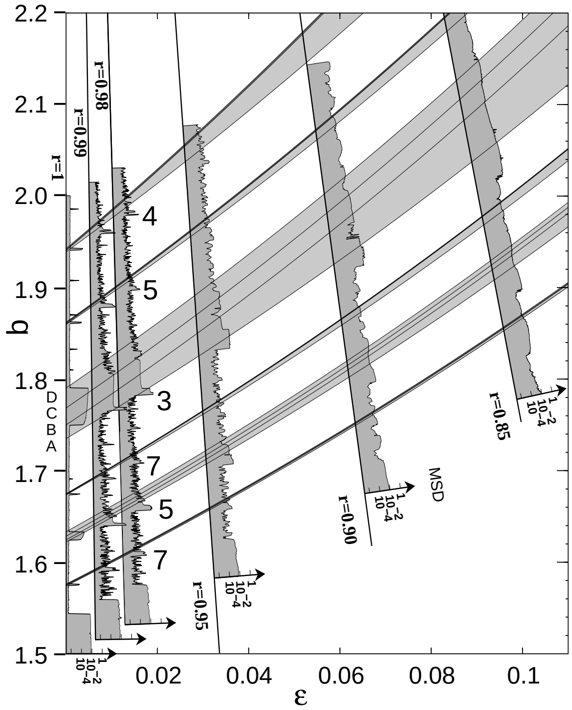

FIG. 1: Foliation of windows $p = 7, 5, 7, 3, 5, 4$ (shadowed bands). A, B, C, D indicate respectively the intermittency starting, the opening, the 1st bifurvation (in a window), and the closing point of $p = 3$ window. Pannels show MSD curves at constant r. ($N = 10^6$). Bottom (MSD=10 7) is aligned with fixed r curve (fitted by a line). Window's effects (PM's) diminish with decreasing r.

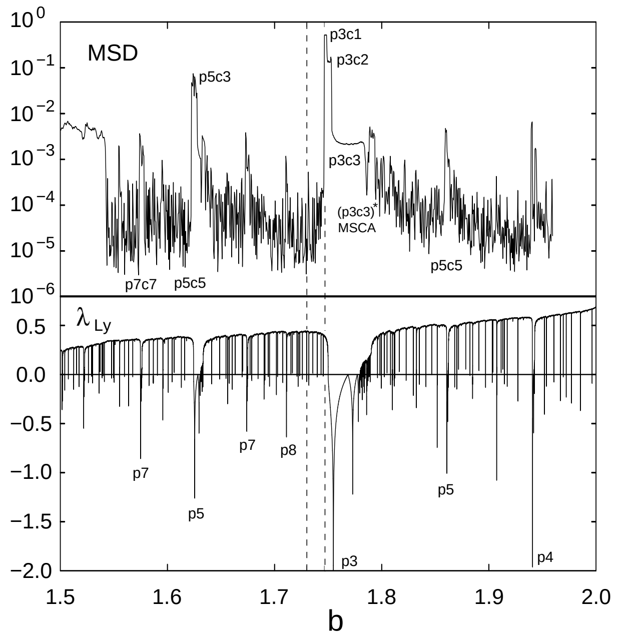

FIG. 2: The MSD of the mean field for GCML at $r = 0.98$ (upper) and the maximum Lyapunov number λ_{Ly} of a single logistic map (lower), both as functions of b. The correspondence between the dominant periodic windows and their MSD valley-peak structures induced by the MSCA and $c = p$ 1, p 2, clusters is clearly seen.

into a canonical form

$$y_i(n+1) = 1 - b\,y_i^2(n),\ i = 1, \cdots, N. \tag{5}$$

Here we find that the nonlinearity of the map is reduced by a factor

$$r \equiv \frac{b}{a} = (1-\varepsilon)(1-\varepsilon+\varepsilon h^*) \approx 1 - 2\varepsilon, \tag{6}$$

and the value of $b = ra$ must be within the range of the period p window of the map (5); x_i's in the MSCA oscillate in period p, so y_i's must also oscillate in period p. Now, let's denote by $y^*(b)$ the long time average of the map (5). Then, from (4), it follows that

$$y^*(b) = \frac{1}{1-\varepsilon+\varepsilon h^*} h^*. \tag{7}$$

Eliminating h^* from (6) and (7), we obtain

$$a = b/r \tag{8}$$

$$\varepsilon = 1 - \frac{ry^*(b)}{2} - \sqrt{r\,(1-y^*(b)) + \left(\frac{ry^*(b)}{2}\right)^2}$$

This determines on the (a, ε) plane a one-parameter (b) family of curves along which the period p MSCA may be formed. These are curves of foliation of periodic windows [6]. In Fig. 1 we observe that near $r = 1$ the MSD curves sensibly reflect the window dynamics of the element maps of GCML and with the decrease of r from one (the larger reduction of non-linearity from a to b), the valley-peak structure of MSD curve diminishes. Accordingly, an extensive study reveals that cluster attractors are formed roughly for $r \geq r_{th}$ and there occur only remnants for $r < r_{th}$ with $r_{th} \approx 0.95$. (We note that the synchronization in the predominant $p3$ window continues to the lower r compared with the other narrower windows.)

In Fig. 2 we compare the MSD curve (sampled at $r = 0.98$) of the GCML with the maximum Lyapunov number λ_{max} of the element map. We find that the MSD curve of the mean field $h(n)$ of GCML is a sensitive mirror of the window dynamics of element maps. In [6] it is pointed out that the MSD curve as a function of ε at fixed a have many valleys and peaks at the smaller ε than for $p3$ foliation, while only few at the larger ε. This anomaly is conjectured as the effect of the difference in the reduction factor r. Present Figures 1 and 2 verify beautifully this conjecture. Below we present our new observations in order.

II. FREE GAS LIMIT AND ADVENT OF CLUSTERS

In Fig. 3 we show how the predominant period three PM's appear in GCML with the decrease of r from one (the increase of ε from zero). The system size is taken as

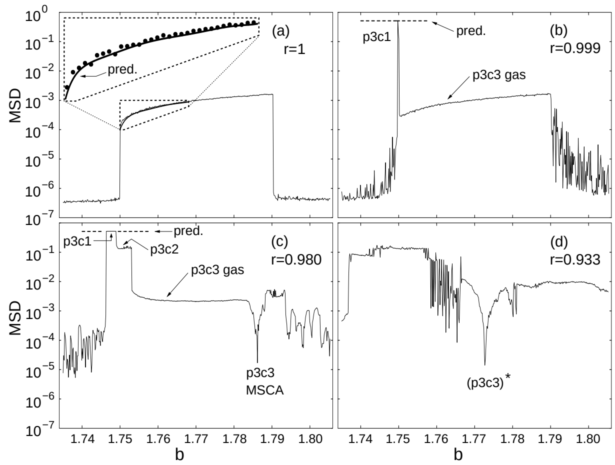

FIG. 3: Variation of the MSD curves with the decrease of r. ($r = 1, 0.999, 0.98, 0.933$.) The inset compares prediction with the measured MSD points (decimated by 1/4 for comparison).

$N = 10^6$ in order to remove noises. In (a) the MSD curve at $r = 1$ is depicted, which corresponds to an ensemble of free N logistic maps. Let's call this as free gas limit of GCML. Even though there is no interaction, the MSD curve already exhibits an interesting structure. Why the mean field of N independent maps at the large N fluctuates in time? This comes from the basin set structure. The GCML evolves from randomly chosen initial numbers for maps. After certain transient steps all the maps come (independently) into period three attractor. (Precisely, for $b = 1.75 - 1.7685$ the attractor is purely period three, then it repeats period bifurcation to chaos within the window.) Let's denote θ_i $(i = A, B, C)$ the population fraction of the maps subject to each of the three bands (with the center value x_A, x_B, x_C) at some time n_0 after the transient. Then, the mean field evolves as

$$\begin{aligned} h(n_0) &= \theta_A x_A + \theta_B x_B + \theta_C x_C \\ h(n_0+1) &= \theta_A x_B + \theta_B x_C + \theta_C x_A \\ h(n_0+2) &= \theta_A x_C + \theta_B x_A + \theta_C x_B \end{aligned}$$

which is clearly not a constant in time; its oscillates in period three with the MSD dictated by the basin structure characterized by the θ's and the period three orbits x's of the single logistic map. We can make a prediction for MSD from the above formula for $h(n)$ (with the variation of the θ's taking into account) and the analytic orbits x_A, x_B, x_C (for b below the first bifurcation in the $p3$ window). It remarkably explains the measured MSD structure of the free gas GCML as exhibited in the inset.

Then, in (b), at $r = 0.999$, we find that remarkably high MSD peak around the threshold of the $p3$ window. The $p3c1$ cluster attractor is now formed. For other b values, the model is still approximately the free gas $p3c3$ state (with population unbalance).

In (c), at $r = 0.98$, we find now all of the PM's. See Fig. 4 for an enlarged plot. The $p3c1$, and $p3c2$ cluster attractors form in the MSD curve the highest and the second high steps respectively. Their evolution is depicted in the respective insets. Then, at higher b, MSD curve shows unbalanced $p3c3$ plateau. Remarkably, around the closing point of the $p3$ window, the MSD valley due to approximate $p3c3$ MSCA is formed. The averaging interaction with $\varepsilon \approx 0.01$ now starts changing the free gas (unbalanced) $p3c3$ into maximally symmetric $p3c3$ cluster attractor ($p3c3$ MSCA).

In (d), at $r = 0.933$, we find $p3c2$ high MSD plateau in the smaller b and a remarkable MSD valley in the middle of the window. The latter is induced by the bifurcated $p3c3$ (that is $p6c6$) as discussed in ref. [6] with analytic consideration on its stability. It is formed around the super-stable point of the $p6$ orbit of the element maps. At this r the GCML dynamics has completely changed from free gas to the synchronization dynamics.

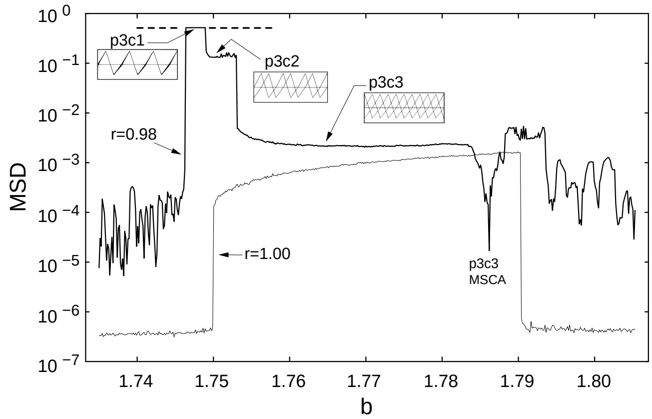

FIG. 4: Change of GCML synchronization with nonlinear parameter b of element maps as seen by the steps of MSD. ($r = 0.98$, $N = 10^6$.) Insets exhibit corresponding cluster attractor. The seagull structure of MSD curve is induced by p3c3 cluster in MSCA configuration. Dashed line is prediction for MSD at $p3c1$ cluster attractor.

III. MECHANISM OF CLUSTERING

Here we clarify the mechanism how the $p3c2$ cluster attractor is realized. It consists of only with two clusters, each in period three motion; a deformed state of $p3c3$ MSCA with a lack of one cluster at the higher coupling. To understand further we adopt a line of argument presented by Shibata and Kaneko to explain the collective motion in GCML [3]. At the $p3c2$ cluster attractor, the mean field oscillate in period three (say, $h_A \to h_B \to h_C \to h_A \to \cdots$). Then, the maps evolve at every three steps by $F_3(x) = F_C(F_B(F_A(x)))$ where

$$\begin{aligned} F_A(x_i) &= (1-\varepsilon) f_a(x_i) + h_A \\ F_B(x_i) &= (1-\varepsilon) f_a(x_i) + h_B \\ F_C(x_i) &= (1-\varepsilon) f_a(x_i) + h_C. \end{aligned}$$

An important observation is that at each step *all* maps obey the *common* logistic map F's. Therefore it suffice to study $F_3(x)$ to investigate $p3c2$ cluster attractor. In Fig. 5, $F_3(x)$ with measured values of h_A, h_B, h_C at $p3c2$ cluster attractor are shown along with the line $y = x$. We clearly observe that the case resembles the tangent bifurcation of a single logistic map, but there is an important difference. Now, we observe that only two crossings are stable and each of them attract maps forming two clusters. This is the mechanism for the realization of $p3c2$ cluster attractor. More analytic treatment involving the prediction of the values of h_A, h_B, h_C is under study.

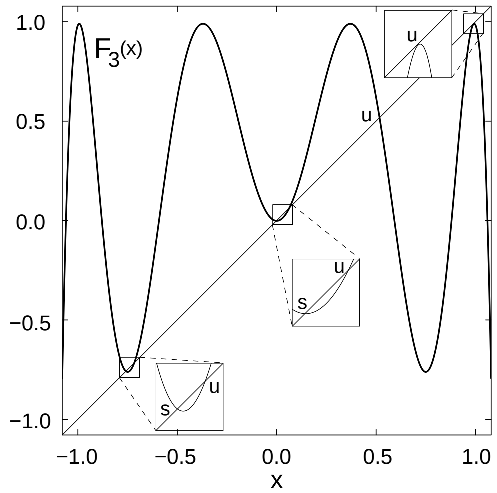

FIG. 5: The mechanism for the $p3p2$ cluster synchronization. $F_3(x) = F_C(F_B(F_A(x)))$ crosses the line $y = x$ at just two stable points, which attract the maps to form eventually two clusters in period 3 motion with $2\pi/3$ mutual phase difference.

IV. MANY SMALL WINDOWS

Up to this point we focused our attention to the predominant period three PM's. Before closing this article we comment on the sharp valleys and peaks in the MSD curve in the lower and upper b regions than the $p3$ window. We show here that they are the reflection of the windows with narrower widths. In fact there is $(2^{p-1} - 1)/p$ windows with a prime number period p [10, 11] and, with the increase of p, they become more dense in the interval of the nonlinear parameter b. Accordingly the width of the window rapidly becomes narrower. We find that it is sufficient to include the windows with period less than 20 in order to account for the valley and peaks in the lower b region than the $p3$ window. In Fig. 6, we show the location of windows by the zeros of the supertruck functions. It can be seen that these windows are responsible for the valley and peak of the MSD curve ($N = 10^6$ GCML sampled at $r = 0.98$).

In summary we have reported our new observations on the periodicity manifestations of the homogeneous logistic GCML. A new phenomena induced by the basin structure in the free gas GCML is reported. The change of the GCML dynamics from the free gas model to the synchronization with the decrease of r from 1 (the increase of ε from zero) is studied in detail. The mechanism realizing $p3c2$ cluster attractor is shown. The relation between the many small valley-peak structure and the periodic windows are exhibited by the supertruck technique.

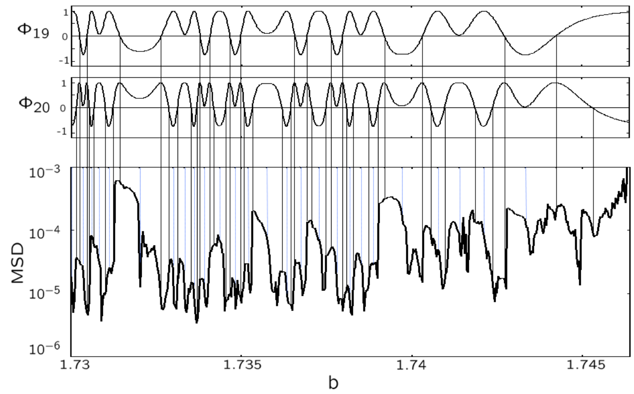

FIG. 6: Valley-peak structure of the MSD curve (lower) and zeros of supertruck curves (upper). Zeros of $p = 19, 20$ windows are shown by solid lines and those with lower period by dotted lines. ($p = 11, 13, 14, 15, 16, 17, 18, 19, 20$ windows contribute respectively $1, 1, 1, 3, 4, 6, 10, 16, 26$ zeros for $b \in [1.73, 1.75]$.)

One of us (TS) thanks Kengo Kikuchi for his enthusiasm in the early stage of this work in 1999.

[1] K. Kaneko, Phys. Rev. Lett. **63**, 219 (1989).
[2] K. Kaneko, Phys. Rev. Lett. **65**, 1391 (1990).
[3] T. Shibata and K. Kaneko, Physica **D**124, 177 (1998).
[4] T. Shibata and K. Kaneko, Phys. Rev. Lett. **81**, 4116 (1998).
[5] A. P. Parravano and M. G. Cosenza, Cluster dynamics in systems with constant mean field coupling, chao-dyn/9808009.
[6] T. Shimada and K. Kikuchi, Phys. Rev. **E**62, pp.3489-3503 (2000)
[7] T. Shimada and K. Kikuchi, Periodic Cluster Attractors and their Stabilities in the Turbulent Globally Coupled Map Lattice, in *Prococeedings of International Symposium on Artificial Life and Robotics*, **2**, 313-316 (2001);
[8] T. Shimada and S. Tukada, Physica **D**168-169, pp. 126-135 (2002).
[9] G. Perez and H. A. Cerdeira, Phys. Rev. **A46**, 7492 (1992).
[10] N. Metropolis, M. L. Stein and P. R. Stein, J. Comb. Theory, **A**15, 25 (1973).
[11] K. Kikuchi and T. Shimada, Transaction of JSCES, paper no. 20020005.

Stability analysis of the wheeled humanoid robot

Hyun-Uk Ha, Sang-Won Ryu, Jang-Myung Lee

Dept. of Electronic Engineering, Pusan National Univ.

(Tel : +82-51-510-1696; Fax :+82-51-514-1693)
(hhook@pusan.ac.kr , ryu5086@pusan.ac.kr , jmlee@pusan.ac.kr)

Abstract: Stability of a mobile inverted pendulum has been analyzed through the kinematic and dynamic analysis of the mobile inverted pendulum based on the proposed model. The motion of the manipulator which is installed on the top of the mobile robot is considered as the unpredictable disturbance. There are several factors that un-stabilize the mobile inverted pendulum: 1. The long response time of tilt sensor and accelerator meter, 2. Accumulated error of gyroscope, 3. The unpredictable motion of the humanoid type manipulator, 4. Quantization error and processing delay of A/D converter, and 5. Limited sampling time based on the processing speed of the processor. The mobile inverted pendulum is similar to the automated segway. Instead of a human on the segway, the humanoid type manipulator is driving the segway. The manipulator motion changes the center of gravity of the mobile inverted pendulum while it is moving, which may cause the unstable fall down of the mobile inverted pendulum. Stability of the mobile inverted pendulum has been proved using Lyapunov stability criterion. Effectiveness of the proposed algorithm has been verified through the real experiments and the results are shown.

Keywords: Mobile inverted pendulum, Segway, Stability, Lyapunov, Service robot

I. INTRODUCTION

This paper focuses on the stability analysis of the wheeled humanoid robot, called 'Segway' or 'Mobile inverted pendulum'. After 'Segway' is invented by Dean Kamen for commercial purpose in 2001[2], its kinematic analysis and dynamic analysis are well studied[1][3][4], but its stability analysis is insufficient. So this paper suggests a stability analysis of the 'Mobile inverted pendulum'. The reliability of the transport in the next generation is hang on 1. the modeling of the 'Mobile inverted pendulum' is reasonable[6] 2. how's the model's stability 3. the simulations can be accepted. In the section 2, derive the pendulum equation and find the equilibrium points using phase portrait, in section 3, stability analysis of the model of 'Mobile inverted pendulum' using Lyapunov stability criterion. In section 4, kinematics and dynamics analysis will be discussed. And last, in section 5, the result of overall block diagram and simulated with rule based fuzzy rule, and dynamic simulation will be shown.

II. Pendulum equation

From the most simple equation of 'Mobile inverted pendulum', conduct real model of the robot. First consider the pendulum state equation from Fig.1. and find its equilibrium point using phase portrait in Matlab[7].

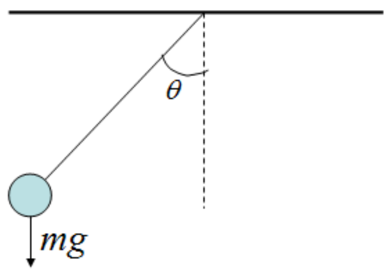

Fig.1. Motion of the pendulum.

Consider the simple pendulum shown in Fig.1., where l indicates the length of the rod and m indicates the mass of the rod. Let θ denotes the angle of the pendulum. Angular velocity is derivative value of angle, and tangential force equation of the pendulum is

$$\dot{x}_1 = x_2 \tag{1-a}$$

$$\dot{x}_2 = -\frac{g}{l}\sin x_1 - \frac{k}{m}x_2 \tag{1-b}$$

Where state x_1 is angle, θ, and state x_2 is angular velocity of the pendulum, g is gravity acceleration, k is friction coefficient term. Using these equations, to find the equilibrium point, set $x_1 = 0$, $x_2 = 0$, and solve for x_1 and x_2.

$$0 = x_2 \tag{2-a}$$

$$0 = -\frac{g}{l}\sin x_1 - \frac{k}{m}x_2 \tag{2-b}$$

©ISAROB 2009

From this equations the equilibrium point in pendulum equation is ($n\pi, 0$), for n=+-1,+-2,… To demonstrate this, draw the phase portrait using equation (1), then we can get Fig.2.

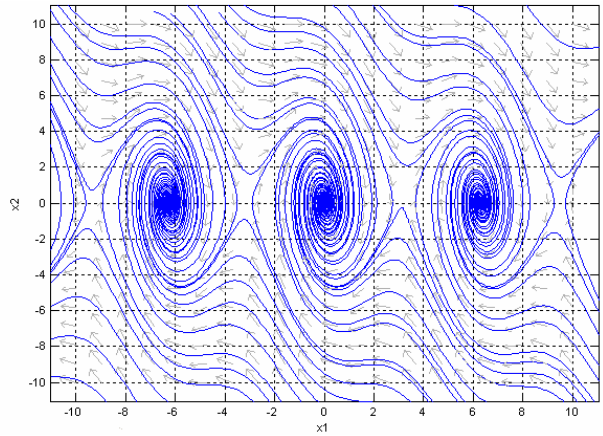

Fig.2. Phase Portrait of mobile inverted pendulum using matlab when $\frac{g}{l}=-10$, $\frac{k}{m}=-1$.

The even number of equilibrium points is stable nodes, and odd number of equilibrium points is saddle points. From the phase portrait, any state of the 'Mobile inverted pendulum' can be estimated.

III. Lyapunov stability

To determine the stability of the 'Mobile inverted pendulum', 1. Set a Lyapunov candidate function, V, from the state equation of section.2. 2. Show that the function, V is Positive definite function, 3. Show that the derivation of the function, $\dot{V}$ is Negative (semi-)definite function, then the system 'Mobile inverted pendulum' is stable in sense of Lyapunov(SISL)[5].

From section 2, the state equation is

$$\dot{x}_1 = x_2 \tag{3-a}$$
$$\dot{x}_2 = -a\sin x_1 - b \tag{3-b}$$

First let Lyapunov candidate function,

$$V(x_1, x_2) = a(1-\cos x_1) + \frac{1}{2}x_2^2 \tag{4}$$

Then derivative of this function is,

$$\dot{V}(x_1, x_2) = a\dot{x}_1 \sin x_1 + x_2\dot{x}_2 \tag{5-a}$$
$$\dot{V}(x_1, x_2) = ax_2 \sin x_1 + x_2(-a\sin x_1 - bx_2) = -bx_2^2 \tag{5-b}$$

This equation is negative semi-definite function, so origin is stable in sense of Lyapunov. From LaSalle's theorem[5], the derivative of Lyapunov candidate function of this system, $\dot{V}$ is Negative definite function. So the origin is asymptotically stable.

IV. Kinematics & Dynamics

In this section, modeling the 'Mobile inverted pendulum' and analyze the kinematics and dynamics. First assume that humanoid robot at the upper body is considered as output disturbance when analyzing the motion of the 'Mobile inverted pendulum'. The model of the 'Mobile inverted pendulum' is shown in Fig.3. Its kinematic analysis is shown in Fig.3.

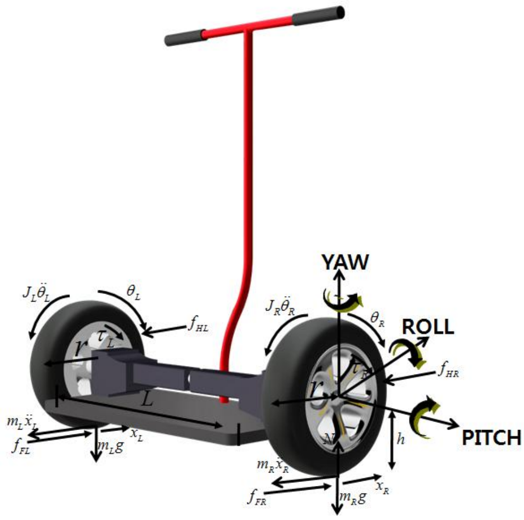

Fig.3. Kinematics of the 'Mobile inverted pendulum'.

Where, J_R, J_L is each wheel inertia, m_R, m_L is mass of each wheel, r is radius of wheel, θ_R, θ_L is angle of each wheel's turn, F_F is friction force of each wheel. But its kinematic model is insufficient to describe the system, so to balance the two wheeled 'Mobile inverted pendulum', the goal should be achieved by dynamic analysis. From Fig.3. model of right wheel is,

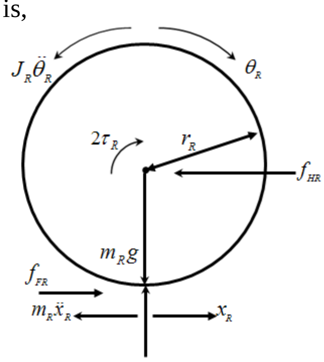

Fig. 4. Kinematic analysis of the right wheel (Left wheel's kinematics is exactly same).

©ISAROB 2009

From Fig.4. J_R is rotational inertia of the wheel, m_R is mass of right wheel, θ_R is angle of right wheel turns, r is radius of the wheel, x is moving distance of 'Mobile inverted pendulum', f_{FR} is friction force between right wheel and ground, f_{HR} is external force to the wheel, τ_R is torque of right motor. The equation of wheel in horizontal axis and vertical axis is,

$$m_R\ddot{x}_R + f_{HR} - f_{FR} = 0 \tag{6-a}$$
$$m_R g - N + f_C = 0 \tag{6-b}$$

where N is normal force from the earth, and f_C is vertical force from the upper body model. From the rotational force in right hand rule is,

$$2\tau_R - J_R\ddot{\theta}_R - f_{FR}r_R = 0\,. \tag{7}$$

We consider the humanoid robot as external disturbance, so humanoid robot can be modeling like chassis like Fig.6.

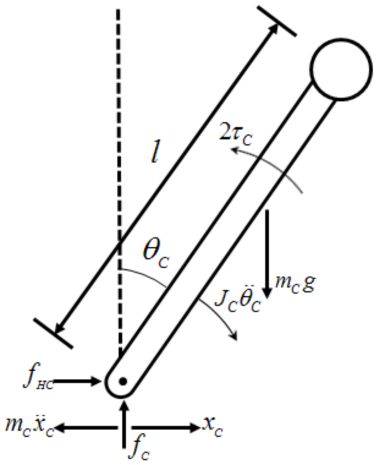

Fig.5. Modeling of the humanoid robot as chassis.

The equation algorithm is same with above wheel equation. The equation of chassis in horizontal axis and vertical axis is,

$$m_C\ddot{x} - f_H = 0 \tag{8-a}$$
$$m_C g - f_C = 0 \tag{8-b}$$

Last, the rotational force equation in right hand rule is,

$$m_C g\sin\theta_C + J_C\ddot{\theta}_C - 2\tau_C = 0 \tag{9}$$

Using the torque to the wheel from Fig.4.,

$$F_{FR} = V_S\left(\frac{K}{r_R R_R}\right) - \dot{\omega}\left(\frac{K}{J_R R_R}\right) - \omega\left(\frac{K^2}{r_R R_R}\right) \tag{10}$$

Using the known equation (10) and the motor equation can be calculated as,

$$-m_C g\sin\theta_C - J_C\ddot{\theta}_C + J_R\ddot{\theta}_R + F_{FR}r_R = 0 \tag{11}$$

From equation (10) and (11),

$$\ddot{\theta}_C = -\frac{g\sin\theta_C}{l^2} + \left(\frac{m_R r}{2m_C l^2} - \frac{J}{rm_C l^2}\right)\ddot{x} + \left(\frac{-K^2}{r_R R_R m_C l^2}\right)\dot{x} + \left(\frac{K}{R_R m_C l^2}\right)V_S \tag{12}$$

Motor equation is substituted into this, then obtain,

$$-m_C\ddot{x} + F_{FR} + m_R\ddot{x} = 0 \tag{13}$$

Inserting F_{FR} and recalculate, then

$$\ddot{x} = -\dot{x}\left(\frac{K^2}{R_R(m_C r_R^2 + J + m_R r_R^2)}\right) + \left(\frac{Kr_R}{R_R(m_C r_R^2 + J + m_R r_R^2)}\right)V_S \tag{14}$$

From these equations, we can get,

$$\dot{x} = v \tag{15-a}$$
$$\dot{v} = -\left(\frac{K^2}{R_R\cdot(m_C r_R^2 + J + m_R r_R^2)}\right)v + \left(\frac{K\cdot r_R}{R_R\cdot(m_C r_R^2 + J + m_R r_R^2)}\right)V_S \tag{15-b}$$
$$\dot{\theta}_C = \omega_C \tag{15-c}$$
$$\ddot{\omega}_C = -\frac{g\cdot\sin\theta_C}{l^2} + \left(\frac{m_R r}{2m_C l^2} - \frac{J}{rm_C l^2}\right)\dot{v} + \left(\frac{-K^2}{r_R R_R m_C l^2}\right)v + \left(\frac{K}{R_R m_C l^2}\right)V_S \tag{15-d}$$

V. Simulations

1. Scheme diagram of 'Mobile inverted pendulum'

Our lab make a real 'Mobile inverted pendulum' from Fig.6. The overall scheme diagram is shown in Fig.6.

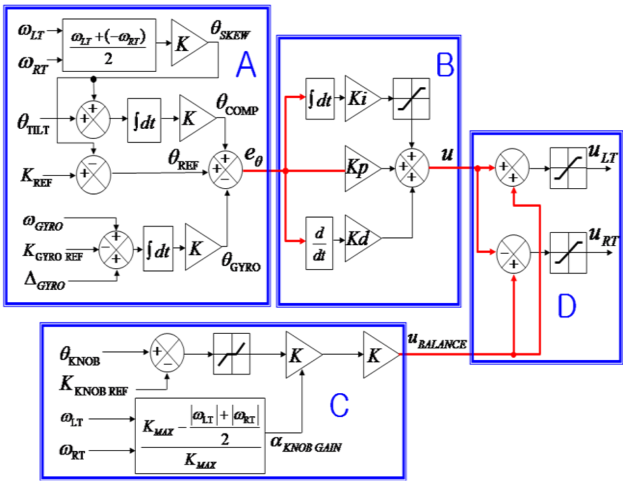

Fig.6. Block scheme diagram of 'Mobile inverted pendulum'.

Part A is sensor part, A/D converted the gyroscope signal and tilt signal and calculate the angle and angular velocity. Part B is PID controller, which gain is auto tuning using adaptive control or user gain tuning while riding the 'Mobile inverted pendulum' on the variable resistor on the PCB board. Part C is streering, we can get the knob signal using A/D converter. And the value determine the direction of the 'Mobile inverted pendulum'. Part D is motor drive, our lab use a 3-phase BLDC motor(200W). Under this specification, the simulator is shown below.

2. Simulation using rule based Fuzzy theorem

Fuzzy theorem is a good tool to simulate the transient response and stability of the 'Mobile inverted pendulum'. So stability can be simulated by fuzzy toolbox in matlab. The result is shown in Fig.7.

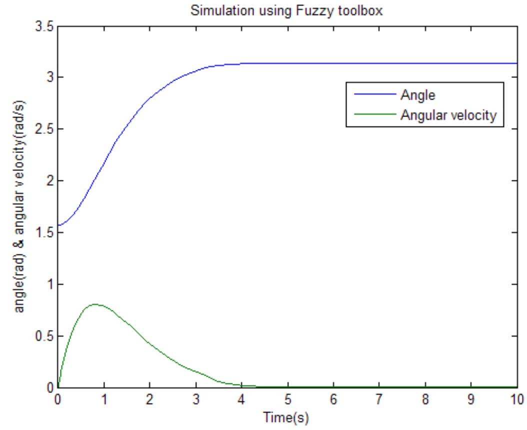

Fig.7. Simulation by 'Rule based fuzzy theory'.

From the Fig.7., the steady state value of angle is π, so simulation result is stable for the fuzzy controller.

VI. CONCLUSION

'Mobile inverted pendulum', or 'Segway', is a good candidate for the next generation personal transportation[8]. As a future business model, the service robot can be built by the 'Mobile inverted pendulum' and a humanoid robot on the mobile platform. The stability analysis of the robot is essential for reliability. In this paper, a method for stability confirmation has been suggested and proved by the simulation. In this paper, the motion of the upper body, that is, humanoid robot is just considered as external disturbances. The motion of humanoid changes COG (Center of Gravity), which makes it difficult to model the 'Mobile inverted pendulum.' Instead of trying to obtain an exact model, this motion as considered as disturbances to the autonomous system. For this, the motion of the upper body has been modeled as time varying state equations using the encoder data at each motor. To apply for the service robot, a CCD camera is used to gather the environment data. The coordination between 'Mobile inverted pendulum' and humanoid manipulator is achieved with PID adaptive and robust control algorithm.

Fig.8. Hardware of the 'Mobile inverted pendulum' and upper body, humanoid manipulator.

VII. ACKNOWLEDGEMENT

"This work was supported by the Korea Research Foundation Grant funded by the Korean Government (MOEHRD)", (KRF-2007-521-D00119), in which main calculations were performed by using the supercomputing resource of the Korea Institute of Science and Technology Information(KISTI)

REFERENCES

[1] F. Grasser, A. D'Arrigo, S. Colombi "JOE: a mobile, inverted pendulum", *IEEE Transactions on industrial electronics*, vol. 49, no. 1, pp. 107-114, Mar. 2002.
[2] S. S. Kim and S. Jung, "Hardware implementation of a real time neural network controller with a DSP and an FPGA board," *in Proc. IEEE ICRA*, pp. 4639–4644, 2004.
[3] M. W. Spong, P. Corke, and R. Lozano, "Nonlinear control of the inertia wheel pendulum," *Automatica*, vol. 37, pp. 1845–1851, 2001.
[4] H. Seraji and A. Howard, "Behavior-based robot navigation on challenging terrain: a fuzzy logic approach," *IEEE Transactions on Robotics and Automation*, vol. 18, no. 3, 2002.
[5] K. Pathak, J. Franch, and S. K. Agrawal, "Velocity and position control of a wheeled inverted pendulum by partial feedback linearization," *IEEE Transactions on Robotics and Automation*, vol. 21, no. 3, pp. 505–513, Jun. 2005.
[6] S. Jung and H. T. Cho, "Decentralized neural network reference compensation technique for PD controlled two degrees of freedom inverted pendulum," *Int. J. Control, Automation., Syst.*, vol. 2, no. 1, pp. 92–99, 2004.

©ISAROB 2009

The Fourteenth International Symposium on Artificial Life and Robotics 2009 (AROB 14th '09),
B-Con Plaza, Beppu, Oita, Japan, February 5 - 7, 2009

Trajectory tracking control of mobile robots without using longitudinal velocity measurement

Koei Maeda, Masahiro Oya, Qiang Wang, Katsuhiro Okumura

Department of Mechanical and Control Engineering, Kyushu Institute of Technology
1-1 Sensui-cho, Tobata-ku, Kitakyushu-shi, Fukuoka, Japan
(Tel: +81-93-884-3186; Fax: +81-93-861-1159)
(E-mail: g344221k@tobata.isc.kyutech.ac.jp)

Abstract: In this paper, a new robust trajectory tracking control scheme for wheeled mobile robots without longitudinal velocity measurement is proposed. In the proposed controller, the velocity observer is used to estimate the velocity of wheeled mobile robot. The developed controller has the following good properties. The developed controller does not require any accurate knowledge of robot parameters and motor parameters. Even if there are the uncertainties in the robot dynamics including motor properties, it can be assured that tracking errors become uniformly ultimately bounded in the closed-loop system using the developed controller. It is shown theoretically that the ultimate norms of tracking errors can be reduced easily by setting only one design parameter.

Keywords: mobile robots, trajectory tracking

I. INTRODUCTION

There are many dangerous tasks for human workers in extreme environments such as stricken areas and planet surfaces. Therefore, mobile robots working instead of human in the environments have become the focus of the attention, and recently, trajectory tracking control schemes for wheeled mobile robots have been developed[1]-[7]. The proposed controllers require full state measurement including velocity measurements. However, in general, full state measurements may not be available due to cost of sensors, weight limitation, effects of noises, and so on. Especially for the longitudinal velocity measurement, the required accuracy may not be achieved in practical applications due to the existence of noises. Most recently, the trajectory tracking control schemes without using velocity measurement have been proposed[8]-[10]. The proposed controllers require some accurate knowledge of robot parameters such as the position of gravity center and radius of wheel. If there are uncertainties in the position of gravity center and radius of wheel, the proposed controllers may give a poor performance and even cause instability. Another observation is that torque inputs are considered in the proposed schemes. Torque inputs are generated by motors in practical application. If there are uncertainties in the motor properties, the control performance can not be achieved in the closed loop system using the developed controllers.

To overcome the problem, based on the dynamic model including properties of motors, a robust trajectory tracking controller without using the longitudinal velocity measurement is proposed in this paper. In general, yaw rate can be measured with a low-cost sensor, and the measurements of the yaw rate sensors are widely used. Thus, we develop a controller using measurements of the position and the yaw rate. For the longitudinal velocity of the mobile robot, a robust estimator is designed.

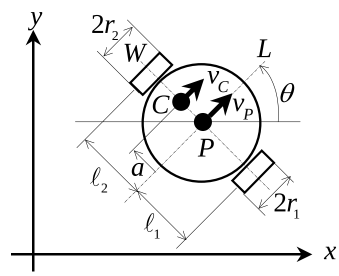

Fig. 1. Two wheels model

II. CONTROLLED OBJECT AND TRACKING ERROR EQUATION

Fig.1 shows 2-wheeled mobile robot model. In Fig.1, the axes x and y denote Cartesian coordinates, C denotes the center of gravity and P denotes the reference point. Longitudinal velocity at the points C and P are denoted by $v_c(t)$ and $v_p(t)$, and oriental angle is given by $\theta(t)$. The symbol a denotes the distance from the reference point P to the center of gravity C. The velocities $v_c(t)$ and $v_p(t)$ satisfy the relation $v_c(t) = v_p(t) - a\dot{\theta}(t)$. Definitions for parameters of wheeled mobile robot are shown in Table 1. Assuming the nonholonomic constraint and nonslipping, dynamic equation is given by the following equations [8].

$$\dot{\boldsymbol{q}}(t) = S(\boldsymbol{q})\boldsymbol{v}(t),\ M_p\dot{\boldsymbol{v}}(t) + D_p\boldsymbol{v}(t) = \Gamma K_{rw}\boldsymbol{u}_m(t) \quad (1)$$

$$\left.\begin{array}{l} \boldsymbol{q}(t) = [x_p(t), y_p(t), \theta(t)]^T, \boldsymbol{v}(t) = [v_p(t), \dot{\theta}(t)]^T \\ \boldsymbol{u}_m(t) = [u_{mR}(t), u_{mL}(t)]^T \\ M = \mathrm{diag}[m,\ I_c],\ R = \mathrm{diag}[1/r_1,\ 1/r_2] \\ J_w = \mathrm{diag}[J_{Rw} + n^2 J_{Rm},\ J_{Lw} + n^2 J_{Lm}] \\ B_w = \mathrm{diag}[n^2 K_{Rt} R_{Ra}^{-1} K_{Rb},\ n^2 K_{Lt} R_{La}^{-1} K_{Lb}] \\ K_w = \mathrm{diag}[n K_{Rt} R_{Ra}^{-1},\ n K_{Lt} R_{La}^{-1}] \\ M_p = (H^T)^{-1} M H^{-1} + \Gamma R J_w R \Gamma^T \\ D_p = \Gamma R B_w R \Gamma^T,\ K_{rw} = R K_w \end{array}\right\} \quad (2)$$

Table 1 Notation of mobile robot model

x_p, y_p	the position of reference point P in $x-y$ coordinates
θ	oriental angle
v_p	longitudinal velocity of mobile robot at the reference point P
m	mass of mobile robot
I_c	moment of inertia for mobile robot around the center of gravity C
ℓ_1, ℓ_2	distances from P to right wheel and left wheel
r_1, r_2	the radius of right wheel and left wheel
a	distance from the reference point P to the center of gravity C
n	gear ratio for motor
u_{mR}, u_{mL}	voltage of right wheel motor and left wheel motor
R_{Ra}, R_{La}	armature resistance
J_{Rw}, J_{Lw}	moment of inertia for right wheel and left wheel
J_{Rm}, J_{Lm}	moment of inertia for right wheel motor and left wheel motor
K_{Rt}, K_{Lt}	torque constant of right wheel motor and left wheel motor
K_{Rb}, K_{Lb}	voltage constant of right wheel motor and left wheel motor

$$S(\boldsymbol{q})=\begin{bmatrix}\cos\theta(t) & 0\\ \sin\theta(t) & 0\\ 0 & 1\end{bmatrix},\ \Gamma=\begin{bmatrix}1 & 1\\ \ell_1 & -\ell_2\end{bmatrix},\ H=\begin{bmatrix}1 & a\\ 0 & 1\end{bmatrix} \qquad (3)$$

Where $\dagger_{R\bullet}$ and $\dagger_{L\bullet}$ denote parameters with respect to right and left wheel including a motor. The control input is the motor voltage $\boldsymbol{u}_m(t) = [u_{mR}(t), u_{mL}(t)]^T$. The reference point P is determined by designer. Thus, it is obvious that the distance ℓ_1 and ℓ_2 are known. Then, the matrix Γ is known matrix. Other system parameters include uncertainties.

Desired trajectory $\boldsymbol{q}_d(t)$ is given by the following equations.

$$\left.\begin{array}{l}\dot{\boldsymbol{q}}_d(t) = S(\boldsymbol{q}_d)\boldsymbol{v}_d(t)\\ \boldsymbol{q}_d(t) = [x_d(t),\ y_d(t),\ \theta_d(t)]^T\\ \boldsymbol{v}_d(t) = [v_{d1}(t), v_{d2}(t)]^T\end{array}\right\} \qquad (4)$$

The tracking error is defined as follows.

$$\left.\begin{array}{l}\widetilde{\boldsymbol{q}}(t) = \boldsymbol{q}(t) - \boldsymbol{q}_d(t) = [\widetilde{x}(t),\ \widetilde{y}(t),\ \widetilde{\theta}(t)]^T\\ \widetilde{x}(t) = x(t) - x_d(t),\ \widetilde{y}(t) = y(t) - y_d(t)\\ \widetilde{\theta}(t) = \theta(t) - \theta_d(t)\end{array}\right\} \qquad (5)$$

Then, using the scheme shown in [8], the new error signal $[w(t),\ \boldsymbol{z}(t)^T]^T \in \boldsymbol{R}^3$, $\boldsymbol{z}(t) = [z_1(t),\ z_2(t)]^T \in \boldsymbol{R}^2$ and signal $\boldsymbol{u}(t)$ are defined as follows.

$$\begin{bmatrix}w(t)\\ \boldsymbol{z}(t)\end{bmatrix} =\begin{bmatrix}-\widetilde{\theta}(t)\cos\theta(t)+2\sin\theta(t) & -\widetilde{\theta}(t)\sin\theta(t)-2\cos\theta(t) & 0\\ 0 & 0 & 1\\ \cos\theta(t) & \sin\theta(t) & 0\end{bmatrix}\widetilde{\boldsymbol{q}}(t) \qquad (6)$$

$$\begin{aligned}\boldsymbol{u}(t) &= T(t)^{-1}\boldsymbol{v}(t) - \begin{bmatrix}v_{d2}(t)\\ v_{d1}(t)\cos z_1(t)\end{bmatrix}\\ &= T(t)^{-1}\boldsymbol{v}(t) - \boldsymbol{f}_u(t)\end{aligned} \qquad (7)$$

$$T(t)=\begin{bmatrix}0.5(w(t)+z_1(t)z_2(t)) & 1\\ 1 & 0\end{bmatrix}=\begin{bmatrix}f_T(t) & 1\\ 1 & 0\end{bmatrix} \qquad (8)$$

Then, the tracking error equation is given by the following equations [8].

$$\left.\begin{array}{l}\dot{w}(t) = \boldsymbol{u}(t)^T J^T \boldsymbol{z}(t) + f(t)\\ \dot{\boldsymbol{z}}(t) = \boldsymbol{u}(t)\\ f(t)=2(v_{d2}(t)z_2(t)-v_{d1}(t)\sin z_1(t)),\ J=\begin{bmatrix}0 & -1\\ 1 & 0\end{bmatrix}\end{array}\right\} \qquad (9)$$

Assuming that the signal $\boldsymbol{u}(t)$ can be used as the control input, the tracking error system (6) can be stabilized by the following controller [8].

$$\boldsymbol{u}(t) = \boldsymbol{u}_a(t) - k_2\boldsymbol{z}(t) \qquad (10)$$

$$\left.\begin{array}{l}\boldsymbol{u}_a(t) = \sigma(t)J\boldsymbol{z}_d(t) + \Omega_1(t)\boldsymbol{z}_d(t)\\ \sigma(t) = \varepsilon_1^{-2}(k_1 w(t) + f(t))\\ \Omega_1(t) = k_2 + w(t)\sigma(t)\\ \dot{\boldsymbol{z}}_d(t) = (\sigma(t)+w(t)\Omega_1(t)J\boldsymbol{z}_d(t),\ \|\boldsymbol{z}_d(0)\|^2 = \varepsilon_1^2\end{array}\right\} \qquad (11)$$

Where $k_i \geq 0, i = 1, 2$, $\varepsilon_1 > 0$ are design parameters. In fact, the signal $\boldsymbol{u}(t)$ can not be used as control input. To struggle the problem, let's consider the designed signal (7) as the desired signal $\boldsymbol{u}_d(t)$ for the signal $\boldsymbol{u}(t)$, and then, the error signal $\boldsymbol{\eta}(t)$ and $\widetilde{\boldsymbol{z}}(t)$ are defined as $\boldsymbol{\eta}(t) = [\eta_1(t), \eta_2(t)]^T = \boldsymbol{u}_d(t) - \boldsymbol{u}(t)$, $\widetilde{\boldsymbol{z}}(t) = \boldsymbol{z}_d(t) - \boldsymbol{z}(t)$. Using the same manner stated in [8], the following error equations can be obtained.

$$\left.\begin{array}{l}\dot{w}(t) = -k_1 w(t) + \boldsymbol{u}_a(t)^T J\widetilde{\boldsymbol{z}}(t) + \boldsymbol{\eta}(t)^T J\boldsymbol{z}(t)\\ \dot{\widetilde{\boldsymbol{z}}}(t) = -k_2\widetilde{\boldsymbol{z}}(t) + w(t)J\boldsymbol{u}_a(t) + \boldsymbol{\eta}(t)\end{array}\right\} \qquad (12)$$

$$\begin{aligned}M_\eta(t)\dot{\boldsymbol{\eta}}(t) = &-(V_\eta(t)+D_\eta(t))\boldsymbol{\eta}(t)+V_\eta(t)\boldsymbol{u}_d(t)\\ &+M_\eta(t)(\dot{\boldsymbol{d}}(t)+v_{d2}(t)\dot{\boldsymbol{h}}(t))+D_\eta(t)\boldsymbol{d}(t)\\ &-T(t)^T\Gamma K_{rw}\boldsymbol{u}_m(t)\end{aligned} \qquad (13)$$

$$\left.\begin{array}{l}M_\eta(t) = T(t)^T M_p T(t),\ V_\eta(t) = T(t)^T M_p \dot{T}(t)\\ D_\eta(t) = T(t)^T D_p T(t)\\ \boldsymbol{d}(t) = \begin{bmatrix}v_{d2}(t)\\ v_{d1}(t)\cos z_1(t)\end{bmatrix} + \boldsymbol{u}_d(t)\\ \boldsymbol{h}(t) = \begin{bmatrix}0\\ 0.5(w(t) + z_1(t)z_2(t))\end{bmatrix}\end{array}\right\} \qquad (14)$$

For the error system (12)$\sim$(14), the following properties hold.

P1 The matrixes $M_\eta(t)$, $V_\eta(t)$ and K_{rw} are positive definite matrixes.

P2 There exist bounded positive constants $\underline{\rho}_{mp}$, $\overline{\rho}_{mp}$, $\underline{\rho}_{dp}$, $\overline{\rho}_{dp}$, $\underline{\rho}_k$, and $\overline{\rho}_k$ satisfying the relations $\underline{\rho}_{mp}\boldsymbol{x}^T\boldsymbol{x} \leq \boldsymbol{x}^T M_p\boldsymbol{x} \leq \overline{\rho}_{mp}\boldsymbol{x}^T\boldsymbol{x}$, $\underline{\rho}_{dp}\boldsymbol{x}^T\boldsymbol{x} \leq \boldsymbol{x}^T D_p\boldsymbol{x} \leq \overline{\rho}_{dp}\boldsymbol{x}^T\boldsymbol{x}$, $\underline{\rho}_k\boldsymbol{x}^T\boldsymbol{x} \leq \boldsymbol{x}^T\Gamma K_{rw}\Gamma^T\boldsymbol{x} \leq \overline{\rho}_k\boldsymbol{x}^T\boldsymbol{x}$, for $\forall\boldsymbol{x}$.

P3 The matrixes $M_\eta(t)$ and $V_\eta(t)$ satisfy the relation $\boldsymbol{x}^T(\dot{M}_\eta(t) - 2V_\eta(t))\boldsymbol{x} = 0$, for $\forall\boldsymbol{x}$.

©ISAROB 2009

III. DEVELOPMENT OF TRACKING CONTROLLER

If the norm of $\boldsymbol{\eta}(t)$ can be reduced to a small value, $\boldsymbol{u}(t)$ converges to the desired signal $\boldsymbol{u}_d(t)$. The norm of error signal $w(t)$ and $\boldsymbol{z}(t)$ become small, and then, the norm of tracking error $\widetilde{\boldsymbol{q}}(t)$ also becomes small. Therefore, the control objective considered here is to develop a controller without using the longitudinal velocity so that the norm of $\|\boldsymbol{\eta}(t)\|$ is reduced to a small value.

To achieve the control objective, the error system (13) is rewritten as follow.

$$
\begin{aligned}
M_\eta(t)\dot{\boldsymbol{\eta}}(t) = &-(V_\eta(t)+D_\eta(t))\boldsymbol{\eta}(t)+M_\eta(t)F_{ud}(t)\boldsymbol{b}\boldsymbol{b}^T\boldsymbol{\eta}(t)\\
&-T(t)^T\Gamma K_{rw}(\boldsymbol{u}_m(t)-\Theta\boldsymbol{\xi}(t))
\end{aligned} \tag{15}
$$

$$
\left.\begin{aligned}
&\Theta = [K_{rw}^{-1}\Gamma^{-1}M_p \;\; K_{rw}^{-1}\Gamma^{-1}D_p]\\
&\boldsymbol{\xi}(t) = \begin{matrix}\boldsymbol{\xi}_a(t)\\ T(t)\boldsymbol{d}(t)\end{matrix}
\end{aligned}\right\} \tag{16}
$$

$$
\left.\begin{aligned}
&\boldsymbol{\xi}_a(t)=T(t)\dot{\boldsymbol{f}}_u(t)+v_{d2}(t)T(t)\dot{\boldsymbol{h}}(t)+\dot{T}(t)\boldsymbol{u}_d(t)\\
&\qquad +T(t)(F_{uda}(t)+F_{ud}(t)\boldsymbol{c}\boldsymbol{c}^T\boldsymbol{\eta}(t))\\
&\dot{\boldsymbol{u}}_d(t) = F_{ud}(t)\boldsymbol{\eta}(t) + F_{uda}(t)\\
&\dot{F}_{ud}(t) = F_{ud1}(t) + F_{ud2}(t)\boldsymbol{b}^T\boldsymbol{\eta}(t)\\
&\boldsymbol{b} = [0\ 1]^T,\ \boldsymbol{c} = [1\ 0]^T
\end{aligned}\right\} \tag{17}
$$

Where the matrix $F_{ud}(t)$, $F_{uda}(t)$, $F_{ud1}(t)$ and $F_{ud2}(t)$ are available. The vector $\boldsymbol{c}\boldsymbol{c}^T\boldsymbol{\eta}(t)$ and $\boldsymbol{b}\boldsymbol{b}^T\boldsymbol{\eta}(t)$ is given as follow.

$$
\left.\begin{aligned}
&\boldsymbol{c}\boldsymbol{c}^T\boldsymbol{\eta}(t)=\boldsymbol{c}(\boldsymbol{c}^T\boldsymbol{u}_d(t)-\boldsymbol{b}^T\boldsymbol{v}(t)+\boldsymbol{c}^T\boldsymbol{f}_u(t))\\
&\boldsymbol{b}\boldsymbol{b}^T\boldsymbol{\eta}(t)=\boldsymbol{b}(\boldsymbol{b}^T\boldsymbol{u}_d(t)-\boldsymbol{c}^T\boldsymbol{v}(t)-f_T(t)\boldsymbol{b}^T\boldsymbol{v}(t)+\boldsymbol{b}^T\boldsymbol{f}_u(t))
\end{aligned}\right\} \tag{18}
$$

In the equation (18), $\boldsymbol{c}\boldsymbol{c}^T\boldsymbol{\eta}(t)$ is not including the longitudinal velocity and available signal. But, $\boldsymbol{b}\boldsymbol{b}^T\boldsymbol{\eta}(t)$ is not available signal.

Based on the system representation (15), we propose the following tracking controller.

$$
\boldsymbol{u}_m(t) = \widehat{\Theta}\boldsymbol{\xi}(t) + k_\eta\Gamma^T T(t)\widehat{\boldsymbol{\eta}}(t) \tag{19}
$$

$$
\begin{aligned}
\widehat{\boldsymbol{\eta}}(t)=&-k_{\tilde{\eta}}\boldsymbol{z}(t)-F_{ud}(t)\boldsymbol{b}\boldsymbol{b}^T\boldsymbol{z}(t)-0.5F_{ud2}(t)\boldsymbol{b}(\boldsymbol{b}^T\boldsymbol{z}(t))^2\\
&-k_\eta T(t)^{-1}\widehat{A}_{MK}T(t)\boldsymbol{b}\boldsymbol{b}^T\boldsymbol{z}(t)+\boldsymbol{\zeta}(t)
\end{aligned} \tag{20}
$$

$$
\begin{aligned}
\dot{\boldsymbol{\zeta}}(t)=&k_{\tilde{\eta}}(\boldsymbol{u}_d(t)-\widehat{\boldsymbol{\eta}}(t))+F_{ud1}(t)\boldsymbol{b}\boldsymbol{b}^T\boldsymbol{z}(t)+F_{ud}(t)\boldsymbol{b}\boldsymbol{b}^T\boldsymbol{u}_d(t)\\
&+F_{ud2}(t)\boldsymbol{b}\boldsymbol{b}^T\boldsymbol{z}(t)\boldsymbol{b}^T\boldsymbol{u}_d(t)+0.5\dot{F}_{ud2}(t)\boldsymbol{b}(\boldsymbol{b}^T\boldsymbol{z}(t))^2\\
&+k_\eta(\dot{T}(t)^{-1}\widehat{A}_{MK}T(t)+T(t)^{-1}\widehat{A}_{MK}\dot{T}(t))\boldsymbol{b}\boldsymbol{b}^T\boldsymbol{z}(t)\\
&+k_\eta(t)T(t)^{-1}\widehat{A}_{MK}T(t)(\boldsymbol{b}\boldsymbol{b}^T\boldsymbol{u}_d(t)+\boldsymbol{c}\boldsymbol{c}^T\boldsymbol{\eta}(t)-\widehat{\boldsymbol{\eta}}(t))\\
&-T(t)^{-1}\widehat{M}_p^{-1}\widehat{D}_pT(t)\widehat{\boldsymbol{\eta}}(t)-T(t)^{-1}\dot{T}(t)\widehat{\boldsymbol{\eta}}(t)
\end{aligned} \tag{21}
$$

$$
\widehat{A}_{MK} = \widehat{M}_p^{-1}\Gamma\widehat{K}_{rw}\Gamma^T,\ K_{\Gamma r} = \Gamma K_{rw}\Gamma^T \tag{22}
$$

Where the constant matrix $\widehat{M}_p$, $\widehat{D}_p$, $\widehat{K}_{rw}$ and $\widehat{\Theta}$ is the estimate for M_p, D_p, K_{rw} and Θ, $\widehat{\boldsymbol{\eta}}(t)$ is the estimate for $\boldsymbol{\eta}(t)$, k_η and $k_{\tilde{\eta}}$ are feedback gain and observer gain, respectively. Differentiating the both side of the equation (20) and using the relation (21), it can be ascertained easily that the estimated error $\widetilde{\boldsymbol{\eta}}(t)$ as $\widetilde{\boldsymbol{\eta}}(t)=\boldsymbol{\eta}(t)-\widehat{\boldsymbol{\eta}}(t)$, satisfies the following error equation.

$$
\begin{aligned}
M_\eta(t)\dot{\widetilde{\boldsymbol{\eta}}}(t) = &-k_{\tilde{\eta}}M_\eta(t)\widetilde{\boldsymbol{\eta}}(t) - k_\eta T(t)^T K_{\Gamma r}T(t)\boldsymbol{\eta}(t)\\
&-(V_\eta(t)+D_\eta(t))\widetilde{\boldsymbol{\eta}}(t)\\
&+T^T(\widetilde{\Theta}_{\tilde{\eta}}\boldsymbol{\xi}_{\tilde{\eta}}(t)+\Gamma K_{rw}\widetilde{\Theta}\boldsymbol{\xi}(t))
\end{aligned} \tag{23}
$$

$$
\left.\begin{aligned}
&\widetilde{\Theta}_{\tilde{\eta}} = [\widetilde{M_p}\;\; \Gamma\widetilde{K}_{rw}\;\; \widetilde{D}_p]\\
&\boldsymbol{\xi}_{\tilde{\eta}}(t)=\begin{bmatrix}-k_\eta\widehat{A}_{MK}T(t)\widetilde{\boldsymbol{\eta}}(t)+\widehat{M}_p^{-1}\widehat{D}_pT(t)(\boldsymbol{\eta}-\widetilde{\boldsymbol{\eta}}(t))\\ k_\eta\Gamma^TT(t)\widetilde{\boldsymbol{\eta}}(t)\\ T(t)(\boldsymbol{\eta}(t)-\widetilde{\boldsymbol{\eta}}(t))\end{bmatrix}
\end{aligned}\right\} \tag{24}
$$

As it is shown in the following theorem, using the developed controller (19)∼(22), the control objective can be realized. To show this fact, for the error system (12)∼(14), (23) and (24), the additional property is shown, and the following assumptions are made.

P4 The signals $\boldsymbol{r}_1(t)$, $\boldsymbol{r}_2(t)$ and $\boldsymbol{e}(t)$ are defined as follows.

$$
\left.\begin{aligned}
&\boldsymbol{r}_1(t)=\boldsymbol{\eta}(t)^TT(t)^T(M_pT(t)F_{ud}(t)\boldsymbol{b}\boldsymbol{b}^T\boldsymbol{\eta}(t)+\Gamma K_{rw}\widetilde{\Theta}\boldsymbol{\xi}(t))\\
&\boldsymbol{r}_2(t)=\widetilde{\boldsymbol{\eta}}(t)^TT(t)^T(\widetilde{\Theta}_{\tilde{\eta}}\boldsymbol{\xi}(t)+\Gamma K_{rw}\widetilde{\Theta}\boldsymbol{\xi}(t))
\end{aligned}\right\} \tag{25}
$$

$$
\left.\begin{aligned}
&\boldsymbol{e}(t) = \begin{bmatrix} w(t)\\ \widetilde{\boldsymbol{z}}(t)\\ \dfrac{1}{k_{max}+1}M_p^{\frac{1}{2}}T(t)\boldsymbol{\eta}(t)\\ \dfrac{1}{k_{max}+1}M_p^{\frac{1}{2}}T(t)\widetilde{\boldsymbol{\eta}}(t)\end{bmatrix}\\
&k_{max} = \max[k_1, k_2]
\end{aligned}\right\} \tag{26}
$$

For the signals $\boldsymbol{r}_1(t)$, $\boldsymbol{r}_2(t)$ and $\boldsymbol{e}(t)$, there exist bounded positive constants $\overline{\rho}_{i,j}, i = 1, 2$ satisfying the following relations.

$$
\begin{aligned}
\|\boldsymbol{r}_i(t)\| \le (k_{max}+1)^2\Bigg\{&\sum_{j=1}^{7}\overline{\rho}_{i,j}\|\boldsymbol{e}(t)\|^j\\
&+\|\widetilde{\Theta}\|\sum_{j=0}^{7}\overline{\rho}_{i,j}\|\boldsymbol{e}(t)\|^j+\overline{\rho}_i\|\widetilde{\Theta}_{\tilde{\eta}}\|\|\boldsymbol{e}(t)\|\Bigg\}
\end{aligned} \tag{27}
$$

A1 The positive constants $\underline{\rho}_{mp}$, $\overline{\rho}_{mp}$, $\underline{\rho}_{dp}$, $\overline{\rho}_{dp}$, $\underline{\rho}_k$ and $\overline{\rho}_k$ are known.

A2 For the positive definite function $V(t) = \boldsymbol{e}(t)^T\boldsymbol{e}(t)$, there exists bounded positive constant $\overline{\rho}_{v0}$ satisfying the relation $V(0) \le \overline{\rho}_{v0}$.

In **P4**, to derive the inequalities, the fact is used that there exists bounded positive constant $\overline{\rho}_T$ satisfying the relation $\|T(t)^{-1}\| \le \overline{\rho}_T\sum_{j=0}^{2}\|\boldsymbol{e}(t)\|^j$. From this fact it can be seen the value of $\overline{\rho}_{i,j}$ can be determimed independent of design parameters k_1, k_2, k_η and $k_{\tilde{\eta}}$. In **A2**, there exists bounded positive constant $\overline{\rho}_{ud}$ satisfying the relation $\|\boldsymbol{u}_d(0)\| \le (k_{max}+1)\overline{\rho}_{ud}$. From this fact it is clear that there exists $\overline{\rho}_{v0}$ independent of design parameters k_1, k_2, k_η and $k_{\tilde{\eta}}$.

The monotonically increasing function $g(V(t))$ is defined as follows.

$$
\begin{aligned}
g(V(t))=&12\|K_{\Gamma r}^{-\frac{1}{2}}\|^2\overline{\rho}_T^2\sum_{j=0}^{2}V(t)^j(V(t)+\frac{1}{2}V(t)^2)\\
&+\overline{\rho}_1\sum_{j=1}^{7}V(t)^j+\overline{\rho}_2\|\widetilde{\Theta}\|^2\sum_{j=0}^{7}V(t)^j+\overline{\rho}_3\|\widetilde{\Theta}_{\tilde{\eta}}\|^2V(t)
\end{aligned} \tag{28}
$$

©ISAROB 2009

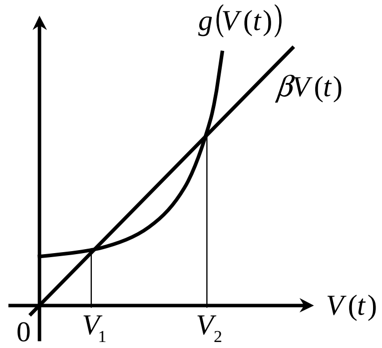

Fig. 2. Real roots of equation $-\beta V(t) + g(V(t)) = 0$

As it is shown in Fig.2, for the design parameter β, there exists $\beta = \underline{\beta} > 0$ such that the equation $-\beta V(t) + g(V(t)) = 0$ has two different real roots $V_i,\ i = 1, 2$. For $V(t) \in [V_1,\ V_2]$, the relation $-\beta V(t) + g(V(t)) \leq 0$ is satisfied. When the design parameter β increases, V_1 is close to zero, and V_2 becomes large.

In the closed loop system using the proposed controller (19)∼(22), the following theorem holds.

Theorem The design parameters $k_i, i = 1, 2,\ k_\eta,\ k_{\tilde{\eta}}$ are set as follows.

$$\left.\begin{array}{l} k_1 = k_2 = \dfrac{\beta}{2},\ \beta > 0 \\ k_\eta = \dfrac{1}{32}(\beta+2)^2(\varepsilon_1^2 + 4) + \dfrac{1}{2}\beta(k_{max}+1)^2 \\ k_{\tilde{\eta}} = \dfrac{1}{8}(\beta+2)^2 + \dfrac{1}{2}\beta(k_{max}+1)^2 \end{array}\right\} \quad (29)$$

Where $\overline{\rho}_{mp}$, $\underline{\rho}_{mp}$, $\overline{\rho}_k$, $\underline{\rho}_k$ and $\underline{\rho}_{dp}$ are known positive values. The parameter β is a design parameter. When the design parameters are fixed except for the design parameter β, there exists $\beta = \underline{\beta} > 0$ such that the real roots V_2 of equation $-\beta V(t) + g(V(t)) = 0$ satisfies the relation $\overline{\rho}_{v0} < V_2$ (see Fig.2). Then, using the design parameter $\beta \geq \underline{\beta}$, the close loop system using the proposed controller (14), (15) becomes stable. Moreover, the error signals $w(t),\ \boldsymbol{z}(t)$ satisfy the following inequalities.

$$\left.\begin{array}{l} |w(t)| \leq \sqrt{\overline{\rho}_{v0} e^{-\beta t} + \dfrac{g(\overline{\rho}_g)}{\beta}} \\ \|\boldsymbol{z}(t)\| \leq \sqrt{\overline{\rho}_{v0} e^{-\beta t} + \dfrac{g(\overline{\rho}_g)}{\beta}} + \varepsilon_1 \\ \overline{\rho}_g = \max[\overline{\rho}_{v0},\ \mathrm{V}_1] \end{array}\right\} \quad (30)$$

Where $\overline{\rho}_{v0},\ \overline{\rho}_g$ are bounded positive constant independent of design parameter β.

The closed loop system is stable but not asymptotically stable. However, from the inequalities (30), the ultimate value of error signals $w(t)$ and $\boldsymbol{z}(t)$ become $|w(t)| \leq \sqrt{g(\overline{\rho}_g)/\beta},\ \|\boldsymbol{z}(t)\| \leq \sqrt{g(\overline{\rho}_g)/\beta} + \varepsilon_1$. Setting the design parameter ε_1 to be a small value and the design parameter β to be a large value, $|w(t)|$ and $\|\boldsymbol{z}(t)\|$ can be reduced to a small value. Moreover, the tracking performance can be improved by increasing the design parameter β.

IV. CONCLUSION

In this paper, a new robust trajectory tracking control scheme is proposed for wheeled mobile robots. In the proposed controller, the velocity observer is used to estimate the velocity of wheeled mobile robot. The proposed controller does not require the longitudinal velocity measurement. The proposed controller has robustness not only for the weight and the moment of inertia but also the position of gravity center, the radius of wheel and the uncertainties of motor. Moreover, it is easy to improve tracking performance by setting only one design parameter.

REFERENCES

[1] W. E. Dixon, D. M. Dawson, and E. Zergeroglu et al (2000), Robust Tracking and Regulation Control for Mobile Robots, Int. J. Robust and Nonlinear Control 10:199-216.

[2] T.C. Lee, K.T. Song, and C.H. Lee et al (2001), Tracking control of unicycle-modeled mobile robots using a saturation feedback controller, IEEE Transactions on Control Systems Technology 9(2):305-318.

[3] W. E. Dixon, M. S. de Queiroz, and D. M. Dawson (2002), Adaptive Tracking and regulation of a Wheeled Mobile Robot with Controller / Update Law Modularity, Proc. IEEE Conf. Robotics and Automation :2620-2625

[4] D.-K. Chwa, J. H. Seo, and P. Kim et al (2002), Sliding Mode Tracking Control of Nonholonimic Wheeled Mobile Robots, Proceedings of the American Control Conference :3991-3996

[5] Wei Ren, Ji-Sang Sun, and Randal W. Beard et al (2005), Nonlinear Tracking Control for Nonholonomic Mobile Robots with Input Constraints: An Experimental Study, Proc. of 2005 American Control Conference, June 8-10,. Portland, OR, USA :4923-4928

[6] L. Lapierre, D. Soetanto, and A. Pascoal (2006), Nonsingular path following control of a unicycle in the presence of parametric modelling uncertainties, Int. J. Robust Nonlinear Control 16:485-503

[7] Jian Wanga, Xiangyang Zhub, and Masahiro Oya (2006), Robust motion tracking control of partially nonholonomic mechanical systems, Robotics and Autonomous Systems 54:332-341

[8] W. E. Dixon, D. M. Dawson, and E. Zergeroglu et al (2001), Nonlinear Control of Wheeled Mobile Robots, Lecture Notes in Control and Information Sciences 262, Springer

[9] K.D. Do, Z.P. Jiang, and J. Pan (2003), Simultaneous tracking and stabilization of mobile robots without velocity measurements, Proceedings of the 42nd IEEE Conference on Decision and Control, Maui, Hawaii USA, December :3852-3857

[10] K.D. Do, and J. Pan (2006), Global output-feedback path tracking of unicycle-type mobile robots, Robotics and Computer-Integrated Manufacturing 22:166-179

©ISAROB 2009

The Fourteenth International Symposium on Artificial Life and Robotics 2009 (AROB 14th '09),
B-Con Plaza, Beppu, Oita, Japan, February 5 - 7, 2009

Integration of stereo vision system and laser range finder for autonomous obstacle avoidance and map construction

Yau-Zen Chang[1], Jung-Fu Hou[2], and Yung-Pyng Chang[3]

[1,2]*Dept. of Mechanical Engineering, Chang Gung University, Tao-Yuan 33302, Taiwan*
[3]*Chung-Shan Institute of Science & Technology, Tao-Yuan 325, Taiwan*
[1]*zen@mail.cgu.edu.tw;* [2]*frid.hou@gmail.com;* [3]*ypc88@yahoo.com.tw*

Abstract: In this paper, we investigate the possibility of integrating a binocular stereo vision system and a laser range finder to construct 3-D map for path planning and navigation. Our proposed system is realized by forming the task as an optimization problem of minimizing the alignment error between scanned local map and selected parts of the developing global map. The problem is then solved using the Simplex method. The computation is further accelerated by reducing the data size by the procedure of Grid Map. To increase the robustness of the searching, multiple initial guesses for the Simplex method are provided. The alignment parameters are used for the data generated by the stereo vision system to be integrated into a 3D map of the environment. Performance of the proposed architecture is verified by experiment results of a real-time mobile vehicle which is also equipped with obstacle avoidance capability.

Keywords: Intelligent Vehicle; Stereo Vision; Autonomous Obstacle Avoidance; Map Construction.

I. INTRODUCTION

Intelligent navigation of a mobile robot requires the capability of simultaneous self localization and mapping, which is usually abbreviated as SLAM. Self localization is the task of finding the location of a robot in a map. Mapping is about the construct of a referable map when the robot is moving in an unknown or changing environment.

There are various kinds of sensors used for these tasks, such as sonar, laser range finders, and video cameras. Sonar is effective in detecting range, but only a narrow region can be detected at one time. Laser range finders can effectively provide 2-D environmental information at high refresh rate, up to 10 frames per sec, but fail to sense black objects and complex 3-D obstacles. Moreover, video cameras can emulate the capability of human eyes, but huge computing power is required for real-time implementation.

Autonomous map construction has been under extensive research for decades. For instance, Chong and Kleeman [1] used a sonar sensor and a positioning sensor, and Jaradat and Langari [2] used a sonar sensor in accordance with the occupancy grid map (OGM) method, where the environment is simplified into occupied and vacant grids. Jose et al. [3] used encoders in cooperation with a laser range finder to detect environments for positioning. Davison and Kita [4] combined an accelerometer and two dynamic video cameras to reconstruct irregular maps. Tomono [5] used baselines as the basis for a video camera to choose the characteristic points for map reconstruction.

II. METHODS

In this paper, we investigate the possibilities to integrate a binocular stereo vision system and a laser range finder to construct map for path planning and navigation.

The URG-04LX laser range finder, provided by Hokuyo Inc., can provide two-dimensional distance information in each scan. The binocular stereo vision system, manufactured by Videre Design Inc., has built-in FPGA accelerated by the MMX instruction set for fast computation that is able to achieve a processing speed of 50 frames per seconds.

1. **The map registration problem**

In each scan, a two-dimensional map is provided by the laser range finder. As the robot moves, the latest local map will be different from the last one. But most of the two maps can be overlapped through a rotation and a linear translation in the general case, if the two maps are obtained on the same plane.

©ISAROB 2009

As shown in Fig.1, the purpose of map registration is to align two pieces of maps such that they can overlap each other as much as possible. Fig. 1(a) shows two patterns before registration, and Fig. 1(b) is the result of an ideal registration.

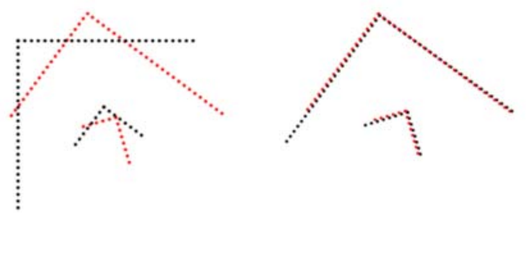

(a) (b)

Fig. 1. The registration of two patterns. **(a)** Before the registration. **(b)** After an ideal registration.

There are three design issues for this registration problem:

1. The choice of parts of these two maps that are used for the registration.
2. The method to find the rotation angle, θ, and the linear translation, denoted as a two-dimensional vector (x, y), that can overlap most portions of the parts.
3. The cost function that can efficiently guide the search by defining the degree of alignment.

As the global map is assumed to be incomplete before the navigation, it is appended gradually with local maps obtained using the laser range finder as the robot maneuvers.

In each registration, part of the global map is selected for the registration with a local map. The selection is based on the direction of last motion. The registration is formulated as an optimization problem solved using the Nelder-Mead simplex algorithm [6][7]. Although the algorithm is a local search method, no objective function derivatives is required, and the search is efficient if initial guess is properly given.

To ease the simplex algorithm and provide continuous grade for the registration, the maps are processed with the chamfer matching method before each optimization operation using the simplex algorithm, as will be described in the next section.

2. The Chamfer Matching Method

The procedure of the chamfer matching method [8] contains a forward operation and a backward operation. There are two masks used in the operations, the forward mask and the backward mask, as shown in Fig. 2.

Fig. 3 shows a landscape obtained by processing a typical map using the chamfer matching method. As shown in the figure, the processed map contains rich distance information that can provide continuous matching degree for the simplex method.

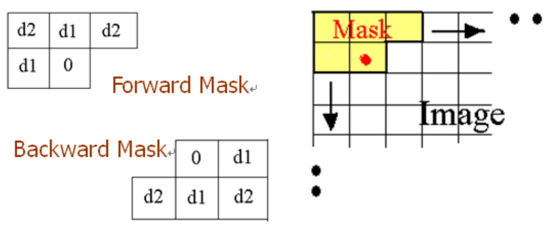

Fig. 2. The masks used in the chamfer matching method.

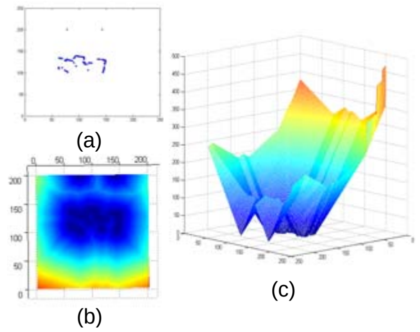

Fig. 3. (a) An example map consists of clustered points representing objects sensed by the laser range finder. **(b)** A 2-D view of the results obtained by processing (a) using the chamfer matching method. **(c)** A 3-D view of (b).

3. The Grid Map Method

To reduce the computation of the chamfer matching method and registration, the maps are represented as coarse grids using the grid map method [9]. The method is shown in Fig. 4. In the figure, the grid size is set at 10 mm.

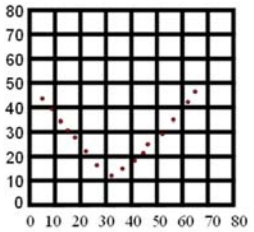

(a) (b)

Fig. 4. The concept of grid map operation. **(a)** Before the operation. **(b)** After the operation.

Fig. 5 compares the map constructed before, (a), and after, (b), the grid map operation. In this example, the grid size is set at 25 mm. Although the amount of data has been reduced about 620 times, the difference between them is indistinguishable.

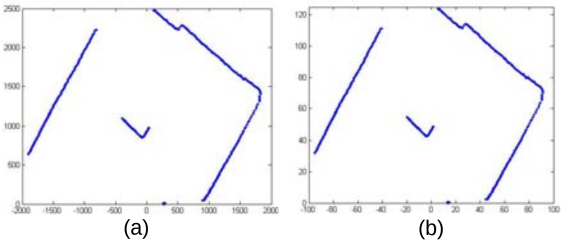

Fig. 5. (a) The original map obtained using the laser range finder. (b) The map reduced by the grid map method.

III. Experimental Results

1. Data collected by the stereo vision system

As shown in Fig. 6, the binocular stereo vision system, manufactured by Videre Design Inc., is able to capture 3-D information through built-in image processing. The disparity images of Fig. 6(b) can be translated into three-dimensional information using a built-in DSP.

However, the information is too rich and inconsistent, if captured from different position, rendering direct 3-D registration with the raw data very difficult, if not impossible.

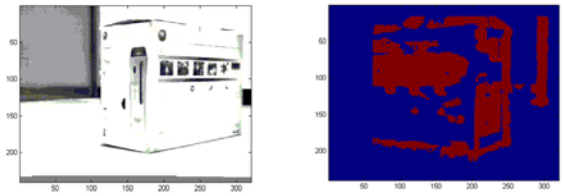

Fig. 6. (a) An object captured by an ordinary camera. (b) The disparity image of the same object captured by the binocular stereo vision system.

2. Performance of the proposed 3-D construction method

In this research, we assume that the relative position between the laser range finder and the binocular stereo vision system are fixed. We can then use the transformation (including rotation and linear translation) obtained from the 2-D registration between local and global maps to construct 3-D map of the environment.

Fig. 7 shows the scenario for the 3-D construction task. As shown in the picture, there are one chair and three boxes located at the corners of a room. The corresponding global map generated using data obtained from the laser ranger finder is shown Fig. 8. Note that not all of the objects are presented in this figure, since the robot only moved within very limited region. Also, the chair legs are absent in Fig. 8 because they are both black and too thin to be detected.

Using the transformation used in Fig. 8 for 2-D map registration, we are able to construct the 3-D map of the scenario with the binocular stereo vision system, as shown in Fig. 9. In this figure, we have that all the 3-D information required for object avoidance and path planning is present, including the chair legs, since the binocular stereo vision system is able to capture black image patterns.

VI. CONCLUSION

In this paper, we proposed a scheme for integrating a binocular stereo vision system and a laser range finder to construct 3-D map for path planning and navigation.

The laser range finder is used to provide information for real-time construction of global map. The alignment between global map and newly obtained local maps is realized by forming the task as an optimization problem and solved by the Simplex method. The computation is further accelerated by reducing the data size by the procedure of Grid Map.

©ISAROB 2009

The alignment parameters are used for the data generated by the stereo vision system to be integrated into a 3D map of the environment. Performance of the proposed architecture is verified by experiment results of a real-time mobile vehicle which is also equipped with obstacle avoidance capability.

Fig. 7. The scenario for the experimental 3-D construction task.

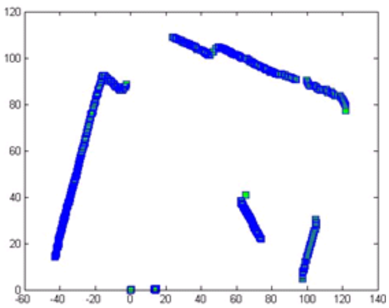

Fig. 8. The global map generated using data obtained from the laser ranger finder for the scenario of Fig. 7.

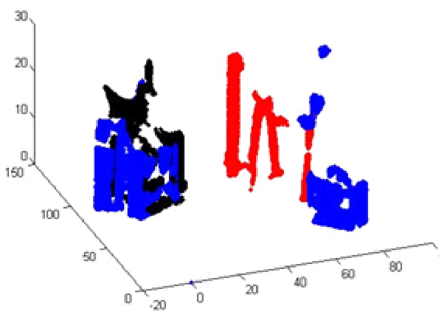

Fig. 9. The 3-D map of the scenario of Fig. 7 using the transformation used in Fig. 8 and the data obtained from the binocular stereo vision system.

ACKNOWLEGMENT

The authors would like to thank the support of Chung-Shan Institute of Science & Technology, Taiwan, R.O.C., under contract number BB97017P068PE. Without the support, the research will be impossible.

REFERENCES

[1] Chong KS and Kleeman L (1996), Mobile Robot Map Building from an Advanced Sonar Array and Accurate Odometry. Technical Report MECSE

[2] Abdel M, Jaradat K and Langari R (2005), Line Map Construction using a Mobile Robot with a Sonar Sensor. IEEE/ASME Int Conf Advanced Intelligent Mechatronics: 1251-1256

[3] Guivant J, Nebot E, and Baiker S (2000), Autonomous Navigation and Map building Using Laser Range Sensors in Outdoor Applications. Journal of Robotic System: 17(10) 565-583

[4] Andrew J and Kita N (2001),3D Simultaneous Localisation and Map-Building Using Active Vision for a Robot Moving on Undulating Terrain. IEEE Computer Society Conf : 384-391

[5] Tomono M (2005), 3-D Localization and Mapping Using a Single Camera Based on Structure-from-Motion with Automatic Baseline Selection. IEEE International Conference on Robotics and Automation: 334.

[6] Nelder JA and Mead R (1965), A simplex method for function minimization. The Computer J 7: 308–313

[7] Press WH, Teukolsky SA, and Vetterling VT (1994), Numerical recipes, the art of scientific computing. Cambridge: Cambridge University Press.

[8] Borgefors G (1988), Hierarchical chamfer matching: A parametric edge matching algorithm. IEEE Trans. Pattern Analysis and Machine Intell:10(6): 849–865

[9] Elfes A and Moravec H (1985), High resolution maps from wide angle sonar. IEEE Int Conference on Robotics and Automation: 116-121

©ISAROB 2009

Concurrent Localization of Multiple Robots

JaeHyun Park, JungYun Cheong, TaeKyung Yang and JangMyung Lee

Dep. Of Electronics and Electrical Engineering
Pusan National University
Busan, Geumjeong Gu, 609-735, Republic of Korea.
(Tel : 82-51-510-1696; Fax : 82-51-514-1693)
(jae-hyun@pusan.ac.kr, cheong2k@pusan.ac.kr, yangpa@pusan.ac.kr, jmlee@pusan.ac.kr)

*Abstract***:** The concurrent localization method for multiple robots using ultrasonic beacons is proposed in this paper. This method provides a high accuracy solution using only low price sensors. To measure the distance of a mobile robot from a beacon at a known position, the mobile robot wakes up one beacon to send out the ultrasonic signal to measure the traveling time from the beacon to the mobile robot. When multiple robots are moving in the same block requiring localization, it needs a scheduling to choose measuring-sequence in order to overcome ultrasonic signal interferences among robots at every time. But the increased time delay to estimate the positions for the multiple robots degrades the localization accuracy. To solve this problem, this paper proposes an efficient localization algorithm for the multiple robots, where the robots are grouped into one master robot and the other slave robots. In this method, when a master robot calls a beacon, all the robots simultaneously receive the identical ultrasonic signal to estimate their positions. Effectiveness of the proposed algorithm has been verified through real experiments.

Keywords: Localization, Mobile robot, Multiple robots, iGS, Concurrent Localization, Master& Slave

I. INTRODUCTION

For the localization of the mobile robot in the indoor environment, there are several schemes using IR [1], laser [2], vision [3], Ultrasonic and etc. The ultrasonic sensors widely used indoor localization system, since they are cheap and easy to be controlled with high accuracy [4]. Even so, they are susceptible to environmental noise [5] and reflection from their propagation characteristics, and they are hard to transmit to long distance because of their decay phenomena.

The typical Systems using the ultrasonic sensors are Active Bat [6] and iGS [7]. The abovementioned systems have a high accuracy of localization about a single mobile robot. However, if the number of robots increases in the same area, they produce a signal collision for increasing signals. That is, they will cause problems for localization. If they do not know concurrently positions of multiple robots, it is not useful because of only applying a single robot.

In this paper, the localization of multiple robots using ultrasonic sensors has been introduced to analyze problems. And efficient method to overcome problems has been proposed.

This paper consists of five sections including this introduction section. In section II, the indoor localization system, iGS, has been introduced in detail and section III describes the concurrent localization of multiple robots that is the major contribution of this paper. In the section IV, the effectiveness and usefulness of the master & slave algorithm have been verified by the real experiments. Finally, In the section V concludes this research, work and mentions future studies related to this research.

II. Indoor Global-localization System(iGS)

1. iGS basic principle

The iGS is composed of a localizer, beacons, and a PC for the user. At first, the active beacon sensor consists of a radio frequency(RF) receiver and an ultrasonic transmitter. A mobile robot can select a specific beacon that has its own ID and position information during the navigation by sending a desired beacon code via RF. When a beacon receives its own ID from the localizer, it sends back an ultrasonic signal to measure the distance from the beacon to the localizer using the time of flight(TOF). Using the distances and the relative beacon position information, the robot position can be computed using the trilateration method. Figure 1 illustrates the basic configuration of iGS.

©ISAROB 2009

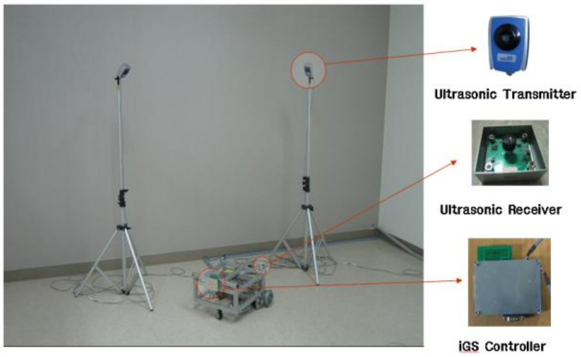

Fig. 1. Configuration of iGS

2. **Position measurement**

Localization of mobile robot is measured by distances from the beacon to the localizer using TOF of ultrasonic. The Distance between beacon and localizer, *r*, can be obtained as the multiplication of v and TOF.

$$r[m] = v[m/\sec] \cdot TOF[\sec] \quad (1)$$

The speed of the ultrasonic signal is function of environment temperature, *T*, and it is represented as

$$v[m/\sec] = 331.5 + 0.6 \times T[^\circ C] \quad (2)$$

In the Equation (2), the transmission velocity of the ultrasonic signal is changing according to the environment temperature. The temperature is assumed to be 20℃ in this research for simplicity in these experiments. The TOF of ultrasonic signal is represented as

$$TOF = n \times T_c - t_d \quad (3)$$

Where *n* is time counter, T_c is counter clock, T_d is the delay of the ultrasonic signal in the circuit.

Figure 2 is concept of the distance measurement of iGS. Since the height, *h*, from the localizer to the beacons is known as a constant, the distance from a beacon, *r*, is mapped to *d*, which is the horizontal distance. With the three distance d_1, d_2, d_3, from the three beacons and the pre-specified beacon locations, (x_1, y_1), (x_2, y_2), (x_3, y_3), the location of the mobile robot, (x_R, y_R), can be obtained as the intersection of the two circles, and they are represented as

$$d = \sqrt{(r^2 - h^2)} \quad (4)$$

$$\begin{bmatrix} (x_R - x_1)^2 + (y_R - y_1)^2 \\ (x_R - x_2)^2 + (y_R - y_2)^2 \\ (x_R - x_3)^2 + (y_R - y_3)^2 \end{bmatrix} = \begin{bmatrix} d_1^2 \\ d_2^2 \\ d_3^2 \end{bmatrix} \quad (5)$$

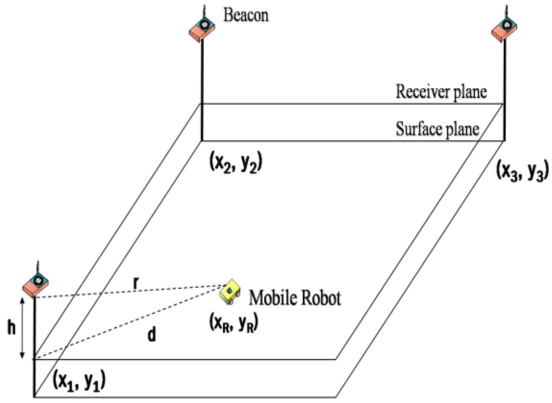

Fig. 2. Mesurement of distance between the beacon and the receiver for trilateration

III. Localization of multiple robots

1. Localization of multiple robots

Localization of multiple robots currently used iGS has some problems. If mobile robots are more than two in the same area, where consist of three beacons, they separately select each beacon for localization. And then a selected beacon and other beacons send ultrasonic signal at once. At this time, mobile robot cannot recognize which beacons send out a useful signal, since signals are concurrently submitted within the transmission time of the ultrasonic signal.

In order to overcome abovementioned problems, each robot and beacons need synchronization for localization. There are two ways of beacons synchronization and mobile robots synchronization. In case of beacons synchronization, all of the beacons are synchronized since a beacon sends out ultrasonic signal once. And at the same, mobile robots are synchronized in order to recognize a specified beacon that sent out ultrasonic signal. It has a disadvantage to add more hardware since the beacons consist of only RF transmitter not receiver. The other way of mobile robots synchronization measure a robot position at once or synchronize a call time of the beacons. It has advantage to have a high accuracy and measuring time in a small number case of robots. But if a number of mobile robots increase, time of measuring the robot position increase also.

Table 1. The time of measuring position of a robot

d_1	d_2	d_3	Trilateration
40ms	40ms	40ms	80ms

Table 1 shows the sampling time of measuring position of a robot. D_n(n = 1,2,3) is the sampling time measuring the distance from the beacons to the mobile robot. All amount of the sampling time measuring the position increase as n times because of increasing in a number of robots. And mentioned two ways have a disadvantage to add controller for synchronization.

2. Master& Slave Method

The method proposed in this paper is kind of ways synchronizing mobile robots only. One robot is designated as the master and the other robots are designated as the slaves. Figure 3 shows the basic structure of the master& slave method.

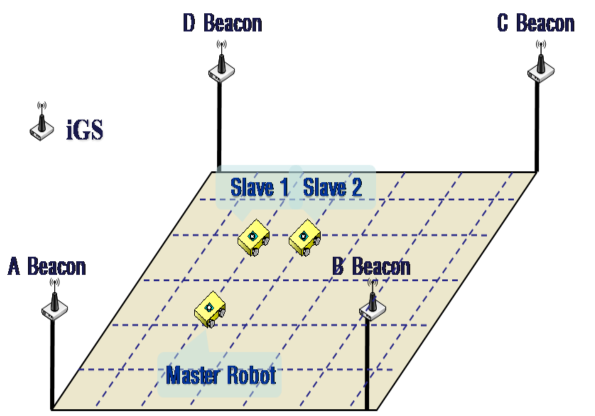

Fig. 3. Basic structure using Master & Slave Method

This method is that only the master robot calls the beacons. Slave robots synchronized with the master receive the ultrasonic signal from a same beacon calling master robot concurrently. The slave is always watching and waiting master's synchronization signal. If the master robot sends out a synchronization signal, slave robots wait ultrasonic signal. And then the master and the slave calculate distances from a beacon to each mobile robot. Finally they measure each position themselves after calculating distances from the next beacons in serial. The master robot considers max transmission time that arrive at each robot because the arrival times of ultrasonic signal are difference. Figure 4 summarize a flowchart of master& slave method.

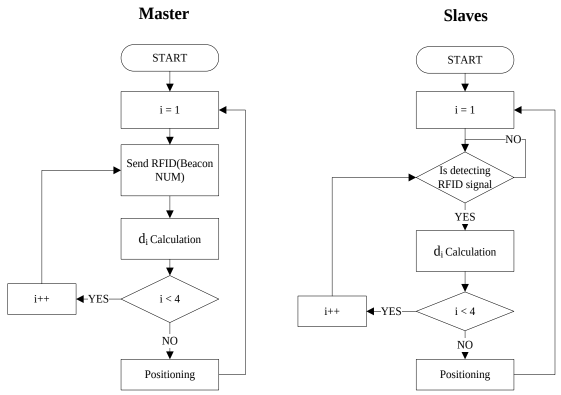

Fig. 4. Flowchart of Master& Slave Algorithm

IV. Experiment

The localizer that was attached to the robot to receive the RF and ultrasonic signals and to measure the distance from the beacons was designed in the Intelligent Robot Laboratory in Pusan National University and Ninety Systems Corp. using DSP TMS320C2406, and the ultrasonic transmitters were designed using MSP430 [Fig. 5].

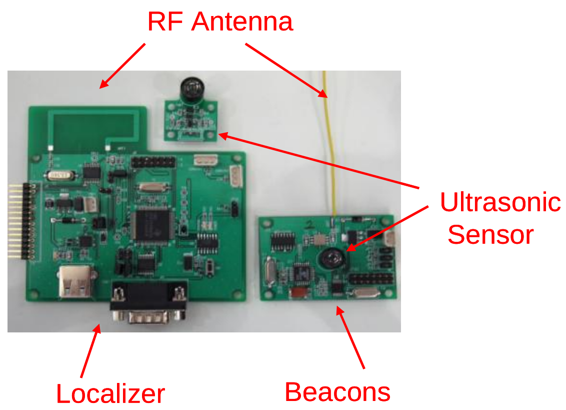

Fig. 5. The beacons and localizer

In order to measure position accuracy and success rate of position recognition according to a number of robots, beacon a, b, c are installed at (0, 0), (2000, 0) and (1000, 2000)[unit: mm]. We assume that the position of each robot will not move at fixed position.

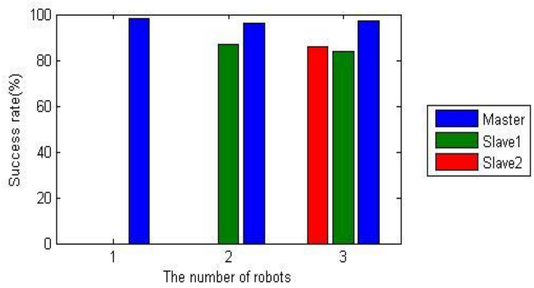

Fig. 6. Success rates of the localization

Figure 6 shows the success rate of position recognition according to a number of robots. In case of measuring position using a master robot only, the success rate is more than 95%. To use two or three robots is confirmed at least more than 80%.

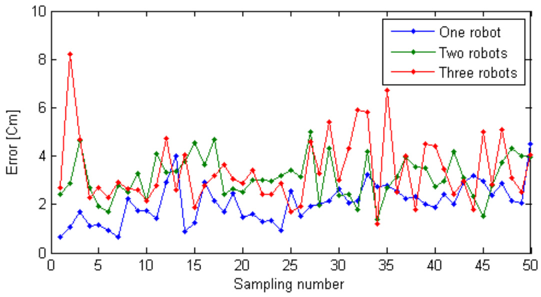

Fig. 7. Localization error according to the number of robots

The position accuracy according to the number of robots is shown in figure 7. The average localization error of using the master robot only is about 2cm. And also using three robots is about 3.4cm. It is stable to increase the number of robots about position accuracy.

V. CONCLUSION

In this paper, the localization of multiple robots using iGS based on the ultrasonic sensors has been proposed and implemented. For the localization, master robot is assigned for each block which wakes up the iGS to send out the ultrasonic signal to all the robots in the block. The communication between the master and the slave has been implemented using the R/F signal. This algorithm is applicable for various environments without additional hardware except the existing iGS. It is proved through the real experiments that the localization system is stable and robust against the robot positions and the number of robots in the working space.

ACKNOWLEDGMENT

This work was supported by the IT R&D program of MKE/IITA [2008-S033-01, Development of Global Seamless Localization Sensor].

REFERENCES

[1] Junqiu Wang, R. Cipolla and Hongbin Zha, "Vision-based Global Localization Using a Visual Vocabulary," *IEEE int. Conf. on Robotics and Automation*, pp. 4230-4235, Apr. 2005.

[2] Yu Zhou, Wenfei Liu and Peisen Huang, "Laser-activate RFID-based Indoor Localization System for Mobile-Robots," *IEEE int. Conf. on Robotics and Automation*, pp. 4600-4605, Apr. 2007.

[3] Weiguo Lin, Songmin Jia, Abe T. and Takase K, "Localization of mobile robot based on ID tag and WEB camera," *IEEE int. Conf. on Robotics, Automation and Mechatronics*, vol. 2, pp. 851-856, Dec. 2004.

[4] Ching Chih Tsai, "A Localization system of a mobile robot by fusing dead-reckoning and ultrasonic," *IEEE Trans. on Instrumentation and Measurement*, vol. 47, pp. 1399-1404, Oct. 1998.

[5] H. Premans and V. Campenhout, "High resolution sensor based on tri-aural perception," *IEEE Trans. on Robotics and Automation*, vol. 9, no. 1, pp. 36-48, 1993.

[6] A. Harter, A. Hopper, P. Steggles, A. Ward and P. Webster. "The Anatomy of a Context-Aware Application," *In 5th ACM International Conference on Mobile Computing and Networking (Mobicom 99)*, pp. 59-68, August 1999.

[7] D. G. Seo and J. M. Lee, "Localization Algorithm for a mobile robot using iGS," *Jour. of inst. of Control, Robotics and system*, vol. 14, no. 3, Mar. 2008.

The Fourteenth International Symposium on Artificial Life and Robotics 2009 (AROB 14th '09),
B-Con Plaza, Beppu, Oita, Japan, February 5 - 7, 2009

Yawing Control of a Single Wheel Robot

BuHwan Ahn , JongMyung Hwang , JuBum Son and JangMyung Lee

Dep. Of Electronics and Electrical Engineering
Pusan National University
Busan, Geumjeong Gu, 609-735, Republic of Korea.
(Tel : 82-51-510-1696; Fax : 82-51-514-1693)
(abssky@pusan.ac.kr, h_kafka@pusan.ac.kr, sonjb81@pusan.ac.kr, jmlee@pusan.ac.kr)

***Abstract*:** The yawing control of a single wheel robot has been proposed to control the rotation angle of the single wheel robot according to the motor torque and rotation velocity. Most researches on the single wheel robot so far focus on the balance control in roll and pitch directions. With this balance control, the robot can move forward and backward for hours and it can go to the desired position finally. However, the robot can not avoid obstacles while it is keeping the balance and moving forward and backward. To provide the obstacle avoidance capability, the left or right rotation control, that is, the yawing control is added to the single wheel robot. With this additional function, the single wheel robot can be used as an autonomous carrying device even though it is operating in an environment shared by people. In this research, the yaw direction control algorithm is developed with the single wheel robot simulator and applied for the real robot. The effectiveness of the yawing controller and control algorithm has been demonstrated through the real experiments.

***Keywords*:** unicycle robot, roll, pitch, yaw, position, balance, angle, rotation control

I. INTRODUCTION

Recently single wheel robots consisted of motor and controller are coming. This robot called the unicycle robot.

Yaw direction rotation controls means, while standing still or movement the obstacle appears on the front, or, robot converts direction of yaw axis for changes the angle θ of the body. Yawing controls are same meaning to yaw direction controls.

Until currently single wheel robots of existing research and development are has many with difficult in Yaw direction rotation controls.

In order to rotate a direction or evade an obstacle, unicycle robot engineer have to research on the method which yaw direction rotary control systems are a kinetic efficiency.

The key issue of this paper is to develop the optimum movement tracking routine without external force to take the rotation of the robot body.

The unicycle robot will be used later at the recreational area where service, dining etc., and medical treatment which assists the old person and disabled person. So the field of research is very high value of the unicycle robot.

II. Analysis of yawing rotation angle

2.1 Relationship of ω and α from Rolling motion

Angular velocity is rotated angle per unit time, and definition θ_1, θ_2 are initial angle and rotated angle, t_1 and t_2 are initial time and after rotated time.

$$\varpi = \frac{\theta_2 - \theta_1}{t_2 - t_1} = \frac{\Delta\theta}{\Delta t} \tag{1}$$

$$\omega = \lim_{\Delta t \to 0} \frac{\Delta\theta}{\Delta t} = \frac{d\theta}{dt} \tag{2}$$

Angular acceleration defines to changing angular velocity per unit time and consisted of average angular acceleration $\bar{\alpha}$ with momentary angular acceleration α .

$$\bar{\alpha} = \frac{\omega_2 - \omega_1}{t_2 - t_1} = \frac{\Delta\omega}{\Delta t} \tag{3}$$

$$\alpha = \lim_{\Delta t \to 0} = \frac{\Delta\omega}{\Delta t} = \frac{d\omega}{dt} \tag{4}$$

By (1) and (2), and (3) and (4), when rigid body (rotation disk) rotates, disk angular velocity and angular acceleration becomes same value from all points. In order to know α of the rigid body which it specifies, we must calculates ω .

The ω and the α refers from the paper are the momentary angular velocity and the momentary average

©ISAROB 2009

angular average acceleration angular. But average terms are attached the word `average' which is before. The rotation torques from the disk's roll motion and standstill motion are vectors which has a size and a direction. Therefore, ω and α which consists torque are also vectors.

2.2 Principle of motion for yawing Disk

[Fig.1.] the yawing Disk which (affixed in DC motor)

The [Fig.1.] is the disk actual object features what is actually affixed in yaw direction rotary simulators.
When DC motors operates initially t_1 second, the disk accelerates to make specific speed at specific time during t_2 second time. And it arrive scheduled speed, the motor move uniform motion.
When the uniform motioning disk arrive programmed time t_3, the motor stop rolling motion and the electric power shut down.
That moment, the torque will occur in proportionately in with angular acceleration. Consequently robots frame rotate by the force F of the vector product propensity occurs. If there's no noise, it shows simply in speed graph of DC motors, like the [Fig. 2.].

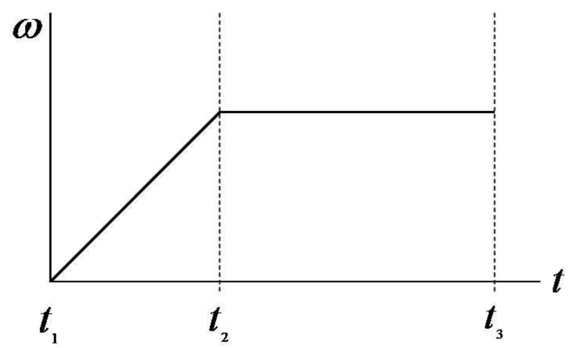

[Fig. 2.] Speed quality graph of DC motors

The [Fig. 2.] appears from t_1 seconds until t_2 seconds to show a precipitous slope price and the motor accelerated motion. But from t_2 seconds until t_3 seconds motion shows without speed changes of DC motor.
In ideal state or free space, we know α and $\bar{\alpha}$ like the [Fig. 2.] almost the same. So, we have the rule of (5).

$$\bar{\alpha} \cong \alpha \tag{5}$$

Uses (5) constraint condition, dividing speed levels of 16 steps of DC motor. And we calculate the torque τ each 16 steps of speed changes.
The disks rotation time and stop time designed respectively in 10 seconds.

$$f = \frac{\omega}{2\pi} \tag{6}$$

$$\omega = 2\pi f \tag{7}$$

Therefore rotational frequency f is rotated frequency per unit time (usually, meaning rpm), it means one rotation same as 2π radian rotations. So, it defines with (6) and (7).
Consequently angular acceleration α and the torque τ are figuring out with (8) relationships.

$$\alpha \propto \tau \tag{8}$$

By using (8) equation, it will be able to derivation the equation (9) of rolling motion from Newton's 2nd law.

$$\tau = mR^2\alpha \tag{9}$$

The (9) shows that mR^2 is the inertia from rolling motion.

The (5) ~ (9) theories will be able to define about the rolling disk torques.

$$\tau = \left(\sum m_i R_i^2\right)\alpha \tag{10}$$

When deriving (10), we used a fact that angular accelerations are same to rotating in the fixed axis.

$$\sum m_i R_i^2 = m_1 R_1^2 + m_2 R_2^2 + m_3 R_3^2 + \cdots + m_n R_n^2$$

From (10), it will be able to define (11) and I is the disk inertia moments.

$$I = \sum m_i R_i^2 \quad (11)$$

Unites with (10) and (11), defines (12).

$$\tau = I\alpha \quad (12)$$

Similarly (9), as (12) that corresponds to the law of Newton's 2nd laws of movement can derive and can be used as the definition of torque τ .

III. Experiment

1. Yawing control techniques

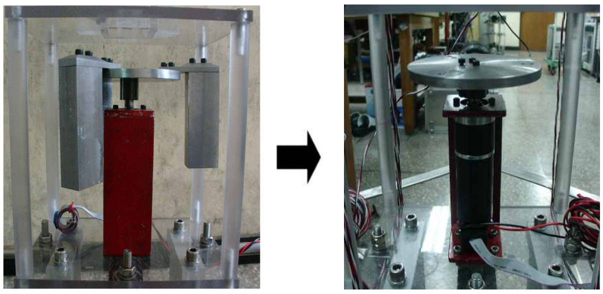

[Fig. 3.] Yawing Disk of the changes

The [Fig. 3.] shows a disk initially form and a postscript form. The Maxon Motor attached the Yaw axis, features are changed because the maximum continuous torque specification is 181mNm, and the optimal load of the weight is 1.7Kg in uniform velocity system. Initially the disk weight is 3.5Kg, it was too weighty. After reduce weight, the disk weight is 1.4Kg. Right figure of the [Fig. 3] shows the disk for the optimum rotation torque.
After changing the load of the motor by 1.4Kg, experiment direction rotating of left and right. To get the rotation torque, repeat switching high-speed rotation and an instantaneous resting state of the disk.

The [Table. 1.] listed rotation angle of the robot body step by step for change yawing rotation motor RPM value. The 0x008f value is the maximum motor RPM character, so it is representative value.

PWM Value	Motor RPM (3 times measurement)	RPM average value	Rotation degrees	Note	PWM Value	Motor RPM (3 times measurement)	RPM average value	Rotation degrees	Note
0x000f	0	0	0°	No change	0x008f	1014.0, 1016.0, 1098.4	1042.8	13°	Max
0x001f	39.9, 38.1, 40.5	39.5	0°	〃	0x009f	991.8, 985.2, 985.1	987.4	11°	Fix
0x002f	110.7, 116.0, 119.2	115.3	0°	〃	0x00af	973.4, 962.0, 976.9	970.8	11°	〃
0x003f	233.9, 253.2, 227.9	238.3	0°	〃	0x00bf	978.3, 978.4, 980.8	979.2	10°	〃
0x004f	335.8, 339.1, 321.4	332.1	0°	〃	0x00cf	980.9, 983.0, 988.8	984.2	12°	〃
0x005f	539.2, 515.1, 511.4	521.9	3°	Start	0x00df	985.4, 974.9, 980.9	980.4	11°	〃
0x006f	690.8, 763.0, 669.2	707.6	5°	〃	0x00ef	994.5, 994.4, 990.2	993.0	12°	〃
0x007f	799.2, 806.8, 772.6	792.9	7°	〃	0x00ff	990.8, 987.7, 984.2	987.6	11°	〃

[Table.1.] List of Motor RPM and rotation degrees by yawing velocity control

2. Yawing rotation experiment

The second experiment is to rotate unicycle body from the resting state where is not the mobile condition.

[Fig. 4.] change in the rotary angle in compliance with Yaw direction rotation wheel track movement

The [Fig. 4.] shows environment of yawing rotation experiments of unicycle robots. The left figure is not open space but rested environment. The middle figure shows 0 degree between unicycle robot and ground. This is reference point of rotation degrees. And the right figure shows after rotated degrees between unicycle robot and ground reference points.

The [Fig. 5.] shows the direction change scene of unicycle robot bodies in compliance with yawing rotation control experiment.

[Fig. 5.] Yawing rotation scenes of unicycle robots

The [Fig. 5.] shows yawing rotation scenes of unicycle robots from resting state. Yaw direction rotating motor repeat the high-speed rotation and an instantaneous resting state 5 times which change degrees. In [Fig. 5.], there are 5 pictures of unicycle body. Looking attentively, there is a black line besides robots single wheel, the rotary angle changes little by little and there is a fact that the direction is exchanged with the right side.

This rotation speed hex character of yawing motor is 0x008f whose rpm value is highest. As one rotation change robot body in 13 degrees right sides, totally 65 degrees right sides by 5 times continuous rotations.

IV. CONCLUSION

This research and experiment to control the rotation of the physically instable unicycle robot with appropriate degrees of rotation could get the desired direction of rotation.

The future directions of research is more smooth rotation of the yawing control, and more efficient rotation by acquiring the value of torque, consequently position control could be the more stable and the more robust.

V. ACKNOWLEDGEMENT

This work was supported by Korea Science and Engineering Foundation (KOSEF) Grant R01-2007-000-10171-0 funded by the Korean Government (MOST).

REFERENCES

[1] M. Iwase., "An Assistant System for Riding a Unicycle" International Journal of ARM VOL. 8, NO. 1, March 2007

[2] Yongsheng Ou., "Balance Control of a Single Wheel Robot",Conference on Intelligent Robots and Systems, October 2002

[3] Jinseok Kim., "The Posture Control of One-wheel Unicyle Robot Using Partial Feedback Linearization", Journal of the Korean Society for Precision Engineering, Vol. 24, No. 4, April 2007

[4] Sheng Z. and Yamafuji K., "Stability and Motion Control of a Unicycle (1st Report: Dynamics of a Human Unicycle and its Modeling by Link Mechanism)", JSME, International Journal, Series C, June, 1995

Robust oscillation control of wheeled mobile robots

Yasutaka Tsuchida, Masahiro Oya, Natsuki Takagi and Qiang Wang

Department of Mechanical and Control Engineering, Kyushu Institute of Technology
1-1 Sensui-cho, Tobata-ku, Kitakyushu-shi, Fukuoka, Japan
(Tel: +81-93-884-3186; Fax: +81-93-861-1159)
(E-mail: g344212y@tobata.isc.kyutech.ac.jp)

Abstract: In the case when wheeled mobile robots run fast on rough surface, due to the body acceleration and oscillation, the sensors mounted on the robot body may be destroyed. In this paper, we propose a scheme to reduce the body acceleration at any specified location on the mobile robot body. To achieve this, a combined ideal robot model is designed. In the combined ideal robot model, the location where the acceleration performance becomes best can be moved easily by setting only two design parameters. Next, a robust model tracking controller is developed so that the behavior of an actual mobile robot tracks that of the combined ideal robot model. It is ascertained by numerical simulations that the body acceleration at any specified location can be improved easily and good robustness for uncertainties of robot mass, pitch and roll moment of inertia of robot body, and the position of the center of gravity is confirmed.

Keywords: Oscillation Control, Robust Tracking Control, Ideal Model, Wheeled Mobile Robot

I. INTRODUCTION

In extreme environment, for example, stricken area and planet surface, there are many dangerous tasks for human workers. Recently, in the environment, mobile robots working instead of human have been developed. Mobile robots developed until now are classified roughly into three large categories based on its mechanism, such as wheeled mobile robots[1]-[4], legged robots[5],[6], and articulated robots[7],[8]. Wheeled mobile robots with the high-speed mobility have an advantage in the case when it is required to gather information as soon as possible. In the developed wheeled mobile robots until now, the main focuses were concentrated on mechanisms to over steps and control scheme for a trajectory tracking. In the case when wheeled mobile robots run on rough surface at high-speed, due to the body acceleration and oscillation, the sensors mounted on the robot body may be destroyed and measurement accuracy of the sensors becomes worse. If instruments to reduce oscillation are equipped for every sensor, this problem can be resolved. However, this method is not suitable for small mobile robots.

Using actuators set at wheels axis, we can control the body acceleration and oscillation. This method is more suitable for small mobile robots. Therefore, in this paper, we propose a scheme to reduce the body acceleration at any specified location for mobile robots with actuators set at wheels axis. To achieve this end, a combined ideal robot model is designed based on the state space description containing the body acceleration. In the combined ideal robot model, the location where the acceleration performance becomes best can be moved easily by setting only two design parameters. Next, a robust model tracking controller is developed so that the behavior of an actual wheeled mobile robot tracks that of the combined ideal robot model.

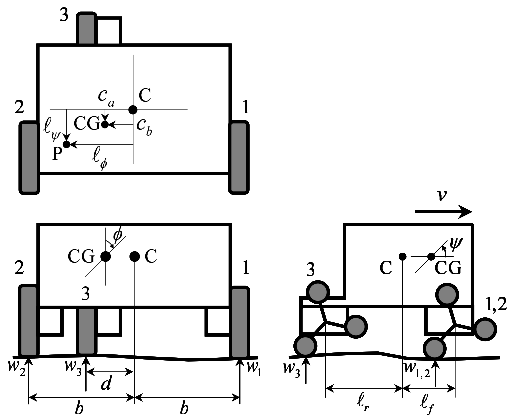

Fig. 1 Illustration of mobile robot

II. WHEELED MOBILE ROBOT

The wheeled mobile robot model is shown in Fig. 1. To simplify the explanation below, each large wheel is labeled as $1, 2, 3$. Each large wheel has three small wheels. In large wheel labeled 1 and 2, small wheels are driving wheels. The wheeled mobile robot has the mechanism that each large wheel can be rotated by the actuators set at the center of large wheels axis. In this paper, the control input to reduce the body acceleration is the voltage added to the actuators. The symbols O_n, I_n used below denote $n\times n$ zero matrix and $n\times n$ unit matrix.

1. Dynamic equation

It is assumed that the pitch angle $\psi(t)$ and the roll angle $\phi(t)$ are small, and then, dynamic equation of the wheeled mobile robot is given as follows. The explanation of parameters is shown in Table 1.

$$M_q\boldsymbol{q}(t)+k_dH^TH\dot{\boldsymbol{q}}(t)=-k_bH^T\boldsymbol{u}(t)+k_JH^T\boldsymbol{w}(t) +k_dH^T\dot{\boldsymbol{w}}(t)-(T_h^T)^{-1}M_c\boldsymbol{g} \quad (1)$$

©ISAROB 2009

Table 1. Notation of wheeled mobile robot

C, CG	center and center of gravity of mobile robot body
z_c	vertical displacement at C
ψ, ϕ	pitch and roll angle
x_1, x_2, x_3	vertical displacement at the center of large wheel
w_1, w_2, w_3	vertical displacement of road disturbance added to large wheels
v	longitudinal velocity of mobile robot
g	acceleration of gravity
m, i_ψ, i_ϕ	robot mass, pitch and roll moment of inertia of robot body
ℓ_f, ℓ_r, b, d	distance from C to large wheels
c_a, c_b	distance from C to CG
ℓ_ψ, ℓ_ϕ	distance from C to P
ℓ	distance from the center of large wheel to the center of small wheel
k_a	voltage and torque conversion constant
r, k_G	reciprocal of armature resistance and gear ratio
j_m, d_m	moment of inertia and viscous damping constant between a motor and wheel center axis

$$\left.\begin{array}{l} \boldsymbol{q}(t) = [z_c(t), \psi(t), \phi(t)]^T \\ \boldsymbol{u}(t) = [u_1(t), u_2(t), u_3(t)]^T \\ \boldsymbol{w}(t) = [w_1(t), w_2(t), w_3(t)]^T \end{array}\right\} \quad (2)$$

$$\left.\begin{array}{l} M_q = (T_h^T)^{-1} M_c (T_h)^{-1} + k_J H^T H \\ M_c = \mathrm{diag}[m, i_\psi, i_\phi], \boldsymbol{g} = [g, 0, 0]^T \\ T_h = I_3 - \boldsymbol{b}[0, c_a, c_b], k_b = \frac{4rk_a}{\sqrt{7}\ell k_G} \\ k_d = \frac{16}{7\ell^2}(d_m + \frac{rk_a^2}{k_G^2}), k_J = \frac{16 j_m}{7\ell^2} \\ H = \begin{bmatrix} 1 & \ell_f & -b \\ 1 & \ell_f & b \\ 1 & -\ell_r & d \end{bmatrix}, \boldsymbol{b} = \begin{bmatrix} 1 \\ 0 \\ 0 \end{bmatrix} \end{array}\right\} \quad (3)$$

Where $u_i(t), i = 1, 2, 3$ is the input voltage to motors at the center of large wheels axis. To simplify the design of a controller, the values of j_m, d_m, r, and k_a are the same in each large wheel.

2. Passive robot

We use the relation that the acceleration $\boldsymbol{y}(\ell_\psi, \ell_\phi, t)$ $= [z_{\ell\psi,\ell\phi}(t), \psi(t), \phi(t)]^T$ at a location (ℓ_ψ, ℓ_ϕ) on the robot body can be described as $\boldsymbol{y}(\ell_\psi, \ell_\phi, t) = (I_3 + \boldsymbol{b}[0, \ell_\psi, \ell_\phi])\boldsymbol{q}(t)$. Where $z_{\ell\psi,\ell\phi}(t)$ denotes the vertical acceleration at the location (ℓ_ψ, ℓ_ϕ). In this paper, the proposed ideal robot model is designed based on the wheeled mobile robot using nominal values shown in Table 2. Using the relation $\boldsymbol{x}(t) = H\boldsymbol{q}(t) - \boldsymbol{w}(t)$, dynamic equation for the vertical displacement at the center of large wheels $\boldsymbol{x}(t) = [x_1(t), x_2(t), x_3(t)]^T$ is given by

$$\left.\begin{array}{l} M_p\boldsymbol{x}(t) + k_d\dot{\boldsymbol{x}}(t) = -k_b\boldsymbol{u}(t) + (k_J I_3 - M_p)\boldsymbol{w}(t) - (T_h^T)^{-1} M_c \boldsymbol{g} \\ M_p = (H^T)^{-1} M_q H^{-1} \end{array}\right\}. \quad (4)$$

Table 2. Nominal values of parameters

m	84.2	kg	i_ψ	1.72	kgm^2
i_ϕ	1.39	kgm^2	ℓ	0.15	m
c_a	0.079	m	c_b	0.011	m
ℓ_f	0.125	m	ℓ_r	0.445	m
b	0.35	m	d	0.011	m
k_a	0.126	N/V	k_G	1/160	
j_m	0.21	kgm^2	d_m	1.73×10^{-4}	Nms/rad
r	0.226	$1/\Omega$			

To add a suspension characteristic to the wheeled mobile robot (4), the following input voltage is used.

$$\boldsymbol{u}(t) = \boldsymbol{u}_a(t) + \frac{k_p}{k_b}\boldsymbol{x}(t) + \frac{k_J}{k_b}\boldsymbol{w}(t) + \boldsymbol{u}_g. \quad (5)$$

Where $\boldsymbol{u}_a(t)$ is new input, $\boldsymbol{u}_g$ is the constant input voltage to hold the center of large wheels in a certain height, and k_p is feedback gain for the suspension characteristics.

To develop a controller achieving small acceleration of the robot body in the following section, the following state space description is introduced. The state is given by $\boldsymbol{\xi}(t) = [\boldsymbol{x}(t)^T, \dot{\boldsymbol{x}}(t)^T, (H\boldsymbol{q}(t))^T]^T$. It should be noted that the body acceleration $\boldsymbol{q}(t)$ is included in the new state $\boldsymbol{\xi}(t)$.

$$\left.\begin{array}{l} \dot{\boldsymbol{\xi}}(t) = (\quad + BF)\boldsymbol{\xi}(t) + B\boldsymbol{\mu}(t) + D_w\boldsymbol{w}(t) \\ \boldsymbol{\mu}(t) = \dot{\boldsymbol{u}}_a(t) + \boldsymbol{u}_a(t) \end{array}\right\} \quad (6)$$

$$\left.\begin{array}{l} = \begin{bmatrix} O_3 & I_3 & O_3 \\ O_3 & O_3 & I_3 \\ O_3 & O_3 & O_3 \end{bmatrix}, B = \begin{bmatrix} O_3 \\ O_3 \\ -k_b M_p^{-1} \end{bmatrix}, D_w = \begin{bmatrix} O_3 \\ -I_3 \\ k_d M_p^{-1} \end{bmatrix} \\ F = \frac{1}{k_b}[k_p I_3, (k_d + k_p)I_3, M_p + k_d I_3] \end{array}\right\} \quad (7)$$

Where $\boldsymbol{\mu}(t)$ is the new input to design a controller. The mobile robot (6) with $\boldsymbol{\mu}(t) = \boldsymbol{0}$ is called as the passive robot.

III. ROBUST TRACKING CONTROLLER

The control objective is to develop a robust controller so that the pitch and roll angle acceleration become small and the vertical acceleration at any specified location (ℓ_ψ, ℓ_ϕ) on the robot body can be reduced to small value easily. Hereafter, the location where the vertical acceleration becomes minimum will be called as the best location. To meet the objective, the following assumptions are made for an actual wheeled mobile robot considered here.

A1 The exact values of parameter except robot mass m, pitch and roll moment of inertia i_ψ, i_ϕ and the position of the center of gravity c_a, c_b are known and do not vary.

A2 Robot body accelerations $z_c(t), \psi(t), \phi(t)$ are measured.

A3 Vertical displacement at the center of large wheels $\boldsymbol{x}(t)$ and its velocity $\dot{\boldsymbol{x}}(t)$ are measured.

A4 Acceleration of road disturbance $\boldsymbol{w}(t)$ is measured and bounded.

©ISAROB 2009

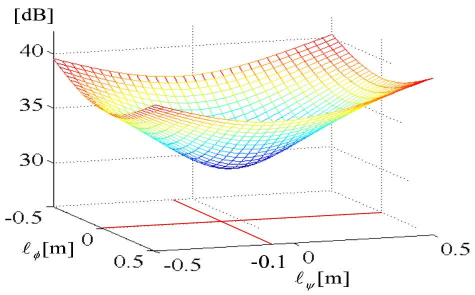

Fig. 2 Maximum gain surface of the passive robot

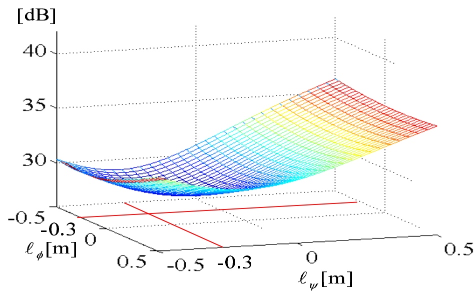

(a) $\ell_{\psi p} = -0.3, \ell_{\phi p} = -0.3$

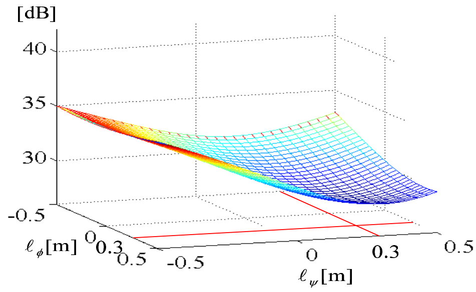

(b) $\ell_{\psi p} = 0.3, \ell_{\phi p} = 0.3$

Fig. 3 Maximum gain surface of the combined ideal robot model

1. Combined ideal robot model

To develop a controller achieving the control objective, using the similar manner proposed in [9], a combined ideal robot model is proposed. The following ideal robot models are developed based on the wheeled mobile robot (6) using nominal values. In the explanation below, the symbol $\dagger_N$ denotes the matrix using nominal values.

$$\left.\begin{array}{l} \dot{\boldsymbol{\xi}}_m(t) = \quad \boldsymbol{\xi}_m(t) + B_N \boldsymbol{f}_m(t) + D_{wN}\boldsymbol{w}(t) \\ \boldsymbol{\xi}_m(t) = [\boldsymbol{x}_m(t)^T, \dot{\boldsymbol{x}}_m(t)^T, (H\boldsymbol{q}_m(t))^T]^T \\ \quad = \sum_{i=1}^{2}\gamma_{\phi i}\sum_{j=1}^{2}\gamma_{\psi j}\boldsymbol{\xi}_{m(2i+j-2)}(t) \end{array}\right\} \quad (8)$$

$$\left.\begin{array}{l} \boldsymbol{f}_m(t) = \sum_{i=1}^{2}\gamma_{\phi i}\sum_{j=1}^{2}\gamma_{\psi j}F_{m(2i+j-2)}\boldsymbol{\xi}_{m(2i+j-2)}(t) \\ \gamma_{\psi i} = \frac{(-1)^{i\ \ 1}\ell_{\psi p}+\ell_{\psi m}}{2\ell_{\psi m}}, \gamma_{\phi i} = \frac{(-1)^{i}\ell_{\phi p}+\ell_{\phi m}}{2\ell_{\phi m}}, i = 1, 2 \\ \boldsymbol{\xi}_{mi}(t) = [\boldsymbol{x}_{mi}(t)^T, \dot{\boldsymbol{x}}_{mi}(t)^T, (H\boldsymbol{q}_{mi}(t))^T]^T \\ \quad = \Omega_i \boldsymbol{\xi}_{di}(t), i = 1, 2, 3, 4 \\ F_{mi} = M_{pN}HT_iH^{-1}M_{pN}^{-1}(F_N - G_i)\Omega_i^{-1}, i = 1, 2, 3, 4 \\ \Omega_i = \mathrm{diag}[HT_iH^{-1}, HT_iH^{-1}, HT_iH^{-1}], i = 1, 2, 3, 4 \\ T_i = I_3 - \boldsymbol{b}[0, \ell_{\psi p} - \ell_{\psi m}, \ell_{\phi p} + (-1)^{i-1}\ell_{\phi m}], i = 1, 2 \\ T_i = I_3 - \boldsymbol{b}[0, \ell_{\psi p} + \ell_{\psi m}, \ell_{\phi p} + (-1)^{i-1}\ell_{\phi m}], i = 3, 4 \end{array}\right\} (9)$$

The design parameters $\ell_{\psi p}, \ell_{\phi p}$ are introduced to specify the location where the vertical acceleration on the robot body must become minimum. The symbols $\boldsymbol{\xi}_{di}(t), i = 1, 2, 3, 4$ denotes the states for the ideal robot models given by

$$\left.\begin{array}{l} \dot{\boldsymbol{\xi}}_{di}(t) = (\quad + B_N(F_N - G_i))\boldsymbol{\xi}_{di}(t) + D_{wN}\boldsymbol{w}(t) \\ \boldsymbol{\xi}_{di}(t) = [\boldsymbol{x}_{di}(t)^T, \dot{\boldsymbol{x}}_{di}(t)^T, (H\boldsymbol{q}_{di}(t))^T]^T, i = 1, 2, 3, 4 \end{array}\right\} (10)$$

Where the feedback gains $G_i, i = 1, 2, 3, 4$ are designed for nominal robot

$$\left.\begin{array}{l} \dot{\boldsymbol{\xi}}_N(t) = (\quad + B_N F_N)\boldsymbol{\xi}_N(t) + B_N\boldsymbol{\mu}_N(t) + D_{wN}\boldsymbol{w}(t) \\ \boldsymbol{\xi}_N(t) = [\boldsymbol{x}_N(t)^T, \dot{\boldsymbol{x}}_N(t)^T, (H\boldsymbol{q}_N(t))^T]^T \end{array}\right\} (11)$$

so that the following quadratic criterion becomes minimum.

$$\left.\begin{array}{l} J = \int_0^\infty (\boldsymbol{q}_{Ni}(t)^T E_{qi}\boldsymbol{q}_{Ni}(t) + \boldsymbol{x}_N(t)^T E_{xi}\boldsymbol{x}_N(t) \\ \quad + \dot{\boldsymbol{x}}_N(t)^T E_{dxi}\dot{\boldsymbol{x}}_N(t) + \boldsymbol{\mu}_N(t)^T R_i \boldsymbol{\mu}_N(t))dt \\ \boldsymbol{q}_{Ni}(t) = [z_{Ni}(t), \theta_N(t)]^T, i = 1, 2, 3, 4 \end{array}\right\} (12)$$

The symbols $E_{qi}, E_{xi}, E_{dxi}, R_i, i = 1, 2, 3, 4$ in (12) denote the weight matrixes for the ideal robot models $\boldsymbol{\xi}_{di}(t), i = 1, 2, 3, 4$. The signals $z_{Ni}(t), i = 1, 2, 3, 4$ denote the vertical acceleration at the specified location $(\ell_\psi = \ell_{\psi m}, \ell_\phi = (-1)^i\ell_{\phi m}), i = 1, 2$ and $(\ell_\psi = -\ell_{\psi m}, \ell_\phi = (-1)^i\ell_{\phi m}), i = 3, 4$. Using the positive definite solution of the Riccati equation

$$\left.\begin{array}{l} (\quad + B_N F_N)^T P_i + P_i(\quad + B_N F_N) - P_i B_N R_i^{-1} B_N^T P_i = -Q_i \\ Q_i = \mathrm{diag}[E_{xi}, E_{dxi}, Q_{qi}], i = 1, 2, 3, 4 \\ Q_{qi} = (H^T)^{-1}(I_3 + \boldsymbol{b}[0, \ell_{\psi m}, (-1)^i\ell_{\phi m}])^T \\ \quad \times E_{qi}(I_3 + \boldsymbol{b}[0, \ell_{\psi m}, (-1)^i\ell_{\phi m}])H^{-1}, i = 1, 2 \\ Q_{qi} = (H^T)^{-1}(I_3 + \boldsymbol{b}[0, -\ell_{\psi m}, (-1)^i\ell_{\phi m}])^T \\ \quad \times E_{qi}(I_3 + \boldsymbol{b}[0, -\ell_{\psi m}, (-1)^i\ell_{\phi m}])H^{-1}, i = 3, 4 \\ E_{qi} = (I_3 + \boldsymbol{b}[0, \ell_{\psi qi}, \ell_{\phi qi}])^T \mathrm{diag}[e_z, e_\psi, e_\phi] \\ \quad \times (I_3 + \boldsymbol{b}[0, \ell_{\psi qi}, \ell_{\phi qi}]), i = 1, 2, 3, 4 \end{array}\right\}, (13)$$

a controller to minimize the criterion (12) is given by

$$\boldsymbol{\mu}_N(t) = -R_i^{-1}B_N^T P_i \boldsymbol{x}_N(t) = -G_i\boldsymbol{x}_N(t), i = 1, 2, 3, 4. \quad (14)$$

The weight matrixes are set so that the vertical acceleration $z_{Ni}(t), i = 1, 2, 3, 4$ becomes minimum, respectively.

The transform matrix $\Omega_i, i = 1, 2, 3, 4$ is introduced to move the location where the vertical acceleration becomes minimum in $\boldsymbol{\xi}_{mi}(t), i = 1, 2, 3, 4$. The combined ideal robot model (8) is designed by combining the ideal robot models $\boldsymbol{\xi}_{mi}(t), i = 1, 2, 3, 4$ linearly. In the combined ideal robot model, the best location can be moved easily by setting the only two design parameters $\ell_{\psi p}$ and $\ell_{\phi p}$.

Figs. 2, 3 show the properties of the passive robot and the proposed combined ideal robot model. To show the gain characteristics relating to the vertical acceleration on the robot body, the maximum value of the norm of transfer function vector from the derivative of road disturbance $\dot{\boldsymbol{w}}(t)$ to the vertical acceleration $z_{\ell\psi,\ell\phi}(t)$ at a location (ℓ_ψ, ℓ_ϕ) is plotted with respect to 10Hz or less frequency of the derivative of road disturbance. Hereafter, the curved surface such as shown in Figs. 2, 3 are called as the maximum gain surface. Fig. 2 shows the maximum gain surface of the passive robot and Fig. 3 shows that of the combined ideal robot model. The two design parameters $\ell_{\psi p}, \ell_{\phi p}$ are set as $\ell_{\psi p} = -0.3, \ell_{\phi p} = -0.3$ in Fig. 3 (a) and $\ell_{\psi p} = 0.3, \ell_{\phi p} = 0.3$ in Fig. 3 (b). It can be seen from Fig. 3, in the combined ideal robot model, the best location can be moved easily by setting the only two design parameters $\ell_{\psi p}$ and $\ell_{\phi p}$.

As stated above, even if actual mobile robot parameters such as robot mass, pitch and roll moment of inertia of robot body, and the position of the center of gravity include uncertainties, the control objective can be achieved if the behavior of the actual wheeled mobile robot tracks that of the combined ideal robot model (8).

2. Trajectory tracking controller

In order to develop a robust controller achieving the control objective, the tracking error between the actual wheeled mobile robot (6) and the combined ideal robot model (8) is defined as $\widetilde{\boldsymbol{\xi}}(t) = \boldsymbol{\xi}(t) - \boldsymbol{\xi}_m(t)$. Then, the tracking error equation is given by

$$\dot{\widetilde{\boldsymbol{\xi}}}(t) = \ {}_{\xi}\widetilde{\boldsymbol{\xi}}(t) + B_\xi M_p^{-1}(-k_b\boldsymbol{\mu}(t) - \boldsymbol{\omega}_1(t) + M_{pN}\boldsymbol{\omega}_2(t) + \Theta\boldsymbol{\omega}(t)), \quad (15)$$

$$\left.\begin{array}{l} {}_{\xi} = \begin{bmatrix} O_3 & I_3 & O_3 \\ O_3 & O_3 & I_3 \\ -I_3 & -3I_3 & -3I_3 \end{bmatrix}, B_\xi = \begin{bmatrix} O_3 \\ O_3 \\ I_3 \end{bmatrix} \\ \Theta = M_p M_{pN}^{-1} - I_3, \boldsymbol{\omega}(t) = M_{pN}\boldsymbol{\omega}_2(t) + k_d\boldsymbol{w}(t) \\ \boldsymbol{\omega}_1(t) = k_p\boldsymbol{x}(t) + (k_d + k_p)\dot{\boldsymbol{x}}(t) + k_d H\boldsymbol{q}(t) \\ \boldsymbol{\omega}_2(t) = k_b M_{pN}^{-1}\boldsymbol{f}_m(t) - H\boldsymbol{q}(t) + \widetilde{\boldsymbol{x}}(t) + 3\dot{\widetilde{\boldsymbol{x}}}(t) + 3H\widetilde{\boldsymbol{q}}(t) \end{array}\right\}. (16)$$

Where Θ is unknown matrix and $\boldsymbol{\omega}(t), \boldsymbol{\omega}_i(t), i = 1, 2$ are known signal vectors. The developed robust controller is given by

$$\boldsymbol{\mu}(t) = \frac{1}{k_b}(-\boldsymbol{\omega}_1(t) + M_{pN}\boldsymbol{\omega}_2(t) + \alpha B_\xi^T P_\xi \widetilde{\boldsymbol{\xi}}(t)). (17)$$

The positive definite matrix P_ξ is the solution of the following Lyapunov equation.

$$ {}_{\xi}^{T} P_\xi + P_\xi \ {}_{\xi} = -\beta I_9 \quad (18)$$

Where α and β are the positive design parameters.

In the controlled wheeled mobile robot using the controller (17), the following theorem holds.

Theorem 1 The controlled wheeled mobile robot using the controller (17) becomes stable, and by analyzing the time derivative of $V(t) = \widetilde{\boldsymbol{\xi}}(t)^T P_\xi \widetilde{\boldsymbol{\xi}}(t)$,the following inequality can be obtained.

$$\dot{V}(t) \leq -\beta\widetilde{\boldsymbol{\xi}}(t)^T\widetilde{\boldsymbol{\xi}}(t) + \frac{\overline{\rho}}{\alpha} \quad (19)$$

where $\overline{\rho}$ is a bounded constant independent of the design parameter α.

It can be concluded from the theorem 1 that the tracking performance can be improved easily by setting the design parameters α and β as large enough.

IV. CONCLUSION

We have proposed the new scheme to achieve good acceleration performance at any specified location on the wheeled mobile robot body. For lack of space, the simulation results for the actual wheeled mobile robot using the developed controller are not shown. However, the following properties have been ascertained by carrying out numerical simulations. Using the proposed scheme, by setting the only two design parameters $\ell_{\psi p}$ and $\ell_{\phi p}$, the location where the acceleration performance becomes best can be moved easily without redesigning a controller. Moreover, good acceleration performance can be achieved even if the actual wheeled mobile robot parameters include uncertainties, such as robot mass, pitch and roll moment of inertia of robot body, and the position of the center of gravity. This research is sponsored by the Robotics Industry Development Council.

REFERENCES

[1] Hoffmann. G. M., Tomlin. C. J. and Montemerlo. M. et al (2007), Autonomous Automobile Trajectory Tracking for Off-Road Driving: Controller Design, Experimental Validation and Racing, American Control Conference, 2296-2301

[2] Terupally. C. R., Zhu. J. J. and Williams. R. L. (2007), Trajectory Tracking and Stair Climbing Capability Assessment for a Skid-Steered Mobile Robot, American Control Conference, 2861-2866

[3] Lhomme-Desages. D., Grand. C. and Guinot. J. -C. (2007), Trajectory Control of a Four-Wheel Skid-Steering Vehicle over Soft Terrain using a Physical Interaction Model, Proc. IEEE Int. Conf. Robotics and Automation, 1164-1169

[4] Bugeja. M. K. and Fabri. S. G. (2007), Dual Adaptive Control for Trajectory Tracking of Mobile Robots, Proc. IEEE Int. Conf. Robotics and Automation, 2215-2220

[5] Takahaashi. M., Yoneda. K. and Hirose. S. (2006), Rough terrain locomotion of a leg-wheel hybrid quadruped robot, Proc. IEEE Int. Conf. Robotics and Automation, 1090-1095

[6] Grand. Ch., BenAmar. F. and Plumet. F. et al (2004), Decoupled control of posture and trajectory of the hybrid wheel-legged robot Hylos, Proc. IEEE Int. Conf. Robotics and Automation, 5111-5116

[7] McKenna. J. C., Anhalt. D. J. and Bronson. F. M. et al (2008), Toroidal skin drive for snake robot locomotion, Proc. IEEE Int. Conf. Robotics and Automation, 1150-1155

[8] Kimura. H., Hirose. S. and Shimizu. K. (2004), Stuck evasion control for active-wheel passive-joint snake-like mobile robot 'Genbu', Proc. IEEE Int. Conf. Robotics and Automation, 5087-5092

[9] Oya. M., Harada. H. and Araki. Y. (2007), An Active Suspension Controller Achieving the Best Ride Comfort at Any Specified Location on A Vehicle, Journal of System Design and Dynamics, 245-256

©ISAROB 2009

Workspace mapping based on multi-sensor information fusion using heterogeneous onboard sensors

Masamichi Miyake, Hiroyuki Takai and Keihachiro Tachibana*

Graduate school of Information Sciences,
Hiroshima City University, Hiroshima, Japan
(Tel : 81-82-830-1628; Fax : 81-82-830-1792)
({miyake,takai}@sys.im.hiroshima-cu.ac.jp)

*Graduate school of Computer Science,
Osaka Gakuin University, Suita, Osaka, Japan
(Tel : 81-6-6381-8434)
(tatibana@ogu.ac.jp)

***Abstract*:** In recent years, multiple robot systems that perform team operations have been developed. These robot systems are expected to execute complicated tasks smoothly in a given congested workspace. In this paper, we propose a workspace mapping algorithm using ultrasonic stereo sonar and an image sensor in order to operate the mobile robots among obstacles. This workspace mapping algorithm involves two steps: 1) the position detection of obstacles using ultrasonic stereo sonar and 2) the shape detection of obstacles using an image sensor. While each robot moves around in the given workspace, the two steps of the mapping algorithm are repeated and sensor data are collected. The robot measures the distance and the direction of obstacles using ultrasonic stereo sonar. The shape of obstacles is also captured using an onboard image sensor. A workspace map is created based on the sensor data accumulated from the proposed method and successful results are also obtained through the experiments.

Keywords: autonomous mobile robot, navigation system, localization, map creation, ultrasonic signal processing, **.**

I. INTRODUCTION

In the last several years, multiple mobile robot systems that perform team operations have been studied. These robot teams are expected to execute complicated tasks such as USAR (urban search and rescue) operations and/or repairing industrial facilities in hazardous environments.

When the number of robots increases in the same workspace, the occurrence of collisions also increases. We think that one of the causes of the collisions is related to the mutual position among the robots and/or the arrangements of the obstacles in the workspace. If the robots follow a plan that is created based on an exact workspace map, they should be able to avoid some of the collisions. In order to decrease the chance of collisions, the robots collect positional information of obstacles in the workspace and share a workspace map that is created from the sensor data.

In order to create and share the workspace map, the robots have to share the global coordinate axis and the point of origin. However, if the robots are operating in an unknown workspace, since there are no artificial landmarks prepared previously, they have to find and choose an obstacle of particular shape in the workspace to position their point of origin. In order to confirm fundamental principles of this map creation method, we have considered an ideal workspace to be a place where the floor is flat and all objects stand perpendicular. This ideal workspace is similar to most buildings where there are many walls and pillars resting on a flat floor. In addition, some of the walls and pillars create "corners (concave) / edges (convex)" in the workspace. As a result, these "corners / edges" can be used as temporary reference points that become candidates for the point of origin in the workspace, since they are easy to detect using onboard sensors.

In order to create the workspace map, the positional information of obstacles uses the Cartesian coordinates as the positional information needs to be normalized. On the other hand conventional sensors output positional data that centers the robot and indicate the distance and the direction from the robot. Therefore, the robot that is creating a workspace map has to transform the coordinates system of the positional information from polar coordinates to Cartesian coordinates. In addition, when the robot moves around in the workspace, since the center position of the detected positional data has been changed, the map-creating robot needs to repeat the transformation of its coordinate systems.

We propose a workspace map-creation algorithm using ultrasonic stereo sonar and an image sensor with a laser line generator. Ultrasonic stereo sonar can measure the distance and the direction of objects at the same time using a simple signal processing algorithm. The image sensor with a laser line generator can take a geo-

©ISAROB 2009

The Fourteenth International Symposium on Artificial Life and Robotics 2009 (AROB 14th '09),
B-Con Plaza, Beppu, Oita, Japan, February 5 - 7, 2009

metrical feature of the object also using simple image processing algorithms. We have considered a method of compiling of positional information detected by both onboard sensors in order to improve the accuracy of map creation.

II. Multi-obstacles position detection algorithm using ultrasonic stereo sonar

1. Distance measurement using ultrasonic sonar

Ultrasonic sonar is one of the major onboard sensors for mobile robot systems. Conventional ultrasonic sonar detects the envelope of the received signal and measures the time period until the envelope exceeds a threshold of signal strength from the ultrasonic emission. However, since the threshold of this method is defined empirically, it has incomplete theoretical background and is mostly guess work. Therefore, this measurement method is slightly flawed.

Another method of distance measurement using ultrasonic sonar measures the time period from when the ultrasonic pulse is emitted until the peak of the envelope of the received signal is reached. However, the peak of the envelope indicates the distance of the maximum reflective cross section and it does not represent true distance.

We examined a signal processing algorithm that estimates the true distance from the received reflected ultrasonic signal. Figure 1 shows a model of time period estimation algorithm. In figure 1, the horizontal axis is time and the vertical axis is amplitude. Several data sets of time and amplitude are measured and then regression lines p and q are computed based on the measured data sets using the least-square method. The intersection of regression lines p and q shows the estimated period t. The distance is derived from the estimated time period t based on the acoustic velocity.

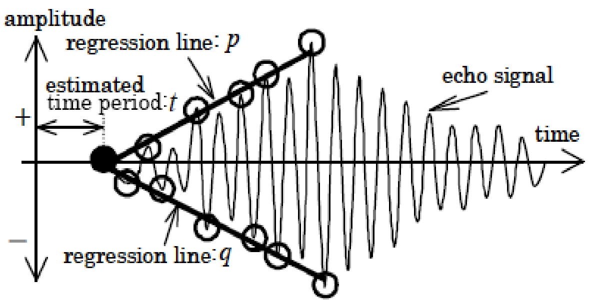

Fig. 1 A model of time period estimation

2. Direction detection using ultrasonic stereo reception

In order to scan surrounding obstacles, conventional ultrasonic sonar needs to rotate mechanically because it receives monaural signals and only measures distance from one frontal point. When the robot moves, and if the sonar also rotates, it may lose the position of obstacles and increase the possibility of collisions. In addition, it is difficult to downsize a mechanical rotator for ultrasonic sonar and to define its scanning width and scanning speed.

We examined ultrasonic stereo reception that receives reflected signals using two ultrasonic microphones. When the beam width of the ultrasonic device is wide, ultrasonic waves spread out not only in front of the device but also to the left and right sides. Two ultrasonic microphones of stereo reception receive the reflected signal that have time differences because the signal is reflected by an obstacle positioned in the left or right side and the distances from the obstacle to the microphones are different. In this method, the distances and the directions of the obstacle can be measured from the time of arrival (ToA) and the time difference of arrival (TDoA) of the received signal. Figure 2 shows a model of ultrasonic stereo reception.

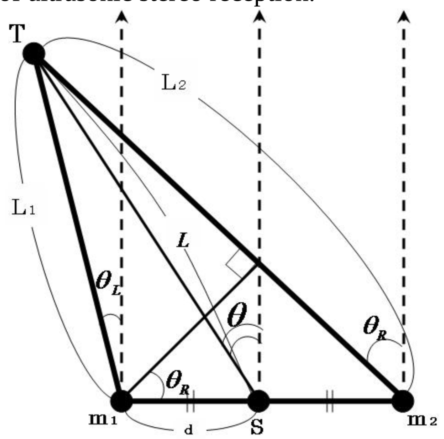

Fig. 2 A model of ultrasonic stereo reception

The parameters in figure 2 indicate below.

T: the position of an obstacle,

S: the position of an ultrasonic speaker,

m_1, m_2 : the position of the left / right microphones,

L : the distance from the speaker to the obstacle,

L_1 ,:the distance from the obstacle to the left microphones,

L_2 :the distance from the obstacle to the right microphones,

θ : the shift angles from the speaker,

θ_L, θ_R : the sift angle the left / right microphone,

d: the intervals between the speaker and microphones.

When the distance L_2 is greater than L_1, the distance L and the direction θ of are calculated by the equation 1. The distance L_1 and L_2, the direction θ_L and θ_R are positioned opposite if the distance L_1 is less than L_2.

$$\theta_R \propto \frac{L_2{}^2 - L_1{}^2 + 4d^2}{4dL_2}$$

$$\theta \propto \frac{L_1 \sin\theta_L + d}{L_1 \cos\theta_L} \tag{1}$$

$$L \propto \frac{L_1 \cos\theta_L}{\cos\theta}$$

III. Obstacle direction detection using image processing

We examined a laser line generator that can draw a straight line on a flat surface as an extra light source for an image sensor. When the laser line generator illuminates an object, an image sensor can capture a visual representation of the geometric features of the object. In order to detect the location and direction of the object, the shape of the object is extracted from the captured image using image processing algorithms. Figure 3 shows an extraction model with reference point using an image sensor.

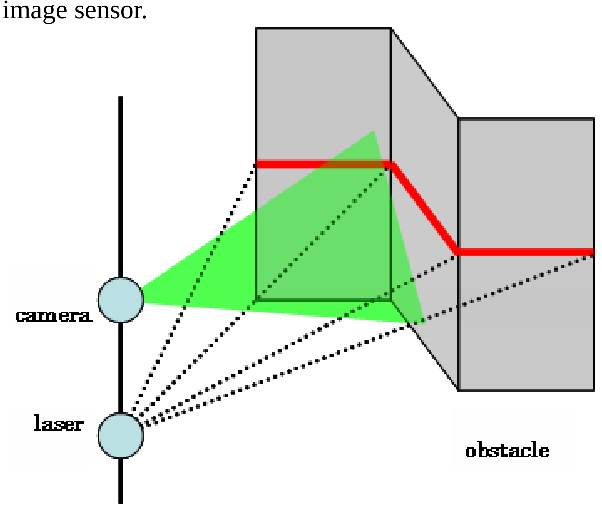

Fig.3 Extraction model with reference point using an image sensor

The shape of an obstacle is calculated by taking the difference between the captured images and background images. Figure 4 shows an example of shape detection using difference image processing. The position of the corner / edge can be calculated from the vertexes of kinked lines that are detected from the difference image.

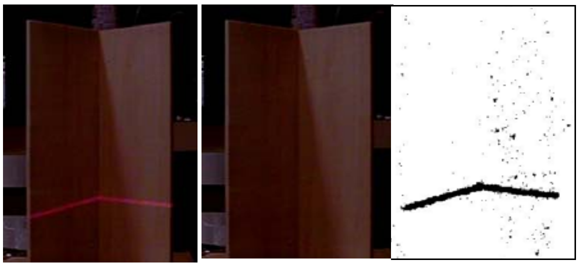

(a) captured (b) background (c) difference

Fig.4 A shape detection using difference image processing

IV. Workspace map creation algorithm

In order to represent an arrangement of objects in the given workspace, we have proposed a map creation algorithm based on the captured sensor data using ultrasonic sonar and image sensors. This has been modified from our previous research [1]. The procedure of the map creation is shown below.

(1) A robot detects the position of neighboring obstacles using ultrasonic stereo sonar.

(2) The robot illuminates obstacles using a laser line generator and captures features of the shape of each obstacle using image sensors.

(3) If a kinked line is detected in the captured image of the geometrical special feature of the object, since "an edge" or "a corner" of the object is mapped onto the image as in the vertex of the kinked line, the map creation algorithm calculates the position of "the edge" or "the corner" as a temporary reference point. Conversely, if a straight line is detected in the captured image, since "a flat surface" of the object is mapped onto the image as in the straight line, the map creation algorithm interprets it as a part of "the flat surface" of the object.

(4) Positional information of a temporary reference point detected by sensors needs to be converted from polar coordinates into a Cartesian coordinates.

(5) The positional information of the temporary reference point detected by sensors needs to be transformed into global coordinates, since the local coordinates of the robot shift along with the motion of the robot.

(6) The positional information of the temporary reference point that was transformed into the global coordinates is compared with the latest workspace map. If the positional information of the reference point has not been registered in the map yet, it is added into the map and the map is then updated.

(7) The robot repeats steps from (1) to (6) as it moves and updates the map.

©ISAROB 2009

VI. Exploratory experiment

We examined the performance of ultrasonic stereo reception. Figure 5 shows three targets in an experimental field. In this figure, ultrasonic speaker and microphones are placed in the left side of the field. In this experiment, Murata MA40B8R/S (Carrier frequency: 40 KHz, Beam width: 50 degrees) is used as the ultrasonic devices.

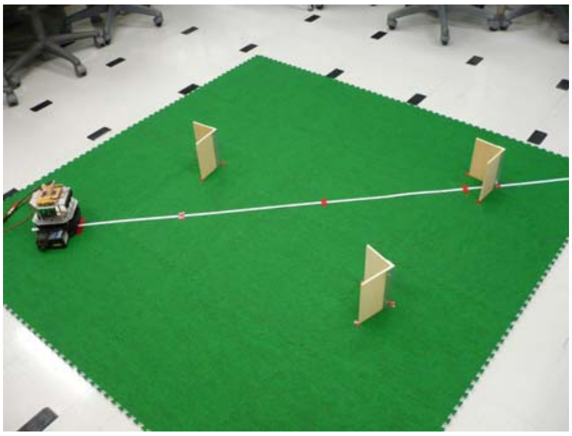

Fig.5 An experimental field with three targets

Figure 6 shows a sample of reflected ultrasonic signals. In figure 6, three target echoes can be found in these received signals. Table 1 shows the experimental results derived from ultrasonic stereo sonar. In this table, the positional information indicated the distance and the direction can be measured using ultrasonic stereo sonar.

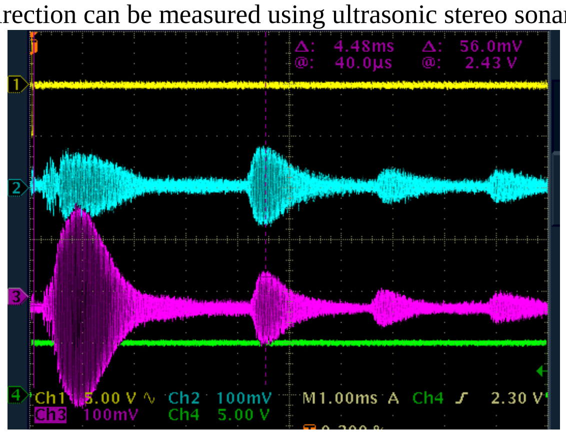

Fig.6 Echoes from the three targets

Table 1. Measurement results of ultrasonic stereo sonar

	Target 1		Target 2		Target 3	
	Distance	Angle	Distance	Angle	Distance	Angle
Theoretical	715.9	24.8L	1118.0	26.6R	1500.0	0.0
Trigger	701.2	21.6L	1094.4	26.4R	1502.5	2.4L
Error (Trig)	-14.7	-3.2	-23.7	-0.2	2.5	2.4
Burst	701.0	20.5L	1128.3	28.2R	1512.1	0.3L
Error (Burst)	-14.9	-4.2	10.3	1.7	12.2	0.3

Unit: distance (mm), angle (degree)

V. Conclusion and Future works

We proposed the ultrasonic stereo sonar system and the target position estimation algorithm using the least-square method. The performance and the accuracy of the target position estimation algorithm were confirmed through the exploratory experiments.

We also proposed the map creation algorithm that was modified from our previous research [1]. The previous algorithm used ultrasonic monaural sonar and the results of its position estimation were inaccurate due to the difficulty of collating to the same coordinate axis given by the ultrasonic sonar and image sensors. The modified algorithm that is proposed in this paper uses ultrasonic stereo sonar and the algorithm can collate the same coordinate axis because both sensors can measure the direction. Figure 7 shows a sample of the workspace map [1].

In future works, these algorithms will be installed into the small mobile robots and workspace maps will be created using these algorithms. We will confirm the accuracy of these algorithms through the workspace map.

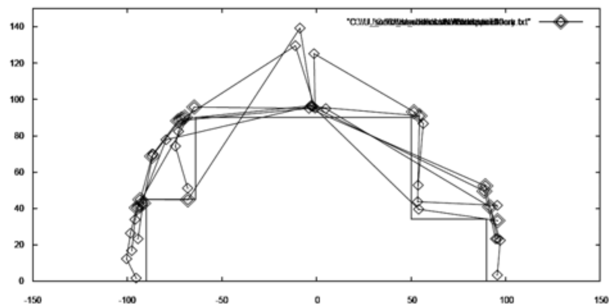

Fig.7 A sample of the workspace map

REFERENCES

[1]H. Takai, J. Mitsuoka, et, al. (2006): "Feasibility study of Sensing Methods on Cooperative Localization for Team Operation of Multiple Mobile Robots", The3rd International Conference on Autonomous Robots and Agents (ICARA2006) pp.379-385, Palmerston North, New Zealand, 2006

[2]H. Takai, M. Miyake, et, al. (2008): "Multi-Robot Cooperative Localization and Mapping using Multi-Sensor Information Fusion" Proceeding of the 39th ISR (International Symposium on Robotics 2008) pp.342-347, Seoul, Korea, 2008

©ISAROB 2009

Simultaneous Localization and Mapping of Wheel based Autonomous Vehicle with Ultrasonic Sensors

†Sungyoung Jung, †Jungmin Kim, †Jungmin Heo, †Sungshin Kim, ††Jong-il Bae

†School of Electronics and Electrical Engineering, Pusan National University, Busan, Korea
Pusan National University 30 Changjeon-dong, Keumjeong-ku, Busan 609-735, Korea
(Tel : 81-51-510-2367; Fax : 81-51-513-0212)
(Email : {pleiades0223, kjm16, hjm1700, sskim}@pusan.ac.kr)

††Division of Electrical and Control Engineering,Pukyong National University, Busan, Korea
San 100, Youngdang-dong, Nam-ku, Busan 608-739, Korea
(Tel : 81-51-629-6314)
(Email : jibae@pknu.ac.kr)

Abstract: Autonomous localization and mapping requires a vehicle to start in an unknown location in an unknown environment and then to incrementally build a map of landmarks present in this environment while simultaneously using this map to compute absolute vehicle location. The theoretical basis of the solution to this problem, known as Simultaneous Localization and Mapping (SLAM), is now well understood. A number of approaches to SLAM have appeared in the recent literature. In this paper, we used ultrasonic sensors and digital magnetic compass for measuring range, and used gyro sensors and encoder for positioning. Fusing ultrasonic sensor and digital magnetic compass have advantages of both economical efficiency and complementary cooperation. Experimental results show that the SLAM algorithm can successfully be executed with high accuracy and reliability.

Keywords: SLAM, Autonomous Vehicle, Ultrasonic sensor, Digital magnetic compass.

I. INTRODUCTION

The currently robot is applied to the fields and objectives more various than the previous robot that wrought simple and recursive work, so it is required to become the intelligent robot that will able to judge and move by itself. To be such intelligent robot need to be consisted of localization technique, path planning technique, map building technique for multi robot. Localization and map building is base technique among to the techniques, those are being studied actively. In the recent years, Technique that integrated localization and map building is named simultaneous localization and mapping (SLAM). This technique can improve the performance of localization using map information that is made by map building technique.

First of all, let us look about map building or map mapping. Those are being studied actively using distance sensors that are laser range finder, vision sensor, Infrared sensor, ultrasonic sensor and etc. [1] Each of sensors has merits and demerits. Laser range finder has very high accuracy, but it is very expensive and has a high electric power than other sensors. In case of vision sensor, can have plenty of environment information, but it have problems that have to operate plenty of data and have an accuracy that is very variable. Infrared sensor is cheap, but it can't guarantee high performance because its maximum range is less than 100cm. On the other hand, ultrasonic sensor is cheap, and can measure more than 300cm. [2] And we can expect high accuracy and credibility because that is strong on noise disturbance.

The sensors that used on localization technique are divided largely global positioning sensor and local positioning sensor. Most sensors for measuring global positioning are expensive, and have restriction on installation environment. On the other hand, sensors for local positioning, such as encoder, gyro, electric compass, and etc. are very cheap and strong on noise disturbance than global positioning sensors. However, those can't calculate the position in absolute coordinate, and have a problem that error is accumulated. In this paper, we aim to find position of robot in absolute coordinate using ultrasonic sensor and encoder, gyro, electric compass.

This paper is consisted as follows. First of all, we present a system configuration of autonomous vehicle in section 2, and techniques related SLAM used in this

Acknowledge - "This work was supported by the Grant of the Korean Ministry of Education, Science and Technology" (The Regional Core Research Program/Institute of Logistics Information Technology)

paper. Finally, we describe experiments and results in section 4.

II. Autonomous Vehicle

1. Measurement System

The Objective of this paper is SLAM technique using five ultrasonic sensor and two encoders, gyro, electric compass. We designed and made an actual autonomous vehicle. The driving part of this vehicle is based on 2 wheels - drive which has linearly 2 - degree of freedom. Fig.1 shows that system configuration of autonomous vehicle. As shown in Fig.1 we used various sensors, such as ultrasonic range finder and encoder, gyro, electric compass which specification of each sensor shown in Table 1. Electric compass data usually affected by magnetic field of own motor. So we used gyro that has high accuracy during vehicle is moving, and electric compass when vehicle is stopped. In this way, we could calculate more accurate orientation angle data for implement SLAM.

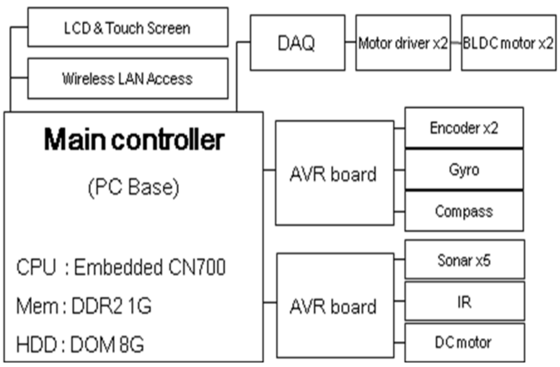

Fig.1. System configuration of autonomous vehicle

Table 1. Specification of sensors used

Item	Specification	
Ultrasonic(SRF04)	Frequency	40kHz
	Range	300~3cm
Encoder(MD200)	Voltage	5V
	R-F Time	300us
Gyro(ADXRS401EB)	Voltage	5V
	Sensitivity	±75 ˚/s
Compass(CMPS03)	Resolution	0.1 ˚
	Accuracy	3~4 ˚ approx.

2. Kinematics

This section will analyze the kinematics of vehicle to calculate the own position. Fig.2 shows kinematics of vehicle. X1-Y1 axis is the absolute coordinate, and X2-Y2 axis is the relative coordinate based on vehicle own position and X2 axis is vehicle's forward moving direction.

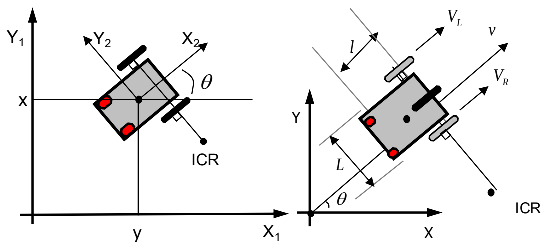

a. Coordinate of robot b. Bicycle model

Fig.2. Kinematics of autonomous vehicle

$$P = (x, y, \theta)^T \qquad (1)$$

P is definition of vehicle's posture. The x, y is coordinate of vehicle, θ is the angle of moving direction. Driving model can represented by bicycle model as shown in Fig.2b. If angular velocity of both wheels are ω_R, ω_L and radius of wheel is r then linear velocity of each wheels are as follows.

$$V_R = r\omega_R \ , \quad V_L = r\omega_L \qquad (2)$$

If distance between both wheels are L, then the angular velocity(ω) and linear velocity(v) of vehicle based on absolute coordinate (X1-X2) are related with kinematics on two-dimensional coordinate system. Also those are represented by equation (3).

$$\begin{aligned} \omega &= \frac{V_R - V_L}{L} = \frac{r}{L} \\ v &= \frac{V_R + V_L}{2} = r\omega \end{aligned} \qquad (3)$$

So we can calculate the posture vector (P) from linear and angular velocity by equation (4).

$$P = \begin{pmatrix} \dot{x} \\ \dot{y} \\ \dot{\theta} \end{pmatrix} = \begin{pmatrix} \cos\theta & 0 \\ \sin\theta & 0 \\ 0 & 1 \end{pmatrix} \begin{pmatrix} v \\ \omega \end{pmatrix} \qquad (4)$$

3. Driving Control

To control driving of vehicle safely, we used fuzzy logic control in -50° ~ +50° section and proportional control in rest of section. (Fig.3)

In case of fuzzy logic control, there is a problem that caused by a plenty of calculation. Thus, we defined membership functions using fuzzy toolbox of MATLAB R2008, and made a lookup table. Main controller loads the lookup table then control the vehicle, so it works well in real-time.

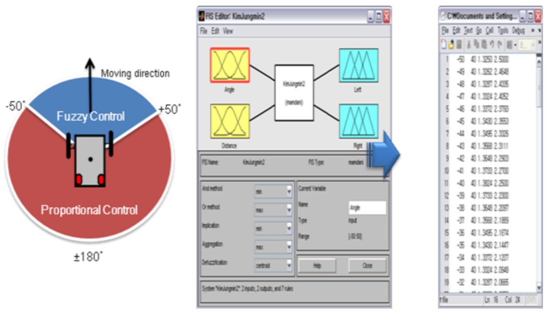

Fig.3. Driving control of autonomous vehicle

III. Simultaneous Localization and Mapping

1. Map Building

Map building must be leaded before implementation of the SLAM, and the performance depending on the accuracy of map building. In general, the map can represent by Grid and Topological, Feature, Hybrid type. Moreover, there are two main map building methods that standard map building and hierarchical map building. [3] Fig.4 compares standard map building and hierarchical map building method by Grid type.

We use two distance variations that measured by ultrasonic range sensor of autonomous vehicle. Global map is consist of every points that moved and measured by vehicle, so this map has duplicated points.(Fig.4a) Also accumulated error of encoder and gyro cause localization error of the entire map. Actually, if vehicle moves 180 meters, then orientation and distance error was about to 6°(degree) and 20 cm. On the other hand topological map is more precise than global map as shown in Fig 4b. t But if the map represented by grid type, system require a very large storage space and real time calculations may be difficult. So, in his paper we represent hierarchical map by feature type. [4]

Fig.5 shows map building by extracted and clustered feature points. The red spots on the top and bottom of the horizontal direction show that the doors of the seminar rooms and lab, and spots on the horizontal direction show lockers and elevators, mirrors, stairs.

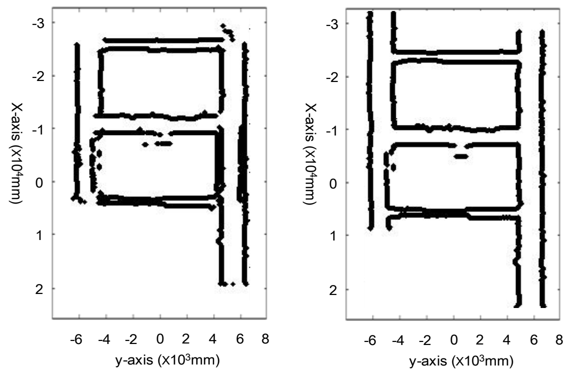

a. General map b. Topological map

Fig.4. Map Building Method

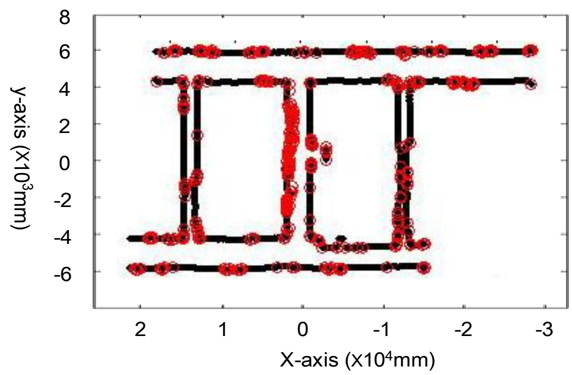

Fig.5. Feature points on the map

2. SLAM

Typically, localization using only gyro and encoder can calculate relative coordinates based on the start position of vehicle. However, absolute position must be known if vehicle want to go to goal position. SLAM algorithm that calculate the absolute position of vehicle in unknown location is as follows flow chart.(Fig.6) First, vehicle that starts in unknown location calculate the orientation of itself by using electronic compass. And calculate the relative angle base on own corridor using distances of ultrasonic range sensors and compass orientation angle. [5] Then vehicle move to the center of the corridor by measured distance, and move through the wall of corridor. Simultaneously compare with feature points that are measured by vehicle and map building features, and calculate the absolute location of vehicle. Our designed vehicle will move to the center of corridor continuously if there are no obstacles. This algorithm is not only calculate absolute position, but how can reduce the error of position during vehicle is moving.

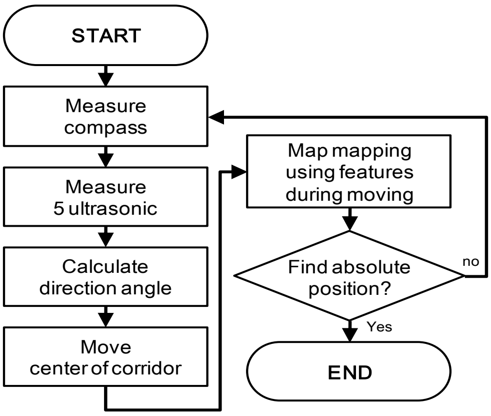

Fig.6. SLAM algorithm

IV. Result

Fig.7 shows autonomous vehicle experimented. Development environment of this autonomous vehicle is Borland C++ 6.0 Builder and Code Vision AVR studio in Window XP. Experiment was performed after map building was done. (vehicle can find out 105 feature points as shown in Fig.5) Then, vehicle located in eight unknown location that is shown in Fig.8. Fig.9 shows measured during time and distance that vehicle was driven, used feature points. Actually in the ⓓ and ⓗ location, it took very long time because extracted map feature was not exactly.

Fig.7. Autonomous Vehicle

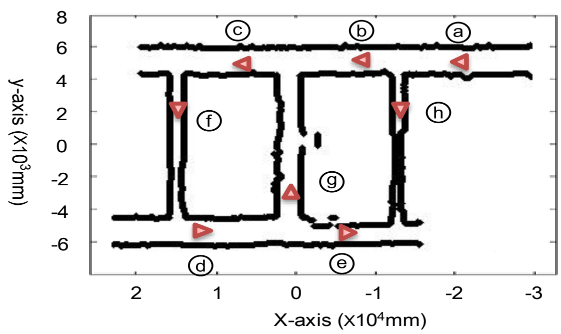

Fig.8. Unknown location at experiment

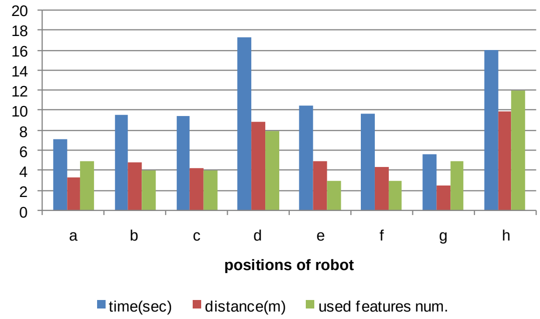

Fig.9. The result of experiment

V. Conclusion

In this paper, we were implemented SLAM using ultrasonic range sensors and encoder, gyro, electric compass. Map building as the previous step of SLAM made by distance variation of ultrasonic range sensor and map was constructed in hierarchical. Then extract feature point from map data. In experiment, vehicle can find out its absolute coordinate in average 10.7s (use five feature points, driving distance is about 5.39m) Applied to the real autonomous vehicle, finding absolute localization in real-time was able to see.

REFERENCES

[1]Ho-Duck Kim, Sang-Wook Seo, In-hun Jang, and Kwee-Bo Sim, "SLAM of Mobile Robot in the indoor Environment with Digital Magnetic Compass and Ultrasonic Sensors", International Conference on Control, Automation and Systems, Seoul, 2007, pp.87-90
[2]Sunghwan Ahn and Wan Kyun Chung, "Efficient SLAM Algorithm with Hybrid Visual Map in an Indoor Environment", International Conference on Control, Automation and Systems, Seoul, 2007, pp.663-667
[3]SungHwan Ahn, Jinwoo Choi, Nakju Lett Doh, Wan Kyun Chung "A practical approach for EKF-SLAM in an indoor environment: fusing ultrasonic sensors and stereo camera", Springer Science+Business Media, LLC 2008, vol.24, pp.315-335
[4]Henrik Andreasson, Andre Treptow and Tom Duckett "Localization for mobile robots using panoramic vision, local features and particle filter" ,Proceedings of the 2005 IEEE, International Conference on Robotics and Automation, Barcelona, 2005, pp.3348-3353
[5]Michael Montemerlo, Sebastian Thrun, William Whittaker. "Conditional particle filters for simultaneous mobile robot locaization and people-tracking", Proceedings of the 2002 IEEE, International Conference on Robotics & Automation, Washington, 2002, pp.695-701

©ISAROB 2009

The Fourteenth International Symposium on Artificial Life and Robotics 2009 (AROB 14th '09),
B-Con Plaza, Beppu, Oita, Japan, February 5 - 7, 2009

Hybridization of Evolutionary Multiobjective Optimization Algorithms by the Adaptive Use of Scalarizing Fitness Function

Noritaka Tsukamoto, Yuji Sakane, Yusuke Nojima, and Hisao Ishibuchi

Department of Computer Science and Intelligent Systems,
Graduate School of Engineering, Osaka Prefecture University
1-1 Gakuen-cho, Naka-ku, Sakai, Osaka 599-8531, Japan
(Tel : 81-72-254-9198; Fax : 81-72-254-9915)
({nori@ci., sakane@ci., nojima@, hisaoi@}cs.osakafu-u.ac.jp)

Abstract: This paper proposes an idea of adaptively using a scalarizing fitness function in evolutionary multiobjective optimization (EMO) algorithms. In our former study, we proposed a hybrid EMO algorithm, where we introduced two probabilities to specify how often the scalarizing fitness function is used for parent selection and generation update in EMO algorithms. In this paper, we use the ratio of non-dominated solutions to specify how often the scalarizing fitness function is used in our hybrid EMO algorithm. Through computational experiments on multiobjective 0/1 knapsack problems, we show the effectiveness of adaptively using a scalarizing fitness function.

Keywords: Evolutionary multiobjective optimization (EMO) algorithms, multiobjective problems, many-objective problems, scalarizing fitness function, multiobjective 0/1 knapsack problems.

I. INTRODUCTION

Evolutionary multiobjective optimization (EMO) is one of the most active research areas of evolutionary computation. Most EMO algorithms use Pareto ranking to evaluate the fitness of each solution. Whereas Pareto ranking-based EMO algorithms usually work well on two-objective problems, their search ability is severely degraded by the increase in the number of objectives. Well-known Pareto ranking-based EMO algorithms such as NSGA-II [1] and SPEA [2] do not work well on many-objective problems with four or more objectives. This is because almost all solutions in each population become non-dominated with each other when they are compared using many objectives. That is, almost all solutions have the same fitness with respect to Pareto ranking. On the other hand, Hughes [3] showed that multiple runs of single-objective evolutionary algorithms (SOEAs) outperformed a single run of EMO algorithms in their applications to many-objective problems. In some studies, EMO algorithms can outperform SOEAs even when they are used to solve single-objective problems. It was also reported that better results were obtained from transforming single-objective problems into multi-objective ones.

Some related studies suggest that SOEAs and EMO algorithms have their own advantages and disadvantages. In our former study [4], we hybridized them into a single algorithm in order to simultaneously utilize their advantages. Following this idea, we implemented a hybrid EMO algorithm using NSGA-II and a weighted sum fitness function. The weighted sum fitness function is probabilistically used for parent selection and generation update in our hybrid EMO algorithm. We introduced two probabilities to specify how often the scalarizing fitness function is used for parent selection and generation update in our hybrid EMO algorithms. We showed that the use of the weighted sum fitness function improved the performance of NSGA-II for multiobjective optimization.

In this paper, we propose an idea of adaptively using the weighted sum fitness function in our hybrid EMO algorithm. We use the ratio of non-dominated solutions to specify how often the weighted sum fitness function is used in our hybrid EMO algorithm. The weighted sum fitness function is adaptively used for parent selection and generation update in this paper. Through computational experiments on multiobjective 0/1 knapsack problems, we show the effectiveness of adaptively using the weighted sum fitness function.

II. HYBRID EMO ALGORITHM

In this section, we explain about our hybrid EMO algorithm. In our former study [4], we implemented a hybrid EMO algorithm by incorporating a weighted sum fitness function into NSGA-II [1]. We introduced two probabilities P_{PS} and P_{GU} to specify how often the

©ISAROB 2009

weighted sum fitness function is used for parent selection and generation update, respectively.

1. NSGA-II

NSGA-II [1] is a well-known and frequently-used EMO algorithm with the $(\mu+\lambda)$-ES generation update mechanism. The outline of NSGA-II is as follows:

[NSGA-II]
Step 1: P = Initialize (P)
Step 2: While the stopping condition is not satisfied, do
Step 3: P' = Parent Selection (P)
Step 4: P'' = Genetic Operations (P')
Step 5: P = Generation Update ($P \cup P''$)
Step 6: End while
Step 7: Return Non-dominated (P)

In NSGA-II, each solution in the current population is evaluated using Pareto ranking and crowding distance in the following manner in Step 3. First, Rank 1 is assigned to all the non-dominated solutions in the current population. Solutions with Rank 1 are tentatively removed from the current population. Next, Rank 2 is assigned to all the non-dominated solutions in the remaining population. Solutions with Rank 2 are tentatively removed from the remaining population. In the same manner, ranks are assigned to all solutions in the current population. Solutions with smaller rank values are viewed as being better than those with larger rank values. A crowding distance is used to compare solutions with the same rank. The crowding distance of a solution is the Manhattan distance between its two adjacent solutions in the objective space (for details, see [1]). When two solutions have the same rank, one solution with a larger value of crowding distance is viewed as being better than the other with a smaller value.

A prespecified number of pairs of parent solutions are selected from the current population by binary tournament selection to form a parent population P' in Step 3. An offspring solution is generated from each pair of parent solutions by genetic operations to form an offspring population P'' in Step 4. The current population and the offspring population are merged to form an enlarged population. Each solution in the enlarged population is evaluated by Pareto ranking and the crowding distance as in the parent selection phase. A prespecified number of the best solutions are chosen from the enlarged population as the next population P in Step 5.

2. Weighted sum fitness function

The weighted sum fitness function of the k objectives is as follows:

$$fitness(\mathbf{x}) = w_1 \cdot f_1(\mathbf{x}) + w_2 \cdot f_2(\mathbf{x}) + \ldots + w_k \cdot f_k(\mathbf{x}) \quad (1)$$

where $f_i(\mathbf{x})$ is the i-th objective value of $\mathbf{x}$, w_i is a non-negative weight value.

We generate a set of non-negative integer vectors satisfying the following relation: $w_1 + w_2 + \ldots + w_k = d$ where d is a prespecified integer. In this paper, we specify $d = 4$ for two, three, and four-objective problems. On the other hand, we specify $d = k$ for five and six-objective problems where k is the number of objectives. For example, we have five integer vectors: (4, 0), (3, 1), (2, 2), (1, 3), and (0, 4) for two-objective problems. For three-objective problems, we have 15 integer vectors: (4, 0, 0), (3, 1, 0), …, (0, 0, 4). For four, five, and six-objective problems, we have 35, 126 and 462 integer vectors, respectively.

3. Hybrid EMO algorithm

Our hybrid EMO algorithm is the same as NSGA-II except for parent selection in Step 3 and generation update in Step 5. When a pair of parent solutions is selected from the current population, the weighted sum fitness function and the NSGA-II fitness evaluation mechanism are used with the probabilities P_{PS} and $(1-P_{\mathrm{PS}})$, respectively. When another pair of parent solutions is to be selected, the probabilistic choice between two fitness evaluation schemes is performed again.

As in the parent selection phase in Step 3, we probabilistically use the weighted sum fitness function in generation update phase in Step 5. When one solution is to be selected and added to the next population, the weighted sum fitness function and the NSGA-II fitness evaluation mechanism are used with the probabilities P_{GU} and $(1-P_{\mathrm{GU}})$, respectively. When another solution is to be selected, the probabilistic choice between two fitness evaluation schemes is performed again.

It should be noted that our hybrid EMO algorithm with $P_{\mathrm{PS}} = 0.0$ and $P_{\mathrm{GU}} = 0.0$ is the same as the pure NSGA-II [1] since the weighted sum fitness function is never used. On the other hand, our hybrid EMO algorithm with $P_{\mathrm{PS}} = 1.0$ and $P_{\mathrm{GU}} = 1.0$ is a weighted sum-based genetic algorithm with the $(\mu+\lambda)$-ES generation update mechanism. In our former study [4], we used fixed values P_{PS} and P_{GU} during the execution of our

Table 1. Hyprevolume measure over 50 runs in subsection 3.2.

	2-500 ($\times 10^8$)	3-500 ($\times 10^{12}$)	4-500 ($\times 10^{17}$)	5-500 ($\times 10^{21}$)	6-500 ($\times 10^{25}$)
NSGA-II	3.80 (0.0160)	6.53 (0.0440)	1.01 (0.0085)	<u>1.74 (0.0185)</u>	<u>2.60 (0.0286)</u>
$\text{Hybrid}_{\text{PS}}$	<u>3.78 (0.0152)</u>	<u>6.48 (0.0388)</u>	<u>1.00 (0.0081)</u>	<u>1.74 (0.0138)</u>	2.62 (0.0237)
$\text{Hybrid}_{\text{GU}}$	3.85 (0.0179)	6.71 (0.0410)	1.08 (0.0070)	1.89 (0.0161)	2.91 (0.0297)
$\text{Hybrid}_{\text{adapt}}$	**3.91 (0.0145)**	**6.87 (0.0409)**	**1.11 (0.0094)**	**1.93 (0.0214)**	**2.92 (0.0381)**

hybrid algorithm.

In this paper, we adaptively use the weighted sum fitness function. In short, we use various values P_{PS} and P_{GU} during the execution of our hybrid algorithm. P_{PS} is the ratio of non-dominated solutions in the current population in Step 3 whereas P_{GU} is the ratio of non-dominated solutions in the enlarged population in Step 5.

III. PERFORMANCE EVALUATION

In this section, we examine the performance of adaptively using the weighted sum fitness function. First, we compare three versions of our idea in subsection 3.2. Next, we compare our idea with our original hybrid algorithm [4] in subsection 3.3.

1. Parameter settings

As test problems, we use a two-objective 500-item, a three-objective 500-item, and a four-objective 500-item knapsack problem in [2]. These test problems are denoted as 2-500, 3-500, and 4-500, respectively. As many-objective problems, we generate a five-objective 500-item (i.e., 5-500) and a six-objective 500-item (i.e., 6-500) knapsack problem in the same manner as [2]. We use the following parameter specifications in this section:

Population size: 200 (i.e., $\mu = \lambda = 200$),
Crossover probability: 0.8 (uniform crossover),
Mutation probability: 1/500 (bit-flip mutation),
Stopping condition: 400,000 fitness evaluations.

Each algorithm is applied to each test problem 50 times. As a performance measure, we use the hypervolume measure [5] that calculates the volume of the dominated region by the non-dominated solution set in the objective space. The hypervolume measure is used as the diversity and the convergence measure. For the 2-500 problem, we show the 50% attainment surface [6] in order to visually show the behavior of each algorithm.

2. Comparison among three versions of our idea

In this subsection, we examine the following versions of our idea:

$\text{Hybrid}_{\text{PS}}$: The weighted sum fitness function is adaptively used for parent selection in Step 3.

$\text{Hybrid}_{\text{GU}}$: The weighted sum fitness function is adaptively used for generation update in Step 5.

$\text{Hybrid}_{\text{adapt}}$: The weighted sum fitness function is adaptively used for parent selection in Step 3 and generation update in Step 5.

We also use the pure NSGA-II [1] to compare three versions of our idea. In Table 1, we show the average value and the standard deviation value (in the parentheses) of the hypervolume measure over 50 runs for each problem. The best value and the worst value are highlighted by bold and underline, respectively.

Table 1 shows that the best result for each problem was obtained from $\text{Hybrid}_{\text{adapt}}$. From this table, we show the effectiveness of adaptively using the weighted sum fitness function for parent selection phase and generation update phase. On the other hand, $\text{Hybrid}_{\text{PS}}$ did not obtain good results for each problem. We cannot observe the effect of adaptively using the weighted sum fitness function only for parent selection phase. In Fig. 1, we show the 50% attainment surface over 50 runs of each algorithm: $\text{Hybrid}_{\text{PS}}$, $\text{Hybrid}_{\text{GU}}$, $\text{Hybrid}_{\text{adapt}}$, and NSGA-II. From Fig. 1, $\text{Hybrid}_{\text{adapt}}$ improved the diversity of obtained non-dominated solutions. On the other hand, $\text{Hybrid}_{\text{PS}}$ obtained the similar result with NSGA-II. From these results, it is shown that adaptively using the weighted sum fitness function only for parent selection phase did not improve the search ability of NSGA-II whereas adaptively using the weighted sum fitness function for generation update phase had a positive effect.

©ISAROB 2009

Table 2. Hyprevolume measure over 50 runs in subsection 3.3.

	2-500 ($\times 10^{8}$)	3-500 ($\times 10^{12}$)	4-500 ($\times 10^{17}$)	5-500 ($\times 10^{21}$)	6-500 ($\times 10^{25}$)
NSGA-II	3.80 (0.0160)	6.53 (0.0440)	1.01 (0.0085)	1.74 (0.0185)	2.60 (0.0286)
Hybrid$_{0.5_0.5}$	3.89 (0.0154)	6.78 (0.0400)	1.08 (0.0069)	1.88 (0.0131)	2.86 (0.0309)
Weighted Sum	**3.95 (0.0121)**	**6.95 (0.0416)**	**1.12 (0.0086)**	**1.93 (0.0193)**	2.86 (0.0377)
Hybrid$_{adapt}$	3.91 (0.0145)	6.87 (0.0409)	1.11 (0.0094)	**1.93 (0.0214)**	**2.92 (0.0381)**

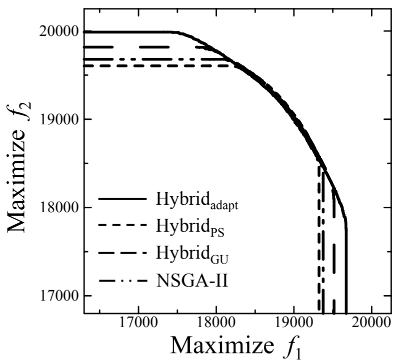

Fig. 1. 50% attainment surface in subsection 3.2.

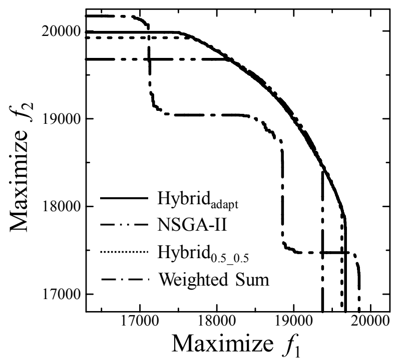

Fig. 2. 50% attainment surface in subsection 3.3.

3. Comparison with original hybrid algorithm

In this subsection, we compare our idea Hybrid$_{adapt}$ with our original hybrid algorithm [4]. In our original hybrid algorithm, we use the following parameters for P_{PS} and P_{GU}:

P_{PS}: 0.0, 0.5, 1.0,
P_{GU}: 0.0, 0.5, 1.0.

We examine the 3 × 3 combinations of the 3 values of P_{PS} and P_{GU}. Due to the page limitation, we use 3 combinations of P_{PS} and P_{GU}: $P_{PS} = P_{GU} = 0.0$, $P_{PS} = P_{GU} = 0.5$, $P_{PS} = P_{GU} = 1.0$. As stated in subsection 2.3, our original hybrid algorithm with $P_{PS} = P_{GU} = 0.0$ is the same as the pure NSGA-II whereas our original hybrid algorithm with $P_{PS} = P_{GU} = 1.0$ is a weighted sum-based genetic algorithm with $(\mu+\lambda)$-ES generation update mechanism. We denote the combination of $P_{PS} = P_{GU} = 0.5$ as Hybrid$_{0.5_0.5}$. In Table 2, we show the average value and the standard deviation value of the hypervolume measure over 50 runs for each problem. From Table 2, Hybrid$_{adapt}$ obtained relatively good results for each problem. Especially, Hybrid$_{adapt}$ obtained the best result for two problems with five or six objectives. In Fig. 2, we show the 50% attainment surface over 50 runs of each algorithm: NSGA-II, Hybrid$_{0.5_0.5}$, Weighted Sum, and Hybrid$_{adapt}$. From Fig. 2, adaptively using the weighted sum fitness function had relatively good effect on the search ability of our original hybrid algorithm.

VI. CONCLUSION

This paper proposed an idea of adaptively using a scalarizing fitness function in our hybrid EMO algorithm. We used the ratio of the non-dominated solutions to specify how often the scalarizing function is used in our hybrid EMO algorithm. Through computational experiments, we showed the effectiveness of our idea.

REFERENCES

[1] K. Deb, A. Pratap, S. Agarwal, and T. Meyarivan (2002), A fast and elitist multiobjective genetic algorithm: NSGA-II, *IEEE Trans. on Evolutionary Computation*, 6, 2, 182-197.
[2] E. Zitzler and L. Thiele (1999), Multiobjective evolutionary algorithms: A comparative case study and the strength pareto approach, *IEEE Trans. on Evolutionary Computation*, 3, 4, 257-271.
[3] E. J. Hughes (2005), Evolutionary many-objective optimization: Many once or one many?, *Proc. of CEC 2005*, 222-227.
[4] H. Ishibuchi, T. Doi, and Y. Nojima (2006), Incorporation of scalarizing fitness functions into evolutionary multiobjective optimization, *LNCS 4193: PPSN IX*, 493-502, Springer, Berlin.
[5] E. Zitler and L. Thiele (1998), Multiobjective optimization using evolutionary algorithms – A comparative case study, *LNCS: 1498: PPSN V*, 292-301, Springer, Berlin.
[6] C. M. Fonseca and P. J. Fleming (1996), On the performance assessment and comparison of stochastic multiobjective optimizers, *LNCS 1141: PPSN IV*, 584-593, Springer, Berlin.

The Fourteenth International Symposium on Artificial Life and Robotics 2009 (AROB 14th '09),
B-Con Plaza, Beppu, Oita, Japan, February 5 - 7, 2009

Development of Programming Language Espace and Its Application to Parallel and Distributed Evolutionary Computation

Takehiko IWAKAWA Satoshi ONO Shigeru NAKAYAMA
Deptartment of Information and Computer Science, Faculty of Engineering
Kagoshima University
1-21-40, Korimoto, Kagohima 890-0065, Japan
{sc100007, ono, shignaka}@ics.kagoshima-u.ac.jp

Abstract

This paper proposes a programming language called "Espace" for parallel and distributed computation. In general, it is difficult to code a distributed, parallel program due to multi threading, message passing, managing clients, and so on. Espace involves a few simple syntax rules added to Java. Developers do not need to know how to write a parallel, distributed program source code in detail. This paper applies Espace to parallelize an evolutionary computation program and shows that the Espace compiler enables to convert an evolutionary computation program written in Java into a distributed, parallel system by adding a few words to the program.

1 Introduction

General evolutionary computation algorithms are stochastic, population-based generate-and-test algorithms which require huge computational cost. They are not an essential way to solve combinatorial explosion but practical resources for cost reduction to develop an evolutionary computation program as a distributed, parallel system.

Distributed models of evolutionary computation are mainly classi ed into two models: island model and evaluation-distributed model. Island model involves some subpopulations, and a few solution candidates immigrating between subpopulations at de ned intervals. Island model is a rough-grained model which can be parallelized by subpopulations and has an advantage in control of search diversi cation. Evaluation-distributed model is a ne-grained parallel and distributed model appropriate for problems which require much computation time to evaluate a solution candidate because evaluation of solution candidates can easily be parallelized.

In the case using the existing libraries or languages, although the above models are e ective to reduce computation time, developers have to code for parallelization procedures such as multi threading, fault tolerance and so on

In general, it is difficult to code a distributed, paralleled program due to multithreading, message passing, managing clients, and so on. To reduce the development cost of distributed, parallel system, some libraries for programming languages producing shared memory or message passing functions are used[1]. There are also other methodologies using compilers, such as programming languages, macros, directions to compilers, which are speci ed to address these problems reducing the cost of distributed, parallel system development [2, 3, 4, 5, 6].

Using these libraries or languages is unfortunately not so easy because of their complicated syntax and discords between base language and extended module. Construction of distributed runtime environment is also a cumbersome procedure. For example, a developer has to set up an operating system on personal computers only for parallel, distributed computation as a cluster, or install middleware to maintain the system's security level[7].

This paper proposes a programming language for parallel and distributed computation called "Espace"[8], and shows that the Espace compiler enables to convert evolutionary computation program written in Java into distributed, parallel system by adding a few words of Espace to the program.

2 Programming Language Espace

2.1 Design policy

Design policies of Espace language proposed in this paper are as follows:

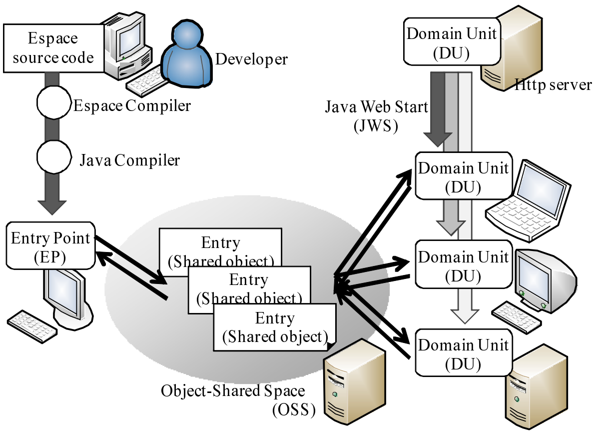

Figure 1: System structure of Espace runtime environment

1. Espace utilizes simple, few syntax rules.
2. Espace abstracts distributed and parallel processing function.
3. Espace produces a distributed runtime environment which can be built up easily.

Espace involves a few simple syntax rules added to Java. The added syntax rules are mainly invocation rules of distributed method and access rules to a distributed object. Therefore, developers do not need to know how to write a parallel, distributed program source code in detail.

2.2 System structure

The distributed runtime environment of Espace is made up of an Object-Shared Space(OSS) server and its clients. Clients communicate with each other via reading or writing shared objects called Entry. The system structure of Espace is shown in Fig. 1. An Espace program is compiled by an Espace Compiler into a Java program called Entry Point(EP). At the same time, EP is conducted with anonymous computation units called Domain Units(DUs) via Java Web Start[9]. DU works as computation resource or as a holder of distributed object. The only operation users need to do is accessing an HTTP server for deploying the DU.

2.3 Syntax rules

Developers can allocate or access distributed objects by inserting the keyword "remote", which indicates that a eld modi ed by the keyword has a remote attribute (remote eld) and can be accessed by any client joining the Espace network.

Invocation syntax rules of distributed method enables developers to write distributed, parallel processing program with extremely reduced cost; adding the keyword "espace" to distributed methods and invoking them in a "distribute" statement. The EBNF definition of a distribute statement is shown in Figure 2. In a "distribute" section, a method modi ed by the keyword has an espace attribute (espace method), and then each espace method is invoked on parallel threads. In addition, it is not necessary for developers to adjust task granularity of parallelization and implement fault tolerance functions on connection or unforeseen situation. Processes de ned at "doing" section are also executed at one time on EP .

```
distribute-statement =
'distribute'
'{' block-statement* '}'
['doing' '{' block-statement* '}' ] ;
```

Figure 2: EBNF de nition of distribute statement.

The keyword can be used to modify a eld. Field instances modi ed by the keyword is shared by DUs while running a "distribute" statement, and the elds become able to be used in espace method.

3 Application to Image Filter Generation by Genetic Programming

3.1 Overview

Over the past few years, studies have been performed on image lter generation(IFG) with genetic algorithm (GA) or genetic programming (GP)[10]. The existing methods generate various lters by combining existing primitive lters. Although lters generated by GP show better output quality than lters generated by GA, chromosome size becomes huge in GP. Uncontrolled chromosome growth, called bloat, makes lter application time worse, and makes it impossible for users to analyze and modify generated lters. The authors of this study propose a GP based image lter generation method that tunes numeric parameters of the primitive lters and restrains surplus chromosome growth[10].

3.2 Process Flow

GP for IFG recieves source and objective image sets as input, and outputs a generated image lter. Each node in a tree-structured chromosome corresponds to a basic lter such as smoothing, edge extraction, inverse, and so on. Some of the basic lters have a parameter such as binarization, addition, maximization and so on, and the parameter should be adjusted so that the basic lter works well.

The process ow of GP for IFG is basically an iteration of recombination of individuals by applying operators of selection, crossover, and mutation, evaluation of the individuals, and parameter adjustment in basic lters.

The parameter adjustment is conducted in a similar way to local search:

Step 1 Choose R_{PA} individuals randomly.

Step 2 Repeat following Step 3 through 4 S_{PA} times.

Step 3 For each individual i, choose a basic lter and generate N_{PA} o springs by changing the parameter of the chosen basic lter.

Step 4 Choose the best o spring and replace i by the best o spring.

In the parameter adjustment, R_{PA} S_{PA} N_{PA} times tness calculation must be conducted, and this is more time-consuming than all other processes in the iteration involving evaluation of all individuals.

3.3 Implemantation

We applied Espace to parallelization of GP for IFG. Here GP for IFG distributed by Espace is called as DGPIFG . In DGPIFG, EP distributes parameter adjustment process for one chromosome to DUs via OSS. DUs get chromosomes from EP via OSS and return the result to EP in every generation.

To parallelize existing GPIFG code with Espace, the following procedure is necessary.

Step1 Add the "espace" keyword to modify the method de ning parameter adjustment processes.

Step2 Add the "distribute" statement outside of the loop invoking the parameter adjustment method repeatedly.

Step3 Add the "espace" keyword to variables read in the parameter adjustment method.

The source code for DGPIFG is shown in Figure3. Method tuneParam is an espace method, and is accessed on a distribute statement. Method calFitnessN is also an espace method, and is accessed on method tuneParam. Each espace method is executed on DUs. Field orgFit, pixGs, pixSs, and weight are espace eld and are accessed on calFitnessN. Instances of these espace elds are assigned to OSS, and shared between DUs. In addition, it is necessary to change declared type of an espace eld to Object class of Java due to inhibited number of connections to OSS. If an espace eld were to be decleared as array, each element in the array would be written to OSS as Entry splitted by dimension, consequentry number of connections would extremely increase causing performance decrement in the case shown in Figure. 3. It is also nessesary to insert cast operation to espace eld. To run the system, the user starts OSS, DUs, and EP, in this order. Because DUs and EP automatically search and connect to OSS, users need not con gure network settings.

3.4 Evaluation

The Espace source code shown in Figure. 3 contains ve espace elds, six espace methods, and a distribute statement. The conversion from Java to Espace was done by adding 12 keywords and a block, changing 4 declared types and adding 24 cast operators. Although it was vexatious to add cast operators, the program structure almost was not changed. It, therefore, seems resonable to conclude that the source code of DGPIF is easy to understand for Java programmers.

4 Conclusions

We have proposed a programming language called Espace which involves simpli ed syntax rules for distributed parallel computation. The experimental result has shown that the Espace compiler enables to convert an evolutionary computation program written in Java into distributed, parallel system by adding a few words of Espace to the program.

In the future we plan to work up experimental implementations of distributed system written in Espace to evaluate usability of the language.

Acknowledgements

Part of this study was supported by IPA Exploratory Software Project.

©ISAROB 2009

```
class GPIF_gp{
  espace Object orgFit;//double[]
  espace Object pixGs;//Pixels[]
  espace Object pixSs;
  espace Object weight;//double[][][]
  void ptNotE() {
    int num=(int)(nC*HIT_RATE);
    int[] targets=new int[num];
    IdvTree tmpElite=null;
    for (int i=0; i<num; i++) {
      targets[i]=(int)((nC)*Math.random()
          *0.99);
    }
    distribute{
      for (int i=0; i<num; i++) {
        tmpElite =tuneParam(popula[targets
            [i]], num);
        popula[targets[i]] = tmpElite;
      }
    }
    ...
  }
  espace IdvTree tuneParam(IdvTree elite,
      int candiNum,
    int prmNum, boolean isRplc) {
    calFitnessN(...);
    ...
  }
  espace IdvTree calFitnessN(IdvTree tree1
      ){
    double[][][] w = (double[][][])weight;
    Pixels[] pixs = ((Pixels[])pixGs);
    Pixels[][] pixSsl = (Pixels[][])pixSs;
    double[] orgFitl = ((double[])orgFit);
    double fitSum;
    int[][][] outPix;
    fitSum = 0.0;
    if (!tree1.isCalculatedFlg()) {
      for (int k = 0; k < NUM_IMG; k++) {
        flt.initImg(pixSsl[k]);
        outPix = filtering(tree1.getChromo
            ());
        ...
      }
      tree1.setFitness(fitSum / inImgNum);
      tree1.setCalculatedFlg(true);
    }
    return tree1;
  }
  ...
}
```

Figure 3: Espace source code example.

References

[1] MPICH2. http://www.mcs.anl.gov/index.php.

[2] Open MP. http://www.openmp.org/drupal/.

[3] Omni OpenMP Compiler Project. `http://phase.hpcc.jp/Omni/`.

[4] Philippe Charles, Christopher Donawa, Kemal Ebcioglu, Christian Grotho , Allan Kielstra, Christoph von Praun, Vijay Saraswat, and Vivek Sarkar. X10: An Object-oriented Approach to Non-Uniform Cluster Computing. In *Proc. 20th Ann. ACM SIGPLAN Conf. Object-Oriented Programming, Systems, Languages, and Applications (OOPSLA 05)*, pages 519–538. ACM Press, 2005.

[5] Eric Allen, David Chase, Joe Hallett, Victor Luchangco, Jan-Willem Maessen, Sukyoung Ryu, Guy L. Steele Jr., and Sam Tobin-Hochstadt. The fortress language speci cation version 1.0, 2008.

[6] Takeshi KAMOGAWA and Takaya YUIZONO. A proposal of programming Language JavaPAN with Static Network Scope. *The transactions of the Institute of Electronics, Information and Communication Engineers. D-I*, 88(2):326–329, 2005.

[7] I Foster and C Kesselman. Globus: A metacomputing infrastructure toolkit. 11(2), 1997.

[8] Takehiko IWAKAWA, Satoshi ONO, and Shigeru NAKAYAMA. Development of a Programming Language Espace for Distributed Parallel Processing. *Transactions of ISCIE*, 19(7), 2006.

[9] Java SE Desktop Technologies - Java Web Start Technology. `http://java.sun.com/javase/technologies/desktop/javawebstart/index.jsp`.

[10] Masaki MAEZONO, Satoshi ONO, and Shigeru NAKAYAMA. Automatic Parameter Tuning and Bloat Restriction in Image Processing Filter Generation Using Genetic Programming. *Transactions of JSCES*, 8(20060021), 2006.

The Fourteenth International Symposium on Artificial Life and Robotics 2009 (AROB 14th '09),
B-Con Plaza, Beppu, Oita, Japan, February 5 - 7, 2009

Competitive Coevolutionary Algorithms can Solve Function Optimization Problems

Tatsuya Sato Takaya Arita
Graduate School of Information Science, Nagoya University
Furo-cho, Chikusa-ku, Nagoya 464-8601, Japan
E-mail: sato@alife.cs.is.nagoya-u.ac.jp, arita@nagoya-u.jp

Abstract

Competitive coevolutionary algorithms (CCEA) have many advantages but their application range has been crucially limited. This study provides a simple, non-problem-specific framework to extend the range. The framework has two coevolving populations: that of candidate solutions and that of criteria, in which these population competitively coevolve with each other. The framework aims to move candidate solutions getting stuck in a local optimum by changing the fitness landscape dynamically. Moreover, the framework has a mechanism in order to establish and maintain proper arms race. We have conducted experiments on two function optimization problems: 1-dimensional function maximization problem and the Rastringin function minimization problem, in order to investigate the basic properties of the framework. The results of the experiments showed that CCEA achieves comparable performance with GA.

Keywords: Competitive Coevolutionary Algorithm, Genetic Algorithm, Evolutionary Computation, Function Optimization, Artificial Evolution

1 Introduction

Since D. Hillis extended the evolutionary computation paradigm by introducing coevolution [1] *et al.*, competitive coevolutionary algorithms (CCEAs) have attracted a lot of attention in the field of evolutionary algorithms (EAs). The framework of CCEA is similar to that of conventional EA except for fitness evaluation, in which the fitness of an individual is based on "competitions" with other individuals instead of an objective function. The difference between CCEA and EA in fitness evaluation have been believed to make a significant difference between them in applicable problems.

Conventional EA can be applied to the problems in which solutions can be evaluated absolutely, such as function optimization, combinatorial optimization. On the other hand, CCEA can find great solutions for problems which can be expressed by using competitive populations in GA framework including sorting-network design (sorting networks vs test cases) [1], cellular automaton density classification (CA rules vs initial states) [2] and the Nim game (first move vs passive move) [3]. It has been shown that CCEA can perform better than EA in this type of problems. However, the range of the problems to which CCEA can be applied has been crucially limited, which has prohibited its progress.

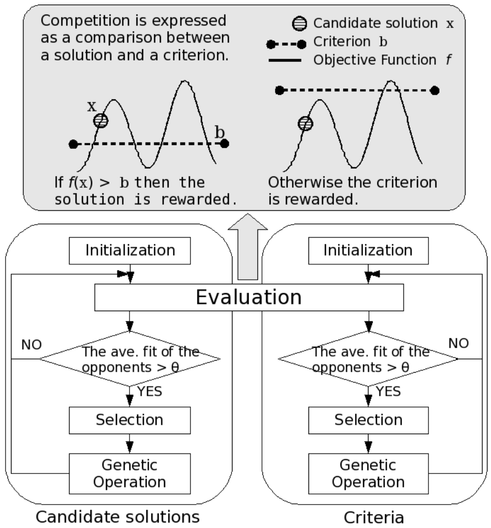

Figure 1: The framework.

There have been a very few researches which investigate the performance and characteristics of CEAs in solving problems in which solutions can be evaluated absolutely [4]. However, unfortunately approaches proposed in these researches are problem specific. In this work, we propose a simple, non-problem-specific framework of CCEA which extends significantly the range of problems to which CCEA can be applied.

2 Framework

Figure 1 shows our proposed framework. In the framework, candidate solutions and criteria (thresh-

©ISAROB 2009

olds) competitively coevolve with each other. A criterion is defined as a real value used to evaluate a candidate solution. Competition between a solution and a criterion in a maximization problem is simply a comparison: If the objective function value of the candidate solution is greater than the criterion then the solution is rewarded, otherwise the criterion is rewarded. The total rewards are used as fitness. The fitness functions of solutions and criteria, denoted by f_{Sol} and f_{Crit} respectively, are defined as follows:

$$f_{\text{Sol}}(x) = \sum_{b \in P_{\text{Crit}}} I_{(\text{Sol},\text{Crit})}(x, b) \quad (1)$$

$$f_{\text{Crit}}(b) = \sum_{x \in P_{\text{Sol}}} I_{(\text{Crit},\text{Sol})}(b, x) \quad (2)$$

$$I_{(\text{Sol},\text{Crit})}(x, b) = \begin{cases} 1 & \text{if } f(x) \geq b \\ 0 & \text{else} \end{cases} \quad (3)$$

$$I_{(\text{Crit},\text{Sol})}(b, x) = 1 - I_{(\text{Sol},\text{Crit})}(x, b) \quad (4)$$

where $I_{(\text{Sol},\text{Crit})}(x, b)$ and $I_{(\text{Crit},\text{Sol})}(b, x)$ represent rewards to a candidate solution x and to a criterion b respectively, P_{Sol} and P_{Crit} represent the population of candidate solutions and that of criteria respectively and $f(x)$ is the objective function of a given problem.

The point of the framework is to utilize the loss of gradient of the dynamic landscape, which has been believed to be detrimental at least in the field of CCEA [5]. Specifically, the more one population outperforms the other, in other words, the less difference in fitness among individuals in each population exist, the more coevolutionary search becomes to random search, which is realized not by an explicit algorithm but by the coevolution implicitly. This mechanism can allow populations stuck in local optima to escape there.

Moreover, this framework has a mechanism in order to establish and maintain proper arms race. Selection and genetic operations are not performed to a population if the average fitness of the opponents is lower than the parameter θ. In other words, if the difference in fitness between two populations goes beyond a certain present value, the preceding population stops evolving until dropping below the value. Thus this framework stops the evolution of a coevolving population according to the condition of the opponents.

This framework is not problem-specific since it uses the objective function of a given problem only.

3 Evolutionary Setup

Our CCEA has two populations: a population of candidate solutions and that of criterion. Each population consists of N individuals. The genotype of a candidate solution is defined as a vector of length n and, as mentioned above, the genotype of a criterion is defined as a real value. For each of these, the genotype is identical to the phenotype. Stochastic Universal Selection [6] is adopted. Mutation is the only genetic operator used in the experiments, which is realized by adding a random number generated according to a normal distribution $\mathcal{N}(0, \sigma_{\text{Sol}})$ for candidate solutions or $\mathcal{N}(0, \sigma_{\text{Crit}})$ for criterion to the value at each locus with a probability p_m. All algorithms evaluated in this experiments terminates when the number of generations reached to $g_{\max}$.

Table 1 shows the values used for these parameters.

Table 1: The values used for parameters.

	1-D function	Rastringin
population size N	30	100
dimension n	1	10
mutation prob. p_m	0.1	0.01
σ_{Sol}	0.25	0.25
σ_{Crit}	0.25	1.0
max. generation $g_{\max}$	1×10^5	5×10^4

4 Results

In order to investigate the basic properties of the framework, we firstly applied it to a 1-dimensional function maximization problem and compared the results of out CCEA to those of three types of genetic algorithms (GAs): a conventional GA, a GA with fitness sharing (GA+FS) which is used to avoid premature convergence [7], a GA with random selection (RANDOM). Each of the algorithms compared is initialized with a population of N individuals whose genotype is 0.

The objective function of this problem is defined as a multimodal function of one variable as follows:

$$f(x) = x + ax \sin(bx) \quad (5)$$

where $x \in [0, \infty]$ and the values of a and b are 0.75 and 3.0 respectively. Local optima of this problem are placed at regular intervals.

Figure 2 shows that the objective value of the best solution which each algorithm found so far. CCEA found better solutions for this problem than GAs. Particularly, CCEA with $\theta = 0$ is the best among the algorithms compared in this experiments, which is 10^2 times as large as GA and is 10 times as large as GA+FS in terms of the objective value of the best solution found up to the last generation (Table 2).

©ISAROB 2009

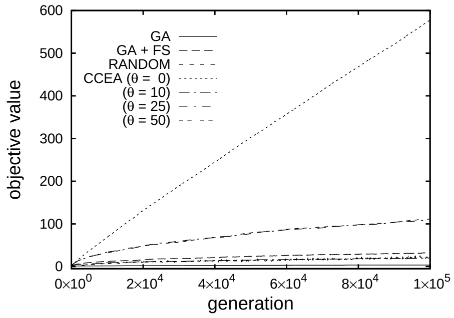

Figure 2: The objective value of the best solution found so far versus generation (averaged over 30 runs).

Table 2: The objective value of the best solution found up to the last generation (averaged over 30 runs).

GA		3.730×10^0
GA+FS		3.312×10^1
RANDOM		1.482×10^1
CCEA	$\theta = 0$	5.777×10^2
	$\theta = 10$	2.012×10^1
	$\theta = 25$	1.095×10^2
	$\theta = 50$	1.118×10^2

Figure 3 illustrates how in CCEA with $\theta = 0$ candidate solutions escape from local optima by utilizing loss of gradient. Candidate solutions can move and pass through valleys among local optima freely while loss of gradient occurs (Fig. 3(a)). The populations start to coevolve competitively again when a good solution whose objective value is larger than some criteria is found (Fig. 3(b)). Though loss of gradient will occur again, this phenomenon moves candidate solutions to a higher peak (Fig. 3(c)).

Furthermore, we applied our framework to the Rastringin function minimization problem [8] which is known as a benchmark problem so as to investigate how our framework would work on more practical problems. Rastringin function is given by the following equation:

$$f(x) = 10n + \sum_{i=1}^{n} \left(x_i^2 - 10\cos(2\pi x_i) \right) \tag{6}$$

where $x_i \in [-5.12, 5.11]$. This problem has the unique global optimum $x^* = (0, 0, \ldots, 0)$ and has many local optima. A population of candidate solutions is initialized randomly and all criterion in the initial population are arranged at regular intervals in the range between the maximum of and the minimum of the objective function values of the initial candidate solutions.

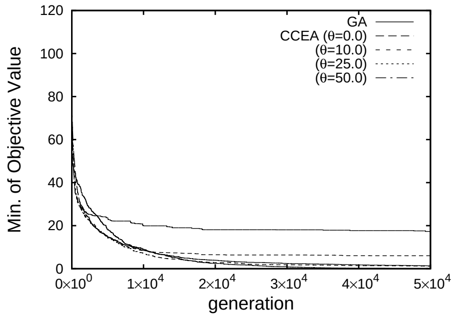

Figure 4: The objective value of the best solution found so far (averaged over 30 runs).

Table 3: The objective value of the best solution found so far (averaged over 30 runs).

GA		6.633×10^{-2}
CCEA	$\theta = 0.0$	1.726×10^1
	$\theta = 10.0$	6.641×10^0
	$\theta = 25.0$	1.923×10^0
	$\theta = 50.0$	1.025×10^0

Figure 4 shows that the objective value of the best solution which each algorithm found so far. This figure indicates that the larger the value of the parameter θ, the better the quality of solutions which CCEA found. However, the performance of CCEA was slightly worse than that of GA (Table 3).

In order to measure the speed of convergence to the global optimum, we measured the expected number of generations taken by each algorithm to find a candidate solution whose objective value is less than a specified threshold (Figure 5)[1]. This analysis reveals that CCEA finds the nearest local optima ($n = 1$) to the global optimum faster than GA.

5 Summary

We have proposed a simple framework of competitive coevolutionary algorithms (CCEA) to extend their application range. We conducted the experiments on two function optimization problems: a 1-dimensional function maximization problem and the

[1] The values of multiplying the objective function value of the nearest local optimum to the global optimum by n ($0 \le n \le 10$) are used for the thresholds. In the figure, the values of all algorithms compared in the experiments at $n = 0$ are equal to 0, which indicates that all algorithm could not find the global optimum.

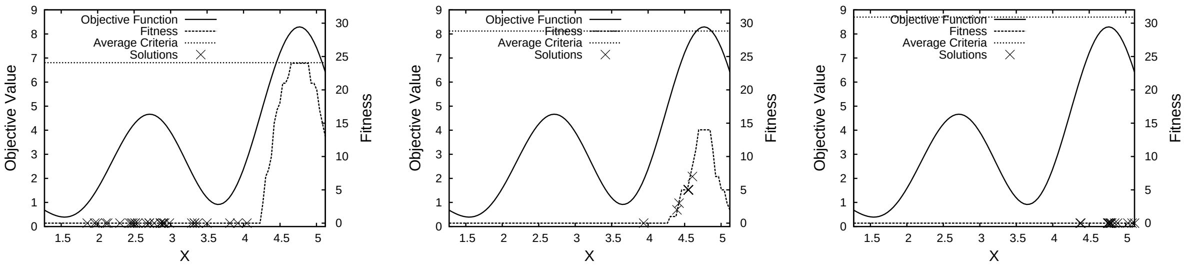

(a) 796th generation. (b) 802th generation. (c) 810th generation.

Figure 3: The changes of the dynamic fitness landscape in a typical run. The solid line indicates the objective function (Equation 5), the dashed line indicates the fitness landscape of candidate solutions and the dotted line indicates the average of criteria. A cross indicates a candidate solution.

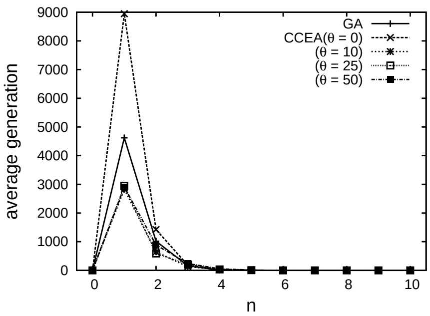

Figure 5: The expected number of generations taken by each algorithm to find a candidate solution whose objective value is less than a certain level. $n = 0$ means the global optimum (averaged over 30 runs).

Rastringin function minimization problem, in order to investigate the basic properties of our framework. The results of the first experiments showed that our CCEA is the best among the algorithms compared in the experiments because it can escape from local optima by utilizing loss of gradient and demonstrated how CCEA utilizes loss of gradient. Moreover, the results of the second experiments showed that CCEA has performance comparable to GA and that, in particular, on a practical problem our CCEA can find an approximate solution faster than GA.

Function optimization is one of the most important optimization problems and has a large application. We believe that this framework will open up an interesting possibility to extend drastically the range of problems to which CCEA can be applied.

Acknowledgments

This work was supported by a Grant-in-Aid for 21st Century COE "Frontiers of Computational Science".

References

[1] W. D. Hillis: "Co-evolving parasites improve simulated evolution as an optimization procedure", *Artificial Life II*, pp. 313–324, 1992.

[2] H. Juillé and J. B. Pollack: "Coevolutionary learning: a case study", *Proc. of the Fifteenth International Conference on Machine Learning*, pp. 251–259, 1998.

[3] C. D. Rosin: "Coevolutionary Search Among Adversaries", *PhD thesis*, University of California, San Diego, CA, 1997.

[4] J. Paredis: "Co-evolutionary constraint satisfication", *Proc. of the International Conference on Evolutionary Computation*, pp. 46–55, 1994.

[5] J. Cartlidge and S. Bullock: "Combating coevolutionary disengagement by reducing parasite virulence", *Evolutionary Computation*, Vol. 12, No. 2, pp. 193–222, 2004.

[6] J. E. Baker: "Reducing bias and inefficiency in the selection algorithm", *Proc. of the Second International Conference on Genetic Algorithms on Genetic algorithms and their application*, pp. 14–21, 1987.

[7] D. E. Goldberg and J. Richardson: "Genetic algorithms with sharing for multimodal function optimization", *Proc. of the Second International Conference on Genetic Algorithms*, pp. 41–49, 1987.

[8] D. Whiteley, S. B. Rana, J. Dzubera and K. E. Mathias: "Evaluating evolutionary algorithms", *Artificial Intelligence*, Vol. 85, Issue 1-2, pp. 245–276, 1996.

©ISAROB 2009

The Fourteenth International Symposium on Artificial Life and Robotics 2009 (AROB 14th '09),
B-Con Plaza, Beppu, Oita, Japan, February 5 - 7, 2009

Pareto-optimal Fuzzy Rule Mining with EMO Algorithms and Its Improvement by Heuristic Initialization

Isao Kuwajima, Yusuke Nojima, and Hisao Ishibuchi

Gakuen-cho 1-1, Naka-ku, Sakai, Osaka 599-8531, Japan
(Tel : 81-072-254-9198; Fax : 81-072-254-9915)
(Email {kuwajima@ci., nojima@, hisaoi@}cs.osakafu-u.ac.jp)

Abstract: In this paper, we apply evolutionary multiobjective optimization (EMO) algorithms to Pareto-optimal fuzzy rule mining. Pareto-optimal rules, which are Pareto-optimal in confidence and support maximization, have an interesting feature that they maximize other various rule evaluation measures. In our method, we use MOEA/D and NSGA-II, which are simple and high-performance EMO algorithms, to efficiently discover Pareto-optimal fuzzy rules. Conventional data mining techniques such as Apriori need to set thresholds on confidence and support to reduce the search space. Our EMO-based method does not need those parameters because EMO algorithms make an efficient search toward confidence-support trade-off curve. Through computational experiments, we show that our EMO-based method can generate Pareto-optimal rules in a short time.

Keywords: Association rule mining, evolutionary multiobjective optimization, knowledge extraction.

I. INTRODUCTION

Association rule mining [1] is a popular and well-known method for discovering interesting relations. In its basic form, all association rules satisfying some constraints on rule evaluation criteria are extracted from a database. There are numerous proposals for the rule evaluation criteria that quantify the interestingness or goodness of a rule. There are two major rule evaluation criteria: confidence and support. Other rule evaluation criteria include gain, variance, chi-squared value, entropy gain, Gini, Laplace, lift, and conviction. It is shown in [2] that Pareto-optimal rules in terms of confidence and support maximization have an interesting feature that the best rule with respect to any of the above-mentioned criteria is included in the Pareto-optimal rules.

In this paper, we apply evolutionary multiobjective optimization (EMO) algorithms to discover Pareto-optimal fuzzy rules. Among EMO algorithms, we use MOEA/D [3] and NSGA-II [4], which are simple and effective EMO algorithms. Conventional data mining techniques such as the Apriori algorithm [1] need to set thresholds on confidence and support or need to set the maximum rule length to reduce the search space. Our EMO-based method does not need to set those parameters because EMO algorithms make an efficient search toward a confidence-support trade-off curve.

The performances of algorithms are examined on the data sets from the UCI machine learning repository. Through computational experiments, we show that our EMO-based method can generate Pareto-optimal rules in a short time compared to data mining techniques especially when we use MOEA/D. We also show that our EMO-based method can obtain better performance because there is no need to set thresholds on confidence and support or to set the maximum rule length.

In addition, we improve the performance of our EMO-based method using problem-specific initialization, which we call *heuristic initialization*. We show that the use of heuristic initialization can improve the performance of our EMO-based method at the early stage of evolution.

II. FUZZY RULES

Let $\mathbf{x} = (x_1, ..., x_n)$ be an n-dimensional pattern vector. Our task is to discover fuzzy rules of the following form:

$$\text{Rule } R : \text{If } x_1 \text{ is } A_1 \text{ and } ... \text{ and } x_n \text{ is } A_n \text{ then Class } C, \tag{1}$$

where $\mathbf{A} = (A_1, ..., A_n)$ are antecedent fuzzy sets and C is a consequent class. We denote the rule R in (1) as $\mathbf{A} \Rightarrow C$. Since we usually have no *a priori* information about appropriate fuzzy sets for each attribute, we use various fuzzy sets to extract candidate fuzzy rules. In computational experiments, we use 14 different triangular fuzzy sets in Fig. 1.

The membership value of the pattern $\mathbf{x}$ to the antecedent part $\mathbf{A}$ is calculated with the product operator as:

$$\mu_{\mathbf{A}}(\mathbf{x}) = \mu_{A_1}(x_1) \cdot ... \cdot \mu_{A_n}(x_n). \tag{2}$$

©ISAROB 2009

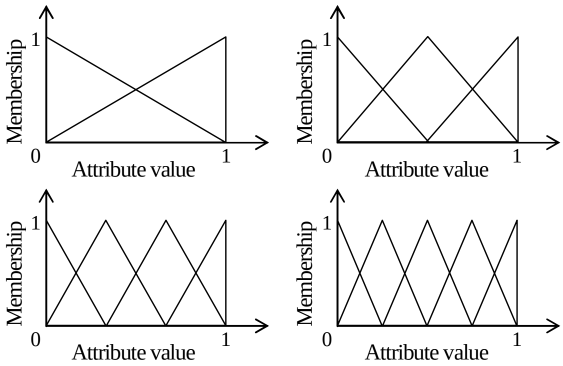

Fig. 1. Fuzzy sets used in the computational experiments.

In the field of data mining, two rule evaluation criteria called confidence and support are widely used to measure the goodness of rules.

Let us assume that we have m training patterns $\mathbf{x}_p$, (p = 1, 2, …, m). The fuzzy version of confidence is defined as follows [5]:

$$confidence(\mathbf{A} \Rightarrow C) = \frac{\sum_{\mathbf{x}_p \in C} \mu_{\mathbf{A}}(\mathbf{x}_p)}{\sum_{p=1}^{m} \mu_{\mathbf{A}}(\mathbf{x}_p)}. \tag{3}$$

In the same manner, support is defined as follows [5]:

$$support(\mathbf{A} \Rightarrow C) = \frac{\sum_{\mathbf{x}_p \in C} \mu_{\mathbf{A}}(\mathbf{x}_p)}{m}. \tag{4}$$

A rule evaluation criterion called coverage can be used instead of support. Coverage is defined as follows:

$$coverage(\mathbf{A} \Rightarrow C) = \frac{\sum_{\mathbf{x}_p \in C} \mu_{\mathbf{A}}(\mathbf{x}_p)}{sup(C)}, \tag{5}$$

where $sup(C)$ is consequent support, which is equal to the number of patterns whose class is C. This measure is often used for the problem of partial classification [6]. This problem is the search for the rules of a specified class. In partial classification, it is often convenient and intuitive to use coverage instead of support. Since the $sup(C)$ is constant in partial classification, the maximization of coverage is the same as that of support. We hereafter use coverage instead of support because the consequent class is fixed in our method.

We call the rules, which are Pareto-optimal in terms of the maximization of confidence and coverage, *Pareto-optimal rules*. Roughly speaking, a solution is Pareto optimal if it cannot result in further improvement of an objective without causing the degradation of another objective. It is shown in [2] that Pareto-optimal rules have the maximum value of other various rule evaluation criteria including gain, variance, chi-squared value, entropy gain, Gini, Laplace, lift, and conviction. Since the number of Pareto-optimal rules is conveniently small, Pareto-optimal rules can be discovered efficiently. In this paper, we discover Pareto-optimal rules using EMO algorithms.

III. PARETO-OPTIMAL RULE MINING WITH EMO ALGORITHMS

EMO algorithms are widely established and well developed for problems with multiple objectives. We apply EMO algorithms in the framework of genetics-based machine learning (GBML). GBML has two approaches: Michigan-style and Pittsburgh-style approach. In the Michigan-style approach, chromosomes are individual rules and a rule set is represented by the entire population. In the Pittsburgh-style approach, each chromosome represents a rule set (i.e., classifier). We adopt the former approach (i.e., Michigan-style approach) in our method where the antecedent part of a rule $\mathbf{A} = (A_1, ..., A_n)$ is encoded as a chromosome. The objectives of EMO algorithms are the maximization of confidence and coverage.

$$\text{maximize} \begin{cases} confidence(\mathbf{A} \Rightarrow C) \\ coverage(\mathbf{A} \Rightarrow C) \end{cases} \tag{6}$$

Among EMO algorithms, we use MOEA/D and NSGA-II. We briefly explain basic characteristics of these two algorithms in the following subsections.

1. MOEA/D

MOEA/D is an EMO algorithm proposed by Zhang [3]. Let P and EP be a current population and an external population, respectively. In MOEA/D, each individual has T neighbors to which one of the uniformly generated weight vectors is assigned. In MOEA/D, genetic operations for each individual are locally performed among its neighbors. The outline of MOEA/D can be written as follows:

```
Initialize P
while a termination condition is not satisfied do
    foreach individual x in P
        Select m, n from the T neighbors of x
        Generate y from m, n by genetic operations
        Update the neighbors of x with y
        Update EP
```

8: **end foreach**
9: **end while**
10: **return** *EP*

First an initial population is generated in line 1. In line 1, a set of uniformly distributed weight vectors is also generated. In line 4, a couple of parents **m** and **n** are randomly selected from the *T* neighbors of **x**. Then in line 5, an offspring **y** is generated from **m** and **n** by using genetic operators. In line 6, if **y** is better than some neighbors of **x**, they are replaced with **y**. The comparison is made by using scalarizing function (i.e., the weighted sum or the weighted Tchebycheff, we use the latter in our experiments). In line 7, all individuals dominated by **y** are removed from *EP*. These procedures are applied for each individual until a termination condition is satisfied.

2. NSGA-II

NSGA-II is an EMO algorithm proposed by Deb [4]. The outline of NSGA-II can be written as follows:

1: *P* = Initialize (*P*)
2: **while** a termination condition is not satisfied **do**
3: *P*' = Selection (*P*)
4: *P*'' = Genetic Operations (*P*')
5: *P* = Replace ($P \cup P''$)
6: **end while**
7: **return** non-dominated solutions (*P*)

First an initial population is generated in line 1. In line 3, parent individuals (i.e., *P*') are selected from the current population *P*. The standard binary tournament selection is used to choose a pair of parent individuals. In line 4, an offspring population *P*'' is generated from the parent population *P*' by genetic operations such as crossover and mutation. In line 5, the best individuals are chosen from the merged population ($P \cup P''$) to generate the next population *P*.

IV. COMPUTATIONAL EXPERIMENTS

Experiments were conducted by using the following seven datasets from the UCI machine learning repository: Breast W, Diabetes, Glass, Heart C, Iris, Sonar, and Wine. The parameter specifications in EMO algorithms are as follows:

Population size: 200 individuals,
Crossover probability: 1.0 (uniform crossover),
Mutation probability: $1/n$,
Termination condition: 1000 generations.

We compare the performance of our method with that of conventional data mining algorithms including the Apriori algorithm and the simple enumeration (SE). For Apriori and SE, we set minimum confidence and coverage as 0.6 and 0.01, respectively. We also set the maximum rule length as two for Sonar and three for the other datasets to alleviate a computational load.

Table 1 shows the average CPU time of 100 runs. The experiment was conducted on Dual Core Xeon 3.6GHz, 4GB RAM workstations. The best result for each class is highlighted in bold. The values in parentheses will be mentioned later. From Table 1, we can see that MOEA/D is faster than the other algorithms for many datasets. While Apriori outperforms MOEA/D for some datasets, it is significantly slow for others.

Figure 2 shows generated fuzzy rules in confidence-coverage space for Class 4 and 5 of Glass. MOEA/D and NSGA-II clearly outperforms Apriori and SE. It should be noted that MOEA/D and NSGA-II can generate fuzzy rules that have four or more antecedent fuzzy sets. This allows MOEA/D and NSGA-II to generate fuzzy rules with high confidence and coverage.

One underlying problem with MOEA/D and NSGA-II is that they cannot discover useful rules when a dataset has a number of attributes. In the case of Sonar which has 60 attributes, all discovered rules by MOEA/D and NSGA-II were zero-confidence and zero-coverage. As the number of attributes increases, the search spaces of MOEA/D and NSGA-II exponentially increase. The size of the search space for Sonar is 15^{60},

Table 1. CPU time (sec.)

Dataset	Class	MOEA/D		NSGA-II		Apriori	SE
Breast W	1	21.1	(21.1)	57.1	(57.6)	**8.1**	48.9
	2	**20.9**	(20.9)	53.6	(53.8)	63.4	49.0
Diabetes	1	21.8	(22.0)	60.3	(61.0)	**13.5**	33.5
	2	21.7	(21.9)	58.0	(58.5)	**15.0**	33.3
Glass	1	**7.4**	(7.4)	29.5	(30.2)	**7.4**	15.3
	2	**7.2**	(7.2)	29.6	(30.5)	13.4	15.4
	3	7.5	(7.6)	29.7	(30.5)	**7.4**	15.3
	4	**7.1**	(7.1)	28.3	(29.6)	14.8	15.4
	5	7.2	(7.2)	27.7	(28.7)	**6.1**	15.3
	6	**7.2**	(7.2)	28.4	(29.6)	13.3	15.4
Heart C	1	**12.2**	(12.1)	38.6	(39.1)	105.0	98.8
	2	**12.7**	(12.5)	38.9	(39.6)	105.9	97.4
	3	**12.6**	(12.5)	39.2	(39.5)	114.7	97.4
	4	**12.6**	(12.5)	39.1	(39.4)	118.5	97.4
	5	**13.0**	(12.9)	38.4	(39.9)	93.2	97.8
Iris	1	3.4	(3.5)	20.1	(20.1)	**0.1**	0.3
	2	3.4	(3.5)	20.2	(20.3)	**0.2**	0.3
	3	3.4	(3.5)	20.3	(20.3)	**0.2**	0.3
Sonar	1	**34.7**	(30.9)	76.4	(81.6)	201.5	82.3
	2	**34.7**	(30.9)	74.9	(81.6)	221.7	82.5
Wine	1	**7.5**	(7.6)	28.2	(28.4)	104.2	58.9
	2	**7.5**	(7.5)	28.3	(28.5)	164.2	58.9
	3	**7.5**	(7.6)	28.3	(28.8)	112.5	59.0

©ISAROB 2009

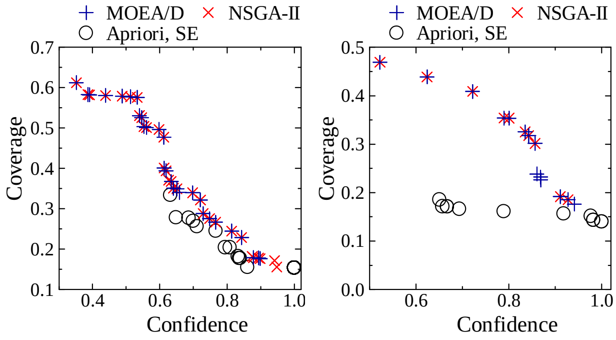

(a) Class 4 (b) Class 5

Fig. 2. Generated fuzzy rules (Glass).

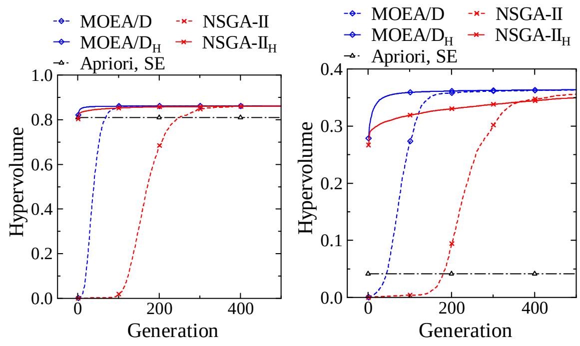

(a) Class 1 (b) Class 2

Fig. 3. Hypervolume measure (Heart C).

which makes the search for Pareto-optimal rules impossible. One possible remedy for this problem is to use problem-specific initialization for improving the search ability.

V. HEURISTIC INITIALIZATION

In the design of fuzzy classifiers, the search ability of fuzzy classifiers can be improved by directly generating initial fuzzy rules from training patterns. Let N_{rule} be the population size. First we randomly select N_{rule} patterns. Then we choose the fuzzy set which has a high membership value. We probabilistically choose an antecedent fuzzy set from the 14 candidates B_k (k = 1, 2, …, 14) in Fig. 1 where each candidate B_k has the following selection probability for the attribute value x_i:

$$P(B_k) = \frac{\mu_{B_j}(x_i)}{\sum_{j=1}^{14} \mu_{B_j}(x_i)}. \tag{7}$$

We conducted the same experiment using heuristic initialization. By using heuristic initialization, MOEA/D and NSGA-II could discover as good rules as Apriori and SE for Sonar. To show the effects of heuristic initialization, we examined the hypervolume measure during evolution. The hypervolume measure, which indicates the size of the portion of objective space that is dominated by the solutions, is often used to assess the performance of EMO algorithms. Figure 3 shows the average value of the hypervolume measure at each generation for Heart C. In Fig. 3, MOEA/D_H and NSGA-II_H shows the results using heuristic initialization. We can see that MOEA/D_H and NSGA-II_H evolves faster than the original ones at the early stage.

The effect of using heuristic initialization on CPU time is not large. The values in parentheses in Table 1 show the CPU time with heuristic initialization. Heuristic initialization made 0.2-second delay for MOEA/D and 6.7-second delay for NSGA-II at most. In some cases (e.g., Heart C and Sonar), MOEA/D with heuristic initialization was faster than the original one.

VI. CONCLUSION

In this paper, we applied MOEA/D and NSGA-II to discover Pareto-optimal fuzzy rules. Through computational experiments, we showed that MOEA/D is faster than Apriori and SE for a number of datasets. Futhermore, the generated rules were better than Apriori and SE. We also showed that the search ability of MOEA/D and NSGA-II was improved by using heuristic initialization without increasing much computation time.

REFERENCES

[1] Agrawal R, Mannila H, Srikant H, Toivonen R, Verkamo AI (1996), Fast discovery of association rules, Advances in Knowledge Discovery and Data Mining: 307–328
[2] Bayardo RJ Jr., Agrawal R (1999), Mining the most interesting rules, Proc. of 5th ACM SIGKDD International Conference on Knowledge Discovery and Data Mining: 145–153
[3] Zhang Q, Li H (2007), MOEA/D: A multiobjective evolutionary algorithm based on decomposition, IEEE Trans. on Evolutionary Computation, 11 (6): 712–731
[4] Deb K, Pratap A, Agarwal S, Meyarivan T (2002), A fast and elitist multiobjective genetic algorithm: NSGA-II, IEEE Trans. on Evolutionary Computation, 6 (2): 182–197
[5] Hong TP (2001), Tradeoff between computation time and number of rules for fuzzy mining from quantitative data, International Journal of Uncertainty, 9 (6): 587–604
[6] Ali S, Manganaris S, Srikant R (1997), Partial classification using association rules, Proc. of the Third International Conference on Knowledge Discovery and Data Mining: 115–118

©ISAROB 2009

The Fourteenth International Symposium on Artificial Life and Robotics 2009 (AROB 14th '09),
B-Con Plaza, Beppu, Oita, Japan, February 5 - 7, 2009

Robust Optimization Using Multi-Objective Particle Swarm Optimization

Satoshi Ono Yohei Yoshitake Shigeru Nakayama
Department of Information and Computer Science,
Faculty of Engineering, Kagoshima University
1-21-40, Korimoto, Kagoshima, 890-0065 Japan
{ono, sc104059, shignaka}@ics.kagoshima-u.ac.jp

Abstract

This paper proposes an algorithm searching for solutions which are robust against small perturbations of design variables. The proposed algorithm formulates robust optimization as a bi-objecitve optimization problem, and finds solutions by Multi-Objective Particle Swarm Optimization (MOPSO). Experimental results have shown that MOPSO has better search performance to find multiple robust solutions than a previous method using multi-objective genetic algorithm.

1 Introduction

Particle Swarm Optimization (PSO)[1] is one of stochastic, population-based optimization algorithms inspired by swarm intelligence of insects which form a group and move such as bird, fish, bee and so on. PSO has recently been investigated and applied to many real-world problems because of its simplicity and good search performance. PSO is effective in problems whose design values are represented by real values in particular. Multi-Objective Particle Swarm Optimization (MOPSO)[2, 3, 4] is also proposed to solve multi-objective optimization problems involving more than one objective function.

In recent years there has been renewal of interest in robust optimization techniques as a practical optimization methodology considering margins of errors, noises, aged deterioration, and other uncertainties on design, production, observation and so on [5, 6, 7, 8, 9]. General optimization algorithms evaluate solution candidates with focusing only on optimality of an objective function. If a solution obtained by the algorithms is sensitive to small perturbations of variables, it may not be appropriate or risky for practical use. Such small variation may cause undesired deviations of engine performance in automobile valuvetrain control, or collisions or interference in controlling machines. Robust optimization[7, 8, 10] finds solutions which are moderately good in terms of optimality and also good in germs of robustness against small perturbations of values, as shown in Figure 1. In many practical optimization tasks, there is a need to search for robust solutions whose value of optimization function is su ciently high and will not change due to the small variation of parameter values.

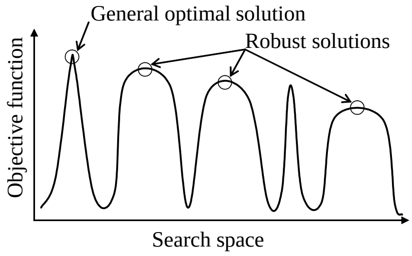

Figure 1: The difference between general optimization and robust optimization.

Design For Six Sigma (DFSS)[11, 12] is a methodology for designing new products or processes and can be considered as a robust optimization algorithm. But in DFSS, an optimization function equation involves weight parameters which must be adjusted manually, and sigma level must be specified before starting a search.

Aiming to resolve the above drawbacks of DFSS, Design For Multi-Objective Six Sigma (DFMOSS) has been proposed[6, 8]. DFMOSS performs Monte Carlo simulation and evaluates solution candidates with two objective functions: mean value of given objective function and its deviation. DFMOSS therefore does not need to adjust the weight parameters in objective function of DFSS, and to specify sigma level in advance. Although DFMOSS can find multiple robust optimal solutions simultaneously, DFMOSS requires high computational cost.

In this paper, we propose a robust optimization method by using MOPSO in order to verify the effectiveness of MOPSO against robust optimization. The

Step 1: Initialize all particles; place them at random positions with random velocities.
Step 2: Evaluate all particles.
Step 3: Store Pareto solutions chosen randomly into the archive.
Step 4: Divide objective function space onto hypercube.
Step 5: Determine personal bests of all solutions.
Step 6: *Until* evaluation time reaches the limit, *repeat* **step 7**:
  Step 7: *For each* particle i, *repeat* **step 8** through **12**.
    Step 8: Update i's velocity and position.
    Step 9: *If* i moves too slowly, reset its position and velocity.
    Step 10: Evaluate i.
    Step 11: Update personal best and the archive.
    Step 12: Redivide the hypercube if necessary.

Figure 2: The outline of the proposed algorithm.

proposed algorithm formulates a robust optimization problem as a multi-objective optimization problem by following the idea of DFMOSS, and utilizes MOPSO to search for robust solutions instead of Multi-Objective Genetic Algorithm in DFMOSS. The proposed algorithm also utilizes hypercube method in order to maintain its archive to be diverse. Experimental results have shown that the proposed algorithm could find robust optimal solutions with higher discovery rate than DFMOSS in a benchmark function.

2 The proposed algorithm

2.1 Overview

The algorithm proposed in this paper finds multiple robust solutions simultaneously based on the following basic ideas:

1. **Formulating robust solution search as a bi-objective optimization problem.** The proposed algorithm replaces single-objective robust solution search to bi-objective optimization problem by using Monte Carlo Simulation (MCS). The two objective functions are mean of the given objective function values at sampled points nearby a particle to be evaluated and their standard deviation.

2. **Using Multi-objective Particle Swarm Optimization (MOPSO).** The proposed method is based on MOPSO[2] whereas the previous work uses MOGA[8]. PSO is promising for problems involving continuous design variables. In MOPSO, a particle moves toward one of known Pareto solutions and searches around the solution exploitatively. Although MOGA uses Pareto ranking scheme to handle multi-objective optimization problem, MOPSO manages Pareto optimal solutions by storing grid-structured archive [13, 2, 4]. Dividing an objective space into hypercubes allows to maintain the diversity of Pareto solutions.

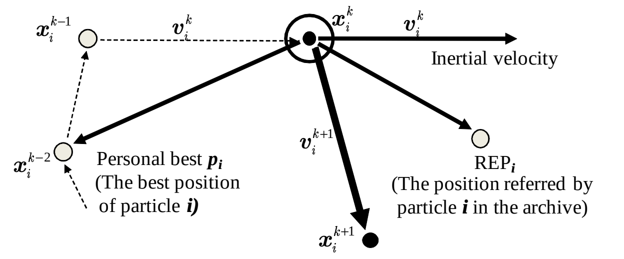

Figure 3: Velocity and position update.

2.2 Search by MOPSO

First, each particle i is initialized; its position $\boldsymbol{x}_i$ and its velocity $\boldsymbol{v}_i$ are defined by random. And then, the archive is initialized by storing Pareto solutions derived from a set of positions chosen randomly from search space. Each position in the archive is assigned to a particle as REP_i by random. Objective space is divided onto $d \times d$ hypercubes by dividing each objective into d equal divisions. Personal best $\boldsymbol{p}_i$ is initialized by $\boldsymbol{x}_i$.

After initialization, the proposed algorithm iterates particles' position and velocity update. As shown in Figure 3, particle velocity is updated considering its personal best position and referring solution's position in archive by following equation:

$$\boldsymbol{v}_i^{k+1} = w\boldsymbol{v}_i^k + c_1 r_1(\boldsymbol{p}_i - \boldsymbol{x}_i^k) + c_2 r_2(REP_h - x_i^k), \quad (1)$$
$$\boldsymbol{x}_i^{k+1} = \boldsymbol{x}_i^k + \boldsymbol{v}_i^{k+1}, \quad (2)$$

where $\boldsymbol{x}_i^k$ and $\boldsymbol{v}_i^k$ indicate position and velocity of particle i at step k, $\boldsymbol{p}_i$ indicates personal best of particle i which is the best position of all positions the particle passed so far, REP_h is a solution in archive which is referred by particle i, c_1 and c_2 are two positive constants called cognitive and social parameter, r_1 and r_2 are random numbers uniformly distributed within [0, 1].

Particle i is evaluated in its current position $\boldsymbol{x}_i^{k+1}$. If the current position dominates personal best $\boldsymbol{p}_i$ of particle i, then the position replaces $\boldsymbol{p}_i$. If neither of the current position and $\boldsymbol{p}_i$ is dominated by the other, $\boldsymbol{p}_i$ is selected from them randomly.

Particle i is reset when it violates the constraint, i.e., it stikcs out of defined domain. Particle i is also reinitialized when satisfying following two conditions:

- Particle i moves too slowly, i.e., its speed $|v_i|$ goes down under a threshold T_v, and

- There is no improvement on $\boldsymbol{p}_i$ for more than Tr steps.

2.3 Particle evaluation

Two objective functions, mean $\mu_f(\boldsymbol{x})$ and standard deviation $\sigma_f(\boldsymbol{x})$ of given objective function values, are statistical values calculated based on Monte Carlo Simulation (MCS). Namely, probability distribution which imitates unevenness of design variables is assumed as Gaussian distribution, mean of the distribution is set to be the value of variables $\boldsymbol{x}^{(i)}$ of individual i and standard deviation of the distribution to be a specified value, and random points are sampled nearby $\boldsymbol{x}^{(i)}$.

The proposed algorithm uses Pareto ranking scheme as DFMOSS, and Pareto solutions are stored in the archive which are divided onto d^2 hypercubes. Fitness sharing is therefore conducted by this archive structure.

Solutions are stored in archive by following two rules:

1. If a particle finds a new good position which dominates the solution the particle is referring, then the solution in the archive is replaced by the new position.

2. If both a solution found by a particle and the solution referred by the particle are non-dominant each other, then the new position is stored in archive without eliminating the referred solution. If the number of solutions in the archive exceeds the limit N_p, a solution is selected randomly from the hypercube which has the most solutions.

Archive is re-partitioned in the case that the maximum or minimum value of a design variable in the archive is updated.

3 Evaluation

A benchmark function $f_t(\boldsymbol{x})$ is defined to experimentally validate search performance of the proposed

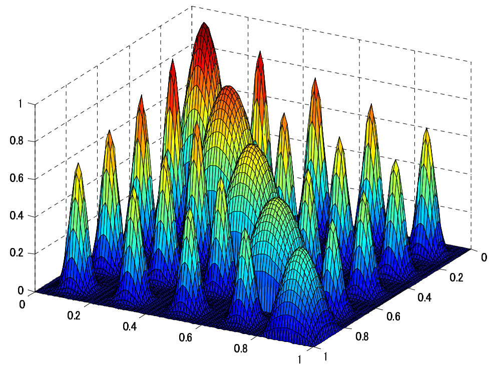

Figure 4: Tested function f_t $(n = 2)$.

algorithm.

$$f_t(\boldsymbol{x}) = \prod_{k=1}^{n} e^{-\frac{x_k \ 0.1}{n}} \left|\sin^{m(\boldsymbol{x})}(5\pi x_k)\right| \qquad (0 \le x_k \le 1) \tag{3}$$

$$m(\boldsymbol{x}) = \begin{cases} 6 & if \displaystyle\bigvee_{\substack{a\in\{0,0.2,\\ \ldots,0.8\}}} \left(\bigwedge_{\substack{k=1,\\ \ldots,n}} a < x_k < a + 0.2 \right) \\ 1 & Otherwise \end{cases} \tag{4}$$

The tested function f_t has five robust solutions, and f_t at $n = 2$ is shown in Fig. 4. We used the function whose dimension n was from 2 to 5. Upper and lower specification limits (USL and LSL) are parameters which should be specified for each target problem[11]; in this experiment, LSL was set to 0.1 and USL was not used.

A robust solution whose mean value $\mu_f(\boldsymbol{x}^{(i)})$ and standard deviation $\sigma_f(\boldsymbol{x}^{(i)})$ of an objective function satisfy the following equation is regarded as sigma level $l\sigma$:

$$\mu_f(\boldsymbol{x}^{(i)}) - l\sigma_f(\boldsymbol{x}^{(i)}) \ge \text{LSL}. \tag{5}$$

The higher l is, the more robust $\boldsymbol{X}^{(i)}$ is against small perturbations of $\boldsymbol{x}^{(i)}$. Sigma levels of solutions found by a tested algorithm were calculated after the search.

Parameters of MOPSO were configured as follows: number of particles was set to 1,000, and w, c_1, c_2, T_v, T_{rs}, N_p, T_r were set to 0.9, 1.2, 1.2, 10^{-3}, 100, 1,000, and 100, respectively. Sampling was performed by using Descriptive Sampling (DS)[14], and sampling number and range of DS were 1,000 and 0.02. Parameters of DFMOSS were configured as follows: population size, crossover method, crossover rate, mutation rate, and a parameter of Pareto ranking c were 100,

©ISAROB 2009

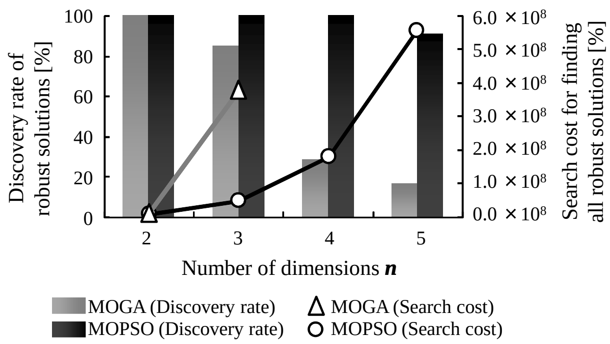

Figure 5: Experimental results.

BLX-α ($\alpha = 0.5$), 1.0, 0.2 and 0.1, respectively. The maximum number of function calls was set to 1.0×10^9.

Figure 5 shows the discovery rate of robust solutions over 30 runs, and search cost that is a function evaluation time for finding all robust solutions averaged over the runs succeeded in finding all robust solutions. The proposed algorithm could find all robust solutions simultaneously even when $n = 4$ and find almost all of solutions when $n = 5$, whereas DFMOSS could find all solutions only when $n = 2$ and found no solutions when $n = 5$.

4 Conclusions

In this paper, we propose an algorithm for robust solution search using multi-objective particle swarm optimization. The proposed algorithm formulates robust optimization as a bi-objective optimization problem which involves two objective functions of mean and standard deviation on sampled values of an objective function.

Experimental results have shown that the proposed MOPSO could find robust solutions better than DFMOSS using MOGA.

In the future, we plan to examine in higher dimensional problems and to adopt multi-objective memetic particle swarm optimization.

Acknowledgements

This research was partially supported by the Ministry of Education, Science, Sports and Culture, Grant-in-Aid for Young Scientist (B), No.20700211, 2008–2010.

References

[1] J. Kennedy and R. Eberhart, "Particle swarm optimization," in *Procedings of the IEEE International Conference on Neural Networks*, vol. 4, 1995, pp. 1942–1948.

[2] C. A. C. Coello, G. T. Pulido, and M. S. Lechuga, "Handling multiple objectives with particle swarm optimization," *IEEE Transactions on Evolutionary Computation*, vol. 8, no. 3, pp. 256–279, 2004.

[3] J. E. Fieldsend, "Multi-objective particle swarm optimization methods," Technical Report #419, Department of Computer Science, University of Exeter, 2004.

[4] L. Cagnina, S. Esquivel, and C. A. C. Coello, "A particle swarm optimizer for multi-objective optimization," *Journal of Computer Science & Technology*, vol. 5, no. 4, pp. 204–210, 2005.

[5] E. Kazancioglu, G. Wu, J. Ko, S. Bohac, Z. Filipi, S. J. Hu, D. Assanis, and K. Saitou, "Robust optimization of an automobile valvetrain using a multiobjective genetic algorithm," in *Proceedings of ASME 2003 Design Engineering Technical Conferences (DETC'03)*, 2003.

[6] K. Shimoyama, K. Fujii, and H. Kobayashi, "Development of realistic optimization method of tsto spaceplane — multi-objective and robust optimization," in *Proceedings of 10th AIAA/ISSMO Multidisciplinary Analysis and Optimization Conference*, 2004.

[7] S. L. Padula, C. R. Gumbert, and W. Li, "Aerospace applications of optimization under uncertainty," *Optimization and Engineering*, vol. 7, no. 3, pp. 317–328, 2006.

[8] K. Shimoyama, "Robust aerodynamic design of mars exploratory airplane wing with a new optimization method," Ph.D. dissertation, University of Tokyo, 2006.

[9] D. Huang, F. Fabozzi, and M. Fukushima, "Robust portfolio selection with uncertain exit time using worst-case var strategy," *Operations Research Letters*, vol. 35, pp. 627–635, 2007.

[10] Y. Jin and J. Branke, "Evolutionary optimization in uncertain environments — a survey," *IEEE Transactions on Evolutionary Computation*, vol. 9, no. 3, pp. 303–317, 2005.

[11] G. Brue and R. G. Launsby, *Design for Six Sigma*. Mcgraw-Hill, 2003.

[12] M. Sokovic, D. Pavletic, and S. Fakin, "Application of six sigma methodology for process design," *Journal of Materials Processing Technology*, vol. 162-163, pp. 777–783, 2005.

[13] K. Deb, *Multi-Objective Optimization using Evolutionary Algorithms*. JohnWiley & Sons, Ltd., 2001.

[14] E. Saliby, "Descriptive sampling: A better approach to monte carlo simulation," *Journal of the Operational Research Society*, vol. 41, no. 12, pp. 1133–1142, 1990.

The Fourteenth International Symposium on Artificial Life and Robotics 2009 (AROB 14th '09),
B-Con Plaza, Beppu, Oita, Japan, February 5 - 7, 2009

Three-dimensional medical image recognition of cancer of the liver by the revised radial basis function (RBF) neural network algorithm

Masahiro Nakagawa, Tadashi Kondo[1)], Tsuyosi Kudo,
Shoichiro Takao and Junji Ueno

Graduate school of Health Sciences, The University of Tokushima
3-18-15 Kuramoto-cho, Tokushima 770-8509, Japan

E-mail:kondo@medsci.tokushima-u.ac.jp[1)]

Abstract: In this study, we propose a revised radial basis function (RBF) neural network algorithm and apply this algorithm to the computer-aided diagnosis (CAD) of the liver. First, the revised RBF neural network algorithm is applied to the recognition of the liver regions and the recognition results are compared with those obtained using the conventional RBF neural network and the conventional multi-layered neural network trained using the back propagation algorithm. It is shown that the revised RBF neural network is accurate and a useful method because the parameters are automatically determined. Then, the revised RBF neural network is applied to CAD of the liver cancer which is called Hepate-Cellular Carcinoma (HCC).

Key words **:**Medical image recognition, Neural network, Radial basis function

I. INTRODUCTION

In the conventional RBF neural network [1], the architectures of the neurons are described using the redial basis function and the neural network has the three layered architecture that is constructed with the input, hidden and output layers. The conventional RBF neural network has the structural parameters such as the mean and the variance of the radial basis function and it is difficult to determine the optimum values of these parameters automatically. So, we must iterate neural network calculations many times changing these parameters so as to find the optimum values of these parameters.

In this paper, we propose the revised RBF neural network algorithm, in which the structural parameters are automatically determined so as to fit the characteristics of the nonlinear system. The means are determined at the training data points and the variances of the radial basis functions are estimated by the regression analysis [2] of the training data and so we do not need to iterate the neural network calculation many times. The revised RBF neural network algorithm is applied the recognition of the liver regions and the recognition results are compared with those obtained using the conventional RBF neural network and the conventional multi-layered neural network trained using the back propagation algorithm. It is shown that the revised RBF neural network is accurate and a useful method because the parameters are automatically determined. Then, we apply the revised RBF neural network algorithm to the computer-aided diagnosis (CAD) of the liver cancer.

Recently, the number of slices scanned by the multi detector raw computed tomography (MDCT) is increasing according to the development of medical imaging technology, and the number of images for the diagnosis becomes large and the doctor's burden is increasing. The CAD for the medical images is expected to reduce the doctor's diagnosis works and to improve diagnosis speed and accuracy. In this study, we applied the revised RBF neural network to the CAD of the liver cancer which is called HCC.

In this application, MDCT images are used. Ten input variables, which are four statistical image features, such as mean, variance, standard variation and range, and four texture features and the two coordinates (x and y) of the neighboring regions are used. The neural network is applied to extract the liver regions and the candidate region images of the HCC are extracted. Then, the density difference image between the early phase and late phase image of MDCT is extracted. The regions of HCC are identified using the density difference images and candidate region images of HCC. These image processing are carried out for all slices of MDCT and 3-dimentionl images of HCC is clearly displayed with the volume rendering software.

II. REVISED RADIAL BASIS FUNCTION NEURAL NETWORK ALGORITHM

In this paper, the regions of the liver and the liver cancer were recognized and extracted using the revised RBF neural network. In this application, the image recognition accuracy of the neural network is very important. The revised RBF neural network had a 3-layered architecture with the input, hidden and output layers. Architecture of the revised RBF neural network is shown in Fig.1. In this figure, x shows the input variable and ϕ shows the output variable and h shows the radial basis function.

In the revised RBF neural network, the structural parameters, which are mean (the center of the neuron)

©ISAROB 2009

and variance of the radial basis function, are calculated automatically using the training data. The revised RBF neural network is calculated as follows:

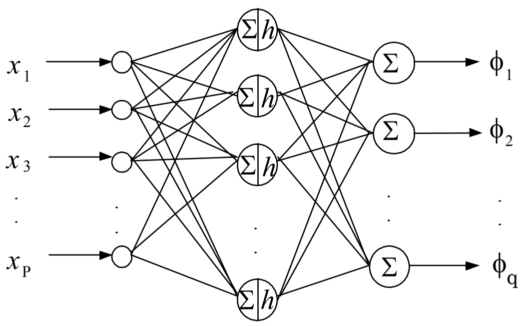

Fig.1 Architecture of the revised RBF neural network

(1)Input layer

$$u_i = x_i \quad (i = 1,2,\ldots,p) \tag{1}$$

Here, x_i is input variable and p is the number of input variables and u_i is the output variable of the input layer.

(2)Hidden layer

In the hidden layer, the output (h_j) of the RBF neuron is calculated by the following equation:

$$h_j = \exp(-z_j^2) \quad (j = 1,2,\ldots,g) \tag{2}$$

Here, z_j is estimated using the regression analysis [2] for the training data.

$$z_j = a_0 + a_1 d_j \tag{3}$$

$$d_j = \|u - c\| \tag{4}$$

Here, a_j ($j=0,1$) are the regression coefficients and d_j are the distance between the training data (u) and the center (c) of the neuron.

(3)Output layer

$$\phi_i(x) = \sum_{j=1}^{g} w_j h_j(u) \quad (i=1,2,\ldots,q) \tag{5}$$

Here, w_j $(j=1,2,\ldots,g)$ are the weights of the neural network and q is the number of neurons in the output layer and $\phi_i(x)(i=1,2,\ldots,q)$are the output variables.

Weights w_j $(j=1,2,\ldots,g)$ are estimated using multiple regression analysis as follows:

$$\underline{w} = (H^T H + \Lambda)^{-1} H^T \underline{\phi}_i \tag{6}$$

Here,

$$H = \begin{bmatrix} h_1(u_1) & h_2(u_1) & \cdots & \cdots & h_g(u_1) \\ h_1(u_2) & h_2(u_2) & \cdots & \cdots & h_g(u_2) \\ \vdots & \cdots & \ddots & \cdots & \vdots \\ \vdots & \cdots & \cdots & \ddots & \vdots \\ h_1(u_n) & h_2(u_n) & \cdots & \cdots & h_g(u_n) \end{bmatrix} \tag{7}$$

$$\Lambda = \begin{bmatrix} \lambda_1 & 0 & \cdots & \cdots & \cdots & 0 \\ 0 & \lambda_2 & 0 & \cdots & \cdots & 0 \\ 0 & 0 & \ddots & 0 & \cdots & 0 \\ 0 & \cdots & 0 & \ddots & 0 & 0 \\ 0 & \cdots & \cdots & 0 & \ddots & 0 \\ 0 & \cdots & \cdots & \cdots & 0 & \lambda_g \end{bmatrix} \tag{8}$$

$$\underline{\phi_i}^T = (\underline{\phi_i}(u_1), \underline{\phi_i}(u_2), \ldots, \underline{\phi_i}(u_n)) \tag{9}$$

$$\underline{w}^T = (w_1, w_2, \ldots, w_g) \tag{10}$$

Here, n is the number of training data.

In the revised RBF-neural network, the structural parameters such as means and variances of the radial basis functions, are automatically determined from the training data as follows. The number of neurons in the hidden layer was set to the number of the training data and the centers (means) of the radial basis functions are located at the training data points. Means are determined at the training data points. Variances are estimated using the regression analysis [2] of the training data to fit the characteristics of the nonlinear system. Using these procedures, the structural parameters such as means and variances of the radial basis functions, are automatically determined from the training data.

III. INPUT VARIABLES OF THE NEURAL NETWORK

In the neural network, ten input variables, which are four statistical image features, such as mean, variance, standard variation and range, and four texture features [3] and two coordinates (x and y) of the neighboring region were used. The four texture features were calculated with a co-occurrence matrix. Co-occurrence matrix is constructed with probability $P_\delta(i,j)$ $(i,j=0,1,\ldots,n-1)$ in the $n \times n$ neighboring region using a parameter $\delta = (r, \theta)$. Here, r is a distance between gray level i and gray level j and θ is an angle. Four texture features are calculated using the co-occurrence matrix as follows;

Angular second moment:

$$ASM = \sum_{i=0}^{n-1} \sum_{j=0}^{n-1} \{P_\delta(i,j)\}^2 \tag{11}$$

Contrast:

$$CON = \sum_{k=0}^{n-1} k^2 \cdot p_{x-y}(k), \quad P_{x-y}(k) = \sum_{i=0}^{n-1} \sum_{\substack{j=0 \\ |i-j|=k}}^{n-1} P_\delta(i,j) \quad k = 0,1,\ldots,n-1 \tag{12}$$

Entropy:

$$ENT = -\sum_{i=0}^{n-1} \sum_{j=0}^{n-1} P_\delta(i,j) \cdot \log\{P_\delta(i,j)\} \tag{13}$$

Inverse difference moment:

$$IDM = \sum_{i=0}^{n-1}\sum_{j=0}^{n-1}\frac{1}{1+(i-j)^2}P_{\delta}(i,j) \qquad (14)$$

VI. MEDICAL IMASGE RECOGNITION OF THE LIVER BY THE REVISED RBF NEURAL NETWORK

In this study, The revised RBF neural network algorithm was applied to the medical image recognition of the liver regions and the recognition results were compared with those obtained using the conventional RBF neural network and the conventional multi-layered neural network trained using the back propagation algorithm. MDCT images of the abdomen were used. An original image shown in Fig.2 was used for organizing the artificial neural networks. Ten input variables, which are four statistical image features and four texture features and the two coordinates (x and y) of the N×N regions were used. The output value of the neural network was zero or one. When N×N pixel region was contained in the region of the liver, the neural network set the pixel value at the center of the N×N pixel region to one and this pixel was shown as the white point. In this study, we set the value of N to 3. Fig.3 shows the output images of neural network. Then we calculated the concordance rate of the liver and outside area of the liver and compared them. Table.1 show the concordance rate of the liver and outside area of the liver. It is shown that the revised RBF neural network is most accurate in three neural networks.

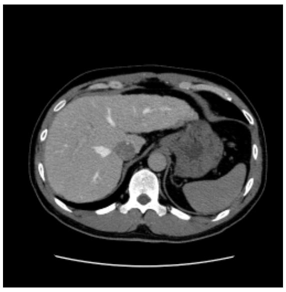

Fig.2 Original image

(a)Revised RBF-NN

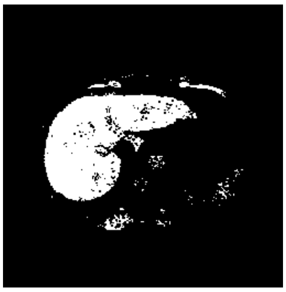

(b)Conventional RBF-NN

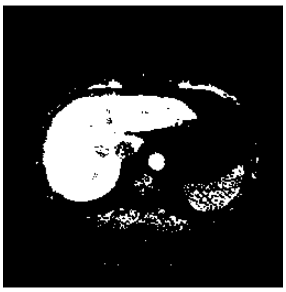

(c)Sigmoid function-NN

Fig.3 The output images of the neural networks

Table.1 The concordance rate of the liver and outside area of the liver

	Revised RBF-NN	Conventional RBF-NN	Sigmoid function-NN
Concordance rate of the liver	0.984	0.905	0.968
Outside area of the liver (pixels)	379	568	1611

V. MEDICAL IMAGE RECOGNITION OF THE LIVER CANCER (HCC)

The revised RBF neural network algorithm was applied to the medical image recognition of HCC. MDCT images of the liver, which are obtained in the early phase and the late phase, were used in this study.

1. Extraction of the liver region

An original image shown in Fig.4 was used for organizing the artificial neural network. This image is an early phase image of MDCT. Ten input variables, which are four statistical image features and four texture features and the two coordinates (x and y) of the N×N regions were used. The output value of the neural network was zero or one. When N×N pixel region was contained in the region of the liver, the neural network set the pixel value at the center of the N×N pixel region to one and this pixel was show as the white point. In this study, we set the value of N to 3. Fig.5 shows the output image after the post processing such as the dilatation and erosion.

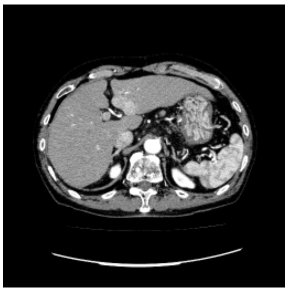

Fig.4 Original image obtained in early phase

Fig.5 Output image of the neural network after the post processing (1)

2. Extraction of HCC regions

The post-processing such as the dilatation and erosion was carried out so as to eliminate the isolate regions in the liver. Fig.6 shows the output image of the liver region including the abnormal regions and the blood vessels regions in the liver. Then the candidate

©ISAROB 2009

regions of the HCC, which contained the abnormal regions and the blood vessels regions in the liver, were subtracted from the liver regions using the output image of the revised RBF neural network after the post-processing. Figure 7 shows the candidate regions of HCC.

Figure 8 shows the late phase image of MDCT. In the late phase image of MDCT, the densities of HCC regions are lower than those of liver regions. In the early phase image (Fig.4) of MDCT, the densities of HCC regions are higher than those of liver regions. Therefore, the density difference image between the early and late phase image contains the HCC regions. The density difference image between the early and late phase image of MDCT was subtracted and the threshold processing was carried out to obtain the binary image. Fig.9 shows the density difference image after the threshold processing.

Fig.6 The liver region after the post-processing(2)

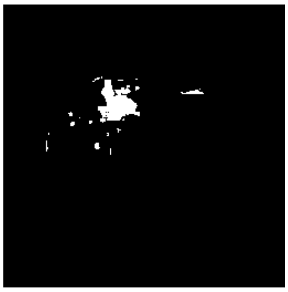

Fig.7 The candidate regions of HCC

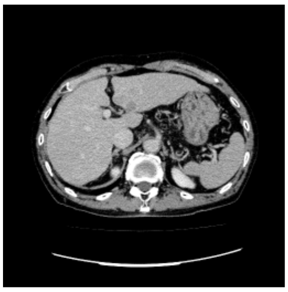

Fig.8 Original image obtained in late phase

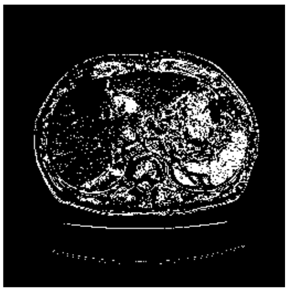

Fig.9 The density difference image

HCC regions were contained in both images in Fig.7 and 9 and so HCC regions can be detected using Fig.7 and Fig.9. The common area between Fig.7 and 9 were subtracted and the post processing analysis was carried out so as to eliminate the small isolated regions such as the blood vessels in the liver and the other regions outside the liver. In the post processing, the image processing such as the circumference length processing and the dilatation and the erosion were carried out to eliminate the small isolate regions. Fig.10 shows the HCC regions after these post processing.

These image processing were carried out for all slices of MDCT images and 3-dimentional images of HCC were displayed clearly with volume rendering software as shown in Fig.11.

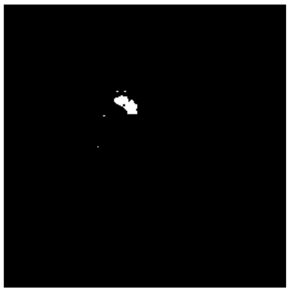

Fig.10 HCC regions after the post processing (3)

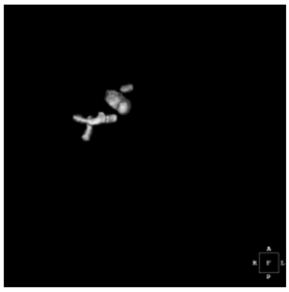

Fig.11 Three-dimensional image of HCC

VI. CONCLUSION

In this paper, we proposed the revised RBF neural network algorithm and applied this algorithm to recognition of the liver regions and extraction of the liver cancer (HCC). In the revised RBF neural network, the structural parameters such as means and variances of the radial basis functions, are automatically determined to fit the characteristics of the nonlinear system. So it is not needed to iterate the neural network calculations many times so as to find the optimum values of the structural parameters. We applied this algorithm to the medical image recognition of the liver and obtained 3-dimensional image of HCC.

REFERENCES

[1] T.Kudo, T.Kondo, T.Matsuki and et.al., Recogniton of 3-dimensional medical images of the head by radial basis function (RBF) neural network, *Proceedings of the 39th ISCIE International Symposium on Stochastic System Theory and Its Applications*, pp.201-206 (2007)

[2] Draper N.R.and Smith H., Applied Regression Analysis, John Wiley and Sons, New York, 1981.

[3] N. Kodama et.al., Application of Textural Features to the Objective Diagnosis of Alzheimer-type Dementia, *Medical Imaging Technology Vol.21 No.1*, pp.41-48(2003) (in Japanese)

©ISAROB 2009

The Fourteenth International Symposium on Artificial Life and Robotics 2009 (AROB 14th '09),
B-Con Plaza, Beppu, Oita, Japan, February 5 - 7, 2009

Remarks on tracking method of neural network weight change for learning type neural network feedforward feedback controller

Takayuki Yamada
Department of Computer and Information Sciences
Faculty of Engineering
Ibaraki University
4-12-1 Nakanarusawa, Hitachi, Ibaraki, 316-8511, Japan

Abstract: Although there are many neural network controllers are proposed, we should still tune several parameters of neural networks in order to obtain well neural network learning performance in practical applications. Our tracking method can be provided as a new aspect for this neural network parameter tuning. It has been applied to an adaptive & a learning type neural network direct controllers and an adaptive type neural network feedforward feedback controller. This paper applied it to a learning type neural network feedforward feedback controller. Simulation results confirmed its usefulness and discussed a transformation of the track on 2D plane to one dimensional value.

Keywords: Neural network, Controller, Learning, Adaptive

I. INTRODUCTION

Many studies have been undertaken in order to apply both the flexibility and the learning capability of neural networks to control systems. Although there are many neural network controllers are proposed, we should still tune several parameters of neural networks in order to obtain well neural network learning performance in practical applications. Learning rules of neural networks are usually designed so as to minimize the squared error between a plant output (or neural network output) and a desired output (teaching signal). This squared error is usually observed in order to tune parameters of neural networks and to examine which neural networks are suitable. However, the essence of neural network learning rules is nothing but the change of the neural network weights. It is not always reflected in the squared error. This is because the object plant has dynamics and the squared error is affected by this plant dynamics. The reason of the use of the squared error is that a usual neural network has huge number of its weights and it is difficult to observe whole neural network weight change in neural network learning progresses. On the other hand, the squared error is a scalar value and it is easily dealt with.

Thus, we proposed a tracking method of neural network weight change as a better examination method for neural network leaning performance.[1] This tracking method derives a weight vector form whole neural network weights. We can calculate an angle between this weight vector and a standard vector. The neural network weight change can be directly drawn on 2D plane by use of the norm of the weight vector and the above angle. Drawn trajectories on 2D plane are not affected by the plant dynamics in comparison with the observation of the squared error. This is because the plant output is not used. Our tracking method is easier to dealt with than observation of whole neural network weight change. We have applied this tracking method to both a learning type and an adaptive type neural network direct controllers and confirmed its usefulness.[1][2] Next, it has been applied to an adaptive type feedforward feedback neural network controller which uses the sum of the neural network output and the feedback loop output as a plant input.[3][4] The feedfoward feedback controller has more complex structure in comparison with the direct controller. This is because the direct controller uses only neural network output as a plant input. However, we can expect more robustness because the feedback loop can compress that the control system becomes to be unstable in earlier learning stage.

This paper applied our tracking method of the neural network weight change to a learning type neural network feedforward feedback controller. The simulation results confirmed its usefulness which is similar to those of both the learning type direct controller and the adaptive type feedforward feedback controller. We noticed through the simulation that it was hard for untrained users to observe the neural network weight performance on 2D plane in some cases. To overcome this problem, this paper also discussed a transformation of the track on 2D plane to one dimensional value.

II. TRACKING METHOD OF NEURAL NETWORK WEIGHT CHANGE

This section explains the tracking method of the neural network weight change briefly. This tracking method is applied to the learning type neural network

©ISAROB 2009

feedforward feedback controller for the SISO plant. In this paper, an output layer of the neural network has one neuron, the weights between the output layer and a hidden layer can be expressed as a vector ω and the weights between the hidden layer and an input layer can be expressed as a matrix W. To simplify, the neuron number of the input layer is equal to that of the hidden layer. That is, the weight matrix W is the square matrix. The tracking method uses the following steps.

(Tracking method of neural network weight change)
(1) We can derive one weight vector Γ from the neural network weight vector ω and weight matrix W as follows:

$$\Gamma^T = [\omega_1 \cdots \omega_n \; W_{11} \cdots W_{1n} W_{21} \cdots W_{2n} \cdots W_{n1} \cdots W_{nn}] \qquad (1)$$

Where n is the neuron number both the input layer and the hidden layer.

(2)We must define a standard vector Γ_0. Any vector, which has same order as that of the weight vector Γ, can be selected as this standard vector, for example, the weight vectors derived from the initial neural network weights, the final neural network weights and so on.

(3) We can calculate an inner product of the weight vector Γ and the standard vector Γ_0 because these vectors have same order. We can also calculate an angle between the weight vector Γ and the standard vector Γ_0 as follows:

$$X = |\Gamma| \cos\theta, \quad Y = |\Gamma| \sin\theta \qquad (2)$$

$$\theta = \cos^{-1}\left(\frac{<\Gamma_0 \cdot \Gamma>}{|\Gamma_0| \cdot |\Gamma|}\right) \qquad (3)$$

Where $<\Gamma_0 \cdot \Gamma>$ is the inner product between the vector Γ_0 and the vector Γ, and $|\Gamma|$ is the norm of the vector Γ.

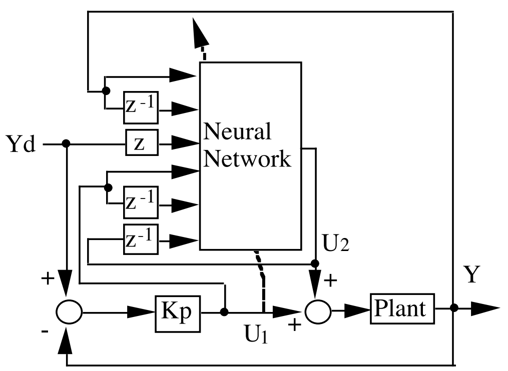

Fig.1 Block diagram of neural network feedforward feedback controller for second order discrete time plant.

(4) We can draw a new weight performance on the 2D plane by the use of X and Y in equations (2) and (3).

III. SIMULATION

This paper applies the tracking method of the neural network weight change to the learning type neural network feedforward feedback controller. The simulated plant is follows:

$$Y(k) = -a_1 Y(k-1) - a_2 Y(k-2) + U(k-1) + bU(k-2) - a_3 Y(k-3) + C_{non} Y^2(k-1) \qquad (4)$$

Where Y(k) is the plant output, U(k) is the plant input, k is the sampling number, a_1, a_2 & b are the plant parameters, a_3 is the parasite term and C_{non} is the nonlinear term. For this simulation, a_1=-1.3, a_2=0.3, b=0.7, a_3=-0.03 and C_{non}=0.2 are selected. The rectangular wave is also selected as the desired value Yd. The output error ε and the cost function J are defined as follows:

$$\varepsilon(k) = Yd(k) - Y(k)$$

$$J(p) = \frac{1}{2} \sum_{k=1}^{\rho} \varepsilon^2(k) \qquad (5)$$

Where p is the trial number and ρ is the sampling number within one trial period.

For this simulated plant, the neuron number n in both the input and hidden layers is 6. The neural network input vector I is defined as the following equation.

$$I^T(k) = [Y_d(k+1) \; Y(k) \; Y(k-1) \; U_2(k-1) \; U_1(k) \; U_1(k-1)] \qquad (6)$$

Where U1(k) and U2(k) are the feedback loop output and the neural network output respectively. We select the following sigmoid function f(x) as the input output relation of the hidden layer neuron.

$$f(x) = \frac{X_g\{1-\exp(-4x/X_g)\}}{2\{1+\exp(-4x/X_g)\}} \qquad (7)$$

Where Xg is the parameter which defines the sigmoid function shape. The neural network output U2(k) is composed as follows:

$$U_2(k) = \omega^T(p) f\{W(p) I(k)\} \qquad (8)$$

When we use the P control (Proportional control), the feedback loop output U1(k) is composed using the feedback gain Kp as shown in the following equation.

$$U_1(k) = Kp\{Yd(k) - Y(k)\} \qquad (9)$$

The plant input U(k) of the feedforward feedback neural network controller is the sum of the neural network output and the feedback loop output as follows:

$$U(k) = U_1(k) + U_2(k) \tag{10}$$

The block diagram of the learning type neural network feedforward feedback controller is shown in Fig.1. The learning rule of this neural network controller is designed so as to minimize the feedback loop output. When we apply the δ rule to this learning rule, it is expressed as follows:

$$W_{ij}(p+1) = W_{ij}(p) + \sum_{k=1}^{\rho} [\eta U_1(k)\omega_i(p) I_j(k-1) \times f'\{\sum_{j=1}^{n} W_{ij}(p) I_j(k-1)\}] \tag{11}$$

$$\omega_i(p+1) = \omega_i(p) + \sum_{k=1}^{\rho} [\eta U_1(k) f\{\sum_{j=1}^{n} W_{ij}(p) I_j(k-1)\}] \tag{12}$$

Where η is the parameter to determine the neural network learning speed. We select the weight vector derived from the initial neural network weights as the standard vector Γ_0 of the equations (2) and (3)

Fig.1 shows the plant output (p=1) before learning. As shown in this figure, there is large output error between the plant output and the desired value. Figs.2 and 3 show the plant output (p=200) after learning and the cost function respectively. As shown in these figures, there is the error remained in the first cycle of the desired value, but it becomes to be small in other parts and the cost function smoothly decreases. This means that the neural network learning performs well.

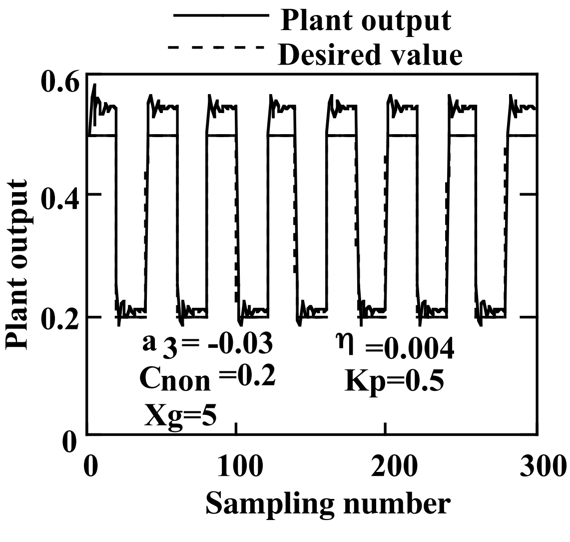

Fig.2 Plant output (p=1) before learning.

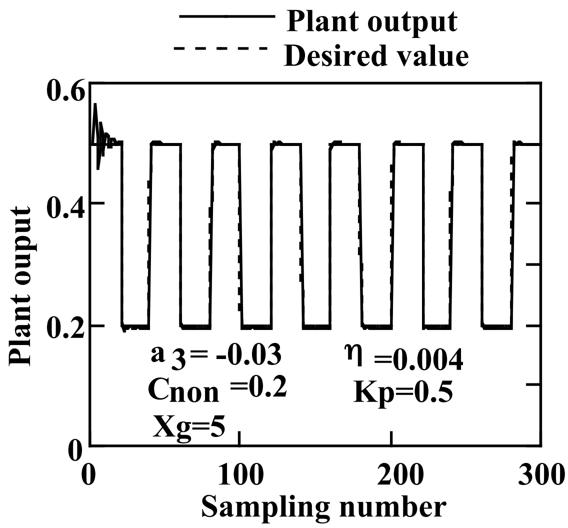

Fig.3 Plant output (p=200) after learning.

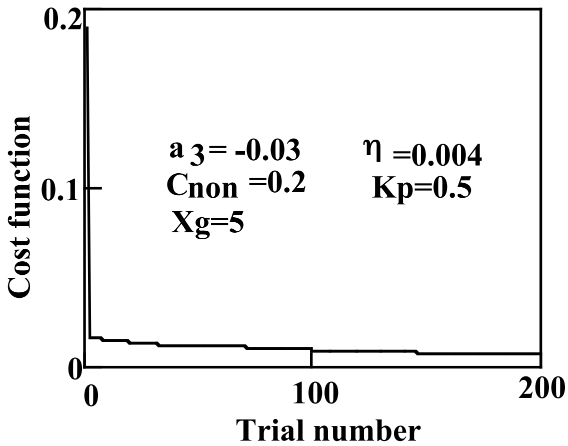

Fig.4 Cost funtion.

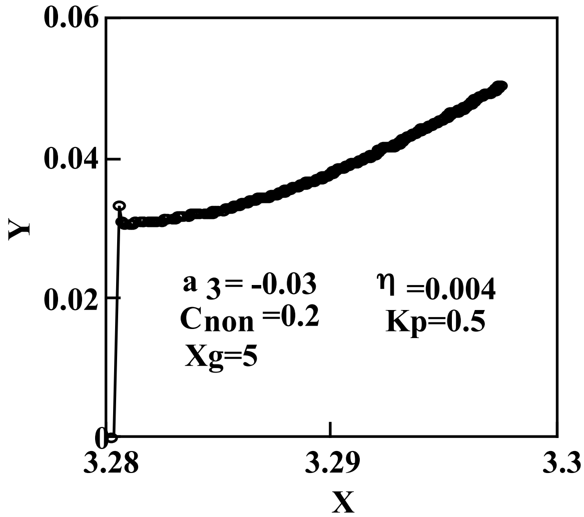

Fig.5 Track of neural network weight change.

©ISAROB 2009

Fig.5 shows the track of the neural network weight change. As shown in this figure, our tracking method is also useful for a learning type neural network feedforward feedback controller.

Fig.6 shows the other example of the track of the neural network weight change. As shown here, it may not be easy for untrained users to distinguish whether the neural network learning performance in fig.6 is well or not. To overcome this problem, one choice is a transformation of the track on 2D plane to one dimensional value. Following equation is one example.

$$V_W(p) = \sqrt{(X(p+1) - X(p))^2 + (Y(p+1) - Y(p))^2} \quad (13)$$

Fig.7 shows the one dimensional value Vw in the initial learning stage. As shown in fig.7, the VW smoothly decreases and this transformation is easily dealt with. This discussion also has another advantage. Fig.8 shows the cost function in initial leaning stage. As shown here, there is little vibration and this may be caused by the plant dynamics. Other possibility is to be caused by the vibration of the neural network weight vector element or the weight matrix element observed only by 2D plane. Advanced study for this problem is our future work.

IV. CONCLUSION

This paper applied the tracking method of the neural network weight change to the learning type neural network feedforward feedback controller. The simulation results confirmed its usefulness. We also discussed a transformation of the track on 2D plane to one dimensional value in order to realize an easier expression of the neural network weight change for untrained users.

ACKNOWLEDGMENT

The author wishes to express his thanks to Mr.Daisuke Suzuki, graduated student, Ibaraki University, for his programming and simulation.

REFERENCES

[1] Takayuki Yamada, "Remarks on tracking method of neural network weight change for learning type neural network direct controller", Proceedings of AROB 10th '05 (The Tenth International Symposium on Artificial Life and Robotics 2005), pp.624-627(2005)

[2] Takayuki Yamada, "Remarks on tracking method of neural network weight change for adaptive type neural network direct controller", Proceedings of AROB 11th '06 (The Eleventh International Symposium on Artificial Life and Robotics 2006), GS19-3 (2006)

[3]TakayukiYamada and TetsuroYabuta, "Adaptive Type Feedforward Feedback Controller Using Neural Networks", Transactions of the Society of Instrument and Control Engineers, Vol.30, No.10, pp.1234-1241(1994)(in Japanese)

[4]Takayuki Yamada, "Remarks on tracking method of neural network weight change for adaptive type neural network feedforward feedback controller", Proceeding of AROB13th '08 (The Thirteenth International Symposium on Artificial Life and Robotics), pp.559-562(2008)

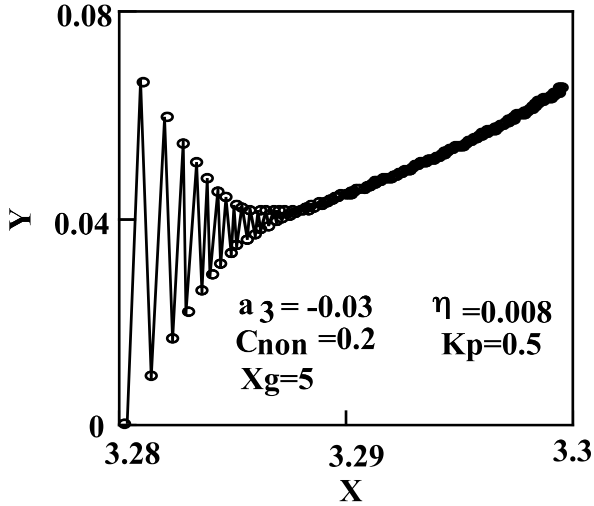

Fig.6 Track of neural network weight change.

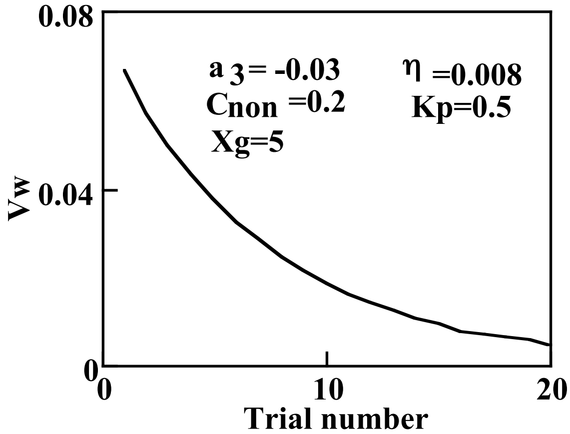

Fig.7 Vw.in initial learning stage.

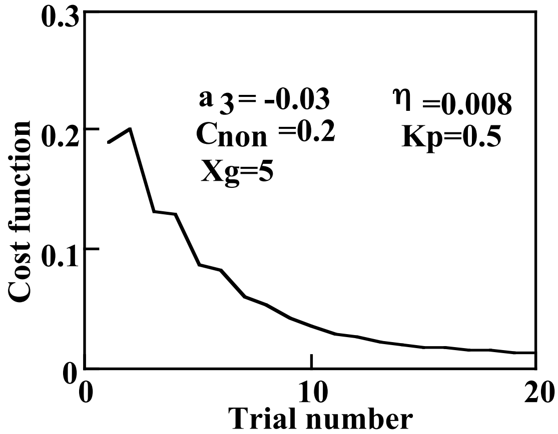

Fig.8 Cost function in initial learning stage.

Multiple Self-Organizing Maps for Visuo-Motor System that uses multiple cameras with different field of views

Nobuhiro Okada, Jinjun Qiu, Nakamura Kenta, and Eiji Kondo

Dept. of Intelligent Machinery & Systems, Kyushu University, 744, motooka, nishi-ku, Fukuoka, 819-0395 Japan
(Tel : 81-92-802-3171; Fax : 81-92-802-0001)
(okada@mech.kyushu-u.ac.jp)

Abstract: This paper proposes multiple self-organizing maps (SOMs) for control of a visuo-motor system that consists of a redundant manipulator and multiple cameras in an unstructured environment. The maps control the manipulator so that it reaches its end-effector to targets given in the camera images. Also the maps make the manipulator take obstacle free poses. Multiple cameras are introduced to avoid occlusions and multiple SOMs are introduced to deal with multiple camera images. Simulation results will be shown.

Keywords: Robot vision systems, Self-organizing maps**.**

I. INTRODUCTION

Vision guide for a manipulator has been one of the major research issues in robotics. Coordination schemes of visuo-motor systems can be classified on the basis of the knowledge about manipulator kinematics and camera parameters. Many researchers have proposed a number of systems that deal with unknown manipulator kinematics and unknown camera parameters. In the studies, visuo-motor models are either estimated analytically during the execution of tasks on-line or learned prior to the execution off-line. Artificial neural networks can be used to learn the non-linear relationships between features in images and the manipulator joint angles. Miller et al. proposed a neural network based on the learning control system, where a cerebeller model arithmetic computer memory was employed for the learning [1]. Carusone et al. used a network to train an un-calibrated industrial robot [2]. In their systems, neural networks provided the estimation of the poses of targets in the manipulator coordinate frames, and the poses were used to guide the manipulator to grasp the objects. However, supervisors were needed in the systems.

Self-organizing map (SOM) based on the Kohonen algorithm is an important unsupervised artificial neural network model [3]. It has shown great potential in application fields such as motor control, pattern recognition, optimization, and so on, and also has provided insights into how mammalian brains are organized [4] [5]. During the past years it has been demonstrated that the SOM can solve the inverse kinematics problem for visuo-motor control. Buessler et al. determined arm movements by tracking an image target [6] [7]. The correlation between an image-defined error and the joint movement was learned on-line using self-organizing algorithm for making the error zero. Multiple neural maps were combined to simplify neural learning in their study. Martinetz et al. and Walter et al. used a three dimensional lattice to learn the nonlinear transformation that specifies the joint angles of a 3-DOF manipulator so that the angles take the tip of the manipulator to a target point given in the coordinates provided by two cameras [8] [9]. In all of these studies, however, they solved the visuo-motor coordination problems with non-redundant manipulators in an environment without obstacles. Such obstacle avoidance problems are important for manipulators that work in real environments. Zeller et al. developed a motion planning for a non-redundant manipulator to avoid collision with obstacles in a cluttered environment by using the TRN model [10]. They used a fact that a locally optimized path can be determined by minimizing the Euclidean distance from the current position to a given goal. Collision check was performed not in the self-organizing process but in the path planning process afterwards. In contrast to these precedent studies, our system is not only for precise positioning of the end-effector but also for ensuring obstacle free poses of the manipulator. We intend to realize coordination for a visuo-motor system with a redundant manipulator in a cluttered environment. The redundancy is then used to

©ISAROB 2009

make the manipulator take obstacle free poses and achieve high manipulability.

In the previous researches, Zha et al. used a SOM to coordinate a visuo-motor system in an environment with obstacles [11]. Collisions between the links and obstacles were, however, not well considered. We introduced a potential field to avoid such collisions only in a 2D space [12]. Han et al. realized collision avoidance for a visuo-motor system in a 3D space [13]. The occlusion problem was, however, not solved effectively even in the system.

Vision systems are generally classified by the number of cameras, camera configurations, the level of calibration and some a priori knowledge about the scene. The binocular configuration is a commonly used configuration. In comparison with the eye-in-hand configuration, it allows a wide field of view and then it makes easy to observe both the manipulator and targets simultaneously. Such a vision system was employed in [13]. However, since they treated spaces occluded by obstacles in the image space as unreachable spaces for the manipulator, the workspace was restricted.

In order to handle the occlusion problem, we have developed a visuo-motor system with multiple related SOMs and a redundant camera system in this paper. The SOMs are directly connected to the cameras and learn to perform manipulator control. Based on the visibility of a target given in the workspace, the appropriate map is selected. The map outputs a joint angle vector which makes the manipulator reach the target with an obstacle free pose. The proposed learning algorithm ensures that the manipulator moves smoothly and consistently in the whole workspace no matter which map is selected. The advantages of the proposed method are: (1) By employing multiple maps, the system overcomes the occlusion problems in cluttered environments. The cooperation and complementation of maps make the manipulator consistently move in the whole workspace. (2) In our self-organizing learning procedure, the visuo-motor system learns not only to position the end-effector precisely but also ensure that the manipulator takes obstacle free poses.

This paper is organized as follows. First, an outline of our visuo-motor system is introduced in the section II. Introduction of a near camera is discussed in the section III. Simulation results are shown in the section IV. Finally, conclusions are given in the section V.

II. OUR VISUO-MOTOR SYSTEM

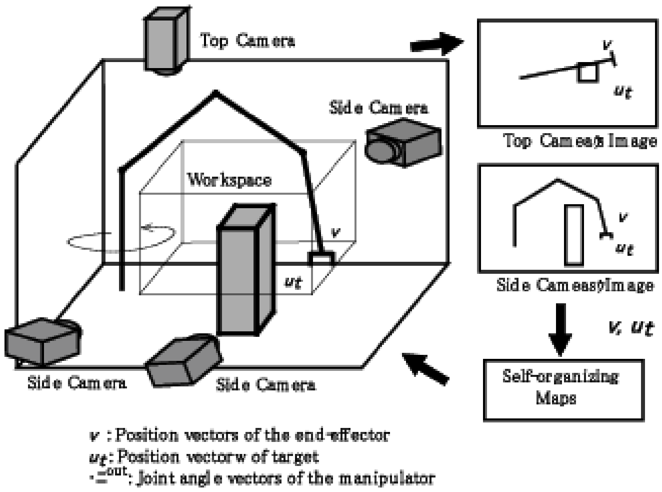

Fig.1. Outline of our visuo-motor system.

Our visuo-motor system is illustrated in Fig.1. The system contains a 4-DOF redundant manipulator, multiple CCD cameras, and multiple related SOMs. The CCD cameras are used to get the target positions, the locations of the end-effector and the manipulator poses. They also acquire information about obstacles by simple using threshold. From visual information provided by the cameras, the SOMs learn projections that convert the position vectors of the targets in the image spaces into the joint angle vectors of the manipulator.

Although stereo camera systems can provide 3D information and we have used such a system in our previous works [12] [13], the system could not well deal with spaces occluded by obstacles. They introduced 3-cameras system to overcome the situation [14]. However, the result was limited. To deal with the occlusion problem, a multiple camera system is presented in this paper. The valid workspace is extended by using the cameras at multiple viewpoints. Related SOMs are simultaneously employed in the visuo-motor system. For the detail of the algorithm using in our system, please refer to our previous study [14].

III. INTRODUCTION OF A NEAR CAMERA

We added a near camera in our system to reduce the positioning error as shown as in Fig.2. This camera has a narrow view than other cameras. And it can only obtain the image coordinates of the neurons that enter given categories.

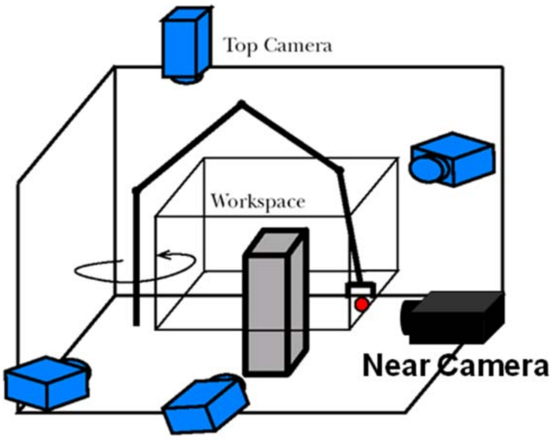

Fig.2. Outline of our visuo-motor system with a near camera

The near camera's SOM has a different learning algorithm from others. First neurons which are generated without the near camera are divided into two groups according to whether the neuron position can be seen by the near camera. The group of the neurons with positions which can be caught in the near camera does the self-organizing maps' learning procedure by using the data from the near camera and updates the neurons' parameters again. On the other hand, the other group of the neurons is left just as it is. The grouping is done for each target. Thus if the target position is in the given categories, by using the near camera we can get the more accurate pose of the manipulator.

IV. SIMULATION RESULTS

We have constructed an experimental system. By simulation and experiments, we have also revealed that a visuo-motor system with 3 CCD cameras and 2 SOMs can control a redundant manipulator and realize collision avoidance in an environment with obstacles.

In this paper, we aim at a system with 5 CCD cameras, 3 SOMs and a 4-DOF redundant manipulator, and show its validity by simulation. The cameras are assumed to be orthographic models and each camera has 640X480 pixel resolution. The simulation model is illustrated in Fig. 3. The length of each link is 120, 135, 110 and 140 pixels in the image spaces. Each SOM involves 240 neurons. 15000 targets were given in the learning process and they were distributed 200X200 pixels with a focus on the obstacle. The time required

Table 1. The average positioning error of the end-effector

	Path 1	Path 2	Path 3	Path 4
Without a near camera	2.91	2.65	2.90	3.35
With a near camera	2.18	1.84	4.37	2.64

for the learning was about 10 minutes using a PC with 3.0GHz Pentium4.

After the learning, the path planning system planned a collision-free path of the end-effector in the top camera image using Laplace potential method, and determined the shortest path in another camera image. Then the planning system divided the path into 34 positions and the SOMs outputted the collision-free poses for the positions. An example of path planning is shown in Fig.4. The average positioning errors of the end-effector for different path are shown in Table 1. And by Fig.5, we can see that the positioning errors of the

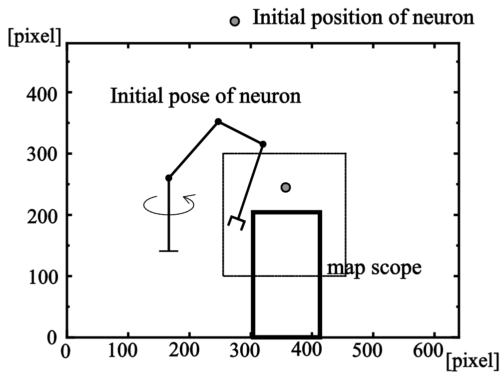

Fig.3. Assumed simulation environment illustrated in the image space of the right camera

end-effector don't change when the manipulator's pose is outside the view of the near camera, but once the target position enters the view of the near camera, the positioning errors are made smaller. In most situations, the average positioning error becomes fewer. However the average positioning error of path 3 becomes larger, we think the reason may be that the neurons are not filled enough in the view of the near camera. Now we are still dealing with that.

V. CONCLUSIONS

We developed a visuo-motor system with multiple self-organizing maps. The system consists of a redundant manipulator, multiple cameras and multiple SOMs corresponding to the cameras. By using the cameras, the system can control the manipulator in an environment with obstacles. To reduce the positioning

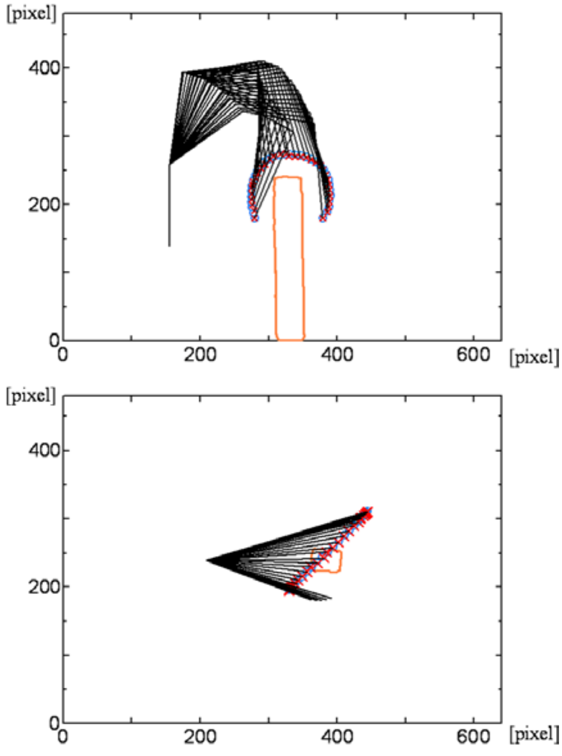

Fig.4. Collision avoidance by the simulation

error of the end-effector, we then added a near camera in our former system. Simulation results showed that by using the near camera we can get the more accurate pose of the manipulator in most situations.

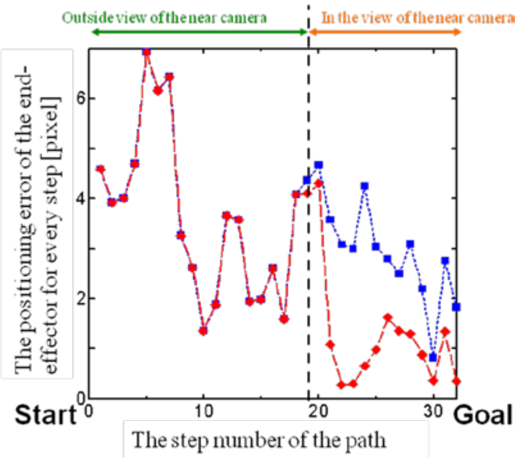

Fig.5. The path 4's positioning error of the end-effector for every step. (The dotted line: without a near camera; the dash line: with a near camera)

REFERENCES

[1]W. Miller (1989), "Real-time application of neural networks for sensor-based control of robots with vision," IEEE Trans. on Systems, Man and Cybernetics, vol.19, No.4, pp.825-831.

[2]J. Carusone and G. Eleurterio (1998), "The feature CMAC: a neural-network based vision system for robotic control," Proc. of the IEEE Int. Conf. on Robotics and Automation, vol.4, pp.2959-2964.

[3]T. Kohonen (1988), "Self-organizing maps and associative memory, Second Edition," Springer information Sciences, vol.8, pp.43-48.

[4]J. Wiener, T.Burwick and W. von Seelen (2000), "Self-organizing maps for visual feature representation based on natural binocular stimuli," Biological Cybernetics, 82, pp.97-110.

[5]L. Behera and N. Kirubanandan (1999), "A hybrid neural control scheme for visuo-motor coordination," IEEE Control Systems, pp.34-41.

[6]J. L. Buessler and J. P. Urban (1998), "Visual guided movements: learning with modular neural maps in robotics," Neural Networks, 11, pp.1395-1415.

[7]J. L. Buessler, R. Kara, P. Wira et al (1999), "Multiple self-organizing maps to facilitate the learning of visuo-motor correlations," Proc. of the IEEE Int. Conf. on Systems, Man and Cybernetics, pp.470-475.

[8]T. Marinetz, H. Ritter, and K. Schulten (1990), "Three-dimensional neural net for learning visuo-motor coordination of a robot arm," IEEE Trans. on neural networks, vol.1, pp.131-136.

[9]J. A. Walter and K. J. Schulten (1993), "Implementation of self-organizing neural networks for visuo-motor control of an industrial robot," IEEE Trans. on Neural Networks, vol.4, pp.86-95.

[10]M. Zeller, R. Sharma and K. Schulten (1997), "Motion planning of a pneumatic robot using a neural network," IEEE Control Systems, 17, pp.89-98.

[11]H. B. Zha, T. Onitsuka and T. Nagata (1996), "A visuo-motor coordination algorithm for controlling arm's movement in environments with obstacles," Proc. of the 4th Int. Conf. on Control, Automation, Robotics and Vision, pp.1013-1017.

[12]N. Okada, Y. Shimizu, Y. Maruki and A. Yoshida (1999), "A self-organizing visuo-motor map for a redundant manipulator in environment with obstacles," Proc. of the 9th Int. Conf. on Advanced Robotics, pp.517-522.

[13]M. Han, N. Okada and E. Kondo (2003), "Collision avoidance for a visuo-motor system using a self-organizing map in a 3D space," 6th Japan-France Congress on Mechatronics, pp.495-500.

[14]M. Han, N. Okada and E. Kondo (2006), "Coordination of an uncalibrated 3-D visuo-motor system based on multiple self-organizing maps," JSME International Journal, Series C, vol.49, pp.230-239.

The Fourteenth International Symposium on Artificial Life and Robotics 2009 (AROB 14th '09),
B-Con Plaza, Beppu, Oita, Japan, February 5 - 7, 2009

Three-dimensional medical image analysis of the heart by the revised GMDH-type neural network self-selecting optimum neural network architecture

C. Kondo[1] and T. Kondo[2]

[1] *Graduate school of Design, Kyushu Univ., 4-9-1shiohara minamiku Fukuoka 815-8540, Japan*
[2] *Graduate School of Health Sci., The Univ. of Tokushima, 3-l8-15 Kuramoto-cho Tokushima 770-8509, Japan*
([2] *kondo@medsci.tokushima-u.ac.jp*)

***Abstract*:** In this study, a revised GMDH-type neural network algorithm self-selecting the optimum neural network architecture is applied to 3-dimensional medical image analysis of the heart. The GMDH-type neural network can automatically organize the neural network architecture by using the heuristic self-organization method which is the basic theory of the GMDH algorism. The heuristic self-organization method is a kind of the evolutional computation methods. In this revised GMDH-type neural network algorithm, the optimum neural network architecture was automatically organized using the polynomial and sigmoid function neurons. Furthermore, the structural parameters such as the number of layers, the number of neurons in the hidden layers and the useful input variables are automatically selected so as to minimize the prediction error criterion defined as Prediction Sum of Squares (PSS).

***Keywords*:** GMDH, Neural network, Medical image recognition

I. INTRODUCTION

In this study, 3-dimensional medical image analysis of the heart by a revised Group Method of Data Handling (GMDH)-type neural network self-selecting optimum neural network architecture [1] is developed. In the medical image recognition, there are many kinds of medical images, such as magnetic resonance imaging (MRI) image, X-ray computed tomography (CT) image, X-ray image, mammography and others, whose characteristics are complex and different from each other. Furthermore, in recent years, 3-dimensional medical images generated by multi-detector row computed tomography (MDCT) and MRI are used in clinical diagnosis. The 3-dimensional medical images contain a lot of information and so computer-aided diagnosis (CAD) systems for the 3-dimensional medical images are needed for many kinds of organs. When we apply artificial neural networks to the medical image analysis and CAD , it is very difficult to find the optimum neural network architecture fitting the characteristics of the medical images.

The revised GMDH-type neural network algorithm proposed in our early work [1] is applied to medical image analysis of the heart. The neural network architecture that fits the complexity of the medical images is automatically organized by the revised GMDH-type neural network algorithm so as to minimize the prediction error criterion defined as PSS [2]. The medical images used in this study are MDCT images of the heart. Statistics of image densities in neighboring regions and x and y coordinates of the centers of the neighboring regions are used as the image features. Only useful image features are selected automatically and the optimum neural network architecture are organized using selected useful image features. The 3-dimensional outlines of the heart are recognized using the neural network organized by the revised GMDH-type neural network algorithm and the regions of the heart are extracted. The results are compared with those obtained using GMDH [2] and show that the revised GMDH-type neural network algorithm is useful for the 3-dimensional medical image analysis of the heart and is very easy to apply the practical complex problem because the optimum neural network architecture is automatically organized so as to minimize the prediction error criterion PSS.

II. REVISED GMDH-TYPE NEURAL NETWRK ALGORITHM.

The revised GMDH-type neural network is shown in Fig.1. Here, nonlinear function g_i is described by the following Kolmogorov-Gabor polynomial [3], [4]:

$$g_i(x_1,x_2,\cdots,x_p)= a_0+\sum_i a_i x_i+\sum_i\sum_j a_{ij}x_i x_j+\cdots \qquad (1)$$

This nonlinear function is automatically organized by using the polynomial type neuron. In the revised GMDH-type neural network, many kinds of nonlinear

©ISAROB 2009

combinations of the input variables are generated by using the polynomial type neurons and only useful nonlinear combinations of the input variables are selected. Optimum neural network architectures are organized by using selected useful combinations of the input variables. The architecture of the revised GMDH-type neural network is produced as follows:

1. The first layer

$$u_j=x_j \qquad (j=1,2,\cdots,p) \qquad (2)$$

where x_j $(j=1,2,\cdots,p)$ are the input variables of the system, and p is the number of input variables.

2. The second layer

Many combinations of two variables (u_i,u_j) are generated. For each combination, the neuron architecture is described by the following equations:

Σ: (Nonlinear function)

$$z_k= w_1u_i+w_2u_j+w_3u_iu_j+w_4u_i^2+w_5u_j^2+w_6u_i^3+w_7u_i^2u_j +w_8u_iu_j^2+w_9u_j^3 - w_0\theta_1 \qquad (3)$$

f : (Linear function)

$$y_k= z_k \qquad (4)$$

where $\theta_1 =1$ and w_i $(i=0,1,2,\cdots,9)$ are weights between the first and second layer. The weights w_i $(i=0,1,2,\cdots,9)$ are estimated by using the revised regression analysis [5]. This procedure is as follows:

First, the values of z_k are calculated by using the following equation:

$$z_k=\log_e(\phi'/(1-\phi')) \qquad (5)$$

where ϕ' is the normalized output variable. Then the weights w_i $(i=0,1,2,\cdots,9)$ are estimated by using the stepwise regression analysis [5] which selects useful input variables by using the PSS [2]. Therefore, only useful terms in (3) are selected and neuron architecture can be organized by these selected useful terms.

From these generated neurons, L neurons which minimize the PSS are selected. The output values (y_k) of L selected neurons are set to the input values of the neurons in the third layer.

3. The third and succeeding layers

In the third and succeeding layers, the same computation of the second layer is continued until the PSS values of L neurons are not decreased. When the iterative computation is terminated, the following calculation of the output layer is carried out.

4. The output layer

In the output layer, the output values of the neural network are calculated from z_k as follows:

$$\phi=1/(1+\exp(-z_k)) \qquad (6)$$

So, in the output layer, the neuron architecture becomes as follows:

Σ: (Nonlinear function)

$$z_k= w_1u_i+w_2u_j+w_3u_iu_j+w_4u_i^2+w_5u_j^2+w_6u_i^3+w_7u_i^2u_j +w_8u_iu_j^2+w_9u_j^3 - w_0\theta_1 \qquad (7)$$

f : (Nonlinear function)

$$\phi =1/(1+\exp(-z_k)) \qquad (8)$$

At last, the complete neural network architecture is produced by selected neuron in each layer.

By using above procedures, the revised GMDH-type neural network can be organized.

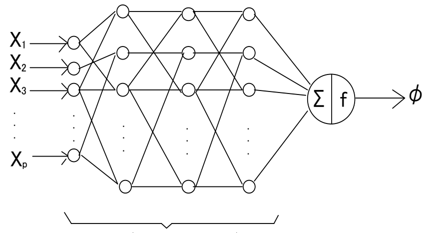

$g_i\,(x_1,x_2,\cdots,x_p)$

Σ : (Nonlinear function)

$z = \sum w_i\, g_i\,(x_1,x_2,\cdots,x_p)$

f : (Nonlinear function)

$\phi =1 / (1+\exp(-z))$

Fig.1 Architecture of revised GMDH-type neural network [1]

III. APPLICATION TO THE MEDICAL IMAGE RECOGNITION.

In the medical image recognition, there are many kinds of medical images, such as MRI image, X-ray CT image, X-ray images, mammography and others, whose characteristics are different each other. So, when we apply neural networks to medical image recognition, it is very difficult to find out the optimum neural network architectures fitting the characteristic of each medical image. The revised GMDH-type neural network can be automatically organized by using the heuristic self-organization method [3],[4]. Furthermore, in the revised GMDH-type neural network, a lot of nonlinear combinations of the input variables are generated and only useful combinations of the input variables are selected so as to minimize the error criterion defined as PSS. Therefore, we can easily apply the revised GMDH-type neural network to medical image recognition. The recognition results obtained by the revised GMDH-type neural network are compared with those obtained by the GMDH.

1. Results of the medical image recognition by using the revised GMDH-type neural network.

The X-ray CT image shown in Fig.2 are used for organizing the neural network. x and y coordinates and the statistics of the image densities in the neighboring regions of the N×N pixels at the positions of the learning points are used as the input variables of the neural network. The statistics used for the recognition are the mean, the standard deviation, the variance, the median, the minimum, the maximum and the range. Only five input variables which are the mean, the standard deviation, the variance and x and y coordinates are automatically selected as useful input variables by the revised GMDH-type neural network. The output value of the neural network is zero or one. When N×N pixel region is contained in the region of the heart, the neural network set the pixel value at the center of the N×N pixel region to one and this pixel is shown as the white point. The neural networks were organized when the values of N were from 3 to 15. It was determined that when N was equal to 4, the neural network architecture had the smallest recognition error. Five useful neurons were selected in each hidden layer. Figure 3 shows the variation of PSS values. PSS values decreased gradually and small PSS value was obtained. The region of the heart was recognized by using the organized neural network and was extracted automatically. Fig.4 shows the output image of the revised GMDH-type neural network. This output image was processed by the post-processing analysis. In the post-processing, the small isolated regions were eliminated and the outlines of the regions of the heart were expanded outside by N/2 pixels. Fig.5 shows the output image after this processing. In order to check the matching between the original image and the output image of the neural network, the output image was overlapped on the original image of Fig.2. The overlapped image is shown in Fig.6. From Fig.6, we can see that the output image was very accurate.

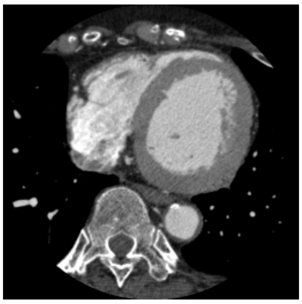

Fig.2 Original image (1)

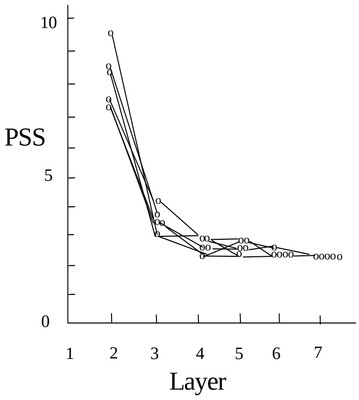

Fig.3 Variation of PSS

Fig.4 Output image of the neural network (1)

Fig.5 Output image after post-processing (1)

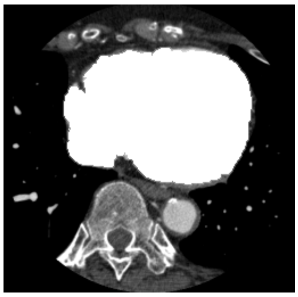

Fig.6 Overlapped image (1)

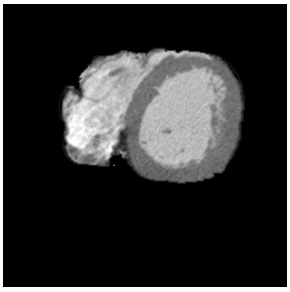

Fig.7 Extracted image (1)

2. Generation of 3-dimensional heart images

Three-dimensional heart images were generated using the following procedures. The heart image shown in Figs. 7 was subtracted from the original images in Fig. 2 using the output images after post-processing in Figs.5. For all MDCT slice images, these image subtractions were conducted and all slice subtracted images of the heart were generated. Then, 3-dimensional heart images were generated from these subtracted images using the rendering software. Figure 8 shows the 3-dimensional heart images generated by the revised GMDH-type neural network.

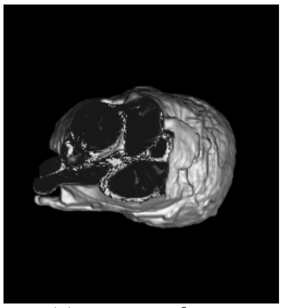

(a) Upper side

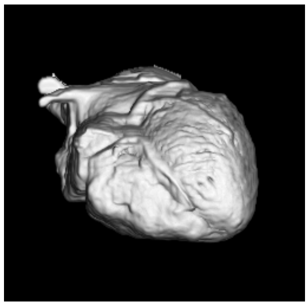

(b) Under side

Fig.8 3-dimensional images of the heart

3. Check of generalization of neural network

In order to check generalization of revised GMDH-type neural network, revised GMDH-type neural network, which was organized by original image of the heart (Fig.2), is applied to another original image of the heart (Fig.9). Revised GMDH-type neural network output the heart image (Fig.10) and post-processing analysis of the heart image was carried out, based on which regions of the heart were extracted. The outline of regions of the heart were expanded outside by N/2 pixels. Fig.11 shows the output image after the post-processing. In order to check matching between the original image and the output image of the neural network, the output image was overlapped on the original image after the post-processing. Overlapped image is shown in Fig.12. From Fig.12, we can see that revised GMDH-type neural network could extract new regions of the heart accurately and it is shown that revised GMDH-type neural network has a good generalization ability. Fig.13 shows the extracted image.

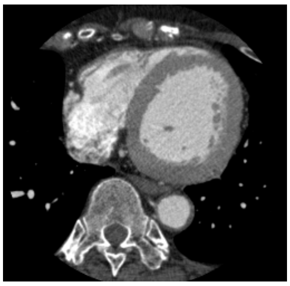

Fig.9 Original image (2)

Fig.10 Output image of the neural network (2)

Fig.11 Output image after post-processing (2)

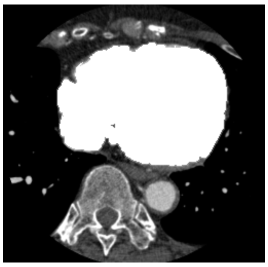

Fig.12 Overlapped image(2)

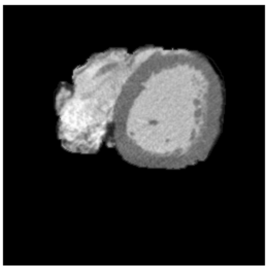

Fig.13 Extracted image (2)

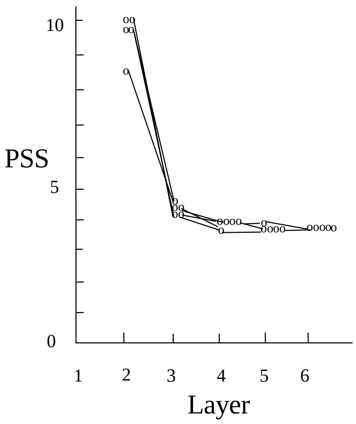

Fig.14 Variation of PSS in GMDH

4. Results of the medical image recognition by using the GMDH [2]

The GMDH was applied to the same recognition problem and the recognition results were compared with the results obtained using the revised GMDH-type neural network. Same five input variables, which were mean, standard deviation and variance, x and y positions were used in the input layer. Figure 14 shows the variation of PSS in the GMDH. The output images are shown in Fig.15 and 16. These images contain more regions not part of the heart than output images obtained using the revised GMDH-type neural network shown in Fig.4 and 10.

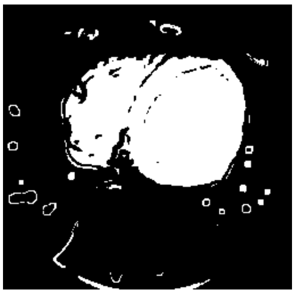

Fig.15 Output image of GMDH (1)

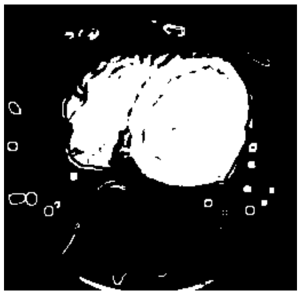

Fig.16 Output image of GMDH (2)

VI. CONCLUSION.

In this study, the revised GMDH-type neural network was applied to the medical image recognition. The revised GMDH-type neural network can automatically organize the optimum neural network architecture fitting the complexity of the medical images. Therefore, we can easily apply the revised GMDH-type neural network to the medical image recognition. It was shown that the revised GMDH-type neural network was very accurate and useful method for the medical image recognition of the heart.

REFERENCES

[1] Kondo T. and J.Ueno, Logistic GMDH-type Neural network and Its Application to identification of X-ray Film Characteristic Curve, *Journal of Advanced Computational Intelligence and Intelligent Informatics*, Voll.11, No.3, PP.312-318, 2007.

[2] Tamura H. and T.Kondo, Heuristics free group method of data handling algorithm of generating optimum partial polynomials with application to air pollution prediction, *Int. J. System Sci.*, Vol.11, No.9, pp.1095-1111, 1980.

[3] Farlow S.J. ed., *Self-organizing methods in modeling, GMDH-type algorithm*, Marcel Dekker, Inc., New York, 1984.

[4] Ivakhnenko A.G., Heuristic self-organization in problems of engineering cybernetics, *Automatica*, Vol.6, No.2, pp.207-219, 1970.

[5] Draper N.R. and Smith H., *Applied Regression Analysis*, John Wiley and Sons, New York, 1981.

The Fourteenth International Symposium on Artificial Life and Robotics 2009 (AROB 14th '09),
B-Con Plaza, Beppu, Oita, Japan, February 5 - 7, 2009

Modeling Artificial Neural Networks using a Visual Programming Paradigm

Kenneth J. Mackin

Dept of Information Systems, Tokyo University of Information Sciences
4-1 Onaridai, Wakaba-ku, Chiba, Japan
(Tel&Fax : 81-43-236-1329)
(mackin@rsch.tuis.ac.jp)

Abstract: The understanding of soft computing methodology often requires grasping abstract concepts or imagining complex interactions of large models over long computing cycles. But this can be difficult for students with weak background in mathematics, especially in the early stages of soft computing education. This paper introduces applying a visual programming paradigm as a tool for educational introduction to soft computing methods. For the visual programming paradigm, IntelligentPad proposed by Y. Tanaka is used. IntelligentPad defines a visual appearance to objects or classes, and allows users to operate and link different objects together using the mouse. This paper reports on using IntelligentPad to teach the basic mechanism of artificial neural networks. The proposed method was applied to 3rd year college students to verify the validity of the proposed teaching method.

Keywords: Visual Programming, IntelligentPad, Artificial neural networks

I. INTRODUCTION

Understanding of soft computing methodology often requires grasping abstract concepts or imagining complex interactions of large models over long computing cycles. But this can be difficult for students with weak background in mathematics, especially in the early stages of soft computing education.

This paper introduces applying a visual programming paradigm as a tool for educational introduction to soft computing methods. For the visual programming paradigm, IntelligentPad proposed by Y. Tanaka[1] is used. IntelligentPad defines a visual appearance to objects or classes, and allows users to operate and link different objects together using the mouse.

Past research on using IntelligentPad for programming education[2] has reported promising results. This paper proposes using IntelligentPad to teach the basic mechanism of artificial neural networks. The proposed method was applied to 3rd year college students to verify the validity of the proposed teaching method.

II. INTELLIGENTPAD

IntelligentPad[1] is a visual programming and runtime paradigm proposed by Y.Tanaka. IntelligentPad is based on an object-oriented programming design, and supports a Model-View-Controller (MVC) model for classes to allow objects to have a visual representation on the screen. This visual object is called a "pad". Public methods or fields are defined as "slots" in a pad. Users can connect slots between different pads to realize message passing between objects. Creation of pads, laying of pads, and connecting slots of pads can all be done by the user using only the mouse.

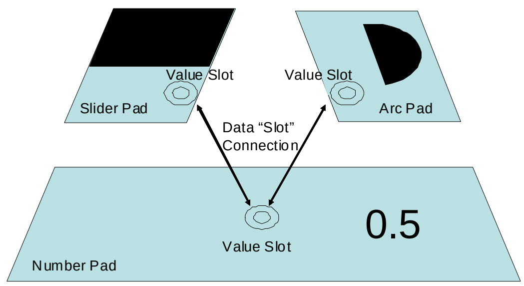

Fig.1. Slot connection of pads on IntelligentPad

III. ARTIFICIAL NEURAL NETWORKS ON INTELLIGENTPAD

In this research, IntelligentPad-Java provided by IntelligentPad Consortium[3] was used. IntelligentPad-Java is an IntelligentPad package implemented in Java, and can be run as either a stand-alone application or Web browser applet.

The educational goal was for the students to understand the basic mechanism of a) a single neuron model and b) a feed-forward neural network model (Fig.2). For the neuron's synapse function, a simple step function with variable threshold value was selected for the purpose of simplicity.

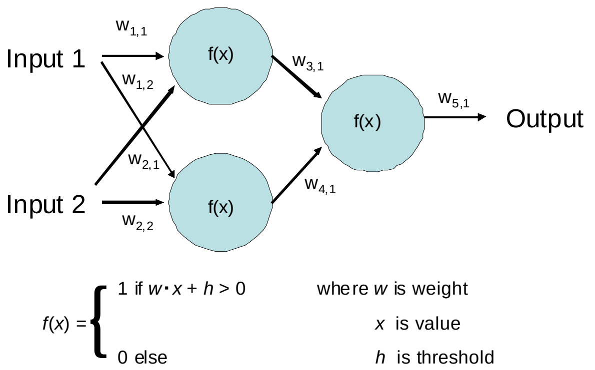

Fig.2. Feed-forward neural network model

The following different pads were provided to the students as basic building blocks of the neural network: number pad, arithmetic pad, comparison pad, switch pad, slider pad, range pad, and neuron pad.

A number pad is a class used to hold a single floating point numerical value. An arithmetic pad is a class that can add, subtract, multiply or divide 2 different numerical values and outputs the results. A comparison pad compares 2 different numerical values and outputs a whether the first input is equal, less than, or greater than the second input. A switch pad works as a toggle switch to display whether a value is either 0 or 1. A slider pad works as a bar or gauge to display a continuous range of values between 0 and 1. A range pad is used to normalize a specified range of values to a range of 0 and 1. The neuron pad takes 2 numerical input values and outputs 1 numerical value, providing the basic feed-forward calculation. The neuron pad also has a threshold slot for setting the synapse threshold.

By combining the provided pads and creating the correct connections between the pad slots, it is possible to create a visual representation of a single neuron model (Fig.3). Next by creating multiple copies of the single neuron and connecting the input and output slots of the neurons, a layered neural network can be created.

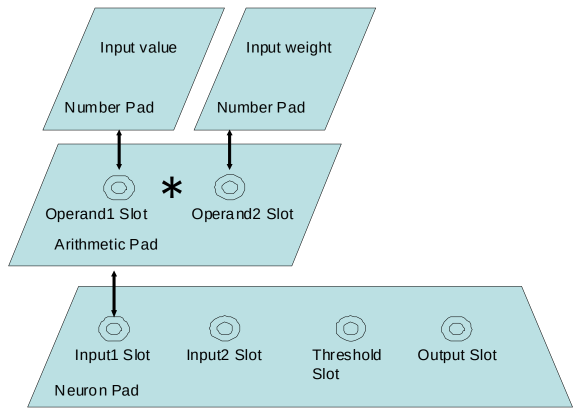

Fig.3. Neuron pad connection model

IV. APPLICATION RESULTS AND CONCLUSION

IntelligentPad-Java and the described pads were provided to 3rd year college students majoring in information systems, directly after a lecture on the mechanism of artificial neural networks. After a short explanation on how to use IntelligentPad, the students were given the task of 1) creating a visual representation of a single neuron and 2) creating a layered feed-forward neural network. With some help, all 13 participating students were able to create a running layered feed-forward neural network within 90 minutes (Fig.4).

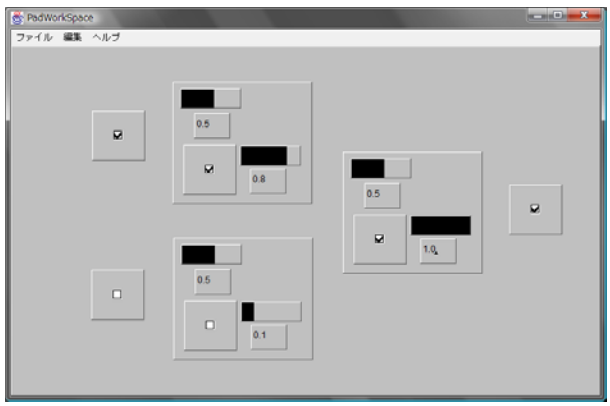

Fig.4. Example of layered network on IntelligentPad

This paper introduced applying a visual programming paradigm as a tool for educational introduction to soft computing methods. IntelligentPad

©ISAROB 2009

is a visual programming paradigm that defines a visual appearance to objects or classes, and allows users to operate and link different objects together using the mouse.

This paper proposed using IntelligentPad to teach the basic mechanism of artificial neural networks. The proposed method was applied to 3rd year college students. In the class, students were able to create a layered feed-forward neural network from basic classes, and greatly improved the students' understanding of the mechanism of artificial neural networks.

For future works, we will consider creating pads to implement the sigmoid function and realize back propagation using IntelligentPad. We also plan to use IntelligentPad for visually representing evolutionary computation methods, fuzzy logic, and other major soft computing algorithms.

REFERENCES

[1] Y. Tanaka (1996), IntelligentPad as meme media and its application to multimedia databases. Information and Software Technology, 38(3), pp.201-211

[2] T. Noguchi (2003), A Programming Learning Environment Using IntelligentPad System (in Japanese). Proceedings for Japanese Society for Engineering Education Annual Conference & Exposition

[3] IntelligentPad Consortium, http://pads.or.jp

The Fourteenth International Symposium on Artificial Life and Robotics 2009 (AROB 14th '09),
B-Con Plaza, Beppu, Oita, Japan, February 5 - 7, 2009

Neuro-based Olfactory Model for Artificial Organoleptic Tests

Zu Soh†, Toshio Tsuji†, Noboru Takiguchi††, and Hisao Ohtake†††

†Graduate School of Engineering, Hiroshima Univ., Hiroshima 739-8527, Japan
††Graduate School of Advanced Sciences of Matter, Hiroshima Univ., Hiroshima 739-8530, Japan
†††Graduate School of Engineering, Osaka Univ., Osaka 565-0871, Japan

Abstract

Recently, the demand for odor processing apparatus in the fragrance and food industries has increased. In this paper, we construct a neural network model of the olfactory system as basis for artificial organoleptic tests that combines possesses the advantages of both human sensory evaluation and machine olfaction. The simulation results indicate that the model can predict odor coding on the glomeruli by appropriately adjusting the parameters involved. Further, the model can simulate the feature extraction ability known *Attention*.

1 Introduction

As considerable evidence has been presented to show that odors have an effect on memory and emotions [1], the importance of odors has begun to be recognized beyond their role as components of flavor. For this reason, the demand for odor processing apparatus in the fragrance and food industries is increasing [2].

Two methods of odor assessment developed so far are the sensory evaluation method and machine olfaction [2]. Generally, the sensory evaluation method is employed because it is based on the characteristics of human perception, although, individual differences due to factors such as personal preference or physical condition can affect the evaluation results. Machine olfaction, in contrast, is an objective assessment method; nevertheless, it tends to ignore the nature of odor perception. Accordingly, a novel odor assessment method combining the advantages of both human sensory evaluation and machine olfaction making it suitable for artificial organoleptic tests is required. To develop such a method, it is first necessary to predict how odorant information is coded in the brain to obtain the perception characteristics of animals. The mechanisms of feature extraction from the neuro-coded odor information must then also be predicted.

Although the ideal scenario would be to analyze the human olfactory system, current biological knowledge regarding the coding manner of odorant information in the human brain remains limited. Given this restriction, the present study focuses on the olfactory system of mice.

An odor is a combination of more than 400,000 kinds of odorant molecules. Mice have approximately 1,000 kinds of odorant receptors, each of which is responsible for detecting a specific group of odorant molecules [3]. The outputs of the receptor neurons evoke an odor-specific activity pattern on glomeruli [4, 5]. As this activity pattern represents fundamental information for odor recognition, it is considered closely linked to the characteristics of perception. We constructed a neural network model [6] using biological data on glomerular activity patterns [5] as inputs, and attempted to simulate the perception characteristics of mice. The model also employed a feature extraction mechanism for *Attention* [7] in which the mice would focus on some of the important molecules in odors. The results of the computer simulation were compared with ones of behavioral experiments [7], and it was confirmed that the model could predict the discrimination ability of mice. However, the scope of our model was limited to odorants with known glomerular activity patterns.

In this paper, we report on the extension of the model to enable the prediction of glomerular activity patterns from odorant properties. For this purpose, 3-layered feed-forward neural network was added and trained by using a known biological data set. Predicted activity patterns were ued as the input of the model for further *Attention* processing. The simulation results were then examined through comparison with the odor discrimination rates obtained from behavioral experiments on mice.

©ISAROB 2009

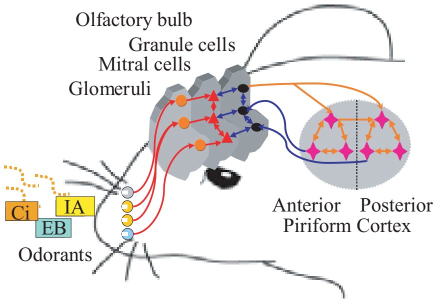

Figure 1: The olfactory system of mice.

2 Biological insight

2.1 Olfactory system of mice

Fig. 1 shows the basic structure of the olfactory system in mice, which consists of three parts: receptor neurons, the olfactory bulb and the piriform cortex. Receptor neurons that distributed on the surface of the nasal chamber express single receptor from among 1,000 different ones, and bind to specific odorants [3]. When odorant molecules bind to the receptor, its neuron is activated and sends signals to the olfactory bulb. The axons from the receptors that express the same gene terminate at the same point on the surface of the olfactory bulb [4]. The terminals of these axons form a small, round cluster called a glomerulus. A 2D map of glomerular distribution can be associated with receptor genes as well as odorants, and is thus called an odor map [4].

Besides the glomeruli, mitral cells and granule cells are the principal neurons in the olfactory bulb. Signals from the glomeruli are inputted to the mitral cells, which are interconnected via the excitatory synapse. The granule cells receive inputs from the mitral cells and send inhibitory signals back to them. In general, the olfactory bulb is considered to perform feature extraction [8].

The mitral cells transmit the signal to the pyramidal cells in the piriform cortex, which then transmit signals back to the granule cells in the olfactory bulb and indirectly inhibit the mitral cells. The piriform cortex is divided into the anterior piriform cortex (APC) and the posterior piriform cortex (PPC); the division of their functions remains slightly unclear. Generally, the piriform cortex is believed to be responsible for the identification of odors [9].

2.2 Attention mechanism in the olfactory system

Okuhara *et al.* [7] conducted a series of odor discrimination experiments on mice [7]. First, the mice

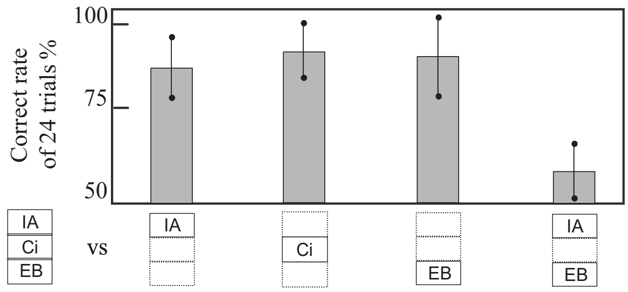

Figure 2: Results of the odor discrimination experiment.

were trained to select a rewarded odor, such as [IA, Ci, EB] composed of three types of odorant. They were then required to discriminate among other odors that contained elements in odor [IA, Ci, EB], such as [IA] or [IA, EB]. Fig. 2 outlines the results of the odor discrimination experiment performed with 10 mice, and indicates that most of them had difficulty in discriminating between [IA, EB] and [IA, Ci, EB]. This implies that they focused on a combination of the odorants [IA] and [EB] when learning the odor [IA, Ci, EB]. This mechanism is called *Attention*, and contributes significantly to the odor perception characteristics of mice as described above.

3 Model of the olfactory system of mice

3.1 Structure of the proposed model

Fig. 3 shows the structure of the proposed neural network model, which consists of three parts: odor reception, the olfactory bulb and the piriform cortex.

The odor reception model is a feed-forward neural network of 3 layers: which are the *preprocessing* layer ($l = 1$), the *odorant* layer ($l = 2$) and the *receptor* layer ($l = 3$). The neuron populations for each layer (${}^{l}N$) are ${}^{1}N = 80$, ${}^{2}N = 500$, and ${}^{3}N = 1,805$, respectively. The olfactory bulb model consists of the *Glomerular* layer ($l = 4$), the *Mitral* layer ($l = 5$), and the *Granule* layer ($l = 6$). The neuron populations in the olfactory bulb are ${}^{4}N = {}^{5}N = {}^{6}N = 1,805$, These populations were determined based on the actual number of glomeruli distributed on the olfactory bulb [10].

The piriform cortex model consists of an *APC* layer ($l = 7$) and a *PPC* layer ($l = 8$) corresponding to the anterior piriform cortex and the posterior piriform cortex, respectively. The neuron populations of the *APC* and the *PPC* layers are ${}^{7}N = 1,000$ and ${}^{8}N = 100$, respectively.

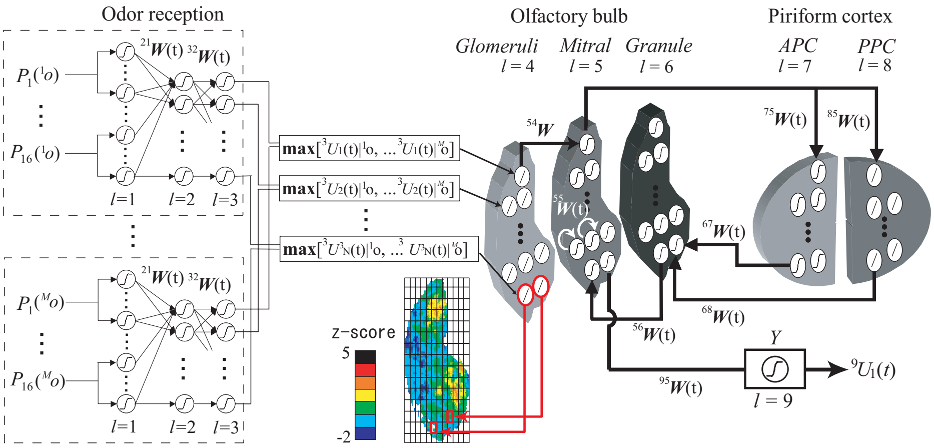

Figure 3: Structure of the proposed model. The activity pattern of glomeruli is cited from literature [5].

The connections between each layer in the olfactory bulb model and the piriform cortex model are set up based on the structure of the olfactory system described in Section 2.1, with the exception that the interconnections in each layer are not included in the model for simplification. In addition, a single neuron layer Y ($l = 9$) is artificially introduced as the output of the model.

The model takes the odorant properties as the input from the *preprocessing* layer. Since there are approximately 400,000 kinds of odorant (forming extremely high-dimensional information), it is impossible to input the odorant information to the model through binary coding. The properties of each odorant are therefore broken down into 16 numeric properties as listed by Johnson *et al.* [11] along with their corresponding activity patterns.

In order to normalize the properties with different units and orders, the *preprocessing* layer converts the value of the properties into activated neuron numbers. This method is introduced based on the concept of population coding [12]. The neurons in the *preprocessing* layer are divided into 16 groups, each of which receives a different kind of odorant property. The input to the neurons in the *preprocessing* layer is given by the following equation:

$$^1u_s(t) = P_i(^m o), \quad (s = (i-1)K + k, \ k = 1, 2...K), \quad (1)$$

where $^1u_s(t)$ is the input to the s^{th} neuron in the *preprocessing* layer ($l = 1$) at time step t, $^m o$ is the m^{th} odorant in odor O, P_i is the i^{th} numeric property of the odorant $^m o$, and K is the maximum number of neurons responsible for property P_i. The activities of the neurons are given by the following sigmoid function:

$$^1U_s(t) = \frac{1}{1 + \exp\{-^1\epsilon_s(^1u_s(t) - ^1\theta_s)\}}. \quad (2)$$

The outputs of sigmoid neurons in other layers are also calculated using the above equation. The threshold $^1\theta_s$ and the gradient $^1\epsilon_s$ of the sigmoid function are determined according to the corresponding property by the following equation:

$$^1\theta_s = k\frac{(P_{i,\max} - P_{i,\min})}{K}, \quad (3)$$

$$^1\epsilon_s = C_s\frac{(P_{i,\max} - P_{i,\min})}{K}, \quad (4)$$

where $P_{i,\max}$ and $P_{i,\min}$ are the maximum and minimum values of the property P_i in an odorant data set, and C_s is a constant.

The output of the *preprocessing* layer ($l = 1$) is inputted to the *odorant* layer ($l = 2$) through a connective weight matrix $^1\mathbf{W}(t)$. The input to the *odorant* layer is given by the following equation:

$$^2u_n(t) = \sum_s {}^{21}w_{ns}(t) \, ^1U_s(t), \quad (5)$$

where $^2u_n(t)$ is the input to the n^{th} neuron in the *odorant* layer, and $^1w_{ns}(t)$ is the connective weight between neuron units n and s, which is an element in the connective weight matrix $^{21}\mathbf{W}(t)$.

The output of the *odorant* layer is inputted to the *receptor* layer ($l = 3$) through $^{32}\mathbf{W}(t)$ in the same manner as the equation (5).

The output of the *receptor* layer ($l = 3$) is passed to the glomerular layer ($l = 4$). According to Lin *et al.* [13], the glomerular activity of an odorant mixture O can be represented by binary addition of the activities evoked by its odorant components. Thus, the input and output of the *Glomerular* layer is determined by the following equation:

$$^4u_e(t) = \max[^3U_r(t)|_{^1o} ... ^3U_r(t)|_{^M o}] \quad (6)$$

©ISAROB 2009

The output ${}^{4}U_e(t)$, which is calculated by equation (2), is an element in the activity pattern vector ${}^{4}U(t)$. Each element corresponds to a divided lattice of the activity patterns provided by Johnson *et al.* [5], as shown in Fig. 3.

The output of the *Glomerular* layer is input to the *Mitral* layer on a one-to-one basis. The detailed structure of the olfactory bulb and piriform cortex part is described in our previous paper [6], where the inputs and outputs of each layer are determined in the same manner as described above.

The inputs of the newly introduced Y $(l = 9)$ layer represent the output of the model. Its output is determined by the input from *Mitral* layer as the following equation:

$$ {}^{9}U_1(t) = \frac{\exp\{-{}^{9}\epsilon_1({}^{9}u_1(t) - {}^{9}\theta_1)\}}{1 + \exp\{-{}^{9}\epsilon_1({}^{9}u_1(t) - {}^{9}\theta_1)\}}. \quad (7) $$

To predict the glomerular activity patterns and perception characteristics affected by attention, the connective weights appearing in each equation must be appropriately adjusted. The next subsection describes the learning algorithm of the model.

3.2 Algorithm of the learning phase

The learning algorithm consists of 2 steps, whose details are described in this subsection.

3.2.1 The 1st step of the learning phase

In the 1st step, the connective weights ${}^{21}\mathbf{W}(t)$ and ${}^{32}\mathbf{W}(t)$ are adjusted for accurate prediction of the activity patterns for the *Glomerular* layer from the input odorants' properties as given by the training set. The connective weights are adjusted to minimize the error energy E:

$$ E = \frac{1}{2}\sum_{i}^{{}^{4}N} e_i = \frac{1}{2}\sum_{i}^{{}^{4}N}(U_i^4 - a_i)^2, \quad (8) $$

where e_i is the mean square error (MSE); U_i^4 is the output of the glomerular layer, and a_i is the activity of actual glomeruli in the i^{th} lattice. For the implementation of weight adjustment, the RPROP algorithm proposed by Riedmiller *et al.* [14] is utilized. This algorithm allows fast error convergence with a reasonable computer memory requirement. The connective weights are iteratively adjusted until a preset maximum iteration number is reached.

3.2.2 The 2nd step of the learning phase

In the 2st step, the connective weights in the olfactory bulb and piriform cortex are modulated based on the algorithm proposed in [6]. Since most of the computational functions of the olfactory system, especially the connection from the piriform cortex to the olfactory bulb, are not yet clearly understood, signal transduction or connective weight modulation are hypothesized based on the odor discrimination experiment outlined in Section 2.2 [7]. We assume that the connection from the piriform cortex to the olfactory bulb plays a role in extracting the most activated regions in the glomeruli. With regard to these assumptions, we propose a learning algorithm that consists of 3 steps outlined below.

In the 1st step, the connective weights ${}^{75}\mathbf{W}(t)$ and ${}^{67}\mathbf{W}(t)$ are modulated to subtract the background activity from the activated part of the *Mitral* layer using the following equation:

$$ {}^{75}W_{zb}(t{+}1) = \alpha^{75}W_{zb}(t) + \beta^{5}U_b(t)|_{^AO}{}^{7}U_z(t)|_{^AO}, \quad (9) $$
$$ {}^{67}W_{gz}(t{+}1) = \alpha^{67}W_{gz}(t) + \beta^{7}U_z(t)|_{^AO}{}^{5}U_b(t)|_{\text{back}}, \quad (10) $$

where α denotes the forgetting term, and β is the learning rate. As a result, when an odor A is input through the connective weights ${}^{75}W(t)$ and ${}^{67}W(t)$, the *Granule* layer can inhibit the background activity of the *Mitral* layer.

In the 2nd step, the most activated neurons in the *Glomerular* layer are extracted. The connective weights between the *Mitral* layer and the *PPC* layer are assumed to form a competitive system, and the corresponding connective weights are adjusted according to Amari *et al.* [15].

In the 3rd step, the activity pattern of the *Mitral* layer resulting from the 2nd step is memorized by adjusting the connective weights ${}^{95}\mathbf{W}(t)$ as in the following equation:

$$ {}^{95}W_{1b}(t) = {}^{5}U_b(t)|_{^AO}. \quad (11) $$

This adjustment enables the model to compare the features of the memorized odor to the inputted odors using the comparison algorithm described in the next subsection.

3.3 Comparison algorithm

In the comparison phase, an arbitrary odor B is inputted to the model. The input to the Y layer can be calculated as follows:

$$ \begin{aligned} {}^{9}u_(t)|_{^BO} &= \sum_b {}^{95}W_{1b}(t){}^{5}U_b(t)|_{^BO} \\ &= \sum_b {}^{5}U_b(t)|_{^AO}{}^{5}U_b(t)|_{^BO}. \quad (12) \end{aligned} $$

©ISAROB 2009

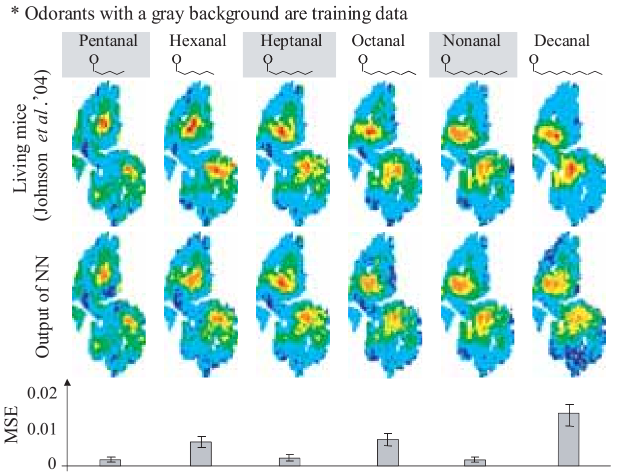

Figure 4: Simulation results of aldehydes.

Accordingly, calculating the input to the Y layer is equivalent to calculating the correlation between the current output ${}^5U_b(t)|_{B_O}$ and the memorized output ${}^5U_b(t)|_{A_O}$ of the $Mitral$ layer. The correlation is then converted to an index of dissimilarity by equation (7). It can be assumed that the mice tend to make wrong decisions when the outputs of the $Mitral$ layer are similar. Accordingly, the output of the model is considered to correspond with the results of the odor discrimination experiments on mice [7].

4 Simulation

This section describes the simulations performed based on the algorithm described in the previous section.

4.1 The 1st step of the simulation

First, data on 70 odorants were selected from the 365 odorants provided by Johnson *et al.* [11] as a training data set. Then, 3 odorants with identical structures but different carbon numbers were chosen and added to the set.

Fig. 4 shows the outputs of the model after the training is completed. In Fig. 4, the molecules in the uppermost row are the inputted odorants followed by the actual activity patterns [5], the output of the model, and the a graph of the mean square errors (MSEs). The odorants with a gray background are included in the training set, while those with no background color are untrained odorants. This figure indicates that the model successfully predicted the activity patterns in the training data set with an prediction error MSE of below 0.002. The predicted activity patterns of untrained odorants were also close to the actual activity patterns with MSEs ranging from about

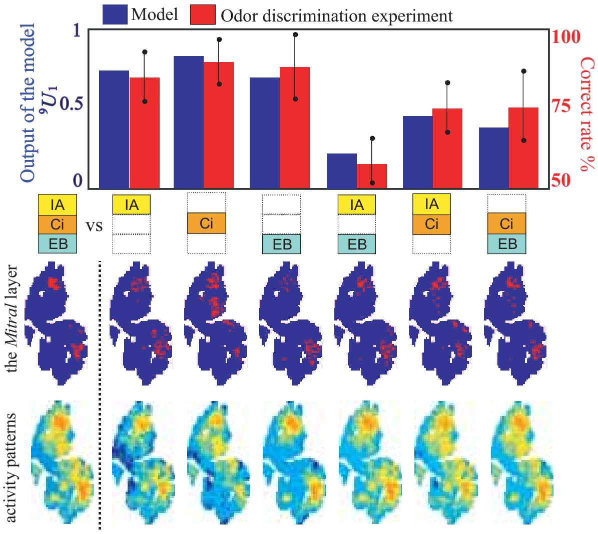

Figure 5: Comparison between the results of the behavior experiments.

0.007 to 0.015. Consequently, the model is capable of predicting the tendency for the activated parts of glomeruli to shift continuously along with the carbon number [5].

4.2 2nd step of the simulation

In the learning phase, an odor [IA, Ci, EB], representing an odorant mixture composed of isoamyl acetate, citral, and ethyl butyrate, is input to the proposed model. The connective weights are then adjusted according to the learning algorithm described in Section 3.2.2. The initial values of the connective weights are determined by uniform random values ranging between -10^{-5} and 10^{-5}.

After the learning phase, 6 different odors [IA], [EB], [Ci], [IA, EB], [IA, Ci], and [Ci, EB] are input to the model. Then, the output of the neuron in the Y layer is compared with the correct rates in odor discrimination experiments on the mice. In this step, the connective weights are fixed on the values determined in the 1st step of the simulation.

The outputs of the *Glomerular* layer to each odor are shown in the bottom row in Fig. 5. The outputs of the $Mitral$ layer after the 2nd learning phase are shown in the middle row, and the outputs of the neurons in the Y layer are plotted at the top. The discrimination rates obtained from the odor discrimination experiment on the mice are also plotted beside the output of the Y layer.

Comparing the activity patterns of the *Glomerular* layer to those of the $Mitral$ layer shows that the activated region becomes narrow, but its activity becomes stronger, which means that most activated regions in

©ISAROB 2009

the *Glomerular* layer were extracted. Fig. 5 indicates a similar tendency between the correct rates and the output of the neuron in the Y layer; the higher the output, the higher the correct rate. From these results, we can conclude that the model is capable of account for the perception characteristics of mice to a certain extent through the assumed *Attention* mechanism.

5 Conclusion

In this paper, we propose a neural network model of the olfactory system of mice. Utilizing this model, we tried to predict the activity pattern in glomeruli evoked by odorants. The simulation results indicated that the model was capable of predicting the activity patterns of untrained odors with different carbon numbers, and showed consistency with those of odor discrimination experiments on mice. This ability to predict perception characteristics makes the model suitable as a basis for artificial organoleptic tests.

However, odors in nature are composed of odorants in different concentrations, which is not accounted for in the proposed model. Future studies must therefore include the odor coding manner for different concentrations. In addition, since the simulations were performed only with on odorants [IA], [Ci], and [EB] using limited experimental data, further behavioral experiments and simulation need to be performed on other odorants to verify the ability of the model.

Acknowledgments.

This work was partially supported by the 21st Century COE Program of JSPS (the Japan Society for the Promotion of Science) on *Hyper Human Technology toward the 21st Century Industrial Revolution.*

References

[1] R.S. Herz and T. Engen, "Odor memory: review and analysis," *Psychonomic Bulletin and Review*, Vol. 3, No. 3, pp. 300–313, 1996.

[2] R. Gutierrez-Osuna, "Pattern Analysis for Machine Olfaction: A Review," *IEEE Sensors Journal*, Vol. 2, No. 3, pp. 189–202, 2002.

[3] L. Buck and R. Axel "A novel multigene family may encode odorant receptors: a molecular basis for odor recognition," *Cell*, Vol. 65, pp.175–187, 1991.

[4] K. Mori and Y. Yoshihara "Molecular recognition and olfactory processing in the mammalian olfactory system," *Progress in Neurobiology*, Vol. 45, pp. 585–619, 1995.

[5] B.A. Johnson and M. Leon "Modular glomerular representations of odorants in the rat olfactory bulb and the effects of stimulus concentration," *The Journal of Comparative Neurology*, Vol. 422, pp. 496–509.

[6] Z. Soh, T. Tsuji, N. Takiguchi, H. Ohtake "A neural network model of the olfactory system of mice Simulated the tendency of attention behavior," *The 13th International Symposium on Artificial Life and Robotics*, pp. 537–542, 2008.

[7] K. Okuhara and T. Nakamura "Explore algorithms in olfactory system of mice," *Software Biology*, Vol.3, pp.20–25, 2005. (in Japanese)

[8] O. Hoshino, Y. Kashimori, and T. Kambara, "Feature extraction from mixed odor stimuli based on spatio-temporalrepresentation of odors in olfactory bulb," *International Conference on Neural Networks*, vol. 1, pp. 344–349, 1997.

[9] D.A. Wilson, "Receptive Fields in the Rat Piriform Cortex," *Chemical Senses*, Vol. 26, No. 5, pp. 577–584, 2001.

[10] B.A. Johnson, H. Farahbod, Z. Xu "Local and global chemotopic organization: general features of the glomerular representations of aliphatic odorants differing in carbon number," *The Journal of Comparative Neurology*, Vol. 480, No. 2, pp. 234–249, 2004.

[11] M. Leon, B. A. Johnson, "Glomerular Response Archive," http://leonserver.bio.uci.edu/.

[12] A.P. Georgopoulos, A.B. Schwartz, R.E. Kettner, "Neuronal population coding of movement direction," *Science*, Vol. 233, Issue. 4771, pp. 1416–1419, 1986.

[13] D.Y. Lin, S.D. Shea, L.C. Katz, "Representation of natural stimuli in the rodent main olfactory bulb," *Neuron*, Vol.50, No. 6, pp. 816–818, 2006.

[14] M. Riedmiller and H. Braun, "A direct adaptive method for faster backpropagation learning: The RPROP algorithm," *Proceedings of the IEEE International Conference on Neural Networks San Francisco*, pp. 586–591, 1993.

[15] S. Amari, M.A. Arbib, "Computation and cooperation in neural nets," *Systems Neuroscience, Academic Press*, pp. 67–117, 1977.

©ISAROB 2009

Revised GMDH-type neural network algorithm self-selecting optimum neural network architecture

C. Kondo[1] and T. Kondo[2]

[1] Graduate school of Design, Kyushu Univ., 4-9-1shiohara minamiku Fukuoka 815-8540, Japan
[2] Graduate School of Health Sci., The Univ. of Tokushima, 3-l8-15 Kuramoto-cho Tokushima 770-8509, Japan
([2] kondo@medsci.tokushima-u.ac.jp)

***Abstract*:** In this study, the revised Group Method of Data Handling (GMDH)-type neural network algorithm self-selecting the optimum neural network architecture is applied to the identification of the nonlinear system. In this algorithm, the optimum neural network architecture is automatically organized using two kinds of the neuron architectures such as the polynomial and sigmoid function neurons. Many combinations of the input variables, in which high order effects of the input variables are contained, are generated using the polynomial neurons and useful combinations are selected using Prediction Sum of Squares (PSS) criterion. These calculations are iterated and the multi-layered architecture is organized. Furthermore, the structural parameters such as the number of layers, the number of neurons in the hidden layers and the useful input variables are automatically selected so as to minimize the prediction error criterion defined as PSS.

***Keywords*:** GMDH, Neural network, Medical image recognition

I. INTRODUCTION

The GMDH-type neural networks [1], [2] are automatically organized by using the heuristic self-organization method [3]. In the GMDH-type neural networks, the structural parameters such as the number of layers, the number of neurons in each layer, useful input variables and optimum neuron architectures are automatically determined. Furthermore, many types of neurons such as polynomial type, sigmoid function type and radial basis function type neurons, are used for organizing neural network architecture and therefore many types of nonlinear systems can be identified by the GMDH-type neural networks.

In this study, the revised GMDH-type neural network [1] is applied to the nonlinear system identification. In the revised GMDH-type neural network, the polynomial type and the sigmoid function type neurons are used for organizing the neural network architecture. A lot of complex nonlinear combinations of the input variables fitting the complexity of the nonlinear system are generated by using the polynomial type neurons and only useful combinations of the input variables are selected for organizing the neural network architecture. In the output layer, the sigmoid function type neurons are used for organizing the neural network and the output values of the neural network become between zero and one. It is shown that the revised GMDH-type neural network is accurate and useful method for the nonlinear system identification.

II. REVISED GMDH-TYPE NEURAL NETWRK ALGORITHM

In the conventional GMDH-type neural network [2], following neuron architectures are used for organizing neural network to fit the complexity of the nonlinear system.

1) First type neuron

Σ: (Nonlinear function)

$$z_k= w_1u_i+w_2u_j+w_3u_iu_j+w_4u_i^2+w_5u_j^2+w_6u_i^3+w_7u_i^2u_j +w_8u_iu_j^2+w_9u_j^3 - w_0\theta_1 \quad (1)$$

f : (Nonlinear function)

$$y_k= 1 / (1+exp (- z_k)) \quad (2)$$

2) Second type neuron

Σ: (Nonlinear function)

$$z_k= w_1u_i+w_2u_j+w_3u_iu_j+w_4u_i^2+w_5u_j^2+w_6u_i^3+w_7u_i^2u_j +w_8u_iu_j^2+w_9u_j^3 - w_0\theta_1 \quad (3)$$

f : (Linear function)

$$y_k= z_k \quad (4)$$

3) Third type neuron

Σ: (Linear function)

$$z_k= w_1u_1+w_2u_2+w_3u_3+ \cdots +w_ru_r - w_0\theta_1 \quad (r<p) \quad (5)$$

f : (Nonlinear function)

$$y_k= 1 / (1+exp (- z_k)) \quad (6)$$

4) Fourth type neuron

Σ: (Linear function)

$$z_k= w_1u_1+w_2u_2+w_3u_3+ \cdots +w_ru_r - w_0\theta_1 \quad (r<p) \quad (7)$$

f : (Linear function)

$$y_k= z_k \quad (8)$$

©ISAROB 2009

5) Fifth type neuron

$\sum$: (Nonlinear function)

$$z_k= w_1u_i+w_2u_j+w_3u_iu_j+w_4u_i^2+w_5u_j^2+w_6u_i^3+w_7u_i^2u_j+w_8u_iu_j^2+w_9u_j^3 - w_0\theta_1 \quad (9)$$

f : (Nonlinear function)

$$y_k= exp\ (- z_k^2) \quad (10)$$

6) Sixth type neuron

$\sum$: (Linear function)

$$z_k= w_1u_1+w_2u_2+w_3u_3+ \cdots +w_ru_r - w_0\theta_1 \quad (r<p) \quad (11)$$

f : (Nonlinear function)

$$y_k= exp\ (- z_k^2) \quad (12)$$

7) Seventh type neuron

$\sum$: (Linear function)

$$z_k= w_1u_1+w_2u_2+w_3u_3+ \cdots +w_ru_r - w_0\theta_1 \quad (r<p) \quad (13)$$

f : (Nonlinear function)

$$y_k= a_0+a_1z_k+a_2z_k^2+ \cdots +a_mz_k^m \quad (14)$$

Here, $\theta_1=1$ and w_i $(i=0,1,2,\cdots)$ are weights between the neurons. The optimum neuron architectures fitting the complexity of the nonlinear system are automatically selected by using the PSS [4]. Therefore, many kinds of nonlinear systems can be automatically identified by using the conventional GMDH-type neural network.

In the revised GMDH-type neural network, many kinds of nonlinear combinations of the input variables are generated by using the polynomial type neurons and only useful nonlinear combinations of the input variables are selected. Optimum neural network architectures are organized by using selected useful combinations of the input variables.

The revised GMDH-type neural network is shown in Fig.1. Here, nonlinear function g_i is described by the following Kolmogorov-Gabor polynomial:

$$g_i\,(x_1,x_2,\cdots,x_p)= a_0+\sum_i a_ix_i+\sum_i\sum_j a_{ij}x_ix_j+ \cdots \quad (15)$$

This nonlinear function is automatically organized by using the second type neuron of the conventional GMDH-type neural network. The architectures of the revised GMDH-type neural network is produced as follows:

First, the architecture of the first layer is organized.

1. The first layer

$$u_j=x_j \qquad (j=1,2,\cdots,p) \quad (16)$$

where x_j $(j=1,2,\cdots,p)$ are the input variables of the system, and p is the number of input variables. In the first layer, input variables are set to the output variables.

2. The second layer

Many combinations of two variables (u_i,u_j) are generated. For each combination, the neuron architecture is described by the following equations:

$\sum$: (Nonlinear function)

$$z_k= w_1u_i+w_2u_j+w_3u_iu_j+w_4u_i^2+w_5u_j^2+w_6u_i^3+w_7u_i^2u_j+w_8u_iu_j^2+w_9u_j^3 - w_0\theta_1 \quad (17)$$

f : (Linear function)

$$y_k= z_k \quad (18)$$

where $\theta_1 =1$ and w_i $(i=0,1,2,\cdots,9)$ are weights between the first and second layer. This neuron is equal to the second type neuron of the conventional GMDH-type neural network. The weights w_i $(i=0,1,2,\cdots,9)$ are estimated by using the revised regression analysis [5]. This procedure is as follows:

First, the values of z_k are calculated by using the following equation:

$$z_k=log_e(\phi'/(1-\phi')) \quad (19)$$

where ϕ' is the normalized output variable. Then the weights w_i $(i=0,1,2,\cdots,9)$ are estimated by using the stepwise regression analysis [5] which selects useful input variables by using the PSS[4]. Therefore, only useful terms in (17) are selected and neuron architecture can be organized by these selected useful terms.

From these generated neurons, L neurons which minimize the PSS are selected. The output values (y_k) of L selected neurons are set to the input values of the neurons in the third layer.

3. The third and succeeding layers

In the third and succeeding layers, the same computation of the second layer is continued until the PSS values of L neurons are not decreased. When the iterative computation is terminated, the following calculation of the output layer is carried out.

4. The output layer

In the output layer, the output values of the neural network are calculated from z_k as follows:

$$\phi =1/(1+exp(-z_k)) \quad (20)$$

So, in the output layer, the neuron architecture becomes as follows:

$\sum$: (Nonlinear function)

$$z_k= w_1u_i+w_2u_j+w_3u_iu_j+w_4u_i^2+w_5u_j^2+w_6u_i^3+w_7u_i^2u_j+w_8u_iu_j^2+w_9u_j^3 - w_0\theta_1 \quad (21)$$

f : (Nonlinear function)

$$\phi =1/(1+exp(-z_k)) \quad (22)$$

This neuron architecture is the same of the first type neuron of the conventional GMDH-type neural network. At last, the complete neural network architecture is produced by selected neurons in each layer.

By using above procedures, the revised GMDH-type neural network can be organized.

©ISAROB 2009

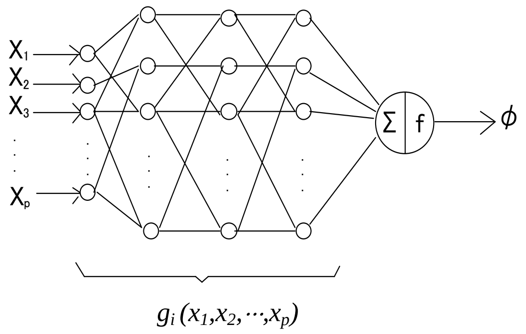

Σ : (Nonlinear function)

$z = \sum w_i g_i (x_1,x_2,\cdots,x_p)$

f : (Nonlinear function)

$\phi = 1 / (1+exp(-z))$

Fig.1 Architecture of revised GMDH-type neural network [1]

III. APPLICTION TO NONLINEAR SYSTEM IDENTIFICATION

Nonlinear system is assumed to be described by the following equations:

$$\phi = f_1 (x_1, x_2, x_3) / f_2 (x_1, x_2, x_3)+\varepsilon \quad (23)$$

$$f_1 (x_1, x_2, x_3)=1.0+2.0\, x_1^2 x_2+3.0\, x_2^2 x_3 \quad (24)$$

$$f_2 (x_1, x, x_3)=1.0+2.0exp(x_1)+3.0exp(x_1x_2)+4.0exp(x_3) \quad (25)$$

Here, ϕ is output variable and $x_1 \sim x_3$ are input variables and ε is Gaussian white noise which is N(0, 0.005^2). An additional input, x_4, is added as input variable of neural network to check that revised GMDH-type neural network can detect and eliminate useless input variables. Neural network is organized by twenty training data. Twenty other data are used to check prediction and generalization ability.

1. Identification results of revised GMDH-type neural network

A. Input variables

Four input variables were used, but useless input variable x_4 was automatically eliminated.

B. Number of selected neurons in each layer

Four neurons were selected in each hidden layer.

C. Variation of PSS

Variation of PSS is shown in Fig.2. PSS values converged at the fifth layer.

D. Architecture of neural network

Calculation of revised GMDH-type neural network was terminated at the fifth layer because PSS values were not decreased. Five layered neural network architecture was organized. The first layer is input layer and the second, the third, the fourth layer are hidden layers and the fifth layer is output layer.

E. Estimation accuracy

Estimation accuracy was evaluated by the following equation:

$$J_1 = \frac{1}{20}\sum_{i=1}^{20}\left|\phi_i - \phi_i^*\right| \quad (26)$$

where ϕ_i $(i=1,2,\cdots,20)$ are actual values with Gaussian white noise ε and ϕ_i^* $(i=1,2,\cdots,20)$ are estimated values by revised GMDH-type neural network. ϕ_i $(i=1,2,\cdots,20)$ were used to organize revised GMDH-type neural network. Value of J_1 is shown in Table1. In this table, Revised GMDH-type NN shows revised GMDH-type neural network developed in this paper and GMDH shows conventional GMDH algorithm.

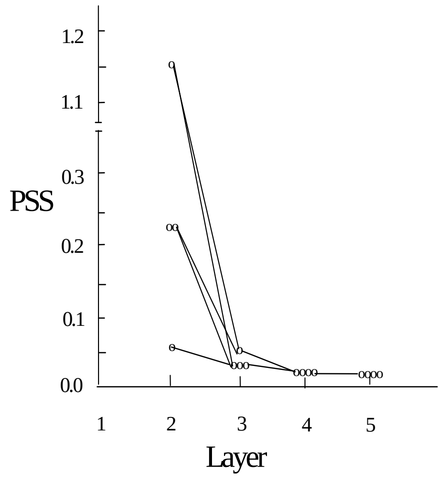

Fig.2 Variation of PSS in revised GMDH-type neural network

Table 1 Identification results of two methods

Method	J1	J2	Layer
Revised GMDH-type NN	0.02274	0.02942	5
GMDH	0.04094	0.03829	5

F. Prediction accuracy

Prediction accuracy was evaluated by using the following equation:

$$J_2 = \frac{1}{20}\sum_{i=21}^{40}\left|\phi_i - \phi_i^*\right| \quad (27)$$

where ϕ_i $(i=21,22,\cdots,40)$ are actual values with Gaussian white noise ε and ϕ_i^* $(i=21,22,\cdots,40)$ are predicted values by revised GMDH-type neural network.

ϕ_i *(i =21,22,···,40)* were not used to organize revised GMDH-type neural network and were used to check generalization ability. Value of J_2 is shown in Table1 and is very small. From this prediction result, we can see that revised GMDH-type neural network do not overfit training data and have good generalization ability.

G. Estimated and predicted values

Estimated and predicted values of ϕ by revised GMDH-type neural network are shown in Fig.3. Estimated values are shown for the data points between the first and 20-th data entities and predicted values are shown for the data points between the 21-th and 40-th data entities. We can see that estimated and predicted values are accurate.

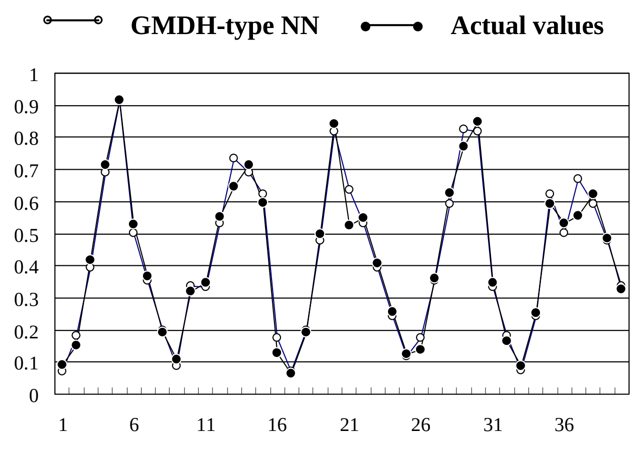

Fig.3 Estimated and predicted values by revised GMDH-type neural network

2. Identification Results of GMDH

Identification results of GMDH algorithm are shown as follows:

Four input variables were used, but again useless input variable x_4 was automatically eliminated. Four intermediate variables were selected in each selection layer. Variation of PSS is shown in Fig.4. PSS converged at the fifth layer. Calculation of GMDH converged at the fifth layer and neurons of the fifth layer had the minimum PSS value. Five layered polynomial network architecture was organized. The first layer is input layer and the second, the third and the fourth layer are hidden layers and the fifth layer is output layer. Estimation accuracy was evaluated by Eq.(26) and value of J_1 is shown in Table1. Prediction accuracy was evaluated by Eq.(27) and value of J_2 is shown in Table1.

VI. CONCLUSION

In this paper, a revised GMDH-type neural network algorithm self-selecting optimum neural network architecture was applied to the nonlinear system identification. In this algorithm, optimum neural network architecture is automatically organized using the polynomial and sigmoid function type neurons. It was shown that revised GMDH-type neural network algorithm was a useful method for the nonlinear system identification.

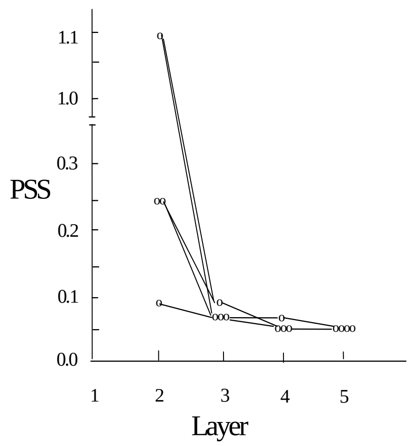

Fig.4 Variation of PSS in GMDH

REFERENCES

[1] Kondo T. and J.Ueno, Logistic GMDH-type Neural network and Its Application to identification of X-ray Film Characteristic Curve, *Journal of Advanced Computational Intelligence and Intelligent Informatics*, Voll.11, No.3, PP.312-318, 2007.

[2]. Kondo T., GMDH neural network algorithm using the heuristic self-organization method and its application to the pattern identification problem, *Proc. of the 37th SICE Annual Conference*, pp.1143-1148,1998.

[3] Ivakhnenko A.G., Heuristic self-organization in problems of engineering cybernetics, *Automatica*, Vo.6, No.2, pp.207-219, 1970.

[4] Tamura H. and T.Kondo, Heuristics free group method of data handling algorithm of generating optimum partial polynomials with application to air pollution prediction, *Int. J. System Sci.*, Vol.11, No.9, pp.1095-1111, 1980.

[5] Draper N.R. and H.Smith, *Applied Regression Analysis*, John Wiley and Sons, New York, 1981.

©ISAROB 2009

PHEROMONE-ORIENTED TRANSMISSION FOR LOAD-BALANCED DATA GATHERING IN WIRELESS SENSOR NETWORKS

Eisuke Orito, Akihide Utani, and Hisao Yamamoto
Faculty of Knowledge Engineering
Musashi Institute of Technology
1-28-1, Tamazutsumi, Setagaya-ku, Tokyo, 158-8557 Japan
{ utani; yamamoto }@si.musashi-tech.ac.jp

Abstract. *In large-scale wireless sensor networks, hundreds or thousands of micro-sensor nodes with such resource limitations as battery capacity, memory, CPU, and communication capacity are deployed in an observation area and used to monitor and gather information of environments. Therefore, a scalable, efficient, and load-balanced data gathering method is needed to prolong the lifetime of wireless sensor networks. This study proposes a novel method for the long-term operation of wireless sensor networks, named the pheromone-oriented transmission method. In the pheromone-oriented transmission method, the load of each sensor node is autonomously balanced. We evaluate the proposed method by computer simulations and discuss its development potential. In simulation experiments, the performance of the proposed method is investigated in detail to verify its effectiveness.*
Keywords: Large scale wireless sensor networks, Multiple sinks, Load balancing, Ant-based routing algorithms

1. Introduction

There is growing expectation for wireless sensor networks as a means of realizing many applications, such as natural environmental monitoring, environmental control in office buildings and factories, object tracking, and precision agriculture. In large-scale wireless sensor networks, hundreds or thousands of micro-sensor nodes with such resource limitations as battery capacity, memory, CPU, and communication capacity are deployed in an observation area and used to monitor and gather information of environments. Therefore, a scalable, efficient, and load-balanced data gathering method is needed to prolong the lifetime of wireless sensor networks. The ant-based routing algorithms[1] have attracted attention as algorithms for saving energy consumption because they are more scalable and efficient than other conventional routing algorithms. In previous studies, we proposed an Advanced Ant-based Routing (AAR) algorithm[2], which is more scalable and efficient than conventional ant-based routing algorithms. This study proposes an AAR-inspired novel method for the long-term operation of wireless sensor networks, named the Pheromone-Oriented Transmission (POT) method. In the POT method, the load of each sensor node is autonomously balanced. We evaluate the proposed POT method by computer simulations and discuss its development potential. In simulation experiments, the performance of the proposed POT method is investigated in detail to verify its effectiveness.

2. Pheromone-Oriented Transmission and Experimental Results

The POT method is a novel method that adaptively reduces the load on load-concentrated nodes and facilitates the long-term operation of wireless sensor networks. The routing table of each node is composed of the pheromone value of every neighbor node. In the POT method, each node determines a relay node of sensing data based on the pheromone value updated by considering the residual energy of neighbor nodes. Consequently, the destination (sink) node and the route to the sink node are determined. The conditions of simulation, which were used in the experiments performed, are shown in Table 1. The routes used by applying the POT method are shown in Fig.1. Of the 2,000 sensing data transmissions from the evaluation node, the routes in (1) were used 1 to 300 times and those in (2) 1 to 2,000 times. The load-balanced data transmissions are achieved. In Fig.2, the transition of the delivery ratio from a total of 20 nodes randomly selected to sink nodes is shown and the lifetime of wireless sensor networks is compared, where the Minimum Route Transmission (MRT) method in the figure is general data transmission method by the shortest route and the Modified Uniform Ant Algorithm (MUAA) is a promising ant-based routing algorithm[1]. From the results, it can be confirmed that the POT method is effective for the long-term operation of wireless sensor networks.

©ISAROB 2009

Table1 Conditions of simulation

Simulation size	*2,400 m × 2,400 m*
The number of sensor nodes	*1,000*
Range of radio wave	*150 m*
The number of sink nodes	*2*

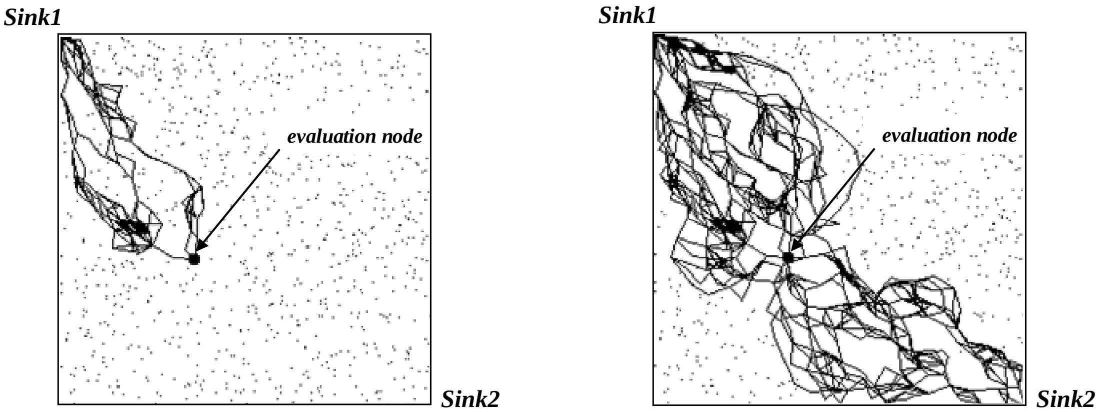

(a) 1 to 300 times (b) 1 to 2,000 times

Fig.1 Routes used by applying the POT method

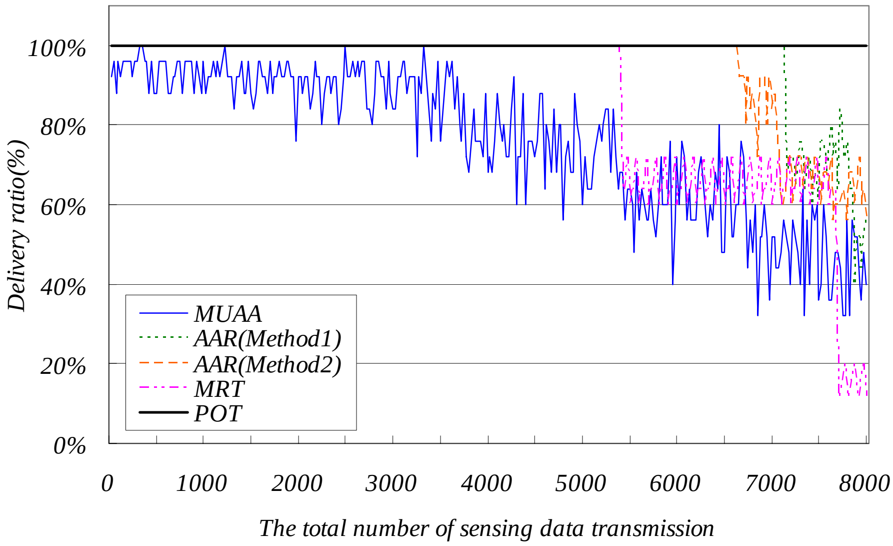

Fig.2 Transition of delivery ratio

3. Conclusions

In this paper, a novel method that adaptively reduces the load on load-concentrated nodes and facilitates the long-term operation of wireless sensor networks, named the Pheromone-Oriented Transmission (POT) method, has been proposed. Through experimental results, it has been confirmed that the proposed POT method has the development potential as a promising method for the long-term operation of wireless sensor networks.

REFERENCES

[1]Ohtaki Y, Wakamiya N, Murata M, Imase M (2006), Scalable and efficient ant-based routing algorithm for ad-hoc networks. IEICE Trans. Commun. E89-B(4): 1231-1238

[2]Utani A, Orito E, Kumamoto A, Yamamoto H (2008), An advanced ant-based routing algorithm for large scale mobile ad-hoc sensor networks (in Japanese). Trans. SICE 44(4): 351-360

A STUDY ON OBJECT OBSERVATION BY LARGE-SCALE WIRELESS SENSOR NETWORK AND AUTONOMOUS MOBILE ROBOT

Kakeru Matsumoto, Akihide Utani, and Hisao Yamamoto
Faculty of Knowledge Engineering
Musashi Institute of Technology
1-28-1, Tamazutsumi, Setagaya-ku, Tokyo, 158-8557 Japan
{ utani; yamamoto }@si.musashi-tech.ac.jp

Abstract. *This paper proposes a new system for object observation by a large-scale wireless sensor network and an autonomous mobile robot, named the Network-Robot system (N-R system) for object observation. In the proposed N-R system, a large-scale wireless sensor network composed of sensor nodes limited resources learns the appearance points of objects and appearance frequency at each point. An autonomous mobile robot with a highly efficient camera obtains learning results from the wireless sensor network and moves to a high point of appearance frequency of objects. In the proposed N-R system, an autonomous mobile robot measures the status of objects in detail at the appearance point. We evaluate the proposed N-R system by computer simulations and discuss its development potential. In simulation experiments, the performance of the proposed N-R system is investigated in detail to verify its effectiveness.*

Keywords: Wireless sensor nodes, Autonomous mobile robot, Large-scale sensor network, Object observation

1. Introduction

Wireless sensor networks have attracted a significant amount of interest from many researchers because they have great potential as a means of obtaining information of various environments remotely[1],[2]. Wireless sensor networks have a wide range of applications, such as environmental monitoring, environmental control, and object tracking[3],[4]. In large-scale wireless sensor networks, hundreds or thousands of sensor nodes are deployed in an observation area and used to monitor and gather information of environments. Each sensor node consists of a simplified sensing function to perceive the appearance of objects, a limited information processing function, and a limited wireless communication function, and operates on a resource of a limited power-supply capacity such as a battery. This paper proposes a new system for object observation by a large-scale wireless sensor network and an autonomous mobile robot, named the Network-Robot system (N-R system). In the proposed N-R system, a large-scale wireless sensor network composed of sensor nodes limited resources learns the appearance points of objects and appearance frequency at each point. An autonomous mobile robot with a highly efficient camera obtains learning results from the wireless sensor network and moves to a high point of appearance frequency of objects. In the proposed N-R system, an autonomous mobile robot measures the status of objects in detail at the appearance point. We evaluate the proposed N-R system by computer simulations and discuss its development potential. In simulation experiments, the performance of the proposed N-R system is investigated in detail to verify its effectiveness.

2. Network-Robot System and Experimental Results

The proposed N-R system consists of the following Phase I and Phase II. In Phase I, a large-scale wireless sensor network composed of sensor nodes limited resources learns the appearance points of objects and appearance frequency at each point. The learning algorithm is based on the Advanced Ant-based Routing (AAR) algorithm[5]. In Phase II, an autonomous mobile robot with a highly efficient camera obtains learning results from the large-scale wireless sensor network and moves to a high point of appearance frequency of objects. As Phase II, we show the results of the pattern that an autonomous mobile robot moves to the highest point of appearance frequency of objects after each learning result from all sensor nodes was gathered.

©ISAROB 2009

The conditions of simulation, which were used in the experiments performed, are shown in Table 1. The simulation configuration is illustrated in Fig.1. Experimental results on average successful ratio of object observation and total energy consumption through a large-scale wireless sensor network are reported in Fig.2. By using the proposed N-R system, the object observation was achieved with acceptable accuracy and stable energy consumption.

Table 1 Conditions of simulation

Simulation size	*400m ✕ 400m*
The number of sensor nodes	*1000*
Sensing Range	*10m*
Range of radio wave	*25m*
Packet size	*10byte*

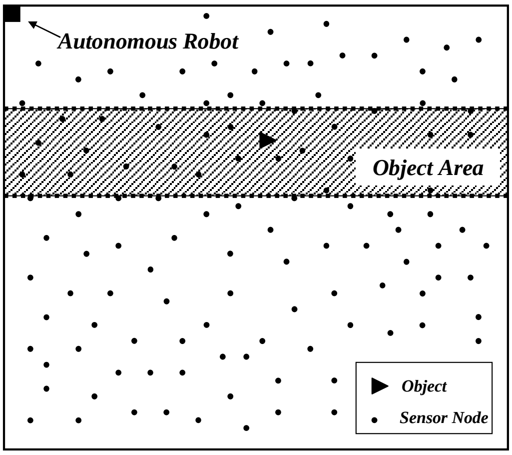

Fig.1 Simulation configuration

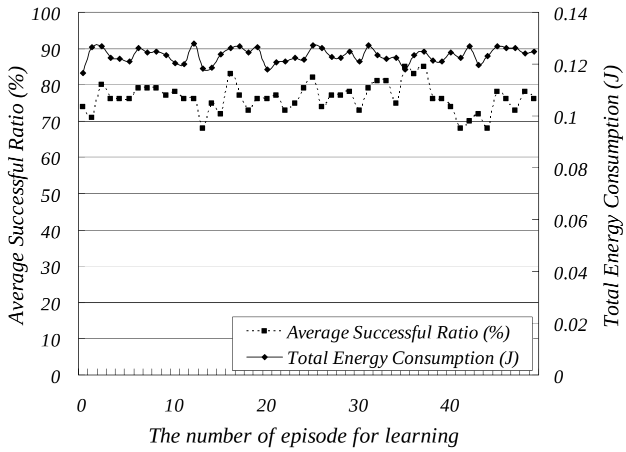

Fig.2 Experimental results

3. Conclusions

In this paper, a new system for object observation by a large-scale wireless sensor network and an autonomous mobile robot, named the Network-Robot system (N-R system), has been proposed. Through experimental results, it has been confirmed that the proposed N-R system has the development potential as a promising system for object observation. Future works include proposal of a more efficient method on Phase II and verification of the effectiveness to various situations.

REFERENCES

[1]Akyildiz I, Su W, Sankarasubramaniam Y, Cayirci E (2002), Wireless sensor networks: A survey. Computer Networks Journal (Elsevier) 38(4): 393-422

[2]Heinzelman WR, Chandrakasan A, Balakrishnan H (2000), Energy-efficient communication protocol for wireless microsensor networks. Proc. Hawaii International Conference on System Sciences, 2000, pp.3005-3014

[3]Tseng VS, Lin KW, Hsieh MH (2008), Energy efficient object tracking in sensor networks by mining temporal moving patterns. Proc. 2008 IEEE International Conference on Sensor Networks, Ubiquitous, and Trustworthy Computing, 2008, pp.170-176

[4]Xu Y, Winter J, Lee WC (2004), Prediction-based strategies for energy saving in object tracking sensor networks. Proc. 2004 IEEE International Conference on Mobile Data Management, 2004, pp.346-357

[5]Utani A, Orito E, Kumamoto A, Yamamoto H (2008), An advanced ant-based routing algorithm for large scale mobile ad-hoc sensor networks (in Japanese). Trans. SICE 44(4): 351-360

DISCRETE PARTICLE SWARM OPTIMIZATION SELECTING FORWARDING NODES FOR QUERY DISSEMINATION IN WIRELESS SENSOR NETWORKS

Junya Nagashima, Akihide Utani, and Hisao Yamamoto
Faculty of Knowledge Engineering
Musashi Institute of Technology
1-28-1, Tamazutsumi, Setagaya-ku, Tokyo, 158-8557 Japan
{ utani; yamamoto }@si.musashi-tech.ac.jp

Abstract. *In wireless sensor networks, flooding is required for the dissemination of queries and event announcements. The original flooding causes the overlap problems. In the original flooding, each sensor node receiving a broadcast message forwards it to its neighbors, resulting in a lot of collisions and duplicate messages. For dense wireless sensor networks, the impact caused by the original flooding may be overwhelming. The original flooding may result in the reduced network lifetime. Therefore, the selection of forwarding nodes for the dissemination of queries and event announcements is needed to prolong the lifetime of wireless sensor networks. In this study, we use the discrete particle swarm optimization method to select forwarding nodes for query dissemination.*

Keywords: Sensor networks, Selecting forwarding nodes, Query dissemination, Particle swarm optimization

1. Introduction

Wireless sensor networks have a wide range of applications, such as environmental monitoring, environmental control, object tracking, and precision agriculture[1]. In wireless sensor networks, flooding is required for the dissemination of queries and event announcements. The original flooding causes the overlap problems. In the original flooding, each sensor node receiving a broadcast message forwards it to its neighbors, resulting in a lot of collisions and duplicate messages. For dense wireless sensor networks, the impact caused by the original flooding may be overwhelming. The original flooding may result in the reduced network lifetime. Therefore, the selection of forwarding nodes for the dissemination of queries and event announcements is needed to prolong the lifetime of wireless sensor networks. In this study, we use the discrete particle swarm optimization method to select forwarding nodes for the dissemination of queries and event announcements. We evaluate the applicability of discrete particle swarm optimization by computer simulations and discuss its development potential. In simulation experiments, the performance of discrete particle swarm optimization is compared with that of genetic algorithm.

2. Discrete Particle Swarm Optimization

The particle swarm optimization method belongs to the category of swarm intelligence methods[2]. It was developed and first introduced as a stochastic optimization algorithm. The ideas that underlie the particle swarm optimization method are inspired not by the evolutionary mechanisms encountered in natural selection, but rather by the social behavior of flocking organisms, such as swarms of birds and fish schools. The particle swarm optimization method can directly handle the variables of continuous type[3]. The discrete particle swarm optimization method is an improved algorithm proposed for combination optimization problems[4].

3. Experimental Results

In the selection of forwarding nodes for the dissemination of queries and event announcements, the network topology information is first collected by a sink node. Forwarding nodes are selected by applying the discrete particle swarm optimization method to a combination optimization problem based on the topology information. The conditions of simulation and the values for the parameters of Discrete Particle Swarm Optimization (DPSO) and Genetic Algorithm (GA) are shown in Table 1 and Table 2. A global optimum solution on forwarding nodes is illustrated in Fig.1. Experimental results are reported in Fig.2, Fig.3, and Fig.4. By using the discrete particle swarm optimization method, a global optimum solution on forwarding nodes was obtained within 200 iterations.

©ISAROB 2009

Table 1 Conditions of simulation

Simulation size	100*m*×100*m*
The Number of sensor nodes	73
Range of radio wave	25*m*

Table 2 Settings for DPSO and GA parameters

DPSO	GA
The number of particle: 30	The number of individual: 30
ω, c1, c2: 1.0, 2.1, 0.8	Mutation rate: 5%

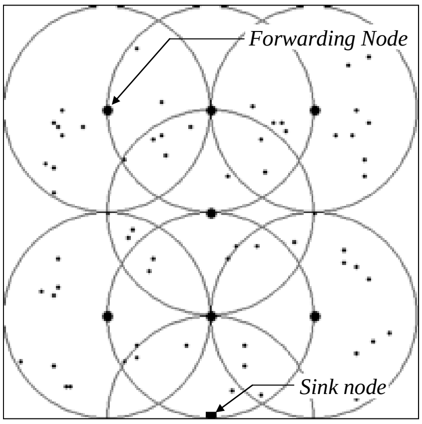

Fig.1 Simulation configuration

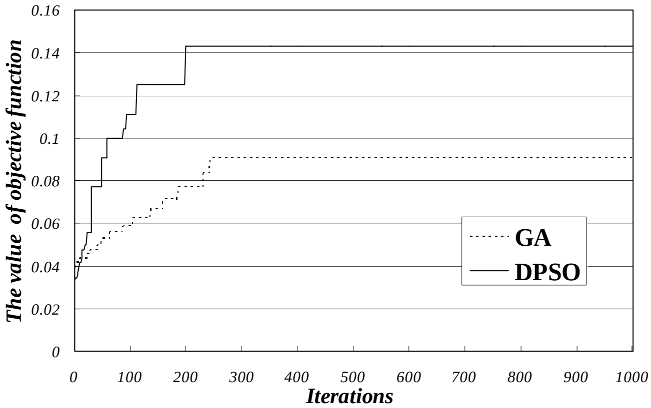

Fig.2 Experimental results

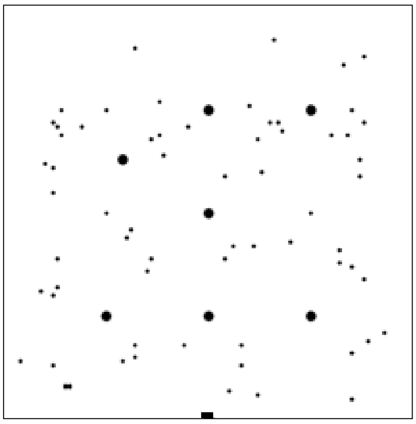
Fig.3 Forwarding nodes selected by DPSO

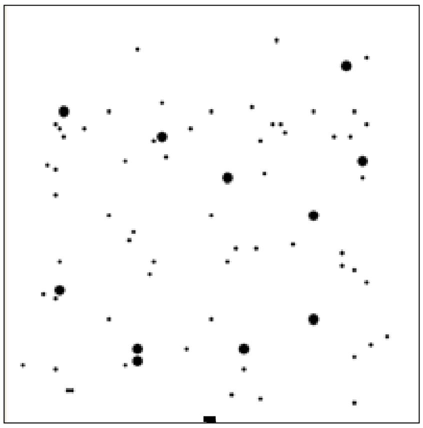
Fig.4 Forwarding nodes selected by GA

4. Conclusions

In this study, the discrete particle swarm optimization method has been used for selecting forwarding nodes for the dissemination of queries and event announcements. Through experimental results, it has been confirmed that the discrete particle swarm optimization method has the development potential as a promising method selecting forwarding nodes for the dissemination of queries and event announcements within an allowable computation time.

REFERENCES

[1]Akyildiz I, Su W, Sankarasubramaniam Y, Cayirci E (2002), Wireless sensor networks: A survey. Computer Networks Journal (Elsevier) 38(4): 393-422
[2]Kennedy J, Eberhart RC (1995), Particle swarm optimization. Proc. IEEE International Conference on Neural Networks, 1995, pp.1942-1948
[3]Kumamoto A, Utani A, Yamamoto H (2008), Improved particle swarm optimization for locating relay-dedicated nodes in wireless sensor networks. Proc. SCIS & ISIS, 2008, pp.1971-1976
[4]Kennedy J, Eberhart RC (1997), A discrete binary version of the particle swarm algorithm. Proc. IEEE International Conference on Systems, Man & Cybernetics, 1997, pp.4104-4108

The Fourteenth International Symposium on Artificial Life and Robotics 2009 (AROB 14th '09),
B-Con Plaza, Beppu, Oita, Japan, February 5 - 7, 2009

Logistic Regression Analysis for Mutation Data of Hemophilia B

Makoto Utsunomiya, Makoto Sakamoto and Hiroshi Furutani

Faculty of Engineering, University of Miyazaki, Miyazaki City, 889-2192

Abstract: Hemophilia B is hereditary disease caused by defects in coagulation factor IX. The compilation of mutation data in the hemophilia B database makes it possible to study this disease at molecular level. The most common mutations reported in the database are amino acid substitutions. We examined the relation between activation level of factor IX and category of amino acid substitution by using the logistic regression analysis. As parameters, we used four physical-chemical parameters of amino acids. We have good results of discrimination for the severity of the disease.

Keywords: hemophilia B, factor IX, amino acid, logistic regression analysis.

I. Introduction

Hemophilia is an X-linked hereditary bleeding disorder caused by a deficient or defective coagulation factor VIII or factor IX [1]. About three-fourths of patients with hemophilia have the A type which is due to deficient factor VIII activity. The B type is less frequent than the A type and is due to deficient factor IX activity [2,3].

Factor IX is a vitamin K dependent plasma protein that participates in the middle phase of blood coagulation [4]. The clinical definition of hemophilia B is based on the individual's factor IX activity level as mild (>5%), moderate (1%-5%), or severe (<1%) [5]. Factor IX is made up of seven regions: (1)Signal peptide, (2)Propeptide, (3)Gla, (4)EGF(1st), (5)EGF(2nd), (6)Activation, and (7)Catalytic. Mutation in factor IX is made up of a majority of point mutations. Substitutions of amino acid sequence are the most common form of point mutation. The effects of amino acid substitutions on the activities of factor IX depends on two factors. One is the combination of native and hemophilic amino acids, the differences of physical-chemical properties of the amino acids. Another is the position of mutation in factor IX protein. In general, substitution in important site and substitution to different character from original amino acid are supposed to the drastic decrease in activity of factor IX. On the other hand, variations in unimportant places and substitution to similar type of amino acid are supposed to be lightly affected. We have introduced distances between 20 amino acids by using the following four physical-chemical properties: (1)Molecular volume, (2)Hydropathy, (3)Polar requirement, and (4)Isoelectric point.

There have been reported a variety of defects in the factor IX gene from hemophilia B patients, and these are summarized in the Haemophilia B Mutation Database [6]. There are 2925 patients data in the database. In this study, we analyzed missense mutations in the database described with factor IX activity values. Among them, the cases with more than single mutations and female patients were excluded from our analysis. We adopted 1494 cases.

We performed the logistic regression analysis for the estimation of factor IX activity by using distances of four amino acid parameters. And, we conducted estimation of factor IX activity and prediction of distinction between severely ill patient and mildly ill patient with result of logistic regression analysis.

II. Methods

Table 1 is a sample of the hemophilia B mutation database. CLOTTING is the factor IX activity level. AA_CHANGE indicates the amino acid substitution.

Table 1. Hemophilia B database

CLOTTING	AA_CHANGE	
	Before	After
4.7	V	L
0	V	F
23	V	A

Distance of amino acid.

We adopted four physical-chemical properties of amino acid.

©ISAROB 2009

(1) Molecular volume.
(2) Hydropathy
(3) Polar requirement
(4) Isoelectric point

For each amino acid parameter, the distance between amino acid *i* and *j* is defined by the next expression,

$$D_{ij} = \left| f_i - f_j \right|,$$

f_i and f_j are values of each amino acid parameter in amino acid *i* and *j*.

Logistic regression analysis.

In this study, we applied the logistic regression analysis, which a collection of p independent variables denoted by $x_1, x_2, \cdots, x_p$ [7]. This study adopts 4 independent variables $x_k = D_{ij}(k)$ corresponding to four amino acid parameters $(k = 1,2,3,4)$. The logistic regression model is given by

$$\pi(x) = \frac{e^{g(x)}}{1 + e^{g(x)}},$$

where $x = (x_1, x_2, x_3, x_4)$. The conditional probability given independent variables x is defined by

$$\pi(x) = P(Y = 1 \mid x),$$

where Y is the severity of a patient with $Y = 0$ for mild case and $Y = 1$ for severe case. Thus in this study, $\pi(x)$ represents the probability that a patient with data x shows severe bleeding symptom. The logit of the multiple logistic regression model $g(x)$ is given by the equation

$$g(x) = \beta_0 + \beta_1 x_1 + \cdots + \beta_4 x_4 .$$

Assume that we have a sample of n independent observations $(y_i, x_{1i}, x_{2i}, x_{3i}, x_{4i})$, $i = 1,2,\cdots,n$, where y_i is the severity of the *i*th patient. As in the univariate case, fitting the model requires the estimates of the parameters $(\beta_0, \beta_1, \cdots, \beta_4)$. The method of estimation is the maximum likelihood.

In this study, we defined severity of hemophilia B as follows. Clotting ≧ 5; mild. Clotting < 5; severe. We used sensitivity and specificity. These are statistical measures of the performance of a binary classification test. Table 2 is relationships among terms in this work. Sensitivity is probability that the test recognizes severe patient as severe. Specificity is probability that the test recognizes mild patient as mild.

$$Sensitivity = \frac{TP}{FN + TP}$$

$$Specificity = \frac{TN}{TN + FP}$$

Table 2. Relationships of among terms

		expected severity		
		mild	severe	
actual severity	mild	True Negative	False Positive	Specificity
	severe	False Negative	True Positive	Sensitivity

III. Results

Case 1.

Table 3 is the result of the logistic regression analysis. We used converted for with the equation of y.

$$y = 1 - (clotting/100)$$

In the following we use the notations of the significance level; ** for p-value < 0.01, * for p-value < 0.05 and blank for p-value > 0.05.

Table 3. Result of logistic regression analysis

	coefficient	p-value
β0	2.1711	**
Molecular volume	0.0063	
Hydropathy	0.1029	
Polar requirement	0.0299	
Isoelectric point	0.1018	
likelihood		-280.67

We defined the expected value of $\pi(x)$ as follows. If $\pi(x) \le 0.95$; mild case. If $\pi(x) > 0.95$; severe case. And, we performed chi-square test for its result. The result is significance on 1% STD. Table 4 is organized list for these data.

Table 4. Frequency of mild and severe case

		expected severity		
		mild	severe	total
actual severity	mild	315	150	465
	severe	277	752	1029
	total	592	902	1494
p-value		**		

Specificity is 67.7%. Sensitivity is 73.1%.

We defined as follows. If $\pi(x) \leq 0.97$; mild case. If $\pi(x) > 0.97$; severe case. And, we performed chi-square test for its result. The result is significance on 1% STD. Table 5 is organized list for these data.

Table 5. Frequency of mild and severe case

		expected severity		
		mild	severe	total
actual severity	mild	442	23	465
	severe	848	181	1029
	total	1290	204	1494
p-value		**		

Specificity is 95.1%. Sensitivity is 17.6%.

We defined as follows. If $\pi(x) \leq 0.93$; mild case. If $\pi(x) > 0.93$; severe case. And, we performed chi-square test for its result. The result is significance on 1% STD. Table 6 is organized list for these data.

Table 6. Frequency of mild and severe case

		expected severity		
		mild	severe	total
actual severity	mild	110	355	465
	severe	90	939	1029
	total	200	1294	1494
p-value		**		

Specificity is 23.7%. Sensitivity is 91.3%.

Case 2.

Table 7 is the result of logistic regression analysis. We converted clotting by the method. If clotting ≧ 5; $y = 0$. If clotting < 5; $y = 1$.

Table 7. Result of logistic regression analysis

	coefficient	p-value
β_0	-1.044	**
Molecular volume	0.0136	**
Hydropathy	0.1844	**
Polar requirement	0.0958	
Isoelectric point	0.2669	**
likelihood		-743.75

The parameters are significance on 1% STD other than polar requirement.

We defined the expected value of $\pi(x)$ as follows. If $\pi(x) \leq 0.5$; mild case. If $\pi(x) > 0.5$; severe case. We performed chi-square test for its result. The result is significance on 1% STD. Table 8 is organized list for these data.

Table 8. Frequency of mild and severe case

		expected severity		
		mild	severe	total
actual severity	mild	187	278	465
	severe	108	921	1029
	total	295	1199	1494
p-value		**		

Specificity is 40.2%. Sensitivity is 89.5%.

We defined as follows. If $\pi(x) \leq 0.7$; mild case. If $\pi(x) > 0.7$; severe case. And, we performed chi-square test for its result. The result is significance on 1% STD. Table 9 is organized list for these data.

Table 9. Frequency of mild and severe case

		expected severity		
		mild	severe	total
actual severity	mild	339	126	465
	severe	330	699	1029
	total	669	825	1494
p-value		**		

Specificity is 72.9%. Sensitivity is 67.9%.

©ISAROB 2009

Case 3.

Table 10 is the result of logistic regression analysis. We converted clotting by the method. If clotting ≧ 5; $y = 0$. If clotting < 5; $y = -\frac{1}{5}(clotting) + 1$.

Table 10. Result of logistic regression analysis

	coefficient	p-value
β_0	-1.2200	**
Molecular volume	0.0123	**
Hydropathy	0.0786	*
Polar requirement	0.0900	*
Isoelectric point	0.1591	**
likelihood		-743.75

Molecular volume and isoelectric point are significance on 1% STD. Hydropathy and polar requirement are significance on 5% STD.

We defined the expected value of $\pi(x)$ as follows. If $\pi(x) \leq 0.5$; mild case. If $\pi(x) > 0.5$; severe case. And, we performed chi-square test for its result. The result is significance on 1% STD. Table 11 is organized list for these data.

Table 11. Frequency of mild and severe case

		expected severity		
		mild	severe	total
actual severity	mild	335	130	465
	severe	316	713	1029
	total	651	843	1494
p-value		**		

Specificity is 72.0%. Sensitivity is 69.3%.

We defined as follows. If $\pi(x) \leq 0.7$; mild case. If $\pi(x) > 0.7$; severe case. And, we performed chi-square test for its result. The result is significance on 1% STD. Table 12 is organized list for these data.

Table 12. Frequency of mild and severe case

		expected severity		
		mild	severe	total
actual severity	mild	440	25	465
	severe	848	181	1029
	total	1288	206	1494
p-value		**		

Specificity is 94.6%. Sensitivity is 17.6%.

IV. Summary

This analysis shows that molecular volume and isoelectric point are important parameters for prediction of hemophilia B severity. In case 1, specificity is 67.7% and sensitivity is 73.1% if we set 0.95 as limits of severity. In case 2, specificity is 72.9% and sensitivity is 67.9% if we set 0.7 as limits of severity. In case 3, specificity is 72.0% and sensitivity is 69.3% if we set 0.5 as limits of severity.

As future work, we would like to develop a method which takes into account the site dependence of mutation.

REFERENCES

[1] Iris Plug, Eveline P. Mauser-Bunschoten, Annette H. J. T. Brocker-Vriends, et al (2006), Bleeding in carriers of hemophilia. BLOOD, 1 JULY 2006 – VOLUME 108, NUMBER 1
[2] Furutani H (1995), A Method to Estimate Effects of Amino Acid Substitutions in Blood Coagulation Factor IX from Hemophilia B Patients. Proceedings of MEDINFO 95, 909
[3] H Furutani (1993), Analysis of Correlation between Amino Acid Substitution and Factor IX Activity in Hemophilia B (in Japanese). Iryoujouhougaku Vol.13 No.4, 211-220
[4] S Yoshitake, Barbara G. Schach, Donald C. Foster, et al (1985), Nucleotide Sequence of the Gene for Human Factor IX. *Biochemistry* 1985, 24, 3736-3750
[5] Da-Yun Jin, Tai-Ping Zhang, Tong Gui, et al (2004), BLOOD, 15 SEPTEMBER 2004・VOLUME 104, NUMBER 6
[6] fixhome : http://www.kcl.ac.uk/ip/petergreen/haemBdatabase.html
[7] David W. Hosmer, Stanley Lemeshow (2000), Applied Logistic Regression Second Edition. WILEY-INTERSCIENCE

©ISAROB 2009

Real-time Estimation System of Gaze Angle Based on Electrooculogram

Xiu Zhang[1, 3], Takenao Sugi[2], Xingyu Wang[1], Masatoshi Nakamura[3]

[1]*Department of Automation, East China University of Science and Technology, 130 St. Meilong, Shanghai, China*
(Tel : 86-21-6425-3386; Fax : 86-21-6425-3386)
(Email: shuyee_zhang@yahoo.com.cn)
[2]*Department of Electrical and Electronic Engineering, Saga University, 1 Honjimachi, Saga, Japan, 840-8502*
(Tel : 81-952-28-8643; Fax : 81-952-28-8666)
(Email: sugi@cntl.ee.saga-u.ac.jp)
[3]*Department of Advanced Systems Control Engineering, Saga University, 1 Honjimachi, Saga, Japan, 840-8502*
(Tel : 81-952-28-8644; Fax : 81-952-28-8666)
(Email: nakamura@cc.saga-u.ac.jp)

Abstract: This paper describes an online eye-tracking method based on electrooculogram (EOG) to estimate gaze angle. The objective is to use biomedical signal EOG as the input of human-machine interface for both disabled and healthy people. In this study, a quadratic function is applied to set the relation between EOG and gaze angle. The estimated gaze angle is decided by three EOG channels with maximum amplitude after compensating shift and smoothing. The results of real-time estimation showed high accuracy, which makes it possible in many application fields, such as assistance robot control, online word processor and so on.

Keywords: electrooculogram, gaze angle, tracking target, real-time estimation**.**

I. INTRODUCTION

In Japan, it is estimated that over 5% of the total population is disabled and the population aged over 65 years will have a ratio at nearly 1 person in 4 in 2020. With the rapid growth of life expectancy in recent years, a large part of elder people will experience functional problems in daily life, such as eating and moving. It is necessary to provide a new human machine interface to increase the quality of life for the elder or disabled people and allow them a more autonomous lifestyle.

In the past years, there has been a significant increase in using neuro-physiological signal such as electrooculogram (EOG) [1], electromyogram (EMG) [2] and electroencephalogram (EEG) [3] as assistive technology for disabled people. EOG is the recording of the steady corneal retinal potential which is proportional to vertical and horizontal movements of the eye [4]. It offers an objective way to quantify the direction of gaze, and is applied widely in assisted wheelchair [1], meal assistance orthosis [5], etc.

In this study, an online estimation system is established to track the gaze angle of user by EOG. The purpose is to use biomedical signal EOG as the input of human-machine interface for both disabled and healthy people. The relation between EOG amplitude and gaze angle is set by a quadratic function. One of the most important features is the use of compensation to improve the performance of estimation. After comparing the target angle and the estimated angle, the results show the quadratic function together with the method of compensation is effective in estimating the gaze angle of the user. The good performance and real-time response make it possible to provide a fast and reliable control input for home assistance robots, online word processor and other kinds of communication by use of eye movements.

II. METHODS

1. General structure of real-time estimation system

The general structure of eye tracking is illustrated in Fig. 1. During the experiment, a target point was moving around a circle at constant speed on the screen. The subject was asked to stare at the moving point. Ten

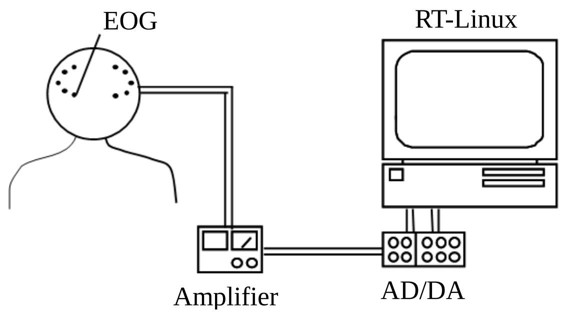

Fig. 1 General structure of estimation system

channels of EOG were acquired, amplified by EEG-1000 with sampling rate of 100Hz, and then sent to RT-Linux system for further processing after AD/DA conversion.

Eleven electrodes are placed on the face, each with an interval of 45 degree, as shown in Fig. 2. Cz is for reference. The mean value of F3 and F4, C3 and C4 is calculated to present the EOG on the vertical direction. So eight channels of EOG (A1, F7, F34, F8, A2, T4, C34, and T3) are used to estimate the gaze angle.

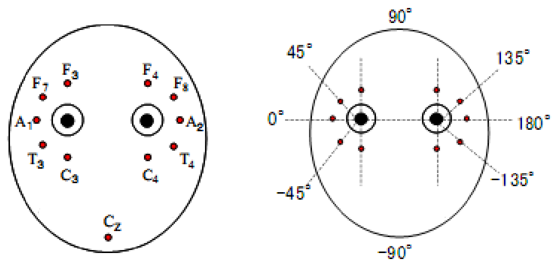

Fig. 2 Placement of electrodes

2. Pre-processing of EOG

A. Band pass filter

EOG is first passed by a Butterworth band pass filter with a cut frequency from 0.1Hz to 10Hz, to remove environment noise.

B. Bias elimination

Average of EOG signal is subtracted from the filtered EOG $A_i(t)$, to eliminate the bias deviation which is caused by the placement of electrodes as (1),

$$A_i^*(t) = A_i(t) - \overline{A_i} \tag{1}$$

where $A_i^*(t)$ is the signal after elimination of bias deviation, $\overline{A_i}$ is the average of EOG, and i is the channel number.

C. Normalization

Normalization is applied to minimize the difference among each channel as (2),

$$A_i'(t) = A_i^*(t) / \left|\overline{A_i^*}\right| \tag{2}$$

where $A_i'(t)$ is the signal after normalization.

3. Estimation of gaze angle by quadratic function

When the iris of eyeball is gazing at one direction, EOG around this direction is positive. EOG around the opposite direction is negative. In a word, EOG from the nearest electrode in the gaze direction has the maximum positive amplitude. The gaze angle is estimated based on such relationship between EOG amplitude and gaze angle.

In this study, a quadratic function is used to model EOG signal from each channel, as (3)

$$A_i'(t) = a\theta_i^2 + b\theta_i + c \tag{3}$$

where θ_i is the angle of electrode. Three EOG channels, the one with maximum EOG amplitude, together with its two neighbor EOG channels are used to determine the acme of quadratic function ($-b/2a$, $c-b^2/4a$), which is the estimated gaze angle and corresponding amplitude.

4. Compensation of estimated gaze angle

As most of bio-potentials, EOG is sensitive to many factors, such as acquisition noise, skin conditions, head movements, processing delay and sudden saccade of eyeballs, so proper compensation is needed to improve the estimated results. Here, two steps of compensation are applied before the real-time estimation by use of training EOG data.

A. Compensation of angle shift

Processing delay may cause the shift of estimated angle. In order to compensate the shift of angle φ, least square method is applied according to the following cost function $J_1(\varphi)$ as (4),

$$J_1(\varphi) = \int [\alpha(t) - \theta(t+\varphi)]^2 dt \tag{4}$$

where $\alpha(t)$ is the target angle, $\theta(t)$ is the estimated angle, φ ranges from -50 to 250. The φ_0 which has the minimum $J_1(\varphi_0)$ is used to compensate the shift.

B. Smoothing

Smoothing is also applied to impair the influence of sudden saccade of eyeballs according to (5),

$$\theta^*(t) = (1-\lambda) \times \theta^*(t-\Delta t) + \lambda \times \frac{\theta(t+\varphi) + \theta(t+\varphi-\Delta t)}{2} \tag{5}$$

where $\theta^*(t)$ is the estimated angle after smoothing. The coefficient λ is decided by least square method according to (6),

$$J_2(\lambda) = \int \left[\alpha(t) - \theta^*(\lambda, t)\right]^2 dt \tag{6}$$

where λ ranges from 0.01 to 0.99 with an interval of 0.01. The λ_0 which has the minimum $J_2(\lambda_0)$ is used to smooth the estimated angle.

After applying the selected coefficients (φ_0, λ_0) into the compensation of delay and smoothing for the

©ISAROB 2009

testing data, $\theta^*(t)$ is got as the final estimated gaze angle.

III. RESULTS

1. Estimated gaze angle without compensation

In the experiment, the red target point was moving round a circle with radius of 10cm at the speed of 10 cm/s. The estimated result was illustrated in a green point, tracking the red target on the screen. The target angle and the estimated angle after pre-processing are illustrated in Fig. 3. There was obvious shift between the target and the estimated one.

2. Estimated gaze angle with compensation

A. Compensation of shift

Different values of delay φ were applied to calculate the cost function $J_1(\varphi)$, as shown in Fig. 4. φ was ranging from -50 to 250, and $J_1(\varphi)$ reached its minimum when φ was 151.

B. Smoothing

Different values of λ were applied to calculated the cost function $J_2(\lambda)$, as shown in Fig. 5. λ was ranging from 0.01 to 0.99 with an interval of 0.01, and $J_2(\lambda)$ reached its minimum when λ was 0.09.

After applying the proper coefficients (φ, λ) of compensation, the estimated gaze angle was improved and was able to chase the target angle as shown in Fig. 6.

IV. DISCUSSION

1. Necessity of compensation

Due to the processing delay, there always exists a shift of angle between the estimated one and the target one, as shown in Fig. 3. We can also find the estimated

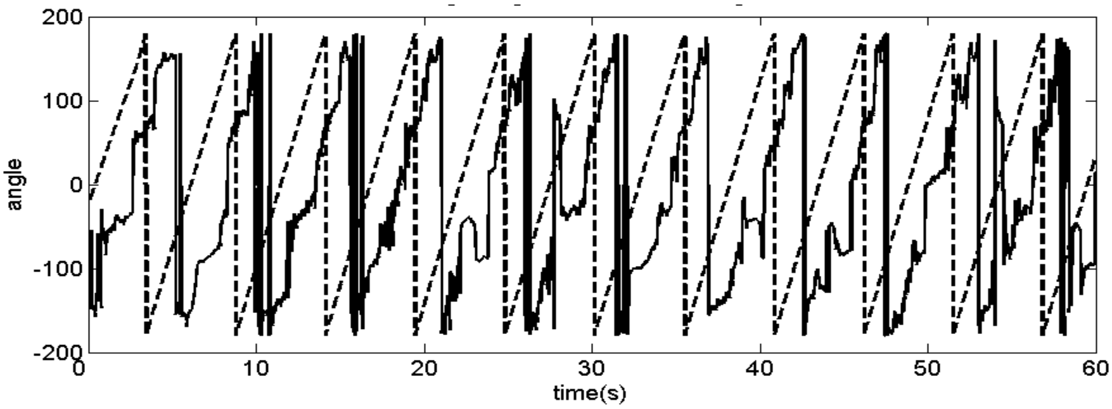

Fig. 3 Target angle and estimated angle without compensation. Dash: target; solid: estimated angle

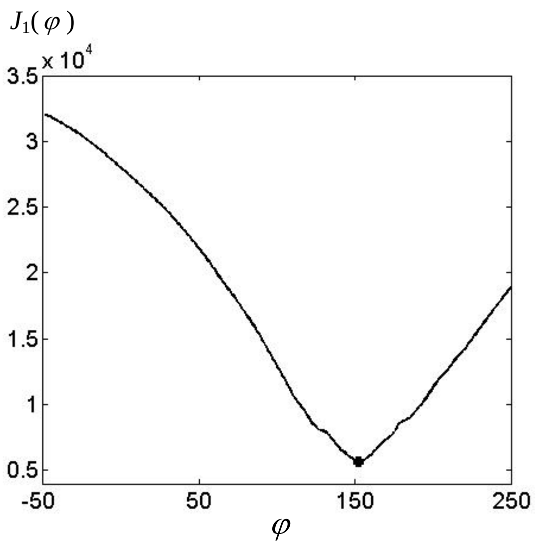

Fig. 4 Cost function of $J_1(\varphi)$. Cost function reached the minimum when φ is equal to 151.

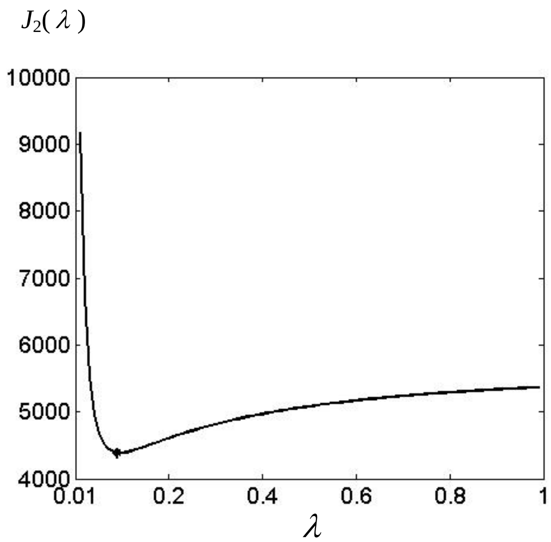

Fig. 5 Cost function of $J_2(\lambda)$. Cost function reached the minimum when λ is equal to 0.09.

©ISAROB 2009

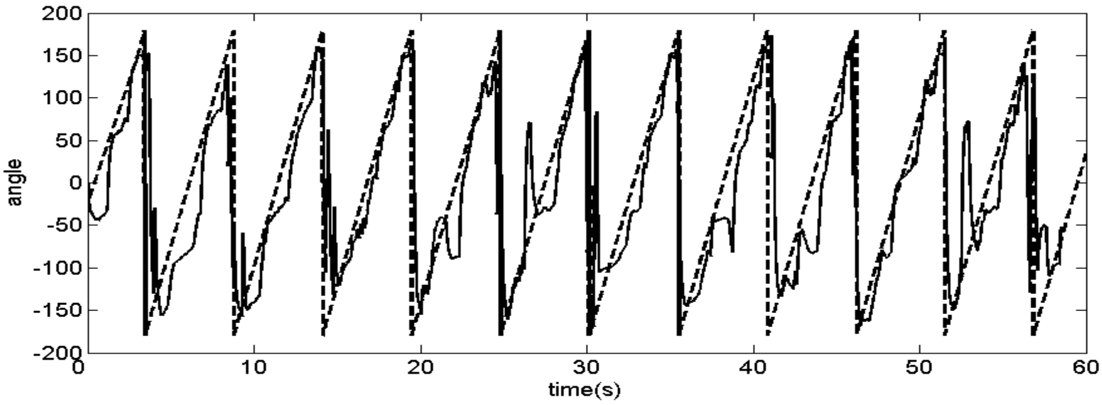

Fig. 6 Target angle and estimated angle with compensation. Dash: target; solid: estimated angle

angle contains many fluctuations. This is probably because EOG is easily influenced by environment noise, such as head movements or blinks. It is essential to use some methods to compensate these deficiencies. Instead of choosing coefficients by experimental experience, here we used cost function $J_1(\varphi)$ and $J_2(\lambda)$ to find proper coefficients by least square method. The whole segment of EOG signals were used as training data to find the coefficients that had the minimum cost functions. The selected coefficients were then applied to estimate the gaze angle of testing data. The effective of this method was illustrated in Fig. 6, in which the estimated angle was quite smooth and was able to track the target angle.

2. Future work

Our future goal is to realize an EOG-based tracking system with more freedom. The target can move at variable speed and in different radius. We would like to investigate the best way to track eye movements by EOG in 2D space.

Another work line is the application part. We would like to develop an EOG based meal assistance robot that serves the disables for eating, or online word processor. Moreover, this kind of achievement can be used for healthy people as novel input of communication and video games.

V. CONCLUSION

In this study, a relationship between EOG amplitude and gaze angle is established by a quadratic function, to estimate the exact gaze angle of eye movements. Compensation of shift and smoothing is applied to improve the performance of estimation by least square method. The real-time estimation system is realized by RT-Linux. The results show the proposed method is quite accurate to estimate the gaze angle. Its high performance in accuracy and response time guarantee the perspective in many fields, such as real-time control of assistance robot, novel input of telephone, word processor for the disables, and video games for healthy people as well.

VI. ACKNOWLEDGMENT

This study is partly supported by Nation Nature Science Foundation of China 60543005, 60674089; and Shanghai Leading Academic Discipline Project, B504.

REFERENCES

[1] Barea R, Boquete L, Mazo M et al. (2002), System for Assisted Mobility Using Eye Movements Based on Electrooculography. IEEE Trans. Neural Sys. & Rehab. Eng. 10(4): 209-218.
[2] Barreto A, Scargle SD, Adjouadi M (2000), A practical EMG-based human-computer interface for users with motor disabilities. J. Rehab. Res. & Develop. 37(1): 53-64.
[3] Shenoy P, Krauledat M, Blankertz B et al. (2006), Towards adaptive classification for BCI. J. Neural Eng. 3: 13-23.
[4] Du Bois-Reymond EH (1848), Untersuchungen Ueber Thierische Elektricitat. G Reimer, German, pp. 56-74
[5] Goto S, Sugi T, Nakamura M (2006), Development of meal assistance orthosis for disabled persons with human intention extraction through EOG signals. SICE-ICASE International Joint Conference, Busan, Korea, Oct. 18-21, 2006, pp.227-232

A study on a postural optimization for bicycle's exercise based on electromyography

S.Matsumoto, T.Tokuyasu, S.Iwao, H.Taniguchi, S.Adachi, S.Shiga and K.Ohba

Oita National College of Technology, 1666 Maki, Oita-city, Oita, Japan

(*Tel : 81-97-552-7403; Fax : 81-97-552-7403*)

(tokuyasu@oita-ct.ac.jp)

Abstract: Against the background of various social issues such as rising crude oil prices, global heating, and diseases associated with adult lifestyle habits, the role of bicycle has been reviewed. In fact, many types of bicycle have been developed, and have been in widespread use all over the country. Various frame size is prepared for the physical size of user and, additionally we can alter the position of bicycle by adjusting the posture of a handle and a saddle. Adjusting position of bicycle against rider's physical properties before exercise makes it possible to improve efficiency of cycle exercise. In this paper, we present an optimization method of determination of saddle height of the bicycle by the use of physical information processing. Especially, we focused on electromyography of leg during cycle exercise and employed both of First Fourier Transformation and analysis of principle components as physical data processing method. In order to accomplish the optimization method of the posture of bicycle exercise, firstly it is necessary to set evaluation standards that we can quantitatively evaluate the performances due to the different settings of saddle height. This paper shows the system structure, introduces our data processing method, and discusses the results of our experiments.

Keywords: Electromyography, First Fourier Transformation, Posture optimization, Cycle exercise, Information Processing.

I. INTRODUCTION

In these days, lifestyle-related diseases, middle-aged health problems mainly caused by the lack of exercises have been a growing concern as a social issue. Besides, reduction of carbon-dioxide emissions against global warming, and increment of the cost of fossil fuels have received considerable attention in recent years. These situations have led to the revision of effectiveness of bicycle, in fact, many types of bicycles including compact folding type and/or electric motor-driven type have been developed by lots of major companies and used in all over the world.

Cycling is currently becoming one of the most popular exercises for physical fitness and recreation for the people who are not specifically trained. From physical load efficiency, briskness, and convenience, the bicycle has also been proactively used in the welfares including rehabilitation. Performance in cycling is affected by a variety of factors, including aerobic and anaerobic capacity, muscular strength and endurance, and body composition [1]. However there is a lack of interests in the importance of the position of bicycle, and its available method have been blurred and given empirically. Within our inquiry, there are few researches evaluating the posture of cycle exercise based on biological information. If it becomes possible to easily make the settings of bicycle better for users, we can use bicycle more effectively and healthfully. And then, this study aims to accomplish the optimization method of the bicycle position based on user's individual physical data. In order to achieve our purpose, firstly we have to reveal what is the good position of the bicycle?

The purpose of this study is to establish an intelligent algorithm to search the bicycle position which can ensure individual best performance. In order to accomplish them, firstly we have to set evaluation standards that we can quantitatively evaluate user's performance during cycling exercise. And then leg electromyography during bicycle exercise has been employed as biological data because these information can be measured non-invasively and tell us the active statements of muscle [2,3]. The following muscles are selected as measurement objects because we can easily patch electrodes on them; vastus lateralis, vastus medialis, gastrocnemius, and biceps femoris. In the following sections, this paper shows the system structure and the graphical user interface we have developed, and shows the experimental results and discusses about them.

II. METHOD

2-1. System structure

Fig. 1 shows a schematic diagram of our developed system, in which it is composed of a computer, a measurement instrument device of electromyography, and a fixed cycle trainer. This computer is running on Windows XP operating system and installed Visual Basic

©ISAROB 2009

2005 in order to construct a real-time instrumentation system. The role of this computer is to measure leg electromyography and controls an automation device which is able to change the height of saddle in 1 kHz sampling frequency. And a graphical user interface is displayed on its screen. We can monitor information of the height of saddle and the leg electromyography of examinee during our experimental measurement.

The saddle control device we have developed is described in Fig. 1, which is composed of a DC servo motor, worm and rack gears, and aluminum covers. As a consequence these gears' combination yields an effect of gravity compensation of this saddle height control device. We applied a common PD control law to control the DC servo motor and its feedback gains are empirically determined. To reduce the noise of linear potentiometer, a software filter is employed. The following equation (1) shows the PD control law and the equation (2) is for the software filter used in our system, where the variable i shows the driving current, K_P and K_D are the feedback gains, x is raw data of the saddle height detected by the linear potentiometer, and z is the filtered saddle height. Especially α is 0.4 which is empirically determined as filter permeability.

$$i = K_P(x_r - z) + K_D(-\dot{z}) \quad (1)$$

$$z_n = \alpha x_n + (1-\alpha) z_{n-1} \quad (2)$$

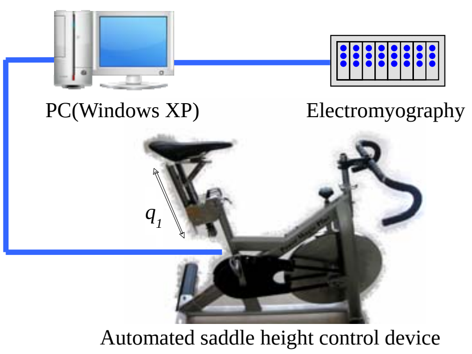

Fig. 1 Automatic saddle height control system muscles

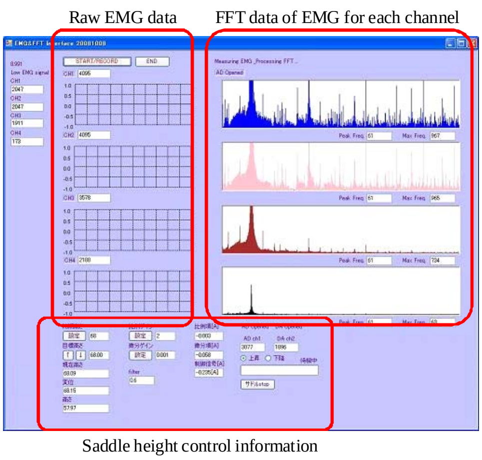

Fig. 2 Graphical user interface

2-2. Human interface

Fig. 2 shows the graphical user interface, which is designed by the basis of dialog base programming of Visual Basic 2005. The computer displaying this user interface on its monitor has to do real-time processing for the saddle height control and the measurement of electromyography. Because of this, we adopted some Windows APIs to realize real-time processing.

Surface electromyography is so called EMG, which is well known as bio-instrumentation system and is a non-invasive technique commonly used to obtain information on muscle activity. And studies of EMG are well accepted by the research community and spreading in sport and clinical physiology as assessment tools.

Generally, muscles generate about 0.5 mV of electric potential when they contract even insensible movement such as eyewink and so on. In short, EMG is sensitive amplification equipment. By using this instrument we can easily know muscular active statement with no effect of HUM noises of 60Hz. In order to distinguish each muscular active during cycling exercise, we patched four electrodes on vastus lateralis, vastus medialis, gastrocnemius, and biceps femoris respectively as shown in Fig. 3. The computer retrieves the output signals from EMG through 12 bit AD/DA conversion board, and transforms these frequency data to electro power spectrum data by using First Fourier Transformation (FFT) method. This translated data is displayed on the graphical user interface with respect to each channel. Table 1 shows our EMG measurement conditions.

2-3. Information processing and experimental conditions

This study experiments with a subject who is an experienced cycling player with more than 10 years athletic career, and measures his EMG by fixing rotation

Table 1 Measurement conditions of electromyograph

Sampling Freq.	1KHz
Lo cut	10Hz
Hi cut	1KHz
A/D resolution	12Bit

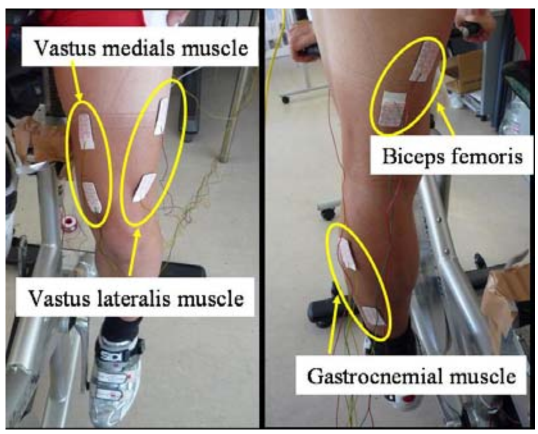

Fig. 3 Measurement muscles of EMG

Table 1 Correlation matrix between four measured muscles

	Vastus medialis muscle	Vastus lateralis muscle	Biceps femoris muscle	Gastrocnemial muscle
Vastus medialis muscle	1			
Vastus lateralis muscle	-0.8834	1		
Biceps femoris muscle	0.9622	-0.9776	1	
Gastrocnemial muscle	-0.8935	0.9998	-0.9820	1

speed of the pedal at 90 rpm. The measurement is performed by following procedures.

1. After starting the pedaling exercise for a while, measurer pushes "start/record" button on the measurement software in Fig. 2 to get the subject's EMG data with the bio-instrumentation system.
2. Measurer pushes the "stop" button to terminate the measurement after the elapse of predetermined time. On the termination of this operation, time series of EMG for each channel both raw data and power spectrum data transformed through FFT are saved as CSV files in a given directory on PC.
3. By putting the files into MS-Excel, changes of EMG are examined by relying on statistics mainly using principal component analysis (PCA).

This study uses FFT to examine the change of muscle activity according to the height of saddle [4]. The system of this study needs on-line and interactive processing to fine-tune the height of saddle quickly. Therefore this study thought FFT is the most suitable technique due to the ability of high computational speed.

As the experimental condition, we collects EMG data of 40 patterns that are obtained at 0.5mm different heights of saddle within the range from 660.5mm to 660.5mm, and each pattern is changed after a lapse of 30 seconds. Here to minimize the effect of muscular fatigue, the measurement time is divided into four and each measurement is given 300 consecutive seconds. The reason giving such the range of height is as follows; the subject has felt 670.0mm as his good position, so we decide to give the measuring range within 10.0mm above or below on the basis of 670.0mm. Similarly, range of motion in automatic saddle height control device is designed by considering generally recommended saddle height. It has well known that length of leg × 0.875 derives a proper saddle height.

In general, professional cycling players have adjusted the height of saddle under 1.0 mm scale, so we give 0.5 mm differences of height to grasp the change of EMG roughly. As an example obtained by the experiment, the time series of EMG and power spectrum of vastus medials muscle at 657.0 mm are shown in Fig. 5 and Fig. 6 respectively. The power spectrum is obtained through FFT in each 1024 milliseconds, so one measurement pattern consists of 30 data of power spectrum distribution. To analyze the muscle activities, this study averages 30 data, and obtains 40 patterns for each muscle, i.e. 160 patterns.

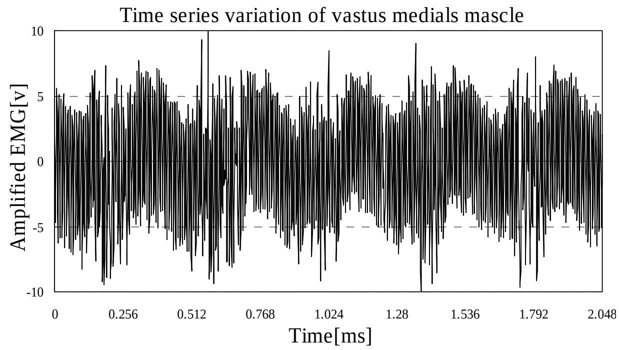

Fig. 4 An example of time series of EMG

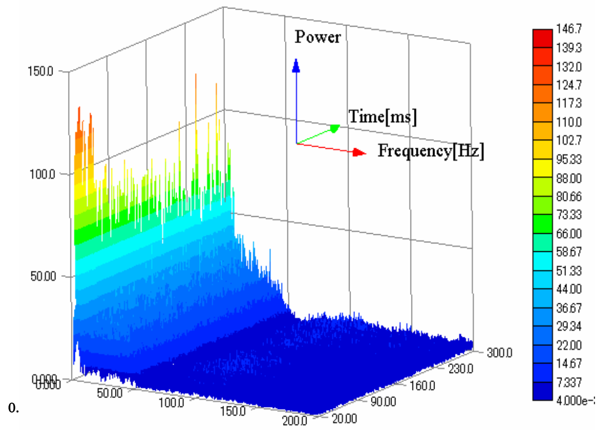

Fig. 5 An example of power spectrum of EMG

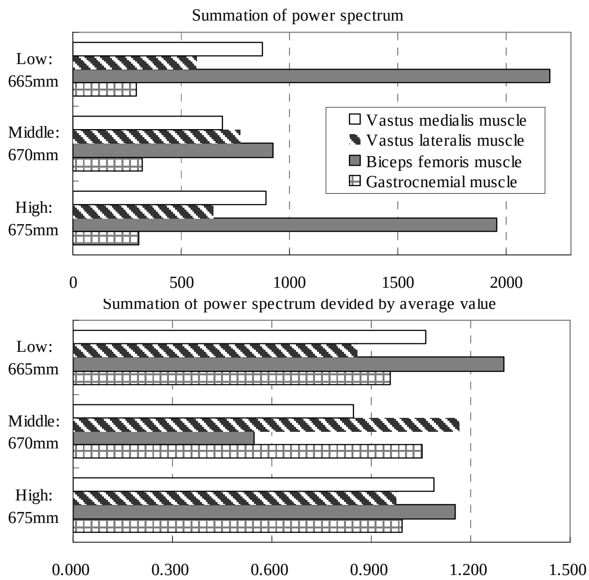

Fig. 6 Summation of maximum power spectrum

©ISAROB 2009

Table 2 Characteristic values in PCA

	Characteristic value	Contribution ratio	Cumulative contribution ratio
1st PC	1.8744	46.86%	46.86%
2nd PC	1.1781	29.45%	76.31%
3rd PC	0.6173	15.43%	91.74%
4th PC	0.3303	8.26%	100.00%

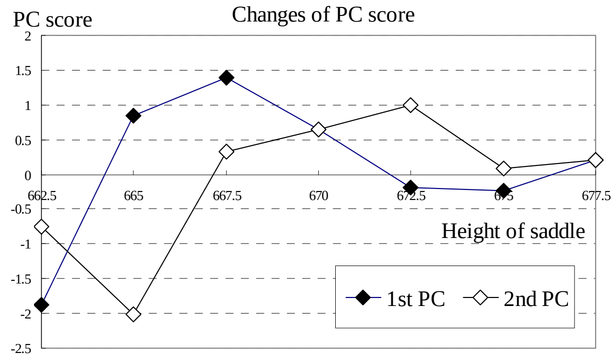

Fig. 7 Changes of PC score from 662.5 to 677.5 mm

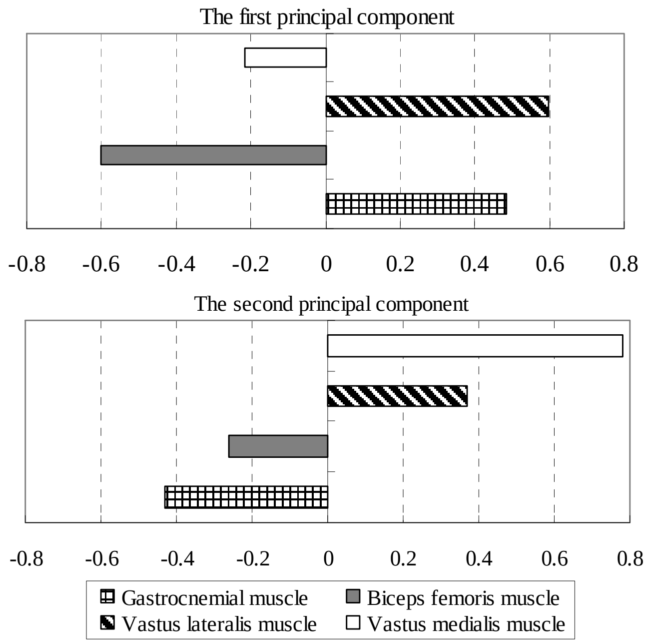

Fig. 8 The first and second principal components

III. Results

The experimental results had shown remarkable differences on the maximum power spectrum depending on the height of saddle, so this paper analyzes variation with time of the maximum power spectrum. This study addresses only the magnitude without the discussion of exact frequency value because most of maximum values are observed in near 1 Hz (see Fig. 5). Summation of the maximum power spectrum at each muscle is shown in Fig. 6, and Fig. 6 shows the differences of magnitude depending on the size of muscle (upper figure is expressed by absolute number, and the lower is after standardization). At first, this study performed correlation analysis, and the result is shown in Table 1. Here we can see the typical positive and negative correlations for all coefficient values, and especially the correlation coefficient value close to 1.0 between gastrocnemial muscle and vastus lateralis muscle can be said as the notable conclusion.

Next, this paper applied PCA to examine the changes of maximum power spectrum. Traditionally, PCA has been performed on the symmetric covariance matrix or on the symmetric correlation matrix. Based on the result shown in Fig. 6, this study shows only the result of correlation matrix that is like a covariance matrix but first the variables, i.e. the columns have been standardized. The results of PCA are shown in Fig. 7 and 8, and the result in Table. 2 are evaluated by the subject and an expert in muscle. The PC scores have varied quite a bit through the heights, so Fig. 8 shows the values averaged within 1.0 mm above or below on the each basis height in Fig. 7 (662.5 mm, 665.0 mm and so on), i.e. the each value in Fig. 7 is five-points average.

IV. Conclusion

From the results of analysis, biceps femoris muscle showed characteristic changes as shown in Fig.6 and 7. Particularly in Fig. 7, the middle position had the lower power spectrum than about the half at high and low position. According to one assumption, the magnitude of power spectrum represents the amount of muscle activity can be said that the position with low power spectrum in biceps femoris muscle is the moderate height of saddle. In Fig. 8, the eigenvector coefficients in 1st PC denoted the approximately-same tendency of the changes in Fig. 6 and 7, but it might be an important consideration that the magnitude of each element is different. As future works, this study will describe fuzzy logic rules [5] based on muscle activity.

Reference

[1] I. Faria, Applied physiology of cycling, *Sports Medicine*, 1, pp.187-204, 1984.
[2] A. Kiduka et al., Surface electromyography (Biomechanisms Library), *Publishing of Tokyo Denki University*, 2006 (In Japanese).
[3] F. Hug et al, Electromyographic analysis of pedaling: A review, *Journal of Electromyography and Kinesiology*, Available online, 2008,
[4] K. Ogawa et al, Break Control of Bicycle Ergometer Based on Muscle Activity , *The transactions of the IEICE*, Vol.J81-D-II, No.2, pp.421-428, 1998 (In Japanese).
[5] S. Nakamura et al., Fuzzy Reasoning Demand Forecasting Model of Season Type, *Journal of JSOFT*,Vol.20,No.2,pp.211-217,2008 (In Japanese).

©ISAROB 2009

The Fourteenth International Symposium on Artificial Life and Robotics 2009 (AROB 14th '09),
B-Con Plaza, Beppu, Oita, Japan, February 5 - 7, 2009

A Movie Rating Prediction System based on Personal Propensity Analysis

Soojin Lee, Taeryong Jeon, Gyeongdong Baek, Jaewoo Cho, and Sungshin Kim

School of Electronics and Electrical Engineering, Pusan National University, Busan, Korea
Pusan National University Changjeon 2 dong, Keumjeong-ku, Busan 609-735, Korea
(Tel : 82-51-510-2367; Fax : 82-51-513-0212)
(Email address: {pooh3887, jtr, gdbaek, jwjw777, and sskim}@ pusan.ac.kr)

Abstract: Most of all the movie recommendation methods need the data for genre of movies and private information of user. As the kinds of movies are getting various, recommendation system for analyzing user's propensity can be required because movie recommendation method by data for genre of movies is limited. The recommendation system for analyzing user's propensity is recommending movies through the movie records and evaluation of the past. This paper proposed active recommendation algorithm which analyzed propensity of user and predicted evaluation of the movies before users look up the data for preferred recent movies.

Keywords: prediction system, data mining, movie recommendation, user propensity analysis

I. INTRODUCTION

As internet service and computer technology are getting better, the personalized recommendation system is actively researched by analyzing user's personal information such as propensity. Web sites about e-commerce are investing development of excellent recommendation system because additional information can be added to user's personal information in the ideal personalized recommend system. Amazon, which is the company merchandising product by online system, and Netflix, which is the company renting movies by online system, are recommending products that considered user's expectation and satisfaction.

Data-mining techniques that are included pattern recognition and information filtering methods have been applied to develop recommendation system. Representative technology of recommendation system is Information filtering technology that divides content-based recommendation and collaborative recommendation [3-4]. Content-based recommendation extracts user's propensity and predicts user's preference. But this recommendation is difficult from missing information about item at that time of the first attempt [5-6]. Collaborative recommendation which is the most popular recommendation analyzes other user information based on similarity to target user.

In this study, the suggestion is predicting evaluation from target movie about target user that Netflix offers data about movies and users. Data consist of users (480,189), movies (17,770), dates of evaluation and points from 1 to 5. Also prove data and qualifying data are given for the performance evaluation of developed system.

II. MOVIE RATING PREDICTION SYSTEM

Each user's personal propensity is analyzed to predict system watched movie evaluation. The analysis method for personal propensity usually is normalizing personal information such as age, sex and occupation. This kind of method can be caused security problems by personal information. And user's satisfactions are lower than expected because user's data also wasn't perfectly matched with personal taste and individuality. This movie rating prediction system that analyzes personal propensity through the previously watched user's movie records is developed.

1. Reorganization of the data set

The raw data of the Netflix are used to build movie rating prediction system. The structure of raw data is shown in Fig. 1 and all data are consisted of text type. The training data is consisted of evaluation and data of 17,770 movies that all users of approximately 4.8 million peoples watched. But the training data isn't properly used by analyzed personal information because classification is about kind of movies. It is the reason why the reorganization is needed before the rating is predicted. The reorganization of the training data that are properly aimed at analysis of personal propensity offered from the Netflix is shown in Fig. 2.

The probe and qualifying files are offered by the Netflix that purposed evaluation of the performance.

©ISAROB 2009

The rating about evaluated movies will be obtained till the first decimal number by estimation algorithm. And each detailed item of evaluation is constituted with ID of the movie, date and ID of the user to predict a point of target movie. In other words, rating will be predicted after target movie is watched by target user. There are difference between probe and qualifying data. The probe data is offered as detailed result of each item of evaluation and qualifying data is offered as calculated total error through the on-line. The performance of system is evaluated to improve and evaluate confidence of movie rating prediction system.

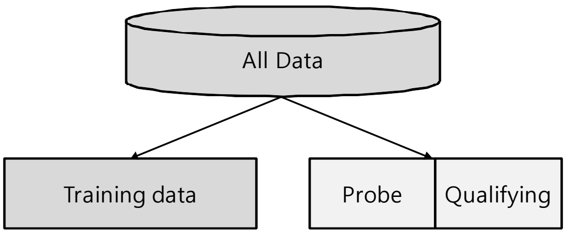

Fig.1. The data structure from the Netflix

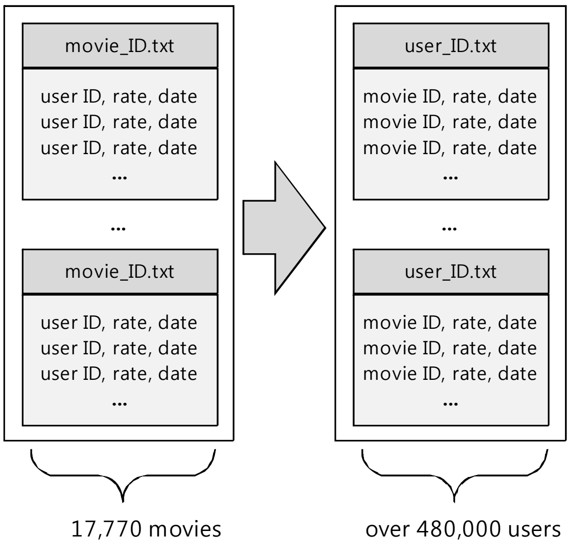

Fig.2. The reorganization of Data set

2. The process of the movie rating prediction system

The prediction process for rating of the movies after target user watched target movie is shown in Fig. 3. First of all, information of target user about target movie is extracted through the probe data. And then related users with target user are subjected for rating of the movie. Probe data is evaluated and predicted through the repetition of the process.

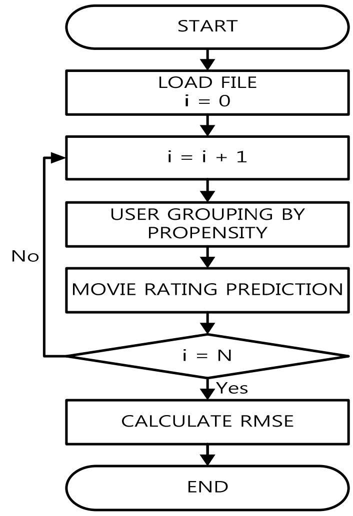

Fig.3. The flow chart of movie rating prediction

3. User grouping classified by user propensity

Users having similar propensity with target user are classified to related user group in order to analyze target user's propensity. The process for each user's propensity is analyzed by target user and related user group about rating records of movie.

The process of classifying related user group is as follows. At first, target user and movie are extracted in the probe data in order to evaluate performance of movie rating prediction system. Secondly, all users that watched target movie except target user are classified related user group.

4. The prediction of movie rating

After user grouping classified by user propensity, similarities are derived from related propensity between target user and related users. The calculating method for similarity is shown in Eq. (1).

$$\mu = \frac{N\left(r_{t,i}, r_{u,i}\right)}{n_t} \tag{1}$$

The rate of evaluated movie i by target user is $r_{t,i}$, the rate of evaluated movie i by related user is $r_{u,i}$ and $N\left(r_{t,i}, r_{u,i}\right)$ is the same number between $r_{t,i}$ and $r_{u,i}$. And n_t is the number of movies that target user watched. If the value of similarity is high, related users have more similar propensity. Each similarity is estimated as follows.

$$Estimated\ Rate = \frac{\sum_{i=1}^{n} \mu_i \times R}{\sum_{i=1}^{n} \mu_i} \tag{2}$$

The similarity of related user is μ_i. *R* is evaluated rate of related user about target movie and *n* is the number of related users, Eq. (2). In other words, the number of related users with target user is *i*. The estimated rate is reflected with evaluated rate through the related user's movie information watched and evaluated.

$$RMSE = \sqrt{\frac{1}{n}\sum_{i=1}^{n}\left(y_i - \hat{y}_i\right)^2} \quad (3)$$

5. Error calculation of prediction system for movie evaluation

Probe data are applied to evaluate performance of the movie rating prediction system and error calculation is taking advantage of the RMSE (root mean square error). The equation of system error, RMSE, is showing in Eq. (3). The actual rate of target user about target movie is y_i and also $\hat{y}_i$ is estimated rate through the analysis of personal propensity. And *n* is the number of items to evaluate in the probe data.

III. AN EXPERIMENT AND RESULTS

1. Experimental Method

Training data is utilized in order to develop the movie rating prediction system that offered movie data (17,770) and evaluation data (480,189) from the Netflix. It takes a lot of times to reorganize data that fits the purpose of analysis of personal propensity. The process of reorganization is accomplished only once per each user transforming database that isn't repeatedly accomplished.

As the amount of training data is getting much, the samples reflected population's attributes are experimented through the random sample method of probabilistic sampling method. And also, the samples are classified as 3 parts, e.g. (100, 300 and 500 users) in order to compare system performances with different sizes of the samples repeatedly 10 times.

2. Experimental results

The visual C++ is utilized for evaluation and development of proposed the movie rating prediction system. The performance of prediction system is evaluated through the calculated estimation error for movie rating of the system. The results of proposed movie rating prediction system, RMSE, are presented to Table 1.

Table 1.RMSE of movie rating prediction system

	100	300	500
1	1.094094	1.057966	0.961277
2	1.084670	0.987677	0.970496
3	1.156681	1.080526	0.940614
4	1.089129	1.062151	0.983205
5	1.025894	1.020257	0.961183
6	1.118859	1.006011	0.974777
7	1.175142	0.991430	0.951108
8	1.076674	1.009890	0.949743
9	1.179335	0.979645	0.981149
10	1.061592	1.008651	0.987640
Avg.	**1.106207**	**1.020420**	**0.966119**

As the number of users is increasing, RMSE is conversely decreasing. In other words, the more users are included, the more detailed prediction is achieved, because information of propensity about related user is also extended.

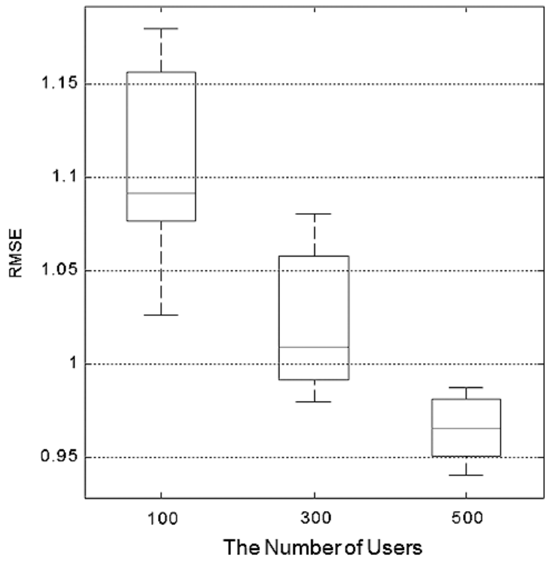

Fig.4.The results of RMSE

The evaluated results of system performance are presented by box-plot graph, Fig. 4. The number of users, e.g. (100, 300 and 500) is projected on the x-axis and the distribution of RMSE is projected on the y-axis. And the ranges of maximum and minimum value are presented through the graph. As the number of users is increasing, the range is decreasing that mean variation of RMSE is also decreased. After the restriction is disappeared such as the number of users, RMSE will be converged to specific point. The performance of proposed system would be properly identified by reorganized structure and detected converging specific point.

The least predicted error among developed systems using opened data from the Netflix is 0.9841 which is estimated by team of Bellkor [11]. It is difficult to compare our system with team of Bellkor because there is difference between the two that our system experimented samples of population and Bellkor's system experimented whole population. But proposed system would contribute to improve performances of previous movie rating prediction system.

IV. CONCLUSION

After target user watched target movie through the analysis of personal propensity, the prediction system of evaluating target movie is proposed. The proposed system is based on opened data from the Netflix. The normalized analysis method through the personal information isn't considered in this paper, but the analysis method is developed with user's satisfaction through the personalized movie information.

The probe data from the Netflix is subjected to performance of movie rating prediction system through the extracted sample of random sample method. The extracted samples are examined by the number of users, e.g. (100, 300 and 500 users) and repeated 10 times per the number of users. The evaluated prediction error is calculated by means of RMSE.

As the similarity is calculated and analyzed by relation of target user and related users, the personal propensity is decided. The proposed movie rating prediction system can be using base technology to recommend movie that is properly capturing the public fancy through the analysis of user's propensity.

Further subject of the research will be considered about data reorganization of whole population for the comparison with previous movie rating prediction system and identified the performance of proposed system.

REFERENCES

[1] Herlocker J, Konstan J, Terveen L, and Riedl J , "Evaluating Collaborative Filtering Recommender Systems," ACM Transactions on Information Systems 22, ACM Press, 5-53, 2004.
[2] G. Adomavicius and A. Tuzhilin, "Towards the Next Generation of Recommender Systems: A Survey of the State-of-the-Art and Possible Extensions," IEEE Transactions on Knowledge and Data Engineering 17, 634-749, 2005.
[3] Ansari,A., Essegaier,S. and RKohli,R., "Internet Recommendation Systems," Journal of Marketing Reserch Vol.37, pp. 363-375, 2000.
[4] Il Im, "Augmenting Knowledge Reuse Using Collaborative Filtering Systems," A Dissertation Presented to the aculty of the graduate school USC (Information Systems), p.191, 2001.
[5] Basu,C., Hirsh,H. and Cohen,W, "Recommendation as Classification : Using Social and Content-based Information in Recommendation," Proc. of the Fifteenth National Conference on Artificial Intelligence (AAAI-98), pp.714-720, 1998.
[6] Pazzani,M., "A Framework for Collaborative , Content-Based and Demographic Filtering," Artificial Intelligent Review13(5-6), pp.393-408, 1999.
[7] D. Goldberg, D. Nichols, B. M. Oki and D. Terry, "Using Collaborative Filtering to Weave an Information Tapestry," Communications of the ACM 35, 61-70, 1992.
[8] Konstan,J., Miller,B., Maltz,D., Herlocker,J., Gordon, K. and Riedl,J. "GroupLens :Applying Collaborative Filtering to Usenet News," Communications of the ACM, Vol.40 No.3, pp.77-87, 1997.
[9] Rensnick,P., Iacovou,N., Suchak,M., Nergstorm,P. and Riedl.,J. "GroupLens : An Open Architecture for Collaborative Filtering of Netnews," Proc. of CSCW '94, pp. 175-186, 1994.
[10] Shardanand,U. and Maes,P., "Social information filtering : Algorithms for automating 'word of mouth'," Proc. of ACM CHI '95 Conference on Human Factors in Computing Systems, pp.210-217, 1995.
[11] Robert M. Bell and Yehuda Koren, "Improved Neighborhood-based Collaborative Filtering, " KDD 2007 Netflix Competition Workshop, 2007.

Electric Wheelchair Control with Gaze Direction and Eye Blinking

Djoko Purwanto[1)], Ronny Mardiyanto[2)] and Kouhei Arai[3)]

[1),2)]*Department of Electrical Engineering ITS, Kampus ITS Sukolilo, Surabaya 60111, Indonesia*
Tel : 62-31-594-7302; Fax : 62-31-593-1237
djoko@ee.its.ac.id, ronny@ee.its.ac.id

[3)]*Department of Information Science, Saga University, 1 Honjo, Saga 840-8502, Japan*
Tel : 81-952-28-8567; Fax : 81-952-28-8650
arai@is.saga-u.ac.jp

Abstract: In this research, the electric wheelchair control with gaze direction and eye blinking is proposed. A camera is set up in front of wheelchair user to capture image information. The sequential captured image is interpreted to obtain the gaze direction and eye blinking properties. The gaze direction is expressed by horizontal angle of gaze, and it is derived from the triangle form formed by the centre positions of eyes and nose. The gaze direction and eye blinking are used to provide the direction and timing command, respectively. The direction command relates to the movement direction of electric wheelchair, and the timing command relates to the time condition when the wheelchair should move. The timing command with eye blinking mechanism is designed to generate ready, backward movement, and stop command for the electric wheelchair. Furthermore, to move in certain velocity, the electric wheelchair also receives the velocity command beside the direction and timing command. The disturbance observer based control system is used to control the direction and velocity. For safety purpose, the emergency stop is generated when electric wheelchair user do not focus the gaze direction consistently in specified time. A number of experiments conducted for the electric wheelchair in a laboratory environment. The simulation results indicate the effectiveness of the proposed electric wheelchair system.

Keywords: electric wheelchair control, gaze estimation, blinking measurement.

I. INTRODUCTION

The ability to move freely is highly value for all people. However, it is sometimes difficult for person with physical disabilities. Nowadays, the electric wheelchair is commercially available for the disable person. It is generally require considerable skill to operate. Moreover, some disabled person cannot drive the electric wheelchair manually, even with a joystick, because they lack the physical ability to control the movement. To enable the disable person to drive a wheelchair safely and easily so that they can enjoy a higher quality of life, researchers proposed some electric wheelchair system. The use of voice command to control an electric wheelchair is one of research results. A small number of command worlds and high performance voice recognition employed in this system. An electric wheelchair control with electrooculography (EOG) techniques proposed. In this case, the different commands for wheelchair derived from electrooculography (EOG) potential signals of eye movement.

A system for electric wheel chair control with human eyes has been proposed in 2007. Commercially available Web camera mounted on Head Mounted Display: HMD of which user wears is used to capture moving pictures of users' face. Computer mounted on the electric chair process the captured imagery data, detecting and tracking of user's eye, estimating line of sight vector and actuate electric wheel chair in the designated directions pointed by human eye. One of the keys of the proposed system is detection and tracking of eye movement so that this paper deals with the experimental results from the eyeball rotation angle estimation accuracy with the acquired eye and its surrounding image. Through the experiments almost 99% success rate was confirmed in terms of matching accuracy the electric wheel chair movement with the desired directions user intended to move[1].

In this research, the topic of electric wheelchair control with gaze direction and eye blinking properties is proposed. A camera is set up in front of wheelchair user to capture image information. The camera direction is focused to the face area of wheelchair user. The camera is connected to a computer with vision processing and electric wheelchair motion control capabilities. With vision processing, the sequential captured image is interpreted to obtain the gaze direction and eye blinking properties. The gaze direction is expressed by horizontal angle of user's gaze, and it is

©ISAROB 2009

derived from the triangle form formed by the centre positions of eyes and nose. The eye blinking properties obtained from blinking time condition. The gaze direction and eye blinking are used to provide the direction and timing command, respectively, for the electric wheelchair. The direction command relates to the electric wheelchair movement direction, and the timing command relates to the time condition when the electric wheelchair should move. The eye blinking mechanism with blinking duration at least 400 ms is designed to generate timing command for moving action. Furthermore, the electric wheelchair also receives the velocity command to move in certain velocity beside the direction and timing command. The disturbance observer based control system is used to control the direction and velocity. For safety purpose, the emergency stop is generated when electric wheelchair user do not focus the gaze direction consistently in specified time.

II. PROPOSED SYSTEM

1. System overview

The electric wheelchair system equipped with a camera is shown in Figure 1. The electronic system for vision processing and control purpose is place on the bottom of wheelchair. The electric wheelchair adopts the differential streering mechanism. The wheelchair design considers 4 important factors as follows: safety, easy to operate, cheap, and convenience.

Fig. 1. The electric wheelchair system

There are 4 commands applied to the electric wheelchair, safety, timing, direction, and velocity command (see figure 2). Safety command is related to situation where wheelchair must stop immediately. The timing command is obtained from eye blinking mechanism and it is used to run and stop the motion. The direction command is derive from properties of triangle points from both eyes and nose of user. The velocity command is set independently and it does not depend on vision system. Both of direction and velocity command refer to wheelchair motion in cartesian space.

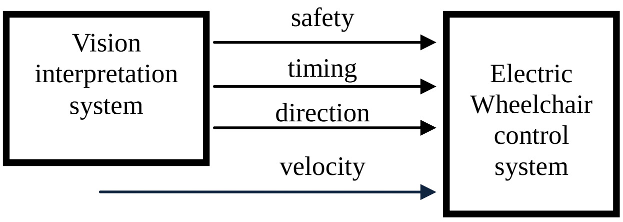

Fig. 2. Command for electric wheelchair

2. Electric wheelchair model

Figure 3 illustrates the differential steering type of electric wheelchair model. The desired wheelchair motion determined by the command value of direction θ and linear velocity v. The wheelchair motion depends on the electric signal applied to motor of each wheel. The angular velocity ω_l and ω_r represent the direct input signal to move the left and right wheel of electric wheelchair. The relation between direction-velocity (θ, v) and angular velocity of wheels (ω_l, ω_r) is written in equation (1), where R_w is radius of wheel, η is gear ratio, and l is distance between wheels.

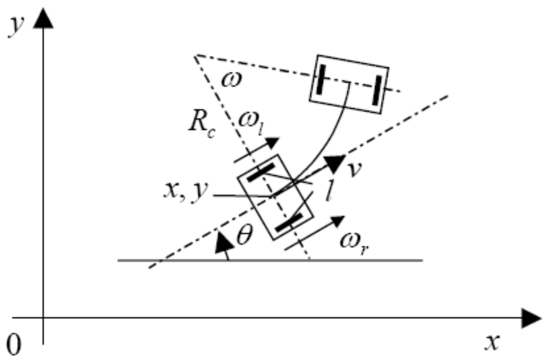

Fig. 3. Electric wheelchair model

$$\begin{bmatrix} v \\ \dot{\theta} \end{bmatrix} = \begin{bmatrix} \frac{R_w}{2\eta} & \frac{R_w}{2\eta} \\ \frac{R_w}{l\eta} & -\frac{R_w}{l\eta} \end{bmatrix} \begin{bmatrix} \omega_l \\ \omega_r \end{bmatrix} \quad (1)$$

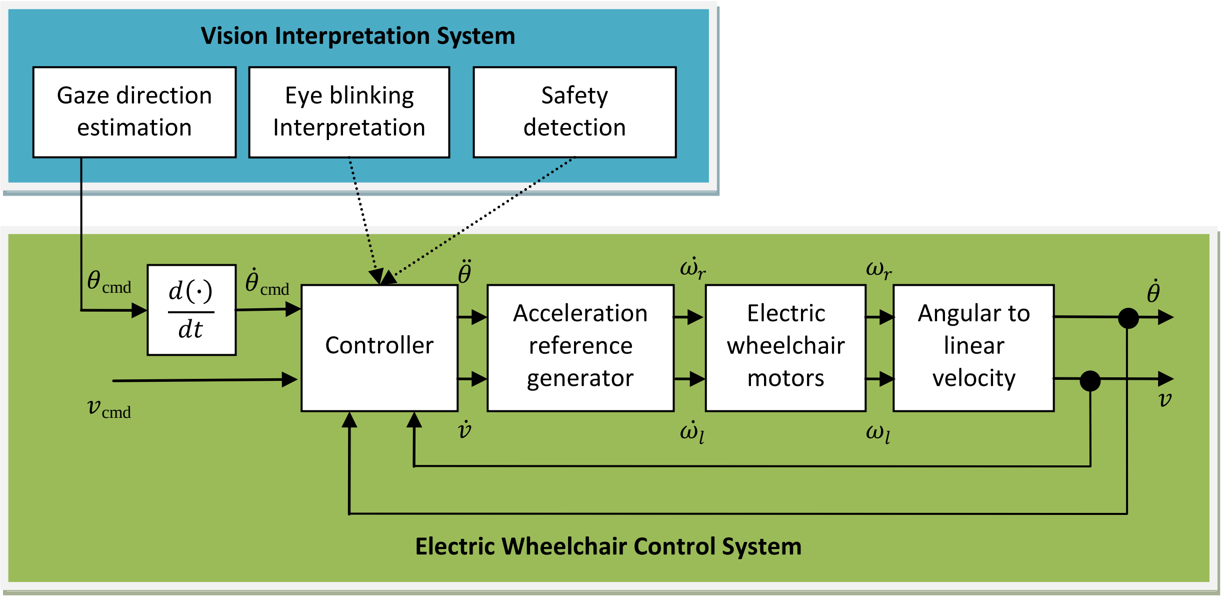

Fig. 3. Electric wheelchair system

3. Electric wheelchair system

The overall block diagram of electric wheelchair system is shown in figure 3. The system consist of vision interpretation system and electric wheelchair control system. All of visual information processing that include gaze direction estimation, eye blinking interpretation, and safety detection, are carried out in vision interpretation system. The gaze direction estimation generate the smooth-running direction command. The eye blinking interpretation and safety detection are generated commands signal directly to the controller. In the wheelchair control system, a disturbance observer based control strategy is applied to solve 2 inputs 2 outputs control problem.

4. Vision interpretation system

A. Gaze direction estimation

The gaze direction is interpreted from 3 positions of both 2 eyes and nose of wheelchair user. As show in figure 4, these 3 positions form a triangle shape that relates to gaze direction. With the parameters of triangle is shown in figure 5, the estimation of gaze direction is formulated as equation (2). The function of $f_1(\cdot)$ is determined during calibration procedure.

$$\hat{\theta} = f_1\left(\frac{a-b}{L}\right) \qquad (2)$$

The direction command θ_{cmd} is derived from the gaze direction estimation $\hat{\theta}$ with smoothing function

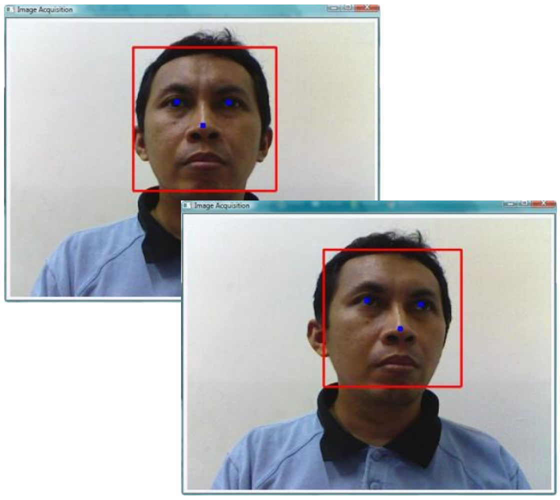

Fig. 4. Relation of triangle shape and gaze

formulation to yield natural change of command and to suppress measurement noise.

$$\theta_{cmd} = f_2(\hat{\theta}) \qquad (3)$$

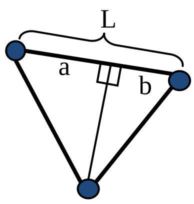

Fig. 5. Triangle shape from eyes and nose

B. Eye blinking interpretation

The interpretation of eye blinking is useful to generate the timing command applied directly to the controller. The eye blinking with duration at least 400 ms is used as timing command. The algorithm of timing command is as follows:

If	<1 time blinking>	**then**	<disable controller>
If	<2 times blinking>	**then**	<enable controller>
If	<long blinking>	**then**	<set move backward>

C. Safety detection

The safety detection monitors the electric wheelchair user behavior and vision system performance. Bad behavior is defined when the user does not focus in wheelchair control. Failed vision system occurs when vision system fails to detect user face. The safety command algorithm is defined as follows:

If	<bad user behavior>	**or**	<face detect failed>
then	<disable controller>		

5. Electric wheelchair control system

A. Electric wheelchair motors and controller

In both of wheelchair motors, the disturbance observer technique is applied. Disturbance observer is a technique to estimate the disturbance existing in a plant and to make the motion controller to be an acceleration controller [3]. With acceleration controller, the wheelchair motors can be modeled as ideal integrator, and the controller block diagram is realized by constant gain *K*.

$$\begin{bmatrix} \dot{v} \\ \ddot{\theta} \end{bmatrix} = \begin{bmatrix} K & 0 \\ 0 & K \end{bmatrix} \begin{bmatrix} v_{\mathrm{cmd}} - v \\ \dot{\theta}_{\mathrm{cmd}} - \dot{\theta} \end{bmatrix} \tag{4}$$

B. Angular to linear velocity conversion and acceleration reference generator

The conversion from angular to linear velocity is formulated in equation (1). Furthermore, the acceleration reference can be derived from equation (1) as follows :

$$\begin{bmatrix} \dot{\omega}_l \\ \dot{\omega}_r \end{bmatrix} = \begin{bmatrix} \frac{R_w}{2\eta} & \frac{R_w}{2\eta} \\ \frac{R_w}{l\eta} & -\frac{R_w}{l\eta} \end{bmatrix}^{-1} \begin{bmatrix} \dot{v} \\ \ddot{\theta} \end{bmatrix} \tag{5}$$

III. RESULTS

To verify the effectiveness of proposed method, several simulations was carried out. Figure 6 shows that the actual response follows the command in specified settling time. Furthermore, the actual response of motor shows that there is difference angular velocity in left and right motor when direction command changes.

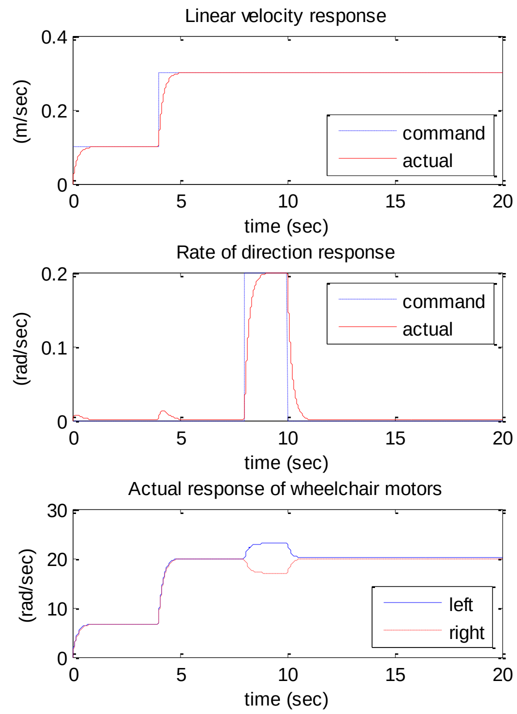

Fig. 6. Simulation results

IV. CONCLUSION

The feature points in triangle shape of eyes and nose positions can be formulated to generate direction command for electric wheelchair. Combining direction, velocity, timing, and safety command yields effective method to control electric wheelchair. With disturbance observer technique applied as control strategy, the design criteria of wheelchair control system can be satisfied easily.

V. ACKNOWLEDGEMENT

I thank to JICA (Japan International Cooperation Agency) for supporting this research project.

VI. REFERENCES

[1]. Kohei Arai, Djoko Purwanto, Electric wheel ch air control with human eye, The 7th International C onference on Optimization : Techniques and Applica tions, Dec 2007, Kobe, Japan.
[2]. Kohei Arai, Computer input system based on v iewing vector estimation with iris center detection f rom the image of users acquired with relatively che ap web camera allowing user movements, Saga Uni versity.
[3]. K. Ohnishi, M. Shibata, and T. Murakami, (1996), Motion control for advance mechatronics, IEEE/ASM E Transaction on Mechatronics, Vol.1 No.1, pp. 56-67.

©ISAROB 2009

The Fourteenth International Symposium on Artificial Life and Robotics 2009 (AROB 14th '09),
B-Con Plaza, Beppu, Oita, Japan, February 5 - 7, 2009

Construction of the robot control system which understands voice and pointing action

Yuki TAKENAKA, Norihiro ABE, Yoshihiro TABUCHI
Kyusyu Institute of Technology
680-4 Kawazu, iizuka, Fukuoka 820-8502, Japan
Email: takenaka@sein.mse.kyutech.ac.jp

Hirokazu TAKI
Wakayama University
930 Sakaedani, Wakayama-shi
Wakayama 680-8510, Japan
Email: taki@sys.wakayama-u.ac.jp

Shoujie He
VuCOMP
Richardson, Texas, USA
Email: hesj@computer.org

*Abstract***:** This research is aiming at making the robot that can go to take an object designated by a user. We produce the robot control system that uses pointing and voice. This system is composed of two systems. One system is the object instruction system that uses pointing, another one is the object instruction system that uses voice. An approximate position of a designated object is recognized by the object instruction system that uses pointing, details of information on a designated object and an instruction operation correction are conveyed by the object instruction system that uses voice. This time, the object instruction system that uses pointing has been designed and verified as the first step. A calculation resource to calculate an approximate position of a designated object is obtained when a user directs the object with pointing. A robot is able to be moved around a designated object by using this system. The object instruction system that uses voice will be constructed in the future.

Keywords: Robotics, Image Processing, Binocular Stereo, Pointing, Voice

I. INTRODUCTION

In this research, to develop the nursing mobile robot which every senior person can easily instruct to attain his/her requirement, the robot control system is proposed which is easily instructed with use of voice and pointing action. When a user tells a robot to carry an object to the user using pointing action and voice like " take it to me", the robot must move to the object and bring it near the user.

For the purpose, the robot has to know the position of the user and the object to attain the goal. We propose the approach which makes a robot calculate the position of an object designated by a user and move to the position. When it is difficult to move a robot near the indicated object with only the first indication, information concerning the object such as color, geometry, and orientation is given with voice to the robot to modify the behavior of the robot. In this paper, the design of an indication system using pointing action and voice and the verification is shown as the first step.

II. SYSTEM CONFIGURATION

The system configuration is shown in Fig.1. The image acquired with network cameras on a robot is sent to PC using wireless LAN, and image processing calculate the position of a user and an object, then a command is sent back to the robot.

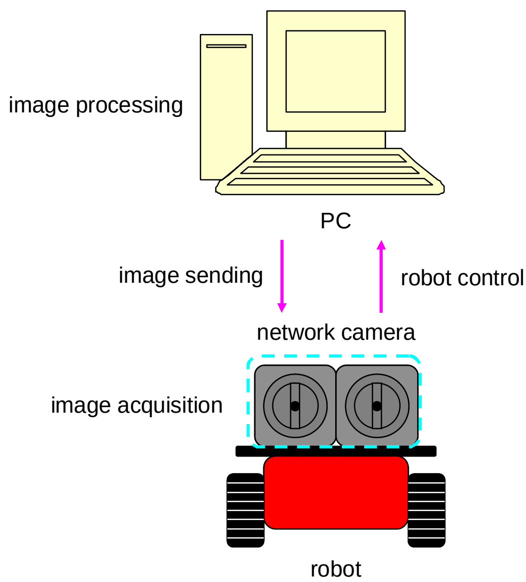

Fig.1.System configuration

III. THE OBJECT INDICATION USING POINTIG ACTION

When a user pointed at an object, it is necessary to make a robot judge where a user is pointing. As it is difficult to calculate the precise decision of position with only pointing action, approximate position of an object is estimated.

Recognizing a face and arm of a user will make it possible to calculate the location of a user and an object in terms of the robot coordination theoretically. Face recognition module realizes the face recognition of a user, and the binocular vision system based on parallax calculated from x coordinate of the center of a face in each camera image will determine the position of the user. An arm vector can be calculated referring to the two characteristic points on an arm based on the binocular vision system in the similar way.

1. Face detection

A face detecting module based on AdaBoost is used because of the speed and precision of the method. Using both features extracted from enormous number of faces saved as data and a classifier learned beforehand, it detects a face from input image.

After a face is recognized, the binocular vision calculates the three dimensional coordinates of the face using center points (two dimensions) of right and left face images.

Fig.3 shows the execution result.

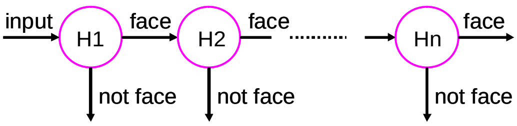

Fig.2.Face detection system

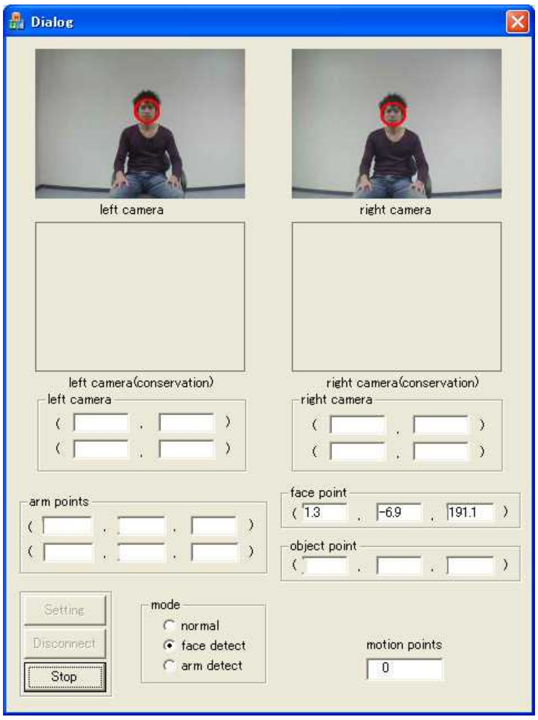

Fig.3.Excution result (Face detection)

2. Arm detection

As parts except for the arm are almost still when pointing action is performed, the arm can be detected by taking difference between consecutive two images.

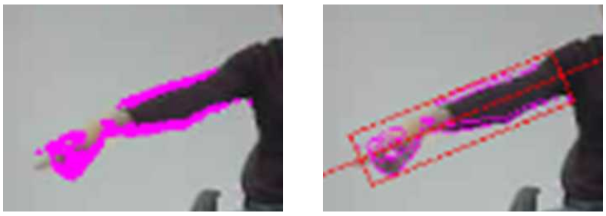

(a) Difference image (b) Arm vector

Fig.4.Arm detector

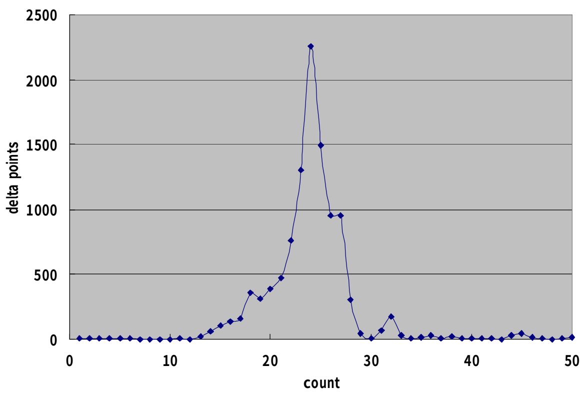

Fig.5.Change in number of difference points

The arm vector is obtained as the line connecting two middle points of two narrow sides of the rectangular which includes difference points. When the number of difference points is quite a few and the difference between consecutive numbers of difference points is negative, pointing action is regarded as completed. Calculating a cross point between the ground and the arm vector obtained when pointing action completed will give the position of the object the user designated by pointing action.

Fig.6 shows the execution result.

©ISAROB 2009

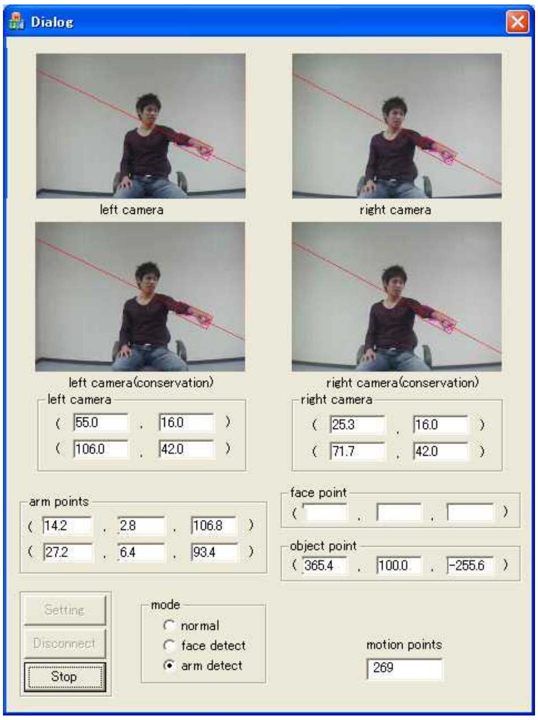

Fig.6.Excution result (Arm detection)

IV. OBJECT RECOGNITION

There is apparently some error in the position of the designated object and it is clear that a robot cannot precisely reach the given goal. These facts make it difficult for a robot reach the position of the object designated. Then additional information on the object must be given to the robot to make the robot modify its behavior. We believe the voice will useful to do this.

Fig.7 shows the current position of a robot and object. It is unnecessary to correct the behavior of a robot when the robot is facing toward the object. In contrast, a robot must correct it heading when the robot is facing to the right or left of the object. In Fig.7, the target object deviates left by θ from front.

Let the distance from a robot to the object be Z, the distance between cameras d, the Focal distance be f and the width of an image plane be width, then the θ is calculated by the following expression;

$$\theta = \tan^{-1}\left(\frac{width}{2f} - \frac{d\_r}{f} - \frac{d}{2Z}\right) \quad \cdots(1)$$

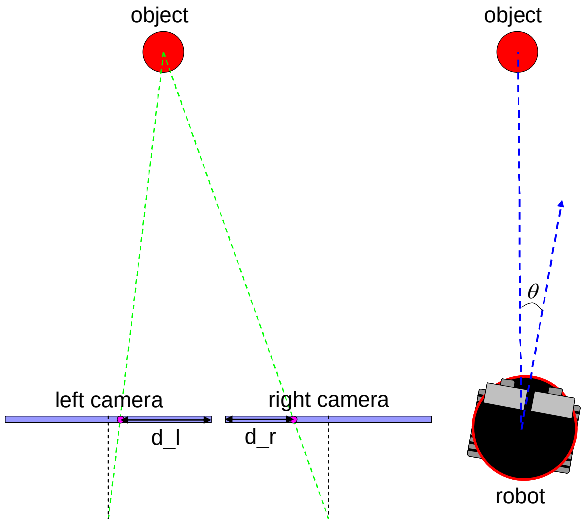

(a) Physical relationship

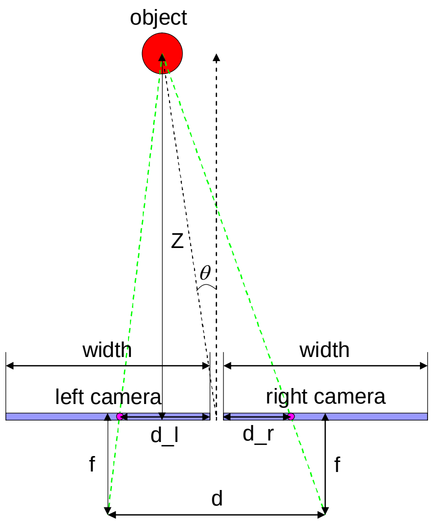

(b) Variable definition

Fig.7.Object recognition (d_l>d_r)

Let the position of the object be P, the position of the object in left camera image be PL, the position of the object in right camera image be PR, the distance between cameras d and the Focal distance be f as shown in Fig.8, then P is calculated by the following expression;

$$\begin{cases} X = \dfrac{dXL}{XL - XR} & \cdots(2) \\ Y = \dfrac{dYL}{XL - XR} & \cdots(3) \\ Z = \left(\dfrac{d}{XL - XR} - 1\right) f & \cdots(4) \end{cases}$$

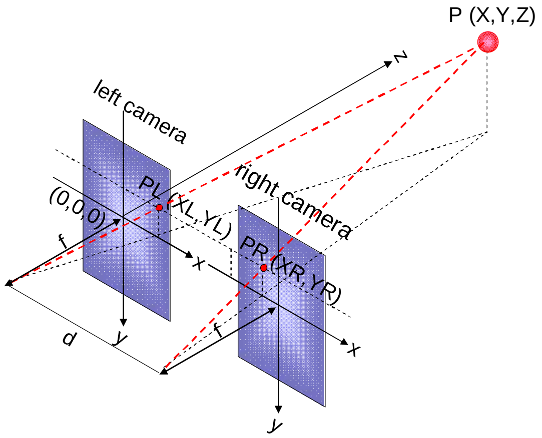

Fig.8.Binocular stereo

According to the deviation from the proper direction, if the behavior of the robot must be corrected, then it will be led to near the position of the designated object.

Fig.9 shows the execution result.

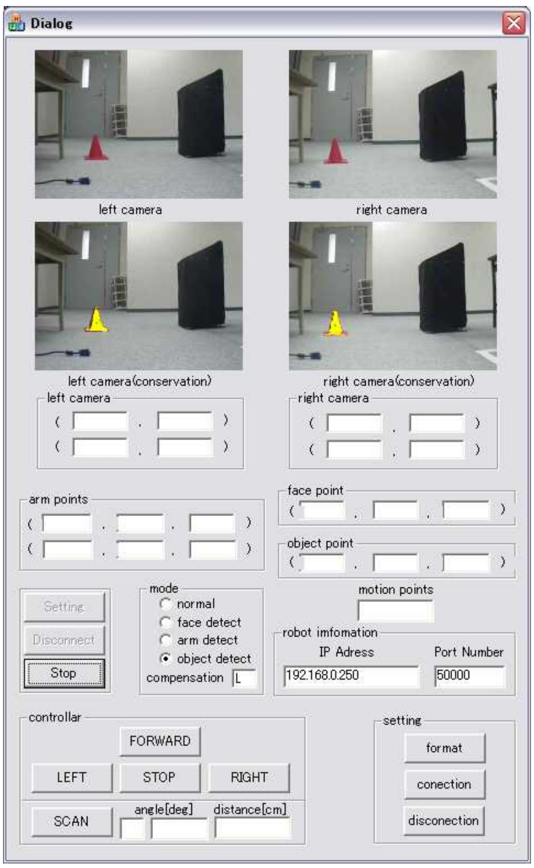

Fig.9.Excution result (Object recognition)

V. CONCLUSION

It is considered possible to calculate the position of the object which a user designates by pointing action. It is confirmed that the proposed method successfully calculates both the user's position by recognizing user's face and the position of the designated object by detecting the user's arm. Calculation results contain errors, but they are considered to be within a tolerance as the behavior of a robot will be corrected with additional voice command from the user when it tries to attain the task given by the user.

The design and implementation of an object indication system using pointing action are generally seemed to be over; the promotion of efficiency of system is attempted while testing it. The validity of the object indication system when the robot is controlled using pointing action, how much correction of robot behavior by voice interruption is necessary must be estimated to aim at developing the robot controlling system using voice and pointing action.

ACKNOWLEDGMENTS

We greatly appreciate the aid of the Grant-in-Aid for Scientific Research (S) and (A).

REFERENCES

[1] M. Inaba, S. Kagami, F. Kanehiro, Y.Hoshino, H. Inoue, Remote-Brained Robot Approach, International Journal of Robotics Research, Vol.19, No.10, pp.933-954, 2000

[2] Yasuhiro Watanabe, Norihiro Abe, Kazuaki Tanaka, Hirokazu Taki, Tetsuya Yagi, Multimodal communication system allowing man and avatar to use voice and beck, 3rd International Conference on Information Technology and Applications(ICITA'2005), pp.161-166

[3] Hiroki Goto, Norihiro Abe, Kazuaki Tanaka, Yoshihiro Tabuchi, Hirokazu Taki, Shoujie He: Usage of Shared Memory for Multimodal Data Processing in an Outdoor Mobile Robot, proc. ISR (36th International Symposium on Robotics) (CD-ROM), 2005

[4] Moez Bellamine, Norihiro Abe, Kazuaki Tanaka, Hirokazu Taki :Remote Diagnosis System for Rotating Machinery Using Virtual Reality, IEICE Transactions,pp.895-903,2005

[5] Toshiaki Oomori, Norihiro Abe, Kazuaki Tanaka, Hirokazu TAKI, Shoujie HE: Concurrent development of Virtual Robots and Real Robots Based on Physical Low, IMEKO / IFAC / IFIP Workshop on Advanced Robot Systems and Virtual Reality.(CD-ROM), . 2005

[6] Norihiro Abe, Yoshihiro Tabuchi, Hirokazu Taki, Shoujie He " Synchronization between Audiovisual and Haptic Feeling for Constructing Edutainment Systems", international journal(Journal of Virtual Reality, accepted, 2006

©ISAROB 2009

The Fourteenth International Symposium on Artificial Life and Robotics 2009 (AROB 14th '09),
B-Con Plaza, Beppu, Oita, Japan, February 5 - 7, 2009

Effective RFID Tag Positioning Strategy for Mobile Robot with Indoor Mapping

Jaewook Shin[1], Moonsoo Chang[1], Gyumin Lee[1], Won-Seok Kang[2], Young-Duk Kim[2], Jinung An[2] and Poogyeon Park[1]

1: Department of Electronic and Electrical Engineering, Pohang University of Science and Technology
(Tel. 82-54-279-558; Fax. 82-54-279-290; E-mail: {shinshingo, gravi, madboys7, ppg}@postech.ac.kr)
2: Daegu Techopark Venture 2nd Plant, 75 Gongdanbuk2gil, Dalseo-gu, Daegu, 704-230, Korea
(Tel. 82-53-431-8601; Fax. 82-53-430-8479; E-mail: {wskang, ydkim, robot}@dgist.ac.kr)

Abstract: To achieve accurate localization of mobile robot in indoor environment, various methods which are based on RFID technology have been developed over the past decade. Especially, the distribution of RFID tags is one of the main issues in real-world applications. In this paper, we propose a new RFID tag arrangement strategy based on the topology of the given map. The proposed method divides the given map into geometric sections by applying Voronoi graph method. To estimate accurate position in local section, we adopt the particle filter; this causes computational complexity. By modified weighting of the particle filter, we can reduce the number of particles.

Keywords: Localization, RFID, Voronoi diagram, Topological map, Mobile Robot

I. INTRODUCTION

Localization is one of major issues for the mobile robot. Usually, the measured position of a mobile robot is different from the true position and this causes serious problems to moving the robot to the desired position.

To overcome this problem, various methods are proposed. The GPS (Global Positioning System) [1] and the RFID (Radio Frequency Identification) [2] provide absolute position information. For the indoor localization, a RFID system is extensively used because the GPS is not available. An RFID system consists of readers and tags and tags can provide absolute/relative position information to the reader in a range manner.

RFID systems can be divided by the way of tag responding into two types: passive or active [2][3][4]. RFID systems also can be categorized by distribution of tags [5]. To estimate the robot position in the map, various types of tag-deploying such as grid, equilateral triangulation and random distribution have been proposed [6].

In this paper, we present a strategy that is based on the geometrical segmentation of the given map. To achieve this result, the Voronoi diagram of the map is used. When the number of RFID tags is not sufficient to make repeatable patterns, the proposed method can help localization.

To estimate more accurate position, we adopt the particle filter that uses the other information from measurement units such as odometry and laser-range-finder. Moreover, we reduce the computational burden of the particle filter by using RFID tags.

This paper is organized as follows. In section II, we will present the method of the geometrical map segmentation and modified version. Then we describe the particle filter and modified application with the RFID information in section III. In section IV, we will

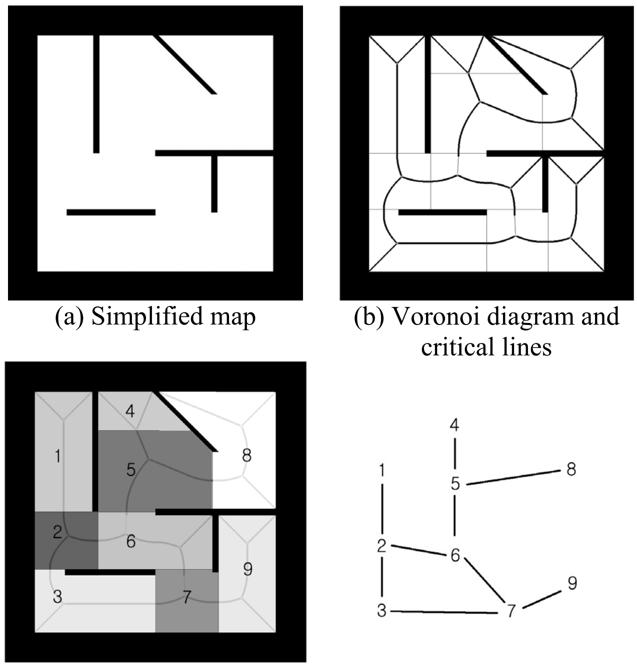

(a) Simplified map (b) Voronoi diagram and critical lines

(c) Regions (d) Topological graph

Fig.1.The result of geometrical map segmentation

propose an effective RFID tag positioning strategy. Then section V gives the result of simulation. Finally, we conclude the presented research work in section VI.

II. GEOMETRICAL MAP SEGMENTATION

The method of the geometrical map segmentation was presented[7]. We use modified version of the method as follows.

1) Thresholding and simplifying

First, we take thresholding. To make all obstacles in

©ISAROB 2009

the given map into convex polygon, small wiggled line should be corrected by some simplify because Voronoi diagram can handle convex figures only(Fig.1(a)).

2) Voronoi diagram

We achieve Voronoi diagram for all possible points and eliminate some points and lines that is out of the bound or in obstacles.

3) Critical points

Critical points are points on the Voronoi diagram that minimize clearance locally.

4) Critical lines

Critical lines are obtained by connecting each critical point with its basis points (Fig.1(b)).

5) Regions

Regions are obtained by dividing map with critical lines(Fig.1(c)).

6) Topological graph

The partitioning is mapped into an isomorphic graph(Fig.1(d)).

III. ESTIMATION WITH PARTICLE FILTER

1. Particle Filter

When we consider nonlinear system with non-gaussian error distribution, the particle filter is more effective method to estimate than classical approaches such as Kalman filter and extended Kalman filter. An implementation of the particle filter is given as follows [8][9].

Algorithm:

1) Initialization:

Generate $x_0^i \sim p_{x_0}, i = 1, \ldots, N$. Each sample of the state vector is referred to as a particle.

2) Measurement Update: Importance weighting

Update the weights by the likelihood.

$w_t^i = w_{t-1}^i p(y_t \mid x_t^i) = w_{t-1}^i p_{e_t}(y_t - h(x_t^i))$,

where $i = 1, 2, \ldots, N$.

After updating, normalize $w_t^i := w_t^i / \sum_i w_t^i$.

3) Resampling

a) Bayesian Bootstrap

Choose N samples with replacing particles from the set $\{x_t^i\}_{i=1}^N$, where the probability to choose sample i is w_t^i. Let $w_t^i = 1/N$. We call this procedure as sampling importance resampling(SIR).

b) Importance Sampling

If the effective number of samples is less than a threshold N_{th}, resampling becomes

$$N_{eff} = \frac{1}{\sum_i (w_t^i)^2} < N_{th},$$

where, $1 \le N_{eff} \le N$. The upper bound is for that all particles have the same weight, and the lower bound is for that only one particle is remained. We choose the threshold as $N_{th} = 2N/3$.

4) Prediction

Simulate the system and derive the prediction

5) $t := t + 1$*, iterate to 2)*

where

x_t state vector;

u_t measured inputs;

y_t measurements;

e_t measurement error;

2. Modifying Particle Filter for RFID

If the mobile robot read one or more tags, the probability of its existence near the tags greatly increases. Applying the RFID information to the particle filter can drastically reduce the number of particles which is required for localization [10].

In this paper, we adopt the modified particle filter for RFID system which can enhance the performance of the localization [11]. While processing the particle filter with the data from the sensor such as wheel-encoder or a laser-range-finder, the importance weighting step of the filter is modified with RFID information. If particles are in the range of responding tags, the likelihood of the particle will be increased (Fig. 1). The modified algorithm is given as follows.

Modified algorithm in particle filter
2) Measurement Update: importance weighting
For each particle after calculating likelihood
Loop *for each responded RFID tag*
If *(the tag matched to the particle)*
$count_m$ ++;
End If
End Loop
If *($count_m$ ==0)*
likelihood = 0;
Else
*likelihood = likelihood * $rate_w$ ^ $count_m$*
End If

where
$count_m$ matched tag count
$rate_w$ weight rate

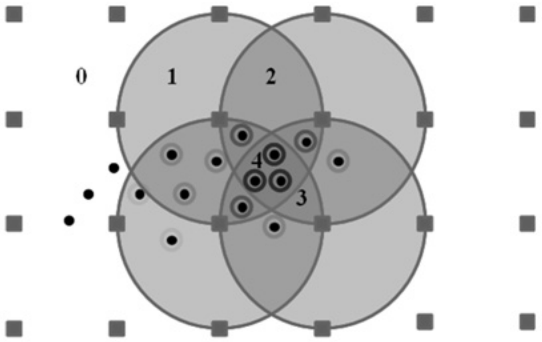

Fig.2. An example of the modified algorithm in particle filter. Each square represents a RFID tag and large circles are responding range of tags. The numbers are for matched tag count on the area and dots are for particles. The density of small circles represents assigned likelihood of each particle.

IV. RFID ARRANGEMENT

First, we define the two parameters: the number of RFID tags, N_{tag} and the number of sections in given map N_r. In the case of $N_{tag} >> N_r$, the distribution strategy is not important. Therefore we focus on the case $N_{tag} \approx N_r$. As shown in Fig.3 (b), patterned distribution does not consider the geometry of the map; some region has no RFID tags. The proposed method placed the RFID tags on the center of gravity of each region. Therefore robot meets the RFID tags once at least for a region. This prevents the error accumulation. Moreover, Voronoi diagram method generates lines which never cross the obstacles; robot in navigating has a tendency to follow the Voronoi diagram lines; a probability of the encounter between robot and RFID tags is increased when RFID tags are placed on the Voronoi diagram or near the Voronoi diagram

V. SIMULATION RESULT

The simulations are performed by using MATLAB. In all simulations, particle filter is used to estimate the position of the robot. The measurement length of Laser-range-finder is same and measurement noise is 20dB.

Fig.4 (a) and (b) uses the particle filter and laser-range-finder but RFID tags are used only in Fig.4 (a). In Fig.4, it is shown that fewer particles are used in Fig. 4(a) because absolute position can be measured.

Fig. 5 shows that the auxiliary sensor information improves the performance of the localization. Two simulations used same number of particles but their trajectory is somewhat different.

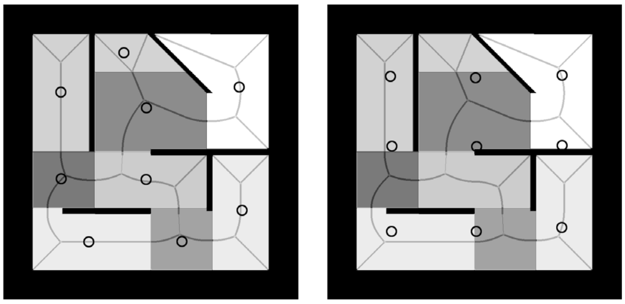

(a)Proposed (b) Patterned distribution

Fig.3. RFID arrangement

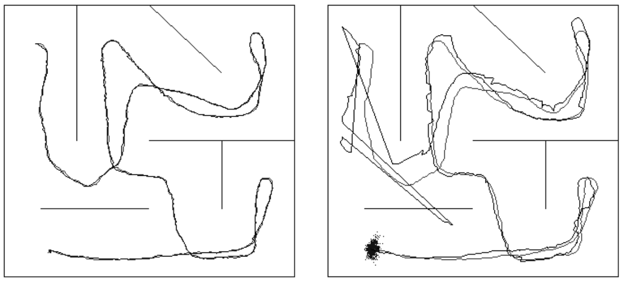

(a) N = 50, with RFID and laser-range-finder (b) N = 800, with laser-range-finder only

Fig.4. Tracking error with / without RFID tags

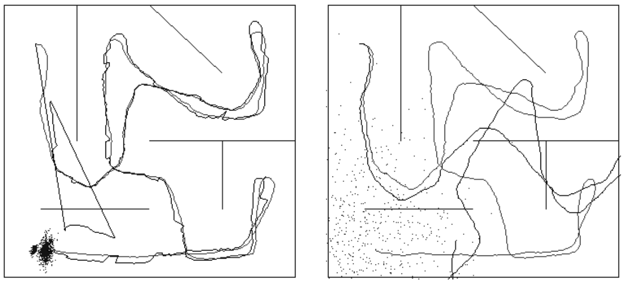

(a) N = 1000, with laser range finder (b) N = 1000, with particle filter only

Fig.5. Tracking error with / without laser-range-finder

VI. CONCLUSION

In this paper, we proposed RFID tags distribution strategy that is based on the geometrical segmentation with the Voronoi diagram. When the number of RFID tags is not sufficient to cover the whole map with patterns, the proposed method still aid the estimation of particle filter.

VII. ACKNOLEDGEMENT

This work was supported by DGIST (Daegu Gyeongbuk Institute of Science and Technology) and funded by MEST, Korea.

This work was supported by the Brain Korea 21 Project in 2008.

©ISAROB 2009

REFERENCES

[1] Garmin Corporation(2001). About GPS. Website, http://www.garmin.com/aboutGPS/

[2] K. Finkenzeller(1999). "RFID Handbook", John Wiley & Sons.

[3] G.-Y. Jin, X.-Y. Lu and M.-S. Park(2006), "An Indoor Localization Mechanism Using Active RFID Tag", IEEE International Conference on Sensor Networks, Ubiquitous, and Trustworthy Computing, Vol 1, pp. 40-43.

[4] L. M. Ni, Y. Liu, Y. C. Lau, and A. P. Patil(2003), "LANDMARC: Indoor location sensing using active RFID". In Proceedings of IEEE PerCom 2003, Dallas, TX, USA.

[5] J. Bohn, F. Mattern(2004), "Super-Distributed RFID Tag Infrastructures," in Proc. of the 2nd European Symposium on Ambient Intelligence (EUSAI 2004), Eindhoven, The Netherlands, pp.1-12.

[6] D.-S. Seo, D.-H. Won and G.-W. Yang et al.(2005), "A probabilistic approach for mobile robot localization under RFID tag infrastructures," ICASE.

[7] S. Thrun(1998). "Learning metric-topological maps for indoor mobile robot navigation", Artificial Intelligence, 99(1):21–71.

[8] M. S. Arulampalam, S. Maskell, N. Gordon, and T. Clapp(2002), "A tutorial on particle filters for online nonlinear/non-Gaussian Bayesian tracking," IEEE Trans. Signal Process., vol. 50, no. 2, pp. 174–188.

[9] F. Gustafsson, F. Gunnarsson, N. Bergman, U. Forssell, J. Jansson, R. Karlsson and P-J. Nordlund(2002), "Particle filters for positioning, navigation and tracking," IEEE Trans. Signal Processing, vol. 50, no. 2, pp. 425–437.

[10] D. Hähnel, W. Burgard, D. Fox, K. Fishkin, and M. Philipose(2003), "Mapping and Localization with RFID Technology", Technical Report IRS-TR-03-014, Intel Research Institute, Seattle, WA.

[11] G. Lee, M. Chang and P. Park(2008), "New Algorithm of Localization Using Odometry and RFID System", IEEK Conference on Information and Control Systems 2008, Korea.

The Fourteenth International Symposium on Artificial Life and Robotics 2009 (AROB 14th '09),
B-Con Plaza, Beppu, Oita, Japan, February 5 - 7, 2009

A New Grasp Quality Measure Considering Physical Limits of Robot Hands

Hyunhwan Jeong Jongwoo Park Joono Cheong
Dept. of Ctrl. & Instr. Engineering
Korea University
Jochiwon, 339-700 S. KOREA
email: {hyunhwanjeong, jekiel, jncheong}@korea.ac.kr

Abstract

In this paper, we introduce the extended grasp wrench space (GWS) to identify the applied location and the magnitude of the critical external wrench, in conjunction with the task wrench space (TWS) that is made up of all the possible external wrenches produced from the unit normal force to the surface points of the grasped object (that is, object wrench space(OWS)) In the extended GWS, the torque bound of each joint of the robot hand is considered in determining the grasp capability. Through the convexity analysis and linear programming technique, we propose a new way to obtaining an enhanced grasp measure which shows the clear physical meaning. We verify the proposed grasp analysis and quality measure using visual grasp simulator and various shaped polygonal objects.

1 Introduction

Despite the long history of research, the grasp planning methods for multi-fingered hands are not so efficient until now. This may be due to the fact that the grasp planning task requires a complicated and time-consuming mathematical computation associated with the convexity theory to confirm that the finite number of friction cones at the fingers' contacts positively spans any external wrench.

Liu et al. [1] introduced the force-closure grasp using ray-shooting technique, and grasp planning using force-closure grasp condition. Recently, Goldfeder et al. [2] presented a grasp planning method by simplifying object shapes using decomposition. Kirkpatrick[3] suggested the largest inscribed sphere that just fits within the convex hull of Grasp Wrench Space (GWS) as a task independent grasp quality measure. Li and Sastry [4] proposed to use the volume of ellipsoid generated by the grasp matrix as a measure of grasp quality. They also suggested Task Wrench Space (TWS). Pollard [5] introduced the Object Wrench Space (OWS) which is generated by object's geometry. Borst et al. [6] proposed a method to define the grasp quality measure using GWS, TWS, and OWS, where, in order to find grasp quality measure, they constructed TWS using OWS and Mass Wrench Space(MWS) and computed the circumscribe ellipsoid to the TWS and calculated the minimum distance from the ellipsoid to the convex hull of GWS.

In this paper, we propose a new grasp qualification measure which can confirm the capability of resiting under the disturbance forces. This measure basically seeks a weakest object position under the external force. The measure is on the basis of the minimal scale value between TWS and GWS, which was originally proposed by Borst et al. [6]. However, instead of using the circumscribed ellipsoid of TWS, we use the exact information of wrenches in TWS in order to obtain the minimal distance to extended GWS. We also apply this method to handle the case where the gravitational force acting on the object is the major source of external force.

The rest of the paper is organized as follows. In section 2, we present the details of our new grasp method, and we verify the theoretical result through the simulation study in section 3. Finally, section 4 addresses the conclusion and future works.

2 Grasp Quality Measure

2.1 Extended grasp wrench space

As shown in Fig.1, the force at the tip of a robot hand has a relation with the joint torque. Using this relation, we generate GWS which contains the information of joint torque range. Since the joints of the robot hand have torque limits, we can calculate the maximum end effector(contact point) force which is generated by the robot hand through the linear programming. We know that force and torque of each

©ISAROB 2009

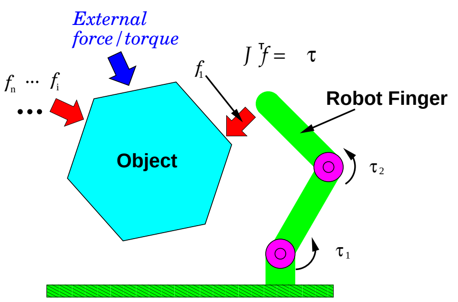

Figure 1: Force-torque relation in a real hand.

finger are related such as

$$\tau_{robot_i} = J_i{}^T f_{end,i}, \tag{1}$$

where $J_i \in \Re^{m \times n}$ is the Jacobian matrix of finger i. If we take the pseudo inverse of J_i to (1), we obtain

$$(J_i J_i{}^T)^{-1} J_i \tau_i = f_{end,i}. \tag{2}$$

Since the finger tip force $f_{end,i}$ indicates a different direction from the normal direction in the object surface, the pure component of $f_{end,i}$ toward the normal is obtained by

$$f_{c_i} = n_{c_i} \cdot f_{end,i}, \tag{3}$$

where n_{c_i} is the normal vector at contact i. Because we know the bound of each finger joint torque, the maximum of f_{c_i} is easily achievable by the linear programming such that:

$$\begin{array}{rl} \text{Objective function}: & f_{c_{i_{max.}}} = n_{c_i} \cdot (J_i J_i{}^T)^{-1} J_i \tau_i \\ \text{subject to}: & \tau_{min.} \le \tau_i \le \tau_{max.}, \end{array} \tag{4}$$

where $f_{c_{i_{max}}}$ is the contact force on the object surface and $f_{e_{max}}$ is the maximum finger tip force. Now we can make the grasp wrench space using these $f_{c_{i_{max}}}$ with the assumption of the friction contacts. While the conventional wrench space does not consider the actual scale of force at the contact point, the current grasp wrench space, i.e., the extended wrench space, takes into consideration the physical ranges of feasible contact forces from the fingers.

2.2 Suggested grasp quality measure

In order to implement our suggested grasp quality measure, we assume that object models are discretized into a sufficient number of facets(polygons) at the surfaces. We suppose that each facet of the object model is possibly subject to a unit external force acting into the normal surface. Thus, we can construct TWS by combining all these unit external forces. Due to the nature of TWS, it has a large number of directional vectors which point from the origin to the wrenches of TWS. The minimal scale value between the convex hull of TWS and that of the extended GWS will be the grasp quality measure we suggest; furthermore, the corresponding location where the minimum of scale is found is the fatal spot. The following is the procedures of finding the minimum distance between TWS and the extended GWS.

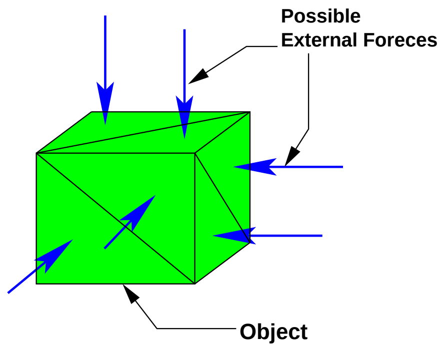

Figure 2: Possible external forces on an object that make OWS.

1. Make a discrete object model and create the corresponding OWS(which becomes the TWS).

2. Calculate convex hull of TWS.

3. Find the wrench vectors in TWS which makes the boundary of the convex hull of TWS.

4. Calculate the distance between convex hull of TWS and convex hull of extended GWS using the ray-shooting method.

The ray-shooting method is implemented as follows: First, define that the *i-th* wrench directional vector of convex hull of TWS is $T_{v_i} \in R^6$ and the *j-th* wrench vector of convex hull of extended GWS is $G_{v_j} \in R^6$. Then, find the hyper-plane equation of the convex hull (extended GWS) intersected to extended line from T_{v_i} by using the linear programming which maximizes the object function z such that

$$\begin{array}{rl} \text{Objective function}: & z = T_{v_i}^T x \\ \text{subject to}: & G_{v_j}^T x \le 1 \quad j = 1, 2, \ldots, N \end{array} \tag{5}$$

Finally, find the minimum scale between T_{v_i} and the intersection point in the boundary of the convex hull of extended GWS for all i. This minimum scale value

©ISAROB 2009

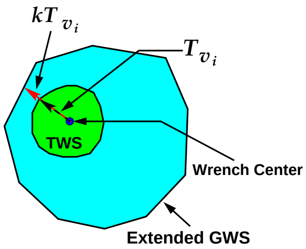

Figure 3: Schematic of the grasp measure.

is the grasp measure, which is mathematically written as

$$Q_g = \{k \in \Re | \min(k), \text{for } \forall T_{v_i} \& \ kT_{v_i} \in \partial(\text{EGWS})\}$$

where k is a scalar constant and ∂(EGWS) denotes the surface of the extended GWS. (Please see Fig.3 for the schematic of the grasp measure.) Thus, it is clear that our measure value directly implies the magnitude of the maximum external force applied normal to a particular facet of the polygonal object without causing unstable grasp. Since we are able to compute that a particular T_{v_i} yields the minimum scale value, the corresponding facet of the object surface where the T_{v_i} is created from the external is the weakest spot.

2.3 Application: Under gravity load

We may apply the proposed grasp measure to verify the grasp stability to the case where the only external force is from the gravity. Since the gravity is acting on each particle of the rigid object as shown in Fig.4(a), it is tricky to handle the distributed load in practice. So an easy way is to use the equivalent single force at a particular point as shown in Fig.4(b). If this equivalent force does not exceed the allowable load at the location, then we can say that the grasp under the gravity load is stable.

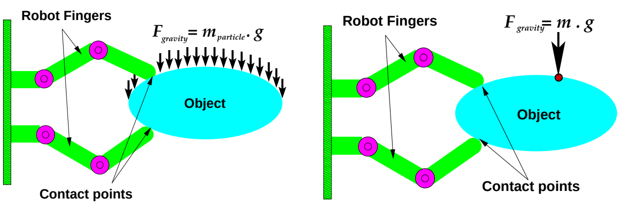

(a) Distributed gravity load (b) Equivalent gravity load

Figure 4: Gravity load.

Table 1: Results of the simulation with different objects.

Object model	Box	Cylinder	Cup	Arbitraty
Grasp type	Pinch	Spherical	Spherical	Spherical
Grasp measure (Q_g)	1.782	1.598	0.745	0.167
Meshes (units)	1200	1044	1740	306
Calculation time (sec.)	0.198	2.122	42.692	1.818
X	0.999	0.000	0.000	0.961
Y	0.000	0.000	0.000	0.260
Z	0.000	0.999	0.998	0.075
Rx	0.000	-0.033	0.053	0.011
Ry	0.0367	0.016	0.011	-0.043
Rz	-0.018	0.000	0.000	-0.002

Table 2: Results of simulation with different grasp types and contact configurations.

Object model	Box	Box	Box
Grasp type	Spherical	Pinch	Pinch
Grasp measure (Q_g)	2.181745	1.821307	0.001641
Meshes (units)	1200	1200	1200
Calculation time (sec.)	0.204855	0.215650	0.225968
X	-0.999179	0.999158	0.999158
Y	0.000000	0.000000	0.000000
Z	0.000000	0.000000	0.000000
Rx	0.000000	0.000000	0.000000
Ry	0.036717	0.036716	0.036716
Rz	-0.017109	-0.018295	-0.018295

3 Simulation

In the simulation, the considered robot hand is assumed to be of the Barret hand type, having three fingers, each being 3-DOFs. So, the total DOFs of the hand are nine. In the simulator, we use taxonomy based preformed grasp for grasping the object and use sampling method to find contact points, which was addressed in [7]. In this simulation, we assume the torque min-max limits of the joints fingers are ± 1.

We use the objects including box, cylinder, cup type and arbitrary shaped object. These 3-D object models which are used in our simulation have hundreds or thousand polygons. In our test, we apply the pinch grasp and spherical grasp for grasping a box object, spherical grasp for grasping a cylinder, a cup and an arbitrary shaped object.

Firstly, we compare the grasp measures for different objects. Fig. 5 shows the screen shots of grasping the target objects, and Table 1 shows the corresponding results such as grasp types, measure values, calculation time and weakest directions. From the figure, we can confirm the validity of the computed weakest position of the object. Secondly, we compared the grasp qualities between grasp configurations. In this test, we test two different sets of contact points, where one is the marginal force-closure and the other one is strict force-closure as illustrated in Fig. 6. The summary of the result is given in Table 2.

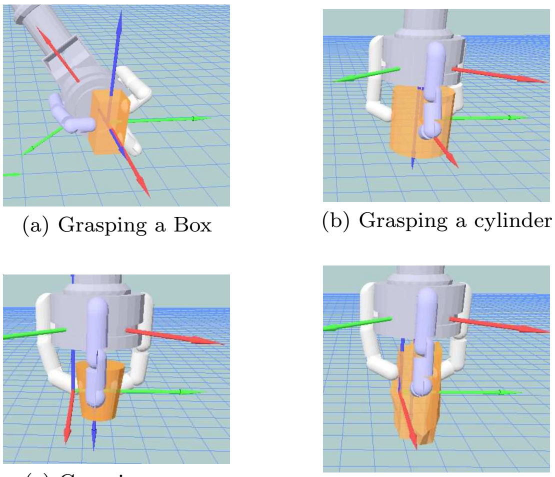

(a) Grasping a Box (b) Grasping a cylinder (c) Grasping a cup (d) Grasping a arbitrary shape

Figure 5: Screen shots of various grasps.

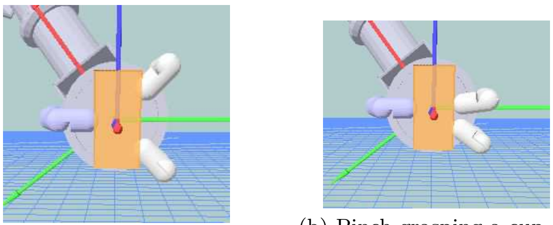

(a) Pinch grasping a cup on the stable contact points (b) Pinch grasping a cup on the marginal contact points

Figure 6: Screen shots of grasps for the different finger configuration and contact position.

4 Conclusion and Future Works

We have proposed the extended grasp wrench space using the robot hand's physical torque limits. Using the extended GWS, a new grasp quality measure has been suggested, along with the procedures of computing the measure. Through the proposed measure, we could find the weakest spot of the object surface under the external force for each finger configuration. We have demonstrated our algorithm for examples of various object grasps. For each example, the grasp quality measure has been computed together with the weakest spot. In the future, a more efficient way to reduce the computation time will be studied on the basis of the proposed framework. Also, we think of extending the algorithm to cope with the gravitational force field as the external force on the object surface.

Acknowledgements

This research was performed under the support of the Intelligent Robotics Development Program, one of the 21st Century Frontier R&D Programs funded by the Ministry of Knowledge Economy, Republic of Korea.

References

[1] Y. H. Liu, D. Ding and M. L. Lam, "3-D Grasp Analysis and synthesis using the ray-shooting technique," *Robotics Welding, Intelligence and Automation*, LNCIS 299, pp. 80-109, 2004.

[2] C. Goldfeder, P. K. Allen, C. Kackner and R. Pelossof, Grasp plannig via decomposition tree, *in Proc. IEEE Int. Conf. Robotics and Automation*, pp. 4679-4684, 2007.

[3] David Kirkpatrick, Bhubaneswar Mishra, and Chee-Keng Yap, "Quantitative Steinitz's Theorem with Applications to Multifingered Grasping," *in Proc. of the 20th ACM symp. on Theory of Computing*, pp. 341-351, 1990.

[4] Zexiang Li and Shankar S. Sastry, "Task-Oriented Oprimal Grasping by Multifingered Robot hands," *IEEE J. of Robotics and Automation*, vol. 4, pp. 32-44, 1988.

[5] Nacy S. Pollard, "Parallel methods for synthesizing whole-hand grsps from generalized prototypes," *Technical Report AI-TR 1464, MIT Artificaial Inteligence Laboratory*, 1994.

[6] Ch. Borst, M. Fischer, G. Hirzinger,"Grasp planning: how to choose a suitable task wrench space," *in Proc. IEEE Int. Conf. Robotics and Automation*, vol. 1, pp. 319-325, 2004.

[7] H. Jeong, J. Park, J. Cheong, F. C. Park, "Grasp planning for Three-Fingerd Robot Hands using Taxonomy-Based Preformed Grasp and Object Primitives," *The Journal of Korea Robotics Society*, vol. 3, pp. 123-130, 2008.

©ISAROB 2009

The Fourteenth International Symposium on Artificial Life and Robotics 2009 (AROB 14th '09),
B-Con Plaza, Beppu, Oita, Japan, February 5 - 7, 2009

Generation of a pick and place trajectory model for the tip of a robotic manipulator arm for an loading and unloading operation

Manjunath TC[1], Ishani Mishra[2], Anil Kumar Satapathy[3]

[1]*Professor & Head, ECE Dept., NHCE, Bangalore-87.*
[2]*Post Graduate M.Tech Student, Dept. of Electronics & Communications Engg.,*
National Institute of Science & Technology, Palur Hills, Berhampur, Ganjan Dist., Orrisa-760018, India.
Email : ishani_mishra2002@yahoo.co.in mishra.ishani@gmail.com
Phone : +91 80 66297777 Extn. 2004 ; Fax : +91 80 28440770 ; Mobile +91 09740097978
[3] *Senior Lead Engineer, General Motors, Bangalore, Karnataka*

Abstract : In the work considered in this paper, a mathematical formulation of a pick and place trajectory is designed for a robotic manipulator arm which is used to do a loading and unloading operation & its simulation done using a graphical user interface developed in C++. Direct kinematics gives the position and orientation of the robot arm in the 3D space. Inverse kinematics gives the sets of joint variables that will satisfy the same position and orientation. In between these two kinematic problems, robot motion comes into the picture. The robot motion from the pick point to the place point (through a number of via points) consists of paths and trajectories. These paths and trajectories are nothing but the various possible routes that are taken by the robot to move from the source (pick point) to the goal / destination (place point) and traversed in a specified amount of time. Trajectory planning schemes helps us to interpolate / approximate between these pick and place points using a smooth motion. This PNP trajectory model which is formulated in the form of 4 matrices is given as input to the robot. The robot picks up the object from one place and keeps it at another place in a specified time through the via points. The trajectory obtained so is called as the PNP trajectory which consists of 4 points plus the intermediate or the via points, viz., the pick point, lift-off points, via (intermediate) points, set-down point, place point. The simulation results show the effectiveness of the method.

Keywords: Robot, Simulation, PNP, Job operation, Trajectory, Model.

I. INTRODUCTION

PNP robots exhibit Pick & Place type of motion or trajectory as shown in Fig. 1. Any typical robotic operation begins with the robot picking up the object. The main function of any robotic manipulator is to pick up an object from one particular place, which is in one particular position and orientation, and keep it at another particular place in another position and orientation [1]. Robot picks up an object from one place, moves along a specified path and keeps it at another place in a specified time, thus giving rise to a trajectory. The trajectory obtained so is called PNP trajectory. The pick and place points has to be explicitly specified by the user, whereas the path can be specified by the user or the robot can judge its own path using computer vision. The path that is taken by the robot to reach the destination may be the shortest one or longest one irrespective of overcoming the obstacles in its path of motion and preventing collisions with them. This operation is called as PNPO (Pick aNd Place Operation). The path or route that is taken by the robot from the pick point to the place point with the time information is called as the four point minimal pick and place trajectory. Any PNP trajectory will have 4 points passing through it, which are discussed in greater detail one in next section. They are the pick point, lift-off point, via points, set-down point & the place point.

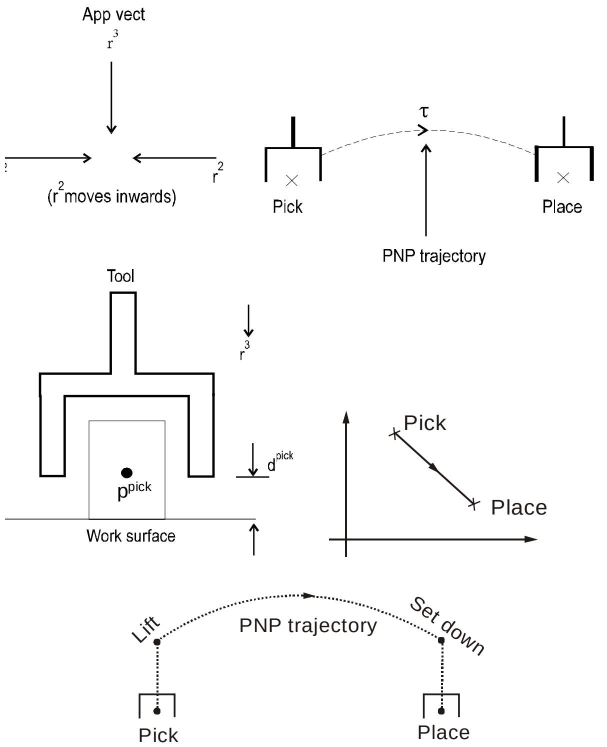

Fig. 1 : Pick point & the approach / sliding vector
A PNP robot & its trajectory

©ISAROB 2009

The Fourteenth International Symposium on Artificial Life and Robotics 2009 (AROB 14th '09),
B-Con Plaza, Beppu, Oita, Japan, February 5 - 7, 2009

2. MATHEMATICAL MODEL OF PNP TRAJECTORY

Pick Point [p^{pick}] is the first point in the PNP trajectory. Object is picked up using the approach vector, which is perpendicular to the work surface, and sliding vector moving inwards (pick using fine motion). Object is picked up at its centroid G, i.e., tool-tip p and G of the object should be same. Here, d^{pick} is the distance of the object from the work surface to the centroid of the object at the pick point p^{pick} and p^{pick} (position of the object at the pick point) and R^{pick} (orientation of the object at the pick point) are to be specified by the user, i.e., the user specifies the pick point. To do this operation, give the matrix T^{Pick} as input to the Inverse Kinematic Problem (IKP). When this matrix is inputted to the IKP, sets of joint variables will be calculated and the tool will be properly configured so as to come and pick up the object. The position and orientation at the pick point is given by [1], [2]

$$T^{pick} = \begin{bmatrix} R^{pick} & p^{pick} \\ 0\ 0\ 0 & 1 \end{bmatrix} \tag{1}$$

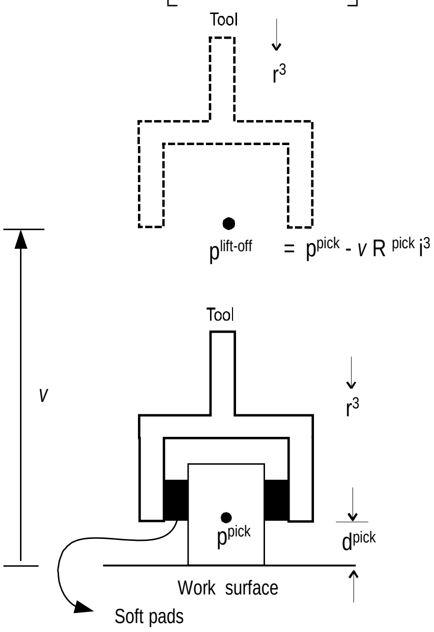

Fig. 2 : Lift-off operation

Lift-off Point [$p^{lift\text{-}off}$] is the second point in the PNP trajectory (Fig. 2). It is a point very near to the pick point, but situated directly above the pick point by a small amount of distance *v* so that the orientation of the tool at lift-off point is the same as that of pick point, i.e., $R^{lift\text{-}off} = R^{pick}$, but position p is different. (use fine motion to bring the object to the lift-off point). Position of the lift-off point is obtained by moving backwards along the approach vector from p^{pick} by a distance *v*, so that $p^{lift\text{-}off} = p^{pick} - v\, R^{pick}\, i^3$. To do this operation, give the matrix $T^{Lift\text{-}off}$ as input to the IKP [3]. When this matrix is inputted to the IKP, sets of joint variables will be calculated, the robot comes from the home position, picks up the object using fine motion and exactly lifts it up using the fine motion and stops at the lift-off point. Note that from the IK, knowing the position of the tip, approach vector, length of the tool, the position of the wrist is obtained by using the equation $p^{wrist} = p - d_n r^3$. The position and orientation at lift-off point is given by

$$T^{Lift\text{-}off} = \begin{bmatrix} R^{Pick} & p^{Pick} - v R^{Pick} i^3 \\ 0 & 1 \end{bmatrix} \tag{2}$$

Set-down Point [$p^{set\text{-}down}$] is the third point in the PNP trajectory and is analogous to the lift-off point as shown in Fig. 3. It is a point very near to the place point and directly above the place point, but situated by a small amount of distance *v* so that the orientation of the tool at the set-down point is same as the orientation of the tool at the place point ; i.e., $R^{set\text{-}down} = R^{place,}$ but position p is different. (bring the object to the set down point using gross motion). Position of the set-down point is obtained by moving backwards along the approach vector from p^{place} by a small amount of distance *v*, so that $p^{set\text{-}down} = p^{place} - v\, R^{place}\, i^3$. It is the point where the initiation of the object placement just begins, i.e., the robot is about to place the object. To do this operation, give the matrix $T^{Set\text{-}down}$ as input to the IKP [4]. When this matrix is inputted to the IKP, sets of joint variables will be calculated, the robot comes from the home position, picks up the object using fine motion and exactly lifts it up using the fine motion and reaches the set-down point using the gross motion. The p and R at set-down point is given by [1]

$$T^{Set\text{-}down} = \begin{bmatrix} R^{Place} & p^{Place} - v R^{Place} i^3 \\ 0 & 1 \end{bmatrix} \tag{3}$$

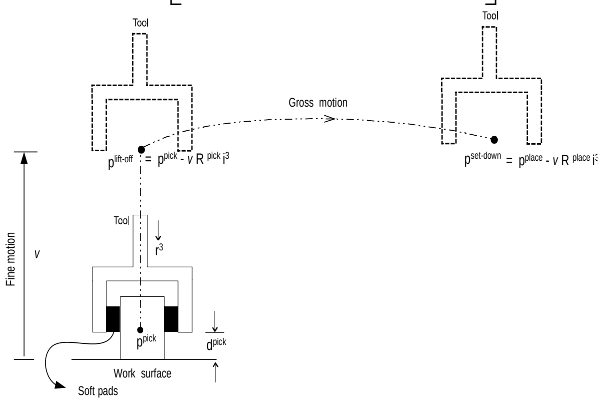

Fig. 3 : Object being lifted from pick to set-down point

Place Point [p^{place}] is the final point of the PNP trajectory. It is the point where the object has to be placed in the desired position and orientation (place using fine motion). Object is placed using the approach vector 90° to the surface & sliding vector moving outwards. d^{place} is the distance from the surface to the centroid of the object at the place point p^{place}. The p^{place} (position of the object at the place point) and R^{place} (orientation of the object at the place point) are to be specified by the user [6]. To do this operation, give the matrix T^{Place} as input to the IKP. When this matrix is inputted to IKP, set of joint variables will be calculated, the robot comes from the home position, picks up the object using fine motion and exactly lifts it up using the fine motion, reaches the set-down point using the gross motion and places the object at the place position in the desired position and orientation using the fine motion as shown in Fig. 4. The p & R at the place point is given by [1], [5]

$$T^{Place} = \begin{bmatrix} R^{Place} & p^{Place} \\ 0\ 0\ 0 & 1 \end{bmatrix} \quad (4)$$

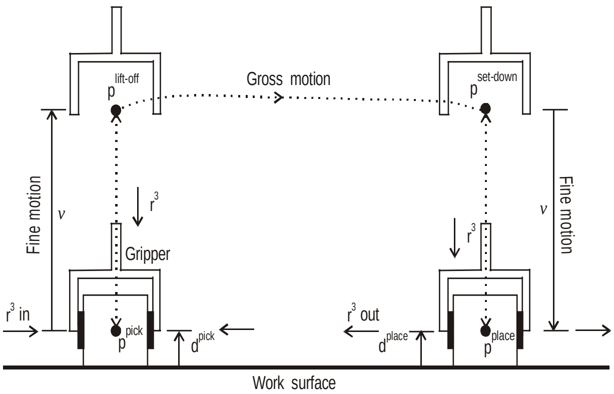

Fig. 4 : Sequence of operations from the pick point to the place point via the lift-off & the set-down point

If all the 4 matrices T^{Pick}, $T^{Lift\text{-}off}$, $T^{set\text{-}down}$ and T^{Place} are given in succession as input to the inverse kinematic problem, the robot comes from the home position, picks up the object (using fine motion) lifts up (using fine motion), transports the part from lift-off point to the set-down point using gross motion, gets ready to place the object and places the object in the desired position and orientation (using fine motion) [8]. If any obstacles are present in the work space, then a number of via points (intermediate points) are used to move round the obstacles to avoid collision by sensing them and circumventing the obstacles as shown in Fig. 5. Note that lift-off and set-down points are visited twice in a PNP trajectory as shown in Fig. 5 [7].

A typical 4 point minimal PNP trajectory is shown in Fig. 5. The constraints for doing PNPO are [1]

- If $d^{place} = d^{pick}$, object is picked up from the work surface and placed exactly on the work surface [1].
- If $d^{place} > d^{pick}$, the placed part or object is unsupported (hanging in air) when it reaches the destination and the robot opens its fingers and the object or the part falls down because of gravity (some inaccuracy has been resulted) [5].
- If $d^{place} < d^{pick}$, an attempt is made by the robot to penetrate the object into the work surface when part is placed, as a result of which the part slides in between the fingers of the gripper if the work surface is hard OR the part moves into the work surface if the work surface is soft [6].
- So, for effective PNPO, the constraint is [1]

$$d^{place} = d^{pick} \quad \& \quad p_3^{Place} = p_3^{Pick} \quad (4)$$

This is shown in the Fig. 6.

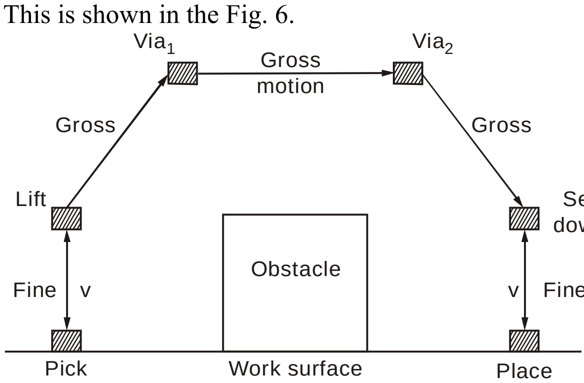

Fig. 5 : A typical 4 point minimal PNP trajectory

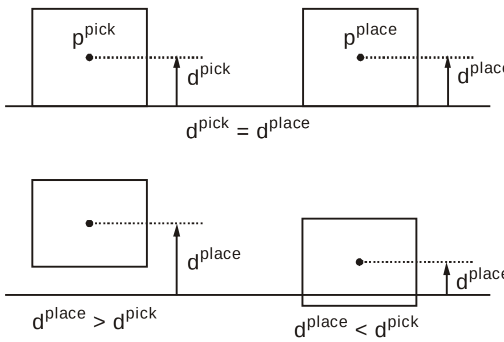

Fig. 6 : Constraints for doing effective PNP operation

The sequence of PNP motions shown in Fig. 5 is called as the minimal four point PNP trajectory. Any PNP trajectory has got 6 knot points (pick, lift-off, via 1, via 2, set-down, place) and 5 individual sub-trajectories (pick-lift off ; lift off-via 1 ; via 1-via 2 ; via 2-set down ; set down-place). A horizontal work surface is assumed for doing the PNP operation [7]. If part feeders etc., are used, then use different PNP surfaces or levels and the height of the stack comes into picture [9].

From the PNP trajectory, we see that robot reaches or approaches the object using fine motion and picks it up. This operation given by T^{Pick}. Using fine motion technique, object or part is lifted from the pick up point to the lift-off point. This operation is given by $T^{Lift\text{-}off}$. Using gross motion, object or part is transported to the set-down point [1]. This operation is given by $T^{Set\text{-}down}$. During this transportation, if any obstacles occur or come in the way of robot motion, a number of via points or intermediate points has to be visited in order to over come the obstacle (move round the obstacle, circumvent the obstacle). This operation is given by $T^{via\text{-}1}$ & $T^{via\text{-}2}$. At set-down point, the robot is about to place the object, i.e., the initiation of the object placement just begins. The robot places the object at the place point using fine motion techniques in the desired p and R and then comes back to its home position. This operation is given by T^{Place}.

3. SIMULATION RESULTS

A graphical user interface (GUI) was developed in C++ language and a 4-axis SCARA robot was used for the simulation purposes. The mathematical model is used to generate the pick and place points. Once the pick & place points are specified as 3D input to the robot, the robot does the PNPO. The results of the simulation are shown in the Figs. 7 to 10 respectively.

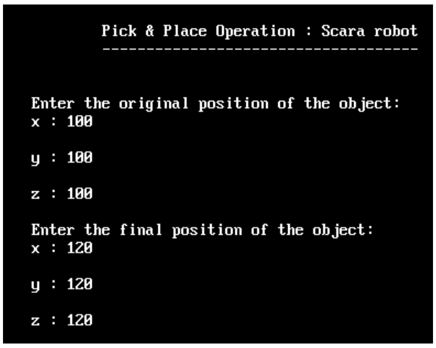

Fig. 7 : Inputs to the PNP operation

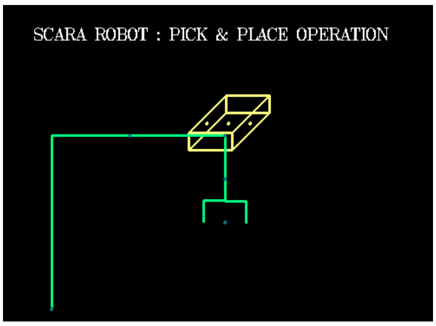

Fig. 8 : SCARA robot in home position (Ref)

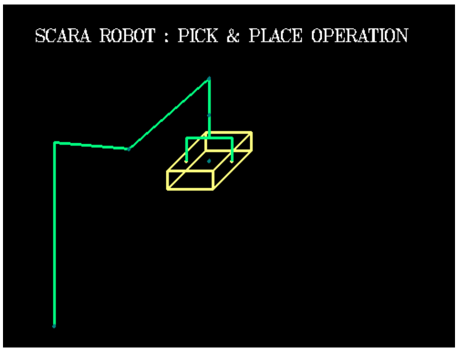

Fig. 9 : SCARA robot coming from home position & picking the object

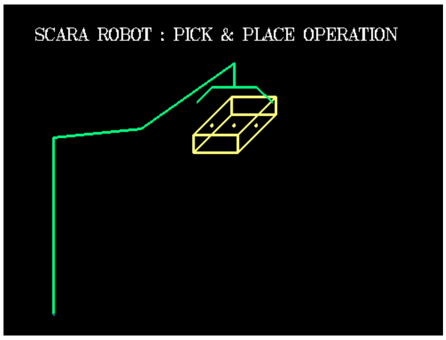

Fig. 10 : SCARA robot coming from home position & placing the object

4. CONCLUSION

A mathematical model of the trajectory generation for a 4-axis SCARA robot was developed and this was used as input to the robot in the simulation performed using a GUI in C++. The simulation results show the effectiveness of the developed method.

REFERENCES

[1] Robert J. Schilling, "Fundamentals of Robotics - Analysis and Control", PHI, New Delhi.
[2] Manjunath T.C., "Fundamentals of Robotics", Fourth edn., Nandu Publishers, Mumbai, 2005.
[3] Craig J, "Introduction to Robotics : Mechanics, Dynamics & Control", Addison Wessely, USA, 1986.
[4] Klafter, Thomas and Negin, "Robotic Engineering", PHI, New Delhi.
[5] Fu, Gonzalez and Lee, "Robotics: Control, Sensing, Vision and Intelligence", McGraw Hill.
[6] Manjunath, T.C., "Fast Track to Robotics", Second edn., Nandu Publishers, Mumbai, 2005.
[7] Groover, Weiss, Nagel and Odrey, "Industrial Robotics", McGraw Hill.
[8] Ranky, P. G., C. Y. Ho, "Robot Modeling, Control & Applications", IFS Publishers, Springer, UK.
[9] Crane, Joseph Duffy, "Kinematic Analysis of Robotic Manipulators", Cambridge Press, UK.

©ISAROB 2009

The Fourteenth International Symposium on Artificial Life and Robotics 2009 (AROB 14th '09),
B-Con Plaza, Beppu, Oita, Japan, February 5 - 7, 2009

Mathematical modeling for morphogenesis of leaf with employing cell automata and reaction-diffusion equation

Koji Ishii[1], Hiroyuki Hamada[1] and Masahiro Okamoto[1,2,3*]

[1]*Laboratory for Bioinformatics, Graduate School of Systems Life Sciences, Kyushu University, Japan*
[2]*Kyushu University Bio-Architecture Center, Japan*
[3]*Metabolic Profiling Group, Redox Navi Institute, Kyushu University, Japan*
**Address correspondence to this author at Laboratory for Bioinformatics, Graduate School of Systems Life Sciences, Kyushu University, 6-10-1 Hakozaki, Higashi-ku, Fukuoka 812-8581, Japan.*
(E-mail add: okahon@brs.kyushu-u.ac.jp)

Abstract: The phenome analysis is used for an elucidation of the leaf morphogenesis. However, it is difficult to identify a complicated biochemical system which exists between genome and phenome. Designing a mathematical model for the morphogenesis has a possibility to infer the complicated system by using the observed data on phenome analysis. We attempted to design a novel mathematical model in order to analyze the effects of the interaction between the expansion of leaf blade and elongation of leaf venation in the development of leaf shape, and discussed an availability of the proposed model on the numerical analysis of development of leaf. The expansion of leaf blade and the elongation of leaf venation were designed by employing the reaction-diffusion equation and cellular automata (CA) theory, respectively. As for the numerical simulation for development of *gingko*'s leaf primordium, the proposed model could realize several well-known biological findings such as a reconnection of leaf venation. Moreover, the numerical analysis demonstrated that the interaction between the elongation of leaf venation and the expansion of leaf blade was indispensable for the complicated pattern formation of leaf venation. These results agreed with biological findings, which implied that the proposed model was useful for elucidating a development of leaf.

Keywords: Morphogenesis, Cellular automata, Reaction-diffusion equation, Pattern formation, Leaf shape, Leaf venation.

I. INTRODUCTION

Morphogenesis of organisms is important process related to a determination of size, shape and mutual arrangement of tissues, and is regulated by a complicated biochemical system which exists between the genotype and the phenotype. The phenome analysis is used for an elucidation of relationship between genotype and phenotype by comparing wild type with mutant strain with using genetic engineering. In particular, the phenome analysis for higher plants such as *Arabidopsis thaliana* was implemented in world wide, and contributed to clarify a mechanism of morphogenesis. Although the analyses identified the genome related to the morphogenesis, it was difficult to infer the complicated biochemical system. Designing of the mathematical model which infers the complicated biochemical system is useful for elucidating a mechanism of morphogenesis in detail. With employing a reaction-diffusion equation, Turing [1] demonstrated that the unstable diffusive dynamics on activator-inhibitor system affected the pattern formation of fish's skin (Turing model). Moreover, Meinhardt *et al.* [2] represented a differentiation of plant cells with applying Turing model, and realized a branching pattern of leaf venation (Meinhardt's model). On the other hand, by employing an automata theory, Lindenmayer [3] designed a mathematical model for a branching pattern formation of tree, and demonstrated that the interactions between tissues were indispensable for the development of organisms. Furthermore, Markus *et al.* [4] designed a mathematical model (Markus's model) for a development of leaf venation based on gene regulation with employing a cellular automata (CA) theory, and realized a pattern formation of leaf venation as same as that seen in Meinhardt's model. Thus, the numerical analysis based on the phenome analysis is useful for elucidating a mechanism of morphogenesis. However, since these conventional models had not considered an expansion of leaf blade, it was difficult to realize several complicated pattern formations of leaf venation such as reconnection phenomena. The mathematical model which considers interaction between the expansion of leaf blade and elongation of leaf venation could elucidate a mechanism of the complicated pattern formation of leaf venation in more detail. In this paper, we attempted to design a novel mathematical model (proposed model) for which interaction between the expansion of leaf blade and elongation of leaf venation

©ISAROB 2009

affects the development of leaf shape. The expansion of leaf blade and the elongation of leaf venation are designed by employing a reaction-diffusion equation and a CA theory, respectively. Next, we shall numerically analyze a development of *gingko*'s leaf primordium, and verify an effect of the expansion of leaf blade in the pattern formation of leaf venation with changing a kinetic parameter. Finally, we shall discuss a validity of the proposed model on the numerical analysis of development of leaf.

II. EXPERIMENTAL PROCEDURES

1. The proposed model

This study assumed that the mesophyll cell of leaf differentiates into either venation cell or blade cell. With using both a set of reaction-diffusion equations and CA theory, the proposed model considered an interaction between an elongation of leaf venation and an expansion of leaf blade.

A. The growth of blade tissue

The growth of blade tissue is depended on a dynamic behavior of Mesophyll Morphogenesis Factor (MMF) such as water and nutrient salts. MMF is supplied from the venation tissue, and is propagated on the blade tissue.

$$\frac{\partial U}{\partial t} = D_x \frac{\partial^2 U}{\partial x^2} + D_y \frac{\partial^2 U}{\partial y^2} - \alpha \qquad (1)$$

where U is level of MMF. Both Dx and Dy are diffusion coefficient to x-axes and y-axes, respectively. The α is consumption rate of MMF on both the blade cell and mesophyll cell. This mathematical model is presumed that the size of the blade tissue is nearly equivalent to the area on which MMF can propagate.

B. The elongation of venation tissue

Venation forming factor (VCF) such as phytohormone is regulated by transport factor, propagated and accumulated on whole cell. With stimulating by VCF, mesophyll cell differentiates into venation cell. Markus et al. [4] designed the mathematical model to represent the differentiation of mesophyll cell into venation cell, in which VCF, transport factor of VCF and gene for venation formation are set to Substrate, Activator and Inhibitor, and Gene, respectively (Markus model). The proposed model is integrated algorism of the Markus model with our algorism (Fig.1). The u, v and s in Fig.1 represent the level of Activator, Inhibitor and Substrate, respectively. According to the procedure, the levels of these factors at the next state are dependent on the current state of these factors. The c, d, γ, δ_1, δ_2, δ_3, δ_4, β_0, β_1 and η represent kinetic parameters for each transient. The ω is the amount of supply of VCF, ε is the threshold for Activator, u_{max} is the upper limit of Activator and g takes the two state, 1 or 2, which determines whether the mesophyll cell differentiates into the venation cell (g=1) or the blade cell (g=0). Step (0) determines whether the procedures from (I) to (VIII) are executed or not at the mesophyll, the venation and the blade cells. Step (VIII) shows the calculation of the moving-average for u,v and s. The initial conditions of u, v and s for the formed mesophyll cell are set to 0.0, 0.0 and 1.0, respectively.

$u_t \rightarrow u^{I} \rightarrow u^{II} \rightarrow u^{III} \rightarrow u^{IV} \rightarrow u^{V} \rightarrow u_{t+1}$
$v_t \rightarrow v^{I} \rightarrow v^{II} \rightarrow v^{III} \rightarrow v_{t+1}$
$s_t \rightarrow s^{I} \rightarrow s_{t+1}$

(0) if U>0, then goto (I)
(I) if $u_t > d \cdot v_t$, then $u_t = c \cdot u_t \cdot s_t$, else $u^{I} = u_t$
(Ia) if $u^{I} > u_{max}$, then $u^{II} = u_{max}$, else $u^{II} = u^{I}$
(II) $u^{III} = \delta_1 \cdot u^{II} - \delta_2$
(IIa) $u^{III} < 0$, then $u^{IV} = 0$, else $u^{IV} = u^{III}$
(III) $v^{I} = \delta_3 \cdot v_t - \delta_4$
(IIIa) if $v^{I} < 0$,then $v^{II} = 0$, else $v^{II} = v^{I}$
(IV) $v^{III} = \gamma \cdot u^{IV} + v^{II}$
(V) $u^{IV} > \varepsilon$, then $g_{t+1}=1$, else $g_{t+1}=0$
(VI) if $g_{t+1}=1$,then $s^{I} = s_t + \omega - \beta 1 \cdot s_t$,
else $s^{I} = s_t + \omega - \beta_0 \cdot s_t$
(VII) if $g_{t+1}=1$,then uV $= u^{IV} + \eta$,else $u^{V} = u^{IV}$
(VIII) $u_{t+1} = < u^{V} >$, $v_{t+1} = < v^{III} >$, $s_{t+1} = < s^{I} >$

Fig. 1. Procedure of the mathematical model with cellular automata theory.

2. Numerical analysis

In this study, the numerical simulations of the proposed model for the spational pattern formation of *gingko*'s leaf primordium are implemented in arbitrary time on two dimensional surfaces (300 × 300 cells) simultaneously. Results are visualized at every 100 time step interval. The number of iterations is 500. Initial conditions of U, u, v and s are set to 1.0, 300.0, 0.0 and 0.2, respectively in only a mesophyll cell at the arbitrary corner (petiole). Numerical simulation result

©ISAROB 2009

with standard kinetic parameter (Table 1) is set to reference pattern. And we examine several effect of variation of diffusion coefficient on the pattern formation of leaf venation. Furthermore we evaluate the time course of both the number of whole cells (*Nwc*) and the development of leaf venation (*Ocp*) to validate the proposed model for simulating the spatiotemporal pattern formation of *gingko*'s leaf primordium. The *Ocp* is the ratio of the number of venation cells (*Nvc*) to *Nwc*, represented by,

$$Ocp = \frac{Nvc}{Nwc} \times 100 \qquad (2)$$

The spatiotemporal development of leaf venation was evaluated by using *Ocp*, which was observed at every 100 time step interval.

Table 1. The value of the standard kinetic parameters for *gingko*'s leaf

D_x	100.0	D_y	100.0
α	0.0001	c	2.7
d	2.0	γ	0.5
$u_{\max}$	250.0	δ_1	0.9
δ_2	1.0	δ_3	0.5
δ_4	2.0	ω	0.3
ε	70.0	η	0.0
β_0	0.2	β_1	1.0

III. RESULTS AND DISCUSSION

To validate adequacy of the proposed model, numerical analysis for the development of *gingko*'s leaf primordium was implemented by using a set of standard kinetic parameter shown in Table 1. Fig.2 shows the time courses of development of *gingko*'s leaf primordium. The venation tissue elongated with the expansion of blade tissue, and generated both the branching and filament pattern formation (Fig.2a: reference pattern). Moreover, blade tissue expanded in the form of fan shape. These results were qualitatively in good agreement with typical pattern formation shown in development of *gingko*'s leaf. When the elongation of venation tissue reached to the tip of leaf blade, the reconnection of leaf venation was generated between existing venation tissues. Berleth *et al.* reported that the reconnection occurred when the venation tissue fully elongated on the leaf blade [5]. This biological finding supported the numerical simulation result, which implied that the proposed model is useful for numerical analysis of the elongation of leaf venation in comparison with the conventional models. With setting *Dx* and *Dy* to 2000.0, since the blade tissue slightly expanded than that seen in the reference pattern, the pattern formation of venation showed a discrepancy with that of reference pattern (Fig.2b). On the other hand, when *Dx* and *Dy* were set to 5, the elongation of venation tissue was inhibited due to a deficiency of an expansion of blade tissue as seen in malnutrition (Fig.2c). These results demonstrated that the expansion of leaf blade affected the pattern formation of leaf venation. Fig.3 shows the time-course of the number of whole cells; both *Dx* and *Dy* increased the number of whole cells. In addition to this, the time-course of the number of whole cells showed an exponential behavior, which corresponded to the typical dynamic behavior of leaf primordium. Furthermore, when Dx and Dy were

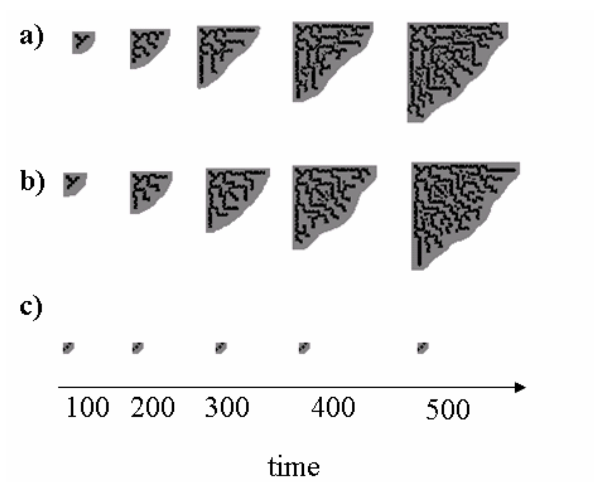

Fig. 2. Effect of kinetic parameters *Dx* and *Dy* on the spatiotemporal development of leaf shape.

a)standard parameters (Table1) b)*Dx* = *Dy*=2000.0 c) *Dx* =*Dy* = 5.0. Black fields and gray fields show venation tissue and blade tissue, respectively.

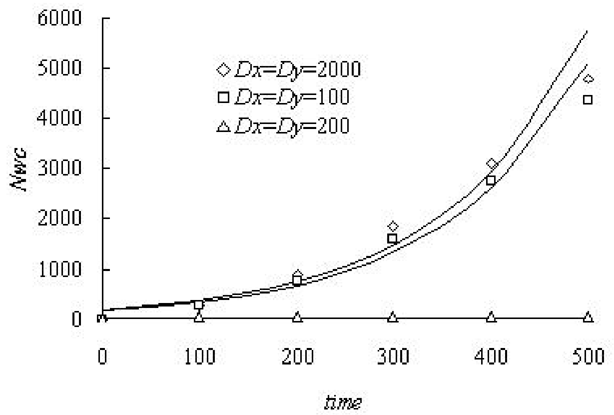

Fig. 3. Time course of the number of whole cells (*Nwc*).

This figure showed effect of *Dx*, *Dy* on the number of *Nwc*. Numerical calculations were executed with *Dx*=*Dy*=5, 100, 2000, respectively.

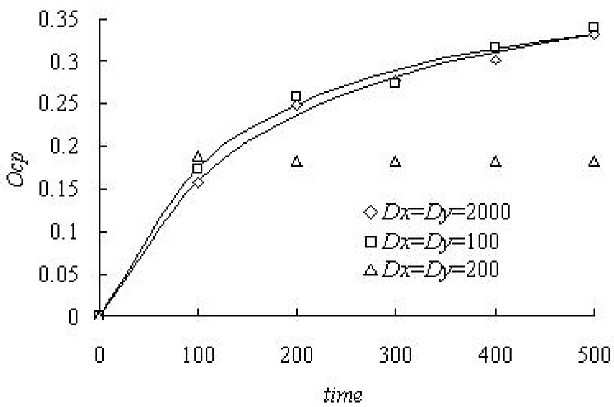

Fig. 4. Time course of the ratio of venation cell to whole cells (*Ocp*).

This figure showed effect of *Dx*, *Dy* on the value of *Ocp*. Numerical calculations were executed with *Dx*=*Dy*=5, 100, 2000, respectively.

set to either 100.0 or 2000.0, as shown in Figs. 3and 4, the number of whole cells is growing with time, however, the ratio of venation cell to whole cells shows saturable with time. Aloni *et al.* reported [6] that the basic skeleton of leaf venation was almost determined in the development process of the leaf primordium. The saturable behavior shown in Fig.4 implied the completion of formation of the basic skeleton of leaf venation, which was in good agreement with the biological finding. Thus, the interaction between the elongation of leaf venation and the expansion of leaf blade is indispensable for the complicated pattern formation of leaf venation. The proposed model with considering the interaction is useful in the numerical analysis of development of leaf in comparison with conventional model.

IV. CONCLUSION

With employing a set of reaction-diffusion equations and CA theory, we designed a novel mathematical model for which an interaction between the elongation of leaf venation and the expansion of leaf blade affects a development of leaf. The proposed model could realize several salient features of development of *gingko*'s leaf primordium such as the reconnection of venation tissues, the branching pattern formation and the fan shape formation of blade tissue, which implied that the interaction between the elongation of leaf venation and the expansion of leaf blade is indispensable for the complicated pattern formation of leaf venation. Therefore the proposed model was useful for the numerical analysis of development of leaf in comparison with the conventional models.

REFERENCES

[1] Turing AM (1952), The chemical basis of morphogenesis. Philos Trans R Soc Lond B Biol Sci 237: 37-72

[2] Meinhardt M (1976), Morphogenesis of Lines and Nets. Differentiation 6: 117-123

[3] Lindenmayer A (1968) Mathematical models for cellular interactions in development. J Theor Biol 18: 280-315

[4] Markus M, Böhm D, Schmick M (1999), Simulation of vessel morphogenesis using cellular automata. Math Biosci 156: 191-206

[5] Berleth T, Scarpella E, Prusinkiewicz P (2007), Towards the systems biology of auxin-transport-mediated patterning. Trends Plant Sci 12: 1360-1385

[6] Aloni R, Schwalm K, Langhans M, Ullrich CI (2003), Gradual shifts in sites of free-auxin production during leaf-primordial development and their role in vascular differentiation and leaf morphogenesis in Arabidopsis. Planta 216: 841-853

An abstract model for investigating the adaptivity of misperception

Jin Akaishi

Department of Information and Electronic Engineering, Yatsushiro National College of Technology,
2627 Hirayama-Shin-Machi, Yatsushiro, Kumamoto 866-8501, Japan
akaishi@as.yatsushiro-nct.ac.jp

Takaya Arita

Graduate School of Information Science, Nagoya University,
Furo-cho, Chikusa-ku, Nagoya 464-8601, Japan
arita@nagoya-u.jp

***Abstract*: We have been focusing on the adaptive property of misperception. Our hypothesis is that misperception can be adaptive because of its beneficial function of increasing diversity in population by reducing the majority bias of collective behavior. In our previous studies, we constructed a simple agent-based model in which agents perform a foraging task. The simulation results showed that misperception could increase diversity in behavior of agents, thus could be adaptive. This paper investigates on the general conditions for misperception to be adaptive based on these preliminary results. For this purpose, we use a mathematical model that does not depend on specific tasks. More specifically, we construct an abstract model in which each agent selects a behavioral choice depending on the rewards for the choices and then obtains a reward based on the distribution of selected behaviors by all agents involved. We evaluate the adaptive property of misperception by considering the balance among environments, cognition and behavior in terms of entropy. It has been shown quantitatively that misperception becomes adaptive by diversifying the distribution of collective perception when agents adopt a behavioral strategy that tends to show overmatching, which decreases the entropy of behavior compared with the entropy of the rewards in environments.**

***Keywords*: Misperception, Diversity, Adaptivity.**

I. INTRODUCTION

Fretwell and Lucas proposed the Ideal Free Distribution (IFD) theory which predicts that individual animals will aggregate in various patches proportionately to the amount of resources available in each [1]. Since then empirical studies have confirmed a tendency toward the IFD in a number of species. In more general context, some studies pointed out a possibility that diversity in collective behavior is autonomously adjusted universally at various levels such as reasoning or communication/language, when fitness contribution of a behavior conducted by an individual of social animals or insects depends on the distribution of their behavior in population [2][3].

However, we can easily imagine situations in human societies where IFD does not hold true. Especially, there is a tendency that a behavior which seems to obtain the best reward is chosen intensively. For instance, if every car driver trusts a source of information on traffic conditions, new traffic jams might be caused as a result. Also, if an information impels many investors to buy a specific stock, many of them might finally have poor profits or suffer a loss owing to the convergence.

We have been focusing on the role of misperception, in other words, the noise at the level of cognition. Our hypothesis is that misperception is adaptive under such circumstances because of its beneficial function of increasing diversity in population by reducing the majority bias of collective behavior. So as to test this hypothesis, we constructed a simple agent-based model in which agents perform a foraging task in our first study. The simulation results showed quantitatively that misperception could increase diversity in behavior of agents, thus could be adaptive, while accurate communication could decrease a diversity of agent behavior, which might decrease fitness. We also discussed the relationship between direct misperception and indirect misperception. Furthermore, we showed that behavioral specificity has dominant effects on adaptive property of misperception [4][5].

We extended the model by introducing the evolution of misperception partly from the evolutionary psychology perspective in our second study. The results showed that while keeping the general tendency towards

©ISAROB 2009

optimal values, uneven distribution of food resources causes a difference between adaptivity at population level and at individual level, which produces a selection pressure toward lower misperception rates [6]. Also, Brumley and others have recently conducted a related study inspired by our first study [7].

This paper investigates on the general conditions for misperception to be adaptive based on these preliminary results. For this purpose, we use a mathematical model that does not depend on specific tasks. More specifically, we construct an abstract model in which each agent selects a behavioral choice depending on the rewards for the choices and then obtains a reward based on the distribution of selected behaviors by all agents involved. We evaluate the adaptive property of misperception by considering the balance among environments, cognition and behavior in terms of entropy.

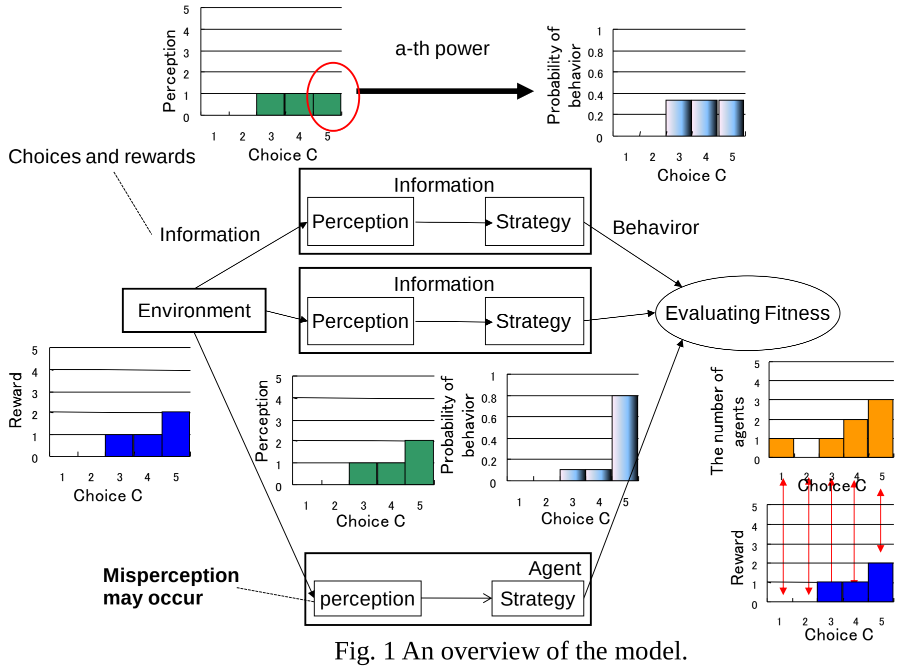

Fig. 1 An overview of the model.

II. MODEL

In this model (Fig. 1), the environment provides agents with the pairs of a choice and a benefit, and each agent can obtain the corresponding reward by choosing one of the choices. We term distributions of benefits among all choices the distribution of reward. There are m choices, each of which is assigned a number c $(1 \le c \le m)$. The amount of the benefit of the choice c, *reward(c)* is decided by Eq. (1) being able to tune distributions by the parameter g. We define a vector consisting of *reward(c)* as **r.**

$$reward(c) = \frac{1}{1+e^{-g(c-m)}} \qquad (1)$$

There are n agents in the environment, each of which is assigned a number i $(1 \le i \le n)$. Agent i perceives a reward at a choice c as *perception*(**r**,i,c). There is a possibility that misperception occurs when an agent perceives a reward. The probability of misperception is defined as p_c. When agent i misperceives a reward, the agent perceives a reward for another choice (other than choice c as the reward for the choice c (Eq. (2)), which diversifies collective distributions of perception.

$$perception(\mathbf{r},i,c) = \begin{cases} reward\ (c) & \text{Prob.}\ 1-p_c \\ reward\ (\text{a choice except } c) & \text{Prob.}\ \dfrac{p_c}{m-1} \end{cases} \qquad (2)$$

We define a vector $\mathbf{p}(i)$ for agent i consisting of *perception*(**r**,i,c) of all choices. Each agent selects a choice based on *strategy*($\mathbf{p}(i)$,i,c) which is the behavioral probability with which agent i chooses the choice c (eq.(3)).

$$strategy\ (\mathbf{p}(i),i,c) = \frac{perception\ \ (\mathbf{r},i,c)^a}{\sum_{k=1}^{m} perception\ \ (\mathbf{r},i,k)^a} \qquad (3)$$

This probability is decided by the relative reward based on individual perceptions. The parameter a, which is common for all agents, adjusts the sensitivity to the distribution of the reward. The distribution corresponds to IFD when a is 1 and misperception does not happen.

A vector consisting of the behavioral probabilities of agent i is defined as $\mathbf{s}(i)$. The result of the choice of agent i is defined as *behavior*($\mathbf{s}(i)$,i,c) (eq. (4)).

$$behavior(\mathbf{s}(i),i,c) = \begin{cases} 1 & \text{if the agent choses } c \\ 0 & \text{otherwise} \end{cases} \qquad (4)$$

We evaluate fitness of the agents based on behaviors. The upper limit that an agent can gain a reward is determined by the total reward divided by the total number of the agents. Agents that chose a choice gain a reward that was equally divided by the number of the agents that chose the choice. Fitness of agent i is defined as $fitness_{ind}$(B,**r**,i). $fitness_{ind}$(B,**r**,i) is calculated by eq. (5), in which B is the matrix that consists of a vector **b**(i) of all agents and the vector **b**(i) consists of *behavior*(***s****(i)*,*i*,*c*).

$$fitness_{ind}(B,\mathbf{r},i) = \sum_{c=1}^{m}\left\{\min\left(\frac{reward\,(c)}{\sum_{d=1}^{m} reward\,(d)}\frac{behavior(\mathbf{s}(i),i,c)}{\sum_{j=1}^{n} behavior(\mathbf{s}(j),j,c)},\ \frac{behavior\,(s(i),i,c)}{n}\right)\right\} \quad (5)$$

The function min(x, y) returns the smallest value in the arguments.

The distribution of rewards, the collective perception of agents and the distributions of behavioral probabilities are evaluated by calculating entropy. The entropy of the distribution of the reward H_{rew} is calculated based on *reward*(*c*) (Eq. (6)).

$$H_{rew} = -\sum_{c=1}^{m}\frac{reward\ (c)}{\sum_{d=1}^{m} reward\ (d)}\log_2\frac{reward\ (c)}{\sum_{d=1}^{m} reward\ (d)} \quad (6)$$

The entropy of the perception H_{perc} (Eq. (8)) is determined by mean perception $P_{perc}(c)$ (Eq. (7)), that is the average perception of all agents on each choice.

$$P_{perc}(c) = \frac{\sum_{i=i}^{n} perception\ (\mathbf{r},i,c)}{\sum_{d=1}^{m}\sum_{i=1}^{n} perception\ (\mathbf{r},i,d)} \quad (7)$$

$$H_{perc} = \sum_{c=0}^{m} P_{perc}(c)\log_2 P_{perc}(c) \quad (8)$$

The entropy of the strategy H_{str} (Eq. (10)) is determined by the mean behavioral probability $P_{str}(c)$ (Eq. (9)), that is the average behavioral probability of all agents on each choice.

$$P_{str}(c) = \frac{\sum_{i=1}^{n} strategy(\mathbf{p}(i), i, c)}{\sum_{d=1}^{m}\sum_{i=1}^{n} strategy(\mathbf{p}(i), i, d)} \quad (9)$$

$$H_{str} = -\sum_{c=1}^{m} P_{str}\,(c)\log_2 P_{str}\,(c) \quad (10)$$

III. RESULTS

We conducted simulation experiments based on the model to measure the effect of changing the distribution of rewards, strategy, and probability of misperception. The following parameters were used in these experiments: *n =1000, m =4 and a = 3*. H_{rew}, H_{perc} and H_{str} were normalized to the range between 0.0 and 1.0. The relative fitness is based on the fitness when the probability of misperception was 0.

The first results are shown in Fig. 2. The probability of misperception and distribution of rewards were changed in order to investigate the effect of misperception on fitness and the relation among fitness, H_{perc}, H_{str} and the difference between H_{rew} and H_{str}. P_{misp} in x-axis and H_{rew} in y-axis indicate the probability of misperception and the entropy of the rewards, respectively. The z-axis indicates the entropy of the perception H_{perc} in Fig. 2(a), the entropy of the strategy H_{str} in Fig. 2(b) and the absolute value of the difference between the distributions of the rewards and the strategy $|H_{str}\text{-}H_{rew}|$ in Fig. 2(c). The fitness in z-axis indicates the mean relative fitness for comparison of effects of misperception.

There was a general tendency that H_{perc} increased as H_{rew} or P_{misp} increased (Fig. 2(a)). Also, H_{str} (Fig. 2(b)) was smaller than H_{perc} (Fig. 2(a)) especially when H_{rew} was small. The results showed that agents were concentrated in choices with more rewards because the parameter *a* was larger than 1.0. In Fig. 2(c) there was a valley, indicating that the difference between H_{rew} and H_{str} was nearly zero, from H_{rew} = 0 and P_{misp} = 0 to H_{rew} = 0.9 and P_{misp} = 0.4. There was a peak of the fitness (Fig. 2(d)) along this valley. This means that the fitness was maximized when H_{str} coincides with H_{rew}. Hence, misperception increased H_{perc} and decreased the

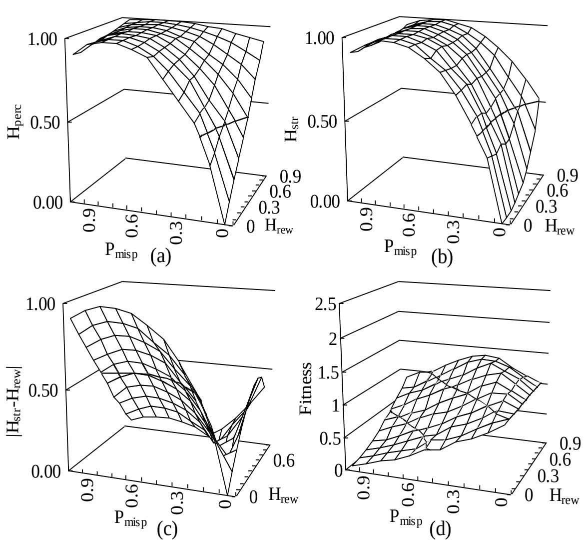

Fig. 2 (a) Entropy of perception, (b) Entropy of strategy, (c) Differences between the distributions of reward and strategy, (d) Fitness (*a*=3.0).

difference between H_{str} and H_{rew}. Fig. 2(d) shows that the higher H_{rew} was, the greater was the adaptive effect of misperception, which shows that the area in which misperception could be adaptive became larger as H_{rew} became higher.

Next, we investigated the effect of the strategy on fitness by changing the parameter of strategy a to be between 0.3 and 10.0 (Fig. 3). We see the area in which misperception is adaptive, that is fitness was greater than 1, tended to grow as the parameter a became greater. Especially, the adaptivity of misperception was not observed when the parameter a was less than or equal to 1.0 (Fig. 3(a) and Fig. 3(b)). We can presume that strategies causing high H_{str} decreased the gap between H_{str} and H_{rew}, and narrowed the range that misperception could diversify behavior. Therefore, misperception could be adaptive when there is the gap due to the concentration on specific choices.

We summarize the relations among misperception, strategy and fitness in Fig. 4, which illustrates the

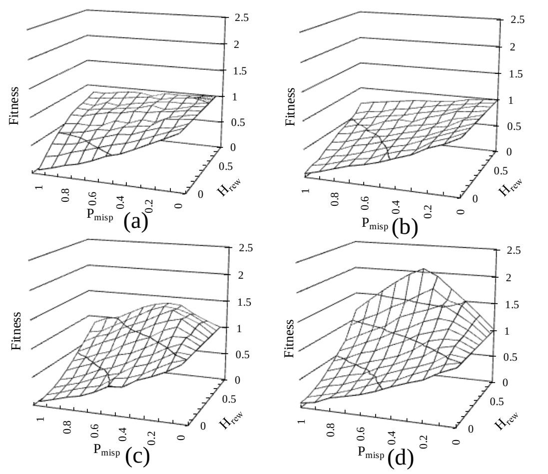

Fig. 3 (a) Fitness (a=0.3), (b) Fitness (a=1.0), (c) Fitness (a=3.0), (d) Fitness (a=10.0).

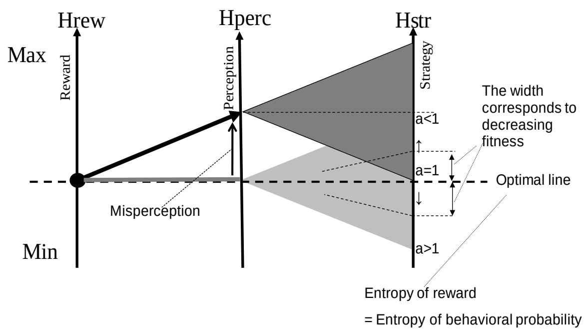

Fig. 4 Relations among misperception, strategy and fitness.

mechanism of the adaptivity of misperception. A strategy with a large a could generate the concentration of collective behavior, which decreased H_{str} below H_{rew}, while misperception has a tendency to increase H_{perc}. As a result, a gap between the distribution of the reward and the distribution of behavioral probability could be filled. Therefore, distribution of agents came closer to the optimal distribution (IFD).

VI. CONCLUSION

We constructed a simple mathematical model to investigate on the mechanism for misperception to be adaptive. When the agents adopt a behavioral strategy that tends to show overmatching, the entropy of behavior decreased. Hence, difference between the entropy of the rewards in environments and the entropy of behavior increased. Misperception increased the entropy of collective perception and thus decreased the difference. As a result, behavior of agents came closer to IFD as the optimal distribution. This result implies the possibility that misperception has a functional role to reduce a cognitive bias (e.g. majority bias) and can be adaptive from the evolutionary viewpoint.

REFERENCES

[1] Fretwell, S. D. and Lucas, H. L., "On territorial behavior and other factors influencing habitat distribution in birds", *Acta Biotheoretica*, Vol. 19, pp. 16-36 (1970).

[2] Arthur, W. B., "Inductive reasoning and bounded rationality", *American Economic Review*, Vol. 84, pp. 406-411 (1994).

[3] Arita, T. and Koyama, Y., "Evolution of linguistic diversity in a simple communication system", *Artificial Life*, Vol. 4, No. 1, pp. 109-124 (1998).

[4] Akaishi, J. and Arita, T., "Misperception, communication and diversity", *Artificial Life VIII*, pp. 350-357 (2002).

[5] Akaishi, J. and Arita, T., "Agent Based Modeling for Investigating Adaptivity of Misperception", *Systems and Computers in Japan*, Vol. 37, No. 12, pp. 96-1066 (2006).

[6] Akaishi, J. and Arita, T., "Agent Based Modeling for Investigating the Evolution of Misperception" (in Japanese), *IEICE Transaction of the Institute of Electronics, Information and Communication Engineers*, Vol. J88-D-I, No. 7, pp. 1161- 1164 (2005).

[7] Brumley, L., Kevin, B. K. and Kopp, C., An "Evolutionary Benefit from Misperception in Foraging Behaviour", *Progress in Artificial Life*, pp. 96-106 (2007).

The Fourteenth International Symposium on Artificial Life and Robotics 2009 (AROB 14th '09),
B-Con Plaza, Beppu, Oita, Japan, February 5 - 7, 2009

Prediction of Human Eye Movements in Facial Discrimination Tasks

S. Nishida, T. Shibata and K. Ikeda
Graduate School of Information Science Nara Institute of Science and Technology
8916-5 Takayama, Ikoma, Nara, 630-0192
{satoshi-n,tom,kazushi}@is.naist.jp

Abstract

Under natural viewing conditions, human observers selectively allocate their attention to subsets of the visual input. Since overt allocation of attention appears as eye-movements, the mechanism of selective attention can be uncovered through computational studies of eye-movement prediction. Since top-down attentional control in a task is expected to modulate eye-movements signi cantly, the models that take a bottom-up approach based on low-level local properties are not expected to suffice for prediction. In this study, we introduce two representative models, apply them to a facial discrimination task with morphed face images, and evaluate their performance by comparing them with the human eye-movement data. The result shows that they cannot predict well the eye-movements in this task.

1 Introduction

Surrounded by complicated visual information, human visual processing selectively allocates limited computing resources such as spatial/feature/object attention. Eye-movements achieve overt allocation of attention by shifting the fovea to the interesting region of a visual scene. Therefore, eye movements are representative of overt attention at the behavioral level, and the mechanism of selective attention can be uncovered through computational models for eye-movement prediction.

Eye-movement controllers are roughly divided into the bottom-up control caused by external factors and top-down control caused by internal factors. While the bottom-up control is based on a static mechanism based on low-level image features such as color, orientation, intensity and so on, the top-down control is based on a dynamic mechanism that depends on semantics, context or task-related factors treated by the high-level cognitive function in the brain.

Recently, a couple of biological models for predicting eye-movements were proposed. One of these models is the saliency-based model[3]. Alternative models utilize Shannon's information theory. These models are designed to explain eye-movements from the viewpoint of minimizing uncertainty in the visual information. Renninger's model[6] is representative of these. In this study, we focus on the saliency-based model and Renninger's model. All of these models are based on bottom-up control.

In this paper, we introduce these two models, and apply them to a discrimination task as well as a free-viewing task of faces to illustrate the possibility of eye-movement prediction in these tasks. Finally, we discuss some characteristics of human eye-movements speci c to facial recognition from the viewpoint of feature selectivity.

2 Methods

2.1 Behavioral Task

Our tasks consisted of a discrimination task and a free-viewing task. One of the purposes of our tasks is verifying that the bottom-up models cannot predict well human eye-movements in facial recognition. The other is analyzing how the goal of discrimination modulates feature selective strategy in the context of facial recognition through comparing the results of these two tasks.

Figure 1 shows a set of morphing images for use in these tasks. To make the set, we generated sixteen morphing images that had continuous change of the mixing ratio of two faces, and extracted eight images that were closer to the half ratio. In the same way, four sets (32 images) were created for these tasks. They were based on face images of six men and two women ranging in age from 22 to 27 years old. The pairs were made of same-sex face images. For morphing, each face image was converted to a gray-scale image, and the background was painted black. The

©ISAROB 2009

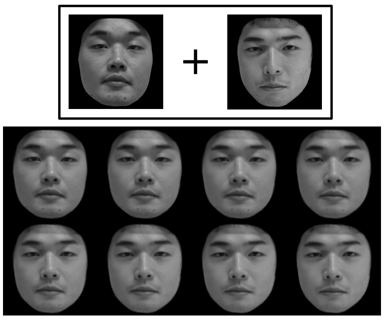

Fig. 1: A set of facial morphing images.

morphing images were created by a morphing software, WinMorph[4], whose algorithm is a eld morphing technique[1].

Subjects were seated 73.5 cm from the display screen and were put on an Eyelink II (SR Research) eye-tracking device. The screen had a size of 31 cm 25 cm, a visual angle of 23.8° 19.3°, a resolution of 1024 pixels 768 pixels and a frame-rate of 59.84 Hz. Eye-position data were acquired at 500 Hz and both eyes were tracked. The stimuli were presented by Matlab's Psychophysics and Eyelink toolbox extensions[2].

In the discrimination task, each session consisted of 8 blocks of 16 trials. At the beginning of each block, calibration of the eye-tracker was executed, and at the beginning of each trial, drift correction was executed. Figure 2 sketches the procedure of each trial. On each trial, subjects pressed a button to begin. First, one of the 32 morphing images (12.5° 12.5°) was presented for 1 sec. It was chosen randomly, but all images appeared at the same times in a session. Then, two original face images (12.5° 12.5°) were displayed together. Until subjects pressed a button to choose the face that was more similar to the rst morphing image, the images did not disappear. Finally, feedback was given.

In the free-viewing task, stimuli were presented under neutral viewing condition without an explicit task goal. Each session consisted of 8 blocks of 16 trials. Calibration and drift correction of the eye-tracker were done in the same way as the discrimination task. On each trial, subjects pressed a button to begin, then only the morphing image (12.5° 12.5°) was displayed for 1 sec.

Three male subjects participated in the experiment. Subjects ranged in age from 23 to 43 years old. All subjects had normal eyesight.

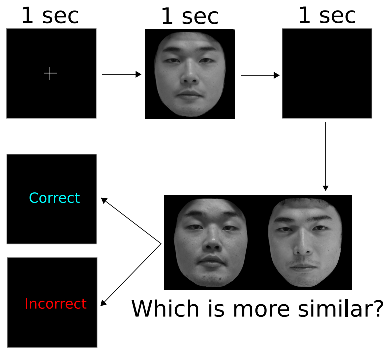

Fig. 2: Procedure of each trial in the facial discrimination task.

2.2 Models for Eye Movement Prediction

Eye-tracking data in the experiment were compared with simulation results of the following models.

2.2.1 Saliency-based Model

This is a model of the visual bottom-up attention mechanism for early visual processing in primates. An input image is decomposed into a set of feature maps, followed by center-surround di erences and normalization of three features (intensity, color and orientation). All feature maps are then combined into a unique topographic saliency map. The winner-take-all network detects the most salient location and directs attention toward it. An inhibition-of-return mechanism transiently suppresses this location in the saliency map, such that attention is autonomously directed to the next most salient image location. This model can plausibly explain eye-movements of the bottom-up control under the context-free viewing condition.

2.2.2 Renninger's Model

This is a model for eye-movement prediction in object discrimination tasks with silhouette images. However, it is also a bottom-up model because the goal of discrimination was not adopted into the evaluation function. One of its characteristics is adoption of foveal and peripheral vision mechanisms. Since discrimination objects are silhouettes, the information needed for the task is the edge orientations. Consequently, the strategy of this model for xation selection is minimization of entropy within edge orientations with respect to variable resolution in the visual eld.

The algorithm of this model is described below. First, edges are decomposed into a collection of edgelets, each of which has one of eight possible orientations. Each edgelet j is given a local region whose size depends on eccentricity $E_j(\mathbf{F})$ from the current xation point $\mathbf{F}$ (using parameters from the vernier acuity literature[5]). The probabilistic distribution of the orientation x_j of edgelet j is generated by the histogram $\mathbf{h}_j(\mathbf{F})$ regarding orientations of all edgelets within the region.

$$P(x_j|\mathbf{h}_j(\mathbf{F}), E_j(\mathbf{F})) = h_{j,x_j}(\mathbf{F})/Z, \qquad (1)$$

where Z is a normalization constant.

Then, a resolution-dependent entropy (RDE) of each pixel i is computed.

$$\mathrm{RDE}_i = \sum_{j \in \text{all edgelet locations within radius } r(E_i(\mathbf{F})) \text{ of } i} H_j \quad , \qquad (2)$$

where $r(E_i(\mathbf{F}))$ is the radius of the circular region determined by the eccentricity $E_i(\mathbf{F})$ from the xation point $\mathbf{F}$, and the entropy H_j of edgelet j is computed by

$$H_j = \quad \sum_{z=1}^{8} P(x_j = z) \log P(x_j = z). \qquad (3)$$

Thus, an RDE map, which represents the uncertainty of shape knowledge at any point, is generated. The next xation is directed towards the maximum point of the map. The new probabilistic distributions, depending on a new xation point, are integrated with the old ones by the Bayesian rule. The posterior probability can be updated for multiple xations $\mathbf{F}_1$ and $\mathbf{F}_2$ by

$$\begin{aligned} &P(x_j|\mathbf{h}_j(\mathbf{F}_1), \mathbf{h}_j(\mathbf{F}_2), E_j(\mathbf{F}_1), E_j(\mathbf{F}_2)) \\ &\qquad = h_{j,x_j}(\mathbf{F}_1) h_{j,x_j}(\mathbf{F}_2)/Z', \end{aligned} \qquad (4)$$

where Z' is a normalization constant.

In addition, this model adopts a human property that saccades to a simple shape or object often landing near the centroid of that object.

$$\begin{bmatrix} f_x \\ f_y \end{bmatrix} = w \begin{bmatrix} C_x \\ C_y \end{bmatrix} + (1 \quad w) \begin{bmatrix} \hat{f}_x \\ \hat{f}_y \end{bmatrix}, \qquad (5)$$

where f is the next xation, $\hat{f}$ is the model-de ned prediction, $\mathbf{C}$ is the centroid, and w is a weight.

3 Results

Three subjects' accuracy rates ranged from 85.9% to 89.5%, and their response times ranged from 0.61 sec to 0.84 sec. Figure 3 shows the average accuracy rate and the average response time of the subjects with respect to distance between two faces. The distance is de ned as the di erence between each mixing ratio of the two source faces of the morphing image, supposing that the distance between the two source faces is 1. The accuracy rate increased and the response time decreased with increasing distance.

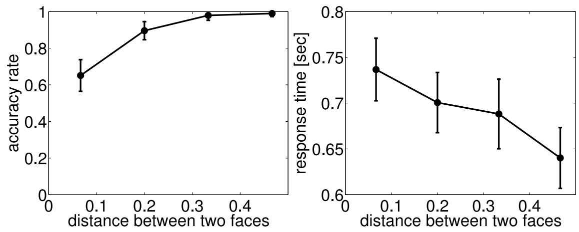

Fig. 3: Accuracy rate (left) and response time (right) with respect to distance between two faces. Error bars indicate 95% con dence intervals.

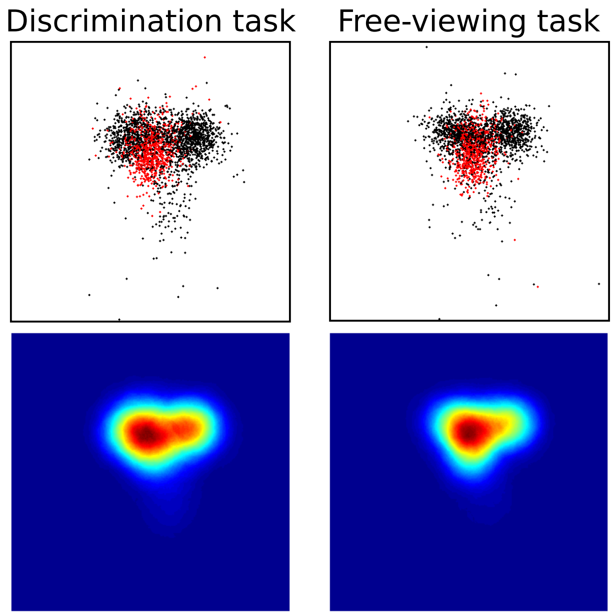

Fig. 4: Fixation distribution (upper) and foveated density (lower).

The upper part of Fig.4 shows the xation distribution. Red points indicate the rst xations. Most of the xations concentrated around the eyes and noses. From the middle points of the eyes, 90% of all xations are distributed within a visual angle of 2.4° and 90% of the rst xations are distributed within a visual angle of 1.9°. The lower part of Fig.4 shows the foveated density generated by the xation distributions with

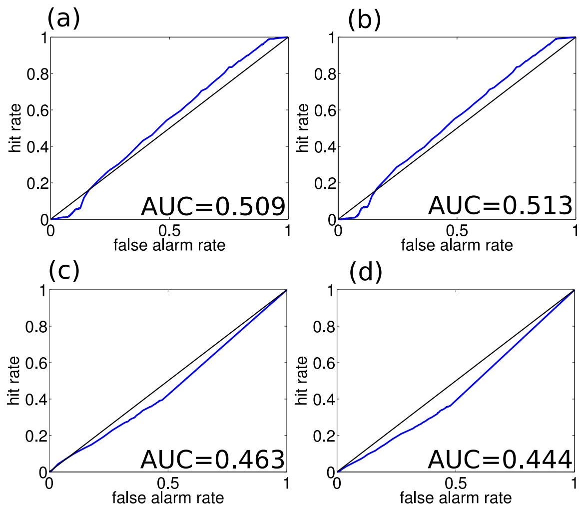

Fig. 5: ROC analysis. Saliency-based model (a,b). Renninger's mode (c,d). Discrimination Task (a,c). Free-viewing Task (b,c)

respect to the visual angle of fovea (2°).

The predictability of the two models discussed above was evaluated with ROC analysis. Figure 5 shows ROC curves and the area-under-the-curve (AUC) of the saliency-based model and Renninger's model (without a centroid bias).

4 Discussion

We found that most xations were concentrated around the eyes and noses under the condition of face recognition. This is also supported by the results that the predictability of Renninger's model with a centroid bias (Eq.5) was higher than one without a centroid bias. Although w ranging from 0.2 to 0.3 made the AUC highest in Renninger's experiment[6], the highest AUC $= 0.573$ is obtained by $w = 0.5$ in our discrimination task and the highest AUC $= 0.565$ is obtained by $w = 0.6$ in our free-viewing task. However, this cannot lead to the conclusion that Renninger's model with a centroid bias is compatible with eye-movements in our tasks. Since psychological or physiological plausibility of a centroid bias in our tasks has not been unproved, this is just a heuristic approach.

In comparison between the discrimination task and free-viewing task (Fig.4, Fig.5), we could not see a clear di erence. This result de ed our expectation that the variability of eye-movements would become greater to obtain more features needed by discrimination. There are two possibilities for the conclusion that this result leads to. One is that using peripheral vision is sufficient to obtain facial features. The other is, in contrast, that the human eye-movement strategy during face viewing involuntarily has the goal of discrimination. These possibilities cannot be examined with our experimental paradigm, but need to be con rmed in further work.

We found that it is difficult for the existing bottom-up models to predict eye-movements in our tasks. The eye-movement predictability of the saliency-based model and Renninger's model is not so di erent from one of random strategy. To explain eye-movements during face viewing, we must clarify a speci c feature space of the face, and consider the mechanism from the viewpoint of feature selection.

Acknowledgements

This work was partly supported by Grant-in-Aid for Scienti c Research from Japan Society for the Promotion of Science, No. 18300101.

References

[1] T. Beier and S. Neely. Feature-based image metamorphosis. *ACM SIGGRAPH Computer Graphics*, Vol. 26, No. 2, pp. 35–42, 1992.

[2] F. W. Cornelissen, E. M. Peters, and J. Palmer. The eyelink toolbox: eye tracking with MATLAB and the psychophysics toolbox. *Behavior Research Methods, Instruments, & Computers*, Vol. 34, No. 4, pp. 613–617, 2002.

[3] L. Itti, C. Koch, and E. Niebur. A model of saliency-based visual attention for rapid scene analysis. *IEEE Transactions on Pattern Analysis and Machine Intelligence*, Vol. 20, pp. 1254–1259, 1998.

[4] S. Kumar. Winmorph [computer software]. http://www.debugmode.com/winmorph/, 2002.

[5] D.M. Levi, S.A. Klein, and AP Aitsebaomo. Vernier acuity, crowding and cortical magni cation. *Vision Research*, Vol. 25, No. 7, pp. 963–977, 1985.

[6] LW Renninger, P. Verghese, and J. Coughlan. Where to look next? Eye movements reduce local uncertainty. *Journal of Vision*, Vol. 7, No. 3, pp. 1–17, 6 2007.

©ISAROB 2009

Origin of the word-initial consonant system of the Japanese-Ryukyuan (JR) language from Oceanic consonant system: Elucidation by JR-Oceanic consonant correspondence laws

Koji Ohnishi and Mayuko Kiriyama

Department of Biology, Faculty of Science, Niigata University, Ikarashi-2, Nishi-Ku, Niigata, 950-2181, Japan (Tel : 81-25-262-6268; Fax : 81-25-262-6116) (E-mail: ohnishi@sc.niigata-u.ac.jp)

***Abstract*:** proto-Japanese-Ryukyuan (pJR) word-initial word-initial consonants were found to regularly correspond to Malayo-Polynesian (MP)/Oceanic (OC) consonants. A nealy complete list of the correspondence laws were obtained based on cognate list of (p)JR and MP/OC. New Caledonian group shows close similarity in cognate comparison with pJR. ***Keywords*:** Consonant-correspondence laws, Oceanic affinity, New Caledonian

I. INTRODUCTION

The Japanese-Ryukyuan (JR) language (or language family) consists of Mainland Japanese (Ml.Jp) and Ryukyuan (Ryukyuan), and has been found to be closely related to Oceanic [1][2][3], although other theories such as Altaic affinities, Dravidian affinity, etc. have long been argued [4]. This paper elucidates Oceanic (especially New Caledonian) affinity of proto-JR (pJR).

II. METHODS, RESULTS, DISCUSSIONS

JR words (Mainland Japanese (Ml.Jpn.), Ryukyuan (Ryu.) were compared with Austronesian (AN) vocabulary listed in Tryon's "Comparative AN Dictionary" (1995) (CAD*). JR-AN cognates thus found are listed in Table 1, from which word-initial consonant correspondence laws have been established in most cases as shown in Table 1 (Revised from [2]). Close phylogenetic affinities of JR to Oceanic/New Caledonian are undoughtedly established.

References: [1] Murayama,S.(1995) "*Nihongo no Hikaku-Kenkyuu (Comparative Study of the Japanese language)*", San'ichi Shobo. **[2]** Ohnishi (1999) Evolution of Mongoloid Languages, Shokado, Kyoto. [3] Ohnishi, K.and Kiriyama, M. (2008): New Caledone an origin of the Japanese-Ryukyuan language elucidated by word -initial consonant correspondence laws, and the importance of Ha teruma dialect. *Materials of the Research Center for Okinawa L anguages (Okinawa Gengo-Kenkyuu Sentaa Shiryou)* #173 (pp. 1-18) (In Japanese with Tables in English). [4] Shibatani,M.: The Languages of Japan, Cambridge Univ. Press., Cambridge.

Table 1.Word-initial consonant correspondeces between proto-Japanese-Ryukyuan (pJR) and Austronesian (AN) languages.

ABBREVIATIONS : |||| *xxxx = reconstructed form, "A < B", "B > A" = A has/had been derived from B, B has/had converted to B, "A < > B" = A is phylogenetically related to B. ; pXX = proto-XX (e.g. pIE, pAN, pMP, pOC),Wr. = Written, [XXX] = closest cognate(s) in AN, dial. = dialect |||
Language names : pX = proto-X (e.g., pJR, pAN, pMP, etc.) ||| JR = Japanese-Ryukyuan : Ml.Jpn.= Mainland Japanese, O.Ml.Jpn.= Old Ml.Jpn. ; RYU = Ryukyuan, Hate.= Hateruma dial. , Kuro.= Kuroshima dial.,Take.=Taketomi dial. ||| AN = Austronesian ; MP = Malayo-Polynesian, pMP = proto-MP. W.MP = Western MP. C.MP = Central MP : SHWNG = South Halmahera and Western New Guiana ; OC = Oceanic. W.OC = Western OC. ReOC = Remote Oceanic, NC = NCal = New Caledonian, MicroN = Micronesian ||| Others: DRA = Dravidian ; pEsk = proto-Eskimo ; pIE=proto-Indo-European; TbB = Tibeto-Burman ||| ||| ||| **Literatures** : ADD* = *An Ainu Dialect Dictionary* (ed. by S. Hattori, Iwanami Shoten, Tokyo, 1964) ||| ANDB* = Austronesian Database (Blast et al.) ||| CAD* = Comparative Austronesian Dictionary, Parts 1-4. ||| Coh* = Cohen, E.M./K. (1999): *Fundamentals of Austronesian roots and etymology. Pacific Linguistics D-94*, Australian National University, Canberra. ||| Handa* = Handa, I.(1999): *Ryuukyu-go Jitten* (半田一郎「*琉球語辞典*」大学書林) ||| IKJ* = Ohno. S. : *Iwanami Kogo Jiten* (Iwanami's Old Japanese Dictionary). Iwanami Shoten ||| Miyara* = Miyara-Zenshuu 8 (Yaeamaa-Goi) (宮良全集8「八重山語彙」第一書房) ||| MRH* =Hirayama, T. (1988)Minami-Ryuukyuu no Hougen Kiso-Goi (平山輝男「南琉球の方言基礎語彙」桜楓社) ||| Mu*95 = 村山七郎 (Murayama. S.) (1995). *日本語の比較研究*. 三一書房. 東京. ||| Pok* = Pokorny. J. (1959) *Indogermanisches etymologisches Woeterbuch I. II.* A. Franke Verlag. Tuebingen und Basel. ||| RHJ* = Nakamatsu. *Ryuukyuu Hougen Jiten (The Dictionary of the Ryukyu Language)*. Naha Shuppansha. Naha. 1987 (中松竹雄「琉球方言辞典」那覇出版社) ||| Zorc* = Zorc, R.D., in CAD*, Part 1, Fasc.2, pp.1105-1197.

I. BILABIALS (m-, p-, p'-, b-, β-) and LABIO-DENTALS (f-, v-) **## 1. [pJR] *m-** ([Old Ml.Jpn] m- /[RYU] (Hate.) (Kuro.) m-) **< [pAN] *m-** |||| **# 1.1. 股 CROTCH:** [Old.Ml Jpn.][Ml.Jpn.]/[RYU](Hate.) mata "crotch" (< [pJR] *mata < *mataŋ) ||| OC: [Kwaio] mataŋ-na "crotch" |||| **# 1.2. 目EYE:** [Ml.Jpn.] ma- "eye" (< *mā < *maa < *mara < [pOC] *mata < [pAN] *maCa "eye") ||| OC: [Lau] mā /[Kwaio] mā(-na) /[Port Sandwitch] mara-n /[Lewo] kila-mara-na //(W.MP) [Adzera] mara- /[Dami] mala /[Takia] mala-n /[Manam. Mabula. Yabem] mata "eye" (< *mata < [pAN] *maCa) |||| **# 1.3. 見る to SEE:** [pJR] *mir-(uŋ) /[Ml.Jpn.] mir-u /[RYU](Hate.) miruŋ. (Kuro.) miri "to see" (< (MP) *mir- "search") ||| OC: (W.OC)[Dami] -mirē- "to search", i-mirē-ya "to seek, to look for" (< i- (3rd person, sing.) + -mirē- "search" + ya (INF))

2. [pJR] *p- ([Old Ml.Jpn.] p- /[Mod.Ml.Jpn.] h-. [RYU] (Hate.) p-) **< (MP) *p-** ||| **[pJR] *p-** //[RYU](Hate.)(Kuro.)(Take.) p- //[Ml.Jpn.] h- |||| **# 2.1. 髭BEARD**: [pJR] *pi-ge$_2$ / [Old Ml.Jpn.] pi$_1$ge$_2$ / //[RYU](Yoron dial.) pigi "beard" (< *pi- "cheek" + *ke$_2$ "hair") ||| OC: [Lewo] pipi-na "cheek" || W.MP: [Bali.] pipi "cheek" ||| **# 2.2. 屁 FART:** [Old Ml.Jpn.] pē (= pe$_2$) "fart" ||| OC: [A'jie] pē /[Xaracuu] pe-a-tapɔ "to break wind"

3. [pJR] *f- ([RYU](Hate.) f- /[Ml.Jpn.] h-) |||| **## 3.1. [pJR] *fu-** ([RYU](Hate.) fu- /(Kuro., Take.) Φu- /[Ml.Jpn.] hu-) **< (MP) *bu- (OC: fu-, vu-, pu-, bu-, βu-)** |||| **# 3.1.1. 吹く to BLOW**: [pJR] *fu-ku(N) /[Ml.Jpn.] huku, Φuku //[RYU] (Hate.) fukuN / (Kuro.) Φuku /(Takeshima) ΦukuN "to blow" (< *fu- "to blow"+ *-ku " verbal suffx meanng "to do. to make", where *fu- < [pMP] *bu- "to blow", and *-ku < (MP) ku ~ gu "to do") ; [Ml.Jpn.] ibuk-u "to blow" (< *i-bu-k-) ||| OC: [Tolai] vuvu " blow " (< *vu < *bu "to blow") ; [Roviana] vua /[Mekeo] (dialects) bua, boa, poa "to blow" (< *bu-a) ; [Maringe] ifu "to blow" (< *i-fu < *i-vu- < *i-bu) "to blow", [Kaulng] βu-βuh /[Lewo] wu"whitsle" (< *bu(h)) ||| ?IE: [pIE] *b(e)u- "to blow" (onomatopoeic) (Pok*) (Cf. [pE] *b(h)ŭ- *bh(e)u- "to blow". Pok*) |||| **# 3.1.2. 蓋COVER:** [Ml. Jpn.] huta /[RYU] (Hate.) futa /(Kuro.)(Takeshima) Φuta "cover" (< *buta) (EML*, p.88) ||| C.MP: [Sika] βuta "cover" (< *buta) || OC: [Takia] futani "to shut, to close" (< *futa-ni < *buta-) |||| **# 3.1.3. 二 TWO:** [pJR] *futa- /[RYU] (Hate.) futa:-tsi / (Kuro.) Φuta-tʃi /[MdernMl.Jpn.] huta-tsu "two" (< *fut-(a) < (OC) *fut- < *buta-) ||| OC: [Tolai] evut, ivut "two" (< *e-vut, *i-vut < *-vut "two")

4. [pJR] *b^w ~ *b- |||||| **## 4.1. [pJR] *b^w- ~ *β-** ([RYU](Hate.) b- /[Ml.Jpn.] w-) ([pJR] *ba-, *bo-, *bi-) **< [pMP][pAN] *b- (0C:** b^w-, p^w-, β-, v-, w-, p-) |||| **# 4.1.1. 腹 BELLY, 内臓 GUTS:** [pJR] *bʷatta ~ *βatta /[RYU](Take.) batta (Hate., Kuro.) bata/(Kabira) bada /(Shuri in Okinawa) (Sani in Amami-Oshima) wata //[Ml.JPN] wata "belly, guts, owels" ||| W.MP: [Konjo] battaŋ /[Javanese] wətcŋ "stomach" (< *bat(t)aŋ) ; [Balinese] basaŋ "stomach, intestines, guts" ; [Molbog] babat (< *bat) "stomach" || SHWNG: [Irarutu] Φəta "stomach" || OC: (NC)[Xaracuu] bʷati /[A'jie] pʷari "stomach" (< *bʷati < *bati ~ *b(a)bati), ?[Adzera] wasaʔ "inside, middle" ; (Vanuatu: from ANDB*) [Tape] vetən /[Nahavaq] βeti "belly" |||| **# 4.1.2. 男 MAN /MALE:** [pJR] *bʷi- ~ *βi "man, male", [RYU] (Hate.) bi-dumu "man" (< [pJR] *bi-domo < *bi- "male, man" + *-domo "nomnal suffix meanng plural", Cf. [Ml.Jpn.] ko-domo "chiild" < orignal meanng: "children".), (Kuro.) biki-dumu "male person" ||| OC: [Kaulong] βi "man" (< *bi), [A'jie] wi "male" (< *bi) |||| **# 4.1.3. 若いYOUNG:** [pJR] *bʷaga- ~ *βaga (< *bag(u)ʔa< *bag(u)ra < (MP) *bagq(u)ra < [pAN] *baq(e)RuH "new") /[RYU] (Hate.) (Take.) baga- /(Kuro.) baha- //[Ml.Jpn.] waka- "young" ||| AN: [pAN] *baq(e)RuH "new", (W.MP)[Aceh] bagʔuh /[Palawan][Murut] bagu /[IndoN][Sasak] baru /[Uma] boʔu "new" || OC: [Yabem] wakuʔ /[Roviana] vagura /[Kilivila] -βau /[Tawala] wou-na /[Nyindrou] haʔu "new" || FORM:[Paiwan] vaḳu-an "new" (< *baqu- ||| Uralic: [proto-Finno-Ugric] *wuð'e- (< *wouð'e- < *boʔuse < *baguH-(e) < [pAN] *baqRuH- "new") |||| |||| **## 4.2. [Ml.Jpn.][RYU] b- < (MP) *b- (mostly onomatopoetic ?)** |||| **# 4.2.1. ブユ GNAT:** JR: [Ml.Jpn.] buyu "gnat" ||| [pAN] *buyuŋ "bumble-bee" |||| **# 4.2.2. 唇 LIP:** JR: [Ml.Jpn.] kuti-biru "lip" (kuti "mouth"), *-biru < (MP) *bir ~ *bil < *biR ~ *bi-biR ||| [pAN] *bi-biR "lip, lips" || W.MP: [Batak Toba][Madurese] bibir /[Sundanese] biwir /[Bali.] bibih /[Isnag, Aklanon, Kagayanen] bibig "lip" (< *bibir) : [Kalinga Limos] sū-bil "lip" (< sū- "mouth" + *bil), [Murut] bibil "upper lip" (< *bil), ǰabil "lower lip" (< *ǰa-bil) || C.MP: [Manggarai] vivir /[Sika] βiβir "lip" || OC: [Kilibila] bilibalo "lip" (< *bili-balo)

II. DENTAL and ALVEOLAR (t-, n-, s-) **## 5. t-** |||||| **## 5.1. [pJR] *t-** {[Ml.Jpn.] t- /[RYU](Hate., Koro., Take.) t- } **< [pMP][pAN] [pOC] *t-** |||| **# 5.1.1. 鳥 BIRD:** [pJR] *toʒri ~ *tori //[Old Jpn.] töri (= toʒri) /[Ml.Jpn.] tori //[RYU] (Hate.) turi /(Kuro.) tuṛi /(Takeshima) tui "bird, fowl" ([pJR] *toʒri < [pJR] *tori < (MP) *toru) ||| C.MP: [Dobel] toru "fowl" |||| **# 5.1.2. 手 HAND:** [Ml.Jpn.] *ta- "hand" (Found in compounds such as; *ta-na-gokoro* "palm of hand", *ta-suku* "to help, to rescue"), [Ml.Jpn.] *ta- < *ta- "hand". ||| W.MP: [Bangingi Sama] [Batak Toba, IndoN, Minangkabau][Javanese, Madurese] taŋan "hand" (< *taŋ-an < *taŋ- "hand" + *-an (= nominalizer meaning "place where (stem) is found/done", CAD*, Part I-1, p.478)) || OC: [Samoan] tapea "elbow" < *ta-pea < *ta- "hand" + pea "?") |||| **# 5.1.3. 太陽 SUN:** [RYU] tīda /(Kuro.) tida /(Shuri) ti:da /(Kumezhima) ti:ra "sun" (< [pJR] *tẽda < (OC) *tẽ-dã < *tẽ- "to shine" + *dã "day") ||| OC: [Lewo] tẽŋo "to shine", [Cemuhi] teát "sun" (< *té-àt < *té- "to shine" + *-àt "sun", where *-àt < *ad "sun" < *adlaw < [pAN] *qal(e)jaw "sun") ; [Raga] rani /[Lau] dani // (NC)[Xaracuu] dã //(MicroN)[Pnapean] rān "day" (< *dani < *daʔani < [pMP(Zorc*)] *daqani "day") |||| |||| **## 5.2. [pJR] *t-** ([Old Ml.Jpn.][Mod.Ml.Jpn.][RYU] t-) **< [pAN] *C-** ||| **# 5.2.1. to HIT with fingers :** JR: [Ml.Jpn.] tutuk-u "to hit wth fingers, stick, etc." (< *tutuk- < [pAN] *Cuk-Cug-) ||| FORM: [Pawan] ȼ-əm-ug-ȼug "to hit wth fingers" (< ȼug-ȼug = [pAN] *Cug-Cug- < *Cug-) ||| Note: Cf. [pMP] dug-dug "to beat, to shake". |||| **# 5.2.2. 人PERSON / HUMAN :** [pJR] pi-toʒ ~ *pu-to /[RTU] (Hate.) pitu /(Take.) hittu /[Old Ml.Jpn.] pi-toʒ-/[Mod.Ml.Jpn.] hito "person" (< *pi-toʒ < *pi- "sun ?" + *-toʒ "person", where *-toʒ < *tow < *tau < *Cau "person, people") ||| OC: [Lau] tō-a /[Motu] tau-dia /[Yabem] [Nyindrou] lau "people" (< *tau- "people" < [pAN] *Cau "person") || W.MP: [Sarangani Blaan] to /[Bugis] tau "person" || FORM: [Tsou] ȼou "person" (= *Cáu) || [pAN] *Cáu "person" |||| |||| **## 5.3. [pJR]** *θ- /[RYU] (Hate.) s-, (Kuro.)(Take.) t- /[Ml.Jpn.] t- < [pMP] *D- (CAD*, 1(1), pp.70-72) ~ *dʒ- (Zorc*)) || (W.MP)[Java.] [Madurese] ḍ- //(OC)[Nengone] θ- /[A'jie] d- /[Ponapean] ṯ- (< [pMP] *D- (CAD*, 1(1), pp.70-72) ~ *dʒ- (Zorc*)) |||| **# 5.3.1. 手 HAND:** JR: [pJR] *θẽ ~*ṯẽ /[Ml.Jpn.] te /[RYU] (Hate.) ʃi: (MRH*)/[Take.] ti: "hand", [RYU] (Hate.) si /(Take.) tii /[Zamami] tee /(Nakiǯin) tii, θii (Handa*, p.888) (< *θẽ "leaf" < *dẽ < *deu < *dəu < *dau < [pMP] *dʒahun ~ *Dahun "leaf") ||| OC (N.CAL): [Nengone] θe-mie "hand" (="leaf-of-arm" < *θẽ - "leaf" + *mie "arm", where *θẽ - < [pMP] *dʒahun ~ *Dahun "leaf") ; [A'jie] dẽ kẽ /[Ponapean] ṯẽ "leaf" (< *dẽ kei "leaf-of-tree" < *dau "leaf" + *kai "tree") ||| C.MP: [Ngada] təke "hand" (< *də- "leaf" + *kei "tree") || W.MP: [Bugis] dau /[Uma] rau /[Javanese] gə-ḍəŋ /[Madurese] ḍaun /[Aklanon] dahun "leaf" |||[Ainu] tek "hand" (< *te-ke "leaf-of-tree") ||| Note: Another example of [Nengone] θ- < [pMP] *D- ~*dʒ- ||| W.MP: [Malagasi Merina] man-ḍʳuviṭʳa "to tear" (< *ḍʳuvi- < *-ḍuvi- < *Dubi- ~ *dʒubi-) || OC: [Nengone] iθuba, θubi (< *(i)θubi < *iDubi) "to divide". |||| |||| **## 5.4. [pRYU] *ti- ~ *ci-** ([RYU] *tʃi- (= ci-)) **< *ti-** |||| **# 5.4.1. 唾 SALIVA:** JR: [RYU] (Tokunoshima) tʃidu /(Sani dial.) tsïdzï "spit", (Nishihara) tsidzi (< *tsidzi) /(Take.) ʃi ⌐dʒi "saliva" (RHJ*) (< [pRYU] *tʃidu < *tidu < *tiduh ~ *ciduh < > [Sundanese] ciduh "spit".) ||| W.MP: [Sasak] tiǰuʔ / [Sundanese] ñiduh (ciduh) (< N- + čiduh) /[Java.] idu "to spit" ; [Sasak] tiǰuʔ < *ti-duʔ < *ti- "water" + *-duh , where *duh < > [pPHIL] *duDaq /[pMP] *luZaq "to spit" ||| KOR: [Mod.Korean] tʃʰŭm "saliva" (= cʰum < *cǰu-m < *ciǰu-m < *tiduʔ- < *ti-duh) ||| [Ainu] ci- "water" (a prefix meaning "water".) < *ti-

6. n- |||||| **## 6. 1. [pJR] *n- < [pMP] [pAN] *n-** |||| **# 6.1.1. 心臓 HEART:** [RYU](Sani dial.) ni "heart" ||| OC: [Yabem] nip-kaləp "heart" (< *ni-p-), [Cemuhi] nime-n "heart" (probably, < *ni-me-) |||| **# 6.1.2. 中 INSIDE / 腹 BELLY:** JR: [Ml.Jpn.] na-ka "inside; belly, stomach, guts" ||| OC: [Cemuhi] nà "stomach", [Ponapean] nan "inside, in" (< *na-n) (Cf. [Paamese] naīn "inside, in" < *na-īn ?) |||| **# 6.1.3. 脚 LEG :** [pJR] *-ne "leg" (< OC: *nẽ "leg"), [Old Jpn.] sune "lower leg, fat of bone-marrow" (< *su- "fat, fluid" + *-ne "leg", [KJ*) ||| OC: [Marshallese] ne /[Ponapean] nẽ "leg", [Roviana] ne-ne "foot" |||| **# 6.1.4. 舐める to LICK:** [pJR] *nam- /[Ml.Jpn.] nam-u //[RYU] (Komi dial., RHJ*, p.141) nam-pisi: "to lick" ||| OC: [North Tanna] nam-n "tongue", nam-namən "flame" (= "tongue of fire") ||| Note: Cf. OC: [Kiribati] nam /[Marshallese] næm "to taste" || [pMP] *ñam+ñam "to taste" (Zorc*) |||| |||| **## 6.2. [pJR] *n- < [pAN] *ŋ-** |||| **# 6.2.1. to BARE the TEETH:** [Old Jpn] nim-u "ro bare the teeth" (< *ŋi-mu < *ŋi- "tooth") ||| OC: [Marshallese] ŋi /[Ponapean][Woleaian] ŋī "tooth" (< *ŋiʔi < *ŋihi ~ *ŋiŋi "tooth") || C.MP: [Ngada] ŋiʔi /[Manggarai] ŋiʔis, ŋīs "tooth" ||| [Ainu] nimák "tooth" (< *ŋi-mák), (Horobetu dial..) nírus /(Sakhalin dal.) niirus "gum" (*nii-rus < [proto-Ainu] *nii- "tooth" + rus "skin", [proto-Ainu] *nii- < *ŋiʔi < *ŋiŋi "tooth") ||| Korean: [Middle Krean] nĩ "tooth" (< *ŋĩ < *ŋiʔi < *ŋiŋi "tooth") |||| **# 6.2.2. 私 I:** [Old Jpn.] na "I" (< *ŋa ~ *ŋã < *ŋau "I") ||| OC: [Xaracuu] nã /[Marshallese] ŋa "I" || Note: Further cognates with; (OC) [Kiribati] ŋŋai /[Takia] ŋai /[Manam] ŋau /[Lau][Kwaio] nau "I" ||| DRAV: [Tamil] nān (< *naun < *ŋau-n) |||| **# 6.2.3. 名NAME:** [Ml..Jpn.] na //[RYU](Hate.) naN (RHJ*), naŋ (Mu*95, p.230) / (Koroshima) na⁻: / (Take.) na: (< [pJR] *nãN , *naaN (Mu*95) < *nãN < *ŋaa-ŋ) ||| W.MP: [Sundanese] [Palawan] ŋaran /[Aklanon] ŋãlan /[Kalinga Limos] ŋādan /[Aceh] nan || C.MP: [Buru] ŋaa-n /[Sika] nara-ŋ (< [pAN] *ŋájan "name") || OC: [Yabem] (ŋa)e / [Nyndrou] ñara-n ; [Maringe] naŋa /[Kwaio] naŋhu |||| |||| **## 6.3. [pJR] *n- < *ñ- < [pAN] *ñ-** |||| **# 6.3.1. なま RAW:** [Ml. Jpn.][RYU(Hate., Kuro., Take.)] nama "raw" (< [pJR] *nama "raw" < OC: ñama-) ||| W.MP: [Isnag] namāta "raw" || OC: [Nyindrou] ñamañak "raw" |||| |||| **## 6.4. [pJR] *n- < [pMP] *N-** |||| **# 6.4.1. 菜 VEGETABLES:** [Ml.Jpn.] na /[RYU(MRH*)] (Ishigaki) na:, (Hate.) naN "vegetables" (< [pJR] *Na(N) ~ *Na(ŋ)) ||| [pAN] *NaCéuaŋ "vegetables" (< *Na-Céuaŋ ?)

7. *s- |||||| **## 7.1. [pJR] *s- < [pMP][pAN] *s-** |||| **# 7.1.1. 腕 ARM/ 手 HAND:** JR: [RYU](Hate.) si: "hand" (RHJ), si: "arm (from shoulder to fingers)" (MRH*) (< *si: < *siu < *siʔu "hand"arm" < *siku "elbow") ||| OC: [Rotuman] siʔu "hand" (< *siku "elbow") (Cf. [Takia] sikuru-n "hand") || C.MP: [Ngada] siiku /[Sika] hiʔu-ŋ "elbow" (< *siku(-ŋ)) ||| Note: Probably further cognates with: (OC) [Nemi] hi-n /[Cemuhi] f-n "hand" (< *hĩ-n < *sĩ- < *si: < *siu- < *siʔu "hand, arm" < *siku "elbow"). |||| **# 7.1.2. BACK:** [Old Ml.Jpn] se, soʒ (IKJ*) /[Ml.Jpn.] se "back (body part)" ||| SHWNG: [Irarutu] sɛ "after" (< *sei "back, backwards") ||| [Ainu] sey "to carry on the back" (< *se-i < *se- "back"), setur "back" (< *se-tur "back-bone" < *se- "back" + *-turi "bone", where *-turi < > [Motu] turia "bone") |||| **# 7.1.3. 太陽 SUN/光 LIGHT:** [pJR] *sina "sun ~ light" ; [RYU](Hate.) ʃina "sun", [Old Ml.Jpn.] sina- "light" (example: sina-teru) ||| OC: [E.Fijian] siŋa "sun", [Lau] snamaru "lightning" (< *sina-) || W.MP: [Kagayanen] sinaŋ /[IndoN] bər- sinar /[Madurese] sunar "to shine", [Konjo] 'sinara "light" ||| [Ainu] sin (= shin) "day, weather" |||| **# 7.1.4. UNDER:** [pJR] *si- "under, belw", [Ml.Jpn.] si-ta; si-mo "area belw", a-si "foot" (< a "foot, leg" + *-si "below") ||| OC: [Yabem] siʔ "downward" (CAD, #12.140), [Kaulng] sii "bottom" |||| **## 7.1a. [RYU](Hate.) ss- < *sVs- (V = vowel)** |||| **# 7.1a.1. 膿 PUS:** [RYU](Hate.) ssi "pus" (< *ssu < *susu) ||| OC: (W.OC)[Kaulong] susu-an "pus" |||| |||| **## 7.2. s- < *S-** |||| **# 7.2.1. 風 WIND:** [Ml.JPN] si "wind", ara-si "storm" (< [pAN] *Siup "to blow" || OC: [Nyindrou] si-yer "wind" |||| **# 7.2.2. WILD BORE / MEAT:** [pJR] *sisi /[Ml.JPN] sisi "wild boar, deer ; meat", [RYU](Shuri) ʃiʃi /(Komi) siːsi "flesh" (< (MP) sisi < [pAN] *Sisi) ||| [pAN] *Sisi "meat" || FORM: [Rukai] ki-sisi "goat" || W.MP: [Yami] aşişi /[Konjo] assi "flesh" || OC: [Mekeo] tsitsi "meat" |||| |||| **## 7.3. s- < (OC) *s- < [pAN] *Z-** |||| **# 7.3.1. 脂肪 FAT / 油 OIL (of MARROW):** [pJR] *sune /[Old Ml.Jpn.] sune "fat (~ oil) of bone-marrow, lower leg" (< [pJR] *su-ne < [pJR] *su- "fluid, liquid, soup" + [pJR] *-ne "leg", IKJ*), [pRYU] *suni /[RYU] (Take.) kara-zuni /(Kuro.) ʃini /(Kabira) sini "leg" (< *zune) ||| OC: [Samoan] sua "liqud, fluid, soup" (< *su-a < *sũ- < suʔu < *suru < [pMP] *ZuRúq "soup, broth"), [Manam] suru / [Yabem] sulu "soup, broth" (< [pMP] *ZuRúq) || C.MP: [Sika] luru "soup, broth" || W.MP: [Murut] dũʔ /[Palawan][Molbog] duruʔ "soup, broth" (< [pMP] *ZuRúq) ||| [Ainu] rúr (ADD*) "soup, broth" (< *ruru ~ *luru < *duru < [pMP] *ZuRúq) ||| Note: [pJR] *-ne "leg" < (OC) *ŋe- "leg, foot" || OC: [Takia] ŋe-n "leg, foot", [Marshallese] ne /[Ponapean] nẽ "leg", [Roviana] ne-ne "foot" (< *ŋe-(n)).

III. VELAR (k-, g-)

8. *k- |||| |||| **## 8.1.** [pJR] ***k-** ([Old Ml.Jpn.][RYU](Hate.,Kuro.,Take.) k- **< (OC) k- < [pMP] *k-** |||| **# 8.1.1. 噛む to BITE:** [pJR] *kam-u(N) /[Ml.Jpn.] kam-u /[RYU](MRH*) (Ishigaki) kamuN /(Hate.) kam̥uN "to bite", [RYU (RHJ*)] (Kohama) kamun "to chew" ||| OC: [Kilivila] kam-kʷam "to chew" ||| [Quechuan] ccamu- (= k'amu-) "to chew" |||| **# 8.1.2. 濃い DENSE** (in colour): [RYU] (Hate.) (Kuro.) kata- "dense" ||| OC: [W.Fijian] kata "dark (in colour)" |||| **# 8.1.3. 声 VOICE:** [pJR] *ko₂we /[Old Ml.Jpn.] ko₂we /[RYU] (Hate., Kuro., Take.) kui (< *koe)/ [Mod.Ml.Jpn.] koe "voce" ||| OC: [A'jie] kõ "loud" |||| |||| **## 8.1a.** [pJR] ***k-** ([Old Ml.Jpn.] k-, [RYU] (Hat.)(Take.) k-, **(Kuro.) h-) < (OC)** k, ɣ-, kʷ- |||| **# 8.1a.1. 噛む to CHEW:** [RYU] (Miyara dial. in Ishigaki Isl.) kantari /(Hate.) kandaruN /(Kuro.) hanzari /(Take.) kandaru(N) "to chew" (RHJ*, p.1421, p.191) < [pRYU] *kantar-uN ~ *kandar-uN "to chew" ||| OC: [Kiribati] kanta "to chew" (< *kan-da < *kan "to eat" + *da "to eat"), [Mbula] -kan /[Port Sandwitch] xan-i /[Raga] ɣani /[Roviana] ɣani-ɣani "to eat" (< *kan- "to eat"); [Xaracuu] da "t o eat" || W.MP: [Wolio] kaⁿde (< *kan-de) /[IndoN][Minangkabau] ma-kan /[Kalinga Limos] maŋan (= maN + kan) "to eat" || FORM: [Paiwan] k-əm-an (= kan + -əm-"INFX") "to eat" ||| Eskimo: [North Buffin dial.] qaniq "mouth" (< *qani-q < *kan-i- ~ *ɣan-i- "to eat" < [pAN] *kan- "to eat") |||| **# 8.1a.2. 肩 SHOULDER:** [Mod. Ml.Jpn.] kata /[RYU] (Hae., Take.) kata, (Kuro.) hata ||| OC: [Nengone] kataʔad (< *kata-ʔad ?) |||| **# 8.1a.3. 風 WIND:** [pJR] *kadza-, *kadzi- /[RYU] (Hate.) katsi / (Kuro.) hadʒi /(Take.) kadʒi "wind", [Ml.Jpn.] kaze, kaza- "wind, cold", kazi-kamu "to numb with coldness" (< *kadzi- "wind" + *kam-u "to bite") ||| OC: [Xaracuu] kʷadɛ "wind" (< *kazai- ?) |||| **# 8.1a.4. 皮SKIN:** [Old Ml.Jpn.] kaΦa, kawa /[RYU] (Take.) kaー: , (Shur) ka: "skin" (< [pJR] *kaΦa ~ *kava "skin" < (MP) *kaba "clothes, clothing"), [RYU] (Hate.) k:nu-ka:, (Kuro.) ki:nu-ha: "bark of tree" (< *kii-no kawa < *kii "ree" + -no + *kawa "skin, bark" ||| OC: [Mbula] kawāla /[Woleaan] xapaȓa "clothes, clothing" (< *kaba-(a)la "clothing"), (Cf. [Dami] ā gabari "bark", ā "tree") || FORM: [Paiwan] kava "clothes, clothing" (< *kaa ~ *gaba ?) ||| Eskimo: [proto-Inuiit] *qavaRuciq "outer skin of whale" |||| |||| **## 8.1b.** [pJR] ***k- < (OC)** g-, ɣ-, k- < [pW.MP][pAN] *k- |||| **# 8.1b.1. 齧る to GNAW:** [Ml.Jpn.] kadir-u (< *kadʒi- < *kač-i- <*kaC-i) ||| OC: [Kilivila] gadi /[Raga] ɣasi /[Paamese] gati /[Port Sandwitch] xač-i (< *kač-i ~ *ɣač-i) /[W.Fijian] kasi-a /[Mele-Fiila] kaji-a /[Maringe] katʰu "to bite" (< * || [pW.MP(Coh*, p.C-40)] *katiʔ "bitten") (< [pAN] *kat+kat "to bite" < > [pW.MP(Coh*, p.C-40)] *katiʔ "bitten") ||| DRA: [Tamil] kaṭi "to bite"(Ohno, 1981). ||| STb: [Thai] kàd "to bite" ||| Note: Cf. [pAN] *kaRat /[Palawan] kagat "to bite" (Zorc*) : ?[pHF?] *gadiŋ "ivory". |||| |||| **## 8.2.**[pJR] ***k- < (MP) *g-** |||| **# 8.2.1. 日 DAY:** [Old Jpn.] [Ml.Jpn.] -ka "day" (for counting)" (< (MP) *gā "sun"). Example: nano-ka "seven days" ||| OC: (W.OC)[Dami] gā "sun" |||| **# 8.2.2. 心 HEART:** [pJR] *ko₂ko₂ro₂ "heart, mind" (< *ko₂ro₂ "heart" < *goru "heart") (> [Old Ml.Jpn.] ko₂ko₂ro₂ "heart, mind", [RYU] (Kuro.) kukuru "mind") ||| OC: [Kwaio] goru "heart" ||| Cf. OC: [Roviana] kor-koro "lung". |||| **# 8.2.3. 口 MOUTH:** [Ml.Jpn.] kutu- "mouth" (in a compound word, *kutu-wa*) (< MP: *gutu "lip"). [Ml.MJpn.] kuti /[RYU] (Hate.) fʉtsi / (Kuro.) (Take.) Φutʃi "mouth"(< [pJR] *kutu-i) ||| OC: [Mele-Fila] gutu "lip" ||| ??[Anu] kut "throat" (< *gut(u) ?)

9. [pJR] *g- (RYU] g- /[Ml. Jpn.] k-) < (MP) *g-, *ᵑg- |||||| **# 9.1.1. 狭い NARROW:** [pJR] *goma- "narrow, (thin)", [RYU] (Kuro.) guma-ha /(Take.) kuma-sa "narrow" (< [pRYU] *guma <] [pJR] *goma-), [Old Ml..pn.][Mod.Ml.Jpn.] koma-ka-, koma- "thin, minute" ||| OC: (W.OC) [Mbula] ᵑgomᵑgomŋa- (< *ᵑgom-(ŋa)-) "narrow" (< *N- + *gomŋa ?) |||| **# 9.1.2. 蜘蛛 SPIDER:** [pJR] *gobu /[RYU (Kabiira dial.) go:Φu /[Ml.Jpn.] (Kushuu dial.) kobu "spider" (Mu*78, p213).||| W.MP: [Murut] lawaʔ-gobuk "wolf-spider" (< lawaʔ- "spiider" + *gobuk)

IV. GLOTTAL (ʔ-, h-) **## 10. [pJR] *ʔ-** |||||| **## 10.1. [RYU** (Yaeyaman)] **ʔ- /[Ml.Jpn.] ø- < [pJR] *ʔ- < (OC) (C.MP)** ʔ- |||| **# 10.1.1. 槍 SPEAR**: [RYU](Hate.) ʔui "spear" (< *ʔui < *ʔuri) ||| OC: [Lau] ʔuia "to shoot" (< *ʔui-a < *ʔuri-) || C.MP: [Dobel] ʔuri "sword" ||| Note: (MP)[Dobel][Lau] ʔ- does not reflct [pAN] *q-, since [Dobel] kʷ- /[Lau] Ø- < [pAN] *q-. Example: [Dobel] kʷusan /[Lau] uta "rain" < [pAN] *quZán "rain".) |||| **# 10.1.2. さつま芋 SWEET POTATO:** [RYU](Kuro.) ʔun "sweet potato", ko:sa:ʔuN "satoimo, a kind of yam" (< [RYU] *ʔun ~ *ʔuN "sweet potato") ||| OC: [Adzera] ʔunas "sweet potato" |||| **# 10.1.3. 織る to WEAVE:** [pJR] *ʔoruN "to sew" (< (MP) *ʔoru-(ŋ)) (> [Old Jpn.] or-u (= o₁r-u) //[RYU](Hate.)(Take.) oruN / (Kuro.) ʔuri (< [pJR] *ʔoruN)) || C.MP: [Sika] ʔoru "to weave" |||| |||| **## 10.2. [RYU] ʔ- /[Ml. Jpn.] Ø- < [pJR] *ʔ- < [pMP][pAN] *q- || (MP) [Manggarai] Ø- /[Dobel] kʷ- / [Adzera] g- /[Tongan] ʔ-** |||| **# 10.2.1. 陰茎 PENIS:** [Ml..Jpn.] tin-tin, tin- "penis" (< [pJpn.] *tin- < *ti-n "penis" < *uti-n < *qútin "penis") ||| OC: [Takia] uti-n /[Manam][Yabem] uti /[Maringe] tʰiti "penis" (< *uti-n < [pAN] *qútin "penis") || C.MP: [Roii] uti-k || NHWNG: [Irarutu] ti (< uti-"penis") ||| [Ainu] ci "pens" (< *ti < *uti < [pAN] *qútin "penis")(Mu*92, p.71) |||| **# 10.2.2. 上 UPSIDE / ABOVE:** [pJR] *ʔu- "(in compunds) up, above" (< *ʔul- "(in compounds) up, above" < > OC: [Tolai] ul- "head (in componunds)" < *ulu- < *ʔulu- < [pAN] *qúluH "head"). [RYU] (Hate.) (Kuro.) ʔui /(Sonai) ui /(Shuri) ʔwi: / [Ml.Jpn.] u-Φe,u-he, u-e (< *ʔu-Φe <*ʔu-pe < *ʔu- "up, above" + *-Φe ~ *-pe) "upside, above" ||| OC: [E.Fijian] ulu- /[Samoan] ulu /[Tongan] ʔulu /[Tolai] ulu, (in compunds) ul- "head" (< *qulu), [Raga] ulu- /[Rotuman] ulu-ŋa /[Samoan] taua-luŋa [Rapanui][MeleFla] ruŋa (< *lu-ŋa < *ulu-ŋa < *qulu-) "top" || W.MP: [Sasak][Bugis] ulu /[Sundanese] hulu "head" || C.MP: [Dobel] kʷulu- "head" (CAD* #04.201) || FORM: [Paiwan] ḳulu "head" ||| Eskimo: [pEsk] *qulə- "area above" ||| TbB: [Atsi] ʔulum "head" (< *ʔulu-m < *qúluH) ||| Korean: [Mod. Korean] ui "upside" (< *ʔu-i). |||| |||| **## 10.3. [pJR] *ʔ- < (MP) *l-** (< *(qa)l-) |||| **# 10.3.1. 五 FIVE:** [pJR] *ʔi- /[RYU](Hate., Kuro., Take.) ʔi- /[Old Ml. Jpn.] [Modern Ml.Jpn.] i "five" (*ʔi- < *li ~ *ri - < *li < *lim < [pAN] *lima "five") ||| OC:[Kaulng] eip (< *e-i-p < *e-i- < *lim) /[Paamese] elim (< *e-lim) /[Sawai] pe-lim /[Motu][Mekeo] ima /[Tahitian(Archaic)] rima (< *lim(a) < [pMP] *lima "five, hand, arm") ; (NC) [Nemi] nim /[Cemuhi] ním (< *lim(a)) "five" || W.MP: [Molbog][Balinese][Konjo] lima /[Da'a] alima "five" (< *lima ~ *alima < *(qa)lima ?), [Aklanon] alima /[Palawan] alima /[Molbog] lima "arm" |||| **# 10.3.2. 注ぐ to POUR** : [Old Ml. Jpn.] ir-u "to pour" (probably, < [pJR] *ʔir- < [pMP] *liR-) ||| MP: [pMP(Zorc*)] *liR "to flow" (< *ʔaliR < [pMP(Coh*)] *qaliR "to flow" ?) |||| |||| **## 10.4. [pJR] *ʔ- <** *l- < [pHF] *L- <[pAN] *L- |||| **# 10.4.1. 臼 MORAR:** [Ml.Jpn.] usu /[RYU] (Hate.) usi / (Kuro.) ʔuʃi /(Taketoami) usu (< [pJR] *ʔusi < *lusu < *lusuŋ < *Lusuŋ) ||| MP: [pHF] *Lesuŋ (CAD* #05.80), *lĕ+suŋ (Zorc*)./[Kalinga Limos] lusuŋ /[Aklanon] ɬusuŋ /[Aceh] lusoŋ "morar" (< *lu+suŋ ~ *lĕ+suŋ) ; [IndoN] ləsuŋ /[Sundanese] lisuŋ (< *lĕ+suŋ)"mortar"; [Sarangan Blaan] suŋ "mortar" || FORM: [Atayal] ɬuhuŋ (< *Lusuŋ)"mortar" ||| Note: Cf. (W.MP)[Sar.Blaan] lu "pestle". [Kalinga Limos] lusuŋ < [Kalnga Limos] lu "pestle" + suŋ "mortar". |||| |||| **## 10.5. [pJR] *ʔ- < *r- < [pMP] *d̥- (Zorc*, Coh*) ~ *D- (Coh*)** || OC: [Raga] d- /[Motu] r- /[Nengone] ḏ- |||| **# 10.5.1. 垢 BODY-DIRT:** [RYU] (Tokunoshima) ʔaki "body-dirt" (< *raki- < (MP) *daki- < [pAN] *dakiH- "dirt, body dirt, dirty") ||| W.MP. [Balinese] daki "dirty" (< *daki), [Aklanon] dakih /[Molbog] daʔki /[Sasak] rəki "dandruff" || C.MP:[Sika] miʔak "dirty" (probably, < *mi-ʔaki)||| OC:[Nyindrou] koʔak "dirty" (probably, < *ko-ʔaki) ||| [Quechua] llequi (= leki < *lki) "body-dirt" |||| **# 10.5.2. 赤い RED:** [pJR] *ʔag(g)a-/[RYU](Hateruuma) ʔaga-haN / (Kuro.) ʔaka-ha / (Take.) ʔakka-saN /[Ml.Jpn.] aka-."red" ([pJR] *ʔag(g)a- < *rag(g)a- < [pAN] *daRaq "blood") ||| OC: [Raga] daγa-./[Manam] dara /[Motu] rara-na /[Paamese] rāk./ [Nengone] ḏa /[Marshallese] ra "blood" (< *daRa-). [Takia] dara-n /[Manam] dara-dara"red" (< [pMP](Zorc*) *d̥aRaq, (Coh*) *d̥aRaq ~ *DaRaq) || W.MP: [Isnag] dāga /[Mnangkabau] darah /[Sasak] ḍara "blood" (< *daRaq "blood") ;[Isnag] daggāŋ "red" |||| **# 10.5.3. 刺 THORN:** [Old Ml.Jpn.(IKJ*)] u-bara /[Mdern Ml.Jpn.] i-bara "thorned wild rose" (< [pMl.Jpn.] *(ʔ)u-bara < *u- "thorn" + -bara "rose", where *(ʔ)u- < *ru- < *rui < *dui < *duRiH "thorn") ||| OC: [Nemi] dui /[Cemuhi] dū-n /[A'jie] ɉū /[Nengone] dun /[Ponapean] ʈī /[E.Fijian] sui /[Tongan] hui /[Motu] turia-na /[Tolai] ur /[Nyindrou] ⁿdʳuwi-n "bone" (< *duri < [pMP] *duRiH "thorn, spine") |||| |||| **## 10.6. [pJR] *ʔ- (~*Ø-) < *r- < *l- < *dʒ- ||| [Wr.Mongolian] d- |||| # 10.6.1. 音 SOUND:** JR: [pJR] *ʔottō /[RYU] (Hate.) ʔuto:, (Kuro.) ʔutu, (Take.) ʔuttu /[Old Ml.Jpn.] o₂to₂ "sound" ([pJR] *ʔottō < *ʔontō < *ʔon- "sound" + *tō "sound, noise", where *ʔon- < (OC) *roŋ ~ *loŋo "to hear" < *loŋo < *doŋol < *duŋol "to hear" < [pAN] *dʒě + ŋěR "to hear", and *tō cognates with [Rotuman] tō /[Lewo] to-na "sound, noise".) ||| OC: [Ponapean] roŋ / [Marshallese] ɽoŋ /[Woleaian] ɽoŋoɽoŋo /[Kiribati] ɽoŋ /[W.Fijian] ɽoŋo-o /[Raga] ɽoŋo / [Paamese] [Lewo][Manam] loŋo "to hear" (< *doŋo "to hear" < [pAN] *dʒě + ŋěR "to hear"). || W.MP: [Kalinga Lmos] doŋol /[Molbog][Murut] doŋog /[Gorrontaro] mo-ʔo-duŋohu "to hear" |||[Mongolc: [Wr.Mong.] duγul- "to hear" (< *duŋul < (W.MP) *duŋol ~ *doŋol) |||| **# 10.6.2. 二 TWO:** [pJR] *-(ʔ)wo (in a compound word, *to₂wo* "ten".) "two" (< *ʔwo < *ʔuwo < *ruo "two" < *duo < *dua "two"), [OldJpn.] to₂wo "ten" (< *to-ʔwo < *to- "arm" + *ʔuwo "two" , where *ʔuwo < *luwo < *duo < *dua "two"< [pAN] *dʒuSá "two") ||| OC: [Kilivila] -luwo-tala "ten" (= "ten(s)-one", -luwo- < *luo < *lua "two" < dua "two", [Lewo] lua-lima "ten" (= "two-hand"), [Yabem] lemeŋ-lu "ten" (= "hand-two") (-lu < *lua < *dua "two") |||| **# 10.6.3. 焼く to BURN:** [pJR] *jagu(N) /[Old Ml.Jpn.] jaku /[RYU] (Hate.) jaguN (< *(ʔ)ia-gu(N) < *(ʔ)iʔa-gu(N) "to burn (v.t.)" < *ʔila-gu(N) < *dʒila-gu(N) "to burn" < *dʒila- "flame (= tongue of fire), tongue" *-gu(N) "suffix for makng a transive verb") ||| W.MP: [Murut] dilaʔ /[Aceh] dilah /[Uma] ǰilaʔ /[Konjo] lila "tongue" || OC: [Easern Fijian] yame- "tongue" (< *ya-mea < *ia-mea < *iʔa-me < *ʔila-mea < *dʒila-mea < *dʒila- "tongue" + *mea "tongue") , [Raga] mea- /[Kwaio] mea "tongue" |||| |||| **## 10.7. [pJR] *ʔ-** /[RYU](Hate.) ʔ-, (Kuro., Take.) **Ø- < (OC) *l- |||| # 10.7.1. 脂肪 FAT / 油 OIL:** [pJR] *ʔabura /[Ml.Jpn.] abura /[RYU] (Hate.) aba, -ʔaba, (Kuro.) ava, (Take.) aba "fat, oil" (< *ʔaᵐbura < *ʔam(u)bura < *lamu-bura "fat, grease" < *lamu- "fat, grease" + *βura "fat, grease"). [RYU] (Hate.) ʔuwa-nu-ʔaba "grease of pig" (ʔuwa "pig") ||| OC: [Paamese] amur "fat, grease" (< *am-ur ~ *am-bur < *ʔam(u)-ʔura ~ *ʔam(u)-bura < *lamu-lura ~ *lamu-bura < *lamu- "fat, grease" + *lura "oil" (< > [Dobel] lura "oil") ~ *βura "fat, grease") || C.MP: [Sika] βura "fat, grease" || W.MP: [Sasak] ləmu /[Indonesan] ləmak /[Minangkabau] ləmu /lamaʔ "fat, grease" |||| **# 10.7.2. 足 FOOT:** [pJR] *ʔa- /[Old Ml.Jpn.] a, a-si "foot, leg" (*ʔa- < *lā "foot"). [RYU](Ishigaki, MRH*) ʔasi-atu "foot print" (< *ʔasi-ato < *ʔa-si- "foot" < *ʔa- "foot" + *-si "below") ||| OC: [Yabem] à /[Cemuhi] á-n /[Rotuman] lā /[West Fijian:] -lā "foot, leg" (*a- < *ʔā- < *lā- "foot"), [Kwaio] ʔā-ʔae "foot" (< *ʔā- "foot" + *ʔae "foot", where *ʔā- < *lā- "foot"). [Lewo] la-na "leg" ||| Note: Cf. [Kiribati] ā /[E.Fijian] rā "down, belw". |||| **# 10.7.3. 馬 HORSE:** [pJR] *ʔuma(-N) /[Ml.Jpn.] uma /[RYU] (Hate.) mmaN "horse" (< *luma) ||| OC: [Lau] luma nia bulumakau / [Lewo] yumama-na puluku "horse" (< *luma) ||| Note: The correspndence, [Ml.Jpn] Ø- /[Lau] l- /[Lewo] y-, completely coincides with [Ml.Jpn.] ma /[Lau] luma "house". ||| Note: Cf. [Rotuman] rī ʔon mənmənu "horse". |||| |||| **## 10.8. [pJR] *(ʔ)V- /[Ml.Jpn] ØV- < *rV- |||| # 10.8.1. 燻す to SMOKE:**[Ml.Jpn.] ibu-su "to smoke" (< *ribu-su < *ribu- "smoke" + *-su "to do") ||| [pW.MP](Coh*) *ribuŋ "smoke" |||| **# 10.8.2. 垢 BODY-DIRT:** [Ml.Jpn] aka "body-dirt" (< *ʔaka < *raga(t)) ||| W.MP:[Javanese] rəgət "diry"

11. [pJR] [pRYU] *h-//[RYU] (Hate.) Ø- /(Take.) h- /[Ml.Jpn.] Ø- < [pRYU][pJR] *h- < [pMP] *h- |||| |||| **# 11.1. 開ける to OPEN:** JR: [pJR] *ha-ku- /[Ml.Jpn.] a-ku "to open (v.i.)", [RYU] (Kuro.) ħaki, (Take.) hattairuN, (Hate.) agiru /[Ml.Jpn.] akeru "to open (v.t.)" ||| [Ainu] ha "empty", hasa "to be open ; to open the mouth" (Ba*) (probably, < *ha-sa < [Ai] ha "empty" + [Ai] sa "(adj.) open, spread out") ||| [pAN] *haŋap (Lopez) "to open mouth" (from WW*) || W.MP: [Aceh] hah "to open" || OC: [Manam] ʔaʔa "to open" (< *ʔa < *ha) ||| IE: [Hittite] ḫaš- (= ḫas) "to open" (< [pIE(K.O.*)] *H₂as- < *has-) **|||| #11.2. ENEMY:** [RYU](Hate.) ha: (< *hā- ~ *ha-(ŋ) ?) ||| FORM: [Tsou] haŋi |||| **# 11.3. 明るい to be LIGHT:** [RYU] (Take.) hai-saN "to be light" (< *hai- < [pJR] *hari "day, sun" ?) ||| W.MP: [Balinese] ai "sun" (< *hai "sun" ~ *hari "day"). ?[IndoN] hari /[Batak Toba] 'ari / [Minangkabau] ari "day" ||| Korean: [Mod.Korean] hǎi "sun"

V. Semivowel (w-) ## 12. [pJR] *w- |||||| ## 12.1. [pJR] *w- /[RYU][Ml.Jpn.] w-< [pMP] *w- || [pDR] *ø- |||| # 12.1. 1. 輪 RING: [Ml.Jpn.] wa "ring, circle, wheel", [RYU](Take.) wa: "wheel" (< [pJR] *wa- ~ *wā "ring, wheel") ||| OC: (NwCAL)[Nengone] waela "round" (< *wa-ela), wačo "sphere, ball" (< *wa-čo), wa-čuen "wheel" ; [Tongan] vaʔe "wheel" (< *va- < *wa-) ||| DRA: [Tamil] āṛi "circle, ring, wheel", [Kannada] āṛi "circle, roundness", āṇi "roundness" (< [pDRA] *ā- "circle, ring" < *wā- ~ *wa- "circle") |||| **# 12.1. 2. 泉 SPRING:** [Old Jpn.] wī (= wi₂) /[Ml.Jpn.] i-, wi "spring, well" (< [pJR] *wi₂ < *wɨ < (OC) *wei ~ *wai < *wahi < [pMP] *wahiR "fresh water"), [Ml.Jpn.] i-dzu-mi, widzu-mi //[RYU](Shuri) ʔidʒuN "spring, well" (< [pJR] *wi₂-du-mi) ||| OC: [Lewo] wi /[Mekeo] vei /[Nemi] we "water" (< *wei < *wai "water"), [Raga][E.&w.Fijian] wai "water" || W.MP: [Bugis] wae /[Kagayanen] waig "water" (< [pMP] *wahiR "fresh water" (Zorc*), *vayey (Dm*)). (Mu*74, p.110). ||| **# 12.1. 3. 太陽 SUN:** [Old Ryukyuan] we "sun" (< *wɛ < *wai < [pMP] *waRi "sun") (Mu*95, p.159) ||| W.MP: [Javanese] wai, we "sun", [Balinese] wai "day" || FORM: [Rukai] vai /[Atayal] wayiʔ "sun"

VI. Disappeared Consonant (Ø-) ## 13. [pJR] *Øi ~ *i̥- < *ʔ- ~ *ʔi̥- < *ri- < [pMP] *d₂i- ~ *Di- |||||| # 13.1. 少し LITTLE: [RYU] (Kohama) ik'ira:-saŋ "little, few" (Murayama, 1995, from Iha) (probably, = iki-ra-saŋ < *(ʔ)iki- "small, litttle" < *d₂iki "small") ||| W.MP: [Konjo] diki "small" (< [pAN] *dikit (Coh*) "small" (Cf. [pAN(Zorc*)] *d₂ikiq "small") ||| ?Mongolic: [Wr.Mongolian] ǰiǰig "small, litttle" (< *ǰi-ǰig < *ǰig < *dig <[pAN] *d₂ikiq "small") |||| **# 13.2. 夜 NIGHT:** [Old Ml.Jpn.] jo₁ "night" (= io < *ʔio < *riō < *diō "darkness" < *dioʔo < *diolo < *diʔolo < *di-holom(o) "darness") ||| OC: [Kiribati] (te) rō (< *riō < *diō) /[Ponapean] rōʈ / [W.Fiijian] dʳiodʳiō (< *dʳiō < *diō < *dioʔo) ||W.MP: [Goronaro] diʔolomo (< *di-holomo) / [Batak Toba] (na) holom "darness" (CAD*, #01.620) ||| Note: Most plausibly, *di-* (in [Goronaro] diʔolomo < *di-holomo) < [pAN] *Di-* in [pAN]*DiRem* "darkness" (Coh*). Cf. [pMP] *d₂e+d₂em* "dark" (Zorc*).

14. [pJR] *Øm- (Ø = disappeared) < *mm- ~ *um < *(ʔ)um- < (OC) *rum- ~ *lum- < [pAN] *Rum-

 # 14.1. 部屋, 間 ROOM: [Ml.Jpn.] ma "room, space" (< *mma ~ *uma < *uma ~ *yuma < *luma ~ *ruma < *rumah < [pAN] *Rumaq "room"), [RYU](Southern Okinawa Island dial.) -ma "place" (Handa*) ||| OC: [Motu] ruma /[Lau][Kwaio] luma /[Raga] imʷa /[Lewo] yumʷa /[North Tanna] nima /[Kwamera] nimʷa /[Cemuhi] mʷà /[A'jie] mʷa /[Xaracuu] mʷā /[Nengone] mma /[Kiribati] (te) uma /[Rotuman] rī "house" || C.MP: [Roti] uma /[Buru] huma "house" ||| W.MP: [Bali.] umah /[Minangkabau] rumah /[Madurese] ruma /[Bangngi Sama] lumaʔ "house"

The Fourteenth International Symposium on Artificial Life and Robotics 2009 (AROB 14th '09),
B-Con Plaza, Beppu, Oita, Japan, February 5 - 7, 2009

A Study on Effect of Morphological Filters on Computer-aided Medical Image Diagnosis

N. Homma, Cyberscience Center, Tohoku University, Sendai, Japan, 980-8579

S. Shimoyama*, Y. Kawai*, T. Ishibashi*, *Graduate School of Medicine, Tohoku University, *Sendai, Japan, 980-8575

M. Yoshizawa, Cyberscience Center, Tohoku University, Sendai, Japan, 980-8579

Abstract

We develop several morphological image filters that can be useful for computer-aided medical image diagnosis. Some computer-aided diagnosis (CAD) systems for lung cancer and breast cancer have been developed to assist radiologist's diagnosis work. The CAD systems for lung cancer can automatically detect pathological changes (pulmonary nodules) with a high true positive rate (TP) even under low false positive rate (FP) conditions. On the other hand, the conventional CAD systems for breast cancer can automatically detect some pathological changes (calcifications and masses), but TP for other changes such as architectural distortion is still very low.

Motivated by the radiologist's cognitive process to increase TP for breast cancer, we propose new methods to extract novel morphological features from X-ray mammography. Simulation results demonstrate the effectiveness of the morphological methods for detecting tumor shadows.

1 Introduction

There may be a great potential demand for using computer-aided diagnosis (CAD) systems in clinics. Lung cancer diagnosis is an example. With the increasing mortality rate for lung cancer, X-ray computed tomography (CT) has been used for detection of lung cancer at early stages [1]. The early stage detection of lung cancer is extremely important for survival rate and this is true for any pathological cells of lung cancer. Using the X-ray CT, pulmonary nodules that are typical shadows of pathological changes of lung cancer can be detected more clearly compared to the chest X-ray examination even if they are at early stages. This is an advantage of the X-ray CT diagnosis. In fact, it has been reported that the survival rate of the later ten years can reach 90% after the detection at early stages using X-ray CT images [2].

On the other hand, using the X-ray CT may exhaust radiologists because the CT generates a large number of images (at least over 30 images per patient) and they must diagnose all of them. The radiologists' exhaustion and physical tiredness might cause a wrong diagnosis especially for a group medical examination where most of CT images are healthy and only very few images involve the pathological changes.

Therefore, some CAD systems for nodule diagnosis have been developed to help their diagnosis work [3, 4]. These CAD systems can automatically detect pulmonary nodules with a high true positive rate (TP), but the false positive rate (FP) is also high. To reduce the FP, several advanced methods such as neural network approaches have been proposed [5, 6]. However, there are still some fundamental problems such as a low discrimination rate for variations of size and positional shift of nodule images. This is because they are still so-called low level or simple image recognition methods with pixel based features compared to the radiologist's complex diagnosis process. For this high FP problem in lung cancer diagnosis, we have demonstrated that a new morphological feature extraction method by using gabor filters can be useful to further reduce [7]. This promising results may imply the effectiveness of morphological filter approaches on the lung cancer CAD systems.

Another example is X-ray mammography screening [8]. The disease rate of the breast cancer is the worst among cancers for women and early detection is also very important for the breast cancer [9]. Although the number of images per patient is less than the X-ray CT screening, diagnosis of the breast cancer using X-ray mammography is more difficult than that of lung nodules and thus it makes more tiredness to diagnose.

For some pathological changes such as calcifications and masses, CAD systems have been developed and they can automatically detect such changes with a high TP [10]. However, TP for other changes of the breast cancer, such as an architectural distortion, is still very low even under a high FP condition [11]. This fact implies the difficulty of the mammography diagnosis.

In this paper, we propose new methods to extract novel morphological features from X-ray mammography images

©ISAROB 2009

to increase TP for breast cancer diagnosis. The extraction of new features are motivated by the radiologist's higher level cognitive process in which several features are combined and integrated to conduct precise diagnosis. Simulation results demonstrate the effectiveness of the new morphological features for enhancing detection rate of architectural distortions of breast cancer.

2 Methods

We consider two principal morphological features of architectural distortions shadow although there are a variety of other minor features involved in the pathological changes of architectural distortions [12]. One of the principal features is a radiate spiculation from a point on the shadow. The other is a local distortion of mammary gland.

To detect candidate shadows with such features, shapes of mammary gland can be an important piece of information. Thus, we first extract the shapes of mammary gland from the original mammography images by using a morphological filter that can detect lines structure [11]. The morphological filter conducts the morphological opening by using multiple linear structuring elements and an square element. Line structure of mammary gland can be extracted by subtracting images between the two opening images. The spiculation feature is approximated by a set of the extracted line segments. Takeo et al. [11] have proposed the following feature of spiculations existence, f, given as

$$f = f_c \times H \tag{1}$$

Here f_c is a concentration feature of line segments on a target point given by

$$f_c = \sum_{i=1}^{n} \cos\theta_i \tag{2}$$

where n denotes the number of line segments and θ_i is the angle between the ith line segment and the straight line containing both the target point and the center point of the ith line segment. On the other hand, H is a distribution entropy of angles θ_i of line segments defined by

$$H = -\sum_{j=1}^{S} P_j \log P_j \tag{3}$$

where $S = 8$ is the number of discrete angles considered in this paper and P_j is the possibility function of the jth angle.

Since the spiculations of architectural distortions consist of radiate line segments with uniformly distributed angles to the target point, both f_c and H may be large. Thus, f becomes large for such local spiculated architectural distortions.

2.1 Modified method 1

The feature of existence f becomes small for spiculations near to the edge of mamma. This is because such spiculations near to the edge consist of line segments with angles not uniformly distributed and thus it makes H be very small.

To overcome this drawback, we modify the definition of the feature of existence, f_m, as follows.

$$f_m = f_c + wH \tag{4}$$

where w is a weighting coefficient. The modification is nothing but to change the product of f_c and H into the weighted sum of two. However, it can be expected that we can detect spiculations near to the edge of mamma by choosing the w appropriately due to the adjustment of the effect of small values of H on f.

2.2 Modified method 2

The difficulty of diagnosis of architectural distortions may also be caused by a wide variety of the distortion shadows in size, shape, and distribution of spiculations. Indeed, there are many spiculations not limited to such shapes concentrating on a target point, but on a target line segments or small regions. The conventional feature f in Eq. (1) becomes small for such cases as well. This is another drawback of the previous method.

To improve the detection capability for such cases, we propose another modification of the feature of existence. The basic idea of a new modification is to use a global structural feature observed commonly in a wide range of spiculations. That is, the general and global structure of mammary gland can be radially symmetric or a tree structure from the nipple. Thus, if the gland directions are inconsistent with the global structure, such gland can be a candidate of architectural distortions.

To formalize this feature, we calculate a global concentration feature, f_g, on the nipple as follows.

$$f_g = -\frac{1}{n}\sum_{k=1}^{n} \cos\theta_k \tag{5}$$

where n is the number of line segments in a local region and θ_k implies the angle θ_i in Eq. (2) with the target point of the nipple. Note that if the gland directions are more consistent with the global structure, the feature is negative with the relatively larger absolute value, i.e., the smaller number. On the other hand, the feature is the relatively larger with smaller absolute value for the inconsistent case. Thus, large values of f_g may imply a candidate point of such strange distortion cases.

©ISAROB 2009

3 Results

3.1 Improvement by the method 1

Fig. 1 shows an example of mammography that involves spiculations near to the edge of mamma for evaluating the proposed method 1. Fig. 2 shows detected candidate regions by using the conventional method (f) and the proposed method 1 (f_m). The weight coefficient w was adjusted to $\frac{5}{3}$ by a trial and error.

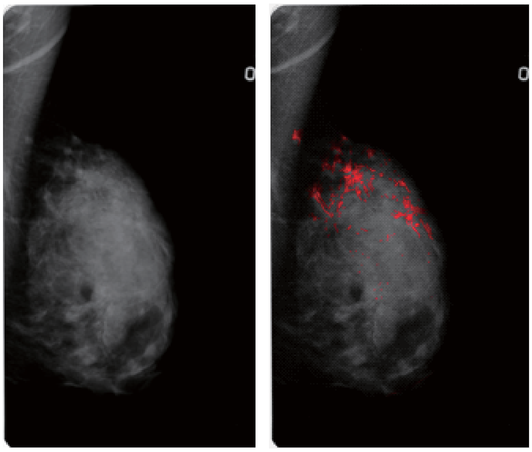

Figure 1: An example of mammography. The original image (left) and diagnosis results by a radiologist (right). The answer sketch is superimposed in red on the original.

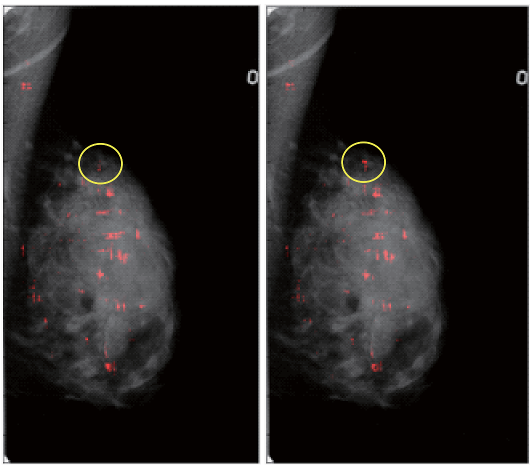

Figure 2: Detected candidate regions by the conventional method (left) and the proposed method 1 (right). Note that TP for spiculations near to the edge of mamma (yellow circle) is improved as expected.

Comparing the results, it can be said that TP for spiculations near to the edge of mamma (yellow circle) is improved by the proposed method 1. Note that this improvement can be achieved without increasing FP. Thus, these results are promising.

3.2 Improvement by the method 2

Another example of mammography that involves a spiculated distortion concentrating on a linear mammary gland is shown in Fig. 3 for evaluating the proposed method 2.

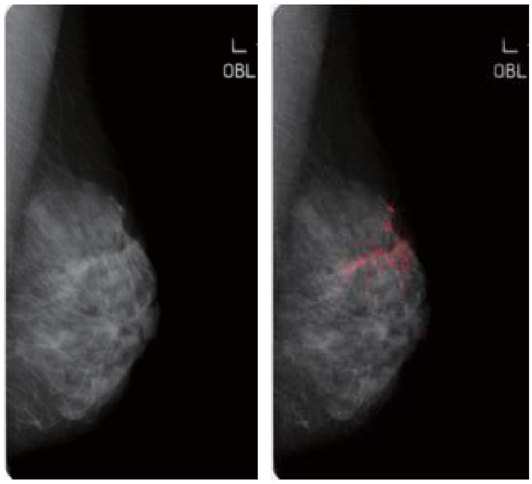

Figure 3: Another example of mammography. The original image (left) and diagnosis results (answer in red) by a radiologist (right).

Figure 4: Detected candidate regions by the conventional method (left) and the proposed method 2 (right). Note that TP for spiculated distortions concentrating on a linear mammary gland (yellow circle) is improved as expected.

©ISAROB 2009

Fig. 4 shows detected candidate regions by using the conventional method (f) and the proposed method 2 (f_g).

As new candidate regions have been detected for spiculated distortions concentrating on a linear mammary gland (yellow circle), TP for such distortions can be improved by the proposed method 2. On the other hand, FP increased for other candidates compared to the conventional method. The reduction of FP can be achieved by the other feature incorporated into the proposed one as a future work that is now in progress.

4 Conclusions

In this paper, we have developed new methods for improving detection capability of architectural distortions in mammography. The results suggest the effectiveness of the proposed methods on the architectural distortions detection. Further reduction of FP and improvement of TP for the other types of distortions are future works.

Acknowledgements

This work was partially supported by The Ministry of Education, Culture, Sports, Science and Technology under Grant-in-Aid for Scientific Research #19500413 and Okawa Foundation.

References

[1] T. Iinuma, Y. Tateno, T. Matsumoto et al., "Preliminary specification of X-ray CT for lung cancer screening (LSCT) and its evaluation on risk-cost-effectiveness," *Nippon Acta Radiologica*, Vol. 52, pp.182-190, 1992 (in Japanese).

[2] International Early Lung Cancer Action Program (I-ELCAP): Survival of Patients with Stage I Lung Cancer Detected on CT Screening, *New England J. Medicine*, Vol. 355, No. 17, pp. 1763-1771, 2006.

[3] T. Okumura, T. Miwa, J. Kako, S. Yamamoto, M. Matsumoto, Y. Tateno, T. Iinuma and T. Matsumoto, "Variable-N-Quoit filter applied for automatic detection of lung cancer by X-ray CT," *Proc. of Computer-Assisted Radiology*, pp.242-247, 1998 (in Japanese).

[4] Y. Lee, T. Hara, H. Fujita, S. Itoh and T. Ishigaki, "Nodule detection on chest helical CT scans by using a genetic algorithm," *Proc. of IASTED International Conference on Intelligent Information Systems*, pp.67-70, 1997.

[5] K. Suzuki, S. G. Armato, F. Le, S. Sone and K. Doi, "Massive training artificial neural network (MTANN) for reduction of false-positives in computerized detection of lung nodules in lowdose computed tomography," *Med. Phys*, Vol. 30, No. 7, pp.1602-1617, 2003.

[6] Y. Nakamura, G. Fukano, H. Takizawa, S. Mizuno, S. Yamamoto, T. Matsumoto, S. Sone. F. Takayama. M. Koyama, S. Wada, "Recognition of X-ray CT image using subspace method considering translation and rotation of pulmonary nodules," *TECHNICAL REPORT OF IEICE*, Vol. 104, No. 580, MI2004-102, pp.119-124, 2005 (in Japanese).

[7] N. Homma, K. Saito, T. Ishibashi, M. M. Gupta, Z.-G. Hou, and A. M. G. Solo: "Shape Features Extraction from Pulmonary Nodules in X-ray CT Images," *Proc. of World Congress on Computational Intelligence*, pp. 3396-3400, June, 2008.

[8] T. Endo: "Trend of Breast Cancer Medical Examination by using Mammography," *Health Culture*, October 2000 (in Japanese).

[9] A. Ito: "Mammography," in *Master Text Book for Radiological Technologists, first volume*, ed. I. Yanagama et al.,2008 (in Japanese).

[10] K. Fujita, T. Hara, Y. Matsubara, D. Fukuoka: "Computer-aided Diagnosis (CAD) in the Field of Breast-cancer Image Diagnosis," *J. Medical Imaging and Informatics*, Vol. 23, No. 2, pp. 19-26, 2006 (in Japanese).

[11] Hideya TAKEO, Kazuo SHIMURA, Takashi IMAMURA, Akinobu SHIMIZU, Hidefumi KOBATAKE: "Development of System for Detecting Abnormal Shadows in CR Mammograms and Its Performance Evaluation," *Medical Imaging Technology*, Vol. 22, No. 4, pp. 201-214, 2004 (in Japanese).

[12] *Mammography Guideline, second edition*, ed. Japan Radiological Society and Japanese Society of Radiological Technology, Gawks-Shorn, 2007 (in Japanese).

©ISAROB 2009

The Fourteenth International Symposium on Artificial Life and Robotics 2009 (AROB 14th '09),
B-Con Plaza, Beppu, Oita, Japan, February 5 - 7, 2009

Group Behavior of Agents with Emotional Model

Satoru Hiroshige*, Hirotoshi ASANO*, Masafumi Uchida** and Hideto IDE*

*Aoyama Gakuin University, 5-10-1 Fuchinobe, Sagamihara-shi, Kanagawa 229-8558, Japan
**The University of Electro-Communications , 1-5-1 tyohugaoka, tyohu-shi, Tokyo 182-8585, Japan
(Tel : 042-759-6419)
(Email address : a5404091@biel.ee.aoyama.ac.jp)

Abstract: Recently, attention has gathered in the study on the form formation of agent group that causes the interaction by agents and invents new functions. We gave agents the action rule based on the interaction of human feelings by using circumplex model. The parameter of feelings had been decided to this model only by two axes. In this report, eight basic action dimensions and pure feelings of four axes corresponding to respectively were given to agents as model of feelings and action based on the multiple factor analysis theory of R.Plutchik, and behavioral characteristic of agent group was examined.

Keywords: Multi Agent System, Emotion Model, R.Plutchik

I. INTRODUCTION

These days, a study on the care robot which is expected in a field of the medical care and the welfare and the petting robot for the purpose of mental healing and entertainment characteristics is prosperous. These robots are different from the robot operating apart from a human being in isolated space such as the industrial robot. The cooperative task in a positive relation with the human being is demanded from these robots. Because the human communicates with emotion, it is important that we design the system that these robots can understand emotion and feeling and can perform cooperative task [1]. On the other hand, there is the study of the multi agent system that plural agents give interaction and produce new functions. This system has the characteristics such as adaptability for the environmental change, flexibility for the work demand, the fault tolerance that some trouble is not connected for total trouble, and the rise of the efficiency by multiple work. The decentralized coordination problem solving by the multi agent system is said to be effective for a complicated large-scale problem. By cooperative relations and organized behavior, the agents achieve a useful purpose as the agent group. The purpose of the study is to design the robot system can understand emotion and perform cooperative task by making use of such a characteristic in a relation with a human being and the robot. If we are able to design the system, we can achieve a purpose without giving a careful order. And the convenience of the robot can improve drastically. We suggest the autonomous action algorithm of a plural number mobile robot new at all which got analogy to the interaction itself of the feelings that were different from the conventional emotion type robot system to choose a task depending on emotion till now. So far, we enabled a morphosis of the agent group by using Circumplex Model expressing two-dimensional structure of feelings that Larsen & Diener proposes as feelings model and giving the agent an action rule based on the interaction of human feelings. In this model, the parameter of feelings was decided only in two axes of a pleasantness value "pleasantness – unpleasantness" and the activity value "activity - non-activity" [2]. In addition, in communication with the human being, the interaction for feelings is possible and can expect that we perform smooth cooperative task by using this model.

In this report, we gave the agent eight basic action dimensions and pure feelings of four axes corresponding to each as a model of feelings and actions by being based on a multiple factor analysis theory of R.Plutchik. Then we examined an action characteristic of the agent group. As a result, because an action about the morphosis such as the set of the agent, disintegration, the running after were seen, we report it.

II. A multiple factor analysis theory of R.Plutchik

The study about human feelings is prosperous in a psychological domain. There are various opinions about the classification method of feelings. For example,

©ISAROB 2009

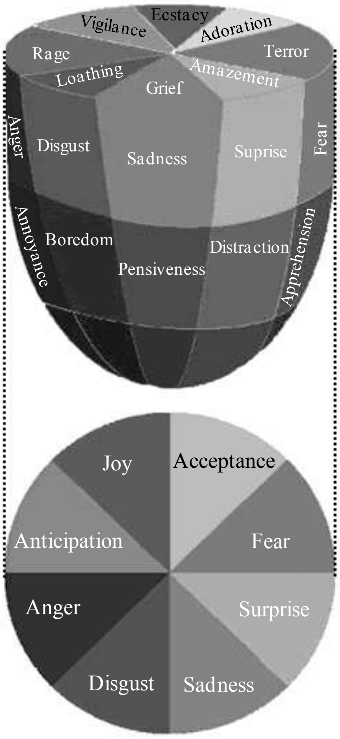

Fig.1. Feelings solid model of R.Plutchik

R.Plutchik is known by having proposed the solid model of feelings. R.Plutchik thinks that we can analyze the complicated feelings to be seen among people in everyday life into some factors and can unify these. R.Plutchik made eight basic emotions and the feelings to belong to a solid by multidimensional scaling method. Feelings structure is expressed by three-dimensional structure such as fig.1. At first R.Plutchik assumed eight basic feelings (acceptance, disgust, anger, fear, joy, sadness, surprise, anticipation) to be common to both an animal and a human being pure feelings. And R.Plutchik assumes that various mixture feelings are made by these strength and a pair. In fig.1, adjacent feelings are the things which are easy to be tied, and the thing in opposite poles is symmetric feelings. In addition, R.Plutchik paid off this adaptation form and assumed it a basic action dimension, and submitted eight action models (union, refusal, destruction, protection, reproduction, reunification, normal position, search). And R.Plutchik make eight pure feelings agree with them. In other words R.Plutchik have it as acceptance for union, disgust for refusal, anger for destruction, fear for protection, joy for reproduction, sadness for reunification, surprise for normal position and anticipation for search. In this study, we used a multiple factor analysis theory of R.Plutchik as feelings model and gave "acceptance - disgust", "anger - fear", "joy - sadness" and "anticipation - surprise" as inside variable of the agents.

III. The definition of the agent

Each agent uses feelings model based on a multiple factor analysis theory of R.Plutchik, we define each axis as "acceptance$^{(+)}$ - disgust$^{(-)}$ value : A ", "anger$^{(+)}$ - fear$^{(-)}$ value : B", "joy$^{(+)}$ - sadness$^{(-)}$ value : C" and "anticipation$^{(+)}$ - surprise$^{(-)}$ value : D" and we give A, B, C, D ($-100 \leqq A$, B, C and $D \leqq 100$) as inside variable of feelings. We assume the general term of A, B, C and D feelings value and feelings value becomes the feelings of (+) in the case of the plus and becomes feelings of the (-) in the case of the minus number. We give the agent field of vision E as a search range. Based on a multiple factor analysis theory of R.Plutchik, we gave each agent following action rule (a) - (h).

- (a) If other agent j in the field of vision is acceptance ($A>0$), agent i approaches agent j
- (b) If other agent j in the field of vision is disgust ($A<0$), agent i grow away from agent j
- (c) If agent i is anger ($B>0$), agent i approaches other agent j in the field of vision and act on destruction
- (d) If agent i is fear ($B<0$), agent i grow away from other agent j in the field of vision
- (e) If agent i is joy ($C>0$), the movement speed of agent i becomes fast
- (f) If agent i is sadness ($C<0$), the movement speed of agent i becomes slow
- (g) If agent i is anticipation ($D>0$), the field of vision of agent i becomes large
- (h) If agent i is surprise ($D<0$), the field of vision of agent i becomes small

We show a rule about the change of the feelings value in (i) - (l).

- (i) When there is other agent in a field of vision, A decreases, B increases, C increases and D decreases
- (j) When there is not other agent in a field of vision, A increases, B nears 0, C decreases and D increases
- (k) When agent was acted on destruction, A decreases, B decreases, C decreases and D decreases
- (l) When agent acted on destruction, B becomes 0

Based on the above-mentioned rule, we set movement vector of an agent V, position vector R and field of vision E of expression (1) - (5). We set a change of the feelings value when there are other agents in a field of vision of expression (6) - (9).

$$\mathbf{V}_{Ai(s)} = \sum_{j=0}^{n} A_{j(s)} \cdot \frac{\mathbf{r}_{ij}}{|\mathbf{r}_{ij}|} \tag{1}$$

$$\mathbf{V}_{Bi(s)} = \sum_{j=0}^{n} B_{i(s)} \cdot \frac{\mathbf{r}_{ij}}{|\mathbf{r}_{ij}|} \tag{2}$$

$$\mathbf{V}_{i(s)} = \left(\mathbf{V}_{i(s-1)} + \frac{\mathbf{V}_{mi(s)}}{|\mathbf{V}_{mi(s)}|} + l \cdot \mathbf{V}_{Ai(s)} + l \cdot \mathbf{V}_{Bi(s)} \right) \cdot \left(\frac{C_{i(s)}}{100} + 1 \right) \tag{3}$$

$$\mathbf{R}_{i(s)} = \mathbf{R}_{i(s-1)} + \mathbf{V}_{i(s-1)} \tag{4}$$

$$E_{i(s)} = \frac{D_{i(s)} + 100}{200} \cdot 360 \tag{5}$$

$$A_{i(s)} = (1 - R_A) A_{i(s-1)} - 100 R_A \tag{6}$$

$$B_{i(s)} = (1 - R_B) B_{i(s-1)} + 100 R_B \tag{7}$$

$$C_{i(s)} = (1 - R_C) C_{i(s-1)} + 100 R_C \tag{8}$$

$$D_{i(s)} = (1 - R_D) D_{i(s-1)} - 100 R_D \tag{9}$$

n : The number of the agents
i : ID-Number of the self
j : ID-Number of the other agents existing in a field of vision
s : The number of the steps
V_A : Approach and estrangement vector by feelings value A
V_B : Approach and estrangement vector by feelings value B
r_{ij} : Direction vectors from agent i to agent j
V : The movement vector of the agent
V_m : The direction vector to the destination of the agent
l : The influence degree of feelings
R : The position vector of the agent
R_A : A value regulation
R_B : B value regulation
R_C : C value regulation
R_D : D value regulation

IV. The basic action characteristic experiment of the agent

We performed an experiment to examine what kind of action plural agents generated by interaction.

1. Experiment environment and setting

The space builds 700×700 two dimensions space. The agent moves from the initial position to the destination. An initial position and the destination assume it random. An initial value assumes it n=30 and l=0.1, A, B, C and D assume it random. All feelings regulation R_A, R_B, R_C and R_D assumes it 0.001. We observed the action of the agent to s=3000.

2. An experiment result and consideration

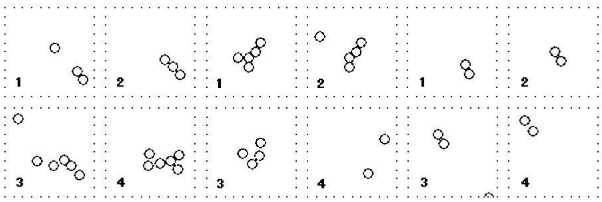

Fig.2. Set Fig.3. Disintegration Fig.4. Running after

As a result of simulation experiment, an action of the set, disintegration and running after such as fig.2, fig.3, fig.4 was confirmed. The number of the lower left in each figure expresses observed order. In fig.2, at first agents of A>0 or B>0 form a set, and then agents having various feelings value gather. In fig.3, agents of A<0 or B<0 increase in the agents which gathered, and then the agent breaks up. In fig.4, in the case of "agent approaches other agent in B>0 and that there is not agent in a field of vision of other agent or that other agent is B<0 or that agent is A<0 is filled" or "other agent approaches agent in A>0 and that there is not agent in a field of vision of other agent or that other agent is B<0 or that agent is A<0 is filled", running after is observed.

V. An evaluation experiment of the feelings value and action characteristic

We performed an experiment to examine relations of feelings regulation (R_A, R_B, R_C and R_D) and the action characteristic observed with Ⅲ .The basic action characteristic experiment of the agent.

1. Experiment environment and setting

The space builds 700*700 two dimensions space. The agent moves from the initial position to the destination. An initial position and the destination assume it random. An initial value assumes it n=30 and l=0.1, A, B, C and D assume it random. We changed feelings regulation and performed simulation to s=3000 ten times in each condition of (i) - (v).

(i) Condition 1 : R_A=0.001, R_B=0.001, R_C=0.001 R_D =0.001
(ii) Condition 2 : R_A=0.1, R_B=0.001, R_C=0.001, R_D =0.001

(iii) Condition 3 : R_A=0.001, R_B=0.1, R_C=0.001, R_D=0.001

(iv) Condition 4 : R_A=0.001, R_B=0.001, R_C=0.1, R_D=0.001

(v) Condition 5 : R_A=0.001, R_B=0.001, R_C=0.001, R_D=0.1

2. An experiment result and consideration

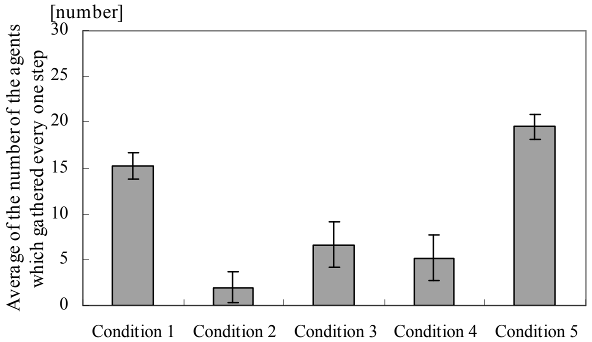

Fig.5. Average of the number of the agents which gathered

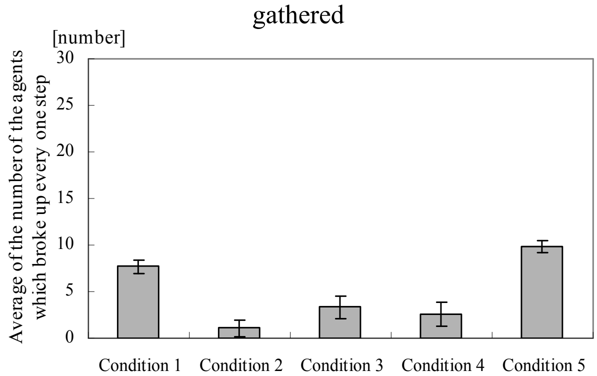

Fig.6. Average of the number of the agents which broke up

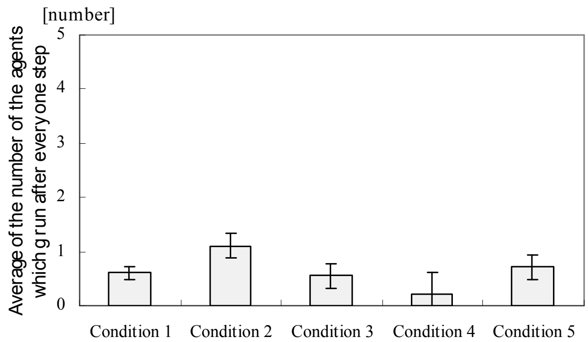

Fig.7. Average of the number of the agents which ran after

Fig.5 expresses average of the number of the agents which gathered every one step in each condition. As a result of having performed t-test between condition 1 and each condition, significant difference was confirmed in a level of significance of 1% between all conditions. From this, when we made R_A, R_B and R_C big, a set is hard to come to happen. And when we made R_D big, a set is easy to come to happen. Fig.6 expresses average of the number of the agents which broke up every one step in each condition. As a result of having performed t-test between condition 1 and each condition, significant difference was confirmed in a level of significance of 1% between all conditions. From this, when we made R_A, R_B and R_C big, disintegration is hard to come to happen. And when we made R_D big, disintegration is easy to come to happen. Fig.7 expresses average of the number of the agents which ran after every one step in each condition. As a result of having performed t-test between condition 1 and each condition, significant difference was confirmed in a level of significance of 1% between condition 1 and 2. Significant difference was confirmed in a level of significance of 5% between condition 1 and 4. Significant difference wasn't confirmed between other conditions. From this, when we made R_A big, running after is easy to come to happen. And when we made R_C big, running after is hard to come to happen.

VI. CONCLUSION

In this report, we gave agent new model of feelings and action based on a multiple factor analysis theory of R.Plutchik and observed analyzed an action as a group. As a result, we understood that the agent group performed action of set, disintegration, running after. In addition, we assumed this action a basic action characteristic of the agent group and examined and the relations of feelings regulation and the basic action characteristic by changing feelings regulation. As a result, we understood that the probability that an action of set, disintegration and running after happens changes. We will examine method to control this set, disintegration, running after in future.

REFERENCES

[1] H.Ishihara (1999), A Study on Emotional Robotics System (in Japanese). JSME ROBOMEC 1999:2P2-79-101

[2] T.Kusano, A.Nozawa, H.Ide (2005), Emergent of Burden Sharing of Robots with Emotion Model (in Japanese). Institute of Electrical Engineers of Japan article magazine C, Vol.124-C, No 7:pp1037-1042

[3] T.Yoshida, M.Tokuhisa, N.Okada (1994), Conceptual Analysis of Emotional Words (in Japanese). Institute of Electronics, Information and Communication Engineers fall meeting lecture memoirs, Vol.19940905:pp341-342

The Fourteenth International Symposium on Artificial Life and Robotics 2009 (AROB 14th '09),
B-Con Plaza, Beppu, Oita, Japan, February 5 - 7, 2009

Basic Examination Concerning Multi Agent Cooperation with Entrainment

Hirotoshi ASANO*, Hiroaki SUZUKI, Masafumi UCHIDA** and Hideto IDE*

*Aoyama Gakuin University, 5-10-1 Fuchinobe, Sagamihara-shi, Kanagawa 229-8558, Japan
**The University of Electro-Communications , 1-5-1 tyohugaoka, tyohu-shi, Tokyo 182-8585, Japan
(Tel : 042-759-6419)
(Email address : hiro@biel.ee.aoyama.ac.jp)

Abstract: The study of multi agent system generating a new function is performed. The coordinate solution such as the multi agent system is effective for a complicated problem. Therefore it is necessary to behave systematically while agen ts build the cooperative relations each other. We pay our attention to an entrainment phenomenon to be seen in the life p henomena such as a cardiac muscle cell or the emission of light of the firefly as an element to promote organized behav ior between agents. We suggest a new system model unlike the conventional system.

Keywords: entrainment**,** van-der-pol oscillator, non-linear oscillator, agent, cooperation movement

I. INTRODUCTION

These days, there is the research of the multi agent system that plural agents give interaction and produce new functions. This system has the characteristics such as adaptability for the environmental change, flexibility for the work demand, the fault tolerance that some trouble is not connected for total trouble, and the rise of the efficiency by multiple work. By cooperative relations and organized behavior, the agents achieve a useful purpose as the agent group. It is an important subject from a viewpoint of smooth problem solution to make cooperative behavior perform to two or more agents[1]. In this environment, since two or more agents influence mutually, overall dynamics becomes complicated. Therefore, it is difficult for a designer to expect the dynamics generated beforehand and to give the suitable directions for agents. Moreover, when change arises by environment, agents need to change a policy into real time[2]. On the other hand, a rhythm is in one of the elements with which a life aligns with the circumference. The system with the rhythm can maintain the same state, even if long time passes. Therefore, a life phenomenon has many things with a rhythm. For example, there are a circadian rhythm, a cycle of cell division, heart pulsation, etc. A rhythm is a nonlinear vibration. There is a form of a characteristic vibration called limit cycle vibration in nonlinear vibration. Limit cycle vibration has stable only amplitude and an only stable cycle in each vibration. Therefore, even if it applies temporary external force to a system, there is the feature of settling in a stable vibration with progress of time[3]-[4]. The dynamics with a nonlinear vibration builds a stable and autonomous system[5]-[6]. Moreover, the problem that control becomes complicated simultaneously is produced[7]-[11]. This means that it is necessary to adjust a system by trial and error. Then, we propose the system which makes the interaction between agents smooth by using entrainment phenomenon. The entrainment phenomenon is a phenomenon in which a vibrator with a different rhythm synchronizes with a vibrator with another stable rhythm. It is thought by building this system that smooth control is attained. This means that a timing synchronization and control of phase difference of various processes can be performed among agents. In this paper, the system was built by computer simulation and the characteristic of a system was checked from the action. Consequently, it turns out that control of the synchronization of timing and phase difference is possible, and the validity of this system was suggested.

II. AGENT DIFINITION

1. Limit Cycle Oscillation

The Van Dell Paul equation is famous as an equation which carries out limit cycle vibration.

$$\frac{d^2x}{dt^2}+\lambda(x^2-1)\frac{dx}{dt}+x=0 \qquad (1)$$

In a formula (1), x expresses an oscillating state (amplitude) and λ is a parameter which shows the degree of un-balancing. Considering the time of $\lambda>0$, a formula (1) becomes the following.

$$\frac{d^2x}{dt^2}=-\lambda(x^2-1)\frac{dx}{dt}-x \qquad (2)$$

It can regard as the formula by which the friction clause joined harmony vibration (single vibration) of a pendulum or a spring treated in physics. This friction is dependent on the friction coefficient x. When the absolute value of x is large, a friction clause is large, and a friction clause becomes small when the absolute

©ISAROB 2009

value of x is small. It means making amplitude small by the fall of friction energy, when amplitude is large, and enlarging amplitude by the increase in negative friction energy, when amplitude is small. Consequently, a stable oscillation (limit cycle oscillation) from which amplitude changes to the time most stable value is obtained. We apply the element of this limit cycle vibration to the interaction between agents.

2. Entrainment Phenomenon

2. 1. Entrainment Phenomenon by Two Oscillation

The formula by two vibrators A and B is shown below.

$$\frac{d^2x_a}{dt^2}+\lambda_a({x_a}^2-1)\frac{dx_a}{dt}+x_a = m_{ab}(x_b-x_a) \qquad (\lambda_a>0) \qquad (3)$$

$$\frac{d^2x_b}{dt^2}+\lambda_b({x_b}^2-1)\frac{dx_b}{dt}+x_b = m_{ba}(x_a-x_b) \qquad (\lambda_b>0) \qquad (4)$$

In a formula 3 and a formula 4, it attaches and a and b of a character show each oscillation A and B. Moreover, m_{ab} and m_{ba} show the strength of drawing in seen from the vibrator, respectively. The element of drawing in of Vibrator B joins the right side of a formula 3. The element of drawing in of Vibrator A joins the right side of a formula 4. The element of this drawing in is applied to the interaction between agents.

2. 2. Entrainment Phenomenon by Three Oscillation

The characteristic of the agent group when increasing the number of vibrators to three is examined. In a formula 5 - a formula 7, it attaches and Characters a,b,c show Vibrator ABC, respectively.

$$\frac{d^2x_a}{dt^2}+\lambda_a({x_a}^2-1)\frac{dx_a}{dt}+x_a = m_{ab}(x_b-x_a)+m_{ac}(x_c-x_a) \quad (\lambda_a>0) \quad (5)$$

$$\frac{d^2x_b}{dt^2}+\lambda_b({x_b}^2-1)\frac{dx_b}{dt}+x_b = m_{ba}(x_a-x_b)+m_{bc}(x_c-x_b) \quad (\lambda_b>0) \quad (6)$$

$$\frac{d^2x_c}{dt^2}+\lambda_c({x_c}^2-1)\frac{dx_c}{dt}+x_c = m_{cb}(x_b-x_c)+m_{ca}(x_a-x_c) \quad (\lambda_c>0) \quad (7)$$

The right of each formula shows external force. The element of drawing in of Vibrator B and Vibrator C joins the right of a formula 5. The element of drawing in of Vibrator A and Vibrator B joins the right of a formula 5. The element of drawing in of Vibrator A and Vibrator B joins the right of a formula 5.

III. SIMULATION RESULT

1. Limit Cycle Oscillation

Fig. 1 - figure 4 is the figure of time change of the Van Dell Paul equation. The value of Parameter λ is changed to 0, 0.1, and 1 and 10. Fig. 1 shows friction being lost if λ=0 is substituted for a formula 1, and taking the amplitude according to arbitrary initial values. This is called harmony vibration. Fig. 5 - figure 7 expresses limit cycle vibration in the space of a phase. It turns out that it carries out asymptotic to stable starting as time passes, even if it starts with which initial value.

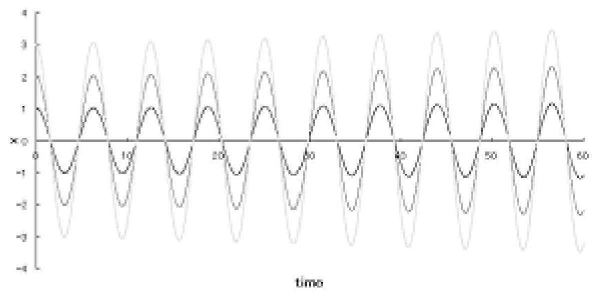

Fig.1. Limit-cycle oscillation
(λ = 0, initival value: x = 1,2,3)

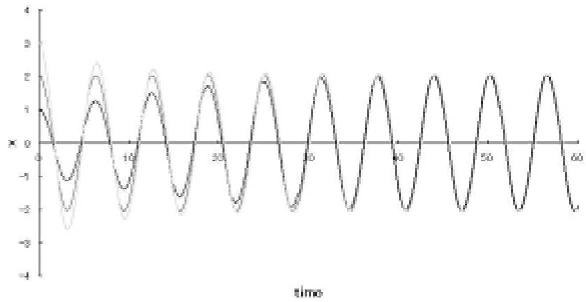

Fig.2. Limit-cycle oscillation
(λ = 0.1, initival value: x = 1,2,3)

2. Entrainment Phenomenon by Two Oscillation

Fig. 8 - figure 11 to three things are understood. One is the time of m_{ab}, $m_{ba} > 0$. It is synchronizing with a reverse phase. Another becomes the same phase when m_{ab}, $m_{ba} < 0$ and an absolute value are small. When m_{ab}, $m_{ba} < 0$ and the absolute value of another are large, it is synchronizing with a reverse phase. Furthermore, when synchronizing by this reverse phase, the cycle is twice the original waveform. When the phenomenon of drawing in occurs, the amplitude and frequency of a

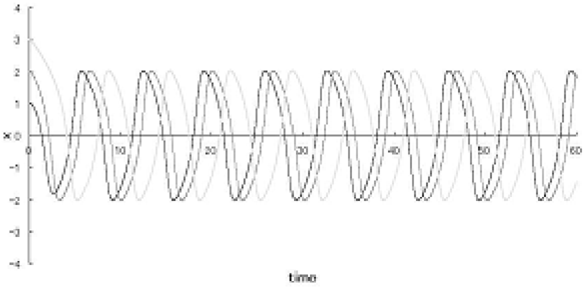

Fig.3. Limit-cycle oscillation
(λ = 1, initival value: x = 1,2,3)

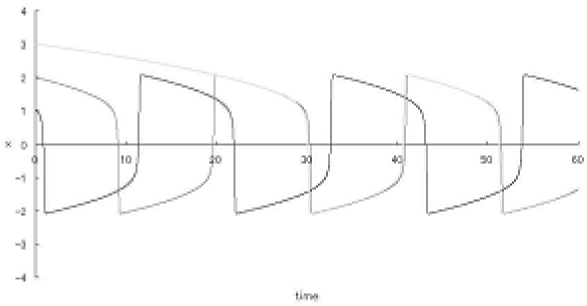

Fig.4. Limit-cycle oscillation
(λ = 10, initival value: x = 1,2,3)

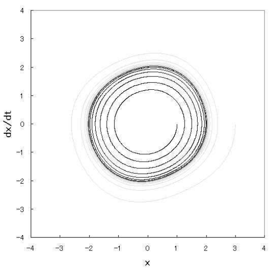

Fig.5. Aspect space
(λ = 0.1)

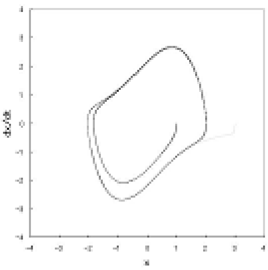

Fig.6. Aspect space
(λ = 1)

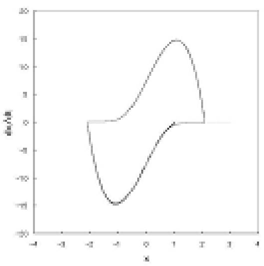

Fig.7. Aspect space
(λ = 10)

oscillation which synchronized may become completely different from the original oscillation. This is the phenomenon of drawing in to a multi agent system. Application A possibility of performing unexpected new action is shown.

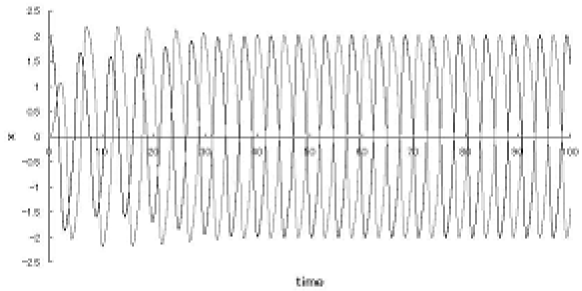

Fig.8. Entrainment (λ = 1 $m_{ab} = m_{ba}$ = 0.3)

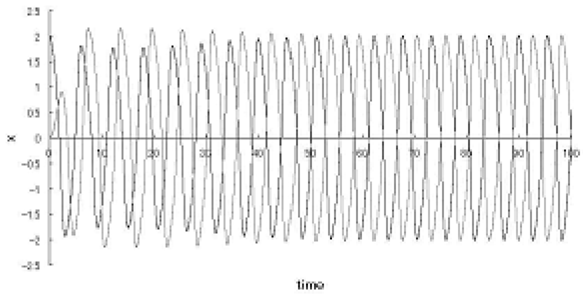

Fig.9. Entrainment (λ = 1 $m_{ab} = m_{ba}$ = 0.2)

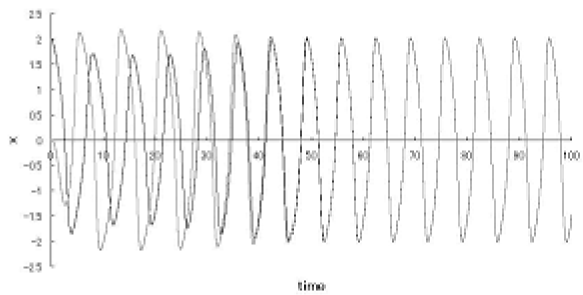

Fig.10. Entrainment (λ = 1 $m_{ab} = m_{ba}$ = -0.
2)

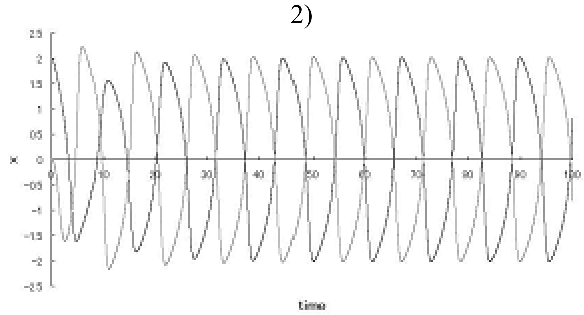

Fig.11. Entrainment (λ = 1 $m_{ab} = m_{ba}$ =
0.3)

3. Entrainment Phenomenon by Three Oscillation

The parameter m= 0.2, -0.2, -0.3 which drew with two oscillation and was used by the phenomenon is substituted at random to the parameter m of a formula 5 to the formula 7. The original oscillation shows what showed a different oscillation in Fig. 12 and Fig. 13. In the other oscillation, it turns out that it is drawn in the same phase or the reverse phase like the time of two vibrators. The 4th Runge-Kutta method is used for the numerical computation of a formula 5 to the formula 7 on linux like the foregoing paragraph. The initial value is set to $x_a = 2$, $x_b = 0$, $x_c = 1$, $dx_a/dt = dx_b/dt = dx_c/dt = 0$. In Fig. 12 and Fig. 13, vibration is complicated compared with the original waveform and nonlinear nature is reflected strongly. Moreover, when time passes, it turns out that a periodic vibration is repeated. The vibrator of each other is drawn and this is considered to have been stabilized periodically.

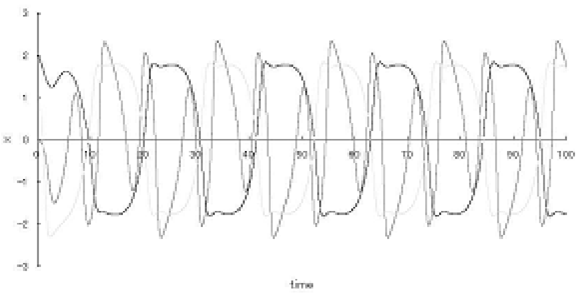

Fig.12. Entrainment ($\lambda = 1$ $m_{ab} = m_{ba} = -0.2$, $m_{ac} = m_{ca} = -0.3$, $m_{cb} = m_{bc} = 0.2$)

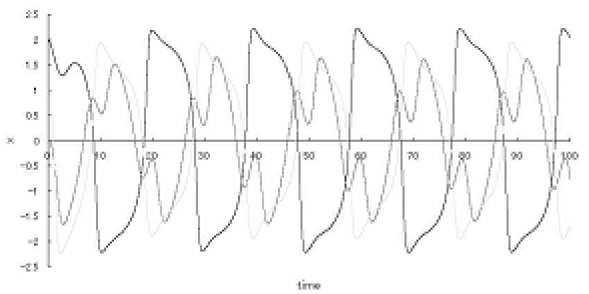

Fig.13. Entrainment ($\lambda = 1$ $m_{ab} = m_{ba} = -0.3$, $m_{ac} = m_{ca} = -0.2$, $m_{cb} = m_{bc} = 0.2$)

IV. CONCLUTION

We performed basic examination for making real time realize simple cooperation. It specifically drew in the interaction between agents, and the phenomenon was applied. And it investigated about the basic characteristic. The experiment showed that a oscillation synchronized with the same phase or a reverse phase in a certain fixed environment. This means being a synchronization and that control of phase difference is possible. Therefore, the possibility of the group cooperation by the multi-agent was able to be suggested. Moreover, when drawing in occurs, oscillation may turn into a oscillation different from the original thing. This has suggested the possibility of the unexpected new group cooperation between agents. From now on, we will verify about the validity of the system when giving an agent a task.

REFERENCES

[1] Tokashi I, Yoshihisa F, An Adventure to The Frontier Knowledge, NTT Press (1999)
[2] Kanji U, Creative action and a multi-agent system, Baifukan Co., Ltd. (2007)
[3] Masayasu M, Yuki K, University of Tokyo Press (2005)
[4] Ryuichi K, A Study on Dependancy of Parameters for Non-linear Oscillators, A Buchelor Thesis, (2002) (in Japanese)
[5] Hiroyuki N, Yoshikazu B, A guide to chaos Analysis mathematical principle of a phenomenon, Baifukan Co., Ltd. (1992)
[6] The volume on Waseda University complexity system high scientific research center, Kyoritsu shuppan-Co., Ltd. (2007)
[7] Hiroto K, A Simple Model of Coupleed Oscillat ion and Multi-agent Simulation of Synchronization. Yamagata College of Industry and Technology Journ al, No.7, pp.38-44 (2001.06) (in Japanese)
[8] Tomoaki K, Mihiro M, Toru M, Models of Relational Adaption in Mutual Interference System and Application of Adaptive Mechanism to Cooperative Walker-Agents, No.98, (1998.06) (in Japanese)
[9] Yoichiro N, Tomoshi O, Kazuhiro O, Kanji U, Self-organization Model of Cooperative Relationships between Agents (Reinforcement Learning by Globally Coupled Chaotic System), Vol.A, No.96-2, pp.730-733 (1996.06) (in Japanese)
[10] Toshihiko K, Hideki S, Yoshio I, Takuji S, The Study Synchronous Flashing of Firefiles using Celluar Automata, pp.183-184 (2000.11.27) (in Japanese)
[11] Toshihiko K, Hideki S, Yoshio I, Simulation of Synchronous Flashung of Firefiles using Cellular Automata, pp.135-136, (2001.03.15) (in Japanese)

The Fourteenth International Symposium on Artificial Life and Robotics 2009 (AROB 14th '09),
B-Con Plaza, Beppu, Oita, Japan, February 5 - 7, 2009

Basics Study about Cooperation Movement of Human and Agent with Entrainment

MASAMAZU Saito*, HIROTOSHI ASANO*, MASAFUMI Uchida** and HIDETO Ide*

*Aoyama Gakuin University, 5-10-1 Fuchinobe, Sagamihara-shi, Kanagawa 229-8558, Japan
**The University of Electro-Communications, 1-5-1 tyohugaoka, tyohu-shi, Tokyo 182-8585, Japan
(Tel : 042-759-6419)
(Email address : masakazu@biel.ee.aoyama.ac.jp)

Abstract: In the environment like the medical treatment, welfare, the construction field, and the home, the use of the ag ent is examined. It is necessary to be able to work cooperatively with human is problems of the agent in that. Then, in this study it pays attention to the phenomenon that is called an entrainment. It is the phenomenon that the rhythm of a certain person and the partner of the communication synchronizes. It sets it as the purpose of this study to perform basic examination for applying an entrainment, in order to realize cooperation operation of man and a agent. Since many of man's rhythms are expressed by the non-linear oscillator, we simulated limit cycle oscillators which are one of the non-linear oscillators of two that caused the interaction each other as a basic examination for the achievement. Consequently, entrainment of the limit cycle oscillator with which rhythms differ has been checked in a certain condition. Thereby, a possibility that cooperation movement could be gained was suggested.

Keywords: entrainment, van der Pol oscillator, non-linear oscillator, agent, cooperation movement

I. INTRODUCTION

In modern society, the use of the agent under a general environment such as medical treatment, welfare field, construction shop floor, and home where a complete automation is difficult begins to be examined. It is said that the following problems exist there. The ordinary persons who have not received special education can communicate with a machine. An agent works in harmony with man. It is autonomously adapted for the environment where it changes every moment, and the early purpose can be attained.[1]

Especially, it is thought that it becomes important that both of man who excels the agent in situation grasp and a agent good at work more exact than man[2] can work in cooperation.

When it considers attaining the purpose while the agent cooperated with man as mentioned above, Reinforcement Learning etc. can be considered as a means for making a agent gain cooperation movement. Although Reinforcement Learning takes the method of giving a value about the combination of a state and action, in environment and learns the optimal action, it is almost impossible to cover all combination in fact. [3] Anyway, it needs more consideration for thing cooperatively working smoothly with man and the cost at the study time though the method such as taking the generalization processing is researched.

In this paper, its attention is paid to a frequency entrainment realization of such a system. Frequency entrainment is a phenomenon that synchronizes with the rhythm as which man's rhythm, the other party of communications or the rhythms of the environment are the same in the human society. In meter of mother's voice and the infant's operation, talker and the listener's nod and breaths, biological rhythm of brain wave, and man's cranial nerve system and environment system of the body, etc. when walking, synchronization is caused, and it connects with promotion of communications of personal and an environment[4].

It is a purpose of this paper to examine the base of man and the agent work cooperatively after this by applying this phenomenon. Concretely, the appearance where frequency entrainment is caused in two non-linear oscillators with a different cycle is considered. The reason for treating a non-linear oscillator is that what is expressed when the rhythm of man's life phenomenon is seen exists mostly.

II. Frequency entrainment

It explains frequency entrainment considered by this paper. First of all, the frequency entrainment is a

©ISAROB 2009

phenomenon of two or more, non-linear oscillators' synchronizing. And, a non-linear oscillator is the one to generate the vibration not proportional to an initial value unlike the harmonic oscillator. The limit cycle oscillation can be enumerated as a feature non-linear oscillator. There are two features of the limit cycle oscillation. The first is that each vibration has only steady amplitude and cycle. The second is to return to a steady vibration if time passes even if the outside power joins temporarily and the vibration falls into disorder. [5]

One of the concrete examples of the limit cycle oscillation is van der Pol oscillator. van der Pol oscillator is shown by the following expression.

$$\frac{d^2x}{dt^2} + \lambda\left(x^2 - 1\right)\frac{d\ x}{dt} + x = 0 \qquad (1)$$

where x is the amplitude and $\lambda > 0$ a parameter. This expression can be seen as expression that the friction term is added to the harmony vibration. When amplitude is large, amplitude is made small by taking energy by friction. When amplitude is small, amplitude is enlarged by pouring in energy by negative friction.[5] Consequently, limit cycle oscillation is obtained. When two or more limit cycle oscillations do an interaction, frequency entrainment may be caused. Two limit cycle oscillations are assumed in this study. Henceforth, each oscillation is named oscillator 1 and oscillator 2, and limit cycle oscillation is only expressed as oscillation. Two oscillations which do an interaction can be expressed with the following expressions.

$$\begin{aligned} \frac{d^2x_1}{dt^2} + \lambda_1\left(x_1^{\ 2} - 1\right)\frac{d\ x_1}{dt} + x_1 &= \alpha\ \left(x_2 - x_1\right) \\ \frac{d^2x_2}{dt^2} + \lambda_2\left(x_2^{\ 2} - 1\right)\frac{d\ x_2}{dt} + x_2 &= \alpha\ \left(x_2 - x_1\right) \end{aligned} \qquad (2)$$

x and λ are the same as that of a expression(1), and oscillator 1 and oscillator 2 correspond to each oscillation. α is a parameter about the strength of an interaction. When the angular frequency of each vibrator is considered as ω_1 and ω_2, it is a s frequency entrainment that two oscillations with different angle frequency synchronize.

III. Simulation experiment

To examine the characteristic of frequency entrainment the simulation experiment was done by using expression (2) while changing the parameter. When performing numerical computation, the fourth Runge-Kutta method was used.

When expressing ω_1 and ω_2 which are the angular frequency of oscillator 1 and oscillator 2, it fixed with $\omega_1 = 1$, and thought as $\omega_2 = \beta\omega_1$. Lapsed time after a simulation start is set to t. And t_2 which is a variable showing the time of oscillator 2 is assumed. Furthermore, the difference in angular frequency was expressed by replacing with $t_2 = \omega_2\, t / \omega_1$.

Next, a synchronous condition in the actual experiment is described. The phase of the start of oscillator 1 at the cycle is assumed to be 0, and it is defined from there to the start at the next cycle as 2π. The phase of oscillator 2 when oscillator 1 is phase 0 is assumed to be θ_i And the phase of oscillator 2 when oscillator 1 is phase 2π is assumed to be θ_{i+1}. When it became $\theta_i = \theta_{i+1}$, it should consider that it synchronized and frequency entrainment should occur.

IV. Experiment result

1. Experiment conditions

It was assumed initial amplitude $x_{01} = x_{02} = 3$, initial acceleration $dx_{01}/dt = dx_{02}/dt = 0$, and $\lambda_0 = \lambda_1 = 1$. ω_1, ω_2 and α of each oscillator were changed, and the simulation was performed.

2. The obtained waveform

As an example as a result of the simulation in which the frequency entrainment occurred, the figure of α = 0.3 and ω_2 = 0.941 is shown. The result of t = 0 and t = 250 was shown in Fig. 1 and Fig. 3. Moreover, in order to compare with what does not do an interaction, the result of α = 0 was shown in Fig. 2 and Fig. 4.

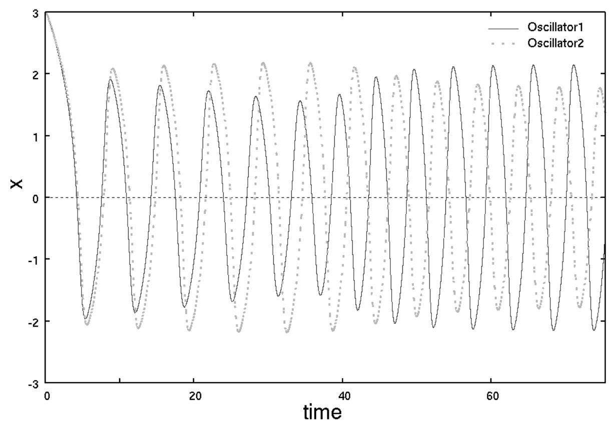

Fig.1. Two oscillators which do an interaction (α=0.3,ω_2=0.941, t=0)

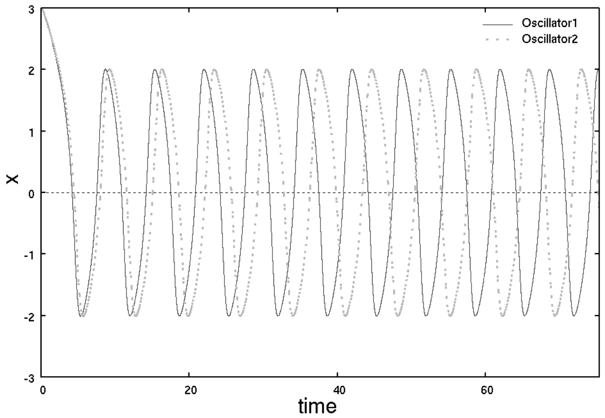

Fig.2.Two oscillators which doesn't do an interaction (α=0, ω_2=0.941, t=0)

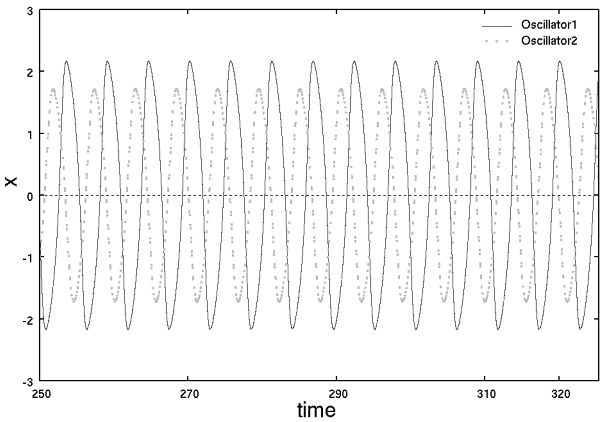

Fig.3. Two oscillators which do an interaction (α=0.3, ω_2=0.941, t=250)

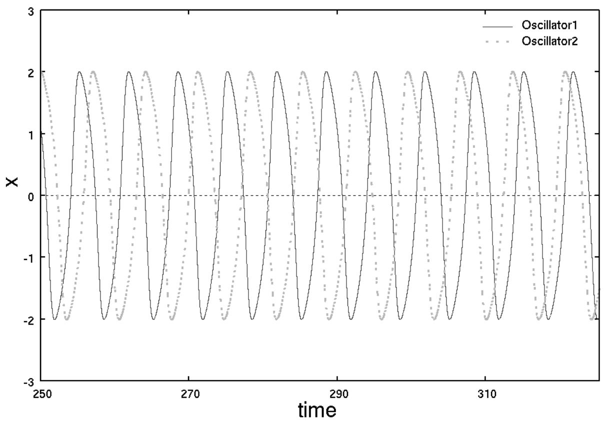

Fig.4. Two oscillators which doesn't do an interaction (α=0, ω_2=0.941, t=250)

When Fig.1 is looked at as compared with Fig.2, the interaction of oscillators shows approaching the stable waveform, changing the form of a wave. And, it is understood to have caused frequency entrainment from the vibration of two oscillators keeping a constant phase lag after the fixed time passes as shown in Figure.3.

3. Return map

Next, whether the result of showing by "2. The obtained waveform" has caused frequency entrainment by drawing return map is examined. Return map is plotting of the relation between θ_i and θ_{i+1}. This time, the plotted time is t=0-500. First of all, Fig. 5 is shown about α=0.3 and ω_2=0.941. This figure shows converging on $\theta_i = \theta_{i+1}$. That is, it was shown that Oscillator 1 and 2 cause frequency entrainment and synchronize. Return map in the conditions of α= 0 and ω_2= 0.941 is shown in Fig. 6. The fact that a locus parallel to the straight line of $\theta_i = \theta_{i+1}$ is drawn, and it does not cross shows that the phase is always shifted. Therefore, not synchronizing was checked.

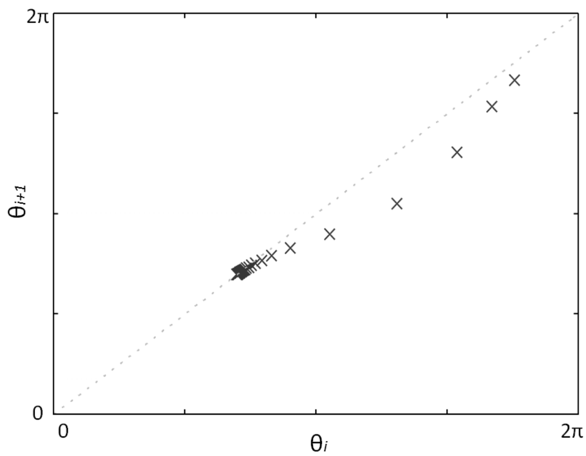

Fig.5. return map (α=0.3, ω_2=0.941)

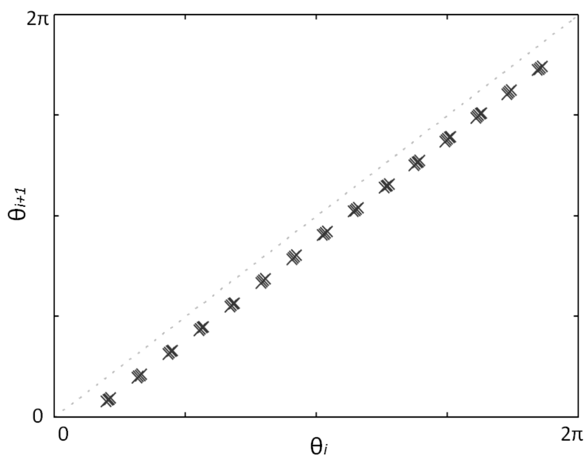

Fig. .6. return map (α=0, ω_2=0.941)

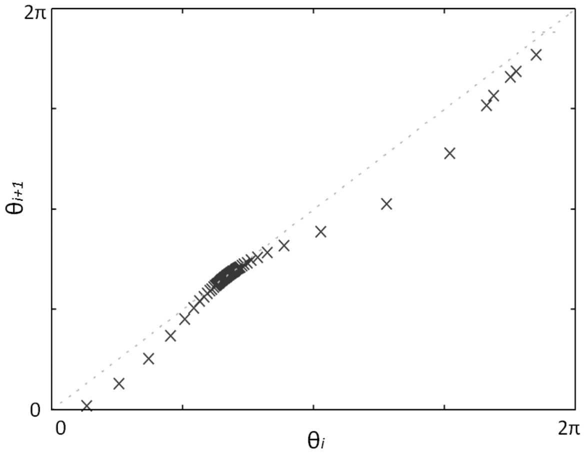

Fig.7. return map (α=0.3, ω_2=0.940)

Furthermore, return map in the conditions of α= 0. 3 and ω_2= 0.940 is shown in Fig. 7. At this time, i t heads for convergence to $\theta_i = \theta_{i+1}$ temporarily. Ho wever, the fact it separated after that and phase dif ference has arisen shows not synchronizing. Therefor e, in α=0.3, it turns out that they are the boundary conditions from which ω_2=0.941 starts frequency entrainment.

4. Synchronous conditions

When changing α by 0.1 units in the range of $0<\alpha \leqq 1$, the simulation of the boundary conditions of which ω_2 causes frequency entrainment was carried out. A result is shown in Fig.8. Frequency entrainment occurs if the interaction grows even if the difference at the angular frequency grows to some degree is understood as a result. When it was set as α = 1, frequency entrainment occurred to ω_2 = 0.597.

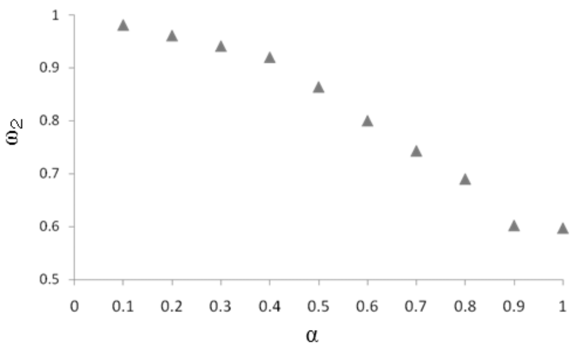

Fig.8. Synchronous conditions
($x_{01} = x_{02} =$ 3,dx_{01}/dt= dx_{02}/dt=0, λ_0=λ_1=1.)

IV. Conclusion

In this paper, frequency entrainment with two oscillators was observed by the simulation as basic examination for the achievement of the cooperation movement by the rhythm of man and the agent. It was observable that two non-linear oscillators with which rhythms differ synchronize from this experiment. The thing that the frequency entrainment can be expected to be caused in thing to express the rhythm from the state and the movement of man and the agent appropriately, and to define the interaction has been understood. A simple case was assumed this time, and frequency entrainment of two non-linear oscillators was observed. The examination problem in the future is thing that analyzes man's operation and chooses as a non-linear oscillator, and thing to consider frequency entrainment of it. It is thought it is for the achievement of a smooth cooperation movement of man and the agent by the thing that ties to the promotion of communications by a frequency entrainment.

REFERENCES

[1] Mamoru E, Junichi K, and Junji S(1999), Devel opment of Human-friendly Robot System Called Ma rvel(in Japanese). OMRON TECHINICS Vol.39 No. 1: 36-41
[2] Hajime A(1996),Elemental Technologies for Collec tive Robots(in Japanese).JSME ROBOMECHA SHIM POJIA the collection of lecture papersVol.1:175-180
[3]Norihiko Y(2003), Soft information processing(in Japanese). Saiensu-Sha Co., Ltd:pp54
[4]Takashi T, Toyoaki N(2003), Manualless interaction by synchronization and modulati on. TECHNICAL REPORT OF IEICE Vol.103 No,5 22: 55-60
[5] Yuki F(2005), The world of rhythm phenomenon, The University of Tokyo publication association

Man-machine Interface for Modular Robot System

Tomotsugu Goto[*1] Masafumi Uchida[*1] Hirotoshi Asano[*3] Akio Nozawa[*2] Hitoshi Onogaki[*4]
Tota Mizuno[*5] Hideto Ide[*3] and Syuichi Yokoyama[*4]

**1 The University of Electro-Communications, 1-5-1, Chofu-ga-oka, Chofu, Tokyo 182-8585*
**2 Meisei University, 2-1-1, Hodokubo, Hino, Tokyo 191-8506*
**3 Aoyama Gakuin University, 5-10-1, Fuchinobe, Sagamihara, Kanagawa 229-8558*
**4 Kogakuin University, 1-24-2, Nishishinjuku, Shinjuku-ku, Tokyo 163-8677*
**5 National Institute of Advanced Industrial Science and Technology (AIST),*
Central 6, 1-1-1 Higashi, Tsukuba, Ibaraki 305-8566

Abstract: A modular robot is composed of multiple modules, each comprising a sensor, an actuator, and a control system. Each module accumulates information about its own sensor, actuator, and connection to other modules and communication information between adjoining modules. The user obtains this information via an interface and can thus recognize the state of the robot and issue commands. However, when the number of modules becomes large, the amount of information sent from the modules becomes too much for the user to deal with effectively. Naturally, it also becomes more difficult for the user to issue commands to the modular robot as the number of modules increases. In this study, we developed an interface to present, in a simple manner, information aggregated in a certain module from other modules, and we examined its effectiveness in a modular robot composed of these modules.

Keywords: modular robot, interface, CDMA

I. INTRODUCTION

A modular robot is composed of multiple modules, each comprising a sensor, an actuator, and a control system. These modules are the fundamental compositional units of the robot body. Each module uses its sensor to collect information about the environment and accumulates that information. To this information it adds information that the module accumulates about itself, such as the state of the actuator and the connections between modules. Communication information between adjoining modules is also accumulated. By obtaining this information via an interface, a user can recognize the state of the robot and can issue commands. However, if the number of modules is increased to several thousand or more, the amount of information sent to the user from the module becomes too much for the user to deal with effectively. Naturally, it also becomes more difficult for the user to issue commands to the modular robot as the number of modules increases.

A multi-arm module used in this study possesses eight arms, that is, four movable arms and four attachable arms, and can be attached to and detached from other modules. A movable arm and an attachable arm are arranged on each diagonal of the generally cube-shaped module. Fig. 1 shows a modular robot constructed using these modules.

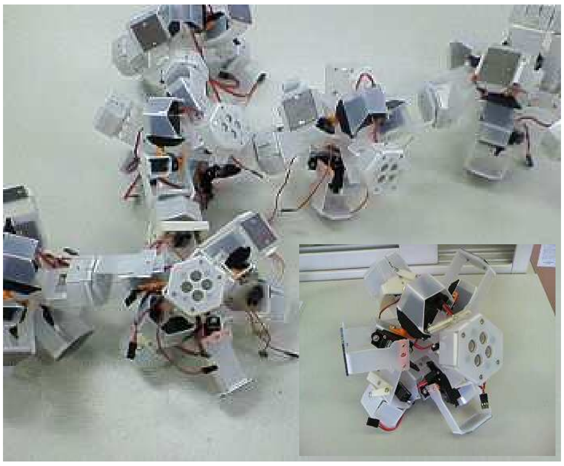

Fig. 1. Modular robot.

In this study, we developed an interface for presenting to the user, in a simple manner, the information aggregated in a certain module from other modules, and we examined its effectiveness in a modular robot composed of these modules. This interface is composed of a communication system, a positional search system that searches for arms of the adjacent module, and a system that aggregates and presents information about the modular robot.

©ISAROB 2009

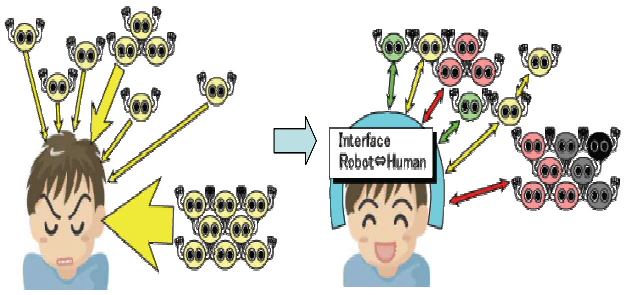

Fig. 2. Man-machine interface.

II. Man-machine Interface

1. Communication system

The communication between modules was assumed to be short-range local communication via infrared light, and the communication distance was assumed to be the same as the module size, about 10 to 15 cm. Code division multiple access (CDMA) was adopted as the communication method so that there were no interruptions even when sending and receiving information between two or more modules simultaneously.

A communication device, either a transmitter or receiver, was installed at the end of each arm, as shown in Fig. 3. The positional search system and the communication system for the arm were implemented with a single device by utilizing the directivity of the communication element (infrared receiver IC).

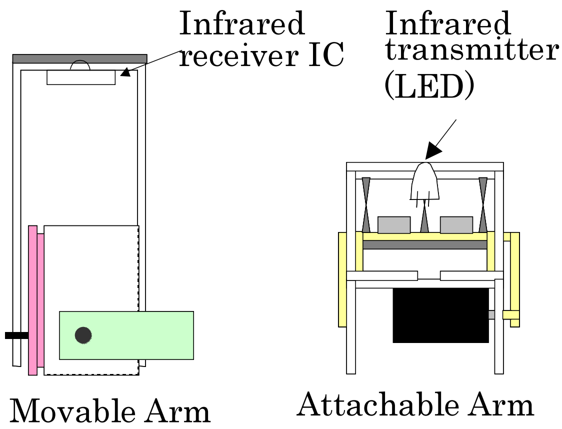

Fig. 3. Communication system.

2. System for aggregating and presenting information

The system that collects and presents information was designed based on a cubic model of each module, where the vertexes of the cube represent the tips of the arms, as shown in Fig. 4. The arm on each corner is of a different kind from the structure of an actual module. A unique ID was assigned to each module, and an identifying number was assigned to each arm of the module. When communicating between modules, the module ID and the arm number used for sending and receiving were transmitted as information. The current shape of the modular robot can be determined by accumulating information about the connections between modules.

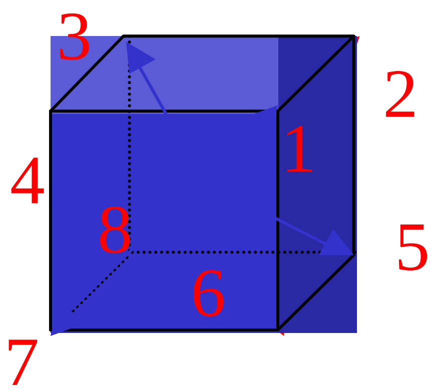

Fig. 4. Module model.

The format of the transmission signal showing the connection between modules was as follows: [Transmission-side module number (Tn), reception-side module number (Rn), reception-side arm number (An)]. Each part was modulated by using a spread-code sequence and transmitted. For the module located at the end of the robot, when its own information was sent, '0' was substituted for the part containing the reception-side module number. At the reception-side module, the module number and arm number were added to the respective parts and transmitted to the next module. Fig. 5 illustrates this.

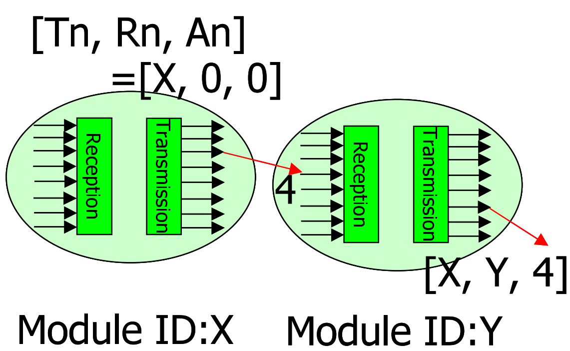

Fig. 5 Transmission format.

Two peripheral interface controllers (PICs) were used, one for receiving and one for transmitting, and pins on the PICs corresponded to module arms. Only information about the connection was transmitted in the transmission part. The acquired data in the reception part was sent to a demodulator in a personal computer (PC), which demodulated the format.

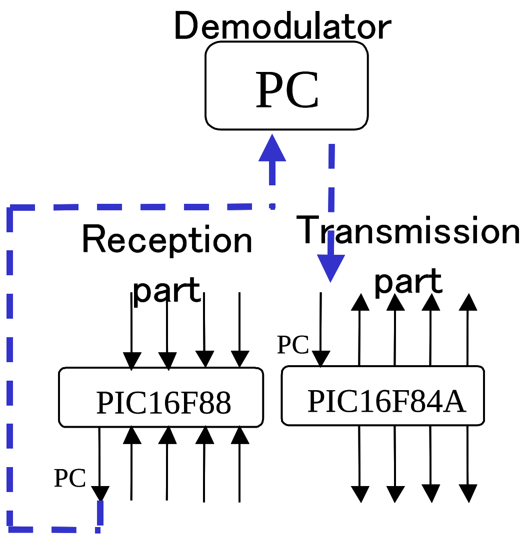

Fig. 6 System configuration.

The communication between modules was performed as shown in Fig. 7, and information was aggregated in the upper right module. This module communicated with the PC, and the PC demodulated the obtained information to determine the configuration of the robot and display it in 3D.

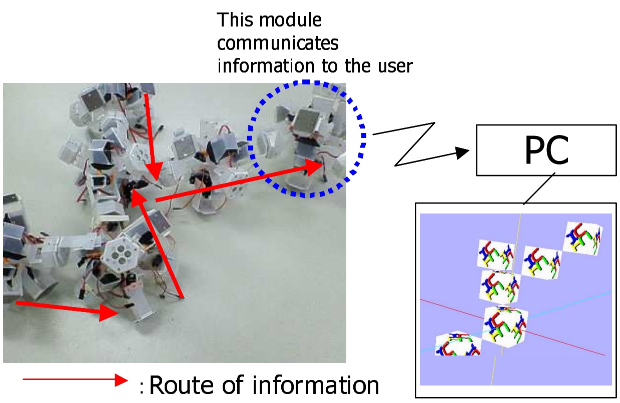

Fig. 7 Reproduction of modular configuration.

When the modules were connected as shown in Fig. 8(a), the result of reproducing the configuration of the modular robot based on information about the connections between modules is shown in Fig. 8(b).

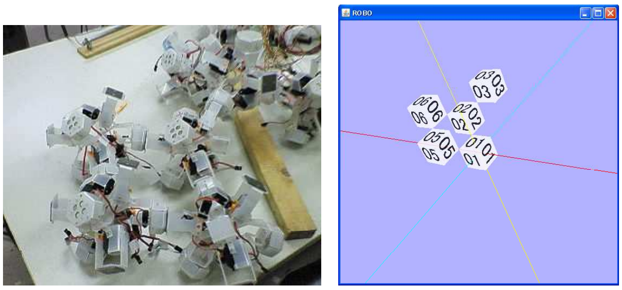

(a) (b)

Fig. 8 Modular configuration (a) and 3D view of reconstructed configuration (b).

III. CONCLUSION

In this study, we constructed a system that aggregates information about the connections between modules of a modular robot, and presents the information to a user in a simple manner. Future work will include investigation of a complementary system for transmitting information (commands) from the user to the modular robot and development of a method for presenting information in a multimodal manner.

Acknowledgements

This work was supported in part by Grant-in-Aid from the Hayao Nakayama Foundation for Science & Technology and Culture, Japan. This support is gratefully acknowledged.

REFERENCES

[1] Michael Rubenstein, Kenneth Payne, Peta Will, and Wei-Mm Shen: "Docking among independent and autonomous CONRO self-reconfigurable robots", 2004 IEEE International Conference on Robotics and Automation, Volume 3, pp. 2877–2882, 26 April-1 May 2004.
[2] Toshio Fukuda, Hidemi Hosokai, Yoshio Kawauchi, and Martin Buss: "Dynamically Reconfigurable Robotic System (DRRS) (System Configuration and Implementation as CEBOT)", Proc. of 5th Int'l Symp. of Robotics Research, pp. 22–28 (1989).
[3] Eiichi Yoshida, Satoshi Murata, Shigeru Kokaji, Kohji Tomita and Haruhisa Kurokawa: "Micro Self-Reconfigurable Robotic System using Shape Memory Alloy", Distributed Autonomous Robotic Systems 4, Lynne E. Parker, George Bekey, and Jacob Barhen, eds., pp. 145–154, 2000 (Knoxville, USA).
[4] Wei-Min Shen, Behanam Salemi, and Peter Will: "Hormone-Inspired Adaptive Communication and Distributed Control for CONRO", IEEE Transactions

©ISAROB 2009

on Robotics and Automation, Vol. 18, No. 5, pp. 700–712, October 2002.

[5] Mitsuru Shiozak, Toshimi Fujii, Kousuke Katayama, Masahiro Ono, and Atsushi Iwata: “The Flexible CDMA Serial Link Network for Robot Control”, Technical Report of IEICE. ICD pp. 51-56, ICD2002-115 IEICE, ISSN:09135685.

[6] KAMIMURA Akiya, MURATA Satoshi, YOSHIDA Eiichi, KUROKAWA Haruhisa, TOMITA Kohji, and KOKAJI Shigeru: “Research on Self-Reconfigurable Modular Robot System: Experiments on Reconfiguration and Locomotion with Several Modules”, Transactions of the Japan Society of Mechanical Engineers C, Vol. 68, No. 667, pp. 886–892 (2002).

[7] Mark Yim, Craig Eldershaw, Ying Zhang, and David Duff: “Self-Reconfigurable Robot Systems: PolyBot”, Journal of the Robotics Society of Japan, Vol. 21, No. 8, pp. 23–26, (2003).

[8] Saburo Matunaga: “Modular Relocatable Manipulators”, Journal of the Robotics Society of Japan, Vol. 21, No. 8, pp. 40–44, 2003.

[9] Norio Inou: “Cellular Robots Forming a Mechanical Structure”, Journal of the Robotics Society of Japan, Vol. 21, No. 8, pp. 45–48, 2003.

[10] Ryoko Matsuo, Michihito Matsuo, Tomoaki Ohtsuki, Tomoyuki Udagawa, Iwao Sasae: “Performance Analysis of Indoor Infrared Wireless Systems Using OOK CDMA on a Diffuse Channel”, Technical Report of IEICE. RCS Vol. 99, No. 220 pp. 85–90, (1999).

[11] Toya Nobuyuki, Muneyasu Mitsuji, Nomura Yasuo, Imanishi Shigeru: “Examination of CDMA-RAKE Receiver for Optical Telemetry Using Indirectly Scattered Light”, IEICE Technical Report. ME and Bio-Cybernetics, Vol. 104, No. 179 pp. 41–44, (2004).

The Fourteenth International Symposium on Artificial Life and Robotics 2009 (AROB 14th '09),
B-Con Plaza, Beppu, Oita, Japan, February 5 - 7, 2009

Autonomous Reconfiguration of Robot Shape by Using Q-learning

Satoshi Shiba*1 Masafumi Uchida*1 Akio Nozawa*2 Hirotoshi Asano*3 Hitoshi Onogaki*4
Tota Mizuno*5 Hideto Ide*3 and Syuichi Yokoyama*4
*1 The University of Electro-Communications, 1–5–1 Chofu-ga-oka, Chofu, Tokyo 182–8585
*2 Meisei University, 2–1–1, Hodokubo, Hino, Tokyo 191–8506
*3 Aoyama Gakuin University, 5–10–1, Fuchinobe, Sagamihara, Kanagawa 229–8558
*4 Kogakuin University, 1–24–2, Nishi-shinjuku, Shinjuku-ku, Tokyo 163–8677
*5 National Institute of Advanced Industrial Science and Technology (AIST),
Central6, 1–1–1 Higashi, Tsukuba, Ibaraki 305–8566

Abstract

A modular robot can be built with a shape and function that match the working environment. We developed a four-arm modular robot system which can be configured in a planar structure. A learning mechanism is incorporated in each module constituting the robot. We aim to control the overall shape of the robot by accumulation of the autonomous actions resulting from the individual learning functions. Considering that the overall shape of the modular robot depends on the learning condition in each module, this control method can be treated as a dispersion control learning method. The learning object is the cooperative motion between adjacent modules. The learning process proceeds based on Q-learning by trial and error. We confirmed the effectiveness of proposed technique by computer simulation.

1 Introduction

Most of traditional robots have been built to perform particular tasks in place of humans. In future, however, robots are expected to be able to perform a wide range of tasks autonomously. Conventional robots are limited to performing just one or two tasks assumed by the designer. It is almost impossible for a single robot to adapt to various kinds of tasks and environments. To overcome this limitation, a modular robot was proposed as a system that can be adapted to various given tasks and unknown environments [1, 2, 5, 6]. A modular robot can be defined as a robotic system constructed from a set of standardized components, so-called "modules". With this approach, the robot body is reconfigured for various complex tasks, instead of designing a new, different robot for each task. Modules, by themselves, cannot perform tasks, but when many of them are connected together, a new system can be obtained to do complicated tasks.

A modular robot changes its shape by changing the connections between modules in order to meet the demands of different tasks or different working environments. Over the last ten years, research in this field has focused on versatility and adaptability aspects, but less effort has been made in the field of self-reconfigurable modular robots that can autonomously change their configuration [10, 11, 12].

In this study, we developed a multi-arm modular robot, and we propose a system that incorporates a learning mechanism of each module constituting the modular robot. We aim to control the overall shape of the modular robot by the accumulation of autonomous actions arising from the learning mechanism of each module. Since the overall shape of the modular robot depends on the learning result of each module, this method can be treated as a dispersion control learning method [7, 8, 9]. The cooperation between a module and an adjacent module is the object of learning. The learning process involves trial and error based on Q-learning [13, 14]. We confirmed the effectiveness of the proposed technique by computer simulation.

2 Function of a module and Q-learning

Figure 1 shows a model of the four-arm module and the assumed modular robot constructed from such modules [3, ?]. Each arm has the ability to be connected to and disconnected from other arms of the module. The shape of the robot can be reconfigured by changing connections with adjacent modules according to preset rules, as shown in Figure 1. Here,

©ISAROB 2009

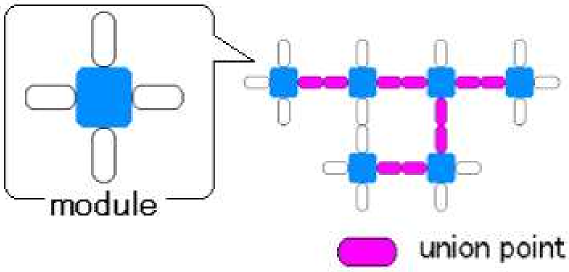

Figure 1. Model of four-arm module and modular robot.

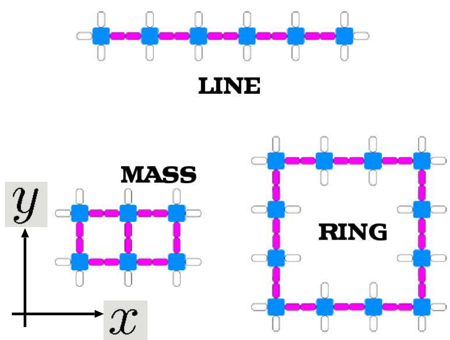

Figure 2. Three robot shapes considered (**LINE**, **MASS** and **RING**).

the connection state of an arm is expressed by two values (binary) as follows: connected ($s = 1$), not connected ($s = 0$). Since there are four arms per module, the connection states of the arms in one module can be expressed by four bits. The following four basic operations are defined for each arm: (i) arm is turned clockwise [**MOVE CW**], (ii) arm is turned counter-clockwise [**MOVE CCW**], (iii) arm is connected [**CONNECT**], and (iv) arm is disconnected [**DISCONNECT**]. These four basic actions cannot be performed by a single module; they are performed by the cooperative behavior of two or more modules. An additional standby action [**STAY**] is also added. As a result, there are 17 kinds of action **a** in total: 4 arms × 4 basic actions + 1 standby action. A module acts in accordance with the rule of state **s** versus action **a**. The appearance probability of an action **a** in the state **s** is optimized by Q-learning.

Figure 2 shows three robot shapes that we consider. They are called the **LINE** shape, **MASS** shape, and **RING** shape. Since the action of each module is decided by Q-learning, the overall shape of the robot is controlled by Q-learning. The reconfiguration process of the robot shape was examined by computer simulation.

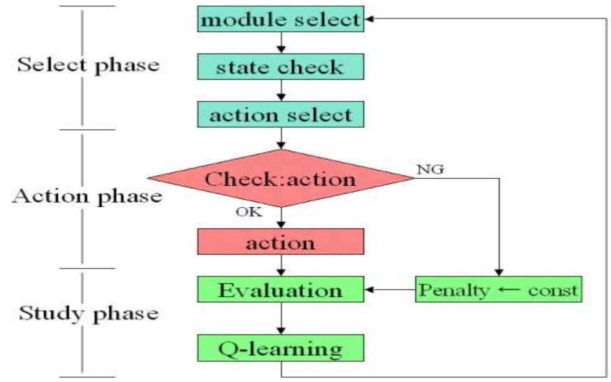

Figure 3. Flow of learning algorithm.

To develop a system in which the shape of the robot is automatically reconfigured, each module proceeds with Q-learning while repeating trial and error actions in the early stage. This Q-learning is not performed uniformly for the entire robot, but is performed independently in each module.

Figure 3 shows the flow of the learning algorithm. First, one module is chosen at random from the group of modules constituting the robot. The chosen module decides an action in accordance with its own Q value. After checking whether the action is valid, the module carries out the action. Next, the action is evaluated, and the Q value is updated in accordance with the evaluation result. This series of processes is defined as one step". The number of modules that act in one step is assumed to be only one. According to an observed state $\mathbf{s}_t$ at time t, an action $\mathbf{a}_k$ for the module is selected with probability $P(s_t, a_k)$ presented in Eq. (1) below through a Boltzmann selection method. If it is judged to be an invalid action, it is not carried out. In that case, this action is dealt with by imposing a penalty value on the Q value. In Eq. (1), $ANUM$ is the total number of actions, and $Q(s_t, a_k)$ is an expectation value of action $\mathbf{a}_k$ ($k = 1, 2, \cdots, ANUM$) in a state $\mathbf{s}_t$. T is the Boltzmann temperature presented in Eq. (2). In Eq. (2), τ is a time constant.

$$P(\mathbf{s}_t, \mathbf{a}_k) = \frac{e^{\frac{Q(\mathbf{s}_t, \mathbf{a}_k)}{T}}}{\sum_{k=1}^{ANUM} e^{\frac{Q(\mathbf{s}_t, \mathbf{a}_k)}{T}}} \tag{1}$$

$$T = 2 \cdot e^{-\frac{t}{\tau}} \tag{2}$$

©ISAROB 2009

Then, $Q(s_t, a_k)$ is updated as shown in Eq. (3) according to an obtained reward $Reward$ by carrying out an action based on Eq. (1).

$$Q(\mathbf{s}_t, \mathbf{a}_k) \leftarrow (1-\alpha)\cdot Q(\mathbf{s}_t, \mathbf{a}_k) + \alpha\left\{Reward + \gamma \max_{\mathbf{a}'} Q(\mathbf{s}_{t+1}, \mathbf{a}')\right\} \quad (3)$$

$$Reward = \frac{Eval_{t-1} - Eval_t}{Eval_t + 1} - Penalty \quad (4)$$

Here, α is a learning rate, γ is a discount rate, $\max_{a'} Q(s_{t+1}, a')$ is a maximum expectation value in state $\mathbf{s}_{t+1}$ observed at the next time step, and $\mathbf{a}'$ is an action indicated by this maximum expectation value. In Eq. (4), $Penalty$ is a penalty value, and $Eval_t$ is an evaluation value of the robot shape at time t.

3 Computer Simulation

We simulated the reconfiguration of the modular robot shape from an initial shape to (i) the **LINE** shape and (ii) the **MASS** shape. The initial shape of the robot was set so that modules formed a chain. The evaluation value is $Eval_t$ when the shape of the robot is evaluated from the viewpoint of an outside observer at time t. First, the shape of the robot was estimated from the positions of all modules in the simulation. Next, $Eval_t$ was calculated from the difference between the estimated shape and the requested shape (**LINE** and **MASS**). In the case of the **LINE** shape, the deviation on either side of the x axis or the y axis is the evaluation value $Eval_t$ concerning the position of all modules. On the other hand, in the case of the **MASS** shape, the deviation of the position of all modules is the evaluation value $Eval_t$.

Minimizing $Eval_t$ is equivalent to achieving the requested shape in both cases. The learning process proceeds by comparing the evaluation value after an action with the evaluation value before the action.

The convergence time in learning and the required memory storage capacity depend on the size of the learning space, calculated by the product of the total number of states $\mathbf{s}$ and the total number of actions $\mathbf{a}$ in the Q-learning. We considered two ways of reducing the learning space to improve the learning efficiency. The first way was to exclude the choice of the arm from the learning object, reducing the number of possible actions from 17 to 5. The learning space was reduced by 70 % as a result. We called this the "action only" method. The second way is to pair the **[CONNECT]** action in one module and the **[DISCONNECT]** action in an adjacent module and to unify them by introducing a new **[REVERSE]** action. As a result, the

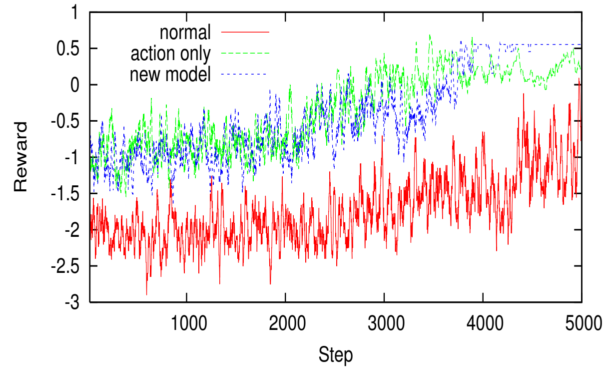

Figure 4. Comparison of 5,000 learning steps (**LINE** shape).

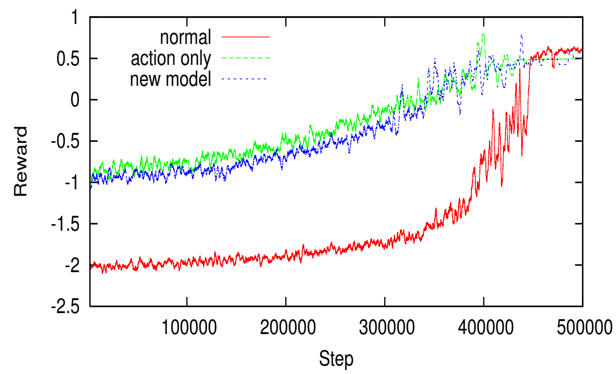

Figure 5. Comparison of 500,000 learning steps (**LINE** shape).

total number of actions decreased from 17 to 7, and the learning space was reduced by 59 %. We called this the "new model" method.

Figures 4 and 5 show the simulation results of reconfiguration based on the evaluation value of the **LINE** shape in a robot body composed of 10 modules. In these two figures, the solid line indicates the results obtained without using either of the methods described above ("normal"). The dotted line indicates the "action only" type, and the broken line indicates the "new model" type. The horizontal axis is the number of learning steps, and the vertical axis is the mean value of $Reward$ for each module. In Figures 4 and 5, the upper limit was set to 5,000 steps and 500,000 steps, respectively. The "action only" type converges earlier to a certain value at the end of the learning step.

As shown in Figure 4, the amount of change in $Reward$ with the "normal" type is large in the ini-

©ISAROB 2009

tial stage of the learning process, and the final convergence is insufficient. On the other hand, the "action only" type has a more expensive *Reward* at the early stage,and *Reward* becomes a constant, stable value at the last stage, showing successful convergence. The "new model" type shows the best result in terms of the rate of rise in *Reward* at the last stage and the stability after reaching convergence. For the "action only" type, the learning object was 5 actions. Therefore, it determines that learning is completed in fewer steps, but there is no optimization related to the choice of arm because arm choice was excluded from the learning object. Therefore, the final convergent value does not reach the optimum value. The learning space of the "new model" type is larger than that of the "action only" type. However, because the choice of arm is contained in the learning object of the "new model" type, the final convergent value reaches the optimum value. As shown in Figure 5, if a sufficient number of learning steps for all three types is ensured, it is possible to achieve a final convergent result that is equivalent to that of the "new model" type. Figure 6 shows one example of the **LINE** shape and the **MASS** shape after learning with the "new model" type. In this figure, the blocks with numbers represent modules (numbers $0, 1, 2, \cdots$ are modules' IDs), and the "**" mark indicates the connections between modules. The resulting shape is not necessarily always optimized. However, we confirmed that the shape of the robot could be controlled to a certain extent without using communication between modules.

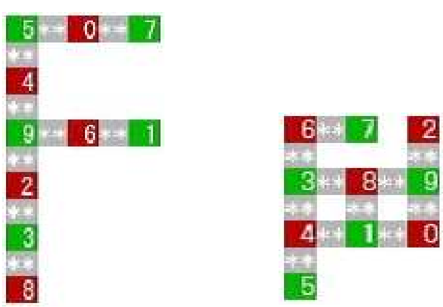

Figure 6. **LINE** shape (left) and **MASS** shape (right) obtained by using the "new model" type.

The evaluation value to form the **RING** shape was defined as follows. The requested radius of the **RING** shape is D_0. An arbitrary module is M. A module adjoining M is M_1. The furthest module from M is M_2. An evaluation value $Eval_t$ is defined by Eq. (5) based on a distance D between the position at distance

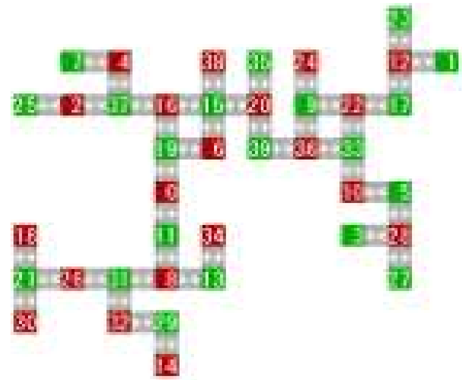

Figure 7. Reconfiguration result for **RING** shape ($D_0 = 9.0$).

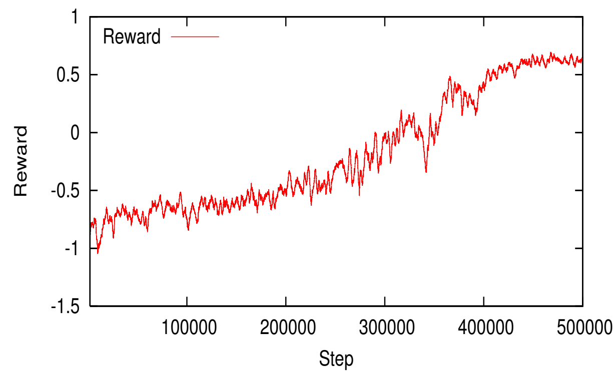

Figure 8. Evolution of *Reward* value in reconfiguration of the **RING** shape ($D_0 = 9.0$).

D_0 and the position of M from the midpoint of M_1 and M_2.

$$Eval_t = e^{(D_0 - D)^2} \tag{5}$$

This rule was established based on the circular alignment algorithm of multi-robot systems[15].

Figures 7 and 8 show the simulation results of reconfiguration based on the evaluation value of the **RING** shape. In this simulation, we specified $D_0 = 9.0$ with 40 modules used, and the number of learning steps was set to 500,000. In Figure 8, the horizontal axis is the learning step number, and the vertical axis is the *Reward* value. As shown in this figure, the *Reward* value increased as the step number increased, showing that the learning function proceeded. However, the modules did not fully converge to the *RING* shape. Figures 9 and 10 show the evolution of the obtained *Reward* value of each module constituting the robot. Figure 9 shows the case of the **LINE** shape,

©ISAROB 2009

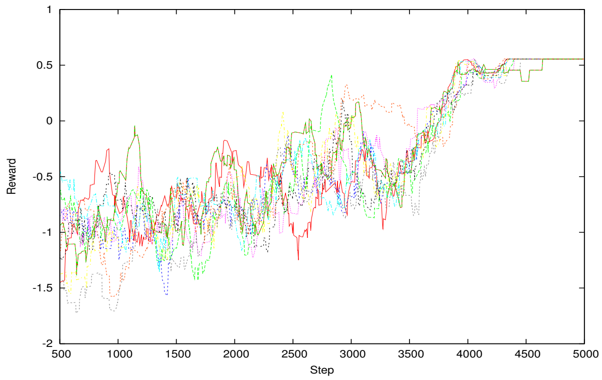

Figure 9. Comparison of evolution of *Reward* value for each module in the case of the **LINE** shape.

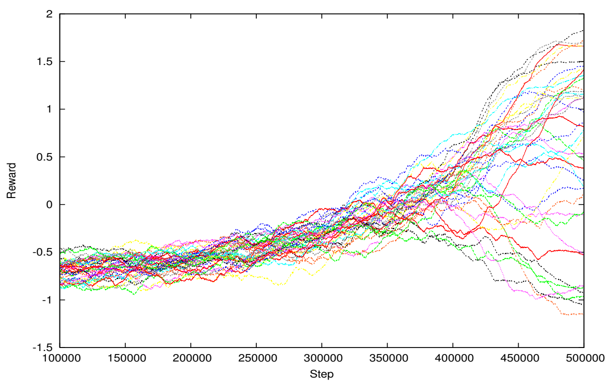

Figure 10. Comparison of evolution of *Reward* value for each module in the case of the **RING** shape ($D_0 = 9.0$).

and Figure 10 shows the case of the **RING** shape with $D_0 = 9.0$. The obtained *Reward* value of all modules tends to increase in the case of the **LINE** shape. The final convergent value for the obtained *Reward* is the same for all modules. Although there was a difference in the obtained *Reward* between the modules in the first half of the learning process, this difference gradually reduced in the latter half. On the other hand, in the case of the **RING** shape, convergence could not be confirmed from the obtained *Reward* between each module in the learning process. The obtained *Reward* values for each module diverged in the latter half of the learning process. Comparing Figure 9 with Figure 10, we found that, in order to obtain a good result, it is necessary to reduce the differences in the obtained reward among the modules. In the learning result shown in Figure 10, the module which converged to the highest obtained *Reward* was ID:7, and the module which converged to the lowest obtained *Reward* was ID:16. Figures 11 and 12 show the number of invalid actions, determined based on the Q value, in module ID:7 and module ID:16, showing the states after 100,000 steps and after 500,000 steps, respectively. In each figure, the left part shows module ID:7, and the right part shows module ID:16. The horizontal axes of the figures show the state of the module, and the vertical axes show action 0:[**STAY**], 1:[**MOVE CW**] for arm No. 1, 2:[**MOVE CCW**] for arm No. 1, 3:[**MOVE CW**] for arm No. 2, 4:[**MOVE CCW**] for arm No. 2, 5:[**REVERSE**] for arm No. 3, and 6:[**REVERSE**] for arm No. 4. Here, arm Nos. 1–4 correspond to the four arms of a module. This figure shows the number of invalid actions that occurred in the first 5,000 steps. The actions in the state indicated by the thick red part shows actions that were often judged invalid.

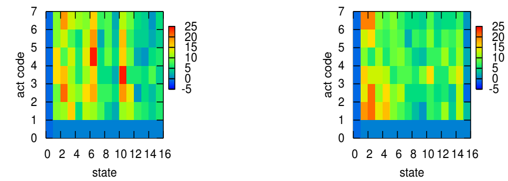

Figure 11. The total number of invalid actions in 100,000 steps for ID:7 (left) and ID:16 (right).

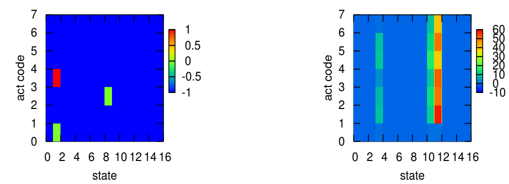

Figure 12. The total number of invalid actions in 500,000 steps for ID:7 (left) and ID:16 (right).

It was confirmed that the number of actions judged invalid gradually reduced as the learning process proceeded. There were more actions judged invalid in the module with ID:16 than in the module with ID:7 in the latter half of the learning process. In other words, the learning process for the module with ID:16 was delayed. An action judged invalid is an action that cannot be carried out in the actual environment. Therefore, when an invalid action is output, the learning process cannot proceed. As a result, the learn-

©ISAROB 2009

ing process of the module that outputs more actions judged invalid is delayed. It is possible that this problem might be improved by making the learning process proceed equally.

4 Conclusion

In this research, we examined the reconfiguration control of the shape of a modular robot. A robot composed of four-arm modules was considered as a model. We proposed providing each module with a learning function based on Q-learning. We verified the validity of the proposed technique by computer simulation. Our results showed that, when learning of each module was integrated in the overall robot, the requested shape of the robot could be realized.

Problems that we currently face in advancing our work include: (1) increasing the number of modules; (2) expanding the approach to a 3-D environment; and (3) verifying the performance in real environments.

Acknowledgements

This work was supported in part by Grant-in-Aid of Hayao Nakayama Foundation for Science & Technology and Culture, Japan. This support is gratefully acknowledged.

References

[1] T. Fukuda and S. Nakagawa: "Dynamically Reconfigurable Robotics System," Proc. of IEEE Int. Conf. Robotics and Automation, pp.1581–1586(1988)

[2] G. S. Chirikjian: "Metamorphic Hyper-Redundant Manipulators," Proc. of JSME Int. Conf. on Advanced Mecatronics, pp.467–472(1993)

[3] K.Kotay and D. Rus: "Locomotion versatility through self-reconfiguration," Robotics and Autonomous Systems, vol.26, pp.217–232(1999)

[4] D. Rus and M. Vona: "Crystalline robots: Self-reconfiguration with unit-compressible modules," Autonomous Robots, vol.10, no.1, pp.107–124(2001)

[5] M. Yim: "New locomotion gaits," Proc. of IEEE ICRA, pp.2508–2514(1994)

[6] C. Paredis, H.B. Brown and P. Khosla: "A rapidly deployable manipulator system," Proc. of IEEE ICRA, pp.1434–1439(1996)

[7] W.-M.Shen, B.Salemi and P.Will: "Hormone-Inspired Adaptive Communication and Distributed Control for CONRO," IEEE Trans. on Robotics and Automation, Vol.18, No.5, pp.700–712 (2002)

[8] J. Walter, J. Welch and N. Amato: "Distributed Reconfiguration of Metamorphic Robot Chains," Proc. of the 19th Annual ACM SIGACTSIGOPS Symposium on Principles of Distributed Computing (PODC 2000), Portland, Oregon, pp.171–180(2000)

[9] Z. Bulter, K. Kotay, D. Rus and K. Tomita: "Cellular Automata for for Decentralized Control of Self-Reconfigurable Robots," Proc. of the 2001 IEEE Int. Conf. of Robotics and Automation workshop on Robotics Modular Robots (2001)

[10] A. Pamecha, I. Ebert-Uphoff and G. Chirikjian: "Useful Metric for Modular Robot Motion Planning," IEEE Trans. on Robotics and Automation, vol.13, no.4, pp.531–545 (1997)

[11] D. Rus and M. Vona: "Crystalline Robots: Self-Reconfiguration with Compressible Unit Modules," Autonomous Robots, vol.10, no.1, pp.107–124 (2001)

[12] C.-H. Chiang and G. Chirikjian: "Modular robot motion planning using similarity metrics," Autonomous Robots, vol.10, no.1, pp.91–106, (2001)

[13] Watkins,C.J.C.H. and Dayan,P.: Technical Note: Q-Learning, Machine Learning 8, pp. 279–292(1992).

[14] R.S. Sutton and A.G.Barti: "Reinforcement Learning: An Introduction," MIT Press(1998)

[15] Koji Ito: “Intelligence and Emergence,” NTT Publishing Co., Ltd.,pp.60-70 (2000)

The Fourteenth International Symposium on Artificial Life and Robotics 2009 (AROB 14th '09),
B-Con Plaza, Beppu, Oita, Japan, February 5 - 7, 2009

Current Control of PWM Power Amplifier by Approximate 2-Degree-of-Freedom Digital Controller

Keisuke FUJITA[1], Kohji HIGUCHI[2], Kazushi NAKANO[3], Koji MATSUSHITA[5] and Fumiho CHINO[6]
[1,2,3,4]Dept.of Electronic Engineering, The University of Electro-Communications
1-5-1 Chofu-ga-oka, Chofu, Tokyo 182-8585, Japan, email : higuchi@ee.uec.ac.jp
nakano@ee.uec.ac.jp, kajikawa@ee.uec.ac.jp
[5,6]NF Corporation
6-3-20 Tunashimahigashi,Kohoku-ku, Yokohama 223-8508, Japan
email:matsushita-k@nfcorp.co.jp, chino-f@nfcorp.co.jp

Abstract

In this paper, a digital robust controller with bumpless mode switching for controlling the current of PWM power amplifier for satisfying the demands and extending the range of inductive load wider is proposed. It is necessary to measure the value of load to implement this bumpless mode switching automatically according to the load range. Thus, a method of estimating inductive load is shown. The bumpless mode switching is automatically performed by estimating a inductive value without specifying the value of inductive load beforehand. The digital controller equipped with the inductance estimation and the bumpless mode switching is realized by a DSP. Some experiments show that the digital controller with the proposed bumpless mode switching can satisfy larger specifications.

1 Introduction

A pulse width modulation (PWM) switching circuit is used for an electric-power conversion circuit, an LCL low-pass filter is inserted between the conversion circuit and the load for noise removal, and a PWM amplifier which constitutes feedback control systems so that the output current supplied to the load might be proportional to a reference input is used as an amplifier itself or as a current supply. If the characteristics and parameters of the load are decided and there is little change in those, satisfactory performances are obtained in general. In many applications, however, loads cannot be specified, i.e., its amplitude is also sharply changed from the zero to the maximum rating. Usually, design conditions are changed for each load and then each controller is re-designed. Then, a so-called robust PWM amplifier which can cover such an extensive load changes and also direct-current power supply voltage changes with one controller is needed. We have recently proposed the different methods for designing a digital controller for PWM voltage amplifiers which can attain such demand. Furthermore, a digital controller which uses mode switching was proposed in order to extend the range of load wider. This mode switching is performed automatically without specifying the value of capacitive load beforehand, i.e., the parameters of the controller are switched automatically. In this paper, a bumpless mode switching method for controlling of the current of PWM power amplifier is proposed. It is necessary to measure the values of the loads to implement this bumpless mode switching automatically according to the load range. Thus, a method of estimating inductive load is shown. The digital controller with the bumpless mode switching function is actually realized by using a DSP. Experimental studies show that the proposed digital controllers can satisfy larger specifications smoothly.

2 PWM power amplifier

The PWM amplifier as shown in **Fig.1** is being manufactured. The carrier frequency of triangular waves are 10-100[kHz], and the amplitude c_m is 10[V] and E is 150[V]. The LCL circuit is a filter for removing carrier and switching noises. The values L_0, C_0 and L_1 of the LCL circuit are determined so that control systems can make their sensitivity to load changes low and reduce noise. If the frequency of input u is smaller enough than that of the carrier, the state equation of the PWM amplifier at inductannce load L_L

©ISAROB 2009

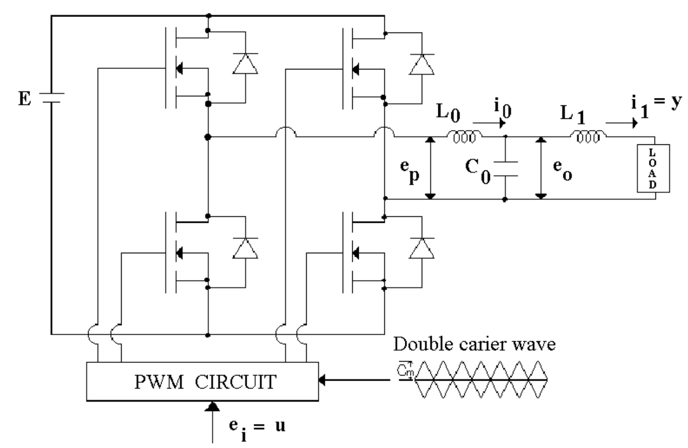

Figure 1: PWM amplifier

in **Fig.1** can be expressed from the state equalizing method as follows:

$$\left\{ \begin{array}{l} \dot{x} = A_c x + B_c u \\ y = Cx \end{array} \right. \quad (1)$$

where

$$\begin{aligned} x &= \left[\begin{array}{ccc} e_o & i_0 & i_1 \end{array} \right]^T \\ A_c &= \left[\begin{array}{ccc} 0 & \frac{1}{C_0} & -\frac{1}{C_0} \\ -\frac{1}{L_0} & -\frac{R_0}{L_0} & 0 \\ \frac{1}{L_1+L_L} & 0 & -\frac{R_1+R_L}{L_1+L_L} \end{array} \right] B_c = \left[\begin{array}{c} 0 \\ \frac{K_p}{L_0} \\ 0 \end{array} \right] \\ C &= \left[\begin{array}{ccc} 0 & 0 & 1 \end{array} \right] \quad u = e_i \quad y = i_1 \quad K_p = -\frac{E}{c_m} \end{aligned}$$

and R_0 is the total resistance of coil, ON resistance of FET, etc. R_1 and R_L are resistances of coil(L_1) and coil(L_L), respctively. When realizing a digital controller by a DSP, a delay time exists between the start point of sampling operation and the output point of control input due to the input computing time and AD/DA conversion times. This delay time is considered to be equivalent to the input dead time which exists in the controlled object. Then the state equation of the system of **Fig.2** is expressed by

$$\left\{ \begin{array}{l} x_d(k+1) = A_d x_d(k) + B_d v(k) \\ y(k) = C_d x_d(k) \end{array} \right. \quad (2)$$

where

$$\begin{aligned} x_d &= \left[\begin{array}{c} x \\ \xi \end{array} \right] \quad \xi(k) = u(k) \quad C_d = \left[\begin{array}{cc} C & 0 \end{array} \right] \\ A_d &= \left[\begin{array}{cc} e^{A_c T} & e^{A_c (T-L_d)} \int_0^{L_d} e^{A_c \tau} B_c d\tau \\ 0 & 0 \end{array} \right] \\ B_d &= \left[\begin{array}{c} \int_0^{T-L_d} e^{A_c \tau} B_c d\tau \\ 1 \end{array} \right] \end{aligned}$$

Now, the PWM amplifier with the following specifications 1-3 is designed and is manufactured by constituting digital control systems to the PWM amplifier (controlled object) at inductive load. Such specification is demanded in Magnetic-Field Current Tracking Control in MRI[?] etc..

1. The band-width of control systems is about 1[kHz] to inductive load, where $0 \leq L_L < 5$[mH].
2. Against the range of inductance load of spec.1, an over-shoot is not allowable in a step response.
3. The specs. 1 and 2 are satisfied regardless of change in large direct-current power supply.

The load changes for the controlled object and the direct-current power supply change are considered as parameter changes in eq.(2). Such parameter changes can be transformed to equivalent disturbances. Therefore, what is necessary is just to constitute the control systems whose pulse transfer functions from equivalent disturbances and to the output become as small as possible in their amplitudes.

3 Design method of approximate 2-degree-of-freedom digital integral-type control system

First, the transfer function between the reference input r and the output y is specified as

$$\begin{aligned} W_{ry} &= \frac{(1+H_1)(1+H_2)(1+H_3)}{(1-n_1)(1-n_2)(1-n_3)} \\ &\times \frac{(1+H_4)(z-n_1)(z-n_2)(z-n_3)}{(z+H_1)(z+H_2)(z+H_3)(z+H_4)} \end{aligned} \quad (3)$$

where n_1 and n_2 are the zeros for discrete-time controlled object (2). It shall be specified that H_1 and H_2, H_3 satisfy the relations $H_1 \gg H_2, H_3, H_4 > 0$. Then $W_{ry}(z)$ can be approximated by the following:

$$W_{ry}(z) \approx W_m(z) = \frac{1+H_1}{z+H_1} \quad (4)$$

We constitute a state feedback system using $u = Fx_d + Gr$ to the controlled object(2), and decide $F = [F(1,1) \; F(1,2) \; F(1,3) \; F(1,4)]$ and G so that $W_{ry}(z)$ becomes eq.(3). The equivalent disturbance is defined as $Q = [q_u \;\; q_{\bar{y}} \;\; q_y]^T$ and the pulse transfer function between Q and the output y of the state feedback system is defined as $W_{Qy}(z)$. The system with an inverse system and a filter added to the state feedback

©ISAROB 2009

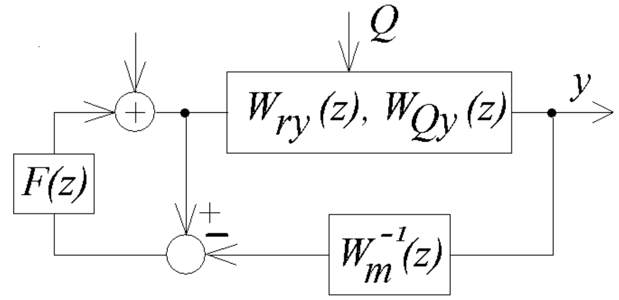

Figure 2: System reconstituted with an inverse system and a filter

system is constituted as shown in **Fig.2**, in which the pulse transfer function $F(z)$ is given by

$$F(z) = \frac{k_z}{z - 1 + k_z} \tag{5}$$

The transfer functions between r and y, Q and y of the system in **Fig.4** are written approximately as

$$y \approx \frac{1 + H_1}{z + H_1} r \tag{6}$$

$$y \approx \frac{z - 1}{z - 1 + k_z} W_{Qy}(z) Q \tag{7}$$

It turns out from eqs.(8) and (9) that the characteristic $r - y$ can be specified with H_1 and the characteristic $Q - y$ can be independently specified with k_z. That is, the systems of **Fig.2** are of approximate 2-degree-of-freedom, and their sensitivity against the disturbance, i.e., load changes becomes lower with the increase of k_z.

Now, if an equivalent conversion of the controller in **Fig.2** is carried out introducing steady state gain g between $r - y$, an approximate 2-degree-of-freedom digital integral-type control systems will be obtained as shown in **Fig.3**.

4 Inductance estimating and controller parameter bumpless switching method

4.1 Inductance estimating method

Load inductance can be estimated from the continuous-time controlled object of eq.(1). If it is $e_o(t) \gg (R_1 + R_l)i$, at an inductive load, the inductance is computed by the voltage of capacity and the

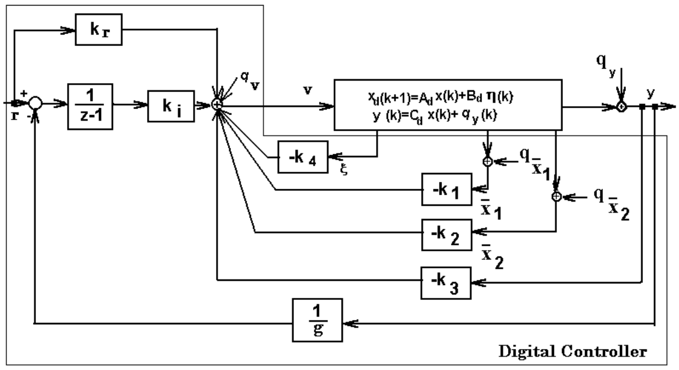

Figure 3: Approximate 2-degree-of-freedom digital integral type control system

derivative of current of load coil such that

$$L_1 + L_L \approx \frac{e_o(t)}{\dot{i}_1(t)} \tag{8}$$

The inductance can be estimated from eq.(11), which is expressed in the discrete approximation form of

$$L_1 + L_L \approx \frac{e_o(k) + e_o(k-1)}{2(i_1(k) - i_1(k-1))} T \tag{9}$$

Eqs.(12) and the filter are implemented by a DSP. The holding function is added.

The control mode is switched with an estimated inductance. If the estimated value is changed due to noise etc. when the load inductance is close to a threshold of change, the problem of frequent mode switching will occur. Therefore, the hysteresis characteristic with mode switching is established. The inductances of $TH - L$ and $TH - H$ used as the width of hysteresis are set up experimentally so that a change does not occur beyond necessity. As for the parameter, Low(L)-mode is chosen at the start of an inductance estimation program. Even when an estimated value exceeds $TH - L$, it does not switch to the High(H)-mode. Only when it exceeds $TH - H$, it switches to the H-mode. At the time of being conversely less than $TH - L$ a switch from the H-mode to the L-mode is performed.

4.2 Bumpless mode switching method

The control mode is switched with an estimated inductance. If the estimated value is changed due to noise etc. when the load inductance is close to a threshold of change, the problem of frequent mode switching will occur. Therefore, the hysteresis characteristic with mode switching is established. If the

©ISAROB 2009

control variable changes rapidly when the controller switches the control mode, a bump will arise in an output. In order to suppress the bump, auxiliary feedback functions are implemented by a combination of H-mode controller and L-mode controller.

5 Experimental studies

A single-chip DSP from Texas Imstruments(TI) is used, which realizes a digital controller as in **Fig.3**. We will design a control system so that all the specifications are satisfied within $0 \leq L_L \leq 3$[mH] and $3 \leq L_L \leq 5$[mH] at L-mode and H-mode, respectively. First of all, in order to set the band-width to about 1[kHz], H_1, H_2 and H_3 are specified as

$$H_1 = -0.89 \quad H_2 = -0.05 \quad H_3 = -0.5 \quad H_4 = -0.4 \tag{10}$$

If it sets up with

$$L_L = 1[\text{mH}] \quad k_z = 0.09 \tag{11}$$

then a specification can be satisfied at L-mode. The parameters of controller become as

$$\begin{aligned} k_{1l} &= -0.04280 \quad k_{2l} = -0.43702 \quad k_{3l} = 0.61873 \\ k_{4l} &= -0.13447 \quad k_{il} = -0.012601 \quad Gg = 0 \end{aligned} \tag{12}$$

Next, H_1, H_2 and H_3 are specified as

$$H_1 = -0.89 \quad H_2 = -0.05 \quad H_3 = -0.01 \quad H_4 = -0.5 \tag{13}$$

If it is set up with

$$L_L = 5[\text{mH}] \quad k_z = 0.45 \tag{14}$$

then a specification can be satisfied at H-mode. The parameters of controller become as

$$\begin{aligned} k_{1h} &= -0.054912 \quad k_{2h} = -0.078368 \quad k_{3h} = 3.962700 \\ k_{4h} &= -3.76630 \quad k_{ih} = -0.31917 \quad Gg = 0 \end{aligned} \tag{15}$$

According to the estimated value, the mode is switched from L to H. When $L_L = 4$[mH] at L-mode, the parameters are switched from L-mode to H-mode. If it switches from L-mode to H-mode, the range of L_L is extended to

$$0 \leq L_L \leq 5[\text{mH}] \tag{16}$$

and then all the specifications are satisfied. **Fig.4** shows a step responses of i_1 and e_i when performing the DDC using the automatic bumpless mode switching from L-mode to H-mode. L and H in **Fig.4** show

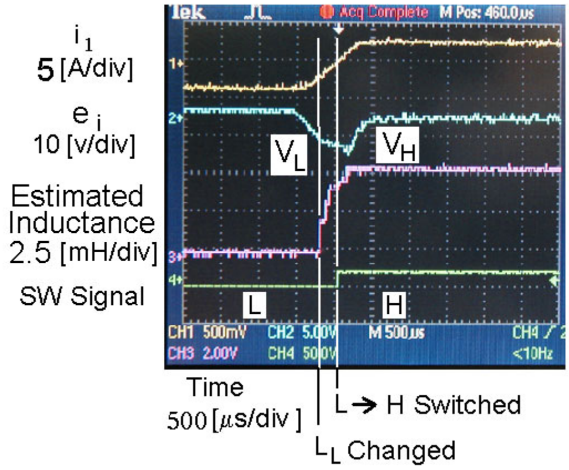

Figure 4: Experimental result of step response at inductive load ($L_L = 5$[mH]) using automatic bumpless switching from L-mode to H-mode

that L-mode and H-mode controllers are operating, respectively. This experimental result shows that the bumpless mode switching can spread the range of the value of inductive load. Fig.14 Experimental result of step response at inductive
load ($L_L = 5$

6 Conclusion

In this paper, the concept of controller with bumpless mode switching to attain the robust control of the current of PWM power amplifier against extensive load changes was given. The proposed digital controller with bumpless mode switching was realized by using a DSP implemented to the controlled object. It was shown from an experiment that a sufficiently robust digital controller is realizable. The range of inductive load can be extended by performing the bumpless mode switching.

References

[1] K.Higuchi, K.Nakano, T.Kajikawa, K.Araki and F.Chino, "Robust Digital Control of PWM Power Amplifier by Approximate 2-Degree-of-Freedom System with Bumpless Mode Switching," *IEEE CDC-2003*, (2003.12).

The Fourteenth International Symposium on Artificial Life and Robotics 2009 (AROB 14th '09),
B-Con Plaza, Beppu, Oita, Japan, February 5 - 7, 2009

Vibration Suppression Control of a Flexible Arm using Non-linear Observer with Simultaneous Perturbation Stochastic Approximation

Jorge Ivan Medina Martinez [1] , Umerujan Sawut [2] , Kazushi Nakano [3]
[1, 3] *Dept. of Electronic Eng., The University of Electro-Communications*
1-5-1 Chofu-ga-oka, Chofu, Tokyo 182-8585, Japan
(Tel: +81-42-443-5190; e-mail: ivan@francis.ee.uec.ac.jp)
[2] *Nikki Co. Ltd.*

Abstract: The main objective in this study concerns to vibration control of a one-link flexible arm system. A variable structure system (VSS)-non-linear observer has been proposed in order to reduce the oscillation in controlling the angle of the flexible arm. The non-linear observer parameters are optimized using a novel version of simultaneous perturbation stochastic approximation (SPSA) algorithm. The SPSA algorithm is especially useful when the number of parameters to be adjusted is large, and makes it possible to estimate them very efficiently. As for the vibration and position control, a model reference sliding-mode control (MR-SMC) has been proposed. The simulations show that the vibration control of a one-link flexible arm system can be achieved more efficiently using our method.

Keywords: Non-linear Observer, Simultaneous Perturbation Method, Flexible Arm System, Fisher Information Matrix, Sliding Mode Control.

I. INTRODUCTION

The robot manipulators are widely used in various industrial applications. In this paper, the main goal is to control the vibration of the flexible arm. Since the feedback of only the motor angle will not be sufficient to suppress the oscillation, a variable structure system (VSS)-non-linear observer is incorporated. Also, a model reference-sliding mode control (MR-SMC) is established as a very efficient control method. However, there are many design parameters for the observer and controller to be determined, so it is difficult to design them in advance. Hence in order to overcome the problem, the simultaneous perturbation stochastic approximation (SPSA) algorithm is used to obtain the parameters of the VSS non-linear observer and controller.

II. DYNAMIC MODELING

The physical configuration of flexible arm is given by Fig.1. The deflection $y(x,t)$ is described by an infinite series of separable modes [1].

$$y(x,t) = \sum_{i=1}^{n} \phi_i(x) q_i(t) \tag{1}$$

where $\phi_i(x)$ is a characteristic function and $q_i(t)$ is a mode function. The kinetic and potential energies can be determined as follows:

$$T_e = \frac{1}{2}\dot{\theta}^2 J + \frac{m}{2L}\sum_{i=1}^{n} A_i \dot{q}_i^2 + \frac{m}{2L}\dot{\theta}\sum_{i=1}^{n} A_i \dot{q}_i^2 + \frac{m}{L}\dot{\theta}\sum_{i=1}^{n} B_i \dot{q}_i + \frac{M}{2}(L^2\dot{\theta}^2 + \sum_{i=1}^{n} C_i^2 \dot{q}_i^2 + \dot{\theta}^2 \sum_{i=1}^{n} C_i^2 q_i^2 + 2L\dot{\theta}\sum_{i=1}^{n} C_i \dot{q}_i) \tag{2}$$

$$V = \frac{EI}{2}\sum_{i=1}^{n} D_i q_i^2 \tag{3}$$

where

$A_i = \int_0^L \phi_i^2(x)dx$, $B_i = \int_0^L x\phi_i(x)dx$, $C_i = \phi_i(L)$ and $D_i = \int_0^L \left[d^2\phi_i(x)/dx^2\right]^2 dx$.

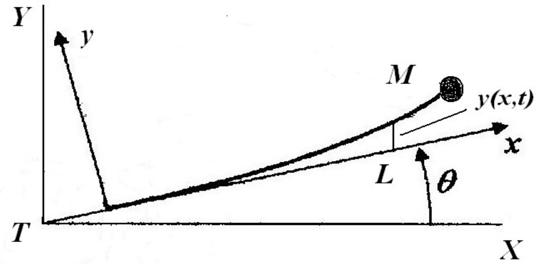

Fig.1. One-link flexible arm.

In the Fig. 1, L is the length of the flexible arm that has a mass m, T is the torque that rotates the elastic arm, M is the payload at the end of the arm and θ is the angle of the joint. The equation of motion is written as follows:

$$EIL\frac{\partial^4 y}{\partial x^4} + m\frac{\partial^2 y}{\partial t^2} = 0 \tag{4}$$

and the boundary conditions are

$$y(0,t) = 0 \quad (5)$$

$$\frac{dy}{dx}(0,t) = 0 \quad (6)$$

$$\frac{d^2y}{dx^2}(L,t) = 0 \quad (7)$$

$$EI\frac{d^3y}{dx^3}(L,t) = m\frac{d^2y}{dt^2}(L,t). \quad (8)$$

From (4) and (5)-(8), we have

$$y_i(x,t) = \phi_i(x)\cos\omega_i t\,. \quad (9)$$

Moreover

$$\begin{aligned}\phi_i(x) = c_{1i}\cos\beta_i x + c_{2i}\cosh\beta_i x + \\ c_{3i}\sin\beta_{ix} + c_{4i}\sinh\beta_i x\end{aligned} \quad (10)$$

$$\omega_i^2 = \frac{EI}{\rho a}\beta_i^4\,. \quad (11)$$

Substituting $\phi_i(x)$ from (10) into (9) and using (5)-(8), β_i and c_{1i}-c_{4i} are determined.

Assuming that only the first mode exists, from (2), (3), and using Lagrange's equations as in [2][3], we obtain

$$\frac{d}{dt}\left(\frac{\partial T_e}{\partial\dot\theta}\right) - \frac{\partial T_e}{\partial\theta} + \frac{\partial V}{\partial\theta} = T \quad (12)$$

$$\frac{d}{dt}\left(\frac{\partial T_e}{\partial\dot q_1}\right) - \frac{\partial T_e}{\partial q_1} + \frac{\partial V}{\partial q_1} = 0 \quad (13)$$

thus, we obtain

$$\begin{bmatrix}\alpha_{00} & \alpha_{01}\\ \alpha_{01} & \alpha_{11}\end{bmatrix}\begin{bmatrix}\ddot\theta\\ \ddot q_1\end{bmatrix} = \begin{bmatrix}T - 2\dot\theta\alpha_{11}q_1\dot q_1\\ -H_1q_1 + \alpha_{11}q_1\dot\theta^2\end{bmatrix} \quad (14)$$

$$y = \theta$$

where $\alpha_{00} = J + ML^2 + \alpha_{11}q_1^2$, T is the motor's shaft torque, J is the moment of inertia, $\alpha_{01} = \omega_1 + ML\phi_{1e}, \alpha_{11} = v_1 + ML + \phi_{1e}^2, v_1 = \rho a\int_0^L \phi_1^2 dx_1$ $H_1 = EI\int_0^L \ddot\phi_1^2 dx_1, \phi_{1e} = \phi_1(L), \omega_1 = \rho a\int_0^L x_1\phi_1 dx_1$, a is the area of the cross section, ρ is the density, E is Young's modulus, I is the area moment of inertia and y is the observation of θ. Defining the state variables such that

$x_1 = \theta$ $x_2 = \dot\theta$, $x_3 = q_1, x_4 = \dot q_1$, we have

$$\begin{bmatrix}\dot x_1\\ \dot x_2\\ \dot x_3\\ \dot x_4\end{bmatrix} = \begin{bmatrix}x_2\\ f_1(x_2,x_3,x_4)\\ x_4\\ f_2(x_2,x_3,x_4)\end{bmatrix} + \begin{bmatrix}0\\ b_1\\ 0\\ b_2\end{bmatrix}T \quad (15)$$

where

$$f_1(x_2,x_3,x_4) = \frac{1}{\alpha_{00}\alpha_{11} - \alpha_{01}^2}$$

$$\cdot\left[-2\alpha_{11}^2x_2x_3x_4 - \alpha_{01}(-H_1x_3 + \alpha_{11}x_3x_2^2)\right]$$

$$f_2(x_2,x_3,x_4) = \frac{1}{\alpha_{00}\alpha_{11} - \alpha_{01}^2}$$

$$\cdot\left[2\alpha_{01}\alpha_{11}^2x_2x_3x_4 - \alpha_{00}(-H_1x_3 + \alpha_{11}x_3x_2^2)\right]$$

$$b_1 = \frac{\alpha_{11}}{\alpha_{00}\alpha_{11} - \alpha_{01}^2}$$

$$b_2 = \frac{\alpha_{01}}{\alpha_{00}\alpha_{11} - \alpha_{01}^2}\,.$$

III. PROPOSED MODIFIED SPSA ALGORITHM

The SPSA is an efficient algorithm for high-dimensional problems in terms of proving a good solution for a relatively small number of measurements of the objective function. The recursions for SPSA algorithms are(basic SPSA algorithm [4]):

$$\hat\theta_{k+1} = \hat\theta_k - \bar a_k\bar{\bar H}_k^{-1}\hat g_k(\hat\theta_k). \quad (16)$$

The second order of simultaneous perturbation stochastic approximation (2SPSA) [5] is :

$$\hat\theta_{k+1} = \hat\theta_k - \bar a_k\bar{\bar H}_k^{-1}\hat g_k(\hat\theta_k),\ \bar{\bar H}_k = f_k(\bar H_k) \quad (17a)$$

$$\bar H_k = \frac{k}{k+1}\bar H_{k-1} + \frac{1}{k+1}\hat H_k\,,\ k=0,1,... \quad (17b)$$

where $\bar a_k$ is a scalar gain, $\hat g_k$ is the simultaneous perturbation that estimates the loss function, $\hat H_k$ is the estimate of the Hessian matrix, and f_k maps an usual non-positive-definite $\bar H_k$ to a positive definite pxp matrix. In our proposed SPSA algorithm, all the parameters are perturbed simultaneously, also it is possible to modify parameters with only two measurements of an evaluation function regardless of the dimension of the parameter. First, we compute the eigenvalues of $\bar H_k$ and sort them into descending order:

$$\Lambda_k = \mathrm{diag}[\lambda_1,\ldots,\lambda_{q-1},\lambda_q,\lambda_{q+1},\ldots,\lambda_p] \quad (18)$$

where

$$\hat\lambda_q = \varepsilon\lambda_{q-1}, \hat\lambda_{q+1} = \varepsilon\hat\lambda_q,\ldots,\hat\lambda_p = \varepsilon\hat\lambda_{p-1} \quad (19)$$

and

$$\varepsilon = (\lambda_{q-1}/\lambda_1)^{q-2}\,. \quad (20)$$

Then, we use the mapping f_k as follows:

$$f_k(\bar H_k) = P_k\hat\Lambda_k P_k^T \quad (21)$$

where $\hat\Lambda_k$ is the diagonal matrix of Λ_k, the 2SPSA algorithm based on the mapping (21) makes the procedure of eliminating the non-positive definiteness of $\bar H_k$. In this part, we use the Fisher information matrix $F(n)$ instead of the Hessian matrix $\bar H_k$ in order to keep and guarantee the estimation matrix be positive-definite. In these estimates, the gain series at each iterations are determined using the 2SPSA algorithm (17a) by replacing $\hat\Lambda_k$ in the mapping f_k of (21) with

©ISAROB 2009

$\hat{\Lambda}_k$ that contains constant diagonal elements

$$\hat{\theta}_{k+1} = \hat{\theta}_k - \bar{a}_k \bar{\lambda}_k^{-1} \hat{g}_k(\hat{\theta}_k) \tag{22}$$

where $\bar{\lambda}_k$ is the geometric mean of all the eigenvalues of $F(n)$

$$\bar{\lambda}_k = (\lambda_1 \ldots \lambda_{q-1} \hat{\lambda}_q \hat{\lambda}_{q+1} \ldots \hat{\lambda}_p)^{1/p}. \tag{23}$$

Recursions (22) and (17b) together with (18)–(20) and (23) form a modified version of the 2SPSA (called 3SPSA). The parameters estimation using our proposed SPSA algorithm is given as follows:

$$\hat{\chi}_{k+n} = \hat{\chi}_{k-1} - \psi_{\frac{k-1}{n+1}} \cdot \left\{ \frac{1}{2} \frac{(W_{k+n} - W_k^T \hat{\chi}_{k-1}^+)^2 - (W_{k+n} - W_{k+n}^T \hat{\chi}_{k-1}^+)^2}{c_{\frac{k-1}{n+1}}} Xs_{k-1} - \begin{bmatrix} \upsilon^2 I_n & 0 \\ 0 & 0 \end{bmatrix} \hat{\chi}_{k-1} \right\} \tag{24}$$

where W_k is measured output, *c* is the perturbation, υ represents the variance, *n, k* are sampling time, χ is the parameter to be estimated, and ψ is a gain coefficient and the subscript in this coefficient represents a fraction. By making use of this, the perturbation vector *c* defined by our proposed SPSA algorithm is added at the same time to all parameters, and finally $\hat{\chi}_{k-1}^+$ is calculated by

$$\hat{\chi}_{k-1}^+ = \hat{\chi}_{k-1} + c_{\frac{k-1}{n+1}} s_{k-1} \tag{25}$$

where s_k is a signed vector.

IV. DESIGN OF NON-LINEAR OBSERVER

Since only the motor angle x_1 is the measurable state variable, the remaining states x_2, x_3 and x_4 are predicted using intelligent state observer design [6]. For this, (14) can be written as

$$\dot{x} = f(x) + g(x)T \tag{26}$$

$$y = Cx, \quad C = [1 \quad 0 \quad 0 \quad 0]. \tag{27}$$

For this non-linear system, we consider a robust VSS observer, which predicts system states and is defined as follows:

$$\dot{\hat{x}} = f(\hat{x}) + g(\hat{x})T + M(\bar{y}) + K(\hat{y} - y) \tag{28}$$

$$\hat{y} = C\hat{x} \tag{29}$$

$$M(\bar{y}) = -g(x) \frac{\bar{y}}{\|\bar{y}\| + \gamma} \varsigma \tag{30}$$

$$\bar{y} = \hat{y} - y = C(\hat{x} - x) \tag{31}$$

where $\hat{x}$ represents the predicted values of system states, *K* is the observer gain matrix, $M(\bar{y})$ is the observer non-linearity term, ς represents the gain, and $\gamma > 0$ is an averaging constant for removing chattering. Now defining the estimation error as

$$e = \hat{x} - x \tag{32}$$

then, we have

$$\dot{e} = f(\hat{x}) - f(x) + [g(\hat{x}) - g(x)]T + KC(\hat{x} - x) + M(\bar{y}). \tag{33}$$

The error system is given as follows:

$$\dot{e} = [f'(x_d) + g'(x_d)T + KC]e + M(\bar{y}) = A_0 e + M(\bar{y}) \tag{34}$$

where

$$A_0 = A + GT + KC \tag{35}$$

$$A = \partial f_i / \partial x_j \tag{36}$$

$$G = \partial g_i / \partial x_j \qquad (i,j=2,3,4). \tag{37}$$

Choosing a Lyapunov function of *e* as

$$V = \frac{1}{2} e^2 \tag{38}$$

and integrating *V* with respect to *e* yields

$$\dot{V} = e\dot{e} = e^2 (A_0 - |g(x)| C \frac{1}{C\|e\| + \gamma} \varsigma). \tag{39}$$

The observer parameters determined by our novel SPSA algorithm are computed with *A* and *G*, so as to ensure the stability of (40) minimizing the following evaluation function:

$$J_0 = \sum (y - \hat{y})^2. \tag{40}$$

The parameters determined are
K=[-339 -19002 15.20 -10109]^T, ς =0.012 , γ =0.013.

V. SLIDING MODE CONTROLLER

The purpose of sliding mode control is to make the states converge to the sliding mode surface. Therefore, we choose the desired response based on a second order reference model given as [6]

$$\begin{bmatrix} \dot{x}_m \\ \ddot{x}_m \end{bmatrix} = \begin{bmatrix} 0 & 1 \\ -\omega_n^2 & -2\omega_n \end{bmatrix} \begin{bmatrix} x_m \\ \dot{x}_m \end{bmatrix} + \begin{bmatrix} 0 \\ \omega_n^2 \end{bmatrix} U_m \tag{41}$$

where ω_n is the eigenvalue of angular frequency and U_m is the model input. Assuming the sliding mode hyper-plane for the system of (14) with the states variables predicted by the observer as

$$\sigma = s_1(x_1 - x_m) + s_2(x_2 - \dot{x}_m) + s_3 x_3 + s_4 x_4 \tag{42}$$

when the sliding mode is in operation, then

$$\sigma = 0 \tag{43}$$

$$\dot{\sigma} = 0. \tag{44}$$

The equivalent control input can be obtained by substituting equation (14) to (44). This gives

$$T_{eq} = 2\alpha_{11} x_2 x_3 x_4 + \frac{\alpha_{01}}{\alpha_{11}}(-H_1 x_3 + \alpha_{11} x_2^2 x_3) - \frac{\Delta}{s_2}\left[s_1(x_2 - \dot{x}_m) - s_2 \ddot{x}_m + s_3 x_4 + s_4 \dot{x}_4\right] \tag{45}$$

where

$$\Delta = (\alpha_{00} - \alpha_{01}^2 / \alpha_{11}) > 0.$$

Now, we consider the design of sliding mode controller, which is the non-linear input to make the states converge in the hyper-plane. In general, the eventual sliding mode input can be considered which is consisted of two independent inputs, namely, the equivalent control input T_{eq} and non-linear control input T_ℓ [6]. In other words

$$T = T_{eq} + T_\ell = T_{eq} - k(x,t)\mathrm{sat}(\sigma) \tag{46}$$

where

$$\mathrm{sat}(\sigma) = \begin{cases} 1 & if \quad \sigma > \delta \\ \dfrac{\sigma}{\delta} & if \quad |\sigma| \le \delta \\ -1 & if \quad \sigma < -\delta \end{cases} \tag{47}$$

and $k(x,t)$ is the control input function. δ is a constant to eliminate the chattering. We choose a Lyapunov function σ to confirm $\sigma = 0$:

$$V = \frac{1}{2}\sigma^2. \tag{48}$$

With this, $\dot V$ is given by

$$\dot V = \sigma\dot\sigma = \sigma\left\{ \frac{s_2}{\Delta}\left[T - 2\alpha_{11}x_2x_3x_4 - \frac{\alpha_{01}}{\alpha_{11}}\left(-H_1x_3 + \alpha_{11}x_2^2x_3 \right)\right] + s_1(x_2 - x_m) - s_2\ddot{x}_m + s_3x_4 + s_4\dot{x}_4 \right\}. \tag{49}$$

Substituting (46) into (49), the existence condition for the sliding mode is given as

$$\dot V = \sigma\left\{ -\frac{s_2}{\Delta}k(x,t)\,\mathrm{sgn}(\sigma)\right\} = -k(x,t)\frac{s_2}{\Delta}|\sigma| < 0. \tag{50}$$

Since $\frac{s_2}{\Delta} > 0$, if we choose $k(x,t) > 0$, then the state variable x will converge in the sliding mode plane and a stable MR-SMC can be realized. The controller gains are determined using our proposed SPSA algorithm so as to minimize the cost function given by

$$J_h = \sum [|L * (x_1 - x_m)| + |x_3|]. \tag{51}$$

The parameters values are $s_1 = 3.4$, s_2=2, s_3=11.23, s_4=-0.58 and δ = 0.43, $k(x,t)$=3.45.

VI. SIMULATION RESULTS

The results are compared with previous simulations without our proposed algorithm [6]. Fig. 2 shows a typical responses of the system at the tip position. This result was improved in comparison with previous simulations.

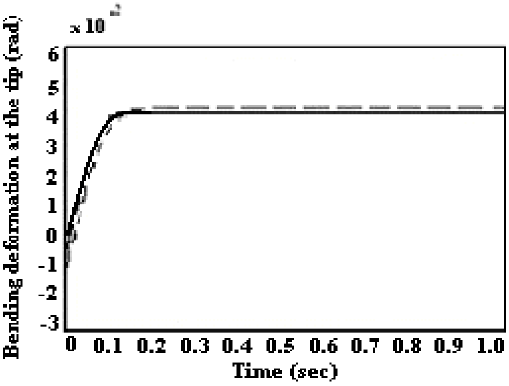

Fig.2. Bending deformation. Without SPSA algorithm (dashed line (- -)). With 3SPSA algorithm and non-linear observer (solid line (-)).

Fig. 3 shows the tip velocity. The algorithm reduces the magnitude of velocity to a small value.

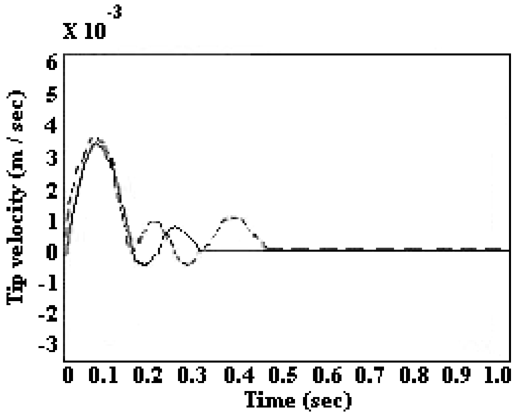

Fig.3. Tip velocity. Without SPSA algorithm (dashed-line(--)). With 3SPSA algorithm and non-linear observer (solid line (-)).

VII. CONCLUSION

We have proposed a MR-SMC method using a non-linear observer for controlling the angular position of a flexible arm by suppressing its oscillation. We also have proposed the use of a novel SPSA algorithm in order to determinate the observer/controller gains. Also, the SPSA algorithm has a very low computational complexity for solving difficult estimation problems in an efficient way. The non-linear observer was successful in predicting the state variables from the motor angular position and the MR-SMC was a very efficient control method. The use of the novel version of SPSA algorithm could determine easily and efficiently, the control parameters and observer gains.

REFERENCES

[1] K. S. Yeung and Y. P. Chen (1989), Regulation of a one-link flexible robot arm using sliding mode technique. Int. journal control 49: 1965-1978.
[2] S. Nicosia, P. Tomei,and A. Tornambe (1989), Non-linear control and observation algorithms for a single-link flexible arm. Int. journal control 49: 827-840.
[3] J. Link, F. L. Lewis (2003), Two-time fuzzy logic controller of flexible link robot arm. Fuzzy sets and system 139:125-149.
[4] J. C. Spall (1997), One-measurement form of simultaneous perturbation stochastic approximation. Automatica 33:109-112.
[5] J. C. Spall (2000), Adaptive stochastic approximation by the simultaneous perturbation method. IEEE Trans. on autom. control 45:1839-1853.
[6] U. Sawut, N. Umeda, T. Hanamoto, T. Tsuji (1999), Applications of non-linear observer in flexible arm control. Trans. of SICE 35(3): 401-406.

©ISAROB 2009

The Fourteenth International Symposium on Artificial Life and Robotics 2009 (AROB 14th '09),
B-Con Plaza, Beppu, Oita, Japan, February 5 - 7, 2009

Multiple Cell Assemblies and Multi-Step Computation in Neural Networks

Makito Oku Kazuyuki Aihara[†,‡]

[*]Department of Mathematical Informatics, Graduate School of Information Science and Technology,
The University of Tokyo, 7-3-1 Hongo, Bunkyo-ku, Tokyo 113-8656, Japan

[†]Institute of Industrial Science, The University of Tokyo, 4-6-1 Komaba, Meguro-ku, Tokyo 153-8505, Japan

[‡]Aihara Complexity Modelling Project, ERATO, Japan Science and Technology Agency (JST),
3-23-5-201 Uehara, Shibuya-ku, Tokyo 151-0064, Japan

e-mail: oku@sat.t.u-tokyo.ac.jp

Abstract

The dynamics of a recurrent neural network model in which localized learning patterns and asymmetric interactions between the patterns are embedded is investigated. In the network, multiple cell assemblies exist at the same time, and the combination of assemblies changes step by step. The network dynamics exhibits characteristic behavior that the timings of each appearance and disappearance of assemblies vary much from trial to trial, while the sequential order of events does not. These features are probably due to the balance between two forces: the feedback within each assembly that stabilizes the network state and the asymmetric inter-assembly connections that keep computation go on. The computational meanings of this 'assembly of assemblies' framework as a mechanism of multi-step computation are discussed.

Key words Cell assembly, multi-step computation

1 Introduction

A cell assembly is a collection of neurons those cooperate temporarily as a functional unit. There are considered a few mechanisms of a cell assembly, i.e., reverberation of excitatory signals[1], populational oscillation at a specific frequency[2,3], and synchronous spiking[4,5]. Functional meanings of a cell assembly include the following. First, an assembly maintains information for a certain time after the input disappears, which is regarded as working memory. At another viewpoint, distant areas in the brain are dynamically interrelated by an assembly so that they can exchange information depending on the situation[6–8].

It comes that the same neuron or connection has multiple meanings, because it may belong to different assemblies at different time. In general, assembly switchings are considered in many contexts. For example, associative thinking and mental imagery are believed to correlate with assembly switchings in the brain. Recently it is also experimentally observed that the ongoing activity in the visual area of cats exhibits spontaneous transitions between different patterns[9]. Theoretical models have also been proposed to explain the mechanism of the switching phenomena[10,11].

By the way, multiple assemblies may coexist at the same time in the real brain. Switchings of multiple assemblies, however, have not been considered so far. Here we propose a framework in which assemblies cooperate to evoke or suppress other assemblies, and then the combination of assemblies in the network changes one after another (see Fig. 1).

In this paper, the above mechanism of multi-step computation is realized by a simple neural network model. In the next section, the model is explained. In section 3, the main results of test simulations are shown. The computational meanings of multi-step computation performed by multiple assemblies are discussed in section 4.

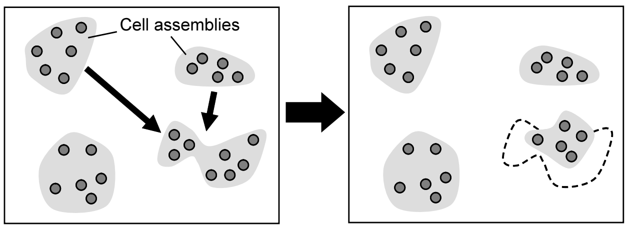

Fig. 1: Mechanism of multi-step computation. In the neural network, multiple cell assemblies exist at the same time. They cooperate to evoke or suppress other assemblies. This triggers subsequent changes, which may cause a chain of assembly switchings.

©ISAROB 2009

2 Model

As a single neuron model, the simplest threshold model with stochastic update is used:

$$y_i = \sum_{j=1}^{N} w_{ij} x_j - \theta_i, \quad (1)$$

$$p_i = \frac{1}{1+\exp(-\epsilon y_i)}, \quad (2)$$

where x_i is the activity of neuron i (1 is spike and 0 is resting), w_{ij} is the synaptic weight from neuron j to neuron i, θ_i is the threshold, and p_i is the probability of the neuron i being on. The order of updating is random.

Now we store in the network localized learning patterns $s^1, \ldots, s^M$, $s^\alpha \in \{-1, 0, 1\}^N$ (see Fig. 2). In addition to symmetric connections that make the patterns self-sustained, we also stored in the network asymmetric inter-assembly connections:

$$W = \sum_{\alpha=1}^{M} s^\alpha.(s^\alpha)^{\mathrm{T}} + \lambda \sum_{(\alpha,\beta)\in A} s^\beta.(s^\alpha)^{\mathrm{T}}, \quad (3)$$

where A is a set of index pairs and $\lambda \geq 0$ is a parameter that determines the strength of asymmetric connections.

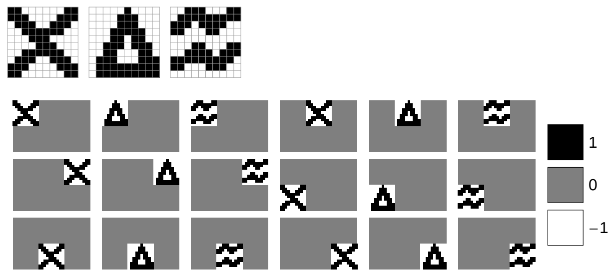

Fig. 2: Localized learning patterns. Three templates of size 10×10 are located in 30×20 space with translation. Blank spaces are zero-padded. Templates are borrowed from Adachi and Aihara (1997)[10].

3 Simulation Results

The default parameter values for the following simulations are shown in Tab. 1. The components of set A are manually decided so that more than two assemblies invoke one new assembly cooperatively, and as long chain of assembly switchings as possible occurs.

Table 1: Parameter settings for the simulations.

Variable	Value	Explanation
N	600	number of neurons
M	18	number of patterns
L	18	number of index pairs in A
ϵ	0.1	slope of sigmoid function
θ_i	0	threshold
λ	0.2	asymmetry coe cient

Figure 3 shows the property of the weight matrix W. First, the average of $|w_{ij}|$ against the distance in the two-dimensional space indicates that short-range connections are dominant in the sense of absolute value. On the other hand, the average of $|w_{ij} - w_{ji}|$ indicates that long-range connections have higher asymmetry degree than short-range connections.

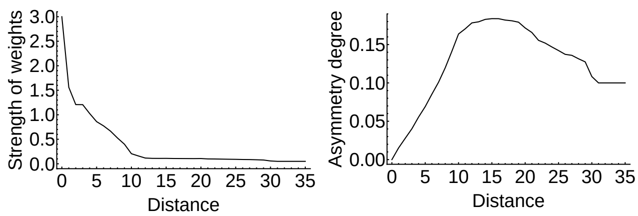

Fig. 3: Property of the weight matrix. (Left) Average of $|w_{ij}|$ against the distance in the two-dimensional space, and (Right) Average of $|w_{ij} - w_{ji}|$ against the distance.

Figure 4 shows an example of time sequence of the state of the network. Starting from the initial state (the top left edge), the combination of assemblies changed step by step. For example, at first the cross-shaped assembly at the bottom left region disappeared, and the triangle-shaped assembly emerged there. Subsequently, another change started at the bottom right region. Totally eight switchings of assemblies occurred. The last state remained stable for longer runs.

The stepwise dynamics is also clearly seen in the plot of the activity of each assembly measured by $< s^\alpha, x > /|s^\alpha|^2$ (see Fig. 5, Left). The time scale of the durations of assemblies was much longer than that of switchings.

Furthermore, the timings of each appearance and disappearance of assemblies varied much from trial to trial (see Fig. 5, right). On the other hand, the sequential order of the assembly switchings was roughly kept in most trials.

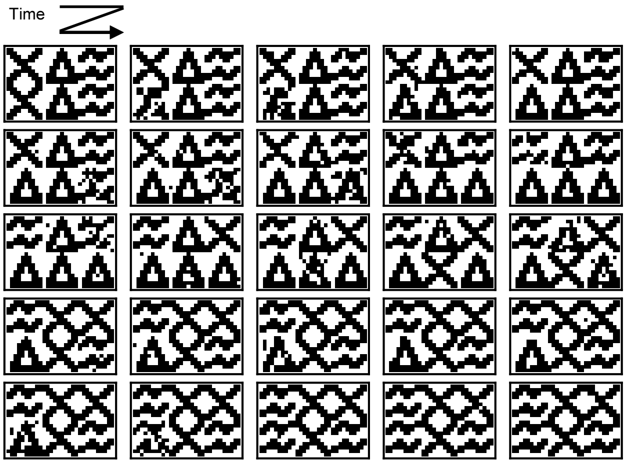

Fig. 4: An example of time sequence of the state of the network. Black and white cells show the firing and resting states, respectively. Intervals between the snapshots are two steps.

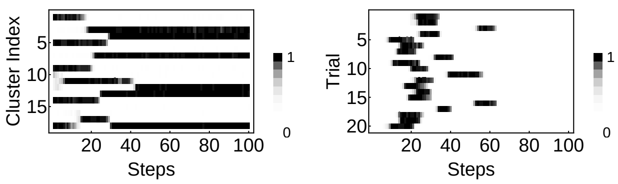

Fig. 5: (Left) Activity plot of the trial in Fig. 4 , and (Right) 20 trials plot of the activity of an assembly (index = 17).

In the limitation of $\epsilon \to \infty$, where the system's dynamics becomes deterministic, the initial state and all the intermediate states were stable.

When the value of λ was increased to 0.5, the whole chain of switchings turned to take shorter time on average. However, the sequential order of switchings became vague, because more than one switchings were likely to occur simultaneously at different regions.

4 Discussion

The observed dynamical characteristics, large fluctuations of the timings of assembly switchings and high rate of reproduction of the similar sequential order, can be explained by the two points below. First, the property of the weight matrix shows that the effect of feedback connections within each assembly dominates the effect of asymmetric inter-assembly connections. Second, the result of the limitation of $\epsilon \to \infty$ shows that each assembly switching is driven by stochastic fluctuations. From these evidences, it is thought that switchings may occur only when the stochastic fluctuations happen to largely overlap the inter-assembly influence, and any other perturbations are repaired by the dominant short-range connections. The balance of the two types of connections may control the speed and accuracy of assembly switchings, which is consistent with the result of larger λ's case. In general, high reliability per step is particularly important for complex computation that needs many steps, because errors in computation accumulate in each step.

Next, it should be clarified what advantage the 'assembly of assemblies' framework has against the assembly of single neurons. The most critical thing is that in principle a single neuron cannot actively sustain the state of itself without continuous external input, while an assembly can do that. Accordingly, the neurons that are involved in a formation of an assembly will be able to be reused for other processing after the target assembly is completed. Of course, by behaving as a group, assemblies perhaps have more robustness against noise or uncertainty and can deal with much complex nonlinear interactions than single neurons. Furthermore, just as a single neuron possesses much more information than whether or not it is activated, an assembly is perhaps able to represent multi-modal information.

Although it is a di cult problem what should be regarded as the output of the network, this framework can be seen as a model that represents the input-output mappings. Given an initial state as an input, the network visits multiple intermediate states until the output is obtained. A benefit for neural networks to use this computational method may be that under a certain limitation of neuron number and wiring complexity, the method is e cient to embed in the network as many input-output correspondence relations as possible. To check this idea, it is necessary to investigate how much information processing ability networks of different structures have on average.

By the way, some of neuroscientists think that in a specific region in the brain information is explicitly coded, and a different region controls it [12,13]. On the other hand, our standpoint is different because in our framework both representation and operation of information are performed in the same place. An explanation why this is possible is that 'drive system' assemblies, which make other assemblies switch, and 'response system' assemblies, which are switched,

©ISAROB 2009

are separated at each moment, but the assignment changes depending on the context.

Finally, how can we measure the validity of this framework? In the first place, there is no strong evidence that neurons dynamically form functional clusters in the real brain. Many neuroscientists, however, predict that there must be neural activities that correlate with our conscious experiences, and that would be dynamically-formed cell assemblies consisting of a number of neurons[13–15]. Such assemblies may be still di cult to observe in the real brain. Furthermore, it is almost impossible to prove the causal relationships between sub-assemblies composing the principal assembly that correlates with the unified consciousness. Therefore, now we can only imply what computational meanings inter-assembly interaction may have.

5 Summary

In this paper, a new framework, multi-step computation performed by multiple cell assemblies, has been proposed, and we constructed a simple neural network model that realize the proposed mechanism and investigated its dynamical characteristics by numerical simulations. The network dynamics is subject to two types of connections, the feedback within each assembly and asymmetrical inter-assembly connections. The former dominates the latter, resulting in accurate transitions in each step.

Although the proposed model used continuous mutual excitations among neurons as a mechanism of cell assembly, the fundamental ideas are probably able to be shared with other mechanisms such as oscillation and synchronization. Even though it is di cult to show experimentally, the proposed mechanism could be used in some form in the real brain.

Acknowledgments

This study is partially supported by Grant-in-Aid No. 17022012 for Scientific Research on Priority Areas System study on higher-order brain functions from the Ministry of Education, Culture, Sports, Science and Technology of Japan.

References

[1] D. O. Hebb, *The organization of behavior*. Wiley, New York, 1949.

[2] G. Buzsáki, *Rhythms of the Brain*. Oxford University Press, USA, 2006.

[3] R. Llinás, U. Ribary, D. Contreras, *et al.*, "The neuronal basis for consciousness.," *Philos Trans R Soc Lond B Biol Sci*, vol. 353, pp. 1841–1849, Nov 1998.

[4] H. Fujii, H. Ito, K. Aihara, *et al.*, "Dynamical cell assembly hypothesis - theoretical possibility of spatio-temporal coding in the cortex.," *Neural Netw*, vol. 9, pp. 1303–1350, Nov 1996.

[5] W. Singer, "Neuronal synchrony: a versatile code for the definition of relations?," *Neuron*, vol. 24, pp. 49–65, 111–25, Sep 1999.

[6] S. Bressler and J. Kelso, "Cortical coordination dynamics and cognition.," *Trends Cogn Sci*, vol. 5, pp. 26–36, Jan 2001.

[7] S. Dehaene, M. Kerszberg, and J. P. Changeux, "A neuronal model of a global workspace in effortful cognitive tasks.," *Proc Natl Acad Sci U S A*, vol. 95, pp. 14529–14534, Nov 1998.

[8] A. Treisman, "Solutions to the binding problem: progress through controversy and convergence.," *Neuron*, vol. 24, pp. 105–10, 111–25, Sep 1999.

[9] T. Kenet, D. Bibitchkov, M. Tsodyks, *et al.*, "Spontaneously emerging cortical representations of visual attributes.," *Nature*, vol. 425, pp. 954–956, Oct 2003.

[10] M. Adachi and K. Aihara, "Associative dynamics in a chaotic neural network.," *Neural Netw*, vol. 10, pp. 83–98, Jan 1997.

[11] S. Nara and P. Davis, "Chaotic wandering and search in a cycle-memory neural network," *Progress of Theoretical Physics*, vol. 88, no. 5, pp. 845–855, 1992.

[12] A. Baddeley, "Working memory: looking back and looking forward.," *Nat Rev Neurosci*, vol. 4, pp. 829–839, Oct 2003.

[13] C. Koch, *The Quest for Consciousness: A Neurobiological Approach*. Roberts & Co, 2004.

[14] F. Crick and C. Koch, "A framework for consciousness.," *Nat Neurosci*, vol. 6, pp. 119–126, Feb 2003.

[15] G. Tononi and G. M. Edelman, "Consciousness and complexity.," *Science*, vol. 282, pp. 1846–1851, Dec 1998. 157.

©ISAROB 2009

The Fourteenth International Symposium on Artificial Life and Robotics 2009 (AROB 14th '09),
B-Con Plaza, Beppu, Oita, Japan, February 5 - 7, 2009

Possible roles of pre-synaptic connections in neural circuits

H. Watanabe
Graduate School of
Information Science and Technology,
The University of Tokyo

Institute of Industrial Science,
University of Tokyo
Tokyo, Komaba 4-6-1. 153-8505

K. Aihara
Graduate School of
Information Science and Technology,
The University of Tokyo,

ERATO Aihara Complexity
Modelling Project, JST
Institute of Industrial Science,
University of Tokyo
Tokyo, Komaba 4-6-1. 153-8505

Abstract

A recent study suggests a new form of inhibitory circuits, in the cortex, in which a pyramidal cell directly excites pre-synaptic terminal of an inhibitory interneuron [1]. This circuit allows action potentials generated in a single pyramidal (excitatory) neuron to evoke reliable constant-latency inhibition in other nearby pyramidal neurons. However, tangible effects of this direct inter-pyramidal inhibition in neural circuits are still unclear. In the present paper, we examine effects of the direct inter-pyramidal inhibition by numerical simulations.

1 Introduction

Inhibitory circuits in the neocortex were thought to be so simple. Excitatory synapses from pyramidal neurons excite the dendrites or soma of interneurons, and generate action potentials that propagates the axons to trigger the release of inhibitory neuronal transmitters onto postsynaptic cells. The neocortex has been thought to have only this classical inhibitory circuit. Recently, however, Ren et al proposed an extraordinary form of synaptic circuitry that allows one pyramidal cell to rapidly inhibit other pyramidal neurons [1]. They suggests a new form of inhibitory circuit, in which the excitatory synaptic terminal from one pyramidal cell directly connects to the presynaptic terminal of an inhibitory interneuron. In the classical inhibitory pathway, considerable integration of synaptic inputs onto interneurons is needed for triggering spikes in the interneurons, one spike in one pyramidal cell is not enough. In contrast, the new circuits suggested by Ren et al allows action potentials generated in a single pyramidal neuron to evoke reliable, constant-latency inhibition in other nearby pyramidal neurons. Instead of weakly exciting one another, pyramidal cells arranged in this way can strongly inhibit one another.

The work of Ren et al suggests both a new inhibitory function and its surprising cellular mechanism that allows one neuron to violate Dale's principle. But there are many problems to be solved. However, one of the most important problems is what the functional differences is between classical inhibitory pathways and this new inhibitory mechanisms. To verify this problem, we simulated the effects of direct inter-pyramidal inhibition on dynamics of neural ensembles using the spiking neuron model. The results shows that there are large differences of network dynamics between classical and new type inhibition, even when all parameters and setting are identical except the type of inhibitory mechanism.

2 Model

2.1 Neural model

In simulations of dynamics of neural ensembles we can use physiologically realistic models like the Hodgkin-Huxley one. However, we have to find a compromise between computational e ciency and physiological plausibility. In this work we use spiking neuron model proposed by Izhikevich [3].

$$\frac{dv}{dt} = 0.04v^2 + 5v + 140 - u + I \tag{1}$$

©ISAROB 2009

$$\frac{du}{dt} = a(bv - u) \tag{2}$$

with the auxiliary after-spike resetting

$$if \quad v \geq 30mV \quad then \quad v \leftarrow c, \quad u \leftarrow u + d \tag{3}$$

Here, the variable v represents the membrane potential of the neuron and u represents a membrane recovery variable, which accounts for the activation of K^+ ionic currents and inactivation of Na^+ ionic currents, and it provides negative feedback to v. The variables a, b, c, and d are dimensionless parameters, and t is the time. After the spike reaches its apex (+30 mV), the membrane voltage and the recovery variable are reset according to the (3). Synaptic currents or injected dc-currents are delivered via the variable I.

The reasons for using this model are that it is as biologically plausible as the Hodgkin-Huxley model, yet as computationally e cient as the integrate-and-fire model, and depending on four parameters, the model reproduces spiking and bursting behavior of known types of cortical neurons (pyramidal neuron, fast spiking neuron and so on).

2.2 Short term synaptic plasticity and Synaptic activity

In the real brain, the synaptic strength of each synapse can be depressed or facilitated on a short time scale of hundreds of milliseconds by a scalar factor (Short term synaptic plasticity). To reconstruct short term synaptic plasticity, this scalar factor, different for each synapse, is modeled by the following one-dimensional equation [4].

$$\frac{dr_{ij}}{dt} = \frac{1 - r_{ij}}{\tau_r} \tag{4}$$

$$if \ presynaptic \ spike \ arrive \ then \ r_{ij} \leftarrow p_r r_{ij} \tag{5}$$

r_{ij} is scalar factor of synapse from neuron j to neuron i. r_{ij} tends to recover to the equilibrium value $r_{ij} = 1$ with the time constant τ_r, and it is reset by each spike of the presynaptic cell to the new value p_r. The parameter $p_r > 1$ decreases r_{ij} and results in short-term synaptic depression, whereas $p_r < 1$ results in short-term synaptic facilitation. (In the present simulation, we use only short-term synaptic depression.)

In addition, synaptic activity is modeled by following one-dimensional equation [4].

$$\frac{dg_{ij}}{dt} = -\frac{g_{ij}}{\tau_g} \tag{6}$$

$$if \ presynaptic \ spike \ arrive \ then \ g_{ij} \leftarrow g_{ij} + w_{ij} r_{ij} \tag{7}$$

Here g_{ij} is the activity of synaptic terminal from neuron j to neuron i, w_{ij} is strength of synaptic connection, and r_{ij} is short term plasticity factor mentioned above. When spike from neuron j reach neuron i with synaptic delay t_{dij}, g_{ij} is increased by $w_{ij} r_{ij}$, and then g_{ij} tends to decrease to the equilibrium value $g_{ij} = 0$ with the time constant τ_g.

After all, total input to neuron i is described by following equation.

$$I_i = (V_E - v_i) \sum g_{ij} + (V_I - v_i) \sum g_{ij} + I_0 \tag{8}$$

Here, v_i is the membrane potential of the neuron i, V_E and V_i represent reversal potentials of excitatory and inhibitory synaptic input, respectively. I_0 is external input.

2.3 Network structure

The network consists of N neurons. The network topology is random, and all neurons are connected with equal probability $\epsilon \in [0, 1]$, regardless of their identity. The only constraint is that all neurons receive same number of excitatory and inhibitory synapses. Figure 1 shows the schematic structure of network we use.

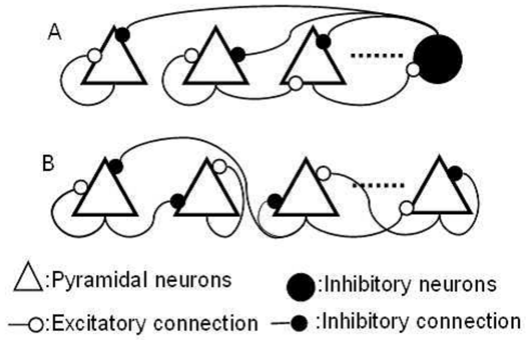

Figure 1: Schematic structure of network. In classical type inhibition system (Figure 1-A), one neuron either excites all postsynaptic neruons or inhibit them. On the other hand, in new type inhibition system (Figure 1-B), one neuron can make both type of synaptic connections for each postsynaptic target.

Small open circle indicate excitatory connections, whereas small filled circle indicate inhibitory connections. Large open triangle indicate a pyramidal neuron, and large filled circle means an inhibitory neuron, respectively.

In figure 1-A, traditional type of inhibition, there are βN excitatory neurons and $(1 - \beta)N$ inhibitory neurons in the network ($\beta \in [0,1]$). On the other hand, in figure 1-B, there are no discrimination between excitatory and inhibitory neuron. Instead, $100\times\beta$ percent of all connections are excitatory, and the others are inhibitory (violation of Dale's principle). In both cases, one neuron receives $\epsilon\beta N$ excitatory synapses and $\epsilon(1-\beta)N$ inhibitory synapses.

3 Simulation and Results

3.1 Simulation settings

To reproduce the behavior of regular spiking neurons, we set parameter $a = 0.02$, $b = 0.2$, $c = -55$, $d = 6$ in the equation (1), (2) and (3). (In the real brain, spiking characteristics are different between excitatory and inhibitory neurons. However, for purely making a comparison of difference by the type of inhibition, we set same parameter to all neurons in both classical type inhibition and new inhibition mechanism suggested by Ren et al.) Initial values of u and v of each neurons are randomly set. And for other parameters, we use following values; $V_E = 0$ (mV), $V_I = -70$ (mV), $\tau_r = 150$ (ms), $\tau_g = 6.0$ (ms), $p_r = 0.6$,

$$w_{ij} = \begin{cases} 0.02 & \text{if the synapse } j \to i \text{ is excitatory} \\ 0.2 & \text{if the synapse } j \to i \text{ is inhibitory} \\ 0 & \text{if the synapse } j \to i \text{ is not exist} \end{cases}$$

and synaptic transmission delay is fixed to 2 (ms).

And we set the number of neurons $N = 250$, proportion of excitatory neurons (synapses) $\beta = 0.8$, and connection probability $\epsilon = 0.8$ (So in classical inhibitory mechanism simulations, there are 200 excitatory neurons and 50 inhibitory neurons.) In both cases, one neuron receives 160 excitatory synapses and 40 inhibitory synapses.

Changing the type of inhibitory mechanism, we observe the spiking dynamics of the network.

3.2 Results

In each type of inhibition mechanism, we ran simulations by 40 times. Figure 2 shows the one example of raster plot and population histograms when we add the constant input to the network ($I_0 = 10.0$). Figure 2-A is the result of classical inhibitory mechanism simulation, and Figure 2-B is that of new type mechanism simulations.

As shown by numerical simulation of otherwise identical systems, the difference of inhibitory mechanism causes the large difference of network dynamics.

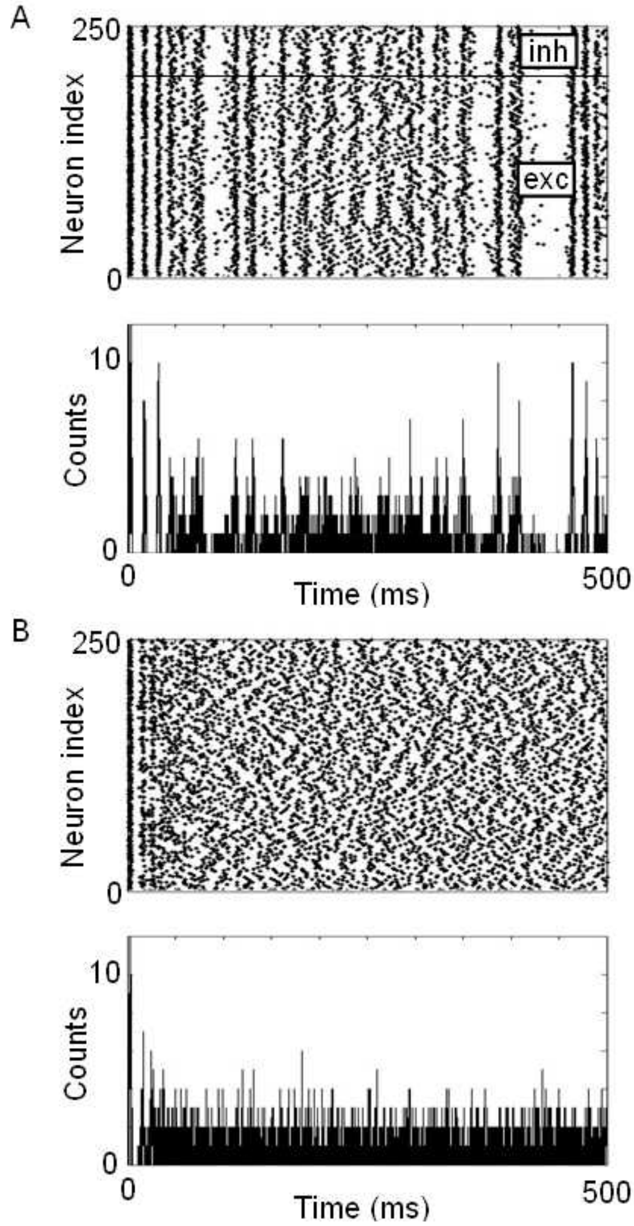

Figure 2: Population spiking activity in classical inhibition mechanisms (Figure 2-A) and new inhibition suggested by Ren et al (Figure 2-B). Spiking activity (dot displays) for networks of size N = 250 neurons (200 excitatory and 50 inhibitory neurons in A) and population histograms (lower panels of each figure; bin size 0.1 ms) in classical inhibition mechanism and new type inhibition (see section 3.1 for network and simulation parameters). Even though all other parameters and the number of synaptic connections are identical, network dynamics are largely different between two type inhibition mechanisms.

The distribution of population spike counts is comparably broad and skewed in classical type inhibition networks, whereas it is narrow and uniform for the new type inhibition network.

The average spike count per one neuron is not so different between two inhibition type (classical type; 19.1866, new type; 20.6374, slightly larger in new type inhibition). However, variance of spike count among neurons in one simulation running is somewhat different. Simulation results show that in new type inhibition, spike count variance is about 5 times larger than in classical type inhibition (classical type; 2.1306, new type; 10.4955). These result suggest that new type inhibition mechanism has stronger desynchronizing effect on network dynamics than classical inhibition.

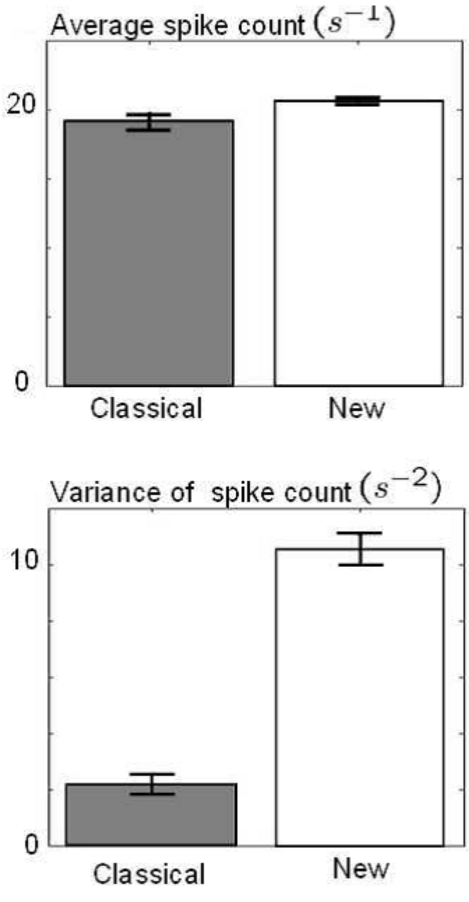

Figure 3: Average spike count (upper panel) and variance of spike count among neurons in one simulation (lower panel). These figure shows the differences of each value averaged over 40 simulations. Error bars mean standard deviation. Spike count variance in new type inhibition is about 5 times larger than that in classical type inhibition, while average spike count per one neuron is not so different.

4 Summary

We have simulated the dynamics of spiking neural networks, and compared the difference of effects on network dynamics between traditional initiatory circuits and new inhibitory circuits suggested by Ren et al. Even though all other parameters and the number of synaptic connections are identical, network dynamics are largely different between two type inhibition mechanisms. Our result has indicated that the new type inhibition mechanism has stronger desynchronizing effects on network dynamics than classical inhibition.

To investigate whether these characteristic features are useful for information processing in the brain cortex is one of our future problems.

Acknowledgements

This work was supported by a *kakenhi* Grant-in-Aid for Scientific Research (A).

References

[1] Ren, M., Yoshimura, Y., Takada, N., Horibe, S., Komatsu, Y. "Specialized inhibitory synaptic actions between nearby neocortical pyramidal neurons" *Science*, Vol. 316, pp. 758-761, 2007.

[2] Connors, B. W., Cruikshank, S. J. "Bypassing interneurons: Inhibition in neocortex," *Nat.Neurosci*, Vol. 10, pp. 808-810, 2007.

[3] Izhikevich, E. M. "Simple model of spiking neurons" *IEEE Transactions on Neural Networks*, Vol. 14, No. 6, pp. 1569-1572, 2003.

[4] Izhikevich, E. M., Edelman G. M. "Large-scale model of mammalian thalamocortical systems" *PNAS*, Vol. 105 No. 9, pp. 3593-3598, 2008.

[5] Dyan, P., Abbot, L. F. *Theoretical Neuroscience*, The MIT Press, 2001.

[6] Shepherd, G. M., *THe Synaptic Organization of the Brain*, The OXFORD University Press, 2004.

[7] Izhikevich, E. M. *Dynamical Systems in Neuroscience*, The MIT Press, 2001.

©ISAROB 2009

The Fourteenth International Symposium on Artificial Life and Robotics 2009 (AROB 14th '09),
B-Con Plaza, Beppu, Oita, Japan, February 5 - 7, 2009

Self-Organization of Orientation Selective and Ocular Dominance Maps through Spike-Timing-Dependent Plasticity

Koji Iwayama(1)
Hideyuki Suzuki(1)(2)
Kazuyuki Aihara(1)(2)(3)
(1)Graduate School of Information Science and Technology,
The University of Tokyo, Tokyo 113-8656, Japan
(2)Institute of Industrial Science, The University of Tokyo, Tokyo 153-8505, Japan
(3)Aihara Complexity Modelling Project, ERATO, JST, Tokyo 153-8505, Japan
(Tel : +81-3-5452-6693; Fax : +81-3-5452-6694)
(Email: koji@sat.t.u-tokyo.ac.jp)

Abstract

In the primary visual cortex, there are orientation selective map and ocular dominance map. These maps correlate with each other. Though many models which explain the formation of the orientation selective map and the ocular dominance map have been proposed, these models contain a physiologically implausible process. It is indicated that spike-timing-dependent plasticity (STDP) can yield "topographic map" without any constraints. We show that large STDP time constants yield the orientation selective map, and small STDP time constants yield the ocular dominance map. This result suggests the relationship between the orientation selective and the ocular dominance maps can be explained by modulation of STDP time constants.

Keywords :Orientations selective map, Ocular Dominance Map, Spike-timing-dependent plasticity

1 Introduction

In sensory cortex, the selective map called " topographic map "consists of stimulus-selective neurons, in which close neurons are selective to a similar stimulus and distant neurons are selective to a different stimulus. In the primary visual cortex, there are orientation selective map and ocular dominance map [1]. Orientation selective map consists of neurons selective to orientation of edge in the input image. Ocular dominance map consists of neurons selective to whether the input comes from the right eye or the left one. These maps have spatial relationships [2]. The borders between different orientation selectivities are tend to intersect the borders between different ocular dominance at right angles. Moreover, many intersections of the borders between different orientation selectivities are in the middle of the regions with same ocular dominance. These relationships indicate two maps have negative correlation.

Correlations between inputs are important for formation of topographic maps. In the primary visual cortex, neurons receive inputs from lateral geniculate nucleus (LGN). LGN has eye-specific layers and their respective ON/OFF sublaminae. In eye-specific layers, neurons are selective to inputs from the contralateral or the ipsilateral eye. ON/OFF sublaminae consist of ON-Center and OFF-Center neurons, respectively. Activities show correlations between neurons in the same sublamina and different sublaminae [3]. Correlation in the same sublamina is the strongest and correlation in the same eye-specific layer is stronger than in different eye-specific layers. Cross-correlation functions within the same and between different eye-specific layers show unimodal distribution and strong peak at zero. However, in finer time scale, central peaks are wider and more peaks at nonzero are observed between different eye-specific layers. These differrences of correlations between neurons in the same sublamina and different sublaminae lead to formation of orientation selective and ocular dominance map.

Many models based on correlation learning which modify synaptic strengths depending on the correlation of pre- and postsynaptic activities explain formation of topographic maps [4] [5] [6]. These models contain, however, physiologically implausible constraints. For example, Malsberg's model normalizes synaptic strength to keep constant sum of synaptic strengths

©ISAROB 2009

subject to one neuron.

It is indicated that long-term potentiation (LTP) and long-term depression (LTD) of synapses depend on relative spike timing of pre- and post-synaptic neurons [7]. Postsynaptic spikes preceding presynaptic spikes induce LTP and postsynaptic spikes following presynaptic spikes induce LTD. Smaller difference between pre- and postsynaptic spikes induce larger synaptic modification. Such synaptic plasticity is called "spike-timing-dependent plasticity" (STDP). It is indicated that STDP can lead to formation of topographic map [8].

There is no model that explains formation of orientation selective and ocular dominance maps without implausible constraints. For unified explanation of formation of orientation selective and ocular dominance maps by STDP, we show that we can switch between formation of orientation selective and ocular dominance maps by modulating time constants of STDP.

2 Model

2.1 Synaptic strengths and STDP

The model network consists of the LGN and the primary visual cortex. Each of the LGN neurons has projections to all of the cortical neurons. All of the cortical neurons are connected to each other with synaptic strengths w^{cor}:

$$w^{cor} = E \exp\left(-\frac{d}{\sigma_e^2}\right) - I \exp\left(-\frac{d}{\sigma_i^2}\right), \qquad (1)$$

where d is the distance between neurons, and E, I, σ_e, σ_i are parameters.

Synaptic strengths $w^{E,C}$ of projections from the LGN eye-specific layer $E \in \{con, ips\}$ whose center type is $C \in \{on, off\}$ to the cortex is modified by STDP as follows:

$$\begin{aligned} w^{E,C} &\leftarrow w^{E,C} + \Delta w^{E,C}, \\ \Delta w^{E,C} &= \begin{cases} A_+ \exp\left(-\frac{\Delta t}{\tau_+}\right) & (\Delta t \geq 0), \\ -A_- \exp\left(\frac{\Delta t}{\tau_-}\right) & (\Delta t < 0), \end{cases} \end{aligned} \qquad (2)$$

when pre- and postsynaptic spikes occur at t_{pre} and t_{post}. Here, $\Delta t = t_{post} - t_{pre}$ is the interval between pre- and postsynaptic spikes. A_+ and τ_+ respectively determine maximum amount and the time constant of LTP and A_- and τ_- respectively determine those of LTD.

Let Δt_1 and Δt_2 are intervals of pre- and postsynaptic spikes and $\Delta t_1 > \Delta t_2$. The difference of modification,

$$\begin{aligned} &|\Delta w_1 - \Delta w_2| = \\ &\begin{cases} A_+ \left(\exp\left(-\frac{\Delta t_2}{\tau_+}\right) - \exp\left(-\frac{\Delta t_1}{\tau_+}\right)\right) & (\Delta t_2 > 0) \\ A_- \left(\exp\left(-\frac{\Delta t_1}{\tau_-}\right) - \exp\left(-\frac{\Delta t_2}{\tau_-}\right)\right) & (0 > \Delta t_1) \end{cases} \end{aligned}$$

is small when τ_+ and τ_- are large. The synaptic modification by STDP is less sensitive to fine difference of the interval between pre- and postsynaptic spikes with large time constants τ_+ and τ_-. There are correlations between neurons in the same and between different eye-specific layers in large time scale. Eye-specific Layers are not distinguished by STDP with the large time constants. Therefore STDP with large τ_+ and τ_- may lead to formation of orientation selective map, and small τ_+ and τ_- may lead to formation of ocular dominance map.

2.2 Primary visual cortex model

The model network consists of 225 cortical neurons and 225 LGN neurons in each sublaminae. We used Izhikevich neuron model [9] for cortical neurons, that is,

$$\begin{aligned} \frac{\mathrm{d}v}{\mathrm{d}t} &= 0.04v^2 + 5v + 140 - u + I, \\ \frac{\mathrm{d}u}{\mathrm{d}t} &= a(bv - u), \\ \text{if } v &\geq 30\,\mathrm{mV} \text{ then, } v \leftarrow c,\ u \leftarrow u + d. \end{aligned} \qquad (3)$$

Here, a, b, c, and d are dimensionless parameters, and the variable I represents synaptic currents. In this simulation, we set parameters, $a = 0.02$, $b = 0.2$, $c = -65$, and $d = 8$. The variable v is the membrane potential. The variable u represents the recovery variable providing negative feedback to v. The cortical neuron i receives synaptic currents I_i:

$$\begin{aligned} I_i &= \sum_{E \in \{con,ips\}} \sum_{C \in \{on,off\}} \sum_j w_{ij}^{E,C} s_j^{E,C} \\ &\quad + \sum_j w_{ij}^{cor} s_j^{cor}, \qquad (4) \\ \frac{\mathrm{d}s_j^{cor}}{\mathrm{d}t} &= -\frac{1}{\tau_s} s_j^{cor} + \delta(t - t_j), \\ \frac{\mathrm{d}s_j^{E,C}}{\mathrm{d}t} &= -\frac{1}{\tau_s} s_j^{E,C} + \delta(t - t_j). \end{aligned}$$

Here, w_{ij} is the synaptic strength from neuron j to neuron i , and δ is the delta function. Synaptic current from cortical neuron j is represented by s_j^{cor}, and synaptic current from LGN neuron j in eye-specific layer E whose center type is C is represented by $s_{ij}^{E,C}$. The presynaptic neuron j generates a spike at t_j.

2.3 LGN model

The LGN neuron j at location (x, y) , location of the center of LGN is $(0, 0)$, generates spikes through Poisson process with the following firing rate:

$$\begin{aligned} \lambda_j^{on} &= 0.015 + 0.015 \exp\left(-\frac{x_\theta^2 + y_\theta^2}{\sigma^2}\right) \cos\left(\frac{2\pi x_\theta}{\lambda^{sp}}\right), \\ \lambda_j^{off} &= 0.015 - 0.015 \exp\left(-\frac{x_\theta^2 + y_\theta^2}{\sigma^2}\right) \cos\left(\frac{2\pi x_\theta}{\lambda^{sp}}\right), \\ x_\theta &= x\cos\theta + y\sin(\theta), \\ y_\theta &= 0.3 \times (-x\sin(\theta) + y\cos(\theta)). \end{aligned} \tag{5}$$

Here, $\theta \in \{0, \pi/6, \pi/3, \pi/2, 2\pi/3, 5\pi/6\}$ is the orientation of the input, and σ and λ^{sp} are parameters determining the spatial variance of the input. The firing rate of the neuron j in the on-center sublamina is λ_j^{on}, and the firing rate of neuron j in the off-center sublamina is λ_j^{off}. In addition, spikes of LGN neurons in the same and different sublaminae are correlated in different time scale as previously indicated (Figure 1).

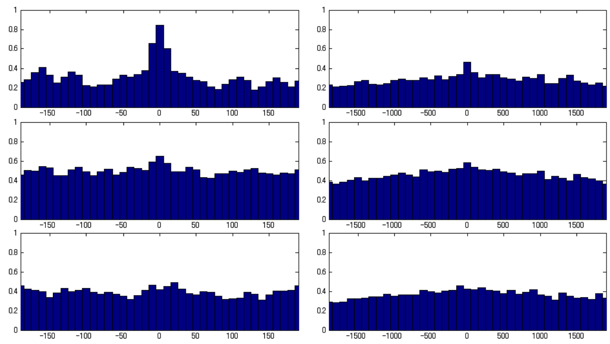

Figure 1: Cross-correlation functions calculated between neurons within the same sublamina (top), between the on-center sublamina and the off-center sublamina within the same eye-specific layer (middle), and between different eye-specific layers (bottom). Spikes were binned into 10 ms (left) and 100 ms (right).

3 Results

We simulated in three conditions, small, medium, and large time constants. We determined A_- in equation (2) to keep the value of $A_-\tau_-$ constant and modified A_+ to balance LTP with LTD (table 1).

Table 1: Parameters of STDP.

τ_+	10	50	100
τ_-	50	250	500
A_+	0.3	0.026	0.008
A_-	0.13	0.026	0.013

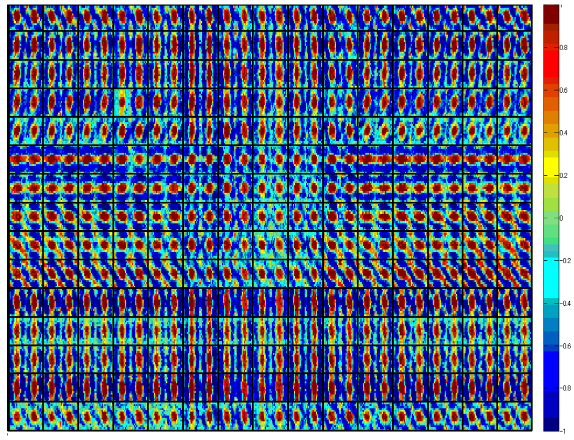

Figure 2: The orientation selective map with $\tau_+ = 50$ and $\tau_- = 250$. One black square represents one cortical neuron. Values of $w_{ij}^{on} - w_{ij}^{off}$ are represented by colors. Here, w_{ij}^{on} and w_{ij}^{off} are same as in equation (6).

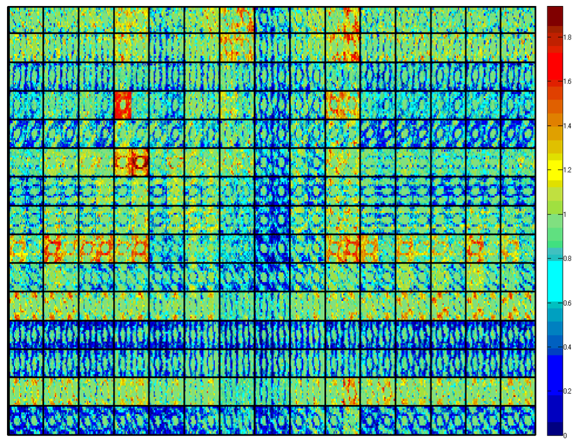

Figure 3: The ocular dominance map with $\tau_+ = 50$ and $\tau_- = 250$.

Figure (2) and figure (3) are the orientation selective map and the ocular dominance map obtained with $\tau_+ = 50$ and $\tau_- = 250$. Though many neurons are se-

©ISAROB 2009

lective to certain orientation, few neurons are selective to contralateral or ipsilateral eye.

To evaluate differences of orientation selectivity and ocular dominance, we defined degrees of orientation selectivity S_i^{OR} and ocular dominance S_i^{OC} of the cortical neuron i below.

$$\begin{aligned} O_i^\theta &= \frac{\sum_j \left(\lambda_j^{on} w_{ij}^{on} + \lambda_j^{off} w_{ij}^{off}\right)}{\sum_j \left(\lambda_j^{on} + \lambda_j^{off}\right)}, \\ \left(S_i^{OR} e^{\mathrm{i}\psi}\right)^2 &= \frac{\sum_\theta \left(e^{\mathrm{i}\theta} O_i^\theta\right)^2}{\sum_\theta \left(O_i^\theta\right)^2}, \qquad (6) \\ S_i^{OC} &= \frac{\left(\sum_j w_{ij}^{con}\right)^2 - \left(\sum_j w_{ij}^{ips}\right)^2}{\left(\sum_j w_{ij}^{con}\right)^2 + \left(\sum_j w_{ij}^{ips}\right)^2}. \end{aligned}$$

Here, θ is the orientation of the input and λ_j^{on} and λ_j^{off} are frequencies of the LGN neuron j. These are defined in equation (5). Synaptic strengths from the on-center and the off-center neurons j are represented by $w_j^{on} = w_j^{con,on} + w_j^{ips,on}$ and $x_j^{off} = w_j^{con,off} + w_j^{ips,off}$. Those from LGN neurons j in eye-specific layers selective to the contralateral eye and the ipsilateral eye are represented by $w_j^{con} = w_j^{con,on} + w_j^{con,off}$ and $w_j^{ips} = w_j^{ips,off} + w_j^{ips,off}$.

Table 2: Selectivity in three conditions of time constants.

τ_+/τ_-	S^{OR}	S^{OC}
10/50	0.2799±0.0919	0.2721±0.2002
50/250	0.3425±0.0779	0.1129±0.0886
100/500	0.3273±0.0715	0.0779±0.0605

The difference between degrees of orientation selectivity $\tau_+ = 10$ and $\tau_+ = 50$ is significant($P < 0.05$, t-test). The difference between $\tau_+ = 50$ and $\tau_+ = 100$ is not significant($P < 0.05$, t-test). About ocular selectivity, though it is significant between $\tau_+ = 50$ and $\tau_+ = 100$, not significant between $\tau_+ = 10$ and $\tau_+ = 50$($P < 0.05$, t-test).

4 Conclusion

We showed that STDP with different time constants result different topographic maps. If cortical neurons could modulate time constants by any way, STDP could explain the negative correlation between the orientation selective and ocular dominance map without implausible constraints. Such modification, however, has not found either in vitro or in vivo.

In our model, we explained formation of orientation selectivity and ocular dominance by differences of correlations of inputs in different time scales. Hence, we can yield other "multiple maps" representing multiple informations, only if inputs have different correlations in different time scales.

References

[1] D. H. Hubel and T. N. Wiesel, "Receptive Fields, Binocular Interaction and Functional Architecture in The Cat's Visual Cortex", *J. Physiol.*, Vol.160, pp. 106-154, 1962.

[2] Mark Hübener, Doron Shoham, Amiram Grinvald, et al., "Spatial Relationships among Three Columnar Systems in Cat Area 17", *J. Neurosci.*, Vol.17, No.23, pp. 9270-9284, 1997.

[3] Michael Weliky and Lawrence C. Katz, "Correlational Structure of Spontaneous Neuronal Activity in the Developing Lateral Geniculate Nucleous in Vivo", *Science*, Vol. 285, pp. 599-604, 1999.

[4] von der Malsburg, "Self-Organization of Orientation Selective Cells in the Striate cortex", *Kybernetik*, Vol. 14, pp. 85-100, 1973.

[5] Ralph Linsker, "From Basic Network Principles to Neural Architecture: Emergence of Orientation Columns", *Proc. of National Academy of Science USA*, Vol. 83, pp. 8779-8783, 1986.

[6] Ed Erwin and Kenneth D. Miller, "Correlation-Based Development of Ocularly Matched Orientation and Ocular Dominance Maps: Determination of Required Input Activities", *J. Neurosci.*, Vol. 18, No. 23, pp. 9870-9895, 1998.

[7] Guo-qiang Bi and Mu-ming Poo, "Synaptic Modifications in Cultured Hippocampal Neurons: Dependence on Spike Timing, Synaptic Strength, and Postsynaptic Cell Type", *J. Neurosci.*, Vol.18, No.24, pp. 10464-10472, 1998.

[8] Sen Song and L.F. Abbott, "Cortical Development and remapping through Spike Timing-Dependent plasticity", Neuron, Vol.32, pp. 339-350, 2001.

[9] Eugene M. Izhikevich, "Simple Model of Spiking Neurons", *IEEE Trans. Neural Networks*, Vol. 14, No. 6, pp. 1569-1572.

©ISAROB 2009

The Fourteenth International Symposium on Artificial Life and Robotics 2009 (AROB 14th '09),
B-Con Plaza, Beppu, Oita, Japan, February 5 - 7, 2009

Integrative Bayesian Model of Two Opposite Types of Sensory Adaptation

Y. Sato[†,‡] and K. Aihara[†,‡,*]

[†] Department of Complexity Science and Technology, Graduate School of Frontier Sciences, University of Tokyo, Japan

[‡] Institute of Industrial Sciences, University of Tokyo, Japan

[*] Aihara Complexity Modelling Project, ERATO, JST, Japan

(Address: 4-6-1 Komaba, Meguro-ku, Tokyo 153-8505, Japan)

(E-mail: yoshi@sat.t.u-tokyo.ac.jp)

Abstract

Adaptation is a fundamental property of human perception. Recently, it was found that there are two opposite types of adaptation to repetitive stimuli with temporal difference. In this paper, we construct an integrative model of adaptation. We model the perception as a Bayesian inference and also model the two types of adaptation as changes in the likelihood function and the prior distribution in the Bayesian inference. We examine our model analytically and show how the type of adaptation depends on model parameters.

Keywords: Bayesian inference, lag adaptation, Bayesian calibration, ventriloquism aftereffect

1 Introduction

Our surrounding world is constantly changing. Our perception has to deal with such changes in statistics of our surroundings, by adjusting the inner representations of those statistics. In addition to those changes in the outer world, there are also changes in our body. For example, when we injure our eyes or ears, our perception would be impaired, due to the change in the inner representation of the physically delivered stimulus in the brain. Such adaptation phenomena are the important aspects of human perception and they themselves are worth to be investigated. In addition to that, by investigating the properties of the adaptation of a particular type of perception or a motor system, its neural mechanism can often be deduced by psychophysical experiments and brain imaging experiments (e.g. [1]).

We showed in earlier works that the ventriloquism aftereffect, which is an adaptation phenomenon in audiovisual spatial perception, can be explained by updating the parameter that determines the mean value of the likelihood function that represents a noise distribution [2].

In the ventriloquism aftereffect, the repeated stimuli are perceived to be presented at the same place. This type of adaptation is also observed in the adaptation to audiovisual temporal difference, that is, the participants perceive the temporal difference in the adapting stimuli to be simultaneous [3]. This type of adaptation is call the "lag adaptation". However, recently, an opposite type of adaptation was found [4] in tactile temporal adaptation. They showed that adaptational effect was opposite to the lag adaptation, that is, the participants were more unlikely to perceive simultaneity for the repeatedly presented stimuli. They showed that the result could be explained by assuming that the participants had learned the prior distribution of stimulus timing. They called the adaptation "Bayesian calibration".

In our earlier work [2], adaptation was modeled as the update of the mean values of likelihood functions. Therefore, lag adaptation can be considered to be changes in the likelihood functions. On the other hand, as Miyazaki et al. showed in [4], Bayesian calibration can be considered to be changes in the prior distributions.

In this paper, we extend our earlier model [2] and investigate the interaction of these two types of adaptation and show what parameters determine the type of adaptation.

2 Integrative Bayesian model of adaptation

We consider an audiovisual localization task. We consider a task in which a pair of sound and light with spatial disparity is presented, and the participant determines which stimulus is presented at the right. If

©ISAROB 2009

The Fourteenth International Symposium on Artificial Life and Robotics 2009 (AROB 14th '09),
B-Con Plaza, Beppu, Oita, Japan, February 5 - 7, 2009

we plot the percentage of "sound right" response for various test stimulus disparities, we obtain a psychometric function. The center point of the psychometric function represents the disparity that the participants judged to be at the same location. During an adaptation period, stimuli with, in most experiments, constant disparity are repeated. The adapting stimuli during the adaptation period are not necessarily constant: they may be drawn from a probability distribution. Then we measure the psychometric function again. The type of adaptation is represented as the difference in the center point of the psychometric function between before and after adaptation period. If the center point is shifted toward the adapting stimuli, it is "lag adaptation" type, and if it is shifted opposite from the adapting stimuli, it is "Bayesian calibration" type.

We formalize the optimal observer that uses Bayesian inference to estimate the true positions of stimuli. We assume that the observer can only observe noisy position of sound and light, denoted as y_A and y_V, respectively, that are deviated from the true positions of stimuli, denoted as x_A and x_V, respectively. The observer is assumed to determine estimators $\hat{x}_A$ and $\hat{x}_V$ from y_A and y_V by maximizing the posterior probability distribution $P(x_A, x_V|y_A, y_V)$. We assume independence between the auditory and visual noise. Then, from Bayes' theorem, it follows that

$$P(x_V, x_A|y_V, y_A) \propto P(y_A|x_A)P(y_V|x_V)P(x_A, x_V), \tag{1}$$

We model the adaptation by changing the mean values of the likelihood function [2], $P(y_A|x_A)$ and $P(y_V|x_V)$, and the prior distribution $P(x_A, x_V)$. We assume that the noise are Gaussian noise and the prior probability of x_A and x_V depends only on their difference $x_A - x_V$. Thus, we assume

$$P(y_V|x_V) = \frac{1}{\sqrt{2\pi}\sigma_V} \exp\left(-\frac{(y_V - x_V - \mu_V)^2}{2\sigma_V^2}\right), \tag{2}$$

$$P(y_A|x_A) = \frac{1}{\sqrt{2\pi}\sigma_A} \exp\left(-\frac{(y_A - x_A - \mu_A)^2}{2\sigma_A^2}\right), \tag{3}$$

$$P(x_A, x_V) = \frac{1}{\sqrt{2\pi}\sigma_p L} \exp\left(-\frac{(x_A - x_V - \mu_p)^2}{2\sigma_p^2}\right), \tag{4}$$

where μ_A, μ_V, and μ_p modifies represent the mean values of distributions.

We interpret the adaptational effect observed in psychophysical experiments as the false update of μ_A and μ_V due to the unnatural stimuli that the participants are exposed to, and the learning of μ_p of such unnatural stimuli. We assume that the real values of μ_A and μ_V are zero and unchanged from their initial values, and that the observer knows the other parameters like σ_A, σ_V, and σ_p. Quantities σ_p and μ_p can be controlled by the experimenter.

Each time the observer receives the adapting audiovisual stimuli, it estimates the corresponding parameters and updates its estimations on μ_V, μ_A, and μ_p based on observations and estimations. We denote these observer's estimations of μ_V, μ_A, and μ_p as $\hat{\mu}_V$, $\hat{\mu}_A$, and $\hat{\mu}_p$. The observer determines MAP estimators $\hat{x}_V$ and $\hat{x}_A$ from y_V and y_A, and updates $\hat{\mu}_V$, $\hat{\mu}_A$, and $\hat{\mu}_p$ as

$$\begin{aligned} \hat{\mu}_A(t+1) &= (1-\alpha_A)\hat{\mu}_A(t) + \alpha_A(y_A - \hat{x}_A), && (5)\\ \hat{\mu}_V(t+1) &= (1-\alpha_V)\hat{\mu}_V(t) + \alpha_V(y_V - \hat{x}_V), && (6)\\ \hat{\mu}_p(t+1) &= (1-\alpha_p)\hat{\mu}_p(t) + \alpha_p(\hat{x_A} - \hat{x}_V), && (7) \end{aligned}$$

where $\hat{\mu}_A(t)$, $\hat{\mu}_V(t)$, and $\hat{\mu}_p(t)$ represent the observer's estimations at time t. Quantities α_A, α_V, and α_p determine the relative adaptation effect in each step, and are assumed to satisfy $0 \leq \alpha_i \leq 1$, where i represents each one of $\{A, V, p\}$. We assume that the initial values of $\hat{\mu}_A$ and $\hat{\mu}_V$ are their true values, that is, zero. We also assume that the initial value of $\hat{\mu}_p$ is zero.

3 Psychometric function

Here, we derive the dependency of the center point of a psychometric function on model parameters.

In our model, the observer's task corresponds to judging the sign of $\hat{x}_A - \hat{x}_V$: if it is positive, sound is on the right. Therefore, the probability that the observer's response is "sound right" given a presented disparity $\;_x \equiv x_A - x_V$ is equivalent to $P(\hat{x}_A - \hat{x}_V > 0|x_A - x_V = \;_x)$. As we will show later, this probability distribution does not depend on the absolute values of x_A or x_V but only on their difference $\;_x$. Thus in our model, the psychometric function, denoted as $Psycho(\;_x)$, can be written as

$$Psycho(\;_x) = P(\hat{x}_A - \hat{x}_V > 0|x_A - x_V = \;_x). \tag{8}$$

In usual experiments, it is known that psychometric function can be approximated by a cumulative Gaussian distribution (e.g. [4]). Therefore, it can be written as

$$Psycho(\;_x) = \int_{-\infty}^{\Delta_x} d\;'_x N(\;'_x; \mu_{psycho}, \sigma^2_{psycho}), \tag{9}$$

where $N(x; \mu, \sigma^2)$ represents a normal probability distribution of x with mean μ and variance σ^2. Thus, by calculating $P(\hat{x}_A - \hat{x}_V > 0|x_A - x_V = \;_x)$ and comparing equations (8) and (9), we can determine how the center point of the psychometric function, i.e. μ_{psycho}, depends on the model parameters.

©ISAROB 2009

By substituting equations (2), (3), and (4) into equation (1) and maximizing it, we obtain

$$\hat{x}_A = \frac{1}{\sigma_{all}^2} \quad (\sigma_V^2 + \sigma_p^2)(y_A - \hat{\mu}_A) + \sigma_A^2(y_V - \hat{\mu}_V) + \sigma_A^2 \hat{\mu}_p \quad , \tag{10}$$

$$\hat{x}_V = \frac{1}{\sigma_{all}^2} \quad \sigma_V^2(y_A - \hat{\mu}_A) + (\sigma_A^2 + \sigma_p^2)(y_V - \hat{\mu}_V) - \sigma_V^2 \hat{\mu}_p \quad , \tag{11}$$

where $\sigma_{all}^2 \equiv \sigma_A^2 + \sigma_V^2 + \sigma_p^2$. From equations (10) and (11), we obtain

$$\hat{~}_x = \frac{\sigma_p^2}{\sigma_{all}^2}(\ _y - \hat{~}_\mu) + \frac{\sigma_A^2 + \sigma_V^2}{\sigma_{all}^2}\hat{\mu}_p, \tag{12}$$

where $\hat{~}_x \equiv \hat{x}_A - \hat{x}_V$, $\ _y \equiv y_A - y_V$, and $\hat{~}_\mu \equiv \hat{\mu}_A - \hat{\mu}_V$.

Then we can calculate $P(\hat{~}_x > 0 |\ _x)$ as follows:

$$P(\hat{~}_x > 0 |\ _x) = \int_{-\infty}^{\Delta_x} d\hat{~}'_x \, N\left(\hat{~}'_x; \hat{~}_\mu - \frac{\sigma_A^2 + \sigma_V^2}{\sigma_p^2}\hat{\mu}_p, \sigma_A^2 + \sigma_V^2\right). \tag{13}$$

Thus, from equations (9) and (13), we obtain

$$\mu_{psycho} = \hat{~}_\mu - \frac{\sigma_A^2 + \sigma_V^2}{\sigma_p^2}\hat{\mu}_p, \tag{14}$$

$$\sigma_{psycho} = \sigma_A^2 + \sigma_V^2. \tag{15}$$

Now that we know how μ_{psycho} depends on model parameters and $\hat{\mu}_A$, $\hat{\mu}_V$, and $\hat{\mu}_p$, next we must investigate the time course of these $\hat{\mu}$s during the adaptation period and their converging values. Thus, we can show how the type of adaptation is determined.

4 Analysis of the model behavior

It can be seen from equations (5), (6), and (7) that the update rules of $\hat{\mu}_A$, $\hat{\mu}_V$, and $\hat{\mu}_p$ are independent from each other given $\hat{x}_A$ and $\hat{x}_V$. However, because $\hat{x}_A$ and $\hat{x}_V$ depend on $\hat{\mu}_A(t)$, $\hat{\mu}_V(t)$, and $\hat{\mu}_p(t)$, the values of $\hat{\mu}$s are not independently changed.

By substituting equations (10) and (11) into equations (5), (6), and (7), we obtain

$$\begin{pmatrix}\hat{\mu}_A(t+1)\\ \hat{\mu}_V(t+1)\\ \hat{\mu}_p(t+1)\end{pmatrix} = \begin{pmatrix}1-a & a & -a\\ v & 1-v & v\\ -p & p & 1-p\end{pmatrix}\begin{pmatrix}\hat{\mu}_A(t)\\ \hat{\mu}_V(t)\\ \hat{\mu}_p(t)\end{pmatrix} + \begin{pmatrix}a\\ -v\\ p\end{pmatrix}\ _y, \tag{16}$$

where a,v, and p are defined by: $a \equiv \alpha_A \frac{\sigma_A^2}{\sigma_{all}^2}$, $v \equiv \alpha_V \frac{\sigma_V^2}{\sigma_{all}^2}$, and $p \equiv \alpha_p \frac{\sigma_p^2}{\sigma_{all}^2}$.

Although, in reality, y_A and y_V are determined randomly from trial to trial, we can pursue the average behavior of the model by fixing each of y_A and y_V to its mean value during the adaptation period. We validate this assumption later by numerical simulations. From equations (2), (3), and (4), and our assumption that the true values of μ_A and μ_V are zero, the mean value of $\ _y \equiv y_A - y_V$ is $\ _{adapt} \equiv \mu_p$. We use the notation $\ _{adapt}$ to avoid confusion of μ_p with $\hat{\mu}_p$.

With this assumption, we can solve equation (16) explicitly with respect to t, which yields

$$\begin{pmatrix}\hat{\mu}_A(t)\\ \hat{\mu}_V(t)\\ \hat{\mu}_p(t)\end{pmatrix} = \begin{pmatrix}\frac{a}{z}\ _y - \frac{a}{z}\ _y(1-z)^t\\ -\frac{v}{z}\ _y + \frac{v}{z}\ _y(1-z)^t\\ \frac{p}{z}\ _y - \frac{p}{z}\ _y(1-z)^t\end{pmatrix}, \tag{17}$$

where $z \equiv a + v + p$.

By definition, z satisfies $0 \leq z \leq 1$, and we omit the case $z = 0$, because it is the case where all αs are zero and the results are trivial. Then $(1 - z)^t$ converges to zero. From equation (17), we can also see that the converging speed of all $\hat{\mu}$s are the same. Because α_i represents the degree of adaptation in each step, at first sight, it seems that the converging speed is different if α_i is different for different i. However, due to the interaction of all $\hat{\mu}$s, their converging speed are the same.

By substituting equation (17) into equation (14), after some calculations, we obtain

$$\mu_{psycho}(t) = \beta\ _{adapt} - \beta\ _{adapt}(1-z)^t, \tag{18}$$

where $\mu_{psycho}(t)$ is the center of the psychometric function measured with $\mu_A(t)$, $\mu_V(t)$, and $\mu_p(t)$, and β is defined as:

$$\beta \equiv \frac{1}{z\sigma_{all}^2}(\alpha_A\sigma_A^2 + \alpha_V\sigma_V^2 - \alpha_p(\sigma_A^2 + \sigma_V^2)). \tag{19}$$

Thus, the direction of the shift in the center point of the psychometric function relative to $\ _{adapt}$ is determined by the sign of β.

In reality, in order to measure $\mu_{psycho}(t)$, test stimuli must be presented to the participant, and such stimuli must change $\hat{\mu}_A(t)$, $\hat{\mu}_V(t)$, and $\hat{\mu}_p(t)$, if presented too many times. Therefore, $\mu_{psycho}(t)$ can only be measured by conducting the whole experiment multiple times, with a small number of test stimuli, and averaging the results, like Miyazaki et al. did in [4].

5 Numerical simulations

In deriving equation (17), we assumed $_y$ was constant with respect to t and investigated the mean behavior of the model. Here, we validate this assumption using numerical simulations.

Parameter values were as follows: $\mu_p = 8$, $\sigma_A = 8$, $\sigma_V = 2.5$, $\sigma_p = 1$, $\alpha_A = 0.01, \alpha_V = 0.01$, and $\alpha_p = 0.005$. At each time step, we sampled x_A from a normal distribution with mean μ_p and variance σ_p^2, while x_V was fixed to 0. We also sampled y_A and y_V according to the noise distributions in equations(2) and (3). Then the model observer judged $\hat{x}_A$ and $\hat{x}_V$ based on equations (10) and (11) and updated $\hat{\mu}_A$, $\hat{\mu}_V$, and $\hat{\mu}_A$ according to equations (5), (6), and (7). This procedure was repeated 1000 times. We also investigated the time course of μ_{psycho}. At each time step, after updating all $\hat{\mu}$s, we measured the psychometric function using the updated $\hat{\mu}s$. We presented test stimuli with $_x$ from -30 to 30 with 1 step, each 1000 times. Then we calculated $\mu_{psycho}(t)$ by fitting the result to equation (9) by minimizing mean squared error.

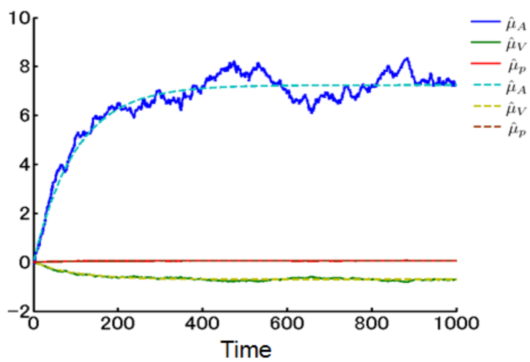

Figure 1: Time course of $\hat{\mu}_A$, $\hat{\mu}_V$, and $\hat{\mu}_A$. Solid lines show numerical simulation results and dashed lines show corresponding analytical results.

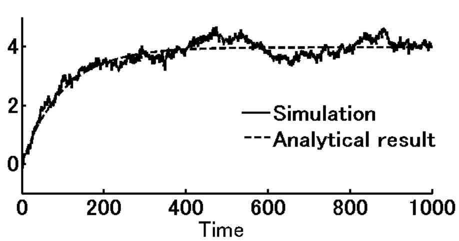

Figure 2: Time course of $\mu_{psycho}(t)$. The solid line shows numerical simulation results and the dashed line shows corresponding analytical result.

Figure 1 shows an example of the simulation result for the time course of $\hat{\mu}_A$, $\hat{\mu}_V$, and $\hat{\mu}_A$, together with the analytical results in equation (17). Figure 2 shows the simulation result for the time course of μ_{psycho}, together with the analytical results in equation (18). These figures clearly show that the analytical results in equations (17) and (18) correctly follow the average behavior of $\hat{\mu}$s or μ_{psycho}.

6 Conclusion

In this paper, we constructed an integrative Bayesian model of adaptation and investigated what factors determine the type of adaptation. We showed that the type of adaptation was determined by the sign of β defined in equation (19). Quantities σ_A, σ_V, and σ_p can be measured or adjusted experimentally. Therefore, according to our model, we might be able to control experimentally the type of adaptation by adjusting the parameters. However, it is not straightforward what determines the adaptation parameters α_A, α_V, and α_p. The investigation of the meaning of them remains as a future work.

Acknowledgments

This work was partially supported by Grant-in-Aid for JSPS Fellows from JSPS (20・8988) and Grant-in-Aid for Scientific Research on Priority Areas –System study on higher-order brain functions– from MEXT, Japan (17022012).

References

[1] R.B.H. Tootell, J.B. Reppas, A.M. Dale et al. Visual motion aftereffect in human cortical area MT revealed by functional magnetic resonance imaging. *Nature*, 375(6527):139–141, 1995.

[2] Y. Sato, T. Toyoizumi, and K. Aihara. Bayesian Inference Explains Perception of Unity and Ventriloquism Aftereffect: Identification of Common Sources of Audiovisual Stimuli. *Neural Computation*, 19(12):3335–3355, 2007.

[3] W. Fujisaki, S. Shimojo, M. Kashino et al. Recalibration of audiovisual simultaneity. *Nature Neuroscience*, 7(7):773–778, 2004.

[4] M. Miyazaki, S. Yamamoto, S. Uchida et al. Bayesian calibration of simultaneity in tactile temporal order judgment. *Nature Neuroscience*, 9(7):875–7, 2006.

The Fourteenth International Symposium on Artificial Life and Robotics 2009 (AROB 14th '09),
B-Con Plaza, Beppu, Oita, Japan, February 5 - 7, 2009

A hub gene in a HIV-1 gene regulatory network is a promising target for anti-HIV-1 drugs

Kouji Harada
Dept. of Knowledge-based Info. Engr.
Toyohasi University of Technology,
1-1, Tenpaku, Toyohashi-shi, Aichi
441-8585, Japan
(E-Mail: harada@tutkie.tut.ac.jp)

Yoshiteru Ishida
Dept. of Knowledge-based Info. Engr.
Toyohasi University of Technology,
1-1, Tenpaku, Toyohashi-shi, Aichi
441-8585, Japan
(E-Mail: ishida@tutkie.tut.ac.jp)

Abstract

Any of the existing anti-HIV-1 drugs has tough problems: side-effects and development of drug resistance. From logical reasoning, the study concludes promising targets of anti-HIV-1 drug without the above problems should bear "hub" and "bottleneck" topological features in HIV-1 gene regulatory networks.

Keywords

Hub gene, Bottleneck gene, Anti-HIV-1 drug, Drug resistance, HAART

I Introduction

Topologies of gene regulatory networks of *Saccharomyces cerevisiae* and yeast were energetically analyzed [1][2]. The analyses revealed all of these networks were scale-free with power-law degree distributions. Further, it was shown that "hub" genes, which regulate multiple genes exist. The hub genes are evolutionary conserved; therefore it is thought that the genes assume important functions.

Recently, another topological feature of genes called "bottleneck" is noted [3]. The bottleneck gene is defined as a sort of a "main bridge" between highly connected sub gene networks (Fig. 1). Thus the bottleneck gene is considered to be requisite for sustaining interactions between sub networks; inhibiting the bottleneck gene leads to block the interaction between them. As an example of the bottleneck gene, Yu et al [3] take up Cak1p in yeast, and reveals Cak1p connects two signal pathways: cell cycle and sporulation.

Except biological networks, topological analyses of the Internet, where many computers are linked by wired or wireless connections have also been carried out. The analyses revealed the network topology of the Internet is the same scale-free as the gene regulatory networks are. Albert et al [4] investigated the scale-free network is immune or vulnerable to what kind of attacks. They demonstrated the scale-free network is fault-resilient against random faults; it receives a death stroke when hub routers or hub servers are taken a shot at.

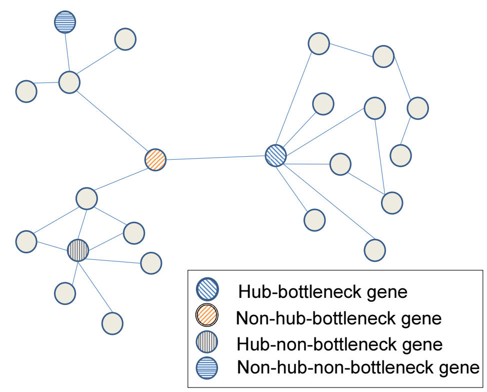

Fig. 1: Schematic view of hub-bottleneck, non-hub-bottleneck, hub-non-bottleneck and non-hub-non-bottleneck gene

With these research backgrounds, this study interests to determine topological features of anti-HIV-1 drug targets with no side-effects and no development of drug resistance.

HIV-1 which is a causal agent of AIDS only has 9 genes. However, functions of each gene are only partly revealed. One of the reasons is that HIV-1 replicates by manipulating intracellular agents so that a large number of interactions between HIV-1 genes and the agents form a web-like complicated pattern. For instance, Tat: the one of HIV-1 genes involves tran-

©ISAROB 2009

scriptional activation of HIV-1 gene expression, but actually its process looks very complex as follows (see. Fig. 2)[5]:

1. The nuclear factor NF-kB, NFAT and Sp1 bind to the long terminal repeat (LTR) region at the end of HIV-1 DNA.
2. By RNA polymerase II (RNAP II), short non-polyadenylated transcripts are synthesized.
3. A Tat protein and an intracellular Cyclin T1 bind to TAR segments of the short transcripts, thereby an intracellular Cdk9 is recruited and activated.
4. The activated Cdk9 phosphorylates the C-terminal domain (CTD) of RNAP II, which starts to elongate eukaryotic transcription.

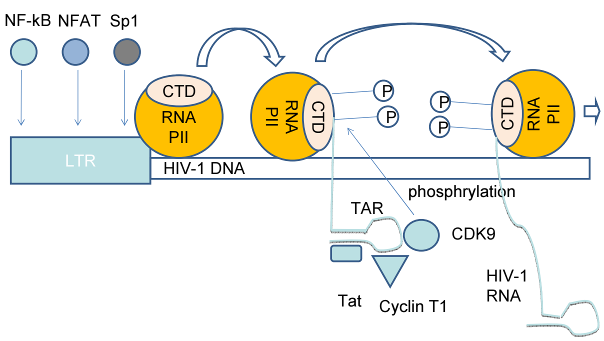

Fig. 2: Transcriptional process by cooperation between HIV-1 genes and intracellular agents

Even this scenario is so simplified that its perfect scenario is still incomprehensible. Actually HIV-1 gene regulatory networks are still not enough uunderstood. Therefore, from logical reasoning approach different from network analyses, the present study derives some topological conditions for anti-HIV-1 drug targets with no side-effects and no drug resistance to satisfy. This study concludes "hub-ness" and "bottleneck-ness" of HIV-1 genes are promising topological features of anti-HIV-1 drug targets.

II Hub-ness for anti-HIV-1 drug targets

II.1 About the drug resistance

Currently, there are 25 anti-HIV-1 drugs and they are divided into 3 classes. The most bothersome problem for the present anti-HIV-1 drugs is development of the drug resistance.The reason why the drug resistance is easy to emerge is HIV-1 is highly mutagenic in nature so that HIV-1 can evolve a virus enzyme's active site which an anti-HIV-1 drug targets; thereby HIV-1 can easily escape from that inhibition. In other words, the problem lies in each anti-HIV-1 drug can only inhibit just "one" active site (i.e. one specific function) of HIV-1 enzyme. For instance, the reverse transcriptase inhibitor which was developed as the earliest anti-HIV-1 drugs blocks a HIV-1 reverse transcriptase (RT)'s active site. Indeed, HIV-1 mutates an active site of RT, for instance, such as K65R, L74V, Y115F and M184V against "Abacavir"(RT inhibitor) [6], thereby the drug resistant strain appears in just two months. This problem is not limited to a particular HIV-1 drug. On "Alazanavir", which belongs in the class of a protease inhibitor, multiple mutations (L10IFV, G16E, K20RMI, L24I and so on) on the active site of its targeting protease are observed [6].

On the other hand, we can expect an anti-hub gene drug can cause a malfunction of all genes under the hub gene's regulation. Even though HIV-1 is highly mutagenic, it seems unlikely that all of the malfunctioning genes can evolve together to recover their functions. From this reasoning, we can conclude that anti-HIV-1 drugs targeting hub genes are immune to drug resistance. This conclusion is validated by the fact that "multiple drugs therapy (HAART)" targeting multiple HIV-1 functions is effective to suppress HIV-1 population growth.

Meanwhile, a hub gene must play a significant role in a HIV-1 gene regulatory network, thus we can expect that the hub gene have to be insusceptible to any mutations. Namely, any mutations to a hub gene to achieve the drug resistance must result in a suicidal action for HIV-1.

From these discussions, we think a hub gene in HIV-1 gene regulatory networks is a promising candidate as anti-HIV-1 drug targets to overcome the drug resistance.

II.2 About the multiple drug therapy

Next we discuss some important problems of multiple drug therapy for AIDS. The problems are 1) an increase of a treatment cost and of a daily dosage and 2) strong side-effects. First, we discuss the primary problem.

The multiple drug therapy produces a strong effect by simultaneously inhibiting multiple HIV-1 enzymic activities by plural anti-HIV-1 drugs. However, unfortunately the therapy just restrains AIDS progres-

©ISAROB 2009

sion and does not bring AIDS patients to recover fully. Therefore, the therapy forces them to continue to take the plural drugs for a long life, so the treatment cost will become high amount. This means that a quite number of AIDS patients in developing countries can not take this treatment by its cost.

On the other hand, as already mentioned, an anti-HIV drug targeting a hub gene can inhibit multiple genes under the hub gene's regulation. Namely we can expect the same effect as the multiple drug therapy by use of a single drug against a hub gene. Additionally we can reduce the treatment cost because the number of drugs necessary for our proposed therapy is the only one: anti-hub gene drug. Therefore AIDS patients in developing countries could use the drug.

Another problem of the multiple drug therapy is side-effects. In the therapy, patients have to take multiple drugs so that a very acute side effect by a synergetic effect of each drug's side-effect is brought into patients. Thereby, quite number of patients quit the treatment. Meanwhile if an anti-HIV-1 drug against a hub gene is used, just one drug suffices to take daily. Therefore, a side effect by the anti-HIV-1 drug targeting a hub gene must be reduced comparing with the one by the multiple drug therapy.

III Bottleneck-ness for anti-HIV-1 drug targets

In the previous section, as a topological condition for new targets of anti-HIV-1 drugs to satisfy, we have took up the "hub" feature of HIV-1 genes. However, the hub feature is not enough. We think the "bottleneck" feature is also important.

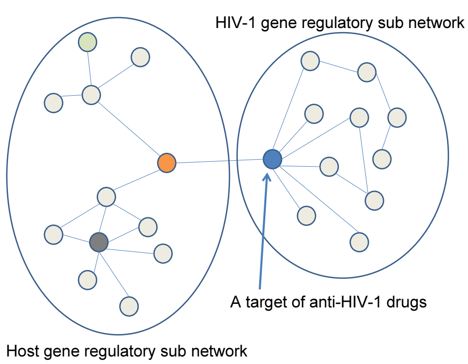

Fig. 3: A candidate of anti-HIV-1 drug targets

The reason why we have to consider the bottleneck feature is due to what HIV-1 replicates by using intracellular agents. Supposing that there exists a bottleneck HIV-1 gene connecting between a sub network composed of intracellular agents and the other sub network of HIV-1 genes, by inhibiting the bottleneck HIV-1 gene, HIV-1 could not utilize cellular agents belonging to the sub intracellular network. This means to block the HIV-1 replication. That is why we place equal importance on the bottleneck-ness and the hubness of anti-HIV-1 drug targets. Fig. 3 shows a "hub-bottleneck" HIV-1 gene which is considered to be ideal as an anti-HIV-1 drug target.

IV Conclusions

Based on logical reasoning, this study has concluded the hub-ness and bottleneck-ness are requisite topological features for anti-HIV-1 drug targets.

To demonstrate the validity of this study's discussions, we would require DNA micro-array time course data on the coexpression of HIV-1 genes and its host genes of each stage of HIV-1 virion synthesis [7]: the HIV-1 binding to the host cell, the HIV-1 uncoating, the reverse transcription from HIV-1 RNA to HIV-1 DNA, the nuclear import of HIV-1 DNA, the integration of HIV-1 DNA into the host DNA, the transcription from a pro-virus, the RNA export, the RNA translation, the assembly of HIV-1 elements, the virus RNA encapsidation, the budding of HIV-1 virions and the maturation of them. In the near future, we expect that these data will be provided in some public databases.

Acknowledgements

This study has been supported by the Grant-in-Aid for Young Scientists (B) No.18700293 of the Ministry of Education, Culture, Sports, Science and Technology (MEXT) from 2006 to 2008. We are grateful for their support.

References

[1] Horak GE, NM Qian J, Bertone P, et al (2002), Complex transcriptional circuitry at the G1/S transition in Saccharomyces cerevisiae. Genes Dev 16:3017-3033

[2] Gavin AG, Bosche M, Krause R, et al (2002), Functional organization of the yeast proteome by systematic analysis of protein complexes. Nature 415:141-147

©ISAROB 2009

[3] Yu H, Kim PM, Sprecher E, et al (2007), The importance of bottlenecks in protein networks: Correlation with gene essentiality and expression dynamics. PLoS Comput Biol 3(4):e59:713-720

[4] Albert R, Jeong H, Barabasi AL (1999), Diameter of the world wide web. Nature 401: 130-131

[5] Green WC, Peterlin B.M (2008), Molecular Biology of HIV: Implications for New Therapies. In: Volberding PA, Sande MA, Warner C, et al (ed), Global HIV/AIDS Medicine, W B Saunders Co, pp.23-38

[6] Okumura N, Hamaguchi M (2006), Careful points after HAART (in Japanese). In: Diagnosis and Treatment, 94, 12, Shindan to chiryo Co, pp.2255-2260

[7] Koyanagi Y (2005), Outline of the HIV replication and its cellular factors: the track of an invader in cell (in Japanese). Virus 55, 2:251-258

Reverse Engineering of Spatiotemporal Patterns in Spatial Prisoner's Dilemma

Takuya Ueda and Yoshiteru Ishida
Department of Knowledge-Based Information Engineering
Toyohashi University of Technology
Toyohashi, Aichi, Japan 441-8580

***Abstract*:** Many complex patterns are produced by spatial prisoner's dilemma such as spatial games [Nowak & May 92] and spatial strategies [Ishida & Mori 04]. We have studied an inverse problem of identifying a game by estimating parameters in the payoff of the game from spatiotemporal patterns.

***Keywords*:** spatial prisoner's dilemma, reverse engineering, cellular automata, fractal

1 Introduction

Many spatiotemporal patterns can be found in nature such as ice crystal, a coastal railroad and shells. A spatial game [1] can produce spatiotemporal patterns. This is an extension of well known Prisoner's Dilemma (PD) in a space dimension.

While a game in general is played by two players, a spatial game is played by multiple players. Each player is placed at a cell in a lattice and interacts with the neighbor players. Fig. 1 shows spatiotemporal patterns generated by one dimensional spatial prisoner's dilemma.

This paper deals with an inverse problem of estimating parameters of spatial game from spatiotemporal patterns (generated by the spatial game). When the space is k-dimensional lattice (k is a natural number), a spatial game can be identified as cellular automata. A spatial game process can be estimated as a transition rule of cellular automata from spatial patterns by the rule identification algorithm [3]. Hence strategies of each player can be inferred by analyzing the spatiotemporal patterns.

2 Spatial Prisoner's Dilemma and Spatiotemporal Patterns

2.1 SPD

Iterated prisoner's dilemma (IPD) iterates prisoner's dilemma N steps. Spatial prisoner's dilemma (SPD) [1, 2] is an extended IPD in spatial axis; i.e. The SPD is played by multiple players placed in the neighborhood cells in a lattice space. Here we restrict ourselves to the case of one dimensional square lattice. In our SPD, a player has a strategy and decides an action at each step based on its strategy. Each player plays with neighbor players (including itself). Score of each play will be calculated from payoff matrix (Table 1) for neighbor players within a radius r. For example, when $r = 1$ and the space is one dimensional square lattice, the number of neighborhood players is three. After every interaction, the strategy of the highest score will be copied to its neighbor players.

Table 1: Payoff matrix. ($T > R > P > S$, $2R > T + S$ and $1.0 < b < 2.0$ [2])

Player \ Adversary	C	D
C	R(1)	S(0)
D	T(b)	P(0)

All-D and All-C are the base strategies [1]. All-D (All-C) chooses D (C) every time. In addition to All-D (All-C), we will study spatial strategies such as k-D (k-C) [2]. k-D (k-C) strategy chooses D (C) when the number of players with D (C) in neighborhood exceeds k. We will also use the strategy code. The 2-D strategy, for example, can be expressed by a strategy code CCD (Table 2).

Table 2: Strategy Codes when $r = 1$ and the space is one dimensional square lattice

Number of D in neighborhood	0	1	2
Action	C	C	D

©ISAROB 2009

2.2 Spatiotemporal patterns generated by SPD

Spatiotemporal patterns found in SPD can involve many interesting ones including fractal patterns. In fact, Fig. 1 shows spatiotemporal patterns with the parameter b 1.5 in Table 1.

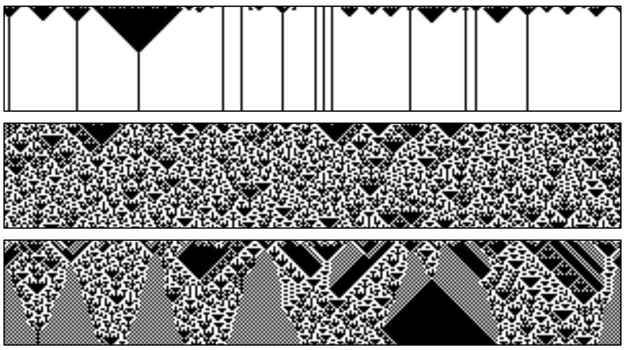

Figure 1: spatiotemporal patterns generated by one dimensional spatial prisoner's dilemma of All-D v.s. All-C. White cells cooperation and black defection. Simulation is carried out in 50 steps with a periodic boundary condition, with the space size is 300 (one dimensional square lattice) and the neighborhood radius : $r = 1$. The pattern above is a result of All-D v.s. All-C, the pattern middle is that All-D v.s. DCD and the pattern below is that of 1-D v.s. DCD. The above pattern is monotonous but the middle and the below involve fractal patterns.

3 SPD with Single Strategy as DCA

SPD can be identified as deterministic cellular automata (DCA) with D as 1, C as 0; and neighborhood radius r_{CA}. Thus we can apply the the rule identification algorithm [3] on spatiotemporal patterns of SPD. Table 3 is a result of rule identification. We use six patterns (Fig. 2) generated by a single strategy of SPD (without interaction and only action update) with payoff matrix of Table 1 and the parameter b 1.5. Each strategy has been tested assuming DCA and $r_{CA} = 1$.

When two strategies are involved, rules cannot be identified as DCA with a binary state and $r_{CA} = 1$. Only in the case of All-C v.s. All-D, rules can be identified as DCA with a binary state and $r_{CA} = 2$).

Table 3: Results of rule identification when single strategy is used. Rules are represented by Wolfram's numbering [5].

Strategy	2-D	CDC	1-D	DCC	DCD	DDC
Rule No.	160	90	250	5	155	95

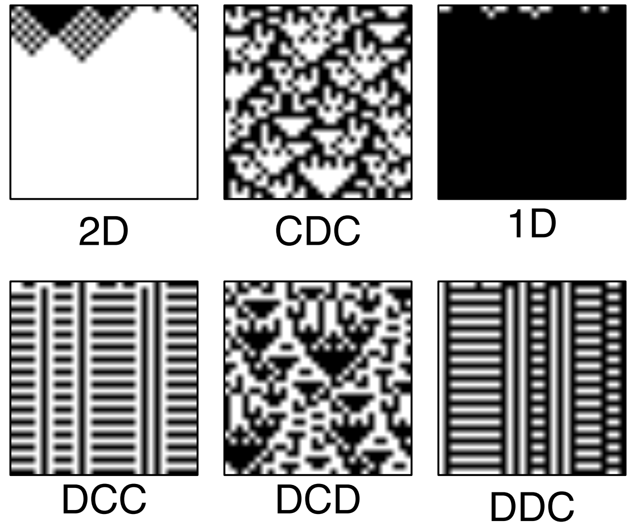

Figure 2: Spatiotemporal patterns generated by a single strategy of SPD with initial random seeds.

4 Estimating the payoff matrix When All-C v.s. All-D

Fig. 3 shows spatiotemporal patterns of All-C v.s. All-D when b is varied. The lattice size is 30 with a periodic boundary condition and simulations are carried out in 30 steps. Cs and Ds are seeded random with an equal probability initially. Table 4 lists the rules identified from the spatiotemporal patterns of Fig. 3. When $1.0 < b \leq 1.5$, rule is identified as $(ECF4EE30)_{16}$ and when $1.5 < b < 2.0$ as $(ECF4EF34)_{16}$. Thus the rule of SPD with All-C v.s. All-D can be identified as either $(ECF4EE30)_{16}$ or $(ECF4EF34)_{16}$ when $r_{CA} = 1$. In other word, we can estimate the range of the parameter b from spatiotemporal patterns generated by All-C v.s. All-D.

Table 4: Rule identification in the case of All-C v.s. All-D when the parameter b varied.

b	1.1	1.3	1.5	1.6	1.7	1.9
Rule No.	$(ECF4EE30)_{16}$			$(ECF4EF34)_{16}$		

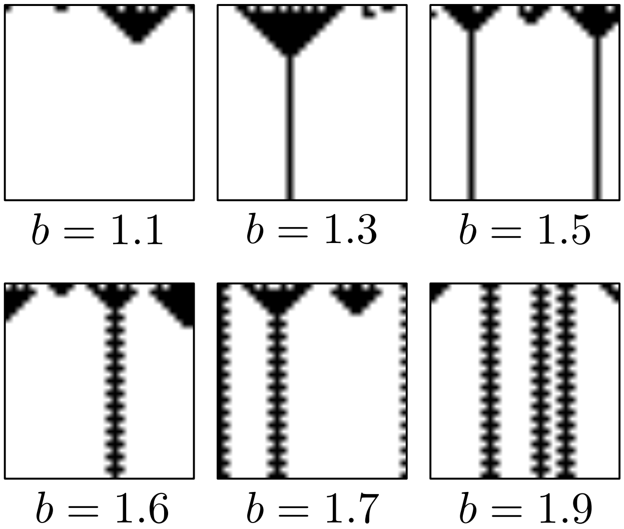

Figure 3: spatiotemporal patterns generated by All-C v.s. All-D in one dimensional lattice with a periodic boundary condition.

5 SPD with Multiple Strategies as PCA

When SPD is analyzed by the probabilistic rule identification algorithm [3], SPD with multiple strategies can be identified as probabilistic cellular automata (PCA) with a binary state and $r_{CA} = 2$ (Table 5).

Table 5: Rule of PCA. p_l indicates the probability of being D.

DDDDD	DDDDC	$\cdots$	CCCCD	CCCCC
p_{31}	p_{30}	$\cdots$	p_1	p_0

Table 6 shows identified rules of SPD as a rule of PCA when All-D v.s. 2-D.

Table 6: SPD identified as a rule of PCA when All-D v.s. 2-D with parameters: lattice size : 500, time steps : 500 steps and b : 1.5. These results are the average of trials of thousand times.

Rule ($r_{CA} = 2$) $p_{31}, p_{30}, \cdots p_0$
1.00, 1.00, 0.48, 0.00, 1.00, 1.00, 0.00, 0.00, 0.49, 0.50, 0.46, 0.49, 0.00, 0.49, 0.00, 0.00, 1.00, 1.00, 0.50, 0.00, 1.00, 1.00, 0.49, 0.00, 0.00, 0.00, 0.49, 0.70, 0.00, 0.00, 0.00, 0.00

6 Estimating the Payoff Matrix with All-D v.s. Other Strategies using PCA

Since SPD with All-C v.s. All-D can be identified as DCA, we can estimate range of the parameter b. But other cases (such as All-D v.s. 1-D) cannot be identified as DCA. However, these cases can be identified as PCA and we can estimate range of the parameter b as well (except the case : All-D v.s. 1-D). Fig. 4, 5 and 6 are binary trees showing stimated range of the parameter b in each game. We can find range of the parameter b by tracing the tree with conditional branches of probability p_l. For example, the parameter b in the case of All-D v.s. 2D with $p_9 \neq 0, p_{18} \neq 0, p_2 = 0, p_8 = 0$ is estimated within the range of $1.0 < b \leq 1.5$.

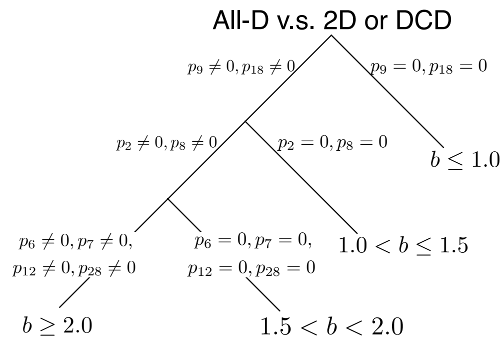

Figure 4: A binary tree showing estimated range of the parameter b when All-D v.s. 2-D or DCD.

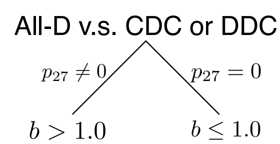

Figure 5: A binary tree showing estimated range of the parameter b when All-D v.s. CDC or DDC.

7 Estimating Strategies from Spatiotemporal Patterns

Since SPD with single strategy can be identified as DCA, we can infer strategies of each player. Fig. 7 above is a spatiotemporal pattern generated by 1-D v.s. DCD. Both below left and right figures in Fig. 7 is a part the pattern above. Table 7 lists a result

©ISAROB 2009

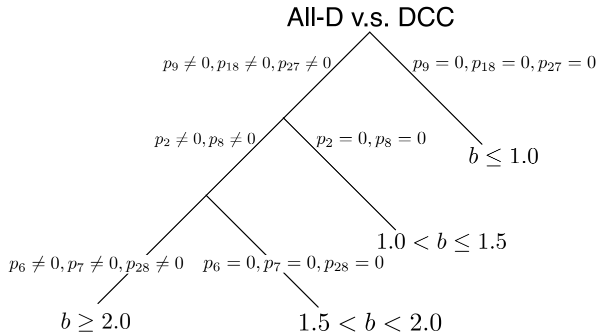

Figure 6: A binary tree showing estimated range of the parameter b when All-D v.s. DCC.

of the rule identification from the strategy cluster-A, and Table 8 from the strategy cluster-B. Upper rows of each table indicate the neighborhood configuration (i.e. CCC) and lower rows indicate the next state of the center. The symbol u (unknown) means that the state cannot be identified from the spatiotemporal patterns. The strategy of cluster-A is 1-D strategy (Table 7), and that of cluster-B is DCD strategy (Table 8). By analyzing a cluster of the spatiotemporal pattern, we can infer possible strategies that could generate the pattern.

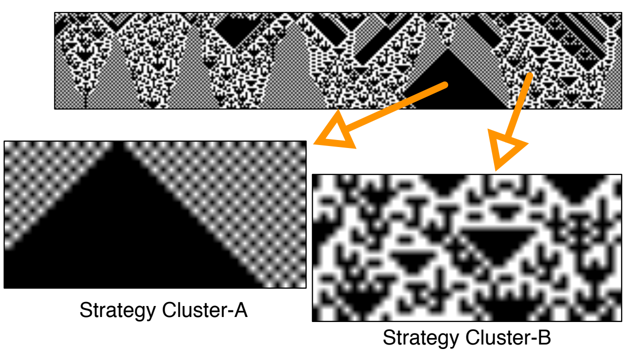

Figure 7: A spatiotemporal pattern generated by 1-D v.s. DCD (above) and its enlarged clusters (below).

Table 7: Identified rule of the cluster-A.

DDD	DDC	DCD	DCC	CDD	CDC	CCD	CCC
D	D	D	u	D	C	u	u

Table 8: Identified rule of the cluster-B.

DDD	DDC	DCD	DCC	CDD	CDC	CCD	CCC
D	C	D	C	C	D	C	D

8 Conclusions

Spatial prisoner's dilemma (SPD) may be considered as cellular automata (CA). Since a reverse engineering on spatiotemporal patterns generated by CA allows recognizing the possible rule generating the patterns, we can likewise infer the possible strategy underlying the game by reverse engineering on the spatiotemporal patterns generated by SPD. We regarded SPD with single spatial strategy as deterministic cellular automata (DCA); and SPD with multiple strategies as probabilistic cellular automata (PCA). Spatiotemporal patterns generated by SPD include sufficient information to estimate range of parameters of SPD (hence identifying the game played when an appropriate space-time frame is used).

Acknowledgments

We are grateful to Hisashi Ohtsuki for the important discussion. This work was supported in part by Grants-in-Aid from Toyohashi University of Technology and CASIO Science Promotion Foundation.

References

[1] M. A. Nowak and R. M. May, "Evolutionnary games and spatial chaos," *Nature*, Vol. 359, p.p.826-829, 1992.

[2] Y. Ishida and T. Mori, "Spatial Strategies on a Generalized Spatial Prisoner's Dilemma," *Artificial Life and Robotics*, Vol. 9, p.p.139-143, 2004.

[3] Y. Ichise and Y. Ishida, "Reverse Engineering of Spatial Patterns in Cellular Automata," *Artificial Life and Robotics*, 2009 to appear.

[4] J.J. von Neumann, *Theory of Self-Reproducing Automata*, edited and completed by A. Burks, *University of Illinois Press*, Champaign, 1966

[5] S. Wolfram, "Universality and Complexity in Cellular Automata," *Physica D*, Vol.10, pp.1-35, 1984

The Fourteenth International Symposium on Artificial Life and Robotics 2009 (AROB 14th '09),
B-Con Plaza, Beppu, Oita, Japan, February 5 - 7, 2009

Using Spatial Strategies to Model Agents' Commitments for a Protocol Formation

Nguyen Duc Thien[1], Yuji Katsumata[1], Masahiro Tokumitsu[1], Yoshiteru Ishida[1,2]

[1]*Department of Knowledge-based Information Engineering*
[2]*Intelligent Sensing System Research Center*
Toyohashi University of Technology,
Tempaku, Toyohashi, 441-8580 Japan

Abstract: In spatial strategies of a spatial prisoner's dilemma (Ishida and Mori '05), it is possible to involve not only geographical configuration of countries but many other relation such as economical relation, historical relation, military relation and so on if they can be expressed by a network. This paper explores the possibility of modeling the agents' commitments using the spatial strategies. Several types of spatiotemporal strategies are discussed in a context of protocol formation in the international communities.

Keywords**:** spatial prisoner's dilemma, spatial strategy, international politics, protocol formation

I. INTRODUCTION

The game theoretical analysis of international problems has received increasing attention in recent years. This paper tries to model the organizing process in a protocol formation using different strategies of a spatial prisoner's dilemma (SPD), as observed in organization of international protocols and agreements such as protocols in the environment problem, free trade agreements, the nuclear non-proliferation treaty and so on. Nowadays, there appear an increasing number of international protocols and agreements on greenhouse gases emission, global warming, nuclear weapons and so on which are not agreed and cooperated by all countries. On the gases emission for example, since the impact of a country on the global pollution level is rather small, each country is reluctant to reduce the emission. Therefore, the reluctant structure is similar to a SPD. The similarity can be conspicuous when cooperation/defection in SPD is corresponded to agreeing/rejecting the protocol.

In this paper, we use a two dimensional lattice to represent spatial circumstances such as geographical configuration of countries, economic circumstance, historical background, military position and so on. On the lattice, we explored the possibility of modeling the agents' commitments using the spatial strategies. A few typical spatial strategies are discussed in a context of protocol formation in international communities.

II. BASIC MODEL

1. The Prisoner's dilemma

Prisoner's dilemma (PD) is a game played by two players with two actions: cooperation C, or defection D (Table 1). If both cooperate, they gain payoff ***R*** (reward) whereas if both defect, they gain payoff ***P*** (punishment) lower than ***R***. But if one player defects when the adversary cooperates, then the defector gains payoff ***T*** (temptation) which is higher than ***R*,** whereas the cooperator's payoff ***S*** (sucker) is the smallest (1). When one player defects, it always gains a higher payoff than that when it cooperates. However, if both players defect, they gain a lower payoff than that when they both cooperate.

In iterated prisoner's dilemma (IPD), PD is carried out repeatedly where double ***R*** higher than ***T*** plus ***S*** (2). Players with possibly distinct strategies are placed at each cell in a lattice. The strategy will determine the next action based on a spatial configuration of C and D in the neighborhood. We called the strategies as spatial strategies (Ishida and Mori '05) in SPD.

$$T > R > P > S \tag{1}$$

$$2R > T + S \tag{2}$$

Table 1. The payoff matrix of the PD game

		Player 2	
		C	*D*
Player 1	*C*	***R, R***	***S, T***
	D	***T, S***	***P, P***

©ISAROB 2009

2. Modeling

We first present a model of an SPD in which $N \times N$ - countries (agents) as players can either cooperate, C or defect, D in a square lattice space with the size $N \times N$. All the countries are divided into two classes: $\boldsymbol{q}$ majors and the rest $N \times N$ -$\boldsymbol{q}$ minors. They are placed at each lattice. Each player interacts with $\boldsymbol{n}$ neighbors (the Moore neighborhood is used, hence eight neighbors). We use the periodic boundary condition. Each country has its own spatial strategy and action. Spatial strategy determines the next action depending upon the spatial pattern of actions in the neighbors. Each country gains the payoff corresponding to their actions after they play the PD game with the neighbors.

Major countries act as major powers. They have a power of influence to make minor countries follow. In this model, the major countries use either All-C (C major) or All-D (D major), and have a higher weight w ($1 \leq w \leq 50$) than minors.

Minor countries have a spatial strategy of ***k***-D (See the next section 3), which determines the next actions based on the neighbors' actions.

Table 2 lists the payoff matrix used. The parameter ***b*** is set to be a minimal value that allows All-D to expand. Fig.1 illustrates a calculation on how to define the parameter [2].

Table 2. The payoff matrix

		Adversary	
		C	*D*
Country	*C*	$R=1$	$S=0$
	D	$T=b$	$P=0$

The score of each country is calculated by summing up all the scores received from PD game with its neighbors (including the self [2]). After ***s*** (strategy update cycle) steps of interactions with the neighbors, the minor country updates its strategy to the strategy that earned the highest score in the neighbors. The strategy update cycle ***s*** is set to be 1 throughout this paper.

3. *k*-D Strategies

The minor countries take ***k***-D strategies to make decisions based on the spatial pattern of actions (C/D) in

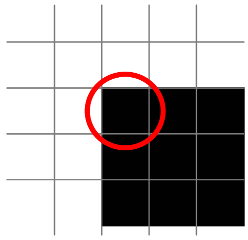

Fig.1 How to calculate the parameter b. C and D are indicated as white and black cells respectively. For All-D in the corner (indicated by the circle) to gain the profit higher than the cooperators, b must satisfy 5b > 9 since the highest payoff of the cooperators is 9.

the neighbors [1, 2]. The integer ***k*** (of ***k***-D) indicates the spatial version of the generosity (how many D actions in the neighbor are tolerated). The ***k***-D strategy determines the next action based on the number of D actions in the neighbor. The ***k***-D strategy will take D if $l \geq k$ where ***l*** is the normalized and weighted sum (with weight ***w***) of Ds in the neighbor excluding the self, and will take C otherwise. Let ***g*** be the number of majors with All-D strategy, hence with D action, and ***h*** be the number of minors with D action then the normalized and weighted sum ***l*** can be expressed as follows:

$$l = \frac{gw+h}{q(w-1)+n} n \tag{1}$$

where ***n*** is the number of neighbors and ***q*** is the number of major countries.

Fig. 2 illustrates example of the action update with a ***k***-D strategy. The country (gray) changes its action to C because the normalized weight ***l*** does not exceed ***k***.

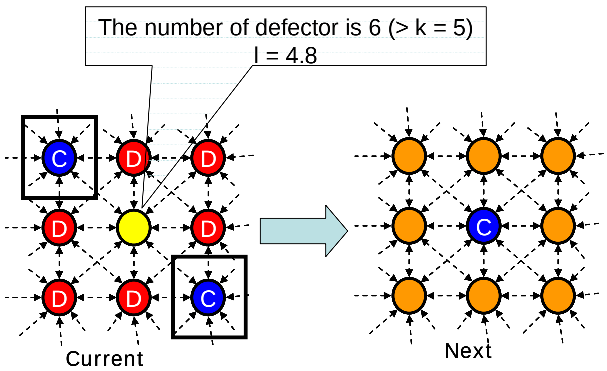

Fig.2. An example of an action update of a *k*-D strategy where *k*=5, *l*=4.8, and weight *w*=2. The black rectangle indicates a major country.

©ISAROB 2009

III. SIMULATIONS

Simulations are conducted with the parameters listed in Table 3. We investigate if the protocol formation (C cluster) is observed when minor countries surround the major countries. We are interested to see if the existence of major countries, those with the All-C strategy (C major) in particular, can enhance the formation of C-cluster or not.

Table 3. List of parameters for simulations

Name	Value
Number of countries N (Lattice size)	50×50
Generosity of k-D strategies	$1 \le k \le 9$
Number of majors q	0,1,5,10,30,50
Ratio of All-C major and All-D	1:1
Weight w of major	1,2,5,10,20,30,50
Bias b for defection in the payoff matrix in Table 2	1.81
Time steps (t)	100
Number of trials	10

In the interaction between All-D vs. ***k***-D rather than All-D vs. All-C (as in Nowak-May's SPD), the clusters of ***k***-D form a membrane (gray) of action D protecting the inner cluster of action C (white). The membrane formation occurs as in our simulation within a certain parameter scope of ***k*** (spatial generosity) and ***b*** [2].

Fig. 3 shows an example of snapshots of the cases where the membrane is formed with both C major country and D major country involved. The membranes of C clusters are not broken in Fig. 3(b) even if it expands through the C major (indicated by the circle). It means that the action (power) of the major country does not affect the neighbors, because the major's effect is almost the same as those with the minors (with the ***k***-D strategies) when the weight ***w*** is low enough. On the other hand, the membrane of C clusters (Fig. 4(b)) is broken when it expanded through the C major country (indicated by the circle). The C major country made the minors in the corner select the action C, because the power of the major country is influential with the high weight ***w***, hence making the normalized and weighted sum relatively small. The D major country made the surrounding minors with the ***k***-D strategy select D

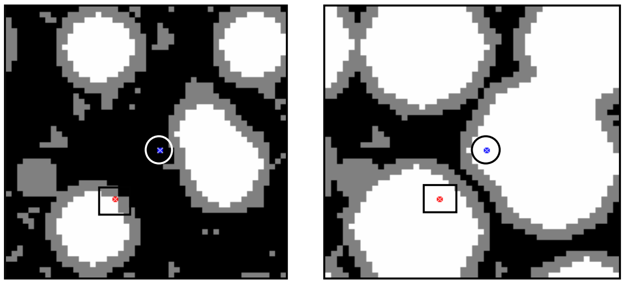

(a) Steps = 12 (b) Steps = 21

Fig.3. Two snapshots showing that membranes are protecting C-clusters with the 6-D strategy where and number of major is 1 for C and D major and weight is 2. Black (white) and gray cells indicate defector (cooperator) and defector of k-D, respectively. Cells in the circle (rectangle) indicate D (C) major.

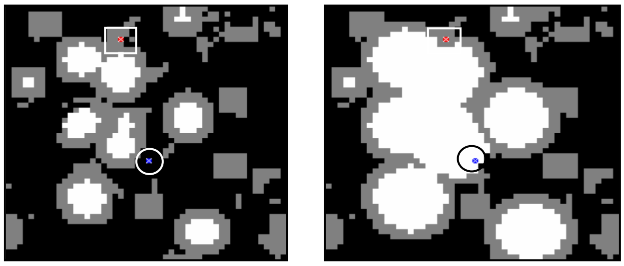

(a) Steps = 6 (b) Steps = 12

Fig.4. A snapshot of breaking membrane where number of major is 1 and weight is 50

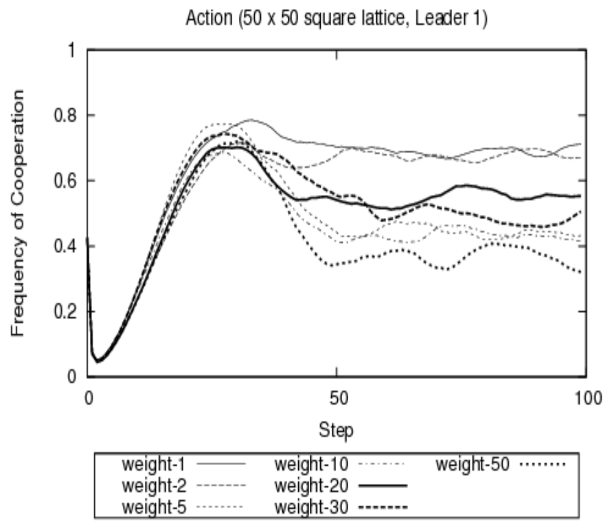

Fig.5. Frequency of cooperators with one C major country and one D major country.

action, because they are affected by the power of the major when the weight ***w*** is high enough.

When the weight ***w*** is low enough, D major countries (indicated by the rectangle) can exploit their neighbors (Fig. 3(b)), because the neighbors are

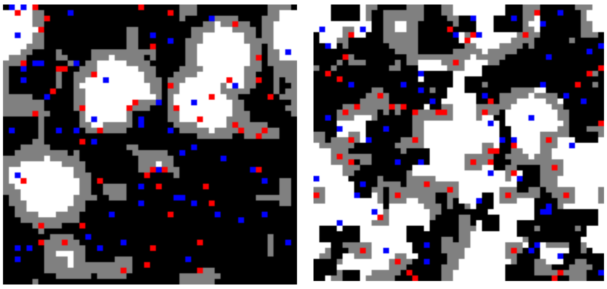

(a) Weight = 2 (b) Weight = 50

Fig.6. A comparison of membrane formation when the weight varies and the number of major is set to be 50.

cooperators. When the weight ***w*** is high enough, however, the neighbors of D major countries exploit their C neighbors, while the D major countries themselves cannot.

Fig. 5 shows the time evolution of cooperator's frequency when the weight ***w*** varies with one C major country and one D major county. The fraction of cooperators becomes larger as the weight ***w*** becomes lower. The membrane can grow without being affected by the majors when the weight is low (Fig. 6(a)). When the weight is high enough, however (as in Fig. 6(b)), the membrane is broken by the D major countries, because the power D major country is strong enough, hence breaching the membrane. Fig. 6 shows a snapshot with weight 2 and that with weight 50, corresponding to those weights in Fig. 5.

IV. DISCUSSION

In the real world, the countries confront to the situation that they have to agree/reject being affected by major countries in the neighbor. Computer simulations revealed that the minors are affected by their neighbor majors when they have enough power. We observed the minor countries implementing the spatial strategy *k*-D can form C-clusters by being protected by a membrane when the influence of major is low enough. However, the fraction of cooperators decreases as the weight of the majors increases (Fig.5). In the problem of organizing international protocols such as Kyoto Protocol, the number of agreed countries tends to be low possibly due to influential majors, or due to too low benefit in the payoff matrix.

V. CONCLUSIONS

This paper applied Prisoner's Dilemma (PD) to the problem of international cooperation in organizing protocols and agreements such as protocols in environment problems, free trade agreements, and the nuclear non-proliferation treaty and so on. We used a spatial strategy *k*-D for minors and the fixed strategy All-C or All-D for majors. The influence of countries is tuned by the weight parameter in counting the number of actions in the neighbor.

Computer simulations with the model revealed that there are cases when the existence of cooperating major countries could hamper the formation of cooperative clusters.

ACKNOWLEDGEMENTS

This work was supported in part by The Japan International Cooperation Agency (JICA) and Grants-in-Aid from Toyohashi University of Technology.

REFERENCES

[1] Ishida Y and Mori T (2005), Spatial strategies in a generalized spatial prisoner's dilemma, Artificial Life and Robotics, 9: 139-143
[2] Katsumata Y and Ishida Y (2008), On a membrane formation in a spatio-temporally Generalized Prisoner's Dilemma, ACRI 2008, Volume 5191/2008: 60-66
[3] Imhofa LA, Fudenbergb D, Nowak MA (2007), Tit-for-tat or win-stay, lose-shift? Journal of Theoretical Biology 247: 574-580

A time-dependent threshold condition to determine an onset of AIDS

Kouji Harada
Dept. of Knowledge-based Info. Engr.
Toyohasi University of Technology,
1-1, Tenpaku, Toyohashi-shi, Aichi
441-8585, Japan
(E-Mail: harada@tutkie.tut.ac.jp)

Yoshiteru Ishida
Dept. of Knowledge-based Info. Engr.
Toyohasi University of Technology,
1-1, Tenpaku, Toyohashi-shi, Aichi
441-8585, Japan
(E-Mail: ishida@tutkie.tut.ac.jp)

Abstract

The present study first considers the effect of "non-infectious" HIV-1 due to fatal mutations in HIV-1 population dynamical models, and the analyses of the model reveal AIDS develops when the number of HIV-1 strains, i.e. antigenic diversity is over a "time-dependent" threshold. This result is quite interesting because it suggests a possibility of an onset of AIDS being dynamically determined. This dynamic behavior of the threshold may make the prediction of AIDS development difficult.

Keywords

HIV-1, Antigenic diversity threshold, noninfectious HIV-1, Double edged sword

I Introduction

AIDS is an infectious disease with HIV-1 and has still been a threat for mankind. HIV-1's proliferation processes are very subtle. HIV-1 infects its host ($CD4^+$Tcell) through a complimentary binding of a GP-120 molecule on its membrane to a CD4 receptor molecule on the host's membrane. Once inside the host cell, a reverse transcriptase of HIV-1 starts to transcribe HIV-1's RNA genome into cDNA. By referring to the cDNA sequence, a double stranded HIV-1 DNA is elaborated, then it is inserted into the host's DNA. Subsequently genetic machineries of the host cell are manipulated to produce mRNA copies of the viral genome and some functional molecules necessary for the synthesis of new HIV-1 particles. After the enough production of such requisite molecules, new HIV-1 particles are assembled inside the host cell. Finally they bud from the host cell; the host cell will be killed[1].

The present study focuses on an inaccurate transcription of the reverse transcriptase[2] and it leads to put HIV-1 in so-called a "double edged sword" situation. It is known that GP-120 gene is coded in HIV-1 RNA genome; some experimental study reports a transcription accuracy of the reverse transcriptase is very low (10^{-4} mutations/basepairs/replication cycle [3]). Thus, in a transcription process, some mutations must occur on GP-120 gene. In other words, a phenotype of a newly synthesized GP-120 molecule must change (see. Fig.1). GP-120 molecule is a requisite molecule for the infection to the host cell, as well as a target molecule (i.e. antigen) for the immune system. So a phenotypic change of a GP-120 molecule by some mutations may give HIV-1 a possibility to escape a specific immune response; it may deprive an infectious ability from HIV-1. That is "double edged sword" situation. By introducing an "noninfectious" HIV-1, the present model considers "double edged sword" situation[4][5].

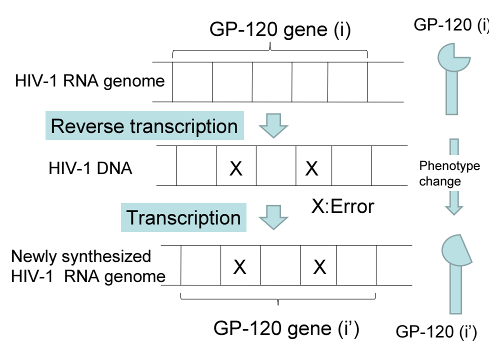

Fig. 1: Mutations on GP-120 gene by a reverse transcriptase

Our study is based on Nowak and May's original work[6]. Our originality is to introduce the noninfectious HIV-1 they did not consider. Their works pro-

©ISAROB 2009

posed antigenic diversity threshold theory[6]. The theory suggests there exists a threshold on the diversity of HIV-1 strains and mentions AIDS develops when the number of HIV-1 strains is over the threshold. Meanwhile the present study demonstrates there exists a threshold for an onset of AIDS despite the introduction of the noninfectious HIV-1. However, the threshold has a time dependency. This point is quite different from the Nowak and May's result: their derived threshold is invariant on time[6]. This time dependency reflects the effect of considering the noninfectious HIV-1, in other words, the double edged sword situation.

II Model

Our proposed model is the following system described as ordinary differential equations:

$$\begin{aligned} \dot{v}_i &= -px_iv_i + \sum_{j=1}^{L} Q_{ij}bv_j \qquad i = 1\dots M & (1)\\ \dot{x}_i &= kv_i - uvx_i \qquad\qquad i = 1\dots M, & (2)\\ v &= \sum_{i=1}^{M} v_i. & (3) \end{aligned}$$

Let v_i denote the population size of HIV strain (or mutant) with the antigen (GP-120) i (we simply call it "HIV strain i") and let x_i denote the magnitude of the specific immune response against the HIV strain i. The differential equation (1) describes a population dynamics of the HIV-1 strain i. The first term means an immune response against the antigen i eliminates the HIV-1 strain i at the rate px_iv_i. The second term means the HIV-1 strain j mutates into the HIV-1 strain i with a definite mutation probability, Q_{ij}. Also an error free replication of HIV-1 strain i is given by $Q_{ii}bv_i$ (Fig. 2).

Our model consists of N different HIV-1 strains by considering the type of antigen (i). M strains ($1 \leq i \leq M$) out of them are survival ones (holding an ability to infect a host cell); the left strains ($M+1 \leq i \leq N$) are noninfectious ones (Fig. 2). From the modeling assumptions, the probability Q_{ij} satisfies the following condition:

$$\sum_{i=1}^{N} Q_{ij} = 1 \qquad (4)$$

and

$$\sum_{i=1}^{M} Q_{ij} < 1 \qquad (5)$$

Meanwhile, the differential equation (2) describes a time evolution of magnitude of an immune response specific for the HIV-1 strain i. The first term means an immune response is stimulated at the rate kv_i, which is proportional to the abundance of the HIV-1 strain i. The second term means the immune response weakens through the decrease of CD4 positive T cells infected by any of HIV-1 strains.

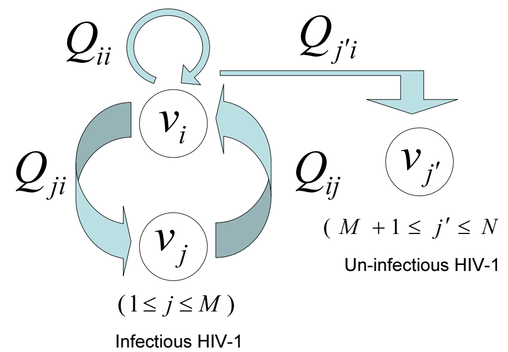

Fig. 2: Schematic view of HIV-1 mutation dynamics

III Time-dependent threshold condition

As the most fundamental case of the proposed model, this study deals with two HIV-1 strains model, i.e. $M = 2$. This section derives conditional equations controlling an onset of AIDS defined as divergence of the total HIV-1 population.

It assumes the variable x_i converges faster to a steady-state level than the variable v_i does. Thus let $\dot{x}_i$ be zero then we obtain $x_i = \frac{kv_i}{uv}$. Substituting x_i into the Eq.(1), we obtain this equation:

$$\begin{aligned} \dot{v}_i &= \sum_{j=1}^{2} Q_{ij}bv_j - \frac{pk}{uv}v_i^2 \\ &= \phi(\sum_{j=1}^{2} w_{ij}v_j - \frac{v_i^2}{v}), \qquad (6) \end{aligned}$$

where $w_{ij} = \frac{Q_{ij}b}{\phi}$ and $\phi = \frac{pk}{u}$.

©ISAROB 2009

Let $\frac{v_i}{v}$ represent $\bar{v_i}$ and we first examines the time evolution of $\bar{v_1}$. Eq.(6) yields

$$\frac{\dot{v_i}}{v} = \phi(\sum_{j=1}^{2} w_{ij}\bar{v_j} - \bar{v_i}^2) \tag{7}$$

Here, concerning to $\dot{\bar{v_1}}$, the following equation:

$$\dot{\bar{v_1}} = (1-\bar{v_1})\frac{\dot{v_1}}{v} - \bar{v_1}\frac{\dot{v_2}}{v} \tag{8}$$

succeeds. Substituting Eq.(7) into Eq.(8), then

$$\begin{aligned} & \dot{\bar{v_1}} \\ = \; & \phi\left((1-\bar{v_1})(\sum_{j=1}^{2} w_{1j}\bar{v_j} - \bar{v_1}^2) - \bar{v_1}(\sum_{j=1}^{2} w_{2j}\bar{v_j} - \bar{v_2}^2)\right) \\ = \; & \phi F(\bar{v_1}) \end{aligned} \tag{9}$$

is obtained. Here $F(\bar{v_1})$ is defined as a third-order expression of the variable $\bar{v_1}$,

$$\begin{aligned} F(\bar{v_1}) = & (1-\bar{v_1})(w_{11}\bar{v_1} + w_{12}(1-\bar{v_1}) - \bar{v_1}^2) \\ & -\bar{v_1}(w_{21}\bar{v_1} + w_{22}(1-\bar{v_1}) - (1-\bar{v_1})^2). \end{aligned} \tag{10}$$

The time evolution of the variable $\bar{v_1}$ is determined by a shape of the function $F(\bar{v_1})$. The function has the following characters:

- The coefficient of $\bar{v_1}^3$ is positive.
- The value of $F(0)$ is w_{12} (>0).
- The value of $F(1)$ is $-w_{21}$ (<0).

These characters suggests there exists $\bar{v_1}^*(0 < \bar{v_1}^* < 1)$ satisfying $F(\bar{v_1}^*)$ is equal to zero. Therefore, the next conditions:

- $F(\bar{v_1}) > 0$ if $0 < \bar{v_1} < \bar{v_1}^*$,
- $F(\bar{v_1}) < 0$ if $\bar{v_1}^* < \bar{v_1} < 1$,

succeed. These conditions imply that the variable $\bar{v_1}$ converges to the value $\bar{v_1}^*$ when the time t goes to the infinite.

Next, we derive a condition on an onset of AIDS defined as divergence of the total HIV-1 population $v(= v_1 + v_2)$.

From Eq.(6), the temporal differentiation of v is described as:

$$\dot{v} = \phi(-\frac{v_1^2 + v_2^2}{v} + \alpha_1 v_1 + \alpha_2 v_2), \tag{11}$$

where $\alpha_i \equiv \sum_{j=1}^{2} w_{ji}(i = 1, 2)$. Furthermore,

$$\begin{aligned} & \frac{d}{dt}(\ln(v)) = \frac{\dot{v}}{v} \\ = \; & \phi(-(\bar{v_1}^2 + \bar{v_2}^2) + \alpha_1\bar{v_1} + \alpha_2\bar{v_2}) \\ = \; & \phi(-(\bar{v_1}^2 + (1-\bar{v_1})^2) + (\alpha_1 - \alpha_2)\bar{v_1} + \alpha_2)) \\ = \; & \phi(-S(\bar{v_1}) + H(\bar{v_1})) \\ = \; & \phi G(\bar{v_1}), \end{aligned} \tag{12}$$

where $G(\bar{v_1}) \equiv -S(\bar{v_1}) + H(\bar{v_1})$, $H(\bar{v_1}) \equiv (\alpha_1 - \alpha_2)\bar{v_1} + \alpha_2$ and $S(\bar{v_1}) \equiv \bar{v_1}^2 + (1-\bar{v_1})^2$. $S(\bar{v_1})$ is called "Simpson index" which is an inverse measure for "antigenic diversity $D(\bar{v_1})$"; $S(\bar{v_1})$ takes a value between 1/2 and 1.

According to the above discussion, the variable $\bar{v_1}$ converges to $\bar{v_1}^*$ $(0 < \bar{v_1}^* < 1)$; there exist the specific time T_0 satisfying $\bar{v_1}(t) \approx \bar{v_1}^*$ $(t \geq T_0)$. Therefore, after the integration of Eq.(12) from the time T_0 to $T(T \gg T_0)$, we obtain

$$\ln\frac{v(T)}{v(T_0)} = \phi\int_{T_0}^{T} G(\bar{v_1})\cdot dt \approx \phi G(\bar{v_1}^*)(T - T_0). \tag{13}$$

From Eq.(13), we can conclude the followings:

1. $\lim_{T\to\infty} v(T) = \infty$ when $G(\bar{v_1}^*) > 0$ i.e. $D(\bar{v_1}^*) > 1/H(\bar{v_1}^*)$,
2. $\lim_{T\to\infty} v(T) = 0$ when $G(\bar{v_1}^*) < 0$ i.e. $D(\bar{v_1}^*) < 1/H(\bar{v_1}^*)$.

The first and the second cases respectively corresponds to conditions of AIDS development and of AIDS suppression. Interestingly, these analyses clarifies there exist the threshold: $1/H(\bar{v_1}^*)$ on the antigenic diversity $D(\bar{v_1})$. It is worth noting that a value of the threshold depends on the time evolution of the variable $\bar{v_1}$. This time-dependency of the threshold is quiet different from Nowak and May's results; their derived threshold is time-independent. This difference is due to the effect of "double edged sword" because if the effect is not considered(i.e. $M = N$), the threshold become a constant value (1).

IV Conclusions

The present study has first considered the effect of "double edged sword" situation concerning to HIV-1 strategy, and the analyses have revealed AIDS development depends on the "time-dependent" threshold on the antigenic diversity. This result is quite interesting because it suggests a possibility of onset of AIDS being dynamically determined. This dynamic behaviour of the threshold may make the prediction of AIDS development difficult.

Acknowledgements

This study has been supported by the Grant-in-Aid for Young Scientists (B) No.18700293 of the Ministry of Education, Culture, Sports, Science and Technology (MEXT) from 2006 to 2008. We are grateful for their support.

References

[1] Green WC, Peterlin B.M (2008), Molecular Biology of HIV: Implications for New Therapies. In: Volberding PA, Sande MA, Warner C, et al (ed), Global HIV/AIDS Medicine, W B Saunders Co, pp.23-38

[2] Preston BD, Poiesz BJ, Loeb LA (1988), Fidelity of HIV-1 reverse transcriptase. Science Nov 25;242(4882):1168-71

[3] de Mercoyrol L, Job C, Job D (1989), Studies on the inhibition by alpha-amanitin of single-step addition reactions and productive RNA synthesis catalysed by wheat-germ RNA polymerase II. Biochem J Feb 15;258(1):165-169

[4] Domingo E (2000), Viruses at the Edge of Adaptation. Virology 270:251-253

[5] Holland JJ, Domingo E (1998), Origin and Evolution of Viruses. Virus Genes 16: 13-21

[6] Nowak MA, RM May (1991), Mathematical biology of HIV infections: antigenic variation and diversity threshold. Math Biosci 106: 1-21

©ISAROB 2009

The Fourteenth International Symposium on Artificial Life and Robotics 2009 (AROB 14th '09),
B-Con Plaza, Beppu, Oita, Japan, February 5 - 7, 2009

Quadruped Virtual Robot Simulation in Virtual Environment Obeying Physical Law

Kouki MIYOSHI, Norihiro ABE, Yoshihiro TABUCHI
Kyusyu Institute of Technology
680-4 Kawazu, iizuka, Fukuoka 820-8502, Japan
Email:miyosi@sein.mse.kyutech.ac.jp

Hirokazu TAKI
Wakayama University
930 Sakaedani, Wakayama-shi
Wakayama 680-8510, Japan
Email: taki@sys.wakayama-u.ac.jp

Shoujie He
VuCOMP
Richardson, Texas, USA
Email: hesj@computer.org

***Abstract*:** In the development of a robot, the validation of a robot with use of real machinery takes much cost and time. Especially it is difficult to validate a robot's behavior at the unsafe place. Then developers have paid attention to virtual debugging. Using a program validated in VR space makes verification of a real machine's behavior more efficient.

In this research, we have a virtual robot walk on a road autonomously by using the program that the virtual robot tracks a line on virtual environment.
Keywords: *VR, Virtual Robots, Virtual Space*

1. INTRODUCTION

In the last few years, many robots are advancing to human society with the development of robot industry, and a robot is expected to be a member of the general public in the near future. However the validation of robot motion control with using real machinery takes much cost and time to develop a real robot and no one deploys any robots in dangerous environment for fear of damage owing to violent fall or collision. If robots damage in real space, it will compel us to pay much time and expense for fixing robots. This will increase in necessary expense and length of a period for robot development.

Then virtual debugging using virtual reality space has gotten attention. Virtual debug enables developers to validate the robot motion in dangerous environment in parallel with development of a real machine after deciding the specification and design of a robot. A debug of a control program using a real machine debug will be shortened using the control program that successfully operates in virtual debug.

In this research, we have a virtual four legged robot built in virtual space based on physics move autonomo usly in a dangerous environment. By analyzing images c aptured with two cameras installed on the four legged ro bot, we have it track a line on the environment including bridges and up down-hills and walk on a road whose edges are white lines.

2. Construction of Virtual Reality Space

In the simulation, it is necessary to construct th e virtual reality space based on a physical rule bec ause of making virtual environment same as real on e as far as possible. So we use the rigid physics c alculation library, Vortex (developed by CMLabs Si mulations, Inc.) to build the virtual reality space. V ortex has the function to create a basic object like plane, box, corn, sphere, and cylinder. We enable to give a constant restraint between objects by using joint. We are able to create a composite object wit h the use of two or more basic objects. Combinatio n of composite objects and joint enables to express a complex object like robot and car.

3. Expression of Virtual Robot

In this research, servomotors of virtual quadruped robot are expressed with a hinge joint between two rectangular solids and two boxes as shown in Fig.1.

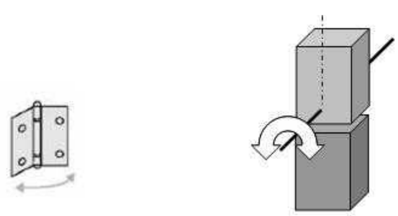

(a) Hinge joint (b) Servomotor
Fig.1. A Virtual Servomotor

©ISAROB 2009

A virtual quadruped robot is composed by 13 composite objects and 12 hinges concatenating them. Shoulders, upper legs, and lower legs consist of boxes and cylinders. These parts are linked with a hinge joint. An appearance of robot is shown in Fig.2.

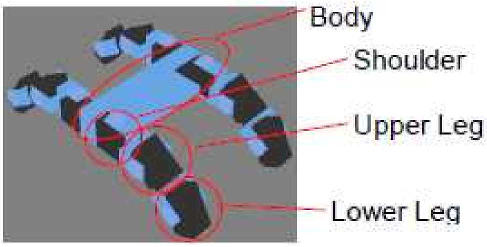

Fig.2. The Quadruped Robot

4. Virtual Sensor

The robot has virtual camera. System gets image buffer from virtual camera to control the robot. However images captured with cameras will decline (shown as Fig.4), when a robot goes ahead. So in addition to cameras, a virtual gradient sensor is installed on the robot to calculate how much cameras decline and compensate the image to make an image processing easy.

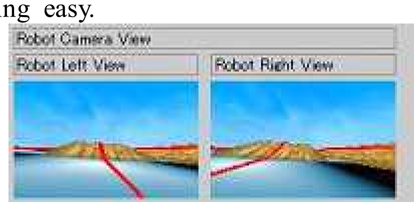

Fig.4. Images from two virtual cameras

A virtual gradient sensor obtains the gradient angle of camera from two coordinates (x_1, y_1) and (x_2, y_2) as shown in Fig.5.

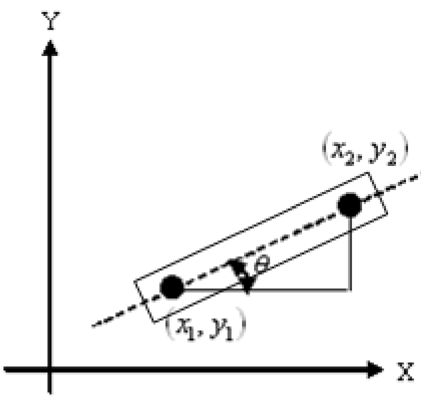

Fig.5. The Virtual Gradient Sensor

The gradient θ is calculated with the use of the expression (1).

$$\theta = \sin^{-1}\left(\frac{x_1 - x_2}{\sqrt{(x_1 - x_2)^2 + (y_1 - y_2)^2}}\right) \qquad (1)$$

5. Image Processing

5.1. Autonomous walk along the line

There is the case where a single continuous line in the original image is cut into several ones after rotation. So System expands the line before rotation. Then the robot tries to find a line to track, but several lines are detected in the images. As it seems that the line to be tracked exists near the robot, initial points to find the corresponding line from each camera are determined based on the proximity to the robot.

To make a walking command, the left image is used as a base image. The first step is to discover a red point from the left image. The second step is to find from the right image the point corresponding to the red one by extending the horizontal line passing through the y coordinate value of the red point in the left image as shown in Fig.6. This process is run over until a red point is found in the both images. The average number of x-coordinate of the right and the left images decides that the robot is on line or deviates from side to side.

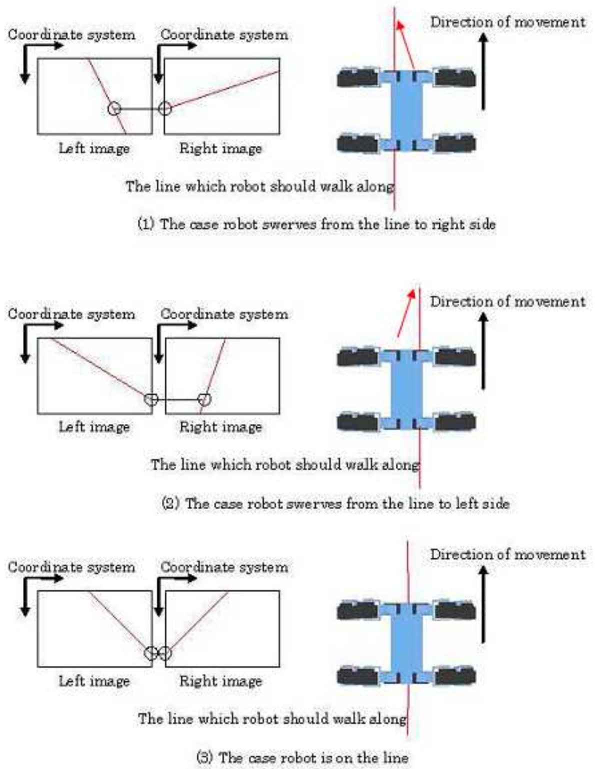

Fig.6. The Decision of a Walk Order

If the robot is on the line, the average x-coordinate is equal to the half size of the image width. If the robot deviates to the right side, the average x-coordinate will be less than the half size of the image width. On the other hand, in case the robot deviates to the left side, the x-coordinate will be more than the half size of the image width (Fig.6). Even if a robot is going straight, as it will shake from side to side, the x-coordinate dose not precisely coincide to the half size of the image width. So the decision of whether the robot is on the line or not is relaxed. If a robot is judged to be on the left side, it will be given a command to move to the right direction, and vice versa.

5.2. Autonomous walk along the road

We make a robot walk along the center line between the left and right white lines. A center line finder looks for cross points where a line parallel to the horizontal line intersects with left or right white lines by moving the line from the bottom of left and right images. If the left and right cross points are found, then the mid point is on the centerline. If only one cross point is found, the center line is extended parallel to the white line found from the end point of the centerline found immediately before. If no cross point is found, as it means a robot to be in a junction, the robot has only to keep going straight until a new white line is found.

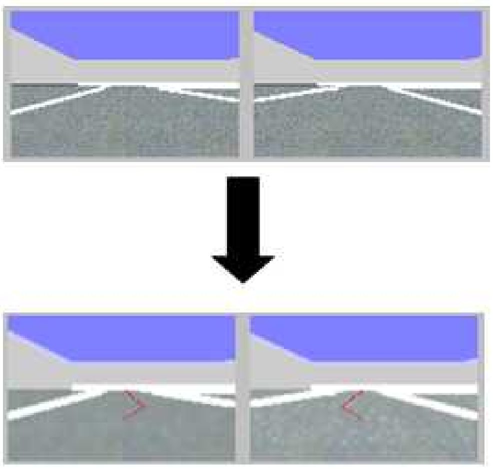

Fig.7.Plot the Imaginary Center Line

6. Conclusions and Future Work

This research's aim is to make a virtual robot a utonomously walk in the Virtual reality space and we successfully implement simulation. Now the rob ot enables to walk autonomously along the line and the road. In the future, we want a robot to walk i n the environment with diverging roads. Given the start point, goal point and a map, we expect a rob ot to go automatically from the start to the goal.

Now, except for up hills or down hills, the syst em successfully simulates the behavior of a robot o n a flat plane with a constant homogeneous friction coefficient. Next we would like to simulate the be havior on rolled ground with variable friction coeffi cients.

7. Acknowledgment

We greatly appreciate the aid of the Grant-in-Aid for Scientific Research (S) and (A).

8. Reference

[1] Norihiro Abe, Yoshinori Takamura, Kazuaki Tanaka, Hirokazu Taki (2003): Construction Of Physics Simulation Environment for Education Using Vortex, In *proceedings of the SCI2003*, 301- 307.
[2] Toshiaki Oomori, Norihiro Abe, Kazuaki Tanaka, Hirokazu TAKI, Shoujie HE (2005): Concurrent development of Virtual Robots and Real Robots Based on Physical Low, *IMEKO / IFAC / IFIP Workshop on Advanced Robot Systems and Virtual Reality. ISMCR2005.*
[3] Toshiaki Oomori, Norihiro Abe, Hiroaki Taki, Shoujie He (2007): A System Allowing Concurrent Design and Implementation of Both Virtual and Real Robots , accepted, *International Symposium on Artificial Life and Robotics (AROB 2007).*
[4] Yi PAN, Norihiro Abe, AND Kazuaki Tanaka (2003): The Virtual Debugging System for Embedded Software Development, *SCI2003*, 78-84.
[5] Yi Pan, Norihiro ABE, Kazuaki Tanaka (2003): The Virtual Debugging System for Embedded Software Development, *VRAI2003.*
[6] Yi Pan, Norihiro Abe, Kazuaki Tanaka, Hirokazu Taki (2004): The Virtual Debugging System for Developing Embedded Software Using Virtual Machinery, In *proceedings. of Embedded and Ubiquitous Computing, International Conference (EUC 2004),* Aizu Japan, 85-95.

Modeling and Deforming Virtual Dense Elastic Object with Haptic Device PHANToM

Hiroshi TAKADA, Norihiro ABE

Kyushu Institute of Technology, 680-4 Kawazu, Iizuka-shi, Fukuoka, 820-8502, JAPAN
(Tel : 81-948-29-7776)
(takada@sein.mse.kyutech.ac.jp)

Yoshimasa KINOSITA

Munakata Suikokai General Hospital
341-1, Kamisaigou, Fukutsu-shi, Fukuoka, 811-3298, JAPAN

Tatsushi TOKUYASU

Oita National College of Technology
1666, Oaza-maki, Oita-shi, Oita, 870-0152, JAPAN

Hirokazu TAKI

Wakayama University
930, Sakaedani, Wakayama 640-8510, JAPAN

Shoujie He

VuCOMP
1231 West Campbell Road Richardson, TX 75080, USA

Abstract: In the recent years there have been various problems in medical treatments, of which the human error by the surgeon in an operation is one of the most serious of problems. In order to minimize the human error in an operation, we need a medical training system by which an inexperienced surgeon can try operating again and again to improve his skill. In this research, we construct the system of modeling a virtual dense elastic object and deforming the object using a haptic device called PHANToM. In the system which we construct, we use two PCs to distribute the process of calculation and SCRAMNet+ is used to connect each PC. PHANToM is used to operate the object and to express the force which is generated from the deformation of the object. We represent the dense object by using Voxels and Tetrahedrons, and the elastic object by using a spring-mass model. A virtual dense elastic object is obtained from CT or MRI to express each patient's organs.

Keywords: Virtual Reality, Simulation, Rendering, Deformation, Haptic Device

I. INTRODUCTION

In the recent years, there have been various problems in medical treatments, of which the human error by the surgeon in an operation is one of the most serious of problems. The major cause is considered to be the insufficient experience of surgeons. A great deal of experience is necessary in medical operation, and tactile or haptic sensation such as manual sensation becomes important to prevent mistakes. It is, however, impossible to use real human body for practicing medical operation. Therefore simulation of the medical operation with a sense of reality as in a real operation is required.

We have studied about the cutting operation using surface model (Koichi [1]), and deformation of surface model (Ryuichirou [2]) and synchronization between audiovisual and haptic feeling (Yoshihiro [3]) in previous research of our laboratory to construct the medical operation training system.

In this research, we approach the construction of the medical operation training system, by creating a virtual human organ model which is not a rigid object but a flexible object which is deformable. The data of the human organ is obtained from CT or MRI.

II. SYSTEM CONFIGURATION

This system consists of two PCs connected with SCRAMNet+: one PC (PC1) renders a virtual dense elastic object with Open GL and the other PC (PC2) calculates haptic feedback given to an operator through

©ISAROB 2009

PHANToM as shown in Fig.1. In this way, we can distribute the process of calculation.

The flowchart of entire process is shown in Fig.2. We use SCRAMNet+ to share the information between PC1 and PC2. Each PC writes and loads the information which is stored in the SCRAMNet.

PHANToM has the original coordinates against the coordinates of the virtual space created with OpenGL. Therefore, we have to multiply the position of PHANToM by the rotation matrix to match the coordinates of the virtual space with that of PHANToM.

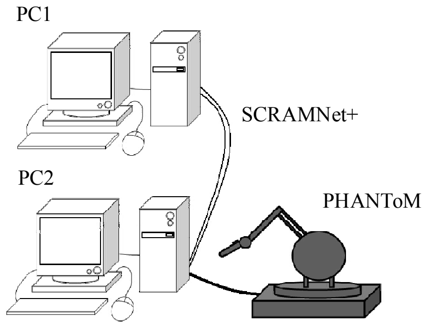

Fig.1. System configuration

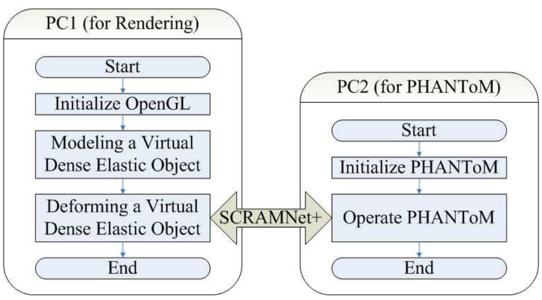

Fig.2. Flowchart of entire process

III. MODELING A VIRTUAL DENSE ELASTIC OBJECT

Rendering a virtual dense elastic object requires the system of drawing the inner tissue obtained from the CT or MRI. In order to construct the virtual dense elastic object, at first Voxels are obtained by dividing Geometry and then Tetrahedrons are generated from each Voxel as shown in Fig.3. We can create a virtual dense elastic object when we set color information (RGBA) to each Tetrahedron. We use CT or MRI data to express any human organs. In order to create the CT or MRI data in original format which can load in our system, we use OpenGL Volumizer.

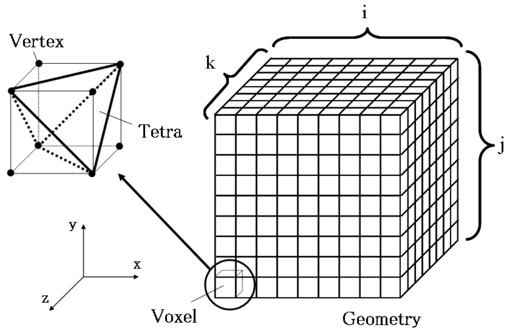

Fig.3. Virtual dense elastic object

1. High Performance of Rendering Process

We set RGBA value to each Tetrahedron as color information to render a virtual dense elastic object. If the partition number of Voxel increases, the number of Tetrahedron also increases and the process of rendering all Tetrahedrons results in bad performance. Therefore we render only the visible part of a virtual dense elastic object from user's viewpoint to improve the performance. The inner object is invisible to the user, so it is not necessary to render. We make a list of visible Tetrahedrons, and we enable high performance of the rendering process by using the list.

2. Spring-Mass Model

A spring-mass model is a model which is a set of the massless spring and the point mass. As shown in Fig.4, we apply the spring-mass model to each Tetrahedron (Koichi [4]).

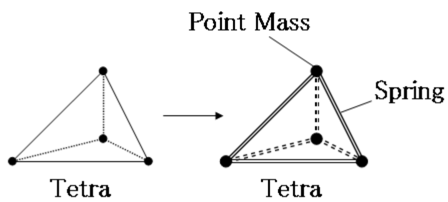

Fig.4. Spring-mass model

We replace each side of Tetrahedron by spring and each Vertex of Tetrahedron by point mass. Tetrahedrons share their Vertices and if the Vertices move, the Tetrahedron deform. So we can represent the deforming process of a virtual dense elastic object as the movement of the Vertices. A spring-mass model is used to realize the deformation based on mechanics.

IV. DEFORMING A VIRTUAL DENSE ELASTIC OBJECT

A virtual dense elastic object must be deformed when it is cut or pushed with a medical tool and the effect must be given to the operator. A medical tool is represented as a rigid stick by PHANToM.

1. Deforming Process

The information such as position, acceleration and force are stored on each Vertex. When a Vertex is moved with a medical tool, a force of spring and damper is induced by the movement of Vertex and the force acts on the connection between Vertices. From the velocity and the displacement between Vertices connected with springs and dampers, each force of the Vertex can be expressed as an equation (1). Here an operator is given the force which is determined from the equation (1) through PHANToM.

$$F_i = \sum \left(\frac{l_{ij}}{|l_{ij}|} k_{ij} \left(|l_{ij}| - |l_{0ij}| \right) + c_{ij} v_i \right) \tag{1}$$

Then we compute the motion equation to obtain each position of the Vertex using the force obtained from the equation (1). Euler method is used to solve dynamically characteristics of a spring-mass model using a motion equation. Then information stored on each Vertex adjacent to the moved Vertex is recomputed and the entire object will deform.

2. Collision Detection of PHANToM

Collision is detected between a Vertex and PHANToM in order to choose the Vertex which is moved with PHANToM. However if we use the position of PHANToM to detect a collision, we have only to detect collision at just one point. The medical operation training system, however, requires operation using a medical tool such as scissors or scalpel. So we make a medical tool as a line made from the position of PHANToM and the angle of rotation of PHANToM. If a deformable dense object is moved with a rigid stick such as a medical tool controlled with PHANToM, the same computation is conducted recursively for all Vertices on the object colliding with the medical tool. Here we explain about collision detection between a Vertex and a medical tool made from PHANToM.

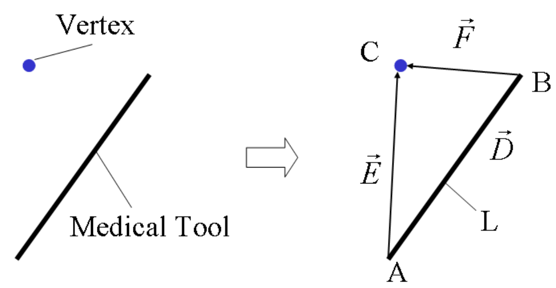

Fig.5. Vectorization of the collision detection model

We use a vector to detect the collision. As shown in Fig.5, we label the edge of a medical tool as *AB* and length of the medical tool as *L*. Also we label the Vertex as *C*. Then we can express the vector *AB*, *AC*, and *BC* as $\vec{D}$, $\vec{E}$ and $\vec{F}$ respectively. Collision is detected when *C* is on the segment *AB*. It is possible to judge whether *C* is on the line *AB* or not by checking whether $\vec{D}$ and $\vec{E}$ are parallel or not using a cross product of the vector. A normal vector can be obtained from a cross product. If the result of the normal vector is zero, then $\vec{D}$ and $\vec{E}$ are parallel, that is to say *C* is on the line *AB*. Next, if *C* is on the line *AB*, check the length of $\vec{E}$ and $\vec{F}$, and if they are less than or equal to *L*, *C* is on the segment *AB*.

3. High Performance of Deforming Process

The process of deforming a virtual dense elastic object requires high computational power when we calculate all Vertices. If the number of Tetrahedron increases, same as rendering process, the process of deformation results in a bad performance. Therefore we calculate only the Vertices of the Tetrahedron which has the color information. We make the list of Tetrahedrons which has the color information and use the list for calculation. Additionally, in order to reduce the computational load of the collision detection process, we search only the Vertices of the Tetrahedron which construct the surface of the object. We use the visible Tetrahedron list which we make in the rendering process for collision detection.

V. EXECUTION RESULT

1. Modeling of a Virtual Dense Elastic Object

A virtual dense object restored from CT is shown in Fig.6 and 7, where the Geometry is (1.0, 1.0, 1.0) and the number of partition of Voxel is (120,120,70). The

©ISAROB 2009

entrails appear as shown in Fig.6 if the threshold amount is changed. This fact shows that a virtual dense object is successfully implemented. Fig.7 shows rendering the data of the blood vessel and it also shows that it is able to rotate.

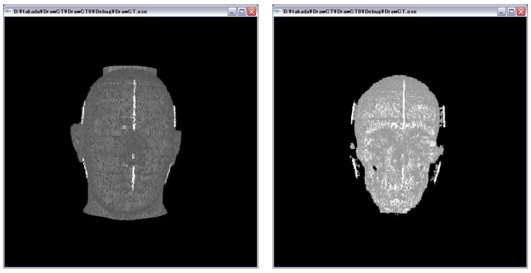

Fig.6. Rendering head

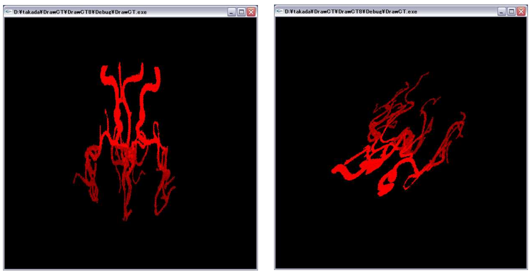

Fig.7. Rendering blood vessel

2. Deformation of a Virtual Dense Elastic Object

Fig.8 shows the situation in which a blood vessel fixed at both ends is deformed to see the invisible object behind the vessel, where Geometry is (0.1, 1.0, 0.1) and the number of partition of Voxel is (1, 10 ,1). The vessel is deformed with a medical tool controlled with PHANToM. In this case, we confirm that the adequate haptic feedback is returned to operator's hand. Additionally, we confirm that the object gets back to its original shape.

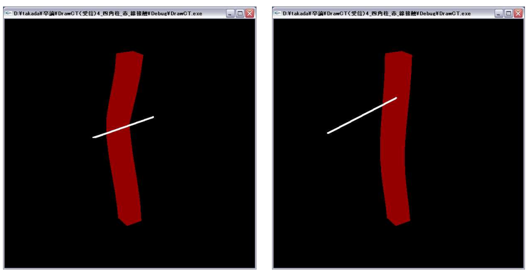

Fig.8. Deforming blood vessel

VI. CONCLUSION

We construct the system of rendering a virtual dense elastic object obtained from CT or MRI data and expressing deformation of tissue in this research to achieve the construction of the medical operation training system. Then we confirm the force generated from deformation of tissue and the real time rendering of a virtual dense elastic object.

However, the size of a virtual dense elastic object which can be deformed is too small to operate as a real medical operation. More the number of Tetrahedrons to be rendered, lesser is the frame rate. In a real medical operation, as the target tissue is only a portion of whole organ, it is sufficient to transform only the target portion into a set of Tetrahedrons and retain the rest as it is or model it roughly to reduce computational load. Also, in this research, we just confirm the force obtained from computing the amount of deformation. In the future, we would like to give a real haptic feeling to an operator. At present, cutting operation with a scalpel or scissors are not implemented. We would like to develop a medical training system in which an inexperienced surgeon is allowed to operate again and again by using a virtual model obtained from each patient's CT or MRI.

ACKNOWLEDGMENTS

We greatly appreciate the aid of the Grant-in-Aid for Scientific Research (S) and (A).

REFERENCES

[1] Koichi Y, Kazuaki T, Norihiro A, et al. (1999), Cutting operation of virtual object and it application to medical simulation.. ICAT'99. 161-165.
[2] Ryuichirou M, Norihiro A, Yoshimasa K, et al. (2007), Simulation of ICSI Procedure Using Virtual Haptic Feedback Model. CME2007. 176-181.
[3] Yoshihiro T, Norihiro A, Hirokazu T, et al. (2008), Synchronization between Audiovisual and Haptic Feeling for Constructing Edutainment Systems. Journal of Virtual Reality. Vol.12, No.1, 27-36.
[4] Koichi S (2006), Introductory Book of Making Dynamic Animation with OpenGL (in Japanese). Morikita Publishing Co, Tokyo, pp 126-152

The Fourteenth International Symposium on Artificial Life and Robotics 2009 (AROB 14th '09),
B-Con Plaza, Beppu, Oita, Japan, February 5 - 7, 2009

Study on communication system between haptic-device for medical operation training system

Yasutaka UCHIDA, Norihiro ABE

Kyushu Institute of Technology, 680-4, Kawazu, Iizuka-shi, Fukuoka, 820-8502, JAPAN
(Tel : 81-948-29-7776)
(*uchida@sein.mse.kyutech.ac.jp)*

Yoshimasa KINOSHITA

Munakata Suikokai General Hospital
341-1, Kamisaigou, Fukutsu-shi, Fukuoka, 811-3298, JAPAN

Tatsushi TOKUYASU

Oita National College of Technology
1666, Oaza-maki, Oita-shi, Oita, 870-0152 JAPAN

Hirokazu TAKI

Wakayama University
930, Sakaedani, Wakayama 640-8510, JAPAN

Shoujie He

VuCOMP
1231 West Campbell Road Richardson, TX 75080 U.S.A

Abstract: Recent years, advances in medical technology are remarkable and the amount of study required to medical students increases year by year. But it is not easy for them to acquire medical operation technique and as a result inexperience in medical operation is feared. But it is difficult to obtain the opportunity of operation practice. The physician has empirically acquired medical technologies through observing medical operation performed by experienced physician in actual condition, but the malpractice really happens occasionally, To solve these problems, it is necessary to give them the same feeling as an experienced doctor feels when he performs a real medical operation. For the purpose, it is needed to give all medical information felt by the experienced doctor to them through a network.

Keywords: PHANTOM**,** Haptic-feedback device, Communication, Education

I. INTRODUCTION

The aim of this research is to have a learner acquire the skill on medical operation by giving him the same visual and haptic sensation as an experienced physician who is conducting operation. As the first step, this research aims at building communication system which synchronously sends/receives simultaneous medical information to distant places.

II. SYSTEM STRUCTURE

Fig.1 shows configuration of this system structure. PHANTOM and PC are connected by particularized lines. Tests using three kinds of communication methods UDP, TCP and Skype communication are conducted. OpenGL draws a virtual organ operated by a skilled person making use of a virtual scalpel controlled with PHANTOM. The purpose of this research's is to compare the quality of each communication method.

1. PHANTOM

Fig.2 shows two PHANTOMs; (a) is Premium 1.5 and (b) is Premium1.0. The basic function is almost the same, but there is considerable differenc e in the movement range.

PHANTOM is a three dimensional haptic feedback device. It has positional sensors from three to six degree of freedom to enable detailed operation.

PHANTOM can give force to an operator. Force is assumed to be force of the spring. The force ca n be changed by providing contact of spring k according

©ISAROB 2009

to Hooke's law.

2. UDP communication

The feature of the UDP communication is enumer ated as follows.(1)

· This System can transmit data to two or more other parties at the same time.

· It is real time and much higher than TCP communication because it does not have a sending again system and congestion control.

· The enhanced feature is not equipped.

· The Diagram of the network is not concealed.

· The connection need not be established before data are exchanged.

· The source PC does not concerned whether data reached the destination PC or not. So data may be broken or lost.

3. TCP communication

The feature of the TCP communication is enumerated as follows.

· It has the function to maintain the data adjustment.

-The sent data is calculated, forwarded, checked with checksum by a destination PC. The data broke n during transmission is omitted and is recognized as the un-received data. So the data is resent from the source PC to the destination PC.

· The flow control is equipped.

-This means the receiving PC can control the se nding PC, that is, the receiving PC sends the number of bytes the sending PC can transmit when the response puts out.

· It is necessary to establish the connection to send or receive data.

4. Skype communication

Skype is internet telephone service and uses P2P technique.(2)(3) It assures a stable call even on a law line or inside firewall. Generally, Skype is used by telephone service and messenger used. An advantage to exploit Skype is to encipher the data and to distinguish the connected status with a companion.

In this research, we use it for a data communication.

5. Open GL

Open GL is programming interface for three – dimensional graphics. It is possible to draw three-dimensional highly accurate image at the very high speed.

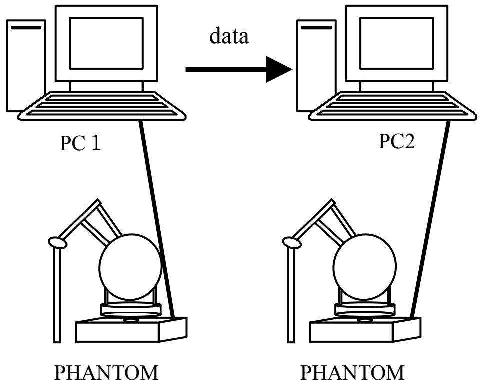

Fig.1 System structure

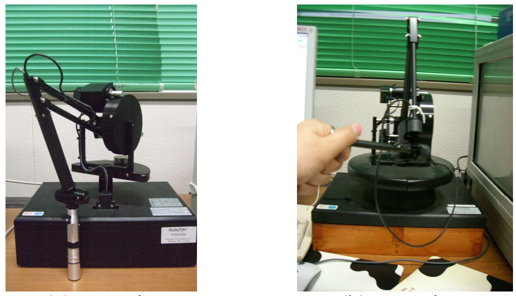

(a) Premium 1.5 (b) Premium 1.0

Fig.2 PHANTOM

III. INTERPOLATION

Data may be lost in UDP communication. So the received PC must interpolate missing data. As methods of interpolation, Lagrange's interpolation and Newton's interpolation are well known. In this case, we have used Newton's interpolation because it is easy to interpolate missing data even when the number of them increases. The dimension will change based on the number of objects in Newton's interpolation. In this research, we develop three expressions- the second, the third, and the fourth dimensions.

Fig.2 shows interpolation. If the data are lost at 2, 6 and 9 when a receiving PC took the data, it prepares an expression and performs interpolation.

It interpolates that individual data before and behind the loss coordinates is used when the number of objects is two, two data ahead of the loss coordinates and the following one coordinates are used when the number of objects is three, and two data before and behind the loss coordinates is used when the number of objects is four. The expressions show (1), (2) and (3).

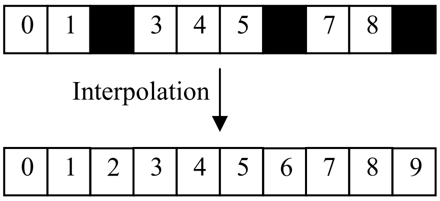

Fig.2 Interpolation

$$f(x)=c_0+c_1(x-x_0)$$
$$c_0=y_0, c_1=\frac{y_1-y_0}{x_1-x_0} \quad (1)$$

$$f(x)=c_0+c_1(x-x_0)+c_2(x-x_0)(x-x_1)$$
$$c_0=y_0, c_1=\frac{y_1-y_0}{x_1-x_0}, c_2=\frac{1}{x_2-x_1}\left(\frac{y_2-y_0}{x_2-x_0}+\frac{y_1-y_0}{x_1-x_0}\right) \quad (2)$$

$$f(x)=c_0+c_1(x-x_0)+c_2(x-x_0)(x-x_1)+c_3(x-x_0)(x-x_1)(x-x_2) \quad (3)$$
$$c_0=y_0, c_1=\frac{y_1-y_0}{x_1-x_0}, c_2=\frac{1}{x_2-x_1}\left(\frac{y_2-y_0}{x_2-x_0}+\frac{y_1-y_0}{x_1-x_0}\right)$$
$$c_3=\frac{1}{x_3-x_2}\left(\frac{y_3-y_0}{(x_3-x_0)(x_3-x_1)}+\frac{c_1}{x_3-x_1}+c_2\right)$$

IV. Verification

We examined what influence will occur when a method of interpolation or a method of communication method is changed. To make the measurement precise as far as possible, the average value is calculated by repeating several times interpolation. This time, the data to be sent is limited to PHANTOM coordinates-x, y and z.

V. RESULTS

1. Operation Screen

Fig.3 shows the display window used in communication test[(4)(5)]. The upper and bottom window which are rendered with Open GL correspond to a sending window and receiving one, respectively. The black point corresponds to the PHANTOM point, and the coordinate values are shown in the right side.

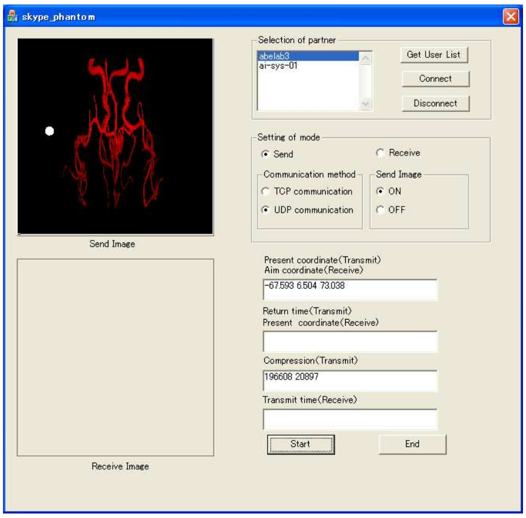

(a) Operation Screen of send PC

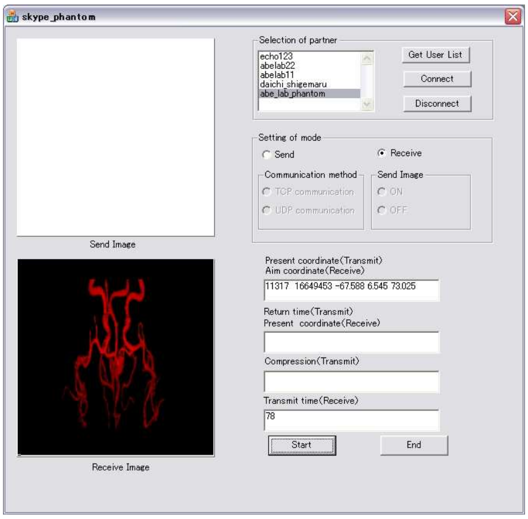

(b) Operation Screen of send PC

Fig.3. Operation screen

2. Result

Comparison between UDP and TCP is shown in Table 1, the lack of data has been caused at UDP communication, but it has not been caused at TCP communication. Communication time by TCP is much more than that by UDP.

Table 1 Time-lag between UDP to TCP

	UDP	TCP
Time-lag(ms)	3.24	111.86

Table.2 shows the error rate calculated based on the difference between the original data and the data restored by interpolation. The table shows how the error rate decreases according to the dimension of the method used when five data are lost during communication.

Table 2 Error average by the number object

point	Two	Three	Four
Error Average	0.003	0.002	0

The above data are obtained form the experiment in which both sending and receiving PC are connected with LAN in our laboratory. To get the result when 2 PCs are connected with WAN, the experiment between our laboratory and Wakayama University has been conducted. In this experiment, image data are also sent.

In this case, there was the apparent difference between the sending and receiving images, and it seemed that movement of Phantom point does not accord with the image. This is due to the difference in computational capability of PCs used, and this is solved by preparing PCs with the same performance. Another way to solve the problem is to thin out image data when the data is sent out. In this case, the number of data eliminated must be determined not to make people feel sense of incongruity. Finding a appropriate number needs further experiment.

VI. CONCLUSION

In this research, we develop communication system using the haptic-feedback device PHANTOM, OpenGL and Microsoft Visual C++ 6.0.

It is confirmed that haptic data are successfully sent 1000 times a second through network, but it is difficult to send image data thirty frames a second. This means that the synchronization between haptic data and image data may not always attained. It is necessary to examine if the haptic data synchronized with image data sent out are successfully restored at the destination or not.

ACKNOWLEDGMENT

We greatly appreciate the aid of the Grant-in-Aid for Scientific Research (S) and (A).

REFERENCE

(1) WinSock2 Programming, Lewis Napper, 2005
(2) S.Uchino, N.Abe, Y.Tabuchi, H.Taki, He, "VR Interactive Dialog System with Verbal and Nonverbal Communication", AROB 13th '08
(3) SkypeAPI, https://developer.skype.com/Docs/ApiDoc
(4) H.Takada, N.Abe, Y.Kinoshita, H.Taki, He, "Deforming Virtual Dense Elastic Object with Force Feedback Device PHANToM" Intution2008
(5) T.Miyagi, N.Abe, Y.Kinoshita, H.Taki, He, "Detection of Blood Vessels and Brain Aneurysm Referring to Medical Images of Head" ,Intution2008

©ISAROB 2009

Detection of brain aneurysm and route searching to brain aneurysm aim at the development of operation simulation system

Toshihide Miyagi, Norihiro Abe
Kyushu Institute of Technology
680-4 Kawazu, Iizuka, Fukuoka 820-8502, Japan
(Email: miyagi@sein.mse.kyutech.ac.jp)

Yoshimasa Kinoshita
Munakata Suikokai General hospital, Japan

Tatsushi Tokuyasu
Oita National College of Technology,

Hirokazu TAKI
Wakayama University
930 Sakaedani, Wakayama-shi, Wkayama 680-8510, Japan

Shoujie He
VuCOMP, USA

Abstract: In this paper, a system is proposed that is necessary for an operation simulation system helping a trainee perform medical operation to make a cerebral aneurysm avoid exploding. The physician has empirically acquired medical technologies through a medical operation in traditional clinical teaching. However, there is a problem with security and a burden to a patient. So, recently as a new approach for training, the medical operation simulation system using Virtual Reality is attracted. Then, aiming at developing the medical operation simulation system for a cerebral aneurysm, we constructed the necessary function such as detecting a brain aneurysm that is a target of operation, searching for a blood vessel to make a plan of the operation.

Keywords: Medical image processing, Operation simulation, Brain aneurysm, Operation planning

I. Introduction

The physician has empirically acquired medical technologies through a medical operation in traditional clinical teaching. However, there is a problem with security and a burden to a patient. The exercise using a pig is difficult to repeat training, and hardship to conduct because of the cost and the protest by a group of protection of animals.

As a new approach for teaching / training in place of the traditional approach, the medical operation simulation system which utilizes virtual reality (VR) attracts attention. The advantage of VR is that it allows trainee to experience various disease state repeatedly and to evaluate know-how quantitatively.

So, this system aims at constructing a medical operation training system for cerebral aneurysm. We will show below the techniques necessary for an operation simulation system.

1. A visual display of an operation object
2. The force feedback using a haptic device
3. A medical operation planning system
4. Implementation of surgical instrument to cut or deform a virtual organ model

Among them, this search tackles 1, 3 to construct a system that detects brain aneurysm from a medical image, and analyzes structures of blood vessels to find a route to brain aneurysm.

This research is conducted based on our experience on both diagnosis of lug cancer or structural analysis of tracheole from CT images [1][2], how to cut a virtual surface model [3] or a virtual voxel model [4] with a scalpel, and simulation of medical manipulation ICSI using a deformable surface model [5].

II. Brain aneurysm

A brain aneurysm generally means a lump or a tumefaction part occurring in a small artery inside the brain. . As a cause of the occurrence, it is considered that there is a weak part on a brain artery wall by nature, and a blood vessel swells out like a lump because blood flow continues meeting with this part for many years. As the result, it occurs at a divergent position between blood vessels.

Treatment for a brain aneurysm is done to prevent an aneurysm from exploding in future. Main treatment is pinching a lump with a clip or inserting coils into a lump.

III. Detection of a cerebral aneurysm

If it is possible to make the location of a brain aneurysm clear in advance before training or diagnosis, it will help not only a trainee confirm a target but also a doctor determine if medical operation is needed or not. .

The appearance of a cerebral aneurysm is a lump shown in Fig. 1. A cerebral aneurysm occurs near the bifurcation between two blood vessels, and the one whose diameter is more than 2[mm] must be detected.

Two methods are used for detecting a cerebral aneurysm; the first one exploits how much a blood vessel is expanded as an index, the second one uses the distance from a bifurcation as an index.

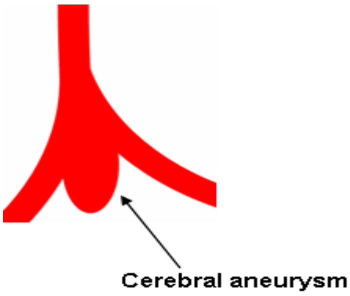

Fig. 1 State of outbreak of cerebral aneurysm

1. Detection of using the domain expansion of a blood vessel

Regarding an aneurysm as a part of a sphere, the domain expansion must be repeated two or more times at the point where a blood vessel swelled like a lump as shown in Fig. 2. In this process, it is necessary to judge the bifurcation of a blood vessel while applying the region growing method. For judging bifurcation, connectedness between the expanded areas is calculated, and if there is no connectedness, then there is a bifurcation between them [6]. When a point included in 27-neighborhoods of the current point labeled with a number i on a blood vessel is judged to be on a blood vessel, it is labeled with the number i+1. Only when there is connection between points given the same label in this process, they are determined to be on the same branch, otherwise, a new branch derives from the point; there is a bifurcation. As shown in Fig.3 the elements given a label 6 are not connected each other, so points labeled with 6 are judged as a bifurcation.

Now let the expansion rate be (A-B)/B, where B and A is the area before and after an expansion, respectively. We define a candidate of a cerebral aneurysm to be the portion where expansion whose expansion rate is more than 1.15 occurred successively at least two times.

In Fig. 2, the areas labeled with a number 4 and 5 are detected as a cerebral aneurysm because it suffices the above condition. But, the area of a peripheral blood vessel is so narrow that the increase rate of the area changes greatly. The goal of the system is to detect an aneurysm of which diameter is more than 2mm, then a small area less than the threshold value is not regarded as a candidate. As the spatial resolution in the axial slices is 0.357[mm], and square measure per one pixel is 0.127[mm^2], the number of pixels necessary to detect a cerebral aneurysm is about 25[pixels].

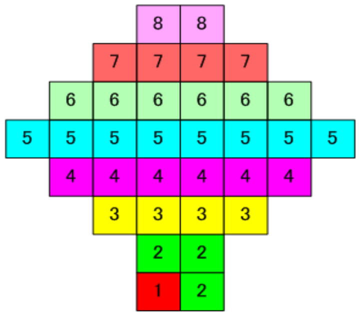

Fig. 2 Detection with the domain expansion

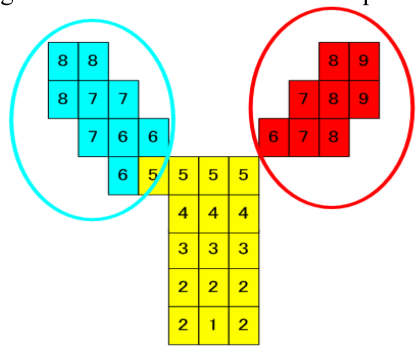

Fig. 3 Detection of the bifurcation

2. Detection using the distance from bifurcations

Though the method described in before section is able to detect candidates of a cerebral aneurysm, this method will cause a thick vessel to be regarded as a cerebral aneurysm. But the fact that a brain aneurysm occurs near a bifurcation will find a real brain aneurysm from candidates detected using the method shown in before section.

But, there are two bifurcations at the both end of one branch, so it needs to decide which one should be used to calculate a distance from an aneurysm to the bifurcation. Then, distance between an aneurysm and two bifurcations are calculated and the nearer one is selected as the bifurcation corresponding to an Aneurysm.

Fig. 4 and Fig. 5 will explain how the method is applied.

In Fig. 4, L1 and L2 show the distance between a candidate aneurysm and two bifurcations; in this case L1 is shorter than L2, so L1 is regarded as a distance to a detected brain aneurysm. In Fig. 5, the lump area at left side is close to the bifurcation, so it is judged as an aneurysm, and the lump area at right side is so far from a bifurcation that it is considered not to be an aneurysm. This system decides whether candidates are an aneurysm or not based on the condition that the distance from an aneurysm to a bifurcation is shorter than 4[mm] or not.

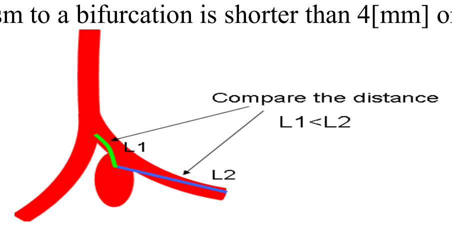

Fig. 4 Compare the distance from bifurcations

©ISAROB 2009

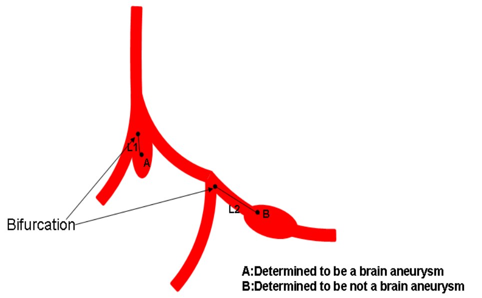

Fig. 5 Detection with the bifurcation distance

IV. Structural analysis of blood vessel for route searching to brain aneurysm

Intravascular operation needs a planning to make a catheter lead to near an aneurysm. Additionally, if the path toward an affected part can be found with a VR system, it is useful not only in an exercise but also in a real operation.

So with use of the result of divergence recognition, a path leading to the affected part is found using A* algorithm.

The process has 3 steps. First, a user decides the aim and start point. Secondly, as an estimate of a cost between the aim point and each bifurcation calculates distance from the aim point to each bifurcation. Finally, it searches the path to the aim point using A* algorithm.

1. Route finding based on structure

Connectivity relation between vertex of blood vessel is necessary to search a path using A* algorithm, but it is generated from the recognition result of bifurcation

Let the label of point be a bifurcation point(i) and that of a branch be branch(j).

The one set of information to be stored includes just a label of bifurcation points that are parent and child of one branch and a label of a branch.

We store this information list structure. The making method of this list is shown in following.

Start the following procedure from i=1, j=1, k=2.

(1) Store point (i) as a parent of branch (j).

(2) Perform a bifurcation recognition, and if a bifurcation point point(k) is found, store point(k) to the an child point of branch(j).

(3) If there are n branches of which parent is point (k), then name the one branch selected from them branch(j+1) and store the rest of them in a stack.

(4) in case point(k) is not an end point, then let i=k, k=k+1, j=j+1, and repeat from (1) to (3).

(5) In case point(k) is an end point and a stack is not empty, then pop up a stack, and set i , k, j to the label of a parent of the selected branch, k+1, j+1, respectively, then repeat from (1) to (3).

(6) In else case, end the process.

The method of this is shown in Fig. 6.

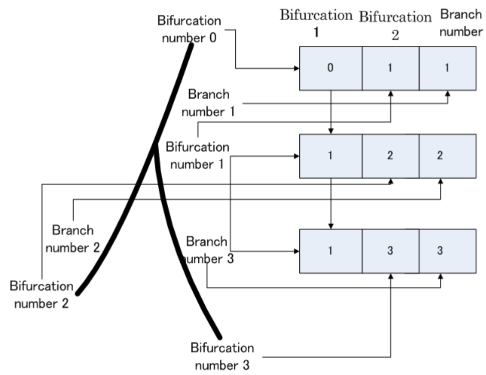

Fig. 6 Acquisition of connection information

V. Execution results

For 4 MRI images provided as samples, detection of brain aneurysm and the route searching to the brain aneurysm using by the structural analysis are tried to verify the validity of the proposed methods. The number of slices is 140, the slice interval is 0.5[mm], and the spatial resolution in the axial slices is 0.357[mm].

1. Detection result of brain aneurysm

Fig. 7 shows detection result using by the proposed method, and candidate of brain aneurysm is colored by yellow.

The proposed method is applied to 4 images and the validity of the method is evaluated based on the criteria shown below. The results are divided into two classes as shown in Table 1; the one uses only the domain expansion information and the other uses both the domain expansion information and the distance from bifurcation.

The number of false positives is used as evaluation criteria. A false positive means that an aneurysm is found in the place where none exists in reality.

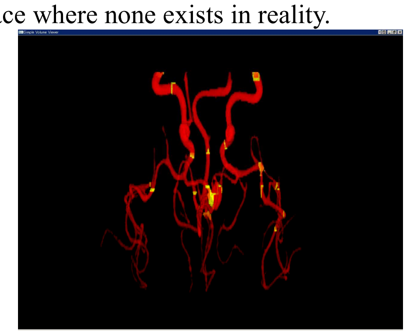

Fig. 7 Detected result of brain aneurysms

Table 1 Result of cerebral aneurysms

	True positive	False Positive [nodules/case]
Not use distance	100%(4/4)	82.25
Use distance	100%(4/4)	36.25

The result of Table 1 shows that proposed method is possible to detect brain aneurysm. And using by the distance from a bifurcation point as an index, the number of false positives decrease about 55.9[%].

But, any other false positives are found in curved portion of vessels. It is because the domain expansion applied to curved portion of a vessel tends to expand the area inside the curve because it is regarded as a part of a vessel.

2. Route searching to brain aneurysm using by the structural of blood vessel

Inserting coils into an aneurysm needs navigation leading a catheter to the diseased part. And before the operation, it needs to plan how to move the coil. So, this system constructs the path planning system from arbitrary part to a brain aneurysm using the analysis result of blood vessels.

The brain aneurysm is decided by referring to the detection result of brain aneurysm.

Fig. 8 shows the aim part (brain aneurysm) and start point. And, Fig. 9 shows the route found by using the structural analysis result of blood vessel and by applying A* algorithm to this analysis result.

The result of Fig. 9 shows that route searching succeeds.

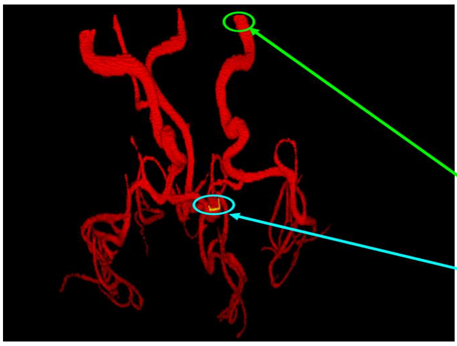

Fig. 8 The aim and start point of search

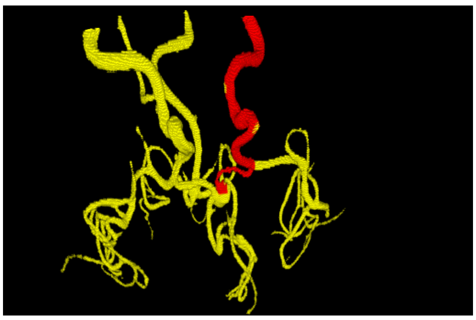

Fig. 9 Route search result to brain aneurysm

VI. Conclusion

Our research aims at building a medical operation training system helping an inexperienced medical student get medical techniques by performing medical operation to a virtual body restored from given sets of CT or MRI images. In this paper, we especially showed detection of a brain aneurysm and route searching to brain aneurysm.

The detection of an aneurysm is attained by reducing false positives using the distance from the bifurcation to the aneurysm as an index, but false positives are still remained. So, improving the precision in detection must be realized by using information on local structural features such as curvature of a blood vessel.

And, a route searching to brain aneurysm succeeds without any troubles. This will contribute to navigate a catheter to an aneurysm to put a set of coils into it to avoid its explosion.

To improve this system, we consider that the addition of samples is necessary to make the system more reliable: we would like to improve the precision in detection by getting much more images.

To build a system making a trainee feel as if he/she were performing real medical operation to the body of a real patient, in addition of drawing the deforming process it is necessary to return the force to a trainee's hand when with a medical tool he/she cuts or pushes tissue inside a head including vessels and brain itself.

VII. Acknowledgement

We greatly appreciate the aid of the Grant-in-Aid for Scientific Research (S) and (A).

REFERENCES

[1] Tetsuya Sato, Norihiro Abe, Yoshimasa Kinoshita, Shoujie He (2006): *Toward Developing Multiple Organs and Diseases Diagnosing Intellectual System referring to Knowledge Base and CT Images*, accepted, CBMS 2006(19th IEEE International Symposium on Computer-Based Medical Systems), 359-364.

[2] Tetsuya Sato, Norihiro Abe, Yoshimasa Kinoshita, Shoujie He (2007): *Toward the Developmentof an Intelligent System for the Diagnosis of Multiple Organs and Diseases*, The Second International Conference on Complex Medical Engineering-CME2007, 703-710.

[3] Koichi Yamamoto, Kazuaki Tanaka, Norihiro Abe, Yoshimasa Kinosita, Akira Yokota (1999): *Cutting operation of virtual object and it application to medical simulation*, ICAT'99, 161-165.

[4] D. Tokumoti, N. Abe, K. Tanaka, H. Taki, Y. Kinoshita (2004): *Cutting of the Voxel ModelUsing a Haptic Feedback Device*, Conference on Systemics, Cybernetics and Informatics (SCI), Orlando, Florida.

[5] Ryutarou Mizokami, Norihiro Abe, Yoshimasa Kinoshita, Shoujie He (2007): *Simulation of ICSI Procedure Using Virtual Haptic Feedback Model*", The Second International Conference on Complex Medical Engineering-CME2007, 176-181.

[6] H. Sekiguchi, N. Sugimoto, S. Eiho, T. Hanakawa, S. URAYAMA (2004): *A Blood Vessel Segmentation for Head MRA Using Branch-Based Region-Growing*, The transactions of the Institute of Electronics, Information and Communication Engineers. D-II, J87-D-II(1), 126-133.

The Fourteenth International Symposium on Artificial Life and Robotics 2009 (AROB 14th '09),
B-Con Plaza, Beppu, Oita, Japan, February 5 - 7, 2009

Development of indoor navigation system for monocular-vision-based autonomous mobile robot

Tomoyuki Kinoshita Eiji Hayashi

Department of Mechanical Information Science and Technology
Faculty of Computer Science and Systems Engineering, Kyushu Institute of Technology
680-4, Kawazu, Iizuka-City, Fukuoka Prefecture, Japan

Abstract: In our research, we developed a technology for our robot that uses an indoor navigation system based on visual methods to provide the required autonomy. For robots to run autonomously, it is extremely important that they be able to recognize the surrounding environment and their current location. Because it was not necessary to use plural external world sensors, we built a navigation system in our test environment that reduced the burden of information processing mainly by using sight information from a monocular camera. In addition, we only used natural landmarks like walls because we assumed the environmental to be a human one. In this paper we discuss and explain two modules: a self-position recognition system and an obstacle recognition system. In both systems, recognition is based on image processing of the sight information provided by the robot's camera. In addition, to provide autonomy for the robot, we use an encoder and information from a two-dimensional space map given beforehand. We explain here the navigation system that integrates these two modules. We applied this system to the robot in an indoor environment and evaluated its performance, and in a discussion of our experimental results we consider the resulting problems.

Keywords: Personal robot, Autonomous driving, Visual Processing

I. Introduction

While an increasing number of robots is being used in manufacturing fields, there is at the same time an increasing need for robots to work in non-manufacturing jobs in home environments, in medical care, and in providing welfare for the aging. To deal with various conditions in these places, robots that function autonomously are required. Therefore, in our laboratory we are attempting to develop autonomous drive-type personal robots that are safe, reliable, and useful to humans.

In our research, we have developed an indoor navigation system based on visual methods that provide the required autonomy. For robots to run autonomously, it is extremely important that they be able to recognize both the surrounding environment and their current location. To date there have been very many studies of indoor navigation systems for robots in which the robots are generally equipped with plural cameras or with scanning type light range sensors that allow them to sufficiently understand their surrounding environment[1][2]. However, building a sensor system based on information processing remains a difficult problem.

We assume that the robot should be autonomous over a long distance in an indoor environment where there are relatively few obstacles. We consider the robot's navigation in such an environment to be a success if it arrives at its destination without crashing into obstacles or walls. Because it was not necessary to use plural external world sensors, we built a navigation system in our test environment that reduced the burden of information processing mainly by using sight information from a monocular camera. In addition, unlike many studies that recognize a robot's position by using artificial landmarks[3], we only used natural landmarks like walls because we assumed the environment to be a human one.

II. Specification of the robot

Our robot has a drive mechanism of two front and two back wheels (Fig.1). The two front wheels are attached to a motor, which operates them independently, while the back wheels are castors. DC servo motors are used for the robot's drive mechanism, and the robot's position and speed control are achieved by the control system of the drive mechanism. One CCD camera is installed on the head of the robot and can be rotated to all sides by two DC motors. This camera is able to make an image of about 300,000 pixels. All devices are controlled by a personal computer, and lead batteries supply electric power. A system overview is shown in Fig. 2.

©ISAROB 2009

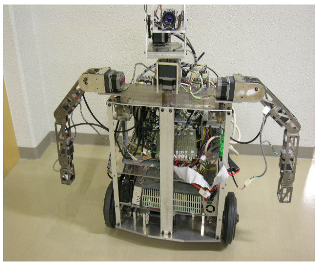

Fig.1 Robot appearance

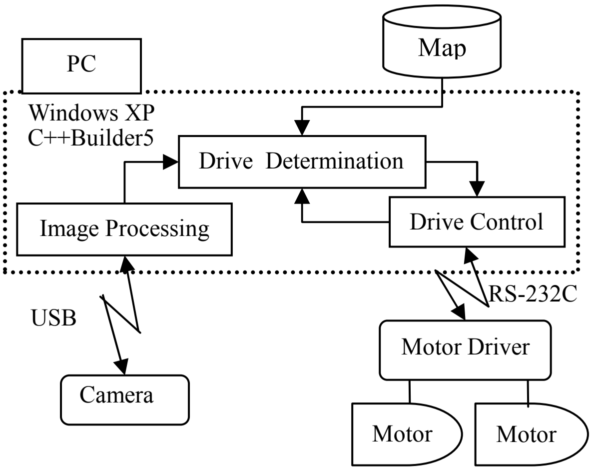

Fig. 2 System overview

Ⅲ. Navigation system

1. Outline

The navigation system consists of two modules: an obstacle recognition system and a self-position recognition system. We explain the systems of each of these modules as well as their integration into the entire system.

2. Obstacle recognition system

The obstacle recognition system is the system which, by processing images that it receives, recognizes still obstacles that exist in the movement environment.

Systems have often failed in recognizing obstacles because they only used color or edge information. Therefore, in this study, the system recognizes obstacles with judgments made by combining plural kinds of information.

At first, the system obtains binarization, floor color, and edge extraction information by processing an image received from a monocular camera. A grayscale image is converted into a binary image according to the threshold that the distinction between aspects of the floor and aspects of obstacles be clear. The binary image is scanned from its bottom to its top end, and the coordinates where black pixels appear are recorded.

Concerning the floor color information, first, a group of image pixels is sampled in a rectangular region at the bottom center of an image. Then, a group of image data inside this region is used as sample image data, which is then used to calculate the deflection. The floor region is extracted in terms of the difference between all the pixels in the image.

Edge extraction information is obtained from edge-enhancement processing with a Sobel operator. Boundary lines between obstacles and the floor can then be recognized by comparing the three above-mentioned kinds of information with each other. Fig. 3 shows the obstacle recognition processing.

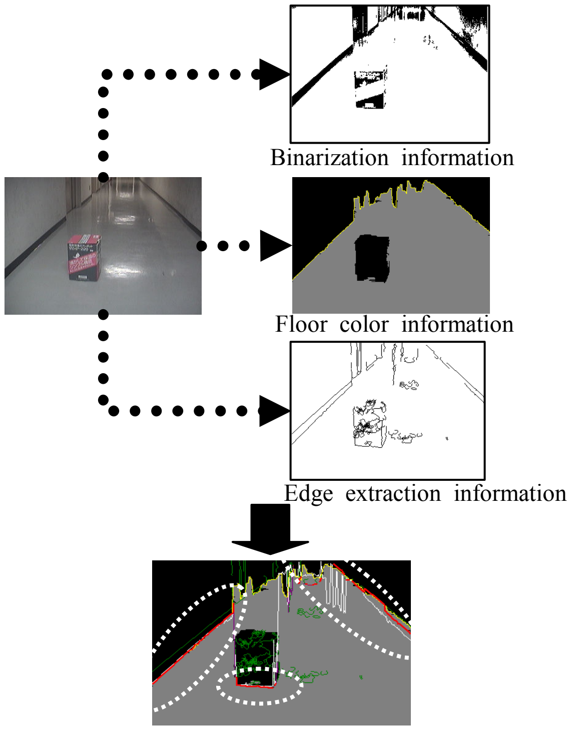

Fig.3 Obstacle recognition system

3. Self-position recognition system

The self-position recognition system is a system for recognizing the self-position of the robot by using landmarks that naturally exist in a movement environment[4]. In this study, because we assume that the robot drives in a corridor environment, we establish relationships between the walls and the robot's position by recognizing the boundary lines between aspects of the floor and walls.

In general, there are characteristic straight lines on right and left sides of a corridor. We make a database of the leaning pattern of these lines on the image that is calculated from the corridor's width and the robot's posture. Next, the two characteristic straight lines are

©ISAROB 2009

detected by performing a Hough transformation of the straight line[5] from the image acquired during the driving. After the degree that these straight lines lean is calculated, we identify the robot's relative position to the characteristic lines by comparing them with the degree of the leaning pattern derived from the database. By allowing a revision of the robot's self-position on the map when it is running, this recognition helps to solve the problem of the dead reckoning error. Fig. 4 shows the self-position recognition processing.

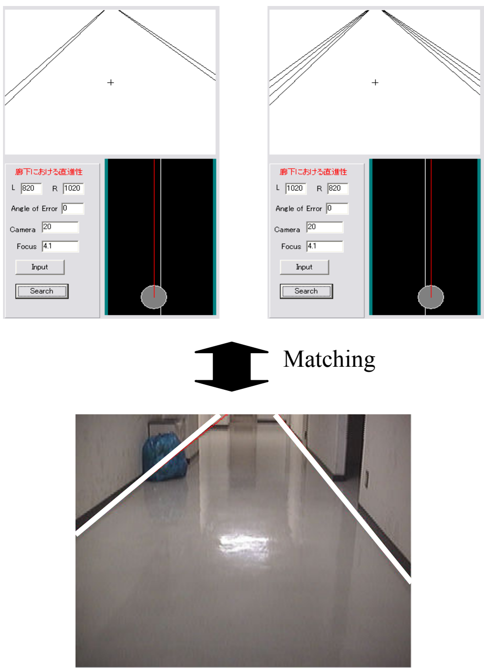

Fig.4 Self-position recognition system

4. Driving plan

4.1 Driving algorithm

The system uses a limited space map, which is a two-dimensional space map given before the driving begins. Fig. 5 shows the driving algorithm. At first, a goal is set up on the map, and a path-finding system searches for a course to arrive at it. Next, the robot starts its movement after having made a driving plan from the course.

As the robot runs along the course plan, it constantly repeats obstacle and self-position recognitions. When obstacles are detected and it appears likely to crash into them, it takes avoidance action. At these times, it does not process the self-position recognition. We illustrate the obstacle avoidance processing in the following chapters in detail. After its finishes avoiding an obstacle, the robot returns to its original course.

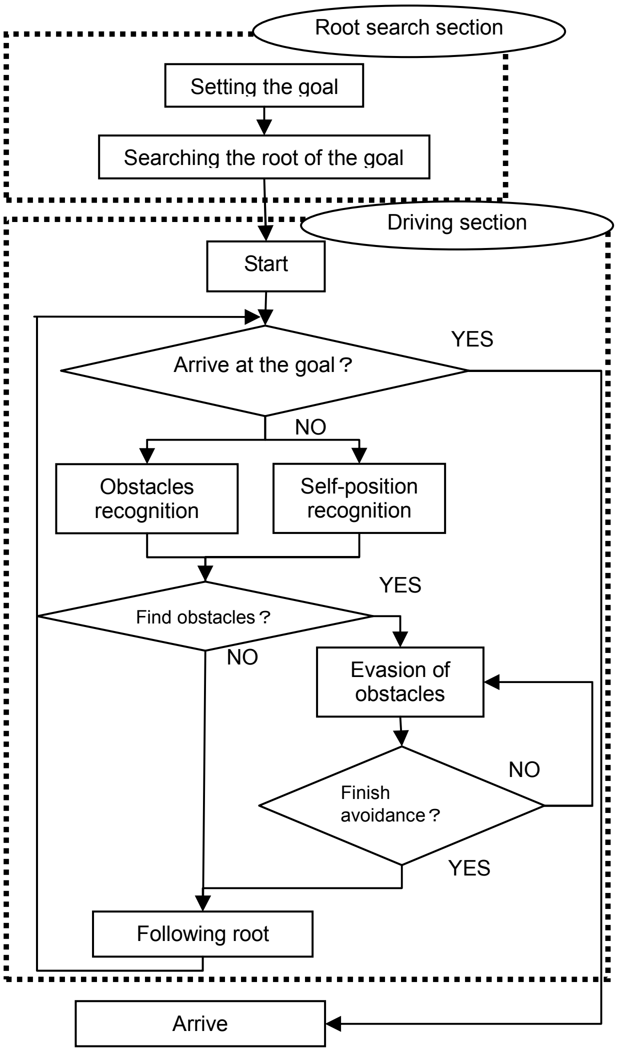

Fig. 5 Driving algorithm

4.2 Obstacles avoidance processing

At first, the system converts the coordinates of obstacles on an image which is recognized by the obstacle recognition processing into coordinates on a map by making calculations from the camera's posture. These are written onto the map. When there is an obstacle in the robot's direction of progress on the map, the systems searches for an avoidance course. It confirms whether or not an obstacle will interfere with the robot's movement in a right, left or straight direction. The attractive potential, U, which represents the energy attracted to the goal from each course's points is calculated by Eq. (1). The robot proceeds in the direction where value of U is the smallest and where is an obstacle won't interfere (shown in Fig. 6). This method enabled the robot to reach its goal after avoiding obstacles.

$$U = A\sqrt{(x_r - x_g)^2 + (y_r - y_g)^2} \qquad (1)$$

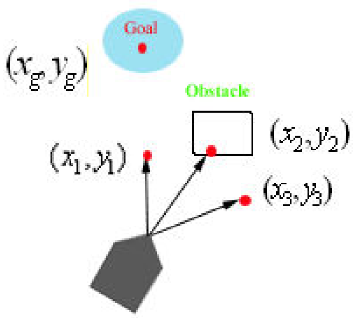

Fig. 6 Obstacles avoidance processing

Ⅳ. Experiment

1. Method of experiment

We conducted drive experiments with the robot in an indoor environment with the same floor pattern and installed obstacles (shown in Fig. 7). If it arrived accurately at the goal while safely avoiding obstacles, the navigation was regarded as a success. Its speed was 0.3 m/s.

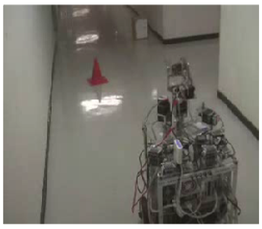

Fig. 7 Environment of experiment

2. Result of experiment

The map after the drive is shown in Fig. 8, and the robot's trajectory data is shown in Fig. 9. Although the robot shifted about 0.05m from the goal, it was able to reach the goal without colliding into two obstacles that were recognized. The error of self-position recognition was about ±0.074m on the average, small enough compared with the passageway width. The average time for each processing is shown in Table.1. It can be said that these speed are sufficiently practical.

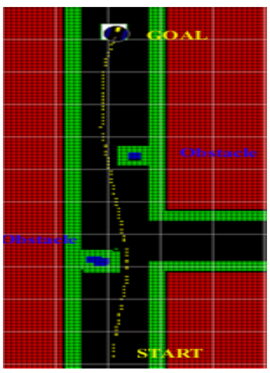

Fig. 8 The map after robot's driving

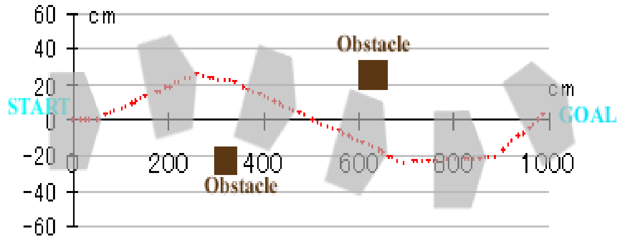

Fig. 9 Robot's trajectory data

Table 1. Average time of processes

	Obstacle recognition	Obstacle recognition and self-position recognition
Time[ms]	181	364

Ⅴ. Conclusions

Based on visual methods, we developed an indoor navigation system for the robot which provides the required autonomy. This system consists of an obstacle recognition system and a self-position recognition system. It is possible for each system to perform simultaneously. The entire system enabled the robot to run safely in an indoor environment where there were relatively few obstacles.

Although the robot can at the present only recognize stationary obstacles, in the future it should also be able to recognize moving obstacles. Moreover, in the future, the navigation system should be able to function in a complicated indoor environment.

References

[1] D.J. Kriegman, E. Triendl, and T.O. Binford(1989), Stereo Vision and Navigation in Buildings for Mobile Robots. IEEE Trans. on Robotics and Automation, vol.5, no.6: pp.792-803

[2] Thorsten Belker and Dirk Schulz (2002), Local Action Planning for Mobile Robot Collision Avoidance. IEEE/RSJ International Conference on Intelligent Robots and Systems '02 IROS: pp. 601–606, 2002.

[3] K. Komoriya, E. Oyama and K.Tani (1992), Planning of Landmark Measurement for the Navigation of a Mobile Robot. IEEE/RSJ International Conference on Intelligent Robot and Systems: pp.1476-1481

[4]Takuma Umeno, Eiji Hayashi (2006), Navigation system for an autonomous robot using an ocellus camera in indoor environment. proceedings of the 11th international symposium on artificial life and robotics, Vol1.11th, Beppu, Oita, Japan, 2006: pp229

[5]D.H.Ballard (1981), Generalizing the Hough transform to detect arbitrary shapes. Pattern Recognition, vol.13, No.2: pp.111-122

©ISAROB 2009

An effective localization and navigation method based on sensor fusion for mobile robot moving in unknown indoor environment

In soo Kim* and Woong keun Hyun*, Jong Jin Yu* and Sung Sub Park**
*Honam Univ, GWANG-JU, KOREA

** Korea Digital Co., KOREA

(Tel : 82-62-940-5482; Fax : 82-62-940-5484)
(wkhyun@honam.ac.kr;kiskisskis@naver.com)

Abstract: Odometry is simple and fast method to estimate the position and orientation of the moving robot. However, there are some errors in detecting the correct position. Moreover, the errors continuously accumulate. To cope with this problems, Absolute position correction is necessary, and they are usually based on external measurements such as electric compass, indoor GPS or landmark recognizing by vision system. This paper presents a sensor fusion localization method by optimal combination of encoder sensor and landmark recognizing method by vision sensor module(STARGAZER). The position error estimated by absolute sensor such as vision system is increased especially when the landmark image is captured during robot is moving. In this paper, a filtering method for removing the wrong estimated position was also proposed. For natural motion of the robot an effective weights control method of position and orientation rate was proposed. We proved this system's validity through field test

Keywords: mobile robot, localization, sensor fusion

I. INTRODUCTION

The goal of this work is to implement an autonomous mobile robot capable of navigating in an unknown indoor environment. For this, the robot requires the capability to estimate accurate position and to build a map of the environment while the robot moving in the indoor space. Map building and navigation is a complex problem because map integrity and localization cannot be sustained by odometry alone due to errors introduced by wheel slippage and distortion. Moreover, neither odometry nor absolute sensory data gives perfect estimation of the robot's position. This paper employs absolute and relative positioning for accurate position estimation in the map building process and navigation. Relative positioning is usually based on odometry, that is, computing a robot's relative motion from the measurement of wheel revolution. In most mobile robots, odometry is implemented by means of optical encoders that monitor the wheel revolutions. A positioning by odometry is simple and fast method to estimate the position and orientation of the moving robot. However, there are some systematic and non-systematic errors in detecting the correct position. Moreover, the errors continuously accumulate. Therefore, the odometry needs to be correct from time to time. The disadvantage of odometry is its unbounded accumulation of errors. To cope with this problems, Absolute position correction is necessary, and they are usually based on external measurements such as electric compass, indoor GPS or landmark recognizing by vision system. This paper presents a sensor fusion localization method by optimal combination of encoder sensor and landmark recognizing method by vision sensor module (STARGAZER). The position error estimated by absolute sensor such as vision system is increased especially when the landmark image is captured during robot is moving. In this paper, a filtering method for removing the wrong estimated position was also proposed. For natural motion of the robot an effective weights control method of position and orientation rate was proposed. The paper is organized as follows: Section 2 describes properties of odometry errors. Section 3 presents a sensor fusion localization method using absolute sensor and relative sensor. Section 4 describes an effective weight control method of position and orientation rate for natural robot moving. Section 5 represents the developed Linux based robot control structure which can deal with multiple sensors effectively. Section 6 and 7 provide successful experiment results for navigation and obstacle avoidance, and conclusions, respectively.

II. A SENSOR FUSION localization method

using absolute sensor and relative sensor

Encoder is low cost and easily equipped relative sensor for position estimation of the mobile robot. A localization by encoder sensor is simple and fast method to estimate the position and orientation of the moving robot. In the differential-drive design of two wheel mobile robot, incremental encoders are mounted onto the two drive motors to count the wheel revolution. Using simple geometric equations, it is straight-forward to compute the momentary position of the vehicle relative to the known starting position. The basic localization equations by using incremental encoder data are given as Eq.(1), (2) and (3).

$$\Delta\theta(t) = \frac{2\pi R}{N} \cdot \frac{\Delta C_R(t) - \Delta C_L(t)}{D} \quad (1)$$

$$\Delta x(t) = \frac{2\pi R}{N} \cdot \frac{\Delta C_R(t) + \Delta C_L(t)}{D} \cdot \cos(\theta(t) + \frac{1}{2}\Delta\theta(t)) \quad (2)$$

$$\Delta y(t) = \frac{2\pi R}{N} \cdot \frac{\Delta C_R(t) + \Delta C_L(t)}{D} \cdot \sin(\theta(t) + \frac{1}{2}\Delta\theta(t)) \quad (3)$$

$$\theta(t) = \theta(t - \Delta t) + \Delta\theta(t) \quad (4)$$

where R, N and D are the radius of wheel, gear rate and distance between wheels, respectively. Δenc_L and Δenc_R are incremental encoder values of right and left wheel, respectirely. For correcting the encoder localization errors, one should realize that there are a few types of error such as systematic errors caused by unequal wheel diameter, simple linealization of the odometry equations as Eq(1) thru (3), and non-systematic errors are caused by lippery floors. A localization by encoder sensor is simple and fast method to estimate the position and orientation of the moving robot. However, there are some systematic and non-systematic errors in detecting the correct position. Moreover, the errors continuously accumulate[5]. Therefore, the odometry needs to be correct from time to time. We propose a sensor fusion method to estimate the robot position using vision sensor module (STARGAZER) and encoder sensor. The sensor estimate the position and heading angle of the robot by analyzing the infrared ray image which is reflected from different ID number-given passive landmarks on the ceiling. It has some drawback that its average position error is much larger than that of odometry , and the sensor can not find robot position when the robot is located in deadzone where the image can not be readable. Position error by image sensor is larger than that by encoder sensor, when the robot follows the straight line path. On the other hand, when the robot moves in corner or circular path, The sensed error by encoder is larger than image sensor. To overcome the short coming of the two sensor and increase the advantages, we propose a sensor fusion method by using absolute and relative sensors.

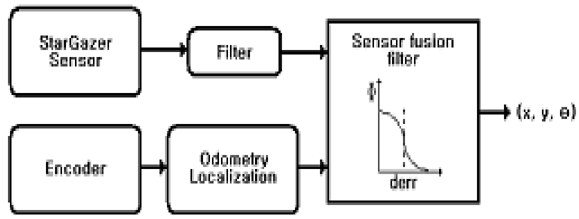

Fig1. The absolute and relative sensor fusion for localization

The Fig 1 represents the block diagram of the proposed sensor fusion method using encoder sensor and image sensor module. The encoder sensor and image sensor module detect the relative position and absolute position of the mobile robot, respectively . The two sensor data are fused by sigmoid function filter as Eq(4) . Xa is a localization position velocity after sensor fusion. The sigmoid function is defined by Eq(5). Where perr is absolute difference value between sensed value by image sensor (Xsg) and sensed value by encoder (Xe). The sensor fusion system described by Eq(5),(6) and (7) is designed by following idea. (1) if the distance error perr is larger than the limit value of image sensor , then the reliable value is that from image sensor, (2) if the perr is smaller than derr, then the appropriate localization value is mixed one of image sensor and encoder and (3) the smaller perr is, the more reliable encoder position localization is. The larger perr is, the more reliable image sensor localization is

$$X_a = (1 - \Phi)X_{SG} + \Phi \cdot X_E \quad (5)$$

$$\Phi = 1 - \frac{1}{1 + e^{-(perr + derr)\cdot k}} \quad (6)$$

$$perr = \sqrt{(X_{SG} - X_E)^2 + (Y_{SG} - Y_E)^2} \quad (7)$$

III. AN EFFECTIVE WEIGHT CONTROL METHOD OF POSITION AND ORIENTATION RATE FOR NATURAL ROBOT MOVING

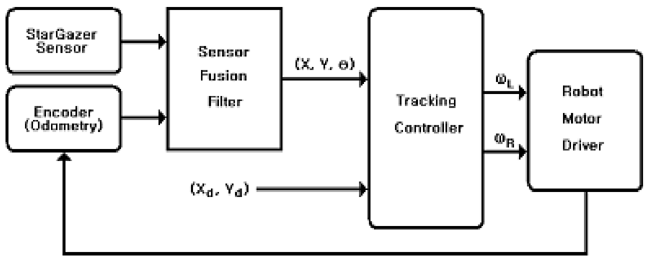

Fig. 2 Block diagram of position controller.

Two wheel velocity commands are decided by Eq.(8)

thru Eq(12). Where γ_1 control the linear velocity of the robot. And γ_2 control the rotation velocity. For the natural motion, it is better for the robot to control direction toward goal position during first 25% of moving distance, and the robot move linearly to the goal during the last 75% distance. These motion can be possible by control the weighting factors γ_1 and γ_2. γ_1 is decided by Eq.(9), where L0 is distance between starting position and goal position. Delta Li is distance between current position and goal position. If we decide the Kg1 and delta L0 as 20.0 and 0.25, then the motion of the robot will be like the trajectory as shown Fig.3.

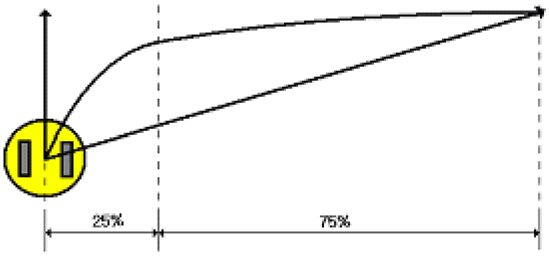

Fig.3 Trajectory of the robot controlled by factors γ_1 and γ_2.

$$\omega_R = V_d\gamma_1 + \gamma_2(kr_p\theta_e + kr_d\dot{\theta}) + \gamma_3 k_{o_R} \quad (8)$$

$$\omega_L = V_d\gamma_1 - \gamma_2(kr_p\theta_e + kr_d\dot{\theta}) - \gamma_3 k_{o_L} \quad (9)$$

$$\gamma_1 = \mathbf{1} - \frac{\mathbf{1}}{\mathbf{1} + e^{-(\delta l_i / L_0 - \delta L_0 / 2)\cdot kg_1}} \quad (10)$$

$$kg_1 = \mathbf{20.0},\ \delta L_0 = \mathbf{0.25} \quad \begin{matrix} \omega_L \le |\omega_{L\max}| \\ \omega_R \le |\omega_{R\max}| \end{matrix} \quad (11)$$

$$\delta L_i = \sqrt{(X_f - X_o)^2 - (Y_f - Y_o)^2} \quad (12)$$

γ_3 is controllable weighting factor for obstacle avoidance. Since the larger γ_3 is, the robot rotates more fast, if the factor γ_3 is controlled according to the distance between robot and obstacle, robot can avoid the moving or static obstacle. The approach velocity to the goal position controlled by γ_1. Therefore, The appropriate change of γ_1, γ_2 and γ_3 can make the robot move to the goal position while avoiding the obstacle.

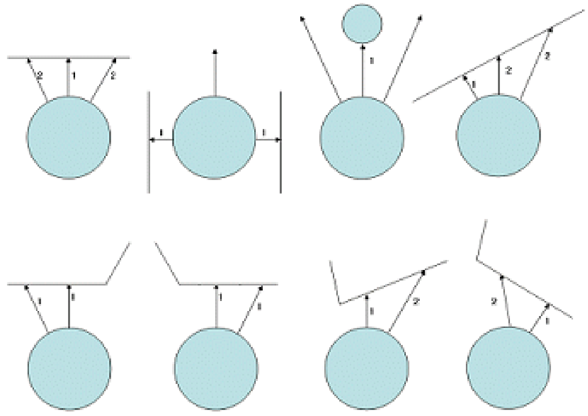

Fig. 4. Obstacle sensing and avoiding according to various obstacle types.

IV. EXPERIMENT RESULTS

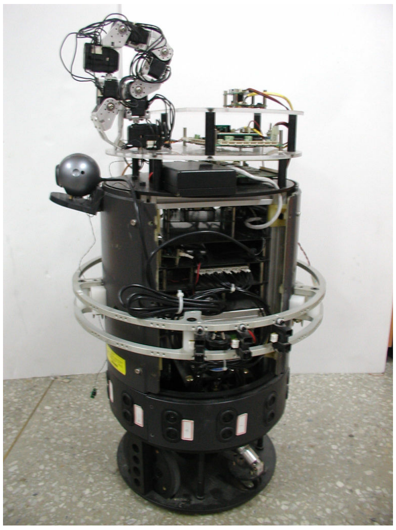

Fig.5 Developed mobile robot and sensor fusion contol system

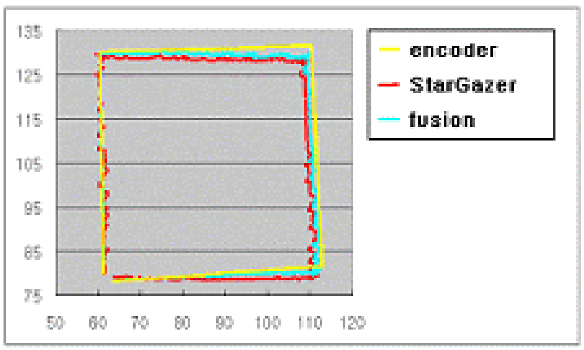

Fig.6 Rectangle trajectories with 3 control method.

The developed sensor controller for sensing of multiple sensor and mobile robot is shown in Fig. 5. Localized trajectories estimated by image sensor module and encoder data are shown in Fig 6. The desired trajectory is rectangle path of 50cmX50cm. The trajectory drawn with bold line is desired one and the trajectory drawn with yellow line is resultant path estimated by odometry. There are some error in edges of the rectangle trajectory owing to slipping and simple linearization of the odometry equation. The trajectory localized by image sensor module is shown in red line. The trajectory has error like noise type. The errors were distributed in whole trajectory, but the errors were not accumulated. The errors in line path of trajectory localized by encoder sensor were much smaller than that by image sensor. Fig.7 shows the result of the proposed natural motion control method by equation (8) thru equation (11). We can see that our proposed method control the rotation and linear velocities well.

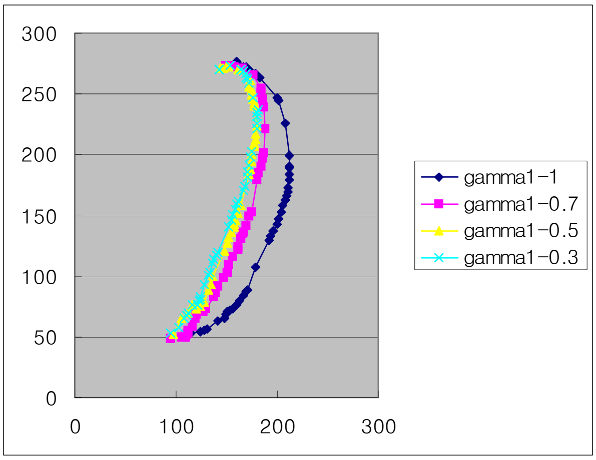

Fig.7 Trajectories with various γ_1 and γ_2 are changed

Obstacle avoidance trajectory while robot moving to the goal position is shown in Fig.8. The robot can avoid the obstacle with control of γ_3 and move to goal position with γ_1 and γ_3.

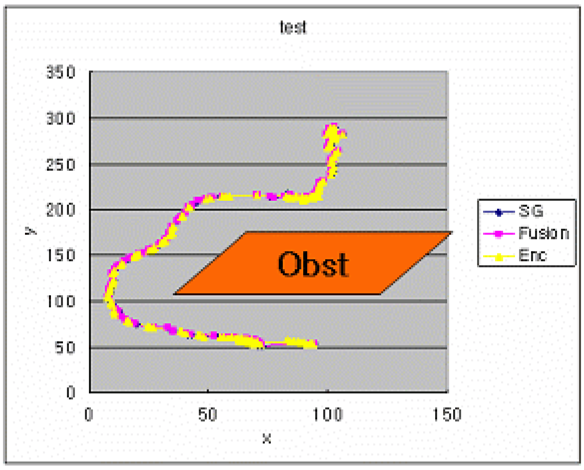

VI. CONCLUSION

This paper presents a sensor fusion localization method by optimal combination of encoder sensor and landmark recognizing method by vision sensor module(STARGAZER). The position error estimated by absolute sensor such as vision system is increased especially when the landmark image is captured during robot is moving. In this paper, a filtering method for removing the wrong estimated position was also proposed. For natural motion of the robot an effective weights control method of position and orientation rate was proposed.

REFERENCES

[1] Woong keun Hyun, Tae Cheol Jung and Chang wan Lee, "Aline based map building and virtual robot modeling for remote controlled mobile robot," ITC-CSCC, 2005, Vol. 1, p281-282

[2] S a D shiv Ghidary, Takahiro Tani, Toshi Takamori, Motofumi Hattori, " *A new Home Robot Positioning System (HRPS) using IR switched multi ultrasonic sensors*"

[3] Chenavier, F. and Crowley, j., 1992, "Position Estimation for a Mobile Robot Using Vision and Odometry." *Proceedings of IEEE International Conference on Robotics and Automation*, Nice, France, May 12-14, pp. 2588-2593.

[4] Feng, L., Borenstein, J., and Everett, B., 1994, "Where am I? Sensors and Methods for Autonomous Mobile Robot Localization." *Technical Report, The University of Michigan, available via anonymous FTP from* ftp,eecs,umich,edu/f/people/jogannb.

[5] Cang Ye, Johann Borenstein, "Characterization of a 2-D Laser Scanner for Mobile Robot Obstacle Negotiation", Proc. IEEE Int. Conf. On Robotics and Automation, Washington, DC, December, pp. 2512-2518,2002

[6] T. Bailey, J. Nieto, and E. Nobot. Consistency of the FastSLAM algorithm. In *Proc. IEEE int. Conf. Robotics and Automation, 2006.*

This research was supported by the program for the Training of Graduate Students in Regional Innovation and the program for Regional Strategic Industries which was conducted by the Ministry of Commerce Industry and Energy of the Korean Government .

An Indoor Autonomously Mobile Robot with Laser Sensor and Image Processing Approach

Akihiro Fujiwara, Norihiro Abe, Yoshihiri Tabuchi

Kyushu Institute of Technology graduate school
680-4 Kawazu Iizaka, Fukuoka 820-8502, Japan
Tel : 08-948-29-7776
a.fujiwara@sein.mse.kyutech.ac.jp

Hirokazu Taki
Wakayama University
930 Sakaedani, Wakayama-shi
Wakayama 680-8510, Japan
taki@sys.wakayama-u.ac.jp

Shoujie He
VuCOMP
USA
shoujie.he@gmail.com

***Abstract*:** Robots have been studied over a couple of decades. Nowadays, a lot of robots have been developed for improving the productivity at factories or helping with the daily chores in offices. A truly autonomous mobile robot will definitely benefit our life in many areas, including nursing care services and office guide. Most of the robots, however, are still at the stage of being controlled remotely or performing a set of predefined tasks. In addition, an autonomous movement in complex geographical features is very difficult. In order to do things autonomously, a robot must be capable of recognizing and interacting with its environment. This research aims at developing an autonomous mobile robot, which will move without collision with obstacles in an indoor environment. This requires the robot to be able to recognize its own location, select routes, and avoid collision with obstacles.

Keywords: robot, Laser Sensor, Image Processing, route selection, self-position recognition, obstacle avoidance.

I. INTRODUCTION

This research aims at developing a robot that moves autonomously in a dynamically changing environment. In order to do so, it is considered a basic capability for the robot to identify obstacles. It is necessary for an autonomous robot to perform several tasks including the self-position recognition, route selection and obstacle avoidance.

At the current stage, our very first goal is to make a robot move autonomously towards the destination in a static environment.

This paper discusses how to identify the current location of a robot by comparing the geographical features and the environmental map and recognize obstacles with a laser sensor and stereo camera.

II. System Structure

1. Mobile Robot System

Fig.1 shows the robot that is developed in this research. A laser sensor, a laptop PC and two cameras are mounted on the mobile robot. The two cameras are at the same altitude with their optical axes in parallel.

A robot recognizes the environment around its current location through the analysis of the distance data. Based on the result of environment recognition, it issues a voltage command to the servo pack through the DA board. The servo packing applies a constant voltage to the motor, and the motor controls the wheel.

At the current stage, this mobile robot is still moving in a static indoor environment. But the ultimate goal of this research is to put the robot in a dynamic environment with moving obstacles.

Fig.1. Mobile Robot

©ISAROB 2009

Fig.2. Communication configuration

2. Autonomous movement

When the robot moves, the control program compares the distance data sampled at 35 degrees on the right side with the distance data at 145 degrees on the left side as shown in Fig. 3. In order to minimize the potential collision, the robot is kept moving along the centerline of the road. When the distance data is almost equal, both wheels will be controlled to move forward. When there are short distance data and long distance data, the wheel with shorter distance data will be controlled to move forward and the wheel on the opposite side move backward. This adjustment keeps going until the robot moves to the point on the centerline.

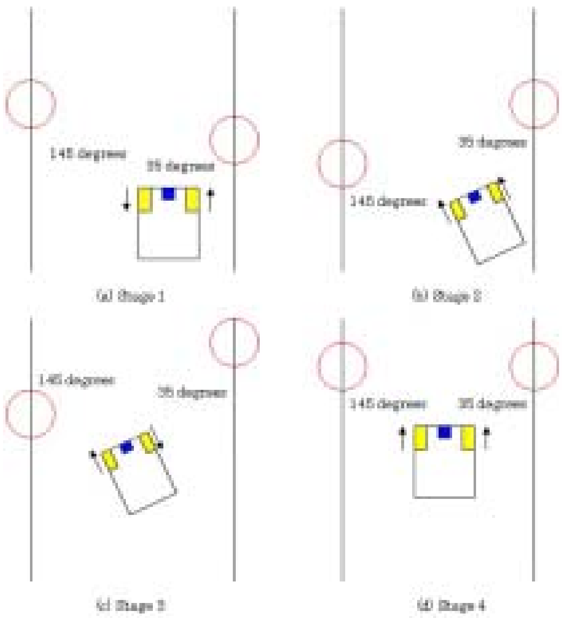

Fig.3. Move to the center

3. Control Program

The environmental map is given to the program in advance. Both an initial position and posture of the robot are also given to the program. Next, the destination is specified. It searches for the route from an initial position to the destination by using the A-star algorithm. Next, a laptop computer obtains the distance data sent from the laser sensor. The robot compares the distance data images made from the distance data with the environmental map image. The present position of the robot is calculated from the result. If the present position of the robot is a destination, the robot is stopped. Oppositely, if the present position of the robot is not a destination, the robot is controlled along the searched route. Figure 4 shows the flow chart of the program.

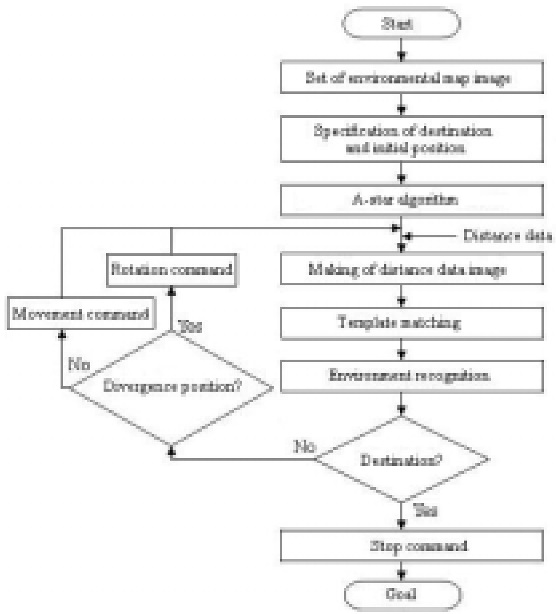

Fig.4. Flow chart

III. Route Selection

A* search algorithm is used for route selection, where the environment map is given; the initial location and posture of the robot are also given. The environmental map is divided into each area at the divergence position as shown in Figure 5. Moreover, the distance between each area is as shown in Figure 5. Once a destination is specified, A* search algorithm will

©ISAROB 2009

find the shortest route from the initial location to the destination.

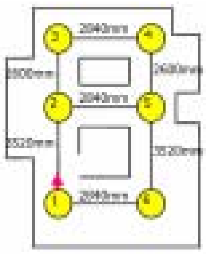

Fig.5. Indoor environmental map

IV. Self-position Recognition

On its way to the destination, the robot needs to be constantly aware of its current location. Otherwise, it will be impossible to reach the destination. Identifying the current location, however, proved to be the most difficult task for developing an autonomous mobile robot. In this study, a new approach is proposed for the identification of the current location. It is basically a template matching method, which compares the geographical features measured with a laser sensor with the pre-given environment map.

At any given location, the robot will first collect the distance data through the laser sensor. The distance data will then be represented as a distance image. At this stage, template matching could be conducted between the distance image and the environment map. However, it is computationally costly to directly match with the entire environment map. Therefore, only the portion of the environment map that is within the neighborhood of the spot where the robot was previously located is selected for the template matching. An image processing software package named Halcon is used for the template matching. As the result of template matching, the current location and the posture of the robot will be determined.

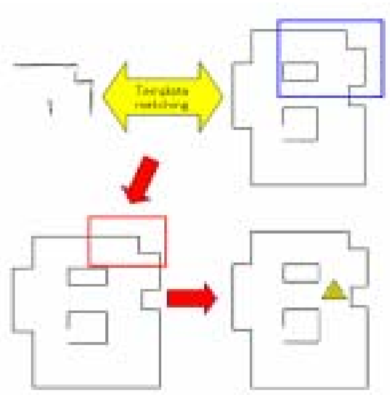

Fig.6. Template Matching

V. Obstacle Avoidance

1. Obstacles avoidance with a laser sensor

Collision with any obstacle that does not exist on the environment map needs to be avoided. Detection of this type of obstacles could simply be done by checking the difference between the distance image and the matched environment map. Since the range covered by the laser sensor is limited, not all the obstacles could be detected solely by the laser sensor. In this experiment, the laser sensor is mounted on the bottom part of the robot. When the robot moves underneath a table, for instance, the legs of the table could be detected by the laser sensor. The table top, however, will not be captured by the laser sensor. Similarly, when an obstacle is hanged from the ceiling or coming out from the side walls, laser sensor will fail to detect them. In order to handle all these cases, optical sensor is needed. Nevertheless, at the current stage, it is assumed that all obstacles are standing on the ground.

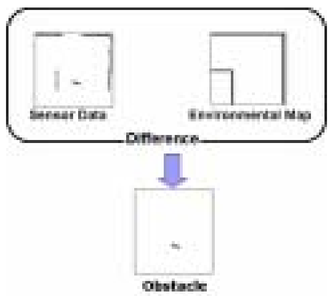

Fig.7. Difference

2. Obstacles avoidance with image processing

Stereo image processing is considered the right methodology for detecting the obstacles out of the coverage of the laser sensor. Two cameras are mounted on the mobile robot with their optical axes in parallel and at the same altitude. Finding corresponding points in the two images captured by the cameras is important for the distance measurement. Features based on color, brightness and shape are used for identifying the corresponding points. As soon as the corresponding points are located, the distance will be calculated. Based on the distance and the speed at which the robot is moving towards the obstacles, a control command will be generated and sent to the robot so that any potential collision will be avoided.

During the stereo matching, the feature points extracted from the right image are used as the references.

©ISAROB 2009

For any point picked on the right image, a corresponding point will be searched in the left image. Here is a constraint that helps with the reduction of the search space. For point (x, y) on the right image, the corresponding point on the left image should have the same coordinate value of y and a larger x because of the way that the two cameras are mounted.

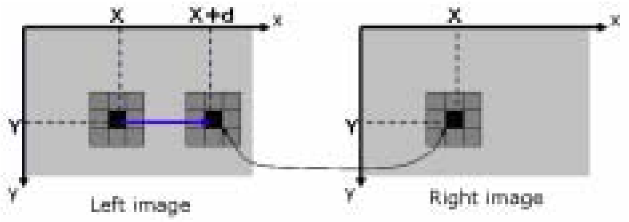

Fig.8. Stereo Matching

Whenever a feature point on the right image is selected, pixels on the left image with similar color, brightness, or shape will be extracted. The probability that a pixel actually corresponds to the feature pixel on the right image is calculated with the Correlation method. Pixels with large correlation coefficients are considered the correspondences. Image processing algorithms for the correspondence detection have been implemented and the performance has been evaluated. For the regions rich in features, the correspondence went well. For the regions with less reliable features, the correspondence is not as good due to the small variance. Therefore, for the regions with small variance, it is more reliable to use edge detection algorithms and search for the correspondence in the vicinity of edge elements.

3. Obstacles avoidance with Database System

When more than one obstacle with uniform color and shape features are captured on the images, however, the current correspondence searching algorithms will not work well. Currently, the alternative is to register all the obstacles in a database. Fig.9 illustrates the case that the robot is moving towards a table. The laser sensor will identify the tables with the information collected through the detection of the table legs. If the table top is lower than the height of the robot, the robot must avoid it referring to the data base.

To identify the table with the laser sensor, however, will be difficult when a long and slender stick exists near the leg of the table. Moreover, any table that is not registered will still cause collision. Further, if a table is put on the floor diagonally against a robot, it may be difficult to walk through under the table. This is one of the future problems to resolve.

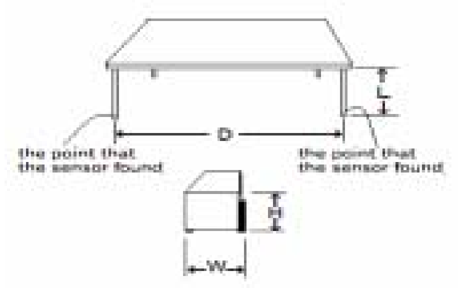

Fig.9. A table is used as an obstacle

VI. CONCLUSION

The present position of the robot was able to be calculated at any time based on the template matching. Moreover, the robot was able to move to the destination along the route calculated by the A-star algorithm. The avoidance of the obstacle will become a problem now. The robot will identify the obstacles referring to the data base.

ACKNOWLEDGMENT

We greatly appreciate the aid of the Grant-in-Aid for Scientific Research (S) and (A)

REFERENCES

[1] Ryoichi Suematsu "Image Processing Engineering", Corona Publishing Co. 2000

[2] Takahiro Kurita, Norihiro Abe, Kazuaki Tanaka, Hirokazu Taki, Shoujie He "Control of Autonomous Mobile Robot through Environmnet Recognition with Laser Sensor" The 60st Joint Conference of Electrical and Electronics Engineers in Kyushu, 2007

[3] TakahiroKurita, "Control of Autonomous Mobile Robot through Environment Recognition with Laser Sensor"(in Japanese), Kyushu Institute of Technology, Master Thesis, 2008

The Fourteenth International Symposium on Artificial Life and Robotics 2009 (AROB 14th '09),
B-Con Plaza, Beppu, Oita, Japan, February 5 - 7, 2009

Development of a Desktop Swarm Robot System based on Pheromone Communication

Naoyuki Kitamura
Advanced Course of Electricity and Control System Engineering
Anan National College of Technology
265 Aoki Minobayashi,
Anan, Tokushima 774-0017, Japan
kitamura@emergence.jp

Yoshiyuki Nakamichi
Department of Systems and Control Engineering
Anan National College of Technology
265 Aoki Minobayashi,
Anan, Tokushima 774-0017, Japan
nakamiti@emergence.jp

Koji Fukuda
Department of Electronic Control Engineering
Gifu National College of Technology
2236-2 Kamimakuwa, Motosu,
Gifu 501-0495, Japan
fukuda@gifu-nct.ac.jp

Abstract

Complex and adaptive behavior of population emerges in social insects. Especially in ants, pheromone communication is the key to understanding their swarm intelligence. This paper proposes a swarm robot system based on pheromone communication and reports our current status of development of the robot system. We believe that the system could be used in swarm robotics and complex systems education.

Key words: multi robot system, pheromone communication, swarm intelligence

1 Introduction

Complex and adaptive behavior of population emerges in social insects. Especially in ants, pheromone communication is the key to understanding their swarm intelligence. The study of mechanisms of pheromone communication and its technological and/or educational application are highlighted in recent year. This paper proposes a desktop swarm robot system based on pheromone communication and reports our current status of development of the robot system. We believe that the system could be used in swarm robotics and complex systems education.

2 Backgrounds

One of main features of pheromone communication is that pheromone di use and evaporate, so its communication media is variable with time. To realize the feature in real robot systems is important for emergence of ant-like swarm intelligence. However it is difficult to treat features of pheromone by using chemical materials in real robot systems.

In past studies, some robot systems based on pheromone communication are using virtual pheromone instead of chemical materials.

For example, Payton proposed "Pheromone Robotics," in which virtual pheromone is expressed by wireless infrared technology [1]. Sugawara conducted ant-like foraging experiments using "V-DEAR" which is composed of the LC projector, the CCD camera and autonomous mobile robots equipped with color sensors [2, 3]. In this system, virtual pheromones were replaced with graphics projected on the ground.

3 A desktop swarm robot system based on pheromone communication

3.1 Concept

One of the goals of our study is development of swarm robot system for educational use. So, the robots should behave on desktop and virtual pheromone should be observable for students. We propose a desktop swarm robot system based on pheromone communication using pen display (Figure 1).

Main components of our system are a pen display and small robots. The pen display shows virtual pheromone, a nest and food resources, and monitors robots' actions. The small robots have color sensors and a pen. The color sensors detect virtual pheromone, nest and food resources shown as graphics on display. The pen of display is used for secreting virtual pheromone.

©ISAROB 2009

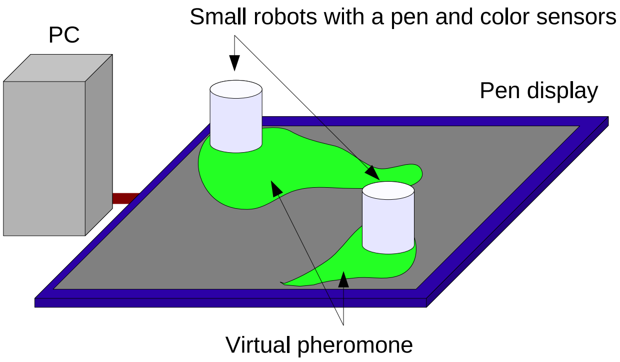

Figure 1: The concept of desktop swarm robot system based on pheromone communication.

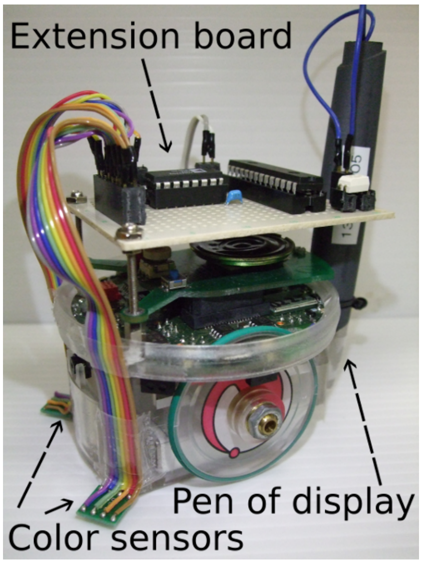

Figure 2: The e-Puck connected with color sensors and a pen of display via extention board.

3.2 Robots

In this study, the e-Puck [4] was adopted as small robot. Two color sensors for detecting colors from display and one pen of display for secreating pheromone were connected to the robot via extension board (Figure 2).

3.3 Pheromone

The 21 inch pen display (Cintiq 21UX) displays virtual pheromone, nest and food as colors on $X \quad Y$ grid like [5, 6].

The robots were able to secrete several types of pheromones at the same point in the environment. However only a pheromone type which is more secreted is displayed on screen.

In the following, the type of pheromone is identified by the subscript v ($v = 1, 2, \quad$). Each robot was capable of depositing pheromones, which subsequently gradually evaporated and diffused. The pen display displayes only diffusing pheromone.

In the following, deposited pheromone and diffusing pheromone are represented by $T_v(x, y)$ and $P_v(x, y)$, respectively, where $T_v(x, y)$ is the intensity of deposited pheromone at position (x, y) and $P_v(x, y)$ is the intensity of diffusing pheromone at position (x, y). The diffusion process was defined by a partial differential equation as follows:

$$T_v^*(x,y) = (1 - \quad_{eva})T_v(x,y) + \sum_{k=1}^{N_a} \Delta T_v^k(x,y) \tag{1}$$

$$\Delta T_v^k(x,y) = \begin{cases} Q_p & \text{if } k\text{-th ant agent on the grid } (x,y) \text{ put the pheromone } v \\ 0 & \text{otherwise} \end{cases} \tag{2}$$

$$\begin{aligned} P_v^*(x,y) = {} & P_v(x,y) + \quad_{dif}(P_v(x-1,y) \\ & + P_v(x,y+1) + P_v(x,y-1) + P_v(x+1,y) \\ & - 5P_v(x,y)) + \quad_{eva}T_v(x,y) \end{aligned} \tag{3}$$

where the parameters $\quad_{eva}$ and $\quad_{dif}$ are the evaporation rate and the diffusion rate of the pheromone per unit time, respectively. The superscript asterisk, "*", denotes the intensity of pheromone at after 200ms, and Q_p is the intensity of the pheromone deposited by a robot.

4 Experiments

Using this system, we conducted the experiments to simulate foraging behaviors of ants. For comparison, we conducted the experiments with robots which was not using pen of display.

4.1 Setting

The robots' behaviors were designed as follows. The robots could secrete two types of pheromone which

©ISAROB 2009

are "food pheromone" and "nest pheromone". The food pheromone, which was deposited by robots on encountering a food resource, indicated the presence of food resources. If robots without food detected this pheromone, they moved along its gradient towards higher pheromone concentrations. The nest pheromone indicated the location of the nest. If robots were in the nest, they deposited this pheromone. If robots that carried food resources detected this pheromone, they moved along its gradient towards higher pheromone concentrations. Figure 3 is the state chart of this behavior.

Table 1 shows meanings of displayed colors. These were distinguishable colors for color sensors in preliminary experiment.

Table 1: Meanings of displayed colors.

Color name	R	G	B	Meaning
White	255	255	255	Nest
Green	34	177	76	Food
Orange	255	126	0	Nest pheromone
Purplish red	153	0	48	Food pheromone
Black	0	0	0	(nothing)

Details of the parameter settings are given in Table 2.

4.2 Results

Figure 4 shows snapshots of experiments.

Table 3 shows average number of times that arrived at the destination (food or nest) per one robot for 15 minutes. One of nding clearly demonstrates the emergence of a pheromone communication that increased the efficiency of foraging in the case of using pheromone. The other is that the efficiency of foraging did not increase with the number of robots because robots obstructed the path of each other and/or pheromone trails were not established.

Table 2: Parameter settings.

X	Y	eva	dif	Q_p
80	60	0.01	0.01	100,000

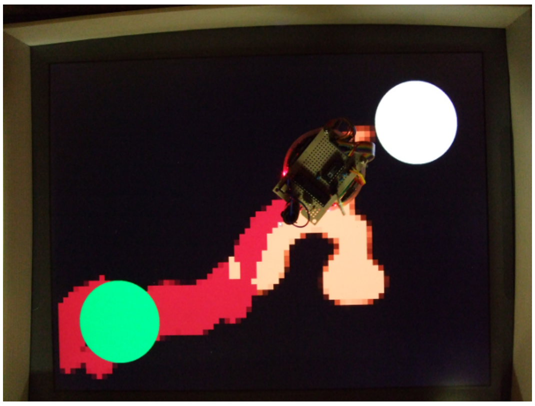

(a) Experiment with one robot.

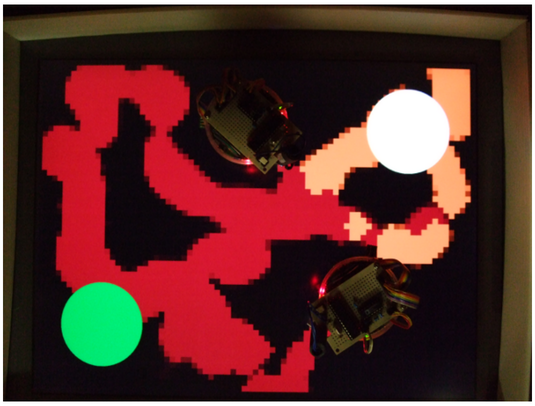

(b) Experiment with two robots.

Figure 4: Snapshots of experiments.

Table 3: Average number of times that arrived at the destination (food or nest) per one robot for 15 minutes.

Number of robots	Pheromone (Pen)	
	Use	Not use
1	25.0	10.0
2	16.5	11.5

5 Conclusion

This paper describes a desktop swarm robot system based on pheromone communication. Using this system, we conducted experiments like ant foraging. In the future works, we will propose using in complex systems education.

©ISAROB 2009

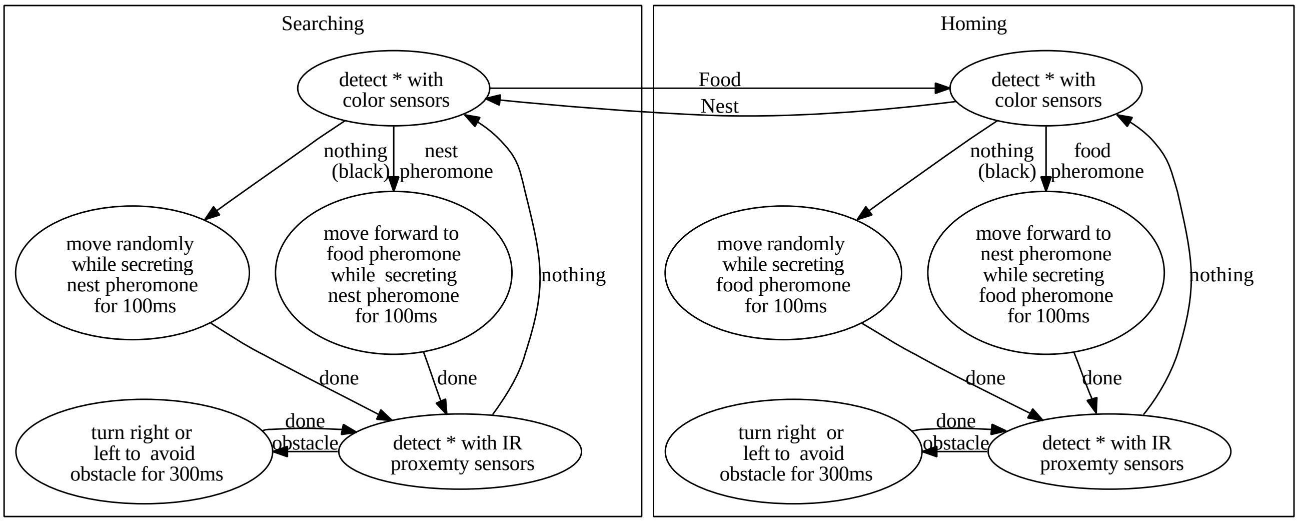

Figure 3: The state chart of robot's behavior.

Acknowledgments

This work was supported by KAKENHI (19700227).

References

[1] D. Payton, M. Daily, R. Estkowski, M. Howard, and C. Lee, "Pheromone robotics," *Autonomous Robots*, vol. 11, no. 3, pp. 319–324, 2001.

[2] T. Kazama, K. Sugawara, and T. Watanabe, "Traffic-like movement on a trail of interacting robots with virtual pheromone," in *Proceedings of the 3rd International Symposium on Autonomous Minirobots for Research and Edutainment (AMiRE 2005)*, pp. 383–388, 2006.

[3] K. Nishinari, K. Sugawara, T. Kazama, A. Schadschneider, and D. Chowdhury, "Modelling of self-driven particles: Foraging ants and pedestrians," *Physica A: Statistical Mechanics and its Applications*, vol. 372, no. 1, pp. 132–141, 2006.

[4] C. M. Cianci, X. Raemy, J. Pugh, and A. Martinoli, "Communication in a swarm of miniature robots: The e-puck as an educational tool for swarm robotics," in *Proceedings of Simulation of Adaptive Behavior (SAB-2006), Swarm Robotics Workshop*, vol. 4433 of *Lecture Notes in Computer Science (LNCS)*, pp. 103–115, 2007.

[5] Y. Nakamichi and T. Arita, *Food Exploitation by Social Insects: Ecological, Behavioral, and Theoretical Approaches*, ch. Evolutionary Simulation of Pheromone Communication in Ant Foraging. CRC Press, in press.

[6] Y. Nakamichi and T. Arita, "An evolutionary simulation of the origin of pheromone communication," *Trans Inform Process Soc Jpn*, vol. 47, no. SIG 1 (TOM 14), pp. 78–88, 2006. (in Japanese).

Subsea Fiber optic cable maintenance using ROV based flux leakage expert system

Md. Reza Hedayati

Scientific-Applied Faculty of Post and Telecommunications
Danesh Blvd., Janah Expressway Azadi Sq., Tehran- Iran
(Tel: +98 21- 446594900, 44654555, Fax: 44659665)
(Email: hedayati@ictfaculty.ir)

Abstract: Word events have increased the demand for secure high band width under water fiber optic communications and at the same time the telecommunications service providers are struggling with maintenance and protection expense containment. As a result of extended usage of the sub sea industries, the number of installed subsea optic services continues to increase and the potential for external aggression resulting to these cables increased.

This paper addresses the evolving subsea especially designed Remotely Operated Vehicle (ROV) with dedicated electromagnetic flux leakage searching arm as a part of associated maintenance arrangement. Current research achievements apply the expert system techniques in the diagnostic system of sub sea fiber optic cables base on the concept of Ampere's law and method of measuring circulating currents without any physical destruction by testing the suspected section which is already subjected to alternating current flow with selected frequencies.

Keywords: Diagnostic, Undersea fiber optic cable, Electromagnetic flux leakage, Expert system

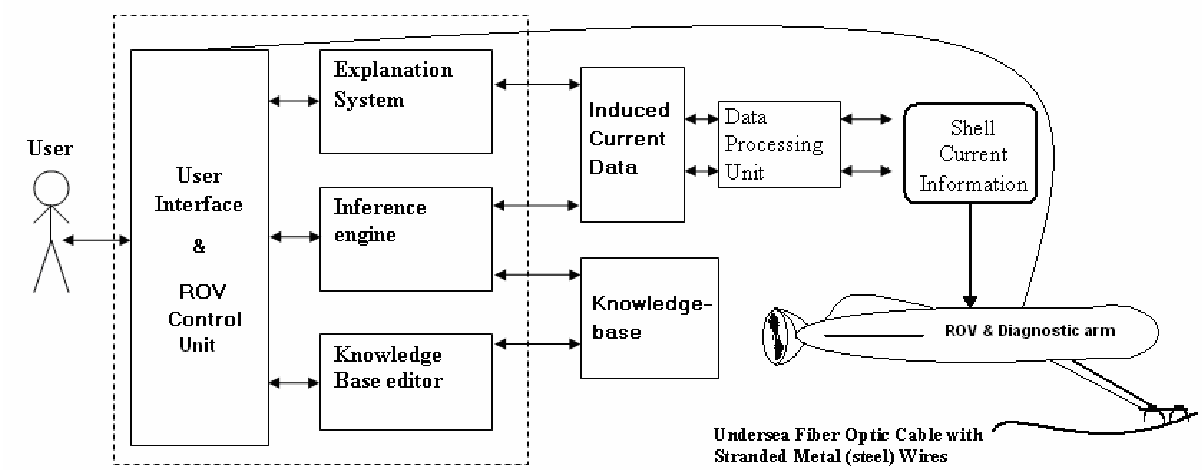

Fig.1. The most important modules of proposed rule-based diagnostic expert system

I. INTRODUCTION

Reduction of the human experts' involvement in the diagnosis process has gradually taken place upon the recent developments in the modern artificial intelligence (AI) tools. Artificial neural networks (ANNs), fuzzy and adaptive fuzzy systems, and expert systems are good candidates for the automation of the diagnostic procedures and e-maintenance application [6, 9]. The present work surveys the principles and criteria of the diagnosis process and introduces these achievements to an expert system technique. In this paper a new sensor design is discussed and experimental results are presented for an expert system application, based on the concept of Ampere's law and method of measuring alternating circulating currents without disturbing their paths for suspected part of undersea fiber optic cable. A transducer using the principle of a toroidal search coil has been tried and considered to be suitable for measuring any probable damage due to irregular phenomenal impact on the suspected superficial portion of the cable. Such transducers are proposed to be the basis for condition monitoring of armored steel structure in the cable by means analyzing the change of e.m.f induced by primary winding of the testing probe.

©ISAROB 2009

The telecommunications service providers have worked out several diagnostic techniques including optical time-domain reflectometer method (OTDR) suiting to individual requirements [1]. Some of these are listed as below:

- Condition monitoring based on video observations
- Leaser detection and monitoring
- Ultrasonic fault and health monitoring device
- Electromagnetic flux leakage (EMFL)diagnostic
- Radiography (X-Ray)

The information already gathered for a healthy cable stored in a data base which can be used by expert system shell. The test personnel interact with the system through a user interface which uses menus and style of interaction. An inference engine is used to reason with both the expert knowledge (extracted from our experienced expert) and data specific to the problem solving. The expert knowledge is in the form of a set of IF-THEN rules. The case specific data includes both data provided by ROV's test personnel (user) and partial conclusions (along with certainty measures) based on this data [4, 6, and 9]. The explanation subsystem, which allows the program to explain its reasoning to the test personnel beside knowledge base editor help the expert or knowledge engineer to easily update and cheek the knowledge base as shown in the Fig (1).

II. Study of Problem

According to the statistics the most important causes of mechanical faults of fiber optic cables in Persian Gulf are included the following:

- Fishing activities
- Aggression due to installation and maintenance of offshore utility installation
- Anchor drop

The effects of the above mentioned activities are in the form of mechanical impact load or stress on the submarine cable which usually it is not possible to diagnosis them through video inspection. The irregular mechanical impact changes the structure of wired steel armor and therefore causes unusual pressure on the fiber housing situated in the middle of the cable. The undersea fiber optic cable which is subjected to these types of unusual mechanical stress is subjected to the disruption of interior fibers in the near future.

The alternating flux generated by semicircular active part of designed sensor is affecting the suspected portion of the cable. In the proposed method asymmetries in the magnetic circuit of damaged section of cable are due to uneven air gap-caused by displacement and misalignment of standard steel wires (armored Surrounding section of the cable). Such asymmetry are inevitable after a high mechanical impact load or stress on the surface of undersea fiber optic cables and changes the permeability of the tested section. Saturation of the steel wire also introduces high order harmonics in the search coil. The important components of induced currents are fundamental, the third and the fifth harmonic, corresponding to the most dominant components in the magnetic field.

The predominance of one component or the other will depend on both the type of the asymmetry and misalignment of the selected wires, which is related to the type of engineering information to be generated with respect to the structure of the armor wires, for the knowledge base which contributes data with the proposed expert system shell through interface engine and knowledge base editor. The half circle transducer clamped around the suspected part of the under surveillance and induced current variation is recorded with respect to healthy portion of the cable.

III. The Principle of EMFL Contact less health monitoring of undersea fiber optic cable

The current value depends on the way the measuring instrument is connected, i.e. the way the connecting leads are laid out. Since it has been seen that in circulating current circuits, the current is the only uniquely defined quantity, its measurement needs grater care than similar measurements in an externally forced current circuit [3, 9]. Whilst the induced emf in the closed contour of the circulating current circuit is a unique value.

$$e = -N\, d\Theta/dt,$$

If the current starts flowing in it, the potential drop between any two points on it is no longer a single-value function. A split type, uniformly wound, flat induction coil with equal cross-section all along the turns, is used for contact less induced cable current measurement, Fig.(4). Such an arrangement facilitates the determination of the enclosed current. If the coil is arranged as a closed loop around a conductor, then the line integral corresponds to the induced cable current in the enclosed conductor. Such a coil must have an inner diameter just more than the diameter at the mounting location. Depending on the type of the coil, it can cover a wide range of induced currents from a few milliamperes to a few tens of miliampers over a wide frequency range, with the help of FFT analyzer. It is well known that the current flowing in a conductor gives rise to the flux around, Fig. (4), illustrating the principle of ampere's law. Mathematically, Ampere's law is expressed as:

$$\oint H.ds \quad = \; I \text{ enclosed}$$

For a circular path C, around suspected part of the cable carrying an induced current. Integrating over the circular contour ,C,

$$B = \mu I / 2\pi r$$

Flux linkage for a toroid of axial length L meter and N turns, of the dimensions as shown in Fig. (4), we have

$$N\Phi = (\mu I L N / 2\pi) [\ln (r_2/r_1)]$$

Voltage induced across the toroidal coil of axial len gth L meters and N turns, and then induced current,

$$i = I_{max} \sin \omega t,$$

$$e_{rms} = \mu L N f [\ln(r_2/r_1)] T_{rms}$$

The above expression is used for designing toroidal search coil used for measurement of current in the suspected part of the cable.

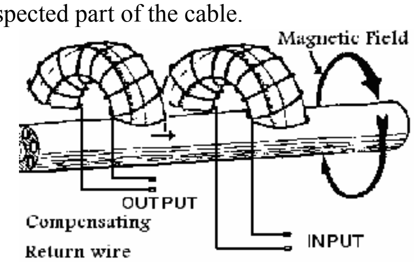

Fig. 4. Current Measurement Principle in the suspected part of subsea fiber optic cable

IV. Typical Test Results

For construction of knowledge base and serving expert system shell, measurement of current in the suspected part of cable, incorporated through data processing unit and induced current data modules. Fabrication, calibration of split toroidal search coil and mounting on the suspected part, resulted to obtain the following induced values on a test cable.

Test results in suspected portion (Which already subjected to mechanical impact load and damaged) indicate that the third harmonic component is predominant. Variation in the behavior and operating condition of the cable will be reflected in the data processing unit and knowledge base module of expert system for proper decision making. Typical induced cable current values are recorded as shown in Fig. (5). for an undersea fiber optic cable.

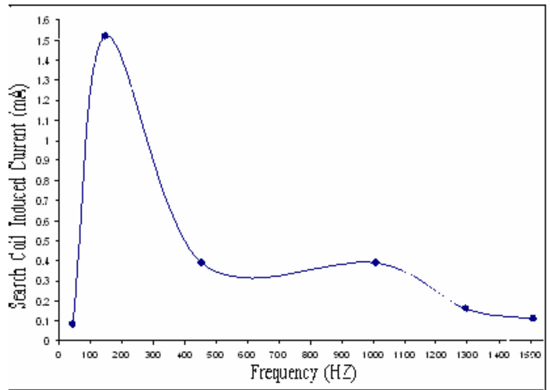

Fig.5. A typical variation of transducer signal for shaft current measurement

Fig. (6) Shows several typical discontinuities and how their corresponding signals may appear on a test screen monitor. Fig.(7) shows the nature of the change can be analyzed and diagnosis made according to the fault and used for construction of knowledge base module.

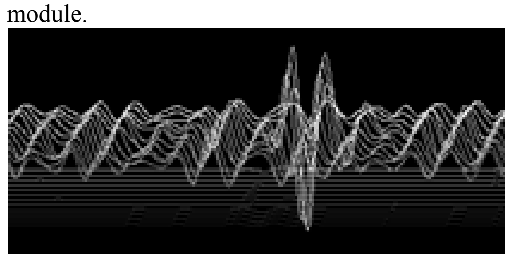

Fig.6: Signal From search coil to data processing unit

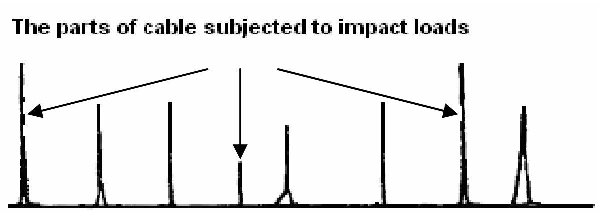

Fig. (7): Samples Data for Knowledge Base Module

V. Conclusions

It is apparent that in the proposed method the perfect undersea fiber optic cable should produce induced voltage more or less than abnormal value. This is never the case, for it is impossible to eliminate all asymmetries in the materials and geometry of the steel wires in the cable. To extract knowledge from the expert the knowledge engineer must become familiar with problem of electromagnetic flux leakage and induced current. The rule base system is goal driven using back ward chaining strategy to test the collected induced current information is true. The case specific data plus the above information with the help of explanation subsystem, allows the program to explain its reasoning to the user and will provide the expert system shell requirements.

Significant difference can exist between the signals created by cable defects. Alternating induced current in undersea fiber optic cable can be measured conveniently and with reasonable accuracy using toroidal coil located by an ROV and proposed diagnostic arm. This device serves as a base for development of expert system monitoring module. The change of reference signal with proposed expert system implies that something within the fiber optic cable structure has altered and diagnosis is made.

References:

[1] Siddique A, Yadava G S, Singh B, (2003) Applications of artificial intelligence techniques for induction machine stator fault diagnostics: review SDEMPED 2003. 4th IEEE International Symposium on Diagnostics for Electric Machines, Power Electronics and Drives 1:29-34

[2] Whitcomb LL (2000) Underwater Robotics: Out of the research laboratory and into the field.IEEE International Conference on Robotics and Automation 1:1-14

[3] Roman H T, Pellegrino B A, Sigrist W R (1993) Pipe crawling inspection robots: an overview IEEE Transaction on Energy Conversion 8 :3:576-583

[4] Han Y, Song Y H, (2003) Condition monitoring techniques for electrical equipment-a literature survey IEEE Transactions on Power Delivery, 1:4-13

[5] Bannon R T (2000) Remotely operated vehicles evolution for maintenance and repair of fiber optic system. OCEANS 2000 MTS/IEEE conference and exhibition 1:489-496

[6] Filippetti, F. Martelli, M. Franceschini, G. Tassoni, C. (1992) Development of expert system knowledge base to on-line diagnosis of rotor electrical faults of induction motors, IEEE Industry Applications Society Annual Meeting, 1:92 - 99

[7] Nandi, S. Toliyat, H.A. (1999) Condition monitoring and fault diagnosis of electrical machines-a review, Industry Applications Conference, IEEE Annual Meeting, 1:115-118

[8] Greska, M (2002) Requirement standards for qualified submarine cable technicians. OCEANS, 2001. MTS/IEEE Conference and Exhibition 1.1: 586-590

[9] Hedayati MR (2004) On-line condition monitoring of locomotives, the 7th Railway conference, Sharif University, (in Persian), Tehran- Iran 1: 60-65

©ISAROB 2009

The Fourteenth International Symposium on Artificial Life and Robotics 2009 (AROB 14th '09),
B-Con Plaza, Beppu, Oita, Japan, February 5 - 7, 2009

Development of A Finger Pointing Interpretation and Speech Recognition System to Operate Virtual World

Takeshi Shiofuku , Norihiro Abe , Yoshihiro Tabuchi
Kyushu Institute of Technology
680-4 Kawadu, Iizuka, Fukuoka 820-8502, Japan
Tel : 81-948-29-7776
shiofuku@sein.mse.kyutech.ac.jp,

Hirokazu Taki
Wakayama University
930 Sakaedani, Wakayama-shi
Wakayama 680-8510, Japan
taki@sys.wakayama-u.ac.jp

Shoujie He
VuCOMP,
hesj@computer.org

Abstract:
In this research, the system constructed achieved the goal of real-time interaction with the virtual world through the interpretation of finger point gestures and speech recognition. Recently, Interaction with a computer is, however, mainly through a mouse and keyboard, which are not user-friendly enough for the majority. So, it is imperative to develop straightforward and easy-to-use user interface for computers. We made the system that was able to operate virtual objects with pointing action and voice without using an expensive, special device such as cyber gloves. The system was divided into voice recognition, pointing gesture recognition, and virtual world managing system as the processing time grew if these systems were executed with one PC. Data was shared by communicating data among them, and the decentralization allows the system to work in real time. The user is now able to specify a virtual object to be operated with pointing action, and will be able to operate it by voice.
Keywords: Pointing action, Speech recognition, Real time

1. INTRODUCTION

With the advancement of data processing and telecommunication technologies, more and more people are using the Internet in their daily life. So far, the Internet had been mainly used for collecting information and sending or receiving email messages. The widely deployed fiber optics based high-speed communication networks and the lower-price and high-performance computers make it possible to telecommunicate the data-intensive content such as voice, images, and video over the Internet. At the same time, VR technologies that used to be time-consuming in data rendering also had attained significant progress.

Interaction with a computer is, however, mainly through a mouse and keyboards, which are not user-friendly enough for the majority. People who are used to such devices could easily collect huge amount of information through the Internet. On the other hand, people who are not familiar with the usage of them could hardly benefit from the availability of the Internet technologies. In order to improve the unbalanced situation in terms of information collection, it is imperative to develop straightforward and easy-to-use user interface for computers.

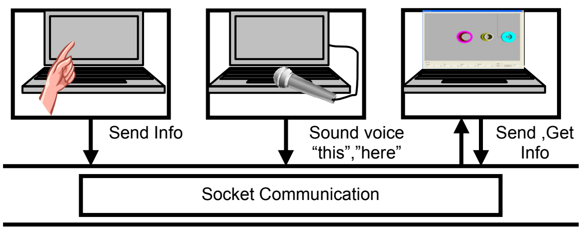

Figure 1: Concurrent processing among 3 PCs.

Then, in this research we developed pointing-recognition and speech-recognition system to operate virtual objects in virtual space. This system consists of three parts: In the vision part, user's pointing action is recognized based on image information obtained from cameras. The language processing part which

©ISAROB 2009

©ISAROB 2009

recognizes user's voice acquired with a mike. The display part shows a virtual world and allows a user to convey the requirement from a user to the system by using voice and action.

2. System Configuration

In this system, the application program is written in C++. The development environment is Microsoft visual C++.Net and we used the voice recognition soft that is called Dragon Naturally Speaking. Then, in order to recognize the gesture of pointing, we used 2 CCD cameras.

Table 1 : System configuration

Graphic library	OpenGL
Gesture recognition	2 CCD Cameras
Develop environment	Microsoft visual C++ . NET
Voice recognition	Dragon Naturally Speaking
Data communication	Socket communication(UDP)

This system does the parallel processing while communicating data each other among three systems managing pointing recognition, voice recognition, and a virtual space, respectively.

2.1 Research Environment

Figure 2 shows the research environment. The two cameras are set at the left side with the optical axes in parallel. It is supposed no fresh colored object to be put in the background.

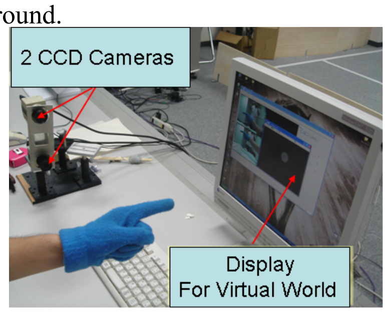

Fig2: Research Environment

3 Theory

3.1 UDP Communication

We use UDP communication protocol for the synchronization among the three PCs. In order to improve reliability, memory of each PC is always updated to the fresh data whenever the system writes data into memory.

3.1.1 Multicast

UDP can simultaneously transmit data to multiple destinations with the multicast option.

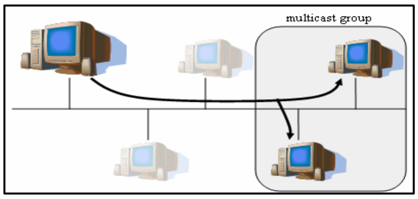

Figure 3: Multicast

In the multicast communication, data are transmitted to the PCs that participate in the multicast group (Figure 3).

- Reliability of data

UDP is a high-speed communication, but it is lack of reliability. The following approach has been taken to improve the reliability.

- Distinction of Information

If only a single port is available, information collides and the data loss will occur at the time when data are transmitted from VR, Voice, and Vision unit (Figure 4).

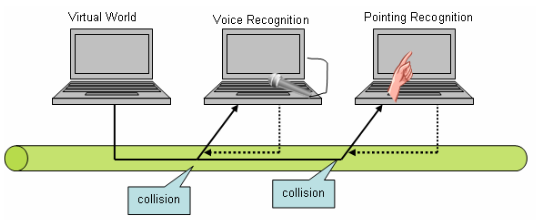

Figure 4: Collision of data

To avoid the collision, three ports are exclusively prepared for VR, Voice recognition system, and Pointing recognition system (Figure 5). This way prevents the data collision from happening.

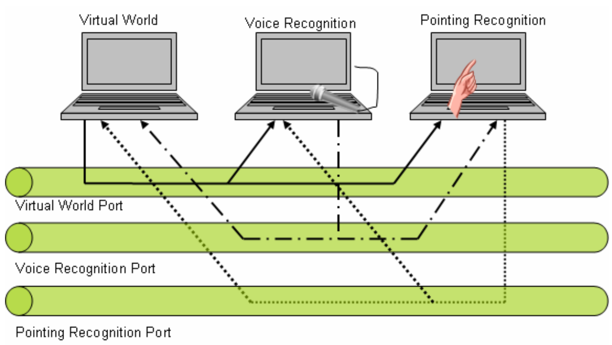

Figure 5: Each port

©ISAROB 2009

3.2 Pointing information acquisition

In order to detect the pointing direction, the system must extract flesh-colored regions from the image and assign a label to each region by removing noises. To calculate the vector of a forefinger, two characteristic points of the forefinger are detected.

3.2.1 HSV conversion

The original image data captured from the camera are in RGB color system. It is, however, difficult to set the range of the target colors in this color system.

This problem could be resolved by using the HSV color system. In the HSV system, the person can express the color sensuously. It is necessary to convert the image data from the RGB color system to the HSV color system. In the HSV color system, it is empirically known that a flesh-colored area is within the following ranges. Figure 3 shows the result with the flesh-colored region extracted.

Hue	: $-75 < H < 40$	(Range : 0~360)
Saturation	: $40 < S < 200$	(Range : 0~255)
Varue	: $0 < V < 255$	(Range : 0~255)

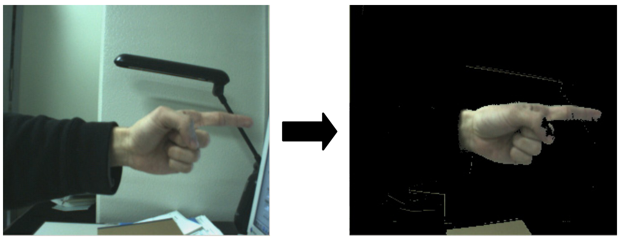

Fig6: The extracted flesh-colored image

3.2.2 Labeling

Labeling is a process of assigning a different label to each of the connected components. In this research, we used the run-length method in which the regions with a small area were removed.

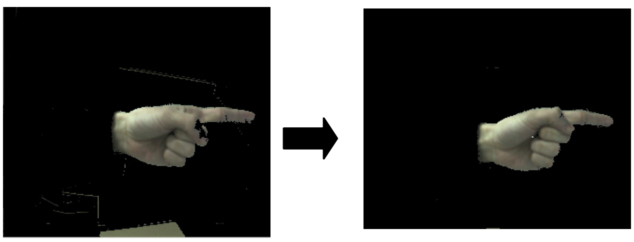

Fig7: The labeling

3.2.3 Characteristic Point Detection

The first characteristic point of a finger is a fingertip point. The other point is decided by comparing the amounts of the pixel forming the finger tip to back the hand.

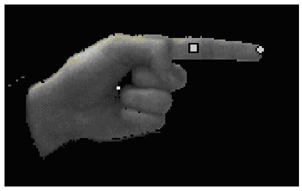

Fig8: Characteristic Point

The comparison equation is as follows. The index i is taken in a horizontal axis and x_dis[i] shows amount of pixels.

$$x\_dis[i] > x\_dis[i+5] * 1.5 \qquad (1)$$

3.2.4 Stereo vision

Stereovision is a method of observing the same object from two different view points and measuring three dimension position of the object by the parallax of characteristic points. As shown in Figure 8, the three-dimensional coordinates of object P can be measured with the formulae (2), (3) and (4). Length in Figure 9 shows the distance between cameras, and f shows the focal length of the cameras.

$$X = Length \frac{(XL + XR)/2}{XL - XR} \qquad (2)$$

$$Y = Length \frac{YL/2}{XL - XR} \qquad (3)$$

$$Z = Length \frac{f}{XL - XR} \qquad (4)$$

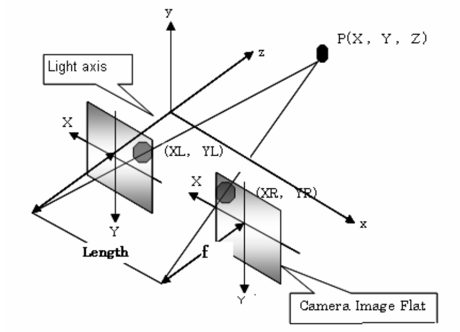

Fig9: Three-dimensional positional coordinates

3.3 Speech Recognition System

Speech recognition is achieved with a software package named Dragon Naturally Speaking. Dragon Naturally Speaking attains highly accurate voice recognition, and can translate the input voice into a sentence consisting of hiragana and Chinese characters. The speech recognition system retrieves the word from the set of words registered beforehand. The registered

©ISAROB 2009

word is limited only to a word set necessary for operating virtual objects.

For example, if the inputted sentence is "Move the paper to the position", the following words are detected: "Move", "Paper" and "Position" from the input voice.

3.4 Virtual World Operating System

The virtual space is constructed with OpenGL, a well-known graphics library. With this rendering technology, it is possible to construct a 3D world, where complex spatial relationships that are impossible to represent in a 2D world are easily handled. This system manipulates virtual objects according to the instruction recognized by the above-mentioned pointing recognition and speech recognition system. Concretely, this system determines which point within the display the user specified by referring to the coordinates acquired by the pointing action recognition system.

If the point is included in one of regions shown in. [Fig10], the system changes the current view point into the point where the user wants as shown in [Fig.11], but the point is included in the region of a virtual objects and if voice input includes a demonstrative pronoun, the system interprets that the user specified a virtual object to be operated.

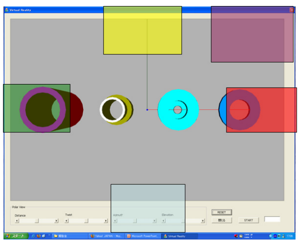

Fig10：Eyes Moved Area

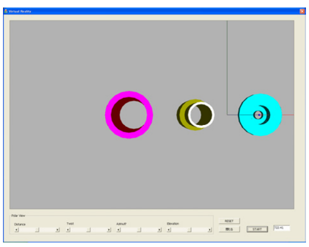

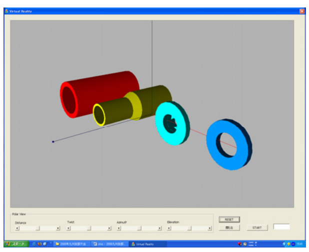

(a)Eyes view movement to the left (b) Rotation around axis
Fig11: Eyes View Movement

4. Conclusions

The system constructed in this research achieves the goal of real-time interaction with the virtual world through the interpretation of finger point gestures and voice without using expensive tool such as a data glove. The translational/rotational movement of a viewpoint in the global coordinate system and manipulation of virtual objects in the local coordinate system are both performed in real-time. Since these operations make assembling/disassembling virtual object intuitive and easy, the high reality feeling as if real objects were manipulated is attained.

5. Future Work

Experimental results shows that the blur of finger caused by hand motion directly affect the accuracy in extracting feature points of a forefinger. In addition, to give much more real feeling, it is necessary to introduce collision detection between virtual objects. This is an issue in the future.

6. Acknowledgement

We greatly appreciate the Grant-in-Aid for Scientific Research(S) and (A).

7. REFERENCES

[1]Yoshiaki Shirai ,Masahiko Taniuchida "Pattern information processing" ohmsha,1998

[2]Yasuhiro Watanabe, Norihiro Abe, Kazuaki Tanaka, Hirokazu Taki, Tetsuya Yagi,Multimodal communication system allowing man and avatar to use voice and beck,3rd International Conference on Information Technology and Applications (ICITA'2005), pp.161-166

[3] Tatsuya Yoshikawa, Syunji Uchino, Norihiro Abe, Kazuaki Tanaka, Hirokazu Taki, Tetsuya Yagi, Shoujie He: Voice and gesture recognition system facilitating Communication between man and virtual agent, INVITE2006 International Conference on Parallel and Distributed Systems), Vol.2, pp.673-677, 2006

[4]Syunji Uchino, Norihiro Abe, Shoujie He, Hirokazu Taki, "Real-time Interactive Dialog System between Person and Virtual Agent", accepted, International Symposium on Artificial Life and Robotics (AROB 2007)

©ISAROB 2009

The Fourteenth International Symposium on Artificial Life and Robotics 2009 (AROB 14th '09),
B-Con Plaza, Beppu, Oita, Japan, February 5 - 7, 2009

Entire Shape Recovery Employing Virtual See-through Cameras

K. Mori, T. Sone, J. K. Tan, H. Kim, S. Ishikawa

Kyushu Institute of Technology
1-1 Sensui-cho, Tobata-ku, Kitakyushu, Fukuoka 804-8550, Japan
(Tel: 81-93-884-3183; Fax: 81-93-884-3183)
(ishikawa@cntl.kyutech.ac.jp)

Abstract: The present paper describes a novel technique for simultaneous entire shape recovery of an object by use of multiple cameras surrounding the object. The rear shape is transformed to frontal view information and it is merged with the frontal view information into an entire shape information to which factorization is applied. This camera system is named a virtual see-through camera system, since the frontal cameras see through the rear shape as if the object is transparent. Experimental results show satisfactory performance of the technique.

Keywords: shape recovery, 3-D modeling, see-through, factorization, computer vision

I. INTRODUCTION

Three-dimensional modeling of our living environment is of great importance in simulating our various activities and planning better life. When we want to buy furniture, we are able to see its fitness in a house by looking into a virtual house equipped with the furniture. Creating a new building should be examined its appearance and fitness in the area where it is to be built by modeling the area and the building in a virtual space. These are the examples of useful applications of a virtual reality technology, in which various 3-D object models are created and employed.

Hence 3-D object modeling techniques employing cameras [1] have been studied rigorously to date in the computer vision community. The technique employing stereo cameras has long been used as a standard technique. This has become much popular since the proposal of the DLT [2] by which one doesn't have to acquire inner as well as outer camera parameters directly. Instead it employs a 3-D calibration tool and acquires the projective relation between the 3-D space and the image plane of an observing camera. The factorization method [3] further simplifies the 3-D modeling strategy. In the method, a single mobile camera takes images of a rigid object from multiple orientations and the method recovers the 3-D shape of the commonly observed part of the object along with recovering the camera motion, although it contains linear approximation in imaging by the camera.

The issue focused in the present paper is 3-D modeling of the entire shape of an object. Normally this is achieved by a set of cameras surrounding the object concerned. In an optical motion capture system, many calibrated cameras are placed fixed in a large studio and capture video images of an actor playing some action from multiple orientations. The basic recovery technique is stereo vision. Every pair of stereo cameras recovers the shape of the object within its view. The shape is partial in most cases, since the fixed camera pair cannot observe an opposite side of the object. The resultant partial 3-D shapes are merged into an entire shape, yielding a 3-D model of the object. In this procedure, registration technique [4] must be employed in order to connect the partial shapes one by one with the least connection errors in a 3-D space. This requests the system strict camera calibration. Simultaneous entire shape recovery without the registration would be the best for reducing computational load.

One also notices by the above explanation that it is not very simple to apply the technique to various kinds of 3-D object modeling. The image taking cameras need be calibrated in advance. How can it then be applied to the 3-D modeling of a street performer who won't wait for the advance camera calibration? How can it be applied to 3-D modeling of a statue around which many people gather in a marketplace? Thus one notices the advantage of a 3-D modeling technique based on image-based camera calibration.

In the present paper, a novel 3-D modeling technique is presented which performs simultaneous entire shape recovery based on image-based camera calibration. A similar technique was invented by some of the authors [5]. It gave restriction on the camera arrangement, however, that a facing cameras need colinearity with their principal axes. The restriction imposed on the proposed technique is that at least three points need be shared among observing cameras around the object concerned. These points in captured images are employed for camera calibration. This simpler constraint can be realized often easily when every camera is set so that it looks down the object. Thus it results in more flexible arrangement of the surrounding cameras compared to [5].

The idea of simultaneous recovery is explained in the following. The proposed technique applies the factorization to the 3-D shape recovery. The factorization [3] claims that, once a point, actually its 2-D image coordinates, is included in a measurement matrix, it recovers the 3-D location by factorizing the measurement matrix. Therefore the locations of rear points on an object are transformed to the locations where the frontal cameras would observe them if the object is transparent, and the transformed points are included in the measurement matrix defined by the frontal points, which yields an entire measurement matrix. By factorizing this matrix, all the specified points that spread over the object recover their 3-D locations and hence the entire 3-D modeling is done. Since the above procedure can be described that frontal cameras see through rear shape of an object as well as its frontal part, they are referred to *virtual see-through cameras*. Formulation of the present technique and experimental results are given in the following with discussion and conclusions.

II. PROCEDURE

The cameras surrounding an object are categorized into frontal cameras C^F and rear cameras C^R. Since the present technique recovers point location, the points for the recovery are specified on an object. They are classified into three sets. The point commonly observable from the both cameras C^F and C^R is denoted by P^{FR} which is an element of a set $G(P^{FR})$: The point observable only from the frontal cameras is denoted by P^{F-} which is an element of a set $G(P^{F-})$: The point observable only from the rear cameras is denoted by P^{-R} which is an element of a set $G(P^{-R})$. Then the set of points which the frontal cameras C^F observe is given by $G(P^F)= G(P^{FR}) \cup G(P^{F-})$, whereas the set of points the rear cameras C^R observe is given by $G(P^R)= G(P^{FR}) \cup G(P^{-R})$. See **Fig. 1** for example.

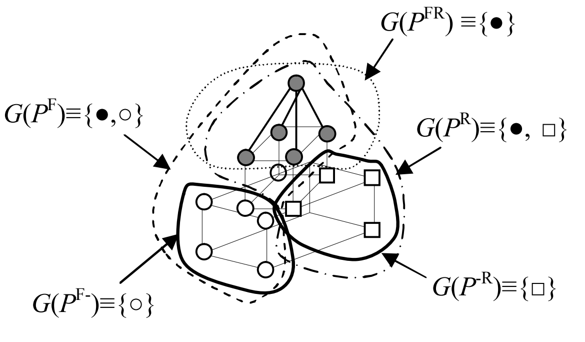

Fig. 1. Categorized points on an object. The points commonly observable from frontal and rear cameras, observable only from frontal cameras, and observable only from rear cameras are denoted by ●, ○, and □, respectively.

The application of the factorization with respect to the frontal cameras and to the points in the set $G(P^F)$ provides the following equation;

$$W^F=M^F S^F \tag{1}$$

Here W^F is a measurement matrix defined by the *xy*-coordinates of the points in the set $G(P^F)$, S^F is a shape matrix containing their 3-D coordinates, and M^F is an orientation matrix giving the orientations of the frontal cameras.

Matrix S^F in Eq. (1) can be decomposed into

$$S^F=\{S^{FR}|S^{F-}\} \tag{2}$$

Here S^{FR} is the shape matrix giving the 3-D coordinates of the points in the set $G(P^{FR})$ and S^{F-} is that giving the 3-D coordinates of the points in the set $G(P^{F-})$.

Employing the matrix S^{FR}, the orientation matrix of rear cameras denoted by M^R satisfies the following relation;

$$W^{FR}=M^R S^{FR} \tag{3}$$

where W^{FR} is the measurement matrix with respect to the points in $G(P^{FR})$. Since W^{FR} is known in an experiment and S^{FR} is given by Eq. (2), we have

$$M^R= W^{FR}[S^{FR}]^T(S^{FR}[S^{FR}]^T)^{-1} \tag{4}$$

The points in the set $G(P^{F-})$ are then projected virtually onto the image planes of the rear cameras by

$$V^{F-}=M^R S^{F-} \tag{5}$$

By this projection, the rear cameras have the measurement matrix W^R that contains all the projected points;

$$W^R=\{W^{FR}|V^{F-}|W^{-R}\} \tag{6}$$

On the other hand, the following holds with the set $G(P^{-R})$;

$$W^{-R}=M^R S^{-R} \tag{7}$$

Since W^{-R} is known and M^R is given by Eq. (4), we have

$$S^{-R}=([M^R]^T M^R)^{-1} \ [M^R]^T W^{-R} \tag{8}$$

The shape matrix S^{-R} gives the 3-D coordinates of the points in the set $G(P^{-R})$. They are projected virtually onto the image planes of the frontal cameras by

$$V^{-R}=M^F S^{-R} \tag{9}$$

Then we have the measurement matrix of the form

$$W^F=\{W^{FR}|\ W^{F-}|V^{-R}\} \tag{10}$$

Finally, from Eqs. (6) and (10), we have an overall measurement matrix W of the form (See also **Fig. 2**.)

$$W = \begin{pmatrix} W^F \\ \cdots\cdots \\ W^R \end{pmatrix} \tag{11}$$

In this way, all the selected points on object O have been projected onto the image planes of all the

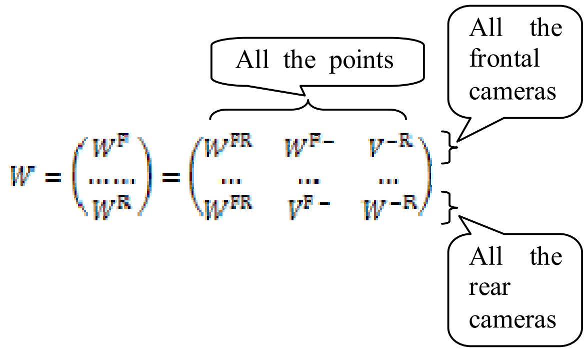

Fig. 2. Matrix *W* containing all the point information with all the surrounding cameras.

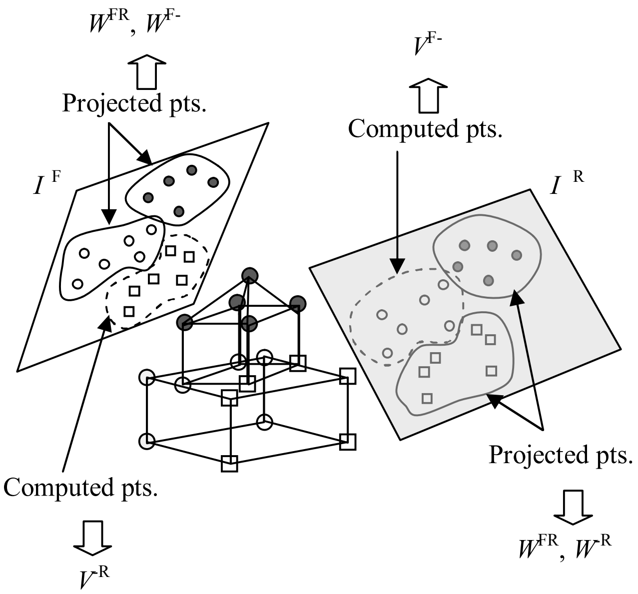

Fig. 3. Virtual see-through camera. Observable points in a scene are projected directly onto the image plane of a camera, whereas unobservable points are computed their projected locations in the image plane and included in it. The points □ cannot be seen from frontal cameras and their locations on the frontal image planes I^F are computed. In the same way, the points ○ are not seen from rear cameras and their locations on the rear image planes I^R are computed.

surrounding cameras. In another expression, all the points on object *O* have been observed by all the virtual see-through cameras. See **Fig. 3** for the idea.

The matrix *W* of Eq. (11) is factorized as

$$W=MS \tag{12}$$

providing the final orientation matrix *M* of all the cameras and the shape matrix *S* of all the points on the object. Matrix *S* gives the 3-D point model of object *O*.

It is noted that Eq. (11) represents the geometrical constraints of all the points on object *O* in the orientation of all the cameras. From the factorization shown by Eq. (12), a 3-D model that satisfies the constraints best in the sense of the LMS errors is obtained.

III. EXPERIMENTAL RESULTS

An experiment was conducted to examine the performance of the proposed technique. Instead of employing multiple cameras, as shown in **Fig. 4**, a single digital video camera and a turntable was used for taking images of a polyhedron from multiple orientations. The turntable was given turns manually. The angles of the turns were not very strict as the values are not employed in the recovery calculation. The employed factorization assumed weak perspective projection with the camera imaging. This linear projection well approximates the imaging by a lens when the thickness of the object concerned is 1/10 or less of the distance from the camera to the object [6].

Figure 5 shows the result of the entire 3-D recovery of a polyhedron. The polyhedral images were taken from 4 to 6 orientations. The recovery errors were calculated with respect to the side lengths and the angles the adjacent sides make at the vertices. The result is shown in **Table 1**. The average recovery error is 1.66% with the side lengths, where it is 2.27% with the angles. The recovery errors decrease monotonically according to the increase of camera observation orientations. As the geometrical constraints increase, more exact recovery is realized.

Fig. 4. Experimental setup: A digital video camera and a turntable on which an object is placed. The turntable is given turns manually for multiple views by the camera.

Table 1. Relative recovery errors of a polyhedron with respect to side lengths and angles at vertices.

No. of camera orientations	Side length	Angle
4	1.85	2.57
5	1.79	2.42
6	1.68	2.14
7	1.54	2.12
8	1.44	2.09

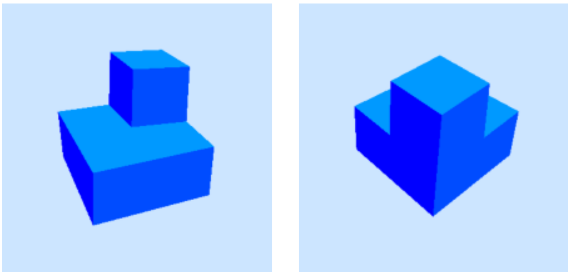

Fig. 5. Recovered polyhedron rendered from its 3-D point model: Frontal view (the left) and rear view (the right).

V. CONCLUSIONS

A technique was presented for recovering entire shape of an object by use of multiple surrounding cameras. The idea was to merge the rear shape information with the frontal shape information, and vice versa. The procedure was described as the information acquisition of the opposite side of an object by a virtual see-through camera. The shape recovery achieved satisfactory performance by taking geometrical constraints in multiple orientations into account simultaneously. This is the most important issue in the technique. The simultaneous consideration of the multiple geometrical constraints may result in less distortion with the recovered shape.

The presented technique can also be applied to non-rigid object recovery [7,8] by arranging multiple cameras around it, instead of a single camera and a turntable. The camera arrangement is more flexible in the technique compared to [8], and it may even be employed outdoors, since camera calibration is done by use of acquired images, i.e., image-based camera calibration.

The presented shape recovery is the recovery of the 3-D location of a point in a 3-D space and it provides a 3-D model of an object in the form of a point set. Hence graphical operation follows the present technique to make a solid model. This is a little disadvantage compared to a back projection technique [9], where a volumetric 3-D model is directly obtained without choosing points on an object, although concave parts cannot recover by the technique.

Those points specified on an object were categorized into three classes, i.e., the class of a point observable commonly from frontal as well as rear cameras, the class of a point observable only from frontal cameras, and the class of a point observable only from rear cameras. This categorization was done manually. It isn't necessarily be automated, since the present subject is 3-D modeling and not automatic recognition. Machine categorization and human examination may, however, realize a time saving and efficient modeling system.

The authors have been developing a man-machine interface system employing a camera mounted on the display of a computer. The system watches a user in front of a computer by the camera and recognizes his/her hand gestures by which a 3-D object in the display moves and rotates in a 3-D way. The present technique is going to be employed for providing the system with 3-D models of objects.

REFERENCES

[1] Gonzalez, R. C., Wintz, P.: *Digital Image Processing*, Addison Wesley, 1987.
[2] Abdel-Aziz, Y. I., Karara, H. M.: "Direct linear transformation from comparator coordinates into object space coordinates in close-range photogrammetry", *Proc. Symp. Close-Range Photogrammetry*, pp.1-18, 1971.
[3] Tomasi, C., Kanade, T.: "Shape from motion under orthography: A factorization method", *Int. J. Comput. Vision*, Vol.9, Vo.2, pp.137-154. 1992.
[4] Cheng, Y., Medioni, G.: "Object modeling by registration of multiple range images", *Image and Vision Computing*, vol.10, no.3, pp.145-155, 1992.
[5] Tan, J. K., Ishikawa, S.: "Recovering entire shape of a deformable object employing a single measurement matrix", *Proc. 1999 IEEE Int. Conf. on Image Processing*, CD-ROM, 27PP5A.4, 1999.
[6] Sato, J.: Computer Vision – Geometry of Vision, Corona Publishing, 1999. (in Japanese)
[7] Tan J. K., Ishikawa S.: "Deformable shape recovery by factorization based on a spatiotemporal measurement matrix", *Computer Vision and Image Understanding*, Vol. 82, No. 2, pp.101-109, 2001.
[8] Tan, J. K., Ishikawa, S., Hirokawa, S.: "A fully 3-D modeling method of non-rigid objects from multiple views", *J. Inst. Image Electron. Eng. Japan*, Vol.32, No.4, pp.483-487, 2003. (in Japanese)
[9] Uchinoumi M., Tan J. K., Ishikawa S.: "A simple structured real-time motion capture system employing silhouette images", *Proc. IEEE Int. Conf. on Systems, Man and Cybernetics*, pp.3094-3098 (Oct., 2004).

The Fourteenth International Symposium on Artificial Life and Robotics 2009 (AROB 14th '09),
B-Con Plaza, Beppu, Oita, Japan, February 5 - 7, 2009

Autonomous Control of Mobile Robots by Image Data Processing and Development of the Simulation System

Ryutaro Mizokami Yoshihiro Tabuchi Norihiro Abe
Kyushu Institute of Technology graduate school Information System Major,
680-4 Kawazu Iizuka, Fukuoka 820-8502, Japan
(Tel 08-948-29-7776)
(E-mail mizokami@sein.mse.kyutech.ac.jp)

Hirokazu Taki
Wakayama University
930 Sakaedani, Wakayama-shi
Wakayama 680-8510, Japan

Shoujie He
VuCOMP,
U.S.A.

Abstract: Recently, the cases where the autonomous mobile robots enter into human society have increased. However, it is rare that a large number of robots share the narrow space, because it is too danger for them to avoid other robots in real time. Therefore, this research aims at developing a system to simulate the behavior of multiple robots when they share the same environment.

This system eventually aims at overcoming a lot of weak points caused when robots are controlled in real space.

As a result, it succeeded in the simultaneous control of two or more robots which use the image processing as a method of measuring environment. .

Keywords: Autonomous mobile robot, Image processing, Virtual realty

I. INTRODUCTION

A lot of robots are widespread together with the development of robot industry. Especially autonomous mobile robots are expected to solve the problems such as "nursing care of the senior citizens" and "decrease in the percentage of working force",

However, their development needs expensive cost. Additionally the behavior of them must be debugged using real machinery in real environment, but it is difficult to test the behavior in various real environments because of the difficulty of building such environment in real space. Further the debugging in the habitat like a slope or stairs is so difficult for fear of destructing robots..

To solve these problems, the simulation system using virtual reality space is brought to attention. "Virtual reality space" is the world actuality made by a computer. The system helps developers to construct robots with high reliability because the algorithm and the specification to control them can be examined before real machinery is made.

Then, this research aims at controlling a large numbers of robots autonomously. As the first step, the concrete target of this research is the following two

1. In a real space, to make a mobile robot with the network camera evade autonomously obstacles.
2. To develop the simulation system of robots control. (in the virtual space, generating multiple numbers of virtual robots with the same configuration as real ones are generated, we would like to solve problems occurring when they move around.)

II. ROBOT CONTROL IN REAL SPACE

In this chapter, it is a purpose to make a single mobile robot equipped with the network camera evades the obstacle autonomously in a real space.

1. System Overview

Our robot's composition is so simple and is equipped with a network camera, a wireless LAN card and a motor driver. This composition makes it possible for a PC outside of the robot to drive the robot by receiving and processing an image from the robot and then transmitting motion commands to the robot. As a result, we succeeded in the miniaturization of the robot because it is needles to mount a PC on a robot.

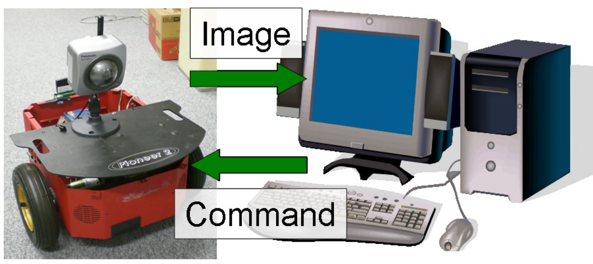

Fig.1. System Overview

As shown in Fig. 2, a network camera is installed forward on the robot. And a motor driver and a wireless LAN card are set up inside and in the rear of the robot, respectively.

©ISAROB 2009

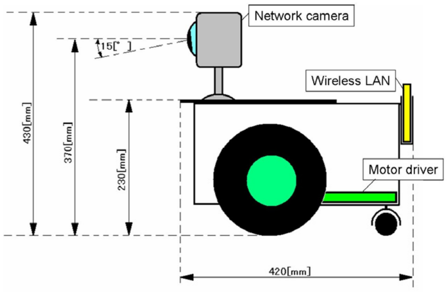

Fig. 2 Robot Overview

2. Algorithm for Dodging Obstacles

The robot recognizes the floor in front of itself to roam indoors. In this algorithm, a robot regards everything except for a floor as obstacles and drives while avoiding them.

A. Floor-Extraction Algorithm

Floor-Extraction is conducted according to the following steps.

Step 1: The image is captured. (Fig. 3 (a))

Step 2: The lower area of the image is extracted. (Fig. 3 (b))

Step 3: Floor surface is extracted based on the floor color information acquired from five yellow points as shown in Fig.3 (c). (Fig. 3(d))

Step 4: A robot keeps the color of a floor updating because a light may give effect to the color.

Note here that the algorithm assumes that no obstacle is in front of the robot immediately before it starts driving and there is no pattern on a floor.

Red area in Fig.3 (d) is regarded as a non-target of image processing because it is far from a robot. Blue area is recognized as the floor while green area is recognized as that including obstacles.

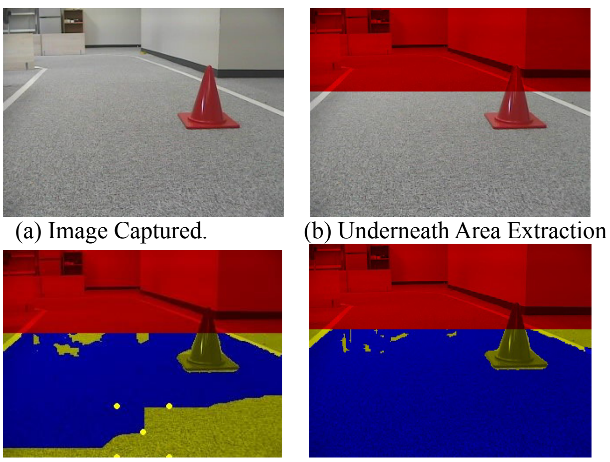

(a) Image Captured. (b) Underneath Area Extraction

(c) Floor-Extraction (d) Resultant image

Fig.3. Appearance of Floor-Extraction

B. Choice of Motion Command

The robot is controlled by five kinds of operation. They are "direct advance", "curve to the left", "curve to the right", "counter-clockwise turning" and "clockwise turning". When a robot confirms an image of the extracted floor, it selects and drives the appropriate operation from them.

It judges the possibility of going straight by examining whether the free area recognized as the floor is included in yellow and green rectangles shown in Fig.4. Otherwise, the free areas included in green rectangles are checked out, and if the occupied area including obstacles is small, it is judged that the robot can take a curve. In the case, the direction where obstacles can be evaded effectively is judged on the comparison of the areas included in the right and left yellow rectangles. Finally, it is judged on the areas included in green rectangles whether a right or left curve can efficiently evade the obstacle.

These results are stored in the memory of 4bit as shown in Fig. 5. The operation corresponding to the lowest bit among bits whose value is 1, in the case shown in the figure LEFT, is selected as the most plausible motion.

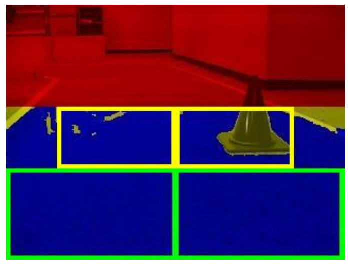

Fig. 4 Rectangle to Choice the Action

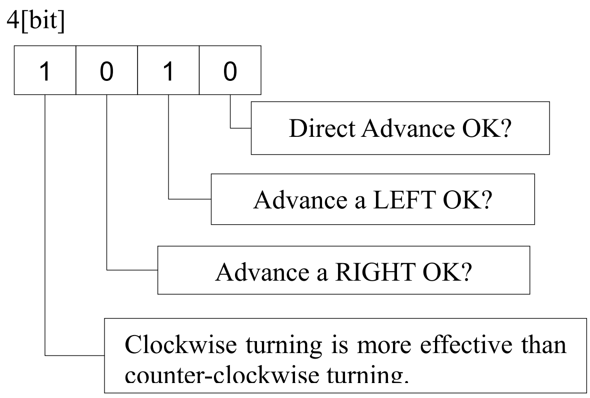

Fig. 5 Storage of Operable Action

C. Algorithm to give a weight to an obstacle

The operation selected by a robot may continuously change when the difference between the amount of a right side floor and that of a left side floor is little. So the algorithm puts a weight on an obstacle so that the operation is stably selected. For example when a clockwise turning is selected, the weight of obstacles in the left rectangle is increased.

4. Experimental Methodology

We had a robot move in the environment shown in Fig. 6. The gray region in Fig. 6 is a course in which a red triangle is an initial position of the robot, and it a blue rectangle is an obstacle.

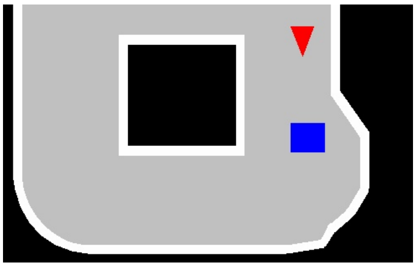

Fig. 6 Experimental environment

5. Result

The robot successfully confirms the floor region and wanders dodging an obstacle in front to of it by selecting suitable operation as shown in Fig. 7. Additionally, it successfully goes along the boundary of the course by recognizing it as well as the obstacle.

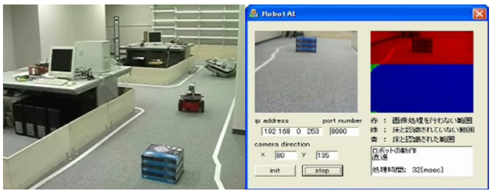

(a) Time = 0.0[sec]

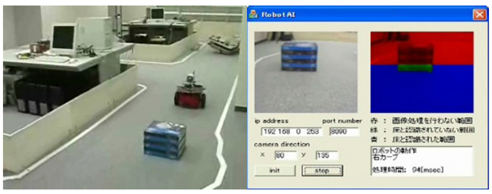

(b) Time = 4.0[sec]

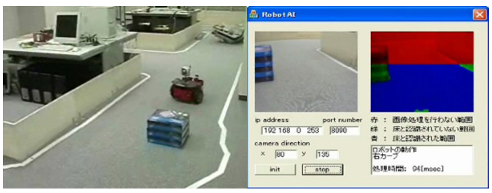

(c) Time = 5.5[sec]

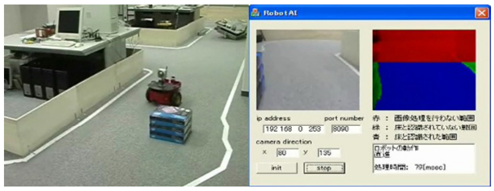

(d) Time = 8.0[sec]

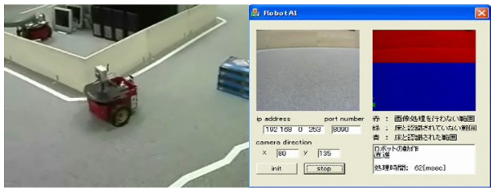

(e) Time = 12.0[sec]

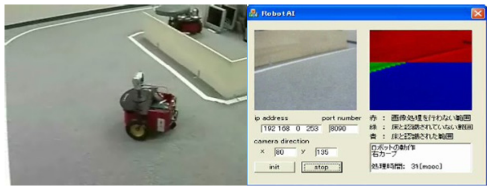

(e) Time = 15.5[sec]

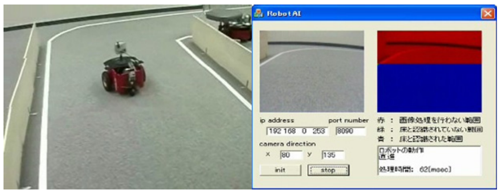

(f) Time = 18.5[sec]

Fig.7. Locus of Robot

III. ROBOT CONTROL IN VIRTUAL SPACE

In this chapter, it is a target to simulate the control of virtual robots in virtual space.

So the specific targets are the following two.

1. To make the system simulate the control of virtual robots.
2. To drive virtual robots of which functions are the same as the real ones.

1. System Overview

One server computer has information of both a virtual space and virtual robots in the simulation system. And each client computer remotely controls one virtual robot allocated to the client.

A virtual robot acquires an image with a virtual camera and sends it to a server. Next it sends the image to a client which performs an image processing, then sends a command to the robot.

This composition reflects the situation in which multiple real robots move in a real space.

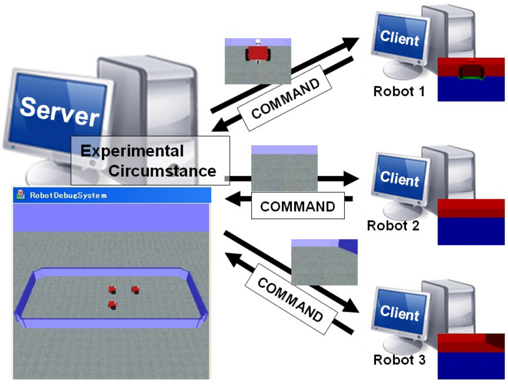

Fig.8. Control of robots in virtual space

2. Virtual Space & Virtual Object

The virtual object consists of three components. They are "Dynamics Element", "Collision Detection Element" and "Graphics Element". Giving these three components the same transformation matrix in the process of simulation allows the system to simulate and render the behavior of a virtual object.

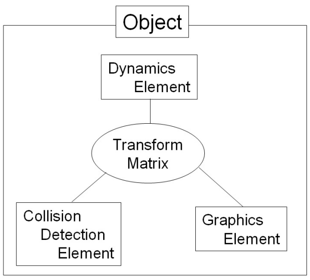

Fig.9. Generation method of virtual object

3. Virtual Network Camera

"A virtual network camera" is used in virtual space as a real one is mounted on a real robot. The virtual camera acquires a three dimensional scene generated by Open GL and then transforms it to two dimensional image. Next the image compressed to make transmission rate high is sent to a client who should analyze it. The client restores it to its original state and processes it.

4. Algorithm Built into Virtual Robots

The algorithm built into virtual robots is the same as that in the real robot. In a word, a virtual robot also evades obstacles by extracting the floor side area. (See II.2. Algorithm for Dodging Obstacles)

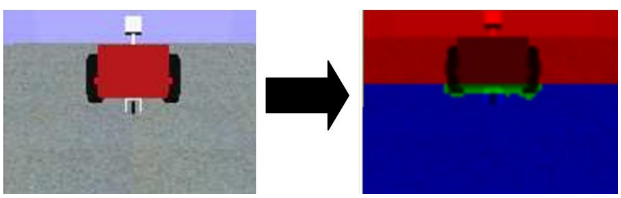

Fig10. Image processing in virtual space

5. Result

It is confirmed that three virtual robots can be controlled while evading obstacles dynamically as shown Fig.11.

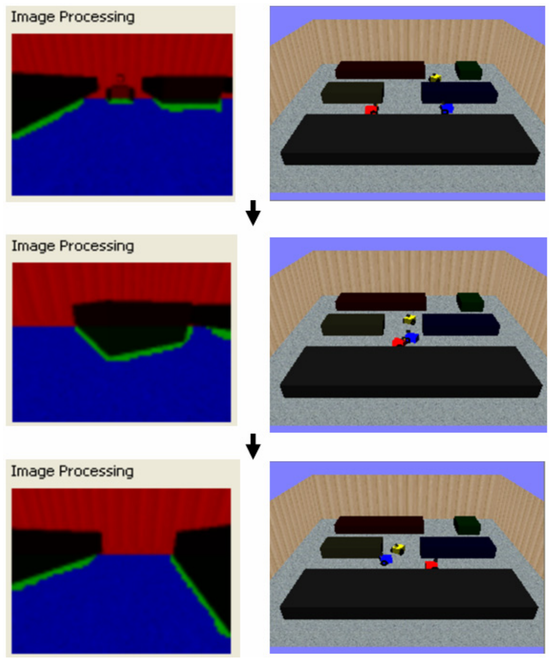

Fig.11. Pictures of simulation
(Left figure is processing result of blue robot)

IV. FEATURE WORK

As two or more robots successfully drive in dynamic virtual space, it seems that the algorithm of obstacle avoidance proposed in this research works well.

The robot, however, can observe only information in front of itself because the network camera is installed ahead of a robot. If robots run side by side while gradually shortening the distance between them, they will collide because the situation makes them invisible each other. Therefore we are planning to give a virtual distance sensor to a virtual robot to make it possible to evade obstacles being at the side of it.

ACKNOWLEDGEMENT

We greatly appreciate the aid of the Grant-in-Aid for Scientific Research (S) and (A).

REFERENCES

[1] Goto Hiroki, "Usage of Shared Memory for Multimodal Data Processing in an Outdoor Mobile Robot"
[2] Mizokami Ryutaro, "Prowl of Autonomous Mobile Robot with Network Camera"

The Fourteenth International Symposium on Artificial Life and Robotics 2009 (AROB 14th '09),
B-Con Plaza, Beppu, Oita, Japan, February 5 - 7, 2009

Construction of super-micro sense of force feedback and visual for micro objects -Develop the haptic device-

Ryo Uehara

Graduate School of Computer Science
And System Engineering
Kyushu Institute of Technology
680-4, Iizuka City, Fukuoka, Japan, 820-8502
uehara@mmcs.mse.kyutech.ac.jp

Eiji Hayashi

Department of Mechanical Information
Science and Technology
Kyushu Institute of Technology
680-4, Iizuka City, Fukuoka, Japan, 820-8502
haya@mse.kyutech.ac.jp

Abstract This research aims to develop a combined sense system that uses both the sense of a force feedback as well as visual feedback in the shape of microscopic features from a micro sample. It is thought that the efficiency of minute work would be improved if the operator could obtain a sense of force while using a manipulator. We used a cantilever to touch a minute object and obtained anti-power from the degree of its bend.

We made a haptic device, which gives a sense of force to the operator, who can feel the force when he touches a sample with a cantilever. In addition, when he uses the haptic device in a simulated manner, he can feel as if he had touched a sample.

Key words: Force feedback, Haptic interface, Simulation

1. Introduction

Technologies that can accurately perform minute work are now being sought for both the medical treatment and semiconductor manufacturing fields. Such minute work is improved by using micro manipulators, but their operation is difficult because the operator cannot have a sense of force; he relies only on sight through a microscope. As a result, a person skilled in the use of this technology is needed for minute work. It is thought that the efficiency of minute work would be improved if the operator could obtain a sense of force while using a manipulator

This study describes the development of a more efficient system for minute operations. Our aim was to develop a system using not only the sense of sight from a microscope but also a sense of force from a manipulator. For this fundamental research, a system was built to anti-power when a minute sample was touched. A cantilever was used to touch the sample, and the anti-power was obtained from the degree of its bend. In addition, we used a haptic device and amplified the force feedback from a virtual object of the minute sample.

2. System Structure

2-1. System Summary

The structure of the system is shown in Fig. 1-1, and the schematic view is shown in Fig. 1-2. This system consisted of a microscope, an automatic x-y stage on the microscope, a piezo stage, a feedback stage controller to control the x-y stage, a piezo stage controller, a haptic device for transmitting force feedback (Fig. 2), a cantilever (Fig. 3), and a PC with which I control and operate these components. The sample was fixed on the X-Y stage by an injector and a holding pipette. Then I touched the sample with the cantilever of the fixed piezo stage. The operator could feel force, as if he had touched the sample using the haptic device. The resolution of piezo stage is 1nm. Table 1 gives the specifics of the injector, and Table 2 gives the specifics of the holding pipette.

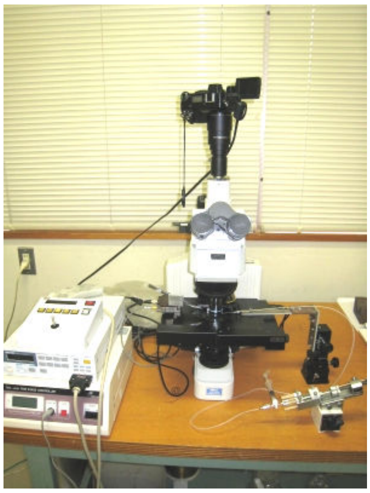

Fig. 1-1 System structure

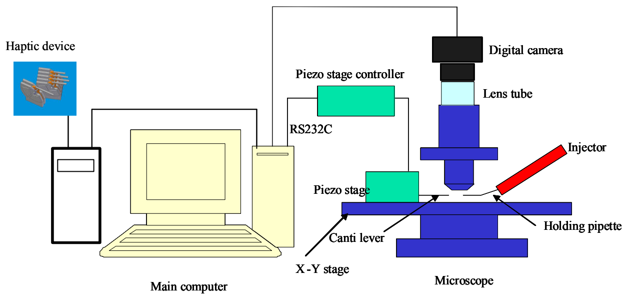

Fig. 1-2 System structure

©ISAROB 2009

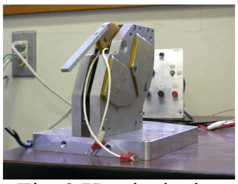

Fig. 2 Haptic device

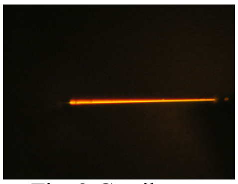

Fig. 3 Cantilever

Table 1 Specifics of injector

drive distance	40mm
braking distance	800 μ ‖
size	200*80*30 mm
weight	2kg

Table 2 Specifics of holding pipette

length	60mm
inside diameter	13 μ m

Fig. 4 Injector

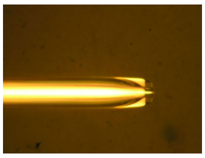

Fig. 5 Tip of holding pipette

2-2. Haptic device

Fig. 6 is a summary figure of the haptic device which we built in this study. It consists mainly of a rotor, laser, and PSD (Position Sensitive Device). We installed a coil on a rotor with a polarity magnet, which generated electromagnetic induction by an electric current and magnetic force. We were able to detect the angle of rotation of the laser and the PSD. We converted the current output into a voltage signal and carried out a positioning of the rotor.

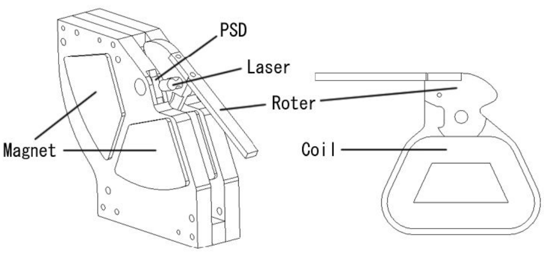

Fig. 6 Summary of haptic device

It is necessary to control an actuator with a servomechanism on an actuator. Therefore the system driving the actuator consists of three actuators: a PC, an AD/DA board inputting and a PC outputting. The system controls the actuator in each part of the process. Fig. 7 shows the system structure of the haptic device.

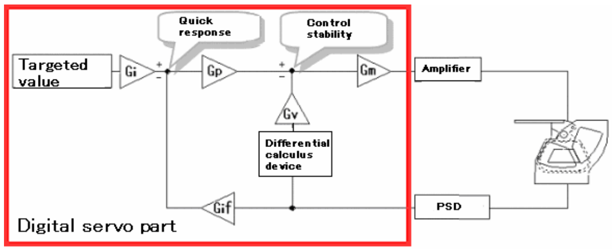

Fig. 7 System structure of haptic device

I drive the actuator by the PD control by operating it with a direct signal and a signal through the digital differential calculus device.

The transfer function of the quadratic function system shown in Fig. 8 is provided when I make an equation for the motion of the actuator and the feedback system of the controller circuit block diagram. The role of each parameter of the control system which I built is to adjust a total offset to a master in Gi / Gif, to regulate the item viscosity / resonance point in Gp / Gv, and to regulate the total gain in Gm.

Table 3 is the servomechanism system control parameter list.

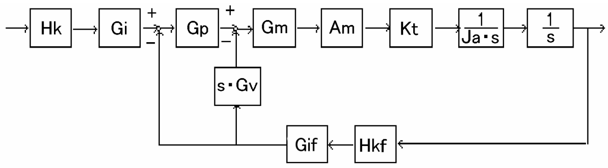

Fig. 8 Servomechanism system block diagram

Table 3 Servomechanism system control parameter list

Parameter	Reference	Unit
Gi	Controller Input Gain	1.0
Gif	Position Feedback Gain	1.0
Gp	Position Gain	1.0
Gv	Velocity Gain	0.0015
Gm	Manipulation Gain	1.0
Hk	Position Voltage Constant	18.531 V/rad
Hkf	Position Voltage Feedback Constant	18.531 V/rad
Am	Amplifier Constant	1.0 A/V
Kt	Torque Constant	2.768 Nm/A
Ja	Moment of Inertia	0.0002147 kg $\cdot m^2$

3. Measure the anti-power

We used anti-power to know the power which is applied by the minute object. In this experiment, we touched the minute object with the cantilever (Fig.3) and obtained the anti-power from the degree of its bend. The environment of the experiment is shown in Fig. 7 and Fig. 8. As a result of this experiment we got anti-power applied from the minute object.

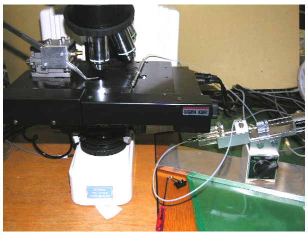

Fig. 9 Environment of the experiment

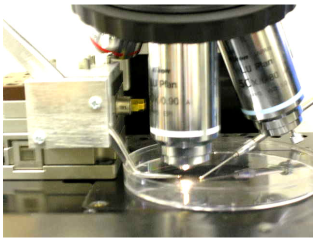

Fig.10 Environment of the experiment

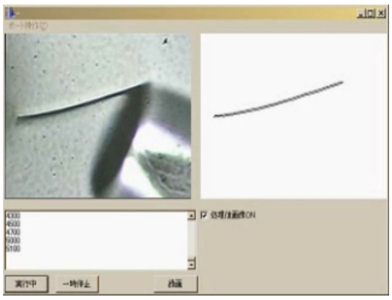

Fig.11 Cantilever touched the sample

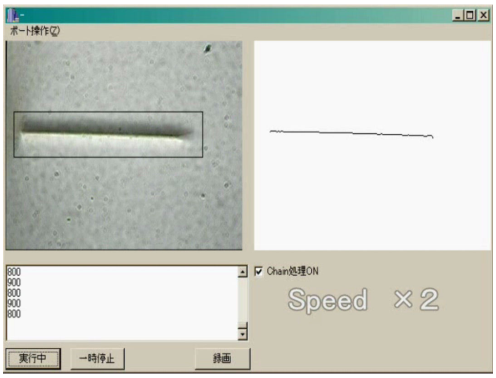

Fig.12 Cantilever detection program

Fig. 11 shows the cantilever touching the sample. The detection of the transaction speed of the cantilever was a problem, but it was possible to reduce this problem by performing tracking processing. (Fig. 12)

We found the anti-power by applying the degree of the cantilever's bend to Hokke's law.

$$\begin{aligned} F &= kx \qquad (1) \\ &= 0.11 * 30 \\ &= 3.3 \quad [\mu\ n] \end{aligned}$$

4. Deform simulation of the sample

In this study, we aimed to build a working system with a microscope, a haptic device and a simulation. A fundamental part was the deform simulation of a minute object. Fig. 13 shows a summary of the GUI. We used OpenGl, a graphic tool to draw the object, and we were able to choose the shape of the sample as a cube or sphere. A dynamic model of the sample consists of a spring-mass array element of mass points in vertical and parallel directions. I arranged the mass points as in Fig. 14. When power was applied at a mass point, this simulation calculated the speed of the mass point and the adjacent mass points. After each calculation, this simulation performs similar processing for the other mass points until it finishes. The image is renewed after ten calculations.

I define a spring as an object that does not have weight but has size, and a rigid body, and I define a mass point as an object that has weight and size and a rigid body. We can stick an arbitrary bitmap on a spring – a mass object. (Fig. 15) In addition, I can watch a sample from various viewpoints and in this way check the deformation of a sample that I cannot look at with the microscope. The shape of this object can be a choice of a cube or sphere. We can choose any point as a fixed point or an operating point.

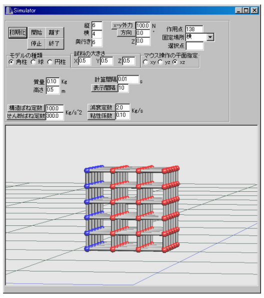

Fig. 13 Simulator

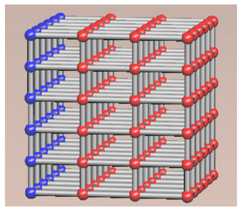

Fig.14 Arranged mass points

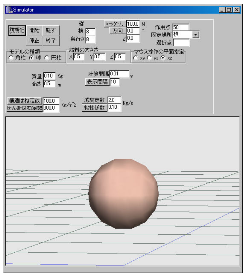

Fig. 15 Sticking on a bitmap

The calculation method for the displacement of each mass point is based on Newton's equation of motion (Expression 1) with the Euler method. A mass point is linked to an adjacent mass point by a spring. When the interval of the mass point is longer or shorter than the natural length of the spring, power acts. (Fig. 16)

$$ma = \Sigma F \qquad (1)$$

©ISAROB 2009

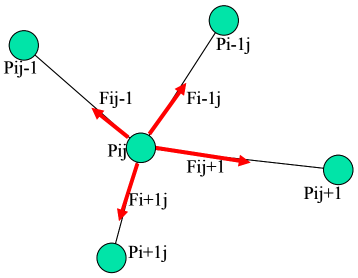

Fig. 16 Elasticity

"F" is summation of the elastic force of a construction spring and a shear spring, the viscous force and the damping force. I show expressions (2) to (5) to describe the detailed changes of each parameter.

To use this calculated result, the displacement of a neighboring mass point is calculated.

$$F_{spring} = \Sigma F_{ij} \quad (2)$$

$$F_{damping} = -C_d v_i \quad (3)$$

$$F_{viscous} = -C_v (v_i - v_j) \quad (4)$$

$$\Sigma F = F_{spring} + F_{damping} + F_{viscous} \quad (5)$$

5. Conclusion

In this paper, we evaluated whether force feedback is amplified by touching a virtual object with a haptic device in a PC. We can amplify the reaction force, but we cannot present a large enough reaction force for a worker to feel its elasticity.

In the future, I plan to build a system to detect and show more precisely an extended minute reaction force. The system will be tested using a smaller sample. Therefore, I will build a manipulator and develop a system around it.

I now carry out in C++ the program for the movement of the haptic device in Windows that I made. However, in the future I will make a control department with a microcomputer, and I anticipate a further performance enhancement from its incorporation into an order in which the PC communicates as a system.

In addition, I will perform an algorithm and a review of the detection method because a big load depends on the image processing part. I will express by a haptic device the power Satoshi information that I get from image processing.

Reference

[1] Xide Li; Zhao Zhang(2008), Probe-type microforce sensor for micro/nano experimental mechanics. Trans Tech Publications Ltd, Stafa-Zurich, Switzerland

[2] Jiangbo Zhang; Ning Xi; Guangyong Li; Chanmin Su(2006), Atomic force microscopy sensing using multiple modes. IEEE, Piscataway, NJ, USA, 2006 IEEE/RSJ International Conference on Intelligent Robots and Systems Beijing, China, 9-15 October 2006

[3] Hrouzek, M(2005).Feedback control in an atomic force microscope used as a nano-manipulator. Acta Polytechnica, Czech Technical University in Prague Volume: 45 Issues: 4 Pages: 65-9 Published: 2005

[4] Ryota Ujihara(2004), Develop the haptic device. Kyushu Institute of Technology.

[5]Yaacoub,F.;Hamam, Y.; Abche, A(2008). Computer-based training system for simulating wrist arthroscopy. Proceedings of the 21st IEEE International Symposium on Computer-Based Medical Systems (CBMS 2008)

[6] Tahmasebi, A.M.; Taati, B.; Mobasser, F.; Hashtrudi-Zaad, K(2005). Dynamic parameter identification and analysis of a PHANToM trade haptic device. 2005 IEEE International Conference on Control Applications (CCA) (IEEE Cat. No.05CH37713)

[7] Takamasa Sonoda(2006). Construction of super-micro sense of force feedback and visual for an elastic body. processings of the 12th international symposium on artificial life and robotics. Beppu, Oita, Japan, 2006

[8] Kotaro Miyamoto(2007), Construction of super-micro sense of force feedback and visual for micro objects. processings of the 12th international symposium on artificial life and robotics. Beppu, Oita, Japan, 2007

Microorganic Engine

K. Naitoh, R. Kubo, R. Miyagawa, K. Ogata, and A. Suzuki
Waseda University, Faculty of Science and Engineering, 3-4-1 Ookubo, Shinjuku, Tokyo, 169-8555 Japan
(Tel : 81-3-5286-3265)
(Email address: k-naito@waseda.jp)

Abstract: Energy systems such as fuel cells and recent combustors including internal combustion engines work at lower temperatures. Recent direct-injection gasoline and diesel engines often operate at relatively low exhaust gas temperatures around 100°C, because their lean-burn combustion process uses less fuel, resulting in burned gases of lower temperatures. The exhaust gas temperatures are close to those at which hyperthermophiles and thermophiles replicate. This situation could give rise to the possibility that thermophiles might proliferate inside the exhaust pipe of internal combustion engines. The nutrient preconditions for proliferation may be sufficient, because soot contains a lot of carbon and sulfur. Air, which is also needed by aerobic microorganisms, is taken in through the intake manifold from the atmosphere and water can be produced after combustion. Aeropyrum pernix (JCM 9820) is a species that is known to proliferate well at temperatures between 80 and 100°C, close to exhaust gas temperatures. In this paper, it is shown that Aeropyrum, a type of aerobic thermophile, proliferates well by eating soot around the temperatures in the presence of only pure water and air. This fusion of artifact and life may offer the possibility of overcoming one of the weak points of internal combustion engines.

Keywords: Aeropyrum, Soot, Engine, Thermophile**.**

I. INTRODUCTION

Recent internal combustion engines with direct-injection diesel or gasoline fuel supply systems for addressing environmental problems and reducing fuel consumption often operate at relatively low exhaust gas temperatures around 100°C. This is because lean-burn operation uses less fuel than a stoichiometric condition, thus producing burned gases of lower temperatures. The lower temperature of the exhaust gas may lead to a condition of catalyst inactivity in the system with a diesel particulate filter (DPF) for trapping soot.[3] A quantum leap is necessary for overcoming the soot problem that is the principal weak point of diesel engines.

The exhaust gas temperatures are close to those at which hyperthermophiles [5] and thermophiles replicate. This situation could give rise to the possibility that thermophiles might proliferate inside the exhaust pipe of internal combustion engines. The nutrient preconditions for proliferation may be sufficient, because soot contains a lot of carbon and sulfur. Air, which is also needed by aerobic microorganisms, is taken in through the intake manifold from the atmosphere and water can be produced during combustion.

II. AEROPYRUM PERNIX

Aeropyrum pernix (JCM 9820)[4] was isolated from a coastal solfataric vent in Japan. This species is aerobic organism. The optimum growth temperature is 90 to 95 degree Celsius at pH7.0 and a salinity of 3.5 %.[4] The isolate was grown in the standard medium referred to as JXT, containing 1g of yeast extract, 1g of trypticase peptone, and 1g of $Na_2S_2O_3$ per liter of water.[4]

III. AEROPYRUM EATING SOOT

In the present study, Aeropyrum pernix (JCM 9820)[4] was cultivated aerobically at temperatures over 85 degree Celsius during a period of thirteen days using soot exhausted from a conventional engine and also that from a diffusion flame burner.

The vial contained only the soot, pure water, and air in the present study, although a yeast extract and trypticase peptone are normally given as the nutrients for this species. A small amount of soot was put in 1 ml of pure water in a 10-ml vial, which was not pressurized. The pH and cultivation temperature were 7.0 and 85°C, respectively.

Figure 1 shows photomicrographs of Aeropyrum per nix cultivated during thirteen days in the vial containing only the soot, pure water, and air. The photographs wer e taken by means of DAPI staining and show densities c lose to that averaged from nine inspection points. (Photographs taken at each inspection point had dimensi ons of about 130 x 90 micrometers.)

Soot was obtained from the end of the exhaust pipe of a conventional piston engine. Several cultivation trials revealed that the density of the species after thirteen days of cultivation was about five times greater than the initial density. (Fig. 2.) Engine soot and soot taken from a methyl alcohol burner yielded approximately the same species density.

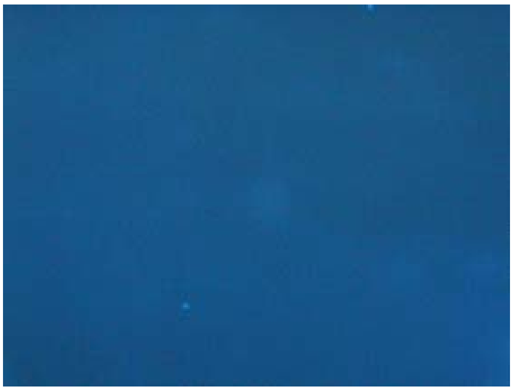

(a)

(b)

Fig.1. Microphotographs of Aeropyrum pernix cultivated during thirteen days at 85℃ in a vial containing only engine soot, pure water, and air. (a) Cultivation start and (b) after thirteen days.

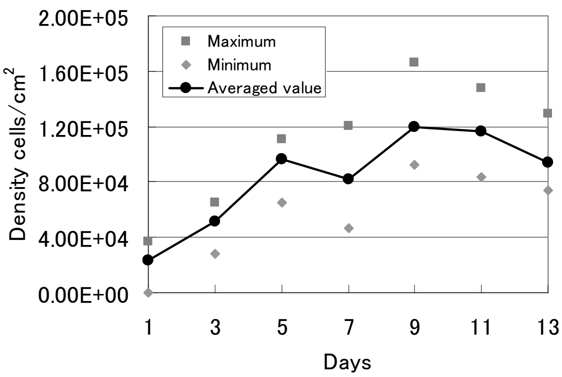

Fig.2. Time history of the density of Aeropyrum pernix cultivated during thirteen days at 85℃ in a vial containing only engine soot, pure water, and air. (The average density of the species calculated from photographs taken at nine inspection points on the glass cover was 2.55 cells per photograph at cultivation start and 10.11 cells per photograph after thirteen days of cultivation.)

V. CONCLUSION

There is a trend toward power systems that work at temperatures close to that of living organisms.[1,2] The present fusion of artifact and life, micro-organic engine, may offer the possibility of overcoming one of the weak points of internal combustion engines. (Fig. 3)

Acknowledgement

The authors express sincere thanks to the Japan Collection of Microorganisms, RIKEN BioResource Center and Prof. Yoshihiko Sako of Kyoto University for supplying the microorganisms of Aeropyrum pernix and the papers related to the species.

(Mr. Ryuta Miyagawa, the third author of this paper, had done the present study under the direction of Ken Naitoh in Waseda University until the end of March, 2008.)

REFERENCES

[1] Naitoh K, (2004) Symbiotic fusion of life and artifact, Proc. of the 9th Int. Symp. On Artificial Life and Robotics (AROB9th '04): 440－442.

[2] Naitoh K, (2004) Fundamental study on the degradation of fuel cell, Proc. of the 2004 JSAE Annual Congress, Japan Society of Automotive Engineers, No.43-04:7-11. (in Japanese)

[3] Ookubo M, Kuroki T, Miwa S, and Yamamoto T, (2 003) Soot incineration of diesel particulate filter using honeycomb nonthermal plasma, SAE paper 2003-01-1886.

[4] Sako Y, Nomura N, Uchida A, Ishida Y, Morii H, Koga Y, Hoaki T, and Maruyama T. (1996) Aeropyrum pernix gen. nov., sp. nov., a novel aerobic hyperthermophilic archaeon growing at temperatures up to 100 degrees C. International Journal of Systematics Bacteriology, 46-4: 1070.

[5] Stetter KO, (1995) Microbial life in hyperthermal en vironments. Am. Soc. for Microbiol. News, 61: 285-290.

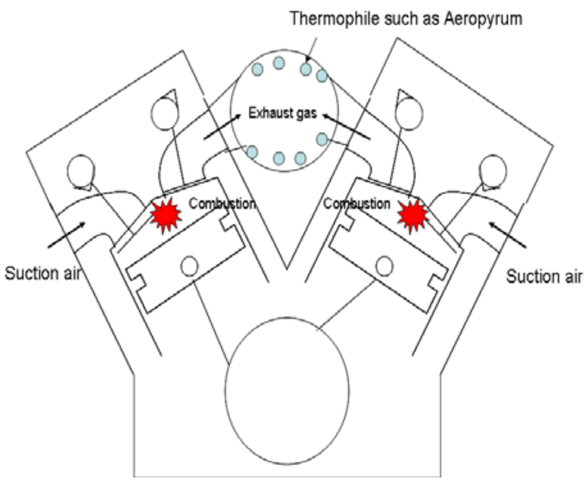

Fig. 3. Micro-organic engine including a combustion engine and thermophile.

The Fourteenth International Symposium on Artificial Life and Robotics 2009 (AROB 14th '09),
B-Con Plaza, Beppu, Oita, Japan, February 5 - 7, 2009

A unified motion planning method for a multifunctional underwater robot

Koichiro Shiraishi and Hajime Kimura
Dept. of Maritime Engineering
Graduate School of Engineering, Kyushu University
744 Motooka, Nishi-ku,Fukuoka, 819-0395 Japan
k-shiraishi@system.nams.kyushu-u.ac.jp and kimura@nams.kyushu-u.ac.jp

Abstract

This paper deals with motion planning for a multifunctional underwater robot which can accomplish various missions, e.g., swimming, walking and grasping objects. Authors have developed a unified motion planning method which can generate motion planning for a variety of task by a single algorithm. In this method, motion planning problems are modeled as finite horizon Markov decision processes. The optimum motion planning is obtained by Dynamic Programming, however Dynamic Programming is sometimes thought to be of limited applicability because of the curse of dimensionality. To avoid the curse of dimensionality, authors applied a random network as a state transition network. The explosion of the number of states can be suppressed by using the random network. The effectiveness of the proposed method is demonstrated through numerical simulations of two types of tasks for multifunctional robots. One is a reaching task, the other is a generating thrust force task.

Keywords: Mutifunctional underwater robot, Fluid Drag Force, Reaching task, Generating thrust force task, Dynamic Programming, Random network

1 Introduction

The field of underwater robotics is currently enjoying a period of high interest and growth. Applications for such robots include exploration of deep sea environment, cable maintenance, monitoring of subsurface structures, and biological surveys [1]. Authors have been developing a multifunctional underwater robot which can accomplish various missions, e.g., swimming, walking and grasping objects [2]. The robot is equipped with a redundant degree of freedom manipulator. It has two excellent features; One is robustness for troubles, the other is multifunction, that is, it can use not only as an arm, but also as a finger for gripping objects, or a fin for swimming.

It is necessary for a robot to generate motion planning according to various missions. The problem is that we must develop the corresponding motion planning algorithms for each individual task. Authors have developed a unified motion planning method that can generate motion planning for a variety of task by a single algorithm. In the method, motion planning problems are modeled as finite horizon Markov decision processes. The optimum motion planning can be acquired by using Dynamic Programming.

This paper presents a new approach which has ability to avoid curse of dimensionality. The number of state increase exponentially with the number of state variables is called the curse of dimensionality. The conventional Dynamic Programming is to discretize state space with full grid points. Due to the exponential growth in the full grid discretization as the number of state variables increases, Dynamic Programming is still commonly considered to be computationally intractable. The proposed method generates a random state transition network by discretizing the state space at random. The random network can prevent from exponentially increasing of the number of states. The optimum motion planning can be acquired by using the Dynamic Programming in the random network.

The effectiveness of the proposed method is demonstrated through numerical simulations of two types of tasks for multifunctional robots. One is a reaching task that is composed of a manipulator posture planning, so that the robot keeps to a minimum of energy consumption [3]. The other is a generating thrust force task that is driving the robot forward by a fluid drag force that acts on a manipulator. The experimental results show that the proposed method could generate reasonable motion planning at two problems of motion planning by a single algorithm. The proposed method used a random network could apply to a high dimension problem, and enabled the computation time to be shortened.

©ISAROB 2009

2 Motion Planning Problem

In this paper, authors dealt with two motion planning problems of a multifunctional underwater robot. The one is a reaching task which is a path planning task for a robotic manipulator. The other is a generating thrust force task for a multifunctional underwater robot. The reaching task is to obtain an optimum sequence of postures in fluid. In the reaching task, the optimum planning minimizes energy consumption caused by the fluid drag force. Authors consider a movable underwater robot equipped with a manipulator in the generating thrust force task. This robot generates fluid drag force to move in front by moving the manipulator. In this task, the objective function is to maximize the advancing distance.

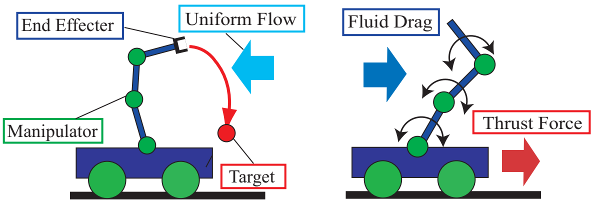

Figure 1: Reaching task and Generating thrust force task

2.1 Coordinate System of a Manipulator

Figure 2 shows the coordinate system and parameters in the manipulator. x and y are horizontal, vertical directions, respectively. l_i is the length of the ith link θ_i is the angle of the ith link. The shape of the links are assumed to be columns. Joints are assumed to be small enough compared with the links, so that fluid drag forces which act on joints are able to be omitted in the calculation. $\boldsymbol{S}$ is defined as a manipulator posture, which is vector composed of angles of the links, given by

$$\boldsymbol{S} = (\theta_1, \theta_2, \cdots, \theta_i, \cdots, \theta_n). \quad (1)$$

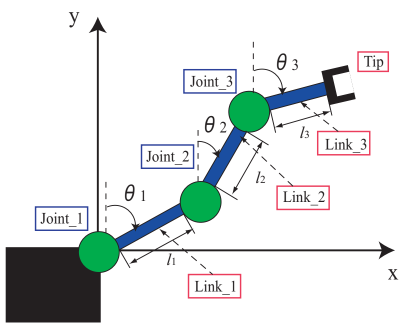

Figure 2: Configuration of three-link manipulator

A point of the nth link's tip becomes the position of the end effecter. The point is given by

$$x_{Tip} = \sum_{i=1}^{n} l_i \sin\theta_i, \quad y_{Tip} = \sum_{i=1}^{n} l_i \cos\theta_i. \quad (2)$$

Coordinates of other links can be provided by using the equation (2). The notation $\boldsymbol{P}$ is a sequence of manipulator postures become target posture from initial posture, It is given by

$$\boldsymbol{P} = (\boldsymbol{S}_{init}, \boldsymbol{S}_2, \cdots, \boldsymbol{S}_j, \cdots, \boldsymbol{S}_{end}), \quad (3)$$

where $\boldsymbol{S}_{init}$ is the initial posture where the manipulator begins to move is an initial posture, $\boldsymbol{S}_{end}$ is the target posture which the end effecter reaches target coordinates, j is the number of posture changes, and $\boldsymbol{S}_j$ is jth manipulator posture.

2.2 The Fluid Drag Force

The Fluid drag force is given by

$$f = C_d \frac{1}{2}\rho D u|u| + C_m \rho \frac{\pi}{4} D^2 \frac{du}{dt}, \quad (4)$$

where D is a diameter of the column, C_d is a drag coefficient, C_m is an added mass coefficient, u is a velocity of a link through the fluid. ρ is a density of the fluid. Since the velocity of the link is small enough, the second term at the right of the equation (4) can be omitted. The fluid drag force acting on each link is shown as follows by the use of the equation (4)

$$F_{x,i} = F_{x,i+1} + f_i \cos\theta_i \quad (5)$$

$$F_{y,i} = F_{y,i+1} - f_i \sin\theta_i \quad (6)$$

$$M_i = M_{i+1} + T_i + F_{x,i+1} l_i \cos\theta_i - F_{y,i+1} l_i \sin\theta_i, \quad (7)$$

where f_i and T_i are given by

$$f_i = \int_0^{l_i} C_d \frac{1}{2} \rho D_i u_i |u_i| dr_i,$$
$$T_i = \int_0^{l_i} C_d \frac{1}{2} \rho D_i u_i |u_i| r_i dr_i.$$

©ISAROB 2009

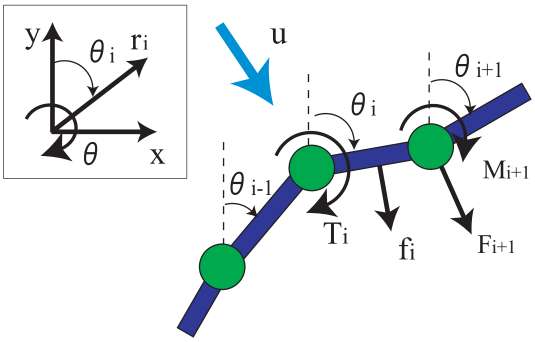

Figure 3: Forces acting on a link

2.3 A Reaching Task

Multifunctional underwater robot is operated under the subsea environment. It is necessary to consider an influence of fluid drag force caused by sea current. Thus, authors consider that a motion planning problem which minimizes energy consumption caused by the fluid drag force. The energy is determined by torque which acts on the joints and the angles of the links moved in a period. In the motion planning problem, the cost function is formulated by using the consumed energy. When a manipulator posture changes from $\boldsymbol{S}_A$ to $\boldsymbol{S}_B$, the cost function is shown approximately in the following,

$$Cost(\boldsymbol{S}_a, \boldsymbol{S}_b) = \sum_{i=1}^{n} \int_{\theta_{S_{a,i}}}^{\theta_{S_{b,i}}} M_i d\theta_i + \Delta E, \tag{8}$$

where n is the number of the links, θ_{S_i} is the angle of the ith link in the manipulator posture S, ΔE denotes energy consumption caused by a mechanical friction. A total cost is provided by the use of the equation (8) as

$$Total\ Cost(\boldsymbol{P}) = \sum_{i=1}^{|\boldsymbol{P}|-1} Cost(\boldsymbol{S}_i, \boldsymbol{S}_{i+1}). \tag{9}$$

In the reaching task, the motion planning problem is formulated as an optimization problem of minimizing a total cost of the equation (9).

$$Optimum\ Planning = \min_{\boldsymbol{P} \in \boldsymbol{P}_{All}} Total\ Cost(\boldsymbol{P}) \tag{10}$$

where $\boldsymbol{P}_{All}$ denotes sets of all executable motion planning in the motion planning problem. In this paper, the positive energy obtained from the current is not considered.

2.4 A Generating Thrust Force Task

In this section, authors describe the motion planning problem of generating thrust force for a movable underwater robot. The robot is able to move in front by using the fluid drag force that acts on the manipulator. In this paper, it is assumed that the body of the robot is constrained by the rail. For a preliminary experiment, the one dimentional motion is considered. For simplicity, the effect of the added mass which is concerned with the fluid is assumed to be negligible. Consider that fluid drag forces that acts on main body and each links. The motion equation of the body is given by

$$M\ddot{x} = F_{body} + \sum_{i=1}^{n} F_{x,i}, \tag{11}$$

where M is a mass of the movable underwater robot. F_{body} denotes the fluid drag force that acts on the body of the robot except for the force on the links. $F_{x,i}$ denotes the fluid drag force of x axial component that acts on the ith link. n is a number of links of the manipulator. In this problem, the optimum planning is a motion to maximize advancement distance of the robot.

3 A Unified Motion Planning Method

The motion planning problem of the multifunctional underwater robots is modeled as finite horizon Markov decision processes. Optimum motion planning for various tasks is obtained by using Dynamic Programming.

3.1 Markov Decision Processes

State transitions of the robot is represented as a network showing Fig.4.

In the network, a node denotes a manipulator posture. A direction of an arrow denotes a direction of the posture change. $f(s_i, s_{i+1})$ is an objective function, when the robot posture changes from s_i to s_{i+1}. In reaching task, an objective function is consumed energy caused by fluid drag force. On the other hand, an objective function is an advancement distance in generating thrust force task. Thus, the motion planning problem is considered as a graph search problem.

Assuming that Markov property is approved, the motion planning problem is considered as a Markov decision process. Markov Decision Processes framework for planning is rich in capturing the essence of purposeful activity in various situations. A Markov decision process is defined by its state and action sets

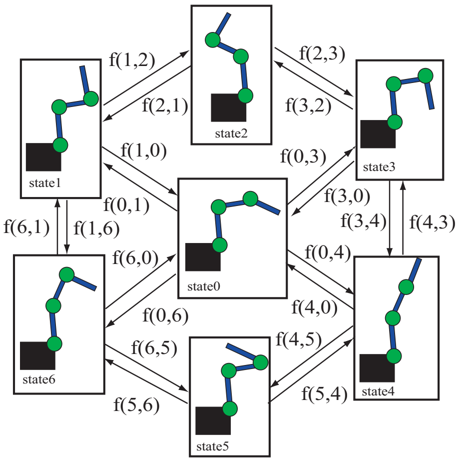

Figure 4: State transition network

and by the one-step dynamics of the environment [4] [5]. A state s is defined as a manipulator posture. An action a is motion of each link in the posture change. A reward $R(s'|s,a)$ is a value of the objective function in the state transition. A value function $V(s)$ denotes the expected total reward starting at state s according to the strategy. In Markov decision process, the Bellman equation is shown by

$$V^*(s) = \max_{a \in A} \sum_{s' \in S} p(s'|s,a) \left(R(s'|s,a) + \gamma V^*(s')\right), \quad (12)$$

where $\boldsymbol{S}$ is state sets, $\boldsymbol{A}$ is action sets, and γ is a discount factor. The optimum policy is obtained by solving the equation (12) by using the standard Dynamic Programming. The policy is the optimum motion planning for various tasks In this paper, a standard value iteration method is used for solving the Bellman equation.

3.2 Discretization of State Space

In this section, authors describe a random network used as a state transition network. State space should be discretized in standard Dynamic Programming. In conventional method, the state space is discretized like a lattice. However, this method is suffered from the curse of dimensionality. The curse of curse of dimensionality is a phenomenon that a number of states increases in exponential. A random network which discretizes the state space at random, is developed as a method to avoid the curse of dimensionality [6] [7]. In this paper, the state transition network is produced by the random network. The optimum motion planning can be obtained by using Dynamic Programming with this network.

4 Experiment and Results

In order to confirm the validity of proposed method, several experiments of two tasks for the multifunctional underwater robots were made. One is the reaching task, the other is the generating thrust force task. Figure 5 shows settings of the multifunctional underwater robot in two tasks.

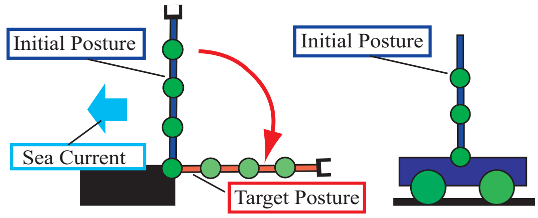

Figure 5: Settings of two Experiments

4.1 Experiment 1: Reaching Task

The aim of Experiment 1 is to verify whether the proposed method could obtain the motion planning minimizing the consumed energy by fluid drag. In the experiment, the 4 D.O.F. manipulator was used. The parameter of the experiment is set as follows: $l_i = 0.7[m], D_i = 0.2[m], C_d = 1.17, \rho = 1.023, |u| = 2.0[m/s]$, and $\theta_{limit} = \pm 1.571[rad]$, where θ_{limit} is the angle where the links of the manipulator can rotate.

In order to compare results, three motion planning were used: Planning 1 is to reach a target posture in the shortest time, Planning 2 is generated by the unified motion planning with the lattice network, and Planning 3 is generated by the unified motion planning with the random network. The lattice network was provided by discretization of the state space like a lattice. Each dimension of the state space is divided evenly into 11 parts. The number of nodes is $11^4 = 14641$, the number of links per a node is 80 in the lattice network. On the other hand, the random network was provided by discretization of the state space at random. The number of nodes is 8000, the number of links per a node is 50 in the random network. The simulation is executed 10 times and the performances are evaluated by the average of the results.

Figure 6, 7, and 8 show the motion planning obtained by simulation of the reaching task. All planning

©ISAROB 2009

could obtain the motion to reach from the initial posture to the target posture. Table 1 show the cost and the computation time on experiment 1. Planning 2 has the smallest cost among the three motions, although the computation time is longest. The computation time of Planning 3 is a half compared with Planning 2. Planning 3 is the most effective solution, considering two points of the computation time and the cost. Authors could notice that the motion of the best solution shown in Figure 7 or Figure 8 takes advantage of the sea current.

Table 1: Simulation results of experiment 1

	Cost[J]	Computation Time[s]
Planning 1	0.93044 ± 0	178.0 ± 0
Planning 2	0.00073 ± 0	661.3 ± 0
Planning 3	0.01326 ± 0.0088	344.5 ± 20.5

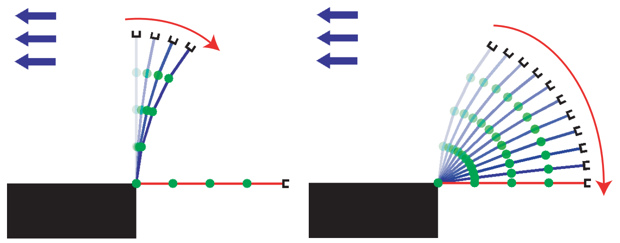

Figure 6: Motion to reach in the shortest time (Planning 1)

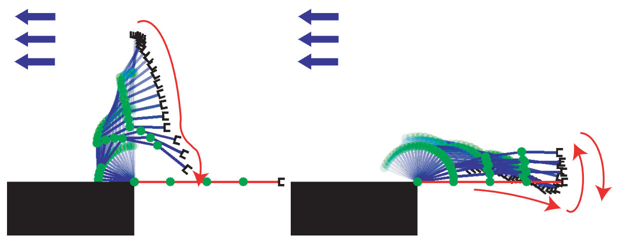

Figure 7: Motion obtained by proposed method with lattice network (Planning 2)

4.2 Experiment 2: Generating Thrust Force Task

The aim of the experiment is to verify whether the proposed method could obtain the generating thrust

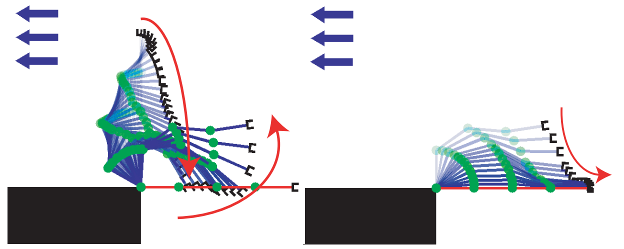

Figure 8: Motion obtained by proposed method with random network (Planning 3)

force motion. In the experiment, the movable underwater robot equipped with the 3 D.O.F manipulator is used. The parameter of the experiment is set as follows : $l_i = 0.5[m], D_i = 0.2[m], C_d = 1.17, M = 5.0[kg], \rho = 1.023, \theta_{limit} = \pm 1.047[rad]$, and $\dot{\theta} = 0.034$ $[rad/s]$, where $\dot{\theta}$ is the velocity of the links of the manipulator. The height and the width of the body is $0.2[m]$ and $0.3[m]$. In the lattice network, the number of nodes is $11^3 = 1331$, the number of links per a node is 26. In the random network, the number of nodes is 600, the number of links per a node is 50. In order to compare results, two motion planning were used : Planning 4 is the motion planning generated by the unified motion planning with a lattice network and Planning 5 is the motion planning generated by the unified motion planning with a random network.

Figure 10 and 11 show the motion planning obtained by simulation of the generating thrust force task. In the both motion the motion of the manipulator is a flutter kick for swimming. Table 2 show the average velocity and the computation time on experiment 2. Planning 4 is superior to Planning 5 in the average velocity. The computation time of Planning 5 is a half compared with Planning 4. Planning 5 is the most effective solution, considering two points of the average velocity and the computation time.

Table 2: Simulation results of experiment 2

	Average velocity [m/s]	Computation Time [s]
Planning 4	0.0271 ± 0	510 ± 0
Planning 5	0.0235 ± 0.0052	248 ± 34.5

5 Summary and Conclusions

In this paper, authors developed the unified motion planning for multifunctional underwater robots. The motion planning problems are modeled as Markov decision processes and optimum motion planning is ob-

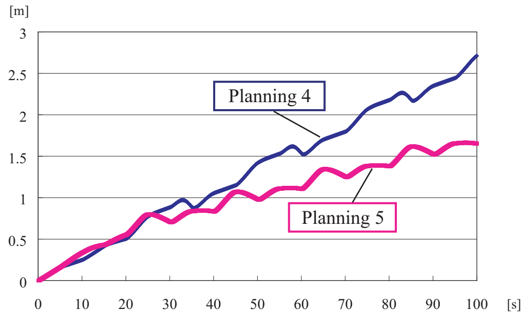

Figure 9: Time series graph for x coordinate value of a movable underwater robot

Figure 10: Motion obtained by proposed method with lattice network (Planning 4)

Figure 11: Motion obtained by proposed method with random network (Planning 5)

tained by standard Dynamic Programming. The proposed method can generate motion planning for a variety of tasks by a single algorithm. In addition, the proposed method used random networks enabled the computation time to be shortened. The method could avoid the curse of dimensionality, since the number of nodes is independent on the number of state variables. The validity of the method was confirmed through two experiments.

The drawback of the random network approach is that the quality of the best solution has large variance because of the random location of the state node. That is, the solution is depending on the initial design of the random network. It is necessary to develop the method to suppress the variance.

In the future work, authors will utilize the conjugate gradient method to solve the problem that the random networks approach has the variance of the solution. The method is an algorithm for finding the nearest local minimum of a function of variables which presupposes that the gradient of the function can be computed. The locations of the nodes in the solution are modified by the conjugate gradient method, so that the quality of the solution is improved. Therefore, this approach could reduce the variance of the solution in the random network.

Acknowledgements

This work partly was supported by the Sasakawa Scientific Research Grant from The Japan Science Society.

References

[1] G. Antonelli, *Underwater Robots: Motion and Force Control of Vehicle-Manipulator Systems*, Springer, 2003.

[2] K. Shiraishi and H. Kimura, "On a Unified Motion Planning for a Multifunctional Underwater Robot," *Proceedings of the 26th Annual Conference of the Robotics Society of Japan*, (in Japanese) 2008.

[3] S. Ishibashi, M. Ito, and E. Shimizu, "Autonomous Motion Planning for a Manipulator Equipped on AUV in a Workspace Divided into Cubes," *Proceedings of the 13th International Offshore and Polar Engineering Conference*, pp. 231-238, 2003.

[4] D. P. Bertsekas and J. N. Tsitsiklis, *Neuro-Dynamic Programming*, Athena Scientific, 1996.

[5] Abhijit Gosavi, *Simulation-Based Optimization*, Kluwer Academic Publishers, 2003.

[6] C. G. Atkeson and B. J. Stephens, "Random Sampling of States in Dynamic Programming," *IEEE Transactions on Systems, Man, and Cybernetics*, Vol. 38, pp. 924-929, 2008.

[7] S. M. LaValle, M. S. Branicky, and S. R. Lindemann, "On the Relationship Between Classical Grid Search and Probabilistic Roadmaps," *International Journal of Robotics Research*, Vol. 23, pp. 673-692, 2004.

The Fourteenth International Symposium on Artificial Life and Robotics 2009 (AROB 14th '09),
B-Con Plaza, Beppu, Oita, Japan, February 5 - 7, 2009

Image data processing for an autonomously moving robot using network

Minami Sato, Yoshihiro Tabuchi, Norihiro Abe
Kyushu Institute of Technology
680-4 Kawadu, Iizuka, Fukuoka 820-8502, Japan
Email: minami@sein.mse.kyutech.ac.jp

Hirokazu Taki
Wakayama University
930 Sakaedani, Wakayama-shi
Wakayama 680-8510, Japan

Shoujie He
VuComp, U.S.A.

Abstract: This research aims at constructing an autonomously moving robot system using network communication tech nologies. All the sensor data are sent to one of nearby access points through a wireless LAN. With this infrastructure, a ny new functionality could be added to the robot system without changing the overall architecture of the robot system. Moreover, there will be no performance impact. Even if an accident happened to the robot during the experiment, the d amage will be minimized. The system includes a mobile robot, two network cameras that are mounted on the robot, a w ireless LAN, and an image processing system. This paper focuses on the image processing system. A computer is dedic ated to the images captured by the cameras, and processes the images. As soon as the images are processed, a set of con trol instructions will be transmitted to the robot. The robot can therefore autonomously move by repeating this process.

Keywords: Robot, Image processing

I. INTRODUCTION

Many robot systems have been developed in the past. The majority of the robot systems, however, is designed to perform one and only predefined task. In order to design a robot system that could help people to perform a variety of tasks, communication with people in a timely fashion is considered one of the basics. It is therefore necessary for a robot system to interact with people through the speech and gesture recognition. For instance, in the case that a user points with his finger to the object that he wants the robot to pick up and carry back to him, the current location of both the robot and the user will be needed for determining the object location. This means that both environment recognition and object location are required to perform a communication task that was considered not directly relevant to the task. As a matter of fact, a couple of different type of information must be processed simultaneously. As soon as a request from the user has been received and successfully interpreted, the robot system must build a plan for the execution of the task. The plan includes the environment recognition necessary for moving toward the target and avoiding obstacles during the movement as well as the actual control sequence of the movement.

As seen from the above mentioned cases, different type of information must be processed in parallel. This requires the robot to be equipped with many high performance computers, which will substantially increase the weight and cost.

To solve these problems, this research proposed an approach that keeps the number of computers mounted on a robot as few as possible. The basic idea is to send all sensor information to one of nearby access points through a wireless LAN. All the data-intensive processing that is needed for the robot to perform the assigned task is actually happening on the computers available through the wireless LAN. Those computers are made available through the wireless LAN anytime and at any physical location as long as they are reachable through the network.

This paper focuses the discussion on the image processing system for the environment recognition, which is used by the robot system.

II. SYSTEM ORGANIZATION

The mobile robot used in this research is 39cm in width, 44cm in length, and 53cm in height. Two network cameras are mounted on the front of the mobile robot. The axes of the two cameras are parallel to each

©ISAROB 2009

other. The distance between the two cameras is about 10cm. Since the speed of the robot is slow, cameras need to capture the images of the nearby environment rather than a distant environment. For this reason, the axial directions of the two cameras are tilted down a little bit. Each of the network cameras has its own IP address, which makes it easy to transmit images through the wireless LAN to server machine. Images are transmitted through an IEEE 802.11b/g wireless router.

As soon as the computer receives the images, it begins image processing. Images are received at a rate of up to 30 images per second. The computer generates the control commands for the movement of the robot at the time of finishing processing the images. The same computer will transmit the control commands back to the robot.

A microcomputer that is capable of handling the network communication is mounted on the robot. The microcomputer receives the control commands and then converts the commands into the motor signals.

Microsoft Visual Studio.NET has been used for the software development. The image processing tasks are executed with the help of OpenCV, an open-source library from Intel. The program code from the Independent JPEG Group was used for the conversion from JPEG to BMP image file format.

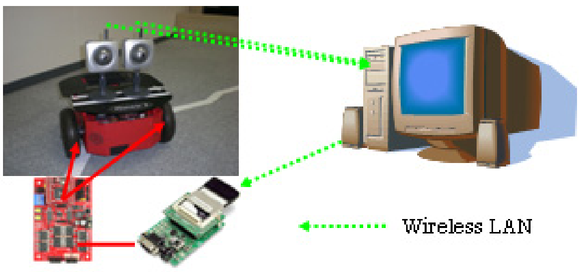

Fig.1 Organization of the robot system

III. IMAGE PROCESSING

White line recognition and the obstacle identification are processed in parallel for the autonomous movement. Depending upon the feature analysis of each of the targets, a corresponding image processing algorithm has been developed. The control commands are generated through the integration of the image processing results.

Since the received images are in the format of JPEG, the images are converted from the JPEG format into the BMP format in the memory. In addition, only a region of interest (ROI) is processed. As a result, the delay of image processing was suppressed to an acceptable extent.

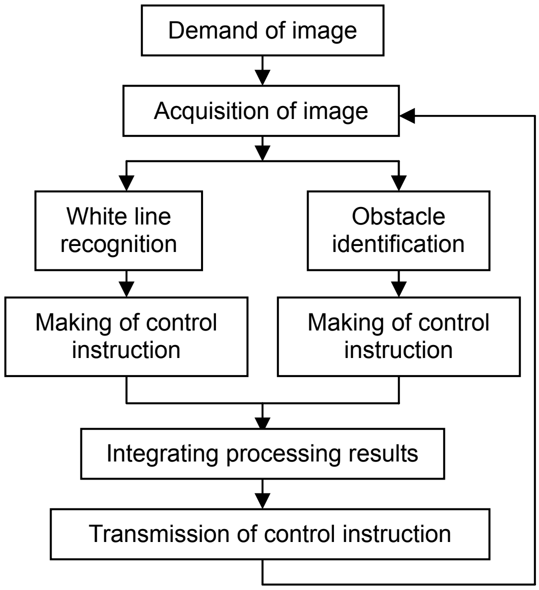

Fig.2 The flow of the entire processing

1. White Line Recognition

The white line recognition is for the purpose of finding out the route along which the robot will move. The white line recognition algorithm uses color and shape information. The white line at the right(left) of the robot is handled with the right(left) side camera. The part on the edge of the image is used to identify whether the robot is approaching to the white line or is moving away. When the white line is extracted in the bottom half of the image, it means the robot is approaching to the white line. Therefore, the control command generated will be "to move away".

(a) Image captured by camera (b) Result

Fig.3 Result of white line recognition

2. Obstacle Identification

The obstacle identification uses the stereo image processing algorithm. The stereo image processing algorithm calculates 3D location of objects from the parallax between the two images. Using the stereo image processing algorithm, it is possible to exclude the patterns on the floor or a thin object such as a piece of paper on the floor from the category of obstacles.

Therefore, the robot will not make the unnecessary obstacle avoiding movement.

The parallax of two images is calculated by using the correlation base. The correlation base calculates all 3D coordinates of the image by using the colour. A 5×5 mask is used to calculate the correlation. The correlation is evaluated by Eqn.1.

$$d = \sum_{m=-2}^{2}\sum_{n=-2}^{2}\left|dl_{i+m,j+n} - dr_{i'+m,j'+n}\right| \qquad (1)$$

dl and dr show pixel value of one pixel. d is a correlation coefficient. Two points are considered correspondence when d is minimized. An area with a small amount of variance will not be processed.

The area where the correspondence had not been found is determined by referring to the surrounding information and labeling results of adjacent regions

Fig.4 (b) shows an actual processing result. Obstacles are displayed in white, and safe areas are displayed in black, and areas that were not able to be judged are displayed in gray. The robot advances in a black area. Because keeping itself the inside of white lines is the principle, the robot never advances to the safety area which is the outside of white lines.

(a)Images captured by the cameras

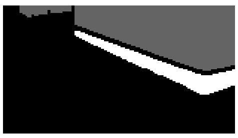

(b)Result

Fig.4 Result of obstacle identification

IV. EXPERIMENTS

An experiment has been conducted to verify the effectiveness and reliability of image processing system.

1. Methodology

Fig 5 shows the route specified in the experiment. As static obstacles a blue colored box and a thin paper are put on a part of the route. Whether the robot is able to advance between white lines are examined. At the same time, whether the robot is able to avoid the obstacles and keep advancing are examined.

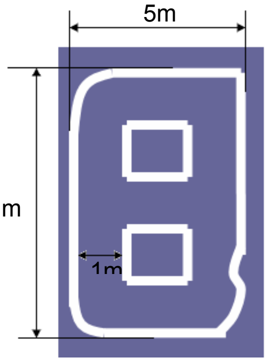

Fig.5 Experimental course

2. Experimental Result

Fig.6 shows appearances of the experiment. The robot was successfully able to run between white lines and avoid the collision with the obstacles. The time necessary for processing was about 300 msec. It was confirmed the robot was able to work in an easy environment by this experiment.

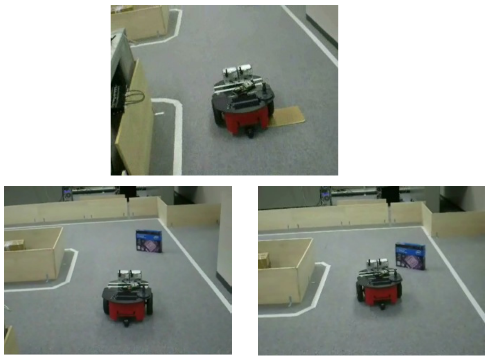

Fig.6 appearances of the experiment

V. DISCUSSIONS

Experimental results demonstrated that the robot can autonomously move in a simple environment. However, the area that cannot be judged in the space exists. To decrease such an area, we should mount a new sensor or device or add a new processing.

At present, the robot works well in a static environment. The robot should move autonomously in a more complex environment such as a dynamically changing environment. If a robot stands still, it is quite easy to determine if the environment is dynamic or not. But as our robot is compelled not to stop unless it is in a dangerous situation, it is not easy to determine if the environment is dynamic or not. Dynamically changing environment could be detected by both measuring the distance between itself and the obstacles and localizing the current position of the robot. The former has been already attained, but the latter must be implemented.

VI. CONCLUSION

This research aimed at the construction of a network-based robot system. This paper presented the image processing system that is capable of recognizing white lines using color information and identifying obstacles using a stereo image processing algorithm. Experimental results proved the feasibility of the proposed network-based approach to the construction of an autonomously moving robot system.

Using the resources available through the network, it is possible to have a complicated computation problem resolved in a distributed and concurrent fashion. At the same time, the robot can be made small and light-weighted.

However, the network sometimes becomes unstable. The construction of the system that considers this instability will be needed in the future.

Moreover, more complex processing is needed. The system should be improved to be adapted to various environments in the future.

Acknowledgment

We greatly appreciate the aid of the Grant-in-Aid for Scientific Research (S) and (A).

REFERENCES

[1] M. Inaba, S. Kagami, F. Kanehiro, Y.Hoshino, H. Inoue, Remote-Brained Robot Approach, International Journal of Robotics Research, Vol.19, No.10, pp.933-954, 2000

[2] Yasuhiro Watanabe, Norihiro Abe, Kazuaki Tanaka, Hirokazu Taki, Tetsuya Yagi, Multimodal communication system allowing man and avatar to use voice and beck, 3rd International Conference on Information Technology and Applications(ICITA'2005), pp.161-166

[3] Hiroki Goto, Norihiro Abe, Kazuaki Tanaka, Yoshihiro Tabuchi, Hirokazu Taki, Shoujie He: Usage of Shared Memory for Multimodal Data Processing in an Outdoor Mobile Robot, proc. ISR (36th International Symposium on Robotics) (CD-ROM), 2005

[4] Moez Bellamine, Norihiro Abe, Kazuaki Tanaka, Hirokazu Taki :Remote Diagnosis System for Rotating Machinery Using Virtual Reality, IEICE Transactions,pp.895-903,2005

[5] Toshiaki Oomori, Norihiro Abe, Kazuaki Tanaka, Hirokazu TAKI, Shoujie HE: Concurrent development of Virtual Robots and Real Robots Based on Physical Low, IMEKO / IFAC / IFIP Workshop on Advanced Robot Systems and Virtual Reality.(CD-ROM), . 2005

[6 Norihiro Abe, Yoshihiro Tabuchi, Hirokazu Taki, Shoujie He " Synchronization between Audiovisual and Haptic Feeling for Constructing Edutainment Systems", international journal(Journal of Virtual Reality, accepted, 2006

©ISAROB 2009

The Fourteenth International Symposium on Artificial Life and Robotics 2009 (AROB 14th '09),
B-Con Plaza, Beppu, Oita, Japan, February 5 - 7, 2009

Cooperative Manipulation of a Floating Object by Some Space Robots with Joint Velocity Controllers
– Application of a Tracking Control Method Using Transpose of Generalized Jacobian Matrix –

Shinichi Sagara† Yuichiro Taira‡

† Department of Control Engineering, Kyushu Institute of Technology
Tobata, Kitakyushu 804-8550, Japan
E-mail: sagara@cntl.kyutech.ac.jp

‡ Department of Ocean Mechanical Engineering, National Fisheries University
Nagata-Honmachi, Shimonoseki 759-6595, Japan
E-mail: taira@fish-u.ac.jp

Abstract

We have studied on a cooperative manipulation of a floating object by some space robots. Moreover, for the cooperative motions we have reported that a tracking control method using the transpose of the Generalized Jacobian Matrix (GJM) can be utilized for the robot having joint torque controllers. In this paper, for the cooperative motions by some space robots with joint velocity controllers, we proposed a tracking control method using the transpose of the GJM. Simulation results show the effectiveness of the proposed control method.

1 Introduction

Space exploration in future will demand robots such tasks that should be achieved by cooperative motions of some space robots. We have studied on control problems for realizing such cooperative manipulation and reported that a system consisting of some space robots having manipulators and a floating object can be treated as a kind of distributed system [1,2]. Using the distributed system representation each robot constituting the distributed system can be designed the control system individually.

For the robots having manipulators many control methods have been proposed [3]. Most of them, however, use the inverse of the generalized Jacobian matrix (GJM) [4] which is a coefficient matrix between the end-effector's velocity and the joint velocity of the manipulator. Therefore, if the robot becomes in a singular configuration, the manipulator is out of control because the inverse of the GJM does not exist. For this problem, we have proposed a joint torque input type discrete time trajectory tracking control method using the transpose of the GJM [5] and reported that the proposed control method can be used for the distributed system described above [6].

It is considered that joint velocity controllers are also used for space robot manipulators. So, we have proposed a control method for joint velocity controller [7]. In this paper, we propose a tracking control method using the transpose of the GJM for handling a floating object cooperatively by some space robots having joint velocity controllers. To validate the control method computer simulations are done. Simulation results show the effectiveness of the control method.

2 Modeling [1,2,6]

2.1 Robot system model

In this paper, we consider a space robot system consisting of M robots with manipulators and a floating object, as shown in Fig. 1. The h-th robot ($h = 1, \cdots, M$) consists of an uncontrolled base and n_h-DOF manipulator with revolute joints. Assumptions and symbols used in this paper are defined as follows:

[Assumptions]

A1) All elements of the space robot are rigid.

A2) The robot system is standing still in an initial state, i. e., the initial linear momentum and angular momentum of the space robots are zero.

A3) No external force acts on the robot system.

A4) Positions and attitude angles of the robots and an object in inertial coordinate frame can be measured.

©ISAROB 2009

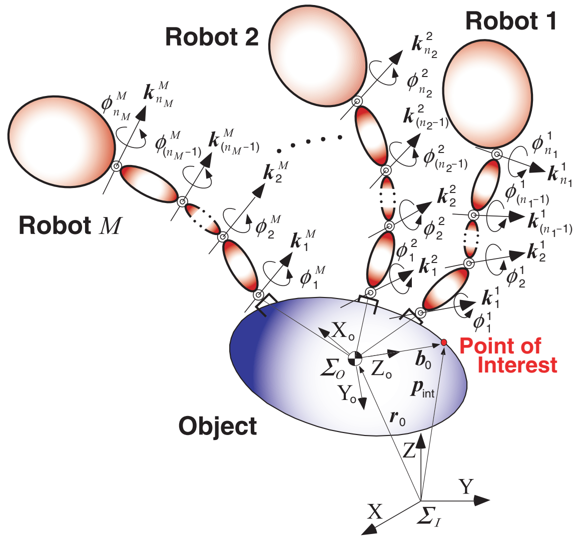

Fig. 1 Model of space robot system

[Symbols]

Σ_I: inertial coordinate frame
$\Sigma_{\rm int}$: point of interest coordinate frame
Σ_T: target coordinate frame
i^h: number of link or joint i of robot h
$\boldsymbol{p}_{\rm int}$: position vector of point of interest
$\boldsymbol{p}_T$: position vector of origin of Σ_T
$\boldsymbol{r}_0$: position vector of mass center of object
$\boldsymbol{v}_*$: linear velocity vector of point of interest ($* =$ int) or mass center of object ($* = 0$)
$\boldsymbol{\omega}_*$: angular velocity vector of point of interest ($* =$ int) or mass center of object ($* = 0$)
$\boldsymbol{p}_i^h$: position vector of joint i^h
$\boldsymbol{r}_i^h$: position vector of mass center of link i^h
$\boldsymbol{k}_i^h$: unit vector indicating joint axis direction of joint i^h
$\boldsymbol{r}_g$: position vector of mass center of system
$\boldsymbol{r}_g^h$: position vector of mass center of robot h
$\boldsymbol{q}$: joint angle vector
${}^I\boldsymbol{A}_*$: rotation matrix from Σ_* ($* =$ int, T) to Σ_I
ϕ_i^h: relative angle of joint i^h
$\boldsymbol{\phi}^h$: joint angle vector of robot h
m_0: mass of object
m_i^h: mass of link i^h
$\boldsymbol{I}_0$: inertia tensor of object
$\boldsymbol{I}_i^h$: inertia tensor of link i^h
$\boldsymbol{E}$: identity matrix

The tilde operator stands for a cross product such that $\tilde{\boldsymbol{r}}\boldsymbol{a} = \boldsymbol{r} \times \boldsymbol{a}$. All position and velocity vectors are defined with respect to the inertial reference frame.

2.2 Kinematic model

The robot system shown in Fig. 1 can be understood as one robot with M manipulators by regarding the object as a robot body, and M robot arms and robot bodies as M manipulators. The kinematic formulation of such space system has been derived by Yoshida et al. [8]. The relation obtained from its geometrical relationships, and the conservation laws of linear momentum and angular momentum under the above assumptions as follows:

$$\boldsymbol{\nu}_{\rm int} = \begin{bmatrix} \dot{\boldsymbol{p}}_{\rm int} \\ \boldsymbol{\omega}_{\rm int} \end{bmatrix} = \boldsymbol{J}_s \begin{bmatrix} \boldsymbol{v}_0 \\ \boldsymbol{\omega}_0 \end{bmatrix}, \quad \boldsymbol{H}_s \begin{bmatrix} \boldsymbol{v}_o \\ \boldsymbol{\omega}_o \end{bmatrix} + \boldsymbol{H}_m \dot{\boldsymbol{\phi}} = \boldsymbol{0} \quad (1)$$

where

$$\boldsymbol{J}_s = \begin{bmatrix} \boldsymbol{E} & \tilde{\boldsymbol{r}}_0 - \tilde{\boldsymbol{p}}_{\rm int} \\ \boldsymbol{0} & \boldsymbol{E} \end{bmatrix}, \quad \boldsymbol{H}_s = \begin{bmatrix} w\boldsymbol{E} & w(\tilde{\boldsymbol{r}}_0 - \tilde{\boldsymbol{r}}_g) \\ w\tilde{\boldsymbol{r}}_g & \boldsymbol{I}_w \end{bmatrix},$$

$$\boldsymbol{H}_m = \begin{bmatrix} \boldsymbol{J}_{T_w} \\ \boldsymbol{I}_\phi \end{bmatrix}, \quad \boldsymbol{\phi} = [(\boldsymbol{\phi}^1)^T, (\boldsymbol{\phi}^2)^T, \cdots, (\boldsymbol{\phi}^M)^T]^T,$$

$$\boldsymbol{I}_w = \sum_{h=1}^{M} \boldsymbol{I}_w^h + \boldsymbol{I}_o, \quad \boldsymbol{J}_{T_w} = \sum_{h=1}^{M} \boldsymbol{J}_{T_w}^h, \quad \boldsymbol{I}_\phi = \sum_{h=1}^{M} \boldsymbol{I}_\phi^h,$$

$$\boldsymbol{I}_w^h = \sum_{i=1}^{n_h} \{\boldsymbol{I}_i^h - m_i^h \tilde{\boldsymbol{r}}_i^h (\tilde{\boldsymbol{r}}_i^h - \tilde{\boldsymbol{r}}_0^h)\}, \quad \boldsymbol{J}_{T_w}^h = \sum_{i=1}^{n_h} m_i^h \boldsymbol{J}_{T_i}^h,$$

$$\boldsymbol{I}_\phi^h = \sum_{i=1}^{n_h} (\boldsymbol{I}_i^h \boldsymbol{J}_{R_i}^h + m_i^h \tilde{\boldsymbol{r}}_i^h \boldsymbol{J}_{T_i}^h),$$

$$\boldsymbol{J}_{T_i}^h = \begin{bmatrix} \boldsymbol{O}_a & \bar{\boldsymbol{J}}_{T_i}^h & \boldsymbol{O}_b \end{bmatrix}, \quad \boldsymbol{J}_{R_i}^h = \begin{bmatrix} \boldsymbol{O}_a & \bar{\boldsymbol{J}}_{R_i}^h & \boldsymbol{O}_b \end{bmatrix},$$

$$\bar{\boldsymbol{J}}_{T_i}^h = \left[\tilde{\boldsymbol{k}}_1^h (\boldsymbol{r}_i^h - \boldsymbol{p}_1^h), \cdots, \tilde{\boldsymbol{k}}_i^h (\boldsymbol{r}_i^h - \boldsymbol{p}_i^h), \boldsymbol{0}, \cdots, \boldsymbol{0} \right],$$

$$\bar{\boldsymbol{J}}_{R_i}^h = \left[\boldsymbol{k}_1^h, \cdots, \boldsymbol{k}_i^h, \boldsymbol{0}, \cdots, \boldsymbol{0} \right],$$

and $\boldsymbol{O}_a \in \boldsymbol{R}^{3\times n_a}$ ($n_a = \sum_{i=1}^{h-1} n_i$) and $\boldsymbol{O}_b \in \boldsymbol{R}^{3\times n_b}$ ($n_b = \sum_{i=h+1}^{M} n_i$) are zero matrices.

Form Eq. (1), the relation between velocity $\boldsymbol{\nu}_{\rm int}$ of the object and joint angular velocity $\dot{\boldsymbol{\phi}}$ of the manipulator can be derived as

$$\boldsymbol{\nu}_{\rm int} = \boldsymbol{J}^* \dot{\boldsymbol{\phi}} \quad (2)$$

where $\boldsymbol{J}^* = -\boldsymbol{J}_s(\boldsymbol{H}_s)^{-1}\boldsymbol{H}_m$ is a GJM of the system shown in Fig. 1.

2.3 System partition

For the system shown in Fig. 1 control systems can be easily constructed by using Eq. (2). However, if the number of robots is changed, Eq. (2) must be recalculated. Furthermore, if the number of robots becomes increased, a large amount of calculation for the system is necessary. To solve the problems described above, This total robot system is regarded as a distributed system.

©ISAROB 2009

By examining parameters and variables included in the matrix $\boldsymbol{H}_s$ and vector $\boldsymbol{H}_m\dot{\boldsymbol{\phi}}$ in Eq. (1), the matrix and vector can be rewritten as

$$\boldsymbol{H}_s = \boldsymbol{H}_s^0 + \sum_{h=1}^{M} \boldsymbol{H}_s^h, \quad \boldsymbol{H}_m\dot{\boldsymbol{\phi}} = \sum_{h=1}^{M} \boldsymbol{H}_m^h\dot{\boldsymbol{\phi}}^h \qquad (3)$$

where

$$\boldsymbol{H}_s^0 = \begin{bmatrix} m_0\boldsymbol{E} & \boldsymbol{0} \\ m_0\tilde{\boldsymbol{r}}_0 & \boldsymbol{I}_0 \end{bmatrix}, \quad \boldsymbol{H}_s^h = \begin{bmatrix} m^h\boldsymbol{E} & m^h(\tilde{\boldsymbol{r}}_0^h - \tilde{\boldsymbol{r}}_g^h) \\ m^h\tilde{\boldsymbol{r}}_g^h & \boldsymbol{I}_w^h \end{bmatrix},$$

$$\boldsymbol{H}_m^h = \begin{bmatrix} \bar{\boldsymbol{J}}_{T_w}^h \\ \bar{\boldsymbol{I}}_\phi^h \end{bmatrix}, \quad m^h = \sum_{i=1}^{n_h} m_i^h,$$

$$\bar{\boldsymbol{J}}_{T_w}^h = \sum_{i=1}^{n_h} m_i^h \bar{\boldsymbol{J}}_{T_i}^h, \quad \bar{\boldsymbol{I}}_\phi^h = \sum_{i=1}^{n_h} \left(\boldsymbol{I}_i^h \bar{\boldsymbol{J}}_{R_i}^h + m_i^h \tilde{\boldsymbol{r}}_i^h \bar{\boldsymbol{J}}_{T_i}^h \right).$$

$\boldsymbol{H}_s^h$ and $\boldsymbol{H}_m^h$ are matrices including parameters the h-th robot only, and $\boldsymbol{H}_s^0$ is a matrix including parameters of the object only.

Eqs. (1) and (3) make the following relation:

$$\left(\boldsymbol{H}_s^0 + \sum_{h=1}^{M} \boldsymbol{H}_s^h \right) \boldsymbol{J}_s^{-1}\boldsymbol{\nu}_{\text{int}} + \sum_{h=1}^{M} \boldsymbol{H}_m^h\dot{\boldsymbol{\phi}}^h = \boldsymbol{0}. \qquad (4)$$

It is clear that the following set of equations is one of solutions of Eq. (4), when a constant and diagonal matrix $\boldsymbol{A}_h$ is introduced.

$$\bar{\boldsymbol{H}}_s^h \boldsymbol{J}_s^{-1}\boldsymbol{\nu}_{\text{int}} + \boldsymbol{H}_m^h\dot{\boldsymbol{\phi}}^h = \boldsymbol{0} \quad (h{=}1,\cdots,M) \qquad (5)$$

where

$$\bar{\boldsymbol{H}}_s^h = \boldsymbol{H}_s^h + \boldsymbol{A}_h\boldsymbol{H}_s^0, \qquad \sum_{h=1}^{M} \boldsymbol{A}_h = \boldsymbol{E}.$$

Then, the following relation can be derived from Eq. (5).

$$\boldsymbol{\nu}_{\text{int}} = -\boldsymbol{J}_s(\bar{\boldsymbol{H}}_s^h)^{-1}\boldsymbol{H}_m^h\dot{\boldsymbol{\phi}}^h \quad (h{=}1,\cdots,M). \qquad (6)$$

Therefore, for each robot of the system the control system can be designed individually.

3 Digital Control

3.1 Torque input type tracking control law [5]

Eq. (6) can be rewritten as

$$\begin{bmatrix} \boldsymbol{v}_{\text{int}}(k) \\ \boldsymbol{\omega}_{\text{int}}(k) \end{bmatrix} = -\boldsymbol{J}_s(\bar{\boldsymbol{H}}_s^h)^{-1}\boldsymbol{H}_m^h\dot{\boldsymbol{\phi}}^h(k) = \begin{bmatrix} \boldsymbol{J}_L^h \\ \boldsymbol{J}_A^h \end{bmatrix} \dot{\boldsymbol{\phi}}^h(k) \quad (7)$$

For Eq. (7) the following digital tracking control law using the transpose of the GJM [5] is utilized:

$$\begin{aligned} \boldsymbol{\tau}_d^h(k) = (\boldsymbol{J}_L^h)^T(k) \left[\hat{k}_L(k)\boldsymbol{e}_L(k) - \hat{\boldsymbol{K}}_L(k)\boldsymbol{v}_{\text{int}}(k) \right] \\ + (\boldsymbol{J}_A^h)^T(k) \left[\hat{k}_A(k)\boldsymbol{e}_A(k) - \hat{\boldsymbol{K}}_A(k)\boldsymbol{\omega}_{\text{int}}(k) \right] \end{aligned} \quad (8)$$

where $\boldsymbol{\tau}_d^h(k)$ is the joint torque input vector and

$$\boldsymbol{e}_L(k) = \boldsymbol{p}_T(k) - \boldsymbol{p}_{\text{int}}(k), \ \boldsymbol{e}_A(k) = -\frac{1}{2}\boldsymbol{E}_X^T(k)\boldsymbol{E}_A(k),$$

$$\boldsymbol{E}_A(k) = \begin{bmatrix} \boldsymbol{n}_T(k) - \boldsymbol{n}_{\text{int}}(k) \\ \boldsymbol{s}_T(k) - \boldsymbol{s}_{\text{int}}(k) \\ \boldsymbol{a}_T(k) - \boldsymbol{a}_{\text{int}}(k) \end{bmatrix}, \quad \boldsymbol{E}_X(k) = \begin{bmatrix} \tilde{\boldsymbol{n}}_{\text{int}}(k) \\ \tilde{\boldsymbol{s}}_{\text{int}}(k) \\ \tilde{\boldsymbol{a}}_{\text{int}}(k) \end{bmatrix},$$

$$\hat{k}_\dagger(k) = k_\dagger\{1 + \alpha_\dagger\nu_\dagger(k)\} \ (\dagger = L, \ A),$$

$$\hat{\boldsymbol{K}}_\dagger(k) = \boldsymbol{K}_\dagger\{1 - \beta_\dagger\nu_\dagger(k)\} \ (\dagger = L, \ A),$$

$$\nu_L(k) = \frac{||\boldsymbol{v}_{\text{int}_d}(k)||}{v_{d_{\max}}}, \quad \nu_A(k) = \frac{||\boldsymbol{\omega}_{\text{int}_d}(k)||}{\omega_{d_{\max}}}.$$

The vectors $\boldsymbol{n}_*$, $\boldsymbol{s}_*$ and $\boldsymbol{a}_*$ ($* = T$, int) are unit vectors along the axes of Σ_* with respect to Σ_I, i. e., ${}^I\boldsymbol{A}_* = [\boldsymbol{n}_*(k) \ \boldsymbol{s}_*(k) \ \boldsymbol{a}_*(k)]$. $*_{\text{int}_d}(k)$ ($* = \boldsymbol{v}, \ \boldsymbol{\omega}$) is the desired velocity of $*_{\text{int}}(k)$, $*_{d_{\max}}$ ($* = v, \ \omega$) is the maximum values of the norm of $*_{\text{int}_d}(k)$, $\alpha_\dagger$ ($\alpha_\dagger \geq 0$) and $\beta_\dagger$ ($0 \leq \beta_\dagger \leq 1$) are setting parameters. Furthermore, $k_\dagger$ is a positive scalar gain, and $\boldsymbol{K}_\dagger$ is a symmetric and positive definite gain matrix.

3.2 Control input of joint velocity

For manipulators with joint velocity controllers the control law (8) cannot be applied directly. To obtain similar control performance to the case of the joint torque controllers, we use the dynamic equation of the robot. Equation of motion of each space robot shown in Fig. 1 can be described as follows [3]:

$$\boldsymbol{M}^h\dot{\boldsymbol{\chi}}(t) + \boldsymbol{C}^h = \boldsymbol{u}^h(t) \qquad (9)$$

where

$$\boldsymbol{\chi} = \begin{bmatrix} \boldsymbol{\eta}_0 \\ \dot{\boldsymbol{\phi}}^h \end{bmatrix}, \quad \boldsymbol{u} = \begin{bmatrix} \boldsymbol{f}^h \\ \boldsymbol{\tau}^h \end{bmatrix},$$

and $\boldsymbol{M}^h$ is the symmetric and positive definite inertia matrix, and $\boldsymbol{C}^h$ is the vector of Coliolis and centrifugal forces, $\boldsymbol{\eta}_0 = [\boldsymbol{v}_0{}^T, \ \boldsymbol{\omega}_0{}^T]^T$ is the velocity of the mass center of object, $\boldsymbol{f}^h$ is the external force affected by other robots.

Discretizing Eq. (9) by the sampling period T_1 ($T = nT_1$, n is positive integer) and applying the Euler approximation to $\ddot{\boldsymbol{q}}(k_1)$, we have [7]

$$\boldsymbol{\chi}^h(k_1) = \boldsymbol{\chi}^h(k_1{-}1) - T_1{\boldsymbol{M}^h}^{-1}(k_1)\left\{\boldsymbol{C}^h(k_1) - \boldsymbol{u}^h(k_1)\right\}. \qquad (10)$$

©ISAROB 2009

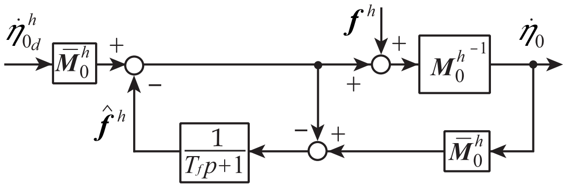

(a) continuous time block diagram

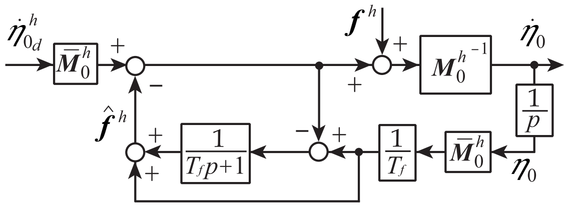

(b) equivalent transformation of (a)

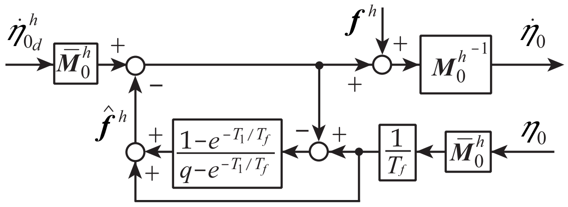

(c) discrete time block diagram

Fig. 2 Disturbance observer

For Eq. (10) the actual joint velocity control input $\dot{\phi}_d^h(k_1)$ is determined as

$$\chi_d^h(k_1) = \chi^h(k_1-1) - T_1 M^{h^{-1}}(k)\left\{C^h(k_1) - u_d^h(k_1)\right\} \quad (11)$$

where

$$\chi_d(k_1) = \begin{bmatrix} \eta_{0_d}^h(k_1) \\ \dot{\phi}_d^h(k_1) \end{bmatrix}, \quad u_d(k_1) = \begin{bmatrix} f^h(k_1) \\ \tau_d^h(k) \end{bmatrix}.$$

Since the value of the external force f_h affected by other robots cannot obtained directly, a disturbance observer in discrete time [9] is used to estimate f_h.

The equation of motion of the floating object with respect to the h-th robot is

$$M_0^h(k_1)\dot{\eta}_0(k_1) = f^h(k_1) + \bar{M}_0^h \eta_{0_d}^h(k_1) \quad (12)$$

where $M_0^h(k_1)$ is the inertia matrix of the floating object and

$$\bar{M}_0^h = A_h \begin{bmatrix} m_0 E & 0 \\ 0 & I_0 \end{bmatrix}$$

is the nominal model of $M_0^h(k_1)$.

For Eq. (12) the estimated value of f_h, $\hat{f}_h$, can be obtained from the disturbance observer as shown in Fig. 2. In this figure, (a), (b) and (c) show the basic configuration in continuous time, the equivalent transformation of (a) and the discrete time version, respectively, T_f is a time constant of a low-pass filter, p and q are the differential and shift operators. From Fig. 2(c), the estimated force can be obtained as follows:

$$\hat{f}^h(k_1) = \hat{f}^h(k_1-1) + \left(1 - e^{-T_1/T_f}\right)\bar{M}_0^h \dot{\eta}_{0_d}(k_1-1) + \frac{1}{T_f}\bar{M}_0^h\left\{\eta_0(k_1) + \left(1 - 2e^{-T_1/T_f}\right)\eta_0(k_1-1)\right\}. \quad (13)$$

Table 1 Physical parameters of robots and object

	Length m	Mass kg	Moment of inertia kg·m^2
Base	3.5	2000	3587.9
Link 2	2.5	50	26.2
Link 1	2.5	50	26.2
hand	0.5	5	0.23
Object	4.0	1200	2400.0

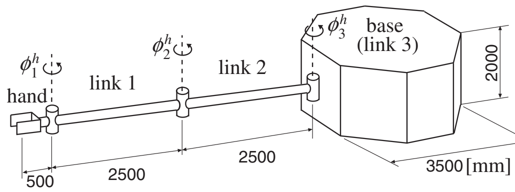

Fig. 3 Space robot

4 Simulation

To examine the performance of the proposed control method described in Section 3, simulations are performed by using three of the horizontal planar 3-DOF robots shown in Fig. 3 and an object.

The physical parameters of the robots and object are shown in Table 1. Simulations are carried out under the following condition. A point of interest on the object moves along a straight path from the initial position to the target position, and the object angle is set up as the initial value. The sampling periods are $T = 0.01$s and $T_1 = 0.001$s ($n = 10$). The coefficient matrices are $A_1 = A_2 = 0.33E$ and $A_3 = 0.34E$. The feedback gains are $k_L = k_A = 2 \times 10^5$, $K_L = \mathrm{diag}\{2\times10^4,\ 2\times10^4\}$ and $K_A = 2\times10^4$. The setting parameters are $\alpha_\dagger = 2$ and $\beta_\dagger = 0.2$ ($\dagger = L,\ A$). The time constant for the low-pass filter is $T_f = 1$s.

Fig. 4 shows the motion of the robot system. From this figure, the object is successfully moved by three robots. Fig. 5 shows the time history of the simulation. This figure also shows the case of constant gains, i. e., $\alpha_\dagger = \beta_\dagger = 0$ except estimated values. From Fig. 5,

©ISAROB 2009

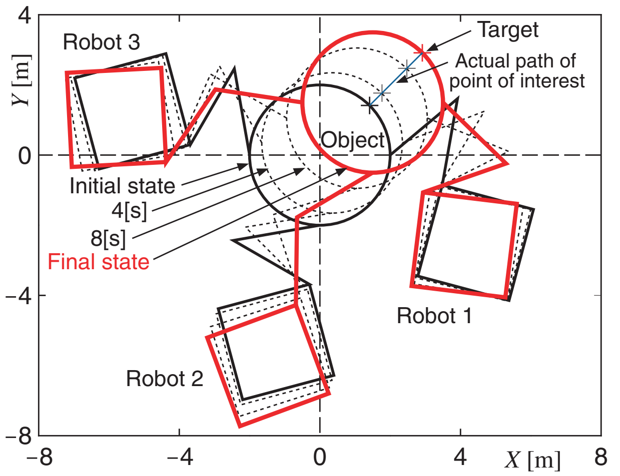

Fig. 4 Motion of the robot system

it can be seen that good control performance can be achieved using the proposed control method.

5 Conclusion

In this paper, we proposed a tracking control method using the transpose of the GJM for handling a floating object cooperatively by some space robots having joint velocity controllers. Simulation results show the effectiveness of the control method.

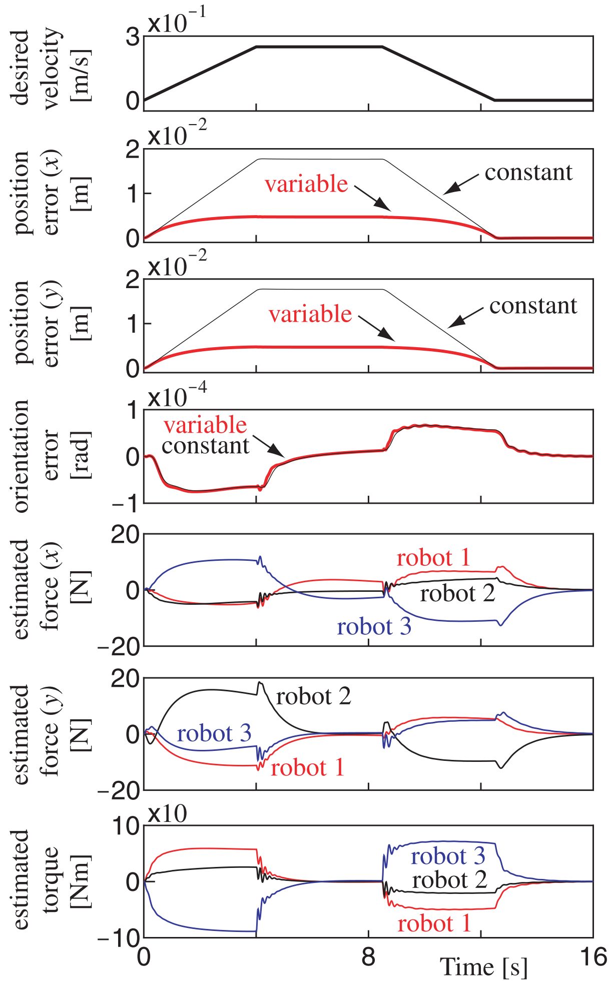

Fig. 5 Simulation result

References

[1] R. Katoh, K. Nakatsuka, S. Sagara, J. Kobayashi, F. Ohkawa, "Manipulation of a Floating Object by Two Space Manipulators", *Proc. IECON'97*, pp. 1397 – 1402, 1997.

[2] S. Sagara, M. Hideura,R. Katoh, T. Yamashita, J. Kobayashi, F. Ohkawa, "Adaptive RMRC for Cooperative Manipulation of a Floating Object by Two Free-Based Space Robots", *Proc. IROS'98*, pp. 1467 – 1472, 1998.

[3] Y. Xu and T. Kanade (eds), *Space Robotics: Dynamics and Control*, Kluwer Academic Publishers, 1993.

[4] K. Yoshida and Y. Umetani, "Control of Space Robot Manipulators with Generalized Jacobian Matrix", In Y. Xu and T. Kanade (eds), *Space Robotics: Dynamics and Control*, Kluwer Academic Publishers, pp. 165–204, 1993.

[5] S. Sagara, Y. Taira, "Digital Tracking Control of Space Robots using Transpose of Generalized Jacobian Matrix", *J. Artif Life Robotics*, Vol. 11, pp. 82 – 86, 2007.

[6] S. Sagara, Y. Taira, "Cooperative Manipulation of a Floating Object by Some Space Robots - Application of a Tracking Control Method Using Transpose of GJM -", *J. Artif Life Robotics*, Vol. 12, pp. 138 – 141, 2008.

[7] S. Sagara, Y. Taira, "Digital Control of Space Robot Manipulators with Velocity Type Joint Controller Using Transpose of Generalized Jacobian Matrix", *Proc. 13th AROB*, pp. 127 – 130, 2008.

[8] K. Yoshida, R. Kurazume, Y. Umetani, "Coordinated Control of Multiple Manipulators in Space Robots", *J. Robotics Society of Japan*, Vol. 9, No. 6, (in Japanese) pp. 718–726, 1991.

[9] I. Godler, H. Honda and K. Ohnishi, "Design Guidelines for Disturbance Observer's Filter in Discrete Time", *Proc. 7th Int. Workshop on Advanced Motion Control*, pp. 390 – 395, 2002.

©ISAROB 2009

Determinate the Time to Contact Using Compound Eye Sensor

Y. Kaneta, Y. Katsuyama and K. Ito

Department of Systems and Control Engineering Hosei University, 3-7-2 Kajinocho Koganei Tokyo Japan 184-8584
(Tel: +81-42-387-6093; Fax: +81-42-387-6381)
(yukimasa.kaneta.y7@gs-eng.hosei.ac.jp, yasuhiro.katsuyama.wn@eng.hosei.ac.jp, ito@hosei.ac.jp)

Abstract: Recently, many control methods for autonomous robot that are based on biological mechanism have been studied. In particular, a concept of time to contact called tau-margin that is studied in ecological psychology is attracting much attention. In conventional works, various approaches to acquire tau-margin have been studied and are applied for timing control of mobile robots. However, in those studies, robot has a light bulb, and direct light from the light bulb is required for acquiring tau-margin. Thus, it is impossible to apply the conventional method for the robots that use in-direct light for acquiring tau-margin. For that purpose, we develop compound eye sensor which is configured by photodiodes. We employ the framework of optical flow to detect objects and we acquire tau-margin from apparent size of the detected objects and their temporal changes. To demonstrate the effectiveness of the proposed compound eye sensor, we employ a mobile robot controlled with this sensor and conduct a fleeing task. The aim of the fleeing task is to flee an obstacle which approaches, and the timing to flee is controlled by using the tau-margin. Experiments have been conducted by using an actual robot, and as a result, fleeing task has been completed successfully. We can conclude that it is possible to estimate tau-margin by using proposed compound eye sensor.

Keywords: time to contact, ecological psychology, compound eye sensor, optical flow

I. INTRODUCTION

Recently robots that operate in unknown environment have attracted much attention, and various robots have been developed. To behave autonomously, the robots have to acquire information of distance from obstacles to construct three dimensional internal models of the environment. So, usually robot has some sensors that measures distance among the robots and obstacles, for example ultrasonic sensors, the infrared distance sensors and so on.

On the other hand, animals and insects can behave adaptively in the unknown environment without distance sensors. In ecological psychology, the mechanism has been studied, and it is considered that animals and insects employ information that means time to contact instead of information of distance [1]. This time to contact is called "tau-margin", and animals and insects perceive it from apparent size of objects and temporal changes of them.

In conventional works, various approaches to acquire tau-margin have been studied, and are applied for timing control of mobile robots. However, in the conventional studies, robot has a light bulb, and direct light from the light bulb is required for acquiring tau-margin [2]. Thus, it is impossible to apply the conventional method for the robots that use in-direct light for acquiring tau-margin.

In this paper, we propose a method for acquiring time to contact under in-direct light condition. To realize this method, we develop compound eye sensor which is configured by photodiodes. In this sensor, we apply the framework of optical flow to acquire tau-margin. We mount this sensor to a mobile robot, and experiments of fleeing task are conducted by using this mobile robot.

II. TAU-MARGIN IN ECOLOGICAL PSYCHOLOGY

1. Problem of the binocular parallax

It is generally known that many animals and insects can perceive distance by using the binocular parallax. However, as distance becomes far, it is difficult to perceive distance with accuracy, because error between perceived distance and actual distance increases. Fig.1 shows the difference of error of distance with the binocular parallax.

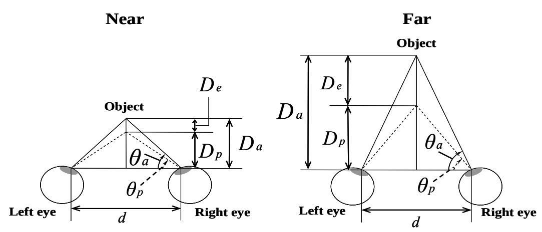

Fig.1. The difference of error of distance

In this figure, the actual distance from the object is described by D_a, and the distance which is recognized visually is described by D_p. θ_a is angular direction to the actual object, and θ_p is angular direction to the perceived object. The error of distance D_e is described by following equation.

$$D_e = \frac{d}{2}(\tan\theta_a - \tan\theta_p) \tag{1}$$

As the angle of θ_a approaches 90 degrees, D_e diverges to the infinite value. So, this equation means that error of distance becomes larger with increasing actual distance.

2. Perception of tau-margin

It is considered that the binocular parallax is not useful for perceiving long distance. So, in addition to the binocular parallax, animals employ another mechanism to perceive relation between own body and environment. In ecological psychology, this mechanism is studied, and these studies have indicated that animals can perceive visual information which means time to contact. This visual information is called tau-margin, and animals perceive it from apparent size of object and its temporal change. Fig.2 shows visual perception of an object.

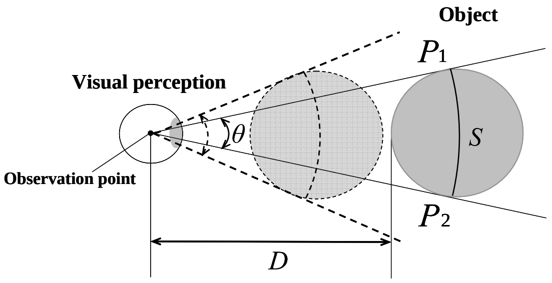

Fig.2. Visual perception of an object

In this figure, S means actual size of the object D means distance between object and visual perception. The apparent size of the object which is represented by θ is described by the equation (2) with S and D.

$$\theta = \frac{S}{D} \tag{2}$$

The temporal change of θ is shown by the equation (3).

$$\dot{\theta} = -\frac{S}{D^2}\dot{D} \tag{3}$$

τ means the tau-margin. It is described by the equation (4).

$$\tau = -\frac{\theta}{\dot{\theta}} = \frac{D}{\dot{D}} \tag{4}$$

This equation means that tau-margin can be perceived directly from the apparent size of object and its temporal change without information of distance or relative velocity to the object.

III. PROPSAL MESTHOD

1. Optical flow

We employ optical flow [3] [4] to acquire apparent size of objects.

Optical flow is one of the popular motion estimate method. It is possible to represent the object motion with velocity vector by analysis of changes in luminance on each pixel. Also, it is possible to estimate direction of the object motion by using the temporal luminance gradient and the spatial luminance gradient.

2. The acquisition method for tau-margin

Fig.3 shows acquisition method for apparent size of object with the compound eye sensor that we propose. In this sensor, each ommatidium is configured by photodiode, and can detect optical flow from optical information of the object.

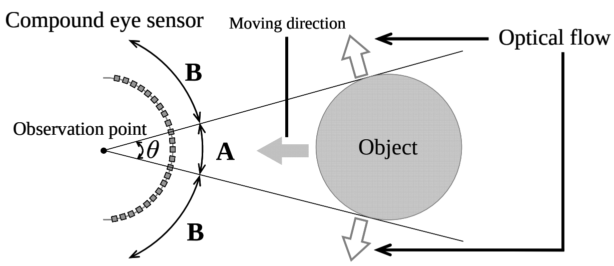

Fig.3 Acquisition method for apparent size of object

As the object approaches to this compound eye sensor, outward optical flow is generated at the region A. And, on the region B, optical flow becomes irregularity. So, it is possible to obtain apparent size of object θ by the outward optical flow.

The temporal change of θ is calculated by an electrical circuit. From these values, tau-margin shown by equation (4) is acquired. Fig. 4 shows processing flow of calculating tau-margin.

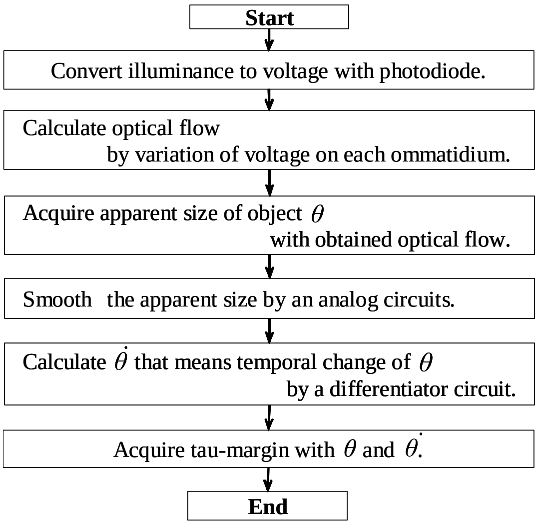

Fig. 4 The processing flow of calculating tau-margin

IV. EXPERIMENTS

1. Compound eye sensor

Fig. 5 and Fig. 6 show the developed compound eye sensor. Fig. 5 is a top view and Fig. 6 is a front view. This sensor is designed so that it can obtain the tau-margin by using some analog circuits which employ 30 photodiode devices. To improve the directivity of the photodiode, a cylinder of black rubber (Fig. 7c) is applied to the photodiode (Fig. 7b). Viewing angle of this sensor is about 160 degrees.

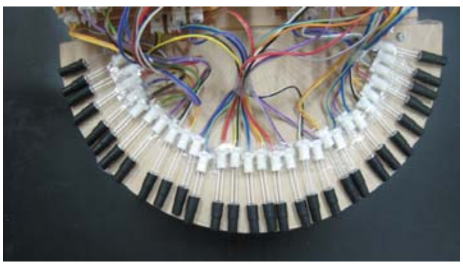

Fig. 5 compound eye sensor (Top view)

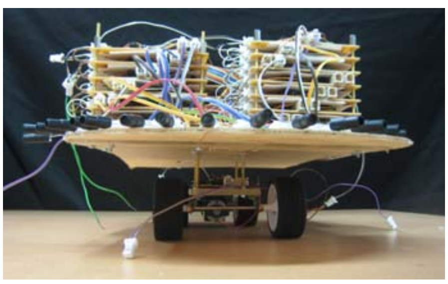

Fig. 6 Compound eye sensor (Front view)

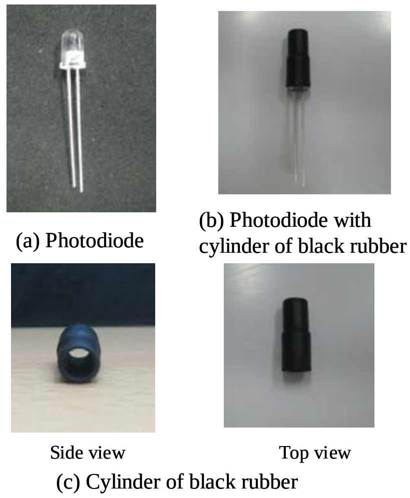

Fig. 7 Photodiode

2. Preliminary experiment

As a preliminary experiment, we obtain the tau-margin with the compound eye sensor when object approaches. Fig. 8 shows the experiment environment. There are white boards around the compound eye sensor. The object is a black board, and it approaches to the compound eye sensor.

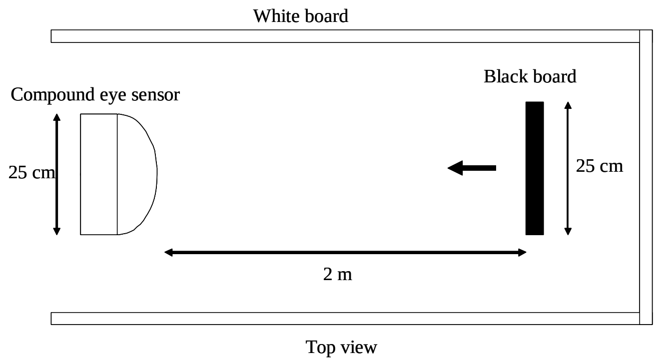

Fig. 8 Experimentation environment

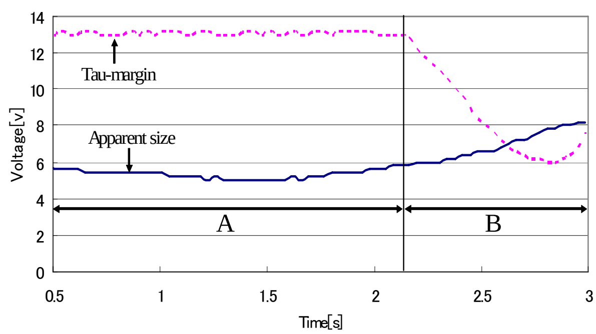

Fig. 9 Apparent size of object and tau-margin

©ISAROB 2009

Fig. 9 shows the result. The solid line is the obtained apparent size of the object and dotted line is the tau-margin. In area B, the apparent size of the object increases and the tau-margin decreases. It means that compound eye sensor can obtain the tau-margin from the apparent size.

3. Fleeing task

To demonstrate the effectiveness of the proposed compound eye sensor, we apply it to timing control of a mobile robot. We conduct fleeing task using real robot. The aim of the fleeing task is to flee from the object when it approaches. In this case, the timing of the mobile robot is controlled by the tau-margin.

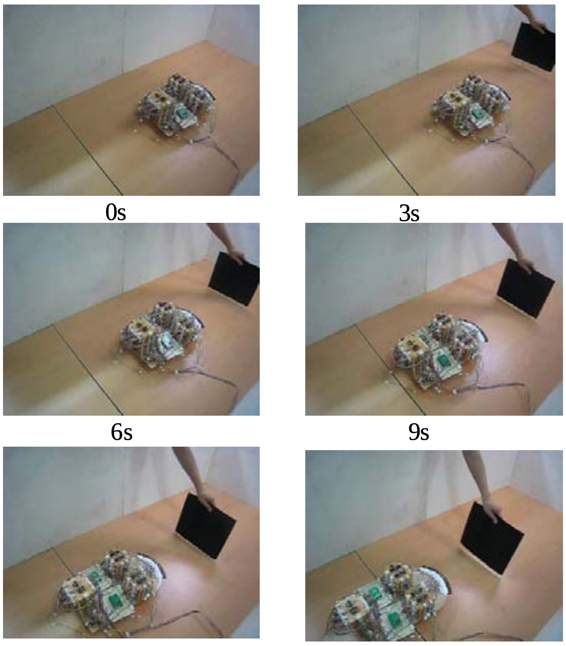

Fig. 10 Fleeing task

Fig. 10 shows a realized motion of the mobile robot in fleeing task. When the object approaches, the robot can operate at the timing to flee. We can consider that the robots behave effectively by using the tau-margin.

4. Discussion

In those experiments, the compound eye sensor does not measure any distance or velocity. However, the fleeing task was able to be achieved by applying the tau-margin. The sensors have obtained the tau-margin in direct light condition. We can confirm that timing control of the mobile robot is realized by the proposed compound eye sensor.

V. CONCLUSION

In this paper, we have considered timing control of a mobile robot and applied the framework of ecological psychology to the robot. We have developed a prototype of the compound eye sensor for obtaining the tau-margin.

We have conducted experiments with the compound eye sensor. As the result, the experiments have been completed successfully. We have confirmed that the compound eye sensor obtained the tau-margin and the robot can operate autonomously by using the tau-margin without any distance or velocity sensors. We can conclude that the proposed compound eye sensor is effective for timing control of the mobile robots.

REFERENCES

[1] Lee DN (1985), Visual timing of interceptive action. Brain mechanisms and spatial vision: 1-30

[2] Tomonori Kai, Yasuhiro Shimada, Kazuyuki Ito (2007), Timing control of the mobile robot using tau-margin. Proceedings of the 13th International Symposium on Artificial Life and Robotics, pp. 907-910

[3] Takashi Fuse, Eihan Shimizu, Morito Tsutsumi (2000), A Comparative Study on Gradient-Based Approaches for Optical Flow Estimation (in Japanese). Proceedings of Applied Survey Technology, Vol. 11, pp. 45-52

[4]Horn B.K.P. and Schunk B.G., Determining optical flow(1981), Artif. Intell. 17, pp.185-203

[5] Kazunori Hoshino (2005), Visual System Inspired by the Insect Compound Eye (in Japanese). Journal of the Robotics Society of Japan, Vol.23, No.1: 32-35

[6] Kazunori Hoshino, Fabrizio Mura, Isao Shimoyama (2001), Fabrication and Performance of Compound Eye Sensors with Scanning Receptor Arrays (in Japanese). Journal of the Robotics Society of Japan, Vol.19, No.3: 408-414

[7] Michiaki SEKINE, Kazunori UMEDA (2001), Construction of compound-eye-type micro vision sensor with simple structure (in Japanese). Journal of the Horological Institute of Japan, Vol.45, No.2: 54-62

[8] Kazunori Hoshino, Fabrizio Mura, Isao Shimoyama (2001), A One-Chip Scanning Retina With an Integrated Micromechanical Scanning Actuator. Journal of Microelectromechanical systems, Vol.10, No.4:492-497

Systematization of Error Recovery in Skill-Based Manipulation

Akira Nakamura and Tetsuo Kotoku

Intelligent Systems Research Institute
National Institute of Advanced Industrial Science and Technology (AIST)
Central 2, 1-1-1 Umezono, Tsukuba, Ibaraki, 305-8568 Japan
a-nakamura@aist.go.jp, t.kotoku@aist.go.jp

Abstract: Dexterous manipulation is an important function for working robots. Manipulator tasks such as assembly and disassembly can generally be divided into several motion primitives. We call such motion primitives "skills" and explain how most manipulator tasks can be composed of sequences of these skills. We are currently planning to construct a maintenance robot for household electrical appliances. We considered hierarchizing the manipulation tasks of this robot since the maintenance of such appliances has become more complex than ever before. Additionally, as errors are seen likely to increase in complex tasks, it is important to implement effective error recovery technology. This paper presents our proposal of a new type of error recovery that uses the concepts of task stratification and error classification.

Key words: manipulation skill, maintenance task, error recovery

1. Introduction

To be useful in wide-ranging fields, manipulation robots need to achieve various tasks using special techniques. We analyzed human motions in such tasks as assembly and disassembly and found that the movements consisted of several significant motion primitives. We call motion primitives "skills" and have demonstrated that most tasks of a manipulator robot can be composed of sequences of skills [1]–[5]. In the hierarchy of manipulator control, skill level control is positioned between task level control and servo level control. Programmers can describe a task program easily as a sequence of skills without needing to take into account servo level control.

We have researched maintenance robots working in various plants, including nuclear power plants. As a target for our future research, we will consider manipulation robots used for the maintenance of household electrical appliances and consumer electronics. At present, we are working toward producing a prototype of a maintenance robot for system components and personal computers (Fig. 1). The robot opens and closes the equipment enclosures and replaces parts. Such maintenance requires the use of many manipulation skills, and the composition of the tasks is complex. Therefore, we considered employing task stratification with the manipulation skills to make the development more manageable.

Manipulation tasks with skills are performed in theory by sequences of visual sensing, geometric modeling, planning and execution. In actual manipulation, however, errors often occur for various reasons and processes are interrupted. Failures can be caused by such errors as execution errors, planning errors, modeling errors and sensing errors. Various approaches for error recovery have been reported [6]–[9], however, few methods for realistic error recovery have been proposed for the various errors that could actually occur during maintenance tasks. We have grouped such errors into several classes according to their potential causes. If an error occurs, the parameters of planning, modeling or sensing are corrected by specifying the class, and then the task process is performed again. We propose a method of error recovery that uses the concept of error classification. Furthermore, we considered error recovery for stratified tasks, and we have been able to apply our approach to complex tasks. In this paper, we explain the concept of manipulation skills and skill-based processes for maintenance tasks, and we propose a method of error recovery that uses the concepts of task stratification and error classification.

The next section explains manipulation skills. The stratification of manipulation tasks and an example of maintenance tasks for electrical appliances is shown in section 3. The classification of errors and error recovery in the task hierarchy are shown in section 4.

2. Manipulation Skills

This section explains our concept of skills. See References [1], [2] for more details.

Skills in which the contact states vary during assembly and disassembly tasks are particularly significant. We considered three fundamental skills of move-to-touch, rotate-to-level and rotate-to-insert, which play an important part in such tasks. First, the move-to-touch skill means the transition from free to vertex-to-face contact between an object grasped by the manipulator and a stationary object in the working environment (Fig. 2). Secondly, the rotate-to-level skill means the transition from vertex-to-face contact to edge-to-face contact for the two objects (Fig. 3). Thirdly, the rotate-to-insert skill means the motion of rotating the object obliquely into a

©ISAROB 2009

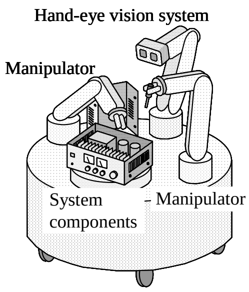

Fig. 1 Maintenance robot for audio-visual system components

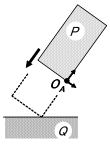

Fig. 2 Move-to-touch skill

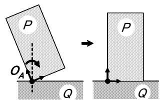

Fig. 3 Rotate-to-level skill

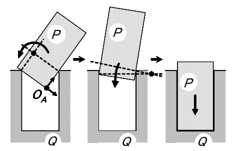

Fig. 4 Rotate-to-insert skill

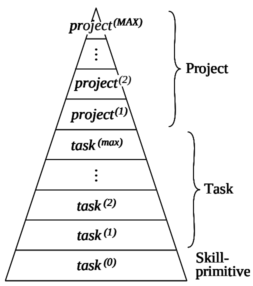

Fig. 5 Manipulation Hierarchy

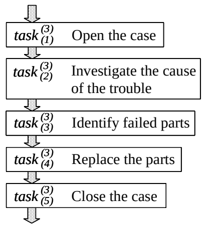

Fig. 6 Maintenance procedure

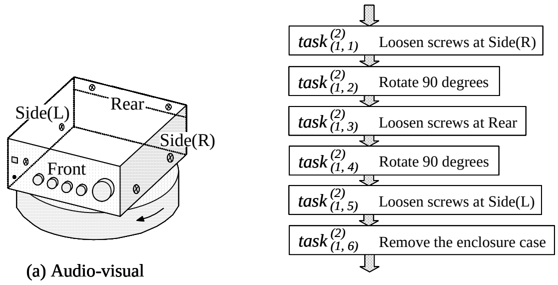

(a) Audio-visual system component

(b) Case opening task sequence

Fig. 7 Task of opening the case of an audio-visual system component

hole in the opposing object to complete the insertion task (Fig. 4). A specific task is composed of sequences of skill primitives such as these move-to-touch, rotate-to-level and rotate-to-insert skills. The skill sequences can be decided by several methods. We have already presented a method that uses variations of the number of contact points in the skill primitives [2].

Moreover, many skills can be defined based on small-change versions of these three fundamental skills. For example, rotate-to-bite and rotate-to-loosen skills that are used in the task of loosening a screw while manipulating a screwdriver are derived by performing small changes of these fundamental skills as shown in section 4.

3. Stratification of Tasks

Manipulation tasks composed of several skills were considered previously as described in Reference [5]. However, the actual tasks composed of many skills are in fact more complex and stratification of tasks is preferable for efficient management and execution.

3.1. Hierarchy of Tasks

We will describe hierarchizing of manipulation tasks based on a bottom-up approach. If we ignore the servo layer, the *skill* layer, which consists of elements such as move-to-touch and rotate-to-bite skills, is located in the lowest rank layer called the $task^{(0)}$ layer. Each skill is performed by the processes of visual sensing, geometric modeling, planning and execution. One tier above the $task^{(0)}$ layer will be called the $task^{(1)}$ layer. Similarly, the $task^{(i+1)}$ is composed of sequences of $task^{(i)}$ elements (Fig. 5). The top layer, where the error recovery loop is closed, will be called $task^{(max)}$ and one tier above $task^{(max)}$ will be called the *project* layer. The *project* layer might also be hierarchized, but we will not discuss this here.

3.2. Stratification of Maintenance Tasks

Let us consider typical tasks involved in the repair of the system components of consumer audio-visual equipment as an example of stratification. The maintenance tasks for an electrical appliance are performed as shown in Fig. 6. The task sequence $\{task^{(2)}_{(1, i2)}\}$ of the case opening $task^{(3)}_{(1)}$ is shown in Fig. 7. If there are two Phillips screws in Side (R), $task^{(2)}_{(1, 1)}$ is composed of two tasks of loosening each of the two Phillips screws using a Phillips screwdriver which can be described as $task^{(1)}_{(1, 1, 1)}$ and $task^{(1)}_{(1, 1, 2)}$, and the skill sequences $\{task^{(0)}_{(1,1,1, i0)}\}$ and $\{task^{(0)}_{(1,1,2, i0)}\}$ are shown in Fig. 8. These skill primitives are described in detail in Reference [5]. The loosening tasks at the Rear and Side (L) called $task^{(2)}_{(1, 3)}$ and $task^{(2)}_{(1, 5)}$, respectively, are similar to $task^{(2)}_{(1, 1)}$ at Side (R). The task of removing the case is composed of the skill sequences $\{task^{(0)}_{(1,6,1, i0)}\}$ shown in Fig. 9. Then, layer $task^{(1)}_{(1, 6, 1)}$, which has no meaning, adds one tier below $task^{(2)}_{(1, 6)}$ to make the number of layers the same. The tasks of rotating 90 degrees using a manipulator in $task^{(2)}_{(1, 2)}$ and $task^{(2)}_{(1, 4)}$ are performed by a procedure that refers to the task of removing the case.

4. Error Recovery in Stratified Tasks

In an ideal environment, the tasks are achieved without any errors occurring. In actual manipulation, however, errors often do occur from various causes. We will show our concept of error classification and process flow with error recovery in the task hierarchy.

4.1. Classification of Errors

The causes of failures can be attributable to several kinds of errors such as control errors, model errors and visual sensing errors. We group the error states into several classes according to possible causes. The classes of errors are described in detail in Reference [5].

・Execution error: This is a mechanical error caused in the manipulator mechanism such as a gear backlash.

・Planning error: This is an error caused by inaccurate

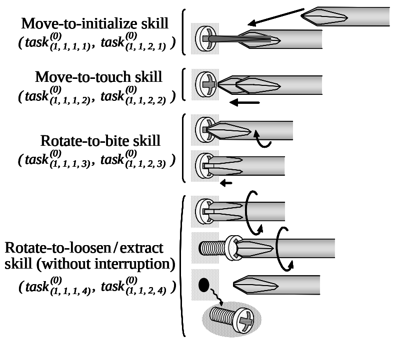

Fig. 8 Skill sequence of loosening a Phillips screw using a Phillips screwdriver

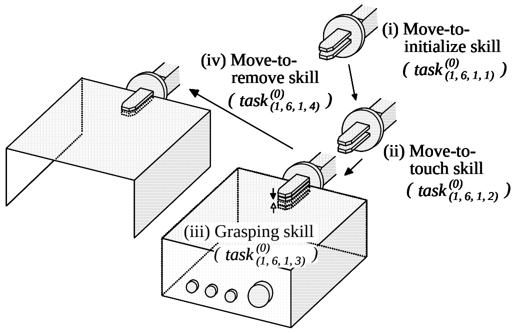

Fig. 9 Task of removing the case

parameter values in the planning.

・Modeling error: This is an error caused by differences in the real object and the geometric model in the software.

・Sensing error: This is an error occurring during visual sensing.

Merely restoring these causes of error does not always solve the problem. It may be necessary to return to a previous step when the working environment is greatly changed by the error.

4.2. Error Recovery based on Classification

A generalized process flow of stratified tasks that takes error recovery into account is shown in Fig. 10. At the Confirmation step in each skill primitive $task^{(0)}_{(i0)}$, whether the result is correct or a failure is judged by an automatic process or by a human operator. Error recovery is performed using the following error classification.

Class 1: When it is judged to be an execution error, $task^{(1)}_{(i1)}$ is executed again without correcting the parameter .

Class 2: When it is judged to be a planning error, $task^{(1)}_{(i1)}$ is executed again with a change in the planning parameters .

Class 3: When it is judged to be a modeling error, $task^{(1)}_{(i1)}$ is executed again with a change in the modeling parameters.

Class $T^{(1)}$: When it is judged to be a sensing error, $task^{(1)}_{(i1)}$ is executed again with a change in the sensing parameters.

Class $T^{(2)}$: $task^{(2)}_{(i2)}$ is executed again after the execution of the necessary changes and returns to the start of one tier above the layer $task^{(1)}_{(i1)}$.

⋮

Class $T^{(max)}$: $task^{(max)}_{(imax)}$ is executed again after the execution of the necessary changes and returns to the start of (max - 1) tier above the layer $task^{(1)}_{(i1)}$.

Class $T^{(max+1)}$: When it is judged that too many changes will be required, the process being executed is interrupted and the process returns to the start of the all-over task.

5. Conclusions

It is necessary to increase the reliability of maintenance robots that work on household appliances. Therefore, error recovery in complex tasks is important, and a processing flow for recovery from errors of various causes has been presented. We have proposed a new method of error recovery that uses the concepts of both task stratification and error classification.

In the future, we will further study optimum adjustment methods for the error recovery parameters and a fully automatic method for confirming skill achievement. We will attempt to apply our method to real maintenance robots.

References

[1] Hasegawa T, Suehiro T, Takase K (1992), A model-based manipulation system with skill-based execution. IEEE Trans Robotics Autom 8(5):535-544
[2] Nakamura A, Ogasawara T, Suehiro T, Tsukune H (1996), Skill-based backprojection for fine motion planning, Proceedings of the IEEE/RSJ International Conference on Intelligent Robots and Systems (IROS '96), Osaka, Japan, Nov 4-8, 1996, pp.526-533
[3] Nakamura A, Ogasawara T, Kitagaki K, Suehiro T (2001), Using robust and simplified geometric models in skill-based manipulation, Proceedings of the IEEE/RSJ International Conference on Intelligent Robots and Systems (IROS 2001), Hawaii, USA, Oct 29-Nov 3, 2001, pp.138-145
[4] Nakamura A, Ogasawara T, Suehiro T, Tsukune H (1998), Fine motion strategy in three-dimensional space using skill-based backprojection. Artificial Life and Robotics 2(3):134-137
[5] Nakamura A, Kitagaki K (2007), Skill-Based Manipulation and Error Recovery in Maintenance Tasks, Proceedings of the 12th International Symposium on Artificial Life and Robotics (AROB 12th '07), Oita, Japan, Jan 25-27, 2007, pp.179-182.
[6] Donald BR (1989), Error detection and recovery in robotics. Springer-Verlag, Berlin Heidelberg New York, pp.1-256
[7] Evans EZ, Lee CSG (1994), Automatic generation of error recovery knowledge through learned reactivity, Proceedings of the IEEE International Conference on Robotics and Automation (IRCA '94), California, USA, May 8-13, 1994, pp.2915-2920
[8] Xue G, Fukuda T, Asama H (1995), Error recovery in the assembly of a self-organizing manipulator by using active visual and force sensing. Autonomous Robots 1(2):179-186
[9] Moon CW, Lee BH (2001), A model-based error recovery scheme for a multi-robot system. Robotica 19(4): 371-380

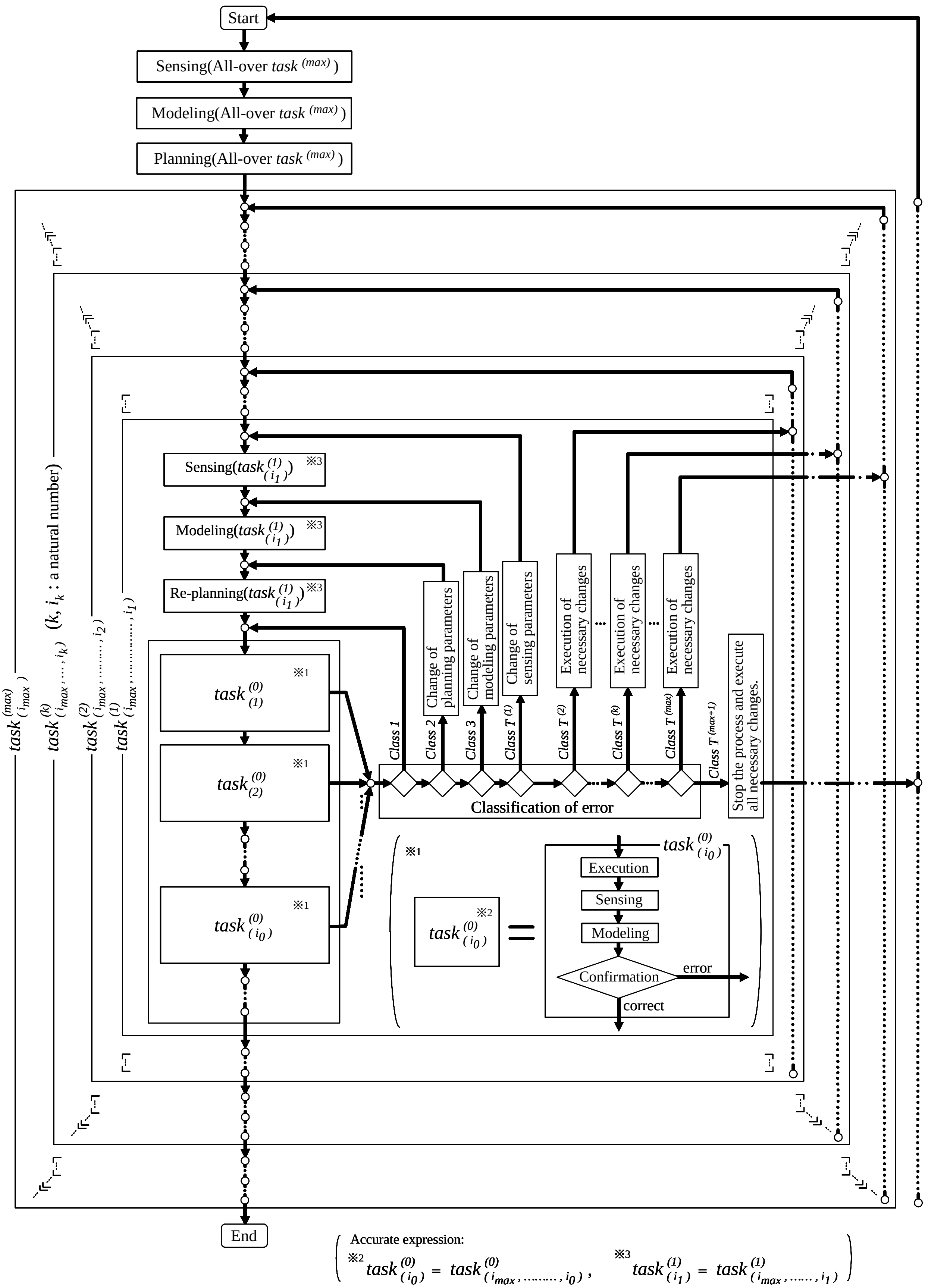

Fig. 10 Generalized process flow with error recovery

The Fourteenth International Symposium on Artificial Life and Robotics 2009 (AROB 14th '09),
B-Con Plaza, Beppu, Oita, Japan, February 5 - 7, 2009

Generating Function of Color Information Detection using Genetic Programming

Takanori Ogawa* Naoki Oshiro** and Hiroshi Kinjo**

*Graduate School of Engineering and Science, University of the Ryukyus
**Faculty of Engineering, University of the Ryukyus
Senbaru 1, Nishihara, Okinawa 903-0213
ogawa@mibai.tec.u-ryukyu.ac.jp

Abstract: This paper proposes a function of color information detection using genetic programming (GP). In the image-processing, object detection is one of important processes. In case the object has complex color domain, the detection becomes more difficult. The authors generate the detection function of complex color domain by using GP. The detection function deals with one pixel of an input image, and it obtains an output image by processing for all pixels. We aim at the time reduction of human consideration of the image-processing system design. In this study, we detect the actual images using the detection function. The results show that the detection function has sufficiently ability for these detection.

Keyword: Genetic Programming, Color Information Detection

1 Introduction

Object detection is one of important processes in the image-processing. In case object has simple color domain, it is possible to detect the object by using basic methods such as the segmentation or the histogram. The detection becomes more difficult when the object has a complex color domain. In this case, an image-processing system is generally constructed by human's trial and error. However, its image-processing system by human consideration depends a specific process. In summery, it is said that the system by human consideration lacks of the generalization ability. Recent studies have reported the filters for the object detection generated by GP or genetic algorithm (GA) [1, 2]. Their methods automatically generates the filters by evolutional process. In the GP system, the generating filter outputs better detection results in image-processing. However, function and terminal nodes in GP are selected by human consideration from among the conventional image filters to solve the problems.

In this paper, our GP method treats the three basic operators of arithmetic and the color informations, without treating the conventional image filters. It generates a function of color information detection. The generating function receives color information from one pixel of an input image, and output a new pixel value into output image. The output image is obtained by repeating this processes for all pixels. Because our method treats only simple operators, we expect that the our proposed method facilitates the construction of GP in the image-processing. We apply this method to detect the complex domain of color images.

2 Detection function evolved by GP

2.1 Genetic Programming

Genetic programming [3] is one of the typical evolutionary method, and it is a method to search the computer programs and the equations for solve the problems. The individuals in GP system can handle tree structures, which is represented with a following S-expression.

$$x^2 + x + 2 \Rightarrow (\ +\ \ (\ *\ \ x\ \ x\ )\ \ (\ +\ \ x\ \ 2\ )\ )\ )$$

Figure 1 shows how to evolve function trees of GP. Trees are updated by repeating crossover and mutation of tree each other.

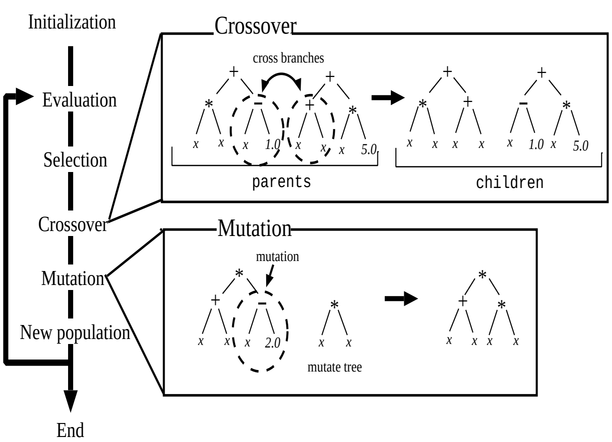

Fig. 1: GP tree evolution

©ISAROB 2009

2.2 Image-processing System by GP tree

In our GP system, it generate the function of color information detection while evolutional process. Figure 2 shows the image-processing system using a tree individual evolved by GP. A tree individual recieves the color information from an optional pixel $I(x, y)$ of input image (size= $W_x \times W_y$), and outputs a value O'. Afterwards, O' is segmented to a value of 0 (white) or 1 (black) according to the following threshold, which is set to new pixel $O(x, y)$.

$$O(x,y) = \begin{cases} 1 \text{ (black)} & O' \geq 0 \\ 0 \text{ (white)} & \text{otherwise} \end{cases} \quad (1)$$

Our image-processing system generates an output image by repeating the above process for all pixels.

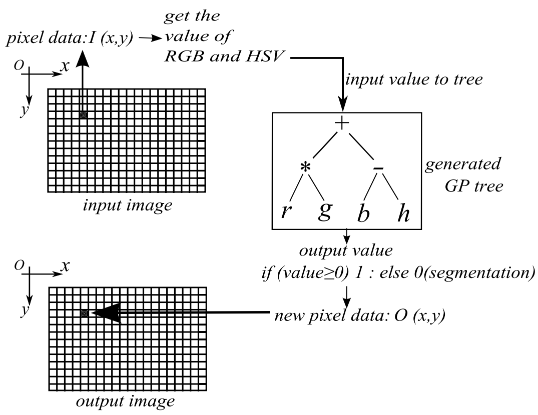

Fig. 2: Image-processing system using GP tree

2.3 Function and terminal nodes

To generate the desired tree structure, we set the function nodes and the terminal nodes as shown in Table 1. The function nodes are the three basic operators of arithmetic, such as addition (+), subtraction (−), multiplication (∗). The terminal nodes are color informations from the optional pixel $I(x, y)$ of the input image, such as values of Red, Green, Blue, Hue, Saturation , Brightness, Luminosity [1]. And moreover, we set the random number which are drawn from the range [-1, 1].

2.4 Evaluation Method

At the begining of evolutional process, we provide the input image, and a target image for the GP (for example: Figure 3). Target image is a mask image of a target object domain. During the evolving, evaluation value E of tree individuals is computed using following [1], and its value is within the range [0, 1].

[1]We consider that the system using GP can detect with an only information of RGB or HSV, whereas we have not achieved its detection yet.

Table 1: Funtion nodes and terminal nodes

node	arity	description
+	2	sum of the branches
−	2	subtract 1 from 2 brances
∗	2	multiply of the branches
r	0	value of Red
g	0	value of Green
b	0	value of Blue
h	0	value of Hue
s	0	value of Saturation
v	0	value of Brightness
y	0	value of Luminosity
rand	0	random number [-1,1]

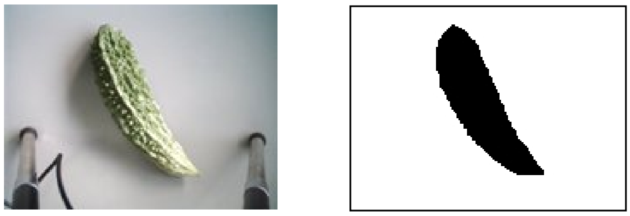

Input image Target image

Fig. 3: Training image set

$$E = 1 - \frac{\sum_{x=1}^{W_x}\sum_{y=1}^{W_y} w(x,y)|O(x,y) - T(x,y)|}{\sum_{x=1}^{W_x}\sum_{y=1}^{W_y} w(x,y) \cdot V_{\max}} \quad (2)$$

$$\begin{cases} O(x,y) & : \text{pixel value in the output image} \\ T(x,y) & : \text{pixel value in the target image} \\ w(x,y) & : \text{evaluation weight of each pixel} \\ V_{\max} & : \text{max gradation value} \end{cases}$$

where, evaluation weight value set to $w(x, y) = 1.0$, and gradation value is $V_{\max} = 1.0$.

3 Simulation

To examine the effectiveness of the proposed method, we prepare the samples shown in Table 2. Parameter of GP is shown in Table 3.

Table 2: Sample images

Sample No.	Image name
1	Balsam pear
2	Hand
3	Sea

Table 3: GP parameter set

Number of population	100
Probability of crossover	0.8
Probability of mutation	0.2
Maximum depth after crossover	14

3.1 Evolutionary Result

Figure 4 shows the evaluation results of GP evolving. It can be seen that all processes acquired good evaluation values until the 100th generation. At the end of evolution, evaluation values E became 0.995 (Sample 1), 0.988 (Sample 2), and 0.984 (Sample 3). Figure 5 shows the input images, and output images using detection functions generated by GP, respectively. Sample 1 and 2 are taken the image in indoor environment. The balsam pear of Sample 1 compounds the complex color information which includes many tones of green, yellow, and near to white. In spite of these difficulties, from Figure 5 (a), it observed that generating detection function could detect the target object. Similarly, the hand of Sample 2 has the complex color domain and complex background, and, from Figure 5 (b), the detection function can detect the target object. Moreover, image of Sample 3 is a landscape image. This image compounds the complex color information both target object and background, and it includes color domain of the sky which is near to color information of target object of the sea. Although we considered that detection of this image is difficult, the sea is detected by the detection function. From these results, we confirmed that it is possible for the detection function evolved by GP to obtain sufficient ability for these detection. Figure 6 shows the detection result of an untrained image using detection function generated by Example 1. From this figure, it can be seen that the detection function could detect not only trained images, but also color domain of the balsam pear in the untrained image. Therefore, it is clear that the generated detection function has the generalization ability.

3.2 Characteristic of Tree Structure

In this paper, we examine the characteristic of tree structure evolved by GP. S-expression in Figure 7 shows the tree for Sample 1. Tree depth is 13, and number of nodes is 77. We set an examination process as follows First, we set an individual node-number to each node like this.

$$(+ \;\; r \; (* \;\; g \;\; b)) \Rightarrow \text{Node-number:}(0 \;\; 1 \; (2 \;\; 3 \;\; 4))$$

Next, we exclude an optional branch according to each node-number. Finally, after exclusion, it computes evaluation value of its tree. In this process, we considered that the branch which decreases evaluation value largely is important in the tree.

Figure 8 shows the change of the evaluation value when tree excludes optional branch. From this figure, evaluation value decreased to the smallest value at the node-number 1 ($E = 0.0049$), and next was node-number 16 ($E = 0.1412$). Because the evalua-

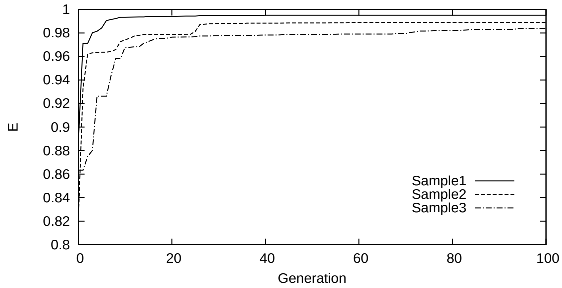

Fig. 4: Evaluation value of GP evolving

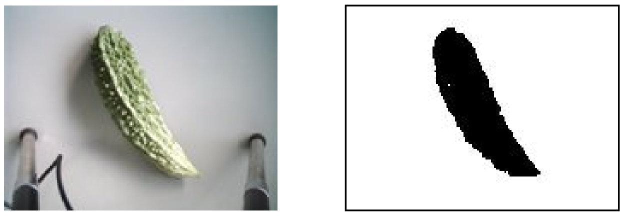

Input image Output image

(a) Sample 1 : a balsam pear ($E = 0.995$)

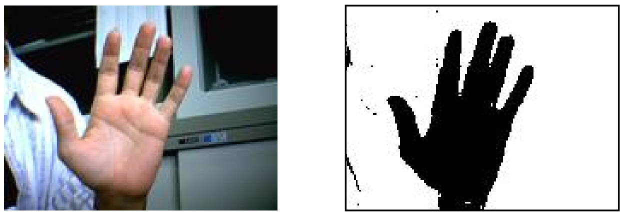

Input image Output image

(b) Sample 2 : a hand ($E = 0.988$)

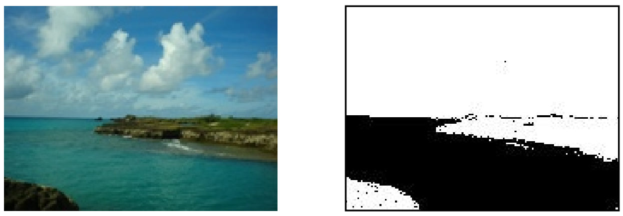

Input image Output image

(c) Sample 3 : the sea ($E = 0.984$)

Fig. 5: Results of detection

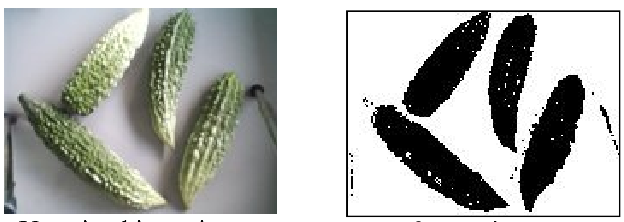

Untrained input image Output image

Fig. 6: Detection of the untrained image

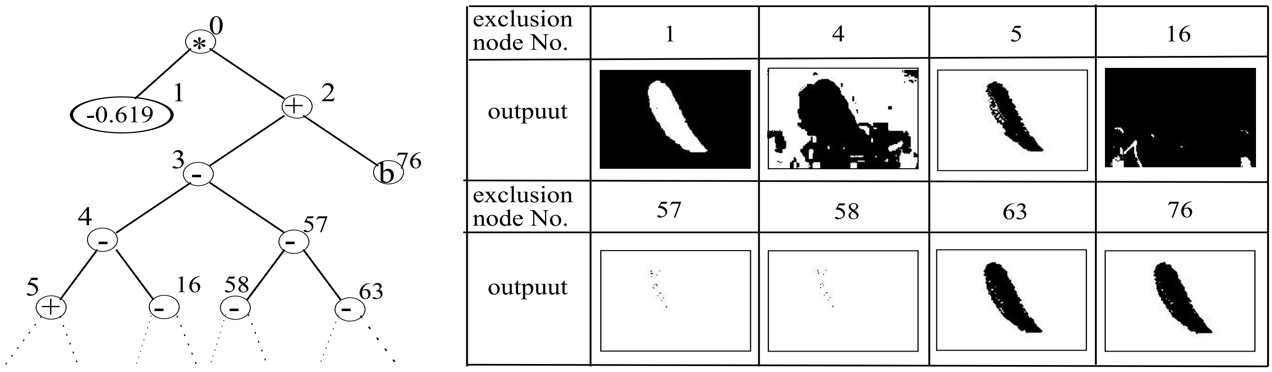

Fig. 9: Examine the tree structure

(* -0.6190547(+(-(-(+(+(-(- r s) v)(- r y)) v)(-(- y(+(* y(*(+(+ s r) s)(-(- r (+ v v) v))(-(-(- g s) v) y))))) 0.5004493))(+ b(*(- r g)(* r(- g(- b g)))))))(- (- g(- b g))(-(+(+(* -0.6292867 v) h) b)(+ s(+ g v))))) b))

Fig. 7: Generation tree of Sample 1

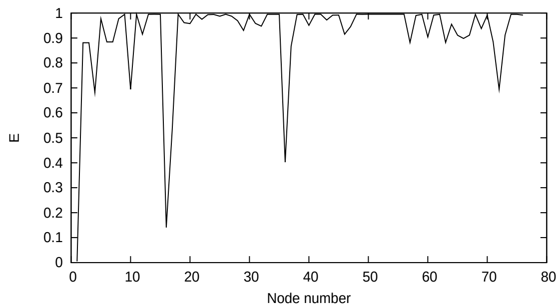

Fig. 8: Change of evaluation value

Table 4: Exclusion branch

node-No.	exclusion branch
1	-0.6190547
16	(-(- y(+(* y(*(+(+ s r) s)(-(- r(* (+ v v) v))(-(-(- g s) v) y)))) 0.5 004493))(+ b(*(- r g)(* r(- g(- b g))))))

tion value decreased largely by excluding their branches, we consider that their branches are important in the tree. Their branches are shown in Table 4. Furthermore, we investigated output images when tree excludes its important branches. Figure 9 shows a part of the tree structure, and shows output images after excluding branches. This tree structure includes the branches of node-number 1 and 16. From output images in the figure, at the excluding branch of node-number 1, tree does not detect the target object, whereas detect the background. Its output image is an inversed image of target image. It can be seen that this excluding branch has a role which reverses a sign of output value from tree. At the excluding branch of Node-number 16, tree not only detect the target object but also background of excepting color domain near to black in input image. Namely, we considered that its branch processes the background domain. Also, from other output images in this figure, it can be confirmed that each branches has various roles in the tree. Therefore, it is clear that generating tree by GP is composed of each branches which has various roles.

4 Conclusion

In this paper, we proposed a method of function generation for color information detection using GP. We set the function nodes and terminal nodes that contain three basic operations of arithmetic and color informations. The evolutionary results showed that GP could generates the function to detect the target domain. Moreover, we confirmed that the branch in generated tree structure influences each other, and its branches compose one detection function for image-processing system.

References

[1] T. Nagao, "Evolutionary image processing", Syouko-do, 2002 (in Japanese).

[2] M. Maezono, S. Ono, S. Nakayama, "Automatic Parameter Tuning and Bloat Restriction in Image Processing Filter Generation Using Genetic Programming", Trans. of JSCES, Paper No.20060021, 2006.

[3] J. Koza, "Genetic Programming, On the Programming of Computers by means of Natural Selection", MIT Press, 1992.

The Fourteenth International Symposium on Artificial Life and Robotics 2009 (AROB 14th '09),
B-Con Plaza, Beppu, Oita, Japan, February 5 - 7, 2009

Swing Up Control of a 3-DOF Acrobot Using Evolutionary Approach

Ryo Fukushima* and Eiho Uezato**

*Graduate School of Engineering and Science, University of the Ryukyus
**Faculty of Engineering, University of the Ryukyus
1 Senbaru, Nishihara, Okinawa. 903-0213
(Tel:098-895-8638 ; Fax:098-895-3636)
(fukushima@mibai.tec.u-ryukyu.ac.jp)

Abstract: This paper discusses a control method for the acrobot. The acrobot is a model of a gymnast on a horizontal bar with three links and two active joints and a passive joint. This robot is a non-holonomic and underactuated system. We propose a control method for the acrobot where swing-up stage is performed by genetic programming (GP) and balancing stage is handled by a linear quadratic regulator (LQR). Here, GP searches for the optimum input torques for swing up so that the acrobot is able to reach the nearly-desired configuration. The LQR is then switched on to stabilize the system. Simulation results show that the proposed method could control the acrobot effectively.

Keyword: Underactuated robot, Nonlinear system, Genetic programming, Acrobot

1 Introduction

The acrobot [1] is a model of a gymnast on a horizontal bar. This robot is a non-holonomic and underactuated system. Various studies have demonstrated for a two-degree-of-freedom acrobot with an active joint and a passive joint[2], but little has been reported on a three-degree-of-freedom (3-DOF) acrobot[3][4]. The 3-DOF acrobot is studied in order to model more realistic system.

In this paper, we discuss a swing up control method for the 3-DOF acrobot with and two active joints and a passive joint. Swing up control is performed by genetic programming (GP)[5]. GP is an approach expanding from genetic algorithm (GA), and it can widely search for optimum input feedback function for design of the acrobot system. A motion control using GP is discussed in [6].

We propose a control method for the 3–DOF acrobot where swing up stage is performed by GP and balancing stage is handled by a linear quadratic regulator (LQR). It is appropriate to use GP for di cult control problem as the acrobot.

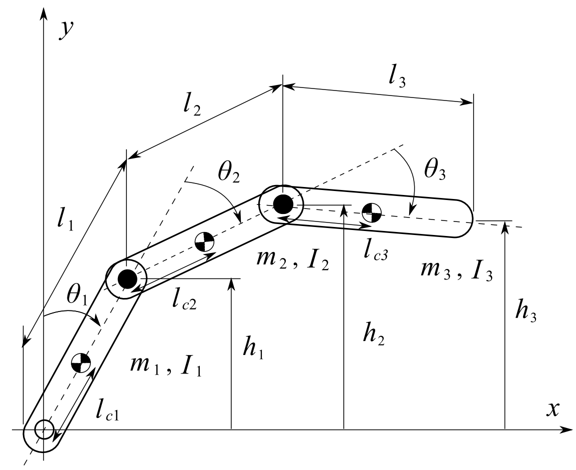

Fig. 1: Model of the acrobot

2 Model of the acrobot

Fig. 1 shows the model of the acrobot. m_i ($i = 1, 2, 3$) and I_i denote mass and moment of inertia, l_i and l_{ci} denote length of link and distance to the center of mass, θ_i is angle, h_i is height to the top of link. Here, u_2 and u_3 are symbolized as actuated torques. The equation of motion of the acrobot system is

$$M(\theta)\theta + C(\theta, \dot{\theta}) + G(\theta) = Hu, \qquad (1)$$

where,

$$\theta = [\ \theta_1,\ \theta_2,\ \theta_3\ ]^T,\ u = [\ u_2,\ u_3\ ]^T.$$

M is an inertial matrix, C is a coriolis term, G is a gravity term and H is constant matrix.

3 Control System

Fig. 2 shows the block diagram for closed-loop system. Su x d represents desired values. We define deviations as $e = \theta_d - \theta$, $\dot{e} = \dot{\theta}_d - \dot{\theta}$. The control goal is to swing the acrobot up to balancing point ($\theta_d = 0$, $\dot{\theta}_d = 0$). We propose a control method for the acrobot where swing up stage is performed by genetic programming (GP) and balancing stage is handled by a linear quadratic regulator (LQR).

The Fourteenth International Symposium on Artificial Life and Robotics 2009 (AROB 14th '09),
B-Con Plaza, Beppu, Oita, Japan, February 5 - 7, 2009

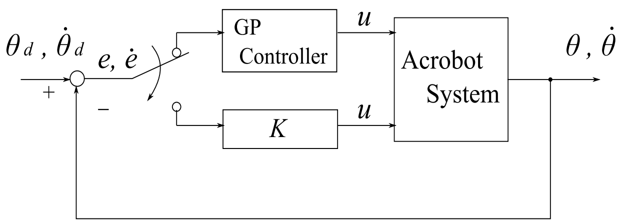

Fig. 2: Block diagram for closed-loop system

3.1 Swing up control of GP

Evolutionary approach is the model of natural selection of genes. As evolution progresses, it is idea of the individuals adapt to a given environmental. GP, which is one of evolutionary approaches, searches for the optimum input torques (feedback input function $u\,(e, \dot{e}\,)$) for swing up. Each individual of GP represents tree structure which stands for a function. Fig. 3 shows an example of a tree structure. Now, we explain the terminology of GP.

Each elements of tree structure are called a node. The node has a function node and a terminal node. According to the tree structure as shown in Fig. 3, the function nodes are "+", "tanh" and "×", the terminal nodes are "x_1", "x_3", "5.2". The function nodes have a branch, for example "+" has two branch as "tanh" and "×", and "tanh" has one branch as "x_1". The rank of tree structure is called depth. For example, in Fig. 3, depth of tree structure is three. The tree structure shown in Fig. 3 represents function as "tanh(x_1)+5.2x_3". We operate the tree structure with genetic crossover and mutation, so that tree structure adapts to the given environment. The elements for design of GP have the function nodes, the terminal nodes, fitness, parameters (crossover rate, mutation rate, population size), termination condition. We will get the desired feedback input function by the five elements set effectively.

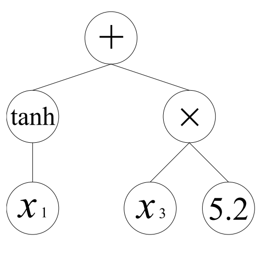

Fig. 3: An example of a tree structure

The following are calculation procedure.
Step 1
Set the number of generation G, and population size is N. Generate a initial population, and evaluate the population with fitness function below.
Step 2
Performs the crossover and mutation operation to the population with mutation rate α.
Step 3
Generate new population up to $N \times \beta$, where, β is crossover rate.
Step4
Evaluate generated population, and individual of the high fitness value is brought down to next generation.
Step5
Until generation reach G, repeat from Step 2. We adopt the excellent individual as the input function of control system.

The fitness function for evaluating the individuals is

$$\begin{aligned} E = \min_{t}\ & w_1(l_1 - h_1)^2 + w_2(l_1 + l_2 - h_2)^2 \\ & + w_3(l_1 + l_2 + l_3 - h_3)^2 + w_4(\dot{\theta}_{r1} - \dot{\theta}_1)^2 \\ & + w_5(\dot{\theta}_{r2} - \dot{\theta}_2)^2 + w_6(\dot{\theta}_{r3} - \dot{\theta}_3)^2\ , \end{aligned} \quad (2)$$

where, t represents time of swing up motion, t_f represents finish time of swing up motion, w_i represents weight coe cient. The lower fitness value, the closer the acrobot locates in the desired position. The "min" in the Eq. (2) is the minimum fitness value of each step from the range of $0 < t \le t_f$. Finally, this minimum fitness value is of the individual. Here, the first, three term in the Eq. (2) are function considering the highest marks of the each link. For considering height of the each link, the farther distance from the balancing point causes high fitness value. θ_1 and θ_2 are restricted in the range of $-\pi < \theta_{2,3} < \pi$ to limit rotated the link 2 and link 3. If θ_1 and θ_2 exceed the range of limit while searching for the desired input function using GP, we add 10^6 to the fitness value of the individual for penalty.

3.2 Stabilize control at balancing point

Stabilizing control uses the LQR at the near balancing point. If θ_i is su ciently small ($\theta_i \approx 0$), we can approximate $\sin\theta_i \approx \theta_i$, $\cos\theta_i \approx 1$ and neglect $\dot{\theta_i}^2$. Thus, the Eq. (1) is simplified

$$\tilde{M}\theta + \tilde{G}\theta = Hu, \quad (3)$$

and eliminate C which is coriolis term from the Eq. (1). Here, state variable defines $x = [\ \theta_1, \theta_2, \theta_3, \dot{\theta}_1, \dot{\theta}_2, \dot{\theta}_3\ ]^T$, and the Eq. (3) is

$$\dot{x} = Ax + Bu. \quad (4)$$

$$A = \begin{bmatrix} 0_{3\times3} & I_{3\times3} \\ -\tilde{M}^{-1}\tilde{G} & 0_{3\times3} \end{bmatrix}, \quad B = \begin{bmatrix} 0_{3\times2} \\ \tilde{M}^{-1}H \end{bmatrix}.$$

©ISAROB 2009

4 Simulation

We carry out simulation as sampling time of 10[ms] and $t_f = 3.0$[s]. Initial values for state variable is $[\ \theta_1, \theta_2, \theta_3, \dot{\theta}_1, \dot{\theta}_2, \dot{\theta}_3\ ] = [\ \pi, 0, 0, 0, 0, 0\ ]$. We set the terminal nodes as e, $\dot{e}$ and random real numbers from the range of $[-10, 10]$. The function nodes are shown in Table 1. We hope that the term tanh in the function node will get better result by inhibiting input torque. We search for the individual (input function) which minimize E by a combination of the terminal nodes and the function nodes. Table 2 shows parameters of GP, and Table 3 shows Parameters of the acrobot system.

Using GNU Octave, the LQR controller was designed with weighting matrices

$$\begin{aligned} Q &= \mathrm{diag}(1,1,1,1,1,1), \\ R &= \mathrm{diag}(1,1), \end{aligned}$$

and the state feedback controller $u = -Kx$, where,

$$K = -\begin{bmatrix} 224.39 & 124.15 & 58.06 \\ 171.39 & 98.91 & 40.69 \end{bmatrix.$$
$$\begin{matrix} 82.26 & 50.04 & 24.15 \\ 62.73 & 39.05 & 17.82 \end{matrix}\Bigg]. \quad (5)$$

Table 1: Nodes of function

Function	Number of arg.	Description
$+$	2	arg.1 $+$ arg.2
$-$	2	arg.1 $-$ arg.2
$*$	2	arg.1 $\times$ arg.2
tanh	1	tanh(arg.1)

Table 2: Parameters of GP

Parameter	Value
Number of generation G	100
Population N	200
Mutation rate α	0.60
Crossover rate β	0.80

Table 3: Parameters of the acrobot

Parameter	Value	Parameter	Value
m_1 [kg]	0.5	l_{c1} [m]	0.25
m_2 [kg]	0.5	l_{c2} [m]	0.25
m_3 [kg]	1.0	l_{c3} [m]	0.5
l_1 [m]	0.5	I_1 [kgm^2]	0.01
l_2 [m]	0.5	I_2 [kgm^2]	0.01
l_3 [m]	1.0	I_3 [kgm^2]	0.083

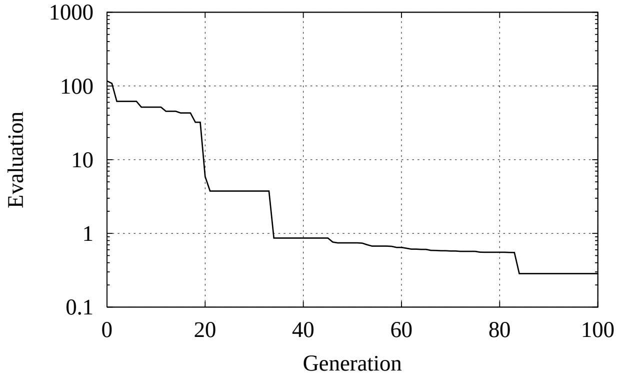

Fig. 4: Evaluation at each generation

5 Results and Discussions

Fig. 4 shows the fitness value of excellent individual at each generation. As the generation proceed, the fitness value tends to the desired position gradually. The fitness function is very important for getting the optimum input torques. Especially, the setting of the weight coe cients of the fitness function affects results strongly, but there is no effective way to determine of the weight coe cients, we have to decide those by trial and error. We evaluate the position of the acrobot considering the highest marks of each link. That is, fitness value become lower at the near balancing point and higher at the far balancing point.

We evaluate the angular velocity of the acrobot considering reaction forces. Each link of the acrobot receives reaction forces from the next link. Thus, if we restrain the angular velocity of the link 2 previously, the angular velocity of the link 1 and link 3 will decrease with decline of the angular velocity of link 2. As a result, the weight coe cients of the fitness function are $w_1 = 40$, $w_2 = 20$, $w_3 = 10$, $w_4 = 1$, $w_5 = 10$, $w_6 = 1$.

Fig. 5 shows successful simulation results of swing up and balancing. θ_1, θ_2 and θ_3 converged on the balance point in about 3.5 seconds. $\dot{\theta}_1$, $\dot{\theta}_2$, $\dot{\theta}_3$, u_2 and u_3 are similar results. A switching time to swing up control from balance control is about 2.15 seconds. The acrobot reaches to the balancing point quickly. We determine the switching time as the step when the lowest fitness value on the simulation.

We obttained the optimum feedback input function using GP. The tree structure of u_2 has number of the nodes of 47 and its depth is 14. The tree structure of u_3 has number of the nodes of 161 and its depth is 27. The input functions are very complex because the depth and number of nodes is large. therefore, we can see that it was very hard to perform swing up control of the 3-DOF acrobot.

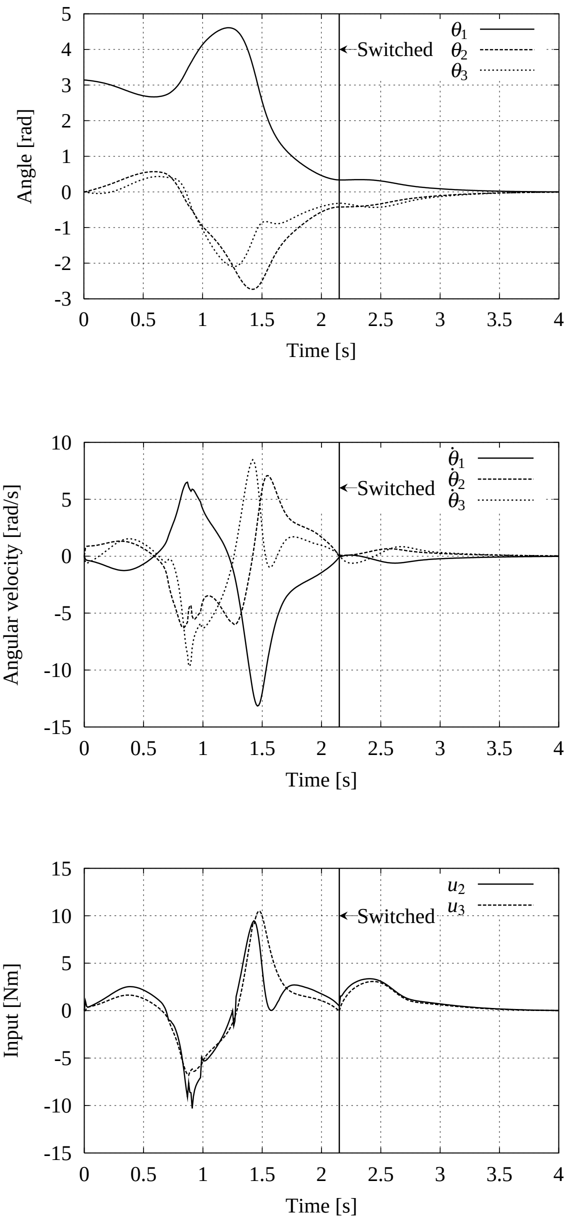

Fig. 5: Simulation results

6 Conclusion

In this paper, we have discussed swing up control for the acrobot. We obtained the optimum input torque using GP. As the simulation results, the acrobot could swing up to the desired position, and the proposed method could control the 3-DOF acrobot effectively.

References

[1] M. W. Spong (1995), The Swing Up Control Problem For The Acrobot. IEEE Control System Magazine, Vol.15, No.2, pp.49–55

[2] K. Kawada, M. Obika, et al (2005), Creating Swing-Up Patterns of a Acrobot Using Evolutionary Computation. Proc. 2005 IEEE Int. Symposium on Computational Intelligence in Robotics and Automation, pp.261–266

[3] X. Xin and M. Kaneda (2007), Swinging–Up Control for a 3–DOF Gymnastic Robot With Passive First Joint: Design and Analysis. IEEE TRANSACTION ON ROBOTICS, Vol.23, No.6, pp.1277–1285

[4] T. Watabe, M. Ymakita and T, Mita (2002), Stabilization of 3 Link Acrobat Robot in Upright Position. Proc. SICE Ann. Conf. 2002 in Osaka (SICE2002), pp.2996–3001

[5] J. Koza (1992), Genetic Programming: On the Programming of Computers by Means of Natural Selection. MIT Press

[6] T. Ogawa, N. Oshiro and H. Kinjo (2008), Backward Movement Control with Two-Trailer Truck System Using Genetic Programming. Proc. of the 13th Int. Symposium on Artificial Life and Robotics, pp.597–600

©ISAROB 2009

Intelligent Control of a Three-DOF Planar Underactuated Manipulator

Sam Chau Duong, Hiroshi Kinjo, Eiho Uezato
Faculty of Engineering, University of the Ryukyus
Senbaru 1, Nishihara, Okinawa 903-0213, Japan

Tetsuhiko Yamamoto
Tokushima Technology College
Itano-gun, Tokushima 779-0108, Japan

Abstract – Recently, computational intelligence has been applied extensively in control engineering, especially for the systems that cannot be easily controlled by conventional means. In this paper, attention is paid to the control of a three-DOF planar underactuated manipulator, also known as the three-link gymnastic robot, by utilizing neural network (NN) and genetic algorithm (GA).

With different swing-up timing constraints, performance of the proposed controller is investigated and control simulations are performed. Numerical simulations show that the control system works effectively and enables us to prespecify swing-up timing.

Keywords – Three-DOF gymnastic robot, Neural Network, Genetic Algorithms, Intelligent Control, Underactuated System.

1 Introduction

For the last decades, underactuated system has been attracted the growing interest in control engineering. The difficulty in control of such a system arises from the fact that it processes fewer actuators than degrees of freedom and usually exhibits highly nonlinear and nonholonomic behaviors [1], [2]. As is well-known, the class of nonholonomic system cannot be stabilized by continuous and time-invariant state feedback control.

One of typical examples of underactuated system is the gymnastic robot, related to the so-called dextrous robots [2]-[4]. A general work on switch control of swing-up and balance of gymnastic robots can be found in the study devoted by Spong M.W. [3].

A two-link mechanism, called the Acrobot [2], has been widely studied in many literature. This system roughly imitates a gymnast on a horizontal bar, it has a passive joint (corresponding to the gymnast's hands on the bar) and an active joint (corresponding to the gymnast bending at the waist). The control problem of the Acrobot involves two processes. The first stage is swing-up which is mainly focused in many researches, and the second control process is stabilizing or balancing control which is easier as it can be linearized. There have been abundant works devoted in developing control methods for the Acrobot system, including classical methods [1]-[3] and advanced techniques, such as, reinforcement learning (RL) [5], [6], fuzzy and genetic algorithms (GAs) [7], [8].

Most previous work has focused on switch controllers which are generally required to satisfy some strict criteria to turn to stabilizing control, thus it is difficult to determine the switching time in advance. In view of limitations of the classical control techniques and there being still a few works on the application of neural network (NN) to the Acrobot control, we have presented a control method using neurocontroller (NC) with GA for such a complex object [9]. The method could provide smooth control process and allow us to flexibly prespecify the swing-up time in advance. However, the simplified two-link Acrobot is not enough to represent human movement on a horizontal bar. Nevertheless, a three-link robot is a more realistic model for a human gymnast and it can generate more complicated skillful motion [10], [11]. It seems that the gymnast's shoulder joint (represented by another active joint in the three-link robot) is very helpful for the swinging motion. Reader can refer to Ref. [12] for a detail study on the motion of the system.

For that reason, this paper focuses on the control of a three-link gymnastic robot. A neurocontrol system is proposed by using NN and GA for swing-up control of the three-DOF manipulator, which is known as one of challenging robotic control problems. We would not use any swing-up or switch condition but shall test the controller with various swing-up timings defined in advance.

This article is organized into five sections. Sect. 2 introduces the model and dynamics of the three-link gymnastic robot. In Sect. 3 the design of the proposed control system is presented. In Sect. 4, the system performance is investigated with various swing-up timings and control simulations are implemented. Lastly, we conclude this research in Sect. 5.

©ISAROB 2009

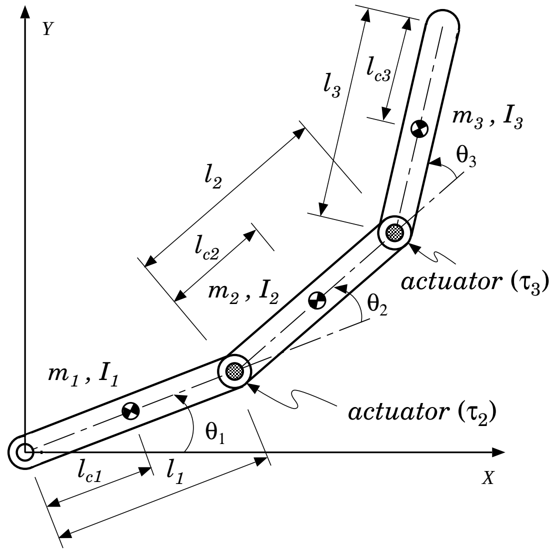

Figure 1: The three-DOF manipulator system

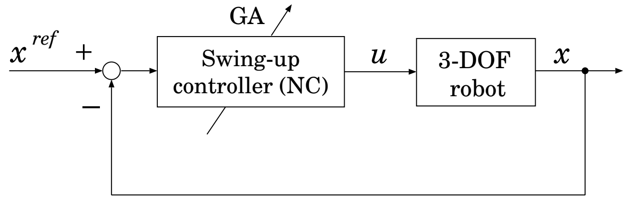

Figure 2: The proposed control system

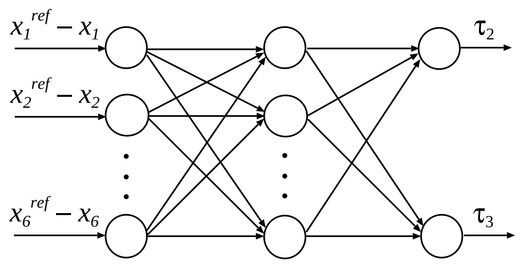

Figure 3: Neurocontroller

2 The Three-DOF Gymnastic Robot System and Dynamics

The three-DOF mechanism is a system having three links with a passive joint at the first joint and two active joints (i.e., with actuators at joints 2 and 3). The model of the gymnastic robot and its basic physical parameters are illustrated in Fig. 1, where m_i, l_i, l_{ci}, I_i are mass, length, distance between joint and the center of mass, and moment of inertia of link i ($i = 1,\ 2,\ 3$). The dynamic equation of the system is in form of

$$M(\theta)\ddot{\theta} + C(\dot{\theta}, \theta) + G(\theta) = Hu \tag{1}$$

where $M(\theta)$ is the inertia matrix, $C(\dot{\theta}, \theta)$ represents the Coriolis and centrifugal terms, $G(\theta)$ represents the gravity term, H is the input matrix, and u represents the control input.

3 Control System for the Gymnastic Robot

3.1 Control System Design

Let $x_1 = \theta_1$, $x_2 = \theta_2$, $x_3 = \theta_3$, $x_4 = \dot{\theta}_1$, $x_5 = \dot{\theta}_2$, $x_6 = \dot{\theta}_3$, the state of the system is defined as $x = [x_1,\ x_2,\ x_3,\ x_4,\ x_5,\ x_6]^T$. The task of the controller is to swing the robot from its stable downward position, which has initial state $x^{init} = [-\pi/2,\ 0,\ 0,\ 0,\ 0,\ 0]^T$, to its unstable position that is very close to the desired vertical with state $x^{ref} = \left[x_1^{ref},\ x_2^{ref},\ x_3^{ref},\ x_4^{ref},\ x_5^{ref},\ x_6^{ref}\right]^T = [\pi/2,\ 0,\ 0,\ 0,\ 0,\ 0]^T$.

Figure 2 shows the proposed control system consisting of an NC optimized by GA for swing-up the robot. From the input $u = [\tau_2,\ \tau_3]^T$, the state x of the above-described gymnastic robot is determined, this state will be feedback and the deviation $\left(x^{ref} - x\right)$ will be the input of the NC for producing torques τ_2 and τ_3. The error between the desired and actual responses (which will be defined in next subsection) is used to update the connection weights of NC by GA.

Figure 3 illustrates the structure of the NC which uses a three-layer NN architecture consisting of input layer, hidden layer, and output layer. Since we desire to control the three links of the robot with six state variables by two input torques τ_2 and τ_3, the neuron number of input layer and output layer of the NC are 6 and 2 neurons, respectively. While a linear activation $f(x) = x$ is used for input and output layers, a hyperbolic tangent activation function $f(x) = \tanh(x)$ is applied to hidden layer of the NC.

3.2 Genetic Algorithm in the Controller Design

In this paper, GA is applied to search the optimal sets of NC connection weights, each of weight is trans-

©ISAROB 2009

formed into the genetic code encoded by 16−bit binary code. The algorithm flow of GA in the controller design can be found in [9]. In GA, Roulette wheel is used to select parents for reproduction in proportion to their relative fitness, which is defined as:

$$F^{(p)} = \frac{1}{1 + E^{(p)}}\ , \qquad p = 1, 2, \cdots, N \tag{2}$$

where N is population size and $E^{(p)}$ is the error function value of p^{th} individual calculated by:

$$E_1^{(p)} = \sum_{k=1}^{6} Q_k \left(x_k^{ref} - x_k^{end}\right)^2 \tag{3}$$

where Q_k are weight coefficients, x_k^{end} are the state variables at the final state of the robot in swing-up term, i.e., at the time t_s in the control simulation.

4 Numerical Simulations

4.1 Test Design and Parameters

In this study, fourth–order $Runge - Kutta$ technique is applied with step size of 0.005 seconds. The parameters of the robot is shown in Table 1 (referring to [2]) and the parameters of GA are depicted in Table 2. A 6-8-2 structured NN is used with the initial weights are drawn randomly from the range [−1.0, 1.0].

In order to analyze the characteristics of the proposed control system, we will perform several tests using different swing-up timings. With each timing, the performance of the controller is evaluated by the rate of successfully-evolved NCs calculated over the 50 replications of changing initial populations. An NC is considered to be successfully evolved when it can obtain an error value less than a required accuracy E_{suc} after GA process.

4.2 Simulation Results

Using the defined parameters the tests were executed. The result on evolving the NCs by GA with different timings is provided in Table 3 which shows that the proposed control system is able to work flexibly with different timings defined in advance. We can observe that the obtained rates are still low and the difficulty in evolving the controller increases when decreasing swing-up time.

For instance, numerical simulations of control are implemented using the resulting NCs evolved with two

Table 1: Parameters of GA

Parameter	Value/ Scheme
Population size N	500
No. of offspring	$0.6 \times N$
No. of generations	5000
Bit number	16
Solution range of NN weights	$[-50, 50]$
Mutation rate	0.3
Selection scheme	Roulette wheel
E_{suc}	0.005
Q_k $(k = 1, 2, \cdots, 6)$	1.0

Table 2: Parameters of the three-DOF robot

Parameter \ Link i	Link 1	Link 2	Link 3
Mass m_i [kg]	1.0	1.0	1.0
Length l_i [m]	1.0	1.0	1.0
Center of mass l_{ci} [m]	0.5	0.5	0.5
Inertial moment I_i [kgm^2]	0.083	0.083	0.083

Table 3: Rates of successfully-evolved NCs [%]

t_s [second]	1.0	2.0	3.0	4.0	5.0
	0	4	6	6	8

timing constraints $t_s = 5$ seconds and $t_s = 2$ seconds as illustrated in Figs. 4 and 5. It is clear that the controlled robot could reach the desired configuration within the given timings.

5 Conclusion

In this research, an intelligent control method was proposed for the swing-up problem of a three-link gymnastic robot. We have investigated the performance of the controller with different swing-up timings, and control simulations have been also demonstrated. It is clear that, while other condition-based methods can not provide the prior information of swing-up time, the proposed control system allows us to predetermine flexibly the swing-up time in advance. However, it is worth mentioning that the rates of successfully-evolved MCs are still low. This is apparently due to the difficulty of the problem. With such a wide range of motion of the links, GA is easily trapped into local optimums. For future work, it is therefore necessary to improve the system performance.

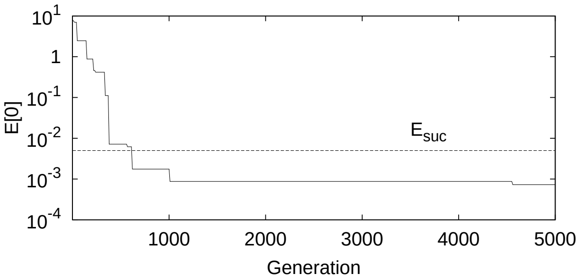

(a) The error value of the best NC at each generation

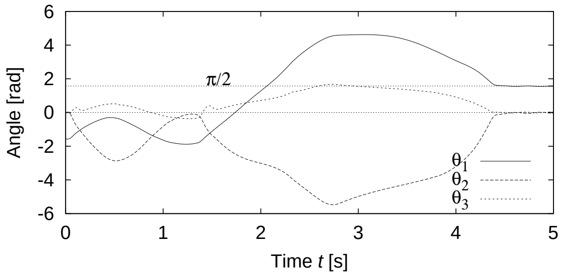

(b) Joint angles

Figure 4: Simulation result with $t_s = 5$ seconds

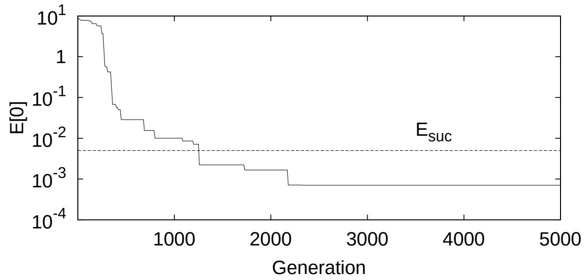

(a) The error value of the best NC at each generation

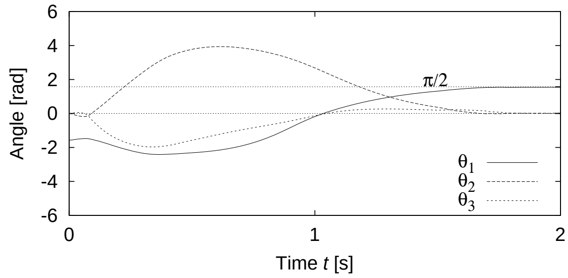

(b) Joint angles

Figure 5: Simulation result with $t_s = 2$ seconds

References

[1] Spong M. W. (1998), "Underactuated Mechanical Systems," in Control Problems in Robotics and Automation, B. Siciliano and K. P. Valavanis Eds., LNCIS, vol. 230, pp. 135-150, Springer Verlag, London.

[2] Spong M.W. (1995), "The Swing Up Control Problem for the Acrobot", IEEE Control Systems Magazine, Vol. 15, No.1, pp. 49–55.

[3] Spong M.W. (2000), "Some Aspects of Switching Control in Robot Locomotion", at-Automatisierungs Technik, Oldenbourg Verlag, Vol. 4, pp. 157-164.

[4] Saito F., Fukuda T., Arai F. (1993), "Swing and Locomotion Control for Two-link Brachiation Robot", Proceedings of IEEE International Conference on Robotics and Automation, pp. 719-724, Atlanta, GA, 1993.

[5] Boone G. (1997), "Efficient Reinforcement Learning: Model-Based Acrobot Control", IEEE International Conference on Robotics and Automation, Vol. 1 pp. 229–234.

[6] Yoshimoto J., Nishimura M., Tokida Y., Ishii S. (2005), "Acrobot Control by Learning the Switching of Multiple Controllers", Artificial Life and Robotics 9, pp. 67–71.

[7] Brown S.C., Passino K.M. (1997), "Intelligent Control for an Acrobot", Journal of Intelligent Systems 18, pp. 209–248.

[8] Kawada K., Obika M., Fujisawa S., Yamamoto T., Mada Y. (2005), "Creating Swing-Up Patterns of an Acrobot Using Evolutionary Computation", IEEJ Trans. EIS Vol. 125, No. 3, pp. 457–462 (*in Japanese*).

[9] Sam C. Duong, Kinjo H., Uezato E., Yamamoto T. (2008), "A Switch Controller Design for the Acrobot using Neural Network and Genetic Algorithm" Proceedings of the 10th IEEE International Conference on Control, Automation, Robotics and Vision, ICARCV-2008, Vietnam (*accepted*).

[10] Michitsuji Y., Sato H., Yamakita M. (2001), "Giant Swing via Forward Upward Circling of the Acrobat-robot", Proceedings of the American Control Conference, Vol.4, pp. 3262-3267, Arlington, VA.

[11] Takashima S. (1991), "Control of Gymnast on a High Bar", Proceedings of IEEE/RSJ International Workshop on Intelligent Robots and Systems, pp. 1423-1429.

[12] Suzuki K., Kawai N., Miyamoto T., Tsuchiya H., Kimura S. (1996), "Mechanics of Kip Motion", Trans. of the Japan Society of Mechanical Engineers (JSME) - C, Vol. 62, No. 602, pp. 3979-3984 (*in Japanese*).

©ISAROB 2009

The Fourteenth International Symposium on Artificial Life and Robotics 2009 (AROB 14th '09),
B-Con Plaza, Beppu, Oita, Japan, February 5 - 7, 2009

Optimal Suppression Control of Load Swing with Disturbance for Rotary Crane System Using Neuro-controller

Kunihiko Nakazono[†], Kosuke Tamanoi[‡], Keijiro Ozaki[‡], and Kouhei Ohnishi[§]

[†] Faculty of Engineering, University of the Ryukyus.
[‡] Graduate School of Engineering and Science, University of the Ryukyus.
[§] Faculty of Science and Techonology, Keio University
[†,‡] 1 Senbaru, Nishihara, Okinawa JAPAN 903–0213
[§] 3–14–1 Hiyoshi, Yokohama JAPAN 222–8522
{nakazono,tamanoi,ozaki}@mibai.tec.u-ryukyu.ac.jp, ohnishi@sd.keio.ac.jp

Abstract: In the paper, we propose a neuro-controller (NC) for suppression of load swing in a crane system rotating around the vertical axis. As in a nonholonomic system, the traditional control method using a static continuous state feedback law cannot stabilize the load swing. It is necessary to design a time-varying feedback controller or a discontinuous feedback controller. We propose a simple three-layered neural network as a controller in order to have control performance even if the load of the rotary crane system swings suddenly (disturbance). The NC is trained by a simple GA. The validity of the proposed NC is verified through computer simulation.

Keyword: neuro-controller, genetic algorithm, load swing suppression, disturbace

1 Introduction

A rotary crane system is used to move a load mass to a desired position through rotating, raising, and lowering the jib arm. These operations are accompanied by oscillation of the load, or load swing. Rotary crane systems are usually operated using both the rotation angle and the lean angle in order to suppress such a load swing. Operation of the rotary crane system rotating around the vertical axis results in a nonholonomic system for which the control problem is complex and necessary to design a time-varying feedback control method or a discontinuous feedback control method [1]. In this paper, we propose a neuro-controller (NC) [2] trained by a genetic algorithm (GA)[3, 4, 5, 6, 7]. It is easy to apply the NC which has simple layered structure and has generalized ability as a controller.

Many control methods for load swing suppression in a rotary crane system have been researched[8, 9, 10, 11, 12]. An example is a control method in which the control law follows the most suitable trajectory along which the load swing will be smallest[8]. The theory of the optimal regulator for linear systems fuzzy reasoning, and feedback law for nonlinear systems are examples of such control methods. These control methods can fundamentally stabilize the load swing in the circumferential direction, but cannot suppress the swing in the radial direction. Some vibration control methods for the crane system with only controllable rotation operation have been reported [10, 11, 12]. Anti-sway control method of the crane system based on a skillful operator's knowledge has been proposed[10]. Load swing suppression based on a linear feedback law by switching two modes in the radial and circumferential directions has been reported[11, 12]. However, all of these control methods require knowledge of difficult control theories. In contrast, a neuro-controller trained by an evolutionary computation technique, such as a genetic algorithm, is substantially simpler to realize than conventional control methods.

In general, the load of the rotary crane system has swung due to disturbance, that is, a gust of wind, a constant wind, and so on. In this paper, we propose the NC which has optimal control performance even if the load swings suddenly. And the performance of the resulting controller is compared with that of a controller without disturbance using computer simulations. The training algorithm of the neural network is a bit-string GA.

2 Model of rotary crane system

Figure 1 shows the crane system rotating around the z axis. x, y, z denote the coordinates of the load mass position, θ denotes the rotation angle. r is the radius of rotation, h is the height from the tip of the jib arm, m is the load mass, and ℓ is the wire length. The control purpose is to suppress load swing from the arbitrary position to the reference position by controlling the rotation motion.

If the swing of the load mass is sufficiently small, we have only to think about three-dimensional space

©ISAROB 2009

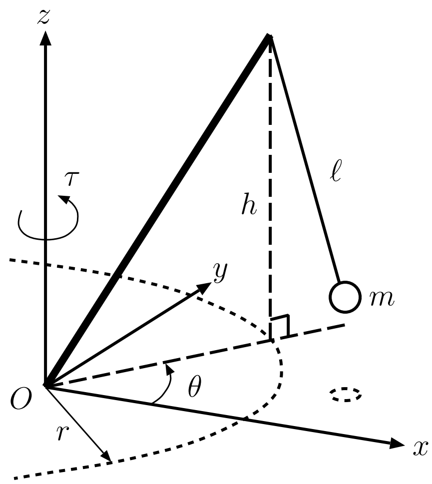

Fig. 1: Rotary crane system

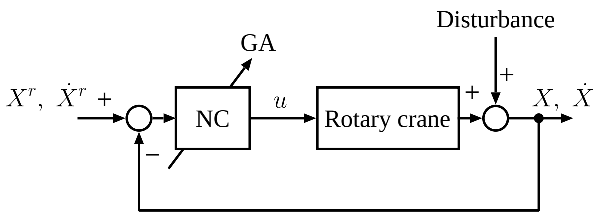

Fig. 2: Control system for rotary crane

but a two-dimensional plane. Using Lagrange equation for the constraint system, the dynamics of the rotary crane system can approximately be described in terms of the following equations:

$$\begin{cases} \ddot{x}(t) &= \omega^2(r\cos\theta(t) - x(t)) \\ \ddot{y}(t) &= \omega^2(r\sin\theta(t) - y(t)) \\ \ddot{\theta}(t) &= Ku \end{cases} \quad (1)$$

where $\omega = \sqrt{g/\ell}$ is natural frequency and K is constant value.

It is difficult for a designer to control the rotation angle of the rotary crane system by conventional methods because the dynamic model is a type of nonholonomic system. As in a nonholonomic system, the control method for the rotary crane system using a static continuous state feedback cannot stabilize the load swing. It is necessary to design a time-varying feedback controller or a discontinuous feedback controller. In this paper, the controller is instead designed using NC optimized by GA.

3 Control system for rotary crane

The control system using NC with GA is shown in Fig.2. In this figure, the state variable is $X = [x, y, \theta]$, and the reference is $X^r = [x^r, y^r, \theta^r]$, respectively. The training method uses a simple GA. The NC receives the position error, the velocity of the load mass, the rotation angle error, and the angular velocity as inputs. And it outputs the control input u. The NC is composed of three hierarchical layers, with 6–5–1 structure. A linear function is used at the input and output layers, and a sigmoid function in range $[-1, 1]$ is used for the hidden layer. The control purposes to suppress the load swing accompanying movement from an arbitrary initial position (x_0, y_0) to the reference position (x^r, y^r) by rotation control.

In general, the load of the rotary crane system has swung due to disturbance, that is, a gust of wind, a constant wind, and so on. In this paper, we propose the NC which has optimal control performance even if the load swings suddenly. The disturbance is as follows: When the control start, position (x, y) of the load suddenly move to position $(x+\Delta x, y+\Delta y)$ on the way. $\Delta x, \Delta y$ are determined by constant random numbers in range $[-\alpha, \alpha]$.

The NC is trained by the bit-string GA in an off-line process. The evolutionary algorithm for the NC is as follows:

STEP 1. Create initial NCs at random. The initial connection weights are set in the range $[-2.0, 2.0]$ and are transformed to the chromosome. The genetic code is transformed to the binary code (12 bit).

STEP 2. Calculate an error function E while demonstrating control simulation for all NCs.

STEP 3. Select the upper NCs by ranking selection in the individuals.

STEP 4. Perform a one-point crossover operation to produce new NCs.

STEP 5. Perform a mutation operation to produce additional new NCs.

STEP 6. Alternate the NCs including the new NCs to the next generation. Iterate from STEP 2 until the evolution process reaches generation 10000.

Table 1 shows further information regarding to the parameters of the GA.

During evolutionary process, an error function E is used to evaluate the performance of each NC. The error function E is defined as

$$E = (X^r - X)^T(X^r - X) + (\dot{X}^r - \dot{X})^T(\dot{X}^r - \dot{X}) \quad (2)$$

The error function is determined so as to settle the load swing at the desired position. In the GA evolution, the connection weights of the NC are modified in order to minimize the error function in Eq. (2).

©ISAROB 2009

Table 1: GA parameters

Parameter	Value/method
No. of initial NCs	40
No. of children	20
Selection	ranking selection
Crossover	one-point
Mutation	bit reverse
Mutation rate	0.1
Final generation	10000

Table 2: Parameters and initial conditions

Parameter/condition	Value
Load mass m [kg]	0.5
Rotation radius r [m]	1.0
Length of wire ℓ [m]	2.0
Acceleration of gravity g [m/s^2]	9.8
Initial rotation angle θ_0 [deg]	90
Reference position (x^r, y^r) [m]	(1, 0)
Constant value K	5.0
Control time [s]	10.0

4 Simulation results

The validity of the NC trained by GA is verified using computer simulations. Runge-Kutta method is used for the system dynamic model, and sampling time is 10 [ms]. The parameters of the rotary crane system and the initial conditions are listed in Table 2.

The aim of the evolution progressed by the GA is to obtain an NC that suppress the load swing of the rotary crane system upon movement from the initial position (x_0, y_0) to the reference position (x^r, y^r). When the initial rotation angle θ_0 is 90 [deg] and the initial position of the load is set $(x_0, y_0) = (\cos\theta_0, \sin\theta_0)$, the evolution process affording the best NC with GA-based training is shown in Fig. 3. The position (x, y) of the load suddenly move to position $(x + \Delta x, y + \Delta y)$ after the control time equals 1 [s]. When $\alpha = 0.03$, it means that the disturbance is set by constant random numbers in range $[-\alpha, \alpha] = [-0.03, 0.03]$. The training involved for 10000 iterations and the values of $\Delta x, \Delta y$ randomly change during each generation in evolutionary process.

The result demonstrates that the GA evolution process of NCs is successful. The error values of the GA initially decrease gradually, then decreases rapidly after 1000 generations until the evolution converges near generation 10000.

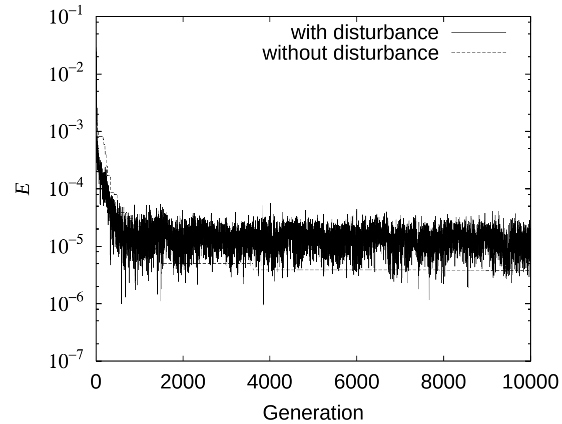

Fig. 3: Evolutionary process

Table 3: Rate of successful control (with disturbance)

Range	$\alpha = 0.03$	$\alpha = 0.04$	$\alpha = 0.05$
Rate[%]	100	93	71

Table 3 shows the successful rate of control performance for the rotary crane system in 100 trials. The position $(x + \Delta x, y + \Delta y)$ of $t = 1$ [s] are randomly set in the ranges $[-\alpha, \alpha]$ at $\alpha = 0.03$. The criterion for success in control is when the squared errors less than 0.0001. It can be seen that the trained NC has good control performance and has generalized ability.

Figure 4 shows the control simulation results using the trained NC. Here, the disturbance is $(\Delta x, \Delta y)$ = $(0.0146, -0.0294)$. Control by the trained NC converges to the reference position on the x and y axes in approximately 8 [s]. The training is therefore effective for achieving good load swing suppression.

Figure 5 shows the trajectory of the load mass in the x–y plane using the trained NC. The load is transferred along the control trajectory with very little swing oscillation.

5 Conclusion

A simple GA was applied to optimeze a neuro-controller for load swing suppression in rotary crane systems involving only rotation about the vertical axis. Simulations confirmed that the bit-string GA training scheme is effective for generating a reliable

©ISAROB 2009

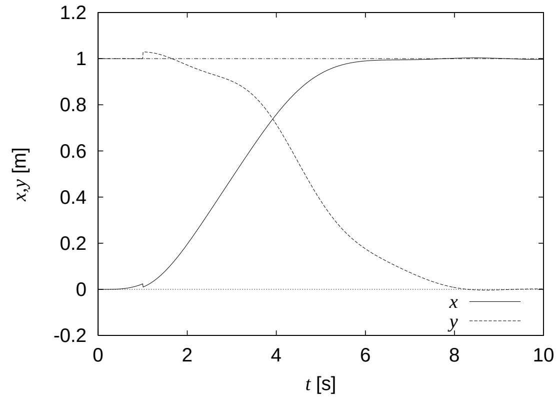

(a) Position

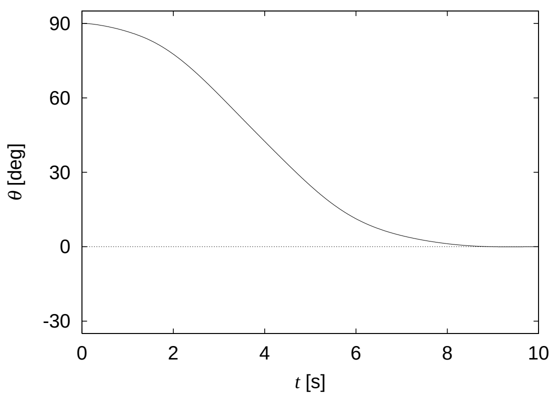

(b) Rotation angle

Fig. 4: Control results

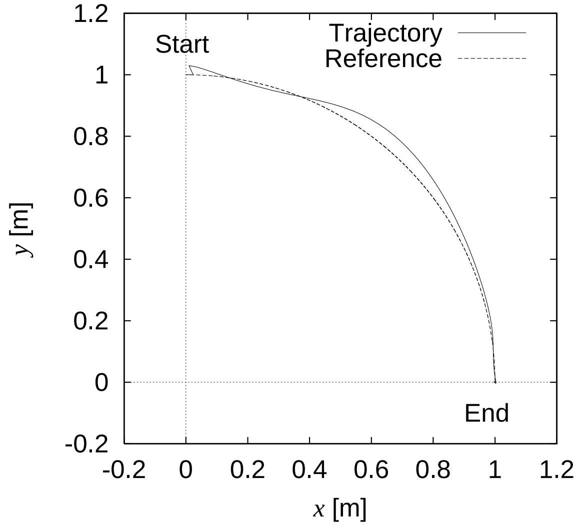

Fig. 5: Trajectory on x–y plane

NC with disturbance for the rotary crane system, with competitive performance to the trained NC without disturbance.

References

[1] M. Sanpei (1997), Feedback Control of Non-holonomic System (in Japanese), Journal of the Society of Instrument and Control Engineers, 36(6):396–403

[2] D. E. Rumelhart, J. L. McClelland, and PDP Research Group (1989), Parallel Distributed Processing, MIT Press

[3] Edited by L. Davis (1991), Handbook of genetic algorithms, Van Nostrand Reinhold, New York

[4] D. B. Forgel (1995), Evolutionary Computation, IEEE Press,

[5] J. H. Holland (1992), Adaptation in Natural and Artificial Systems: An Introductory Analysis with Applications to Biology, Control, and Artificial Intelligence, MIT Press

[6] D. E. Goldberg (1989), Genetic Algorithms in Search, Optimization & Machine Learning, Addison–Wesley

[7] L. J. Eshelman, D. J. Schaffer (1993), Real–Coded Genetic Algorithms and Interval–Schemata, Foundations of Genetic Algorithms 2, Morgan Kaufmann Publishers, :187–202

[8] S. Yamazaki, T. Itoh, and T. Hisamura (1979), Theoretical Consideration on a Control of Jib-Crane, Transaction of the Society of Instrument and Control Engineers, 15(6):826–832

[9] Y. Sakawa and Y. Shindo (1982), Optimal Control of Container Cranes, Automatica, 18(3)3:257-266

[10] M. Ohto and S. Yasunobu (1997), A Rotary Crane Control Method Based on a Skillful Operator's Knowledge, Transaction of the Society of Instrument and Control Engineers, 33(9):923–929

[11] R. Kondo and S. Shimahara (2005), Anti-Sway Control of a Rotary Crane via Two-Mode Switching Control, Transaction of the Society of Instrument and Control Engineers, 41(4):307–313

[12] R. Kondo (2006), Vibration Control of Rotary Crane via Two-Mode Switching Control (in Japanese), Journal of the Society of Instrument and Control Engineers, 45(7):632–637

Japanese companies and those introductions of the American management technique

Seiichi Fujii

Hiroshima University Graduate School, 1-1-89,Higashisenda-chou,naka-ku,Hiroshima-city730-0053,Japan
(Tel : +81-82-542-6962; Fax : +81-82-542-6964)
(fujii@dear.ne.jp)

Abstract: Straying is seen in the American companies shown weakness by a financial crisis. There was the time when the sick Japanese companies were going to take again in a domination of the strong American companies all together more than ten years before it. The experimental study was done how the Japanese companies had approached the American companies by technique introduction of American companies while clarifying the characteristic of the Japanese companies and the American companies. As a result, it is conducted that many companies still maintained the accumulation and the long-term intention that was the superiority of the Japanese companies. On the other hand, it is found that there was partly the company which had Americanized. As a result of having inspected how a product market strategy was practiced for the introduction period of the American management technique while allotting the financial resources mainly on human resources with a focus, it became clear that the characteristic of each company appeared to the divisions of the business or the decision-making structure.

Keywords: accumulation, long-term intention, a product market, business rebuilding, securities reports, household appliance industry

I. Introduction

Many Japanese companies followed the back of American companies in rapid economic growth period, and took in various management techniques, such as a quality control and improvement activities. As a result, it grew up, by the time it caught up at last and passed in the beginning of the 1980s, and it became world No.1 which was commented. However, it considered that the status was temporary prosperity by the collapse of the 'bubble' economy, and many Japanese companies lost confidence. The motion which takes in the management technique became strong after the 1990s, regarding the American companies which regained vitality as leadership in the world again. However, American companies began land subsidence by collapse of the financial bubble this time. Moreover, the failure example in the introduction of the American management technique was reported [1]. Furthermore, the capability at the spot of the production in Japanese companies has indication that it has still high competitive power [2], so the voice to review strength of the Japanese type became strong. Then, how Japanese companies had been Americanized by this deployment of the American type management technique? It is a question of the beginning of this research.

In order to search for this answer, firstly previous study is reviewed about introduction of American management technique. Next, the trend for the latest 20 years of the companies belonging to household appliance industry is analyzed based on the knowledge acquired through the review. After that, the Sharp which has finished steady growth, and Sanyo Electric which has made little increase are taken up, and it inquires in detail. And finally the result obtained by these analyses is summarized, and a future subject is arranged.

II. Introduction of the American management technique by the Japanese companies

Firstly, it is reviewed about essential factor that came to pay attention to the American companies. Kono and Clegg [3], Yamasaki et al [4], and Itami et al[5] presented an inner factor and an external factor as the interaction. Fujimoto [2] pointed out the importance of synchronization with the market from the standpoint in the research of the production site. Similarly, Ikeo [6] proposed that the change in the consumer characteristic was the root of the environmental transformation. When approaching from all the administrative functions, the start of the problem was showed in the change of the market as "Quality from the Amount" or "Maturation of consumption".

Next, it is reviewed about point aimed at and details in technique introduction. Miura [7] and Kono and Clegg [3] stated that the management target changed greatly. Ohtsubo [8] took up a problem of the diversification and explained that the rebuilding of the business was

©ISAROB 2009

pressed for. Abegglen [9] and Itami et al [5] studied diversification , Moriya [1] studied human resource management, Cho [10] studied management financial affairs, analyzed them in the business restructuring.

Finally, finding obtained from previous study is arranged and specific of analysis viewpoint is given. Previous researches were reviewed from two aspects, essential factor and development. Almost researchers are describing about the feature of a Japanese type and the American type. Albert [11] compared "Success of the group and long-term profit" and "Individual success and short-term profit". Ishii [12] had allegorized as "Resource preceding" and "Purpose and reasonable". Mishina[13] were expressed, "Accumulation" and "Procurement".

So, in this research, the business rebuilding based on the market is mainly considered. And, how the feature of the Japanese type and the feature of the American type are seen is examined. In that case, it assumed that the Japanese type is accumulation and a long-term intentions, the American type is procurement and a short-term intention.

III. A proof study：The change of the household appliance industry

Household appliance industry is an about 45 trillion yen scale near the market size of the automobile industry among the manufacturing industries, and history of companies is only a long-life company exceeding 50 years. Moreover, there are many major companies representing Japan, they have export manufacture typical for Japan, and high long global competitiveness has been maintained. In addition, there are many precedence researches. In this research, nine companies (Hitachi, Panasonic, Sony, Toshiba, Fujitsu, NEC, Mitsubishi Electric, Sharp, Sanyo Electric) are dealt with in the household appliance industry which has such a feature.

1. Indicator setup

Its attention in this research is paid to securities reports to which the booklet object from 1961 is opened. Furthermore, the methodology which makes this data applicable to research is already shown that validity [Kida, Bowman].Firstly, Securities reports were examined, and the scope was limited based on the policy of making the one related to the resource that was the medium of accumulation and procurement a center. Next, when the indicators are set, it is necessary to think about two elements greatly. They are the indicators concerning the achievement and the indicators concerning the resource. These relate mutually. As the first indicators, five items (sales amount, operating income, pure profit and loss, sales of each business, and profit of each business) were set. As the second indicators, ten items (number of employees, representative's on the register years, number of outside executives, number of trueborn executives, amount of capital investment, R&D spending, number of single employees, average age of single employees, single employees' average length of service, single employees' average salary per year) are taken up. There is a detailed description on a part of these indicators, and they are targeted when it is necessary.

2. Analysis of the household appliance industry by indicator

Firstly, all of the nine companies are the expansion almost keynotes as sales are shown in Figure 1 for 20 years after the collapse of the economic bubble. The operating income had been dropped to 0.9 times though sales of nine companies total had expanded to about 1.6 times for the earlier half ten years. But, for the latter half ten years, the operating income had been extended to 3.3 times though sales had been about 1.3 times. In a word, it can be thought that the business objective changed from sales and the market share to the profit.

Continuously, such an improving one's physical condition and the restructuring of the business is considered from the aspect of the resource allocation. Some tendencies were seen when analyzing it according to the business. The first is to center on the main business respectively and to raise sales and the profit. The second is to turn a lot of human resources to a leading business without sticking to productivity. And, the third has been to have redefined the business frequently. In addition, the fourth is to be done the anticipatory investment like equipment and R&D to non-final products that is called module, electronic device, and parts positively. The fifth at the end is to be seen the difference in the achievement of the non-final products business.

Then, the decision-making machinery is considered. First of all, it falls overall though a trueborn (work for the enterprise for 20 years or more) ratio of executives was about 70~90% in the first half of the 90's. Especially in Sony, it had dropped on about 30% in 2004 though it had exceeded 70-90% in the 90 year. The change is conspicuous. Next, on the average representative's tenure, the shortest is 2.5 years of NEC, the longest is 6.0 years of Sharp. It was clarified that the constituent member of the decision-making institution was changing greatly from these facts in these 20 years. It is thought that the continuance of the idea and the climate is high, and it tends to stand in a long-term intention when the representative alternates regularly and the representative is selected from trueborn. It was clarified to do the decision making that stared at the future while maintaining employment by most enterprises.

3. Consideration concerning change to the Americanized

To consider it more objectively, the correlation coefficient was asked for all 15 items (9 companies) of 20 years. As a result, a strong correlation was confirmed at the single average age and the single average length of service. Moreover, the average age, the annual average salary, and the single average length of service have increased every year. From these facts, it is guessed that it is required the person is not employed from various labor markets by the mid-career hiring but to employ the new graduate and to employ it long. However, only Sony's situation is different in recent years. Single employee's average age and average length of service are level-offs after 1998, the scale expansion is intended putting it in to the business by M&A, the trueborn rate of executives has decreased rapidly since 2002, and so on. In Sony, the feature of the American companies as procurement and a short-term intention appears. In a word, it is considered that only Sony had progress the change to Americanized and shifts the business structure greatly in these 20 years. On the other hand, in eight other companies, it was clarified that accumulation and a long-term intention of the resource that centered on talent were maintained. In one side, it has been understood that a big difference is seen in the achievement by eight that has maintained the feature of the Japanese companies for a long term. It appears in the rate of profit in Table 1. Sharp's operating profit margin and the pure profit and loss rate are the highest from this table. And, the change is small, and with stability. However, both operating profits and the current term net profit or losses of the accumulation are deficits in Sanyo Electric. The comparison of Sharp and Sanyo Electric is necessary as the following consideration.

IV. Comparison of Sharp and Sanyo Electric

1. Comparison of capabilities to be related to achievement

Set indicators are combined, employee's sales a person, employee's the operating profit, and employee's the current term net profit or loss are examined. Sanyo Electric is sluggish while Sharp has extended it almost well in three indicators. Therefore, Sharp is thought to be demonstrating an ability employee individual enough and the achievement is pushed up. But, there is some existence of inefficiency in Sanyo Electric somewhere.

2. Consideration concerning capabilities difference

The place where the capabilities was accumulated when the product market selects and method of decision making are considered.

First of all, the business definition of Sharp is very simple. It is only two kinds that are the electronic marvel and the electronic parts for 20 years. It doesn't divide by the consumer goods and the industrial goods when these content are examined. It is the final products and the non-final products. In other words, electronic parts are non-final products of the industrial goods though the electronic marvel has been divided into the final products of consumer goods and the final products of the industrial goods. While the final products accounts for about 65% of the whole on the sales scale among these, non-final products is reversed with about 60% in the profit. The intention of expanding the market from such a composition with the final products, and bringing earnings with non-final products can be clearly read. Moreover, it is guessed that the decision making that stares at a long term has been done about the distribution of management resources because presidents on the register years are long.

On the other hand, the business division of Sanyo Electric approaches Sharp. However, it is shape that non-final products pulls both sales and operating profits according to the business, and it is different from Sharp. Moreover, the ratio has changed by fiscal year though a lot of investments are distributed to non-final products. It is thought that it originates the fact that the constituent member of the decision-making machinery has been changed as each year. In a word, representative's on the register period is short, there are a lot of outside executives, and the trueborn rate of the executives is low. So, the policy concerning the resource allocation is blurred, and it is guessed that it might be a short-term intention consequentially. It is considered that it has brought the difference of the achievement.

V. Figures/Tables

1. Figures

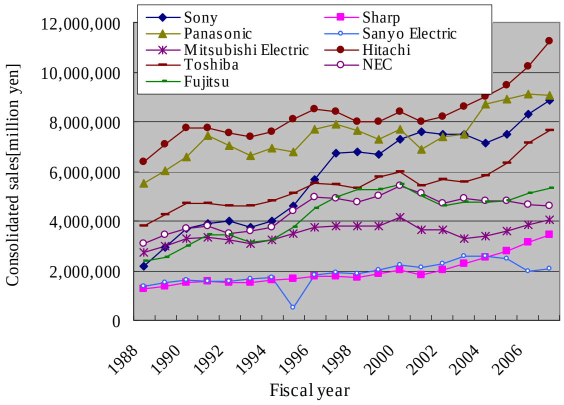

Fig.1. Consolidated sales changes of household appliance 9 companies

2. Tables

Table 1. Rate of consolidated profit of each company for 20 years

		Sony	Sharp	Sanyo	Hitachi	NEC
Consolidated operating income ratio	Average	3.85%	4.65%	2.59%	3.19%	0.40%
	Standard deviation	0.71%	0.25%	0.28%	0.47%	0.53%
	Range	14.28%	3.78%	5.45%	8.55%	11.04%
	Total	76.98%	93.05%	51.78%	63.85%	8.00%
Consolidated pure profit and loss rate	Average	1.56%	2.30%	-0.52%	0.43%	0.27%
	Standard deviation	0.54%	0.19%	0.60%	0.49%	0.44%
	Range	11.53%	2.99%	10.16%	9.03%	8.59%
	Total	31.14%	46.03%	-10.39%	8.56%	5.34%

VI. Conclusion

In the end, the result in this research is brought together, and the conclusion is obtained. To verify whether a Japanese companies had changed to American type, it was assumed that the feature of a Japanese type and the American type was caught as "Accumulation and long-term intention" and Procurement and short-term intention", based on the finding obtained from the previous studies. It applied it to nine consumer electronic industry companies, and the transition of 20 years was analyzed and considered. As a result, although only Sony had changed to the American type company, it turned out that other eight companies do not change and the feature of the Japan type company is maintained. While those companies with this feature redefined the business, it turned out that employment is secured at a long period of time, and know-how and technology are accumulated in the spot. Moreover, the highest decision-making function found that there were many patterns which are the necessary personnel raised from the inside and are constituted. It will not be different from before 20 years, and accumulation and a long-term intention are maintained. Furthermore, it became clear that the difference of the mechanism for changing the accumulated capability brings about the difference of achievements by comparing two companies, the Sharp and Sanyo Electric which have the feature of the same Japan type company. Moreover, it turned out that it is very important also for the definition of the business which is the essential subject of marketing.

And, some future subjects were discovered. First, it is important for Sony to consider the process by what kind of circumstances to have converted into the American type, and its time. Secondary, consideration is required, how the American management technique was taken in and attaches. The last subject is clarifying the structure of circulation with finished goods and non-finished goods in detail.

REFERENCES

[1] Moriya T (2005), Performance-based evaluation i ntroduction into Japanese enterprise(in Japanese).p50
[2] Fujimoto T (2004), Japanese manufacturing philosophy (in Japanese).p55
[3] Kono T and Clegg S (2001) Trends in Japanese Management: Continuing Strengths, Current Problem and Changing Priorities.p5
[4] Yamasaki H and Business History Society of Japan (2004), (in Japanese).p364
[5] Itami H and Hitotsubashi MBA Strategy workshop (2002), Analysis of strategy 2001 in Japanese enterprise (in Japanese).p16
[6] Ikeo K(1999), Innovation of Japanese type marketing (in Japanese).p61
[7] Miura M(2004), A management organization {Tashiro Y compilation ,The business administration of the modern Japanese company }(in Japanese).pp74-75
[8]Ohtsubo M (2005), Restructuring of Japanese enterprise (in Japanese).p13
[9] Abegglen, J.C. （2004） 21st Century Japanese Management: New Systems, Lasting Values .p52
[10] Cho E(2004), A consideration of corporate governance reform in Japan (in Japanese). The Ritsumeikan business review 43(4):p121
[11] Albert M(1991),Capitalisme contre capitalisme.p148
[12] Ishi J(1993), Myth of marketing (in Japanese).p194
[13] Mishina K (1997), "Accumulation" Versus "Combination" (in Japanese).Business Review 45(2):p76

The Fourteenth International Symposium on Artificial Life and Robotics 2009 (AROB 14th '09),
B-Con Plaza, Beppu, Oita, Japan, February 5 - 7, 2009

A Consideration of Management of the Value Co-Creation with Customers: A Case of the Grocery Retailers

Yoshirou Fujioka

Graduate School of Hiroshima University , 1-1-89 Higashisenda Nakaku,Hirosima JAPAN

(Tel : 082-542-7037; Fax : 082-542-7037)
(y.fujioka@purecook.jp)

Abstract: The focus on customer has been recognized as a key success factor of company and considerable research has been conducted in the field of management and marketing. This case study aims to fill in this gap by focusing on the way how grocery retailers co-create value with customers by using a new technology called CalNeCo. The study emphasizes that the traditional analogue system and the new digital system are co-exist and used interactively in the practice of grocery retailers. In the case of a grocery retail management, the management style was not characterized by conventional top-down management and there were multiple needs but not single needs in creating customer relationship.

Keywords: value co-creation, relationship, experience, Service Dominant Logic, CalNeCo

I.LITERATURE REVIEW

The purpose of this paper is to consider how comp any co-creates value with customers.

The focus on customer has been recognized as a key success factor of company and considerable research has been conducted in the field of management and marketing. The concept of "value co-creation jointly with customers" has been presented by Prahalad and Ramaswamy,2004.

The new starting premise is that the consumer and the firm co-create value, and so the basis of value. The co-creation experience (not the offering) is the basis of unique value for each individual.

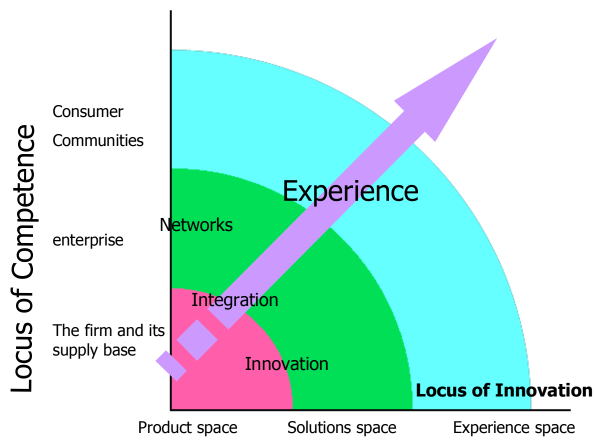

Source : Prahalad and Ramaswamy,2004.p.147.
Fig.1.The New Competitive Space

On the one hand, the study focused on the topic of the relationship with customers and co-creation of value with them has become one of the most popular studies in these fields, but on the other hand, their focus is still on the conceptual level. In other words, many studies focused on *what* is co-creation of value but not *how* company co-creates value with customers. In addition to this, most early studies have focused on large manufacturing firms where they merely contact directly with customers.

Therefore, the study in retail industry where they often have direct contact with customers through their stores has not been conducted enough. Since this technology is quite new, this case study aims to examine how grocery retailers utilize this new technology to manage co-creation of value with customer.

The study emphasizes that the traditional analogue system and the new digital system are co-exist and used interactively in the practice of grocery retailers. In the case of a grocery retail management, the management style was not characterized by conventional top-down management and there were multiple needs but not single needs in creating customer relationship.

Vargo and Lusch point out the importance of shift on focus from goods to service by introducing the new concept called "Service Dominant Logic"(2004).Thus marketing focus shifts to customer (co-create value).
S-D logic is strategic and traditional marketing mix is tactics.

S-D logic moves the totality of marketing from a product-centric focus to a customer- and knowledge centric focus. Marketing is thus seen as the means by which organizations and societies are able to creat value

©ISAROB 2009

by the voluntary exchange of knowledge and skills (Lusch and Vargo 2006).

This paper point out the service centered view of marketing is customer-centric and market driven. A service-centered dominant logic implies that value is defined by and co-created with the consumer rather than embedded in output.

Table 1. Marketing Mix versus S-D Logic

Traditional Marketing Mix (tactical)	**Service-Dominant Logic (strategic)**
Product	Co-Creating service(s)
Price	Co-creating value proposition
Promotion	Co-creating conversation and dialogue
Place (Channel of Distribution)	Co-creating value processes and networks

Source : Lusch and vargo,2006.p.408.

Pine II presents the experience economy. Each successive offering commodities goods services and experiences greatly increases in value because the buyer finds each more relevant to what customer truly wants.

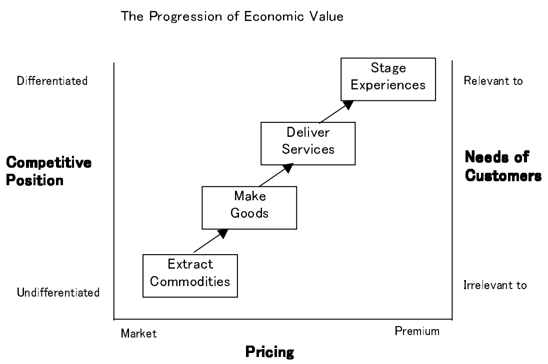

Source : Prahalad and Ramaswamy,2004.p.147.
Fig.2.The Progression of Economic Value

I considered a precedent study. I understood that new viewpoints such as service or the experience.

A new viewpoint appeared in management and marketing. In particular this study considers how co-create value is performed.

II. FRAMEWORK

Figure2 represents a framework for a consideration of management of the value co-creation with customers.

I research the co-creation process with company and customers. First, company set the place where exchange of information between company and customers. In the place manager work them to give their opinion. Manager combines customer's opinion with value.

The point of research is consideration of communication process, and I view how operate the capability of medium-sized and small companies. Retailer and customer perform interaction through point of contact.

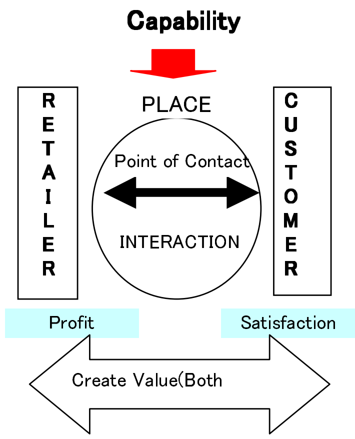

Fig.3.Framework for a consideration

And I set point of view to consider through a framework. Firstly the retailer sets the point of customer contact place.

The retailer performs interactive communication with the customer next. This is ability for relation-ship construction for the customer. And the retailer reacts to the voice of the customer.

This is organization reaction ability. organization reaction ability has 2types which are ability for out side and ability for inside.

I consider it in the above-mentioned analysis point of view through an example of CalNeCo system.

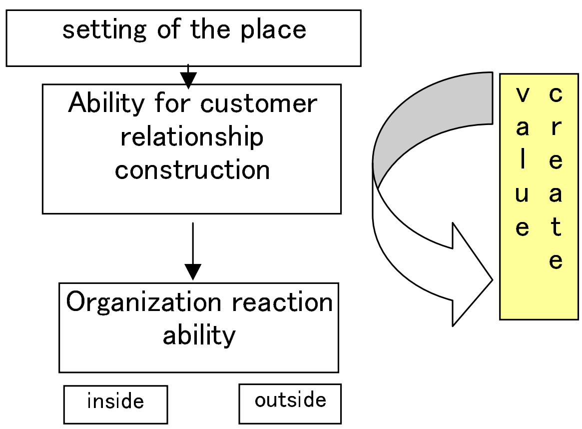

Fig.4. Consideration Point of View

III. CalNeCo SYSTEM

This case study aims to fill in this gap by focusing on the way how grocery retailers co-create value with customers by using a new technology called CalNeCo.

CalNeCo (abbreviation of Calendar, Network and Com munication) is the system which supports the co-creation of value with customer by providing informa-tion of customers at the store.

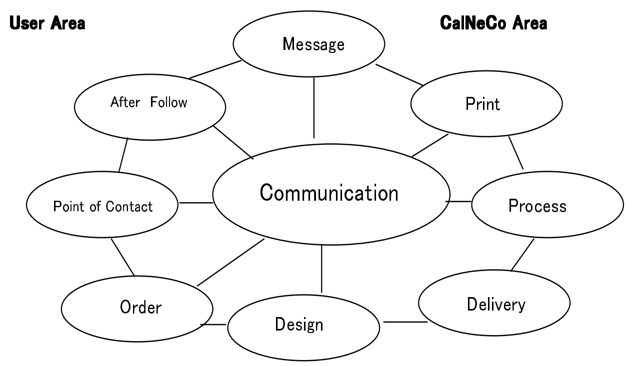

Source : CalNeCo

Fig.5. Total CalNeCo system

In the first place, CalNeCo system was made for the maker.

CalNeCo system has been developed in retail i ndustry and recently implemented on a trial basis in som e grocery retailers. The Point of Sales System (POS) is probably most famous and popular technology used in grocery retailers. However it has been pointed out that information based on POS does not provide any relevan t information about why and how particular items are sold since it does provide information only about what, when, by whom and how many items are sold. To com-plement these limitations of POS, grocery retailers start ed adopting CalNeCo system.

Now CalNeCo consists of 178 members. Almost member is loyal customer of store. F company's card data is Table2. Upper 30% customers occupy 67.5% of all sales.

Table 2. Analysis(Three months :90 days)

	Customer	amount of mone	ratio(%)		unit price	frequency
Decil 1	302	33,938,324	34.8	34.8	2,014	55.8
Decil 2	302	18,566,136	19.0	53.8	1,694	36.9
Decil 3	302	13,335,635	13.7	67.5	1,591	28.1
Decil 4	302	9,982,286	10.2	77.7	1,479	22.4
Decil 5	302	7,507,885	7.7	85.4	1,365	18.6
Decil 6	302	5,690,554	5.8	91.2	1,273	15.0
Decil 7	302	4,023,534	4.1	95.3	1,178	11.3
Decil 8	302	2,616,578	2.7	98.0	1,126	7.9
Decil 9	302	1,487,376	1.5	99.6	1,026	4.9
Decil 10	302	469,136	0.5	100.0	829	1.9
	3020	97,617,444	100.0		1,609	20.3

Source : F company's card data

Figure4 represents a point of contact of CalNeCo system. The retailer communicates with a customer through CalNeCo system. Retailer can acquire information of customer easily.

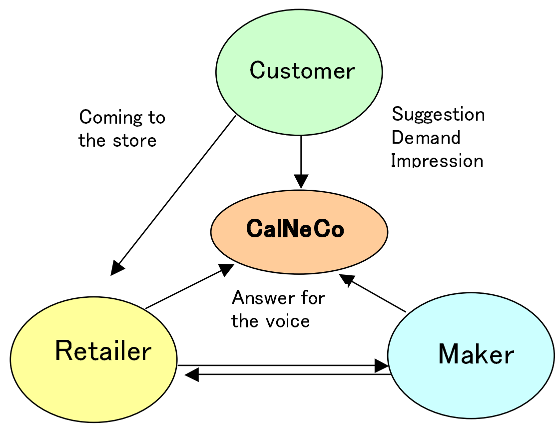

Fig.6.Point of Contact

Customers come to the store. Loyal customer (decil 1)come to the store 55.8 times in 90 days. Therefore, Loyal customer request to high level service for a store.

Example:Voice of Customer (Voc)

Voc1: selection of Japanese sweet

Voc2:have a good selection of cheeses

Voc3:suggestion about today's menu

Voc4:evaluation about service

Voc5:complaint about freshness

Voc6:knowledge about cooking

Voc7: skill to eat delicious

Many various opinions are given from customer through CalNeCo system. And retailer reacts to voice of the customer.

Example:Reaction of Retailer(Ror)

Ror1: improvement of the merchandising

Ror2. improvement of the information contents

Ror3: education training of the salesperson

Ror4: article development

Ror5: improvement of the sales system

I introduce the example that led to article development by react to Voc1.Retailer put good quality sweet in the shop in response to the demand of the customer. The buyer has thought high sweet are not sell till the voice of the customer arrived. But good quality sweet became the hot seller when buyer sold it.

Table 3. Pos Data

brand name	amount of sale	Sales figures	margin
X	196,739	800	31
Y	59,350	262	29
Z	111,208	456	33
total	367,297	1,518	

IV. FINDINGS

I would consider co-create value through CalNeCo system in analysis point of view.

The first is setting of a place of the customer point of contact. This is performed through a CalNeCo system such as figure 4. Second, ability for customer relationship construction is capability for organization promoting information exchange with the customer. The retailer performs the information exchange with the customer through a system. However, retailer and maker gather regularly and perform the organization inside and the outside correspondence. The retail trade got possible to simplify the information exchange by development of the IT technology. However, the communication of the face to face becomes important.

A merit of the information exchange of the face to face is the following points.

(1) A participant can communicate immediately.
(2) A participant is easy to convey intention.

Next it is necessary that the manager switch a management method. And it is necessary for technique of the management to switch from top-down type. It becomes important that the manager manages the atmosphere of the place.

(1) The manager promotes free information exchange in nature.
(2) The manager promotes the information exchange that the density is high.
(3) The manager promotes the interchange of feelings and psychological stimulation.

Ability of these managers is ability to receive the information of the customer. And ability to promote the atmosphere of the place than controlling a subordinate is important for a manager.

REFERENCES

[1] Lusch, R.F. & Vargo, S.L. ［2006］ *"Service-Dominant Logic as a Foundation for a General Theory"* The Service-Dominant Logic of Marketing, Lusch, R.F.＆Vargo, S.L., M.E.Sharpe.pp.406-420.
[2] Pine□, B.J.Gilmore, J.H. ［1999］ *The Experience Economy*,Harvard Business School .
[3] Prahalad, C.K. & Rawaswamy, V. ［2004］ *The Future of Competition：Co-Creating Unique Value with Custmers,*Harvard Business School.
[4] Vargo, S.L.＆Lusch, R.F. ［2004］ "Evolving to a New Dominant Logic for Marketing"*Journal of Marketing, Vol.68, January.pp.1-17.*

A relationship analysis between centrality and module production in the Keiretsu of Mazda

Hiroshi Kimura[1], Takao Ito[1]*, Zengyu Xia[2]

[1]*Dept. of Business Administration, Ube National College of Technology, Yamaguchi, 755-8555, JAPAN*
[2]*School of Management, Wenzhou University, Zhejiang,, 325035, China*

Abstract: Relationship analysis is one of the most interesting issues in inter-organizational management. Relationship between auto maker and parts suppliers in the Keiretsu of Japan, as one of the special cases, has been changed greatly due to the diffusion of module production recently. Parts suppliers are required to develop their capacity of R&D and parts integration to cope with the new situation. In order to measure the transactional relationship between centrality and module production, we review the literature of module production and inter-organizational research from the viewpoint of network, and measure eigenvector, one of the centrality indices, of the transaction network in the keiretsu of Mazda using the two fiscal years of 1995 and 2005. We analyze the changes of inter-organizational relationship between the years of 1995 and 2005, and identify the relationship between centrality and module system. Furthermore, we discuss the implications of our new findings of the transactional network in Mazda.

Keywords: module production, supplier, network analysis

I. INTRODUCTION

Module production, as one of the new production system, has been introduced in the keiretsu of Mazda from 2000. Two different types of module production exist in Mazda. The first is sub-assy (assembly) type. Most of the component-parts assembled to a certain extent are called sub-assy type. They can be delivered to Mazda directly. The second is functional integration type. All of the parts integrated functionally based on the idea of combining related parts into one unit called functional integration type.

The formation of keiretsu has been changed greatly because the module production and open policy of the parts transaction are adopted in Mazda. Mazda not only deals with the members of keiretsu of Mazda, but also with the members of other keiretsu such as Toyota and Nissan. Therefore, all of the powerful suppliers such as foreign parts-makers and other parts-makers of other keiretsu would be considered as the competitive rivals for the suppliers of Mazda in Hiroshima area. In order to keep up with the new trend, most of the suppliers concentrate on integrating the production of related parts. One of the most interesting issues is what kind of changes has been taken place in the keiretsu of Mazda.

In this paper, we apply centrality analysis of network theory to the keiretsu of Mazda for identifying the central suppliers. We examine the features of those central suppliers, and analyze the relationship between centrality and module production.

The main contribution of this paper is to provide an empirical perspective to identify the relationship between the centrality and module production in the keiretsu of Mazda. We measure eigenvector, one of the centrality indices, of the transaction network in the keiretsu of Mazda using the two fiscal years of 1995 and 2005. We analyze the change of inter-organizational relationship between the years of 1995 and 2005, and identify the relationship between centrality and module system. Furthermore, the implications of our new findings are discussed in this paper.

This paper is organized as follows. In Section 2, we review some relevant literature of the module production and network research. And then, we introduce the measurement of eigenvector and calculate this index in Section 3. We analyze the results and discuss the implication of our analysis in Section 4. Finally we conclude in Section 5.

II. Background

Whilst module production is not new conception [1], it appears that more and more automotive manufacturers are now realizing that modular strategies for production can offer potential long-term benefits to suppliers and customers. There has been a plethora of discussions of module production given in the literature. For instance, Fujimoto, Takeishi, and Aoshima [2] propose that four kinds of architecture could be classified based on the features of product-process: integral architecture, modular architecture, closed architecture, and open architecture. The integral-closed type product is adopted in the Japanese automobile industry.

©ISAROB 2009

Egusa [3] investigated the module production in Mazda and found that the module production is carried out in the production of front-end field, cockpit field, center panel field, door field, and fuel tank field. These parts are composed of many different kinds of parts. One of the most important issues for teir-1 suppliers is to improve their ability of parts integration. The adjustment problem occurred in the supplier is that what kind of parts should be integrated for the module production.

We investigated the keiretsu of Mazda and found that module production has close relationship with transaction. In other words, it is not enough to study module production without considering the transaction among the firms of keiretsu. Inter-organizational relationships in keiretsu have been analyzed with quantitative analysis tools such as centrality analysis [4]. Fukuoka et al. [5] reported a new trend in relationships between firms in the keiretsu of Nissan from the viewpoint of network organization. Furthermore,

Kimura and Ito [6] analyze the transactional network using influence index, and find that the suppliers in Hiroshima area have lower power of influence compared with other suppliers. Furthermore, Kimura and Ito [7] measure the keiretsu network of Mazda with the centrality index of information and eigenvector; and found that most of the suppliers in Hiroshima area occupy an important position although part of them are not ranked at the high centrality group.

III. Measurement

1. Eigenvector

Many methods have been developed to measure the centrality of a network. Eigenvector index of the largest positive eigenvector is a measure of centrality. It also called Bonacich centrality. Eigenvector follows that the centralities will be the elements of the corresponding eigenvector. Given an adjacency matrix 'A', the centrality of node k (denoted c_k), is given by $c_k = a\sum A_{ij}c_j$ where 'A' is a parameter [8].

We apply eigenvector, one of the centrality indices, to measure central suppliers in the keiretsu of Mazda.

2. Measurement

Every car maker has its supplier's organization in Japan. They are called '*Kyoryokukai*'. The *Kyoryokukai* of Mazda is called '*Yokokai*'. *Yokokai*, the cooperative organization of parts suppliers of Mazda, is composed of three regional sub-organizations of Kanto, Kansai, and Nishi Nihon. In order to identify the influence of the module production on transaction, we measure eigenvector of the transaction network in Mazda using the two fiscal years of 1995 and 2005 in this paper.

The total number of the firms in the keiretsu of Mazda in 1995 and 2005 is 192 and 181 respectively. They can be illustrated as in Figure 1 and Figure 2.

Fig.1. Transactional network of Yokokai in 1995

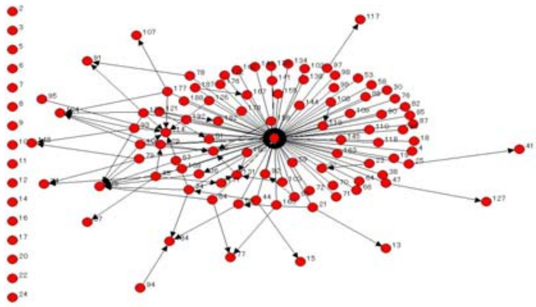

Fig.2. Transactional network of Yokokai in 2005

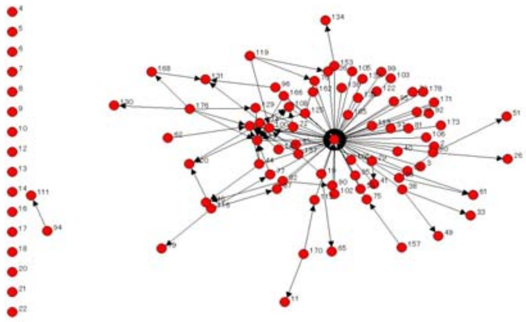

The result of the measurement is shown in Table 1.

Table 1. Top 10 suppliers in 1995

	Firms	Value
1	Toyo Seat	0.240
2	Mazda Parts Industry	0.228
3	Miura Industry	0.222
4	Hiroshima Seiken Kogyo	0.205
5	Mitsuba Industry	0.205
6	Delta	0.198
7	Sumino Kogyo	0.191
8	Microtecno Corporation	0.189
9	Hiroshima Aluminum Industry	0.176
10	Hirotani	0.164

In 1995, Toyo Seat is ranked at the top in Table 1. Toyo Seat is a firm of supplying seat of compact car to Mazda. Delta, ranked at the sixth, is also a seat supplier of Mazda. It is obviously that Toyo Seat, located in Hiroshima area, is the most central firms in the transactional network. Miura Industry is ranked at the third. Dash panel and rear-end panel are its main products. Mitsuba Industry is ranked at the fifth. The main products of Mitsuba Industry is cross-member and door arm. Sumino Kogyo specializes in the small parts press is ranked at the seventh.

In order to compare with the result in 1995, we measure the centrality of 2005. The result is shown in table 2.

Table2. Top 10 suppliers in 2005

	Firms	Value
1	Keylex	0.275
2	Japan Climate Systems	0.271
3	Sumino Kogyo	0.255
4	Nishikawa Kasei	0.253
5	Futaba Kogyo	0.207
6	Niitec	0.185
7	Hiroshima Aluminum Industry	0.178
8	Kurashiki Kako	0.161
9	Kokusan Buhin Industry	0.115
10	Meiwa Industry	0.107

In 2005, Keylex is ranked at the top in Table 2. This is a joint-stock company of Miura Industry and Kurata in 2001. The rank of Miura (Keylex) has risen up from the 3rd to the 1st. It covers a wide area with the hood, dash panel, trunk, rear-end panel. The number 2 supplier is Japan Climate Systems. This is a car air-conditioner manufacturer established by the joint investment of Mazda, Matsushita Electric Industrial (Panasonic), and Visteon AP. The rank of Sumino Kogyo has risen up from number 7 to 3. The fourth supplier is Nishikawa Kasei, a plasticization supplier of producing cockpit and other parts. The fifth supplier is Futaba Kogyo. It is a supplier that manufactures the press parts of body in Hiroshima region. The sixth supplier is Niitec. Door parts are produced in Niitec. The main product of the next Hiroshima Aluminum Industry is engine parts made by the plastic and mold. The number eighth is the head office of Kurashiki Kako. It is located in Okayama prefecture, neighbor of Hiroshima. In other words, Kurashiki Kako is one of the suppliers out of Hiroshima area. This firm sells rubber parts from the engine to the wheel widely. The following two suppliers are also not located in Hiroshima area. Their assembly plant is located in the suburbs of Hiroshima City and Hofu City, nearby the Mazda assembly plant, respectively.

IV. Analysis and Implications

1. Analysis

Many interesting results will be found based upon our measurement. The first is the seat and body suppliers such as Toyo Seat and Delta have high value of centrality. The common feature of these parts is large scale with high transportation cost. Therefore, for saving the transportation cost, the nearby suppliers become important supplier of Mazda. The second is some suppliers which produce small parts also have high value of centrality. We find that the firm will become important one when it occupy at an important position in the network of parts transaction, even if it is a small-scale supplier. The third is the fact that some suppliers such as Keylex and Japan Climate Systems in Table 1 and Table 2 will merge other companies for the purpose of expanding their operations aiming at an increase of their long term profitability in the future.

2. M&A and module production

M&A (Merger and acquisition) is one of the most important features in the keiretsu of Mazda. Most of the M&A have close relationship with the module production.

On of the typical examples is Keylex. Keylex is established under the proposal from Mazda. One of the purposes is to improve the ability of the parts manufacturing with global standard. Keylex can produce a variety of parts form dash panel, rear-end panel to bonnet, and trunk after M&A. Therefore, the ability of integration has been improved. The brief outline of Keylex is shown in the Table3.

Table3. The outline of Keylex

	Kurata	Miura Industry
Head office	Hiroshima	Hatsukaichi
Plants	Hiroshima, Yano, Yuu (Yamaguchi)	Saeki, Tsuwano (Shimane)
Capital	150 Million Yen	90 Million Yen
Employee	481	394
Sales(2005)	16,600 Million Yen	8,700 Million Yen
Parts	Bonnet, Trunk	Dash Panel, Rear-end Panel
↓		
	Keylex	
Head office	Hiroshima, Kaita	
Capital	240 Million Yen	
Employee	797	
Sales	27,600 Million Yen	
Parts	Front-end Module, Rear-end Module	

Daikyo Nishikawa, a joint-stock company of Nishikawa Kasei and GP Daikyo, is established in 2007. Nishikawa Kasei manufactures plastic parts of interior and exterior, and GP Daikyo produces plastic parts of engine mainly. The purpose of this M&A is to enlarge its business scale and to get competitive advantage. The basic information of Daikyo Nishikawa is shown in the Table 4.

Table4. Basic information of Daikyo Nishikawa

	GP Daikyo	Nishikawa Kasei
Head office	Higashi-Hiroshima	Hiroshima
Plants	Higashi-Hiroshima Hofu (Yamaguchi)	Hiroshima, Hofu (Yamaguchi)
Capital	100 Million Yen	343.5 Million Yen
Employee	1,069	780
Sales(2005)	55,930 Million Yen	45,905 Million Yen
Parts	Plastic (Interior, Exterior, Engine)	Plastic (instrument panel)
	↓	
	Daikyo Nishikawa	
Head office	Hiroshima-Aki county	
Capital	443.5 Million Yen	
Employee	2,100	
Sales	108,000 Million Yen	
Parts	Plastic (Interior, Exterior, Engine, Instrument panel)	

For improving the abilities of module production, one of the basic conditions is to enlarge its business scale. Therefore, M&A could be considered as one of the most important factors for module production.

3. Centrality and module production

Most of the firms with high value of centrality, not only the large-scale parts suppliers, but also the small-scale suppliers are developing their module production. We investigate these suppliers, and found that some of them are not suitable for the module production. For instance, Sumino Kogyo, one of the small-scale suppliers in Hiroshima area, has high value of centrality in the two years. This firm is producing many kinds of small press parts. All kinds of the parts produced in Sumino Kogyo reaches about 2,500. These parts are used in many large-scale parts, for example, engine, transmission, chassis, and body. It is the subcontractor of other suppliers which manufacture large-scale parts such as seat and body. This firm has main transactional relationship with Mazda, Japan Climate Systems, Nihon Seiko, Visteon AP and other large-scale supplier. So Sumino Kogyo is hardly to be considered as a module oriented company.

V. Conclusion

We identified the central firms of transaction network in Mazda using one of the centrality indices, eigenvector. And we analyzed the relationship between centrality and module production in the keiretsu of Mazda. Most of the central firms with high eigenvector are module oriented companies. They expand their business via M&A in order to improve their integration ability. Module production would be one of the important architectures, but it is obviously not the best practice for all of the suppliers.

Despite some meaningful new findings, the work had several limitations. First, we focused on the analysis of module production, but we did not investigate the actual situation in these firms. Second, not only module architecture, but also other architectures such as integral architecture and open architecture should be discussed. Third, only two fiscal years data was limited in our measurement of Eigenvector. Much more data should be collected to analyze the relationship between centrality and production system.

REFERENCES

[1] Starr M. K. (1965), Modula Production – a New Concept, *Harvard Business Review*, Vol. 43, Nov-Dec, pp.131-142.
[2] Fujimoto T., Takeishi A., and Aoshima Y. (2001), *Business Architecture* (Japanese Edition), Yuhikaku.
[3] Egusa H. (2004), Module Production in the Automobile Industry of Hiroshima Region (Japanese Edition), *Research Chugoku* 55 (661), pp.107-118.
[4] Ito, T. (2004) Quantitative analysis of a firm's relationship in the Keiretsu of Toyota group, *Innovations through Information Technology*, pp.1078- 1079, IRMA 2004 International Conference, New Orleans, USA.
[5] Fukuoka S., Ito T., Passerini K., and Sakamoto M. (2006), An Analysis between Transaction and Cross Shareholdings in the Keiretsu of Nissan, Proceedings of the 6th International Business Information Management, International Conference, *Managing Information in the Digital Economy Issues & Solutions*, pp. 163-169, June 19-21, Bonn, Germany.
[6] Kimura H., and Ito T. (2007), Network Analysis of Auto-Parts Suppliers in Mazda (Japanese Edition), Kyushu Keizaigakkai Nenpo 45:59-64.
[7]Kimura H., and Ito T. et al. (2007), Influence Analysis in the Keiretsu of Mazda, Proceedings of the 2007 Information Resources Management Association, International Conference, *Managing Worldwide Operations and Communications with Information technology*, pp.892-897, May 19-23, 2007, Vancouver, Canada.
[8]Bonacich P. (1972), Factoring and weighing approaches to status scores and clique identification, *Journal of Mathematical Sociology* 2, pp.113-120.

* Takao Ito is visiting research professor of School of Management, New Jersey Institute of Technology in USA from March 29, 2008 to March 28, 2009.

©ISAROB 2009

The Fourteenth International Symposium on Artificial Life and Robotics 2009 (AROB 14th '09),
B-Con Plaza, Beppu, Oita, Japan, February 5 - 7, 2009

Marketing strategy with introduction of Customer Relationship Management -Case of Japanese financial institutions-

Takahisa Yamaguchi

Department of Socio-Information, Faculty of Informatics,Okayama University of Science,
1-1 Ridai-cho, Okayama-city, 700-0005, Japan
(Tel,Fax : 81-86-256-9752)
(t- yama@soci.ous.ac.jp)

Abstract: Also in the financial institution of our country, the measure for relationship marketing (customer relationship management) is progressing by leaps and bounds in the past several years. So, in this paper, the customer relationship management strategy of financial institutions was studied by conducting questionnaire surveys and company interviews. In order to operate overall structure changed by customer relationship management implementation effectively, clarify missions of each departments and employees. Moreover, it is important to evaluate fairly to raise awareness and motivation of employees.

Keywords: Customer relationship management, marketing strategy, IT strategy, retail banking, financial institutions

I. INTRODUCTION

1. Awareness of the issue

Environment surrounding corporate, from service providers to industrial manufacturers, in present Japan, 1) more competition because of ripe markets, 2) price competition, 3)difficulty in differentiation of products and services as shared issues.

In order for corporate to survive in the difficult business environment in which such issues are exist, I thought it was very important to maintain long-term relationships with existing customers and came to believe the need for conducting research "Relationships marketing (Customer Relationship Management)" that puts focus on long-term business relationship and customer sharing.

2. Selection of Research subject

Recently, also in Japan, the number of corporate that implements "relationship marketing" by introducing customer relationship management system (herein after referred to as "CRM") from USA to manage and analyze customer information is increasing.

However, as indicated by a study conducted by Rigby et. al ("DIAMOND Harvard Business Review" July, 2002 issue) which concluded 55% of corporate implemented CRM had not achieved certain success", it is a fact for many corporate introduced CRM have not been able to maintain relationship with their customers.

By studying series of researches on relationship marketing conducted so far, following questions were raised. "Is customer relationships maintainable by utilization of CRM?" "What do corporate successfully introduced CRM use as the basic strategy for CRM utilization?" So, I decided to conduct research on corporate that have introduced CRM.

3. Hypothesis

While studying about "relationship marketing" and CRM, I came up with an idea that successful corporate in CRM introduction might reform whole business processes to address CRM introduction in order to utilize customer's information inside the corporate and I established the following hypothesis.

<u>(Hypothesis)</u> "The company which reforms its operation processes to address CRM introduction has been successful in maintaining relationships by utilization of CRM".

II. Company questionnaire survey and interview

In Japan, the effort by financial institutions for CRM has been growing rapidly in the past several years. Then, I conducted "Questionnaire survey on the actual status regarding CRM" (26 items of question, 116 banks in total, consisting of five major banks, 64 regional banks, 47 second regional banks, 94 effective replies (among them, 12 replies contains partial deficiencies)) and interviewed by visiting 11 regional financial institutions in which whole components of CRM system have been introduced. Then, I selected a regional financial

©ISAROB 2009

institution (Tottori Bank) that has realized profitability increase by CRM implementation in order to verify the hypothesis.

1. Customer Relationship Management in Tottori Bank

Tottori Bank, a regional financial institution, its headquarter is located in Tottori-city Tottori, has declared its specialization in retail banking and has achieved 47% of personal loan ratio that ranks one of the highest among regional financial institutions (as of September, 2007). Moreover, it has realized high profitability since CRM system introduction in April 2004. So, it can be called as a company successful in CRM introduction.

Purposes of CRM introduction are to sophisticate and streamline its sales promotion activities and to establish long-term trust relationship by unification of customer information including customer needs and constant and timely approaches. Moreover, all customers information are integrated in CRM and customer data and contact histories can be browsed on real time at all customer contact points (Fig. 1).

2. Success factor

Analysis of Tottori Bank's success in CRM introduction shows, as in Fig 2, following five factors; "personal loan specialization strategy", strengthening "customer contact points", "products and services development", "awareness and system reforms" and "system evolution" as its success factors.

2-1. personal loan specialization strategy

Tottori Bank's target customers are not one who are considered as excellent customers by other banks including salaried-workers employed by major companies and government officials but who borrow money even if the interest of loan is little bit higher because other banks are reluctant to lend even though they have repayment capacities. This is why Tottori Bank does not need to participate in lower interest competitions and is able to maintain high profitability.

(Example of target)- single working female, customer who is having health problem and whose loan application is rejected by other bank. system engineer or employee of foreign-affiliated firm who tend to change workplace repeatedly , salaried worker who considers purchasing apartment not for habitation but for an investment purpose (target in urban markets),etc.

2-2. customer contact points

2-2-1. customer contact points' excellent ability in proposal

Compared with other banks, Tottori Bank is superior to in the proposed type business at each shop front by utilizing CRM. Sales activities are efficiently performed by registering the customers information obtained at all customer contact points including information gained through conversations with customers at branches and call centers to CRM and sharing such data among all customer contact points. For example, existing customers are categorized into five classes according to their contents of dealings, and profitability. And with understanding of each customer's position, employees perform sales activities. Moreover, it has developed systems that utilizes customer contact point's capabilities at maximum extent by CRM, which includes displaying of cross-sell (recommendation of related products) products on a CRM system screen based on each customer's dealing history.

2-2-2. expansion of sales channels

Housing loan centers have been established in Tokyo and the urban areas of Osaka, in where many target customers reside, and employees with specialized qualifications are assigned there to strengthen housing loan sales channels in urban areas. As of April 2004, housing loan for urban area accounts for more than 30% of its total housing loan. Moreover, it started banking business on the internet earlier than other neighboring banks and has created easy-to-use environment for customers. User application is acceptable from nationwide.

3. Products and services development capability

Headquarters is developing new products and services based on proposals that reflect customer's opinions gained at customer contact points through the built-in board established on CRM and shared by headquarters and branches.

4. Awareness and system reform

4-1. awareness sharing /motivation improvement

Company-wide issues are studied with CRM and younger employees' opinions and suggestions are actively harnessed in management through the built-in board that has a function to make proposals to management and age-based trainings. Realization of proposals especially contributes to establish trust relationship between employees and management in a way that management listen their opinions and corporate culture in which branches actively express their opinions to headquarters.

4-2. clarification of roles of organizations and each employee

In accordance to CRM introduction, whole operation processes were reconstructed and missions of branches and employees were clarified. For example, branches as "sales and service channels", clerks of each branches as "who perform sales activities" and headquarters, by transferring backyard/examination businesses of branches to headquarters, as thoroughly supporting body for branches. Furthermore, function and target customers of each branch were reviewed and clarified. Various branch styles including "In-store branch" in hypermarkets, opens on Saturdays and Sundays, small scale "Money plaza" operates only retail banking around station areas and "Loan plaza" specializes housing loans were successively established. To address these changes of missions of branches and employees, organization and evaluation system are under reform. Quick management decision is secured by Flattening of the organization and efforts for fair and highly transparent personal evaluation has been made by adopting balanced score cards.

5. System evolution

5-1. evolution of CRM

CRM is continuously evolving in easier-to-use way with each employee's ideas and various know-how. Function addition and display change to CRM are always made to reflect requests and opinions from branches.

5-2. Upgrading of automated screening system

Based on the accumulated data through personal loans, products that utilize automated screening system and self-line examination are developed and very quick screening of loan not available at other banks has became possible. This screening is based on repayment capability of each individual in stead of collateral and effectively used in new products development.

III. Verification of hypothesis

1. Operation process reform

In Tottori Bank, whole operation process of the bank has been reformed and missions of branches and bank clerks were clarified. These measures are considered to have established the basis of effective implementation of CRM.

2. About customer relationship

In Tottori Bank, it is possible to make suggestions on products suitable to customer's needs on time through appropriate channel by clerk's active utilization of accumulated customer information on CRM at customer contact points. CRM-strengthened proposing capability of customer contact points realizes maintaining relationship with existing customers. Moreover, taking advantage of the ideas obtained from the data analyzed by CRM and dialogues with customers etc., it has created products and services other banks do not have or cannot imitate. These have brought success in acquiring new customers as well as maintaining existing customers.

Ⅳ. Figures/Tables

1. Figures

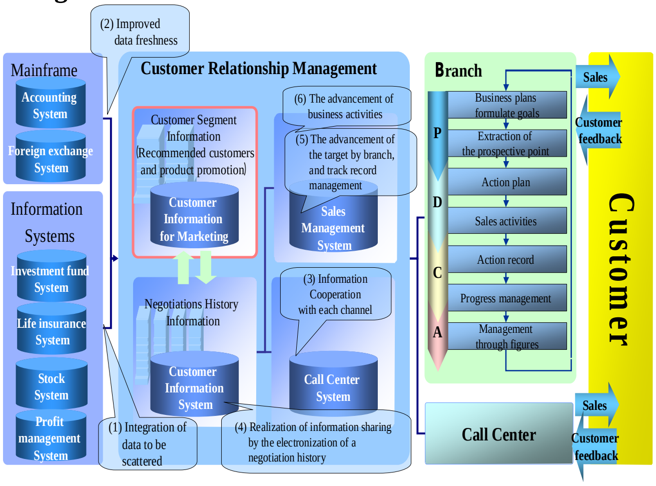

Fig.1. CRM in Tottori Bank

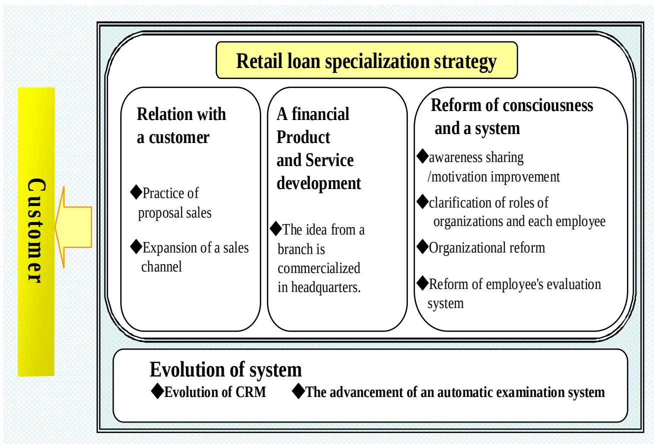

Fig. 2. Success factors of Tottori Bank

Ⅴ. Conclusion

The questionnaire survey and interviews brought me the following two strong impressions. 1) In order to utilize CRM and maintain relationship with customers, it is important not only to introduce the latest CRM but to reform whole business process of a company and to clarify missions of each business units and employees. 2) In order to operate effectively overall structure changed by CRM, it is important by fair evaluation in accordance with each mission of business unit and employee to raise awareness and motivation of employees. The importance of clarification of missions, fair evaluation and raising awareness and motivation of employees was re-recognized by this survey and research.

Tottori Bank analyzed in this paper shares and utilizes integrated data collected from all customer contact points including teller, call center operator, internet banking and ATM as well as branch clerks in charge of personal and corporate and branch managers. This example of new usage can be called "Real CRM" and will attract big attention from now on with many financial institutions have not been able to expand system implementation since CRM introduction.

CRM is not a strategy of which result shows up quickly. In implementing CRM, it is important to keep tolerance and energy to repeat continuously the basic cycle of "collection and accumulation of customer information", "Analysis of customer information", "Customer approach based on the analysis" and "measurement, evaluation and feedback based on the results of approach".

For that purpose, company-wide awareness reform should be promoted under management's understanding and strong support, need of CRM etc. should be thoroughly discussed until consensus are obtained from all employees, and if necessary, organization structure and performance evaluation should also be reformed.

Approximately 10 years have passed since the first introduction of CRM in financial institutions in Japan. And even in this 10-year, lifecycle of customers and environment surrounding financial institutions are rapidly changing in line with the development of information society. From now on, financial institution's way of communication with customers is believed to change dramatically along with further development of infrastructure for realization of ubiquitous society.

Meanwhile, it becomes important for each financial institution to review preconditions constantly for establishing relationship that has been considered as given nature. Furthermore, I would like to study further in future research about the state of CRM from the viewpoint of "Relationship".

REFERENCES

[1]Takahisa Yamaguchi (2006) "Consumer behaviors in purchasing financial products and services -perceived risks and information search behaviors-)" edited by Japan Management Diagnosis Association, "Japan management diagnosis association papers 7", Doyukan(in Japanese).pp278-279

[2]Takuo Yoda (2005) "Strategic logic of customer relations" Hakuto shobo(in Japanese).pp156-157

[3]Koji Nishikubo (1999) "Formation factors of customer satisfaction in financial products and management results " "Life insurance management (Seimei hoken keiei)" Japan Institute of Life Insuranc(in Japanese).p87

[4]Heide, Jan B.(1994) "Interorganizational Governance in Marketing Channels" Journal of Marketing, Vol.58 (1).pp.88-92

[5]Schmitt, B.H.(1999) "Experiential Marketing", The Free Press. Translated by Kazue Shimamura and Morikazu Hirose "Experienctial marketing " Diamond Inc., 2000(in Japanese).p261

[6]Tatsuo Watanabe(1996) "Trends and issues of relationship marketing researches - indication of development in Europe-""Distribution Economics"(in Japanese).p126

[7]Hiroshi Ueno and Tetsuo Fujita (2000) "Retail financial institutions of new century" Kindai-Sales-Sha(in Japanese).pp46-47

[8]Koji Mitani (2003) "CRM marketing strategies" Toyo Keizai Inc(in Japanese).p119

[9]Yaichi Aoshima and Toshihiko Katou (2003) "Strategic management" Toyo Keizai Inc(in Japanese).p132

[10]Tomoo Asaoka, Satoshi Ishii and Kenji Koyama (1999) "To CRE from CRM" JMA Management Center(in Japanese).p66

[11]the Center for Financial Industry Information System (2006) "White paper on the financial information systems (FY2007 version)", Zaikei Shouhou-Sha(in Japanese).pp78-79

[12]Masanori Tamura (2002) "Financial retail reconstruction", Chikura Shobo (in Japanese) .p19,216

©ISAROB 2009

An empirical investigation of the determinants of IS outsourcing in Japan

Seigo Matsuno[1], Takao Ito[1]*, Zengyu Xia[2]

[1]*Dept. of Business Administration, Ube National College of Technology, Yamaguchi, 755-8555, Japan*
[2]*School of Management, Wenzhou University, Zhejiang, 325035, China*

Abstract: Two typical different patterns of Information Systems (IS) outsourcing are considered as the most effective approaches in supply chain management. They are conventional outsourcing and quasi-outsourcing. Generally the later is often adopted in large-scale organizations in Japan. In order to design an effective strategy, we should identify the factors which will give important impact on the performance of IS outsourcing. In this paper, we review the relevant literature of IS outsourcing, and propose four hypotheses. We test these four hypotheses by logistic regression analysis based on our original questionnaire survey from Japanese companies in order to find the relationship between the IS outsourcing and its determinants. And finally implications of this study are discussed. Therefore, this paper provides an empirical perspective to identify the determinants of conventional outsourcing versus quasi-outsourcing in Japan.

Keywords: IS outsourcing, outsourcing decision, logistic regression analysis

I. INTRODUCTION

Outsourcing of Information Systems (IS) is considered as one of the most important strategies in corporate management. Recently an increasing large number of companies outsource their information systems. In Japan, many companies try to keep their capital alliance with their external vendors or to dissolve the partnership with their subsidiaries by selling the whole stocks. On the other hand, some subsidiaries are internalized as a functional department of their parent company and/or their group businesses.

Generally, the outsourcing of information systems can be classified into two typical different patterns: conventional outsourcing and quasi-outsourcing. The former involves the transfer of the management and/or daily execution of an entire business function to an external service provider and so on. In addition, the later means to set up their own IS subsidiaries, which is defined as "a firm that is partially owned by the parent, but independently managed" (Ito [1]).

The main contribution of this paper is to provide an empirical perspective to identify the determinants of conventional outsourcing versus quasi-outsourcing in Japan. We propose four hypotheses of IS outsourcing after reviewing the relevant literature, and test these four hypotheses by logistic regression analysis based on our original questionnaire survey from Japanese companies in order to find the relationship between the IS outsourcing and the determinants of IS outsourcing. Finally, implications of this study are discussed.

This paper is organized as follows. In Section 2, we briefly review some previous literature of IS outsourcing. After reviewing relevant literature on IS outsourcing, we propose four hypotheses about factors that influence IS sourcing strategy and test them based on our original survey in Section 3. Section 4 introduces research method. Implications of our results are discussed in Section 5. Finally, in Section 6 we conclude by a summary of this paper.

II. BACKGROUND

In the previous study of IS outsourcing, some research focused on identifying the determinant factors of the two patterns. For instance, Barthelemy and Geyer [2] show that the decision of conventional outsourcing versus quasi-outsourcing is strongly influenced by both internal and external determinants. They focused on testing five hypotheses, which was built based on Transaction Cost Economics (TCE) (Coase [3]). Aubert et al. [4] find IT operation activities, such as asset outsourcing and uncertainty will influence the level of their outsourcing relying on transaction costs and incomplete contracts theories. Other studies show that different effects and problems of IS outsourcing caused from the different patterns. However, many studies found different effects of IS outsourcing between conventional outsourcing and quasi-outsourcing. For instance, the issue is still under discussion whether the effects of "cost reduction" and "improvement of planning and development of IS skill" of these two patterns of outsourcing are different or not while the effect of "using new technology" of conventional outsourcing is higher than that of quasi-outsourcing is overall supported (Negoro and Tamura [5]).

©ISAROB 2009

IS sourcing strategy is considered broadly as the decisions of "make-or-buy" and of making of procurement resources such as functions, technology and personnel for IS activities in this paper. We propose the following four hypotheses on the determinants of conventional outsourcing versus quasi-outsourcing after reviewing the relevant literature on IS outsourcing, and test them using a binomial logistic regression analysis based on our original survey.

III. RESEARCH HYPOTHESES

1. Size of consignor

Since IS subsidiaries basically expect to receive a certain amount of orders from their parent company and/or group businesses which are their consignor, they can be setting up as a spin-off. Therefore, they can enjoy the economies of scale and their role can be switched from shared service to a profit center in the future. Hence, we propose the following hypothesis.

Hypothesis 1. *The larger the size of consignor is, the more quasi-outsourcing is selected.*

2. Category of industry of consignor

There is not enough discussion of whether or not a specific industry classification has a meaningful influence on a necessity of the companies' holding their IS subsidiaries and the IS outsourcing patterns. In general, as Barthelemy and Geyer [2] pointed out, industries such as bank, security, and insurance have "IT-intensive" characteristics so that these financial sectors tend to have quasi-outsourcing, compare to the other industries.

Hypothesis 2. *Industries belonging to financial sectors tend to select quasi-outsourcing.*

3. Asset specificity of IS activity

Asset specificity for IS outsourcing has two aspects; for business of consignor supported by the developed information systems and for technologies which external vendors utilize. If a business that the consignor outsources is unusual, external vendors have to be familiar with the business so that the asset specificity will occur on mainly human resources. If technology used by external vendors is specific, it will be hard to use the information systems for other purposes on the consignor. Investment to these unusual assets causes a fundamental transformation. Therefore, the transaction costs would increase.

Hence, if it is necessary to reduce the risk of opportunism resulted in asset specificity and to restrict the increase of transaction costs, quasi-outsourcing would be selected. This is because the consignor can wield an influence on its IS subsidiaries depending on its investment ratio under the operation of quasi-outsourcing.

Hypothesis 3. *Firms having high asset specificity on IS activity tend to select quasi-outsourcing.*

4. Contribution of IS activity to the core business

According to the resource-based view (RBV) (Barney [6], Bharadwaj [7]), the company tends to select insourcing or quasi-outsourcing by the IS subsidiaries if the company's original resources and unique abilities and/or capabilities on IS activity are regarded as a core competence which can not be imitated and implemented by other companies easily or IS activity has a great contribution to the development of business based on the core competence. Hence, the following hypothesis can be proposed in general.

Hypothesis 4. *The greater IS activity that contributes the core business the company has, the more it tends to select quasi-outsourcing.*

IV. RESEARCH METHOD

1. Data collection

We conducted an original questionnaire survey by mailing to IT representatives from 700 corporations all over Japan chosen at random from July through September 2007 (Matsuno and Taoda [8]). However, industries such as communication, traffic, real estate and information service have not been used for this survey. 195 companies out of 700 sent us their responses back and 181 responses were valid. The valid response rate was 25.9%.

The practice rate of IS outsourcing was 58.0% and 32 companies adopted quasi-outsourcing while 66 companies adopted conventional outsourcing.

2. Construct operationalization

Dependent variable

The dependent variable of logistic regression model is encoded into "0-1" dummy variable depending on whether the 98 companies using IS outsourcing adopt quasi-outsourcing or not. While there are various controlling share, from 100% to under 50%, of investment from consignor to its IS subsidiary on quasi-outsourcing, but only the fact of whether the consignor has a capital relation with the outsourcer or not was used as the criterion to judge on quasi-outsourcing here.

Independent variables

We briefly explain about independent variables, which is essential to test four hypotheses mentioned above.

First, scales to measure the size of consignor is required to test Hypothesis 1. In this case, that would be either market capital, number of employees, or amount of sales, and we chose market capital (logarithmic transformed) as the criterion in this study, without having any sub-scales.

To test Hypothesis 2, we decided to use a scale encoded into a dummy variable depending on the sample companies applicable to "finance/insurance" in the major classification of business type on the classification table determined by Securities Identification Code Committee in Japan.

To test Hypothesis 3 and 4, we use observed variables for each question item of our survey. These measurement data are the ordinal scale if they follow a strict level of measurement, but they are regarded as the interval scale expediently in this analysis. In addition, major questions were chosen to make sub-scales to compound an explanatory variable by referring to the findings obtained from previous studies. Therefore, the process of factor analysis was skipped, and instead of it, we examined the reliability of test scale (Cronbach's α) and confirmed the correlation coefficient between each question item, considering a great influence of a number of items on Cronbach's α.

The sum of each measurement data on the following two questions was used to test Hypothesis 3 (α =.43, r =.27).

(1) Development method of mission critical systems (4-point Likert scale: "use packages only" =1, "use packages mainly, but partially use self-developments" =2, "use packages partially" =3, "use original self-developments wholly" =4).

(2) Familiarity of business knowledge of the company is required to develop and use information systems (6-point Likert scale: from "strongly disagree" =1 to "strongly agree" =6).

The measurement data of the following each 2-question items are used to test Hypothesis 4 (use 6-point Likert scale for each item).

The sum of each measurement data of the following 2-question items were used as a scale to measure the contribution degree of IS activity for the development of core business groups (α =.57, r =.40).

(1) The company's original information system has a big role for a development of both new products and technologies.

(2) Information systems are unified and integral with a performance of the company's core business groups.

In addition, the sum of each measurement data of the following 2-question items is used to examine the influence of burden of IS activity contributing to the core business groups (α =.82, r =.69).

(1) Enormous investment for a development and use of information systems is required to perform core business groups.

(2) Specification change and maintenance/repair of information systems are often required to perform core business groups.

In this way, we have five independent variables to test these four hypotheses mentioned above in this study.

V. RESULTS AND DISCUSSION

Binomial logistic regression analysis was conducted by the forced entry method including all independent variables mentioned above with all of the 98 companies using IS outsourcing. Quasi-outsourcing is treated as dependent variable in this paper. Table 1 shows the results of the analysis.

Table 1. Results of the logistic regression analysis

Valuables	β	S.E.	p- value	odds ratio
Size of consignor	0.66	0.17	0.00	1.94
Category of industry of consignor	-0.20	0.94	0.84	0.82
Asset specificity of IS activity	0.43	0.20	0.04	1.54
Contribution of IS activity to the core business	0.05	0.16	0.74	1.05
Burden degree of IS activity for contributtion to the core business	-0.40	0.16	0.01	0.67
Intercept	-7.18	2.18	0.00	
N	98			
χ^2 with 5 d.f.	29.86		0.00	
-2 log likelihood	93.96			
Error rate	21.4%			

We apply maximum likelihood method to estimate the partial regression coefficient, and use a property of Wald statistic amount's following to χ^2 distribution to test the estimation. Because of Hosmer-Lemeshow test, we got χ^2 = 5.42, df =8, p =.71 as a conformity of predicted value and observed value, and the null hypothesis for a conformity of this model was not rejected.

First, partial regression coefficient on "size of consignor" is positive and it is clear that this has a significant influence on the selection of quasi-outsourcing. This result supports Hypothesis 1. Moreover, adjusted odds ratio is 1.94 times, which is the highest in the independent variables.

Second, "category of industry of consignor" has a negative partial regression coefficient, and this has a different result from Hypothesis 2. In addition, the test result is not meaningful. Therefore, Hypothesis 2 is not supported.

Third, "asset specificity of IS activity" has a significantly positive influence on the selection of quasi-outsourcing, and this result supports Hypothesis 3. It can be considered that selection of quasi-outsourcing is effective in restraining the transaction costs, which resulted in opportunistic behavior by external vendors.

We test Hypothesis 4 lastly. "Contribution of IS activity to the core business" and "burden degree of IS activity for contribution to the core business" are prepared as independent variables. The former variable does not have a meaningful influence on the selection of quasi-outsourcing even though it has a positive partial regression coefficient. On the other hand, the latter variable has a negative partial regression coefficient and a significant negative influence on the selection of quasi- outsourcing. For this reason, Hypothesis 4 should be discussed more carefully.

Based on the RBV, if there is an economic value being hard to be imitated which becomes a resource for IS activity and a source of competitive advantage, or IS activity has integrally unified contribution on the development of core business groups, quasi-outsourcing is more likely to be selected. However, from the result of our analysis, it is hard to say that the quasi-outsourcing is selected when huge amount of investment is required to develop and use the information systems, and also specification change and maintenance/repair of information systems are often required to accomplish their core business groups.

VI. CONCLUSION

In this study, we had a limited analysis based on the data of our survey, but we analyzed the determinants of IS outsourcing and examined a consistency with the major theories such as TCE and the RBV. However, there is still an issue of reliability of the sample data itself used for this analysis and a validity of sub-scales, which construct independent variables.

On recent phenomena, there are many cases that IS activities, assets and personnel which were outsourced in the past are insourced again, especially in finance and insurance industries in the U.S. Also in Japan, the role of IS subsidiaries is changing to work on new management issues such as internal control and information security and so on.

In the future, we will elaborate a method of statistical analysis, including introducing of methods other than logistic regression analysis, and have theoretical and empirical approaches about IS sourcing strategy, especially arrangement of IS subsidiaries belonging to companies which adopt quasi-outsourcing.

REFERENCES

[1] Ito K (1995), Japanese spin-offs: unexpected survival strategies. Strategic Management Journal 16:431-446
[2] Barthelemy J, Geyer D (2005), An empirical investigation of IT outsourcing versus quasi-outsourcing in France and Germany. Information and Management 42(4):533-542
[3] Coase R (1937), The nature of the firm. Economica 4(16):386-405
[4] Aubert B, Rivard S, Patry M (2004), A transaction cost model of IT outsourcing. Information and Management 41(7):921-932
[5] Negoro T, Tamura K (2005), Investigation Report: Feature according to types of IT outsourcing (in Japanese). Research Institute of IT & Management, Waseda University
[6] Barney J (1991), Firm resources and sustained competitive advantage. Journal of Management 17(1):99-120
[7] Bharadwaj A (2000), A resource-based perspective on information technology capability and firm performance: an empirical investigation. MIS Quarterly 24(1):169-196
[8] Matsuno S, Taoda Y (2007), An analysis of factors that influence the arrangement of IS subsidiary (in Japanese). Trans. of the Japan Society Production Management 14(1):55-60

*Takao Ito is visiting research professor of School of Management, New Jersey Institute of Technology in USA from March 29, 2008 to March 28, 2009.

The Fourteenth International Symposium on Artificial Life and Robotics 2009 (AROB 14th '09),
B-Con Plaza, Beppu, Oita, Japan, February 5 - 7, 2009

Study of Genetic Algorithms with Mutation by Markov Chains and Diffusion Model

Yu-an Zhang Makoto Sakamoto Hiroshi Furutani
Faculty of Engineering University of Miyazaki
Miyazaki City 889-2192 Japan

Abstract

This paper treats the performance of Genetics Algorithms (GAs) by means of stochastic models. We consider the success probability S of GA on the multiplicative landscape, and study the effect of mutation on S. The success probability S is defines as the probability of obtaining the optimum solution in the limit of reaching the stationary distribution. If we choose the mutation rate p_m properly, we can greatly increase the success probability S. We discuss the roles of mutation on S within the framework of the stochastic schema theory using the Markov chain and diffusion models.

1 Introduction

In the application of GAs, it is in general very difficult to choose an optimal set of calculation parameters. For example, the performance of GA is influenced by population size(N), string length (ℓ), crossover rate (p_c) and mutation rate (p_m), and these parameters play important roles on the results of optimization. However, to date, the complete theory for parameter selection is still not well established[1, 2]. Therefore, what is the best way for parameter selection becomes more and more important for future study.

The theoretical analysis of GAs with finite N is far more complicated than the deterministic approach assuming infinitely large N. The most representative approach is Markov chain analysis. This model includes selection, mutation and crossover, and can calculate the exact transition matrix. However, it is in general difficult to obtain an analytical expression of Markov process in closed form. Furthermore, the dimension of the transition matrix increases exponentially with string length ℓ and population size N. This makes numerical simulations almost impossible for realistic values of ℓ and N. In population genetics, researchers also encountered this type of difficulties in treating the evolution of a finite population by Markov chain model. They found another approach to get out of it, the diffusion model.

Generally speaking, the success probability may increase under the condition of finite mutation [3, 4]. In this study, GA on the multiplicative landscape was performed to make comparison and analysis on relationship among success probability, string length and mutation rate in theories and experiments. The diffusion model was also used to investigate the distribution of the first order schema.

2 Models and Methods

In this paper, we studied the genetic algorithm on the multiplicative landscape with selection, crossover and mutation by markov chains, and among them mutation is very carefully investigated. We used the fitness proportionate selection and uniform crossover.

An individual is represented by a binary string of fixed length ℓ, and the genotype is given by the integer i with $i = 0, \ldots, n-1, n = 2^l$. In our notation $i(k)$ is the kth bit of integer i. We use the frequency $N_i(t)$ and relative frequency $x_i(t)$ of the ith genotype at generation t. The population size N is assumed to be time-independent, and

$$N = \sum_{i=0}^{n-1} N_i(t),$$

The relative frequency $x_i(t)$ is defined by

$$x_i(t) = \frac{N_i(t)}{\sum_{i=0}^{n-1} N_i(t)}.$$

If a population is in linkage equilibrium, the distribution of individuals depends only on the frequencies of the first order schemata. Therefore, the relative frequency x_i is represented by

$$x_i = \prod_{k=1}^{\ell} h_{i(k)}, \tag{1}$$

©ISAROB 2009

where $h_{i(k)}$ is the frequency of the first order schema corresponding to $i(k)$. This decomposition enables us to treat the population by using the schema theory of exact form [5].

2.1 Deterministic Model

We consider the evolution of the GA on the multiplicative landscape in the deterministic model. The fitness function has a multiplicative form

$$f_i = \prod_{k=1}^{\ell} \{1 + s\, i(k)\}, \tag{2}$$

where s is a parameter of selection strength. The theory of the infinite population model on the multiplicative landscape tells that the assumption of linkage equilibrium holds at all generations if the initial state is at linkage equilibrium. Thus the evolution process of the first order schema $i(k) = 1$ isgiven by the following difference equation

$$h_1(t+1) = \frac{(1+s)\, h_1(t)}{1 + s\, h_1(t)}. \tag{3}$$

The effect of mutation on the first order schemata is give by

$$h_1'(t+1) = (1-p_m)\, h_1(t+1) + p_m h_0(t+1),$$
$$h_0'(t+1) = (1-p_m)\, h_0(t+1) + p_m h_1(t+1).$$

2.2 Markov Chains

We suppose that the population is of total size N and let the two alleles be A and a. We assume that the A genes have selective advantage $1+s$ while a genes have selective advantage unity. The number of A genes in any generation is a Markovian variable with the transition matrix P give by

$$p_{ij} = P(j|i) = \binom{N}{j} a^j \, (1-a)^{N-j}, \tag{4}$$

Where

$$a = \frac{(1+s)\, i}{(1+s)\, i + N - i}. \tag{5}$$

The matrix element p_{ij} is the probability that the number of A individuals selected at the $t+1$ th generation is j, given that the number of A individuals in the t th generation is i. The evolution of GA population is given by

$$\pi_j(t+1) = \sum_{i=0}^{N} \pi_i(t)\, p_{ij}, \tag{6}$$

where π_i is the probability that there are i A individuals in the population. In general, it is very difficult to solve this equation analytically. The states $i = 0$ and $i = N$ are absorbing states of Markov chain, and the population goes to these absorbing states as $t \to \infty$.

To take into account the effect of mutation with mutation rate p_m, we replace a by b in equation (4)

$$b = (1 - 2p_m) a + p_m, \tag{7}$$

and we have

$$P(j|i) = \binom{N}{j} b^j \, (1-b)^{N-j}. \tag{8}$$

2.3 Diffusion Equations

In the field of theoretical population genetics, the evolution equation is solved by the use of the diffusion model, where the Kolmogorov equations play a fundamental role. The Wright-Fisher model can be approximated by diffusion equations if N is not too small. The diffusion equation derived from equation (4) is

$$\frac{\partial \psi(p,t)}{\partial t} = \frac{V(p)}{2} \frac{\partial^2 \psi(p,t)}{\partial p^2} + M(p) \frac{\partial \psi(p,t)}{\partial p}, \tag{9}$$

where p is the initial value of the relative frequency $y = i/N$ at time $t = 0$, and

$$V(p) = \frac{p(1-p)}{N}, \quad M(p) = s\,p(1-p). \tag{10}$$

We define the ultimate fixation probability by $u(p) = \lim_{t\to\infty} \psi(p,t)$, and the solution is

$$u(p) = \frac{1 - \exp(-2Nsp)}{1 - \exp(-2Ns)}. \tag{11}$$

We also define the ultimate extinction probability by $v(p) = 1 - u(p)$.

We define the success probability S that there is at least one optimum individual in the stationary state. This probability is approximately given by $u(p)$

$$S = u(p)^{\ell} = (1 - v(p))^{\ell}. \tag{12}$$

3 Results

We performed numerical calculations of GA with roulette wheel selection on the multiplicative landscape. The results were compared with the deterministic and stochastic models of the first order schema. We

©ISAROB 2009

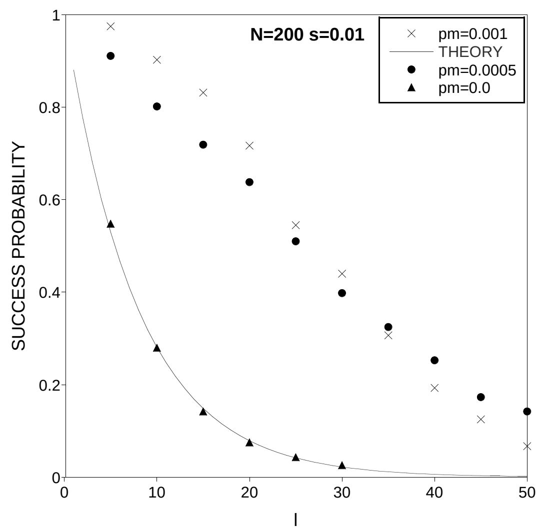

Figure 1: Success probability S with $s = 0.01$ and $p_c = 1.0$. Mutation rate are $p_m = 0.001, 0.0005$ and 0. The horizontal axis represents string length (ℓ).

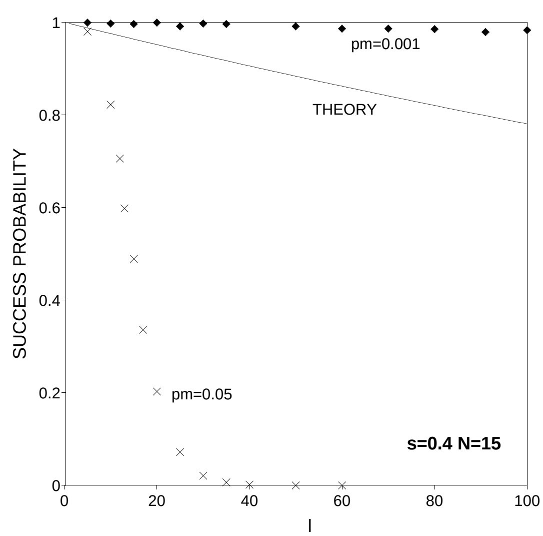

Figure 2: Success probability S with $s = 0.4$ and $p_c = 1.0$. Mutation rate are $p_m = 0.001$ and 0.05. The horizontal axis represents string length (ℓ).

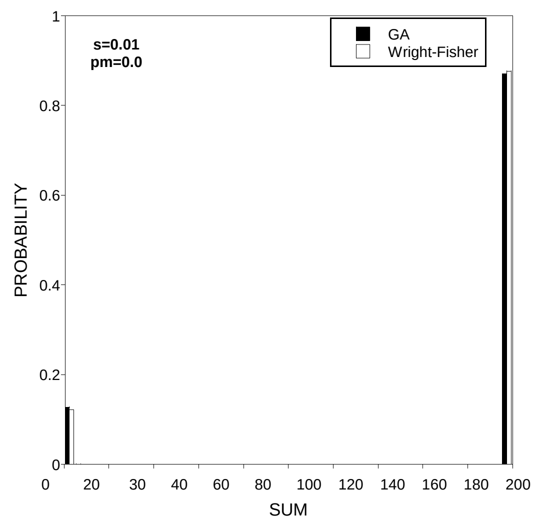

Figure 3: The distribution of the first order schemata with $s = 0.01$,$N = 200$ and $p_m = 0.0$.

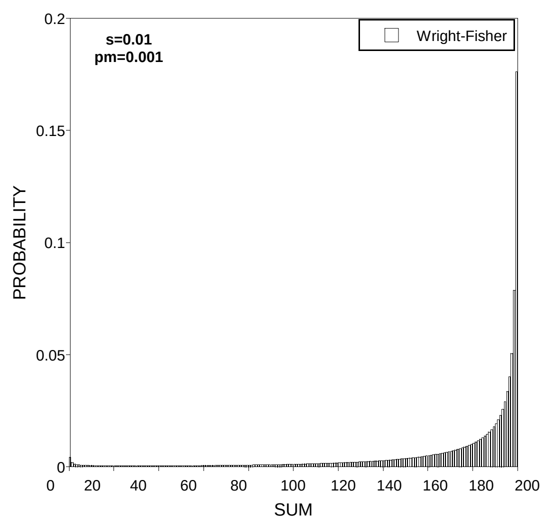

Figure 4: The distribution of the first order schemata with $s = 0.01$,$N = 200$ and $p_m = 0.001$.

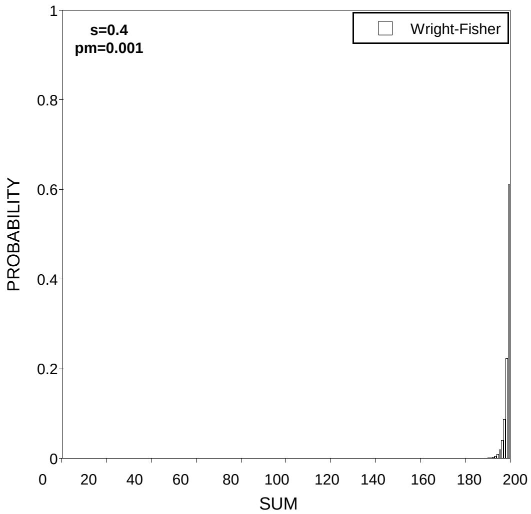

Figure 5: The distribution of the first order schemata with $s = 0.4$,$N = 200$ and $p_m = 0.001$.

compared results of selection with $s = 0.01$ and $s = 0.4$. Crossover was done with the uniform crossover of crossover rate p_c. We used mutation rates p_m from 0 to 0.05 and compared their results. The initial value of the first order schema was $h_1 = 1/2$. The calculations were performed repeatedly, and results were averaged over 1000 runs.

Figure 1 shows success probability S with $s = 0.01$ and $p_c = 1.0$. Mutation rate are $p_m = 0.001, 0.0005$ and 0. The horizontal axis represents string length (ℓ). The solid line represents the prediction of diffusion model given by equation (12). It shows that the success probability is improved by mutation with weak selection ($s = 0.01$).

Figure 2 shows success probability S with $s = 0.4$ and $p_c = 1.0$. Mutation rate are $p_m = 0.001$ and 0.05. It also illustrates the relationship between string length (ℓ) and success probability (S), and shows that the success probability improves according to moderate mutation rate $p_m = 0.001$ and $s = 0.4$, but too strong mutation may destroy the optimum solution.

Figures 3 , 4 and 5 show the probability distribution of the first-order schemata. In these figures, 0 value in the horizontal axis is the ultimate extinction probability $v(p)$, and value at N is the ultimate fixation probability $u(p)$. The $v(p)$ is the probability when all the first order bit value is 0 , and $u(p)$ is the probability when all the first order bit value is 1. We find the Wright-Fisher model of equation (8) well reproduces the distribution of the first-order schemata. As can be seen from graphs, the ultimate extinction probability $v(p)$ and ultimate fixation probability $u(p)$ are on the decline, and the decline of $v(p)$ is stronger than $u(p)$.

4 Summary

In this study, the relationship between mutation rate and success probability is studied. The results reveal that the success probability is improved by mutation with weak selection $s = 0.01$, and the success probability improves according to moderate mutation rate $p_m = 0.001$ and $s = 0.4$, but too strong mutation may destroy the optimum solution. The results also show that ultimate extinction probability $v(p)$ and ultimate fixation probability $u(p)$ are on the decline, and the decline of $v(p)$ is stronger than $u(p)$, so that the success probability S increases. Therefore, the good effect on success probability is obtained by adding the properly selected mutation.

References

[1] H. Furutani, T. Fujimaru, Y. Zhang and M. Sakamoto: Effects of Population Size on Computational Performance of Genetic Algorithm on Multiplicative Landscape, *Proceedings of Third International Conference on Natural Computation*, Vol.3, 488–493 (2007).

[2] H. Furutani, S. Katayama, M. Sakamoto and M. Ito: Stochastic Analysis of Schema Distribution in a Multiplicative Landscape, *Artificial Life and Robotics*, **11**, (2007) 101–104.

[3] Y. Zhang, M.Sakamoto, H. Furutani: Effects of Population Size and Mutation Rate on Results of Genetic Algorithm, *Proceedings of Third International Conference on Natural Computation*, Vol.3, (2008) 70–75.

[4] Y. Zhang, M.Sakamoto, H. Furutani: Effects of Population Size on Performance of Genetic Algorithms and Roles of Crossover and Mutation, *The Thirteenth International Symposium on Artificial Life and Robotics (AROB 13th'08)*, (2008) 861–864 .

[5] H. Furutani: Schema Analysis of OneMax Problem, *Foundations of Genetic Algorithms* 7, Morgan Kaufmann, San Francisco, (2003), 9–26.

©ISAROB 2009

The Fourteenth International Symposium on Artificial Life and Robotics 2009 (AROB 14th '09),
B-Con Plaza, Beppu, Oita, Japan, February 5 - 7, 2009

A Visual-inspection System Using Self-organizing Map

Ikeda Keiko, Yasunaga Moritoshi, Yamaguchi Yoshiki, Yamamoto Yorihisa, Yoshihara Ikuo
University of Tsukuba, Graduate School of Systems and Information Engineering
‡Yamamoto System Design Corp.
§Faculty of Engineering, University of Miyazaki
Tsukuba, Ibaraki 305-8573, JAPAN
ikeda@islab.cs.tsukuba.ac.jp

Abstract

The visual inspection task is generally difficult for a machine, and is carried out by examiners usually. The task is desired to be mechanized and automated because it often causes bottleneck of production processes.

In order to satisfy the requirement, we study an image recognition using the self-organizing map (SOM) for visual inspection equipments. The SOM maps high-dimensional input data onto a low-dimensional (typically two-dimensional) space. And the data are clustered based on their similarity. On the map, input data is thus classi ed based on its position of the mapped data. The reason we use the SOM for inspections is that it can visualize the results of clustering. With the visualized results, the user can understand data classi cation intuitively.

We have implemented a visual-inspection system based on the SOM and tested it using actual product images. In the implementation, we preprocess the images to decrease data size before input them into the SOM because large input data size causes poor clustering. The image data is preprocessed in three steps, that is, binarization, 2D-FFT and converting to one-dimensional data.

We rst considered only one inspection point, and obtained high recognition accuracy of 98%. We second considered two inspection points, and also obtained high recognition accuracy of 96%.

Keywords: Image Recognition, Self-Organizing Map, Visual Inspection, FFT

1 Introduction

Many visual inspection tasks are carried out by examiners, because the task is generally difficult for a machine. As the examiners check products by hand, the task often causes bottleneck of production processes. And the task has serious problems that training of examiners and securing of manpower of the task are indispensable. It also causes another problem that the results of inspection di er from person to person. Therefore, the visual inspection is desired to be mechanized and automated.

In order to satisfy the requirement, we study image recognition using the SOM (Self-Organizing Map) for visual inspection. The SOM is one of neural networks, and is used as a clustering method by unsupervised learning and a data visualization method by dimensional reduction. We use the SOM to cluster the image data of test object products. The reason we use the SOM is that it can visualize the results of clustering. With the visualized results, the user can understand data classi cation intuitively.

2 Self-Organizing Map

The Self-Organizing Map (SOM) is proposed by Kohonen [1]. Its feature is mapping high-dimensional input data onto a low-dimensional (typically two-dimensional map) space, where the map consists of grid nodes usually. Each node has n-dimensional data vector called the weight vector, $m_{i,j}$. The input data x is also n-dimensional vector data. The values of all weight vectors are randomly initialized. The learning of the map is performed by repeating the following steps.

1. One input data is fed into the map, and its Euclidean distances to all weight vectors are computed.
2. The node with the smallest distance to the input data vector gets selected as the winner node.
3. The neighbor nodes of the winner node are updated as follows:

$$m_{i,j} := m_{i,j} + \quad (i,j)\{x \quad m_{i,j}\}$$

©ISAROB 2009

where hc(x) is called neighborhood function. As the result of the updating, the distance between weight vectors of updated nodes and input vector is smaller.

Repeating the above steps for di erent input data makes the data clusters on the map. On the map, input data is classi ed based on the position of the mapped data. In other words, similar data are put close to each other on the map, and di erent data are put far separately.

After learning of the map, test object data are input into the map, and each datum's cluster is judged. The SOM also decides the winner node for the test object data. On the map the cluster which this winner node belong to is the one which the test object data belong to. The boundary of each cluster is shown on the map, but the SOM doesn't de ne the boundary clearly. The boundary is able to be de ned arbitrarily by the user.

3 Test Object Products

Fig.1 shows the product we use as the target for our visual-inspection system. It is a dental injection needle made from plastic and is currently examined by examiners. The sample products are provided from the BETHEL Inc. in Japan. In the actually examination, some inspection points are considered, but in this paper, we focus on two inspection points, that is, burr and foreign object. Fig.2 shows the closeup of the acceptable product (a) and the disquali ed ones (b), (c). Fig.2 (b) shows the disquali ed product with a burr, and (c) shows the one with foreign object.

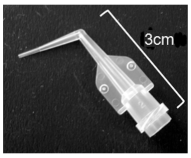

Figure 1: Objective Product (Dental Injection Needle)

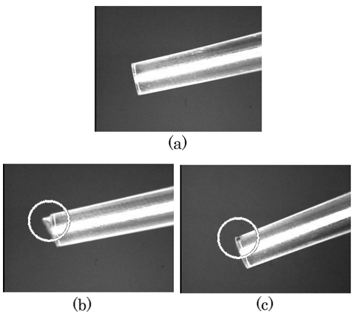

Figure 2: The Acceptable Product and Disquali ed Products

4 Preprocessing

We basically use the image data as the input into the SOM. But the size of the original image is too large. Large input data size causes huge amounts of calculation time and poor clustering in the SOM. We thus decrease the images data size. (Fig.3)

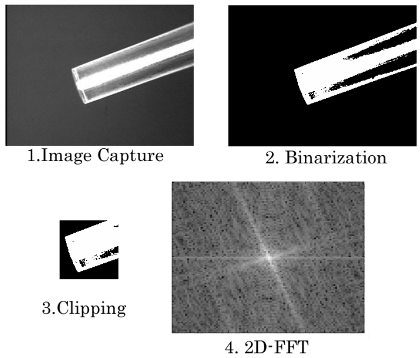

Figure 3: Preprocessing

First, we binarize the closeup image of the product. Second, the image of the point of the product is clipped to 100x100 pixels. Third, the image is transformed into one in the frequency space by 2D-FFT. It is expected that the transformation extracts the feature more e ectively. Finally, the data is converted to one-dimensional data in frequency space. The frequency data are concentrically averaged as shown in Fig.4 [2]. As a result, the image data are converted 70 dimension data.

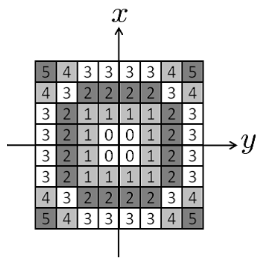

Figure 4: Concentrically Average

5 Experiments And Results

5.1 Experimentation Environment

We have implemented the SOM using the C-language. The map consists of 100x100 nodes. The map has the torus structure to eliminate the edge effect of the map [3]. The sample products that have been previously examined by examiners are provided for the test. We have used cross validation method to evaluate recognition rate. The map rst trained by the learning data, and after training, the test object data is examined by inputting it into the learned map. In one learning cycle of the SOM, all learning data are input to the map, and the learning is repeated 100 times.

5.1.1 One Inspection Point Experiment

We rst consider only one inspection point that is burr at the needle point. 100 sample data has used, where 50 data are acceptable products data and 50 data are disquali ed ones with burr. We have evaluated the recognition accuracy 5 times using cross validation method as shown Table 1, and averaged the results.

Table 1: The Cross Validation Method

# of Test	Learning Data Sets	Test Data Sets
1	ABCD A'B'C'D'	E E'
2	ABCE A'B'C'E'	D D'
3	ABDE A'B'E'E'	C C'
4	ACDE A'C'D'E'	B B'
5	BCDE B'C'D'E'	A A'

50 acceptable data and 50 disquali ed data are divided into 5 sets of A,B,C,D,E and A',B',C',D',E' , respectively.

The result of the examination is shown in Table 2, and resultant maps are shown in Figs 5 and 6. In Figs 5 and 6, the acceptable nodes, whose weight vector is similar to the acceptable data, are shaded. When a test object is input into the learned map, the good judgment is that its winner node is selected from the group of right nodes [4]. On the map, acceptable data nodes and burr data nodes are clustered each other.

As shown Table 2, we have obtained high recognition accuracy of 98 % for the disquali ed data.

Table 2: The Recognition accuracy (One Inspection Point)

Acceptable Data	100%
Disquali ed Data (Burr)	98%

5.2 Two Inspection Points Experiments

We consider two inspection points that are burr at the needle point and foreign object in the needle. 40 disquali ed products data with foreign object are added to the sample data. These data are generated from the acceptable images arti cially. We have tested the map using the same method as the one inspection point experiment above.

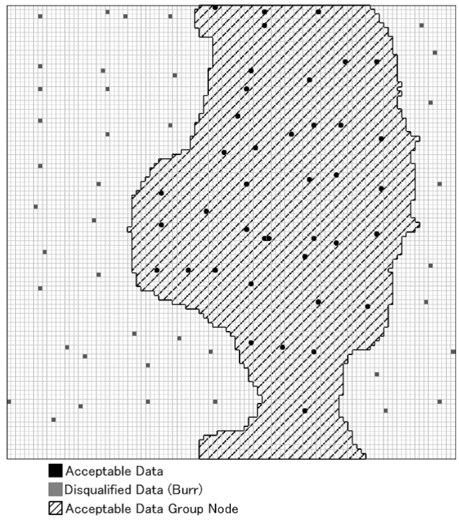

Figure 5: The Learned Map (One Inspection Point)

The result is shown in Table 3, and resultant maps are shown in Figs 7 and 8. In Figs 7 and 8, nodes to the disquali ed data with foreign object are dotted. On the map, burr and foreign object data nodes are clustered each other as well as acceptable data nodes.

As shown Table 3, we have also obtained high recognition accuracy of 96% for the disquali ed data.

Table 3: The Recognition accuracy (Two Inspection Points)

Acceptable Data	100%
Disquali ed Data (Burr)	96%
Disquali ed Data (foreign object)	100%

5.3 Discussion

One of the goals of the visual inspection is to screen the disquali ed products completely. To achieve the goal, we newly propose the method in which the user can arbitrarily move the boundary of acceptable data and disquali ed data.

On the map, the boundary of cluster is not shown, and it can be de ned arbitrarily and interactively. Thus the user can de ne the boundary that picks out only acceptable data, and check the data easily as expert examiners.

6 Conclusion and Further Work

In this paper, we proposed the visual inspection system using the Self-Organizing Map. We have implemented the map by the C-language and tested it using actual products. As the result, we have visualized the

©ISAROB 2009

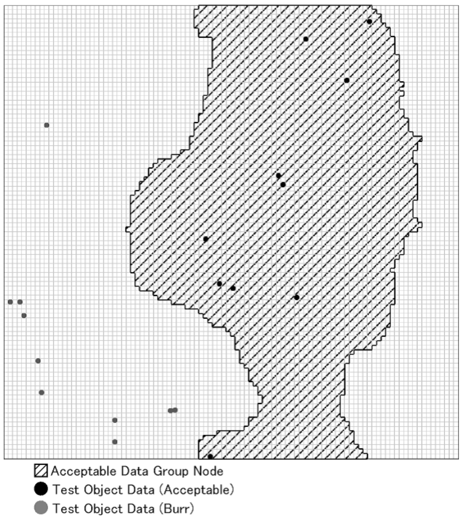

Figure 6: The Result of Inputting Test Object Data (One Inspection Point)

clustering results, and obtained high recognition accuracy.

In the further work, we are planning to test using more sample data. The recognition accuracy using more data must be measured for the practical use. And we are going to implement the function that the user can arbitrarily de ne the boundary on the map.

References

[1] Teuvo Kohonen, "The self-organizing map," *Neurocomputing*,Vol. 21, pp. 1-6, 1998.

[2] Onishi Takahisa, "Improvement of the feature extraction using 2D-FFT on Dried Sardine Selection System (in Japanese)", Kochi University of Technology Undergraduate Thesis, 2006.

[3] Ito Masahiro, Miyoshi Tsutomu, Masuyama Hiroshi, "The characteristecs of the torus Self Organizing Map (in Japanese)," *16th Fuzzy System Symposium*, pp. 373-374, 2000.

[4] Ikeda Kazutaka, Hashimoto Yoshihito, Ishiguro Takehiro, "Automated Sensory Inspection Based on Vibration and Acoustic Information (in Japanese)", *Matsushita Electric Works Technical Report*, Vol. 54, pp. 42-48, 2006.

[5] Ikeda Keiko, Yasunaga Moritoshi, Yamaguchi Yoshiki, Yamamoto Yorihisa, "A Study on Image Recognition by Self-Organizing map for Visual Inspection Equipment (in Japanese)," *Technicak Report of IEICE* ,Vol. FIIS08, No.235, 2008.

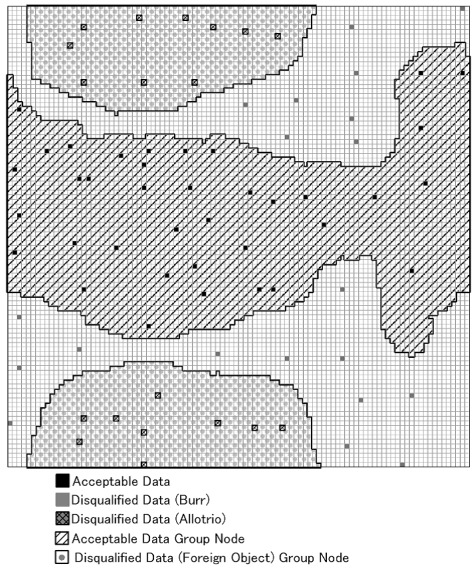

Figure 7: The Learned Map (Two Inspection Points)

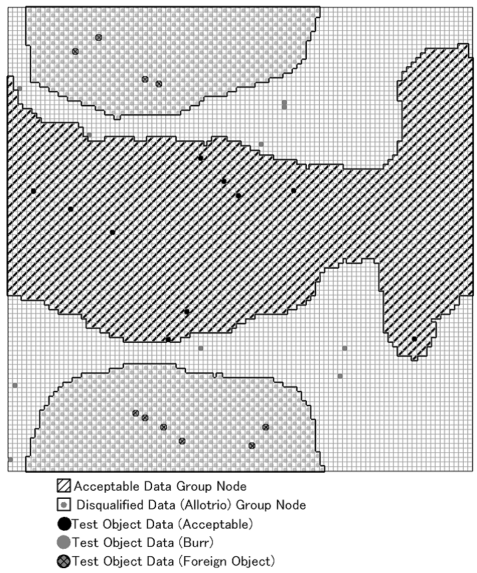

Figure 8: The Result of Inputting Test Object Data (Two Inspection Points)

Development of Physiological Activity Estimation Method of Foods Using Amplitude Extended Neural Networks

Toru KUNO[1)], Mayumi KAMIGUCHI[1)], Kunihito YAMAMORI[2)], Ikuo YOSHIHARA[2)], Kiyoko NAGAHAMA[2)]

[1)]1-1, Gakuen Kibanadai-nishi, Miyazaki, 889-2192, Japan, Graduate School of Engineering, University of Miyazaki
[2)]1-1, Gakuen Kibanadai-nishi, Miyazaki, 889-2192 , Japan, University of Miyazaki
[3)] 16500-2, Higashi Kami-Naka, Sadowara, 880-0303, Japan, Miyazaki Prefectural Industrial Foundation

(Tel : +81 985 58 7589; Fax : +81 985 58 7589)
(Email address {kuno, yamamori}@taurus.cs.miyazaki-u.ac.jp)

Abstract: We developed a system to estimate physiological activities of foods from protein expression levels using artificial neural networks (ANNs). Since protein expression levels and physiological activities are measured in multiple times for a constituent, we employ a simple regression analysis to find appropriate correspondence between physiological activities and protein expression levels. The range of physiological activities are from 0 to Z (Z >1), they cannot directly use training signals of ANNs because the output of a neuron is limited from zero to one. To tackle this problem, we introduce two parameters K and l to the activation function of our system like as ($\boldsymbol{f(x)} = \frac{\boldsymbol{K}}{\boldsymbol{1+e^{-lx}}}$). Our system is based on three-layer ANN and back-propagation algorithm is employed as training algorithm. Experimental results showed that our system can estimate more accurate than that of ANNs with normalized training samples for antioxidant stress activity.

Keywords: physiological activity, protein expression level, functional foods, artificial neural networks

I. INTRODUCTION

Since the third function of foods which is effect to physiological activities for human is useful to keep health and prevent diseases, many people pay attention to some foods that have relatively large effect [1]. A way to evaluate the function of foods is direct measurement of their physiological activities. However, it is difficult because there are many kinds of foods in the world, and their physiological activities are also different in seasons and places. The other way to evaluate the function of foods is estimation from their constituents, but it is also difficult because it needs to be clear the complicated interactions between these constituents and human. So a new method to estimate physiological activities of foods is required.

Some researchers proposed methods to estimate physiological activities by artificial neural networks (ANNs) [2]-[5]. For example, Tsukuda *et al*. [2] showed that artificial neural networks (ANNs) could achieve good accuracy to estimate some physiological activities. In this research, ANNs train the relations between the protein expression levels and the physiological activities when constituents of foods are poured for human cells. After training process, the protein expression levels by extraction of foods are presented to ANNs.

ANNs need many appropriate training samples to make a better model equation. Protein expression levels and physiological activities are measured in multiple times for a constituent. However, previous works took an average of measured values, then these average values were composed to a training sample. This operation decreases the total number of training samples. To solve is problem, we utilize all measured values to make enough numbers of training samples. Because the physiological activities and the protein expression levels were independently measured for a constituent, it is needed to find an appropriate correspondence between them. To find an appropriate correspondence, we employ simple regression analysis. The correspondence with the smallest p-value is selected from all the available correspondences.

The range of physiological activities as the training signals are from 0 to Z (Z > 1), physiological activities are usually normalized because the output of neurons is limited from zero to one. At that time, acceptable error will become too small to terminate training process by normalization. To solve this problem, we use amplitude extended neural networks (AENNs). AENNs have two parameters K and l in the activation function of our system like as $f(x) = \frac{K}{1+e^{-lx}}$. The K adjusts amplitude of sigmoid function and the l adjusts slope of sigmoid function. By using the sigmoid function with these parameters, it does not need to normalize training signals.

©ISAROB 2009

Table 1 A part of constituents and concentrations for training samples.

		concentrations(μM)		
aliphatic acid	RosmarinicAcid	5	15	50
	LipoicAcid	100	300	1000
	ArachidonicAcid	15	45	100
	CLA12C	1	3	10
	CLA9C	10	30	100
…				
anti-virus	IFN	100	300	1000
	Ribavirin	2	10	30

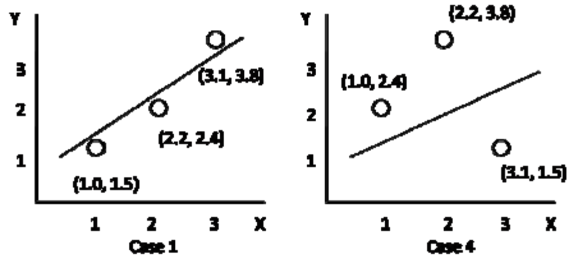

Fig.1 Correspondence between the protein expression levels and the physiological activities.

II. PREPROCESSING

1. Constituents for training sample

We use thirty kinds of constituents of foods and medicines, a part of them is shown in Table 1. The constituents and medicines are poured over HepG2 cells in three concentration levels, then protein expression levels and physiological activities are measured, respectively. The protein expression levels and physiological activities are measured in six times for each constituent. So the number of training sample is 540($=30\times3\times6$). The kinds of proteins are as follows; Thioredoxin, Survivin, HSP70, XIAP, FADD, TXNRD1, HSP90, MxA, tNOX, NQO1, ERK2, p53 and Bcl2. We adopt the following three physiological activities; anti-proliferative activity, anti-inflammatory activity and anti-oxidant stress activity.

2. Correspondence of protein expression levels with physiological activities

Since the protein expression levels and the physiological activities are respectively measured, it is needed to find an appropriate correspondence between the protein expression levels and the physiological activities even if they are observed by the same constituent and the same concentration. For this correspondence, we use simple regression analysis, whose concept is illustrated in Fig.1. The X-axis and

Table 2 Correspondence and p-value.

case	(X_1, Y_1)	(X_2, Y_2)	(X_3, Y_3)	p-value
1	(1.0, 1.5)	(2.2, 2.4)	(3.1, 3.8)	0.13
2	(1.0, 1.5)	(2.2, 3.8)	(3.1, 2.4)	0.69
3	(1.0, 2.4)	(2.2, 1.5)	(3.1, 3.8)	0.64
4	(1.0, 2.4)	(2.2, 3.8)	(3.1, 1.5)	0.80
5	(1.0, 3.8)	(2.2, 1.5)	(3.1, 2.4)	0.53
6	(1.0, 3.8)	(2.2, 2.4)	(3.1, 1.5)	0.03

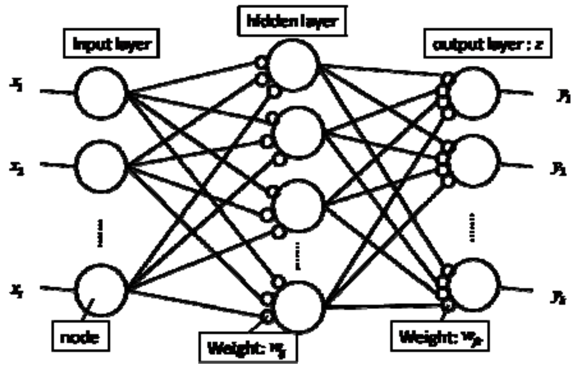

Fig.2 The structure of ANNs.

the Y-axis in Fig.1 denote the protein expression levels and the physiological activities, respectively.

Here explains how to correspond between protein expression levels and physiological activities by simple regression analysis. Let the protein expression levels be measured as {1.0, 2.2, 3.1}, and let the physiological activities be measured as {1.5, 2.4, 3.8}. In this case, six combinations of correspondence are available as shown in Table 2. We execute single regression analysis for all combinations. In Fig.1 the left shows the case 1 and the right shows the case 4. We select the case with minimum *p*-value among all combinations, then case 6 is selected. The *p*-value expresses probability that the protein expression levels have no relation with the physiological activities.

III. AMPLITUDE EXTENDED NEURAL NETWORKS

Fig.2 shows a sample of three layers ANNs [6]. The ANNs has an input layer, a hidden layer and an output layer. A node of the input layer connects all nodes in the hidden layer, and a node of the hidden layer connects all nodes in the output layer. Equation (1) and Equation (2) express the input and output in the neuron *j* on the layer *L*, respectively.

$$x_j^L = \sum_i O_i^{L-1} w_{L-1,i}^{L,j}, \tag{1}$$

$$O_j^L = f(x_j^L), \tag{2}$$

where $w_{L-1,i}^{L,j}$ denotes the weight from the neuron *i* on the layer *L*-1 to the neuron *j* on the layer *L*. Sigmoid function described in Equation (3) is usually used as activation function,

©ISAROB 2009

Table 3 Training parameters.

	K	l	Physiological activity		Accept error	η	ε	Max iteration	Hidden neurons
			Min.	Max.					
anti-proliferative activity	2.0	0.8	0.30	1.14	0.06	0.4	0.7	20000	6
anti-inflammatory activity	2.0	0.8	0.06	1.59	0.14				
antioxidant stress activity	2.5	0.2	0.01	2.68	0.2				

$$f(x) = \frac{1}{1+e^{-x}}. \quad (3)$$

Since the range of physiological activities as the training signals are from zero to Z (Z >1), the training signals are usually divided by the maximum physiological activity for normalization. At that time acceptable error is also divided, it will become too small to terminate training process. To avoid normalization of physiological activities, we employed two parameters K and l in sigmoid function,

$$f(x) = \frac{K}{1+e^{-lx}}. \quad (4)$$

K adjusts the amplitude of sigmoid function and the l adjusts the slope of sigmoid function. By using sigmoid function with these parameters, it does not need to normalize training signals.

The error E is defined as follow,

$$E(p) = \frac{1}{2}\left(T(p) - O_i^L(p)\right)^2, \quad (5)$$

for the training sample p. To minimize $E(p)$, we obtain the following rule derived from $\frac{\partial \mathrm{E}}{\partial \mathrm{w}_{\mathrm{L-1,i}}^{\mathrm{L,j}}} = 0$.

$$\Delta w_{L-1,i}^{L,j}(p) = \eta \cdot f'(\mathrm{x}_\mathrm{j}^\mathrm{L}(p)) \cdot \left(T(p) - O_i^L(p)\right) + \varepsilon \Delta w_{L-1,i}^{L,j}(p-1), \quad (6)$$

$$f'(\mathrm{x}_\mathrm{j}^\mathrm{L}(p)) = \frac{l \cdot K \cdot e^{-lx_j^L(p)}}{(1+e^{-lx_j^L(p)})^2}, \quad (7)$$

where η is rate parameter and ε is inertia parameter. The error of hidden neurons is defined by Equation (8),

$$\delta_\mathrm{i}^{\mathrm{L-1}} = \sum_\mathrm{j} \mathrm{w}_{\mathrm{L-1,i}}^{\mathrm{L,j}}\, \delta_\mathrm{j}^\mathrm{L}(p), \quad (8)$$

$$\delta_\mathrm{j}^\mathrm{L}(p) = f'\left(\mathrm{x}_\mathrm{j}^\mathrm{L}(p)\right) \cdot \left(T(p) - O_i^L(p)\right), \quad (9)$$

where z is the index of the output layer. The weight update rule is obtained as Equation (10).

$$w_{L-1,i}^{L,j}(p+1) = w_{L-1,i}^{L,j}(p) + \Delta w_{L-1,i}^{L,j}(p). \quad (10)$$

IV. EXPERIMENTS AND DISCUSSIONS

We compared estimation accuracy between convention ANNs with normalized samples and our AENNs without normalization. The parameters of experiments are as follows;

- Network size : 13-6-1 (13 input neurons, 6 hidden neurons, 1 output neuron)
- runs : 10 run
- number of test sample : 72
  - 4 extracts
    - extract of blueberry leaf by boiled water
    - extract of blueberry leaf by ethanol
    - extract of onion leaf by boiled water
    - extract of tea leaf by boiled water
  - 3 concentrations
  - 6 samples

We change K from 1.0 to 3.0 with 0.5 step and we also change l from 0.1 to 1.0 with 0.2 step. These K and l were decided by preprimary experiments. The conditions of experiments are summarized in Table 3.

A. Anti-proliferative activity

Fig.3 shows the average estimated value of anti-proliferativity activity. ANN can estimate the anti-proliferativity activity 4 samples within acceptable error for all 12 samples (4/12). AENNs can estimate the anti-proliferativity activity 3 samples within acceptable error for all 12 samples (3/12). The result by ANNs without averaging was 39/72 and that of AENNs was 36/72.This results showed that ANNs and AENNs could estimate activity with the almost same accuracy.

B. Anti-inflammatory activity

Fig.4 shows the average estimated value of anti-inflammatory activity. ANN can estimate 8/12 and AENNs can estimate 7/12 for anti- inflammatory activity. The result by ANN without averaging was 43/72 and that of AENNs was 40/72. ANN and AENNs could estimate activity with the almost same accuracy.

C. Antioxidant activity

Fig.5 shows the average estimated value of antioxidant stress activity. ANN can estimate 8/12 and

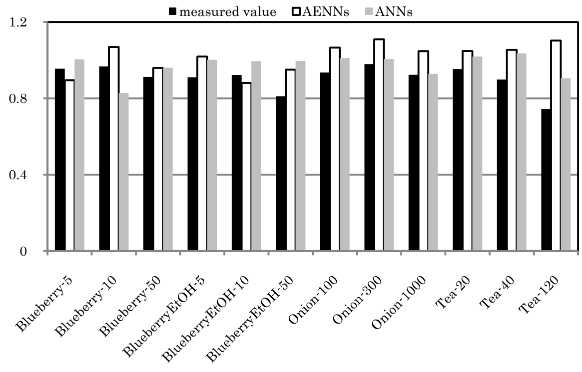

Fig.3 Estimated values of anti-proliferativity activity

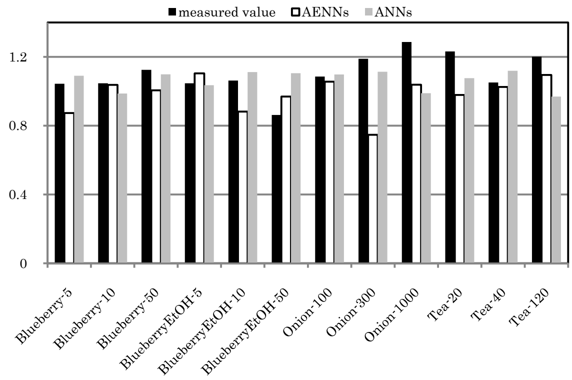

Fig.4 Estimated values of anti-inflammatory activity

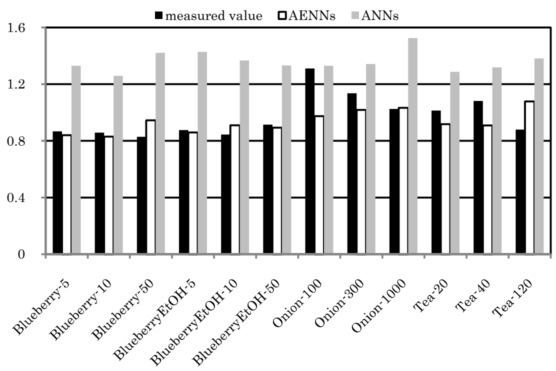

Fig.5 Estimated values of antioxidant stress activity

AENNs can estimate 7/12 for anti- inflammatory activity. The result by ANN without averaging was 15/72 and that of AENNs was 46/72. The error of conventional ANN is large, because the error is multiplied by the maximum value of the training samples as the inverted normalization process on other hand, out AENNs does not need the inverted normalization process, so it can be said that the AENNs are suitable for estimation with large physiological activities.

V. CONCLUSIONS

We develop a physiological activity estimation system from protein expression levels using amplitude extended neural networks. Since protein expression levels and physiological activities are separately measured, we employ simple regression analysis for finding an appropriate correspondence between protein expression levels and physiological activities. And AENNs adjust the amplitude of sigmoid function to avoid normalization of physiological activities, it is suitable to estimate some kinds of large physiological activities. The experimental result showed that our system could estimate antioxidant stress activity more accurate than conventional ANNs with normalization.

It remains to adjust the parameters K and l automatically through training process as a future work.

ACKNOWLEDGEMENT

A part of this research is supported by JST Grant-In-Aid of Miyazaki Prefecture Collaboration of Regional Entities for the Advancement of Technological Excellence.

REFERENCES

[1] S. Arai, K. Abe, K. Kanazawa, T. Yoshikawa, S. Watanabe (2007), Cyclopedia of Functional Foods (in Japanese), Asakura Publishing Co., Ltd.

[2] K. Yamamori, S. Tsukuda, I. Yoshihara (2007), Estimation of Physiology Activity in Foods by Neural Network from Insufficient Protein Activities, Memoirs of the Faculty of Engineering, University of miyazaki, 36, 345-350

[3] E. Kolarzyk M. Stepniewski, A, Mendyk, M.Kitlinski, A. Pietrzycka (2006), The usefulness of artificial neural networks in the evaluation of pulmonary efficiency and antioxidant capacity of welders. Int. J. Hyg. Environ.-Health, 209, 385-392

[4] M. A. Chamjangali, M. Beglari, G. Bagherian (2007), Prediction of cytotoxicity data (CC_{50}) of anti-HIV 5-pheny-l-phenylamino-1H-imidazole derivatives by artificial neural network trained with Levenberg-Marquardt algorithm, J. Mol. Graph. Model. doi: 10.1016/j. jmgm. 2007.01.005

[5] Y. Ni, C. Liu (1999), Artificial neural networks and multivariate calibration for spectrophotometric differential kinetic determinations of food antioxidants. Analytica Chemica Acta, 396, 221-230

[6] P. H. Winston (1992), Artificial Intelligence Third Edition, Addison-Wesley Company

The Fourteenth International Symposium on Artificial Life and Robotics 2009 (AROB 14th '09),
B-Con Plaza, Beppu, Oita, Japan, February 5 - 7, 2009

Roll of Rhythmic Component in Proactive Control of Human Hand

Yoshikatsu Hayashi[1,2], Yurie Tamura [1,3], Fumihiko Ishida[4], Ken Sugawara[3], Yasuji Sawada[2]

[1] Department of Research and Developement NPO natural science
[2] Tohoku Institute of Technology
[3] Department of Liberal arts, Tohoku Gakuin University [4] The University of Electro-Communications

Abstract

Evolutionally, the strategy of catching prey should have been important to survive in constantly changing environment. Prediction mechanism should have developed to compensate the delay of sensory-motor system. In previous study, "proactive control" was found, in which motion of hands preceded the virtual moving target. The results implied that the positive phase shift of the hand motion represents the proactive nature of the visual-motor control system to minimize the transient error of the hand motion when the target changes unexpectedly. In our study, visual target moves in circle (13cm in diameter) in computer screen, and each subject is asked to keep track with the target motion in circle by the motion of a cursor. As frequency of target increases, rhythmic component in velocity of cursor was found in spite of the fact that velocity of target is constant. The generation of rhythmic component cannot be explained by only feedback mechanism for the phase shift of target and cursor in sensory-motor system. Therefore, it implies that rhythmic component was generated to predict the velocity of target, which is feed forward mechanism in sensory-motor system. In presentation, we discuss the generation of rhythmic component and its roll in feed forward mechanism.

1 Introduction

Evolutionally, the strategy of catching prey should have been important to survive in constantly changing environment. Prediction mechanism should have developed to compensate the delay of sensory-motor system. In previous study, "proactive control" was found([1],[2]), in which motion of hands preceded the virtual moving target. The results implied that the positive phase shift of the hand motion represents the proactive nature of the visual-motor control system to minimize the transient error of the hand motion when the target changes unexpectedly.

In this paper, we studied the enhancement of proactivity by discretization of visual information in human visual-motor system by performing hand tracking experiments. The results showed that the magnitudes of the phase di erence of the hand motion with respect to the target motion increased when the target is shown intermittently. As frequency of target increases, rhythmic component in velocity of cursor was found in spite of the fact that velocity of target is constant. The generation of rhythmic component cannot be explained by only feedback mechanism for the phase shift of target and cursor in sensory-motor system. Therefore, it implies that rhythmic component was generated to predict the velocity of target, which is feed forward mechanism in sensory-motor system. In this research, we discuss the generation of rhythmic component and its roll in feed forward mechanism.

2 Method and Analysis

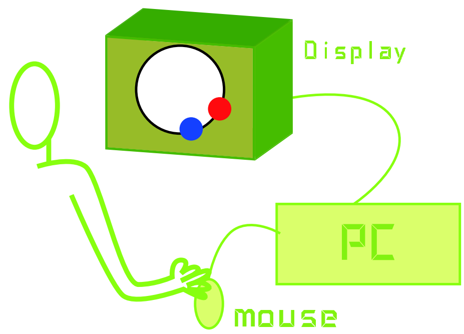

Figure1: Schematic picture of the hand tracking experiment

A subject was seated at 50cm in front of computer screen, and was asked to trace a moving visual target (red circle of 6mm diameter) as accurately as possible by the motion of a cursor (blue

©ISAROB 2009

circle of 6mm diameter) in the screen produced by hand motion through a mechanical computer mouse(Fig.1).

Experiments are performed in two conditions; in a rst condition, target in circle trajectory is shown continuously, in a second condition, target is intermittently shown, i.e., the target is shown for only 40 percent of trajectory. subject rst follow the moving target, and when the target disapears, subject has to follow the circle line in a process of guessing target velocity and position. We analyze following physical quantities;

1. Phase shift between target and tracer
2. Velocity of tracer as a function of time
3. Frequency analysis of tracer velocity

3 Results and Discussion

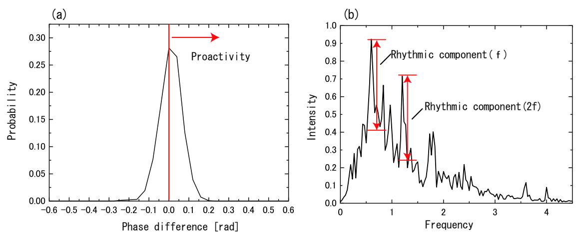

Figure2: (a) Distribution of phase shift (b) Frequency analysis of tarcer velocity

Proactivity of hand motion is caluculated as follows. Distribution of phase shift between target and tracer is tted by gaussan distribution and center of gaussin function is obtained. To nd rhythmic component of hand motion, frequency analysis is performed on velocity of tracer. The strength of rhythmic component was measured by a height of peak as shown in Fig.2.

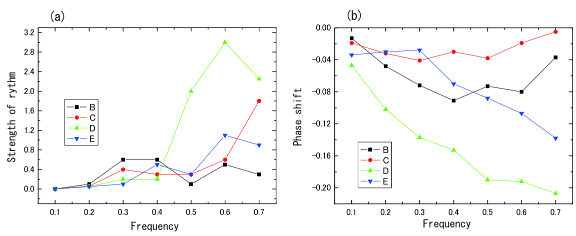

Figure3: In continuous trajectory of target (a) The strength of rhythmic component as a function of frequency (b) Proactivity as a function of frequency

In a rst experimental condition when the target was shown continuously in circle orbital, Rhythmic component in hand movement was enhanced as the frequency of target increases(Fig.3). However, phase shift was negative in all frequency; hand motion of the subject delayed the target motion. In a second condition when the target was shown intermittently, one subject showed proactivity(Fig.4), i.e., hand motion of the subject preceded the target motion. In the inter-stimulus-interval(when the target is not shown), correction motion to decrease phase shift between target and tracer can not perform(feed-back mechanism), thus, only feed-forward mechanism in which the velocity of target is estimated would work. In this case, the strengh of rhythmic component increased, thus the rhythmic component might play a role in feed-forward mechanism. These considerations indicate that proactivity emerges when feed-forward mechanism works more than feed-back of position correction. In the presentation, we would like to talk about detail analysis based on the emergence of rhythmic component and its roll in feed forward mechanism in visual-motor system.

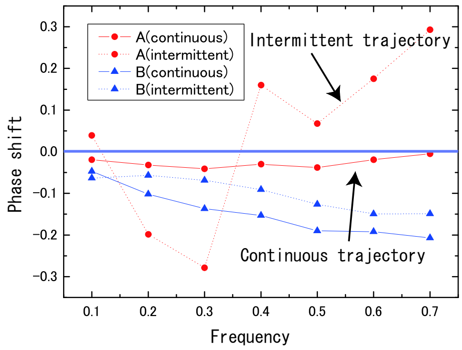

Figure4: Proactivity as a function of frequency in two experimental condition

References

[1] F. Ishida and Y. Sawada: Human hand moves proactively to the external stimulus: An evolutional strategy for minimizing transient error. *Physical Review Letter*, 93, 168105 (2004)

[2] J. R. Carl and R. S Gellman: Human smooth pursuit: stimulus-dependent responses. *Journal of Neurophysiology*, 57, 1446/1463 (1987)

©ISAROB 2009

The Fourteenth International Symposium on Artificial Life and Robotics 2009 (AROB 14th '09),
B-Con Plaza, Beppu, Oita, Japan, February 5 - 7, 2009

Modeling of Patrol Behavior of *Diacamma*'s Gamergate

Kazuyuki Yaegashi[1)2)], Ken Sugawara[3)], Yoshikatsu Hayashi[2)]
1) Tohoku University, Aoba, Aramaki, Aoba-ku, Sendai 980-8579 JAPAN
2) natural science NPO, 4-7 kitame-cho Aoba-ku, Sendai 980-0023 JAPAN
3) Tohoku Gakuin University, 2-1-1, Tenjinzawa, Izumi-ku, Sendai 981-3193 JAPAN
(Tel : 81-22-773-3306; Fax : 81-22-773-3306)
(sugawara@cs.tohoku-gakuin.ac.jp)

Abstract: Gamergate (generally called "queen") of *Diacamma sp.* walks around in the nest and comes in contact with the workers. The gamergate informs its presence to the workers by the physical contact. This behavior is called "patrol." In previous works, it is reported the gamergate controls the patrolling time depending on the colony size. How does the gamergate know the colony size and control the patrolling time? In this paper, we propose a simple dynamics to explain this behavior. We assume the gamergate and the workers have internal state which interacts by physical contacts. By numerical simulations, we confirm the patrol time of the proposed model depends on the size of colony.

Keywords: *Diacamma sp*, gamergate, patrol behavior, modeling

I. INTRODUCTION

It is well-known that ants' colonies are highly organized and exhibit number of remarkable behaviors. Their colonies consist of numerous individuals and each individual engages in nest construction/maintenance, defending, foraging, taking care of eggs and so on.

In the colony of *Diacamma sp*, which lives in Okinawa and several islands, the gamergate (generally called "queen") randomly repeats walking and quiescence in the nest and comes in contact with workers. This behavior is called "patrol." The aim of patrol is considered to rule its colony.

In previous works, following facts have been reported[1-5]:

(1) The gamergate walks around in the nest and comes in contact with the workers.

(2) Each worker has an egg production performance, but it is inhibited when the gamergate exists in the nest.

(3) Presence of the gamergate is detected by physical contact between the gamergate and the worker.

(4) The gamergate transfers the information about its presence by chemical signals.

(5) When the gamergate disappears from the nest, each worker starts to lay eggs 3 to 6 hours later.

(6) The gamergate can detect the condition of worker's ovary.

It was also reported that the gamergate increases the number of patrolling time as the colony grows. It seems the gamergate knows the size of its colony. How does the gamergate know the colony size and control the patrolling time? In this paper, we propose a simple model to explain the mechanism of colony size dependent patrolling behavior by introducing internal state which interacts by physical contacts.

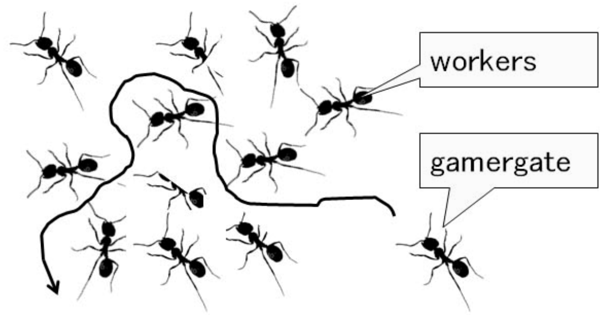

Fig.1. Patrolling behavior of *Diacamma* in the nest.

II. MODELING OF PATROL BEHAVIOR

From experimental results, it is natural to introduce an internal state for each individual. We assume the gamergate has an internal state I_g which controls patrolling behavior, and each worker has an internal state I_{wi} which implies the condition of ovary. Based on the facts described in previous section, we consider I_g is increased by the internal value of i-th worker, which the gamergate contacts.

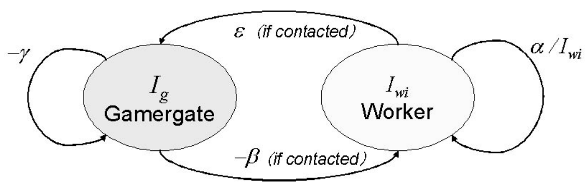

Fig.2. Diagram of proposed model

As the egg production performance of each worker is inhibited by the physical contact, we assume the internal value of the worker decreases when it encounters the gamergate. Fig.2 shows the interaction of I_g and I_{wi}, and the dynamics of the system is described as follows:

$$\dot{I}_g = -\gamma \cdot I_g + \varepsilon \cdot \delta(\vec{x}_g - \vec{x}_{w_i}) \cdot I_{w_i}$$
$$\dot{I}_{w_i} = \alpha / I_{w_i} - \beta \cdot \delta(\vec{x}_{w_i} - \vec{x}_g) \cdot I_{w_i}, \qquad (1)$$

where x_g, x_{wi} denote the position of the gamergate and the worker i, respectively. $\alpha, \beta, \varepsilon, \gamma$ are constant. $\delta(r)$ denotes delta function.
We assume quiescence time τ_q and walking time τ_w of the gamergate depend on the probability as follows:

$$\tau_q = \langle C_0 \cdot I_g \rangle$$
$$\tau_w = \langle C_1 \rangle \qquad (2)$$

where C_0 and C_1 are constant.

III. RESULTS AND DISCUSSION

In this section, we show the results obtained by numerical simulation. Fig.3 shows distribution of walking time of the gamergate in case of colony size N=70. Here the mean and SD are 83.6 and 82.9. Experimental result in case of N=75 shows those are 81.1 and 70.9[5]. We obtained similar results in case of other colony sizes.

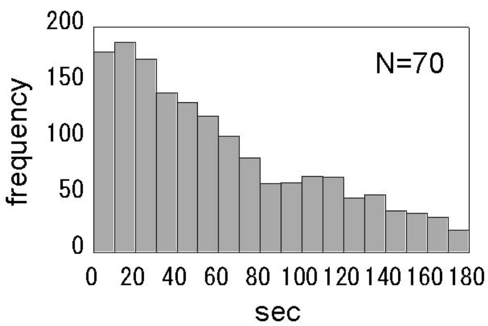

Fig.3. Frequency of walking duration of gamergate.

Fig.4 shows the total patrol time and total number of patrolling. Horizontal axis is the colony size, bar graph expresses the total patrolling time, and dots are the total number of patrolling behavior. This figure shows the activity for patrolling is in proportion to the colony size as observed in the experiment. We can conclude proposed model describes the characteristics of *Diacamma*'s behaviors qualitatively.

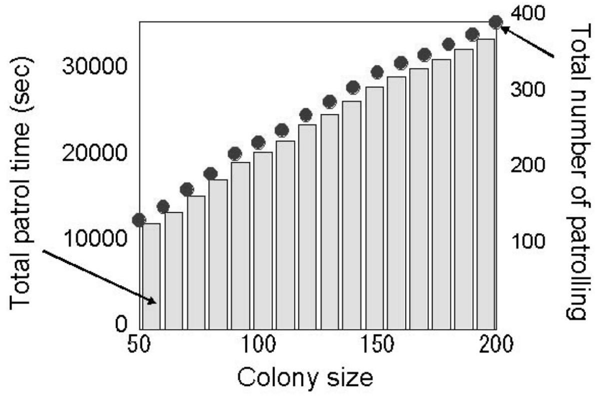

Fig.4. Total patrol time and total number of patrolling.

We are considering the behavior of the gamergate in *Diacamma*'s colony is applicable to multi-robot system. One of the possible applications is a cooperative mining system, in which small robots as "the worker" engage in mining and a large robot irregularly moves around the field and collects the material from the worker robots. Now we are designing and evaluating this type of mining system.

ACKNOWLEDGEMENT

This work is partially supported by a Grant-in-Aid for Scientific Research on Priority Areas "Emergence of Adaptive Motor Function through Interaction between Body, Brain and Environment" from the Japanese Ministry of Education, Culture, Sports, Science and Technology.

REFERENCES

[1] Kikuta N, Tsuji K (1999), Queen and worker policing in the monogynous and monandrous ant, Diacamma sp, Behavioral Ecology and Sociobiology 46 :180–189.
[2] Kawabata S, Tsuji K (2005), The policing behavior 'immobilization' towards ovary-developed workers in the ant, Diacamma sp. from Japan, Insectes Sociaux 52:89–95.
[3] Tsuji K, Peeters C and Hölldobler B (1998), Experimental investigation of the mechanism of reproductive differentiation in the queenless ant, Diacamma sp., from Japan, Ethology 104:633–643.
[4] Tsuji K, Egashira K, Holldobler B (1999), Regulation of worker reproduction by direct physical contact in the ant Diacamma sp. from Japan, Animal Behaviour, 58, 337.
[5] Kikuchi T, Nakagawa T, Tsuji K (2008), Changes in relative importance of multiple social regulatory forces with colony size in the ant Diacamma sp. from Japan. Animal Behavior (in press).

©ISAROB 2009

Analysis and Modeling of *Diacamma* workers' Behavior

Mai Yuki, Yoshikatsu Hayashi*, Ken Sugawara
Tohoku Gakuin University, 2-1-1, Tenjinzawa, Izumi-ku, Sendai 981-3193 JAPAN
** natural science NPO, 4-7 kitame-cho Aoba-ku, Sendai 980-0023 JAPAN*
(Tel : 81-22-773-3306; Fax : 81-22-773-3306)
(sugawara@cs.tohoku-gakuin.ac.jp)

Abstract: It is well-known that social insects such as ants show interesting collective behaviors. How do they organize such behaviors? To expand understanding of collective behaviors of social insects, we focused on ants, *Diacamma*, and analyzed the behavior of a few individuals. In an experimental set-up, ants are placed in hemisphere without a nest and food and the trajectory of ants is recorded. From this bottom-up approach, we found following characteristics: 1. Activity of individuals increases and decreases periodically. 2. Spontaneous meeting process is observed between two ants and meeting spot of two ants is localized in the experimental field.

Keywords: social insects, ant, meeting process, multi-body dynamics

I. INTRODUCTION

Social insects have some interesting characteristics and show organized group behaviors. Especially, ants' colonies are highly organized and exhibit number of remarkable behaviors. Their colonies consist of numerous individuals and engage in nest construction/ maintenance, taking care of eggs, defending, foraging and so on by well-organized division of labor. These collective behaviors do not require a special individual that controls the behavior of the entire group. Hereditarily homogeneous individuals achieve these collective behaviors by interacting with each other through direct sight or chemical materials, such as pheromones.

Many researchers have been investigating behaviors of ants[1-3] and lots of interesting results have reported. However, not so large number of researches have treated single or some ants' behaviors[4,5]. This means the knowledge of the relationship between the colony-level behaviors and the individual level behaviors is not enough.

We consider the modeling of the behaviors is one of the most effective approaches to combine the individual-level behaviors and colony-level behaviors. Our final goal is to describe ants' behavior as the dynamics of interacting self-driven particles. By treating ants' behaviors from physical viewpoint, we aim to construct a universal model of ants' behaviors. It is also expected to be applied to engineering systems such as muti-robot system[6-8]. In our previous work, we reported a fluctuation of velocity on single ant walk[9]. In their walking, we found the time correlation of walking velocity. From the spectrum of walking velocity, we can see a long-term correlation in the velocity dispersion. We also found the fluctuation is in proportion to the time scale. In spite of long-term correlation in velocity, from the actual value of average velocity and the velocity dispersion, we can regard ants as a random walker.

Then what happens when a few ants is placed in a closed field? It is known that ants from the same colony tend to get together and stay in contact. It means the behavior of a few ants is considerably different from solitary ant. In this paper, we discuss the behaviors of a few ants mainly focusing on a movement of each ant.

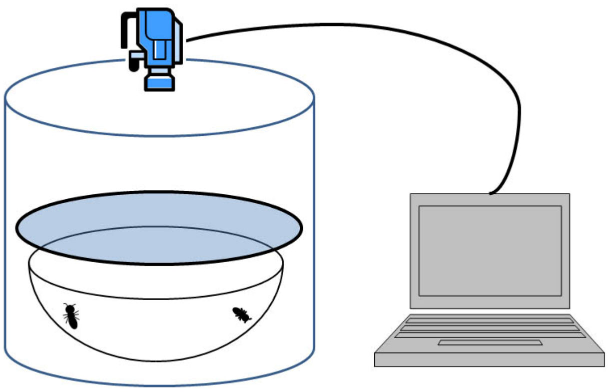

Fig.1: Experimental set up: Ants are released in hemisphere and covered by the clear plate. Trajectory of ants is recorded by CCD camera.

II. METHODS AND ANALYSIS

We observed the behaviors of *Diacamma*, which lives in Okinawa and several islands. In our experiment, one to several ants are randomly picked up and placed in acrylic hemisphere (30cm in diameter) field. The hemisphere is covered by a transparent acrylic board during the experiment. CCD camera is equipped at the top of the experimental equipment, which size is 40cm x 40cm x 90cm height(Fig.1). Trajectory of ants walking in hemisphere is recorded and we analyze the trajectory of ants as a function of time.

III. RESULTS AND DISCUSSION

1. Analysis of trajectory of single to multi ants

Firstly, we measured the trajectory of single ant. During the first 30 minutes, the trajectory of ants spreads in the field. The space distribution of the trajectory, however, becomes localized after 30 minutes.

Next, we measured the trajectory of two ants. As time proceeds, they walk less and less and eventually halt at one place. Space distribution of ant position is localized as well.

To further investigate the walking distance more quantit atively, we analyzed the walking distance of single ant s ummed up in every 10 minutes. Walking distance gradu ally decreases and eventually becomes inactive at 120 minutes. The walking distance can be interpreted as acti vity of ant. After 120minutes, it shows that single ant re peats active and inactive role. Further result shows that t he activity of single ant changes periodically. This indic ates that the single ant has some rhythmic component in its activity.

In the case of two ants placed in hemisphere, we suggest that there should be two stages in ants' behavior from the result of walking distance.

(1)At former stage, the difference of walking distance between two ants is small (Fig.2), thus, both of two ants are active, i.e., they travel around the surface of hemisphere. 60 minutes later, both of them become inactive. Compared with trajectory of two ants, it is considered that they finish exploring the unknown environment within 90 minutes.

(2)At latter stage, the difference of walking distance bet ween two ants becomes larger, thus, one of them becom es inactive. There seems to be an exchange of active and inactive role between two ants..

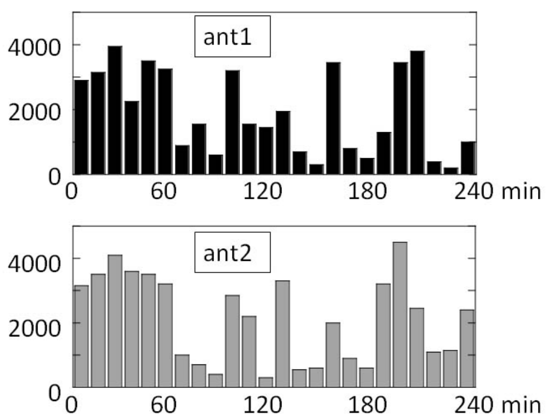

Fig.2: Walking distance of two ants summed in every 10 minutes as a function of time: Red column denotes ant A, and blue column denotes ant B.

2. Analysis of meeting spot of ants' behaviors

By the observation of two ants’ behavior, a few meeting spot of two ants appear in the experimental field (Fig.3). We suggest that one or some chemicals affect to organize the spots, and build a simple model to investigate the mechanism of emergence of meeting spot.

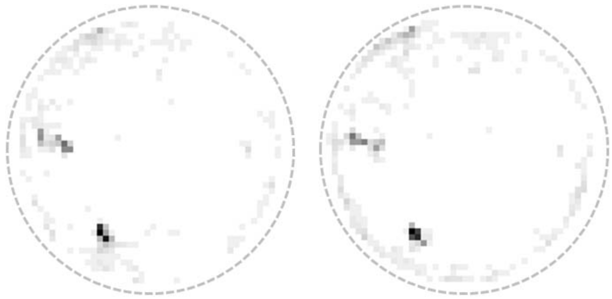

Fig.3. Existing rate of ant 1 (left) and ant 2 (right). Degree of darkness is in proportion to the rate.

ACKNOWLEDGEMENT

This work is partially supported by a Grant-in-Aid for Scientific Research on Priority Areas "Emergence of Adaptive Motor Function through Interaction between Body, Brain and Environment" from the Japanese Ministry of Education, Culture, Sports, Science and Technology.

REFERENCES

[1] Hölldobler B, Wilson EO (1990), The Ants. Harvard University Press.

[2] Hölldobler B, Wilson EO (1995), Journey to the Ants: A Story of Scientific Exploration, Harvard University Press.

[3] Gordon D (2000), Ants at Work, W W Norton & Co Inc.

[4] Cole BJ (1992), Short-term activity cycles in ants. Behav. Ecol. Sociobiol. 31:181-187.

[5] Cole BJ, Cheshire D (1996), Mobile Cellular Automata Models of Ant Behavior. Am. Naturalist 148: 1-15.

[6] Bonabeau E, Theraulaz G, Dorigo M (1999), Swarm Intelligence: From Natural to Artificial Systems, Oxford Univ Press.

[7] Krieger MJB, Billeter JB, Keller L (2000), Ant-like task allocation and recruitment in cooperative robots. Nature 406:992-995.

[8] Balch T, Parker LE (2002), Robot Teams: From Diversity to Polymorphism, A K Peters Ltd.

[9] Uchikawa T, Sugawara K, Kikuchi T, Tsuji K and Hayakawa Y (2007), Time-series analysis of ant behavior and its modeling (in Japanese). IEICE tech. report. Nonlinear problems, 106(573) 20070226 : 27-30.

Modeling and Robostic Control of Reduction Car Using the Ultrasonic Satellite System

Hyung Jun Park*, Seong Man Yoon*,Su Yong Kim*,Jong Il Bae, Man Hyung Lee***

**Department of Mechanical and Intelligent Systems Engineering Pusan National University,*
Busan, 609-735,Korea (Tel : 82-51-510-1456; Fax : 82-51-512-9835)
(flatronaron@naver.com)
*** Department of electrical engneering, Pukyong National University*
Busan, 609-735, (Tel : 82-51-629-6314; Fax :)
(jibae@pknu.ac.kr)

Abstract: In this paper In this paper, which is one of the part of the development for the automation system in the navigation process, covers the car system. Local detection system based on pseudo-satellite was used to be able to detect the space coordinates and the absolute location with four ultrasonic transmitters and two receivers. Using this system wH_∞ e get the lateral dynamic model of a reduced car by using system identification methods and design a lateral controller. The system input is the steering wheel angle of the vehicle with constant speed and the output is the yaw of the vehicle. With system identification for a basis, to achieve a control objective, we design a controller using the model equation.

***Keywords*: USAT, localization, positioning, mobile robot**

I. INTRODUCTION

Research centered on ITS (Intelligent Transportation System), PATH (Partners for Advanced Transit and Highways) and AHS (Automated Highway System) has led to the development of the autonomous vehicle (Broggi *et al., 1999*) Although magnetoresistive (MR) and vision sensors play an enabling part in autonomous vehicle operation, they are not sufficient to permit operation under all conditions (Huei et al., 1992). For example, MR sensors require marked magnet points on the road and are susceptible to stochastic error. A disadvantage of vision sensors is that they are sensitive to weather conditions and light (Lee et al., 2002; Lee et al., 2006).

In this paper, as a part of this study we make a reduced car adopted H_∞ based on USAT(Ultrasonic satellite system) and design a controller. H_∞ control system as acontroller, which uses the feedback of the yaw angle error, was used to design a robust lateral control against modeling uncertainty (Shladover, 1991). The performance of this algorithm is compared to that of the PID controller. In order to obtain the system model equation, we use system identification.

2. ULTRASONIC SATTELLITE SYSTEM

The measurement of the distance using the ultrasonic waves is calculated with sound velocity and the delivering time. TOF (Time of Flight) is defined as the time difference between transmitter and receiver. Pseudo-satellite system(or Ultrasonic satellite system) consist of four transmitters and two receivers. Ultrasonic transmitters function as ultrasonic satellites and locate on the fixed places whose coordinates are known. So ultrasonic receivers receive ultrasonic waves transferred from ultrasonic satellites and the distance between ultrasonic receivers and ultrasonic satellites is calculated. The basic idea of U-SAT is similar to that of GPS. Although ultrasonic receivers exist in the ultrasonic satellites, the position of ultrasonic receiver is calculated respectively. We obtain the UCT position data from U-SAT and obtain the yaw data between prior position and present position.

3. SYSTEM IDENTIFICATION

Discrete time subspace system identification methods have attracted much attention during the past few years due to ability of identifying multivariable linear processes directly from the input-output data. Compared with the classical PEM and IVM, these subspace methods do not suffer from a parameterization and nonlinear optimization. Also, their properties and common features have been analyzed well (Van Overshee *et al.* [2]) and their extensions to closed-loop process data have been developed (Chou *et al.* [3], and Ljung *et al.* [4]). The objective of discrete-time subspace system identification methods is identifying the system matrices as well as the process order of the discrete-time state space model.

In general, linear time invariant system represented

$$x(t+1) = Ax(t) + Bu(t) \quad (3.1)$$

$$y(t) = Cx(t) + Du(t) + v(t) \quad (3.2)$$

System identification tool is used discrete state-space model. Discrete state-space equation is

$$x(kT+T) = Ax(kT) + Bu(kT) + Ke(kT) \quad (3.3)$$

$$y(kT) = Cx(kT) + Du(kT) + e(kT) \quad (3.4)$$

$$x(0) = x_0 \quad (3.5)$$

In order to design a PID controller, eq. (2), (3), and (4) is transformed the continuous state space equation

$$\dot{x}(t) = Fx(t) + Gu(t) + \tilde{K}\,w(t) \quad (3.6)$$

$$y(t) = Hx(t) + Du(t) + w(t) \quad (3.7)$$

$$x(0) = x_0 \quad (3.8)$$

The relation discrete time state matrices A, B, C, D have relation with continuous time state matrices F, G, H, D

$$A = e^{FT} \quad (3.9)$$

$$B = \int_0^T e^{F\tau} G d\tau \quad (3.10)$$

$$C = H \quad (3.11)$$

This relation accomplish when input is piecewise-constant in time interval. Where is state transition matrix. If the system has no noise, we approximate $v(t) \approx 0$, $K \approx 0$ and we rewrite the Eq. (3.6), (3.7), (3.8) as Eq. (3.1), (3.2).

A least squares problem to obtain the state space matrices solve Eq. (3.12).

$$\begin{pmatrix} \hat{A} & \hat{B} \\ \hat{C} & \hat{D} \end{pmatrix} = \min_{A,B,C,D} \left\| \begin{pmatrix} \hat{x}_{i+1} & \hat{x}_{i+1} & \cdots & \hat{x}_{i+j} \\ y_i & y_{i+1} & \cdots & y_{i+j-1} \end{pmatrix} - \begin{pmatrix} A & B \\ C & D \end{pmatrix} \begin{pmatrix} \hat{x}_i & \hat{x}_{i+1} & \cdots & \hat{x}_{i+j-1} \\ u_i & u_{i+1} & \cdots & u_{i+j-1} \end{pmatrix} \right\|_F^2 \quad (3.12)$$

Where $\|\cdot\|_F$ denotes the Frobenius-norm of a matrix[5]. As soon as the order of the model and the state sequences X_i and X_{i+1} are known, the state space matrices A, B, C, D can be solved form

$$\begin{pmatrix} X_{i+1} \\ Y_{i|i} \end{pmatrix} = \begin{pmatrix} A & B \\ C & D \end{pmatrix} \begin{pmatrix} X_i \\ U_{i|i} \end{pmatrix} \quad (3.13)$$

Where $U_{i|i}$, $Y_{i|i}$ are block Hankel matrices with only one block row of inputs respectively outputs, namely $U_{i|i} = \begin{pmatrix} u_i & u_{i+1} & \cdots & u_{i+j-1} \end{pmatrix}$ and similarly for $Y_{i|i}$. This set of equations can be solved. As there is no noise, it is consistent.

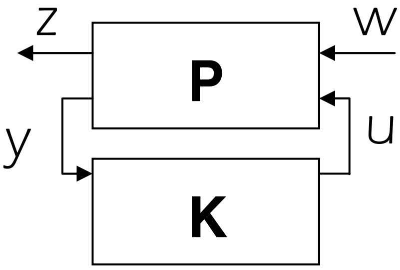

Fig 4.1. H_∞ controller block diagram

4. H∞ LATERAL CONTROL OF AUTRONOMOUS VEHICLES

Figure 1 shows the H∞ control block diagram. The components of w are all the exogenous inputs to the system (Kemin, 1998). These typically consist of disturbances, sensor noise reference commands and fictitious signals that drive frequency weights and models of the uncertainty in the dynamics of the system. The components of z are all the variables we wish to control, such as tracking errors and actuator signals. The inputs generated by the controller are denoted u. The sensor measurements used by the feedback controller are denoted y.

The generalized plant P, which is assumed to be linear and time-invariant, contains all the information that is favorable to incorporate into the synthesis of the controller, K. System dynamics, models of the uncertainty in the system's dynamics, frequency weights to influence the controller synthesis, actuator dynamics, sensor dynamics and implementation hardware dynamics are all included in P

$$z=P_{11}w+P_{12}u \quad (4.1)$$

$$y=P_{21}w+P_{22}u \quad (4.2)$$

$$u=Ky \quad (4.3)$$

The relationship between the variable z and the exogenous input is $z = T_{zw}w$. The H∞ control is represented as follows:

$$\| T_{zw} \|_\infty \le r\,. \quad (4.4)$$

Equation (4.4) motivates the design of a stable controller of P to maintain a less infinite norm of Tzw than the given scalar γ.

The H∞ control is represented as Equation (4.5) with the method of Glever and Doyle (John et al., 1989).

$$\left\| \begin{matrix} w_1 & s \\ w_3 & s \end{matrix} \right\|_\infty \le r\,. \quad .(4.5)$$

In the mixed-sensitivity problem, W1 and W3 are

weighting functions for improving the performance of the system. In addition, S and T are the sensitivity function and the loop transfer function of the system, respectively.
The selection of weighting functions for a specific design problem often involves ad hoc fixing, many iterations and fine tuning. It is challnging to generate a general formula for weighting functions that applies to every case. Based on the time domain performance specifications, the corresponding requirements in a frequency domain in terms of the bandwidth w_b and the peak sensitivity Ms can be determined. This assumes that the steady state error of the step response ε has to satisfy $|w_1(0)| \geq 1/\varepsilon$. A possible choice of w_1 can be obtained by modifying the weighting function as follows:

$$w_1 = \frac{s/M_S + w_b}{s + w_b\varepsilon}. \quad (4.6)$$

W1 is selected to improve the disturbance-reject and command-tracking, as follows:

$$w_1 = \frac{0.38s^2 + 15.5s + 1.38}{s^2 + 3s + 0.26}. \quad (4.7)$$

Additionally, the magnitude of $|KS|$ in the low frequency range is essentially limited by the allowable cost of control effort and saturation limit of the actuators;
hence, in general, the maximum gain M_T of KS can be fairly large, while the high-frequency gain is essentially limited by the controller bandwidth (w_{bc}) and the sensor nois frequencies. A candidate weight w_3 would be

$$w_3 = \frac{s + w_{bc}/M_T}{\varepsilon_1 s + w_{bc}} \quad . \quad (4.8)$$

for a small $\varepsilon_1 > 0$. Considering the roll off performance of the controller w_3 is selected to reject noise, as follows:

$$w_3 = \frac{s^3 + 600}{80000}. \quad (4.9)$$

Figure 4.2 is the frequency domain performance of each weighting function.

5. SIMULATION

To evaluate performance of controller reference path is set and a simulation performanced. To evaluate how the vehicle trace well to the designated point using Navigation algorithm PTP(point to point). Reference path is randomly set and base on state using system identification degree of tracing is evaluated. In real experiment performance fluctuates according to external condition nonlinealy system identification. Considering system identification method is designed on nonlinearty. Nonlinearty can be ignored in simulation to compare the performance of controller with disturbance and noise with the performance of controller without them.

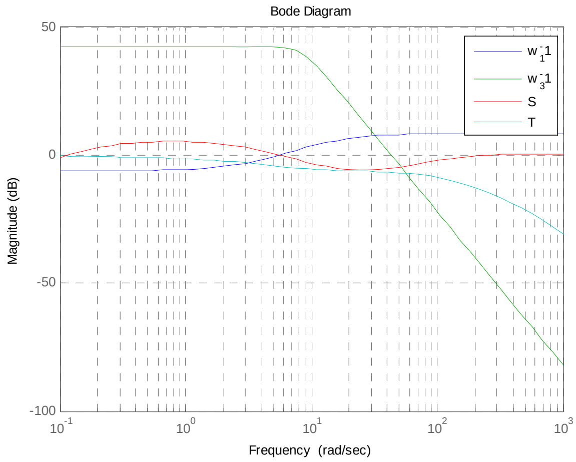

Fig 4.2 weighting function w_1, w_3 frequency domain performance

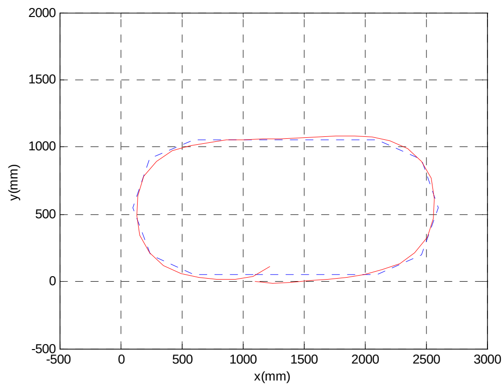

Fig 5.1 simulation result(0.3m/s)

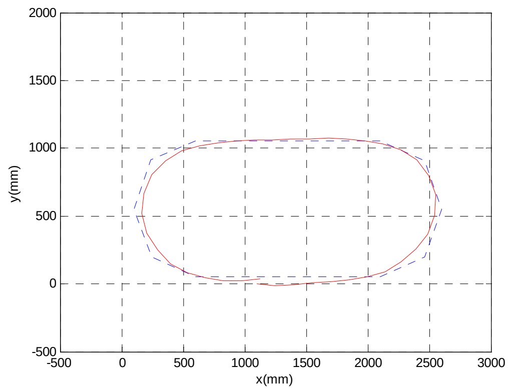

Fig 5.2 simulation result(0.35m/s)

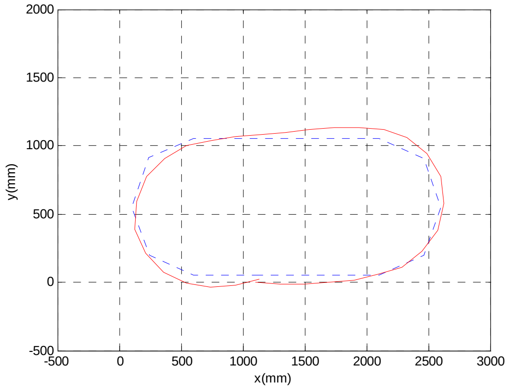

Fig 5.3 simulation result(0.4m/s)

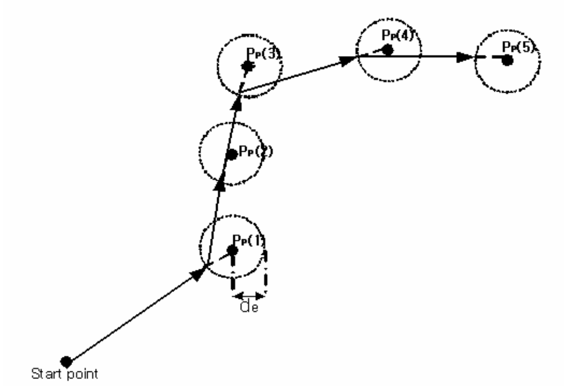

Fig 6.1 Navigation algorithm

6.NAVIGATION ALGORITHM

Fig. 6 represents the unmanned navigation algorithm. Navigation algorithm is PTP(Point To Point) method. UCT moves from the point on the reference path $P_p(i)$ to $P_p(i+1)$. If the reduced car arrives the target point, system continuously determined the next target point. And if the distance error between current position and $P_p(i)$ is smaller than d_e , system correct the next target point $P_p(i)$ to $P_p(i+1)$. d_e is selected by the velocity of reduced car and error of position measurement.

7. CONCLUSION

In this paper, we determined the system model of an autonomous vehicle for lateral control that is important to design parameter based controller in unmanned vehicle system. Using the subspace system identification method, we confirmed that the simulation is very accurate. It is important to design a controller that uses system parameters. We minimized the modeling error using system identification that using system input-output data. and we made a reduced car adopted H_∞ based on USAT(Ultrasonic satellite system) and design a controller. The performance of the compensated system that based on the system identification deserves satisfied. We will research the vehicle system identification with other dynamic and system condition. we design controller that is robust to system disturbance and parameter uncertainty.

REFERENCES

[1] K.S. Yun, D.H. Lee, J.G. Kang, K.S. Lee amd J.M. Lee, *UCT/AGV Design and Implementation Using Steering Function in Automizing Port System,* Korean Institute of Navigation and Port Research, Vol. 14, No. 2, pp. 199-207, 2000.

[2] Van Overschee, P. and De Moor, B. A (1995), *unifying theorem for three subspace system identification algorithms*, Automatica, 31:1855-1864.

[3] Chou, C.T. and Verhagegen, M. (1997), *Subspace algorithms for the identification of multivariable dynamic errors-in-variables models*, Automatica, 33:1857-1869.

[4] Ljung, L. and McKelvey, T. (1996), *Subspace identification from closed-loop data*, Signal processing, 1996, 52, 209-215

[5] Seong Man Yoon, Seong Taek Hwang, and Jae Heon Ryu and Man Hyung Lee, *System Identification and Controller Design for Lateral Control of an Unmanned Vehicle*, The Thirteenth International Symposium on Artificial Life and Robotics 2008(AROB 13th '08), 2008

[6] Y. H. Lee, S. I. Kim, M. W. Suh, H. S. Son and S. H. Kim, *Linearized Dynamic Analysis of a Four-Wheel Steering Vehicle*, The Korean Society of Automotive Engineers, Vol. 2, No. 5, 1994, pp. 101-109.

[7] J. H. Ryu, C. S. KIM, S. H. LEE and Man Hyung Lee, H_∞ Lateral Control of an Autonomous Vehicle Using the RTK-DGPS, *International Journal of Automotive Technology*, Vol.8, No.5, October 2007, 583-591

The Fourteenth International Symposium on Artificial Life and Robotics 2009 (AROB 14th '09),
B-Con Plaza, Beppu, Oita, Japan, February 5 - 7, 2009

Development of an autonomous-drive personal robot (Self-position recognition by characteristic point detection)

Seiki Matsuura *Eiji Hayashi*
Department of Mechanical Information Science and Technology
Faculty of Computer Science and Systems Engineering, Kyushu Institute of Technology
680-4, Kawazu, Iizuka-City, Fukuoka Prefecture, Japan

Abstract : We are attempting to develop an autonomous personal robot that has the ability to perform practical tasks in a human living environment by using information derived from sensors and a knowledge database. When a robot is made to function in a human environment, the issue of safety must be considered in regard to its autonomous movements. Thus, robots absolutely require systems that can recognize the external world and maintain correct driving control. We have thus developed a navigation system for an autonomous robot. The system requires only image data captured by an ocellus CCD camera. This study paid attention to the necessary self-position recognition so that the robot can move precisely. We limited the environment in which it drove to a corridor. In this system, the robot recognizes a door from an image provided by an ocellus CCD camera, and it calculates its position relative to the door. In addition, it recognizes its self-position by comparing the calculated result about the door to map information that we registered beforehand. From all of this and based on the understanding of its self-position that it has developed, the robot performs safe and correct movements without hitting walls.

KeyWords : Personal robot, Autonomous driving, Ocellus camera

Ⅰ. Introduction

Currently, autonomous self-driving robots are expected to provide various services within humans' living environments. Such robotic technology is already seeing practical use in industry. But so far the robots for industry simply follow motions given by humans. Therefore, we are developing an autonomous personal robot with the ability to perform practical tasks in a human living environment by using information derived from sensors and a knowledge database.

Our robot has a drive mechanism consisting of two front wheels and one back wheel. The front wheels are attached to a motor that operates the wheels on either side independently, while the back wheel is a passive castor wheel. This method has the advantage that a far smaller turn can be negotiated than, for instance, that using a steering system that turns the wheel of a passenger car. DC servo motors are used for the robot's drive mechanism, and position control and speed control are achieved by the drive mechanism's control system. An installed wireless LAN can provide a remote control for humans. All devices are controlled by a PC, and lead batteries supply electric power.

The navigation system uses only an ocellus CCD camera and processes the image information displayed by that camera. This study paid attention to necessary self-position recognition so that the robot can move precisely. We limited the environment that it drove in to a corridor. A human being in a corridor recognizes his own rough movement distance and current position by placements such as a door, a window, and a fire hydrant. Therefore, in order for our robot to drive correctly, it recognizes a mise en scene with the sight information that a CCD stemma camera like a human being's eyes provides it. We have registered a map of the life space with the robot beforehand and intend to develop a system in which the robot's self-position is determined by its recognition of a door as the standard marker of its position than a CCD camera.

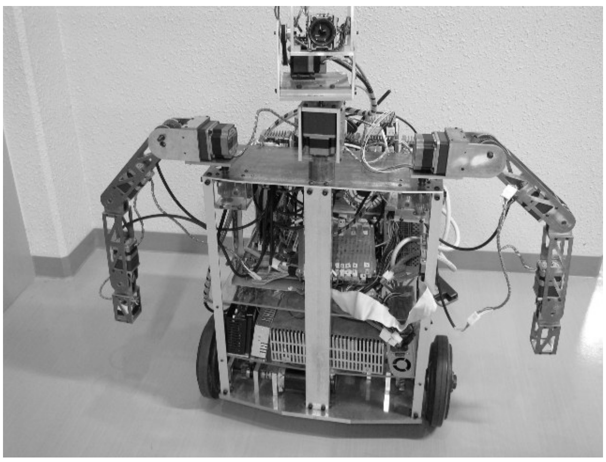

Fig.1. Robot appearance

The map of the life space can indicate a dangerous domain that will prevent the robot from colliding with walls, a door and other obstacles. One pixel in its map represents a true distance of 5cm, and the robot moves with the map as a standard. The map of the life space is shown in Fig. 2.

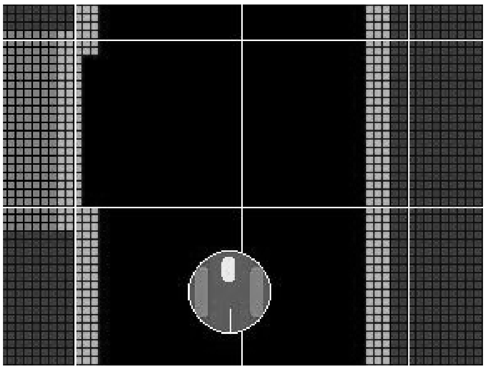

Fig. 2. Map of life space

Ⅱ. A self-position recognition system

This system extracts a straight line ingredient from an image provided from the ocellus CCD camera and distinguishes the door from information about the color of a domain that is surrounded by a straight line.
This system's flowchart is shown in Fig. 3.

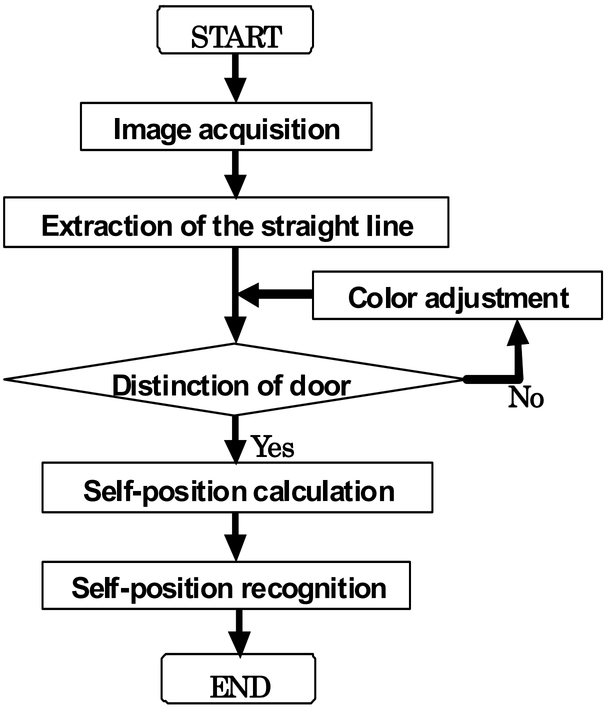

Fig. 3. System flowchart

1. Image acquisition
The image acquired from the ocellus CCD camera has a size of 320×240 pixels and is a 24-bit color image in the RGB form.

2. Extraction of the straight line
The system performs Hough transform processing of the acquired image in order to extract straight lines and circles from points that lie scattered on the image. The extraction of the straight lines is intended to distinguish the boundary lines between the door and wall and between the floor and wall.
First, this system performs an edge extraction to determine the border of each domain. The edge extraction detects a discontinuity in the color density by the use of a differential calculus filter. I consider that detected discontinuous ingredients represent the border of a door and the wall or the floor. With a Hough transform, the system converts these ingredients into a straight line that divides domains. A chart of the extraction of a straight line is shown in Fig. 4.

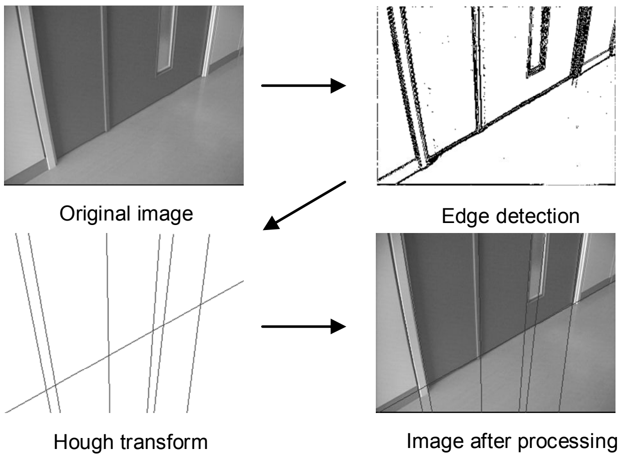

Fig. 4. Extraction of a straight line

3. Distinction of door
By extracting a straight line, the system distinguishes the domain of a door from an image divided into plural domains. I consider a line straight when its lurch is within 0 to 0.9 that of the boundary line of a wall and the floor. In addition, I consider the door to be a domain on this straight line, and I calculate the average of the pixel values in the upper part of each domain . As a result, when the domain satisfies a condition set by every working environment, the system distinguishes the domain from a door. To calculate the distance to a door, the system takes a point on the intersection between the door and the domain that is distinguished from a door. considers two points in the outside the both ends of the door most, and record them.

4. Color adjustment
When there is no big difference between the color of a door and the wall in a working or living environment,

the system performs a color revision. This is a method to increase contrasts by expanding the distribution in a histogram showing the brightness of the image. The histogram when it revises a color is shown in Fig. 4.

It is easy to increase the distinction when there are slight color differences between a door and the wall by performing this processing. The result of this is shown in Fig. 5 and Table 1.

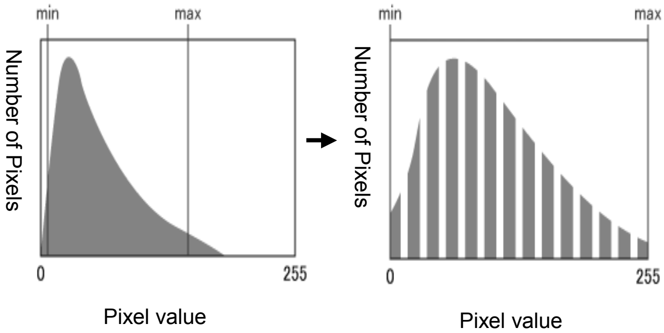

Fig. 4. Color adjustments

(a) Before revision (b) After revision
Fig. 5. Result of color revision

Table 1. Result of color revision

	Before revision			After revision		
	R	G	B	R	G	B
Wall	138	137	136	152	160	158
Door	139	132	129	157	141	132

5. Self-position calculation

・The angle of pan calculation of the camera

This process calculates the angle of the pan of the camera so that it can distinguish a door. Like the distinction of the door, I consider a straight line that declines the most as the boundary line between a wall and the floor. The system acquires two points of suitable coordinates from this and calculates the degree of leaning.

・The distance calculation to a door

From the above, with the points at both ends of the door which it recorded for door identification and from the angle of pan of the camera which it calculated, the system calculates the distance between the robot and the edge of door based on its movement direction and also the shortest distance to the wall.

When the system is not able to detect a door, it calculates only the distance to the wall.

6. Self-position recognition

The system compares the distance between the robot and the edge of the door based on its movement direction and the distance between the robot and the wall based on the angle of the pan of the camera, which it calculated with a map and which allowed it to revise its self-position. I suppose that the door on the map is the door which it detected according to its movement distance and has been provided from the encoder and the initial position of the robot which I set.

It does not perform a revision for the movement distance when it is unable to detect a door. However, it revises only the distance beween the wall and the robot.

The result of the self-position revision on the map is shown in Fig. 6.

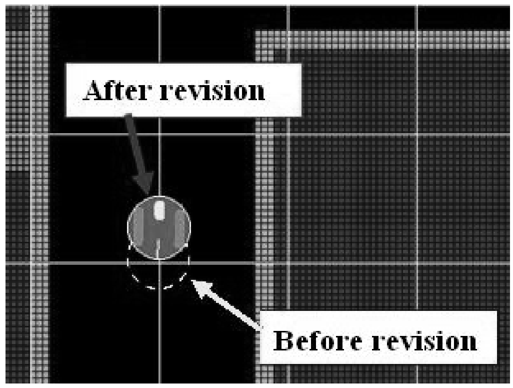

Fig. 6. Self-position revision

Ⅲ. System evaluation experiment

1. Experiment procedure

An obstacle avoidance system was developed in this laboratory from a conventional study. However, I understand that a big movement error occurs when the robot evades an obstacle using this system. Therefore, I performed a system evaluation by revising this movement error.

In this experiment, the height of the ocellus CCD camera was set at 87.5cm from the floor and the angle of declination at 30 degrees, and the mileage of the robot was set at 750cm. In addition, the position of the obstacle was set at a spot 300cm from the robot. The position of the door was set at a spot 650cm. from the robot

A robot performed movements and revisions ten times in the above-mentioned condition. From the results, I confirmed the length between the destination and the position of the robot slip off and consider it.

2. Experiment result

The experiment result is shown in Table 2. Without revisions, the average error became 57.1cm, and the greatest error became 70cm. With the revisions to this system, the average error became 6.49cm, and the greatest error became 11cm.

This system, then, was able to reduce the movement error to nearly 10% of its previous value. This error is around a 1 pixel error on the map. Therefore, I believe that sufficient revision is possible.

It is considered that an error in the straight line extraction by the Hough transform and a calculation error from the resolution caused the error that occurred by this system.

Table 2. Experiment result

	Average error (cm)	Maximum error (cm)
No revision	57.1	70
Revision	6.49	11

Ⅳ. Conclusions

This system was able to reduce an error of around 60cm to around 6cm. This is a minute error in a map with regard to the standards of the movement, and it may be said that it is a sufficient revision.

With this system, the robot stops and makes calculations from the acquired image. Therefore, there is a problem of its taking too much time when it moves in a corridor. There is the need to develop a system for self-position revision along with movement in order to solve this problem. In addition, identification of a door becomes difficult when robot is too far from a wall when a robot is over by a wall. I have to integrate the solution to this problem with the movement angle error revision system developed in this laboratory.

References

[1]Takuma Umeno, Eiji Hayashi, Navigation system for an autonomous robot using an ocellus camera in indoor environment, proceedings of the 11th international symposium on artificial life and robotics, Vol1.11th, pp229., Beppu, Oita, Japan, 2006.

[2] Hiroshi Mizoguchi, Eiji Hayashi, Development of an obstacle recognition system for autonomous robots in indoor environment, proceedings of the 12th international symposium on artificial life and robotics, Vol1.12th, pp.348, Beppu, Oita, Japan, 2007

[3] Tomoyuki Kinoshita, Eiji Hayashi, Development of distance recognition using an ocellus camera for an autonomous personal robot, proceedings of the 13th international symposium on artificial life and robotics, Vol1.13th, Beppu, Oita, Japan, 2008

The Fourteenth International Symposium on Artificial Life and Robotics 2009 (AROB 14th '09),
B-Con Plaza, Beppu, Oita, Japan, February 5 - 7, 2009

The recognition of multiple people using an ocellus camera

Seiichi Tanaka **Eiji Hayashi**
Department of Mechanical Information Science and Technology
Faculty of Computer Science and Systems Engineering, Kyushu Institute of Technology
680-4, Kawazu, Iizuka-City, Fukuoka Prefecture, Japan
(0948-29-7793)
(tanaka@mmcs.mse.kyutech.ac.jp)

Abstract: Communication between a person and a robot is necessary for the robot to be able to function in a human living environment in such a way as to be helpful to the humans. A human being needs to send a command to a robot without having to use exclusive equipment, and this requires that the robot recognize the human being. For this purpose, I have developed in this study a system for recognizing multiple human beings whose images appear in a CCD camera. The purpose of this system is to enable a robot to recognize the position of a user with a stemma camera image.

From this image, the system detects an object which moves, and it then carries out a search in its data domain. It pays attention to the shape and color of the object and narrows it down to either a non-human object or a human being. In addition, it determines the position of a human face and decides if it is a human being from the color, size, and position of the face that it detected.

Keywords**:** Robotics, Image processing, Multiple people recognition

1 Introduction

Due to the insufficient number of workers in Japan's low-birthrate society, autonomous self-driving robots will be called upon to provide various services within human living environments. Robots are currently used in industry, where they simply perform a given motion previously made by humans. However, such robots are less useful for tasks in the home. We are developing an autonomous personal robot with the ability to perform practical tasks in a human living environment using information derived from sensors and a knowledge database.

Our robot has a drive mechanism composed of two front wheels and two back wheels. The two front wheels are attached to a motor, which operates them independently, while the back wheels are castor wheels. DC servo motors are used for the robot's drive mechanism, and position control and speed control are achieved by means of the control system for the drive mechanism. One CCD camera is installed on the head of the robot. It can be rotated to some sides (90 degrees in the top direction, 65 degrees to lower degrees, 90 degrees in the right direction, and 90 degrees in the left direction) by two DC motors. This camera contains approximately 300,000 pixels. All devices are controlled by a personal computer, and electric power is supplied by lead batteries.

To work, the robot needs to receive a command from the human. The robot can be easily sent instructions from devices such as remote controls, personal computers and so on. However, because this step is inconvenient, I developed a system which can recognize multiple human beings who appear in camera images.

With this system, I detect an object which moves from an image that is provided from a CCD stemma camera image, and then I search a data domain. I pay attention to the shape and color of an object which moves, and determine whether it is a human being and then estimate the position of the human face. Furthermore, I determine whether it is a human being by its size and color and the color under a thought, the position of the face which I detected when a human being is piled up.

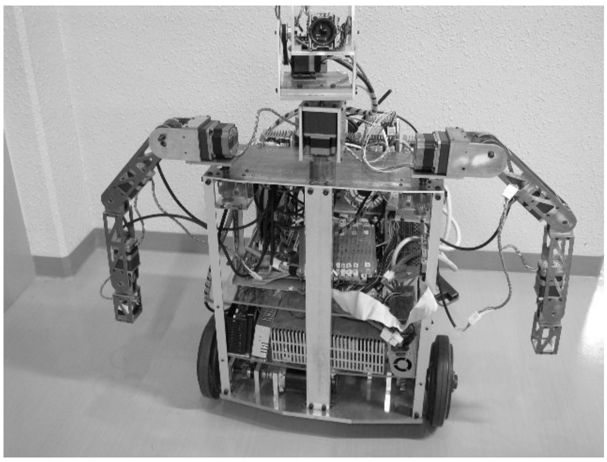

Fig. 1 Robot appearance

2 The recognition of multiple people system

©ISAROB 2009

2.1 Outline of the system

From an image provided by a CCD stemma camera, the system detects an object which moves and carries out a search in its data domain. It pays attention to the shape and color of an object and determines whether it is either a non-human object or a human being. In addition, it determines the position of a human face and whether it is a human being from the color, size, and position of the face that it detected.

2.2 Method for recognition of multiple people

Here in Section 2, we explain the method for obstacle detection. The flow for the recognition of multiple people is shown in Fig. 2.

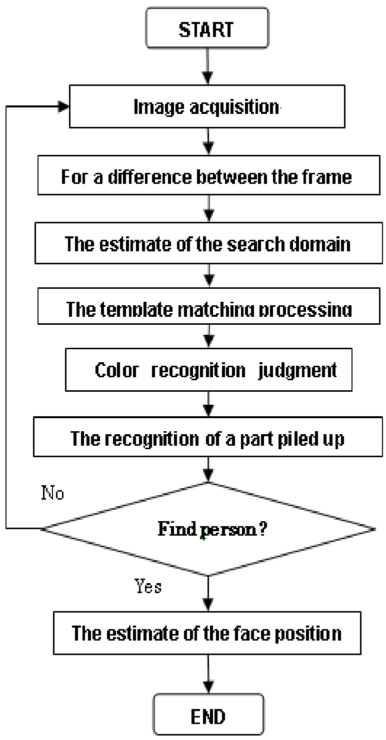

Fig. 2 System flow

Ⅰ. Image Acquisition

The image obtained by the CCD camera is read into a PC in the robot.

Ⅱ. Processing using the difference between frames

We use the difference between frames to extract certain objects moving within the camera's view. Because the system is not easily affected by changes in the background, it can resist the effects of such changes. First, our robot acquires an image from the camera and saves it. Next, it acquires a succession of images and compares them with the first image until differences greater than 2% appear. When differences in the RGB color model exceed this threshold, the system determines that a significant difference has appeared. If it does not detect a moving object, even if it has performed ten comparisons, it photographs the first image again. An image made from differences between frames is shown in Fig. 3.

Ⅲ. The estimate of the search domain

This process estimates the domain of a human being is from the information provided by the differences between the frames.

ⅰ. The detection of the maximum height

This system detects the maximum height Y of each X point in the image from the differential image which it acquired from the differences between the frames. The image from these detections is shown in Fig. 4.

ⅱ. Average

This system makes a smooth graph by creating an average by 40 pixels of values of the height Y which it detected at the maximum, because the position sensing of the domain is difficult only at the maximum height Y. The image of the average values is shown in Fig. 5.

ⅲ. The detection of the search domain

From the graph, the system detects the part which is at the top and estimates the position of a human being. Next, it scans from a person's position and detects the point below the top or the point that is lower than 1/3 from the height of the person's position. I assume that a part surrounded by points is a search domain.

Fig. 3 For a difference

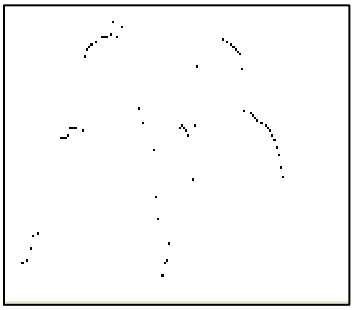

Fig. 4 Height at the maximum

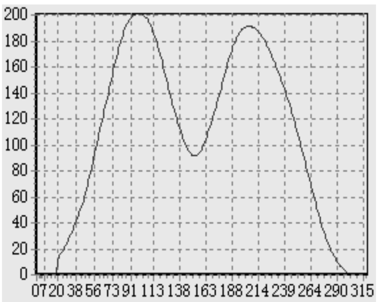

Fig. 5 The graph of the average

Ⅳ. Template matching processing

When this system begins its operation, it reads the template that imitates the head of a person. The outline acquired in the previous process is compared with the template. The size of the template changes according to size of the search range. Generally, this process requires a great deal of calculation time. Real time operation is achieved by reducing the number of comparisons. When the matching rate is higher than the threshold and reaches its maximum, the position is output as the position of a human face.

Ⅴ. Confirmation by using color information

An image is difficult to identify using only conventional processing. The system has to finally confirm that the image is that of a human being. Thus, skin color is used to ultimately determine this, using the template matching process to decide the identity and position of the human image. In this case, color information processing uses the HSV color model.

Ⅵ.The recognition of a part piled up

HSV converts the lower domain that this system took as a human face. Then it detects the part of the external color and performs 2 value. It makes a histogram of external color pixels for the X and Y coordinates and judges the position of the face from the histogram. The image which detected as an external color part is shown in Fig. 6. The image of the histogram is shown in Fig. 7.

When our system performs these processes and determines that the head of a person is in view, it outputs the position information.

Fig. 6 External color extraction

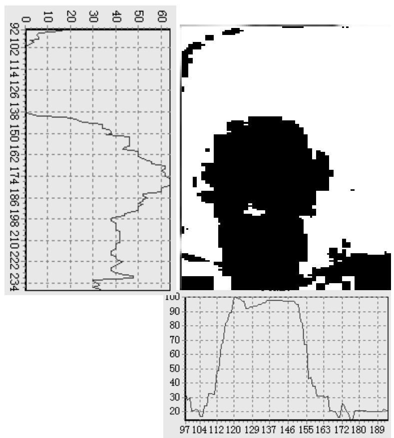

Fig.7 Histogram

2.3 Experiment

The system's performance was evaluated under two conditions.

A: Multiple people under normal lighting
B: A great number of people under normal lighting
C: Multiple people under strong lighting

The strong lighting condition in case C was made by guessing a fluorescent lamp and sunlight right. The experiments were conducted in a conventional human living environment..

In case A, this system was seen to operate effectively. In case B, it was seen to detect a human, but when a head overlaps, detection is difficult. In case C, the system has a slight difficulty in identifying the person's color, so the robot's ability to follow the person under this condition deteriorates.

We consider that these results demonstrate that the system can detect multiple people.

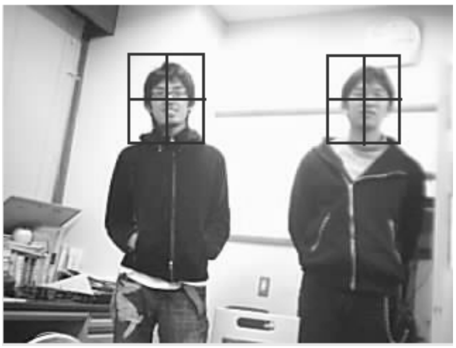

(A)

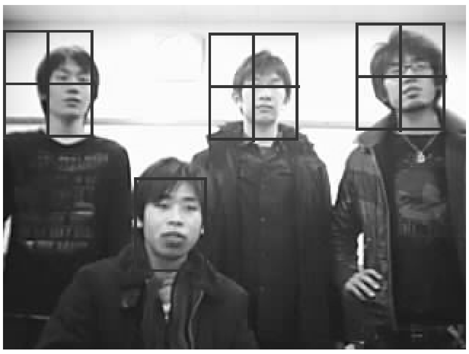

(B)

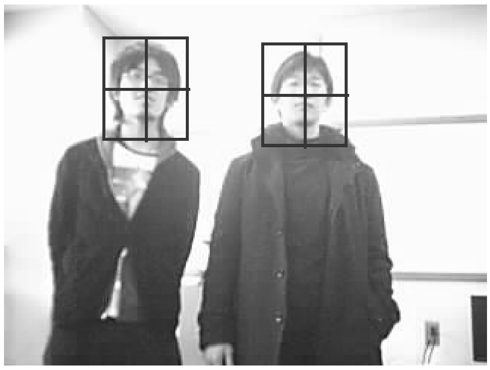

(C)

Fig. 8 Experiment

3. Conclusions

We have proposed a system, composed of an ocellus camera and intended for use in a indoor environment, that extracts a human's position from a field of view. This system constitutes the beginning for communication between a robot and a human being.

Our next subject of study is the development of a program to recognize the position of the user.

References

[1] Toru Azuma, Yoshihiro Takenaga, Eiji Hayashi, Development of a self-driven personal robot、Artificial Life and Robotics(AROB 8th '03)、pp.1-3、Oita, Japan, 2003

[2] Yoshitaka Hane, Eiji Hayashi, User-recognition system for an autonomous robotin human li ving environments Artificial Life and Robotics(AROB 12th '07)、Oita, Japan, 2007

The Fourteenth International Symposium on Artificial Life and Robotics 2009 (AROB 14th '09),
B-Con Plaza, Beppu, Oita, Japan, February 5 - 7, 2009

Robust Object Instance Registration to Robot-centered Knowledge Framework

Dae Sic Lee, Gi Hyun Lim, and Il Hong Suh
dslee@incorl.hanyang.ac.kr and {hmetal, ihsuh}@hanyang.ac.kr
Dept. of Electrical and Computer Engineering
Hanyang University
Seoul, Korea, 133-791

Abstract

Robot-centered knowledge enables a robot to perform complicated service tasks. It requires that robot knowledge robustly be instantiated for logical rigidness. However, there are some misidentifications in object recognition using a single camera. In this study, robust object instance registration method is proposed to detect misidentifications of object recognition. There are four types of properties for reasoning mechanisms: confidence of recognition of objects for statistical reasoning, inherent properties of object for ontological reasoning, spatial relation between objects for spatial reasoning and temporal relation of intervals between object detections for temporal reasoning. Validity of recognition of an object will be proved by using rules of reasoning mechanisms, since the object may not be assured to be correctly identified at the time of recognition. Additionally, action recommendation rules are applied to confirm the authenticity of object recognition when an object is not proved for a given period of time. To show the validity of proposed robust object instance registration method, several experimental results will be presented in an indoor environment.

1 Introduction

Semantic knowledge is required for a service robot to perform service tasks only with an object-based environment map. Suppose that you visit your friend's house and ask him/her where a cup is located. Then, he/she will answer, for example, "Go to the kitchen. A cup may be on a dinner table, or in a cupboard." In this case, Nobody says as follows; "a cup is at (x, y)." Humans will use semantic information instead of using such a metric data. In our previous works [1], we proposed robot-centered semantic knowledge framework, called Ontology-based Robot Knowledge Framework (OMRKF) which is developed for robot-centered knowledge representation. OMRKF includes four knowledge classes: perception, object, space, context, and action. And, in OMRKF, there are available domain specific rules to verify relations between knowledge classes. For robot-centered knowledge, it is required to robustly instantiate robot knowledge classes. Instances are often created by using object recognition algorithms. However, there will be some misidentifications such as false positives and/or false negatives because of imperfect object recognition algorithms. Also it is difficult to know if recognized objects are true positives or not. Inconsistent knowledge instances created from false recognition can prevent robot-centered knowledge from working for inference correctly.

There are research works that attempt to detect or control false data using rules-based [2] or randomization-based method [3]. Detection of misidentification in object recognition can be said to be one of uncertain problems. To cope with any uncertainty or vagueness using rule-based approaches, some methods are presented on various areas [4]. And there are also attempts to manage uncertainty in logic programming [5] [6]. For uncertainty, probability is considered to be the most useful approach. However it has some weaknesses, such as a scale problem that occurs when another new element is added to it. Rule-based system has advantages, such as locality, detachment, and truth-functionality. Thus, rule-based system such as expert system helps humans to make decision in a specific problem domain with rules which is gathered from expert's knowledge [7]. So, we consider cafefully object recognition in indoor environment, and extract rules to detect misidentifications.

Actually, at the time of recognition, nobody can assure that an object is correctly recognized. Therefore the recognized object cannot be registered at the time of recognition. Thus, we propose a robust object instance registration method for robot-centered knowledge framework, where the four types of properties

©ISAROB 2009

are considered to be used in reasoning mechanisms: confidence of recognition of objects for statistical reasoning, inherent properties of object including mobility for ontological reasoning, spatial relation between objects for spatial reasoning and temporal relation of intervals between object detections for temporal reasoning. Object properties are designed by using ontology to assure the consistency of robot knowledge base. Spatial relations and temporal relations, as supplementary information, are employed to verify authenticity of object recognition. Additionally, for the case when an object is not proved for a given period of time, actions of a robot are recommended to confirm the authenticity of object recognition.

To verify the proposed approaches, some experimental results will be provided for an indoor lab environment, where 20 objects are distributed over the environments.

2 Ontology-based Robot Knowledge Framework (OMRKF)

From a need of semantic information for service robot, we proposed robot-centered knowledge framework, called OMRKF, which has four knowledge classes, such as perception, model, context and activity [1]. The robot-centered knowledge is integrated by using ontology from low level sensory-motor data such as visual feature, atomic behaviors to high level information such as objects, spaces, contexts, and service tasks. It ensures consistency for all instances created by using this scheme. And there are domain specific rules that support bi-directional reasoning means. OMRKF gives robots more opportunities to complete complicated missions. Fig.1 shows the system concept of OMRKF.

Figure 1: System concept of OMRKF

3 Misidentification in Object Recognition

For the robot centered knowledge, it is required to robustly instantiate robot knowledge classes for logical ridigness. Instances in the robot-centered knowledge are often created by using object recognition algorithms. However, there will be some false object identification such as false positives and/or false negatives because of imperfect object recognition algorithms. Also it is difficult to know if recognized objects are true positives or not. We made robot taking snaps consecutively, recognizing objects and localizing by using the Evolution Robotics Software Platform (ERSP) [8] in an indoor lab environment, where objects are distributed over the environments.

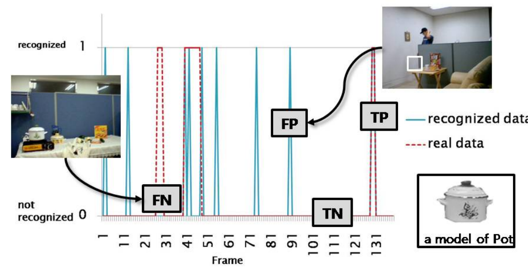

Figure 2: Object Recognition for Pot using ERSP

Fig.2 shows object recognition for pot and corresponding ground truth-data. The solid lines in this figure show the recognition of pot using ERSP vision module, and dotted lines show that there is a pot in the snaps for real. Here, there are misidentifications, such as false positives and/or false negatives, quite frequently in object recognition. Inconsistent knowledge instances created from false recognition can prevent robot-centered knowledge from correctly working for inference.

4 Overview of Proposed Rule-based Object Detection Method

4.1 System concept

To deal with misidentifications of object recognition, we propose a robust object instance registration method for the robot-centered knowledge framework.

Fig.3 illustrates system concept of our proposed method. We have designed rules to confirm authenticity of object recognition. For the rules, the following reasoning mechanisms are conidered: statistical reasoning, ontological reasoning, spatial reasoning and temporal reasoning. First of all, recognized objects are stored to buffers, such as p-buffer and/or n-buffer. Applying rules on the objects in buffers, the recognition of the objects is proved to be true or not. Finally,

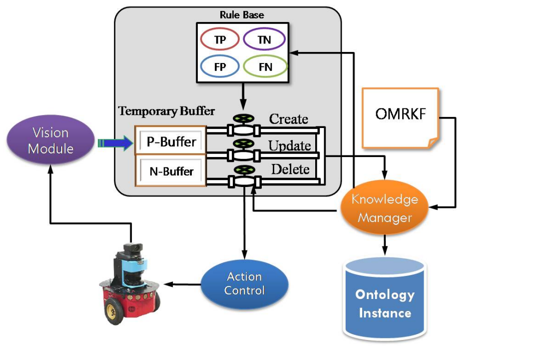

Figure 3: System concept of proposed object instance registration method

the proven objects will be settled into ontology instance database by Knowledge Manager through the three functions: create, update, or delete.

4.2 Temporary Buffers and Intervals

Because of misidentifications, the recognized objects cannot be registered at the time of recognition. To cope with this problem, two buffers, named positive buffer and negative buffer, are designed to store recognized objects until they are proved to be true or not. The buffers consists of fields of time string, object id, whether or not the object is recognized, localized x and y position. The recognized objects, before the objects are instantiated, are stored in the positive buffer (p-buffer). So are the objects recognized on different positions when compared to one in instance database. And the unrecognized objects that were registered and supposed to be recognized according to view of a robot are stored in the negative buffer (n-buffer). To confirm whether the recognition of the objects in the buffers are true or not, intervals are measured between instants at which the same object is or has to be recognized and localized. There are two types of intervals, named *is*-Interval and *has-to-be*-interval. all objects in the buffers have its own intervals. Those intervals are composed from buffers by a localized position. Fig.4 shows an example of buffers and intervals.

Suppose that a robot was moving around from time T1 to T5, recognizing the object A that is not yet instantiated. A was recognized and localized on (150, 100) at time T1, then a region for A is created around localized position by threshold (here, the threshold is assumed as ±30.) The recognitions of A from T1 to T5 have been stored continuously in p-buffer. However, the recognized result of A at T3 is not included in *is*-interval of A at T5, because localized position at T3 was out of the region.

When an interval satisfys one of rules, the object in the interval will be settled into ontology instance database by one of functions; create or update for the object in *is*-interval, and delete for the object in *has-to-be*-interval.

4.3 Properties in Reasoning Mechanisms

Four properties are utilized in reasoning mechanisms to build rules in our proposed method: inherent properties of object for ontological reasoning, spatial reasoning, and temporal reasoning, and confidence of recognition of objects for statistical reasoning.

Object properties are designed by using ontology to assure the consistency of robot knowledge base. Mobility, spatial relations, temporal relations and confidence of recognition, as supplementary information, are employed to verify authenticity of object recognition. These properties are used for ontological reasoning, spatial reasoning, temporal reasoning and statistical reasoning. Object properties are placed in robot-centered ontology scheme and/or instance database. So they are provided to rules by Knowledge Manager(KM).

Mobility of each object represents how easily the object can be moved. In the case of cups, pots, and snacks, their values of mobility property are true. On the other hand, the values of mobility property are false for television, refrigerator, and desk.

Spatial relations among objects, such as left, right, above and so on, are generated from localized position between objects by spatial reasoning, when object instances are created. Spatial relations are used to provide additional information to efficiently prove the object recognition to be true or not.

Temporal relation represents relations of intervals between object detections using before, met-by, overlapped-by and so on. Temporal relations are used

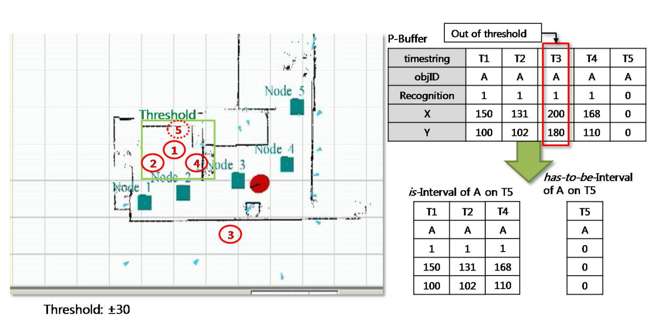

Figure 4: Example of buffers and intervals

for temporal reasoning which was proposed in [9] to reason about if some objects are recognized together or not for several periods of times.

Confidence of recognition is computed by interval-counter(γ) from recognition rate of each object to be used for statistical reasoning. Recognition rate of each object in the proposed method is obtained as follows: suppose that a robot took 100 snaps of object A while moving around. And A was recognized in 80 snaps. Then the recognition rate of object A is 80%. Recognition rates of objects in our method are supposed to be given by experts before rules are applied.

If the recognition rate of object A is x, (1-x) is the probability for that the recognition of A can be false. From that, (1-x)$^\gamma$ can be calculated to define probability when the vaues of γ consecutive recognition are all false. If the result of (1-x)$^\gamma$ is less than 5%, then it can be said that the recognition are reached 95% of confidence level. The interval-counter at that case is represented as follows;

$$\gamma : (1-x)^\gamma \geq 0.05. \quad (1)$$

Suppose that two objects A and B are recognized together and they have spatial reations to each other. Then we can measure confidence of recognition for multi objects and it can be expected to enable object recognition to be proved, although the confidence of recognition for multi objects is less than confidence recognition for each object. Interval-counter for multi objects, that makes confidence of recognition reached 95% of confidence level, is derived as follows;

$$\gamma_{multi} : (\Pi_{i=1}^{n}(1-x_{obji}))^{\gamma_{multi}} \geq 0.05. \quad (2)$$

Interval-counter for multi objects(γ_{multi}) will be used only to update or delete object instances in instance database.

5 Rules

Using the four properties, we have designed rules to confirm the object recognition. The rules can be clissified into three categories by reasoning mechanisms: statistical reasoning rules, spatial & temporal reasoning rules, and action recommendation rules. If objects which are already registered are recognized on the registered position, the recognized object will be considered to be proved as true.

5.1 Statistical Reasoning Rules

Rules in this category are called as statistical reasoning rules, used for most cases in object recognition. The statistical reasoning rules are used for the first instantiation of objects, update of instances caused by object mobility, or unrecognized objects that were supposed to be recognized according to view of a robot. Recognized objects are stored in buffers with lapse of time as a robot is moving over and over, and magnitude of intervals becomes growing. When *is*-interval of an obejct reaches over some confidence level, the recognition of the object is proved to be successfull. The statistical reasoning rules given above will look like;

```
IF an is-Interval of TV AND
  length of the Interval is over 3
  (interval-counter of TV)
THEN The data are proved as true.
```

5.2 Spatial & Temporal Reasoning Rules

Rules in this category are used to update or delete object instances in instance database. If an object A is identified and, there are spatial relations or temporal relations with other objects B's, and B's are recognized with same spatial or temporal relations with A, then recognition of object A can be proved by applying γ_{multi} even at a confidence level which is lower than the confidence level employed in the first remedy described above. Rules given in this category will look like;

```
IF An is-Interval of Clock AND
  DeskLamp has spatial relation with Clock AND
  DeskLamp also has is-interval AND
  the intervals are overlapped AND
  length of the overlapped intervals is over 2
  (interval-counter for the objects)
THEN the recognitions are proved to be true.
```

5.3 Action Recommendation Rules

There are cases that an object is not proved for a period of time with the above-mentioned rules. It is necessary to handle with this object. Therefore, in the proposed method, actions like an object re-searching are used with object properties. Action is special property of robot, which makes robot different from regular computer. There are three types of action recommendation rules.

First, when an object is not proved for a given period of time, magnitude of the intervals will be growing

©ISAROB 2009

over and over. To deal with this object, actions of a robot and mobility of objects can be utilized. For example, if the object does not have mobility, we can think the *is*-intervals are true, because the obejct is recognized on one position for a given period of time and it is hard to be thought that the object could be moved frequently for that moment. In the case when the object has mobility, it cannot be proved easily, so it is necessary to re-search the object around the localized position. These kinds of rules will look like as follows;

```
IF length of all Intervals of Cup is over two
  times of 5 (interval-counter for Cup) AND
  Cup has mobility
THEN re-search around Cup.
```

Second, there could be a case where object A has been proved as true negative but A does not have mobility. In this case, it could be either that object was truely moved or not. The object could not be recognized by other reasons. We cannot easily be sure of the reasons. Therefore, re-searching the object could be useful for correcting additional information to confirm the result. These rules will look like as follows;

```
IF Fridge has been proved as TN AND
  Fridge has not mobility property
THEN re-search around Fridge.
```

Third, we can come up with some cases where object A has been proved as true negative but object B which has spatial relation with A has been considered as true positive. In this case, A could not be recognized from a variation of view caused by position of a robot. Through the actions refering spatial relation between the objects, the result of A can be confirmed. These rules can be represented as follows;

```
IF Keyboard has been proved as TN AND
  Monitor that has spatial relation
  with Keyboard has been proved as TP
THEN re-search around Monitor.
```

6 Experiment

6.1 Experimental Environment

Our experimental environment is made up of a kitchen and a living room. We made models for 20 objects and assumed that there is only one object for each object model in the environment. The recognition rate of each object is derived from the recognized object data in 213 snaps. A robot took snaps with a single camera attached on the robot and recognized the objects using ERSP vision module, as moving along with nodes.

6.2 Experimental Result

Fig.5 shows how proposed method works to confirm misidentifications and correct them. (a) in Fig.6 is about detection of false negative in recognition of TV using statistical reasoning rules. The recognitions of TV were stored in p-buffer. And two *is*-intervlas and a *has-to-be*-interval are generated for TV from the p-buffer. Interval counter(γ) for TV was measured as 3 in our experiment. The positive results of TV in buffers are proved to be true from the sec-

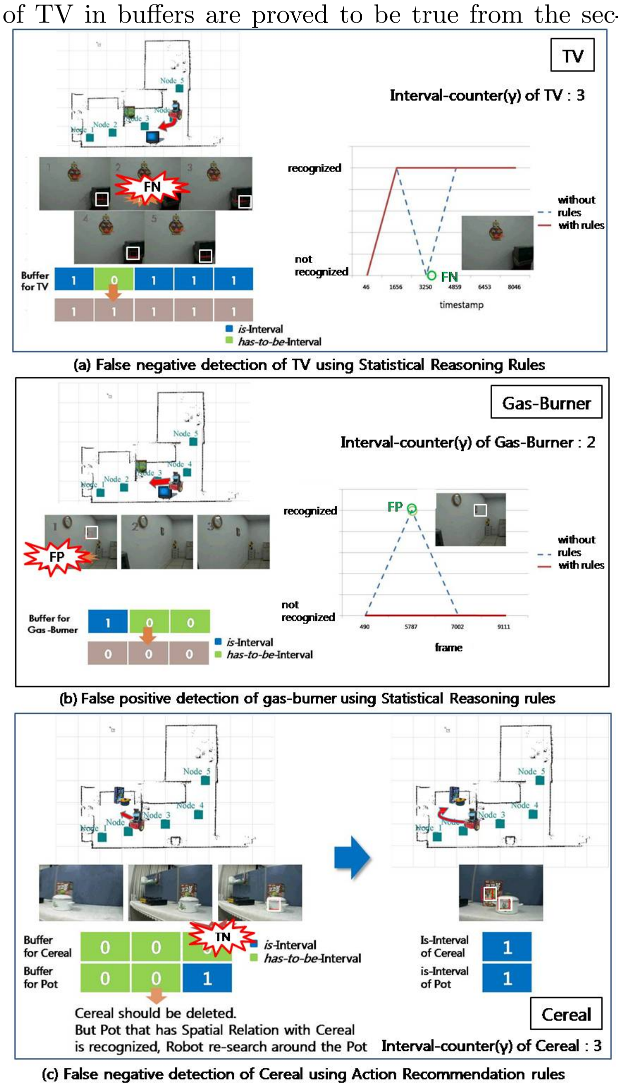

(a) False negative detection of TV using Statistical Reasoning Rules

(b) False positive detection of gas-burner using Statistical Reasoning rules

(c) False negative detection of Cereal using Action Recommendation rules

Figure 5: The results of object recognition using the proposed method.

Table 1: Misidentification rate

	without rules	with rules
TV	19.67%	9.83%
Cereal	23.80%	4.76%
Gas-burner	46.15%	23.07%

ond is-interval as it is reached the confidence level by applying statistical reasoning rules. Thus the negative results in *has-to-be*-interval at the second frame is considered as false and it is corrected to be true.

(c) in Fig.5 shows detection misidentification of cereal instance using action recommendation rules. Spatial relation between pot and cereal instances were generated when the instances were created. When the robot was watching the position where the pot and the cereal were, the cereal happened to be considered as true negative because it was patially shaded by the pot. At the moment when the cereal was proved as true negative, the pot was considered as true positive, so that the robot was asked to re-search around the pot by action recommendation rules. Finally, from changing the view by actions of robot, the cereal instance was found and the negative results of the cereal were ignored, then the instance of the cereal was kept in instance database.

Table 1 shows the rate of misidentifications about TV, gas-burner, and cereal without and with rules. From the result in table 1, we showed that the misidentification rate were reduced through the proposed method.

7 Conclusion

We proposed robust object instance registration method to robot centered knowledge framework, where statistical reasoning rules, spatial and temporal reasoning rules, and action recommendataion rules are employed. To verify authenticity of object recognition that cannot assure an object is correctly recognized at the time of recognition, buffers, named *p*-buffer and *n*-buffer, and intervals, named *is*-interval and *has-to-be*-interval, are designed. In addition, we showed that misidentifications in object recognition can be detected and corrected by using the proposed method, so that robot centered knowledge framework can be managed robustly.

Acknowledgements

This work was performed by a grant of the Second Stage of BK21 Research Division for Advanced IT Education Program on Industrial Demand, and for the Intelligent Robotics Development Program, one of the 21st Century Frontier R&D Programs funded by Korea Ministry of Knowledge Economy.

References

[1] Suh IH, Lim GH, Hwan WI et al.(2007), "Ontology-based Multi-layered Robot Knowledge Framework(OMRKF) for Robot Intelligence," *IEEE/RSJ International Conference on Intelligent Robots and Systems 2007*, p429-436, San Diego, CA, USA, Oct 29-Nov 2, 2007

[2] Kyoshgoftaar TM, Seliya N, Gao K(2004), "Rule-Based Noise Detection forSoftware Measurement Data," *In IRI*, pages 302-307, 2004.

[3] Jahanian H, Soltanian-Zadeh H, Hossein-Zadeh SA(2004), "Controlling the False Poritive Detection Rate in Fuzzy Clustering of FMRI Data," *IEEE International Symposium Biomedical Imaging: Macro to Nano 2004*, p388-391, April 15-18, 2004

[4] Yang J, Liu J, Wang J et al.(2006), "A generic rule-base inference methodology using the evidential reasoning approach - RIMER," *IEEE Trans. on Sys., Man, and Cyb. (Part A: Systems and Humans) 2006*, p.266-285, March 2006

[5] Damasio CV, Pan JZ, Stoilos G et al., "Representing Uncertainty in RuleML," *IOS Press*, 2008

[6] Loyer Y, Straccia U, "Default Knowledge in Logic Programs with Uncertainty," *In International Conference on Logic Programming*, volume 2916 of LNCS,pages 466?480, Mumbai, India, 2003.

[7] Shortliffe EH(1976), "Computer Based Medical Consultations: MYCIN." *in Computer Based Medical Consultations: MYCIN*

[8] Munich M, Ostrowski J, Pirjanian P(2005), "ERSP: A software platform and architecture for the service robotics industry," *in Proc. IEEE International Conference on Intelligent Robots and Systems*, 2005.

[9] Allen JF(1991), "Planning as Temporal Reasoning," *the Second International Conference on Principles of Knowledge Representation and Reasoning*, Cambridge, MA April, 1991

©ISAROB 2009

Developing High-Level Management Facilities for Distributed Unmanned Systems

Peter Sapaty
Institute of Mathematical Machines and Systems, National Academy of Sciences
Glushkova Ave 42, 03187 Kiev, Ukraine, sapaty@immsp.kiev.ua

Klaus-Dieter Kuhnert
Institute of Real-Time Learning Systems, University of Siegen
Hölderlinstr. 3, D-57068 Siegen, Germany, kuhnert@fb12.uni-siegen.de

Masanori Sugisaka
Department of Mechanical and Electrical Engineering, Nippon Bunri University
1727 Oaza Itiki, Oita, 870-0397, Japan, ms@alife-robotics.co.jp

Robert Finkelstein
Robotic Technology Inc.11424 Palatine Drive, Potomac MD, USA
RobertFinkelstein@compuserve.com

Abstract

Due to increasing complexity of tasks delegated to unmanned vehicles, their collective use is becoming of paramount importance for performing any reasonable jobs. An approach is offered where group behaviors are accomplished automatically rather than set up manually, as usual. Missions in the Distributed Scenario Language (DSL) can be executed jointly by communicating interpreters in robotic units. Scenarios like reconnaissance, camp security, convoy, mule, and EOD in DSL, oriented on different numbers of cooperating vehicles, are demonstrated. The approach may allow us to effectively manage any robotic teams, both homogeneous and heterogeneous, regardless of the number of vehicles in them.

Keywords: unmanned systems, scenario language, robotic teams, swarms, distributed interpretation, reconnaissance, camp security, convoys, EOD, high-level management.

1 Introduction

With the world dynamics increasing due to global warming, numerous natural and manmade disasters, military conflicts, and international terrorism, using unmanned (ground, sea, underwater, and air) systems can alleviate many problems and save lives in hazardous environments. Because of the complexity of tasks delegated to unmanned solutions and still insufficient capabilities of existing robotic vehicles, their simultaneous, collective use may be of paramount importance to perform any reasonable jobs. Operating together, the unmanned groups, often called swarms, can fulfill the required objectives despite possible runtime damages to individual units.

We are offering a novel approach to organization of unmanned swarms, oriented from the very beginning on parallel solutions in physical spaces, with swarm behaviors resulting naturally and accomplished automatically, rather than programmed manually. A mission scenario, written in a special high-level language and reflecting semantics of what to be done in a distributed space rather than details of implementation, is executed in a cooperative manner by dynamically networked unmanned units.

The current paper is inspired by the European Land Robotic Trial ELROB 2008 [1], in which the authors participated. It was conducted to provide trials as close as possible to operational scenarios for UGVs/UAVs with focus on short-term realizable robot systems. The day and night trials were organized within the following five main scenarios: non-urban reconnaissance, camp security, transport convoy, transport mule, and explosive ordnance disposal. Only a limited number of robotic units was engaged in every scenario, just one or two, whereas every scenario could potentially be executed with much higher efficiency if using robotic teams with many units, which cooperate with each other.

The paper reflects an initial state of the international project under sponsorship of Alexander von Humboldt Foundation (AvH) in Germany. Its aim is formalization of known mission scenarios in such a way that they could be performed by any available numbers of robotic vehicles, with the management burden shifted to self-organized robotic teams--thus relieving human operators from tedious routines and allowing them concentrate on mission goals and overall efficiency.

The main features of the Distributed Scenario Language and its parallel interpretation in distributed environments are briefed, with more details on the underlying paradigm and its applications easily obtainable from the previous publications [2-4]. The formalization and expression in DSL of the main ELROB 2008 scenarios is provided on a semantic level, with the scenarios to be potentially executed by any number of mobile robots, and overall management of robotic swarms fully shifted to the self-organized network of DSL interpreters.

The scenario examples in DSL (unfortunately, without detailed comments, due to page limits) show compactness of the DSL code, which can be written on the fly, thus timely responding on dynamics of the environment and changing system goals. More on the underlying spatial algorithms and related DSL code interpretation will be in subsequent publications, including the forthcoming project report for AvH.

2 Distributed Scenario Language (DSL)

Our approach is based on the Distributed Scenario Language (DSL), describing what to do in distributed spaces rather than how to do, and by which resources, leaving the latter to an effective automatic interpretation in networked environments. The DSL main features include:

- Association of different actions (which may be performed in parallel) with positions in physical, virtual, or combined spaces
- Working with both information and physical matter
- Runtime creation of distributed knowledge networks
- Distributed decision making
- Automatic command and control

DSL has a recursive syntax that can be expressed on the top level as follows (square brackets are for an optional construct, braces mean construct repetition with a delimiter at the right, and vertical bar separates alternatives).

wave → *constant* | *variable* | [*rule*] ({*wave* , })
constant → *information* | *matter*
variable → *nodal* | *frontal* | *environmental*
rule → *evolution* | *fusion* | *verification* | *essence*
evolution → *expansion* | *branching* | *advancing* | *repetition* | *granting*
fusion → *echoing* | *processing* | *constructing* | *assignment*
verification → *comparison* | *membership* | *linkage*
essence → *type* | *usage*

A rule is a general construct which can be:

- Elementary arithmetic, string or logic operation
- Hop in a physical, virtual, or combined space
- Hierarchical fusion and return of (remote) data
- Parallel and distributed control
- Special context for navigation in space
- Sense of a value for its proper interpretation

Different types of variables, especially when used together, allow us to create efficient spatial algorithms which work *in between* components of distributed systems rather than *in* them. The *nodal* variables can store and access local results in the system points visited, while other ones can transfer data in space together with the evolving control (*frontal* variables) or access and impact the internal and external world (*environmental* variables).

Due to peculiar syntax and semantics, the language parallel interpretation in distributed systems is transparent and straightforward, and does not need any central resources. DSL can dramatically simplify application programming in distributed environments, which is often much more concise and simple than in traditional programming languages.

3 Distributed DSL Interpreter

The DSL interpreter may be embedded in internet hosts, robots, mobile phones, or smart sensors (the interpreter can also be a human being herself, understanding and executing high-level orders in DSL and communicating with other humans or robots via the language syntax). The interpreter copies may be concealed, if needed (say, to work in a hostile environment); they can also migrate freely, collectively executing (mobile too) mission scenarios, resulting altogether in a flexible and ubiquitous system organization.

The interpreter [3] consists of a number of specialized modules working in parallel and handling & sharing specific data structures, which are supporting both persistent virtual worlds and temporary hierarchical control mechanisms. The heart of the distributed interpreter is its spatial track system enabling hierarchical command and control and remote data and code access, with high integrity (or "consciousness") of emerging parallel and distributed solutions, achievable without any central facilities.

In application to robotic communities, the approach allows us to convert any group of mobile robots into a goal-directed cooperative system by integrating copies of the DSL interpreter, as a universal control module U on Fig. 1, with traditional robotic functionalities, like the ones described in [5]. (The figure uses pictures of mobile robots participated in the ELROB 2008 trial.)

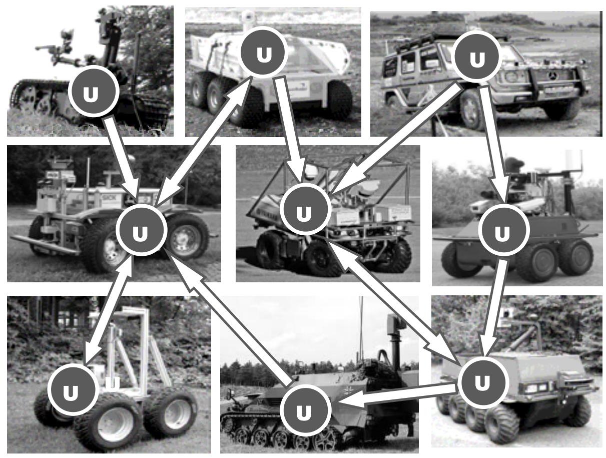

Figure 1. Heterogeneous robotic teaming using embedded DSL interpreters.

Any mission scenario in DSL can start from any robot, covering and tasking the whole system (or its parts needed) at runtime and in parallel. Subordination between the units and dynamic command and control are established automatically--as a derivative of the mission scenario and current state of environment.

Due to fully interpretive nature of the technology, the scenarios can self-recover from any point, timely reacting on failures of robots. The whole group may remain fully functional and global-goal-oriented even in case of indiscriminate damages to individual units.

4 Non-urban / Reconnaissance

For this scenario, it is supposed that a group of unknown vehicles is located in some distance in a non-urban area (defined, say, with the position of a center and area's radius), with security situation unclear there, so the reconnaissance should be done by robotic vehicles for not risking own personnel. The objective is to go to this target area and search for vehicles with specific characteristics. If found, they should be examined in detail, with their parameters collected and reported to the control station.

The general picture is shown in Fig. 2, where the reconnaissance facilities should first go to the target area (i.e. its center), observe the area by cameras/sensors to roughly locate most probable targets (by their size, for example). The next will be to move directly to these selected targets and sense & collect their detailed parameters, with sending the results to the control point where they are stored and analyzed.

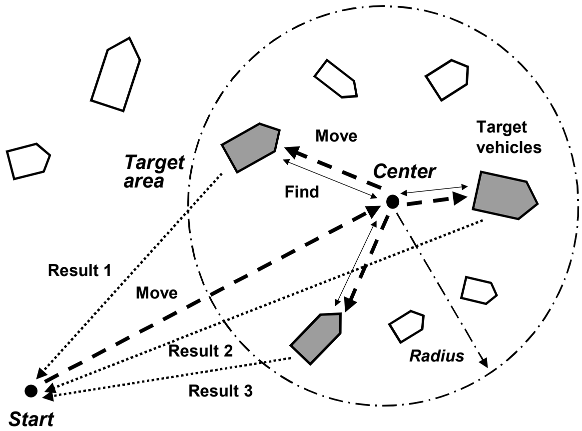

Figure 2. The reconnaissance scenario.

Parallel solution. This solution in DSL may allow us to use as many reconnaissance vehicles as possible (a single one including), potentially involving individual vehicles for each target identified, for their detailed examination.

```
USER = (
 move (start); WHERE = center;
 Targets = recognize (radius, features);
 split (Targets); WHERE = VALUE;
 collect (size, type, speed))
```

Explicitly sequential solution. The following DSL program just details navigation and organization procedures to execute the reconnaissance scenario in a strictly sequential way, which may be useful for optimization of the use of a single vehicle only.

```
move (start); WHERE = center;
Targets = recognize (radius, features);
loop (
 (Next = withdraw (Targets, 1)) != nil;
 WHERE = Next;
 Result &= collect (size, type, speed));
USER = Result
```

Avoiding obstacles. The movement to the target area and inside it may be complicated due to presence of obstacles, as shown in Fig. 3. The following DSL program, for the move from *Start* to *Center*, uses an external procedure `approach_or_stop` to detect obstacles and stop to avoid collision, and the procedure `suitable` to find next suitable waypoint on the way to the destination, from which the move should continue.

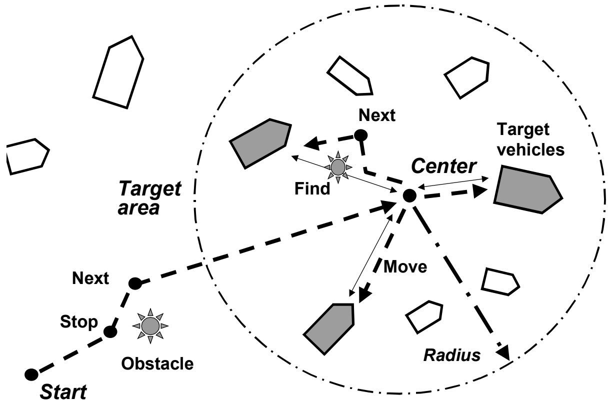

Figure 3. Avoiding obstacles.

```
move (start);
loop (approach_or_stop (center);
      WHERE ! = center;
      Next = suitable (depth, center);
      WHERE = Next)
```

5 Camp Security

For the camp security scenarios, a defined urban area has to be monitored (think military camp) and this should be executed by robotic vehicles too, to minimize risk to human personnel. The objective is to detect and report irregularities in the area, like intruders, while acquiring their positions and imagery, and transmitting to control station.

The general picture is shown in Fig. 4, where the camp units (numbered 1 to 6) are simultaneously patrolled by a number of robotic vehicles moving along the paths between and around the buildings.

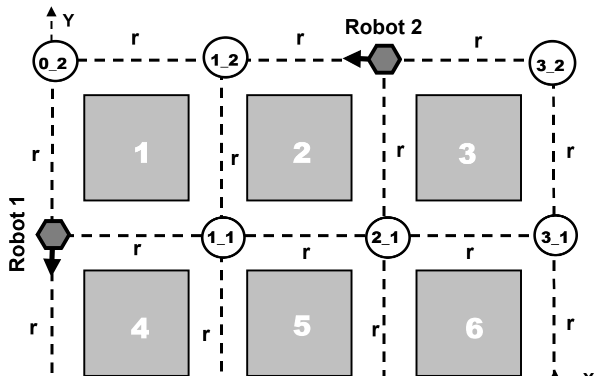

Figure 4. Camp security scenario.

Distributed campus map. The proper routing of vehicles and resolution of possible conflicts between them (like collision avoidance) can be assisted by the creation of a distributed map of the campus area (just reflecting Fig. 4) by the following DSL program (with node names reflecting X-Y coordinates of the crossings, and all links named `r`):

```
create (#3_1; F1=A; r#2_1; F2=A;
 r#1_1; F3=A; r#0_1;
```

```
  (r#0_2; r#1_2; r#F3, (r#2_2; r#F2,
   (r#3_2; r#F1))),
  (r#0_0; r#1_0; r#F3, (r#2_0; r#F2,
   (r#3_0; r#F1))))
```

Random movement. The next program organizes duty performance by three parallel processes (which may be executed by three robots) using the created distributed map, with random choice of the next-hop crossing and activation of the external service procedure `move_check_report` to analyze the local security situation while on the move.

```
hop (0_1, 2_2, 3_0);
WHERE = CONTENT;
repeat (
 or (
  (hop (link (random));
   grasp (Mark == nil; Mark = 1);
   (hop (BACK); Mark) = nil;
   move_check_report (CONTENT)),
  stay))
```

Movement via predetermined routes. If to use predetermined routes only, like shown in Fig. 5 (one route using links named `r1` and another one `r2`), the collisions between robots can be avoided in full.

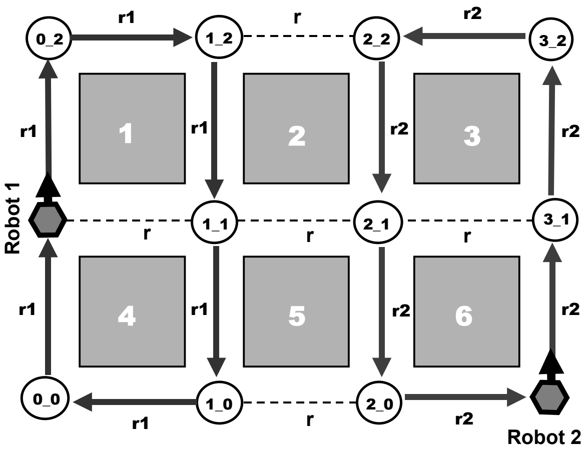

Figure 5. Using predetermined routes

Additional links `r1` and `r2` in the campus map can be installed by the following DSL program:

```
Linkup (
 (#0_2; r1#1_2; r1#1_1; r1#1_0; r1#0_0;
  r1#0_1; r1#0_2),
 (#3_2; r1#2_2; r1#2_1; r1#2_0; r1#3_0;
  r1#3_1; r1#3_2))
```

And two independent spatial processes navigating the campus via the new links (which may engage two robots) can be organized by the following parallel DSL code:

```
(hop (0_1); Flink = +r1),
(hop (3_0); Flink = +r2);
WHERE = CONTENT;
repeat (
  hop (link (Flink));
  move_check_report (CONTENT))
```

Any imaginable combinations of different types of simultaneous movement through the camp (like those by predetermined routes and/or by free, random, wandering) with collision avoidance can also be easily organized in DSL.

6 Transport Convoy

Imagine there is a delivery for a camp located in some distance. The objective is to move at least two vehicles to the target location, where only the first one can be manned and the second should follow the route of the first one, on a certain distance from it. We will consider a fully robotic solution for such a convoy, with two and also any number of vehicles, where only the first vehicle knows (and follows) waypoints toward the target location, while others dynamically chaining with, and following the previous ones on the move.

Two-unit convoy. It is represented by the communicating `Leader` and `Follower`, where the first one defines its movement by a sequence of waypoints, and the second one, regularly requesting the Leader, moves to the positions previously occupied by it, while keeping a certain threshold distance. This is shown in Fig. 6, and by the DSL program that follows

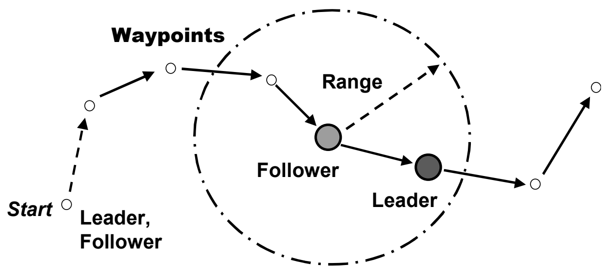

Figure 6. Two-unit convoy.

```
move (start);
(create (Leader);
 Waypoints = (w1, w2, w3, …);
 loop (
  (Next = withdraw (Waypoints,1))!= nil;
   WHERE = Next)),
(create (Follower);
 sling (
  Lcoord = (hop (range, any); WHERE);
  distance (WHERE, Lcoord) > threshold;
  WHERE = Lcoord))
```

Multiple-unit convoy. A scenario for the convoy with any number of chained processes (to be materialized by robotic units) is described by the following DSL program and depicted in Fig. 7. For this case, only the first process is a pure leader and the last process is a pure follower, while all other processes combine both functionalities, i.e. being followers for the previous processes and leaders for the subsequent ones.

```
move (start);
cycle (N < number; create (N += 1));
(NAME == 1; Waypoints = (w1, w2, w3, …);
 loop (
  (Next = withdraw(Waypoints, 1))!= nil;
   WHERE = Next)),
(NAME != 1;
 sling (
  Lcoord = (hop (range, NAME-1); WHERE);
```

```
distance (WHERE, Lcoord) > threshold;
WHERE = Lcoord))
```

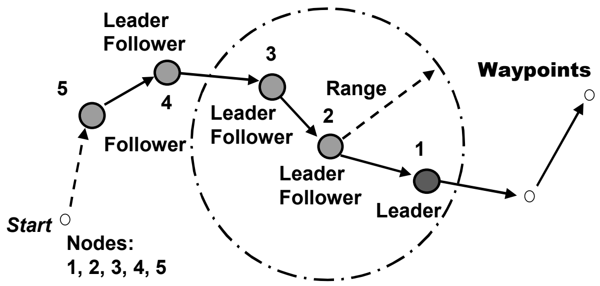

Figure 7. Multiple-unit convoy.

7 Transport Mule

Fir this scenario, there are two camps with a certain distance in between, and a cargo with a given weight should be transferred between the camps. We will consider here different possibilities to deliver payload between the camps, using unmanned vehicles as "mules".

In a single piece. This may be the case if cargo's weight allows it to be put on a single vehicle, as shown ion Fig. 8.

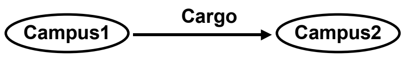

Figure 8. Single piece cargo delivery.

The related DSL program will be as follows:

```
move (Campus1);
frontal (Cargo) ="substance";
move (Campus2); Store = Cargo
```

Shuttling between camps. For this option, the process shuttles as often as possible between the two camps after partitioning the cargo into portions for the weight allowed, unless all the cargo is delivered, as shown in Fig. 9 and by the following program.

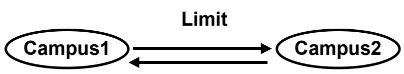

Figure 9. Shuttling delivery.

```
move (Campus1); frontal (Load);
Cargo = "substance"; Limit = 50;
loop (
 or (
 (weight (Cargo) > Limit;
  Load = withdraw (Cargo, Limit)),
 (weight (Cargo) > 0; Load = Cargo));
 hop (Campus2); Store += Load;
 hop (Campus1))
```

Multiple, parallel delivery. For this case, different processes (vehicles) are considered to be independent from each other, each moving to the destination as quickly as possible on its own (see Fig. 10 and the following program).

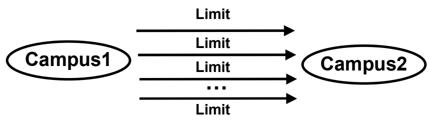

Figure 10. Parallel cargo delivery.

```
move (Campus1); frontal (Load);
Cargo = "substance"; Limit = 50;
cycle (
 or (
 (weight (Cargo) > Limit;
  Load = withdraw (Cargo, Limit)),
 (weight (Cargo) > 0; Load = Cargo)));
move (Campus2); Store += Load
```

Multiple, convoy delivery. For this scenario, the vehicles, each with a limited partition of cargo, are dynamically chaining in a column for a cohesive movement towards the destination (see Fig. 11 and the subsequent DSL program).

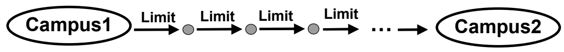

Figure 11. Delivery in a convoy.

```
move (Campus1); frontal (Load);
Cargo = "substance"; Limit = 50;
cycle (
 Or (
   (weight (Cargo) > Limit;
    Load = withdraw (Cargo, Limit)),
   (weight (Cargo) > 0; Load = Cargo));
 create (N += 1));
(NAME == 1; move (Campus2)),
(NAME != 1;
 loop (WHERE != Campus2;
       WHERE = (hop (NAME-1); WHERE));
Store += Load
```

8 Explosive Ordnance Disposal

Explosive Ordnance Disposal (EOD) means the detection, identification, onsite evaluation, rendering safe, recovery, and final disposal of Unexploded Ordnance (UXO) including detonation and burning. It is often said that the EOD operation is a 3 Ds one, which is Dangerous, Dirty and Demanding (or Difficult) job. Using robotic vehicles, especially multiple ones, is therefore becoming the most promising EOD option.

Various kinds of EOD scenarios for navigation and examination of the target territory may be offered. We will just hint here on the simplest two options, easily expressible in DSL.

Sequential territory search. This represents a single-thread process (oriented on a single vehicle), where the whole territory is incrementally scanned unless all being searched, as described by the following program and depicted in Fig. 12.

```
X1 =…, X2 =…; Y = Y1; Y2 =…; DY =…;
loop (WHERE = (X1, Y); (Y += DY) < Y2;
      WHERE = (X2, Y); (Y += DY) < Y2)
```

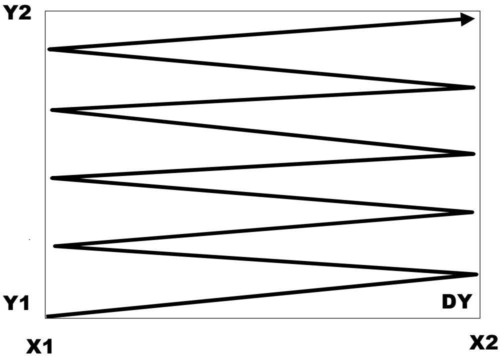

Figure 12. Sequential navigation.

Parallel territory search. This can be represented by a number of independent processes, each starting from a different location, and navigating altogether the whole region in parallel, as depicted by Fig. 13 and explained by the DSL program that follows.

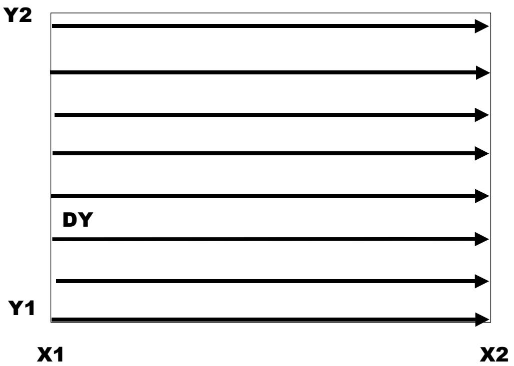

Figure 13. Parallel navigation.

```
X1 = …; X2 = …; Y1 = …; Y2 = …; DY = …;
frontal (Y) = Y1; DDY = 0;
cycle ((Y += DDY) < Y2; DDY += DY);
WHERE = (X1, Y); WHERE = (X2, Y)
```

9 Conclusions

Programming multi-robot scenarios in distributed and dynamic environments using DSL may not be more complex than, say, programming routine data processing tasks in traditional languages like Fortran, C, or Java, where the latter can run on parallel computers using any available number of processors. In our case, any multi-robot system may also be treated as a universal parallel computer (more correctly: parallel machine, as it operates not only with information but with physical matter or objects too).

The mission scenario in DSL may set up top level semantics of what, and generally how, should be done in a distributed space, and which key decisions should be taken in different spatial locations, to fulfill the objectives, regardless of the number of available robotic units, which may vary overtime (as some robots can be destroyed while others entering the operational field at runtime). This may essentially (and in many cases completely) relieve the human manager from traditional tedious routines of handling distributed multi-component systems, shifting the organizational burden to parallel scenario interpretation in the self-organized network of DSL interpreters.

This also gives us new opportunities for self-recovery in hostile environments as, first, the DSL scenarios may be free from mentioning any hardware robotic components (like computational problems in Fortran not mentioning computer registers or functional units and data transfers between them), and failures or recovery of particular robots may not be the business of the application program but rather of the internal system organization. And, second, due to fully interpretative nature of DSL, self-spreading scenarios in it may themselves recover from any point (robot), or even be self-relaunching from the beginning in most unfavorable situations. Using DSL, the human operator may effectively control distributed robotic swarms regardless of the number of units in them, just like controlling a single robot remotely, due to high self-organizational level of the swarms within the technology offered.

The current work is in progress, and in parallel with re-implementation of the technology on new, robotic, platforms (its existing public domain is mostly used for intelligent network management), we are considering various scenarios of engagement of heterogeneous unmanned systems for solving complex tasks. One of these is investigation and development of exemplary behaviors integrating energy (e.g. biofuel) seeking foraging robots [6] with other types of vehicles having specific payloads (the latter supposedly consuming the energy produced by the former). The foraging robots are dedicated to operate autonomously and for a long time in remote unpopulated areas, and heterogeneous swarms with them may represent a promising approach for advanced applications.

We also hope that the current project may help the next, ELROB 10, event to use more cooperating robots and even their swarms within the scenarios discussed, and, possibly, quite new ones.

Acknowledgment. This work has been funded by the Alexander von Humboldt Foundation in Germany.

References

[1] Military European Land-Robot Trial, M-ELROB 2008: 30 June – 03 July 2008, Hammelburg, Germany, http://www.m-elrob.eu/.

[2] P. Sapaty, M. Sugisaka, R. Finkelstein, J. Delgado-Frias, N. Mirenkov, "Advanced IT Support of Crisis Relief Missions", Journal of Emergency Management, Vol.4, No.4, ISSN 1543-5865, July/August 2006.

[3] P. S. Sapaty, Ruling Distributed Dynamic Worlds, John Wiley & Sons, New York, May 2005, ISBN 0-471-65575-9.

[4] P. Sapaty, Distributed Technology for Global Dominance, Proceedings of SPIE – Volume 6981, Defense Transformation and Net-Centric Systems 2008.

[5] K.-D. Kuhnert, M. Krödel: Autonomous Vehicle Steering Based on Evaluative Feedback by Reinforcement Learning, MLDM 2005.

[6] R. Finkelstein, EATR: Energetically Autonomous Tactical Robot, DARPA Contract W31P4Q-08-C-0292.

USAT(Ultrasonic Satellite System) and Gyro Integrated System Using Kalman Filter

Yun Sang Yeom, Ji Hoon Kang, Su Yong Kim, Jong Il Bae, Man Hyung Lee

Department of Mechanical and
Intelligent Systems Engineering
Pusan National University,
Busan, 609-735, KOREA
(Tel : 82-51-510-1456; Fax : 82-51-512-9835)
(yunsang77@dreamwiz.com)

***Abstract*:** The localization of mobile robot is an important part of control problem. USAT(Ultrasonic Satellite System) is the method to find an absolute position by using ultrasonic sensor. USAT can be able to estimate the position of mobile robot precisely, in which errors are not accumulated. USAT insure a high accuracy on static state. But mobile robot moves as fast as an estimated position errors are increased. In this paper, we propose a compensation method to increase the accuracy of estimated position on moving robot by using USAT and Gyro. USAT take a 400 milliseconds to estimate mobile robot's position one time. This method can calculate a position on increased sampling period, 100 milliseconds at once. Also a Kalman filter is employed for USAT and Gyro integration. This integrated system provides more accuracy of mobile robot position. The performance of USAT and Gyro integrated system showed its effectiveness from the result of the simulation and the experiment.

Keywords: USAT, localization, positioning, mobile robot

I. INTRODUCTION

The process of finding mobile robot in environment is a major concern in robot navigation. Nowadays, especially the need for the navigation of mobile robot has rapidly increased. To measure the position of robot, generally presented two methods. The one is absolute positioning method and another is relative positioning method. Absolute positioning is accomplished by using a active/passive landmark, beacon, map matching, CCD camera or GPS. The method of relative positioning widely uses the encoded information which gains from the wheels to determine the position of robot. But because of wheel slippage, mechanical tolerance and surface roughness, this method has its unbounded accumulation of errors. So the real position is hardly maintained as it moves longer distance [1].

The ultrasonic positioning system is very similar to GPS. It measures distances from emitters to a measuring point. Then it solves the equations to determine its position. Since ultrasonic waves are much slower than radiowaves, it is easier to count the spent time that diffused waves need to reach the measuring points than it does for GPS. However, waves radiated from other emitters interfere with each other. Thus, only one emitter can radiate ultrasonic waves at a time. Since all the transmitters radiate their waves by turns, it takes more time to measure all the distances from different transmitters. Therefore the faster mobile robot moves the more estimated position errors increased.[2],[3]

In this paper, a compensation method to increase the accuracy of estimated position on moving robot by using USAT(Ultrasonic Satellite System) and Gyro Integrated system is presented. Also a Kalman filter is employed for USAT and Gyro integration and finally the simulation and experimental result are given.

II. SYSTEM CONFIGURATION

2.1 System Modeling

Generally, the non-linear model is need to analyze a dynamic characteristics of vehicle. however, if the vehicle moves under 4 m/s(approx.). The characteristics of vehicle can be analyzed by linear model of 2 degree of freedom(bicycle model). It is verified through experiments [4],[5].

In linear model, we can substitute both right and left wheels by single equivalent wheel on centerline axle of the vehicle. so, easily figure out dynamic performance of the car ignoring many factors such as motion of suspension, transition of lateral force, and negative and positive acceleration. Herein 2 degree of freedom are a yaw and a lateral displacement.

Fig. 1. shows the 2 degrees of freedom model which shows the general linear model. Motion equation of linear model is equation (2.1) and Matrix form is equation (2.2).

$$\dot{x}(t) = Ax(t) + Bu(t) \tag{2.1}$$

$$\begin{bmatrix} \dot{v} \\ \dot{\gamma} \end{bmatrix} = \begin{bmatrix} a_{11} & a_{12} \\ a_{21} & a_{22} \end{bmatrix} \begin{bmatrix} v \\ \gamma \end{bmatrix} + \begin{bmatrix} b_{11} & b_{12} \\ b_{21} & b_{22} \end{bmatrix} \begin{bmatrix} \delta_f \\ \delta_r \end{bmatrix} \tag{2.2}$$

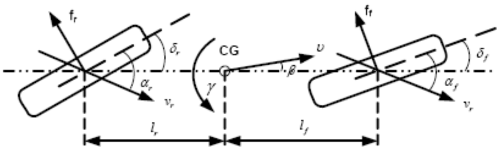

Fig. 1. Bicycle model of 4WS

Elements of matrix A and B shows equation (2.3).

$$a_{11} = -\frac{(c_r + c_f)}{mv},\quad a_{12} = -\frac{(c_f l_f + c_r l_r)}{mv} - v$$

$$a_{21} = -\frac{(c_f l_f - c_r l_r)}{Jv},\quad a_{22} = -\frac{(c_f l_f^2 + c_r l_r^2)}{Jv} \qquad (2.3)$$

$$b_{11} = \frac{c_f}{m},\quad b_{12} = \frac{c_r}{m}$$

$$b_{21} = \frac{c_f l_f}{J},\quad b_{22} = \frac{c_r l_r}{J}$$

Turning radius of vehicle can be reduced in a low speed and a constant speed of it. Also to improve controllability, we adopted inverse phased wheel in rear wheel of 4WS system. So, in same magnitude, the input to rear wheel has opposite sign to the input to the front wheel. In this way, single input system(SISO) can be modeled instead of 2 input system(MIMO). Equation (2.4) is showing this.

$$\begin{bmatrix} \dot{v} \\ \dot{\gamma} \\ \dot{\theta} \end{bmatrix} = \begin{bmatrix} a_{11} & a_{12} & 0 \\ a_{21} & a_{22} & 0 \\ 0 & 1 & 0 \end{bmatrix} \begin{bmatrix} v \\ \gamma \\ \theta \end{bmatrix} + \begin{bmatrix} b_{11} - b_{12} \\ b_{21} - b_{22} \\ 0 \end{bmatrix} \begin{bmatrix} \delta_{fr} \end{bmatrix} \qquad (2.4)$$

2.2 PD Controller

Getting feedback signal that is proportional to the derivative of error with respect to time, PD controller shows good performance of increasing damping ratio and decreasing overshoot. This kind of controller(PD) is frequently applied in industrial field due to easier adjustment of control parameter (Kp,Kd). Controller transfer function K(s) is (2.5)

$$K(s) = K_p(1 + T_d s) \qquad (2.5)$$

Actually, control gain as real experiment differs from it of simulation due to unstable driving voltage and vehicle's nonlinearity, and moreover, the vehicle sometimes doesn't response to input signal. So, in this research, verified values of control gain from the previous research is applied to Kp, Kd, (Kp =1.6, Kd = 0.2)

2.3 The Positioning System

U-SAT (Ultra Satellite System) is provided by Korea LPS Co. as positioning systems for unmanned navigation using as shown in Fig. 2.[6]. The USAT operates like GPS (Global Positioning System), Using ultrasonic sensor it measures distances that are needed.

4 unit of 40 Khz ultrasonic transmitters is attached on the ceiling, and the vehicle is equipped with 2 receivers.

When the vehicle receives the RF (Radio Frequency) signal, transmitters are synchronized with receivers. RF

Transmitters transmit signal in regular the intervals of 0.4sec, and the system calculate TOF(Time of Flight),

and then, the distance between transmitters and receivers can be measured..

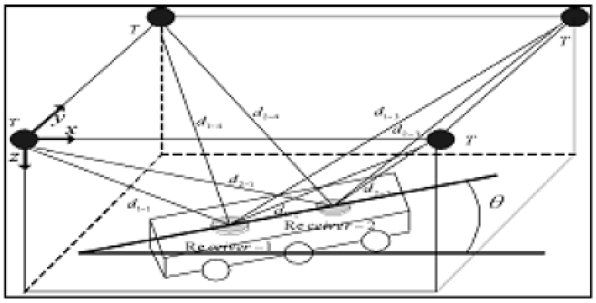

Fig. 2. Placement of sensor USAT

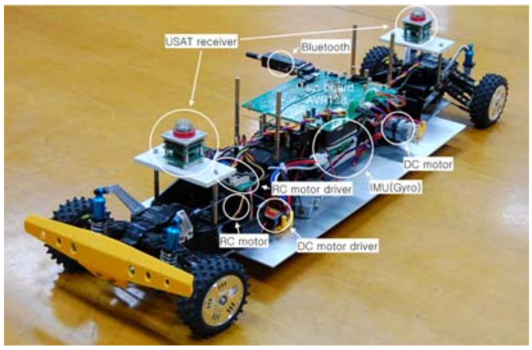

Fig. 3. Test model of unmanned vehicle

Using 2 receivers the absolute position based on 3 dimensional space(X,Y,Z) and angle of direction θ can be measured. Fig. 2. shows way of measuring position (X,Y,Z) and angle of direction θ using USAT . and Fig. 3. shows the test model.

2.4 Detecting Angle of Direction Using USAT

Getting information about where the vehicle is moving to is important as well as getting to know the position of it. As you see on Fig. 4 the vehicle is equipped with 2 Ultra sonic receiver to get information of angle of direction as well as of position of the vehicle. After the position of the vehicle is decided, an angle of direction of the vehicle can be calculated by below equation (2.6)

$$\theta = \tan^{-1}\left(\frac{y_{front} - y_{rear}}{x_{front} - x_{rear}}\right) \qquad (2.6)$$

Herein, θ is angle between X axis and the direction the vehicle is forwarded to. Degrees of Angle increases in a clockwise direction from X axis

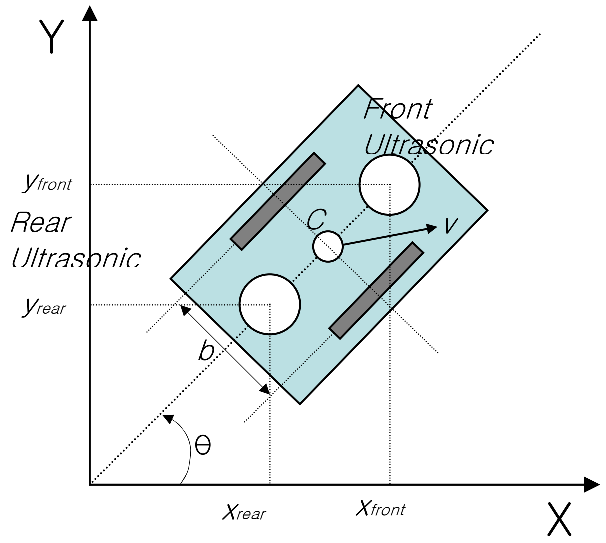

Fig. 4 Mobile robot position and heading angle

2.5 Application of Kalman Filter

Getting data from Gyro sensor and USAT, adopted Kalman filter estimates more precise angle of direction than before using the filter

To acquire angle of direction, let state variable as below

$$x = \begin{bmatrix} \theta \\ \hline \varphi \end{bmatrix} \qquad (2.7)$$

θ is angle of direction of the vehicle φ is angular speed of rotation.

State space equation model(2.8) can be obtained in continuous time model.

$$\dot{x} = \begin{bmatrix} 0 & 1 \\ 0 & 0 \end{bmatrix} x + Q \qquad (2.8)$$

Letting sampling period Δt and discretizing the continuous time model, Φ_k can be obtained as below

$$\Phi_k = \begin{pmatrix} 1 & \Delta t \\ 0 & 1 \end{pmatrix} \qquad (2.9)$$

$$Q_k = \int_0^{\delta t} \Phi(\tau)\Gamma Q \Gamma^T \Phi(\tau)^T d\tau$$

$$= \begin{pmatrix} \frac{W}{3}\Delta t & \frac{W}{2}\Delta t \\ \frac{W}{2}\Delta t & W\Delta t \end{pmatrix} \qquad (2.10)$$

Getting data as azimuth angle from USAT

The measurement equation can be obtained as below

$$[\theta] = H(k)x(k)$$

$$H_k = [1 \quad 0] \qquad (2.11)$$

Using Kalman filter with data from the above state space model and the measurement equation, optimal angle of direction can be obtained minimizing covariance as an gap between the reference and data from Gyro and USAT.

III. EXPERIMENT

On Fig 3.1, The circle(small circle) through all the points scattered on the coordinate plane is given reference route. And the other circle(large circle) is path followed by the vehicle. We can see the vehicle traced given path smoothly.

Fig 3.2 shows a variation of the vehicle's angle using Kalman filter while it moves around in given path . Stable steering characteristic in circular movement can be seen. Having 180 degree at the point of departure the angle of vehicle's direction increases from 180 to 360 (0), and to 180 degree.

Fig 3.3 shows angular gap between given reference and vehicle heading direction. It fluctuates approximately between -10 and 30 degrees of angle.

Fig 3.4 shows distance gap between given reference and vehicle's position. It ranges within 220mm.

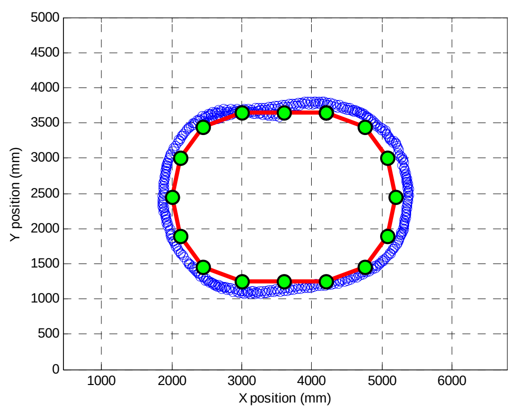

Fig.3.1 Position Estimation at Vehicle speed 0.38(m/s)

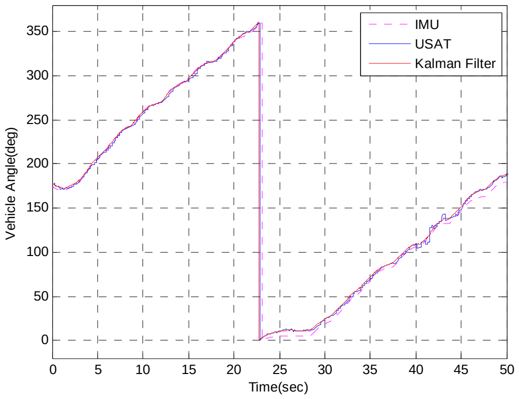

Fig.3.2. Vehicle angle using Kalman filter

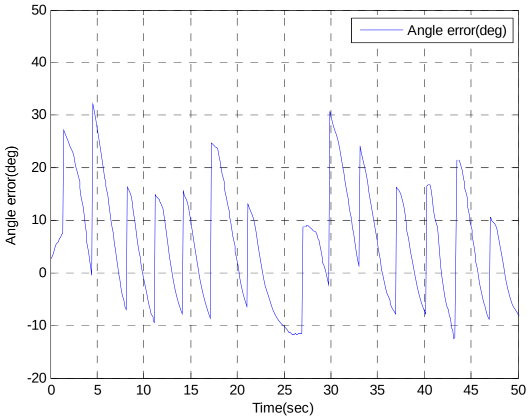

Fig 3.3 Angular gap (error) between vehicle and given reference

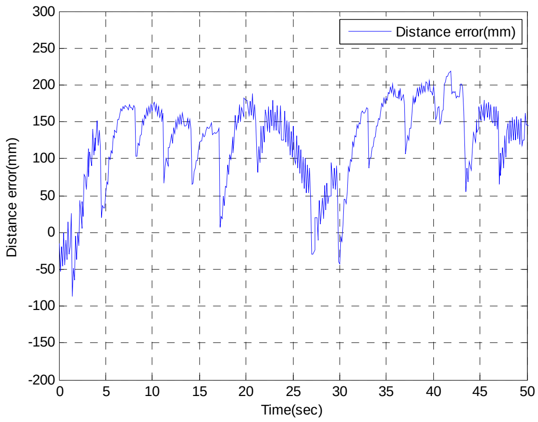

Fig 3.4 Distance gap (error) between vehicle and given reference

IV. CONCLUSION

The localization of mobile robot is an important part of control problem. USAT is useful device as a positioning detection system. But, To have better performance while the vehicle trace a given path as an reference. We adopted Gyro and Kalman filter as compensation of positioning detection with USAT.

Gyro compensate the vehicle's position for position error from measured angular speed of rotation and adopted Kalman filter adjusts feedback signal from estimated vehicle's direction of angle.

The vehicle trace given path well with the result of angular error within 30 degrees and distance error within 220mm.

REFERENCES

[1] Jae Hwan Kim and Poong Hyun Seong, "Experiments on orientation recovery and steering of autonomous mobile robot using encoded magnetic compass disc," *IEEE Transactions on, Instrumentation and Measurement*, Vol. 45, Feb, 1996, pp. 271~274.

[2] D. H. Lee, S. Y. Kim, K. S. Yoon, and M. H. Lee, "A Long Range Accurate Ultrasonic Distance Measurement System by Using Period Detecting Method," *Journal of the Korean Society for Precision Engineering*, Vol. 24, No.8 Aug 2007, pp. 41~49.

[3] S. Y. Kim, D. H. Lee, H. T. An, S. H. Lee, Y.H. Koh, and M. H. Lee "Analysis of UPS (ultrasonic positioning system) using DGPS," *Industrial Electronics Society, 2004. IECON 2004.30th Annual Conference of IEEE,* Vol. 1, pp. 609~613, 2004

[4] K. S. Lee, T. Y. Shin, S. Y. Kim, J. M. Lee and M. H. Lee, "Lateral Control of 4WS Unmanned Container Transporter Using U-SAT", ICASE 2006

[5] Y. H. Lee, S. I. Kim, M. W. Suh, H.S Son and S.H. Kim, "Liberalized Dynamic Analysis of a Four-Wheel Steering Vehicle", Vol.5, No. 5, pp. 101-109, 1994

[6] Jung-Min Lee, Dong Hwal Lee, Hee Tae An, Nam Huh, Myoung Kook Kim and Man Hyung Lee, "Ultrasonic Satellite System for the Positioning of Mobile Robots", Industrial Electronics Society 2004, IECON 2004, Annual Conference of IEEE, Vol. 1, pp. 448-453, November 2004.

The Fourteenth International Symposium on Artificial Life and Robotics 2009 (AROB 14th '09),
B-Con Plaza, Beppu, Oita, Japan, February 5 - 7, 2009

Development of an Autonomous Flexible Robot that Uses No Explicit Sensors or Controllers

R. Anzai and K. Ito

Department of Systems and Control Engineering, Hosei University, 3-7-2 Kajino-cho, Koganei, Tokyo, Japan
(Tel: 81-42-387-6093; Fax: 81-42-387-6381)
(ryota.anzai.rp@gs-eng.hosei.ac.jp, ito@hosei.ac.jp)

Abstract: Recently, various robots that have many degrees of freedom have been developed and applications for practical use like a rescue operation, domestic robot, and so on, have attracted much attention. However, it is difficult to control the robot autonomously in the real environment, because, in order to control the many degrees of freedom, we have to observe many states, calculate huge amount of information, and operate many actuators. In this paper, we consider a flexible robot that perceives inclination of a slope and goes up the slope without sensors or controllers. To demonstrate the effectiveness of the proposed framework, we have developed a prototype robot and conducted experiments. As a result, the robot has perceived inclination and has been able to go up a gentle slope autonomously. We can conclude that by designing the body for utilizing the properties of the environment, we can realize autonomous robot that has no explicit sensors or controllers.

Keywords: Flexible robot, Column robot, Autonomous robot, Properties of the real world,

I. INTRODUCTION

Recently, various robots that have many degrees of freedom have been developed and applications for practical use like a rescue operation, domestic robot, and so on, have attracted much attention[1]-[5]. However, it is difficult to control the robot autonomously in real environment, because, in order to control the many degrees of freedom, we have to observe many states, calculate huge amount of information, and operate many actuators in real-time.

On the other hand, insects and lower animals can behave autonomously in spite of the fact that their brains are very small and calculation abilities are restricted [6]. The reason why they can behave adaptively have not been clarified completely, but, it is consider that their bodies play important roles and reduce load of the brain [7].

In our conventional works [1]-[3], we have considered reinforcement learning for a real snake-like robot, and to reduce the size of the state action space, we focused on mechanical design of the robot and showed that time for learning can be extremely reduced and acquired policy can obtain generality by just utilizing the properties of the body without adding any modification to the algorithm of Q-learning. But these works, a computer is employed as a controller.

In this paper, we consider an autonomously flexible robot that perceives inclination of a slope and goes up the slope without sensors or controllers as the simplest example. To control the robot, we employ physical and chemical properties of the real world. We employ sodium hydrogen carbonate and citric acid. They are in the tanks of the robot and by mixing them with water, carbon dioxide is generated. The pressure of the carbon dioxide moves water, and the center of gravity of the robot moves. Thus, the robot moves with rotating. Inclination of the slope is perceived by the water without sensors, and many degrees of the robot are controlled by the physical dynamics. So, the robot can move autonomously without sensors or controllers.

To demonstrate the effectiveness of the proposed framework, we have developed a prototype robot and conducts experiments.

Ⅱ. PROBLEM OF CONVENTIONAL FRAMEWORK

In this paper, we consider that the problem of conventional framework is to assume the computer the brain. In general, animals have a brain, and it is considered that the brain is the origin of intelligence, and we tend to consider that the computer works as the brain, and the computer is indispensable for realizing intelligent behaviors. So, conventional robots have many sensors, and actuators, and a computer. The computer is used for processing information from the sensors to generate control signal of the actuators.

©ISAROB 2009

However, it is difficult to control robots with many degrees of freedom autonomously in real environment by conventional frameworks. Because, in order to control the many degrees of freedom, we have to observe many states, calculate huge amount of information, and operate many actuators in real-time.

In this section, to explain problems of the conventional framework, we divide them into three problems written below.

P1 PROBLEM OF MEASUREMENT

The number of sensors that robot can be installed has limitation. And in addition, there are same physical parameters that can not be measured. So, it is impossible to acquire all of necessary information of the real environment.

P2 PROBLEM OF MODELING

There are some physical parameters that we can not identify in advance, because the environment is unknown. Thus, we can not construct a model for the controller.

P3 PROBLEM OF REAL-TIME PROCESSING

As the complexity of environment increases, it is difficult to process all the necessary information in real-time, because the computational costs increase exponentially.

From the problem P1 to P3, it is difficult to apply conventional framework of control theory to autonomous robots that operate in the real environment.

On the other hand, insects and lower animals can behave autonomously in spite of the fact that their brains are very small and calculation abilities are restricted. Especially, adaptability of the animals is respectable. They can behave adequately at various situations, in spite of the fact that the situations are always different and the same situations never occur again. The mechanism how to realize the adaptability has not been clarified completely, but it is considered that their bodies play important roles and reduce load of the brains. For instance, by designing the mechanism and the parameters of the body adequately, the body can adapt itself to the environment without sensors or controllers. The adaptive behavior is realized by interaction with environment. So, states of the environment affect the body directly, and movement of the body is determined by dynamics of the environment. Thus, sensors and controllers are not required.

Ⅲ. PROPOSED FRAMEWORK

In this paper, we consider an autonomous flexible robot that uses no sensors or controllers as the simplest example. Fig.1 shows the proposed mechanism. In Fig. 1 (i), to explain clearly, only hoses between Ta and Tb are illustrated, and illustrations of the other hoses are omitted. Fig. 1 (ii) is the extended figure of Ta and Tb in Fig. 1 (ii). The shape of the robot is a column and the robot moves by rotating. To control the robot, we employ physical and chemical properties of the environment. The robot consists of flexible sheets, and has six tanks that contain water, and has twelve valves.

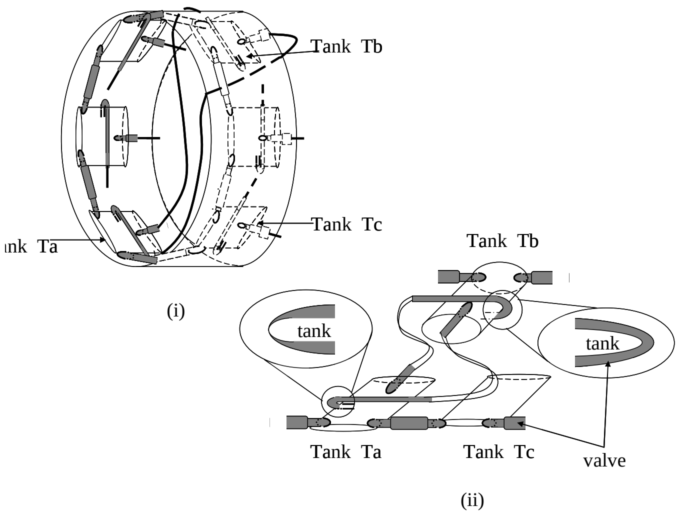

Fig. 1 Proposed mechanism

The tanks are made from flexible material. Fig. 2 (i) shows a tank. Each tank has three valves. Fig. 2 (ii) shows connection between tanks and valves. Va is the valve for deflating carbon dioxide of Tb, and Vd is the valve for deflating carbon dioxide of Ta. Ha and Hb are the hoses which connect Ta with Tb. Va and Vd are installed to a head of Ha and Hb. Vb and Vc are the valves for controlling water in the tanks.

As a beginning, we explain the valve which controls the pressure of the tanks. Opening and shutting of Va and Vd are switched passively with changing the shape of the body as shown in Fig. 2 (ii). In that case Ta is contracting and Tb is expanding. Fig. 2 (ii) shows Va is shut and V(d) is open. Therefore the pressure of Tb remains and the pressure of Ta deflates. By the chemical reaction, when Ta is expand, Va is open, and pressure of Tb is deflated.

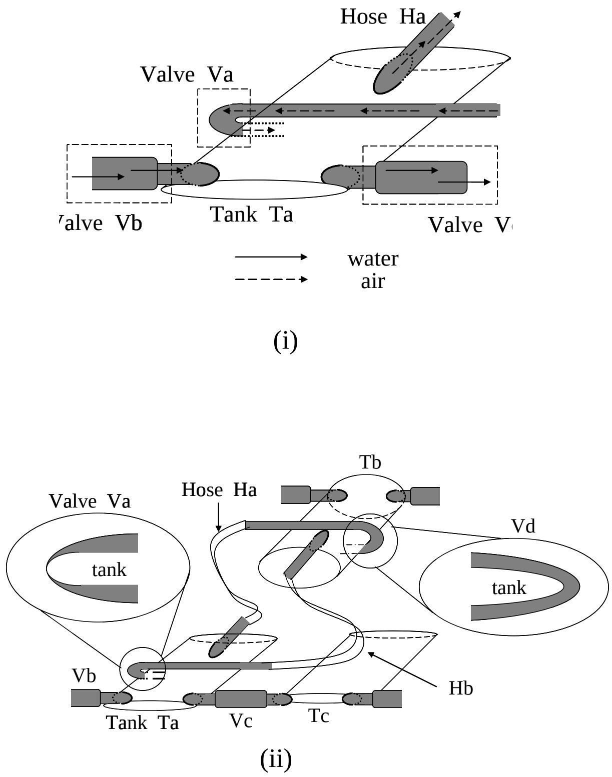

Fig. 2 Mechanism of tank

Next, we explain the valve that controls water in the tanks. Fig. 3(i) shows the valve that is open and Fig. 3(ii) shows the valve that is shut. These valves are controlled by changing of the body as shown in Fig. 4. As the shape of the body is decided autonomously with changing the pressure of carbon dioxide and weight of itself, the valves which are integrated with the body are controlled autonomously too.

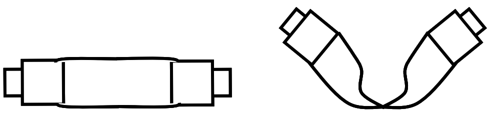

(i) (ii)

Fig. 3 Water valve

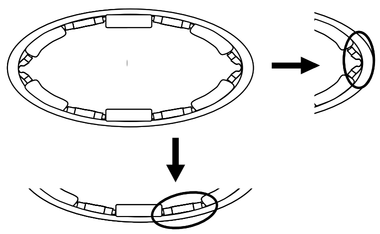

Fig. 4 Mechanism of valve

When the robot is put at slope, the water in the tank moves the lowest tank. The water is mixed to the sodium hydrogen carbonate and citric acid. Then, carbon dioxide is generated. By the pressure of the carbon dioxide, the water is pushed and moves to the next tank through the open valve. Fig. 5 shows a method of transference. Opening and shutting of the valve are switched with changing the shape of the body as shown in Fig. 4. The lower side of the body is twisted by the gravity, and the valve of the lower side is shut. So, water goes up as shown in Fig. 5. By the movement of the water, the center of gravity of the robot moves. Thus, the robot goes up the slope with rotating. When the robot rotated half around, the valve of lowest tank is opened and carbon dioxide of the highest tank is released. By repeating these cycles, robot can move. In the proposed mechanism, slope is perceived as the position of the water and the shape of the body, and control of the valves is realized with changing the shape of the body. Thus, no sensors and controllers are required.

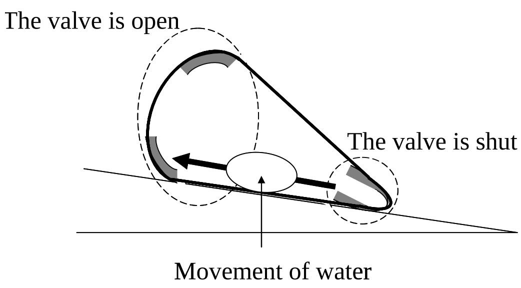

Fig.5 Method of transference

IV. EXPERIMENT

We have conducted experiment in order to confirm the behavior of the proposed robot.

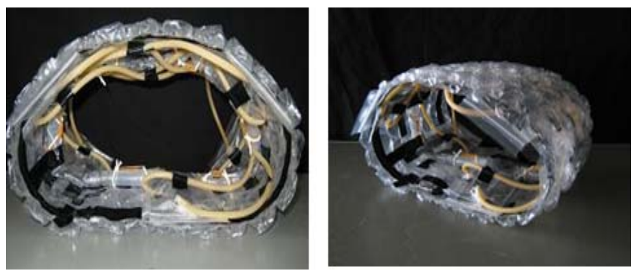

Fig. 6 Flexible robot

Fig. 7 shows experiment result. The robot perceives inclination of the slope and goes up the slope autonomously. The maximum angle of the slope the robot can go up was 4deg. We can confirm that the proposed robot perceived inclination of the slope and goes up the slope autonomously without sensors or controllers. So, by employing the properties of the real world, we can realize the autonomous robot that has no use sensors, and controllers.

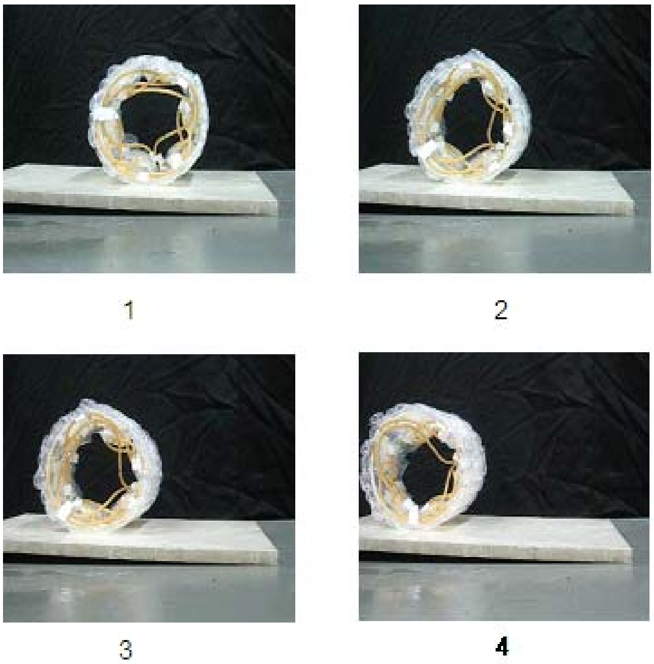

Fig. 8 Experiment result of 2deg

V. DISCUSSION.

First, we consider the method of perceiving inclination of a slope. The result clearly shows that the water can perceive inclination of the slope by the position of itself, and the robot can decide direction of movement autonomously.

Second, we consider rotating motion of the robots. In this paper, we used the valves which control the movement of water and the pressure of carbon dioxide. These valves behave adequately and autonomously by the mechanisms of the body and properties of the real world. So, we can regard every part of the robot as the processors. In the other words, we can consider that the real world is the information processing system. In the information processing system, as the necessary information is contained in itself, sensors are not required. And in addition, realizing of motion and processing of information are unified, so all information is processed in real-time. Thus, we can realize autonomous robot without sensors and controllers.

VI. CONCLUSION

In this paper, we have considered a flexible robot that perceives inclination of a slope and goes up the slope without sensors and controllers. We have developed a prototype and conducted experiments. As results, effective behaviors of the proposed framework have been demonstrated.

We can conclude that our proposed framework is effective for solving the problem of measurement, modeling, and real-time processing.

REFERENCES

[1] Ito K, Fukumori Y (2006), Proposal of new framework of controller design based on conceptual quantity, (in Japanese) Transactions of the Society of Instrument and Control Engineers vol.24 2006, pp.436-445

[2] Ito K (2006), Autonomous control of a snake-like robot utilizing passive mechanism. Proceeding of the 2006 IEEE International Conference on Robotics and Automation, pp.381-386

[3] Ito K, Fukumori Y, Takayama (2007), Autonomous Control of Real Snake-Like Robot Using Reinforcement Learning, Intelligent Sensors, Sensor Networks and Information, 2007. ISSNIP 2007. 3rd International Conference on, pp.389-394

[4] Sugiyama Y, Hirai S (2006), Soft Robots for Crawling and Jumping via Deformation (in Japanese), Journal of Robotics Society of Japan, vol.24, pp.378-387

[5] Kimura H, Maruyama D, Kajimaru F, Koseki M, Inou N, Hermetically (2007), Sealed Flexible Mobile Robot with Hydrostatic Skeleton (in Japanese), Journal of Robotics Society of Japan, vol.25, pp.1092-1099

[6] Lee DN (1985), Visual timing of interceptive action. Brain mechanisms and spatial vision: 1-30

[7] Pfeifer R, Iida F, Gomez G, Designing Intelligent Robots (2006), Journal of Robotics Society of Japan, vol.24, pp.783-790

©ISAROB 2009

Development of an autonomous-drive personal robot "object recognition system using a monocular camera"

Yuki Moritaka Eiji Hayashi
Department of Mechanical Information Science and Technology
Faculty of Computer Science and Systems Engineering , Kyushu Institute of Technology
680-4, Kawazu, Iizuka-City, Fukuoka Prefecture, Japan

Abstract: We are developing an autonomous personal robot able to perform practical tasks in a human environment based on information derived from camera images and a knowledge database. In the robot's adjustment to a human environment, it is very important that it be able to recognize the external world and identify specific objects. If an object cannot be identified, the robot cannot determine its next action plan. For this reason, we have developed an object-recognition system that allows an autonomous robot to identify objects within its environment. This object-recognition system is composed of both shape- and color-recognition systems that are based on a sensor using only a monocular camera. The shape-recognition system discerns objects' domains from their background by using region splitting processing. In the shape-recognition system, an object is identified based on its distinctive shape. The color-recognition system identifies an object based on its color information. Here we explain the algorithm used for the object search and the method for processing images. In addition, we describe the results of an experiment carried out to evaluate the system as it performed an object search.

Keywords: Personal robot, monocular camera, Image processing, Object recognition, Region splitting

Ⅰ.Introduction

In the near future, autonomous self-driving robots are expected to provide various services in human living environments. For this to occur, the robots must have a grasp of their driving environment. Therefore, systems to provide environmental recognition from the use of image information are being widely studied. However, they are very difficult to recognize only with the image information, because it is difficult to differentiate objects from their background. We, therefore, are developing an autonomous personal robot able to perform practical tasks in a human environment based on information derived from camera images and a knowledge database.

This object-recognition system is composed of both shape- and color-recognition systems that are based on a sensor using only a monocular camera. The object is identified by processing the image information which is provided by the camera. At first, the shape-recognition system checks to determine if the object is lying on a desk. Next, it discerns objects from their background by using region-splitting processing. This processing is performed based on HSV and RGB information in the camera image, and the system extracts only objects. The shape-recognition system identifies specified object shapes by comparing a shape template in the database to information about the extracted objects. The color-recognition system identifies an object based on its color information. In the processing flow, the system makes a histogram from the hue data based on the object's HSV information and in addition makes a histogram from the object data in the database. It then identifies the object by comparing these two histograms. An object-recognition system searches for the object using both of these recognition systems.

Ⅱ.System for robot

Our robot has a drive mechanism consisting of two front wheels and two back wheels. The front wheels are attached to a motor that operates the wheels on either side independently, while the back wheels function as castor wheels. This method has the advantage of allowing a small turning radius. In addition, in order to acquire image information, a single CCD camera with approximately 300,000 pixels is installed on the head of the robot and can be rotated to all sides by two motors. DC servo motors are used for the robot's drive mechanism, and position and speed control are achieved by the control system of the drive mechanism. The robot also has two arms and hands equipped with sensors, which enable it to respond to the various demands of humans. Finally, an installed wireless LAN can provide remote control for humans. All devices are controlled by a PC, and lead batteries supply the robot's electric power.

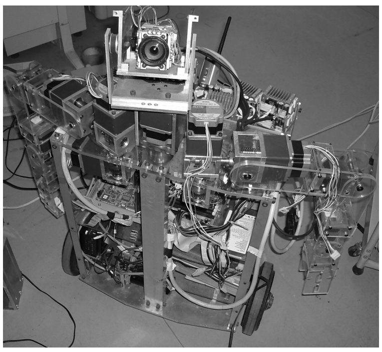

Fig. 1 Our developed robot

©ISAROB 2009

Ⅲ Object-recognition system.

3.1 Outline of the system

We developed an object-recognition system for robots that can search objects with image information captured by a monocular CCD camera. This system can search for an object on the assumption, for example, that the object is put on a desk. The system then searches for an object with the shape and color of the object registered by the database. The system notes the shape and color of the object and then step by step narrows down the objects.

3.2 shape-recognition system

In the shape-recognition system, an object is identified based on its shape. Objects that are carried in the hand in daily life are generally not complex in shape, so in this system especially notice the two-dimensional display of the object. The processing flow is as follows.

Ⅰ. Image Acquisition

The image obtained by the monocular CCD camera is read into a PC in the robot. This image is a 24-bit full-color image of the RGB data form.

Ⅱ. HSV conversion

The system converts 24-bit RGB image data into HSV data.

.

Ⅲ. Extraction processing of the desk surface

First, the robot extracts the desk surface which assumed that there is an object. In the processing flow, the system obtains image data from the desk surface by sampling. The robot then calculates the standard deviation of each HSV parameter from the acquired sample data. If the pixel of the image is within a value of threshold of the standard deviation, it is extracted as the surface of the desk.

Ⅳ. Presumption of an object domain

At first, the system performs label processing for all pixel groups except those recognized by the desk surface extraction process. The group of image pixels that lead to the search of an object is distinguished by this process. The system cannot judge accurate shape about the group of image pixels in contacting with the frame of the image. Therefore, this area around the image frame is excluded from the object region. The system determines the size of the object domain of the search object by using width data of the extracted object domain. The size of the object domain is calculated based on registered data for each object in the database. Figure 2 shows an example of the object domain established by this processing.

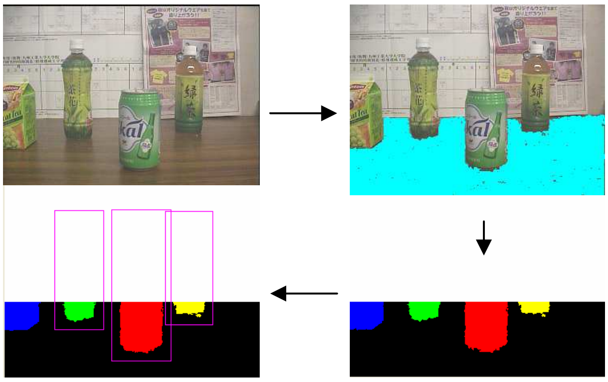

Fig. 2 Object extraction processing

Ⅴ. Region splitting processing

The system uses a plural region-splitting method to acquire only the object domain. The system distinguishes between the object domain and the background by this processing. The region-splitting processing uses two methods. One is a method that splits the domain by using integrated processing of the domain, and the other is a method that splits the domain by using the histogram of the image. The system has previously established knowledge of the desk domain, so it eliminates the desk domain from the processing area at this time. The system is able to extract only the object domain by combining these processes. Figure 3 shows the object domain extracted by this region-splitting processing.

Fig. 3 Result image of region splitting processing

Ⅵ. Template matching processing

This type of processing compares the shape of the extracted object domain with a template (shape data that was registered by the database). The size of the template changes according to size of the width of the object domain. The system partially computes the matching rate of the object shape. By this method, the system can obtain results that take into consideration differences in the shapes of the objects. The system calculates two matching rates, and determines the shape and position of the object as a shape of the template if it is both higher than the threshold and reaches its maximum.

©ISAROB 2009

3.3 Color-recognition system

The color-recognition system searches for an object based on color data for the object. The system acquires color data for the object which is searched for by the shape-recognition system. It compares the color data that was registered by the database with the color data of that object, which is then searched for by the shape-recognition system. If the feature of color data of two type accords, it judges as a search object by this processing. The processing flow is as follows.

Ⅰ. Color data Acquisition

The system acquires the color data for the object that was searched for with the shape-recognition system. The color data use information regarding Hue from the HSV information for the object.

Ⅱ. Making the histogram

The image is regarded as an assemblage of pixel values. The color data of Hue for the object is expressed as a value between 0 and 360. This processing divides the Hue data into 72 groups and counts the frequency of each pixel value. Figure 4 shows the histogram.

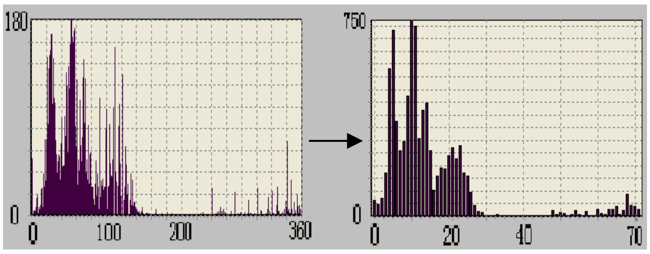

Fig. 4. Histogram

Ⅲ. Comparison of the histogram

Next, in order to identify color similarities, the system analyzes the correlation between the histogram of the object domain that was recognized by the shape-recognition system and the histogram of the search object that was registered by the database. First, the system calculates the regularization histogram. Next, two regularization histograms are overlapped, and the minimum value of the pair of values is taken. The total value from all these minimum values is set as a similarity. Color similarity becomes high when overlap of the histograms is large. In addition, this processing compares the average pixel value and the pixel value that appears most frequently. Figure 5 shows the overlapped regularization histograms obtained by this processing.

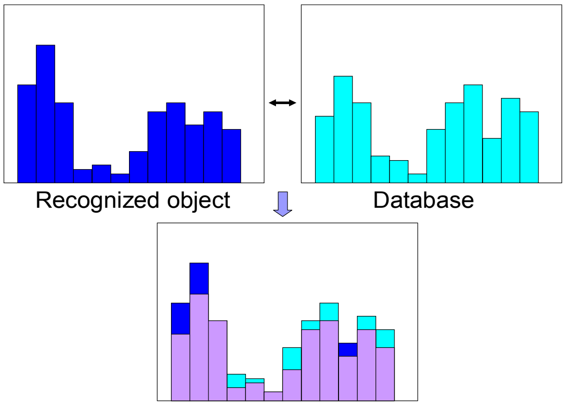

Fig. 5 Comparison of the histogram

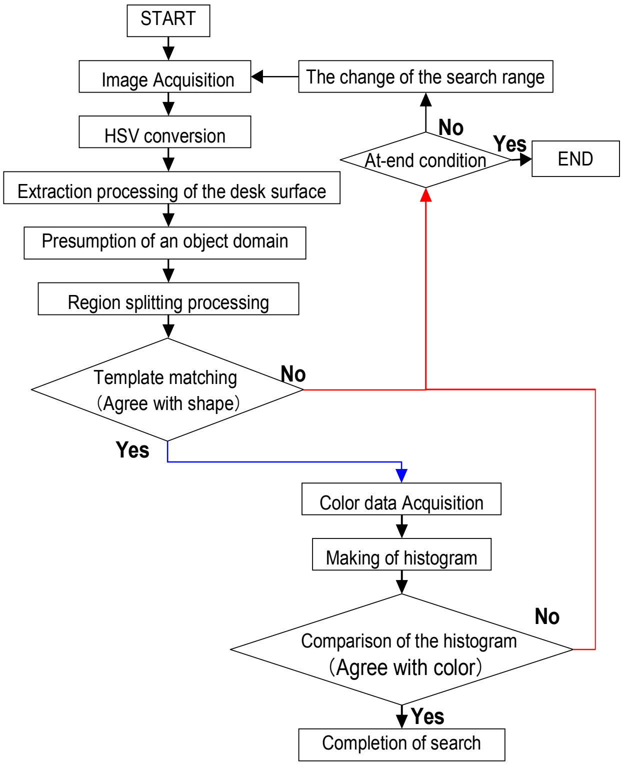

Fig. 6 System flow

Ⅳ. Experiment

We performed the following experiment to evaluate the performance of this system that searches for an object with the shape and color of the object registered by the database.

A: Experiments related to object shape

We conducted an experiment that involved searching for several different types of object forms.

B: Experiments related to object color.

We performed an experiment that involved searching for a specified object from an object that had been searched for by a shape-recognition system using color data that was registered by the database.

©ISAROB 2009

In the case of A, the experimental results show that an object of simple shape could be searched for with high probability. However, there was a case in which the system misidentified the object of similar form. There was also a case in which the system could not recognize depending on the results of region-splitting processing. In the case of B, the system was almost able to search for the object by using color data that was registered by the database because the histogram did not appear to be influenced by the visibility of the object. However, there was a case in which the system could not successfully carry out the search depending on the object. Figure 7 shows an example of results for the shape-recognition system, and Fig. 8 shows an example of results for the color-recognition system.

Fig. 7 Shape recognition system

Fig. 8 Color recognition system

Ⅴ.Conclusions

We have proposed a system that searches for objects using only a monocular camera. It is thought that objects held in the hand in daily life are generally not complex in shape. Experimental results show that objects of simple shape can be searched for with high probability. However, there was a case in which the system could not successfully search for the object based on various factors. We therefore must improve the accuracy of the object-recognition system by combination with other processing methods such as those that can display an object in three dimensions. For these reasons, we believe that the present system requires further improvement. In addition, the robot cannot yet acquire distance information of the object. We therefore want to mount on the robot this function. Our next subject of study is to develop a system that makes possible a holding function for the recognized object and a carrying task.

References

[1] Takuma Umeno, Eiji Hayashi, Development of an au tonomous personal robot "The visual processing system for autonomous driving", proceedings of the 10th intern ational symposium on artificial life and robotics、Vol.10th, pp.44, Beppu, Oita, Japan, 2005

[2]Yoshitaka Hane, Eiji Hayashi, User-recognition system for an autonomous robot in human living environments, proceedings of The twelfth international symposium on artificial life and robotics、Vol.12th,pp72-75, Beppu, Oita, Japan, 2007

[3]Toshifumi Uewaki, Eiji Hayashi, Development of an autonomous mobile system for an autonomous robot in an indoor environment, proceedings of The twelfth international symposium on artificial life and robotics、Vol.12th, pp52-55, Beppu, Oita, Japan, 2007

[4]K. Belloulata and J. Konrad, Fractal Image compression with region-based functionality, *IEEE Transactions on Image Processing*11 (2002) , p. 351

The Fourteenth International Symposium on Artificial Life and Robotics 2009 (AROB 14th '09),
B-Con Plaza, Beppu, Oita, Japan, February 5 - 7, 2009

An algorithm for automatic generation of assembly process of modular fixture parts

Takayoshi YAMADA[1], Ken-ichi KURODA[1], Yasuyuki FUNAHASHI[2], Hidehiko YAMAMOTO[3]

[1.] Nagoya Institute of Technology, Gokiso, Showa, Nagoya, Aichi 466-8555, Japan, yamada.takayoshi@nitech.ac.jp

[2.] Chukyo University, 101 Tokodachi, Kaizu, Toyota, Aichi 470-0393, Japan, funa-@life.chukyo-u.ac.jp

[3.] Gifu University, 1-1 Yanagido, Gifu 501-1193, Japan, yam-h@gifu-u.ac.jp

Abstract: In metal mold production systems, rapid, high-quality, and low-cost production technologies are needed. In the systems, assembly tasks of fixtures to immobilize the mold are required. The mold must be firmly fixed by fixtures, in order to resist force generated by NC machine tools. In this paper, we discuss automatic generation of assembly process for modular fixture parts in the systems. The assembly drawing of the parts is obtained from STEP/AP203, which is a text file of CAD/CAF data. In the data, the shape and the configuration of all assembled fixtures are included. The shape of each fixture is constructed with planar, cylindrical, and conical surfaces. From the data, the number of surfaces contacting with the others is derived in each part. And valid contacts are judged with degree of importance. Tree of contacts among all fixtures are derived. In numerical examples, assembly process is automatically generated by our proposed method. It is shown that suitable assembly process is provided.

Keywords: Assembly process planning, modular fixture parts, CAD/CAF, STEP/AP203, assembly drawing.

I. INTRODUCTION

In metal mold production systems, rapid, high-quality, and low-cost production technologies are needed. For this reason, integrated production systems have already been constructed, which include CAD, CAF (Computer Aided Fixturing), CAM, and NC machine tools, as shown in Fig. 1.

In the production systems, assembly tasks of fixtures to immobilize the mold are required. As shown in Fig. 2, the mold must be firmly fixed by fixtures, in order to resist force generated by NC machine tools. Characteristics of the metal mold productions are a diverse-types-and-small-quantity production, a variety of shape of fixtures, complex contact types among fixtures, and so on. From these reasons, recognition, adaptability, and dexterity of humans are required for the assembly tasks. Hence, at present, the assembly tasks are carried out by human beings with handwork, while they are checking the assembly drawing. In the tasks, however, human beings sometimes make mistakes such as inadmissible position and different assembly process of fixtures. As a result of them, we have serious problems leading to destruction of the metal mold and the machine tools. To overcome the problems, automatic assembly tasks must be realized without humans.

In Refs. [1]-[4], the authors explored elemental technologies for the assembly tasks. Refs. [1] and [2] analyzed grasp stability for the parts handling. Refs. [3] and [4] identified contact conditions between a grasped part and an external environment (the other parts). In this paper, we discuss automatic generation of assembly process planning for modular fixture parts.

In Refs. [5]-[8], fixture planning is treated. Babu et al [5] and Wu et al. [6] explored automatic fixture layout planning. Ames et al. [7] and Yi et al. [8] provided assembly planning for a given modular fixture

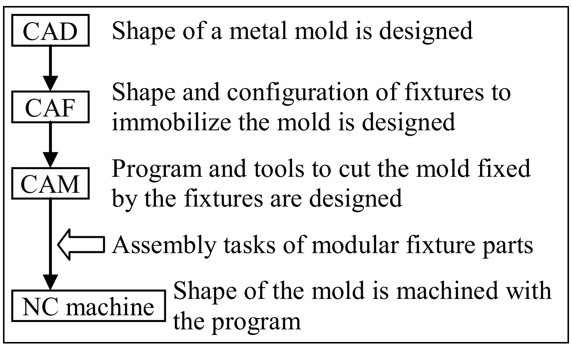

Fig. 1. Production process of a metal mold.

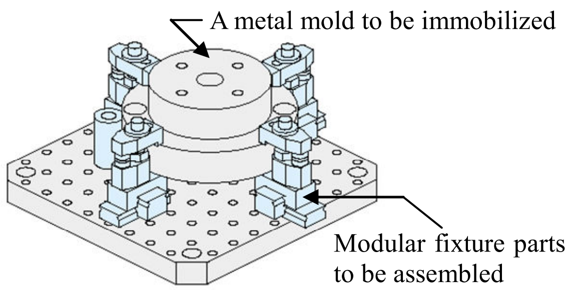

Fig. 2. Assembly drawing of a metal mold and modular fixture parts.

configuration. It is difficult to say to be used practicably. The similar problem of Refs. [7] and [8] is treated in this paper, to carry out the assembly tasks by robots with the technologies of Refs. [1]-[4].

In this paper, the assembly drawing is obtained from STEP/AP203, which is a text file of CAD/CAF data. In the data, the shape and the configuration of all assembled fixtures are included. The shape of each fixture is constructed with planar, cylindrical, and conical surfaces. From the data, the number of surfaces contacting with the others is derived in each part. Then, tree of contacts among all fixtures are derived. To eliminate redundant contacts and closed loop contacts in the tree, valid contacts are judged with degree of importance. In numerical examples, assembly process is automatically generated by our proposed method. It is shown that suitable assembly process is provided.

II. DATA EXTRACTION

1. STEP/AP203

A variety of CAD software is marketed for the mechanical design. The STEP form is an intermediate file of the text form used to exchange data among a variety of CAD systems. In the assembly drawing as shown in Figure 2, the shape and the configuration of the modular fixture parts are recorded.

Each part is constructed with a variety of geometry. In this paper, we discuss simple geometries such as planar, cylindrical, conical geometries. Local shape of the parts is extracted by the following methods.

2. Elements of planar geometry

The information of planar geometry is obtained from the commands such as Table 1. The detail of the geometry is extracted by searching the command number "#NUMBER". We obtain an outer unit normal vector $\boldsymbol{n}$, vertex points $\boldsymbol{v}_i$ (i=1,2,...,n), and edge vectors $\boldsymbol{e}_i$ (i=1,2,...,n).

3. Elements of cylindrical geometry

The information of cylindrical geometry is obtained from the commands such as Table 2. We obtain center points $\boldsymbol{c}_i$ (i=1,2) of both ends and radius r. The unit vector of the centerline is calculated by

$$\boldsymbol{l} = (\boldsymbol{c}_1 - \boldsymbol{c}_2)/\|\boldsymbol{c}_1 - \boldsymbol{c}_2\| . \qquad (1)$$

4. Elements of conical geometry

The information of conical geometry is obtained from the commands such as Table 3. We obtain center point $\boldsymbol{c}_i$ (i=1,2) and radius r_i (i=1,2) of both ends. The unit vector of the centerline is given by Eq. (1). The slope rate is calculated by

$$s = (r_1 - r_2)/\|\boldsymbol{c}_1 - \boldsymbol{c}_2\| . \qquad (2)$$

III. JUDGMENT OF CONTACTS AMONG THE PARTS

By using the elements extracted in Section II, it is judged whether each part is in contact with the other parts. And the number of contact surfaces of the part is derived. Then, a tree of contacts among all parts is produced.

1. Judgment of planar contact

Firstly, we choose one of the planar surfaces. It is denoted by A. The other planar surfaces are denoted by Bj, (j=1,2,...,m). In the following steps, we judge whether plane A is in contact with the others.

Step 1: (Direction) The unit normal vectors of planes A and Bj are evaluated. Plane A is parallel to plane Bj, if we have

$$\boldsymbol{n}_A^T \boldsymbol{n}_{Bj} = -1 . \qquad (3)$$

Step 2: (Distance) The vertex points within planes A and Bj are evaluated. The two planes have zero distance from each other, if we have

$$\boldsymbol{n}_A^T (\boldsymbol{v}_{Bj} - \boldsymbol{v}_A) = 0 . \qquad (4)$$

Step 3: (Common area) The two planes are in contact with each other, if plane A has common area with plane Bj.

2. Judgment of cylindrical contact

In a similar way of III.1, we choose cylindrical surfaces A and Bj, (j=1,2,...,m).

Step 1: (Radius) The radius of cylinders A and Bj are evaluated. We check

$$r_A = r_{Bj} . \qquad (5)$$

Step 2: (Direction) The directions of cylinders A and

Table 1. Commands of planar geometry

```
#2094=ADVANCED_FACE('NONE',(#13593,#13594),...
#13593=FACE_BOUND('NONE',#1792,.T.);
#13594=FACE_OUTER_BOUND('NONE',#25,.T.);
#13595=PLANE('NONE',#13596);
```

Table 2. Commands of cylindrical geometry

```
#7218=ADVANCED_FACE('NONE',(#17267),#17268,...
#17267=FACE_OUTER_BOUND('NONE',#6914,.T.);
#6914=EDGE_LOOP('NONE',(#6274,#5646,#4277,....
#17268=CYLINDRICAL_SURFACE('NONE',#17269,.....
```

Table 3. Commands of conical geometry

```
#1814=ADVANCED_FACE('NONE',(#13427),#13428,...
#13427=FACE_OUTER_BOUND('NONE',#1527,.T.);
#1527=EDGE_LOOP('NONE',(#884,#20855,#19480,...
#13428=CONICAL_SURFACE('NONE',#13429,.........
```

©ISAROB 2009

Bj are evaluated. The directions of the cylinders are parallel to each other, if we have

$$\left| \boldsymbol{l}_A^T \boldsymbol{l}_{Bj} \right| = 1 . \qquad (6)$$

Step 3: (Distance) The centerlines are located on the same line, if we have

$$\boldsymbol{l}_A \times (\boldsymbol{p}_{Bj} - \boldsymbol{p}_A) = 0 . \qquad (7)$$

Step 4: (Common region) We check whether the both ends of cylinder *A* has common area with cylinder *Bj*.

3. Judgment of conical contact

In a similar way of III.1, we choose conical surfaces *A* and *Bj*, (j=1,2,...,m).

Step 1: (Slope rate) The slope rates of cones *A* and *Bj* are evaluated. We check

$$s_A = s_{Bj} \qquad (8)$$

Step 2: (Direction) The directions of conical surfaces *A* and *Bj* are evaluated. The directions are parallel to each other, if we have Eq. (6).

Step 3: (Distance) The centerlines are located on the same line, if we have Eq. (7).

Step 4: (Common region) We check whether the both ends of conical surface *A* has common area with conical surface *Bj*.

IV. GENERATION OF ASSEMBLY PROCESS

In the contact tree, generally, closed loop contact among more than three parts exits. For simplicity of the analysis, this paper considers the case of the loop with less than four parts.

1. Screws

Each screw is assembled at the last order from the contacted parts.

2. Number of contact surfaces

In order to enhance the connection of two parts, the next part to be assembled is selected with the evaluation of the largest number of contact surfaces from the remainder of the parts (Fig. 3).

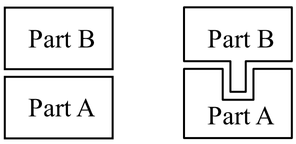

(a) (b)

Fig. 3. Difference of the number of contact surfaces.

3. Generation of Assembly Process

We describe the assembly process with the following assumptions.

(A1) Screws and baseplates are listed in other files. The serial number of them is written in the files.

(A2) The serial number of each part is written in the STEP file of assembly drawing.

(A3) CAD data is not for machining (no chamfer).

From the contact information described above, we produce the assembly process by the following conditions:

(C1) A baseplate is picked up at first from the extracted parts.

(C2) The process is generated by the contact tree of the parts.

(C3) The part maximizing the number of contact surfaces is selected, if the previous part is in contact with two parts.

V. NUMERICAL EXAMPLES

We generate assembly process from the assembly drawing shown in Fig. 4. The drawing is constructed with 41 parts listed in Table 4. These parts are classified into 11 types. The details of the parts are shown in Ref. [9]. These data are obtained from a STEP/AP203 file including more than 20000 command lines. The shape and the configuration of the fixtures are also obtained from the STEP file. Contacts among 41 fixtures are judged. Redundant contacts and closed loop contacts are eliminated in the contact tree. Finally, assembly process is automatically generated.

The generated assembly process is listed in Table 5. "Extracted number" means the extracted order from the STEP/AP203 file. "Extracted contact parts" mean a list of the parts contacting with each part, where the number is described in "Extracted number". "Assembly sequence" means the sequence of the assembly task. Several numbers are eliminated in the sequence, because three parts contact exist in the tree. In the assembly task, each part is selected in ascending order. It is shown that suitable assembly process is provided.

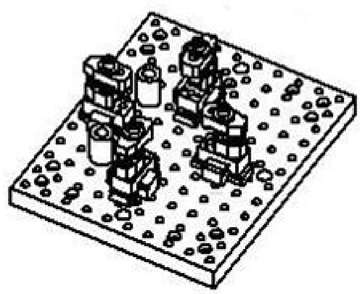

Fig. 4. Example of the assembly drawing.

©ISAROB 2009

Table 4. List of modular fixture parts included in Fig. 4

Name	Serial number	Quantity
Baseplate	BJ010-5060-16	1
Slide unit 1	FJ20-16063_01	4
Slide unit 2	FJ20-16063_02	4
Slide unit 3	FJ20-16063_03	4
Quick nut	FJ42-16001	4
System clamp 1	FJ40-16055S_01	4
System clamp 2	FJ40-16055S_02	4
System clamp 3	FJ40-16055S_03	4
Baseplate screw	CSB M16X40	8
Locator	BJ400-16075	2
Locator screw	BJ701-16055	2

Table 5. Generated assembly sequence.

Extracted number	Serial number	Extracted contact parts	Assembly sequence
1	FJ40-16055S_03	5,9	43
2	FJ20-16063_01	3,4,7,8,10	15
3	FJ20-16063_02	2,4	24
4	FJ20-16063_03	2,3,6,9	28
5	FJ40-16055S_01	1	47
6	FJ42-16001	4,9	35
7	CSB M16X40	2,10	16
8	CSB M16X40	2,10	17
9	FJ40-16055S_02	1,4,6	39
10	BJ010-5060-16	2,7,8,13,17,18 20,21,25,26,30 32,33,39,40,41	1
11	FJ20-16063_02	12,18	18
12	FJ20-16063_03	11,15,18,19	25
13	CSB M16X40	10,18	3
14	FJ40-16055S_03	15,16	40
15	FJ40-16055S_02	12,14,19	36
16	FJ40-16055S_01	14	44
17	CSB M16X40	10,18	4
18	FJ20-16063_01	10,11,12,13,17	2
19	FJ42-16001	12,15	30
20	BJ400-16075	10,21	5
21	BJ701-16055	10,20	6
22	FJ42-16001	28,29	31
23	FJ40-16055S_01	24	45
24	FJ40-16055S_03	23,28	41
25	FJ20-16063_01	10,26,27,29,30	7
26	CSB M16X40	10,25	8
27	FJ20-16063_02	25,29	20
28	FJ40-16055S_02	22,24,29	37
29	FJ20-16063_03	22,25,27,28	26
30	CSB M16X40	10,25	9
31	FJ40-16055S_01	35	46
32	FJ20-16063_01	10,33,36,37,39	10
33	CSB M16X40	10,32	11
34	FJ40-16055S_02	35,37,38	38
35	FJ40-16055S_03	31,34	42
36	FJ20-16063_02	32,37	22
37	FJ20-16063_03	32,34,36,38	27
38	FJ42-16001	34,37	33
39	CSB M16X40	10,32	12
40	BJ400-16075	10,41	13
41	BJ701-16055	10,40	14

VI. CONCLUSION

We have discussed an algorithm for automatic generation of assembly process of modular fixture parts. In this method, the geometry and the location of each part is extracted from STEP/AP203 file. The tree of contacts among all parts is derived. Then assembly process is automatically generated.

In this paper, we have discussed simple geometries such as planar, cylindrical, and conical surfaces. In the future work, we will discuss more complex geometries. And we aim to carry out the automatic assembly of the modular fixture parts by robots.

VI. ACKNOWLEDGMENT

We would like to thank IMAO Corporation for providing us with the modular fixture parts and helpful suggestions.

REFERENCES

[1] T. Yamada, T. Koishikura, Y. Mizuno, N. Mimura, Y. Funahashi (2001), Stability Analysis of 3D Grasps by A Multifingered Hand, Proc. of the IEEE ICRA, pp. 2466-2473.
[2] T. Yamada, T. Ooba, T. Yamamoto, N. Mimura, Y. Funahashi (2005), Grasp Stability Analysis of Two Objects in Two Dimensions, Proc. of the IEEE ICRA, pp. 772-777.
[3] T. Mouri, T. Yamada, N. Mimura, Y. Funahashi (1999), Identification of Contact Conditions from Contaminated Data of Contact Moment, Proc. of the IEEE ICRA, pp. 585-591.
[4] T. Yamada, T. Mouri, K. Shimosaka, N. Mimura, Y. Funahashi (2008), Uncertainty of Estimated Parameters of Contact Conditions by Active Force Sensing, Proc. of the IEEE Int. Conf. on Robotics and Biomimetics, Accepted for Publication.
[5] B. S. Babu, P. M. Valli, A. V. V. A. Kumar, D. N. Rao (2005), Automatic modular fixture generation in computer-aided process planning systems, Proc. IMechE, Vol. 219, Part C: J. of Mechanical Engineering Science, pp. 1147-1152.
[6] Y. Wu, S. Gao, Z. Chen (2008), Automatic modular fixture planning based on linkage mechanism theory, Robotics and Computer-Integrated Manufacturing, Vol. 24, pp. 38-49.
[7] A. L. Ames, T. L. Calton, R. E. Jones, S. G. Kaufman, C. A. Laguna, R. H. Wilson (1995), Lessons Learned from a Second Generation Assembly Planning System, Proc. of the IEEE Int. Symp. on Assembly and Task Planning, pp. 41-47.
[8] C. Yi, G. A. Bekey (1996), Assembly Planning for Modular Fixtures, Proc. of the IEEE IROS, pp. 704-711.
[9] http://www.imao.co.jp/whs/top.

Optimization of robot path using off-line simulation and method for changing tool using a wireless communication device

Ishani Mishra[1], Abhro Mukherjee[2], Ajay Gopalswamy[3], Anil Kumar Satapathy[4], Manjunath TC[5]

[1]*Post Graduate M.Tech Student, Dept. of Electronics & Communications Engg., National Institute of Science & Technology, Palur Hills, Berhampur, Ganjan Dist., Orrisa-760018, India.*
Email : ishani_mishra2002@yahoo.co.in mishra.ishani@gmail.com
Phone : +91 80 66297777 Extn. 2004 ; Fax : +91 80 28440770 ; Mobile +91 09740097978
[2] *Assistant Professor, Electronics & Instrumentation Dept., NIST, Berhampur, Orrisa, India*
[3] *Director, Difacto Robotics & Automation Pvt. Ltd., Bangalore, Karnataka*
[4] *Senior Lead Engineer, General Motors, Bangalore, Karnataka*
[5]*Professor & Head, ECE Dept., NHCE, Bangalore-87.*

Abstract: This paper presents an effective method of performing an optimization of the robot path using an off-line simulation concept along with a method for changing the robot tool using a wireless communication device. The robot controller was also worked upon & the control concept was being developed with the help of a native robot programming language. The method for changing the tool for a robotic manipulator comprised of a wireless communication device for controlling the data communication on the tool. The simulation and the off-line programming was carried out successfully. This not only saved the time and improved the quality, but also boosted the customer's confidence. The focus on the work considered in this paper was to practice the simulation and the off-line programming tools used in the robotic research in the day-to-day activities and deliver the end result meeting and exceeding the customer's requirements and expectations. During this research work, various concepts of simulation and off-line programming were used at different phases for the completion of the spray-painting application underneath the body of an automobile. A method for changing the tool in an industrial robotic manipulator using a wireless communication device thus reduced the hard wiring and increased the reliability in the system. Here, the communication or the control cables are not necessary between the robot arm and the moveable robot tool, which is at the end of the robot manipulator. The simulation results show the effectiveness of the developed method.

Keywords: Automation, Robot controller, Simulation, Robot programming language, Wireless communication, Tool.

I. INTRODUCTION

In recent years, automation has become an integral part of the modern manufacturing facilities. There is no surprise with this trend of automation, because manufacturing enterprises are under increasing pressure to bring in consistency in quality and reduce the cost. Robots are used to achieve this full-fledged automation. Industrial robots are being used more & more in many fields of industry where they are replacing the human operators engaged in repetitive, onerous & potentially hazardous tasks [1]. Robots have revolutionized the industrial workplace. Thus, thousands of manufacturers rely on the productivity, high-performance & savings provided by the modern day industrial automation. According to the Robotic Institute of America (RIA) ; a robot is defined as a re-programmable multifunctional manipulator designed to move various objects, tools, materials or specialized devices through various programmed motions for the performance of a variety of tasks. In the current practice, before a robot does a particular job, first the task is being simulated and then, it is carried on forward to the implementation stage.

The objective of the work considered in this paper is the robot cell simulation & the off-line programming. Also, the verification & running the developed off-line programs with the changing of a robot tool using an wireless communication means is discussed.

2. ROBOT SIMULATIONS

Simulation of any job is defined as the "the first step of the engineering process for system design". Simulation is the process of imitating the real dynamics of a robot with a set of mathematical formulas. Simulation tools provide an off line system to represent what equipment and parts are included in a work cell and how the overall robotic system does its job in terms of process throughput, cycle time etc. PC based simulation provides a way to verify the layout, interferences, robot reach, and fixturing requirements of a work cell. The simulation reduces a great amount of costs & time that would have incurred due to experimentation otherwise. Simulation is a graphical software tool but also, and probably more importantly, is an engineering method. Two packages are used here.

©ISAROB 2009

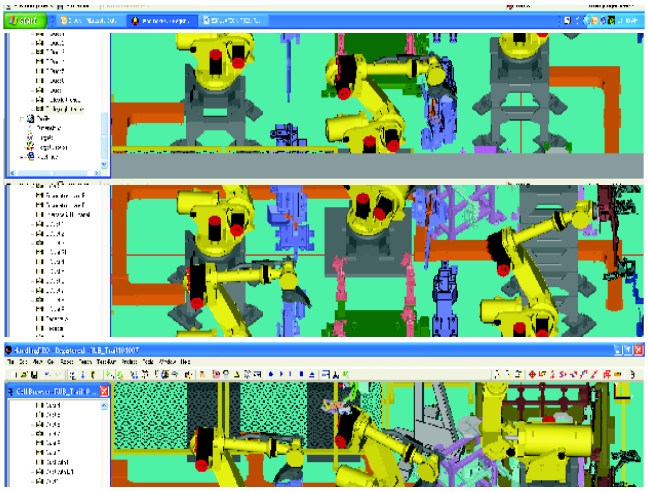

Fig. 1 : Simulation using FANUC Robo-guide

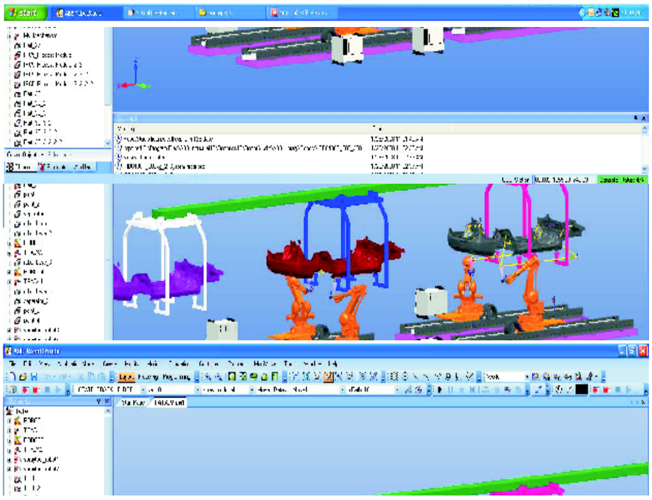

Fig. 2 : Simulation using ABB Robot studio

The benefits of robot simulation and offline programming exhibited in our work are as follows. They are : slashes time and money, provides profitability and affordability, avoids costly mistakes, allows for graphical programming, provides PC based programming, eliminates costly larger systems, provides high accuracy, provides sophisticated calibration, promotes concurrent engineering, promotes design for manufacturability, reduces scarp and costly rework & reduces the requirement of the skilled laborers on the shop floor [2]. Two simulations using Fanuc robot guide and ABB robot studio are shown in the Figs. 1 & 2 respectively [3].

3. REQUIREMENT STUDY

The customer requirement is to automate the underbody spraying application of an automobile using robots, in order to achieve some objectives, such as to increase productivity, to achieve uniform coating, reduce wastage, reduce human intervention as the PVC may be harmful, adaptation, to reduce the time of production and quick changing over to new models. The customer gave the following inputs to commence the work [4]. They are : CAD models of the various car body and hanger (that carries the car body), the quality requirements in terms of coating thickness, the space availability, cycle time and the process details. The following process related inputs were also provided for the project's simulation study. They included the paint/ coat specifications, such as the pogoplast A104-RT / 21055, which is PVC based PU paint with high noise suppression qualities and basically used as a anticorrosion anti-chip agent. The spraying method with compressed air (pneumatic) & a spraying speed of 0.9-1.0 m/s is also provided [5].

4. WORK CELL CREATION

The generation of the work cell in the simulated environment using the simulation package is described as follows. The current project's work cell consists of 2 identical stations, placed at a particular pitch. The car bodies are mounted on the specially designed hangers. A motorized chain conveyor drives these hangers. Each station consists of the 2 nos. of ABB robots mounted on linear rails on either side of the car body, 2 nos. of robot controllers for each robot. Each of the above robots is equipped with the spraying nozzles, the hoses, and pneumatic valves for spraying [6]. There are 2 nos. of sealant dispensing units & 1 set of body identification system with 1 set of hanger stopping and clamping mechanism. Some of the 3D models of cell components are shown in Fig. 3.

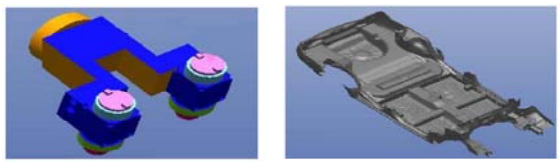

(a) Spraying nozzle with adapter (b) underbody of car

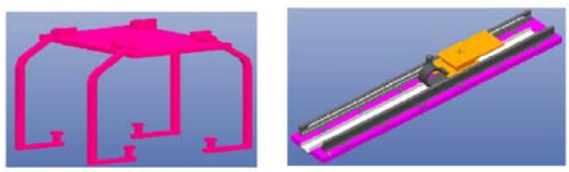

(c) Hangars (d) slide units for robots

Fig. 3 : 3D models of cell components

The WC creation includes the basic activities such as 3-D solid modeling and data translation, robot selection, robot end effector selection, robot tool adapter design, cell kinematics, robot programming including path and work coordinate creation, ergonomics analysis, sequence of operation - SOP definition, production layout and material flow optimization [7]. Before creating the cell, the required things are made in 3D software and then transferred to the simulation software. The required robot is selected by considering some parameters such as work envelope, payload, and applications. By taking this parameters ABB's IRB 2400/16 with S4C+ controller is selected. The robot end effector and tool adapter design is carried out in 3D software and then transferred to simulation software [8]. The selected robot, end effector and tool adapter are shown in the Fig. 4. After modeling of all the required data the complete cell components were imported and placed in the work cell in Fig. 5.

Fig. 4 : Robot selected for spray painting with the end-effector and the tool adapted in the simulation

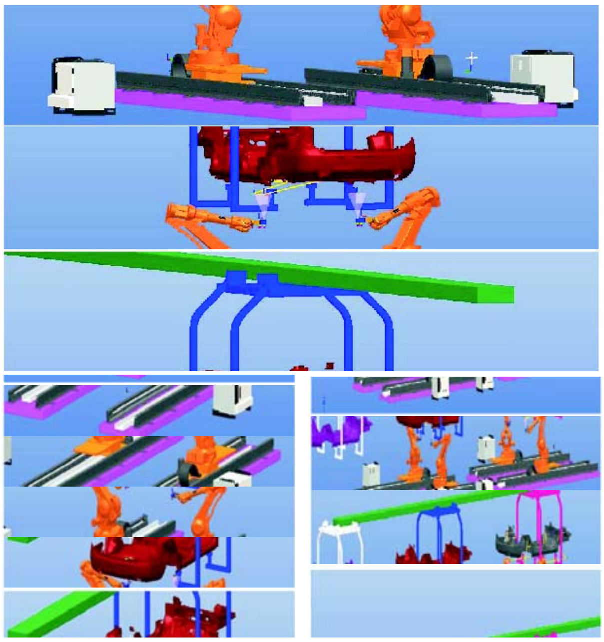

Fig. 5 : Work cell creation for spray-painting

5. Path Creation

The activities carried out in the sequence they appear prior to the path generation are creating targets and paths, checking target orientation, checking reachability, synchronizing the program to the virtual controller, performing text based editing, collision detection, testing the program [9]. The simulated tool path created in the simulation is shown in Fig. 6 with the sample program code is shown in Fig. 7.

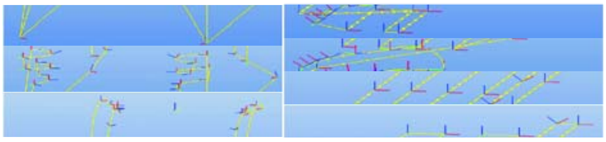

Fig. 6 : Creation of the tool path in the 3D space

"MOVE L	P1	V1000	Z50	tool0"
A	B	C	D	E

Fig. 7 : Program code

A - The name of the instruction, which moves the robot linearly

B - The value of the instruction's position

C - Determines the velocity of the robot

D - Determines the precision of the robot's position

E - Specifies which tool is active

6. ETHERNET COMMUNICATION

Ethernet / IP is a communication system suitable for use in industrial environments & allows industrial devices to exchange time-critical application information. These devices include simple I/O devices such as sensors, transmitters / receivers, actuators as well as complex control devices such as PLC, welders, and process controllers. The robot supports one adapter connection [10]. This connection is normally to a cell controller or PLC to exchange cell interface I/O data. The Ethernet / IP Adapter option is to be loaded to support this functionality. The robot supports upto 7 scanner connections. The IP address is next configured so that bi-directional data transfer takes place. All these facilities are incorporated in the simulation study.

7. METHOD FOR CHANGING THE TOOL OF AN ROBOT USING WIRELESS MEANS

This is a proposed method for changing a tool for a robot or manipulator comprising a wireless communication device for control and/or data communication on the tool. Communication or control cables may not be necessary between the robot arm and the moveable robot tool. One or more wireless communication members comprised on the robot tool may also be powered by the contact less power supply in another embodiment.

Tool changes are time consuming & may cause production delays. It is important that tool changes are carried out in a predictable way so that technical specifications related to quality do not vary and that planned production is not disrupted. The present study provides improvements to methods for controlling an industrial robot arranged with at least one arm arranged with a tool comprising a wireless communication member which wirelessly controlled tool may be changed or exchanged automatically. The method is described briefly as follows [11].

This study may be described as comprising a control method for an industrial robot equipped with a wirelessly controlled tool, the method comprising of registering at some point in the architecture of the control system information that a tool change will take place. Preferably and not exclusively, this comprises providing the information to a wireless base station that the tool change is planned to take place [12].

Providing this information allows the control system, or at least the wireless base station, to "expect" communication loss from a given wireless tool, and thus communication of an error or alarm for this event is prevented. One or more embodiments of the simulation study further describes that this improvement may conveniently be achieved by reserving a certain field in the communication link between the overlying control system (e.g., robot controller or PLC) and the wireless radio base station, which field may be reserved for information regarding a tool change [13].

Then, when a tool change is scheduled, the overlying control system sends that information to the radio base station. When the base station reads information regarding a tool change it "knows" that it will loose contact with a specific node at a time in the near future and can therefore prepare a safe disconnection of the radio link. This will ensure that a planned tool change is distinguished from an unplanned loss of communication and will give the overlying control system improved control of the wireless system by eliminating alarms or errors due to predictable communication disruptions [14].

8. CONCLUSION

The optimization of robot tool path using off-line simulation and method for changing tool using a wireless (ethernet) communication device was briefly discussed in this research paper. The simulation and the off-line programming were successfully carried out. This not only saves production time, but also improves the quality of finished product so that all errors are rectified in simulation stage itself. During this work, various concepts of simulation & offline programming were used at different phases of simulation & the research work gave us excellent results.

This paper suggests a method for changing the tools in an industrial robot using a wireless communication device, thus reducing the hard wiring and increasing the reliability in the system. Here, communication or control cables are not necessary between the robot arm and the movable robot tool. After the completion of simulation and offline programming, the programs have to be downloaded in the real robot controller and then experimentally verified, which is not the concept of this paper. The authors like to acknowledge Difacto Robotics, Bangalore, for their coordination & help rendered during the completion of this research work.

REFERENCES

[1] Kris Gunnarsson, "Robotic simulation and offline teaching system", RIA conference, Michigan, 2000.
[2] Manjunath, T.C., "Fundamentals of Robotics", Fourth edn., Nandu Publishers, Mumbai, 2005.
[3] Manjunath, T.C., "Fast Track to Robotics", Second edn., Nandu Publishers, Mumbai, 2005.
[4] Kris Gunnarsson, "New concepts and ideas for robotic simulation and offline teaching system", Pittsburg, Mar. 2000.
[5] Bennett Brumson, "Painting with the Sims", Robotics online technical paper, Michigan, Jan. 2006.
[6] Carl Traynor, "Optimize production by computerized simulation of robots", Robotics online technical paper, Michigan, Jan. 2006.
[7] Saeed B. Niku, "Introduction to robotics analysis, systems & applications" 2nd edition, Pearson education publication.
[8] John J. Craig, "Introduction to robotics mechanics and control", 2nd edn., Addison-Wesley publication.
[9] Mikell P Grover, Mitchell Weiss, Roger N Nagel, Nicholas G Ordey, "Industrial robotics - Technology, Programming and Applications", Mc. Graw Hill Book Co., Singapore, 1986.
[10] Ishani Mishra, "Optimization of robot path using off-line simulation and method for changing tool using a wireless communication device", M.Tech. Project report, ECE Dept., NIST, Berhampur, Orrisa, India, 2008.
[11] Phillip John Mckerrow, "Introduction to robotics", Addision-Wesley Publishers Ltd., Singapore, 1991.
[12] YU G. Kozyrew and A.A Kudinov, "Robot Work Cells", Moscow, Mir Publishers, 1989.
[13] E.P. Poppov and E.I.Yurevich, "Robotics", Moscow, Mir publishers, 1984.
[14] ABB Robot studio user guide.

Implementation of Ant Colony System for DNA Sequence Optimization

Zuwairie Ibrahim, Tri Basuki Kurniawan, Noor Khafifah Khalid, and Marzuki Khalid

Centre for Artificial Intelligence and Robotics (CAIRO), Department of Mechatronics and Robotics, Faculty of Electrical Engineering, Universiti Teknologi Malaysia, 81310 UTM Skudai, Johor Darul Takzim, Malaysia.

(zuwairiee@fke.utm.my; tribasukikurniawan@yahoo.com; ifah_khalid@yahoo.com; marzuki@utmkl.utm.my)

Abstract: DNA computation as a new paradigm has the computational power of molecules for information processing and many computational models have been proposed for solving mathematical problems in laboratory experiments. In order to achieve the correct computation, a set good of DNA sequences is crucial, because the code determines the way to process information on sequences in the experiments. Much works have focused on designing the DNA sequences to archive a reliable molecular computation and many algorithms have been proposed to obtain a set of good DNA sequences. In this paper, Ant Colony System (ACS) is proposed to solve the DNA sequence design problem. ACS used some ants to get their solutions based on the pheromone in their colony. A model is prepared which consists of four nodes representing four DNA bases. The results of the proposed approach are compared with the other methods such as Genetic Algorithm.

Keywords: Ant Colony Optimization, Ant Colony System, DNA sequence optimization**.**

I. INTRODUCTION

DNA computation has been extensively researched as a new computation paradigm in recent ten years. It has the ability to perform calculation using specific biochemical reaction between different DNA bases by Watson-Crick complementary base pairing, and has a number of useful properties such as massive parallelism and a huge memory capacity [1].

Although there have been many achievements, DNA computing faces some hurdles due to the technological difficulty of handling biochemistry process. To overcome these drawbacks, some works have focused on the design of DNA sequences to reduce the possibility for illegal reactions [2].

The necessity of DNA sequence design appears not only in DNA computation, but also in other biotechnology fields, such as the design of DNA chips for mutational analysis and for sequencing [2]. In these approaches, sequences are designed such that each element uniquely hybridizes to its complementary sequence, but not to any other sequence. Due to the differences in experimental requirements, however, it seems impossible to establish an all-purpose library of sequences that effectively caters to the requirements of all laboratory experiments [3]. Although the design of DNA sequences is dependent on the protocol of biological experiments, it is highly required to establish a method for the systematic design of DNA sequences, which could be applied to various design constraints [4].

Various kinds of methods and strategies for DNA sequence optimization have been proposed to date, such as template-map strategy [5], graph method [6], stochastic methods [7], and nearest-neighbour thermodynamic [8]. An Ant Colony Optimization (ACO) approach for DNA sequence design has been previously proposed [9], which used thermodynamic values as heuristic information. However, in DNA sequence design, since there is actually no information could be used as heuristic information, in this study, DNA sequences are designed based on Ant Colony System (ACS) without any heuristic information.

II. THE DNA SEQUENCE OPTIMIZATION

The objective of the DNA sequence optimization problem is basically to obtain a set of DNA sequences, where each sequence is unique or cannot be hybridized with other sequences in the set. In this paper, the objective functions and constraints from [9] are used. Two objective functions, namely $H_{measure}$ and *similarity*, are chosen to estimate the uniqueness of each DNA sequence. Moreover, two additional objective functions, which are *hairpin* and *continuity*, are used in order to prevent secondary structure of a DNA sequence. Furthermore, two constraints, which are $GC_{content}$ and melting temperature, are used to keep uniform chemical characteristics.

DNA sequence optimization is actually a multi-objective optimization problem. However, the problem is converted into single-objective problem, which can be formulated as follows:

$$\min f_{DNA} = \sum_i \omega_i f_i \tag{1}$$

subjected to Tm and GCcontent constraints, where fi is the objective function for each i∈ {$H_{measure}$, *similarity, hairpin, continuity*}, and ω_i is the weight for each f_i. In this study, the weights are defined by the user.

III. ANT COLONY SYSTEM

The studies of natural systems and the models of these systems have been beneficial for solving difficult

©ISAROB 2009

and complex real-world problems. ACO, as one of the natural systems, is inspired by the behavior of ants in finding the shortest path from the nest to the food place.

There are several additional or modification algorithms of ACO have been proposed, such as ACS, which has achieved performance improvements through the introduction of new mechanisms based on ideas not included in the original AS [10] Those mechanisms are state transition rule, global updating rule, and local pheromone updating rule [11].

A. State transition rule

Difference between ACS and AS is in the decision rule used by the ants during the construction process. The ACS transition rule, also referred as a *pseudo-random-proportional* rule was developed to explicitly balance the exploration and exploitation abilities of the algorithm. In ACS the probability for an ant to move from city i to city j depends on a random variable q and q_0 likes shown in Eq. (2);

$$j = \begin{cases} \arg\max_{u \in J_k(r)} \left\{ [\tau(r,u)] \cdot [\eta(r,u)]^{\beta} \right\} & \text{if } q \le q_0 \\ S & \text{otherwise} \end{cases} \qquad (2)$$

where q is a uniformly distributed random variable [0,1], q_0 value is between 0 and 1, and S is another random variable selected according to the probability distribution.

B. Global updating rule

The global pheromone update is applied at the end o f the each iteration by only one ant, which can be either the *iteration-best* or the *best-so-far*. The global updatin g rule is formulated as,

$$\tau(r,s) = (1-\rho)\cdot\tau(r,s) + \Delta\tau(r,s) \qquad (3)$$

where ρ is the pheromone evaporation for global u pdating and $\Delta\tau(r,s)$ shown in Eq. (4).

$$\Delta\tau(r,s) = \begin{cases} 1/Q & \text{if } (r,s) \in \text{sequence done by ant } k \\ 0 & \text{otherwise} \end{cases} \qquad (4)$$

where Q is the sum of all objective calculated for a sequence.

C. Local pheromone updating rule

The local pheromone update is performed by all the ants after each construction step using Eq. (5);

$$\tau(r,s) = (1-\zeta)\cdot\tau(r,s) + \tau_0 \qquad (5)$$

where $\zeta \in [0, 1]$ is the pheromone decay coefficient, and τ_0 is the initial value of the pheromone and in Eq. (5);

$$\tau_0 = 1/C \qquad (6)$$

where C is average values of Q for a set sequences, which are obtained randomly in the initialization process.

After that, each ant applied a state transition rule as defined in Eq. (2) to construct the solution until all ants have build a complete solution. After that, a local pheromone updating is applied. The objective function is calculated based on the problem being solved and then the global updating rule is applied based on Eq. (3) for all solutions.

IV. METHODOLOGY

The implementation of process in solving the DNA sequence design problem has been started by modeling the problem based on ACO methods. After that, the algorithms are developed to achieve the best solution of the problem.

In order to model the DNA sequence design problem into ACO methods, a model similar to finite state machine, which has four nodes, is proposed. In this model, the nodes represent A, C, G, and T of DNA bases. Every node is connected to each other, including its own node, as shown in Fig 1.

As illustrated in Fig 1, if an ant is placed (randomly) at node A (Fig 1a), and then if the ant moves to node T (Fig 1b), the formed path by the ant can be translated into 'AT' sequence of DNA. Next, if the ant moves from node T to node C (Fig 1c), the DNA sequence 'ATC' is formed. The tours of the ant continue until the number of required sequences has been produced.

Since DNA sequence design problem offers no information, which can be directly used as heuristic information, this model only uses pheromone information for ACO computations. Taillard and Gambardella [12], in their proposed approach, Fast Ant, also have used pheromone information only for Quadratic Assignment Problem (QAP).

During the initialization step, all parameters, such as α and ρ are set determined based on the default parameters for ACO [13] as presented in Table 1. The DNA parameters are initialized as listed in Table 2 [4].

In this paper, a multi-objective optimization problem is simplified into single-objective problem. Since it difficult to find the proper weight value to every objective [14], the weights in Eq. (1) are set as 1.

In the main process, every ant is placed randomly at the start node, at first. After that, every ant will be moving from one node to the other nodes to construct the DNA sequence. During the tour, the ant chooses the next node by applying the state transition rule, as in Eq. (2).

Since the required solution is a set of DNA sequences, a mechanism is needed to store the DNA sequence in an archive to be analyzed. The updating archive process is done only when the total of DNA

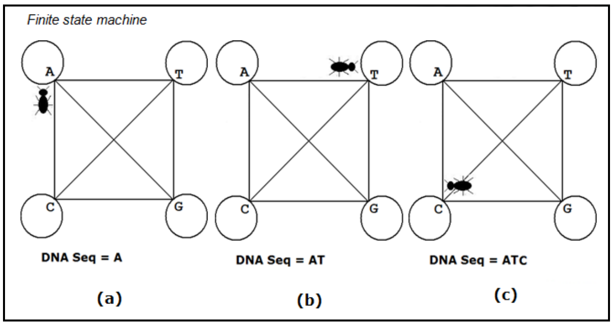

Fig 1. Finite state machine as a model for constructing a DNA sequence.

Table 1. Parameter for Ant Colony Optimization

Parameter	ACS
α	-
β	*0*
ζ	*0.1*
ρ	*0.1*
q_0	*0.9*
N	*half of ants*
Number of Sequences = 7 (*no. of ants-* n_k) Length of DNA Sequence = 20 (*no. of tours*) Max. Number of Iteration (*tmax*) = 500	

Table 2. DNA Sequence Parameter

DNA Sequence Parameter		
Parameter		**Value**
$h_{measure}$	h_{con}	6
	h_{dis}	0.17%
similarity	s_{con}	6
	s_{dis}	0.17%
t (continuity threshold)		2
hairpin	R_{min}	6
	P_{min}	6
GC%	*Min*	50
	Max	60
Tm	*Min*	40°C
	Max	80°C

The ACS algorithm for DNA sequence optimization is summarized in Algorithm 1;

Algorithm 1. Ant Colony System for DNA Sequence Optimization

// --- *Initialization step*
Initialize parameter *t*, α, ρ, q_0, n_k, *N, and all DNA parameters, such as* h_{con}, h_{dis}, s_{con}, s_{dis};
Calculate τ_o;
For each link(*i*, *j*) **do**
$\tau(i, j) = \tau_o$; // --- *Pheromone initialize*
end
t= 0; // --- *initialize no of iteration.*
Repeat
Repeat
Place all ants, *k* =1, …, n_k; // --- (n_k *= number of ants*)
For each ant *k* =1, …, n_k **do**
Repeat // --- *State Transition Rule*
Each ant applies a ***state transition rule*** (Eq. 34) to incrementally build a DNA sequence;
A ***local pheromone updating rule*** (Eq. 32) is applied;
Until all ants have build a complete a DNA sequence;
Next
If no. of DNA sequences in archive are equal with the number of ants (full) **Then**
Calculate all DNA sequences in archive bases on four objective functions and then sort in descending order ;
N-DNA sequences which have higher value in archive is removed;
EndIf
Calculate all DNA sequences bases on four objective functions and then sort in ascending order;
For each DNA sequence **do**
Checked for $GC_{content}$ and T_m constraints;
If passed and archive is not full **Then** stored DNA sequence to archive;
Next
A ***global pheromone updating rule*** (Eq. 30) is applied;
Until number of DNA sequences in archive are equal with the number of ants;
t = *t* + 1;
// --- *maximum no. of (tmax) iteration is reached.*
Until End_Condition

sequences in archive is equal to number of ants (n_k). The process calculates the objective values for each DNA sequence and sorted them in descending order. The *N*-first worst DNA sequences will be selected and the next process, storing archive, remove them from the archive to be replaced by *N* new DNA sequences.

The storing archive process also calculates the objective values for each new DNA sequence and sorted them by ascending order. The DNA sequences are placed in the archive started from the smallest objective values, if the range of $GC_{content}$ and *melting temperature* constraints are satisfied. The process continues until the archive is full. In the last process, global updating rule is applied for all new DNA sequences.

V. RESULTS AND DISCUSSION

Based on the proposed model and algorithm, one hundred independent runs of the ACS approach for DNA sequence design have been executed, and average of over these runs reported. The comparison results between our result with previous work [9], and GA approach taken from the result of Deaton *et al* [15] as shown in Table 3 and Fig 2.

Since this optimization process is finding the minimum values for the objective function, the smallest value is the best. Also, since the multi-objective problem is converted into single objective problem, the overall results only considered by the total objective values.

Table 3 and Fig 2 show the new proposed approach obtained the much lower in total objective values than the GA [15] and ACS [9]. The new approach has quite lower in *continuity*, *hairpin*, and $H_{measure}$ objective

Table 3. The comparison result of ACS approach, ACS [9], and GA [15]

The Average value of objective for 100 times running of ACS approach					
	C	*Hr*	*Hm*	*Sm*	*Total*
Average	1.0	0.1	35.4	58.8	95.4
Standard Deviation	*1.2*	*0.3*	*5.0*	*4.5*	*2.31*
The DNA Sequences taken from [9]					
Average	0.0	0.0	54.1	51.9	106.0
Standard Deviation	*0.0*	*0.0*	*12.4*	*7.8*	*10.5*
The DNA Sequences taken from [15]					
Average	11.7	0.6	63.4	48.3	124.0
Standard Deviation	14.8	1.5	7.1	7.4	14.7

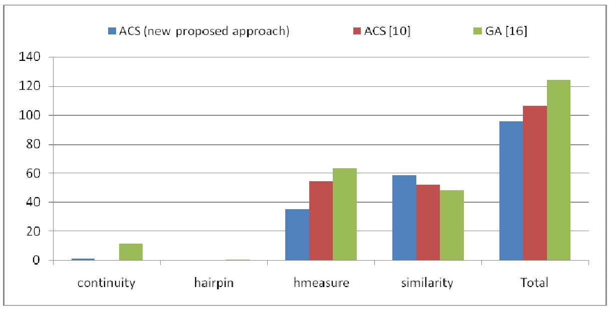

Fig 2. The comparison result of ACS approach, ACS [9], and GA [15]

values, but has higher in *similarity* than other results. For sequences generated by ACS [9], no *continuity* is observed, whereas the *continuity* value of sequences generated by the proposed approach and GA [15] are 1.0 and 11.7, respectively.

VI. CONCLUSION

ACS was implemented without heuristic information for DNA sequence optimization with four objective functions: $H_{measure}$, *similarity*, *continuity*, and *hairpin* and two constraints: $GC_{content}$ and *melting temperature*. The DNA sequences obtained from proposed approach were compared with those designed by previous work and GA approach. The results show that ACS can generate relatively better in total objective values than other approaches.

ACKNOWLEDGEMENT

This research is supported financially by the Ministry of Science, Technology, and Innovation (MOSTI), Malaysia, under eScienceFund Research Funding (Vot 79034) and the Ministry of Higher Education (MOHE), Malaysia, under Fundamental Research Grant Scheme (FRGS) (Vot 78225).

REFERENCES

[1] C.C. Maley, DNA computing: Theory, practice, and prospects, *Evol. Comp*, vol 6(3), 1998, pp. 201-229.

[2] A. Brenneman and A. Condon, Strand design for biomolecular computation, *Theory: Comput. Sci,* vol. 287, 2002, pp. 39-58.

[3] S. Kashiwamura, A. Kameda, M. Yamamoto, A. Ohuchi, Two-step Search for DNA Sequence Design, *Proceedings of the 2003 (ITC-CSCC 03)*, 2003, pp. 1815–1818.

[4] S.Y. Shin, I.H. Lee, D. Kim, B.T. Zhang, Multiobjective evolutionary optimization of DNA sequences for reliable DNA computing, *IEEE Transaction on Evolutionary Computation*, vol. 9(2), 2005, pp. 143-158.

[5] A.G. Frutos, A.J. Thiel, A.E. Condon, L.M. Smith, and R.M. Corn, DNA computing at surfaces: four base mismatch word design, *Proceedings of the 3rd DIMACS Workshop DNA Based Computers*, 1997.

[6] U. Feldkamp, S. Saghafi, W. Banzhaf, and H. Rauhe, DNA sequence generator - A program for the construction of DNA sequences, *Proceedings of the 7th International Workshop DNA Based Computers*, 2001, pp. 179–188.

[7] F. Tanaka, M. Nakatsugawa, M. Yamamoto, T. Shiba, and A. Ohuchi, Developing support system for sequence design in DNA computing, *Proceedings of the 7th International Workshop DNA Based Computers*, 2001, pp. 340–349.

[8] F. Tanaka, A. Kameda, M. Yamamoto, and A. Ohuchi, Thermodynamic parameter based on nearest-neighbor model for DNA sequences with a single-bulge loop, *Biochemistry*, vol. 43(22), 2004, pp. 7143–7150.

[9] T.B. Kurniawan, N.K. Khalid, Z. Ibrahim, M. Khalid, and M. Middendorf, An ant colony system for DNA sequence design based on thermodynamics, *Proceedings of IASTED-ACST*, 2008, pp. 144-149.

[10] M. Dorigo, Optimization, learning and natural algorithms, *PhD Thesis," Dipartimento di Elettronica, Politechico di Milano, Italy*, 1992.

[11] M. Dorigo, M.G. Luca, Ant Colony System: A cooperative learning approach to the Traveling Salesman Problem, *IEEE Trans. Ev. Com,* vol. 1, 1997.

[12] E.D. Taillard, L,-M. Gambardella, 1997, Adaptive memories for the Quadratic Assignment Problems, *Technical report* IDSIA-87-97, IDSIA, Lugano.

[13] M. Dorigo, and T. Stutzle, Ant Colony Optimization, *Massachusets Institute of Technology*, 2004.

[14] Y. Jin. M. Olhofer, B. Sendhoff, 2001. Dynamic Weighted Aggregation for Evolutionary Multi-Objective Optimization: How does it work and How?, *In Proceeding of GECCO 2001 Conference.*

[15] R. Deaton, R. C. Murphy, M. Garzon, D. R. Franceschetti, and S. E.Stevens, Jr., Good encodings for DNA-based solutions to combinatorial problems, *Proc. 2nd Annu. Meeting DNA Based Comp.,* 1996, pp. 247–258.

©ISAROB 2009

The Fourteenth International Symposium on Artificial Life and Robotics 2009 (AROB 14th '09),
B-Con Plaza, Beppu, Oita, Japan, February 5 - 7, 2009

Understanding User Commands by Evaluating Fuzzy Linguistic Information Based on Visual Attention

Buddhika Jayasekara Keigo Watanabe Kiyotaka Izumi
Department of Advanced Systems Control Engineering
Saga University
Saga 840-8502, Japan.

Abstract

This paper proposes a method for understanding the user commands based on visual attention. Visual attention system is implemented to evaluate the fuzzy linguistic information based on the environmental conditions. It is assumed that the corresponding distance value for a particular fuzzy linguistic command depends on the spatial arrangement of the surrounding objects. A fuzzy logic based voice command evaluation system (VCES) is proposed to assess the uncertain information in user commands. A situation of object manipulation for rearranging the users working space is simulated to illustrate the system. It is demonstrated with PA-10 robot manipulator.

1 Introduction

Natural human-human like interaction plays a major role in human friendly robotic system. Voice communication is significant in human-robot interaction. Human user may use subjective, uncertain information to convey their idea. Therefore, the ability of the robot companion to understand the uncertain information is crucial in effective human-robot interaction. An intelligent service robot would increase the functional capacity of the aged and possibly even improve their state of health. In addition, a successful human-friendly robot equipped with human-like voice communication capabilities will be able to help disabled people, to help in complex tasks such as surgery, etc. [1], [2].

The ability to understand the fuzzy linguistic information plays a key role in human-robot interaction. In Pulasinghe et al. [3], robot controlling by using rich voice commands such as "move little right" has been studied. Jayawardena et al. [4] proposed a natural language command based robot learning method using fuzzy coach-player systems. In evaluating the fuzzy linguistic information, they have assumed that the actual amount traversed as the response to a distance command depends on the distance traversed immediately before that. In addition, the system of understanding and quantifying the uncertain information in voice commands is predetermined. However, the ability to adapt the system for understanding the fuzzy linguistic information based on the environment conditions is vital. In addition, human learner may adjust their output for instructions including uncertain information by acquiring the environmental conditions through visual attention.

The capability to acquire the environmental conditions through vision is important in human-robot interaction. In addition, object identification plays a major role in an interaction with the environment. The object features and corresponding lexical symbols are taught to achieve the object identification. The natural language object references, which consist of combination of lexical symbols such as "small green cube," have been studied [5]. A vision system is studied to identify and locate objects for object manipulation tasks in natural, domestic environments [6]. But, these methods still fall sort of a system, which can evaluate the fuzzy linguistic information by acquiring environmental conditions through visual attention.

Therefore, this paper proposes a method to understand the fuzzy linguistic information by acquiring the environmental conditions through visual attention. The system overview is discussed in section 2. Next section 3 discusses the visual attention system for acquiring the environmental conditions. The evaluation process of voice commands is presented in section 4. Finally, summary is presented.

2 System Overview

The functional overview of the system is shown in Fig. 1. The system consists of fuzzy logic based voice command evaluation system (VCES), visual attention system (VAS), and interaction manager (IM). The voice interaction between human user and the robot is managed by the IM. The voice recognition and understanding are implemented by the IBM ViaVoice software development kit. Conversational grammar patterns and basic dialogue phrases are

©ISAROB 2009

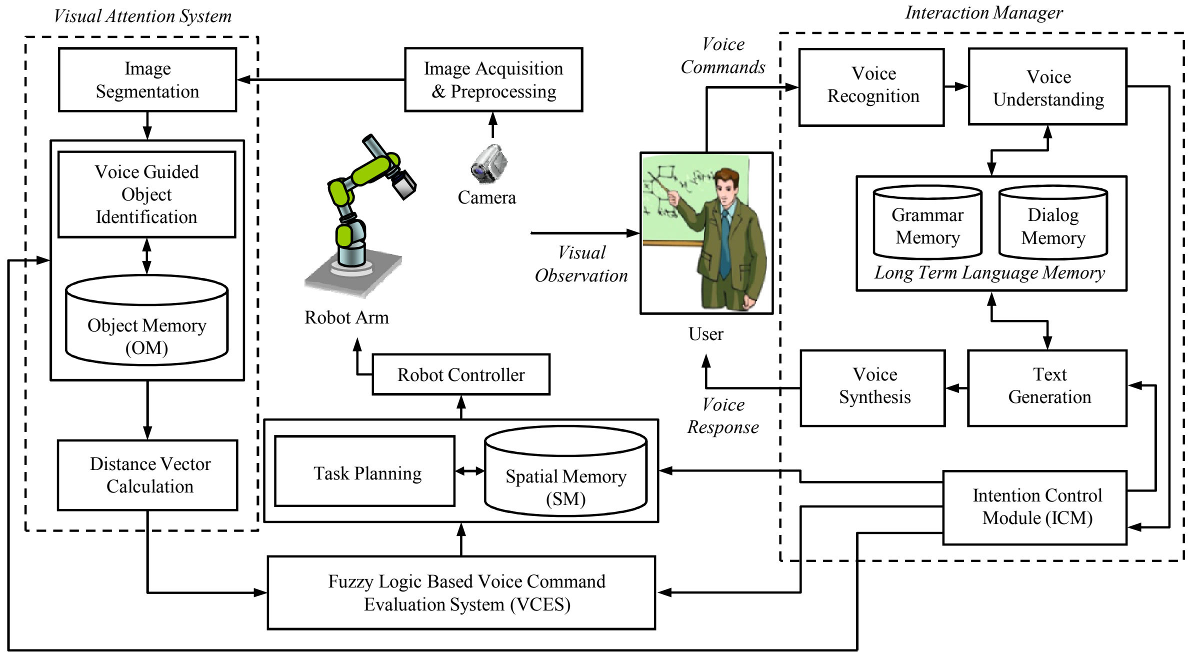

Figure 1: System overview.

stored in the long term language memory. The speech synthesis is a text-to-speech (TTS) conversion, which is implemented by using the Microsoft speech SDK.

The VAS is used to percept the spatial data of surrounding objects. VCES is introduced to evaluate the fuzzy linguistic information in the user commands. A task planner is deployed to identify the primitive behavior sequence, which is required to fulfill the task. A spatial memory (SM) is proposed to remember the corresponding position control vectors for visual-motor mapping. It is implemented by a neural map with a competitive layer [7]. Finally, the task planner guides the robot controller with the support of SM.

The presented system is capable of moving an existing object based on the user voice commands. In addition, new objects can be taught to the system by interactive dialogue.

3 Visual Attention System

VAS is introduced to capture the spatial arrangement of the objects in the surrounding area. First, the work space images are captured using a camera and they are preprocessed to remove the irregularities. Then, images are segmented to extract the objects. The corresponding object is identified based on the lexical symbol, which is included in the user command [5]. The object memory (OM) is used to store the direct mapping between the lexical symbol of the object and the feature vector. Here, average RGB color values and the Hu descriptors are considered as the feature set. The space around the corresponding object is divided into four main regions to compute the distance vector as in Fig. 2. The neighborhood is identified based on a ratio ζ, which determines the neighborhood region:

$$\zeta = \frac{r}{r} \tag{1}$$

Here, r is the radial distance to the nearest object in the region and r is the corresponding neighborhood. The average distance to the surrounding objects d_{avg} is calculated based on the average distances of each region as in (2):

$$d_{avg} = \psi^T d \tag{2}$$

where

$$\begin{aligned} \psi &= (\psi_1, \psi_2, \psi_3, \psi_4)^T, \quad \sum_{i=1}^{4} \psi_i = 1 \\ d &= (d_1, d_2, d_3, d_4)^T \end{aligned}$$

Here, d_i, where $i = 1, 2, 3, 4$, is the average distance to the surrounding objects in the neighborhood of region i. ψ consists of the corresponding weighting factors for the regions. ψ_j, where $j = 1, 2, 3, 4$, is the corresponding weight for region j. In addition, the distance to the nearest object in the target direction X and the distance to the farthest object from all regions D are also obtained.

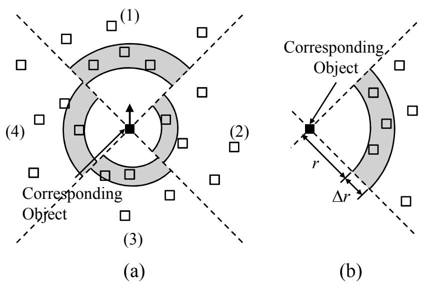

Figure 2: (a) and (b) illustrate the spatial arrangement of the corresponding object and the neighbor objects. Here, □s represent the neighbor objects of the corresponding object ■.

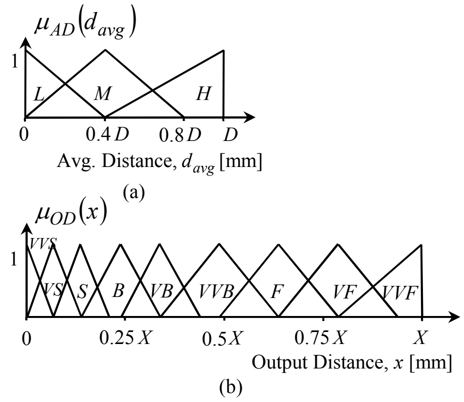

Figure 3: (a) and (b) represent the membership functions for average distance d_{avg} and output distance x. Fuzzy labels are defined by, L: Low, M: Medium, H: High for d_{avg} and VVS: Very Very Small, VS: Very Small, S: Small, B: Big, VB: Very Big, VVB: Very Very Big, F: Far, VF: Very Far, VVF: Very Very Far for x.

4 Voice Command Evaluation

VCES is implemented by using a fuzzy inference system to evaluate the fuzzy linguistic information in user commands based on the spatial arrangement of the surrounding objects. Here, it is assumed that the corresponding distance value for a particular fuzzy linguistic command depends on the spatial arrangement of the surrounding objects in the environment. The user command and the average distance to the surrounding objects are the inputs of VCES. The output is the corresponding output distance x_{out} for the user command. The membership functions for the average distance to the surrounding objects $\mu_{AD}(d_{avg})$ and the output distance $\mu_{OD}(x)$ are shown in Fig. 3. Here, the input spaces of $\mu_{AD}(d_{avg})$ and $\mu_{OD}(x)$

Input Memberships		Average Distance		
		Low	Medium	High
User Command	Very Little	*VVS*	*VS*	*S*
	Little	*S*	*B*	*VB*
	(Medium)	*VB*	*VVB*	*F*
	Far	*F*	*VF*	*VVF*

Figure 4: User commands are interpreted based on these fuzzy rules. Fuzzy labels are similar to that in Fig. 3.

Table 1: Basic actions and fuzzy predicates.

Action	Fuzzy predicate
move right	very little
move left	little
move forward	(medium)
move backward	far

are adjusted based on D and X respectively. This yields the adaptation of the system towards the environmental conditions. The considered rule base is given in Fig. 4. The possible set of actions and fuzzy predicates for action modification are shown in Table 1. The user command is structured by including the action and action modification as "Move" + <Lexical symbol of object> + <Fuzzy predicate> + <Direction component of action> (e.g. "Move blue Box very little backward").

5 Summary

The proposed system was implemented based on PA-10 robot manipulator. A working space of 0.5×0.8 m was used to manipulate the objects. A camera image of 1280×960 resolution was captured for each situation. The parameters of VAS are chosen as $\zeta = 0.5$ and $\psi = (0.3, 0.2, 0.3, 0.2)^T$. Here, ψ is selected by considering the natural human tendency. Normally, humans pay more attention to the objects in the moving direction. It is simulated by selecting higher values for ψ_1 and ψ_3. Different visual situations are achieved by changing the position of the idle objects in the environment and they are illustrated in Fig. 5. A set of user commands and the corresponding output movements are shown in Table 2. (a)–(d) visual situations are used to highlight the effectiveness of capturing the spatial arrangement by VAS. A situation with few actual objects is considered in (f).

A method has been proposed to understand the fuzzy

Table 2: User commands and corresponding output distances.

	User command	X (mm)	D (mm)	Average distances to objects (mm)				d_{avg} (mm)	x_{out} (mm)
				d_1	d_2	d_3	d_4		
(a)	Move blue Box little right	108.4	265.5	227.9	166.7	197.2	143.0	189.4	32.2
(b)		104.5	250.4	197.8	148.7	126.0	142.8	155.4	30.1
(c)		56.2	230.3	128.5	169.1	195.9	131.4	157.4	16.5
(d)		158.1	305.4	235.4	99.2	253.1	110.9	188.6	45.5
(e)	Move blue Box very little right	140.4	245.2	225.5	137.8	186.8	160.6	183.3	15.8
	Move blue Box right	140.4	245.2	225.5	137.8	186.8	160.6	183.3	81.5
	Move blue Box left	135.3	245.2	186.8	160.6	225.5	137.8	183.3	78.6
	Move blue Box little forward	70.9	245.2	160.6	225.5	137.8	186.8	172.0	20.9
(f)	Move Biscuit packet far left	81.5	402.7	236.4	204.1	328.4	261.6	262.6	72.9
	Move Biscuit packet little forward	112.3	402.7	204.1	328.4	261.6	236.4	252.7	32.4

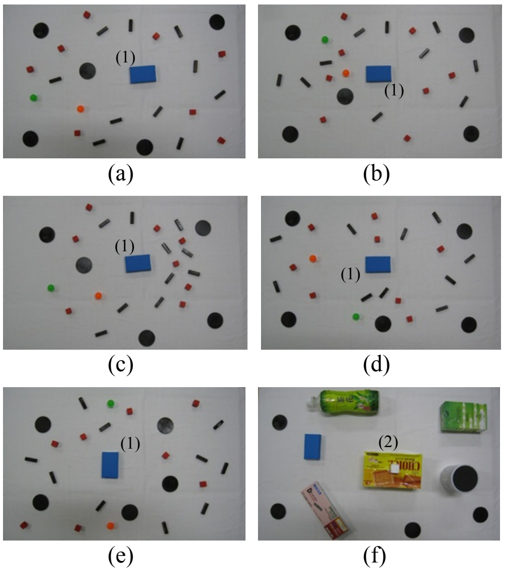

Figure 5: (a)–(f) represent up camera view of visual situations. The movement of blue Box (1) is considered in (a)–(e) and the movement of Biscuit packet (2) is considered in situation (f). Other idle objects are used to change the surrounding environment by changing the positions.

linguistic information by visual attention. The proposed system is an effective method to manipulate the objects based on user commands, which includes fuzzy linguistic information.

References

[1] C. Crangle and P. Suppes, *Language and Learning for Robots*, CSLI Publications, Stanford, CA, 1994.

[2] P. Menzel and F. D'Aluisio, *Robosapiens*, The MIT Press, England, 2000.

[3] K. Pulasinghe, K. Watanabe, K. Izumi, and K. Kiguchi, "A modular fuzzy-neuro controller driven by spoken language commands," *IEEE Trans. on Systems, Man, and Cybernetics-Part B:Cybernetics*, vol. 34, pp. 293–302, 2004.

[4] C. Jayawardena, K. Watanabe, and K. Izumi, "Knowledge acquisition by a sub-coach in a coach player system for controlling a robot," in *Proc. of the 4th Intl. Conf. on Advanced Mechatronics*, Hokkaido, Japan, Oct. 2004, pp. 601–606.

[5] C. Jayawardena, K. Watanabe, and K. Izumi, "Learning of object identification by robots commanded by natural language," in *Proc. of the 9th Intl. Conf. on Intelligent Autonomous Systems*, Tokyo, Japan, Mar. 2006, pp. 913–920.

[6] D. Kragic, M. Bjorkman, H.I. Christensen, and J. Eklundh, "Vision for robotic object manipulation in domestic settings," *Robotics and Autonomous Systems*, vol. 52, pp. 85–100, 2005.

[7] B. Jayasekara, K. Watanabe, and K. Izumi, "Controlling a robot manipulator with fuzzy voice commands guided by visual motor coordination learning," in *Proc. of the Intl. Conf. on Instrumentation, Control and Information Technology*, Tokyo, Japan, Aug. 2008, pp. 2540–2544.

Biomimetic Intelligent Creatures and Artificial Muscles

Maki K. Habib[1,2] Keigo Watanabe[2], Kiyotaka Izumi[2]
[1]Mechanical Engineering Department, School of Sciences and engineering,
The American University in Cairo, Egypt
[2]Saga University, Saga, Japan
maki@ieee.org

Abstract- **Biomimetics is an interdisciplinary scientific research focuses on making nature as a model of creative inspiration to study, analyze and design of new efficient engineering systems and modern technology. Smart materials are the foundation supporting the development of new biomimetic based technology. Wide range of biologically inspired robots and intelligent systems has been developed. However, engineering such biomimetic intelligent creatures were hampered by physical and technological constraints, and it is still a challenge. Making robots and intelligent creatures that are actuated by biologically inspired artificial muscles would create new reality with great potentials. This paper provides the concept of Biomimetic as an interdisciplinary field, discusses the enabling technologies, and presents the development of biologically inspired actuators.**

I. Introduction

The evolution of nature led to the introduction of highly effective and power efficient biological mechanisms. Nature tested every field of science and engineering leading to inventions that work well, can adapt and last. Biological systems exhibit remarkable physical properties and have been always a source of inspiration. Adopting mechanisms and capabilities from nature and the use of scientific approaches led to effective materials, structures, tools, mechanisms, processes, algorithms, methods, systems and many other benefits. Nature has always served as a model for mimicking and inspiration to humans in their efforts to improve their life. Humans throughout history have always sought to mimic the appearance, mobility, functionality, intelligent operation, and thinking process of biological creatures [1].

Maturing conventional technologies are associated with constraints and inadequate performance and this foster the demand for new solutions to maximize functionality while minimizing costs in energy and materials. The need to seek for new solutions is driving science to consider nature as biologically inspired model. The driving force behind attempting to merge biological principles and physics applications stems from the recognition that, there are a number of areas where biological methods are more efficient, environmentally and ecologically friendly, and overall superior to current technology. Hence, understanding biological systems presents unique opportunities for wide range development of innovative ideas, paradigms, concepts and methods for engineering solutions, and helps to create new generations of smart materials, novel advanced structures, intelligent devices and technologies. Engineers are increasingly turning to biologists to understand and learn how living organisms function and solve problems. This leads to fuse the best solutions from nature with artificially engineered components to develop systems that are better in functions and efficiency than existing conventional approaches, and this science and technology became known as "Biomimetics" or the 'Mimicry of Nature'. Researchers diverge in precisely how they define biomimetics [2]. However, the use of inspiration instead of mimics is a more accurate description since mimicry is neither possible nor desirable.

From the view point of the author, Biomimetics can be defined as a new interdisciplinary scientific field featured by technology outcome (hardware and software), and it lies at the interface between biology, physics, chemistry, information, and engineering sciences [7]. Biomimetics focuses on making nature as a model of inspiration that would immensely help conscious abstraction of new principles and ideas, foster innovative design collections, find out new techniques and functionalities, seek new paradigms and methods, develop new materials, and design new streams of intelligent machines, robots, systems, devices, algorithms, etc. Biomimetics incorporates building novel materials at nature's scale and techniques drawn from naturally made substances, and resembles biological systems in structure and/or function as necessary. In the field of sensing and actuations, biomimetics devices can provide an efficient way of converting mechanical energy into electrical or chemical forms and vice versa. Scientists hope this blending may one day lead to stronger, cost- and energy-efficient, and intelligent products that are attractive ecologically.

Today, researchers are looking for any insights they can find into how other biological species do things that the current class of robots cannot with aim at developing a new class of biologically inspired robots that exhibit greater robustness and better performance in unstructured and dynamic environments. This new generation of robots will be substantially more compliant and stable than current robots, and will take advantage of new developments in materials, fabrication technologies, sensors and actuators. Technologies that enable the development of biologically inspired systems are increasingly emerging, such as MEMS and NEMS, artificial muscles, AI and computational intelligence, computer vision, etc. as well as biomimetic capabilities in materials science,

©ISAROB 2009

mechanics, electronics, computing science, information technology, etc. Making creatures that look and behave like a biological model, such as robots and toys that are greatly inspired by science fiction, have established perceptions and expectations that are far beyond the reach of current engineering capabilities, which are constrained by laws of physics and current state-of-the-art. However, innovative robot design should not be restricted by an animal model's design rather to fuse the best solutions from nature with artificially engineered components.

Researchers in the field of robotics can apply the available research outcomes and lessons that already learnt from biology to practice. How birds fly, how fish swim, how dolphins locate objects, and how humans and other species walk, etc. might best be discovered and understood by trying to understand and abstract the key knowledge from relevant bio-systems. Some of the developed robot design inspired by the biological shape and motion mechanisms selected from the bio-systems family. Such robots may perform combinations of locomotion techniques including legged (two legs [3] four legs [4, 5], six legs [5,6], eight legs [8], etc.), hopping [4, 9], walking and jumping [11], running [4], climbing [12], walking and climbing [13], rolling [14], snake like[16], crawling [17], swimming (underwater, shallow water) [18, 20], water striding [22], flying [23-25], etc. Other development was inspired by behaviors of bio-systems, such as, sensing, navigation, formation, tracking, etc. [27, 29, 30].

In spite of such development, current robots lack the robustness and performance of even the simplest insect or animal when operating in dynamic, unstructured and complex environments. Even if the design of biomimetic robots is inspired from biology, however, their realizations were in most cases compromised by the complexity and fragility that result due to the use of traditional engineering materials and manufacturing methods [6]. It should be kept in mind that mimicking animals, or even plants, requires deep investigation of new materials, mechanisms, sensors, actuators, and control schemes and can lead to breakthrough advances of robotics technologies.

II. BIOMIMETICS AND ENABLING TECHNOLOGIES

The growing effect of interdisciplinary technology is changing the world across all dimension of life: social, health, education, manufacturing, industry, economic, political, personal, etc. The revolution of information technology, information availability and utilities continue to influence the world in all life dimensions. Biotechnology is revolutionizing our life by enabling us to identify, understand, manipulate, improve, and control every aspect of living organisms. Smart materials, agile manufacturing, and nanotechnology are inspiring, enabling, and offering the promise of a new dimension in innovation of new devices with unforeseen capabilities that we have not seen. Biotechnology relies heavily on laboratory equipment providing lab-on-a-chip analysis as well as progress in bioinformatics. Many of the advances in lowering energy intensity have come from developments in the materials and chemical sciences, such as new magnetic materials; high strength, lightweight alloys and composites; novel electronic materials; and new catalysts, with a host of energy technology applications. Materials sciences are helping in the development of energy generation, conversion, transmission, and use, while chemical sciences provide the necessary understanding of the interactions of atoms, molecules, and ions with photons and electrons; the making and breaking of chemical bonds in gas phase, in solutions, at interfaces, and on surfaces; and the energy transfer processes within and between molecules.

Our bodies can be viewed as complex assembles of molecular-level machines [21]. Biolmolecular motors are individual protein complexes that are ultimately responsible for all active biological motion involving internal material transport. They perform tasks vital to life of the organism, such as muscle contraction, damage repair, cell division, intracellular transport and genomic transcription [10]. The success of future molecule-driven actuators most likely lies in the development of artificial molecular motors because of their ability to provide large forces from low voltage inputs while featuring bistable actuation characteristics and molecular design flexibility. In order to develop mechanical parts in the nanometer range, and thereby create nano-electromechanical systems (NEMS) [26] that may be used beyond those satisfied by current MEMS devices, different fabrication methods have been initiated [10, 19, 28]. Biomimetic synthetics are being used to encourage bone regeneration and interaction with human implants and orthopaedic implants. The smaller the particle size of the material used, the better the result as far as tissue growth and regeneration. Recent developments are using nanotechnology to produce molecular level changes to materials in order to mimic natural found materials

Nano- and smart materials technologies are changing the way structures and electronics are made, and promise the development of useful components, products and systems for desired characteristics that are highly stronger, smaller (composed of just a few atoms and molecules), smarter, high resolution, lighter weight, faster, accurate, reliable, structural functionality and flexible, and self-repairing, multi-functional, user and environment friendly, efficient energy conversion and storage, more survivable, customizable, etc. The revolution in genomics research has the potential to provide entirely new ways of producing forms of energy, sequestering carbon, and generating materials that require less energy to produce. It includes research to investigate the underlying biological processes of plants and microorganisms, potentially leading to new processes and products for energy applications.

Different materials with sensing and actuation capabilities are increasingly used to combine these capabilities in response to various needs, such as, new smart and specialized equipment and systems; monitoring and diagnosis for health, industry, structures and environment; security and tracking; realizing new clothes that can respond to weather and health or comfort, interface with information systems, monitor vital signs, deliver medicines, and protect wounds; personal identification; supporting new trends in building intelligent transportation systems, etc. Rapid prototyping, and flexible manufacturing together with embedded sensors and systems, has provided a means for accelerated and affordable design and development of complex components and systems. Hardware advances for exponentially smaller, faster, and cheaper semiconductors are supporting the growth of information technology. This trend in technology increases the availability of low-cost computing, high memory devices, and enable the development of ubiquitous embedded sensors and computational systems in consumer products, intelligent system, appliances, and environments. The evolution of these technologies is leading to the development of new trend of instrumentation and measurement technologies along with chemical, fluidic, optical, mechanical, and biological integrated micro- and nano-scale components, which are integrated with computational logic in chip designs. Increases in materials performance for power sources, sensing, and actuation could also enable new and more sophisticated classes of robots and remotely guided vehicles based on biological models. A potential long-term solution to overcome possible limitation in computational power is to shift the basis of computation to devices that take advantage of various quantum effects. In addition, another approach known as molecular electronics would use chemically assembled logic switches organized in large numbers to form sophisticated devices and computers. These concepts are attractive because of the huge number of parallel, low-power devices that could be developed.

The biomimetics field is highly interdisciplinary and all of the mentioned technologies that contribute to its progress are highly inter-related and heavily synergized, which makes the progress of each area leads to accelerate progress in each of the other areas. In addition, biomimetics is demanding to increase the importance of continued interdisciplinary education, training and research. The progress of the mentioned fields is highly contributing to improve life quality by having better disease control, new medicines and treatments, gene therapy, age mitigation and reversal, prosthetics, bionic implants, animal transplants, and many other advances. The accelerating pace of the advancements in the field of biomimetics seems to make evident that the emergence of machines as our peers is imminent. Further advancement and the actual realization of these possibilities depends on a number of factors, including local acceptance of technological change, levels of technology and infrastructure investments, market drivers and limitations, and technology breakthroughs and advancements.

III. Bioinpiration and Actuation materials

Along with limitations in current control methodologies, actuation presents constraints to novel designs of intelligent mechanisms. Three types of conventional actuation are considered as the core of motion and force power for all motion based systems: Hydraulic, Pneumatic, and Electromagnetic actuators. However, the challenges of energy inefficiency, flexibility, robustness and other technical motivations have been many in getting robots to perform bio-inspired motion, such as that of human, animal, insect, etc. Hence, there are demands to develop technologies that would drive robots with efficient, high power density actuation and achieve lifelike motion performance. The most significant difficulty in achieving lifelike performance or appearance is the lack of actuator technology that can truly mimic natural muscles even at its most basic performance. Natural muscles are essential to the mobility and manipulation capabilities of biological creatures. This highlights the need and the necessity to develop actuators that emulate and supersede the behavior and performance of real muscles. The potential to make such actuators is increasingly becoming feasible with the emergence of new development. Recently, many new types of actuators and materials have been used or currently under development to provide the necessary motion and force input. Examples of these actuators are Shape Memory Alloys, Electro-Rheological Fluids, Magneto-Active Transducers, single Crystal Piezoelectric ceramics, Carbon nano-tubes, Electrostatic, and Electroactive Polymers.

Electroactive polymers artificial muscles (EPAM), dielectric elastomers (DE), electroelastromers are terms used to indicate to electroactive polymers (EPA) [31]. The basic architecture of EPAM actuator is made up of a dielectric polymer film sandwiched between two compliant electrodes, typically 10 to 200 um thick that is coated on both sides with an expandable and compliant film of a conducting electrode material, such as carbon impregnated elastomer. The potential of this technology is immense as electroactive polymers that perform muscles activities by expanding and contracting silently based on small variable voltage input levels. The good electromechanical response of EPAM, as well as other characteristics such as good environmental tolerance and long-term durability, suggests a wide range of possible applications. The significant advantage EPAM has over electromagnetic actuators is energy density, i.e., more energy created per unit mass of the actuator itself. In addition, EPAM has a significant direct displacement advantage compared to other evolving technologies. The EPAM materials can be easily formed in various shapes and their properties can be engineered and they can potentially be integrated with micro-electro-mechanical-system (MEMS) sensors to produce smart actuators. EPAM has the ability to be configured and tailored to particular applications. These include rolled actuators, actuators based on stretched films on rigid frames, bimorph and unimorph actuators, diaphragms, and bowtie actuators (so called because the top and bottom rigid end pieces, together with the flexible sides that come in at an angle, make the shape of a bowtie) [15]. Furthermore, one can have multi layer of EPAM to get additional displacement or stroke as well as getting higher exerted forces. These layers can be constructed in multiple planar configurations or in linear rolls. The EPAM can be patterned to pinpoint actuation in multiple locations. The overall displacement is a function of the area of EPAM, and the force exerted is a function of the number of layers of EPAM.

Dielectric elastomers have the ability to emulate the operation of biological muscles with high fracture toughness, large actuation strain and inherent vibration damping. Their unique characteristics make them promising materials in electromechanical transduction and active vibration damping Many prototypes have been developed seeking to embody the advantages of the dielectric elastomers and create biologically inspired intelligent robots and machines [31-33]. Nevertheless, the EAP materials that have been developed so far are still exhibiting low conversion efficiency, are not robust, and there is a need for developing adequate understanding of EAP materials' behavior, as well as processing and characterization techniques [33].

IV. CONCLUSIONS

Duplicating nature's designs is not an easy task and it is not always necessary either. A reality check reveals that creative inspiration comes a lot easier than imitation. By studying and analyzing biological systems, one may be able to derive or understand the relevant principles and use them to help solve engineering problems. However, the main challenge facing the development of Biomimetics robots and systems is the available technology, materials and the methods of fabrication as it is still in their infancy compared to nature's evolution. Biomaterials are expected to become the dominant focus of materials research, as it would lead to down-sizing of engineered components and the up-scaling incorporation of biomimetic concepts and processes. The inspiration of nature is expected to continue leading to technology improvements and the impact is expected to be felt in every aspect of human life. Finally, in order to achieve desirable lifelike motion, actuators must be able to reproduce the important features of natural muscle.

REFERENCES

[1] Y. Bar-Cohen, "Biologically Inspired Intelligent Robotics", In Proceedings of the SPIE Smart Structures Conference, March 2003. Paper 5051-02,
[2] L. D. Paulson, "Biomimetic Robots", IEEE Computer, 2004, pp. 48-53.
[3] J. H. Park and K. D. Kim, "Biped robot Walking using Gravity-Compensated Inverted Pendulum Mode and Computed Torque Control", In Proceedings of the IEEE International Conference on Robotics and Automation (ICRA'1998), Leuven-Belgium, 1998, pp. 3528–3533.
[4] M. H. Raibert, "Legged Robots that Balance," MIT Press, MA, 1986.
[5] M. Buehler, "Dynamic Locomotion with one, Four and Six-legged Robots", J. of the Robotics Soc. of Japan, Vol. 20, No. 3, 2000, pp.15-20.
[6] J. G. Cham, J. K. Karpick and M. R. Cutkosky, "Stride Period Adaptation for a Biomimetic Running Hexapod," International Journal of Robotics Research, Vol. 23, No. 2, 2004, pp. 141-153.
[7] M. K. Habib, K. Watanabe, and K. Izumi, ""Biomimetics Intelligent Robots and Biological Inspiration", Int. Conf. on Control, Instrumentation and Mechatronics 'CIM'2007', Johor-Malaysia, 2007, pp. 824-832.
[8] B. Klaassen, R. Linnemann, D. Spenneberg and F. Kirchner, "Biologically Inspired Robot Design and Modeling", In Proceedings of ICAR'2003, Coimbra-Portugal, 2003, pp. 576-581.
[9] W.J. Schwind and D.E. Koditchek, "Control of Forward Velocity for a Simplified pPanar Hopping Robot", In Proceedings of the 1995 IEEE ICRA'1995, Nagoya-Japan, 1995, pp. 691–696.
[10] T. J. Huang, Y. Liu, B. Brough, A. H. Flood, P. Bonvallet, H.-R. Tseng, M. Baller, S. Magonov, J. F. Stoddart, and C.-M. Ho, "A Nano-Chemo-Mechanical Actuator Based on Artificial Molecular Machines," MEMS Miami, FL, 2005, pp. 871-874.
[11] K. S. Aschenbeck, N.I. Kern, R.J. Bachmann, and R.D. Quinn, "Design of a Quadruped Robot Driven by Air Muscles," In Proceedings of the IEEE/RAS-EMBS International Conference on BioRob'06), Pisa, 2006.
[12] B. L. Luk, A.A. Collie, V. Piefort, and G.S. Virk, "Robug III: A Tele-operated Climbing and Walking Robot," UKACC International Conference on Control, Vol. 1, No. 427, 1996.
[13] S. Hirose, A. Nagakubo, and R. Toyama, "Machine that can Walk and Climb on Floors, Walls and Ceilings," In Proceedings of 5^{th} International Conference on Advanced Robotics, Pisa, 1991, pp.753-758
[14] S. Bhattacharya and S. K. Agrawal, "Spherical Rolling Robot: A Design and Motion Planning Studies," IEEE Transactions on Robotics and Automation, Vol. 16, No. 16, 2000, pp.835–839.
[15] R. Kornbluh, R. Pelrine, Q. Pei, and V. Shastri, "Application of Dielectric EAP Actuators," Electroactive Polymer (EAP) Actuators as Artificial Muscles—Reality, Potential and Challenges," ed. Y. Bar-Cohen, SPIE Press, 2001, Ch. 16, pp. 457–495.
[16] S. Hirose and E. Fukushima, "Snakes and Strings: New Robotic Components for Rescue Operations," Experimental Robotics VIII 2002, pp. 48-61.
[17 J. A. Galvez, P.G. de Santos, and F. Pfeiffer, "Intrinsic Tactile Sensing for the Optimization of Force Distribution in a Pipe Crawling Robot," IEEE/ASME Transactions on Mechatronics, Vol. 6, No. 1, 2001.
[18] A. M. Anderson, K. Streitlien, D. S. Barrett and M. S. Triantafyllou, "Oscillating Foils of High Propulsive Efficiency," Journal of Fluid Mech, Vol. 360, 1998, pp. 41-72.
[19] V. Balzani, A. Gredi, F. M. Ramyo, and J. F. Stoddart, "Artificial molecular machines," Angew. Chem. Int. Ed., Vol. 39, 2000, pp. 3348-3391.
[20] J. Ayers, Witting, N. McGruer, C. Olcott, D. Massa, "Lobster Robots," In Proceedings of the International Symposium on Aqua Biomechanisms, T. Wu and N, Kato, [eds], Tokai University, 2000.
[21] D. S. Goodsell, "Our molecular Nature: The body's Motors, Machines and Messages," Copernicus, New York, 1996.
[22] S. H. Suhr, Y. S. Song, S. J. Lee, and M. Sitti, "Biologically Inspired Miniature Water Strider Robot," Robotics: Science and Systems, June 2005, pp. 42
[23] J. Yan, R. J. Wood, S. Avadhanula, M. Sitti and R. S. Fearing, "Towards Flapping Wing Control of a Micromechanical Flying Insect," IEEE ICRA'2000, Seoul-Korea, 2000.
[24] R. Madangopal, Z. A. Khan and S. K. Agrawal, "Biologically Inspired Design of Small Flapping Wing Air Vehicles using Four-bar Mechanisms and Quasi-steady Aerodynamics," Journal of Mechanical Design, Vol. 127, July 2005, pp. 809-816.
[25] R. C. Michelson and M. A. Naqvi, "Beyond Biologically-Inspired Insect Flight," von Karman Institute for Fluid Dynamics RTO/AVT Lecture Series on Low Reynolds Number Aerodynamics on Aircraft Including Applications in Emergening UAV Technology, Brussels, 2003.
[26] H. G. Graighead, "Nanoelectromechanical Systems," Science, Vol. 290, 2000, pp. 1532-1535.
[27] W. A. Lewinger, C.M. Harley, R.E. Ritzmann, M.S. Branicky, and R.D. Quinn. "Insect-like Antennal Sensing for Climbing and Tunneling Behavior in a Biologically-Inspired Mobile Robot," In Proceedings of the IEEE ICRA'05, Barcelona, Spain, April 2005.
[28] J.-P. Sauvage, C. Dietrich-Buchecker, "Molecular catenanes rotaxanes and knots," Wiely-VCH, Weinheim, 1999.
[29] W.-M. Shen, P. Will, A. Galstyan, and C.-M. Chuong, "Hormone-inspired Self-organization and Distributed Control of Robotic Swarms," Autonomous Robots, Vol. 17, No. 1, July 2004, pp. 93–105.
[30] S. Viollet, and N. Franceschini, "Aerial Minirobot that Stabilizes and Tracks with a Bio-inspired Visual Scanning Sensor," Biorobotics, B. Webb and T. Consi (Eds), MIT Press, Cambridge, 2001, pp. 67-73.
[31] Y. Bar-Cohen (Ed.), "Electroactive Polymer (EAP) actuators as artificial muscles: reality, potential and challenges," SPIE, Vol. PM98, 2001.
[32] SRI International, http://www.sri.com/esd/automation/actuators.html
[33] Y. Bar-Cohen, "Biologically Inspired Robots as Artificial Inspectors," NDT.net, Vol. 7 No.1, Jan. 2002.

Voice-based Control of a Robotic Forceps by Using Displayed Image and Auxiliary Information

Keigo Watanabe, Takuya Tokunaga, and Kiyotaka Izumi
Department of Advanced Systems Control Engineering
Graduate School of Science and Engineering, Saga University
1-Honjomachi, Saga 840-8502, Japan

Abstract

A method of using an image related to three-dimensional movement and of auxiliary information is proposed for controlling a robotic forceps with voice instructions, where information on the tip-position in three-dimension and on the distance of the previous movement is viewed as the auxiliary one. A degree-related adverb included in the voice instruction is quantified by using fuzzy reasoning, in which such auxiliary information is also applied to update the membership functions so as to realize a user-friendly interface.

1 Introduction

In recent years, robots come to be regarded as very natural in a home, a company, etc., and are utilized for various users. Among them, there have been many cases using a voice interface as means of the communication between human being and robots. Since the voice is the easiest communication approach of human beings, the operation by exclusive input devices, such as a keyboard, is unnecessary, and therefore it can be easily used also for elderly people or the handicapped.

However, in the case that the voice is used for an interface, a certain problem arises. For example, when ambiguous expressions, such as "go to that," are included, the interpretation of "that" depends on each user's subjective scale. Therefore, if a particular setting is carried out for a specific user, then other users may feel inconvenient when using it, without resetting of it. About the interpretation of a voice command, there are a method that interprets a voice command in consideration of a user's viewpoint [1], a method that quantifies the degree-related adverbs contained in a voice command by fuzzy reasoning [2],[3],[4], etc.

In this paper, for the movement control of a robotic forceps operated by the voice that may be used in a laparoscopy, an approach using the image and the auxiliary information on the movement indication in a three-dimensional direction is proposed, together with considering the ambiguity included in the voice instruction. A fuzzy coach-player system [5] is applied as a voice instruction system, using the positional information at the arm tip in three-dimension and the latest movement distance as auxiliary information, where it is aiming at realizing a user-friendly interface by updating membership functions using auxiliary information.

2 Fuzzy Coach-Player System

2.1 Overview of the System

In order for a man and a robot to perform a cooperative task smoothly, mutual intellectual information needs to be exchanged. The fuzzy coach player system used in this research considers the concern between a man and a robot to be a concern between a coach and a player, and takes in the ambiguity included in the voice instruction, the subjective evaluation of the coach, etc.

2.2 Voice Commands from the Coach

Assume that at time step t, an input sequence of fuzzy voice instruction uttered by the coach and collected from a microphone, $v(t)$, is handed over by a voice recognizer, and it can be split into an unnecessary language variable to the motion command, $v_a(t)$, a verb $v_b(t)$, a noun $v_c(t)$, and an adverb (or adverb phrase) $v_d(t)$. Here, $v(k) \in \mathcal{V}$, $v_a(t) \in \mathcal{V}$, $v_b(t) \in \mathcal{V}$, $v_c(t) \in \mathcal{V}$, and $v_d(t) \in \mathcal{V}$, where $\mathcal{V}$ denotes a voice space that represents a time series in signal or character level. Effective language variables to the motion command, $v_b(t)$, $v_c(t)$, and $v_d(t)$ are available to generate a command to the robot.

2.3 System Structure

The structure of an experimental setup in this research consists of a microphone for gathering voice input, a camera for image input, a PC for control, a forceps for grasping an object, and a robot manipulator with 7-dof (called PA10, which is provided by the Mitsubishi Heavy Industries Ltd.) where the forceps is attached on the manipulator tip. The outline of the system is depicted in Fig. 1.

The task is to pick up the object allocated on a cylinder in the work table and convey it to a box. The work coordinate is the same as the base coordinate and the forceps coordinate in the arm tip is shown in Fig. 2.

3 Generation of Voice Commands

3.1 Voice Processing

In the voice processing part, the voice input $v(t)$ coming from the microphone is processed in turn for the voice

©ISAROB 2009

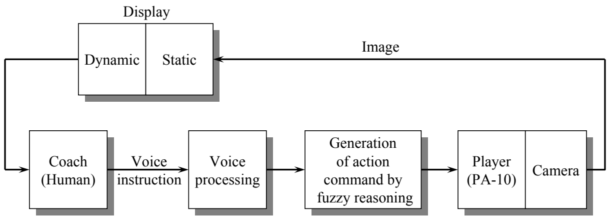

Figure 1: Construction of speech based interface with visual feedback

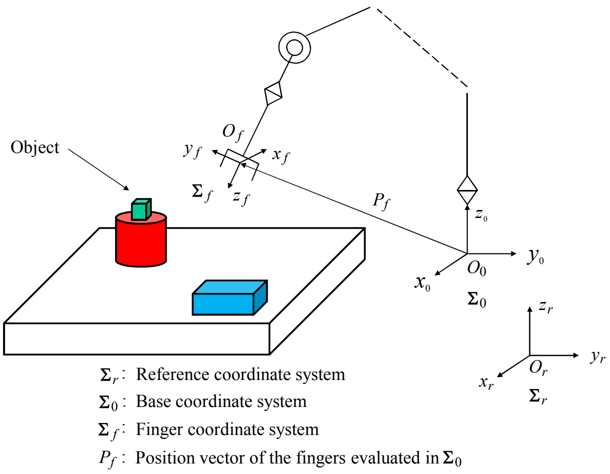

Figure 2: Coordinate system

recognition, the morphological analysis, and the pattern matching in order to generate words $v_b(t)$, $v_c(t)$, and $v_d(t)$ that are related to the motion, the direction, and the degree, respectively.

For the voice recognition, the voice uttered by the user is inputted to the PC through the microphone and then it is transformed into a text by a voice-recognition software, IBM Via Voice. The morphological analysis decomposes the text obtained in the voice recognition into several fundamental words by morphological software, where Chasen, which is a free morphological analyzer for Japanese, was used here. The pattern matching extracts some necessary words by comparing the fundamental words in the text level obtained from the morphological analysis with the keywords tabulated in Table 1.

3.2 Action Generation

The action of the robot arm is generally determined by using $v_b(t)$ and/or $v_c(t)$ obtained in the voice processing. For the actions associated with $v_b(t)$, "hold" and "release" are related to the closing and opening of the forceps, whereas "go" is related to the carrying of an object to the desired position, gripping it. Note that the amount to move is quantified for the forceps by fuzzy reasoning described below, according to $v_d(t)$ included in $v(t)$.

Table 1: Keywords in voice instruction

	Examples
Direction	right, left, up, down, ahead, back
Degree	more, little, very little
Action	go, hold, release

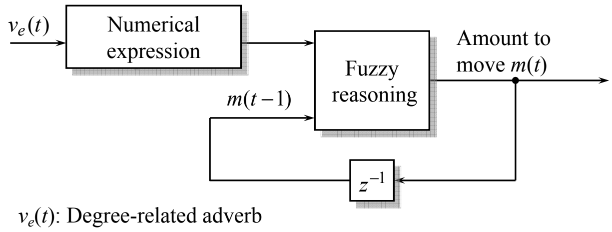

Figure 3: Flow of quantification for degree-related adverbs

The keywords for $v(t)$ are set in Table 1. When "go" is input to $v_b(t)$, the movement direction of the hand tip is determined according to $v_c(t)$. Here, "right" and "left" in $v_c(t)$ are assigned to the direction of x_f-axis in Σ_f, "up" and "down" correspond to the direction of y_f-axis, and "back" and "ahead" are related to the direction of z_f-axis in Σ_f.

4 Fuzzy Rule Extraction Using Auxiliary Information

4.1 Auxiliary Information

The three-dimensional position information on the forceps tip and the amount of movement due to the voice instruction are shown in a display as the auxiliary information giving for the user. It is assumed that such information is composed of a position vector P_f evaluated in the base coordinate.

4.2 Extraction of Fuzzy Rules

4.2.1 Fuzzy Reasoning

The degree-related adverb $v_d(t)$ included in the voice instruction is quantified by fuzzy reasoning, as shown in Fig. 3, where the fuzzy reasoning is assumed to be a simplified one, which consists of two-inputs, one-output, and 16 rules in total.

The first input to the fuzzy reasoning is the voice command $v_d(t)$, where it is labeled and numerically expressed in v_e (i.e., as singleton values) as shown in Table 2. The previous direction of the forceps in x_f, y_f and z_f, i.e., the amount of movement $m_i(t-1)$ [mm] is the second input to the reasoning, and the resultant output is just $m_i(t)$ [mm], where $i = x_f, y_f, z_f$ and the reasoning in each axis is assumed to be performed independently.

©ISAROB 2009

Table 2: Numerical expression for degree-related adverbs

Voice command	Very little	Little	Nothing	More
Label	SS	S	M	L
$v_e(t)$	0.2	0.4	0.6	0.8

Table 3: Amount of previous movement

Amount of previous movement	Nothing	Very small	Small	Medium	Large
Label	–	SS	S	M	L
$m_i(t-1)$	0	50	80	150	200

Table 4: Amount of current movement to be output

Amount of current movement to be output	Very small	Small	Medium	Large
Label	SS	S	M	L
$m_i(t)$	30	60	120	180

Table 5: Fuzzy rules

		Voice command (degree-related adverbs)			
		SS	S	M	L
Amount of previous movement	SS	SS	SS	SS	S
	S	SS	SS	S	M
	M	SS	S	M	L
	L	S	M	L	L

The membership functions for $v_e(t)$, $m_i(t-1)$, and $m_i(t)$ are set as shown in Fig. 4. For the previous and current amounts to move, the corresponding labels and the central (or singleton) values for their membership functions are shown in Table 3 and Table 4 respectively, where the membership functions are assumed to be triangular or singleton, whose values are assumed to be used as the initial ones for the update.

The resultant fuzzy rules is shown in Table 5.

4.2.2 Extraction Method of Fuzzy Rules

It is assumed that in the extraction of fuzzy rules, $a_1, \ldots, a_4$ and $b_1, \ldots, b_4$ in Fig. 4 are updated according to the current position for the forceps tip, the content of the voice instruction, and the amount of the previous movement, keeping the number of fuzzy rules. Here, a_i denotes the center value of each membership function on the support set of $m_i(t-1)$ and b_i denotes the position of the singleton for each membership function on the support set of $m_i(t)$.

Set the initial values for the update of a_i and b_i as given in Table 3 and 4, and update the allocation of all membership functions per each axis by the following method. Note here that in what follows, "the position of the forceps tip is positive" means the case when the value of any axis coordinate takes a positive value, whereas the negative means the case when it takes a negative values. Additionally, "the direction of the voice instruction is positive" implies the case when $v_c(t)$ takes any word out of "right," "up," and "ahead," whereas the negative means the case when it takes any word out of "left," "down," and "back."

1. The update by using the position of the forceps tip and the content of the voice instruction
   - If the position of the forceps tip is positive and the direction of the voice instruction is negative, or the position of the forceps tip is negative and the direction of the voice instruction is positive, then
     $a_i := a_i \times 1.2, \quad b_i := b_i \times 1.2$
   - If the position of the forceps tip is positive and the direction of the voice instruction is positive, or the position of the forceps tip is negative and the direction of the voice instruction is negative, then
     $a_i := a_i \times 0.8, \quad b_i := b_i \times 0.8$
2. The update by using the amount of the previous movement and the degree-related word included in the voice instruction
   - If $m_i(t-1) < 20.0$ and the voice instruction contains "very little," then
     $a_i := a_i \times 0.8, \quad b_i := b_i \times 0.8$
   - If $m_i(t-1) < 20.0$ and the voice instruction contains "more," then
     $a_i := a_i \times 2.0, \quad b_i := b_i \times 2.0$
   - If $30.0 < m_i(t-1) < 50.0$ and the voice instruction contains "very little," then
     $a_i := a_i \times 0.7, \quad b_i := b_i \times 0.6$
   - If $30.0 < m_i(t-1) < 50.0$ and the voice instruction contains "more," then
     $a_i := a_i \times 1.8, \quad b_i := b_i \times 1.8$
   - If $100.0 < m_i(t-1)$ and the voice instruction contains "more," then
     $a_i := a_i \times 1.2, \quad b_i := b_i \times 1.2$

5 Actual Experiment

In this research, the holding transference of an object controlled by the voice instruction is conducted as actual experiment. The user indicates with the voice, seeing the image provided on the display and taking account of auxiliary information. When it needs to tune the location finely, a forceps is moved to the desired location by following a command, such as "go very little right." The object on the red cylinder is grasped by the indication of "hold" and is

©ISAROB 2009

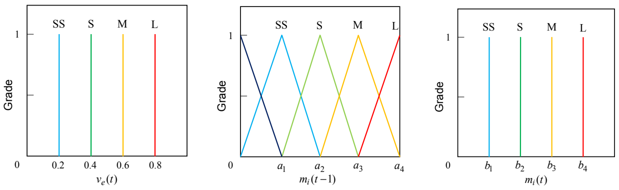

(a) (b) (c)

Figure 4: Membership functions: (a) for the degree-related adverb $v_e(t)$, (b) for the amount of previous movement $m_i(t-1)$, and (c) for the output $m_i(t)$

Table 6: A series of voice instructions

Step number	Command	x_f [mm]	y_f [mm]	z_f [mm]
1	Go more right	60.0	0	0
2	Go right	88.0	0	0
3	Go up	0	108.34	0
4	Go little ahead	0	0	76.80
5	Go very little ahead	0	0	30.17
6	Hold it	0	0	0
7	Go back	0	0	-37.30
8	Go more left	-189.06	0	0
9	Go down	0	-189.06	0
10	Go very little left	0	-72.49	0
11	Release it	0	0	0

conveyed to the blue box, where it is set there after receiving the indication of "release."

As an operational example, a series of performing directional indications is shown in Table 6 where the corresponding updates of the allocation for membership functions are given in Table 7 and Table 8.

6 Conclusions

In this research, it has been demonstrated that in the fuzzy coach-player system using voice instruction, the operation in three-dimensional space became easy by providing the auxiliary information such as the forceps tip position etc., together with using the image information, to the user. For the interpretation of the voice instruction, the user was able to give an instruction such as "go very little right" to the robot, because an ambiguous expression included in the voice instruction was quantified by using a fuzzy reasoning. In addition, the voice instruction became much easier than the conventional method, because the allocation parameters for membership functions were updated by applying auxiliary information so that the fuzzy reasoning was performed using the relevant rules according to the situation.

Table 7: Update of membership allocation for the amount of previous movement

Step number	a_1 [mm]	a_2 [mm]	a_3 [mm]	a_4 [mm]
1	50.00	80.00	150.00	200.00
2	40.00	64.00	120.00	160.00
3	32.00	51.20	96.00	128.00
4	32.00	51.20	96.00	128.00
5	32.00	51.20	96.00	128.00
6	32.00	51.20	96.00	128.00
7	69.12	110.59	207.36	276.48
8	82.94	132.71	248.83	331.78
9	82.94	132.71	248.83	331.78
10	99.53	159.25	298.60	398.13
11	99.53	159.25	298.60	398.13

Table 8: Update of membership allocation for the amount of current movement

Step number	b_1 [mm]	b_2 [mm]	b_3 [mm]	b_4 [mm]
1	30.00	60.00	120.00	180.00
2	24.00	48.00	96.00	144.00
3	19.20	38.40	76.80	115.20
4	19.20	38.40	76.80	115.20
5	19.20	38.40	76.80	115.20
6	19.20	38.40	76.80	115.20
7	41.47	82.94	165.89	248.83
8	49.72	99.53	199.07	298.60
9	49.72	99.53	199.07	298.60
10	59.72	119.44	238.88	300.00
11	59.72	119.44	238.88	300.00

References

[1] Y. Shinyama, T. Tokunaga, and H. Tanaka, "Kairai—Software robots understanding natural language," *J. of Information Processing Society of Japan*, vol. 42, no. 6, pp. 1359–1367, 2001.

[2] H. Kitagami, K. Nishihara, T. Yoshidome, and N. Kawarazaki "A robot operation system based on voice instruction by a quantitative expression," in *Proc. of 2001 JSME Conf. on Robotics and Mechatronics*, 2P2-N8, 2001.

[3] S. Kajiwara, S. Hiratsuka, T. Ishihara, and H. Inooka, "Position control using voice instruction with ambiguous degree expression," *Trans. of the Japan Society of Mechanical Engineers*, C, vol. 69, no. 686, pp. 2735–2742, 2003.

[4] K. Kankubo and S. Kobayashi, "Basic research on application of adverb instruction to robot," Memoirs of the Yuge National College of Maritime Technology, vol. 29, no. 9, pp. 49–55, 2007.

[5] K. Izumi, S. Ishii, and K. Watanabe, "Voice control of a robotic forceps using hierarchical instructions," in *Proc. of 2008 Int. Conf. on Control, Automation and Systems (ICCAS 2008)*, Seoul, Korea, 2008, pp. 810–815.

©ISAROB 2009

The Fourteenth International Symposium on Artificial Life and Robotics 2009 (AROB 14th '09),
B-Con Plaza, Beppu, Oita, Japan, February 5 - 7, 2009

Unconstrained and Noninvasive Measurement of Bioelectric Signals from Small Fish

Mitsuru Terawaki, Akira Hirano, Zu Soh, Toshio Tsuji

Graduate School of Engineering, Hiroshima Univ., Hiroshima, 739-8527, Japan

Abstract

Recently, the technique of fish bioassay has attracted attention as a method for constant monitoring of aquatic contamination. The respiratory rhythms of fish are considered an efficient indicator for the monitoring of water quality, since they are sensitive to chemicals and can be indirectly measured from bioelectric signals generated by breathing. However, no method has yet been established to measure signals in small free-swimming fish.

In this paper, we propose a system to measure bioelectric signals in small fish and monitor the frequency component in real time. To cover the large measurement range required in a free-swimming environment, the signals are measured using multiple electrodes. Further, the system focuses on the frequency component of the signal to assess the condition of fish using frequency analysis and a band-pass filter. Experiments were conducted with the purpose of enabling remote sensing and environment estimation. First, it was verified that the measured signals were synchronized with breathing. Then, a remote sensing experiment was performed using medaka (Oryzias latipes) that were allowed to swim freely in a measurement aquarium. The results confirmed that bioelectric signals synchronized with breathing could be measured in unconstrained and noninvasive conditions.

1 Introduction

Currently, incidents involving the contamination of water sources by industrial effluent are reported every year in Japan. Accordingly, the quality of tap water is monitored in water treatment plants to prevent contaminated water from being supplied to homes. In this monitoring, chemical concentration levels in water are analyzed and checked to ensure that safety standards for tap water are met. Not all tests, however, can be performed frequently because of limitations in terms of time and cost. As a result, only three items are inspected each day, and other checks are carried out just once a month [1]. Consequently, aquatic contamination may not be discovered until it causes a health hazard after a contamination incident occurs. This situation has led the Ministry of Health, Labour and Welfare to recommend introducing the bioassay system together with chemical analysis [2].

Bioassay is a method of estimating environmental changes from biological responses. In general, fish are used in the examination of water. Since it has been reported that bioelectric signals from fish are sensitive to changes [3], these signals are expected to make early detection possible, and several research projects on a bioassay system using bioelectric signals have therefore been conducted. Shedd et al. [4], for example, proposed a system that calculates ventilatory frequency from signals and evaluates aquatic contamination from changes in breathing. However, this system limits the movement range of fish to improve the quality of signal measurement, which can cause stress and influence breathing conditions. Additionally, Taue et al. [5] proposed a system using small fish in free-swimming conditions. However, the system can only assess whether fish are dead or alive, as it relies solely on the amplitude information of the signal for assessment.

The aim of this study was to develop a bioassay system using bioelectric signals from small fish in free-swimming conditions. As the first step, this paper proposes a method to measure the bioelectric signals of medaka (Oryzias latipes) in unconstrained and noninvasive conditions to minimize their levels of stress. Instead of amplitude information, the system utilizes frequency information that has been proven to be quite stable in free-swimming conditions.

2 Ventilatory signals

The medaka is suitable as a test fish for the bioassay system because it is relatively sensitive to chemicals, and is recommended in the OECD Guidelines for the Testing of Chemicals [6]. In our research, ventilatory signals were selected as the measurement target.

It is already known that it is possible to observe the electrical field around a fish's body by which peri-

©ISAROB 2009

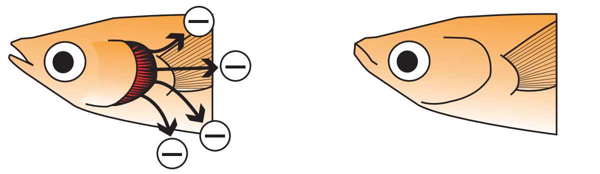

Figure 1: Relationship between gill cover movement and ion movement

odic potential is generated [7]. The main source of the potential difference is considered to be the ionic concentration difference between the inside and outside of the body caused by the osmotic mechanism [8].

As shown in Fig. 1(a), when the gill cover is opened, ions move to the outside of the body, generating electric potential. On the other hand, when the gill cover is closed, ionic movement is shut off (Fig. 1(b)). The potential around the fish is thus synchronized with the open-close movement of gill covers [9].

3 The ventilatory signal measurement system

The system established to measure the ventilatory signals of the medaka is shown in Fig. 2, and consists of a signal measuring part and a signal processing part. This section describes the system configuration.

3.1 Signal measuring part

The signal measuring part plays the role of inputting measured signals into a PC, and is composed of a measurement aquarium, electrodes, amplifiers and A/D converters.

Signals are measured using disposable medical electrodes (Ag-AgCl). n pairs of active electrodes (+, $-$) and a reference electrode (GND) are placed in the aquarium to enable differential amplification for signal denoising. Since the measured signals are faint (i.e., in μV order), they are amplified using a bioelectric amplifier (time constant: 3 [ms], high cutoff frequency: 30 [Hz]; Nihon Kohden Corporation). AD processing (sampling frequency: 1,000 [Hz]) is then conducted to input the signals into a PC using an interface module (PCI-3521, Interface Inc.).

3.2 Signal processing part

In the signal processing part, the input signals are filtered and converted into the frequency domain, and both are monitored on the PC screen.

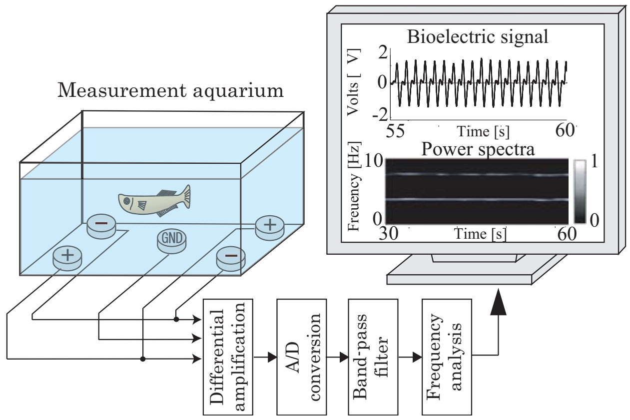

Figure 2: Structure of the measurement and signal analysis system

First, input signals are filtered by band-pass filters (low cutoff frequency: 0.053 [Hz]; high cutoff frequency: 10 [Hz]). Then, frequency analysis is conducted using an AR model, which is less influenced by unexpected noise. The AR model is given by the following equation:

$$x(n) = -\sum_{k=1}^{K} a(k)x(n-k) + \varepsilon(n), \tag{1}$$

where $x(n-k)$ is the measured signal and $\varepsilon(n)$ is the prediction error (white noise). This model predicts future data $x(n)$ from measured signals by appropriately adjusting AR parameter $a(k)$.

Power spectrum density (PSD) $P(f)$ is calculated for every second using an AR model of order $K = 200$ using equation (2).

$$P(f) = \frac{\sigma_\varepsilon^2}{\left|1 + \sum_{k=1}^{K} a(k)e^{j2\pi kf}\right|^2}, \tag{2}$$

where σ_ε^2 is the prediction error variance. $P(f)$ is normalized in the range of 0 to 10 [Hz] using equation (3) to monitor peak frequency per unit of time.

$$P_{\mathrm{n}}(f) = \frac{P(f)}{\max_f (P(f))} \quad : (f = [0, 10]), \tag{3}$$

Normalized PSD $P(f)$ is displayed in grayscale on the PC screen, as shown in Fig. 2. This system can measure the ventilatory signals of medaka in real time and monitor the frequency component.

©ISAROB 2009

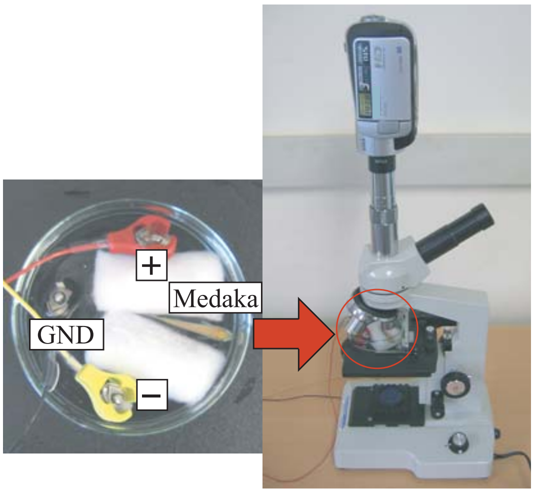

Figure 3: Experimental apparatus for the verification experiment

4 Measurement under constrained conditions

Ventilatory signal measurements of medaka were conducted under constrained conditions as a basis for later experiments in free-swimming conditions. First, synchronization between measured signals and breathing was confirmed. Then, the influence of electrode distance on the signal quality was examined to enable remote sensing. The water used for the experiment was dechlorinated ahead of time. The temperature and electrical conductivity were also measured before the experiment, and the temperature was kept constant during the testing period.

4.1 Experiment to verify ventilatory signals

The correlation between the measured signals and gill cover movement was examined to verify that the measured signals are synchronized with breathing. First, a medaka was placed on a petri dish, and its range of movement was limited using absorbent cotton as shown in Fig. 3. Then, a pair of active electrodes (+, −) and a reference electrode (GND) were placed in the petri dish for signal measurement. At the same time, the gill cover movements were recorded using a video camera (frame rate 29.97 [fps]) mounted on a microscope to quantify the movements by image analysis.

The video images were analyzed using Cosmos32 image analysis software (Library Inc.). The picture was converted into a binary image, and the area of gill cover corresponding to the number of black pixels

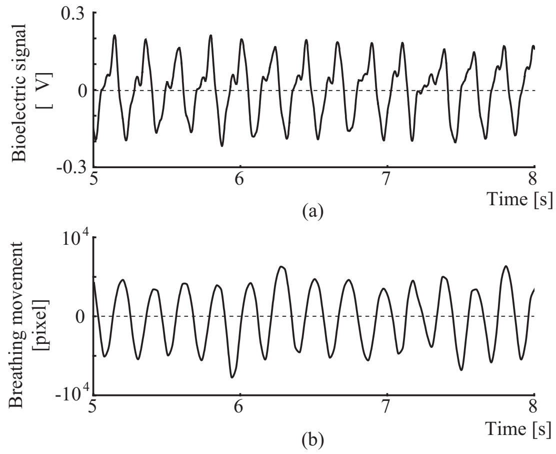

Figure 4: Examples of the results experimental verification

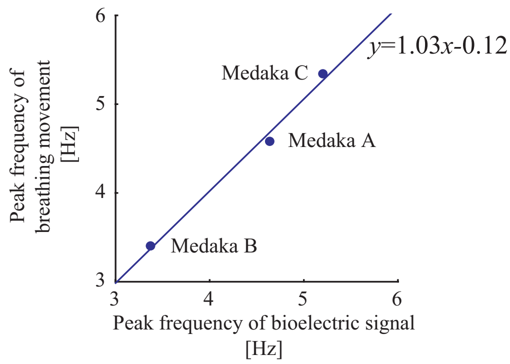

Figure 5: Relation between signal frequency and ventilatory frequency

was calculated. The same process was performed on all frames of the video, and the number of black pixels in each frame was obtained. Then, the number data were processed using a band-pass filter (low cutoff frequency 1 [Hz], high cutoff frequency 10 [Hz]), and the data thus obtained were used to define the breathing movement.

Fig. 4 shows an example of the experimental results obtained from three subjects. (a) shows a measured signal. The horizontal axis represents time, and the vertical axis is the electric potential. (b) shows the breathing movement. The horizontal axis represents time, and the vertical axis is the number of black pixels. Both the measured signal and the gill cover movements showed a periodic wave pattern, as seen in Fig. 4.

Fig. 5 shows the correlation between the peak frequencies of the signals and gill cover movements as calculated using data from a 60-second period. The result for the correlation coefficient of each point shows a value of 0.995. This high correlation verified that the

©ISAROB 2009

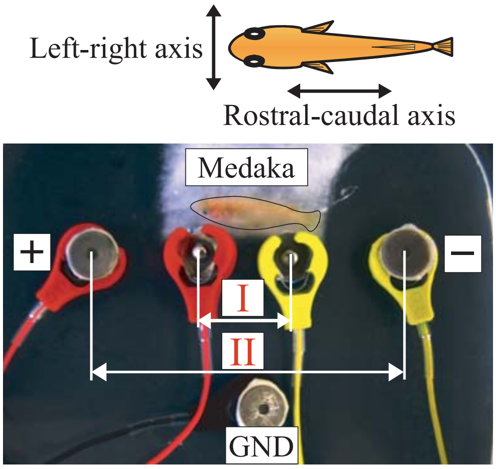

Figure 6: Electrode arrangement for the measuring experiment with different interelectrode distances

measured signals were synchronized with breathing.

4.2 The measuring experiment in different interelectrode distance

Next, we conducted a measuring experiment with different interelectrode distances to confirm the influence of this distance with medaka. The fish was constrained using absorbent cotton to confine the motion of its fins. The size of the aquarium used for measurement was 500(W)×350(D)×200(H) [mm], and two pairs of active electrodes were used, as shown in Fig. 6. Electrode pair I was attached to the fish to measure the low-noise standard signal with an interelectrode distance of 20 [mm]. The interelectrode distance of electrode pair II was changed from 40 to 300 [mm] in increments of 20 [mm]. The experiments were conducted under two sets of conditions: one with the direction of the electrode pair along the rostral-caudal axis, and the other along the left-right axis against the axis of the fish's body.

Experiments were conducted with four subjects. Figs. 7, 8 and 9 show the results when the electrode pairs were placed along the rostral-caudal axis. Fig. 7 shows an example of the ventilatory signals measured when the interelectrode distance of electrode pair II was 100 [mm]. The relationship between the interelectrode distance and the signals is shown in Fig. 8. The vertical axis denotes the ratio of effective value (V_2/V_1). V_1 and V_2 are the effective values of electrode pairs I and II. Fig. 9 shows the relationship between the interelectrode distance and the peak frequency of the signals. The differences in the signal amplitude were confirmed by the differences in distance, as shown

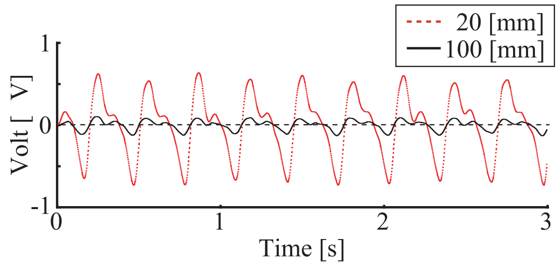

Figure 7: An example of the experimental results under constrained conditions

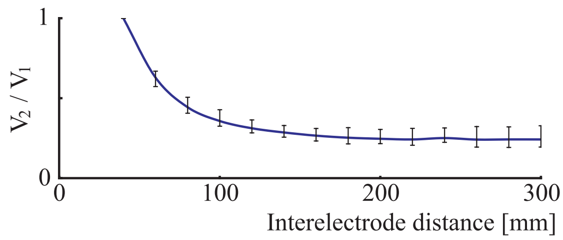

Figure 8: Effective value of measured bioelectric signals with different interelectrode distances

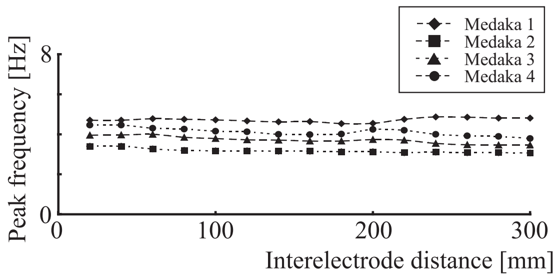

Figure 9: Peak frequency with different interelectrode distances

in Fig. 7, and the amplitude decreased as the electrode distance increased, as shown in Fig. 8. This is due to increased electrical resistance between the subject and the electrodes. In contrast, the peak frequency bore no relation to the distance, and remained almost constant as shown in Fig. 9. Similar results were obtained under the condition in which the electrode pairs were placed on the left-right axis. From the results described above, it can be considered that the information on signal frequency is more suitable for evaluating the changes in the conditions of fish than amplitude in unconstrained and noninvasive conditions, because medaka would move freely around the aquarium causing constant changes in amplitude information.

5 Measuring experiment under free-swimming conditions

It is necessary to measure ventilatory signals under no-stress conditions from the viewpoint of developing a

©ISAROB 2009

practical bioassay system. Accordingly, we conducted an experiment under free-swimming conditions using a medaka in a polyethylene resin measurement aquarium with dimensions 150(W)×100(D)×50(H) [mm] (Fig. 10). The size was determined based on the measurement results described in the previous section and further preliminary experimentation. Electrodes were placed on the four lower corners of the aquarium to keep the medaka between the active electrodes (+, −). The other experimental conditions were the same as those described in Section 4.2. The water temperature and electrical conductivity were 20.2 [°C] and 12.08 [μS/mm], respectively.

Figure 10: Measuring aquarium for the experiment under free-swimming conditions

5.1 Ventilatory signals under free-swimming conditions

We performed an experiment to verify the feasibility of measuring ventilatory signals from medaka allowed to swim freely using the proposed system. Fig. 11 shows an example of the experimental results. (a) shows the signals measured in the period between 300 and 310 [s]. (b) is the spectrum variation of the signals from 290 – 320 [s]. The magnitude of PSD is expressed in grayscale. (c) shows the trajectory of the medaka from 290 – 320 [s]. It was confirmed that ventilatory signals could be measured even from medaka under free-swimming conditions, as shown in Fig. 11. It was also confirmed that the amplitude of signals changed according to the position of the medaka as shown in (a), but the signal frequency was almost constant during swimming, as shown in (b). An unexpected change in frequency was recorded when the medaka rushed to the aquarium wall (310 – 320[s]). These results imply that signal frequency can be affected by mechanical stimulus and possibly utilized to monitor abnormal behavior in the subject.

5.2 Response of signals to breach exposure

A water contamination experiment was performed to confirm the response of ventilatory signals to chemical irritation. The experiment started with the same conditions as those described in the previous subsection. Then, 4 [ml] of household bleach mainly consisting of NaClO was poured into the aquarium at 180 [s].

Fig. 12 shows an example of the experimental results after the exposure. (a) shows the signals measured from 330 – 340 [s], and (b) shows the spectrum variation of the signals from 320 – 350 [s]. (c) shows the trajectory of the medaka from 320 – 350 [s]. In comparison with Fig. 11, it can be seen that both the spectrum and the amplitude of the signals showed a marked change after exposure. Note that the signal changes were not evoked by movement; the medaka stayed in the same position, as shown in Fig. 12 (c). It is therefore suggested that aquatic contamination can be detected using ventilatory signals.

6 Conclusion

In this paper, we propose a system to measure the ventilatory signals of medaka and report on the experiment conducted to measure these signals. The results confirm that the system can successfully measure signals from medaka in unconstrained and noninvasive conditions. Further, it was suggested that signal frequency could be an important factor in estimating levels of water contamination. In the future, we plan to analyze changes in the patterns of bioelectric signals in line with exposure to different toxic substances, and to develop a system that can discriminate aquatic contamination from bioelectric signals.

Acknowledgements

This work was partially supported by the 21st Century COE Program of the JSPS (Japan Society for the Promotion of Science) on *Hyper Human Technology toward the 21st Century Industrial Revolution.*

References

[1] Ministry of Health, Labour and Welfare (2007), Enforcement Regulation of Water Supply Law (in Japanese)

[2] Ministry of Health, Labour and Welfare (2001), Anti-terrorism Policy (in Japanese) http:// www.mhlw.go.jp /houdou /0110 /h1005-1.html

[3] M. Thomas, A. Florion (1996), A New Warning Biomonitor Using a Weakly Electric Fish,

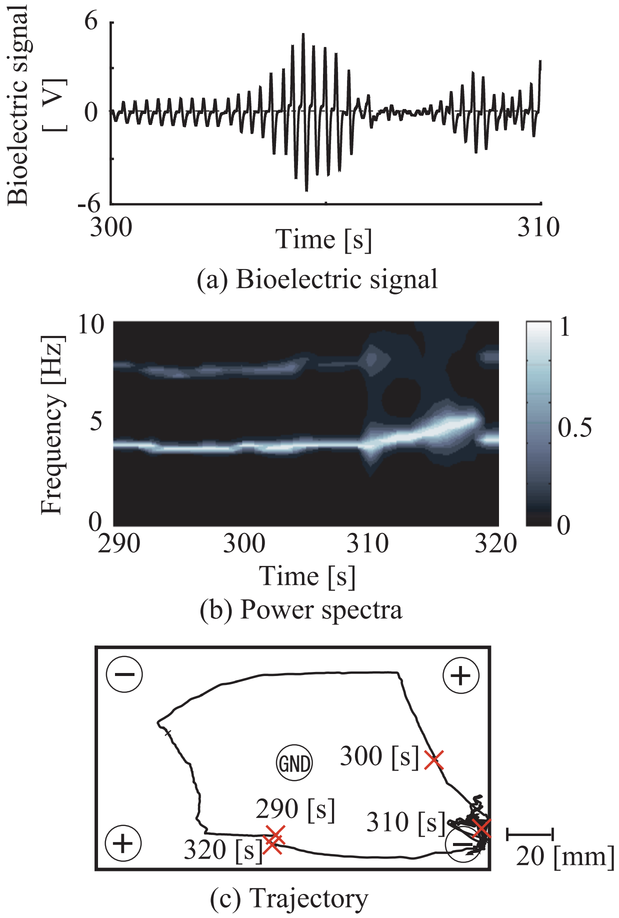

(a) Bioelectric signal

(b) Power spectra

(c) Trajectory

Figure 11: An example of the experimental results under free-swimming conditions

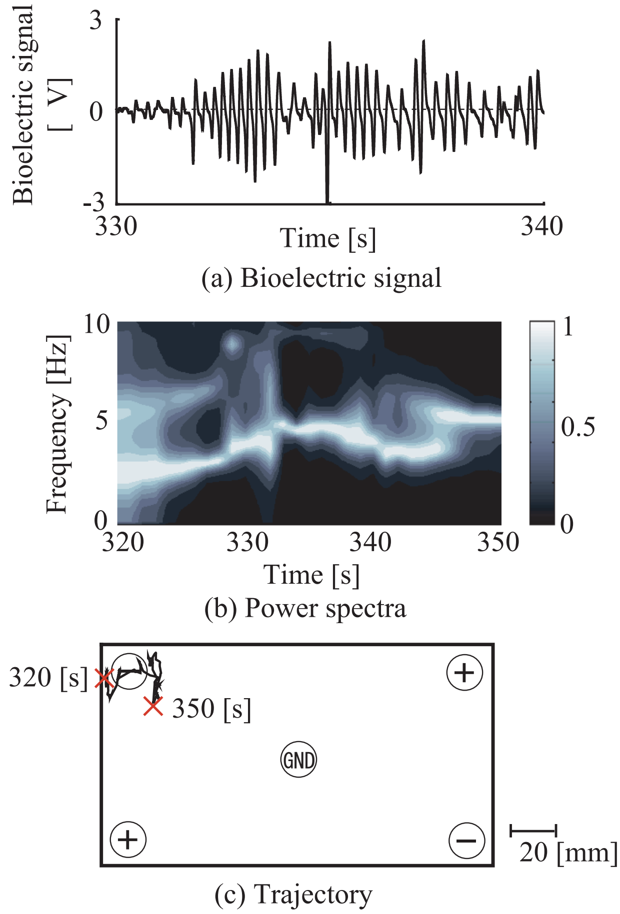

(a) Bioelectric signal

(b) Power spectra

(c) Trajectory

Figure 12: An example of the results from the bleach exposure experiment

Apteronotus Albifrons (Gymnotiformes), and The Effect of Temperature on The Bioelectric Responses. Environmental Monitoring and Assessment 51:605-620

[4] T. R. Shedd, W. H. van der Schalie (2001), Long-Term Operation of an Automated Fish Biomonitoring System for Continuous Effluent Acute Toxicity Surveillance. Burrows Bulletin of Environmental Contamination and Toxicology 66:392-399

[5] S. Taue, R. Hashimoto (2006), Unirelief water quality monitoring system, Jarnal of Resources and Environment (in Japanese). 42(2):73-77

[6] Organisation for Economic Co-operation and Development (OECD) (1992), OECD Guidelines for the Testing of Chemicals No. 203. Fish, Acute Toxicity Test

[7] R. C. Peters et. al (1974), Distribution of Electroreceptors, Bioelectric Field Patterns, and Skin Resistance in the Catfish, *Ictalurus nebulosus* LeS. Journal of Comparative Physiology A 92(1):11-22

[8] C. M. Wood, P. Part (1997), Cultured Branchial Epithelia From Freshwater Fish Gills. Journal of Experimental Biology 200:1047-1059

[9] R. C. Peters, R. J. A. Buwalda (1972), Frequency Response of the Electroreceptors (“Small Pit Organs”) of the Catfish. Ictalurus nebulosus LeS. Journal of Comparative Physiology A 79(1):29-38

[10] S. Umezawa, H. Watanabe (1973), On the Resperation of the Killifish Oryzias Latipes. Journal of Experimental Biology 58:305-325

[11] W. H. van der Schalie, T. R. Shedd (2004), Response Characteristics of an Aquatic Biomonitor Used for Rapid Toxicity Detection. Journal of Appleid Toxicology 24:387-394

©ISAROB 2009

The Fourteenth International Symposium on Artificial Life and Robotics 2009 (AROB 14th '09),
B-Con Plaza, Beppu, Oita, Japan, February 5 - 7, 2009

Three-dimensional Human Motion Modeling by Back Projection Based on Image-based Camera Calibration

S. Masaoka, J. K. Tan, H. Kim and S. Ishikawa

Kyushu Institute of Technology,
1-1 Sensui-cho, Tobata-ku, Kitakyushu-shi, Fukuoka, 804-8550, Japans
(Tel : 81-93-884-3191; Fax : 81-93-884-3191)
(masaoka@ss10.cntl.kyutech.ac.jp)

Abstract: This paper proposes a back projection technique for 3-D human motion modeling that performs camera calibration using obtained multiple video sequences. This technique calculates an affine camera matrix from the factorization method and performs back projection under the affine camera model. The proposed technique needs neither 3-D camera calibration tool nor markers for shape recovery, and can recover a human motion from silhouette images. In this paper, we also propose a shadow detector and eliminator using color information and normalized cross correlation for robust extraction and elimination of shadows. Experimental results show effectiveness of the proposed technique.

Keywords: motion capture, back projection, factorization, affine camera model

I. INTRODUCTION

Human motion recovery from video sequences is an important as well as interesting subject of study in computer vision with various applications in the fields of video media and sports. One of the advantages of the optical technique employing cameras should be its limitless nature with respect to human motion range and its environment. However many of conventional techniques need camera calibration using a 3-D tool in order to acquire three-dimensional coordinates in a real space. Thus these techniques are not suitable for human motion modeling in outdoor scenes. A technique of 3-D modeling without camera calibration [1] and a mobile stereo technique employing image-based self-calibration [2] have already been proposed as calibrationless techniques before image capture. They are suitable in various outdoor scenes. However, its post-processing is complicated because of the modeling based on markers. As a markerless technique, the back projection technique is proposed [3]. The post-processing of this technique is simpler than other techniques because it performs 3-D modeling from only a silhouette image. But, this technique need to perform camera calibration employing a 3-D tool before video capture.

This paper proposes a back projection technique that performs camera calibration using obtained video sequences without a 3-D calibration tool and markers. It employs the factorization technique [4] for deriving camera orientations and performs back projection of the multiple silhouette images of the object interested by making use of the camera orientations.

We use background subtraction to acquire silhouette images. However, this technique cannot be simply employed in outdoor scenes because of shadows. We then propose a shadow detector and eliminator using color information and normalized cross correlation for robust extraction and elimination of shadows. The proposed technique is improved based on a normalized RGB color space compared to the existing normalized cross correlation technique [5]. By employing the color information, the shadow detection gains much robustness. Furthermore, the threshold is set adaptive with respect to various scenes in each frame by approximating the normalized cross correlation by a Gaussian distribution.

II. PROPOSED TECHNIQUE

1. Affine camera model and the factorization

As a projection model, we consider an affine camera model such as week-perspective projection. When a three-dimensional point $\boldsymbol{X}=(X,Y,Z)$ in the world coordinate system is projected on an image point $\boldsymbol{x}=(x,y)$ in an image coordinate system, it is expressed in a homogeneous coordinate system as follows;

$$\tilde{\mathbf{x}} = P_a \tilde{\mathbf{X}} \tag{1a}$$

$$P_a = \begin{pmatrix} \hat{P}_a & \mathbf{t} \\ \mathbf{0} & 1 \end{pmatrix} \tag{1b}$$

©ISAROB 2009

where P_a is a 3×4 affine camera matrix. It consists of a 2×3 matrix $\hat{P}_a$ and a 2-component column vector $\boldsymbol{t}$.

Equation (1a) is expressed in the Euclid coordinate system as follows;

$$\mathbf{x} = \hat{P}_a \mathbf{X} + \mathbf{t} \qquad (2)$$

In Eq. (2), when $\boldsymbol{X}$=0, $\boldsymbol{t}$ is a projected point of the origin of the world coordinate system to the camera image, because $\boldsymbol{x}$=$\boldsymbol{t}$. We can therefore assume that the origin of the camera image is $\boldsymbol{t}$. Let $\boldsymbol{x}$ be deviation from $\boldsymbol{t}$, and the following equation holds.

$$\mathbf{x} = \hat{P}_a \mathbf{X} \qquad (3)$$

Suppose that the points $\boldsymbol{X}_p$ (p=1,2,…,P) in the space is projected to the points $\boldsymbol{x}_p$ on the image plane of a fixed camera f (f=1,2,…,F). Then, by Eq. (3),

$$\mathbf{x}_{fp} = \hat{P}_{a,f} \mathbf{X}_p \qquad (4)$$

In the case of F cameras, we have

$$\begin{pmatrix} \mathbf{x}_{11} & \mathbf{x}_{12} & \cdots & \mathbf{x}_{1P} \\ \mathbf{x}_{21} & \mathbf{x}_{22} & \cdots & \mathbf{x}_{2P} \\ \vdots & \vdots & \ddots & \vdots \\ \mathbf{x}_{F1} & \mathbf{x}_{F2} & \cdots & \mathbf{x}_{FP} \end{pmatrix} = \begin{pmatrix} \hat{P}_{a,1} \\ \hat{P}_{a,2} \\ \vdots \\ \hat{P}_{a,F} \end{pmatrix} (\mathbf{X}_1, \mathbf{X}_2, \ldots, \mathbf{X}_P) \qquad (5)$$

Let the left-hand side matrix be denoted by W. W is the $2F \times P$ matrix. By performing the factorization to W, the following decomposition is obtained;

$$W = MS \qquad (6)$$

where M is a camera orientation matrix, and S is a 3-D shape matrix of points $\boldsymbol{X}_i$. The matrix M is given by

$$M \equiv \begin{pmatrix} \hat{P}_{a,1} \\ \hat{P}_{a,2} \\ \vdots \\ \hat{P}_{a,F} \end{pmatrix} \qquad (7)$$

On the plane which is perpendicular to an optical axis via a lens center of camera f, let $\boldsymbol{i}_f$ be a horizontal unit vector to the lens center, and $\boldsymbol{j}_f$ be a vertical unit vector. Then $\hat{P}_{a,f}$ is given by;

$$\hat{P}_{a,f} = \begin{pmatrix} \mathbf{i}_f^{\mathrm{T}} \\ \mathbf{j}_f^{\mathrm{T}} \end{pmatrix} \qquad (8)$$

So, if the points x_{fp} $(f = 1,2,\ldots,F;\ p = 1,2,\ldots,P)$ on the image are obtained, $\hat{P}_{a,f}$ is acquired by Eqs. (6) and (8).

2. The back projection technique based on the affine camera model

The back projection technique is a modeling technique that projects silhouette images on camera image planes back to the 3-D space and obtain a 3-D object model by taking the common region of the back projected images. The conventional back projection technique needs to perform camera calibration using a 3-D calibration tool because of a camera projection model. Here we propose a back projection technique based on the affine camera model. It performs the factorization and the back projection employing the calculated affine matrices. By this approach, the proposed technique needs neither 3-D camera calibration tool nor markers for shape recovery, and can recover a human motion from silhouette images. This technique is described in the following.

A pixel $\boldsymbol{x}_f \in S_f$ in the silhouette S_f on the fixed camera image f is projected back to the 3-D space by Eq. (1a). Then the set of the points is given as follows;

$$BP(\mathbf{x}_f) = \{\mathbf{X} \mid \lambda \tilde{\mathbf{x}}_f = P_{a,f} \tilde{\mathbf{X}}\} \qquad (9)$$

where P_f is the affine camera matrix of camera f. The set of the points $BP(S_f)$ that contains all the projected pixels in the S_f is defined by

$$BP(S_f) = \bigcup_{\mathbf{x}_f \in S_f} BP(\mathbf{x}_f) \qquad (10)$$

A 3-D model V employing the back projection is finally obtained by

$$V = \bigcap_{f=1,2,\ldots,F} BP(S_f) \qquad (11)$$

3. Shadow detection and elimination

In this paper, we perform a silhouette extraction by using a background subtraction technique. However, it is often difficult to extract a silhouette image because of the shadow of the object. Therefore, we propose a shadow detection and elimination technique using color information and normalized cross correlation. This is more robust than employing existing techniques.

In the first place, the proposed technique extracts a foreground area including the shadow as follows;

$$\begin{cases} 1 & if\ L_{th} < |T - B| < H_{th} \\ 0 & otherwise \end{cases} \qquad (12)$$

where T and B are the sum of each channel of RGB in an input image and in a background image, respectively. L_{th} and H_{th} are the thresholds for extracting the area including the shadow. The shadow detection is applied to all the pixels that satisfy Eq. (12). In the second, we calculate a feature quantity that mixes the color information with the texture information. In the color information, we use the normalized RGB color space. The conversion from RGB color space to normalized RGB color space is given by

$$\begin{cases} r = \dfrac{R}{R+G+B} \\ g = \dfrac{G}{R+G+B} \\ b = \dfrac{B}{R+G+B} (=1-r-g) \end{cases} \tag{13}$$

In the texture information, we use the normalized cross correlation which is defined in the normalized RGB color space as follows;

$$NCC(i,j) = \frac{\sum_{k=r,g}\sum_{n=-N}^{N}\sum_{m=-N}^{N} B_k(i+n,j+m)T_k(i+n,j+m)}{\sqrt{\sum_{k=r,g}\sum_{n=-N}^{N}\sum_{m=-N}^{N} B_k(i+n,j+m)}\sqrt{\sum_{k=r,g}\sum_{n=-N}^{N}\sum_{m=-N}^{N} T_k(i+n,j+m)}} \tag{14}$$

where $T_k(i,j)$ is the value of r and g in a pixel $T(i,j)$ of the input image, and $B_k(i,j)$ is that in a pixel $B(i,j)$ of the background image. N is the size of a window. Furthermore, the threshold is set adaptive with respect to various scenes in each frame by approximating it by a Gaussian distribution as follows;

$$f(x,\sigma^2/n) = \frac{1}{\sqrt{2\pi(\sigma^2/n)}} \exp\left(-\frac{(x-1)^2}{2(\sigma^2/n)}\right) \tag{15}$$

where σ^2 is a variance of the correlation value, and n is the number of samples. Finally the shadow area is defined as the pixel that satisfies the following relation;

$$NCC(i,j) > 1.0 - c\frac{\sigma}{\sqrt{n}} \tag{16}$$

where c is a parameter. An example of the proposed shadow detection and elimination is shown in Fig.1.

III. EXPERIMENTAL RESULTS

We performed an experiment of a human motion recovery by employing 4 cameras in an outdoor environment. We fixed the distance from the cameras to a human about 5m, and the angle between the set cameras about 45 degrees. We extracted 39 points manually for the factorization method. A sample of the video sequences is shown in Fig.2. The result of the shadow detection and elimination is shown in Fig.3. Examples of silhouette images are shown in Fig.4.

The result of the 3-D recovery is depicted in Fig.5. In order to evaluate the proposed technique, we examined the number of true positive voxels contained in the recovery results employing ground truth data. To compare the proposed technique with a conventional technique, we calibrated the video taking system with the DLT technique using a 3-D calibration tool. The precision of the 3-D recovery is shown in Table.1.

IV. DISCUSSION

The precision of the motion recovery was 83.0% in the proposed technique, whereas it was 86.4% in the back projection technique employing the DLT method. The result is not much difference in spite of the approximation by an affine camera model. It should be noted that the proposed technique is more adaptable to various usages including outdoor motion capture than the existing back projection technique. It is indeed convenient for the modeling of transient, or unrepeated motions, since one only has to take their images on the spot and can calibrate the cameras afterword in the lab using the obtained videos. Thus the proposed technique may contribute to expanding motion capture technology to various new fields.

An increasing error in Camera2 has been attributed to the effect of a moving distance of a human in the direction of the optical axis. Because the human in Camera2 is moving largely in the direction of the depth compared with other cameras, it may result in larger computational errors than other cameras. On the other hand, in Camera4, the error is the smallest, since there was the least moving distance by the human.

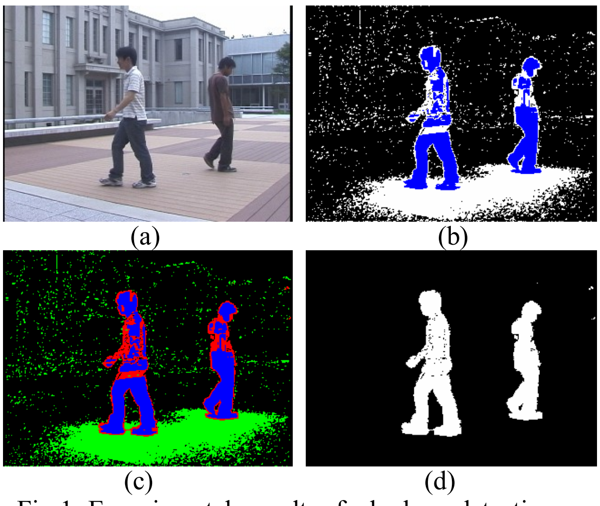

Fig.1 Experimental result of shadow detection and removal. (a) Input image. (b) Foreground image. (c) Result of the shadow detection. (d) Result of the shadow removal.

V. CONCLUSIONS

In this paper, we proposed a back projection technique with simpler camera calibration. The proposed technique does not need a 3-D calibration tool. Instead it performs camera calibration by employing video sequences. The technique calculates an affine camera matrix from the factorization method, and performs back projection under the affine camera model. We also proposed a shadow detection and elimination technique using color information of the scene. This is more effective than employing light intensity to a textured scene. Future works include the recovery of a human motion in various outdoor scenes.

Table.1 True Positive Rate

	The DLT technique	The Proposed technique
Camera1	86.3 %	84.7 %
Camera2	87.8 %	80.1 %
Camara3	86.4 %	82.1 %
Camera4	85.0 %	85.0 %
Average	86.4 %	83.0 %

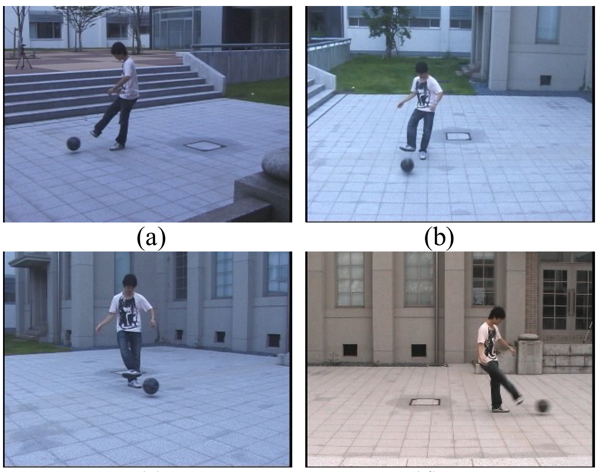

(a) (b) (c) (d)

Fig.2 Video sequence. (a)Camera1, (b)Camera2, (c)Cam era3, (d)Cmaera4.

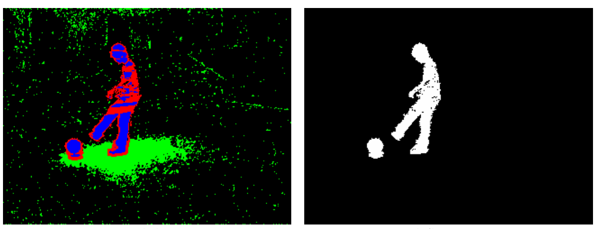

(c) (d)

Fig.3 Experimental result of shadow detection and elimination. (a)Shadow detection,(b)shadow elimination.

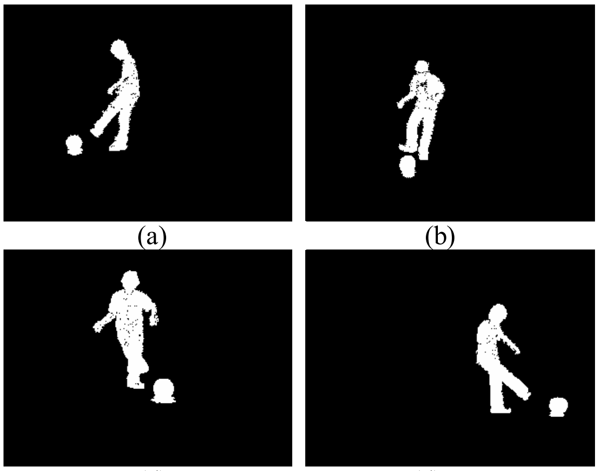

(a) (b) (d) (d)

Fig.4 Silhouette image. (a) Camera1, (b) Camera2, (c) Camera3, (d) Cmaera4.

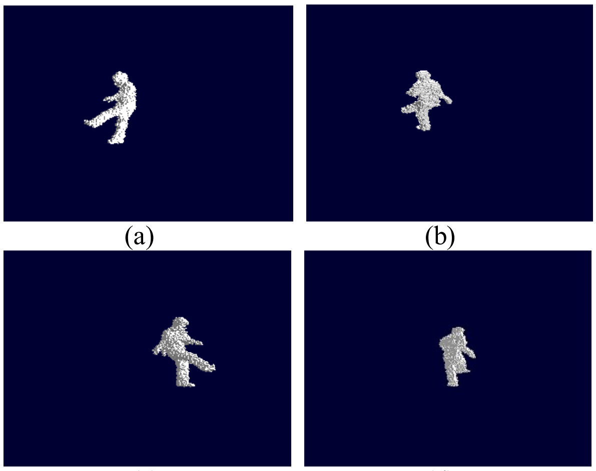

(a) (b) (c) (d)

Fig.5 Experimental result of human motion recovery. (a) View1, (b) View2, (c)View3, (d)View4.

REFERENCES

[1] Tan J. K., Ishikawa S.: "Deformable shape recovery by factorization based on a spatiotemporal measurement matrix", *Computer Vision and Image Understanding*, Vol. 82, No. 2, pp.101-109, 2001.

[2] Yamaguchi I., Tan J. K., Ishikawa S.: "A mobile motion capture technique excelling in 3-D modeling of temporary events", *Proc. IEEE Int. Conf. on Systems, Man and Cybernetics*, pp.1613-1617, 2006.

[3] Uchinoumi M., Tan J. K., Ishikawa S.: "A simple structured real-time motion capture system employing silhouette images", *Proc. IEEE Int. Conf. on Systems, Man and Cybernetics*, pp. 3094-3098 (Oct., 2004).

[4] Tomasi C., Kanade T.: "Shape and motion from image streams: a factorization method", Technical Report CMU-CS-91-172, CMU, 1991.

[5] Jacques Jr., J. C. S., Jung C. R., Musse S. R.: "Background subtraction and shadow detection in grayscale video sequences", *Proceedings of SIGGRAPH*, pp.189-196, 2005.

©ISAROB 2009

The Fourteenth International Symposium on Artificial Life and Robotics 2009 (AROB 14th '09),
B-Con Plaza, Beppu, Oita, Japan, February 5 - 7, 2009

RESEARCH ON THE INTELLIGENT CONTROL ALGORITHM FOR A SOFT JOINT ACTUATED BY MCKIBBEN MUSCLES

Enyu Jiang[1] Huailin Zhao[2](zhao_huailin@yahoo.com) Masanori Sugisaka[3] Fengzhi Dai[4] Wuyun Quan[5]

[1]School of Physics Eng., zhengzhou university, China [2]School of Mec. & Aut. Eng., Shanghai Institute of Technology, China

[3]Mec. & Ele. Course, Nippon Bunri University, Japan [4]Dep. Of Control Eng., Matsue National College of Technology, Japan

[5]School of Microelectronics, Fudan University, China

Abstract: In view of certain McKibben muscle model and the joint model which actuated by it,we design effective compound control algorithm which based on the CMAC neural network and the PID. The PID controller is to realize the feedback control in order to guarantee system's stability. And the CMAC function forward feed compensator realizes system's counter dynamic model, the parallel controller's output takes system's control action.Through the CMAC learning process so that the PID output tends to zero, making thereby systematic, control action comes into being from CMAC.Digital simulation's result had proven this parallel algorithm has the very high track capacity and the interference immunity, and robustness is strong and the response speed is quick, suits in the nonlinear real-time control.

Key word: McKibben muscle, neural network, CMAC, PID, Control algorithm.

1 Introduction

The Mckibben muscle is one kind of relatively new-style drive. It is one kind of the movement engine which is drived by the barometric pressure may contract. The major characteristic of it is light and supple, meanwhile it can produce enough strength. Because of the similarity with the biological muscle, when it is used in the robot, the robot is easy to produce animal-like movement. Because of its inborn flexibility, this kind of robot, when with environment alternately, it is easy to produce gentle touching and relative security operation, therefore in area of industry assembly, spray coating, capture brittle goods and so on, it has the latent huge application value[1].

At present, the anti-outside disturbance ability of PID control method which is widely used in robot joint controls is bad, and the adaptiveness to system's design parameter change is not good, too. It also affects control system's robustness. However,the development of robot system reqires the robot control to have the fast track capacity, high tracking accuracy and fine robustness. This article uses the CMAC neural network and the PID compound control algorithm。It can fully reflect feature of CMAC that are reducing output errors, good real time performance and strong robusticity in order to control the movement of joint effectively.

2 The McKibben muscle model and the joint model

2.1 McKibben muscle synopsis

The McKibben muscle was invented by American Dr. McKibben in the 1950s which is one kind of the pneumatic driving artificial muscle. Its main body is composed by an expandable rubber pipe of inner layer and the outer layer is of fabric shell constituted by textile fiber, the both sides of the shell and the both sides of rubber pipe both continually in together (Fig. 1). After McKibben muscle has sufficient pressure, the rubber tube starts to expand, as a result of the fibrous layer to the rubber tube movement's restraint, the rubber tube's radial direction expansive power is transformed to the McKibben muscle axial shrinkage force. Thus causes the McKibben muscle to have the radial swelling movement and the axial contractive motion[1]. In the contraction process, its pulling force reduces gradually, enables the McKibben muscle to be able to finally achieve the expectation position. Its shrinkage character is similar to animal's muscle contracture. Afterward, people research and develope and the pneumatic driving artificial muscle one after another, like Japan, some company produced Rubbertuator, some British company produced Air Musule and so on, all take the McKibben muscle as the primary form, and is applied in the industrial field, sometimes it is generally called the McKibben muscle.

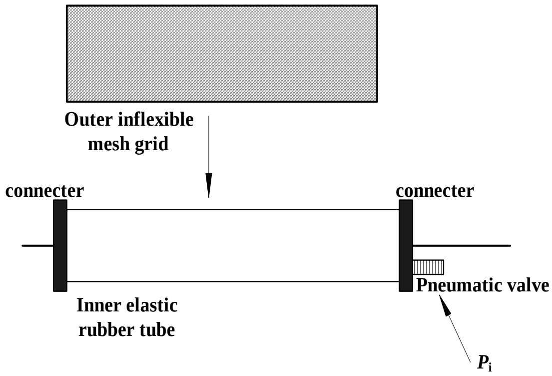

Fig.1 Structure model of McKibben muscle

©ISAROB 2009

2.2 McKibben muscle's mathematical model

As an artificial muscle, the shrinkage must be its important concept,.Generally the literature pointed out that its greatest shrinkage is 20%~40%. It is defined as

$$R_c = (L_0 - L) / L_0 \times 100\% \tag{1}$$

And, R_c is the shrinkage, L is the current length, L_0 is the initial length.

Regards the McKibben muscle as the ideal circular cylinder, establishes its geometric model, as shown in Fig. 2. Here we have neglected the non-column shapes of the two sides of muscle, and thought that the internal aerocyst wall thickness is small enough. L is the current length of circular cylinder, D is the current diameter, n is the outer layer textile fiber winding turn, b is the simple root textile fiber length. θ is the outer layer trace angle of bank. When muscle bearing radial swelling, θ increases, L reduces, but b maintains invariable. By now pulling force F is:

$$F = Pb^2(3L^2 / b^2 - 1) / (4\pi n^2) \tag{2}$$

Formula (2) is the McKibben muscle's theory strength - length characteristic. After having the barometric pressure inputs, the strength output and the barometric pressure value are proportional, becomes the misalignment relations with the length, in addition concerns with the design parameter.

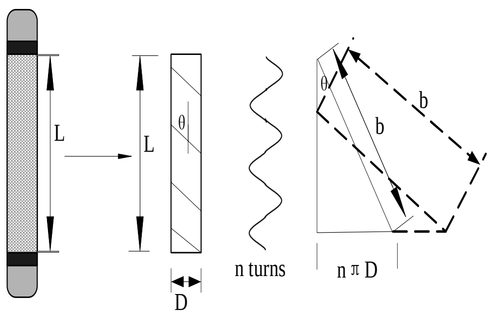

Fig.2 Mathematical model of McKibben muscle

2.3 The Joint actuated by the McKibben muscle

Shown in Fig. 3 for the symmetrical arrangement of two McKibben muscle joint schematic drawing. When the joint is at the initial state of equilibrium, two muscles have same shrinkage R_c and initial intensity of pressure P_0. Records R is the joint transfers the column radius, $F1$ and $F2$ represent pulling force produced by the two McKibben muscles when the joint rotates.When a McKibben muscle's input intensity of pressure change Δp, at the same time another McKibben muscle's input intensity of pressure reverse direction change Δp, transfers an angle ω through the change of McKibben muscle pulling force actuation joint. Then joint static state moment of force.

$$M_s = R(F1 - F2) \tag{3}$$

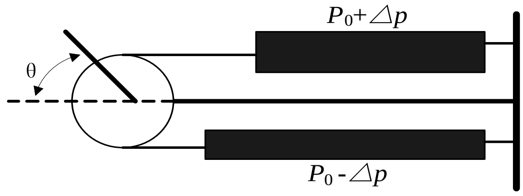

Fig.3 Joint model

Because in the joint rotation process, it is inevitable to introduce joint's dynamic model, namely increases to a speed damping consideration. For different factories, speed damping of different material's product is different. Regarding this joint system, two McKibben muscle resistance establishment actuation joint, two McKibben muscle's speed damping action effect must be more obvious than simple root's function effect, because no matter is the flexure process or stretches out straight in front of oneself the process two muscle's speed damping action effects is superimposes mutually compared to simple root's function effect, and when the contraction speed is big, the speed damping action will be more remarkable, therefore it is the essential consideration to increase the acceleration damping item in the static moment of force foundation. Suppose M_v is the joint angular speed damping item, M_0 is the dynamic moment of force, then:

$$M_0 = M_s - M_v \tag{4}$$

The literature had proven the McKibben muscle's speed damping's existence, through experiments we establish the M_v available equation below expression:

$$M_v = c(P1 + P2)d\omega / dt \tag{5}$$

And c is the speed damping factor, its size is decided by experimental.By the joint dynamic physical model we can know:

$$M_0 = Jd^2\omega / dt^2 \tag{6}$$

And J is the rotor inertia, suppose joint transfers the column for the circle columnar, then:

$$J = \int r^2 dm \tag{7}$$

By take the above equation (3) - (7) we can konw joint's dynamic mathematical model is:

$$J \cdot d^2\omega / dt^2 = R(F1 - F2) - c(P1 + P2)d\omega / dt \tag{8}$$

3 Cerebellum model joint controller neural network (CMAC)

Cereballar Model Articulation Controller is proposed by J.S.Albus in 1975.The simple CMAC principle structural model is shown in Fig. 4, it is constituted by the network input, the concept mapping, the physical mapping and the network outputs[2,3].

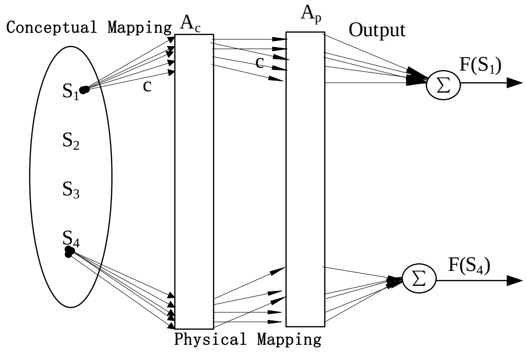

Fig 4 CMAC model

In Fig. 4, A_c is the concept memory cell, A_p is physics memory cell, $F(S_i)$ is the CMAC neural network output. In input state space, each spot in S corresponds to C unit in the concept storage space A_c, also corresponds to c memory cell in the actual storage space A_p, but neural network's output $F(S_i)$ is the sum in these c unit value saves(network weight).

CMAC uses the following learning algorithm: uses δ to study rule adjustment weight, the weight adjustment target:

$$E = \frac{1}{2c} e^2(t) \tag{9}$$

In the formula, $e(t) = r(t) - y(t)$ is according to gradient descent method. Weight adjustment is as follows:

$$\Delta w_j = -\eta \frac{\partial E}{\partial w} = \eta \frac{r(t) - y(t)}{c} \cdot \frac{\partial y}{\partial w} = \eta \frac{e(t)}{c} \tag{10}$$

$$w_j(t) = w_j(t-1) + \Delta w_j(t) + \alpha(w_j(t-1) - w_j(t-2)) \tag{11}$$

In the formula, α is the inertial coefficient.

4 CMAC and PID compound control algorithm

CMAC and PID compound control structure is shown in Fig. 5:

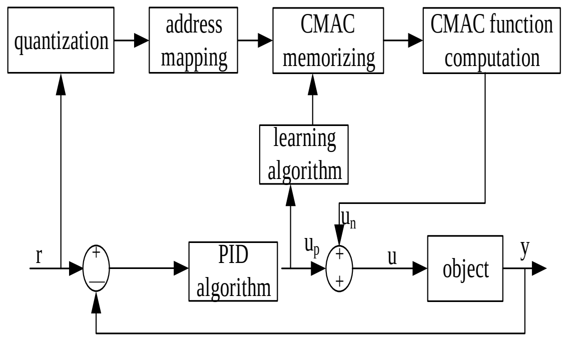

Fig 5 Compound control structure

This system realizes the forward feed reaction control through CMAC and the PID compound control, its characteristic is:

(1) The cerebellum model nerve controller realizes the feed-forward control, realizes the controlled plant counter dynamic model;

(2) The conventional controller realizes the reaction control, guarantee system's stability, and suppresses the perturbation. the this system's control algorithm is:

$$u_n(k) = \sum_{i=1}^{c} w_i a_i \tag{12}$$

$$u(k) = u_n(k) + u_p(k) \tag{13}$$

In the formula, a_i is the binary choice vector, c is the CMAC network pan-parameter, $u_n(k)$ is the corresponding output which CMAC produces, $u_p(k)$ is the output which conventional controller PID produces.

The CMAC adjustment target is:

$$E(k) = \frac{1}{2}(u(k) - u_n(k))^2 \cdot \frac{a_i}{c} \tag{14}$$

$$\Delta w(k) = \eta \frac{u(k) - u_n(k)}{c} a_i = \eta \frac{u_p(k)}{c} a_i \tag{15}$$

$$w(k) = w(k-1) + \Delta w(k) - \alpha(w(k) - w(k-1)) \tag{16}$$

In the formula, η for the speed of network study , $\eta \in (0,1)$, α is the inertia quantity, $\alpha \in (0,1)$.

5 The pneumatic joint's compound control simulation testing

System mathematical model is given in the formula (8):

©ISAROB 2009

$$J \cdot d^2\omega / dt^2 = R(F1 - F2) - c(P1 + P2)d\omega / dt \qquad (17)$$

Input is unit step signal. PID controller's parameters are: $K_p = 99, K_i = 0, K_d = 0.75$. Sampling time $t_s = 0.001$. Add disturbance at $t = 0.15$ s.Program and simulate under MATLAB. Output curves of PD controller, CMAC neural network controller and parallel controller are shown in Fig 6.

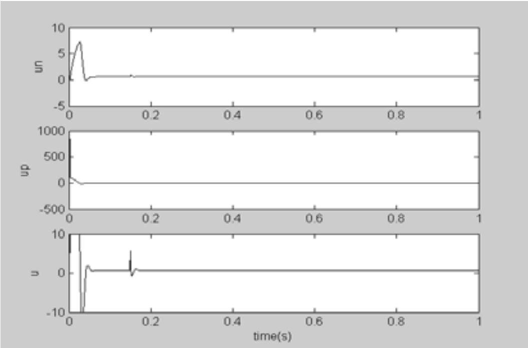

Fig 6 Output curves

We see through the simulation result that: the PD controller has an effect at first,then CMAC controller unceasing study from the outputs of the PD controller and gradually in stead of PD controller .CMAC makes the result of control much better than only use PID . This method realized the feedback control by using traditional PID controller and realized the feed forward control by using CMAC neural network to increase the response speed and control precision.

After added disturbance, the system which is under the disturbance will quickly returen to stable state due to CMAC. CMAC and PID parallel controller can overcome some disadvantages which the PID controller cannot avoid to some extent and improve the effect of controlling.

The Fig.7 and Fig.8 show that CMAC and PID parallel controller can ruduce overshoot of system, Speed up the control response speed and fully reflect feature of CMAC, namely, reducing output errors, good real time performance and strong robusticity.

6 **Conclusion**

In view of complex the mathematical model of which a soft joint actuated by McKibben muscles. This article uses CMAC and the PID parallel controller .Compared with traditional PID or the neural network control method, CMAC and the PID parallel controller has great adaptability and easy to realize.The simulation result proof that this algorithm has the very big enhancement in the control quality and display the very good performance in dynamic response speed, stability and adaptability.

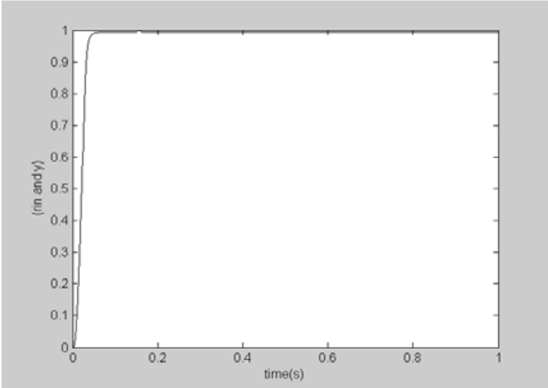

Fig.7 Unit step response curve of CMAC and PID parallel controller

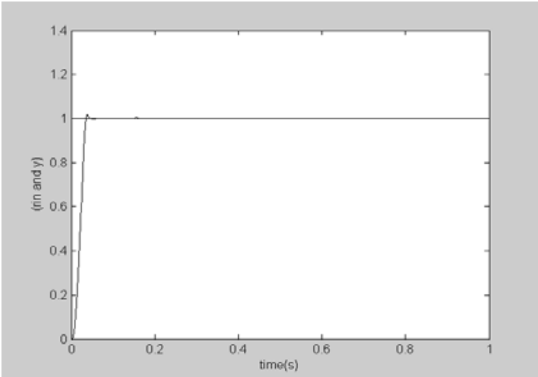

Fig.8 Unit step response curve of only PID controller

Acknowledgement

This study is supported by the project from Dep. of Science & Technology, Henan Province, China (the project No. 072102240022).

Reference:

[1] H.L.Zhao, D.T.Yu, G.Li, "A Humanoid Joint Actuated by Mckibben Muscles", Journal of University of Science and Technology Beijing, 2006(11). pp1096-1100

[2] J.K.Liu, "Advanced PID control and MATLAB simulation", Beijing: Publishing House of Electronics Industry, 2003

[3] C.Y.Zhu, D.H.Yue, X.C.Wang, "The Application of CMAC-PID Parallel control Algorithm in Electro-hydraulic Servo ystem", Chinese Hydraulcs&Pneumatics, 2006(11). pp54-57

©ISAROB 2009

Cooperating Systems of Three-Dimensional Finite Automata

Tomoya Matsukawa[1], Makoto Sakamoto[1], Yasuo Uchida[2], Ayumi Taniue[1], Masatsugu Fukuda[1], Kaoru Kajisa[1], Satoshi Okatani[1], Takao Ito[2], Hiroshi Furutani[1], and Michio Kono[1]

[1] Dept. of Computer Science and Systems Engineering, University of Miyazaki, Miyazaki 889-2192, JAPAN
[2] Dept. of Business Administration, Ube National College of Technology, Ube 755-8555, JAPAN

Abstract

In 1967, M.Blum and C.Hewitt first proposed two-dimensional automata as a computational model of two-dimensional pattern processing, and investigated their pattern recognition abilities. Since then, a lot of researchers in this field have been investigating many properties about automata on a two-dimensional tape. On the other hand, the question of whether processing three-dimensional digital patterns is much more difficult than two-dimensional ones is of great interest from the theoretical and practical standpoints. Thus, the study of three-dimensional automata as a computasional model of three-dimensional pattern processing has been meaningful. This paper introduces a cooperating system of three-dimensional finite automata as one model of three-dimensional automata. A cooperating system of three-dimensional finite automata consists of a finite number of three-dimensional finite automata and a three-dimensional input tape where these finite automata work independently (in parallel). Those finite automata whose input heads scan the same cell of the input tape can communicate with each other, that is, every finite automaton is allowed to know the internal states of other finite automata on the same cell it is scanning at the moment. In this paper, we mainly investigate several accepting powers of a cooperating system of five-way three-dimensional finite automata. The five-way three-dimensional finite automaton is a three-dimensional finite automaton whose input head can move east,west,south,north,or down,but not up on a three-dimensional input tape.

Key Words **:** computational complexity, cooperating system, finite automaton, multihead, three-dimension

1 Introduction

A cooperating system of three-dimensional finite automata (CS-3-FA) [2,3,4] consists of a finite number of three-dimensional finite automata and a three-dimensional input tape where these finite automata work independently (in parallel). Those finite automata whose input heads scan the same cell of the input tape can communicate with each other, that is, every finite automaton is allowed to know the internal states of other finite automata on the same cell it is scanning at the moment.

In this paper, we propose a cooperating system of five-way three-dimensional finite automata (CS-FV3-FA) which is a restricted version of CS-3-FA's, and mainly investigate its several properties as three-dimensional language acceptors. The five-way three-dimensional finite automaton [7] is a three-dimensional finite automaton [1] whose input head can move east,west,south,north,or down, but not up.

The paper has six sections in addition to this Introduction. Section 2 contains some definitions and notions. Section 3 investigates a relationship between five-way three-dimensional simple multihead finite automata (FV3-SPMHFA's) and CS-FV3-FA's. It is shown that FV3-SPMHFA's and CS-FV3-FA's are equivalent in accepting power if the input tapes are restricted to cubic ones. Section 4 investigates the difference between the accepting powers of CS-FV3-FA's and CS-3-FA's, and shows that CS-FV3-FA's are less powerful than CS-3-FA's. Section 5 investigates the difference between the accepting powers of deterministic and nondeterministic CS-FV3-FA's, and shows that deterministic CS-FV3-FA's are less powerful than nondeterministic CS-FV3-FA's. Section 6 concludes by giving some open problems. In this paper only cubic input tapes are considered.

2 Preliminaries

Definition 2.1. Let $\sum$ be a finite set of symbols. A *three-dimensional tape* over $\sum$ is a three-dimensional rectangular array of elements of $\sum$. The set of all three-dimensional tapes over $\sum$ is denoted by $\sum^{(3)}$. Given a tape $x \in \sum^{(3)}$, for each integer $j (1 \leq j \leq 3)$, we let $l_j(x)$ be the length of x along the jth axis. The set of all $x \in \sum^{(3)}$ with $l_1(x) = n_1$, $l_2(x) = n_2$, and $l_3(x) = n_3$ is denoted by $\sum^{(n_1,n_2,n_3)}$. When $1 \leq i_j \leq l_j(x)$ for each $j (1 \leq j \leq 3)$, let $x(i_1, i_2, i_3)$ denote the symbol in x with coordinates (i_1, i_2, i_3). Furthermore, we define

$$x[(i_1, i_2, i_3), (i'_1, i'_2, i'_3)],$$

©ISAROB 2009

when $1 \leq i_j \leq i'_j \leq l_j(x)$ for each integer $j(1 \leq j \leq 3)$, as the three-dimensional input tape y satisfying the follwing conditions:

(i) for each $j(1 \leq j \leq 3)$, $l_j(y) = i'_j - i_j + 1$;

(ii) for each $r_1, r_2, r_3(1 \leq r_1 \leq l_1(y), 1 \leq r_2 \leq l_2(y), 1 \leq r_3 \leq l_3(y)), y(r_1, r_2, r_3) = x(r_1 + i_1 - 1, r_2 + i_2 - 1, r_3 + i_3 - 1)$. (We call $x[(i_1, i_2, i_3), (i'_1, i'_2, i'_3)]$ the $[(i_1, i_2, i_3), (i'_1, i'_2, i'_3)]$-*segment* of x.)

We recall a *five-way three-dimentional simple k-head finite automaton* (FV3-SPk-HFA)[5,6]. An FV3-SPk-HFA M is a finite automaton with k read-only input heads operating on a three-dimentional input tape surrounded by boundary symbols $\sharp$'s. The only one head(called the '*reading*' head) of M is capable of distinguishing the symbols in the input alphabet, and the other heads(called *'counting'* heads) of M can only detect whether they are on the boundary symbols or a symbol in the input alphabet. When an input tape x is a presented to M, M determines the next state of the finite control, the next move direction (east,west,south,north,down,or no move) of each input head, depending on the present state of the finite contorol, the symbol read by the reading head, and on whether or not the symbol read by each counting head is boundary symbol. We say that M *accepts* x if M, when started in its initial state with all its input heads on $x(1, 1, 1)$, eventually halts in an accepting state with all its heads on the bottom boundary symbols of x. As usual, we define nondeterministic and dterministic FV3-SPk-HFA's.

A *five-way three-dimentional sensing simple k-head finite automaton*(FV3-SNSPk-HFA) is the same device as a FV3-SPk-HFA except that the former can detect coincidence of the input heads.

We denote a deterministic(nondeterministic) FV3-SPk-HFA by FV3-SPk-HDFA(FV3-SPk-HNFA), and denote a deterministic (nondeterministic)FV3-SNSPk-HFA by FV3-SNSPk-HDFA(FV3-SNSPk-HNFA).

We now give formal definition of a *cooperating system of k three-dimensional deterministic finite automata* (CS-3-DFA(k)) as an acceptor.

Definition 2.2. A CS-3-DFA(k) is a k-tuple $M = (\mathrm{FA}_1, \mathrm{FA}_2, \ldots, \mathrm{FA}_k)$, $k \geq 1$, such that for each $1 \leq i \leq k$,

$$\mathrm{FA}_i = (\textstyle\sum, Q_i, X_i, \delta_i, q_0 i, F_i, \phi, \sharp),$$

where

1. $\sum$ is a finite set of *input symbols.*
2. Q_i is a finite set of *states.*
3. $X_i = (Q_1 \cup \{\phi\}) \times \cdots \times (Q_{i-1} \cup \{\phi\}) \times (Q_{i+1} \cup \{\phi\}) \times \cdots \times (Q_k \cup \{\phi\})$, where '$\phi$' is a special state not in $(Q_1 \cup Q_2 \cup \cdots \cup Q_k)$.
4. $\delta_i : (\sum \cup \{\sharp\}) \times X_i \times Q_i \to Q_i \times \{\mathrm{east}(= (0, +1, 0))$, $\mathrm{west}(= (0, -1, 0))$, $\mathrm{south}(= (+1, 0, 0))$, $north(=(-1,0,0))$, $\mathrm{up}(= (0, 0, -1))$, $down(=(0,0,+1))\}$, no move$(= (0, 0, 0))\}$ is the *next move function*, where '$\sharp$' is the *boundary symbol* not in $\sum$.
5. $q_{0i} \in Q_i$ is the *initial state* of FA_i.
6. $F_i \subseteq Q_i$ is the set of *accepting states* of FA_i.

Every automaton of M independently (in parallel) works step by step on the same three-dimentional tape x over $\sum$ surrounded by boundary symbols $\sharp$'s. Each step is assumed to require exactly one time for its completion. For each $i(1 \leq i \leq k)$, let q_i be the state of FA_i at time 't'. Then each FA_i, enters the next state 'p_i' at time '$t+1$' according to the function

$$\delta_i(x(\alpha, \beta, \gamma), (q'_1, \ldots, q'_{i-1}, q'_{i+1}, \ldots, q'_k), q_i) = (p_i, (d_1, d_2, d_3)),$$

where $x(\alpha, \beta, \gamma)$ is the symbol read by the input head of FA_i at time 't' and for each $j \in \{1, \ldots, i-1, i+1, \ldots, k\}$,

$$q'_j = \begin{cases} \mathrm{q}_j \in Q_j & \text{if the input heads of } \mathrm{FA}_i \text{ and } \mathrm{FA}_j, \\ & \text{are on the same input position at} \\ & \text{the moment '}t\text{';} \\ \phi & \text{otherwise,} \end{cases}$$

and moves 1st input head to $x(\alpha + d_1, \beta + d_2, \gamma + d_3)$ at time '$t+1$'. We assume that the input head of FA_i never falls off the tape beyond boundary symbols.

When an input tape $x \in \sum^{(3)}$ is presented to M, we say that M *accepts* the tape x if each automaton of M, when started in its initial state with its input head on $x(1, 1, 1)$, eventually enters an accepting state with its input head on one of the bottom boundary symbols.

We next introduce a *cooperating system of k five-way three-dimensional deteministic finite automata* (CS-FV3-DFA(k)), with which we are mainly concerned in this paper.

Definition 2.3. A CS-FV3-DFA(k) is a CS-3-DFA(k) $M = (\mathrm{FA}_1, \mathrm{FA}_2, \ldots, \mathrm{FA}_k)$ such that the input head of each FA_i can only move east, west, south, north, or down, but not up.

To give the formal definition of a *cooperating system of k three-dimensional nondeterministic finite automata* (CS-3-NFA(k)) and a *cooperating system of k five-way three-dimensional nondeterministic finite* *automata* (CS-FV3-NFA(k)) is left to the reader.

For each $X \in$ {FV3-SPk-HDFA,FV3-SPk-HNFA,FV3-SNSPk-HDFA,FV3-SNSPk-HNFA,CS-3-DFA(k),CS-3-NFA(k),CS-FV3-DFA(k),CS-FV3-NFA(k)}, by X^c we denote an X whose input tapes are restricted to cubic ones; by $\mathcal{L}[X](\mathcal{L}([X^c])$ we denote the class of sets of input tapes accepted by X's(X^c's). We will focuse our attention on the acceptors whose input tapes are restricted to cubic ones.

3 Relationship between FV3-SPMHFA's and CS-FV3-FA's

In this section, we establish a relation between the accepting powers of five-way three-dimensional simple multihead finite automata and cooperating systems of five-way three-dimensional finite sutomata over cubic input tapes. This result will be used in the latter sections.

Lemma 3.1. *For any $k \geq 1$ and $X \in \{N, D\}$,*

$$\mathcal{L}[\text{FV3-SNSP}k\text{-HXFA}^c] \subseteq \mathcal{L}[\text{CS-FV3-XFA}(2k)^c]$$

Proof. Let M be an FV3-SNSPk-HFA^c. We will construct a CS-FV3-XFA$(2k)^c$ M' to simulate M. M' acts as follws:

1. M' simulates the moves of the reading head of M and all the east,west,south,or north moves of counting heads of M by using its $(k+1)$ finite automata.
2. M' simulates all the down moves of counting heads of M by making the east moves of input heads of its other $(k-1)$ finite automata.
3. During the simulation, if M moves its reading head down, then M' makes all of input heads of finite automata of M' move down so that all the automata of M' can keep their input heads on the same plane and can communicate with each other in that plane.

It is easy to see that M' can simulate M. □

Lemma 3.2. *For any $k \geq 1$ and any $X \in \{N, D\}$,*

$$\mathcal{L}[\text{CS-FV3-XFA}(k)^c] \subseteq \mathcal{L}[\text{FV3-SNSP}(2k^2-k+1)\text{-HXFA}^c].$$

Proof. Let $M =$ (FA$_1$,FA$_2$,...,FA$_k$)be a CS-FV3-XFA$(k)^c$. We will construct an FV3-SNSP$(2k^2-k+1)$-HXFA^c M' to simulate M. Let R denote the reading head of M', and $h_1, h_2, \ldots, h_{2k^2-k}$ denote the $2k^2-k$ counting heads of M'. M' acts as follws:

1. M' stores the internal states of FA$_1$, FA_2,...,FA$_k$ in its finite contorol.
2. For each plane of the input tape:
   - **(a)** M' simulates the east,west,south,or north moves of input heads of FA$_1$, FA_2,...,FA$_k$ by using R and $h_1, h_2, \ldots, h_k$.
   - **(b)** M' stores in its finite control the internal state of each FA$_i$, $1 \leq i \leq k$, when the input head of FA$_i$ leaves the plane and the order, $(d_1, d_2, \ldots, d_k)$, in which the input heads of FA$_1$, FA$_2$, ..., FA$_k$ leave the plane subsequently (i.e., FA$_{d_1}$ firstly moves its input head down from the plane. FA$_{d_2}$ secondly moves its input head down from the plane, and so on.), and M' keeps the position where the input head of each FA$_i$, $1 \leq i \leq k$, leaves the plane by the positions of $h_1, h_2, \ldots, h_k$.
   - **(c)** Furthermore, for each $i(1 \leq i \leq k-1)$, the interval between the times at which FA$_{d_i}$ and FA$_{d_{i+1}}$ move their input heads down from the plane is stored by a counter with $O(n^{4k})$ space bound, which can be realized by using $h_{(2i-1)k-1}$, $h_{(2i-1)k-2}, \ldots, h_{(2i-1)k}$, where n is the number of rows (or columns or planes) of the input tape.

Note that M works in $O(n^{4k})$ time, that is, if an input tape with n rows (or columns or planes) is accepted by M, then it can be accepted by M in $O(n^{4k})$ time. Thus, it is easy to verify that M' can simulate M. □

From [5],it follows that $\cup_{1\leq k<\infty}\mathcal{L}$[FV3-SP$k$-HXFA^c] $= \cup_{1\leq k<\infty}\mathcal{L}$[FV3-SNSP$k$-HXFA^c] for any $X \in \{N, D\}$. Combining this result with Lemmas 3.1 and 3.2, we have the follwing thorem.

Theorem 3.1. $\cup_{1<\infty}\mathcal{L}$[FV3-SP$k$-HXFA^c] $= \cup_{1\leq k<\infty}\mathcal{L}$[CS-FV3-XFA$(k)^c$] for any $X \in \{N, D\}$.

Corolary 3.1. *For any $k \geq 1$, there is no* CS-FV3-NFA(k) *that accepts the set of connected patterns.*

Remark 3.1. It is easy to see that for each $k \leq 1$, (1)three-dimensional sensing simple k head finite automata [5] are simulated by cooperating systems of $(k+1)$ three-dimensional finite automata, and (2) cooperating systems of k three-dimensional finite automata are simulated by three-dimensional sensing simple $(k+1)$ head finite automata.

©ISAROB 2009

Remark 3.2. It is shown in [8] that (one-dimensional) one-way simple multihead finite automata snd cooperating systems of (one-dimensional) one-way deterministic finite automata are incomparable in accepting power. From this fact, it follows that FV3-SPMHFA's and CS-FV3-DFA's are incomparable in accepting power if the input tapes are restricted to those x such that $l_3(x) > l_1(x) = l_2(x)$. We can also show that FV3-SPMHFA's are more powerful than CS-FV3-DFA's if the input tapes are restricted to those x such that $l_3(x) < l_1(x) = l_2(x)$.

4 Five-Way versus Six-Way

In this section, we investigate the difference between the accepting powers of CS-3-DFA$(k)^c$'s [CS-3-NFA$(k)^c$'s] and CS-FV3-DFA$(k)^c$'s [CS-FV3-NFA$(k)^c$'s].

Theorem 4.1. *For each* $X \in \{N, D\}$, $\mathcal{L}$ [CS-3-DFA$(1)^c$]$- \cup_{1 \leq k < \infty} \mathcal{L}$[CS-FV3-XFA$(k)^c$] $\neq \emptyset$.

Proof. Let $T_1 = \{x \in \{0,1\}^{(3)} | (\exists m \geq 2)[l_1(x) = l_2(x) = l_3(x) = m \ \& \ x[(1,1,1),(m,m,1)] = x[(1,1,2),(m,m,2)]]\}$. Clearly, $T_1 \in \mathcal{L}$[CS-3-DFA$(1)^c$]. From [5], it is easy to see that T_1 is not in $\cup_{1 \leq k < \infty}\mathcal{L}$[FV3-SP$k$-HNFA^c]. From this fact and Theorem 3.1, the theorem follows. □

From Theorem 4.1, we can get the following corollary.

Corollary 4.1. *For each* $k \geq 1$ *and* $X \in \{N, D\}$, (1)$\mathcal{L}$[CS-TR2-XFA$(k)^c$]$\subsetneq$ $\mathcal{L}$[CS-2-XFA$(k)^c$], *and* (2) $\cup_{1 \leq k < \infty}\mathcal{L}$[CS-TR2-XFA$(k)^c$] $\subsetneq \cup_{1 \leq k < \infty}\mathcal{L}$[CS-2-XFA$(k)^c$].

5 Nondeterminism versus Determinism

In this section, we investigate the difference between the accpting powers of CS-FV3-NFA$(k)^c$'s and CS-FV3-DFA$(k)^c$'s.

Theorem 5.1. $\mathcal{L}$[CS-FV3-NFA$(1)^c$] $- \cup_{1 \leq k < \infty}\mathcal{L}$[CS-FV3-DFA$(k)^c$] $\neq \emptyset$.

Proof. Let $T_2 = \{x \in \{0,1\}^{(3)} | (\exists m \geq 2)[l_1(x) = l_2(x) = l_3(x) = m]$ & $\exists_i, \exists_j (1 \leq i \leq m, 1 \leq j \leq m)[x(i,j,1) = x(i,j,2) = 1]$. Clearly, $T_2 \in$ [CS-FV3-NFA$(1)^c$]. From [5], it is easy to see that T_2 is not in $\cup_{1 \leq k < \infty}\mathcal{L}$[FV3-SP$k$-HDFA^c]. From this fact and Theorem 3.1, the theorem follows. □

From Theorem 5.1, we get the following corollary.

Corollary 5.1. *For each* $k \geq 1$, (1)$\mathcal{L}$[CS-FV3-DFA$(k)^c$] $\subsetneq \mathcal{L}$[CS-FV3-NFA$(k)^c$], *and*(2) $\cup_{1 \leq k < \infty}\mathcal{L}$[CS-FV3-DFA$(k)^c$] $\subsetneq \cup_{1 \leq k < \infty}\mathcal{L}$[CS-FV3-NFA$(k)^c$].

6 Conclusion

We conclude this paper by giving several open problems except the open problem stated in the previous section.

In this paper, we introduced a cooperating system of three-dimensional finite automata, and investigated several basic accepting powers. We conclude this paper by giving an open problem as follows.

For each $k \geq 2$,

$$\mathcal{L}[\text{CS-3-DFA}(k)^c] \subsetneq \mathcal{L}[\text{CS-3-NFA}(k)^c] \ ?$$

References

[1] M.Blum and C.Hewitt, Automata on a two-dimensional tape, *in* IEEE *Symp. Switching Automata Theory*,pp.155-160,1967.

[2] M.Blum and K.Kozen, On the power of the compass, in *Processings of the 19th Annual Simp. on Foundations of Computer Science*,1987.

[3] M.Blum and W.J.Sakoda, On the capability of finite automata in 2 and 3 dimensional space, *in Processings of the 18th Annual Simp. on Foundations of Computer Science* pp.147-161,1977.

[4] A.Hemmerling, Normed two-plane trapes for finite system of cooperating compass automata, *in EIK* 23(8/9),pp.453-470,1978.

[5] K.Inoue, I.Takanami, and H.Taniguchi, Three-way two-dimensional simple multihead finite automata – hierarchical properties (in Japanese), *IECE Jan. Trans.*(D),pp.65-72,1979.

[6] K.Inoue, I.Takanami, and H.Taniguchi, Three-way two-dimensional simple multihead finite automata – closure properties (in Japanese),*IECE Jan. Trans.*(D),pp.273-280,1979.

[7] M.Sakamoto, Three-dimensional alternating Turing machines, *Ph.D.Thesis, Yamaguchi University*,1999.

[8] Y.Wang, K.Inoue, and I.Takanami, Some properties of cooperating systems of one-way finite automata (in Japanese), *IECE Jan. Trans.*(D-I) No.7,pp.391-399,1992.

©ISAROB 2009

The Fourteenth International Symposium on Artificial Life and Robotics 2009 (AROB 14th '09),
B-Con Plaza, Beppu, Oita, Japan, February 5 - 7, 2009

Hierarchies Based on the Number of Cooperating Systems of Three-Dimensional Finite Automata

Yasuo UCHIDA[1], Makoto SAKAMOTO[2], Satoshi OKATANI[2], Kaoru KAJISA[2], Masatsugu FUKUDA[2], Tomoya MATSUKAWA[2], Ayumi TANIUE[2], Takao ITO[1], Hiroshi FURUTANI[2], and Michio KONO[2]

[1] Dept. of Business Administration, Ube National College of Technology, Ube 755-8555, JAPAN
[2] Dept. of Computer Science and Systems Engineering, University of Miyazaki, Miyazaki 889-2192, JAPAN

Abstract

The question of whether processing three-dimensional digital patterns is much more difficult than two-dimensional ones is of great interest from the theoretical and practical standpoints. Recently, due to the advances in many application areas such as computer vision, robotics, and so forth, it has become increasingly apparent that the study of three-dimensional pattern processing has been of crucial importance. Thus, the study of three-dimensional automata as a computational model of three-dimensional pattern processing has been meaningfull. This paper introduces a cooperating system of three-dimensional finite automata as one model of three-dimensional automata. A cooperating system of three-dimensional finite automata consists of a finite number of three-dimensional finite automata and a three-dimensional input tape where these finite automata work independently (in parallel). Those finite automata whose input heads scan the same cell of the input tape can communicate with each other, that is, every finite automaton is allowed to know the internal states of other finite automata on the same cell it is scanning at the moment. In this paper, we continue the study of cooperating systems of three-dimensional finite automata, and mainly investigate hierarchies based on the number of their cooperating systems.

Key Words **:** computational complexity, cooperating system, finite automaton, hierarchy, three-dimension

1 Introduction

It has become increasingly apparent that the study of three-dimensional pattern processing has been of crucial importance. Thus, the study of three-dimensional automata as a computational model of three-dimensional pattern processing has also been meaningful. For example, in 1982, three-dimensional finite automata were introduced.

A cooperating system of three-dimensional finite automata (*CS*-2-*FA*) [2,3,4] consists of a finite number of three-dimensional finite automata and a three-dimensional input tape where these finite automata work independently (in parallel). Those finite automata whose input heads scan the same cell of the input tape can communicate with each other, that is, every finite automaton is allowed to know the internal states of other finite automata on the same cell it is scannig at the moment.

In this paper, we propose a cooperating system of five-way three-dimensional finite automata (*CS-FV*3-*FA*) which is a resticted version of *CS*-3-*FA*'s, and mainly investigate the hierarchies can be obtained by varying the number of finite automata in the system for classes of sets accepted by *CS-FV*3-*FA*'s and *CS*-3-*FA*'s.The five-way three-dimensional finite automaton [7] is a three-dimensional finite automaton [1] whose input head can move east, west, south, north, or down, but not up.

2 Preliminaries

Definition 2.1. Let Σ be a finite set of symbols. A *three-dimesional tape* over Σ is a three-dimensional rectangular array of elements of Σ. The set of all three-dimesional tapes over Σ is denoted by $\Sigma^{(3)}$. Given a tape $x \in \Sigma^{(3)}$, for each integer $j(1 \leq j \leq 3)$, we let $l_j(x)$ be the length of x along the jth axis. The set of all $x \in \Sigma^{(3)}$ with $l_1(x)$=n_1, $l_2(x)$=n_2, and $l_3(x)$=n_3 is denoted by $\Sigma^{(n_1,n_2,n_3)}$. When $1 \leq i_j \leq l_j(x)$ for each $j(1 \leq j \leq 3)$, let $x(i_1,i_2,i_3)$ denote the symbol in x with coordinates (i_1,i_2,i_3). Furthermore, we define

$$x[(i_1,i_2,i_3),(i'_1,i'_2,i'_3)],$$

when $1 \leq i_j \leq i'_j \leq l_j(x)$ for each integer $j(1 \leq j \leq 3)$, as the three-dimensional input tape y satisfying the following conditions :

(i)for each $j(1\leq j \leq 3)$, $l_j(y)$=i'_j-i_j+1;

(ii)for each $r_1,r_2,r_3(i \leq r_1 \leq l_1(y)$, $i \leq r_2 \leq l_2(y)$, $i \leq r_3 \leq l_3(y))$, $y(r_1,r_2,r_3)$=$x(r_1$+i_1-1, r_2+i_2-1, r_3+i_3-1). (We call $x[(i_1,i_2,i_3),\ (i'_1,i'_2,i'_3)]$ the $[(i_1,i_2,i_3),\ (i'_1,i'_2,i'_3)]$-*segment* of x.)

We recall a *five-way three-dimensional simple k-head finite automaton* (*FV*3-*SPk*-*HFA*) [5,6]. An *FV*3-*SPk*-*HFA* M is a finite automaton with k read-only input heads operating on a three-dimensional input

©ISAROB 2009

tape surrounded by boundary symbols #'s. The only one head (called the *'reading'* head) of M is capable of distinguishing the symbols in the input alphabet, and the other heads (called the *'counting'* heads) of M can only detect whether they are on the boundary symbols or a symbol in the input alphabet. When an input tape x is presented to M, M determines the next state of the finite control, the next move direction (east, west, south, nouth, down, or no move) of each input head, depending on the present state of the finite control, the symbol read by the reading head, and on whether or not the symbol read by each counting head is boundary symbol. We say that M *accepts* x if M, when started in its initial state with all its input heads on $x(1,1,1)$, eventually halts in an accepting state with all its heads on the bottom boundary symbols of x. As usual, we define nondeterministic and deterministic $FV3$-*SPk*-*HFA*'s.

A *five-way three-dimensional sensing simple k-head finite automaton* ($FV3$-*SNSPk*-*HFA*) is the same device as an $FV3$-*SPk*-*HFA* except that the former can detect coincidence of the input heads.

We denote a deterministic (nondeterministic) $FV3$-*SPk*-*HFA* by $FV3$-*SPk*-*HDFA* ($FV3$-*SPk*-*HNFA*), and denote a deterministic (nondeterministic) $FV3$-*SNSPk*-*HFA* by $FV3$-*SNSPk*-*HDFA* ($FV3$-*SNSPk*-*HNFA*).

We now give a formal definition of a *cooperating system of k three-dimensional deterministic finite automata* (*CS*-3-*DFA*(k)) as an acceptor.

Definition 2.2. A *CS*-3-*DFA*(k) is a k-tuple $M = (FA_1, FA_2, \cdots, FA_k)$, $k \geq 1$, such that for each $1 \leq i \leq k$,

$$FA_i = (\Sigma, Q_i, X_i, \delta_i, q_{0i}, F_i, \phi, \#),$$

where

1. Σ is a finite set of *input symbols*.
2. Q_i is a finite set of *states*.
3. $X_i = (Q_1 \cup \{\phi\}) \times \cdots \times (Q_{i-1} \cup \{\phi\}) \times (Q_{i+1} \cup \{\phi\}) \times \cdots \times (Q_k \cup \{\phi\})$,where '$\phi$' is a special state not in $(Q_1 \cup Q_2 \cup \cdots \cup Q_k)$.
4. $\delta_i = (\Sigma \cup \{\#\}) \times X_i \times Q_i \rightarrow Q_i \times \{$east(=(0,+1,0)), west(=(0,-1,0)),south(=(+1,0,0)),north(=(-1,0,0)),up(=(0,0,-1)),down(=(0,0,-1)),no move (=(0,0,0))$\}$ is the *next move function*, where '#' is the *boundary symbol* not in Σ.
5. $q_{0i} \in Q_i$ is the *initial state* of FA_i.
6. $F_i \subseteq Q_i$ is the set of *accepting state* of FA_i.

Every automaton of M independently (in parallel) works step by step on the same three-dimensional tape x over Σ surrounded by boundary symbols #'s. Each step is assumed to require exactly one time for its completion. For each i ($1 \leq i \leq k$), let q_i be the state of FA_i at time 't'. Then each FA_i enters the next state 'p_i' at time '$t+1$' according to the function

$$\begin{aligned}\delta_i(x(\alpha,\beta,\gamma),(q'_1,\cdots,q'_{i-1},q'_{i+1},\cdots,q'_k),q_i)\\ =(p_i,(d_1,d_2,d_3)),\end{aligned}$$

where $x(\alpha, \beta, \gamma)$ is the symbol read by the input head of FA_i at time 't' and for each $j \in \{1, \cdots, i-1, i+1, \cdots, k\}$,

$$q'_j = \begin{cases} q_j \in Q_j & \text{if the input heads of } FA_i \text{ and } FA_j \text{ are on the same input position at the moment '}t\text{';} \\ \phi & \text{otherwise,} \end{cases}$$

and moves 1st input head to $x(\alpha + d_1, \beta + d_2, \gamma + d_3)$ at time '$t+1$'. We assume that the input head of FA_i never falls off the tape beyond boundary symbols.

When an input tape $x \in \Sigma^{(3)}$ is presented to M, we say that M*accepts* the tape x if each automaton of M, when started in its initial state with its input head on $x(1,1,1)$, eventually enters an accepting state with its input head on one of the bottom boundary symbols.

We next introduce a *cooperating system of k five-way three-dimensional deterministic finite automata* (*CS*-$FV3$-*DFA*(k)), with which we are mainly concerned in this paper.

Definition 2.3. A *CS*-$FV3$-*DFA*(k) is a *CS*-3-*DFA*(k) $M = (FA_1, FA_2, \cdots, FA_k)$ such that the input head of each FA_i can only move east, west, south, north, or down, but not up.

To give the formal definition of a *cooperating system of k three-dimensional nondeterministic finite automata* (*CS*-3-*NFA*(k)) and a *cooperating system of k five-way three-dimensional nondeterministic finite automata* (*CS*-$FV3$-*NFA*(k)) is left to the reader.

For each $X \in \{FV3$-*SPk*-*HDFA*, $FV3$-*SPk*-*HNFA*, $FV3$-*SNSPk*-*HDFA*, $FV3$-*SNSPk*-*HNFA*, *CS*-3-*DFA*(k), *CS*-3-*NFA*(k), *CS*-$FV3$-*DFA*(k), *CS*-$FV3$-*NFA*(k)$\}$, by X^c we denote an X whose input tapes are restricted to cubic ones; by $\mathcal{L}[X]$ ($\mathcal{L}[X^c]$) we denote the class of sets of input tapes accepted by X's (X^c's). We will focus our attention on the acceptors whose input tapes are restricted to cubic ones.

3 Hierarchies Based on the Number of Automata

3.1. Six-Way Case

We first investigate how the number of automata of *CS*-3-*FA*^{c}'s affects the accepting power.

Theorem 3.1.1.

For each $k \geq 1$ and each $X \in \{N, D\}$, $\mathcal{L}[CS\text{-}3\text{-}XFA_{\{0\}}(k)^c] \subsetneq \mathcal{L}[CS\text{-}3\text{-}XFA_{\{0\}}(k+2)^c]$, where $\mathcal{L}[CS\text{-}3\text{-}XFA_{\{0\}}(k)^c]$ denote the class of sets of cubic tapes over a one-letter alphabet accepted by $CS\text{-}3\text{-}XFA(k)$'s.

Proof. It is easy to prove that every CS-3-$DFA(k)$[CS-3-$NFA(k)$] can be simulated by a (six-way) three-dimesional sensing deterministic [nondeterministic] k-head finite automaton, and every (six-way) three-dimensional sensing deterministic [nondeterministic] k-head finite automaton can be simulated by a CS-3-$DFA(k+1)$[CS-3-$NFA(k+1)$]. From [8], for sets of cubic tapes over a one-letter alphabet, (six-way) three-dimensional sensing deterministic [nondeterministic] (k+1)-head finite automata are more powerful than the cooresponding k-head finite automata. From these facts, the theorem follows. □

Unfortunately, it is unknown whether $\mathcal{L}[CS\text{-}3\text{-}XFA_{\{0\}}(k)^c] \subsetneq \mathcal{L}[CS\text{-}3\text{-}XFA_{\{0\}}(k+1)^c]$ for any $k \geq 1$ and for any $X \in \{D, N\}$. It is also unknown wtether $\mathcal{L}[CS\text{-}3\text{-}XFA(k)^c] \subsetneq \mathcal{L}[CS\text{-}3\text{-}XFA(k+1)^c]$ for any $k \geq 2$ and for any $X \in \{D, N\}$. (It is easy to show that $\mathcal{L}[CS\text{-}3\text{-}XFA(1)^c] \subsetneq \mathcal{L}[CS\text{-}3\text{-}XFA(2)^c]$.)

3.2. Five-Way Case

We next investigate how the number of automata of $CS\text{-}FV3\text{-}FA^c$'s affects the accepting power.

For each $n \geq 1$, let $T(n) = \{x \in \{0,1\}^{(3)} | (^\exists m \geq n)$ $[l_1(x) = l_2(x) = l_3(x) = m$ & $x[(1,1,1),(m,m,1)] = x[(1,1,2),(m,m,2)]\} \in R_n(m)$ & $x[(1,1,3),(m,m,m)] \in \{0\}^{(3)}]\}$, where $R_n(m) = \{x \in \{0,1\}^{(3)} |\ l_1(x) = m, l_2(x) = m, l_3(x) = m$ & (x has exactly n 1's)$\}$ for each $m \geq n$. It is obvious that for any fixed positive integer n, $T(n)$ can be accepted by a $CS\text{-}FV3\text{-}DFA(n)$.

We first consider the following problem: given a fixed positive integer n, find a $CS\text{-}FV3\text{-}FA$ which accepts $T(n)$ and uses the minimum number of automata. Unfortunately, we cannot generally solve the problem in the present paper, but we give the lower and upper bounds. Let $f(n)$ denote the minimum number of automata required for deterministic $CS\text{-}FV3\text{-}FA^c$'s to accept $T(n)$, and $g(n)$ denote the minimum number of automata required for nondeterministic $CS\text{-}FV3\text{-}FA^c$'s to accept $T(n)$. Clearly, $g(n) \leq f(n)$ for any $n \geq 1$.

Theorem 3.2.1. *For each $k \geq 1$, (1) $f(k^2+k-1) \leq 2k-1$, (2) $f(k^2+2k) \leq 2k$, and (3) $f(k(k-1)/2+1) \geq k$.*

Proof. The proofs of (1) and (2) are similar. We only give the proof of (2) here. To prove (2) is equivalent to proving that: for each $k \geq 1$, $T(k^2+2k) \in \mathcal{L}[CS\text{-}FV3\text{-}DFA(2k)^c]$.

For each $n \leq 1$, let $T'(n) = \{x[(1,1,1),(l_1(x),l_2(x),2)] | x \in T(n)\}$. For convenience, we prove by induction on k that $T'(k^2+2k) \in \mathcal{L}[CS\text{-}FV3\text{-}DFA(2k)]$. It will be obvious that (2) follows from this fact.

We now prove (3). Suppose that there is a $CS\text{-}FV3\text{-}DFA(k-1)^c$ $M(k-1) = (FA_1, FA_2, \cdots, FA_{k-1})$ accepting $T(k(k-1)/2+1)$. Let h_i denote the input of FA_i for each $i \in \{1,2,\cdots,k-1\}$.

For each $m \geq k(k-1)/2+1$, let $V(m) = \{x \in T(k(k-1)/2+1) | l_1(x) = l_2(x) = l_3(x) = m\}$, and for each permutation $\sigma : \{1,2,\cdots,k-1\} \to \{1,2,\cdots,k-1\}$, let $W_\sigma(m)$ be the set of all input tapes $x \in V(m)$ such that during the accepting computation of $M(k-1)$ on x, input heads $h_{\sigma(1)}, h_{\sigma(2)}, \cdots, h_{\sigma(k-1)}$ leave the first plane of x in this order. Then there must exist some permutation τ such that

$$|W_\tau(m)| \geq |V(m)|/(k-1)! = \Omega(m^{2(k(k-1)/2+1)}).$$

For each $x \in W_\tau(m)$ and each $1 \leq i \leq k-1$, let $q_{\tau(i)}(x), p_{\tau(i)}(x)$ and $t_{\tau(i)}(x)$ denote the internal state of $FA_{\tau(i)}$, the position of $h_{\tau(i)}$ and the time, respectively, when $h_{\tau(i)}$ leaves the first plane during the accepting computation of $M(k-1)$ on x.

For each $x \in W_\tau(m)$, let

$$t(x) = (t_{\tau(2)}(x) - t_{\tau(1)}(x), t_{\tau(3)}(x) - t_{\tau(2)}(x), \cdots, t_{\tau(k-1)}(x) - t_{\tau(k-2)}(x)),$$

and

$$u(x) = ((q_{\tau(1)}(x), p_{\tau(1)}(x)), \cdots, (q_{\tau(k-1)}(x), p_{\tau(k-1)}(x)), t(x)).$$

Clearly, for each $2 \leq i \leq k-1$, $t_{\tau(i)}(x) - t_{\tau(i-1)}(x) = O(m^{k-i})$, because otherwise $FA_{\tau(i)}, \cdots, FA_{\tau(k-1)}$ would enter a loop on the first plane, and thus $M(k-1)$ would never accept x. So $|\{u(x)|x \in W_\tau(m)\}| = O(m^{k(k-1)})$. Therefore, it follows that for large m

$$|W_\tau(m)| > |\{u(x)|x \in W_\tau(m)\}|,$$

and so there exist two diffirent input tapes $x, y \in W_\tau(m)$ such that $u(x) = u(y)$. Let z be the tape obtained from x by replacing the second plane of x with the second plane of y. It follows that z is also accepted by $M(k-1)$. This is a contradiction, because z in not in $T(k(k-1)/2+1)$. This completes the proof of (3). □

Theorem 3.2.2. $g(2k^2-5k+4) \geq k$, for $k \geq 1$.

Proof. The proof is very similar to that of (3) of Theorem 3.2.1. Suppose, to the contrary, that there is a $CS\text{-}FV3\text{-}NFA(k-1)^c$ $M(k-1) = (FA_1, FA_2, \cdots, FA_{k-1})$ accepting $T(2k^2-5k+4)$. Let h_i denote the input head of FA_i for each $i \in \{1,2,\cdots,k-1\}$.

For each $m \geq 2k^2-5k+4$, let $V(m) = \{x \in T(2k^2-5k+4) | l_1(x) = l_2(x) = l_3(x) = m\}$. With each $x \in V(m)$, we associate one fixed accepting computation, $c(x)$, of $M(k-1)$ on x in which $M(k-1)$ operates in $O(m^{4(k-1)})$ time. Furthermore, for each permutation $\sigma:\{1,2,\cdots,k-1\} \rightarrow \{1,2,\cdots,k-1\}$, let $W_\sigma(m)$ be the set of all input tapes $x \in V(m)$ such that during $c(x)$, input heads $h_{\sigma(1)}, h_{\sigma(2)}, \cdots, h_{\sigma(k-1)}$ leave the first plane of x in this order. Then there must exist some permutation τ such that

$$|W_\tau(m)| \geq |V(m)|/(k-1)! = \Omega(m^{4k^2-10k+8}).$$

For each $x \in W_\tau(m)$ and each $1 \leq i \leq k-1$, let $q_{\tau(i)}(x), p_{\tau(i)}(x)$ *and* $t_{\tau(i)}(x)$ denote the internal state of $FA_{\tau(i)}$, the position of $h_{\tau(i)}$ and the time, respectively, when $h_{\tau(i)}$ leaves the first plane of x during $c(x)$.

For each $x \in W_\tau(m)$, let

$$t(x) = (t_{\tau(2)}(x) - t_{\tau(1)}(x), t_{\tau(3)}(x) - t_{\tau(2)}(x), \cdots, t_{\tau(k-1)}(x) - t_{\tau(k-2)}(x)),$$

and

$$u(x) = ((q_{\tau(1)}(x), p_{\tau(1)}(x)), \cdots, (q_{\tau(k-1)}(x), p_{\tau(k-1)}(x)), t(x)).$$

Clearly, for each $2 \leq i \leq k-1, t_{\tau(i)}(x) - t_{\tau(i-1)}(x) = O(m^{4(k-1)})$. So $|\{u(x)|x \in W_\tau(m)\}| = O(m^{4k^2-10k+6})$. Therefore, it follows that for large m

$$|W_\tau(m)| > |\{u(x)|x \in W_\tau(m)\}|,$$

and so there exist two different input tapes $x, y \in W_\tau(m)$ such that $u(x) = u(y)$. Let z be the tape obtained from x by replacing the second plane of x with the second plane of y. Clearly, from $c(m)$ and $c(y)$, we can construct an accepting computation of $M(k-1)$ on z. This is a contradiction, because z in not in $T(2k^2-5k+4)$. This completes the proof of the thereom. □

From Theorems 3.2.1 and 3.2.2, we can get the following theorem.

Theorem 3.2.3. *For each* $k \geq 1$ *and each* $X \in \{D, N\}$, $\mathcal{L}[CS\text{-}FV3\text{-}XFA(k)^c] \subsetneq \mathcal{L}[CS\text{-}FV3\text{-}XFA(k+1)^c]$.

Proof. For each $k \geq 1$, let $D(k)$=max$\{n|f(n) = k\}$ and $N(k)$=max$\{n|g(n) = k\}$. From Theorem 3.2.1 (3) and Thorem 3.2.2, we have

$$D(k) \leq k(k+1)/2 \text{ and } N(k) \leq 2k^2 - k,$$

respectively.

For each $X \in \{D, N\}$, let M be a CS-$FV3$-$XFA(k)^c$ accepting $T(X(k))$. From M, we can easily construct a CS-$FV3$-$XFA(k+1)^c M'$ which accepts $T(X(k)+1)$. Thus $T(X(k)+1) \in \mathcal{L}[CS$-$FV3$-$XFA(k+1)^c]$. From this and the fact that $T(X(k)+1) \notin \mathcal{L}[CS$-$FV3$-$XFA(k)^c]$, it follows that $T(X(k)+1) \in \mathcal{L}[CS$-$FV3$-$XFA(k+1)^c] - \mathcal{L}[CS$-$FV3$-$XFA(k)^c]$. □

4 Conclusion

We conclude this paper by giving two open problems.

1. For each $k \geq 1$, and each $X \in \{D, N\}$, $\mathcal{L}[CS\text{-}FV3\text{-}XFA_{\{0\}}(k)^c] \subsetneq \mathcal{L}[CS\text{-}FV3\text{-}XFA_{\{0\}}(k+1)^c]$, where $\mathcal{L}[CS\text{-}FV3\text{-}XFA_{\{0\}}(k)^c]$ denote the class of sets of cubic tapes over a one-letter alphabet accepted by CS-$FV3$-$XFA(k)$'s?

2. For $n \geq 4$, $g(n) < f(n)$? (It is easy to show that for $1 \leq n \leq 3$, $g(n) = f(n)$.)

References

[1] M.Blum and C.Hewitt, Automata on a two-dimensional tape, *in* IEEE *Symp. Switching Automata Theory*,pp.155-160,1967.

[2] M.Blum and K.Kozen, On the power of the compass, in *Processings of the 19th Annual Simp. on Foundations of Computer Science*,1987.

[3] M.Blum and W.J.Sakoda, On the capability of finite automata in 2 and 3 dimensional space, *in Processings of the 18th Annual Simp. on Foundations of Computer Science* pp.147-161,1977.

[4] A.Hemmerling, Normed two-plane trapes for finite system of cooperating compass automata, *in EIK* 23(8/9),pp.453-470,1978.

[5] K.Inoue, I.Takanami, and H.Taniguchi, Three-way two-dimensional simple multihead finite automata – hierarchical properties (in Japanese), *IECE Jan. Trans.*(D),pp.65-72,1979.

[6] K.Inoue, I.Takanami, and H.Taniguchi, Three-way two-dimensional simple multihead finite automata – closure properties (in Japanese),*IECE Jan. Trans.*(D),pp.273-280,1979.

[7] M.Sakamoto, Three-dimensional alternating Turing machines, *Ph.D.Thesis, Yamaguchi University*,1999.

[8] Y.Wang, K.Inoue, and I.Takanami, Some hierarchy results on multihead automata over a one-letter alphabet, in *IEICE Jan. Trans.*(E76-D),No.6,pp.625-633,1993.

The Fourteenth International Symposium on Artificial Life and Robotics 2009 (AROB 14th '09),
B-Con Plaza, Beppu, Oita, Japan, February 5 - 7, 2009

Robust l_∞ Preview Control for Biped Walking Pattern Generation

Sadaaki Kunimatsu, Takahiro Fukuda, Makoto Kumon and Mitsuaki Ishitobi
Graduate School of Science and Technology, Kumamoto University
Kurokami 2-39-1, Kumamoto, 860-8555, JAPAN

Abstract

We propose robust l_∞ preview control for biped walking pattern generation. First, we state robust l_∞ preview control with robustness against initial value and apply it to the cart-table model. Next, we propose a method to reduce the conservativeness of the robust l_∞ preview control and an algorithm to solve it. Finally, the effectiveness of our proposed methods is illustrated by simulation.

1 Introduction

Recently, attention has been focused on the study of biped walking for life size humanoid robots. Generally, an approach to biped walking is the method of adjusting futural ZMP(Zero Moment Point) proposed in Reference [2]. ZMP changes as a step function when the humanoid robot shifts the way of supporting from one leg to both legs. Moreover, it is known that the change of ZMP generates after that of the center of gravity does. Therefore, we cannot use normal servo control in regarding ZMP as a step input. This problem is solved by applying the preview control with the performance index of l_2 norm [3] that use futural information of reference inputs [2]. However, since the performance index of l_2 norm minimizes the integral square of the error between references and outputs, the maximal value of the error is not always small. Therefore, there exists possibility of resulting in toppling. There are several researches using the maximal value as performance index [1, 4, 6]. We propoesed l_∞ preview control via LMI(Linear Matrix Inequality [1]) optimization problem by using l_∞ norm as the performance index [5]. Since l_∞ norm can evaluate ZMP error directly, it is expected that this approach prevents the humanoid robot from toppling. However, the upper bound of performance index of robust l_∞ preview control was conservative in spite of having good performance in simulation.

In this paper, we propose a method to reduce the conservativeness of the robust l_∞ preview control and an algorithm to solve it. Finally, the effectiveness of our proposed methods is illustrated by simulation.

2 Walking pattern generation based on cart-table model

We consider a cart-table model [2] as follows:

$$p = x_c - \frac{z_c}{g}\ddot{x}_c \tag{1}$$

where p is the position of ZMP, z_c is the height of the center of gravity, g is the gravity acceleration, x_c is the position of the cart. We define the input as the time derivative of the horizontal acceleration of the cart and construct a continuous-time state space system. With discretizing the system as the sampling time h, the discrete-time state space equation is transformed into the following equation.

$$x_{k+1} = Ax_k + Bu_k \tag{2a}$$
$$p_k = Cx_k \tag{2b}$$

where

$$A := \begin{bmatrix} 1 & h & \frac{h^2}{2} \\ 0 & 1 & h \\ 0 & 0 & 1 \end{bmatrix}, \quad B := \begin{bmatrix} \frac{h^3}{6} \\ \frac{h^2}{2} \\ h \end{bmatrix},$$
$$C := \begin{matrix} 1 & 0 & -\frac{z_c}{g} \end{matrix}$$

We define the error e_k between the reference ZMP p_k^{ref} and the measured ZMP p_k as follows:

$$e_k := p_k^{ref} - p_k \tag{3}$$

In order to eliminate the steady state error, we construct the error system with the first-order difference value of the state and the error as the state variable.

$$\bar{x}_{k+1} = \bar{A}\bar{x}_k + \bar{B}\Delta u_k + B_R \Delta p_{k+1}^{ref}, \tag{4a}$$
$$e_k = \bar{C}\bar{x}_k \tag{4b}$$

©ISAROB 2009

where

$$\bar{A} := \begin{bmatrix} I & -CA \\ 0 & A \end{bmatrix}, \quad \bar{B} := \begin{bmatrix} -CB \\ B \end{bmatrix},$$

$$B_R := \begin{bmatrix} I \\ 0 \end{bmatrix}, \quad \bar{C} := \begin{bmatrix} 1 & 0 & 0 & 0 \end{bmatrix},$$

$$\bar{x}_k := \begin{bmatrix} e_k \\ \Delta x_k \end{bmatrix},$$

$$\Delta x_k := x_k - x_{k-1},$$

$$\Delta u_k := u_k - u_{k-1},$$

$$\Delta p_k^{ref} := p_k^{ref} - p_{k-1}^{ref}$$

Then, by using $\bar{x}_k$ and the reference up to N-step future, the preview control input Δu is given by

$$\Delta u_k = -F\bar{x}_k + \sum_{j=1}^{N} f_j \Delta p_{k+j}^{ref} \tag{5}$$

3 l preview control

In order to apply l_∞ control, we transform the system (4) into the following augmented error system with $\Delta p_{k+1}^{ref} \sim \Delta p_{k+N}^{ref}$ [3].

$$\tilde{x}_{k+1} = \tilde{A}\tilde{x}_k + \tilde{B}\Delta u_k \tag{6a}$$

$$\tilde{e}_k = \tilde{C}\tilde{x}_k \tag{6b}$$

where

$$\tilde{x}_k := \begin{bmatrix} \bar{x}_k \\ \Delta p_{k+1}^{ref} \\ \Delta p_{k+2}^{ref} \\ \vdots \\ \Delta p_{k+N}^{ref} \end{bmatrix}, \quad \tilde{A} := \begin{bmatrix} \bar{A} & B_R & 0 & \cdots & 0 \\ 0 & 0 & I & 0 & 0 \\ \vdots & \vdots & 0 & \ddots & 0 \\ \vdots & 0 & 0 & 0 & I \\ 0 & 0 & 0 & \cdots & 0 \end{bmatrix}$$

$$\tilde{B} := \begin{bmatrix} \bar{B} & 0 & \cdots & \cdots & 0 \end{bmatrix}^T,$$

$$\tilde{C} := \begin{bmatrix} \bar{C} & 0 & \cdots & 0 \end{bmatrix},$$

$$p_{k+N+\alpha}^{ref} := p_{k+N}^{ref}$$

The preview input Δu_k is also transformed as follows:

$$\Delta u_k = -\tilde{F}\tilde{x}_k \tag{7}$$

where $\tilde{F} := \begin{bmatrix} F & -f_1 & \cdots & -f_N \end{bmatrix}$. Here, we give an initial value defined by

$$\tilde{x}_0 := \begin{bmatrix} \bar{x}_0^T, \Delta p_1^{ref}, \Delta p_2^{ref}, \cdots, \Delta p_N^{ref} \end{bmatrix}^T$$

As performance index, we consider the l_∞ norm to evaluate the maximum of the error as follows:

$$\Gamma_\infty := \max_{k \geq 0} \left(\tilde{e}_k^T \tilde{e}_k \right)^{1/2} \tag{8}$$

Then we can obtain l_∞ preview controller minimizing the upper bound of the performance index (8) (See Reference [5]).

4 Robust l preview control

In order to avoid obstacles, it is necessary to change walking pattern of humanoid robots on the way. This means that the preview trajectory need be adjusted from the scheduled preview trajectory. The l_∞ preview control is dependent on the initial value and its influence is crucial. We consider l_∞ preview control with robustness against the initial value.

4.1 l preview control with robustness against initial value

Let us consider the set Ω defined by

$$\Omega(\tilde{x}_0) := \mathrm{Co}\{\tilde{x}_0^{[1]},\ \tilde{x}_0^{[2]},\ \cdots, \tilde{x}_0^{[M]}\} \tag{9}$$

where Co denotes the convex hull. If $\tilde{x}_0 \in \Omega$, then $\tilde{x}_0$ satisfies

$$\tilde{x}_0 = \sum_{i=1}^{M} \alpha_i \tilde{x}_0^{[i]} \tag{10}$$

where

$$\alpha_i \geq 0, \quad \sum_{i=1}^{M} \alpha_i = 1 \tag{11}$$

In order to evaluate the worst case of (8) for $\tilde{x}_0 \in \Omega$, we introduce new performance index defined by

$$\Gamma_\infty^{\max} := \max_{\tilde{x}_0 \in \Omega} \Gamma_\infty \tag{12}$$

Then we obtain the following lemma on the upper bound of $\Gamma_\infty^{\max}$.

Lemma 1 [5] *Assume that $\tilde{x}_0 \in \Omega$ in the system (6). The upper bound γ_∞ satisfying $\Gamma_\infty^{\max} \leq \gamma_\infty$ can be obtained by solving the following LMI optimization problem with respect to $Q > 0$, L and $\gamma_\infty > 0$. Then the optimal feedback gain of (7) is given by $\tilde{F} = LQ^{-1}$.*

$$\min_{Q,\, L} \gamma_\infty \tag{13}$$

©ISAROB 2009

subject to

$$\begin{matrix} -Q & (\tilde{A}Q - \tilde{B}L)^T \\ \tilde{A}Q - \tilde{B}L & -Q \end{matrix} < 0 \tag{14a}$$

$$\begin{bmatrix} -Q & \tilde{x}_0^{[i]} \\ (\tilde{x}_0^{[i]})^T & -\gamma_\infty \end{bmatrix} \le 0, \quad \text{for} \quad i = 1,\, 2,\, \cdots,\, M \tag{14b}$$

$$\begin{matrix} -Q & (\tilde{C}Q)^T \\ \tilde{C}Q & -\gamma_\infty I \end{matrix} \le 0 \tag{14c}$$

4.2 Reduction of conservativeness

Since the upper bound γ_∞ of $\mathit{\Gamma}_\infty^{\max}$ obtained by Lemma 1 becomes coservative [5], we consider reducing the conservativeness. Experientially, the l_∞ preview control has almost the maximal value $\mathit{\Gamma}_\infty$ in time $k = 1$. We obtain the next theorem by using this fact.

Theorem 1 *Assume that* $\tilde{x}_0 \in \Omega$ *in the system (6) and* $\|\tilde{e}_0\| \le \|\tilde{e}_1\|$*. Then the upper bound* γ_∞ *satisfying* $\mathit{\Gamma}_\infty^{\max} \le \gamma_\infty$ *can be obtained by solving the following BMI(Bilinear Matrix Inequality) optimization problem with respect to* $Q > 0,\ \tilde{F}$ *and* $\gamma_\infty > 0$.

$$\min_{Q,\,\tilde{F}} \ \gamma_\infty \tag{15}$$

subject to

$$\begin{matrix} -Q & (\tilde{A}Q - \tilde{B}\tilde{F}Q)^T \\ \tilde{A}Q - \tilde{B}\tilde{F}Q & -Q \end{matrix} < 0 \tag{16a}$$

$$\begin{bmatrix} -Q & (\tilde{A} - \tilde{B}\tilde{F})\tilde{x}_0^{[i]} \\ (\tilde{x}_0^{[i]})^T(\tilde{A} - \tilde{B}\tilde{F})^T & -\gamma_\infty \end{bmatrix} \le 0$$

$$\text{for} \quad i = 1,\, 2,\, \cdots,\, M \tag{16b}$$

$$\begin{matrix} -Q & (\tilde{C}Q)^T \\ \tilde{C}Q & -\gamma_\infty I \end{matrix} \le 0 \tag{16c}$$

Proof: From (11) and (16b), we obtain

$$\begin{matrix} -Q & \hat{x}_1 \\ (\hat{x}_1)^T & -\gamma_\infty \end{matrix}$$
$$= \begin{bmatrix} -Q\sum_{i=1}^M \alpha_i & \sum_{i=1}^M \alpha_i \hat{x}_1^{[i]} \\ (\sum_{i=1}^M \alpha_i \hat{x}_1^{[i]})^T & -\gamma_\infty \sum_{i=1}^M \alpha_i \end{bmatrix}$$
$$= \sum_{i=1}^M \left(\alpha_i \begin{bmatrix} -Q & (\tilde{A} - \tilde{B}\tilde{F})\hat{x}_0^{[i]} \\ (\hat{x}_0^{[i]})^T(\tilde{A} - \tilde{B}\tilde{F})^T & -\gamma_\infty \end{bmatrix} \right) \le 0$$

The above means $\hat{x}_1^T Q^{-1} \hat{x}_1 \le \gamma_\infty$. By using this fact, (16a) and (16b), we obtain the following inequality.

$$\gamma_\infty^{-1} \hat{x}_k^T \hat{C}^T \hat{C} \hat{x}_k \le \hat{x}_k^T Q^{-1} \hat{x}_k \le \hat{x}_1^T Q^{-1} \hat{x}_1 \le \gamma_\infty$$

By $\|\tilde{e}_0\| \le \|\tilde{e}_1\|$, this implies $\mathit{\Gamma}_\infty^{\max} \le \gamma_\infty$. ♠

If the maximal value $\mathit{\Gamma}_\infty$ is in time $k = 1$, the invariant ellipsoid is not conservative. Therefore, it is important to choose $\Omega(\tilde{x}_0)$ appropriately.

We apply the following LMI-based iterative algorithm to solve Theorem 1.

Iterative algorithm

Step1: Obtain an initial solution $\tilde{F}^{(0)}$ by Lemma 1.

Step2: Solve the follwoing two problems alternately when $k = 1,\ 2,\ \cdots$
  a) Minimize $\gamma_\infty^{(k)}$ subject to (16) for given $\tilde{F}^{(k)}$ where $\gamma_\infty^{(k)} := \min_Q \gamma_\infty$.
  b) Obtain $\tilde{F}^{(k+1)}$ minimizing $\hat{\gamma}_\infty^{(k+1)}$ subject to (16) for given $Q^{(k)}$ where $\hat{\gamma}_\infty^{(k+1)} := \gamma_\infty$.

Step3: Repeat Step2 until $|\gamma_\infty^{(k+1)} - \gamma_\infty^{(k)}| < \varepsilon$ for some $\varepsilon > 0$. ♠

By using the above algorithm, we obtain Theorem 2.

Theorem 2 *Given a certain initial solution of* $\tilde{F}^{(0)}$*, the above LMI-based iterative algorithm is always feasible, and the gain* $\tilde{F}^{(k+1)}$ *obtained in Step2-b satisfies*

$$\begin{aligned} \mathit{\Gamma}_\infty^{\max} &\le \cdots \le \gamma_\infty^{(k+1)} \le \hat{\gamma}_\infty^{(k+1)} \le \gamma_\infty^{(k)} \\ &\le \cdots \le \hat{\gamma}_\infty^{(1)} \le \gamma_\infty^{(0)} \end{aligned} \tag{17}$$

5 Simulation on biped walking pattern generation

We made simulation of shifting the reference ZMP into 0.2[m] with the control approach of Section 2. We give $z_c = 0.85$[m], $g = 9.81$[m/s^2] and $h = 0.04$[s] in this simulation. We also give $N = 50$ as the number of preview steps.

We state the case that the reference ZMP is changed in 2.8[s] from the scheduled preview trajectory. We show the simulation results of the trajectories of the reference and measured ZMPs and those of the reference ZMP and the center of gravity in Figure 1 and 2, respectively. We also show the magnified figure of Figure 1 in Figure 3. When we calculated the upper bound of the worst case of l_∞ norm by the approach of Lemma 1 and Theorem 2, we obtained $\gamma_\infty = 0.104$[m] and $\gamma_\infty = 0.0499$[m] for the following $\Omega(\tilde{x}_0)$, respectively.

$$\Omega(\tilde{x}_0) := \mathrm{Co}\{\tilde{x}_0^{[1]},\ \tilde{x}_0^{[2]},\ \tilde{x}_0^{[3]}, \tilde{x}_0^{[4]}\}$$

where $\tilde{x}_0^{[1]} := [e + \delta_1, \Delta x^{[1]} + \delta_2, \Delta x^{[2]}, \Delta x^{[3]}, \Delta p_1^{ref}, \cdots, \Delta p_N^{ref}]$, $\tilde{x}_0^{[2]} := [e + \delta_1, \Delta x^{[1]} - \delta_2/2, \Delta x^{[2]},$

©ISAROB 2009

$\Delta x^{[3]}, \Delta p_1^{ref}, \cdots, \Delta p_N^{ref}]$, $\tilde{x}_0^{[3]} := [e - \delta_1/2, \Delta x^{[1]} + \delta_2, \Delta x^{[2]}, \Delta x^{[3]}, \Delta p_1^{ref}, \cdots, \Delta p_N^{ref}]$, $\tilde{x}_0^{[4]} := [e - \delta_1, \Delta x^{[1]} - \delta_2, \Delta x^{[2]}, \Delta x^{[3]}, \Delta p_1^{ref}, \cdots, \Delta p_N^{ref}]$ and $e := 3.97 \times 10^{-3}$, $x^{[1]} := 7.28 \times 10^{-3}$, $\Delta x^{[2]} := 1.82 \times 10^{-2}$, $\Delta x^{[3]} := 8.78 \times 10^{-2}$, $\delta_1 := 5.00 \times 10^{-3}$, $\delta_2 := 5.00 \times 10^{-4}$, $\Delta p_6^{ref} = 0.1$, $\Delta p_i^{ref} = 0$ $(i = 1, \cdots, 50, i \neq 6)$. In Figures 1, 2 and 3, the solid line denotes the controller by Theorem 2, the dashed line does the controller by Lemma 1 and the dotted line does the reference ZMP with change in 2.8[s]. In Figure 3, the maximum of the error between the reference and measured ZMPs in using the the controller by Theorem 2 is smaller than that in using the controller by Lemma 1. Therefore, we see that the conservativeness is reduced.

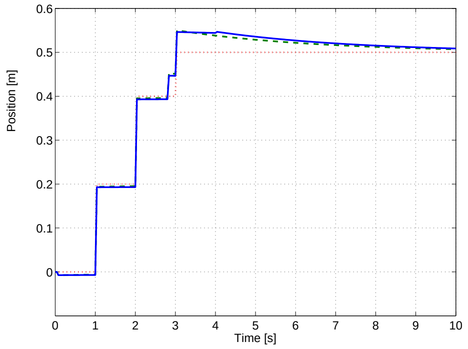

Figure 1: Trajectory of reference and measured ZMPs

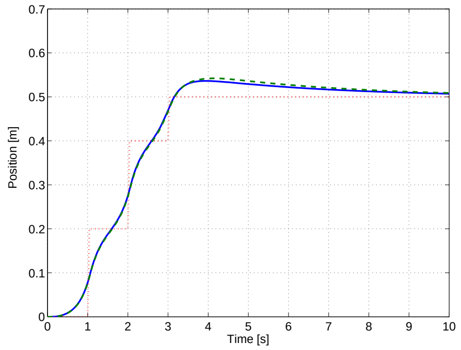

Figure 2: Trajectory of center of gravity

6 Conclusion

In this paper, we proposed the robust l_∞ preview control for biped walking pattern generation. First, we showed l_∞ preview control with robustness against initial value. Next, we proposed a method to reduce the conservativeness of Lemma 1 and an algorithm to solve it. Finally, we showed the effectiveness of our proposed method by simulation.

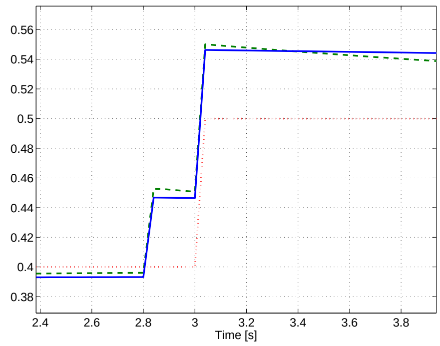

Figure 3: Trajectory of reference and measured ZMPs (Magnified figure of Fig. 1)

Acknowledgements

This research was partially supported by Grant-in-Aid for Young Scientists (B) (19760287).

References

[1] S. Boyd, L. El Ghaoui, E. Feron and V. Balakrishnan: Linear Matrix Inequalities in System and Control Theory; *SIAM*, 1994.

[2] Kajita et al.: Biped Walking Pattern Generation by using Preview Control of Zero-Moment Point; *Proc. of 2003 IEEE Int. Conf. on Robotics and Automation*, pp. 1620–1626, 2003.

[3] T. Katayama, T. Ohki, T. Inoue and T. Kato: Design of a Optimal Controller for a Discrete Time System Subject to Previewable Demand; *Int. Journal of Control*, Vol. 41, No. 3, pp. 677–699, 1985.

[4] S. Kunimatsu and T. Fujii: Analysis and Synthesis of Model Reference ILQ Servo System using Robust l_∞ Performance Measure for a Fixed Input, *Trans. of SICE*, Vol. 41, No. 1, pp. 46–52, 2005.

[5] S. Kunimatsu, T. Fukuda, K. Nakasaki and M. Ishitobi: l_∞ Preview Control for Biped Walking Pattern Generation; *Proc. of SICE Annual Conference 2008*, pp. 1916-1919, 2008.

[6] H. Tokunaga, T. Iwasaki and S. Hara: Analysis and Synthesis of the Robust Impulse-to-Peak Performance; *Automatica*, Vol. 34 No. 11, pp. 1473–1477, 1998.

©ISAROB 2009

Robust Control Method for the Inverted Pendulum System with Structured Uncertainty Caused by Measurement Error

N. Takahashi, T. Morikubo, O. Sato and M. Kono

Department of Computer Science and Systems Engineering,
Faculty of Engineering, University of Miyazaki,
1-1 Gakuenkibanadai Nishi, Miyazaki, 889-2192, Japan
E-mail : ntaka@cs.miyazaki-u.ac.jp

Abstract

In this paper, we propose a design method of the inverted pendulum system with structured uncertainty. We consider such uncertainty is caused by a measurement error in the rotation angle of the pendulum and causes to the system structure that can not be included in the nominal parameter. For the obtained uncertain system, we apply the integral tracking control and guaranteed cost control to design a robust stable tracking control system. At the last, we show the effectiveness of our method through numerical example.

1 Introduction

In the robust control problem, it is important how to evaluate effect of uncertainty. Such uncertainty effects a bad influence to the system performance. In general, such uncertainty is not contained in the nominal system, then, for the design of the robust stable control system, it is need to express the structural property of the instrument. Kimura showed the derivation method of the structured uncertainty that is caused from the higher order terms in the Taylor expansion[1]. In this paper, we consider the effect of uncertainty to the performance of system that is caused by measurement error. The effect of uncertainty is formulated as the structured uncertainty corresponds to the system matrices. For this system, to show the effectiveness of our proposed method, we apply the integral tracking control system and guaranteed cost control design method.

In section 2, we will propose the formulate method of the robust inverted pendulum-car system model which included uncertain element. In section 3, we will apply the integral tracking control system to the obtained system, and guaranteed cost control method. In section 4, we will present a numerical solution and a simulation result.

2 Derivation of the Uncertain Inverted Pendulum Model

In this section, we will derivate the linear system of the inverted pendulum-car model with structured uncertainties. Now we consider the inverted pendulum-car model that takes following parameters,

M : a Mass of the Car [kg]
m : a Mass of the Pendulum [kg]
I : the Inertia Moment of the Pendulum [$\mathrm{kg \cdot m^2}$]
L : the Distance from the Rotation Axis to the Center of Gravity of Pendulum [m]
g : Gravity [$\mathrm{m/sec^2}$]
$\theta(t)$: an Angle of the Pendulum [rad]
$u(t)$: an External Force on the Car [N] (Input)
$z(t)$: a Position of the Car [m] (Output)

The system state variables are obtained by the measured value of sensors in the instrument or observation equipments, e.g. potentiometer, image data of video camera. Unfortunately, these measurement values contain measurement deviation caused by a lower resolution limit of the sensor, noise of sensor and so on. Then it needs to include the effects of such disturbance in the system dynamics. To deal with this problem, we will introduce following uncertainty in the angle of pendulum.

$$\theta(t) = \theta_0(t) + \varDelta\theta \tag{1}$$

where, $\theta(t)$ is a measured angle of the pendulum consist with $\theta_0(t)$ and $\varDelta\theta$. $\theta_0(t)$ is a nominal element and

©ISAROB 2009

$\Delta\theta$ is a disturbance element which caused by measurement error. From the fundamental formulae of the trigonometric functions, we have

$$\begin{aligned}\sin(\theta(t)) &= \sin(\theta_0(t)+\Delta\theta)\\ &= \sin(\theta_0(t))\cos(\Delta\theta)+\cos(\theta_0(t))\sin(\Delta\theta),\\ \cos(\theta(t)) &= \cos(\theta_0(t)+\Delta\theta)\\ &= \cos(\theta_0(t))\cos(\Delta\theta)-\sin(\theta_0(t))\sin(\Delta\theta)\end{aligned}$$

Here we assume that $\Delta\theta$ takes very small value, then $\sin(\Delta\theta)\to 0$. We estimate a maximum variation value of $\cos(\Delta\theta)$ as constant value Δc. From the linearization by using Taylor expansion, we have $\sin(\theta_0(t))\approx\theta_0(t), \cos(\theta_0(t))\approx 1$. Thus,

$$\sin(\theta(t))\approx\Delta c\cdot\theta_0(t), \quad (2)$$

$$\cos(\theta(t))\approx\Delta c, \quad (3)$$

$$\frac{d^2}{dt^2}(\sin(\theta(t)))\approx\Delta c\cdot\ddot{\theta}_0(t), \quad (4)$$

$$\frac{d^2}{dt^2}(\cos(\theta(t)))\approx 0. \quad (5)$$

A dynamics of the inverted pendulum-car system is expressed as

$$\begin{aligned}I\ddot{\theta}_0(t) &= VL\sin(\theta_0(t))-HL\cos(\theta_0(t)),\\ H &= m\ddot{z}(t)+ML\cdot\frac{d^2}{dt^2}(\sin(\theta_0(t))),\\ V &= mL\cdot\frac{d^2}{dt^2}(\cos(\theta_0(t)))+mg,\\ H &= u-M\ddot{z}(t).\end{aligned}$$

In virtue of (2)-(5), we have

$$\begin{aligned}\ddot{z}(t) &= -\frac{\Delta c^2\cdot m^2gL^2}{I(m+M)+\Delta c^2\cdot mML}\theta_0(t)\\ &\quad+\frac{\Delta c^2\cdot mL^2+I}{I(m+M)+\Delta c^2\cdot mML}u(t), \quad (6)\end{aligned}$$

$$\begin{aligned}\ddot{\theta}_0(t) &= \frac{\Delta c\cdot mgL(M+m)}{I(m+M)+\Delta c^2\cdot mL^2}\theta_0(t)\\ &\quad-\frac{\Delta c\cdot mL}{I(m+M)+\Delta c^2\cdot mL^2}u(t). \quad (7)\end{aligned}$$

Here we define the state vector of a linear system is

$$\boldsymbol{x}(t)=[\ \theta_0(t)\ \ \dot{\theta}_0(t)\ \ z(t)\ \ \dot{z}(t)\ ]^{\mathrm{T}}$$

and the system matrices are

$$A(\xi)=\begin{bmatrix}0 & 1 & 0 & 0\\ \frac{\Delta c\cdot mgL(M+m)}{I(m+M)+\Delta c^2\cdot mL^2} & 0 & 0 & 0\\ 0 & 0 & 0 & 1\\ -\frac{\Delta c^2\cdot m^2gL^2}{I(m+M)+\Delta c^2\cdot mL^2} & 0 & 0 & 0\end{bmatrix},$$

$$B(\zeta)=\begin{bmatrix}0\\ -\frac{\Delta c\cdot mL}{I(m+M)+\Delta c^2\cdot mL^2}\\ 0\\ \frac{\Delta c^2\cdot mL^2+I}{I(m+M)+\Delta c^2\cdot mL^2}\end{bmatrix}.$$

Here we clarified a structure of the effect of the uncertainty about axis of the pendulum. Note that if $\Delta\theta=0$, that is $\Delta c=1$, $A(\xi)$ and $B(\zeta)$ equivalent to nominal system A_0 and B_0. Let A_D and B_D are disturbanced system with the maximum value of the variety of uncertainty $\Delta\theta_0$,

$$\begin{aligned}A_1 &= A_0-A_D,\\ B_1 &= B_0-B_D.\end{aligned}$$

Consequently, we obtain LTI system with structured uncertainties.

$$\dot{\boldsymbol{x}}(t)=A(\xi)\boldsymbol{x}(t)+B(\zeta)\boldsymbol{u}(t) \quad (8)$$

where, $A(\xi)$ and $B(\zeta)$ are real matrices of appropriate size.

$$A(\xi) = A_0+\Delta A, \quad (9)$$

$$B(\zeta) = B_0+\Delta B. \quad (10)$$

A_0 and B_0 are the nominal elements, ΔA and ΔB are the uncertain elements of the system.

$$\Delta A = \sum_{i=1}^{p}\xi_iA_i,\ |\xi_i|\le 1,\ p=1, \quad (11)$$

$$\Delta B = \sum_{j=1}^{q}\zeta_jB_j,\ |\zeta_j|\le 1,\ q=1. \quad (12)$$

ξ_i and ζ_j are scalar values which denote the size of uncertainties. A_i and B_j are matrices of structure of the uncertainties.

Here we define output $y(t)=z(t)$, then the output matrix C is obtained as

$$y(t)=C\boldsymbol{x}(t)=[\ 0\ \ 0\ \ 1\ \ 0\ ]\,\boldsymbol{x}(t) \quad (13)$$

All system matrices are of appropriate dimension.

3 Stabilization of the Inverted Pendulum System

In this section, for the structured uncertain inverted pendulum system, we synthesize the integral tracking control system. Next, we design the robust control system by using guaranteed cost control methd[2].

©ISAROB 2009

3.1 The Integral Tracking Control System

In this paper, we assume that the controller can use the system state vector $\boldsymbol{x}(t)$. Input signal to the system is $v(t) = v$. Error $e(t)$ of output signal of nominal system $y(t)$ and
input signal $v(t)$ is given as

$$e(t) = v - y(t) = v - C\boldsymbol{x}(t).$$

The derivative of the deflection $e(t)$ is

$$\dot{e}(t) = -C\dot{\boldsymbol{x}}(t) \tag{14}$$

Here we differentiate the system (8), we have

$$\ddot{\boldsymbol{x}}(t) = A(\xi)\dot{\boldsymbol{x}}(t) + B(\zeta)\dot{\boldsymbol{u}}(t) \tag{15}$$

From (14) and (15), we obtain the augmented system

$$\dot{\boldsymbol{x}}_e(t) = A_e(\xi)\boldsymbol{x}_e(t) + B_e(\zeta)u_e(t) \tag{16}$$

where input vector is $u_e(t) = \dot{u}(t)$, state vector is

$$\boldsymbol{x}_e(t) = [\ \dot{\boldsymbol{x}}(t)^{\mathrm{T}} \quad e(t)\ ]^{\mathrm{T}}$$

System matrices are defined as follows

$$\begin{aligned} A_e(\xi) &= \begin{bmatrix} A(\xi) & \mathrm{O}_{4\times1} \\ -C & 0 \end{bmatrix}, \\ B_e(\zeta) &= \begin{bmatrix} B(\zeta) \\ 0 \end{bmatrix}, \end{aligned}$$

Augmented nominal and uncertain system matrices $A_{e0},\ B_{e0}, A_{ei}$ and B_{ej} are defined as same form in (11) and (12) corresponding to based system matrices A_0, B_0, A_i and B_j.

3.2 Stabilization by using Guaranteed Cost Control

Here, we apply the guaranteed cost control design method to the augmented integral tracking control system (16). Let us consider the following performance index.

$$J = \int_0^\infty \{\boldsymbol{x}_e^{\mathrm{T}}(t)Q\boldsymbol{x}_e(t) + u_e^{\mathrm{T}}(t)Ru_e(t)\}dt \tag{17}$$

The stochastic algebraic Riccati equation based on the eigenvalue upperbound is

$$\begin{aligned} &C^{\mathrm{T}}C + PA_{e0} + A_{e0}^{\mathrm{T}}P - PB_{e0}R^{-1}B_{e0}^{\mathrm{T}}P \\ &\quad + U_E(\varDelta A_e(\xi), \varDelta B_e(\zeta), P, R) = \mathrm{O}_{5\times5} \end{aligned} \tag{18}$$

where, $\varDelta A_e(\xi)$ and $\varDelta B_e(\zeta)$ are uncertainties defined in (11) and (12). Upper bound matrix $U_E(\cdot)$ is

$$\begin{aligned} &U_E(\varDelta A_e(\xi), \varDelta B_e(\zeta), P, R) \\ &\quad = \sum_{i=1}^{p} L_i|\Lambda_i|L_i^{\mathrm{T}} + \sum_{j=1}^{q} M_i|\Gamma_i|M_i^{\mathrm{T}} \end{aligned} \tag{19}$$

where, $|\cdot|$ denotes matrix that have absolute value of each elements. L_i, M_i, Λ_i and Γ_i are

$$L_i^{\mathrm{T}}(PA_{ei} + A_{ei}^{\mathrm{T}}P)L_i = \Lambda_i \tag{20}$$

$$M_i^{\mathrm{T}}P(B_{ei}R^{-1}B_{e0}^{\mathrm{T}} + B_{e0}R^{-1}B_{ei}^{\mathrm{T}})PM_i = \Gamma_i \tag{21}$$

where, Λ_i and Γ_i are diagonal matrices which have eigenvalues on the diagonal elements. L_i and M_i are orthogonal matrices which constructed from the corresponding orthogonal vectors. From the solution P of (18), we obtain the feedback gain matrix F_e

$$F_e = -R^{-1}B_{e0}^{\mathrm{T}}P \tag{22}$$

we divide the matrix F_e into F_{e1} and F_{e2} correspond to the structure of state vector $\boldsymbol{x}(t)$.

$$\begin{aligned} u_e(t) &= -F_e\boldsymbol{x}_e(t) \\ &= -[\ F_{e1} \quad F_{e2}\ ]\begin{bmatrix} \dot{\boldsymbol{x}}(t) \\ e(t) \end{bmatrix} \\ &= -F_{e1}\dot{\boldsymbol{x}}(t) - F_{e2}e(t) \end{aligned} \tag{23}$$

To obtain input vector $u(t)$, we integrate (23).

$$\begin{aligned} \int u_e(t)dt &= -\int F_{e1}\dot{\boldsymbol{x}}(t)dt - F_{e2}\int e(t)dt \\ u(t) &= -F_{e1}\boldsymbol{x}(t) - F_{e2}\int e(t)dt \end{aligned} \tag{24}$$

The block diagram of this system is illustrated in fig.1.

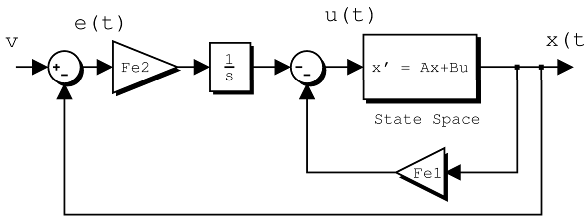

Fig.1 : Block diagram of the Integral Tracking System

4 Numerical Example

We used MATLAB software to solve the problem and simulate the system by using SIMULINK.

The stochastic algebraic Riccati equation is solved by Runge-Kutta method, standard linear quadratic regulator problem is solved by function `lqr` of control system toolbox in MATLAB.

System parameters are $m = 1, M = 1, L = 1, I = 1/3, g = 9.8$ and $\Delta\theta = 0.07$. The weighting matrices of performance index are $Q = [\ 1,\ 1,\ 0.01,\ 0.01,\ 1\ ], R = 1$. The solution of the stochastic algebraic Riccati equation (Proposed method) is

$$P = \begin{bmatrix} 801.8824 & 280.2749 & 93.5159 & 119.8140 & -28.1920 \\ 280.2749 & 99.3540 & 35.0210 & 44.7910 & -10.4630 \\ 93.5159 & 35.0210 & 21.2097 & 20.9584 & -7.7061 \\ 119.8140 & 44.7910 & 20.9584 & 25.4665 & -6.3596 \\ -28.1920 & -10.4630 & -7.7061 & -6.3596 & 5.0472 \end{bmatrix}$$

Feedback gain is

$$F_{e1} = \begin{bmatrix} -72.3137 & -23.7796 & -4.2459 & -6.5014 \end{bmatrix},$$

$$F_{e2} = \begin{bmatrix} 1.1901 \end{bmatrix}$$

Eigenvalues of the closed-loop system are

$$(\ -0.7374,\ -3.7640,\ -3.3146,\ -0.6253 \pm 0.6080i\ )$$

The solution of the algebraic Riccati equation (Ordinary method) is

$$P^* = \begin{bmatrix} 621.7728 & 213.4494 & 57.1646 & 80.2692 & -20.6857 \\ 213.4494 & 74.4296 & 21.2874 & 29.9650 & -7.6877 \\ 57.1646 & 21.2874 & 10.8762 & 12.0466 & -4.9095 \\ 80.2692 & 29.9650 & 12.0466 & 16.3369 & -4.5157 \\ -20.6857 & -7.6877 & -4.9095 & -4.5157 & 3.1351 \end{bmatrix},$$

Feedback gain is

$$F^*_{e1} = \begin{bmatrix} -63.8542 & -20.6857 & -3.1351 & -4.9095 \end{bmatrix},$$

$$F^*_{e2} = \begin{bmatrix} 1.0000 \end{bmatrix}$$

Eigenvalues of the closed-loop system are

$$(\ -3.7314,\ -3.1562,\ -0.7844,\ -0.4059 \pm 0.6868i\ )$$

Table 1: Comparison of the results

	Ordinary	Proposed
Overshoot [%]	7	0.5
Delay Time [sec]	5.28	5.42

For these two cases, we simulate the disturbed system. In time interval $[0, 3)$, the reference is $v = 0$, In $[3, 20)$, $v = 0.1$ and $[20, -40)$, $v = 0$. Overshoot and delay time of the position of the car are in Table 1. The simulation result shows that our proposed method barely increase the delay time (1.02% increased), but widely reduce the overshoot (93.9% decreased).

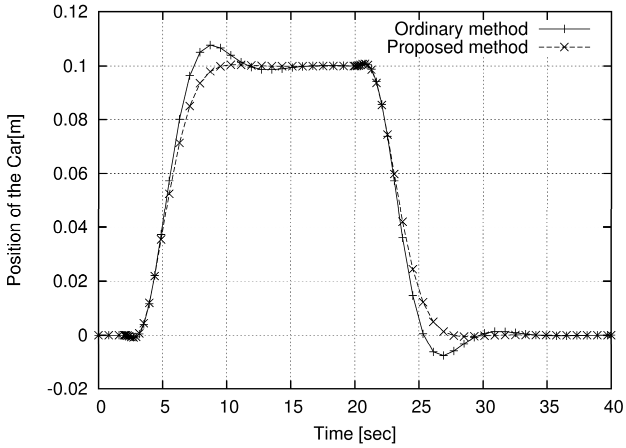

Fig.2 : Simulation results

5 Conclusion

In this paper, we considered the effect of the uncertainty in rotation angle and proposed the design method for the robust inverted pendulum-car system model with structured uncertainty. We extended this system to the integral tracking control system and applied guaranteed cost control design method to obtain the robust stable tracking control system. Through the numerical example, we showed the effectiveness of our proposed method. Future study is to apply our method for more complex model, e.g. double inverted pendulum system.

References

[1] S. Yamamoto, Q. Shen and H. Kimura, "Quadratic stabilization for a class of uncertain linear systems and its application to a magnetic levitation system", *Trans. of the Society of Instrument and Control Engineers*, Vol.29, pp.334-339, 1993.

[2] N. Takahashi, M. Kono, K. Hiranuma and O. Sato, "Generalization of guaranteed cost control", *Trans. of the Japan Society of Mechanical Engineers (Series C)*, Vol.66, No.645, pp.1531-1536, 2000.

[3] H. Kimura, T. Fujii and T. Mori, Robust Control, Corona, 1994.

[4] T. Kimura, M. Kono, N. Takahashi and M. Ishitobi, "Guaranteed cost control of tracking problem in a helicopter", *The 48th annual conference of Joint Automatic Control Conference*, pp. 241-244, 2005.

©ISAROB 2009

Gene Subset Selection Using an Iterative Approach Based on Genetic Algorithms

M.S. Mohamad[1,2] S. Omatu[1] S. Deris[2] and M. Yoshioka[1]

[1]*Department of Computer Science and Intelligent Systems, Graduate School of Engineering, Osaka Prefecture University, Sakai, Osaka 599-8531, Japan*
(Tel : 81-72-254-9278; Fax : 81-72-257-1788)
(mohd.saberi@sig.cs.osakafu-u.ac.jp; omatu@cs.osakafu-u.ac.jp; yoshioka@cs.osakafu-u.ac.jp)

[2]*Department of Software Engineering, Faculty of Computer Science and Information Systems, Universiti Teknologi Malaysia, 81310 Skudai, Johore, Malaysia*
(Tel : 60-7-553-7784; Fax : 60-7-556-5044)
(safaai@utm.my)

Abstract: Microarray data are expected to be useful for cancer classification. The main problem that needs to be addressed is the selection of a smaller subset of genes from the thousands of genes in the data that contributes to a disease. This selection process is difficult due to many irrelevant genes, noisy genes, and the availability of a small number of samples compared to a huge number of genes (higher-dimensional data). Hence, this paper aims to select a near-optimal (smaller) subset of informative genes that is most relevant for the cancer classification. To achieve the aim, an iterative approach based on genetic algorithms has been proposed. Experimental results show that the performance of the proposed approach is superior to other related previous works as well as four methods experimented in this work. In addition a list of informative genes in the best gene subsets is also presented for biological usage.

Keywords: Gene selection, Genetic algorithm, Iterative approach, Microarray data**.**

I. INTRODUCTION

Advances in the area of microarray-based gene expression analyses have led to a promising future of cancer diagnosis using new molecular-based approaches. This microarray technology is used to measure the expression levels of thousands of genes simultaneously, and finally produce microarray data. A comparison between the gene expression levels of cancerous and normal tissues can also be done. This comparison is useful to select those genes that might anticipate the clinical behaviour of cancers. Thus, there is a need to select informative genes that contribute to a cancerous state. However, the gene selection process poses a major challenge because of the characteristics of microarray data: the huge number of genes compared to the small number of samples (higher-dimensional data), irrelevant genes, and noisy data.

To overcome the challenge, a gene selection method is used to select a subset of genes that increases the classifier's ability to classify samples more accurately. The gene selection method has several advantages such as improving classification accuracy, reducing the dimensionality of data, and removing irrelevant and noisy genes.

There are two types of gene selection methods: [1,2] if a gene selection method is carried out independently from a classifier, it belongs to the filter approach; otherwise, it is said to follow a hybrid (wrapper) approach. In the early era of microarray analysis, most previous works have used the filter approach to select genes because it is computationally more efficient than the hybrid approach. However, the hybrid approach usually provides greater accuracy than the filter approach since the genes are selected by considering and optimising relations among genes.[3] Until now, several hybrid methods, especially a combination between a genetic algorithm (GA) and a support vector machine (SVM) classifier (GASVM), have been implemented to select informative genes.[1,2,4,5] The drawbacks of the hybrid methods (GASVM-based methods) in the previous works are:[1,2,4,5] 1) intractable to efficiently produce a near-optimal subset of informative genes when the total number of genes is too large (higher-dimensional data) due to the drawback of binary chromosome representation; 2) the high risk of over-fitting problems. The over-fitting problem that occurred on hybrid methods (e.g., GASVM-based methods) is also reported in a review paper in Saeys *et al.* [3]

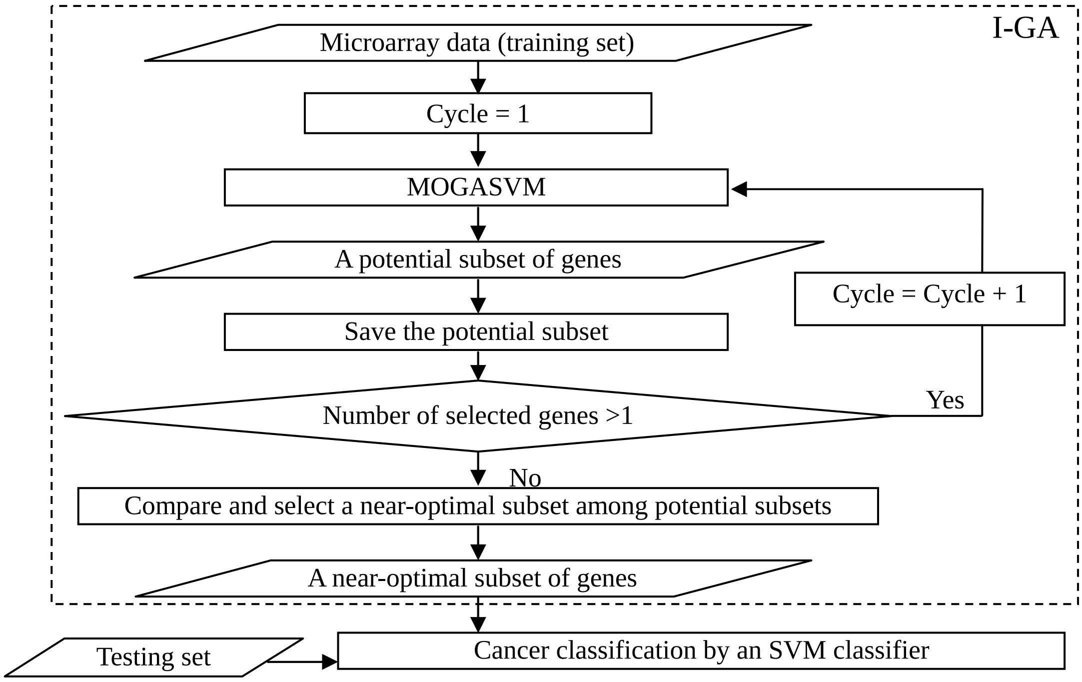

Fig.1. The general procedure of I-GA

In order to overcome the limitations of the previous works and solve the problems derived from microarray data, we propose an iterative approach based on multi-objective GASVM (MOGASVM). The ultimate goal of this paper is to automatically select a near-optimal (smaller) subset of informative genes that is most relevant for the cancer classification. To achieve the goal, we adopt the proposed method. It is evaluated on two real microarray data sets.

II. THE PROPOSED ITERATIVE APPROACH BASED ON MOGASVM (I-GA)

In this paper, we propose I-GA to overcome the problems derived from the previous works and microarray data.[1,2,4,5] I-GA is a hybrid approach based on MOGASVM. Details of MOGASVM can be found in Mohamad *et al*.[4] I-GA in our work differs from the methods in the previous works in one major part.[1,2,4,5] The major difference is that our proposed method involves an iterative approach, whereas the previous works did not use any iterative process for gene selection. The general procedure of I-GA is shown in Fig. 1.

Basically, I-GA repeats the process of MOGASVM to reduce the dimensionality of data iteratively. The description of each step is explained as follows:

Step 1: Starting an iterative process. It is repeated until the number of selected genes in the potential subset of the current cycle c is equal or less than 1. Every cycle is started here. In each cycle of I-GA, a number of selected genes are automatically selected by MOGASVM and the dimensionality is iteratively reduced.

Step 2: Starting MOGASVM to find and produce a potential subset of genes.

Step 3: Producing and saving the potential subset of selected genes. This potential subset is used for the next cycle (cycle c+1) as an input set. The selection of genes in the next cycle (cycle c+1) only uses genes in the potential subset that is resulted by the previous cycle (cycle c). Therefore, the dimensionality and complexity of solution spaces can be decreased on a cycle by cycle basis.

Step 4: A near-optimal subset is selected among the potential subsets based on the highest fitness value (the highest LOOCV accuracy with the smallest number of selected genes).

Step 5: An iterative process (Steps 1-4) results a near-optimal subset of genes. This subset is possible to be found due to the dimensionality of data has been iteratively reduced. The near-optimal subset is then used to construct an SVM classifier, and the constructed SVM is tested by using the test set.

III. EXPERIMENTS

3.1. Data Sets

Two real microarray data sets are used to evaluate I-GA: Leukaemia cancer and lung cancer. The leukaemia data set contains the expression levels of 7,129 genes and can be obtained at http://www.broad.mit.edu/cgi-bin/cancer/datasets.cgi. it has two cancer classes: acute lymphoblastic leukaemia, acute myeloid leukaemia. In this data set, bone marrow and blood samples were taken from 72 patients (the training set contains 38 samples; the test set consists 34 samples). There are 181 samples in the lung cancer data set (the training set contains 32; the test set consists 149 samples). It has two tumour classes (malignant pleural mesothelioma and adenocarcinoma) and can be obtained at http://chestsurg.org/publications/2002-microarray.aspx.

3.2. Experimental Setup

Three criteria following their importance are considered to evaluate the performances of I-GA and other experimental methods: test accuracy, leave-one-out-cross-validation (LOOCV) accuracy, and the number of selected genes. Several experiments are conducted 10 times on each data set using I-GA and other experimental methods such as GASVM MOGASVM, GASVM version 2 (GASVM-II), and SVM. Next, an average result of the 10 independent runs is obtained. A near-optimal subset that produces the highest classification accuracies with the possible least number of genes is selected as the best subset.

3.3. Experimental Results

Table 1 shows the classification accuracy for each run using I-GA on both data sets. Interestingly, all runs have achieved 100% LOOCV accuracy on the data sets. This has proven that I-GA has efficiently selected and produced a near-optimal solution in a solution space. This is due to the fact of its ability to automatically reduce the dimensionality and complexity of the solution space on a cycle by cycle basis. Therefore, I-GA yields the near-optimal gene subset (a smaller subset of informative genes with higher classification accuracy) successfully.

Table 1. Classification accuracies for each run using I-GA

Run#	Leukaemia Data Set			Lung Data Set		
	LOOCV (%)	Test (%)	#Selected Genes	LOOCV (%)	Test (%)	#Selected Genes
1	100	85.35	5	100	90.60	2
2	100	91.18	5	100	95.30	2
3	100	91.18	3	100	93.29	3
4	100	85.29	5	100	95.30	4
5	100	85.29	5	100	85.24	2
6	100	82.35	5	100	83.22	3
7	100	82.35	4	100	92.62	2
8	100	100	5	100	97.32	2
9	100	88.24	5	100	96.64	2
10	100	85.29	4	100	95.30	3
Average ± S.D	100 ± 0	87.65 ± 5.33	4.60 ± 0.70	100 ± 0	92.48 ± 4.80	2.5 ± 0.71

Note: Results of the best subsets shown in shaded cells. S.D. denotes the standard deviation, whereas #Selected Genes represent a number of selected genes.

Table 2. The list of informative genes in the best gene subsets

Data Set	Run#	Probe-set Name	Gene Description
Leukaemia	8	L15388_at	G PROTEIN-COUPLED RECEPTOR KINASE GRK5
		M95678_at	PLCB2 Phospholipase C, beta 2
		X15357_at	GB DEF = Natriuretic peptide receptor (ANP-A receptor)
		X55668_at	PRTN3 Proteinase 3
		S76473_s_at	TrkB [human, brain, mRNA, 3194 nt]
Lung	8	33328_at	ESTs
		609_f_at	Highly similar to SMHU1B metallothionein 1B [H.sapiens]

Note: Run# denotes a run number.

©ISAROB 2009

Table 3. The benchmark of the proposed I-GA with the other experimental methods and related previous works

Method	**Leukaemia Data Set (Average ± S.D; The Best)**			**Lung Data Set (Average ± S.D; The Best)**		
	#Selected Genes	**Accuracy (%)**		**#Selected Genes**	**Accuracy (%)**	
		LOOCV	**Test**		**LOOCV**	**Test**
I-GA	(4.60 ± 0.70; 5)	(100 ± 0; 100)	(87.65 ± 5.33; 100)	(2.5 ± 0.71; 2)	(100 ± 0; 100)	(92.48 ± 4.80; 97.32)
GASVM-II [2]	(10 ± 0; 10)	(100 ± 0; 100)	(81.18 ± 10.21; 94.12)	(10 ± 0; 10)	(100 ± 0; 100)	(59.33 ± 29.32; 97.32)
MOGASVM [4]	(2,212.6 ± 26.63; 2,189)	(95.53 ± 1.27; 97.37)	(84.41 ± 2.42; 88.24)	(4,418.5 ± 50.19; 4,433)	(75.31 ± 0.99; 78.13)	(85.84 ± 3.97; 93.29)
GASVM [2]	(3,574.9 ± 40.05; 3,531)	(94.74 ± 0; 94.74)	(83.53 ± 2.48; 88.24)	(6,267.8 ± 56.34; 6,342)	(75 ± 0; 75)	(84.77 ± 2.53; 87.92)
SVM [2]	(7,129 ± 0; 7,129)	(94.74 ± 0; 94.74)	(85.29 ± 0; 85.29)	(12,533 ± 0; 12,533)	(65.63 ± 0; 65.63)	(85.91 ± 0; 85.91)
Li *et al.*[1]	(4 ± NA; NA)	(100 ± NA; NA)	NA	NA	NA	NA
Peng *et al.*[5]	(6 ± NA; NA)	(100 ± NA; NA)	NA	NA	NA	NA

Note: The best result shown in shaded cells. S.D. denotes the standard deviation, whereas #Selected Genes represent a number of selected genes. 'NA' means that a result is not reported in the related previous works. Methods in *italic* style are experimented in this work.

Informative genes in the best gene subsets as produced by the proposed I-GA and reported in Table 1 are listed in Table 2. These informative genes among the thousand of genes may be the excellent candidates for clinical and medical investigations. Biologists can save much time since they can directly refer to the genes that have higher possibility to be useful for cancer diagnosis and drug target in the future.

According to Table 3, I-GA has outperformed the other experimental methods and previous works in terms of LOOCV accuracy, test accuracy, and the number of selected genes. The gap between LOOCV accuracy and test accuracy that resulted by I-GA was also lower. This small gap shows that the risk of the over-fitting problem can be reduced. Therefore, I-GA is more efficient than other experimental methods since it has produced the higher classification accuracies, smaller number of selected genes, smaller standard deviations, and smaller gap between LOOCV accuracy and test accuracy. However, due to the iterative process, I-GA is computationally more extensive than other methods.

IV. CONCLUSION

In this paper, I-GA has been proposed and tested for gene selection on two real microarray data. Based on the experimental results, the performance of I-GA was superior to the other experimental methods and related previous works. This is due to the fact that I-GA can automatically reduce the dimensionality of the data on a cycle by cycle basis. When the dimensionality was reduced, the combination of genes and the complexity of solution spaces can also be automatically decreased iteratively. This iterative process is done to generate potential gene subsets in higher-dimensional data (microarray data), and finally produce a near-optimal subset of informative genes. Hence, the gene selection using I-GA is needed to produce a near-optimal (smaller) subset of informative genes for better cancer classification. Moreover, focusing the attention on the informative genes in the best subset may provide insights into the mechanisms responsible for the cancer itself. Even though I-GA has classified tumours with higher accuracy, it is still not able to completely avoid the over-fitting problem. Therefore, a combination between a constraint approach and a hybrid approach will be developed to solve the problem.

REFERENCES

[1] Li S, Wu X, Hu X (2008) Gene selection using genetic algorithm and support vectors machines. Soft Comput 12:693–698

[2] Mohamad MS, Deris S, Illias RM (2005) A hybrid of genetic algorithm and support vector machine for features selection and classification of gene expression microarray. J Comput Intell Appl 5:1–17

[3] Saeys Y, Inza I, Larranaga P (2007) A review of feature selection techniques in bioinformatics. Bioinformatics 23(19):2507–2517

[4] Mohamad MS, Omatu S, Deris S, *et al.* (Appear in press) A multi-objective strategy in genetic algorithm for gene selection of gene expression data. Int J Artif Life & Rob 13(2)

[5] Peng S, Xu Q, Ling XB, *et al.* (2003) Molecular classification of cancer types from microarray data using the combination of genetic algorithms and support vector machines. FEBS Lett 555:358–362

©ISAROB 2009

Particle Swarm Optimization for Gene Selection in Classifying Cancer Classes

M.S. Mohamad[1,2] S. Omatu[1] S. Deris[2] and M. Yoshioka[1]

[1]*Department of Computer Science and Intelligent Systems, Graduate School of Engineering,*
Osaka Prefecture University, Sakai, Osaka 599-8531, Japan
(Tel : 81-72-254-9278; Fax : 81-72-257-1788)
(mohd.saberi@sig.cs.osakafu-u.ac.jp; omatu@cs.osakafu-u.ac.jp; yoshioka@cs.osakafu-u.ac.jp)

[2]*Department of Software Engineering, Faculty of Computer Science and Information Systems,*
Universiti Teknologi Malaysia, 81310 Skudai, Johore, Malaysia
(Tel : 60-7-553-7784; Fax : 60-7-556-5044)
(safaai@utm.my)

Abstract: The application of microarray data for cancer classification has recently gained in popularity. The main problem that needs to be addressed is the selection of a smaller subset of genes from the thousands of genes in the data that contributes to a disease. This selection process is difficult due to the availability of a small number of samples compared to the huge number of genes, many irrelevant genes, and noisy genes. Therefore, this paper proposes an improved binary particle swarm optimization to select a near-optimal (smaller) subset of informative genes that is relevant for cancer classification. Experimental results show that the performance of the proposed method is superior to the experimental method and other related previous works in terms of classification accuracy and the number of selected genes.

Keywords: Gene selection, Hybrid approach, Microarray data, Particle swarm optimization**.**

I. INTRODUCTION

Microarray technology is a device that can be employed in measuring expression levels of thousands of genes simultaneously. It finally produces microarray data that contain useful information of biological, diagnostic, and prognostic for researchers.[1] Thus, there is a need to select informative genes that contribute to a cancerous state. However, the gene selection process poses a major challenge because of the following characteristics of microarray data: the huge number of genes compared to the small number of samples (higher-dimensional data), irrelevant genes, and noisy data. To overcome this challenge, a gene selection method is used to select a subset of genes that increases the classifier's ability to classify samples more accurately.

Recently, several methods based on particle swarm optimization (PSO) are proposed to select informative genes from microarray data.[2,3,4] PSO is a new evolutionary computation technique proposed by Kennedy and Eberhart.[5] It was motivated from the simulation of social behaviour of organisms such as bird flocking and fish schooling. The work of Shen *et al*. has proposed a hybrid of PSO and tabu search approaches for gene selection.[2] However, the results obtained by using the proposed hybrid method are less significant because the application of tabu approaches in PSO is unable to search into all possible search spaces. Next, an improved binary PSO have been proposed by the work of Chuang *et al*.[3] This approach produced 100% classification accuracy in many data sets, but it used a high number of selected genes to achieve the good result. This is due to all global best particles are reset to the same position when their fitness values does not change after three consecutive iterations. Li *et al*. introduced a hybrid of PSO and GA for the same purpose.[4] Unfortunately, the accuracy result is still not high and many genes selected for cancer classification since there is no probability relations between GA and PSO in the proposed hybrid method. Generally, the proposed methods that based on PSO[2,3,4] are intractable to efficiently produce a near-optimal (smaller) subset of informative genes for higher classification accuracy. This is mainly because the total number of genes in microarray data is too large (higher-dimensional data).

The diagnostic goal is to develop a medical procedure based on the least number of possible genes that needed to detect diseases. Thus, we propose an

©ISAROB 2009

improved binary PSO to select a smaller (near-optimal) subset of informative genes that is most relevant for the cancer classification. The proposed method is evaluated on two real microarray data sets.

II. METHODS

2.1. The Standard Version of Binary PSO

Binary PSO is initialized with a population of particles. At each iteration, all particles move in the problem space to find the optimal solution. A particle represents a potential solution (gene subset) in an n-dimensional space.[6] Each particle has a position and velocity vectors for directing its movement. The position vector and velocity vector of the ith particle in the n-dimension can be represented as $X_i = (x_i^1, x_i^2, ..., x_i^n)$ and $V_i = (v_i^1, v_i^2, ..., v_i^n)$, respectively, where v_i^d in the range $[0, V_{\max}]$, whereas x_i^d is a binary bit, i=1,2,..m (m is the total number of particles); d=1,2,..n (n is the dimension of data).

Hence, the vector of particle positions is represented by a binary bit string of length n, where n is the dimension of data (the total number of genes). Each vector denotes a gene subset. If the value of the bit is 1, it means that the corresponding gene is selected. Otherwise, the value of 0 means that the corresponding gene is not selected. Each particle in the tth iteration updates its own position and velocity according to the following equations:

$$v_i^d(t+1) = w * v_i^d(t) + c_1 r_1 * (pbest_i^d(t) - x_i^d(t)) + c_2 r_2 * (gbest^d(t) - x_i^d(t)) \quad (1)$$

$$Sig(v_i^d(t+1)) = \frac{1}{1+e^{-v_i^d(t+1)}} \quad (2)$$

$$\text{if } Sig(v_i^d(t+1)) > r_3, \text{ then } x_i^d(t+1) = 1; \text{ else } x_i^d(t+1) = 0 \quad (3)$$

where w is the inertia weight. c_1 and c_2 are the acceleration constants in the interval [0,2]. r_1, r_2, and r_3 are random values in the range [0,1]. $Pbest_i = (pbest_i^1, pbest_i^2, ..., pbest_i^n)$ and $Gbest = (gbest^1, gbest^2, ..., gbest^n)$ represent the best previous position of the ith particle and the global best position of the swarm (all particles), respectively.

2.2. An Improved Binary PSO (IPSO)

In this paper we propose IPSO for gene selection. It is introduced to solve the problems derived from the microarray data, overcome the limitation of the previous works[2,3,4], and inline with the diagnostic goal. IPSO in our work differs from the methods in the previous works in one major part. The major difference is that we modify the existing rule (Eq. 3) for the position update in our proposed IPSO, whereas the previous works used a standard rule (Eq. 3) for the position update in their PSO. Firstly, we analyze the sigmoid function (Eq. 2). This function represents a probability for $x_i^d(t+1)$ to be 0 or 1 ($P(x_i^d(t+1)=0)$ or $P(x_i^d(t+1)=1)$). It has the properties as follows:

$$Sig(v_i^d(t+1)) \in [0,1]$$

$$\lim_{v_i^d(t+1)\to\infty} Sig(v_i^d(t+1)) = 1 \quad (4)$$

$$\lim_{v_i^d(t+1)\to-\infty} Sig(v_i^d(t+1)) = 0 \quad (5)$$

$$\text{if } v_i^d(t+1) = 0 \text{ then}$$

$$P(x_i^d(t+1)=1) = 0.5 \text{ or } Sig(0) = 0.5 \quad (6)$$

$$\text{if } v_i^d(t+1) < 0 \text{ then}$$

$$P(x_i^d(t+1)=1) < 0.5 \text{ or } Sig(v_i^d(t+1) < 0) < 0.5 \quad (7)$$

$$\text{if } v_i^d(t+1) > 0 \text{ then}$$

$$P(x_i^d(t+1)=1) > 0.5 \text{ or } Sig(v_i^d(t+1) > 0) > 0.5 \quad (8)$$

$$P(x_i^d(t+1)=0) = 1 - P(x_i^d(t+1)=1) \quad (9)$$

Also note that the value of $x_i^d(t+1)$ can change even if the value of $v_i^d(t+1)$ does not change, due to the random number r_3 in the Eq. 3. To propose IPSO, the first three items below are suggested:

A. A Simple Modification of the formula of velocity update (Eq. 1)

$$V_i(t+1) = w * V_i(t) + c_1 r_1 * (Pbest_i(t) - X_i(t)) + c_2 r_2 * (Gbest(t) - X_i(t)) \quad (10)$$

where $V_i \in [0, V_{\max}]$.

B. Calculation for the distance of two positions

The number of different bits between two particles relates to the difference between their positions. For example, $Gbest(t) = [1011101001]$ and $X_i(t) = [0100110101]$. The difference between $Gbest(t)$ and $X_i(t)$ is $[1 -1 1 1 0 -1 1 -1 0 0]$. A value of 1 indicates that compared with the best position, this bit (gene) should be selected, but is not selected, which may decrease classification quality and lead to a lower fitness value. In contrast, a value of -1 indicates that, compared with the best position, this bit should not be selected, but is selected. The selection of irrelevant genes makes the length of the subset longer and leads to a lower fitness value. Assume that the number of 1 is a, whereas the number of -1 is b. We use the absolute value of $(a-b)$ to express the distance between two positions. Such variation makes particles exhibit the ability of exploration within the solution space. In this

©ISAROB 2009

example, $(a-b)=4-3$, so the distance between $Gbest(t)$ and $X_i(t)$ is $Gbest(t)-X_i(t)=1$.

C. Modify the existing rule of position update (Eq. 3).

In order to support the diagnostic goal that needs the least number of genes for accurate cancer classification, the rule of position update is simple modified as follows:

if $S(V_i(t+1)) > r_3$, then $x_i^d(t+1)=0$; else
$x_i^d(t+1)=1$ (11)

Please note that the value of $V_i(t+1)$ is always a positive real number. Based on this velocity value, Eq. 2, and Eq. 11, the possibility of $x_i^d(t+1)=1$ is too small. This situation causes a smaller number of genes is selected in order to produce a near-optimal gene subset from higher dimensional data.

D. Fitness function

The fitness value of a particle (a gene subset) is calculated as follows:

$$fitness(X_i) = w_1 \times A(X_i) + (w_2(M - R(X_i))/M) \quad (12)$$

in which $A(X_i) \in [0,1]$ is leave-one-out-cross-validation (LOOCV) accuracy on the training set using the only genes in X_i. This accuracy is provided by an SVM classifier. $R(X_i)$ is the number of selected genes in X_i. M is the total number of genes for each sample in the training set. w_1 and w_2 are two priority weights corresponding to the importance of accuracy and the number of selected genes, respectively, where $w_1 \in [0.1, 0.9]$ and $w_2 = 1 - w_1$.

III. EXPERIMENTS

3.1. Data Sets and Experimental Setup

Two benchmark microarray data sets are used to evaluate IPSO: leukaemia cancer and colon cancer data sets. The leukaemia data set contains the expression levels of 7,129 genes and can be obtained at http://www.broad.mit.edu/cgi-bin/cancer/datasets.cgi. It has 72 samples. For the colon cancer data set, there are 62 samples. It can be obtained at http://chestsurg.org/publications/2002-microarray.aspx.

Firstly, we applied the gain ratio technique to pre-select 500-top-ranked genes. These genes are then used by IPSO in the next process. In this paper, LOOCV is used to measure classification accuracy of a gene subset that produced by IPSO. The implementation of LOOCV is in exactly the same way as did by Chuang *et al*.[3] Two criteria following their importance are considered to evaluate the performance of IPSO: LOOCV accuracy, and the number of selected genes. A near-optimal subset that produces the highest classification accuracy with the smallest number of genes is selected as the best subset. Several experiments are independently conducted 10 times on each data set using IPSO and a standard version of PSO. Next, an average result of the 10 independent runs is obtained.

3.2. Experimental Results

Based on the standard deviations of classification accuracy and the number of selected genes in Table 1, results that produced by IPSO were nearly consistent on both data sets. Interestingly, all runs have achieved 100% LOOCV accuracy on the leukaemia data set with less than 5 selected genes.

According to the Table 2, overall, it is worthwhile to mention that the classification accuracy and the number of selected genes of IPSO are superior to the standard version of binary PSO in terms of the best, average, and standard deviation results.

For an objective comparison, we only compare our work with related previous works that used PSO in their methods.[2,3,4] It is shown in Table 3. For the leukaemia data set, the averages of LOOCV accuracy and the number of selected genes of our work were 100% and 3.5 genes, respectively. The latest previous work also came up with the similar LOOCV result to ours, but they used more than 1,000 genes to obtain the same result.[3] Overall, this work has outperformed the related previous works on both the data sets in terms of LOOCV accuracy and the number of selected genes.

According to Tables 1-3, IPSO is reliable for gene selection since it has produced the near-optimal solution from microarray data. This is due to the modification of position update that causes the selection of a smaller number of genes. Therefore, IPSO yields the optimal gene subset (a smaller subset of informative genes with higher classification accuracy) for cancer classification.

IV. CONCLUSION

In this paper, IPSO has been proposed and tested for gene selection on two real microarray data. Based on the experimental results, the performance of IPSO was superior to the standard version of binary PSO and related previous works. This is due to the fact that the modified rule of position update in IPSO causes a smaller number of genes is selected in each iterative, and finally produce a near-optimal subset of informative genes for better cancer classification. For future work, a combination between a constraint approach and PSO will be proposed to increase the classification accuracy.

Table 1. Classification accuracies for each run using IPSO

Run#	Leukaemia Data Set		Colon Data Set	
	Classification Accuracy (%)	#Selected Genes	Classification Accuracy (%)	#Selected Genes
1	100	4	93.55	5
2	100	2	93.55	5
3	100	4	96.77	4
4	100	4	93.55	5
5	100	3	93.55	4
6	100	4	95.16	5
7	100	4	93.55	4
8	100	3	95.16	4
9	100	4	93.55	5
10	100	3	93.55	4
Average ± S.D	100 ± 0	3.50 ± 0.71	94.19 ± 1.13	4.5 ± 0.53

Note: Results of the best subsets shown in shaded cells. S.D. denotes the standard deviation, whereas #Selected Genes and Run# represent the number of selected genes and a run number, respectively.

Table 2. A comparison in terms of statistical results of the proposed IPSO and the standard version of PSO

Data	Method / Evaluation	IPSO			The standard version of binary PSO		
		The Best	Average	S.D	The Best	Average	S.D
Leukaemia	Classfication Accuracy (%)	100	100	0	98.61	98.61	0
	#Selected Genes	2	3.50	0.71	216	224.70	5.23
Colon	Classfication Accuracy (%)	96.77	94.19	1.13	87.10	86.94	0.51
	#Selected Genes	4	4.50	0.53	214	231	10.19

Note: The best result of each data set shown in shaded cells. S.D. denotes the standard deviation, whereas #Selected Genes represents the number of selected genes.

Table 3. A comparison between our method (IPSO) and other previous methods based on PSO

Data	Method / Evaluation	This work	PSOTS [Shen et al.[2]]	IBPSO [Chuang et al.[3]]	PSOGA [Li et al.[4]]
Leukaemia	Classfication Accuracy (%)	(100)	(98.61)	100	(95.1)
	#Selected Genes	(3.5)	(7)	1034	(21)
Colon	Classfication Accuracy (%)	(94.19)	(93.55)	-	(88.7)
	# Selected Genes	(4.50)	(8)	-	(16.8)

Note: The results of the best subsets shown in shaded cells. '-' means that a result is not reported in the related previous work. A result in '( )' denotes an average result. #Selected Genes represents the number of selected genes.
PSOTS = A hybrid of PSO and tabu search. IBPSO = An improved binary PSO. PSOGA = A hybrid of PSO and GA

REFERENCES

[1] Knudsen S (2002) A biologist's guide to analysis of DNA Microarray Data. John Wiley & Sons.
[2] Shen Q, Shi WM, Kong W (2008) Hybrid particle swarm optimization and tabu search approach for selecting genes for tumor classification using gene expression data. Comput Biol Chem 32:53–60
[3] Chuang LY, Chang HW, Tu CJ, *et al.* (2008) Improved binary PSO for feature selection using gene expression data. Comput Biol Chem 32:29–38
[4] Li S, Wu X, Tan M (2008) Gene selection using hybrid particle swarm optimization and genetic algorithm. Soft Comput 12:1039–1048
[5] Kennedy J, Eberhart R (1995) Particle swarm optimization. Proceedings of the IEEE International Conference on Neural Networks 4:1942–1948
[6] Kennedy J, Eberhart R (1997) A discrete binary version of the particle swarm algorithm. Proceedings of the IEEE International Conference on Systems, Man, and Cybernetics 5:4104–4108

The Fourteenth International Symposium on Artificial Life and Robotics 2009 (AROB 14th '09),
B-Con Plaza, Beppu, Oita, Japan, February 5 - 7, 2009

An analysis of epression data using Support Vector Machine and feature selection methods

Michifumi Yoshioka, Norihiro Shimoda, Sigeru Omatu
Dept. of conputer science and intelligent System
Osaka Prefecture University
Sakai, Osaka, Japan

Abstract

Gene expression data is signi cantly expected as aid in the development of efficient cancer diagnosis and classi cation platforms. However, Gene expression data is high dimensional and the number of samples is small in comparison to the dimension of the data, and furthermore, noisy inherently. Therefore, we would be better o using not all genes but part of genes in order to classify gene expression data. Previous works introduce a method of hybrid Genetic Algorithm and Support Vector Machine (GASVM) for nding the small subset of informative genes which maximize the classi cation accuracy. However, these methods have some problems. Firstly, previous works cost a large amount of calculation because of SVM using high dimensional data and its iteration. Secondly, previous works use only accuracy of SVM as a criterion for gene selection. This might cause over tting. Thus, we introduce a criterion named "Con dence Margin". The criterion means a "goodness" of hyperplane made by SVM. Using " Con dence Margin ", proposed method cut o iteration, and, cost less amount of calculation than previous works. Furthermore, proposed method shows as a high accuracy as previous works.

1 introduction

DNA microarray has been the key technology in recently biology and helped us to understand the biological system because of its ability to monitor the expression levels of thousands of genes simultaneously. The expression levels mean the hereditary activities in each genes. Therefore, gene expression data is created by a process known as microarray and represents the activation level of each gene within an organism at a particular point of time, and the class label means which class a person belongs to. Thus, gene expression data is signi cantly expected as aid in the development of efficient cancer diagnosis and classi cation platforms.

This work deals with the way of classi cation using gene expression data. From the classi cation point of view, it is well known that, when the number of samples is much smaller than the number of features, classi cation methods may lead to data over tting, meaning that one can easily nd a decision function that correctly classi es the training data but this function may behave very poorly on the test data. In order to classify gene expression data, it is necessary to reduce the data dimension by selecting a subset of features that are relevant for classi cation, that is, we should not use all genes but part of genes which contribute to classi cation [1]. Previous works introduce a method of hybrid Genetic Algorithm and Support Vector Machine (GASVM) [2], and extended-GASVM (New-GASVM) [3]for gene selection and classi cation tasks. The methods consists of two parts. GA part works for feature selection and evaluation, that is, makes gene subsets and evaluate its goodness, and SVM part measures accuracy of gene subsets from GA part. Then, the accuracy is used to evaluate gene subsets in GA part. As seen above, the method using accuracy of a classi er as criterion is called " Wrapper tequniques "[4]. The method shows very high accuracy of the benchmark datasets. However, previous works have two problems. Firstly, previous works cost a large amount of calculation because of SVM for high dimensional data and LOOCV (Leave-One-Out Cross-Validation). Secondly, previous works use only accuracy of SVM as a criterion. Therefore, the result (optimal gene subset) show high accuracy for training data, but might not show high accuracy for unknown data, so-called " over tting ". In order to resolve these problems, we focus on data distribution in feature space, and select features so that two data constellation are isolated each other. In concrete terms, we use criterion named "Con dence Margin" [5]. The criterion means a "goodness" of hyperplane made by

©ISAROB 2009

SVM. Using "Con dence Margin", we have proposed a new method that selects genes and classi es gene expression data. Proposed method achieve drastically reduction of calculation amount because of cutting o iteration(LOOCV) when selected gene sbset are evaluated. Concequently, proposed method belongs to" Filter techniques "[4].

By the way, Filter tequniques carry out feature selection as preparation. Usually, lter techniques select features as preparation. As a result, lter techniques tend to show smaller amount of calculation than Wrapper techniques, but lower accuracy simultaneously. However, proposed method shows smaller amount of calculation and higher or equal accuracy than previous works which belongs to wrapper method.

2 Previous Works

2.1 GASVM

GASVM consists of two main components: GA and SVM classi er. The GA will select the subsets of features and then the SVM classi er evaluates the subsets during a classi cation process. The result of the classi cation process is used for the tness value of GA. We describe the outline of GASVM as below.

[individual representation] An individual represents a selecded gene subsets. The chromosome (individual) is represented by binary vector whose dimension are equal to the number of genes in gene expression data. If a bit is 1, it means that the corresponding feature is selected, and If a bit is 0, it indicates that the corresponding feature is not selected.
[making gene subsets] According to the rule described "individual representation", gene subsets are made of each chromosome by comparison with gene expression data.
[evaluation of tness] The tness function of each individual is determined by evaluating the SVM using a training set. Hence, this research is used with a tness function containing classi cation accuracy as mentioned below,

$$Fitness(x) = accuracySVM(x) \tag{1}$$

where $accuracySVM(x)$ is the LOOCV accuracy of the classi er with the features subset selection which is represented by x.
[GA operation] Using tness, the individual is applied to some normal evolution steps in GA, that is, selection, crossover and mutation.

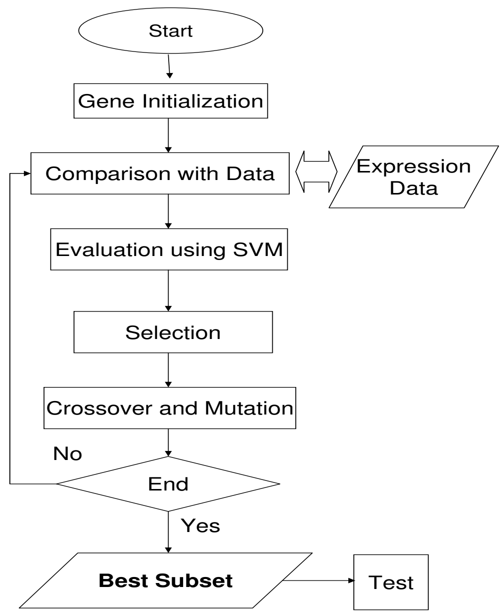

Figure 1: A ow chart of GASVM

The GA is used to maximize the tness value in order to nd the optimal features subset which has been achieved the highest LOOCV accuracy. The optimal subset from training set is used to construct SVM classi er.The Flow chart of GASVM are shown in Figure 1.

2.2 Difficulty of GASVM

GASVM investigate the optimal gene subset which maximizes the accuracy of SVM using the accuracy of SVM itself, and the number of samples is much smaller than the number of features in gene expression data in this case. Therefore, the selected gene subset lead to over tting, and lacks the foundation why these genes are optimal. Hence, it is a better way to select gene subset according to another criterion outside the accuracy of SVM ,and that result in high accuracy simultaneously.

©ISAROB 2009

3 Proposed Method

3.1 GASVM-CM

As an another criterion, we have employed the distance between two data constellation. There is some measurements which mean distance in SVM. Hence, taking into account the fact that gene expression data is linear inseparable and noisy, we adopt" Con dence Margin ". "Con dence Margin" is "Margin"[6] multiplied by "Con dence" [7]. Here, Con dence Margin is

$$ConfidenceMargin = Confidence \quad Margin \qquad (2)$$

where $Margin$ means distance from hyperplane to support vector, that is, $Margin$ means the geometric distance between two data constellation. $Confidence$ is the distance which imposes penalties on the misclassi ed samples. Therefore, $ConfidenceMargin$ is the distance which takes into account the misclassi- ed sample, that is, it means goodness of hyperplane made by SVM. We have proposed a new method of gene selection and classi cation which use "Con dence Margin" in place of accuracy of SVM in GASVM, and named it GASVM-CM. The proposed method is used with a tness function as mentioned below.

$$Fitness(x) = ConfidenceMargin(x) \qquad (3)$$

where $fitness(x)$ is tness value of individual x, and $ConfidenceMargin(x)$ is Con dence Margin of individual x. GASVM-CM remains basically the same with GASVM. However, it has the di erent way of evaluating individuals from GASVM. The outline of evaluating individuals in GASVM-CM are described as below.

[measurement of Margin] SVM are trained by gene subset made from each individuals. As a result, support vector and hyperplane are determined in each individuals, and then, Margin is able to measured.

[measurement of Con dence] We can measure distance from determined margin to each samples taking into account its class label, and then, average these distance. It is Con dence in each individuals.

[Calculation of Con dence Margin] Con dence Margin is calculated by Margin and Con dence from previous step.

The proposed method searches combination of genes (individual) which maximizes Con dence Margin.

4 Experiment

4.1 Benchmark datasets

The rst benchmark gene exression microarray dataset is Colon Cancer. The data contains expressin levels of 2000 genes from 40 tumor and 22 normal colon tissues. The dataset has only 62 samples for training data, originally analyzed by Alon et al[8] and downloaded from http://microarray.princeton.edu/oncology/ The second benchmark gene expression microarray dataset is Leukemia Cancer. The data contains examples of human acute leukemia, originally analyzed by Golub et al[9]. The dataset containing expression levels of 7129 genes can be obtained at http://www.broad.mit.edu/cgi-bin/cancer/datasets.cgi . The bone marrow or blood samples were taken from 72 patients, 47 with acute myloid leukemia (AML) and 25 with acute lymphoblastic leukemia (ALL). The training data consists of 38 samples and the remaining 34 samples were used as testing data.

4.2 Coventional approaches

In order to evaluate performance of proposed method, we experiment on GASVM, GASVM-CM, and comventional approaches. We introduce two methods which use only Margin, and Con dence as a criterion respectively. Those are named GASVM-M (Margin only) and GASVM-C (Con dence only). The comventional approaches are used a tness function as mentoned below,

$$fitness(x) = Margin(x) \qquad (4)$$

$$fitness(x) = Confidence(x) \qquad (5)$$

where $fitness(x)$ a tness value of individual x. $Margin(x)$ is a Margin from individual x , $Confidence(x)$ is a Con dence from imdividual x.

4.3 Result of experiment and discussion

Tables 1. and 2. show the results of the experiments for Colon Cancer and Leukemia Cancer datasets. Number of genes means the number of optimal gene subset in each method. Accuracy means accuracy of SVM on test data using optimal gene subset from training data. However, only LOOCV procedure was used to measure the classi cation accuracy on Colon Cancer dataset because this data set had only the training set.

©ISAROB 2009

Table 1: The Experimental Result of Colon

	Number of genes	Run-time (minute)	Accuracy (%)
GASVM	11	1380	87.10
GASVM-CM	29	420	88.71
GASVM-M	17	8	72.58
GASVM-C	70	450	72.58

Table 2: The Experimental Result of Leukemia

	Number of genes	Run-time (minute)	Accuracy (%)
GASVM	5	600	82.35
GASVM-CM	33	240	88.24
GASVM-M	10	7	73.53
GASVM-C	93	240	70.59

Comparing GASVM with GASVM-CM rstly, GASVM-CM have achieved the higher accuracy than GASVM, and the less amount of calculation. This is the comparison between wrapper technique and Filter technique. E ectiveness of our proposed method is con rmed because it means that the proposed method is able to avoid over tting.

Comparing GASVM-CM with comventional approaches secandly, GASVM-CM have achieve the higher accuracy than comventional approaches, however, the greater amount of calculation basically. The result is also very contented because it means that the proposed method can higher accuracy than comventional approaches. The result about Run-time is appropriate because Con dence Margin are calculated by Margin and Con dence measured in advance. As mentioned above, e ectiveness of using Con dence Margin as a criterion of feature selection on SVM is con rmed.

5 Conclusion

This paper have introduced Con dence Margin and proposed a method using Con dence Margin. Proposed method belongs to Filter method. Generally, Filter techniques tend to show smaller amount of calculation than Wrapper techniques but lower accuracy simultaneously. However, proposed method shows smaller amount of calculation and higher or equal accuracy than previous works which belongs to wrapper method.

References

[1] M. S. Mohamad and S. Deris, "Feature selection method using genetic algorithm for the classi cation of small and high dimension data" *Proc. Int. Symp. Info. Com. Tech*, p.13-16(2004)

[2] Edmundo Bonilla Huerta, Beatrice Duval, and Jin-Kao, "A Hybrid GA/SVM Approach for Gene Selection and Classi cation of Microarray Data" Proc. ofEvoWorkshops 2006, LNCS 3907, p.34-44, 2006.

[3] MOHAD SAVERI MOHAD ad SAFAAI DERIS , "A HYBRID OF GENETIC ALGORITHM AND SUPPORT VECTOR MACHINE FOR FEATURES SELECTION AND CLASSIFICATION OF GENE EXPRESSION MICROARRAY" *International Journal of Computational Inteligence and Apprications*, Vol.5, No.1 pp.91-107, 2005.

[4] Yvan Saeys Inaki Inza, and Pedro Larranaga, "A review of feature selection techniques in bioinformatics", *Bioinformatics*, Vol.123, No.19 pp.91-177, 2007.

[5] K.Aoki, S. Kuroyanagi, M. KUGULER, A. S. NUGROHO, and A. IWATA, "Feature selection Using Con dent Margin for SVM", *IEICE TRANS D-II*, No.12 pp2291-2300, 2005.

[6] Nello Cistianini, John Shawe-Taylor, *An Introduction to Spport Vector Machines and other kernel-based learning methods*, Cambridge University Press, 2000.

[7] Ling Li, Amrit Pratap, Hsuan-Tien Lin, and Yaser S. abu-Mostafa, "Improving Generatio by Data Categorization", *PKDD 2005*, LNAI 3721, pp.157-168, 2005.

[8] U. Alon, N. Barkai, D. A. Notterman, K. Gish, S. Ybarra, D. Mack, and A.J Levine, "Broad patterns of gene expression revealed by clustering analysis of tumor and normal colon tissues probed by oligonucleotide arrays", *Proc. Natnl. Acad. Sci. USA*, volume 96, 1999.

[9] T. R. Golub, D. K. Slnim, P. Tamayo, C. Huarg, M. Gaasenbeek, J. P Mesirov, H. Coller, M. L. Loh, J. R. Downing, M. A. Caligiuri, C. D. Bloom- eld, and E. S. Lander, "Molecular classi cation of cancer: Class discovery and class prediction by gene expression monitoring", *Science*, 286:531-537, 1999.

©ISAROB 2009

The Fourteenth International Symposium on Artificial Life and Robotics 2009 (AROB 14th '09),
B-Con Plaza, Beppu, Oita, Japan, February 5 - 7, 2009

Audio-Signal Separation by Independent Component Analysis

Michifumi Yoshioka andSigeru Omatu
Computer and Systems Sciences, Graduate School of Engineering,
Osaka Prefecture University, 1-1 Gakuen-cho, Sakai City, 599-8531

Abstract

In this paper, a method of separating the acoustic signals of motors and gears of mechanical devices by using the independent component analysis (ICA) with band-pass filters is proposed. The frequency distribution of a recorded acoustic signal of the operating mechanical device can be divided into three fields, the low-frequency field, which corresponds to the frequency characteristics of the gear, the medium-frequency field, which is mixed with the frequency characteristics of the gear and the motor, and the high-frequency field, which corresponds to the frequency characteristics of the motor. Since only the medium-frequency components are the mixture of acoustic signals of gears and motors, the ICA with band-pass filters is expected to separate the acoustic signals of motors and gears more accurately than the conventional ICA. The simulation and experimental results show that the proposed method can separate the acoustic signals of motors and gears of mechanical devices successfully.

Keywords: ICA, Signal processing, Neural Networks

1 Introduction

In the quality evaluation of mechanical devices, it is important to separate the acoustic signals of motors and gears in order to identify the causes of failures. The ICA method, which is developed to solve the cocktail-party problem, can separate two independent acoustic signals from their mixtures by using the information measure of statistically independent properties [1]-[3]. However, many applications in practice denote that the ICA does not perform well in separation by using the observed acoustic signals directly [4]-[5]. In order to separate the independent acoustic signals correctly, additional data processing is necessary before applying the ICA.

By applying the fast fourier transform (FFT) to a recorded acoustic signal of the operating mechanical device, we observe that its frequency distribution can be divided into three fields, the low-frequency field, which corresponds to the frequency characteristics of the gear, the medium-frequency field, which is mixed with the frequency characteristics of the gear and the motor, and the high-frequency field, which corresponds to the frequency characteristics of the motor. Since the frequencies of a motor may be harmonics of the fundamental frequencies of a gear, which causes the independence assumption of the sources to fail and affects the separation accuracy. Therefore, the mixed acoustic signals with less frequency components are expected to be separated more accurately. In this paper, the ICA with band-pass filters is used to separate the acoustic signals of gears and motors. We first record the acoustic signals of the operating mechanical devices. By applying the band-pass filters, the respective components of low-frequency, medium-frequency and high-frequency can be obtained. Then the medium-frequency components are given to the ICA. After separation, the acoustic signals of gears and motors are recovered by adding the low-frequency and high-frequency components to the separated results, respectively. In this paper, the mixtures of two independent signals are also designed to simulate the separation process of acoustic signals of a gear and a motor. Both the simulation results and the experimental results show that the better separation results can be obtained by using the mixed medium-frequency field than using the whole frequency field.

2 Simulation Results

Suppose there are two independent signals s_1 and s_2, their frequency characteristics are illustrated in Figs. 1 and 2, respectively where f_1, f_2 and f_4 are constant and f_3 is variable.

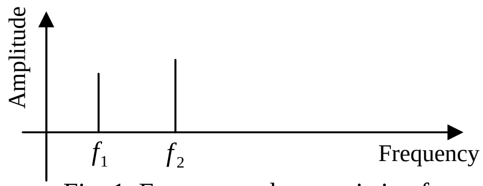

Fig. 1. Frequency characteristic of s_1.

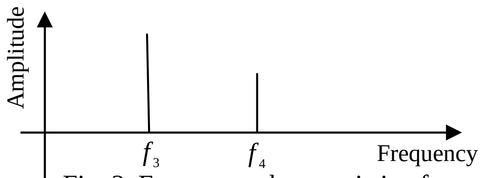

Fig. 2. Frequency characteristic of s_2.

If we use two microphones to record the acoustic signals, we have two observed signals $x_1(t) = a_{11}s_1 + a_{12}s_2$, $x_2(t) = a_{21}s_1 + a_{22}s_2$. We use the ICA to separate the two independent signals s_1 and s_2 from the observed signals. Table I shows the separation results where "Y" denotes that the independent signals s_1 and s_2 can be separated correctly and "N" denotes that they cannot be separated correctly. From Table I, it can be seen that sometimes we fail in separating the acoustic signals s_1 and s_2 by using the observed signals x_1 and x_2 directly.

©ISAROB 2009

Table I. Separation results of observed signals (unit: Hz).

f_3	30	40	50	60	70	80	90	100	110
Y/N	Y	Y	Y	N	Y	Y	Y	N	Y
f_3	120	130	150	160	170	180	190	200	210
Y/N	N	Y	Y	Y	Y	N	Y	Y	Y
f_3	220	230	$f_1 = 20$, $f_2 = 140$, $f_4 = 240$						
Y/N	Y	Y							

However, after filtering the frequency components f_1 and f_4 with a band-pass filter, the frequency components f_2 and f_3 can be separated successfully by using the ICA. Thus, the original acoustic signals s_1 and s_2 can be obtained by adding the frequency components f_1 and f_4 to the separation results of the ICA, respectively. As an example, Figs. 3 and 4 show the frequency characteristics of separated signals s_1' and s_2' by using the ICA with band-pass filters, respectively where $f_3 = 100$ Hz. From these figures, it can be seen that the two acoustic signals of s_1 and s_2 are separated correctly.

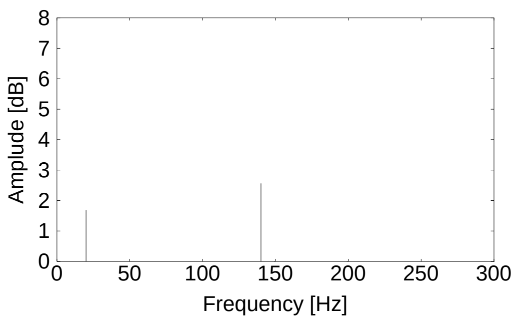

Fig. 3. Frequency characteristic of separated signal s_1' with band-pass filters.

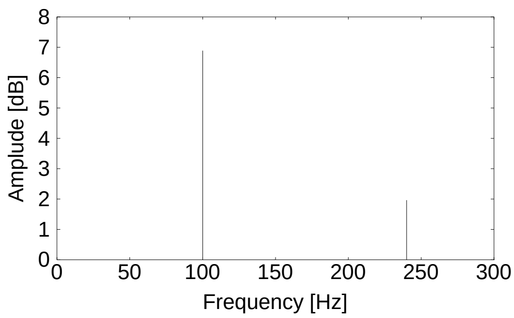

Fig. 4. Frequency characteristic of separated signal s_2' with band-pass filters.

Similarly, other unsuccessful separation experiments of Table I are redone by using the ICA with band-pass filters. The simulation results show that all the signals are separated successfully. And the separation experiments of mixed acoustic signals with multi-frequencies also show that the ICA with band-pass filters performs better than the conventional ICA in acoustic signals separation.

3 Experimental Results

According to the above simulation results, we separate the acoustic signals of motors and gears of mechanical devices by using the ICA with band-pass filters. The acoustic signals recording system is shown in Fig.5. Two microphones, which are held in different locations, are used to record the acoustic signals of operating mechanical devices. By applying the band-pass filters, we obtain the respective components of low-frequency, medium-frequency and high-frequency. Since only the medium-frequency components are the mixture of acoustic signals of gears and motors, we input the medium-frequency components to the ICA. Then the acoustic signals of gears and motors can be recovered by adding the low-frequency and high-frequency components to the separation results of the ICA, respectively.

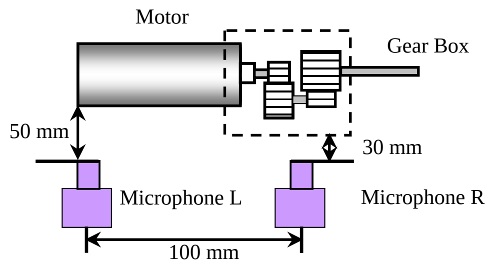

Fig. 5. The acoustic signals recording system.

An example of acoustic signals recorded by microphones L and R are shown in Figs. 6 and 7, respectively where the sampling rate is 8,000. Their frequency characteristics are shown in Figs. 8 and 9.

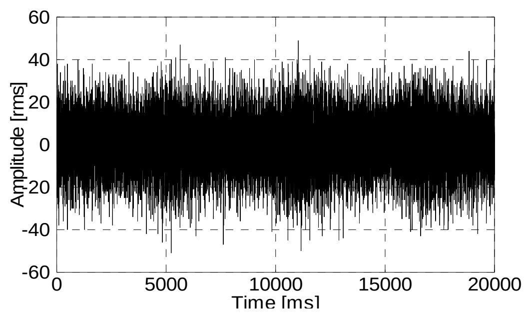

Fig. 6. Acoustic signal recorded by the left microphone.

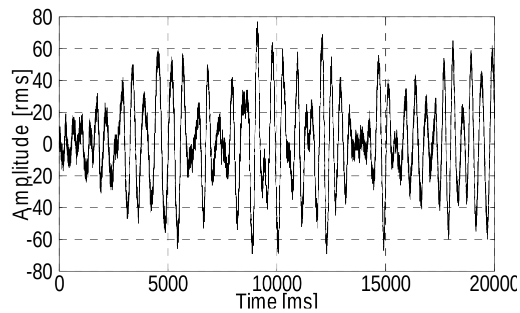

Fig. 7. Acoustic signal recorded by the right microphone.

Since the rotational speed of the motor is 3600 rpm and the rotor has 12 poles, the fundamental frequency of the motor is about 360 Hz. Similarly, since the gear ratio is 30:1, the fundamental frequency of the gear is about 12 Hz. Thus, it can be considered that the medium-frequency is the range of 300 to 2,000 Hz and the relevant band-pass filters are designed.

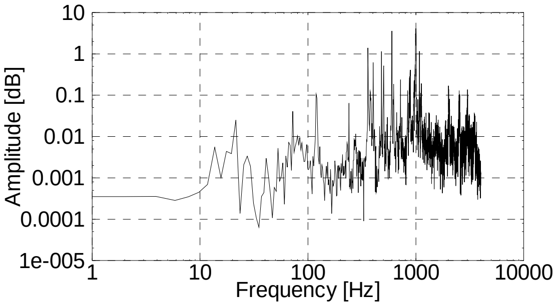

Fig. 8. Spectrum of acoustic signal of left microphone.

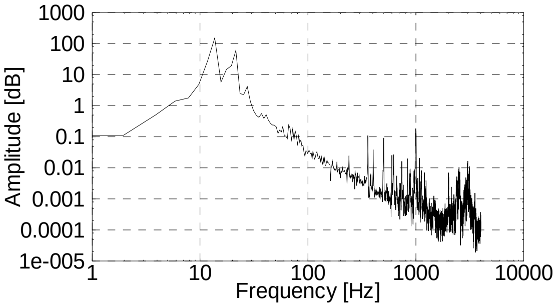

Fig. 9. Spectrum of acoustic signal of right microphone.

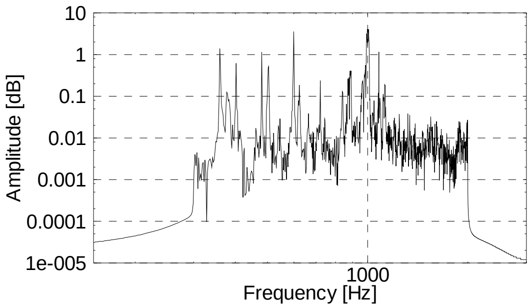

Fig. 10. Spectrum of Fig. 8 with a band-pass filter.

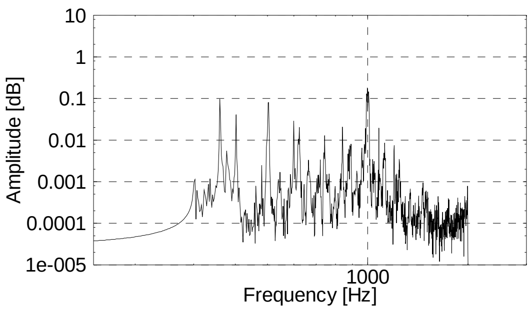

Fig. 11. Spectrum of Fig. 9 with a band-pass filter.

In Figs. 10 and 11, the medium-frequency fields of acoustic signals of left and right microphones with the band-pass filter are given respectively. The filtered signals are used as the input of the ICA. The spectra of the separated acoustic signals are shown in Figs. 12 and 13. Since a peak of amplitude nearby 1,000 Hz, which is about 3 times of the fundamental frequency of the motor, can be observed in Fig. 12, it is regarded that Figs. 12 and 13 show the medium-frequency fields of acoustic signals of the motor and the gear, respectively.

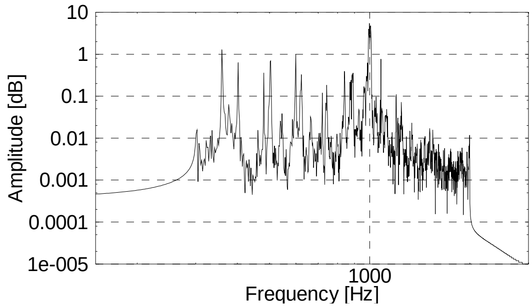

Fig. 12. Spectrum of the separated acoustic signal by using the ICA with a band-pass filter (motor).

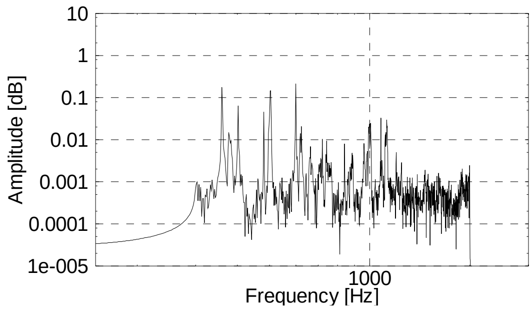

Fig. 13. Spectrum of the separated acoustic signal by using the ICA with a band filter-pass (gear).

To verify the effectiveness of our proposed method, we also give the separation results by applying the recorded acoustic signals of mechanical devices to the ICA directly. The frequency characteristics of the separated acoustic signal are shown in Figs. 14 (a) and 15 (a), and the medium-frequency characteristics are shown in Figs. 14 (b) and 15 (b). Comparing with Figs. 8 and 9, it can be concluded that Figs. 14 and 15 show the frequency characteristics of the motor and the gear, respectively.

From the above figures, it can be seen that the ICA with band-pass filters performs better than the conventional ICA in acoustic signals separation. The spectrum of Fig. 14 (b) is similar with the one of Fig. 15 (b), especially the peaks of amplitudes appeared in both figures, which are located in the multiple of fundamental frequency of the motor, denote that the separation results of acoustic signals of the motor and the gear are not good.

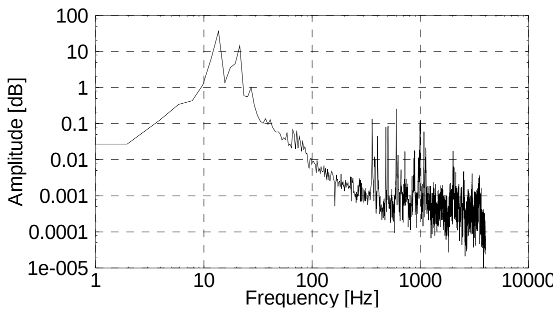

Fig. 14 (a). Frequency characteristics of the separated acoustic signal by using the ICA (motor).

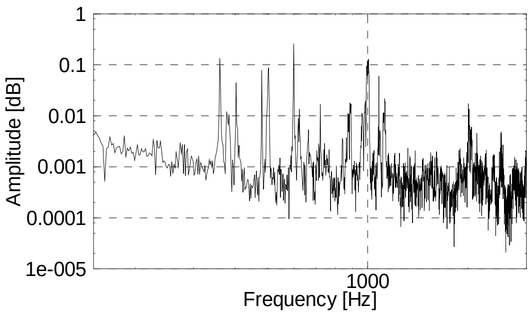

Fig. 14 (b). Medium-frequency characteristics of the separated acoustic signal by using the ICA (motor).

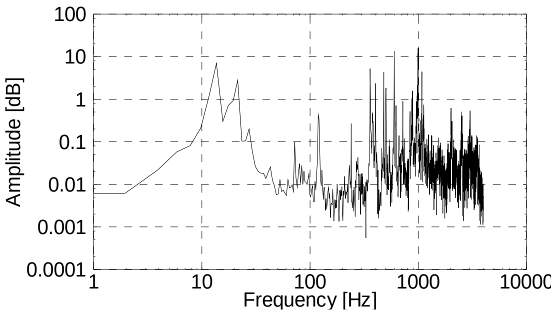

Fig. 15 (a). Frequency characteristics of the separated acoustic signal by using the ICA (gear).

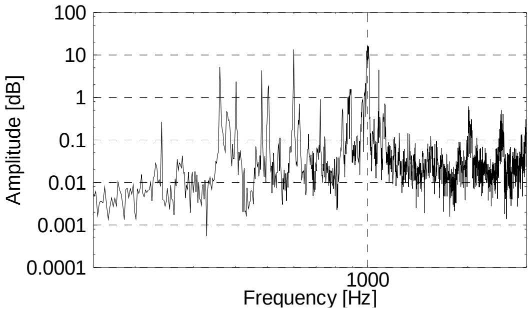

Fig. 15 (b). Medium-frequency characteristics of the separated acoustic signal by using the ICA (gear).

The acoustic signals of the gear and the motor are recovered by adding the low-frequency and high-frequency components to the separation results of Figs. 12 and 13, respectively. The spectra of recovered acoustic signals of the gear and the motor are shown in Figs. 16 and 17 where the amplitudes of medium-frequency are adjusted according to the amplitudes of low-frequency and high-frequency, respectively. Comparing with the above figures, it can be concluded that the separation results are reasonable. The separated acoustic signals of the gear and the motor are also checked by a technician, the sounds of the motor and the gear denote that the acoustic signals of the gear and the motor are separated successfully by using the ICA with band-pass filters.

6. Conclusion

In this paper, a method of separating the acoustic signals of gears and motors of mechanical devices by using the ICA with band-pass filter is proposed. The simulation results denote that the mixed acoustic signals with less frequency components can achieve better separation performance by using the ICA. Therefore, for those independent signals which are mixed only in medium-frequency field, the ICA with band-pass filters can separate the independent original signals more accurately than the conventional ICA. Using the proposed method, we have solved the acoustic signals separation problem of gears and motors of mechanical devices successfully.

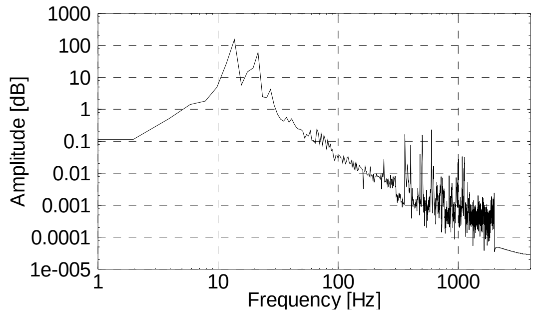

Fig. 16. Spectrum of recovered acoustic signal of the gear.

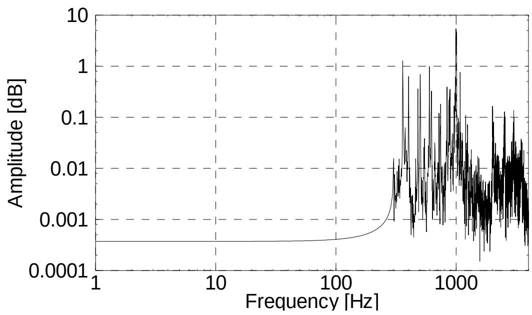

Fig. 17. Spectrum of recovered acoustic signal of the motor.

References

(1) A. Hyvarinen, J. Karhumen, and E. Oja, Independent Component Analysis, Wiley Publisher, New York, 2001.

(2) E.Bingham, and A. Hyvarinen, " A fast fixed-point algorithm for independent component analysis of complex valued signals," International Journal of Neural Systems, Vol. 10, No. 1, pp. 1-8, 2000.

(3) S. Hochreiter, and J. Schmidhuber, "LOCOCODE performs nonlinear ICA without knowing the number of sources," Proceedings of the First International Workshop on ICA and Signal Separation, Aussois, France, 1999, pp. 149-154.

(4) T. W. Lee, Independent Component Analysis: Theory and Applications, Kluwer Academic Publishers, Boston, 1998.

(5) A. Cichocki, and S. Amari, Adaptive Blind Signal and Image Processing: Learning Alogarithms and Applications, Wiley Publisher, New York, 2002.

The Fourteenth International Symposium on Artificial Life and Robotics 2009 (AROB 14th '09),
B-Con Plaza, Beppu, Oita, Japan, February 5 - 7, 2009

Crack detection method using rotational morphology

M. Yoshioka
Osaka Pref. Univ.
Sakai, Osaka 599-8531

S. Omatu
Osaka Pref. Univ.
Sakai, Osaka 599-8531

Abstract

Recently, in the factory, it becomes very important to detect cracks on products automatically. In order to achieve this purpose, auto crack detection systems using photo images from digital camera have been proposed. However, in conventional methods using detected edge lines extracted by such as Sobel filter, it is di cult to distinguish between the original lines on the product surface and those of cracks in the case of noisy images. In order to overcome this di culties, we have proposed the new method using rotational morphology. The rotational morphology is a kind of mathematical morpholgy with structuring element rotation. Finally, some simulations are carried out for confirming the effectiveness of our proposed method.

1 Introduction

In these latter years, in the factory, it becomes very important to detect cracks on products automatically, because cracks on products reduce the lifetime of them and it costs much time to detect small cracks by human check. In order to achieve this purpose, auto crack detection systems using photo images from digital camera have been proposed. However, in conventional methods using detected edge lines extracted by such as Sobel filter, it is di cult to distinguish between the lines from the product surface texture and those from cracks in the case of noisy images(Fig.1,5,7). For example, Fig.1 is the sample image which has the noisy surface texture, and Figs.2 and 3 are the results of vertical and horizontal Sobel filter from it. Figs.2 and 3 are filtered with different threshold values th. In this case, it is di cult to find cracks by using Sobel filter and its threshold value optimization because the intensities of image in crack and product texture are almost same. In order to overcome this di culties, we have proposed the new method using rotational morphology. The rotational morphology is a kind of mathematical morpholgy with the rotated structuring element. Finally, some simulations are carried out for confirming the effectiveness of our proposed method.

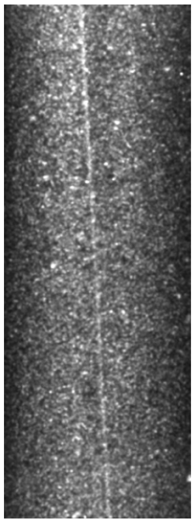

Figure 1: Sample image 1.

2 Proposed method

In order to improve the crack detection in noisy images, we have proposed the new crack detection method using rotational morphology. At first, we introduce rotational morphology briefly and mention about our proposed method.

2.1 Rotational morphology

Mathematical morphology [1] is one of the well known methods for image processing. It has many operators which are dilation, erosion and etc. Particularly in edge detection from noisy images, mathematical morphology is used with the top-hat operator. Rotational morphology [2] is the expansion of the mathematical morphology with rotated structuring elements. By using rotated structuring elements, it fits not only one direction but also the other directions.

©ISAROB 2009

The Fourteenth International Symposium on Artificial Life and Robotics 2009 (AROB 14th '09),
B-Con Plaza, Beppu, Oita, Japan, February 5 - 7, 2009

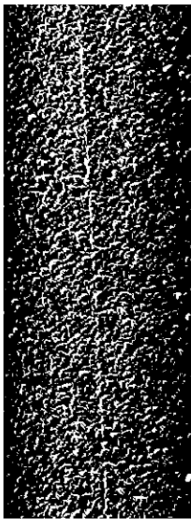

Figure 2: Filtered image 1 (th=10).

Figure 3: Filtered image 1 (th=20).

2.2 Flexible structuring element

In conventional mathematical morphology, structuring elements need to be selected along the target edges for detection. However, it is di cult to select suitable one because there are many kinds of cracks in length, width and depth. In order to resolve this point, we have proposed the flexible structuring element instead of conventional one (Fig.4), where L, K and D in Fig.4 are parameters for determining the size of the structuring element. By using this as a structuring element and fitting it to intensity surface, the fitting error is able to be used for the criterion whether there is crack. The fitting error is defined as following equations:

$$E = \sum_{x,y \in A_1} (D - I(x,y) - \alpha)^2 + \sum_{x,y \in A_2} (I(x,y) + \alpha)^2 \quad (1)$$

where the area A_1 and A_2 indicate the top and bottom surface of the structuring element, and E and $I(x,y)$ indicate the fitting error and the intensity of images at position (x,y). The α is the optimized parameter which minimizes the fitting error E.

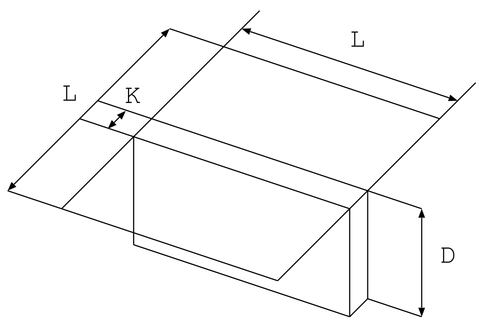

Figure 4: Structuring element.

3 Simulations

In order to confirm the effectiveness our proposed method, simulations for crack detection are performed using Figs. 1,5 and 7. Results of simulations are shown in Figs.8-13. Parameters determining the structuring element size and used for simulations are indicated in the figure captions, and θ and th are the rotation angle of the structuring element and threshold value of cracks respectively. As the results of simulations, cracks are clearly detected from noisy images, and the effectiveness of our proposed method is confirmed.

4 Conclusions

In order to develop the crack detection method in noisy images, we have just proposed the new method using the rotational morphology. As the result of simulations, the effectiveness of our proposed method is confirmed. As the future work, we need to develop automatic parameter optimization and reduce computation time.

©ISAROB 2009

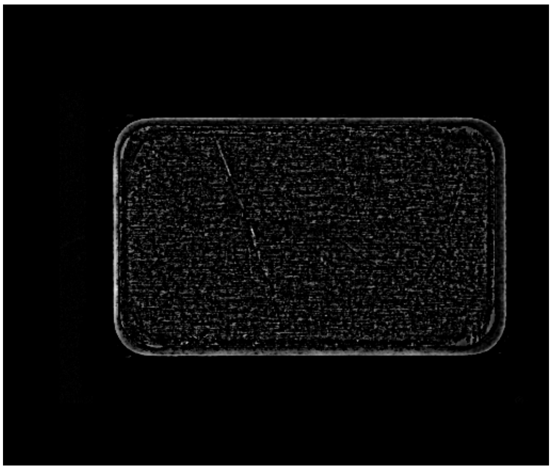

Figure 5: Sample image 2.

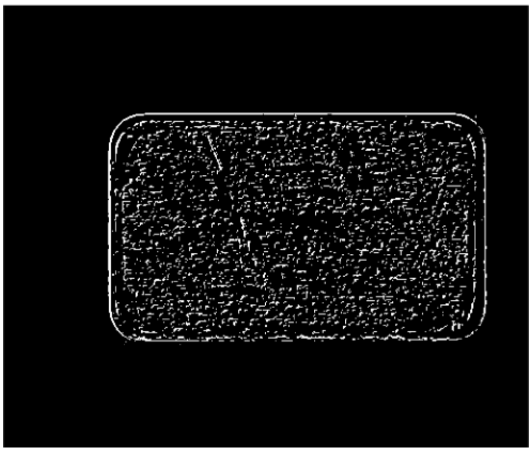

Figure 6: Filtered image 2(th=20).

References

[1] Jean Serra, *Mathematical Morphology volume II*, Academic press, London, 1988.

[2] K. Yoshitaka, O. Yosuke, I. Norihiko, B. Norio and K. Eisaku, "A procedure to analyze surface profiles of the protein molecules visualized by quick-freeze deep-etch replica electron microscopy", *Ultramicroscopy*, Vol. 107, No. 1, pp 25-39, 2007.

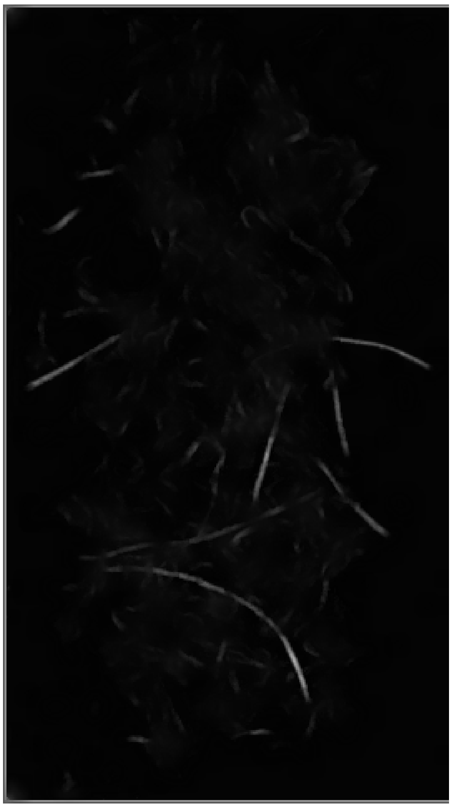

Figure 7: Sample image 3.

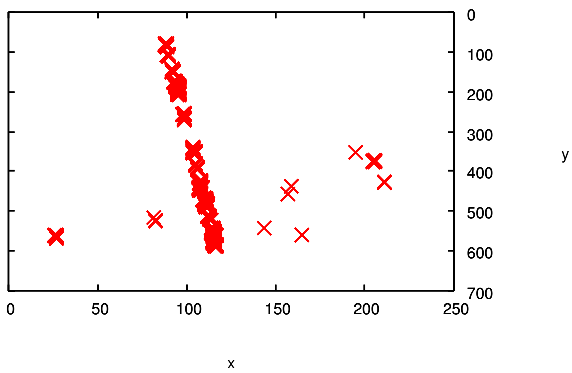

Figure 8: Detected crack in Image 1 ($\theta = 85, L = 20, K = 4, D = 100, th < 500000$).

©ISAROB 2009

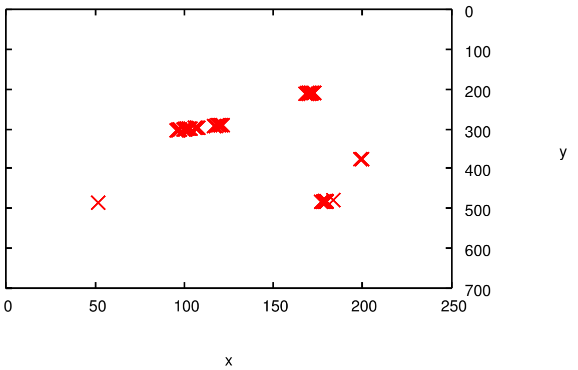

Figure 9: Detected crack in Image 1 ($\theta = -30, L = 20, K = 4, D = 100, th < 500000$).

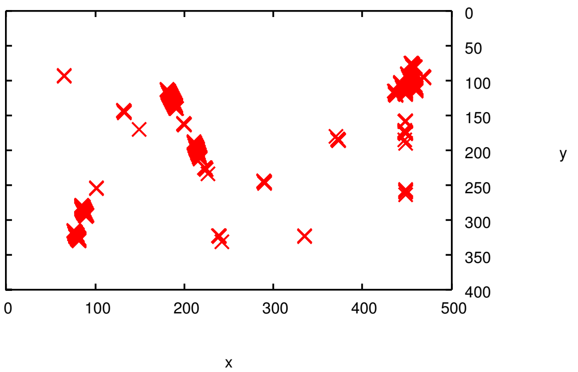

Figure 10: Detected crack in Image 2 ($\theta = 70, L = 20, K = 3, D = 200, th < 1800000$).

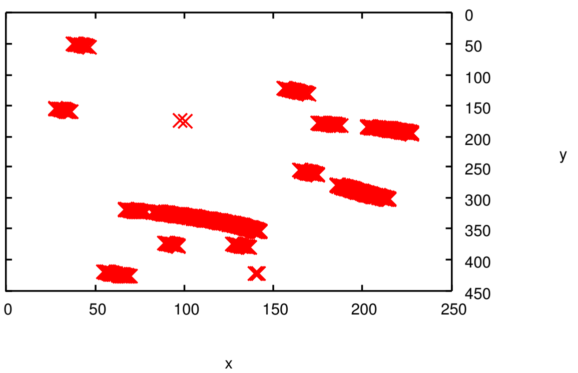

Figure 11: Detected crack in Image 3 ($\theta = 30, L = 20, K = 4, D = 100, th < 550000$).

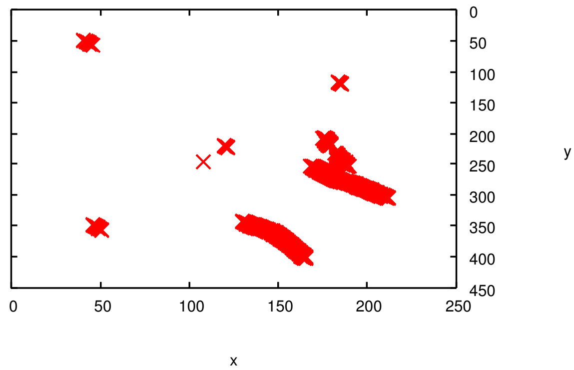

Figure 12: Detected crack in Image 3 ($\theta = 60, L = 20, K = 4, D = 100, th < 550000$).

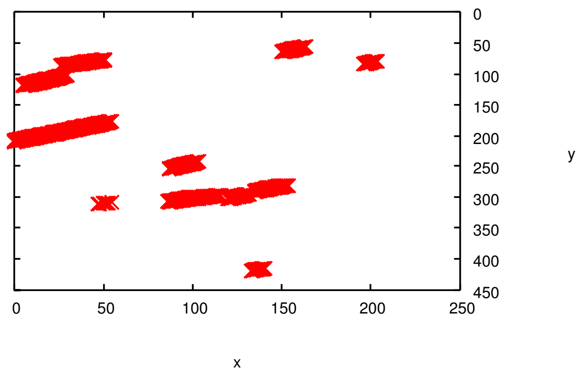

Figure 13: Detected crack in Image 3 ($\theta = -30, L = 20, K = 4, D = 100, th < 550000$).

Estimation of the optimal image resolution using the SIFT

M. Yoshioka, Y. Maeda and S. Omatu

Osaka Pref. Univ.
1-1 Gakuen-tyo Naka-ku Sakai-city, Osaka Japan 599-8531
(Tel : 81-72-254-9279)

Abstract

The image processing is used to check products in many factories. If we use down-sampled images, we can reduce the calculation time and the image noise. However, the accuracy of the detection also becomes low. The purpose of this paper is to estimate the optimal image resolution for the detection, keeping the accuracy of detection high. To achieve our purpose, we adopt the SIFT(Scale Invariant Feature Transform)as the criterion of the optimal image resolution. Finally we confirm that our proposed method is useful by the simulation.

Keywords: SIFT, Lanczos, Normalized-correlation, MSE.

I. INTRODUCTION

Checking products in the factory, the image includes blur, noise and so on. Using the original size image, we need long computation time and the accuracy of the detection becomes lower on account of blur and noise. If we use down-sampled image, we can reduce the calculation time, blur and noise. However, the accuracy of the detection also becomes low and there are a few researches to estimate the optimal resolution for the detection. So, our purpose is to propose new criterion that is independent of input images and determined only by the template image. Using down-sampled images, we need to use the feature that is scale invariant in order to achieve our purpose. We adopt the SIFT[1] feature and improve the SIFT. We have proposed new criterion by using the SIFT feature, the normalized correlation and the MSE. Finally we have confirmed that our proposed method is useful by the simulation.

II. IMPROVEMENT ON THE SIFT

We compute the SIFT feature of the template and the input image and use them for estimation of the

Fig.1. Using simple algorithm

$$\begin{aligned} G(2x, 2y) &= I(x,y) \\ G(2x+1,2y) &= (I(x,y)+I(x+1,y))/2 \\ G(2x,2y+1) &= (I(x,y)+I(x,y+1))/2 \\ G(2x+1,2y+1) &= (I(x,y)+I(x+1,y)+ \\ &\quad I(x,y+1)+I(x+1,y+1))/4 \end{aligned} \tag{1}$$

$$G(x,y): Output \quad I(x,y): Input$$

optimal image resolution and the detection. In the first stage of the SIFT, the image is up-sampled and down-sampled by using simple algorithms which do not interpolate in order to reduce the computation time. The down-sampling algorithm is the 4 neighbor averaging and the up-sampling algorithm is defined as the above equation.

We show the example using simple algorithm in Fig.1(double scale). The image in Fig.1 is not high quality and loses some features, because we use algorithms which do not interpolate. Thus, we need to change simple algorithm for advanced algorithm which interpolate not to lose features. We adopt three famous interpolation algorithms (Lanczos3[2], Bicubic, Bilinear). We experiment with the best combination of up-sampling and down-sampling algorithms on 9 following images. The original resolution of these images are VGA and we use down-sampled images from 160x120 to 80x60[pixel]. We compute corresponded keypoints between original resolution images and down-sampled images by using SIFT feature and show the result following Table1.

©ISAROB 2009

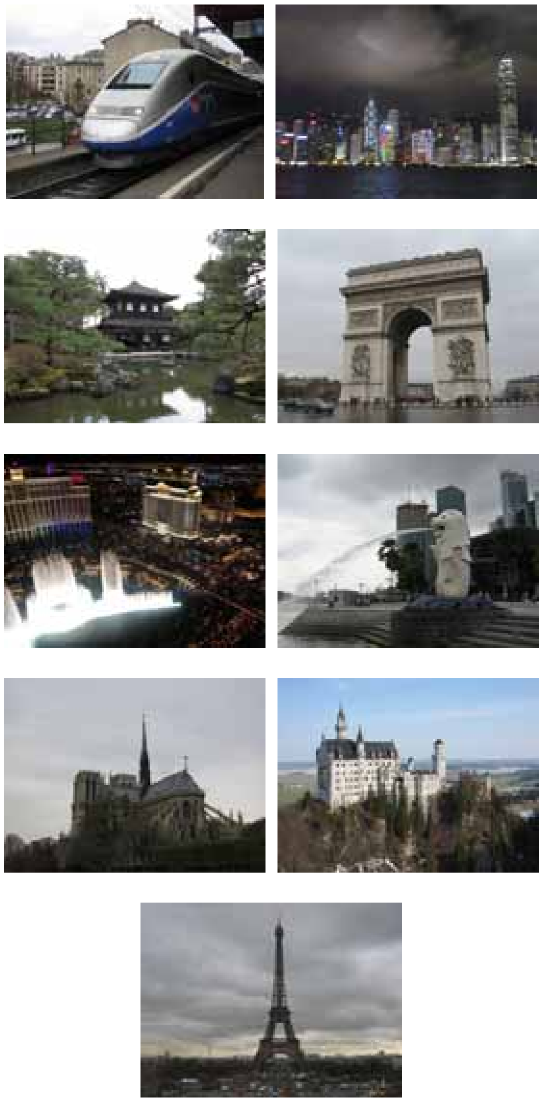

Fig.2. Using images

Table.1. Matching rate (%)

Up \ Down	Original	Bi linear	Bi cubic	Lanc zos3
Original	39.1	39.8	29.3	31.4
Bilinear	38.2	38.9	28.1	30.4
Bicubic	39.4	42.7	30.7	33.0
Lanczos3	39.5	42.9	32.9	34.5

As the results, the best combination is the bilinear as the up-sampling algorithm and the lanczos3 as the down-sampling algorithm and the matching rate is improved and 14% as Max and 3.8% as average are achieved. We use this improved SIFT in this paper.

As the resolution become lower, the number of SIFT keypoints and matching SIFT keypoints to original resolution changes.

Fig.3. Template image

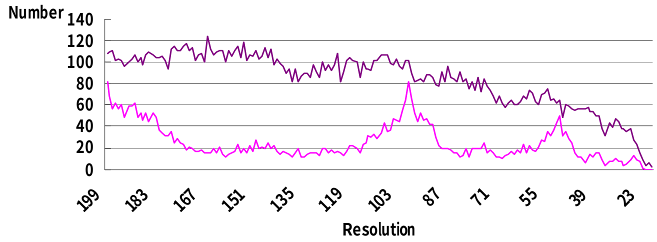

Fig.4. Number of keypoints and matching Keypoints of Fig.3

The original resolution of the template image is 200x200 [pixel]. The purple line shows the number of keypoints and the pink line shows the number of matching keypoints to ones in the original resolution in Fig.4.

The minimum resolution that has matching keypoints to ones in the original resolution is 23 x 23[pixel]. The input image of the SIFT is converted to double size, half size and …. of the original resolution in computing the SIFT feature. Thus, at 1/2 size and 1/4 size…. of the original resolution, there are many matching keypoints. From Fig3., purple and pink line do not show simple behavior. So, we need to use not only the SIFT feature but also other feature for proposing new criterion.

III. OUR PROPOSED METHOD

1. Normalized correlation and MSE

The SIFT feature is described by using neighbor gradients of the keypoint. So, the SIFT feature describes not global features of the image but local features of the image. Therefore we need to combine it with global features of the image to estimate the optimal image resolution. So, we adopt the normalized correlation and the MSE as the global feature. We compute them between original resolution of the template image and the down-sampled template image. There is a little difference in the normalized correlation between them and a large difference in the MSE between them.

©ISAROB 2009

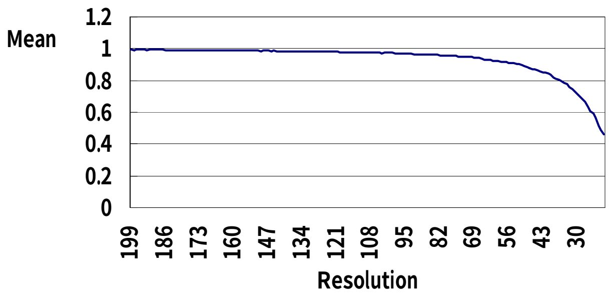

Fig.5. Mean between the NC and the 1-normalized MSE

So, we use the mean of the normalized correlation and the MSE. However, as the resolution becomes lower, the normalized correlation becomes lower and the MSE becomes higher. So, we reverse the MSE. We need to normalize the MSE because maximums of the MSE and the normalized correlation are not same. We normalize the MSE with the maximum of it. We compute the mean between the normalized correlation and (1 - normalized MSE). We use this mean as the global feature of the image. We show the value of mean between normalized correlation and (1 –normalized MSE) in Fig.5.

2. OUR CRITERION

In this section, we propose new criterion to estimate the optimal image resolution by using the SIFT feature, the normalized correlation and the MSE. We define the new fitness function:

$$F(x)=\left(0.9g(x)+0.1\frac{x}{K}\right)\left(\frac{NC+(1-normalizedMSE)}{2}\right) \quad (2)$$

$$g(x)=\left(1-\frac{1}{1+\left(\frac{x}{4}\right)^2}\right)$$

where x the number of matching keypoints to ones in the original resolution, K the number of keypoints and NC the value of the normalized correlation. The x / k means the matching rate, g(x) means the function of the number of matching keypoints and the mean of the normalized correlation and the reversed and normalized MSE means the criterion of the global features of the image. We show the behavior of g(x) in Fig.6. We use normalized value as the global features of image, so we use the normalized value as the local feature of the image. We adopt the function of the number of matching keypoints and matching rate as the local feature of the image because

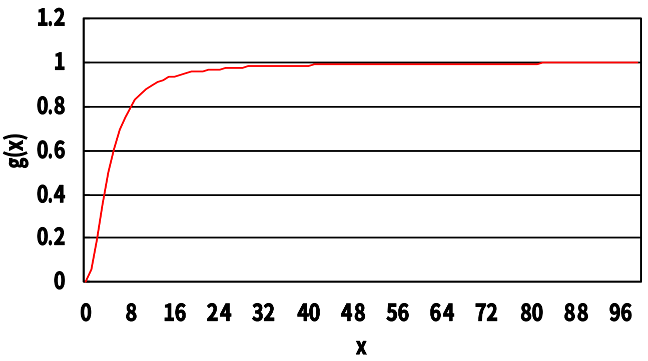

Fig6. g(x) the function of number of matching keypoints

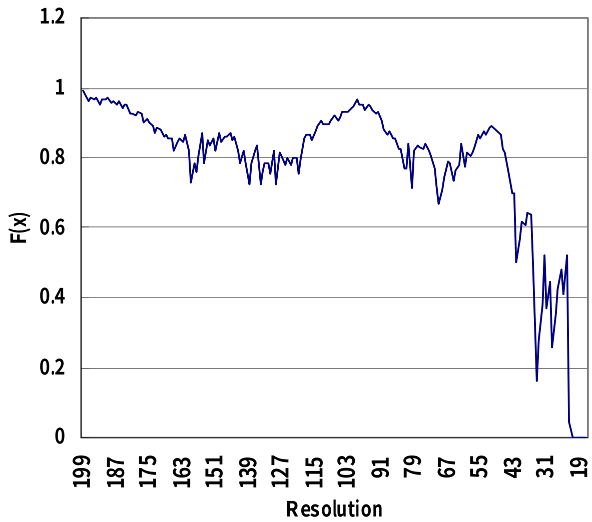

Fig.7 Fitness function of the optimal resolution

they mean how many local features the down-sampled image keeps. If there are two other resolution which have same matching keypoints, we select the resolution which has higher matching rate than another resolution. However the number of matching keypoints is more important than the matching rate. So, we weight the function of matching keypoints.

If the value of this fitness function is more than 0.4 at some resolution, that resolution is better. The minimum resolution where the value of our fitness function is more than 0.4 is the optimal resolution. We show the value of our fitness function with the template image in Fig.7. The behavior of our fitness function is not smooth. The half size, the quarter size and the 1/8 size images of the original resolution have more matching keypoints than other size images because the input image of the SIFT is converted to double size, half size, quarter size … of the original resolution in computing the SIFT feature. So, our fitness function has high value at 100, 50, 25.

©ISAROB 2009

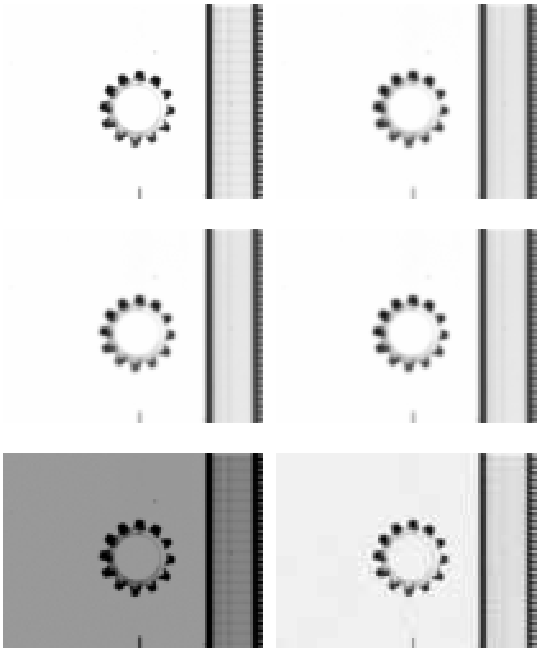

Fig.8. Input images

IV. SIMULATION

We show input images used for simulation in Fig.8. Original resolutions of them are VGA size. Checking products in factories, images include blur, noise and so on. So, we use not only the normal image but also three blur images, the noise image and the dark image as input . All input images are made from the normal image. Gaussian radiuses of three blur images are 5, 7 and 10. The dark image is 40 point darker than the normal image in brightness. The noise image is made by RGB diffusion and its parameters are 0.3 respectively. Based on our proposed criterion, the optimal image resolution is 24 x 24[pixel] in all resolution. So, down-sampling rate is 12%. The template image and input images are down-sampled to 12% and check whether we can detect or not. We show result in Table.2. In all input images, there are more than 5 matching keypoints, so we can detect the template from input images. We have confirmed that our proposed criterion is useful for not only the normal image but also blur, noise and dark input images. And we simulate with 11.5% down-sampled template and input images. There is no matching keypoints, so we can not detect the template from the noise image. Therefore, the down-sampling rate, at 12%, is the optimal and our proposed fitness function is effective. We use only one template image in this simulation. So, we need to simulate with more other template images and input images.

Table.2. Result of the detection (12%)

	Normal	Blur.5	Blur.7
Detection	○	○	○
	Blur.10	Dark	Noise
Detection	○	○	○

Table.3. Result of the detection (11.5%)

	Normal	Blur.5	Blur.7
Detection	○	○	○
	Blur.10	Dark	Noise
Detection	○	○	×

V. CONCLUSION

We have improved the SIFT feature by changing up-sampling and down-sampling algorithm and confirmed usefulness by the experiment. We have proposed the criterion that is independent of input images and robust. We have confirmed that our proposed method is useful by simulation. As the future work, we improve the SIFT feature and our criterion and use other image features such as edge.

REFERENCES

[1]David.G.Lowe, "Distinctive Image Feaures from Scale-Invariant Keypoints". International Journal of Computer Vision Vol.60,No.2,pp.91-110, 2004

[2]Ken.Turkowski. "Filters for Common Re-sampling Tasks" Graphic Gems I, Academic Press, p p. 147-165, 1990

[3]Mikio Takagi and Haruhisa Shimda, "Handbook o f Image Analysis [Revised Edition]", University ofTo kyo Press, 2004

[4]Philippe Thevanaz et al, "Image Interpolation and Resampling", Handbook f Medical Imaging, Proce-ssing and Analysis, I.N.Bankman, ED., Academic Press, San Diego CA, USA, pp. 393-420, 2000

©ISAROB 2009

Smell Classification by Neural Networks

Michifumi Yoshioka+, Toru Fujinaka++, and Sigeru Omatu+
Osaka Prefecture University, Sakai, Osaka 599-8531, Japan
: omatu@cs.osakafu-u.ac.jp
++Hiroshima University, Higashihiroshima, 739-8524, Japan

Abastract

In this paper, a reliable electronic nose (EN) system designed from the combination of various metal oxide gas sensors (MOGS) is applied to detect the early stage of fire from various sources. The time series signals of the same source of fire in every repetition data are highly correlated and each source of fire has a unique pattern of time series data. Therefore, the error back propagation (BP) method can classify the tested smell with 99.6% of correct classification by using only a single training data from each source of fire. The results of the k-means algorithms can be achieved 98.3% of correct classification which also show the high ability of the EN to detect the early stage of fire from various sources accurately.

1. Introduction

Every year the damage from the household fire disaster brings about not only severe loss to property assets, but also physical and psychological injuries of the people. Although most of the residences have installed the fire detectors system such as smoke detectors, those devices cannot detect the early stage of fire since their warning signals are triggered by the high smoke density or the high air temperature. In this paper, the reliability of a new electronic nose (EN) system developed from various metal oxide gas sensors (MOGSs) to specify the smell from various sources of fire is presented.

Jame A. Milke [1] has proved that two kinds of MOGSs have the ability to classify several sources of fire more precisely than conventional smoke detector. However, his results can be achieved only 85% of correct classification. In this paper, a new EN that has been successfully applied to classify not only the same smell from different brands, but also the same smell at different concentration levels [2] is applied to measure smells from various sources of fire such as household burning materials, cooking smells, the leakage from the liquid petroleum gas (LPG). The time series signals of the MOGSs from the beginning to the time until the MOGSs are fully absorbed the smell from each source of fire are recorded and analyzed by the error back propagation (BP) neural networks and the k-means algorithms. The average classification rate of 99.6% can be achieved by using the BP method with only a single training data from each source of fire. The results from the k-means algorithm can be achieved 98.3% of correct classification that also confirms the reliability of this new device to be able to detect various sources of fire in the early stage much better than the results of Jame A. Mike [1].

2. Metal Oxide Gas Sensors for EN

A commercial MOGS has been developed widely for more than thirty years.

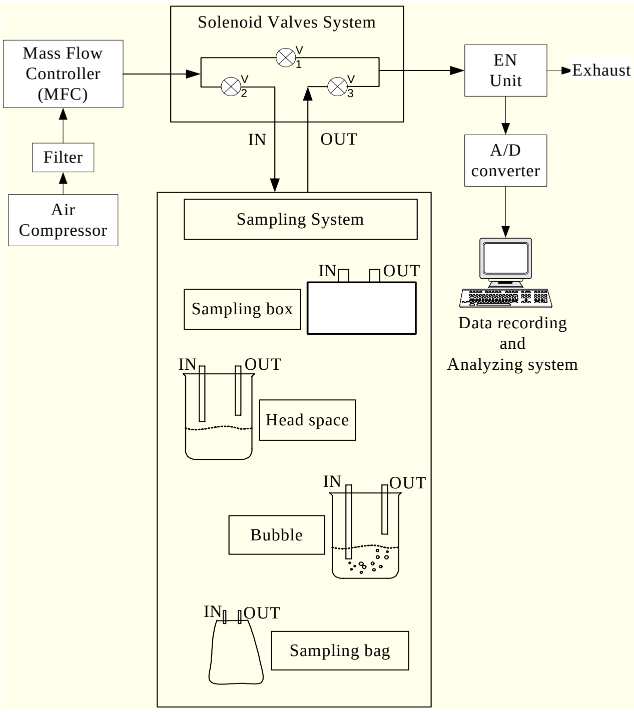

Fig. 1 Schematic diagram of the electronic nose system.

Generally, it is designed to detect some specific smell in electrical appliances such as an air purifier, a breath

©ISAROB 2009

alcohol checker, and so on. Each type of MOGS has its own characteristics to response to different gases. When combining many MOGSs together, the ability to detect the smell is increased. An EN system shown in Fig. 1 has been developed based on the concept of human olfactory system by using the combination of MOGSs from FIS Inc. listed in Table I as the olfactory receptors in the human nose. The MOGSs unit is combined with the air flow system to flow the air and the tested smell into the MOGSs unit. The data logger converts the analog signals to digital signals and stores them in the data recording system before being analyzed by multivariate analytical methods, such as the BP method and the k-means algorithms.

The main part of the MOGS is the metal oxide element on the surface of the sensor. When this element is heated at a certain high temperature, the oxygen is absorbed on the crystal surface with the negative charge. The reaction between the negative charge of the metal oxide surface and deoxidizing gas makes the resistance of the sensor vary as the partial pressure of oxygen changes [3]. Based on this characteristic, we can measure the total voltage changes during the sensors absorbing the tested odor.

Table I List of MOGSs from the FIS Inc.

Sensor Model	Main Detection Gas
SP-53	Ammonia, Ethanol
SP-MW0	Alcohol, Hydrogen
SP-32	Alcohol
SP-42A	Freon
SP-31	Hydrocarbon
SP-19	Hydrogen
SP-11	Methane, Hydrocarbon
SP-MW1	Cooking vapor

Since the MOGS is sensitive to the temperature and the humidity, the MOGSs unit is put in a small chamber that has a heating system to increase the air temperature during winter season. The heating unit can also decrease the air humidity in the chamber. The clean water is manually sprayed into the chamber when the humidity drops lower than the control level. In this experiment the temperature in the chamber is kept between 20-30°C and the humidity is kept between 30-40%RH. The tested smell is sucked to mix with the fresh air before passing to the MOGSs unit. The distance from the tested smell to the MOGSs unit is approximately 1.5 m.

3. Experimental Data Collection

The smell from twelve sources of fire listed in Table II are measured by the EN system explained in previous section. Each source of fire has been tested with forty repetition data measured in different days in order to check the repeatability response of the MOGSs to the same smell.

For each data, the voltage signal of the normal air is measured every second for one minute and its average value, $\bar{v}_{air}$, is used as an air reference point. After that, the voltage signals of the sensors when absorbing tested smell, $v_{smell,t}$, are collected every two minutes for each smell sample. Finally, the total change in signals at each period, $V_{smell,t}$, is calculated by

$$V_{smell,t} = v_{smell,t} - \bar{v}_{air}$$

where t is the time from 1 to 120s.

After testing one smell the MOGSs need to be cleaned by removing the tested smell and supplying only the fresh air until the MOGSs return to stable point before testing the new sample. This process is just like the human nose which need to breath the fresh air before able to recognize the new smell accurately. Some time series data from the experiment in Fig.2 show that all smells approach the saturation stages within the measuring periods. The signals from the same source of fire in every repetition data are similar in most data sources. The results using the BP method and the k-means algorithm to analyze the time series data from each source of fire every two seconds and the average signals during the saturation stages(time 100-120s) are discussed in Section V.

Table II List of Burning Materials in the Experiment

Sources of fire	Abbreviation
Steam from boiling water	Steam
Burning joss stick	Joss
Burning mosquito coil	Mos
Aroma oil	Aroma
Aroma candle	Candle
Flame from liquid petroleum gas(LPG)	Flame
Leakage of LPG	LPG
Steam from Japanese soup called "oden"	Oden
Boiling vegetable oil	Oil
Toasted bread	Toast
Burning paper	Paper
Burning wood	Wood

4 Correlation of the Experimental Data

Before classifying each source of data, the correlation of each data source is investigated by using the similarity index (SI) and the principal components analysis (PCA).

4.1. Similarity index

In the statistical application, the correlation value developed mainly by Karl Pearson is widely used to find the relationship between two random variables. In this paper, we call the correlation value as a similarity index (SI). The SI value varies from -1 to 1. Two random variables with a SI of either 1 or 1 are highly correlated because knowledge of one provides precise knowledge of the other. However, the SI provides information only about linear relationships between random variables.

©ISAROB 2009

Random variables could have a nonlinear relationship but still have a SI close to 0 [4]. Therefore, we make an assumption on this application that each data pattern has nearly linear relationship to the other data patterns. The SI value between two data is calculated by

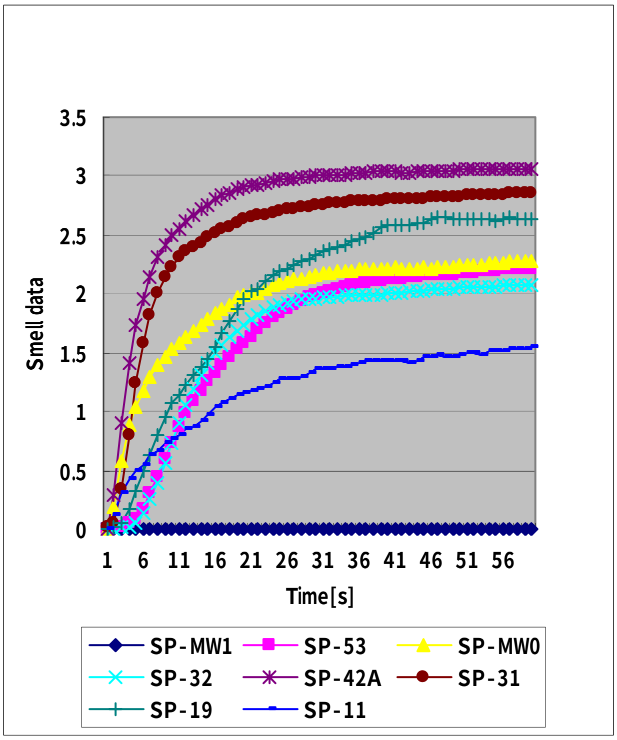

Fig.2 Time series data from some sources of fire in the experiment.

$$r_{xy} = \frac{\sum_{i=1}^{n} x_i y_i - n\overline{x}\overline{y}}{\sqrt{(\sum_{i=1}^{n} x_i^2 - \overline{x}^2)(\sum_{i=1}^{n} y_i^2 - \overline{y}^2)}}$$

where r_{xy} is the SI value, x and y are the comparing data, $\overline{x} = \frac{1}{n}\sum_{i=1}^{n} x_i$, $\overline{y} = \frac{1}{n}\sum_{i=1}^{n} y_i$, and n is the size of each data which equals 480 (60 periodsx8 sensors).

By using the SI to find the relationship between the repetition data of each data source, we found that all data sources except the paper and the wood have high average SI values above 0.99. During the experiment, the paper and the wood have inconsistent burning rates, therefore the signals from the repetition data of these sources are more fluctuated than the other sources that have better consistent burning rate.

4.2 Principal components analysis

In this paper, the well known PCA is applied to analyze two cases of the experimental data. The full time series data case uses the data signals every two seconds, but the saturation stage data case uses only the average data from time 100 to 120s for analyzing.

The plots of two main components are shown in Fig.3. The distribution of the paper and the wood burning smell are more scattered than the other kinds of smells especially in the case of saturation stage data. Most of the tested data are separated into their own clusters with some overlap zones between different data source.

5. Experimental Results and Discussion

5.1 Experimental result

Two case of data are analyzed by the BP method and k-means algorithm. The full time series data (TSD) case uses the data from all MOGSs every two seconds as the input data. The saturation stage data (SSD) case uses only the average value from time 100 to120s of all sensors as the input data.

The BP structure contains three layers. The input layer of the TSD case, and the SSD case consists of four hundred eighty nodes (8 sensors x 60 periods), and eight nodes(average signal from 8 sensors), respectively. For the hidden layer, we have tried with several values and the size that gives a good accuracy and a reasonable training time for both data cases is forty nodes. The output layer contains twelve nodes, each node represents one data source. The learning rate, the momentum rate, and the minimum mean square error (MSE) during the training period are set by trial and error method to 0.1, 0.001, and 0.0003, respectively.

Based on the information during investigating the correlation of the data, most data sources are highly correlated to their repetition data with high SI values. Therefore, only one data that has the highest average SI value to the other repetition data from each sources of fire are used as the training data for the BP and the rest of the data are used as the test data. We assume that a pattern is classified correctly if (output $\leq$ 0.7 and target=1) or (output $\leq$ 0.3 and target =0). For the k-means algorithm, the training data of the BP method are used as the initialize data and then assigns the data patterns to the nearest cluster center by calculating the Euclidean distance. After that, the new cluster center is recalculated. The process continues until the position of the cluster center is not changed. The final results of this experiment are shown in Table III.

The results using the TSD from both the BP method and the k-means algorithm are sufficiently effective. The data signals from the MOGSs are affected by many factors, such as the sampling condition, the inconsistency burning rate, the fluctuation from the standard air, and so on. Therefore, the saturation stages of the data are varied by those factors. By including the signal before approaching the saturation stage, the accuracy to classify all smell is increased.

5.2 Discussion

Although the distribution of PCA shown in Fig. 3 cannot clearly separate similar smell such as the aroma oil and the aroma candle, the BP method and the k-means algorithms are able to classify them perfectly as shown in Table III. The results of TSD using the BP method have only two incorrect classified data. These two data are not misclassified as the other smells. Only the output values of their paper node are not high enough to classify them as the paper. The output values of these two data on the paper node are only 0.4951, and 0.4799, respectively and the output of the others output nodes are nearly 0. The results are much better than the results from [1] which used two kinds of MOGSs to classify several sources of fire into three fire condition levels, flaming, smoldering, and nuisance, with only 85% of correct classification. The smoke density of the tested data is not high enough to trigger the alarm of the smoke detector. In case of unusual burning smells in the residences such as the wood burning, flaming from the LPG, or the leakage LPG, it is necessary to have a proper device to detect these sources before unable to stop the fire. We can conclude that the new EN system shown in this paper is a proper device for this application.

6. Conclusions

We have proposed a new EN system designed from various kinds of MOGSs. The EN has the ability to identify various sources of fire in the early stage with more than 99% of accuracy by using only a single training data in the BP case. The results from the k-means algorithm are also able to predict the sources of fire with more than 98% of accuracy. It can be concluded that the EN is suitable for detecting the early stage of fire.

References

[1] Jame A.Mike, "Applicaiton of Neural Networks for Discriminating Fire Detectors", International Conference on Automatic Fire Detection, AUBE'95, 10th, Duisburg, Germany, pp.213-222, April 4-6, 1995.

[2] Bancha Charumporn, Michifumi Yoshioka, Toru Fujinaka, and SigeruOmatu, "An Electronic Nose System Using Back Propagation Neural Networks with a Centroid Training Data Set", proceeding of the Eight International Symposium on Artificial Life and Robotics, Japan, pp.605-608, January 24-26, 2003

[3] General Information for TGS sensors, Figaro Engineering, available at www.figarosensor.com/products/general.pdf. M. Tanaka, "Modeling of Mixtures of Principal Component Analysis Model with Genetic Algorithm," Proc. 31st Int'l Symposium on Stochastic Systems Theory and Its Applications, pp. 157-162, Yokohama, Japan, 1999.

[4] William L. Carlson and Betty Thorne, Applied Statistical Methods, Prentice Hall International, 1997

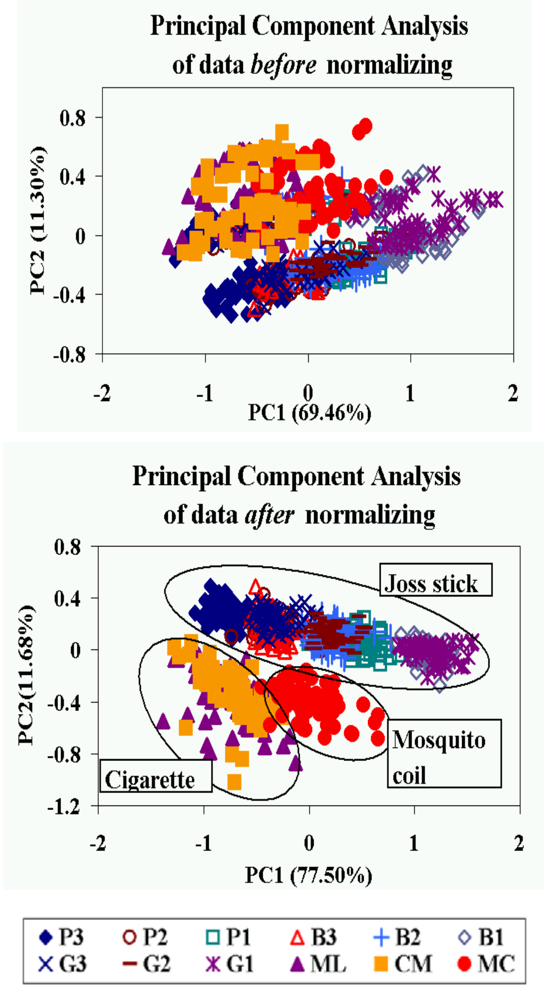

Fig.3. Two main components of the experimental data using the PCA.

Table III Experimental Results

Sources	TSD				SSD			
	BP		k-means					
	True	%	True	%	True	%	True	%
Steam	39/39	100	40/40	100	38/39	97	39/40	98
Joss	39/39	100	40/40	100	39/39	100	40/40	100
Mos	39/39	100	40/40	100	39/39	100	40/40	100
Aroma	39/39	100	40/40	100	39/39	100	40/40	100
Candle	39/39	100	40/40	100	39/39	100	40/40	100
Flame	39/39	100	40/40	100	39/39	100	40/40	100
LPG	39/39	100	40/40	100	39/39	100	40/40	100
Oden	39/39	100	40/40	100	39/39	100	40/40	100
Oil	39/39	100	40/40	100	38/39	97	37/40	93
Toast	39/39	100	40/40	100	38/39	97	40/40	100
Paper	38/39	95	35/40	88	31/39	80	28/40	70
Wood	39/39	100	37/40	93	32/39	82	28/40	70
Average		99		98		96		94

©ISAROB 2009

The Fourteenth International Symposium on Artificial Life and Robotics 2009 (AROB 14th '09),
B-Con Plaza, Beppu, Oita, Japan, February 5 - 7, 2009

Bill Money Classification by Neural Networks

Michifumi Yoshioka[+],Sigeru Omatu[+], and Toshihisa Kosaka[++],
[+]Osaka Prefecture University, Sakai, Osaka 599-8531, Japan
: omatu@cs.osakafu-u.ac.jp
[++]Glory TD Himeji, Hyougo 670-8567 Japan

ABATRACT

For the pattern classification problems the neuro-pattern recognition which is the pattern recognition based on the neural network approach has been paid an attention since it can classify various patterns like human beings. In this paper, we adopt the learning vector quantization(LVQ) method to classify the various money. The reasons to use the LVQ are that it can process the unsupervised classification and treat many input data with small computational burdens. We will construct the LVQ network to classify the Italian Liras. Compared with a conventional pattern matching technique, which has been adopted as a classification method, the proposed method has shown excellent classification results.

1. INTRODUCTION

Bill money classification by transaction machines has been important to make progress the office automation[1]. Since sizes of bills are different according to kinds of bills, the measurement data of bills include various variations. Human being can classify the bills correctly even if they are suffered from those variations such as rotation and shift. But usual pattern recognition using a conventional transaction machine cannot give us the correct classification result under such cases since the basic method is a pattern matching principle. Furthermore, the conventional pattern matching method requires many template patterns for many kinds of bills, which takes much time and needs much experience[1].

Recently, neural networks which are based on the biological mechanism of human brain have been focussed since they have intelligent pattern recognition ability[2]. In this paper, we will apply the neural network approach to classify the bill money under various conditions by using transaction machines. The learning vector quantization(LVQ) has been used to classify the bills since it can treat high dimensional input and has simple learning structure[3]. The LVQ network adopted here has 64x15 units in the input layer and many units at the output layer. The bills are Italian Liras of of 8 kinds, 1,000, 2,000, 5,000, 10,000, 50,000 (new), 50,000 (old), 100,000 (new), 100,000 (old) Liras with four directions A,B,C, and D where A and B mean the normal direction and the upside down direction and C and D mean the reverse version of A and B. The simulation results show that the proposed method can produce the excellent classification results.

2. COMPETITIVE NEURAL NETWORKS

We will explain the competitive neural networks that are used to classify the bill money. The structure of a LVQ competitive network is shown in Fig. 1. The input for the LVQ is bill money data where an original image consists of 128x64 pixels and the input data to the network is compressed as 64x15 pixels to decrease the computational load. The output of the network consists of the Italian Liras of 8 kinds, 1,000, 2,000, 5,000, 10,000, 50,000 (new), 50,000 (old), 100,000 (new), 100,000 (old) Liras with four directions A,B,C, and D where A and B mean the normal direction and the upside down direction and C and D mean the reverse version of A and B.

In the input layer the original bill money data are applied and all the units at the input layer are connected to all the neurons at the output layer with connection weight W_{ij} . W_{ij} denotes the connection weight from the unit j in the input layer to unit i in the output layer. The output layer will output only one neuron which is called winner neuron. The winner neuron is selected as the neuron with the minimum distance between an input vector and its connection weight vector. The connection weights W_{ij} are set by the random number at the beginning. Here, we set the mean vector of the cluster plus small random number. Then the following learning algorithm of the connection weight vector is used.

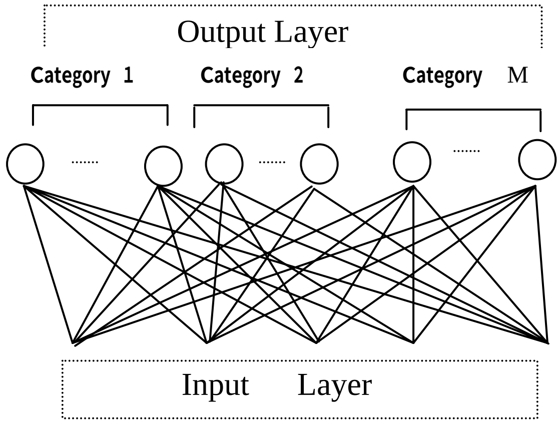

Fig. 1. Structure of the LVQ networks.

LVQ algorithm

Step 1. Find the unit c at the output layer which has the minimum distance from the input data **x** (t)

$$\|\mathbf{x}(t)-\mathbf{W}_c\| = \min_i \|\mathbf{x}(t)-\mathbf{W}_i\|$$

where $\|\ \|$ denotes the Euclidean norm and t denotes the iteration time.

Step 2. If the input **x** (t) belongs to Category c, then

$$\mathbf{w}_c(t+1) = \mathbf{w}_c(t) + \alpha(t)(\mathbf{x}(t) - \mathbf{w}_c(t))$$

$$\mathbf{w}_i(t+1) = \mathbf{w}_i(t)\ ,\quad i \neq c$$

and if input **x** (t) belongs to the other Category j (j$\neq$c), then

$$\mathbf{w}_c(t+1) = \mathbf{w}_c(t) - \alpha(t)(\mathbf{x}(t) - \mathbf{w}_c(t))$$

$$\mathbf{w}_i(t+1) = \mathbf{w}_i(t)\ ,\quad i \neq c$$

where $\alpha(t)$ is a positive function and denotes learning rate.

In the usual LVQ $\alpha(t)$ is given by $\alpha(t) = \alpha_0(1-\frac{t}{T})$

where (0<α_0<1) is a positive and T is a total number of learning iterations.

The above algorithm for selection of new weight vector Wc(t+1) can be explained graphically as Fig. 2 .

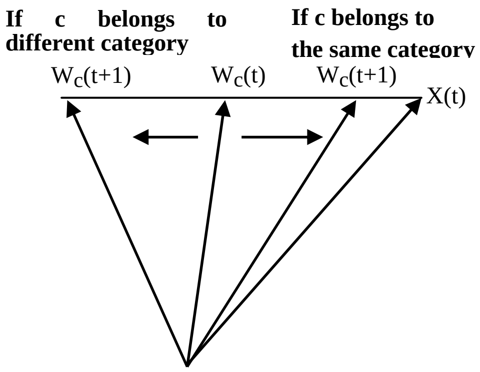

Fig.2. Principle of the LVQ algorithm where the right hand side shows the same category case of **x**(t) and Category c and the left hand side denotes the different category case.

In the above LVQ algorithm, the learning rate $\alpha(t)$ plays an important role for convergence. To adjust the parameter, Kohonen has proposed an optimization method without proof as follows:

$$\alpha_c(t) = \frac{\alpha_c(t-1)}{1+s(t-1)\alpha_c(t-1)}$$

where s(t) =1 if **x**(t) belongs to the same Category c and s(t)=-1 if **x**(t) does not belong to the same Category c. Here, $\alpha_c(t)$ denotes the learning rate for the pattern of Category C.

3. PREPROCESSING ALGORITHM

The images obtained by transaction machine, there are variations such as rotation or shift. Therefore, we must adjust the images such that the variations may be reduced as much as possible by using the preprocessing. The flow char of the preprocessing procedure is illustrated in Figure 3. In this figure, the original image with 128x64 pixels are observed at the transaction machine in which rotation and shit are included. After correction of these effects, we select a suitable aria which show the bill image and compressed as the image with 64x15 pixels to the neural networks. Although the neural network of the LVQ type could process any order of the dimension of the input data, the small size is better to achieve the fast convergence result. Thus, we have selected the above size of the image.

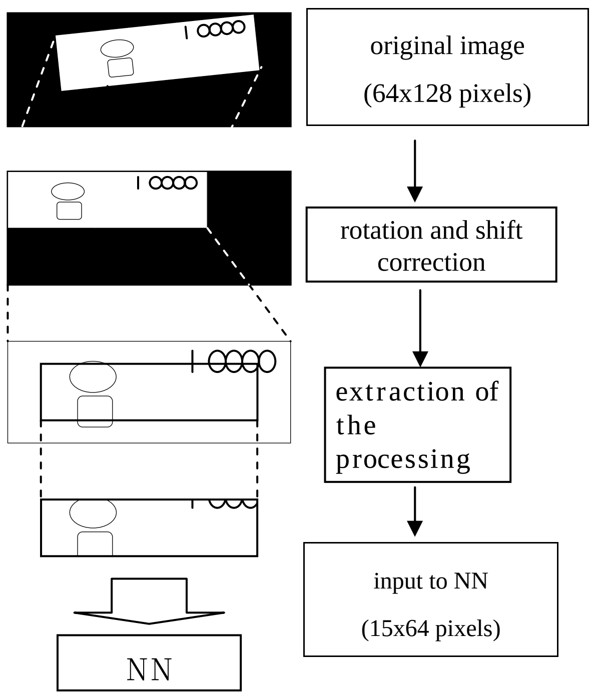

Fig. 3. Preprocessing algorithm.

4. ITALIAN LIRA CLASSIFICATION

The bills used here are Italian liras, which have 8 kinds such as 1,000 Liras, 2,000 Liras, 5,000 Liras, 10,000 Liras, new 50,000 Liras, old 50,000 Liras, new 100,000 Liras, and old 100,000 liras. Those Lira bills are used at the input of the transaction machine where

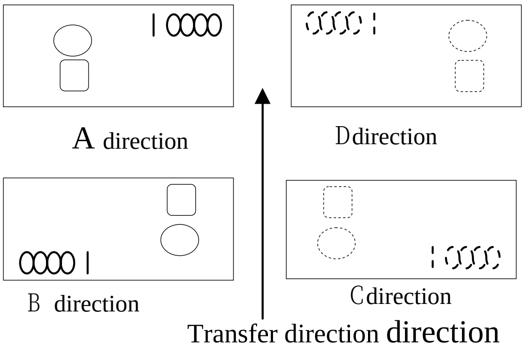

Fig. 4. Four directions of bill money.

(a) A direction of 1,000Lira

(b) B direction of 1,000 Lira

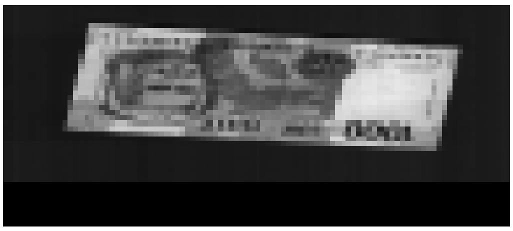

(c) C direction of 1,000 Lira

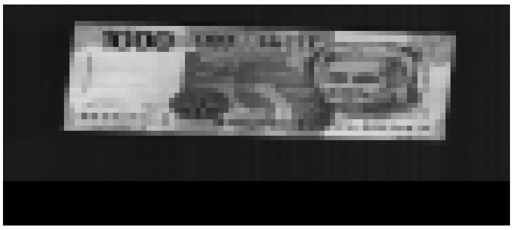

(d) D direction of 1,000 Lira

Fig.5. Image of four directions of 1,000 Lira.

four directions such as A, B, C, and D appear since normal direction, reverse direction, and their upside down directions occur at the input as shown in Fig.4.

The typical images of 1,000 Lira for four directions are shown in Fig.5. Thus, thirty-two bill images are one set of the classification pattern of the experiment. Total number of data sets is 30 and 10 data sets are used for training of the network and the remaining 20 data sets are used to test the network. In order to reduce the misclassification, we have set the threshold value d_θ such that if $d_c > d_\theta$, unit c is not fired. This means that if the minimum distance is not less than d_θ, the input data is not classified. The parameters of the neural network used here are as follows:

Number of units in the input layer=960

Number of units in the output layer in the initial state=32 where every 50 iterations the number has been adjusted.

Total learning timeT=150

$\alpha_i(0) = 0.5,\ i = 1,\cdots M$

Initial values of the weight vectors=mean vectors for training patterns

$d_\theta = \min_c (m_c + 4.5\sigma_c)$

After training the neural network, 20 data sets are tested how well the LVQ network could work. Table 1 denotes the recognition rate in the beginning(t=0), which means the result by the conventional pattern matching method. Table 2 shows the number of not fired numbers at t=0. Tables 3 and 4 show those values at t=160. We can see the improvement by learning. Table 5 shows the number of the neuron units at t=160 which are determined by increasing them.

From the original image data we can see that the difference between 50,000 Lira old and new is slight and the difference between old and new100,000 Liras. Therefore, it is rather difficult to recognize them so perfectly. but in this case the misclassification like old and new bills within the same values is not serious. Thus, we have regarded these misclassification as the correct one. Furthermore, we have introduced the threshold value to prevent from occurring the misclassification. Thus, even if the minimum distance criterion results in the correct classification, we have decided these bells are unknown. Without these threshold constraint, we could obtain 100% recognition rate in any case.

6. CONCLUSIONS

We have proposed a new classification method of Italian Liras by using the OLVQ1 algorithm. The experimental results show the effectiveness of the proposed algorithm compared with the conventional pattern matching method.

©ISAROB 2009

REFERENCES

[1] S. Fukuda, T. Kosaka, and S. Omatu: Bill Money Classification of Japanese Yen Using Time Series Data, Trans. Of IEE of Japan, Vol.115-C, No.3, pp.354-360, 9995(in Japanese).

[2] J. Dayhoff: Neural Network Architectures: An Introduction, International Thompson Computer Press, New York, 1990.

[3] T. Kohonen: Self-Organizing Maps, Springer, Berlin, 1995.

Table 1. Recognition rate(%) at t=0.

		Directions			
		A	B	C	D
Italian Liras	1,000	100	100	100	100
	2,000	100	100	100	100
	5,000	100	100	100	100
	10,000	100	100	100	100
	50,000(new)	100	100	100	100
	50,000(old)	85	100	80	95
	100,000(new)	100	100	90	100
	100,000(old)	100	100	95	90

Table 2. Not fired rate(%) at t=0.

		Directions			
		A	B	C	D
Italian Liras	1,000	20	15	15	10
	2,000	5	10	25	25
	5,000	15	20	5	0
	10,000	10	10	10	5
	50,000(new)	5	0	20	5
	50,000(old)	0	0	0	0
	100,000(new)	0	0	0	0
	100,000(old)	0	5	0	0

Table 3. Recognition rate(%) at t=160.

		Directions			
		A	B	C	D
Italian Liras	1,000	100	100	100	100
	2,000	100	100	100	100
	5,000	100	100	100	100
	10,000	100	100	100	100
	50,000(new)	100	100	100	100
	50,000(old)	100	100	95	95
	100,000(new)	100	100	90	100
	100,000(old)	100	100	95	90

Table 4. Not fired rate(%) at t=160.

		Directions			
		A	B	C	D
Italian Liras	1,000	5	0	5	0
	2,000	0	10	25	25
	5,000	15	20	5	0
	10,000	10	0	0	5
	50,000(new)	5	0	0	0
	50,000(old)	0	5	0	0
	100,000(new)	0	0	0	0
	100,000(old)	0	5	0	0

Table 5. Number of units after learning.

		Directions			
		A	B	C	D
Italian Liras	1,000	2	2	2	2
	2,000	2	1	1	1
	5,000	1	1	1	1
	10,000	1	2	2	1
	50,000(new)	2	1	1	1
	50,000(old)	2	1	3	1
	100,000(new)	1	1	1	1
	100,000(old)	1	1	1	1

©ISAROB 2009

Motion Analysis of Tripod Parallel Mechanism

Yasunobu HITAKA*, Yoshito TANAKA*, Yutaka TANAKA** and Ken ICHIRYU***

** Kitakyushu National College of Technology*
Tel : +81-93-964-7244
Email hitaka@kct.ac.jp

*** Hosei University*
**** KIKUCHI SEISAKUSHO*

Abstract: The Tripod Parallel Mechanism consists of three links of fixed length and a rigid platform, and they are connected by revolute joints. The platform can be achieved six-degree-of freedom (6-DOF) motion by the movement of the bottom ends of the three links on the horizontal plane. This mechanism has advantages over the common six extendible parallel manipulators. It has a much larger work space, simple structure and so on.

In this paper, it is shown that the vector analysis for this Tripod Parallel Mechanism and derive the positions of the bottom ends of three links for the attitude of platform by the inverse kinematics and the conditions of geometrically-constraint. And then, the trajectories of bottom ends of three links by numerical simulation are shown.

Keywords: tripod parallel mechanism, six degree of freedom, inverse kinematics, geometrically constraint

I. INTRODUCTION

The Stewart type Parallel Mechanism which achieves 6-DOF motion by coordinated motion of six actuators has many advantages compared with the conventional serial link mechanism [1]. They are:

- higher payload-to-weight ratio since the payload is carried by six cylinders in parallel,
- higher accuracy due to non-cumulative joint error,
- higher structural rigidity,
- simpler solution of the inverse kinematics equations.

On the other hand, this type manipulator has some weaknesses that are:

- small work space,
- complex structure

A different type of parallel mechanism is proposed in [2]. It consists of three links of fixed length and a rigid platform, and they are connected by revolute joints. The platform can be achieved 6-DOF motion by the coordinated movement of the bottom ends of the three links of fixed length on the horizontal plane. This mechanism has a much larger work space and simpler configuration than the Stewart type parallel mechanism.

Figure1 shows the same type of above parallel mechanism which is produced experimentally by us. We call this mechanism, "The tripod parallel mechanism". For our parallel mechanism, the planer motion of the bottom end of three links is actualized by the X-Y unit which consists of two linear drive actuators. From the experimental results, it was confirmed that the tripod parallel mechanism has much larger work space than the Stewart type parallel mechanism.

Fig.1. Tripod parallel mechanism

In this paper, as the next step of the research, it is reported that a vector analysis of the tripod parallel mechanism and a derivation method of the positions of bottom ends of three fixed links for the attitude of platform by the inverse kinematics and conditions of geometrically-constraint. And then, the trajectories of bottom ends of three links by numerical simulation are shown.

©ISAROB 2009

II. MOTION ANALYSIS

Manipulation tasks are usually given as a set of positions and orientations in the world reference frame of the platform trajectory. To achieve these tasks it is necessary to transform the platform trajectory into the motion of bottom ends of fixed length links. This transformation is known as the inverse kinematic problem and in this case, it is the calculation of the position of the three bottom ends from a given position and orientation of the movable platform.

1. Structure of the tripod parallel mechanism

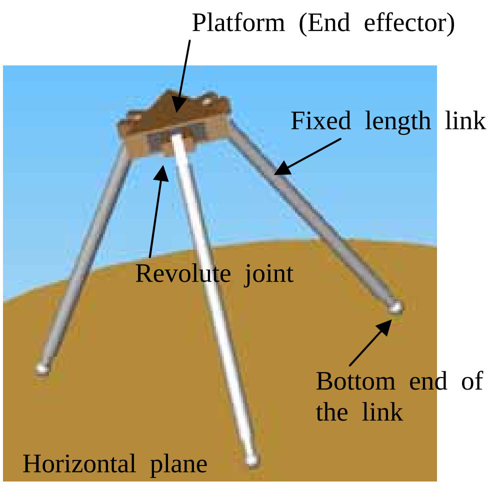

Fig.2. Simplified diagram of Tripod mechanism

As the preparation for motion analysis, we describe the structure of tripod parallel mechanism. As shown in Fig.2, the tripod parallel mechanism consists of a platform (end-effector) and three fixed length links, and they are connected by revolute joints. The bottom ends of three links are given two degree of freedom motion on the horizontal plane with any way. In the case of our experimental setup, this motion can be actualized by the pair of linear actuators.

Coordinated motion of three bottom ends of links is converted through a spatial mechanism with fixed length links, into a six-degree-of-freedom motion of the platform.

2. Vector analysis

Figure3 shows the vector diagram of the tripod parallel mechanism. Upper triangle plate "a_1, a_2, a_3" is platform and the sphere "○" is bottom end of link. These three bottom ends are constrained on the Horizontal plane. This system has two reference frames, $(\mathbf{i},\mathbf{j},\mathbf{k})^T$ and $(\mathbf{e}_1,\mathbf{e}_2,\mathbf{e}_3)^T$. (Using this notation that $\mathbf{i},\mathbf{j},\mathbf{k}$ and $\mathbf{e}_i$ denote the unit vectors along the respective coordinate axes for each of the two frames). The one is the motion frame which is located at the centroid of the platform. The other is the world reference frame. Sign $\mathbf{O}'$ denotes the origin of the motion frame and sign $\mathbf{O}$ denotes the origin of the world reference frame.

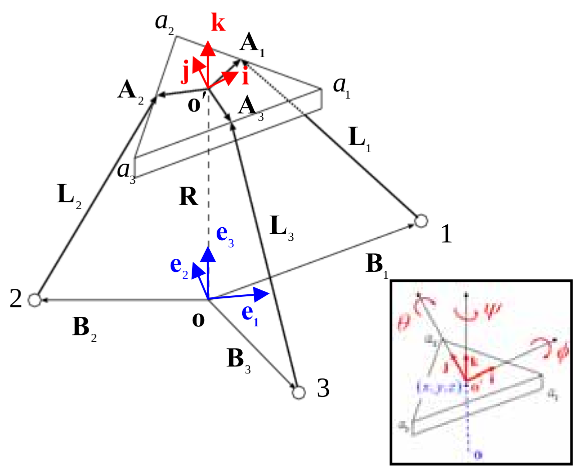

Fig.3. Vector diagram of Tripod parallel mechanism

Vector $\mathbf{A}_i = (a_{i1}, a_{i2}, a_{i3})(\mathbf{e}_1,\mathbf{e}_2,\mathbf{e}_3)^T \quad (i=1,2,3)$ denotes the revolute joint which connects the platform and the fixed length link, $\mathbf{B}_i = (b_{i1}, b_{i2}, b_{i3})(\mathbf{e}_1,\mathbf{e}_2,\mathbf{e}_3)^T \quad (i=1,2,3)$ is position vector of the bottom end of link and $\mathbf{R} = (x,y,z)(\mathbf{e}_1,\mathbf{e}_2,\mathbf{e}_3)^T$ is the position vector of centroid $\mathbf{O}'$ with respect to the world reference frame. For the foregoing vectors and the fixed length link vector $\mathbf{L}_i = (l_{i1}, l_{i2}, l_{i3})(\mathbf{e}_1,\mathbf{e}_2,\mathbf{e}_3)^T \quad (i=1,2,3)$, the following relation exists:

$$\mathbf{L}_i = \mathbf{A}_i + \mathbf{R} - \mathbf{B}_i \qquad (i=1,2,3)\,. \tag{1}$$

Using vector $\mathbf{A}_{im} = (a_{im1}, a_{im2}, a_{im3})(\mathbf{i},\mathbf{j},\mathbf{k})^T \quad (i=1,2,3)$ which denotes the revolute joint with respect to the motion frame and the coordinate transform matrix

$$\mathbf{T} = \begin{bmatrix} \cos\theta\cos\psi & \cos\theta\sin\psi & -\sin\theta \\ \sin\phi\sin\theta\cos\psi - \cos\phi\sin\psi & \sin\phi\sin\theta\sin\psi + \cos\phi\cos\psi & \sin\phi\cos\theta \\ \cos\phi\sin\theta\cos\psi - \sin\phi\sin\psi & \cos\phi\sin\theta\sin\psi - \sin\phi\cos\psi & \cos\phi\cos\theta \end{bmatrix}$$

, where ϕ, θ and ψ are "roll", "pitch" and "yaw" angles about $\mathbf{i},\mathbf{j},\mathbf{k}$ axes, respectively, link vector $\mathbf{L}_i$ can be rewrite as

$$\mathbf{L}_i = \mathbf{A}_{im}\mathbf{T} + \mathbf{R} - \mathbf{B}_i \qquad (i=1,2,3)\,. \tag{2}$$

Equation (2) denotes the relationship between 6-DOF attitude of platform (x,y,z,ϕ,θ,ψ) and link vector $\mathbf{L}_i$. This equation is called the inverse kinematic equation.

©ISAROB 2009

3. Derivation of bottom end position

Our purpose is to derive the bottom end of fixed length link vector $\mathbf{B}_i$ from an arbitrary six-degree-of freedom attitude $(x, y, z, \phi, \theta, \psi)$ of platform. However, the inverse kinematic equation (2) has another unknown vector, that is link vector $\mathbf{L}_i$. Thus, vector $\mathbf{B}_i$ can't be calculated by using only equation (2).

Here, we note the geometrically-constraint of tripod parallel mechanism. There are three conditions of the constraint. First, the length of each link is fixed. This condition can be described as follows:

$$|\mathbf{L}_i|^2 = \mathbf{L}_i \mathbf{L}_i^T = l^2, \quad (i = 1,2,3) \tag{3}$$

where l is the fixed length of link. Expanding equation (3), a quadratic vector equation

$$\begin{aligned} &\mathbf{A}_{im}\mathbf{A}_{im}^T + \mathbf{R}\mathbf{R}^T + \mathbf{B}_i\mathbf{B}_i^T \\ &+2\mathbf{R}\mathbf{T}^T\mathbf{A}_{im}^T - 2\mathbf{B}_i\mathbf{T}^T\mathbf{A}_{im}^T - 2\mathbf{R}\mathbf{B}_i^T - l^2 = 0 \quad (i = 1,2,3) \end{aligned} \tag{4}$$

, which has one unknown vector $\mathbf{B}_i$ is obtained. At this moment, considering second condition that the position of the bottom end of link is constrained on the horizontal plane, the component b_{i3} of vector $\mathbf{B}_i$ is equal to zero, that is, $\mathbf{B}_i = (b_{i1}, b_{i2}, 0)$. Third condition is that the link vector $\mathbf{L}_i$ and the lateral side vectors of platform, which are represented by

$$\overrightarrow{a_1 a_2} = (\alpha_1, \alpha_2, \alpha_3)(\mathbf{i}, \mathbf{j}, \mathbf{k})^T = \boldsymbol{\alpha}_1$$
$$\overrightarrow{a_2 a_3} = \boldsymbol{\alpha}_2, \quad \overrightarrow{a_3 a_1} = \boldsymbol{\alpha}_3$$

are consistently orthogonal. That is, inner product of both vectors is equal to zero as follows:

$$\boldsymbol{\alpha}_i \mathbf{T} \cdot \mathbf{L}_i = 0 \,. \tag{5}$$

Equation (5) is rewrite as

$$(\alpha_{i1}, \alpha_{i2}, \alpha_{i3})\mathbf{T} \cdot (\mathbf{A}_{im}\mathbf{T} + \mathbf{R} - \mathbf{B}_i) = 0 \,. \tag{6}$$

Equation (6) is a liner vector equation where $\mathbf{B}_i$ is the unknown vector. For equation (6), the component b_{i1} (or b_{i2}) is represented as

$$b_{i1} = P_{i1} b_{i2} + Q_{i1} \quad (\text{or} \quad b_{i2} = P_{i2} b_{i1} + Q_{i2}) \tag{7}$$

where P_{i1}, P_{i2}, Q_{i1} and Q_{i2} are coefficient vectors. Thus, the unknown vector $\mathbf{B}_i = (b_{i1}, b_{i2}, 0)$ can be derivative to solve the quadric equation (4) with equation (7). When the bottom end of link vector $\mathbf{B}_i$ can be derived, the link vector $\mathbf{L}_i$ can also be derived by equation (2).

4. Condition of solution

In the previous section, we presented the derivation of the position of bottom end of link. This method provides two solutions for each link since it is the derivation for the quadratic equation. This situation is shown in Fig.4.

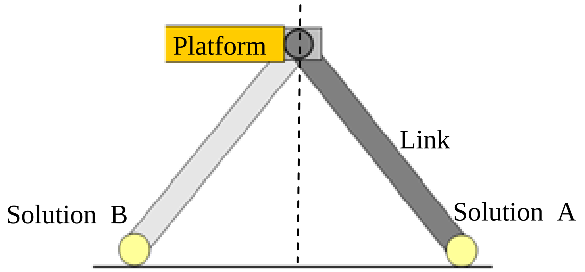

Fig.4. Existence of two candidates of solution

To avoid three links interfere with each other, and from the structural constraint that the link cannot revolve toward the platform from the vertical line through the upper revolute joint, we choose a solution which is outer region from the vertical line.

III. Numerical simulation

In this section, the numerical simulation results based on our analysis are shown. For this simulation, the length of each link is set to 250(mm) and three revolute joints are assigned from 30(deg) in the world reference frame at intervals of 120(deg) on the circumference of circle with radius 31.5(mm). The initial position of platform is set as [x_0, y_0, z_0] = [0.0, 0.0, 125] (mm) and initial orientation of platform is set as [ϕ_0, θ_0, ψ_0] =[0.0, 0.0, 0.0](mm). For the initial condition, we give three rotational motions. They are roll, pitch and yaw motion.

Figure 5 shows the trajectories of bottom ends of links for the roll motion of the platform. Where, the top is 3D graph where the vertical axis denotes the roll angle ϕ and sign B1, B2, B3 denote the bottom ends of 1st, 2nd and 3rd link, respectively. In this simulation, due to the condition of solution in the last chapter, the operating range of roll angle is restricted in -53.08 ~ 56.47(deg). This operating range is asymmetric since the assignments of links are asymmetric for roll axis.

Figure 6 and 7 show the results of pitch motion and yaw motion, respectively. As the simulation result for pitch motion, the operating range of pitch angle is restricted in -53.97 ~ 53.97(deg). This operating range is symmetric since the assignments of links are symmetric for pitch axis. For yaw motion, the operating area of each bottom end of link is not restricted. Thus, the operating range of yaw angle is not restricted.

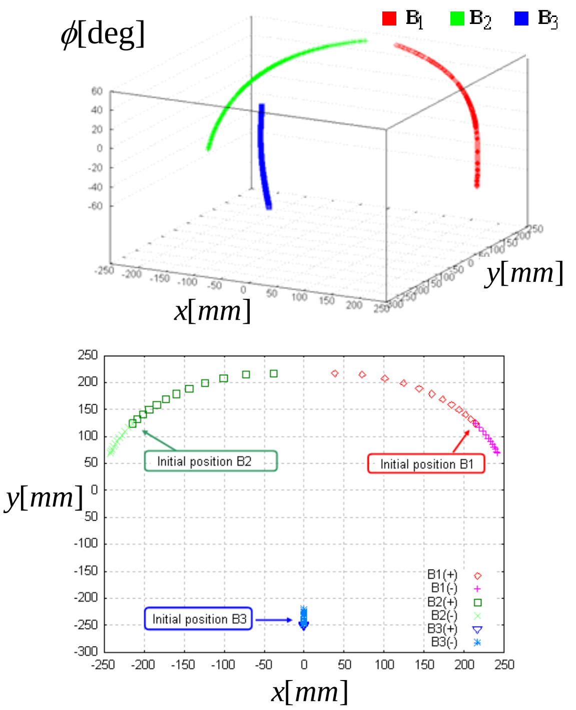

Fig.5 Result for roll motion

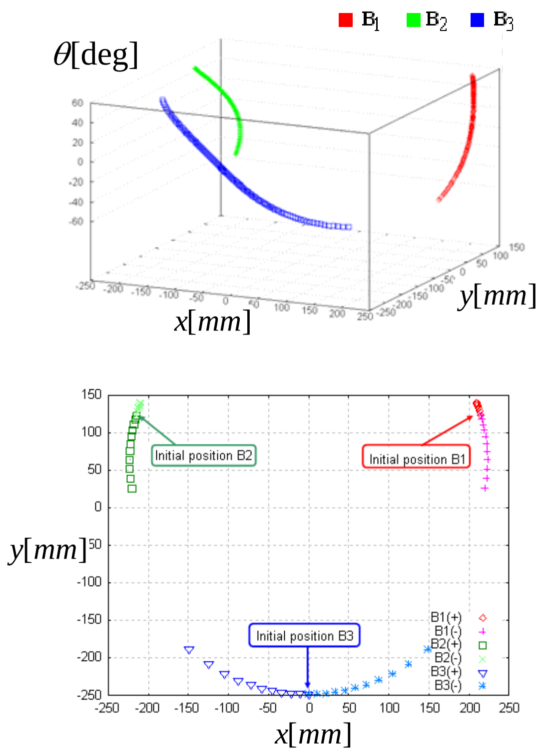

Fig.6 Result for pitch motion

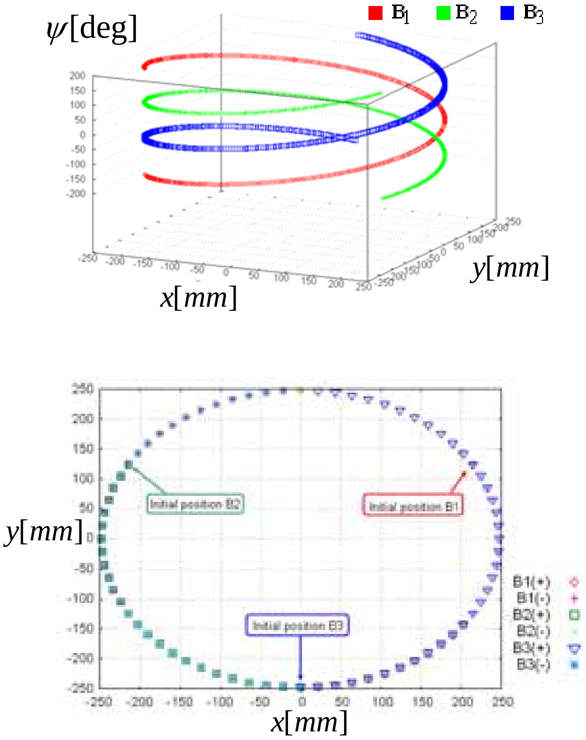

Fig.7 Result for yaw motion

Ⅳ. CONCLUSION

In this paper, we produced the vector analysis of the tripod parallel mechanism and derivation method of the position of bottom ends of three links for the attitude of platform by the inverse kinematics and conditions of geometrically-constraint. And then, we presented the numerical simulation results for our analysis.

In the future work, we'll confirm the analysis by a comparison between the simulation and the experiments for the actual tripod parallel mechanism.

REFERENCES

[1] Stewart.D, A Platform with 6 degrees of freedom, Proc. Inst Mech. Eng, Vol.180,Part 1, No15, pp.371-386, 1965-66.

[2] Ronen Ben-Horin, Moshe Shoham, and Shlomo Djerassi(1998),"Kinematics, Dynamics and construction of a planarly actuated parallel robot." Robotics and Computer-Integrated Manufacturing 14, 163-172

Development of a new positioning system for underwater robot based on sensor network

Bin Fu*, Feifei Zhang*, Masanori Ito*, Yoshitaka Watanabe**, Taro Aoki**

**Marine System Engineering, Tokyo Univ. of Marine Science & Technology, Tokyo, Japan*
***Japan Agency for Marine-Earth Science and Technology (JAMSTEC), Kanagawa, Japan*
(Tel : 81-3-5245-7422; Fax : 81-2-5245-7422)
(b_fujp@yahoo.co.jp)

Abstract: We are developing a new positioning system for underwater vehicle based on sound power decreasing with transmitted distance and sensor network technology. Conventional positioning system is using the difference between sounded time at station and received time on vehicle. However it is so much expensive, requires high operational cost and measuring field is not so wide. Then we need some new positioning system of low cost, easy operation, easy maintenance and high accuracy. Our system is expected to satisfy such kinds of requirements. At the first stage, we confirmed the principal with theoretical and experimental method. In the research, we treated only the directly arrived wave in the received data. It showed a good precision for short range of distance but also showed that it was easily affected by the reflected wave, and positioning area was limited with in only several hundred meters when the reflective surface existed near to receiver. Those were reported in AROB2008. Therefore, we tried a new idea that is using a low frequency sound and sending plural frequency sounds simultaneously, as the second stage of this study. We are trying to confirm the performance of the method. This paper showed the results of the simulation and the water tank experiment. With these improvements, the influence of reflection was suppressed and positioning area became larger than former research. Then the under water positioning system using sound power transmission loss will come to useful.

Keywords: Underwater positioning, Sensor network, Propagation loss

I. INTRODUCTION

Depending on the needs for natural resources inquiry, environmental protection and prediction of earthquake, the role of underwater vehicle becomes more and more important. In particular, the functional improvements for Autonomous Underwater Vehicle (AUV) which can achieve a given mission automatically without support of operator or mother ship in deep sea, is becoming an urgent matter. Recently, AUV-Urashima of the Japan Agency for Marine-Earth Science and Technology (JAMSTEC) has succeeded in the autonomous underwater navigation of 317km. [1] However, it proved that the conventional positioning system was not convenient and cannot perform the ability of AUV's autonomy completely. For this reason, a new type of underwater positioning system which is covering wide area, easy operation, easy maintenance, high accuracy and not so expensive is thought to be necessary for AUV's effective work.

Depending on these needs, we started to develop a new positioning system for underwater vehicle based on sound power decreasing with transmitted distance and sensor network technology. It is using monotone sound, so the system configuration becomes very simple, and system cost is lower than conventional system, which is using time difference between station and vehicle measured with high accurate clock. And sensor network can cover wide area. Then our system is expected to satisfy such kinds of requirements.

At the first stage, we confirmed the principal with theoretical and experimental method. In the research, we treated only the directly arrived wave in the received data. It showed a good accuracy for short range of distance but also showed that it was easily affected by the reflected wave, and measuring distance was not so long when the reflective surface was near. Those were reported in AROB2008[2][3]. Therefore, we tried a new idea that is using a low frequency and sending plural frequency sounds simultaneously, as the second stage of this study. We are trying to confirm the performance of the method. This paper showed the results of the simulation and the water tank experiments.

II. PRINCIPLE OF MEASUREMENT

We define sound power decreasing as that the amplitude of sound becomes small depending on a distance when a sound is propagating in a medium.

©ISAROB 2009

Sound power decreasing is composed of a diffusion decreasing, an absorption decreasing and a reflection decreasing. When the distance to reflective surfaces is far, we can get typical signal like Fig.1 (a). In this case, direct wave and reflected wave are divided clearly, then r[m] (Propagation can be calculated with PL[dB] (Propagation Loss) easily.[2][3] But when reflective surface is near or the propagation distance is far, the reflected wave is so near to direct wave and they become hard to separate as Fig.1 (b). fr[kHz] is Sound frequency.

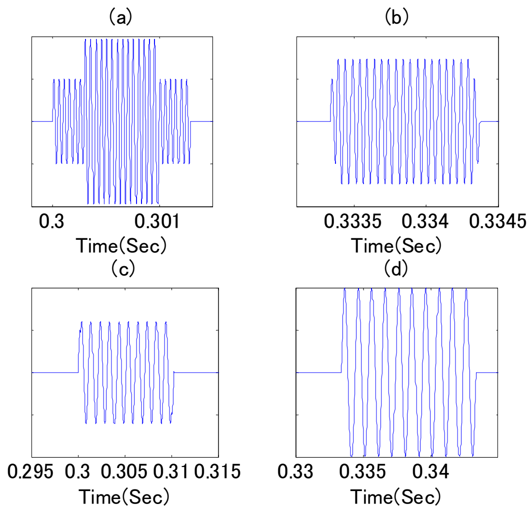

Fig.1. Examples of simulation
(a) fr=20kHz, r=450m; (b) fr=20kHz, r=3500m
(c) fr=1kHz, r=450m; (b) fr=1kHz, r=3500m

We could suppose that a sound wave produces specular reflection when it comes across flat-water surface, like Fig.2. [4] Evidently accompanied with the distance between sender and receiver, the difference of arrival time between direct wave and reflected wave becomes short.

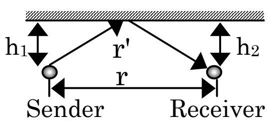

Fig.2. Reflection model
h_1: Depths of sender; h_2: Depths of receiver;
r: Propagation distance of the direct wave;
r': Propagation distance of the reflected wave;

In this case, if send a sound wave of lower frequency, we can find direct wave and reflected wave are nearly piled up with same phase as Fig.1 (d). The total energy of received wave can be calculated with the sums of energy of both waves. And the energy of reflected wave is proportional to the direct wave. So we suppose that the received power becomes k times of PL of the direct wave and error A, as Eq. (1). Here, k is influenced by reflectance, and it is measured on the site.

$$PL = k(20\log10(r)+\alpha r)+A \qquad (1)$$

However, this equation is only effective when the phase difference of both waves is smaller than $\pi/4$, and the error is affected with the phase difference. For example, when send sound waves of 1 kHz similarly, the phase difference of r=3500[m] is smaller than r=450[m] as Fig.1(c), (d). So the error by the phase difference shrinking. On the other hand, PL can also be calculated as Eq. (2).

$$PL = 20\log10(Te) + Tx + Rx + Rg - 20\log10(Re) \qquad (2)$$

Here, Te is a power of send signal and Re is of received signal, and calculated with FFT. Transmission sensitivity Tx [dB], receiving sensitivity Rx [dB] and reception gain Rg [dB] are constants.

III. DATA PROCESSING

This section is explains the calculation process for distance r from recorded wave signal. At first, we measure the receiver's depth and height with depth sensor and altimeter. Then we estimate the phase difference between direct wave and reflected wave, and choose the handling method of signal. When it fills the mode of direct wave, it can be handled as references [2] [3]. Or else, it can be handled as Fig.3. We firstly use band pass filter to reduce the influence of noise and find the initial point of the received signal. Then separate necessary data from received data and calculate signal power Re [dB] with FFT, so Propagation Loss PL [dB] can be calculated. In other hand we calculate error A with using h_1,h_2, and calculate true value of propagation distance r[m] with using Eq. (1) and Eq. (2).

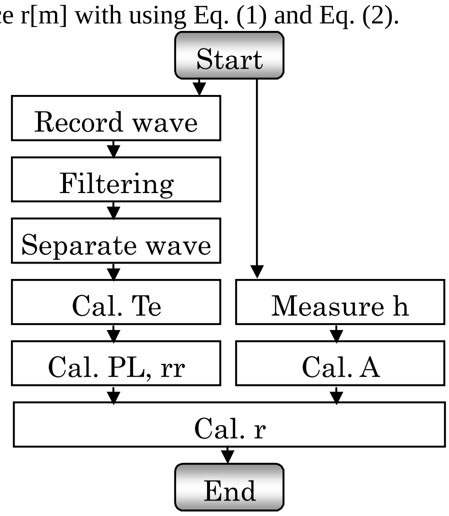

Fig.3. Signal processing flow

©ISAROB 2009

Fig.4 shows an example of data processing. Fig.4 (a) is a measured data. It shows the signal is sounded every 0.5sec, including more reflected waves and hard to distinguish the direct wave. After filtering, we get clear wave (Fig.4-(b)). Fig.4-(c) is pick-upped wave from (b) with separation and (d) is the result of FFT. In the sea area, as the most remarkable reflection is from surface or sea floor, we can suppose that the wave of only one time reflection is countable.

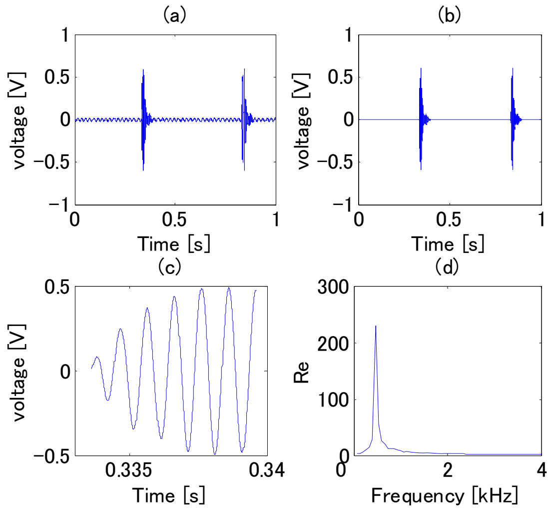

Fig.4. Example of received data

IV. WATER TANK EXPERIMENTS

1. EXPERIMENTAL CONTENTS

To confirm the practical performance for this new idea, we accomplished the experiments with using ultrasonic signal transmission and reception system in the water tank of JAMSTEC.

Fig.5 is the tank used for this experiment.

.

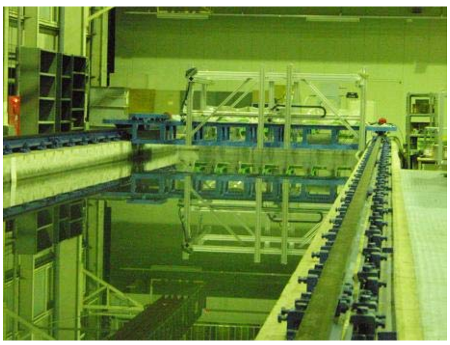

Fig.5. Water tank

In this study we used a lower frequency sound of fr = 1[kHz], and omni-directional transducer, and set it at middle position of the depth and center position of tank width as shown in Fig.6. Then the reflected waves from surface and bottom arrived at transducer in the same time approximately. The reflection waves from right and left sidewall are also same condition.

Fig.6. Transducer (sender)

Fig.7 shows the outline of the experimental system. It is consisted of a function generator, a power amp, a transducer (sender), a transducer (receiver), a pre-amplifier, an AD converter and a PC. In this experiment, we used software band-pass filter instead of hardware.

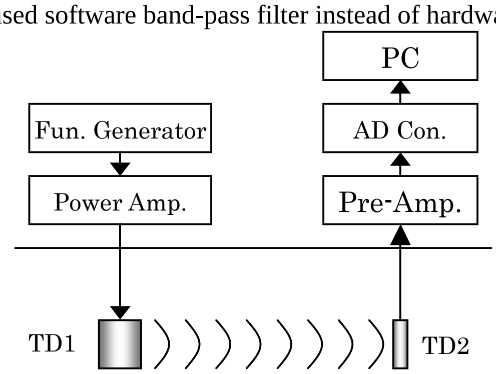

Fig.7. Configuration of experimental system

Then we set the sampling frequency of received wave in 200 kHz, measured the true distance with ruler, and record the data with changing distance from 3 meter to 25meter with every 1 meter. Table.1 shows the condition of this experiment.

Table 1. Condition of water tank experiment

Sound frequency	1[kHz]
Size of water tank	40[m](L)×4[m](W) ×2[m](D)
Size of transducer	Sender: 16.6[in.](D)×12.9[in.](H) Receiver: 3[in.](D)×10[in](H)
Signal pattern	10[Waves/10msec], 2Times/sec
Distance	3-25[m], pitched with 1[m]

2. EXPERIMENTAL CONFIRMATION

In this section we'll show the results of simulation and water-tank experiment without error compensation. At first, we show the result of Simulation in Fig. 8. In the simulation we supposed that tank size is same as experimental tank, and sound come out from point source and receiver is also point. In Fig. 8, the horizontal axis is propagation distance and vertical axis is power loss.

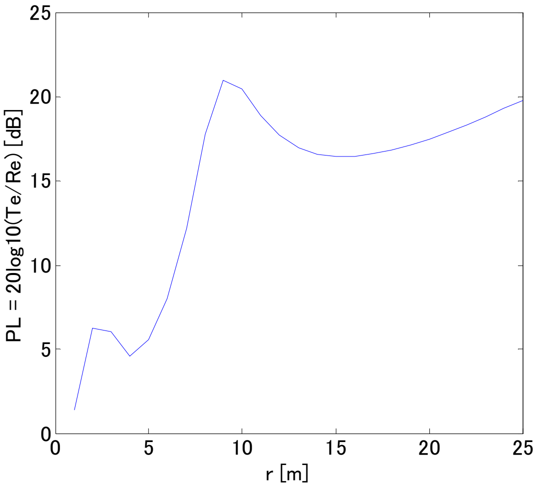

Fig.8. Simulation result of r

Fig.9 shows the experimental results of PL. It is calculated with received wave of water-tank experiment data. We can say that this result has a rough similarity to the result of simulation in shape. But there is some disturbance on the waves caused of second reflections or third reflections.

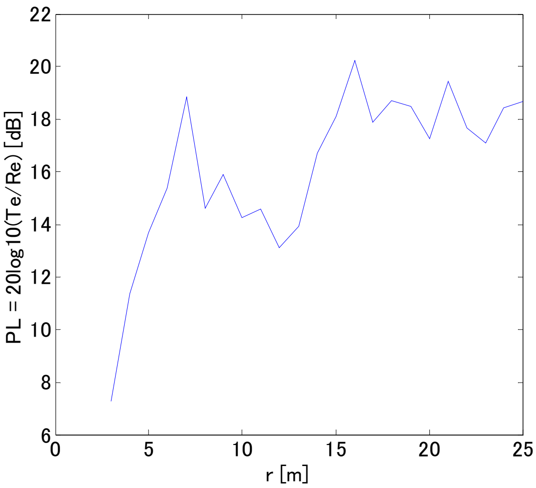

Fig.9. Result of water-tank experiment

Fig.10 shows the error compensation of the water-tank experiment. Errors became small with k. As Fig.10, area A is available of positioning with direct wave, area B has an influence of phase difference and area C is using the suggested method in this study. We think that using multi-frequency as sending signal the error depending on a phase difference can be suppressed.

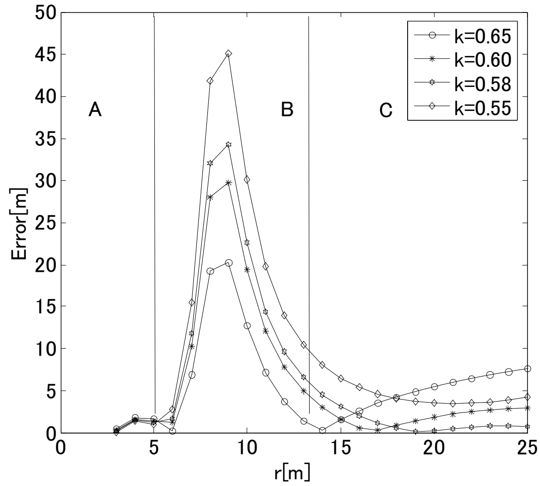

Fig.9. Error compensation of water-tank experiment

V. CONCLUSION

In this study we confirmed a new method that is using both of direct wave and reflected wave. This method is suited to the case that sensor is near to surface or bottom. If the power of sender is sufficiently large, they can fix the position in wide area. Although secondly and thirdly reflected wave had a big influence in water tank experiment, those waves can be separated in T-zone in case of sea area. We found when we use plural sensors more than 2 and take the average of them, can decrease this error. In addition, the difference of PL for each sensor can be used for phase difference detection. Consequently, using this method correct positioning is possible without time synchronization of the transmission and reception side.

REFERENCES

[1] Maeda T. Ishiguro S. Yokoyama K., et al (2006), Fuel Cell AUV "URASHIMA" (in Japanese). Mitsubishi Technical review, 43(1): 24-25
[2] Fu B. Zhang F. Ito M. et al (2009), Development of a new underwater positioning system based on sensor network. J-AROB 13(1): 45-49
[3] Fu B. Zhang F. Ito M. et al (2007), A new underwater positioning technique based on sound propagation loss (in Japanese). Proceeding of SICE Symposium on Industrial Application Systems 2007: 25-30
[4] Marine Acoustics Society of Japan (2004), The basics and application of Marine Acoustics, Seizando, 22-24, 26-34

The Fourteenth International Symposium on Artificial Life and Robotics 2009 (AROB 14th '09),
B-Con Plaza, Beppu, Oita, Japan, February 5 - 7, 2009

Motion Estimation Based on Optical Flow and ANN

Jiafeng. Zhang, *Feifei. Zhang, *Masanori. Ito

Tokyo University of Marine Science and Technology, 2-1-6, Etchujima Koto-Ku, Tokyo
(Tel : 81-3-5245-7422; Fax : 81-3-5245-7422)
(fnfnzhang78@yahoo.co.jp)

Abstract: Motion estimation provides an attractive choice to cumbersome interface devices for human computer interaction (HCI). Worthy of note, visual recognition of hand gestures can help achieving in an easy and natural way for interaction between human and computer. The interfaces of HCI and other virtual reality systems depend on accurate, real-time hand and fingertip tracking for association between real objects and relative digital information. They cost expensively and complicated operations make them troublesome. We are developing a real-time, view-based gesture recognition system. Optical flow is estimated and segmented into motion fragments. Using artificial neural network (ANN), it can compute and estimate the motion of gesture. Comparing with the traditional approaches, theoretical and experimental results show that this method has more simple hardware and algorithm demands but more effectiveness. It can be used in moving object recognition system for understanding the human body languages.

Keywords: motion estimation; optical flow; ANN**.**

I. INTRODUCTION

In order to meet human requirements better, motion estimation at a distance has recently gained more and more interests from computer vision researchers. It has a particularly attractive modality from a surveillance perspective, such as human computer interaction (HCI) or more generally human-machine interaction (HMI) etc.

Up to now, the most popular modes of HCI/HMI are based on mechanical devices, such as motion-capture system, remote controller or fingertip-tracking system. All these devices have shown more and more disadvantages such as inconvenience, high expense, complex manipulation, and even causing injuries to users.

To make it more humanized, a natural approach of speech recognition has been employed in HCI/HMI [1]. Although the vocabulary used in a speech HCI/HMI is much less than in human-human interaction (HHI), it is too hard to make a speech HCI/HMI applicable for every linguistic form of variety of languages, even for individual accents or localism. And, to make use of speech recognizing of HCI/HMI is not a good choice in a place where silence is required, or a noisy surrounding. Relevant experiments have shown that in a noisy surrounding blind people can only understand 23% of the speech contents averagely, while the others who are not blinded can understand 65% with the same speech. It proves that visual and auditory sensations are both important in HHI, and human vision system does great help for speech understanding. In fact, body motion and gesture are kinds of shape languages which do not depend on the individua1 characters or various linguistic forms, on which voice languages do. To make the communication between human and machine more natural and humanized, a lot of works have been spent to motion estimation and gesture recognition of HCI/HMI.

General motions include walking, jumping, turning around or gestures such as moving up, moving down, waving hand etc. can be divided into a series of motion states corresponding a image sequence. According to these states, human can easily track and recognize motions or gestures. How do we make computer be able to replicate such recognition ability? Initially motion analysis was devoted to the complete recovery of motion information from image sequences known as an ill-posed problem [2].

However, it is not necessary to obtain information so detailed for further analysis of dynamic content in image sequences. On the other hand, in terms of various motions, necessary information for the motion may usually change. In this paper, a visual approach based on gesture recognition is proposed.

To recognize a hand gesture from a complex backside image essentially, the three stages of detection, segmentation and recognition for a number of gestures which are assigned as some control commands must be included (Fig.1).

©ISAROB 2009

Details of the method and preliminary experimental results will be shown below.

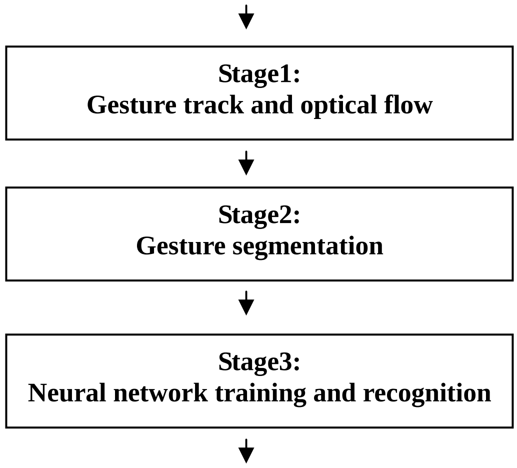

Fig.1. Three stages of gesture recognition

II. OPTICAL FLOW ESTIMATION

The major milestone of the concept of optical flow was firstly advanced and attempted to calculate by Horn and Schunck. They define optical flow as "the distribution of apparent velocities of movement of brightness patterns in an image" [3]. If the velocities of the brightness patterns (objects within the image) are known, then a robot or vision system using the optical flow techniques will have some knowledge of how its surroundings are changing.

To compute the optical flow, we assume that the object being imaged is a flat surface and the illumination on the image is constant and uniform. It is also assumed that the reflectance of the object varies smoothly and has no spatial discontinuities. These assumptions assure that the image brightness or intensity is differentiable.

Let $I = I(x, y, t)$ denote the continuous space-time intensity distribution. If the intensity remains constant along a motion path, that is,

$$I(x, y, t) = I(x + \Delta x, y + \Delta y, t + \Delta t) \tag{1}$$

then $dI(x, y, t)/dt = 0$. This latter condition can also be written as

$$\frac{\partial I}{\partial x}u + \frac{\partial I}{\partial y}v + \frac{\partial I}{\partial t} = 0 \tag{2}$$

where $u = \frac{dx}{dt}$ and $v = \frac{dy}{dt}$ denote the components of the coordinate velocity vector in terms of the continuous spatial coordinates. Equation (2) is known as the optical flow equation (OFE). The OFE is not sufficient to uniquely specify the 2-D velocity field. The remainder of this section outlines the methods employed in this study to estimate the velocity field.

1. Horn and Schunck method

The Horn and Schunck method seeks a motion field that satisfies the OFE with the minimum pixel-to-pixel variation among the velocity vectors. The pixel-to-pixel variation of the velocity vectors can be quantified by

$$\iint [(I_x u + I_y v + I_t)^2 + \lambda^2 (\|\nabla_u\|_2^2 + \|\nabla_v\|_2^2)] dxdy \tag{3}$$

Horn and Shunck proposed the following iteration to estimate the optical flow

$$u_{n+1} = u_n - \frac{I_x[I_x u_n + I_y v_n + I_t]}{\alpha^2 + I_x^2 + I_y^2}$$
$$v_{n+1} = v_n - \frac{I_y[I_x u_n + I_y v_n + I_t]}{\alpha^2 + I_x^2 + I_y^2} \tag{4}$$

where n is the iteration counter and all partial derivatives are evaluated at the point (x, y, t)

2. Lucas and Kanade method

Following Lucas and Kanade [4], we implemented a weighted least-squares (LS) fit of local first-order constraints (2) to a constant model for (u, v) in each small spatial neighborhood D by minimizing

$$\sum_D W^2(x, y)(I_x u + I_y v + I_t)^2 \tag{5}$$

where $W(x, y)$ denotes a window function that gives more influence to constraints at the center of the neighborhood than those at the periphery. I_x, I_y, I_t denote the partial derivative of $I(x, y, t)$ at point (x_i, y_i). Using LS, the solution to (5) is given by

$$u\sum_D W^2(x,y)I_x^2 + v\sum_D W^2(x,y)I_x I_y + \sum_D W^2(x,y)I_t I_x = 0 \tag{6}$$

$$u\sum_D W^2(x,y)I_x I_y + v\sum_D W^2(x,y)I_y^2 + \sum_D W^2(x,y)I_t I_y = 0 \tag{7}$$

The solution to (6) and (7) is

$$\begin{pmatrix} u \\ v \end{pmatrix} = \begin{pmatrix} \sum W^2(x,y)I_x^2 & \sum W^2(x,y)I_x I_y \\ \sum W^2(x,y)I_x I_y & \sum W^2(x,y)I_y^2 \end{pmatrix}^{-1} \begin{pmatrix} -\sum W^2(x,y)I_t & I_x \\ -\sum W^2(x,y)I_t & I_y \end{pmatrix} \tag{8}$$

Barron et al[5] compared many computing approach used for optical flow calculation and Lucas and Kanade method shows better veracity and stability. Further more, it is relatively speedy and easy in computation and implementation, and we adopt it in this paper.

©ISAROB 2009

3. Real-time gesture tracking and optical flow

In our experiment system, a standard 2.4GHz Pentium 4 PC was used with a monochrome Sony XC-HR50 digital video camera.

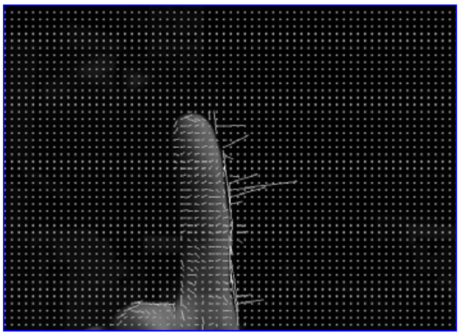

Fig.2. The optical flow of a forefinger motion (from left to right)

Fig.2 shows the moving velocity (from left to right) extracted from the real-time video stream by utilizing the Lucas and Kanade optical flow method outlined in this paper. The values of velocity are indicated by lines (the rectangles denote the origin in the former frame). Fig.2 also shows the velocity field of moving area.

4. Flow estimation confidence measurement

There exists a significant problem outlined in sections II.1-II.2, that is, for those methods that integrate normal constraints with global (regularization) smoothness constraints, these measurements are lack of confidence.

In Fig.2, we can see undesired optical flow on the edges of the moving parts. This kind of undesired optical flow is evident in the process using matching methods or with some degree of dilation and so on.

To evaluate the confidence in the flow estimation, for example, Anandan [6] fitted a cubic surface to the SSD values and defined a confidence measurement based on the curvatures of the surface. Another way to verify the optical flow was to use the left-right check [7], which is, computing the flow for frame I_t with respect to I_{t+1}, then repeating for I_{t+1} with respect to I_t. Only the flow whose estimation results were same (or close) should be used. Although these techniques gave good results, they required massive calculations. Here, we use a simple way depending on the histogram of optical flow to eliminate the common flow estimate errors, and it has been proved that for our later analysis this technique has given sufficient flow estimation.

Fig.3 shows the flow histogram in x-direction and y-direction; and Fig.4 only shows the most important optical flow we expected by removing the flow noise in optical flow field through histogram.

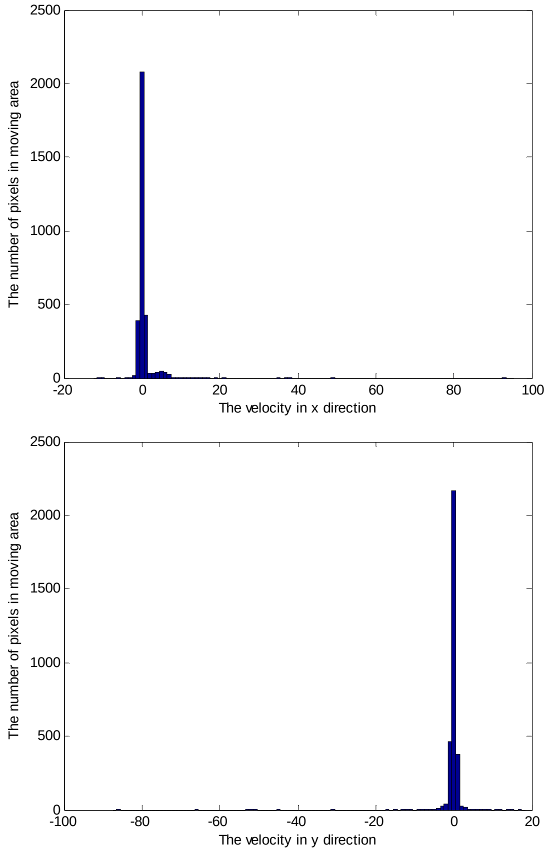

Fig.3. The histogram of flow velocity

Fig.4. Using histogram to get the main flow

From the histogram of Fig.3, we can set a threshold to get rid of the undesirable flow.

III. SEGMENTATION AND RECOGNITION

1. Gesture segmentation with optical flow

The first task is to work out how the optical flow vectors we get from each frame in II can be presented to the ANN. In our experiments, we represented a kind of motion segmentation as a series of 12 vectors, which

©ISAROB 2009

come from consecutive video frames. Fig.5 shows how the gesture for Right Arrow can be represented as a series of vectors.

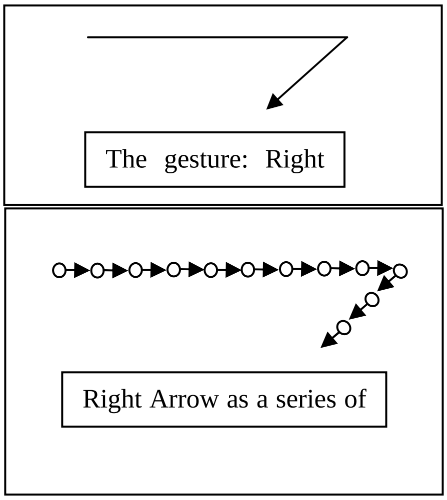

Fig.5. Gestures as vectors

Each vector can be got by calculating the mean value of optical flow in the corresponding frame. To aid training, these vectors are normalized before becoming part of the training set. Therefore, all the inputs into the network have been standardized. In this way, additional advantage is that, when we come to process the gestures made by users, we can achieve even distribution of the vectors through the gesture pattern, which will aid the ANN in the recognition process.

In our experiment, we predefined 10 gestures to express different semantic.

Table1. Predefined 10 basic gestures for semantic

Gesture	Command	Gesture	Command
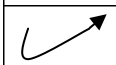	Begin		Down
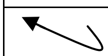	Stop	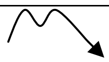	Right
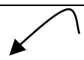	Forward	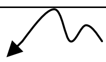	Left
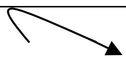	Backward	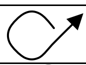	Take up
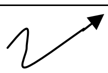	Up	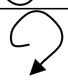	Put down

IV. Recognition by BP network

Backpropagation (BP network)[8], works as follows: First create a network with one or more hidden layers and randomize all the weights. Then present a pattern to the network and compute error value. This error value is then used to determine how the weights from the layer below the output layer are adjusted. Once the weights for the current layer have been adjusted, the same thing is repeated for the previous layer and so on until the first hidden layer is reached. The next time the input pattern is presented, the output will be a little bit closer to the target output. This whole process is then repeated with all the different input patterns many times until the error value is coming to an acceptable limit for the recognition system.

Using BP network, the recognition rate achieved 83.3% in our experiments for the predefined gestures.

V. CONCLUSION

In this paper, we have utilized optical flow method to segment human's gesture motions from real-time video stream. A histogram technique for getting rid of flow noise is proposed, and using BP networks, we can recognize a set of gestures, which are defined by optical flow vectors in a context of motion segmentation. Using this system, the recognition rate achieved 83.3% in our experiments for the predefined gestures. Future work for this system includes: adding more gestures and enhancing recognition rate; using HMM to make the gesture recognition more robust.

REFERENCES

[1] Pavlovi'c VI, Sharma R, Huang TS (1997) Visual interpretation of hand gestures for human-computer interaction: a review. IEEE Transactions on Pattern Analysis and Machine Intelligence 19:677-695
[2] Bertero M, Poggio T, Torre V (1988) Ill-posed problems in early vision. Proc. of the IEEE 76(8): 869-890
[3] Horn BKP, Schunk BG (1981) Determining optical flow. Artificial Intelligence 17:185–203
[4] Lucas B, Kanade T (1981) An iterative image registration technique with an application to stereo vision. DARPA Image Understanding Workshop 2:121--130
[5] Barron JL, Fleet DJ, Beauchemin SS, Burkitt TA (1992) Performance of optical flow techniques. CVPR
[6] Anandan P (1989) A computational framework and an algorithm for the measurement of visual motion. International Journal of Computer Vision 2:283–310
[7] Faugeras O, Hotz B, Mathieu H et al. (1993) Real time correlation based stereo: algorithm implementations and applications. Technical Report 2013
[8] Freeman JA, Skapura DM (1992) Backpropagation Neural Networks Algorithm Applications and Programming Techniques, pp 89-125.

©ISAROB 2009

Development for on-board use anti-tilting table with Horizontally slider type parallel mechanism
――Analysis on Inverse Kinematics and Work-space of the Mechanism

Yunzhi Zhang, Etsuro Shimizu, Feifei Zhang and Masanori Ito

Tokyo University of Marine Science and Technology
Etchujima 2-1-6, Kotou-ku, Tokyo, 135-8533 Japan
(*Tel : 81-03-5245-7300; Fax : 81-03-5245-7422*)
(*Email sfzyz@pub.sz.jsinfo.net*)

***Abstract*:** In this paper, the authors propose a new type of parallel mechanism, i.e. 6-STRT parallel mechanisms, and its applications. This mechanism is consisted of 6-sliders of horizontal motion attached on a base plate and 6-links of which lower ends are connected to sliders and upper ends to end plate via universal joints, so the end plate can be moved in 6 degree of freedom. The authors are intending to apply this mechanism making perfectly stable stage on the ship regardless all kind of ship motion such as rolling, pitching or heaving.

In this paper, the authors introduce the specialty and kinematics of this mechanism with the matrix-vector method as the first step of our research. The searching algorithm of work-space boundary in this research is characterized with simplicity, wide range of application, clearness of physical meaning, preciseness of mathematical logic, and easiness of programming method and it is thought to be very practical method on the robot design. The work-space and configuration of the parallel robot is analyze in terms of the relationship between work-space and structural parameter of parallel mechanism.

Keywords: Parallel mechanism, Inverse kinematics, Work-space.

I. INTRODUCTION

The initial application of parallel robot can be traced back to 1930s. Really arouse interests in the field of kinematics of machinery was the 6 degrees of freedom parallel mechanism i.e. Stewart-platform[1] proposed by Stewart in 1965. Until 1978, the Professor Hunt used parallel mechanism as the robot structure for the first time which opened the prelude to the study of parallel robot[2].With light structure, stiffness non-cumulative error and other unique nature, parallel robot has become a hot spot in robotic research since the 1990s.There are many types of parallel mechanism, such a stretch type represented in Stewart platform, such a rotating structure represented in Delta mechanism[3] or linear motion mechanism[4]. Those mechanisms have many merits, but many shortages for the application to ship. Then the authors have developed a new type of parallel robot, as shown in Fig.1.

This paper introduces a new type of parallel robot developed by the authors, see Fig.1. The motion of 6 degrees of freedom of end plate is driven by six links, which are driven by the movement of six sliders installed in the base plate. The merits of the structure are as follows.

1. The distance between base plate and end plate become minimum in the parallel mechanism.

2. The stiffness of this mechanism is better than stretch type and rotary type.

3. As a result of screw driver, this mechanism has higher output power and better safety.

4. As the actuators installed in the base plate, the mass and inertia of moving parts is smaller and the output response is faster.

The following is the structure sketch of this parallel mechanism.

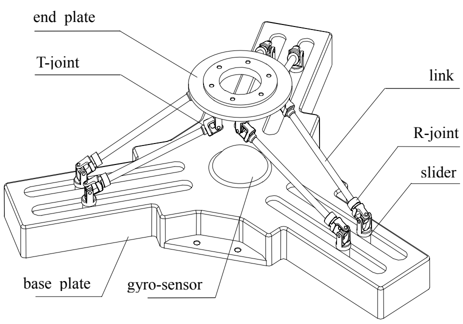

Fig.1. the 6-STRT Parallel mechanism

II. MODELING OF KINEMATICS

1. Modeling of Inverse Kinematics

The authors propose to use a minimal set of parame-

©ISAROB 2009

ters in order to derive the inverse kinematic models: the main feature of this set is the definition of two coordinate systems:

$\Sigma_b(\,o_b - x_b y_b z_b)$: The coordinate system is fixed on the base plate and the origin is coincident with the center point of the base plate, as shown in Fig.2.

$\Sigma_t\,(o_t - x_t y_t z_t)$: The coordinate system is fixed on the end plate and the origin of coordinate is coincident with the center point of the end plate, as shown in Fig.3. Here we define some parameters used in this paper as follows:

x, y, z : position parameter of the end plate.

α, β, γ : posture parameter of the end plate.

E: length of link.

L_{ij}: displacement of sliders.

${}^{A}_{B}R$: transformation matrix.

d: distance of joint to its symmetry center line.

h: distance of joint to center point of end plate.

e: distance of slider to its symmetry center line.

δ_i: allocation angle of the end plate.

$\emptyset_i$: allocation angle of the base plate.

Here, we show two numbers of slider sets with i (=1,2,3) and divide each slider with j (=1,2).

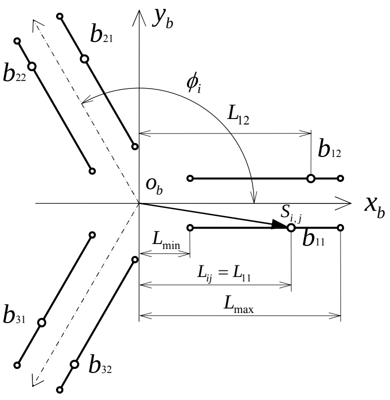

Fig.2 Kinematics model of base plate

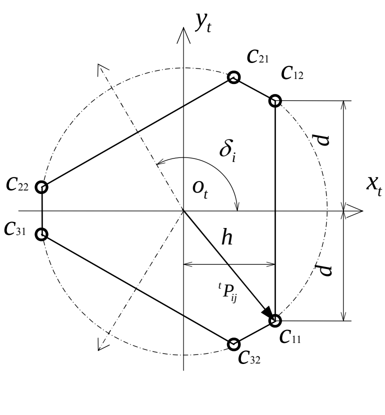

Fig.3 Kinematics model of end plate

Let us take out one motion chain, which represents the relationship between the relative position of two coordinate systems (i.e. Σ_b and Σ_t).

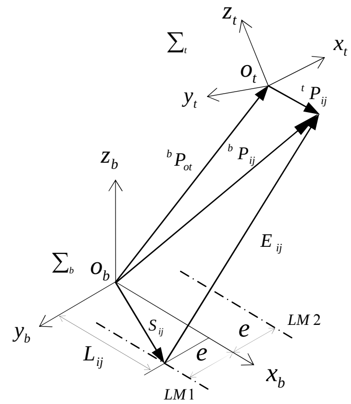

Fig.4 Model of a motion chain

According to Fig.4, the relations of each vector are as follows:

$$ {}^bP_{ij} = {}^bP_{ot} + {}^{A}_{B}R\ {}^tP_{ij} \tag{1}$$

$$ {}^bP_{ot} = \begin{bmatrix} x & y & z \end{bmatrix}^T \tag{2}$$

$$ E_{ij} = {}^bP_{ot} + {}^{A}_{B}R\ {}^tP_{ij} - S_{ij} \tag{3}$$

$$ {}^{A}_{B}R = \begin{bmatrix} c\alpha c\beta & c\alpha s\beta s\gamma - s\alpha c\gamma & c\alpha s\beta c\gamma + s\alpha s\gamma \\ s\alpha c\beta & s\alpha s\beta s\gamma + c\alpha c\gamma & s\alpha s\beta c\gamma - c\alpha s\gamma \\ -s\beta & c\beta s\gamma & c\beta c\gamma \end{bmatrix} $$

with: $c\alpha = \cos\alpha \quad s\alpha = \sin\alpha \quad c\beta = \cos\beta$

$s\beta = \sin\beta \quad c\gamma = \cos\gamma \quad s\gamma = \sin\gamma$

The authors first express the vectors of each joint on the end plate in the frame Σ_t, which can be written as:

$$ {}^tP_{ij} = \begin{bmatrix} \cos\delta_i & -\sin\delta_i & 0 \\ \sin\delta_i & \cos\delta_i & 0 \\ 0 & 0 & 1 \end{bmatrix} \begin{bmatrix} h \\ (-1)^j d \\ 0 \end{bmatrix} \tag{4}$$

with: $\delta_i = 2\pi(i-1)/3 \quad i = 1,2,3$

Besides, we can write the vectors of each slider on the base plate in the frame Σ_b:

$$ S_{ij} = \begin{bmatrix} \cos\phi_i & -\sin\phi_i & 0 \\ \sin\phi_i & \cos\phi_i & 0 \\ 0 & 0 & 1 \end{bmatrix} \begin{bmatrix} L_{ij} \\ (-1)^j e \\ 0 \end{bmatrix} \tag{5}$$

with: $\phi_i = 2\pi(i-1)/3 \quad i = 1,2,3$

Let us note coordinates of each slider in the frame Σ_b: (x_{ij}, y_{ij}, z_{ij}), besides, coordinates of each joint in the frame Σ_b:(X_{ij}, Y_{ij}, Z_{ij}), then following equation stands:

$$ (X_{ij} - x_{ij})^2 + (Y_{ij} - y_{ij})^2 + Z_{ij}^2 = E^2 \tag{6}$$

The previous calculations give the solution to the inverse kinematics model of the parallel robot:

$$L_{ij} = B_{ij} + \sqrt{B_{ij}^2 - C_{ij}} \tag{7}$$

where:

$$B_{ij} = X_{ij} \cos \phi_i + Y_{ij} \sin \phi_i$$

$$C_{ij} = 2(-1)^j e(X_{ij} \sin \phi_i - Y_{ij} \cos \phi_i) + X_{ij}^2 + Y_{ij}^2 + Z_{ij}^2 + e^2 - E^2$$

2. Velocity and Acceleration of the Mechanism

From equation (7), the displacement of each slider L_{ij} is the function of the parameters with regard to position and posture of end plate, which can be written as follows:

$$L_{ij} = f_{ij}(x, y, z, \alpha, \beta, \gamma) \tag{8}$$

When we partial differentiate both sides by t(time), then we get the velocity of the each slider.

$$V_{i,j} = \begin{bmatrix} \frac{\partial f_{ij}}{\partial x} & \frac{\partial f_{ij}}{\partial y} & \cdots & \frac{\partial f_{ij}}{\partial \gamma} \end{bmatrix} \begin{bmatrix} v_p \\ \omega_p \end{bmatrix} = J_a \begin{bmatrix} v_p \\ \omega_p \end{bmatrix} \tag{9}$$

where: J_a denotes Jacobin matrix.

v_p, ω_p: Velocity and angular velocity of the end plate.

If Jacobin matrix J_a is none-singular matrix, then we can get the velocity of end plate from velocity of each slider.

As the same manner, with differentiating equation (9) by t(time) we get the acceleration of each slider.

$$a_{ij} = A_{ij} \begin{bmatrix} v_p \\ \omega_p \end{bmatrix} + J_a \begin{bmatrix} a_p \\ \varepsilon_p \end{bmatrix} \tag{10}$$

with: $$A_{ij} = \begin{bmatrix} \frac{\partial^2 f_{ij}}{\partial x^2} & \frac{\partial^2 f_{ij}}{\partial y^2} & \cdots & \frac{\partial^2 f_{ij}}{\partial \gamma^2} \end{bmatrix}$$

a_p, ε_p: acceleration and angle acceleration of the end plate.

Similarly, if J_a is none-singular matrix, we can get the acceleration of the end plate from acceleration of each slider.

3. Constraints of Inverse Kinematics

According to Geometric relationship and material properties of the parallel mechanism, the constraint condition of motion of each slider is as follows.

$$L_{\min} \geq h$$
$$L_{\max} \leq h + \sqrt{E^2 - d^2 - e^2 + 2ed} \tag{11}$$

III. ANALYSIS ON WORK-SPACE

Generally, the shape of work-space of parallel robot is thought to be very complicated and difficult. We would like to introduce a simple algorithm to search the work-space boundary in this paper.

1. Cylindrical Coordinate Search Method

As the motion of proposed parallel mechanism is concentrated in a cylindrical space, it is easy to imagine that its work-space should be searched under cylindrical coordinate. At first, we consider a cutting plane through *z*-axis and ρ-axis. The ρ-axis exists on a *x*-*y* plane and makes an angle of $\theta(m)(= m \cdot \Delta\gamma)$ to *x*-axis as shown in Fig.5. Here $\Delta\gamma$ is a small angle divided cylindrical space with circular direction and *m* is a counted number of $\Delta\gamma$ from *x*-axis. Now, we will search for $\rho - z$ plane. We divide this plane with a strip of $\Delta\rho$ width along ρ-axis and Δz width along *z*-axis. Then the block position of *s*th along ρ-axis and *n*th along z-axis in $\rho - z$ plane are shown as following.

$$\rho(s) = s \cdot \Delta\rho, \ z(n) = n \cdot \Delta z$$

The coordinate (x, y, z) in this space are presented with using (ρ, θ, z).

$$x = x(s, m) = \rho(s) \cos(\theta(m))$$
$$y = y(s, m) = \rho(s) \sin(\theta(m)) \tag{12}$$
$$z = z(n) = z(n)$$

Here, $s, m, n \geq 0$

Now we confirm the existence of solution for all (*s*, *m*, *n*) with inverse kinematics.

The principle of the cylindrical coordinate search method is as follows:

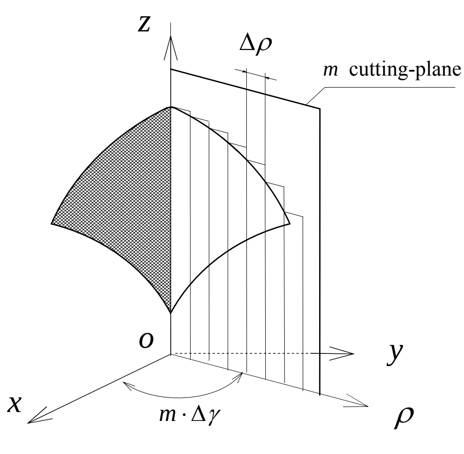

Fig. 5 Principle of cylindrical coordinate search

2. Analysis on Work-space of 6-STRT Parallel Robot

The authors analyze the work-space of 6-STRT type parallel robot of which link length are l_1, l_2 and l_3 by cylindrical coordinate search method.

The Fig.6 is y-z section of work-space boundary of 6-STRT type parallel robot of which link length are l_1, l_2 and l_3.

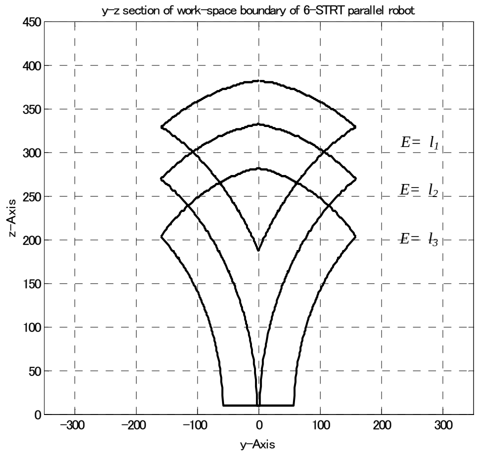

Fig.6 y-z section of work-space boundary

The x-z section of work-space boundary is shown in Fig.7.

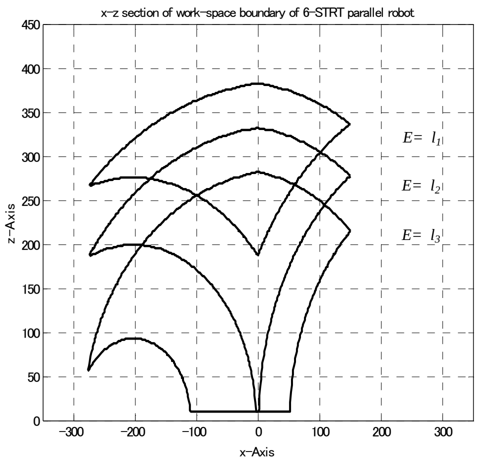

Fig.7 x-z section of work-space boundary

We can conclude to the above mentioned analysis, with the growth of the length of link, the center of work-space will move upward and the work-space will be gradually becoming smaller. This conclusion is significant for the optimal design of the parallel mechanism.

Certainly, there are some factors else will influence the work-space of parallel robot for example location of each joint, etc, but we will not discuss in this paper, as the effect is not large.

Finally, the authors show the three-dimensional work-space of the 6-STRT type parallel robot got with the cylindrical coordinate search method in Fig.8.

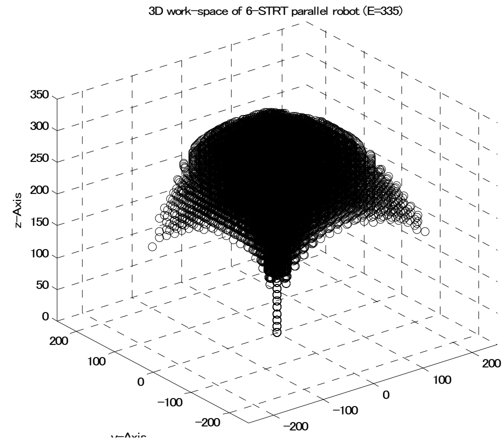

Fig.8 3D work-space of the parallel robot

IV. CONCLUSION

In this paper the authors propose a new type of the parallel mechanism; this mechanism consists of 6-sliders of horizontal motion and 6-links of which lower ends are connected to sliders and upper ends to end plate with universal joints. This mechanism can move the end plate in 6 degree of freedom, with higher power than conventional parallel mechanism, so the authors are thought to apply this mechanism to make a stable surface on ship. In the first of this research, the authors analyze inverse kinematics by the matrix-vector method and present the mathematical algorithm of work-space based on cylindrical coordinate of this mechanism for optimal design.

REFERENCES

[1] D. Stewart, A Platform six Degree of Freedom Proceedings of the Institute of mechanical Engineers. 1965, 180 (5) Part1: pp.371-386.

[2] K. H. Hunt, Kinematic Geometry of Mechanisms. Clarendon Press. Oxford. 1978, pp. 421-426.

[3] F.Pierrot, A. Fournier and P. Dauchez, Towards a Fully parallel 6-DOF robot for high-speed applic ations. IEEE Transactions on Robotics and Automation, Sacra mento, Califomia(1991-4), France. pp.1289-1292.

[4] Takanori Masuta, Motoyoshi Fujiwara and Tatsuo Arai. Specific Kinematic Changes in a Linear-Actuated Parallel Mechanism According to Differences in Actuator Arrangement. JSME, Vol65-659(2001-7).

A Method for Expressing Human Posture as 3DCG Using Thermal Image Processing and 3D Model Fitting

T. Asada[1] and Y. Yoshitomi[2]

1: Dept. of Environmental Information Graduate School of Human Environment Science Kyoto Prefectural University, Shimogamo Sakyo-ku Kyoto 606-8522 JAPAN, E-mail: t_asada@aoi.kpu.ac.jp
2: Div. of Environmental Sciences Graduate School of Life and Environmental Sciences Kyoto Prefectural University Shimogamo Sakyo-ku Kyoto 606-8522 JAPAN, E-mail: yoshitomi@kpu.ac.jp

Abstract: An imitation of human motion has been used as a promising technique for a development of robot. Some techniques such as motion capture systems and data-gloves are used for analyzing a human motion. However, since those methods need (a) environmental restrictions such as preparation of two or more cameras and strict control on brightness condition and (b) physical restrictions such as wearing of markers and/or data-gloves, they are far from the method for recognizing a human motion on the natural condition. In this paper, we propose a method that makes a 3-dimensional CG (3DCG) by transforming a feature vector of human posture on a thermal image into a 3DCG model. The 3DCG models as training data are made with manual model fitting. Then, the human models synthesized by our method are geometrically evaluated in CG space. The average error in position is about 10 cm. Such a relatively small error might be acceptable in several cases of both the 3DCG animation generation and the imitation of human motion by a robot. Our method needs neither the physical nor environmental restrictions. The rotation-angles at each joint obtained by our method can be used for imitating a human posture by a robot.

Keywords: Human posture, Thermal image, Computer graphics, Model fitting, Feature vector.

I. INTRODUCTION

In recent years, various computer graphics (CG) animations have been appearing on television or in movie. Such a CG animation is usually made through tough analyses on a human motion. Some techniques such as motion capture systems and data-gloves are used for analyzing a human motion. There have been many researches for acquiring the information on a human posture from an image [1-4]. However, since those methods need (a) environmental restrictions such as preparation of two or more cameras and strict control on brightness condition and (b) physical restrictions such as wearing of markers and/or data-gloves, they are far from the method for recognizing human motion on the natural condition.

In order to overcome the issues coming from these restrictions, the method with thermal images was studied [5]. However, the difficulty in making a 3-dimensional (3D) information on posture from a 2-dimensional (2D) one has been still kept in the reported method [5].

In this paper, a method for expressing a human posture as a CG with human thermal image taken under no special restrictions on a person is proposed. Based on a geometrical relationship among the feature vector of human posture on the test image and those of the training images, the 3DCG models for test images are produced from some 3DCG models, which have been produced by manual model fitting beforehand through referring each human posture on a training image. Then, the human models synthesized by our method are geometrically evaluated in CG space. Our method needs neither the physical nor environmental restrictions. Our method might be useful at least in making a 3DCG for several limited human postures. Moreover, the rotation-angles at each joint obtained by our method can be used for imitating a human posture by a robot.

II. BASIC ALGORITHM

A basic algorithm for producing a CG for expressing a human posture is as follows.

<Step1> Several thermal images expressing one human posture per image are collected as training images. Through referring each training image expressing one human posture, the 3DCG model expressing the corresponding human posture is made by manual model fitting and stored in a computer. Then, the feature vectors for human postures of training images are calculated and stored in the computer.
<Step 2> The test image is inputted into the computer and then the corresponding feature vector for human posture on the image is calculated.
<Step 3> The human model corresponding to the test image is made from those of training images, according to the geometrical relationship in the feature vector

©ISAROB 2009

space among the feature vector of the test image and those of the training images.

For each motion in gesture on thermal image, a 3-dimensional CG (3DCG) animation can be made by changing continuously the rotation-angles at joints in a 3DCG model corresponding to the test image at the start time into those at the end time [6].

III. THERMAL IMAGE GENERATION

In this study, thermal images having a human posture per an image are produced by a Thermal Video System (TVS-700) (Nippon Avionics) with infrared rays and these images are recorded in digital videotape as a Mpeg1 file. Then, several thermal images with BMP format having a spatial resolution of 380×460 pixels and a gray level of 256 are obtained from the Mpeg1 file.

IV. HUMAN MODEL

The human model has 10 joints. All rotation-angles at 10 joints are stored in a file. Fig.1 shows the human model, the standard posture and its structure.

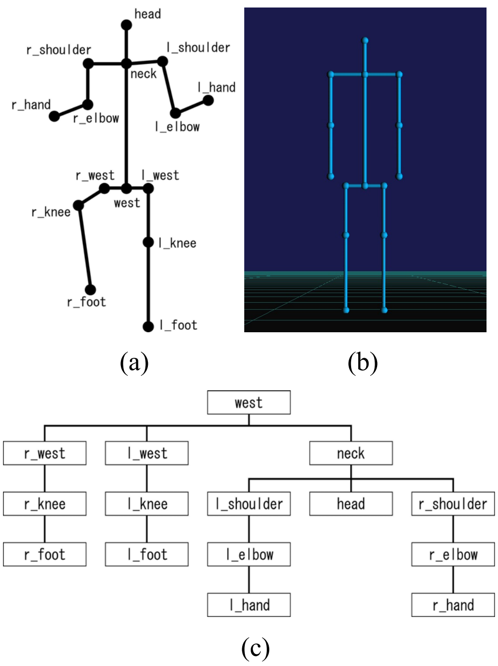

Fig.1. Human model (a), standard posture (b) and structure of human model (c)

V. MODEL FITTING

Fig.2 demonstrates the process of manual model fitting for making a human model corresponding to a human posture on a thermal image. Through the manual model fitting, all rotation-angles at 10 joints are stored in a file

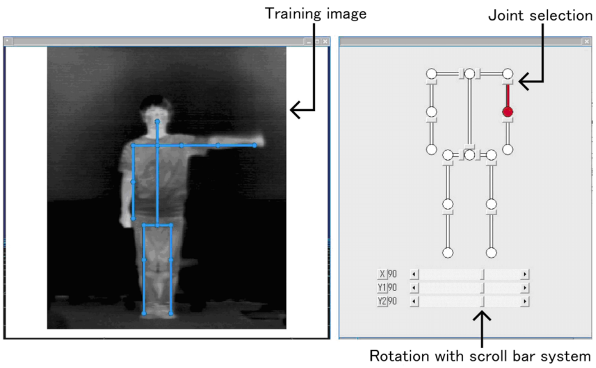

Fig.2. Manual model fitting

VI. FEATURE VECTOR GENERATION

After processing for standardizing the position and the size, the mosaic image is generated from the training image after subtracting the gray level of background image from the training image (Fig.3). The gray levels of mosaic image having 14×14 blocks, each of which has the average gray level on 25×25 pixels, are used as the components of feature vector.

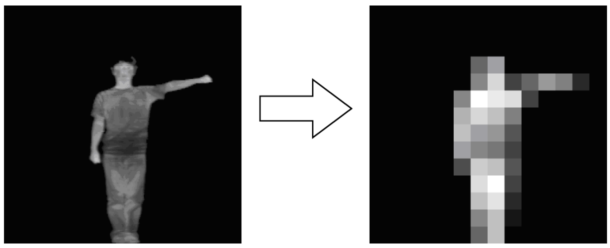

Fig.3. Mosaic image for making feature vector

VII. HUMAN POSTURE ESTIMATION

We assume $\{\boldsymbol{X}_m\}(m=1,2,\cdots,M)$ to be a set of posture pattern made from training images. $\boldsymbol{X}_m$ indicates a N-dimensional feature vector having gray levels of mosaic image as components.

Assuming the feature vector of test image, the feature vector of the class c to be $\boldsymbol{f}=(f_1,f_2,\cdots,f_N), \boldsymbol{f}_c=(f_{c,1},f_{c,2},\cdots,f_{c,N})$ respectively. In the conventional way, the test image is recognized as class j when the Euclid distance d_c, defined by the equation (1) as a discriminant function, gives the minimum value for class j among all classes.

©ISAROB 2009

$$d_c = \left\{ \sum_{i=1}^{N} \left(f_i - f_{c,i}\right)^2 \right\}^{1/2} \qquad (1)$$

However, this conventional method for pattern recognition needs various kinds of training images for recognizing many test-images with good accuracy. Therefore it is not practical to produce the CG model corresponding to the test image, with this conventional pattern recognition.

In this study, for transforming the test image into the corresponding 3DCG model, a stepwise approximation to the feature vector of test image is performed in the following way. Hereinafter, the shortest distance among those of all pairs of feature vectors coming from training images is referred as R.

<Step1> The approximate feature vector is obtained as that having the shortest distance (hereinafter referred as $d_{\min}$) to the feature vector of the test image among those of all training images. When $d_{\min}$ is under the half of R, go to the step 5, getting from the database all rotation-angles at 10 joints on the model corresponding to the class whose training image gives $d_{\min}$ to the test image. Otherwise, go to the step 2.

<Step2> In the feature vector space, every length of the perpendicular drawn from the position of the test image to the straight line passing a pair of the positions of feature vectors of training images is calculated. The approximate feature vector is obtained as the position vector of intersection of the shortest perpendicular, which is expressed as H_0, from the position of the test image on the straight line passing the positions of a pair of training images. The selected two feature vectors of the training images for making the approximate feature vector are expressed as $f_{a,0}, f_{b,0}$. When the geometrical relationship of the approximate feature vector for the test image to two selected feature vectors of training images is inside linear interpolation and the length of H_0 is under the half of R, go to the step 5, getting all rotation-angles at 10 joints on the models corresponding to the compounded feature vector obtained by the inside linear interpolation with its ratio and all rotation-angles at 10 joints on the models corresponding to two feature vector used for the inside linear interpolation (Fig.4). Otherwise, set $n = 0$ and go to the step 3.

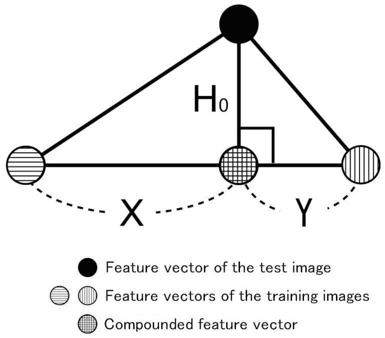

Fig.4. Schematic diagram showing inside linear interpolation for getting the second-step approximate feature vector

<Step3> The feature vector $f_{a,n+1}$ corresponding to the position vector of intersection of the shortest perpendicular from the position of the test image on the straight line passing the positions of a pair of $f_{a,n}$ and $f_{b,n}$ is generated. Then, every length of the perpendicular drawn from the position of the test image to the straight line passing a pair of the positions of $f_{a,n+1}$ and the feature vector of training image is calculated. The approximate feature vector is obtained as the position vector of intersection of the shortest perpendicular, which is expressed as H_{n+1}, on the straight line passing the positions of a pair of $f_{a,n+1}$ and the feature vector of training image. The selected feature vector for making the approximate feature vector is expressed as $f_{b,n+1}$. When the geometrical relationship of the approximate feature vector for the test image to $f_{a,n+1}$ and $f_{b,n+1}$ is inside linear interpolation and the length of H_{n+1} is under the half of R, go to the step 5, getting all rotation-angles at 10 joints on the model corresponding to the compounded feature vector obtained by the inside linear interpolation with its ratio and all rotation-angles at 10 joints on the models corresponding to two feature vector used for the inside linear interpolation. Otherwise, go to the step 4.

<Step4>
$n := n+1$, then go to the step 3.

<Step5>
The model is produced with the rotation-angles finally obtained in the above step(s) at 10 joints.

Figs. 5 and 6 (1) demonstrate the above approximation of the feature vector of test image, using a simple case. Fig.5 (a) and (c) illustrate the training

©ISAROB 2009

images while Fig.5 (b) illustrates the test image. Fig.6 (1) demonstrates the relationship among the values of components of feature vectors of the three images illustrated in Fig.5. In this case, the feature vector of the test image (b) is compounded by the inside linear interpolation with the feature vectors of the training images (a) and (c). We extend this idea of approximation to the more general case shown in Fig.6 (2), where (d) denotes the position of the feature vector of test image. Fig.6 corresponds to Fig.4 with which the second step is demonstrated.

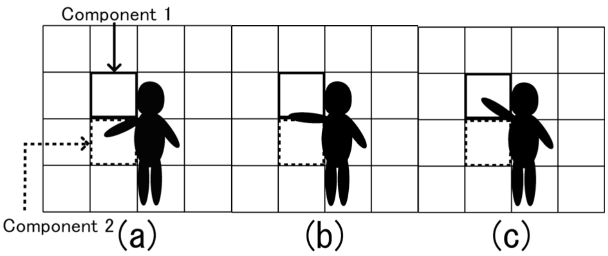

Fig.5. Schematic diagram on images; (a)& (c) training, (b) test

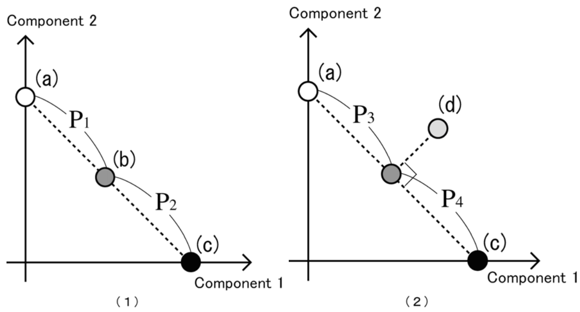

Fig.6. Schematic diagram on compound of feature vector, (1) simple, (2) more general

VIII. ESTIMATION OF POSITION ERROR IN CG SPACE

In the experiments, a personal computer, Dell Dimension 8300 (CPU: Pentium IV 3.2 GHz, main memory: 2.0 GB, OS: Windows XP), is used. For programming, Microsoft Visual C++ 6.0 is used. For the evaluation of our method, several marks are attached to the subject and the model in CG space (Fig.7). Then, the model is manually fitted to the human posture. For fitting the model to the human posture, we do not use the markers. The markers are used only for measuring the position-errors of markers on the human model (Fig.8). We use the motion capture system named as Radish (Library) for measuring the position of markers attached on the subject. We use 28 training-images shown in Fig.9 and 10 test-images shown in Fig.10. In the case of 8 test images (a-h), each image has very similar human posture on training images (No.1-8) respectively, while 2 test images (i, j) do not have very similar human posture on training images (No.1-24).

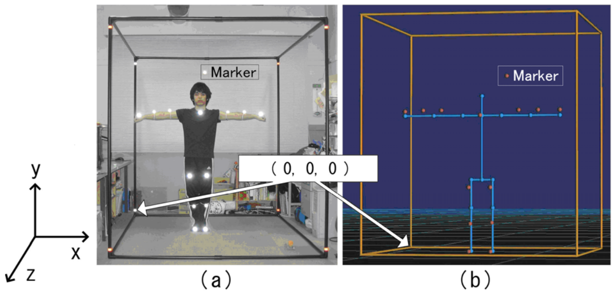

Fig.7. Scene in measuring three-dimensional positions (a), CG space corresponding to real space (b)

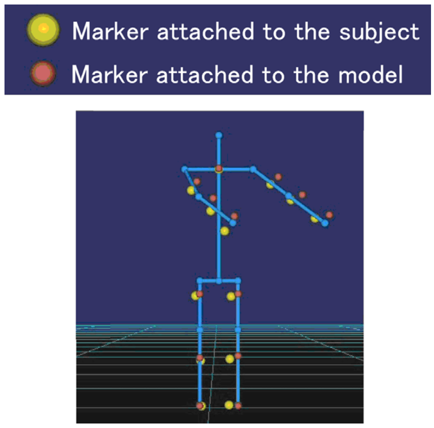

Fig.8. A model with markers

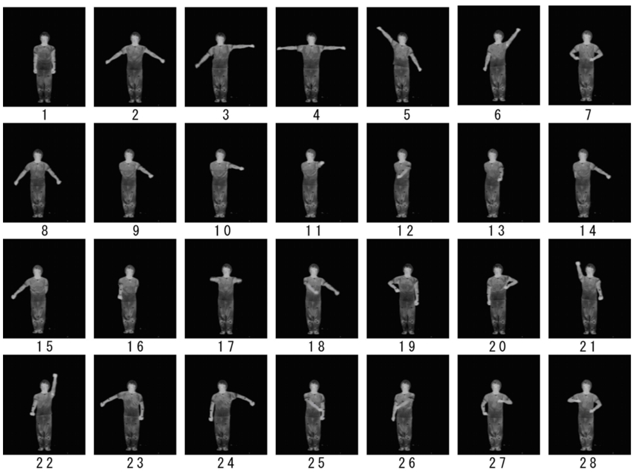

Fig.9. Training images for position measuring

©ISAROB 2009

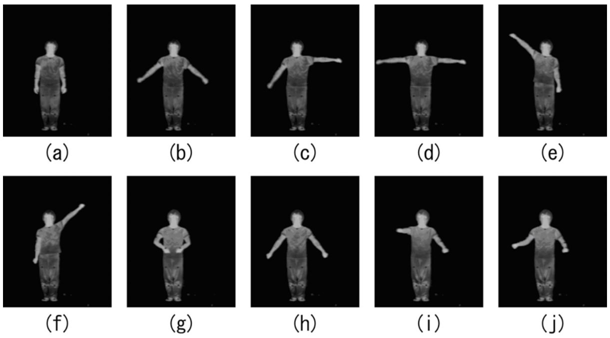

(a)～(h): Test images having the same posture patterns as training images 1～8
(i) (j): Unknown test images

Fig.10. Test images for position measuring

Table 1 shows the position-errors of markers on the human model for the training images. As the total, the average and maximum position-errors of markers are 6.2 and 13.6 cm respectively. Tables 2 and 3 show the position-errors of markers on the human model for the test images. As the total, the average and maximum position-errors of markers are 7.5 and 20.4 cm for the images a-h respectively, while those are 8.9 and 24.3 cm for the images i,j respectively. As the total, both the average and maximum position-errors of markers for the images i,j, which do not have very similar image on the training images (No.1-28), are slightly bigger than those for the images a-h, each of which has very similar image on the training images (No.1-8). Since, the average position-errors of markers for test images are about 10 cm, we think that our method is useful for estimating a human posture roughly. Figs 11 and 12 show the human models for test images i, j respectively. Fig. 13 demonstrates the synthetic process of feature vector in the case of test image j. The process is terminated at the step 3. When using the conventional way, the test image j having the shortest distance in the feature vector space to the training image No.7 is recognized as the class of training image No.7. Since the human model shown in Fig. 12 is more similar to the human posture of the test image j than that of Fig.14, our method might have an advantage over the conventional way. It takes about one minute for making a human model with manual model fitting, while it takes about 0.6 second for estimating a human posture and making a human model for a test image.

Our method needs neither the physical nor environmental restrictions. The rotation-angles at each joint obtained by our method can be used for imitating a human posture by a robot.

Table 1. Position-errors of makers on human model (Training images No.1−8)

No.	1	2	3	4	5	6	7	8	Total
Average	4.4	7.5	5.4	5.5	7.3	5.4	7.4	6.4	6.2
Maximum	6.8	23	10	13	11	16	14	15	13.6

(cm)

Table 2. Position-errors of makers on human model (Test images a−h)

	a	b	c	d	e	f	g	h	Total
Average	5.0	6.6	7.4	7.1	8.4	5.4	11.9	8.2	7.5
Maximum	12.4	24.0	20.2	13.5	27.1	16.0	26.7	23.5	20.4

(cm)

Table 3. Position-errors of makers on human model (Unknown test images i,j)

Image	i	j	Total
Average	8.1	9.6	8.9
Maximum	25.4	23.2	24.3

(cm)

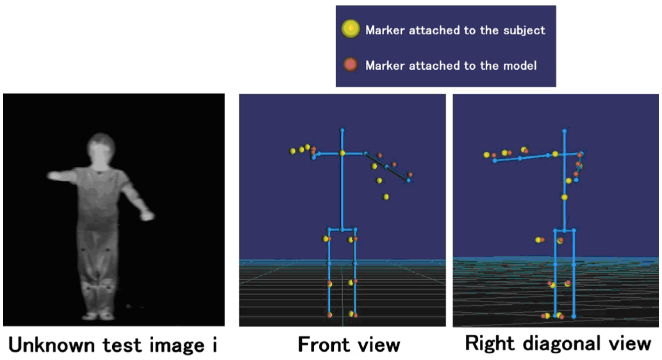

Fig.11. Unknown test image i and corresponding CG

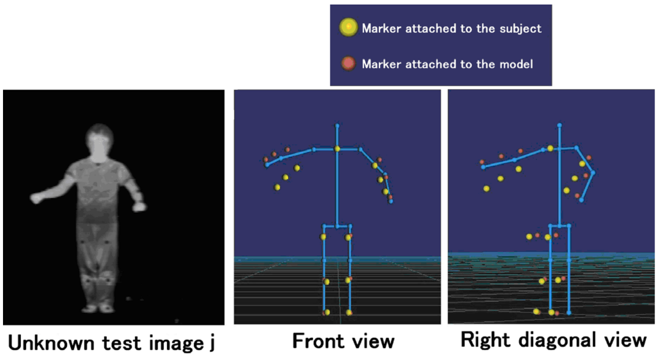

Fig.12. Unknown test image j and corresponding CG

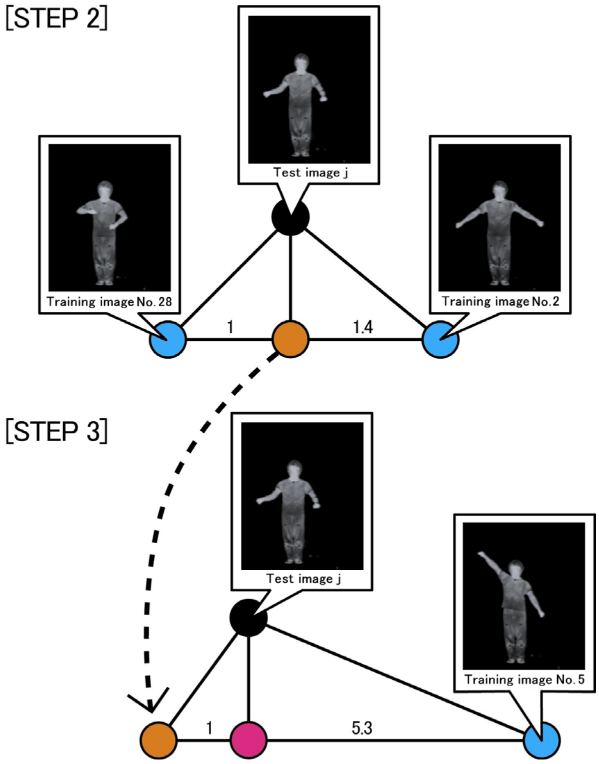

Fig.13. Synthetic process of feature vector for unknown test image j

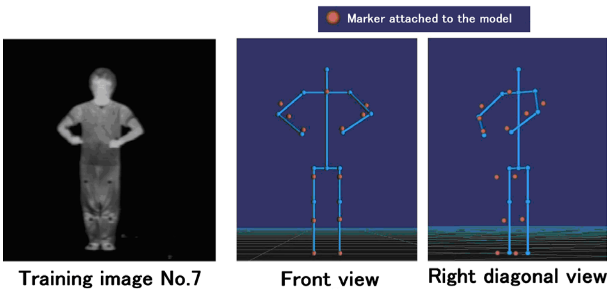

Fig.14. CG for training image No.7

IX. CONCLUSION

We propose a method that makes a 3DCG by transforming a feature vector of posture on a thermal image into a 3DCG model. The 3DCG models as training data are made with manual model fitting. The average error in position is about 10 cm. Such a relatively small error might be acceptable in several cases of both the 3DCG animation generation and the imitation of human motion by a robot. Our method needs neither the physical nor environmental restrictions.

REFERENCES

[1]Pentland A (1990), Automatic extraction of deformable part models, Int. Journal of Computer Vision 4(2):107-126

[2]Pentland A and Sclaroff S (1991), Closed-form solutions for physically based shape modeling and recognition. IEEE Trans. on Pattern Analysis and Machine Intelligence 13(7):715-729

[3]Ohya J and Kishino F (1994), Human posture estimation from multiple images using genetic algorithm. Proc. 12th ICPR:750-753

[4]Wren C, Azarbayejani A, Darrel T and Pentland A (1996), Pfinder, real-time tracking of the human body. Proc. 2nd Int. Conf. on Automatic Face and Gesture Recognition:51-56

[5]Iwasawa S, Ebihara K, Ohya J, Nakatsu R and Morishima S (1997), Real-time estimation of human body postures from monocular thermal images (in Japanese). Journal of the Institute of Image Information and Television Engineers 51(8):1270-1274

[6]Asada T, Uragami K, Ikeno Y, Tanijiri T, and Yoshitomi Y (2004), A method for synthesizing computer graphics animation by transforming feature vector of posture on thermal image into 3-dimensional model. Proc. 13th IEEE Workshop on Robot and Human Interactive Communication:325-330